CODEN: JASMAN

The Journal of the Acoustical Society of America

ISSN: 0001-4966

Vol. 119, No. 1 January 2006

(Continued)

CONTENTS—*Continued from preceding page*

UNDERWATER SOUND [30]

ULTRASONICS, QUANTUM ACOUSTICS, AND PHYSICAL EFFECTS OF SOUND [35]

TRANSDUCTION [38]

STRUCTURAL ACOUSTICS AND VIBRATION [40]

NOISE: ITS EFFECTS AND CONTROL [50]

ARCHITECTURAL ACOUSTICS [55]

(Continued)

CONTENTS—*Continued from preceding page*

ACOUSTICAL MEASUREMENTS AND INSTRUMENTATION [58]

ACOUSTIC SIGNAL PROCESSING [60]

PHYSIOLOGICAL ACOUSTICS [64]

PSYCHOLOGICAL ACOUSTICS [66]

(Continued)

CONTENTS—*Continued from preceding page*

SPEECH PRODUCTION [70]

SPEECH PERCEPTION [71]

SPEECH PROCESSING AND COMMUNICATION SYSTEMS [72]

BIOACOUSTICS [80]

CUMULATIVE AUTHOR INDEX

ACOUSTICAL NEWS—USA

E Moran
Acoustical Society of America, Suite 1NO1, 2 Huntington Quadrangle, Melville, NY 11747–4502

Editor's Note: *Readers of this journal are encouraged to submit news items on awards, appointments, and other activities about themselves or their colleagues. Deadline dates for news and notices are 2 months prior to publication.*

Announcement of the 2006 Election

In accordance with the provisions of the bylaws, the following Nominating Committee was appointed to prepare a slate for the election to take place on 26 May 2006: Ilene J. Busch-Vishniac, Chair; Dani Byrd; Christy K. Holland; John Perkins; and Kevin Shepherd.

The bylaws of the Society require that the Executive Director publish in the *Journal*, at least 90 days prior to the election date, an announcement of the election and the Nominating Committee's nominations for the offices to be filled. Additional candidates for these offices may be provided by any Member or Fellow in good standing by letter received by the Executive Director not less than 60 days prior to the election date, and the name of any eligible candidate so proposed by 20 Members or Fellows shall be entered on the ballot.

Biographical information about the candidates and statements of objectives of the candidates for President-Elect and Vice President-Elect will be mailed with the ballots.

CHARLES E. SCHMID
Executive Director

The Nominating Committee has submitted the following slate:

For President-Elect

Gilles A. Daigle

Henrik Schmidt

For Vice President-Elect

George V. Frisk

K. Anthony Hoover

 0001-4966/2006/119(1)/1/3/$22.50

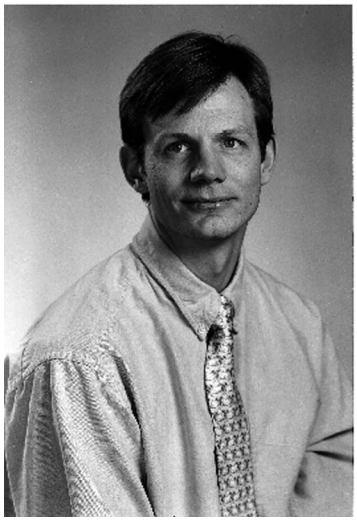

Robin O. Cleveland

Randy L. Diehl

Peggy B. Nelson

Brigitte Schulte-Fortkamp

Peter F. Worcester

Wayne M. Wright

USA Meetings Calendar

Listed below is a summary of meetings related to acoustics to be held in the U.S. in the near future. The month/year notation refers to the issue in which a complete meeting announcement appeared.

2006

9–12 Feb. 46th Annual Convention, Illinois Speech-Language-Hearing Association, Rosemont, IL [ISHA, 230 E. Ohio St., Suite 400, Chicago, IL 60611-3265; Tel.: 312-644-0828; Fax: 315-644-8557; Web: www.aishil.org].

16–18 Feb. 31st Annual Conference, National Hearing Conservation Association, Tampa, FL [NHCA, 7995 E. Prentice Ave., Suite 100 East, Greenwood Village, CO 80111-2710; Tel: 303-224-9022; Fax: 303-770-1614; E-mail: nhca@gwami.com; WWW: www-.hearingconservation.org].

6–9 June 151st Meeting of the Acoustical Society of America, Providence Rhode Island [Acoustical Society of America, Suite 1NO1, 2 Huntington Quadrangle, Melville, NY 11747-4502; Tel.: 516-576-2360; Fax: 516-576-2377; E-mail: asa@aip.org; WWW: http://asa.aip.org].

17–21 Sept. INTERSPEECH 2006 (ICSLP 2006), Pittsburgh, PA [www.interspeech2006.org ⟨http://www.interspeech2006.org/⟩].

28 Nov–2 Dec 152nd Meeting of the Acoustical Society of America joint with the Acoustical Society of Japan, Honolulu, Hawaii [Acoustical Society of America, Suite 1NO1, 2 Huntington Quadrangle, Melville, NY 11747- 4502; Tel.: 516-576-2360; Fax: 516-576-2377; E-mail: asa@aip.org; WWW: http://asa.aip.org]. Deadline for receipt of abstracts: 30 June 2006.

2007

4–8 June 153rd Meeting of the Acoustical Society of America, Salt Lake City, Utah [Acoustical Society of America, Suite 1NO1, 2 Huntington Quadrangle, Melville, NY 11747-4502; Tel.: 516-576-2360; Fax: 516-576-2377; E-mail: asa@aip.org; WWW: http://asa.aip.or].

27 Nov–2 Dec 154th Meeting of the Acoustical Society of America, New Orleans, Louisiana (note Tuesday through Saturday) [Acoustical Society of America, Suite 1NO1, 2 Huntington Quadrangle, Melville, NY 11747-4502; Tel.: 516-576-2360; Fax: 516-576-2377; E-mail: asa@aip.org; WWW: http://asa.aip.org].

2008

28 July–1 Aug 9th International Congress on Noise as a Public Health Problem (Quintennial meeting of ICBEN, the International Commission on Biological Effects of Noise). Foxwoods Resort, Mashantucket, CT [Jerry V. Tobias, ICBEN 9, Post Office Box 1609, Groton CT 06340-1609, Tel. 860-572-0680; Web: www.icben.org. E-mail: icben2008@att.net.

Cumulative Indexes to the *Journal of the Acoustical Society of America*

Ordering information: Orders must be paid by check or money order in U.S. funds drawn on a U.S. bank or by Mastercard, Visa, or American Express credit cards. Send orders to Circulation and Fulfillment Division, American Institute of Physics, Suite 1NO1, 2 Huntington Quadrangle, Melville, NY 11747-4502; Tel.: 516-576-2270. Non-U.S. orders add $11 per index.

Some indexes are out of print as noted below.

Volumes 1–10, 1929–1938: JASA, and Contemporary Literature, 1937–1939. Classified by subject and indexed by author. Pp. 131. Price: ASA members $5; Nonmembers $10.

Volumes 11–20, 1939–1948: JASA, Contemporary Literature and Patents. Classified by subject and indexed by author and inventor. Pp. 395. Out of print.

Volumes 21–30, 1949–1958: JASA, Contemporary Literature and Patents. Classified by subject and indexed by author and inventor. Pp. 952. Price: ASA members $20; Nonmembers $75.

Volumes 31–35, 1959–1963: JASA, Contemporary Literature and Patents. Classified by subject and indexed by author and inventor. Pp. 1140. Price: ASA members $20; Nonmembers $90.

Volumes 36–44, 1964–1968: JASA and Patents. Classified by subject and indexed by author and inventor. Pp. 485. Out of print.

Volumes 36–44, 1964–1968: Contemporary Literature. Classified by subject and indexed by author. Pp. 1060. Out of print.

Volumes 45–54, 1969–1973: JASA and Patents. Classified by subject and indexed by author and inventor. Pp. 540. Price: $20 (paperbound); ASA members $25 (clothbound); Nonmembers $60 (clothbound).

Volumes 55–64, 1974–1978: JASA and Patents. Classified by subject and indexed by author and inventor. Pp. 816. Price: $20 (paperbound); ASA members $25 (clothbound); Nonmembers $60 (clothbound).

Volumes 65–74, 1979–1983: JASA and Patents. Classified by subject and indexed by author and inventor. Pp. 624. Price: ASA members $25 (paperbound); Nonmembers $75 (clothbound).

Volumes 75–84, 1984–1988: JASA and Patents. Classified by subject and indexed by author and inventor. Pp. 625. Price: ASA members $30 (paperbound); Nonmembers $80 (clothbound).

Volumes 85–94, 1989–1993: JASA and Patents. Classified by subject and indexed by author and inventor. Pp. 736. Price: ASA members $30 (paperbound); Nonmembers $80 (clothbound).

Volumes 95–104, 1994–1998: JASA and Patents. Classified by subject and indexed by author and inventor. Pp. 632, Price: ASA members $40 (paperbound); Nonmembers $90 (clothbound).

Volumes 105–114, 1999–2003: JASA and Patents. Classified by subject and indexed by author and inventor. Pp.616, Price: ASA members $50; Nonmembers $90 (paperbound).

ACOUSTICAL STANDARDS NEWS

Susan B. Blaeser, Standards Manager
ASA Standards Secretariat

George S. K. Wong
Acoustical Standards, Institute for National Measurement Standards, National Research Council, Ottawa, Ontario K1A 0R6, Canada [Tel.: (613) 993-6159; Fax: (613) 990-8765; e-mail: george.wong@nrc.ca]

American National Standards (ANSI Standards) developed by Accredited Standards Committees S1, S2, S3, and S12 in the areas of acoustics, mechanical vibration and shock, bioacoustics, and noise, respectively, are published by the Acoustical Society of America (ASA). In addition to these standards, ASA publishes Catalogs of Acoustical Standards, both National and International. To receive copies of the latest Standards Catalogs, please, contact Susan B. Blaeser.

Comments are welcomed on all material in Acoustical Standards News.

This Acoustical Standards News section in JASA, as well as the National and International Catalogs of Acoustical Standards, and other information on the Standards Program of the Acoustical Society of America, are available via the ASA home page: http://asa.aip.org.

Standards on Acoustics, Vibration, Bioacoustics, and Noise Now Available for Classroom Use

The Acoustical Society of America (ASA) recently announced its new initiative to encourage classroom use of its American National Standards on acoustics, vibration, bioacoustics and noise. Under this new program, teachers who are ASA members can obtain a site license to reproduce Standards needed in the classroom, including one copy for the teacher. Teachers who are not ASA members will need to purchase one copy of the current standard at full cost to then obtain a site license for their class.

Nearly 120 American National Standards developed by Accredited Standards Committee S1 Acoustics, S2 Mechanical Vibration and Shock, S3 Bioacoustics, and S12 Noise, are available under this program. While the normal price of these standards ranges around $100 per copy, student copies will be available at $5 each. Students will receive a complete copy of the latest edition of the standard.

William A. Yost, ASA President, said, "Standards are essential in trade and commerce, and their importance grows as we move more and more towards a world economy. Students need to learn the role and use of Standards, and this is an outstanding opportunity to introduce the use of Standards in the classroom."

Teachers who wish to participate should contact the ASA Standards Secretariat at 631 390–0215. The complete list of American National Standards offered under this program can be seen at the ASA Standards Store at http://asastore.aip.org/ or request a catalog from the Secretariat.

S1/WG 25 Specification for Acoustical Calibrators, chaired by Phil Battenberg.

News from the Minneapolis Meeting

The Standards Committees and U.S. TAGs did not meet in Minneapolis, nevertheless there were a number of Standards-related activities. The ASA Committee on Standards (ASACOS) met as did the ASACOS Steering Committee. Nine working groups took advantage of the opportunity to meet during the week, as well. We were able to get photos of a few of the groups.

S1/WG26 Frequency Calibration of the Pressure Sensitivity of Microphones by Means of Measurements in the Free-Field, Chaired by Allan Zuckerwar.

S1/WG28 Passive Acoustic Monitoring for Marine Mammal Mitigation for Seismic Surveys, Chaired by Aaron Thode.

S3/WG48 Hearing Aids, Chaired by David Preves.

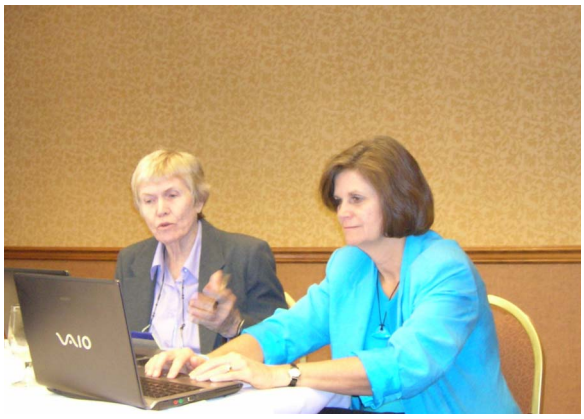

The Co-Chairs of S3/WG81 Hearing Assistance Technologies, Laura Ann Wilber (l) and Linda Thibodeau (r).

S12/WG14 Measurement of the Noise Attenuation of Active and/or Passive Level Depended Hearing Protective Devices, Chaired by William Murphy.

ASA Committee on Standards, Chaired by Paul Schomer.

The ASACOS Steering Committee, Chaired by Paul Schomer.

Standards Meetings Calendar—National

In conjunction with the 151st ASA Meeting, Providence, RI, 5–9 June 2006, the ASA Committee on Standards (ASACOS), ASACOS STEERING Committees, and Accredited Standards Committees S1 Acoustics, S2 Mechanical Vibration and Shock, S3 Bioacoustics, and S12 Noise, and the Standards Plenary Group will meet as follows:

• ***Monday, 5 June 2006***

ASACOS Steering Committee

• ***Tuesday, 6 June 2006***

ASA Committee on Standards (ASACOS). Meeting of the Committee that directs the Standards Program of the Acoustical Society.

• ***Tuesday, 6 June 2006***

Standards Plenary Group. To discuss national and international items relevant to Accredited Standards Committees S1, S2, S3, and S12. This meeting also includes the annual meetings of the U.S. Technical Advisory Groups (TAGs) for ISO/TC 43 Acoustics; ISO/TC 43/SC 1 Noise; IEC/TC 29 Electroacoustics; ISO/TC 108 Mechanical Vibration and Shock; ISO/TC 108/SC 2 Measurement and Evaluation of Mechanical Vibration and Shock as applied to Machines, Vehicles and Structures; ISO/TC 108/SC 3 Use and Calibration of Vibration and Shock Measuring Instruments; ISO/TC 108/SC 4 Human Exposure to Mechanical Vibration and Shock; ISO/TC 108/SC 5 Condition Monitoring and Diagnostics of Machines; and ISO/TC 108/SC 6 Vibration and Shock Generating Systems.

• ***Tuesday, 6 June 2006***

Accredited Standards Committee S3 on Bioacoustics.

• ***Tuesday, 6 June 2006***

Accredited Standards Committee S12 on Noise.

• ***Wednesday, 7 June 2006***

Accredited Standards Committee S2 on Mechanical Vibration and Shock.

• ***Wednesday, 7 June 2006***

Accredited Standards Committee S1 on Acoustics.

Accredited Standards Committee on Acoustics, S1

(J. P. Seiler, Chair; G. S. K. Wong, Vice Chair)

Scope: Standards, specifications, methods of measurement and test, and terminology in the field of physical acoustics, including architectural acoustics, electroacoustics, sonics and ultrasonics, and underwater sound, but

excluding those aspects that pertain to biological safety, tolerance, and comfort.

S1 Working Groups

S1/Advisory—Advisory Planning Committee to S1 (G. S. K. Wong);
S1/WG1—Standard Microphones and their Calibration (V. Nedzelnitsky);
S1/WG4—Measurement of Sound Pressure Levels in Air (M. Nobile);
S1/WG5—Band Filter Sets (A. H. Marsh);
S1/WG17—Sound Level Meters and Integrating Sound Level Meters (B. M. Brooks);
S1/WG19—Insertion Loss of Windscreens (A. J. Campanella);
S1/WG20—Ground Impedance (K. Attenborough, Chair; J. Sabatier, Vice Chair);
S1/WG22—Bubble Detection and Cavitation Monitoring (Vacant);
S1/WG25—Specification for Acoustical Calibrators (P. Battenberg);
S1/WG26—High Frequency Calibration of the Pressure Sensitivity of Microphones (A. Zuckerwar);
S1/WG27—Acoustical Terminology (J. Vipperman);
S1/WG28—Passive Acoustic Monitoring for Marine Mammal Mitigation for Seismic Surveys (A. Thode).
S1 Inactive Working Groups:
S1/WG16—FFT Acoustical Analyzers (R. J. Peppin, Chair)

S1 STANDARDS ON ACOUSTICS

ANSI S1.1-1994 (R 2004) American National Standard Acoustical Terminology
ANSI S1.4-1983 (R 2001) American National Standard Specification for Sound Level Meters
ANSI S1.4A-1985 (R 2001) Amendment to ANSI S1.4-1983
ANSI S1.6-1984 (R 2001) American National Standard Preferred Frequencies, Frequency Levels, and Band Numbers for Acoustical Measurements
ANSI S1.8-1989 (R 2001) American National Standard Reference Quantities for Acoustical Levels
ANSI S1.9-1996 (R 2001) American National Standard Instruments for the Measurement of Sound Intensity
ANSI S1.11-2004 American National Standard Specification for Octave-Band and Fractional-Octave-Band Analog and Digital Filters
ANSI S1.13-2005 American National Standard Measurement of Sound Pressure Levels in Air
ANSI S1.14-1998 (R 2003) American National Standard Recommendations for Specifying and Testing the Susceptibility of Acoustical Instruments to Radiated Radio-Frequency Electromagnetic Fields, 25 MHz to 1 GHz
ANSI S1.15-1997/Part 1 (R 2001) American National Standard Measurement Microphones, Part 1: Specifications for Laboratory Standard Microphones
ANSI S1.15-2005/Part 2 American National Standard Measurement Microphones, Part 2: Primary Method for Pressure Calibration of Laboratory Standard Microphones by the Reciprocity Technique
ANSI S1.16-2000 (R 2005) American National Standard Method for Measuring the Performance of Noise Discriminating and Noise Canceling Microphones
ANSI S1.17-2004/Part 1 American National Standard Microphone Windscreens—Part 1: Measurements and Specification of Insertion Loss in Still or Slightly Moving Air
ANSI S1.18-1999 (R 2004) American National Standard Template Method for Ground Impedance
ANSI S1.20-1988 (R 2003) American National Standard Procedures for Calibration of Underwater Electroacoustic Transducers
ANSI S1.22-1992 (R 2002) American National Standard Scales and Sizes for Frequency Characteristics and Polar Diagrams in Acoustics
ANSI S1.24 TR-2002 ANSI Technical Report Bubble Detection and Cavitation Monitoring
ANSI S1.25-1991 (R 2002) American National Standard Specification for Personal Noise Dosimeters
ANSI S1.26-1995 (R 2004) American National Standard Method for Calculation of the Absorption of Sound by the Atmosphere
ANSI S1.40-1984 (R 2001) American National Standard Specification for Acoustical Calibrators
ANSI S1.42-2001 American National Standard Design Response of Weighting Networks for Acoustical Measurements
ANSI S1.43-1997 (R 2002) American National Standard Specifications for Integrating-Averaging Sound Level Meters

Accredited Standards Committee on Mechanical Vibration and Shock, S2

(R. J. Peppin, Chair; D. J. Evans, Vice Chair)

Scope: Standards, specifications, methods of measurement and test, and terminology in the field of mechanical vibration and shock, and condition monitoring and diagnostics of machines, including the effects of mechanical vibration and shock on humans, including those aspects which pertain to biological safety, tolerance, and comfort.

S2 Working Groups

S2/WG1—S2 Advisory Planning Committee (D. J. Evans);
S2/WG2—Terminology and Nomenclature in the Field of Mechanical Vibration and Shock and Condition Monitoring and Diagnostics of Machines (D. J. Evans);
S2/WG3—Signal Processing Methods (T. S. Edwards);
S2/WG4—Characterization of the Dynamic Mechanical Properties of Viscoelastic Polymers (W. M. Madigosky, Chair; J. Niemic, Vice Chair);
S2/WG5—Use and Calibration of Vibration and Shock Measuring Instruments (D. J. Evans, Chair; B. E. Douglas, Vice Chair);
S2/WG6—Vibration and Shock Actuators (G. Booth);
S2/WG7—Acquisition of Mechanical Vibration and Shock Measurement Data (B. E. Douglas);
S2/WG8—Analysis Methods of Structural Dynamics (B. E. Douglas);
S2/WG9—Training and Accreditation (R. Eshleman, Chair);
S2/WG10—Measurement and Evaluation of Machinery for Acceptance and Condition (R. Eshleman, Chair; H. Pusey, Vice Chair);
S2/WG10/Panel 1—Balancing (R. Eshleman);
S2/WG10/Panel 2—Operational Monitoring and Condition Evaluation—R. Bankert);
S2/WG10/Panel 3—Machinery Testing (R. Eshleman);
S2/WG10/Panel 4—Prognosis (R. Eshleman);
S2/WG10/Panel 5—Data Processing, Communication, and Presentation (K. Bever);
S2/WG11—Measurement and Evaluation of Mechanical Vibration of Vehicles (A. F. Kilcullen);
S2/WG12—Measurement and Evaluation of Structures and Structural Systems for Assessment and Condition Monitoring (B. E. Douglas, Chair; R. J. Peppin, Vice Chair);
S2/WG13—Shock Test Requirements for Commercial Electronic Systems (P. D. Loeffler);
S2/WG39 (S3)—Human Exposure to Mechanical Vibration and Shock—Parallel to ISO/TC 108/SC 4 (D. D. Reynolds, Chair; H. E. von Gierke, Vice Chair).
S2 Inactive Working Group:
S2/WG54—Atmospheric Blast Effects (J. W. Reed)

S2 Standards on Mechanical Vibration and Shock

ANSI S2.1-2000 ISO 2041:1990 Nationally Adopted International Standard Vibration and Shock—Vocabulary
ANSI S2.2-1959 (R 2001) American National Standard Methods for the Calibration of Shock and Vibration Pickups
ANSI S2.4-1976 (R 2004) American National Standard Method for Specifying the Characteristics of Auxiliary Analog Equipment for Shock and Vibration Measurements
ANSI S2.7-1982 (R 2004) American National Standard Balancing Terminology
ANSI S2.8-1972 (R 2001) American National Standard Guide for Describing the Characteristics of Resilient Mountings
ANSI S2.9-1976 (R 2001) American National Standard Nomenclature for Specifying Damping Properties of Materials

ANSI S2.13-1996/Part 1 (R 2001) American National Standard Mechanical Vibration of Non-Reciprocating Machines—Measurements on Rotating Shafts and Evaluation, Part 1: General Guidelines

ANSI S2.16-1997 (R 2001) American National Standard Vibratory Noise Measurements and Acceptance Criteria of Shipboard Equipment

ANSI S2.17-1980 (R 2004) American National Standard Techniques of Machinery Vibration Measurement

ANSI S2.19-1999 (R 2004) American National Standard Mechanical Vibration—Balance Quality Requirements of Rigid Rotors, Part 1: Determination of Permissible Residual Unbalance, Including Marine Applications

ANSI S2.20-1983 (R 2001) American National Standard Estimating Airblast Characteristics for Single Point Explosions in Air, with a Guide to Evaluation of Atmospheric Propagation and Effects

ANSI S2.21-1998 (R 2002) American National Standard Method for Preparation of a Standard Material for Dynamic Mechanical Measurements

ANSI S2.22-1998 (R 2002) American National Standard Resonance Method for Measuring the Dynamic Mechanical Properties of Viscoelastic Materials

ANSI S2.23-1998 (R 2002) American National Standard Single Cantilever Beam Method for Measuring the Dynamic Mechanical Properties of Viscoelastic Materials

ANSI S2.24-2001 American National Standard Graphical Presentation of the Complex Modulus of Viscoelastic Materials

ANSI S2.25-2004 American National Standard Guide for the Measurement, Reporting, and Evaluation of Hull and Superstructure Vibration in Ships

ANSI S2.26-2001 American National Standard Vibration Testing Requirements and Acceptance Criteria for Shipboard Equipment

ANSI S2.27-2002 American National Standard Guidelines for the Measurement and Evaluation of Vibration of Ship Propulsion Machinery

ANSI S2.28-2003 American National Standard Guidelines for the Measurement and Evaluation of Vibration of Shipboard Machinery

ANSI S2.29-2003 American National Standard Guidelines for the Measurement and Evaluation of Vibration of Marine Shafts on Shipboard Machinery

ANSI S2.31-1979 (R 2004) American National Standard Method for the Experimental Determination of Mechanical Mobility, Part 1: Basic Definitions and Transducers

ANSI S2.32-1982 (R 2004) American National Standard Methods for the Experimental Determination of Mechanical Mobility, Part 2: Measurements Using Single-Point Translational Excitation

ANSI S2.34-1984 (R 2005) American National Standard Guide to the Experimental Determination of Rotational Mobility Properties and the Complete Mobility Matrix

ANSI S2.41-1985 (R 2001) American National Standard Mechanical Vibration of Large Rotating Machines with Speed Range from 10 to 200 rev/s—Measurement and Evaluation of Vibration Severity *in situ*

ANSI S2.42-1982 (R 2004) American National Standard Procedures for Balancing Flexible Rotors

ANSI S2.43-1984 (R 2005) American National Standard Criteria for Evaluating Flexible Rotor Balance

ANSI S2.46-1989 (R 2005) American National Standard Characteristics to be Specified for Seismic Transducers

ANSI S2.47-1990 (R 2001) American National Standard Vibrations of Buildings—Guidelines for the Measurements of Vibrations and Evaluation of their Effects on Buildings

ANSI S2.48-1993 (R 2001) American National Standard Servo-Hydraulic Test Equipment for Generating Vibration—Methods of Describing Characteristics

ANSI S2.60-1987 (R 2005) American National Standard Balancing Machines—Enclosures and Other Safety Measures

ANSI S2.61-1989 (R 2005) American National Standard Guide to the Mechanical Mounting of Accelerometers

ANSI S3.18-2002 ISO 2631-1:1997 Nationally Adopted International Standard Mechanical vibration and shock—Evaluation of human exposure to whole-body vibration—Part 1: General requirements

ANSI S3.18-2003 ISO 2631-4: 2001 Nationally Adopted International Standard Mechanical vibration and shock—Evaluation of human exposure to whole body vibration—Part 4: Guidelines for the evaluation of the effects of vibration and rotational motion on passenger and crew comfort in fixed-guideway transport systems

ANSI S3.29-1983 (R 2001) American National Standard Guide to the Evaluation of Human Exposure to Vibration in Buildings

ANSI S3.34-1986 (R 1997) American National Standard Guide for the Measurement and Evaluation of Human Exposure to Vibration Transmitted to the Hand

ANSI S3.40-2002 ISO 10819:1996 Nationally Adopted International Standard Mechanical vibration and shock—Hand–arm vibration—Method for the measurement and evaluation of the vibration transmissibility of gloves at the palm of the hand

Accredited Standards Committee on Bioacoustics, S3

(R. F. Burkard, Chair; C. A, Champlin, Vice Chair)

Scope: Standards, specifications, methods of measurement and test, and terminology in the fields of psychological and physiological acoustics, including aspects of general acoustics, which pertain to biological safety, tolerance and comfort.

S3 Working Groups

S3/Advisory—Advisory Planning Committee to S3 (R. F. Burkard);
S3/WG35—Audiometers (R. L. Grason);
S3/WG36—Speech Intelligibility (R. S. Schlauch);
S3/WG37—Coupler Calibration of Earphones (B. Kruger);
S3/WG43—Method for Calibration of Bone Conduction Vibrator (J. Durrant);
S3/WG48—Hearing Aids (D. A. Preves);
S3/WG51—Auditory Magnitudes (R. P. Hellman);
S3/WG56—Criteria for Background Noise for Audiometric Testing (J. Franks);
S3/WG59—Measurement of Speech Levels (M. C. Killion and L. A. Wilber, Co-Chairs);
S3/WG60—Measurement of Acoustic Impedance and Admittance of the Ear (Vacant);
S3/WG62—Impulse Noise with Respect to Hearing Hazard (J. H. Patterson);
S3/WG67—Manikins (M. D. Burkhard);
S3/WG72—Measurement of Auditory Evoked Potentials (R. F. Burkard);
S3/WG76—Computerized Audiometry (A. J. Miltich);
S3/WG78—Thresholds (W. A. Yost);
S3/WG79—Methods for Calculation of the Speech Intelligibility Index (C. V. Pavlovic);
S3/WG81—Hearing Assistance Technologies (L. Thibodeau and L. A. Wilber, Co-chairs);
S3/WG82—Basic Vestibular Function Test Battery (C. Wall, III);
S3/WG83—Sound Field Audiometry (T. R. Letowski);
S3/WG84—Otoacoustic Emission (G. R. Long);
S3/WG86—Audiometric Data Structures (W. A. Cole and B. Kruger, Co-Chairs);
S3/WG87—Human Response to Repetitive Mechanical Shock (N. Alem);
S3/WG88—Standard Audible Emergency Evacuation and Other Signals (I. Mande);
S3/WG89—Spatial Audiometry in Real and Virtual Environments (J. Besing);
S3/WG90—Animal Bioacoustics (A. E. Bowles);
S3/WG91—Text-to-Speech Synthesis Systems (A. K. Syrdal and C. Bickley, Co-Chairs);
S3/WG92—Effects of Sound on Fish and Turtles (R. R. Fay and A. N. Popper, Co-Chairs)
S2/WG39 (S3)—Human Exposure to Mechanical Vibration and Shock—Parallel to ISO/TC 108/SC 4 (D. D. Reynolds).

S3 Liaison Group:

S3/L-1 S3 U. S. TAG Liaison to IEC/TC 87 Ultrasonics (W. L. Nyborg).
S3 Inactive Working Groups:
S3/WG71 Artificial Mouths (R. L. McKinley);

S3/WG80 Probe-tube Measurements of Hearing Aid Performance (W. A. Cole);
S3/WG58 Hearing Conservation Criteria.

S3 Standards on Bioacoustics

ANSI S3.1-1999 (R 2003) American National Standard Maximum Permissible Ambient Noise Levels for Audiometric Test Rooms
ANSI S3.2-1989 (R 1999) American National Standard Method for Measuring the Intelligibility of Speech over Communication Systems
ANSI S3.4-2005 American National Standard Procedure for the Computation of Loudness of Steady Sound
ANSI S3.5-1997 (R 2002) American National Standard Methods for Calculation of the Speech Intelligibility Index
ANSI S3.6-2004 American National Standard Specification for Audiometers
ANSI S3.7-1995 (R 2003) American National Standard Method for Coupler Calibration of Earphones
ANSI S3.13-1987 (R 2002) American National Standard Mechanical Coupler for Measurement of Bone Vibrators
ANSI S3.14-1977 (R 1997) American National Standard for Rating Noise with Respect to Speech Interference
ANSI S3.20-1995 (R 2003) American National Standard Bioacoustical Terminology
ANSI S3.21-2004 American National Standard Methods for Manual Pure-Tone Threshold Audiometry
ANSI S3.22-2003 American National Standards Specification of Hearing Aid Characteristics
ANSI S3.25-1989 (R 2003) American National Standard for an Occluded Ear Simulator
ANSI S3.35-2004 American National Standard Method of Measurement of Performance Characteristics of Hearing Aids under Simulated Real-Ear Working Conditions
ANSI S3.36-1985 (R 2001) American National Standard Specification for a Manikin for Simulated *in situ* Airborne Acoustic Measurements
ANSI S3.37-1987 (R 2002) American National Standard Preferred Earhook Nozzle Thread for Postauricular Hearing Aids
ANSI S3.39-1987 (R 2002) American National Standard Specifications for Instruments to Measure Aural Acoustic Impedance and Admittance (Aural Acoustic Immittance)
ANSI S3.41-1990 (R 2001) American National Standard Audible Emergency Evacuation Signal
ANSI S3.42-1992 (R 2002) American National Standard Testing Hearing Aids with a Broad-band Noise Signal
ANSI S3.44-1996 (R 2001) American National Standard Determination of Occupational Noise Exposure and Estimation of Noise-Induced Hearing Impairment
ANSI S3.45-1999 American National Standard Procedure for Testing Basic Vestibular Function
ANSI S3.46-1997 (R 2002) American National Standard Methods of Measurement of Real-Ear Performance Characteristics of Hearing Aids

Accredited Standards Committee on Noise, S12

(R. D. Hellweg, Chair; W. J. Murphy, Vice Chair)

Scope: Standards, specifications, and terminology in the field of acoustical noise pertaining to methods of measurement, evaluation, and control; including biological safety, tolerance and comfort, and physical acoustics, as related to environmental and occupational noise.

S12 Working Groups

S12/Advisory—Advisory Planning Committee to S12 (R. D. Hellweg);
S12/WG3—Measurement of Noise from Information Technology and Telecommunications Equipment (K. X. C. Man);
S12/WG11—Hearing Protector Attenuation and Performance (E. H. Berger);
S12/WG12—Evaluation of Hearing Conservation Programs (J. D. Royster, Chair; E. H. Berger, Vice Chair);
S12/WG13—Method for the Selection of Hearing Protectors that Optimize the Ability to Communicate (D. Byrne);
12/WG14—Measurement of the Noise Attenuation of Active and /or Passive Level Dependent Hearing Protective Devices (J. Kalb, Chair; W. J. Murphy, Vice Chair);
S12/WG15—Measurement and Evaluation of Outdoor Community Noise (P. D. Schomer);
S12/WG18—Criteria for Room Noise (R. J. Peppin);
S12/WG23—Determination of Sound Power (R. J. Peppin and B. M. Brooks, Co-Chairs);
S12/WG31—Predicting Sound Pressure Levels Outdoors (R. J. Peppin);
S12/WG32—Revision of ANSI S12.7-1986 Methods for Measurement of Impulse Noise (A. H. Marsh);
S12/WG33—Revision of ANSI S5.1-1971 Test Code for the Measurement of Sound from Pneumatic Equipment (B. M. Brooks);
S12/WG36—Development of Methods for Using Sound Quality (G. L. Ebbit and P. Davies, Co-Chairs);
S12/WG38—Noise Labeling in Products (R. D. Hellweg and J. Pope, Co-Chairs);
S12/WG40—Measurement of the Noise Aboard Ships (S. Antonides, Chair; S. Fisher, Vice Chair);
S12/WG41—Model Community Noise Ordinances (L. Finegold, Chair; B. M. Brooks, Vice Chair);
S12/WG43—Rating Noise with Respect to Speech Interference (M. Alexander).

S12 Liaison Groups:

S12/L-1 IEEE 85 Committee for TAG Liaison—Noise Emitted by Rotating Electrical Machines (Parallel to ISO/TC 43/SC 1/WG 13) (R. G. Bartheld);
S12/L-2 Measurement of Noise from Pneumatic Compressors Tools and Machines (Parallel to ISO/TC 43/SC 1/WG 9) (Vacant);
S12/L-3 SAE Committee for TAG Liaison on Measurement and Evaluation of Motor Vehicle Noise (parallel to ISO/TC 43/SC 1/WG 8) (R. F. Schumacher and J. Johnson);
S12/L-4 SAE Committee A-21 for TAG Liaison on Measurement and Evaluation of Aircraft Noise (J. Brooks);
S12/L-5 ASTM E-33 on Environmental Acoustics (to include activities of ASTM E33.06 on Building Acoustics, parallel to ISO/TC 43/SC 2 and ASTM E33.09 on Community Noise) (K. P. Roy);
S12/L-6 SAE Construction-Agricultural Sound Level Committee (I. Douell);
S12/L-7 SAE Specialized Vehicle and Equipment Sound Level Committee (T. Disch);
S12/L-8 ASTM PTC 36 Measurement of Industrial Sound (R. A. Putnam, Chair; B. M. Brooks, Vice Chair).

S12 Inactive Working Groups:

S12/WG27 Outdoor Measurement of Sound Pressure Level (G. Daigle)
S12/WG8 Determination of Interference of Noise with Speech Intelligibility (L. Marshall)
S12/WG9 Annoyance Response to Impulsive Noise (L. C. Sutherland)
S12/WG19 Measurement of Occupational Noise Exposure (J. P. Barry/R. Goodwin, Co-chairs);
S12/WG29 Field Measurement of the Sound Output of Audible Public-Warning Devices (Sirens) (P. Graham)
S12/WG 34—Methodology for Implementing a Hearing Conservation Program (J. P. Barry)
S12/WG37—Measuring Sleep Disturbance Due to Noise (K. S. Pearsons);

S12 Standards on Noise

ANSI S12.1-1983 (R 2001) American National Standard Guidelines for the Preparation of Standard Procedures to Determine the Noise Emission from Sources
ANSI S12.2-1995 (R 1999) American National Standard Criteria for Evaluating Room Noise
ANSI S12.3-1985 (R 2001) American National Standard Statistical Methods for Determining and Verifying Stated Noise Emission Values of Machinery and Equipment

ANSI S12.5-1990 (R 1997) American National Standard Requirements for the Performance and Calibration of Reference Sound Sources

ANSI S12.6-1997 (R 2002) American National Standard Methods for Measuring the Real-Ear Attenuation of Hearing Protectors

ANSI S12.7-1986 (R 1998) American National Standard Methods for Measurements of Impulse Noise

ANSI S12.8-1998 (R 2003) American National Standard Methods for Determining the Insertion Loss of Outdoor Noise Barriers

ANSI S12.9-1988/Part 1 (R 2003) American National Standard Quantities and Procedures for Description and Measurement of Environmental Sound, Part 1

ANSI S12.9-1992/Part 2 (R 2003) American National Standard Quantities and Procedures for Description and Measurement of Environmental Sound, Part 2: Measurement of Long-Term, Wide-Area Sound

ANSI S12.9-1993/Part 3 (R 2003) American National Standard Quantities and Procedures for Description and Measurement of Environmental Sound, Part 3: Short-Term Measurements with an Observer Present

ANSI S12.9-1996/Part 4 (R 2001) American National Standard Quantities and Procedures for Description and Measurement of Environmental Sound, Part 4: Noise Assessment and Prediction of Long-Term Community Response

ANSI S12.9-1998/Part 5 (R 2003) American National Standard Quantities and Procedures for Description and Measurement of Environmental Sound, Part 5: Sound Level Descriptors for Determination of Compatible Land Use

ANSI S12.9-2000/Part 6 (R 2005) American National Standard Quantities and Procedures for Description and Measurement of Environmental Sound, Part 6: Methods for Estimation of Awakenings Associated with Aircraft Noise Events Heard in Homes

ANSI S12.10-2002/ISO 7779:1999 Nationally Adopted International Standard Acoustics—Measurement of airborne noise emitted by information technology and telecommunications equipment

ANSI S12.11-2003/Part 1/ISO 10302: 1996 (MOD) American National Standard Acoustics—Measurement of noise and vibration of small air-moving devices—Part 1: Airborne noise emission

ANSI S12.11-2003/Part 2 American National Standard Acoustics—Measurement of Noise and Vibration of Small Air-Moving Devices—Part 2: Structure-Borne Vibration

ANSI S12.12-1992 (R2002) American National Standard Engineering Method for the Determination of Sound Power Levels of Noise Sources Using Sound Intensity

ANSI S12.13 TR-2002 ANSI Technical Report Evaluating the Effectiveness of Hearing Conservation Programs through Audiometric Data Base Analysis

ANSI S12.14-1992 (R 2002) American National Standard Methods for the Field Measurement of the Sound Output of Audible Public Warning Devices Installed at Fixed Locations Outdoors

ANSI S12.15-1992 (R 2002) American National Standard For Acoustics *B* Portable Electric Power Tools, Stationary and Fixed Electric Power Tools, and Gardening Appliances—Measurement of Sound Emitted

ANSI S12.16-1992 (R 2002) American National Standard Guidelines for the Specification of Noise of New Machinery

ANSI S12.17-1996 (R 2001) American National Standard Impulse Sound Propagation for Environmental Noise Assessment

ANSI S12.18-1994 (R 2004) American National Standard Procedures for Outdoor Measurement of Sound Pressure Level

ANSI S12.19-1996 (R 2001) American National Standard Measurement of Occupational Noise Exposure

ANSI S12.23-1989 (R 2001) American National Standard Method for the Designation of Sound Power Emitted by Machinery and Equipment

ANSI S12.30-1990 (R 2002) American National Standard Guidelines for the Use of Sound Power Standards and for the Preparation of Noise Test Codes

ANSI S12.35-1990 (R 2001) American National Standard Precision Methods for the Determination of Sound Power Levels of Noise Sources in Anechoic and Hemi-Anechoic Rooms

ANSI S12.42-1995 (R 2004) American National Standard Microphone-in-Real-Ear and Acoustic Test Fixture Methods for the Measurement of Insertion Loss of Circumaural Hearing Protection Devices

ANSI S12.43-1997 (R 2002) American National Standard Methods for Measurement of Sound Emitted by Machinery and Equipment at Workstations and other Specified Positions

ANSI S12.44-1997 (R 2002) American National Standard Methods for Calculation of Sound Emitted by Machinery and Equipment at Workstations and other Specified Positions from Sound Power Level

ANSI S12.50-2002/ISO 3740:2000 Nationally Adopted International Standard Acoustics—Determination of sound power levels of noise sources—Guidelines for the use of basic standards

ANSI S12.51-2002 / ISO 3741:1999 Nationally Adopted International Standard Acoustics—Determination of sound power levels of noise sources using sound pressure—Precision method for reverberation rooms

ANSI S12.53/1-1999 (R 2004)/ISO 3743-1:1994 Nationally Adopted International Standard Acoustics—Determination of sound power levels of noise sources—Engineering methods for small, movable sources in reverberant fields—Part 1: Comparison method for hard-walled test rooms

ANSI S12.53/2-1999 (R 2004)/ISO 3743-2:1994 Nationally Adopted International Standard Acoustics—Determination of sound power levels of noise sources using sound pressure—Engineering methods for small, movable sources in reverberant fields—Part 2: Methods for special reverberation test rooms

ANSI S12.54-1999 (R 2004)/ISO 3744:1994 Nationally Adopted International Standard Acoustics—Determination of sound power levels of noise sources using sound pressure—Engineering method in an essentially free field over a reflecting plane

ANSI S12.56-1999/ISO 3746:1995 Nationally Adopted International Standard Acoustics—Determination of sound power levels of noise sources using sound pressure—Survey method using an enveloping measurement surface over a reflecting plane

ANSI S12.57-2002 / ISO 3747:2000 Nationally Adopted International Standard Acoustics—Determination of sound power levels of noise sources using sound pressure—Comparison method *in situ*

ANSI S12.60-2002 American National Standard Acoustical Performance Criteria, Design Requirements, and Guidelines for Schools

ASA Committee on Standards (ASACOS)

ASACOS (P. D. Schomer, Chair and ASA Standards Director)

U. S. Technical Advisory Groups (TAGS) for International Standards Committees

ISO/TC 43 Acoustics, **ISO/TC 43/SC 1** Noise (P. D. Schomer, U.S. TAG Chair)

ISO/TC 108 Mechanical Vibration and Shock (D. J. Evans, U.S. TAG Chair)

ISO/TC 108/SC2 Measurement and Evaluation of Mechanical Vibration and Shock as Applied to Machines, Vehicles and Structures (A. F. Kilcullen, and R. F. Taddeo, U.S. TAG Co-Chairs)

ISO/TC 108/SC3 Use and Calibration of Vibration and Shock Measuring Instruments (D. J. Evans, U.S. TAG Chair)

ISO/TC 108/SC4 Human Exposure to Mechanical Vibration and Shock (D. D. Reynolds, U.S. TAG Chair)

ISO/TC 108/SC5 Condition Monitoring and Diagnostic Machines (D. J. Vendittis, U.S. TAG Chair)

ISO/TC 108/SC6 Vibration and Shock Generating Systems (G. Booth, U.S. TAG Chair)

IEC/TC 29 Electroacoustics (V. Nedzelnitsky, U.S. Technical Advisor)

Standards News from the United States

(Partially derived from *ANSI Reporter*, and *ANSI Standards Action*, with appreciation)

American National Standards Call for Comment on Proposals Listed

This section solicits comments on proposed new American National Standards and on proposals to revise, reaffirm, or withdraw approval of existing standards. The dates listed in parentheses are for information only.

ASA (ASC S2) (Acoustical Society of America)

REVISIONS

BSR S2.70-200x, Guide for the Measurement and Evaluation of Human Exposure to Vibration Transmitted to the Hand [revision and redesignation of ANSI S3.34-1986 (R1997)]

Specifies recommended method for measurement, data analysis, vibration and health risk assessments, and reporting of human exposure to hand-transmitted vibration. Specifies format for measurement, data analysis, vibration and health risk assessments, and reporting of hand-transmitted vibration, periodic or random, in three orthogonal axes, in the frequency range from 5.6 to 1400 Hz. Four normative annexes address risk assessments, mitigation, training, and medical surveillance. One informative annex provides guidance on the measurement of hand-transmitted vibration. (28 November 2005)

ASA (ASC S12) (Acoustical Society of America)

REVISIONS

BSR S12.2-200X, Criteria for Evaluating Room Noise [revision of ANSI S12.2-1995 (R1999)]

This standard provides three primary methods for evaluating room noise:—a survey method that employs the A-weighted sound level;—an engineering method that employs expanded noise criteria (NC) curves; and—a precision method that employs room noise criterion (RNC) curves.

BSR S12.9-Part 4-2005, Quantities and Procedures for Description and Measurement of Environmental Sound—Part 4: Noise Assessment and Prediction of Long-Term Community Response [revision of ANSI S12.9-Part 4-1996 (R2001)]

Specifies methods to assess environmental sounds and to predict the annoyance response of communities to long-term noise from any and all types of environmental sounds produced by one or more distinct or distributed sound sources. The sources may be separate or in various combinations. Application of the method is limited to areas where people reside and related long-term land uses. (28 November 2005)

REAFFIRMATIONS

BSR S12.9-Part 6-2000 (R2005), Quantities and Procedures for Description and Measurement of Environmental Sound—Part 6: Methods for Estimation of Awakenings Associated with Aircraft Noise Events Heard in Homes (reaffirmation of ANSI S12.9-Part 6-2000)

Provides a method to predict sleep disturbance in terms of percent awakenings associated with the noise level of events in terms of sound exposure level (SEL). The Standard was developed using field studies of behavioral awakening primarily in homes near areas of routine aircraft takeoff and landing operations. The database used in derivation of the dose-response relationship consists of more than 5000 subject nights of observations in a variety of communities in the United States.

American National Standards

Errata

ANSI S1.11-2004, American National Standard Specification for Octave-Band and Fractional—Octave-Band Analog and Digital Filters

Accredited Standards Committee S1, Acoustics, will publish the following errata to correct two errors in ANSI S1.11-2004 American National Standard Specification for Octave-Band and Fractional-Octave-Band Analog and Digital Filters **Page 4**: The definition in 3.32 contains extra, unrelated text. Delete the text at the bottom of the right-hand column beginning with the word "according" and ending with the word "instrument." **Page 9**: Three words were omitted from subclause 4.14.2. The omitted words are underlined below. The clause should read: **4.14.2 Relative humidity**. The manufacturer shall state the range of relative humidity and corresponding air temperature over which the instrument can operate continuously. After a 24 hour exposure to the humid atmosphere at a relative humidity of 75%, and at an ambient air temperature of +40 C and without condensation on internal components of the instrument under test, the relative attenuation at the nominal midband frequency for any filter available in the instrument shall not deviate from the relative attenuation at the same frequency under reference environmental conditions by more than ±0.15, ±0.3, and ±0.5 dB for class 0, 1, and 2 instruments, respectively.

ITSDF (Industrial Truck Standards Development Foundation, Inc.)

REAFFIRMATIONS

ANSI/ITSDF B56.11.5-2005, Measurement of Sound Emitted by Low Lift, High Lift, and Rough Terrain Powered Industrial Trucks [reaffirmation and redesignation of ANSI/ASME B56.11.5-1992 (R2000)]: (19 September 2005)

AMCA (Air Movement and Control Association)

REVISIONS

ANSI/AMCA 204–2005, Balance Quality and Vibration Levels for Fans (revision of ANSI/AMCA 204-1996): (23 September 2005)

ATIS (Alliance for Telecommunications Industry Solutions)

BSR ATIS 0600005-200x, Acoustic Measurement (new standard)

This standard identifies sound power as the preferred method of measuring the emission of acoustic noise from telecommunications equipment. The main focus is to use sound power to gain repeatability and accuracy over sound pressure methods. This standard will also provide the emission limits for the temperature-controlled environment (i.e., Central Office, data centers) for the North American environment. (5 December 2005)

IEEE (Institute of Electrical and Electronics Engineers)

REVISIONS

BSR/IEEE 1100-200x, Recommended Practice for Powering and Grounding Electronic Equipment (revision of ANSI/IEEE 1100–1999)

Presents recommended design, installation, and maintenance practices for electrical power and grounding (including both safety and noise control) and protection of electronic loads such as industrial controllers, computers and other information technology equipment used in commercial and industrial applications.

REAFFIRMATIONS

BSR/IEEE C57.136-2000 (R200x), Guide for Sound Level Abatement and Determination for Liquid-Immersed Power Transformers and Shunt Reactors Rated Over 500 kVA (reaffirmation of ANSI/IEEE C57.136-2000)

Guidelines are provided for the selection of suitable sound reduction methods in oil-immersed power transformers and shunt reactors over 500 kVA

Project Initiation Notification System (PINS)

ANSI Procedures require notification of ANSI by ANSI-accredited standards developers of the initiation and scope of activities expected to result in new or revised American National Standards. This information is a key element in planning and coordinating American National Standards.

The following is a list of proposed new American National Standards or revisions to existing American National Standards that have been received from ANSI-accredited standards developers that utilize the periodic maintenance option in connection with their standards. Directly and materially affected interests wishing to receive more information should contact the standards developer directly.

ASA (ASC S3) (Acoustical Society of America)

BSR S3.47-200x, Hearing Assistance Device Systems (new standard)

Describes definitions and measurements suitable for the specification and evaluation of Hearing Assistance Devices/Systems (HADS). HADS are a group of physically configured instruments that are intended to facilitate hearing by providing amplification of an acoustic signal and/or improving the signal-to-noise ratio by means of a non-acoustic signal

transmission method. Project Need: To verify Hearing Assistive Devices using standardized procedures so that professionals will know performance characteristics.

ISA (ISA-The Instrumentation, Systems, and Automation Society)

BSR/ISA RP77.60.02-200x, Fossil Fuel Power Plant Human-Machine Interface Alarms (new standard)

This recommended practice is provided for the benefit of design engineers and, ultimately, plant operators. Use of this recommended practice will result in a more coherent and useful application of plant alarms for operations personnel. The goal of this recommended practice is to reduce alarm discrepancies, clutter, excessive noise levels, and information overload. This recommended practice will address the following alarm-related issues: (a) Functional grouping; (b) Prioritization; (c) Order and consistency; (d) Colors; (e) Formats and displays; (f) Audio tone and pitch; (g) Acknowledge, reset, and test functions; and (h) Nuisance alarms. Project Need: Provides advice and guidance in the development and design of plant alarm systems.

Standards News from Abroad

(Partially derived from *ANSI Reporter* and *ANSI Standards Action*, with appreciation)

International Organization for Standardization (ISO)

Call for New Secretary

Relinquishment of ISO Subcommittee Secretariat ISO/TC 135/SC 3—Nondestructive testing—Acoustical methods

ANSI has been advised that ASTM no longer wish to serve as Secretary for this International Subcommittee. The work of this subcommittee is covered by the scope of ISO/TC 135 as follows: Standardization covering non-destructive testing as applied generally to constructional materials, components and assemblies, by means of: glossary of terms; methods of test; performance specifications for testing equipment and ancillary apparatus. Excluded: quality levels; specifications for electrical equipment and apparatus, which fall within the range of IEC Committees. Any organization wishing to assume the role of US delegated Secretariat, please contact Henrietta Scully via email: hscully@ansi.org; (7 November 2005)

Newly Published ISO and IEC Standards

Listed here are new and revised standards recently approved and promulgated by ISO—the International Organization for Standardization

ISO Standards

Acoustics (TC 43)

ISO 3095:2005, Railway applications—Acoustics—Measurement of noise emitted by railbound vehicles,

ISO 3381:2005, Railway applications—Acoustics—Measurement of noise inside railbound vehicles

IEC Standards

Power Transformers (TC 14)

IEC 60076-10 Ed. 1.0 b:2005, Power transformers—Part 10: Determination of sound levels

ISO Draft Standards

Acoustics (TC 43)

ISO/DIS 389-6, Acoustics—Reference zero for the calibration of audiometric equipment—Part 6: Reference hearing threshold levels for test signals of short duration—(5 January 2006)

ISO 4869-3, Acoustics—Hearing protectors—Part 3: Measurement of insertion loss of earmuff-type protectors using an acoustic test fixture—(5 January 2006)

Mechanical Vibration and Shock (TC 108)

ISO/DIS 15230, Mechanical vibration and shock—Coupling forces at the machine–man interface for hand-transmitted vibration—(22 December 2005)

Quantities, Units, Symbols, Conversion Factors (TC 12)

ISO/DIS 80000-8, Quantities and units—Part 8: Acoustics—(24 December 2008)

International documents submitted to the U. S. for vote and/or comment

Some of the documents processed recently by the ASA Standards Secretariat. Dates in parentheses are deadlines for the submission of comments and recommendation for vote, and they are for information only.

U.S. TAG	ISO and IEC documents
S1	**IEC/FDIS 60118-7 (29/585/FDIS)** "Electroacoustics—Hearing aids—Part 7: Measurement of the performance characteristics of hearing aids for production, supply and delivery quality assurance purposes" (22 August 2005)
S1 & S3	**ISO/DIS 389-6** "Acoustics—Reference zero for the calibration of audiometric equipment—Part 6: Reference hearing threshold levels for test signals of short duration" (13 February 2006)
S12	**ISO/CD 13474** "Acoustics—Impulse sound propagation for environmental noise assessment" (16 November 2005) **ISO/DIS 4869-3** "Acoustics—Hearing protectors—Part 3: Measurement of insertion loss of earmuff-type protectors using an acoustic test fixture" (13 February 2006)**ISO/DTS 4869-5** "Acoustics—Hearing protectors—Part 5: Method for estimation of noise reduction using fitting by inexperienced test subjects" (Renumbered from 4869 Part 7) (12 October 2005)

BOOK REVIEWS

P. L. Marston
Physics Department, Washington State University, Pullman, Washington 99164

These reviews of books and other forms of information express the opinions of the individual reviewers and are not necessarily endorsed by the Editorial Board of this Journal.

Editorial Policy: *If there is a negative review, the author of the book will be given a chance to respond to the review in this section of the Journal and the reviewer will be allowed to respond to the author's comments. [See "Book Reviews Editor's Note," J. Acoust. Soc. Am.* **81***, 1651 (May 1987).]*

Physical Acoustics in the Solid State

B. Lüthi

Springer, Berlin, 2005. 428 pp. Price $179.00 (hardcover). ISBN: 3540229108.

The speeds of sound and the elasticity of condensed matter depend fundamentally and strongly on the most important thermodynamic properties and are of comparable importance to specific heat, thermal expansion, magnetic susceptibility, and dielectric constant. Unlike, however, most of the quantities measured by experimentalists, the elastic constants are fourth-rank tensors which means that they contain a wealth of detail, directional information, and consistency constraints that, when used correctly and completely, provide some of the most powerful tests of theories of condensed matter. Moreover, the measurement of the speeds of sound, one route to the elastic constants, also connects to an important transport property—ultrasonic attenuation. In fact, it was the measurement of ultrasonic attenuation that enabled observation of the "freezing" of the normal electrons in a superconductor (masked, of course, when electrical conductivity becomes infinite) that was the first experimental confirmation of the famous Bardeen-Cooper-Schreiffer theory of superconductivity.

Accordingly, there is an enormous body of knowledge in print covering the study of condensed matter using acoustics, and one might be tempted to miss just another monograph. However, with this book by Lüthi, one of the most renowned physical acousticians, comes a special compendium of connections to microscopic physics. The book begins by surveying, once again, methods for the measurement of elastic moduli primarily through acousticlike processes, the theory of elasticity, and some thermodynamics. Though the beginning is neither pedagogical nor tutorial, it does provide a useful referent for what follows, and contains for the most part very-well-referenced sections on experimental techniques, elastic moduli, and more.

However, once Lüthi makes it through the introductory chapters, what remains must become required reading for anyone attempting to understand the value and relationships between ultrasound, ultrasonic attenuation, correlated-electron systems, magnetism, and superconductivity.

Lüthi covers magnetic ions, magnetic phase transitions, and structural transitions in three chapters where the overview is very rewarding. Of great importance is that while the basics are covered, sometimes quite quickly, many nasty little exceptions and surprises in phenomena ordinarily taken to be simple are dug out, described, and most importantly referenced. Accompanying tables, connected to theory and measurements, give the theorist and experimentalist alike a way of making a first cut at determining whether some behavior newly observed fits with previous work done by others on other systems.

Much of this book is devoted to cataloging unusual responses of many materials to doping, temperature, and, especially, magnetic field—all studied via ultrasound, but with sufficient contact and comparison with other measurements techniques. A whirlwind tour through metals and semiconductors, Kondo and mixed-valent materials, and such non-Fermi-liquid effects as quantum criticality is no substitute for delving deeply into each topic via the copious references provided, but Lüthi provides real value with many, many paragraph-length definitions of most of the strange physical phenomena cataloged by the condensed-matter physics community in recent years. These paragraphs are an excellent initial referent for further study, connecting the physics to the named investigator important to its discovery. If you need a decoder ring to go from names to the physics behind them, here it is.

Often neglected in many solid-state compendia on ultrasound are symmetry-breaking effects, so important in magnetic fields and low-symmetry systems. This topic is well covered, with, in a fashion similar to the rest of the book, careful note of exceptions, surprises, and obscure effects.

Of course, in any book with this breadth, some things are weak or missing, including connections to thermoelectric materials and discussion of polycrystal effects. One must also be careful to check formulas—there are a few typographic errors that are important. The index is very sparse—a CD-ROM version of the book would greatly increase its value because of this, but an unusually useful index to all the materials is provided. The overall strength of this book remains the ability to inform the reader about hundreds of fascinating phenomena of solid state physics and their exploration via physical acoustics.

ALBERT MIGLIORI
National High Magnetic Field Laboratory,
Los Alamos National Laboratory,
Los Alamos, New Mexico 87545

 0001-4966/2006/119(1)/13/1/$22.50

Radiation Acoustics

Leonid M. Lyamshev

CRC Press, Boca Raton, FL, 2004. 376 pp. Price $139.95 (hardcover) ISBN: 0415309999

Leonid Lyamshev's monograph on radiation acoustics is a review of sound generation by optical radiation, nuclear decay, and the interactions of elementary particles with condensed matter. Many of the processes described by the author that convert the energy in nuclear radiation to sound act in a manner directly analogous to optical absorption and heat liberation followed by thermal expansion; hence, the reader familiar with the photoacoustic effect will find much of the mathematics and the physics of sound production described in the text to be instructive and intriguing.

The first two chapters of the book describe basic interactions between elementary particles and condensed matter, such as energy loss by electrons, heavy particles, and nuclear cascade showers, and how the various interactions with matter lead to the production of ultrasound. Of particular note is the concise review in the second chapter of topics such as thermal expansion, microscopic shock production, bubble formation, electrostriction, momentum transfer, and electron and heavy particle deceleration, all of which generate ultrasound.

In chapter 3, starting from the linearized equations of fluid mechanics, the author proceeds to derive the basic equations for sound generation from a source of penetrating radiation, giving a detailed discussion of the restrictions on the validity of the resulting wave equation. In the following chapters, the book covers the excitation of sound in infinite media and in media where the effects of boundaries determine the spatial and temporal characteristics of the acoustic wave. The use of a reciprocity theorem developed by the author is illustrated by several examples in chapters 3 and 4.

The chapter describing the pulsed generation of sound in isotropic solids is notable for its lucid description of thermoacoustic wave generation in solids. Although the equations for sound generation in solids are not derived from first principles, the text gives a concise exposition on the origin of the fundamental equations, and a clear discussion of the range of validity of the resulting wave equation. Also found in *Radiation Acoustics* is a review of wave generation by moving radiation sources, including a description of the effects of a thermal source that moves at the wave speed, producing a wave where energy deposition over time is cumulative. The last chapters in *Radiation Acoustics* review experimental work related to the theoretical discussions of the first chapters, including directional properties of ultrasound produced by a source that penetrates a liquid surface, sound produced by a sequence of pulses, surface acoustic waves, and ultrasound generation by x rays, electrons, positrons, protons, and ion beams. Short reviews of ion-acoustic and scanning laser acoustic microscopy are given as well.

The author's lucid derivations of the basic equations of sound generation, together with his coverage of a wide range of topics, makes the book an excellent introduction not only to radiation acoustics, but to photoacoustics in general. Aside from the text's value as an excellent review of the production of sound from the interactions of radiation with matter, it also provides a valuable introduction to the physics of sound generation for graduate students or researchers wishing to familiarize themselves with the fundamentals of photoacoustics. For the reader conversant with photoacoustic and photothermal phenomena, the book is delightful reading, giving summaries and detailed discussions of the imaginative research that has been conducted in this field.

GERALD DIEBOLD
Department of Chemistry
Brown University
Providence, RI

 0001-4966/2006/119(1)/14/1/$22.50

Radiation Acoustics

Leonid M. Lyamshev

CRC Press, Boca Raton, FL, 2004. 376 pp. Price $139.95 (hardcover) ISBN: 0415309999

Leonid Lyamshev's monograph on radiation acoustics is a review of sound generation by optical radiation, nuclear decay, and the interactions of elementary particles with condensed matter. Many of the processes described by the author that convert the energy in nuclear radiation to sound act in a manner directly analogous to optical absorption and heat liberation followed by thermal expansion; hence, the reader familiar with the photoacoustic effect will find much of the mathematics and the physics of sound production described in the text to be instructive and intriguing.

The first two chapters of the book describe basic interactions between elementary particles and condensed matter, such as energy loss by electrons, heavy particles, and nuclear cascade showers, and how the various interactions with matter lead to the production of ultrasound. Of particular note is the concise review in the second chapter of topics such as thermal expansion, microscopic shock production, bubble formation, electrostriction, momentum transfer, and electron and heavy particle deceleration, all of which generate ultrasound.

In chapter 3, starting from the linearized equations of fluid mechanics, the author proceeds to derive the basic equations for sound generation from a source of penetrating radiation, giving a detailed discussion of the restrictions on the validity of the resulting wave equation. In the following chapters, the book covers the excitation of sound in infinite media and in media where the effects of boundaries determine the spatial and temporal characteristics of the acoustic wave. The use of a reciprocity theorem developed by the author is illustrated by several examples in chapters 3 and 4.

The chapter describing the pulsed generation of sound in isotropic solids is notable for its lucid description of thermoacoustic wave generation in solids. Although the equations for sound generation in solids are not derived from first principles, the text gives a concise exposition on the origin of the fundamental equations, and a clear discussion of the range of validity of the resulting wave equation. Also found in *Radiation Acoustics* is a review of wave generation by moving radiation sources, including a description of the effects of a thermal source that moves at the wave speed, producing a wave where energy deposition over time is cumulative. The last chapters in *Radiation Acoustics* review experimental work related to the theoretical discussions of the first chapters, including directional properties of ultrasound produced by a source that penetrates a liquid surface, sound produced by a sequence of pulses, surface acoustic waves, and ultrasound generation by x rays, electrons, positrons, protons, and ion beams. Short reviews of ion-acoustic and scanning laser acoustic microscopy are given as well.

The author's lucid derivations of the basic equations of sound generation, together with his coverage of a wide range of topics, makes the book an excellent introduction not only to radiation acoustics, but to photoacoustics in general. Aside from the text's value as an excellent review of the production of sound from the interactions of radiation with matter, it also provides a valuable introduction to the physics of sound generation for graduate students or researchers wishing to familiarize themselves with the fundamentals of photoacoustics. For the reader conversant with photoacoustic and photothermal phenomena, the book is delightful reading, giving summaries and detailed discussions of the imaginative research that has been conducted in this field.

GERALD DIEBOLD
Department of Chemistry
Brown University
Providence, RI

 0001-4966/2006/119(1)/14/1/$22.50

REVIEWS OF ACOUSTICAL PATENTS

Lloyd Rice
11222 Flatiron Drive, Lafayette, Colorado 80026

The purpose of these acoustical patent reviews is to provide enough information for a Journal reader to decide whether to seek more information from the patent itself. Any opinions expressed here are those of reviewers as individuals and are not legal opinions. Printed copies of United States Patents may be ordered at $3.00 each from the Commissioner of Patents and Trademarks, Washington, DC 20231. Patents are available via the Internet at http://www.uspto.gov.

Reviewers for this issue:

GEORGE L. AUGSPURGER, *Perception, Incorporated, Box 39536, Los Angeles, California 90039*
JOHN M. EARGLE, *JME Consulting Corporation, 7034 Macapa Drive, Los Angeles, California 90068*
SEAN A. FULOP, *California State University, Fresno, 5245 N. Backer Avenue M/S PB92, Fresno, California 93740-8001*
JEROME A. HELFFRICH, *Southwest Research Institute, San Antonio, Texas 78228*
MARK KAHRS, *Department of Electrical Engineering, University of Pittsburgh, Pittsburgh, Pennsylvania 15261*
DAVID PREVES, *Starkey Laboratories, 6600 Washington Ave. S., Eden Prarie, Minnesota 55344*
DANIEL R. RAICHEL, *2727 Moore Lane, Fort Collins, Colorado 80526*
CARL J. ROSENBERG, *Acentech Incorporated, 33 Moulton Street, Cambridge, Massachusetts 02138*
NEIL A. SHAW, *Menlo Scientific Acoustics, Inc., Post Office Box 1610, Topanga, California 90290*
WILLIAM THOMPSON, JR., *Pennsylvania State University, University Park, Pennsylvania 16802*
ERIC E. UNGAR, *Acentech, Incorporated, 33 Moulton Street, Cambridge, Massachusetts 02138*
ROBERT C. WAAG, *University of Rochester, Department of Electrical and Computer Engineering, Rochester, New York 14627*

6,923,105

43.30.Wi GUN-ARMED COUNTERMEASURE

Thomas J. Gieseke and Robert Kuklinski, assignors to The United States of America as represented by the Secretary of the Navy
2 August 2005 (Class 89/1.13); filed 6 October 2003

An armed underwater countermeasure is described. It comprises a hollow cylindrical tube **12** within which is mounted a gun **14** with barrel **16**. Item **30** is a compressed air source used to clear the barrel **16** prior to firing its projectile at an incoming target. Acoustic array panels **20**, which may be

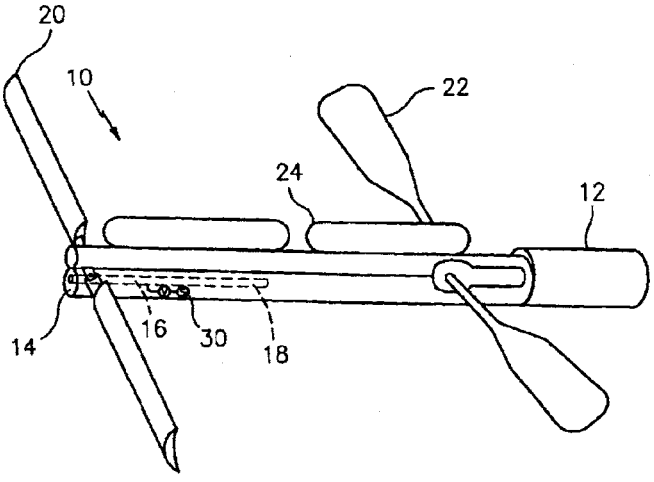

active as well as passive, are used to detect and localize the target. The transducer elements are of conventional design. Thrusters **22**, such as flapping foils, orient the device. Inflatable chambers **24** allow the device to hover at a chosen depth.—WT

6,921,366

43.35.Sx APPARATUS AND METHOD FOR NON-INVASIVELY MEASURING BIO-FLUID CONCENTRATIONS USING PHOTOACOUSTIC SPECTROSCOPY

Kye-jin Jeon *et al.*, assignors to Samsung Electronics Company, Limited
26 July 2005 (Class 600/309); filed in the Republic of Korea 20 March 2002

This is an apparatus for noninvasively measuring biofluid concentrations. A light source produces incident light containing a specific waveband that can be absorbed into a targeted part of the body. A signal generator produces an acoustic signal having a frequency band similar to that of a photoacoustic signal that is generated when the incident light is absorbed into the targeted component. An ultrasonic transducer detects the photo-

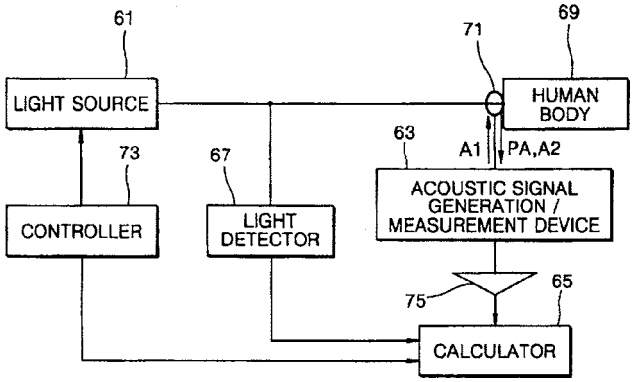

acoustic signal and a second signal modulated by the acoustic signal. A controller generates the acoustic signal in a predetermined frequency band. A light detector detects the intensity of the incident light and a processor calculates a signal compensation value based on the incident light and the photoacoustic signal, and also computes the biofluid concentration of the targeted components.—DRR

 0001-4966/2006/119(1)/15/14/$22.50

6,922,498

43.35.Sx FIBER-OPTIC MATRIX SWITCH USING PHASED ARRAY ACOUSTO-OPTIC DEVICE

Manhar L. Shah, assignor to MVM Electronics, Incorporated
26 July 2005 (Class 385/17); filed 5 February 2003

This design represents an attempt to provide a high-speed, high-isolation fiber optic switch through the use of a single acousto-optic device with phase-arrayed transducers. A single structure is disclosed which consists of a 2×2 fiber-optic matrix switch with one phased transducer. Use of a single, shared lens instead of individual lenses at the input and output fiber arrays is said to reduce the complexity and cost of the customary acousto-optic-based fiber optic switches.—DRR

6,898,978

43.35.Yb GEOMETRY FOR PULSED ACOUSTIC MEASUREMENTS OF PARTICLE SIZE

Richard O'Brien and David W. Cannon, assignors to Colloidal Dynamics Pty Limited
31 May 2005 (Class 73/613); filed in Australia 26 February 2001

An improved means of measuring particle size and the zeta potential in colloids is described wherein the cross talk between the measurement trans-

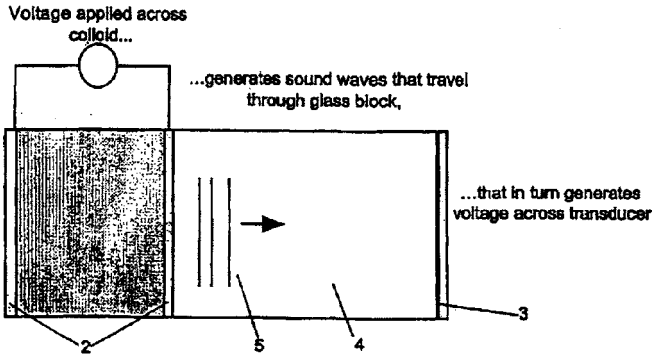

ducer **3** and the excitation electrodes **2** is reduced by using a pulsed signal and a physical delay line **4**.—NAS

6,924,587

43.38.Ar PIEZOELECTRIC TRANSDUCER, MANUFACTURING METHOD OF PIEZOELECTRIC TRANSDUCER AND PULSE WAVE DETECTOR

Hiroyuki Muramatsu *et al.*, assignors to Seiko Instruments Incorporated
2 August 2005 (Class 310/334); filed in Japan 16 November 2001

This patent describes various aspects of impedance matching ultrasonic transducers such as electroding methods, matching layers, and transducer shaping. None of this is gone into in any detail, but no matter—it can all be found elsewhere in the literature. It is hard to see why these inventors were granted a patent.—JAH

6,920,230

43.38.Ar ELECTROMAGNETIC TRANSDUCER AND PORTABLE COMMUNICATION DEVICE

Sawako Usuki and Shuji Saiki, assignors to Matsushita Electric Industrial Company, Limited
19 July 2005 (Class 381/396); filed in Japan 22 May 2000

This interesting patent describes a fairly complex armature-type transducer in which dual diaphragms and magnets interact with a fixed coil to create enhanced output. As the patent states, "In accordance with such an electromagnetic transducer, it is possible to maintain a high driving force

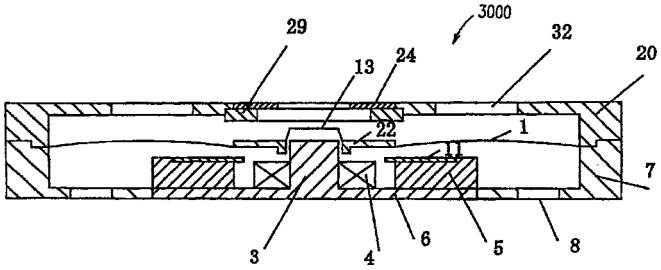

even when a magnetic gap along the height direction is increased, by merely altering existing components. Thus, a high sound-pressure level and low frequency-range reproduction are realized."—JME

6,921,952

43.38.Ar TORSION SPRING FOR MEMS STRUCTURE

Hee-moon Jeong, assignor to Samsung Electronics Company, Limited
26 July 2005 (Class 257/417); filed in the Republic of Korea 7 February 2002

This is a torsion spring designed specifically for vertically oriented construction, i.e., using silicon micromachining processes. The design basi-

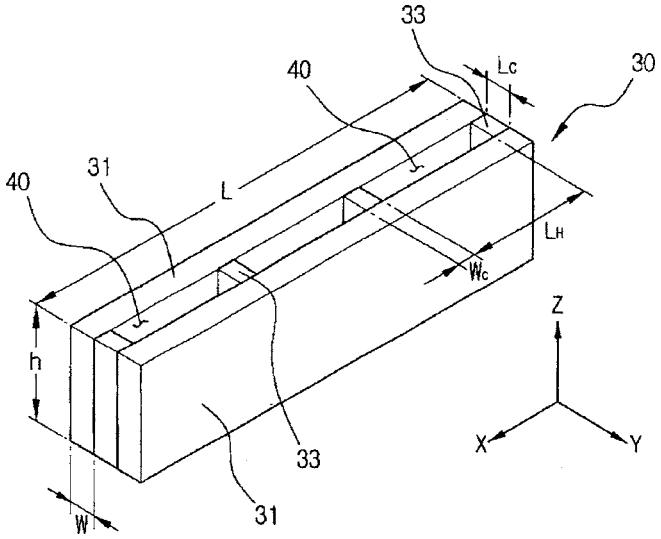

cally consist of holes through a rectangular beam such as in the figure. There is nothing really new here.—JAH

6,922,475

43.38.Ar SHOCKPROOF MICROPHONE SUPPORT DEVICE

Wu-Hong Hsieh, Lu Chou City, Taipei Hsien, Taiwan, Province of China

26 July 2005 (Class 381/368); filed 16 August 2001

The patent describes a relatively simple elastic loop of material to

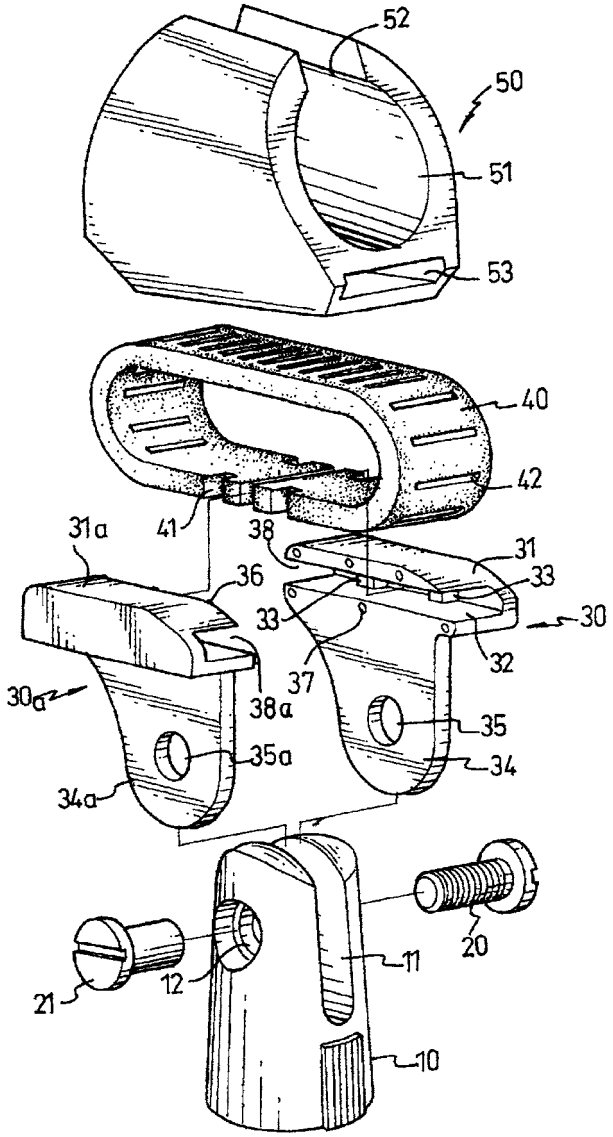

isolate a microphone from the stand on which it is mounted. Similar approaches have been used in the microphone accessory business.—JME

6,925,868

43.38.Ar ACOUSTIC VOLUME INDICATOR

Winston B. Young and Huey Wai, assignors to Young Manufacturing & Engineering, Incorporated

9 August 2005 (Class 73/290 V); filed 20 June 2002

"Volume" here refers to the volume of liquid contents, such as oil or gas, in a storage tank. Working noninvasively, from outside the tank, an oscillator produces a sound at the resonant frequency of the tank. An accelerometer or microphone picks up the tank response to the pulse and a processor computes the tank's liquid contents. There is no discussion of how the device is to be calibrated.—DLR

6,928,173

43.38.Ar CAPACITOR MICROPHONE

Hiroshi Akino, assignor to Kabushiki Kaisha Audio-Technica

9 August 2005 (Class 381/111); filed in Japan 6 July 2001

There are a few microphones on the current professional market that are called "digital," but which make use of traditional dc biasing to achieve an analog signal that is subsequently digitized. The procedure described in this patent is even "more digital." The transducing capacitor is in the tuned circuit of an oscillator, and that oscillator produces a frequency-modulated

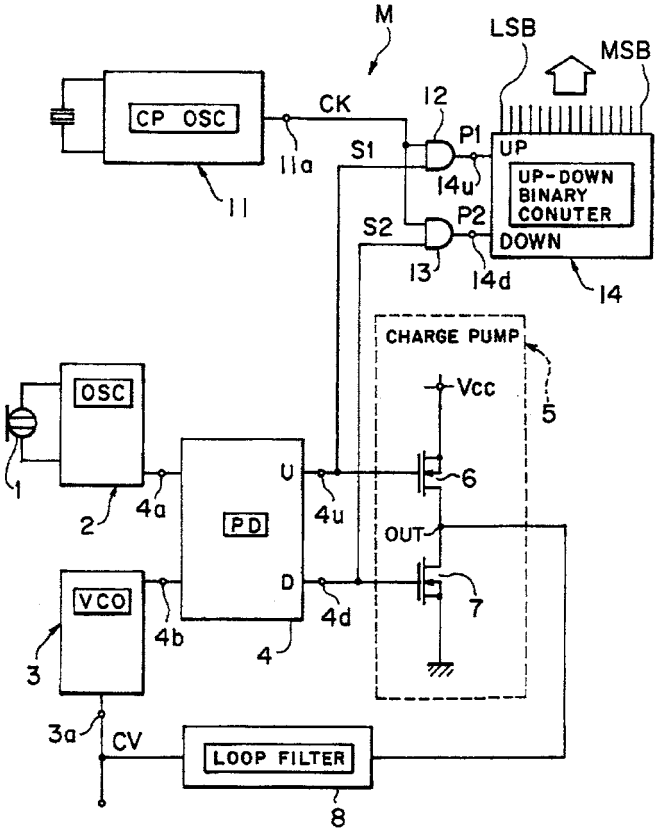

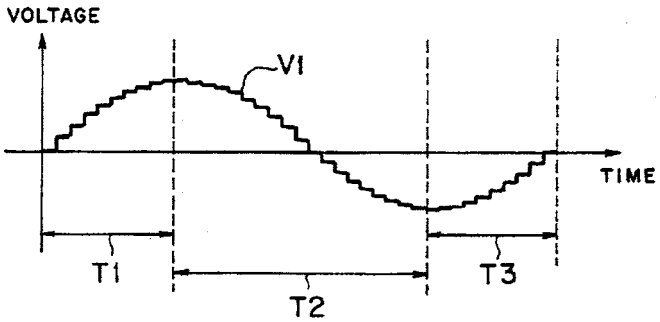

output proportional to the change in capacitance caused by sound vibrations. A second oscillator has a fixed output, which is compared with the variable output of the first oscillator. The phase difference between the two is then digitized directly.—JME

6,924,583

43.38.Bs FILM BULK ACOUSTIC DEVICE WITH INTEGRATED TUNABLE AND TRIMMABLE DEVICE

Chung-Hsien Lin *et al.*, assignors to Asia Pacific Microsystems, Incorporated
2 August 2005 (Class 310/324); filed in Taiwan, Province of China 3 May 2002

This patent discloses several more or less obvious methods of trimming a resonator with variable capacitors and inductors. The patent is brief but the English is difficult and hard to understand. Of the tuning methods presented, the comb electrode activated capacitor illustrated is probably the

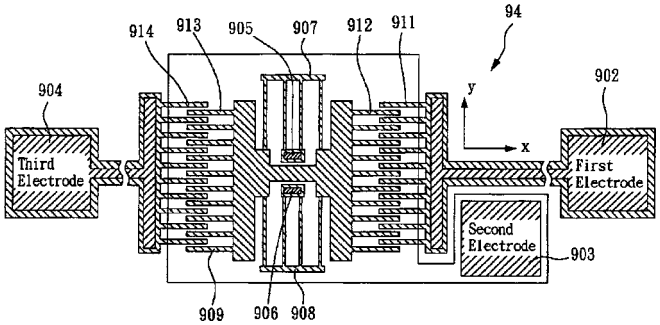

most interesting. This shows a gating arrangement wherein a voltage applied to electrode **903** alters the geometry between **902** and **904**, lowering the capacitance between them.—JAH

6,924,717

43.38.Fx TAPERED ELECTRODE IN AN ACOUSTIC RESONATOR

Eyal Ginsburg *et al.*, assignors to Intel Corporation
2 August 2005 (Class 333/187); filed 30 June 2003

This brief patent describes a fabrication technique for electroding piezoelectric layers as found in bulk acoustic wave resonators. In it, the authors purport to have discovered the method of tapering metal electrodes to reduce piezo (AlN, ZnO) crystal dislocations generated by steps in the substrate that it is being deposited on. There are no realistic prescriptions for how this tapering is to be accomplished in the world of semiconductor processing. There is nothing here that would warrant looking up the patent.—JAH

6,924,733

43.38.Fx HOSE SEPARATION TRANSMITTER SYSTEM AND METHODS

Samuel E. McTier *et al.*, assignors to McTier Supply Company
2 August 2005 (Class 340/425.5); filed 21 August 2003

An application is described in which a piezo transducer is placed in the truck-attachment end of a gas or oil delivery hose. If the hose becomes detached from the truck, the sensor detects the shock of the hose end hitting the ground. A signal is sent to the truck, which causes the delivery pump to shut down.—DLR

6,924,584

43.38.Hz PIEZOELECTRIC TRANSDUCERS UTILIZING SUB-DIAPHRAGMS

Steven A. Buhler *et al.*, assignors to Palo Alto Research Center Incorporated
2 August 2005 (Class 310/324); filed 13 December 2002

This patent describes a way of dividing membranes that are piezo-coupled into separate subdiaphragms in order to increase stiffness. What seems to be the inventor's goal is to increase the resonant frequency of a given moving area. What is not stated is that this reduces the displacement available. The value of doing this is not clear, unless the individual sensors are independently addressable.—JAH

6,899,794

43.38.Ja SPEAKER DEVICE, AND METHOD AND DEVICE FOR PRODUCING THE SAME

Teruho Yamada *et al.*, assignors to Mitsubishi Denki Kabushiki Kaisha
31 May 2005 (Class 162/219); filed 6 October 2000

Metal frames for loudspeakers can resonate, have manufacturing defects, can take time to manufacture, have a cost, can divert magnetic flux from the motor circuit, and may present disposal problems at the end of their lives, among other things. The patent describes a paper frame solution for

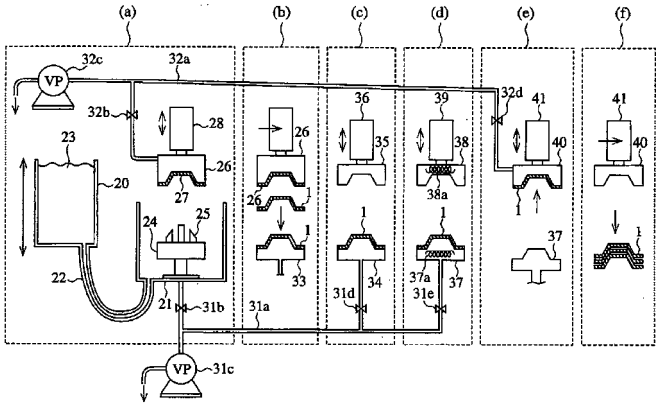

these problems as well as describing a means to manufacture the paper skimmed frames. The figure may remind one of the steps that can be used to manufacture paper cones. As such, the properties of the paper frame can be varied as needed.—NAS

6,904,154

43.38.Ja ACOUSTIC DEVICE

Henry Firouz Azima *et al.*, assignors to New Transducers Limited
7 June 2005 (Class 381/152); filed in the United Kingdom 2 September 1995

We find 52 columns of text, 66 figures (some with more than one part), and 16 claims about loudspeaker/microphone systems that use bending wave mechanisms (sometimes described as distributed mode resonators, distributed mode panels, distributed mode loudspeakers, or DML) for conversion of mechanical energy into/from acoustic energy by electrodynamic, and other means. Various implementations including, but apparently not limited

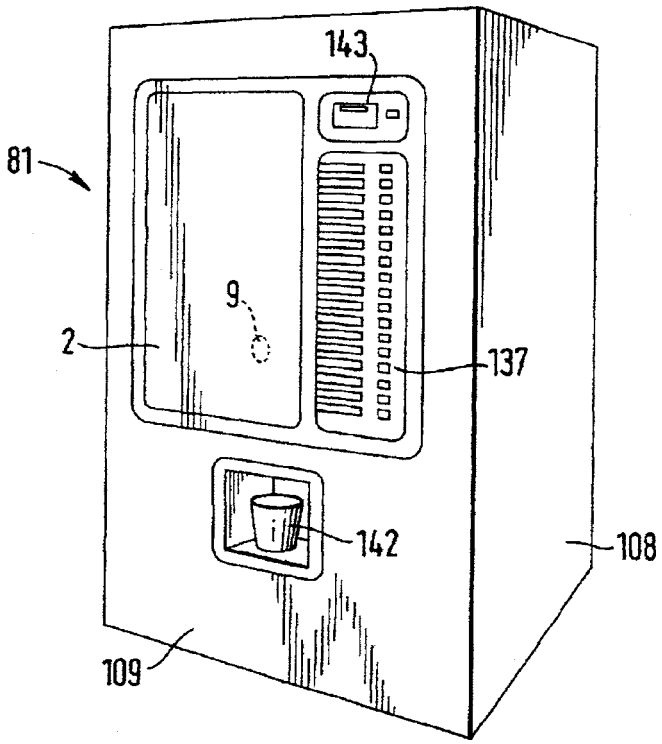

to, musical instruments, home and commercial theaters, portable equipment (such as computers and personal listening devices), vending machines, automobiles, and airplanes are described. The assignee is a company that has built up a large stable of patents around transduction via bending wave mechanisms.—NAS

6,910,549

43.38.Ja EMBEDDED MULTIMEDIA SPEAKER STRUCTURE

Hsien-Chin Kung, Junghe, Taipei, Taiwan, Province of China
28 June 2005 (Class 181/199); filed 16 June 2003

Many desktop computers have auxiliary loudspeakers that are placed on either side of the computer monitor and these may add to the clutter of the desktop, as opposed to the one on the computer monitor. To alleviate desktop clutter, these multimedia speakers are mounted in a case that fits in

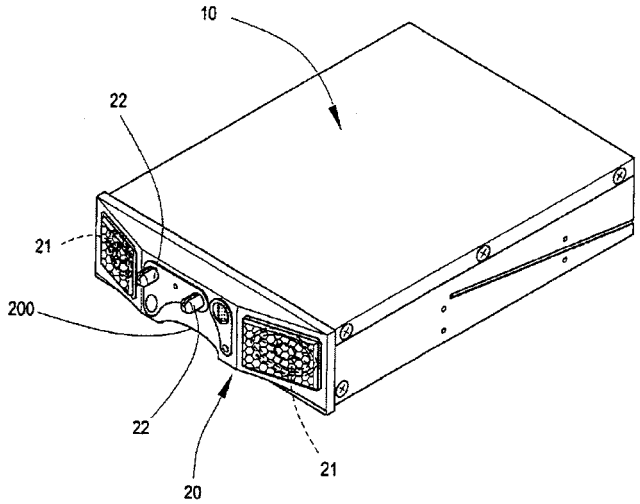

a 5.25 in. disk drive slot. All well and good if the desktop computer sits under the monitor so that the disk drive speaker is correctly positioned, but what if it is mounted below the desk or is in fact a tower (which is shown in one of the figures)?—NAS

6,920,957

43.38.Ja LOUDSPEAKER DIAPHRAGM

Sawako Usuki and Shuji Saiki, assignors to Matsushita Electric Industrial Company, Limited
26 July 2005 (Class 181/173); filed in Japan 24 June 2002

Although this patent is mainly concerned with shallow loudspeakers using oval diaphragms, the claims are broad enough to cover almost any configuration. One or more stiffening ribs **202** are formed within the central

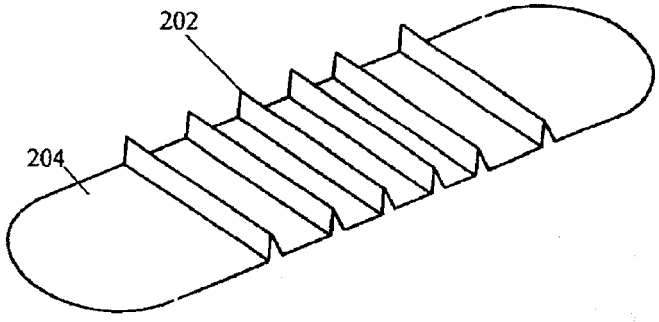

portion of the diaphragm. These allow the overall assembly to be lighter and also extend high-frequency performance.—GLA

6,925,187

43.38.Ja HORN ARRAY EMITTER

Elwood G. Norris and James J. Croft III, assignors to American Technology Corporation
2 August 2005 (Class 381/191); filed 27 March 2001

The invention has its main application in the generation of ultrasonic sound. An array of small horns is formed in rigid plate **11**. A deformable membrane **20** is attached directly to the underside of the plate. Thus, the

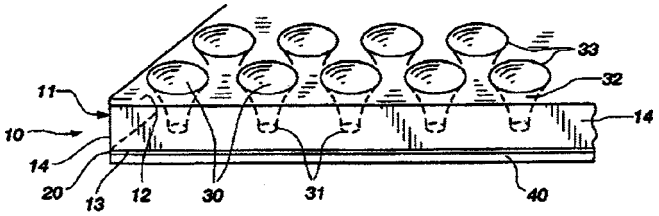

areas stretched across individual horn throats are free to vibrate and can be driven electrostatically or by other means. The patent describes a number of practical embodiments.—GLA

6,919,771

43.38.Lc DIGITAL AMPLIFIER

Kouji Nakajima, assignor to Denon, Limited
19 July 2005 (Class 332/109); filed in Japan 6 January 2003

An all-digital audio amplifier has a number of advantages for use in portable CD players and the like. Such an amplifier might include gain regulation and digital filtering (tone controls) before conversion to pulse-width modulation. If the user stops the unit or sets the gain to zero, the

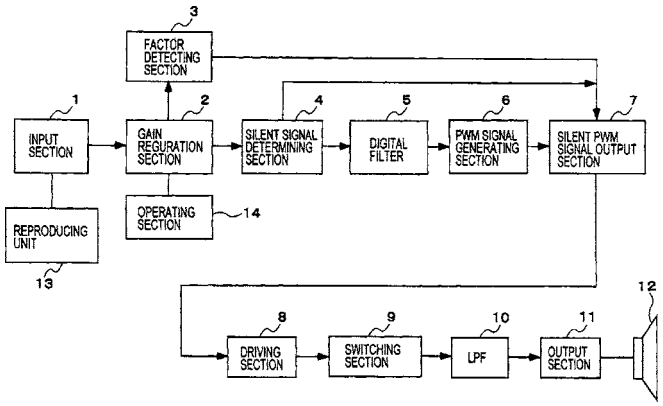

digital filter continues to process data already in the pipeline, resulting in a brief ''tail'' of unwanted sound. This patent describes additional circuitry to detect these situations and instantly set the PWM driving signal to the desired 50% duty cycle.—GLA

6,922,474

43.38.Lc SHOCK SOUND PREVENTION CIRCUIT

Koichi Hayama, assignor to Sanyo Electric Company, Limited
26 July 2005 (Class 381/94.5); filed in Japan 23 April 2002

When transistorized audio equipment first became available, loud turn-on transients (''shock sounds'') were an annoying problem. Today, the inexpensive circuits used to provide beep tones in portable cameras and the like suffer from the same failing. ''On that account, there arises a problem

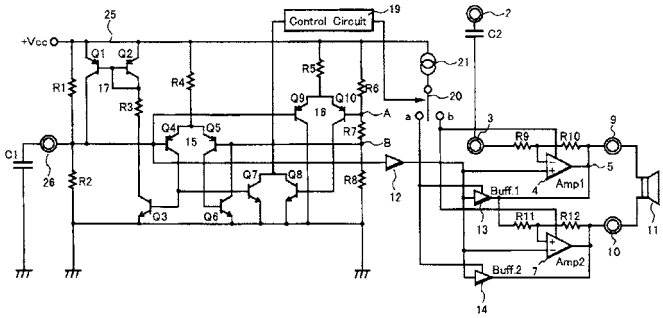

that the shock sound disturbs the beep sound.'' A fairly sophisticated turn-on delay arrangement is described which does not require the use of large capacitors.—GLA

6,917,689

43.38.Md SOUND MIXING EQUIPMENT

Lung-En Cheng, assignor to Hanpin Electron Company, Limited
12 July 2005 (Class 381/119); filed 30 July 2002

The inventor fears that shaft encoders are not robust enough to withstand smoky, dirty dance halls, so an electro-optical mixer is proposed. Light is emitted by LED **11** and reflects off of paddle **15**, which lengthens or

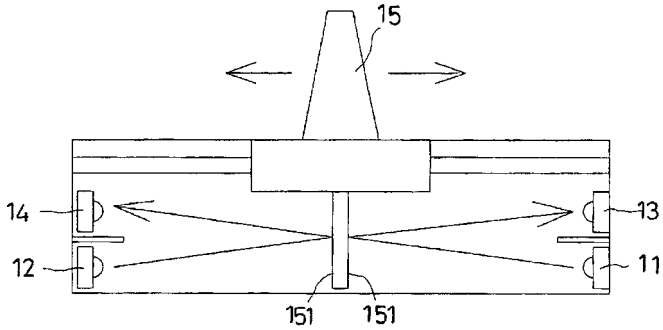

shortens the light path. A phototransistor **13** receives the signal and delivers it to a two-channel electronic balance circuit.—MK

6,927,373

43.38.Md COOKING APPARATUS EQUIPPED WITH AUDIO PLAYER

Sei Ill Jeon, assignor to Samsung Electronics Company, Limited
9 August 2005 (Class 219/702); filed in the Republic of Korea 22 February 2003

At present, the only sound of the microwave oven is the cooling fan of the magnetron. Wouldn't your reheat experience be enhanced with an attached CD player? Why is putting a CD player in a microwave novel enough to be granted a patent?—MK

6,928,433

43.38.Md AUTOMATIC HIERARCHICAL CATEGORIZATION OF MUSIC BY METADATA

Ron Goodman and Howard N. Egan, assignors to Creative Technology Limited
9 August 2005 (Class 707/4); filed 5 January 2001

As an opening battle in the MP3 player wars, this is possibly the most contentious patent to be reviewed this year. At issue is the graphical user interface presented to the listener. In this disclosure, Creative Technology stakes its claim on the Zen(™) user interface. The basic idea is that the metadata can be presented to the user in a number of ways: by artist, by track, by album, etc. However, this is what is known in database theory as a ''view.'' The final issue—whether applying a well-established database principle to audio players is novel enough for a patent—will probably land before a court.—MK

6,920,228

43.38.Si LIGHTWEIGHT HEADSET FOR HIGH NOISE ENVIRONMENTS

Karl W. Redmer *et al.*, assignors to Otto Engineering, Incorporated
19 July 2005 (Class 381/370); filed 20 August 2002

In this lightweight headset, a single driver **40** transmits sound to both ears via flexible tubes **12**. This is said to be more comfortable than the more

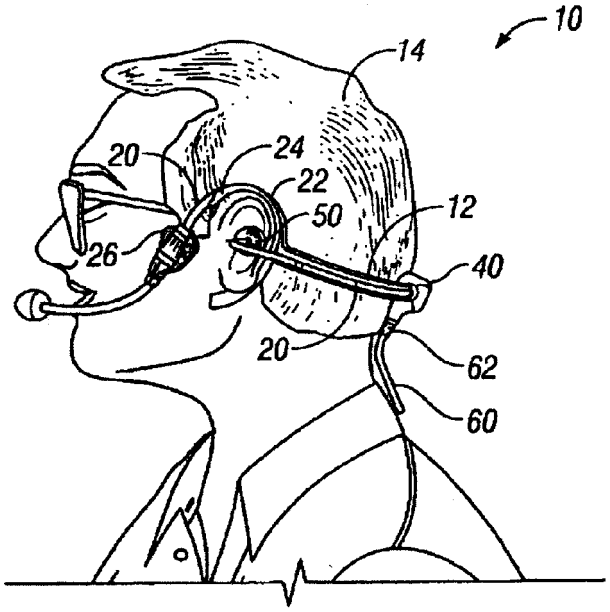

conventional two-transducer arrangement. Removable in-ear inserts allow the headset to be configured for a variety of applications.—GLA

6,925,296

43.38.Si SOUND-BASED PROXIMITY DETECTOR

Sven Mattisson, assignor to Telefonaktiebolaget L M Ericsson (publ)
2 August 2005 (Class 455/355); filed in Sweden 28 December 2000

Your cell phone rings. You hold it at some distance, initiate the off-the-hook response, and say, ''Hello.'' After a few words between you and the caller, you decide to continue the conversation and bring the phone to your ear. The problem with this scenario is that the loudspeaker volume must somehow be turned up when the phone is held at a distance and then reduced when it is brought to your ear. This patent describes an automatic

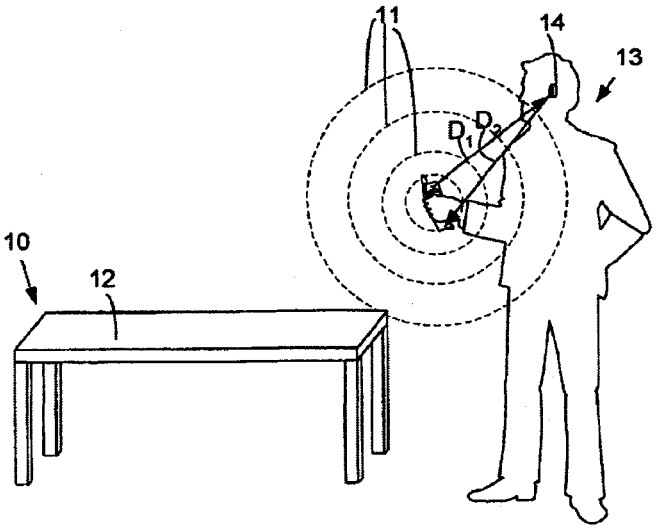

ranging system that initiates a repetitive control signal when the phone is taken off the hook and then measures the elapsed time and intensity of the signal when it is received by the microphone. Some fancy computer processing then utilizes this information to determine the distance between you and the phone without being misled by reflections from other objects.—GLA

6,928,306

43.38.Si PORTABLE MOBILE UNIT

Masayuki Matsuda *et al.*, assignors to Hitachi, Limited
9 August 2005 (Class 455/567); filed in Japan 7 January 2000

Providing customized ring tones for cell phones is a multimillion dollar business in the U.S. alone and a large volume of prior art already exists in this specialized field. It would be convenient if the user could program the

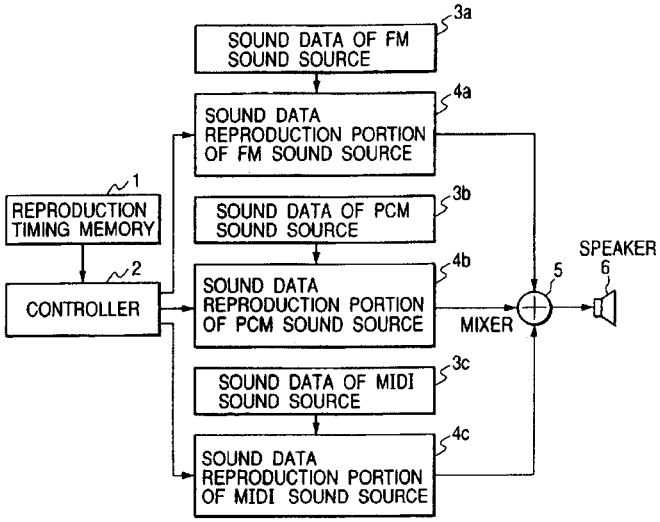

selection of different customized tones depending on, say, caller identification, time of day, or a particular date. Some might argue that implementing such a simple program would be self-evident to anyone skilled in the art. However, the method described in this patent conserves memory by composing such specialized tones from shorter common building blocks.—GLA

6,918,461

43.38.Vk DUAL MONO CENTER CHANNEL

Cary L. Christie, Incline Village, Nevada
19 July 2005 (Class 181/148); filed 20 February 2003

This is a wonderful example of a vanity patent. Almost all present-day TV sets include two loudspeakers at the sides of the screen. When processing surround sound, a phantom center is created by adding equal amounts of the center signal to the left and right signals. The matrixing circuit may consist of a few resistors and costs perhaps 25¢. A similar matrixing capability is included in most home theater receivers for the occasional situation

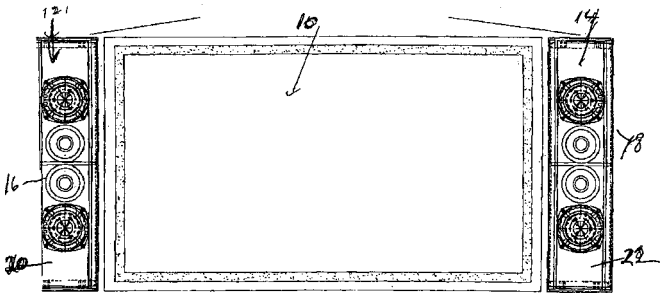

in which there is no space for a center loudspeaker. None of this prior art is mentioned here. Instead, the patent describes a mind-boggling alternative approach in which a duplicate set of left and right loudspeakers is driven from the center channel amplifier. The patent attorney has somehow managed to create 25 well-crafted claims from an idea that is of interest to no one except the inventor himself.—GLA

6,925,426

43.38.Vk PROCESS FOR HIGH FIDELITY SOUND RECORDING AND REPRODUCTION OF MUSICAL SOUND

William M. Hartmann, assignor to Board of Trustees operating Michigan State University
2 August 2005 (Class 703/5); filed 22 February 2000

The patent describes a multichannel recording system in which each instrument in an ensemble is itself recorded with multiple contact pickups on various parts of the instrument. (As an example, a string quartet might require, say, 20 recording channels.) Playback is by way of loudspeaker clusters, one set for each instrument, in which the radiation pattern for the

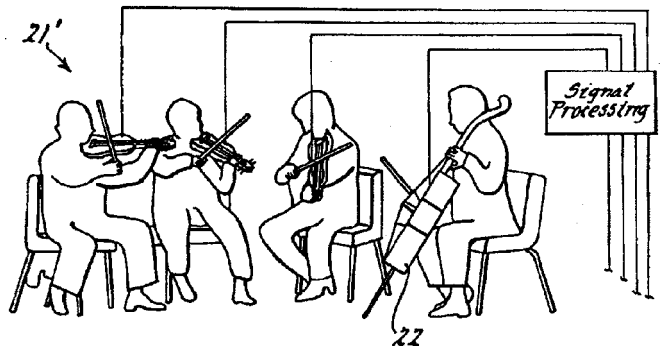

target instrument is substantially duplicated. The intention is not to create a ''you are there'' impression for the listener, but rather to create a ''they are here'' effect. Properly implemented, you could truly recreate the sound of a small instrumental group in your living room, parallax and all.—JME

6,928,168

43.38.Vk TRANSPARENT STEREO WIDENING ALGORITHM FOR LOUDSPEAKERS

Ole Kirkeby, assignor to Nokia Corporation
9 August 2005 (Class 381/1); filed 19 January 2001

This is another in a long line of patents dealing with widening the apparent width of the reproduced stereo soundstage through the use of interchannel crosstalk. This method uses both delay and frequency shaping in the crosstalk paths to optimize the effect.—JME

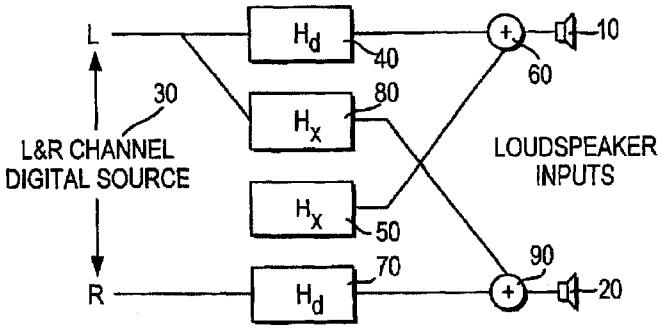

6,918,884

43.40.Ng VIBRATING LUMBAR SUPPORT

John Knelsen and Reinold Kosciuw, assignors to L&P Property Management Company
19 July 2005 (Class 601/57); filed 14 September 2001

In a preferred embodiment, an electromagnet, positioned between two vertical guide rods, is shaped to function with an arching lumbar support. The arched pressure surface slides along these rods at an upper and lower sliding connection. The shape of the arch is adjustable by the user through a traction device, namely a Bowden cable. After adjustment, the pressure surface remains in the selected shape until the next readjustment. The guide rods are sandwiched between two plates which transmit vibration from the electromagnet through the vibration plates, through the guide rods, and then through the arched pressure surface and finally through the seat cushion to the passenger. This reviewer has noted elsewhere that Mercedes-Benz is already using a similar system in some of its ultra-luxury models.—DRR

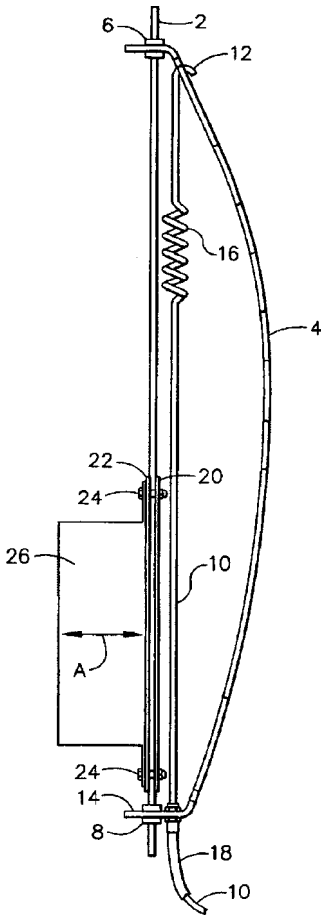

6,920,967

43.40.Tm CONTROLLER FOR REDUCING EXCESSIVE AMPLITUDE OF OSCILLATION OF FREE PISTON

James Gary Wood, assignor to Sunpower, Incorporated
26 July 2005 (Class 188/380); filed 3 April 2003

A dynamic absorber consisting of a spring-supported mass is attached to the outside of the cylinder of a free-piston, Stirling-cycle engine. If motion of the mass exceeding a predetermined threshold is detected (via a vibration or displacement sensor), signifying excessive motion of the machine, a controller reduces the fuel fed to the engine.—EEU

6,923,298

43.40.Tm SHOCK, VIBRATION AND ACOUSTIC ISOLATION SYSTEM

Edward T. Tanner, assignor to Northrop Grumman Corporation
2 August 2005 (Class 188/267); filed 20 May 2004

This self-contained system is intended to provide effective vibration isolation in the 10–200-Hz range, as well as isolation from a variety of shocks. A semiactive damper is disposed in mechanical parallel within a spring arrangement and adapted for providing a selectively variable reaction force in response to relative motion between the ends of the spring. The damper may be based on an electrorheological or magnetorheological fluid, activated via a controller.—EEU

6,920,959

43.50.Gf INLET AND OUTLET DUCT UNITS FOR AIR SUPPLY FAN

Ming Hui Han and Pradeep Guar, assignors to M & I Heat Transfer Products Limited
26 July 2005 (Class 181/224); filed 30 May 2003

This duct unit delivers air to an air-supply fan while providing sound attenuation. One version consists of a narrow input section followed by a second transition-type section and a third wide, sound-attenuating section. Spaced-apart splitters containing sound-deadening materials and having side walls of perforated metal are mounted in the third section. The splitters include a central splitter and outer splitters that converge inwardly toward the center of the third section. The duct also features an elbow-shaped section connected between the upstream end of the third section and the downstream end of a fan.—DRR

6,920,723

43.55.Vj IMPACT SOUND INSULATION

Paul Charles Downey, assignor to Dodge-Regupol, Incorporated
26 July 2005 (Class 52/144); filed 16 August 2001

This mat is an underlayment for fancy, finished floor systems that will reduce impact energy, such as foot-fall sound. The underlayment incorporates voids between particles of rubber that provide static deflection to the mat, which in turn absorbs impact energy.—CJR

6,927,651

43.58.Kr ACOUSTIC RESONATOR DEVICES HAVING MULTIPLE RESONANT FREQUENCIES AND METHODS OF MAKING THE SAME

John D. Larson III and Yury Oshmyansky, assignors to Agilent Technologies, Incorporated
9 August 2005 (Class 333/189); filed 12 May 2003

This brief patent describes a technique for depositing piezoelectric layers in thin-film bulk acoustic wave resonators so as to stagger-tune the fundamental thickness resonance. The authors teach that the layers are deposited with their crystal axes intentionally misaligned so as to create a lack of electrical coupling between them, but mechanical coupling is fostered. The result is a pair of resonances in the composite structure, and this device is shown used in ladder networks, as an example. While the authors maintain that they have discovered this, it seems to this reviewer that the idea of layering materials with different properties and/or crystallographic orientations to obtain a composite response is not new. There is some fabrication information here, but no design equations for how to get the desired impedances and resonant frequencies.—JAH

6,923,708

43.58.Wc NOISE GENERATING DEVICE

Craig Coons, Whitestone, New York
2 August 2005 (Class 446/397); filed 19 February 2004

Is the sound of a fly or mosquito annoying? Why not invent a portable, annoying-insect sound generator? You can use it to bother guests who stay

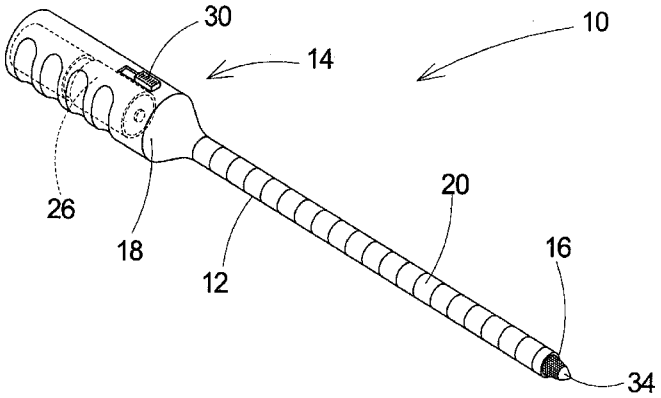

too long, door-to-door sales people, and maybe fool the neighbourhood frogs. The possibilities are endless.—MK

6,928,031

43.58.Wc ALARM CLOCK SYSTEM, METHOD OF OPERATION AND PROGRAM PRODUCT THEREFOR

Dimitri Kanevsky and Wlodek Zadrozny, assignors to International Business Machines Corporation
9 August 2005 (Class 368/12); filed 24 April 2000

The inventors believe that waking up with an alarm during REM (rapid eye movement) sleep is very rude. So they propose nightly attaching a brain activity sensor to the skull, and then connecting it to a computer, so that the sleeper can be awakened at the nearest non-REM sleep phase (within reason). Acoustically speaking, the output of the alarm is not specified.—MK

6,924,895

43.60.Bf SENSOR FOR OPTICALLY SENSING AIR BORNE ACOUSTIC WAVES

Joseph Lawrence Chovan *et al.*, assignors to Lockheed Martin Corporation
2 August 2005 (Class 356/484); filed 1 August 2003

This succinct and well-written patent describes a method of sensing acoustic waves in air. According to the abstract, ''The sensor comprises means for producing mutually coherent optical sampling and reference beams, which may be combined to form an intermediate frequency carrier, the sampling beam being exposed to the acoustic field in which acoustic wave induced density variations occur. These density variations produce a variation in the index of refraction and thereupon a phase modulation of the

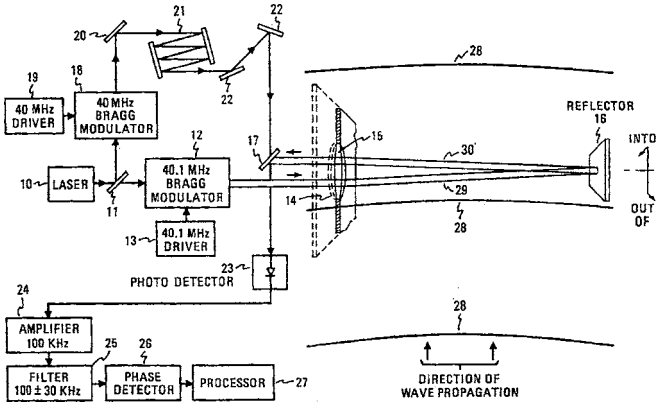

sampling beam. This phase modulation may be recovered by an optical detector and a phase detector as an electrical signal representative of the acoustical signal.'' The primary application of the process is in surveillance activities.—JME

6,928,170

43.60.Bf WIRELESS MICROPHONE HAVING A SPLIT-BAND AUDIO FREQUENCY COMPANDING SYSTEM THAT PROVIDES IMPROVED NOISE REDUCTION AND SOUND QUALITY

Kelly Statham, assignor to Audio Technica, Incorporated
9 August 2005 (Class 381/92); filed 2 November 2000

Virtually all wireless microphone systems in use today use companding (compression with inverse expansion) to improve the effective dynamic range of the overall system. In addition, pre- and postemphasis are used to reduce the audibility of noise modulation. This patent describes the advantages of split-band companding to further minimize the audibility of these artifacts.—JME

6,928,172

43.60.Bf AUTOMATIC SOUND FIELD CORRECTING SYSTEM

Yoshiki Ohta, assignor to Pioneer Corporation
9 August 2005 (Class 381/98); filed in Japan 14 February 2000

With the proliferation of surround-sound systems in the home—and the availability of low-cost DSP—it is now possible to design mid-priced systems that are self-calibrating in terms of equal playback levels, channel

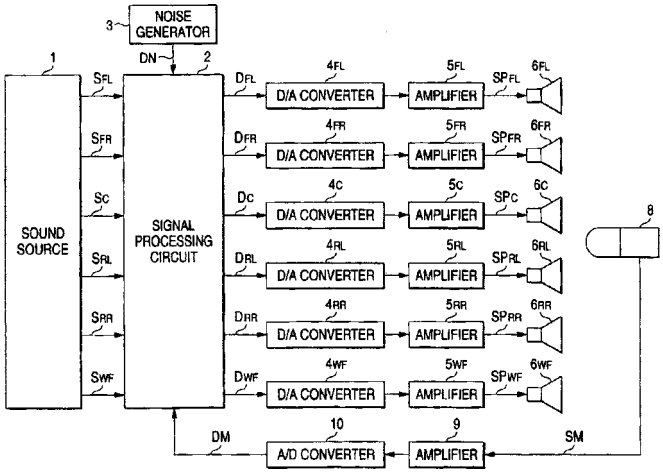

polarity, uniform frequency response, and equal arrival times at the primary listening position.—JME

6,910,011

43.60.Dh NOISY ACOUSTIC SIGNAL ENHANCEMENT

Pierre Zakarauskas, assignor to Haman Becker Automotive Systems-Wavemakers, Incorporated
21 June 2005 (Class 704/233); filed 16 August 1999

Reducing the noise in signals has been a goal since the beginning of communications by electrical means. A method, apparatus, and computer program are described that enhance the quality of an acoustic signal by means of an acoustic model that estimates the noise and isolates transients, and by training the model with comparison to known templates. The invention is said to have applications in voice communications, automatic speech recognition, and hearing aids, among others.—NAS

6,922,206

43.60.Fg VIDEOCONFERENCING SYSTEM WITH HORIZONTAL AND VERTICAL MICROPHONE ARRAYS

Peter L. Chu *et al.*, assignors to Polycom, Incorporated
26 July 2005 (Class 348/14.09); filed 15 April 2003

Vertical and horizontal microphone arrays are used in an adaptive system to locate a sound source. A video camera can then be trained on the source.—JME

6,925,189

43.60.Fg HYBRID ADAPTIVE BEAMFORMER

Walter S. Koroljow and Gary L. Gibian, assignors to Planning Systems, Incorporated
2 August 2005 (Class 381/313); filed 11 October 2000

The patent describes a forward-oriented microphone array installed in the ear clip of a pair of spectacles for the hearing impaired. The associated

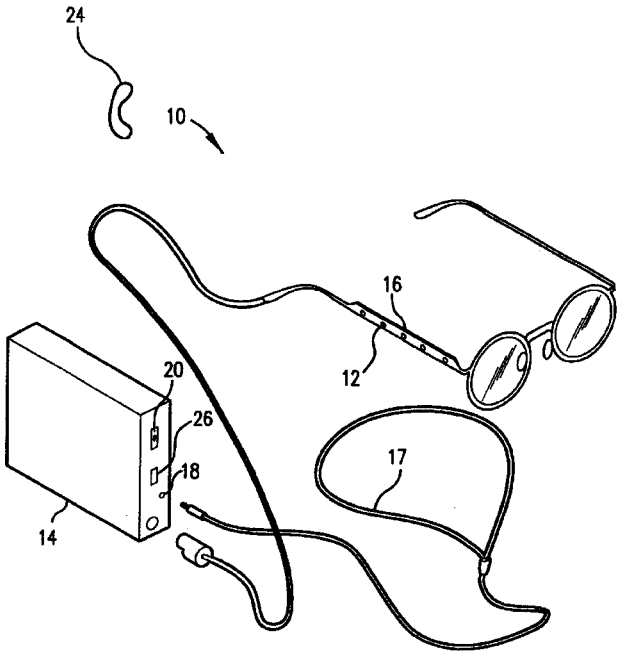

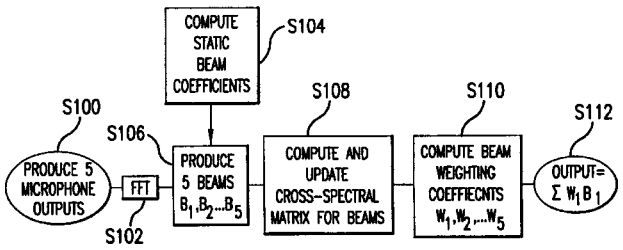

adaptive system senses the ambient noise level in the environment and adjusts the synthesized microphone pattern between first and second order, as required for maximum intelligibility.—JME

6,923,064

43.60.Vx METHOD AND DEVICE FOR DETECTION, IDENTIFICATION AND DENSIMETRIC QUANTIFICATION OF GRAIN-EATING INSECTS IN STOCKS OF CEREALS

Pedro Rodriguez Gobernado *et al.*, assignors to Solween Technologies (Societe a Responsabilite Limited)
2 August 2005 (Class 73/587); filed in France 8 June 2001

This method provides a means for detecting, classifying, and densimetrically quantifying granivorous (cereal-loving) insects in stacks of cereals. The methodology includes recording the actual noises in the cereal stock, eliminating known random noises, detecting the resulting energy envelope corresponding to energy peaks, and determining therefrom the mean

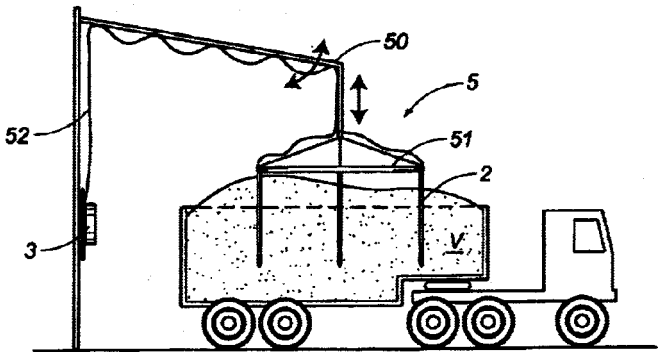

frequency, the spectral width, and the global energy. These windows are compared with windows of known characteristics to obtain a taxonomic classification. As for getting rid of the insects, that is another matter not addressed here.—DRR

6,927,204

43.64.Ld TREATMENT OF INNER EAR HAIR CELLS

Wei-Qiang Gao, assignor to Genentech, Incorporated
9 August 2005 (Class 514/2); filed 9 June 2003

This represents a noble attempt to promote the growth, proliferation, or regeneration of inner ear epithelial hair cells. The patent covers methods, compositions, and devices for prophylactic and therapeutic treatment of inner ear disorders and conditions. The methods entail the administration of insulinlike growth factor-1 (2GF-1) and/or fibroblast growth factor-2 (FGF-2), or their agonists.—DRR

6,923,760

43.64.Yp ENDOSCOPIC AUDITORY CANAL CLEANING APPARATUS

Yoshiharu Koda and Kojiro Koda, assignors to Coden Company, Limited
2 August 2005 (Class 600/200); filed in Japan 6 June 2003

This is an endoscopic auditory canal cleaning device that incorporates a guide light, an ear-picking main body shaped so as to guide the light, and an ear picking part furnished with a surface layer made of a fibrous material

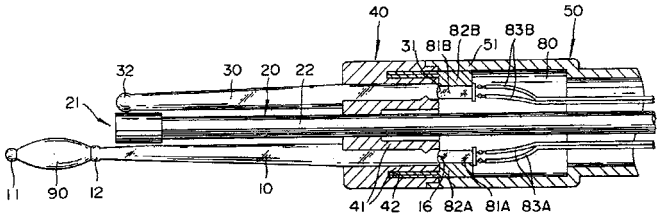

adapted to be discarded after use. The ear picking body rotates about the light guide containing micro lens used to acquire an image. The fibrous part of the ear picking part is used to remove ear wax.—DRR

6,920,452

43.66.Lj SOUND PATTERN FEEDBACK FOR INFORMATIONAL EVENTS DURING TYPING

Andreas Dieberger, assignor to International Business Machines Corporation
19 July 2005 (Class 707/6); filed 26 April 2001

What is presented here is a system of beeps and clicks produced by a computer to aid the user in performing specific tasks. A number of similar prior-art patents are described, but, it is argued, the system covered here involves a more comprehensive application of psychological principles in the choices and presentation of the various sounds used for alarms and status indications.—DLR

6,920,226

43.66.Ts HEARING AID HAVING A DEACTIVATABLE SIGNAL PROCESSING DEVICE, AND DEACTIVATION METHOD

Gunter Sauer, assignor to Siemens Aktiengesellschaft
19 July 2005 (Class 381/312); filed in Germany 14 March 2002

When there is little or no signal activity, the input to a signal process-

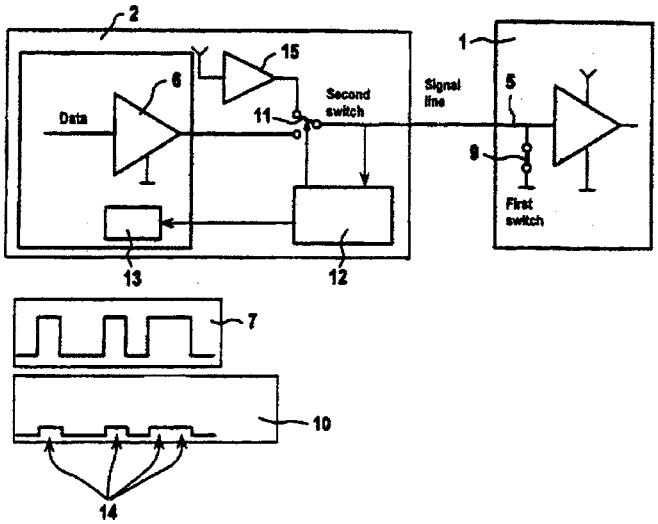

ing amplifier is shunted to ground and the signal line connected to a preamp output is switched to a lower power driver.—DAP

6,920,227

43.66.Ts ACTIVE NOISE SUPPRESSION FOR A HEARING AID DEVICE WHICH CAN BE WORN IN THE EAR OR A HEARING AID DEVICE WITH OTOPLASTIC WHICH CAN BE WORN IN THE EAR

Josef Chalupper *et al.*, assignors to Siemens Audiologische Technik GmbH
19 July 2005 (Class 381/312); filed in Germany 16 July 2003

To cancel sound traveling into the ear canal via the hearing-aid vent, a second microphone picks up the sound in a first region of the vent and plays it back into a second region in the vent after phase shifting it with a filter so

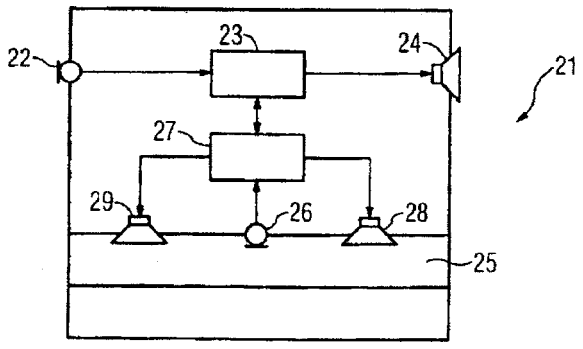

as to cancel the direct sound. The same mechanism applies as well to cancel sound fed back through the vent from the opposite direction.—DAP

6,920,414

43.66.Ts CAD/CAM SYSTEM FOR DESIGNING A HEARING AID

Jan Tøpholm, assignor to Widex A/S
19 July 2005 (Class 703/1); filed in the European Patent Office 26 March 2001

Methodology is described for computer-assisted design and manufacturing of a custom hearing aid. The shell for the earmold and faceplate for mounting components such microphone and circuitry are contoured using a

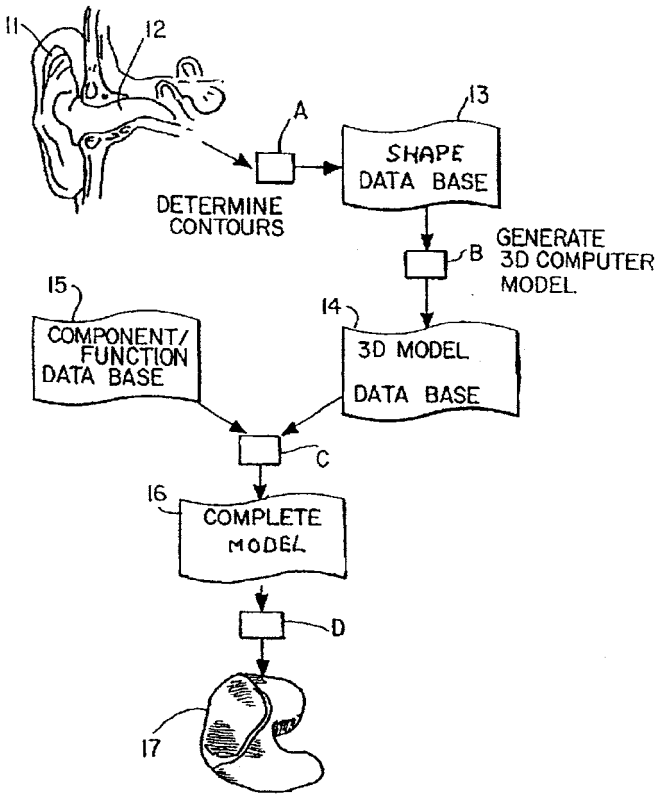

three-dimensional model of the wearer's outer ear and auditory canal.—DAP

6,928,171

43.66.Ts CIRCUIT AND METHOD FOR THE ADAPTIVE SUPPRESSION OF NOISE

Remo Leber, assignor to Bernafon AG
9 August 2005 (Class 381/94.1); filed in Switzerland 2 February 2000

The output signals of two hearing-aid microphones are categorized as either desired or interfering signals by means of blind signal separation. One goal is to make the signal-to-noise ratio of one microphone always greater than that of a second microphone. Filter coefficients for each microphone signal are updated via crosscorrelation.—DAP

6,920,423

43.72.Ar METHODS FOR SPEECH PROCESSING

Achim Mueller and Hans-Georg Zimmermann, assignors to Siemens Aktiengesellschaft
19 July 2005 (Class 704/232); filed in Germany 22 September 2000

New techniques for de-emphasizing speech parameters (input variables) are presented which attempt to detect the irrelevance of certain parameters to the processed output variables. The suggested procedures involve iterated reweighting of the input parameters using neural networks, to successively eliminate those input variables whose values are not correlated with any output variable.—SAF

6,925,438

43.72.Ja METHOD AND APPARATUS FOR PROVIDING AN ANIMATED DISPLAY WITH TRANSLATED SPEECH

Magdi A. Mohamed *et al.*, assignors to Motorola, Incorporated
2 August 2005 (Class 704/276); filed 8 October 2002

This system consists of three essential components, a text-based language translator, a text-to-speech system in the target language, and a talking-head generator with facial shape tables for sounds in the target language. In addition to the phonetic text transmitted to the target-language subsystem, various special annotations are also transmitted, which may include phonetic parsing details or observed facial expression details. The receiving end may optionally use these to customize the display, or may visually present the target speaker using arbitrary facial features and expressions.—DLR

6,920,425

43.72.Ne VISUAL INTERACTIVE RESPONSE SYSTEM AND METHOD TRANSLATED FROM INTERACTIVE VOICE RESPONSE FOR TELEPHONE UTILITY

Craig A. Will and Wayne N. Shelley, assignors to Nortel Networks Limited
19 July 2005 (Class 704/275); filed 16 May 2000

The patent describes several modes of telephone/computer interactions using different languages, particularly the voice-enabled adaptations of XML. The server includes the ability to translate between voice-control

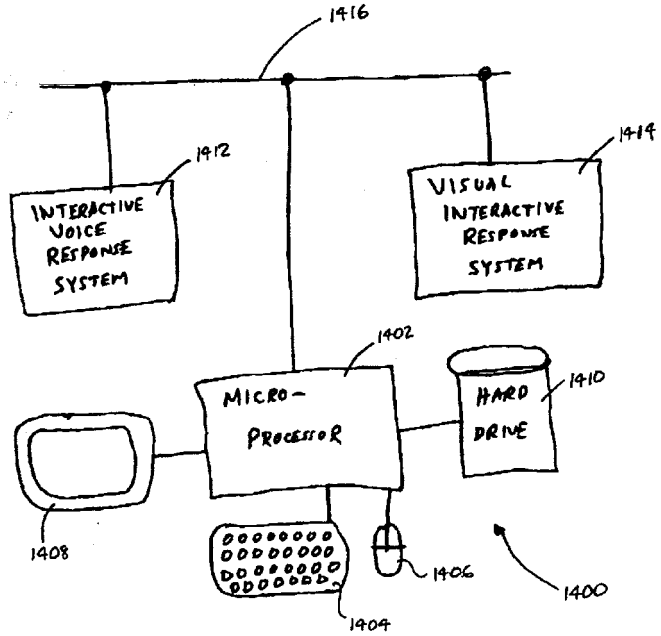

scripts and visual scripts, allowing inputs in either modality to perform the mode switch. Command parsing is dicussed, although not in great detail. The patent hits a new low in figure quality. Perhaps the assignee is having problems we don't know about.—DLR

6,925,436

43.72.Ne INDEXING WITH TRANSLATION MODEL FOR FEATURE REGULARIZATION

Martin Franz and Jeffrey Scott McCarley, assignors to International Business Machines Corporation
2 August 2005 (Class 704/235); filed 28 January 2000

In an audio-to-text system using speech recognition and/or feature extraction, a statistical translation model is trained on parallel sets of automatically and hand-corrected transcribed text data to reduce errors in audio indexing.—DAP

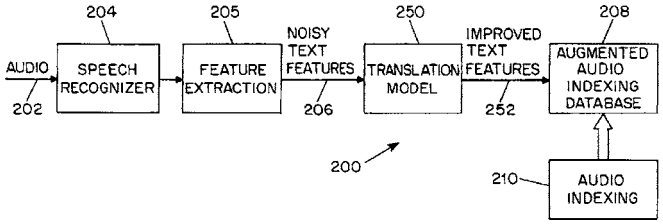

6,919,502

43.75.Wx MUSICAL TONE GENERATION APPARATUS INSTALLING EXTENSION BOARD FOR EXPANSION OF TONE COLORS AND EFFECTS

Takao Yamamoto, assignor to Yamaha Corporation
19 July 2005 (Class 84/622); filed in Japan 2 June 1999

This astounding patent observes that if you add an external board with a sequencer and synthesizer, then it can be used for "tone color" synthesis. This is plain and obvious to those "skilled in the art."—MK

6,919,503

43.75.Wx MUSICAL TONE GENERATION CONTROL SYSTEM, MUSICAL TONE GENERATION CONTROL METHOD, AND PROGRAM FOR IMPLEMENTING THE METHOD

Yoshiki Nishitani *et al.*, assignors to Yamaha Corporation
19 July 2005 (Class 84/633); filed in Japan 17 October 2001

This invention uses radio-linked batons that transmit positional information in 3-D. This can be used by an automated composition program and synthesizer to entertain the assembled crowd. Unfortunately, there is no mention of Mathews' earlier Radio Baton (United States Patents 4,980,519 and 6,222,522) which anticipates many of the claims.—MK

6,928,181

43.80.Gx METHOD AND SYSTEM FOR BIOMETRIC RECOGNITION USING UNIQUE INTERNAL DISTINGUISHING CHARACTERISTICS

Juliana H. J. Brooks, assignor to Berkshire Labs
9 August 2005 (Class 382/115); filed 29 October 2003

In this biometric security system, ultrasonic signals are transmitted into a region of the body in an area, such as a finger, which has regions of variable density to reflect the acoustic signal. Body regions, such as bone,

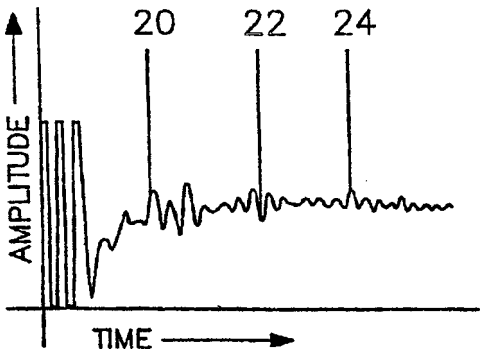

fat, cartilage, muscle, or nerve fibers, are said to produce distinctive "representative patterns." The analysis methods presented in the patent seem to be relatively rudimentary.—DLR

6,918,876

43.80.Qf ULTRASOUND DIAGNOSTIC APPARATUS

Naohisa Kamiyama, assignor to Kabushiki Kaisha Toshiba
19 July 2005 (Class 600/447); filed in Japan 29 October 1999

The goal of this apparatus is to provide ultrasound diagnoses enhanced as uniformly as possible within specific slices by an ultrasound contrast agent. The system consists of an ultrasound apparatus for obtaining an image of a subject into which a contrast agent composed mainly of microbubbles is injected. A probe is included, configured to transmit or receive an ultrasound wave to or from the subject. A transmission circuit drives the probe to transmit a sound wave while sequentially changing the direction of the transmission lines. A reception circuit generates reception line data from the echoes. An image processing unit generates an ultrasound image from the reception line data.—DRR

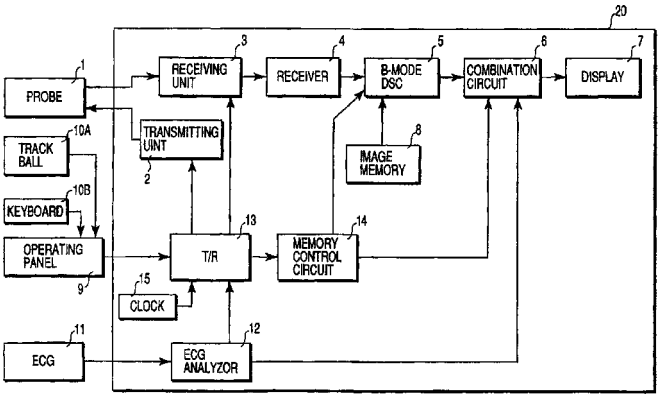

6,926,672

43.80.Qf ELECTRET ACOUSTIC TRANSDUCER ARRAY FOR COMPUTERIZED ULTRASOUND RISK EVALUATION SYSTEM

Thomas L. Moore and Karl A. Fisher, assignors to Barbara Ann Karmanos Cancer Institute
9 August 2005 (Class 600/459); filed 18 December 2002

The idea behind using an electret-based acoustic transducer array instead of the more usual array of piezoelectric transducers for ultrasound examination of tissue is to meet the goal of reducing manufacturing costs,

such costs being influenced by the need for high sensitivity and small size. In one embodiment, the acoustic transducer array is formed within a substrate that contains several distinct cells. Within each of these cells is an acoustic transducing element formed of electret material. A conductive membrane is placed over the distinct cells and it may be made flexible. The distinct cells may be arrayed linearly or in a two-dimensional arrangement. In some embodiments, a number of amplifiers may also be contained within the substrate, each connected with one of the acoustic transducing elements.—DRR

6,921,371

43.80.Sh ULTRASOUND RADIATING MEMBERS FOR CATHETER

Richard R. Wilson, assignor to Ekos Corporation
26 July 2005 (Class 601/2); filed 14 October 2003

As an alternative to cylindrical and rectangular ultrasound radiating elements, a method is described for providing a substantially planar slab of piezoelectric material. The method entails drilling multiple holes through the top surface and into the slab and making a number of cuts through the top surface and into the slab. These cuts form a series of polygons that center about one of the holes. It is asserted that this type of radiating material is cheaper to produce than cylindrical elements, is more reliable in operation, and provides a more uniform radial distribution of sound energy than rectangular elements.—DRR

6,923,768

43.80.Vj METHOD AND APPARATUS FOR ACQUIRING AND DISPLAYING A MEDICAL INSTRUMENT INTRODUCED INTO A CAVITY ORGAN OF A PATIENT TO BE EXAMINED OR TREATED

Estelle Camus *et al.*, assignors to Siemens Aktiengesellschaft
2 August 2005 (Class 600/463); filed in Germany 11 March 2002

An ultrasound probe that includes position sensing is used, along with another instrument such as an endoscope or catheter that also includes position sensing, to acquire a set of ultrasound images that span three dimensions as the ultrasound probe is moved. An ECG signal is employed to display the three-dimensional ultrasound data at the same phase of the cardiac cycle along with the position of the other instrument. Images from an x-ray fluoroscope may also be registered in the coordinate system of the three-dimensional ultrasound image data.—RCW

6,926,673

43.80.Vj OPTICAL TRACKING SYSTEMS

Patricia Roberts *et al.*, assignors to Roke Manor Research Limited
9 August 2005 (Class 600/464); filed in the United Kingdom 28 November 2000

The position and orientation of an ultrasound probe are tracked optically as the probe is moved and used to calculate the position and orientation of ultrasound images from a model of the beam-scan geometry.—RCW

LETTERS TO THE EDITOR

This Letters section is for publishing (a) brief acoustical research or applied acoustical reports, (b) comments on articles or letters previously published in this Journal, and (c) a reply by the article author to criticism by the Letter author in (b). Extensive reports should be submitted as articles, not in a letter series. Letters are peer-reviewed on the same basis as articles, but usually require less review time before acceptance. Letters cannot exceed four printed pages (approximately 3000–4000 words) including figures, tables, references, and a required abstract of about 100 words.

Alternate proof of the optical theorem for impenetrable targets (L)

G. A. Kriegsmann
Department of Mathematical Sciences, Center for Applied Mathematics and Statistics, New Jersey Institute of Technology, University Heights, Newark, New Jersey 07102

(Received 6 October 2005; accepted 14 October 2005)

The optical theorem is proven for impenetrable targets without using the method of stationary phase. The proof depends upon the divergence theorem, the Helmholtz representation of the scattered field, and the law of cosines. © *2006 Acoustical Society of America.* [DOI: 10.1121/1.2139071]

PACS number(s): 43.20.Fn, 43.20.Bi [AJMD] Pages: 31–32

I. INTRODUCTION

The optical theorem is an important relationship that relates the total cross section of a scattered wave with its forward scattered amplitude and with the power dissipated within the target. It is a manifestation of the conservation of power. This relationship follows from integrating the total flux of the acoustic wave in the region between the target and a large sphere at infinity, from applying the divergence theorem, and from using the method of stationary phase.[1,2]

In this note a proof is given which does not depend upon the method of stationary phase. The argument presented here uses, in its place, the Helmholtz representation of the scattered field and an application of the law of cosines.

II. FORMULATION

A incident plane acoustic wave, $P_{inc}=e^{ikx}$, propagating in the x direction impinges upon an smooth, bounded, impenetrable target Ω and scatters from it. The total acoustic pressure in the region exterior to the target is given by

$$P = P_{inc} + P_S, \tag{1}$$

where P_S is the scattered field. The total pressure, as well as the incident and scattered, all satisfy the Helmholtz equation

$$\nabla^2 P + k^2 P = 0 \tag{2}$$

in the region exterior to the target, where $k=\omega/c$, ω is the angular frequency of the incident wave, and c is the sound speed. In the far field where $r=\sqrt{x^2+y^2=z^2}\to\infty$ the scattered field is given approximately by

$$P_S = A(\theta,\phi,k)\frac{e^{ikr}}{r}, \tag{3}$$

where A is the far field pattern and θ and ϕ are the spherical coordinates of the observation point.

The total field is required to satisfy a boundary condition on the surface $\partial\Omega$ of the target. The most general boundary condition is

$$\frac{\partial}{\partial n}P + ZP = 0, \quad \mathbf{x} \in \partial\Omega, \tag{4}$$

where Z is a prescribed complex number and $\partial/\partial n$ denotes the normal derivative. If $Z=0(\infty)$, then the body is soft (hard). If $Z\neq 0$, then (4) is an impedance condition which models the physics of the target.

One of the most important problems of scattering theory is to determine the scattering cross section A. This function satisfies the optical theorem[1,2]

$$\|A\|^2 = \frac{4\pi}{k}\,\mathrm{Im}(A_{FS}) - \frac{1}{k}\mathcal{L}(P), \tag{5a}$$

where A_{FS} is the value of the scattering cross section in the forward scattered direction, i.e., $\theta=\pi/2$ and $\phi=0$, Im denotes the imaginary part of a complex number,

$$\|A\|^2 = \int_0^{2\pi}\int_0^{\pi} |A|^2 \sin(\theta)\, d\theta\, d\phi, \tag{5b}$$

and

$$\mathcal{L}(P) = \mathrm{Im}() \int\int_{\partial\Omega} Z|P|^2\, da. \tag{5c}$$

The term $\mathcal{L}(P)$ represents the power absorbed by the target. If $\mathrm{Im}(Z)=0$, then the scatterer is lossless and the optical theorem simplifies accordingly. The optical theorem is also true for hard targets where $(\partial/\partial n)P=0$ on $\partial\Omega$ and for soft targets where $P=0$ on $\partial\Omega$. In both cases (5a) holds with the term $\mathcal{L}(P)$ set to zero.

III. THE PROOF

Since both P and its complex conjugate P^* both satisfy (2), it follows that

$$\mathrm{Im}(\nabla \cdot P^* \nabla P) = 0. \tag{6}$$

Integrating this equation in the region exterior to Ω and within the circumscribing sphere $r=r_0$, applying the divergence theorem, applying (1) and (3) on $r=r_0$ and (4) on $\partial\Omega$ yields

$$k\|A\|^2 + I_1 + I_2 = -\mathcal{L}(P). \tag{7a}$$

$$I_1 = \mathrm{Im}\left\{ \int\int_{r=r_0} P^*_{inc} \frac{\partial}{\partial r} P_{inc}\, da \right\}, \tag{7b}$$

$$I_2 = \mathrm{Im}\left\{ \int\int_{r=r_0} \left[P^*_{\mathrm{inc}} \frac{\partial}{\partial r} P_S + P^*_S \frac{\partial}{\partial r} P_{\mathrm{inc}} \right] da \right\}. \tag{7c}$$

Inserting $P_{\mathrm{inc}}=e^{ikx}$ into (7b) and carrying out the integration readily given $I_1=0$.

Now the scattered field at a point $\mathbf{x}$ exterior to Ω is related to its values on the surface $\partial\Omega$ by the Helmholtz representation[1]

$$P_S(\mathbf{x}) = \int\int_{\partial\Omega} \left(P_S \frac{\partial}{\partial n'} G - G \frac{\partial}{\partial n'} P_S \right) da', \tag{8a}$$

where the prime denotes values on the surface and G is the free space Green's function

$$G = \frac{e^{ik|\mathbf{x}-\mathbf{x}'}}{4\pi|\mathbf{x}-\mathbf{x}'|}. \tag{8b}$$

An application of the law of cosines shows in the far field, where $|\mathbf{x}| \gg |\mathbf{x}'|$, that the distance $|\mathbf{x}-\mathbf{x}'| \sim r - \mathbf{x}' \cdot \hat{\mathbf{r}}$. Here the unit vector $\hat{r}$ points in the direction of the observation point, i.e., $\mathbf{x}=r\hat{\mathbf{r}}$. Inserting this approximation into (8), setting $\hat{r}=(1,0,0)$, i.e., the forward scattered direction, and using (3) yields

$$A_{FS} = \int\int_{\partial\Omega} \left\{ P_S \frac{\partial}{\partial r} P^*_{\mathrm{inc}} - P^*_{\mathrm{inc}} \frac{\partial}{\partial r} P_S \right\} \frac{da}{4\pi}, \tag{9a}$$

where the primes have been dropped.

Now since P_S and P^*_{inc} both satisfy (2) it follows that $\nabla \cdot \{P_S \nabla P^*_{\mathrm{inc}} - P^*_{\mathrm{inc}} \nabla P_S\} = 0$. Integrating this expression in the region exterior to Ω and within the circumscribing sphere of radius r_0 and applying the divergence theorem gives

$$A_{FS} = \int\int_{r=r_0} \left\{ P_S \frac{\partial}{\partial n} P^*_{\mathrm{inc}} - P^*_{\mathrm{inc}} \frac{\partial}{\partial n} P_S \right\} \frac{da}{4\pi}. \tag{9b}$$

Finally, taking the imaginary part of (9b) and recalling that $\mathrm{Im}(z)=-\mathrm{Im}(z^*)$, for any complex number z, it follows that $I_2=-4\pi\,\mathrm{Im}(A_{FS})$. Using this result along with $I_1=0$ and (7a) yields the optical theorem (5).

If the body is hard, then $(\partial/\partial n)P=0$ on the surface of the scatterer. Equivalently, the impedance $Z=0$ and the right-hand side of (7a) vanishes. Thus, the optical theorem is true for hard targets. If the body is soft, then $P=0$ on the surface of the scatterer. Recalling that before the application of (4) the right-hand side of (7a) originally was $\int\int_{\partial\Omega} P^*(\partial/\partial n)P da$, it follows that this integral vanishes and the optical theorem is true for soft targets.

[1] D. S. Jones, *Acoustic and Electromagnetic Waves* (Oxford U.P., Oxford, 1998).
[2] M. Born and E. Wolf, *Principles of Optics*, 7th ed. (Cambridge U.P., Cambridge, 1999).

A study of the influence of mounting conditions on the measured sound absorption in laboratory tests of suspended ceilings (L)

Marcelo de Godoy and Peter J. Barry
Institute for Technological Research, 05508-901, São Paulo, SP, Brazil

Sylvio R. Bistafa
Department of Technology, School of Architecture and Urban Planning, University of São Paulo, SP, 05508-900, Brazil

(Received 23 May 2005; revised 6 September 2005; accepted 22 October 2005)

This letter presents the results of an investigation into the influence of mounting conditions on the measured sound absorption coefficients of a suspended ceiling specimen. A series of measurements and analyses were carried out using a fixed standard sample, varying independently different mounting parameters and introducing controlled leaks. A correction of room volume in the calculation of the sound absorption coefficients was also examined. The tests were carried out in accordance with the ISO 354:2003 standard (International Organisation for Standardisation, Geneva, 2003), using the type E mounting. The test specimen consisted of fiberglass wool panels covered with a plastic film. Some of the experiments resulted in no statistically significant alteration. This included, unexpectedly, the sealing requirements of E type mountings. © *2006 Acoustical Society of America.* [DOI: 10.1121/1.2139076]

PACS number(s): 43.55.Ev, 43.55.Dt [NX] Pages: 33–36

I. INTRODUCTION

A suspended ceiling system is a very common component in enclosed spaces, being used in offices, classrooms, auditoria, supermarkets, and a host of other applications.

In laboratory sound absorption tests of such suspended material, the ISO standard 354:2003,[1] "type E" mounting, attempts to simulate such practical applications. (Note: The ISO standard is technically equivalent to the ASTM C423[2] standard and the 2003 revision has adopted the mounting types of ASTM E795.[3])

It is frequently unviable to install, in a reverberation room, a suspended ceiling system with a plenum in its normal orientation, Hence, the type E mounting, as defined in ISO 354, proposes a system to simulate the ceiling, but placed on the floor of the reverberation room instead. This consists of a horizontal support (commonly a metal railing) into which the test specimen is placed with the test surface visible, i.e., in an upside down position. This support is raised a given distance off the floor and the sides closed with heavy material. The whole support structure delimits a volume of air, simulating a plenum.

This type of structure is the most widely used worldwide to test ceilings with a plenum. Notwithstanding, large variations of absorption coefficients between different laboratories have been registered.[4,5] The present work proposed analyzing some variables of "the type E" mounting system in order to identify and quantify the principal causes of interference in the test results of sound absorption in reverberant rooms, due to specimen mounting details. Some calculation parameters were also analyzed.

II. METHODS

A series of measurements was carried out using a specimen set up according to the ISO 354:2003 standard type E-300 mount. The same system, materials, and positioning were used in all tests, in order to reduce the effects of variables which were not the object of the investigation, such as the uniformity of the diffuse sound field. Different parameters were varied independently, one at a time.

The specimen for all measurements consisted of ceiling panels, ISOVER®, Sirius 60×2.0, made of fiberglass wool covered on the visible surface with a texturized plastic film. Each panel measured $1240\times615\times20$ mm^3 and had an average density of approximately 60 kg/m^3.

The test structure into which the specimen was accommodated consisted of wood boards, 300 m high and 22 mm thick, forming a rectangle of 3795×3125 mm^2. The panel support structure consisted of "T" aluminum railing, commonly used for installing this type of ceiling.

The reverberation times were obtained using an indirect integrated impulse response method with MLS sound signal excitation. The calculations of the sound absorption coefficient were made according to ISO 354:2003.

It is desirable to use a statistical test to evaluate the significance of the standardized condition in relation to the altered condition. To do this, the uncertainties involved in the experiments were obtained. The principals of these uncertainties are the spatial variations of the reverberation decay times, as represented by the standard deviations of decay times from a number of microphone/source positions. Other uncertainties, considerably smaller, include room volume, specimen size, temperature, relative humidity, and instrument calibration. From the set of uncertainties, the standard

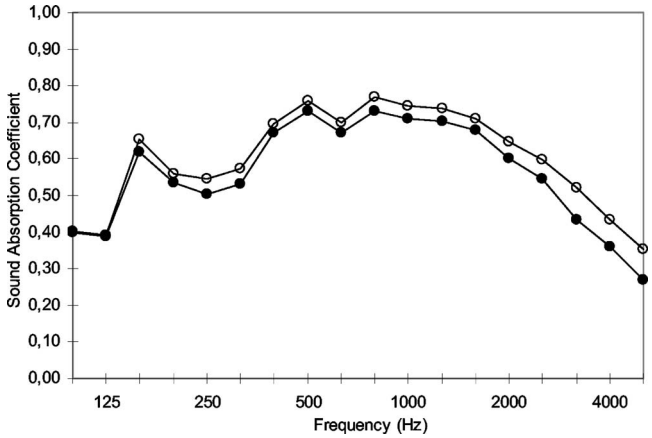

FIG. 1. Comparison of the sound absorption coefficients calculated using empty room reverberation times measured with and without the supporting structure. —○— ISO 354:2003 procedure; —●— Alternative procedure.

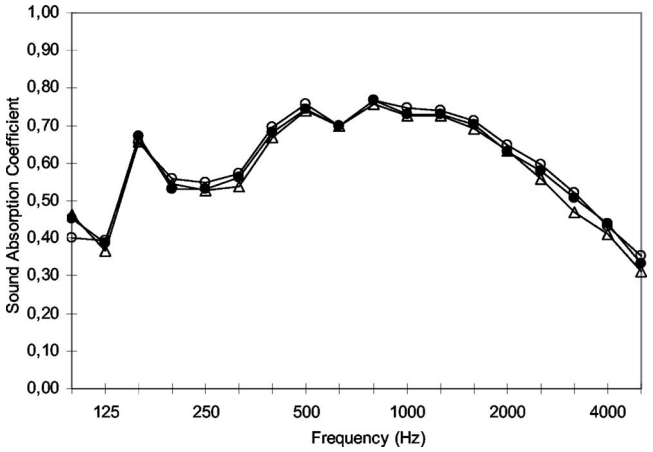

FIG. 2. Comparison of the sound absorption coefficients with different floor-structure sealing conditions. —○— No sealing. —●— Partial sealing. —△— Complete sealing.

combined uncertainty and the corresponding number of degrees of freedom of each test were calculated.[6] The standard combined uncertainty represents the resultant standard deviation of the absorption coefficient and thus permits the use of the Student t test.

In each $\frac{1}{3}$ oct band Student's t variable was obtained, and a nonpaired, two-sided test of the difference between two means was made, with a significance level of 0.025.

III. TEST PARAMETERS AND RESULTS

A. Influence of the support structure

The ISO 354:2003 standard specifies that the reverberation times in the empty room be measured without the supporting structure. In this case, the support was made of wooden boards, which, although varnished, may present some residual absorption, thus affecting the results. Figure 1 shows the sound absorption coefficients, obtained from the reverberation times of the empty room, measured without the supporting structure (standard procedure, ISO 354:2003) and with the support remaining during the measurements (alternative procedure).

The Student t tests show a significant modification at all frequency bands except at 100 and 125 Hz.

This result is undesirable as the support is not part of the ceiling, but simply a device to simulate a plenum.

B. Sealing between the support structure and the floor

Annex B of the ISO 354:2003 standard explicitly specifies that there must be good sealing between the support structure and the floor, but does not indicate how this should be done.

Due to irregularities in the reverberation room floor surface and the boards (total length 14.28 m), the interface between the structure and the floor had gaps, 2–5 mm in places, thus linking the enclosed airspace with the external space.

To evaluate the effect of these leaks, tests were made as follows:

(i) with no sealing;
(ii) sealing between the floor and supporting structure, using a substantial adhesive tape, covering all the perimeter except for a 500-mm stretch having the most pronounced gap; and
(iii) sealing of the complete perimeter of the supporting structure.

The graph of Fig. 2 shows the measured sound absorption coefficients for the three situations.

The Student t tests show no significant modification at any frequency bands for the partial sealing conditions and, for the complete sealing condition, showed a significant difference only for the 315- and 3150-Hz frequency bands. These results do not corroborate the requirements of the standard.

C. Exposure of the specimen panel sides

In a real installation, the ceiling panels are usually placed in an inverted-T-shaped railing, where the panels sit on the side lugs of the T. In this arrangement, any clearance in the seating of the panel is not exposed. In the test setup, however, the panel is inverted to expose the test surface, but the railing remains in the same position and the side lugs are now covered by the panel instead of vice versa. Any slack now leaves small spaces between the panels and the vertical section of the railing, thus exposing the panel sides. This is illustrated in Fig. 3.

In the present experiments, these gaps were left uncovered to facilitate material handling in view of the large number of tests made.

However, for the test specimen used, the exposed fiberglass wool would be more absorbing than the plastic-covered surface, and the effective specimen area is increased—about 5%, assuming half the sides exposed. The effect of the increased absorption may be considerable.

To investigate the influence of this condition, three configurations were tested:

(i) no sealing—the gaps were left uncovered;
(ii) sealing with a layer of thick adhesive tape; and
(iii) sealing with a double layer of thick adhesive tape.

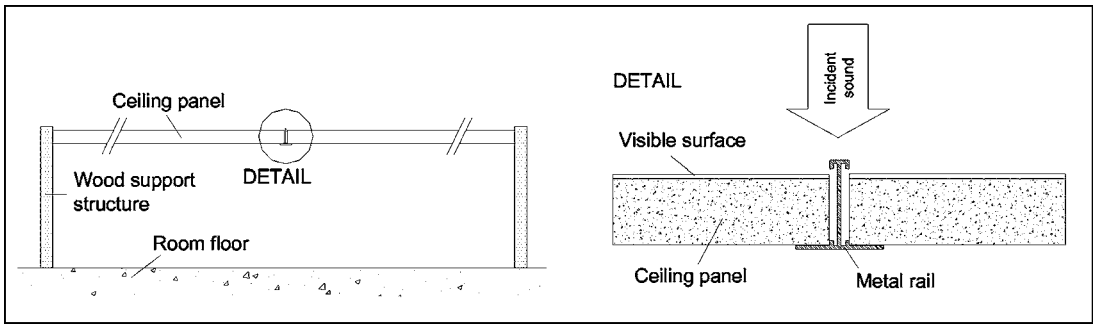

FIG. 3. Detail showing the seating of the ceiling panels on the metal railing.

Figure 4 shows the sound absorption coefficients for these three conditions.

For the single layer condition, the Student *t* tests show a significant influence of the sealing at all frequency bands except at 125 and 630 Hz. For the double layer condition, only the 125-Hz frequency band did not show a significant influence.

These results show evidence that the sealing of the gaps between panels and the vertical section of the T railing exercises a strong influence on the measured sound absorption coefficients.

The pronounced reduction in the sound absorption coefficients between 160 and 400 Hz may be due to the increased stiffness of the panel mounting conditions provided by the sealing tape, which tends to reduce the low-frequency panel vibrations and, as a result, the sound absorption coefficient.

D. Influence of acoustic modes within the plenum

This part of the study attempted to identify a possible influence on the results of low-frequency standing waves between the parallel sides of the specimen support structure. In a real situation, these standing waves would not so readily occur, as, in the absence of the test structure sidewalls, the plenum would have much greater lateral dimensions. The presence of the test structure then constitutes a distortion of the real situation.

To investigate the influence of possible standing waves, a board was placed diagonally across the plenum effectively blocking possible first-, second-, and third-order axial standing waves within the enclosed space. The board, of length 3078 mm, height 225 mm, and thickness 30 mm, was positioned diagonally across the plenum space, but without touching either the sides of the support structure or the test panels.

Figure 5 shows the measured sound absorption coefficients with and without the diagonal dividing board.

The Student *t* tests show no significant alteration due to the presence of the diagonal dividing board except for the 315-Hz frequency band, showing that any influence of low-frequency standing waves on the sound absorption coefficients could not be confirmed.

E. Change of reverberation room volume due to the test specimen

The volume enclosed by the E-300 support structure and the panels is approximately equal to 3.6 m^3, which is equivalent to 1.6% of the volume of the reverberation room (224 m^3). The calculation of the sound absorption coefficients, established in the ISO 354:2003 standard, makes no allowance for a change in the volume of the reverberation room for the calculation of the sound absorption with the test

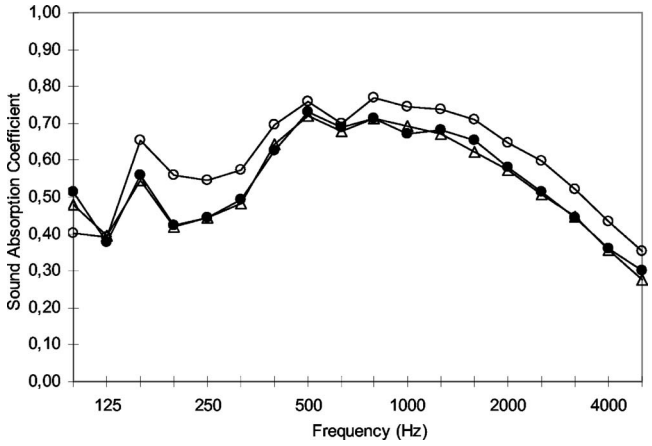

FIG. 4. The effects of different sealing conditions of the gaps between the panels and the vertical section of the "T" railing on the sound absorption coefficients. —○— No sealing between panels. —●— Sealing with one layer of tape. —△— Sealing with double layer of tape.

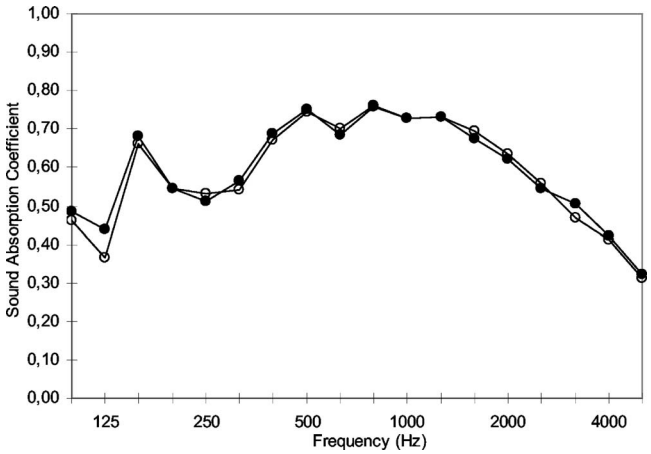

FIG. 5. Comparison of the sound absorption coefficients under different plenum conditions. —○— Without dividing board. —●— With dividing board.

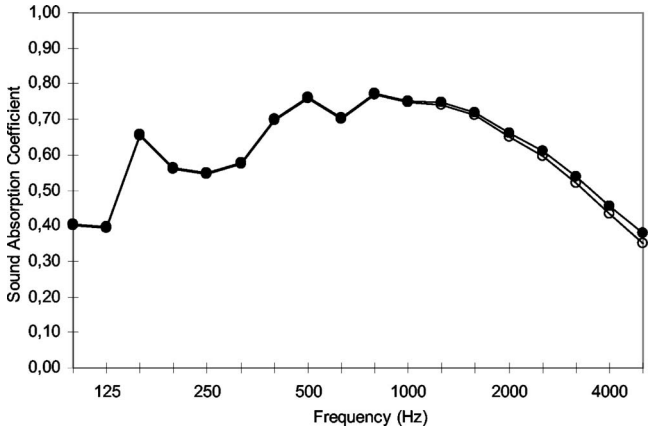

FIG. 6. Comparison of the sound absorption coefficients obtained via two calculation procedures. —○— ISO 354:2003 calculation. —●— Alternative calculation.

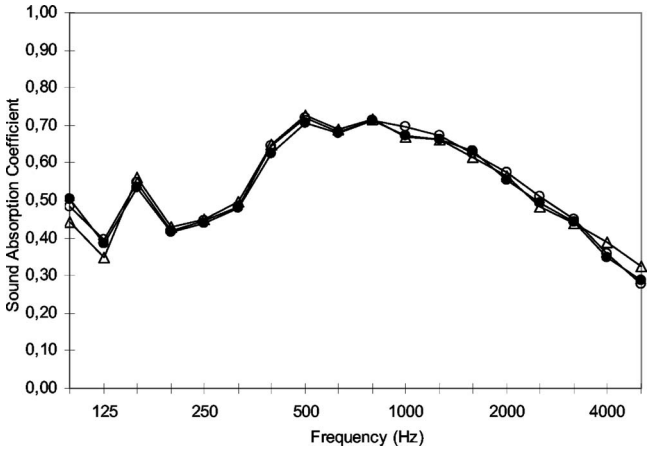

FIG. 7. Sound absorption coefficients obtained with openings of different areas in the surface of the panels in comparison with the no-opening case. —○— No opening. —●— Opening 100×100 mm^2. —△— Opening 200×200 mm^2.

specimen present in the room, using the value for the empty chamber. Plausibly, this difference may alter the value of the calculated sound absorption coefficients.

Figure 6 shows the sound absorption coefficients calculated using the procedures of the ISO 354:2003 standard and an alternative method, considering the difference in volume.

The Student t tests show no significant modification in the measured sound absorption coefficients at any frequency band, when the volume of the reverberation chamber used in the calculations is reduced by the volume enclosed by the E-300 support structure and test panels.

F. Influence of openings in the specimen surface

In view of the robustness of the test method with regard to the sealing, or rather the lack of sealing, of the specimen support structure, tests were made to investigate the influence of openings made in the surface of the absorbing panels, linking directly the enclosed airspace with the exterior environment of the reverberation room.

Two openings with different areas were made in the surface of the panels. These openings were created in the center of one of the panels by removing the panel material from a square section—with sides of 100 and 200 mm. For these tests, the boundaries of the panels were covered with adhesive tape (see Sec. III C), as was the interface of the support structure with the floor (see Sec. III B).

Figure 7 shows the sound absorption coefficients with the two openings and for the no opening condition.

The Student t tests show no significant influence at any frequency band for a 100×100 mm^2 opening and only at the 1000-Hz frequency band for a 200×200 mm^2 opening.

These results are similar to the results reported in Sec. III B (sealing of the floor/support structure interface) and are more evidence that the control of leakage is not the major factor in the measured results.

IV. CONCLUSIONS

The parameters that showed the greatest influence on the measured results of the sound absorption coefficients, for the conditions and materials adopted, were (a) the reverberation decay of the empty room measured with the support structure remaining in the room and (b) the exposure of the sides of the fiberwool panels. By contrast, parameters that showed the least sensitivity to change were those related to the sealing of the enclosed airspace, specifically the sealing between the support structure and the floor and the presence of openings in the exposed surface.

We conclude that a covering of the junction between panels is necessary. However, the use of adhesive tape results in a reduction of absorption at low frequencies, a phenomenon possibly caused by the stiffening of the suspended specimen. A metal strip or H-shaped railing might then be more appropriate. The usual practice of the laboratory is to tape seal the junction of panels when using a "type A" mounting configuration. Not being suspended, the stiffening is probably not a factor here.

The ISO 354:2003 standard does not make specific mounting recommendations, with the exception of the sealing between structure and floor. However, the measured results were persistently insensitive to the sealing between the support structure and the floor and the presence of openings in the test surface.

We do not suggest abolishing the ISO recommendation on sealing without further study, including interlaboratory programs, but suggest that it is not a major concern, nor do we suggest that the support structure remain in the room during the measurements of the decay times for the empty room. This may introduce greater errors than it removes.

[1]ISO 354, "Acoustics —Measurement of sound absorption in a reverberation room," International Organisation for Standardisation, Geneva, 2003.
[2]ASTM C423, "Standard test method for sound absorption and sound absorption coefficients by the reverberation room method," ASTM International, 2002.
[3]ASTM E795, "Standard Practices for Mounting Test Specimens During Sound Absorption Tests," ASTM International, 2000.
[4]R. E. Halliwell, "Sound absorption variation caused by modifications to a standard mounting," J. Acoust. Soc. Am. **72**, 1634–1636 (1982).
[5]R. E. Halliwell, "Interlaboratory variability of sound absorption measurement," J. Acoust. Soc. Am. **73**, 880–886 (1983).
[6]IEC, *Guide to the Expression of Uncertainty in Measurement* (International Electrotechnical Commission, Geneva, 1997).

Discrimination of depth of sinusoidal amplitude modulation with and without roved carrier levels (L)

Mark A. Stellmack,[a] Neal F. Viemeister, and Andrew J. Byrne
Department of Psychology, University of Minnesota, Minneapolis, Minnesota 55455

(Received 16 May 2005; revised 13 September 2005; accepted 12 October 2005)

Thresholds for the discrimination of the depth of sinusoidal amplitude modulation with a broadband noise carrier were measured for three listeners in a two-alternative, forced-choice task for modulation frequencies of 8, 32, and 128 Hz. Thresholds were measured with the spectrum level of the carrier fixed at 20 dB across all trials and, separately, with the carrier spectrum level roved randomly over a 20-dB range (10–30 dB) in each interval. Mean thresholds were equal or slightly lower (but not significantly so) for the fixed conditions relative to the roved conditions, and the differences between thresholds were too small to be explained by assuming that listeners compared instantaneous intensity at corresponding phases of the modulation cycle (for example, in the troughs). Rather, it appears that listeners discriminated modulation depth by extracting an estimate of the modulation depth within each interval that was independent of the overall level. Consequently, models of envelope extraction must include normalization of the envelope fluctuations to the envelope dc. [DOI: 10.1121/1.2133576]

PACS number(s): 43.66.Mk [JHG] Pages: 37–40

I. INTRODUCTION

Amplitude modulation is an important information-bearing characteristic of sound. The ability of listeners to extract and utilize amplitude modulation has been assessed in tasks involving detection (e.g., Viemeister, 1979; Forrest and Green, 1987), discrimination of modulation depth (e.g., Ozimek and Sek, 1988; Wakefield and Viemeister, 1990; Ewert and Dau, 2004), and discrimination of envelope shape (e.g., Strickland and Viemeister, 1996), among others. Typically, the ability to perform these tasks is modeled on the basis of computation of a decision statistic that is related to the range of fluctuations in the amplitude of the stimulus envelope, such as the rms envelope power, ratio of maximum to minimum envelope amplitudes, or the ratio of the envelope maximum to envelope rms (e.g., Strickland and Viemeister, 1996). The efficiency of the auditory system in extracting these statistics is affected by its ability to encode the envelope (which varies with modulation rate) and by variability in the decision statistic either from internal or external (stimulus-based) sources of noise.

In amplitude modulation-detection tasks, one must control for the increase in power and potential concomitant loudness cue that occurs when a signal is amplitude modulated. One way in which the loudness cue can be controlled is to scale the modulated stimulus to compensate for the known increase in power (Viemeister, 1979). Another way is to impose a random rove in carrier level across trials such that the change in power associated with the presence of amplitude modulation will be so small relative to the overall rove as to be ineffective as a cue (Forrest and Green, 1987). Forrest and Green (1987) found that modulation detection thresholds for a broadband noise carrier were unaffected when they roved the carrier level over a 20-dB range (relative to thresholds with a fixed carrier level). One implication of this observation is that a successful model of modulation detection must include some normalization of the modulation envelope to its dc value in order to remove effects of a roved carrier level. The max-min statistic proposed by Forrest and Green, for example, implicitly incorporates such a normalization.

In tasks involving discrimination of the depth of amplitude modulation, the loudness cue associated with changes in power also may be a concern. In a study of modulation depth discrimination, Wakefield and Viemeister (1990) controlled for the loudness cue by compensating for the changes in total power associated with changes in the depth of sinusoidal amplitude modulation. They attempted to account for their data with a leaky-integrator model based on that of Viemeister (1979). In Wakefield and Viemeister's implementation of the model, the stimulus envelope was extracted through a process of half-wave rectification and low-pass filtering. Decisions were based on differences in the ac-coupled rms power of the extracted envelopes. The leaky-integrator model accurately predicted thresholds for standard modulation depths up to about -12.5 dB ($10 \log m^2$) but for higher standard modulation depths it predicted much lower thresholds than those measured behaviorally.

In their study of envelope discrimination, Strickland and Viemeister (1996) studied the ability of listeners to discriminate envelopes by measuring thresholds for detection of a signal modulator in the presence of a masker modulator, with both modulators applied to a single carrier. Adding the signal modulator to the masker modulator changes the effective modulation depth of the stimulus envelope. Like Wakefield and Viemeister (1990), Strickland and Viemeister (1996) controlled for loudness cues related to the signal modulator by compensating for the change in total power associated with its presence or absence. Strickland and Viemeister evaluated five different decision statistics in terms of their

[a]Electronic mail: stell006@umn.edu

ability to account for the data. The relevant point here is that all of the decision statistics evaluated by Strickland and Viemeister were based on representations of the envelope that were normalized to the envelope dc value and thus none predict an effect of a roved carrier level. The same is true of the model employed by Ewert and Dau (2004) to account for their modulation depth discrimination data.

While measuring modulation depth-discrimination thresholds in the context of a different study, it became apparent to the present authors that another possible cue existed for the depth-discrimination task that was not based upon estimates of the modulation depths *per se* of the standard and comparison stimuli or upon differences in overall loudness. In listening to the stimuli, it seemed that in some cases, particularly for large standard modulation depths and low modulation frequencies (below about 10 Hz), the cue for discrimination of modulation depth was related to the intensity in the troughs of the stimulus envelopes. In these cases, higher modulation depths were perceived as having gaps or brief moments of silence in the troughs of the intervals while the lower modulation depths seemed to have troughs that were "filled in." In other words, it seemed that modulation depth discrimination was based on detection of energy in the modulation troughs or discrimination of an estimate of instantaneous intensity in the troughs.

The present experiment was conducted to test whether or not a model based on discrimination of the intensities of the stimulus envelopes at corresponding modulator phases, such as at the modulator troughs, might account for modulation depth-discrimination thresholds to any extent. To our knowledge, this possibility has not been tested. The rationale behind the experiment is that if listeners were basing decisions on a comparison of instantaneous intensity across intervals, then an intensity rove imposed on the carrier across intervals should drastically interfere with modulation depth discrimination. In the present experiment, depth discrimination thresholds were measured with the spectrum level of the carrier fixed at 20 dB across intervals and, in separate conditions, with the spectrum level of the carrier randomly roved over a 20-dB range (10–30 dB). It will be seen that modulation depth discrimination thresholds were very similar in the two conditions, suggesting that listeners perform the depth discrimination task by comparing estimates of the modulation depths extracted from the standard and comparison stimuli rather than comparing estimates of instantaneous intensity across stimuli.

II. METHODS

Modulation depth-discrimination thresholds were measured in a two-interval, two-alternative forced-choice task. The stimulus within each interval was defined as

$$s(t) = A[1 + m\cos(2\pi f_m t + \phi)]n(t), \quad (1)$$

where $n(t)$ was a broadband Gaussian noise, m was the modulation depth ranging from 0 to 1, f_m was the modulation frequency, ϕ was the starting phase of the modulator, and A was a scaling factor that determined overall stimulus level. One interval, chosen randomly with equal *a priori* probability from trial to trial, contained a stimulus carrying the standard modulation depth ($m=m_s$, fixed across trials within a block) while the stimulus in the remaining interval carried the comparison modulation depth ($m=m_c$), which was always less than the standard depth. The modulation frequency, f_m, was held constant within each block of trials at 8, 32, or 128 Hz. The starting phase of the modulator, ϕ, was randomized across intervals in order to minimize cues associated with differences in intensity at stimulus onset. Each stimulus was 1 s in duration with 500 ms of silence between the two intervals of each trial. Subjects were instructed to select the interval containing the larger (standard) modulation depth. Visual feedback indicating the "correct" interval was presented after each trial.

In one set of conditions, the unroved or fixed conditions, A in Eq. (1) was held constant across all trials such that the spectrum level of the noise carrier was fixed at 20 dB (measured at 1 kHz). In a second set of conditions, the roved conditions, the spectrum level (in dB) of every stimulus presentation was selected randomly and independently from a uniform distribution over the interval 10–30 dB. For a broadband noise carrier, detectability of amplitude modulation is independent of carrier level over a wide range of levels (Viemeister, 1979). In the fixed conditions, the rms amplitude of the signal interval was set equal to that of the nonsignal interval in order to minimize loudness cues associated with a difference in modulation depth (Viemeister, 1979). In practice, this control probably was unnecessary because the rms amplitudes of the signal and nonsignal intervals were essentially equal for these stimuli with identical carriers.

Thresholds were measured for standard modulation depths of 0, −6, and −12 dB ($10\log m_s^2$). By varying the modulation depth of the comparison, the difference between the modulation depths of the standard and comparison was varied adaptively from trial to trial in units of $10\log(m_s^2 - m_c^2)$, the intensity difference between the modulation depths of the standard and comparison expressed in dB. These units were chosen because Wakefield and Viemeister (1990) showed that psychometric functions expressed in terms of $\log d'$ vs $10\log(m_c^2 - m_s^2)$ are approximately parallel. (In the Wakefield and Viemeister experiment, the comparison modulation depth was always larger than the standard, thus the terms m_c^2 and m_s^2 are transposed in their expression.) The quantity $10\log(m_s^2 - m_c^2)$ was varied using a two-down, one-up procedure that estimated the 70.7% correct point on the psychometric function (Levitt, 1971). At the start of each block of trials, the value of $10\log(m_s^2 - m_c^2)$ was set 6 dB lower than $10\log m_s^2$. For example, when the standard modulation depth was −6 dB, $10\log(m_s^2 - m_c^2)$ was initialized to −12 dB. The initial step size in the adaptive procedure was set to 2 dB and was reduced to 0.5 dB after the first four reversals. Each block of trials was terminated after 12 reversals and the threshold was computed as the mean value of $10\log(m_s^2 - m_c^2)$ at the final eight reversals. The mean of four such threshold estimates was taken as the final estimate of threshold in each condition.

All stimuli were generated digitally in MATLAB at a sampling frequency of 44.1 kHz. For each trial, a 1-s broadband

noise signal was generated in the frequency domain by drawing amplitudes from a Rayleigh distribution and starting phases from a uniform distribution for all components below 10 kHz (except for the dc component, which had an amplitude of zero). A time-domain signal was produced by applying an inverse fast Fourier transform (FFT) to the resulting spectrum. Cosine-squared ramps, 20 ms in duration, were applied to the onset and offset of each noise signal. The same noise carrier, $n(t)$, was presented in both intervals of a trial but an independent carrier was generated for each trial. The noise carrier was multiplied by the appropriate modulator to produce the stimulus for each interval.

The digital signals were generated and converted to analog signals on a PC equipped with a high-quality, 24-bit sound card (Echo Audio Gina). Stimuli were presented over Sony MDR-V6 stereo headphones to listeners seated in an IAC sound-attenuating chamber. Each block of trials was initiated by the listener. On each trial, a "ready" light flashed on the computer screen for 250 ms followed by a 100-ms pause after which a trial was presented. The intervals were marked visually by lights on the computer monitor. Listeners entered their responses on the computer keyboard at which time the correct response was indicated on the screen. Listeners were run in 2-h sessions, during which approximately 10–12 blocks of trials were run, until all stimulus conditions were completed.

All data for the conditions in which $10 \log m_s^2 = -6$ were gathered first. Within those conditions, two blocks of unroved-carrier trials were run at each modulation frequency, followed by two blocks of roved-carrier trials, then the sequence was repeated such that roved and unroved blocks of trials were interleaved. Data were gathered in the same way for standard modulation depths of −12 dB and then 0 dB. All listeners ran conditions with different standard depths on different days, alleviating concerns about the use of different standard modulation depths in successive blocks of trials (Wakefield and Viemeister, 1990; Ewert and Dau, 2004).

The three listeners consisted of the first and third authors and a female undergraduate student from the University of Minnesota who was paid to participate in the study. All listeners had pure-tone thresholds of 15 dB HL or better at octave frequencies from 250 to 8000 Hz. Listeners practiced the modulation depth-discrimination task with various modulation frequencies and standard depths until their thresholds stabilized.

III. RESULTS AND DISCUSSION

The performance of the three listeners was very similar, so only the mean data are shown. In Fig. 1, mean threshold values of $10 \log(m_s^2 - m_c^2)$ are plotted as a function of modulation frequency. The top, middle, and lower panels show data for $10 \log m_s^2 = 0$, −6, and −12 dB, respectively. Open symbols represent thresholds measured in the fixed conditions and closed symbols represent thresholds measured in the roved conditions. The error bars represent the standard error of the mean computed across the three threshold values of the three listeners.

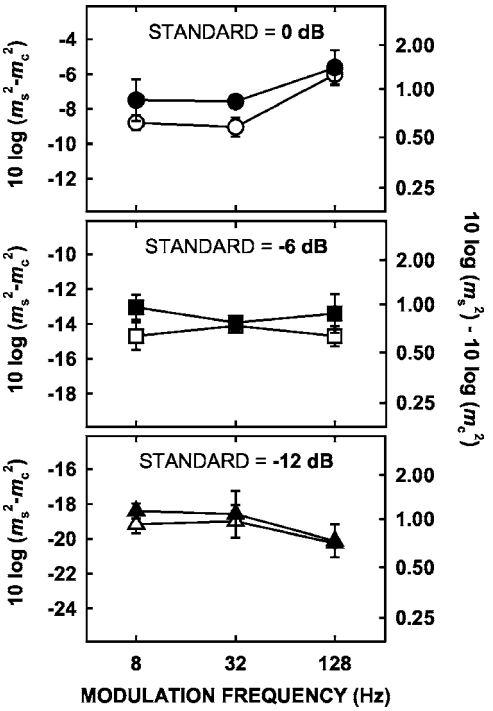

FIG. 1. Mean thresholds for three listeners in terms of the intensity difference between the modulation depths of the standard and comparison (in dB) as a function of modulation frequency. The right-hand axis scales the thresholds in terms of the modulation depth of the standard minus the modulation depth of the comparison (both expressed as $10 \log m^2$). Open symbols represent conditions in which the carrier level was fixed across trials. Closed symbols represent conditions in which the carrier level was randomly chosen from a 20-dB range of spectrum levels (between 10 and 30 dB). Error bars represent standard errors of the mean. Each panel shows data for a different standard depth (as indicated in the panels).

A three-factor, repeated measures ANOVA was performed on the thresholds expressed in terms of the dB difference between m for the standard and comparison (the right-hand axis of Fig. 1). The three factors were standard modulation depth (three levels), modulation frequency (three levels), and fixed versus roved carrier level. No main effects or interactions were statistically significant ($\alpha = 0.05$). The only visually apparent trend in Fig. 1 is that thresholds appeared to vary across standard modulation depth for $f_m = 128$ Hz, but once again this trend was not statistically significant. Most importantly in the present context, the main effect of fixed versus roved carrier level was not significant. It should be noted that an ideal observer that compares the intensities of the waveforms at corresponding points in the modulation cycle (for example, in the troughs, where the difference between instantaneous intensities is largest across intervals for modulated stimuli with fixed carrier levels) would require a change in m of approximately 8 dB in the presence of a 20-dB carrier rove in order to attain 70% correct by simply discriminating intensity at the troughs of the modulation.

The results suggest that listeners performed the modulation depth discrimination task by extracting an estimate of modulation depth that is independent of overall level. Based on the data presented here, it seems that it is appropriate and

necessary for models of amplitude modulation processing, such as those noted in Sec. I, to include a normalization stage in which the modulation component of the envelope is normalized relative to its dc component, thereby eliminating effects of a rove of the carrier level.

ACKNOWLEDGMENTS

The authors thank Dr. John Grose and an anonymous reviewer for their comments. This work was supported by Research Grant No. R01 DC 00683 from the National Institute on Deafness and Communication Disorders, National Institutes of Health.

Ewert, S. D., and Dau, T. (**2004**). "External and internal limitations in amplitude-modulation processing," J. Acoust. Soc. Am. **116**, 478–490.
Forrest, T. G., and Green, D. M. (**1987**). "Detection of partially filled gaps in noise and the temporal modulation transfer function," J. Acoust. Soc. Am. **82**, 1933–1943.
Levitt, H. (**1971**). "Transformed up-down methods in psychoacoustics," J. Acoust. Soc. Am. **49**, 467–477.
Ozimek, E., and Sek, A. (**1988**). "AM difference limens for noise bands," Acustica **66**, 153–160.
Strickland, E. A., and Viemeister, N. F. (**1996**). "Cues for discrimination of envelopes," J. Acoust. Soc. Am. **99**, 3638–3646.
Viemeister, N. F. (**1979**). "Temporal modulation transfer functions based upon modulation thresholds," J. Acoust. Soc. Am. **66**, 1364–1380.
Wakefield, G. H., and Viemeister, N. F. (**1990**). "Discrimination of modulation depth of sinusoidal amplitude modulation (SAM) noise," J. Acoust. Soc. Am. **88**, 1367–1373.

Measuring the acoustic effects of compression amplification on speech in noise (L)

Pamela E. Souza, Lorienne M. Jenstad,[a] and Kumiko T. Boike[b]
Department of Speech and Hearing Sciences, University of Washington, Seattle, Washington 98105

(Received 22 November 2004; revised 15 August 2005; accepted 2 September 2005)

This letter contains a description of an inversion technique that allows for separation of speech and noise and its application to quantifying the acoustic effects of wide-dynamic-range compression (WDRC) on speech in background noise. Three main findings are reported: that fast-acting WDRC further degrades signal-to-noise ratio; that the effective compression ratio is lower for speech in noise than speech in quiet; and that in contrast to speech in quiet, the amplitude envelope of speech is mostly unaffected when compressed in background noise. © *2006 Acoustical Society of America.* [DOI: 10.1121/1.2108861]

PACS number(s): 43.66.Ts [JHG] Pages: 41–44

I. INTRODUCTION

Fast, acting wide-dynamic range compression (WDRC) amplification is a commonly used amplification strategy which is intended to improve speech audibility (and, by association, speech recognition) over linear amplification. With few exceptions, investigators have been unable to demonstrate improved speech understanding in background noise with this strategy. In fact, WDRC often reduces recognition of speech in noise [see Souza (2002) for a recent review]. Why this occurs has been difficult to determine, in part because available techniques did not permit separation and analysis of speech and noise signals at the output of the compressor. Attempts at acoustic analysis were therefore limited to acoustic analysis of speech in quiet, or to hypotheses based on listener performance without direct examination of the signal received by the listener.

In this study, we pose two possible reasons for these findings. The first is that signal-to-noise ratio (SNR) may be reduced with WDRC amplification. The SNR is a critical determinant of performance. For some test materials, a 1- or 2-dB change in signal-to-noise ratio can make a substantial difference in speech recognition. Currently, no data are available regarding the effect of fast-acting WDRC on SNR.

The second possibility is that when WDRC is applied to speech in noise, the range of short-term speech levels is not reduced as expected. The expected improvement in speech recognition with WDRC is tied to improved audibility. Specifically, fast-acting WDRC is assumed to improve audibility by increasing the level of low-intensity sounds relative to high-intensity sounds, that is, by compressing the dynamic range of speech. The most straightforward way to test this is to look directly at the amplitude variations of the speech signal. The expected effect is an overall smoothing of the amplitude envelope whereby low-intensity consonants are amplified to a greater extent than high-intensity consonants. This can improve performance for speech in quiet, primarily due to improved consonant audibility (Jenstad and Souza, 2005). It is possible that when WDRC is applied to speech in noise, this change does not occur to the same extent.

Another way to measure changes to the amplitude envelope is to measure the effective compression ratio, which is the actual compression ratio achieved for speech. For a speech input, the modulation period of the input signal varies and is usually less than the attack and release times of the compressor. That is, the speech level typically decreases or increases prior to the point of maximum or minimum compression, resulting in a lower effective compression ratio than that noted in the hearing aid specifications (e.g., Stone and Moore, 1992). How much lower has been a point of debate; a few researchers have measured effective compression ratios in quiet (Souza and Turner 1999; Stelmachowicz *et al.*, 1994) but previous techniques did not allow for separation of speech and noise in a compressed signal, preventing such measurements in background noise.

A recently developed inversion technique (Hagerman and Olofsson, 2002) offers an opportunity to examine these issues. Although not intended specifically for compression amplification, this method offers a means to separate and examine speech and noise signals at the output of the signal processing stage. Accordingly, the goals of the present study were (1) to measure the effect of WDRC amplification on signal-to-noise ratio and (2) to measure the effect of WDRC amplification on the speech dynamic range by measuring (a) effective compression ratio and (b) amplitude envelope.

II. METHOD

The inversion technique described by Hagerman and Oloffson (2002) can be used to isolate either speech or noise from the output signal. We will describe the general application of the method first. This method can be used in any waveform editing program that includes a function to invert the phase of the digital signal or can be easily implemented in a programming environment such as MatLab. Next, we describe the specific method for each of our research ques-

[a]Current affiliation: School of Audiology and Speech Sciences, Faculty of Medicine, University of British Columbia, Vancouver, BC.
[b]Current affiliation: Department of Speech and Hearing Science, Arizona State University, Tempe, AZ.

tions. The speech stimuli and compression parameters vary slightly across questions because the acoustic stimuli were originally designed for separate experiments.

A. Inversion technique

A speech signal is digitally recorded into a waveform editing program. A copy of the speech file is phase inverted and saved as a separate file. Auditorily, the original and inverted files sound identical, with no perceptible noise or distortion. Mixing the original speech and inverted speech results in silence (i.e., no waveform).

A noise signal is digitally recorded into the waveform editing program. This can be a multitalker babble, a speech spectrum noise, or other noise. A copy of the noise file is phase inverted and saved as a separate file.

Three speech-plus-noise files are created: (1) the original speech and original noise, (2) the original speech and inverted noise, and (3) the inverted speech and original noise. In each case, speech and noise are mixed at the desired (input) signal-to-noise ratio by adjusting the digital level in each channel (with speech in channel one and noise in channel two) of a two-channel waveform file. At this point, the speech-plus-noise files can be manipulated by any signal processing strategy (e.g., amplitude compression, digital noise reduction, frequency shaping). Amplitude compression processing is described in this example.

After the speech-plus-noise files are processed, the speech or noise files are ready to be extracted. To obtain the waveform of the *speech* after compression, two files are digitally mixed: the compressed original speech with original noise and the compressed original speech with inverted noise. Mixing these files phase cancels the noise, leaving only the speech. To accomplish this, the two files must be exactly aligned in time. Because the extracted speech-alone digital file represents a doubled speech file, the speech level is reduced by 6 dB to obtain accurate speech levels.

To obtain the waveform of the *noise* after amplitude compression, two files are digitally mixed: the compressed original speech with original noise and the compressed inverted speech with original noise. Mixing these files phase cancels the speech, leaving only the noise. Because this digital file represents a doubled noise file, the noise level is reduced by 6 dB.

To verify the method, we can process signals without amplitude compression to ensure that the method results in undistorted versions of the original signals. The retrieved speech and noise files were virtually identical to the original versions with respect to the long-term spectra ($\frac{1}{3}$ octave band levels), the sampled waveform amplitude as a function of time (Pearson $r=0.98$), and in informal listening comparisons.

B. Measuring the effect of WDRC on SNR

For the measurement of the effect of WDRC on SNR, the test signal is a concatenated set of ten sentences taken from a single passage of the Connected Speech Test (Cox *et al.*, 1987), spoken by a female talker. The background noise is a steady-state noise shaped to match the long-term spectrum of the speech. Four speech-plus-noise files are created by digitally mixing speech and noise at a range of signal-to-noise ratios: −2, +2, +6, and +10 dB. Three versions of each SNR file are created: (1) the original speech and original noise; (2) the original speech and inverted noise; and (3) the inverted speech and original noise, for a total of 12 files.

The speech-plus-noise files are amplitude compressed using a compression algorithm implemented in C code. This mimics the action of the input compression stage of a WDRC amplification hearing aid. The input level of the digital speech file is adjusted to the desired speech input level. For each digital waveform point the rms level of the preceding speech segment is determined with a moving exponential window. If this value exceeds the specified compression threshold, the point value is adjusted to yield the desired compression ratio. The length of the preceding speech segment and the exponent of the window control the attack and release times (ANSI, 1996).

1. Single-channel compression

A representative set of compression parameters is used, consisting of a compression ratio of 2:1, attack time 5 ms, release time 50 ms, and a compression threshold of 45 dB SPL. The input to the compression algorithm always reflects a speech input level of 70 dB SPL, with noise level adjusted according to the desired SNR. The output file represents the processing effects of compression on the combined speech in noise signal without frequency shaping or output limiting.

2. Multichannel compression

The input speech-plus-noise signals are filtered into two channels, using a 1200-Hz crossover frequency. Each channel is separately compressed, using the same parameters as for the single-channel condition. The compressed channels are then mixed together. As for the single-channel compression, the output files represent the processing effects of compression on the combined speech-in-noise signals without frequency shaping or output limiting. After compression, the compressed speech and compressed noise levels are retrieved using the inversion technique described above. Finally, the overall level (average rms power) of each retrieved digital file is determined.

3. Control condition

A linear control condition is created for each SNR. Processing for the linear condition is identical to that described above, minus the compression algorithm.

C. Effect of fast-acting WDRC on speech dynamic range

1. Effective compression ratio

Using the retrieved speech files described above, we can measure a series of short-term speech levels (98.66-ms window) in each one-third octave band (200–8000 Hz) using a locally developed algorithm. These values are tabulated and used to obtain the short-term speech level range (5th to 95th

percentile levels) in each band. The effective compression ratio is calculated as the input speech range divided by the compressed (output) speech range.

2. Effect of WDRC on amplitude envelope

To directly examine the effects of varying compression parameters, including both fast- and slow-acting WDRC, on the amplitude envelope of speech, we use a set of ten digitally recorded sentences from the Speech Perception in Noise (SPIN) test (Bilger *et al.*, 1984), spoken by a male talker. The sentences are digitally recorded in quiet and at a +8 dB SNR. The SNR is defined as the difference in rms level between the speech (ten sentences, minus pauses between words and between sentences) and the noise, and therefore does not represent moment-to-moment changes in signal level relative to noise level. The noise is the standard 12-talker babble used in the SPIN test, which is spectrally matched to the test sentences.

For the purposes of understanding the effects of compression on *speech*, only two speech-plus-noise files are necessary: (1) original speech and original noise and (2) original speech and inverted noise. The speech-plus-noise files are digitally compressed using a two-channel compression algorithm with a 1200-Hz crossover frequency. The compression threshold is 40 dB SPL and the attack time is 6 ms. We present the effects of varying compression ratio (2:1, 4:1, 10:1) and varying release time from compression (12, 100, 800, and 1600 ms), as well as the interactions among these settings.

To quantify the effects of compression on the amplitude envelope, we use a calculation called the Envelope Difference Index (EDI) (Fortune *et al.*, 1994). Briefly, the EDI calculates a single number to represent the overall difference between two amplitude envelopes, regardless of differences in level. The EDI value can range from 0 to 1, with 0 representing identical waveforms and 1 representing opposite waveforms (such as two sine waves that are 180° out of phase). We calculate the EDI on the difference between the amplitude envelope of the uncompressed speech signal and the compressed speech signal for each sentence to quantify the effects of compression.[1]

III. RESULTS AND DISCUSSION

A. Effect of WDRC on SNR

Table I shows the signal-to-noise ratios after compression and after linear processing. As expected, linear processing does not alter the SNRs relative to those of the input signal. However, for all of the speech-in-noise signals the SNRs are *worse* after WDRC processing. This effect is unexpected but may provide one explanation as to why previous work has consistently failed to show an advantage of single-channel, fast-acting WDRC amplification for speech in background noise. We hypothesize that this effect occurs when the compression amplifier increases low-level noise during pauses in the speech signal. The variation across SNRs is in good agreement with this hypothesis. At a +10 input SNR there is little change in the output SNR, perhaps because the noise level is below the compression threshold, too low to trigger increased gain during pauses in the speech.

TABLE I. Signal-to-noise ratio before and after WDRC processing. At less favorable SNRs (−2 to +6 dB), the resulting SNR is even less favorable after compression. At the most favorable SNR (+10 dB), compression has little effect upon the output SNR. Note that the SNR is unchanged by linear processing.

Single-channel compression		
Input SNR (dB)	Output SNR (dB) after compression processing	Output SNR (dB) after linear processing
−2	−5	−2
+2	−2	+2
+6	+2	+6
+10	+9	+10
Multichannel compression		
−2	−3	−2
+2	0	+2
+6	+3	+6
+10	+7	+10

For most of the input SNRs, the decrement in SNR is smaller for the two-channel than for the single-channel compressor. This is consistent with the expected ability of multichannel compression to selectively adjust gain across frequency. Put another way, low-frequency noise in a single-channel compressor will cause a gain reduction across all frequencies and may reduce audibility of high-frequency speech regardless of the high-frequency noise level. In contrast, low-frequency noise in a two-channel compressor will reduce gain only in the low-frequency channel, maintaining high-frequency speech audibility. However, the greater SNR degradation seen in the two-channel compressor for the +10 dB input SNR underlies the complexity of this relationship.

B. Speech dynamic range and effective compression ratio

Table II shows the effective compression ratios for linear (unprocessed) speech, compressed speech in quiet, and compressed speech in noise at a range of SNRs. Because these values are very similar across frequency, we average across all frequency bands to obtain a single value. Effective compression ratio is always lower than the nominal compression

TABLE II. The range of speech levels (5th to 95th percentile levels) after single-channel compression for each SNR and in quiet (mean across $\frac{1}{3}$ octave bands from 250 to 8000 Hz). The effective compression ratio is calculated as the unprocessed speech range divided by the processed speech range.

SNR condition	Range of speech levels (dB)	Effective compression ratio
−2 dB	27.6	1.06
+2 dB	27.1	1.08
+6 dB	26.8	1.09
+10 dB	26.0	1.12
Quiet	26.0	1.12
Uncompressed	29.2	N/A

TABLE III. The envelope difference index (EDI) values for speech compressed with a two-channel compressor and various compression parameters. Each cell shows the mean EDI across ten sentences for speech compressed in quiet and in noise. For the background noise condition, noise was removed prior to calculations using the noise inversion procedure described. (Key to EDI values: 0 represents no difference between two amplitude envelopes and 1 represents complete difference between two amplitude envelopes.)

			Release time from compression (ms)			
			12	100	800	1600
Compression ratio (Nominal)	2:1	Quiet	0.14	0.13	0.10	0.10
		Noise	*0.08*	*0.08*	*0.08*	*0.08*
	4:1	Quiet	0.25	0.24	0.16	0.15
		Noise	*0.12*	*0.12*	*0.11*	*0.10*
	10:1	Quiet	0.34	0.34	0.25	0.21
		Noise	*0.15*	*0.14*	*0.13*	*0.13*

ratio of 2:1. The effective compression ratio decreases systematically as the noise level increases. Generally, the more background noise, the smaller the effects of compression. These results are consistent with the finding that single-channel compression does not improve performance in background noise over linear amplification (Souza, 2002). The apparent effect is that there is little to no change in the audibility of the compressed speech signal.

C. Speech dynamic range and amplitude envelope

Qualitatively, compression has a large effect on speech in quiet by reducing the differences between the peaks and valleys of the envelope. The effect is not as pronounced for WDRC-processed speech in noise, despite the relatively favorable (+8 dB) SNR.

Table III summarizes the EDI values for our compression conditions, in both noise and quiet. The EDI values are greater for speech in quiet than speech compressed in background noise. The values also vary with compression parameters: as the parameters are made more extreme, either by increasing the compression ratio or shortening the release time, the effects on the amplitude envelope are greater. Again, this effect is more apparent for speech in quiet than speech compressed in background noise.

These data are consistent with our finding that the effective compression ratio is not as great for speech compressed in a background of steady noise as for speech in quiet. Put another way, the reason there is little change in the effective compression ratio is because the amplitude of low-intensity sounds is not being increased relative to high-intensity sounds. Also, when background noise is present, the precise compression parameters make little difference, because the effect of compression on the speech envelope is so minimal.

IV. CONCLUSIONS

The general picture is that high levels of background noise essentially negate the acoustic effects of compression, ranging from the desired reduction of the speech intensity range to changes (favorable or unfavorable) to the speech envelope. This finding is similar across all of the speech and test conditions examined here: male and female talkers, a range of SNRs, and a variety of compression parameters. There is also an unexpected detrimental effect whereby compression degrades the signal-to-noise ratio, perhaps because noise is amplified during speech pauses. Such effects in conjunction with other demonstrated acoustic changes, such as degradation of the temporal envelope (Souza and Turner, 1998), may help to explain one of the puzzling aspects of compression amplification with a small number of channels: its failure to improve speech recognition in noise. These quantifications of compression for speech in noise are not possible without the inversion technique described here. However, additional research is needed to delineate the exact effects of compression on speech acoustics.

ACKNOWLEDGMENTS

This research was supported by the National Institutes of Health (P. Souza: DC006014; K. Boike: F31DC05092) and by the Canadian Institutes of Health Research and the American Speech-Language-Hearing Foundation (L. Jenstad).

[1]Although the EDI was originally proposed for short speech segments, such as syllables, we have expanded its application to entire sentences. When obtained under similar compression conditions, the values for syllables and sentences are similar.

American National Standards Institute (**1996**). "Specification of hearing aid characteristics," ANSI S3.22-1996 (ANSI, New York).

Bilger, R. C., Nuetzel, J. AL, Rabinowitz, W. M., and Rzeczkowski, C. (**1984**). "Standardization of a test of speech perception in noise," J. Speech Hear. Res. **27**, 32–48.

Cox, R. M., Alexander, G. C., and Gilmore, C. (**1987**). "Development of the Connected Speech Test (CST)," Ear Hear. **8**, 119S–126S.

Fortune, T. W., Woodruff, B. D., and Preves, D. A. (**1994**). "A new technique for quantifying amplitude envelope contrasts," Ear Hear. **15**, 93–99.

Hagerman, B., and Olofsson, A. (**2002**). "A method to measure the effects of noise reduction algorithms using simultaneous speech and noise," presentation at International Hearing Aid Research Conference, Lake Tahoe, CA.

Jenstad, L. M., and Souza, P. E. (**2005**). "Quantifying the effect of compression hearing aid release time on speech acoustics and intelligibility," J. Speech Lang. Hear. Res. **48**, 651.

Souza, P. E. (**2002**). "Effects of compression on speech acoustics, intelligibility, and speech quality," Trends Amplification **6**, 131–165.

Souza, P. E., and Turner, C. W. (**1998**). "Multichannel compression, temporal cues and audibility," J. Speech Lang. Hear. Res. 41, 315–326.

Souza, P. E., and Turner, C. W. (**1999**). "Quantifying the contribution of audibility to recognition of compression-amplified speech," Ear Hear. **20**, 12–20.

Stelmachowicz, P., Lewis, D., Kalberer, A., and Creutz, T. (**1994**). "Situational hearing aid response profile users manual (SHARP, v 2.0)," Boys Town National Research Hospital, Omaha, NE.

Stone, M. A., and Moore, B. C. (**1992**). "Syllabic compression: effective compression ratios for signals modulated at different rates." Br. J. Audiol. **26**, 351–361.

Hybrid compliance-stiffness matrix method for stable analysis of elastic wave propagation in multilayered anisotropic media

Eng Leong Tan[a)]
Nanyang Technological University, South Spine, Block S2, Nanyang Avenue, Singapore 639798, Singapore

(Received 25 May 2005; revised 10 October 2005; accepted 24 October 2005)

This paper presents the hybrid compliance-stiffness matrix method for stable analysis of elastic wave propagation in multilayered anisotropic media. The method utilizes the hybrid matrix of each layer in a recursive algorithm to deduce the stack hybrid matrix for a multilayered structure. Like the stiffness matrix method, the hybrid matrix method is able to eliminate the numerical instability of transfer matrix method. By operating with total stresses and displacements, it also preserves the convenience for incorporating imperfect or perfect interfaces. However, unlike the stiffness matrix, the hybrid matrix remains to be well-conditioned and accurate even for zero or small thicknesses. The stability of hybrid matrix method has been demonstrated by the numerical results of reflection and transmission coefficients. These results have been determined efficiently based on the surface hybrid matrix method involving only a subset of hybrid submatrices. In conjunction with the recursive asymptotic method, the hybrid matrix method is self-sufficient without hybrid asymptotic method and may achieve low error level over a wide range of sublayer thickness or the number of recursive operations. © *2006 Acoustical Society of America.* [DOI: 10.1121/1.2139617]

PACS number(s): 43.20.Bi, 43.20.Fn, 43.20.Gp [JJM] Pages: 45–53

I. INTRODUCTION

For many years there has been considerable interest in the elastic wave propagation in multilayered anisotropic media due to its many applications in composite materials, nondestructive evaluation, geophysics, SAW devices, etc. One of the celebrated techniques for analysis of such media is based on the transfer matrix method.[1,2] This method facilitates the transition of field variables from one layer to the next while satisfying the interfacial condition between them. Although the transfer matrix method is applicable in principle, its direct implementation has been found to suffer from numerical instabilities. These instabilities often occur when the frequency is high and/or the thickness is large.

Many researchers have proposed various techniques to overcome the numerical instability of transfer matrix method. An early reformulation based on the delta operator technique has been developed to alleviate the problem for isotropic media.[3] The technique has been extended to anisotropic media but it requires the computation of large-order delta matrices.[4] An alternative approach that is able to circumvent the numerical instability is the direct global matrix method.[5–7] The method involves a global banded matrix whose size grows with the number of layers. For many layers, it will lead to substantial memory storage and computation time. Another stable approach that involves a constant-size matrix is the reflection matrix method (sometimes called invariant imbedding method).[8–10] This method utilizes a recursive scheme to build up the overall response of a stratified medium from the scattering properties of each interface. The original implementation of the reflection matrix method has been made more efficient and concise in our scattering matrix method.[11,12] Through the transition region reflection and transmission operators, the invariant imbedding method has also been applied to transversely inhomogeneous multilayers.[13]

Recently, a different approach called the stiffness matrix method[14,15] has been proposed to resolve the numerical instability of transfer matrix method. The method operates with total stresses and displacements via the stiffness matrix applied in a recursive algorithm. Using these total field variables makes it more convenient to incorporate imperfect interfaces that must be considered in certain ultrasonic problems.[16,17] It also constitutes naturally the framework of recursive asymptotic method,[18,19] which is a simple asymptotic method that obviates the need to compute the exact wave propagation solution. When not all submatrices of the stiffness matrix are required, e.g., for a layered half-space, a partial algorithm of surface stiffness (or impedance) matrix method can be utilized.[20] This method deals with surface matrices that are of smaller dimension at each recursion, thus giving rise to higher computation speed. Although the stiffness matrix method has been demonstrated to be computationally stable for large layer thickness, it becomes inaccurate and approaches being singular when the layer thickness reduces toward zero.

In this paper, we develop an alternative recursive hybrid compliance-stiffness matrix method for stable analysis of elastic wave propagation in multilayered anisotropic media. The method utilizes the hybrid matrix of each layer in a recursive algorithm to deduce the stack hybrid matrix for a multilayered structure. Like the stiffness matrix method, the hybrid matrix method is able to eliminate the numerical instability of transfer matrix method. By operating with total

a)Electronic mail: eeltan@ntu.edu.sg

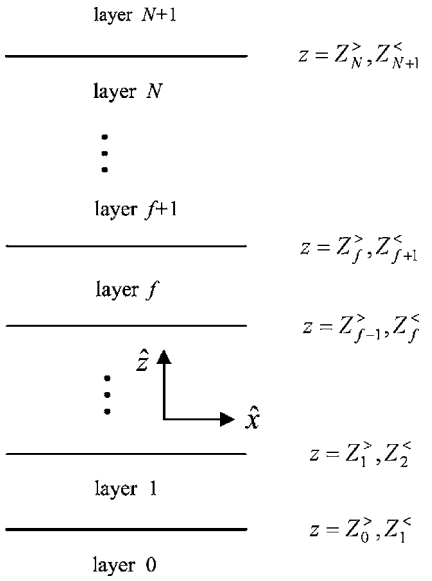

FIG. 1. Geometry of a planar multilayered anisotropic media embedded in two exterior regions (layers 0 and $N+1$). The upper and lower bounding interfaces of each layer f are denoted by $Z_f^>$ and $Z_f^<$, respectively.

stresses and displacements, it also preserves the convenience of stiffness matrix method for incorporating imperfect interfaces. However, contrary to the stiffness matrix, the hybrid matrix remains to be well-conditioned and accurate even for zero or small thicknesses encountered in thin layer modeling. The stability of hybrid matrix method is demonstrated by the numerical results of reflection and transmission coefficients. These results can be determined efficiently based on the surface hybrid matrix method involving only a subset of hybrid submatrices. In conjunction with the recursive asymptotic method, it will be shown that the hybrid matrix method is self-sufficient without hybrid asymptotic method[19] and may achieve low error level over a wide range of sublayer thickness or the number of recursive operations.

II. HYBRID COMPLIANCE-STIFFNESS MATRIX METHOD

A. Formulation of layer hybrid matrix

Figure 1 depicts the geometry of a planar multilayered structure comprising N arbitrarily anisotropic layers stratified in $\hat{\mathbf{z}}$ direction. For each layer f ($f=1,2,\ldots,N$) of thickness h_f, its upper and lower bounding interfaces are denoted, respectively by $Z_f^>$ and $Z_f^<$ such that $Z_f^> \geqslant z$ and $Z_f^< \leqslant z$ for z within the layer. Let the fields in each layer f be described by a 6×1 field vector $\mathbf{f}_f$ formed by the elements of displacement vector $\mathbf{u}_f$ and normal stress vector $\boldsymbol{\sigma}_f$, i.e.,

$$\mathbf{f}_f = \begin{bmatrix} \mathbf{u}_f \\ \boldsymbol{\sigma}_f \end{bmatrix}. \tag{1}$$

Assuming plane harmonic wave with $\exp(j\omega t)$ time dependence, each field vector satisfies a first-order 6×6 matrix differential system (see Refs. 10 and 11, and references therein)

$$\frac{d}{dz}\mathbf{f}_f = \mathbf{\Lambda}_f \mathbf{f}_f, \tag{2}$$

$$\mathbf{\Lambda}_f = \begin{bmatrix} jk_x(\mathbf{\Gamma}_{33}^f)^{-1}\mathbf{\Gamma}_{31}^f & (\mathbf{\Gamma}_{33}^f)^{-1} \\ k_x^2[\mathbf{\Gamma}_{11}^f - \mathbf{\Gamma}_{13}^f(\mathbf{\Gamma}_{33}^f)^{-1}\mathbf{\Gamma}_{31}^f] - \omega^2\rho_f\mathbf{I} & jk_x\mathbf{\Gamma}_{13}^f(\mathbf{\Gamma}_{33}^f)^{-1} \end{bmatrix}. \tag{3}$$

Here, k_x is the transverse wave number along $\hat{\mathbf{x}}$ direction, ρ_f is the mass density, $\mathbf{I}$ is the 3×3 identity matrix and $\mathbf{\Gamma}$'s can be constructed from the stiffness constants using the abbreviated subscripts.[21]

Based on the solutions to a standard eigenvalue problem of Eq. (2), the field vector can be written in terms of the superposition of eigenwaves as

$$\mathbf{f}_f(z) = \mathbf{\Psi}_f\mathbf{P}_f(z)\mathbf{c}_f = \mathbf{\Psi}_f\mathbf{w}_f(z). \tag{4}$$

Here, $\mathbf{\Psi}_f$ is a 6×6 eigenmatrix formed by the eigenvectors $\boldsymbol{\psi}_f^i$ of the system matrix $\mathbf{\Lambda}_f$ in Eq. (3); $\mathbf{P}_f(z)$ is a diagonal matrix whose elements consist of the eigenvalues $\lambda_f^i = -jk_{zf}^i$ in their exponentials as $\exp(-jk_{zf}^i z)$, with k_{zf}^i being the ith wave number along the $\hat{\mathbf{z}}$ direction; $\mathbf{c}_f$ is a 6×1 coefficient vector containing the unknown constants to be determined; $\mathbf{w}_f(z)$ is another 6×1 vector that conveniently lumps the coefficients and exponential terms together. Note that $\mathbf{f}_f(Z_f^>) = \mathbf{f}_{f+1}(Z_{f+1}^<)$ but $\mathbf{w}_f(Z_f^>) \neq \mathbf{w}_{f+1}(Z_{f+1}^<)$.

Henceforth, it will be assumed that the wave numbers for $i=1,2,3$ and $i=4,5,6$ along with their associated eigenwaves correspond to the upward-bounded and downward-bounded (or upward-propagating and downward-propagating) waves whose amplitudes remain bounded in the upward ($z\to+\infty$) and downward ($z\to-\infty$) directions, respectively. Under such association, the matrices and vectors in Eq. (4) can be decomposed into 3×3 and 3×1 partitions:

$$\mathbf{\Psi}_f = \begin{bmatrix} \mathbf{u}_f^> & \mathbf{u}_f^< \\ \boldsymbol{\sigma}_f^> & \boldsymbol{\sigma}_f^< \end{bmatrix}, \tag{5}$$

$$\mathbf{P}_f(z) = \begin{bmatrix} \mathbf{P}_f^>(z) & \mathbf{0} \\ \mathbf{0} & \mathbf{P}_f^<(z) \end{bmatrix}, \tag{6}$$

$$\mathbf{c}_f = \begin{bmatrix} \mathbf{c}_f^> \\ \mathbf{c}_f^< \end{bmatrix}, \quad \mathbf{w}_f(z) = \begin{bmatrix} \mathbf{w}_f^<(z) \\ \mathbf{w}_f^<(z) \end{bmatrix}. \tag{7}$$

($\mathbf{0}$ is the 3×3 null matrix). We have used the superscripts ">" and "<" to stand for "upward-bounded" and "downward-bounded" decomposition, respectively. To keep our notations in coherence with the field vector composition of $\mathbf{u}_f$ and $\boldsymbol{\sigma}_f$ in Eq. (1), the 3×3 eigen-submatrices of $\mathbf{\Psi}_f$ in Eq. (4) have been designated by $\mathbf{u}_f^{\gtrless}$ and $\boldsymbol{\sigma}_f^{\gtrless}$ accordingly.

With the eigensolutions available, we are ready to deduce for each layer f the matrix relations among the field vector elements ordered as

$$\begin{bmatrix} \mathbf{u}_f(Z_f^<) \\ \boldsymbol{\sigma}_f(Z_f^>) \end{bmatrix} = \mathbf{H}^f \begin{bmatrix} \boldsymbol{\sigma}_f(Z_f^<) \\ \mathbf{u}_f(Z_f^>) \end{bmatrix}. \tag{8}$$

The pertaining matrix $\mathbf{H}^f$ is called the layer hybrid compliance-stiffness matrix, or simply layer hybrid matrix, since its elements are a mixture of compliance, stiffness, and dimensionless transfer quantities. In particular, letting the 3×3 partitions of $\mathbf{H}^f$ be denoted by

$$\mathbf{H}^f = \begin{bmatrix} \mathbf{H}_{11}^f & \mathbf{H}_{12}^f \\ \mathbf{H}_{21}^f & \mathbf{H}_{22}^f \end{bmatrix}, \tag{9}$$

one can readily recognize their respective physical significance as follows: $\mathbf{H}_{11}^f$ is the compliance matrix at the lower surface $z=Z_f^<$ when the upper surface $z=Z_f^>$ is clamped; $\mathbf{H}_{22}^f$ is the stiffness matrix at the upper surface when the lower surface is free; $\mathbf{H}_{12}^f$ is the downward displacement transfer matrix when the lower surface is free; $\mathbf{H}_{21}^f$ is the upward stress transfer matrix when the upper surface is clamped. By performing some manipulations onto Eqs. (4)–(8), the hybrid matrix can be determined in terms of the eigensolutions as

$$\mathbf{H}^f = \begin{bmatrix} \mathbf{u}_f^> & \mathbf{u}_f^< \mathbf{P}_f^<(-h_f) \\ \boldsymbol{\sigma}_f^> \mathbf{P}_f^>(h_f) & \boldsymbol{\sigma}_f^< \end{bmatrix} \cdot \begin{bmatrix} \boldsymbol{\sigma}_f^> & \boldsymbol{\sigma}_f^< \mathbf{P}_f^<(-h_f) \\ \mathbf{u}_f^> \mathbf{P}_f^>(h_f) & \mathbf{u}_f^< \end{bmatrix}^{-1}. \tag{10}$$

Prior to discussing its numerical characteristics, it will be instructive to consider first the relation of hybrid matrix to other layer matrices employed previously.

B. Relation to transfer matrix and stiffness matrix

For each layer f, the transfer matrix $\mathbf{T}^f$ relates the displacement and stress at the upper surface to those at the lower surface via

$$\begin{bmatrix} \mathbf{u}_f(Z_f^>) \\ \boldsymbol{\sigma}_f(Z_f^>) \end{bmatrix} = \mathbf{T}^f \begin{bmatrix} \mathbf{u}_f(Z_f^<) \\ \boldsymbol{\sigma}_f(Z_f^<) \end{bmatrix}. \tag{11}$$

Using the eigensolutions of Eqs. (4)–(7), the transfer matrix can be written as

$$\mathbf{T}^f = \begin{bmatrix} \mathbf{u}_f^> \mathbf{P}_f^>(h_f) & \mathbf{u}_f^< \\ \boldsymbol{\sigma}_f^> \mathbf{P}_f^>(h_f) & \boldsymbol{\sigma}_f^< \end{bmatrix} \begin{bmatrix} \mathbf{u}_f^> & \mathbf{u}_f^< \mathbf{P}_f^<(-h_f) \\ \boldsymbol{\sigma}_f^> & \boldsymbol{\sigma}_f^< \mathbf{P}_f^<(-h_f) \end{bmatrix}^{-1}. \tag{12}$$

Alternatively, it can be deduced from the hybrid matrix partitions of Sec. II A as

$$\mathbf{T}^f = \begin{bmatrix} (\mathbf{H}_{12}^f)^{-1} & -(\mathbf{H}_{12}^f)^{-1}\mathbf{H}_{11}^f \\ \mathbf{H}_{22}^f(\mathbf{H}_{12}^f)^{-1} & \mathbf{H}_{21}^f - \mathbf{H}_{22}^f(\mathbf{H}_{12}^f)^{-1}\mathbf{H}_{11}^f \end{bmatrix}. \tag{13}$$

In turn, the hybrid matrix can be related to the transfer matrix partitions by

$$\mathbf{H}^f = \begin{bmatrix} -(\mathbf{T}_{11}^f)^{-1}\mathbf{T}_{12}^f & (\mathbf{T}_{11}^f)^{-1} \\ \mathbf{T}_{22}^f - \mathbf{T}_{21}^f(\mathbf{T}_{11}^f)^{-1}\mathbf{T}_{12}^f & \mathbf{T}_{21}^f(\mathbf{T}_{11}^f)^{-1} \end{bmatrix}. \tag{14}$$

For the stiffness matrix $\mathbf{K}^f$, it relates the stresses at the bottom and top surfaces of each layer f to the displacements therein via[15]

$$\begin{bmatrix} \boldsymbol{\sigma}_f(Z_f^<) \\ \boldsymbol{\sigma}_f(Z_f^>) \end{bmatrix} = \mathbf{K}^f \begin{bmatrix} \mathbf{u}_f(Z_f^<) \\ \mathbf{u}_f(Z_f^>) \end{bmatrix}. \tag{15}$$

[According to the geometry in Ref. 15, $\mathbf{K}^f$ of that paper has been defined by swapping the top and bottom surfaces in Eq. (15).] The stiffness matrix can be expressed in terms of the eigensolutions as

$$\mathbf{K}^f = \begin{bmatrix} \boldsymbol{\sigma}_f^> & \boldsymbol{\sigma}_f^< \mathbf{P}_f^<(-h_f) \\ \boldsymbol{\sigma}_f^> \mathbf{P}_f^>(h_f) & \boldsymbol{\sigma}_f^< \end{bmatrix} \cdot \begin{bmatrix} \mathbf{u}_f^> & \mathbf{u}_f^< \mathbf{P}_f^<(-h_f) \\ \mathbf{u}_f^> \mathbf{P}_f^>(h_f) & \mathbf{u}_f^< \end{bmatrix}^{-1}. \tag{16}$$

Its relationships with the hybrid matrix are given by

$$\mathbf{K}^f = \begin{bmatrix} (\mathbf{H}_{11}^f)^{-1} & -(\mathbf{H}_{11}^f)^{-1}\mathbf{H}_{12}^f \\ \mathbf{H}_{21}^f(\mathbf{H}_{11}^f)^{-1} & \mathbf{H}_{22}^f - \mathbf{H}_{21}^f(\mathbf{H}_{11}^f)^{-1}\mathbf{H}_{12}^f \end{bmatrix}, \tag{17}$$

$$\mathbf{H}^f = \begin{bmatrix} (\mathbf{K}_{11}^f)^{-1} & -(\mathbf{K}_{11}^f)^{-1}\mathbf{K}_{12}^f \\ \mathbf{K}_{21}^f(\mathbf{K}_{11}^f)^{-1} & \mathbf{K}_{22}^f - \mathbf{K}_{21}^f(\mathbf{K}_{11}^f)^{-1}\mathbf{K}_{12}^f \end{bmatrix}. \tag{18}$$

From Eqs. (8), (11), and (15), one can see that the hybrid matrix, transfer matrix, and stiffness matrix are merely the resultant matrices for different arrangements of the vector elements to be related in their definitions. It is possible to rearrange and relate the vector elements in more different ways which will lead to more other variants, e.g., the matrices signified by the inverses $(\mathbf{H}^f)^{-1}$, $(\mathbf{T}^f)^{-1}$, and $(\mathbf{K}^f)^{-1}$. The last one is just the compliance matrix denoted by $\mathbf{S}^f$ in Ref. 15. Numerical wise these inverse matrices perform similarly as their counterparts and so they will not be discussed separately in the following. From the pedagogical point of view, the hybrid matrix is less attractive compared to the transfer or stiffness matrix since it does not lead to easy interpretation at first sight. This is unlike the transfer matrix which describes and transfers the field vectors conveniently as a whole, or the stiffness matrix which carries all elements of the same dimensions with the significance of stiffnesses (or impedances). In spite of that, the hybrid matrix does possess certain important numerical advantages, particularly in regards to its numerical stability and accuracy that are often of primary concern.

C. Numerical stability and accuracy

1. Condition when $h_f \to \infty$

When the layer thickness h_f, or equivalently the frequency of elastic waves, increases to infinity, some or all of the elements in the diagonal matrices $\mathbf{P}_f^>(h_f)$ and $\mathbf{P}_f^<(-h_f)$ may diminish to zero. Assuming that all eigenwaves have become inhomogeneous, which is the physical case when the medium includes at least slight loss, the hybrid matrix of Eq. (10) with $h_f \to \infty$ reduces to

$$\mathbf{H}^f|_{h_f\to\infty} = \begin{bmatrix} \mathbf{u}_f^>(\boldsymbol{\sigma}_f^>)^{-1} & \mathbf{0} \\ \mathbf{0} & \boldsymbol{\sigma}_f^<(\mathbf{u}_f^<)^{-1} \end{bmatrix}. \tag{19}$$

Thus it can be seen that the hybrid matrix for thick layer asymptotically decomposes into compliance and stiffness matrices at the lower and upper surfaces. Moreover, such reduction to the asymptotic hybrid matrix is numerically stable because only the decreasing exponential terms are involved and the matrices are well conditioned. The asymptotic hybrid matrix will be particularly useful to characterize the exterior semi-infinite regions.

On the other hand, it is known that when the thickness or frequency approaches infinity, the transfer matrix of Eq. (12) becomes[15]

$$\mathbf{T}^f|_{h_f\to\infty} = \begin{bmatrix} \mathbf{0} & \mathbf{u}_f^< \\ \mathbf{0} & \boldsymbol{\sigma}_f^< \end{bmatrix} \begin{bmatrix} \mathbf{u}_f^> & \mathbf{0} \\ \boldsymbol{\sigma}_f^> & \mathbf{0} \end{bmatrix}^{-1}, \tag{20}$$

which is obviously not computable (overflow) numerically. Similar deduction can also be made from Eq. (13) where $\mathbf{H}_{12}^f$ is a null matrix as seen from Eq. (19). In practice, numerical difficulty also occurs for transfer matrix at high frequency/thickness even before the extreme state of being overflow. This is due to the mixture of exponentially growing and decaying terms that lead to loss of precision during computations. When the incorporation of transfer matrix such as Eqs. (13) and (14) is unavoidable or desirable, the layer thickness should be kept sufficiently small so that the computations do not suffer significant loss of accuracy.

For the stiffness matrix of Eq. (16), its asymptotic solution has been obtained for thickness or frequency approaching infinity as[15]

$$\mathbf{K}^f|_{h_f\to\infty} = \begin{bmatrix} \boldsymbol{\sigma}_f^>(\mathbf{u}_f^>)^{-1} & \mathbf{0} \\ \mathbf{0} & \boldsymbol{\sigma}_f^<(\mathbf{u}_f^<)^{-1} \end{bmatrix}. \tag{21}$$

Thus it can be seen that the stiffness matrix is regular and computationally stable for very thick layer. The asymptotic stiffness matrix in Eq. (21) bears the same structure as the asymptotic hybrid matrix in Eq. (19). Both of them can be specified directly from each other by noting that $\mathbf{K}_{11}^f\mathbf{H}_{11}^f=\mathbf{I}$ and $\mathbf{K}_{22}^f=\mathbf{H}_{22}^f$ when $h_f\to\infty$. With their expressions given in terms of eigensolutions, it brings better insight as to how the stiffness and hybrid matrices eliminate the numerical instability associated with the transfer matrix.

2. Condition when $h_f\to 0$

When the layer thickness h_f tends to zero, both hybrid and transfer matrices do not encounter much numerical difficulty. This is evident from their expressions, which when $h_f=0$ become simply

$$\mathbf{H}^f|_{h_f=0} = \begin{bmatrix} \mathbf{0} & \mathbf{I} \\ \mathbf{I} & \mathbf{0} \end{bmatrix}, \tag{22}$$

$$\mathbf{T}^f|_{h_f=0} = \begin{bmatrix} \mathbf{I} & \mathbf{0} \\ \mathbf{0} & \mathbf{I} \end{bmatrix}. \tag{23}$$

These reductions can be used to initiate the subsequent recursive and iterative algorithms for the hybrid and transfer matrices, respectively.

On the contrary, the stiffness matrix is not immune to numerical difficulty when the thickness reduces toward zero. This can be understood easily from its expression (16) in terms of eigensolutions with $h_f=0$:

$$\mathbf{K}^f|_{h_f=0} = \begin{bmatrix} \boldsymbol{\sigma}_f^> & \boldsymbol{\sigma}_f^< \\ \boldsymbol{\sigma}_f^> & \boldsymbol{\sigma}_f^< \end{bmatrix} \begin{bmatrix} \mathbf{u}_f^> & \mathbf{u}_f^< \\ \mathbf{u}_f^> & \mathbf{u}_f^< \end{bmatrix}^{-1}. \tag{24}$$

The matrix at the right is obviously not invertible due to its repeated rows and columns, thus Eq. (24) will give rise to numerical singularity. Similar deduction can also be made from the stiffness matrix expression (17) in terms of hybrid matrix, which degrades to Eq. (22) with $\mathbf{H}_{11}^f$ not invertible. Although absolute zero thickness may be exempted in practice, computation accuracy would be affected when one is close to singularity for small but finite thicknesses encountered in thin layer modeling.

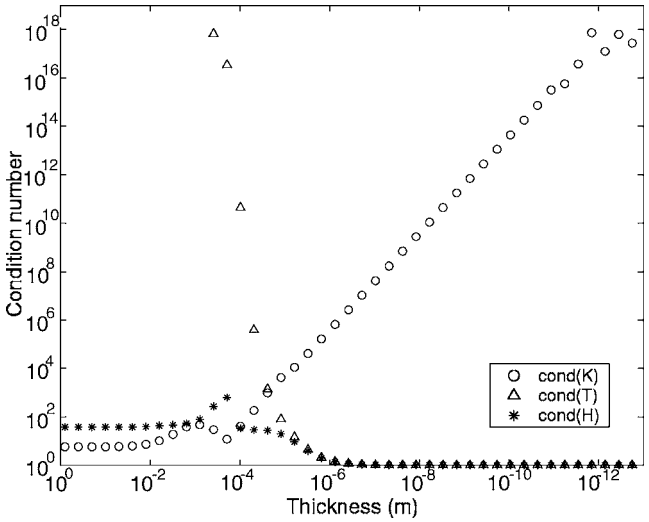

FIG. 2. Condition numbers of stiffness (**K**), transfer (**T**), and hybrid (**H**) matrices vs layer thickness.

For illustration, Fig. 2 plots the condition number of the stiffness matrix for a range of layer thickness. The range considered includes some physically realistic thicknesses as well as purely numerical ones adopted for thin layer approximation and recursive asymptotic method of Sec. III. (The parameters used are specified in that section although the observation here is representative of general cases.) It is evident that the condition number of stiffness matrix grows when the thickness becomes smaller. To demonstrate how the computation accuracy is affected, one can perform a certain number (say 25) of recursions using the stiffness matrix for various thickness repeatedly and compare with that of the resultant stack deduced from Eq. (16) directly. For example, it has been found that the relative error of the stiffness matrix element with largest magnitude increases from $\sim 10^{-14}$ at 0.1 mm to $\sim 10^{-5}$ at 10^{-13} m, and continues to rise further for thinner layers. Also shown in Fig. 2 are the condition numbers of transfer and hybrid matrices. As expected, the transfer matrix is extremely ill-conditioned for large thicknesses. Conversely, the hybrid matrix is rather well-conditioned throughout all the thicknesses.

From the above discussions, one can see that the stable and accurate range of layer thickness for transfer matrix and stiffness matrix is not complete but somewhat complements each other. In particular, the transfer matrix is usually stable only for very small thicknesses and becomes inaccurate or unstable when the thickness increases. The stiffness matrix is mostly stable and accurate for all but very small thicknesses. This leaves us with the hybrid matrix, which has been shown earlier to preserve the numerical stability and accuracy even at zero and infinite thicknesses. In this sense the hybrid matrix is superior to both transfer and stiffness matrices for its

robustness to accommodate the complete range of layer thickness. (Note that there may still exist instabilities at discrete thickness values that correspond to the resonance or guided modes within a layer bounded by certain boundary conditions. These instabilities may appear for transfer, stiffness, or hybrid matrices and can be alleviated with the inclusion of slight loss.)

D. Imperfect interface conditions

For imperfect interface between two solid layers, one can make use of the simple approximate model based on the asymptotic expansion of thin layer transfer matrix.[16,17] For instance, the first-order asymptotic transfer matrix that omits the coupling terms and includes only the spring and inertial terms reads

$$\mathbf{T}^{\text{imp}} = \begin{bmatrix} \mathbf{I} & \mathbb{K}^{-1} \\ -\mathbb{M} & \mathbf{I} \end{bmatrix}, \tag{25}$$

where $\mathbb{K}=\text{diag}\{K_{t1}, K_{t2}, K_n\}$ and $\mathbb{M}=\text{diag}\{\omega^2 M_{p1}, \omega^2 M_{p2}, \omega^2 M_n\}$. Substituting Eq. (25) into Eq. (14), we obtain the corresponding hybrid matrix that characterizes an imperfect interfacial layer as

$$\mathbf{H}^{\text{imp}} = \begin{bmatrix} -\mathbb{K}^{-1} & \mathbf{I} \\ \mathbf{I}+\mathbb{M}\mathbb{K}^{-1} & -\mathbb{M} \end{bmatrix}. \tag{26}$$

In the Appendix, we present the hybrid matrix that includes also the coupling terms. For more accurate modeling of the interfacial layer, one may utilize the second-order asymptotic approximation which is also useful in the recursive asymptotic method of Sec. III.

If one recalls the expressions of spring (K's) and inertial (M's) terms,[16] it is seen that the elements of both transfer and hybrid matrices in Eqs. (25) and (26) do not invoke any term inversely proportional to layer thickness. This is unlike the stiffness matrix given by[15]

$$\mathbf{K}^{\text{imp}} = \begin{bmatrix} -\mathbb{K} & \mathbb{K} \\ -\mathbb{M}-\mathbb{K} & \mathbb{K} \end{bmatrix}, \tag{27}$$

where the elements with K_{ti} and K_n will grow with $1/h_f$ as the layer thickness shrinks toward zero. On the other hand, the hybrid matrix (26) stays bounded no matter how small the interfacial layer thickness could be. Using such hybrid matrix also makes it convenient for incorporating imperfect or perfect interfaces especially when it is included in the recursive algorithm of the following.

E. Hybrid matrix recursive algorithm

For a stack of multilayers from f to N, the relationships among the displacements and stresses at the bottom and top surfaces can be described via a stack hybrid matrix as

$$\begin{bmatrix} \mathbf{u}_f(Z_f^<) \\ \boldsymbol{\sigma}_N(Z_N^>) \end{bmatrix} = \mathbf{H}^{(f)} \begin{bmatrix} \boldsymbol{\sigma}_f(Z_f^<) \\ \mathbf{u}_N(Z_N^>) \end{bmatrix}. \tag{28}$$

The notation here is that the superscript f in brackets denotes the stack matrix for layers from f to (always) N, in contrast to the earlier superscript without brackets denoting merely the individual layer matrix. Upon introducing another stack hybrid matrix for layers from $f+1$ to N, i.e., $\mathbf{H}^{(f+1)}$, along with use of the layer hybrid matrix in Eq. (8) and the field continuity $\mathbf{f}_f(Z_f^>)=\mathbf{f}_{f+1}(Z_{f+1}^<)$ (Fig. 1), the stack hybrid matrix partitions of Eq. (28) can be determined from

$$\mathbf{H}_{11}^{(f)} = \mathbf{H}_{11}^f + \mathbf{H}_{12}^f \mathbf{H}_{11}^{(f+1)} [\mathbf{I} - \mathbf{H}_{22}^f \mathbf{H}_{11}^{(f+1)}]^{-1} \mathbf{H}_{21}^f, \tag{29}$$

$$\mathbf{H}_{12}^{(f)} = \mathbf{H}_{12}^f \{\mathbf{I} + \mathbf{H}_{11}^{(f+1)} [\mathbf{I} - \mathbf{H}_{22}^f \mathbf{H}_{11}^{(f+1)}]^{-1} \mathbf{H}_{22}^f\} \mathbf{H}_{12}^{(f+1)}, \tag{30}$$

$$\mathbf{H}_{21}^{(f)} = \mathbf{H}_{21}^{(f+1)} [\mathbf{I} - \mathbf{H}_{22}^f \mathbf{H}_{11}^{(f+1)}]^{-1} \mathbf{H}_{21}^f, \tag{31}$$

$$\mathbf{H}_{22}^{(f)} = \mathbf{H}_{22}^{(f+1)} + \mathbf{H}_{21}^{(f+1)} [\mathbf{I} - \mathbf{H}_{22}^f \mathbf{H}_{11}^{(f+1)}]^{-1} \mathbf{H}_{22}^f \mathbf{H}_{12}^{(f+1)}. \tag{32}$$

Equations (29)–(32) constitute the recursive algorithm of hybrid matrix method. It can be found that they involve one type of inverse $[\mathbf{I}-\mathbf{H}_{22}^f \mathbf{H}_{11}^{(f+1)}]^{-1}$ that is regular even when the layer or stack thickness is infinite or zero. By using another type of inverse that is also regular, Eqs. (30) and (32) can be written in the form dual to Eqs. (31) and (29):

$$\mathbf{H}_{12}^{(f)} = \mathbf{H}_{12}^f [\mathbf{I} - \mathbf{H}_{11}^{(f+1)} \mathbf{H}_{22}^f]^{-1} \mathbf{H}_{12}^{(f+1)}, \tag{33}$$

$$\mathbf{H}_{22}^{(f)} = \mathbf{H}_{22}^{(f+1)} + \mathbf{H}_{21}^{(f+1)} \mathbf{H}_{22}^f [\mathbf{I} - \mathbf{H}_{11}^{(f+1)} \mathbf{H}_{22}^f]^{-1} \mathbf{H}_{12}^{(f+1)}. \tag{34}$$

The recursive algorithm in Eqs. (29)–(34) starts from layer N by setting stack $\mathbf{H}^{(N)}$ equals to layer $\mathbf{H}^N$. Then it progresses to layer $f<N$ involving all intervening layer hybrid matrices one at a time. In an alternative manner as mentioned earlier, the recursion may be initiated with $f=N$ and $\mathbf{H}^{(f+1)}$ given by the matrix in Eq. (22). This of course yields the same $\mathbf{H}^{(N)}=\mathbf{H}^N$ as before after one iteration. Still there is a third initialization approach possible that will be described in Sec. III. The recursion process terminates when $\mathbf{H}^{(1)}$ for the entire stack of multilayers has been obtained.

For comparison, the stack stiffness matrix that relates the stresses to displacements at the bottom and top surfaces of a multilayered stack is defined and determined as[14,15]

$$\begin{bmatrix} \boldsymbol{\sigma}_f(Z_f^<) \\ \boldsymbol{\sigma}_N(Z_N^>) \end{bmatrix} = \mathbf{K}^{(f)} \begin{bmatrix} \mathbf{u}_f(Z_f^<) \\ \mathbf{u}_N(Z_N^>) \end{bmatrix}, \tag{35}$$

$$\mathbf{K}_{11}^{(f)} = \mathbf{K}_{11}^f + \mathbf{K}_{12}^f [\mathbf{K}_{11}^{(f+1)} - \mathbf{K}_{22}^f]^{-1} \mathbf{K}_{21}^f, \tag{36}$$

$$\mathbf{K}_{12}^{(f)} = -\mathbf{K}_{12}^f [\mathbf{K}_{11}^{(f+1)} - \mathbf{K}_{22}^f]^{-1} \mathbf{K}_{12}^{(f+1)}, \tag{37}$$

$$\mathbf{K}_{21}^{(f)} = \mathbf{K}_{21}^{(f+1)} [\mathbf{K}_{11}^{(f+1)} - \mathbf{K}_{22}^f]^{-1} \mathbf{K}_{21}^f, \tag{38}$$

$$\mathbf{K}_{22}^{(f)} = \mathbf{K}_{22}^{(f+1)} - \mathbf{K}_{21}^{(f+1)} [\mathbf{K}_{11}^{(f+1)} - \mathbf{K}_{22}^f]^{-1} \mathbf{K}_{12}^{(f+1)}. \tag{39}$$

$\mathbf{K}^{(f)}$ denotes the stack stiffness matrix for layers from f to N, while $\mathbf{K}^{(f+1)}$ denotes that from $f+1$ to N. The recurrence relations in Eqs. (36)–(39) require fewer operations than those of Eqs. (29), (33), (31), and (34), respectively. However, in contrast to the stack hybrid matrix case, they cannot be initiated with the layer or stack stiffness matrix for zero thickness since Eq. (24) is singular. Moreover, when the layer thickness is very small, the implementation of stiffness matrix method leads to more accumulation of round-off errors (see Secs. II C 2 and III B).

For collation, the stack transfer matrix is defined and determined iteratively as

$$\begin{bmatrix} \mathbf{u}_N(Z_N^>) \\ \boldsymbol{\sigma}_N(Z_N^>) \end{bmatrix} = \mathbf{T}^{(f)} \begin{bmatrix} \mathbf{u}_f(Z_f^<) \\ \boldsymbol{\sigma}_f(Z_f^<) \end{bmatrix}, \tag{40}$$

$$\mathbf{T}^{(f)} = \mathbf{T}^{(f+1)}\mathbf{T}^f. \tag{41}$$

The number of matrix operations required for this iterative algorithm is slightly fewer than that of hybrid matrix recursive algorithm and slightly more than that of stiffness matrix one. Still they all take the amount of computation time that is proportional to the number of layers N. However, the transfer matrix method becomes inaccurate or unstable when the layer or stack thickness increases.

III. APPLICATIONS OF HYBRID MATRIX METHOD AND NUMERICAL EXAMPLES

A. Reflection and transmission coefficients

Having obtained the stack hybrid matrix for a multilayered structure, one can readily determine the reflection and transmission coefficients for the structure bounded by two anisotropic solids. Assuming that the wave is incident from layer 0, let the reflection ($\mathbf{r}_{0,1}$) and transmission ($\mathbf{t}_{0,N+1}$) coefficient matrices be defined as

$$\mathbf{w}_0^<(Z_0^>) = \mathbf{r}_{0,1}\mathbf{w}_0^>(Z_0^>), \tag{42}$$

$$\mathbf{w}_{N+1}^>(Z_{N+1}^<) = \mathbf{t}_{0,N+1}\mathbf{w}_0^>(Z_0^>). \tag{43}$$

Substituting Eqs. (42) and (43) into Eqs. (4)–(7), the field radiation and continuity conditions are imposed to be

$$\begin{bmatrix} \mathbf{u}_0^< - \mathbf{H}_{11}^{(1)}\boldsymbol{\sigma}_0^< & -\mathbf{H}_{12}^{(1)}\mathbf{u}_{N+1}^> \\ -\mathbf{H}_{21}^{(1)}\boldsymbol{\sigma}_0^< & \boldsymbol{\sigma}_{N+1}^> - \mathbf{H}_{22}^{(1)}\mathbf{u}_{N+1}^> \end{bmatrix} \begin{bmatrix} \mathbf{r}_{0,1} \\ \mathbf{t}_{0,N+1} \end{bmatrix} = \begin{bmatrix} \mathbf{H}_{11}^{(1)}\boldsymbol{\sigma}_0^> - \mathbf{u}_0^> \\ \mathbf{H}_{21}^{(1)}\boldsymbol{\sigma}_0^> \end{bmatrix}. \tag{44}$$

Equation (44) takes the same form as Eq. (31) of Ref. 15, which is expressed in terms of the stack stiffness submatrices. If desired, it can be solved explicitly for the reflection and transmission coefficient matrices

$$\mathbf{r}_{0,1} = [\mathbf{H}_S\boldsymbol{\sigma}_0^< - \mathbf{u}_0^<]^{-1}[\mathbf{u}_0^> - \mathbf{H}_S\boldsymbol{\sigma}_0^>], \tag{45}$$

$$\mathbf{t}_{0,N+1} = [\boldsymbol{\sigma}_{N+1}^> - \mathbf{H}_{22}^{(1)}\mathbf{u}_{N+1}^>]^{-1}\mathbf{H}_{21}^{(1)}[\boldsymbol{\sigma}_0^> + \boldsymbol{\sigma}_0^<\mathbf{r}_{0,1}]. \tag{46}$$

In Eq. (45), the compliance matrix $\mathbf{H}_S$ is given by

$$\mathbf{H}_S = \mathbf{H}_{11}^{(1)} + \mathbf{H}_{12}^{(1)}[\boldsymbol{\sigma}_{N+1}^>(\mathbf{u}_{N+1}^>)^{-1} - \mathbf{H}_{22}^{(1)}]^{-1}\mathbf{H}_{21}^{(1)}, \tag{47}$$

which can be seen to incorporate the radiation condition in layer $N+1$ through the term $\boldsymbol{\sigma}_{N+1}^>(\mathbf{u}_{N+1}^>)^{-1}$. This matrix actually corresponds to the stiffness matrix $\mathbf{K}_S$ in Eq. (33) of Ref. 14, which has also been defined for the multilayered stack on a half-space.

Equations (44)–(47) call for all four submatrices of the stack hybrid matrix $\mathbf{H}^{(1)}$. The determination of this stack matrix has been described earlier and can be summarized in the procedure below to obtain the reflection and transmission matrices:

(1) Initialize $\mathbf{H}^{(N)}$ with $\mathbf{H}^N$ or $\mathbf{H}^{(N+1)}$ with Eq. (22).
(2) Apply the recursion relations for all four stack hybrid submatrices in Eqs. (29)–(34).
(3) Repeat step (2) until $\mathbf{H}^{(1)}$ is made available.
(4) Incorporate the radiation condition into the compliance matrix $\mathbf{H}_S$ of Eq. (47).
(5) Calculate the reflection and transmission matrices via Eqs. (45) and (46).

To increase the computation speed, one may resort to alternative procedure as follows:
(1′) Incorporate the radiation condition into the hybrid matrix initialized with $\mathbf{H}_{11}^{\{N+1\}} = \mathbf{u}_{N+1}^>(\boldsymbol{\sigma}_{N+1}^>)^{-1}$ and $\mathbf{H}_{21}^{\{N+1\}} = \mathbf{I} \neq \mathbf{0}$ [despite $\mathbf{H}_{21}^{N+1} = \mathbf{0}$ from Eq. (19)].
(2′) Apply the recursion relations for two hybrid submatrices in

$$\mathbf{H}_{11}^{\{f\}} = \mathbf{H}_{11}^f + \mathbf{H}_{12}^f\mathbf{H}_{11}^{\{f+1\}}[\mathbf{I} - \mathbf{H}_{22}^f\mathbf{H}_{11}^{\{f+1\}}]^{-1}\mathbf{H}_{21}^f, \tag{48}$$

$$\mathbf{H}_{21}^{\{f\}} = \mathbf{H}_{21}^{\{f+1\}}[\mathbf{I} - \mathbf{H}_{22}^f\mathbf{H}_{11}^{\{f+1\}}]^{-1}\mathbf{H}_{21}^f. \tag{49}$$

(3′) Repeat step (2′) until $\mathbf{H}_{11}^{\{1\}}$ and $\mathbf{H}_{21}^{\{1\}}$ are made available.
(4′) Calculate the reflection and transmission matrices via

$$\mathbf{r}_{0,1} = [\mathbf{H}_{11}^{\{1\}}\boldsymbol{\sigma}_0^< - \mathbf{u}_0^<]^{-1}[\mathbf{u}_0^> - \mathbf{H}_{11}^{\{1\}}\boldsymbol{\sigma}_0^>], \tag{50}$$

$$\mathbf{t}_{0,N+1} = (\boldsymbol{\sigma}_{N+1}^>)^{-1}\mathbf{H}_{21}^{\{1\}}[\boldsymbol{\sigma}_0^> + \boldsymbol{\sigma}_0^<\mathbf{r}_{0,1}]. \tag{51}$$

In the procedure (1′)–(4′), one starts by imposing the radiation (or other boundary) condition at the outset in step (1′), rather than at later stage in step (4) of the previous procedure (1)–(5). This allows only a subset of hybrid submatrices need to be computed, thus reducing the number of operations in the recursive algorithm. Specifically when only the reflection response is of interest, the size of matrix to be dealt with in steps (2′) and (3′), i.e., $\mathbf{H}_{11}^{\{f\}}$ of Eq. (48), is divided by four from that of steps (2) and (3), i.e., $\mathbf{H}^{(f)}$ of Eqs. (29)–(34). In consequence, the computations of procedure (1′)–(4′) will be faster than procedure (1)–(5) in the same manner and spirit as Ref. 20. Adopting their designation of surface impedance or stiffness matrix method, Eqs. (48) and (49) can be regarded as the surface hybrid matrix method. Apart from being efficient, the surface hybrid matrix method shares the well-conditioning and accuracy advantages of the full matrix method described in the previous section. Although Eqs. (48) and (49) take the form of Eqs. (29) and (31), their implications are somewhat different. In particular, the former hybrid submatrices (superscripted by curly braces) have incorporated radiation/boundary condition "globally," while the latter ones (superscripted by brackets) have not and characterize only the "local" stack. Of course, these global and local hybrid matrices are closely related, e.g.,

$$\mathbf{H}_{21}^{\{1\}} = [\mathbf{I} - \mathbf{H}_{22}^{(1)}\mathbf{H}_{11}^{\{N+1\}}]^{-1}\mathbf{H}_{21}^{(1)}. \tag{52}$$

The above-noted discussions can be adapted readily to determine the reflection and transmission coefficients for a multilayered stack immersed in fluids (rather than solids). This can be achieved by taking into account the vanishing of shear stress components at the top and bottom surfaces accordingly. To save space, we shall not present the equations but provide only their numerical results. These results also

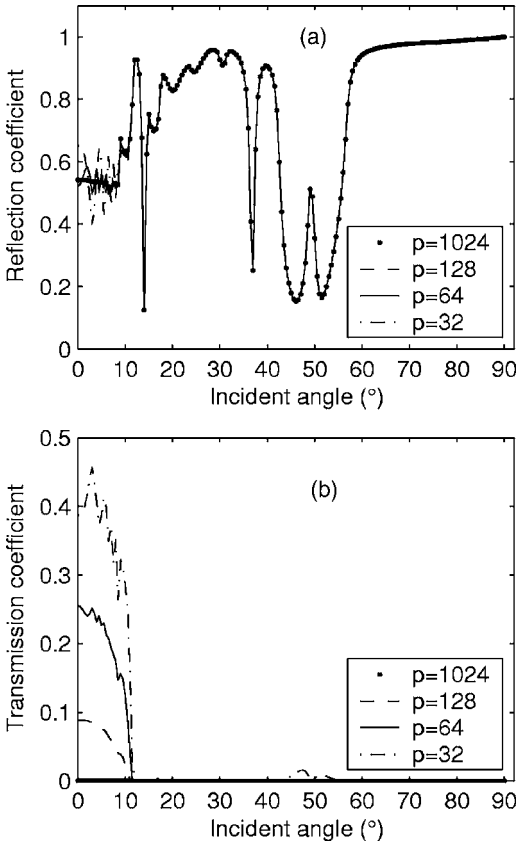

FIG. 3. (a) Reflection and (b) transmission coefficients for a lossy multi-ply composite $[0°/45°/90°/-45°]_p$ immersed in water. The incidence is in $\phi=0°$ plane, the frequency is 3 MHz, and the lamina properties are given in Table I.

serve to demonstrate the numerical stability of hybrid matrix method. For illustration, let us consider the case study of Ref. 15. Figures 3(a) and 3(b) show the reflection and transmission coefficients for a lossy multi-ply composite $[0°/45°/90°/-45°]_p$ $(p=32,64,128)$ immersed in water. The incidence is in $\phi=0°$ plane, the frequency is 3 MHz, and the lamina properties are given in Table I. Similar to the stiffness matrix method, no numerical instability has been encountered, even when the repetition is increased to a much larger value. For example, we are also able to reproduce the reflection coefficient for $[0°/45°/90°/-45°]_{1024}$ using the hybrid matrix method as depicted by the dots in Fig. 3, cf. Fig. 4(b) of Ref. 15. It can be observed that when the lamina attenuation is included, the reflection response of the stack with 64 repetitions has approached quite well that of the stack with 1024 repetitions especially for the incidence above 10°.

TABLE I. Lamina properties (Ref. 15).

C_{11}	$143.2-j0.32$ GPa
C_{22}	$15.8-j0.11$ GPa
C_{12}	$7.5-j0.031$ GPa
C_{23}	$8.2-j0.002$ GPa
C_{55}	$7.0-j0.07$ GPa
ρ	1.6 g/cm^3
h	0.194 mm

B. Recursive asymptotic method for hybrid matrix

Having demonstrated the numerical stability for thick multilayered structure, we next illustrate the use of hybrid matrix method in conjunction with the recursive asymptotic method.[18,19] Recall that the original recursive asymptotic method uses an asymptotic representation of the thin layer transfer matrix to construct the solutions for thick layers. For simplicity, we consider the second-order asymptotic transfer matrix that can be written as[17]

$$\mathbf{T}_{\mathrm{II}}=\left[\mathbf{I}_6-\frac{h}{2}\mathbf{\Lambda}\right]^{-1}\left[\mathbf{I}_6+\frac{h}{2}\mathbf{\Lambda}\right] \tag{53}$$

with $\mathbf{I}_6$ being the 6×6 identity matrix. The representation (53) has the advantage that it satisfies energy balance and does not introduce any scattering in a homogeneous medium, but it is accurate only for sufficiently thin layers. For a thick layer with thickness H, one can subdivide it into a stack of N thin layers of thickness $h=H/N$ each and approximate the stack transfer matrix as the product of thin layer transfer matrices in Eq. (53). When N is selected as a power of 2, i.e., $N=2^n$, the stack transfer matrix can be calculated very efficiently by n repeated squarings.

As soon as the stack thickness increases, it will be prudent for one to deal with the stack stiffness matrix since the transfer matrix may become inaccurate or unstable. To that end, the second-order asymptotic transfer matrix of Eq. (53) is first transformed into the corresponding asymptotic stiffness matrix $\mathbf{K}_{\mathrm{II}}$ via the relation[15,19]

$$\mathbf{K}=\begin{bmatrix}-(\mathbf{T}_{12})^{-1}\mathbf{T}_{11} & (\mathbf{T}_{12})^{-1}\\ \mathbf{T}_{21}-\mathbf{T}_{22}(\mathbf{T}_{12})^{-1}\mathbf{T}_{11} & \mathbf{T}_{22}(\mathbf{T}_{12})^{-1}\end{bmatrix}. \tag{54}$$

By using the resultant $\mathbf{K}_{\mathrm{II}}$ to initiate a series of n self-recursions,[18,19] the stiffness matrix for thick stack can be computed more stably and accurately than the transfer matrix. In the similar manner, one may resort to dealing with the stack hybrid matrix instead of the stack transfer or stiffness matrix above. The asymptotic hybrid matrix $\mathbf{H}_{\mathrm{II}}$ is deduced from Eqs. (53) and (14), and then applied to initiate the self-recursions

$$\mathbf{H}_{11}^{(f)}=\mathbf{H}_{11}^{(f+1)}+\mathbf{H}_{12}^{(f+1)}\mathbf{H}_{11}^{(f+1)}[\mathbf{I}-\mathbf{H}_{22}^{(f+1)}\mathbf{H}_{11}^{(f+1)}]^{-1}\mathbf{H}_{21}^{(f+1)}, \tag{55}$$

$$\mathbf{H}_{12}^{(f)}=\mathbf{H}_{12}^{(f+1)}[\mathbf{I}-\mathbf{H}_{11}^{(f+1)}\mathbf{H}_{22}^{(f+1)}]^{-1}\mathbf{H}_{12}^{(f+1)}, \tag{56}$$

$$\mathbf{H}_{21}^{(f)}=\mathbf{H}_{21}^{(f+1)}[\mathbf{I}-\mathbf{H}_{22}^{(f+1)}\mathbf{H}_{11}^{(f+1)}]^{-1}\mathbf{H}_{21}^{(f+1)}, \tag{57}$$

$$\mathbf{H}_{22}^{(f)}=\mathbf{H}_{22}^{(f+1)}+\mathbf{H}_{21}^{(f+1)}\mathbf{H}_{22}^{(f+1)}[\mathbf{I}-\mathbf{H}_{11}^{(f+1)}\mathbf{H}_{22}^{(f+1)}]^{-1}\mathbf{H}_{12}^{(f+1)}, \tag{58}$$

With this method, the stack hybrid matrix can also be computed stably and accurately even for very thick stack.

To assess the accuracy of various recursive asymptotic methods, let us define the average relative errors[19] adapted for non-piezoelectric media as

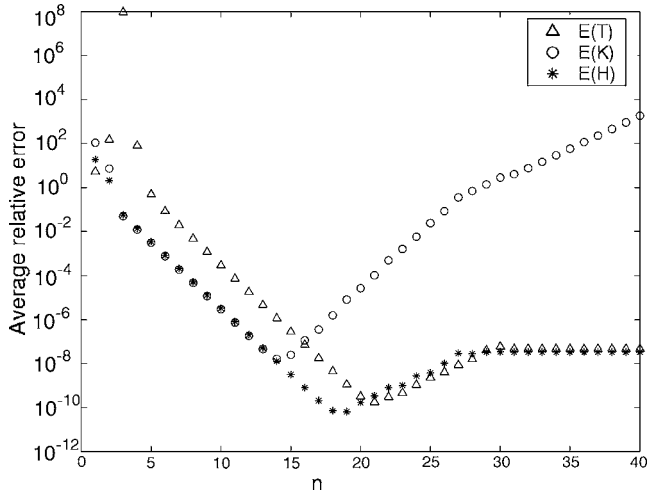

FIG. 4. Average relative errors of transfer (**T**), stiffness (**K**), and hybrid (**H**) matrices computed by recursive asymptotic methods vs the number of recursive operations n, for one lamina of Table I oriented at 45° with $N=2^n$ subdivisions. The errors have been averaged over the transverse wave numbers k_x ranging from 1 to 40 mm^{-1} at frequency 3 MHz.

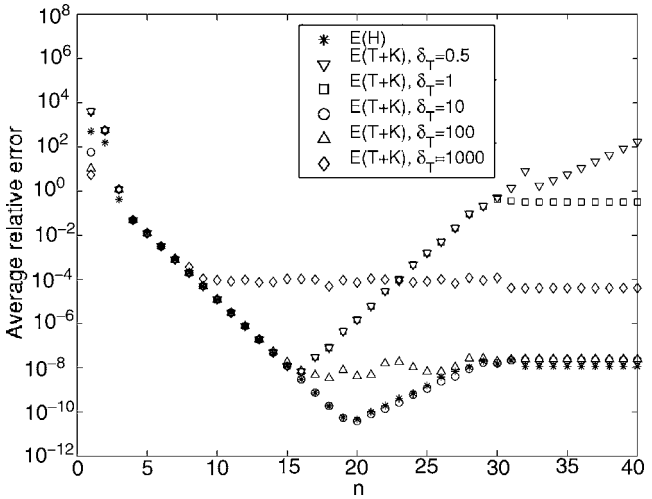

FIG. 5. Average relative errors using hybrid matrix (**H**) method and hybrid asymptotic (**T**+**K**) method for different δ_T vs the number of recursive operations n. All parameters are the same as Fig. 4 except that the errors have been averaged over the transverse wave numbers k_x ranging from 20 to 60 mm^{-1}.

$$E(\mathbf{X}) = \frac{1}{36}\sum_{i=1}^{6}\sum_{j=1}^{6} |(\mathbf{X}_a[i,j] - \mathbf{X}_e[i,j])/\mathbf{X}_e[i,j]|. \tag{59}$$

Here, $\mathbf{X}_a$ represents the asymptotic transfer ($\mathbf{T}_a$), stiffness ($\mathbf{K}_a$), or hybrid ($\mathbf{H}_a$) matrix obtained from the repeated squarings or self-recursions described earlier. $\mathbf{X}_e$ represents the "exact" transfer ($\mathbf{T}_e$), stiffness ($\mathbf{K}_e$), or hybrid ($\mathbf{H}_e$) matrix obtained from the eigensolutions in Eq. (12), (16), or (10), respectively (with thickness H). To investigate the error change with the number of subdivisions $N=2^n$, let us consider one lamina of Sec. III A oriented at 45°. Figure 4 plots the average relative errors versus the number of recursive operations n. The errors $E(\mathbf{X})$ have been averaged over the transverse wave numbers k_x ranging from 1 to 40 mm^{-1} at frequency 3 MHz. It can be seen that the error trends for the transfer and stiffness matrices follow closely the decay and growth rates observable in Fig. 2 of Ref. 19 (despite for non-piezoelectric media). In particular, the errors of both decrease initially at a rate proportional to $(1/2^n)^2$ due to the smaller truncation error for smaller sublayer thickness. After certain minimum points, the errors start to increase with the rates proportional to 2^n for the transfer matrix and $(2^n)^2$ for the stiffness matrix. Furthermore, the minimum error achievable by the stiffness matrix is higher than that of the transfer matrix.

On the other hand, it is observed that the error trend for the hybrid matrix is similar to that for the transfer matrix, having growth rate and minimum error lower than those of the stiffness matrix. Moreover, when the number of recursive operations n is increased further, the errors for both hybrid and transfer matrices actually reach a plateau while the stiffness matrix error continues to grow. If one takes a closer look at Fig. 2 of Ref. 19, similar plateau can also be observed for its transfer matrix error plot after $n>25$, whereas the corresponding plot for the stiffness matrix error rise has been cropped out by the figure window. Furthermore, one can attain low error level $[E(\mathbf{H}) \lesssim 3\times 10^{-8}]$ over a wider range of n values ($14 \leqslant n \leqslant 40$) for the hybrid matrix as compared to only around the minimum point ($n=14,15$) for the stiffness matrix [with $E(\mathbf{K}) \sim 3\times 10^{-8}$]. For small n values and large thicknesses, the transfer matrix is still prone to instability with occurrence of very large errors.

In view of the inadequacy of transfer or stiffness matrix itself, a hybrid asymptotic **T**+**K** method has been proposed in Ref. 19. [The hybrid asymptotic (**T**+**K**) method should not be confused with the hybrid matrix (**H**) method.] In this method, the transfer matrix is first used for thin layers in the beginning. At each iteration, one also calculates a control parameter adapted for non-piezoelectric media as

$$\delta = \frac{1}{6}\sum_{i=1}^{6} |\mathbf{T}_a(i,i)|. \tag{60}$$

When δ exceeds certain threshold δ_T, the transfer matrix is converted into stiffness matrix using Eq. (54). Then the process continues with the self-recursions of stiffness matrix. Figure 5 shows the average relative errors using hybrid asymptotic method for different δ_T. All parameters are the same as Fig. 4 except that the errors $E(\mathbf{T}+\mathbf{K})$ have been averaged over the transverse wave numbers k_x ranging from 20 to 60 mm^{-1}. Note that the threshold cannot be selected too large so as to safeguard against the instability or inaccuracy of transfer matrix, cf. $\delta_T=1000$. Also, it should not be too small for otherwise the error rise may persist like the pure stiffness matrix method, cf. $\delta_T=0.5$. In the optimal case of $\delta_T=10$, one has the error $E(\mathbf{T}+\mathbf{K}) \lesssim 3\times 10^{-8}$ over $15 \leqslant n \leqslant 40$, which is comparable to $E(\mathbf{H})$ of hybrid matrix method like the above-mentioned case. While the hybrid asymptotic method requires continued checking against the proper threshold, the hybrid matrix method bypasses such unnecessary checking process and does not leave one to any risk of instability or inaccuracy of transfer matrix. Therefore it is simpler and worthwhile adopting the hybrid matrix in conjunction with the recur-

sive asymptotic method for its overall high accuracy, stability, and self-sufficiency.

IV. CONCLUSIONS

This paper has presented the hybrid compliance-stiffness matrix method for stable analysis of elastic wave propagation in multilayered anisotropic media. The hybrid matrix method has eliminated the numerical instability of transfer matrix method and preserves the convenience for incorporating imperfect or perfect interfaces. It also remains to be well-conditioned and accurate even for zero or small thicknesses encountered in thin layer modeling. The stability of hybrid matrix method has been demonstrated by the numerical results of reflection and transmission coefficients. These results have been determined efficiently based on the surface hybrid matrix method involving only a subset of hybrid submatrices. In conjunction with the recursive asymptotic method, the hybrid matrix method is self-sufficient without hybrid asymptotic method and may achieve low error level over a wide range of sublayer thickness or the number of recursive operations. With its robustness to accommodate the complete range of layer thickness, the method may find much usefulness in other applications as well including modal solutions, Green's functions, ultrasonic time response, composite design, etc.

APPENDIX: ASYMPTOTIC HYBRID MATRIX INCLUDING COUPLING TERMS

The first-order asymptotic transfer matrix that describes an imperfect interfacial layer with coupling terms included has been provided in Ref. 16. Using Eq. (14), the corresponding hybrid matrix is $\mathbf{H}^{\text{imp}}=[H_{ij}]$, where (in terms of the variables defined therein[16])

$$H_{11} = -(1/K_{t1} + c'_{36}b_{13}^2 b_{15})/D,$$

$$H_{12} = -(c'_{36}b_{13}^2/K_{t2} + b_{15})/D,$$

$$H_{13} = b_{13}/(K_n D), \quad H_{14} = 1/D,$$

$$H_{15} = c'_{36}b_{13}^2/D, \quad H_{16} = -b_{13}/D,$$

$$H_{21} = -b_{15}, \quad H_{22} = -1/K_{t2},$$

$$H_{23} = H_{24} = H_{26} = 0, \quad H_{25} = 1,$$

$$H_{31} = (c'_{13}/K_{t1} + c'_{36}b_{15})b_{13}/D,$$

$$H_{32} = (c'_{36}/K_{t2} + c'_{13}b_{15})b_{13}/D,$$

$$H_{33} = -1/(K_n D), \quad H_{34} = -c'_{13}b_{13}/D,$$

$$H_{35} = -c'_{36}b_{13}/D, \quad H_{36} = 1/D,$$

$$H_{4i} = -\omega^2 M_{p1}H_{1i} + b_{51}H_{2i} + \delta_{i1} + c'_{13}b_{13}\delta_{i3},$$

$$H_{5i} = b_{51}H_{1i} - \omega^2 M_{p2}H_{2i} + \delta_{i2} + c'_{36}b_{13}\delta_{i3},$$

$$H_{6i} = -\omega^2 M_n H_{3i} + \delta_{i3} + b_{13}\delta_{i1},$$

$$D = 1 - c'_{13}b_{13}^2, \quad \delta_{ij} = \text{Kronecker delta},$$

$$c'_{13} = C_{13}/C_{33}, \quad c'_{36} = C_{36}/C_{33}.$$

[1] W. T. Thomson, "Transmission of elastic waves through a stratified solid medium," J. Appl. Phys. **21**, 89–93 (1950).
[2] N. A. Haskell, "The dispersion of surface waves on multilayered media," Bull. Seismol. Soc. Am. **43**, 17–34 (1953).
[3] J. W. Dunkin, "Computation of modal solutions in layered elastic media at high frequencies," Bull. Seismol. Soc. Am. **55**, 335–358 (1965).
[4] M. Castaings and B. Hosten, "Delta operator technique to improve the Thomson-Haskell method stability for propagation in multilayered anisotropic absorbing plates," J. Acoust. Soc. Am. **95**, 1931–1941 (1994).
[5] L. Knopoff, "A matrix method for elastic wave problems," Bull. Seismol. Soc. Am. **54**, 431–438 (1964).
[6] H. Schmidt and F. B. Jensen, "A full wave solution for propagation in multilayered viscoelastic media with application to Gaussian beam reflection at fluid-solid interfaces," J. Acoust. Soc. Am. **77**, 813–825 (1985).
[7] A. K. Mal, "Wave propagation in layered composite laminates under periodic surface loads," Wave Motion **10**, 257–266 (1988).
[8] B. L. N. Kennett, *Seismic Wave Propagation in Stratified Media* (Cambridge University Press, Cambridge, 1983).
[9] D. C. Booth and S. Crampin, "The anisotropic reflectivity technique: Theory," Geophys. J. R. Astron. Soc. **72**, 755–766 (1983).
[10] G. J. Fryer and L. N. Frazer, "Seismic waves in a stratified anisotropic media," Geophys. J. R. Astron. Soc. **78**, 691–710 (1984).
[11] E. L. Tan, "A robust formulation of SAW Green's functions for arbitrarily thick multilayers at high frequencies," IEEE Trans. Ultrason. Ferroelectr. Freq. Control **49**, 929–936 (2002).
[12] E. L. Tan, "A concise and efficient scattering matrix formalism for stable analysis of elastic wave propagation in multilayered anisotropic solids," Ultrasonics **41**, 229–236 (2003).
[13] J. McCoy and L. N. Frazer, "Propagation modelling based on wavefield factorization and invariant imbedding," Geophys. J. R. Astron. Soc. **86**, 703–717 (1986).
[14] L. Wang and S. I. Rokhlin, "Stable reformulation of transfer matrix method for wave propagation in layered anisotropic media," Ultrasonics **39**, 413–424 (2001).
[15] S. I. Rokhlin and L. Wang, "Stable recursive algorithm for elastic wave propagation in layered anisotropic media: Stiffness matrix method," J. Acoust. Soc. Am. **112**, 822–834 (2002).
[16] S. I. Rokhlin and W. Huang, "Ultrasonic wave interaction with a thin anisotropic layer between two anisotropic solids: Exact and asymptotic-boundary-condition methods," J. Acoust. Soc. Am. **92**, 1729–1742 (1992).
[17] S. I. Rokhlin and W. Huang, "Ultrasonic wave interaction with a thin anisotropic layer between two anisotropic solids. II. Second-order asymptotic boundary conditions," J. Acoust. Soc. Am. **93**, 3405–3420 (1993).
[18] L. Wang and S. I. Rokhlin, "Recursive asymptotic stiffness matrix method for analysis of surface acoustic wave devices on layered piezoelectric media," Appl. Phys. Lett. **81**, 4049–4051 (2002).
[19] L. Wang and S. I. Rokhlin, "Modeling of wave propagation in layered piezoelectric media by a recursive asymptotic matrix method," IEEE Trans. Ultrason. Ferroelectr. Freq. Control **51**, 1060–1071 (2004).
[20] B. Hosten and M. Castaings, "Surface impedance matrices to model the propagation in multilayered media," Ultramicroscopy **41**, 501–507 (2003).
[21] B. A. Auld, *Acoustic Fields and Waves in Solids* (Krieger, Malabar, 1990), Vol. **I**.

A large ultrasonic bounded acoustic pulse transducer for acoustic transmission goniometry: Modeling and calibration

Youcef Bouzidi[a] and Douglas R. Schmitt[b]
Institute for Geophysical Research, Department of Physics, University of Alberta, Edmonton, Alberta T6G 2J1, Canada

(Received 24 June 2005; revised 11 October 2005; accepted 12 October 2005)

A large, flat ultrasonic transmitter and a small receiver are developed for studies of material properties in acoustic transmission goniometry. While the character of the wave field produced by the transmitter can be considered as a plane wave as observed by the receiver, diffraction effects are noticeable near critical angles and result in the appearance of weak but detectable arrivals. Transmitted ultrasonic waveforms are acquired in one elastic silicate glass and two visco-elastic acrylic glass sample plates as a function of the angle of incidence. Phase velocities are determined from modeling of the shape of curves of the observed arrival times versus angle of incidence. The waveform observations are modeled using a phase propagation technique that incorporates full wave behavior including attenuation. Subtle diffraction effects are captured in addition to the main bounded pulse propagation. The full propagation modeling allows for various arrivals to be unambiguously interpreted. The results of the plane wave solution are close to the full wave propagation modeling without any corrections to the observed wave field. This is an advantage as it places confidence that later analyses can use simpler plane wave solutions without the need for additional diffraction corrections. A further advantage is that the uniform bounded acoustic pulse allows for the detection of weak arrivals such as a low energy edge diffraction observed in our experiments. © *2006 Acoustical Society of America.* [DOI: 10.1121/1.2133683]

PACS number(s): 43.20.Gp, 43.20.Jr, 43.20.Ye, 43.35.Cg [YHB] Pages: 54–64

I. INTRODUCTION

A great deal of information on the mechanical properties of solids is obtained by studying transmitted and reflected acoustic waves. Observations of the angle-of-incidence-dependent variations of the complex transmission and reflection coefficients can be used to quantitatively determine elastic constants, wave velocities, and attenuation. As such, acoustic goniometry, in which a fluid-loaded plate (i.e., a plate completely immersed in a liquid) is insonified with acoustic energy at a variety of angles of incidence and analyzed in either the time or frequency domain, has long been popular in material property studies. Transmission goniometry techniques, in particular, have been used for studies of high-resolution imaging,[1] complex wave propagation in visco-elastic and anisotropic,[2–4] thin,[5,6] and saturated poro-elastic[7–11] media.

Ultrasonic goniometry experiments are carried out with a variety of geometries. One problem ubiquitous to all these geometries, however, is that the transmitting and receiving transducers are of finite dimension and limited frequency bandwidth. As a result, the analysis of real measurements requires that transducer diffraction,[12,13] such as beam divergence, edge effects, and off-axis wave-number components, be considered in the experimental design and analysis. The energy propagating from such transducers is contained within a continuous bounded beam or a transient bounded pulse. The most dramatic example of bounded beam or pulse effects is nonspecular reflection produced near critical angles[14,15] that results in broadening of reflectivity coefficient maxima and apparent lateral shifting of the reflected beam upon reflection near the Rayleigh critical angle. As such, the influence of such diffraction affects on both transmissivity and reflectivity; the phase must be considered particularly as the S-wave critical angle is approached.

Most theoretical developments in acoustics are constructed with the assumption that monochromatic plane-wave fronts propagate through a medium. Ideally, experimental measurements consequently strive to reduce the imperfect, diffraction-limited observations to a form from which a plane wave interpretation can be employed. This is especially pertinent for more fundamental measurements of reflection and transmission coefficients,[16] intrinsic attenuation,[17] and inversion of anisotropic properties.[18] A variety of strategies are used to overcome this limitation. The most common is to correct the observed amplitudes waveforms for changes due to beam characteristics.[16,19–23] Another approach is to mimic plane wave transducers by superposition of the time domain waveforms acquired during the systematic scanning of a transmitted wave field[24] or by synthetic aperture arrays[25,26] in which the effective dimensions of the transducers are artificially increased.

In principal, the same effects can be obtained by use of large transducers directly. The larger the transducer relative

[a]Now at Geo-X Systems Ltd., Suite 500, 440 2nd Avenue S.W. Electronic mail: youcef@geo-x.com
[b]Author to whom correspondence should be addressed. Electronic mail: doug@phys.ualberta.ca

to the distance to the receiver and the wavelength of the propagating acoustic energy, the more the wave field approaches plane wave behavior. Construction of large aperture transducers is problematic and there is little discussion in the literature of their use in material characterization. However, Hosten and co-workers[27,28] have more recently employed specially constructed large (40×80 mm^2) high-frequency (3.2 MHz) transducers. Using these transducers, the frequency dependence of transmissivity of isotropic glass was measured at a variety of angles of incidence and these agreed with the predictions calculated using simpler plane wave theory. In contrast, the transmissivities obtained using a pair of smaller transducers (~19 mm diameter) differed substantially from the plane wave theory even after laterally shifting the receiver to correct for refraction of the beam within the plate. Consequently, the information obtained from the near-plane wave could be inverted for material properties without having to make transducer diffraction corrections, corrections that would increase the uncertainty of the measurements. This was found to be particularly important in the determination of the imaginary components of the complex moduli that indicate the attenuation.

A similar experimental configuration consisting of a (102×76 mm^2) transmitter but with a much smaller (1.9×1.9 mm^2) receiver is described in this contribution, an ultimate goal of which is to have a system sufficiently sensitive for the study of attenuation and wave propagation in complex materials. The large transmitter is intended to create an acoustic pulse the character of which approaches that of a plane wave. Conversely, the small receiver is intended to sense the pressure at a point in the transmitted wave field. The purpose of this is to eliminate any corrections due to diffraction effects of the transmitted wave field that lead to a nonuniform distribution of pressure over the surface area of the receiver. So, in this context the somewhat subjective term of "large" is taken to mean that which will yield a transmitted wave front that is flat over dimensions greater than the aperture of the "small" receiver. This combination allows for sensitive detection of weak and unanticipated arrivals. The experimental configuration and transducer characterizations are described in Sec. I. In Sec. II a procedure for modeling of the bounded pulse produced in the tests is described. The angle of incidence dependence of the wave fields transmitted through isotropic silica and acrylic glass plates is compared to the wave field modeling in Sec. III, some diffraction effects are noted even for this experimental configuration. The contribution concludes with some directions for future work in Sec. IV.

II. EXPERIMENTAL APPARATUS

A. Experimental configuration

A familiar experimental configuration for measuring the transmissivity of plates is employed.[7] The experiments are conducted in a tank filled with de-ionized water (Fig. 1) to avoid deposition of calcium deposits from normal tap water in our region. The large (102×76 mm^2) transmitting source and the small (1.9×1.9 mm^2) receiver are coaxially mounted 17 cm apart with the alignment confirmed using a laser mounted in the same position as the receiver both before and after measurements were made. The sample plate is mounted vertically (Fig. 2) on a horizontal rotating goniometer table between the transmitter and the receiver. During measurements the plate is manually rotated to successive angles of incidence θ; the plate can be rotated to both negative and positive θ with a precision better than 0.1°. The large dimensions of the transmitter typically limit the range of incidence angles to ±50° and the wave field is sampled at increments of 1° with 101 records obtained in a given transmission test.

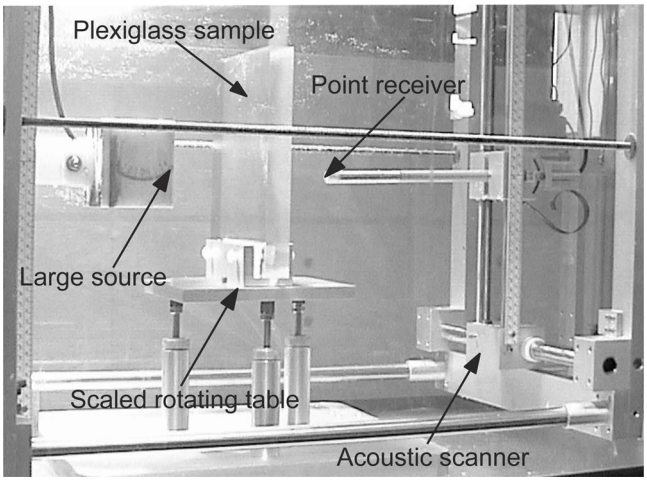

FIG. 1. Photograph of measurement system.

During the transmission goniometry measurements, the transmitter and receiver are aligned and then left stationary. Both, however, are mounted with a manual scanner that has the capacity to sample the wave field in three dimensions to a precision of better than 0.5 mm over 15 cm in the x-y plane and 2 mm over 35 cm along the z axis. Wave field scanning was also used in characterization of the transducers and to provide the initial input for modeling as is described shortly.

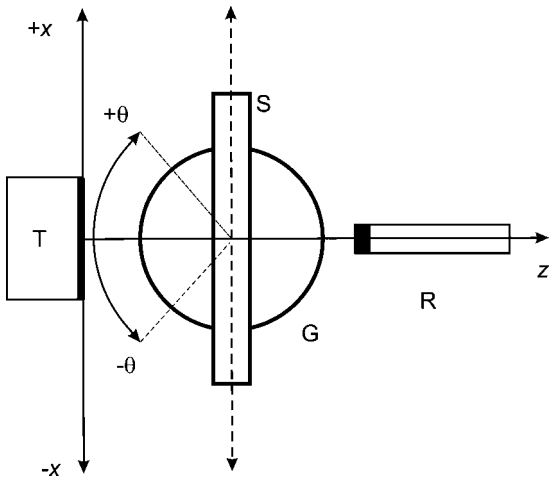

FIG. 2. Simplified diagram of the experimental configuration as seen from above. Coordinate system x-z has origin at the center of the face of the large transmitter T. Receiver R mounted on alignment rod and sample plate S mounted on goniometer table G are both centered on z axis. The angle of incidence θ is equivalent to the angle that the sample face normal makes with respect to the z axis; measurements are made at both negative and positive θ.

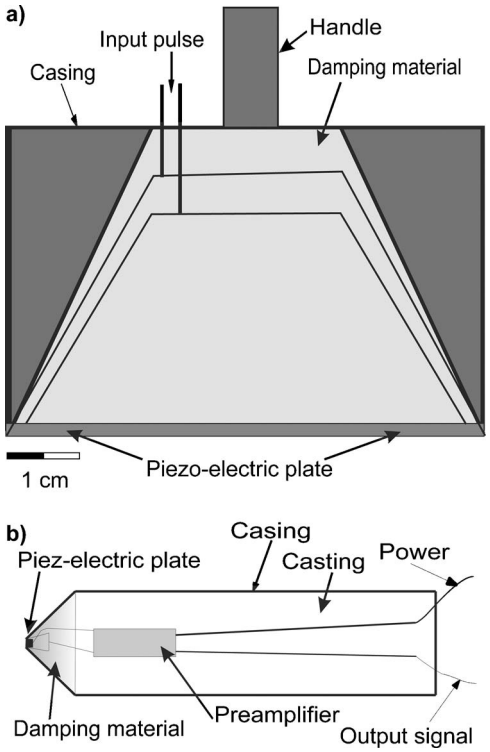

FIG. 3. Cut-away views of the (a) large transmitter and (b) small receiver.

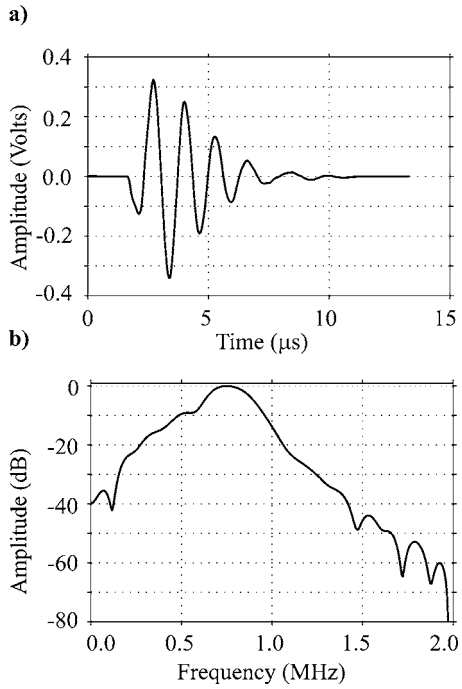

FIG. 4. Typical waveform recorded 2 cm along the axis of the large transducer in the (a) time domain and (b) normalized amplitude spectrum.

The transmitter and receiver were specially constructed for this study. The transmitter [Fig. 3(a)] consists of a 2.54-mm-thick rectangular sheet (102×76 mm^2) of piezo-electric ceramic (PZT-840, American Piezo Ceramics Inc., Mackayville, PA) that has a 780-kHz free resonant frequency in the longitudinal thickness mode. The back face of the ceramic is bonded to a copper sheet and backed by a thick shaped block of a urethane-tungsten mixture that mechanically damps the oscillations producing a broadband signal. The front face of the ceramic is covered with a thin layer of conductive epoxy which is in turn isolated from the surrounding water by a thin layer of electronic lacquer (G C Electronics polystyrene Q dope). For protection and further isolation from the water, this assembly is packed into a plastic housing.

In contrast, the receiver [Fig. 3(b)] is constructed from a small (1.9×1.9 mm^2) and thin (2.01 mm) piezo-electric piece (PZT-850, American Piezo Ceramics, Mackayville, PA) prepared in a manner similar to the transmitter. These dimensions are of the order of the ultrasonic wavelengths in water and as such allow this transducer to be considered as a small receiver. The transmitted wave field, particularly near its center, is uniform over distances much larger than the width of the receiver. Consequently, no additional corrections are necessary to account for spatial variations in the wave field intensity. The area of the receiver (~3.6 mm^2) is only 0.046% that of the transmitter (7752 mm^2). The received signal is increased two to four times by a preamplifier mounted near the ceramic in order to reduce noise. Tests on the receiver have shown that it is highly directional and senses mainly wave arrivals with wave fronts parallel to the surface of the transducer; this minimizes the effect of nondirected scattered energy. The use of this small transducer is effective because of the large energy provided by the transmitter as demonstrated later.

The experiments here are conducted in a pulsed mode and as such the wave field produced by the transmitter is considered to be a bounded pulse being limited both spatially and temporally. The pulse is created by a 200-V, 5-ns rise time square step with energies between 12.5 to 100 μJ (Panametrics Pulse Model 5800) supplied to the transmitter. The receiver senses the pressure and its preamplified signal is digitally obtained (Tektronix TDS 420A) at a 40-ns sampling period after stacking 300 individual pulses. The digital records are immediately stored to a computer for later analysis. The received waveform pulse in the water has a duration of approximately 8 μs [Fig. 4(a)] and significant bandwidth from 200 kHz to 1.2 MHz [Fig. 4(b)].

B. Samples

Three isotropic blocks composed of soda-lime silicate and acrylic (polymethyl methacrylate) glasses were used as test pieces. The low attenuation of silicate glass allows it to be considered as a nearly elastic medium and the quality factors of pure silica glasses are high[29] ($Q\sim10^6$) in the frequencies used here and as such it is difficult even to obtain reliable values for them; it is assumed in this study that the glass is representative of an elastic medium. In contrast, the visco-elastic properties of acrylic glass are well studied with representative quality factors[30] Q of ~50 and ~10 for the longitudinal and shear waves, respectively. The faces of all the samples were of the same dimensions of 22×22 cm^2 but of variable thicknesses (Table I). The two acrylic glass samples were taken from sheets of differing thicknesses and consequently were not from the same batch as made apparent

TABLE I. Sample characteristics.

Sample	Soda-lime glass	Thick acrylic	Thin acrylic
Thickness (cm)	1.9	3.64	2.46
Density (g/cm^3)	2492	1153±35	1153±35
V_P (m/s)	5900	2765±80	2675±30
V_S (m/s)	3400	1390±10	1390±10
α_P (Np/m)	~0	9.4±0.9	9.4±0.9
α_S (Np/m)	~0	26.5±2.7	26.5±2.7
V_l (m/s)	1500±10	1510±10	1490±10
θ_c^P (°)	14.7	33.1	33.9
θ_c^S (°)	26.2	N/A	N/A

by the differences in the longitudinal V_P and shear V_S wave speeds. The greater thickness of the larger plate did not allow for as great a range of angles of incidence to be sampled. The wave speed values given in Table I were measured using *P*- and *S*-wave transducers in direct contact with the plates in a through transmission experiment.

III. WAVE FIELD CHARACTERIZATION AND MODELING

Proper interpretation of any experimental results requires that the wave field and any diffraction limitations be well understood. In particular, it is important to know how flat the bounded acoustic pulse will be and the distances to which the bounded acoustic pulse retains a planar character. This was accomplished by both scanning and modeling the propagating bounded acoustic pulse.

Below, some of the quantitative amplitude information is given in the form of the peak value of the magnitude of the analytic signal as determined using a Hilbert transform. The evaluation of the amplitude envelope of the signal is obtained via the analytical signal given by

$$f_c(t) = s(t) + iH^t\{s(t)\}, \tag{1}$$

where $s(t)$ is a real signal and H^t denotes the Hilbert transform. The amplitude envelope $A(t)$ is simply the magnitude of the analytic signal

$$A(t) = \sqrt{f_c(t) f_c^*(t)}, \tag{2}$$

where * denotes the complex conjugate.

A. Observations of the free bounded acoustic pulse propagation

Here we take a free bounded acoustic pulse to be one that is freely propagating through the water only. The response of the receiver to the free bounded pulse is first sampled along x and y lines in increments of 1 and 2 mm, respectively, and at z=2 cm from the transmitter face at a digitization period of 40 ns. This recorded wave field is reconstructed by plotting the recorded waveforms, normalized with respect to the direct arrival recorded with the sample removed, with only the shorter vertical dimension shown [Fig. 5(a)]. The observed bounded acoustic pulse generated has a uniform arrival time and a nearly constant amplitude in a x-y large area centered around the axis of propagation.

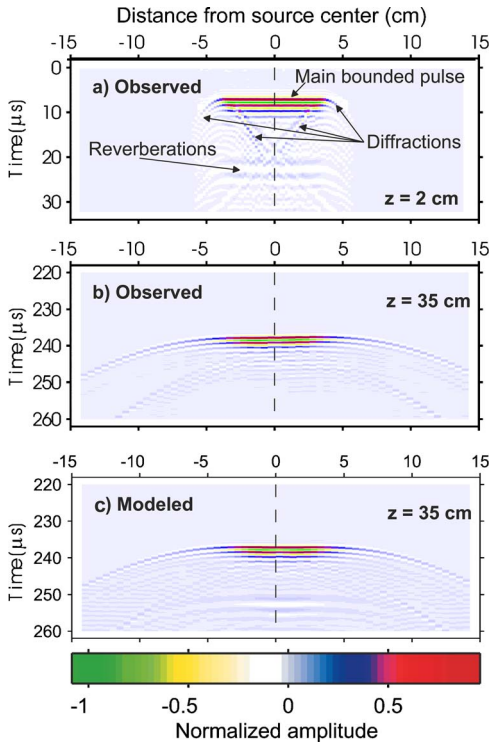

FIG. 5. (Color online) Images of diffraction behavior of the large transducer in water. Scans of the bounded pulse recorded with the receiver along the short dimension of the large transducer at distances from its surface of (a) 2 cm and (b) 35 cm. (c) Modeled scan at 35 cm calculated using the input of (a).

Although not shown, the bounded acoustic pulse is wider in the horizontal x direction than in the vertical y direction according to the lateral dimensions of the source. Also in Fig. 5(a), some lower frequency coherent noise is noticeable at times greater than 15 μs. These events have been generated by reverberations between the transmitter and the receiver. Hyperbolic diffractions from each edge of the transducer are also clearly apparent. However, at the center of the bounded acoustic pulse the diffractions and reverberations do not interfere with the planar front which has uniform amplitude and phase over a distance greater than 9 cm [Fig. 6(a)] in the x direction.

In contrast to the near field [Fig. 5(a)], the edge diffractions become increasingly important with distance. Despite appearing flat over ~7 cm width at 35 cm [Fig. 5(b)], the edge diffractions now contaminate the main front; there are no longer any sharp edges to the bounded pulse in contrast to its early character [Fig. 5(a)]. These edge effects are also quantitatively apparent when variations in amplitudes across the bounded pulse are measured [Fig. 6(b)]. The edge diffractions do not significantly influence the observed amplitude along the z axis of propagation until approximately a distance of z=28 cm [Fig. 6(c)].

B. Modeling of free bounded acoustic pulse propagation

As noted earlier, it is important that we understand the bounded acoustic pulse. One critical aspect of this is being able to predict how the pulse will change with propagation

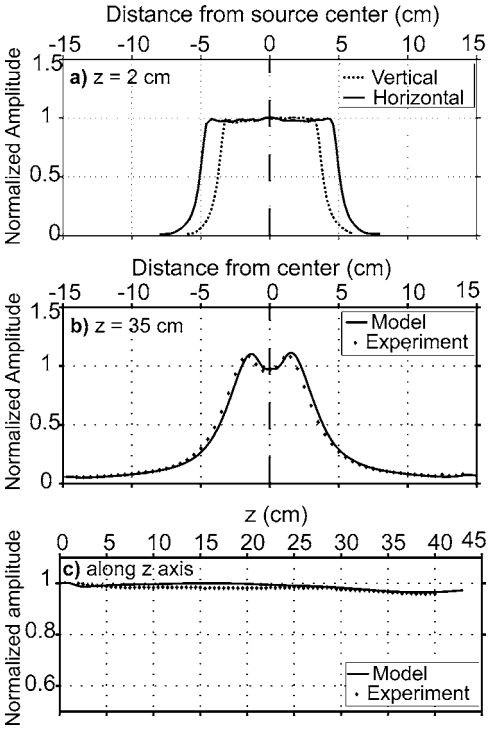

FIG. 6. Quantitative comparison of observed and model peak envelope amplitudes. (a) Peak pulse amplitudes observed 2 cm from large transducer surface along its long and short dimensions. Comparison of observed and modeled peak pulse amplitudes (b) along the long transducer dimension perpendicular to the bounded pulse propagation axis 35 cm from the surface of the large transducer, and (c) with distance from the transmitter surface along the bounded beam axis.

distance. Using as a starting point the early observed wave field of Fig. 5(a), the evolution of the wave field as it propagates through the water is modeled. This modeling will be compared to the observations at greater distances in order to assist in characterization of the bounded pulse and to develop a predictive tool for the analysis of the more complicated reflection and transmission experiments. Specifically, the wave field shape and amplitude at $z=35$ cm are calculated and compared to that observed.

A phase advance technique is employed to carry out the calculations in the two-dimensional plane (x,z). In this contribution the wave front is considered two-dimensional because the measurements are taken within the transmitter's central x-z plane at $y=0$. This allowed selection of a convenient coordinate system (Fig. 2) such that only the components of the wave number in the x-z plane are necessary in modeling. In this two-dimensional propagation, the out-of-plane components are ignored and the freely propagating wave field $\phi(x,z,t)$ is described using an integral,

$$\phi(x,z,t) = \frac{1}{4\pi^2}\int_{-\infty}^{+\infty}\int_{-\infty}^{+\infty}\Phi(k_x,0,\omega)e^{ik_x x}e^{ik_z z}e^{i\omega t}\,dk_x\,d\omega, \qquad (3)$$

where $\Phi(k_x,0,\omega)$ is the wave field recorded on the plane $z=0$ once transformed into the Fourier domain (k_x,ω). k_x and k_z are the horizontal (x) and the vertical (z) wave numbers, respectively. Essentially, this equation describes the superpositioning of monofrequency plane waves with different frequencies and propagation directions within the x-z plane that form the final bounded pulse. These wave numbers are related to each other by $k_x^2+k_z^2=\omega^2/v^2$, where v is the speed of the wave in the medium under consideration. $\Phi(x,z,t)$ is the wave field everywhere in the space (x,z) and at any time t. Note that $\Phi(x,z,t)$ can be any component (i.e., pressure, particle displacement, etc.) describing the wave as it propagates. This is simply the phase shift method of forward modeling often used in seismic migration corrections.[31] The implementation of this procedure is briefly described below.

Using Eq. (3), the wave field recorded 2 cm above the source is propagated to a distance of 35 cm. This is accomplished by first taking the double Fourier transform of the wave field recorded at $z=2$ cm in time and x, phase shifting this result in the frequency domain by multiplication with $e^{ik_z z}$ where $z=0.33$ m, and finally taking the double inverse Fourier transform to obtain the wave field at $z=35$ cm. To speed up the process the fast Fourier transform algorithm can be used. Depending on memory availability the process can be done in one step or in steps in the z direction that sum up to the desired distance (here 33 cm).

The wave fields observed and modeled at a distance of 35 cm are compared in Fig. 5. We notice that these are in excellent agreement despite the reverberations present in the model. This distance of 35 cm is greater than the source-receiver distance of 17 cm used in the transmission experiments. We notice that the "reverberation events" are present in the model above 250 μs but not in the observed data. This further supports the contention that these result from the proximity of the source and receiver (2 cm) when the input wave field data are acquired.

The maximum value of the amplitude envelope of both the observed and the modeled wave fields at distances of 2 and 35 cm are compared Fig. 6. At 2 cm both the vertical and horizontal wave fields show a large area around the axis of propagation where the amplitude is nearly constant. However, the horizontal bounded acoustic pulse is wider than the vertical one. At 35 cm the model and the observed amplitudes are in agreement despite a misalignment of about 2 mm; this is due to the precision of the scanner positioning system at the 35-cm distance. The edges of the bounded acoustic pulse increase in amplitude and migrate inwards towards the center as predicted by the theoretical model. This is evident in the amplitude envelope of the cross section of the acoustic bounded acoustic pulse as it propagates in the fluid as shown in the composite image of Fig. 7. The wave field as predicted by the model given by Eq. (1) spreads energy both outwards and inwards by diffraction as it propagates. The amplitude at the center of the acoustic bounded acoustic pulse as a function of propagation distance is given in Fig. 6(c) with the model superimposed. We see that they are in very good agreement. This confirms that the forward modeling of the bounded acoustic pulse using Eq. (1) adequately and effectively describes the wave field at any point in front of the acoustic source and places further confidence in the theoretical model.

Equation (3) still holds for an acoustic bounded wave field transmitted through a solid material plate immersed in a fluid and recorded by a point receiver on the opposite side of

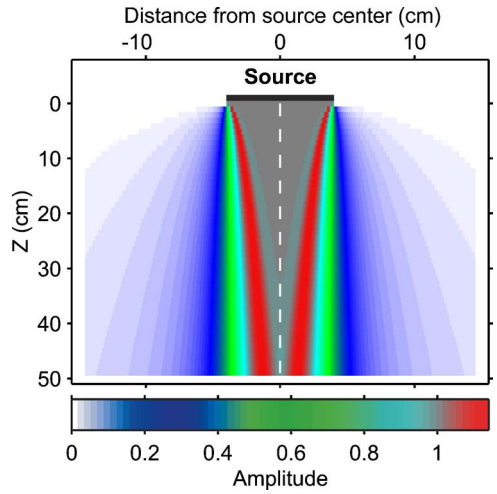

FIG. 7. (Color online) Modeled bounded pulse energy along the propagation path as represented by the maximum of the Hilbert amplitude envelope.

the source provided that the appropriate transmission coefficients were used. Indeed Eq. (3) can be modified for such experiment with thick plates as follows:

$$\phi(x,z,t) = \frac{1}{4\pi^2}\int_{-\infty}^{+\infty}\int_{-\infty}^{+\infty} T_1 T_2 \Phi(k_x,0,\omega) e^{ik_x x} e^{ik_z z} e^{i\omega t}\, dk_x\, d\omega, \tag{4}$$

where T_1 and T_2 are the transmission coefficients at interfaces 1 and 2, respectively. For the sake of completeness, for the reflected wave field the equation can be written as

$$\phi(x,z,t) = \frac{1}{4\pi^2}\int_{-\infty}^{+\infty}\int_{-\infty}^{+\infty} R_1 \Phi(k_x,0,\omega) e^{ik_x x} e^{ik_z z} e^{i\omega t}\, dk_x\, d\omega, \tag{5}$$

where R_1 is the reflection coefficient at the first interface. It needs to be noted here that both Eqs. (4) and (5) apply to a thick plate in the sense that we are describing only the primary reflections and ignoring later events that are well separated in time. We leave studies of reflected pulses for later contributions due to the added difficulties encountered at critical angles.[32,33] It is important to note that the transmission and reflection coefficients in Eqs. (4) and (5) should be properly calculated to include the material properties particularly the *P*-wave and shear-wave attenuations.

Equations (3)–(5) describe precisely the propagation, the transmission, and the reflection of a bounded acoustic pulse. These are tools in modeling such experiments with various materials provided that the reflection and transmission coefficients are properly calculated for the materials under consideration. The reflection and transmission coefficients for elastic isotropic materials can be found in many text books. It is most useful to write these coefficients in terms of the wave numbers that implicitly contain the angle of incidence.

C. Pattern of transmission mode arrival times

The results below are presented as composite images of the amplitudes of adjacent time traces versus the angle of incidence here referred to as a θ-t plot; as this is not a conventional format some discussion of what is to be expected is

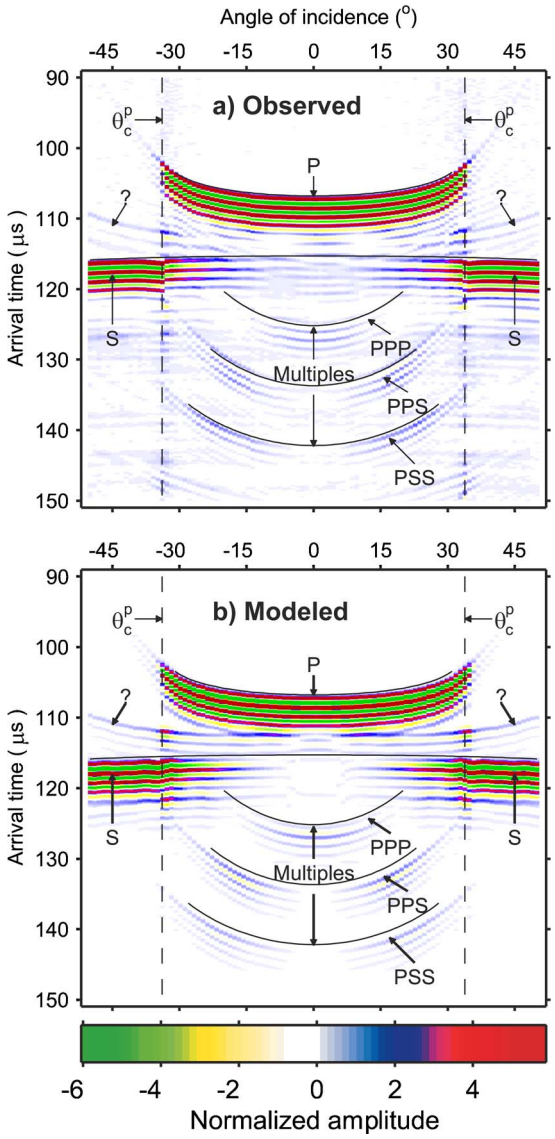

FIG. 8. (Color online) Observed (a) and modeled (b) θ-t composite images for the thin (2.46 cm) acrylic glass. Each trace is normalized to its rms value and amplitudes greater than $\frac{1}{3}$ of the maximum amplitude are clipped in order for small amplitudes to display properly.

useful. The propagation of the bounded pulse from the transmitter to the receiver through the fluid-loaded plate is influenced by both refraction and mode conversion. Despite the fact that the transducers are held fixed, the pulse's transit time necessarily changes with angle of incidence due to variations in the length of the path through the fluid and solid plate. Along the plate axis and in the near field such that the side diffractions do not interfere, the transit time can readily be determined using Snell's law ray tracing. When viewed as a function of the angle of incidence, the travel time loci (Fig. 8) curve upwards or downwards depending on whether the wave speed in the plate is respectively greater or less than that of the surrounding fluid (speed V_1). For example, in a material with $V_P > V_l > V_S$ the longitudinal wave arrivals will be concave upwards while the converted shear wave arrival is concave downwards. When the wave speed in the solid equals that of the surrounding liquid, the arrival time curve is flat. In later figures, the calculated travel time loci are super-

imposed on the θ-t images. The designations **P** and **S** indicate the directly arriving longitudinal and converted shear wave modes, although it must be kept in mind that all of these arrivals are sensed by the receiver in the water as a longitudinal mode. Primary multiple reverberations are indicated by three letters, for example **PPS** represents those arrivals with two passes of the longitudinal wave and one with a converted shear wave through the plate.

IV. TRANSMISSION RESULTS

A. Thin acrylic glass plate

A number of classic plane-wave features are seen in the θ-t image (Fig. 8) for the thin acrylic glass plate. The most notable and strongest are the direct longitudinal (P) and converted shear (S) wave arrivals. The faster longitudinal arrival curves upwards with angle of incidence due to the longer path through the faster material. $V_S < V_l$ and this slower speed of the converted shear wave is manifest as a weakly concave downward curve. As $V_S < V_l < V_P$ only the longitudinal critical angle θ_c^P exists as apparent by the loss of the strong longitudinal arrival at ±33.9° after which the strength of the S arrival is dominant. As anticipated, the converted shear arrival is weak at normal incidence (θ=0) and is not observable near this angle in the later multiple reverberations **PSS** and **PPS**. Phase shifts near θ_c^P appear to give the **S** locus an apparent discontinuity.

Diffraction effects of the finite transmitter still add complications. First, the locus of the direct **P** arrivals extends to angles greater than θ_c^P although this post critical energy is weak. Second, another weak arrival denoted by "**?**" appears between those for **P** and **S** and may exist at all angles of incidence although it is lost in the strong **P** arrival near normal incidence. This latter arrival complicated our preliminary interpretations of θ-t images acquired in more complex materials than discussed here; it will shortly be demonstrated that it is a transducer diffraction effect. The modeled transmitted wave field [Fig. 8(a)] is close to the observed wave field [Fig. 8(b)].

B. Thick acrylic glass plate

The θ-t images for both acrylic plates essentially display the same information including the "**?**" arrival but with some differences. The most obvious are the P and S mode travel times that are respectively advanced and delayed for the thick plate (Fig. 9). The P mode arrives earlier because of its higher speed in the acrylic relative to the water. In contrast the S mode is retarded because the shear wave speed is lower than that in the water (Table I). The pulse propagates through more acrylic material in the thicker plate and consequently is more attenuated. This is evident in the lengthening of the observed pulse waveform and weakening of the amplitudes relative to the thin plate. Here again the modeled transmitted wave field [Fig. 9(a)] is close to the observed wave field [Fig. 9(b)] and it is important to note that attenuation needed to be considered in the modeling.

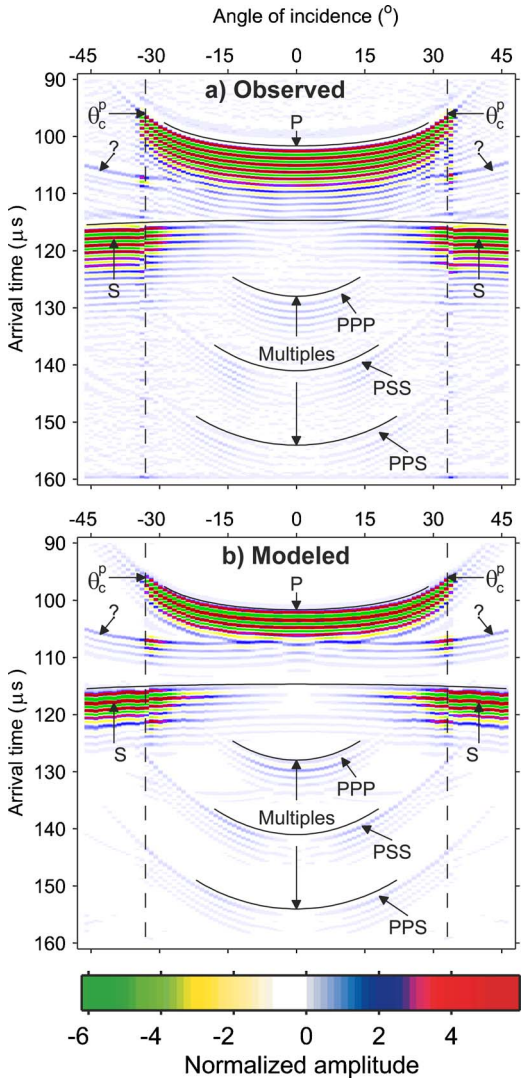

FIG. 9. (Color online) Observed (a) and modeled (b) θ-t composite images for the thick (3.64 cm) acrylic glass. Each trace is normalized to its rms value and amplitudes greater than $\frac{1}{3}$ of the true amplitudes are clipped in order for small amplitudes to display properly.

C. Thin soda-lime glass plate

The elastic properties of the soda-lime glass plate are essentially elastic and hence simpler to model than those for the acrylic. This same material simplicity together with the larger wave speeds (Table I), however, makes for a more complex θ-t image (Fig 10). In this case $V_P > V_S > V_l$ and two critical angles exist (Table I), both of which are apparent. Due to the high velocities, the P, the S, and the later multiple reverberations overlap and are difficult to separate; the loci shown in Fig. 10 are calculated using the known wave speeds. The amplitudes of the S post θ_c^P are substantially smaller in a relative sense than those for the acrylics due to the greater loss of energy on reflection from the first surface of the glass due to its higher elastic impedance relative to the surrounding water. One of the arrivals is labeled by "**??**" that cannot be explained by simple direct or multiply reflected longitudinal or shear waves within the plate is also highlighted. However, in this case it is a diffracted shear wave. At post-shear-critical angle of incidence this wave ap-

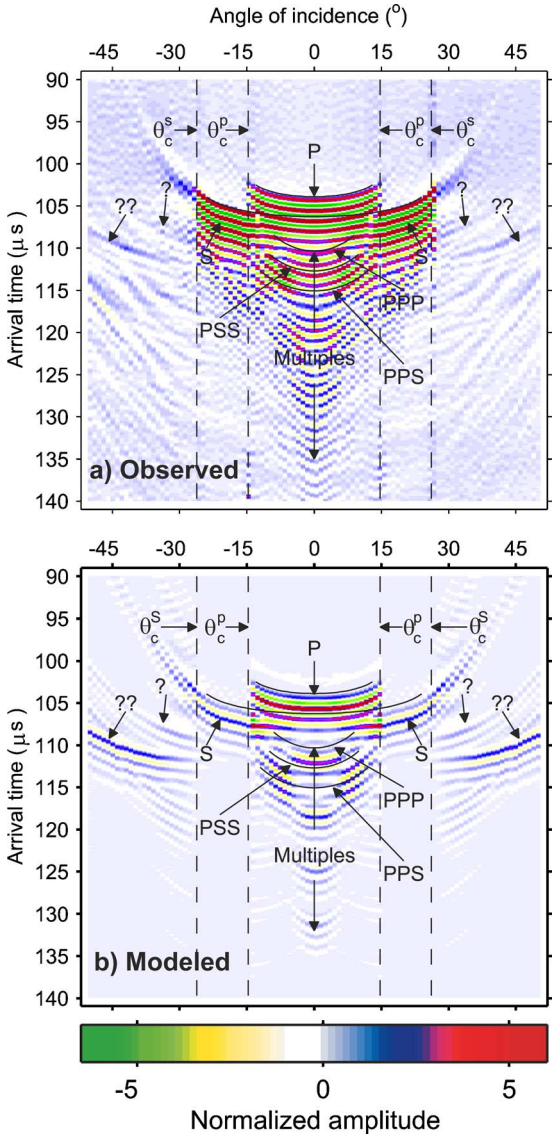

FIG. 10. (Color online) Observed (a) and modeled (b) θ-t composite images for the soda-lime (1.9 cm) glass plate. Each trace at angles less than the S critical angle is normalized with respect to its rms value and traces at angles greater than the S critical angle to three times their rms values.

pears in same manner of that seen in the acrylic samples as a P wave. The P wave at P-post-critical angle labeled "**?**" of incidence is diluted within the S wave first arrival and consequently cannot be clearly identified and shows better in the model. Other similar types of arrivals are seen at later times in this low attenuation material and are multiple reflections of this diffracted mode.

V. DISCUSSION

In this section, the modeling of the bounded pulse in the plate transmission experiments is developed and used to compare with the observed wave fields. The modeling technique used is able to explain without ambiguity the "**?**" arrivals.

A. Modeling of bounded pulse transmission

Modeling of the plate transmission is accomplished in the same manner as described earlier for the free propagation of the bounded pulse but with the added complications of refraction and attenuation via Eq. (4). All the transmitted wave modes detected by the small receiver including all types of multiples can be modeled via the phase shift $e^{ik_z z}$ and by appropriately calculating the transmission and reflection coefficients at each boundary and including the P and S wave attenuations of the material when applicable. The **PPS** multiple, for example, can be modeled by first taking the Fourier transform of the wave field generated by the source (at the angle of incidence under consideration) both in time and space (x direction). Let k_p and k_s denote the wave numbers of the P and S waves in the solid, respectively, and let k denote the wave number in the fluid. It is important here to note that the x component of any wave mode is equal to the projection of the wave number in the fluid on the x axis (Snell's law). Then the following steps are to be performed to obtain the wave field at the small receiver.

(1) Propagation in the fluid to the first interface via $e^{ik_z z}$ where $k_z=(k^2-k_x^2)^{1/2}$.
(2) Multiplication by the transmission coefficient (incident P) between the fluid and the solid to obtain the P wave transmitted into the solid.
(3) P-wave propagation in the solid to the second interface via $e^{ik_z z}$ where $k_z=(k_p^2-k_x^2)^{1/2}$.
(4) Multiplication by the reflection coefficient (incident P) between the solid and the fluid to obtain the reflected P wave from the second interface.
(5) P-wave propagation in the solid to the first interface via $e^{ik_z z}$ where $k_z=(k_p^2-k_x^2)^{1/2}$.
(6) Multiplication by the reflection coefficient (incident P) between the solid and the fluid to obtain the reflected S wave from the solid-fluid interface.
(7) S-wave propagation in the solid to the second interface via $e^{ik_z z}$ where $k_z=(k_s^2-k_x^2)^{1/2}$.
(8) Multiplication by the transmission coefficient (incident S) between the solid and the fluid to obtain the transmitted P wave into the fluid.
(9) P-wave propagation in the fluid to the receiver via $e^{ik_z z}$ where $k_z=(k^2-k_x^2)^{1/2}$.

These steps are performed for each wave mode. The wave field at the receiver is then recorded as the modeled trace and the procedure is repeated for each angle of incidence. Temporal snapshots of the wave field at a series of times during the propagation of the pulse 20° incident to the thin elastic plate highlight the precritical behavior (Fig. 11) and illustrate the modeling. Only the **P** and **S** transmitted arrivals are considered in the modeling of Fig. 11; multiples have not been included. The first panel [Fig. 11(a)] shows the bounded pulse immediately prior to contact with the plate. At a time 42 μs later half the pulse front has intersected the first surface of the plate and the P and S [Fig. 11(b)] and both the **P** and **S** arrivals are propagating through the plate while another 64 μs later the main direct portions of the P and S

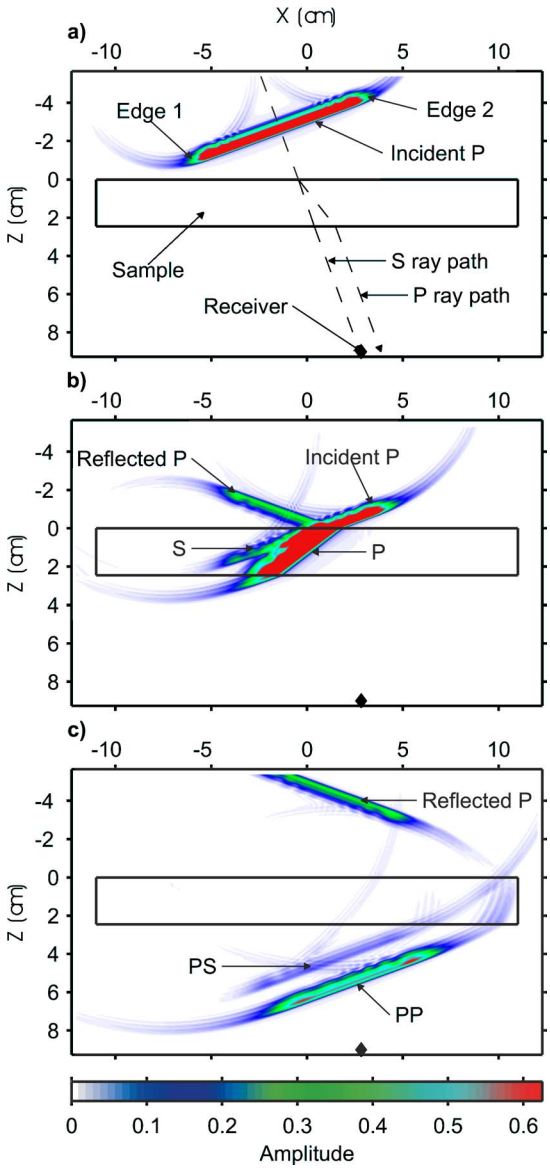

FIG. 11. (Color online) Modeled propagation of the bounded pulse precritically incident at 20° upon the thin (2.46 cm) acrylic glass plate immersed in water. Display is shown to scale and amplitudes greater than half of the maximum true amplitude are clipped in order for small amplitudes to display properly. The critical angle in this case is $\theta_p^C = 33.9°$. The origin of the center bounded acoustic pulse is not shown and is located at $z = -6.6$ cm and $x = -2.85$ cm. The direct distance between the source and the receiver is 0.17 cm. Visualizations of some of the components of the wave field at times of (a) 42 μs with bounded pulse in water incident to first surface, (b) 64 μs partway through contact of pulse with first surface (note generation of a reflected and transmitted **P** and a converted transmitted **S** arrival, and (c) at 93 μs showing nearly completed reflected and transmitted pulses.

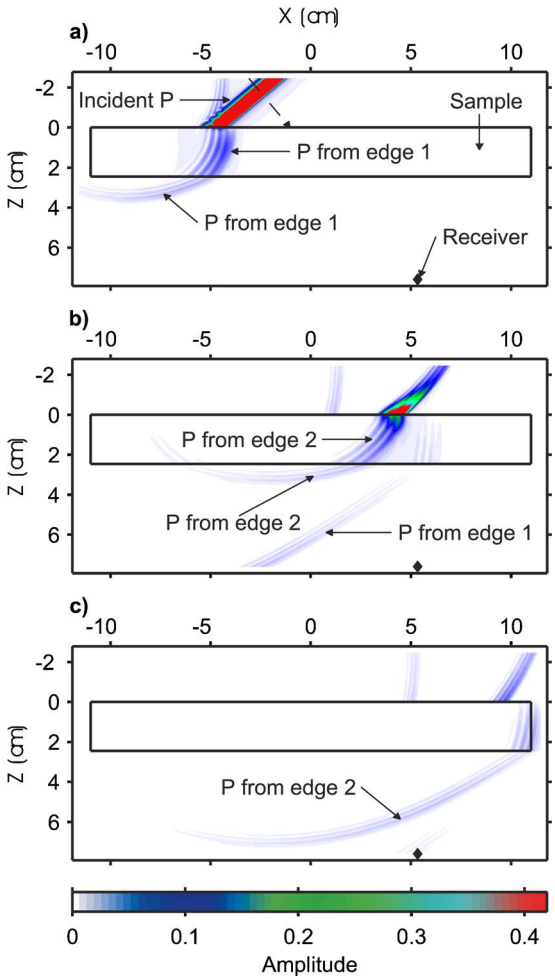

FIG. 12. (Color online) Modeled propagation of the bounded pulse postcritically incident at 40° upon the thin (2.46 cm) acrylic glass plate immersed in water that includes only the edge diffraction arrivals; the primary reflection from the first surface and any induced multiples are not included in the model. Display is shown to scale and amplitudes greater than one-third of the maximum true amplitude are clipped in order for small amplitudes to display properly. The origin of the center of the bounded pulse is located at $z = -3.7$ cm and $x = -4.14$ cm. (a) 42 μs at a time after edge 1 has contacted the first surface with the diffractions transmitted into the plate and the underlying water. (b) 80 μs at a time after the diffracted arrival from edge 2 has contacted the first surface with the diffractions transmitted into the plate and the underlying water. (c) 106 μs after both edge diffractions have propagated through the plate. See Fig. 11 for "edge 1 and edge 2 labels."

arrivals have left the sample. It is important to note that the new **P** component is shifted to greater values of x because of refraction in the plate.

This procedure is very accurate in adequately modeling all arrivals with the correct amplitude and phase including the arrival labeled "**?**" in Figs. 8–10. The modeling is repeated for a postcritical incidence of 40° (Fig. 12). In order to explain the origin of the "**?**" arrival, recall that the spatially and temporally limited bounded pulse will have a wide range of wave numbers in its Fourier domain decomposition. Past the critical angle for the dominant wave numbers some components with wave numbers smaller than the critical angle are still refracted into the solid and then to the water at the second interface. Snell's law does not explain the transit times of these arrivals. To establish its ray path it is important to consider the width of the original spatially bounded pulse and how it evolves in space as it propagates in the water. The flat part of the acoustic wave field shrinks as it propagates through the medium and its edges contain most of the wave numbers deviating from the main propagation angle. Consequently, the path of the edge diffractions must be taken into account with the point upon which the incident pulse first intersects the first surface taken as the departure point for rays refracted into the solid and then emerging into the water through the second interface. Even when this procedure is followed it is difficult to predict the behavior of the

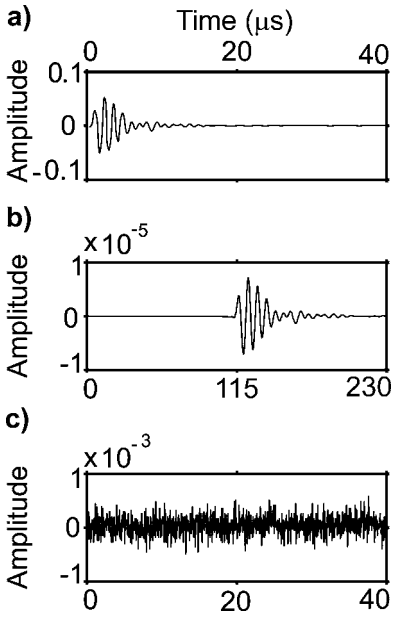

FIG. 13. (a) Observed wave field produced by the large transmitter. (b) Modeled wave field propagated to a distance of 17 cm for a small 2-mm-diam spherical source for illustration. (c) Recorded passive noise.

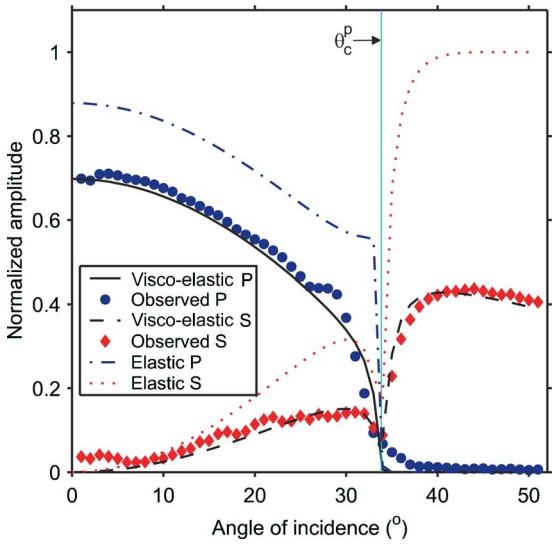

FIG. 14. (Color online) Comparison of the P and S transmitted amplitudes both observed and calculated using plane wave assumptions both with and without attenuation for the thin acrylic glass sample.

diffractions and therefore ray tracing would not lead to the exact path. The results from this modeling show the development of the edge diffractions from edges 1 and 2 in Figs. 12(a) and 12(b), respectively. It is important to note that the strongest parts of the edge 1 diffraction do not propagate to the receiver and the energy that does arrive there is considerably weakened such that it is not reliably observed in the real θ-t images (Figs. 8–10). In contrast portions of the edge 2 diffraction are much stronger at the receiver and are readily detected as the "**?**" arrival (Figs. 8–10). This modeling conclusively demonstrates that the "**?**" arrival is yet another diffraction effect that must be properly accounted for in analysis of the goniometric records.

A complete modeling of all the angles of incidence measured for the thin acrylic glass sample [Fig. 12(b)] displays all the same behavior observed in the recorded traces [Fig. 12(a)]. The travel times for the various arrivals are shown as determined from the modeling also.

B. Advantage of large transmitter

The experimental method described can detect wave modes that would otherwise be lost within the background noise if a small source transmitter is used. Here a model for the waves propagating through the thin acrylic plate (2.46 cm thick) transmitted from a transducer of 2 mm in diameter is presented. It is assumed that the source would produce as much energy per surface as the large transmitter used in these experiments. The resulting direct arrival to the same distance of 17 cm [Fig. 13(b)] is shown as a true amplitude normalized with respect to the amplitude of the free pulse at 2 mm away from the source [Fig. 13(a)]. As is expected, the peak modeled amplitude of Fig. 13(b) is much weaker (approximately four orders of magnitude) than that obtained using the large transmitter [Fig. 13(a)]. Indeed, the background noise measured during passive listening produced amplitudes significantly above those produced using a small source [Fig. 13(c)].

One additional advantage of the larger transmitter is that the wave field smearing due to diffractions are also substantially reduced. As such, critical angle phenomena are clearly apparent.

Finally, while the full modeling of the wave fields is useful here in interpreting the observations, and in particular the edge diffraction "**?**" arrivals, this full modeling is not needed in all cases to determine the effective transmissivity of a plate of material. An original motivation for use of the large transmitter was to reduce the level of complexity required to appropriately model and interpret observed waveforms by allowing use of simpler plane wave theory without the need to account for diffractions. A comparison of the observed **P** and **S** amplitudes transmitted through the thin acrylic plate with those calculated using visco-elastic plane wave theory agree well (Fig. 14). In the precritical range, the observed and calculated amplitudes differ by a small amount on average. At θ_c^P, however, some residual diffracted **P** remains that cannot exist for the pure plane wave solution. This residual observed *P* rapidly vanishes and good agreement between the observed and modeled **S** amplitudes exist. The elastic response (i.e., neglecting attenuation) curves obviously diverge from the visco-elastic ones.

VI. CONCLUSION

A new laboratory method to probe various materials with acoustic waves was developed. The method utilizes a large area source piezoelectric transmitter and a small-receiver piezoelectric receiver. The source produces an acoustic wave field bounded both spatially and temporally. The amplitude along the axis of propagation stays nearly constant to distances up to 30 cm away from the source. The large amount of energy carried by the wave field further makes the detection of subtle arrivals, even in the absence of

amplification, events that would be difficult to observe with a small source transducer. The source-receiver developed here was well characterized and can be used with great confidence in various experiments such as in transmission-reflection laboratory tests on various materials.

In the event that not all characteristics of the wave field are understood, the entire wave field may be modeled using a phase propagation procedure. The advantage of this procedure is that the evolution of independent components of the wave field may be studied. However, once details of the wave field are sufficiently known, the transmissivity of plates may be understood using less onerous calculations involving only plane wave concepts with some care exercised in the vicinity of critical angles.

The goniometer has been used in the characterization of saturated porous materials. Use of the same system in reflectivity studies will be forthcoming in a companion contribution.

ACKNOWLEDGMENTS

This work would not have been possible without the dedication of L. Tober, G. Lachat, A. Paget, and P. Zimmerman. Funding for this work was provided by NSERC and the Canada Research Chairs program. DRS thanks the Research School of Earth Science, Australian National University and in particular Professor I. Jackson for access to facilities during the completion of this manuscript.

[1]Y. E. Shigong, J. Wu, and J. Peach, "Ultrasound shear wave imaging for bone," Ultrasound Med. Biol. **26**, 833–837 (2000).
[2]S. I. Rokhlin and W. Wang, "Double through-transmission bulk wave method for ultrasonic phase velocity measurement and determination of elastic constants of composite materials," J. Acoust. Soc. Am. **91**, 3303–3312 (1992).
[3]B. Hosten, "Ultrasonic through-transmission method for measuring the complex stiffness moduli of composite materials," in *Handbook of Elastic Properties of Solids, Liquids, and Gases*, edited by M. Levy, H. E. Bass, and R. R. Stern (Academic, New York, 2001), Vol. **1**, Chap. 4, pp. 87–106.
[4]A. B. Temsamani, S. Vandenplas, and L. vanBiesen, "Experimental investigation of bounded beam reflection from plane interfaces in the vicinity of leaky wave angles," Ultrasonics **38**, 749–753 (2000).
[5]A. I. Lavrentyev and S. I. Rokhlin, "Ultrasonic study of environmental damage initiation and evolution in adhesive joints," Res. Nondestruct. Eval. **10**, 17–41 (1998).
[6]J. Wu, "Determination of velocity and attenuation of shear waves using ultrasonic spectroscopy," J. Acoust. Soc. Am. **99**, 2871–2875 (1996).
[7]T. J. Plona, "Observation of a second bulk compressional wave in a porous medium at ultrasonic frequencies," Appl. Phys. Lett. **36**, 259–261 (1980).
[8]P. N. J. Rasolofosaon, "Importance of interface hydraulic condition on the generation of the second bulk compressional wave in porous media," Appl. Phys. Lett. **52**, 780–782 (1988).
[9]B. Gurevich, O. Kelder, and D. M. J. Smeulders, "Validation of the slow compressional wave in porous media: comparison of experiments and numerical simulations," Transp. Porous Media **36**, 149–160 (1999).
[10]D. L. Johnson, T. J. Plona, and H. Kojima, "Probing porous media with first and second sound. II. Acoustic properties of water saturated porous media," J. Appl. Phys. **76**, 115–125 (1994).
[11]O. Kelder and D. M. J. Smeulders, "Observation of the Biot slow wave in water-saturated Nivelsteiner sandstone," Geophysics **62**, 1794–1796 (1997).
[12]R. Bass, "Diffraction effects in the ultrasonic field of a piston source," J. Acoust. Soc. Am. **30**, 602 (1958).
[13]P. H. Rogers and A. L. Van Buren, "An exact expression for the Lommel diffraction correction integral," J. Acoust. Soc. Am. **55**, 724 (1974).
[14]H. L. Bertoni and T. Tamir, "Unified theory of Rayleigh-angle phenomena for acoustic beams at liquid-solid interfaces," Appl. Phys. **2**, 157–172 (1973).
[15]T. J. Plona, L. E. Pitts, and W. G. Mayer, "Ultrasonic bounded beam reflection and transmission effects at a liquid/solid-plate/liquid interface," J. Acoust. Soc. Am. **59**, 1324–1328 (1976).
[16]L. Wang, A. I. Larentyev, and S. I. Roklin, "Beam and phase effects in angle-beam-through-transmission method of ultrasonic velocity measurement," J. Acoust. Soc. Am. **113**, 1551–1559 (2003).
[17]K. W. Winkler and T. J. Plona, "Technique for measuring ultrasonic velocity and attenuation spectra in rocks under pressure," J. Geophys. Res. **87**, 776–780 (1982).
[18]M. Mah and D. R. Schmitt, Determination of the complete elastic stiffnesses from ultrasonic phase velocity measurements, J. Geophys. Res. **108**(B1), 2016 (2003).
[19]W. Xu and J. J. Kaufman, "Diffraction correction methods for insertion ultrasound attenuation estimation," IEEE Trans. Biomed. Eng. **40**, 563–570 (1993).
[20]O. I. Lobkis, A. Safaeinili, and D. E. Chimenti, "Precision ultrasonic reflection studies in fluid-coupled plates," J. Acoust. Soc. Am. **99**, 2727–2736 (1996).
[21]O. I. Lobkis and D. E. Chimenti, "Three-dimensional transducer voltage in anisotropic materials characterization," J. Acoust. Soc. Am. **106**, 36–45 (1999).
[22]P. He and J. Zheng, "Acoustic dispersion and attenuation measurement using both transmitted and reflected pulses," Ultrasonics **39**, 27–32 (2001).
[23]M. Arakawa, J. Kushibiki, and N. Aoki, "An evaluation of effective radiuses of bulk-wave ultrasonic transducers as circular piston sources for accurate velocity measurements," IEEE Trans. Ultrason. Ferroelectr. Freq. Control **51**, 496–501 (2004).
[24]B. Hosten and M. Castings, "Transfer-matrix of multilayered absorbing and anisotropic media—Measurements and simulations of ultrasonic wave-propagation through composite-materials," J. Acoust. Soc. Am. **94**(Part 1), 1488–1495 (1993).
[25]D. Fei, D. E. Chimenti, and S. V. Teles, "Material property estimation in thin plates using focused, synthetic-aperture acoustic beams," J. Acoust. Soc. Am. **113**, 2599–2610 (2003).
[26]O. I. Lobkis and D. E. Chimenti, "Equivalence of Gaussian and piston ultrasonic transducer voltages," J. Acoust. Soc. Am. **114**, 3155–3166 (2003).
[27]P. Cawley and B. Hosten, "The use of large ultrasonic transducers to improve transmission coefficient measurements on visco-elastic anisotropic plates," J. Acoust. Soc. Am. **101**, 1373–1379 (1997).
[28]M. Castaings, B. Hosten, and T. Kundu, "Inversion of ultrasonic, plane-wave transmission data in composite plates to infer visco-elastic material properties," NDT & E Int. **33**, 377–392 (2000).
[29]W. J. Startin, M. A. Beilby, and P. R. Saulson, "Mechanical quality factors of fused silica resonators," Rev. Sci. Instrum. **69**, 3681–3689 (1998).
[30]E. Juliac, J. Arman, and D. Harran, "Ultrasonic interferences in polymer plates," J. Acoust. Soc. Am. **104**, 1232–1241 (Part 1) (1998).
[31]J. Gazdag, "Wave equation migration with the phase shift method," Geophysics **43**, 1342–1351 (1997).
[32]A. Schoch, "Schallrelexion, schallbrechung und schallbeugung," Ergeb. Exakten Naturwiss. **23**, 127–234 (1950).
[33]L. C. Brekhovskikh, "Waves in layered media," in *Applied Mathematics and Mechanics*, edited by R. T. Beyer (Academic, New York, 1960), pp. 100–122.

Inverse potential scattering in duct acoustics

Barbara J. Forbes[a)]
Phonologica Ltd., P.O. Box 43925, London NW2 1DJ, United Kingdom

E. Roy Pike
Department of Physics, King's College London, Strand, London, WC2R 2LS, United Kingdom

David B. Sharp
Department of Environmental and Mechanical Engineering, The Open University, Walton Hall, Milton Keynes, MK7 6AA, United Kingdom

Tuncay Aktosun
Department of Mathematics and Statistics, Mississippi State University, Mississippi State, Mississippi 3976

(Received 14 June 2005; accepted 24 October 2005)

The inverse problem of the noninvasive measurement of the shape of an acoustical duct in which one-dimensional wave propagation can be assumed is examined within the theoretical framework of the governing Klein–Gordon equation. Previous deterministic methods developed over the last 40 years have all required direct measurement of the reflectance or input impedance but now, by application of the methods of inverse quantum scattering to the acoustical system, it is shown that the reflectance can be algorithmically derived from the radiated wave. The potential and area functions of the duct can subsequently be reconstructed. The results are discussed with particular reference to acoustic pulse reflectometry. © *2006 Acoustical Society of America.* [DOI: 10.1121/1.2139618]

PACS number(s): 43.20.Mv, 43.20.Ye, 43.58.Gn, 43.60.Pt [SFW] Pages: 65–73

I. INTRODUCTION

The noninvasive measurement of the internal geometry of an acoustical duct is a problem that has long interested researchers in all of mechanical engineering, medical diagnostics, musical acoustics, and speech analysis (see Refs. 1 and 2 for a review). Although it has been established for some 40 years that the transfer function of such a duct does not uniquely determine its area function,[2] even in the lossless case, it is also well known that the area function is completely specified by the input impedance or, equivalently, the reflectance.[3–8] In recent years, accurate and fast duct reconstructions have been obtained by the acoustic pulse reflectometry (APR) method[9–16] which, since the experimental apparatus is relatively portable, has also proved ideally suited to field measurements. Despite this efficiacy, the APR methodology demands that the temporal reflectance be measured directly, and so the experimental protocol requires up to 12 m of extraneous control tubing for the elimination of secondary reflections from the source boundary. Further, all measurements must be taken in the same place and so the method cannot be used to probe the shape of the vocal tract during normal phonation at the glottis. Indeed, due to the nonuniqueness, it is known that the vocal-tract area function cannot be deterministically reconstructed from the radiated speech wave alone, although statistical methods have been attempted.[17–21] Nevertheless, recent results from the mathematical literature report existence proofs for the temporal inversion of the Webster equation from radiated data and known initial conditions.[22–24]

In this paper, a novel and computationally efficient, frequency-domain method for the deterministic acoustical duct inversion is presented, which makes no demands on the direct measurement of either reflectance or impedance. Rather, the reflectance is mathematically derived from the wave radiated in response to a high-impedance source. Since the algorithms naturally incorporate any number of reflections between the source and radiating end, which may be any distance apart, the results are of relevance both in acoustic pulse reflectometry and to the speech inverse problem in particular.

Section II reviews standard inversion methods that reconstruct the area function of an acoustical duct from measurements of the reflected wave. Section III presents an alternative methodology that allows the wave-mechanical reflectance to be derived from the resonance spectrum of the radiated wave, yielding the "potential" function of the duct. The relationship between the potential and area functions is discussed. Section IV validates the proposed inversion methodology through numerical simulations at varying bandwidth. Section V discusses further issues that become relevant in experimental contexts.

II. BACKGROUND

Figure 1 gives a schematic diagram of an acoustic pulse reflectometer,[1,10] typically used for the noninvasive measurement of narrow bore acoustical ducts. An electrical pulse

[a)]Also at: Department of Physics, King's College London, Strand, London, WC2R 2LS, UK; electronic mail: forbes@phonologica.com

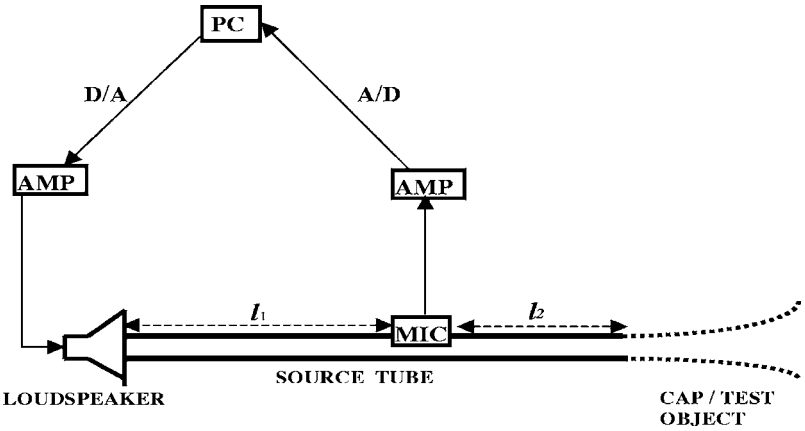

FIG. 1. A schematic diagram of the acoustic pulse reflectometer.

produced by D/A conversion of a digital array is amplified and the resultant pressure wave travels along a length of control tubing, the "source" tube. Reflections from the test object are recorded at the microphone, before A/D conversion and analysis. In the determination of the unknown input impulse response or filter function, $z(t)$, two consecutive measurements are necessary: a calibration measurement of the input pulse, the source function $x(t)$, obtained by sampling the signal reflected back from the rigid termination of the source tube capped with a removable end piece; and one of the reflections, $y(t)$, obtained when the cap is replaced by the test object. The control length l_1 gives the approximation of a source at infinity, allowing $y(t)$ to be cleanly sampled without interference from higher-order reflections at the boundary.[11] If reflections are to be measured for a time $T=50$ ms, for example, l_1 must be set to around 8.5 m. The length l_2, typically[13] set to 4 m, ensures that the incident pulse has completely passed the microphone before recording of the reflections begins.

The system is described by a Fredholm equation of the first kind, namely

$$y(t) = \int_0^t x(t-\tau)z(\tau)d\tau, \quad 0 \leqslant t \leqslant T, \tag{1}$$

from which $z(t)$ must be obtained by a deconvolution procedure before being submitted to a bore reconstruction algorithm.[1,25] It is known[6,26] that this deconvolution is ill posed in the context of finite experimental bandwidths, and previous work by the authors[1] has discussed both theoretical and experimental regularization procedures. However, it was shown by us that propagation losses[27] (−2dB/m at 1 kHz) within the long lengths of control tubing can reduce the effective range of the loudspeaker from the nominal limit of 18 kHz to around just 6 kHz. Since the axial resolution, Δ, in the bore reconstruction is defined by the effective signal bandwidth, f_{eff}, as

$$\Delta = \frac{c}{4f_{\text{eff}}}, \tag{2}$$

for c the speed of sound in free space, neglecting dissipation (taken to be 344 m s^{-1} at 20 °C), it was thus shown that the control tubing causes an increase in resolution from a nominal value of 3.9 mm (at 44.1 kHz sampling) to just 1.6 cm (around four sample points). Clearly, the APR apparatus could be substantially streamlined and the precision and accuracy of the duct reconstruction much improved if an alternative to the direct measurement of the reflections, $y(t)$, could be found.

Available bore reconstruction algorithms assume plane-wave propagation,[25,28] and previous work[1] has noted that the inverse mapping from reflectance (or impedance) to area function will only be fully regularized for algorithms that take into account higher mode solutions,[29–32] which may propagate at high bandwidth in wide and/or strongly expanding objects. To assess the relative contribution of propagation losses and experimental higher modes to the ill-posedness of the bore reconstruction problem, therefore, numerical simulations were made of a conical horn of length 7.5 cm and input and terminating radii $r_0=4.8$ mm and $r_l=3$ cm, respectively. A lead-in tube of 34.4 cm length was assumed for the control of pressure offsets[15] and an ideal closed termination ($Z_{\text{rad}} \to \infty$) was chosen to minimize the effect of the radiation impedance, elucidating multimodal phenomena due to changes in the bore.

The multimodal PAK[29,30] algorithms were implemented numerically at varying mode order, and "forward" solutions for the input impedance were obtained, yielding impulse responses, $z(t)$, that were implemented in a standard, plane-wave, inversion. Lossy forms of both the forward and inverse algorithms were adopted.[31,33] [Due to strongly evanescent higher order modes, convergence in the numerical solution of the PAK algorithms may require an extremely small cylindrical discretization, d, which should be smaller than the spatial sampling length. The reported simulations, for example, were run at $d=0.1$ mm (one-mode solution), and $d=0.02$ mm (four-mode solution), $\Delta=0.2$ mm, with numerical problems due to the inversion of singular matrices becoming evident at higher orders. For these parameters, a one-mode solution takes around 30 min to compute on a 1.8 GHz PC with 512 Mbytes RAM under MATLAB for Windows.] Results were obtained first at an idealized, high bandwidth of 400 kHz, corresponding to an axial resolution of 0.2 mm.

Figure 2(a) illustrates that, when plane-wave propagation is assumed in both the forward and inverse algorithms, the bore reconstruction agrees with the nominal bore radius to within a maximum numerical error of around 0.7% at the mouth. When the first higher mode is included in the forward

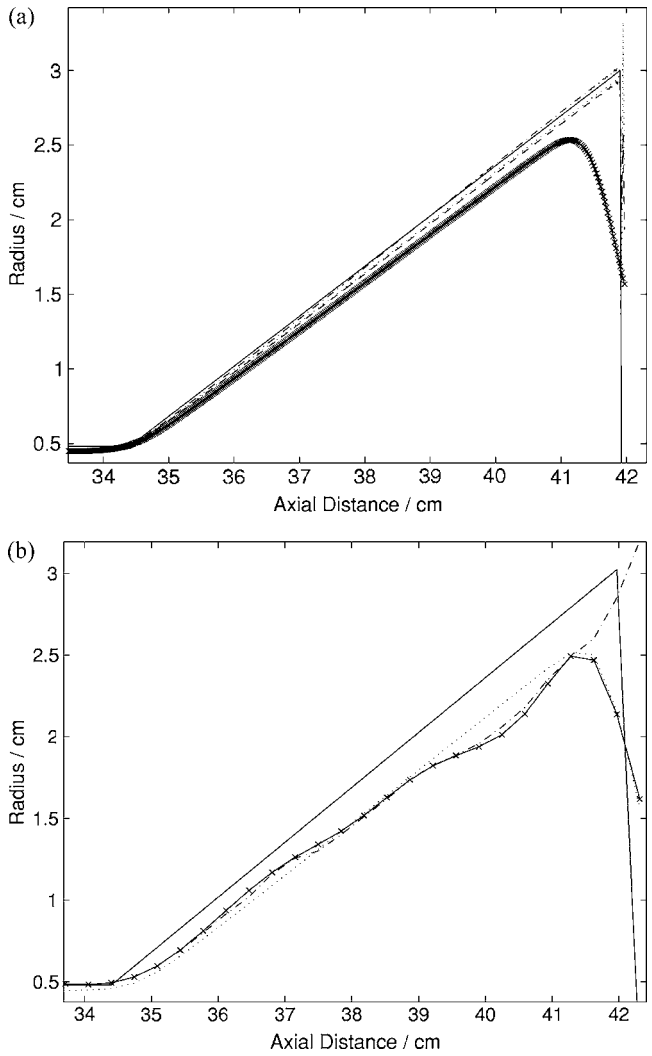

FIG. 2. (a) Conical duct inversion for multimodal impulse response: theoretical radius (—), one mode (---), two mode (···), three mode (---), one mode filtered at 6 kHz (×). (b) Conical duct inversion for multimodal impulse response: theoretical radius (—), one mode filtered at 6 kHz (···), experimental (×), experimental open-ended (---). Both reconstructions include a 34.4 cm lead-in tube.

simulation (cut-on 7 kHz), the error rises to some 1.7% due to the ill-posedness of the plane-wave reconstruction. Adding the second higher mode (cut-on 13 kHz) increases the error by around 1%, to 2.7%. However, this error remains stable with the addition of the next higher mode (cut-on 19 kHz). A far more dramatic effect is found by filtering the plane-wave solution at a half-power point of 6 kHz, below higher mode cut-on but representative of the reduced experimental bandwidth that results from propagation losses. Figure 2(a) now shows that the effective axial resolution falls to around 1.6 cm so that rapid changes in the bore profile take three to four nominal sample points to manifest, introducing an underestimation in the bore reconstruction that rises to as much as 30%.

Indeed, Fig. 2(b) shows that there is good agreement between the simulated, filtered, plane-wave solution and that found by experiment. [An experimental cone with a removable flat metal plate at the termination was machined to the dimensions of the simulations. The reconstruction for a closed end agreed with that for an open end, on removal of the plate, to better than 3%–4% within the main part of the bore.] Figure 2(b) also shows the experimental reconstruction of an open-ended cone, in which additional multimodal effects (*albeit* evanescent) can be assumed. Despite this, the closed and open-ended reconstructions are in close agreement in the main part of the cone.

These results therefore suggest that experimental errors arising from propagation losses may well outweigh those that would arise from higher mode solutions if high bandwidths could be attained. Thus, it can be concluded that methods for eliminating the need for control tubing in the APR apparatus are required.

III. REGULARIZED METHODOLOGY

Although methods for simplifying the APR apparatus have been proposed,[7,11,16] all are constrained by the requirement that the impulse response, $z(t)$, be estimated by direct measurement of the reflections, $y(t)$. It is now possible to present a method that allows $y(t)$ to be derived from noninvasive measurements of the radiated wave. Since multiple reflections are a natural part of the theoretical model, no control tubing is required in the experimental methodology so that propagation losses within the system are dramatically reduced. The concommitant increase in bandwidth substantially regularizes the deconvolution of Eq. (1) and, hence, the duct reconstruction problem.

A. Forward problem: The acoustical Klein–Gordon equation

The results of the previous section suggest that, for many applications in duct acoustics, a plane-wave approximation is effective. It can now be shown that a particularly elegant description exists within the theoretical framework of the governing Klein–Gordon equation.

It has previously been shown that the Webster equation, valid for one-dimensional compressible flow in the linear, adiabatic and nonviscous approximations, can be reduced to a Klein-Gordon equation,[34–38] namely

$$\frac{\partial^2\Psi(x,t)}{\partial t^2} = c^2\left\{\frac{\partial^2\Psi(x,t)}{\partial x^2} - U(x)\Psi(x,t)\right\}, \tag{3}$$

for a "wave function," $\Psi(x,t)$, such that for $p(x,t)$ the excess pressure and $S(x)$ the cross-sectional area of the wave front,

$$\Psi(x,t) = p(x,t)\sqrt{S(x)}. \tag{4}$$

The parameter $U(x)$ is defined as

$$U(x) = \frac{d^2\sqrt{S(x)}/dx^2}{\sqrt{S(x)}}, \tag{5}$$

and is mathematically analogous to the potential function of quantum mechanics. Where no confusion is likely to arise, such as in the present paper, it can thus be referred to as the "potential function." Otherwise, since it refers to a geometry rather than an energy, it should be referred to as the horn function.[34] A unique area function can be found from the

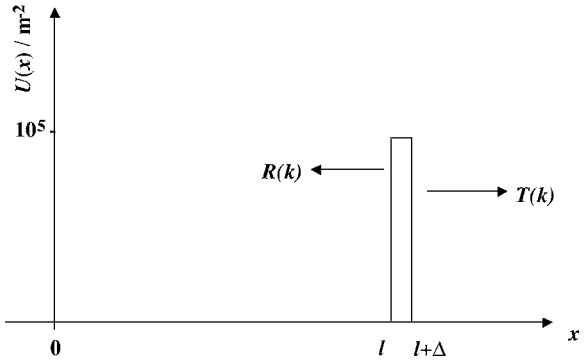

FIG. 3. Schematic potential-function profile of duct terminated in barrier equivalent to a radiation impedance, $U_0=10^5$ m^{-2}, $\Delta=1$ mm.

"potential" function by solution of the homogeneous equation

$$\frac{d^2\sqrt{S(x)}}{dx^2} - U(x)\sqrt{S(x)} = 0, \tag{6}$$

given two known initial conditions on the area.

Previous work[35,36] has considered piecewise constant potential functions, for which $U(x)=U_0$, and it has been shown that a wave-mechanical barrier of approximate height $U_0=1.0\times10^5$ m^{-2} and width $\Delta=1$ mm shares the major characteristics of standard impedance approximations, such as the infinite baffle. In fact, the square barrier corresponds to an infinite cone, whose initial radius and slope are continuous with those of the duct and in which the pressure amplitude falls off with $1/x$, as for a spherically outgoing wave. For analytic and numerical modeling purposes, therefore, the square barrier may be used as a one-dimensional equivalent to commonly adopted radiation impedances. The main advantage of this is that the singularity in the plane-wave potential function, as noted by Benade and Jansson,[34] can be approximated by finite parameters. Subsequently, both the wave function and its first derivative can be matched across the point of expansion into free space, yielding an analytic expression[35,36] for the radiated wave in which energy is fully conserved. This is in contrast to the Wertzel–Kramers–Brillouin approximation adopted by Benade and Jansson, which neglects backward traveling solutions within the lip region and is, in fact, known to be quite inappropriate for changes that occur on scales short in comparison to a wavelength.[39]

A barrier equivalent to the radiation impedance for a duct of length l is illustrated in Fig. 3, along with its transmitted, $T(k)$, and reflected, $R(k)$, waves, for k the free space wave number and $\omega=ck$. For a single barrier, analytic expressions for $T(k)$ and $R(k)$ have been found to be[35,36]

$$R(k) = e^{-2ikl}\frac{(k^2-\hat{k}^2)\sin\hat{k}\Delta}{(k^2+\hat{k}^2)\sin\hat{k}\Delta - i2k\hat{k}\cos\hat{k}\Delta}, \tag{7}$$

and

$$T(k) = \frac{-2ik\hat{k}e^{ik\Delta}}{(k^2+\hat{k}^2)\sin\hat{k}\Delta - i2k\hat{k}\cos\hat{k}\Delta} \tag{8}$$

for $\hat{k}=\sqrt{k^2-U_0}$. It is straightforward to show that $|R|^2+|T|^2=1$, as required for conservation of energy.

For a high-impedance source and a duct that is uniform at the origin, so that $dS(x)/dx=0$ at $x=0$, the Euler equation states the volume velocity excitation, $u(0,t)$, to be

$$u(0,t) = -\frac{\sqrt{S(0)}}{\rho_0}\int_0^t \left.\frac{\partial\Psi(x,\tau)}{\partial x}\right|_{x=0} d\tau, \tag{9}$$

for ρ_0 the equilibrium density of air. (For a discussion of the effects of a bore that is sloped or curved at the input, see Ref. 38.) Setting $u(0,t)=e^{i\omega t}$ thus yields[35,36] the analytic Green's function for the impulse response radiated into the free field, as

$$G_f(x|0|\omega) = \frac{\rho_0 c}{\sqrt{S(0)}}\left(\frac{T(k)}{1-R(k)}\right)e^{-ik[x-(l+\Delta)]}. \tag{10}$$

The power spectrum is therefore

$$|G_f(x|0|\omega)|^2 = \frac{\rho_0^2c^2}{S(0)}g(k), \tag{11}$$

where

$$g(k) = \left|\frac{T(k)}{1-R(k)}\right|^2. \tag{12}$$

The time-independent pressure spectrum, $|P(k)|^2$, a measurable quantity at a point $x=L$ in the free field, is then

$$|P(k)|^2 = \beta g(k), \tag{13}$$

where β is a frequency-independent normalization constant,

$$\beta = \frac{\rho_0^2c^2}{S(0)S(L)}. \tag{14}$$

It may be noted that β is not directly measurable, since it depends on the area, $S(L)$, of the virtual infinite cone. For measurements near the duct mouth, however, it can be approximated as

$$\beta = \frac{\rho_0^2c^2}{S(0)S(l)}, \tag{15}$$

which is measurable. Since the foregoing analysis applies equally to sequences of potential functions (which may include, for example, an arbitrary baffle at the termination) for which $R(k)$ is the matricial reflection coefficient taken at the origin,[35,36] it is now possible to present an inverse solution for the noninvasive reconstruction of the potential and area functions of an unknown duct.

B. Inverse problem: Inverse potential scattering in duct acoustics

By adopting the simplifying assumption of one-dimensional propagation, it has been possible to derive an energy-conserving expression for the normalized, radiated spectrum that is a function of only the transmission and re-

flection coefficients of the duct potential function. Subsequently, since it is known in the quantum mechanical literature[40,41] that the potential function of a scattering system can be reconstructed from $R(k)$, but not from $T(k)$ alone, it becomes sensible to ask whether the unknown potential function can be reconstructed from the combined term, $T(k)/(1-R(k))$. More specifically, it may be asked whether $R(k)$ can be obtained from the radiated pressure, $g(k)$ (13). An answer in the affirmative would also allow quantities such as the input impedance to be derived, in situations where they cannot be measured.

In fact, it has been been proved by Aktosun,[42] in a quantum-mechanical context that generalizes completely to the acoustical setting, that $g(k)$ is equivalent to the real part of the quantity $[1+R(k)]/[1-R(k)]$. Letting $R(k)=a+ib$, the proof is straightforwardly derived since

$$\Re\left\{\frac{1+R(k)}{1-R(k)}\right\}=\Re\left\{\frac{[1+a+ib][1-(a-ib)]}{[1-(a+ib)][1-(a-ib)]}\right\} \tag{16}$$

so that

$$\Re\left\{\frac{1+R(k)}{1-R(k)}\right\}=\frac{\Re(1-|R|^2+2ib)}{|1-R(k)|^2}. \tag{17}$$

Since in an energy-conserving system such as the one presented here, it must be the case that $|T(k)|^2+|R(k)|^2=1$, it can be immediately seen that

$$\Re\left\{\frac{1+R(k)}{1-R(k)}\right\}=\frac{|T(k)|^2}{|1-R(k)|^2}, \tag{18}$$

cf. Eq. (12). Beginning from the quantum-mechanical Jost solution in terms of e^{ikx} for a wave propagating in the positive x direction, Aktosun has gone on to show that the imaginary part, $\lambda(k)$, of a complex quantity, $\Lambda(k)$, where

$$\Re[\Lambda(k)]=\Re\left\{\frac{1+R(k)}{1-R(k)}-1\right\}, \tag{19}$$

can be obtained by analytic continuation in the complex plane as

$$\lambda(k)=-\frac{1}{\pi}\mathrm{CPV}\int_{-\infty}^{\infty}\frac{\Re[\Lambda(s)]}{s-k}ds, \tag{20}$$

where CPV means that the integral must be evaluated as a Cauchy principal value. Setting $\Lambda(k)=\Re[\Lambda(k)]+i\lambda(k)$, substitution of Eq. (12) into Eq. (19) leads to the derivation of the reflectance, $R(k)$, from $g(k)$ as

$$R(k)=\frac{\Lambda(-k)}{2+\Lambda(-k)}. \tag{21}$$

[Note that, in contrast to the description given in, Ref. 42 the right-hand side of Eq. (21) depends on $-k$ rather than k. This is due to the acoustical convention that a wave propagating in the positive x direction be represented as e^{-ikx}.] For a duct that is uniform near the origin,[38] the input impedance is immediately identified as

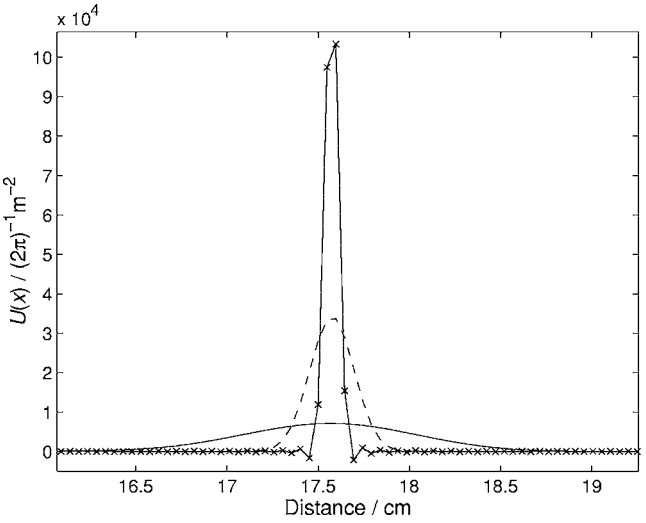

FIG. 4. Reconstruction of single barrier (see Fig. 3) from analytic data, at 180 (×), 20 (---) and 5 (—) kHz bandwiths, respectively.

$$Z_0=\frac{\rho c}{S(0)}\frac{1+R(k)}{1-R(k)}. \tag{22}$$

Transformation of $R(k)$ to the time domain then allows the potential function, $U(x)$, to be obtained by solution of the Marchenko integral equation.[40] Berryman and Greene[28] have proposed a fast matrix method for the numerical solution that also allows the area function to be recovered in terms of cylindrical segments if an initial value of $S(0)$ is supplied. Otherwise, the area function may be obtained[35,36] from Eq. (6), given initial values for $S(0)$ and $dS(x)/dx$ (although care must be taken with conditioning of the solution).

In this section, it has been shown that by conserving energy in a one-dimensional approximation to acoustic scattering, the wave-mechanical model of sound propagation allows the reflectance to be derived noninvasively from the radiated wave without any additional knowledge of the radiation impedance. We may now go on to examine the method through numerical simulations.

IV. NUMERICAL SIMULATIONS AND VALIDATION

First, the stability of the fast matrix method of Berryman and Greene[28] was affirmed. The method is preferred for computational solution of the Marchenko equation and inversion to the potential function from a temporal reflectance, $L(t)$. $R(k)$ was evaluated from the exact analytic expression of Eq. (7) at parameters appropriate to the barrier configuration of Fig. 3, for $l=17.5$ cm. Inverse Fourier transformation yielded $L(t)$. This initial step highlighted the problem of the "Gibbs phenomenon" in simulated data, since it is known that the Fourier transformation of band-limited data leads to numerical errors from windowing convolutions and ripple.[43] To avoid these numerical artifacts, $R(k)$ was first obtained at a high bandwidth of around 180 kHz and then low-pass filtered using a Gaussian filter over experimental ranges before transformation. The Berryman–Greene routines[28] were then coded in MATLAB. Figure 4 shows the resulting reconstruction of the single barrier from data simulated at high bandwidth, and data filtered at half-power points of 20 kHz (the

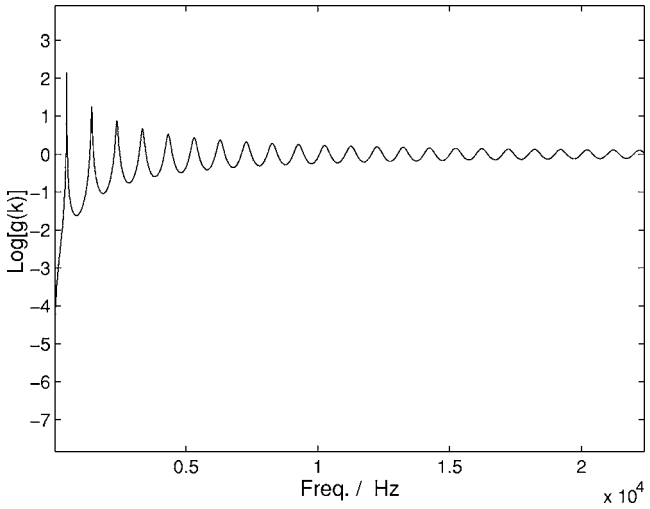

FIG. 5. Log$[g(k)]$ for configuration of Fig. 3 taken up to 20 kHz bandwidth.

loudspeaker range) and 5 kHz (around experimental bandwidths and the plane-wave limit in speech acoustics). At high bandwidth, the square barrier is reconstructed to within 3% maximum error (up to a scaling factor of 2π) over three sample points, agreeing well with the spatial resolution of 0.48 mm predicted by Eq. (2). The effects of the Gibbs phenomenon manifest as a small amount of ripple around discontinuities. In contrast, for filtered data the spatial resolution falls to around 4 mm at a half-power point of 20 kHz and to 1.7 cm at 5 kHz, so that the Gibbs ringing is also smoothed. These results are in precise agreement with the predictions of Eq. (2) and it was concluded that numerical errors in the Berryman–Greene routines, and those due to transformation of simulated data, were effectively controlled.

Subsequently, the Aktosun integral equation (20) was solved by trapezium rule implemented in MATLAB, the two major numerical considerations being the avoidance of the poles at $s=k$ and the effect of truncating the limits of integration. The frequency-dependent part of the radiated power spectrum, $g(k)$, was obtained from Eq. (12) at a resolution of $\delta=10$ Hz and integrated up to $k \mp \delta$. A significantly narrower

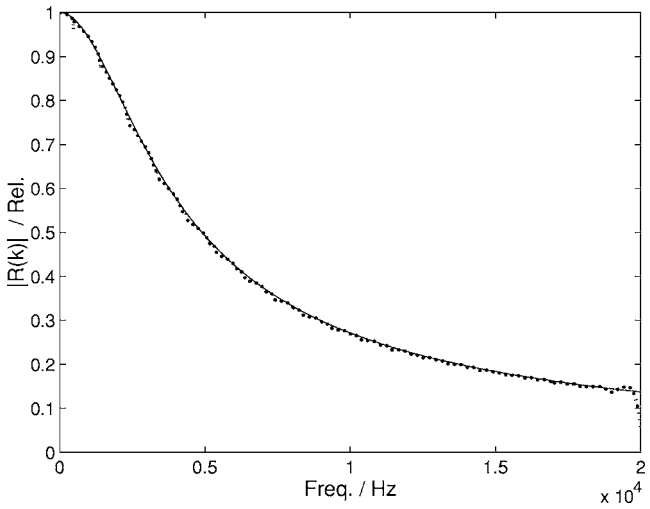

FIG. 6. $R(k)$: analytic (—) and derived by Aktosun method (···) at 20 kHz bandwidth.

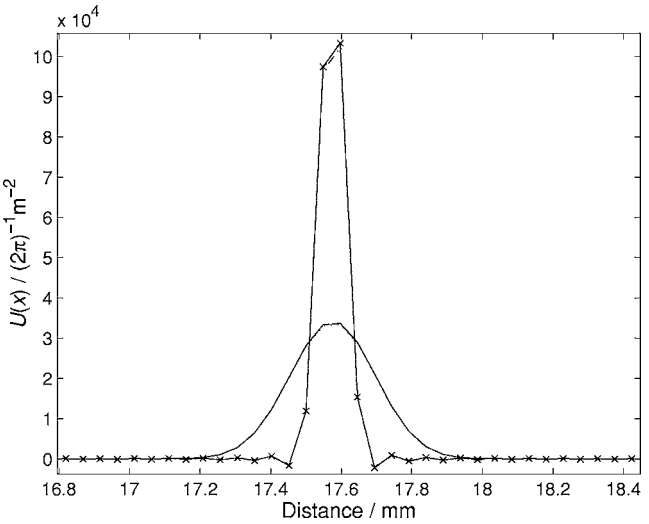

FIG. 7. Reconstruction of single barrier at 180 kHz bandwidth, from analytic data (×) and that obtained by Aktosun method (---). Reconstruction of single barrier at 20 kHz bandwidth, from analytic data (—) and that obtained by Aktosun method (···).

discretization will tend to lead to "divide by zero" errors around the poles and a wider discretization fails to resolve rapid variation in the spectrum. Equation (21) was then solved for varying limits in Eq. (20) to yield $R(k)$. At an effectively infinite bandwidth of 180 kHz, by which limits $g(k)=1$, it was found that the rms error in the derived reflectance [in comparison to the exact analytic solution (7)] was just 1.4×10^{-3}. Figure 5 shows that the oscillations in $g(k)$ are still evident at 20 kHz and thus, on truncation to these limits, the rms error rose slightly to 6.1×10^{-3}. Figure 6 demonstrates the nevertheless-close correspondence between the derived and analytic data. At 5 kHz truncation limits, the rms error increased to 7.5×10^{-3}, still only 0.8% of the maximum, however. Figure 7 shows that the potential-function reconstructions obtained from analytic and derived data agree to better than 1% maximum error, affirming the validity of the Aktosun proofs and numerical integration routines.

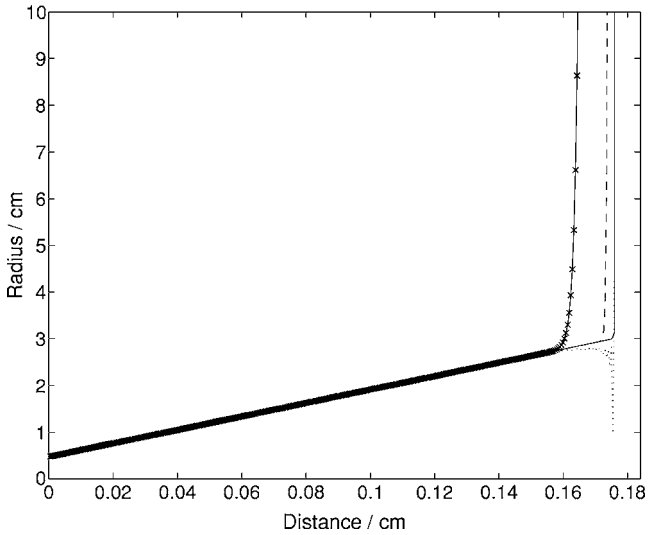

FIG. 8. Reconstruction of conical bore at 180 (···), 20 (---), and 5 (×) kHz bandwidths. Also shown: nominal radius (—).

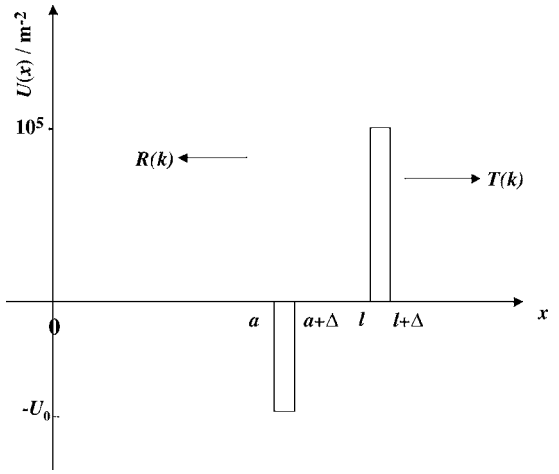

FIG. 9. Schematic potential-function profile of well-barrier pair, $U_0=6.0\times10^4$ m^{-2}, $\Delta=1$ mm, $a=17.1$ cm, $l=17.5$ cm.

(At experimental limits below 20 kHz, it was found that the integral can be performed more or less in real time on a 3.2 GHz PC with 2 Gbytes RAM.)

Figure 8 illustrates the area functions obtained from the reconstructed potential functions by solution of Eq. (6) for initial conditions $r_0=4.8$ mm, $r_l=3$ cm, and $dr(x)/dx|_{x=0}=(r_l-r_0)/l$. The expansion into the infinite conical baffle is narrowly resolved to around 0.5 mm at high bandwidth, with slight Gibbs ringing evident as before. The spatial resolution falls to around 4 mm and 1.7 cm at 20 and 5 kHz, respectively, again in full agreement with the predictions of Eq. (2).

Figure 9 illustrates a schematic well-barrier pair, a configuration generally corresponding to a negative curvature and duct constriction that will lower or raise a resonance depending on its position relative to the standing wave pattern.[37] Figure 10 illustrates the stability and narrow localization of this potential function reconstruction over space, affirming that cumulative errors found in other recursive layer-peeling algorithms[25] are well controlled in the Marchenko inversion. Figure 11 gives a magnified view; the errors and spatial resolutions at ideal and experimental bandwidths

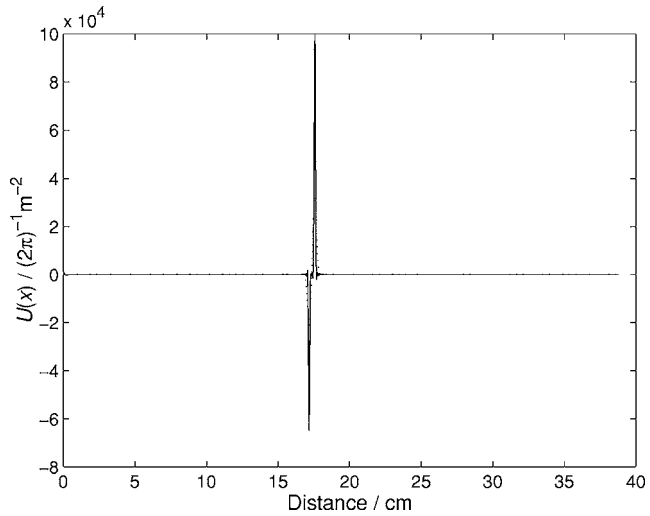

FIG. 10. Reconstruction of well-barrier corresponding to Fig. 9, from data derived by Aktosun method at 180 kHz bandwidth.

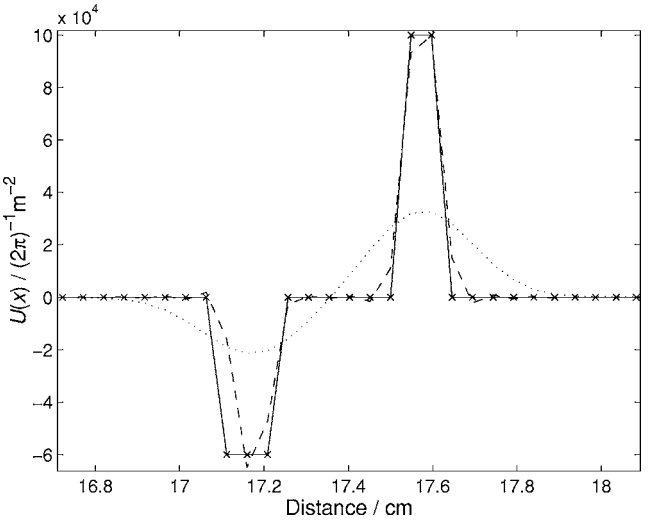

FIG. 11. Magnified view of Fig. 10. Nominal solution (×); data derived at 180 kHz (---) and 20 kHz (···) bandwidths.

are completely in line with previous results. On assumption of a cylindrical discretization of the duct and for a given value of $S(0)$, the Berryman–Greene also yields an area function in the equivalence set corresponding to any potential function. Figure 12 illustrates one such area function, reconstructed at various bandwidths and shown against the exact analytic solution defined by Eq. (6). As before, the resolution of the rapid changes in curvature is around 4 mm at 20 kHz bandwidth, falling to 1.7 cm at 5 kHz. It is clearly seen that the 4 mm resolution yields the bore profile rather accurately, in fact to better than 2.5% at the point of maximum constriction.

In this section, an analytic proof for deriving the wave-mechanical reflectance from the Jost solution has been validated in a one-dimensional approximation to duct acoustics. From the reflectance, the Marchenko equation for inversion to the potential function has been solved by the fast matrix method of Berryman and Greene and related area functions have also been obtained. The "wave mechanical" method has

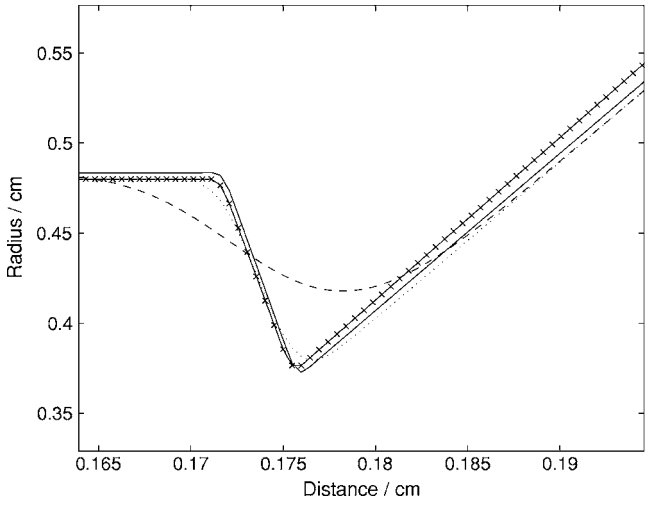

FIG. 12. Reconstruction of radius function corresponding to Figs. 9 and 11. Nominal solution (×), and from data derived at 180 (—), 20 (···), and 5 (---) kHz bandwidths.

been tested on both barriers and wells and so generalizes completely to compound potential functions that characterize highly localized constrictions and expansions,[37] which may correspond to leaks and blockages in a pipe.

V. DISCUSSION

Although the wave-mechanical method for the noninvasive measurement of the shape of an acoustical duct has been validated in principle, the experimental implementation will require consideration of several, familiar, details. First, the method assumes a high-impedance, flat spectrum, source. Recent work has described[44] such a source in terms of the maximum length sequence excitation of a piezoelectric driver mounted in a rigid plate, for example. Alternatively the "sine-wave packet" technique, already in use for APR measurements,[13] could be tried. Nevertheless, deconvolution of the input pulse from the measured data, a well-known problem,[1] will be necessary, requiring initial measurements with a nonreflecting tube.

Second, the scale factor β (14) must be calibrated and normalized. As discussed, it may be estimated from Eq. (15) for measurements near the mouth. Subsequently, a short lead-in tube of known dimensions could be reconstructed by iterative adjustment of β to an acceptable level of accuracy. Indeed, a similar procedure is currently standard practice in the control of pressure offsets.[15]

Third, the Marchenko equation does not allow for propagation losses and so the Berryman–Greene method is unlikely to be suitable for the reconstruction of long or very narrow objects in which boundary layer viscous and thermal effects, described by a complex wave number,[27] become significant. However, it is a great advantage of the Aktosun method that it does, in fact, generalize to a wave number in the upper half of the complex plane. Further work can, therefore, examine the derivation of the lossy reflectance, which would allow the application of standard lossy layer peeling algorithms.

Finally, the method is especially promising for application to the "classic" low-frequency problem of the inversion to the vocal tract shape from the speech signal,[45] although further consideration must be given to the deconvolution of the glottal wave form[46,47] and to calibration of the scale factor.

VI. CONCLUSIONS

The proposed wave-mechanical method for reconstruction of the potential and area functions of an unknown object from the radiated wave demonstrates highly satisfactory numerical stability and accuracy on simulated data, and is a promising technique for noninvasive acoustical measurements. In particular, it indicates how the long lengths of control tubing necessary for direct measurement of the reflectance can be eliminated, substantially reducing propagation losses at high frequency. Although the technique promises up to a fourfold improvement in spatial resolution, improvements will be limited in practice as the one-dimensional approximation to the radiation impedance becomes less appropriate over the increased frequency range. A more detailed examination of the trade off between improved losses and limits of the one-dimensional model remains to be undertaken. Nevertheless, the results presented here are likely be immediately relevant to many narrow bore applications, and to be particularly interesting for the speech inverse problem.

ACKNOWLEDGMENTS

The authors gratefully acknowledge the support in the UK of EPSRC Grant No. GR/S72177/01. They also thank Jonathan Kemp for many valuable discussions on higher-mode theory and Brendan Aengenheister in the Open University workshop for the construction of test cones.

[1] B. J. Forbes, D. B. Sharp, J. A. Kemp, and A. Li, "Singular system methods in acoustic pulse reflectometry," Acta. Acust. Acust. **89**, 743–753 (2003).
[2] J. Schroeter and M. M. Sondhi, "Techniques for estimating vocal-tract shapes from the speech signal," IEEE Trans. Speech Audio Process. **2**, 133–150 (1994).
[3] M. R. Schroeder, "Determination of the geometry of the human vocal tract by acoustic measurements," J. Acoust. Soc. Am. **41**, 1002–1010 (1967).
[4] P. Mermelstein, "Determination of the vocal tract shape from measured formant frequencies," J. Acoust. Soc. Am. **41**, 1283–1294 (1967).
[5] M. M. Sondhi and B. Gopinath, "Determination of vocal tract shape from impulse response at lips," J. Acoust. Soc. Am. **49**, 1867–1873 (1971).
[6] M. M. Sondhi and J. R. Resnick, "The inverse problem for the vocal tract: Numerical methods, acoustical experiments and speech synthesis," J. Acoust. Soc. Am. **73**, 985–1002 (1983).
[7] I. Marshall, "Acoustic reflectometry with an arbitrarily short source tube," J. Acoust. Soc. Am. **91**, 3558–3564 (1992).
[8] I. Marshall, "Impedance reconstruction methods for pulse reflectometry," Acustica **76**, 118–128 (1992).
[9] D. B. Sharp, "Increasing the length of tubular objects that can be measured using acoustic pulse reflectometry," Meas. Sci. Technol. **9**, 1469–1479 (1997).
[10] D. B. Sharp and D. M. Campbell, "Leak detection in pipes using acoustic pulse reflectometry," Acust. Acta Acust. **83**, 560–566 (1997).
[11] J. A. Kemp, J. M. Buick, and D. M. Campbell, "Practical improvements to acoustic pulse reflectometry," Proceedings of the International Symposium on Musical Acoustics Perugia, Italy 2001, No. 2, pp. 391–394.
[12] J. M. Buick, J. A. Kemp, D. B. Sharp *et al.*, "Distinguishing between similar tubular objects using pulse reflectometry: A study of trumpet and cornet leadpipes," Meas. Sci. Technol. **13**, 750–757 (2002).
[13] A. Li, D. B. Sharp, and B. J. Forbes, "Improving the high frequency content of the input signal in acoustic pulse reflectometry," Proceedings of the International Symposium on Musical Acoustics, Perugia, Italy, 2001, pp. 391–394.
[14] B. J. Forbes, J. A. Kemp, and D. B. Sharp, "Pulse reflectometry as an acoustical inverse problem: Regularisation of the bore reconstruction," Proceedings of the First Pan-American/Iberian Meeting on Acoustics incorporating the 144th Meeting of the A.S.A, Cancun, Mexico, 2002.
[15] A. Li, D. B. Sharp, B. J. Forbes, and J. A. Kemp, "The problem of DC offset in the measurement of impulse response using acoustic pulse reflectometry," Proceedings of the Institute of Acoustics, Salford, UK, 2002, Vol. 24, No. 2.
[16] A. Li and D. B. Sharp, "Reducing the source tube to improve the bandwidth of acoustic pulse reflectometry," Proceedings of the Stockholm Music Acoustics Conference (SMAC), Stockholm, Sweden, 2003.
[17] P. Ladefoged, R. Harshman, L. Goldstein, and L. Rice, "Generating vocal tract shapes from formant frequencies," J. Acoust. Soc. Am. **64**, 1027–1035 (1978).
[18] L.-J. Boë, P. Perrier, and G. Bailly, "The geometric vocal tract variables controlled for vowel production: Proposals for constraining acoustic-to-articulatory inversion," J. Phonetics **20**, 27–38 (1992).
[19] J. Schoentgen and S. Ciocea, "Kinematic formant-to-area mapping," Speech Commun. **21**, 227–244 (1997).
[20] P. Badin, D. Beautemps, R. Laboissière *et al.*, "Recovery of vocal-tract geometry from formants for vowels and fricative consonants using a midsaggital-to-area function conversion model," J. Phonetics **23**, 221–229 (1995).

[21]D. Beautemps, P. Badin, and R. Laboissière, "Deriving vocal-tract area functions from midsaggital profiles and formant frequencies: A new model for vowels and fricative consonants based on experimental data," Speech Commun. **16**, 27–47 (1995).
[22]J. Claerbout, *Fundamentals of Geophysical Data Processing* (McGraw-Hill, New York, 1976.
[23]Rakesh, "Impedance inversion from transmission data for the wave equation," Wave Motion **24**, 263–274 (1996).
[24]Rakesh and P. Sacks, "Characterisation of transmission data for Webster's horn equation," Inverse Probl. **16**, L9–L24 (2000).
[25]N. Amir, G. Rosenhouse, and U. Shimony, "A discrete model for tubular acoustic systems with varying cross-section—The direct and inverse problems. I II. Theory and experiment," Acustica **81**, 450–474 (1995).
[26]J. Agulló and S. Cardona, "Time-domain deconvolution to measure reflection functions for discontinuities in waveguides," J. Acoust. Soc. Am. **97**, 1950–1957 (1995).
[27]D. H. Keefe, "Acoustical wave propagation in cylindrical ducts: Transmission line parameter approximations for isothermal and nonisothermal boundary conditions," J. Acoust. Soc. Am. **75**, 58–62 (1984).
[28]J. G. Berryman and R. R. Greene, "Discrete inverse methods for elastic waves in layered media," Geophysics **45**, 213–233 (1980).
[29]V. Pagneux, N. Amir, and J. Kergomard, "A study of wave propagation in varying cross-section waveguides by modal decomposition. I. Theory and validation," J. Acoust. Soc. Am. **100**, 2034–2048 (1996).
[30]C. Hazard and V. Pagneux, "Improved multimodal approach in waveguides with varying cross-section," Proceedings of the 17th International Congress on Acoustics, Rome, 2001, Vol. 25, No. 1–3, pp. 3, 4.
[31]J. A. Kemp, "Multimodal propagation in acoustic horns," Proceedings of the International Symposium on Musical Acoustics, Perugia, Italy, 2001, Vol. 2, pp. 521–524.
[32]J. A. Kemp, "Theoretical and experimental study of wave propagation in brass musical instruments," Ph.D. thesis, University of Edinburgh, 2002.
[33]A. M. Bruneau, M. Bruneau, P. H. Herzog, and J. Kergomard, "Boundary layer attenuation of higher order modes in waveguides," J. Sound Vib. **119**, 15–27 (1987).
[34]A. H. Benade and E. V. Jansson, "On plane and spherical waves with nonuniform flare. I. Theory of radiation, resonance frequencies and mode conversion," Acustica **31**, 79–98 (1974).
[35]B. J. Forbes, "A potential-function analysis of speech acoustics," Ph.D. thesis, Department of Physics, King's College London, Strand, London WC2R 2LS, 2000.
[36]B. J. Forbes, E. R. Pike, and D. B. Sharp, "The acoustical Klein-Gordon equation: The wave-mechanical step and barrier functions," J. Acoust. Soc. Am. **114**, 1291–1302 (2003).
[37]B. J. Forbes and E. R. Pike, "The acoustical Klein-Gordon equation: A time-independent perturbation analysis," Phys. Rev. Lett. **93**, 1–4 (2004).
[38]B. J. Forbes, "The acoustical impedance defined by 'wave function' solutions of the reduced Webster equation," Phys. Rev. E **72**(1), 1–4 (2005).
[39]S. Gasiorowicz, *Quantum Physics* (Wiley, New York, 1974) pp. 469–471.
[40]K. Chadan and P. C. Sabatier, *Inverse Problems in Quantum Scattering Theory*, 2nd ed., (Springer, New York, 1989), Chap. XVII.
[41]Rakesh, "Potential inversion from transmission data for the one-dimensional wave equation," Wave Motion **25**, 319–329 (1997).
[42]T. Aktosun, "Construction of the half line potential from the Jost function," Inverse Probl. **20**, 859–876 (2004).
[43]N. Amir, U. Shimony, and G. Rosenhouse, "Losses in tubular acoustic systems—Theory and experiment in the sampled time and frequency domains," Acust. Acta Acust. **82**, 1–8 (1996).
[44]M. H. F. de Salis, N. V. Movchan, and D. J. Oldham, "Characterising holes in duct walls using resonance frequencies," J. Acoust. Soc. Am. **111**, 2583–2593 (2002).
[45]T. Aktosun, "Inverse scattering for vowel articulation with frequency-domain data," Inverse Probl. **21**, 899–914 (2005).
[46]A. Kounoudes, P. A. Naylor, and M. Brookes, "The DYPSA algorithm for estimation of glottal closure instants in voiced speech," Proc. ICASSP, 2002.
[47]J. Epps, J. R. Smith, and J. Wolfe, "A novel instrument to measure acoustic resonances of the vocal tract during phonation," Meas. Sci. Technol. **8**, 1112–1121 (1997).

An ultrasonic method for dynamic monitoring of fatigue crack initiation and growth

Bao Mi, Jennifer E. Michaels,[a] and Thomas E. Michaels
School of Electrical and Computer Engineering, Georgia Institute of Technology, Atlanta, Georgia 30332-0250

(Received 13 June 2005; revised 24 October 2005; accepted 27 October 2005)

Attached ultrasonic sensors can detect changes caused by crack initiation and growth if the wave path is directed through the area of critical crack formation. Dynamics of cracks opening and closing under load cause nonlinear modulation of received ultrasonic signals, enabling small cracks to be detected by stationary sensors. A methodology is presented based upon the behavior of ultrasonic signals versus applied load to detect and monitor formation and growth of cracks originating from fastener holes. Shear wave angle beam transducers operating in through transmission mode are mounted on either side of the hole such that the transmitted wave travels through the area of expected cracking. Time shift is linear with respect to load, and is well explained by path changes due to strain combined with wave speed changes due to acoustoelasticity. During subsequent *in situ* monitoring with unknown loads, the measured time of flight is used to estimate the load, and behavior of the received energy as a function of load is the basis for crack detection. Results are presented from low cycle fatigue tests of several aluminum specimens and illustrate the efficacy of the method in both determining the applied load and monitoring crack initiation and growth. [DOI: 10.1121/1.2139647]

PACS number(s): 43.25.Zx, 43.35.Yb, 43.25.Dc, 43.35.Cg [YHB] Pages: 74–85

I. INTRODUCTION

The remaining life of many complex structures is often assumed to be correlated to usage, where usage is estimated by simple quantities such as flight hours for aircraft, years for bridges and roads, and number of starts for diesel engines.[1] However, uneven and unknown loading conditions and unpredictable environmental disturbances cause some structural components to accumulate more damage than others with identical service lives. If a structural component is retired based simply on its service life, both safety and economics are compromised. Nondestructive evaluation (NDE) has provided one way to obtain information necessary to determine the current health condition of a structure. NDE methods are implemented either with hand-held equipment following a well-defined inspection procedure or by using automated inspection systems. Either can be quite costly, particularly when intervals between inspections are short. Reducing inspection costs by integrating sensors with structural components has motivated development of *in situ*, real time methods for structural health monitoring (SHM).

In structures made of ductile alloys that are subjected to fatigue failure, a large part of the service life is spent in crack initiation and the presence of very small cracks. One of the major concerns with metallic aircraft in general is fatigue cracking, and developing methods for *in situ* monitoring of the onset and growth of cracks in such critical structures is of growing interest and importance for SHM.[1,2] Ultrasonic methods have been extensively applied to crack detection and sizing for NDE during scheduled maintenance, and are thus a strong candidate for SHM.[3]

Early research efforts on characterizing cracks ultrasonically have primarily been motivated by the need for NDE of critical components. The time-of-flight diffraction technique has been used for bulk crack detection and sizing.[4,5] Surface wave scattering[6] has been deployed for detection and sizing of surface-breaking cracks, and Lamb waves have been investigated for detecting rivet hole cracks in a plate.[7,8] Physical and numerical models have been developed to predict the ultrasonic response to cracks in given materials or structures,[9,10] and these models lay a foundation for interpretation of ultrasonic signals. Recent work on ultrasonic characterization of cracks and flaws has included SHM applications with the goal of *in situ* monitoring of structural integrity. Examples include using an array of surface-mounted PZT wafer elements for monitoring crack growth in a uniaxial specimen exposed to cyclic loading,[11] modulation of surface acoustic waves by cracks opening and closing under load,[12] vibration modal analysis to characterize fatigue cracks in a steel beam,[13] and modulation of torsional waves in a cracked rod.[14]

Described here is an ultrasonic-based SHM method that has been developed for real time, *in situ* monitoring of fastener hole cracks in aluminum components. The fastener hole is monitored using an angle beam through transmission technique incorporating two transducers, one on each side of the hole. As the applied tensile stress is increased, the received signal shifts in time due to a combination of specimen elongation and change in ultrasonic velocity arising from the acoustoelastic effect. If a crack is present, the received signal also decreases in amplitude as the crack opens under stress. If this applied tensile stress is sufficiently large to open the crack, then the ratio of the received ultrasonic energy under stress to that with no stress is a reliable indicator of the

[a]Electronic address: jennifer.michaels@ece.gatech.edu

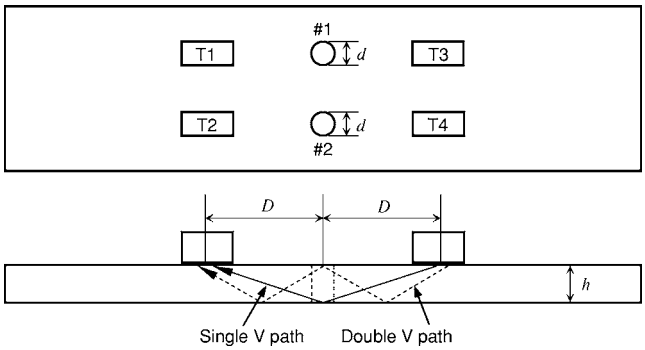

FIG. 1. Specimen geometry including transducer locations and ultrasonic beam paths (thickness $h=5.72$ mm and hole diameter $d=4.83$ mm).

presence of the crack, and growth of the crack can be monitored by tracking this energy ratio during the fatiguing process.[15] When making these measurements in the laboratory, either the fatiguing process can be stopped and measurements made under controlled loading conditions, or a suitable data acquisition system can be interfaced to the fatigue machine to record applied loads and resulting strains. However, it is generally neither feasible nor possible to record actual applied stresses for such an SHM system that is deployed on a real structure. To overcome this problem, the method reported here utilizes the time shift of the ultrasonic signal to deduce the applied stress, and thus enables real time, *in situ* monitoring of crack growth by means of the through transmission energy ratio.[16]

Experimental procedures for both the fatigue tests and the ultrasonic measurements are described in Sec. II. Data analysis methods are explained in Sec. III, and a theoretical analysis of the time shift due to loading is given in Sec. IV. Results are shown in Sec. V and concluding remarks are made in Sec. VI.

II. EXPERIMENTAL PROCEDURES

Coupons for fatigue testing were fabricated of 7075-T7351 and 7075-T651 aluminum as shown in Fig. 1. Fastener holes are simulated by two holes of 4.83 mm diameter machined in the center of the 5.72-mm-thick coupons. A two-hole coupon was chosen to obtain a slightly asymmetric stress field typical of that experienced by a fastener hole at the end of a row of holes. Specimens were fatigued with a uniaxial load at a rate of 5 Hz using an aperiodic loading spectrum as illustrated in Fig. 2 to simulate the variable loads on a structure during service. The maximum load value in the spectrum; i.e., the 100% value, was 75620 N (1700 lb), which corresponds to a maximum uniaxial stress of 279 MPa (40447 psi) based upon the unreduced cross-sectional area. The average stress over the cross section going through the center of the holes was 350 MPa, which represents approximately 75% of the yield point for this material. The load cycles were grouped into blocks of 2640 cycles each, and typical time to failure was between 15 and 20 blocks.

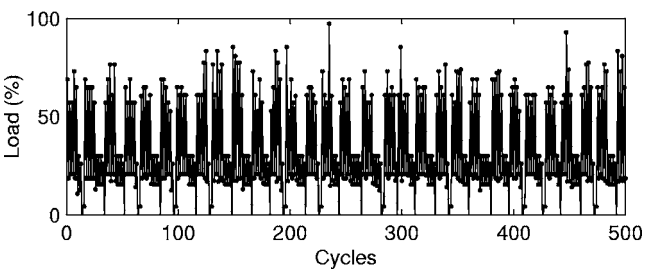

FIG. 2. Typical 500-cycle segment from the fatigue loading spectrum where the 100% value corresponds to 75620 N (17000 lb).

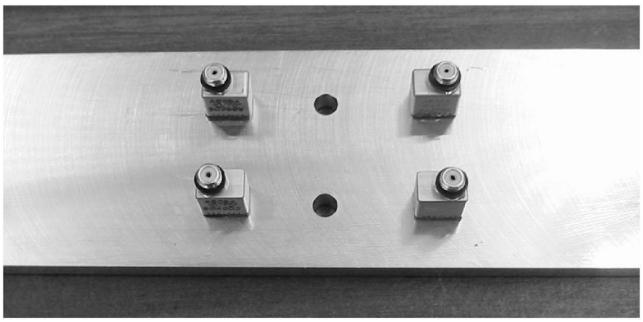

FIG. 3. Photograph of a two-hole fatigue coupon with attached angle beam transducers.

Fatigue testing was halted between blocks to take "static" measurements of ultrasonic response versus load. Ultrasonic measurements were also recorded during the fatiguing process, and these measurements are referred to as the "dynamic" measurements. The dynamic measurements were taken at random times so that the actual load associated with each waveform was not known, but a sufficient number of waveforms were recorded to ensure that waveforms were obtained throughout the entire load range.

Two pairs of 70° shear wave angle beam transducers (Panametrics model A5054, 10 MHz center frequency) were bonded to the coupons using a five minute, two-part epoxy as pictured in Fig. 3. Each transducer was positioned and aligned with the hole based upon the pulse-echo signal reflected from the hole. The distance from the transducer to the hole was set so that the shear wave half and full V reflections from the bottom and top of the hole were approximately balanced in amplitude. This configuration is equivalent to the transducer location where the center of the beam hits the midpoint of the hole, but due to beam spread, both corner reflections are present. This pulse-echo signal was used to monitor the transducer attaching process for all four transducers. In principle, the proper transducer location could be calculated from the beam angle and the thickness of the specimen. In practice, however, it was found necessary to monitor the pulse-echo signals during the transducer attachment process due to both beam skew and transducer-to-transducer refracted angle variations.

Both static and dynamic ultrasonic measurements were performed throughout the fatigue tests. For the static measurements, fatiguing was paused and static loads were applied from 0 to 44482 N (0 to 10000 lb) in 4448 N (1000 lb) increments, which corresponds to stresses ranging from 0 to a maximum of 164 MPa (23793 psi) away from the holes. Dynamic measurements were taken at random times near the beginning of each block of fatigue cycles. All measurements were made using a Panametrics 5072PR

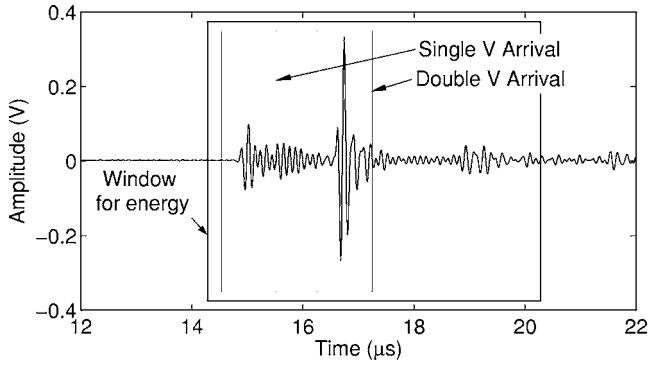

FIG. 4. Typical angle beam through transmission signal showing the single and double V path arrivals.

pulser receiver, and were recorded with a Tektronix TDS5034 digital oscilloscope operating at a sampling frequency of 125 MHz.

III. DATA ANALYSIS

When both angle beam transducers in the pair are aligned as described, the through-transmission ultrasonic signal has two dominant echoes as shown in Fig. 4. These echoes correspond to the single and double V paths illustrated in Fig. 1, and vary in two ways during fatigue loading. First, the amplitudes of the echoes vary as a function of both load and damage, and second, the echoes shift slightly in time with increasing load. Figure 5(a) shows the time shift prior to crack formation, and Fig. 5(b) shows the amplitude change that occurs after cracks have formed. Data analysis consists of characterizing the amplitude change by means of an energy ratio parameter, and measuring the time shift of both the single and double V echoes.

A. Energy ratio from static measurements

In previous work by the authors, a normalized energy ratio method was shown to be a robust and self-calibrating method for crack monitoring.[15] To obtain this energy ratio, fatigue tests were interrupted to apply known static loads and make ultrasonic through transmission measurements as a function of load. This technique is reviewed here.

The first step in determining the energy ratio is to calculate energy values for a windowed portion of the recorded through transmission ultrasonic waveform as a function of applied load expressed in terms of stress, σ, where $x(t;\sigma)$ is the recorded waveform,

$$E(\sigma) = \int_{t_1}^{t_2} x^2(t;\sigma)dt. \tag{1}$$

Next, a ratio is formed of the energy at two different loads: a reference load and no load,

$$R = \frac{E(\sigma = \sigma_{\text{ref}})}{E(\sigma = 0)}. \tag{2}$$

Finally, the energy ratio is normalized by the energy ratio value obtained before the fatigue loading was initiated, i.e., the no-damage condition,

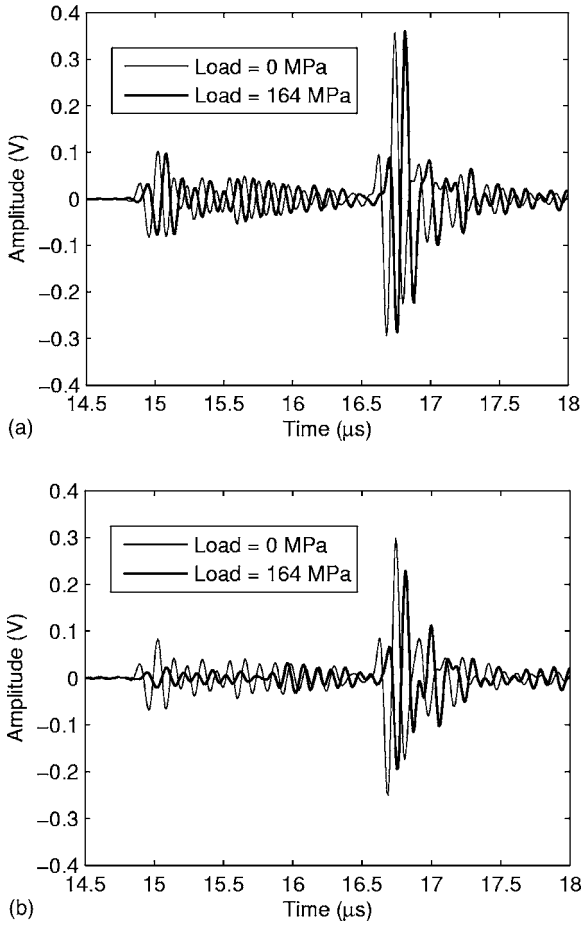

FIG. 5. Effects of tensile loading on the received through transmission angle beam signals. (a) Before the onset of cracking, the ultrasonic signal is shifted in time as load is applied but the amplitude is unaffected. (b) After crack initiation, increasing load causes the ultrasonic signal to both shift in time and decrease in amplitude.

$$R_{\text{norm}} = \frac{R}{R_{\text{initial}}}. \tag{3}$$

For the work reported here, a 6.0 μs time window encompassing both the single and double V echoes was used for calculation of energy as shown by the larger box in Fig. 4. Static ultrasonic measurements were made and energy ratios were calculated after each block of fatigue cycles. These energy ratios are the ones used as benchmarks for comparison with those obtained from the dynamic measurements. It was experimentally determined by observing the through transmission response that a load of 22241 N (5000 lbs) was sufficient to open a crack, and the corresponding stress of 82 MPa (11896 psi) is the value used for σ_{ref}.

B. Determination of load from time shift

The axial loading exerted on the specimen shifts the ultrasonic signals in time, as can be seen in Figs. 5(a) and 5(b). Following previous work by Mi *et al.*,[16] the time shift between the signals under the two loading conditions, referred to as the "delta time-of-flight" (ΔTOF), was calculated from the time of the peak of the cross-correlation function of the two signals. A 1.0 μs time window was used to individu-

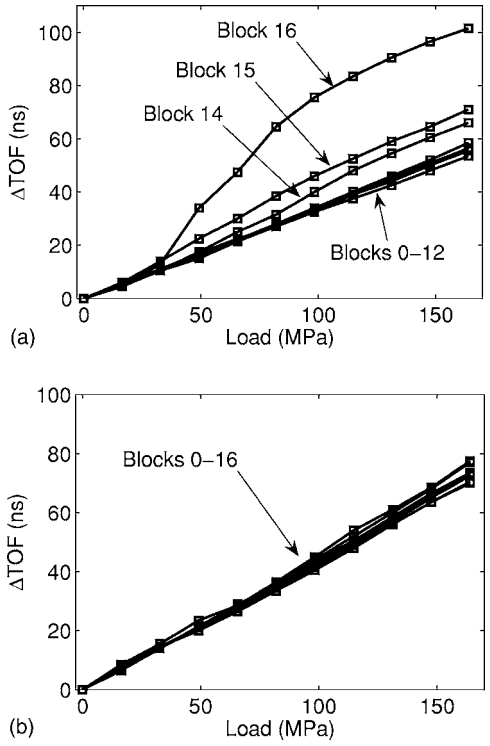

FIG. 6. Change in time of flight of the ultrasonic signal versus load referenced to the zero-load time at the start of each fatigue block. (a) Single V arrival. (b) Double V arrival.

ally gate the single and double V echoes as shown by the two smaller boxes in Fig. 4 since these two peaks are shifted by different amounts. The resolution of the peak location is within one sampling interval of the digitized signal, i.e., 8 ns at the sampling frequency of 125 MHz, and it was improved to 0.8 ns by using piecewise cubic spline interpolation.

Experimentally determined values of ΔTOF versus applied load are shown in Fig. 6 for a specimen that failed in the 17th block of fatigue cycles. For this specimen, static measurements were taken for the initial no-damage condition and after each block of fatigue cycles, and the ΔTOF values are referenced to the zero-load state at each block. Figure 6(a) shows the single V path results, and Fig. 6(b) shows the double V path results. The curves are very consistent until near the end of life when sizable cracks are present. If the curves are referenced to the initial no-damage state, there is a progressively increasing offset at zero load of up to approximately 20 ns as fatiguing progresses. It is believed that most if not all of this offset is due to a combination of permanent specimen deformation increasing the ultrasonic path and an increase in temperature during fatiguing caused by internal friction.

Note that the double V path curves are less affected by the presence of a large crack than the single V path curves. This result is not unexpected because, for this specimen, the amplitude of the double V path echo is much larger than that of the single V path echo. Thus its shape would tend to be less affected by the crack because small signals scattered from the crack would contribute less to the overall echo, and the signal could sustain more of a loss in amplitude before it is reduced to the same level as the background coherent and

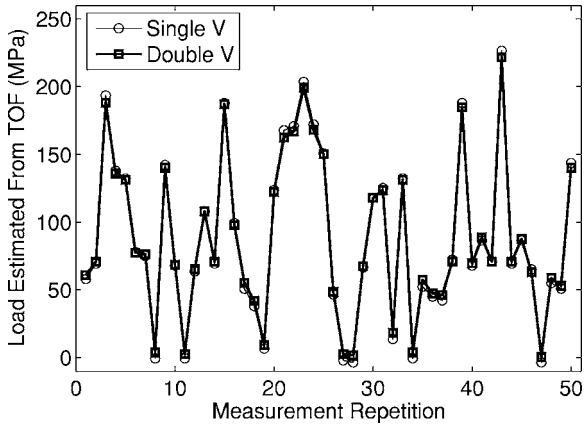

FIG. 7. Loads calculated from the change in ultrasonic time of flight as determined from 50 consecutive dynamic measurements.

random noise. If two echoes have similar shapes, then the cross-correlation method will provide a good estimate of the time shift between them. Therefore, ΔTOF curves from the shear wave double V path are better suited than those from the single V path for deducing actual loads from the recorded dynamic waveforms. As shown in Fig. 6, axial loading exerted on the specimen shifts the ultrasonic signals linearly about 50 ns per 150 MPa for the single V path signal, and about 75 ns per 150 MPa for the double V signal.

The statically determined ΔTOF versus applied load data from the initial no-damage state are referred to as calibration curves for both single and double V arrivals. These piecewise linear curves were subsequently used to determine the effective applied load from measured single and double V echo times as referenced to zero-load values. Typical results are shown in Fig. 7 from 50 dynamically measured ultrasonic waveforms using both single and double V calibration curves; they are in good agreement with each other. The estimated loads, although not measured directly and thus unverified, fall within the expected range based upon the load spectrum. However, as mentioned previously, the double V ΔTOF curve is least affected by the presence of cracks emerging from the fastener holes and thus is more accurate near the end of fatigue life.

C. Energy ratio from dynamic measurements

Dynamic measurements are made by randomly acquiring waveforms during fatigue loading as previously explained, and the ΔTOF calibration curves are used to assign an applied load to each dynamically measured signal.[16] The specific steps used for calculating energy ratios from these dynamic measurements are as follows:

1. A calibration curve relating applied load to ΔTOF is obtained from static measurements prior to fatiguing.
2. Ultrasonic waveforms are randomly recorded during fatigue loading.
3. The ΔTOF is obtained by cross-correlating each signal with the corresponding static no-load signal.
4. The ΔTOF curves obtained from static calibrations are used to assign an effective axial load value to each waveform.

5. The energy is calculated for each waveform as per Eq. (1).
6. Energy is plotted versus load, and data are locally averaged to reduce noise.
7. The energy at both zero load and the reference load is obtained by a local linear fit.
8. The energy ratio is computed from these energy values as per Eq. (2).
9. The energy ratio is normalized by that obtained at the beginning of the fatigue test as per Eq. (3).

In this manner the normalized ultrasonic energy ratio can be monitored using dynamic data acquired during the fatigue life of a specimen.

IV. THEORETICAL ANALYSIS OF TIME SHIFT CAUSED BY LOADING

Critical to determining applied load from dynamic measurements is consistent time shifting of the ultrasonic signal resulting from the load. Many factors can affect the ultrasonic time of flight during loading; these include changes in geometry, acoustic velocity, crack size, ultrasound beam bending, plastic deformation, and measurement conditions. Among these, changes in geometry and acoustic velocity are hypothesized to be the two dominating factors. The effects of the crack itself and plastic deformation around the hole on the time of flight are very localized, affecting only a small portion of the ultrasonic beam path, and can be safely ignored, particularly during early stages of fatiguing. Near the end of life the crack size becomes significant and its effect on the ultrasonic time of flight becomes obvious, as can be seen in Figs. 6(a) and 6(b). Modeling the effect of the crack is extremely difficult, if not impossible, due to uncertainties in initiation, orientation, and location. In the following analysis, change of geometry and acoustoelasticity will be considered in order to determine if they are indeed the dominant factors.

For a generic ultrasonic wave arrival, the time of flight is given by

$$\mathrm{TOF} = \frac{P}{v}, \tag{4}$$

where P is the total propagation path and v is the ultrasonic velocity. Small changes in time of flight are due to small changes in both the path and the ultrasonic velocity,

$$\Delta\mathrm{TOF} = \frac{\partial \mathrm{TOF}}{\partial P}\Delta P + \frac{\partial \mathrm{TOF}}{\partial v}\Delta v = \frac{1}{v}\Delta P - \frac{P}{v^2}\Delta v. \tag{5}$$

The two components of the total change in time of flight are defined as

$$\Delta\mathrm{TOF}_G = \frac{1}{v}\Delta P, \tag{6}$$

$$\Delta\mathrm{TOF}_A = -\frac{P}{v^2}\Delta v, \tag{7}$$

where $\Delta\mathrm{TOF}_G$ is the relative time of flight caused by geometry (change in propagation path), and $\Delta\mathrm{TOF}_A$ is the relative time of flight caused by acoustoelasticity (change in ultrasonic velocity).

A. Time shift due to geometry

Axial loading results in an elongation of the specimen in the loading direction and a contraction in the transverse directions due to the Poisson effect. These strains are assumed to be uniform between the two transducers, and local plastic deformation around the hole is ignored. The ultrasonic beam path is approximated by straight lines from the center of the transmitter to the edge of the hole and ending at the receiver. The ultrasonic velocity for the entire path is assumed to be the shear velocity; the effect of the creeping wave around the edge of the hole is ignored. Referring to Fig. 1, the single and double V paths in the unstrained specimen are

$$P_1 = 2\sqrt{D^2 + h^2 + \left(\frac{d}{2}\right)^2}, \tag{8}$$

$$P_2 = 2\sqrt{D^2 + (2h)^2 + \left(\frac{d}{2}\right)^2}, \tag{9}$$

where P_1 is the single V path, P_2 is the double V path, D is the distance from the transducer to the center of the hole, h is the thickness of the specimen, and d is the diameter of the fastener hole.

Changes in the paths P_1 and P_2 due to small changes in D and h are expressed as

$$\Delta P_1 = \frac{\partial P_1}{\partial D}\Delta D + \frac{\partial P_1}{\partial h}\Delta h, \tag{10}$$

$$\Delta P_2 = \frac{\partial P_2}{\partial D}\Delta D + \frac{\partial P_2}{\partial h}\Delta h. \tag{11}$$

If ϵ is the strain in the direction of loading, then $\Delta D = \epsilon D$ and $\Delta h = -\nu\epsilon h$, where ν is Poisson's ratio. Then ΔP_1 and ΔP_2 can be expressed in terms of ϵ,

$$\Delta P_1 = \frac{4(D^2 - \nu h^2)}{P_1}\epsilon, \tag{12}$$

$$\Delta P_2 = \frac{4(D^2 - 4\nu h^2)}{P_2}\epsilon. \tag{13}$$

Thus, changes in time of flight due to geometry for single and double V paths are

$$\Delta\mathrm{TOF}_{G1} = \frac{\Delta P_1}{v} = \frac{4(D^2 - \nu h^2)}{P_1 v}\epsilon, \tag{14}$$

$$\Delta\mathrm{TOF}_{G2} = \frac{\Delta P_2}{v} = \frac{4(D^2 - 4\nu h^2)}{P_2 v}\epsilon. \tag{15}$$

Figure 8 shows the calculated ΔTOF versus load curves for the single V and double V arrivals based on geometry change only. The distance D from the center of the hole to the nominal exit point of the shear wave from the transducer was measured to be 17.7 mm. The nominal thickness of the specimen, h, was 5.72 mm and the hole diameter, d, was 4.83 mm. Compared to the experimental data of Fig. 6, the

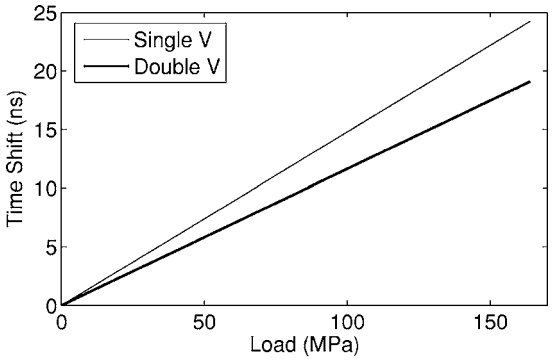

FIG. 8. Calculated change in time of flight versus load for both single and double V arrivals due to geometrical effects only.

geometry change accounts for less than half of the change in time of flight due to loading. It is interesting to note that in Fig. 8 the double V curve shows a smaller time shift than the single V curve because more of the double V propagation path is in the thickness direction, which is reduced due to the Poisson effect. Since the actual behavior is reversed with the double V curve exhibiting the larger time shift, it is clear that geometry changes alone cannot explain the observed time shifts.

B. Time shift due to acoustoelasticity

The acoustoelastic effect refers to the change in acoustic wave velocities in a material as a function of applied stress. The theory of acoustoelasticity is based on a continuum theory of small disturbances superimposed on an elastically deformed body. There is a long history of theoretical and experimental work on acoustoelasticity with an early version of the modern theory developed by Hughes and Kelly[17] in 1953. Pao *et al.* reviewed the theory of acoustoelasticity in 1984 with an emphasis on measurement of residual stresses.[18] Pao and Gamer considered acoustoelasticity in orthotropic media due to an arbitrary homogeneous elastic or plastic strain field,[19] and Qu and Liu investigated acoustoelasticity for guided wave propagation in layered media.[20] Acoustoelasticity has also been experimentally investigated for damage detection.[21]

For a specific experiment, an acoustoelastic constant K can be defined that linearly relates change in velocity v to applied stress σ,

$$\frac{\Delta v}{v} = K\sigma. \tag{16}$$

The constant K is dependent upon the specific wave mode, propagation direction, and stress orientation, and is a function of second- and third-order elastic constants.

For the work presented here, consider a coordinate system with the x_1 axis aligned along the direction of propagation of the shear wave, as shown in Fig. 9. We are interested in the vertically polarized shear wave (SV wave) with particle motion in the x_2 direction and assume a uniaxial stress field, neglecting the stress concentration in the vicinity of the hole. The effective acoustoelastic constant for this SV wave due to the applied uniaxial stress field is of the form

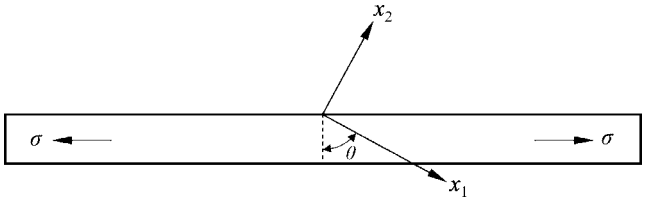

FIG. 9. Coordinate system definition for acoustoelasticity analysis of angle beam ultrasonic wave propagation.

$$\frac{\Delta v}{v} = [K_1 \sin^2\theta + K_2 \cos^2\theta]\sigma = K(\theta)\sigma, \tag{17}$$

where θ is the refracted angle, and K_1 and K_2 are defined as

$$K_1 = \frac{4\mu(\lambda+\mu) + \mu m + \frac{1}{4}\lambda n}{2\mu^2(3\lambda+2\mu)}, \tag{18}$$

$$K_2 = \frac{\mu(\lambda+2\mu) + \mu m + \frac{1}{4}\lambda n}{2\mu^2(3\lambda+2\mu)}. \tag{19}$$

In these equations λ and μ are the Lamé constants, and l, m, and n are the Murnaghan third-order elastic constants. The derivation of these equations is given in the Appendix. It can be seen that K_1 is the acoustoelastic constant for a shear wave propagating in the direction of applied stress (θ=90°), and that K_2 is the acoustoelastic constant for a shear wave propagating perpendicular to the direction of applied stress and with parallel polarization (θ=0°).

The change in wave velocity is

$$\Delta v = vK(\theta)\sigma. \tag{20}$$

The resulting change in time of flight due to this change in wave velocity for the single and double V paths is determined by substituting Eq. (20) into Eq. (7),

$$\Delta \mathrm{TOF}_{A1} = -\frac{P_1}{v^2}\Delta v = -\left[\frac{K(\theta_1)P_1}{v}\right]\sigma = -\left[\frac{2K(\theta_1)\sqrt{D^2+h^2+(d/2)^2}}{v}\right]\sigma, \tag{21}$$

$$\Delta \mathrm{TOF}_{A2} = -\frac{P_2}{v^2}\Delta v = -\left[\frac{K(\theta_2)P_2}{v}\right]\sigma = -\left[\frac{2K(\theta_2)\sqrt{D^2+(2h)^2+(d/2)^2}}{v}\right]\sigma. \tag{22}$$

Note that θ_1 and θ_2 refer to the refracted angles for the two V paths, which are different. If θ_i and the corresponding acoustoelastic constant $K(\theta_i)$ are known, then the time shift can be readily calculated for any value of stress.

Calculation of $K(\theta)$ can be done either directly from Eq. (17) if K_1 and K_2 are known from experimental measurements, or by first calculating K_1 and K_2 from the elastic constants as per Eqs. (18) and (19). Numerical values for acoustoelastic constants for most materials are not readily available due to the difficulty in making the measurements.

TABLE I. Lamé second-order elastic constants (λ and μ) and Murnaghan third-order elastic constants (l, m and n) for 7075-T651 aluminum.[22]

Constant	Value (GPa)
λ	54.9
μ	26.5
l	−252.2
m	−325.0
n	−351.2

Similarly, since values for third-order elastic constants are usually determined from measurements of acoustoelasticity, they are also not readily available. Here we use values of λ, μ, l, m, and n determined by Stobbe[22] for 7075-T651 aluminum and summarized in Table I to calculate K_1 and K_2; values are -1.571×10^{-11} and -3.458×10^{-11} Pa^{-1}, respectively. The velocity of the shear wave speed in the undeformed material is determined from $c=\sqrt{\mu/\rho}$ and is calculated to be 3.076 mm/μs using a value of 2800 kg/m^3 for the density ρ. The refracted angles of the single and double V paths were calculated to be 72° and 57°, respectively, based upon a measured value of 17.7 mm for D.

Figure 10(a) shows the comparison between the experimentally measured ΔTOF and the theoretical predictions using the above parameters. The theoretical calculation includes the ΔTOF based on the elastic deformation [Eqs. (14) and (15)] and the ΔTOF based on the acoustoelastic effect [Eqs. (21) and (22)]. Note that the two theoretical curves fall between the two experimental curves, suggesting that there is a geometrical term not accounted for in the model rather than errors in the elastic constants. One assumption that is clearly an approximation is that the single and double V propagation paths originate from the same point on the surface of the specimen. In reality, due to beam spreading in the transducer wedge, the single V path originates slightly closer to the hole and the double V path originates slightly further away from the hole; these distances were estimated to be 1 mm based upon visual inspection of the wedge geometry, resulting in a value of D equal to 16.7 mm for the single V path and 18.7 mm for the double V path. Using these values, theoretical curves were recalculated and are shown in Fig. 10(b), now exhibiting excellent agreement with the experimental results. The fact that the theoretical calculations agree well with the experimental measurements supports the assumption that the ΔTOF is caused primarily by elastic deformation and acoustoelasticity resulting from a uniaxial stress field, and that other effects can be neglected.

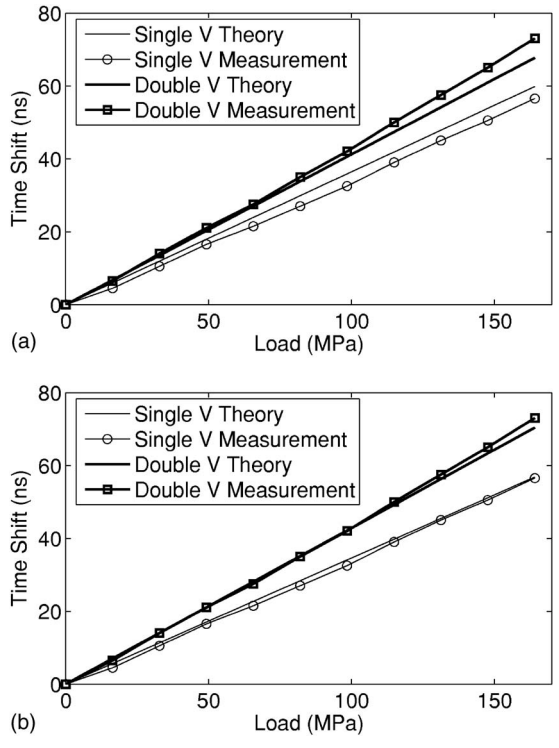

FIG. 10. Theoretical change in time of flight compared to measurements for data recorded after six fatigue blocks. (a) Calculations using the same transducer-hole distance D for both single V and double V paths. (b) Transducer-hole distances adjusted to compensate for differences in single V and double V paths.

C. Temperature effects

Although not specifically investigated here, a discussion of time shifts would not be complete without considering temperature effects. Temperature changes are unavoidable outside of the laboratory and are well known to cause time shifts in received ultrasonic signals due to both thermal expansion and change in acoustic velocity with temperature. Changes in temperature can contribute to both offset and change in slope of the ΔTOF versus load curves.

In considering temperature changes, we assume that they are quasistatic, occurring over a longer time scale than load changes. Thus load effects are considered to be superimposed on the temperature effects. Changes in propagation path P and acoustic velocity v due to a change in temperature of ΔT are

$$\Delta P = P\alpha\Delta T, \tag{23}$$

$$\Delta v = \kappa\Delta T, \tag{24}$$

where α is the coefficient of thermal expansion and κ is the change in acoustic velocity for a unit change in temperature. Substituting these expressions into Eq. (5) gives the change in time of flight due to a temperature change of ΔT assuming that there is no applied load,

$$\Delta\mathrm{TOF} = \frac{P}{v}\left[\alpha - \frac{\kappa}{v}\right]\Delta T. \tag{25}$$

Typical values for α and κ for aluminum are $2.43\times10^{-5}/^\circ$C and -0.752 m/s/°C, respectively.[23] Using these values, we calculate the quantity in square brackets in Eq. (25) to be $2.64\times10^{-4}/^\circ$C. For the double V path, a 10 °C change in temperature results in a ΔTOF of 36 ns, which would cause the overall ΔTOF versus load curve to be offset by this amount. Although this time shift is quite

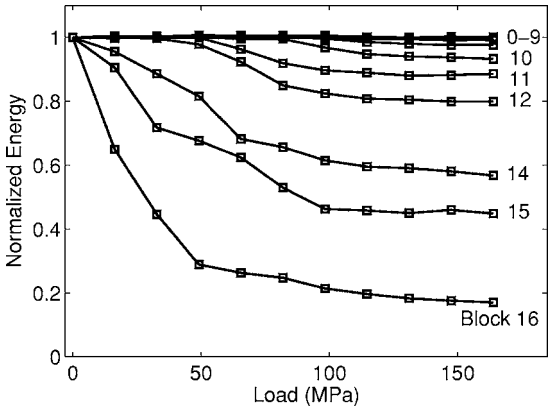

FIG. 11. Energy versus load at various fatigue blocks where energy is normalized to the zero load value for each block.

significant, compensation can be made by referencing the ΔTOF versus load curves to zero load values, as was done in Fig. 6.

To understand how a temperature change affects the slope of the ΔTOF versus load curve, the initial linear dimensions and velocity are perturbed as per Eqs. (23) and (24) to reflect the quasistatic temperature change of ΔT. The various changes in time of flight are then calculated as per Eqs. (14), (15), (21), and (22), dropping terms higher than quadratic in the perturbations ϵ, $\Delta P/P$, and $\Delta v/v$. The result is a general expression for how the change in time of flight due to applied load is affected by a quasistatic change in temperature,

$$\Delta\mathrm{TOF}(\sigma;\Delta T) = \Delta\mathrm{TOF}(\sigma;\Delta T = 0)\left[1 + \left(\alpha - \frac{\kappa}{v}\right)\Delta T\right]. \tag{26}$$

The quantity in square brackets changes the slope of the ΔTOF versus load curve. For an extreme temperature change of 50 °C, this quantity is only 1.0132, causing an insignificant error of approximately 1 ns for a typical ΔTOF of 80 ns. Thus, as long as changes in time of flight are referenced to no-load values at the same temperature, and temperature changes are truly quasistatic relative to changes in load, temperature effects can be safely neglected.

V. RESULTS

Since practical implementation of this *in situ* ultrasonic approach depends upon dynamic data acquisition without interruption of service, the key is to accurately estimate the load under which the dynamic measurements are taken because the ultrasonic features are dependent upon load. This is especially true when cracks are present since the opening and closing of the cracks by the load modulate the ultrasonic signals. As an example, Fig. 11 shows the ultrasonic energy as a function of applied load for various fatigue blocks. This figure demonstrates that the energy changes with applied load, particularly for the later fatigue blocks as the crack size increases.

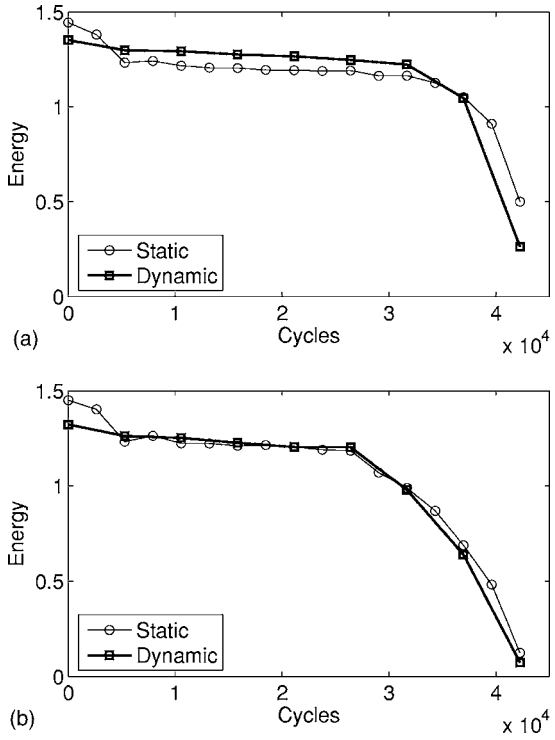

FIG. 12. Comparison of energy versus fatigue cycles as determined from both static and dynamic measurements. (a) No load. (b) Load of 82 MPa.

Figure 12 compares results from static and dynamic measurements in the form of energy versus fatigue cycle curves for the unloaded and loaded specimen. For the dynamic measurements, the load was estimated from the time of flight relative to the minimum recorded for that fatigue block (assumed to be the no-load reference) using the ΔTOF calibration curve established from the undamaged specimen. The energy was calculated by averaging the energy from signals in the neighborhood of the target load. Overall, the static and dynamic curves agree reasonably well for both no load as shown in Fig. 12(a) and under a load of 82 MPa as shown in Fig. 12(b) except for the first few blocks. This inconsistency, which is not always observed to be present, is suspected to be due to coupling stabilization and initial strain hardening.

The through-transmission energy curve measured at 82 GPa begins to decrease when the cracks inside the fastener hole approach a surface length of approximately 0.25 mm (0.01 in.), which is when they are just visible using a 10× magnifier. For the last 40% of the fatigue life, the drop is approximately linear and approaches a relative energy of zero at 100% of expended life. The no-load curve also exhibits a drop, but not until approximately 80% of life expended. After 80% of life, the no-load and 82 GPa load curves maintain a clear separation for the remainder of the specimen life. This difference in response between no-load and loaded crack conditions is consistent with the assumption that the opening of the crack under load blocks the ultrasonic energy from propagating across the crack.

Figure 13 shows a comparison of the normalized energy ratio for two specimens as calculated from Eq. (3). The first specimen was fatigued until failure with the crack fully de-

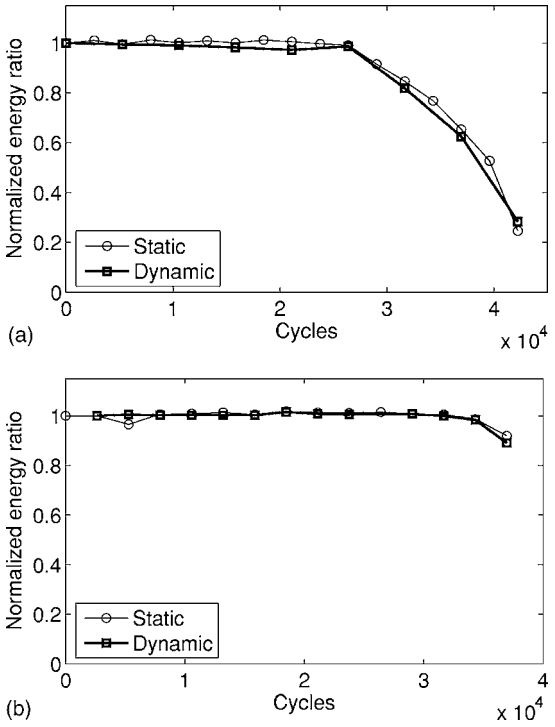

FIG. 13. Comparison of normalized energy ratio versus fatigue cycles as determined from both static and dynamic measurements for two specimens. (a) S3-0001 (7075-T7351). (b) S4-0030 (7075-T651).

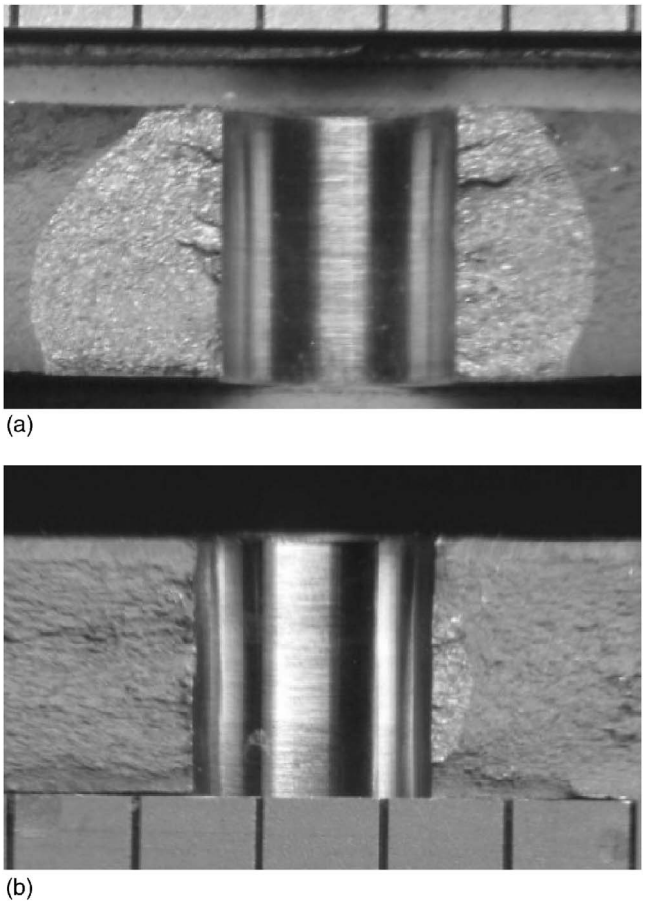

FIG. 14. Cross-sectional images of two holes after coupons were fractured. (a) S3-0001 (7075-T7351). (b) S4-0030 (7075-T651).

veloped, and the second specimen was fatigued until shortly after the crack was detectable. The cross-sectional images of the cracks after the specimens were fractured are shown in Fig. 14. In both cases, the dynamic measurements agree very well with the static measurements. Not considered here is estimation of crack sizes, which is the topic of another paper,[24] but results here confirm that crack size estimates based upon dynamic data should be in good agreement with those determined from static measurements.

VI. SUMMARY AND CONCLUSIONS

An ultrasonic method has been developed to monitor initiation and growth of fatigue cracks emerging from fastener holes during the fatiguing process, and has been verified in aluminum two-hole coupons. This method uses permanently mounted miniature angle beam transducers, which transmit ultrasonic shear waves through a region near a fastener hole that is targeted for monitoring. The energy of the ultrasonic waves transmitted through the affected region is reduced due to the presence of cracks and, further, this energy is modulated by the applied load during fatiguing due to opening and closing of the crack. A normalized energy ratio is calculated as a robust metric for monitoring progression of crack growth, which requires measurement of ultrasonic waveforms as a function of applied load. The work reported here shows results from development of a new method based upon making "dynamic" measurements during fatiguing without either interrupting the test or measuring loads. Waveforms are acquired at random times unsynchronized with the load spectrum, and small shifts in the arrival times of various shear wave components are used to estimate the uniaxial load associated with each waveform, thereby enabling calculation of energy ratios as a function of load. Results agree well with those obtained from static measurements for which fatiguing was interrupted and ultrasonic measurements were made as a function of known applied load.

A theoretical analysis of time shift versus applied load shows that change in path due to elastic deformation combined with the acoustoelastic effect adequately explains the measurements. Both temperature changes and plastic deformation can be ignored as long as the times are referenced to those obtained under no load at the same temperature and state of plastic deformation. Alternatively, measured temperatures could be used to compensate the ultrasonically measured times.

The eventual application of this method is expected to be *in situ* ultrasonic monitoring of crack initiation and growth near "hot spots" in service critical structures. The opening and closing of cracks under applied load modulate the ultrasonic energy that can be transmitted through a crack. In order to properly interpret results under unmeasured and variable loading, it will be necessary to know the actual stress conditions near the crack, and the time-of-flight method demonstrated in this paper is expected to play a key role.

ACKNOWLEDGMENTS

The work of D. M. Stobbe and A. C. Cobb in assisting with the measurements and analysis is gratefully acknowledged. The authors acknowledge and appreciate the support of the Defense Advanced Research Projects Agency (DARPA), Defense Sciences Office, Structural Integrity Prognosis System Program, Contract No. HR0011-04-0003 to Northrop Grumman Corporation, Integrated Systems. This paper is approved for public release with unlimited distribution.

APPENDIX: EQUATIONS OF ACOUSTOELASTICITY FOR ANGLE BEAM SV WAVES

Acoustoelasticity theory is based upon the propagation of a small-amplitude elastic wave in a material subjected to a finite strain. Here we follow the derivation given by Pao[19] for propagation of plane elastic waves in a homogeneous orthotropic medium with initial strains. The equations of motion in the natural (unstrained) coordinates for the elastic wave are

$$A_{\alpha\beta\gamma\delta}\frac{\partial^2 u_\gamma}{\partial a_\beta \partial a_\delta} = \rho_o \ddot{u}_\alpha, \tag{A1}$$

where a_i are the natural coordinates, u_i are the components of displacement, and ρ_o is the density in the natural state. Summation over repeated indices is implied in this and subsequent equations. The coefficients are given by

$$A_{\alpha\beta\gamma\delta} = C_{\beta\delta\epsilon\zeta} e^i_{\epsilon\zeta} \delta_{\alpha\gamma} + \Gamma_{\alpha\beta\gamma\delta}. \tag{A2}$$

The $C_{\beta\delta\epsilon\zeta}$ are the second-order elastic constants, $e^i_{\epsilon\zeta}$ is the initial finite strain tensor, $\delta_{\alpha\gamma}$ is the Kronecker delta function, and $\Gamma_{\alpha\beta\gamma\delta}$ is given by

$$\Gamma_{\alpha\beta\gamma\delta} = C_{\alpha\beta\gamma\delta} + C_{\alpha\beta\lambda\delta}\frac{\partial u^i_\gamma}{\partial a_\lambda} + C_{\lambda\beta\gamma\delta}\frac{\partial u^i_\alpha}{\partial a_\lambda} + C_{\alpha\beta\gamma\delta\epsilon\zeta} e^i_{\epsilon\zeta}. \tag{A3}$$

Here the $C_{\alpha\beta\gamma\delta\epsilon\zeta}$ are the third-order elastic constants. These equations are derived by Pao,[19] Dorfi,[25] and others for an arbitrary homogeneous strain field.

Here we consider propagation of a plane wave in the x_1 direction, which is rotated from the direction of applied uniaxial stress as shown in Fig. 9 where θ is the refracted angle. The Christoffel equation obtained from Eq. (A1) is

$$(A_{\alpha 1 \gamma 1} - \rho_o V^2 \delta_{\alpha\gamma}) U_\alpha = 0. \tag{A4}$$

In this equation, V is the acoustic velocity and U_α, the eigenvector, is the polarization vector. We are interested in the SV wave, which corresponds to the eigenvector that is primarily in the x_2 direction.

Calculation of the nine $A_{\alpha 1 \gamma 1}$ coefficients requires knowledge of the stress and strain tensors. The stress tensor in this rotated coordinate system resulting from a uniaxial stress of σ is given by

$$\tilde{\sigma} = \begin{bmatrix} \sigma \sin^2\theta & -\sigma \sin\theta\cos\theta & 0 \\ -\sigma \sin\theta\cos\theta & \sigma\cos^2\theta & 0 \\ 0 & 0 & 0 \end{bmatrix}. \tag{A5}$$

For a homogeneous and isotropic material, which is assumed to be the case here, there are two independent second-order elastic constants and three independent third-order elastic constants. We use the Lamé constants λ and μ and the Murnaghan constants l, m, and n. Relationships between various third-order elastic constants are given by Norris.[26] The resulting strain tensor can then be calculated as

$$\tilde{\epsilon} = \sigma \begin{bmatrix} \dfrac{2(\lambda+\mu)\sin^2\theta - \lambda\cos^2\theta}{2\mu(3\lambda+2\mu)} & \dfrac{-\sin\theta\cos\theta}{2\mu} & 0 \\ \dfrac{-\sin\theta\cos\theta}{2\mu} & \dfrac{-\lambda\sin^2\theta + 2(\lambda+\mu)\cos^2\theta}{2\mu(3\lambda+2\mu)} & 0 \\ 0 & 0 & \dfrac{-\lambda}{2\mu(3\lambda+2\mu)} \end{bmatrix}. \tag{A6}$$

Both second- and third-order elastic constants are needed to calculate the $A_{\alpha 1 \gamma 1}$.

Calculation of all nine of the $A_{\alpha 1 \gamma 1}$ coefficients is not necessary to determine the velocity of the SV wave. Consider the eigenvalue problem of Eq. (A4) expressed in matrix form,

$$\begin{bmatrix} A_{1111} - \rho_o V^2 & A_{1121} & A_{1131} \\ A_{2111} & A_{2121} - \rho_o V^2 & A_{2131} \\ A_{3111} & A_{3121} & A_{3131} - \rho_o V^2 \end{bmatrix} \begin{bmatrix} U_1 \\ U_2 \\ U_3 \end{bmatrix} = \begin{bmatrix} 0 \\ 0 \\ 0 \end{bmatrix}. \tag{A7}$$

If there is no initial strain, then the off-diagonal terms are zero and the polarization vectors are aligned with the coordinate axes. The finite strain field both perturbs the diagonal terms and introduces small off-diagonal components, but the diagonal terms dominate. Thus, only the A_{2121} term is needed to provide a good estimate of the SV wave velocity.[19] After much algebra and dropping all rotation terms, this component is

$$A_{2121} = \mu + \sigma\left[\frac{2\mu(\lambda+\mu)+\mu m+\frac{1}{4}\lambda n}{\mu(3\lambda+2\mu)}\right] \tag{A8}$$

and the corresponding velocity of the SV wave is

$$V = \sqrt{\frac{\mu}{\rho_o}+\frac{\sigma}{\rho_o}\left[\frac{2\mu(\lambda+\mu)+\mu m+\frac{1}{4}\lambda n}{\mu(3\lambda+2\mu)}\right]}. \tag{A9}$$

Recognizing that the second term under the radical is much smaller than the first, the velocity can be approximated by

$$V = \sqrt{\frac{\mu}{\rho_o}}\left\{1+\sigma\left[\frac{2\mu(\lambda+\mu)+\mu m+\frac{1}{4}\lambda n}{2\mu^2(3\lambda+2\mu)}\right]\right\} = V_o\left(1+\frac{\Delta V}{V_o}\right), \tag{A10}$$

where $V_o=\sqrt{\mu/\rho_o}$. This equation clearly reduces to the usual expression for the shear wave speed when the applied stress is zero.

It is interesting to note that this equation for V has no dependence on θ, the refracted angle. Recall that the above analysis is in reference to the natural, or unstrained, coordinates. A correction term must be applied to obtain the velocity v in the initial, or strained, coordinate system to compensate for the change in path length due to the initial strain,

$$\begin{aligned} v &= V(1+\epsilon_{11}) = V_o\left(1+\frac{\Delta V}{V_o}\right)(1+\epsilon_{11}) \\ &\simeq V_o\left(1+\frac{\Delta V}{V_o}+\epsilon_{11}\right). \end{aligned} \tag{A11}$$

Here ϵ_{11} is the strain in the direction of propagation and is given in Eq. (A6). Upon substitution and after some algebra, we obtain

$$\begin{aligned} v = \sqrt{\frac{\mu}{\rho_o}}\Bigg\{1 &+ \sin^2\theta\left[\frac{4\mu(\lambda+\mu)+\mu m+\frac{1}{4}\lambda n}{2\mu^2(3\lambda+2\mu)}\right] \\ &+ \cos^2\theta\left[\frac{\mu(\lambda+2\mu)+\mu m+\frac{1}{4}\lambda n}{2\mu^2(3\lambda+2\mu)}\right]\Bigg\}\sigma. \end{aligned} \tag{A12}$$

Relative changes in velocity are thus

$$\begin{aligned} \frac{\Delta v}{v_o} = \Bigg\{&\sin^2\theta\left[\frac{4\mu(\lambda+\mu)+\mu m+\frac{1}{4}\lambda n}{2\mu^2(3\lambda+2\mu)}\right] \\ &+ \cos^2\theta\left[\frac{\mu(\lambda+2\mu)+\mu m+\frac{1}{4}\lambda n}{2\mu^2(3\lambda+2\mu)}\right]\Bigg\}\sigma, \end{aligned} \tag{A13}$$

where $v_o=\sqrt{\mu/\rho_o}=V_o$. This equation is in agreement with Eqs. (17)–(19) of Sec. IV B, and is also consistent with equations derived by Hughes and Kelly[17] for $\theta=0°$ and $\theta=90°$. In particular, $\theta=90°$ corresponds to shear wave propagation along the direction of applied stress, and $\theta=0°$ corresponds to shear wave propagation perpendicular to the applied stress and with parallel polarization.

[1] E. Keller and A. Ray, "Real-time nondestructive evaluation of airframe structures for health monitoring and residual life prediction," in *Proceedings of the 20th Digital Avionics Systems Conference* (IEEE, Piscataway, NJ, 2001), Vol. **1**, pp. 3D51–3D512.

[2] G. Bartelds, "Aircraft structural health monitoring, prospects for smart solutions from a European viewpoint," J. Intell. Mater. Syst. Struct. **9**, 906–910 (1999).

[3] C. Boller, "Next generation structural health monitoring and its integration into aircraft design," Int. J. Syst. Sci. **31**, 1333–1349 (2000).

[4] M. G. Silk, "The transfer of ultrasonic energy in the diffraction technique for crack sizing," Ultrasonics **17**, 113–121 (1979).

[5] F. A. Ravenscroft, K. Newton, and C. B. Scruby, "Diffraction of ultrasound by cracks: Comparison of experiment with theory," Ultrasonics **29**, 29–37 (1991).

[6] P. A. Doyle and C. M. Scala, "Depth measurement for corner cracks of arbitrary angle using Rayleigh waves," Ultrasonics **28**, 77–82 (1990).

[7] Z. Chang and A. Mal, "Scattering of Lamb waves from a rivet hole with edge cracks," Mech. Mater. **31**, 197–204 (1999).

[8] P. Fromme and M. B. Sayir, "Detection of cracks at rivet holes using guided waves," Ultrasonics **40**, 199–203 (2002).

[9] P. Bövik and A. Boström, "A model of ultrasonic nondestructive testing for internal and subsurface cracks," J. Acoust. Soc. Am. **102**, 2723–2733 (1997).

[10] J. D. Achenbach, "Modeling for quantitative non-destructive evaluation," Ultrasonics **40**, 1–10 (2002).

[11] N. Rajic, S. C. Galea, and W. K. Chiu, "Autonomous detection of crack initiation using surface-mounted piezotransducers," Smart Mater. Struct. **11**, 107–114 (2002).

[12] J. Y. Kim, V. A. Yakovlev, and S. I. Rokhlin, "Surface acoustic wave modulation on a partially closed fatigue crack," J. Acoust. Soc. Am. **115**, 1961–1972 (2004).

[13] S. Vanlanduit, E. Parloo, and P. Guillaume, "An on-line combined linear-nonlinear fatigue crack detection technique," NDT & E Int. **37**, 41–45 (2004).

[14] A. E. Ekimov, I. N. Didenkulov, and V. V. Kazakov, "Modulation of torsional waves in a rod with a crack," J. Acoust. Soc. Am. **106**, 1289–1292 (1999).

[15] J. E. Michaels, T. E. Michaels, B. Mi, A. C. Cobb, and D. M. Stobbe, "Self-calibrating ultrasonic methods for in-situ monitoring of fatigue crack progression," in *Review of Progress in Quantitative Nondestructive Evaluation*, edited by D. O. Thompson and D. E. Chimenti (American Institute of Physics, New York, 2005), Vol. **24B**, pp. 1765–1772.

[16] B. Mi, T. E. Michaels, and J. E. Michaels, "In-situ monitoring of crack growth under static and dynamic loading conditions," in *Proceedings of the SPIE Conference on Nondestructive Evaluation and Health Monitoring of Aerospace Materials, Composites, and Civil Infrastructure IV*, edited by P. J. Shull, A. L. Gyekenyesi, and A. A. Mufti (SPIE, Bellingham, WA, 2005), Vol. 5767, pp. 1–9.

[17] D. S. Hughes and J. L. Kelly, "Second-order elastic deformation of solids," Phys. Rev. **92**(1), 1145–1149 (1953).

[18] Y.-H. Pao, W. Sachse, and H. Fukuoka, "Acoustoelasticity and ultrasonic measurements of residual stress," in *Physical Acoustics Volume XVII*, edited by W. P. Mason and R. N. Thurston (Academic Press, New York, 1984), pp. 61–143.

[19] Y.-H. Pao and U. Gamer, "Acoustoelastic waves in orthotropic media," J. Acoust. Soc. Am. **77**, 806–812 (1985).

[20] J. Qu and G. Liu, "Effects of residual stress on guided waves in layered media," in *Review of Progress in Quantitative Nondestructive Evaluation*, edited by D. O. Thompson and D. E. Chimenti (American Institute of Physics, New York, 1998), Vol. **17**, pp. 1635–1642.

[21] X. H. Min and H. Kato, "Change in ultrasonic parameters with loading/unloading process in cyclic loading of aluminum alloy," Mater. Sci. Eng., A **372**, 269–277 (2004).

[22] D. M. Stobbe, "Acoustoelasticity in 7075-T651 aluminum and dependence of third order elastic constants on fatigue damage," Master's thesis, Georgia Institute of Technology, 2005.

[23]Y. Lu and J. E. Michaels, "A methodology for structural health monitoring with diffuse ultrasonic waves in the presence of temperature variations," Ultrasonics **43**, 717–731 (2005).
[24]J. E. Michaels, T. E. Michaels, and B. Mi, "An ultrasonic angle beam method for in situ sizing of fastener hole cracks," J. Nondestruct. Eval. (to be published).
[25]H. R. Dorfi, H. R. Busby, and M. Janssen, "Ultrasonic stress measurements based on the generalized acoustic ratio technique," Int. J. Solids Struct. **33**, 1157–1174 (1996).
[26]A. N. Norris, "Finite-amplitude waves in solids," in *Nonlinear Acoustics*, edited by M. F. Hamilton and D. T. Blackstock (Academic Press, New York, 1998), pp. 263–277.

The near-ground structure of the nocturnal sound field

Roger Waxler, Carrick L. Talmadge, Shantharam Dravida, and Kenneth E. Gilbert
National Center for Physical Acoustics, University of Mississippi, University, Mississippi 38677

(Received 31 January 2005; revised 9 August 2005; accepted 27 October 2005)

The near-ground behavior of the low-frequency (100 Hz to 500 Hz) sound field in the nocturnal sound duct is studied theoretically and experimentally. In the first few meters of the atmosphere, narrow-band sound fields are found to have a characteristic vertical structure. The sound field is the superposition of a "surface mode," whose magnitude decreases monotonically with altitude, with a sum of "higher modes," each of whose magnitudes has a pronounced minimum a few meters from the ground at approximately the same height. The surface mode attenuates to negligible levels after a few hundred meters from the source. Consequently, more than a few hundred meters from a narrow-band source, there is a "quiet height" at which the sound level is reduced by 10 to 15 dB relative to its value on the ground. The narrow-band quiet height is shown to be a robust feature of nocturnal sound propagation. © *2006 Acoustical Society of America.* [DOI: 10.1121/1.2139654]

PACS number(s): 43.28.Fp, 43.28.Gq [DKW] Pages: 86–95

I. INTRODUCTION

In this paper, sound propagation outdoors at night is studied. It is shown theoretically and verified experimentally that, for narrow-band signals received at long ranges from the source, there is a robust and stable quiet height a few meters from the ground at which sound pressure levels are significantly reduced.

Downward refraction of sound is typical of the nocturnal environment.[1–4] The cooling of the ground during and after sunset causes the air near the ground to be cooler than the air above so that, near the ground, the sound speed increases with altitude. Wind can have a large effect on the sound propagation, however for sound propagating long distances from a source near the ground to a receiver near the ground, the effective sound speed approximation[1,3,5,6] may be used to account for the effect of the winds. In this approximation, the thermodynamic sound speed in the wave equation is replaced with an effective sound speed given by the thermodynamic sound speed plus the horizontal component of the wind velocity in the direction of propagation. Assuming it depends only on altitude z, $c_{\text{eff}}(z)$ will be used to denote effective sound speed as a function of height. A model[4] nocturnal effective sound speed profile is shown in Fig. 1. Some measured profiles can be found in Fig. 8 of Ref. 2 and Fig. 16 of Ref. 7.

Generally speaking, nocturnal effective sound speed profiles have a steep positive gradient near the ground and a maximum at an inversion height, z_I, above which they begin to decrease.[4] The effective sound speed gradient typically satisfies

$$\frac{dc_{\text{eff}}}{dz} \gg \frac{c_{\text{eff}}(z_I) - c_{\text{eff}}(0)}{z_I} \tag{1}$$

for small z and decreases to zero at the inversion height. The region between the ground and the inversion height will be referred to as the effective sound speed inversion. Note that such profiles are downward refracting in the inversion but upward refracting above the inversion.

Sound propagation is also influenced by interaction with the ground. To account for the effect of the ground, the local impedance approximation may be used.[8] In this approximation, an impedance boundary condition is imposed at the ground surface. The impedance has both real and imaginary parts to model the attenuation by and compliance of the ground, respectively. A variety of ground impedance models are discussed in the textbook cited in Ref. 3. In this paper the ground impedance model from Zwicker and Kosten[9] described in Appendix C of Ref. 3 is used. The free parameters in this model are chosen (in a way to be discussed) to model the site where the experiments were performed. The resulting ground impedance is shown in Fig. 2.

For outdoor sound propagation in atmospheres which are downward refracting near the ground there is a sound duct so that at large distances from the source the sound field exhibits structure associated with the superposition of modes in a duct.[2,10–12] Figure 3 shows the sound field produced by a 150 Hz unit point source on the ground. The sound field is modeled using the methods of Ref. 11 and Ref. 12 for the sound speed profile in Fig. 1 and the ground impedance model shown in Fig. 2. A gray scale plot of the sound pressure level in dB relative to spherical spreading, $20\log[rP(r)/P(1)]$, where P is acoustic pressure and r is range, is depicted as a function of altitude and range. Levels are plotted here relative to spherical spreading to compensate for the geometrical cylindrical spreading of the pressure field as well as for the added attenuation due to atmosphere and ground.

One sees in this plot the interference patterns common to ducted propagation. Note that, beginning less than a kilometer from the source, one sees a height, about 3.5 m in this example, at which the magnitude of the sound field is markedly reduced. As opposed to the minima which are visible across the plot at varying heights and ranges, this minimum occurs at an approximately fixed height independent of range. This is the quiet height alluded to above.

In this paper, it will be shown that the existence of this quiet height depends only on the sound speed having a steep

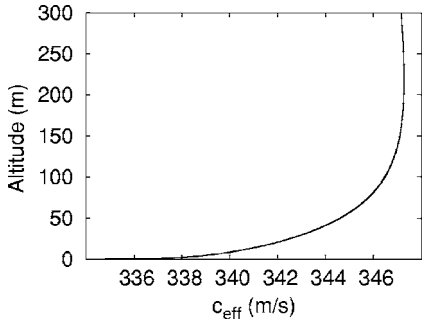

FIG. 1. A model nocturnal effective sound speed profile, $c_{\text{eff}}(z)$. The explicit form taken here for $c_{\text{eff}}(z)$ is discussed in Sec. II B.

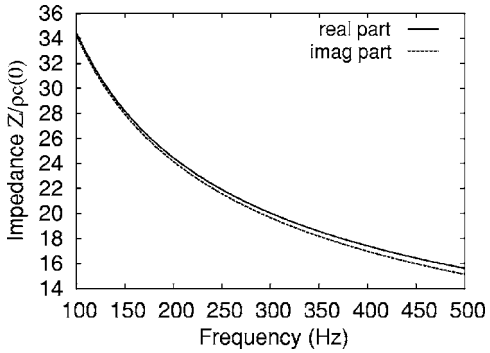

FIG. 2. Normalized ground impedance $\mathcal{Z}/\rho_0 c(0)$. Here, ρ_0 is the mean density of air and $c(0)$ is the thermodynamic soundspeed on the ground. The Zwicker–Kosten model from Appendix C of Ref. 3 is used. The explicit form is discussed in Sec. II B.

near-ground gradient, Eq. (1), on the sound speed having an inversion and on the ground attenuating the sound. These are all typical features of sound propagation outdoors at night. Further, the quiet height is shown to reflect mode shapes and attenuation rather than an interference pattern produced by superposition. Thus, unlike modal interference minima, the quiet height is stable against small changes in sound speed.

An experiment was devised to test these predictions of a quiet height. The experiment was performed in the evening, beginning shortly before sunset, in fair weather. The experimental site was a farm field in the Mississippi Delta,[13] chosen because it is quiet and flat. A vertical array of microphones was placed 1.8 km from a loudspeaker which broadcast tones swept from 100 Hz to 500 Hz. The experiment is illustrated in Fig. 4. Both the existence and stability of the quiet height were validated by the experimental results.

We see the current investigation as the first direct experimental evidence demonstrating the validity of the modal picture of nocturnal sound propagation. The results presented here suggest that it may be possible to use long-range acoustic propagation measurements with short vertical arrays (several meters tall) at a fixed range to remotely monitor the nocturnal boundary layer.

The paper is organized as follows. The theoretical arguments are presented in Sec. II. The description of the experiment and discussions of the experimental results are presented in Sec. III. Our conclusions are contained in Sec. IV.

II. THEORY

A. The nocturnal modes

The theoretical arguments given here are based on a modal picture of the nocturnal sound field.[11,12] At ranges greater than about 0.5 km, a narrow-band sound field propagating in the duct caused by the effective sound speed inversion is given by a sum over vertical modes. Explicitly, if P is the acoustic pressure field produced by a unit point source at height z_0, f the cyclic frequency, $\omega=2\pi f$ the angular frequency, r the range from the source, and z the altitude, then

$$P(\omega,r,z) = -\sqrt{\frac{i}{8\pi r}}\sum_{j=0}^{N}\frac{e^{ik_j r}}{\sqrt{k_j}}\phi_j(z_0)\phi_j(z). \tag{2}$$

Here ϕ_j is the jth vertical mode and k_j is the mode's horizontal wave number; modes are listed in order of decreasing real parts of the horizontal wave numbers beginning with the largest at $j=0$ and the smallest at $j=N$. The modes and horizontal wave numbers are determined by the condition that

$$\left(\frac{d^2}{dz^2} + k(z)^2 - k_j^2\right)\phi_j(z) = 0. \tag{3}$$

Here, $k(z)=\omega/c_{\text{eff}}(z)+i\alpha(\omega)$ is the wave number, $c_{\text{eff}}(z)$ is the sound speed, $\alpha(\omega)$ is the atmospheric attenuation coefficient,[14–16] and ϕ_j is the suitably normalized[11,12] asymptotically exponentially decreasing solution satisfying the boundary condition

$$\phi_j'(0) = -\mathcal{C}(\omega)\phi_j(0) \tag{4}$$

where, for ground impedance[3] $\mathcal{Z}(\omega)$ and ambient density of the air ρ_0,

$$\mathcal{C}(\omega) = \frac{i\omega\rho_0}{\mathcal{Z}(\omega)}. \tag{5}$$

Note that $\mathcal{Z}$ generally has both real and imaginary parts. Consequently, the imaginary parts of the k_j are generally larger than the atmospheric attenuation coefficient, the increased attenuation being due to interaction with the ground.

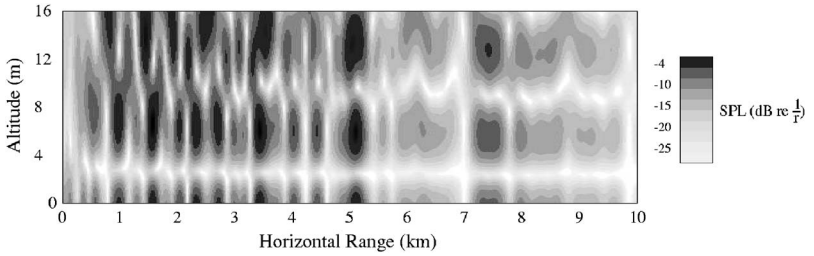

FIG. 3. The sound field produced at 150 Hz by a point source on the ground in the sound speed profile shown in Fig. 1 as predicted by the modal model developed in Refs. 11 and 12. Explicitly, $20\log(rP(r)/P(1))$ is plotted where P is pressure and r is range in meters.

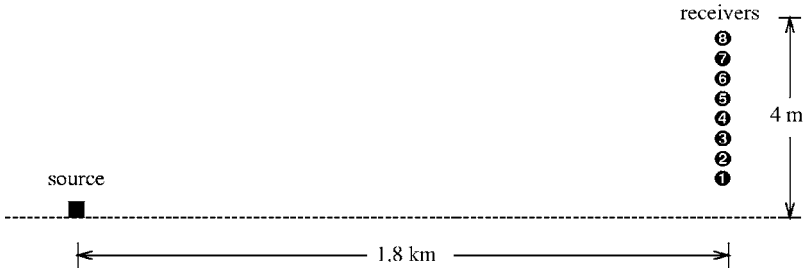

FIG. 4. The experimental setup: A source (only the source on the ground is depicted) and a vertical array of microphones placed 1.8 km from the source.

For propagation in sound speed profiles such as in Fig. 1 over ground with impedances such as in Fig. 2, the modes ϕ_j and wave numbers k_j can be determined using the analytical methods developed in Refs. 11 and 12. The procedure is to first approximate the modes and their horizontal wave numbers by replacing the sound speed profile with one that is constant above the inversion height, equal to the sound speed at inversion. The effect of the upward refraction above the sound speed inversion can then be treated perturbatively. To obtain the first approximation, the analytical methods developed in Ref. 11 have been implemented numerically by discretizing Eq. (3) using a central difference approximation for the second derivative and solving the resulting eigenvalue problem using Sturm's method.[17,18] The corrections due to the upward refraction above the sound speed inversion can be obtained as in Ref. 12. It is found, however, that for the ranges considered here (a few kilometers) these corrections have little effect on the propagation and thus have not been included.

B. An example

The results of this section are valid as long as the sound speed has an inversion and satisfies Eq. (1) and as long as the ground impedance has positive real and imaginary parts. However, to illustrate with an example explicit forms for sound speed and impedance must be chosen. For an example, sound speed profile take the temperature to be given by an exponential model[4]

$$T(z) = T(0) + \Delta T(1 - e^{-\alpha z}) - \Gamma z, \tag{6}$$

and the wind velocity by a logarithmic model[4]

$$\mathbf{v}(z) = \begin{cases} 0 & \text{for } z < h_1 \\ \mathbf{v}(h_2)\dfrac{\log(z/h_1)}{\log(h_2/h_1)} & \text{for } z \geqslant h_1 \end{cases}. \tag{7}$$

Here, $T(0)$ is the temperature on the ground, taken to be 290 K, and Γ is the temperature lapse rate, taken to be the adiabatic value[4] for dry air $\Gamma \approx 0.00975$ K/m.[19] The parameters ΔT and α are free parameters. Similarly, $\mathbf{v}(h_2)$ is the wind velocity at height h_2; h_1 is the stagnation height. The effective sound speed is taken to be

$$c_{\text{eff}}(z) = \sqrt{\gamma RT(z)} + \mathbf{n} \cdot \mathbf{v}(z), \tag{8}$$

where γ is the specific heat ratio for air, R is the gas constant, and $\mathbf{n}$ is a horizontal unit vector pointing from source to receiver. The example ground impedance used is the Zwicker–Kosten model given by Eqs. (C9) through (C11) of Ref. 3. This model has three free parameters: Flow resistivity, porosity, and shape factor.

The explicit forms plotted in Figs. 1 and 2 were obtained by choosing the free parameters above so as to give quantitative agreement with the experimental data to be presented in the next section. The mean horizontal wind speed was measured during the experiment to be 3.3 m/sec at elevation $h_2 = 3.4$ m. The propagation path in the experiment was close to downwind so that $\mathbf{n} \cdot \mathbf{v}(h_2) = 3.4$ was fixed. The stagnation height was taken to be 0.1 m. A least-squares algorithm[17] was used to determine ΔT, α, flow resistivity, and porosity. The shape factor was fixed at 0.6. The values of the various parameters, whether determined by the least-squares algorithm or fixed, are tabulated in Tables I and II.

In Fig. 5, the modal horizontal wave numbers for this model are displayed as functions of frequency. Figure 5(a) shows $\text{Re}\, k_j/k_I$, the real parts of the horizontal wave numbers normalized by the wave number $k_I = \text{Re}\, k(z_I)$ at the turning height. Figure 5(b) shows the attenuation coefficients, $\text{Im}\, k_j$. In Fig. 6, the modes at 150 Hz are shown. Figure 6(a) shows the modes superimposed on the wave number profile which produced them. Each mode function is shifted by the real part of its modal horizontal wave number $\text{Re}\, k_j$. Figure 6(b) shows a near-ground detail of the magnitudes of the modes.

Note that the first mode, labeled with a subscript 0, is a special case. It will be referred to as the "surface mode." The other modes will be referred to as the "higher modes." There is a large gap between the surface mode wave number and the higher mode wave numbers. In addition, the attenuation of the surface mode by the ground is an order of magnitude greater than that of any of the higher modes. Consequently, the surface mode attenuates rapidly with range, becoming

TABLE I. Model parameters for the effective sound speed, either as determined by the least-squares method or fixed.

Temperature offset, ΔT	11.1 K	Least squares
Exponential factor, α	0.021 m^{-1}	Least squares
Ground temperature, $T(0)$	290 K	Fixed
Wind speed, $\mathbf{n} \cdot \mathbf{v}\|_{z=3.4\text{ m}}$	3.4 m/s	Fixed
Stagnation height, h_1	0.1 m	Fixed

TABLE II. Model parameters determined for the ground impedance model, either as determined by the least-squares method or fixed.

Flow resistivity	1164 kPa s/m^2	Least squares
Porosity	0.64	Least squares
Shape factor	6	Fixed

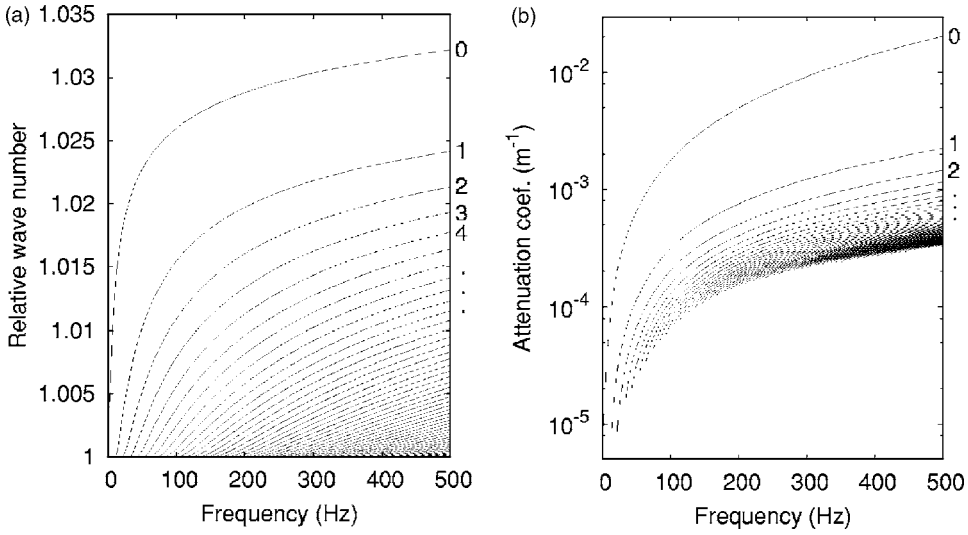

FIG. 5. The modal wave numbers for the sound speed profile of Fig. 1 and the ground impedance model described in the text. (a) Real parts normalized by the wave number at the turning height, $\mathrm{Re}\, k_j/k_I$. (b) Attenuation coefficients, $\mathrm{Im}\, k_j$. The mode numbers of the first few modes are to the right of the wave number curve.

negligible after a few hundred meters, while the higher modes persist for kilometers. Further, the surface mode's magnitude is monotonically decreasing with increasing altitude, while the magnitudes of each of the higher modes has a deep first minimum near the ground. Surprisingly, the lowest minima of each of these higher modes lie close to each other. In the example shown in Fig. 6(b), they lie in a band between 2.2 and 3.25 m elevation. In the sum Eq. (2), the surface mode ($j=0$), the single mode without a minimum, attenuates rapidly while the remaining modes ($j>0$) persist, but all have a minimum at about the same height. This explains the quiet height seen in Fig. 3.

C. The quiet height

The existence of the quiet height seen at long ranges in the example above is a general feature of nocturnal sound propagation over flat terrain. Generally, the sound speed gradient is quite steep near the ground, as in Eq. (1), but decreases to zero as the altitude increases to the inversion height. The resulting sound duct is relatively narrow near the ground, widening as the height increases to the inversion height. As a consequence, the spacing between adjacent modal wave numbers decreases with increasing mode number. The steep gradient near the ground exaggerates the gap between the surface mode's wave number and the higher mode wave numbers. The width of the duct near the inversion causes higher mode wave numbers, k_j, to cluster below $k_I=\mathrm{Re}\, k(z_I)$, the wave number at the inversion height, as j increases.

Note that the jth mode becomes evanescent, decreasing rapidly with altitude for z, at which $\mathrm{Re}\, k_j>\mathrm{Re}\, k(z)$. It follows that the gap between the surface mode wave number and the higher mode wave numbers causes the surface mode to be concentrated more closely to the ground than the higher modes. The greater interaction with the ground causes the surface mode to attenuate much more rapidly with distance than the higher modes. Figure 5(b) shows that in the example considered above and for frequencies greater than 100 Hz, the surface mode is insignificant after a few hundred meters. The remaining sound field is a superposition of higher modes.

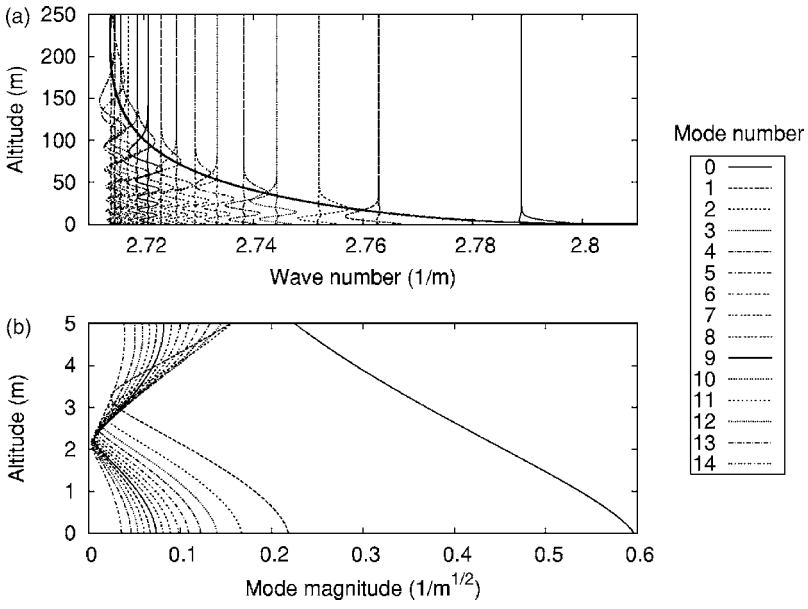

FIG. 6. The modes for the sound speed profile of Fig. 1 at 150 Hz. (a) Real and imaginary parts of the mode functions, shifted by the real part of the modal wave number, superimposed on the wave number profile. (b) Magnitudes of the modes near the ground.

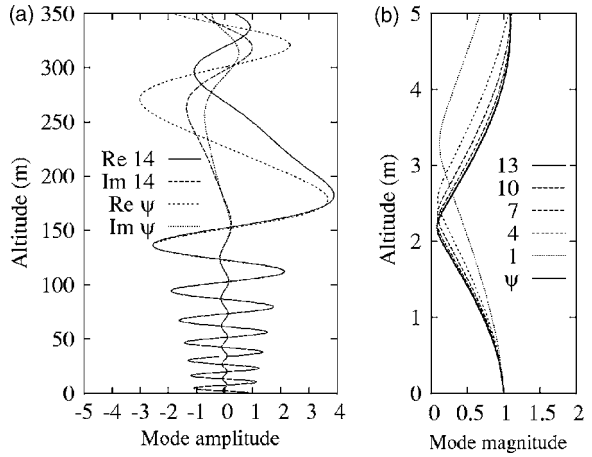

FIG. 7. (a) Comparing real and imaginary parts of the mode at inversion, ψ, to the real and imaginary parts of the last mode, mode 14, normalized by its value at $z=0$, for the sound speed profile of Fig. 1 at 150 Hz. At low altitudes the two are identical. (b) Comparing the normalized magnitudes of the modes to the mode at inversion.

That the lowest minima of the higher modes should be close to each other is a consequence of their wave number's clustering. For large enough j, the modal wave number, k_j, is close to the wave number at the top of the inversion, k_I. Let ψ be the solution of Eq. (3) with $k_j=k_I$,

$$\left(\frac{d^2}{dz^2}+k(z)^2-k_{\mathrm{I}}^2\right)\psi(z)=0,$$

satisfying Eq. (4) and $\psi(0)=1$. For large enough j and for sufficiently small z, one can replace k_j with k_I in Eq. (3) so that

$$\frac{\phi_j(z)}{\phi_j(0)}\approx\psi(z). \tag{9}$$

In Fig. 7(a), Eq. (9) is tested for the highest mode, $j=14$, for the example above at 150 Hz. At low altitudes, Eq. (9) is a very good approximation. In Fig. 7(b), it is seen that Eq. (9) becomes less accurate as j decreases. The magnitudes of several of the modes, normalized by their value on the ground, $|\phi_j(z)/\phi_j(0)|$, are compared to $|\psi(z)|$ in the first few meters of the atmosphere. Note that Eq. (9) is rigorously true for larger j, getting worse as j decreases. However, it remains qualitatively true for all of the higher modes. Thus, as solutions to Eq. (3), in the first few meters there is little difference between the different higher modes other than normalization. In particular, the altitude of the lowest minimum of $|\phi_j|$ is close to the altitude of the lowest minimum of $|\psi|$. Further, Eq. (9) suggests that near the ground, the shape of the higher modes are stable against atmospheric fluctuations. For small z, the difference between the k_I and $k(z)$ is large compared to perturbations in wave number. Consequently, such perturbations will have little effect on the approximate mode shape $\psi(z)$ near the ground.

The example shown in Fig. 6(b) shows Eq. (9) to be only qualitatively true for smaller j. However, the modal attenuation rates decrease with increasing j. As a consequence, the quiet height will vary slowly with range as the modes with smaller j attenuate. Asymptotically with increasing range, the quiet height is given by the altitude of the lowest minimum of $|\psi|$.

As a simple example, consider the case in which, for small z, $k(z)$ can be expanded in a Taylor series about $z=0$ (note that this is the case for the example considered in Sec. II B only if the wind speed is zero). Then, one can solve Eq. (3) by expanding in powers of z,[20]

$$k(z)=k(0)+k'(0)z+\ldots$$

and

$$\phi_j(z)=\phi_j(0)+\phi_j'(0)z+\frac{1}{2}\phi_j''(0)z^2+\ldots.$$

Substituting in Eq. (3) and using Eq. (5) to determine $\phi_j'(0)$, one obtains the small z asymptotic form

$$\phi_j(z)\approx\phi_j(0)\left(1-\mathcal{C}z-\frac{1}{2}(k(0)^2-k_j^2)z^2+\ldots\right).$$

Note that

$$\psi(z)=1-\mathcal{C}z-\frac{1}{2}(k(0)^2-k_{\mathrm{I}}^2)z^2+\ldots.$$

Note that $\mathcal{C}/k(0)=i\rho_0c(0)/\mathcal{Z}$ is fairly small. Thus, the height of the lowest minimum of the jth mode, z_j, can be approximated by setting $\mathcal{C}=0$. One obtains

$$z_j\approx\sqrt{\frac{2}{k(0)^2-k_j^2}}.$$

In this case, the long-range asymptotic quiet height is $\sqrt{2/(k(0)^2-k_I^2)}$ and depends only on the values of the effective sound speed on the ground and at the top of the inversion.

Finally, note that there is a quiet height for sound radiation as well as reception. Holding the receiver fixed and varying the altitude of the source amounts to holding z fixed in Eq. (2) and asking how the received pressure varies as a function of z_0. The conclusions are clearly unchanged. This is not a consequence of the classical reciprocity principle since exchanging source and receiver changes the propagation path and thus can change the effective sound speed. In particular, the quiet height can depend on the direction of propagation. Rather, it is a consequence of an extended reciprocity principle in which source and receiver are exchanged and wind direction reversed.[21]

D. The stability of the quiet height

Some comments are in order on the comparison of Eq. (2) with observations. The modal expansion given in Eq. (2) assumes a temporally and horizontally constant sound speed profile. This leads to the fixed interference minima and maxima seen in Fig. 3. In reality, the sound speed profile fluctuates both temporally and spatially due to turbulent flow and buoyancy waves.[7,22] In the presence of such fluctuations, the delicate phase relationships responsible for the interference patterns cannot be expected to be stable. One expects that the interference patterns shift around as the atmosphere

fluctuates, so that the interference minima are perceived as sound randomly fading in and out rather than as stable quiet spots. In order for the quiet height to truly be a quiet height, it must be stable against atmospheric fluctuations. While a detailed discussion of the effects of the fluctuations of the nocturnal boundary layer is well beyond the scope of this paper, a discussion of the stability of the quiet height will be given. Furthermore, the statistical procedure used in comparing theoretical predictions to experimental results will be discussed.

In comparing theoretical predictions to experimental data, a common procedure is to consider the power spectral density of the measured acoustic pressure, given by the mean square of the Fourier transform of the signal at the receiver.[23] If $\langle\ \rangle$ denotes an average over many runs of an experiment, and if $P(\omega)$ is the Fourier transform of the received signal, then the power spectral density is given by $\langle|P(\omega)|^2\rangle$.

To compute the power spectrum theoretically, it will be assumed that as the atmosphere fluctuates, it remains close enough to being stationary and range independent so that a modal expansion as given in Eq. (2) is valid. Then, one has

$$\langle|P(\omega,r,z)|^2\rangle = \frac{1}{8\pi r}\sum_{j,n=0}^{N}\left\langle \frac{e^{i(k_j-k_n^*)r}}{\sqrt{k_j k_n^*}}\phi_j(z_0)\phi_j(z)\phi_n(z_0)^*\phi_n(z)^*\right\rangle. \quad (10)$$

For sufficiently long ranges r, the surface mode contributions can be dropped from Eq. (10). Further, it has been argued that, near the ground, the shapes of the higher modes are all approximately the same, given by Eq. (9) up to a normalization factor, and do not vary significantly as the atmosphere fluctuates. Dropping the surface mode contributions and, assuming the receiver height z to be near the ground, substituting Eq. (9) in Eq. (10) for the higher modes, the mode shapes can be factored out of both the sum and the average giving

$$\langle|P(\omega,r,z)|^2\rangle \approx \frac{1}{8\pi r}|\psi(z)|^2\sum_{j,n=1}^{N}\left\langle \frac{e^{i(k_j-k_n^*)r}}{\sqrt{k_j k_n^*}}\phi_j(z_0)\phi_j(0)\phi_n(z_0)^*\phi_n(0)^*\right\rangle.$$

Substituting Eq. (9) in Eq. (2), one finds that, if normalized by their values at some representative near-ground altitude, say z_{ref}, the root-mean-square sound pressure and the actual sound pressures will be approximately equal near the ground:

$$\frac{|P(\omega,r,z)|}{|P(\omega,r,z_{\mathrm{ref}})|}\approx\frac{|\psi(z)|}{|\psi(z_{\mathrm{ref}})|}\approx\sqrt{\frac{\langle|P(\omega,r,z)|^2\rangle}{\langle|P(\omega,r,z_{\mathrm{ref}})|^2\rangle}}. \quad (11)$$

Equation (11) is based on Eq. (9) and cannot be expected to be numerically precise. We can, however, conjecture that in a fluctuating atmosphere the normalized pressure amplitude $|P(\omega,r,z)/P(\omega,r,z_{\mathrm{ref}})|$ has considerably less variability for small z than the pressure amplitude $|P(\omega,r,z)|$ alone.

To see how well Eq. (11) works in practice, we consider an example. A simple theoretical averaging procedure is to assume random relative phases between the modes. With this assumption the cross terms between different modes in Eq. (10) vanish and one arrives at

$$\langle|P|^2\rangle\approx-\frac{1}{8\pi r}\sum_{j=1}^{N}\frac{e^{-2\ \mathrm{Im}\ k_j r}}{|k_j|}|\phi_j(z_0)\phi_j(z)|^2. \quad (12)$$

The square root of the expression Eq. (12) for the power spectral density is often referred to as the incoherent modal sum for the root-mean-square pressure magnitude.[18] The form given in Eq. (2) will be referred to hereafter as the coherent modal sum.

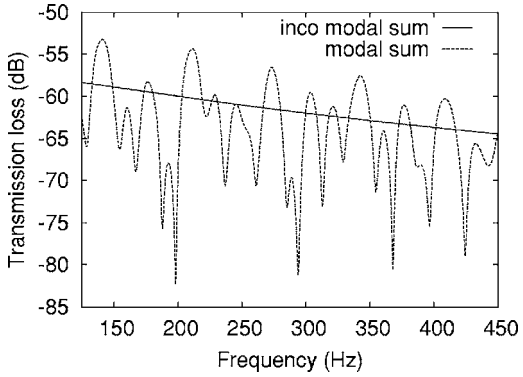

FIG. 8. Coherent and incoherent modal sums for the transmission loss for ground to ground propagation in the sound speed profile of Fig. 1 and ground impedance of Fig. 2 at a range of 1.8 km as a function of frequency.

In Fig. 8, the coherent and incoherent modal sums at 1.8 km for the transmission loss[18] [in this paper, the formula $20\log(4\pi|P|)$, with P given by Eq. (2) for the coherent sum and by the square root of Eq. (12) for the incoherent sum, is used for transmission loss] for ground to ground propagation in the sound speed profile of Fig. 1 and ground impedance of Fig. 2 are shown as functions of frequency. Note that the incoherent modal sum gives a smoothly varying function of frequency as compared to the coherent modal sum which shows considerable variability. In Fig. 9, the coherent and incoherent modal sums for the pressure magnitude at 150 Hz, normalized by their respective values on the ground, $|P(\omega,r,z)/P(\omega,r,0)|$ and $\sqrt{\langle|P(\omega,r,z)|^2\rangle/\langle|P(\omega,r,0)|^2\rangle}$, are shown at several ranges. The normalized coherent sums in Fig. 9 show considerably more structure at higher altitudes than the normalized incoherent sums. Near the ground, at altitudes of 5 m or less, they are remarkably similar.

In Fig. 9, a height at which the sound pressure magnitude has a distinct minimum (the quiet height) is clearly visible in both coherent and incoherent sums. Consider the dependence of the quiet height on frequency. In Fig. 10, the quiet height for the sound speed profile of Fig. 1 and ground impedance of Fig. 2 is plotted as a function of frequency at a fixed range of 1.8 km (the range used in the experiment is discussed in the next section). Figure 10 shows that the quiet height is roughly inversely proportional to frequency.

Figure 11 shows the coherent and incoherent sums for the transmission loss for a source on the ground and receiver at 1.5 m elevation at fixed range (1.8 km) as a function of frequency. The quiet height can be seen centered at 250 Hz.

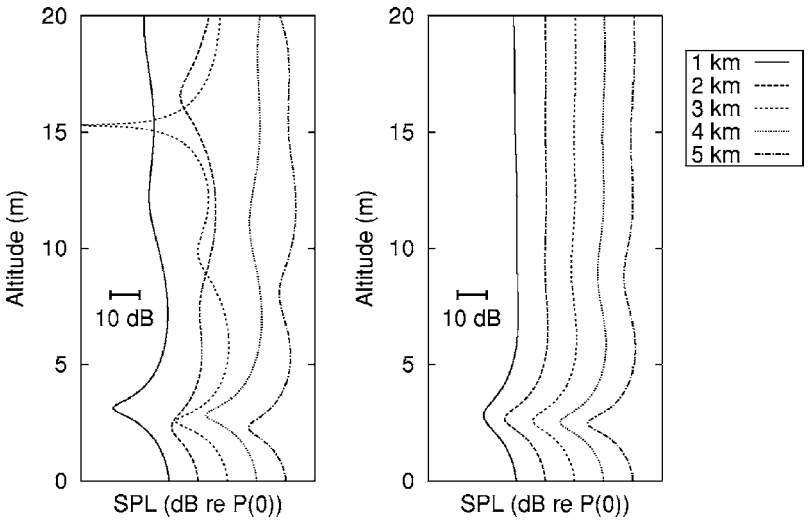

FIG. 9. Coherent and incoherent modal sums for the pressure field magnitude in dB relative to their value on the ground, $20\log(|P(\omega,r,z)/P(\omega,r,0)|)$, at various ranges; 1 km, 2 km, 3 km, 4 km, and 5 km; due to a point source on the ground at 150 Hz in the sound speed profile of Fig. 1 and ground impedance of Fig. 2. (a) Coherent sum. (b) Incoherent sum. Successive curves are displaced by 10 dB so as to be more clearly visible.

In Fig. 6(b), the height of the lowest minimum of the higher modes decreases with increasing j. Further, the attenuation coefficients generally decrease with increasing j, so that at increasing ranges the modes with smaller j become less significant. Thus, one expects that the quiet height should decrease with increasing range as the lower modes attenuate. This effect is visible in the incoherent sum shown in Fig. 9, and in Fig. 12 in which the quiet height at 150 Hz is shown as a function of range.

The variations of the coherent modal sum relative to the incoherent modal sum seen in Figs. 10–12 do not imply that the quiet height itself varies. Rather, modal interference can cause the sound pressure magnitude to have a minimum, lower than that produced by the modal minima, above or below the quiet height. However, as seen in both Figs. 3 and 9, the quiet height is always an altitude at which the sound pressure level is low.

III. EXPERIMENT

A. Methodology

An experiment was performed to study the stability of the normalized pressure amplitude profile and to verify the existence of the quiet height. The experiment was performed on a farm in the Mississippi Delta region where the ground is very flat and there are few trees or houses to complicate the propagation. The experiment consisted of two loudspeakers and a vertical array of microphones placed approximately 1.8 km away from the loudspeakers. The experimental setup is depicted in Fig. 4.

The loudspeakers were Philips LBC3700 horns (Koninklijke Philips Electronics N.V., Eindhoven, Netherlands), chosen because they have a fairly flat response over the frequency band of interest and are designed for outdoor use. One was placed on the ground and a second was mounted on the top of a 10 m tower.

The microphone array consisted of a 4 m tower instrumented with eight Brüel and Kjaer (Naerum, Denmark) type 4191 microphones spaced vertically 0.4 m apart, beginning with the lowest microphone at 0.8 m elevation. The transfer function for the amplifier loudspeaker system was determined in an anechoic chamber. The microphones were calibrated to better than 0.1 dB using a Brüel and Kjaer type 4226 absolute pressure calibrator.

The experiment was performed on April 10, 2004 between 7:40 PM (19:40) and 9:00 PM (21:00), Central Standard Time. Over the course of the experiment, the mean wind velocity was monitored using a Campbell Scientific (Logan, Utah) CSAT3 sonic anemometer mounted at an altitude of 3.4 m. The mean wind speed was 3.3 m/s with a

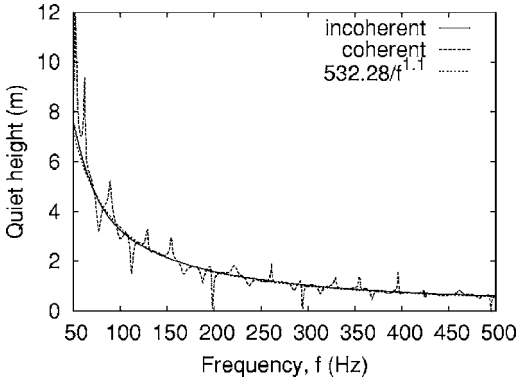

FIG. 10. The quiet height as a function of frequency at a fixed range (1.8 km). The quiet height is determined from both coherent and incoherent modal sums. The sound field is that of a point source on the ground in the sound speed profile of Fig. 1 and ground impedance of Fig. 2.

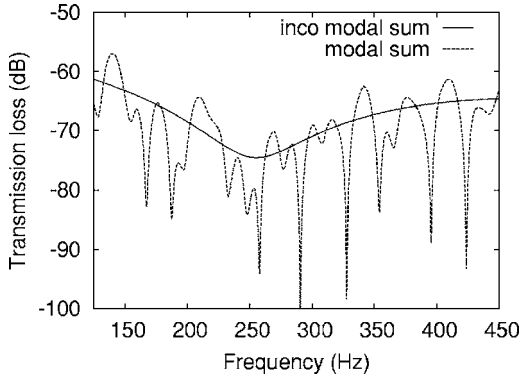

FIG. 11. Coherent and incoherent modal sums for the transmission loss at $z=1.5$ m in the sound speed profile of Fig. 1 and ground impedance of Fig. 2 as a function of frequency.

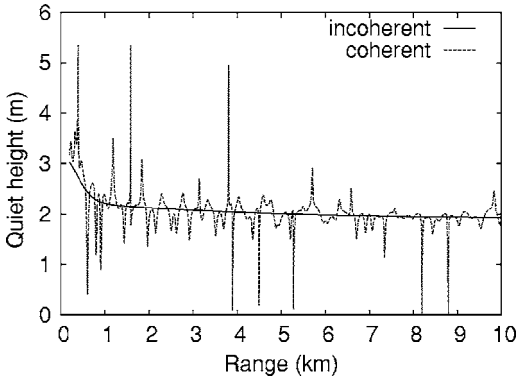

FIG. 12. The quiet height as a function of range at 150 Hz determined from both coherent and incoherent modal sums. The sound field is that of a point source on the ground in the sound speed profile of Fig. 1 and ground impedance of Fig. 2.

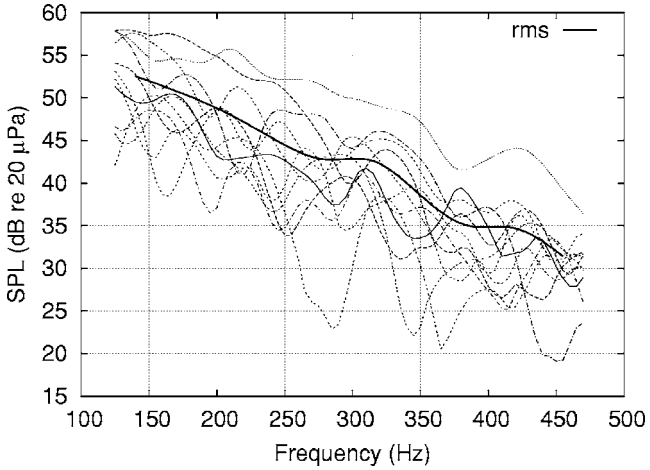

FIG. 13. The SPL measured at the lowest microphone during the run at 20:28. The results of the individual sweeps and their root-mean square are displayed as functions of frequency.

standard deviation of approximately 0.47 m/s. The direction of the prevailing wind near the ground was less than 30° relative to a line from the source to the receiver. Both mean wind speed and direction were approximately constant through the duration of the experiment.

The signals from the loudspeakers were 10 s long linearly swept tones from 100 Hz to 500 Hz. The linear sweeps were generated on a laptop computer using customized software and converted to an analog signal using a MOTU (Cambridge, Massachusetts) 828 mk2ii audio interface (24-bit, 44,100 samples per second). The received signals at the microphones was digitized using a second MOTU 828 mk2ii audio interface and data were acquired on a second computer using customized software.

The two loudspeakers were played separately, each run consisting of 12 consecutive sweeps from one of the loudspeakers. The ground and elevated source were alternated between runs, with a few minutes between runs. The free space sound spectrum level of the speakers was 107 dB (all spectrum levels given here and below are relative to 20 μPa and are in 1 Hz frequency bins) extrapolated to 1 m from the source across the frequency band 100 Hz to 500 Hz. Received spectrum levels at the tower were from 55 dB at 100 Hz to 30 dB at 500 Hz. The ambient noise spectrum levels were from 25 dB at 100 Hz to −10 dB at 500 Hz. The signal-to-noise ratio was more than 25 dB across the entire frequency band.

The data were analyzed using an adaptive least-squares filter to determine the frequency response[24] for transmission from the speaker to the microphone array. A Hann-windowed 50 Hz frequency average was performed. The measurements were averaged over the last 11 sweeps in the run. The first sweep allowed for the amplifier's settling time.

B. Results

All of the runs produced qualitatively similar results, regardless of the source elevation and regardless of the time the run was performed. Measurements from the run performed at 20:28, in which the source was the loudspeaker on the ground, are displayed in detail in Figs. 13–15.

In Fig. 13, the received sound pressure levels at the lowest microphone for the eleven sweeps are compared to their root-mean-square level. The standard deviation of the eleven sweeps ranges from 2.5 to 5 dB. Note that this is consistent with the variability of the coherent model sum as compared to the incoherent modal sum as seen in Fig. 8. It is also consistent with published results, Ref. 7, in which standard deviations of 2 to 3.5 dB where reported in the frequency band 150 Hz to 350 Hz at a distance of 566 m from the source.

Let p_n represent the response of the nth microphone. Let $\langle\ \rangle_{\mathrm{sw}}$ represent the average over the 11 sweeps in the run and let $\overline{p_n^2}=\langle p_n^2\rangle_{\mathrm{sw}}$ be the mean square pressure. To test the validity of Eq. (11), the correlation,[25]

$$\frac{\langle(p_n^2-\overline{p_n^2})(p_1^2-\overline{p_1^2})\rangle_{\mathrm{sw}}}{\sqrt{\langle(p_n^2-\overline{p_n^2})^2\rangle_{\mathrm{sw}}\langle(p_1^2-\overline{p_1^2})^2\rangle_{\mathrm{sw}}}},$$

between the square of the pressure magnitudes registered at the lowest microphone and those registered at the other microphones is computed. In Fig. 14, these correlations are displayed for a representative set of frequencies, 150, 200,

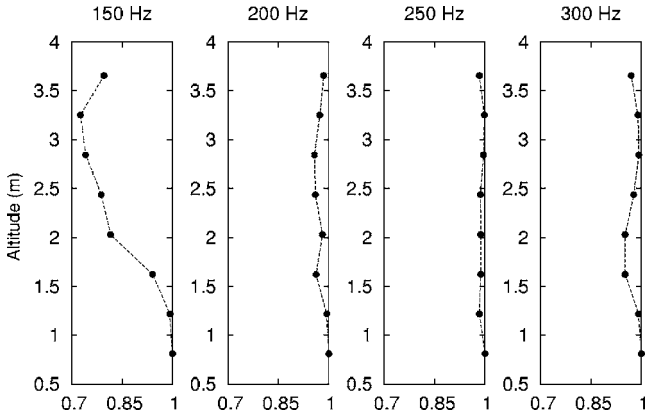

FIG. 14. The correlation between the pressure magnitude at the lowest microphone and the other microphones from the run at 20:28 as a function of altitude for the measured responses centered at 150 Hz, 200 Hz, 250 Hz, and 300 Hz.

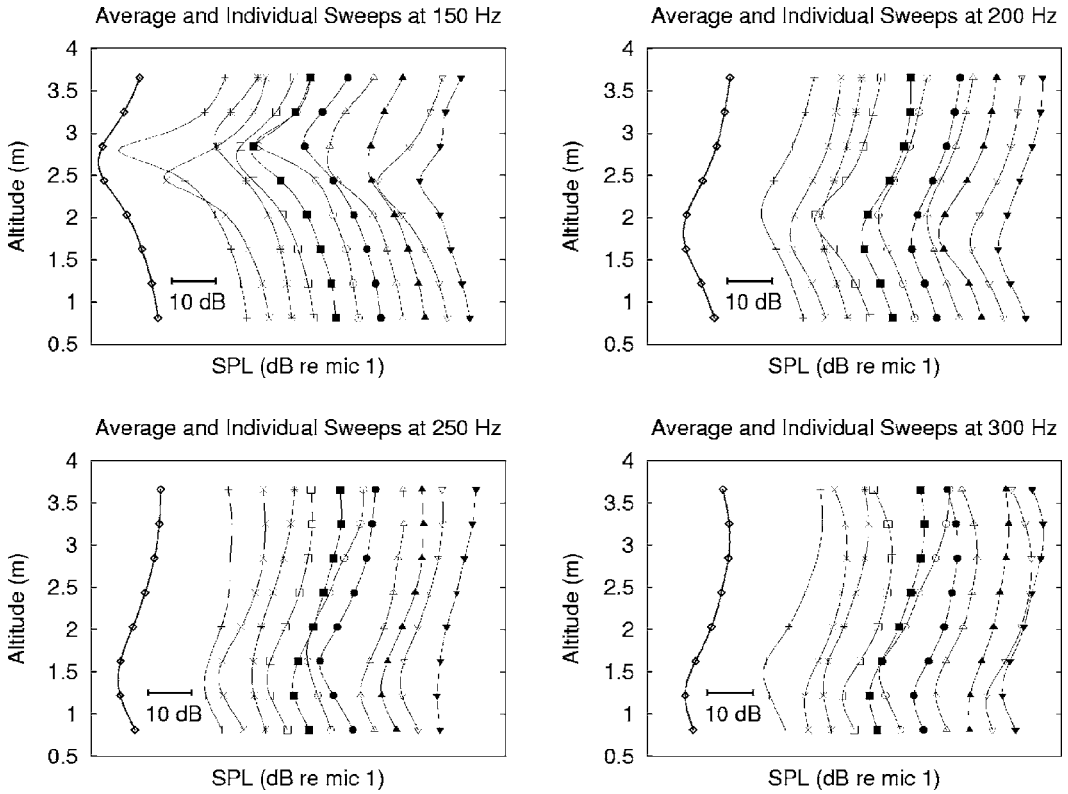

FIG. 15. Measured SPLs in dB relative to the pressure at the lowest microphone from the run at 20:28 as a function of altitude. The curve furthest to the left is the rms average over the eleven individual sweeps (relative to the average pressure at the lowest microphone). The remaining curves are the individual sweeps themselves. Measured responses centered at 150 Hz, 200 Hz, 250 Hz, and 300 Hz are displayed. So as to be more easily viewed, the profile from the first sweep is displaced by 20 dB from the profile of the root-mean squares. The profiles for each succesive sweep are displaced by 5 dB.

250, and 300 Hz (these are the central frequencies of the Hann windowed 50 Hz averages). Correlations were 0.95 or higher, except for 150 Hz for which (in this particular run) the correlation degraded to 0.7 near the top of the array. The high degree of correlation supports the prediction Eq. (11) that the relative sound pressure profile (here, relative to the pressure at the lowest microphone) is insensitive to fluctuations of the sound speed.

The high degree of correlation is displayed graphically in Fig. 15 in which the magnitudes, p_n/p_1, of the relative sound pressure profiles obtained from each individual sweep are displayed to the right of the profiles of the mean levels, $\sqrt{\langle p_n^2\rangle_{\mathrm{sw}}}/\sqrt{\langle p_1^2\rangle_{\mathrm{sw}}}$, of the 11 sweeps. The same central frequencies as above (150, 200, 250, and 300 Hz) are displayed. Note that the quiet height is clearly visible in the relative sound pressure profiles of each individual sweep.

It can be concluded that the quiet height exists and is a regular feature of nocturnal sound propagation. Further, it can be concluded that despite the significant fluctuations one finds in received sound pressure levels, near the ground the fluctuations of the relative vertical profile of the sound pressure are minor. We take this as evidence that while fluctuations of the sound speed can cause the modal wave numbers to fluctuate, the modes shapes themselves are stable near the ground.

Finally, a nonlinear least-squares algorithm[17] was used to obtain a quantitative fit between the data and a physical model. The theoretical model used is the incoherent modal sum for propagation in the sound speed profiles and ground impedances discussed in Sec. II B. The prediction of the normalized incoherent modal sum for the relative root-mean-square sound pressure profiles are fit to the relative profiles of the root-mean-square measured sound pressures. Explicitly,

$$\sum_{n=2}^{8}\sum_{f=125\ \mathrm{Hz}}^{350\ \mathrm{Hz}}\left(\frac{\langle p_n^2\rangle_{\mathrm{sw}}}{\langle p_1^2\rangle_{\mathrm{sw}}}-\frac{\langle|P(2\pi f,1.8\ \mathrm{km},z_n)|^2\rangle}{\langle|P(2\pi f,1.8\ \mathrm{km},z_1)|^2\rangle}\right)^2,$$

with the frequency f summed in steps of 25 Hz, is minimized. The values determined by the least squares algorithm are tabulated in Tables I and II.

The resulting fit is displayed in Fig. 16 where the relative profiles of the mean levels are overlayed on the predictions of the incoherent modal sum. As a check on consistency, in Fig. 17, the mean of the received sound pressure level at the lowest microphone are compared to the levels predicted by the incoherent modal sum. The error bars indicate the standard error of the mean, given by the standard deviation divided by the square root of the number of samples.[25]

Both the received mean sound pressure levels and the normalized mean pressure level profiles are well described by the incoherent modal sum using the sound speed profile and ground impedance models described above. Although the sound speed and ground impedance are physically reasonable, no claim is made that they accurately represent the actual conditions during the experiment, only that the data can be fit with a physically plausible model. A systematic

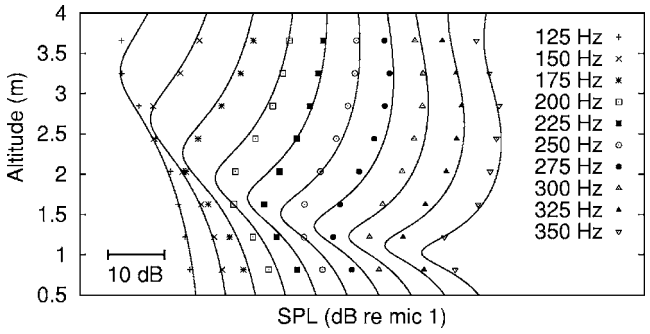

FIG. 16. The root-mean-square pressure magnitudes from the 20:28 run are compared to the predictions of the incoherent modal sum for propagation in the sound speed profile shown in Fig. 1 and ground impedance shown in Fig. 2. All pressures have been normalized by the pressure at the lowest microphone's position so that magnitudes are in dB relative to the magnitude at the lowest microphone. Profiles for succesive frequencies are displaced by 5 dB.

study of how one might invert acoustic data to obtain reliable estimates for the sound speed and ground impedance could be considered for future work.

IV. CONCLUSIONS

It has been predicted theoretically and verified experimentally that for long-range narrow-band sound propagation outdoors under downward refracting conditions over flat ground, there is a quiet height a few meters from the ground at which the sound pressure level is reduced by 10 to 15 dB. The quiet height is a robust feature of outdoor sound propagation at night. It depends only on the effective sound speed having a steep (positive) gradient near the ground and on the sound being attenuated by the ground. Furthermore, in the first few meters of the atmosphere, the dependence of the sound pressure level on elevation, relative to the sound pressure level at a fixed height, is insensitive to fluctuations of the effective sound speed. Finally, the concept of a quiet height applies to sound sources as well as to receivers.

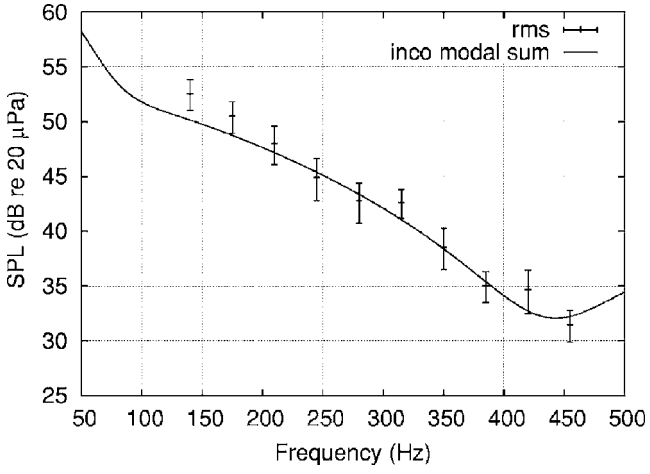

FIG. 17. The root-mean-square SPLs at the lowest microphone for the run at 20:28 compared to the levels predicted by the incoherent modal sum for the sound speed profile of Fig. 1 and ground impedance of Fig. 2.

ACKNOWLEDGMENTS

The authors would like to thank Ty Pitman for allowing them to set up equipment and run experiments on his farm. They are also grateful to Mack Young, county agent of Quitman County, Mississippi, for legwork and introductions. This work was supported by the Space Missile Defense Command and by Miltec Corporation.

[1]D. C. Pridmore-Brown, "Sound propagation in a temperature and wind stratified medium," J. Acoust. Soc. Am. **34**(4), 438–443 (1962).
[2]I. P. Chunchuzov, G. A. Bush, and S. N. Kulichkov, "On acoustical impulse propagation in a moving inhomogeneous atmospheric layer," J. Acoust. Soc. Am. **88**(1), 455–461 (1990).
[3]E. M. Salomons, *Computational Atmospheric Acoustics* (Kluwer, Dordrecht, 2001).
[4]R. B. Stull, *An Introduction to Boundary Layer Meteorology* (Kluwer, Dordrecht, 1991).
[5]V. E. Ostashev, *Acoustics in Moving Inhomogeneous Media* (E & FN Spon, London, 1997).
[6]O. A. Godin, "An effective quiescent medium for sound propagating through an inhomogeneous, moving fluid," J. Acoust. Soc. Am. **112**(4), 1269–1275 (2002).
[7]D. K. Wilson, J. M. Noble, and Mark A. Coleman, "Sound propagation in the nocturnal boundary layer," J. Atmos. Sci. **60**(20), 2473–2486 (2003).
[8]K. Attenborough, "Acoustical impedance models for outdoor ground surfaces," J. Sound Vib. **99**, 521–544 (1985).
[9]C. Zwicker and C. W. Kosten, *Sound Absorbing Materials* (Elsevier, Amsterdam, 1949).
[10]R. Raspet, G. Baird, and W. Wu, "Normal mode solution for low-frequency sound propagation in a downward refracting atmosphere above a complex impedence plane," J. Acoust. Soc. Am. **91**, 1341–1352 (1992).
[11]R. Waxler, "A vertical eigenfunction expansion for the propagation of sound in a downward refracting atmosphere over a complex impedance plane," J. Acoust. Soc. Am. **112**(6), 2540–2552 (2002).
[12]R. Waxler, "Modal expansions for sound propagation in the nocturnal boundary layer," J. Acoust. Soc. Am. **115**(4), 1437–1448 (2004).
[13]The experiment was performed on Ty Pitman's farm outside of Marks, Mississippi. This region of the country is very flat and sparsely populated, affording us long fetch and few obstructions.
[14]H. E. Bass, L. C. Sutherland, J. Piercy, and L. Evans, "Absorption of sound by the atmosphere," *Physical Acoustics*, edited by W. P. Mason and R. N. Thurston (Academic, New York, 1984).
[15]A. D. Pierce, *Acoustics* (Acoustical Society of America, Woodbury, New York, 1989).
[16]American National Standard, "Method of calculation of the absorption of sound by the atmosphere," ANSI S1-26-1995 (ASA 13-1995).
[17]J. Stoer and R. Bulirsch, *Introduction to Numerical Analysis*, 2nd ed. (Springer, New York, 1991).
[18]F. B. Jensen, W. A. Kuperman, M. B. Porter, and H. Schmidt, *Computational Ocean Acoustics* (American Institute of Physics, New York, 1994).
[19]Although the value of the lapse rate does not itself have a significant effect on the propagation at the ranges considered here, its value does determine the inversion height in this model and thus some value must be given.
[20]W. E. Boyce and R. C. DiPrima, *Elementary Differential Equations and Boundary Value Problems*, 4th ed. (Wiley, New York, 1986).
[21]O. A. Godin, "Reciprocity and energy theorems for waves in a compressible homogeneous moving fluid," Wave Motion **25**, 143–167 (1997).
[22]I. P. Chunchuzov, A. I. Otrezov, I. V. Petenko, V. N. Tovchigrechko, A. I. Svertilov, A. L. Fogel, and V. E. Fridman, "Travel time fluctuations of acoustic pulses propagating in the atmospheric boundary layer," Izv., Russ. Acad. Sci., Atmos. Oceanic Phys. **3**, 324–338 (1997).
[23]J. S. Bendat, and A. G. Piersol, *Random Data, Analysis and Measurement Procedures*, 3rd Ed. (Wiley, New York, 2000).
[24]S. Haykin, *Adaptive Filtering Theory*, 4th Ed. (Prentice–Hall, Englewood Cliffs, New Jersey, 2002).
[25]J. Mandel, *The Statistical Analysis of Experimental Data* (Dover, New York, 1964).

Singular meshless method using double layer potentials for exterior acoustics

D. L. Young,[a] K. H. Chen,[b] and C. W. Lee
Department of Civil Engineering and Hydrotech Research Institute, National Taiwan University, Taipei, 106 Taiwan

(Received 15 November 2004; revised 31 October 2005; accepted 1 November 2005)

Time-harmonic exterior acoustic problems are solved by using a singular meshless method in this paper. It is well known that the source points cannot be located on the real boundary, when the method of fundamental solutions (MFS) is used due to the singularity of the adopted kernel functions. Hence, if the source points are right on the boundary the diagonal terms of the influence matrices cannot be derived. Herein we present an approach to obtain the diagonal terms of the influence matrices of the MFS for the numerical treatment of exterior acoustics. By using the regularization technique to regularize the singularity and hypersingularity of the proposed kernel functions, the source points can be located on the real boundary and therefore the diagonal terms of influence matrices are determined. We also maintain the prominent features of the MFS, that it is free from mesh, singularity, and numerical integration. The normal derivative of the fundamental solution of the Helmholtz equation is composed of a two-point function, which is one of the radial basis functions. The solution of the problem is expressed in terms of a double-layer potential representation on the physical boundary based on the potential theory. The solutions of three selected examples are used to compare with the results of the exact solution, conventional MFS, boundary element method, and Dirichlet-to-Neumann finite element method. Good numerical performance is demonstrated by close agreement with other solutions. [DOI: 10.1121/1.2141130]

PACS number(s): 43.28.Js [SFU] Pages: 96–107

I. INTRODUCTION

For practical engineers, the boundary element method (BEM) has been more useful than the finite element method (FEM) during the last two decades, since the model setup takes less time for one-dimension reduction. Science and engineering communities have recently started paying attention to meshless methods that are element free. For the foreseeable future this mesh reduction technique will provide a significant and promising alternative to dominant numerical methods such as the FEM and BEM. Since neither domain nor surface meshing is required for the meshless methods, they could be more attractive for engineers to use. In this paper, we will develop a singular meshless method (SMM) as an efficient and novel numerical technique for solving two-dimensional (2D) exterior acoustics.

The mesh-free methods have become popular tools for scientific computing in recent years because of the strong demand for the reduction of mesh generation in higher dimensional domains. These methods are considered as promising alternatives to the FEM and BEM in solving physical problems numerically. Meshless methods have been successfully applied to some realistic problems[1] but not previously in acoustics. Several important types of meshless methods with their applications have been reported in the literature.[2–15,1,16–20]

Among the above-mentioned mesh-free studies, the method of fundamental solutions (MFS) is extensively applied to solve certain engineering problems.[11,13,17–19] The MFS is one kind of meshless method, since only boundary nodes are needed. Comprehensive reviews of the MFS were published by Fairweather and Karageorghis[11] and Golberg and Chen.[13] In order to avoid the problem of singularity, the solution is presented as a set of single layer potentials (corresponding to the fundamental solutions) on a nonphysical boundary (namely a fictitious boundary). The unknown densities of the fundamental solutions are determined in such a way that the boundary conditions (BCs) are satisfied by the method of collocation. The kernel function is composed of a two-point function that is one kind of radial basis function (RBF). A regular meshless formulation and singularity-free method are then obtained, which are attractive and relatively easy to use. However the MFS has not become a popular numerical method because it involves a controversial artificial boundary outside the physical domain. In general a fictitious boundary is difficult to choose for a complicated geometry. This will produce a restriction on the implementation of the MFS, since the locations of the source points require good estimates. The diagonal coefficients of the influence matrices are divergent in common cases when the off-set boundary approaches the real boundary. Despite the lack of singularities, the influence matrices become ill posed when the off-set boundary is far away from the real boundary. The results become very sensitive, since the condition number gets very large.

[a]Electronic mail: dlyoung@ntu.edu.tw
[b]Present address: Department of Information Management, Toko University, No. 51, Sec. 2, University Road, Pu-Tsu, Chia-Yi, 613, Taiwan.

An improved approach called the boundary knot method (BKM) or the boundary collocation method (BCM) was introduced recently by Chen and co-workers,[3–8] Kang and collaborators,[14,15] and Chen and co-workers.[9,10] Nonsingular kernels were employed to evaluate the complementary solutions instead of using singular fundamental solutions. Many types of problems have been successfully treated with these methods. The major differences between the nonsingular schemes and MFS formulations are that the BKM and BCM choose nonsingular general solutions while MFS uses more effective singular kernel functions such as the RBFs. The Trefftz method is also one improved method for MFS. The Trefftz method uses the complementary set of fundamental solutions, i.e., the solutions of homogeneous differential equations. Hence it does not encounter the singularity since the RBFs are regular. On the other hand the MFS uses fundamental solutions of inhomogeneous differential equations which are appropriate as well. It is worth noticing that MFS and the Trefftz method are mathematically equivalent in spite of their essentially minor and apparent differences in formulation. The link between the Trefftz method and the MFS has been discussed in detail in Refs. 6 and 7. The study on the similarities between the Trefftz method and the MFS has been emphasized recently.

In the above-mentioned references, these methods only work well in regular geometry with Dirichlet and Neumann BCs. Even though those methods can locate the source points on the physical boundary and have nonsingular kernels, it still is an ill-posed problem. Further, for exterior acoustics problems the satisfaction of the BC at infinity such as Sommerfeld radiation condition becomes difficult. However the singular kernel functions for the MFS and proposed SMM will automatically satisfy the Sommerfeld radiation condition. The goal of this paper is to develop a new meshless method with the source points on the physical boundary to solve scattering and radiation problems without the above-mentioned difficulty of BKM, BCM, conventional MFS, and the Trefftz method. We present an alternative approach for the numerical treatment of exterior acoustics, retaining the salient MFS meshless characteristics and selecting the normal derivative of the fundamental solution of the Helmholtz equation as the RBF. The proposed method can be viewed as a special case of indirect BEM using the discrete double layer potential method[21–23] as well as an expansion method of the MFS.[20] The solution of the problem is expressed in terms of a double-layer potential instead of a single-layer potential representation on the physical boundary without the integral process. By comparison with other meshless or mesh reduction schemes such as BKM, BCM, or BEM, the discretization processes or regularization techniques are still needed for those methods and can be found in Refs. 22–25. However the proposed SMM behaves like the MFS by improving the singularity evaluation of diagonal terms, when the source and boundary points are coincident to avoid the ambiguity of off-set distance of the fictitious boundary for the conventional MFS.

By using the proposed regularization technique of subtracting and adding-back, the singularity and hypersingularity of the kernel functions can be regularized. The main idea is to add one singular term in the series and then to subtract the same singular term from the series of the solution representation. The two singular terms are equal and the sum of the augmented series is zero. In general the diagonal terms of the influence matrices can then be derived by using the proposed technique for an arbitrary domain. Also, the influence coefficients for a circular domain are computed analytically by using separable kernels and circulants, and the validity of the diagonal terms can be verified by using the proposed regularization technique. The main part of this paper deals with the strongly singular and hypersingular kernel functions without integration. Furthermore, the innovative concept of this study is that this regularization technique has never been used in the context of meshless methods, except for the writers' recent publication on potential problems.[20] Finally, we present several case studies using the developed singular meshless program to demonstrate that the proposed scheme can be utilized to solve 2D acoustic radiation and scattering problems in circular and square domains subject to Dirichlet and Neumann BCs.

II. FORMULATION

Acoustic problems are usually modeled by the Helmholtz equation. By making the time harmonic assumption, $p(\mathbf{x},t)=\mathrm{Re}\{\phi(x)e^{i\omega t}\}$, the classical wave equation then reduces to the Helmholtz equation as follows:

$$\nabla^2\phi(x)+k^2\phi=0, \quad x\in D^e \tag{1}$$

with the two kinds of BCs as

$$\phi(x)=\bar{\phi}, \quad x\in B \tag{2}$$

or

$$\psi(x)=\bar{\psi}, \quad x\in B, \tag{3}$$

where ∇^2 is the Laplacian, $\phi(x)$ is the acoustic pressure, $\psi(x)=\partial\phi(x)/\partial n_x$ is the normal derivative, n_x is the outward normal vector, k is the wave number, and D^e is the domain of the exterior problem. The two BCs in Eqs. (2) and (3) are stated as follows: Eq. (2) is the essential boundary (Dirichlet boundary) on which the potential is prescribed as $\bar{\phi}$ and Eq. (3) is the natural boundary (Neumann boundary) on which the flux is prescribed as $\bar{\psi}$. B is the boundary of the domain D^e. Furthermore, in order to obtain a well-posed problem; the pressure field is constrained to vanish at infinity. This is accomplished by imposing a radiation condition at infinity. An appropriate radiation condition at infinity is given by the Sommerfeld radiation condition[23,26] as

$$\lim_{r\to\infty} r^{(1/2)(d-1)}\left(\frac{\partial\phi}{\partial r}-ik\phi\right)=0, \quad r\to\infty, \tag{4}$$

where d is the dimension ($d=2$ in this study). Equation (4) stems from the Sommerfeld radiation condition which ensures that no sources at infinity contribute to the acoustic field. Only outgoing traveling waves are acceptable, guaranteeing a net acoustic energy flow toward infinity. This BC implies an integral form, the Rellich–Sommerfeld radiation condition in the form

$$\lim_{r\to\infty}\int_{B_r}\left|\frac{\partial\phi}{\partial r}-ik\phi\right|^2 dB=0, \tag{5}$$

where B_r is the surface of a sphere with a radius r. The radiation condition requires the energy flux at infinity to be positive, thereby assuring a unique solution to the boundary-value problem (1)–(4). Appropriate representation of this condition is crucial to the reliability of any numerical formulation of the problem. A correct and exhaustive presentation of the radiation decay condition has been given in Ref. 27.

By employing the RBF technique, the solution for an exterior problem can be approximated in terms of the strengths of the singularities (s^j) as

$$\phi(x^i)=\sum_{j=1}^{N}A^e(s^j,x^i)\alpha^j,\quad x\in D^e, \tag{6}$$

$$\psi(x^i)=\sum_{j=1}^{N}B^e(s^j,x^i)\alpha^j,\quad x\in D^e, \tag{7}$$

where $A^e(s^j,x^i)$ is the RBF in which the superscript denotes the exterior domain, α^j are the unknown coefficients, N is the number of source points, s^j, and

$$B^e(s^j,x^i)=\frac{\partial A^e(s^j,x^i)}{\partial n_x}.$$

The coefficients $\{\alpha^j\}_{j=1}^N$ are determined, such that BC is satisfied at the boundary points ($\{x^i\}_{i=1}^N$). By collocating N observation points, x^i, to match the BCs from Eq. (2) for Dirichlet problems and Eq. (3) for Neumann problems, we have the following $N\times N$ linear systems in the form of

$$\{\bar{\phi}^i\}=\begin{bmatrix}a_{1,1}&a_{1,2}&\cdots&a_{1,N}\\a_{2,1}&a_{2,2}&\cdots&a_{2,N}\\\vdots&\vdots&\ddots&\vdots\\a_{N,1}&a_{N,2}&\cdots&a_{N,N}\end{bmatrix}\{\alpha^j\}=[A^e]\{\alpha^j\}, \tag{8}$$

$$\{\bar{\psi}^i\}=\begin{bmatrix}b_{1,1}&b_{1,2}&\cdots&b_{1,N}\\b_{2,1}&b_{2,2}&\cdots&b_{2,N}\\\vdots&\vdots&\ddots&\vdots\\b_{N,1}&b_{N,2}&\cdots&b_{N,N}\end{bmatrix}\{\alpha^j\}=[B^e]\{\alpha^j\}, \tag{9}$$

where

$$a_{i,j}=A^e(s^j,x^i),\quad i,j=1,2,\ldots,N, \tag{10}$$

$$b_{i,j}=B^e(s^j,x^i),\quad i,j=1,2,\ldots,N. \tag{11}$$

The chosen RBFs are the double layer potentials from potential theory given as

$$A^e(s^j,x^i)=-\frac{i\pi k}{2}H_1^{(1)}(kr_{ij})\frac{n_k y_k}{r_{ij}}, \tag{12}$$

$$B^e(s^j,x^i)=\frac{i\pi k}{2}\left\{k(H_2^{(1)})(kr_{ij})\frac{y_k y_l n_k\bar{n}_l}{r_{ij}^2}-H_1^{(1)}(kr_{ij})\frac{n_k\bar{n}_k}{r_{ij}}\right\}, \tag{13}$$

where $H_1^{(1)}(kr_{ij})$ and $H_2^{(1)}(kr_{ij})$ are the Hankel functions of the first kind of the first and second order, respectively. $r_{ij}=\Sigma_{k=1}^2|s_k^j-x_k^i|$, $y_k n_k=\Sigma_{k=1}^2(x_k^i-s_k^j)n_k$, n_k is the kth component of the outward normal vector at source point s^j; $\bar{n}_k$ is the kth component of the outward normal vector at field point x^i. It is noted that the double layer potentials in Eqs. (12) and (13) have both singularity and hypersingularity at the origin, which lead to troublesome singular kernels and a controversial auxiliary boundary for the MFS. The off-set distance between the off-set (auxiliary) boundary (B') and the real boundary (B) needs to be chosen deliberately. To overcome this drawback, s^j is distributed on the real boundary by using the following proposed regularization techniques. The rationale for choosing the double layer potential instead of single layer potential as used in the proposed method for the form of RBFs is to take advantage of the regularization of the subtracting and adding-back technique, so that no off-set distance is needed when evaluating the diagonal coefficients of influence matrices as explained in Sec. III. The single layer potentials cannot be chosen as RBFs, because Eqs. (20) and (21) in the following text of Sec. III are not satisfied. If the single layer potential is used, the regularization technique of subtracting and adding-back will fail.

III. DERIVATION OF DIAGONAL COEFFICIENTS OF INFLUENCE MATRICES FOR AN ARBITRARY DOMAIN USING SMM

When the collocation point x^i approaches the source point s^j, Eqs. (12) and (13) will be approximated by

$$\lim_{x_i\to s_j}A^e(s^j,x^i)=\bar{A}^e(s^j,x^i)=\frac{n_k y_k}{r_{ij}^2}, \tag{14}$$

$$\lim_{x_i\to s_j}B^e(s^j,x^i)=\bar{B}^e(s^j,x^i)=\left(2\frac{y_k y_l n_k\bar{n}_l}{r_{ij}^4}-\frac{n_k\bar{n}_k}{r_{ij}^2}\right)+\frac{k^2}{4}i, \tag{15}$$

by using the limiting form for small arguments and the identities from the generalized function as shown in the following:[28]

$$\lim_{r_{ij}\to 0}H_1^{(1)}(kr_{ij})=\frac{kr_{ij}}{2}+\frac{2}{\pi kr_{ij}}i, \tag{16}$$

$$\lim_{r_{ij}\to 0}H_2^{(1)}(kr_{ij})=\frac{(kr_{ij})^2}{8}+\frac{4}{\pi(kr_{ij})^2}i. \tag{17}$$

The kernels in Eqs. (14) and (15) have the same singularity strength as the Laplace equation.[20] Therefore, Eqs. (6) and (7) for the exterior problem need to be regularized by using special treatment such as

$$\bar{\phi}(x^i) = \sum_{j=1}^{N} A^e(s^j,x^i)\alpha^j - \sum_{j=1}^{N} \bar{A}^e(s^j,x^i)\alpha^i$$
$$= \sum_{j=1}^{i-1} A^e(s^j,x^i)\alpha^j + \sum_{j=i+1}^{N} A^e(s^j,x^i)\alpha^j - \left[\sum_{m=1}^{N} \bar{A}^e(s^m,x^i) - A^e(s^i,x^i)\right]\alpha^i, \quad x^i \in B, \tag{18}$$

$$\bar{\psi}(x^i) = \sum_{j=1}^{N} B^e(s^j,x^i)\alpha^j - \sum_{j=1}^{N} \bar{B}^e(s^j,x^i)\alpha^i$$
$$= \sum_{j=1}^{i-1} B^e(s^j,x^i)\alpha^j + \sum_{j=i+1}^{N} B^e(s^j,x^i)\alpha^j - \left[\sum_{m=1}^{N} \bar{B}^e(s^m,x^i) - B^e(s^i,x^i)\right]\alpha^i, \quad x^i \in B, \tag{19}$$

where $\bar{A}^e(s^j,x^i)$ and $\bar{B}^e(s^j,x^i)$ are the double layer potentials of the exterior problem of the Laplace equation for the same domain, in which

$$\sum_{j=1}^{N} \bar{A}^e(s^j,x^i) = 0, \tag{20}$$

$$\sum_{j=1}^{N} \bar{B}^e(s^j,x^i) = 0. \tag{21}$$

The detailed derivations of Eqs. (20) and (21) are given in Appendix A. The original singular terms of $A^e(s^i,x^i)$ and $B^e(s^i,x^i)$ in Eqs. (6) and (7) have been transformed into regular terms $-[\Sigma_{m=1}^{N}\bar{A}^e(s^m,x^i) - A^e(s^i,x^i)]$ and $-[\Sigma_{m=1}^{N}\bar{B}^e(s^m,x^i) - B^e(s^i,x^i)]$ in Eqs. (18) and (19), respectively. The terms of $\Sigma_{m=1}^{N}\bar{A}^e(s^m,x^i)$ and $\Sigma_{m=1}^{N}\bar{B}^e(s^m,x^i)$ are the adding-back terms and the terms of $A^e(s^i,x^i)$ and $B^e(s^i,x^i)$ are the subtracting terms in the two brackets for the special treatment technique. After using the regularization technique of subtracting and adding-back, we are able to remove the singularity and hypersingularity of the kernel functions. Therefore, the diagonal coefficients for the exterior problem can be extracted out as

$$\{\bar{\phi}^i\} = \begin{bmatrix} \sum_{m=1}^{N} \bar{a}_{1,m} - a_{1,1} & a_{1,2} & \cdots & a_{1,N} \\ a_{2,1} & \sum_{m=1}^{N} \bar{a}_{2,m} - a_{2,2} & \cdots & a_{2,N} \\ \vdots & \vdots & \ddots & \vdots \\ a_{N,1} & a_{N,2} & \cdots & \sum_{m=1}^{N} \bar{a}_{N,m} - a_{N,N} \end{bmatrix} \{\alpha^j\}, \tag{22}$$

$$\{\bar{\psi}^i\} = \begin{bmatrix} -\left(\sum_{m=1}^{N} \bar{b}_{1,m} - b_{1,1}\right) & b_{1,2} & \cdots & b_{1,N} \\ b_{2,1} & -\left(\sum_{m=1}^{N} \bar{b}_{2,m} - b_{2,2}\right) & \cdots & b_{2,N} \\ \vdots & \vdots & \ddots & \vdots \\ b_{N,1} & b_{N,2} & \cdots & -\left(\sum_{m=1}^{N} \bar{b}_{N,m} - b_{N,N}\right) \end{bmatrix} \{\alpha^j\}, \tag{23}$$

where $a_{ij}=A^e(s^j,x^i)$, $\bar{a}_{ij}=\bar{A}^e(s^j,x^i)$, $b_{ij}=B^e(s^j,x^i)$, and $\bar{b}_{ij}=\bar{B}^e(s^j,x^i)$.

By collocating N observation points to match the BCs from Eq. (2) for Dirichlet BCs and Eq. (3) for Neumann BCs, we can get the final system of Eqs. (8) and (9). For mixed-type problems, a linear combination of Eqs. (8) and (9) is made to satisfy the mixed-type BCs. After the unknown density, $\{\alpha^j\}_{j=1}^{N}$, is solved by using the linear algebraic solver, the solutions for the domain of interest can be calculated by using the field equations (6) and (7) since the unknown density function $\{\alpha^j\}$ is solved by Eqs. (22) and (23). The numerical procedure of SMM can be found in Fig. 1.

The diagonal terms of the two influence matrices for exterior problems can also be derived analytically for a circular domain as shown in Eqs. (B21) and (B22).

IV. NUMERICAL RESULTS

In order to show the accuracy and validity of the proposed method, three case studies, involving radiation and

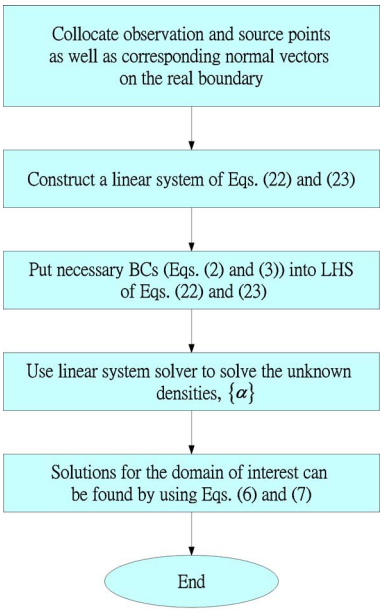

FIG. 1. (Color online) Flow chart of SMM.

scattering problems with circular and square domains subject to Dirichlet and Neumann BCs, are given in the following examples.

1. Radiation problem (Dirichlet BC). For the first case, a nonuniform radiation problem from a sector of a circular cylinder[26] is considered. The BC has a constant nonzero value on the arc $(-\alpha/2 \leqslant \theta \leqslant \alpha/2)$ and zero elsewhere. Two points of discontinuity of the BC can be found. Problem sketch and nodes distribution by using SMM are plotted in Figs. 2 and 3, respectively. The normalized analytical solution is available as follows:

$$\phi(r,\theta) = -\frac{2}{\pi}\sum_{n=0}^{\infty} \varepsilon_n \frac{\sin(n\alpha)}{n} \frac{H_n^{(1)}(kr)}{H_n^{(1)}(ka)} \cos(n\theta), \tag{24}$$

where ε_n is the Neumann factor and a is the radius of the circular cylinder. We choose $\alpha=\pi/9$. After collocating 100 nodes on the physical boundary, both the real and imaginary components for ϕ on $r=2a$ for $ka=1$ are plotted in Figs. 4(a) and 4(b), respectively. The results are used for comparison with the exact solution and the conventional Cauchy singular

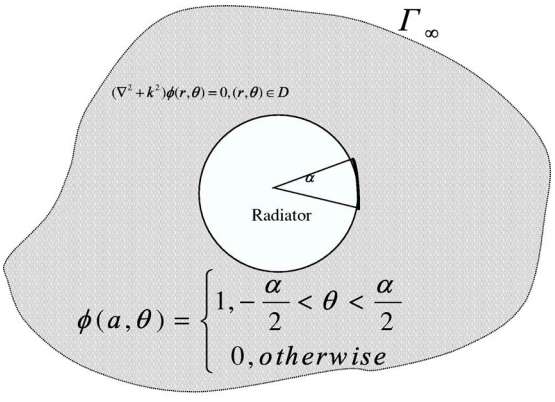

FIG. 2. The nonuniform radiation problem for a circular cylinder subject to Dirichlet BC in Case 1.

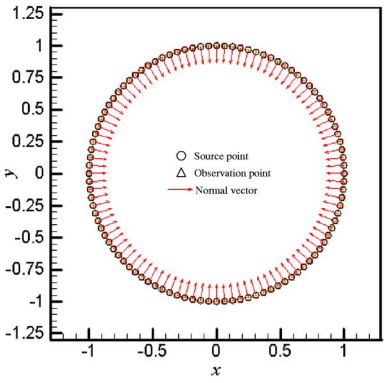

FIG. 3. (Color online) Nodes distribution (100 nodes) in Case 1.

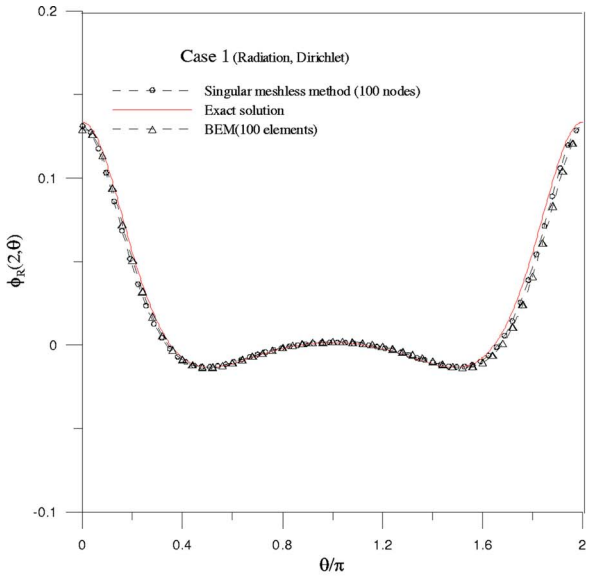

(a) Real part

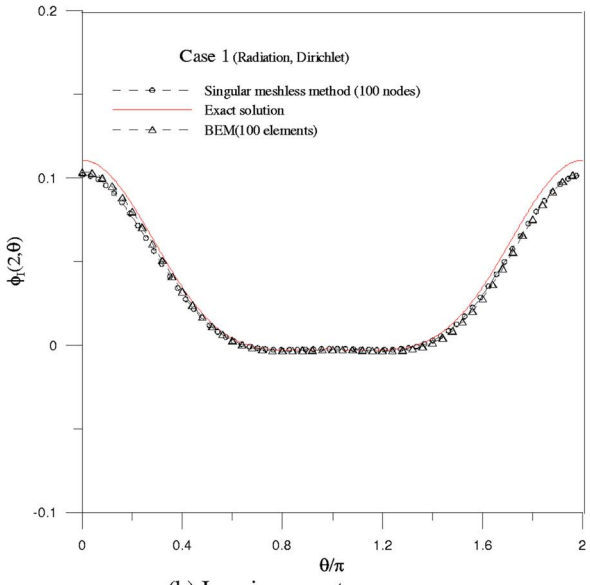

(b) Imaginary part

FIG. 4. (Color online) Nonuniform radiation for a circular cylinder subject to Dirichlet BC in Case 1 for $ka=1$, $r=2a$: (a) real part, (b) imaginary part.

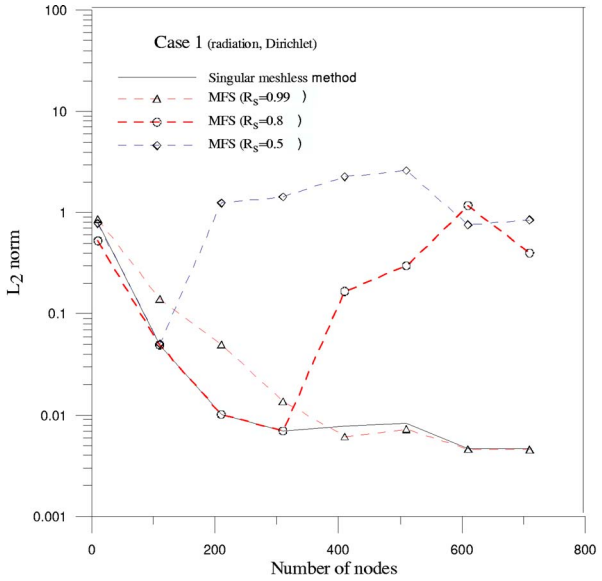

FIG. 5. (Color online) Comparison of error norms using the conventional MFS and proposed SMM for Case 1.

BEM solution. The discretization method of the BEM is collocation discretization with constant elements. These results demonstrate the convergence of the proposed method. The comparison of error norms between the present SMM using double layer potentials and the conventional MFS utilizing single layer potentials with different off-boundary distances (R_s=the radius of source points=0.5,0.8,0.99) is shown in Fig. 5. This illustrates the drawback of the location of source being dubious when the conventional MFS is used. The result using the present method is more efficient than the solution using the conventional MFS with the same number of nodes. Figures 6(a), 6(b), and 6(c) show the contour plots for the real part of the potential for $ka=1$ by adopting the analytical solution, the proposed SMM, and the BEM. The result from using the present method matches the exact solution and the BEM result very well.

2. Radiation problem (Neumann BC). The second example is the same as the first problem except the Dirichlet BC is replaced by the Neumann BC as depicted in Fig. 7. The nodes distribution employing the proposed method is shown in Fig. 8. The discontinuous BC is as follows:

$$\psi(a,\theta)=\begin{cases}1, & -\dfrac{\alpha}{2}<\theta<\dfrac{\alpha}{2}\\ 0, & \text{otherwise}.\end{cases} \tag{25}$$

In this case, the analytical solution is found as follows:[26]

$$\phi(r,\theta)=-\frac{2}{\pi k}\sum_{n=0}^{\infty}\varepsilon_n\frac{\sin(n\alpha)}{n}\frac{H_n^{(1)}(kr)}{H_n^{(1)}(ka)}\cos(n\theta), \tag{26}$$

We select $\alpha=\pi/9$. By collocating 100 nodes on the circular boundary, both the real and imaginary components for ϕ on $r=2a$ for $ka=1$ are plotted in Figs. 9(a) and 9(b), respectively. They are used for comparison with the results of exact solution and the conventional Cauchy singular BEM solution with constant elements. These results demonstrate the convergence of the proposed method. The comparison of error

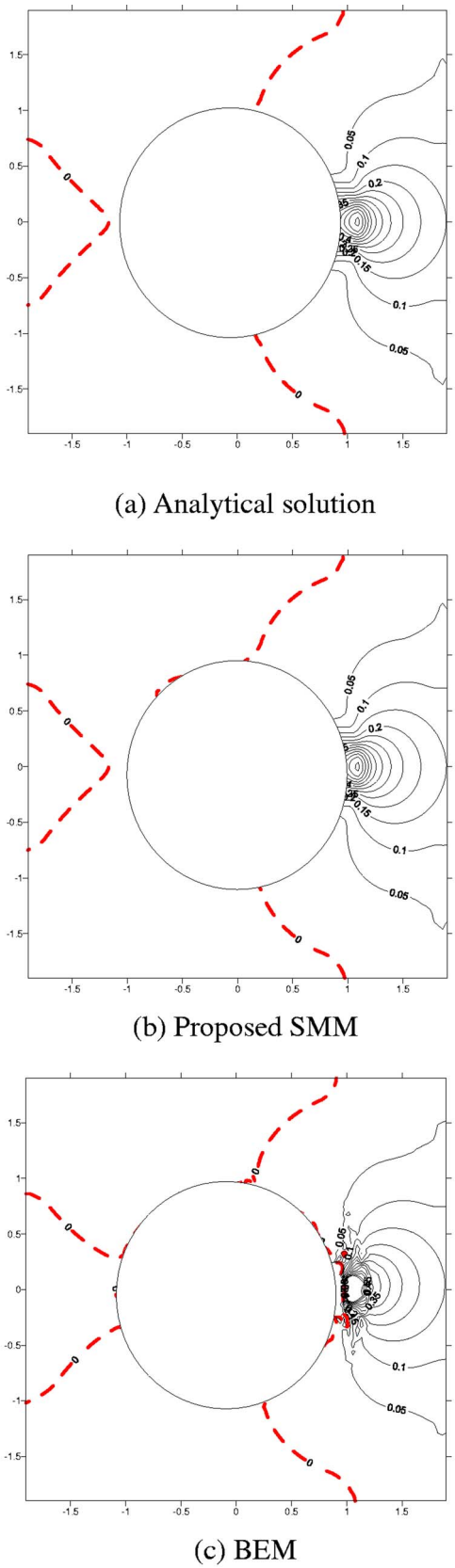

FIG. 6. (Color online) The contour plots for the real-part solutions in Case 1: (a) analytical solution, (b) proposed SMM (100 nodes), (c) BEM (100 elements).

norms between the present SMM and the conventional MFS with different off-boundary distances (R_s=0.5,0.8,0.99) is shown in Fig. 10. This illustrates again the drawback of the well known ill-posed influence matrices when the con-

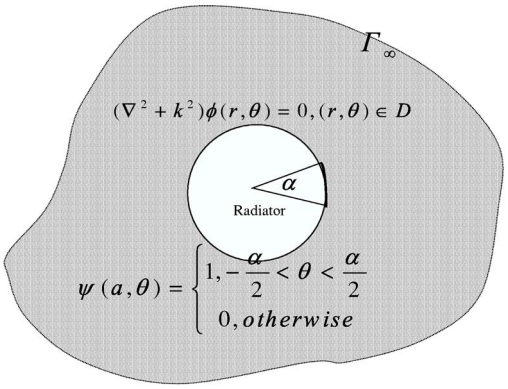

FIG. 7. The nonuniform radiation problem for a circular cylinder subject to Neumann BC in Case 2.

ventional MFS is used. The solution using the present SMM is more efficient than the conventional MFS, if the same number of nodes is used. The contour plots for the real part of the potential for $ka=1$ by adopting the analytical solution, the proposed SMM, and the BEM are shown in Figs. 11(a), 11(b), and 11(c), respectively. Figure 11 reveals that the present model provides very promising results as compared to the analytic and BEM solutions.

3. Scattering problem for a square rod (Neumann BC). Having demonstrated the present technique on a circular cylinder, we proceed to a scattering problem for a square rod (square measure=4), as shown in Fig. 12 in which the exact solution is not available.[29] Due to nonsmooth boundaries at the four corners of the square, the scattering by the square rod becomes multidirectional. By collocating 120 nodes on the square boundary as depicted in Fig. 13, both the real and imaginary components for ϕ on $r=1/0.425$ for $ka=4\pi$ are plotted in Figs. 14(a) and 14(b), respectively, for comparison with the BEM and Dirichlet-to-Neumann (DtN) FEM results. The type of finite elements used is linear triangle elements. The DtN-FEM evaluation uses the h-refinement and Galerkin least-squares finite element formulation with fully coupled DtN BCs. These results demonstrate the numerical convergence and easy treatment of BCs for exterior acoustics problems by the proposed technique. The contour plots of field solution for the real part of the potential for $ka=4\pi$ by adopting the proposed SMM, the FEM with DtN method,[29] and the BEM are shown in Figs. 15(a), 15(b), and 15(c), respectively. Figure 15 shows the better convergence of the present solution in comparison with the other two numerical solutions, BEM and DtN FEM.

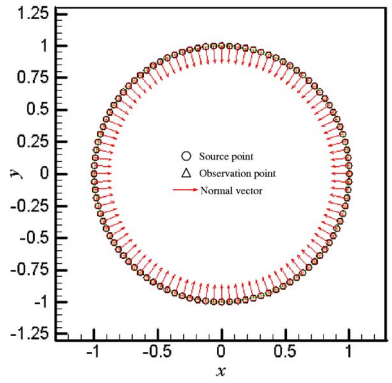

FIG. 8. (Color online) Nodes distribution (100 nodes) in Case 2.

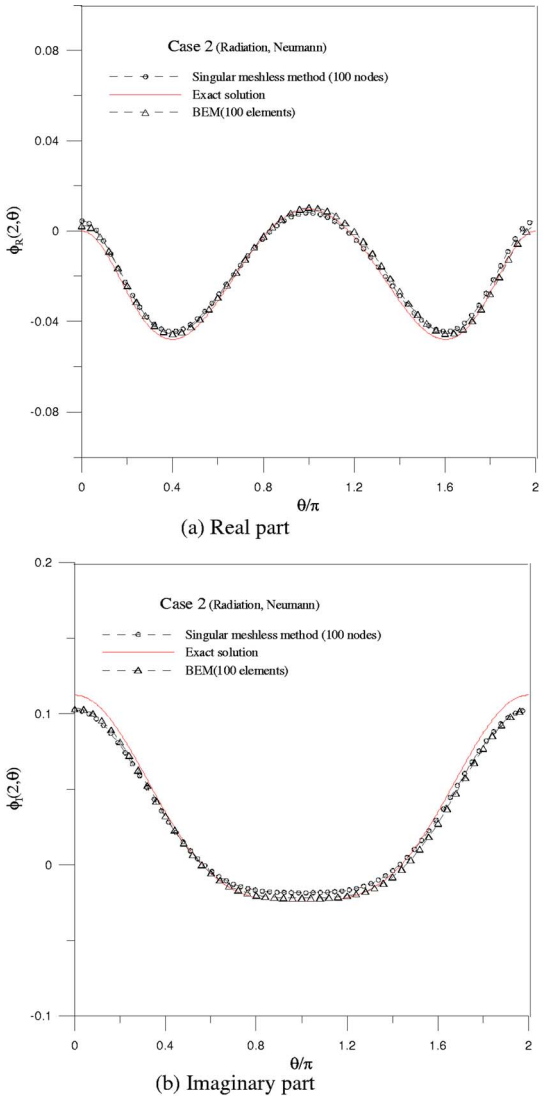

FIG. 9. Nonuniform radiation for a circular cylinder subject to Neumann BC in Case 2 for $ka=1$, $r=2a$: (a) real part, (b) imaginary part.

V. CONCLUSIONS

In this study, we implement a singular meshless method using double layer potentials to solve radiation and scattering problems in two dimensions. Only the boundary nodes on the real boundary are required. The major difficulty of the coincidence of the source and collocation points that causes singularity in the conventional MFS is circumvented. The finite values of the diagonal terms for the influence matrices have been subtracted off by the proposed regularization technique to regularize the singularity and hypersingularity of the kernel functions, when the source and boundary points are coincident. The numerical results obtained by using the presented SMM for the three examples match very well with the analytical solutions and other numerical solutions using con-

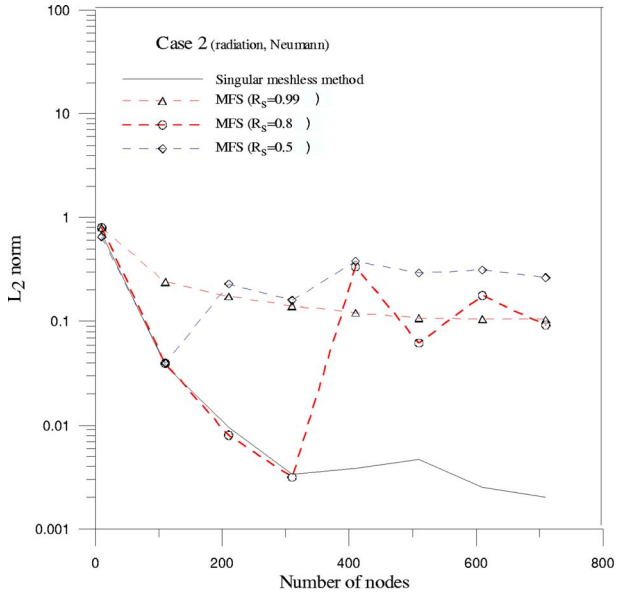

FIG. 10. (Color online) Comparison of error norms using the conventional MFS and proposed SMM for Case 2.

ventional MFS, BEM, or DtN FEM. A much simpler meshless numerical method is claimed as far as modeling of 2D exterior acoustics is concerned.

ACKNOWLEDGMENTS

Financial support from the National Taiwan University, and from the National Science Council of Taiwan under Grant No. NSC-92-2281-E-002-020, are gratefully appreciated. We would like to thank Professor A. S. Muleshkov of the University of Nevada at Las Vegas for discussing and editing the manuscript when D.L.Y. visited the Department of Mathematical Sciences at UNLV. We are also very grateful for constructive comments by the referees to improve our paper.

APPENDIX A: THE DETAILED DERIVATIONS OF EQS. (20) and (21)

The null-fields of the boundary integral equations (BIEs) based on the direct method are

$$0 = \int_B \frac{\partial \Phi^{(e)}(s,x^i)}{\partial n_s} \phi(s) dB(s) - \int_B \Phi^{(e)}(s,x^i) \frac{\partial \phi(s)}{\partial n_s} dB(s), \quad x^i \in D^e, \tag{A1}$$

$$0 = \int_B \frac{\partial^2 \Phi^{(e)}(s,x^i)}{\partial n_s \partial_{x^i}} \phi(s) dB(s) - \int_B \frac{\partial \Phi^{(e)}(s,x^i)}{\partial n_{x^i}} \frac{\partial \phi(s)}{\partial n_s} dB(s), \quad x^i \in D^e, \tag{A2}$$

where the superscript e denotes the exterior domain, Φ is the single layer potential, and is equal to $\ln(r_{ij})$ for the 2D Laplace problem. Let $[\partial \Phi^{(e)}(s,x^i)]/\partial n_s = \bar{A}^{(e)}(s,x^i)$, and $[\partial^2 \Phi^{(e)}(s,x^i)]/\partial n_s \partial n_{x^i} = \bar{B}^{(e)}(s,x^i)$. By employing the simple test method ($\partial \phi(s)/\partial n_s = 0$ when $\phi(s) = 1$), we can write Eqs. (A1) and (A2) as follows:

$$\int_B \bar{A}^e(s,x^i) dB(s) = 0 \quad x^i \in D^e, \tag{A3}$$

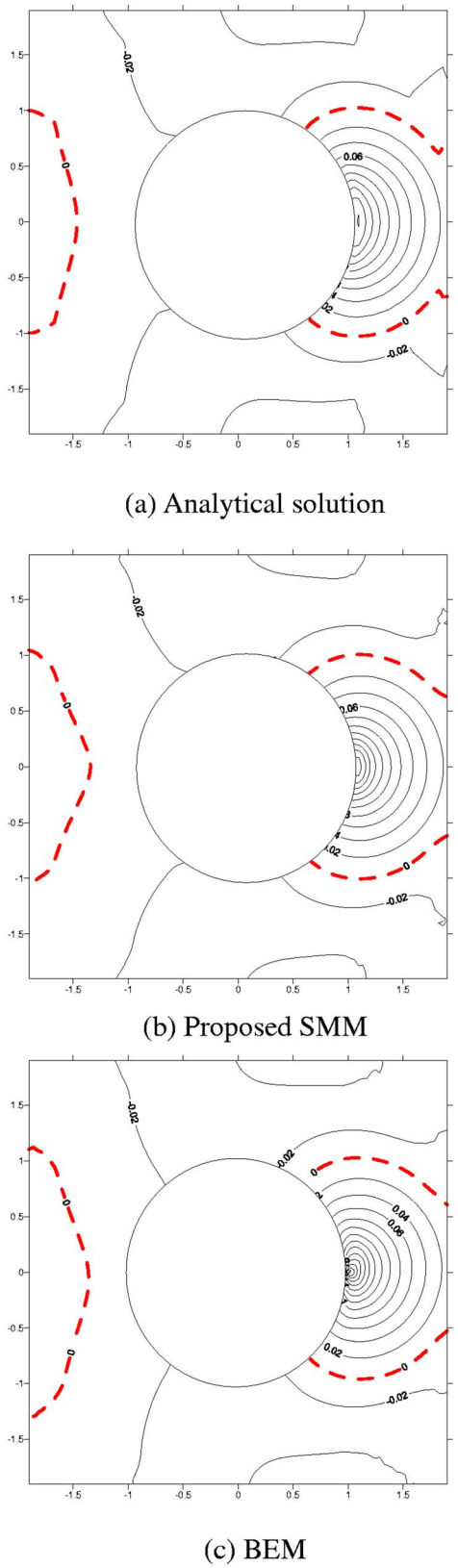

FIG. 11. (Color online) The contour plots for the real-part solutions in Case 2: (a) analytical solution, (b) proposed SMM (100 nodes), (c) BEM (100 elements).

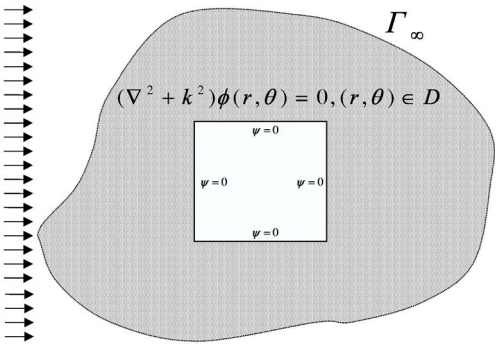

FIG. 12. The scattering problem for a square rod subject to Neumann BC in Case 3.

$$\int_B \bar{B}^e(s,x^i)dB(s) = 0, \quad x^i \in D^e. \tag{A4}$$

When the field point x^i approaches the boundary, we can discretize Eqs. (A3) and (A4) as follows:

$$\sum_{j=1}^{N} \bar{A}^{(e)}(s^j,x^i)\ell^j = 0, \quad x^i \in B, \tag{A5}$$

$$\sum_{j=1}^{N} \bar{B}^{(e)}(s^j,x^i)\ell^j = 0, \quad x^i \in B, \tag{A6}$$

where ℓ^j is the half distance of the $(j-1)$th source point and the $(j+1)$th source point. When the distribution of nodes is uniform, we are able to reduce Eqs. (A5) and (A6) to the following:

$$\sum_{j=1}^{N} \bar{A}^{(e)}(s^j,x^i) = 0, \quad x^i \in B, \tag{A7}$$

$$\sum_{j=1}^{N} \bar{B}^{(e)}(s^j,x^i) = 0, \quad x^i \in B, \tag{A8}$$

where

$$\bar{A}^{(e)}(s^j,x^i) = \frac{\partial \Phi^{(e)}(s^j,x^i)}{\partial n_s} = \frac{n_k y_k}{r_{ij}^2}, \tag{A9}$$

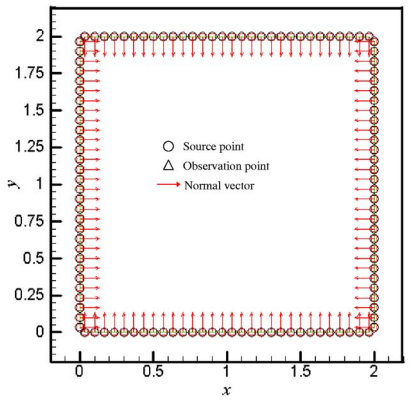

FIG. 13. (Color online) Nodes distribution (120 nodes) in Case 3.

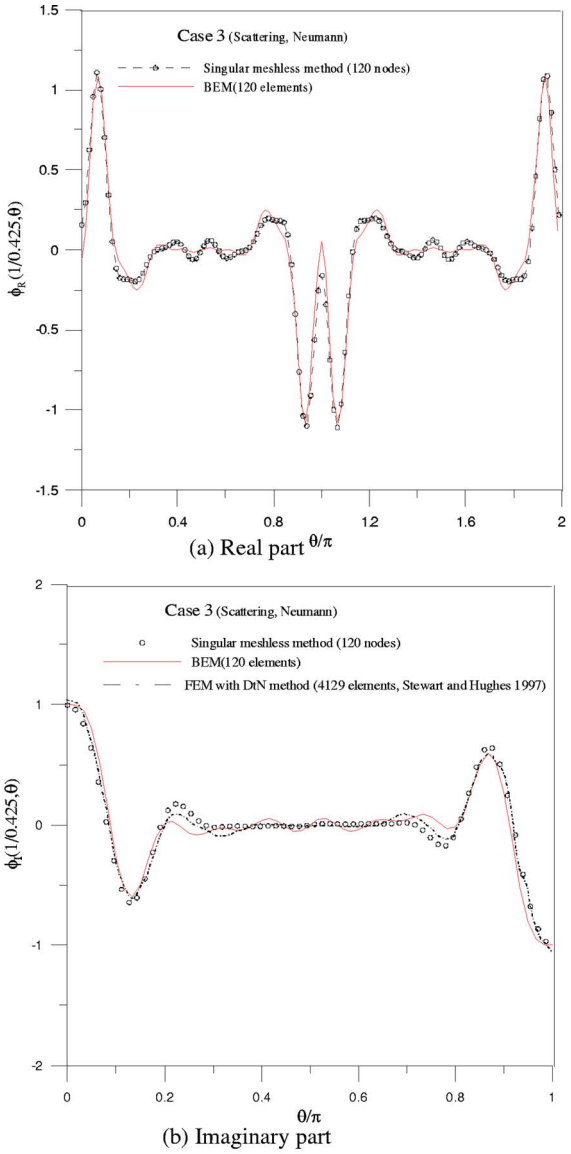

FIG. 14. (Color online) Plane wave scattering for a square rod subject to Neumann BC in Case 3 for $ka=4\pi$, $r=0.425$: (a) real part, (b) imaginary part (only the top half of the boundary is plotted).

$$\bar{B}^{(e)}(s^j,x^i) = \frac{\partial^2 \Phi^{(e)}(s^j,x^i)}{\partial n_{sj} \partial n_{x^i}} = 2\frac{y_k y_l n_k \bar{n}_l}{r_{ij}^4} - \frac{n_k \bar{n}_k}{r_{ij}^2}, \tag{A10}$$

which are Eqs. (20) and (21) in the text of Sec. III.

APPENDIX B: ANALYTICAL DERIVATION OF DIAGONAL COEFFICIENTS OF INFLUENCE MATRICES FOR CIRCULAR DOMAIN USING SEPARABLE KERNELS AND CIRCULANTS

By adopting the addition theorem, in a special case of the circular domain the two kernels in Eqs. (12) and (13) are expanded into separable kernels which segregate the field point, x, and source point, s, as follows:[2]

$$A^e(s,x) = \sum_{m=-\infty}^{\infty} \frac{\pi k}{2}[-iJ_m(k\rho) + Y_m(k\rho)] \times J'_m(kR)\cos(m(\theta-\varphi)), \quad \rho > R, \tag{B1}$$

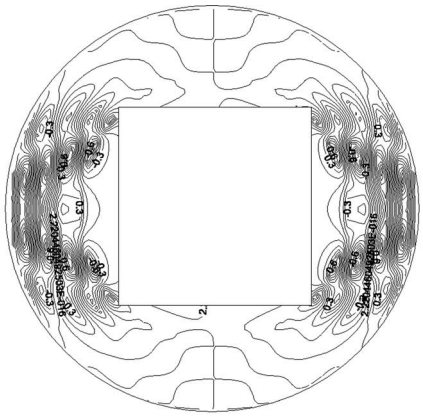

(a) Proposed SMM

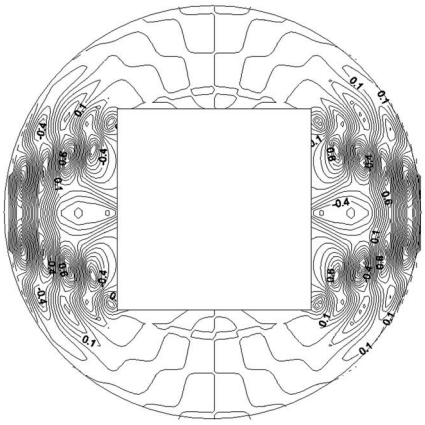

(b) BEM

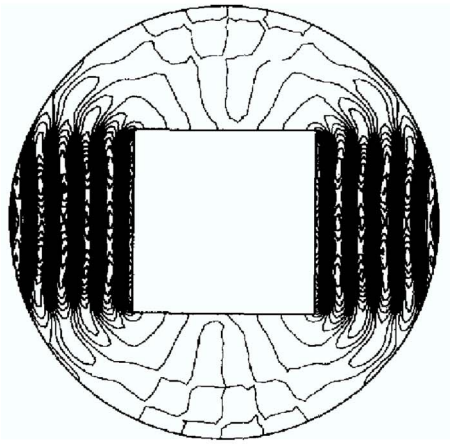

(c) FEM

FIG. 15. The contour plots for the real-part solutions in Case 3: (a) proposed SMM (120 nodes), (b) BEM (120 elements), (c) FEM with DtN method [4129 elements, Stewart and Hughes (1997)].

$$B^e(s,x) = \sum_{m=-\infty}^{\infty} \frac{\pi k}{2}[-i \times J'_m(k\rho) + Y'_m(k\rho)]J'_m(kR)\cos(m(\theta-\varphi)), \quad \rho > R, \tag{B2}$$

where $s=(R,\theta)$ and $x=(\rho,\varphi)$ in polar coordinates and the superscript denotes the derivative operator. Since the rotation symmetry is preserved for a circular boundary, the two influence matrices in Eqs. (8) and (9) are circulants with the elements

$$K_{ij} = K(R,\theta_j;\rho,\varphi_i), \tag{B3}$$

where the kernel K can be A^e or B^e in Eqs. (8) and (9) for the exterior problem, θ_j, φ_i are the angles of collocation and source points, respectively. By superimposing N lumped strength along the boundary, we have the influence matrices,

$$[K] = \begin{bmatrix} k_0 & k_1 & \cdots & k_{N-1} \\ k_{N-1} & k_0 & \cdots & k_{N-2} \\ \vdots & \vdots & \ddots & \vdots \\ k_1 & k_2 & \cdots & k_0 \end{bmatrix}, \tag{B4}$$

where the elements of the first row can be obtained from

$$k_j = K(R,\theta_j;\rho,0), \tag{B5}$$

in which $\varphi=0$ is set without loss of generality. The matrix $[K]$ in Eq. (A4) is found to be a circulant, since the rotational symmetry for the influence coefficients is observed. By introducing the following bases for the circulants, I, $(C_N)^1$, $(C_N)^2,\ldots$, and $(C_N)^{N-1}$, we can expand $[K]$ into

$$[K] = k_0 I + k_1 (C_N)^1 + k_2 (C_N)^2 + \cdots + k_{N-1}(C_N)^{N-1}, \tag{B6}$$

where I is the unit matrix and

$$C_N = \begin{bmatrix} 0 & 1 & 0 & \cdots & 0 & 0 \\ 0 & 0 & 1 & \cdots & 0 & 0 \\ \vdots & \vdots & \vdots & \ddots & \vdots & \vdots \\ 1 & 0 & 0 & \cdots & 0 & 0 \end{bmatrix}_{N\times N}. \tag{B7}$$

Based on the circulant theory, the eigenvalues for the influence matrix, $[K]$, are found as follows:

$$\lambda_l = k_0 + k_1\alpha_l + k_2(\alpha_l)^2 + \cdots + k_{2N-1}(\alpha_l)^{N-1}, \quad l = 0,1,2,\ldots,(N-1), \tag{B8}$$

where λ_l and α_l are the eigenvalues of $[K]$ and $[C_N]$, respectively. It is found that the eigenvalues of the circulants $[C_N]$ are the roots of $\alpha^N=1$, as shown in the following:

$$\alpha_l = e^{i(2\pi l/N)} \quad l = 0,1,2,\ldots,N-1. \tag{B9}$$

Substituting Eq. (B9) into Eq. (B8), we obtain

$$\lambda_l = \sum_{m=0}^{N-1} k_m \alpha_l^m = \sum_{m=0}^{N-1} k_m e^{i(2\pi ml/N)}, \quad l = 0,1,2,\ldots,(N-1). \tag{B10}$$

According to the definition of k_m in Eq. (B5), we have

$$k_m = k_{N-m}, \quad m = 0,1,2,\ldots,N-1. \tag{B11}$$

Substitution of Eq. (B11) into Eq. (B10) yields

$$\lambda_l = k_0 + \sum_{m=1}^{N-1} k_m(\alpha_l^m + \alpha_l^{N-m})$$

$$= \sum_{m=0}^{N-1} k_m \cos\left(\frac{2\pi ml}{N}\right), \quad l = 0,1,2,\ldots,N-1. \tag{B12}$$

By setting $\varphi=0$, without loss of generality, the Riemann sum reduces to the following integral:

$$\lambda_l = \frac{1}{\Delta\theta} \lim_{N\to\infty} \sum_{m=0}^{N-1} K(m\Delta\theta,0)\cos(ml\Delta\theta)\Delta\theta$$

$$= \frac{N}{2\pi}\int_0^{2\pi} \cos(l\theta)K(\theta,0)d\theta, \tag{B13}$$

where $\Delta\theta=2\pi/N$.

By employing the separable kernel $A^e(s,x)$ for exterior problem ($R<\rho$) in Eq. (B1) and the orthogonal conditions, Eq. (B13) then reduces to

$$\lambda_l = \pi k\frac{N}{2}[-iJ_l(k\rho) + Y_l(k\rho)]$$

$$\times J_l'(kR), \quad l = 0,1,2,3,\ldots,N-1. \tag{B14}$$

Similarly, we have

$$\upsilon_l = \pi k^2\frac{N}{2}[-iJ_l'(k\rho) + Y_l'(k\rho)]$$

$$\times J_l'(kR), \quad l = 0,1,2,3,\ldots,N-1 \tag{B15}$$

where λ_l and υ_l are the eigenvalues of $[A^e]$ and $[B^e]$, respectively.

Employing the invariant property of the influence matrices, the first invariant is the sum of all the eigenvalues. The diagonal coefficients of the two matrices for the exterior problem are obtained by the addition of all eigenvalues and are shown as

$$Na_{jj} = \sum_{l=0}^{N-1} \lambda_l, \tag{B16}$$

$$Nb_{jj} = \sum_{l=0}^{N-1} \upsilon_l. \tag{B17}$$

Substituting Eqs. (B14) and (B15) into Eqs. (B16) and (B17), we obtain

$$a_{jj} = -\frac{ik\pi}{4}\sum_{l=0}^{N-1} H_l^{(1)}(kR)[J_{l-1}(kR) - J_{l+1}(kR)], \tag{B18}$$

$$b_{jj} = -\frac{ik^2\pi}{4}\sum_{l=0}^{N-1} [H_{l-1}^{(1)}(kR) - H_{l+1}^{(1)}(kR)][J_{l-1}(kR)$$

$$- J_{l+1}(kR)]. \tag{B19}$$

Applying the addition theorem for the Bessel function, the limiting forms for small argument and approaching the collocation point to the source point, we obtain

$$\lim_{N\to\infty}\left(-\frac{4kR\pi}{N} + \frac{2Ni}{kR\pi}\right) = \lim_{N\to\infty}\sum_{l=0}^{N-1} H_l^{(1)}(kR)[J_{l-1}(kR)$$

$$- J_{l+1}(kR)]. \tag{B20}$$

Hence, the diagonal elements are easily determined from Eqs. (B18) and (B19) as follows:

$$a_{jj} = \frac{\pi}{\frac{2\pi R}{N}}, \quad N \gg 1. \tag{B21}$$

Similarly, we have

$$b_{jj} = \frac{(1+N)N}{8R^2} + \frac{\pi k^2}{4}i, \quad N \gg 1. \tag{B22}$$

It is worth noticing that diagonal terms for general domains of Eqs. (22) and (23) are analogous to Eqs. (B21) and (B22) for the special circular domain.

[1] S. Li and W. K. Liu, "Meshfree and particle methods and their application," Appl. Mech. Rev. **55**(1), (2002).

[2] T. Belytschko, L. Gu, and Y. Lu, "Fracture and crack growth by element-free Galerkin methods," Modell. Simul. Mater. Sci. Eng. **2**, 519–534 (1994).

[3] J. T. Chen, S. R. Kuo, K. H. Chen, and Y. C. Cheng, "Comments on vibration analysis of arbitrary shaped membranes using non-dimensional dynamic influence function," J. Sound Vib. **235**, 156–171 (2000).

[4] J. T. Chen, M. H. Chang, K. H. Chen, and S. R. Lin, "The boundary collocation method with meshless concept for acoustic eigenanalysis of two-dimensional cavities using radial basis function," J. Sound Vib. **257**, 667–711 (2002).

[5] J. T. Chen, M. H. Chang, and K. H. Chen, "Boundary collocation method for acoustic eigenanalysis of three-dimensional cavities using radial basis function," Comput. Mech. **29**, 392–408 (2002).

[6] J. T. Chen, I. L. Chen, and C. S. Wu, "On the equivalence of MFS and Trefftz method for Laplace problems," Proceedings of the Global Chinese Workshop on Boundary Element and Meshless Method, Hebei, China, 2003.

[7] J. T. Chen, C. S. Wu, Y. T. Lee, and K. H. Chen, "On the equivalence of the Trefftz method and method of fundamental solutions for Laplace and biharmonic equations," Comput. Math. Appl. (to be published).

[8] J. T. Chen, I. L. Chen, K. H. Chen, Y. T. Yeh, and Y. T. Lee, "A meshless method for free vibration of arbitrarily shaped plates with clamped boundaries using radial basis function," Eng. Anal. Boundary Elem. **28**, 535–545 (2005).

[9] W. Chen and M. Tanaka, "A meshfree, integration-free and boundary-only RBF technique," Comput. Math. Appl. **43**, 379–391 (2002).

[10] W. Chen and Y. C. Hon, "Numerical investigation on convergence of boundary knot method in the analysis of homogeneous Helmholtz, modified Helmholtz and convection-diffusion problems," Comput. Methods Appl. Mech. Eng. **192**, 1859–1875 (2003).

[11] G. Fairweather and A. Karageorghis, "The method of fundamental solutions for elliptic boundary value problems," Adv. Comput. Math. **9**, 69–95 (1998).

[12] R. A. Gingold and J. J. Maraghan, "Smoothed particle hydrodynamics: Theory and applications to non-spherical stars," Man. Not. Astro. Soc. **181**, 375–389 (1977).

[13] M. A. Golberg and C. S. Chen, "The method of fundamental solution for potential, Helmholtz and diffusion problems," in *Boundary Integral Methods-Numerical and Mathematical Aspects*, edited by M. A. Golberg (Computational Mechanics, 1998) pp. 103–176.

[14] S. W. Kang, J. M. Lee, and Y. J. Kang, "Vibration analysis of arbitrary shaped membranes using non-dimensional dynamic influence function," J. Sound Vib. **221**, 117–132 (1999).

[15] S. W. Kang and J. M. Lee, "Application of free vibration analysis of membranes using the non-dimensional dynamic influence function," J. Sound Vib. **234**, 455–470 (2000).

[16] W. K. Liu, S. Jun, S. Li, J. T. Adee, and T. Belyschko, "Reproducing kernel particle methods for structural dynamics," Int. J. Numer. Methods

Eng. **38**, 1655–1679 (1995).
[17]C. C. Tsai, D. L. Young, and A. H. D. Cheng, "Meshless BEM for three-dimensional Stokes flows," Comput. Model. Eng. Sci. **3**, 117–128 (2002).
[18]Y. S. Smyrlis and A. Karageorghis, "Some aspects of the method of fundamental solutions for certain harmonic problems," J. Sci. Comput. **16**, 341–371 (2001).
[19]D. L. Young, C. C. Tsai, T. I. Eldho, and A. H. D. Cheng, "Solution of Stokes flow using an iterative DRBEM based on compactly-supported, positive definite radial basis function," Comput. Math. Appl. **43**, 607–619 (2002).
[20]D. L. Young, K. H. Chen, and C. W. Lee, "Novel meshless method for solving the potential problems with arbitrary domains," J. Comput. Phys. **209**, 290–321 (2005).
[21]K. E. Atkinson, *The Numerical Solution of Integral Equations of the Second Kind*, 1st ed. (Cambridge University Press, Cambridge, 1997).
[22]M. Guiggiani, "Formulation and numerical treatment of boundary integral equations with hypersingular kernels," in V. Sladek and J. Sladek, editors, *Singular Integrals in Boundary Element Methods* (Computational Mechanics, 1998), Chap. 3, pp. 85–124.
[23]M. Guiggiani, G. Krishnasamy, T. J. Rudolphi, and F. J. Rizzo, "A general algorithm for the numerical solution of hypersingular boundary integral equations," ASME J. Appl. Mech. **59**, 604–614 (1992).
[24]*Singular Integrals in Boundary Element Methods*, edited by V. Sladek and J. Sladek (Computational Mechanics, Southampton, 1998).
[25]M. Tanaka, V. Sladek, and J. Sladek, "Regularization techniques applied to boundary element methods," Appl. Mech. Rev. **47**, 457–499 (1994).
[26]I. Harari, P. E. Barbone, M. Slavutin, and R. Shalom, "Boundary infinite elements for the Helmholtz equation in exterior domains," Int. J. Numer. Methods Eng. **41**, 1105–1131 (1998).
[27]F. Ihlenburg, *Finite Element Analysis of Acoustic Scattering*, Applied Mathematical Sciences (Springer, Berlin, 1998), p. 132.
[28]M. Abramowitz and I. A. Stegun, *Handbook of Mathematical Functions with Formulation Graphs and Mathematical Tables* (Dover, New York, 1972).
[29]J. R. Stewart and T. J. R. Hughes, "*h*-adaptive finite element computation of time-harmonic exterior acoustics problems in two dimensions," Comput. Methods Appl. Mech. Eng. **146**, 65–89 (1997).

High frequency formulation for the acoustic power spectrum due to cascade-turbulence interaction

Cheolung Cheong
Acoustics and Vibration Group, Division of Physical Metrology, Korea Research Institute of Standards and Science, Daejeon 305-340, Korea

Phillip Joseph[a)]
Institute of Sound and Vibration Research, University of Southampton, Highfield, Southampton, SO17 1BJ, United Kingdom

Soogab Lee
Center for Environmental Noise and Vibration Research, School of Mechanical and Aerospace Engineering, Seoul National University, Seoul 151-742, Korea

(Received 14 April 2005; revised 1 September 2005; accepted 25 October 2005)

This paper investigates the noise radiated by a cascade of flat-plate airfoils interacting with homogeneous, isotropic turbulence. An analytic formulation for the spectrum of acoustic power of a two-dimensional flat-plate is derived. The main finding of this paper is that the acoustic power spectrum from the cascade of flat airfoils may be split into two distinct frequency regions of low frequency and high frequency, separated by a critical frequency. Below this frequency, cascade effects due to the interaction between neighboring airfoils are shown to be important. At frequencies above the critical frequency, cascade effects are shown to be relatively weak. In this frequency range, acoustic power is shown to be approximately proportional to the number of blades. Based on this finding at high frequencies, an approximate expression is derived for the power spectrum that is valid above the critical frequency and which is in excellent agreement with the exact expression for the broadband power spectrum. The formulation is used to perform a parametric study on the effects on the power spectrum of the blade number, stagger angle, gap-chord ratio, and Mach number. The theory is also shown to provide a close fit to the measured spectrum of rotor-stator interaction. © *2006 Acoustical Society of America.* [DOI: 10.1121/1.2139626]

PACS number(s): 43.28.Ra, 43.50.Cb [GCL] Pages: 108–122

I. INTRODUCTION

This paper deals with the broadband noise due to the interaction between turbulence and a cascade of flat-plate airfoils. This problem is relevant to broadband noise generation in an aero-engine due to interaction of the turbulent rotor wake with the stator vanes, and to the interaction of ingested turbulence with the rotor blades.

The acoustic radiation from a uniformly spaced cascade of blades due to an impinging turbulent gust may be predicted by Fourier synthesis of the response to a harmonic vortical gust. A number of different approaches have been developed to address this problem. Kaji and Okazaki[1,2] have considered sound propagation upstream through a two-dimensional cascade of flat-plate airfoils by solving for the distribution of dipole source strength on the blade surfaces. Based on a similar approach, Smith[3] has developed the first numerical solution for predicting the unsteady blade loading and the acoustic field upstream or downstream of a two-dimensional cascade of flat-plate airfoils perfectly aligned with a uniform mean flow. Further details are presented in Whitehead.[4] Mani and Hovray[5] have developed other methods for solving this problem using an approximate solution based on the Wiener Hopf method. Koch[6] extended the Wiener Hopf analysis of Mani and Hovray[5] to blades with finite chord and gave the transmission and reflection coefficient for both upstream and downstream propagating acoustic waves. Peake[7] has extended Koch's analysis to give the unsteady loading on the blades caused by an incoming vortical gust, and has also developed analytic tools[8,9] to enable the rapid computation of the function required for the Wiener Hopf solution. [5,6] The effects of blade sweep and oblique gust arrival angles were investigated by Glegg,[10] who has developed an analytic expression for the unsteady blade loading, acoustic mode amplitude, and sound power output of a three-dimensional rectilinear cascade of blades with finite chord excited by a three-dimensional vortical gust.

Hanson and Horan[11] have investigated the broadband noise due to turbulence interacting with a flat-plate cascade, using the cascade response theory due to Glegg.[10] Hanson[12,13] has also extended the theory in Ref. 11 to include the effects of lean and sweep on the broadband noise spectrum. Evers and Peake[14] have recently investigated the effects of small, but nonzero, camber and thickness on the upstream acoustic power.

In the present study, the theory of broadband noise from a cascade of two-dimensional flat airfoils subject to homogeneous frozen turbulent gust is investigated in detail. Emphasis is given to the physical interpretation of the acoustic field above a critical frequency, where it is shown that the sound

[a)]Electronic mail: pfj@isvr.soton.ac.uk

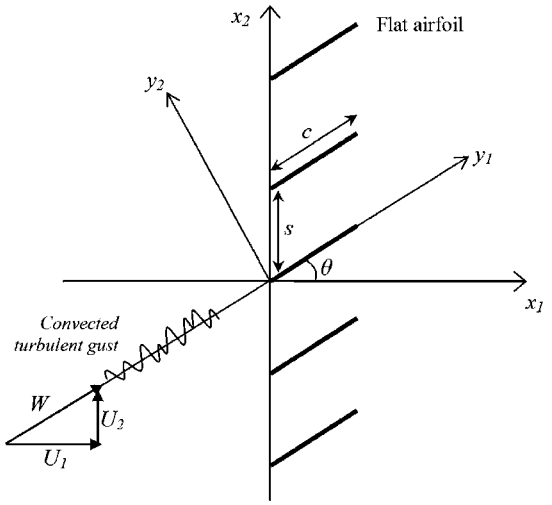

FIG. 1. The cascade geometry and the convected turbulence gust.

power is proportional to the blade number suggesting that for turbulent gusts, interaction effects between the blades is weak.

The main contributions of this paper are threefold. First, we define the concept of a critical frequency which divides the acoustic response of the flat-airfoil cascade to impinging turbulence into two distinct frequency regions. Below the critical frequency, the effects of interaction between the neighboring airfoils are significant and only some of the wave number components of turbulence contribute to the acoustic field. Above the critical frequency, all the wave number components of turbulence contribute to the acoustic field and the interaction between the adjacent airfoils is weak, so that the power from each blade is additive. Second, a simple expression is derived for the broadband power spectrum that is rapid to compute and is in excellent agreement with the exact calculation above the critical frequency. Finally, a parametric study is presented that includes a comparison between experimental data and predictions obtained using the exact and approximate expressions. This shows that overall predictions closely match those of Hanson[11,13] obtained using a three-dimensional theory, thereby suggesting that the contribution from oblique gusts to the radiated sound is comparatively weak.

II. FORMULATION OF ACOUSTIC FIELD

A. Basic equations

The cascade geometry and coordinate system investigated in this paper is shown in Fig. 1. A two-dimensional cascade of flat-plate airfoils with stagger angle θ is assumed to be located in a two-dimensional uniform flow moving in the direction parallel to the chord, i.e., with zero angle of incidence. Turbulence is assumed to be convected with the mean flow W as a "frozen gust pattern." In Fig. 1, (x_1,x_2) is the unwrapped duct coordinate system, and (y_1,y_2) is the cascade-fixed coordinate system. Following Smith, Ref. 3, nontrivial, single-frequency solutions of the linearized Euler equations of the form,

$$\begin{pmatrix} u_1 \\ u_2 \\ p \end{pmatrix} = \begin{pmatrix} \bar{u}_1 \\ \bar{u}_2 \\ \bar{p} \end{pmatrix} e^{i(\omega t+\alpha x_1+\beta x_2)}, \tag{1}$$

are obtained for

$$(\omega + U_1\alpha + U_2\beta)^2 - a^2(\alpha^2+\beta^2) = 0, \tag{2}$$

or

$$(\omega + U_1\alpha + U_2\beta) = 0, \tag{3}$$

where $\bar{u}$ and $\bar{p}$ are complex amplitudes, and α and β are the wave numbers of the perturbation quantities in the axial and gap-wise directions, respectively, and U_j is the mean velocity in the x_j direction, u_i is the unsteady velocity perturbation in the x_i direction, ρ_0 is the mean density, and p is the (acoustic) pressure. The dispersion relations of Eqs. (2) and (3) relate solely to acoustic waves and to vorticity waves, respectively. A single wave number component (k_1,k_2) of impinging turbulence has a phase angle σ between adjacent blades separated by a gap s given by

$$\sigma = (k_1 \sin\theta + k_2 \cos\theta)s. \tag{4}$$

The phase angle $\beta_r s$ between adjacent blades of the rth acoustic wave generated from the cascade due to a single wave number component of vorticity (k_1,k_2) is of the form $\beta_r s = \sigma - 2\pi r (r = -\infty, \ldots, -1, 0, 1, \ldots, \infty)$. The acoustic circumferential wave number β_r of the rth acoustic wave is therefore given by

$$\beta_r = \frac{(k_1 \sin\theta + k_2 \cos\theta)s - 2\pi r}{s}. \tag{5}$$

Equation (2) is a quadratic equation of the axial wave number α, whose solution can be expressed in terms of β_r and ω as follows:

$$\alpha_r^{\pm} = \frac{M_1(\omega/a + M_2\beta_r) \pm \sqrt{(\omega/a + M_2\beta_r)^2 - (1-M_1^2)\beta_r^2}}{1-M_1^2}. \tag{6}$$

The two solutions for α_r correspond to upstream-going (+) and downstream-going (−) acoustic waves. Note that β_r takes an infinite number of values, corresponding to an infinite number of cascade modes. However, Eq. (6) indicates that only a finite number of these can modes can propagate unattenuated. The amplitude of the cascade modes due to a harmonic gust can be obtained by following the procedure presented by Smith.[3] For a harmonic gust of the form,

$$w(y_1,y_2,t) = w_0 e^{i[k_1(y_1-Wt)+k_2 y_2]}, \tag{7}$$

the acoustic pressure upstream and downstream of the cascade (+,−) is of the form,

$$p^{\pm}(x_1,x_2,t) = \rho_0 W w_0 \sum_{r=-\infty}^{\infty} R_r^{\pm} e^{i(k_1 Wt+\alpha_r x_1+\beta_r x_2)}, \tag{8}$$

where $R_r^{\pm}$ is the cascade response function, which is completely defined by the parameters of $s/c, \theta, M, \lambda$, and σ, where λ is the reduced frequency $\omega c/W$.

B. Acoustic power spectrum

The analysis of sound radiation due to an incident sinusoidal vortical gust can be extended to broadband turbulent velocity distributions via the Fourier transform. It is assumed here that the turbulence can be regarded as a "frozen gust pattern" convecting with the free stream velocity W. This is a reasonable assumption because turbulence velocities are generally much smaller than convection velocities and hence change only slightly as they are convected past any airfoil in the cascade. Equation (8) can be generalized to give the acoustic pressure radiated from a cascade subject to the impinging turbulent gust, in the form,

$$p^{\pm}(x_1,x_2,t) = \rho_0 W \int_{-\infty}^{\infty}\int_{-\infty}^{\infty} \hat{\hat{w}}(k_1,k_2) \sum_{r=-\infty}^{\infty} R_r^{\pm}(k_1,k_2) \times e^{i(k_1 Wt + \alpha_r^{\pm} x_1 + \beta_r x_2)} dk_1 dk_2, \tag{9}$$

where $\hat{\hat{w}}(k_1,k_2)$ is the two-dimensional wave number spectrum of the turbulence velocity evaluated in the moving reference frame. Taking the Fourier transform of Eq. (9) with respect to t gives

$$\tilde{p}_T^{\pm}(\mathbf{x},\omega) = \rho_0 \int_{-\infty}^{\infty} \hat{\hat{w}}(K_1,k_2) \sum_{r=-\infty}^{\infty} R_r^{\pm}(K_1,k_2) e^{i(\alpha_r^{\pm} x_1 + \beta_r x_2)} dk_2, \tag{10}$$

where $\tilde{p}_T^{\pm}(\mathbf{x},\omega) = (1/2\pi)\lim_{T\to\infty}\int_{-T}^{T} p^{\pm}(\mathbf{x},t) e^{-i\omega t} dt$ and $K_1 = \omega/W$. Equation (10) substituted into the linearized momentum equation gives the following expressions for the acoustic particle velocities in the axial and gap-wise directions, respectively,

$$\tilde{u}_{1,T}^{\pm}(\mathbf{x},\omega) = \rho_0 \int_{-\infty}^{\infty} \hat{\hat{w}}(K_1,k_2) \sum_{r=-\infty}^{\infty} \frac{-\alpha_r^{\pm} R_r^{\pm}(K_1,k_2) e^{i(\alpha_r^{\pm} x_1 + \beta_r x_2)}}{\rho_0(\omega + U_1\alpha_r^{\pm} + U_2\beta_r)} dk_2, \tag{11}$$

$$\tilde{u}_{2,T}^{\pm}(\mathbf{x},\omega) = \rho_0 \int_{-\infty}^{\infty} \hat{\hat{w}}(K_1,k_2) \sum_{r=-\infty}^{\infty} \frac{-\beta_r R_r^{\pm}(K_1,k_2) e^{i(\alpha_r^{\pm} x_1 + \beta_r x_2)}}{\rho_0(\omega + U_1\alpha_r^{\pm} + U_2\beta_r)} dk_2. \tag{12}$$

In a fluid moving at uniform velocity, the intensity spectrum is given by[15]

$$I^{\pm}(\omega) = \lim_{T\to\infty} \frac{\pi}{T} \mathrm{Re}\left\{ \left(\frac{\tilde{p}_T(\omega)}{\rho_0} + U_1 \tilde{u}_{1,T}^{\pm}(\omega) + U_2 \tilde{u}_{2,T}^{\pm}(\omega) \right) \times \left(\rho_0 \tilde{u}_{1,T}^{\pm *}(\omega) + \frac{U_1 \tilde{p}_T^{*}(\omega)}{a^2} \right) \right\}. \tag{13}$$

Inserting Eqs. (10)–(12) into Eq. (13), and treating w as a random variable, leads to

$$I^{\pm}(\mathbf{x},\omega) = \rho_0 \int_{-\infty}^{\infty}\int_{-\infty}^{\infty} \left[\begin{array}{l} \lim_{T\to\infty} \frac{\pi}{T} E[\hat{\hat{w}}(K_1,k_2)\hat{\hat{w}}^{*}(K_1,k_2')] \\ \sum_{r=-\infty}^{\infty} \sum_{r'=-\infty}^{\infty} \mathrm{Re}\left\{ \begin{array}{l} \frac{\omega(-\alpha_{r'}^{\pm *} + M_1(\omega/a + M_1\alpha_{r'}^{\pm *} + M_2\beta_{r'}))}{(\omega + U_1\alpha_r^{\pm} + U_2\beta_r)(\omega + U_1\alpha_{r'}^{\pm *} + U_2\beta_{r'})} \\ \times R_r^{\pm}(K_1,k_2) R_{r'}^{\pm *}(K_1,k_2) e^{i[(\alpha_r^{\pm} - \alpha_{r'}^{\pm *})x_1 + (\beta_r - \beta_{r'})x_2]} \end{array} \right\} \end{array} \right] dk_2 dk_2', \tag{14}$$

where E[ ] denotes the expected value, or ensemble average value. Assuming that $\hat{\hat{w}}$ is a statistically random variable, and that the velocities at different wave number are uncorrelated, Amiet[16] shows that

$$\lim_{T\to\infty} \frac{\pi}{T} E[\hat{\hat{w}}(K_1,k_2)\hat{\hat{w}}^{*}(K_1,k_2')] = W\delta(k_2 - k_2')\Phi_{ww}(K_1,k_2'), \tag{15}$$

where $\Phi_{ww}(K_1,k_2')$ is the turbulence velocity wave number spectrum evaluated in the moving reference frame. Substituting Eq. (15) into Eq. (14) and performing the k_2' integration leads to

$$I^{\pm}(\mathbf{x},\omega) = \rho_0 M \int_{-\infty}^{\infty} \Phi_{ww}(K_1,k_2) \sum_{r=-\infty}^{\infty} \sum_{r'=-\infty}^{\infty} \times \mathrm{Re}\left\{ \begin{array}{l} \frac{\omega(-a\alpha_{r'}^{\pm *} + M_1(\omega + U_1\alpha_{r'}^{\pm *} + U_2\beta_{r'}))}{(\omega + U_1\alpha_r^{\pm} + U_2\beta_r)(\omega + U_1\alpha_{r'}^{\pm *} + U_2\beta_{r'})} \\ \times R_r^{\pm}(K_1,k_2) R_{r'}^{\pm *}(K_1,k_2) e^{i[(\alpha_r^{\pm} - \alpha_{r'}^{\pm *})x_1 + (\beta_r - \beta_{r'})x_2]} \end{array} \right\} dk_2. \tag{16}$$

The acoustic power per unit span can be obtained by integrating Eq. (16) in the x_2 direction over a distance of Bs.

Since the gap-wise wave numbers β_r and $\beta_{r'}$ are periodic over the distance Bs, this integral is of the form

$$\int_0^{Bs} e^{i(\beta_r-\beta_{r'})x_2}dx_2 = Bs\,\delta_{rr'}, \tag{17}$$

where the Kroneker delta function $\delta_{rr'}$ enables the r' summation in Eq. (16) to be eliminated. The acoustic power spectrum per unit span can therefore be expressed as

$$\mathcal{P}^{\pm}(\omega) = \rho_0 MBs \int_{-\infty}^{\infty} \Phi_{ww}(K_1,k_2) \sum_{r=-\infty}^{\infty} |R_r^{\pm}(K_1,k_2)|^2 \times \frac{\omega \mathrm{Re}\{-a\alpha_r^{\pm} + M_1(\omega + U_1\alpha_r^{\pm} + U_2\beta_r)\}}{|\omega + U_1\alpha_r^{\pm} + U_2\beta_r|^2} dk_2. \tag{18}$$

The periodicity of the turbulence in the x_2 direction (circumferential direction) allows the transverse Fourier integrals in k_2 to be converted to a Fourier series. Since the basic spatial period of the flow is the circumference Bs of the annulus under consideration, the wave number in the y_2 direction, as indicated by the relationship between the (x_1,x_2) and (y_1,y_2) coordinate systems in Fig. 1, must satisfy

$$k_{2,m} = \frac{2\pi m}{Bs\cos\theta} - K_1 \tan\theta, \tag{19}$$

where m is the vortical mode number in the circumferential direction. From Eq. (19), integration over k_2 at constant frequency (or K_1) requires that the elemental wave number $dk_{2,m}$ must be replaced by

$$dk_{2,m} \to \frac{2\pi\Delta m}{Bs\cos\theta}, \tag{20}$$

where $\Delta m = 1$. Thus, the k_2 integral may be written as a summation and Eq. (18) therefore becomes

$$\mathcal{P}^{\pm}(\omega) = \frac{2\pi\rho_0 M}{\cos\theta} \sum_{m=-\infty}^{\infty} \Phi_{ww}(K_1,k_{2,m}) \sum_{r=-\infty}^{\infty} |R_r^{\pm}(K_1,k_{2,m})|^2 \times \frac{\omega\,\mathrm{Re}\{-a\alpha_r^{\pm} + M_1(\omega + U_1\alpha_r^{\pm} + U_2\beta_r)}{|\omega + U_1\alpha_r^{\pm} + U_2\beta_r|^2}. \tag{21}$$

The radiated noise is therefore the sum of contributions from an infinite number of vortical modes, each of which scatters to produce an infinite number of acoustic modes. Equation (21) for the spectrum of sound power is not efficient for computation since $R_r^{\pm}$ appears inside the double summations of m and r. A transformation of the summation indices can be used to move $R_r^{\pm}$ out from the double summation into a single summation at the expense of moving the turbulence spectrum Φ_{ww} under the double summation. Overall, this is advantageous since Φ_{ww} will normally be computed from a simple algebraic expression, whereas $R_r^{\pm}$ requires another infinite summation of the so-called "cascade-waves" and the numerical computation of the upwash integral equation in Ref. 3. Since the basic spatial period of the flow is Bs, the acoustic wave number in the x_2 direction must satisfy

$$\beta_l = \frac{2\pi}{Bs} l, \tag{22}$$

where l is an arbitrary integer and denotes the order of the acoustic mode in the x_2 direction. Note that l is equivalent to the circumferential mode index m used in duct acoustic theory. Inserting Eqs. (19) and (22) into Eq. (5), the mth vortical wave number may be written in terms of the acoustic mode number l and the cascade scattering index r as

$$m = l + Br. \tag{23}$$

Equation (23) specifies the scattering rule for the generation of acoustic mode due to interaction of vortical modes with the cascade. Inserting Eq. (23) into Eq. (19) gives

$$k_{2,l+Br} = \frac{2\pi}{Bs\cos\theta}(l + Br) - K_1 \tan\theta. \tag{24}$$

By using Eq. (24), Eq. (21) can be rearranged as

$$\mathcal{P}^{\pm}(\omega) = \frac{2\pi\rho_0 M}{\cos\theta} \sum_{l=-\infty}^{\infty} Q_l^{\pm}(K_1) \sum_{r=-\infty}^{\infty} \Phi_{ww}(K_1,k_{2,l+Br}), \tag{25}$$

where $Q_l^{\pm}$ is a nondimensional modal power response function given by

$$Q_l^{\pm}(K_1) = |R_l^{\pm}(K_1,k_{2,\mathrm{mod}(l,B)})|^2 \times \frac{\omega\,\mathrm{Re}\{-a\alpha_l^{\pm} + M_1(\omega + U_1\alpha_l^{\pm} + U_2\beta_l)\}}{|\omega + U_1\alpha_l^{\pm} + U_2\beta_l|^2}. \tag{26}$$

The function, $\mathrm{mod}(l,B)$, denotes the remainder when the first argument is divided by the second argument. The modulus function emerges from the form of the cascade response function in Ref. 3, which has the property $K_{ji}^{-1}(\sigma_{l+Br})W_i = K_{ji}^{-1}(\sigma_{\mathrm{mod}(l,B)})W_i$. If we consider only the cut-on modal components in Eq. (25), the infinite summation over l in Eq. (25) becomes finite at a given frequency. In a subsonic flow, $W < a$, propagating modes corresponding to real values of $\alpha_r^{\pm}$ in Eq. (6), which occur over the range of β_l given by

$$\frac{M_2 - (1-M_1^2)^{1/2}}{1-M^2}\omega \leqslant a\beta_l \leqslant \frac{M_2 + (1-M_1^2)^{1/2}}{1-M^2}\omega. \tag{27}$$

We denote by $L_{\max}$ and $L_{\min}$ the maximum and minimum integers of the acoustic mode number l satisfying the upper and lower inequality of Eq. (27), respectively. These correspond to acoustic modes traveling in the direction of the swirl velocity U_2, and against it, respectively. Equation (25) can now be written as

$$\mathcal{P}^{\pm}(\omega) = \frac{2\pi\rho_0 M}{\cos\theta} \sum_{l=L_{\min}}^{L_{\max}} Q_l^{\pm}(K_1) \sum_{r=-\infty}^{\infty} \Phi_{ww}(K_1,k_{2,l+Br}), \tag{28}$$

where the range of r is chosen to ensure convergence. The corresponding sound power integrated over the frequency bandwidth $\omega_L \leqslant \omega \leqslant \omega_H$ can therefore be written as

$$\Pi^{\pm} = \frac{2\pi\rho_0 M}{\cos\theta} \int_{\omega_L}^{\omega_H} \sum_{l=L_{\min}}^{L_{\max}} Q_l^{\pm}(K_1) \sum_{r=-\infty}^{\infty} \Phi_{ww}(K_1, k_{2,l+Br}) d\omega. \tag{29}$$

The integration over ω in Eq. (29) is performed numerically in this paper.

C. Turbulence spectra

For simplicity we assume that the turbulence impinging on the cascade is homogeneous and isotropic. A suitable model for wave number PSD, which is consistent with these requirements, is the Liepmann spectrum $\Phi_{ww}(k_1,k_2,k_3)$ of the form,

$$\Phi_{ww}(k_1,k_2,k_3) = \frac{2\overline{w^2}\Lambda^3}{\pi^2} \frac{\Lambda^2(k_1^2+k_3^2)}{[1+\Lambda^2(k_1^2+k_2^2+k_3^2)]^3}, \tag{30}$$

where $\overline{w^2}$ is the mean square value of turbulence velocity in the direction normal to the chord and Λ is the turbulence integral length-scale. Integrating over k_3 gives the two-dimensional spectrum required in Eqs. (28) and (29) of the form,

$$\Phi_{ww}(k_1,k_2) = \frac{\overline{w^2}\Lambda^2}{4\pi} \frac{[1+\Lambda^2(4k_1^2+k_2^2)]}{[1+\Lambda^2(k_1^2+k_2^2)]^{5/2}}. \tag{31}$$

III. CHARACTERISTICS OF THE ACOUSTIC POWER SPECTRUM

In the following the above-developed theory to predict the acoustic power spectrum upstream and downstream of a two-dimensional flat-airfoil cascade interacting with homogeneous turbulence is now used to investigate the characteristics of the broadband sound field. These findings will be subsequently used to derive an expression for the acoustic power spectrum that is valid above a certain critical frequency. Unless otherwise stated, all the computations in this section were performed with a Mach number $M=0.5$, a stagger angle of $\theta=0°$, a turbulence intensity of $\overline{w^2}/W^2=4\times10^{-4}$, a turbulence integral length-scale of $\Lambda/c=0.05$, and a radius of $R/c=9/2\pi$ (i.e., $Bs/c=9$).

A. Critical frequency

Figure 2 presents the predicted acoustic power spectrum for the blade numbers of $B=4:4:24$ plotted against nondimensional frequency, $\omega/\Delta\omega_{\pm}$, where $\Delta\omega_{\pm}$ is the frequency separation between successive modal cut-on frequencies (note that $\Delta\omega_+=\Delta\omega_-$ for $\theta=0°$). The spectra contain a number of peaks occurring at integer values of $\omega/\Delta\omega_{\pm}$. These peaks can be divided into two categories. The first mostly occurs in the upstream spectra, at $\omega/\Delta\omega_{\pm}=nB$ ($n=1,2,3,\ldots$) and are characterized by narrow bandwidth and comparatively large amplitude. The other, smoother, peaks, occurring at the other integer values of $\omega/\Delta\omega_{\pm}$, except $\omega/\Delta\omega_{\pm}=nB$, have smaller amplitude and are closer together in frequency. These peaks occur at the cut-on frequencies of the cascade acoustic modes, defined by Eq. (27). The cut-on frequency of the lth cascade mode therefore occurs at

$$\omega_{l\pm} = l\Delta\omega_{\pm}, \tag{32}$$

where l is the acoustic mode number defined by the scattering rule $l=m-Br$ in Eq. (23) and $\Delta\omega_{\pm}$ is given by

$$\Delta\omega_{\pm} = \frac{1-M^2}{M_2 \pm (1-M_1^2)^{1/2}} \frac{2\pi a}{Bs}. \tag{33}$$

At frequencies below the cut-on frequency, the mode is cutoff and decays exponentially from the cascade. In this paper we refer to the lowest frequency of the large peak $l=B$ [i.e., plus sign in Eqs. (32) and (33)] as "the critical frequency," defined by

$$\omega_c = B\Delta\omega_+ = \frac{1-M^2}{M_2+(1-M_1^2)^{1/2}} \frac{2\pi a}{s}. \tag{34}$$

The significance of this frequency for cascade-turbulence interaction noise is twofold. First, the wavelength in the x_2 direction of the cascade acoustic mode, $l=B$, equals the blade spacing s. As the frequency increases above the critical frequency, the number of cut-on acoustic modes whose wavelength in the x_2 direction are less than the blade spacing s increases. These modes are therefore anticipated to have relatively weak interaction with the cascade. This property is employed in the next section in order to obtain a modal average value for the sound power. Second, it may be shown that at the critical frequency, all wave number components of turbulence excite propagating cascade modes, whereas below it, only some of the wave number components excite cut-on modes. Consequently, we will show that at frequencies below the critical frequency the acoustic field radiated from the cascade is sensitive to the interaction between neighboring blades. Above the critical frequency the acoustic field is relatively independent of interaction effects and therefore the radiated sound power from the different blades is additive. In order to demonstrate this phenomenon we compute the sound power versus blade number in a frequency band below the critical frequency for $B=24$ and in a frequency band above it. The results are shown in Fig. 3, nondimensionalized on $\rho_0 W^3 c$.

The results in Figs. 3(a) and 3(b) for the lower frequency band vary nonlinearly with the blade number B. In the higher frequency band, Figs. 3(c) and 3(d), however, the acoustic power is roughly proportional to B. The power at these high frequencies for the different blade numbers is therefore additive, suggesting that the interaction between blades is weak. The sensitivity of broadband noise radiation to cascade geometry therefore diminishes once the integration over all k_2 wave numbers is performed, as indicated in Eq. (18).

B. Approximate expression for the acoustic power spectrum

Here, we will derive an approximate expression for the acoustic power spectrum of Eq. (28) based on the findings obtained in Sec. III A. We now make the approximation in Eq. (28) that Φ_{ww} is a slowly varying function of k_2 such that the summation of Φ_{ww} over r is a weak function of l and may therefore be taken out from the summation over l. Correspondingly, we make the substitution,

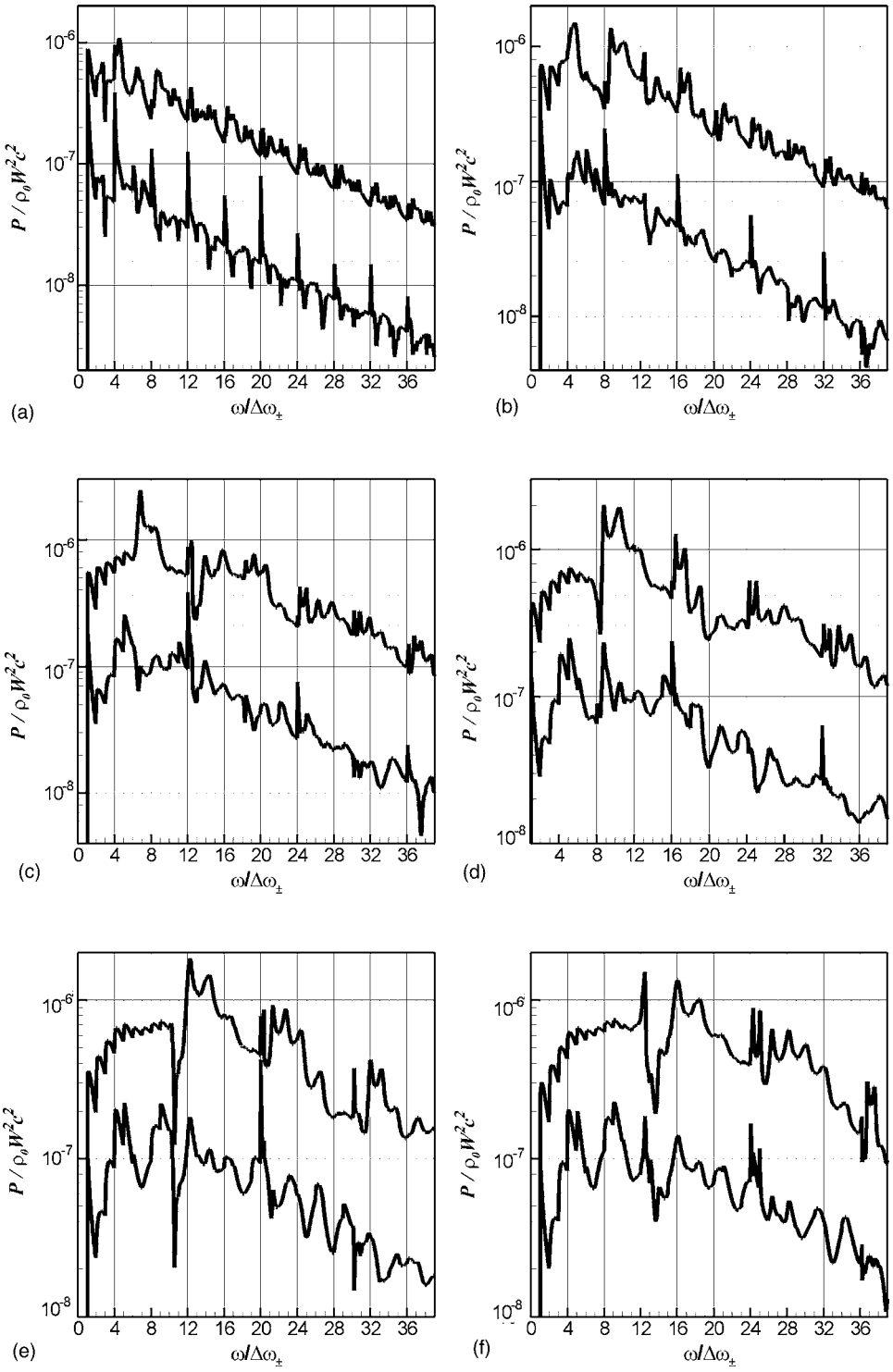

FIG. 2. Predicted spectrum of acoustic PSD: (a) $B=4$, (b) $B=8$, (c) $B=12$, (d) $B=16$, (e) $B=20$, and (f) $B=24$ where lower spectrum denotes the upstream spectrum and upper spectrum denotes the downstream spectrum.

$$\sum_{r=-\infty}^{\infty} \Phi_{ww}(K_1, k_{2,l+Br}) \approx \frac{1}{B} \sum_{m=-\infty}^{\infty} \Phi_{ww}(K_1, k_{2,m}), \tag{35}$$

such that the dependence on l can now be dropped. Equations (24) and (35) suggest that this is a valid approximation at high frequencies and integral length-scales small compared to the blade spacing, i.e., $\Lambda/s < 1$. Insertion of Eq. (35) into Eq. (28) leads to

$$\mathcal{P}^{\pm}(\omega) \approx \frac{2\pi\rho_0 M}{B\cos\theta} \sum_{m=-\infty}^{\infty} \Phi_{ww}(K_1, k_{2,m}) \sum_{l=L_{\min}}^{L_{\max}} Q_l^{\pm}(K_1) \quad \text{for } \omega > \omega_c. \tag{36}$$

This procedure has the effect of decoupling the turbulence wave number spectrum from the cascade response function. In order to verify the validity of Eq. (36), the power spectrum for $B=24$ and $\Lambda/c=0.1$ are computed using the exact expression of Eq. (28) and the approximate expression of Eq. (36). The error between the two predictions, calcu-

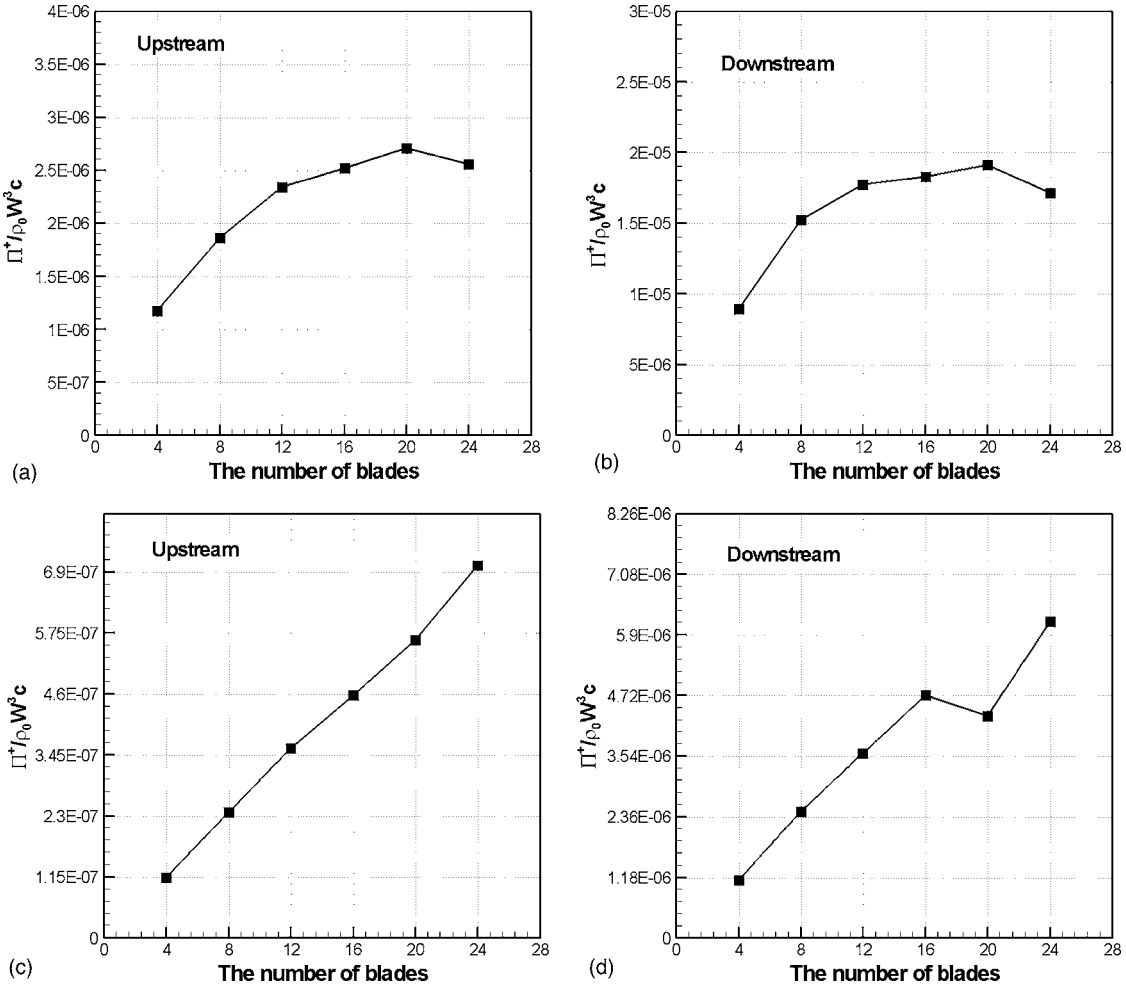

FIG. 3. Predicted band acoustic power with various blade number: (a) and (b) on lower bandwidth, $\omega<(\omega_c)_{B=24}$; (c) and (d) on higher bandwidth, $\omega>(\omega_c)_{B=24}$.

lated from $\epsilon=|(\mathcal{P}^{\pm}(\omega)-\tilde{\mathcal{P}}^{\pm}(\omega))/\mathcal{P}^{\pm}(\omega)|$ where the tilde denotes the approximate prediction, is plotted in Fig. 4. The error between the exact and approximate solutions is negligible at all frequencies, especially above the critical frequency where typical error is less than 1%. Figure 4 suggests that the error associated with Eq. (36) is negligible even at frequencies below the critical frequency. The requirement that the frequency range is above the critical frequency for Eq. (36) to be valid may therefore be relaxed.

We now introduce a further simplification to the sound power expression that is only valid at frequencies above the critical frequency. The basis for the technique involves replacing the frequency-dependence of $Q_l(K_1)$ in Eq. (36) by its high frequency asymptotic dependence. In order to ascertain this dependence, the function $\Sigma_{l=L_{\min}}^{L_{\max}} Q_l^{\pm}(K_1)$ appearing in Eq. (28) is computed for different blade numbers. The results are plotted in Fig. 5.

Also shown in these figures are the curves proportional to B^2/K_1, which provide a good fit to the exact behaviors at frequencies greater than their respective critical frequencies. Based on this goodness of fit, we write the high frequency response function of the cascade in the form,

$$\sum_{l=L_{\min}}^{L_{\max}} Q_l^{\pm}(K_1) \approx \frac{Bs\omega(1-M_1^2)^{1/2}}{\pi a(1-M^2)} \frac{aF^{\pm}(M,\theta)}{W\lambda^2(s/c)^2}, \tag{37}$$

where $F^{\pm}(M,\theta)$ is a nondimensional function that must only depend on M and θ. The argument leading to this formulation is presented in Appendix A.

The first term on the right-hand side of Eq. (37), as demonstrated by Eq. (27), approximates the number of cut-on modes. The second term therefore specifies the modal averaged acoustic power response, and is introduced such that the final form of Eq. (37) is proportional to B^2/K_1 while retaining the nondimensionality. Note that the chord length c cancels in the term, $\lambda^2(s/c)^2$. Insertion of Eq. (37) into Eq. (36) gives an approximation to the power spectral density of the form,

$$\mathcal{P}^{\pm}(\omega) \approx F^{\pm}(M,\theta)\frac{2\rho_0 MW(1-M_1^2)^{1/2}}{\omega s\cos\theta(1-M^2)} \sum_{m=-\infty}^{\infty} \Phi_{ww}(K_1,k_{2,m}) \quad \text{for } \omega \geqslant \omega_c. \tag{38}$$

Converting the $k_{2,m}$ summation into k_2 integration by the use of the inverse relation of Eq. (20) leads to

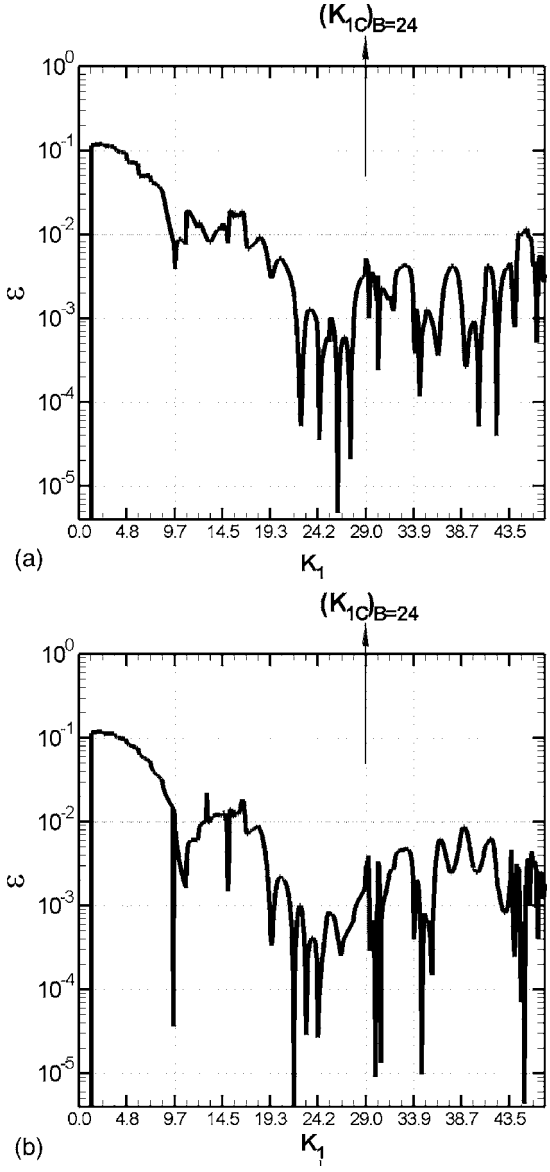

FIG. 4. Calculated error between the exact and approximate predictions for $B=24$ and $\Lambda=0.1$. Error is defined as $\epsilon=|(\mathcal{P}^{\pm}(\omega)-\tilde{\mathcal{P}}^{\pm}(\omega))/\mathcal{P}^{\pm}(\omega)|$ where a tilde denotes the prediction using the approximate equation, Eq. (36): (a) upstream and (b) downstream.

$$\mathcal{P}^{\pm}(\omega) \approx F^{\pm}(M,\theta)\frac{B\rho_0 M(1-M_1^2)^{1/2}}{\pi(1-M^2)}\frac{\Phi_{ww}(K_1)}{K_1} \quad \text{for } \omega \geqslant \omega_c, \tag{39}$$

where the turbulence one-dimensional (frequency) spectrum is given by $\Phi_{ww}(K_1)=\int_{-\infty}^{\infty}\Phi_{ww}(K_1,k_2)dk_2$. This formulation makes explicit that the acoustic power above the critical frequency is proportional to blade number and independent of the airfoil chord and solidity. In order to verify these dependencies from numerical predictions, we define a normalized acoustic power over the bandwidth $(\omega_c)_{B=4n} \leqslant \omega \leqslant (\omega_c)_{B=4n+4}$ in Fig. 2, given by

$$\bar{\Pi}_n^{\pm} = \frac{\int_{(\omega_c)_{B=4n}}^{(\omega_c)_{B=4n+4}}\mathcal{P}^{\pm}(\omega)d\omega}{\int_{(\omega_c)_{B=4n}}^{(\omega_c)_{B=4n+4}}\Phi_{ww}(K_1)/K_1 d\omega}. \tag{40}$$

If the approximate solution of Eq. (39) is valid, then $\bar{\Pi}_n \propto B$ for $B=4,\ldots,4n$ for the same values of M and θ, and the resultant curve of $\bar{\Pi}_n$ collapses onto a single curve proportional to the blade number. Equation (40) was computed using the same parameters used in Fig. 2, except with a solidity of $s/c=1$, i.e., $c=9/B$. In this computation, acoustic power was computed using the exact expression of Eq. (29). The result is plotted in Fig. 6. The normalized power is shown to be a function only of B, thereby confirming the validity of the approximate expression of Eq. (39) above the critical frequency.

The approximate power expression of Eq. (39) predicts explicitly that the acoustic power spectrum falls off as $\Phi_{ww}(K_1)/K_1$. The form of this function is obtained by integrating Eq. (31) over k_2 to give

$$\frac{\Phi_{ww}(K_1)}{K_1} = \frac{\overline{w^2}\Lambda}{2\pi}\frac{(1+3\Lambda^2K_1^2)}{K_1(1+\Lambda^2K_1^2)^2}, \tag{41}$$

which falls off as ω^{-3} as $\Lambda\omega/W(=\Lambda K_1)\to\infty$. Inserting Eq. (41) into Eq. (39) gives the spectrum of sound power per unit span at frequencies above the critical frequency as

$$\mathcal{P}^{\pm}(\omega) \approx F^{\pm}(M,\theta)\frac{B\rho_0\Lambda\overline{w^2}W}{2\pi^2\omega}\frac{M(1-M_1^2)^{1/2}}{(1-M^2)}\frac{(1+3\Lambda^2K_1^2)}{(1+\Lambda^2K_1^2)^2} \quad \text{for } \omega_c \geqslant \omega. \tag{42}$$

C. Characteristics of $F^{\pm}(M,\theta)$

In order to complete the approximate expression of Eq. (42), the cascade response function $F^{\pm}(M,\theta)$ defined by Eq. (37) must be known. In order to compute the dependence of $F^{\pm}(M,\theta)$ on M and θ, the acoustic power in frequency bands above critical frequency for $B=4$ were computed exactly using Eq. (28) for various values of M and θ, and their results equated to Eq. (42) to obtain $F^{\pm}(M,\theta)$. The function $F^{\pm}(M,\theta)$ is plotted in Fig. 7 over the range of values: $M=0.2:0.1:0.8$ and $\theta=15°:15°:75°$. Note that the values of $F^{\pm}$ computed from other values of B are within 0.1% for F^{+} and within 1% for F^{-}. The data were used to calculate the coefficients $a_{m,n}^{\pm}$ in a polynomial of least-squares fit, of the form $\hat{F}^{\pm}(M,\theta)=\Sigma_{m=0}^{2}\Sigma_{n=0}^{4}a_{m,n}^{\pm}\theta^n M^m$. The coefficients are tabulated in Appendix B. This function is plotted as the continuous curves in Fig. 7.

The accuracy of the approximate power expression of Eq. (42), combined with the results for $F^{\pm}(M,\theta)$ in Fig. 7, was verified by using it to compute the acoustic power spectral density of the exact results presented in Fig. 2. The results are shown in Fig. 8. Excellent agreement is obtained at frequencies above the critical frequencies. Below the critical frequency, however, agreement is poor, as expected.

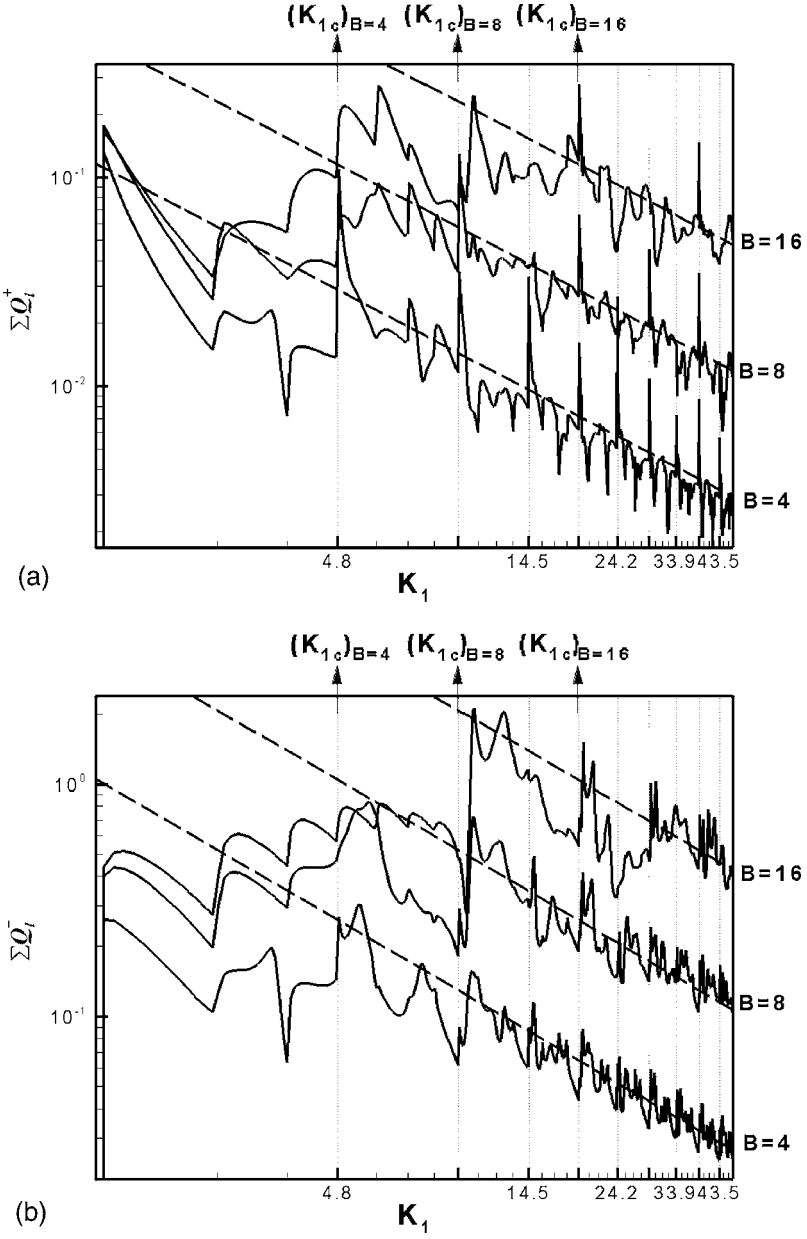

FIG. 5. Modal sum, $\Sigma_{l=L_{\min}}^{L_{\max}} Q_l^{\pm}(K_1)$, for different blade numbers and asymptotic lines. (—) Prediction results of $\Sigma_{l=L_{\min}}^{L_{\max}} Q_l^{\pm}(K_1)$ from Eq. (37) and (- - -) lines of const $\times B^2/K_1$: (a) upstream and (b) downstream.

IV. COMPARISON WITH MEASURED DATA

This section presents a comparison between the prediction and measured data for turbulence-cascade interaction noise. The spectra are expressed in decibels as a power level (PWL) defined as

$$\mathrm{PWL}^{\pm} = 10 \log_{10}\left(\frac{2\Pi^{\pm}\Delta R}{10^{-12}}\right), \tag{43}$$

where the factor of 2 is used to convert from a two-sided spectrum to a one-sided spectrum and ΔR denotes the width of the cascade in the spanwise direction.

Figure 9 shows a comparison between the sound power spectra predicted using the exact expression of Eq. (28), the approximate formulation of Eq. (42), and the experimental data obtained from a model test in a wind tunnel at NASA-Lewis.[11,13] The noise below 300 Hz was reported to be due to sources other than the fan. The stator is modeled by the two-dimensional geometry of Fig. 1, with a mean flow speed corresponding to that at the tip of the stator. The computations were performed for $M=0.5$, $B=45$, $s/c=0.8$, $\theta=30°$, $\overline{w^2}/W^2=4\times10^{-4}$, and $\Lambda/R=0.035$ at a radius of $R=0.80$ m. The calculation was performed with a frequency resolution of $\Delta\omega/W=\pi/40\ \mathrm{m}^{-1}$ and for simplicity we assume that $\Delta R=R/2$. The turbulence length-scale and intensity were adjusted to provide a best match to the measured data.

Although the computation was carried out using two-dimensional theory, and the turbulence properties are represented simply by a single value of intensity and length scale, agreement overall is good. In particular, the rate of high-frequency roll-off closely matches that of the experimental data. Similar levels of agreement were obtained by Hanson[11,13] using three-dimensional theory with approxi-

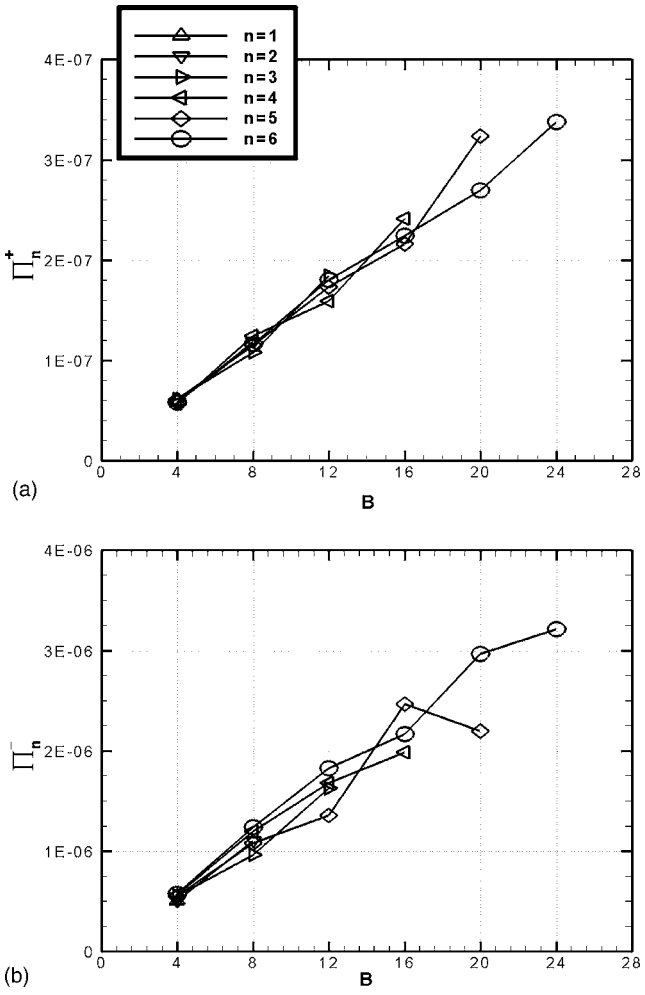

FIG. 6. Normalized characteristic band acoustic power: (a) upstream and (b) downstream.

mately the same values of Λ and $\bar{w}^2$. The use of two-dimensional theory to give comparable results with the three-dimensional theory suggests that three-dimensional effects, such as the contribution from oblique gusts, are comparatively weak.

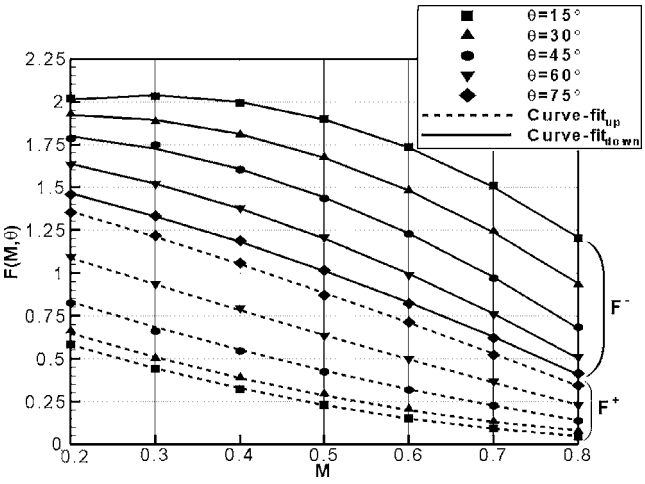

FIG. 7. The dependence of the function $F^{\pm}$ on Mach numbers and stagger angles for $B=4$. Symbols denote the calculation and lines denote a polynominal of least-squares fit.

V. PARAMETRIC STUDY

For the parametric study presented in the following, a baseline case is chosen to correspond to that in Sec. IV, except that the vane count was changed to 30. Vane count is a major consideration for tonal noise since the use of large vane numbers leads to cutoff of the first blade passing frequency. In designing stators, there is usually a preferred solidity for aerodynamic efficiency purpose, but some variability in the vane count is permitted.

Figure 10 shows the variation of power levels, in one-third octave band frequencies, for $B=15,30$, and 60 while keeping solidity, and hence the wetted area, constant. The solid lines represent the predictions obtained using the approximate expression of Eq. (42). Excellent agreement between the exact and approximate predictions is observed at frequencies above the critical frequencies of 660.9, 1321.8, and 2643.6 Hz for $B=30,45$, and 60, respectively. The power above the critical frequency is observed to be proportional to B, as predicted explicitly by Eq. (42). The poor agreement between the exact and approximate calculations below the critical frequencies is due to interactions between neighboring vanes. The center frequency of the "hump" in the spectra is also observed to be proportional to B. Figure 10 suggests that below the critical frequency there exists a saturation blade number, above which the overall acoustic power ceases to increase.

Figure 11 shows the power spectrum for the stagger angles of 15° and 45° for $B=30$. Again, excellent agreement is obtained between the exact and approximate predictions above the critical frequency. Due to convection effects, the high frequency upstream power spectrum increases with increasing stagger angle and decreases for the downstream power spectrum. However, the effect of stagger angle on the downstream spectrum is generally small, particularly at high frequencies.

Figure 12 shows the variation of power spectra for the three gap-chord ratios of $s/c=0.4$, 0.8, and 1.2 for $B=30$ and $\theta=30°$. The approximate expression of Eq. (42) predicts that the sound power is independent of gap-chord ratio (or solidity) above the critical frequency, as confirmed by the exact calculation. Chord length therefore has little effect on sound radiation, especially at high frequencies.

In order to investigate the effect of flow speed Mach number on broadband noise generation, acoustic power spectra were computed for Mach numbers of $M=0.4$, 0.5, and 0.6 using the exact and approximate expressions. The results are plotted in Fig. 13. Again, close agreement is obtained above the critical frequency.

A similar parametric study was carried out by Hanson[11,13] over a range of mean-flow and cascade parameters similar to those above. Overall trends with the various parameters obtained here closely match those predicted by Hanson,[11,13] using a three-dimensional theory. The significant difference in our study is that these trends are predicted

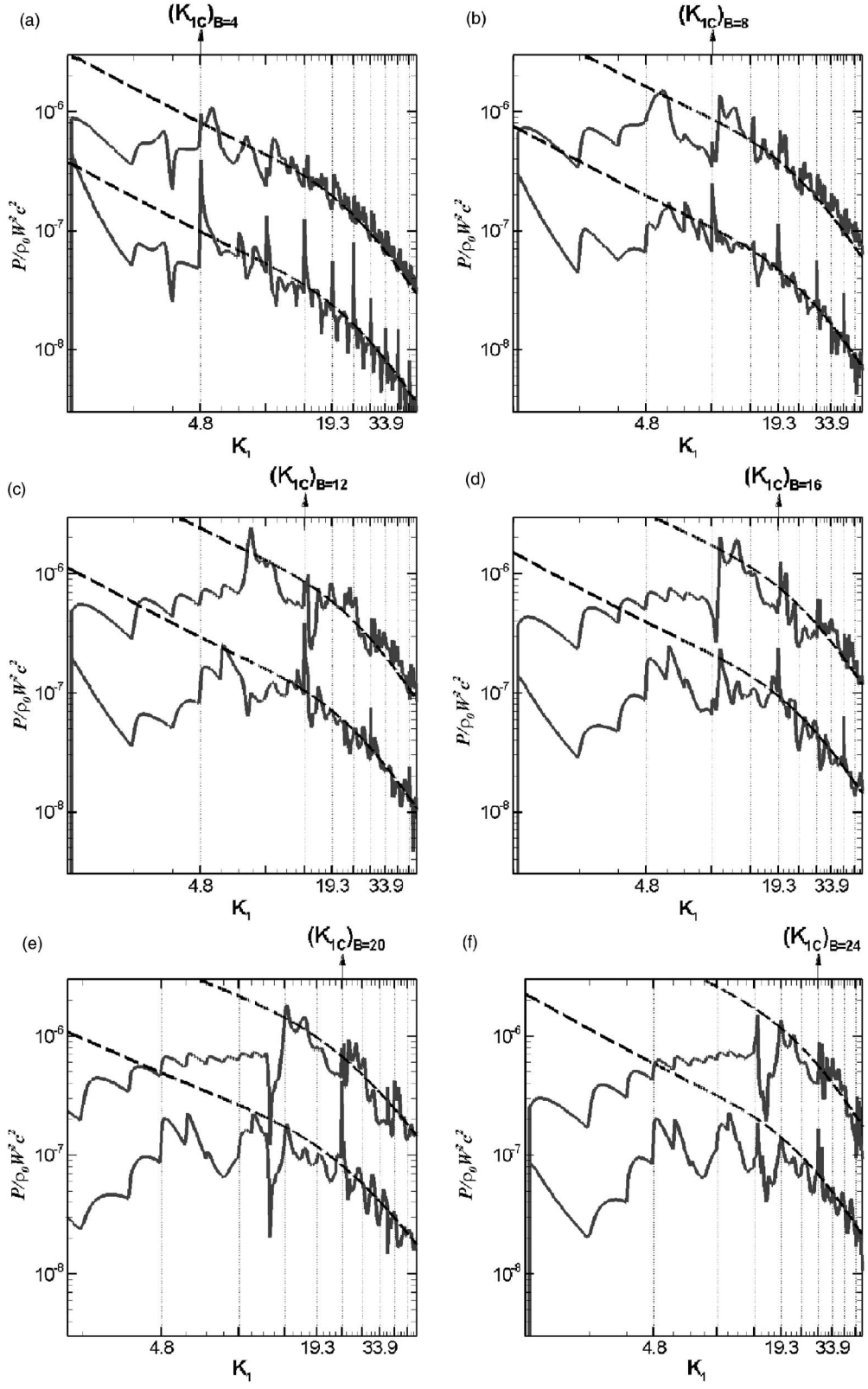

FIG. 8. Comparison of power spectral density between the exact and approximate predictions [exact solutions (—), approximate solutions (- - -)]: (a) $B=4$, (b) $B=8$, (c) $B=12$, (d) $B=16$, (e) $B=20$, and (f) $B=24$.

explicitly by the approximate high frequency result of Eq. (42).

VI. CONCLUSION

The power spectrum of the upstream and downstream sound field due to an isotropic frozen turbulent gust impinging on a cascade of flat-plate airfoils has been computed. The theory has been developed using an analytic formulation of the two-dimensional response by a cascade of flat plates derived from the theory due to Smith[3] and the LINSUB computer code by Whitehead.[4] It is found that the acoustic power spectrum can be categorized into two distinct frequency regions,

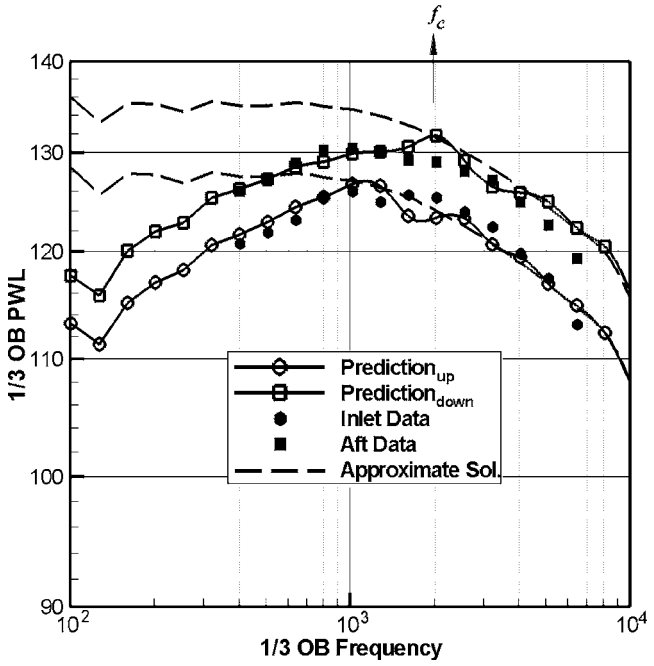

FIG. 9. Comparison of theoretical prediction with measured noise spectra for model data.

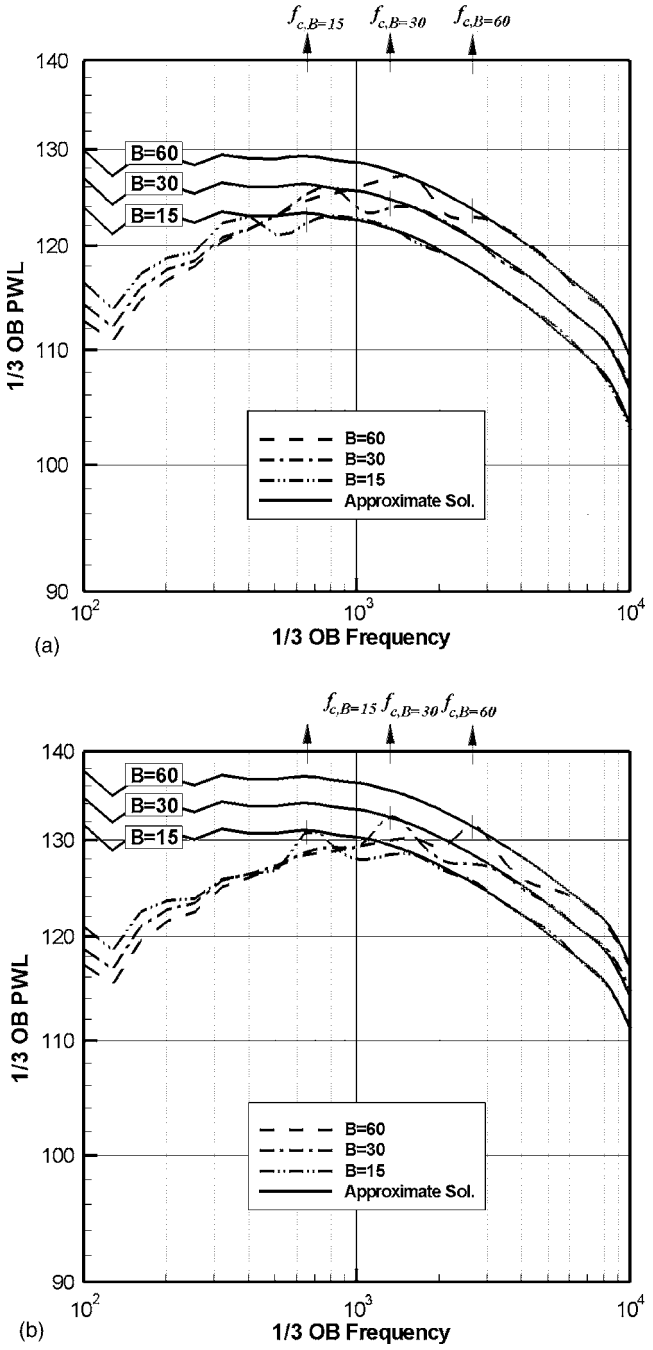

FIG. 10. Variation of acoustic power spectrum with blade number, B; solid lines denote approximate predictions and the other lines exact predictions; vertical line "|" denotes the location of critical frequency: (a) upstream and (b) downstream.

which are separated by a critical frequency. This critical frequency corresponds to the cutoff frequency of the mode $l=B$, i.e., when the gap-wise wavelength equals the blade space. Below this frequency, only some spectral components of turbulence excite cuton acoustic modes. Above the critical frequency, all wave number components of turbulence contribute to cut-on acoustic modes and interaction between acoustic waves radiated from each blade is weak. The blades therefore radiate incoherently and their sound powers are additive. Based on this finding, a simplified, cascade-response/turbulence-spectrum decoupled expression has been derived for the acoustic power spectrum at frequencies above the critical frequency. This expression explicitly predicts that the acoustic power above the critical frequency is proportional to the blade number, independent of the blade chord, and varies with frequencies as $\Phi_{ww}(\omega/W)/\omega$, where $\Phi_{ww}(\omega/W)$ is the wave number spectrum of the turbulence velocity. The theory was utilized to perform a parametric study which shows that overall predictions and trend closely match those predicted by Hanson[11,13] obtained using a three-dimensional theory. This result suggests that three-dimensional effects such as the contribution to the power from oblique gusts are comparatively weak. Through the comparison between experimental data and predictions using the exact and approximated expressions, the approximate expression is shown to provide a highly efficient means of computing the power spectrum at high frequencies above the critical frequency, which for realistic engine parameters, corresponds to about 1 kHz.

Future work is aimed at extending the approximate formula to the prediction of broadband noise due to three-dimensional excitation by inhomogeneous turbulence impinging on a rectilinear cascade of flat-plate airfoils.

ACKNOWLEDGMENTS

This work was supported by the Post-doctoral Fellowship Program of Korea Science & Engineering Foundation (KOSEF) and by the International Cooperation Research Program of the Ministry of Science & Technology. The authors would also like to thank Vincent Jurdic for detecting an error in an earlier draft of this paper.

Nomenclature

a = sound speed

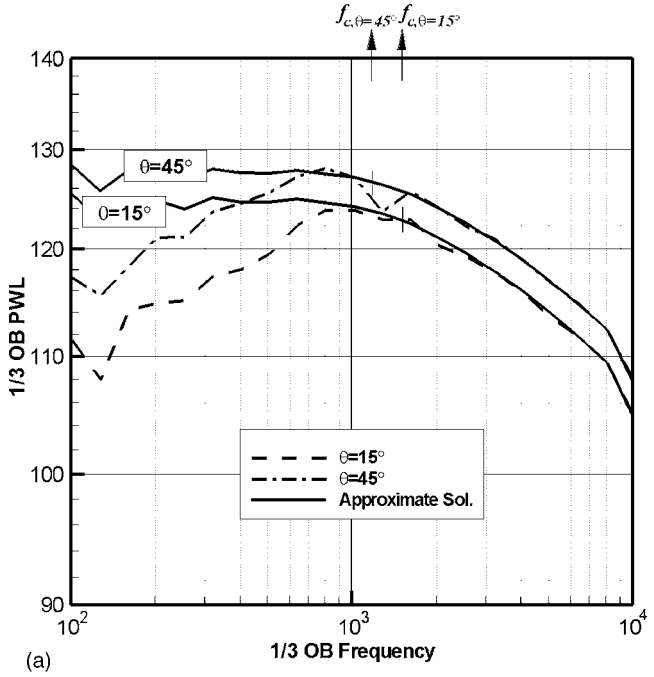

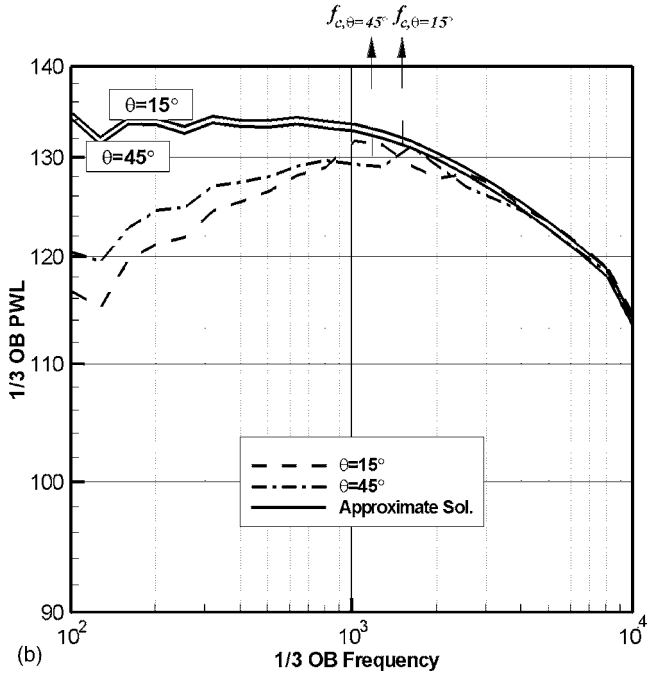

FIG. 11. Variation of acoustic power spectrum with stagger angle, θ; solid lines denote approximate predictions and the other lines exact predictions; vertical line "|" denotes the location of critical frequency: (a) upstream and (b) downstream.

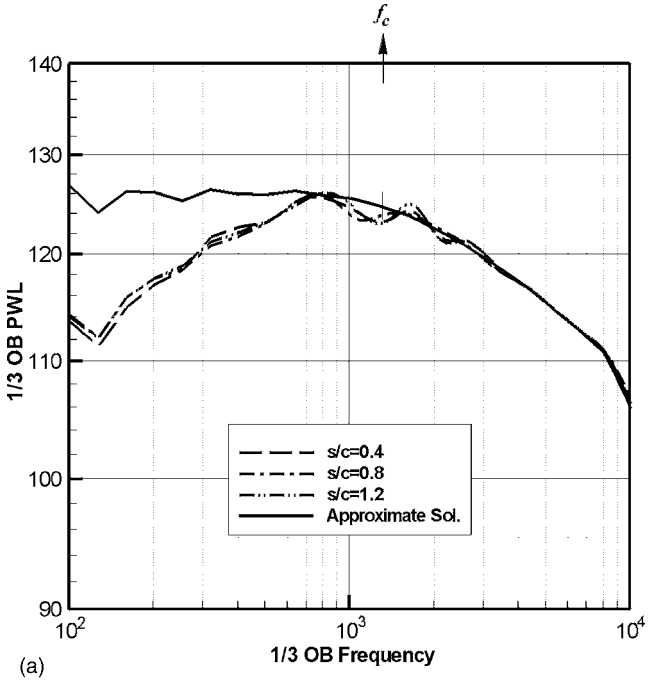

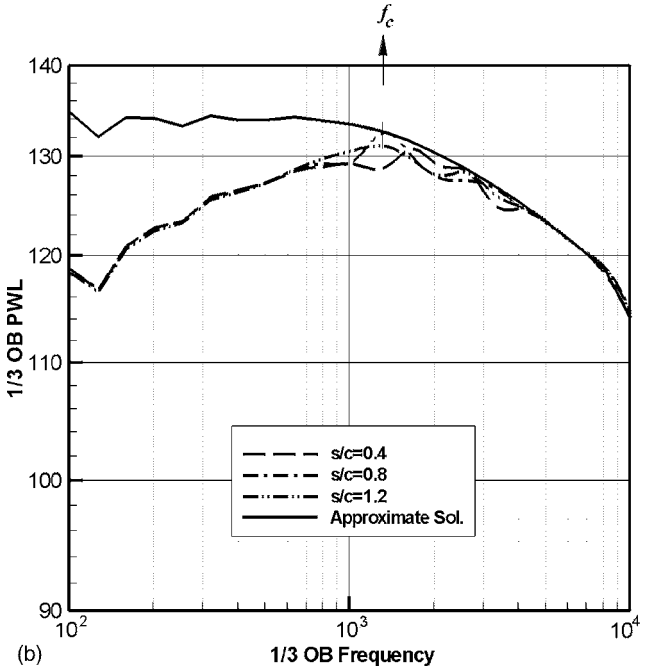

FIG. 12. Variation of acoustic power spectrum with gap-chord ratio s/c (or reciprocal of solidity); solid lines denote approximate predictions and the other lines exact predictions; vertical line "|" denotes the location of critical frequency: (a) upstream and (b) downstream.

B = the number of airfoils in a cascade
c = airfoil chord length
l = acoustic mode number in the gap-wise direction
m = vortical mode number in the gap-wise direction
M = Mach number of mean-flow
M_1 = Mach number in the axial direction, $M \cos \theta$
M_2 = Mach number in the gap-wise direction, $M \sin \theta$
k_i = wave number of ingested turbulence gust in Cartesian coordinate system
K_1 = ω/W
p = pressure perturbation
r = scattering index for a cascade of airfoils
R = radius or cascade response function
s = blade spacing or entropy
t = time
u_i = velocity perturbation in x_i direction
U_i = mean velocity in x_i direction
w = upwash velocity perturbation

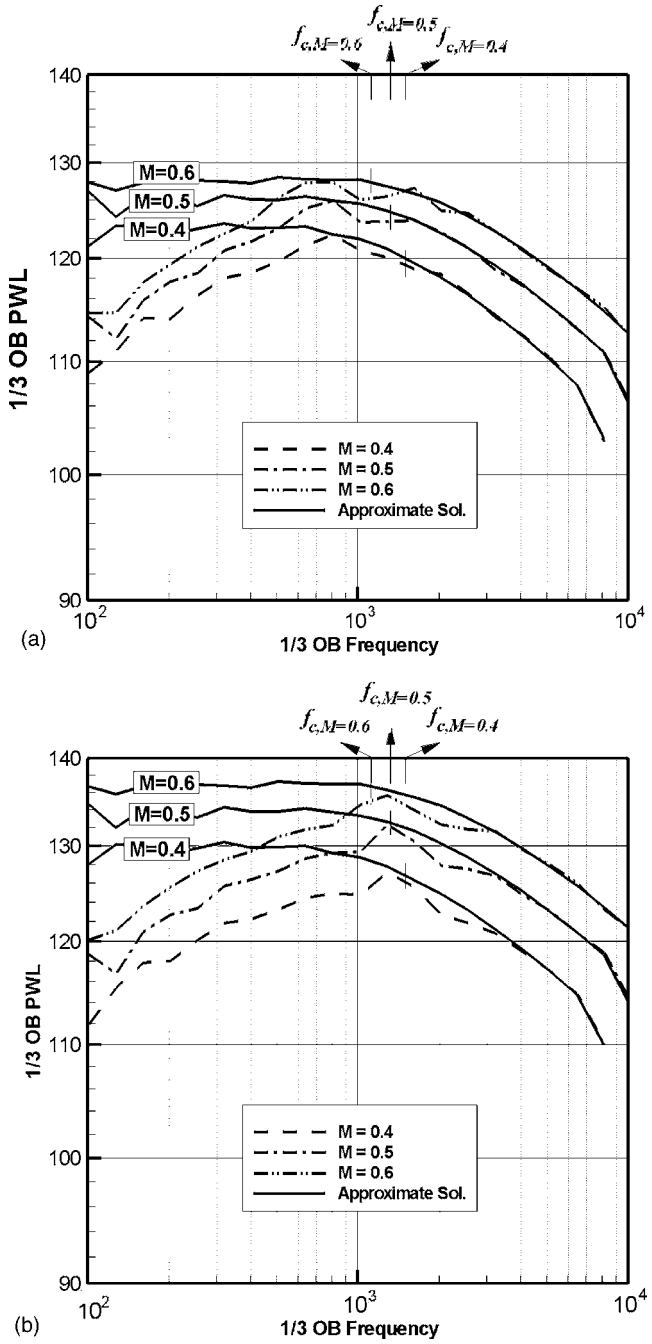

FIG. 13. Variation of acoustic power spectrum with Mach number, M; solid lines denote approximate predictions and the other lines exact predictions; vertical line "|" denotes the location of critical frequency: (a) upstream and (b) downstream.

W = mean-flow speed, $\sqrt{U_1^2+U_2^2}$
x_i = Cartesian duct coordinate system, Fig. 1
y_i = Cartesian cascade-fixed coordinate system, Fig. 1
z = coordinate measured in direction of airfoil chord, Fig. 1
α = wave number of the generated disturbance in the axial direction
β = wave number of the generated disturbance in the gap-wise direction
Γ = vortex strength
Φ_{ww} = turbulence spectrum
θ = stagger angle, $\tan^{-1}(U_2/U_1)$
λ = reduced frequency $\omega c/W$
ρ = density perturbation
ρ_0 = mean-stream density
σ = interblade phase angle
ω = angular frequency
PSD = power spectral density

Superscripts

$+$ = upstream running acoustic wave
$-$ = downstream running acoustic wave
$\wedge$ = convected vorticity wave

APPENDIX A: ARGUMENT FOR THE ANALYTIC FORM OF EQ. (37)

This appendix presents the reasoning for Eq. (37), which is reproduced in the following, for the modal power response function summed over all propagating modes,

$$\sum_{l=L_{\min}}^{L_{\max}} Q_l^{\pm}(K_1) \approx \frac{Bs\omega(1-M_1^2)^{1/2}}{\pi a(1-M^2)} \frac{aF^{\pm}(M,\theta)}{W\lambda^2(s/c)^2}.$$

The form of the right-hand side of this equation may be derived from the following observations:

i. From Sec. III A, the band acoustic power above the critical frequency is proportional to B.
ii. From Eq. (35), the contribution of the wave number spectrum of the turbulence to the acoustic power varies as B^{-1}.
iii. Observations i and ii suggest that the power term, $\Sigma Q_l^{\pm}(K_1)$, in Eq. (28) must be proportional to B^2.
iv. From Fig. 5, $\Sigma Q_l^{\pm}(K_1)$ is inversely proportional to K_1.

Based on i–iv, dimensional analysis was used to derive Eq. (37) for $\Sigma Q_l^{\pm}(K_1)$ to give the desired dependence of B^2/K_1. The first term on the right-hand side of Eq. (37) represents the number of cut-on modes and is proportional to K_1 ($Bs=2\pi R$, i.e., constant). The second term must therefore be proportional to B^2/K_1^2. This second term there has the interpretation as the modal averaged cascade response function of Smith in Ref. 3, which is uniquely defined by the gap-chord ratio s/c, stagger angle θ, Mach number M, and reduced frequency λ. Note that, unlike for harmonic gusts, the phase angle σ has no physical meaning for turbulent gusts and can therefore be neglected as an input parameter in the dimensional analysis. We assume the form, $(s/c)^{\alpha}\lambda^{\eta}F^{\pm}(M,\theta)$ for this second term. First, we must have $\eta=-2$ and $\alpha=-2$ in order to give the required frequency dependence of K_1^{-2} and B dependence of B^2 identified in iii and iv, since s^{-1} is proportional to B ($B=2\pi R/s$). The precise dependence on M and θ cannot be determined from the observations i–iv, and so their dependence is incorporated into the function $F^{\pm}(M,\theta)$. The term of a/W in Eq. (37) is introduced to cancel the same term in the first term on the right-hand side. This procedure leads to the final form of Eq. (37).

TABLE I. The calculated coefficients, $a^{\pm}_{n,m}$ in the polynomial of least-squares fit for the function $F^{\pm}$: $\hat{F}^{\pm}(M,\theta)=\sum_{m=0}^{2}\sum_{n=0}^{4}a^{\pm}_{m,n}\theta^n M^m$.

		m		
n		0	1	2
0	$a^{+}_{0,m}$	1.069 02	−2.072 80	1.008 61
	$a^{-}_{0,m}$	1.507 91	3.955 33	−5.245 09
1	$a^{+}_{1,m}$	−1.080 14	1.290 47	−0.064 344 3
	$a^{-}_{1,m}$	1.696 50	−12.853 7	13.722 7
2	$a^{+}_{2,m}$	2.090 42	−2.119 89	−0.174 021
	$a^{-}_{2,m}$	−3.357 71	23.786 6	−29.140 3
3	$a^{+}_{3,m}$	−0.712 208	1.205 46	−0.451 791
	$a^{-}_{3,m}$	2.886 37	−22.734 3	28.229 1
4	$a^{+}_{4,m}$	0	0	0
	$a^{-}_{4,m}$	−0.944 190	7.565 42	−9.185 14

APPENDIX B: A POLYNOMIAL OF LEAST-SQUARES FIT FOR $F^{\pm}(M,\Theta)$—TABLE I

[1]S. Kaji and T. Okazaki, "Propagation of sound waves through a blade row II. Analysis based on the acceleration potential method," J. Sound Vib. **11**, 355–375 (1970).

[2]S. Kaji and T. Okazaki, "Generation of sound by a rotor stator interaction," J. Sound Vib. **13**, 281–307 (1970).

[3]S. N. Smith, "Discrete frequency sound generation in axial flow turbomachines," Reports and Memoranda No. 3709, Aeronautical Research Control Council, London, 1972.

[4]D. S. Whitehead, "Classical two-dimensional methods," in *Unsteady Turbomachinery Aerodynamics* (AGARD-AG-298), edited by M. F. Platzer and F. O. Carta, AGARD Manual on Aeroelasticity in Axial Flow Turbomachines, Vol. 1 (Neuilly sur Seine, France, 1987), Chap. 3.

[5]R. Mani and G. Hovray, "Sound transmission through blade rows," J. Sound Vib. **12**, 59–83 (1971).

[6]W. Koch, "On transmission of sound through a blade row," J. Sound Vib. **18**, 111–128 (1971).

[7]N. Peake, "The scattering of vorticity waves by an infinite cascade of flat plates in subsonic flow," Wave Motion **18**, 255–271 (1993).

[8]N. Peake, "The interaction between a high frequency gust and a blade row," J. Fluid Mech. **241**, 261–289 (1992).

[9]N. Peake and E. J. Kerschen, "Uniform asymptotic approximation for high frequency unsteady cascade flow," Proc. R. Soc. London London **449**, 177–186 (1995).

[10]S. A. L. Glegg, "The response of a swept blade row to a three-dimensional gust," J. Sound Vib. **227**, 29–64 (1999).

[11]D. B. Hanson and K. P. Horan, "Turbulence/cascade interaction: Spectra of inflow, cascade response, and noise," AIAA-98-2319, 1998.

[12]D. B. Hanson, "Influence of lean and sweep on noise of cascades with turbulent inflow," AIAA-99-1863, 1999.

[13]D. B. Hanson, "Theory for broadband noise of rotor and stator cascades with inhomogeneous inflow turbulence including effects of lean and sweep," NASA Contract Rep. NASA CR **2001**-210762 (2001).

[14]I. Evers and N. Peake, "On sound generation by the interaction between turbulence and a cascade of airfoils with non-uniform mean flow," J. Fluid Mech. **463**, 25–52 (2002).

[15]M. E. Goldstein, *Aeroacoustics* (McGraw-Hill, New York, 1976).

[16]R. K. Amiet, "Acoustic radiation from an airfoil in a turbulent stream," J. Sound Vib. **41**, 407–420 (1975).

On the acoustic field in a Pekeris waveguide with attenuation in the bottom half-space

Michael J. Buckingham[a] and Eric M. Giddens
Marine Physical Laboratory, Scripps Institution of Oceanography, University of California—San Diego, 9500 Gilman Drive, La Jolla, California 92093-0238

(Received 4 April 2005; revised 1 November 2005; accepted 2 November 2005)

The acoustic field in a Pekeris channel with an attenuating basement is critically examined, based on contour integrations of the wave number integrals for the two domains. In both regions, the field consists of a finite sum of proper (square integrable) normal modes plus a branch line integral around a hyperbolic cut. For low bottom attenuation, only "trapped" modes exist but as the loss increases additional "dissipation" modes contribute to the mode sum. A Newton-Raphson iterative procedure is introduced for finding the complex eigenvalues of the modes and a new expression is derived which shows that the total number of proper (trapped plus dissipation) modes supported by the waveguide increases essentially linearly with rising bottom attenuation. Approximations for the complex shape functions of the modes in the water column and the basement are developed and compared with the exact shape functions determined from the Newton-Raphson procedure. An expression derived for the modal attenuation coefficient scales in proportion to the square of the mode number and inversely with the square of the frequency. Stationary-phase approximations for the branch line integrals for both domains are developed, which serve to illustrate the asymptotic range dependence of the lateral wave but otherwise have little utility. [DOI: 10.1121/1.2141212]

PACS number(s): 43.30.Bp, 43.20.Bi [AIT] Pages: 123–142

I. INTRODUCTION

A solution of the wave equation for the sound field in an iso-speed ocean channel overlying a homogeneous fluid half-space was developed and published over half a century ago in a classic paper by Pekeris.[1] His solution for the acoustic pressure consists of a sum of normal modes plus a branch line integral, the latter originating in the so-called Pekeris branch cut, which runs vertically in the complex-wave-number plane, parallel to the imaginary axis. Pekeris was careful not to specify how many modes are included in his mode sum, although he did make it clear that, because of the density discontinuity at the bottom interface, the modes are not orthogonal over either the water column or the entire fluid domain. As for the branch-line integral, Pekeris was vague about its physical interpretation.

Over 25 years later, in describing the Pekeris solution, Stickler[2] stated that it consists of three components: a finite sum of M "proper" modes, each of which decays exponentially with depth in the basement and hence is convergent (i.e., square integrable); an infinite sum of "improper" modes, each of which is divergent, growing exponentially with depth in the basement; and a contribution from the contour integration around the vertical branch cut. The presence of the unphysical improper modes is noteworthy because, by diverging to infinity in the basement, they violate one of the radiation conditions upon which Pekeris predicated his analysis. It should be appreciated, however, that Pekeris[1] himself made no reference to diverging modes in the basement.

An alternative to the Pekeris solution, also described by Stickler,[2] is based on a hyperbolic branch line that is attributed to Ewing, Jardetzky, and Press[3] and commonly referred to as the EJP cut. In this case, the solution consists of two components, a finite sum of M normal modes (identical to the proper modes in the Pekeris solution) plus a branch line integral taken around the EJP branch line. Both the mode sum and the EJP branch line integral are well behaved in that they approach zero asymptotically in the limit of infinite depth in the basement. The EJP branch-line integral represents two physically identifiable components of the acoustic field: the lateral or head wave, which propagates along the interface between the channel and the fluid basement, reradiating energy into the water column at the critical angle as it progresses, and the continuous field, which, in shallow water, penetrates through the bottom boundary into the basement and is thus lost to the water column.

In the absence of loss in the basement, the number, M_o, of proper normal modes obtained with either the Pekeris or EJP cut is readily determined[4] from the Pekeris dispersion relation.[1] The criterion used in deriving M_o is the geometrical condition that the grazing angle of the highest-order modal equivalent ray be no greater than the critical grazing angle of the bottom interface (assuming the sound speed in the bottom to be greater than that in the water column). Under this constraint, all the modes up to and including mode number M_o experience no loss from bottom interactions, since their equivalent rays are totally reflected (with a phase change) from the bottom boundary, and hence such modes

[a]Also affiliated to the: Institute of Sound and Vibration Research, The University, Southampton SO17 1BJ, England. Electronic mail: mjb@mpl.ucsd.edu

are said to be "trapped" in the water column. The shape functions describing the depth dependence of the trapped modes are real, showing oscillatory behavior in the channel and an exponential decay in the basement. The poles associated with the trapped modes lie on the real axis of the wave number complex plane, between $-k_2$ and $-k_1$, the (real) acoustic wave numbers in the basement and water column, respectively.

When attenuation is introduced into the basement, the acoustic wave number k_2 becomes complex and may be written as $k_2 - i\alpha$, where the imaginary part, α, is the attenuation coefficient of plane waves in the bottom. The properties of the field are then modified in ways that are not immediately apparent. For instance, in the presence of a lossy bottom, the number of proper normal modes remains finite but increases to $M \geqslant M_o$. The additional, higher-order modes, with mode numbers greater than M_o and less than or equal to M, appear solely as a result of dissipation in the semi-infinite basement. The term "dissipation" modes is introduced here to distinguish these additional modes from the more familiar trapped modes, the latter having mode numbers that are less than or equal to M_o. The shape functions of all M modes are complex, although the imaginary part of each trapped mode remains negligibly small, whereas the real and imaginary parts of the dissipation modes are comparable. Since the trapped and dissipation modes are all proper modes, each is convergent, being square integrable over the semi-infinite depth of the channel and the basement.

In this article, in order to investigate the properties of the field in a Pekeris waveguide with a lossy basement, a brief but complete derivation of the acoustic field in the water column and the bottom half-space is developed. The analysis is based on the EJP branch cut and leads to the familiar wave-number-integral formulation of the field in both regions. The Pekeris dispersion relation emerges in the usual way from these integrals and, since it governs the properties of the modes, forms the basis of much of the remaining discussion. By definition, a proper mode is taken to be any solution of the Pekeris dispersion relation that *also satisfies the radiation condition at infinite depth in the basement*. In fact, this radiation condition dictates that the EJP cut be chosen when performing the contour integrations in the complex plane. As a corollary to this choice of branch cut, the improper modes discussed by Stickler,[2] which do not satisfy the radiation condition at infinite depth, are automatically excluded from the exact solution.

From the transcendental dispersion relation, new analytical approximations are developed for (1) the total number of proper modes, M, in the lossy waveguide, (2) the complex mode shape functions in the water column and in the basement, and (3) the modal attenuation coefficients. Additionally, a simple, rapidly convergent algorithm is introduced for finding the M complex roots of the dispersion relation numerically. This numerical routine is useful not only for checking the analytical solutions but also as a guide to the positions of the poles in the complex plane. It shows immediately that the poles are not confined to the vertical strip of the complex plane between real $(-k_2)$ and $-k_1$, but are distributed along the lower side of the EJP branch cut. To provide a foundation for the subsequent analytical and numerical developments, the discussion begins with a standard derivation of the wave-number-integral solution for the field in the channel and the semi-infinite basement.

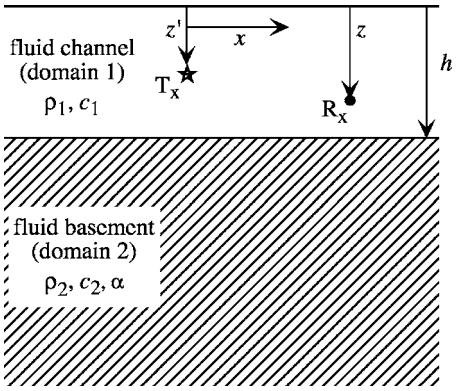

FIG. 1. The Pekeris waveguide with lossless, iso-speed channel (domain 1) overlying a homogeneous, fluid half-space (domain 2) with attenuation coefficient α.

II. PEKERIS WAVEGUIDE

To keep the analysis as straightforward as possible, while retaining the essential elements of the argument, a two-dimensional geometry is considered, as illustrated in Fig. 1. Cartesian coordinates are used, with x and z, respectively, representing horizontal range and depth; the channel surface is taken to be at $z=0$ and the bottom at $z=h$. An impulsive line source normal to the plane of the diagram is at depth z' in the channel and at horizontal range $x=0$. The use of Cartesian rather than the more usual cylindrical coordinates offers a minor reduction in complexity in that the horizontal range dependence of the field will be given by an exponential function instead of a Hankel function.

The wave equations to be solved for the field in the channel and the basement are

$$\frac{\partial^2 \phi_1}{\partial x^2} + \frac{\partial^2 \phi_1}{\partial z^2} - \frac{1}{c_1^2}\frac{\partial^2 \phi_1}{\partial t^2} = -Q\,\delta(z-z')\,\delta(x)\,\delta(t), \quad 0 \leqslant z \leqslant h \tag{1}$$

$$\frac{\partial^2 \phi_2}{\partial x^2} + \frac{\partial^2 \phi_2}{\partial z^2} - \frac{1}{c_2^2}\frac{\partial^2 \phi_2}{\partial t^2} = 0, \quad z > h, \tag{2}$$

where $\phi_j = \phi_j(x,z,t)$ is the velocity potential in layer $j=1$ or 2, c_j are the sound speeds in the layers, Q is the source strength with dimensions of (length)^2, t is time, and $\delta(\cdot)$ is the Dirac delta function. Across the bottom boundary, the pressure and normal component of particle velocity are continuous, as expressed through the conditions

$$\rho_1 \phi_1(h) = \rho_2 \phi_2(h), \tag{3}$$

$$\phi_1'(h) = \phi_2'(h), \tag{4}$$

where ρ_j, $j=1,2$ are the densities in the two domains and, for convenience, the abbreviated forms $\phi_j(h) = \phi_j(x,h,t)$ and $\phi_j'(h) = [\partial \phi_j(x,z,t)/\partial z]|_{z=h}$ have been introduced. The sur-

face of the channel is taken to be a pressure-release boundary, that is, $\phi_1(0)=0$.

To solve Eqs. (1)–(4) for the field in the two domains, standard Fourier transform techniques are adopted. The temporal transform and its inverse are, respectively,

$$\phi_{j\omega}=\int_{-\infty}^{\infty}\phi_j(x,z,t)\exp(-i\omega t)dt \tag{5}$$

and

$$\phi_j(x,z,t)=\frac{1}{2\pi}\int_{-\infty}^{\infty}\phi_{j\omega}\exp(i\omega t)d\omega, \tag{6}$$

where ω is angular frequency and $i=\sqrt{-1}$. Note the use of the transform variable as a subscript to denote the transformed field, a convention which is convenient when multiple transforms are employed. Identical, bilateral transforms to those in Eqs. (5) and (6) are used in horizontal range, except that the variables are x instead of t and horizontal wave number p in place of angular frequency ω.

After transforming Eqs. (1) and (2) with respect to x and t, they reduce to

$$\frac{\partial^2\phi_{1\omega p}}{\partial z^2}+\eta_1^2\phi_{1\omega p}=-Q\delta(z-z') \tag{7}$$

and

$$\frac{\partial^2\phi_{2\omega p}}{\partial z^2}+\eta_2^2\phi_{2\omega p}=0, \tag{8}$$

where $k_j=\omega/c_j$, $j=1,2$, are the acoustic wave numbers in the two domains and η_j are vertical wave numbers given by the radicals

$$\eta_1=\sqrt{k_1^2-p^2} \tag{9}$$

and

$$\eta_2=\sqrt{k_2^2-p^2}. \tag{10}$$

Implicit in Eqs. (7) and (8) are radiation conditions which require that the field and its first derivatives with respect to time and horizontal range go to zero in the limit as $|x|$ and $|t|$ go to infinity.

Equation (8) is a homogeneous second-order ordinary differential equation (ODE) whose solution may be written in the usual way as a sum of two exponentials with arguments of opposite sign. Since the radiation condition requires that the field decay to zero in the limit of infinite depth, the coefficient of the divergent exponential must be set to zero, in which case the solution is

$$\phi_{2\omega p}(z)=\phi_{2\omega p}(h)\exp[-i\eta_2(z-h)],\quad z>h. \tag{11}$$

With the sign convention chosen for the argument of the exponential in Eq. (11), the field in the basement will always decay exponentially with depth provided that

$$\mathrm{imag}(\eta_2)<0. \tag{12}$$

As Stickler[2] recognized, this is the condition that is violated by the improper modes associated with the Pekeris cut. Equation (12) will be critically important later, when it comes to evaluating inversion integrals in the complex wavenumber plane, since it dictates the choice of branch cut.

To complete the solution for the field, a finite Fourier transform with respect to depth, z, is applied to Eq. (7). The finite transform is defined here as

$$\phi_{1q}=\int_0^h\phi_1(z)\exp(-iqz)dz \tag{13}$$

and standard Fourier techniques reveal its inverse to be

$$\phi_1(z)=\frac{1}{2\pi}\int_{-\infty}^{\infty}\phi_{1q}\exp(iqz)dq, \tag{14}$$

where the transform variable, q, is the vertical wave number. When Eq. (13) acts on the second derivative with respect to z, it yields, through partial integration,

$$\int_0^h\phi_1''(z)\exp(-iqz)dz=\phi_1'(h)e^{-iqh}-\phi_1'(0)+iq\phi_1(h)e^{-iqh}-q^2\phi_{1q}, \tag{15}$$

where, as in Eqs. (3) and (4), the prime on a field function denotes differentiation with respect to z. The integrated terms in Eq. (15) are to be determined from the boundary conditions.

On Fourier transforming Eq. (7) with respect to z, an algebraic equation is obtained for the triply transformed field whose solution is

$$\phi_{1\omega pq}=\frac{-Qe^{-iqz'}-\phi_{1\omega p}'(h)e^{-iqh}-iq\phi_{1\omega p}(h)e^{-iqh}+\phi_{1\omega p}'(0)}{(\eta_1^2-q^2)}. \tag{16}$$

Since the (unknown) boundary values of the field and its derivative with respect to z in this expression are independent of q, an inverse transform with respect to q may be performed directly on Eq. (16). The integrals involved are all known forms,[5] allowing the inverse transform to be expressed explicitly. On combining the result with the boundary conditions in Eqs. (3) and (4), solutions are obtained for the unknown terms $\phi_{1\omega p}(h)$, $\phi_{2\omega p}(h)$, $\phi_{1\omega p}'(0)$, and $\phi_{1\omega p}'(h)$. Then, after performing a Fourier inversion with respect to horizontal wave number, p, the fields in the water column [from Eq. (16)] and the basement [from Eq. (11)] are found to be

$$\phi_{1\omega}(x,z)=\frac{Q}{2\pi}\int_{-\infty}^{\infty}F_1(\eta_1,\eta_2)e^{ipx}\,dp,\quad \text{for } 0\leqslant z\leqslant h, \tag{17}$$

and

$$\phi_{2\omega}(x,z)=\frac{b_{12}Q}{2\pi}\int_{-\infty}^{\infty}F_2(\eta_1,\eta_2)e^{ipx}\,dp,\quad \text{for } h<z. \tag{18}$$

The two functions of η_1 and η_2 in the integrands of these inversion integrals are

$$F_1(\eta_1,\eta_2)=\frac{\sin(\eta_1 z_<)}{\eta_1}\frac{\{\eta_1\cos[\eta_1(h-z_>)]+ib_{12}\eta_2\sin[\eta_1(h-z_>)]\}}{[\eta_1\cos(\eta_1 h)+ib_{12}\eta_2\sin(\eta_1 h)]} \tag{19}$$

and

$$F_2(\eta_1,\eta_2)=\frac{\sin(\eta_1 z')e^{-i\eta_2(z-h)}}{[\eta_1\cos(\eta_1 h)+ib_{12}\eta_2\sin(\eta_1 h)]}, \tag{20}$$

where $z_>(z_<)$ is the greater (lesser) of z and z'. Note that F_1 and F_2 are even in η_1 and mixed in η_2.

The Fourier wave-number integrals in Eqs. (17) and (18) constitute an exact solution for the two-dimensional field from a horizontal line source in the Pekeris waveguide. They are precisely analogous to the Hankel-transform solution for the three-dimensional field from a point source derived by Pekeris.[1] Mathematically, the two- and three-dimensional solutions differ only in the kernels of the integral transforms, an exponential function for the line source and a Hankel function for the point source. The functions F_1 and F_2 in Eqs. (19) and (20), which characterize the poles and branch points in the complex plane, are identical to the corresponding functions derived by Pekeris.[1] Moreover, it is clear from Eq. (20), taken in conjunction with the condition on η_2 in Eq. (12), that F_2 decays exponentially with depth in the basement. It follows that the total field in the basement, as given by the wave-number integral in Eq. (18), also satisfies the required radiation condition by converging to zero in the limit of infinite depth in the lower half-space.

III. THE COMPLEX WAVE-NUMBER PLANE

By contour integration around the complex p plane, the wave-number integrals in Eqs. (17) and (18) can be converted into a sum of normal modes and a branch-line integral, the latter associated with the radical η_2, defined in Eq. (10). There is no contribution from the branch cut associated with η_1 because F_1 and F_2 are even functions of η_1, as a result of which the contributions to the integral from either side of the η_1 branch cut cancel. Thus, the only branch points that need be considered in the analysis are at $p=\pm k_2$.

A. The dispersion relation

The functions F_1 and F_2 have the same denominator:

$$D=\eta_1\cos(\eta_1 h)+ib_{12}\eta_2\sin(\eta_1 h), \tag{21}$$

which, in both cases, determines the position of the (simple) poles in the complex p plane. Thus, the poles for the water column are identical to the poles for the basement, which is only to be expected since a mode is a single entity extending throughout the channel and the underlying half-space. These poles occur at the zeros of Eq. (21), that is, they are the roots of the classic dispersion relation derived by Pekeris:[1]

$$\tan(\eta_1 h)=i\frac{\eta_1}{b_{12}\eta_2}. \tag{22}$$

This equation may be expressed solely in terms of η_1 as follows:

$$\tan(\eta_1 h)=-\frac{\eta_1}{b_{12}\sqrt{k_1^2-k_2^2-\eta_1^2}}, \tag{23}$$

where, for consistency with the condition on η_2 in Eq. (12), the real part of the radical must be positive. Equation (23) can always be written in the form

$$\eta_1 h=m\pi-\tan^{-1}\left(\frac{\eta_1}{b_{12}\sqrt{k_1^2-k_2^2-\eta_1^2}}\right),\quad m=1,2,\ldots,M, \tag{24}$$

where the integer m may be identified as the mode number. The modes themselves are, of course, the residues of the integrands in Eqs. (17) and (18) evaluated at the poles, p_m, which are the complex eigenvalues found from the solutions of Eq. (24).

Equation (24) has only a finite number of solutions that also satisfy the required inequality in Eq. (12). Thus, the set of modes is finite, with M being the maximum mode number. For the special case of a lossless basement, it is clear from the form of the dispersion relation in Eq. (23) that the eigenvalues lie on the real axis between $-k_1$ and $-k_2$, but, in general, the eigenvalues are complex, appearing in the second quadrant of the complex p plane. The value of M, along with an iterative algorithm for solving Eq. (24) numerically for the complex eigenvalues, p_m, will be discussed later.

Meanwhile, an approximate solution of Eq. (24) for the trapped modes is obtained by expanding the arctan function to first order in η_1:

$$\eta_1 h\approx m\pi-\frac{\eta_1 h}{b_{12}k_1\sin(\alpha_c)}, \tag{25}$$

where $\alpha_c=\cos^{-1}(k_2/k_1)$ is the critical grazing angle of the bottom interface. It is implicit here that k_2 is real, or nearly so, corresponding to a basement layer that exhibits negligible loss. The solution of Eq. (25) can be immediately written as

$$\eta_{1m}\approx\frac{m\pi}{h_e}, \tag{26}$$

where

$$h_e=h\left[1+\frac{1}{b_{12}k_1 h\sin(\alpha_c)}\right] \tag{27}$$

is the "effective depth" of the channel, which was originally derived by Weston[6] from an argument involving the Rayleigh reflection coefficient. To the same level of approxima-

tion as in Eq. (26), it follows from Eqs. (9) and (10) that the vertical wave number of the mth mode in the basement is

$$\eta_{2m} \approx -ik_1 \sin(\alpha_c)\sqrt{1-\frac{m^2\pi^2}{k_1^2 h_e^2 \sin^2(\alpha_c)}}, \tag{28}$$

and the corresponding eigenvalue is

$$p_m \approx -k_1\sqrt{1-\frac{m^2\pi^2}{k_1^2 h_e^2}}. \tag{29}$$

Physically, the effective depth in Eq. (27) expresses the idea that the phase change experienced by a modal equivalent ray undergoing total reflection from the bottom is approximately equal to the geometrical phase change from a fictitious, pressure-release boundary displaced beneath the actual interface by a distance $(h_e - h)$. Although h_e depends weakly on frequency, through the presence of the acoustic wave number k_1, it possesses the desirable property of being independent of mode number. This has proved useful in the analyses of array performance in shallow water[7] and acoustic propagation in a three-dimensional, penetrable wedge.[8]

From the approximate expressions given above, it is apparent that the effective depth, rather than the actual depth, is the factor that controls the trapped-mode shapes in the water column [Eq. (26)], the modal decay in the basement [Eq. (28)], and the modal attenuation coefficients [from an extension of Eq. (29) to be discussed below]. On the other hand, the total number of trapped modes, M_o, supported by the channel is governed by the actual depth, not the effective depth.

B. The branch cut

The vertical wave number η_2 has branch points at $p = \pm k_2$ in the complex p plane, which, with the sign convention adopted here, fall in the second and fourth quadrants, as shown in Fig. 2. With x positive, the contour used to evaluate the wave-number integrals in Eqs. (17) and (18) must be taken around the upper half-plane (from Cauchy's theorem and Jordan's lemma) and everywhere within that contour the imaginary part of η_2 must be negative in order to avoid violating the constraint in Eq. (12). This condition is achieved by choosing a branch cut such that the imaginary part of η_2 is negative everywhere on the top Riemann sheet, where the integration is to be performed, and positive everywhere on the bottom Riemann sheet. The appropriate branch cut is the locus of η_2 when the imaginary part is identically zero, a choice which, as discussed by Felsen and Marcuvitz,[9] yields a hyperbola in the complex p plane (Fig. 2). This hyperbolic branch line is the familiar EJP cut.

C. Normal modes and the branch line integral

By indenting the D-shaped integration contour in the upper half-plane around the EJP cut, as shown in Fig. 2, the field expressions in Eqs. (17) and (18) may be expressed as

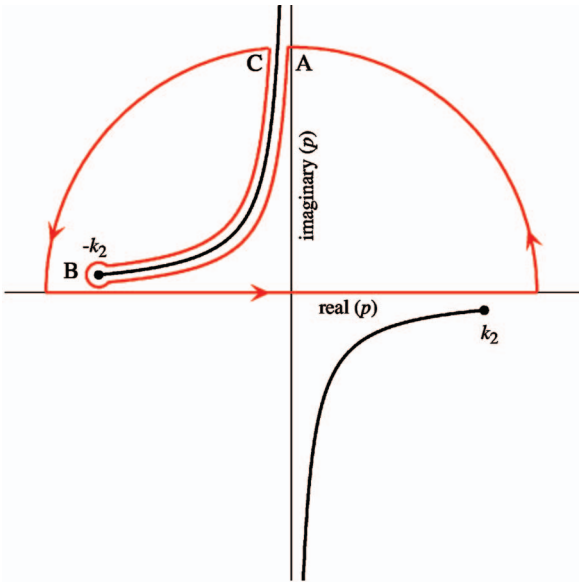

FIG. 2. Sketch of the complex p plane showing branch points at $\pm k_2$ and the corresponding hyperbolic EJP branch cuts, which ensure that everywhere on the top Riemann sheet the imaginary part of η_2 is less than zero. The D contour (red line) of infinite radius in the upper half-plane is used for evaluating the wave number integrals [Eqs. (17) and (18)] for the field in the channel and the basement.

$$\phi_{1\omega}(x,z) = \frac{Q}{2\pi}\left\{2\pi i\sum_{m=1}^{M}\mathrm{Res}[F_1(\eta_{1m},\eta_{2m})e^{ip_m x}] + \oint_{\mathrm{EJP}} F_1(\eta_1,\eta_2)e^{ipx}\,dp\right\} \tag{30}$$

and

$$\phi_{2\omega}(x,z) = \frac{b_{12}Q}{2\pi}\left\{2\pi i\sum_{m=1}^{M}\mathrm{Res}[F_2(\eta_{1m},\eta_{2m})e^{ip_m x}] + \oint_{\mathrm{EJP}} F_2(\eta_1,\eta_2)e^{ipx}\,dp\right\}, \tag{31}$$

where η_{1m}, η_{2m} are the vertical wave numbers evaluated at the poles.

Following the usual procedure to evaluate the residues in these expressions, the function D in Eq. (21) is expanded to first order in a Taylor series about the eigenvalue p_m. After eliminating η_{2m} using the dispersion relation in Eq. (22), the result is

$$\begin{aligned} D &= (p-p_m)\left.\frac{\partial D}{\partial p}\right|_{p=p_m} + \cdots \\ &= \frac{p_m}{\eta_{1m}\sin(\eta_{1m}h)}[\eta_{1m}h - \sin(\eta_{1m}h)\cos(\eta_{1m}h) \\ &\quad - b_{12}^2\sin(\eta_{1m}h)\tan(\eta_{1m}h)](p-p_m) + \cdots. \end{aligned} \tag{32}$$

Some straightforward algebra then yields the residues of these simple poles as

$$\mathrm{Res}[F_1(\eta_{1m},\eta_{2m})e^{ip_m x}] = \frac{\eta_{1m}\sin(\eta_{1m}z)\sin(\eta_{1m}z')}{p_m[\eta_{1m}h - \sin(\eta_{1m}h)\cos(\eta_{1m}h) - b_{12}^2\sin(\eta_{1m}h)\tan(\eta_{1m}h)]}e^{ip_m x} \tag{33}$$

and

$$\mathrm{Res}[F_2(\eta_{1m},\eta_{2m})e^{ip_m x}] = \frac{\eta_{1m}\sin(\eta_{1m}h)\sin(\eta_{1m}z')\exp[-i\eta_{2m}(z-h)]}{p_m[\eta_{1m}h - \sin(\eta_{1m}h)\cos(\eta_{1m}h) - b_{12}^2\sin(\eta_{1m}h)\tan(\eta_{1m}h)]}e^{ip_m x}. \tag{34}$$

The expression for the normal modes in Eq. (33) is valid for all z and z' in the channel, irrespective of which is the greater, and, under the constraint in Eq. (12), it is clear that the mode functions in Eq. (34) all decay to zero in the limit of infinite depth. For a wave traveling away from the source in the positive x direction, the real part of the eigenvalue, p_m, is chosen to be negative, in which case the imaginary part is positive, as required if the modes are to attenuate with increasing distance. Notice that the residues in Eqs. (33) and (34), representing a line source, contain no geometrical decay factor, unlike the modes from a point source, which undergo cylindrical spreading, falling off as $1/\sqrt{x}$ in the far field.

The branch line integrals in Eqs. (30) and (31) are taken along the contour ABC around the EJP cut in Fig. 2. Since, by definition, η_2 is real everywhere along the EJP branch line, with phases of $-\pi$ and zero, respectively, on the upper and lower edges of the cut, a change of integration variable from p to η_2 allows the branch line integrals to be converted to definite integrals over infinite limits:

$$\begin{aligned}\phi_{1\omega\mathrm{EJP}}(x,z) &= \frac{Q}{2\pi}\oint_{\mathrm{EJP}} F_1(\eta_1,\eta_2)e^{ipx}\,dp \\ &= \frac{Q}{2\pi}\int_{-\infty}^{\infty}\frac{\eta_2}{\sqrt{k_2^2-\eta_2^2}}F_1(\eta_1,\eta_2)e^{-i\sqrt{k_2^2-\eta_2^2}x}\,d\eta_2\end{aligned} \tag{35}$$

and

$$\begin{aligned}\phi_{2\omega\mathrm{EJP}}(x,z) &= \frac{Q}{2\pi}\oint_{\mathrm{EJP}} F_2(\eta_1,\eta_2)e^{ipx}\,dp \\ &= \frac{Q}{2\pi}\int_{-\infty}^{\infty}\frac{\eta_2}{\sqrt{k_2^2-\eta_2^2}}F_2(\eta_1,\eta_2)e^{-i\sqrt{k_2^2-\eta_2^2}x}\,d\eta_2,\end{aligned} \tag{36}$$

where the explicit negative sign preceding the radical in the argument of the exponential function ensures that $p = -\sqrt{k_2^2-\eta_2^2}$ falls in the second quadrant of the complex p plane.

Two physically identifiable field components are represented by the branch line integrals in Eqs. (35) and (36): the lateral or head wave and the so-called continuous field. The lateral wave, discussed in Sec. VIII B, travels along the bottom interface, reradiating energy into the water column at the critical grazing angle, with an accompanying evanescent component in the basement. As the name suggests, the continuous field propagates over a continuum of grazing angles and possesses properties that depend largely on the depth of the channel relative to a wavelength. In a shallow channel with a nominally lossless bottom, the continuous field includes significant wave-number components that propagate at grazing angles steeper than the critical. Much of this high-angle energy penetrates the bottom boundary to radiate away into the basement, thus being lost to the water column. However, the partial reflections from the bottom give rise to an interference field in the water column, which may be approximated by an infinite set of "virtual" modes (see Sec. VIII C). The situation is different in deep channels, where the effect of bottom reflections on the field in the water column is negligible. In this case, the continuous field corresponds to the direct and surface-reflected arrivals at the receiver, as discussed in Sec. VIII A.

Since the solution embodied in Eqs. (30) and (31) for the total field in the Pekeris waveguide satisfies the radiation conditions in horizontal range and depth, it is well behaved everywhere. Each of the proper modes appearing in the summations spans the full vertical extent of the waveguide, that is, the water column and basement. Two criteria must be satisfied for such a mode to exist: the eigenvalue, p_m, must be a solution of the dispersion relation in Eq. (24) and the imaginary part of the associated vertical wave number in the basement, η_{2m}, must be negative [Eq. (12)]. Only M eigenvalues satisfy these two conditions and hence no proper modes exist other than those represented by the discrete, convergent terms under the summation signs in Eqs. (30) and (31).

IV. NUMERICAL EVALUATION OF THE EIGENVALUES

As mentioned earlier, with a lossless basement, the eigenvalues lie on the negative real axis of the complex p plane, falling between the real acoustic wave numbers $-k_2$ and $-k_1$. In practice, dissipation is always present, in which case the eigenvalues become complex, migrating away from the real axis into the second quadrant of the p plane. Provided the attenuation is "small," the number, M, of such eigenvalues remains equal to M_o, the same as in the lossless case. However, as the attenuation rises beyond a certain level, the trend is for the total number, M, of eigenvalues to increase beyond M_o. Various iterative techniques for solving the dispersion relation in Eq. (23) for the complex eigenvalues have been discussed by several authors,[10–12] all of which are based on variants of the effective depth in Eq. (27).

A more direct approach to solving the dispersion relation for its complex roots is introduced here, based on a straight-

forward application of the elementary Newton-Raphson algorithm.[13] By a slight modification of Eq. (24), the equation to be solved can be written as

$$f(X) = X - \left(m - \frac{1}{2}\right)\pi - \tan^{-1}[g(X)] = 0,$$

$$m = 1,2,\ldots,M, \tag{37}$$

where

$$X = \eta_1 h, \tag{38}$$

$$g(X) = b_{12}\frac{\sqrt{A^2 - X^2}}{X}, \tag{39}$$

and

$$A = \sqrt{k_1^2 - k_2^2}h. \tag{40}$$

In this formulation, bottom attenuation is accommodated by the usual device of allowing the acoustic wave number k_2 to be complex. The derivative of the function in Eq. (37) with respect to the complex variable X is

$$f'(X) = \frac{df}{dX} = 1 + \frac{1}{X(1+g^2)}\left\{g + \frac{b_{12}^2}{g}\right\}. \tag{41}$$

If the nth approximation for the root is X_n, then an improved estimate is

$$X_{n+1} = X_n - \frac{f(X_n)}{f'(X_n)}, \tag{42}$$

which, with a starting value of $X_o = (m - \frac{1}{2})\pi$, converges to the required complex solution for the vertical wave number, η_{1m}, of mode m after just a few iterations. Once the vertical wave numbers of the modes in the water column have been determined, the eigenvalues are obtained from the expression

$$p_m = -\sqrt{k_1^2 - \eta_{1m}^2}, \quad m = 1,2,\ldots,M, \tag{43}$$

where, again, the minus sign in front of the radical indicates that the real part of p_m is negative, thus placing the pole in the second quadrant of the complex p plane, consistent with an outward-going, attenuating wave.

The total number of proper modes, M, is returned directly by the Newton-Raphson algorithm, since M is identified as the mode whose vertical wave number, η_2, in the basement has the smallest (i.e., nearest to zero) negative imaginary part. When $m > M$, the Newton-Raphson algorithm still returns roots of the dispersion relation, all of which have $\mathrm{imag}(\eta_2) > 0$. This puts them on the lower Riemann sheet of the complex p plane, outside the integration contour in Fig. 2. Such roots, representing improper modes, do not therefore contribute to the exact solution for the field in Eqs. (30) and (31).

As a check on the complex-root-finding procedure in Eq. (42), the Newton-Raphson iteration was performed for the Zhang and Tindle[12] channel ($h = 54$ m, $c_1 = 1500$ m/s, $c_2 = 1600$ m/s, $b_{12} = 0.8$) using their seabed attenuation of 0.3125 dB/m/kHz. At their frequency of $f = 100$ Hz, only three proper modes are supported, that is, $M = 3$, with complex eigenvalues, as returned by the Newton-Raphson algorithm in Eq. (42), that are identical to those shown for the first three modes in Zhang and Tindle's Table I.

The eigenvalues for modes $m = 4$, 5, and 6 that appear in Zhang and Tindle's Table I are also given identically by the Newton-Raphson procedure. However, these eigenvalues, corresponding to mode numbers $m > M$, represent improper modes with vertical wave numbers in the basement having a positive imaginary part. Thus, these improper modes, which are not part of the solution for the field in Eqs. (30) and (31), exhibit exponentially diverging oscillations with increasing depth in the basement, of the type illustrated in Fig. 5.8 of Jensen *et al.*[14]

V. MODE COUNTING

A. Lossless basement

With a lossless basement, since there can be no dissipation modes, only the trapped modes exist in the Pekeris waveguide, the total number being M_o. A well-known analytical expression[4] exists for M_o, which is derived from the dispersion relation in Eq. (24) under the condition that the largest mode number occurs when $\eta_1 = \sqrt{k_1^2 - k_2^2}$. The arctan function then equals $\pi/2$. Physically, this cutoff condition corresponds to the situation where the modal equivalent ray is at the critical grazing angle, in which case the bottom acts as an acoustically rigid interface. The number of trapped modes is immediately found to be

$$M_o = \frac{k_1 h}{\pi}\sin(\alpha_c) + \frac{1}{2}, \tag{44}$$

where $\alpha_c = \cos^{-1}(c_1/c_2)$ is the critical grazing angle of the interface and, since M_o is a whole number, it is implicit in Eq. (44) that the right side is to be rounded down to the nearest integer. At a frequency of 200 Hz, Eq. (44) yields $M_o = 5$ for Zhang and Tindle's channel[12] with no bottom loss. When their attenuation of 0.3125 dB/m/kHz is taken into account, the total number of modes increases to $M = 7$ [evaluated from the Newton-Raphson procedure in Eq. (42)], that is, five trapped modes and two dissipation modes. As frequency increases, the number of dissipation modes rises rapidly. Evidently, in a typical shallow-water environment, over a commonly used frequency band, attenuation in the basement significantly increases the number of proper modes supported by the waveguide.

B. Lossy basement

In general, attenuation in the basement increases the total number of proper modes to $M \geqslant M_o$, although it is considerably more difficult to derive an analytical expression for M than for M_o. For the moment, falling back on the Newton-Raphson procedure in Eq. (42), it is found that for bottom attenuations of one, two, five, and ten times that used by Zhang and Tindle[12] in their Table I, with all else the same, including their frequency of 100 Hz, the corresponding proper mode counts are $M = 3$, 4, 7, and 12 (cf. $M_o = 3$ trapped modes). Figure 3 shows the positions of all the eigenvalues in the complex p plane for these four levels of attenuation at 100 Hz in the Zhang and Tindle channel. The

TABLE I. Mode properties at $f=100$ Hz for the Zhang and Tindle channel, from the Newton-Raphson algorithm [Eq. (42)]. The letters in the first column denote bottom attenuation: $A=0.3125$, $B=0.625$, $C=0.9375$, $D=1.25$ dB/m/kHz. Mode numbers 4 and higher are dissipation modes.

α	m	p_m	η_{2m}	α_m (dB/m)
A	1	−0.415 853 5+0.000 054 7i	0.010 128 5−0.137 248 1i	0.000 475
A	2	−0.406 681 2+0.000 239 2i	0.012 352 5−0.106 501 2i	0.002 078
A	3	−0.391 841 2+0.001 321 5i	0.035 848 7−0.024 966 6i	0.011 479
B	1	−0.415 839 2+0.000 106 4i	0.020 091 5−0.138 438 2i	0.000 925
B	2	−0.406 613 3+0.000 462 4i	0.024 318 0−0.108 465 4i	0.004 017
B	3	−0.391 211 1+0.001 870 2i	0.052 215 7−0.040 103 7i	0.016 245
B	4	−0.365 643 4+0.006 496 3i	0.143 240 2−0.003 144 0i	0.056 426
C	1	−0.415 759 7+0.000 226 5i	0.047 810 8−0.145 784 1i	0.001 968
C	2	−0.406 256 2+0.000 956 8i	0.055 870 9−0.119 481 3i	0.008 311
C	3	−0.389 833 8+0.002 712 0i	0.083 944 5−0.071 559 3i	0.023 556
C	4	−0.364 025 6+0.006 528 3i	0.149 659 9−0.031 322 8i	0.056 704
C	5	−0.325 411 9+0.011 754 5i	0.219 889 2−0.014 731 0i	0.102 098
C	6	−0.269 242 6+0.019 399 4i	0.286 033 5−0.006 436 6i	0.168 501
C	7	−0.181 554 0+0.036 212 9i	0.349 629 0−0.001 400 5i	0.314 542
D	1	−0.415 607 1+0.000 312 7i	0.085 107 0−0.164 481 7i	0.002 716
D	2	−0.405 619 9+0.001 288 7i	0.094 805 5−0.143 512 3i	0.011 194
D	3	−0.388 269 5+0.003 166 2i	0.118 458 5−0.108 891 8i	0.027 501
D	4	−0.361 832 5+0.006 463 4i	0.164 790 1−0.071 544 4i	0.056 141
D	5	−0.323 101 3+0.011 432 7i	0.225 383 7−0.046 296 9i	0.099 303
D	6	−0.266 693 9+0.019 067 9i	0.288 339 7−0.031 363 0i	0.165 622
D	7	−0.178 137 4+0.036 215 8i	0.350 679 4−0.021 892 0i	0.314 567
D	8	−0.055 333 3+0.140 697 0i	0.412 175 8−0.015 389 7i	1.222 078
D	9	−0.033 917 4+0.268 035 6i	0.472 995 0−0.010 650 1i	2.328 127
D	10	−0.028 526 8+0.363 678 9i	0.533 306 9−0.007 038 9i	3.158 875
D	11	−0.026 050 5+0.446 850 4i	0.593 238 9−0.004 193 6i	3.881 293
D	12	−0.024 633 9+0.523 392 7i	0.652 881 9−0.001 892 1i	4.546 131

numerical values of the poles depicted in the four panels of Fig. 3, the corresponding vertical wave numbers in the basement, and the associated modal attenuation coefficients are listed in Table I.

It is also found form Eq. (42) that, as the frequency increases, with the bottom attenuation fixed, the proper-mode count, M, rises more rapidly than M_o. For example, for frequencies of 100, 200, and 500 Hz in the Zhang and Tindle[12] channel, with their bottom attenuation of 0.3125 dB/m/kHz, the corresponding proper mode counts are $M=3$, 7, and 32 (cf. $M_o=3$, 5 and 13 trapped modes).

Apart from the fact that the number of poles increases with rising levels of dissipation and increasing frequency, it is immediately apparent from Fig. 3 that the poles are not confined to the vertical strip between real$(-k_2)$ and $(-k_1)$. Indeed, with the higher levels of attenuation, most of the poles lie well beyond this strip, tending to track the lower side of the EJP branch cut. It is also evident that, as the attenuation rises, the shape of the branch line changes, although it always follows a hyperbolic trajectory passing through the branch point at $-k_2$.

As derived below, an analytical approximation for the total number of modes in the Pekeris waveguide with attenuation in the basement is

$$M \approx \left[1 - \frac{\gamma^2 \cot^4(\alpha_c)}{R^4}\right] \frac{R k_1 h \sin(\alpha_c)}{\pi} + \frac{1}{2}, \tag{45a}$$

where

$$R = \sqrt{1 + \gamma^2 \cot^2(\alpha_c) \left\{1 + \left(\frac{k_1 h \cos(\alpha_c)}{\tanh^{-1}(b_{12})}\right)^2\right\}} \tag{45b}$$

and γ is the loss tangent in the basement (defined below). As before, $\alpha_c=\cos^{-1}(c_1/c_2)$ is the critical grazing angle of the bottom interface and the value of M returned by Eq. (45a) is to be rounded down to the nearest integer. Notice that when γ goes to zero, representing an absence of attenuation in the basement, the expression for M in Eq. (45a) reduces correctly to M_o in Eq. (44). Note also that M depends on the density ratio b_{12}, which appears in the expression for R in Eq. (45b), whereas M_o is independent of density.

Although an approximation, Eq. (45a) is surprisingly accurate, predicting a mode count that is either the same as the exact result returned by the Newton-Raphson procedure in Eq. (42) or differs from it by at most one. When this difference occurs, it is a consequence of the discrete nature of the process: M increments by unity at combinations of the pa-

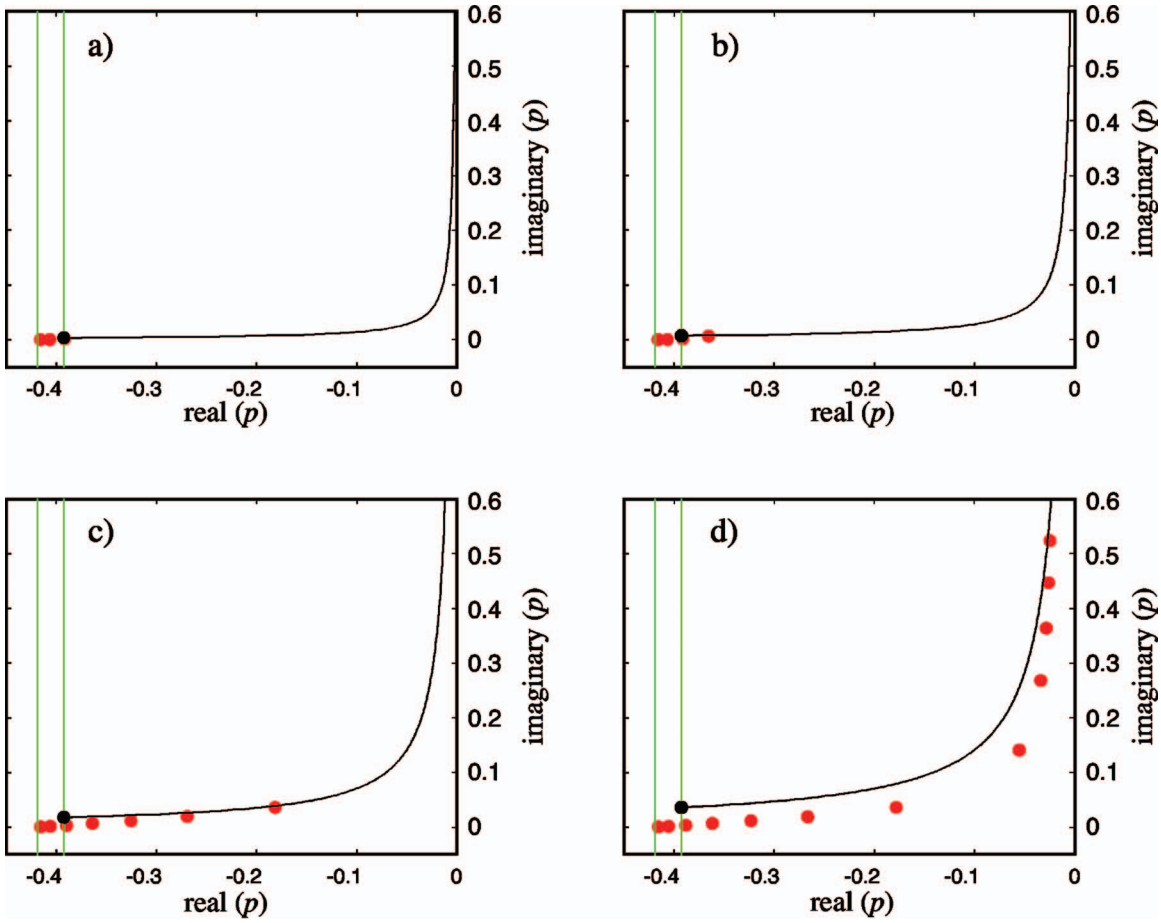

FIG. 3. Second quadrant of the complex p plane showing the branch point at $-k_2$ (black circle), the hyperbolic EJP branch cut (black line), the boundaries of the strip between the real parts of $-k_1$ and $-k_2$ (green vertical lines) and the poles (red circles), as returned by the Newton-Raphson algorithm in Eq. (42), under increasing levels of bottom attenuation (which is taken to scale linearly with the frequency): (a) 0.3125 dB/m/kHz, (b) 0.625 dB/m/kHz, (c) 1.5625 dB/m/kHz, and (d) 3.125 dB/m/kHz. The remaining parameters used in the computation were those of the Zhang and Tindle channel: $h=54$ m, $c_1=1500$ m/s, $c_2=1600$ m/s, $b_{12}=0.8$, and $f=100$ Hz.

rameter values (notably attenuation and frequency) which may differ marginally between the exact and approximate calculations of the total mode number.

The derivation of Eq. (45a) proceeds as follows. In the presence of bottom attenuation, the acoustic wave number in the basement becomes complex and may be expressed as $\bar{k}_2=k_2(1-i\gamma)$, where $k_2=\omega/c_2$ is still real. From the polar representation of $\bar{k}_2$, γ is identified as the loss tangent (i.e., the tangent of the phase angle of the complex number $\bar{k}_2$), in terms of which the plane-wave attenuation coefficient of the basement is $\alpha=\gamma k_2$. For many marine sediments, the attenuation coefficient scales essentially linearly with the frequency, in which case γ is independent of frequency, typically taking a value close to 0.01. On recalling Eq. (24), the dispersion relation, to be solved for $m=M$, is

$$\eta_1 h = M\pi - \tan^{-1}\left(\frac{\eta_1}{b_{12}\sqrt{k_1^2-k_2^2(1-i\gamma)^2-\eta_1^2}}\right). \tag{46}$$

To obtain the solution for M, the vertical wave number in the water column is expressed in terms of its real and imaginary parts:

$$\eta_1 h = w + iy. \tag{47}$$

Now, the physical condition that characterizes the Mth mode is a zero decay of the mode amplitude with increasing depth in the basement. This criterion is satisfied by setting the imaginary part of the term under the radical in Eq. (46) to zero, which yields

$$wy = k_2^2 h^2 \gamma = k_1^2 h^2 \gamma \cos^2(\alpha_c). \tag{48}$$

The arctan function in Eq. (46) is then approximated as

$$\tan^{-1}\left(\frac{\eta_1}{b_{12}\sqrt{k_1^2-k_2^2(1-i\gamma)^2-\eta_1^2}}\right) \approx \frac{\sqrt{w^2-y^2-a^2}}{w^2+y^2}(y+iw)\tanh^{-1}(b_{12}), \tag{49}$$

where

$$a = k_1 h \sin(\alpha_c)\sqrt{1+\gamma^2\cot^2(\alpha_c)}. \tag{50}$$

On substituting Eq. (49) into Eq. (46) and equating the real and imaginary parts, the following pair of simultaneous equations in w, y is obtained, with the highest proper-mode number, M, as a parameter:

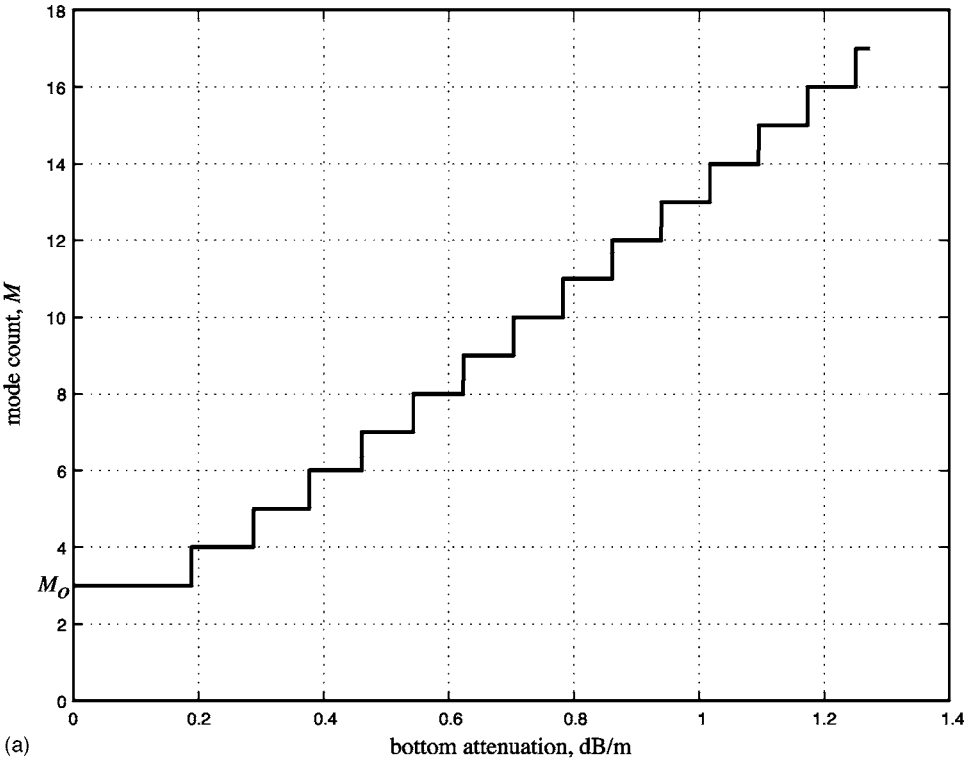

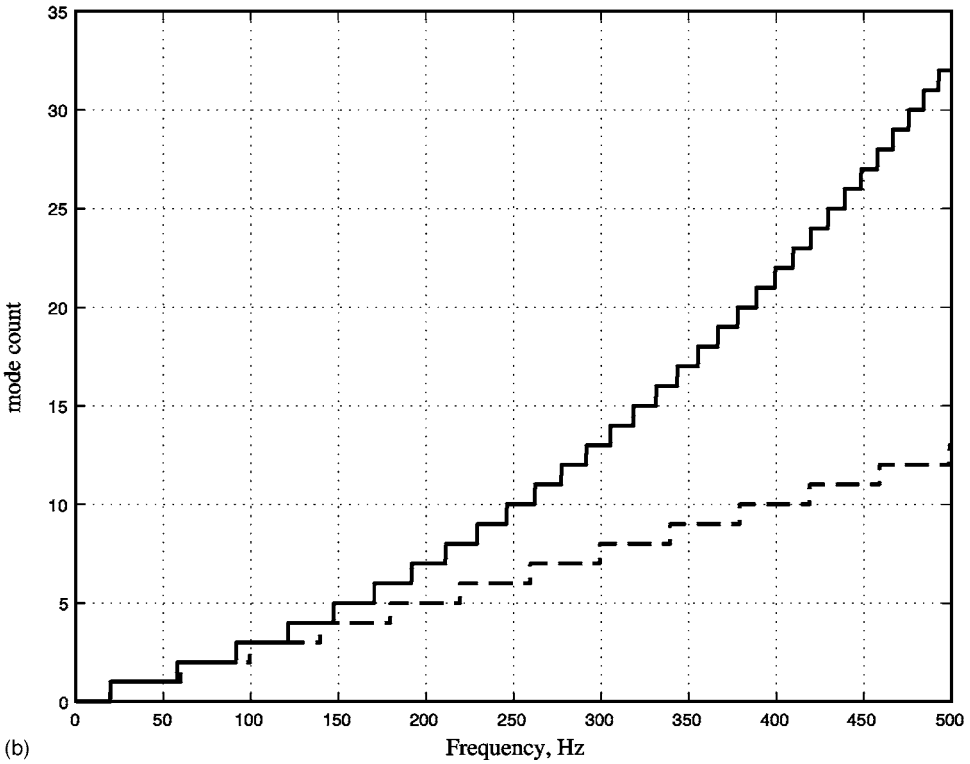

FIG. 4. (a) Mode count, M, evaluated from Eq. (45) as a function of the bottom attenuation at a frequency of 100 Hz and (b) M [Eq. (45), solid line] and M_o [Eq. (44), dashed line] as functions of frequency with a bottom attenuation of 0.3125 dB/m/kHz. The channel parameters are those of Zhang and Tindle, as cited in the legend to Fig. 3.

$$w = (M - 0.5)\pi + \frac{y\sqrt{w^2 - y^2 - a^2}}{w^2 + y^2} \tanh^{-1}(b_{12}), \tag{51}$$

$$y = \frac{w\sqrt{w^2 - y^2 - a^2}}{w^2 + y^2} \tanh^{-1}(b_{12}). \tag{52}$$

Since $y \ll w$ even for unrealistically large values of bottom attenuation, the term y^2 in the denominators of these expressions may be neglected, allowing w to be eliminated from Eqs. (48) and (52). The result is a bi-quadratic equation in y, whose solution is

$$y = k_1^2 h^2 \gamma \cos^2(\alpha_c) \left\{ a^2 + \frac{k_1^4 h^4 \gamma^2 \cos^4(\alpha_c)}{[\tanh^{-1}(b_{12})]^2} \right\}^{-1/2}, \tag{53}$$

which leads to

$$w = \left\{ a^2 + \frac{k_1^4 h^4 \gamma^2 \cos^4(\alpha_c)}{[\tanh^{-1}(b_{12})]^2} \right\}^{1/2}, \tag{54}$$

and hence from Eq. (51) M is found to be as given in Eq. (45a).

Figure 4(a) shows the stair-step behavior of the mode count in Eq. (45a) as a function of attenuation in the basement for the Zhang and Tindle[12] channel at a frequency of 100 Hz. Note that with an (unrealistically high) attenuation of 3.125 dB/m/kHz, the mode count from Fig. 4(a) [and also from the Newton-Raphson algorithm in Eq. (42)] is $M=12$, as shown in Fig. 3(d). Thus, in this case, in addition to the three trapped modes, there are nine dissipation modes, making 12 proper modes in total. For the same channel, but with the attenuation fixed at Zhang and Tindle's (realistic) value of 0.3125 dB/m/kHz, Fig. 4(b) shows the proper-mode count from Eq. (45a) as a function of frequency. Also shown in Fig. 4(b) for comparison is M_o. It is clear from this example, which is typical of many coastal ocean environments, that at commonly used frequencies, the total number of proper modes may exceed significantly the number of trapped modes. In fact, it is easy to verify many realistic combinations of waveguide parameters (i.e., channel depth, density ratio, critical angle, and bottom attenuation) and frequency return mode counts that are higher than M_o.

An inspection of Fig. 4(a) reveals that the trend is for the number of proper modes, M, to increase linearly with the attenuation, γ, in the basement. Such behavior is exhibited when the "high-loss" condition, $k_1 h \gamma \gg 1$, holds, in which case the expression for the mode count, M, in Eq. (45a) reduces to the simpler, linear form

$$M \approx \frac{k_1^2 h^2 \gamma \cos^2(\alpha_c)}{\pi \tanh^{-1}(b_{12})} + \frac{1}{2}. \tag{55}$$

Although not quite as accurate as Eq. (45a), Eq. (55) illustrates clearly the linear connection between the total number of proper modes, M, and the attenuation in the basement, γ. Obviously, since it is a high-loss approximation, Eq. (55) does not reduce to M_o in the limit of zero bottom loss.

VI. MODE SHAPE FUNCTIONS

The depth dependence of the residues for the discrete field in Eqs. (33) and (34) may be conveniently represented in terms of mode shape functions:

$$S_m(z) = \begin{cases} \sin(\eta_{1m} z), & 0 \leqslant z \leqslant h, \\ \sin(\eta_{1m} h)\exp[-i\eta_{2m}(z-h)], & z > h, \end{cases} \tag{56}$$

which is valid for all proper modes, $1 \leqslant m \leqslant M$. In the presence of bottom loss, the vertical wave number in the water column is complex and so too are the shape functions. In the case of the dissipation modes, the real and imaginary parts of each shape function have comparable amplitudes. In contrast, the vertical wave numbers of the trapped modes, η_{1m} and η_{2m}, are essentially real and imaginary, respectively, even in the presence of high bottom loss, and hence the shape functions of the trapped modes are predominantly real with negligible imaginary parts.

A. Trapped modes

Since the shapes of the trapped modes are insensitive to bottom loss, an approximate expression for the shape functions may be derived in terms of the (lossless) effective depth, h_e [Eq. (27)]. With the aid of the expressions for the vertical wave numbers in Eqs. (26) and (28), the shape functions for $1 \leqslant m \leqslant M_o$ are

$$S_m(z) \approx \begin{cases} \sin\left(\dfrac{m\pi z}{h_e}\right), & 0 \leqslant z \leqslant h, \\ \sin\left(\dfrac{m\pi h}{h_e}\right)\exp\left[-k_1(z-h)\sin(\alpha_c)\sqrt{1-\dfrac{m^2\pi^2}{k_1^2 h_e^2 \sin^2(\alpha_c)}}\right], & z > h. \end{cases} \tag{57a}$$

The first of these expressions yields the familiar oscillatory shapes of the modes in the water column and the second returns the evanescent modal tails in the basement. The exponential decay of the latter may be characterized in terms of an e-folding depth,

$$L_m = \frac{1}{|\mathrm{imag}(\eta_{2m})|} \approx \left\{ k_1 \sin(\alpha_c)\sqrt{1-\frac{m^2\pi^2}{k_1^2 h_e^2 \sin^2(\alpha_c)}} \right\}^{-1} \quad \text{for } 1 \leqslant m \leqslant M_o. \tag{57b}$$

According to Eq. (57a), the oscillatory shapes of the trapped modes in a Pekeris channel of depth h are essentially the same as those in a "perfect" waveguide with two pressure-release boundaries and of depth $h_e > h$. In the case of the Zhang and Tindle[12] channel, at their frequency of $f=100$ Hz, the effective depth from Eq. (27) is $h_e=62.6$ m, compared with the actual depth, $h=54$ m. In this case, from Eq. (57b), the approximate e-folding depths of the three trapped modes are, in order of ascending mode number, 7.3, 9.5, and 26.4 m. The corresponding e-folding depths, as evaluated "exactly" from the Newton-Raphson procedure in Eq. (42), are 7.3, 9.4, and 40.1 m. In this example, the approximation returns accurate values of the e-folding depths of the first two modes but underestimates that of mode 3. The reason for this discrepancy is that the equivalent ray of the third mode is close to the critical grazing angle, a condition under which the effective depth approximation begins to degrade.

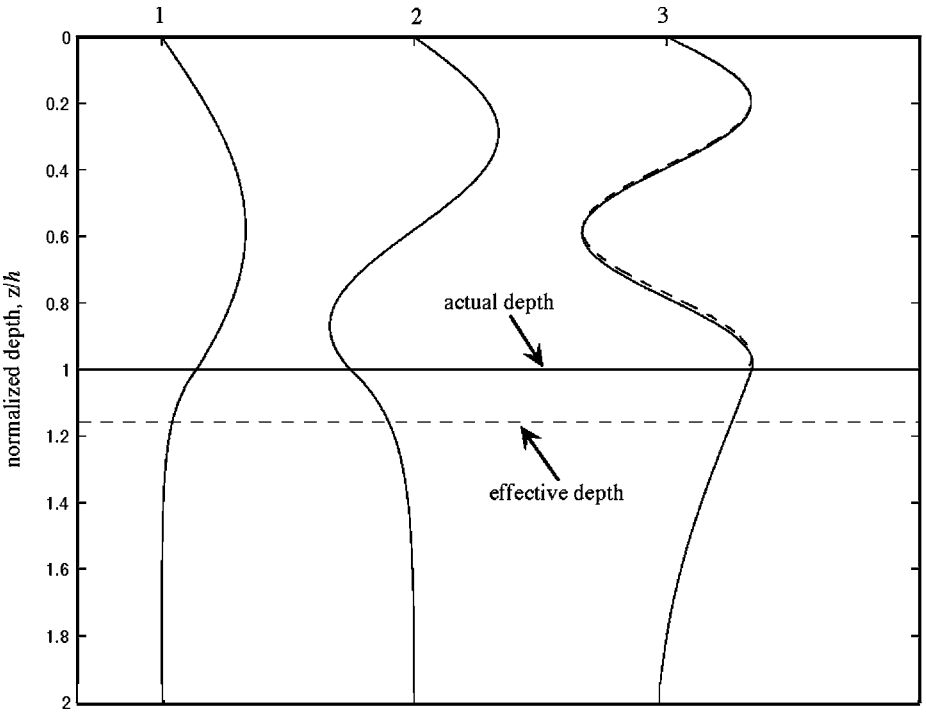

FIG. 5. Shapes of the three trapped modes in the Zhang and Tindle waveguide, as specified in Fig. 3, with a bottom attenuation of 0.3125 dB/m/kHz. The mode numbers are at the top of the panel. The solid curves were computed from the real part of the exact expression in Eq. (56), using the Newton-Raphson procedure in Eq. (42), and the dashed curves were evaluated from the approximation in Eq. (57a).

Figure 5 shows the three proper modes supported by the Zhang and Tindle[12] channel when the bottom attenuation is at their level of 0.3125 dB/m/kHz. The mode shapes were evaluated from the approximate expression in Eq. (57a) and also, for comparison, from the real part of the exact expression in Eq. (56) combined with Eq. (42). For modes 1 and 2 the approximate and exact shape functions are indistinguishable throughout the water column and basement. Even mode 3, which is very near cutoff, is quite reasonably approximated in the water column by Eq. (57a); but in the basement, the radical in Eq. (57a) is no longer real but imaginary, signifying that the approximation fails. Accordingly, in the basement, no approximate form of mode 3 is plotted in Fig. 5.

Figure 6 shows the real and imaginary parts of the seven proper modes supported by the Zhang and Tindle channel when the bottom attenuation is five times their level, at 1.625 dB/m/kHz. These mode shapes were computed using the exact expression in Eq. (56) in conjunction with Eq. (42). At this level of attenuation, four dissipation modes appear in addition to the three trapped modes, the latter exhibiting essentially the same shapes as those in Fig. 5.

B. Dissipation modes

Dissipation modes are "leaky" in the sense that they represent partial transmissions through the bottom of the channel but they still qualify as proper modes since their eigenvalues satisfy both the dispersion relation in Eq. (24) as well as the condition in Eq. (12) on the vertical wave number in the basement. Energy leakage through the bottom occurs because the equivalent rays of the dissipation modes are steeper than the critical grazing angle. As illustrated in Fig. 6, the real and imaginary parts of the dissipation modes exhibit oscillations beneath the bottom interface, the amplitudes of which decay with increasing depth, consistent with Eq. (12). Notice that at the interface itself, both the imaginary part and the depth-gradient of the real part of the dissipation modes are essentially zero.

Approximate expressions for the shapes of the dissipation modes may be developed by introducing a slight modification to the analysis in Sec. V B for the maximum mode number M. When $M_o < m < M$, the condition in Eq. (48) no longer holds but, with M replaced by m, Eqs. (51) and (52) remain valid. Expanding these two expressions to first order in the small quantities y and γ yields

$$\eta_{1m}h \approx \left(m - \tfrac{1}{2}\right)\pi + i \tanh^{-1}(b_{12}) \tag{58a}$$

and

$$\eta_{2m}h \approx \left(m - \frac{1}{2}\right)\pi - i\left(\frac{k_2^2 h^2 \gamma}{\left(m - \frac{1}{2}\right)\pi} - \tanh^{-1}(b_{12})\right). \tag{58b}$$

Taken in conjunction with Eq. (56), these expressions give rise to the following approximate forms for the shape functions of the dissipation modes:

$$S_m(z) \approx \sin\left[\left(m - \frac{1}{2}\right)\frac{\pi z}{h}\right]\cosh\left[\frac{z}{h}\tanh^{-1}(b_{12})\right] + i\cos\left[\left(m - \frac{1}{2}\right)\frac{\pi z}{h}\right]\sinh\left[\frac{z}{h}\tanh^{-1}(b_{12})\right], \quad 0 \leqslant z \leqslant h, \tag{59a}$$

and

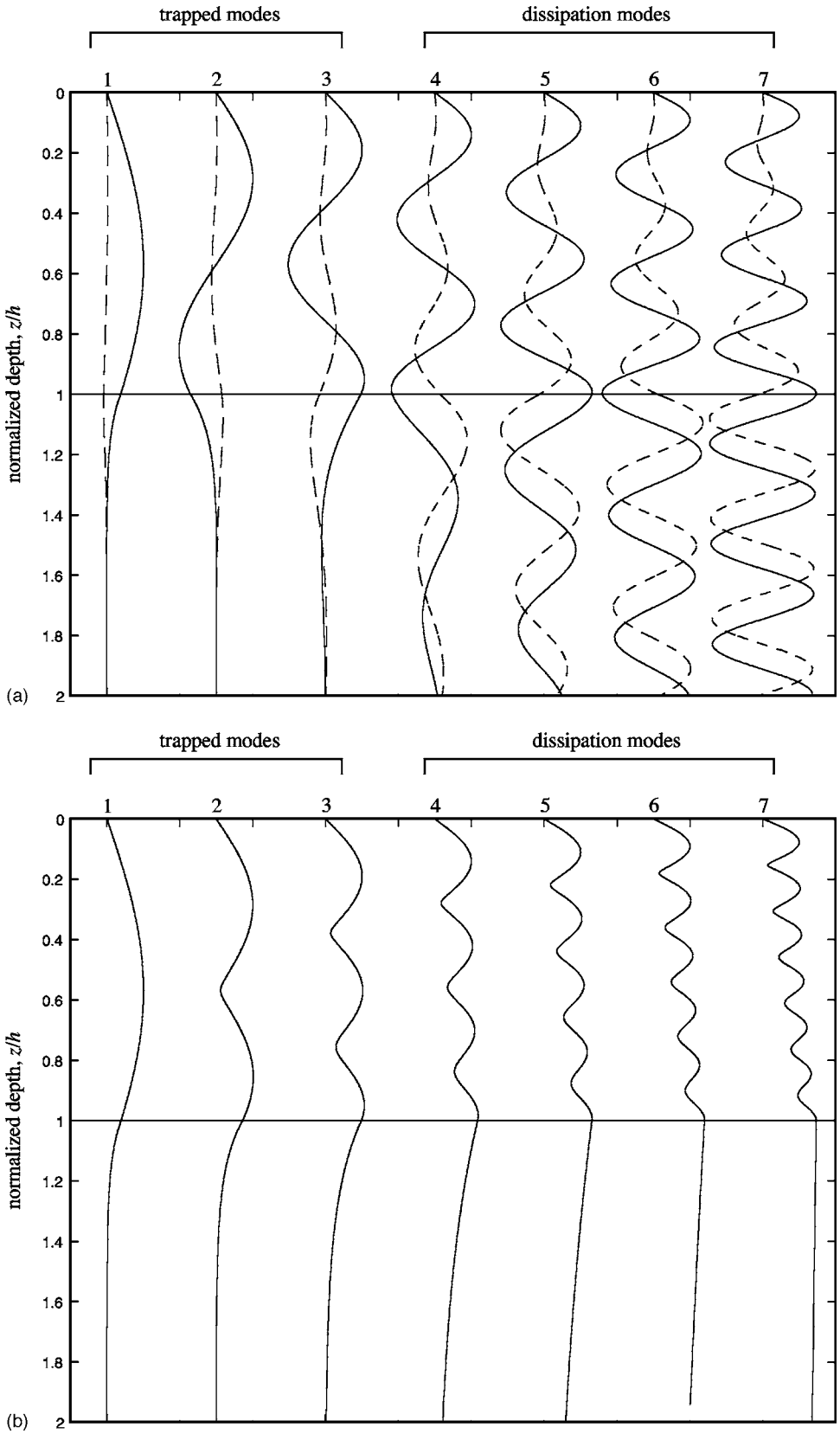

FIG. 6. Numerical evaluation of the complex mode shapes in the Zhang and Tindle waveguide, with the bottom attenuation set at 1.625 dB/m/kHz and the remaining parameters as specified in Fig. 3. The vertical wave numbers were computed from the Newton-Raphson algorithm in Eq. (42) and the mode shapes then evaluated from Eq. (56). The horizontal solid line represents the bottom of the water column and the modes are identified by the numbers at the top of the panels. (a) The real (solid curve) and imaginary (dashed curve) parts of the mode shape functions and (b) the modal envelopes.

$$S_m(z) \approx (-1)^{m+1} \cosh[\tanh^{-1}(b_{12})] \times \exp\left\{-\left[\frac{k_2^2 h^2 \gamma}{\left(m-\frac{1}{2}\right)\pi} - \tanh^{-1}(b_{12})\right]\frac{(z-h)}{h}\right\} \times \left\{\cos\left[\left(m-\frac{1}{2}\right)\frac{\pi(z-h)}{h}\right] - i\sin\left[\left(m-\frac{1}{2}\right)\frac{\pi(z-h)}{h}\right]\right\}, \quad z > h. \tag{59b}$$

According to Eq. (59a), both the imaginary part of the shape functions and the normal gradient of the real part are zero at the bottom interface, in agreement with the exact mode shapes shown in Fig. 6. The exponentially decaying oscillations in the basement, as represented by Eq. (59b), are also consistent with the exact shapes of the dissipation modes shown in Fig. 6.

The approximations leading to Eqs. (59a) and (59b) are valid under the same high-loss condition, $k_1 h\gamma \gg 1$, that underlies the approximate expression for the mode count, M, in Eq. (55). Indeed, Eq. (55) is recovered identically from Eq. (59b) by setting the argument of the exponential decay term to zero, which is the condition that characterizes the Mth proper mode.

VII. MODAL ATTENUATION

From the expressions for the residues in Eqs. (33) and (34), it is evident that if the imaginary parts of the eigenvalues are greater than zero, the modes will be attenuated as they propagate horizontally through the Pekeris waveguide. In the absence of loss in the basement, the eigenvalues are real and hence no such lateral decay occurs, but in general the modal attenuation coefficient is nonzero and given by

$$\alpha_m = \mathrm{imag}(p_m). \tag{60}$$

As shown below, the modal attenuation increases essentially as the square of the mode number and inversely as the square of the frequency. Thus, at a fixed frequency, higher-order modes are effectively removed from the field at shorter ranges, a phenomenon known as mode stripping. A given mode, on the other hand, experiences a rapid reduction in attenuation as the frequency rises, which enhances propagation to longer ranges.

A. Mode stripping

An approximate solution for α_m is obtained from the dispersion relation in Eq. (46) with the arctan function represented by the first term in its Taylor expansion:

$$\eta_1 h \approx m\pi - \left(\frac{\eta_1}{b_{12}\sqrt{k_1^2 - k_2^2(1-i\gamma)^2 - \eta_1^2}}\right). \tag{61}$$

On solving for η_1 and retaining only terms up to first order in both η_1 and the small loss tangent, γ, the following expression is obtained:

$$\eta_{1m} \approx \frac{m\pi}{h_e}\left[1 + i\gamma\frac{\cot^2(\alpha_c)}{b_{12}k_1 h_e \sin(\alpha_c)}\right]. \tag{62}$$

The real part of this result is the lowest-order approximation for the vertical wave number in the water column, which has already been presented in Eq. (26).

To first order in γ, the mth eigenvalue is

$$p_m = -\sqrt{k_1^2 - \eta_{1m}^2} \approx -\sqrt{k_1^2 - \frac{m^2\pi^2}{h_e^2}} + i\gamma\frac{m^2\pi^2\cos^2(\alpha_c)}{b_{12}k_1^2 h_e^3 \sin(\alpha_c)\sqrt{1 - m^2\pi^2/k_1^2 h_e^2}} \tag{63}$$

and, hence, to the same level of approximation, the modal attenuation coefficient is

$$\alpha_m = \begin{cases} \gamma\dfrac{m^2\pi^2\cot^2(\alpha_c)}{b_{12}k_1 h_e^2 \sin(\alpha_c)\sqrt{k_1^2 h_e^2 - m^2\pi^2}} & \text{for } m < \dfrac{k_1 h_e}{\pi}, \\ \dfrac{1}{h_e}\sqrt{m^2\pi^2 - k_1^2 h_e^2} & \text{for } \dfrac{k_1 h_e}{\pi} < m \leqslant M. \end{cases} \tag{64}$$

The inclusion of the term $(m\pi)^2$ under the radical in the first of these expressions has only a minor effect on the predicted modal attenuation but it improves the approximation marginally for values of $m\pi$ close to $k_1 h$. If this term were neglected, the top expression in Eq. (64) would reduce to a form that was originally derived by Buckingham,[7] according to which the modal attenuation is proportional to the square of the mode number. This quadratic scaling with mode number had been recognized earlier by Kornhauser and Raney.[15] Assuming that the loss tangent, γ, is independent of frequency, as it is for many marine sediments,[16,17] and neglecting the weak frequency dependence of the effective depth, h_e, in Eq. (27), then the modal attenuation given by the top expression in Eq. (64) can be seen to scale inversely with the square of the frequency.

The approximation for the modal attenuation coefficient in Eq. (64) is surprisingly good for all the modes, as illustrated in Fig. 7 for the Zhang and Tindle[12] channel with four levels of attenuation in the basement. In this example, the upper expression in Eq. (64) applies for all three trapped modes and for dissipation modes from 4 up to and including 8, which covers all the modes shown in Figs. 7(a)–7(c), while the lower expression holds for dissipation modes 9–12, which appear only in Fig. 7(d). For comparison with the approximate predictions of Eq. (64), the exact modal attenuation coefficients, as computed using the Newton-Raphson algorithm in Eq. (42), are included in Fig. 7.

B. High bottom loss

With the relatively low level of bottom loss in Figs. 7(a) and 7(b), the attenuation coefficient of the highest-order mode does not exceed the attenuation in the basement. In fact, provided that the loss tangent satisfies the inequality

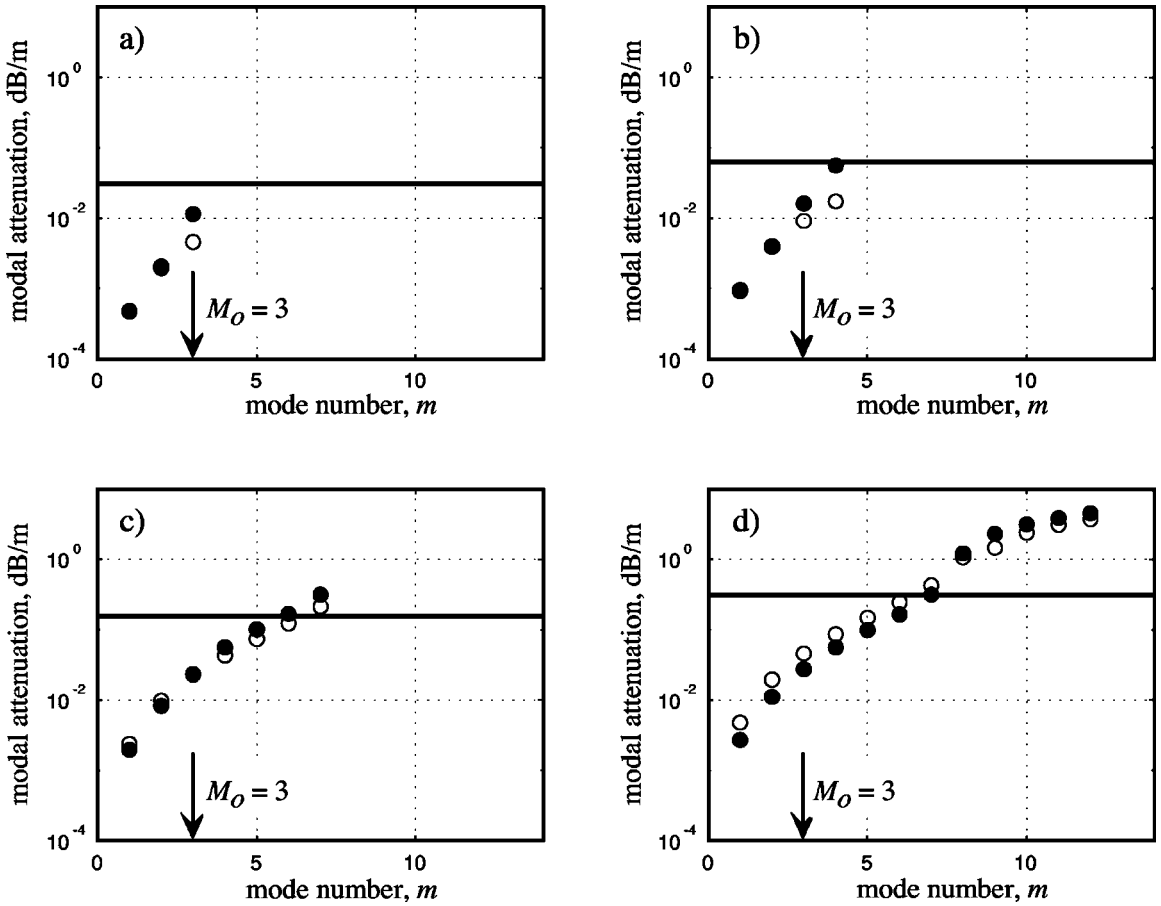

FIG. 7. Modal attenuation at 100 Hz as a function of mode number for the Zhang and Tindle channel parameters of Fig. 3 with increasing levels of attenuation in the basement: (a) 0.3125 dB/m/kHz, (b) 0.625 dB/m/kHz, (c) 1.5625 dB/m/kHz, and (d) 3.125 dB/m/kHz. The open circles derive from the approximate expression in Eq. (64) and the solid circles were computed from the "exact" Newton-Raphson algorithm in Eq. (42). The solid horizontal lines represent the plane-wave attenuation in the basement at $f=100$ Hz. The loss tangent, γ, is taken to be independent of frequency.

$$\gamma < \frac{\tanh^{-1}(b_{12})}{k_2 h}, \tag{65}$$

it is straightforward to show, from Eqs. (46) and (47) combined with the solutions for y and w in Eqs. (53) and (54), that the attenuation coefficient of the Mth mode is the same as the attenuation in the bottom:

$$\alpha_M \approx \gamma k_2. \tag{66}$$

This is a familiar result with a simple interpretation based on Snell's law.

At higher levels of attenuation, Eq. (66) no longer holds, as can be seen in Figs. 7(c) and 7(d), where the attenuation coefficients of the higher-order modes exceed the attenuation in the bottom. Under the high-loss condition

$$\gamma > \frac{\tanh^{-1}(b_{12})}{k_2 h}, \tag{67}$$

it turns out that one of the second-order terms in γ is dominant in the expression for the eigenvalue of the Mth mode. The term in question may be identified by writing the Mth eigenvalue in terms of y and w, as given, respectively, in Eqs. (53) and (54):

$$\begin{aligned} p_M &= -\frac{1}{h}\sqrt{k_1^2 h^2 - \eta_{1M}^2 h^2} \\ &= -\frac{1}{h}\sqrt{k_1^2 h^2 - w^2 + y^2 - 2iwy} \\ &\approx -\frac{1}{h}\sqrt{k_2^2 h^2 - k_2^4 h^4 \gamma^2/\{\tanh^{-1}(b_{12})\}^2 - 2ik_2^2 h^2 \gamma}. \end{aligned} \tag{68}$$

When the inequality in Eq. (67) holds, the second-order term in γ makes the real part of the term under the radical negative, in which case the attenuation coefficient may be roughly approximated as

$$\alpha_M \approx \frac{k_2^2 h \gamma}{\tanh^{-1}(b_{12})}. \tag{69}$$

This expression is greater than the attenuation in the bottom, γk_2, by the factor $k_2 h/\tanh^{-1}(b_{12})$, which is consistent with the excess attenuation exhibited by the highest-order mode shown in Figs. 7(c) and 7(d).

C. Observability of dissipation modes

Given the quadratic scaling of the modal attenuation with mode number [Eq. (64)], it is reasonable to ask whether dissipation modes will be too heavily attenuated to be ob-

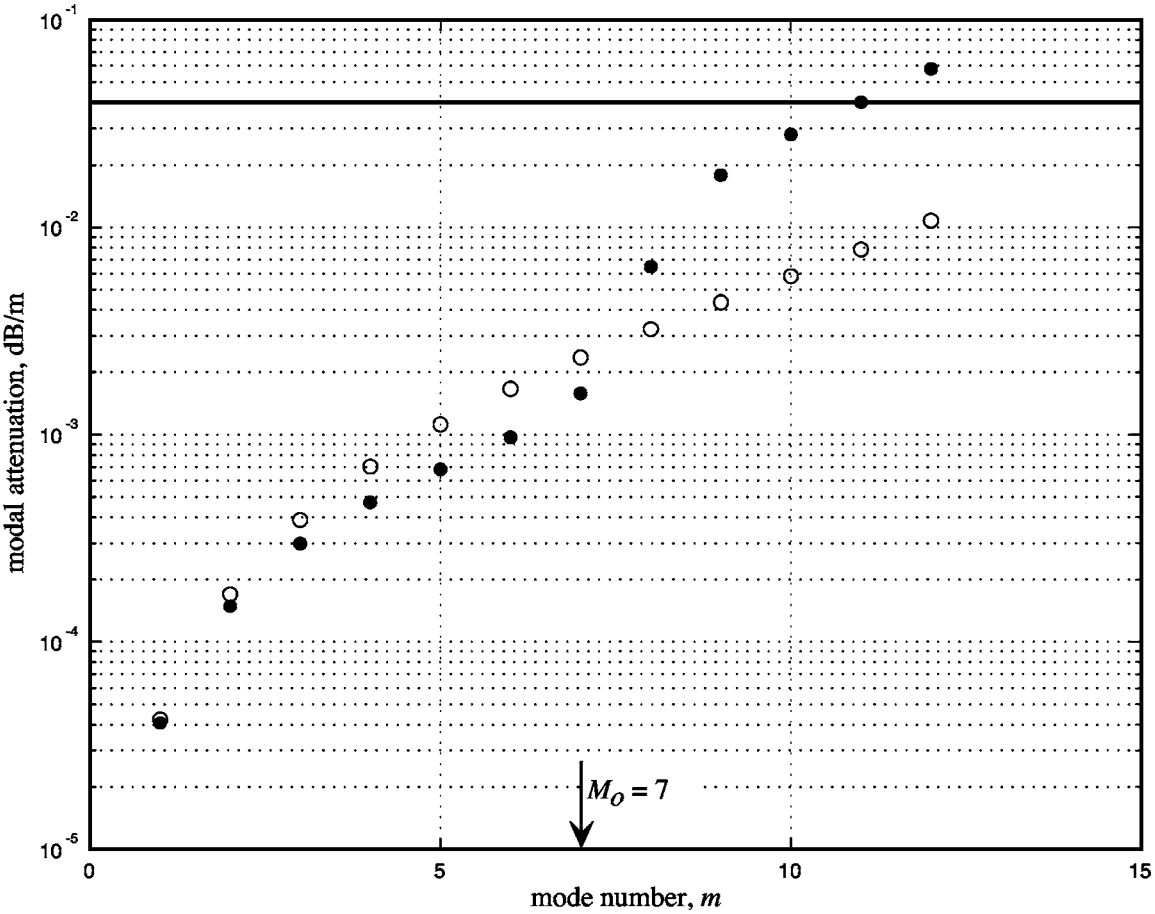

FIG. 8. Modal attenuation as a function of mode number for a frequency of 100 Hz in a 100-m channel overlying a coarse-sand sediment. See text for the bottom parameters. The open circles derive from the approximate expression in Eq. (64) and the solid circles were computed from the "exact" Newton-Raphson algorithm in Eq. (42). The solid horizontal line represents the plane-wave attenuation in the sediment at 100 Hz.

served in typical ocean channels. As an admittedly arbitrary criterion of detectability, suppose that the attenuation of the mode in question is required to be less than 10 dB over a range equal to ten times the channel depth in order to be observable. It is clear that none of the dissipation modes illustrated in Fig. 7 satisfy this condition. For instance, the first (and only) dissipation mode in Fig. 7(b) is mode 4, which is attenuated by approximately 43 dB over a range of $10h=540$ m.

However, in other circumstances that are commonly encountered in shallow ocean channels, dissipation modes which do satisfy the detectability criterion are found to exist. As an example, consider a coarse sand sediment[17] with sound speed of 1800 m/s, a density of 2.05 times the density of seawater, and an attenuation of 0.04 dB/m at 100 Hz. Assuming a channel depth $h=100$ m, a frequency of 100 Hz, and a sound speed in seawater of 1500 m/s, a total of 12 modes are supported (7 trapped and 5 dissipation modes), with attenuations as shown in Fig. 8. Mode 8, the first dissipation mode, has an attenuation $\alpha_8=0.00646$ dB/m, that is, 6.46 dB over a range of $10h=1$ km, which does indeed satisfy the detectability criterion stated above.

It is clear from the top expression in Eq. (64) that, with all else fixed, the higher the critical grazing angle of the bottom, the lower the attenuation of a given mode. Therefore, dissipation modes are most likely to be observed in channels where the sound speed in the basement is considerably higher than that in the water column, a condition that is associated with the coarser marine sediments. As illustrated in Fig. 8, at least one dissipation mode may be readily observable in an ocean channel overlying a fast sediment of coarse sand with a sound speed of 1800 m/s or higher. On the other hand, a slower, fine-grained material such as silt would not be expected to support any weakly attenuated dissipation modes. Even the very-fine-sand of the Zhang and Tindle channel, with a sound speed of 1600 m/s, is barely fast enough to support a detectable dissipation mode over a reasonable range.

VIII. BRANCH LINE INTEGRALS

Each of the branch line integrals, Eq. (35) for the water column and Eq. (36) for the basement, represents two wave components, the head wave and the continuous field. In general, these integrals cannot be expressed explicitly. The one exception to this is the case of an infinitely deep channel, where the water-column integral reduces identically to a sum of two elementary terms, one of which represents the direct and the other the surface-reflected arrival. In shallow water, where the bottom has a significant effect on the field, the branch line integrals cannot be reduced to explicit expressions, but it is possible to develop an asymptotic approxima-

tion for the lateral wave, which is valid in both the water column and the basement. It is also possible to approximate the continuous field in the water column in terms of an infinite sum of "virtual" modes.

A. Direct and surface-reflected arrivals in deep water

When the fluids constituting the channel and the basement are identical, that is, $b_{12}=1$, $k_1=k_2=k$, and $\eta_1=\eta_2=\eta$, the Pekeris waveguide becomes a homogeneous fluid halfspace with a pressure-release surface. The branch line integral in Eq. (35) can then be written in the form

$$\phi_{1\omega\mathrm{EJP}}(x,z)=\frac{Q}{2\pi}\int_0^\infty \frac{\eta}{\sqrt{k^2-\eta^2}}[F_1(\eta,\eta) - F_1(\eta,-\eta)]e^{-i\sqrt{k^2-\eta^2}x}\,d\eta \tag{70}$$

and, from the expression for F_1 in Eq. (19), it follows that

$$[F_1(\eta,\eta)-F_1(\eta,-\eta)] = -\frac{2i}{\eta}\sin(\eta z)\sin(\eta z') = \frac{i}{\eta}\{\cos[\eta(z+z')]-\cos[\eta(z-z')]\}. \tag{71}$$

By expressing each cosine as a Bessel function of the first kind, $J_{-1/2}(\cdots)$, and the exponential function in Eq. (60) as a modified Bessel function of the third kind, $K_{1/2}(\cdots)$, the branch line integral becomes

$$\phi_{1\omega\mathrm{EJP}}(x,z)=\frac{Q}{2\pi}\sqrt{\frac{x(z-z')}{\pi}}\int_0^\infty \eta^{1/2}J_{-1/2}[\eta(z-z')] \times\frac{K_{1/2}[\sqrt{\eta^2-k^2}x]}{(\eta^2-k^2)^{1/4}}\,d\eta-\frac{Q}{2\pi}\sqrt{\frac{x(z+z')}{\pi}} \times\int_0^\infty \eta^{1/2}J_{-1/2}[\eta(z +z')]\frac{K_{1/2}[\sqrt{\eta^2-k^2}x]}{(\eta^2-k^2)^{1/4}}\,d\eta. \tag{72}$$

The integrals here are special cases of Gegenbauer's discontinuous integral, which can be expressed explicitly in terms of Bessel functions,[18] yielding the following result for the branch line contribution to the field in the half space:

$$\phi_{1\omega\mathrm{EJP}}(x,z)=-\frac{iQ}{4\pi}\{H_0^{(2)}[k\sqrt{x^2+(z-z')^2}] - H_0^{(2)}[k\sqrt{x^2+(z+z')^2}]\}, \tag{73}$$

where $H_0^{(2)}(\cdots)$ are Hankel functions of the second kind of order zero.

Equation (73) is the expected result, since the first and second terms on the right represent, respectively, the field from the horizontal line source and its negative image in the pressure-release surface. The source term exhibits a logarithmic singularity at the origin, where the argument is zero; and both terms show a cylindrical-spreading type of decay at longer ranges. These properties are, of course, all characteristic of a line source.

B. The lateral wave in shallow water

For large x, the asymptotic behavior of the branch line integrals in Eqs. (35) and (36) may be approximated by using the method of stationary phase.[19] The analysis is fairly standard apart from one subtlety: the stationary point of the phase function occurs at zero, which returns a null value for the integrals in Eqs. (35) and (36). This difficulty is circumvented by adopting a limiting procedure.

To illustrate the approach, consider the field in the water column when losses everywhere are negligible, in which case the acoustic wave numbers k_1 and k_2 are real. Some straightforward algebraic manipulation of the function $F_1(\eta_1,\eta_2)$ allows the integral in Eq. (35) to be written in the form

$$\phi_{1\omega\mathrm{EJP}}(x,z)=-\frac{ib_{12}Q}{2\pi}\int_{-\infty}^{\infty}\frac{\eta_2^2}{\sqrt{k_2^2-\eta_2^2}}\frac{\sin(\eta_1 z)\sin(\eta_1 z')}{[\eta_1^2\cos^2(\eta_1 h)+b_{12}^2\eta_2^2\sin^2(\eta_1 h)]}e^{-i\sqrt{k_2^2-\eta_2^2}x}\,d\eta_2, \tag{74}$$

where the negative sign in the argument of the exponential function has been written explicitly with the understanding that the real part of the radical is positive, thus ensuring that the horizontal wave number falls in the second quadrant of the complex plane. Since η_1 depends on η_2 through the expression

$$\eta_1=\sqrt{\eta_2^2+k_1^2-k_2^2}, \tag{75}$$

the integrand in Eq. (74) may expressed as a function of η_2 alone.

The quadratic multiplier in the numerator of the integrand of Eq. (74) is now written as the limit

$$\eta_2^2=i\lim_{s\to 0}\frac{d}{ds}\exp(-i\eta_2^2 s), \tag{76}$$

where s is a vanishingly small dummy variable. The integral $\phi_{1\omega EJP}(x,z)$ then consists of a sum of four integrals, each of the form

$$I = \lim_{s\to 0} \frac{d}{ds} \int_{-\infty}^{\infty} \frac{\exp i\{\eta_1 Z - \sqrt{k_2^2 - \eta_2^2}\, x - \eta_2^2 s\}}{\sqrt{k_2^2 - \eta_2^2}[\eta_1^2 \cos^2(k_1 h) + b_{12}^2 \eta_2^2 \sin^2(k_1 h)]}\, d\eta_2, \tag{77}$$

where the four possible sign combinations are represented by $Z = \pm(z \pm z')$. Assuming that, for large x, the exponential in the numerator of the integrand varies much more rapidly than the denominator, the integral may be evaluated by the method of stationary phase. The phase function is

$$\theta(\eta_2) = \sqrt{\eta_2^2 + k_1^2 - k_2^2}\, Z - \sqrt{k_2^2 - \eta_2^2}\, x - \eta_2^2 s, \tag{78}$$

the first two derivatives of which are

$$\theta'(\eta_2) = \frac{\eta_2 Z}{\sqrt{\eta_2^2 + k_1^2 - k_2^2}} + \frac{\eta_2 x}{\sqrt{k_2^2 - \eta_2^2}} - 2\eta_2 s \tag{79}$$

and

$$\theta''(\eta_2) = \frac{(k_1^2 - k_2^2) Z}{(\eta_2^2 + k_1^2 - k_2^2)^{3/2}} + \frac{k_2^2 x}{(k_2^2 - \eta_2^2)^{3/2}} - 2s. \tag{80}$$

Equation (79) has a real root,

$$\eta_2 = 0, \tag{81}$$

at which point the phase function in Eq. (78) is

$$\theta(0) = \sqrt{k_1^2 - k_2^2}\, Z - k_2 x \tag{82}$$

and the second derivative in Eq. (80) is

$$\theta''(0) = \frac{Z}{\sqrt{k_1^2 - k_2^2}} + \frac{x}{k_2} - 2s. \tag{83}$$

The condition in Eq. (81) on the vertical wave number, η_2, is characteristic of the lateral wave, which travels horizontally through the lower medium and, in the water column, is incident on the bottom boundary at precisely the critical angle.

Since the second derivative in Eq. (83) is positive for large x, the turning point in Eq. (82) is a minimum, corresponding to a point of stationary phase, which yields

$$I \approx b_{12}\sqrt{2\pi}\left[\frac{1}{k_2(k_1^2 - k_2^2)\cos^2(\sqrt{k_1^2 - k_2^2}\, h)} \times \exp i\left\{\sqrt{k_1^2 - k_2^2}\, Z - k_2 x + \frac{\pi}{4}\right\}\right] \times \lim_{s\to 0} \frac{d}{ds}[\theta''(0)]^{-1/2}. \tag{84}$$

On evaluating the limit in this expression and recombining the four integrals, the asymptotic approximation for the lateral wave in the water column is found to be

$$\phi_{1\omega\text{lateral}}(x,z) \approx b_{12} Q \sqrt{\frac{\cos(\alpha_c)}{2\pi}} \frac{\sin\{k_1 z \sin(\alpha_c)\}\sin\{k_1 z' \sin(\alpha_c)\}}{(k_1 x)^{3/2} \sin^2(\alpha_c)\cos^2\{k_1 h \sin(\alpha_c\ \}} \times e^{-i\{k_1 x \cos(\alpha_c) - \pi/4\}}, \tag{85}$$

where $\alpha_c = \cos^{-1}(k_2/k_1)$ is the critical grazing angle. Following a similar development, the branch line integral in Eq. (36) for the lateral wave in the basement is approximated by the stationary phase expression

$$\phi_{2\omega\text{lateral}}(x,z) \approx b_{12} Q \sqrt{\frac{\cos(\alpha_c)}{2\pi}} \frac{\sin\{k_1 z' \sin(\alpha_c)\}}{(k_1 x)^{3/2} \sin^2(\alpha_c)\cos^2\{k_1 h \sin(\alpha_c)\}} \times e^{-i\{k_1 x \cos(\alpha_c) - \pi/4\}}[b_{12} \sin\{k_1 h \sin(\alpha_c)\} + k_1(z - h)\sin(\alpha_c)\cos\{k_1 h \sin(\alpha_c)\}], \tag{86}$$

where $k_1(z-h)\sin(\alpha_c)$ is taken to be small compared with unity.

Analogous expressions to those in Eqs. (85) and (86) were stated without proof by Pekeris[1] for the case of a point source. Apart from revealing that the amplitude of the lateral wave reduces rapidly with increasing range, decaying asymptotically as $x^{-3/2}$, the approximations in Eqs. (85) and (86) have little utility. Indeed, when $k_1 h \sin(\alpha_c)$ is a zero of the cosine in the denominator, it is evident that these expressions fail completely, since they diverge to infinity.

C. Virtual modes in shallow water

In an effort to improve the efficiency of shallow-water transmission loss computations, an approximate formulation of the continuous field in the water column was developed by Tindle *et al.*[20] and subsequently extended by Tindle[21] and Stickler and Ammicht.[22] Based on a technique introduced by Labianca,[23] these authors showed that the integrand of the EJP branch line integral for the continuous field in the water column exhibits resonance peaks, which arise from partial reflections off the bottom of wave-number components that are steeper than the critical grazing angle. It is implicit in these analyses that bottom loss is negligible, in which case the channel supports M_o trapped modes and no dissipation modes. By integrating over packets of wave numbers centered on the resonance peaks, Tindle *et al.*[20] approximated the branch line integral as an infinite sum of discrete "virtual" modes, each of which is oscillatory in depth with a shape function that is real and of the form

$$S_m(z) = \sin\left\{\left(m - \frac{1}{2}\right)\frac{\pi z}{h}\right\} \quad \text{for } 0 \leqslant z \leqslant h \text{ and } M_o < m \leqslant \infty. \tag{87}$$

These shape functions are the same as if the bottom were a rigid boundary.

It is perhaps worth emphasizing that virtual modes are quite distinct from dissipation modes. Virtual modes are not exact solutions of the wave equation and hence are neither "proper" nor "improper" modes. The set of *real* virtual modes is infinite with each member being a discrete *approxi-*

mation for the EJP branch line integral representing the continuous field, and the virtual-mode approximation holds even in the absence of bottom loss. In contrast, each of the finite set of *complex* dissipation modes represents an *exact*, convergent, discrete solution of the wave equation and such solutions exist solely because attenuation is present in the basement.

IX. CONCLUDING REMARKS

Acoustic propagation in a Pekeris waveguide with an attenuating, semi-infinite fluid basement is critically examined in this article. The analysis hinges on familiar contour integrations around the complex wave-number plane for the field in the water column and the basement. Based on the EJP branch cut, it is argued that the exact solution for the field in both domains consists of a finite sum of proper normal modes plus a branch line integral. Both of these components of the field are well behaved in the sense that they converge to zero in the limit of infinite depth in the basement. Improper modes, with exponentially diverging tails in the basement, do not contribute to the solution.

A rapidly convergent, iterative algorithm is introduced for solving the dispersion relationship for the complex modal eigenvalues. From this numerical solution, it is demonstrated that the number of proper modes supported by the waveguide rises essentially linearly with increasing attenuation in the bottom. These proper modes comprise the familiar trapped modes and, in addition, dissipation modes that exist solely as a result of attenuation in the basement. An approximate but accurate analytical expression is derived for the total mode count [Eq. (45a)], which depends on the bottom attenuation, the ratio of densities in the water column and the basement, the water depth, and the critical angle of the bottom. The total number of proper modes predicted by this expression is almost indistinguishable from the mode count returned by the exact iterative procedure. Moreover, it is shown that for realistic combinations of the parameters, the number of proper modes supported by the waveguide may be considerably higher in the presence of bottom attenuation than in the lossless case.

The attenuation of each mode is given by the imaginary part of its eigenvalue. An approximate expression is derived for the modal attenuation coefficient [Eq. (64)], which scales with the square of the mode number. This quadratic dependence on mode number accounts for the phenomenon of mode stripping, whereby higher-order modes are effectively removed from the water column at shorter ranges than lower-order modes. Assuming a frequency-independent loss tangent for the basement layer, as is typical of many marine sediments, the modal attenuation coefficient scales inversely with the square of the frequency, indicating that as frequency rises a given mode may propagate to greater ranges. Although higher-order modes undergo increasing attenuation, dissipation modes may still be of practical significance since they could be detectable in real ocean channels, provided the bottom material has a sufficiently high sound speed. This is illustrated by an example involving an channel overlying a realistic coarse-sand sediment with a sound speed of 1800 m/s.

The depth dependence of the proper modes is described in terms of complex shape functions. In the case of trapped modes, the imaginary component of the shape function is negligible and the real part is essentially the same as in the absence of bottom loss. In contrast, the real and imaginary parts of the shape functions of the dissipation modes are comparable. Approximate expressions [Eqs. (59)] are developed for the shape functions of the dissipation modes in the water column and the basement.

The EJP branch line integrals, representing the lateral wave and the continuous spectrum in the water column and the basement, are also examined. Stationary phase approximations [Eqs. (85) and (86)] for these integrals reveal the asymptotic range dependence of the lateral wave but otherwise serve little useful purpose. Indeed, in certain cases, these asymptotic approximations for the lateral wave fail completely by diverging to infinity.

ACKNOWLEDGMENT

This work was supported by Dr. Ellen Livingston, Ocean Acoustics Code, the Office of Naval Research, under Grant No. N00014-04-1-0063.

[1]C. L. Pekeris, "Theory of propagation of explosive sound in shallow water," in *Propagation of Sound in the Ocean*, Geological Society of America, Memoir 27 (Geological Society of America, New York, 1948), pp. 1–117.
[2]D. C. Stickler, "Normal-mode program with both the discrete and branch line contributions," J. Acoust. Soc. Am. **57**, 856–861 (1975).
[3]W. M. Ewing, W. S. Jardetzky, and F. Press, *Elastic Waves in Layered Media* (McGraw-Hill, New York, 1957).
[4]G. V. Frisk, *Ocean and Seabed Acoustics: A Theory of Wave Propagation* (Prentice-Hall, Englewood Cliffs, NJ, 1994).
[5]A. Erdélyi, *Tables of Integral Transforms, Volume 1* (McGraw-Hill, New York, 1954).
[6]D. E. Weston, "A Moiré fringe analog of sound propagation in shallow water," J. Acoust. Soc. Am. **32**, 647–654 (1960).
[7]M. J. Buckingham, "Array gain of a broadside vertical line array in shallow water," J. Acoust. Soc. Am. **65**, 148–161 (1979).
[8]M. J. Buckingham, "Theory of three-dimensional acoustic propagation in a wedge-like ocean with a penetrable bottom," J. Acoust. Soc. Am. **82**, 198–210 (1987).
[9]L. B. Felsen and N. Marcuvitz, *Radiation and Scattering of Waves* (Prentice-Hall, Englewood Cliffs, NJ, 1973).
[10]D. M. E. Chapman, P. D. Ward, and D. D. Ellis, "The effective depth of a Pekeris ocean waveguide, including shear wave effects," J. Acoust. Soc. Am. **85**, 648–653 (1989).
[11]P. Balasubramanian and M. M. Muni, "A note on "The effective depth of a Pekeris ocean waveguide, including shear effects" [Chapman *et al.*, J. Acoust. Soc. Am. **85**, 648–653 (1989)]," **88**, 564–565 (1990).
[12]Z. Y. Zhang and C. T. Tindle, "Complex effective depth of the ocean bottom," J. Acoust. Soc. Am. **93**, 205–213 (1993).
[13]R. Courant, *Differential and Integral Calculus*, 2nd ed. (Blackie & Son, London, 1937).
[14]F. B. Jensen, W. A. Kuperman, M. B. Porter, and H. Schmidt, *Computational Ocean Acoustics* (American Institute of Physics, New York, 1994).
[15]E. T. Kornhauser and W. P. Raney, "Attenuation in shallow-water propagation due to an absorbing bottom," J. Acoust. Soc. Am. **27**, 689–692 (1955).
[16]E. L. Hamilton, "Compressional-wave attenuation in marine sediments," Geophysics **37**, 620–646 (1972).
[17]M. J. Buckingham, "Compressional and shear wave properties of marine

sediments: comparisons between theory and data," J. Acoust. Soc. Am. **117**, 137–152 (2005).
[18]G. N. Watson, *A Treatise on the Theory of Bessel Functions*, 2nd ed., (Cambridge U. P., London, 1958).
[19]J. N. Newman, *Marine Hydrodynamics* (MIT, Cambridge, MA, 1977).
[20]C. T. Tindle, A. P. Stamp, and K. M. Guthrie, "Virtual modes and the surface boundary condition in underwater acoustics," J. Sound Vib. **49**, 231–240 (1976).
[21]C. T. Tindle, "Virtual modes and mode amplitudes near cutoff," J. Acoust. Soc. Am. **65**, 1423–1428 (1979).
[22]D. C. Stickler and E. Ammicht, "Uniform asymptotic evaluation of the continuous spectrum contribution for the Pekeris model," J. Acoust. Soc. Am. **67**, 2018–2024 (1980).
[23]F. M. Labianca, "Normal modes, virtual modes, and alternative representations in the theory of surface duct sound propagation," J. Acoust. Soc. Am. **53**, 1137–1147 (1973).

Broadband modeling of downslope propagation in a penetrable wedge

T. W. Yudichak, G. S. Royal, D. P. Knobles, M. Gray, R. A. Koch, and S. A. Stotts
Applied Research Laboratories, The University of Texas at Austin, P. O. Box 8029, Austin, Texas 78713-8029

(Received 21 November 2003; revised 1 November 2005; accepted 2 November 2005)

Sound propagation in a wedge-shaped environment with a penetrable bottom is simulated with broadband adiabatic mode, coupled mode, and parabolic equation model computations. Simulated results are compared to measured data taken in a tank experiment by Tindle *et al.* The coupled mode formalism is shown to predict, in agreement with that experiment, that modal wave fronts in penetrable wedges are approximately circular arcs centered at the apex of the wedge for a source near the apex. It is also shown that for wedge angles up to 6°, the received waveforms are well approximated by the adiabatic waveforms time-shifted by a depth-dependent interval to account for the curvature of the modal wave fronts. A small deviation from circularity in the modal wave fronts is possibly observed in the 6° case. © *2006 Acoustical Society of America.*
[DOI: 10.1121/1.2141265]

PACS number(s): 43.30.Bp, 43.20.Ks, 43.30.Zk [WLS] Pages: 143–152

I. INTRODUCTION

A topic of ongoing interest in the underwater acoustics community is the nature of sound propagation in range-dependent, shallow-water environments. The partial differential equations (PDE) describing range-dependent propagation are typically nonseparable and therefore require numerical methods of solution. Several such approaches exist, including finite difference methods, the parabolic equation (PE) approximation, and one- and two-way coupled normal mode approaches. Like finite difference schemes, two-way coupled mode approaches introduce no approximations to the PDE apart from those necessary to discretize the problem (which may include neglecting a continuum in the form of a branch line integral). Coupled mode schemes have been used to study wave propagation in range-dependent environments, not only in underwater acoustics,[1–5] but in seismology[6] and electromagnetics[7–9] as well.

An important example of a range-dependent environment is a wedge-shaped waveguide. Such a geometry approximates the region of an ocean over a continental slope, and a significant effort has gone into studying this problem.[10–21] Wedge-shaped waveguides find applications in other fields as well, such as electromagnetics.[7–9,22–24] The case of a point source in a three-dimensional wedge with perfectly reflecting boundaries and homogeneous medium leads to a separable PDE. Buckingham derived an exact solution[10,11] for the case where both boundaries are pressure-release surfaces, and Frisk[25] did so for the case of one pressure release and one rigid boundary. In both cases, the solution is characterized by a decomposition into independently propagating normal modes with curved wave fronts that are circular arcs. These modes have been given the name *wedge modes*.

To examine the applicability of the wedge mode idea to downslope propagation over penetrable bottoms, Tindle *et al.* conducted experiments in a tank with an adjustable bottom slope.[20,21] In these experiments, pulses of short time duration were produced at the shallow end of the tank, and the resulting signals were measured downslope at a range of several hundred wavelengths at various depths. In this experimental geometry, propagation by wedge modes would lead one to expect the wave front of the received signal to also be a circular arc. Indeed, the arrival times of the signal at any given range were shown to increase with depth, confirming propagation with circular-arc wave fronts.

The experiments of Tindle *et al.* have received considerable attention and have led to single-frequency calculations using various approaches, including one using the PE approximation[17] and one based on wedge modes.[19] However, the most important phenomenon demonstrated by the experiments, the depth dependence of signal arrival times, can only be fully analyzed with a broadband computation, the implementation of which is one goal of this paper.

A previous study by Royal[1] presented a broadband analysis of these experiments. This was based on a one-way coupled mode model that neglected modes that penetrate into the sediment. However, another goal of the analysis in the present paper is to investigate the possibility of departures—possibly undetectable at the precision of the experiments of Tindle *et al.*—from propagation with circular arc wave fronts. To this end, an analysis that involves as few approximations as possible is desirable. By treating the sediment layer as a separate fluid layer bounded below by a nearly rigid halfspace within a two-way coupled mode theory, the physics of the experiment is represented more fully. The main approximations are the treatment of the sediment as a fluid layer and the neglect of coupling to the rigid halfspace. The first is a common approximation; the second is expected to have little effect on the propagation in the water column, given the depth of the halfspace in the sediment. For computational reasons, other approximations are also made in this paper. One is that a two-dimensional approximation to the true tank geometry is used that neglects diffraction ef-

fects near the apex of the wedge. (The approximate geometry has a sharp corner directly below the source, but possible spurious diffractive effects from this are neglected with the neglect of the steepest propagation angles that results from truncation of the modal sum.) Also, the discretization necessary for a numerical implementation of the model may introduce spurious physics into the problem; these are expected to be minimized with a sufficiently fine discretization.

While the two-way coupled normal mode model provides an accurate accounting of range-dependent propagation, insight can be gained by examining the effectiveness of other, approximate models. The adiabatic normal mode model neglects coupling between modes; thus, a comparison between it and the coupled mode results isolates the effects of mode coupling. In fact, for the slope angles considered in this paper, the received waveforms predicted by the adiabatic approximation have nearly the same shape as those predicted by the coupled normal mode model. However, the adiabatic approximation predicts no depth-dependent time shift, and so it can be used as a standard for measuring this time shift in the coupled mode result.

The depth-dependent time shifts predicted by this method are shown in this paper to agree within experimental uncertainty with the results reported by Tindle *et al.* However, the results in this paper also suggest that small deviations from the circular arc wave front prediction could occur for higher angles of bottom slope, and these would require more precise methods to detect.

The structure of the paper is as follows: Sec. II briefly describes the tank experiment of Tindle *et al.* and gives the geoacoustic parameters used to model this experiment. Section III outlines the two-way coupled mode formalism, discusses the problem of mode capture—important for downslope propagation—and describes aspects of propagation with a curved wave front. Section IV gives details of the numerical solution of the problem. Section V contains a description of the results of the computations followed by a discussion. Section VI provides a short summary.

II. MODELING THE TANK EXPERIMENT

The experiment simulated in this paper was described in Ref. 21. The apparatus employed was described in detail in Ref. 20. It consisted of a sand-filled stainless steel tray suspended in a tank of water. The tray was 10 m long, 93 cm wide, and 20 cm deep. The slope of the tray could be adjusted to any angle up to 9°.

The present paper, is concerned with results measured in tanks having bottom slopes of 1°, 3°, and 6°. In each case, a source pulse in the band 60–100 kHz was emitted at a depth of 4.7 cm in a water depth of 10 cm. A probe with adjustable depth was used to record signals at a range of 6.5 m downslope from the source. Waveforms were recorded at eight depths for each bottom angle, which are summarized in Table I.

TABLE I. Receiver depths for 1°, 3°, and 6° wedge configurations.

Receiver No.	1°	3°	6°
1	1.9 cm	5 cm	7 cm
2	4.5 cm	10 cm	16 cm
3	7.0 cm	15 cm	25 cm
4	9.5 cm	20 cm	34 cm
5	12.1 cm	25 cm	43 cm
6	14.6 cm	30 cm	52 cm
7	17.2 cm	35 cm	61 cm
8	19.7 cm	40 cm	70 cm

For the computations reported in this paper, the experimental setup is modeled as a waveguide with two fluid layers with a density ratio $\rho_2/\rho_1=1.97\pm0.01$, that lay above a steel halfspace. The top water-filled layer is taken to have a constant sound speed $c_1=1490\pm1$ m/s. The sand-filled layer is modeled as a 20 cm thick layer with constant sound speed $c_2=1784\pm27$ m/s, and attenuation coefficient $\alpha=(0.063\pm0.009)f$ nepers/m/kHz, where f is acoustic frequency in kHz. These values were suggested by Tindle *et al.*[20,21] and were supported by Westwood, who modeled the 0° slope results of the tank experiment, obtaining good agreement with the data.[26] The steel halfspace is taken to have a sound speed of $c=5700$ m/s, density of $\rho=7.8$ g/cm^3, and compressional attenuation of $\alpha=0.05f$ nepers/m/kHz.

III. THEORY

A. General coupled mode formalism

Though the coupled mode formalism is fairly standard and described elsewhere,[2,3] we include the following summary for the convenience of the reader. The basic problem is to determine the acoustic pressure P in a waveguide consisting of a water layer bounded above by a pressure-release surface and below by a penetrable sediment represented as a fluid layer, which is in turn bounded below by a nearly rigid penetrable halfspace at a depth D below the water-sediment interface. We assume cylindrical symmetry; the depth coordinate z_{bot} of the water-sediment interface can be described by a single function of the range coordinate r: $z_{\text{bot}}=H(r)$. The experimental geometry considered in this paper is not cylindrically symmetric, but because the receivers are located directly downslope from the source, we expect refraction in the horizontal direction to be negligible. Thus the plane containing the source and receivers is approximated as a slice of a cylindrically symmetric environment wherein the bottom is a circular cone, and the source is located directly above the apex of this cone. As mentioned in the Introduction, this idealization also has the result of neglecting diffraction near the tank apex. We also assume constant sound speed c and density ρ in each layer,

$$c(r,z)=\begin{cases} c_1 & z\leqslant H(r) \\ c_2 & H(r)<z\leqslant H(r)+D \\ c_3 & z>H(r)+D, \end{cases} \tag{1}$$

and

$$\rho(r,z)=\begin{cases}\rho_1 & z\leqslant H(r)\\ \rho_2 & H(r)<z\leqslant H(r)+D\\ \rho_3 & z>H(r)+D.\end{cases} \tag{2}$$

If a point source is located on the symmetry axis at depth $z=z_0$, the pressure P satisfies the Helmholtz equation,

$$\left\{\frac{\partial^2}{\partial r^2}+\frac{1}{r}\frac{\partial}{\partial r}+\frac{\partial^2}{\partial z^2}+k^2(r,z)\right\}P(r,z,z_0) = -S(f)\frac{1}{2\pi}\frac{\delta(r)}{r}\delta(z-z_0), \tag{3}$$

where $k(r,z)=2\pi f/c(r,z)$, f denotes the frequency, and $S(f)$ denotes the source spectrum level. The pressure also satisfies suitable boundary and matching conditions between layers.[2]

The coupled mode solution of Eq. (3) proceeds by assuming the pressure can be written in the form

$$P(r,z,z_0)=\sum_{m=1}^{\infty}\phi_m(z,r)R_m(r,z_0), \tag{4}$$

where the functions $\phi_m(z,r)$ satisfy the same (depth) boundary conditions as $P(r,z)$ as well as the local vertical eigenvalue equation

$$\frac{1}{\rho(z,r)}\frac{d^2\phi_m}{dz^2}(z,r)+\frac{d}{dz}\left(\frac{1}{\rho(z,r)}\right)\frac{d\phi_m}{dz}(z,r)+(k^2(z,r)-k_m^2(r))\phi_m(z,r)=0. \tag{5}$$

It can be shown[3] that by requiring the ϕ_m to satisfy Eq. (5), and the orthonormality condition

$$\int_0^{\infty}\frac{1}{\rho(z)}\phi_m(z,r)\phi_n(z,r)dz=\delta_{mn}, \tag{6}$$

the modal coefficients $R_m(r)$ satisfy an integral equation of the form

$$R_m(r)=\int_0^{\infty}g_m(r,r')\left[\Theta_m(r')+\sum_n C_{mn}(r')R_n(r')\right]r'dr'. \tag{7}$$

The functions g_m and Θ_m denote the adiabatic Green's function and modal component of the point source for mode m, respectively.[3] The coupling operator is denoted $C_{mn}(r)$. This is a differential operator and can be conveniently decomposed as

$$C_{mn}(r)=A_{mn}(r)+\alpha_{mn}(r)+\frac{B_{mn}(r)}{r}+(2B_{mn}(r)+\beta_{mn}(r))\frac{d}{dr}. \tag{8}$$

The four matrices used in this definition are defined as follows.[2] The matrices determined by overall mode structure are

$$B_{mn}(r)=\int_0^{\infty}\frac{1}{\rho(z)}\phi_m(r,z)\frac{\partial\phi_n}{\partial r}(r,z)dz, \tag{9}$$

$$A_{mn}(r)=\int_0^{\infty}\frac{1}{\rho(z)}\phi_m(r,z)\frac{\partial^2\phi_n}{\partial r^2}(r,z)dz, \tag{10}$$

and the matrices arising from the sloping interface are

$$\beta_{mn}(r)=\frac{dH}{dr}(r)\phi_m(r,H(r))\phi_n(r,H(r))\left(\frac{1}{\rho_2}-\frac{1}{\rho_1}\right), \tag{11}$$

$$\alpha_{mn}(r)=\frac{dH}{dr}(r)\phi_m(r,H(r))\times\left(\frac{1}{\rho_2}\frac{\partial\phi_n}{\partial r}(r,H^+(r))-\frac{1}{\rho_1}\frac{\partial\phi_n}{\partial r}(r,H^-(r))\right), \tag{12}$$

where the superscripts + and − indicate depths just below and just above the interface between the layers, respectively.

B. Propagation in the sediment and mode capture

In many applications of a normal mode model to waveguide propagation, it is a good approximation to truncate the sum in the mode expansion in Eq. (4) to include only the trapped modes. These modes are defined as having phase velocities less than the sound speed of the bottom at the interface and are those modes that carry energy in the water column.[27,28] The approximation is usually good because the sediment has a significantly higher attenuation than the water, so modes penetrating into the sediment rapidly lose their energy with range.

In downslope propagation, the number of trapped modes increases with water depth. Thus, modes that propagate in the sediment in the shallower regions of the waveguide are progressively converted into modes trapped in the water column, a phenomenon known as mode capture. One might try to account for this by merely making the upper limit of the sum in Eq. (4) range dependent and setting it to the number of trapped modes at that range. However, with a steep enough slope, some of the modes that propagate in the sediment can be trapped in the water column before losing all their energy. Perhaps more importantly, mode coupling allows for energy to be transferred from trapped modes to modes that propagate in the sediment. Therefore, it may be a poor approximation to truncate Eq. (4) at the number of trapped modes at any given range.

The strategy of retaining only the trapped modes was followed in Royal's analysis of the experiment of Tindle *et al.*[1] While the computational results for slopes of 1° and 3° were very good, the results showed noticeable degradation for slopes of 6°. Royal attributed this to the neglect of the modes that propagate in the sediment. To eliminate this possible source of inaccuracy, modes that propagate in the sediment (at least for some of the length of the wedge) are retained for the computations in this paper.

C. Wavefront curvature and time delays

As described in the Introduction, the acoustic field in a wedge-shaped waveguide with perfectly reflecting boundaries propagates as a set of normal modes with circular wave fronts centered at the apex of the wedge. For the experimental geometry of Tindle *et al.*, the curvature of the modal wave

fronts is manifest in a depth-dependent time delay in the arrival of the full signal at the range of the receivers. For wave fronts traveling at a constant speed c, the delay observed at a receiver of depth z and range R, as measured from the wedge apex, is

$$\Delta t = \frac{\sqrt{R^2 + z^2} - R}{c}. \tag{13}$$

While the depth-dependent time delay in the (measured or simulated) signal from a broadband source is difficult to estimate directly because of overlapping modal arrivals, several alternatives exist.

The first is to apply mode filtering to the received waveforms while accounting for the curvature of the modal wave front. This was the method pursued by Tindle *et al.*[21] Mode filtering makes use of both the orthonormality [Eq. (6)] and the approximate frequency independence of the mode functions to isolate the contribution of each mode to the waveform. For discretely sampled data, mode filtering is accomplished by a matrix multiplication,

$$\mathbf{M}(t) = \mathbf{P} \cdot \mathbf{W}(t). \tag{14}$$

In Eq. (14),$\mathbf{W}(t)$ is a matrix containing the waveform time series from each receiver, $\mathbf{P}$ is a matrix containing mode profiles sampled at each receiver depth, and $\mathbf{M}(t)$ contains the filtered time series corresponding to each mode. To account for modal wave front curvature, the received waveforms were synchronized by calculating the expected time delay (these were not reported, however), and time shifting them accordingly. Mode filtering was then applied to the set of synchronized waveforms. Because this procedure resulted in smooth single pulses for the modal waveforms, Tindle *et al.* concluded that sound was indeed propagating via modes with curved wave fronts.

A second method of time-delay estimation makes use of the adiabatic approximation to the coupled-mode equations. In this approximation, coupling between modes is neglected by setting $C_{mn}=0$ in Eq. (7). Since the degree of mode coupling increases with bottom slope, the validity of the adiabatic approximation decreases with bottom slope. However, the manner in which it loses validity still gives it some utility. A primary observation by Tindle *et al.*[21] is that the adiabatic approximation predicts vertical instead of curved modal wave fronts, but is still sufficient to predict modal group velocities. Thus, as long as the dominant modes in a signal have sufficiently similar group velocities, the exact waveforms should differ from the adiabatic waveforms primarily by a time shift given by substituting a representative group velocity for c into Eq. (13). (In fact, as the results will demonstrate, it is a good approximation to use the sound speed in water for the purpose of computing the time shifts.)

To estimate the time shift between coupled mode and adiabatic waveforms, and to quantify the extent to which the waveforms have the same shape, the cross-correlation $C(t)$ between the two waveforms can be computed,

$$C(t) = \frac{\int_{-\infty}^{\infty} P_{\mathrm{cm}}(\omega) P_{\mathrm{ad}}^{*}(\omega) e^{-i\omega t} d\omega}{\sqrt{\int_{-\infty}^{\infty} |P_{\mathrm{cm}}(\omega)|^2 d\omega \int_{-\infty}^{\infty} |P_{\mathrm{ad}}(\omega)|^2 d\omega}}, \tag{15}$$

where $P_{\mathrm{cm}}(\omega)$ is the spectrum of the coupled mode waveform, $P_{\mathrm{ad}}(\omega)$ is the spectrum of the adiabatic waveform, and the asterisk denotes complex conjugation. The time at which the maximum of $C(t)$ occurs can be identified as the time shift between the waveforms. At the same time, the peak cross-correlation value provides a measure of the difference in shape between the two waveforms, giving a sense of the range of validity of this method of comparison.

IV. NUMERICAL SOLUTION OF THE COUPLED MODE EQUATIONS

For each measurement geometry considered, Fourier components of the pressure were computed at 33 frequencies between 70 kHz and 90 kHz. Time series were generated from these spectra using an inverse fast Fourier transform (IFFT) of size 1024 and a sampling rate of 640 kHz.[30] The resulting time series are plotted in Figs. 1–3 in the lower curve for each receiver depth. The temporal resolution thus obtained is comparable to the experimental resolution of $\pm 1/8$ of the carrier frequency cycle reported in Ref. 20. Because the spectral signature of the experimental source was unknown, a boxcar filter (smoothed with half Hanning windows of width 2 kHz at each end) from 70 kHz to 90 kHz was applied to the computed spectra before the IFFT.

The depth eigenvalue problem in Eq. (5) was solved in the complex plane with the ORCA normal mode model at 6501 range mesh points spaced every mm.[29] Since the receivers are located at one endpoint of this mesh, the coupled mode computation neglects backscatter from points downslope from the receivers.

To estimate the number of modes to retain in Eq. (4), range-dependent transmission loss (TL) from the source was computed for a receiver at a depth of 3 cm and a frequency of 70 kHz. Convergence of TL at every range within 0.5 dB was taken as a preliminary criterion for the number of modes to be used. For the 1° and 3° wedges, the modal expansion was truncated at twelve modes, and for the 6° wedge, 27 modes were retained.

Using the local depth eigenfunctions thus computed, the coupling coefficient integrals in Eqs. (9) and (10) were evaluated by extended Simpson's quadrature.[30] A depth mesh with 0.5 mm spacing was used to sample the mode functions, and the upper limit of the integral was taken to be the depth of the steel halfspace at the specified range. After the coupling coefficients and local eigenvalues were determined, the coupled mode amplitude integral equation in Eq. (7) was solved using a method developed by Udagawa and Kim that transforms this equation into an auxiliary equation that can be conveniently solved with the Lanczos method.[31] In this approach, an expansion with unknown coefficients of orthonormal vector-valued functions is used to solve for the vector

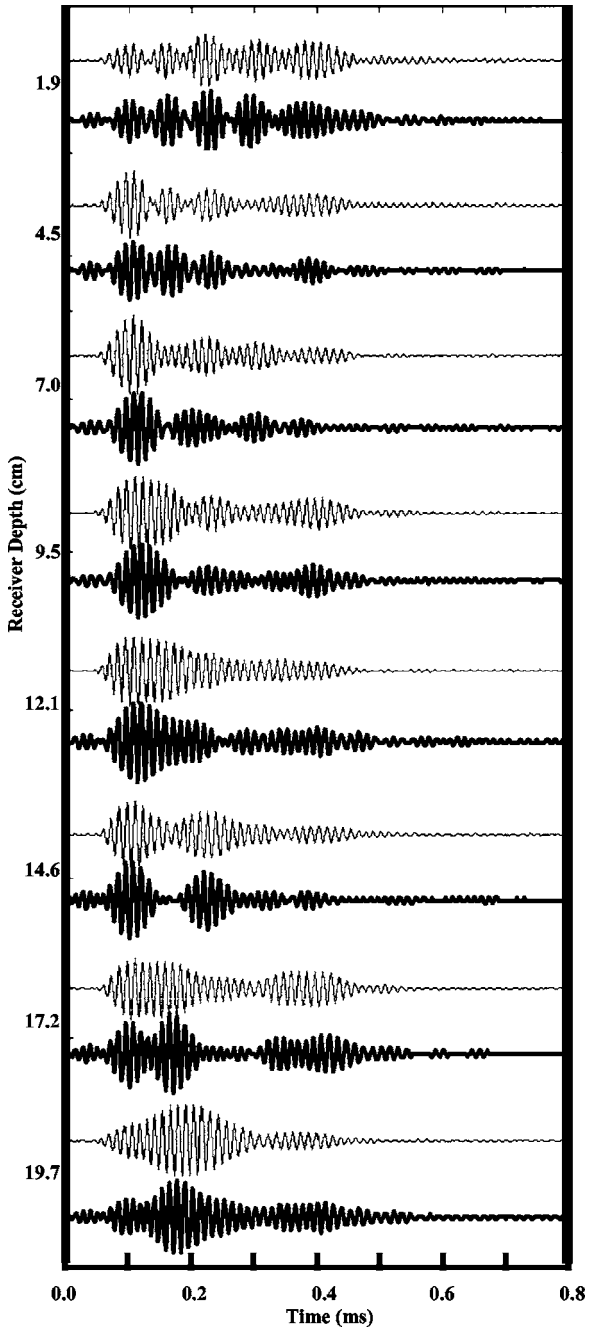

FIG. 1. Comparison of time series measured experimentally and simulated by a two-way coupled mode model for the 1° wedge. For each receiver depth there are two plots: the upper plot of each pair is a plot of the experimentally measured time series, while the lower plot of each pair is a plot of a simulated time series.

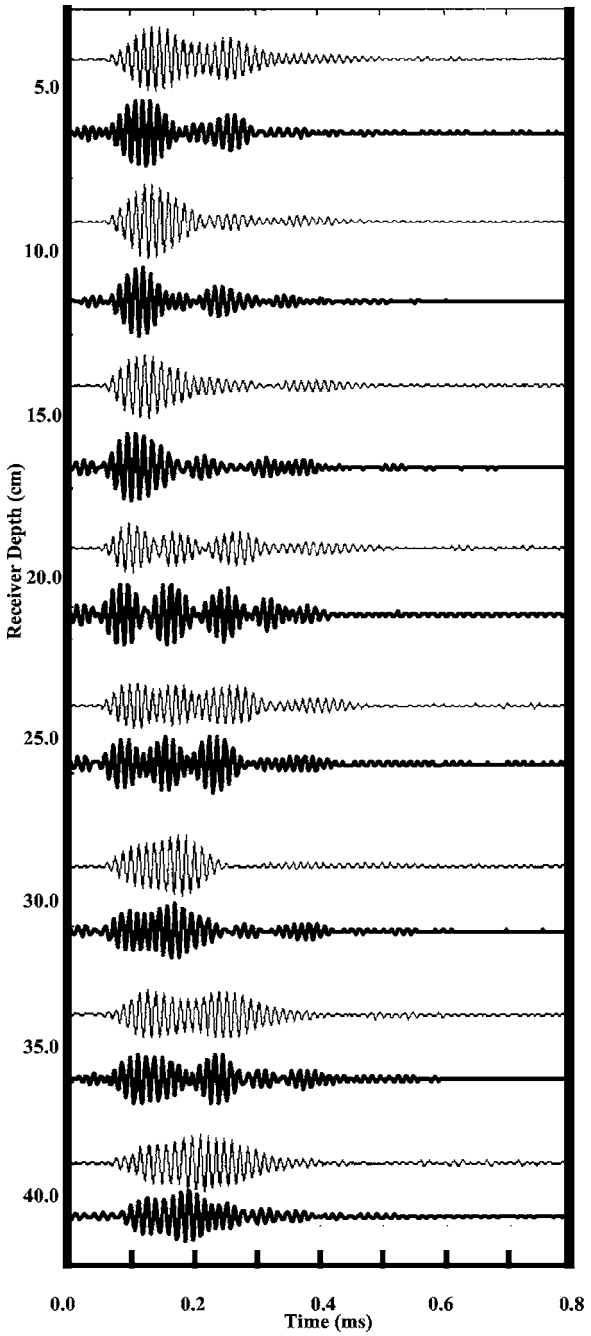

FIG. 2. Comparison of time series measured experimentally and simulated by a two-way coupled mode model for the 3° wedge.

of mode amplitude functions (see Knobles *et al.*[3] for details). The orthonormal vectors are determined by an iterative Gram-Schmidt algorithm.

The number of vectors required for convergence of this method increased with the angle of the wedge. For 1°, ten vectors were used; for 3°, 30 vectors were used, and for 6°, 100 vectors were used. For the six-degree computation, the coefficient of the final vector in the expansion had a magnitude at least 10^{-3} smaller than the magnitude of the initial coefficient. (The final coefficients for the one-degree and three-degree computations were several orders of magnitude smaller.) The rate of convergence of the six-degree computation was so slow for some frequencies that the results are possibly not as accurate as indicated by the relative magnitudes of the coefficients, but temporal constraints prevented a more thorough computation with this method.

The extent of the numerical error in the time lags predicted by the coupled mode computation was gauged by a comparison to results independently simulated by a broadband version of the PE RAM 1.5 algorithm.[32] For these computations, five Padé coefficients were used, and the range and depth mesh sizes were set to $2\lambda/3$ and $\lambda/60$, respectively, where λ is the acoustic wavelength for a given frequency. A pressure-release boundary was placed at a constant depth below the water-air interface such that it was 400 mm below

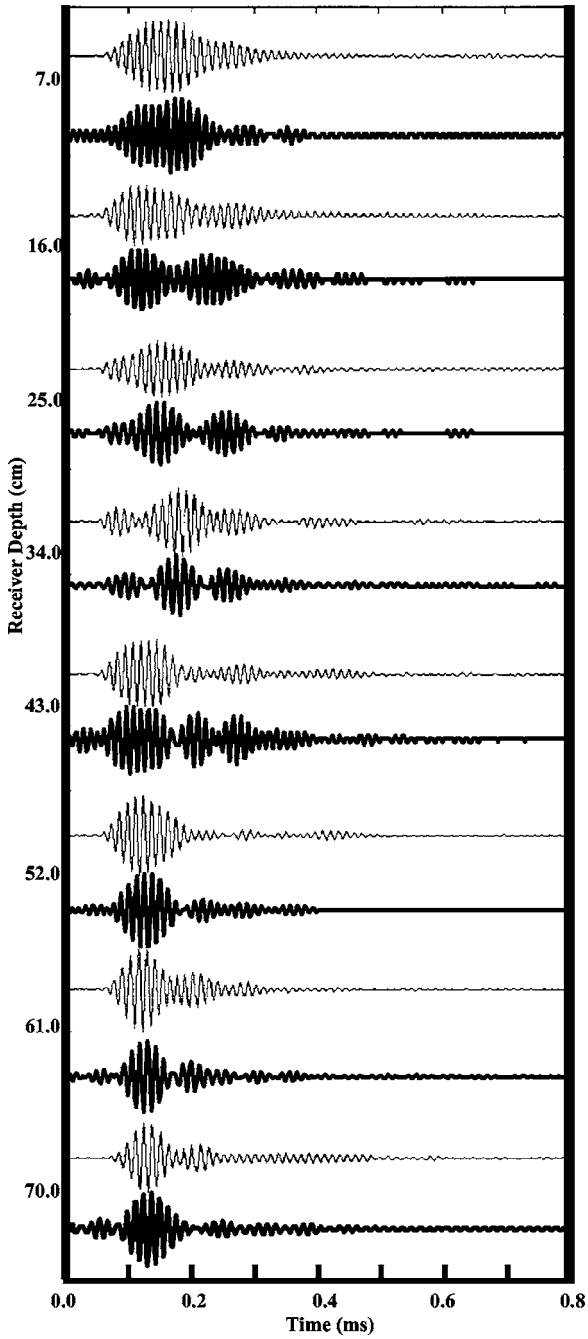

FIG. 3. Comparison of time series measured experimentally and simulated by a two-way coupled mode model for the 6° wedge.

the water-sediment interface at the receiver position. A small absorptive layer was placed above this surface to negate spurious reflections. The time series thus simulated were cross-correlated using Eq. (15) with the time series generated by the coupled mode approach. For all cases, the peak correlation values (all above 0.90) occurred at zero lag, so they agree with the time-delay results discussed in Sec. V.

The cross-correlation function between the coupled mode and adiabatic time series given in Eq. (15) was obtained by IFFT, and the time delays plotted in Figs. 4–6 were taken to be the time lags at which the peak values of the cross-correlation occurred. The peak cross-correlation values appear in Table II. The mode filtering results displayed in

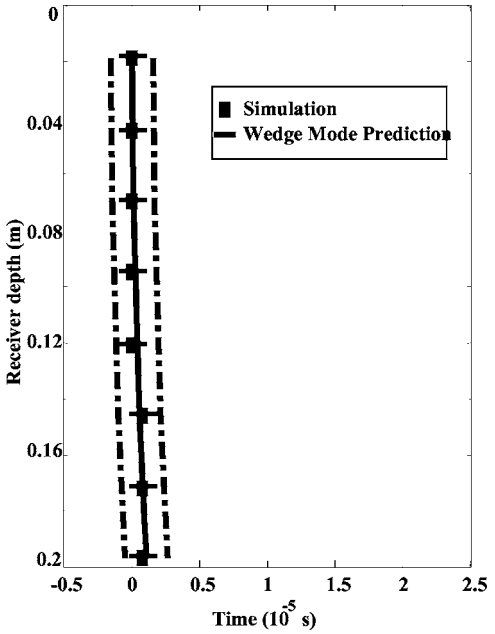

FIG. 4. Comparison of depth-dependent time delays measured from simulated time series with time delays predicted by assuming a circular-arc wave front for the 1° wedge. The error bars on the simulation results represent the FFT time resolution. The region bounded laterally by dotted-dashed lines around the circular-arc prediction represents the precision of the tank experiment of Tindle *et al.*

Figs. 7–9 were produced for modes 1–6 using Eq. (14). For each plot, $\mathbf{W}(t)$ was an 8×1024 matrix containing time series synchronized to account for a curved wave front (and time shifted to a convenient place in the time window), and $\mathbf{P}$ was a 6×8 matrix containing the values at the receiver positions of the mode profiles computed at 80 kHz. Two different synchronizations were applied before mode filtering. The lower curves for each mode number represent the results

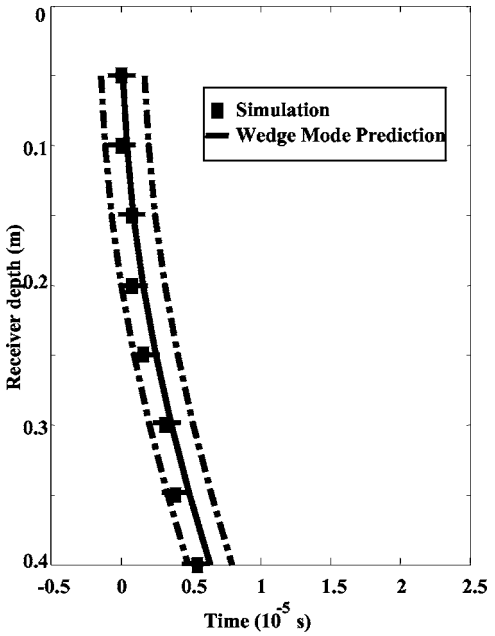

FIG. 5. Comparison of depth-dependent time delays measured from simulated time series with time delays predicted by assuming a circular-arc wave front for the 3° wedge.

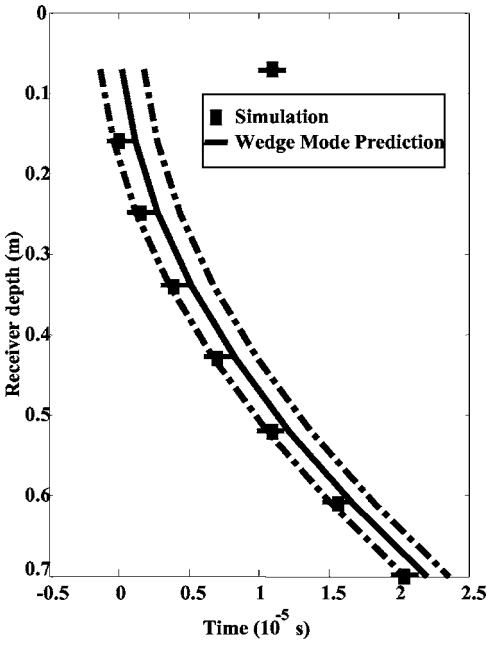

FIG. 6. Comparison of depth-dependent time delays measured from simulated time series with time delays predicted by assuming a circular-arc wave front for the 6° wedge.

after synchronizing according to the predictions of Eq. (13), and the upper curves represent the results after synchronizing according to the time delays computed by the cross-correlation of the adiabatic and coupled mode time series.

V. RESULTS AND DISCUSSION

A. Results

Simulated time series were computed in order to analyze experimental results for acoustic propagation down slopes of 1°, 3°, and 6°. Unfortunately, the measured time series exist only in the form of hard copy plots. A direct comparison between simulation and data has been attempted by juxtaposing the plots of the simulated time series with plots made by digitizing (scanning in) the hard copies, as shown in Figs. 1–3. At best, only qualitative statements can be made on the basis of this comparison. Inspection of these figures shows that while there are phase discrepancies in many of the plots, there is a fairly good agreement between the envelopes of the measured and the simulated results.

Figures 4–6 show the comparison between the time delays predicted for propagation by wedge modes in Eq. (13),

TABLE II. Peak correlation values for adiabatic-coupled mode comparison.

Recever No.	1°	3°	6°
1	0.9973	0.9765	0.9624
2	0.9990	0.9949	0.8829
3	0.9999	0.9703	0.9255
4	0.9987	0.9487	0.9022
5	0.9924	0.9970	0.8838
6	0.9775	0.9826	0.9807
7	0.9491	0.9466	0.9813
8	0.9362	0.9534	0.9825

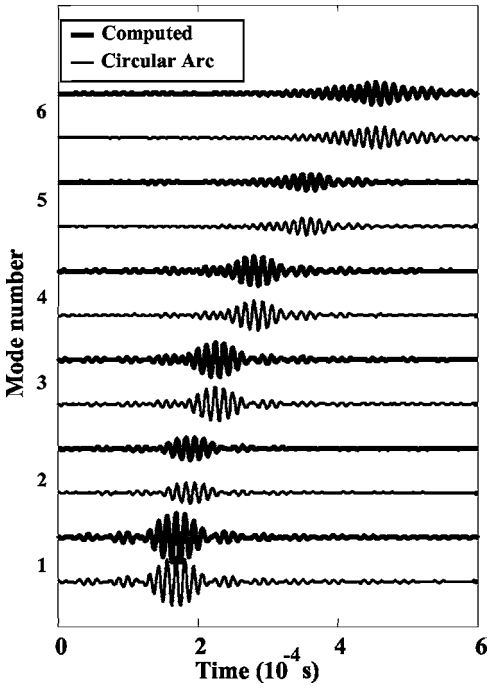

FIG. 7. Results of mode filtering for the 1° wedge. For each mode number, there are two plots: the lower plot represents mode filtering after synchronization assuming a circular-arc wave front; the upper plot represents mode filtering after synchronization using the time delays computed from the simulated time series.

using a water sound speed of $c=1490$ m/s and the time delays found by cross-correlating the adiabatic and coupled mode results using Eq. (15). The time lags reported in these figures were actually generated by finding the Fourier coefficients from time series linearly interpolated at twice the sampling rate. This was done to reduce artifacts as is discussed at the end of Sec. V B. The error bars on the compu-

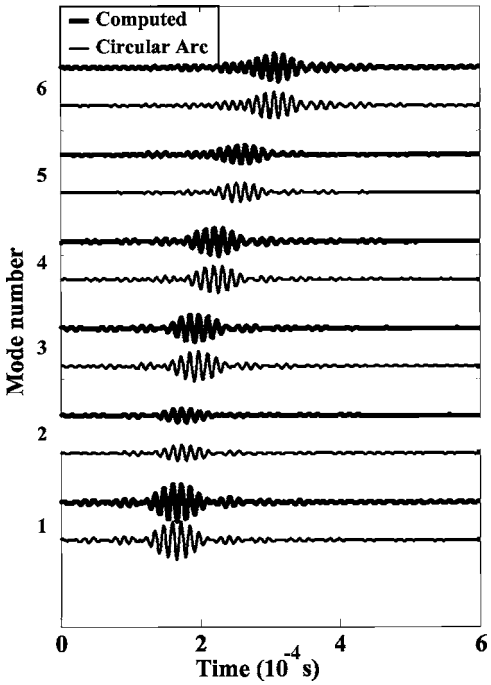

FIG. 8. Results of mode filtering for the 3° wedge.

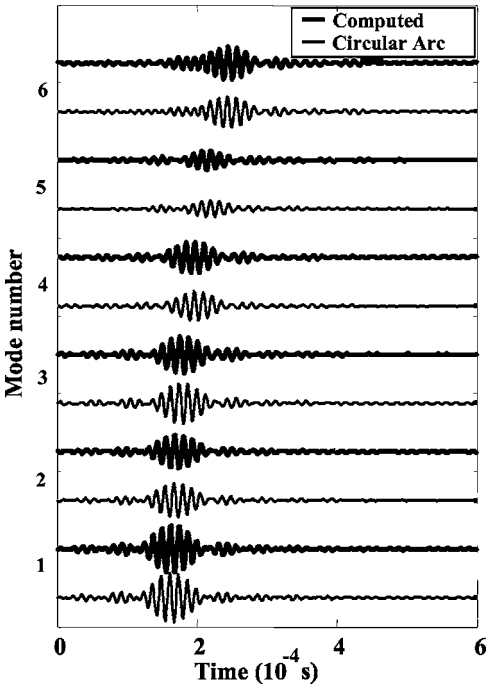

FIG. 9. Results of mode filtering for the 6° wedge.

tational results represent the time resolution of the IFFT. Note that in Figs. 4 and 5, the predicted time shift at the shallowest receivers lies within the IFFT time resolution, and that the computational results at those receivers reflect this time discretization.

The actual time shifts used in the synchronization of waveforms as discussed in Sec. III C were not reported explicitly. Thus a direct comparison of numerical and experimental results is not possible. However, it was reported that the time delays were consistent with propagation by modes with circular wave fronts.[21] Therefore, to convey the resolution [$\pm 1/8$ of a carrier frequency (80 kHz) cycle] at which the experiments confirmed the curved modal wave front prediction, a region bounded by dotted-dashed lines has also been plotted around the theoretical prediction in Figs. 4–6. The maximum values of the cross-correlation of the adiabatic and coupled mode waveforms are displayed in Table II.

The results of mode filtering the coupled-mode waveforms for the first six modes by means of Eq.(14) are displayed in Figs. 7–9. The lower curves for each mode number represent the results of mode filtering accomplished after first synchronizing the waveforms using the predictions of Eq. (13), with a sound speed value $c=1490$ m/s. The upper curves for each mode number represent the results of mode filtering after the curves have been synchronized using the time delays computed by cross-correlating the adiabatic and coupled mode waveforms (the delays plotted in Figs. 4–6).

B. Discussion

Overall, the computational results show good agreement with the experimental conclusion that sound propagates (to a very good approximation) in a wedge-shaped waveguide by means of modes with curved wave fronts, even in the presence of a penetrable bottom. This agreement is apparent in both the time delays determined by cross-correlating the coupled-mode with the adiabatic results plotted in Figs. 4–6 and in the single smooth pulses that appear in Figs. 7–9 resulting from filtering for modes with curved wave fronts.

Furthermore, at slopes of 1° and 3°, the exact waveforms are well approximated by simply time shifting the waveforms predicted by the adiabatic approximation to account for the curvature of the wave front. However, the numerical results do suggest that the approximation of penetrable wedge modes by time-shifted adiabatic modes begins to break down for 6° slopes.

The breakdown of this "wedge-corrected" adiabatic approximation would be expected to emerge more clearly as the degree of mode coupling in the waveguide increases. Such a progression is apparent in the results displayed in Figs. 4–6. Indeed, the 1° case is essentially a null result, given that the theoretical prediction lies mostly within the numerical resolution of zero time shift. The 3° case shows very good agreement with the theoretical prediction within the experimentally reported precision, and even good agreement with the bare theoretical prediction. However, the 6° case in Fig. 6 displays an unambiguous trend of computed time delays falling below the bare theoretical prediction (apart from the artifact at the shallowest receiver, which is discussed below). It is possible that this is partially the result of numerical error, but the fact that the PE generated time series were synchronized with the coupled-mode generated time series argues against this.

A more likely explanation is that the adiabatic approximation for the 6° slope has degraded enough to become an unreliable yardstick by which to measure time delays in the coupled mode results. In fact, Table II does show a general decline in the peak values of the adiabatic-coupled mode cross-correlations as the bottom slope angle (and thus degree of mode coupling) increases. In other words, while the predominant effect of mode coupling in a wedge is a depth-dependent time shift of the adiabatic time series, at higher slopes, distortion of the shape of these time series becomes important.

The final possibility is that this discrepancy is an effect of the penetrable bottom. Figure 9 shows that this effect is subtle enough to have escaped detection by the mode filtering in the experiment.[21] In that experiment, the waveforms filtered after synchronizing to correct for a circular wave front are smooth, single pulses. When the same synchronization is applied to the coupled mode waveforms, smooth, single pulses also result (the lower curves in Fig. 9). However, if the waveforms are synchronized according to the time delays estimated by cross-correlating the coupled mode to the adiabatic results, smooth, single pulses likewise result (the upper curves). Thus, mode filtering after synchronization is not sensitive to a small deviation from the circularity of the wave front. While there is a slight difference in arrival times of the modal pulses, depending on which synchronization is used, it is smaller than the uncertainty in the experimental results. Experiments and computations conducted with higher angle slopes would be valuable in determining whether the effects of the penetrable bottom cause a devia-

tion from the circular arc wavefront predicted in an ideal wedge, but are outside the scope of this paper.

We conclude this section with a discussion of an anomaly in the numerical results. The reason the result for the shallowest receiver on Fig. 6 greatly differs from its expected value is easily demonstrated. The time discrepancy with the theoretical value amounts to exactly one cycle of the 80 kHz carrier frequency. This is likely an artifact of the discretization. Visual comparison of the coupled-mode time series with the adiabatic time series at this receiver shows no lag. Also, the delay for the third receiver differs from its expected value by the same amount when time lags are computed using time series at the original sampling rate.

VI. CONCLUSION

Broadband coupled normal mode propagation simulations have been made for wedge-shaped environments with penetrable bottoms for varying angles of inclination. The results of these simulations were compared to the results of tank experiments by Tindle *et al.*, and were shown to agree for bottom slopes up to 6°, with the central observation that sound propagates down penetrable wedges by means of modes having curved wave fronts. This agreement was demonstrated using two methods: first, by the success of mode filtering the simulated time series after correcting for a curved wave front, and second, by measuring a depth-dependent time delay in the coupled mode results consistent with propagation with a curved wave front. We conclude that the experimentally observed propagation by modes with curved wave fronts is correctly described by the coupled normal mode formalism.

Furthermore, we find that for slopes of 1° and 3°, the coupled mode results are well approximated by results of the adiabatic approximation that have been corrected by applying to them a depth-dependent time shift in accordance with a curved wave front. For a 6° slope, this is still a good, but somewhat degraded, approximation. The primary effect of mode coupling for these relatively small slopes is thus the introduction of a time shift.

The results for the 6° slope suggest that, in the presence of a penetrable bottom, the curved modal wave fronts may deviate slightly from the circular arc characteristic of propagation in an ideal wedge, but this would have been undetectable by the experiment of Tindle *et al.*

ACKNOWLEDGMENTS

The authors would like to thank Professor Chris Tindle, Physics Department, University of Auckland, New Zealand, for providing originals of the tank experiment data, and Donna Bustamantes for her work in editing this paper. A portion of this work was supported by the Office of Naval Research.

[1]G. S. Royal, "Shallow water time series simulation using normal mode theory in range-dependent environments," Master's thesis, University of Texas at Austin (1995).
[2]J. A. Fawcett, "A derivation of the differential equations of coupled-mode propagation," J. Acoust. Soc. Am. **92**, 290–295 (1992).
[3]D. P. Knobles, S. A. Stotts, R. A. Koch, and T. Udagawa, "Integral equation coupled mode approach applied to internal wave problems," J. Comput. Acoust. **9**, 149–167 (2001).
[4]S. A. Stotts, "Coupled-mode solutions in generalized ocean environments," J. Acoust. Soc. Am. **111**, 1623–1643 (2002).
[5]D. P. Knobles, S. A. Stotts, and R. A. Koch, "Low frequency coupled mode sound propagation over a continental shelf," J. Acoust. Soc. Am. **113**, 781–787 (2003).
[6]B. L. N. Kennett, "Guided wave propagation in laterally varying media. I. Theoretical development," Geophys. J. R. Astron. Soc. **79**, 235–255 (1984).
[7]K. G. Budden, "The critical coupling of modes in a tapered earth-ionosphere waveguide," Math. Proc. Cambridge Philos. Soc. **77**, 567–580 (1975).
[8]J. R. Wait, "Coupled mode analysis for a nonuniform tropospheric wave guide," Radio Sci. **15**, 667–673 (1980).
[9]H. Überall, A. Nagl, and J. B. Seaborn, "Coupled-mode propagation in the ionosphere day-night transition region," Radio Sci. **17**, 870–878 (1982).
[10]M. J. Buckingham, "Acoustic propagation in a wedge-shaped ocean," *Acoustics and the Sea-Bed*, edited by N. G. Pace (Bath University Press, Bath, UK, 1983), pp. 251–259.
[11]M. J. Buckingham, "Acoustic propagation in a wedge-shaped ocean with perfectly reflecting boundaries," NRL Report No. 8793 (1984).
[12]J. M. Arnold and L. B. Felsen, "Intrinsic modes in a nonseparable ocean waveguide," J. Acoust. Soc. Am. **76**, 850–860 (1984).
[13]E. K. Westwood, "Ray model solutions to the benchmark wedge problems," J. Acoust. Soc. Am. **87**, 1539–1545 (1990).
[14]R. D. Graves, A. Nagl, H. Überall, and G. L. Zarur, "Range-dependent normal modes in underwater sound propagation: Application to the wedge-shaped ocean," J. Acoust. Soc. Am. **58**, 1171–1177 (1975).
[15]F. B. Jensen and W. A. Kuperman, "Sound propagation in a wedge shaped ocean with a penetrable bottom," J. Acoust. Soc. Am. **67**, 1564–1566 (1980).
[16]F. B. Jensen and C. M. Ferla, "Numerical solutions of range-dependent benchmark problems in ocean acoustics," J. Acoust. Soc. Am. **87**, 1499–1513 (1990).
[17]F. B. Jensen and C. T. Tindle, "Numerical modeling results for mode propagation in a wedge," J. Acoust. Soc. Am. **82**, 211–216 (1987).
[18]Y. Desaubies and K. Dysthe, "Normal-mode propagation in slowly varying ocean waveguides," J. Acoust. Soc. Am. **97**, 933–946 (1995).
[19]H. Primack and K. E. Gilbert, "A two-dimensional downslope propagation model based on coupled wedge modes," J. Acoust. Soc. Am. **90**, 3254–3263 (1991).
[20]C. T. Tindle, H. Hobaek, and T. G. Muir, "Downslope propagation of normal modes in a shallow water wedge," J. Acoust. Soc. Am. **81**, 275–286 (1987).
[21]C. T. Tindle, H. Hobaek, and T. G. Muir, "Normal mode filtering for downslope propagation in a shallow water wedge," J. Acoust. Soc. Am. **81**, 287–294 (1987).
[22]L. B. Felsen and L. Sevgi, "Adiabatic and intrinsic modes for wave propagation in guiding environments with longitudinal and transverse variation: formulation and canonical test," IEEE Trans. Antennas Propag. **39**, 1130–1136 (1991).
[23]A. Baghdadi and A. Safaai-Jazi, "Propagation properties of a dielectric wedge waveguide bounded by conducting planes," Microwave Opt. Technol. Lett. **22**, 160–164 (1999).
[24]E. A. Romanova, L. A. Melnikov, and E. V. Bekker, "Scattering of the total field from the slow-tapered and step like discontinuities of dielectric waveguides," Microwave Opt. Technol. Lett. **25**, 27 (2000).
[25]G. V. Frisk, *Ocean and Seabed Acoustics: A Theory of Wave Propagation* (P T R Prentice-Hall, Englewood Cliffs, New Jersey, 1994).
[26]E. K. Westwood and C. T. Tindle, "Shallow water time-series simulation using ray theory," J. Acoust. Soc. Am. **81**, 1752–1761 (1987).
[27]W. M. Ewing, W. S. Jardetzky, and F. Press, *Elastic Waves in Layered Media* (McGraw-Hill, New York, 1957), pp. 126–151.
[28]E. K. Westwood and R. A. Koch, "Elimination of branch cuts from the normal mode solution using gradient halfspaces," J. Acoust. Soc. Am. **106**, 2513–2523 (1999).

[29]E. K. Westwood, C. T. Tindle, and N. R. Chapman, "A normal mode model for acoustic-elastic ocean environments," J. Acoust. Soc. Am. **100**, 3631–3645 (1996).
[30]W. H. Press, S. A. Teukolsky, W. T. Vetterling, and B. P. Flannery, *Numerical Recipes in C: The Art of Scientific Computing* (Cambridge University Press, Cambridge, 1992).
[31]T. Udagawa and B. T. Kim, "Random phase approximation calculations of nuclear response in the continuum," Phys. Rev. C **40**, 2271 (1989).
[32]M. D. Collins, "A split step Padé solution for the parabolic equation method," J. Acoust. Soc. Am. **93**, 1736 (1993).

A reflected energy prediction model for long-range hydroacoustic reflection in the oceans[a)]

Zachary M. Upton,[b)] Jay J. Pulli, Brian Myhre, and David Blau
BBN Technologies, Arlington, Virginia 22209

(Received 16 May 2005; revised 21 October 2005; accepted 2 November 2005)

Acoustic energy from underwater earthquakes and explosions can propagate over long distances with very little attenuation in the deep ocean. When this sound encounters a seamount, island, or continental margin, it can scatter and again propagate over long distances. Hydrophones in the deep sound channel can detect these reflections tens of minutes or hours after arrivals from the direct source-to-receiver path. This paper presents the Reflected Energy Prediction (REP) model, a model for predicting these reflected arrivals. For a given source and receiver, the REP model uses a detailed knowledge of the underwater environment and components of the Hydroacoustic Coverage Assessment Model, HydroCAM, to predict the impulse response of the ocean. When this impulse response is convolved with a source function, a waveform envelope prediction is made that can be compared with recorded data. In this paper we present the model and a few applications of the model using data recorded from earthquakes and explosions in the Atlantic and Indian Oceans. These examples illustrate the use of the model and initial steps toward model calibration. © *2006 Acoustical Society of America.* [DOI: 10.1121/1.2141234]

PACS number(s): 43.30.Gv, 43.30.Zk, 43.30.Qd [RAS] Pages: 153–160

I. INTRODUCTION

Hydroacoustic arrivals from large amplitude events such as explosions and earthquakes have been studied since shortly after World War II. Early research also showed that when sound traveling underwater encountered a change in impedance like a seamount, island, or continental shelf, some of the energy could be scattered or reflected. In the late 1960s and early 1970s, researchers such as Kibblewhite and Denham (1969) and Northrop (1968) began studying these reflected acoustic arrivals and identifying the bathymetric reflectors that caused them. In both cases, the authors analyze acoustic arrival times in terms of the travel time from the source to a reflector and on to a receiver in order to identify potential bathymetric reflectors. Kibblewhite and Denham also confirmed reflectors by estimating the acoustic arrival azimuth using the time delay between two spaced hydrophones.

In most of these early studies, the researchers were limited in their analyses by analog recordings that were played back through filter banks and output onto paper for analysis. They were also limited by computing capability for long-range propagation studies. Modern studies have benefited from high-quality sensor systems, digital data, global environmental data (Teague *et al.*, 1990) and long-range propagation modeling software.

Recent studies of long-range hydroacoustic reflections by Pulli *et al.* (1999, 2000); Hanson *et al.* (2001, 2002), Harben and Boro (2001), and Upton and Pulli (2002) have been focused on identifying bathymetric reflectors via data analysis and modeling. These efforts have sought to apply an understanding of these reflections to issues like detection and localization that pertain to global monitoring for underwater nuclear explosions. For the purpose of this model, long-range hydroacoustic propagation is defined as acoustic propagation in deep water, where sound is continuously refracted in the deep water sound channel called the sound fixing and ranging or SOFAR channel (Urick, 1983).

Figure 1 shows an example of the horizontal propagation and reflection that are of particular interest in this study. At the source location, a high-energy event occurs. Acoustic energy from this event is trapped in the so-called Sound Fixing and Ranging (SOFAR) channel and propagates over a long distance. When the energy encounters a seamount, island, or continental shelf that intersects the SOFAR channel, the acoustic energy is scattered back into the channel, changing direction. The reflected energy, albeit attenuated, can then travel additional distances before being received at a hydrophone. In some cases, acoustic energy arrives at the receiver from both the most direct acoustic path and from reflected paths. The reflected arrivals can occur tens of minutes or even hours after the direct arrival.

The monitoring and verification regime for the Comprehensive Nuclear Test Ban Treaty is an immediate application for the understanding of these hydroacoustic reflections. This treaty will require a global monitoring system to ensure treaty compliance. The monitoring system, known as the International Monitoring System (IMS), will include seismic sensors, hydroacoustic sensors in the oceans, infrasound sensors, and radionuclide sensors (United Nations, 1996,

[a)]Portions of this work were presented in "Modeling long-range hydroacoustic reflections in the Atlantic and Pacific Oceans," *Proceedings of the 22nd Seismic Research Symposium*, New Orleans, LA, September 2000, "Localization of sub-sea earthquakes using hydroacoustic reflections and matched-field processing," *24th Seismic Research Review*, *Ponte Vedra Beach*, FL, September 2002, and "Hydroacoustic reflections in the Indian Ocean: Comparison of model predictions and recorded data," *6th International Hydroacoustics Workshop*, Victoria, British Columbia, Canada, May 2005.

[b)]Electronic mail: zupton@bbn.com

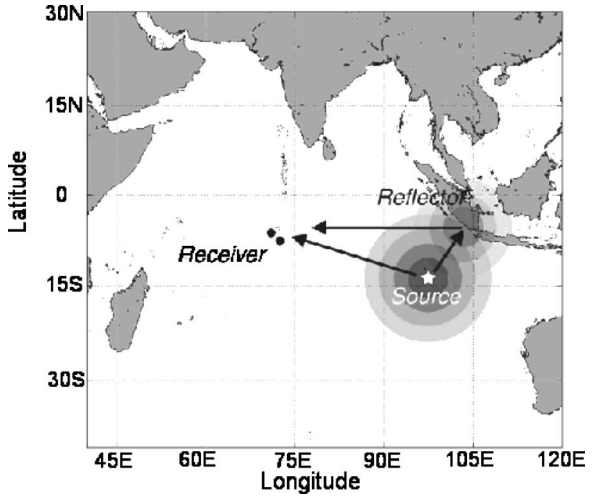

FIG. 1. A geographic example of long-range hydroacoustic reflection. In this example, energy radiating from the source travels in all directions. Some of this energy will travel to the source over the most direct hydroacoustic path. In addition, some of this energy can interact with bathymetry-like islands and continental shelves and scatter toward the receiver, arriving after the direct arrival.

Lawrence *et al.*, 2001). There will be only 11 stations in the hydroacoustic network responsible for monitoring approximately 70% of the Earth's surface.

An understanding of hydroacoustic reflections could aid in the coverage, arrival identification, and event localization ability of the IMS. Hydroacoustic stations record a wealth of signals including earthquakes, marine mammal vocalizations, ice-sheet movements, airguns, and shipping noise (Tolstoy and Bohnenstiehl, 2002). The monitoring system is tasked with sorting out all of these arrivals and detecting explosions. In addition, if the monitoring system could use reflected arrivals in conjunction with or independent of direct arrivals to locate the source of nuclear test explosions, it is possible that the system coverage could be expanded without adding additional expensive hydroacoustic stations. In some cases, the direct source–receiver path may be blocked by bathymetry and reflected arrivals may be the only observable signals.

The first hydroacoustic station in the IMS came online at Diego Garcia in the Indian Ocean in the summer of 2000. Since then, several other stations have been installed. These stations are an excellent source of hydroacoustic data and provide scientists an opportunity to develop and test signal-processing algorithms that will be necessary for the IMS. Central to this understanding is the development of a model that will predict where hydroacoustic reflections will occur, as well as the reflection travel times for a given source–receiver pair.

In this paper we will describe the Reflected Energy Prediction (REP) model and demonstrate its use in a few case studies. In Sec. II we will explain how the Reflected Energy Prediction (REP) model calculates the impulse response of an ocean for a given source and receiver and the method for using this impulse response to create synthetic waveform envelopes of the received signal. In Sec. III, predicted waveform envelopes for earthquake and explosion events in the Atlantic and Indian Oceans are used to demonstrate the model. Finally, potential applications, conclusions, and future study are discussed.

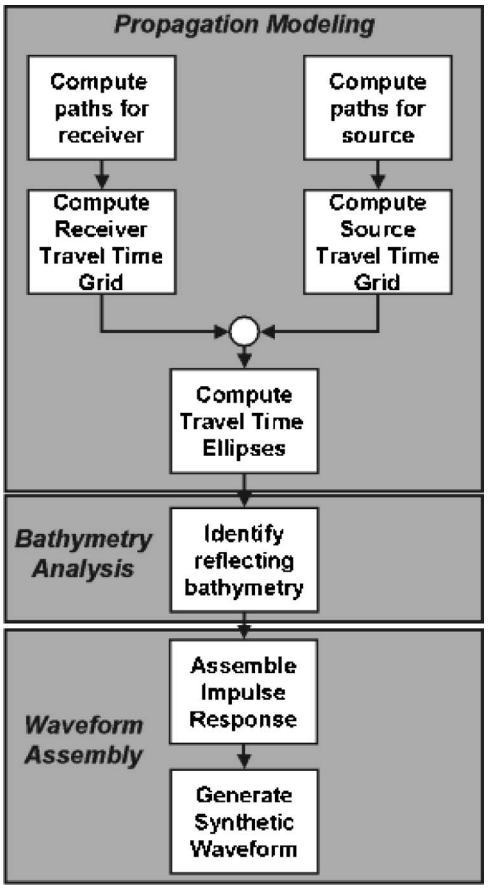

FIG. 2. Flow chart showing the top-level organization of the Reflected Energy Prediction (REP) model.

II. PREDICTING THE IMPULSE RESPONSE OF AN OCEAN BASIN

As stated in the Introduction, the goal of this model is to predict acoustic arrivals from reflected energy after the arrival from the direct source-to-receiver path. To this end, an effective comparison is one between predicted arrival times and recorded arrival times. The REP model is logically divided into three sections that lead to the prediction of a synthetic waveform envelope representing the direct arrival and arrivals from bathymetric reflections in the ocean basin. Figure 2 is a flow chart outlining the top-level flow of the model, from propagation modeling, through bathymetric analysis, to the assembly of the waveform envelope prediction. This introduction to the model is a short overview and the details of the model will be discussed in the following sections.

For both the source and receiver, acoustic ray path predictions are made to determine the travel time along propagation paths throughout the ocean. These rays are then interpolated onto uniform grids in latitude and longitude. Combining the source-and-receiver travel time grids, the bistatic path travel times from source to each grid point to

receiver can be predicted. When these calculations are sorted in increasing time, they describe equal time of arrival ellipses in geographic coordinates.

For each travel time ellipse, the bathymetry along that ellipse is analyzed to identify bathymetric features that might reflect energy propagating in the SOFAR channel. These "bathymetric reflectors," sorted in time, are weighted for reflection strength and propagation losses, and an impulse response of the ocean is formed. Finally, the impulse response is convolved with a model source function to create a synthetic waveform envelope that represents the REP model prediction of the arrivals at the receiver due to the source and the reflections from the ocean basin.

In this reflection model, it is assumed that, in order to reflect enough energy toward the source that a reflection can be detected, that reflection must be specular in nature and from a relatively large bathymetric surface area. The limiting bathymetric characteristics (i.e., minimum surface area) have not been determined.

A. Propagation modeling

During the planning phase of the hydrophone installation in the late 1990s, it became necessary to produce a model to predict long-range propagation in the ocean, accounting for the ellipsoidal earth, horizontal refraction, and the potential detection and localization capability of the planned network. HydroCAM, the Hydroacoustic Coverage Assessment Model, combines ocean environment databases, parametric databases, and hydroacoustic modeling capability to allow researchers to analyze long-range propagation and to predict the detection and possible localization performance of global hydroacoustic monitoring networks (Upton *et al.*, 2005b). Two of HydroCAM's components, the GlobeRay horizontal ray path prediction model, and the PathtoGrid interpolation algorithm, are used as the first steps to predicting the impulse response of the ocean for a single source and receiver.

Long-range acoustic propagation is significantly different from short-range propagation normally modeled for applications such as antisubmarine warfare (ASW) (Upton *et al.*, 2005b). Energy from these large-amplitude signals is trapped in the SOFAR channel and continuously refracted, without significant interaction with the ocean surface and bottom, and can propagate over thousands of kilometers with minimal attenuation. However, as this sound propagates, geographic changes in bathymetry and sound speed cause horizontal refraction that is not present in short-range models. Also, when modeling propagation over thousands of kilometers, the nonspherical nature of the Earth must be taken into account in order to accurately compute the travel time.

The GlobeRay model is based on the Global-Scale Ocean Acoustic Raytrace (GSOAR) model developed by the United States Naval Research Lab (NRL). The model uses a variety of local and global-scale environment databases to predict horizontal acoustic paths in the ocean. The model leverages the work of Heaney *et al.* (1991) and an interpolation/extrapolation technique (Upton *et al.*, 2005b) to predict the discretized propagation path. A detailed description of the GlobeRay model is beyond the scope of this paper, however, the method that GlobeRay uses for calculating the travel time is poignant to this discussion. Once the path is computed, the model integrates over the acoustic group speed along that path to determine the travel time along the path at each path step,

$$t = \int \frac{1}{u_n(s)} ds$$

where $u_s(s)$ is the group speed obtained by bilinear interpolation of the best resolution group speed database available at different locations. (Upton *et al.* 2005b) A detailed discussion of the GlobeRay model is given in (Upton *et al.* 2005b).

The Path-to-Grid algorithm was designed to take the calculated ray fans and interpolate them into rectangular grids. Rectangular grids allow analysts to examine the path characteristics in terms of a uniform grid in latitude and longitude.

1. Travel time ellipse creation

Using the travel time grids for the source and receiver location computed by HydroCAM, the travel time from the source to each potential reflector and from the receiver to each potential reflector is known. The travel time ellipse algorithm sorts these travel time calculations using bistatic ray path characteristics.

For a given source receiver pair, if an acoustically opaque object does not block the path, there will be a direct acoustic path over which sound will travel from the source and arrive at the receiver. Sound from this source can also travel in other directions, reflect off of bodies with different impedances than the water, and be scattered back toward the receiver. The reflected sound will arrive later in time than the direct arrival. Without any knowledge of the azimuth of the reflected arrival, ellipse theory can be employed to demonstrate the possible reflectors at a given reflection time.

In this application, the source and receiver travel time grids are combined by adding them to calculate the travel times along the path from the source, to the potential reflector, and then to receiver. The outputs of this algorithm are locations in latitude and longitude, sorted by reflected arrival time, in a series of equal time of arrival ellipses.

The bathymetric analysis algorithm uses these ellipses to begin at the direct arrival time and move out in increasing time, looking for potential reflectors. Figure 3 illustrates two travel time ellipses, separated by 10 min, and how they might look in relation to the source and receiver.

B. Bathymetric analysis

For each travel time ellipse, the bathymetric feature finder takes each geographic point on the travel time ellipse and analyzes the slope of the bathymetry in the direction of increasing time. The model assumes that bathymetric features of greater slope would present a larger surface area to the incident plane wave and thereby reflect more energy. Therefore, a threshold is set and only slopes greater than an empirically determined maximum are designated potential reflectors.

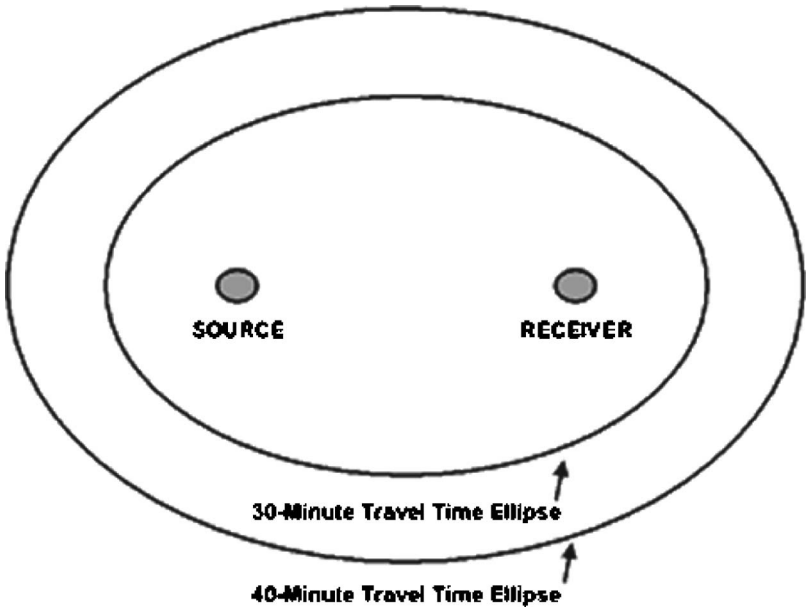

FIG. 3. Diagram illustrating a source, a receiver, and two equal-time-of-arrival ellipses. As time increases, the ellipses get larger, maintaining the source and receiver as the foci of the ellipse.

The determination of slope, although simple in concept, was actually rather difficult to implement because of the relatively low (i.e., 2 min) resolution of available bathymetry for an entire ocean. Instead of slope, the measure of total relief is used (the difference between maximum and minimum depths) as an approximation of slope. This slope is taken at an angle that would create a specular reflection in the direction between source and receiver (Pulli *et al.*, 2000).

Since the majority of the acoustic energy that will propagate over thousands of kilometers is trapped in the SOFAR channel, bathymetric features that do not intersect the SOFAR channel can be eliminated as potential reflectors. Further, reflectors that only partially intersect the SOFAR channel will not scatter as strongly as those that completely break the SOFAR channel.

The boundaries of the SOFAR channel are not well defined in environmental databases. However, the point of minimum sound speed in the channel, or the sound channel axis (SCA), is easily calculated using sound velocity profile data. SCA depths were calculated using HydroCAM and the "Database Description for the Master Generalized Digital Environment Model (GDEM), Version 5.0." SCA data are generally not available at the same resolution as bathymetry data, so a 2-D interpolation must be made before the two databases can be compared (Pulli *et al.*, 2000). The depth of the reflector with respect to the depth of the SCA is used to estimate scattering strength. The mathematical model used to describe this relationship is explained in the following section.

C. Waveform envelope assembly

Once all features for all of the travel time ellipses have been calculated, the impulse response model of the ocean can be created. To create the impulse response, the reflector's contribution to the response must be weighted according to their depth with respect to the sound channel axis depth. The weighting function used in this model is shown in Fig. 4 (Pulli *et al.*, 2000). Features that are well below the SOFAR channel will not reflect hydroacoustic energy, whereas features near or above the SOFAR channel will reflect energy. Once the SOFAR channel is completely blocked, additional elevation does not contribute to the vertical component of the scattering area. Here, we model the relative reflector strength with an arctangent function:

$$f(x) = \frac{1}{2}\left(\frac{\arctan\left(\frac{x}{100}\right)}{\max[\arctan(x)]} + 1\right),$$

where x is an array containing the difference between each bathymetric reflector depth and the respective SCA depth. The arctangent function was chosen over a linear profile to account for the difference between single SCA depths and the range of SOFAR channel depths.

Following the SOFAR channel weighting, each of the impulses that represent the bathymetric features is scaled for propagation losses and attenuation along the propagation path. The output is the impulse response model of the ocean basin for the source–receiver pair in question.

To create a synthetic waveform envelope using this impulse response, the impulse response is convolved with a

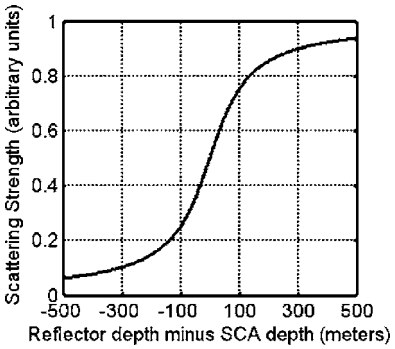

FIG. 4. Model for the scattering strength of a bathymetric feature versus its depth with respect to the SCA. The reflector scattering strength is modeled as an arctangent of the difference of the reflector depth and the sound channel axis depth.

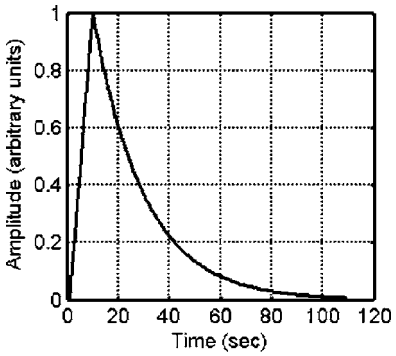

FIG. 5. Source function used to create a synthetic waveform envelope output of the REP model.

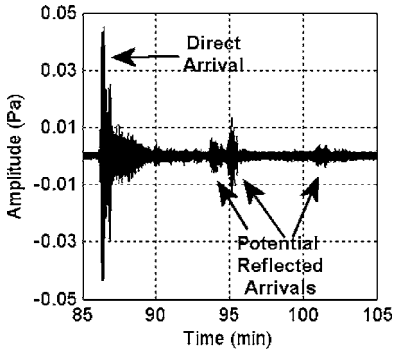

FIG. 7. Hydroacoustic recording of the Chase 21 explosion at Ascension Island. The waveform shown is the full bandwidth (0–100 Hz) of the recording.

source function. A sample source function, derived by examining explosion envelopes, is shown in Fig. 5. Only the first, and highest, energy peak of the explosion is used in the model.

III. MODEL DEMONSTRATION

To demonstrate the REP model, model results are compared visually to recorded waveform envelopes. In addition, for events recorded on the three-element receiver stations of the IMS, the bearing and time of reflected arrivals can be compared with the locations of the reflecting bathymetry identified by the model. Two examples are presented here. The first is an explosion in the Atlantic recorded on Missile Impact Location Study (MILS) hydrophones. The second is a subsea earthquake in the Indian Ocean recorded on the IMS station at Diego Garcia.

A. Atlantic Ocean explosion example

The first example of the model's application is for the Chase 21 explosion recorded at Ascension Island. This event, which occurred on June 25, 1970, was a ship-scuttling explosion on the continental shelf off the coast of New Jersey at a depth of 540 ft. The explosive charge was 614.5 tons. Although the explosion occurred above the SOFAR channel depth, energy was trapped in the channel and excellent recordings were obtained at the Ascension hydrophone array. Figure 6 is a map of the location of the Chase 21 explosion and the Ascension hydrophone array.

The recording made at Ascension station FS27 is shown in Fig. 7. A prominent feature of this signal is the presumed set of reflected arrivals that are seen at travel times between 94 and 97 min. Previous studies of this arrival, based on travel time and back azimuth calculations, indicate that the Guiana Plateau, a bathymetric feature off the northeast coast of South America, is the source of this reflected energy (Pulli *et al.*, 2000). A smaller potential reflection arrives at a travel time of approximately 102 min.

The REP model was run for a travel time window between 85 and 115 min, which should include reflected arrivals corresponding to the available data. The algorithm identified 309 possible bathymetric features, shown in the map in Fig. 8. A histogram of the feature depths is shown in the top half of Fig. 9. Most features are located at depths of between 2000 and 4000 m. A histogram of the SOFAR channel axis depth in the equatorial Atlantic (40°S to 40°N latitude) is shown in the bottom half of Fig. 9. It can be seen that the SOFAR channel axis occurs mostly at depths of between 500 and 1200 m. Hence, only a few of the identified bathymetric features will reflect hydroacoustic energy from the SOFAR channel. Eliminating all of the features that fall 500 m below the SOFAR channel axis leaves 31 of the original 309 potential reflectors. These reflectors are shown on a map in Fig. 10.

The top half of Fig. 11 shows the impulse response model derived from the bathymetry analysis. The amplitude corresponding to each scatterer has been scaled with the function shown in Fig. 4 as well as with geometrical spread-

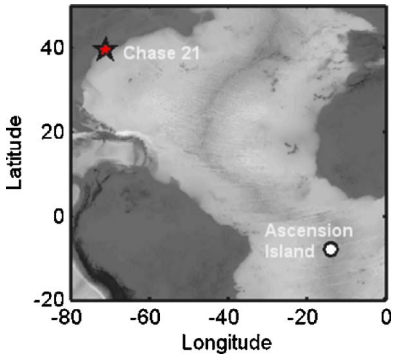

FIG. 6. Location of the Chase 21 explosion (star) and the Ascension Island hydrophone array (round dot).

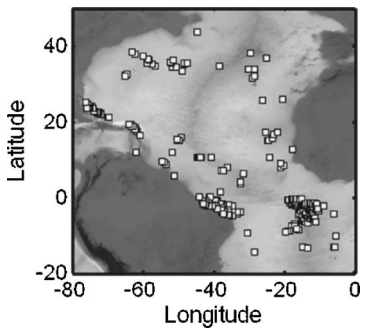

FIG. 8. Bathymetric features identified by the REP model as possible reflectors in the equatorial Atlantic Ocean for the case of Chase 21 to Ascension Island.

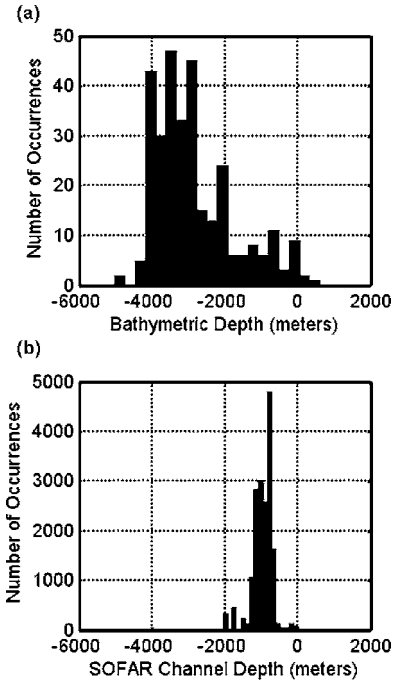

FIG. 9. The top graph (a) shows a histogram of bathymetric feature depths in the equatorial Atlantic for the Chase 21 to Ascension case (Sandwell and Smith, 1977). The bottom graph (b) shows a histogram of SOFAR channel axis depths in the equatorial Atlantic (GDEM, 1995).

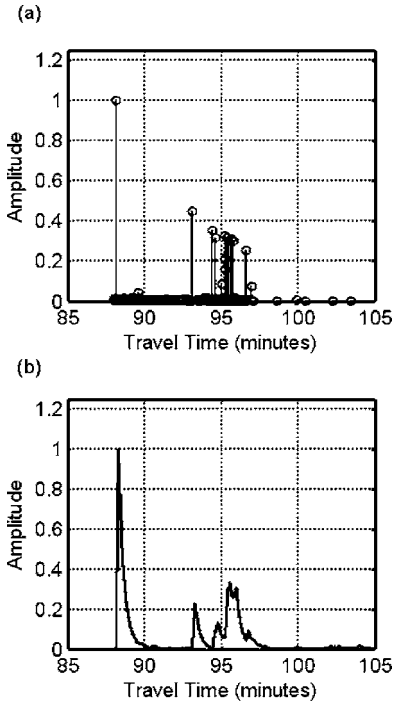

FIG. 11. The top graph (a) shows the REP impulse response model of the equatorial Atlantic for the case of Chase 21 to Ascension Island. The bottom graph (b) shows the result of convolving that impulse response with the source function shown in Fig. 5.

ing and attenuation. After the direct arrival at 88 min, there is a sequence of six large impulses that are much higher in amplitude than the data. At 95 min there is a cluster of arrivals that correspond to scatterers at the Guiana Plateau (Angell *et al.*, 1998; Pulli *et al.*, 1999). This site has been identified, using a combination of bearing and travel time analysis, as the source of the reflected arrival at Ascension. At 100 min there is an additional arrival; however, the data in Fig. 7 show an arrival two minutes later. The bottom half of Fig. 11 shows the final output of the model. The impulse response has been convolved with a source envelope model. Note the cluster of arrivals at 95–96 min that matches those seen in the data shown in Fig. 7. This similarity between modeled and actual data contributes to the validation of the REP model.

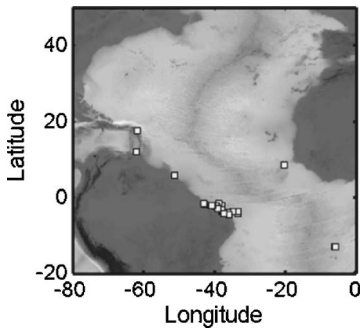

FIG. 10. The remaining bathymetric features, identified by the REP model, after a comparison between reflector depth and SOFAR channel axis depth is used to remove deep features that would not reflect acoustic energy traveling in the SOFAR channel.

B. Indian Ocean earthquake example

This second application of the model demonstrates its results using signals recorded on the IMS hydrophones for which it was designed. These results are primarily presented to demonstrate the model using both travel time matching and comparing the identified bathymetric reflectors with the acoustic arrival azimuths. These azimuths are calculated using intersensor cross-correlation to measure time delays over the three elements of the array.

The event in this example is an earthquake along one of the mid-ocean ridges in the Indian Ocean called the Carlsberg Ridge. The event had a calculated seismic magnitude of 4.8, and was located to the northwest of the Diego Garcia IMS hydrophone station. A map of this event is shown in the top half of Fig. 12. The bottom half of the figure shows the bathymetric features that were identified as reflectors by the REP model. Figure 13 shows a comparison of the recorded waveform envelope at the north hydrophones at Diego Garcia and the REP model prediction. The shaded areas represent times when the recorded waveform envelope and predicted waveform envelope show a high correlation, indicating a possible reflected arrival. In this case, there are other arrivals in the signal that are not predicted by the REP model. These could be aftershocks, other earthquakes, or signals from other sources in the noisy Indian Ocean. In the nuclear monitoring application, an analyst deciphering this signal using REP model results could relate the shaded areas to the direct arrival of this earthquake as reflections from the same source.

To confirm some of these reflections, the back-azimuth of the arrivals at the hydrophone station can be calculated

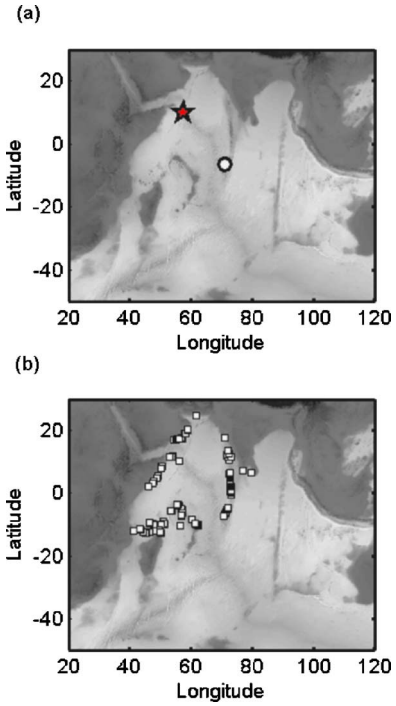

FIG. 12. The top map (a) shows the locations of the May 31, 2001, Carlsberg Ridge Earthquake and the hydrophone station at Diego Garcia. The bottom map (b) shows the bathymetric reflectors identified by the REP model as possible reflection points.

using intersensor cross-correlation techniques (Hanson, 2001). The IMS hydrophone installations consists of a three-hydrophone array installed in a triangle layout so that intersensor cross-correlations can be used to predict arrival bearing using a plane wave assumption and intersensor time delays. Figure 14 shows the result for the arrival near 32.5 min in the waveform envelope shown in Fig. 13. The

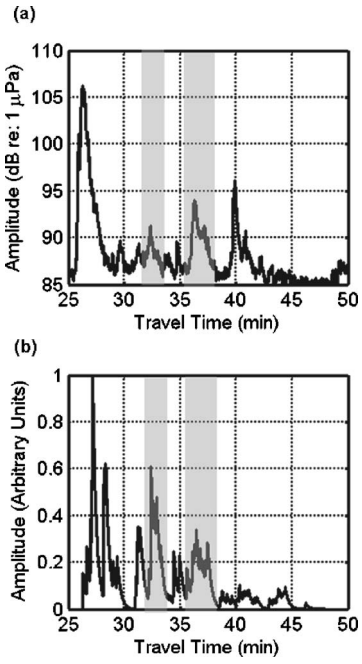

FIG. 13. A comparison between the recorded waveform envelope (a) (at Diego Garcia North) and the REP model synthetic (b). The shaded areas indicate times when the model and data are highly correlated.

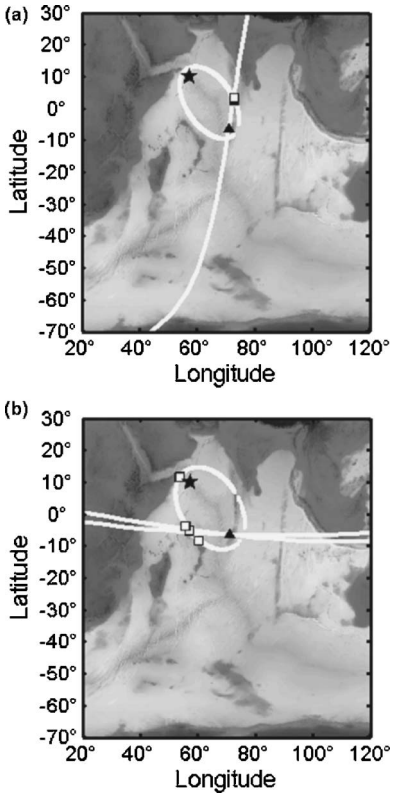

FIG. 14. The top map (a) shows the travel time ellipse representing all possible locations of reflected signals arriving at approximately 32.5 min, the REP model prediction for possible reflection at that time, and a ray showing the computed back-azimuth of the arrivals at approximately 32.5 min in the recorded data. The bottom map (b) shows the same information at approximately 36 min.

map shows the travel time ellipse associated with this arrival time, the bathymetric features identified by the model, and a geodesic ray extending from the receiver at the calculated azimuth of 2°. The bottom half of the figure shows the same information for the arrival near 36 min. Note that in both cases, the ray intersects a patch of bathymetry that was identified by the model as a potential reflector during the time period of the arrival in the recorded data. This time and bearing correlation of the model and recorded data further substantiate the use of this method to predict reflected arrivals.

IV. CONCLUSIONS AND FUTURE STUDY

Signals from large-amplitude events can be seen from both the most direct acoustic path and, in some cases, reflected paths. The arrivals from these reflected paths can be associated to the event using travel time and back-azimuth calculations. The model presented in this paper demonstrates that these reflections can also be predicted by creating an impulse response model of the ocean basin using travel time models and bathymetry data. When this impulse response is convolved with a modeled source function, prediction-to-data comparisons show a correlation in time between predictions and recorded data. In addition, using the bathymetric features selected by the model, equal time of arrival ellipses, and array processing, the reflecting bathymetry can be confirmed.

A future development of this model will be focused on applications to the Comprehensive Test Ban Treaty's International Monitoring System. In the second example shown here, the earthquake is modeled, using its reported epicenter as the source location, calculating travel times from that location using hydroacoustic propagation speeds. Research in the area of energy conversion from the seismic to acoustic regimes has shown that the energy from an earthquake can travel for kilometers in the earth before the conversion to hydroacoustic energy occurs (Shurbet and Ewing, 1957; Chapman, 2004). Thus, for seismic events, the REP model predictions could be improved by accounting for the faster propagation in the Earth prior to the conversion to the acoustic domain.

In the REP model, an acoustic path that is blocked by an island, seamount, or ridge is stopped. It could cause a reflection at that point, and thus an impulse in the model, but the propagating energy will not continue, via diffraction around or transmission through this feature. Recent research on this blockage demonstrates that diffracted and transmitted signals should not be overlooked in nuclear monitoring applications (Upton *et al.*, 2005a). Although the reflection process would further attenuate these signals, they could be accounted for in the model to make the model prediction more realistic.

The model source function could be improved to better represent a source of interest. In addition, the scaling of impulse amplitudes for scattering strength and propagation loss could be improved by integrating better predictions of sediment characteristics and propagation losses.

There are a number of potential applications of this model. For example, localization using reflections is an attractive topic as it can extend the number of arrivals used in event localization of nuclear explosions. Also, identifying reflections to help analysts filter through arrivals and eliminate false alarms could be a very valuable application.

ACKNOWLEDGMENTS

The research presented here was funded in part by the Defense Threat Reduction Agency and the Preparatory Commission for the Comprehensive Nuclear-Test-Ban Treaty Organization. The authors would also like to acknowledge the technical advice and support of Phil Harben, Robert Gibson, Ted Farrell, and Anthony Lyons.

Angell, J., Farrell, T., and Pulli, J. (**1998**). "Characterization of reflected hydroacoustic signals," *Proceedings of the 20th Annual Seismic Research Symposium*, Department of Defense, NTP, pp. 650–659.

Chapman, R. (**2004**). "Directionality of acoustic T-phase signals from shallow underwater earthquakes," J. Acoust. Soc. Am. **115**, 2445.

Comprehensive Nuclear-Test-Ban-Treaty (1996). United Nations, Annex 1, pp. 180–181.

GDEM, Database Description for the Master Generalized Digital Environment Model (GDEM) Version 5.0 (1995). OAML DBD-20F, Naval Oceanographic Office, Stennis Space Center MS.

Hanson, J. (**2001**). "Initial analysis of data from the New Diego Garcia Hydroacoustic Station," *23rd Seismic Research Review*, Jackson Hole, WY, Department of Energy, LA-UR-01-4454, Vol. **II**, pp. 12–22.

Hanson, J., Bowman, R., and Beall, G. (**2002**). "An advanced concept demonstration for monitoring the Indian Ocean," *24th Seismic Research Review*, Ponte Vedra Beach, FL, Department of Energy, LA-UR-02-5048, pp. 632–642.

Harben, P., and Boro, C. (**2001**). "Implosion Source Development and Diego Garcia Reflections," *23rd Seismic Research Review*, Jackson Hole, WY, Department of Energy, LA-UR-01–4454, Vol. **II**, pp. 23–31.

Heaney, K., Kuperman, W., and McDonald, B. (**1991**). "Perth–Bermuda sound propagation (1960): Adiabatic mode interpretations," J. Acoust. Soc. Am. **90**, 2586–2594.

Kibblewhite, A. C., and Denham, R. N. (**1969**). "Hydroacoustic signals from the CHASE V explosion," J. Acoust. Soc. Am. **45**, 944–956.

Lawrence, M., Galindo, M., Grenard, P., and Newton, J. (**2001**). "Hydroacoustic monitoring system for the Comprehensive Nuclear Test Ban Treaty," Kerntechnik **66**, 90–95.

Northrop, J. (**1968**). "Submarine topographic echoes from Chase V," J. Geophys. Res. **73**, 3909–3916.

Pulli, J. J., Farrell, T., and Gibson, R. (**1999**). "Characterization and utilization of hydroacoustic signals reflected from continents and bathymetric features," *21st Seismic Research Symposium*, Las Vegas, NV, Department of Defense, LA-UR-99-4700.

Pulli, J. J., Upton, Z., Gibson, R., and Farrell, T. (**2000**). "Modeling long-range hydroacoustic reflections in the Atlantic and Pacific Oceans," *Proceedings of the 22nd Seismic Research Symposium*, New Orleans, LA, Defense Threat Reduction Agency, OMB No. 0704-0188. Vol. **III**, pp. 75–84.

Shurbet, D., and Ewing, M. (**1957**). "T-phases at Bermuda and transformation of elastic waves," Bull. Seismol. Soc. Am. **47**, 251–262.

Teague, W. J., Carron, M. J., and Hogan, P. J. (**1990**). "A comparison between the generalized digital environment model and levitus climatologies," J. Geophys. Res. **95**, 7167–7183.

Tolstoy, M., and Bohnenstiehl, D. R. (**2002**). "Analysis of hydroacoustic signals in the Indian Ocean, *24th Seismic Research Review*, Ponte Vedra Beach, FL, Department of Energy, LA-UR-02-5048, pp. 666–675.

Upton, Z. M., and Pulli, J. (**2002**). "Localization of sub-sea earthquakes using hydroacoustic reflections and matched-field processing," *24th Seismic Research Review*, Ponte Vedra Beach, FL, Department of Energy, LA-UR-02-5048, pp. 676–685.

Upton, Z., Bhattacharyya, J., Pulli, J., Shah, S., and Collins, M. (**2005a**). "Improving the physical understanding of hydroacoustic blockage: Statistical and model based studies," *27th Seismic Research Review*, Rancho Mirage, CA, Department of Energy, LA-UR-05-6407, pp. 749–758.

Upton, Z., Farrell, T., LePage, K., Barklay, C., Angell, J., and Barger, M. (2005b). "HydroCAM Horizontal Path Prediction: The Globeray Model," BBN Technical Memorandum W-2060, BBN Technologies, 1300 N. 17th Street, Arlington, VA 22209.

Urick, R. (**1983**). *Principles of Underwater Sound*, 3rd ed. (McGraw-Hill, New York), pp. 159–164.

Stepwise coupled mode scattering of ambient noise by a cylindrically symmetric seamount

Richard B. Evans
Science Applications International, Corp., 23 Clara Drive, Suite 203, Mystic, Connecticut 06355

(Received 11 April 2005; revised 12 September 2005; accepted 11 October 2005)

The question of how underwater ambient noise, at low frequencies, interacts with seamounts is addressed. The vertical directivity of the ambient noise, with and without the seamount interaction, is of particular interest. The problem of ambient noise scattering by seamounts motivates the development of a numerical modeling procedure, based on stepwise coupled modes. The procedure is designed to analyze scattering from a cylindrically symmetric seamount. The stepwise coupled mode procedure is extended to more general boundary conditions and brought up to date in the process. An example, using the geometry of the Dickins seamount, suggests that the seamount removes energy from the steeply traveling ambient noise, for this case. The energy is not converted into angles near the horizontal; the energy is lost through bottom interaction and attenuation. [DOI: 10.1121/1.2133240]

PACS number(s): 43.30.Nb [RAS] Pages: 161–167

I. INTRODUCTION

Down slope conversion of energy from ships over slopes can produce energy at the horizontal.[1] The mechanism for down slope conversion is shown graphically by Wagstaff[1] in his Fig. 1 (a) and (b). Bottom-interacting rays have their grazing angles reduced by twice the slope angle at each bottom interaction. In contrast, noise from distant shipping in the deep ocean is, theoretically, peaked around nonzero angles above and below the horizontal, with a notch at the horizontal. A secondary noise scattering problem occurs where a seamount intrudes into the sound channel and is bathed by the ambient noise field from distant deep-ocean shipping. The latter problem is the focus of this article.

Secondary seamount scattering is an alternative mechanism to explain how ambient noise, in the deep ocean, can get into the sound channel. The geometry of seamounts and their distribution in the world's oceans suggests that this alternative mechanism could contribute to noise at the horizontal. This article describes a solution, based on stepwise coupled modes,[2] to the problem of determining if any of the steeply propagating ambient noise field, in the deep ocean, is scattered into the sound channel by a cylindrically symmetric seamount.

The effects of seamounts on underwater acoustic propagation have been the focus of experiments reported by Ebbeson and Turner[3] and scale model tests, accompanied by ray theoretic modeling, due to Medwin *et al.*[4] A perfectly reflecting conical geometry, which touched the surface, was used by Buckingham[5] to obtain an integral representation of scattering by a cone. A three-dimensional coupled mode solution, based on a cylindrically symmetric inclusion with an asymmetric incident field, was developed by Evans[6] and applied by Fawcett[7] to a single region, penetrable inclusion. A three-dimensional coupled mode solution for a multi-layered cylindrically symmetric inclusion was developed by Taroudakis.[8] Numerical problems restricted the method of Taroudakis[8] to a single-region fluid-inclusion, at very low frequency.

Coupled elastic modes have been used by Stange and Friederich[9] for elastic cylindrical inclusions, while finite difference methods have been used for a small scale, elastic seamount by Burns.[10]

The present article applies the three-dimensional stepwise coupled mode technique[6] to a multi-layered cylindrically symmetric fluid seamount with a cylindrically symmetric incident ambient noise field. A variation of the decoupling procedure[11] is used to address stability issues. The novel numerical aspect of this work is the application to multiple regions, at a modest frequency, and the control of the resulting stability problems. The symmetry of the incident field makes the problem numerically feasible. A gradual asymmetry of the incident noise field, based on azimuthal Fourier synthesis,[6] is briefly discussed.

II. INCIDENT NOISE FIELD

The azimuthal dependence of low-frequency underwater ambient noise, due to distant deep-water shipping, is controlled by features such as shipping lanes.[12] The vertical directivity of this noise, as already described, is determined by the shallowness of the source, the water depth, and the distance from the noise sources. The restriction of our attention to gradual azimuthal dependence is justified under the assumption that some intensity averaging is done. Since we are not proposing to do random realizations and intensity averaging, it is necessary to propose a coherent incident field that has the same general features as the incident ambient noise field. This is similar to doing a coherent transmission loss calculation to predict the result of a fluctuating acoustic field measurement.

As an example of the problem at hand, consider an ambient noise field in a horizontally stratified ocean that has no preferential horizontal direction, but has a vertical directivity that is peaked above and below the horizontal. The main component of shipping noise is at frequencies of less than 200 Hz, so the vertical structure of the ambient noise field

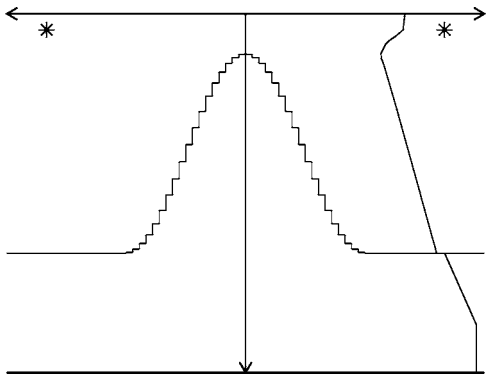

FIG. 1. A cross section of a cylindrically symmetric seamount is shown with a representative sound speed profile and the ring source location.

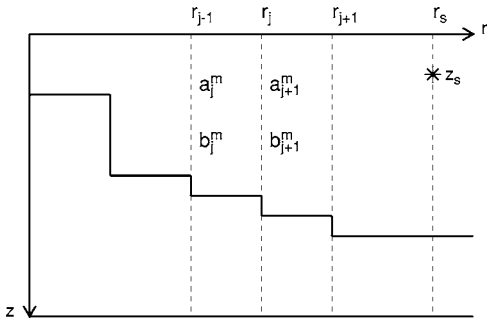

FIG. 2. The range discretization for the stepwise coupled mode solution is shown with the modal coefficients of the outgoing (a's) and ingoing (b's) waves in two adjoining regions.

can be assumed to be modal. At a substantial distance from the noise sources, each mode propagates as a plane wave in the horizontal. If each of the plane waves were randomly phased, then a departure from cylindrical symmetry would be incurred. The expected value of the noise field intensity could be obtained as an average over realizations, but this case is beyond the scope of the method proposed here.

Alternatively, consider an ambient noise field that is cylindrically symmetric, with the same axis of symmetry as the cylindrically symmetric seamount. This way the seamount scattering problem can be considered as a two-dimensional stepwise coupled mode problem. The scattered coupled mode field will have an amplitude and vertical directivity determined by the incident field and the seamount. This is a problem that can be solved using stepwise coupled modes.

A cylindrically symmetric acoustic field can be constructed from plane waves in the horizontal (x,y) plane. The field consists of a sum of terms of the form $\exp[i\vec{k}(\theta)\cdot\vec{r}]$ where $\vec{k}(\theta)=k(\cos\theta,\sin\theta)$ and $\vec{r}=(x,y)=r(\cos\psi,\sin\psi)$. The angles θ and ψ are the direction angles of the plane wave and the observation point. The average over all of the plane wave directions can be evaluated using the integral representation[13] of the Bessel function, of order zero, of the first kind:

$$\frac{1}{2\pi}\int_0^{2\pi}\exp\left[i\vec{k}(\theta)\vec{r}\right]d\theta=J_0(kr). \tag{1}$$

The plane waves, in the integral in Eq. (1), are coherent and all have the same phase at the origin $\vec{r}=(0,0)$. The field in Eq. (1) is cylindrically symmetric, with a peak value of 1 at the origin, assuming that k is real. Complex values of k are encountered when the propagation medium is attenuating.

III. STEPWISE COUPLED MODES

A cylindrically symmetric seamount will be represented as a sequence of N locally flat cylindrically symmetric regions, shown schematically (in cross section) in Fig. 1. Each region has the same total vertical thickness, including an artificial absorber deep in the bottom. Region 1 contains the axis of the seamount. It has the smallest diameter and encloses the top of the seamount. Region N is the source of the incident ambient noise field and contains the base of the seamount.

The stepwise coupled mode representation[2] of the noise field in region j, shown in Fig. 2, with $r_{j-1}\leqslant r\leqslant r_j$, is given in terms of the Hankel functions $H_0^{(i)}, i=1,2$, of order zero, type one and two. The stepwise coupled mode representation (also see Jensen *et al.*[14]) is

$$N^j(r,z)=\sum_{m=1}^{M}\left[a_m^j\frac{H_0^{(1)}(k_m^j r)}{H_0^{(1)}(k_m^j r_{j-1})}+b_m^j\frac{H_0^{(2)}(k_m^j r)}{H_0^{(2)}(k_m^j r_{j-1})}\right]\phi_m^j(z), \tag{2}$$

where k_m^j, ϕ_m^j, $m=1,M$, $j=1,N$, are the complex horizontal wave numbers and normal modes determined by the locally flat environments of Fig. 1. The imaginary parts of the horizontal wave numbers k_m^j are assumed to be non-negative. The normal modes are required to be zero at the surface and below the artificial absorber. The Hankel function ratios are designed to be one at r_{j-1} and are convenient for applying matching conditions at r_{j-1}. Region 1, with $0\leqslant r\leqslant r_1$, is a special case: The Hankel function ratios are designed to be 1 at r_1, not 0. The coefficients a_m^j, b_m^j, $m=1,M$, $j=1,N$, need to be determined by the boundary and interface conditions in the multi-region waveguide in Fig. 2.

The interface conditions and the boundary conditions are combined to form a matrix two-point boundary problem that may be solved for the unknown coefficients in Eq. (2). The interface conditions are the usual continuity of pressure and horizontal particle velocity.[2] The boundary conditions for the seamount scattering problem are different from the commonly encountered case of a point source at the origin and a radiation condition at infinity. The boundary conditions for the seamount scattering problem are developed next.

Generalizing Eq. (1), the modal representation of the incident noise field in region N with $r_{N-1}\leqslant r$ is

$$N_{inc}(r,z)=S\sum_{m=1}^{M}n_m[H_0^{(1)}(k_m^N r)+H_0^{(2)}(k_m^N r)]\phi_m^N(z), \tag{3}$$

where n_m is determined by the modal distribution of the incident noise and S is a scaling factor. The peaks in the vertical distribution of the noise are created by weighting the modes according to

$$n_m=\exp(ik_m^N r_s)\phi_m^N(z_s). \tag{4}$$

The source depth z_s is small, representing a near-surface source and emphasizing the higher order modes. The range

$r_s > r_{N-1}$ is large, corresponding to a distant source while attenuating the highest order modes.

When attenuation is present, the horizontal wave numbers have positive imaginary parts and the incident field, in Eq. (3), becomes large as r becomes large. The magnitude of the incident field is controlled by restricting the region N to the interval $r_{N-1} \leqslant r < r_s$ and viewing the incident field as arising from a ring source at r_s (see Figs. 1 and 2). The incident field, in Eq. (3) with $r < r_s$, is a scaled approximation of the lowest azimuthal order component of the Fourier expansion of the Green's function. The Fourier expansion of the Green's function, in the underwater acoustic setting,[15] is given by

$$G(r,z,\theta,r_s,z_s,\theta_s) = i\pi \sum_{\ell=-L}^{L} \sum_{m=1}^{M} J_\ell(k_m^N r) H_\ell^{(1)}(k_m^N r_s) \phi_m^N(z) \phi_m^N(z_s) \times \exp[i\ell(\theta - \theta_s)], \quad (5)$$

for $r < r_s$ where θ is the azimuth of the receiver, θ_s is the azimuth of the source, and ℓ is the azimuthal order. The $\ell = 0$ ring source solution has a derivative discontinuity at $r = r_s$, but is bounded[15] in the region $r > r_s$. In the following, region N refers to the restricted interval $r_{N-1} \leqslant r < r_s$. We will return to Eq. (5) in connection with an asymmetry in the incident noise field.

In scattering problems, the scattered field is defined as the difference between the total field and the incident field: $N(r,z) = N_{inc}(r,z) + N_{scat}(r,z)$. Usually, the incident field is a progressive wave from a fixed direction, but the incident noise field is coming from every direction and is a standing wave. This feature of the seamount noise scattering problem complicates the usual intuitive interpretation of the scattering problem.

Retaining the above formal definition of the scattered field, we proceed to obtain a second modal representation of the total field in the horizontally stratified region away from the seamount. Note that the total field in region $j=N$, in Eq. (2), may be interpreted as consisting of outgoing waves with coefficients a_m^N and incoming waves with coefficients b_m^N. The incident field in region $j=N$, in Eq. (3), has the same structure. The scattered field must be outgoing because the region away from the seamount is horizontally stratified and absorbing; the geometry supports the Raleigh hypothesis.[16] The total field in the horizontally stratified region $j=N$ should have the modal representation

$$N(r,z) = \sum_{m=1}^{M} [(Sn_m + s_m) H_0^{(1)}(k_m^N r) + Sn_m H_0^{(2)}(k_m^N r)] \phi_m^N(z), \quad (6)$$

where s_m are the coefficients in the expansion of the scattered field. In comparing Eqs. (6) and (2) in region N, it is convenient to multiply the Hankel functions in Eq. (6) by one in the form of ratios of the (same) Hankel functions at r_{N-1}.

The boundary condition in region N is found by matching the incoming components in Eqs. (2) and (6) at $r = r_{N-1}$. The resulting equation is

$$b_m^N = Sn_m H_0^{(2)}(k_m^N r_{N-1}), \quad (7)$$

where n_m is defined in Eq. (4). The boundary condition in region 1 is obtained by observing that the total field is finite at the origin. The two terms in Eq. (2) must combine to produce the Bessel function J_0 and hence

$$a_m^1 = \frac{H_0^{(1)}(k_m^1 r_1)}{H_0^{(2)}(k_m^1 r_1)} b_m^1. \quad (8)$$

The boundary conditions in Eqs. (7) and (8) require a modification to the decoupling procedure[11] to obtain a fundamental matrix solution.

Once the boundary value problem is solved and the coefficients a_m^N and b_m^N are found, the scattered field may be recovered using

$$(Sn_m + s_m) H_0^{(1)}(k_m^N r_{N-1}) = a_m^N.$$

The introduction of the scattered field, although not completely necessary, assisted in establishing the boundary condition in Eq. (7). In view of the nonintuitive nature of the scattered field, already discussed, we will emphasize comparisons between incident and total fields as well as ingoing and outgoing waves in the example to follow, in Sec. IV.

Sections III A and III B provide details of the computational procedure while Sec. III C discusses gradual azimuthal dependence.

A. Fundamental matrix solution

The procedure for solving a matrix two-point boundary problem described by Evans[11] assumed a radiation condition at infinity. As a result, the most general solution of the matrix recursion was not obtained. To entertain the more general boundary conditions encountered above, a fundamental matrix solution, with linearly independent columns, needs to be found. A procedure for finding a fundamental matrix solution (they are not unique) has been described by Mattheij and Staarink[17] and is summarized here for an incoming wave in region N and a regularity condition at the origin. This case is needed for the seamount scattering problem.

The matrix-vector recursion for modal expansion coefficients in Eq. (2) has the form

$$\vec{x}_{j+1} = R_j \vec{x}_j, \quad j = 1, N-1, \quad (9)$$

where R_j is a $2M \times 2M$ propagator matrix[11] that advances the modal expansion coefficients from one region to the next. The coefficients have been stored in the $2M \times 1$ column vector $\vec{x}_j = \mathrm{col}[\vec{b}_j, \vec{a}_j]$, $j = 1, N$ (Jensen *et al.*[14] use a different arrangement). A fundamental matrix solution of Eq. (9) is obtained from the matrix recursion

$$X_{j+1} = R_j X_j, \quad j = 1, N-1, \quad (10)$$

by starting with the initial value $X_1 = I$. Any vector solution of Eq. (9) can be written as $\vec{x}_j = X_j \vec{c}$ for the appropriate choice of the $2M \times 1$ column vector $\vec{c} = \mathrm{col}[\vec{c}_2, \vec{c}_1]$. The generation

of the matrix X_j using Eq. (10) is unstable and the columns of X_j lose their linear independence as j increases.

B. Decoupling algorithm

It is better to generate a fundamental matrix solution, using the decoupling algorithm (repeated orthogonalization). The decoupling algorithm is based on the factorization $X_j = T_j Y_j$ where T_j is a unitary matrix and Y_j is an upper triangular matrix satisfying the upper triangular recursion $Y_{j+1} = U_j Y_j$. The matrices T_{j+1} and U_j are found by orthogonalization of the columns of $R_j T_j = T_{j+1} U_j$ with $T_1 = I$. It is convenient to partition the $2M \times 2M$ matrices T_j and Y_j into four $M \times M$ submatrices given by

$$T_j = \begin{bmatrix} T_{4,j} & T_{3,j} \\ T_{2,j} & T_{1,j} \end{bmatrix}$$

and

$$Y_j = \begin{bmatrix} Y_{4,j} & Y_{3,j} \\ 0 & Y_{1,j} \end{bmatrix}.$$

The procedure for finding T_j and Y_j is a double sweep. It starts with $T_1 = I$, $Y_{2,1} = 0$, and $Y_{1,1} = I$; it proceeds, with increasing j, to obtain T_j, $Y_{2,j} = 0$, and $Y_{1,j}$, $j = 2, N$. The first half of the decoupling procedure is exactly as has previously[11] been described. The second half is different from the previously described procedure. After obtaining T_N, $Y_{2,N} = 0$, and $Y_{1,N}$, then the alternate strategy[17] is employed. The matrices $Y_{4,N} = I$ and $Y_{3,N} = 0$ are defined and the reverse sweep, with decreasing j, is used to find $Y_{4,j}$ and $Y_{3,j}$, $j = N - 1, 1$. Both $Y_{4,j}$ and $Y_{3,j}$ are obtained by back-substitution, based on $Y_{4,j+1}$ and $Y_{3,j+1}$. The decoupling algorithm eliminates the instability associated with Eq. (10), since the double sweep computes the outgoing and ingoing waves in decaying directions.

The fundamental matrix solution $X_j = T_j Y_j$ can now be used to solve the two-point matrix boundary value problem. The solution is $\vec{x}_j = T_j Y_j \vec{c}$, but the boundary conditions at $j = 1$ and N need to be enforced by the choice of $\vec{c}$. The solution at $j = 1$ is

$$\begin{bmatrix} \vec{b}_1 \\ \vec{a}_1 \end{bmatrix} = \begin{bmatrix} Y_{4,1} & Y_{3,1} \\ 0 & I \end{bmatrix} \begin{bmatrix} \vec{c}_2 \\ \vec{c}_1 \end{bmatrix} \tag{11}$$

and the solution at $j = N$ is

$$\begin{bmatrix} \vec{b}_N \\ \vec{a}_N \end{bmatrix} = \begin{bmatrix} T_{4,N} & T_{3,N} Y_{1,N} \\ T_{2,N} & T_{1,N} Y_{1,N} \end{bmatrix} \begin{bmatrix} \vec{c}_2 \\ \vec{c}_1 \end{bmatrix}. \tag{12}$$

The boundary condition for the incoming wave in region N is $\vec{b}_N = \vec{n}$, where $\vec{n}$ is the vector on the right-hand side of Eq. (7). The regularity condition, at the origin, has the form $\vec{a}_1 = D\vec{b}_1$, where D is the diagonal matrix multiplying $\vec{b}_1$ on the right-hand side of Eq. (8). The boundary conditions can be consolidated into a single matrix-vector equation for $\vec{c}$ based on Eqs. (11) and (12) given by

$$\begin{bmatrix} T_{4,N} & T_{3,N} Y_{1,N} \\ -DY_{4,1} & I - DY_{3,1} \end{bmatrix} \begin{bmatrix} \vec{c}_2 \\ \vec{c}_1 \end{bmatrix} = \begin{bmatrix} \vec{n} \\ \vec{0} \end{bmatrix}. \tag{13}$$

Equation (13) may be solved for $\vec{c}$ by Gaussian elimination with partial pivoting. The conditioning of Eq. (13) can be improved by multiplying the top row by $T_{4,N}^H$, where the superscript H stands for complex conjugate transpose, and by using the fact that the block matrix T_N is unitary.

The field in Eq. (2) may be constructed using the modal coefficients obtained from $\vec{x}_j = T_j Y_j \vec{c}$ where $T_j Y_j$ is the fundamental matrix solution generated with the decoupling algorithm.

The complexity of the decoupling algorithm should not disguise the fact that a (linear) matrix two-point boundary value problem has been solved. All the expansion coefficients and fields obtained are proportional to the amplitude of the incident field, through the factor S that appears in the vector $\vec{n}$ on the right-hand side of Eq. (13).

C. Gradual azimuthal dependence

The method proposed by Evans[6] and implemented by Fawcett[7] is designed for a cylindrically symmetric inclusion with an asymmetric incident field. The incident field is the Green's function in Eq. (5). The orthogonality of the cylindrical waves implies that each of the azimuthal orders decouples.[6,7] Each of the azimuthal orders gives rise to a separate matrix two-point boundary value problem. Once the two-point boundary value problems are solved, the azimuthal dependence of the total solution is obtained as a Fourier synthesis, in azimuth. The Fourier synthesis has the same form as the expansion of the incident field.

The implementation of the azimuthal Fourier synthesis method,[6] for a strong asymmetry in the incident field, requires evaluations of Hankel functions for both large arguments and large orders and leads to significant difficulties.[8] A solution for a problem with a gradual asymmetry in the incident field, requiring only additional azimuthal orders of $\ell = \pm 1, \pm 2$, can be obtained based on the usual large argument approximations.[18] The leading order error in the large argument approximations for the Hankel functions is equal to $(\lambda/r)(4\ell^2 - 1)/(16\pi)$ where λ is the wave length. The leading order error is less than 0.15, as compared to 1, for $r > 2\lambda$ and $\ell = \pm 2$. It is even smaller for $\ell = \pm 1$.

The use of the usual large argument approximations of the Hankel function implies that the ratios used in the stepwise coupled mode representation of each azimuthal order in Eq. (2) are independent of the order. The same is true for the corresponding propagator matrices in Eq. (9). The only difference in the matrix two-point boundary value problems, for the azimuthal orders $\ell = 0, \pm 1, \pm 2$, are the coefficients in the Fourier expansion of the incident wave. These differences lead to different vectors $\vec{n}$ on the right-hand side of Eq. (13). The total energy in the incident wave is partitioned across azimuthal orders. The exchange of energy, in the vertical, is determined by the matrix on the left-hand side of Eq. (13) and is the same for each $\ell = 0, \pm 1, \pm 2$ in the large argument approximation.

The above interpretation is valid for a gradual azimuthal dependence of the incident noise field. When there is a stronger asymmetry in the incident field, higher azimuthal orders are needed and both sides of Eq. (13) depend on azimuthal

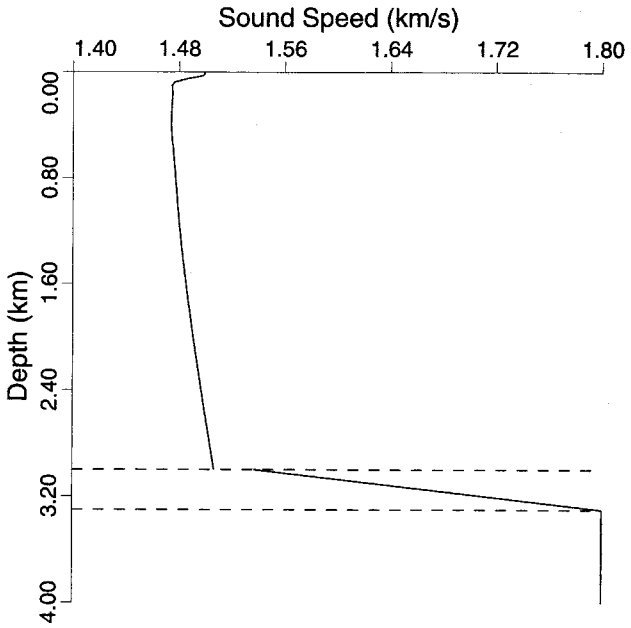

FIG. 3. The sound speed and bottom profile used for the area surrounding the Dickins seamount is plotted versus depth. The water depth is 3000 m. The refracting sediment is 300 m thick. The acoustic basement has a sound speed of 1.8 km/s.

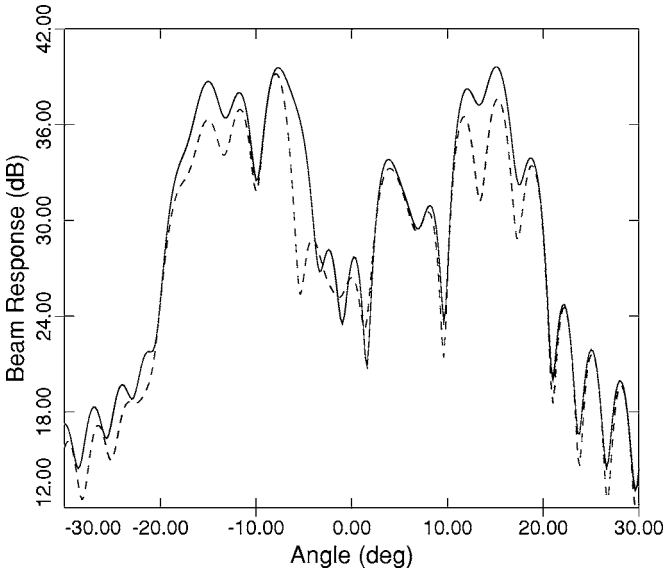

FIG. 4. The beam response of the incident noise field and total (incident plus scattered) fields is shown versus elevation angle. The solid curve is the incident noise field, without the seamount, and the dashed curve is the total field, with the seamount present. The vertical directivity of both fields is similar except in regard to level: the total field intensity is reduced by interaction with the seamount.

order. The total energy in the incident wave is still partitioned across azimuth, but the exchange of energy, in the vertical, can vary among the higher azimuthal orders.

IV. DICKINS SEAMOUNT EXAMPLE

The general characteristics of the Dickins seamount, in the North Pacific, are used to provide an example of the procedure described above, for a cylindrically symmetric incident field. The cylindrically symmetric seamount geometry is similar to the ridge geometry considered by Jensen *et al.*[19] A representative water sound speed and bottom sound speed profile, for the area surrounding the Dickins seamount, is shown in Fig. 3. The depth variation of the sound speed is handled using the Galerkin method described by Evans and Gilbert[20] and reviewed by Fawcett.[7]

The water sound speed has a minimum of 1473.9 m/s at a depth of 400 m and a maximum of 1506.9 m/s at the water sediment interface at a depth of 3000 m. The sound speed in the bottom increases from 1537 m/s, at the water sediment interface, to 1800 m/s at a depth of 300 m into the sediment, where it remains constant for another 700 m. The total thickness of the problem is 4000 m. The bottom has a constant density of 1.5 g/cm^3. The attenuation is 0.5 dB/λ in the first 300 m of the bottom sediment and then gradually increases in the last 700 m, to form an artificial absorber.

The seamount has a slope of about 14°. It rises from the seafloor, at 3000 m, to a depth of 500 m in a range interval of 10 km. The sound speed in the seamount is taken to be a constant equal to 1800 m/s and is the same as the acoustic basement in the surrounding region. The calculations described here are done at 50 Hz and the frequency determines[21] how many stair steps are needed to represent the seamount bathymetry to obtain an accurate representation of the scattered noise field. Convergence tests lead to the use of 1400 steps and 200 modes. The first region had a depth of 500 m and ends at $r_1=30$ m. The last region had a depth of 3000 m and starts at $r_{N-1}=10$ km. There are around 110 propagating modes in 3000 m of water at 50 Hz, although 200 modes are used to resolve higher angles and supplement the Galerkin procedure.

The incident noise field is determined by using a source depth of $z_s=7.5$ m and a source range of $r_s=100$ km in Eq. (4). The source depth is consistent with a merchant ship. A vertical array of 41 receivers, 15 m apart, spanning the depth interval 100 to 700 m, is used in the calculations. Its purpose is to determine the vertical directivity of the incident and total fields using plane wave beamforming.

A plane wave beamformer (phase delay and sum followed by amplitude squaring and $10\log_{10}$) is applied to the incident and total complex pressure fields. The phase delays are based on the sound speed at the sound channel axis at the midpoint of the array. The amplitude of the incident field (through the factor S) is chosen to yield a positive beam response, in dB, over a range of angles. The physical units are not provided since all the fields displayed scale with S. The greater the beam response, the better the match to a plane wave arriving from that angle, above or below the horizontal.

The beam response for the incident and total fields is intensity averaged over the range interval 18 to 19 km away from the axis of the seamount. The averaging is done in an attempt to minimize coherent effects that are not a feature of ambient noise. The 1-km intensity averaged beam response of the incident and total fields are shown in Fig. 4. The solid curve is the beam response of the incident field and shows the expected vertical distribution, with a notch at the horizontal. The dashed curve is the beam response of the total

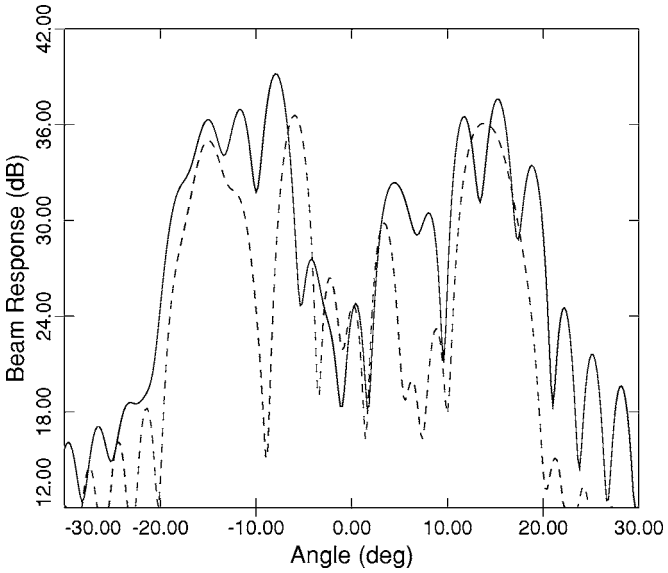

FIG. 5. The beam response of the ingoing and outgoing incident noise fields, without the seamount, is plotted versus elevation angle. The solid curve is the ingoing noise field and the dashed curve is the outgoing noise field.

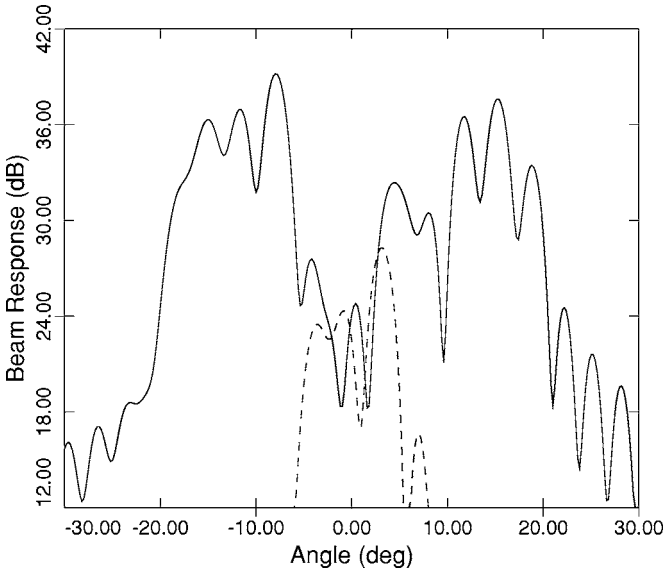

FIG. 6. The beam response of the ingoing and outgoing components of the total field, with the seamount present, is plotted versus elevation angle. The solid curve is the ingoing field and the dashed curve is the outgoing field. The ingoing component of the total field is the same as the ingoing component of the incident noise field in Fig. 5. The outgoing component is reduced in level by interaction with the seamount.

field, with the seamount present. The beam response levels are generally less, when the seamount is present, due to interaction with the seamount and the associated attenuation. There is little evidence of the incident noise being redirected into the nearly horizontal elevation angles, as simulated by a vertical array, in this case.

A vertical array cannot distinguish between waves propagating in different directions, in the horizontal. A three-dimensional array, with both transverse and longitudinal horizontal aperture, can resolve ingoing and outgoing waves. It is possible to simulate the beam response of an idealized three-dimensional array because the computational procedure separates the total field into ingoing and outgoing waves in the region away from the seamount. As a reference point, the intensity averaged beam response due to the ingoing and outgoing components of the incident noise field, without the seamount present, are shown in Fig. 5. The solid curve is the ingoing component and the dashed curve is the outgoing component. The range average in Fig. 5, and subsequent plots, is the same as the range average used in Fig. 4.

The intensity averaged beam response due to the ingoing and outgoing components of the total field, with the seamount present, are shown in Fig. 6. The solid and dashed curves are the ingoing and outgoing components, respectively. Note that the ingoing component of the total field with the seamount present, in Fig. 6, is identical to the ingoing component of the incident noise field, in Fig. 5. It is apparent, from Fig. 6, that much of the outgoing component of the incident noise is lost due to interaction with the seamount. The small fraction that remains is at elevation angles near the horizontal but its intensity level is comparable to the levels in the notch that existed before the seamount was introduced.

Although the scattered field coherently combines with the incident noise field, the theoretical simulation can separate the incident field and the scattered field, in the region away from the seamount. The intensity averaged beam response due to the incident field and the scattered field is shown in Fig. 7. The solid curve is the incident noise field that appeared in Fig. 4. The dashed curve is the scattered field, which is strikingly similar to the outgoing component of the incident noise field in Fig. 5. While the beam response is nonlinear (not additive), the above similarity supports the fact that cancellation occurs between the two apposing fields, leading to the significantly reduced levels of the outgoing component of the total field in Fig. 6. The analogous situa-

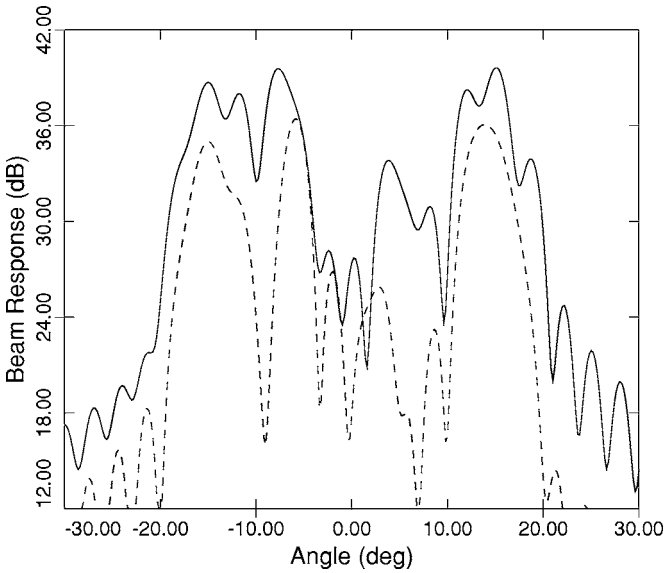

FIG. 7. The beam response of the incident noise field and the scattered field is shown versus elevation angle. The solid curve is the incident noise field, without the seamount, and is the same as the solid curve plotted in Fig. 4. The dashed curve is the scattered field and appears similar to the outgoing component of the incident noise field plotted in Fig. 5.

tion occurs in an acoustic shadow where the incident and scattered field have comparable magnitudes, but are 180° out of phase.

V. CONCLUSIONS

The problem of ambient noise scattering by a cylindrically symmetric seamount motivated and guided the development of a stepwise coupled mode procedure for computing the total and scattered field. The resulting hybrid analytical-numerical solution provides insight into where to look for the effects of scattering by a seamount. The particular example of scattering by the Dickins seamount was used as an exercise in analyzing the total, incoming, outgoing, and scattered fields in the region away from the seamount. While a parametric study was not undertaken, the results of the example were as follows:

The stepwise coupled mode calculations, of ambient noise scattering by a cylindrically symmetric representation of the Dickins seamount, indicated that the seamount interaction served to remove energy from the higher angles. The energy was lost to attenuation, through bottom interaction, and was not necessarily transferred into lower angles. The numerical results of the example were obtained for a cylindrically symmetric incident noise field. The theoretical discussion in Sec. III C implies that the effect of the seamount, on the vertical distribution of scattered ambient noise, would remain the same with a gradual asymmetry in the incident noise field.

The energy loss through bottom interaction is, obviously, not restricted to three dimensions. The same effect could be simulated with a two-dimensional range-dependent propagation model and a ridge[19] in place of the seamount. The logical transition, in the other direction, from two to three dimensions is not as obvious.

ACKNOWLEDGMENT

The author has benefited from the support of SAIC, in analyzing seamount scattering, over a continuing time period on multiple projects. The constructive criticism of Herb Freese and Chuck Spofford is particularly noteworthy.

[1]R. A. Wagstaff, "Low-frequency ambient noise in the deep sound channel-The missing component," J. Acoust. Soc. Am. **69**, 1009–1014 (1981).
[2]R. B. Evans, "A coupled mode solution for acoustic propagation in a waveguide with stepwise depth variations of a penetrable bottom," J. Acoust. Soc. Am. **74**, 188–195 (1983).
[3]G. R. Ebbeson and R. G. Turner, "Sound propagation over Dickins Seamount in the Northeast Pacific Ocean," J. Acoust. Soc. Am. **73**, 143–152 (1983).
[4]H. Medwin, E. Childs, E. A. Jordan, and R. A. Spaulding, Jr., "Sound scattering and shadowing at a seamount: Hybrid physical solutions in two and three dimensions," J. Acoust. Soc. Am. **75**, 1478–1490 (1984).
[5]M. J. Buckingham, "Theory of acoustic propagation around a conical seamount," J. Acoust. Soc. Am. **80**, 265–277 (1986).
[6]R. B. Evans, "Three dimensional scattering from a cylindrical inclusion in a waveguide," in *Computational Acoustics, Vol. 2.*, edited by D. Lee, A. Cakmak, and R. Vichnevetsky (North-Holland, New York, 1990).
[7]J. A. Fawcett, "Coupled-mode modeling of acoustic scattering from three-dimensional, axisymmertic objects," J. Acoust. Soc. Am. **102**, 3387–3393 (1997).
[8]M. I. Taroudakis, "A coupled-mode formulation for the solution of the Helmholtz equation in water in the presence of a conical sea-mount," J. Comput. Acoust. **4**, 101–121 (1996).
[9]S. Stange and W. Friederich, "Guided wave propagation across sharp lateral heterogeneities: the complete wavefield at a cylindrical inclusion," Geophys. J. Int. **111**, 470–482 (1992).
[10]D. R. Burns, "Acoustic and elastic scattering from a seamount in three dimensions-A numerical study," J. Acoust. Soc. Am. **92**, 2784–2791 (1992).
[11]R. B. Evans, "The decoupling of stepwise coupled modes," J. Acoust. Soc. Am. **80**, 1414–1418 (1986).
[12]R. J. Urick, *Ambient Noise in the Sea* (Peninsula, Los Altos, CA, 1984), p. 5-20.
[13]M. Abramowitz and I. A. Stegun, *Handbook of Mathematical Functions* (Dover, New York, 1972), p. 360.
[14]F. B. Jensen, W. A. Kuperman, M. B. Porter, and H. Schmidt, *Computational Ocean Acoustics* (AIP, New York, 1994), pp. 315–319.
[15]A. Haug, R. D. Graves, and H. Uberall, "Normal-mode theory of underwater sound propagation from directional multipole sources," J. Acoust. Soc. Am. **56**, 387–388 (1974).
[16]J. A. DeSanto, "Theoretical methods in ocean acoustics," in *Ocean Acoustics*, edited by J. A. DeSanto, *Topics in Current Physics*, Vol. **8** (Springer-Verlag, New York, 1979), pp. 55–57.
[17]R. M. M. Mattheij and G. W. M. Staarink, "An efficient algorithm for solving general linear two point BVP," SIAM (Soc. Ind. Appl. Math.) J. Sci. Stat. Comput. **5**, 745–763 (1984).
[18]Reference 13, p. 364.
[19]Reference 14, pp. 404–405.
[20]R. B. Evans and K. E. Gilbert, "Acoustic propagation in an refracting ocean waveguide with an irregular interface," Comput. Math. Appl. **11**, 795–805 (1985).
[21]F. B. Jensen, "On the use of stair steps to approximate bathymetry changes in ocean acoustic models," J. Acoust. Soc. Am. **104**, 1310–1315 (1998).

Ocean acoustic hurricane classification

Joshua D. Wilson and Nicholas C. Makris
Massachusetts Institute of Technology, Cambridge, Massachusetts 02139

(Received 18 August 2005; accepted 7 October 2005)

Theoretical and empirical evidence are combined to show that underwater acoustic sensing techniques may be valuable for measuring the wind speed and determining the destructive power of a hurricane. This is done by first developing a model for the acoustic intensity and mutual intensity in an ocean waveguide due to a hurricane and then determining the relationship between local wind speed and underwater acoustic intensity. From this it is shown that it should be feasible to accurately measure the local wind speed and classify the destructive power of a hurricane if its eye wall passes directly over a single underwater acoustic sensor. The potential advantages and disadvantages of the proposed acoustic method are weighed against those of currently employed techniques. © *2006 Acoustical Society of America.* [DOI: 10.1121/1.2130961]

PACS number(s): 43.30.Nb, 43.30.Pc [ADP] Pages: 168–181

I. INTRODUCTION

A case is made that it may be practical to safely and inexpensively determine local wind speed and classify the destructive power of a hurricane by measuring its underwater acoustic noise intensity. Sea-surface agitation from the action of wind and waves is a dominant source of ambient noise in the ocean.[1,2] This noise can be described as a sum of fields radiated from many random sources on the sea surface.[3–8] If the surface noise sources have the same statistical distribution, Ingenito and Wolf have shown that wind-generated noise spectral intensity is the product of two separate factors, a waveguide propagation factor and a "universal ambient noise"[9] source factor which is a function of wind speed but otherwise is expected to be effectively independent of horizontal position.

The concept of using underwater sound to estimate wind speed was first considered by Shaw *et al.*[10] for spatially uniform wind speed distributions. They found sound pressure level in dB to be linearly related to the log of the wind speed. The idea of a universal ambient noise source factor was implicit in their approach. We will show that the slope of their linear relationship corresponds to the universal ambient noise factor and the intercept to the waveguide propagation factor. Evans *et al.* demonstrated that these estimates could be made to within ±1 m/s in the 5 to 10 m/s wind speed range,[11] which is much less than hurricane wind speeds.

Many experiments have been conducted to determine the relationship between local wind speed and underwater noise intensity as noted in Ref. 12. A common difficulty in these experiments has been contamination from shipping noise.[12,13] This typically leads to poorer correlation and greater variance in estimates of the relationship between wind speed and noise intensity.[12] Two experimental studies conducted over many months that minimized this contamination show that a consistent high-correlation power-law relationship exists.[11,14] They also show underwater noise intensity to be linearly proportional to wind speed to a frequency-dependent power, ranging from two to four, for wind speeds between 5 and 20 m/s. While no measured data have been published relating ambient noise and wind speed in a hurricane, the only known mechanism that would cause a roll-off in the extrapolation of these power laws is attenuation by bubbles.[15] This attenuation, however, is insignificant at low frequencies and can be accurately measured and modeled at high frequencies.

We find that it may be possible to estimate local hurricane wind speed by generalizing the approach of Shaw *et al.*[10] We show that the wind-generated noise received by a single underwater acoustic sensor in a hurricane can be well approximated by sea-surface contributions so local that wind speed and surface source intensity can be taken as nearly constant. With these findings, noise intensity can be well approximated as the product of a local universal ambient noise source factor and a waveguide propagation factor even for the range-dependent wind speeds of a hurricane.

At low frequencies, below roughly 100 Hz, we show that attenuation by wind-induced bubbles in the upper-ocean boundary layer should be insignificant even in hurricane conditions. *Temporal variations* in underwater noise intensity should then be primarily caused by the universal ambient noise source factor which is expected to depend on local wind speed and will vary as a hurricane advects over a fixed receiver. By extrapolating known relationships[14] between wind speed and noise level in this frequency range, the ambient noise level should increase monotonically with wind speed, and it should be possible to directly estimate local wind speed from measured noise level.

At higher frequencies temporal variations in underwater noise intensity may also be caused by attenuation due to scattering from bubbles in the upper-ocean boundary layer. This attenuation increases with wind speed and acoustic frequency. Farmer and Lemon[16] experimentally show that this leads to a frequency-dependent peak in noise level versus wind speed at frequencies above 8 kHz and wind speeds above 15 m/s. We analytically show that such a peak may also exist for frequencies above 100 Hz in typical hurricane wind speeds. Since the shape of the ambient noise versus wind speed curve and the location of its peak vary strongly with frequency, we show that wind speed may still be unambiguously estimated from broadband ambient noise measure-

ments in hurricane conditions above 100 Hz once the corresponding universal source dependence is empirically determined.

The accuracy of underwater acoustic wind speed estimates depends on the signal-to-noise ratio (SNR) of the underwater ambient noise intensity measurements upon which they are based. Piggott[14] and Perrone[17] have consistently measured wind noise with a standard deviation of less than 1 dB, as expected from theory where the variance of the intensity measurement can be reduced by stationary averaging.[8,18,19] For the measured power-law relationships that range from quartic to square,[11,14] a 1-dB standard deviation in sound pressure level corresponds to a 6% to 12% respective error in estimated wind speed. If realizable in hurricane conditions, this may provide a useful alternative to current satellite-based techniques.

Ocean acoustics then has serious potential for providing accurate and inexpensive hurricane classification estimates. Since a single hydrophone effectively measures only the local surface noise, it will effectively cut a swath through the hurricane, yielding local wind speed estimates as the storm passes over. At low frequencies, current evidence suggests a simple power-law relationship between noise intensity and wind speed. At higher frequencies, a frequency-dependent roll-off is expected in the relationship due to attenuation by bubbles. Wind speed can still be uniquely estimated, however, by making broadband measurements at higher frequency.

While current satellite technology has made it possible to effectively detect and track hurricanes, it is still difficult to accurately measure the wind speeds and classify the destructive power of a hurricane from satellite measurements. The standard method for hurricane classification by satellite, the Dvorak method,[20–23] often yields errors in wind speed estimates as high as 40%.[24–28] For example, of the eight North Atlantic hurricanes of 2000, three of them[24–26] experienced Dvorak errors over 40% and three more[29–31] experienced Dvorak errors over 20% when compared to the best estimate of wind speed from aircraft measurements. Several satellite microwave techniques show some promise for measuring hurricane wind speed[32] but, because of resolution and accuracy issues, the Dvorak method is still the standard for satellite hurricane classification.[23] In the North Atlantic the limitations of satellite technology are overcome by use of reconnaissance aircraft. These fly through the center of a hurricane to make the accurate measurements of wind speed necessary for classification. Unfortunately the expense of these aircraft prevents their routine use outside the United States.[33] For example, the cost to purchase a WC-130 aircraft is roughly $78 million,[34] adjusted for inflation to year 2003 dollars, and the deployment cost is $155 000 per flight.[35]

Classification of a hurricane's total destructive power, which is proportional to the cube of the hurricane's maximum wind speed,[36] is critical for hurricane planning. For example, inaccurate classification can lead to poor forecasting and unnecessary evacuations,[37] which are expensive, or missed evacuations, which can result in loss of life. These fatalities and costs can be reduced if the public is given timely and accurate advanced warning, but this depends on the ability to accurately classify hurricanes while they are still far from land. To give some background, in 1992 Hurricane Andrew became the most costly natural disaster in United States history causing an estimated 25 billion dollars in damage[33,38] and in 1900 an unnamed hurricane became the most deadly disaster in United States history killing over 6000 people.[39] Overseas the worst hurricane in history killed over 300 000 people in Bangladesh in 1970.[33]

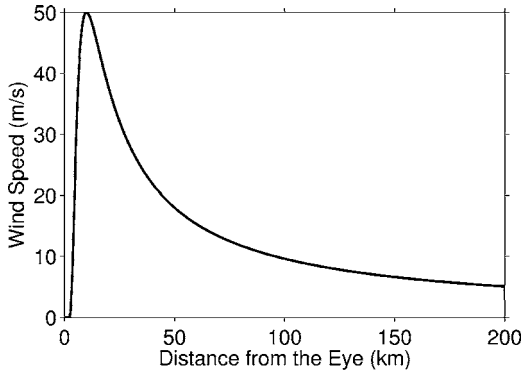

FIG. 1. Hurricane wind speed as a function of distance from the hurricane center based on Holland's model[36] with parameters $A=72.44$, $B=1.86$, $p_c=96\,300$ Pa, $p_n=100\,500$ Pa, and $\rho_{\mathrm{AIR}}=1.15$ kg/m^3. The zero wind speed region at the center of the hurricane (0 km) is called the eye and the high wind speed region (10 km) is the eye wall. The total destructive power of the hurricane is proportional to the cube of the maximum wind speed, which occurs in the eye wall.[40]

In this paper we review models for the spatial wind speed dependence of a hurricane that will be used to model ambient noise, past experiments that measured the relationship between underwater noise intensity and wind speed, and models for range-dependent noise in the ocean. We then develop a model for wind generated noise from a hurricane for both single sensors and arrays. We use this model to demonstrate the potential usefulness of classifying hurricanes with underwater acoustic sensors.

II. HURRICANE STRUCTURE AND CLASSIFICATION

Hurricanes are severe storms characterized by surface winds from 33 to over 80 m/s (Ref. 33) that circulate around a central low pressure zone called the eye. Holland[36] gives an analytic model for the surface wind speed profile as a function of range from the eye since hurricanes are typically cylindrically symmetric,

$$V=\sqrt{AB(p_n-p_c)\frac{\exp\{-A/r^B\}}{\rho_a r^B}} \tag{1}$$

where V is wind speed at a height of 10 m above the sea surface, p_c and p_n are the atmospheric pressure in the eye and outside the hurricane, respectively, ρ_a is the density of the air, and A and B are empirical values. Using this model, the surface wind speed profile for a moderate hurricane is given in Fig. 1, where wind speed in the eye is zero and rapidly increases to a maximum of 50 m/s at what is known as the eye wall. Outside of the eye wall, which is on the order of 10 km thick, wind speed slowly decreases to the edge of the hurricane which is typically hundreds of kilometers from the eye. Most of a hurri-

cane's destructive power then comes from the high winds in the eye wall since this power is roughly proportional to the cube of the maximum wind speed.[40]

The standard approach for classifying a hurricane's destructive power, the Dvorak method,[20–22] is effectively a pattern-recognition technique where satellite images, in the visible and infrared spectrum, are used to classify the hurricane based on features like the size and the geometry of cloud patterns. As discussed in the Introduction, this method often yielded wind speed estimates with errors of over 40% in several recent hurricanes.[24–28] Despite these errors, the Dvorak method is still the primary technique for classifying the destructive power of a hurricane from satellite measurements.[23] A satellite-based pattern-recognition technique similar to the Dvorak method using SSM/I satellite microwave (85 GHz) instead of optical and infrared images has recently been developed but gives similar errors to the Dvorak method.[41]

Satellite classification of hurricanes with microwave sounding units (MSU)[42] is secondary to the primary Dvorak method[23] due to the limited spatial resolution of the unit. The 55-GHz microwave radiation given off by warm air in the hurricane's eye is used to estimate temperature and then infer the hurricane's power. Because of the small size of the satellite array its spatial resolution is about 48 km,[43] which is often larger than the diameter of the eye, resulting in a blurred image of the hurricane and potential errors in estimates of destructive power.[42,43]

Other satellite techniques for estimating hurricane wind speed and destructive power are under development. For an overview see the article by Katsaros *et al.*[32] These techniques, however, are not yet used operationally for hurricane classification and disaster planning.[44]

To overcome the limitations of satellite techniques, specially equipped aircraft, like the Air Force's WC-130s and NOAA's WP-3s, are flown through the center of a hurricane.[44] Using on-board sensors and expendable dropsondes, accurate wind speed estimates with errors less than 5 m/s can be obtained.[44] Unfortunately these aircraft are expensive to purchase and operate and are currently only used by the United States.[33]

III. WIND-GENERATED SURFACE NOISE

Here we develop a model for the surface-generated noise intensity and mutual intensity from a hurricane received by a hydrophone or hydrophone array submerged in an ocean waveguide. The geometry of the problem is shown in Fig. 2. The hurricane is centered at the origin and is surrounded by ambient winds, all of which cause local sea-surface agitation. This agitation leads to sound sources with amplitude dependent on the local wind speed, modeled as a sheet of monopoles on a source plane at a depth z_0 within a quarter wavelength of the free surface following ocean acoustic noise modeling convention.[5–7] Intensity and mutual intensity are determined by directly integrating the surface source contributions using the waveguide Green function.

Several previous authors have addressed similar surface noise problems; however, their derivations are intertwined

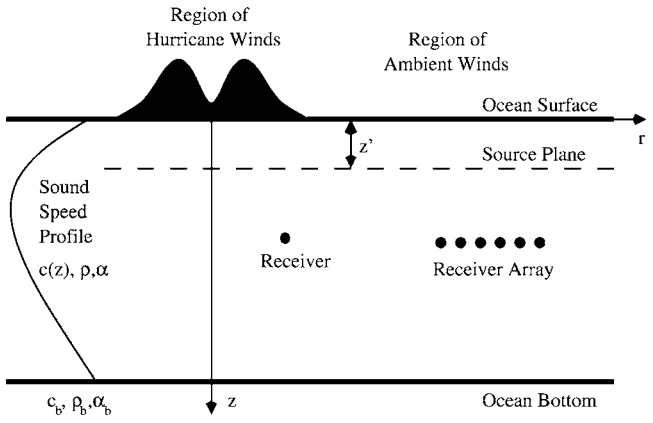

FIG. 2. Cross section of the stratified ocean waveguide showing the geometry of the surface noise problem (not to scale). On the surface is the area covered by the hurricane and surrounding area covered by 5 m/s ambient winds. The surface noise sources are modeled as a plane of monopoles a small depth z_0 below the surface and the sound field is measured by a single point receiver or reciever array.

with approximations or parametrizations that are not suitable for modeling hurricane noise. Kuperman and Ingenito[5] developed a widely used surface noise model; however, embedded in their derivation is the assumption that the source field is range independent. This is not true for hurricane-generated noise where the wind speed and source level change drastically with position.

Using an adiabatic normal mode formulation Perkins *et al.*[7] extended the model of Kuperman and Ingenito to range-dependent source fields and mildly range-dependent waveguides. They did this by dividing the surface area into smaller subareas over which the source field could be considered constant. They used far-field approximations for each subarea. These were coupled with the further approximation that the cross-spectral density for each subarea could be expressed as a single sum over modes. This approximation is only valid when the inverse of the difference between the horizontal wavenumber of the modes is much less than the dimension of the subarea.[45,46] For the highly range-dependent winds of a hurricane in an otherwise range-independent waveguide, this approach proves to be less accurate, more cumbersome, and less efficient to implement than direct integration.[47] Carey *et al.*[6] have developed a computational approach based on the parabolic equation approximation for calculating range-dependent surface noise. We find that steep angle contributions dominate the intensity measured by a single sensor and so require direct integration of local noise sources with a full-field model for the Green function rather than an elevation-angle-restricted parabolic approximation.

It is useful to briefly derive the direct integration approach used here since it has not explicitly appeared in the previous literature even though many essential elements are implicit in the work of Perkins *et al.*[7] For uncorrelated sources the cross-spectral density of the noise field can be written as

$$C(\mathbf{r_1},\mathbf{r_2},f)=\int_{\infty} d^2\boldsymbol{\rho_0}\frac{S_{qq}(V(\boldsymbol{\rho_0}),f)}{\Delta A}g(\mathbf{r_1}|\mathbf{r_0},f)g^*(\mathbf{r_2}|\mathbf{r_0},f) \tag{2}$$

as shown in Appendix A where $S_{qq}(V(\boldsymbol{\rho_0}),f)$ is the source power-spectral density, which is a function of wind speed V and frequency f, ΔA is a small area increment of integration at least the size of the horizontal coherence area of the source distribution, and $g(\mathbf{r_j}|\mathbf{r_0},f)$ is the waveguide Green function. Throughout this paper a cylindrical coordinate system in used where $\mathbf{r}=(\boldsymbol{\rho},z)=(\rho,\theta,z)$, $\boldsymbol{\rho}$ is the horizontal location vector, ρ is distance from the origin, θ is azimuth angle, and z is depth measured with positive downward from the surface. The locations $\mathbf{r_1}$ and $\mathbf{r_2}$ are receivers and $\mathbf{r_0}$ is the source. Green functions are calculated by a combination of wavenumber integration at short ranges and the normal mode approximation at long ranges. The integration over surface source area is computed numerically. This expression is valid for range-dependent source fields and environments.

The source depth z_0 is taken to be a quarter wavelength for all simulations in the present paper. This follows noise modeling convention[5–7] since source depths of a quarter wavelength or less lead to a downward-directed dipole source radiation pattern. Hamson has shown that on average wind-generated noise in the ocean radiates with a downward directed pattern that closely fits a dipole for wind speeds between 5 and 20 m/s and frequencies from 400 Hz to 3.2 kHz.[48] This is true even for average source depths greater than a quarter wavelength and sea-surface roughness much larger than the wavelength[48,49] as in a hurricane where wave heights may exceed 10 m. This is understandable since surface noise is believed to arise from many monopole sources, in particular bubbles, randomly distributed near the sea surface. All of these, by the method of images, have main downward directed lobes and varying side-lobes which tend to cancel.

As discussed in the Introduction, the source power-spectral density has been shown to follow

$$S_{qq}(V,f)=s_0(f)V^{n(f)} \tag{3}$$

for certain frequency and wind speed ranges. While experiments[14] at wind speeds below 20 m/s give $n=3.1\pm0.3$, values in the broader $n=1$ to $n=4$ range will be used here for illustrative purposes. If it is later found that wind speed and noise intensity are related by some other function, the power-law relationships considered here will provide a basis for piecewise construction of this more complicated dependence.

Farmer has shown experimentally that clouds of bubbles near the ocean surface may, through scattering and absorption, lower ambient noise levels at frequencies above 8 kHz and wind speeds above 15 m/s.[16] While such attenuation has never been observed at lower frequencies, we will consider its possibility in the high winds of a hurricane.

Attenuation, in dB/m, can be written as $\alpha=10\log(e)\sigma n_v$, where σ is the extinction cross section of an individual bubble and n_v is the number of bubbles per unit volume.[15] Using this expression, Weston[15] provides a model for attenuation by sea surface bubble clouds, based on the extinction cross section and spatial distribution of wind-generated bubbles as a function of wind speed and frequency. This attenuation can then be included in the Green function in Eq. (2) to determine its effect on the underwater noise field. This is done by calculating the Green function for a waveguide with an effective attenuation in dB/m of

$$\alpha(V,f)=\begin{cases}9.35\times10^{-7}\sqrt{f}V^3, & f<1.5\text{ kHz},\\ 2.44\times10^{-8}fV^3, & f>1.5\text{ kHz},\end{cases} \tag{4}$$

in a layer at the sea surface as given by Weston.[15]

IV. SINGLE HYDROPHONE ANALYSIS

Here it is shown that the noise intensity measured by a single sensor in a hurricane is dominated by local sea-surface sources rather than sound propagating from longer ranges. Underwater acoustic intensity can then be used to estimate the wind speed within a local resolution area since wind speed in a hurricane is also found to be effectively constant over this scale.

Beginning with the cross-spectral density of the noise field in a hurricane, Eq. (2), the spectral intensity of the sound field received at $\mathbf{r}$ can written as

$$I(\mathbf{r},f)=\frac{C(\mathbf{r},\mathbf{r},f)}{\rho_w c}=\int_{-\infty}^{\infty} d^2\boldsymbol{\rho_0}\frac{S_{qq}(V(\boldsymbol{\rho_0}),f)}{\rho_w c\Delta A}|g(\mathbf{r}|\mathbf{r_0},f,V(\boldsymbol{\rho_0}))|^2, \tag{5}$$

where the total instantaneous intensity is given by

$$\mathcal{I}(\mathbf{r})=\int_0^{\infty} I(\mathbf{r},f)df. \tag{6}$$

The Green function $g(\mathbf{r}|\mathbf{r_0},f,V(\boldsymbol{\rho_0}))$ depends on local wind speed $V(\boldsymbol{\rho_0})$ because it includes attenuation due to wind-generated sea-surface bubbles. We show that this wind speed dependence is negligible at frequencies less than 100 Hz for typical hurricane wind speeds, but needs to be accounted for at higher frequencies. Surface wind speed V is given by the Holland model of Fig. 1 for a hurricane, while the surrounding ambient wind speed is taken to be 5 m/s.

Two hurricane-prone ocean environments surrounded by densely populated coastal communities, the North Atlantic and the Bay of Bengal, are considered. Their sound speed profiles are shown in Fig. 3. The difference in water depth between these two environments leads to fundamental differences in propagation. Typical near-surface sound sources will lead to refractive propagation with excess depth in the North Atlantic but not in the Bay of Bengal. In the former, sound may propagate efficiently to long ranges via the deep-sound channel, while in the latter, it will multiply reflect from the lossy bottom leading to far greater transmission loss. Although hurricanes decrease the temperature of the local sea surface by roughly 1 °C near the eye wall to roughly 35-m depth, the corresponding small change in sound speed[50] of roughly 4 m/s is also local and so has a negligible effect on the curvature of both local and long-range sound paths.

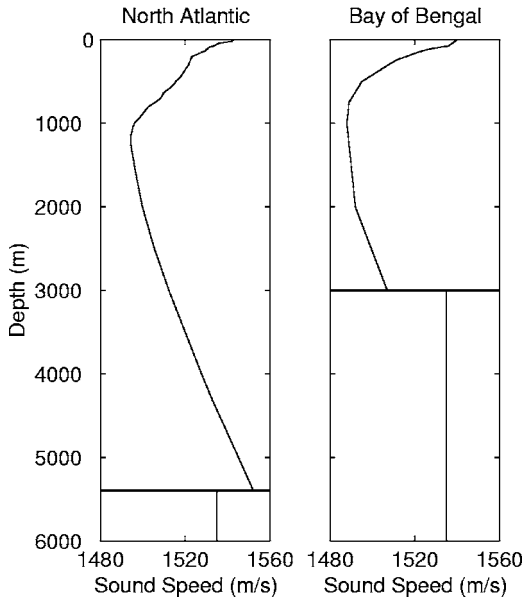

FIG. 3. Sound speed profiles $c(z)$ for the North Atlantic[65] and the Bay of Bengal.[66,67] The bottom has a density of 1.38 g/cm and an attenuation of 0.3 dB/λ corresponding to the deep silty sediment layers of the Bay of Bengal[68,69] and the North Atlantic Abyssal plain.[70,71] The water has a density of 1 g/cm and an attenuation of 6×10^{-5} dB/λ.

The spectral intensity level, given by

$$L_I = 10\log\left(\frac{I(\mathbf{r},f)}{I_{\mathrm{ref}}(f)}\right) \tag{7}$$

in dB *re* $I_{\mathrm{ref}}(f)$, of hurricane-generated noise is computed by the direct integration of Eq. (5) as a function of receiver range ρ and depth z from an origin at the center of the hurricane on the sea-surface. For convenience in the present paper the reference level $I_{\mathrm{ref}}(f)$ is taken to be the spectral intensity at a reference depth $z_{\mathrm{ref}}=200$ m for a reference 10-m altitude wind speed of $V_{\mathrm{ref}}=5$ m/s over the entire ocean

$$I_{\mathrm{ref}}(f) \equiv I(\mathbf{r}_{\mathrm{ref}},f) = \int_{-\infty}^{\infty} d^2\boldsymbol{\rho_0}\frac{S_{qq}(V_{\mathrm{ref}},f)}{\rho_w c\Delta A}|g(\mathbf{r}_{\mathrm{ref}}|\mathbf{r_0},f,V_{\mathrm{ref}})|^2, \tag{8}$$

where $\mathbf{r}_{\mathrm{ref}}=(\boldsymbol{\rho},z_{\mathrm{ref}})$. Noise intensity has been measured for 5 m/s wind speed in many ocean environments and at similar depths.[14,17,51,52] In an experimental scenario other reference values could be chosen.

Spectral intensity level is shown in Fig. 4 for frequencies of 50, 400, and 3200 Hz, spaced three octaves apart, using Eqs. (3)–(8) and assuming $n=3$. The choice of $n=3$ is within measured power-laws[14] and has been chosen out of convenience since it is linearly related to the power of the wind.[53] The wind speed profile of the hurricane and surroundings based on the Holland model at an altitude of 10 m from the sea surface is also plotted with the spectral intensity level at a depth of 200 m. The most apparent feature in Figs. 4(a) and 4(c) is the effectively linear relationship at low frequency, 50 Hz, between spectral intensity level L_I and the log of the wind speed. This is roughly independent of depth as can be seen in Figs. 4(b) and 4(d). At higher frequencies,

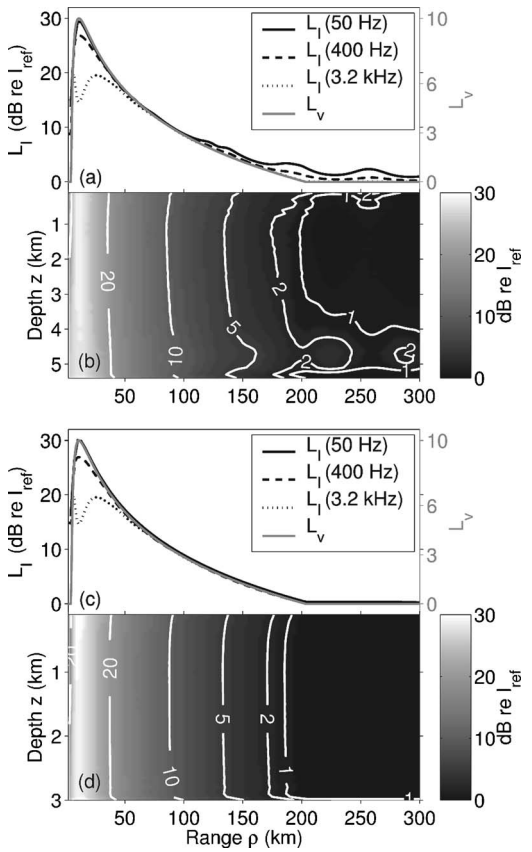

FIG. 4. Noise spectral level (dB *re* I_{ref}) in the North Atlantic [(a) and (b)] and the Bay of Bengal [(c) and (d)] for $n=3$. (a) and (c) show the level as a function of range at a depth of 200 m for 50, 400, and 3200 Hz frequencies. $L_V(\boldsymbol{\rho})=10\log(V(\boldsymbol{\rho})/V_{\mathrm{ref}})$ is plotted for comparison where $V_{\mathrm{ref}}=5$ m/s. $L_V=0$ is equivalent to $V=5$ m/s and $L_V=10$ is equivalent to $V=50$ m/s. (b) and (d) show the level as a function of range and depth at 50 Hz. In both waveguide environments the noise level closely follows the local wind speed. In the North Atlantic there is a convergence zone structure due to sound that propagates from the hurricane's eye wall. Note the convergence zone near the surface at a range of 257 km and the ray vertex depth of 4.7 km.

sea-surface bubbles significantly attenuate sound in the high-wind-speed, eye-wall region of the hurricane but the noise still follows local wind speed with a more complicated nonlinear dependence as will be shown in the next section. The small increase in level in the North Atlantic outside the hurricane at ranges of 193 and 257 km and at a depth of 4.7 km is caused by convergence zone propagation from the powerful sources in the eye wall. This convergence zone structure indicates an efficient mechanism exists for the long-range propagation of hurricane noise in this environment that will be considered in Sec. V.

A. Local noise dominates

The effectively linear relationship between the log of local wind speed and underwater acoustic spectral intensity shown in Fig. 4 suggests a possible simplifying approximation to our formulation. In particular the areal integral of Eq. (5) can be approximated by integrating only over local sources in the hurricane. These fall within a disc of area $A=\pi R^2$ centered at the horizontal location of the receiver $\boldsymbol{\rho}$

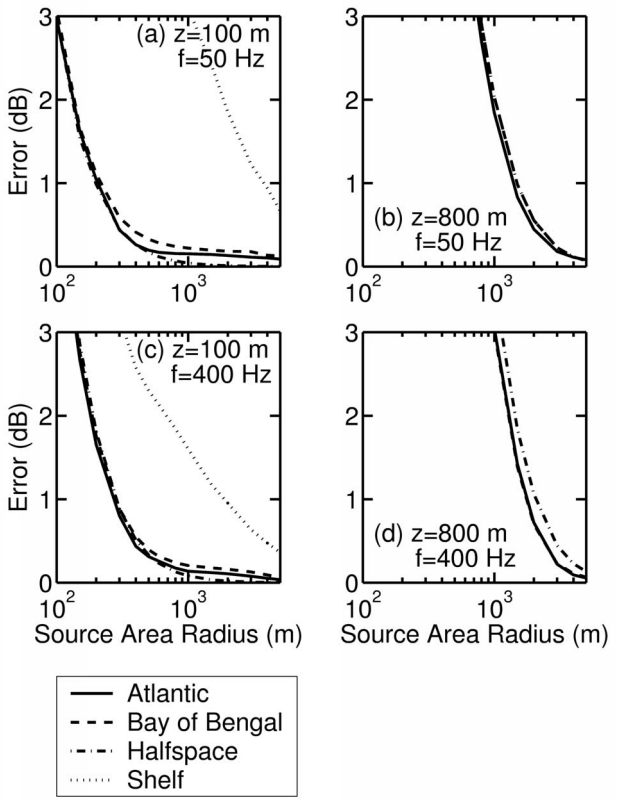

FIG. 5. Error induced by the local area approximation [Eq. (9)] as a function of local source area radius R_{local} for a single sensor under the maximum winds in the eye wall of a hurricane. Curves are shown for the North Atlantic and the Bay of Bengal environments used in this paper as well as for infinite half-space and shallow water continental shelf environments. Plots are given for sensor depths of 100 m [(a) and (c)] and 800 m [(b) and (d)] and for frequencies of 50 Hz [(a) and (b)] and 400 Hz [(c) and (d)]. While these plots are given for $n=3$ the difference for values $n=1$ to 4 is less than 0.1 dB. The North Atlantic, Bay of Bengal, and infinite half-space environments are very similar. In these deep-water environments, for the shallow 100-m sensor depth, we see that for R_{local} greater than 300 m the approximation error is negligible. For the deeper 800-m sensor depth, the R_{local} for which the error is negligible is roughly 2 km. In shallow water the error in the local area approximation is higher leading to a larger R_{local}. This is likely due to the strong reflection of sound off bottom. In deep water environments bottom reflections have little effect and most of the sound measured by a receiver propagates via direct path from the surface source.

which provides the dominant contribution in the exact integral [Eq. (5)]. The spectral intensity can then be approximated as

$$I(\mathbf{r},f) \approx \int_A d^2\boldsymbol{\rho}_\mathbf{0}' \frac{S_{qq}(V(\boldsymbol{\rho}_\mathbf{0}'),f)}{\rho_w c \Delta A} |g(\mathbf{r}|\mathbf{r}_\mathbf{0}',f,V(\boldsymbol{\rho}_\mathbf{0}'))|^2 \tag{9}$$

where $\boldsymbol{\rho}_\mathbf{0}'=\boldsymbol{\rho}_\mathbf{0}-\boldsymbol{\rho}$. Such a simplification can potentially lead to errors if R is too small.

To quantify the potential error of this local approximation, the approximate equation (9) is evaluated for a receiver under the eye wall of the hurricane where wind speed varies most drastically. When compared to the exact result of Eq. (5), we take the error induced by the local approximation to be negligible, less than or equal to 1 dB, for R greater than a minimum length R_{local}. The error as a function of R is given in Fig. 5 where, for deep-water environments, $R_{\text{local}}=300$ to 2000 m depending on sensor depth.

It is noteworthy that the deep-ocean North Atlantic and Bay of Bengal error curves closely match those of the infinite half-space. This shows that bottom reflections and variations in sound speed profile do not have a significant effect on R_{local} in deep water. For a bottom-mounted sensor in a typical shallow water environment $R_{\text{local}}=2$ to 3 km in the 50 to 400 Hz range. Our computations also show that R_{local} does not change significantly for the expected source power-spectral densities and attenuations considered in this paper.

The wind speeds in a hurricane do not change significantly over R_{local} and can be approximated as constant in Eq. (9). This leads to less than 0.2 dB additional error in the spectral intensity level, which can then be approximated as

$$\begin{aligned} I(\mathbf{r},f) &\approx \frac{S_{qq}(V(\boldsymbol{\rho}),f)}{\rho_w c \Delta A} \int_0^{2\pi} \int_0^{R_{\text{local}}} \rho_0' d\rho_0' d\theta_0' |g(\mathbf{r}|\mathbf{r}_\mathbf{0}',f,V(\boldsymbol{\rho}))|^2 \\ &\equiv S_{qq}(V(\boldsymbol{\rho}),f) W(\mathbf{r},f,V(\boldsymbol{\rho})) \end{aligned} \tag{10}$$

where only the local wind speed $V(\boldsymbol{\rho})$ directly above the receiver has a significant effect on both the source factor $S_{qq}(V(\boldsymbol{\rho}),f)$ and the waveguide propagation factor $W(\mathbf{r},f,V(\boldsymbol{\rho}))$. The source factor is universal in that it does not depend on propagation parameters and should be the same for any waveguide environment so long as the ocean depth greatly exceeds the ocean-atmosphere boundary layer. While the propagation factor does depend on the environment, ocean waveguides typically change gradually with horizontal position. The wind-speed-independent functionality of $W(\mathbf{r},f,V(\boldsymbol{\rho}))$ should then be effectively constant over R_{local} and over the horizontal extent of a hurricane, on the order of 100 km. Both factors may be characterized numerically or empirically to develop a set of curves to estimate wind speed from acoustic intensity. In the next section we find that it is possible to simplify these factors and develop an approximate analytic equation for wind speed estimation.

The approximate Eq. (10) for *range-dependent* sources and potentially *range-dependent* waveguides is similar to Kuperman and Ingenito's[5] exact Eq. (30) for *range-independent* sources and waveguides in that spectral intensity is the product of a "universal ambient noise" source factor, following Ingenito and Wolf[9] and here defined as $S_{qq}(V(\boldsymbol{\rho}),f)$, and a waveguide propagation factor $W(\mathbf{r},f,V(\boldsymbol{\rho}))$. The implicit assumption of formulations of this kind is that variations in source depth can be accounted for as equivalent variations in $S_{qq}(V(\boldsymbol{\rho}),f)$. This is consistent with the measured dipole behavior of ambient noise in the ocean.[48]

Taking the log of Eq. (10) leads to a useful approximate equation for spectral intensity level,

$$L_I(\mathbf{r},f) \approx L_S(V(\boldsymbol{\rho}),f) + L_W(\mathbf{r},f,V(\boldsymbol{\rho})) \tag{11}$$

in dB *re* $I_{\text{ref}}(f)$ where

$$L_S(V(\boldsymbol{\rho}),f) = 10\log\left(\frac{S_{qq}(V(\boldsymbol{\rho}),f)}{S_{qq}(V_{\text{ref}},f)}\right), \tag{12}$$

$$L_W(\mathbf{r},f,V(\boldsymbol{\rho})) = 10\log\left(\frac{W(\mathbf{r},f,V(\boldsymbol{\rho}))}{W_{\text{ref}}(f)}\right), \tag{13}$$

and

$$I_{\text{ref}}(f) = S_{qq}(V_{\text{ref}},f)W(\mathbf{r}_{\text{ref}},f,V_{\text{ref}}) = S_{qq}(V_{\text{ref}},f)W_{\text{ref}}(f). \tag{14}$$

Here $L_S(V(\boldsymbol{\rho}),f)$ is a universal ambient noise source term that is independent of waveguide propagation parameters, while $L_W(\mathbf{r},f,V(\boldsymbol{\rho}))$ is a waveguide propagation term. The functional dependencies of the first term can be determined empirically in any waveguide where the ocean depth greatly exceeds the ocean-atmosphere boundary layer, while the functional dependencies of the second term should be locally determined.

If $S_{qq}(V(\boldsymbol{\rho}),f)$ follows a power-law, such as Eq. (3), then universal ambient noise source level is linearly related by

$$L_S(V(\boldsymbol{\rho}),f) = 10n(f)\log\left(\frac{V(\boldsymbol{\rho})}{V_{\text{ref}}}\right) \tag{15}$$

to the log of wind speed. The slope of this linear relationship $10n(f)$ has been previously measured in the 13 Hz to 14.5 kHz frequency range and 1 to 20 m/s wind speed range.[10,11,14,51,52]

To estimate wind speed from ambient noise measurements using Eq. (11), the dependence of $L_W(\mathbf{r},f,V(\boldsymbol{\rho}))$ on wind-dependent attenuation by sea-surface bubbles needs to be established. This may be done empirically, numerically, or analytically as in the next section.

B. Separating the effect of attenuation by bubbles from local waveguide propagation

Analytic expressions are derived to show how attenuation can be separated from other waveguide propagation effects so that $L_W(\mathbf{r},f,V(\boldsymbol{\rho}))$ can be split into a universal wind-speed-dependent attenuation term and a local waveguide calibration term that is wind-speed independent. These analytic expressions also demonstrate the uniqueness of a wind speed estimate based on broadband underwater noise measurements. They also enable analytic expressions for estimation error to be obtained in some important cases.

Underwater spectral intensity level is calculated over a range of wind speeds and frequencies relevant to hurricane classification as illustrated in Fig. 6 using the full areal integration of Eq. (5). The spectral intensity level exhibits a maxima that depends on wind speed and frequency. For wind speeds and frequencies below this maxima, attenuation by bubbles is negligible so that $L_W(\mathbf{r},f,V(\boldsymbol{\rho}))$ is only a function of the local waveguide environment and spectral intensity level $L_I(\mathbf{r},f)$ should depend on the log of wind speed only through Eq. (15) given the power-law $n=3$ assumption of the simulation. For higher wind speeds and frequencies, attenuation by bubbles is significant and eventually leads to a roll-off in the spectral intensity so that $L_W(\mathbf{r},f,V(\boldsymbol{\rho}))$ is a separable function of both wind-speed-dependent and wind-speed-independent terms.

While the dependence of spectral intensity on wind speed and frequency including attenuation by bubbles can be

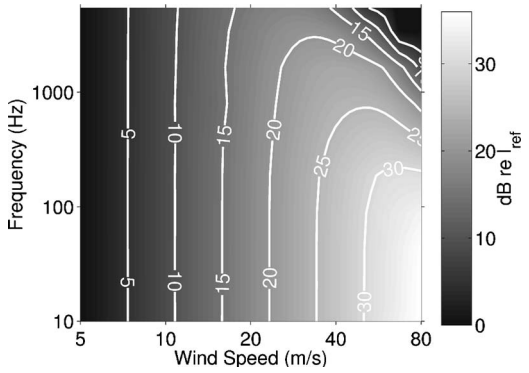

FIG. 6. Simulated noise spectral level (dB *re* I_{ref}) in the North Atlantic for range-independent winds as a function of wind speed and frequency including attenuation by sea-surface bubbles assuming $n=3$ from Eq. (5). Below 100 Hz the power-law relationship between noise intensity and wind speed is unaffected by bubble attenuation even up to the 80 m/s wind speeds of a hurricane. As frequency increases, attenuation affects the noise level at progressively lower wind speeds. For a given frequency the noise level increases linearly with wind speed, peaks, and then decays exponentially.

calculated exactly using the full areal integration of Eq. (5) or the local integral approximations of Eqs. (9) and (10), a useful first-order approximation leads to the analytic result

$$W(\mathbf{r},f,V(\boldsymbol{\rho})) = W_0(\mathbf{r},f)\frac{4\pi^2|A(V(\boldsymbol{\rho}),f,k_r=0)|^2}{z_0^2}, \tag{16}$$

where

$$W_0(\mathbf{r},f) = W(\mathbf{r},f,0) \tag{17}$$

and

$$A(V(\boldsymbol{\rho}),f,k_r=0) = \frac{\sin(kz_0)}{2i\pi[\alpha/(20\log(e))]\cos(kL) + [2\pi\omega/c(z_0)]e^{-ikL}} \tag{18}$$

is the downward plane-wave amplitude for a source in an attenuating sea-surface bubble layer following the Pekeris solution.[54] The complex wavenumber

$$k = \frac{\omega}{c(z_0)} + i\frac{\alpha(V(\boldsymbol{\rho}),f)}{20\log(e)}$$

is used in Eq. (18) where $\alpha(V(\boldsymbol{\rho}),f)$ is given in Eq. (4).

The spectral intensity level of Eq. (11) can then be approximated as

$$L_I(\mathbf{r},f) \approx L_S(V(\boldsymbol{\rho}),f) + L_A(V(\boldsymbol{\rho}),f) + L_{W_0}(\mathbf{r},f) \tag{19}$$

where

$$L_A(V(\boldsymbol{\rho}),f) = 20\log\left(\frac{2\pi|A(V(\boldsymbol{\rho}),f,k_r=0)|}{z_0}\right) \tag{20}$$

and

$$L_{W_0}(\mathbf{r},f) = 10\log\left(\frac{W_0(\mathbf{r},f)}{W_{\text{ref}}(f)}\right) \tag{21}$$

The approximation of Eq. (19) is in agreement with the full areal integration of Eq. (5) to within 1 dB for frequencies below 500 Hz even at hurricane wind speeds as shown in Fig. 7.

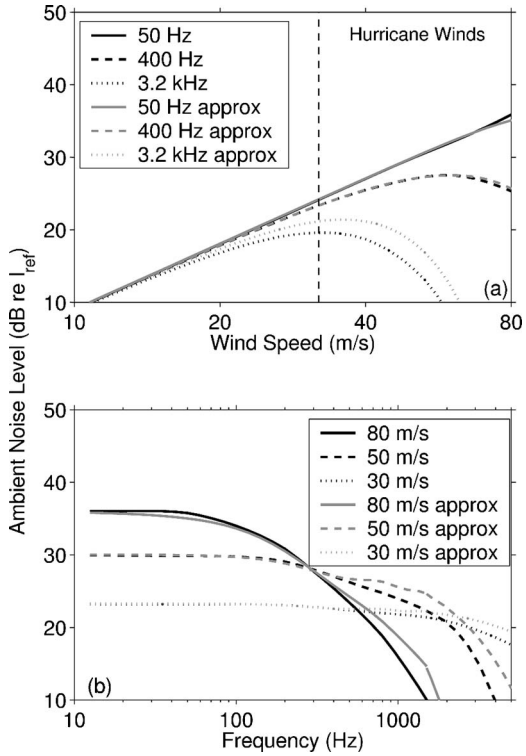

FIG. 7. (a) Noise spectral level (dB *re* I_{ref}) as a function of wind speed at several frequencies, assuming $n=3$. The black curves show the attenuation, caused by bubbles, at 50 Hz, 400 Hz, and 4 kHz. The range of wind speeds typical of a hurricane is also shown. (b) Noise spectral level curves as a function of frequency for typical hurricane wind speeds of 30, 50, and 80 m/s. The black curves show the full areal integration from Eq. (5) and the gray curves show the first-order approximation of the field given by Eq. (19) with Eqs. (15), (20), and (21).

By splitting the local waveguide and bubble attenuation effects of $L_W(\mathbf{r},f,V(\boldsymbol{\rho}))$ into two terms, $L_A(V(\boldsymbol{\rho}),f)$ and $L_{W_0}(\mathbf{r},f)$, wind speed can now be estimated from ambient noise using Eq. (19), where $L_A(V(\boldsymbol{\rho}),f)$ is a universal attenuation term that depends on local wind speed but like $L_S(V(\boldsymbol{\rho}),f)$ is also independent of waveguide parameters. The last term of Eq. (19), $L_{W_0}(\mathbf{r},f)$, is a local waveguide calibration that is independent of wind speed.

At frequencies below 100 Hz where attenuation α due to bubbles is negligible at hurricane wind speeds, $L_A(V(\boldsymbol{\rho}),f)$ goes to zero, as expected from Fig. 6. In this important case, if $S_{qq}(V(\boldsymbol{\rho}),f)$ follows a power law, Eq. (19) reduces to a linear equation in the log of wind speed,

$$L_I(\mathbf{r},f) \approx 10n(f)\log\left(\frac{V(\boldsymbol{\rho})}{V_{\text{ref}}}\right) + L_{W_0}(\mathbf{r},f), \tag{22}$$

where $10n(f)$ is a universal empirically determined slope and $L_{W_0}(\mathbf{r},f)$ is a local calibration intercept. The log of wind speed can be then found from measurements of ambient noise level by standard linear least squares estimation, as has been done in Refs. 10 and 11 at low wind speed.

As frequency increases, bubble-layer thickness exceeds a quarter wavelength and the $L_A(V(\boldsymbol{\rho}),f)$ term can be approximated as

$$L_A(V(\boldsymbol{\rho}),f) \approx -\alpha(V(\boldsymbol{\rho}),f)L. \tag{23}$$

If we use for illustrative purposes the $L=1.2$ m layer thickness given by Weston,[15] then Eqs. (20) and (23) agree to within 1 dB above 300 Hz and to within 2 dB between 100 and 300 Hz. While Weston notes that the assumption of a bubble layer of constant thickness may be poor at high wind speeds, any future improvements in our knowledge of the parameter L can be incorporated in Eqs. (18) and (23).

The locations of maxima in noise spectral level correspond to the ridge in Fig. 6. These can now be approximated analytically by substituting Eqs. (15), (21), and (23) into Eq. (19) and taking the derivative with respect to wind speed to obtain

$$V_{max} \approx \begin{cases} (1/(2.15\times10^{-7}L\sqrt{f}))^{1/3}, & 300 < f < 1.5 \text{ kHz}, \\ (1/(5.63\times10^{-9}Lf))^{1/3}, & f > 1.5 \text{ kHz}, \end{cases} \tag{24}$$

here assuming $n=3$ and $\alpha(V(\boldsymbol{\rho}),f)$ from Eq. (4).

C. Accuracy of underwater acoustic wind speed estimates

By standard stationary averaging, it should be possible to reduce the variance of an underwater acoustic wind speed estimate enough to be useful for meteorological purposes. Given the relationship $V=H(I)$ between the true wind speed V and true ambient noise intensity I, the maximum likelihood estimate (MLE) of the wind speed $\hat{V}$ given a measurement of ambient noise intensity $\hat{I}$ is $\hat{V}=H(\hat{I})$ by the invariance of the MLE.[55] The function H can be found either numerically from the exact integration, Eq. (5), or analytically from one of the approximations, Eqs. (11), (19), and (22). We define the percent root-mean-square error (RMSE) of the wind speed estimate $\hat{V}$ as

$$\nu_{\text{RMSE}} = 100\frac{\sqrt{\langle|\hat{V}-V|^2\rangle}}{\langle\hat{V}\rangle} \tag{25}$$

and the percent bias as

$$\nu_{\text{bias}} = 100\frac{|\langle\hat{V}\rangle - V|}{V} \tag{26}$$

given

$$\langle\hat{V}^m\rangle = \int_0^\infty H^m(\hat{I})p(\hat{I})d\hat{I}, \tag{27}$$

where $p(\hat{I})$ is the probability density function of the measured intensity $\hat{I}$. For the hurricane noise measurements considered here, where the contributions from a large number of independent sources are received simultaneously, the acoustic field is expected to be a circular complex Gaussian random variable. The time-averaged measured intensity $\hat{I}$ is then expected to follow a gamma distribution[8,19]

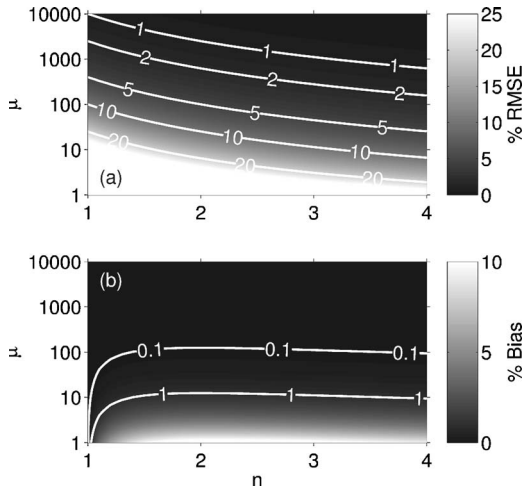

FIG. 8. The percent RMSE ν_{RMSE} (a) and percent bias ν_{bias} (b) of the wind speed estimate $\hat{V}$ where attenuation by sea-surface bubbles is insignificant, evaluated numerically from Eqs. (5) and (27). For time-bandwidth products $\mu > 5$ the estimate becomes unbiased and the RMSE attains the Cramer-Rao lower bound. Piggott[14] and Perrone[59] have measured wind noise level with standard deviations less than 1 dB which corresponds to $\mu > 19$. For $\mu = 19$ the percent RMSE in the wind speed estimate ranges from 6% to 25% depending on n which is a significant improvement over the primary satellite classification method.

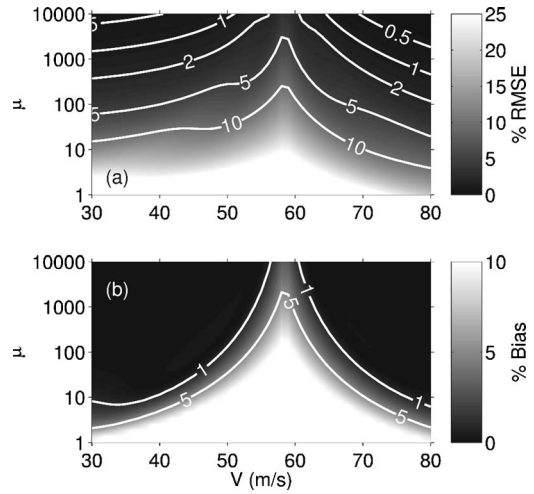

FIG. 9. The percent RMSE ν_{RMSE} (a) and percent bias ν_{bias} (b) of the wind speed estimate $\hat{V}$ including the effect of attenuation calculated numerically from Eqs. (5) and (27), assuming $n=3$, at $f=400$ Hz where $V_{\max}=58$ m/s. The error and bias increase for $V \approx V_{\max}$ but for $\mu > 5$ and for values of V where $\nu_{\mathrm{bias}} < 1\%$ the percent RMSE decreases and attains the Cramer-Rao lower bound. For spectral intensity measurements with $\mu = 19$ the percent RMSE in this example is between 9% and 20%.

$$p(\hat{I}) = \frac{(\mu/\bar{I})^{\mu}\hat{I}^{\mu-1}\exp\{-\mu(\hat{I}/\bar{I})\}}{\Gamma(\mu)}, \tag{28}$$

where μ is the time-bandwidth product and $\bar{I}$ is the mean of the noise measurement.

From the full areal integration of Eqs. (5) we can numerically find the percent RMSE and percent bias of the wind speed estimate $\hat{V}$. For frequencies below 100 Hz, where attenuation α is insignificant, we find that the percent RMSE and percent bias are functions of n and μ as shown in Fig. 8. At higher frequencies, where attenuation is significant, the percent RMSE and percent bias are also functions of frequency and wind speed. This is illustrated in Fig. 9 at a frequency of 400 Hz assuming $n=3$.

Following the standard practice of stationary averaging, the variance of noise measurements is reduced by inverse the number of stationary samples, $1/\mu$. In typical ocean acoustic applications, such as matched filtering, μ's in excess of 100 are common.[56–58] For example, Piggott[14] and Perrone[59] have obtained measurements of wind noise level with standard deviations less than 1 dB corresponding[8,18,19] to $\mu > 19$.

Given a spectral intensity measurement with $\mu > 19$, underwater acoustic wind speed estimates with errors similar to the 6% to 15% errors of hurricane-hunting aircraft[44] are possible. For example, at low frequencies where attenuation is insignificant, a measurement of noise spectral level with $\mu = 19$ would yield a corresponding percent RMSE in estimated wind speed of 6% to 25% for the range of published values for n as shown in Fig. 8. For the higher frequency 400 Hz example in Fig. 9, where attenuation is significant, a spectral intensity measurement with $\mu = 19$ will yield percent RMSEs from 9% to 20%. Even larger errors are common for remote satellite techniques, as high as 40% as noted in the Introduction. From this error analysis we find that underwater acoustic measurements may be worthwhile for estimating hurricane wind speed. Additional errors related to the practical application of the underwater acoustic technique will be discussed in Sec. IV D.

At low frequencies, less than 100 Hz, where attenuation α from bubbles becomes insignificant, the moments of $\hat{V}$ can also be evaluated analytically from the first-order approximation of Eq. (22) to illustrate the fundamental parameters affecting a wind speed estimate. The mean of the wind speed estimate can then be written as

$$\langle \hat{V} \rangle \approx \frac{\Gamma(\mu + 1/n)}{\Gamma(\mu)} \left(\frac{I(f)}{s_0 w_0 \mu} \right)^{1/n} = \frac{\Gamma(\mu + 1/n)}{\Gamma(\mu)\mu^{1/n}} V \tag{29}$$

and the standard deviation as

$$\sigma_{\hat{V}} \approx \left(\frac{I(f)}{s_0 w_0 \mu} \right)^{1/n} \sqrt{\frac{\Gamma(\mu + 2/n)}{\Gamma(\mu)} - \left(\frac{\Gamma(\mu + 1/n)}{\Gamma(\mu)} \right)^2}. \tag{30}$$

At these low frequencies the percent bias can then be approximated as

$$\nu_{\mathrm{bias}} \approx 100 \left| \frac{\Gamma(\mu + 1/n)}{\Gamma(\mu)\mu^{1/n}} - 1 \right| \tag{31}$$

and the percent RMSE as

$$\nu_{\mathrm{RMSE}} \approx 100 \sqrt{\frac{\Gamma(\mu + 2/n)\Gamma(\mu)}{\Gamma(\mu + 1/n)^2} - 2\frac{\Gamma(\mu)\mu^{1/n}}{\Gamma(\mu + 1/n)} + \frac{\Gamma(\mu)^2 \mu^{2/n}}{\Gamma(\mu + 1/n^2)}}. \tag{32}$$

These analytic expressions for the percent RMSE and percent bias match those calculated numerically from Eqs. (5) and (27) and shown in Fig. 8 to within 1%.

At low frequencies, where attenuation is insignificant, the Cramer-Rao lower bound can be derived from the first-

order approximation, Eq. (22), as shown in Appendix B. This provides a straightforward analytic method for calculating the percent RMSE as

$$\nu_{\mathrm{RMSE}} \approx 100\frac{\sqrt{Var_{\mathrm{asymptotic}}(\hat{V})}}{\langle \hat{V} \rangle} = 100\frac{1}{n\sqrt{\mu}}, \tag{33}$$

which matches the numerically computed value in Fig. 8 for $\mu > 5$. This is expected since the Cramer-Rao lower bound is the asymptotic variance for large μ. The Cramer-Rao lower bound can also be used to calculate the percent RMSE at frequencies above 300 Hz from the first-order approximation in Eqs. (19) with Eqs. (15), (21), and (23) yielding

$$\nu_{\mathrm{RMSE}} \approx 100\frac{\sqrt{Var_{\mathrm{asymptotic}}(\hat{V})}}{\langle \hat{V} \rangle} = 100\begin{cases} \dfrac{1}{\sqrt{\mu}(n - 6.46 \times 10^{-7} L\sqrt{f}V^3)}, & f < 1.5 \text{ kHz}, \\ \dfrac{1}{\sqrt{\mu}(n - 1.69 \times 10^{-8} LfV^3)}, & f > 1.5 \text{ kHz}, \end{cases} \tag{34}$$

which matches the numerical results in Fig. 9 when $\mu > 5$ and $\nu_{\mathrm{bias}} < 1\%$.

D. Practical issues

We have shown that a single underwater acoustic sensor provides significant potential as a measurement tool to accurately estimate local wind speed in a hurricane. There are practical issues, however, to consider when deploying such sensors to monitor a hurricane. While this is not a definitive discussion of all the issues that might be involved, we will attempt to illustrate how an underwater acoustic measurement system might be implemented. For example, how would one deploy these sensors, how many sensors would be needed to fully characterize a hurricane, and how much would it cost.

One possible scenario would be to deploy multiple sonobouys, similar to those used in weather classification experiments by Nystuen and Selsor,[60] from aircraft or ships in the path of an oncoming hurricane. As the hurricane passes over each sonobouy the sensor would cut a swath through the storm recording the wind speeds overhead. The swaths from multiple sonobouys could give a fairly complete measurement of the wind speeds in the hurricane. This is similar to the current measurements made by hurricane-hunting aircraft which fly through the storm cutting a swath and measuring wind speed. For both methods, sonobouys or hurricane-hunting aircraft, the sensors must pass through the eye wall of the hurricane where the winds are strongest. For aircraft this means actively piloting the plane through the storm, whereas with stationary sonobouys, one would deploy many sensors along a line that crosses the expected path of the hurricane to insure that at least one sonobouy cuts through the eye wall. For example, a line of 20 sonobouys spaced 5 km apart across the hurricane's path would span almost 100 km, assuring several measurements of the wind speed in the eye wall.

The advantage of deploying sonobouys in advance of a hurricane is that the ship or aircraft never has to enter the storm and would not need to be as expensive as the specialized hurricane-hunting aircraft used today. The cost of a typical hurricane-hunting aircraft such as the WC-130 is \$78 million (inflation adjusted to year 2003 dollars)[34] and the cost of a single flight[35] is roughly \$155,000. Between two and eight aircraft flights are made per day[44] for potentially landfalling hurricanes in the North Atlantic where the lifespan of a hurricane can be several weeks. Twenty sonobouys, at \$500 each,[61] could be deployed from inexpensive nonspecialized ships or aircraft in the path of an oncoming hurricane well before conditions are dangerous for roughly \$10,000.

An alternative scenario would be to deploy hundreds of permanent shore-cabled hydrophone systems, at \$10,000 to \$20,000 each depending on cable length, in strategic hurricane-prone areas for a few million dollars. As noted before, this is much less than the purchase price of a WC-130 hurricane-hunting aircraft.

Such underwater acoustic systems would likely be used in conjunction with *a priori* location estimates from satellites. Satellites would determine the path of the hurricane relative to the hydrophone and show whether the sensor passed through the high winds of the eye wall. The underwater acoustic measurement would then provide an estimate of the wind speeds for the portions of the hurricane that passed overhead. If a hydrophone does not pass through the powerful eye wall but rather through the weaker surrounding winds it would still provide a lower bound or threshold measurement of wind speed and it may be possible to extrapolate these lower wind speeds to determine the higher wind speeds of the eye wall.

V. HYDROPHONE ARRAY ANALYSIS

The analysis in the previous sections demonstrates how omnidirectional sensors may be used to accurately measure the local winds and classify the destructive power of a hurricane as it passes overhead. It may be possible to use arrays of hydrophones to beamform on the acoustic field from a hurricane at long range. For illustrative purposes we will consider horizontal linear arrays of the type that might be towed from an oceanographic or naval vessel; however, other array configurations, such as moored arrays, might also be useful. Arrays might also be useful for directionally filtering out other noise sources, such as ships and surf, in local measurements.

Using the expression for the cross-spectral density of the noise field of Eq. (2) we find the angular spectral density of the noise received by an N-element array, or beamformed output, to be

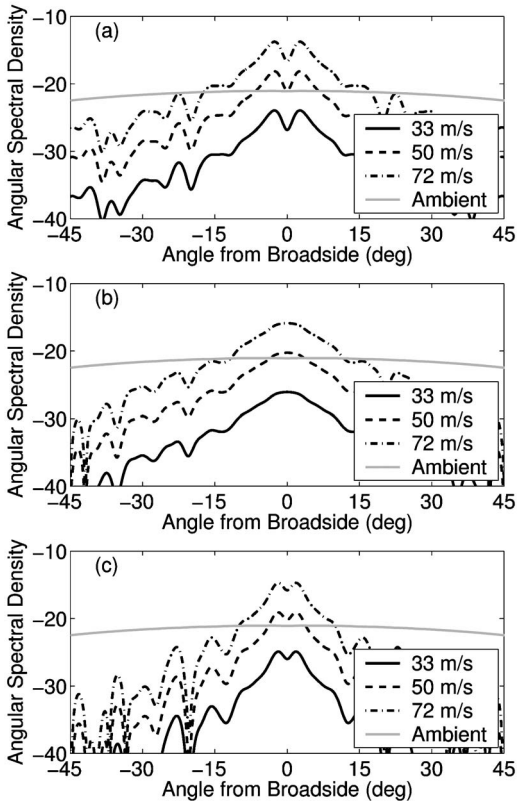

FIG. 10. Angular spectral density level $10\log(B(\Omega,f))\cdot(\mathrm{dB}\ re\ \rho_w c I_{\mathrm{ref}}/sr^2)$ at 100 Hz for a 64-element $\lambda/2$-spaced horizontal broadside array as a function of steering angle for hurricane-generated noise in the North Atlantic at ranges of 257 km (a), 289 km (b), and 385 km (c) from the eye of the hurricane, assuming $n=3$. Ranges of 257 and 385 km correspond to the fourth and sixth convergence zones from the center of the hurricane. The range of 289 km is exactly between the fourth and fifth convergence zones. Curves are shown for a powerful 72-m/s hurricane, a medium 50-m/s hurricane and a weak 33-m/s hurricane. The angular spectral density level from ambient noise is plotted for comparison. A steering angle of 0° corresponds to the array steered toward the calm eye of the hurricane and the powerful eye wall is located at ±3°. This array has an angular resolution of 1.8°, which at a range of 257 km corresponds to an 8-km spatial resolution.

$$B(\Omega,f)=\frac{1}{N^2}\sum_{m=1}^{N}\sum_{n=1}^{N}e^{-j\mathbf{k}\cdot\mathbf{r_m}}C(\mathbf{r_m},\mathbf{r_n},f)e^{j\mathbf{k}\cdot\mathbf{r_n}} \tag{35}$$

with units of $\mu\mathrm{Pa}^2/\mathrm{sr}^2$ Hz, where $\mathbf{k}=(2\pi f/c)\mathbf{i}_{\mathbf{\Omega}}$, $\mathbf{i}_{\mathbf{\Omega}}$ is a unit vector in the steering direction Ω, and $\mathbf{r_m}$ is the position of the mth hydrophone on the array.

We define the hurricane wind-generated noise source area to include sources within 200 km of the hurricane's center as shown in Fig. 1 and the ambient noise source area to include sources generated by the 5-m/s winds surrounding the hurricane. To show how an array might be able to measure the destructive power of a hurricane, the angular spectral density of the noise will be calculated for a hurricane as a function of maximum wind speed.

The angular spectral density of Eq. (35) in the direction of the hurricane increases with maximum wind speed, as shown in Fig. 10 for an array at 200-m depth at a range far from the hurricane eye. The difference in spectral density between the strong 72-m/s-wind-speed and weak 33-m/s-wind-speed hurricanes of Fig. 10 is roughly 10 dB given the assumption here that $n=3$. The difference in spectral density would be greater for larger n.

A practical horizontal array can resolve the important features of the hurricane such as the eye wall, which has dimensions of tens of kilometers, when placed in a convergence zone as in Figs. 10(a) and 10(c). This is not possible for an array just outside the convergence zone as shown in Fig. 10(b). In the former case, the length L of an array, oriented at broadside to the hurricane, would have to be

$$L>R\lambda/l \tag{36}$$

where R is the range from the array to the hurricane and l is the size of the eye-wall. Typical linear arrays[56] have lengths L on the order of $100\lambda/2$. In the example of Fig. 10, a broadside array with $L=32\lambda$, similar to the ONR FORA array,[62] images the hurricane with 10-km resolution at a range of 320 km. The width of the convergence zone must also be sufficiently small to resolve the eye wall in range. For the given environment and ranges considered, this condition is satisfied because the convergence zone width is roughly 5 km, which is less than the width of the eye wall.

A horizontal array oriented at end-fire to the hurricane has the advantage that it discriminates against local surface noise coming from near broadside in favor of sound that travels from long distances at shallow angles in the waveguide. This could potentially lead to longer hurricane detection ranges. Unfortunately, at end-fire, the length of the array must satisfy

$$L>2\lambda(R/l)^2 \tag{37}$$

to resolve the eye-wall. For example, an impractically long $L=2000\lambda$ end-fire array would be needed to achieve 10-km resolution at a range of 320 km.

The analysis presented here for the North Atlantic shows that it may be possible to image the features of a hurricane using linear broadside arrays of sufficient length. Waveguides that lack excess depth, such as the Bay of Bengal, do not exhibit the convergence zone structure seen in the North Atlantic. This probably makes it extremely difficult to even detect hurricanes using practical linear arrays at long ranges in these environments.

VI. CONCLUSIONS

We have shown that the wind-generated noise received by a single underwater acoustic sensor in a hurricane can be well approximated by sea-surface contributions so local that wind speed and surface source intensity can be taken as nearly constant. Two terms with empirically and analytically determined dependencies may be used to estimate wind speed from measured ambient noise spectral level: (1) a universal ambient noise source term and (2) a local waveguide calibration term. At low frequencies, current evidence suggests a simple power-law relationship exists between noise intensity and wind speed so that the log of wind speed may be estimated accurately from spectral ambient noise level by linear least square estimation. At higher frequencies, a non-

linear relationship is expected but we show that it should be possible to make unambiguous low-variance wind speed estimates from broadband noise measurements.

ACKNOWLEDGMENTS

The idea for this work arose during a conversation with Kerry Emanuel of MIT and we thank him for many useful discussions about hurricanes and hurricane classification.

APPENDIX A: NOISE CORRELATION FROM RANDOM SURFACE SOURCES

Previous models for sea-surface noise[5–7] contain approximations or parametrizations that are not valid for the rapidly spatially varying source levels of a hurricane, particularly in the case where the hydrophone is near or under the hurricane. Because of this an alternative expression for calculating the spatial cross-spectral density of the noise field is necessary. The geometry for modeling the spatial cross-spectral density from uncorrelated noise sources at the surface of a stratified ocean waveguide is shown in Fig. 2.

The pressure field created by each surface source is given by the solution to the Helmholtz equation

$$\phi(\mathbf{r},f) = q(\mathbf{r_0},f)g(\mathbf{r}|\mathbf{r_0},f), \tag{A1}$$

where $\phi(\mathbf{r},f)$ is the pressure at $\mathbf{r}$ given a source spectral amplitude $q(\mathbf{r_0},f)$ at $\mathbf{r_0}$ and $g(\mathbf{r}|\mathbf{r_0},f)$ is the waveguide Green function. The total noise field $\phi_S(\mathbf{r},f)$ is the sum of the fields radiated from each source:

$$\phi_S(\mathbf{r},f) = \sum_m^M \phi(\mathbf{r},f) = \sum_m^M q(\mathbf{r_m},f)g(\mathbf{r}|\mathbf{r_m},f). \tag{A2}$$

The spatial correlation of the total field between two receivers $\mathbf{r_1}$ and $\mathbf{r_2}$ can then be written as

$$\begin{aligned} R(\mathbf{r_1},\mathbf{r_2},f',f'') &= \langle \phi_S(\mathbf{r_1},f')\phi_S^*(\mathbf{r_2},f'')\rangle \\ &= \sum_m \sum_n \langle q(\mathbf{r_m},f')q^*(\mathbf{r'_n},f'')\rangle g(\mathbf{r_1}|\mathbf{r_m},f')g^*(\mathbf{r_2}|\mathbf{r_n},f''). \end{aligned} \tag{A3}$$

If the sources have zero mean and are uncorrelated, then $\langle q(\mathbf{r_m},f')q^*(\mathbf{r_n},f'')\rangle = \delta_{m,n}\langle q(\mathbf{r_m},f')q^*(\mathbf{r_n},f'')\rangle$, where $\delta_{m,n}$ is the Kronecker delta function and the correlation simplifies to

$$R(\mathbf{r_1},\mathbf{r_2},f',f'') = \sum_m \langle q(\mathbf{r_m},f')q^*(\mathbf{r_m},f'')\rangle g(\mathbf{r_1}|\mathbf{r_m},f')g^*(\mathbf{r_2}|\mathbf{r_m},f''). \tag{A4}$$

Assuming that the source function q and the received field ϕ_S can be taken to follow a stationary random process in time, at least over the measurement period, then[63] $\langle \phi_S(\mathbf{r_1},f)\phi_S^*(\mathbf{r_2},f')\rangle = C(\mathbf{r_1},\mathbf{r_2},f)\delta(f-f')$ and $\langle q(f)q^*(f')\rangle = S_{qq}(f)\delta(f-f')$ where $S_{qq}(f)$ is the power-spectral density of q and

$$C(\mathbf{r_1},\mathbf{r_2},f) = \sum_m S_{qq}(\mathbf{r_m},f)g(\mathbf{r_1}|\mathbf{r_m},f)g^*(\mathbf{r_2}|\mathbf{r_m},f) \tag{A5}$$

is the cross-spectral density of $\phi_S(\mathbf{r_1})$ and $\phi_S(\mathbf{r_2})$.

For dense source concentrations, this sum can be expressed as an area integral,

$$C(\mathbf{r_1},\mathbf{r_2},f) = \int d^2\boldsymbol{\rho_0} \frac{S_{qq}(\mathbf{r_0},f)}{\Delta A} g(\mathbf{r_1}|\mathbf{r_0},f)g^*(\mathbf{r_2}|\mathbf{r_0},f), \tag{A6}$$

where ΔA is equal to or greater than the coherence area of the random source distribution and corresponds to the smallest differential area summable.

The variance of the source amplitude equals the integrated power spectral density $\langle |q(t)|^2\rangle = \int S_{qq}(f)df$. Since this variance is asymptotically approximated by the sample variance $\langle |q(t)|^2\rangle \approx (1/T)\int_0^T |q(t)|^2\,dt$ for large measurement windows T and since Parseval's theorem has $(1/T)\int_0^T |q(t)|^2\,dt = (1/T)\int_{-\infty}^{\infty} |Q(f)|^2\,df$, we may deduce that

$$S_{qq}(f) \approx \frac{1}{T}|Q(f)|^2, \tag{A7}$$

which relates S_{qq} to practical measurements.

Equation (A6) is similar to an intermediate expression derived by Perkins *et al.* [Eq. (6) of Ref. 7] derived for a significantly different physical scenario as noted in Sec. III. Equation (A6) can be used to model the spatial correlation of the noise field for uncorrelated surface-generated noise when the source distribution or waveguide is range dependent. When the source distribution and environment are range independent, Eq. (A6) reduces to

$$C(\mathbf{r_1},\mathbf{r_2},f) = \frac{2\pi S_{qq}(f)}{\Delta A} \int_{k_r} k_r\,dk_r g(k_r,z_1,z_0)g^*(k_r,z_2,z_0)J_0(k_r|\boldsymbol{\rho_1}-\boldsymbol{\rho_2}|), \tag{A8}$$

following the Kuperman and Ingenito approach[5] where $g(k_r,z_1,z_0)$ is the wavenumber transform of $g(\mathbf{r_1}|\mathbf{r_0},f)$.

APPENDIX B: ASYMPTOTIC VARIANCE FOR WIND SPEED ESTIMATES

The variance of a wind-speed estimate is evaluated numerically in Sec. IV C for some specific scenarios. A general analytic expression is derived here for the asymptotic variance of the wind speed estimate for large sample size μ using Fisher information. For the expected intensity I of an acoustic measurement with a signal-to-noise ratio or time-bandwidth product μ, the inverse Fisher information or Cramer-Rao lower bound (CRLB) of a wind speed estimate $\hat{V}$ is given as[19,64]

$$\mathrm{Var}_{\mathrm{asymptotic}}(\hat{V}) = \left(\frac{\mu}{I^2}\left(\frac{\partial I}{\partial V}\right)^2\right)^{-1}, \tag{B1}$$

which is the asymptotic variance.[63]

At low frequencies the relationship between intensity and wind speed can be expressed using Eq. (22), which, when inserted into Eq. (B1), yields

$$\mathrm{Var}_{\mathrm{asymptotic}}(\hat{V}) = \frac{V^2}{\mu n^2}. \tag{B2}$$

At higher frequencies, where attenuation due to bubbles becomes important, the relationship between intensity and wind speed follows Eq. (19), substituting Eqs. (15), (21), and (23), so that

$$\mathrm{Var}_{\mathrm{asymptotic}}(\hat{V}) = \frac{V^2}{\mu\{n - [VL/(10\log(e))](\partial\alpha/\partial V)\}^2}. \tag{B3}$$

For the attenuation $\alpha(V,f)$ described by Weston[15] in Eq. (4), the CRLB becomes

$$\mathrm{Var}_{\mathrm{asymptotic}}(\hat{V}) = \begin{cases} \dfrac{V^2}{\mu(n - 6.46\times 10^{-7} LV^3\sqrt{f})^2}, & f < 1.5\ \mathrm{kHz}, \\ \dfrac{V^2}{\mu(n - 1.69\times 10^{-8} LV^3 f)^2}, & f > 1.5\ \mathrm{kHz}. \end{cases} \tag{B4}$$

For $V = V_{\max}$ where $V_{\max}$ is given in Eq. (24), the CRLB goes to infinity, indicating that an unbiased estimate of wind speed is not possible for that wind speed and frequency. This problem can be overcome by broadband intensity measurements. For a wind speed estimate given intensity measurements at multiple frequencies, Eq. (B4) becomes

$$\begin{aligned} \mathrm{Var}_{\mathrm{asymptotic}}(\hat{V}) &= \left(\sum_f \frac{\mu(f)}{I(f)^2}\left(\frac{\partial I(f)}{\partial V}\right)^2\right)^{-1} \\ &\approx \begin{cases} \left(\sum_f \dfrac{\mu(f)}{V^2}(n - 6.46\times 10^{-7} LV^3\sqrt{f})^2\right)^{-1}, & f < 1.5\ \mathrm{kHz}, \\ \left(\sum_f \dfrac{\mu(f)}{V^2}(n - 1.69\times 10^{-8} LV^3 f)^2\right)^{-1}, & f > 1.5\ \mathrm{kHz}, \end{cases} \end{aligned} \tag{B5}$$

which remains finite and can be made small by increasing the time-bandwidth product μ.

[1] V. O. Knudsen, R. S. Alford, and J. W. Emling, "Underwater ambient noise," J. Mar. Res. **7**, 410–429 (1948).
[2] G. W. Wenz, "Acoustic ambient noise in the ocean: Spectra and sources," J. Acoust. Soc. Am. **34**, 1936–1956 (1962).
[3] B. F. Cron and C. H. Sherman, "Spatial-correlation functions for various noise models," J. Acoust. Soc. Am. **34**, 1732–1736 (1962).
[4] W. S. Liggett and M. J. Jacobsen, "Covariance of surface-generated noise in a deep ocean," J. Acoust. Soc. Am. **38**, 303–312 (1965).
[5] W. A. Kuperman and F. Ingenito, "Spatial correlation of surface generated noise in a stratified ocean," J. Acoust. Soc. Am. **67**(6), 1988–1996 (1980).
[6] W. M. Carey, R. B. Evans, J. A. Davis, and G. Botseas, "Deep-ocean vertical noise directionality," IEEE J. Ocean. Eng. **15**(4), 324–334 (1990).
[7] J. S. Perkins, W. A. Kuperman, F. Ingenito, L. T. Fialkowski, and J. Glattetre, "Modeling ambient noise in three-dimensional ocean environments," J. Acoust. Soc. Am. **93**, 739–752 (1993).
[8] N. C. Makris, "The statistics of ocean-acoustic ambient noise," in *Sea Surface Sound '97*, edited by T. Leighton (Kluwer Academic, Dordrecht, 1997).
[9] F. Ingenito and S. N. Wolf, "Site dependence of wind-dominated ambient noise in shallow water," J. Acoust. Soc. Am. **85**, 141–145 (1989).
[10] P. T. Shaw, D. R. Watts, and H. T. Rossby, "On the estimation of oceanic wind speed and stress from ambient noise measurements," Deep-Sea Res. **25**, 1225–1233 (1978).
[11] D. L. Evans, D. R. Watts, D. Halpern, and S. Bourassa, "Oceanic winds measured from the seafloor," J. Geophys. Res. **89**(C3), 3457–3461 (1984).
[12] W. M. Carey and D. Browning, "Low frequency ocean ambient noise: Measurements and theory," in *Sea Surface Sound* (Kluwer Academic, Dordrecht, 1988).
[13] A. C. Kibblewhite, "Panel discussion report, wave and turbulence noise," in *Sea Surface Sound* (Kluwer Academic, Dordrecht, 1988).
[14] C. L. Piggott, "Ambient sea noise at low frequencies in shallow water of the Scotian Shelf," J. Acoust. Soc. Am. **36**, 2152–2163 (1964).
[15] D. E. Weston, "On the losses due to storm bubbles in oceanic sound transmission," J. Acoust. Soc. Am. **86**, 1546–1553 (1989).
[16] D. M. Farmer and D. D. Lemon, "The influence of bubbles on ambient noise in the ocean at high wind speeds," J. Phys. Oceanogr. **14**, 1762–1778 (1984).
[17] A. J. Perrone, "Ambient-noise-spectrum levels as a function of water depth," J. Acoust. Soc. Am. **48**, 362–368 (1970).
[18] A. D. Pierce, *Acoustics: An Introduction to Its Physical Principles and Applications* (McGraw-Hill, New York, 1991).
[19] N. C. Makris, "The effect of saturated transmission scintillation on ocean acoustic intensity measurements," J. Acoust. Soc. Am. **100**, 769–783 (1996).
[20] V. F. Dvorak, "Tropical cyclone intensity analysis and forecasting from satellite imagery," Mon. Weather Rev. **103**, 420–430 (1975).
[21] V. F. Dvorak, *Tropical Cyclone Intensity Analysis Using Satellite Data*, NOAA Tech. Rep. NESDIS 11, Washington, DC (1984).
[22] C. S. Velden, T. L. Olander, and R. M. Zehr, "Development of an objective scheme to estimate tropical cyclone intensity from digital geostationary satellite imagery," Weather Forecast. **13**, 172–186 (1998).
[23] J. L. Franklin, L. A. Avila, J. L. Bevin II, M. B. Lawrence, R. J. Pasch, and D. R. Stewart, "Eastern North Pacific hurricane season of 2002," Mon. Weather Rev. **131**, 2379–2393 (2003).
[24] R. J. Pasch, *Tropical Cyclone Report, Hurricane Debby, 19–24 August 2000*, National Hurricane Center, 2000.
[25] J. L. Franklin, *Tropical Cyclone Report, Hurricane Florence, 10–17 September 2000*, National Hurricane Center, 2000.
[26] J. Beven, *Tropical Cyclone Report, Hurricane Keith, 28 September–6 October 2000*, National Hurricane Center, 2000.
[27] L. A. Avila, *Tropical Cyclone Report, Hurricane Iris, 4–9 October 2001*, National Hurricane Center, 2001.
[28] S. R. Stewart, *Tropical Cyclone Report, Hurricane Kyle, 20 September–12 October 2002*, National Hurricane Center, 2002.
[29] R. J. Pasch, *Tropical Cyclone Report, Hurricane Isaac, 21 September–1 October 2000*, National Hurricane Center, 2000.
[30] M. B. Lawrence, *Tropical Cyclone Report, Hurricane Joyce, 25 September–2 October 2000*, National Hurricane Center, 2000.
[31] S. R. Stewart, *Tropical Cyclone Report, Hurricane Michael, 17–19 October 2000*, National Hurricane Center, 2000.
[32] K. B. Katsaros, P. W. Vachon, W. T. Liu, and P. G. Black, "Microwave remote sensing of tropical cyclones from space," J. Phys. Oceanogr. **58**, 137–151 (2002).
[33] G. J. Holland (ed.), *Global Guide to Tropical Cyclone Forecasting* (World Meteorological Organization, Geneva, 1993).
[34] Air Force Reserve Command, Office of Public Affairs, "U. S. air force fact sheet, WC-130 hercules," www.af. mil/factsheets/factsheet.asp?fsID=132
[35] Lt. D. Barr (personal communication, 27 October 2003).
[36] G. J. Holland, "An analytic model of the wind and pressure profiles in hurricanes," Mon. Weather Rev. **108**, 1212–1218 (1980).
[37] K. A. Emanuel, "Thermodynamic control of hurricane intensity," Nature (London) **401**, 665–669 (1999).
[38] R. A. Pielke, Jr. and C. W. Landsea, "Normalized hurricane damages in the U.S.: 1925–1995," Weather Forecast. **13**, 621–631 (1998).
[39] P. J. Hebert, J. D. Jarrell, and M. Mayfield, *The Deadliest, Costliest, and Most Intense United States Hurricanes of this Century (and Other Frequently Requested Hurricane Facts)*, NOAA Tech. Memo., NWS NHC-31, Washington, DC (1993).
[40] G. J. Holland, "The maximum potential intensity of tropical cyclones," J. Atmos. Sci. **54**, 2519–2541 (1997).
[41] R. L. Bankert and P. M. Tag, "An automated method to estimate tropical cyclone intensity using SSM/I imagery," J. Appl. Meteorol. **41**, 461–472 (2002).
[42] C. S. Velden, "Observational analyses of North Atlantic tropical cyclones from NOAA polar-orbiting satellite microwave data," J. Appl. Meteorol. **28**, 59–70 (1989).
[43] S. Q. Kidder, M. D. Goldberg, R. M. Zehr, M. DeMaria, J. F. W. Purdom, C. S. Velden, N. C. Grody, and S. J. Kusselson, "Satellite analysis of

tropical cyclones using the advanced microwave sounding unit (AMSU)," Bull. Am. Meteorol. Soc. **81**(6), 1241–1259 (2000).
[44]Federal Coordinator for Meteorological Services and Supporting Research, *National Hurricane Operations Plan*, U. S. Dept of Commerce/Nat. Oceanic and Atmospheric Administration, FCM-P12-2003 (2003).
[45]P. Ratilal, *Remote Sensing of Submerged Objects and Geomorphology in Continental Shelf Waters with Acoustic Waveguide Scattering*, Ph.D. thesis, Massachusetts Institute of Technology, 2002.
[46]P. Ratilal and N. C. Makris, "Mean and covariance of the forward field propagated through a stratified ocean waveguide with three-dimensional random inhomogeneities," J. Acoust. Soc. Am. (in press).
[47]J. D. Wilson and N. C. Makris, "Full field spatial correlation of range dependent surface generated noise in a stratified ocean with application to hurricane sensing," 143rd Meeting of the Acoustical Society of America, Pittsburgh, PA, June 2002.
[48]R. M. Hamson, "The modeling of ambient noise due to shipping and wind sources in complex environments," Appl. Acoust. **51**(3), 251–287 (1997).
[49]W. J. Pierson and L. Moskowitz, "A proposed spectral form for fully developed wind seas based on the similarity theory of S. A. Kitaigardski," J. Geophys. Res. **69**, 5181–5190 (1964).
[50]D. Hutt, J. Osler, and D. Ellis, "Effect of hurricane Michael on the underwater acoustic environment of the scotian shelf," in *Impact of Littoral Environmental Variability on Acoustic Predictions and Sonar Performance*, edited by N. G. Pace and F. B. Jensen (Kluwer Academic, Dordrecht, Netherlands, 2002).
[51]N. R. Chapman and J. W. Cornish, "Wind dependence of deep ocean ambient noise at low frequencies," J. Acoust. Soc. Am. **93**, 782–789 (1993).
[52]D. H. Cato, "Ambient sea noise in waters near Australia," J. Acoust. Soc. Am. **60**, 320–328 (1976).
[53]V. L. Streeter (ed.), *Handbook of Fluid Dynamics* (McGraw-Hill, New York, 1961).
[54]W. E. Ewing, W. S. Jardetzky, and F. Press, *Elastic Waves in Layered Media* (McGraw-Hill, New York, 1957), pp. 126–130.
[55]S. M. Kay, *Fundamentals of Statistical Signal Processing, Estimation Theory* (Prentice Hall, Englewood Cliffs, NJ, 1993).
[56]R. J. Urick, *Principles of Underwater Sound* (McGraw-Hill, New York, 1983), pp. 57, 389.
[57]C. S. Clay and H. Medwin, *Acoustics Oceanography: Principles & Applications* (Wiley, New York, 1977).
[58]W. S. Burdic, *Underwater Acoustic System Analysis* (Prentice-Hall, Englewood Cliffs, NJ, 1984).
[59]A. J. Perrone, "Deep-ocean ambient-noise spectra in the Northwest Atlantic," J. Acoust. Soc. Am. **3**, 762–770 (1969).
[60]J. A. Nystuen and H. D. Selsor, "Weather classification using passive acoustic drifters," J. Acoust. Soc. Am. **14**, 656–666 (1997).
[61]M. May (personal communication, 15 September, 2004).
[62]*Main Acoustic Clutter Experiment, Initial Report, April 24–May 24*, Office of Naval Research, pp. 53–54.
[63]A. Papoulis and S. U. Pillai, *Probability, Random Variables and Stochastic Processes* (McGraw Hill, Boston, 2002), pp. 513–515, 537–538.
[64]N. C. Makris, "A foundation for logarithmic measures of fluctuating intensity in pattern recognition," Opt. Lett. **20**(19), 2012–2014 (1995).
[65]N. C. Makris, L. Z. Avelino, and R. Menis, "Deterministic reverberation from ocean ridges," J. Acoust. Soc. Am. **97**, 3547–3574 (1995).
[66]S. P. Kumar, T. V. R. Murty, Y. K. Somayajulu, P. V. Chodankar, and C. S. Murty, "Reference sound speed profile and related ray acoustics of Bay of Bengal for tomographic studies," Acustica **80**, 127–137 (1994).
[67]K. D. K. M. Sarma and B. Mathew, "Sound speed structure in the upper layers of equatorial Indian Ocean and Central Bay of Bengal during summer monsoon season," J. Acoust. Soc. India **17**(3-4), 218–221 (1989).
[68]C. Subrahmanyam, N. K. Thakur, T. G. Rao, R. Khanna, M. V. Ramana, and V. Subrahmanyam, "Tectonics of the Bay of Bengal: New insights from satellite-gravity and ship-borne geophysical data," Earth Planet. Sci. Lett. **171**, 237–251 (1999).
[69]E. L. Hamilton, "Geoacoustic modeling of the sea floor," J. Acoust. Soc. Am. **68**, 1313–1340 (1980).
[70]E. L. Hamilton, "Sound velocity as a function of depth in marine sediments," J. Acoust. Soc. Am. **78**, 1348–1355 (1985).
[71]B. E. Tocholke, "Acoustic environment of the Hatteras and Nares Abyssal Plains, Western North Atlantic Ocean, determined from velocities and physical properties of sediment cores," J. Acoust. Soc. Am. **68**, 1376–1390 (1980).

Sounds from an oil production island in the Beaufort Sea in summer: Characteristics and contribution of vessels

Susanna B. Blackwell[a] and Charles R. Greene, Jr.
Greeneridge Sciences, Inc., 1411 Firestone Road, Goleta, California 93117

(Received 30 December 2004; revised 13 October 2005; accepted 29 October 2005)

The objective of this study was to determine the levels, characteristics, and range dependence of underwater and in-air sounds produced during the open-water seasons of 2000–2003 by the Northstar oil development, located in nearshore waters of the Alaskan Beaufort Sea. Specifically, sounds originating at the island itself (from construction, drilling, and oil production activities) were compared with sounds produced by vessels performing island support. Sounds were obtained with boat-based recordings (at distances up to 37 km from Northstar), a cabled hydrophone (distance ~450 m), and with autonomous seafloor recorders (distance ~22 km). Vessels (crew boat, tugs, self-propelled barges) were the main contributors to the underwater sound field and were often detectable underwater as much as ~30 km offshore. Without vessels, broadband island sounds reached background values at 2–4 km. Island sound levels showed more variation (lower min, higher max) during construction than during drilling and production. In-air broadband measurements were not affected by the presence of vessels and reached background values 1–4 km from Northstar. However, one airborne tone (81 Hz) believed to originate at Northstar was still detectable in the spectrum 37 km away. © *2006 Acoustical Society of America.*
[DOI: 10.1121/1.2140907]

PACS number(s): 43.30.Nb, 43.50.Rq [KGF] Pages: 182–196

I. INTRODUCTION

A. Background

Northstar is an artificial oil production island located ~5 km offshore of the barrier islands northwest of Prudhoe Bay, in nearshore waters of the Alaskan Beaufort Sea [position 70.49°N, 148.70°W, see Fig. 1 and Blackwell *et al.* (2004a, b)]. The island is made of gravel and is located in shallow water (12 m). BP Exploration (Alaska) Inc. began construction during the winter of 1999–2000 and the first oil was produced on 31 October 2001.

A few studies have reported on the underwater sounds produced by man-made oil exploration islands in the Arctic during summer [e.g., Davis *et al.*, 1985; Johnson *et al.*, 1986; see Richardson *et al.* (1995) for a review]. These studies indicate that sound levels during construction and drilling are lower when emanating from gravel islands than from other types of offshore platforms used in the Arctic (e.g., caissons, drillships). Reasons for this difference probably have to do with the different construction or emplacement procedures and the various ways in which sounds are coupled to the water. Corresponding data on in-air sounds are virtually nonexistent in the published literature. Measurements of underwater and airborne sound during oil production from offshore facilities of any type during the Arctic summer are also lacking, but Gales (1982) reported on sounds from drilling and production operations in temperate waters.

Concern over the short- and long-term effects of anthropogenic sounds on the ocean environment has been growing in recent years (Richardson *et al.*, 1995; NRC, 2003). Shipping traffic and coastal industrial development have contributed to an increase in average levels of underwater sound in several ocean regions since the 1950s (Ross, 1976, 1993; Andrew *et al.*, 2002; NRC, 2003). Ice cover for most of the year shields the Arctic from much boat traffic, but the quest for new oilfields has resulted in exploration for and production of oil from offshore developments in the Beaufort Sea and elsewhere. In northern Alaska, groups concerned about underwater noise include, in addition to industry itself (in this case BP), federal agencies such as the National Marine Fisheries Service (NMFS) and the Minerals Management Service and local government such as the North Slope Borough (NSB). These and other cooperating groups operate under a "permit" process and associated procedures that aim to document and minimize the sounds produced during offshore industrial projects, and their effects on marine mammals. In this respect, the U.S. Marine Mammal Protection Act (16 U.S.C. 1361) has been a major influence on these types of studies.

B. Objectives and approach

To help assess possible effects of Northstar on marine mammals (mainly bowhead whales, *Balaena mysticetus*, and ringed seals, *Phoca hispida*), underwater and airborne measurements of island sounds were needed during all phases of the Northstar project, from construction to production. Also, acoustical measurements were required to satisfy the provisions of (1) the NSB zoning ordinance for Northstar and (2) Letters of Authorization (LoA) issued by NMFS to BP with respect to possible disturbance of whales and seals during Northstar construction and production.

The objective of the present work was to measure and

[a]Corresponding author; electronic mail: susanna@greeneridge.com

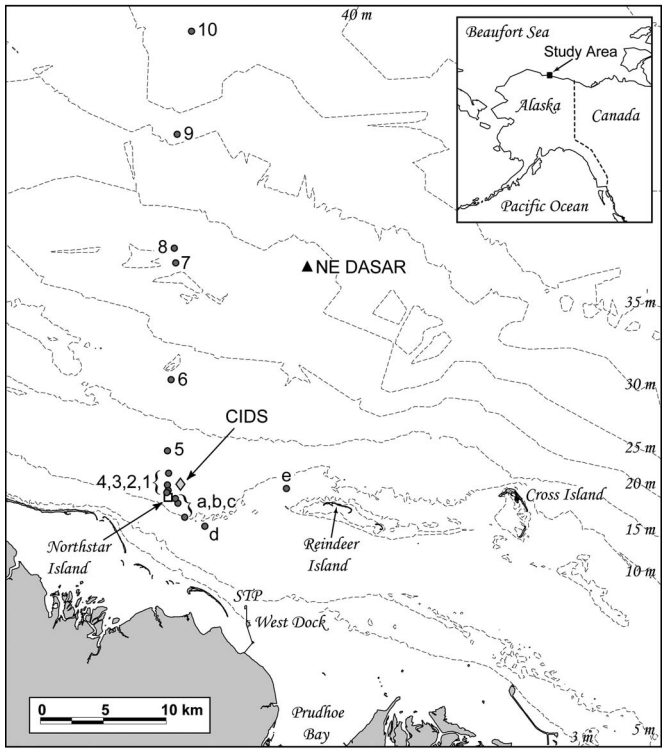

FIG. 1. Acoustic recording locations near Northstar Island, Beaufort Sea, Alaska, 30 August, 1, and 17 September 2000; 10 and 12 August 2001; 5, 6, and 12 September 2002; and 11 August 2003. Northstar Island is shown as a white square, the CIDS caisson as a gray diamond, the NE DASAR as a black triangle, and the recording stations as filled circles. The station numbers indicated refer to Table I.

document the levels, characteristics, and range dependence of sounds produced by Northstar-related industrial activities during the open-water seasons (August–October) of 2000, 2001, 2002, and 2003. In particular, we aimed to compare sounds originating at the island itself (from construction, drilling, and oil production activities) with sounds produced by vessels operating in support of the island. The planned approach relied on two main types of measurements: (1) boat-based recordings of sounds in air and in the water during different activities at Northstar, at a range of distances from targeted sound sources, and (2) continuous underwater recordings at fixed sites over periods of several weeks, obtained by deploying instrumentation on the sea floor, either self-contained or with a cable to shore. Companion studies provided related acoustic data during winter when the sea around Northstar was ice-covered (Blackwell *et al.*, 2004a; Greene and McLennan, 2004).

C. Island activities during study period

The chronology of BP's activities at Northstar during the study period is described in Williams and Rodrigues (2004). During all types of recordings, we collected as much information as possible on any sound producing activities occurring on or around Northstar Island. However, we had no control over any of the island activities and many of the recordings were opportunistic in nature. The main events taking place during each open-water season were the following:

FIG. 2. Sealift barge 400 carrying two process modules, upon its arrival at Northstar Island's southern dock on 10 August 2001. The Ocean-class tug *Navigator* can be seen alongside the barge on one side.

(i) 2000: The gravel island was built up during the ice-covered season in early 2000, and construction continued during the summer (open-water season). The permanent living quarters and the drill rig were brought by sealift barges in August and installed on the island in September. One or two self-propelled barges (440 hp each) were used as moveable docks for transfer of island personnel as well as goods. The barge was positioned on the leeward side of the island, perpendicular to the shore, and maintained that position by "pushing" against the shore. Consequently, the barge's propellers were engaged as long as it remained at the island (sometimes several days). Drilling for wells began in December, after freeze-up.

(ii) 2001: Northstar was still under construction. In August, three sealift barges and seven accompanying tugs brought modular buildings and oil production equipment, which were installed on the island in August and September. The biggest shipment included two process modules; the barge carrying them, along with one of the associated Ocean-class tugs, is shown in Fig. 2. Tugs included Ocean-class (OC, 7200 hp), Point-class (PC, 2100 hp), and River-class (RC, 1095 hp) categories. The self-propelled barges were replaced with floating docks on the island's eastern and western shores. Drilling was suspended in mid-June and resumed in November. On 24 October, the island's primary power was switched from diesel-powered generators to three generators powered by Solar gas turbines, each 13 000 hp. Two gas compressors, powered by two additional gas-turbine engines (each 32 000 hp max), were also installed for reinjection of gas into the oil reservoir. Oil production started on 31 October.

(iii) 2002 and 2003: Northstar was producing oil, but drilling for new wells continued nearly continuously until late October 2002 using a top-drive drill-rig on the island. In August 2003 an underwater berm surrounding the island (part of the island's protection against

ice) was reconstructed by the placement of additional gravel. This operation required a gravel barge, a PC tug, and a RC tug.

The vessels used in the Northstar area during all 4 years were of the following four categories: (1) One or two 19-m crew boats (400 hp), which made several daily round trips between the mainland (West Dock, see Fig. 1) and the island. During 2003, a small hovercraft also traveled periodically between the mainland and Northstar (Blackwell and Greene, 2005). (2) Barges and their associated tugs (~17 vessels total). This category includes the barges used for daily transport of cargo, monthly transport of fuel, and yearly transport of buildings and other large items (sealift). It also includes the two self-propelled barges used as movable docks in 2000 and occasionally thereafter. (3) Spill response vessels (~11 total) performing exercises and routines related to oil spill response preparedness. (4) General vessel traffic (not related to Northstar) transiting through the Northstar development area.

II. METHODS

The data presented in this paper are based on two types of recordings (see Fig. 1 for locations):

(i) Boat-based recordings at variable ranges from targeted sound sources. These recordings include transects at distances of 0.29–37.1 km from Northstar Island. Underwater and in-air recordings were made on nine days: 30 August 2000, 1 and 17 September 2000; 10 and 12 August 2001; 5, 6, and 12 September 2002; and 11 August 2003.

(ii) Continuous underwater recordings from two fixed locations:

(a) A reference location, as far from industrial sounds as possible. A Directional Autonomous Seafloor Acoustic Recorder (DASAR, Greene *et al.*, 2004) was deployed ~22 km northeast of the island as part of a related study (Fig. 1). This DASAR (location "NE") provided continuous recordings during the periods 29 August–30 September 2001, 30 August–3 October 2002 and 29 August–28 September 2003.

(b) A near-island location, 420–550 m northeast of the north shore of Northstar. Island sounds were recorded with a cabled hydrophone (CH) during the periods 28 August–3 October 2001, 31 August–1 October 2002, and 30 August–16 September 2003. A DASAR also recorded island sounds during the period 18–28 September 2003.

A. Equipment and field procedures

1. Boat-based recordings

The sensors included a hydrophone and microphone. The hydrophone was an International Transducer Corporation (ITC) model 6050C. (Two serial numbers were used, calibrated by the manufacturer in 1985 and 2000 for one, 1986 and 1999 for the other. Both hydrophones showed a change in sensitivity of less than 1.3 dB between the two calibrations.) This includes a low-noise preamplifier next to the sensor and a 30-m cable. This cable was attached with cable ties to a fairing to minimize possible strumming problems. Prior to recording, the hydrophone signals were amplified with an adjustable-gain postamplifier (fixed 10-dB steps, changes noted in a log book and on the recorder's voice channel). In 2000, the omnidirectional microphone was an ACO model 7013 condenser microphone (calibrated by the manufacturer in 1999 and 2000) with a 4012 preamplifier. In 2001–2003, we used a G.R.A.S. Sound and Vibration 1/2-in. prepolarized free-field microphone model 40AE (calibrated by the manufacturer in 2001) with an ICP preamplifier model TMS426C01.

Hydrophone and microphone signals were recorded on two channels of a SONY model PC208Ax instrumentation-quality digital audiotape (DAT) recorder, at a sampling rate of 24 kHz. All recorded sensor data were equalized in the laboratory so that the calibrated spectral response of each sensor was flat between 4 and 10 000 Hz. Quantization was 16 bits, providing a dynamic range of >80 dB between an overloaded signal and the quantization noise. A memo channel on the tape recorder was used for voice announcements, and the date and time were recorded automatically.

All recordings were obtained using an Alaska Clean Seas (ACS) "Bay" vessel of length 12.8 m as a recording platform. Recordings were made to distances of 37.1 km north and 9.3 km east of Northstar (Fig. 1). After selecting an appropriate recording location, the boat was stopped and the hydrophone and spar buoy to which it was connected were lowered into the water. The hydrophone depth was 9.5–10.5 m (water depth ranged from 10 to 37 m, see Fig. 1). A depth reading was taken with the recording vessel's depth sounder before all sound-generating devices (engines, generator, depth sounder) on the vessel were turned off.[1] The microphone was positioned on the deck of the vessel in such a way that it had an unobstructed path to the sound source (Northstar or vessel) at all times. During recording the recording vessel drifted with the wind and current. A GPS position (Garmin model 12XL) was obtained at the beginning and end of each recording. These positions were used to calculate a mean distance of each station from the northern or eastern shore of Northstar Island. A laser rangefinder (Bushnell model no. 20-0880) was used for distances <800 m or during recordings targeting a mobile sound source such as a vessel. In 2000 and 2001, hourly wind speed and direction were obtained from the Northstar weather station, accessed on the website http://www.resdat.com/mms. In 2002 and 2003, wind speed and direction were recorded over a period of ~4 min at each station with a Kestrel 2000 Pocket Thermo Wind meter (Nielsen Kellerman, Chester, PA 19013); these data are shown in Table I. During all years, notes on wave height were made at each recording station in order to determine sea state, upon which overall ambient levels depend. All recordings were made in relatively calm conditions, at sea state <3. A total of 75, 136, 123, and 18 min of boat-based recordings were obtained during the four consecutive years, respectively.

TABLE I. Sampling date and direction from Northstar (N*), station ID, distance from N*, water depth, sea state, and mean wind speed for all acoustic recording locations, open water seasons 2000–2003.

Date (North or East)	ID	Distance from N* (m)	Depth (m)	Sea State	Wind (m/s)	Date (North or East)	ID	Distance from N* (m)	Depth (m)	Sea State	Wind (m/s)
30 August 2000 (N)	1	450	11.7	2–3	7–10	12 August 2001 (N)	7	18 190	21.9	2–3	5–9
	2	590	12.3	2	7–10	(cont.)	8	19 740	25.0	$\frac{1}{2}$	5–9
	3	970	13.0	2	7–10	12 August 2001 (E)	a	530	12.2	2–3	5–9
	4	1930	13.9	2	7–10		b	890	10.7	2–3	5–9
	5	3740	13.3	2	7–10		c	2050	11.0	2–3	5–9
	6	9500	19.0	2	7–10		d	3700	11.0	2–3	5–9
	7	19 300	23.9	3	7–10		e	9400	8.2	2–3	5–9
	9	28 630	28.5	3	7–10	5 September 2002 (N)	2	500	14.0	0	0.9
1 September 2000 (N)	1	300	11.5	1	2.5		3	1000	14.3	$\frac{1}{2}$	0.9
	2	590	12.6	1	2.5		4	1960	15.2	$\frac{1}{2}$	0.9
	3	1010	13.3	1	2.5	6 September 2002 (N)	2	530	14.0	0	1.0
	4	1930	14.2	1	2.5		3	950	14.3	0	0.8
	5	3730	14.5	1	2.5		4	1820	15.2	0	1.0
	6	9280	19.7	1	2.5		5	3410	14.6	$\frac{1}{2}$	0.9
	7	19 120	23.9	1	2.5		6	9270	20.1	$\frac{1}{2}$	0.8
	9	28 930	28.5	1	2.5		7	18 500	24.4	$\frac{1}{2}$	1.3
17 September 2000 (N)	1	350	12.6	$\frac{1}{2}$–1	1–2		10	37 050	36.9	$\frac{1}{2}$	0.7
	2	570	12.9	$\frac{1}{2}$–1	1–2	12 Sep. 2002 (N)	2	570	13.1	2	8.5
	3	920	13.3	$\frac{1}{2}$–1	1–2		3	960	13.7	2	2.3
	4	2060	14.2	$\frac{1}{2}$–1	1–2		4	1940	14.2	2	3.5
	5	3870	13.7	$\frac{1}{2}$–1	1–2		5	3760	13.7	2	4.9
	6	9450	19.1	$\frac{1}{2}$–1	1–2		6	9180	19.2	2.5	8.9
	7	18 620	21.8	$\frac{1}{2}$–1	1–2		7	18 600	23.5	2.5	6.0
10 August 2001 (N)	4	1700	14.3	2–3	5–7		10	37 080	36.0	2.5	7.4
	5	3340	14.9	1	5–7	11 August 2003 (N)	1	290	13.1	$\frac{1}{2}$–1	1.8
	6	9170	19.5	1	5–7		2	700	12.8	$\frac{1}{2}$–1	1.8
12 August 2001 (N)	4	1970	14.6	2–3	5–9		4	1800	14.3	$\frac{1}{2}$–1	1.8
	5	3840	14.0	2–3	5–9		6	9580	19.5	$\frac{1}{2}$–1	1.8
	6	9460	20.1	2–3	5–9						

2. Cabled hydrophones

The cabled hydrophone (CH) system, deployed 420–460 m north (offshore) of Northstar, was designed to provide a continuous record of sounds emanating from the island (plus ambient noise) over an extended period.

An ITC model 8212 hydrophone (calibrated by the manufacturer in 2000), containing a low-noise preamplifier, was spliced to the conductors of a 550-m double-armored well-logging cable to form a CH. The recorders themselves and the batteries to power them were housed inside a small shelter hanging on the outside of Northstar's northern sheet-pile wall. A battery powered the preamplifier and the hydrophone. The hydrophone signals were connected to electronics similar to those used in DASARs (see below). This equipment provided for signal conditioning and recording on 10- and 30-GB (gigabyte) disks. Sampling was at 2 kHz to permit recording sounds at frequencies up to 1 kHz. Quantization was 16 bits. The disk capacity and battery life were sufficient to record without interruption for over 40 days.

The hydrophone was mounted on a small iron stand 25 cm above the bottom (water depth 12–13 m) and was deployed by boat 440 m (2001), 420 m (2002), and 460 m (2003) from the north shore of the island. Recording was continuous except for a 1-h period in 2002 to swap disks. On 16 September 2003 the CH was destroyed by a storm and was replaced (on 18 September) by a DASAR (see below) at a location 550 m from the north shore of the island.

3. DASARs

For details on DASARs see Greene *et al.* (2004). Each recorder comprised a DIFAR sensor (Sparton Electronics, De Leon Springs, FL), which includes a compass, two horizontal, orthogonal directional sensors, and an omnidirectional pressure sensor to sense an acoustic field. The three DIFAR channels were recorded directly to an embedded Persistor Instruments CF1 computer, which is a 3.3-V 68338 Computer Module with CompactFlash Operating System. The computer controls signal acquisition, which involved sampling the acoustic signals and storing the resulting data in a continuous stream on a 25.38-GB disk drive. The acoustic data received over a 46.6-min period were stored in buffer memory; the disk then operated for about 25 s while the data were written onto disk. To achieve frequency coverage from 10 to almost 500 Hz, a sample frequency of 1 kHz was selected.

DASARs were configured for deployment by connecting one end of the instrument's aluminum frame to a 100-m line and a 2-kg Danforth anchor. After deploying the anchor, the

line was laid out straight and the DASAR was lowered to the bottom with a rope. The GPS locations of both the anchor and DASAR were recorded during deployment. For retrieval, a double grapnel anchor assembly with 6 m of chain was towed perpendicular to the 100-m line and across it.

B. Signal analysis

1. Boat-based recordings

The recorded, digitized hydrophone signals were transferred directly to a computer hard disk drive as time series. They were then equalized and calibrated in units of sound pressure with flat frequency response over the data bandwidth (10–10 000 Hz). Analysis was done using MATLAB (The MathWorks, Natick, MA) routines and custom programs. For each recording, a sound-pressure time series (SPTS) was generated and the sound was played via a speaker to help the analyst match notes from the field with the recorded sounds. The sound waveform was used to select representative segments for further analysis. These included the stronger and weaker sections of the recording and all the types of sources that could be differentiated. Artifact sounds were avoided, such as those produced by waves slapping against the hull of the recording vessel. Three to 12 8.5-s segments selected from each recording were analyzed.

Frequency composition was determined by calculating the sound-pressure spectral density levels (SPSDLs) by Fourier analysis. The Blackman-Harris minimum three-term window (Harris, 1978) was applied to each 1-s block of samples transformed. The averaging time for such measurements was 8.5 s. With windowing, the spectral resolution was 1.7 Hz with 1-Hz cell separation. Transforms were overlapped by 50% and therefore 16 power spectral densities were averaged for each 8.5-s segment. A tone was identified when the SPSDL for a given frequency cell was greater than the SPSDL for both adjacent frequency cells and at least 5 dB above the nearest minimum SPSDL at a lower frequency.

Microphone data were transcribed to disk files and analyzed in the same way as hydrophone data. Microphone data were A-weighted (and results are expressed in dBA *re*: 20 μPa) to allow comparisons with common airborne sounds described in the literature (Kinsler *et al.*, 2000; Kryter, 1985). Narrow-band data were not A-weighted and are expressed in dB *re*: $(20\ \mu\text{Pa})^2/\text{Hz}$, respectively.

When appropriate, we fitted a simple propagation model to the broadband levels received by both hydrophone and microphone in order to develop equations that characterize propagation loss underwater and in air. The model used was based on logarithmic spreading loss, appropriate for describing sound loss versus distance when used within the range of distances for which measurements were obtained:

$$\text{Received Level } (\mathbf{RL}) = A - B\log(R), \tag{1}$$

where R is range in meters and the units for **RL** are dB *re*: 1 μPa for underwater SPLs and dB or dBA *re*: 20 μPa for in-air SPLs. The spreading loss term (B) varies with the dominant frequency, water depth, bottom topography, and bottom composition. When fitting the model to the data, recordings were included at increasing distances from the sound source until the point at which levels reached a minimum and remained constant (within $\sim\pm 2$ dB). This level was referred to as the background level.

2. Cabled hydrophones

The CH signals were low-pass filtered at 900 Hz and sampled at 2 kHz before being stored on disk. Sound spectral densities based on a 1-s Fourier transform length were computed for 1 min of sound every 4.37 min (4 min 22 s), or $\sim$330 times per 24-h day. These data were used to determine broadband and one-third-octave band levels in the 10–1000 Hz frequency range and to provide a continual record of the levels and spectral characteristics of low-frequency underwater sounds near Northstar during the study period.

3. DASARs

The underwater sound levels reported here required only the omnidirectional hydrophone channel in a DASAR [see Greene *et al.* (2004) for a description of the directional processing]. For antialiasing, the acoustic channel was low-pass filtered at 400 Hz. Broadband and one-third-octave band levels in the 10–500-Hz range were determined as for the CH data.

III. RESULTS

A. Underwater sounds

1. Broadband levels

To distinguish the sounds produced by the island itself (e.g., drilling or production) from those produced by vessels around the island, the data will be presented as a function of the presence or absence of boats at Northstar.

a. Levels versus distance. Received levels of broadband (10–10 000 Hz) underwater sound, as a function of distance from the source, are shown in Fig. 3. Figure 3(a) shows broadband levels for 14 recordings of island-related tug or crew boat activities. These were obtained while the sealift was at Northstar in 2001, and during the reconstruction of the island berm in 2003. The crew boat recordings were obtained in 2002. The best of these recordings, i.e., with minimal contamination from other sound sources and with measurements over a maximal span of distances, was that of barge 400's arrival at Northstar, shown with solid blue circles in Fig. 3(a). Therefore, the logarithmic sound propagation model [Eq. (1)] was fitted to these specific data, as shown in Fig. 3(a).

Figure 3(b) shows received levels of broadband (10–10 000 Hz) sound as a function of distance from Northstar, for recordings in which boats were present near the island (solid lines) and recordings with no boats present to our knowledge (green dotted lines). These boat-based recordings were obtained during eight transects north and east of Northstar (see Table I and Fig. 1). Recording transects northward extended as far as possible from the island and were limited either by the pack ice (2000–2001) or by logistical constraints (2002–2003). The boats present in Fig. 3(b) were

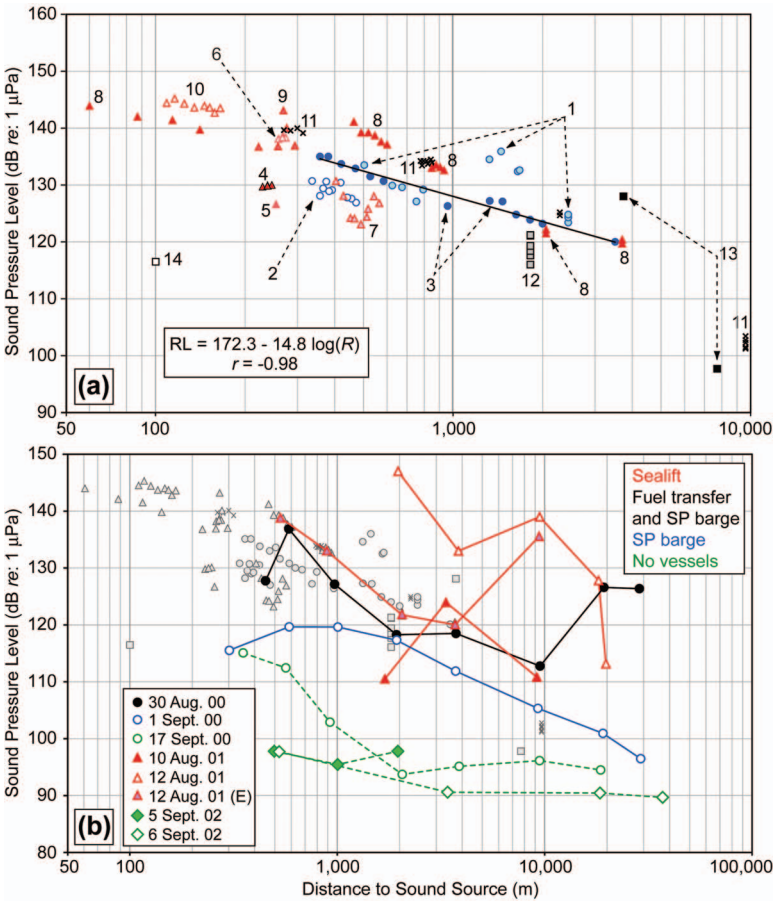

FIG. 3. (a) Broadband (10–10 000 Hz) levels of underwater sound for 14 types of island-related vessel (mainly tugs and crew boat) activities, as a function of distance from sound source. Data are split into three broad categories. *(I) Sounds during arrival at Northstar of three sealift barges* (August 2001, blue circles), specifically (1) arrival of barges 420 and 411 with three accompanying tugs; (2) barge 411 and tug, bow aspect; (3) barge 400 and tug, stern aspect. *(II) Sounds during tug activities*, consisting mainly of holding and maneuvering barges at the Northstar dock during various operations (August 2001, red triangles, and August 2003, black crosses): (4) River-class (RC) tug pushing on barge while ocean-class (OC) tug is standing by. (5) Two tugs idling (one RC and one OC). (6) OC tug pushing on barge while RC tug is standing by. (7) RC and OC tug maneuvering a barge and (8) holding it in place during offloading of equipment. Two other tugs were present but were standing by, idling. (9) Tugs holding barge 420 immediately preceding the offloading of a compressor module and (10) during the offloading. Four tugs (one OC and three RC) were present but usually only two were working at any point in time. (11) Point-class (PC) and RC tugs holding a gravel barge during reconstruction of the island's gravel berm. *(III) Crew vessel sounds* (September 2002, squares), specifically (12) crew boat arriving (bow aspect); (13) crew boat leaving (stern aspect); and (14) hovercraft (from Blackwell and Greene, 2005). The logarithmic regression model shown was fitted to recording (3) only (R is in meters, see text). (b) Broadband (10–10 000 Hz) levels of underwater sound as a function of distance from Northstar, while vessels were present or absent at the island. Line colors indicate the vessel types involved: sealift tugs (red), fuel transfer vessels and a self-propelled (SP) barge (black), a self-propelled barge alone (blue), or no vessels present (green). Data collected on 30 August, 1 and 17 September 2000; 10 and 12 August 2001; 5 and 6 September 2002. For comparison, levels for the island-related vessel activities [Fig. 3(a)] are also shown in gray shading.

the following:

(i) On 30 August 2000 an impending fuel transfer at the island led to the presence of several spill response boats. In addition, a self-propelled barge was used as a movable dock at Northstar. It maintained itself by pushing continuously against the island shore.
(ii) On 1 September 2000 a self-propelled barge was again pushing against Northstar.
(iii) On 10 and 12 August 2001 three sealift barges and a total of seven tugs were in the immediate vicinity of Northstar. The tugs included two OC, three RC, and two PC vessels.

The highest received broadband level (147 dB *re*: 1 μPa) was obtained 2 km from Northstar on 12 August 2001 while the sealift was near the island. With boats present, SPLs showed considerable variation, apparently depending as much or more on boat activities as on distance from the island. At comparable distances, the lowest SPLs were always found in the absence of boats. These recordings happened to coincide with the calmest days (lowest sea states, see Table I), which would tend to emphasize the difference in broadband levels between "boat" and "no boat" recordings. The lowest broadband levels were obtained on 6 September 2002, which had the best recording conditions of any day (sea state $0-\frac{1}{2}$, see Table I). On that date, received levels reached a minimum of ~90 dB *re*: 1 μPa within 3.4 km from Northstar and remained the same until the farthest station (37 km).

b. Variability over time. Broadband (10–500 Hz) levels of underwater sound are shown in Fig. 4 for recordings by the CH 420–440 m from Northstar and the NE DASAR

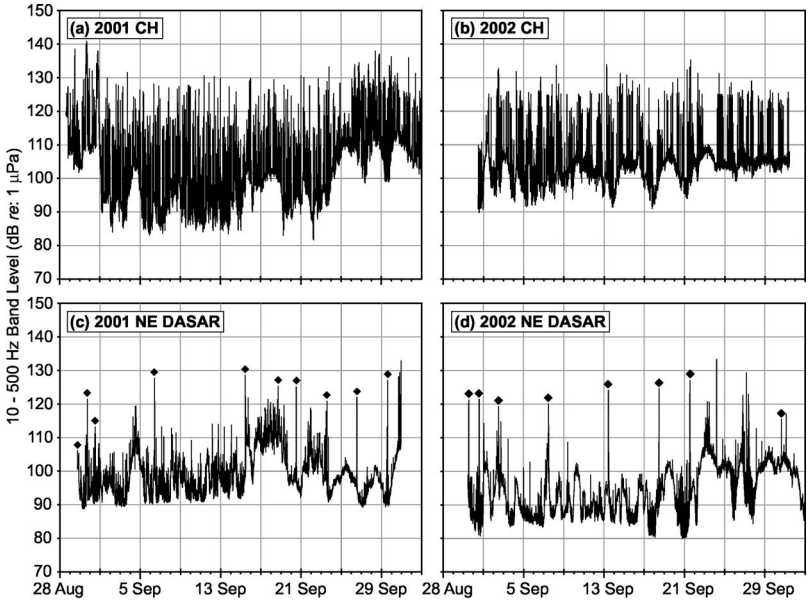

FIG. 4. Variability in broadband (10–500 Hz) levels of underwater sound at fixed locations as recorded continuously by the near-island CH [(a), (b)] and the NE DASAR [(c), (d)] during 36-day periods in September 2001 and 2002. In (c) and (d), black diamonds indicate sound spikes created when the acoustics crew's vessel approached the DASAR instrumentation for servicing.

~22 km away during extended periods in 2001 and 2002. The near-island CH recording in 2001 showed a wider range of SPLs than in 2002, ~82–140 dB versus ~90–135 dB [Fig. 4(a) versus 4(b)]. Tall "spikes" in the SPTS were mainly attributable to boats (see below). In 2001 these spikes were spread across all hours of the day, whereas in 2002 they mainly occurred during daytime and with a more regular pattern. In 2003 (not shown) minimum and maximum sound levels were similar to those in 2002, but there were fewer spikes as crew boat traffic to the island was reduced.

Days with increased wind speeds and sea states led to higher "baseline" levels; here, baseline refers to the lower edge of an "envelope" around the plotted SPTS. For example, on 23 September 2002 stormy weather increased baseline levels for both recorders, but particularly the DASAR [Fig. 4(d)], which was located farther out at sea. On that day all boat traffic was shut down in the Northstar area; this is evident by the complete absence of sound spikes from the 23 September part of Fig. 4(b). Higher wind speeds also accounted for the increased baseline levels in late September 2001.

The NE DASAR data show many fewer spikes than the near-island CH recordings; the large spikes marked with a diamond correspond to boat trips to the DASAR array by the acoustic team to check or service the instrumentation. The NE DASAR was located ~22 km northeast of Northstar and ~39 km north of the mainland (Prudhoe Bay) and was the least influenced by Northstar boat traffic. It was, however, near the routes taken by barges and commercial vessels transiting through the area, and it is likely that some of the spikes were caused by such boat traffic.

On 31 August 2001, the CIDS (concrete island drilling structure) was towed away from the Northstar area by two tugs accompanied by an icebreaker. The CIDS drilling caisson had been grounded and stored 1.1 km northeast of Northstar (see Fig. 1) since August 2000. This departure created the last large spike seen in the CH data [Fig. 4(a)] on 31 August 2001. Mean baseline levels measured via the CH 440 m north of Northstar (and 620 m from CIDS) were 16 dB lower after than before the CIDS' departure. Prior to its departure tugs frequently maneuvered near CIDS as well as near Northstar. The largest spike, on 30 August, was caused by the departure of two sealift barges escorted by an OC tug.

Table II summarizes broadband percentile levels of sound from the near-island and remote locations during all 3 years of data collection. The sampling rate was 1 kHz for DASARs and 2 kHz for CHs, providing acoustic data to 0.5 and 1 kHz, respectively. To allow comparisons, results are given for both the 10–500- and the 10–1000-Hz bands. Near the island, minimum values were lower and maximum values were higher in 2001 than in 2002 and 2003. Despite these differences, and the year-to-year changes in island activities, median levels of underwater sound close to Northstar were very similar during the 3 years of sampling. At the NE DASAR levels were higher in 2001 than other years for all percentiles except the maximum. However, in 2001 the DASARs were housed in a different type of enclosure that led to a heightened sound floor, so a direct comparison of the 2001 data with other years is probably not valid, at least not for the lower percentile levels (i.e., min, 5th percentile, etc.). Levels in 2003 were similar to or somewhat lower than those in 2002. Note that the maximum values were most likely collected during the weekly servicing of DASAR NE by the acoustics crew. Variability (max-min) was similar in 2002 and 2003 (53 vs. 50 dB, respectively).

To further illustrate the connection between sound spikes and vessel traffic, Fig. 5 shows broadband levels as received by the CH on each of four days: 4 and 5 September 2001 and 13 and 14 September 2002. These days included representative amounts of boat traffic. The scheduled crew boat runs (14 daily runs in 2001, 8 in 2002) are shown as shaded bars, each 35 min in duration. The shading begins 10 min before the scheduled arrival time, includes the 15 min during which the crew boat remained at the island, maintaining itself at the eastern or western dock by backing against it with propellers turning, and ends 10 min after the scheduled departure. Daily barge runs for both years are plot-

TABLE II. Broadband (10–500 and 10–1000 Hz) percentile levels of underwater sound ~500 m and ~22 km from Northstar Island in 2001, 2002, and 2003, in dB *re*: 1 μPa. The near-island sound levels were obtained using a cabled hydrophone (CH) located 420–460 m from Northstar or a DASAR (NS) located 550 m from Northstar. The distant sound recordings were obtained using a DASAR (NE) located about 22 km northeast of Northstar.

	0% (min)	5%	25%	50% (median)	75%	95%	100% (max)
Near-island							
2001							
CH (10–500 Hz)[a]	80.9	87.3	94.0	101.9	109.6	122.7	140.6
CH (10–1000 Hz)[a]	81.6	87.8	94.7	102.6	110.1	122.8	140.9
2002							
CH (10–500 Hz)[b]	89.7	94.9	100.3	103.6	105.8	117.5	135.0
CH (10–1000 Hz)[b]	89.8	95.5	100.8	104.0	106.3	118.2	135.3
2003							
CH (10–500 Hz)[c]	91.8	95.3	99.3	102.1	105.2	116.9	136.8
CH (10–1000 Hz)[c]	92.3	96.1	100.4	103.2	106.0	117.3	137.0
DASAR NS (10–500 Hz)[d]	91.1	92.3	96.3	103.6	108.3	124.5	130.4
Distant							
2001							
DASAR NE (10–500 Hz)[e]	88.5	90.9	93.7	97.2	101.9	110.4	132.4
2002							
DASAR NE (10–500 Hz)[f]	80.0	84.1	87.3	92.7	99.9	104.9	133.3
2003							
DASAR NE (10–500 Hz)[g]	76.8	80.5	87.6	94.4	99.1	103.1	127.0

Deployment dates:
[a]28 August–3 October.
[b]31 August–1 October.
[c]30 August–16 September.
[d]18–28 September.
[e]29 August–30 September.
[f]30 August–3 October.
[g]29 August–28 September.

ted as darker-gray bands, marked with diamond symbols; these correspond to the 15-min periods preceding the arrival and following the departure of the barge, respectively. While at the island, the tug either idled or helped maintain the barge in place at the island's southern dock. Northstar therefore served as an acoustic shield between the tug and the CH north of the island, resulting in relative quiet during the barge's stay at the island.

The crew boat runs shown in Fig. 5 correspond to the official schedule, but it was not unusual for runs to be delayed due to weather, cancelled, or added according to need. We have little information on these changes. However, on 13 and 14 September 2002 island records indicate that the crew boat ran seven out of the eight scheduled trips each day. From the broadband levels we can infer that the midnight trip was skipped on both days. On 14 September, there is an excellent match between broadband spikes and scheduled boat runs. On 13 September, crew boat and barge runs accounted for five spikes. An ACS vessel stopped at Northstar between 16:00 and 17:00 and likely produced the pair of spikes occurring at that time. The weather was windy and it appears that the crew boat scheduled for ~20:00 was delayed. As the crew boat did make seven runs that day, the remaining two spikes at ~13:00 and 22:00 were likely rescheduled crew boat trips. In summary, CH data from 4 days shown in Fig. 5 suggest that, during September 2001 and 2002, most sharp spikes in broadband levels as received near Northstar were attributable to the crew boat and barge trips.

c. Broadband propagation loss. The sound propagation model [Eq. (1)] was fitted to data recorded at various distances from Northstar on 30 August 2000, 1 and 17 September 2000, as well as 5 and 6 September 2002 combined (Fig. 6). Data from stations <500 m from the island were not included, as the underwater topography adjacent to the island (island slope and protective gravel berm) may have caused unexpectedly low values, which were seen in several recordings.

On 30 August and 1 September 2000, measurements were made while one or more boats were near Northstar. On 1 September received levels continued decreasing until the farthest distance sampled (27 km), indicating that background levels were not reached. On 30 August received levels were high at the two farthest stations, but since this was likely due to the presence of other vessels nearby during those particular recordings, the data were not included in the regression. Spreading loss terms were 18.3 and 14.4 dB/tenfold change in distance, respectively.

In contrast, on 17 September 2000 and 5 and 6 September 2002, boats were not present at the island and recording conditions were very good (sea state of $0-\frac{1}{2}$). The island was in a construction phase in 2000 versus a drilling and produc-

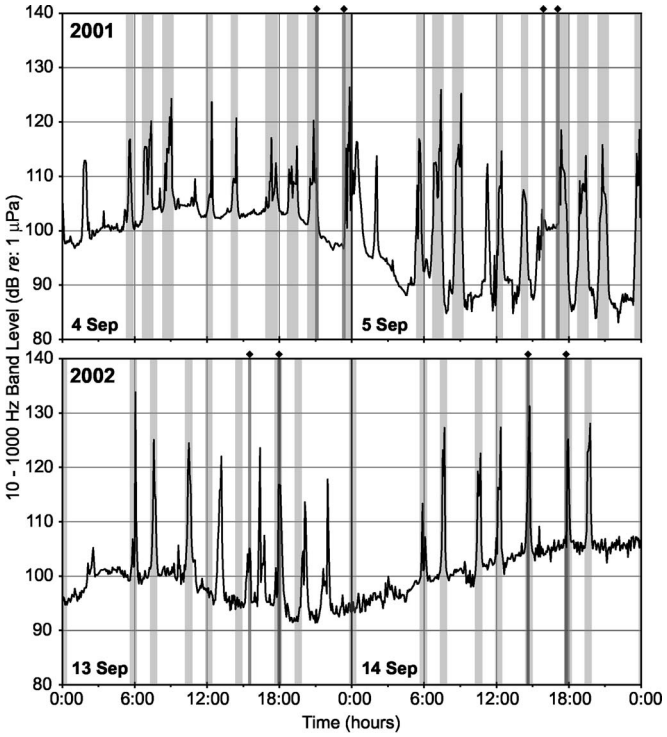

FIG. 5. Broadband (10–1000 Hz) levels as recorded by a cabled hydrophone, located 420–440 m north of Northstar, for two days in September during each of 2001 and 2002. Light-gray shading shows 35-min periods corresponding to the scheduled daily crew boat trips (14 in 2001, 8 in 2002, see text). In 2001, five pairs of crew boat runs (i.e., a total of 10) were close enough in time that their 35-min periods overlap. Dark-gray shading with diamond symbols shows 15-min periods corresponding to the arrival and departure of the daily barge and associated tug.

tion phase in 2002. Received levels remained at ~94 dB *re*: 1 μPa beyond 2.1 km in 2000, and at 90 dB *re*: 1 μPa beyond 3.4 km in 2002 (Fig. 6). Those long-range data, presumably representing background levels, were excluded when estimating spreading loss. Even so, spreading loss terms were variable, 32.6 and 6.3 dB/decade, respectively.

2. Spectral analysis

a. Island sounds. Diesel-powered generators provided the island's primary power from August 2000 until 24 October 2001, when they were replaced by a series of three Solar gas-turbine generators. We estimated the relative contribution of these two types of generators to island sounds by comparing the quietest 1-min period of CH recordings in 2001 and 2002. These occurred at 06:12 on 22 September 2001 [Fig. 4(a)] and at 13:37 on 31 August 2002 [Fig. 4(b)]. The corresponding SPSDLs (Fig. 7, black line for 2001 and dark gray line for 2002) show that received levels were noticeably higher for frequencies below 100 Hz in 2002, when gas-turbine generators were running. At low frequencies, the largest peaks or tones in the 2001 spectrum are at 30 and 75 Hz. In 2002 they are found at or near 30, 40, 60, 81, and 90 Hz. At frequencies above ~100 Hz received levels were similar but again the 2002 spectrum contained many more tones, many of which (44%) were multiples of 60 or 80 Hz. In addition, all of the 27 major tones above 100 Hz were separated from each other by multiples of 20 Hz.

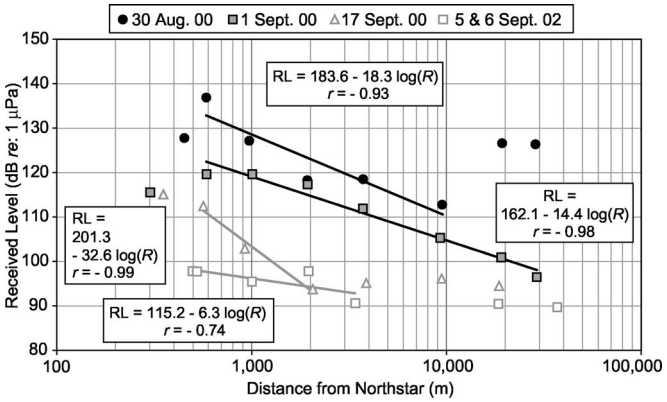

FIG. 6. Propagation loss as calculated using boat-based recordings from 2000 and 2002. The logarithmic spreading loss model [Eq. (1)] was fitted to broadband (10–10 000 Hz) levels of underwater sound. Filled and empty symbols indicate measurements made with and without boats present at Northstar, respectively. See text for rationale for excluding some data points.

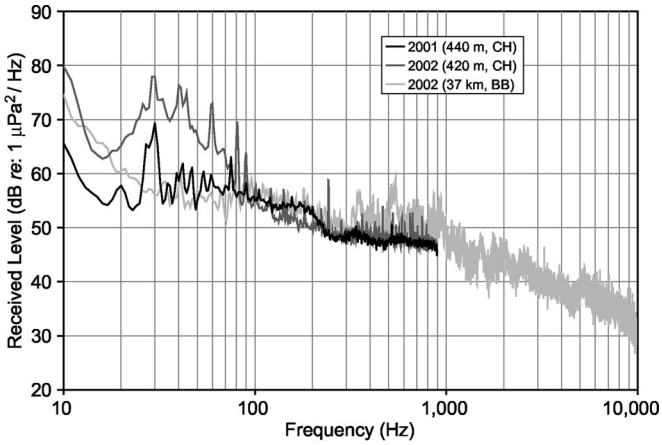

FIG. 7. Underwater sound-pressure density spectra near Northstar, with diesel versus gas turbine generators, and away from the island. The black and dark gray lines show spectra for the quietest 1-min periods in 2001 and 2002, respectively, as recorded by the cabled hydrophone (CH) near the island (frequency range 10–900 Hz). The island's primary power was provided by a diesel-powered generator in 2001 versus a series of Solar gas-turbine generators (of which two were generally running) in 2002. The light gray line shows spectra for a representative sample obtained 37 km from Northstar on a quiet day (6 September 2002), during boat-based (BB) recordings (frequency range 10–10 000 Hz).

Drilling and production were the main island activities after the end of construction. Figure 8 shows two representative SPSDLs obtained during production, with and without concurrent drilling. To enable seeing both spectra on the same graph they are offset from each other by 10 dB. The segments were obtained ~500 m from Northstar within 90 s of each other on 5 September 2002, just before and after the onset of drilling. The spectra are similar, with most of the sound energy below 100 Hz and numerous tones and peaks, mostly of unknown origin. The broadband (10–10 000 Hz) level ~500 m from Northstar was ~2 dB higher during drilling than without, but relatively low in both cases (99 vs. 97 dB *re*: 1 μPa).

The continuous CH recordings allowed us to get information on the island's average spectral composition (up to 1 kHz) over many days, in contrast to the "snapshots" provided by the boat-based recordings. To separate (as much as possible) island sounds from boat sounds in the CH record-

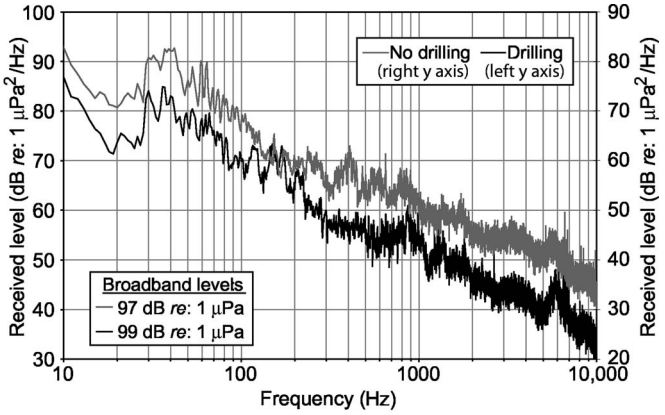

FIG. 8. Underwater sound-pressure density spectra (10–10 000 Hz) during production, with and without drilling, 5 September 2002 (range ~500 m). Received spectrum levels for the black and gray plots are to be read on the left and right *y* axes, respectively. Broadband levels shown are for the frequency range 10–10 000 Hz.

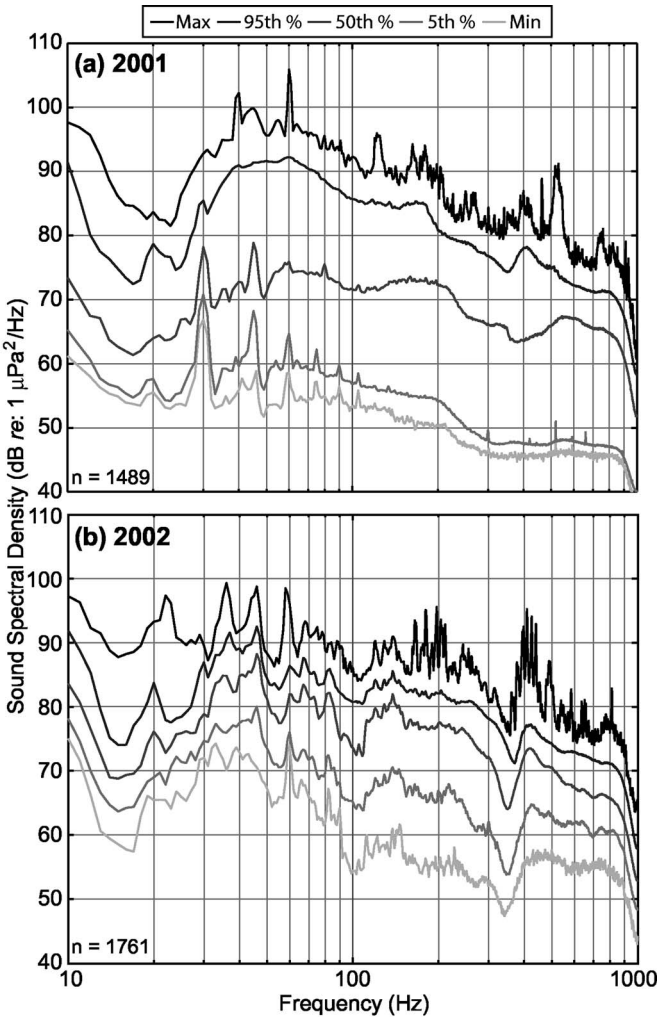

FIG. 9. Percentile sound spectral densities of underwater island sound versus frequency (10–1000 Hz), as recorded by CH in (a) 2001 at range 440 m and (b) 2002 at range 420 m. Six days of data were used each year. Spikes of boat sound (see Fig. 5) were removed from the analysis. The statistical spectra in each graph are based on the number of 1-min measurements shown in the lower left corner. See text for details.

ings, we selected 6 days each year during which the match between large spikes in the SPTS and scheduled crew boat runs was very good (see, for example 14 September 2002 in Fig. 5). For these days, we removed 35- and 15-min sections from the SPTS, corresponding to each of the crew boat and daily Northstar barge runs, respectively (see Fig. 5). The remaining samples were presumed to be largely devoid of boat sounds and were used to calculate the statistical spectra shown in Fig. 9. Thus, the upper curve in each panel shows, for each frequency, the highest spectrum density levels observed in all of the 1-min samples analyzed. The spectrum below the maximum shows the 95th percentile values in each individual frequency bin: 95% of the time the sound level was at or below the plotted value for each frequency. Similarly, the lower curves represent the median, 5th percentile, and minimum spectral density levels.

The presence of tones in these statistical spectra is significant, indicating the regular occurrence of harmonic families from machinery. Depending on their strength, tones can be more prominent when background levels are lower, e.g., tones at 30, 45, 60, 75, and 80 Hz stand out more in the 5th than in the 95th percentile spectrum in 2001. In 2001, island power came from a diesel generator, and there was no drilling and no oil production during the recording sessions. In 2002, island power came from gas-turbine generators, and there was production and periodic drilling. Overall, the strongest components were generally in the 30–100-Hz range, but at times there were prominent clusters of tones at other frequencies (i.e., ~400 Hz in 2002). The low received levels of components below 30 Hz in both years are indicative of the rapid attenuation of low-frequency long-wavelength sounds in shallow water (~12 m).

b. Vessel sounds. The principal vessels around Northstar were the crew boat and several tugs. Representative SPSDLs for those two types of vessels are shown in Fig. 10(a). The OC tug was recorded during the sealift operation in 2001. This tug had a maximum prop shaft rate of 210 rpm and five-bladed propellers. The expected maximum for the blade rate was therefore 17.5 Hz (i.e., $210\times5/60$); this tone is visible as a large peak in Fig. 10(a). The crew boat was recorded as it left Northstar and headed for the mainland. The crew boat had a maximum prop shaft rate of 900 rpm and four-bladed propellers; the expected maximum blade rate was therefore 60 Hz (i.e., $900\times4/60$). A tone at 60 Hz was not seen in the crew boat recordings; instead peaks at 22–26 and 52–55 Hz were found in every recording that included the crew boat and are visible in Fig. 10(a). If the shaft or one of the propeller blades of the vessel has damage (e.g., a blade nicked or a shaft that is not quite straight), the shaft rate can become very prominent. It is therefore likely that the 52–53-Hz peak is the crew boat's blade rate and the 26-Hz peak is a harmonic of the shaft rate (in this case 13 Hz), which is at a frequency too low to propagate well in the shallow waters around Northstar. A comparison of Fig. 10(a) with Fig. 7 also shows that both types of vessels produced substantial broadband sound in the range 50–2000 Hz, which could at least in part be accounted for by propeller cavitation (Ross, 1976).

The island sounds summarized in Fig. 9 were obtained by removing samples recorded by the CH while the crew

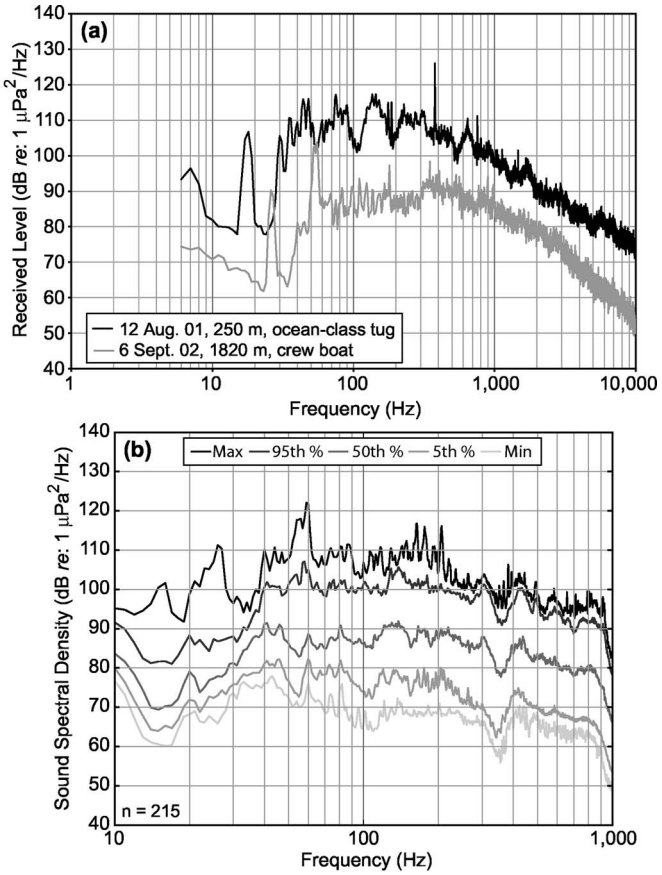

FIG. 10. Underwater narrow-band spectra of vessel sounds near Northstar. (a) Sound-pressure density spectra (6–10 000 Hz) of an Ocean-class tug (at 250 m) and a crew boat (at 1820 m). (b) Percentile sound spectral densities of underwater sound from vessels versus frequency, as recorded by a cabled hydrophone in 2002. Data in (b) consist of the boat-affected segments (215 1-min samples) excluded from the analysis in Fig. 9(b); otherwise, they were analyzed and plotted as in Fig. 9.

boat or daily barge (and tug) were at Northstar. In Fig. 10(b), the removed samples from 2002 were used to calculate statistical spectra. Because boats are the strongest sources of sound recorded commonly by the CH, the maximum and 95th percentile values should be representative of boat sounds near Northstar. For example, the 26-Hz peak mentioned above for the crew boat is prominent in Fig. 10(b). Overall, the spectrum levels were typically much higher during the periods when boats were near Northstar than in the remainder of 2002 [Fig. 10(b) versus 9(b); note difference in y axes].

c. Ambient sounds. The 37-km station was the farthest from Northstar. Spectral density levels for a representative sample from this station are shown in Fig. 7 (light gray line), together with levels from the quietest cabled hydrophone samples in 2001 (black line) and 2002 (dark gray line). Up to 1 kHz levels at 37 km and ~430 m are similar, except the near island samples contain more island-related tones at low frequencies. Above 1 kHz spectral density levels decrease with increasing frequency, reaching a minimum of about 27 dB *re*: 1 μPa^2/Hz at 10 kHz (Fig. 7).

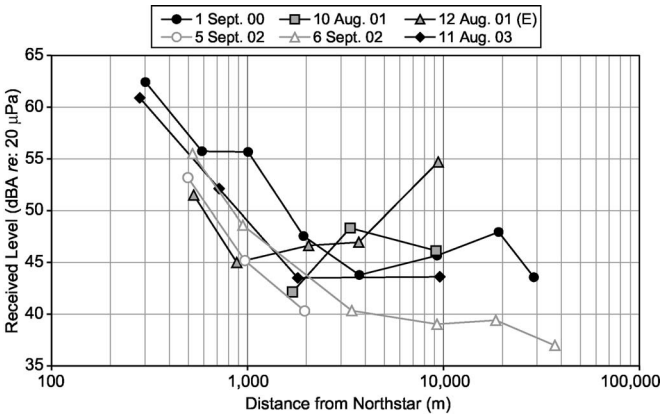

FIG. 11. Broadband (10–10 000 Hz) A-weighted levels of in-air sound as a function of distance from Northstar and presence of boats. Filled and empty symbols indicate measurements made, respectively, with and without boats present at Northstar. All recordings were made north of Northstar except for a transect east (E) of the island on 12 August 2001.

B. Airborne sounds

1. Broadband levels

A-weighted broadband (10–10 000 Hz) SPLs are shown in Fig. 11 for in-air recordings made on six dates at various distances north and east of Northstar, distinguishing cases with and without active boats. To avoid much contamination by wind noise, only data obtained with wind speed <6 m/s are plotted. The highest value (62 dBA *re*: 20 μPa) was obtained 300 m from the island on 1 September 2000, while the island was in construction and boats were present. Background values were reached 1–4 km from the island, at values that were probably more related to sea state and wind speed rather than to the presence of boats. The lowest values (37–40 dBA *re*: 20 μPa) were obtained on 5 and 6 September 2002, days with ideal recording conditions (Table I). The sound propagation model [Eq. (1)] was fitted to the data obtained on 1 September 2000, 5 September 2002, 6 September 2002, and 11 August 2003, excluding longer-range values at background levels. The resulting spreading loss rates were similar, 17–22 dBA/tenfold change in distance (not shown).

2. Spectral analysis

Figure 12 shows SPSDLs of island sounds (i.e., without the presence of boats) from a close (525 m) and distant (37 km) station on 6 September 2002. The most prominent feature is a tone at 81 Hz, detectable even at the station farthest from Northstar. This tone was also found in the underwater data (see Fig. 7) and was present in 94% (30/32) of analyzed airborne segments. Its source is unknown but is likely on the island. The tone's received level decreased by 24 dB/tenfold change in distance from Northstar [Eq. (1): $RL = 148.9 - 24.2 \times \log(R)$, $r = -0.90$]. For frequencies up to ~2 kHz, received levels were 15–20 dB higher at the near station (Fig. 12), and background levels were reached ~1.8 km from Northstar, i.e., spectra beyond that distance overlapped (not shown). Above 5 kHz, received levels were apparently at background levels even at 525 m.

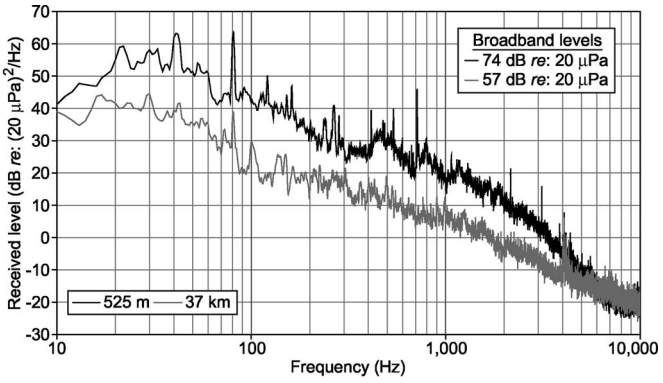

FIG. 12. Airborne sound-pressure density spectra of island sounds, as recorded from a near (525 m) and distant (37 km) station on 6 September 2002. Broadband levels shown are for the frequency range 10–10 000 Hz, unweighted.

IV. DISCUSSION

A. Underwater sounds

Underwater propagation can be affected by physical factors such as the temperature and salinity of the water, or the topography and composition of the sea bottom. In this study these variables were not measured. Therefore we report our results "as is," without attempting to explain the physics of sound propagation in our study area.

1. Island sounds

Recordings obtained in the absence of vessels allowed us to characterize the underwater sounds produced by the island itself. These can be summarized in the following points:

(i) During both the construction phase in 2000 and the drilling and production phase in 2002, broadband island sounds reached background values at distances of 2–4 km. Figure 3(b) shows that broadband (10–10 000 Hz) levels reached a minimum at ~94 and 90 dB *re*: 1 μPa in 2000 and 2002, respectively. This 4-dB difference in background levels can probably be explained by the difference in sea state on the recording days: $\frac{1}{2}$–1 on 17 September 2000 and 0–$\frac{1}{2}$ on 5 and 6 September 2002 (Table I). Boat-based samples are particularly sensitive to differences in recording conditions, specifically sea state. For example, on 12 August 2001 sea state at the 18-km station was 2–3 and broadband levels were 128 dB *re*: 1 μPa. The next recording, at 20 km, was within the pack ice where sea state was $\frac{1}{2}$, and broadband levels had dropped by 15 dB [Fig. 3(b)]. This difference is in agreement with Wenz's (1962) compilation of ambient noise versus sea state, in which spectrum (and therefore broadband) levels for sea state $\frac{1}{2}$ versus 2–3 differ by 12–16 dB.

(ii) In the absence of boats, construction activities led to higher broadband levels close to the island [i.e., compare 17 September 2000 with 5 and 6 September 2002 in Fig. 3(b)]. The small spreading loss term in 2002 (6.3 dB/tenfold change in distance, Fig. 6) is likely due to the larger relative contribution of background noise in these measurements. The higher spreading loss on 17 September 2000 (32.6 dB/decade, Fig. 6) is more difficult to explain, but may be the result of temporal variability of sound sources within the time while recordings were made at various distances. Such variability is to be expected during island construction.

(iii) Figure 7 suggests that diesel generators, which were the main island power source during construction, produced lower sound levels than gas-turbine generators in use during drilling and production. This is supported by the fact that the minimum and 5th percentile plots in Fig. 9, representing "boat-less" samples from 6 days each year, are also lower in 2001 than in 2002.

(iv) Island sounds had strong tonal components (Figs. 7 and 9). In 2001, with diesel generators, they were mainly found at low frequencies: 20, 30, 45, 60, 75, 90, and 105 Hz. The presence of some of these tones or peaks in both the minimum and maximum SPSDLs indicates that they were ever-present and probably had to do with power generation. The power line frequency 60 Hz is, as expected, one of these tones. In 2002, with gas-turbine generators and compressors, some of the low-frequency tones were present (i.e., 20, 30, 45, and 60 Hz), but new groups had also appeared, i.e., at 105–150 and 390–440 Hz.

(v) The maximum SPSDL was higher and the minimum was lower in 2001 than in 2002 (Fig. 9, see also Fig. 4). Greater variation would be expected during the island's construction phase, when activities on and around the island often changed on a daily (or more frequent) basis. The variability in sound levels was reduced as the island moved into the more routine production phase in 2002 and 2003 (see Table II), and this trend continued in 2004 (Blackwell *et al.*, 2005). The new tones that appeared in 2002 (see Figs. 7 and 9) were presumably associated with the changeover in the island power supply and the onset of production and drilling, which were not taking place in September 2001. Production was nearly constant during the 2002 open-water season, and drilling occurred on 97% of days.

Thus, in the absence of boats, underwater broadband sounds from Northstar Island (during construction, drilling, and production) reached background values 2–4 km away in quiet ambient conditions. Compared to caissons emplaced on the ocean bottom, platforms standing on legs, or drilling vessels, offshore drilling from natural or man-made islands generally produces underwater sounds that are weak and do not propagate beyond a few kilometers (Richardson *et al.*, 1995). Davis *et al.* (1985) measured underwater sound in open-water conditions at Seal Island, the artificial island that used to exist on the Northstar site. When nothing but power generation was taking place at the island, it could not be detected underwater 2.3 km away. During well-logging, the detection range increased to ~5 km. Johnson *et al.* (1986) measured drilling sounds from Sandpiper Island, a similar

artificial island in the same area northwest of Prudhoe Bay. As in this study, the sound levels produced were low but notable. They reported tones at 20 and 40 Hz, which they attributed to power production. The tones, as well as broadband (20–1000 Hz) levels, increased during drilling by 6–24 and 8–10 dB, respectively. The tones were weakly detectable at 3.7 km during drilling.

Underwater sounds from production operations are apparently also weaker during production from man-made islands than during production from most or all other types of offshore facilities (Richardson *et al.*, 1995). Gales (1982) summarized the sounds received from 11 production platforms and one man-made island (all in temperate waters) and rated the sounds from the man-made Rincon production island as "very quiet." He surmised that poor conduction of sound through the rock and fill island, and poor conduction of low-frequency sound in shallow water, both resulted in the low levels of production noise in the sea. Similar conditions occurred in the present study, although in this case the island was primarily gravel, not rock. We were not able to detect any differences in broadband SPLs with and without drilling while production was taking place. The two plots in Fig. 8 overlap when plotted on the same scale and are only distinguished by the different tones.

2. Vessel sounds

Crewboats, tugs, and self-propelled barges were the usual vessels around Northstar. Vessels were the most important sound source during all phases of the Northstar operation that were studied, i.e., construction, drilling, and production. Since vessels were the strongest routine sources of sound around Northstar, the 95th percentile SPSDLs (and to some extent the maximum) are good indicators of the boat contribution to the sound field. Indeed, the 95th percentile and maximum SPSDLs, as obtained from the CH recordings, showed a mean decrease of 20 and 19 dB in 2002, respectively, when boats were removed from the analysis [Fig. 10(b) versus Fig. 9(b)]. Background levels were not reached in any of the open-water recordings with boats present at Northstar [Fig. 3(b)]. The only vessel that was noticeably quieter underwater was the hovercraft (Blackwell and Greene, 2005).

Propagation loss for vessel (mainly tug) sounds in the waters surrounding Northstar (~12 m deep) was about 15 dB/tenfold change in distance over distances from a few hundred meters to a few kilometers [Fig. 3(a)]. Expected broadband SPLs at distances of 50 and 100 m were ~145 and 140 dB *re*: 1 μPa, respectively, which is comparable to other measurements of sounds from vessels of that size [see Richardson *et al.* (1995) for a review; also Ross (1976)]. Considering the variety of sound sources and recording conditions, there was general agreement in received SPLs as a function of distance. The variation in received levels seen in Fig. 3(a) can be accounted for by four main factors: (1) The number of "other" (nontargeted) vessels within a 2-km radius from the hydrophone during recordings varied between 1 and 7. (2) Recordings were made at a range of distances from Northstar Island, which means that the contribution of island sounds to the tug recordings was variable. (3) Three classes of tugs (River-class, Point-class, and Ocean-class) and the crew boat were involved, each with different engine and propeller characteristics and therefore sound outputs. For example, broadband levels from an OC tug were ~8 dB higher than from a RC tug performing the same activity at a comparable distance [Fig. 3(a), items 4 and 6]. (4) Recordings were made in different sea states.

A large fraction of the sound spikes recorded by the CH and NE DASAR during September 2001 and 2002 were accounted for by the three vessels for which we had accurate scheduling information: the crew boat and daily supply barge and tug (Fig. 5) plus the ACS vessel used by the acoustics crew to service the recorders [Figs. 4(c) and 4(d)]. Other vessels known to operate near the island were likely responsible for additional periods of high-level sound, particularly in 2000 and 2001, but cannot be quantified. These included a small outboard for surveying and support during construction activities, ACS vessels during spill response exercises or while monitoring fuel transfers, and self-propelled barges during island construction. There was also, in all years, a sizeable amount of vessel traffic not associated with BP's Northstar Development and not specifically concentrated around Northstar Island: barges traveling between industrial sites or North Slope communities, boat traffic associated with subsistence whaling (based on Cross Island, see Fig. 1), seismic and shallow-hazards surveys in 2000 and 2001, and a pipeline route survey in 2001 (Williams and Rodrigues, 2004). In 2002, for example, 84 one-way trips of these types were recorded during the 28 August–19 September period, or 3.7 per day on average. This total did not include subsistence whaling vessels. We expect this vessel traffic to have raised background sound levels in the Northstar area, but we were not able to identify or quantify contributions of individual "non-Northstar" vessels to the SPTS.

The SPSDLs shown in Fig. 10(a) for a tug and the crew boat match published descriptions for vessel sounds: broadband in nature (primarily because of propeller cavitation and flow noise) and with tones at specific frequencies, generally below 50 Hz for medium to large vessels (Ross, 1976). The tugs and crew boat all had medium to high-speed diesel engines, which are considered noisy (Richardson *et al.*, 1995).

3. Ambient sounds

Burgess and Greene (1999) used seafloor recorders to measure ambient sound levels in the central Alaskan Beaufort Sea over periods of several weeks in August and September 1998, away from industrial activities, at distances of 41–94 km from Seal Island (which used to exist on the Northstar site). Therefore, their measurements serve as a "pre-Northstar" reference to which we can compare our values. Percentile levels of broadband (20–1000 Hz) ambient sound (computed over the entire 30-day deployment time) were 68, 79, 99, 114, and 132 dB *re*: 1 μPa for the minimum, 5th, 50th, and 95th percentiles, and maximum, respectively. For the same frequency range our lowest mean broadband value, 90 dB *re*: 1 μPa in the absence of boats at Northstar (Fig. 6), falls midway between their 5th and 50th percentile levels. Considering the fact that our values were obtained in optimal conditions (sea state $\frac{1}{2}$, Table I), sound

levels as obtained 37 km from Northstar were somewhat elevated compared to ambient values for the central Beaufort Sea. We were not able to compare spectral density levels as these were not reported in Burgess and Greene (1999).

B. Airborne sounds

The strongest broadband airborne sounds were recorded ~300 m from Northstar Island (in the presence of vessels) and reached 61–62 dBA *re*: 20 μPa (Fig. 11). In-air broadband sounds generally reached a minimum 1–4 km from the island, with or without the presence of boats. Beyond that distance, they were affected principally by wind. For example, up to a distance of 1 km values obtained on 12 August 2001, in the presence of the sealift, and 5 September 2002, in the absence of boats at Northstar, were the same. Beyond that distance values in 2001 stabilized or increased due to deteriorating weather conditions (wind speed >5 m/s), whereas values in 2002 continued decreasing because of the very calm recording conditions (wind speed 0.9 m/s). However, a tone at 81 Hz was detected on nearly every in-air recording (Fig. 12), and its received level decreased with increasing distance from Northstar, out to the farthest station (37 km). The source of this tone is not known.

V. CONCLUSION

The data presented in this paper show that the Northstar artificial island for oil production raised broadband underwater SPLs above background out to distances of less than 5 km in normal to quiet environmental conditions. In contrast, the vessels associated with the operation, mainly tugs and crew boats, significantly raised the underwater SPLs produced by the entire operation. With vessels at Northstar, broadband levels remained elevated above background values for distances on the order of 30–40 km at times with low-to-moderate background noise. In-air broadband SPLs were not much different with or without the presence of boats at the island, and reached background levels at distances of 1–4 km. However, spectral analysis revealed that at least one specific tone (81 Hz) was detectable out to the farthest station (37 km) in air.

The southern edge of the bowhead whale migration corridor during the fall is only a few kilometers north of Northstar. Bowhead hearing sensitivity is not known, but is presumed to be good at low frequencies (Richardson *et al.*, 1995), where much of the sound from Northstar and its associated vessels is produced. The measurements presented in this paper are being used (in part) to assess the effects, if any, of Northstar sounds on the whales' migratory pathway (Richardson *et al.*, 2004). Because of concerns about possible reactions of marine mammals to Northstar-associated vessels, BP has reduced its vessel operations in support of Northstar, especially during the early autumn when bowhead whales migrate past. As of the 2004 open-water season the crew boat has been replaced by a hovercraft for personnel and equipment transfer to the island.

ACKNOWLEDGMENTS

This study was funded by BP Exploration (Alaska) Inc. to fulfill monitoring and documentation requirements associated with BP's Northstar oil development. We thank Jonah Leavitt from LGL Alaska for help in the field, and J. Hanover, W. Henry, F. McAdams, J. Nevels, K. Pulliam, B. Rutherford, M. Theriault and the captains and crew from Alaska Clean Seas for their expert boating skills. M. Williams, S. Schwenn, and C. Perham from LGL Alaska helped with logistics, and T. Elliott (LGL) produced Fig. 1. For logistical support and problem solving at Northstar we thank J. Huey of BP and W. Cullor and A. Erickson from BP's Environmental Studies Group. R. Norman and Dr. W. Burgess, Greeneridge Sciences Inc., helped with the analysis and problem solving. We thank Dr. W.J. Richardson, LGL Ltd., for providing program direction and guidance as well as helpful criticism of this paper. Finally, we thank Dr. R. Jakubczak, Dr. W. Streever, and D. Trudgen of BP for their support, and Dr. Streever, Dr. K.G. Foote, and two anonymous referees for their critical review.

[1]A note of caution to investigators making vessel-based recordings: during one set of battery-powered underwater recordings in 2002 the boat's inverter was accidentally left on. This led to a series of tones between 10 and 19 kHz (spaced apart by 120 or 240 Hz) and a more pronounced increase in levels at 13.5–15.5 kHz.

Andrew, R. K., Howe, B. M., Mercer, J. A., and Dzieciuch, M. A. (**2002**). "Ocean ambient sound: comparing the 1960s with the 1990s for a receiver off the California coast," ARLO **3**(2), 65–70.

Blackwell, S. B., and Greene, C. R., Jr. (**2005**). "Underwater and in-air sounds from a small hovercraft," J. Acoust. Soc. Am. **118**(6), 3646–3652.

Blackwell, S. B., Greene, C. R., Jr., and Richardson, W. J. (**2004a**). "Drilling and operational sounds from an oil production island in the ice-covered Beaufort Sea," J. Acoust. Soc. Am. **116**, 3199–3211.

Blackwell, S. B., Lawson, J. W., and Williams, M. T. (**2004b**). "Tolerance by ringed seals (*Phoca hispida*) to impact pipe-driving and construction sounds at an oil production island," J. Acoust. Soc. Am. **115**, 2346–2357.

Blackwell, S. B., Norman, R. G., Greene, C. R., Jr., McLennan, M. W., McDonald, T. L., and Richardson, W. J. (**2005**). "Acoustic monitoring of bowhead whale migration, autumn 2004," in "Monitoring of industrial sounds, seals, and bowhead whales near BP's Northstar oil development, Alaskan Beaufort Sea, 2004: summary report," LGL Report TA4143-2, Rep. from LGL Ltd., King City, Ont., Greeneridge Sciences Inc., Santa Barbara, CA, and WEST Inc., Cheyenne, WY, for BP Explor. (Alaska) Inc., Anchorage, AK, edited by W. J. Richardson and M. T. Williams, pp. 2-1–2-39.

Burgess, W. C., and Greene, C. R. (**1999**). "Physical acoustics measurements," in "Marine mammal and acoustical monitoring of Western Geophysical's open-water seismic program in the Alaskan Beaufort Sea, 1998," edited by W. J. Richardson, LGL Rep. TA2230-3, Report from LGL Ltd., King City, Ont., and Greeneridge Sciences Inc., Santa Barbara, CA, for Western Geophysical, Houston, TX, and Nat. Mar. Fish. Serv., Anchorage, AK, and Silver Spring, MD, pp. 3-1–3-65.

Davis, R. A., Greene, C. R., and McLaren, P. L. (**1985**). "Studies of the potential for drilling activities on Seal Island to influence fall migration of bowhead whales through Alaskan nearshore waters," Rep. from LGL Ltd., King City, Ont., for Shell Western E&P Inc., Anchorage, AK.

Gales, R. S. (**1982**). "Effects of noise of offshore oil and gas operations on marine mammals—An introductory assessment," NOSC TR 844, 2 vol. U.S. Naval Ocean Systems Cent., San Diego, CA, NTIS AD-A123699 + AD-A123700.

Greene, C. R., Jr., and McLennan, M. W. (**2004**). "Sounds and vibrations during initial construction of a gravel island in the frozen Beaufort Sea," in "Monitoring of industrial sounds, seals, and bowhead whales near BP's Northstar oil development, Alaskan Beaufort Sea, 1999–2003," edited by

W. J. Richardson and M. T. Williams, LGL Report TA2426-2, Rep. from LGL Ltd., King City, Ont., Greeneridge Sciences Inc., Santa Barbara, CA, and WEST Inc., Cheyenne, WY, for BP Explor. (Alaska) Inc., Anchorage, AK, pp. 1–21 in Appendix G.

Greene, C. R., Jr., McLennan, M. W., Norman, R. G., McDonald, T. L., Jakubczak, R. S., and Richardson, W. J. (**2004**). "DIFAR sensors in seafloor recorders to locate calling bowhead whales during their fall migration," J. Acoust. Soc. Am. **115**, 2346–2357.

Harris, F. J. (**1978**). "On the use of windows for harmonic analysis with the discrete Fourier transform," Proc. IEEE **66**(1), 51–83.

Johnson, S. R., Greene, C. R., Davis, R. A., and Richardson, W. J. (**1986**). "Bowhead whales and underwater noise near the Sandpiper Island drillsite, Alaskan Beaufort Sea, autumn 1985," Report from LGL Ltd., King City, Ont., and Greeneridge Sciences Inc., Santa Barbara, CA, for Shell Western E&P Inc., Anchorage, AK.

Kinsler, L. E., Frey, A. R., Coppens, A. B., and Sanders, J. V. (**2000**). *Fundamentals of Acoustics*, 4th ed. (Wiley, New York), pp. 360–361.

Kryter, K. D. (**1985**). *The Effects of Noise on Man*, 2nd ed. (Academic, Orlando, FL.).

NRC (National Research Council). (**2003**). "Ocean noise and marine mammals," Report by the Committee on Potential Impacts of Ambient Noise in the Ocean on Marine Mammals for the Ocean Studies Board, Division of Earth and Life Studies (National Academies, Washington, DC), pp. 12–16, 57.

Richardson, W. J., Greene, C. R., Jr., Malme, C. I., and Thomson, D. H. (**1995**). *Marine Mammals and Noise* (Academic, San Diego, CA.), pp. 1–2, 110–117, 127–135.

Richardson, W. J., McDonald, T. L., Greene, C. R., Jr., and Blackwell, S. B. (**2004**). "Acoustic localization of bowhead whales near Northstar, 2001–2003: evidence of deflection at high-noise times?" in "Monitoring of industrial sounds, seals, and bowhead whales near BP's Northstar oil development, Alaskan Beaufort Sea, 1999–2003," LGL Rep. TA4002-8, Report from LGL Ltd., King City, Ont., Greeneridge Sciences Inc., Santa Barbara, CA, and WEST Inc., Cheyenne, WY, for BP Explor. (Alaska) Inc., Anchorage, AK, edited by W. J. Richardson and M. T. Williams, pp. 8-1–8-73.

Ross, D. (**1976**). *Mechanics of Underwater Noise* (Pergamon, New York) (reprinted 1987, Peninsula, Los Altos, CA), pp. 202–285.

Ross, D. G. (**1993**). "On ocean underwater ambient noise," UK Inst. Acoust. Bull. **18**(1), 5–8.

Wenz, G. M. (**1962**). "Acoustic ambient noise in the ocean: spectra and sources," J. Acoust. Soc. Am. **34**, 1936–1956.

Williams, M. T., and Rodrigues, R. (**2004**). "BP's activities at Northstar, 1999–2003," in "Monitoring of industrial sounds, seals and bowhead whales near BP's Northstar oil development, Alaskan Beaufort Sea, 1999–2003," LGL Rep. TA4002-2, Report from LGL Ltd., King City, Ont., Greeneridge Sciences Inc., Santa Barbara, CA, and WEST Inc., Cheyenne, WY, for BP Explor. (Alaska) Inc., Anchorage, AK, edited by W. J. Richardson and M. T. Williams, pp. 2-1–2-40.

Uncertainty analysis in matched-field geoacoustic inversions

Chen-Fen Huang,[a] Peter Gerstoft, and William S. Hodgkiss
Marine Physical Laboratory, Scripps Institution of Oceanography, La Jolla, California 92093-0238

(Received 29 April 2005; revised 18 October 2005; accepted 19 October 2005)

Quantifying uncertainty for parameter estimates obtained from matched-field geoacoustic inversions using a Bayesian approach requires estimation of the uncertainties in the data due to ambient noise as well as modeling errors. In this study, the variance parameter of the Gaussian error model, hereafter called error variance, is assumed to describe the data uncertainty. In practice, this parameter is not known *a priori*, and choosing a particular value is often difficult. Hence, to account for the uncertainty in error variance, several methods are introduced for implementing both the full and empirical Bayesian approaches. A full Bayesian approach that permits uncertainty of the error variance to propagate through the parameter estimation processes is a natural way of incorporating the uncertainty of error variance. Due to the large number of unknown parameters in the full Bayesian uncertainty analysis, an alternative, the empirical Bayesian approach, is developed, in which the posterior distributions of model parameters are conditioned on a point estimate of the error variance. Comparisons between the full and empirical Bayesian inferences of model parameters are presented using both synthetic and experimental data. [DOI: 10.1121/1.2139075]

PACS number(s): 43.30.Pc, 43.60.Pt [AIT] Pages: 197–207

I. INTRODUCTION

Ocean acoustic data inversions typically have focused just on inverting the parameters for one environmental model,[1–5] but some researchers have also considered selecting the best environmental parametrization over a family of geoacoustic models.[6,7] Under the Bayesian framework, all inferences are based on the posterior distribution $p(\mathbf{m}|\mathbf{d}, \boldsymbol{\eta}_0)$ given by

$$p(\mathbf{m}|\mathbf{d}, \boldsymbol{\eta}_0) \propto p(\mathbf{d}|\mathbf{m}, \boldsymbol{\eta}_0)p(\mathbf{m}|\boldsymbol{\eta}_0), \tag{1}$$

where $\mathbf{m}$ represents the geoacoustic model parameter vector, $\mathbf{d}$ represents the data, and $p(\mathbf{d}|\mathbf{m}, \boldsymbol{\eta}_0)$ and $p(\mathbf{m}|\boldsymbol{\eta}_0)$ represent the likelihood and prior distribution conditioned on $\boldsymbol{\eta}_0$, respectively. The symbol $\boldsymbol{\eta}$ refers to other possible unknown quantities in our mathematical model, such as uncertainty in signal characteristics as well as uncertainty of other parameters not included in $\mathbf{m}$ (e.g., ocean water column sound speed parameters). As indicated above, it is customary to keep these quantities at fixed values $\boldsymbol{\eta}_0$.

Under the Bayesian approach, unless there is absolute certainty regarding the value of $\boldsymbol{\eta}$, inference of $\mathbf{m}$ should be made by integrating out the effect of $\boldsymbol{\eta}$ from the joint posterior probability $p(\mathbf{m}, \boldsymbol{\eta}|\mathbf{d})$:

$$p(\mathbf{m}|\mathbf{d}) = \int p(\mathbf{m}, \boldsymbol{\eta}|\mathbf{d})\, d\boldsymbol{\eta} \tag{2}$$

$$= \int p(\mathbf{m}|\mathbf{d}, \boldsymbol{\eta})p(\boldsymbol{\eta}|\mathbf{d})\, d\boldsymbol{\eta}. \tag{3}$$

The second representation shows that the posterior distribution of interest, $p(\mathbf{m}|\mathbf{d})$, is a mixture of the conditional posterior distributions as shown in Eq. (1) given a fixed $\boldsymbol{\eta}$ where $p(\boldsymbol{\eta}|\mathbf{d})$ is a weighting function for the different possible values of $\boldsymbol{\eta}$. This is referred to as a full Bayesian approach. A major problem with this approach is that the number of possible parameters to include in the uncertainty analysis might be quite large.

An alternative, the empirical Bayesian approach,[8] is to replace $\boldsymbol{\eta}$ by a single estimate $\hat{\boldsymbol{\eta}}$ obtained from the data. Inference of $\mathbf{m}$ is now based on the estimated posterior distribution

$$p(\mathbf{m}|\mathbf{d}, \hat{\boldsymbol{\eta}}). \tag{4}$$

This simplified approach essentially replaces the integration in Eq. (2) by an estimation step. Since the full Bayesian approach accounts explicitly for the uncertainty in $\boldsymbol{\eta}$, the inference of $\mathbf{m}$ based on Eq. (2) should produce a more correct distribution than that based on Eq. (4). For the linear forward model case, adjustments to account for the uncertainty induced by estimating $\boldsymbol{\eta}$, especially to produce valid parameter variances, can be found in Ref. 8.

This study discusses several methods for implementing both the full and empirical Bayesian approaches with a focus on one important parameter usually not included in the Bayesian analysis: the error variance ν in a Gaussian error model. However, our methods are applicable to any nuisance parameter. The error variance is influenced by both errors in the data and systematic errors in modeling the data. While error

[a]To whom correspondence should be addressed. E-mail: chenfen@mpl.ucsd.edu

in the data, also known as noise, usually can be determined directly from the data (e.g., in the absence of signal), the systematic error is more difficult to assess. The error variance is important because incorrect choices for this parameter can seriously skew the posterior probability density (PPD) for the model parameters of interest.

The full Bayesian approach requires integrating out the nuisance parameters in Eq. (2) and either numerical or analytical *integration* can be used. Numerical integration is the most general approach as it can be carried out for any likelihood or prior distribution (see Sec. III A). Analytical integration is only possible for certain parameters with specific likelihood functions and prior distributions. For the error variance parameter in a Gaussian model, integrating out the error variance analytically (Sec. III B) makes this an attractive approach from both a computational and an analytical point of view.

For the empirical Bayesian approach, inferences are conditional on point estimates of the nuisance parameters in Eq. (4) and these can be estimated by either numerical or analytical *optimization* (as opposed to the integration used in the full Bayesian approach). Numerical optimization of the posterior probability with respect to both nuisance parameters and model parameters can easily be applied to most parameters and likelihood functions using standard optimization procedures[9,10] (Sec. III C). Analytic optimization is only feasible for certain combinations of likelihood functions and prior distributions. Assuming a Gaussian error model, it is possible to estimate the error variance analytically[2] (Sec. III D) and thus it is not necessary to use numerical optimization.

When estimating the error variance an interesting alternative to the point estimate (fixing the error variance at some specified value) is to use the analytic estimator of the error variance for each value of the model parameter vector.[11] This gives the same form of the posterior distribution as the full Bayesian approach (Sec. III D).

An objective of this study is the analysis of error variance. Since the computational expenses are of little concern for the example, an exhaustive evaluation of $p(\mathbf{m}|\mathbf{d})$ over a grid of parameter space combined with ordinary numerical integration is employed. This is a robust and accurate approach and is recommended for inverse problems with only a few parameters (e.g., less than eight parameters). However, if the number of parameters is large, Monte Carlo methods of numerical integration[4,7] should be used.

For the exhaustive integration, it is easier to assess the convergence than for the complex Monte Carlo methods. The convergence was assured by running the exhaustive search with a certain discretization and then comparing the result to a down sampled result. The integration is done by simply summing the enumerated values over the grid, since the parameters near the edge of the parameter space usually have less contribution to the integral.

The motivation of developing the full Bayesian approach is to avoid under/overestimating the data error variance and to understand how the data error uncertainty influences the uncertainty of the parameters of interest. The obtained parameter distributions can be used to make statistical predictions of various quantities of interest (e.g., transmission loss, as in Ref. 12).

The remainder of this paper is organized as follows. In the next section, the formulation of the inverse problem using the Bayesian approach is reviewed briefly. Section III outlines the approaches for handling error variance. Section IV provides an analytic expression for posterior probability distribution (PPD) of error variance. Section V presents the results and compares the model parameter posterior probability distributions using both synthetic and experimental data. Lastly, a few concluding remarks are made in Sec. VI.

II. FORMULATION OF THE INVERSE PROBLEM

In a Bayesian approach for geoacoustic inversions, inferences about the model parameter vector $\mathbf{m}$ based upon an observed data vector $\mathbf{d}$ are made in terms of probability density functions (pdf's). The basic formula for Bayesian parameter estimation is represented by the posterior probability density function, $p(\mathbf{m}|\mathbf{d})$, which by Bayes' theorem is given by

$$p(\mathbf{m}|\mathbf{d}) = \frac{p(\mathbf{d}|\mathbf{m})p(\mathbf{m})}{p(\mathbf{d})}, \tag{5}$$

where $p(\mathbf{m})$ is the pdf associated with our *a priori* understanding of $\mathbf{m}$ before having access to the data $\mathbf{d}$.

The posterior probability density provides the full description of the state of knowledge about model parameters after observing the data. To interpret the multidimensional PPD, marginalization is used to summarize the PPD for a single parameter m_i by integrating over the remaining parameters $\mathbf{m}'$:

$$p(m_i|\mathbf{d}) = \int p(m_i,\mathbf{m}'|\mathbf{d})\, d\mathbf{m}'. \tag{6}$$

Also, 2-D marginal probability distributions of paired parameters can be obtained in a similar way. Further, the structure of the marginal posterior distribution is captured by the highest posterior density (HPD) interval (or region in the 2-D marginal) at a specified level of probability[13] (Sec. V A).

A. Single-frequency matched-field likelihood function

For matched-field geoacoustic inversions, the relationship between the observed complex-valued pressure field at a single frequency sampled at an N-element array and the predicted pressure field, at the frequency of interest, is described by the data model:

$$\mathbf{d} = \mathbf{D}(\mathbf{m}) + \mathbf{n}, \tag{7}$$

where $\mathbf{d}$ is the observed data and $\mathbf{D}(\mathbf{m})$ is the modeled data based upon a parametrized environmental model. In general, the modeled data is nonlinear with respect to the model parameter vector $\mathbf{m}$. The residual vector $\mathbf{n}$ represents the error terms. Typically, the residual vector is ambient noise but here the interpretation of $\mathbf{n}$ is broadened to include modeling errors.

If we assume that the error vector $\mathbf{n}$ is zero-mean complex Gaussian with covariance matrix $\mathbf{C}_D$, i.e., $\mathbf{n} \sim \mathcal{CN}(0, \mathbf{C}_D)$, then the likelihood function $p(\mathbf{d}|\mathbf{m})$ may be expressed as

$$p(\mathbf{d}|\mathbf{m}, \mathbf{C}_D) = \pi^{-N}|\mathbf{C}_D|^{-1} \times \exp[-(\mathbf{d}-\mathbf{D}(\mathbf{m}))^{\dagger}\mathbf{C}_D^{-1}(\mathbf{d}-\mathbf{D}(\mathbf{m}))], \quad (8)$$

where N is the number of elements in the array and superscript † denotes the complex conjugate transpose. Here, for simplicity, we also assume that the error terms may be described by independent and identically distributed (IID) complex Gaussian random variables with common variance ν, i.e., $\mathbf{C}_D = \nu\mathbf{I}$. This IID type of assumption is useful for convenience, but it may not completely model all the errors of interest. In what follows we shall always refer to the variable ν as the variance of the data errors.

The likelihood of the model parameter vector $\mathbf{m}$ for a given set of data may be written as

$$\mathcal{L}(\mathbf{m}, \nu, s) \equiv p(\mathbf{d}|\mathbf{m}, \nu, s) = \frac{1}{\pi^N \nu^N}\exp\left(-\frac{\|\mathbf{d}-\mathbf{d}(\mathbf{m})s\|^2}{\nu}\right), \quad (9)$$

in which the modeled data $\mathbf{D}(\mathbf{m})$ is represented by $\mathbf{D}(\mathbf{m}) = \mathbf{d}(\mathbf{m})s$, where $\mathbf{d}(\mathbf{m})$ is the replica field vector (or normalized signal field) computed using an acoustic propagation model for the model parameters $\mathbf{m}$, and s is the complex-valued source signature at the frequency of interest.

The source signature can be estimated either by the maximum-likelihood (ML) estimator, i.e., finding the value of s that maximizes the likelihood function,[2] or, should we have no interest in its value, by treating s as a nuisance parameter and eliminating it by integration (as will be discussed in Sec. III). Here we adopt the former method and obtain the ML estimate of the source parameter s as $s_{ML} = \mathbf{d}^{\dagger}(\mathbf{m})\mathbf{d}/\|\mathbf{d}(\mathbf{m})\|^2$. Substituting this relationship into Eq. (9) yields[2]

$$\mathcal{L}(\mathbf{m}, \nu) = \frac{1}{\pi^N \nu^N}\exp\left(-\frac{\phi(\mathbf{m})}{\nu}\right), \quad (10)$$

where $\phi(\mathbf{m})$ denotes an objective function defined as

$$\phi(\mathbf{m}) = \|\mathbf{d}\|^2\left[1 - \frac{|\mathbf{d}(\mathbf{m})^{\dagger}\mathbf{d}|^2}{\|\mathbf{d}\|^2\|\mathbf{d}(\mathbf{m})\|^2}\right] \quad (11)$$

in which the second term in the bracket is the normalized Bartlett power objective function[14] measuring the correlation between the data and the replica vectors. The objective function in Eq. (11) can be generalized[2] when multiple data snapshots are available.

B. Multi-frequency matched-field likelihood function

Assuming that the data errors are statistically independent across frequencies, then the multi-frequency matched-field likelihood function is the product of the single frequency counterparts:

$$\mathcal{L}(\mathbf{m}, \nu_1, \ldots, \nu_J) = \prod_j^J \mathcal{L}_j(\mathbf{m}, \nu_j), \quad (12)$$

where J indicates the number of the processed frequencies and $\mathcal{L}_j(\mathbf{m}, \nu_j)$ is the jth frequency likelihood with the error variance denoted by ν_j as in Eq. (10). To illuminate the significance of ν_j, Eq. (10) is rewritten as

$$\mathcal{L}_j(\mathbf{m}, \nu_j) \propto \exp\left(-\frac{\phi_j(\mathbf{m})}{\nu_j} - N\ln\nu_j\right) \quad (13)$$

in which $1/\nu_j^N$ has been expressed as $\exp(-N\ln\nu_j)$ and the constant π^{-N} is omitted.

1. Frequency-dependent error variance

Error variance is frequency dependent. Not only does ambient noise vary across frequency but the error due to modeling mismatch also varies across frequency. With the assumption that errors are independent across frequencies, as in Eq. (12), the likelihood of $\mathbf{m}$ for multi-frequency cases is the product of the marginal likelihoods of $\mathbf{m}$ for each frequency, with ν_j being integrated out:

$$\mathcal{L}(\mathbf{m}) = \prod_j^J \int_{\nu_j} \mathcal{L}_j(\mathbf{m}, \nu_j)p(\nu_j)\,d\nu_j, \quad (14)$$

where $p(\nu_j)$ is the prior distribution of ν_j which will be specified in Sec. II C.

2. A single global error variance

A common approach is to assume the variation of the data error variances ν_j over the selected frequencies is negligible and model them by a single variable ν_0, i.e.,

$$\nu_j = \nu_0, \quad \text{for } j = 1, \ldots, J. \quad (15)$$

The likelihood for the selected frequencies with a common error variance ν_0 can be written as

$$\mathcal{L}(\mathbf{m}, \nu_0) \propto \exp\left(-\frac{J}{\nu_0}\bar{\phi}^a(\mathbf{m}) - JN\ln\nu_0\right), \quad (16)$$

where $\bar{\phi}^a(\mathbf{m}) = (1/J)\Sigma\,\phi_j(\mathbf{m})$ is the arithmetic mean of the objective function over frequencies.

Equations (14) and (16) hold under the assumption that the errors are independent for each frequency. However, when the errors due to frequency-dependent modeling mismatch are the dominant source of error, the modeling error may not be independent across the frequencies used. Therefore, the number of frequencies J must be replaced with an effective number of frequencies J_{eff}.

C. Noninformative priors

Before applying Bayes' theorem to make inference of parameters, one needs to specify their prior pdf's. The natural choice for a prior pdf is the distribution that allows for the greatest uncertainty while obeying the constraints imposed by prior knowledge. We treat here the case where very little is known about $\mathbf{m}$ and ν *a priori*.

Starting from the model parameters $\mathbf{m}$, all one knows is that the values of the parameters are within lower bounds l_i

TABLE I. Summary of the approaches (single frequency[a]).

Section: Approach	PPD of $\mathbf{m}$	Error variance	Remark
III A: Full Bayesian (numerical)	$\int p(\mathbf{m},\nu\|\mathbf{d})\,d\nu$	$\int p(\mathbf{m},\nu\|\mathbf{d})\,d\mathbf{m}$	Theoretically preferred but computationally expensive
III B: Full Bayesian (analytic)	$\dfrac{1}{\phi^N(\mathbf{m})}$	$\nu^{-[(2N-M^*)/2+1]}\exp\left(-\dfrac{\phi(\hat{\mathbf{m}})}{\nu}\right)$[b]	Theoretically & computationally preferred
III C: Empirical Bayesian (numerical)	$p(\mathbf{m}\|\mathbf{d},\nu_{\mathrm{MAP}})$	$\nu_{\mathrm{MAP}}=\arg\max_{\nu} p(\mathbf{m},\nu\|\mathbf{d})$	Computationally efficient
III D: Empirical Bayesian (analytic)	$p(\mathbf{m}\|\mathbf{d},\nu_{\mathrm{ML}})$	$\nu_{\mathrm{ML}}=\dfrac{\phi(\hat{\mathbf{m}})}{N}$	Computationally preferred

[a]As for the multi-frequency data, see Eq. (24) for the details.
[b]The formula is derived in Sec. IV.

and upper bounds u_i based upon the measurements independent of the acoustic data. We assume that there is no prior preference for any value over any other; then a uniform distribution over that range is a practical choice for the prior,

$$p(m_i)=\frac{1}{u_i-l_i},\quad l_i<m_i<u_i. \tag{17}$$

For the error variance parameter ν, all one knows about this parameter *a priori* is that it is always positive and one is equally ignorant about its value or any of its powers (e.g., a standard deviation or a variance). The appropriate distribution for this parameter is a uniform pdf on $\ln\nu$.[15] In practice, the limits of this prior do not go all the way to zero and infinity. We usually know in advance that ν cannot be much less than the ambient noise variance estimate (ν_{AN}) and cannot be much greater than the maximum likelihood estimate (ν_{ML}). Thus,

$$p(\nu)\propto\frac{1}{\nu},\quad 0.1\nu_{\mathrm{AN}}<\nu<10\nu_{\mathrm{ML}}. \tag{18}$$

Note that using broader limits for the error variance is to obtain a full distribution where the upper and lower ends have zero probability.

With the additional assumption that all model parameters $(m_1,\ldots,m_M)$ and ν are mutually independent, the prior distribution is the product of the prior distributions for each parameter:

$$p(\mathbf{m},\nu)=p(\mathbf{m})p(\nu)=\prod_i^M p(m_i)p(\nu)\propto\frac{1}{\nu} \tag{19}$$

over the interval where prior probability of $\mathbf{m}$ is nonzero. Then, based upon Bayes' theorem, the posterior distribution is as follows:

$$p(\mathbf{m},\nu|\mathbf{d})\propto p(\mathbf{d}|\mathbf{m},\nu)p(\mathbf{m},\nu)\propto\mathcal{L}(\mathbf{m},\nu)\frac{1}{\nu}$$
$$\propto\exp\left(-\frac{\phi(\mathbf{m})}{\nu}-(N+1)\ln\nu\right) \tag{20}$$

with the scale factor that makes the posterior distribution integrate to one being omitted. The final representation of Eq. (20) will be extensively used in this analysis.

Note that the posterior distribution for a uniform prior on ν or for a uniform prior on $\ln\nu$ differs only in an N or $N+1$ in front of $\ln\nu$ [Eq. (20)]. This suggests that for reasonably large N their respective PPDs are similar.

III. ERROR VARIANCE AS A NUISANCE PARAMETER

In this section, we shall treat the error variance in a Gaussian error model as a nuisance parameter and discuss both the full and empirical Bayesian methods from an implementation perspective. For convenience of comparison, the approaches discussed below are summarized in Table I.

A. Full Bayesian estimation—numerical integration

The full Bayesian approach is a natural way of incorporating the uncertainty of error variance in the analysis. The approach does not assume the error variance at a particular value, rather, it regards the error variance as an unknown in the parameter space. In this way, the approach allows the data uncertainty to propagate through the parameter estimation processes and, at the end, reflect uncertainty in the error variance in the resulting parameter estimation.

Therefore, the true posterior distribution of the model parameters is obtained by integrating out ν from the joint posterior distribution of $\mathbf{m}$ and ν:

$$p(\mathbf{m}|\mathbf{d})=\int p(\mathbf{m},\nu|\mathbf{d})\,d\nu. \tag{21}$$

B. Full Bayesian estimation—analytic integration

In this approach, the error variance is considered as a nuisance parameter and is eliminated by integrating the likelihood function weighted by the prior distribution of ν over the entire range:[16]

$$p(\mathbf{m}|\mathbf{d}) = \int_0^\infty p(\mathbf{m}, \nu|\mathbf{d})\, d\nu$$

$$\propto p(\mathbf{m}) \underbrace{\int_0^\infty p(\mathbf{d}|\mathbf{m}, \nu) p(\nu)\, d\nu}_{p(\mathbf{d}|\mathbf{m})}. \tag{22}$$

Incorporating the noninformative prior of ν in Eq. (18), the exact expression of $p(\mathbf{d}|\mathbf{m})$ can be shown to be of the form[17]

$$p(\mathbf{d}|\mathbf{m}) = \frac{1}{\pi^N} \frac{(N-1)!}{\phi^N(\mathbf{m})}. \tag{23}$$

This likelihood function is preferable in estimating PPD of model parameters for two reasons. Theoretically, this formula is derived based on a full Bayesian methodology. Computationally, this method is faster than a computer-based numerical integration of the full Bayesian procedure.

The above analytic solution, Eq. (23), can be extended straightforwardly to the multi-frequency data set. From Eq. (14), the multi-frequency likelihood function can be written in a concise form:

$$\mathcal{L}(\mathbf{m}) \propto \left(\frac{1}{\bar{\phi}^g(\mathbf{m})} \right)^{NJ} \tag{24}$$

where $\bar{\phi}^g(\mathbf{m}) = \sqrt[J]{\Pi \phi_j(\mathbf{m})}$ is the geometric mean of the objective function over frequency when the error variance is frequency dependent. However, for the case where the error variance is assumed to be constant over the processed frequencies, the arithmetic mean $\bar{\phi}^a(\mathbf{m})$ is used instead of $\bar{\phi}^g(\mathbf{m})$ in Eq. (24) in a manner analogous to that used by Ref. 11.

C. Empirical Bayesian estimation—optimizing error variance jointly with model parameters

The main idea behind this approach is to consider the error variance on the same level as the model parameters and optimize the joint posterior probability $p(\mathbf{m}, \nu|\mathbf{d})$ to find the estimate of ν:

$$\nu_{\mathrm{MAP}} = \arg\max_{\nu} p(\mathbf{m}, \nu|\mathbf{d}). \tag{25}$$

Then, the posterior distribution of the model parameters is approximated by fixing the error variance at ν_{MAP}:

$$p(\mathbf{m}|\mathbf{d}) \approx p(\mathbf{m}|\mathbf{d}, \nu_{\mathrm{MAP}}) \propto \exp\left[-\frac{\phi(\mathbf{m})}{\nu_{\mathrm{MAP}}} \right]. \tag{26}$$

This approach is easier to implement numerically compared to the full Bayesian approach because the value of the error variance can be found by any efficient optimization procedure, such as simulated annealing or genetic algorithms.[18]

D. Empirical Bayesian estimation—maximum likelihood estimate

The maximum likelihood estimator for the error variance can be obtained analytically

$$\nu_{\mathrm{ML}}(\mathbf{m}) = \frac{\phi(\mathbf{m})}{N}. \tag{27}$$

Two approaches for implementing this estimator in ocean acoustic inversions have been proposed by Mecklenbräuker and Gerstoft.[11]

Following an empirical Bayesian methodology, one requires only an estimate of the error variance. First, the ML solution of model parameter vector, $\hat{\mathbf{m}}$, is found [by minimizing the objective function, Eq. (11), over all $\mathbf{m}$]. Second, an estimate of error variance is obtained:[2]

$$\nu_{\mathrm{ML}}(\hat{\mathbf{m}}) = \frac{\phi(\hat{\mathbf{m}})}{N}. \tag{28}$$

Then, the PPD of $\mathbf{m}$ is approximated by fixing ν at $\nu_{\mathrm{ML}}(\hat{\mathbf{m}})$:

$$p(\mathbf{m}|\mathbf{d}, \nu_{\mathrm{ML}}(\hat{\mathbf{m}})) \propto \exp\left[-\frac{\phi(\mathbf{m})}{\nu_{\mathrm{ML}}} \right]. \tag{29}$$

The error variance estimated from either ν_{MAP} [Eq. (25)] or ν_{ML} [Eq. (28)] often results in overly optimistic posterior distributions of the model parameters since a single value of the error variance may not be representative.

The other approach proposed in Ref. 11 is to substitute Eq. (27) into the likelihood formula [Eq. (10)] without fixing a value for ν. With the noninformative prior for $\mathbf{m}$, the PPD of $\mathbf{m}$ is proportional to the likelihood function

$$p(\mathbf{m}|\mathbf{d}, \nu_{\mathrm{ML}}(\mathbf{m})) \propto p(\mathbf{m}) \mathcal{L}(\mathbf{m}, \nu_{\mathrm{ML}}(\mathbf{m})) \propto \mathcal{L}(\mathbf{m}, \nu_{\mathrm{ML}}(\mathbf{m}))$$

$$\propto \frac{1}{\phi^N(\mathbf{m})}. \tag{30}$$

Note that the likelihood formula derived in Sec. III B [Eq. (23)] and the result derived above [the third representation of Eq. (30)] possess the same functional form.

IV. PPD OF THE ERROR VARIANCE

The posterior distribution of ν is obtained by integrating the joint PPD over the model parameter vector:

$$p(\nu|\mathbf{d}) = \int p(\mathbf{m}, \nu|\mathbf{d})\, d\mathbf{m}. \tag{31}$$

One could always evaluate the integral in Eq. (31) numerically, but an analytic expression can be obtained under the simplifying Gaussian approximation for the PPD of the model parameters. This approach is known as Laplace's method, a family of asymptotic techniques used to approximate integrals.[19]

Inspired by Malinverno,[20] let us assume that, for any value of ν, the PPD of the model parameter vector is approximated by a Gaussian function of $\mathbf{m}$ centered on the MAP solution $\hat{\mathbf{m}}$ (Ref. 21) with the posterior covariance matrix of model parameters $\hat{\mathbf{C}}_{\mathrm{M}}$ (the hat is used to denote the quantity inferred *a posteriori*):

$$p(\mathbf{m}, \nu|\mathbf{d}) \approx p(\hat{\mathbf{m}}, \nu|\mathbf{d}) \exp\left(-\frac{(\mathbf{m}-\hat{\mathbf{m}})^T \hat{\mathbf{C}}_{\mathrm{M}}^{-1} (\mathbf{m}-\hat{\mathbf{m}})}{2} \right). \tag{32}$$

Since an unnormalized Gaussian pdf has the following constant,

$$\int \exp\left(-\frac{\mathbf{m}^T\hat{\mathbf{C}}_{\mathrm{M}}^{-1}\mathbf{m}}{2}\right) d\mathbf{m} = (2\pi)^{M/2}\sqrt{|\hat{\mathbf{C}}_{\mathrm{M}}|}, \tag{33}$$

substituting Eq. (20) into $p(\hat{\mathbf{m}}, \nu|\mathbf{d})$ yields the approximation to the marginal PPD of ν:

$$p(\nu|\mathbf{d}) \approx \frac{a}{\nu^{N+1}} \exp\left(-\frac{\phi(\hat{\mathbf{m}})}{\nu}\right)\sqrt{|\hat{\mathbf{C}}_{\mathrm{M}}|}, \tag{34}$$

where a is a scale factor that makes $p(\nu|\mathbf{d})$ integrate to one.

To evaluate the posterior covariance matrix of model parameters $\hat{\mathbf{C}}_{\mathrm{M}}$, the forward model is linearized with respect to the best-fit model vector

$$\mathbf{D}(\mathbf{m}) \approx \mathbf{K}(\mathbf{m}-\hat{\mathbf{m}}) + \mathbf{D}(\hat{\mathbf{m}}), \tag{35}$$

where $\mathbf{K} = [\partial\mathbf{D}(\mathbf{m})/\partial\mathbf{m}]|_{\mathbf{m}=\hat{\mathbf{m}}}$ is an $N \times M$ matrix of Fréchet derivatives evaluated at the best-fit model solution $\hat{\mathbf{m}}$. Comparing the exponent of Eq. (32) with Eq. (8) in which the nonlinear forward model is substituted by Eq. (35) gives

$$\hat{\mathbf{C}}_{\mathrm{M}} = (2\mathbf{K}^{\dagger}\mathbf{C}_{\mathrm{D}}^{-1}\mathbf{K})^{-1}. \tag{36}$$

Since the data errors are expected *a priori* to be IID with variance ν ($\mathbf{C}_{\mathrm{D}} = \nu\mathbf{I}$) and with the further assumption that the model parameters are resolved by the data set, the determinant of $\hat{\mathbf{C}}_{\mathrm{M}}$ is

$$|\hat{\mathbf{C}}_{\mathrm{M}}| = \left|\frac{\nu}{2}(\mathbf{K}^{\dagger}\mathbf{K})^{-1}\right| \propto |\nu\mathbf{I}_{M^*}| \propto \nu^{M^*}, \tag{37}$$

where M^* is the number of model parameters resolved by the data. Generally speaking, M^* is determined by the number of elements in the model parameter vector when $\mathbf{K}$ has full rank (all the model parameters are constrained by $\mathbf{K}$). However, due to the presence of noise, the parameter sensitivity and the possibility of linear dependence between the model parameters, not all of these may be estimated to a useful accuracy. Therefore, $M^* \leq M$. Then, substituting Eq. (37) into Eq. (34), we obtain the following approximation

$$p(\nu|\mathbf{d}) \propto \nu^{-[(2N-M^*)/2+1]} \exp\left(-\frac{\phi(\hat{\mathbf{m}})}{\nu}\right). \tag{38}$$

This approximation to the marginal PPD of ν is the so-called inverse chi-square distribution used in Bayesian analysis (see Ref. 13, Sec. 2.3.1). However, the inverse chi-square distribution presented in Ref. 13 is based on real-valued Gaussian random variables. For the complex-valued Gaussian random variables, the scaled error variance $\nu/(2\phi(\hat{\mathbf{m}}))$ has the inverse chi-square probability density with $2N-M^*$ degrees of freedom.

Notice that M^* can be found from comparing the analytic result with the PPD of ν obtained from the numerical integration of the full Bayesian, or it can be estimated from the rank of the posterior covariance matrix of the model parameters $\hat{\mathbf{C}}_{\mathrm{M}}$.

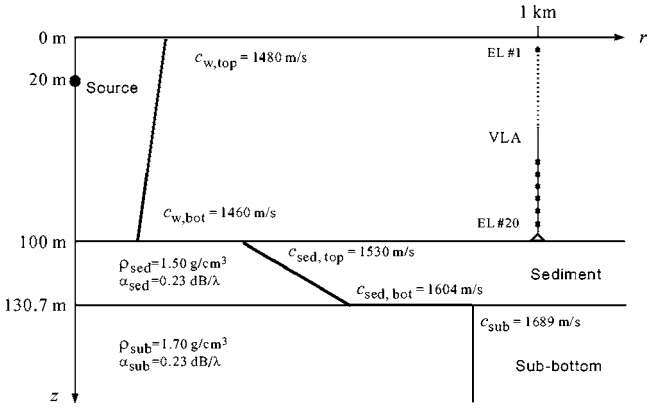

FIG. 1. The **sdc** environment from the Geo-Acoustic Inversion [22] shown here for the parameters corresponding to ground true.

V. RESULTS AND DISCUSSION

A. Synthetic data

To illustrate the various approaches presented in Sec. III, a data set is synthesized using the environmental model employed in the Geo-Acoustic Inversion Workshop 1997.[22] Figure 1 shows the baseline model that consists of a downward refracting sound speed profile overlying a positive-gradient sediment layer atop of a homogeneous subbottom layer. The vertical array consists of 20 hydrophones equally spaced over a 95-m interval with the first phone at 5-m depth, and the source located at 1-km range and 20-m depth, transmitting CW tones at 100 and 200 Hz. The calculations of acoustic fields are performed by the normal-mode propagation model ORCA.[23] The interaction of acoustic fields with the baseline environment for these two frequencies is plotted in Fig. 2.

In order to demonstrate the effect of error variance on the parameter estimation, the amount of noise corresponding to 20-dB SNR [equivalent to $\nu_{\mathrm{true}} = 0.0083$, see Eq. (A6) in the Appendix] is purposely added to the data. The parameters to be estimated are the geoacoustic parameters, including sediment thickness d, top and bottom sediment sound speeds $c_{\mathrm{sed,top}}$ and $c_{\mathrm{sed,bot}}$, subbottom sound speed c_{sub}, and the error variance ν. Figure 3 shows the parameter estimate using the full Bayesian approach for a frequency of 100 Hz. The line subplots along the diagonal are the one-dimensional (1-D) marginal PPDs for each parameter, $p(m_i|\mathbf{d})$, and the contour subplots in the upper triangle are the 2-D marginal PPDs corresponding to the paired parameters in the bottom-most and left-most line subplots, $p(m_b, m_l|\mathbf{d})$. In each contour plot, the gray-scale coloring from darkest to lightest represents 50%, 75%, and 95% highest posterior density (HPD). The β% HPD describes a region which contains β% of the total probability.[13] Due to the nonlinearity of the forward model, the PPD of model parameters is no longer Gaussian. Therefore, the best-fit model (cross signs in 2-D contours or arrow lines in 1-D plots) is not necessarily coincident with those from the mode of the marginal (plus signs in 2-D).

The 1-D and 2-D marginal PPDs reveal the uncertainty of the parameter estimation but in addition the 2-D PPDs also show the correlations between the paired parameters. For example, the contour subplot on row 1 and column 3

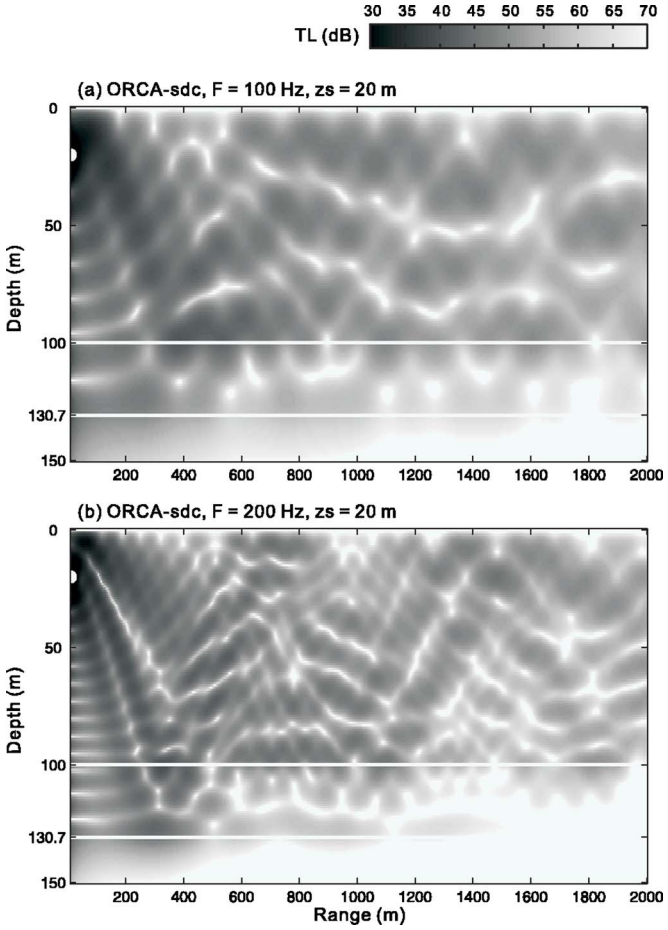

FIG. 2. Range-depth transmission loss for (a) $F=100$ and (b) 200 Hz, respectively, using the **sdc** environment. The two white lines mark the water-sediment (top) and sediment-subbottom (bottom) interfaces.

shows the correlation between bottom sediment sound speed $c_{\text{sed,bot}}$ and sediment thickness d. The result suggests that there is a strong positive coupling between these two parameters. Therefore, the interparameter correlation results in a relatively flat distribution in the 1-D marginal PPDs for the parameters $c_{\text{sed,bot}}$ and d. If more information about one of these two parameters could be obtained, then the 1-D marginal of the other could be sharpened. Likewise, the parameters of $c_{\text{sed,bot}}$ and $c_{\text{sed,top}}$ are strongly correlated in a negative manner. However, the 2-D PPDs for each pair of m_i and ν show that the error variance has little correlation with any other geoacoustic parameters, i.e., $p(m_i,\nu|\mathbf{d})=p(m_i|\mathbf{d})p(\nu|\mathbf{d})$.

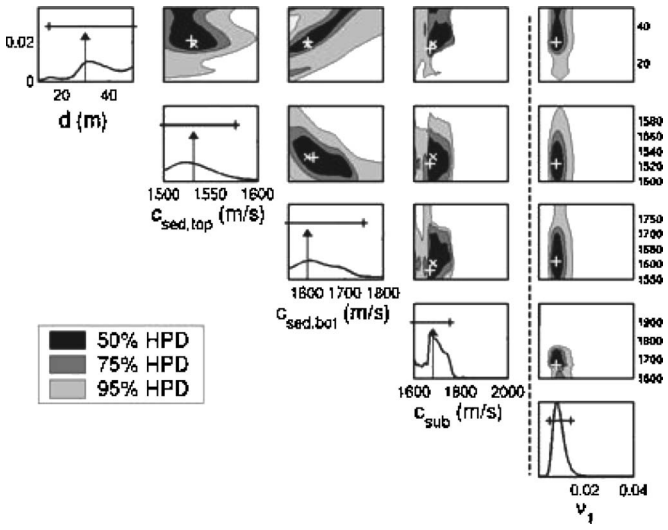

FIG. 3. Marginal posterior probability densities (PPDs) of the geoacoustic parameters as well as the error variance for $F=100$ Hz. In each 1-D marginal, the horizontal error bar shows 95% highest posterior density (HPD) interval.

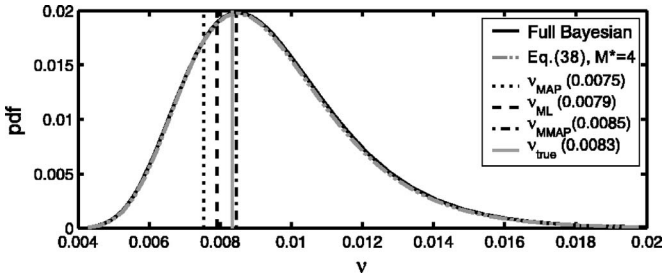

FIG. 4. The enlarged version of the marginal posterior distribution of the error variance in Fig. 3. Note that ν^{MMAP} is the MAP estimate of the marginal PPD of ν; it is not to be confused with the MAP estimate of the multidimensional joint PPD, ν^{MAP}

The error variances estimated from the various approaches are summarized in Fig. 4. First, the PPD of ν obtained from the numerical integration is compared with that from the analytic integration. We find that by setting the parameter $M^*=4$ in the analytic formula of the error variance distribution [Eq. (38)], the analytic result (dash-dot-dot curve) has excellent agreement with the numerical integration result (solid curve). Note that even though the PPDs of the geoacoustic parameters are only very approximately Gaussian, the PPD of ν follows an inverse chi-squared density. In this example, the analytic expression of the posterior distribution of ν agrees well with the full Bayesian result, given the number of well-determined parameters used.

Second, the point estimates of error variance from the empirical Bayesian approaches are summarized in Fig. 4. Since the error variance is distributed *a posteriori* as an inverse chi-square with $(2N-4)$ degrees of freedom, one may consider the peak of this marginal posterior distribution as an estimate of the error variance, named as the marginal MAP (MMAP) value of error variance, ν_{MMAP}. The solid vertical line shows the actual value of the error variance added to the data (0.0083). The ML (dash), MAP (dot), and MMAP (dash-dot) estimates of error variance are also shown. Among the various point estimates of error variance, ν_{MMAP} is the largest since it automatically takes into account the reduction in the degrees of freedom (for the inverse chi-square distribution) in the process of integration over the model parameters. The difference between the MAP and ML estimates of the error variance is due to the $1/\nu$ prior being used. In this synthetic data case, since the only uncertainty is the random error added to the data, there is not much difference in the estimated error variances among the various approaches.

The comparison of the marginal PPDs for each of the geoacoustic parameters is given in Fig. 5. The 1-D PPDs are estimated using full Bayesian treatment of error variance via numerical integration (solid; Sec. III A) and these using the

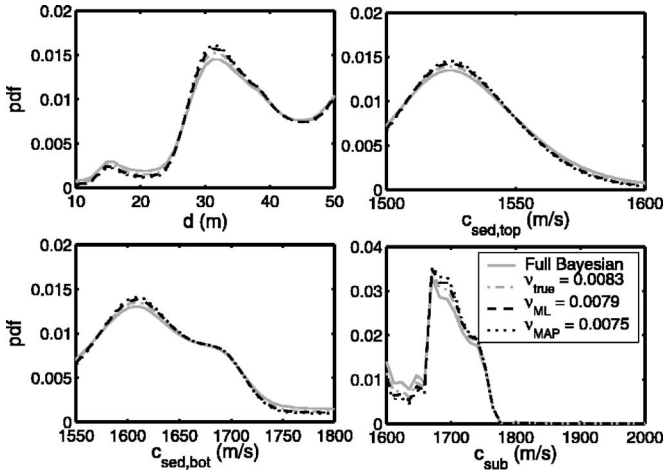

FIG. 5. Comparison of the marginal PPDs for the geoacoustic parameters using different approaches in handling the error variance. $F=100$ Hz).

empirical Bayesian methods based on the true value (dash-dot) and the ML (dash) and MAP (dot) estimates of the error variance. In addition, the PPDs using the analytic integration of the full Bayesian approach (Sec. III B) are identical to these using numerical integration (solid). From the simulations, the empirical Bayesian method using an ML or MAP estimate of the error variance is a good approximation to the full Bayesian approach:

$$p(\mathbf{m}|\mathbf{d}) \approx p(\mathbf{m}|\mathbf{d},\nu). \tag{39}$$

However, the difference would become more distinguishable when the number of inverted parameters is similar to the number of the data points.

Figure 6 shows the marginal PPDs for the same parameter set using 200-Hz frequency data with the additive noise corresponding to 15-dB SNR ($\nu_{true}=0.0194$) in contrast to the 20-dB SNR noise added to the 100-Hz data. Except for $c_{sed,top}$, the geoacoustic parameters are poorly estimated in comparison of Fig. 3. Since the higher frequency has higher

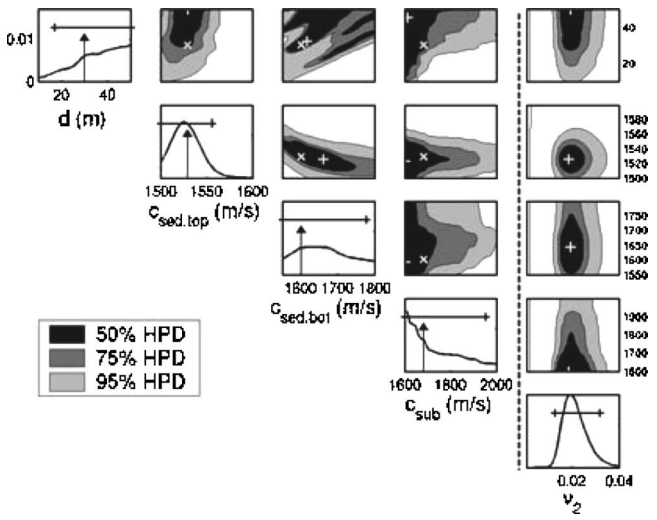

FIG. 6. Full Bayesian approach. 1-D and 2-D marginal PPDs of the geoacoustic parameters as well as the error variance for 200 Hz. The actual value of the error variance added to the data is equivalent to 15–dB SNR ($\nu^{true}=0.0194$). The format is the same as Fig 3

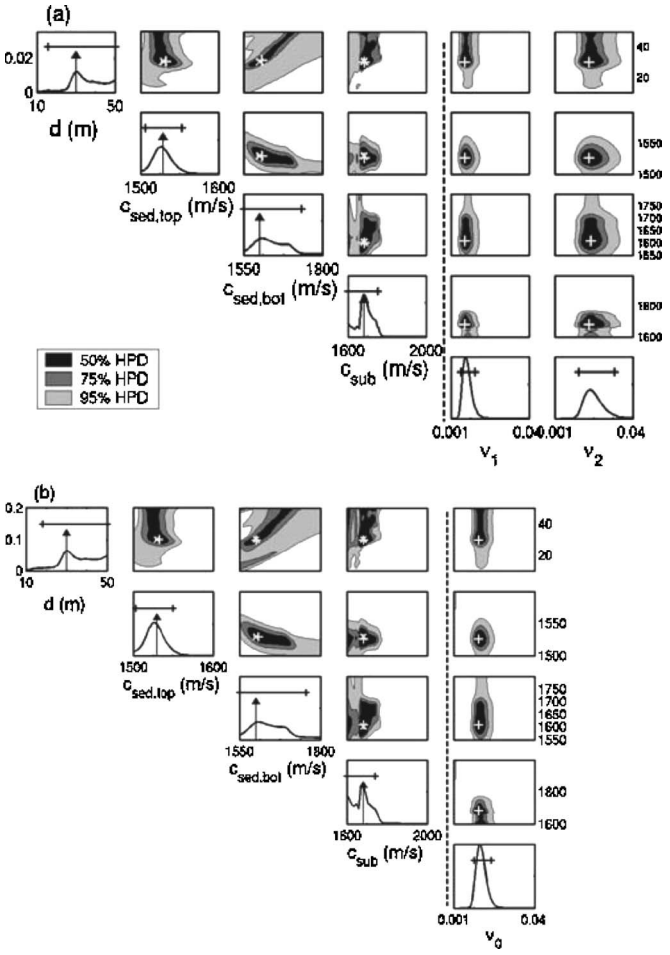

FIG. 7. Full Bayesian approach for the multi-frequency case (a) 1-D and 2-D marginal PPDs of the geoacoustic parameters as well as the error variance for frequency of 100 and 200 Hz. (b) The marginal PPDs of geoacoustic parameters as well as the global error variance. The format is the same as in Fig. 3.

resolution in the upper sediment (more structure in the acoustic field at the water-sediment, as seen in Fig. 2) but shorter penetration depth, only $c_{sed,top}$ is better resolved at 200-Hz frequency.

Having estimated the marginal PPDs using data at 100- and 200-Hz frequencies separately, we then estimate the PPDs using data from both frequencies which have different error variances. Figure 7 demonstrates the multi-frequency case: (a) the error variance are appropriately accounted for (modeled by ν_1 and ν_2) and (b) the error variance are assumed the same over these two frequencies (modeled by ν_0). In addition, the 1-D PPDs using the analytic integration of full Bayesian method, Eq. (24), are shown in both figures, where the geometric mean is used for Fig. 7(a) and the arithmetic mean for Fig. 7(b). The results are not distinguishable from those using the numerical integration.

Comparing Fig. 7(a) with Fig. 7(b), we see there is a slight difference between the two treatments of error variance. The uncertainties of the geoacoustic parameters using two frequencies (Fig. 7) are reduced significantly in contrast to those using single frequency (Figs. 3 and 6), in agreement with Refs. 1–4.

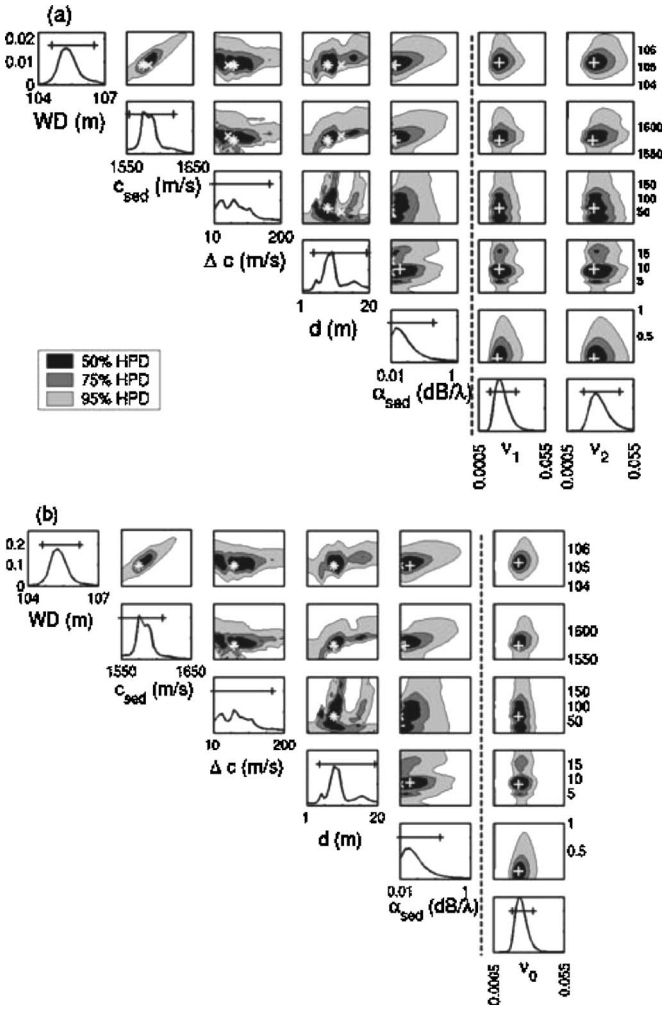

FIG. 8. Full Bayesian approach for the multi-frequency case (a) 1-D and 2-D marginal PPDs fo the geoacoustic parameters as well as the error variances for the freuqenices 195 and 395 Hz. (b) 1-D and 2-D marginal PPDs of the geoacoustic parameters as well as the global error variance. The format is the same as in Fig. 3.

B. Experimental data

Data acquired during the ASIAEX 2001 East China Sea experiment (see Ref. 24) are used to illustrate the approaches for incorporating uncertainty in the error variance. A 16-element vertical line array was deployed in 105-m-deep water (element 4 failed during deployment). The source was towed at a depth of about 48 m. A general bathymetric and geological survey has indicated that in the neighborhood of the experimental site, the environment is nearly range independent. Therefore, the ocean environment is modeled as an ocean layer overlying a uniform sediment layer atop of a basement. All layers are assumed to be range independent.

In our previous study,[24] matched-field geoacoustic inversion using the frequencies 195, 295, and 395 Hz was carried out to invert for the seafloor parameters. Based upon the GPS position of R/V *Melville*, the observed data $\mathbf{d}$ was approximately 1.7 km away from the source. To reduce mismatch in water depth, source position, array geometry, and ocean sound-speed profile, we have inverted for a total of 13 model parameters. In order to estimate the model parameters, a global optimization method, based on genetic algorithms, along

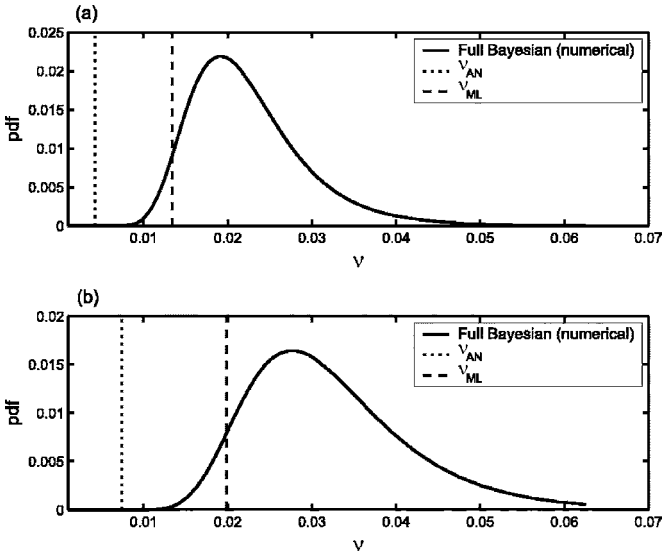

FIG. 9. Posterior marginal distribution of the error variance obtained from the numerical integration. (a) $F=195$ Hz and (b) $F=395$ Hz. The vertical lines show the different estimates of error variance.

with the normal-mode propagation model SNAP[25] was used.

We inspect here the posterior probability densities of the following five model parameters: water depth (WD), sediment sound speed (c_{sed}), basement sound speed increase (Δc), sediment thickness (d), and sediment attenuation (α_{sed}), with all other parameters fixed at their optimal values (using the empirical Bayesian treatment). The same data set is used in this analysis but with the selected frequencies of 195 and 395 Hz. Therefore, we are finding the PPDs of a total of seven parameters (the five model parameters plus the error variances at the two frequencies).

Figure 8 shows the full Bayesian approach for the multi-frequency case: (a) the frequency-dependent error variances are considered and (b) the error variances are assumed constant over frequencies. The error variances do not vary too much across the processed frequencies, therefore, the PPDs of the model parameters do not have a significant difference between the two treatments of error variances.

Figure 9 shows the posterior marginal distributions of error variance obtained from the numerical integration: (a) $F=195$ Hz and (b) $F=395$ Hz. The error estimates from the other examined approaches are superimposed on the PPD of ν. The dotted line represents the ambient noise estimated directly from the data (corresponding to SNR=23 and 21 dB, respectively) and the dashed line denotes the ML estimate of the error variance. The marginal distribution of the error variance captures that the effective error variance may be larger than the ambient noise estimate.

In the experimental data, with the high SNR, the modeling error in the parametrized environment is the dominant source of error in the estimation procedure. Because the modeling error may not be independent across the receivers, the IID assumption in the likelihood function is no longer appropriate; a full data uncertainty covariance matrix $\mathbf{C}_{\text{D}}$ is needed. Therefore, to describe the data uncertainty for N complex-valued measurements, a huge number of quantities, N^2, needs to

be estimated. A way to fix the defect of the likelihood function is to down sample the observations as adopted by Ref. 26. In the experimental data used here, due to the large separation of the array elements (5-m interelement spacing and 15 hydrophones in total), it was not necessary to down sample the data.

Finally, the comparison of PPDs for the model parameters using different error variance estimates is shown in Fig. 10. The PPD of the model parameters using the ambient noise variance (dotted) yields too optimistic an uncertainty estimate. The PPD based on the ML estimate of error variance (dash) is similar to the one obtained by the full Bayesian approach (solid). It is noteworthy that, in the 1-D marginal PPDs of WD and c_{sed}, the location of the peaks varies with different values of error variance. The reason is that there exists nonsymmetrically distributed HPD contours in the joint marginal PPD, and when using a lower value of the error variance, the lower probability density in the 2-D marginal contributes more into the 1-D marginal distribution.

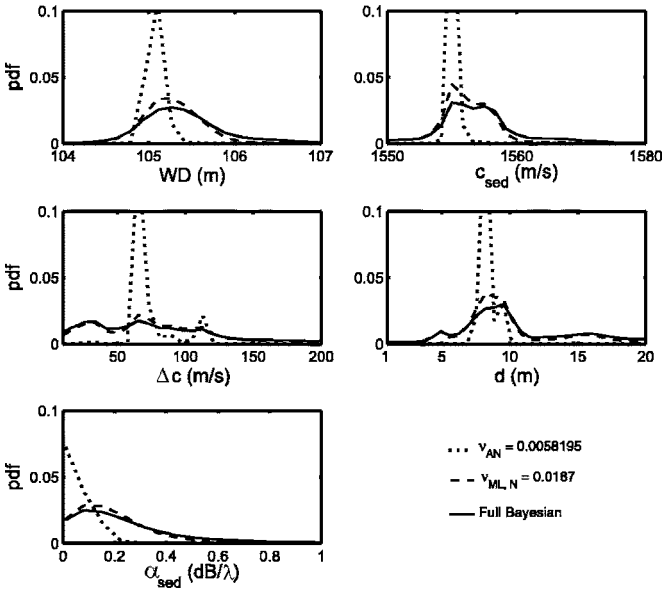

FIG. 10. Comparison of the marginal PPDs for the model parameters using different approaches in the error variance.

VI. CONCLUSIONS

This paper describes several methods for handling nuisance parameters based on both the full and empirical Bayesian approaches. In a full Bayesian approach, the inference is made from the joint posterior probability distribution (PPD) of the model parameters and the nuisance parameters, whereas in an empirical Bayesian approach the PPD of the model parameters is conditioned on a point estimate of the nuisance parameters. The full Bayesian approach takes more complete accounting of uncertainty in the nuisance parameters, but it is computationally expensive. The applications of the approaches to the error variance parameters in a Gaussian error model were examined.

Following a full Bayesian methodology, the analytic expression of PPD of the model parameters was derived for both single frequency [Eq. (23)] and multi-frequency data [Eq. (24)]. The results (Figs. 3, 6, and 7) show that the PPD of the model parameters using this analytic formula cannot be distinguished from that using numerical integration of the full Bayesian approach. Therefore, the analytic integration of the full Bayesian approach is theoretically and computationally preferred.

The analytic expression for the PPD of the error variance was derived and follows the so-called inverse chi-square distribution. This analytic result agrees well with the distribution obtained using numerical integration of the full Bayesian approach.

The empirical Bayesian approach using either the maximum likelihood or the maximum *a posteriori* estimate of the error variance was implemented. For the examples presented here, the 1-D PPDs of the model parameters using both the empirical and full Bayesian approaches yield similar results, but this is most likely not true in general.

ACKNOWLEDGMENTS

This work was supported by the Office of Naval Research under Grant No. N00014-05-1-0264.

APPENDIX: ADDITIVE NOISE

For the case that the observed data are written in the form of the cross-spectral density matrix (CSDM), the noise-contaminated data with error variance ν_0 are synthesized, based on true data $\mathbf{d}$, by

$$\mathbf{R} = \mathbf{d}\mathbf{d}^{\dagger} + \nu_0 \mathbf{I}. \tag{A1}$$

The *array* signal-to-noise ratio (SNR) is the ratio of signal and noise powers:

$$\text{SNR} = 10 \log \frac{\mathbf{d}^{\dagger}\mathbf{d}}{\nu_0}. \tag{A2}$$

Equation (11) can be generalized as

$$\phi_0(\mathbf{m}) = \text{Tr}\,\mathbf{R}\left[1 - \frac{\mathbf{d}(\mathbf{m})^{\dagger}\mathbf{R}\mathbf{d}(\mathbf{m})}{\text{Tr}\,\mathbf{R}}\right]. \tag{A3}$$

Note that the replica field vector $\mathbf{d}(\mathbf{m})$ is computed from an acoustic model for the vector of unknown parameters $\mathbf{m}$ and is normalized to have unit length. If we normalize the objective function by the trace of the CSDM, denoted by Tr $\mathbf{R}$ (the total intensity of the acoustic field recorded at the receivers),

$$\phi_n(\mathbf{m}) = \frac{\phi_0(\mathbf{m})}{\text{Tr}\,\mathbf{R}}, \tag{A4}$$

the noise estimate needs to be scaled by Tr $\mathbf{R}$,

$$\nu_n = \frac{\nu_0}{\text{Tr}\,\mathbf{R}} = \frac{\nu_0}{\mathbf{d}^{\dagger}\mathbf{d} + N\nu_0}, \tag{A5}$$

and is written in terms of the *array* SNR

$$\nu_n = \frac{1}{10^{\text{SNR}/10} + N}. \tag{A6}$$

[1]J. P. Hermand and P. Gerstoft, "Inversion of broadband multi-tone acoustic data from the YELLOW SHARK summer experiment," IEEE J. Ocean. Eng. **21**, 324–346 (1996).
[2]P. Gerstoft and C. F. Mecklenbräuker, "Ocean acoustic inversion with estimation of *a posteriori* probability distributions," J. Acoust. Soc. Am. **104**, 808–819 (1998).
[3]N. R. Chapman and C. E. Lindsay, "Matched-field inversion for geoacoustic model parameters in shallow water," IEEE J. Ocean. Eng. **21**(4), 347–354 (1996).
[4]S. E. Dosso, "Quantifying uncertainty in geoacoustic inversion. I. A fast Gibbs sampler approach," J. Acoust. Soc. Am. **111**, 129–142 (2002).
[5]S. E. Dosso and P. L. Nielsen, "Quantifying uncertainty in geoacoustic inversion. II. Application to broadband, shallow-water data," J. Acoust. Soc. Am. **111**, 143–159 (2002).
[6]C. F. Mecklenbräuker, P. Gerstoft, J. Bohme, and P. Chung, "Hypothesis testing for geoacoustic environmental models using likelihood ratio," J. Acoust. Soc. Am. **105**, 1738–1748 (1999).
[7]D. Battle, P. Gerstoft, W. S. Hodgkiss, W. A. Kuperman, and P. Nielsen, "Bayesian model selection applied to self-noise geoacoustic inversion," J. Acoust. Soc. Am. **116**, 2043–2056 (2004).
[8]B. P. Carlin and T. A. Louis, *Bayes and Empirical Bayes Methods for Data Analysis*, 2nd ed. (Chapman and Hall, London, 2000).
[9]Z. -H. Michalopoulou and M. Picarelli, "A Gibbs sampling approach to maximum *a posteriori* time delay and amplitude estimation," in *Proceedings of IEEE ICASSP '02* (IEEE, New York, 2002), Vol. **3**, pp. 3001–3004.
[10]S. E. Dosso, "Probabilistic geoacoustic inversion," J. Acoust. Soc. Am. **113**, 2189–2190 (2003).
[11]C. F. Mecklenbräuker and P. Gerstoft, "Objective functions for ocean acoustic inversion derived by likelihood methods," J. Comput. Acoust. **8**, 259–270 (2000).
[12]P. Gerstoft, C. -F. Huang, and W. S. Hodgkiss, "Estimation of transmission loss in the presence of geoacoustic inversion uncertainty," IEEE J. Ocean. Eng. (in press 2005).
[13]G. E. P. Box and G. C. Tiao, *Bayesian Inference in Statistical Analysis* (Addison-Wesley, Reading, MA, 1992).
[14]A. B. Baggeroer, W. A. Kuperman, and H. Schmidt, "Matched field processing: Source localization in correlated noise as an optimum estimation problem," J. Acoust. Soc. Am. **83**, 571–587 (1988).
[15]H. Jeffreys, *Theory of Probability* (Oxford U.P., Oxford, 1939).
[16]J. J. K. Ó Ruanaidh and W. J. Fitzgerald, *Numerical Bayesian Methods Applied to Signal Processing*, Statistics and Computing Series (Springer, New York, 1996).
[17]The derivation of the following formula Eq. (23) requires substituting Eqs. (10) and (18) into Eq. (22) and completing the integrand by the use of the gamma integral of the form $\int_0^\infty x^{m-1}\exp(-ax)\,dx = a^{-m}\Gamma(m)$. Strictly speaking, the limits of the integration do not have to go from zero to infinity, since this prior is multiplied by a Gaussian likelihood function which dies away rapidly as $\nu \to 0$ and $\nu \to \infty$ (e.g., Refs. 16 and 27).
[18]P. Gerstoft, *SAGA Users Guide 5.0, an Inversion Software Package*, An updated version of "SAGA Users Guide 2.0, an inversion software package," SACLANT Undersea Research Centre, SM–333, La Spezia, Italy, 1997.
[19]C. M. Bender and S. A. Orszag, *Advanced Mathematical Methods for Scientists and Engineers: Asymptotic Methods and Perturbation Theory* (Springer-Verlag, New York, 1999).
[20]A. Malinverno, "A Bayesian criterion for simplicity in inverse problem parametrization," Geophys. J. Int. **140**, 267–285 (2000).
[21]Note that the symbol $\hat{\mathbf{m}}$ refers to both MAP and ML estimates of $\mathbf{m}$. In the absence of prior information on $\mathbf{m}$, the $\mathbf{m}$ that maximizes the likelihood function, the ML solution, is the same as the MAP solution that maximizes the posterior pdf $p(\mathbf{m}|\mathbf{d})$.
[22]A. Tolstoy, N. R. Chapman, and G. Brooke, "Workshop'97: Benchmarking for geoacoustic inversion in shallow water," J. Comput. Acoust. **6**(1&2), 1–28 (1998).
[23]E. K. Westwood, C. T. Tindle, and N. R. Chapman, "A normal mode model for acoustoelastic ocean environments," J. Acoust. Soc. Am. **100**, 3631–3645 (1996).
[24]C. -F. Huang and W. S. Hodgkiss, "Matched field geoacoustic inversion of low frequency source tow data from the ASIAEX East China Sea experiment," IEEE J. Ocean. Eng. **29**, 952–963 (2004).
[25]F. B. Jensen and M. C. Ferla, SNAP: the SACLANTCEN normal-mode acoustic propagation model, SACLANT Undersea Research Centre, SM–121, La Spezia, Italy, 1979.
[26]M. J. Wilmut, S. E. Dosso, and J. Dettmer, "Data error estimation for matched-field geoacoustic inversion," J. Acoust. Soc. Am. **115**(5), 2408–2409 (2004).
[27]G. L. Bretthorst, *Bayesian Spectrum Analysis and Parameter Estimation* (Springer-Verlag, New York, 1988).

Data error covariance in matched-field geoacoustic inversion

Stan E. Dosso[a)]
School of Earth and Ocean Sciences, University of Victoria, Victoria, British Columbia V8W 3P6, Canada

Peter L. Nielsen
NATO Undersea Research Centre, Viale San Bartolomeo 400, 19138 La Spezia, Italy

Michael J. Wilmut
School of Earth and Ocean Sciences, University of Victoria, Victoria, British Columbia, V8W 3P6, Canada

(Received 24 June 2005; revised 22 October 2005; accepted 25 October 2005)

Many approaches to geoacoustic inversion are based implicitly on the assumptions that data errors are Gaussian-distributed and spatially uncorrelated (i.e., have a diagonal covariance matrix). However, the latter assumption is often not valid due to theory errors, and can lead to reduced accuracy for geoacoustic parameter estimates and underestimation of parameter uncertainties. This paper examines the effects of data error (residual) covariance in matched-field geoacoustic inversion. An inversion approach is developed based on a nonparametric method of estimating the full covariance matrix (including off-diagonal terms) from the data residuals and explicitly including this covariance in the misfit function. Qualitative and quantitative statistical tests for Gaussianity and for correlations in complex residuals are considered to validate the inversion results. The approach is illustrated for Bayesian geoacoustic inversion of broadband, vertical-array acoustic data measured in the Mediterranean Sea. © *2006 Acoustical Society of America.* [DOI: 10.1121/1.2139625]

PACS number(s): 43.30.Pc, 43.60.Pt [AIT] Pages: 208–219

I. INTRODUCTION

Estimating seabed geoacoustic parameters from ocean acoustic-field measurements at an array of sensors (matched-field inversion) is an important but challenging problem that has received considerable attention in recent years (e.g., Refs. 1–20). Matched-field inversion represents a strongly nonlinear inverse problem with no direct solution. The majority of work to date has involved estimating optimal geoacoustic model parameters by minimizing a measure of the misfit between the measured acoustic field and modeled replica fields. Substantial effort has been applied to develop effective optimization algorithms, including grid searches,[1–3] global search methods such as simulated annealing[4–7] and genetic algorithms,[7–11] and hybrid optimizations that combine global and local methods.[12–16] More recently, Markov-chain Monte Carlo methods have been applied to estimate parameter uncertainties by Gibbs sampling the misfit function.[17–19] However, much less work has been applied to the formulation of misfit itself,[20,21] particularly to the important issue of quantifying and incorporating data error statistics.

Within a Bayesian approach to inversion,[22–24] the misfit is based on the likelihood function, which represents the conditional data uncertainty distribution interpreted as a function of the model parameters for the (fixed) measured data. Hence, specifying data uncertainties is an integral component of formulating the misfit. Data uncertainties must include both measurement error (e.g., errors due to instrumentation and ambient noise) and theory error (due to the simplified model parametrization and idealized treatment of the forward problem).[22] Theory error, in particular, is generally difficult to estimate independently, and in most cases physically reasonable assumptions are required about the form of the data uncertainty distribution. Data errors are typically assumed to be Gaussian distributed and spatially uncorrelated (i.e., represented by a diagonal covariance matrix). However, the assumption of uncorrelated errors is often not valid due to theory errors. Spatially correlated errors arise in matched-field problems due, in part, to mismatch of the depth-dependent mode functions which comprise the propagating acoustic field. The use of modern arrays with a large numbers of sensors at small spacings only exacerbates error correlations.

Neglecting significant error correlations misrepresents data uncertainties and portrays the data as more informative than they actually are. This can lead to decreased accuracy of optimal parameter estimates and to underestimation of parameter uncertainties[25] (the primary focus of this paper). There are two general approaches to address error correlations in inversion.[25] One is to attempt to ameliorate the causative theory errors, e.g., by refining the model parametrization and/or adopting a more accurate or appropriate forward model. However, this can be a difficult task subject to practical constraints, and success is often limited at best. The second approach, which is considered here, requires quantifying the error correlations and incorporating them within the inversion formulation. For the present application, this involves estimating full data covariance matrices, including off-diagonal elements, for inclusion in an appropriate misfit

[a)]Electronic mail: sdosso@uvic.ca

 0001-4966/2006/119(1)/208/12/$22.50

function. A third approach that has been applied previously in matched-field inversion is to attempt to compensate for neglecting off-diagonal covariance elements by effectively increasing the size of the diagonal (variance) elements.[17,19]

A variety of methods exist for estimating data covariance.[25–27] As little is known about the form of the covariance for the present problem, a nonparametric approach is applied here based on estimating a covariance matrix of Toeplitz form from the autocovariance function of the data residuals (difference between measured and modeled data for the optimal model). Since the covariance matrix is itself required to estimate the optimal model, an iterative procedure is applied. The formulation developed here differs from standard regression theory in that matched-field problems are typically based on multifrequency complex data with incomplete knowledge of the source spectrum (amplitude and phase), and, hence, residuals cannot be calculated directly as data differences. To address this, an analytic maximum-likelihood estimate is used for the complex source strength, leading to straightforward expressions for the covariance matrix estimate and to a misfit function consisting of the sum over frequency of covariance-weighted Bartlett mismatches. The covariance matrix estimates and the assumed form of the likelihood function should be validated *a posteriori* by applying statistical tests for Gaussianity and correlation to the final data residuals.[25,26] Similar tests have been applied recently in seabed reflection inversion,[28,29] but do not appear to have been used to data in matched-field inversion where the complex residuals require more comprehensive tests.

In this paper, covariance matrix estimation, Bayesian geoacoustic inversion, and posterior validation are illustrated for multifrequency, shallow-water acoustic data collected in the Mediterranean Sea as part of the PROSIM'97 experiment.[30,31] The geoacoustic inversion results obtained using full covariance estimation are compared to results obtained neglecting error correlations (i.e., estimating variances only), and to results obtained with effective-variance estimates that attempt to compensate for neglected covariances.

The remainder of this paper is organized as follows. Section II presents the theoretical development, including a brief review of Bayesian inversion, the formulation of the likelihood function, methodology for covariance estimation, and posterior statistical validation. Section III applies the analysis to measured data, and includes descriptions of the experiment, covariance estimation, inversion results, and statistical tests. Finally, Sec. IV summarizes and discusses this work.

II. THEORY

A. Bayesian geoacoustic inversion

This section briefly summarizes the Bayesian approach to geoacoustic inversion employed in this paper;[18,19] more general treatments of Bayesian theory can be found elsewhere.[22–24] Let $\mathbf{m}$ and $\mathbf{d}$ represent model and data vectors, respectively, with elements of both considered to be random variables. Bayes' rule may be written

$$P(\mathbf{m}|\mathbf{d}) \propto P(\mathbf{d}|\mathbf{m})P(\mathbf{m}), \tag{1}$$

in which the posterior probability density (PPD), $P(\mathbf{m}|\mathbf{d})$, represents the state of information for the model parameters incorporating both data information, $P(\mathbf{d}|\mathbf{m})$, and prior information, $P(\mathbf{m})$. Interpreting the conditional probability $P(\mathbf{d}|\mathbf{m})$ as a function of $\mathbf{m}$ for the (fixed) measured data defines the likelihood function $L(\mathbf{m})$, which can generally be expressed $L(\mathbf{m}) \propto \exp[-E(\mathbf{m})]$ where E is a measure of data misfit (considered in Sec. II B). The PPD can then be written

$$P(\mathbf{m}|\mathbf{d}) = \frac{\exp[-\phi(\mathbf{m})]}{\int \exp[-\phi(\mathbf{m}')]\mathrm{d}\mathbf{m}'}, \tag{2}$$

where a generalized misfit function (combining data and prior) is defined

$$\phi(\mathbf{m}) = E(\mathbf{m}) - \log_e P(\mathbf{m}) \tag{3}$$

and the domain of integration spans the model parameter space.

The multidimensional PPD is interpreted in terms of properties defining parameter estimates and uncertainties, such as the maximum *a posteriori* (MAP) estimate (i.e., the most probable model) and marginal probability distributions, defined as

$$\hat{\mathbf{m}} = \mathrm{Arg}_{\max}\{P(\mathbf{m}|\mathbf{d})\}, \tag{4}$$

$$P(m_i|\mathbf{d}) = \int \delta(m_i' - m_i)P(\mathbf{m}'|\mathbf{d})d\mathbf{m}', \tag{5}$$

where δ is the Dirac delta function. Parameter uncertainties can also be quantified in terms of credibility intervals, such as the $\beta\%$ highest-probability density (HPD) interval, representing the interval of minimum width containing $\beta\%$ of the area of the marginal distribution.

For nonlinear problems, analytic solutions to Eqs. (4) and (5) generally do not exist and numerical approaches must be applied. In this paper, optimal estimates $\hat{\mathbf{m}}$ are determined by minimizing $\phi(\mathbf{m})$ using adaptive simplex simulated annealing, an efficient hybrid optimization algorithm that combines the local downhill-simplex method with a very fast simulated annealing global search.[16] Marginal probability distributions are determined by applying the Markov-chain Monte Carlo method of fast Gibbs sampling to sample $\phi(\mathbf{m})$.[18,19] Fast Gibbs sampling efficiently computes integral properties of the PPD using an adaptive Metropolis Gibbs sampling scheme in a principal-component parameter space where the parameter axes are aligned with the dominant correlation directions (estimated from initial sampling).

The prior employed in this paper consists of a uniform distribution for each parameter on a bounded interval $m_i^- \leqslant m_i \leqslant m_i^+$, with limits designed to impose physical reality, but wide enough so that the data primarily determine the inversion results. In terms of the generalized misfit ϕ in Eq. (3), this prior can be expressed

$$\log_e P(\mathbf{m}) = \begin{cases} \text{constant} & \text{if } m_i^- \leq m_i^+,\ i = 1, M \\ -\infty & \text{otherwise.} \end{cases} \tag{6}$$

Applying this prior is equivalent to simply constraining the search space to within the parameter bounds, and the remainder of this paper will consider only the likelihood function. However, it is also straightforward to apply nonuniform priors, given some reason to favor particular parameter values (e.g., previous experimental results).

B. Likelihood function

Specifying the data uncertainty (error) distribution, which defines the likelihood function, is an important component of quantifying model parameter uncertainties in any inverse problem. Since data uncertainties are generally not known due to theory errors, physically reasonable assumptions are required about the form of the uncertainty distribution. The numerical inversion described in the preceding section is general, with no constraint on the form of the data uncertainty. However, in many practical cases, lack of specific information about the uncertainty distribution suggests that a simple distribution (e.g., Gaussian) be assumed, as considered in this section. Statistical parameters associated with the assumed error distribution can then be estimated from the data, as described in Sec. II C. These estimates and the assumed form of the data uncertainty distribution should be validated *a posteriori* (Sec. II D).

Let $\mathbf{d}_f$ be vectors of complex acoustic pressure data at N sensors for each of $f=1,\ F$ frequencies. Assuming the data errors are complex, zero-mean Gaussian-distributed random variables which are uncorrelated from frequency to frequency but potentially correlated spatially with covariance matrix $\mathbf{C}_f$ at the fth frequency, the likelihood function is given by

$$L(\mathbf{m}) = \prod_{f=1}^{F} \frac{1}{\pi^N |\mathbf{C}_f|} \exp[-[\mathbf{d}_f - \mathbf{d}_f(\mathbf{m})]^\dagger \mathbf{C}_f^{-1} [\mathbf{d}_f - \mathbf{d}_f(\mathbf{m})]], \tag{7}$$

where the dagger indicates Hermitian (conjugate) transpose and $\mathbf{d}_f(\mathbf{m})$ is the modeled (replica) acoustic pressure computed for model $\mathbf{m}$. Likelihood (7) is in the form $L(\mathbf{m}) \propto \exp[-E(\mathbf{m})]$ with misfit function

$$E(\mathbf{m}) = [\mathbf{d}_f - \mathbf{d}_f(\mathbf{m})]^\dagger \mathbf{C}_f^{-1} [\mathbf{d}_f - \mathbf{d}_f(\mathbf{m})]. \tag{8}$$

Note that if $\mathbf{d}_f(\mathbf{m})$ represents a nonlinear function of $\mathbf{m}$, as in acoustic propagation modeling, the likelihood is not a Gaussian function of $\mathbf{m}$.

Matched-field methods are typically applied in cases with incomplete knowledge of the complex source spectrum. When no source information is available, the modeled data can be expressed

$$\mathbf{d}_f(\mathbf{m}) = A_f e^{i\theta_f} \mathbf{p}_f(\mathbf{m}), \tag{9}$$

where $\mathbf{p}_f(\mathbf{m})$ is the acoustic pressure computed via a numerical propagation model with arbitrary source amplitude and phase, and A_f and θ_f represent the unknown amplitude and phase.[20] Substituting Eq. (9) into Eq. (7), the likelihood can be maximized with respect to the source by setting $\partial L/\partial A_f = \partial L/\partial \theta_f = 0$, leading to

$$A_f e^{i\theta_f} = \frac{\mathbf{p}_f^\dagger(\mathbf{m}) \mathbf{C}_f^{-1} \mathbf{d}_f}{\mathbf{p}_f^\dagger(\mathbf{m}) \mathbf{C}_f^{-1} \mathbf{p}_f(\mathbf{m})}. \tag{10}$$

Using Eq. (10) in Eq. (7), the likelihood function for incoherent processing becomes

$$L(\mathbf{m}) = \prod_{f=1}^{F} \frac{1}{\pi^N |\mathbf{C}_f|} \exp[-B_f(\mathbf{m})], \tag{11}$$

where $B_f(\mathbf{m})$ represents a covariance-weighted Bartlett mismatch defined as

$$B_f(\mathbf{m}) = \mathbf{d}_f^\dagger \mathbf{C}_f^{-1} \mathbf{d}_f - \frac{|\mathbf{p}_f^\dagger(\mathbf{m}) \mathbf{C}_f^{-1} \mathbf{d}_f|^2}{\mathbf{p}_f^\dagger(\mathbf{m}) \mathbf{C}_f^{-1} \mathbf{p}_f(\mathbf{m})}. \tag{12}$$

The corresponding misfit function

$$E(\mathbf{m}) = \sum_{f=1}^{F} B_f(\mathbf{m}) \tag{13}$$

is appropriate for matched-field inversion (parameter optimization and uncertainty estimation, as outlined in Sec. II A) taking into account data-error covariance. If source spectral information is available in some form, other misfit functions (e.g., coherent or semicoherent processors) can be derived in a similar manner.[20,21]

C. Covariance estimation

The development in Sec. II B assumes prior knowledge of the data covariance matrix $\mathbf{C}_f$; however, this is rarely available due to unknown theory errors. Formally, the data covariance matrix is defined

$$\mathbf{C}_f = \langle (\mathbf{d}_f - \langle \mathbf{d}_f \rangle)(\mathbf{d}_f - \langle \mathbf{d}_f \rangle)^\dagger \rangle, \tag{14}$$

where $\langle \cdot \rangle$ represents an ensemble average over many realizations of the error process. However, this definition generally cannot be applied in practice. In many cases only a single measured data set is available, and even if multiple data sets are collected, it is difficult to establish that they represent a representative sampling over theory errors. However, if the error process can be assumed to be stationary and ergodic, the covariance can be estimated by approximating the ensemble averaging of Eq. (14) by finite spatial averaging over the array measurements.[25] The covariance matrix can then be estimated from the data using an iterative, nonparametric procedure described in the following. For generality, the procedure is presented first for the standard case from regression theory,[25] and then subsequently specialized to matched-field inversion (i.e., unknown source amplitude and phase).

Consider first the common approximation of a diagonal covariance matrix $\mathbf{C}_f = \sigma_f^2 \mathbf{I}$ (i.e., neglecting covariances), where σ_f is the (unknown) standard deviation at the fth frequency and $\mathbf{I}$ is the identity matrix. In this case, the standard form of the likelihood function representing complex Gaussian errors is

$$L(\mathbf{m}) = \prod_{f=1}^{F} \frac{1}{\pi^N \sigma_f^{2N}} \exp[-|\mathbf{d}_f - \mathbf{d}_f(\mathbf{m})|^2/\sigma_f^2]. \quad (15)$$

To estimate standard deviations, the likelihood is maximized over σ_f: setting $\partial L/\partial \sigma_f = 0$ leads to

$$\hat{\sigma}_f^2 = |\mathbf{d}_f - \mathbf{d}_f(\mathbf{m})|^2/N. \quad (16)$$

To obtain an appropriate estimate for $\mathbf{m}$ in Eq. (16), substitute $\hat{\sigma}_f$ for σ_f in Eq. (15) to obtain likelihood function

$$L(\mathbf{m}) \propto \exp\left[-N \sum_{f=1}^{F} \log_e |\mathbf{d}_f - \mathbf{d}_f(\mathbf{m})|^2 \right], \quad (17)$$

and misfit function

$$E(\mathbf{m}) = N \sum_{f=1}^{F} \log_e |\mathbf{d}_f - \mathbf{d}_f(\mathbf{m})|^2. \quad (18)$$

The model estimate $\hat{\mathbf{m}}$ is obtained by minimizing $E(\mathbf{m})$ given by Eq. (18) (plus prior) using numerical optimization. The standard deviations of the original diagonal covariance matrix can be estimated by substituting $\hat{\mathbf{m}}$ into Eq. (16) to give

$$\hat{\sigma}_f^2 = |\mathbf{d}_f - \mathbf{d}_f(\hat{\mathbf{m}})|^2/N. \quad (19)$$

Equations (15)–(19) neglect off-diagonal elements of the covariance matrix which represent error correlations. As discussed earlier, this can lead to underestimation of parameter uncertainties. An approach that has been applied in matched-field geoacoustic inversion is to increase the variance (diagonal-element) estimates in an attempt to compensate for the neglected off-diagonal elements. In particular, an effective variance estimate,[17,19]

$$\hat{\sigma}_f^2 = |\mathbf{d}_f - \mathbf{d}_f(\hat{\mathbf{m}})|^2/N_E, \quad (20)$$

has been used, where $N_E < N$ represents the effective number of uncorrelated data. For matched-field inversion, the value for N_E has been estimated as the number of significant propagating modes as determined by principle-component analysis.[17,19] While increasing the variance in this manner has the effect of increasing model parameter uncertainty estimates, it is generally not clear to what extent neglected covariance terms can be be properly compensated for by increased variances (this issue is examined in Sec. III).

This paper develops an alternative approach of estimating the full covariance matrix, including off-diagonal terms. A first estimate of the full covariance matrix can be obtained from the data residuals evaluated for the optimal model $\hat{\mathbf{m}}$ obtained by minimizing Eq. (18),

$$\mathbf{r}_f(\hat{\mathbf{m}}) = \mathbf{d}_f - \mathbf{d}_f(\hat{\mathbf{m}}). \quad (21)$$

These residuals can be considered a sample or realization of the underlying error process. Assuming the residuals represent a stationary, ergodic random process, the ensemble average in Eq. (14) can be approximated by a finite spatial average, and the covariance matrix estimated from the residuals as

$$\hat{C}_{ij} = \frac{1}{N} \sum_{k=1}^{N-|i-j|} (r_k - \bar{r})^* (r_{k+|i-j|} - \bar{r}), \quad i = 1,N, \quad j = 1,N, \quad (22)$$

where the asterisk indicates complex conjugation and $\bar{r}$ represents the residual mean (the dependence of all terms on $\hat{\mathbf{m}}$ and the subscript f representing frequency are suppressed in this equation for clarity). According to Eq. (22), the ith row of the covariance matrix estimate consists of N elements of the $2N-1$ element autocovariance function for the residuals, shifted so that the zero-lag (variance) value occurs at element i (hence, the matrix is in Toeplitz form). Note that for zero-mean residuals, the variance estimates ($i=j$) from Eq. (22) are equivalent to those of Eq. (19).

Elements of the covariance matrix in Eq. (22) that are located far off the main diagonal represent covariances between widely spaced measurement points. These are expected to be small (compared to near-diagonal elements) and are often poorly estimated due to the small number of samples of widely spaced points included in the average of Eq. (22). Hence, it is often beneficial to damp elements that are sufficiently far off the main diagonal, while maintaining the positive-definiteness of the covariance matrix. An appropriate damping function for the ith row of the covariance matrix is

$$s_j = \cos^l \frac{\pi |i-j|}{2(N-1)}, \quad j = 1,N, \quad (23)$$

with $l > 1$. This damping function is relatively flat near the main diagonal ($i \approx j$) but drops off at an increasing rate away from the diagonal, with the drop-off rate determined by l in Eq. (23). The inversion results are relatively insensitive to the precise damping rate; a value $l=20$ is used in this to achieve covariance matrix rows that go to (approximately) zero by $N/2$ elements away from the main diagonal (see Sec. III).

The residuals used in the first estimate of the full covariance matrix are based on an optimal model $\hat{\mathbf{m}}$ obtained neglecting off-diagonal covariance terms [i.e., minimizing Eq. (18)]. This estimated covariance matrix can subsequently be used to compute a new optimal model which takes the full covariance into account by minimizing the misfit defined in Sec. II B with estimate $\hat{\mathbf{C}}_f$ replacing $\mathbf{C}_f$. An updated covariance matrix can then be computed for the new model using Eqs. (21)–(23). This procedure is repeated iteratively until convergence (i.e., the covariance matrix stops changing significantly between iterations) to arrive at the final model and covariance estimates.

To apply the above-noted formalism to matched-field inversion with no knowledge of the source spectrum, the substitutions

$$\mathbf{d}_f(\mathbf{m}) = \frac{\mathbf{p}_f^\dagger(\mathbf{m})\mathbf{d}_f}{|\mathbf{p}_f(\mathbf{m})|^2} \mathbf{p}_f(\mathbf{m}), \quad (24)$$

$$|\mathbf{d}_f - \mathbf{d}_f(\mathbf{m})|^2 = |\mathbf{d}_f|^2 - \frac{|\mathbf{p}_f^\dagger(\mathbf{m})\mathbf{d}_f|^2}{|\mathbf{p}_f(\mathbf{m})|^2} \tag{25}$$

are applied in Eqs. (15)–(22) to employ maximum-likelihood estimates for source amplitude and phase (see Sec. II B).

D. Likelihood and covariance validation

The validity of the assumed form of the likelihood function and of the estimated covariance matrix can be examined *a posteriori* by applying appropriate statistical tests to the standardized data residuals,[25] which are defined

$$\mathbf{w}_f(\hat{\mathbf{m}}) = [\hat{\mathbf{C}}_f^{-1/2}]^\dagger[\mathbf{d}_f - \mathbf{d}_f(\hat{\mathbf{m}})], \tag{26}$$

or, for matched-field inversion,

$$\mathbf{w}_f(\hat{\mathbf{m}}) = [\hat{\mathbf{C}}_f^{-1/2}]^\dagger\left[\mathbf{d}_f - \frac{\mathbf{p}_f^\dagger(\hat{\mathbf{m}})\mathbf{d}_f}{|\mathbf{p}_f(\hat{\mathbf{m}})|^2}\mathbf{p}_f(\hat{\mathbf{m}})\right]. \tag{27}$$

In Eq. (26) and (27) $\hat{\mathbf{C}}_f^{1/2}$ represents the upper-triangular Cholesky decomposition (square root) of the estimated covariance matrix $\hat{\mathbf{C}}_f$, defined according to[32]

$$\hat{\mathbf{C}}_f = [\hat{\mathbf{C}}_f^{1/2}]^\dagger\hat{\mathbf{C}}_f^{1/2}. \tag{28}$$

Under the assumption that the errors represent a complex Gaussian-distributed random process with covariance matrix $\hat{\mathbf{C}}_f$, the standardized residuals should represent an uncorrelated complex Gaussian random process with zero mean and unit standard deviation (the standard complex Gaussian distribution). These assumptions can be tested both qualitatively and quantitatively, as described in the following.

The assumption of Gaussian-distributed errors can be examined qualitatively by comparing (normalized) histograms of the standardized residuals with the theoretical Gaussian distribution. Quantitatively, the Kolmogorov-Smirnov (KS) test can be applied to test the null hypothesis H_0 that the standardized residuals are from the standard Gaussian distribution against the alternate hypothesis H_1 that the observations are not from this distribution.[25,26] The KS test statistic is based on the maximum difference between the cumulative marginal distributions of the residuals and the standard Gaussian. The corresponding p value represents the probability of obtaining a test statistic at least as extreme as that observed assuming the null hypothesis is true; hence, the p value quantifies the strength of the evidence against H_0 in favor of H_1. Commonly, $p \geqslant 0.05$ is considered to provide no significant evidence against H_0 while $0.01 \leqslant p < 0.05$ provides significant evidence against H_0, $0.005 \leqslant p < 0.01$ provides highly significant evidence, and $p < 0.005$ provides extremely significant evidence.

Considering the randomness of a set of complex data residuals requires examining the residuals in several ways. First, it must be established that both the real parts and the imaginary parts, individually, represent spatially uncorrelated processes. Second, it must be established that the real parts are spatially uncorrelated with the imaginary parts (i.e., from sensor to sensor). Finally, it must be established that the real and imaginary parts of the residuals at each individual sensor are uncorrelated. To consider correlations between real and imaginary parts, statistical tests can be applied to their difference and/or product. Spatial randomness of the real parts and of imaginary parts (individually) can be examined qualitatively by plotting their auto-correlation function. For random errors, the autocorrelation should exhibit a narrow peak at zero lag; a wide peak indicates that successive residuals tend to have the same sign and may be correlated.

Regarding quantitative tests for randomness, nonparametric statistical tests, which do not depend on the Gaussianity of the residuals or the form of the covariance, are appropriate in the present application.[25] For instance, the runs test (median-delta test) tests the null hypothesis that a set of residuals are random versus the alternative hypothesis that they are serially correlated, with the test statistic consisting of the number of runs of residuals on either side of the median value.[25,26] The runs test can be applied to test for spatial correlation within the real parts and the imaginary parts individually (i.e., autocorrelations). In this case, a one-tailed test for positive correlations is generally appropriate (and more powerful), since error processes causing negative serial autocorrelations are rare.[25] The runs test can also be applied to test for spatial correlation between the real and imaginary residuals (i.e., cross correlation) by considering the set of their differences. In this case, a two-tailed test is appropriate, as positive or negative cross correlations can exist. To test for correlation between real and imaginary parts of the residuals at individual sensors, the sign test[25] can be applied to the set of their products to test the null hypothesis that this set has a median value of zero (i.e., is distributed equally with positive and negative signs).

Applying statistical tests to the residual *a posteriori* allows quantitative examination of the validity of the covariance estimates and the underlying assumptions. However, lack of evidence against the null hypotheses of uncorrelated, Gaussian errors cannot be construed as proof the hypotheses are true. Further, it should be noted that it is not necessary for the assumptions to be strictly satisfied for inversion results to be of value.[25] Rather, reasonable agreement is required, since small departures from the assumptions generally have only a small effect on the inversion results. However, substantial violations of the assumptions can substantially degrade results.

III. INVERSION EXAMPLE

A. Experiment, data, and model

The PROSIM'97 shallow-water geoacoustic experiment was carried out by the SACLANT Undersea Research Centre in the Mediterranean Sea off the west coast of Italy near Elba Island. The experiment and data have been considered previously[19,30,31] and will be described only briefly here, as the purpose for this paper is to illustrate data covariance effects in practical inversion. The experiment consisted of recording acoustic signals from a transducer towed at approximately 10 m depth over a series of shallow-water tracks; the data considered here are for a track with nearly range-independent bathymetry (water depth ~132 m). The source emitted a 0.5 s linear frequency-modulated signal over the band 300–800 Hz every 0.25 km along the track.

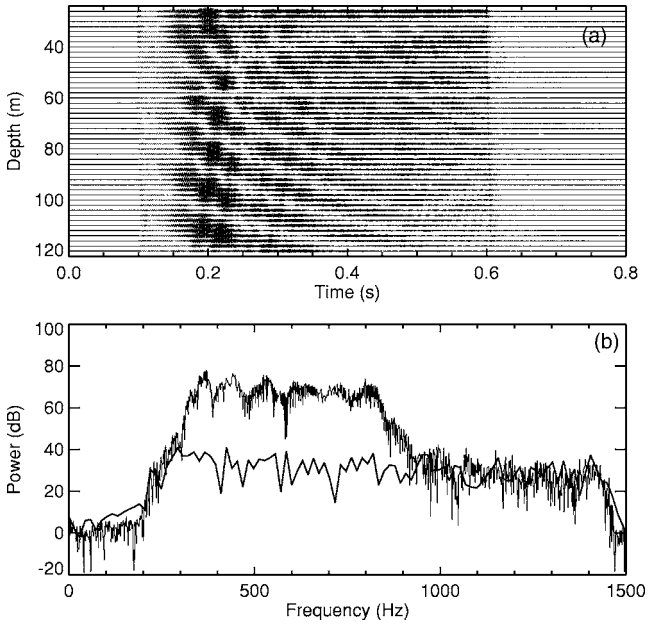

FIG. 1. Acoustic data recorded for a nominal source-receiver range of 3.9 km in the PROSIM'97 experiment. (a) Time-domain data at the 48-sensor VLA (arbitrary origin time). (b) Frequency domain data for a mid-water column receiver (arbitrary reference level) with the signal (plus noise) power indicated by the thin line and noise power (recorded prior to the signal) by the thick line.

The signals were received at a bottom-moored vertical line array (VLA) of hydrophones which spanned from 26 to 120 m depth with a 2 m sensor spacing. The acoustic pressure at each hydrophone was sampled at 3 kHz and transmitted from the VLA to the source ship via a radio-frequency data link, where it was recorded on optical disc. The ocean sound-speed profile was measured during the experiment and found to be stable both spatially and temporally, consisting of a weakly downward-refracting gradient that varied from about 1520 to 1510 m/s over the water column. The data set analyzed here was recorded for a source-receiver range of approximately 3.9 km. The acoustic signals and ambient noise recorded at the VLA are shown in Fig. 1 in both the time and frequency domains.

The geometric and geoacoustic parameters included in the model **m** to represent the experiment and environment

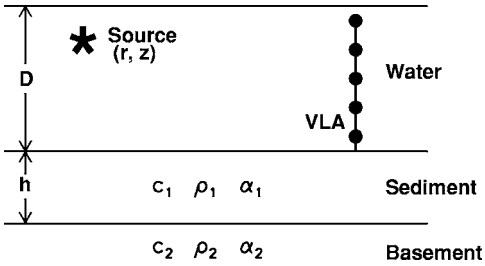

FIG. 2. Schematic diagram of the ocean environment for the synthetic test cases, identifying the geoacoustic and geometric parameters included in the model.

are illustrated in Fig. 2. The acoustic source is at depth z and range r from the VLA in water of depth D. The geoacoustic parameters include the thickness h of an upper sediment layer with sound speed c_1, density ρ_1, and attenuation α_1, overlying a semi-infinite basement with speed c_2, density ρ_2, and attenuation α_2. The search intervals (i.e., the bounds for uniform prior distributions) assumed for all parameters are given in Table I.

B. Covariance estimation

The data covariance matrix for the PROSIM'97 data was estimated using the iterative procedure outlined in Sec. II, employing the normal-mode acoustic propagation model ORCA[33] for forward modeling. Convergence of this procedure is discussed later in this section, and the optimal (final) geoacoustic model is considered in the following section. Examples of the measured and modeled acoustic data for the final model are given in Fig. 3 at frequencies of 300, 500, and 800 Hz. The modal structure of the complex acoustic fields (real and imaginary parts) is evident in this figure, with the content of higher-order modes increasing with frequency. The modeled data are generally a good fit to the measured data over depth and frequency (quantified in the following section). The difference between the measured and modeled data defines the data residuals [Eqs. (21) and (24)], which are considered a sample of the data errors. Figure 3 shows that the residuals are spatially correlated, i.e., the differences do not oscillate randomly about zero along the array, but tend to maintain the same sign over a finite spatial scale.

TABLE I. Summary of inversion results including optimal (MAP) parameters estimated using both full-covariance and diagonal-variance estimates, and 95% HPD credibility intervals estimated using full-covariance, diagonal-variance, and effective variance estimates.

Parameter and units	Search bounds	MAP (Full Cov)	MAP (Diag Var)	95% HPD (Full Cov)	95% HPD (Diag Var)	95% HPD (Eff Var)
h (m)	[0, 30]	9.0	10.5	[7.0, 10.9]	[9.3, 11.5]	[3.3, 9.9]
c_1 (m/s)	[1450, 1600]	1494	1502	[1486, 1504]	[1496, 1505]	[1450, 1501]
c_2 (m/s)	[1500, 1650]	1529	1529	[1524, 1531]	[1528, 1530]	[1524, 1532]
ρ_1 (g/cm^3)	[1.0, 1.7]	1.38	1.45	[1.3, 1.7]	[1.3, 1.7]	[1.2, 1.7]
ρ_2 (g/cm^3)	[1.5, 2.2]	1.52	1.54	[1.5, 2.1]	[1.5, 1.6]	[1.5, 2.2]
α_1 (dB/λ)	[0, 1]	0.02	0.00	(0.0, 0.17)	[0.0, 0.02]	[0.0, 0.32]
α_2 (dB/λ)	[0, 1]	0.22	0.17	[0.0, 0.51]	[0.1, 0.30]	[0.0, 0.51]
r (km)	[3.6, 4.0]	3.95	3.96	[3.93, 4.00]	[3.92, 4.00]	[3.84, 4.00]
z (m)	[6, 12]	10.2	9.9	[8.0, 10.9]	[9.1, 10.3]	[6.00, 10.9]
D (m)	[128, 135]	130.1	130.0	[130.0, 132.3]	[130.0, 130.3]	[130.2, 135.0]

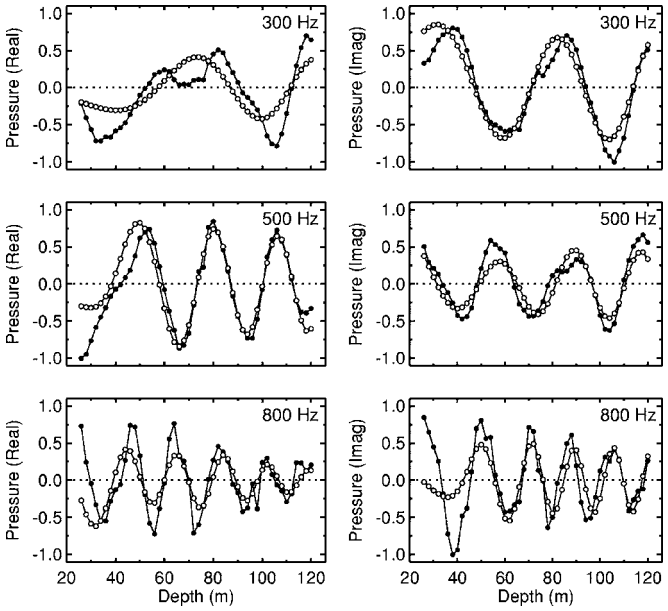

FIG. 3. Measured (closed circles) and modeled (open circles) complex acoustic data at frequencies of 300, 500, and 800 Hz as indicated (left and right columns show real and imaginary parts, respectively).

To illustrate the covariance structure estimated from the residuals, Fig. 4 shows the middle row of the covariance matrices at frequencies of 300, 500, and 800 Hz. Since the covariance matrix is Hermitian, the real part of the middle row is symmetric about its center point and the imaginary part is antisymmetric. In fact, it is straightforward to show from Eq. (14) that the real part of the covariance matrix consists of the sum of the individual covariances of the real and imaginary parts of the residuals, while the imaginary part of the covariance matrix is related to the cross covariances between real and imaginary residuals. For data errors that represent an uncorrelated random process, the covariance matrix should approximate a real, diagonal matrix. The substantially different structure in Fig. 4 (e.g., the wide central lobe of the real parts and nonzero imaginary parts) arises from error correlations. The decreasing width of the central lobe (and other structural features) with increasing frequency in Fig. 4 is consistent with a decrease in the characteristic correlation length scale of the errors with increased higher-mode content and more rapidly fluctuating acoustic fields (Fig. 3).

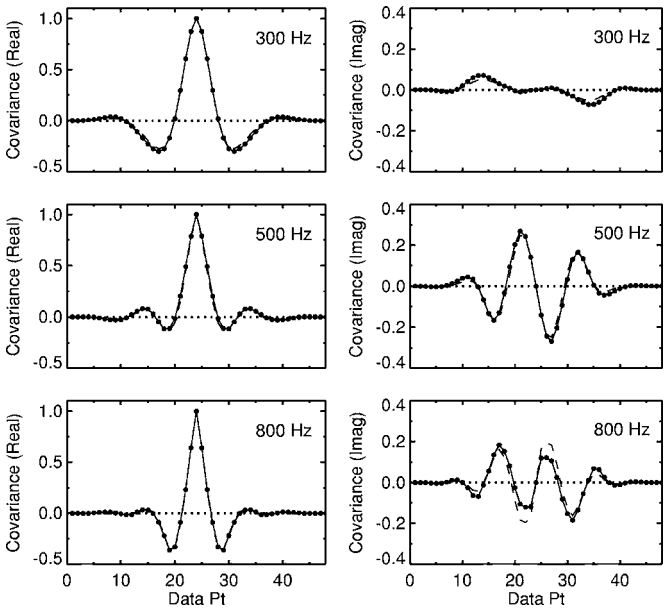

FIG. 4. Middle row of the estimated complex covariance matrix at frequencies of 300, 500, and 800 Hz. Left and right columns show real and imaginary parts, respectively, normalized at each frequency by the maximum value of the real part (i.e., the variance). Dashed lines and solid lines (with circles) show results after one and three iterations of the covariance estimation procedure.

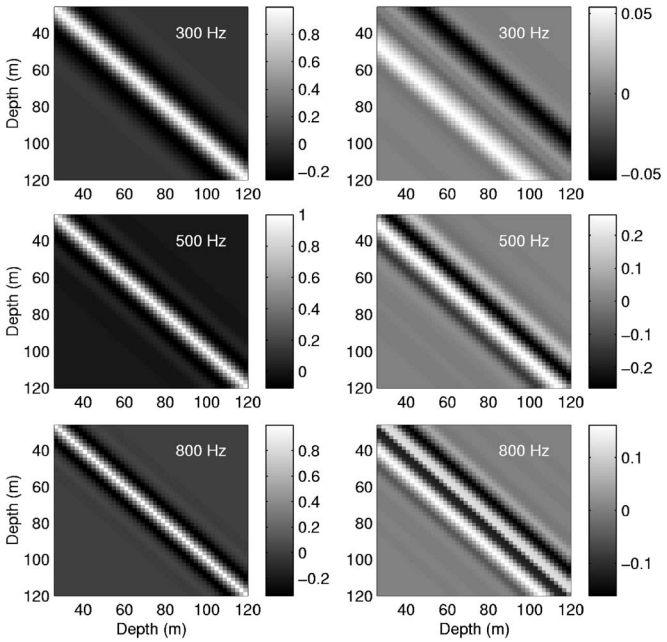

FIG. 5. Estimated complex covariance matrices at frequencies of 300, 500, and 800 Hz. At each frequency, the real and imaginary parts (left and right columns) are normalized by the maximum value of the real part (variance).

The convergence of the iterative covariance estimation procedure is also illustrated in Fig. 4. It was found that there were only small differences between the covariance matrices obtained at successive iterations, but that the differences did not go to zero with many iterations. This is likely due to the nonuniqueness inherent in matched-field inversion and the resulting ambiguity in numerical optimization, which often produces slightly different results even when applied repeatedly to exactly the same problem.[34] Figure 4 shows only very minor differences between the covariance matrices obtained at the first and third iterations. This indicates that, in practice, a single iteration of the covariance estimation could be sufficient; however, the covariance matrix from the third iteration is used in this paper. Full two-dimensional covariance matrices at frequencies of 300, 500, and 800 Hz are illustrated in Fig. 5.

C. Inversion results

The following presents the results of the matched-field geoacoustic inversion for the PROSIM'97 data. Table I gives the parameter values for the optimal model estimated by minimizing the covariance-weighted misfit [Eqs. (12) and (13) using the covariance matrix estimate given in Sec.

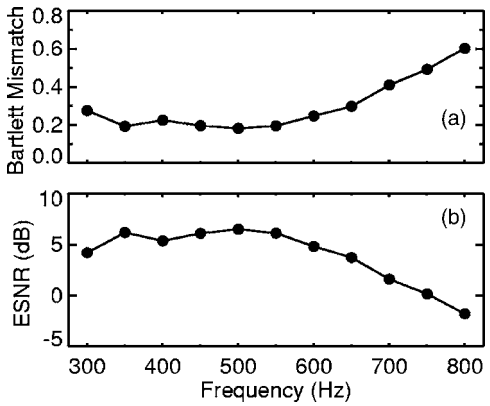

FIG. 6. Data fit achieved for optimal model estimate: (a) the normalized Bartlett mismatch (no covariance weighting), and (b) ESNR.

III B]. To quantify how well this model fits the acoustic data, Fig. 6 gives the (unweighted) normalized Bartlett mismatch, defined as

$$b_f(\mathbf{m}) = 1 - \frac{|\mathbf{p}_f^\dagger(\mathbf{m})\mathbf{d}_f|^2}{|\mathbf{p}_f(\mathbf{m})|^2|\mathbf{d}_f|^2}. \tag{29}$$

The mismatch in Eq. (29) does not include weighting due to data covariance at each frequency, but is given here as it represents a commonly used measure of mismatch that varies between 0 and 1. Figure 6(a) shows that the normalized mismatch for the optimal model is approximately 0.2 for frequencies below 600 Hz, increasing to about 0.6 at 800 Hz (due to theory errors that increase with frequency). Since Eq. (12) rather than Eq. (29) was employed in the inversion, smaller normalized mismatches could likely be obtained for this data set; however, minimizing the covariance-weighted mismatch should produce superior parameter estimates. Figure 1(b) indicates that the signal level is approximately 30–40 dB above the measurement noise level (i.e., ambient and system noise) over the signal frequency band. However, for the purposes of inversion, a more useful measure is the effective signal-to-noise ratio (ESNR), defined.[19]

$$\mathrm{ESNR}_f = 10\log_{10}\frac{1 - b_f(\hat{\mathbf{m}})}{b_f(\hat{\mathbf{m}})} \quad \text{(dB)}, \tag{30}$$

where $\hat{\mathbf{m}}$ represents the optimal model estimate. The ESNR provides a measure of the signal level to all sources of error (measurement and theory). Figure 3(b) shows that the ESNR decreases from approximately 6 to −2 dB over the signal band.

To examine the inversion results and the effects of data-error covariance in detail, Fig. 7 shows marginal posterior probability distributions computed for the geoacoustic parameters three ways: (i) using full covariance matrices at each frequency estimated as described in Sec. III B; (ii) using diagonal covariance matrices consisting of variance estimates [computed using Eqs. (19) and (25)] on the main diagonal at each frequency; and (iii) using diagonal covariance matrices with effective variance estimates [Eqs. (20) and (25)]. In this paper, these three approaches are referred to as the full-covariance, diagonal-variance, and effective-variance

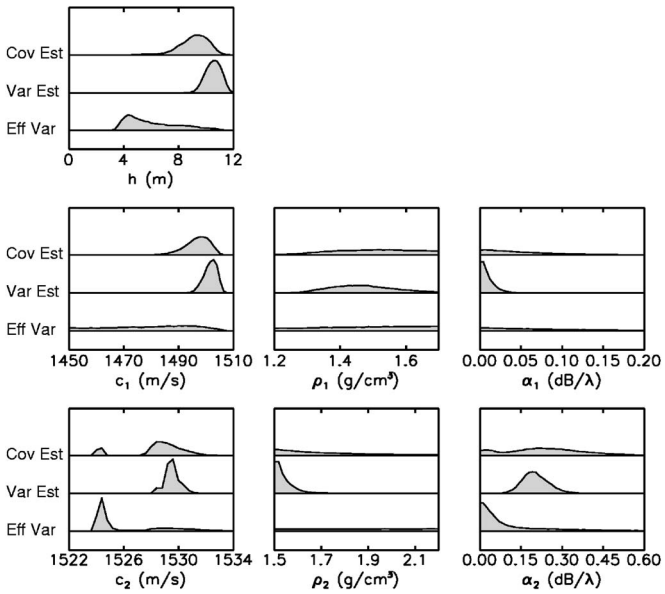

FIG. 7. Marginal probability distributions for geoacoustic parameters computed via Gibbs sampling inversion of measured data using: (i) full covariance matrix estimates (Cov Est), (ii) diagonal-covariance matrices based on variance estimates (Var Est), and (iii) diagonal-covariance matrices based on effective variance estimates (Eff Var).

estimates, respectively. The optimal model used for computing the variance and effective-variance estimates was obtained by minimizing Eqs. (18) and (25) and is given in Table I. For the effective variance estimates, the number of uncorrelated data at each frequency was taken to be $N_E = 5$ as previously determined for the PROSIM'97 data over this frequency band using principle-component analysis of multiple data sets along the source track to determine the number of modes carrying >90% of the acoustic energy[19] (the same effective number over this frequency band has also been estimated for other similar data sets[17]). Table I also gives 95% HPD credibility intervals for the model parameters for each of the three approaches to inversions.

The results in Fig. 7 and Table I indicate substantial differences between the parameter uncertainty distributions computed using the three types of covariance matrix. It is worth emphasizing here that the goal of Bayesian inversion is not to compute the smallest parameter uncertainties, but rather the correct parameter uncertainties (i.e., uncertainties that correctly quantify the geoacoustic information content of the data). As discussed earlier, neglecting off-diagonal covariance elements has the effect of representing the data as more informative than they actually are, and can lead to too-narrow parameter uncertainty distributions. Figure 7 and Table I show that the marginal PPDs computed using diagonal-variance estimates are significantly narrower for all parameters than those for full covariance estimates. For the sediment thickness and sound speed, h and c_1, the 95% HPD intervals are approximately a factor of 2 narrower for diagonal variances. The uncertainty distribution for the basement sound speed, c_2, is also substantially narrower and completely excludes a secondary peak near 1524 m/s. For the less sensitive geoacoustic parameters $(\rho_1, \rho_2, \alpha_1, \alpha_2)$, the results for diagonal variances suggest reasonably well-

determined estimates, while the full-covariance results indicate these parameters are, in fact, poorly determined or undetermined. The narrow uncertainty distribution for the basement density (well known to be insensitive in geoacoustic inversion) obtained using diagonal variances is particularly unrealistic.

The use of effective-variance estimates is intended to compensate for neglected off-diagonal covariance elements by increasing the size of the diagonal elements (variances). The results in Fig. 7 and Table I show that the use of effective variances produces much wider parameter uncertainty distributions than diagonal-variance estimates. However, the uncertainty distributions obtained with effective variances are generally poor approximations to those for full-covariance estimates. The HPD intervals obtained for h and c_1 for effective variances are wider by factors of about 2 and 3, respectively, than for full covariances. Interestingly, the marginal PPD for c_2 emphasizes a different localized peak for effective variances than for full covariances. Finally, the marginal PPD for α_2 is much more compact (unrealistically so) for the effective variances than for full covariances.

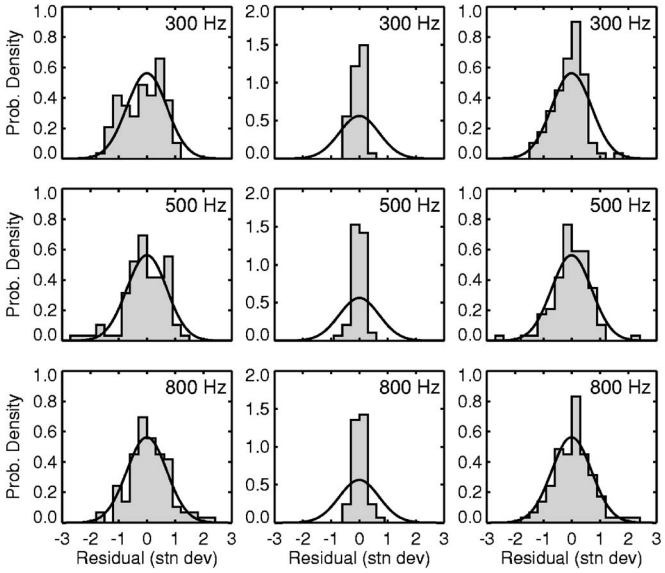

FIG. 8. Histograms of standardized data residuals (in units of standard deviation) compared to theoretical Gaussian distributions (heavy solid line) for frequencies of 300, 500, and 800 Hz. Left, center, and right columns show results using variance (diagonal-covariance) estimates, effective variance estimates, and full covariance estimates, respectively.

D. Statistical validation

The geoacoustic inversion results in Sec. III C are based on the assumption of zero-mean, complex Gaussian-distributed data errors with an estimated covariance matrix at each frequency. To test the validity of these assumptions and of the different approaches to estimating covariance matrices, the Cholesky decomposition of a particular covariance estimate is applied to form standardized residuals according to Eq. (27). If the assumptions and covariance estimate are valid, the standardized residuals should represent an uncorrelated, complex Gaussian-distributed random process with unit variance. In this section, statistical tests for Gaussianity and randomness (outlined in Sec. II D) are applied to standardized residuals from the three approaches to inversion considered in Sec. III C (i.e., diagonal-variance, effective-variance, and full-covariance estimation).

To consider the assumption of Gaussian-distributed errors, Fig. 8 compares histograms of standardized residuals (including both real and imaginary parts) to the standard Gaussian distribution at frequencies of 300, 500, and 800 Hz. Good general agreement is achieved for the diagonal-variance and full-covariance estimates. However, the residual histograms for the effective-variance estimates are much too narrow, which is consistent with purposefully overestimating the variance. For a quantitative comparison, p values from the KS test comparing the residuals to a standard complex Gaussian distribution are given in Fig. 9. For the diagonal-variance estimates, Fig. 9(a) shows that there is no significant evidence at the 0.05 confidence level against the the null hypothesis of Gaussian-distributed residuals in 18 out of 22 cases (real and imaginary residuals considered separately at 11 frequencies). For the effective-variance estimates, Fig. 9(b) indicates extremely significant evidence against the standard Gaussian distribution in all cases. Finally, for the full-covariance estimates, Fig. 9(c) shows that the Gaussian hypothesis passes at the 0.05 level in 21 out of 22 cases.

Examining correlations in complex residuals requires several tests, as described in the following. In the following, note that since the effective-variance covariance matrix estimates represent a simple scaling of the diagonal-variance estimates, the residual correlations are essentially identical for these two approaches and, hence, the results of correlation tests for the effective variance are not considered separately here.

A qualitative test for spatial (serial) correlation is illus-

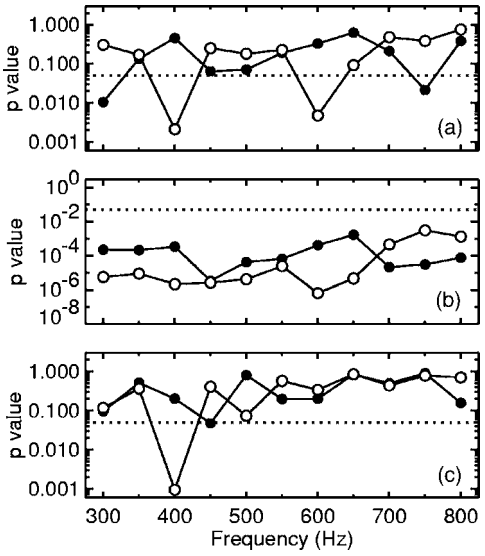

FIG. 9. KS test p values computed for the null hypothesis that the standardized data residuals (real—closed circles; imaginary—open circles) are Gaussian distributed using: (a) variance (diagonal-covariance) estimates, (b) effective variance estimates, and (c) full covariance matrix estimates. Dotted lines indicate the 0.05 level.

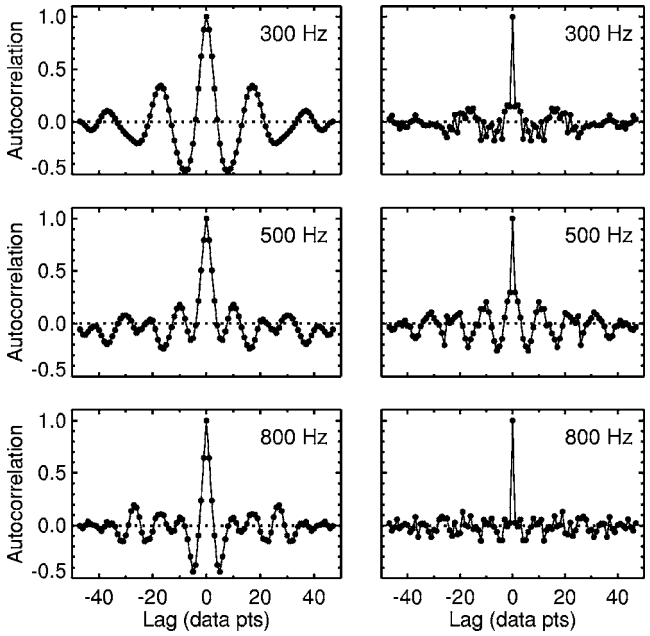

FIG. 10. Autocorrelation of standardized data residuals for frequencies of 300, 500, and 800 Hz. Left and right columns show results using variance (diagonal-covariance) estimates and full covariance estimates, respectively. Results for effective-variance estimates are essentially identical to variance results.

trated in Fig. 10, which shows the real part of the autocorrelation function of the complex standardized residuals (equivalent to the sum of the autocorrelation functions of the real and the imaginary residuals). Figure 10 indicates strong correlations in the standardized residuals using the diagonal-variance estimates, with wide central peaks in the autocorrelation functions (although peak width decreases with frequency). Correlation effects are greatly reduced for the full-covariance estimates, with central peaks a single point wide at 300 and 800 Hz. The standardized residuals do not appear to be fully decorrelated at 500 Hz, although the autocorrelation value is down by a factor of 3 at one lag point. The one-tailed runs test provides a quantitative test for (positive) correlations within a set of residuals. Figure 11 gives runs-test p values for the real and imaginary residuals. For the

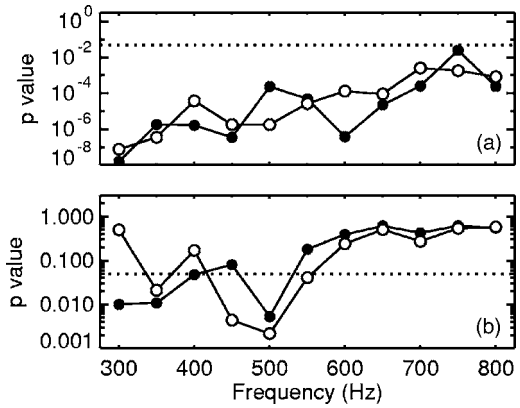

FIG. 11. One-tailed runs-test p values computed for the null hypothesis that standardized residuals (real—closed circles; imaginary—open circles) are random using: (a) diagonal variance estimates and (b) full covariance matrix estimates. Dotted lines indicate the 0.05 level.

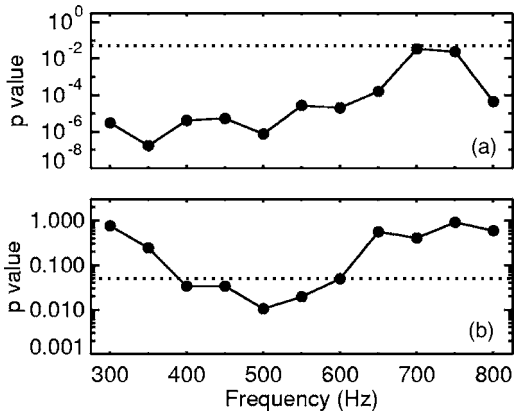

FIG. 12. Two-tailed runs-test p values computed for the null hypothesis that the difference between the real and imaginary parts of the standardized residuals are random using: (a) diagonal variance estimates, and (b) full covariance matrix estimates. Dotted lines indicate the 0.05 level.

diagonal-variance estimate, Fig. 11(a) shows extremely significant evidence against the null hypothesis of random residuals at all frequencies (with the exception of the real residuals at 750 Hz, where there is significant evidence against). The p values in Fig. 11(a) generally increase with frequency, consistent with reduced correlation effects at higher frequencies. For the full-covariance estimates, Fig. 11(b) indicates no significant evidence against the hypothesis of random residuals in 16 out of 22 cases, with significant and highly significant evidence against in 3 cases each. The smallest p value for both real and imaginary residuals occurs at 500 Hz (the autocorrelation at this frequency is shown in Fig. 10).

Figures 10 and 11 consider spatial correlations within the real and the imaginary parts of the standardized residuals (autocorrelations). To consider spatial correlations between the real and imaginary parts (cross correlations), Fig. 12 gives p values for the two-tailed runs test applied to the difference between the real and imaginary residuals. For the diagonal-variance estimates, Fig. 12(a) indicates extremely significant evidence against the hypothesis of uncorrelated real and imaginary parts at all but 2 frequencies (where significant evidence exists). For the full-covariance estimates, Fig. 12(b) shows no significant evidence against uncorrelated real and imaginary parts at 7 of 11 frequencies and significant evidence at the remaining frequencies, with the smallest p value occurring (again) at 500 Hz.

To consider correlations between the real and imaginary parts of the standardized residuals at individual sensors, the sign test can be applied to set of their products to test if this set has a zero median value. Figure 13 shows p values for this test. For the diagonal-variance estimates, Fig. 13(a) indicates no significant evidence against the hypothesis of no correlation at 9 to 11 frequencies, but extremely significant evidence against at the remaining frequencies. For the full-covariance estimates, Fig. 13(b) shows no significant evidence against at 10 of 11 frequencies, and significant evidence against at a single frequency (550 Hz).

Finally, the initial assumption that the data errors are uncorrelated from frequency to frequency (Sec. II B) can be validated by applying the runs test to data residuals across

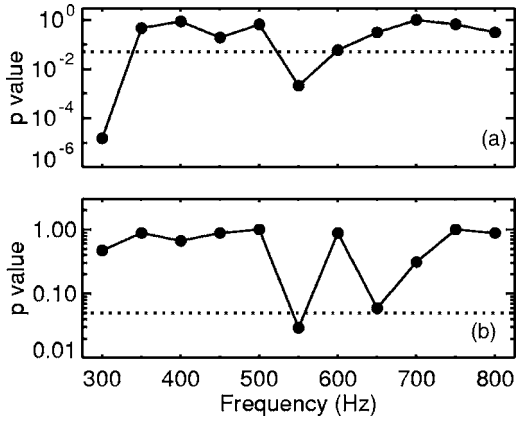

FIG. 13. Sign-test p values computed for the null hypothesis that the real and imaginary parts of the standardized residuals at each sensor are uncorrelated (their products have zero mean) using: (a) variance (diagonal-covariance) estimates and (b) full covariance matrix estimates. Dotted lines indicate the 0.05 level.

frequency at individual sensors. The frequency-series residuals pass the runs test at the 0.05 level for 46/48 hydrophones, indicating that for the 50 Hz frequency spacing used here there is no evidence against the assumption of uncorrelated errors in frequency.

IV. SUMMARY AND DISCUSSION

Many approaches to matched-field geoacoustic inversion are based on the implicit assumption of spatially uncorrelated data errors, although in practice strong correlations often exist due to unknown theory errors. Neglecting error correlations has the effect of representing the data as more informative than they actually are, and can lead to significant underestimation of geoacoustic parameter uncertainties. This paper developed a general approach to matched-field inversion based on estimating full data covariance matrices (including off-diagonal terms representing error correlations), and incorporating the covariance explicitly in a Bayesian formulation. An iterative, nonparametric approach is applied to estimate covariance matrices from the autocovariance function of the (complex) data residuals, replacing ensemble averaging by finite spatial averaging under the assumption of ergodicity. Qualitative and quantitative statistical tests can be applied *a posteriori* to the standardized residuals (i.e., residuals scaled and decorrelated via the covariance estimate) to examine the validity of the covariance matrix estimates and of the underlying assumption of Gaussian-distributed errors.

The above-noted inversion approach was applied to multifrequency, vertical-array data from the PROSIM'97 shallow-water geoacoustic experiment carried out in the Mediterranean sea. Plots of the measured and modeled complex acoustic pressures showed strong residual correlations over depth, related to the modal structure of the acoustic fields. Optimal geoacoustic models, marginal probability distributions, and posterior residual statistics were compared for three approaches to inversion which involved: (i) full covariance matrix estimation, (ii) diagonal covariance matrix estimation (i.e., variance estimation), and (iii) diagonal covariance matrix estimation with effective variances (increased in an attempt to compensate for neglected covariances).

Marginal PPDs computed for the diagonal-variance estimates were found to be substantially narrower than those for the full-covariance estimates. This indicates that neglecting error correlations significantly affects the geoacoustic inversion results for this data set. However, marginal PPDs for the effective-variance estimates were generally much wider than for the full-covariance estimates, indicating that although the effective-variance correction is in the right direction, it does not properly compensate for neglected covariances.

Posterior statistical tests on the residual distributions were consistent with the assumption of Gaussian errors for inversion based on the full-covariance and diagonal-variance estimates. Residual histograms agreed well with the theoretical Gaussian distribution, and the Kolomogorov-Smirnov test provided no significant evidence against Gaussianity at the 0.05 confidence level for almost all frequencies (slightly better results were obtained for the full-covariance estimates). Inversion residuals based on effective-variance estimates were not consistent with the standard Gaussian distribution; however, this is an expected consequence of purposefully overestimating the variances.

Posterior statistical tests for randomness indicated that inversions based on the diagonal-variance and effective-variance estimates left strong error correlations unaccounted for, and hence the inversion results are likely invalid. Plots of the autocorrelation function for the standardized residuals exhibited wide peaks near zero lag, and runs tests yielded extremely significant evidence against the hypothesis that the standardized residuals were random. In particular, spatial correlations were indicated within both the real and the imaginary parts of the standardized residuals (autocorrelations) and between real and imaginary parts (cross correlations). By contrast, inversions based on full-covariance matrix estimates appeared to largely account for error correlations with narrow autocorrelations and no significant evidence against randomness at most frequencies. However, significant evidence against randomness did occur at some frequencies. This indicates that the full covariance matrix did not completely characterized the error correlations in all cases. Hence, even with full-covariance estimates the parameter uncertainty distributions could be slightly optimistic. Finally, the inversion results obtained here are consistent with the limited independent information about the geoacoustic parameters at the experiment site,[18,30,31] but the independent information is not sufficiently accurate to be useful in differentiating between the various results.

[1]A. Tolstoy, "Using matched-field processing to estimate shallow water bottom properties from shot data taken in the Mediterranean Sea," IEEE J. Ocean. Eng. **21**, 471–479 (1996).
[2]A. Tolstoy, "MFP benchmark inversions via the RIGS method," J. Comput. Acoust. **6**, 185–203 (1998).
[3]Z.-H. Michalopoulou, "Matched-impulse-response processing for shallow-water localization and geoacoustic inversion," J. Acoust. Soc. Am. **108**, 2082–2090 (2000).
[4]M. D. Collins, W. A. Kuperman, and H. Schmidt, "Nonlinear inversion for ocean-bottom properties," J. Acoust. Soc. Am. **92**, 2770–2783 (1992).
[5]S. E. Dosso, M. L. Yeremey, J. M. Ozard, and N. R. Chapman, "Estima-

tion of ocean-bottom properties by matched-field inversion of acoustic field data," IEEE J. Ocean. Eng. **18**, 232–239 (1993).
[6]M. R. Fallat and S. E. Dosso, "Geoacoustic inversion for the Workshop97 benchmark test cases using simulated annealing," J. Comput. Acoust. **6**, 29–43 (1998).
[7]P. Gerstoft and Z.-H. Michalopoulou, "Global optimization in matched field inversion," *Proceedings of the Fourth European Conference on Underwater Acoustics*, edited by A. Alippi and G. B. Canneli (Italian National Research Council, Rome, 2000), pp. 27–32.
[8]P. Gerstoft, "Inversion of seismoacoustic data using genetic algorithms and *a posteriori* probability distributions," J. Acoust. Soc. Am. **95**, 770–782 (1994).
[9]M. Siderius, P. Gerstoft, and P. Nielsen, "Broadband geoacoustic inversion from sparse data using genetic algorithms," J. Comput. Acoust. **6**, 117–134 (1998).
[10]M. I. Taroudakis and M. G. Markaki, "Bottom geoacoustic inversion by 'broadband' matched-field processing," J. Comput. Acoust. **6**, 167–184 (1998).
[11]G. J. Heard, D. Hannay, and S. Carr, "Genetic algorithm inversion of the 1997 geoacoustic inversion workshop test case data," J. Comput. Acoust. **6**, 61–71 (1998).
[12]P. Gerstoft, "Inversion of acoustic data using a combination of genetic algorithms and the Gauss-Newton approach," J. Acoust. Soc. Am. **97**, 2181–2190 (1995).
[13]M. I. Taroudakis and M. G. Markaki, "On the use of matched-field processing and hybrid algorithms for vertical slice tomography," J. Acoust. Soc. Am. **102**, 885–895 (1997).
[14]M. R. Fallat and S. E. Dosso, "Geoacoustic inversion via local, global and hybrid algorithms," J. Acoust. Soc. Am. **105**, 3219–3230 (1999).
[15]M. Musil, M. J. Wilmut, and N. R. Chapman, "A hybrid simplex genetic algorithm for estimating geoacoustic parameters using matched-field inversion," IEEE J. Ocean. Eng. **24**, 358–369 (1999).
[16]S. E. Dosso, M. J. Wilmut, and A. L. Lapinski, "An adaptive hybrid algorithm for geoacoustic inversion," IEEE J. Ocean. Eng. **26**, 324–336 (2001).
[17]P. Gerstoft and C. F. Mecklenbräuker, "Ocean acoustic inversion with estimation of *a posteriori* probability distributions," J. Acoust. Soc. Am. **104**, 808–819 (1998).
[18]S. E. Dosso, "Quantifying uncertainty in geoacoustic inversion. I. A fast Gibbs sampler approach," J. Acoust. Soc. Am. **111**, 129–142 (2002).
[19]S. E. Dosso and P. L. Nielsen, "Quantifying uncertainty in geoacoustic inversion. II. Application to broadband, shallow-water data," J. Acoust. Soc. Am. **111**, 143–159 (2002).
[20]C. F. Mecklenbräuker and P. Gerstoft, "Objective functions for ocean acoustic inversion derived by likelihood methods," J. Comput. Acoust. **6**, 1–28 (2000).
[21]S. E. Dosso and M. J. Wilmut, "Effects of incoherent and coherent source spectral information in geoacoustic inversion," J. Acoust. Soc. Am. **112**, 1390–1398 (2002).
[22]A. Tarantola, *Inverse Problem Theory: Methods for Data Fitting and Model Parameter Estimation* (Elsevier, Amsterdam 1987).
[23]M. K. Sen and P. L. Stoffa, "Bayesian inference, Gibbs' sampler and uncertainty estimation in geophysical inversion," Geophys. Prospect. **44**, 313–350 (1996).
[24]W. R. Gilks, S. Richardson, and G. J. Spiegelhalter, *Markov Chain Monte Carlo in Practice* (Chapman and Hall, London, 1996).
[25]D. C. Montgomery and E. A. Peck, *Introduction to Linear Regression Analysis* (Wiley, New York, 1992).
[26]M. H. DeGroot, *Probability and Statistics* (Addison-Wesley, Reading, MA, 1975).
[27]R. H. Jones and A. V. Vecchia, "Fitting continuous ARMA models to unequally spaced spatial data," J. Am. Stat. Assoc. **88**, 947–954 (1993).
[28]S. E. Dosso and C. W. Holland, "Geoacoustic uncertainties from viscoelastic inversion of seabed reflection data," IEEE J. Ocean. Eng. (in press).
[29]C. W. Holland, J. Dettmer, and S. E. Dosso, "Remote sensing of density and velocity gradients in the transition layer," J. Acoust. Soc. Am. **118**, 163–177 (2005).
[30]P. L. Nielsen, F. Bini-Verona, and F. B. Jensen, "Environmental and acoustic data collected south of the island of Elba during the PROSIM'97 experiment," SACLANT-CEN document SM-357, SACLANT Undersea Research Centre, La Spezia, Italy, 1999.
[31]M. R. Fallat, P. L. Nielsen, and S. E. Dosso, "Hybrid geoacoustic inversion of broadband Mediterranean Sea data," J. Acoust. Soc. Am. **107**, 1967–1977 (2000).
[32]W. H. Press, S. A. Teukolsky, W. T. Vetterling, and B. P. Flannery, *Numerical Recipes in FORTRAN*, (Cambridge University Press, Cambridge, 1992), pp. 655.
[33]E. K. Westwood, C. T. Tindle, and N. R. Chapman, "A normal mode model for acousto-elastic ocean environments," J. Acoust. Soc. Am. **100**, 3631–3645 (1996).
[34]M. R. Fallat, S. E. Dosso, and P. L. Nielsen, "Investigation of algorithm-induced variability in matched-field geoacoustic inversion," IEEE J. Ocean. Eng. **29**, 78–87 (2004).

Validity of the Markov approximation in ocean acoustics[a)]

Frank S. Henyey[b)] and Terry E. Ewart[c)]
Applied Physics Laboratory, University of Washington, Seattle, Washington 98105

(Received 22 August 2005; accepted 7 October 2005)

Moment equations and path integrals for wave propagation in random media have been applied to many ocean acoustics problems. Both these techniques make use of the Markov approximation. The expansion parameter, which must be less than one for the Markov approximation to be valid, is the subject of this paper. There is a standard parameter (the Kubo number) which various authors have shown to be sufficient. Fourth moment equations have been successfully used to predict the experimentally measured frequency spectrum of intensity in the mid-ocean acoustic transmission experiment (MATE). Yet, in spite of this success, the Kubo number is greater than 1 for the measured index of refraction variability for MATE, arriving at a contradiction. Here, that contradiction is resolved by showing that the Kubo parameter is far too pessimistic for the ocean case. Using the methodology of van Kampen, another parameter is found which appears to be both necessary and sufficient, and is much smaller than the Kubo number when phase fluctuations are dominated by large scales in the medium. This parameter is shown to be small for the experimental regime of MATE, justifying the applications of the moment equations to that experiment. © *2006 Acoustical Society of America.* [DOI: 10.1121/1.2130963]

PACS number(s): 43.30.Re [ADP] Pages: 220–231

I. INTRODUCTION

The Markov approximation is a fundamental part of theories of acoustic propagation through the internal wave field. In moment equation approaches, the Markov approximation leads to equations with a single range variable, allowing one to avoid the complications of explicitly including the range extent of correlations in the internal wave sound speed fluctuations. In path integral approaches, the Markov approximation reduces the dimensionality of integrals that need to be done. The moment equation and path integral formalisms are reviewed by Henyey and Macaskill (1996). In practice, the Markov approximation consists of replacing the actual sound-speed fluctuation correlation function by an effective correlation function that includes a delta function of the range difference, but is otherwise similar to an ordinary correlation function. The effective correlation function is the product of the delta function and a factor that is somewhat misleadingly called the "transverse correlation function," but would better be called the "Markovian correlation function."

Due to the strong anisotropy of the ocean, this effective correlation function, unlike the true correlation function, is a strong function of the angle of propagation, and due to the depth inhomogeneity, it is a weak function of the depth of propagation. The angle and depth dependence can cause problems (for long-range propagation) in calculations, as the angle and depth distributions are properties of the solutions, not something one knows *a priori*. Standard approaches assume the angle and depth can be approximated by unperturbed values, which becomes increasingly incorrect with increasing range. This problem is serious and unsolved, but will not be investigated in this paper—it is concerned with shorter-range applications.

There are two parameters (at least) that must be small in order for the Markov approximation as used in practice to be valid. These parameters refer to two quite different aspects of the Markov approximation. One relates to the effective correlation being a function, rather than, more generally, an operator. For an isotropic medium, this condition requires the scattering angle to be small for each uncorrelated scattering. This has been generally recognized, for example, by Uscinski (1977) in the moment equation context, and by Dashen (1979) in the path integral context. The correct extension of this parameter to the anisotropic case is given by Beran and McCoy (1974). The scattering angle must not only be small, it must be smaller than the vertical to horizontal aspect ratio of the fluctuations. This parameter is not the subject of this paper. The Beran and McCoy parameter is typically small in oceanic applications.

The other aspect, of more fundamental importance, allows there to be a range delta function at all, without consideration of whether the coefficient is a function or an operator. The parameter associated with this aspect is a strength parameter; it depends on the magnitude of sound speed fluctuations. There is a standard answer as given, for example, by Uscinski for the wave propagation problem, and by many authors in contexts much more general than ocean acoustics. This paper uses the formalism of van Kampen (1992), who discusses the parameter in detail. He refers to it as the "Kubo number." This parameter was not identified by Dashen in his path integral papers, which presented the other parameter as the only condition of validity. Both parameters were discussed as applied to both formalisms, by Codona *et al.*

[a)]Portions of this work were presented in "Some validity issues in the theory and modeling of WPRM," by Terry Ewart and Frank Henyey at the 143rd Meeting of the Acoustical Society of America [J. Acoust. Soc. Am. 111, 2351 (2002)].

[b)]Electronic mail: frank@apl.washington.edu
[c)]Electronic mail: ewart@apl.washington.edu

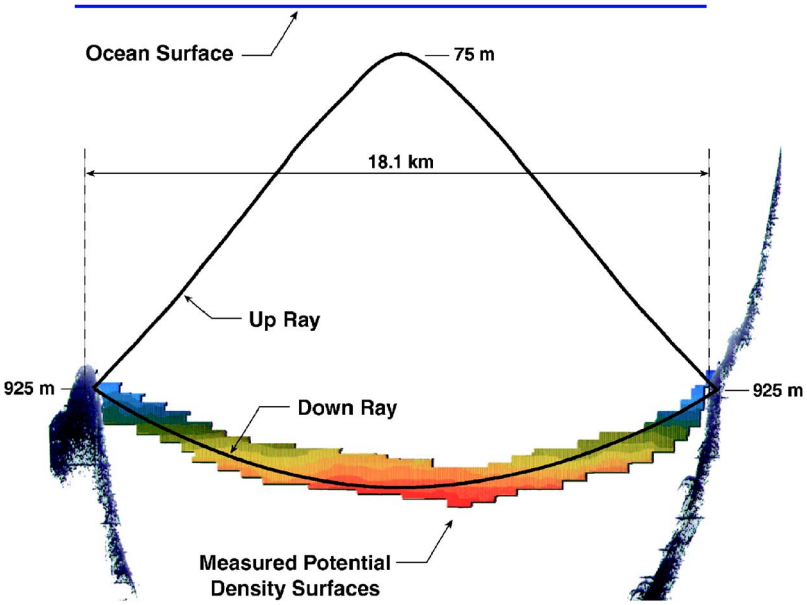

FIG. 1. (Color online) Local bathymetry from the precision depth recorder, upper path and lower path eigenrays traced using the mean sound speed profile, and potential density contours taken with an autonomous vehicle, SPURV, depth cycling over the lower ray. The grayscale are equally spaced, with a total range of 0.2 Kg/m^3.

(1986). It has been repeatedly shown that the smallness of this parameter is sufficient for the (more general) Markov approximation to be valid. The parameter is identified in the literature as

$$k\mu_{\rm rms}L_p/2, \tag{1}$$

where k is the acoustic wave number, $\mu_{\rm rms}$ is the root mean square fluctuation in the index of refraction, and $L_p/2$ is the range correlation length of the sound speed fluctuations. The division by 2 is because L_p is defined as the distance over which the sound speed fluctuation is correlated with that at a given point. As the other point can be either earlier or later in range, L_p is twice the correlation length, which is approximately the largest separation at which sound speeds are correlated.

Clearly, the square root involved in calculating $\mu_{\rm rms}$ does not appear in power series expansions, so the expansion parameter is expected to be the square,

$$\epsilon = k^2\langle\mu^2\rangle L_p^2/4. \tag{2}$$

This is identified as the parameter by Rytov *et al.* (1989), although unfortunately they describe $\epsilon \ll 1$ as a necessary condition after showing it to be a sufficient condition. Codona *et al.* (1986) also incorrectly identify the smallness of ϵ as a necessary condition.

The parameter ϵ is closely related to phase fluctuations (at not-too-long ranges). The phase variance is

$$\Phi^2 = k^2\langle\mu^2\rangle L_p R, \tag{3}$$

where R is the range of the experiment (assumed large relative to L_p). Thus

$$\epsilon = \frac{\Phi^2 L_p}{4R}. \tag{4}$$

(Since $\langle\mu^2\rangle$ and L_p vary with range due to the angle and depth variation, an appropriately averaged L_p is meant in this expression.)

This paper was initiated by an evaluation of ϵ for an experiment in which the theory using the Markov approximation is known to fit data very well. It turns out that ϵ is not small. Clearly, the sufficient condition is too pessimistic. There must be a smaller parameter whose smallness is a sufficient condition in ocean acoustics for the Markov approximation. This paper derives that smaller parameter and presents its value for the MATE oceanic conditions.

Section II shows the evaluation of ϵ for the MATE experiment, Sec. III discusses why ϵ is too pessimistic a parameter because the internal wave spectrum is red, Sec. IV obtains a formula for a smaller sufficient parameter, and Sec. V evaluates the new parameter for MATE. Section VI extends the theory to higher moments than the first, and summarizes the results.

II. EXPERIMENTAL VALUES

In this section ϵ is evaluated for the MATE experiment (Ewart and Reynolds, 1984). First the experiment and the associated modeling are described. In Macaskill and Ewart (1996), predictions of the fourth moment of the MATE complex signals (second moment of intensity) using the Markov approximation are shown to match the experimental results very accurately. Then, ϵ, computed for the experimental oceanographic data, is shown to be greater than 1, which has been expected to make the Markov approximation invalid. This paradox is the reason for this research.

The mid-ocean acoustic transmission experiment (MATE), shown schematically in Fig. 1, was carried out at Cobb Seamount, on the same site as an earlier experiment known in the literature as the "Cobb experiment" (Ewart, 1976; Ewart *et al.*, 1983). The earlier experiment was carried out to study the effects of ocean fluctuations on sonar bearing error, which the experiment determined to be very small; whereas MATE was done to test the modeling of acoustic fluctuations due to internal wave processes. Cobb Seamount (275 miles west of Grays Harbor, Washington) is a large shield volcano that comes almost to the ocean surface; it is

surrounded by several subsidiaries, and much smaller and deeper seamounts. Sound pulses were transmitted over an 18 km path from a single tower on one of the subsidiary peaks to two receiving towers (separated by 253 meters transverse to the acoustic paths) located on the flank of Cobb Seamount. The depth of all the towers was 975±3 m, and pulsed tone and FM slide pulses at center frequencies of 2083, 4167, 8333, and 12 500 Hz, hereafter designated 2, 4, 8, 12.5 kHz, were employed. The eight pulse types were sent in sequence every 15.728 64 seconds, or 125.83 seconds between pulses of the same type. All the frequencies and the repetition rates were generated from a 15 microsecond period signal generated from precision "Austron" quartz crystal oscillators in each tower, which were used as the experiment time base. Using this technique, the travel time to the autonomous receivers was known to a few parts in 10^{12} per day. The 12.5 kHz acoustic data is judged to be less accurate because the lower path was at the edge of the source beam pattern's main lobe; it therefore is not discussed in this paper. Two paths between the towers were studied, the lower and upper paths seen in the figure. Most of the acoustic measurements and almost all the oceanographic data were concentrated on the lower path. This paper is also focused on the lower path results for several reasons. The oceanography is not well known for the upper path, and there have not been any successful calculations of the moments for the upper path. Other approximations that were made are likely at fault, so we do not know if the expansion parameter should be small or large. Moreover, the assumptions needed below to derive a new expansion parameter are not valid for the upper path.

The oceanography at the MATE site is typical of the open ocean, with the exception that the internal tides are characterized by displacements of about 10 m. Another possible exception, the observed high vertical wave number fluctuations with frequencies below those of the internal waves (termed fine structure) were used in the modeling. The dynamical interpretation is that fine structure is neutrally buoyant, relatively high wave number, low frequency intrusions, with possible potential vorticity content. The inertial frequency, ω_I, is 1.7×10^{-5} Hz, and the buoyancy frequency, ω_B, is 3.0×10^{-4} Hz. The potential density surfaces shown in the figure are one example of those measured during MATE by a depth cycling autonomous vehicle, SPURV, that was deployed many times during the experiment. In this deployment SPURV was depth cycled above and below the lower path measuring pressure, salinity, and temperature at two points separated in depth by 1 m. This provides a relatively synoptic picture of the internal wave displacements and gradients as seen by the propagating acoustic field. Three temperature and velocity moorings, located in the center of the transmission path and spanning the depth of the lower ray, were deployed for the duration (23.7 days) of the experiment. Conductivity and temperature versus depth measurements were made throughout the experiment. The oceanographic data and its interpretation are found in papers by Levine and Irish (1981) and Levine *et al.* (1986).

In Fig. 2 the moored displacement spectrum is shown. It has been normalized to have integral one. The fine structure,

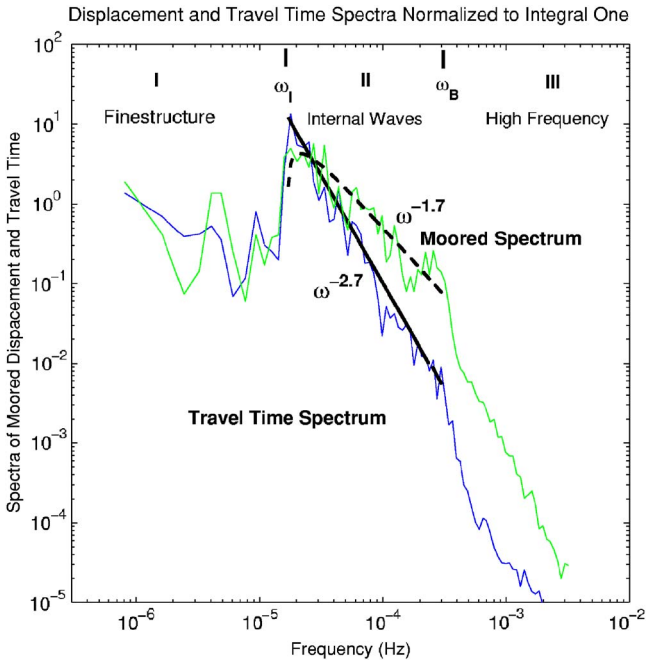

FIG. 2. (Color online) Spectra of the moored displacement and travel time measured during MATE (normalized to integral one). The fit of the model to the moored spectrum and its prediction for the travel time spectrum are shown.

internal wave, and high frequency bands are shown as I, II, III, respectively. The internal wave displacements have a frequency spectrum with a power law $\omega^{-1.7}$, differing from the Garrett-Munk ω^{-2}. A similar deviation from Garrett-Munk has been observed elsewhere, such as in IWEX (Frankignoul and Joyce, 1979) and AFAR (Reynolds *et al.*, 1985). The moored spectrum also has a rolloff near the inertial frequency. The tides have been removed by a simultaneous least squares fit of tidal components at K1, M2, S2, M4 frequencies and a stochastic model of the internal waves and fine structure. The internal wave model fit to the displacement data is shown as a dashed line.

The acoustic data were reduced to travel times and amplitudes for single path transmissions using a multiple dimensional matched filter analysis (Bell and Ewart, 1986). The single path hypothesis fits the data well. The application of this analysis is discussed in Ewart and Reynolds (1984). Also plotted in Fig. 2 is the measured frequency spectrum of the 8 kHz travel time, with the tides removed in the same way as above, for the full 14 days of the MATE lower path record. (The travel time records are virtually independent of acoustic frequency, indicating a geometric phase condition.) The integral is normalized to one as for the displacements. The MATE ocean model is used in the standard way to obtain the predicted spectrum of travel time, shown as a solid black line. This model curve has a power law $\omega^{-2.7}$, one power lower than the moored spectrum. This decrement by one in the power law and the absence of the rolloff near the inertial frequency are a result of the linear internal wave dispersion relation. The agreement with the model curve provides further confidence in the MATE ocean model, because the theory for the travel time is well established, as discussed in Sec. III.

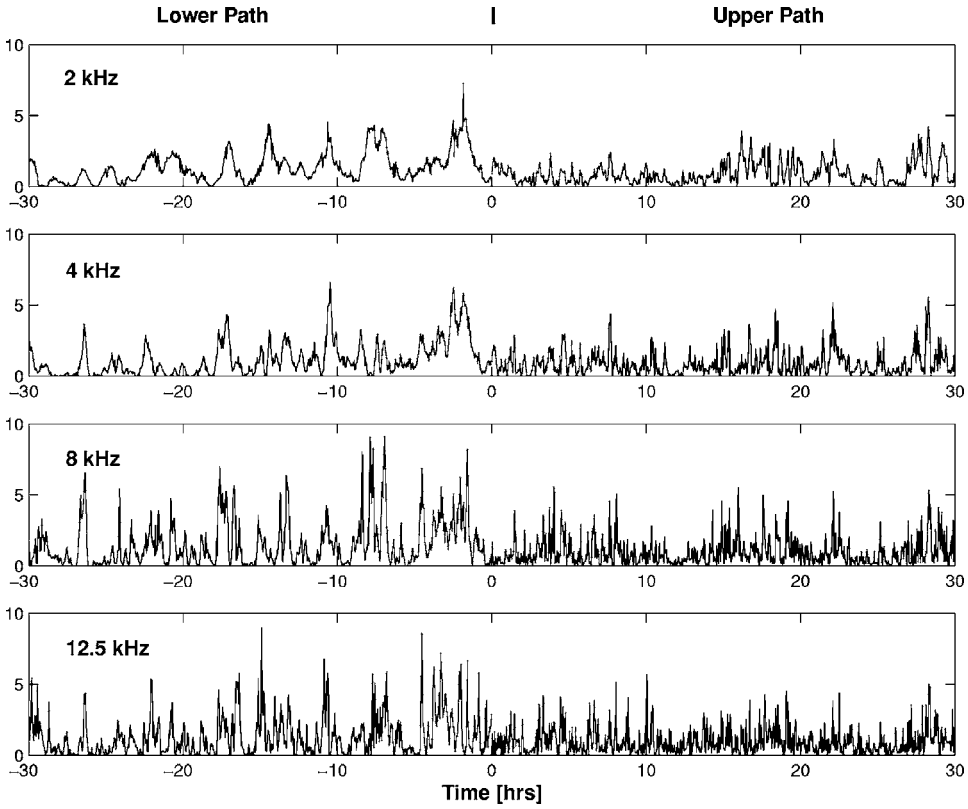

FIG. 3. Intensity for the four frequencies of MATE taken during the last 66 hours of the experiment with equal time records of the lower path and upper path results.

Normalized intensity records, measured in MATE during the last 66 hours of the experiment, are shown in Fig. 3. Plotted for the four frequencies of MATE are equal time periods; the first half where the experiment was run on the path with a lower turning point (1200 m), and the second half where the experiment tracked the path with an upper turning point (75 m). This plot shows that the spectral content of the variance for this data are strong functions of oceanic frequency, acoustic frequency, and very different for the lower path compared to the upper path. As a result of the high intensity spikes shown in the figure, the intensity pdf's are high tailed distributions. This figure demonstrates the complexity involved in modeling the acoustic intensity moments.

Theoretical predictions of the 4, 8 kHz "Cobb Experiment" log intensity spectra using Rytov theory were presented by Munk and Zachariasen (1976), Desaubies (1976, 1978), and by Flatté *et al.* (1979) and Flatté (1983). In all of those references, the Rytov predictions of the log intensity spectra differ in shape and scaling from the observations. The Rytov prediction is proportional to acoustic frequency; this contrasts to the absence of such dependence in the observations from Cobb or MATE at low oceanic frequencies. On the other hand, predictions of the intensity spectra using the moment equations (Shishov, 1968), with internal wave models only, are presented by Uscinski (1977) and Ewart and Reynolds (1984). These theories, which inherently make the Markov approximation, are closer to the observed intensity spectra. In particular, the log intensity spectral slopes are considerably smaller than the phase spectral slopes both in the data (Ewart, 1976) and in the moment equation predictions, whereas Rytov predicts them to be equal. Moreover, the Rytov scaling is absent from these predictions, as it is from the data. In Macaskill and Ewart (1996), the fine structure discussed above was included in addition to the internal waves, and the predictions were obtained by numerical integration of the fourth moment equation without any approximations other than those that underlie the moment equations. Both these features improve the agreement with data. The intensity spectra and these predictions are shown in Fig. 4. The internal wave band and higher frequency predictions are very close to the observations.

Since the moment equations are valid in any scattering regime where the Rytov approximation is valid, the Rytov approximation is invalid in any regime where the moment equations and Rytov differ. As discussed above, Rytov and moment equation methods differ strongly for MATE. Therefore, even in the absence of acoustic data, we could have concluded that Rytov is incorrect for the MATE conditions.

Flatté *et al.* (1979) present a theory dividing experimental conditions into various scattering regimes. Their divisions place the Cobb and MATE experiments into the weak scattering region. They characterize this region by two features, single path propagation rather than multipathing and Rytov valid. As mentioned earlier, Cobb and MATE are well fit with the arrival of a single path. Moreover, the discussion above shows Rytov to be invalid. Therefore these two features, identified in that theory as occurring together, actually occur in noncoincident regions of experimental conditions.

We have shown that the phase and intensity spectra are well predicted with moment theory. The condition for the validity of Markov as presented in previous literature, Eq. (2), is relatively simple to evaluate. The results of this evaluation in Fig. 5 show the expansion parameter, ϵ, for the

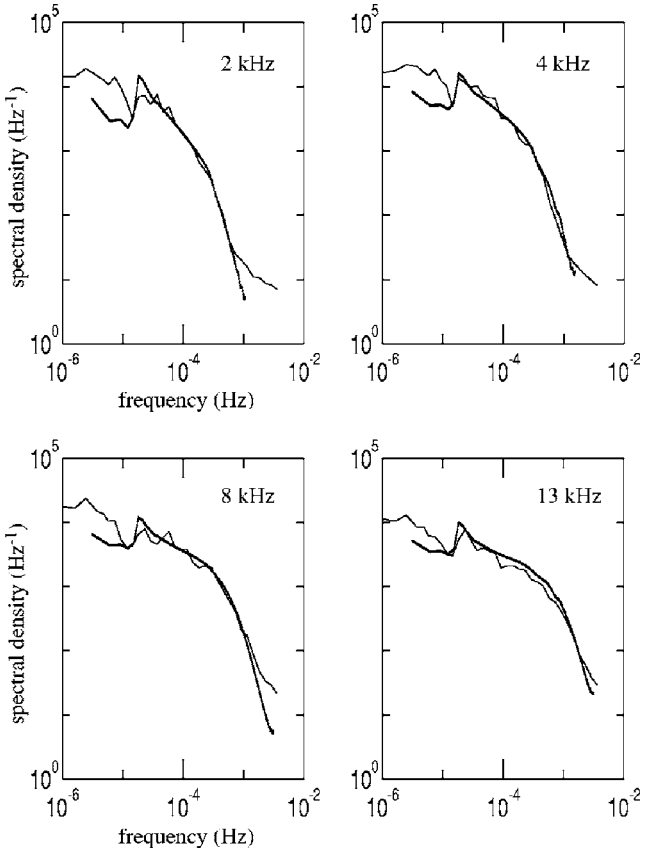

FIG. 4. Intensity spectra for the four frequencies of MATE with the moment theory predictions of Macaskill and Ewart (1996) superimposed. The inertial frequency is 1.7×10^{-5} Hz, and the buoyancy frequency is 3.0×10^{-4} Hz.

MATE lower path at 2, 4, and 8 kHz. One is immediately drawn to the fact that all of the values are above one. This indicates that the predictions in Fig. 4 should not work—yet they clearly work very well. This paradox indicated to us that another parameter may come into the theory; this is the focus of this work.

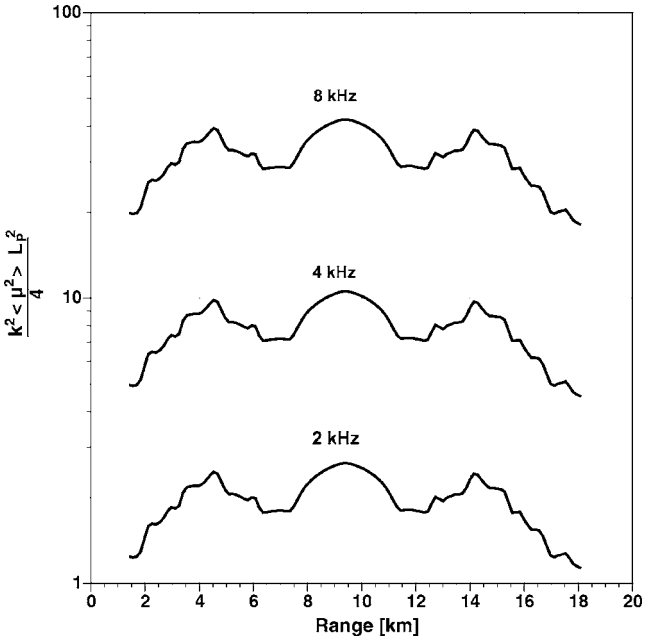

FIG. 5. Expansion parameter, ϵ, according to the literature for 2, 4, and 8 kHz computed using the MATE lower path oceanographic data. Since these values are above 1, the Markov approximation is called into question.

We know that the fourth moment equation does not work well for the upper path (see Macaskill and Ewart, 1996). Thus, the MATE upper path results clearly indicate that a new theoretical approach is required. The value of ϵ for the upper path can be estimated, and is larger than that for the lower path, but as it does not apply to the lower path, there is no reason to think it should apply to the upper path. Since the moment theory does not work well for the upper path, there is no paradox as there is for the lower path. We turn our attention now to the derivation of a modified expansion parameter for the lower path; necessary technical assumptions do not apply to the upper path, so we are unable to provide an expansion parameter with confidence to that case.

III. THE EFFECT OF LARGE VERTICAL SCALES IN THE OCEAN

In this section, we examine the effects of sound speed variations that have a large vertical scale. To keep the discussion simple, we take the largest possible scale, namely no vertical variation at all. For this artificial problem, the moment equation used in ocean acoustics is exact, no matter how large the fluctuations or their correlation scale in range. Thus, the expansion parameter for this case is zero rather than the expression in Eq. (2). This situation is contrasted with another moment equation, the equation with memory. The equation with memory does not fare as well; Eq. (2) is the expansion parameter for that equation.

Throughout this paper, we use the narrow-angle "parabolic" equation (Tappert and Hardin, 1973) for the pressure p,

$$i\frac{\partial p}{\partial x}=\frac{-1}{2k_0}\frac{\partial^2 p}{\partial z^2}+k_0U(z)p+k_0\mu(x,z)p \tag{5}$$

to estimate corrections to the Markov approximations. The fluctuation μ is assumed to have zero ensemble average. The Markov approximation first moment equation is

$$i\frac{\partial\langle p\rangle}{\partial x}=\frac{-1}{2k_0}\frac{\partial^2\langle p\rangle}{\partial z^2}+k_0U(z)\langle p\rangle-\frac{i}{2}k_0^2\langle\mu^2\rangle L_p\langle p\rangle \tag{6}$$

(Uscinski, 1977), where

$$\langle\mu^2\rangle L_p=\int_{-\infty}^{\infty}dx'\langle\mu(x,z)\ \mu(x',z')\rangle\big|_{z'=z+s(x'-x)} \tag{7}$$

and s is the unperturbed slope of the sound wave number vector (the ray slope in the geometrical approximation). With a nonconstant $U(z)$, the assumption of constant slope is only an approximation, made for simplicity. This approximation is irrelevant for the considerations of this paper, and a more exact expression could be used.

This moment equation can be compared to the moment equation with "memory." This equation is derived by substituting p as given by the integral equation equivalent to Eq. (5) into the last term and taking the ensemble average. As in Eq. (7), the unperturbed propagation is taken at constant slope. The resulting equation is

$$i\frac{\partial\langle p(x,z)\rangle}{\partial x}=\frac{-1}{2k_0}\frac{\partial^2\langle p(x,z)\rangle}{\partial z^2}+k_0U(z)\langle p(x,z)\rangle - ik_0^2\int_{-\infty}^{x}dx'\langle\mu(x,z)\ \mu(x',z') \times p(x',z')\rangle\big|_{z'=z+s(x'-x)}. \tag{8}$$

A closure approximation

$$\langle\mu(x,z)\ \mu(x',z')\ p(x',z')\rangle=\langle\mu(x,z)\ \mu(x',z')\rangle\ \langle p(x',z')\rangle$$

turns this into the moment equation with memory

$$i\frac{\partial\langle p(x,z)\rangle}{\partial x}=\frac{-1}{2k_0}\frac{\partial^2\langle p(x,z)\rangle}{\partial z^2}+k_0U(z)\langle p(x,z)\rangle - ik_0^2\int_{-\infty}^{x}dx'\langle\mu(x,z)\ \mu(x',z')\rangle \times\langle p(x',z')\rangle\big|_{z'=z+s(x'-x)}. \tag{9}$$

van Kampen (1974, 1992) asserts that the moment equation without memory is no worse than that with memory.

Let us examine the largest possible vertical scale perturbation—that which has no z dependence at all, $\mu=\mu(x)$. If p_0 is the solution of Eq. (5) with $\mu=0$, then with a z-independent perturbation, the exact solution is

$$p=p_0\exp\left(ik_0\int_0^x\mu(x')dx'\right). \tag{10}$$

Assuming a zero-mean stationary Gaussian process for μ, and ignoring the initial transient,

$$\langle p\rangle=p_0\exp\left(-\frac{k_0^2}{2}\langle\mu^2\rangle L_p x\right). \tag{11}$$

This is an exact solution of the moment equation without memory.

To see how the moment equation with memory fares, we must assume something about the autocorrelation function of $\mu(x)$. To show the order of magnitude effect, we will take an exponential form

$$\langle\mu(x)\mu(x')\rangle=\langle\mu^2\rangle\exp\left(-\frac{2|x-x'|}{L_p}\right). \tag{12}$$

By homogeneity of the equation, the solution must be of the form

$$\langle p\rangle=p_0\exp(-Ax). \tag{13}$$

Setting this ansatz into Eq. (9) (ignoring the initial transient), we find

$$A=k_0^2\langle\mu^2\rangle\int_{-\infty}^{x}dx'\ \exp\left(-\frac{2(x-x')}{L_p}+A(x-x')\right) =\frac{k_0^2\langle\mu^2\rangle}{\left(\frac{2}{L_p}+A\right)}. \tag{14}$$

Assuming A to be small,

$$A=\frac{k_0^2}{2}\langle\mu^2\rangle L_p+\frac{k_0^4}{8}\langle\mu^2\rangle^2L_p^3+\cdots. \tag{15}$$

The fractional error in A is

$$\frac{k_0^2\langle\mu^2\rangle L_p^2}{4}. \tag{16}$$

This is ϵ from Eq. (2). This result is the reason for van Kampen's assertion; the fractional difference between the solution without memory and with memory is the same as the identified expansion parameter ϵ. However, we see that for a z-independent fluctuation, not only is the solution without memory no worse than the solution with memory, it is much better because it is exact.

For perturbations of large vertical size, their main effect is the phase shift

$$k_0\int_0^x\mu(x',z')dx' \tag{17}$$

which the moment equation without memory gets right. The expansion parameter is not ϵ, but only the residual small-scale contribution to ϵ. However, the dividing line between what is large-scale and what is small-scale needs to be determined. The method used here for determining that division, and estimating the actual expansion parameter, is to actually evaluate the next term in the series beyond the Markov approximation. It turns out in the next section that the dividing scale between large and small scales is on the order of the Fresnel radius for propagating a distance of the correlation length L_p.

For the moment equation without memory, with only large scale fluctuations, this section showed that the expansion parameter is nearly zero. When small scale fluctuations are present, the next section shows the expansion parameter is not zero, but is much smaller than ϵ. We have established that the expansion parameter for the equation with memory is ϵ, and therefore that equation is much worse than the equation without memory.

IV. DERIVATION OF THE NEW EXPANSION PARAMETER

In this section the fourth order correction to the Markov approximation in van Kampen's expansion in powers of μ of the transport coefficient is estimated. The expansion parameter is estimated as the ratio of the fourth order and the second order terms for the first moment $\langle p\rangle$. Of course, there can be a factor of order unity multiplying the expansion parameter in the ratio, and it turns out in the calculation below that this factor is very small for horizontal propagation.

van Kampen has presented a systematic expansion of a sequence of moment equations, of which the Markov approximation is the first. These moment equations are related by truncating the same infinite series in powers of μ for the transport coefficient at different orders. The following assumptions are made:

(1) The narrow angle "parabolic" equation is adequate for estimating the expansion parameter.

(2) The sound speed fluctuations are adequately modeled as a mean zero Gaussian process. The process is stationary in time and the horizontal, and the correlation function in the vertical is diagonal when expressed in terms of dynamic oceanic modes.
(3) Both acoustic and oceanic modes can be approximated by traveling Fourier modes over the local vertical extent important for the sound propagating between a given source and a given receiver.
(4) The unperturbed ocean is horizontally homogeneous.

These assumptions are standard in this subject. The third assumption, though commonly made, is in fact not universally valid. It is expected to be valid for the lower path in MATE, but not for the upper path. Neither the acoustic modes nor the oceanic modes are Fourier in regions of strong stratification. The reason that the third assumption makes the calculations tractable is that the product of an acoustic mode with an oceanic mode is a single acoustic mode if all modes are Fourier. Modes diagonalize the propagation operator in a horizontally homogeneous ocean; i.e., the propagation of a mode from one range to another, ignoring internal waves, is given by the factor $e^{ik\delta x}$, where k is the horizontal wave number of the mode and δx is the range extent of that propagation.

A derivation of the van Kampen expression is not given here. The interested reader can find the derivation in van Kampen's book (van Kampen, 1992) and his extension to higher orders (powers of μ) in van Kampen (1974), or in Codona *et al.* (1986). At every order of μ in the expansion, a moment equation exists. (The reader must not conclude, however, that there is an exact moment equation. The series for the coefficient in the expansion is almost certainly asymptotic rather than convergent.) As will be explicitly demonstrated, due to the assumptions made above, a single Fourier mode is a solution of the moment equation. (This would not be true if standing wave modes or non-Fourier modes were required.) Thus, van Kampen's expansion yields a series in μ for the coefficient A_j in

$$\frac{\partial\langle p_j\rangle}{\partial x} = ik_j\langle p_j\rangle + A_j\langle p_j\rangle, \tag{18}$$

where $\langle p_j\rangle$ is the amplitude of the jth mode, and k_j is its unperturbed horizontal wave number. It is given, in the narrow angle PE approximation, as a function $\kappa(q_j)$, where q_j is the vertical wave number of the mode,

$$k_j = \kappa(q_j) = k_0 - \frac{q_j^2}{2k_0}, \tag{19}$$

where k_0 is the unperturbed wave number. The interaction rate is $ik_0\mu$, where μ is the fractional sound speed perturbation. μ is expanded in terms of the oceanic modes, here assumed Fourier,

$$\mu = \int dKdQ\,\tilde{\mu}(K,Q)e^{iKx+Qz}. \tag{20}$$

The oceanic mode amplitudes satisfy

$$\langle\tilde{\mu}^*(K,Q)\tilde{\mu}(K',Q')\rangle = \frac{S(K,Q)}{2}\delta(K-K')\delta(Q-Q'), \tag{21}$$

where S is the spectrum. The factor of $\frac{1}{2}$ is included so that S is the conventional standing wave spectrum, whereas $\tilde{\mu}$ is defined for waves traveling either up or down in the vertical. The integral of $S(K,Q)$ over positive Q's and all K's gives the variance of μ.

We start with the lowest order, Markov, term. Only even orders occur, as we are assuming a mean zero Gaussian process for the fluctuations. Therefore, the lowest order is quadratic in the interaction. In van Kampen's expansion, one of the interactions occurs at the range x at which the coefficient A_j is being evaluated, while other interactions occur earlier in range. For the Markov term, the earlier range of the second interaction will be denoted as x_1.

The terms are compactly written in matrix notation. Let Π be the vector of mode amplitudes, Λ be the diagonal matrix with k_j in the jth position on the diagonal, and $\Gamma(x)$ be the matrix made from μ, Fourier transformed to the mode representation,

$$\Gamma_{jj'} = k_0\int dK\tilde{\mu}(K,q_{j'}-q_j)e^{iKx}. \tag{22}$$

The coefficients of the transport equation can be found in van Kampen's work. However, we obtain them here to provide a framework for the calculations. From van Kampen's derivation, we accept that a moment equation exists in which the transport coefficient can be expanded in powers of μ. The equation should apply under conditions that include the case that $\mu x \ll 1$. We pick that regime to evaluate the coefficients. The matrix equation for the mode amplitudes is

$$\partial\Pi/\partial x = i\Lambda\Pi + i\Gamma\Pi. \tag{23}$$

The perturbative (Born) series solution, valid for small μx, is

$$\begin{aligned}\Pi = \Bigg[&\exp(i\Lambda(x)) + \int_0^x dx_1 \exp(i\Lambda(x-x_1))i\Gamma(x_1)\\ &\times\exp(-i\Lambda x_1) + \int_0^x dx_1\int_0^{x_1} dx_2\\ &\times\exp(i\Lambda(x-x_1))i\Gamma(x_1)\exp(i\Lambda(x_1-x_2))i\Gamma(x_2)\\ &\times\exp(-i\Lambda x_2) + \cdots\Bigg]\Pi(0).\end{aligned} \tag{24}$$

In taking the ensemble average, the odd terms drop out from the assumption of Gaussian statistics for Γ. The result is

$$\begin{aligned}\langle\Pi\rangle = \Bigg[&\exp(i\Lambda(x)) + \int_0^x dx_1\int_0^{x_1} dx_2\\ &\times\langle\exp(i\Lambda(x-x_1))i\Gamma(x_1)\exp(i\Lambda(x_1-x_2))\\ &\times i\Gamma(x_2)\exp(i\Lambda x_2)\rangle\\ &+ \int_0^x dx_1\int_0^{x_1} dx_2\int_0^{x_2} dx_3\int_0^{x_3} dx_4\end{aligned}$$

$$\times\langle\exp(i\Lambda(x-x_1))i\Gamma(x_1)\exp(i\Lambda(x_1-x_2))i\Gamma(x_2)\exp(i\Lambda(x_2-x_3))i\Gamma(x_3)\exp(i\Lambda(x_3-x_4))i\Gamma(x_4)\times\exp(i\Lambda x_4))\rangle+\cdots\Big]\Pi(0). \tag{25}$$

We now assume a transport equation of the form

$$\frac{\partial\langle\Pi\rangle}{\partial x}=i\Lambda\langle\Pi\rangle+[A_{(2)}+A_{(4)}+\cdots]\quad\langle\Pi\rangle, \tag{26}$$

where the subscript is the order in powers of μ. Its perturbative solution is

$$\langle\Pi\rangle=\Big[\exp(i\Lambda(x))+\int_0^x dx_1\exp(i\Lambda(x-x_1))\times[A_{(2)}+A_{(4)}]\exp(i\Lambda x_1)+\int_0^x dx_1\int_0^{x_1}dx_2\times\exp(i\Lambda(x-x_1))A_{(2)}\exp(i\Lambda(x_1-x_2))A_{(2)}\times\exp(i\Lambda x_2)+\cdots\Big]\Pi(0). \tag{27}$$

The x_1 integrals in Eq. (25) and Eq. (27) can be removed by taking the x derivative and subtracting $i\Lambda\langle\Pi\rangle$. By equating terms of the same order in the two equations, one can solve for $A_{(2)}$, $A_{(4)}$, etc. For later reference, $A_{(4)}$ is the difference between the fourth order term obtained from Eq. (25) and that obtained from the second line of Eq. (27), i.e., it is the difference between the contributions correctly calculated, and incorrectly calculated from the lower order moment equation (containing only $A_{(2)}$). Equating terms quadratic in μ results in the Markov approximation result (e.g., Eq. 2.7 on p. 400 of van Kampen, 1992),

$$\frac{\partial\langle\Pi\rangle}{\partial x}=i\Lambda\langle\Pi\rangle+\int_0^x dx_1\langle i\Gamma(x)\exp(i\Lambda(x-x_1))i\Gamma(x_1)\times\exp(-i\Lambda(x-x_1))\rangle\langle\Pi\rangle, \tag{28}$$

Γ is a Hermitian matrix; $\Gamma(x)$ can be replaced by its Hermitian conjugate, while $\Gamma(x_1)$ is left as is, so that Eq. (21) can be used. When this is done, one can see that the matrix in the second term is diagonal due to the $\delta(Q-Q')$ in Eq. (21). The factor $\exp(-i\Lambda(x-x_1))$ backs up the $\langle\Pi\rangle$ from x to x_1.

The diagonal A_j is evaluated to be

$$A_j^{\text{Markov}}=\int_0^x dx_1 e^{-ikj(x-x_1)}\times\int dKdQ(ik_0)^2\frac{S(K,Q)}{2}e^{-iK(x-x_1)}\times e^{i\kappa(q_j+Q)(x-x_1)}. \tag{29}$$

The factor $(ik_0)^2[S(K,Q)/2]e^{iK(x-x_1)}$ is the expectation of the product of the two interactions. The vertical structure of the first interaction changes the acoustic vertical wave number from q_j to $q_{j'}=q_j+Q$, so $\kappa(q_j+Q)$ is the horizontal wave number with which the sound propagates between the two interactions.

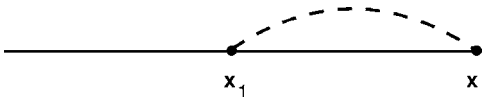

FIG. 6. A diagrammatic representation of Eq. (29). The horizontal represents range, while the vertical does not have a similar meaning. The solid line represents the factor for propagation of the acoustic field, e^{ikjx} for mode j. The dots indicate interaction factors $k\mu$, and the dashed line represents that these interactions are to be correlated. Not indicated is the integration over the range variable x_1 with $x_1<x$, nor is the factor in front of the K,Q integral, that relates the unscattered field at x to that at x_1, indicated. In Eq. (29), the correlation function is expressed in terms of the spectrum.

The expression can be represented diagrammatically, as shown in Fig. 6. The use of diagrams such as the ones used here is described in detail by Rytov *et al.* (1989), Chap. 4.

To simplify the look of this equation, two new quantities are introduced,

$$\alpha=\kappa(q_j+Q)-k_j-K=-K-\frac{q_jQ}{k_0}-\frac{Q^2}{2k_0}, \tag{30}$$

$$\xi=x-x_1. \tag{31}$$

The quantity α is the deviation from resonance, while ξ is the distance in range between the paired interactions. Assuming that x is beyond the initial transient, the lower limit of the x_1 integral can be replaced by $-\infty$, so that

$$A_j^{\text{Markov}}=-k_0^2\int_0^\infty d\xi\int dKdQ\frac{S(K,Q)}{2}e^{i\alpha\xi}. \tag{32}$$

The next step should be to interchange the orders of the integrations. However, the integral over ξ is divergent if that is done. In order to be allowed to interchange the orders, a trick common in quantum scattering theory is used. The integrand is multiplied by $e^{-\eta\xi}$, where η is a small positive number. The integrals can now be rigorously interchanged, and in the end η is set to 0 (as a limit). The result is

$$A_j^{\text{Markov}}=-k_0^2\int_0^\infty dKdQ\frac{S(K,Q)}{2}\frac{1}{\eta-i\alpha}. \tag{33}$$

To obtain the standard expression, $Q^2/2k_0$ is dropped in the expression for α; the justification is that the scattering angle is supposed to be very small compared to the aspect ratio of the ocean, according to Beran and McCoy (1974). With that approximation, α is an odd function of the pair K,Q, whereas the spectrum is even. Therefore, only the even part of $1/\eta-i\alpha$, namely $\eta/\eta^2+\alpha^2$, survives the integral. For small η, this is a delta function, multiplied by π.

$$A_j^{\text{Markov}}=-k_0^2\int dKdQ\frac{S(K,Q)}{2}\pi\delta\left(K+\frac{q_jQ}{k_0}\right). \tag{34}$$

The oceanic correlation function integrated along a straight line with slope s is

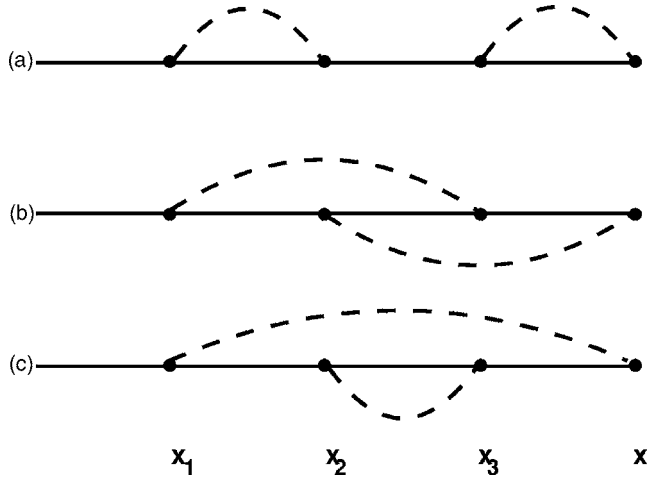

FIG. 7. The three ways of pairing four interactions. The fourth moment of the internal wave field can be expressed in terms of correlated pairs because of the assumption that it comprises a zero mean Gaussian process. These diagrams can be interpreted as parts of the contribution from the medium fourth moment, using the same interpretation as in Fig. 6. Integrations over x_1, x_2, x_3 are understood with $x_1<x_2<x_3<x$.

$$\langle\mu^2\rangle L_p = \int_{-\infty}^{\infty} dx\langle\mu(0,0)\mu(x,z=sx)\rangle$$
$$= \int_{-\infty}^{\infty} dx \int dKdQ\frac{S(K,Q)}{2}e^{i(Kx+Qsx)}$$
$$= \int dKdQ\frac{S(K,Q)}{2}2\pi\delta(K+sQ). \tag{35}$$

Therefore

$$A_j^{\text{Markov}} = \frac{-k_0^2\langle\mu^2\rangle L_p(s_j)}{2}, \tag{36}$$

where $L_p(s_j)$ is evaluated along a line with slope

$$s_j = -\frac{q_j}{k_0}. \tag{37}$$

The narrow angle PE does not distinguish between $\sin\theta = q_j/k_0$ and $\tan\theta = q_j/k_j$. Thus L_p is evaluated in the direction of the propagation of the acoustic wave vector.

A_j^{Markov} turns out to be real and negative, giving a loss of coherence. If the $Q^2/2k_0$ had been retained, there would also have been a small wave number shift from the imaginary part (which is the subject of another paper by Codona *et al.*, 1985).

Now we turn to the fourth order term. The four interactions happen at ranges x_1, x_2, x_3, and x, with $x_1<x_2<x_3<x$. For a Gaussian process, the ensemble average of a product of interactions is the sum of product of correlations from the different ways of pairing up the interactions. These are shown in Fig. 7. Their contributions as calculated by solving the moment equation is shown in Fig. 8; each pair is separate from the others. One sees that the first way of pairing the interactions is correctly calculated in the Markov approximation. van Kampen's result [Eq. (33) of van Kampen, 1974] is that the next order term in A_j is the difference between the

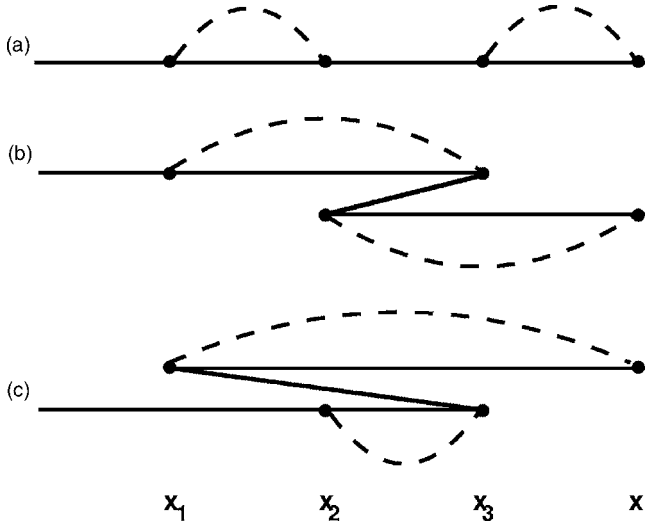

FIG. 8. A diagrammatic representation of how the three contributions of Fig. 7 occur in the solution, Eq. (39), of Eq. (18) with Eq. (29) (Fig. 6) for A_j. No interactions occur between a correlated pair. The correction to Eq. (29) is the difference between Figs. 7 and Fig. 8. The contribution a is correctly given, whereas b and c are different in Figs. 7 and 8. The diagonal lines represent "backward" propagation. For example, in Fig. 8(b) the factor is $e^{-ikj(x_3-x_2)}$. van Kampen gives a purely algebraic method of constructing the correction, so the diagrams should be taken as only interpretational, not as necessary for obtaining the expressions.

contributions correctly calculated, as shown in Figs. 7(b) and 7(c), and incorrectly calculated, as shown in Figs. 8(b) and 8(c).

In terms of the matrices, the correct ordering is

$$\int_{x_1<x_2<x_3<x} \langle i\Gamma(x)\exp(i\Lambda(x-x_3))i\Gamma(x_3)$$
$$\times\exp(i\Lambda(x_3-x_2))i\Gamma(x_2)\exp(i\Lambda(x_2-x_1))i\Gamma(x_1)\rangle$$
$$\times\exp(-i\Lambda(x-x_1))dx_1dx_2dx_3 \tag{38}$$

while the contribution as calculated by solving the moment equation is

$$\int_{x'<x} A_j^{\text{Markov}}(x)A_j^{\text{Markov}}(x')dx'. \tag{39}$$

Equation (28) contains A_j^{Markov} as an integral over range. Thus, Eq. (39) contains three range integrals. Choosing $x_1<x_2<x_3<x$ as the order of the variables, x' can either be x_3 or x_2. If x' is x_3, the integration variable in $A_j^{\text{Markov}}(x')$ can be either x_2 or x_1. These three possibilities are the three possibilities shown in Fig. 8. Each one corresponds to a way of pairing the four Γ's in Eq. (38), shown in Fig. 7.

The oceanic spectrum enters twice. We label the oceanic variables as K_1,Q_1 and K_2,Q_2. We define α and ξ variables,

$$\alpha_1 = \kappa(q_j+Q_1)-k_j-K_1 = -K_1-\frac{q_jQ_1}{k_0}-\frac{Q_1^2}{2k_0}, \tag{40}$$

$$\alpha_2 = \kappa(q_j+Q_2)-k_j-K_2 = -K_2-\frac{q_jQ_2}{k_0}-\frac{Q_2^2}{2k_0}, \tag{41}$$

$$\alpha_{12} = \kappa(q_j + Q_1 + Q_2) - k_j - K_1 = -K_1 - K_2 - \frac{q_j Q_1 + q_j Q_2}{k_0} - \frac{(Q_1^2 + Q_2)^2}{2k_0}, \tag{42}$$

$$\xi_1 = x_2 - x_1, \tag{43}$$

$$\xi_2 = x_3 - x_2, \tag{44}$$

$$\xi_3 = x - x_3. \tag{45}$$

Each of these four terms has the form [by analogy with Eq. (29)]

$$k_0^4 \int_0^\infty d\xi_1 \int_0^\infty d\xi_2 \int_0^\infty d\xi_3 \int dK_1 dQ_1 \frac{S(K_1,Q_1)}{2} \times \int dK_2 dQ_2 \frac{S(K_2,Q_2)}{2} e^{i\Psi}. \tag{46}$$

The phase Ψ is easily worked out to be

$$\Psi = \alpha_1\xi_1 + \alpha_{12}\xi_2 + \alpha_2\xi_3 \quad \text{for Fig. 7(b)}, \tag{47}$$

$$\Psi = \alpha_1\xi_1 + \alpha_{12}\xi_2 + \alpha_1\xi_3 \quad \text{for Fig. 7(c)}, \tag{48}$$

$$\Psi = \alpha_1\xi_1 + (\alpha_1 + \alpha_2)\xi_2 + \alpha_2\xi_3 \quad \text{for Fig. 8(b)}, \tag{49}$$

$$\Psi = \alpha_1\xi_1 + (\alpha_1 + \alpha_2)\xi_2 + \alpha_1\xi_3 \quad \text{for Fig. 8(c)}. \tag{50}$$

Note that the Fig. 8 contributions are related to the Fig. 7 contributions by replacing α_{12} with $\alpha_1 + \alpha_2$.

A factor $e^{-\eta(\xi_1+\xi_2+\xi_3)}$ is put in to allow the interchange of the order in which the integrals are carried out. The ξ integrals give

$$k_0^4 \int dK_1 dQ_1 \frac{S(K_1,Q_1)}{2} \int dK_2 dQ_2 \frac{S(K_2,Q_2)}{2} \times \frac{1}{\eta - i\alpha_1} \frac{1}{\eta - i\alpha_2} \frac{1}{\eta - i\alpha_{12}} \tag{51}$$

for Fig. 7(b) and

$$k_0^4 \int dK_1 dQ_1 \frac{S(K_1,Q_1)}{2} \int dK_2 dQ_2 \frac{S(K_2,Q_2)}{2} \times \left(\frac{1}{\eta - i\alpha_1}\right)^2 \frac{1}{\eta - i\alpha_{12}} \tag{52}$$

for Fig. 7(c).

This last contribution can be written symmetrically as half the way it is given in Eq. (52) plus half the form with the subscripts 1 and 2 interchanged. The two contributions add together to give

$$\frac{k_0^4}{2} \int dK_1 dQ_1 \frac{S(K_1,Q_1)}{2} \int dK_2 dQ_2 \frac{S(K_2,Q_2)}{2} \times \left(\frac{1}{\eta - i\alpha_1} + \frac{1}{\eta - i\alpha_2}\right)^2 \frac{1}{\eta - i\alpha_{12}}. \tag{53}$$

We subtract the Fig. 8 terms, obtained by replacing α_{12} with $\alpha_1 + \alpha_2$, to get

$$A_j^{(4)} = \frac{k_0^4}{2} \int dK_1 dQ_1 \frac{S(K_1,Q_1)}{2} \int dK_2 dQ_2 \frac{S(K_2,Q_2)}{2} \times \left(\frac{1}{\eta - i\alpha_1} + \frac{1}{\eta - i\alpha_2}\right)^2 \times \left(\frac{1}{\eta - i\alpha_{12}} - \frac{1}{\eta - i\alpha_1 - i\alpha_2}\right). \tag{54}$$

The inclusion of η in the denominators is crucial; however η's can be inserted or dropped at will in the numerators. Doing a little algebra, with numerator η's dropped, results in

$$A_j^{(4)} = \frac{k_0^4}{2} \int dK_1 dQ_1 \frac{S(K_1,Q_1)}{2} \int dK_2 dQ_2 \frac{S(K_2,Q_2)}{2} \times (i\alpha_{12} - i\alpha_1 - i\alpha_2) \times \left(\frac{1}{\eta - i\alpha_1} \frac{1}{\eta - i\alpha_2}\right)^2 \times \left(\frac{-i\alpha_1 - i\alpha_2}{\eta - i\alpha_{12}}\right). \tag{55}$$

From the definitions of the α's,

$$\alpha_{12} - \alpha_1 - \alpha_2 = \frac{Q_1 Q_2}{k_0}. \tag{56}$$

If the Beran and McCoy parameter is small, this difference is small relative to other terms that appear in the α's; $\alpha_{12} \approx \alpha_1 + \alpha_2$. Therefore, the last factor in Eq. (55) can be approximated by unity. With this approximation, the expression simplifies greatly,

$$A_j^{(4)} = \frac{ik_0^3}{2} I^2, \tag{57}$$

where

$$I = \int dK dQ \frac{S(K,Q)}{2} \frac{Q}{(\eta - i\alpha)^2}. \tag{58}$$

Making the same approximation as in the Markov term,

$$\alpha \approx -K - sQ \tag{59}$$

we find, by differentiating Eq. (33) with respect to s,

$$I = -\frac{i}{2} \frac{\partial \langle\mu\rangle^2 L_p}{\partial s}, \tag{60}$$

$\langle\mu^2\rangle$ does not depend on direction, so

$$I = -\frac{i}{2} \langle\mu^2\rangle \frac{\partial L_p}{\partial s}. \tag{61}$$

Setting everything together, and dividing by the Markov term,

$$\left| \frac{A_j^{(4)}}{A_j^{\text{Markov}}} \right| = \frac{k_0 \langle\mu^2\rangle}{4L_p} \left(\frac{\partial L_p}{\partial s}\right)^2. \tag{62}$$

The cancellation equation

$$\alpha_{12} - \alpha_1 - \alpha_2 = \frac{Q_1 Q_2}{k_0} \tag{63}$$

is crucial in obtaining this result. There is only one power of k_0 instead of two because of the k_0 in the denominator, and the product of the two Q's suppresses the large scale (small Q) part of the spectrum. The dominant part of α, given in Eq. (30), is the negative of the medium wave number in the direction of propagation. Thus, there is an effective cancellation if the right-hand side of Eq. (63) is smaller than this wave number. Taking reciprocals, inserting factors of 2π, and ignoring that two waves are involved, this condition is, up to a factor of order 1, $\Lambda_\perp^2 > \lambda\Lambda_\parallel$, where $\Lambda_\parallel$ and $\Lambda_\perp$ are the medium wavelengths along and transverse to the propagation direction, and λ is the acoustic wavelength. The right-hand side is recognized as (up to a factor) the square of the Fresnel zone for propagation over a distance $\Lambda_\parallel$. Thus, scales larger than that Fresnel zone are suppressed. For a single scale medium, $\Lambda_\parallel$ can be estimated as L_p. In that case, the dividing line between large and small scales is the Fresnel zone for propagating a distance L_p.

The correlation length L_p is an even function of the slope s. Therefore, I in Eq. (61) vanishes at $s=0$. This does not mean, of course, that the Markov approximation is perfect. The contribution that is higher order in the Beran-McCoy parameter has been dropped. However, even dropping the Beran-McCoy parameter, the expansion parameter is very unlikely to be zero. The term of sixth order in μ is presumably nonzero, and the expansion parameter could be estimated (if the sixth order term could be estimated) as the square root of the ratio of that term to the second order term. Just as the fourth order term, the sixth order term involves differences between the contribution to the propagation calculated correctly and that induced by lower orders. Thus, the cancellation of Eq. (63) still applies, and the expansion parameter will be similar to what we have obtained at nonzero slopes.

V. EVALUATION OF THE NEW PARAMETER FOR MATE

In preceding sections, we assumed homogeneity in the vertical and no sound channel. For the real world, these assumptions must be relaxed. With the assumption, L_P is to be evaluated along the direction of propagation of the mode. In the real world, the direction of the mode depends on depth. For the frequencies and range of MATE, the field near the ray connecting the source and receiver can be thought of as a plane wave travelling in the direction of the ray. Thus, evaluation of ϵ for MATE involves only the computation of the values of $\langle\mu^2\rangle$ and L_P along the ray from source to receiver. The modified parameter

$$\frac{k_0\langle\mu^2\rangle}{4L_p}\left(\frac{\partial L_p}{\partial \tan(\theta)}\right)^2 \tag{64}$$

must be evaluated using two adjacent rays so that the partial derivative with respect to direction can be evaluated holding the depth fixed; this precaution would be unnecessary in the vertically homogeneous case.

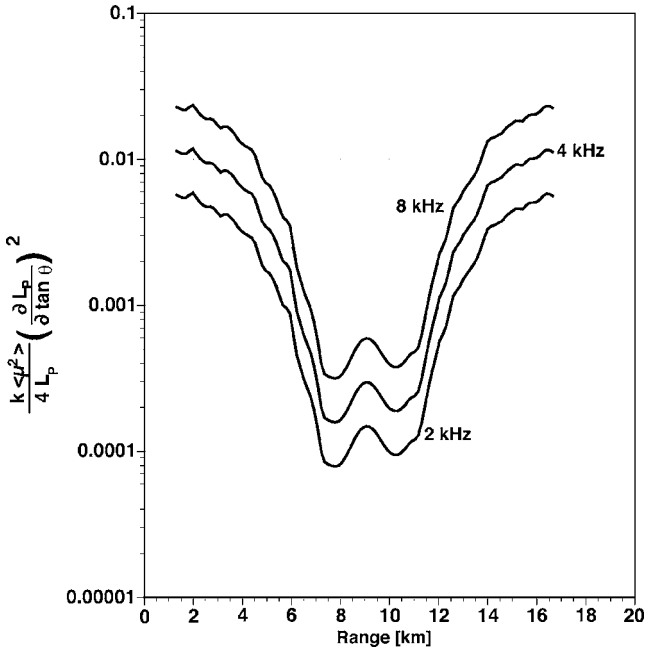

FIG. 9. Estimate of the modified expansion parameter computed from the MATE oceanographic data for the lower path. These values are below 1, so the Markov approximation is valid. The vanishing at the center of the path is not to be understood as the Markov approximation being better there. Rather, the fourth order happens to have a factor multiplying the expansion parameter that is small there.

The ray traces were carried out using the MATE average sound speed profile. Figure 9 shows the results of this evaluation for 2, 4, and 8 kHz. Clearly, the modified expansion parameter is less than one over the entire ray. Hence, one would expect the Markov approximation to hold and the basic conditions for the Macaskill and Ewart predictions are validated.

VI. DISCUSSION AND CONCLUSIONS

The theoretical considerations have involved the first moment, whereas the experimental results of interest are higher moments, especially moments insensitive to wander (i.e., those invariant under multiplying the amplitude by $e^{-i\omega T}$ for an arbitrary time shift T). Such moments include the average intensity, the intensity variance, and other second and fourth moments at a single frequency. The intensity statistics at short to medium ranges are insensitive to the larger scales of the medium. Rytov *et al.* (1989) point out that this means Eq. (2) is not relevant to intensity statistics, because the ϵ defined there depends almost exclusively on the large scales.

As a simple example, consider the vertical correlation function of the received signal. If the separation of the assumed receivers is small, the result is dominated by small separations at all positions between the source and receiver. The interaction depends on the sound speed difference between the two points (the structure function). This sound speed difference is very insensitive to the large scales (which are nearly equal at the two points), so only small scales contribute. The analog of $k^2\langle\mu^2\rangle L_p^2/4$ for this moment is then similar in value to the new expansion parameter for the first moment. If, on the other hand, the separation is large, not

only is the moment very small, but for the same reasons as for the first moment, the large scales are correctly handled by the Markov approximation. Therefore, the improved expansion parameter is also appropriate in that case. Thus, it is reasonable to interpret the expansion parameter derived for the first moment as applying to all moments, and the formalism for the fourth moment, discussed in Henyey and Macaskill (1996), can be appropriately applied in the successful predictions of the MATE intensity correlations in Macaskill and Ewart (1996).

It can also be seen that the new parameter is also a necessary condition (except for accidental cancellations in integrating the moment equation) for the validity of the general Markov approximation. This is because it is actually the ratio of the lowest order non-Markov term to the Markov term. For the specific Markov approximations used in practice, other conditions are required. In particular the Beran and McCoy parameter must be small, and there is a range limit (which has not been quantified) due to the strong angular dependence of L_p.

The application of the first moment expansion parameter to the higher moments has been justified here by a plausibility argument. A more rigorous demonstration would be desirable, to make sure that the division between large and small scales is the same for all moments. We have left out consideration of the upper turning point in ducted oceanic propagation. Our calculation with Fourier modes is inappropriate for the upper path; both the important acoustic modes and the internal wave modes are close to turning points. It is clear that the Markov approximation for the upper path is unlikely to be valid at the same frequencies for which the lower path Markov approximation works. Indeed, (unpublished calculations by Ballard, Ewart, and Uscinski) the moment equations have not been successful when applied to the upper path at MATE. The issue of validity of Markov is very important both to this upper path, and to our understanding of long range (megameter) propagation that involves multiple upper turning points.

We have found that the Markov approximation cannot be taken for granted. An improved parameter has been found to assess its validity, when the standard parameter suggests that it might not be valid. In most applications of the moment equation or path integrals there are other approximations made, whose validity is in even more question than the one we have addressed. All of the approximations need to be addressed in order to really have confidence that a prediction is reliable.

ACKNOWLEDGMENTS

The authors thank Barry Uscinski for conversations and Darrell Jackson for suggestions on improving the paper. This work was supported by the Office of Naval Research.

Bell, B., and Ewart, T. E. (**1986**). "Separating multipaths by global optimization of a multidimensional matched filter," IEEE Trans. Acoust., Speech, Signal Process. **ASSP-34**, 1029–1037.

Beran, M. J., and McCoy, J. J. (**1974**). "Propagation through an anisotropic random medium," J. Math. Phys. **15**, 1901–1912.

Codona, J. L., Creamer, D. B., Flatté, S. M., Frehlich, R. G., and Henyey, F. S. (**1985**). "Average arrival time of wave pulses through continuous random media," Phys. Rev. Lett. **55**, 9–11.

Codona, J. L., Creamer, D. B., Flatté, S. M., Frehlich, R. G., and Henyey, F. S. (**1986**). "Moment-equation and path-integral techniques for wave propagation in random media," J. Math. Phys. **27**, 171–177.

Dashen, R. (**1979**). "Path integrals for waves in random media," J. Math. Phys. **20**, 894–920.

Desaubies, Y. J. F. (**1976**). "Acoustic-phase fluctuations induced by internal waves in the ocean," J. Acoust. Soc. Am. **60**, 795–800.

Desaubies, Y. J. F. (**1978**). "On the scattering of sound by internal waves in the ocean," J. Acoust. Soc. Am. **64**, 1460–1469.

Ewart, T. E. (**1976**). "Acoustic fluctuations in the open ocean—a measurement using a fixed refracted path," J. Acoust. Soc. Am. **60**, 46–59.

Ewart, T. E., Macaskill, C., and Uscinski, B. J. (**1983**). "Intensity fluctuations. Part II: Comparison with the Cobb experiment," J. Acoust. Soc. Am. **74**, 1484–1499.

Ewart, T. E., and Reynolds, S. A. (**1984**). "The mid-ocean acoustic transmission experiment—MATE," J. Acoust. Soc. Am. **75**, 785–802.

Flatté, S. M., Dashen, R., Munk, W. H., Watson, K. M., and Zachariasen, F. (**1979**). *Sound Transmission through a Fluctuating Ocean* (Cambridge University Press, Cambridge).

Flatté, S. M. (**1983**). "Wave propagation through random media: Contributions from ocean acoustics," Proc. IEEE **71**, 1267–1294.

Frankignoul, C., and Joyce, T. M. (**1979**). "On the internal wave variability during the internal wave experiment (IWEX)," J. Geophys. Res. **84**, 769–776.

Henyey, F., and Macaskill, C. (**1996**). "Sound through the internal wave field," in *Stochastic Modelling in Physical Oceanography*, edited by R. J. Adler, P. Müller, and B. L. Rozovskii (Birkhäuser, Boston), p. 141—184.

Levine, M. D., and Irish, J. D. (**1981**). "A statistical description of temperature fine structure in the presence of internal waves," J. Phys. Oceanogr. **11**, 676–691.

Levine, M. D., Irish, J. D., Ewart, T. E., and Reynolds, S. A. (**1986**). "Simultaneous spatial and temporal measurements of the internal wave field during MATE," J. Geophys. Res. **91**, 9709–9719.

Macaskill, C., and Ewart, T. E. (**1996**). "Numerical solution of the fourth moment equation for acoustic intensity correlations and comparison with the mid-ocean acoustic transmission experiment," J. Acoust. Soc. Am. **99**, 1419–1429.

Munk, W. H., and Zachariasen, F. (**1976**). "Sound propagation through a fluctuating stratified ocean—theory and observation," J. Acoust. Soc. Am. **59**, 818–838.

Reynolds, S. A., Flatté, S. M., Dashen, R., Buehler, B., and Maciejewski, P. (**1985**). "AFAR measurements of acoustic mutual coherence functions of time and frequency," J. Acoust. Soc. Am. **77**, 1723–1731.

Rytov, S. M., Kravtsov, Yu. A., and Tatarskii, V. I. (**1989**). *Principles of Statistical Radiophysics 4 Wave Propagation Through Random Media* (Springer-Verlag, Berlin).

Shishov, V. I. (**1968**). "Theory of wave propagation in random media," Izv. Vyssh. Uchebn. Zaved., Radiofiz. **11**, 866–875.

Tappert, F. D., and Hardin, R. H. (1973). "A synopsis of the AESD workshop on acoustic modeling by non-ray tracing techniques," AESD Tech. Note TN 73-05.

Uscinski, B. J. (**1977**). *The Elements of Wave Propagation in Random Media* (McGraw-Hill, New York).

van Kampen, N. G. (**1974**). "A cumulant expansion for stochastic linear differential equations. I," Physica (Utrecht) (Utrecht) **74**, 215–238.

van Kampen, N. G. (**1992**). *Stochastic Processes in Physics and Chemistry*, 2nd ed. (Elsevier, Amsterdam), Chap. XVI.

Improved parameterization of Antarctic krill target strength models

Gareth L. Lawson,[a] Peter H. Wiebe, and Carin J. Ashjian
Biology Department, Woods Hole Oceanographic Institution, Woods Hole, Massachusetts 02543

Dezhang Chu and Timothy K. Stanton
Applied Ocean Physics and Engineering Department, Woods Hole Oceanographic Institution, Woods Hole, Massachusetts 02543

(Received 20 April 2005; revised 31 October 2005; accepted 2 November 2005)

There are historical discrepancies between empirical observations of Antarctic krill target strength and predictions using theoretical scattering models. These differences are addressed through improved understanding of key model parameters. The scattering process was modeled using the distorted-wave Born approximation, representing the shape of the animal as a bent and tapered cylinder. Recently published length-based regressions were used to constrain the sound speed and density contrasts between the animal and the surrounding seawater, rather than the earlier approach of using single values for all lengths. To constrain the parameter governing the orientation of the animal relative to the incident acoustic wave, direct measurements of the orientation of krill *in situ* were made with a video plankton recorder. In contrast to previous indirect and aquarium-based observations, krill were observed to orient themselves mostly horizontally. Averaging predicted scattering over the measured distribution of orientations resulted in predictions of target strength consistent with *in situ* measurements of target strength of large krill (mean length 40–43 mm) at four frequencies (43–420 kHz), but smaller than expected under the semi-empirical model traditionally used to estimate krill target strength. [DOI: 10.1121/1.2141229]

PACS number(s): 43.30.Sf, 43.20.Fn, 43.30.Ft [KGF] Pages: 232–242

I. INTRODUCTION

The Antarctic krill, *Euphausia superba* (henceforth referred to as "krill"), is a key species of marine zooplankton linking primary producers and higher predators in the Southern Ocean (Laws, 1985) and is also the subject of a commercial fishery (Ichii, 2000). Abundance surveys for krill stock assessments and ecological studies typically employ acoustic techniques, as acoustics offer the advantage of continuous surveying over large areas in a short period of time. In order to relate acoustic measurements of echo energy to biological quantities like absolute abundance, however, it is critical to understand the efficiency with which the krill scatter sound, expressed in terms of their target strength. The present work seeks to address certain discrepancies that have resulted between theoretical and empirical approaches to understanding krill target strength.

Most modern acoustic surveys for krill, including those conducted by the international Committee for the Conservation of Antarctic Marine Living Resources (CCAMLR; SC-CAMLR, 1991), employ the semi-empirical target strength model of Greene *et al.* (1991). This model relates target strength at the common survey frequency of 120 kHz linearly to the logarithm of krill length and was derived on a theoretical basis from empirical observations at 420 kHz of a variety of crustacean taxa in an enclosure (Greene *et al.*, 1989; Wiebe *et al.*, 1990). Measurements of Antarctic krill swimming freely in an enclosure (Foote *et al.*, 1990) and *in situ* observations (Hewitt and Demer, 1991) have yielded estimates of krill target strength consistent with the Greene *et al.* (1991) model.

Substantial progress has been made in the theoretical, physics-based modeling of the target strength of fluidlike crustacean zooplankton such as krill (reviewed in Stanton and Chu, 2000). State-of-the-art models employ the distorted-wave Born approximation (DWBA) to estimate the scattering using a simplified description of the shape of the animal. Such an approach accounts for the fact that scattering is a complicated function of the animal's length, shape, orientation, and acoustic material properties, as well as the frequency being used. In the case of euphausiids (the order encompassing Antarctic krill), the shape has typically been modeled as some kind of deformed cylinder. Scattering is integrated along the lengthwise axis of the cylinder, taking into account the phase shift arising from deformation of this axis due to curvature and variations in cross-sectional radius (Chu *et al.*, 1993; Stanton *et al.*, 1993; McGehee *et al.*, 1998; Stanton *et al.*, 1998; Demer and Conti, 2003). Lavery *et al.* (2002) employed the DWBA to estimate scattering as the volume integral over a fully 3-D representation of the animal derived from computerized tomography. Target strengths predicted by these theoretical models have been verified by tank observations of individual tethered animals at a variety of frequencies, animal sizes, and angles of orientation relative to the incident acoustic wave.

[a]Electronic mail: glawson@whoi.edu

Although theoretical predictions are mostly consistent with tank-based measurements where the exact size, shape, and angle of orientation of the animal are known, problems have arisen in parameterizing the models in such a way that their predictions are consistent with the Greene *et al.* (1991) relationship, while keeping the parameters within biologically plausible ranges (Demer and Conti, 2003, 2005). In particular, the greatest uncertainty has surrounded the parameters governing the orientation of the animal and its acoustic material properties. As an individual krill goes from a horizontal to vertical orientation, its target strength as observed by a vertically aimed echosounder decreases by two or more orders of magnitude (Stanton *et al.*, 1998; McGehee *et al.*, 1998). Similarly, it has long been recognized that for bodies filled with fluid similar to the surrounding medium, target strength is highly sensitive to small changes in the contrasts between the sound speed and density within the body and those of the medium (i.e., the "acoustic material properties") (Anderson, 1950; Johnson, 1977; Holliday and Pieper, 1980; Greenlaw and Johnson, 1982; Chu *et al.*, 2000).

In order to make field-applicable predictions of target strength, it is thus highly important to constrain properly these parameters governing orientation and acoustic material properties, but very little information exists concerning their natural distribution. Chu *et al.* (1993) and Demer and Conti (2005) have estimated krill orientation indirectly from measurements of volume backscattering and target strength, respectively, but no direct and quantitative measurements exist of krill *in situ* orientation. Acoustic material properties are typically assumed to be uniform within the animal's body and constant with respect to animal length, although Chu and Wiebe (2005) have shown that in the Antarctic krill both the sound speed and density contrasts are significantly related to length. When McGehee *et al.* (1998) used the then best-available observations made by Kils (1981) of krill orientation in an aquarium and by Foote (1990) of krill acoustic material properties to parameterize a DWBA-based scattering model, their predictions of krill target strength were ca. 6 dB lower than predicted by the Greene *et al.* (1991) semi-empirical relationship.

Motivated by these discrepancies between the predictions of theoretical scattering models and the Greene *et al.* relationship, we seek to improve model parameterization. Backscattering from individual krill is predicted using the DWBA, representing the shape of the animal as a uniformly bent and smoothly tapered cylinder. Improved parameterization is achieved by making direct observations of krill *in situ* orientation with a video plankton recorder (VPR; Davis *et al.*, 1992). In contrast to previous studies where single values of the acoustic material properties have been used for all lengths of krill, we also apply Chu and Wiebe's (2005) length-based regressions of krill sound speed and density contrasts. We further assess the validity of this parameterization by making *in situ* observations of krill target strength at four frequencies.

II. METHODS

A. Theoretical krill scattering model

The scattering model employed here is the DWBA-based deformed cylinder model with homogeneous acoustic material properties first used by Chu *et al.* (1993) and Stanton *et al.* (1993) and expressed more explicitly in Stanton *et al.* (1998). The general formulation of the DWBA gives the far-field scattering amplitude in the backscatter direction (f_{bs}) for a body of finite-length as an integral over the body's volume (Morse and Ingard, 1968). The DWBA assumes that the contrasts between the speed of sound and density within the body and the surrounding seawater are small (i.e., weakly scattering bodies) and that the body has negligible elastic properties, thereby not supporting shear waves (i.e., fluid-like).

Under the assumption that the shape of the animal can be approximated as a deformed cylinder (elongated and circular in cross section), Stanton *et al.* (1998) showed that the volume integral of the general DWBA formulation can be reduced to a line integral along the cylinder's lengthwise axis. Various kinds of cylinders have been used to represent the krill's irregular shape, ranging through a progression of complexity including straight, smoothly tapered, uniformly bent, and randomly rough cylinders, as well as the case where nonuniform variations in cross-sectional radius are used to represent appendages (Stanton and Chu, 2000). We choose to model the krill's shape as a uniformly bent and smoothly tapered cylinder. This representation only coarsely captures the actual shape of the animal; additional justification for not using a higher resolution shape description is provided in the discussion.

In the case of a uniformly bent cylinder with radius of curvature ρ_c, Stanton *et al.* (1998) give the expression for the scattering amplitude as

$$f_{\mathrm{bs}} = \frac{k_1 \rho_c}{4} e^{i2k_2\rho_c} \int a(\gamma_\kappa - \gamma_\rho) e^{-i2k_2\rho_c \cos\beta_{\mathrm{tilt}}} \times \frac{J_1(2k_2 a \cos\beta_{\mathrm{tilt}})}{\cos\beta_{\mathrm{tilt}}} \, d\beta_{\mathrm{tilt}}, \quad (1)$$

where k is the acoustic wave number in the surrounding seawater (subscript 1) and the body (subscript 2); a is the cross-sectional radius of the cylinder; γ_κ and γ_ρ are related to the densities (ρ) and sound speeds (c) of the surrounding seawater (1) and the body (2) following $\gamma_\kappa = (\kappa_2 - \kappa_1)/\kappa_1$, $\gamma_\rho = (\rho_2 - \rho_1)/\rho_2$, and $\kappa = (\rho c^2)^{-1}$, where κ is the compressibility; J_1 is the Bessel function of the first kind of order one; and β_{tilt} is the angle between the incident wave ($\mathbf{k}_i$) and the cross section of the cylinder at each point along its axis (Stanton *et al.*, 1998).

To accommodate further the actual shape of the krill, the ends of the cylinder are tapered by making the radius a function of position along the lengthwise axis (z):

$$a(z) = a_0 \sqrt{1 - \left(\frac{z}{L/2}\right)^T}, \quad (2)$$

where a_0 is the radius of the cylinder at its mid-point, T is a parameter controlling how quickly the cylinder tapers, and L

TABLE I. Definitions of standard lengths (SL) for krill, from Mauchline (1980). Different lengths were required for the various purposes of the present study due to differences in how previous workers have defined krill length.

Name	Definition	Use in the present work	Relation to SL3
SL 1	Anterior tip of rostrum to posterior end of uropods	Length used in sound speed and density contrast regression equations	$1.236 \times$ SL3
SL 2	Anterior of eye to end of sixth abdominal segment	Length of the equivalent cylinder used to represent the krill in modeling target strength	$1.069 \times$ SL3
SL 3	Posterior base of eye stalk to end of sixth abdominal segment	Length measured in silhouette analysis of MOCNESS catches	…

is the cylinder's length with $z=0$ the animal's midpoint (Chu *et al.*, 1993, who set T=10).

Approximate solutions can be found for limiting expressions of Eq. (1) with respect to wavelength, but, more typically, the cylinder is discretized into a series of thin disk-shaped differential elements and the integral performed numerically.

The differential backscattering cross section (σ_{bs}) is defined as the square of the magnitude of the backscattering amplitude, and target strength (TS) is simply σ_{bs} in decibel form (dB relative to 1 m^2):

$$\mathrm{TS} = 10 \log \sigma_{bs} = 10 \log |f_{bs}|^2. \quad (3)$$

B. Model parameterization

Predictions of target strength using the above model are clearly dependent on a variety of parameters, including those governing the animal's shape (L, a_0, T, and ρ_c), its acoustic material properties (γ_κ and γ_ρ), and its orientation (β_{tilt}). As indicated above, the parameters γ_κ and γ_ρ are themselves functions of the sound speed and density contrasts between the animal and the surrounding medium ($h=c_2/c_1$ and $g=\rho_2/\rho_1$, respectively). The emphasis here is on properly constraining the key parameters of krill orientation and acoustic material properties.

Target strength was therefore predicted on the basis of various combinations of orientation and sound speed and density contrast values. Predictions at a frequency of 120 kHz were made for cylinder lengths of 4 to 70 mm, in 1-mm increments. Predictions were also made holding length constant at 43.3 mm, for frequencies of 5–500 kHz, in 5-kHz increments.

The equivalent cylinder used to represent the krill's shape was defined on the basis of the animal's average radius (a_0) and length (L), defined as standard length 2 of Mauchline (1980) (Table I), following the approach of Stanton and Chu (2000). Other than length, the shape parameters were held constant for all simulations: a slight taper parameter T of 10 was used, and the cross-sectional radius of the cylinder at its mid-section was related to length via $a_0=L/18.4$. This constant was derived by measuring the length and average radius (averaged over ten measurements along the animal's length) of 50 preserved krill captured with nets (see below). The radius of curvature was taken to be $\rho_c=3L$, based on measurements of 50 randomly chosen krill observed with the video plankton recorder, but note that backscattering cross sections averaged over a range of angles of orientation (as is done here, see below) are mostly independent of the cylinder's bend, for $\rho_c \geq 2L$ (Stanton *et al.*, 1993).

1. Sound speed and density contrasts

Chu and Wiebe (2005) showed that the sound speed and density contrasts of Antarctic krill are significantly related to animal length. The g and h values used to parameterize the scattering model were therefore estimated from their regression equations:

$$g = 5.439 \times 10^{-4} L(\mathrm{mm}) + 1.002, \quad (4)$$

$$h = 4.981 \times 10^{-4} L(\mathrm{mm}) + 1.009, \quad (5)$$

where length (L) is standard length 1 (Table I). The acoustic material properties were assumed not to vary within the animal, and so single values for each of these parameters were calculated for each krill length examined. For comparison, predictions of target strength were also made based on the length-invariant krill material property measurements of Foote (1990) ($g=1.0357, h=1.0279$). The minimum size of animal examined by Chu and Wiebe (2005) was 25 mm. Extrapolating for lengths smaller than this increasingly produced implausibly small estimates of g and h. The material properties estimated from the regressions for a 25-mm-long animal therefore were used for lengths smaller than 25 mm. Note that the Chu and Wiebe (2005) measurements were made on krill collected in the same study area and at the same time of year (austral fall) as the empirical observations of krill orientation and target strength described below, but a year later (2002).

2. Animal orientation

Equation (1) allows the scattering amplitude to be predicted for an individual animal of a given length at a single angle of orientation (θ), defined as the angle between the line joining the bent cylinder's ends and the horizontal plane. Assuming a vertically aimed echosounder, an animal oriented horizontally in the water ($\theta=0^\circ$) is at normal acoustic incidence. At the cylinder's mid-point, the relationship between β_{tilt} and θ is simply $\beta_{tilt}=\theta$, while elsewhere along the cylinder's axis, it varies due to the cylinder's curvature.

In linear echo-integration theory, the echoes from individual animals within the acoustic beam are assumed to sum incoherently to yield measurements of volume backscattering. In order to simulate the averaging over ensembles of many individuals that occurs during echo-integration sur-

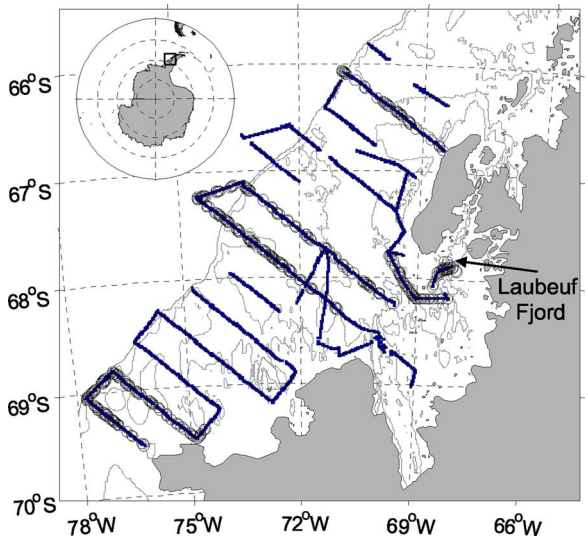

FIG. 1. Study site, covering a region of the continental shelf west of the Western Antarctic Peninsula. Black lines show survey transects along which acoustic, video, and environmental data were collected. Circles indicate the subsections of these lines where video images of krill were captured and analyzed. Contours show the 450- and 1000-m isobaths. Laubeuf Fjord is the region where direct measurements were made of krill target strength and where two net tows sampled acoustically identified krill patches.

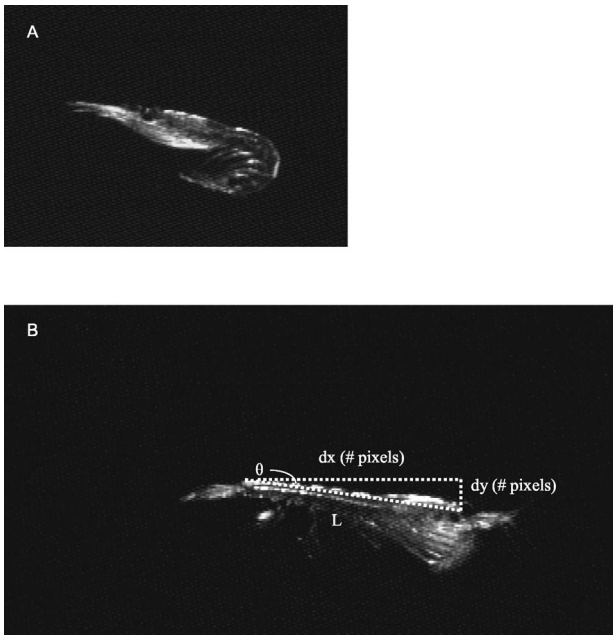

FIG. 2. Representative krill images. (a) A typical krill exhibiting the tail-flip escape response. (b) A krill of length 11.1 mm oriented at −9.4° relative to the horizontal. The horizontal (dx) and vertical (dy) excursions from the animal's tail to its eye were measured in pixels. Knowing the size of the field of view in both pixels and distance, the animal's orientation relative to horizontal (θ) and length (L) were then calculated.

veys, average scattering for each krill length investigated was calculated over a probability density function of angles of orientation $[w(\theta)]$, following

$$\bar{\sigma}_{\mathrm{bs}} = \int_{\theta} \sigma_{\mathrm{bs}}(\theta) w(\theta)\, \mathrm{d}\theta. \tag{6}$$

Average target strength was then defined as the decibel form of $\bar{\sigma}_{\mathrm{bs}}$.

Average scattering was calculated in this way for the observed probability density function of angles of orientation described below. For comparison, average scattering was also calculated over the normal distribution of orientations observed in an aquarium by Kils (1981), $N(\bar{\theta}, \sigma_{\theta}) = N(45.3^{\circ}, 30.4^{\circ})$, where $\bar{\theta}$ is the mean angle of orientation and σ_{θ} is the associated standard deviation. Similarly, for some comparisons, a length-averaged predicted scattering was calculated at each length under investigation by averaging over a distribution of neighboring animal lengths.

C. Empirical approach

Video, acoustic, and environmental data were collected from the RVIB *N.B. Palmer* in April–June of 2001, as part of the U.S. Southern Ocean GLOBal ECosystems Dynamics program (GLOBEC; Hofmann *et al.*, 2002). The study site was a continental shelf region west of the Western Antarctic Peninsula (Fig. 1). All data were collected with the BIo-Optical Multi-frequency Acoustical and Physical Environmental Recorder (BIOMAPER-II; Wiebe *et al.*, 2002), a towed system consisting of a multi-frequency echosounder with both up- and down-looking transducers, a video plankton recorder (VPR), and an environmental sensor package (conductivity, temperature, and depth sensor; fluorometer; transmissometer). The BIOMAPER-II was "towyoed" obliquely up and down through the water column between 20- and 300-m depth as the vessel proceeded along the track-line between stations at 4 to 6 knots, and surveying was conducted around the clock. Data were collected along 13 transect lines running across the continental shelf and perpendicular to the Peninsula coastline; subsections of these lines were selected for analysis of krill orientation (Fig. 1).

1. Measuring the in situ orientation of krill

Measurements of krill *in situ* orientation were made directly from still digital images captured from video collected with the VPR, in a similar manner to Benfield *et al.* (2000). The VPR consisted of a camera and 16-W strobe mounted on the towbody forward of the tow point, separated by 0.5 m, and aimed towards one another and perpendicular to the direction of the body's motion. The field of view of the camera was calibrated using a translucent grid placed in the center of focus and was found to be 31×24.5 mm (width by height). The camera sampled at a rate of 60 Hz, synchronized to the strobe. Video fields were time stamped and digitized at a resolution of 640 by 207 pixels. Regions of each field that were in focus were automatically extracted and saved as tagged image file format (tif) images [see Davis *et al.* (1996) for additional details].

These images were then visually examined and only images that were definitely krill, where the animal's whole body was in the frame and the image was in focus, were used for further analysis. In response to vigorous disturbances, krill are known to perform a rapid tail-flip response (O'Brien, 1987). Animals performing such a tail-flip often were captured in video images [Fig. 2(a)]; such images were excluded from analysis.

For the remaining images, the horizontal (dx) and verti-

cal (dy) excursions in pixels from the tail of each krill to its eye were measured [Fig. 2(b)] and the animal's angle of orientation (θ) calculated as

$$\theta = \tan^{-1}\left(dy \frac{\text{fov height mm}}{\text{fov height pixels}} \Big/ dx \frac{\text{fov width mm}}{\text{fov width pixels}} \right), \quad (7)$$

where fov denotes the field of view. Length (L) was calculated via the Pythagorean theorem. An animal oriented perfectly horizontal was defined as being at an angle of 0° and one oriented belly-up as 180°, with positive angles indicating a head upwards tilt.

In order to use the horizontal and vertical extent of the animal from the image to calculate orientation relative to the horizontal, only images where the krill was perpendicular to the direction faced by the camera, and where the animal was in side-view, were analyzed (Benfield *et al.*, 2000). Identifying animals in side-view was done by looking for overlap of the eyes and inspecting the legs. Determining whether animals were plane to the camera was done by visually assessing the ratio of the vertical to horizontal extent of different segments of the animal.

To confirm that the detection and extraction of krill images by the VPR system were not biased against any particular angles of orientation due to insufficient illumination or focus level, segments of the raw videotapes were examined and the intensity and focus level of extracted krill images were analyzed in relation to the measured angle of orientation. No such bias was evident.

These measurements of krill orientation relative to the reference frame of the camera then had to be corrected for the pitch of the towed body in order to give the orientation relative to true horizontal. Data were collected on the pitch of the BIOMAPER-II every 5 s. To capture the gross behavior of the body while reducing error associated with high-frequency variability, the pitch data were subjected to a ten-point median filter. The filtered pitch observation made nearest in time to each image was then used to correct the measured angles of orientation. Corrections were also made based on interpolations of the raw and median-filtered pitch data, but the resulting distributions of orientations differed little from the previously described correction protocol. Since the body's pitch was especially variable when the vessel was on station, only images collected while the vessel was moving along survey transects were considered.

2. Measuring the in situ target strength of krill

Measurements of acoustic target strength were made at frequencies of 43, 120, 200, and 420 kHz, for comparison with theoretical predictions. All transducers were circular and split-beam, with 3° half-power beamwidths, other than the 7°-wide 43-kHz transducers. Each transducer was acoustically calibrated by the manufacturer (Hydroacoustic Technologies Inc., Seattle, WA, USA) prior to the cruise for source level, receive sensitivity, electro-mechanical "stiffness" (used to determine the position of a target within the split-beam), and transmit and receive beam patterns. An *in situ* calibration with a 38-mm tungsten carbide (6% cobalt) standard target also was performed during a cruise later that year. A 10-kHz bandwidth chirp pulse was used, with an effective pulse duration of 0.18 ms, and a ping rate of 0.3 pings s^{-1}. The system's dynamic range allowed target strength data to be collected between −100 and −40 dB. Profiles of noise levels (ship's noise, ambient noise, and system noise combined) versus depth were made *in situ* near the start of each cruise. Target strength measurements smaller than these noise levels were not recorded. Information on the target's location within the beam from split-beam analysis was used to remove the effects of beam pattern. In order to reduce the likelihood that multiple targets were mistakenly accepted as individual target strengths, only measurements made at a beam pattern factor (an indicator of off-axis position) between 0 and −3 dB, where the length of the received acoustic pulse at half-power was within 12.5% of the transmitted pulse, and at a range of less than 13 m (8 m for the 43 kHz) were included for analysis. Densities of krill larger than 15 mm in the aggregations were estimated to be ca. 5 individuals m^{-3}, and so the selected maximum ranges limited observations to cases where on average there was less than one animal per ensonified volume.

Measurements of target strength were made continuously over the course of the survey. Due to uncertainties in associating particular target strength observations with particular taxa, the focus here is on measurements made in Laubeuf Fjord at the end of the cruise (Fig. 1). Large patches of enhanced volume backscattering were present in this location (Lawson *et al.*, 2004; Wiebe *et al.*, 2004). Using a 1 -m^2 Multiple Opening/Closing Net and Environmental Sensing System (MOCNESS; Wiebe *et al.*, 1985), eight discrete samples were collected through these patches at depths between 50 and 100 m, at each of two closely separated tow locations within the fjord (tow numbers M21 and M22; Wiebe *et al.*, 2004). Both net catches and VPR observations confirmed that these acoustically observed patches were composed almost exclusively of krill. The net catches provide an estimate of the length distribution of the krill in these patches, allowing the observations of target strength to be associated with a particular length range of krill. Krill lengths were measured for an aliquot of each net sample using the silhouette method of Davis and Wiebe (1985) as standard length 3 and multiplied by constant scaling factors to arrive at the lengths used for modeling target strength and estimating g and h (Table I).

III. RESULTS

A. *In situ* observations of krill orientation

In total, the orientations of 972 individual krill were measured. The median and mean of the entire distribution of measured angles, for all lengths of krill observed combined, were −0.5° and 9.7°, respectively, with a standard deviation of 59.3° (Fig. 3). Defining the dominant mode as all observations between −100° and 100°, the median and mean of this mode were −3.4° and 0°, respectively, with a standard deviation of 27.3° (Fig. 3). Two smaller modes also were evident, centered near 140° and −160°.

Between day (0900–1500 h) and night (1700–0700 h), the central mode shifted from slightly above 0° to slightly below (t test for day/night differences $t=6.02$, $p<1\times10^{-8}$).

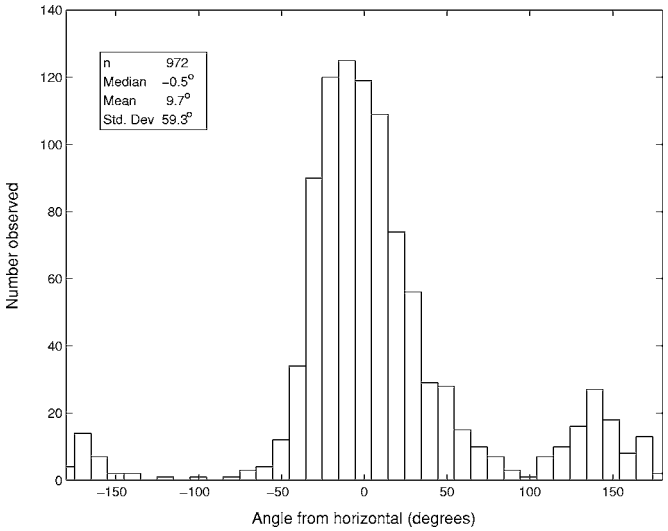

FIG. 3. Frequency distribution of angles of orientation for all lengths of krill combined, after correction for the pitch of the towed body. The median and mean of the entire distribution were −0.5° and 9.7°, respectively, with a standard deviation of 59.3°. Defining the central mode as all observations between −100° and 100°, the median and mean of this mode were −3.4° and 0°, respectively, with a standard deviation of 27.3°.

More observations were made by night (625) than by day (211), perhaps explaining why the distribution over all measurements was slightly negative. The distribution of observed orientations broadened with estimated krill length for lengths between 4 and 6 mm and then narrowed for greater lengths (Fig. 4). At estimated lengths greater than 6 mm, the smaller modes near 140° and −160° were no longer evident.

B. Scattering model predictions

Averaging scattering predictions from the DWBA-based deformed cylinder model over this VPR-derived distribution of angles of orientation following Eq. (6) resulted in higher average target strengths at 120 kHz relative to krill length than with the Kils (1981) distribution (Fig. 5). Although scattering is a complex function of animal length, shape, orientation, material properties, and frequency, we choose to plot target strength in relation to length (standard length 2) as this

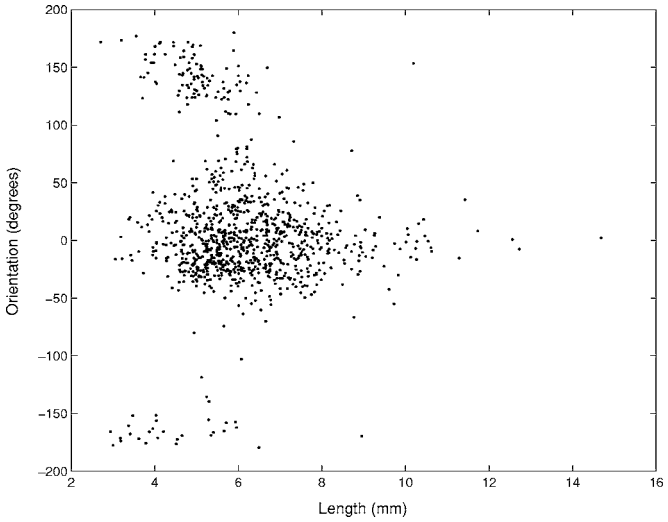

FIG. 4. Measured orientations in relation to krill length (mm).

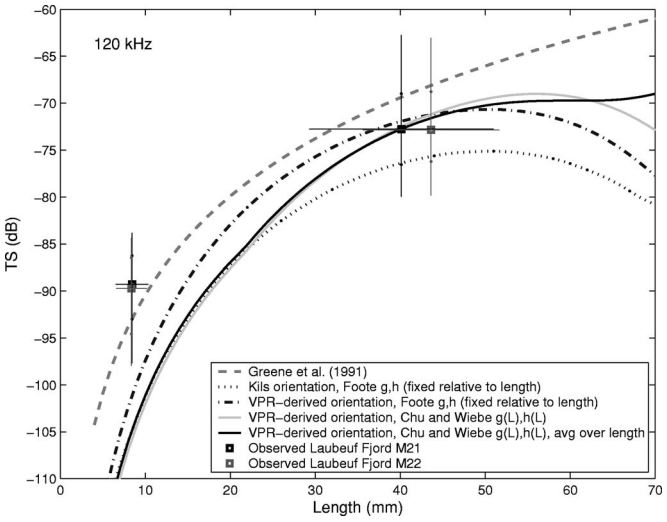

FIG. 5. Krill target strength ($\overline{TS}$) at 120 kHz in relation to length (mm; SL 2 in Table I), averaged over orientation. Dashed gray line shows the Greene *et al.* (1991) and SC-CCAMLR (1991) empirical regression line $TS = -127.45 + 34.85 \log_{10}$ (length in mm), where length is SL 1. All other lines indicate different parameterizations of the theoretical DWBA-based bent cylinder model, involving various combinations of the Foote (1990) length-invariant sound speed (h) and density (g) contrast measurements, the Chu and Wiebe (2005) g and h vs length (L) regressions, Kils' (1981) aquarium observations of krill orientation, and the present VPR-derived *in situ* orientation measurements. The solid black line indicates predicted scattering averaged over a distribution of lengths (standard deviation = 15% of the mean). Squares show median *in situ* measurements of krill target strength made in Laubeuf Fjord relative to the mean length of krill sampled at the same depths and locations as the two net tows (M21 and M22 as black and gray squares, respectively). Vertical lines show 10th and 90th percentiles of target strength measurements; dots show the 25th and 75th percentiles. Horizontal lines represent one standard deviation from the mean length.

is the parameter most familiar to biologists and most relevant to ecological studies. These predictions were made with Foote's (1990) single values for the sound speed and density contrast parameters for all krill lengths and with averaging only over orientation and not over length. Note also that the VPR-derived orientation distribution observed for krill of length 3–15 mm is being applied to a broader range of lengths (4–70 mm). No difference was evident in model predictions for the daytime distribution of orientations as compared to that measured at night (not shown).

When the length-based regressions of Chu and Wiebe (2005) were used to estimate the material properties for each length examined, and these parameters were used in combination with the VPR-derived distribution of orientations, modeled target strengths were smaller than with the Foote (1990) values for lengths below 43 mm but larger for animals above this length. To simulate further the averaging over ensembles of individuals that occurs during echo-integration surveys, length-averaged predicted scattering at each length under investigation was calculated over a normal distribution of neighboring animal lengths with a standard deviation of 15% of the mean (corresponding to the observed length variability from net tow M22). This resulted in a smoothing of the null in the target strength versus length relationship beyond 55 mm (Fig. 5).

In comparison to the Greene *et al.* (1991) semi-empirical target strength model, the present model parameterized with Chu and Wiebe's (2005) material property relationships and

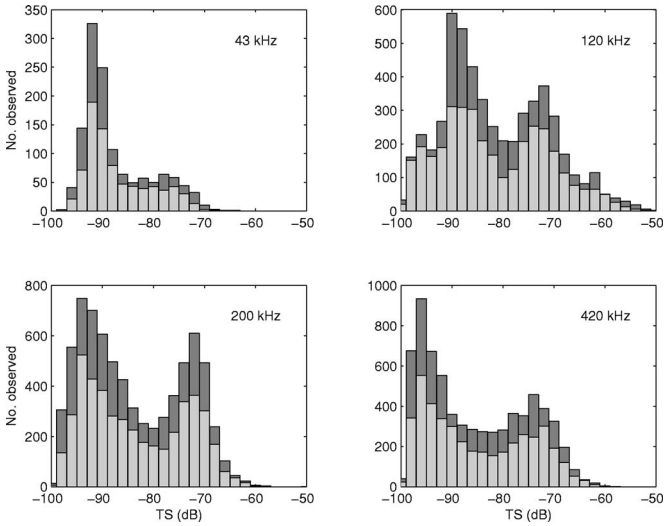

FIG. 6. Frequency distributions of *in situ* observed target strengths at 43, 120, 200, and 420 kHz measured at the two net tow locations in Laubeuf Fjord (M21 and M22 indicated by dark and light gray bars, respectively).

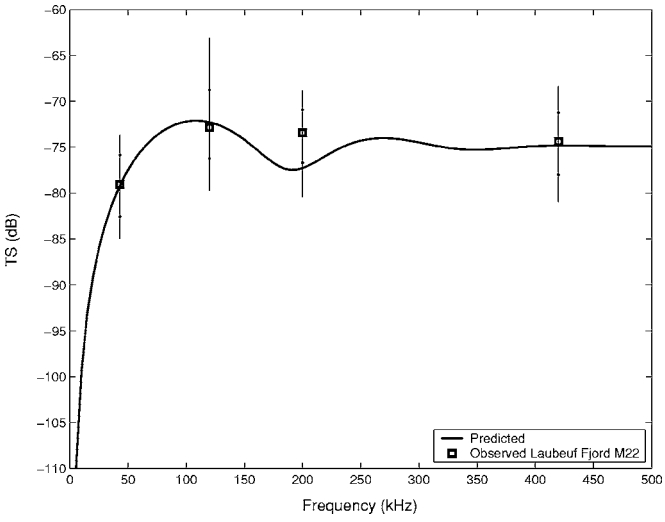

FIG. 7. Average target strength in relation to acoustic frequency (kHz). The solid line shows the predictions from the DWBA bent cylinder model parameterized with the Chu and Wiebe (2005) material property relationships and the VPR-derived orientation distribution. Predicted differential backscattering cross sections were averaged over a normal length distribution with mean 43.3 mm and a standard deviation=15% of the mean, corresponding to the observed length distribution from tow M22. Squares indicate median observed target strengths at the four BIOMAPER-II frequencies (43, 120, 200, and 420 kHz) in the vicinity of tow M22. Vertical lines show the 10th and 90th percentiles of observed target strength; dots show the 25th and 75th percentiles.

the VPR-derived orientation distribution resulted in lower target strength predictions for all krill lengths, particularly for animals smaller than 25 mm and larger than 55 mm.

C. Model verification with empirical *in situ* target strength observations

In situ observations of target strength within the acoustically observed patches in the vicinity of the two net tow locations in Laubeuf Fjord were bimodal at all four frequencies employed here (Fig. 6). The length distributions of krill sampled in the two net tows were similarly bimodal [see appendices in Wiebe *et al.* (2004)], allowing the small and large modes of the target strength distributions to be associated with the corresponding modes evident in the length distributions. The small and large modes of the length distribution from tow M21 had means of 8.4 and 40.5 mm, respectively, and for tow M22 were 8.4 and 43.3 mm. For both tows, the standard deviations of length were 22% and 15% of the mean, for the small and large modes, respectively.

Determining the central tendencies for the target strength modes was less straightforward, since the left-hand tail of the smaller mode was cut of by the system's threshold of −100 dB, while the right-hand tail of the smaller mode overlapped with the left-hand tail of the larger one (Fig. 6). Such issues of overlap and thresholding are well appreciated (Foote *et al.*, 1986). For simplicity, the krill target strengths were assumed to be Rayleigh distributed, even though it is known that this is often not the case (Stanton *et al.*, 2004). A Rayleigh distribution was fit to the smaller mode and used to extrapolate the target strength distributions below the −100 -dB threshold and above the point where overlap began with the larger mode (−83 dB at 43 kHz, and −80 dB at 120, 200, and 420 kHz); the larger mode distribution was similarly extrapolated below this point of overlap. Following extrapolation, the median of each target strength mode was calculated. The magnitude of the difference between the medians of the original truncated data and the extrapolated data never exceeded 1 dB.

After extrapolation, the median of the larger target strength mode at 120 kHz was found to be −72.8 dB in the vicinity of both net tow locations. This median target strength for the sampled length range is consistent with our newly parameterized target strength model (Fig. 5). We consider the median rather than the mean of the target strength distributions in order to reduce any potential bias towards higher values due to erroneous acceptance of multiple targets. The smaller mode of the 120-kHz target strength distribution was centered at −89.3 dB for tow M21 and −89.7 dB for tow M22 (Fig. 5).

The DWBA bent cylinder model parameterized with the VPR-derived distribution of orientations and the Chu and Wiebe (2005) material property relationships was also used to predict the target strengths at increasing frequencies for a normal distribution of animals with mean length 43.3 mm and a standard deviation of 15%. Median target strengths after extrapolation for the larger modes of our direct measurements of target strength at all four frequencies were generally consistent with the theoretical predictions (Fig. 7). The measurements at 200 kHz compared less favorably to the predictions, likely due to error associated with the transducers at this frequency being calibrated less exhaustively than the others.

IV. DISCUSSION

Krill observed in this study were found to orient themselves in a mostly horizontal fashion. This corresponds to normal acoustic incidence relative to a standard vertically aimed echosounder. When applied in conjunction with the length-based sound speed and density contrast relationships of Chu and Wiebe (2005), the observed distribution of orientations produced target strength predictions from a theoret-

ical DWBA-based scattering model that are consistent with *in situ* observations of large krill target strength, but smaller than expected from the semi-empirical model of Greene *et al.* (1991).

Very few previous studies have examined directly the orientation of Antarctic krill or other euphausiids. Based on the qualitative observations of divers, Hamner *et al.* (1983) reported that schooling krill are always aligned uniformly and horizontally within aggregations, and that even when ascending or descending they orient at no more than a 5° to 10° angle. Similar to the present study, Kristensen and Dalen (1986) used underwater photography to measure the orientation of euphausiids (*Meganyctiphanes norvegica* and *Thysanoessa* spp.) in two Norwegian fjords and found that the mean orientation changed from slightly positive by night to slightly negative during the day. In contrast, observations made with a camera of the *in situ* orientation of similar euphausiid species in the Gulf of St. Lawrence revealed a shift in mean orientation from 27° at 1400 to 51° at 0200, albeit with fairly high variability about this trend (Sameoto, 1980).

Quantitative observations of krill in ship-board aquaria (with volumes of 0.06–0.22 m^3) have indicated that krill hover at a mean angle of approximately 45° from horizontal (Kils, 1981; Endo, 1993). Kils (1981) also calculated, however, that it is energetically more favorable for krill to swim at speeds of 3–10 cm s^{-1} than to hover, due to hydrodynamic lift. Kils (1981) further observed increasingly horizontal orientations at greater swimming speeds, with speeds of 3–10 cm s^{-1} corresponding to angles of 30° to $<10°$ [similar to observations by Miyashita *et al.* (1996) of *E. pacifica*]. Our measurements of Antarctic krill orientation are thus consistent with these aquarium studies, if the wild krill are mostly swimming rather than hovering. Supporting this latter notion, observations of *M. norvegica* swimming behavior via acoustic target tracking revealed that this euphausiid swims at a modal speed of ca. 4 cm s^{-1}, and there were virtually no observations of stationary individuals (Klevjer and Kaartvedt, 2003).

Krill orientation has also been estimated indirectly from acoustic observations. On the basis of Foote *et al.*'s (1990) measurements of krill target strengths at 38 and 120 kHz in an experimental enclosure, and using the same theoretical scattering model as employed here, Chu *et al.* (1993) inferred that the krill oriented on average at 20° from horizontal [$N(20°, 20°)$]. More recently, Demer and Conti (2005) used a related theoretical scattering model to estimate an orientation distribution of $N(15°, 5°)$ from measurements of volume backscattering at 38 and 120 kHz attributed to krill. These results are encouragingly similar to the present observations; the means from both studies fall within less than one standard deviation of the dominant mode of the VPR-derived measurements. In order to infer orientation from observations of volume backscattering or target strength, however, it is necessary to know that the acoustic measurements stem uniquely from krill and not from other scatterers, and all other parameters in the scattering model must be properly constrained. Discrepancies between our measurements of orientation and those from earlier indirect studies may stem from uncertainty in these factors. In the case of the Chu *et al.* (1993) study, the estimated distribution of orientations may also have been affected by the krill being in an enclosure where some of them may have been hovering. Our approach to measuring krill orientation is appealing as it captures directly the *in situ* orientation of the krill in the vicinity of a towed acoustic system. The similarity between our measurements of orientation and the estimates made by Demer and Conti (2005) from a vessel-mounted transducer may suggest that the krill are not substantially disturbed by the passage of the survey vessel.

In using the distribution of krill orientations measured here to parameterize the theoretical krill target strength model, we make two important assumptions. First, we assume that the orientation distribution for the sizes of krill captured by the video system (~3–15 mm) also applies to larger individuals. Krill start to exhibit schooling behavior at 10 mm in length, and schools of krill at this size display characteristics identical to those of adults, including uniform orientation and spacing (Hamner *et al.*, 1989). In the absence of any other information, it thus seems reasonable to assume that both large and small krill possess similar schooling behaviors and thereby similar orientations.

Second, we assume that the orientations of the animals observed were not influenced by the presence of the towed body. Hamner and Hamner (2000) found that krill responded to a diver transport vehicle towed at 1 kn by swimming horizontally away, but that tow speeds of 2–4 kn elicited the well-known tail-flip escape response. At a horizontal tow speed of 4–6 kn, and a vertical speed of ca. 0.2 kn, any krill able to respond to the BIOMAPER-II towed body before being captured by the video system would be expected to employ the tail-flip response. Many images of krill exhibiting such a response were indeed captured, but excluded from analysis.

Although the dominant mode of krill orientation distribution was centered at 0°, lesser modes were present near 140° and −160°. The exact behavior underlying this observation is not known, but it is worth noting that no krill larger than 6 mm were observed in this "belly-up" orientation (although fewer observations were made of such larger animals). Excluding these smaller modes of angles from the orientation distribution used to parameterize the acoustic scattering model had a negligible effect on predicted target strengths. This is due to the small size of these modes and because a bent cylinder in ventral aspect scatters sound in a very similar fashion to one in dorsal aspect.

The approach to modeling krill scattering employed here represents the krill's shape as a uniformly bent and smoothly tapered cylinder and assumes that the acoustic material properties do not vary within the animal. More sophisticated formulations employ higher resolution shape descriptions to account for appendages and allow for variations in the sound speed and density contrasts along the animal's length (McGehee *et al.*, 1998; Stanton *et al.*, 1998; Stanton and Chu, 2000; Lavery *et al.*, 2002). Similarly, the addition of a stochastic phase component to scattering models has been used to address differences evident at angles away from normal between model predictions of krill scattering and tank-based measurements (Stanton *et al.*, 1998; Demer and Conti,

2003). When studying the single ping returns from individual animals at discrete angles of orientation (e.g., in the laboratory), the increased accuracy of these more complicated models is desirable. When examining ensembles of animals, as is the case in measurements of volume backscattering strength, and where predicted scattering averaged over a distribution of orientations is dominated by scattering at normal acoustic incidence, errors due to simplifications in the shape description and along-axis variations in material properties become negligible, as do the effects of random phase variability (Stanton and Chu, 2000). Since the animals here are oriented mostly horizontally, and since our interest in knowing krill target strength stems from a desire to make estimates of biologically meaningful quantities from survey measurements of volume backscattering, there is no need to move beyond the lower resolution model nor to include a random phase component. Higher resolution shape models require the digitization of the animal's shape in 2- or 3-D, rather than the simple measurements of length, curvature, and the ratio of length to radius required by the bent cylinder model used here. This latter model thus has the advantage of ease of application (Stanton and Chu, 2000).

Parameterizing the theoretical DWBA-based bent and tapered cylinder model with the distribution of orientations measured here and Chu and Wiebe's (2005) length-based material property regressions resulted in predictions of target strength in relation to length and frequency that for larger krill are consistent with the present *in situ* empirical observations of krill target strength. The congruence in theoretical predictions and empirical measurements provides support for this model parameterization for the larger animals at least. It is these larger krill that are the subject of the krill fishery and the target of most krill acoustic surveys.

In contrast, *in situ* observations of the target strength of smaller krill were much higher than predicted. As krill length decreases, the size of the animal's structural features relative to the acoustic wavelength becomes correspondingly smaller, making the model less sensitive to specific choices of parameter values and giving us confidence in its predictions for the small krill. The empirical measurements for these small krill, however, are subject to a number of likely sources of error. For example, they are undoubtedly biased upwards due to their being so near to both the noise and processing thresholds (which on-axis were –94 and –100 dB and at the edge of the beam –88 and –94 dB, for the down- and up-looking 120 kHz transducers respectively). The density of small krill estimated from the net tows was also higher than for the large krill (Wiebe *et al.*, 2004), increasing the likelihood that multiple targets were erroneously accepted as single targets for these smaller akrill, which would further tend to bias positively the latter's measured target strengths. No animals larger than krill were sampled with the nets, but we also cannot exclude the possibility of confounding sources of scattering such as small zooplankton (e.g., copepods or pteropods) or microstructure. Such scattering would be too weak to be confused with the larger krill target strengths, but might be marginally stronger than the scattering from the small krill, inflating the measurements we are attributing to this size class.

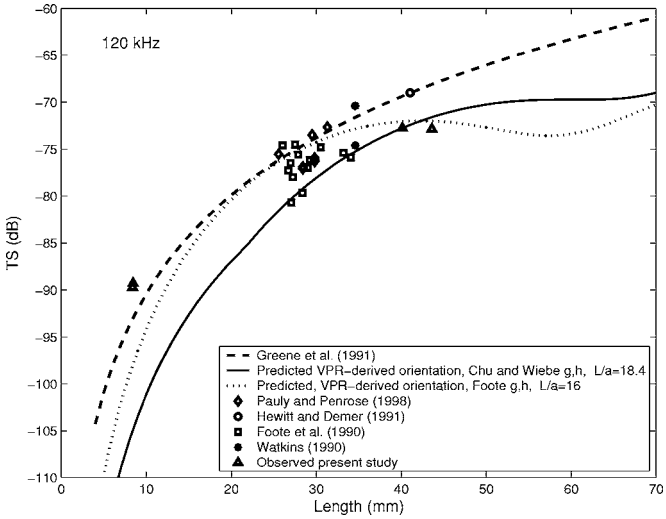

FIG. 8. Target strength at 120 kHz in relation to krill length (mm), showing the Greene *et al.* (1991) model; the DWBA bent cylinder model parameterized with the present VPR-derived distribution of orientations, Chu and Wiebe's (2005) g and h vs length (L) regressions, and an L/a_0 of 18.4 (measured for animals in the present study area); and the model parameterized with the VPR-derived distribution of orientations, Foote's (1990) g and h values, and an L/a_0 of 16. Also shown are the empirical target strength observations made in the present study, as well as the measurements made by Foote *et al.* (1990) of krill in an enclosure, by Hewitt and Demer (1991) of krill *in situ*, and by Pauly and Penrose (1998) of krill in the laboratory, and the target strength estimates made by Watkins (1991) of krill *in situ* from volume backscattering measurements and photographic estimates of krill density. For the latter study, the plotted points indicate the range of estimated target strength.

Foote *et al.* (1992) provide a comprehensive review of the then-up-to-date measurements of target strength for a variety of euphausiid species. The Antarctic krill data reviewed were of varying quality, but the measurements of krill target strength at 120 kHz by Foote *et al.* (1990) and Watkins (1991) were deemed to be of high quality. Since the Foote *et al.* (1992) review, Hewitt and Demer (1991) and Pauly and Penrose (1998) have also reported observations of krill target strength. Most of these earlier observations lie above our newly parameterized scattering model (Fig. 8). This difference likely stems from two sources. First, experimental error may tend to bias the empirical observations; the Hewitt and Demer (1991) *in situ* measurements, for instance, are thought to be positively biased by erroneous acceptance of multiple targets as individual target strengths (Demer and Conti, 2005), and the true target strengths for the krill they observed likely fall closer to the predictions of the present model.

Second, there may have existed differences in the exact shape and nutritional status of the different krill populations under investigation, which would require different model parameter values. Our surveys were conducted during austral fall/winter when food resources are low, while previous studies were mostly of krill during summer. The stronger target strengths measured in these earlier studies may relate to the krill being fatter in summer. Properly modeling the target strengths of these summertime krill thus may require a smaller ratio of length to radius (L/a_0) than the value of 18.4 used here. Similarly, the acoustic material properties may vary seasonally: Foote (1990) measured material properties for krill in summer that lead to larger target strength predic-

tions for the length range of krill he examined than the material property regressions employed here. Indeed, parameterizing the present scattering model with $L/a_0=16$ [used previously by Chu *et al.* (1993) for summertime krill] and Foote's (1990) material property measurements results in predictions of target strength that compare more favorably to the higher values in the range of previous measurements of krill target strength (Fig. 8). This highlights the importance of understanding and measuring wherever possible model parameters appropriate to each particular situation. In the present modeling exercises, all parameters were measured for animals in the actual study region at the time of surveying, and reasonable congruence was achieved between model predictions and empirical observations. Given the low wintertime food conditions experienced by the krill in our study, our target strength predictions should perhaps be taken as a lower bound.

The Greene *et al.* (1991) semi-empirical model of krill target strength at 120 kHz as a function of length enjoys widespread use in acoustic studies of Antarctic krill. Similar to the findings of earlier studies (McGehee *et al.*, 1998; Demer and Conti, 2003, 2005), the present predictions of krill target strength using the novel model parameterization are at least 4.4 dB smaller than expected under the Greene *et al.* (1991) relationship, for all animal lengths investigated. This divergence is particularly strong for small lengths, but Greene *et al.* (1991) did not intend their model to be used in the Rayleigh scattering region ($ka<1$). Their model was derived from a linear regression of empirical target strength measurements made at 420 kHz in relation to individual length (Greene *et al.*, 1989; Wiebe *et al.*, 1990). The regression line was then related to anticipated target strengths at the more typical survey frequency of 120 kHz, on the theoretical basis of a linearized version of the straight finite cylinder scattering model (Wiebe *et al.*, 1990). This approach assumes a linear relationship between target strength and animal length, although both theoretical and empirical studies indicate that this relationship is nonlinear, due to the complicating influences of animal length, shape, orientation, and material properties. Furthermore, the target strengths of a variety of crustacean species were combined into the target strength to length regression, including the euphausiid *Euphausia pacifica* but not the Antarctic krill itself. Some of the taxa were of quite different body shapes to krill (e.g., decapods and copepods), and the larger body depth to length ratios of these animals may explain much of the difference between the Greene *et al.* (1991) line and the current model predictions for the relatively thin Antarctic krill.

Greene *et al.* (1991) recognized that the linearization of the target strength to length relationship constituted a simplification of the scattering process and proposed their model as a practical and highly useful means of estimating krill target strength "until these theoretical models are better developed." Since the Greene *et al.* (1991) study, DWBA-based approximate theoretical models of zooplankton scattering have progressed considerably and been extensively validated for normal acoustic incidence or averages dominated by normal incidence, especially for euphausiids [reviewed in Stanton and Chu (2000)]. Modern theoretical approaches to modeling zooplankton scattering seek to capture the nonlinearities in the target strength versus length relationship, are not limited to any particular frequency (or assumptions concerning the scaling of data from one frequency to another), and include numerous parameters for animal size, shape, orientation, and material properties. These parameters can be adjusted for different taxa, animal behaviors, and body conditions, respectively, thereby providing wide applicability and substantial flexibility. The strong variability in target strength measurements evident in Fig. 8 would suggest that such flexibility is highly desirable.

V. CONCLUSIONS

Improved understanding of key model parameters through direct observations of Antarctic krill orientation and application of recently published regressions relating sound speed and density contrasts to krill length has yielded predictions from a theoretical DWBA-based scattering model that compare favorably to *in situ* measurements of target strength of large krill. The congruence in theoretical predictions and empirical observations provides support for this new model parameterization, as well as further validation of the DWBA-based approach to modeling zooplankton scattering. Arguably, the semi-empirical model of Greene *et al.* (1991) should be replaced by the use of fully parameterized and field-validated theoretical scattering models like the one developed here, although care must be taken to constrain properly all parameters for the particular krill population at hand. Application of such models will allow more accurate estimates of biologically meaningful quantities like krill abundance and stock biomass from observations of volume backscattering (Everson *et al.*, 1990).

ACKNOWLEDGMENTS

Chuck Greene provided the initial impetus for this project, when he remarked over lunch that the question of krill target strength had never been fully resolved, and he was amazed that people were still using the Greene *et al.* (1991) regression model 15 years later. A. Lavery, S. Kaartvedt, Y. Endo, and C. Greene, provided very insightful comments on earlier manuscript drafts. We warmly acknowledge the contributions of C. Davis and S. Gallager, coprimary investigators on the zooplankton broad-scale distribution component of the Southern Ocean GLOBEC project. C. Davis and Q. Hu provided much appreciated help in assessing possible sources of error in the VPR observations. We further thank all officers and crew of the RVIB *N. B. Palmer*; the Raytheon Polar Services Technical Support group; the BIOMAPER-II and MOCNESS teams consisting of C. Davis, M. Dennett, K. Fisher, S. Gallager, A. Girard, E. Horgan, M. Taylor, J. Szelag, and J. Warren; as well as P. Alatalo, M.-Q. Chu, N. Copley, L. Gray, P. Hull, and G. Rosenwaks, for lab analyses of net catches. This project was supported by NSF U.S. Antarctic Program Grant No. OPP-9910307. G. Lawson was supported by an Office of Naval Research Graduate Traineeship Award in Ocean Acoustics (Grant No. N000 14-03-1-0212), a Fulbright Scholarship, a Natural Sciences and Engineering Research Council of

Canada Post-Graduate Scholarship, and the Woods Hole Oceanographic Institution Academic Programs Office. This is U.S. GLOBEC Contribution No. 259.

Anderson, V. C. (**1950**). "Sound scattering from a fluid sphere," J. Acoust. Soc. Am. **22**, 426–431.

Benfield, M. C., Davis, C. S., and Gallager, S. M. (**2000**). "Estimating the *in situ* orientation of *Calanus finmarchicus* on Georges Bank using the Video Plankton Recorder," Plankton Biol. Ecol. **47**, 69–72.

Chu, D., and Wiebe, P. H. (**2005**). "Measurements of acoustic material properties of zooplankton in Antarctic waters," ICES J. Mar. Sci. **62**, 818–831.

Chu, D., Foote, K. G., and Stanton, T. K. (**1993**). "Further analysis of target strength measurements of Antarctic krill at 38 and 120 kHz: Comparison with deformed cylinder model and inference of orientation distribution," J. Acoust. Soc. Am. **93**, 2985–2988.

Chu, D., Wiebe, P. H., and Copley, N. (**2000**). "Inference of material properties of zooplankton from acoustic and resistivity measurements," ICES J. Mar. Sci. **57**, 1128–1142.

Davis, C. S., and Wiebe, P. H. (**1985**). "Macrozooplankton biomass in a warm-core Gulf Stream ring: Time series changes in size structure, taxonomic composition, and vertical distribution," J. Geophys. Res. **90**, 8871–8882.

Davis, C. S., Gallager, S. M., and Solow, A. R. (**1992**). "Microaggregations of oceanic plankton observed by towed video microscopy," Science **257**, 230–232.

Davis, C. S., Gallager, S. M., Marra, M., and Stewart, W. K. (**1996**). "Rapid visualization of plankton abundance and taxonomic composition using the Video Plankton Recorder," Deep-Sea Res., Part II, **43**, 1947–1970.

Demer, D. A., and Conti, S. G. (**2003**). "Reconciling theoretical versus empirical target strengths of krill: effects of phase variability on the distorted-wave Born approximation," ICES J. Mar. Sci. **60**, 429–434.

Demer, D. A., and Conti, S. G. (**2005**). "New target-strength model indicates more krill in the Southern Ocean," ICES J. Mar. Sci. **62**, 25–32.

Endo, Y. (**1993**). "Orientation of Antarctic krill in an aquarium," Nippon Suisan Gakkaishi **59**, 465–468.

Everson, I., Watkins, J. L., Bone, D. G., and Foote, K. G. (**1990**). "Implications of a new acoustic target strength for abundance estimates of Antarctic krill," Nature (London) **345**, 338–339.

Foote, K. G. (**1990**). "Speed of sound in *Euphausia superba*," J. Acoust. Soc. Am. **87**, 1405–1408.

Foote, K. G., Aglen, A., and Nakken, O. (**1986**). "Measurement of fish target strength with a split-beam echo sounder," J. Acoust. Soc. Am. **80**, 612–621.

Foote, K. G., Chu, D., and Stanton, T. K. (**1992**). "Status of krill target strength," in *Selected Scientific Papers, 1992, SC-CAMLR-SSP/9* (Committee for the Conservation of Antarctic Marine Living Resources, Hobart, Australia), pp. 101–126.

Foote, K. G., Everson, I., Watkins, J. L., and Bone, D. G. (**1990**). "Target strengths of Antarctic krill (*Euphausia superba*) at 38 and 120 kHz," J. Acoust. Soc. Am. **87**, 16–24.

Greene, C. H., Wiebe, P. H., and Burczynski, J. (**1989**). "Analyzing zooplankton size distributions using high-frequency sound," Limnol. Oceanogr. **34**, 129–139.

Greene, C. H., Stanton, T. K., Wiebe, P. H., and McClatchie, S. (**1991**). "Acoustic estimates of Antarctic krill," Nature (London) **349**, 110.

Greenlaw, C. F., and Johnson, R. K. (**1982**). "Physical and acoustical properties of zooplankton," J. Acoust. Soc. Am. **72**, 1706–1710.

Hamner, W. M., and Hamner, P. P. (**2000**). "Behavior of Antarctic krill (*Euphausia superba*): schooling, foraging, and antipredatory behavior," Can. J. Fish. Aquat. Sci. (Suppl. 3) **57**, 192–202.

Hamner, W. M., Hamner, P. P., Obst, B. S., and Carleton, J. H. (**1989**). "Field observations on the ontogeny of schooling of *Euphausia superba* furciliae and its relationship to ice in Antarctic waters," Limnol. Oceanogr. **34**, 451–456.

Hamner, W. M., Hamner, P. P., Strand, S. W., and Gilmer, R. W. (**1983**). "Behavior of Antarctic krill, *Euphausia superba*: Chemoreception, feeding, schooling, and molting," Science **220**, 433–435.

Hewitt, R. P., and Demer, D. A. (**1991**). "Target strength of Antarctic krill," Nature (London) **353**, 310.

Hofmann, E. E., Klinck, J. M., Costa, D. P., Daly, K. D., Torres, J. J., and Fraser, W. R. (**2002**). "U.S. Southern Ocean Global Ocean Ecosystem Dynamics Program," Oceanogr. **15**, 64–74.

Holliday, D. V., and Pieper, R. E. (**1980**). "Volume scattering strengths and zooplankton distributions at acoustic frequencies between 0.5 and 3 MHz," J. Acoust. Soc. Am. **67**, 135–146.

Ichii, T. (**2000**). "Krill harvesting," in *Krill: Biology, Ecology and Fisheries*, edited by I. Everson (Blackwell Science, Oxford), pp. 228–261.

Johnson, R. K. (**1977**). "Sound scattering from a fluid sphere revisited," J. Acoust. Soc. Am. **61**, 375–377.

Kils, U. (**1981**). "The swimming behavior, swimming performance and energy balance of Antarctic krill, *Euphauisa superba*," BIOMASS Sci. Ser. No. 3.

Klevjer, T. A., and Kaartvedt, S. (**2003**). "Split-beam target tracking can be used to study the swimming behavior of deep-living plankton *in situ*," Aquat. Liv. Res. **16**, 293–298.

Kristensen, Å., and Dalen, J. (**1986**). "Acoustic estimation of size distribution and abundance of zooplankton," J. Acoust. Soc. Am. **80**, 601–611.

Lavery, A. C., Stanton, T. K., McGehee, D. E., and Chu, D. (**2002**). "Three-dimensional modeling of acoustic backscattering from fluid-like zooplankton," J. Acoust. Soc. Am. **111**, 1197–1210.

Laws, R. M. (**1985**). "The ecology of the Southern Ocean," Am. Sci. **73**, 26–40.

Lawson, G. L., Wiebe, P. H., Ashjian, C. J., Gallager, S. M., Davis, C. S., and Warren, J. D. (**2004**). "Acoustically-inferred zooplankton distribution in relation to hydrography west of the Antarctic Peninsula," Deep-Sea Res., Part II, **51**, 2041–2072.

Mauchline, J. (**1980**). "Measurement of body length of *Euphausia superba* Dana," BIOMASS Handbook No. 4, pp. 4–9.

McGehee, D. E., O'Driscoll, R. L., and Martin-Traykovski, L. V. (**1998**). "Effects of orientation on acoustic scattering for Antarctic krill at 120 kHz," Deep-Sea Res., Part II, **45**, 1273–1294.

Miyashita, K., Aoki, I., and Inagaki, T. (**1996**). "Swimming behavior and target strength of isada krill (*Euphausia pacifica*)," ICES J. Mar. Sci. **53**, 303–308.

Morse, P. M., and Ingard, K. U. (**1968**). *Theoretical Acoustics* (Princeton U. P., Princeton, NJ).

O'Brien, D. P. (**1987**). "Description of escape responses of krill (Crustacea: Euphausiacea), with particular reference to swarming behavior and the size and proximity of the predator," J. Crust. Biol. **7**, 449–457.

Pauly, T., and Penrose, J. D. (**1998**). "Laboratory target strength measurements of free-swimming Antarctic krill (*Euphausia superba*)," J. Acoust. Soc. Am. **103**, 3268–3280.

Sameoto, D. D. (**1980**). "Quantitative measurements of euphausiids using a 120 kHz sounder and their *in situ* orientation," Can. J. Fish. Aquat. Sci. **37**, 693–702.

SC-CAMLR (**1991**). *Report of the 10th Meeting of the Scientific Committee (SC-CAMLR-X)* (CCAMLR, Hobart, Australia), pp. 117–121.

Stanton, T. K., and Chu, D. (**2000**). "Review and recommendations for the modeling of acoustic scattering by fluid-like elongated zooplankton: euphausiids and copepods," ICES J. Mar. Sci. **57**, 793–807.

Stanton, T. K., Chu, D., and Reeder, D. B. (**2004**). "Non-Rayleigh acoustic scattering characteristics of individual fish and zooplankton," IEEE J. Ocean. Eng. **29**, 260–268.

Stanton, T. K., Chu, D., and Wiebe, P. H. (**1998**). "Sound scattering by several zooplankton groups. II. Scattering models," J. Acoust. Soc. Am. **103**, 236–253.

Stanton, T. K., Chu, D., Wiebe, P. H., and Clay, C. S. (**1993**). "Average echoes from randomly oriented random-length finite cylinders: Zooplankton models," J. Acoust. Soc. Am. **94**, 3463–3472.

Watkins, J. L. (**1991**). "Krill target strength estimated by underwater photography and acoustics," (WG-Krill-91-40), CCAMLR, Hobart, Australia [as cited in Foote *et al.* (1992)].

Wiebe, P. H., Greene, C. H., Stanton, T. K., and Burczynski, J. (**1990**). "Sound scattering by live zooplankton and micronekton: Empirical studies with a dual-beam acoustical system," J. Acoust. Soc. Am. **88**, 2346–2360.

Wiebe, P. H., Ashjian, C., Gallager, S., Davis, C., Lawson, G. L., and Copley, N. (**2004**). "Using a High Powered Strobe Light to Increase the Catch of Antarctic Krill," Mar. Biol. (Berlin) **144**, 493–502.

Wiebe, P. H., Morton, A. W., Bradley, A. M., Backus, R. H., Craddock, J. E., Cowles, T. J., Barber, V. A., and Flierl, G. R. (**1985**). "New developments in the MOCNESS, an apparatus for sampling zooplankton and micronekton," Mar. Biol. (Berlin) **87**, 313–323.

Wiebe, P. H., Stanton, T. K., Greene, C. H., Benfield, M. C., Sosik, H. M., Austin, T., Warren, J. A., and Hammar, T. (**2002**). "BIOMAPER II: An integrated instrument platform for coupled biological and physical measurements in coastal and oceanic regimes," IEEE J. Ocean. Eng. **27**, 700–716.

Acoustic waves generated by a laser point pulse in a transversely isotropic cylinder

Y. Pan[a)]
Institute of Acoustics, Tongji University, 200092, Shanghai, People's Republic of China

M. Perton, B. Audoin, and C. Rossignol
Laboratoire de Mécanique Physique, UMR CNRS 8469, Université Bordeaux 1, 33405 Talence, France

(Received 21 June 2005; revised 26 October 2005; accepted 27 October 2005)

A three-dimensional (3D) model is presented to predict the acoustic waves generated by a laser point pulse in a transversely isotropic cylinder. The Fourier series expansion and the two-dimensional Fourier transform are introduced to calculate the 3D transient response under either the ablation or the thermoelastic generation. The presented physical model and the numerical inverse scheme are applied to a fiber reinforced composite cylinder with a strong anisotropy. Experimental radial displacements of the cylinder surface are detected by the laser ultrasonic technique and analyzed by the ray trajectories for both generation regimes. Corresponding theoretical displacements are obtained numerically and compared to the experimental signals. Good agreement is found between theoretical and experimental results. The focusing effects that anisotropy gives rise to are observed in both theory and experiment under either regime. © *2006 Acoustical Society of America.* [DOI: 10.1121/1.2139648]

PACS number(s): 43.35.Cg, 43.35.Zc, 43.20.Bi [YHB] Pages: 243–250

I. INTRODUCTION

Many cylindrical components, such as wires, rods, and pipes, are usually transversely isotropic (TI) due to their manufacturing processes. To provide a high strength-to-weight ratio along the cylinder axis, the transverse isotropy is often desirable for many structural applications, especially in the aeronautic and aerospace industries. There is thus an obvious demand for the nondestructive evaluation (NDE) of the TI cylinder, such as the elastic constants measurement.

In the literature, many studies are available on the wave propagation in a TI cylinder. Early in 1965, Mirsky[1] theoretically investigated the propagation of free harmonic waves in such a cylinder. He found the frequency equation, i.e., the characteristic or dispersion equation for the steady-state free vibrations, and some dispersion curves were obtained numerically. Such a harmonic wave propagation was also documented in the text by Payton.[2] The similar wave propagation in a fluid-loaded TI cylinder was theoretically studied recently.[3] The axisymmetric free vibrations of a finite TI rod were analyzed for the purpose of determining the elastic constants.[4] As studied by Zemanek[5] for an isotropic cylinder, the piezoelectric drivers should be properly mounted to the sample in order to excite the free vibration experimentally, and the fine identification of the resonance peaks is required.

There is an effort in studying the acoustic scattering of a TI cylinder for the NDE purpose. Honarvar and Sinclair analyzed the influence of the elastic constants of a TI cylinder to the resonance spectrum resulting from the oblique insonification by a plane acoustic wave,[6] and evaluated the elastic properties by observing the resonances experimentally.[7] For this technique, the sample must be immersed in a fluid, usually water. This requirement limits the capability of the ultrasonic immersion method when measurements are performed, for instance, at elevated temperatures.

The above research works do not deliver the capability of evaluating the sample without any contact. Fortunately, this deficiency is overcome with the laser-based ultrasonic technique,[8] in which the ultrasonic waves are generated and detected at a distance, without any contact to the sample. Early in 1967, Viktorov[9] calculated the dispersion curve for an isotropic cylinder and made comparison to experimental data detected by conventional piezoelectric transducers, however few experimental results were reported until the development of the laser ultrasonic technique. With the remarkable features of noncontact, high space, and time resolutions introduced by this technique, the transient wave propagation, instead of the previous steady-state vibration, can be observed experimentally. The transient surface wave propagating on an isotropic sphere was observed experimentally in 1988.[10] The dispersion of the surface wave propagating on an isotropic cylinder was observed and compared to the theoretical results very recently.[11,12]

For an anisotropic material, the two-dimensional (2D) transient wave propagation in a half-space was solved theoretically by Burridge[13] in 1971, and the 3D transient wave propagation in a half-space was solved recently by many methods.[14–16] Due to the existence of the circular boundary, the wave propagation in a cylinder is more complicated than in a half-space. For example, contrary to that in a half-space, the cylindrical Rayleigh wave for an isotropic cylinder is dispersive.[9,11,12] As pointed out by Payton,[2] a transversely isotropic cylinder is anisotropic in any plane containing the symmetric axis, and the corresponding group velocity curve most likely has a cuspidal shape. Moreover, owing to phonon focusing, waves may be observed off the cusp edges. This

[a)]Electronic mail: ypan@mail.tongji.edu.cn

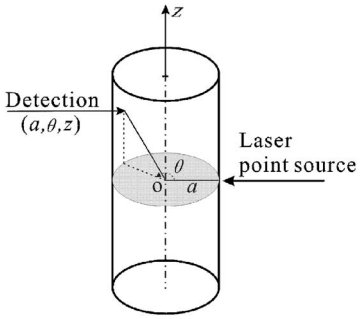

FIG. 1. Problem geometry.

phenomenon is called internal diffraction, since these waves could not be predicted by the ray theory.[17] The cuspidal shape along with the circular boundary further complicates the transient wave propagation. To the best of our knowledge, no work on the 3D transient wave propagation in a TI cylinder has been reported in the literature.

Very recently, the authors presented a 2D model[18] to successfully predict the acoustic waves generated by a laser line pulse in a transversely isotropic cylinder. As the laser was represented by a transient line source, this model does not describe the wave propagation along the cylinder axis. A 3D model[19] was developed soon after to predict successfully the acoustic waves generated by a laser point pulse in an isotropic cylinder by modeling the laser as a transient point source. But the possible anisotropy of a cylindrical material was not accounted for in that work. In this paper, a 3D model is presented to predict the acoustic waves generated by a laser point pulse in a transversely isotropic cylinder under either the ablation or the thermoelastic regime. The corresponding theoretical solutions and a numerical inverse scheme are proposed. Experimental radial displacements generated under either regime are detected by the laser ultrasonic technique for a fiber reinforced composite cylinder. Theoretical displacements are calculated and compared with the corresponding experimental waveforms. The focusing effect that anisotropy gives rise to is discussed.

II. GENERAL FORMULATION

Let us consider a homogeneous and transversely isotropic cylinder of infinite length, radius a, and density ρ. As shown in Fig. 1, the symmetrical axis of the cylinder is assumed to coincide with the z axis of the system of cylindrical coordinates (r, θ, z). A pulsed laser beam focused by a spherical lens impacts the cylinder to generate acoustic waves. These waves are experimentally observed with an optical detection technique.[8] To denote the point detection position, the cylindrical coordinates (a, z, θ) are chosen, considering $\theta=0°$ and $z=0$ for the source position.

Let c_{ij} $(i, j=1,\ldots,6)$ denote the stiffness coefficients of the transversely isotropic material in contracted Voigt notations. Here axes 1, 2, and 3 correspond to the radial, circumferential, and z-axis directions in the cylindrical coordinate system. Owing to the symmetry of the material, the stiffness tensor has five independent coefficients. The components of the displacement vector depend on three space variables r, θ, z and on time t. These components, denoted as u_r, u_θ, and u_z, can be expressed in terms of three scalar potentials φ, ψ, and χ as[20]

$$u_r(r,\theta,z,t) = \frac{\partial \varphi}{\partial r} + \frac{1}{r}\frac{\partial \chi}{\partial \theta},$$

$$u_\theta(r,\theta,z,t) = \frac{1}{r}\frac{\partial \varphi}{\partial \theta} - \frac{\partial \chi}{\partial r}, \tag{1}$$

$$u_z(r,\theta,z,t) = \frac{\partial \psi}{\partial z},$$

where these potentials are governed by the following wave motion equations:

$$c_{11}\left(\nabla^2 - \frac{\partial^2}{\partial z^2}\right)\varphi + c_{44}\frac{\partial^2 \varphi}{\partial z^2} + (c_{13}+c_{44})\frac{\partial^2 \psi}{\partial z^2} = \rho\frac{\partial^2 \varphi}{\partial t^2},$$

$$(c_{13}+c_{44})\left(\nabla^2 - \frac{\partial^2}{\partial z^2}\right)\varphi + c_{44}\left(\nabla^2 - \frac{\partial^2}{\partial z^2}\right)\psi + c_{33}\frac{\partial^2 \psi}{\partial z^2} = \rho\frac{\partial^2 \psi}{\partial t^2}, \tag{2}$$

$$c_{66}\left(\nabla^2 - \frac{\partial^2}{\partial z^2}\right)\chi + c_{44}\frac{\partial^2 \chi}{\partial z^2} = \rho\frac{\partial^2 \chi}{\partial t^2}.$$

In Eqs. (2), the potentials φ and ψ, which represent the harmonic wave propagation of the longitudinal (L) and vertically polarized quasitransverse (T_q) waves, are coupled, and the potential χ, which represents the harmonic wave propagation of the horizontally polarized pure transverse wave (T_p), is independent of the others. To further represent the transient wave propagation, the three potentials must satisfy the following boundary conditions. For a source at position $\theta=0°$ and $z=0$, components σ_{rr}, $\sigma_{r\theta}$, and σ_{rz} of the stress tensor at any point of the cylinder surface are determined by either

$$\sigma_{rr}|_{r=a} = -F_A\delta(t)\delta(z)\delta(\theta),$$

$$\sigma_{r\theta}|_{r=a} = 0, \tag{3}$$

$$\sigma_{rz}|_{r=a} = 0$$

for the ablation generation,[21] or

$$\sigma_{rr}|_{r=a} = 0,$$

$$\sigma_{r\theta}|_{r=a} = -F_T h(t)\delta(z)\delta'(\theta), \tag{4}$$

$$\sigma_{rz}|_{r=a} = -F_T a h(t)\delta'(z)\delta(\theta)$$

for the thermoelastic generation.[22] F_A is a certain loading in N μs m^{-1} for Eqs. (3), and F_T is a certain loading in N m^{-1} for Eqs. (4). They are related to the intensity of the laser point pulse, and their magnitudes are fixed to unity for the corresponding calculations in the following part. Here a delta function of time $\delta(t)$ and a Heaviside step function of time $h(t)$ are used for the ablation and thermoelastic generations, respectively; $\delta'(\theta)$ denotes the derivative of the delta function $\delta(\theta)$, and $\delta'(z)$ denotes the derivative of the delta func-

tion $\delta(z)$. In Eqs. (3), a delta force is postulated in time and space to represent the sudden normal loading in the ablation regime.[21] In Eqs. (4), a Heaviside step function in time is considered in the thermoelastic regime, since thermal diffusion is neglected.[22] Owing to the interface, two dipolar forces are thus considered for the source shape.[23] Here setting the range for θ from $-\pi$ to π instead of from $-\infty$ to $+\infty$ in Ref. 18 also accounts for the periodicity of the cylindrical structure as presented in the following section.

III. TRANSFORMED SOLUTIONS AND NUMERICAL INVERSE SCHEME

To avoid the integration along the wave number ν ($\nu = k_\theta a$, where k_θ is the component of the wave vector k along the θ direction) necessitated by the numerical inversion scheme in Ref. 18, the definition of the Fourier series expansion is introduced for the coordinate θ. In addition, the 2D Fourier transform is considered for time t and coordinate z; and the angular frequency ω and the wave component k along the z direction are thus introduced. Doing so, the displacement field $u_i(r,\theta,z,t)$ $(i=r,\theta,z)$ is now transformed to $U_i(r,\nu,k,\omega)$ as the following form:

$$U_i(r,\nu,k,\omega) = \int_{-\infty}^{+\infty}\int_{-\infty}^{+\infty}\left(\int_{-\pi}^{\pi} u_i(r,\theta,z,t)e^{j\nu\theta}d\theta\right)e^{j(kz-\omega t)}dzdt. \tag{5}$$

Applying the Fourier series expansion and the 2D Fourier transform, the wave motion equations and the boundary equations can be linearized, providing explicit solution forms for the potentials φ, ψ, and χ under either generation regime. At any position on the cylinder surface, the transformed displacement components $U_i(r,\nu,k,\omega)$ are then obtained for the ablation generation as

$$\begin{aligned} U_r(a,\nu,k,\omega) &= -\frac{F_A a}{2c_{66}D(\nu,k,\omega)}\{A_1B_1 - jkaq_2A_2B_2 - j\nu A_3\},\\ U_\theta(a,\nu,k,\omega) &= -\frac{F_A a}{2c_{66}D(\nu,k,\omega)}\{-j\nu A_1 - \nu kaq_2A_2 - A_3B_3\},\\ U_z(a,\nu,k,\omega) &= -\frac{F_A a}{2c_{66}D(\nu,k,\omega)}\{-jkaq_1A_1 + A_2\}, \end{aligned} \tag{6}$$

and for the thermoelastic generation as

$$\begin{aligned} U_r(a,\nu,k,\omega) &= \frac{F_T aH(\omega)}{2c_{66}D(\nu,k,\omega)}\{T_1B_1 - jkaq_2T_2B_2 - j\nu T_3\},\\ U_\theta(a,\nu,k,\omega) &= \frac{F_T aH(\omega)}{2c_{66}D(\nu,k,\omega)}\{-j\nu T_1 - \nu kaq_2T_2 - T_3B_3\},\\ U_z(a,\nu,k,\omega) &= \frac{F_T aH(\omega)}{2c_{66}D(\nu,k,\omega)}\{-jkaq_1T_1 + T_2\}. \end{aligned} \tag{7}$$

In the above equations, coefficients q_1 and q_2 are determined by the following equations:

$$\begin{aligned} q_1 &= \frac{(c_{13}+c_{44})(\rho\omega^2 - c_{44}k^2)}{(c_{13}+c_{44})^2k^2 + c_{11}(\rho\omega^2 - c_{33}k^2) - \beta_1^2c_{11}c_{44}},\\ q_2 &= \frac{(c_{13}+c_{44})}{(c_{11}\beta_2^2 + c_{44}k^2 - \rho\omega^2)a^2}, \end{aligned} \tag{8}$$

where

$$\begin{aligned} \beta_1 &= \sqrt{(E-\Delta)/(2c_{11}c_{44})},\\ \beta_2 &= \sqrt{(E+\Delta)/(2c_{11}c_{44})}, \end{aligned} \tag{9}$$

and

$$\begin{aligned} E &= (c_{13}+c_{44})^2k^2 + c_{11}(\rho\omega^2 - c_{33}k^2) + c_{44}(\rho\omega^2 - c_{44}k^2),\\ \Delta &= \sqrt{E^2 - 4c_{11}c_{44}(\rho\omega^2 - c_{33}k^2)(\rho\omega^2 - c_{44}k^2)}. \end{aligned} \tag{10}$$

And coefficients B_1, B_2, and B_3 are determined by the following equations:

$$\begin{aligned} B_1 &= \beta_1 aJ_\nu'(\beta_1 a)/J_\nu(\beta_1 a),\\ B_2 &= \beta_2 aJ_\nu'(\beta_2 a)/J_\nu(\beta_2 a),\\ B_3 &= \gamma aJ_\nu'(\gamma a)/J_\nu(\gamma a), \end{aligned} \tag{11}$$

with

$$\gamma = \sqrt{(\rho\omega^2 - c_{44}k^2)/c_{66}}. \tag{12}$$

Here, $J_\nu'(x)$ is the derivative of the Bessel function $J_\nu(x)$; β_1, β_2, and γ are the wave numbers for the L, T_q, and T_p waves, respectively. In Eqs. (6), parameters A_1, A_2, and A_3 are

$$\begin{aligned} A_1 &= (m_{22}m_{33} - m_{23}m_{32}),\\ A_2 &= (m_{23}m_{31} - m_{21}m_{33}),\\ A_3 &= (m_{21}m_{32} - m_{22}m_{31}) \end{aligned} \tag{13}$$

for the ablation generation; and in Eqs. (7), parameters T_1, T_2, and T_3 are

$$\begin{aligned} T_1 &= j\nu(m_{13}m_{32} - m_{33}m_{12}) + jka(m_{12}m_{23} - m_{22}m_{13}),\\ T_2 &= j\nu(m_{11}m_{33} - m_{31}m_{13}) + jka(m_{21}m_{13} - m_{11}m_{23}),\\ T_3 &= j\nu(m_{31}m_{12} - m_{11}m_{32}) + jka(m_{11}m_{22} - m_{21}m_{12}) \end{aligned} \tag{14}$$

for the thermoelastic generation. Parameters A_i and T_i, $i=1,2,3$ are determined by the elements in the following matrix:

$$\{m_{ij}\}=\begin{bmatrix} \nu^2-B_1-(c_{11}\beta_1^2+q_1c_{13}k^2)a^2/2c_{66} & jka\{(q_2c_{11}\beta_2^2a^2-c_{13})/2c_{66}-q_2(\nu^2-B_2)\} & j\nu(1-B_3) \\ j\nu(1-B_1) & \nu ka q_2(1-B_2) & \gamma^2a^2/2-\nu^2+B_3 \\ -jka(1+q_1)B_1c_{44}/2c_{66} & (1-k^2a^2q_2)B_2c_{44}/2c_{66} & -\nu kac_{44}/2c_{66} \end{bmatrix}. \tag{15}$$

Note that in Eqs. (6) and (7), $D(\nu,k,\omega)=\det(m_{ij})$ is the determinant of the above matrix $\{m_{ij}\}$. In Eqs. (7), $H(\omega)$ is the Fourier transform of the Heaviside step function $h(t)$.

The explicit forms [Eqs. (6) and (7)] of the displacement field for a transversely isotropic cylinder also represent that for an isotropic cylinder.[19] Let $k_L=\omega\sqrt{\rho/c_{11}}$ and $k_T=\omega\sqrt{\rho/c_{66}}$ denote the wave numbers of the longitudinal and transverse waves in the isotropic plane of the transversely isotropic cylinder, respectively. Here c_{11} and c_{66} are the two independent stiffness coefficients in this isotropic plane. The stiffness coefficients of the isotropic cylinder are related to the Lamé coefficients λ and μ by $c_{11}=c_{33}=\lambda+2\mu$, $c_{13}=\lambda$, and $c_{44}=c_{66}=\mu$. From Eqs. (9)–(12), one gets $\beta_1=\beta=\sqrt{k_L^2-k^2}$, $\beta_2=\gamma=\sqrt{k_T^2-k^2}$, $B_1=B_L=\beta aJ_\nu'(\beta a)/J_\nu(\beta a)$, and $B_2=B_3=B_T$. Equations (8) simplify in $q_1=1$, $q_2=(\gamma a)^{-2}$. Thus the matrix in Eq. (15) becomes

$$\{m_{ij}\}=\begin{bmatrix} \nu^2-k_T^2a^2/2+k^2a^2-B_L & jka\{1-(\nu^2-B_T)/\gamma^2a^2\} & j\nu(1-B_T) \\ j\nu(1-B_L) & \nu ka(1-B_T)/\gamma^2a^2 & \gamma^2a^2/2-\nu^2+B_T \\ -jkaB_L & (k_T^2/2-k^2)B_T/\gamma^2 & -\nu ka/2 \end{bmatrix}. \tag{16}$$

The solutions for the displacements under the ablation regime [Eqs. (6)] and under the thermoelastic regime [Eqs. (7)] are thus identical to the corresponding forms Eqs. (6) and Eqs. (7) in Ref. 19.

The explicit forms [Eqs. (6) and (7)] for the 3D transient wave propagation generated by a laser point source also represent that for the 2D transient wave propagation generated by a laser line source.[18] Generally, the laser line source is orientated along the z direction, and setting $k=0$ represents such an invariance in the z variable. From Eqs. (9)–(12), one then gets $\beta_1=\omega\sqrt{\rho/c_{11}}=k_L$, $\beta_2=\omega\sqrt{\rho/c_{44}}$, $\gamma=\omega\sqrt{\rho/c_{66}}=k_T$, and $B_1=B_L=k_LaJ_\nu'(k_La)/J_\nu(k_La)$. Equations (8) simplify in $q_1=(c_{13}+c_{44})/(c_{11}-c_{44})$, $q_2=q_1c_{44}/\rho\omega^2$. Thus the matrix in Eq. (15) is as follows:

$$\{m_{ij}\}=\begin{bmatrix} \nu^2-k_T^2a^2/2-B_L & 0 & j\nu(1-B_T) \\ j\nu(1-B_L) & 0 & k_T^2a^2/2-\nu^2+B_T \\ 0 & B_2c_{44}/2c_{66} & 0 \end{bmatrix}. \tag{17}$$

Moreover from Eqs. (9) and (10), it is found that $A_2=T_2=0$, and then $U_z(a,\nu,k,\omega)=0$. Finally, the solutions for the radial displacement under the ablation regime [Eqs. (6)] and under the thermoelastic regime [Eqs. (7)] are identical to the corresponding forms Eqs. (6) and Eqs. (7) in Ref. 18. From the above analyses, it is certain that the current theoretical solutions [Eqs. (6) and (7)] could deal with the specific cases for an isotropic cylinder or the 2D wave propagation. Therefore, the results of the authors' previous papers support the current solutions, which, of course, are more general.

Now, it is time to focus on the calculation of the displacement field over coordinates θ, z, and time t by the inverse form of Eq. (5). The calculation of the inverse form meets discontinuities for a particular set of ω, ν, and k values. They correspond to poles associated with the zeros of the dispersion equation,

$$D(\nu,k,\omega)=0. \tag{18}$$

Specifically, when $k=0$, this equation yields

$$(\nu^2-k_T^2a^2/2)^2-\nu^2+k_T^2a^2(B_L+B_T)/2+(1-\nu^2)B_LB_T=0, \tag{19}$$

which is identical to $D_\nu=0$ for Eq. (8) of Ref. 18. These poles describe the cylindrical Rayleigh waves[9] and Whispering Gallery waves.[24] Thus the integration cannot be carried out numerically. Therefore, a small constant δ is introduced as the imaginary part ω as discussed in the previous paper.[18] With this change, the inverse form of Eq. (5) becomes

$$u_i(a,\theta,t)=(2\pi)^{-3}e^{\delta t}\int_{-\infty}^{+\infty}\int_{-\infty}^{+\infty} \times\left(\sum_{\upsilon=-\infty}^{+\infty}U_i(a,\nu,\omega-j\delta)e^{-j\nu\theta}\right)e^{-j(kz-\omega t)}dkd\omega. \tag{20}$$

Doing so, ω becomes complex, ω-$j\delta$, and the poles are moved off the real axis of variable ν. Now the integration can be calculated numerically. The value $\delta=0.06$ rad μs^{-1} is chosen for the auxiliary parameter in the following numerical calculations. Various numerical results along with a comparison of the experimental displacements are going to demonstrate the capability of this numerical inverse scheme in the next section.

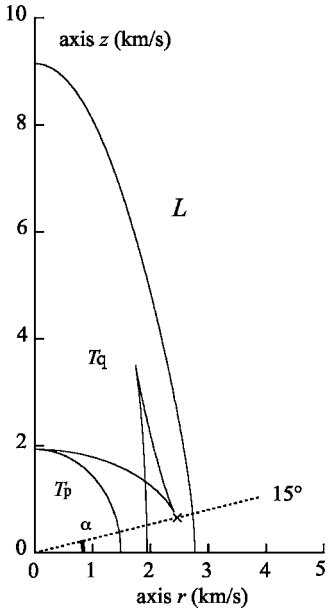

FIG. 2. Group velocity curves of the longitudinal (L), vertically (T_q), or horizontally (T_p) polarized transverse waves for a transversely isotropic cylinder.

IV. ACOUSTIC WAVES GENERATED UNDER THE ABLATION REGIME

To demonstrate the presented theoretical model and the numerical inverse scheme, a fiber reinforced composite cylinder with the transverse isotropy was chosen for both experiments and numerical calculations. This composite has a density of 1.6 g/cm^3 and a diameter of $2a=5.94$ mm. Its complex elastic coefficients are chosen to be (in GPa) $c_{11}=12.26+0.043j$, $c_{66}=7.08+0.027j$, $c_{13}=5.93+0.016j$, $c_{33}=133.81+0.4j$, $c_{44}=6.0+0.015j$, with the imaginary parts accounting for the material's viscoelasticity. These values were measured by a laser ultrasonic method developed for a plate sample.[25] The group wave velocity curves for this material are shown in Fig. 2. Two cuspidal shapes are observed in the corresponding curve for the vertically polarized quasitransverse wave owing to a strong anisotropy.

A laser ultrasonic system was set up to carry the experiments. A Nd:YAG laser was used for the ultrasonic wave generation under either the ablation or the thermoelastic regime. The pulse duration is about 20 ns and the infrared light emission was obtained at 1064 nm with a maximum burst energy output of 340 mJ. The collimated optical beam was focused by means of a spherical lens with a focus length of 150 mm. The obtained laser spot is about 0.2 mm in diameter with a Gaussian distribution. An optical heterodyne probe was used to detect the radial displacement at the cylinder surface. This laser interferometer has a power output of 100 mW and a sensitivity[10] of 10^{-14} m/$\sqrt{\text{Hz}}$. For the ablation generation, the signal was averaged by 20 shots; and for the thermoelastic generation, the signal was averaged by 400 shots. See Ref. 25 for details about the experimental setup.

The experimental system was adjusted to locate the epicenter detection position. This position corresponds to $r=a$, $\theta=180°$, and $z=0$ in the theoretical formulation. The nonepicenter experimental displacements were observed by scanning the laser source by a step of 0.4 mm along the z direction of the cylinder sample with the fixed angle $\theta=180°$. For comparisons, the corresponding theoretical displacements are obtained numerically by applying the transformed theoretical solutions and the numerical inverse scheme discussed in the previous section.

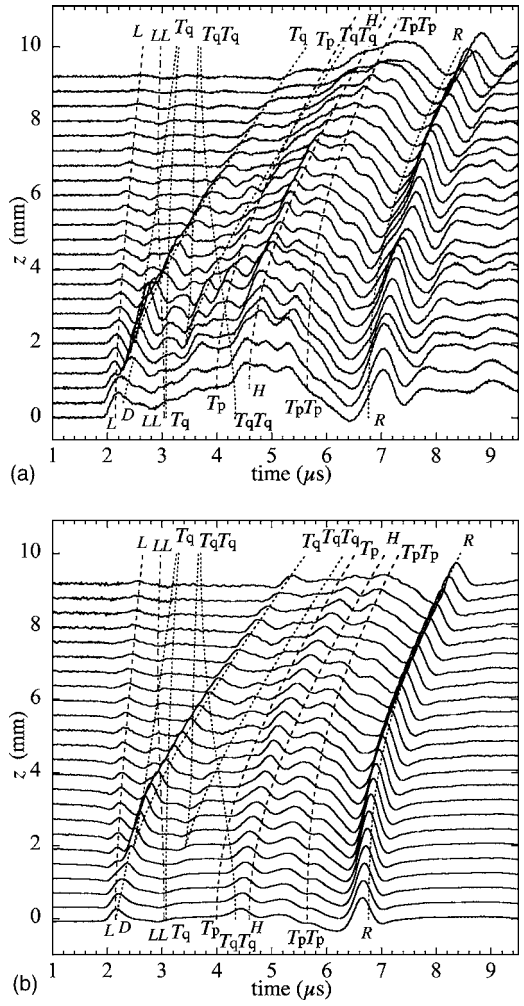

FIG. 3. Waterfall plots of (a) experimental and (b) calculated displacements generated by a laser point pulse under the ablation regime at $z=0, 0.4, \ldots,$ and 9.2 mm for a composite cylinder.

Interest is now focused on the acoustic waves generated under the ablation regime. As shown in Figs. 3(a) and 3(b), the waterfall plots of the experimental and calculated displacements reveal several waves. The detailed description of the abbreviations and symbols marked in Fig. 3 and in the following figures are tabulated in Table I. The experimental and theoretical waveforms at each corresponding detection position are in good agreement regarding the time arrival, shape, and the relative amplitude. The direct longitudinal (L) and vertically polarized quasitransverse (T_q) waves are clearly observable. Their once reflected counterparts (LL) and (T_qT_q) are also observable with decreased amplitudes due to the different directivities and an energy loss between the reflection. Especially, the cuspidal shape in the group velocity curve (Fig. 2) of the vertically polarized quasitransverse wave appears in both arrivals of T_q and T_qT_q waves. In addition, the direct horizontally polarized pure transverse

TABLE I. The abbreviations and detailed descriptions of the acoustic waves discussed in this paper.

Abbreviations	L	LL	T_q	T_qT_q	T_p	T_pT_p	H	R	D
Descriptions	direct longitudinal wave	reflected	direct vertically polarized quasitransverse wave	reflected	direct horizontally polarized pure transverse wave	reflected	Head wave	Rayleigh wave	wave diffracted by the cusp edge

wave (T_p) is less observable than the direct vertically polarized quasitransverse wave T_q, because its amplitude contributes less along the radial direction due to its polarization. Its once-reflected counterpart (T_pT_p) is more observable, as the polarization favors the radial detection after the reflection. These bulk waves have the corresponding ray trajectories shown in Fig. 4(a). Their arrival times are calculated based on their corresponding group wave velocities in Fig. 2, and are displayed as dashed lines in Fig. 3. The cylindrical Rayleigh wave (R) and its dispersive behavior are clearly discernible. A head wave (H) converted from the horizontally polarized pure transverse (T_p) wave is observed. Their time arrivals are in agreement with that of the ray trajectory shown in Fig. 4(b). Here since the cylindrical Rayleigh wave is dispersive, its group wave velocity is approximated by that for an anisotropic half-space. Other waves such as the twice-reflected longitudinal wave ($3L$) observed in an isotropic cylinder,[19] or the head waves converted from the vertically polarized quasitransverse wave, are not illustrated here. They have a low amplitude and they are possibly overlapped by the marked waves in Figs. 3(a) and 3(b).

To emphasize the capability of the modeling, the experimental and calculated displacements are further compared at the epicenter ($z=0$) and non-epicenter ($z=1.6$ mm) positions of the laser point detection, respectively. The calculated waveforms were scaled vertically by a constant to account for the source strength. As shown in Figs. 5(a) and 5(b), the experimental and theoretical waveforms are in agreement. The time, shape, and relative amplitude of most marked wave arrivals are almost identical. Small discrepancies occur that may be caused by the imperfect nature of the actual composite material, and by a tiny aluminum film stuck on the sample surface to improve the signal-to-noise ratio of the interferometer. This film causes the deviation of the Rayleigh wave arrivals between theory and experiment. Under both waveforms, the L, LL, T_pT_p, H, and R waves are clearly observable. For the epicenter observation, the theoretical waveform (solid line) obtained by the current 3D model is almost identical to that (dashed line) by the previous 2D model;[18] the slight deviation is due to the different directivity of the source. Moreover, the direct transverse waves T_p and T_q almost disappear, because the directivity of the generated transverse wave has no contribution along this direction.[8] For a non-epicenter observation, these two waves likely appear as the directivity shows nonzero amplitude. Meanwhile, the amplitude evolution of the L wave is in agreement with the directivity of the generated longitudinal wave for this ablation regime.

Specifically, a wave denoted as D is clearly observed both in theory and experiment, as shown in Fig. 5(b). This non-epicenter position corresponds to an observation angle

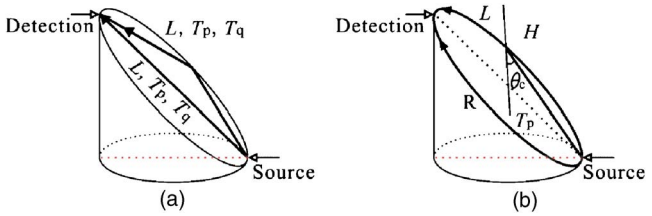

FIG. 4. Ray trajectories of (a) bulk waves L, LL, T_q, T_qT_q, T_p, T_pT_p, (b) head and Raleigh waves H, R, observed in Figs. 2 and 6. Here θ_c is the critical angle for the composite cylinder.

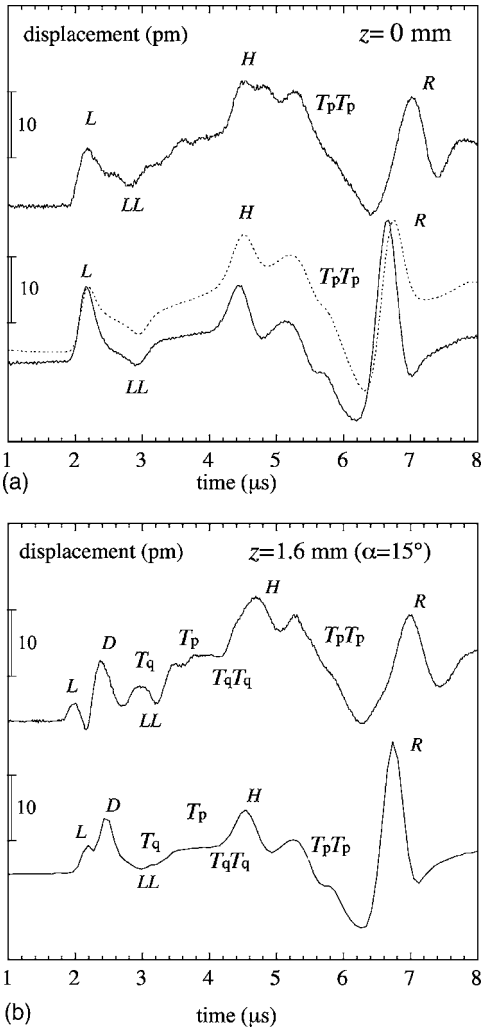

FIG. 5. Experimental (top) and calculated (below) radial displacements of the composite cylinder at (a) the epicenter $z=0$ and (b) a non-epicenter $z=1.6$ mm ($\alpha=15°$) positions of the laser point detection under the ablation generation. For the epicenter observation, the waveform in the dashed line is the corresponding displacement calculated for a laser line pulse generation.

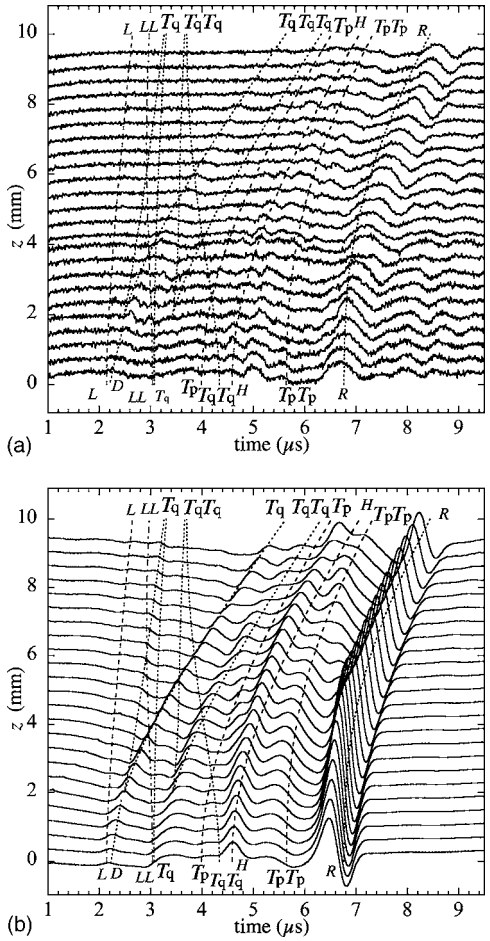

FIG. 6. Waterfall plots of (a) experimental and (b) calculated displacements generated by a laser point pulse under the thermoelastic regime at $z=0, 0.4, \ldots$, and 9.2 mm for a composite cylinder.

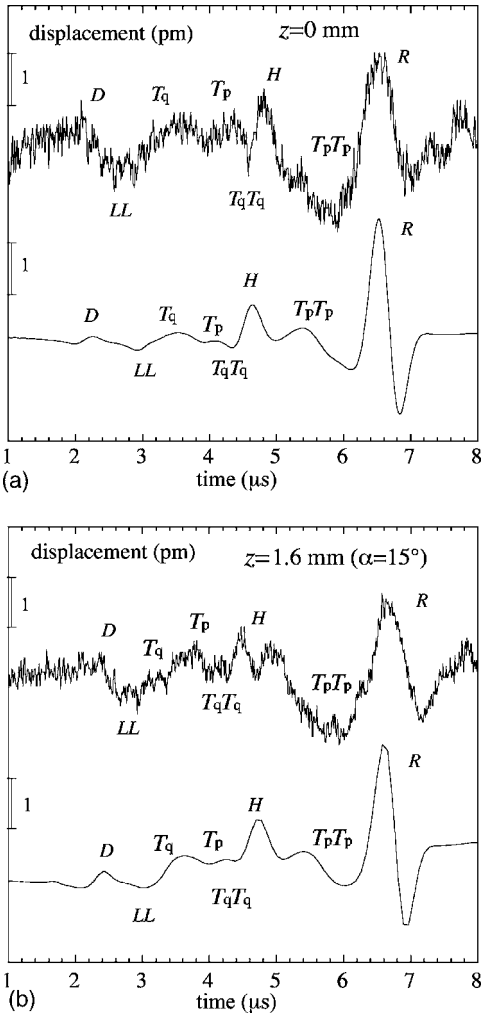

FIG. 7. Experimental (top) and calculated (below) radial displacements of the composite cylinder at (a) the epicenter $z=0$ and (b) the non-epicenter $z=1.6$ mm ($\alpha=15°$) positions of the laser point detection under the thermoelastic generation.

of $\alpha=15°$ shown as a dashed line in the group velocity curve in Fig. 2, which is close to the sharp point of the cuspidal shape. The velocity of this wave is identical to the value marked as a cross on the dashed line. This wave, resulting from the proximity of the cusp, cannot be predicted by the ray theory, since it does not originate from a homogeneous wave, but instead from an inhomogeneous one.[26] As shown in Figs. 3(a) and 3(b), the amplitude evolution of the D wave supports such an interpretation. This phenomenon is the so-called diffraction by the cusp edges, which does not exist for an isotropic material. The D wave and the cuspidal shape of the T_q and T_qT_q wave arrivals were not observed for an isotropic cylinder.[19]

V. ACOUSTIC WAVES GENERATED UNDER THE THERMOELASTIC REGIME

Interest is now focused on the acoustic waves generated under the thermoelastic regime. Despite averaging, the signal-to-noise ratio is less for this regime restricted to low laser intensity. However, the waterfall plots of the experimental and calculated displacements, Figs. 6(a) and 6(b), show that the waveforms at each corresponding detection position are in good agreement. As in the ablation regime, the vertically polarized quasitransverse (T_q) wave and its once reflected counterparts (T_qT_q) are clearly observable with the same cuspidal shape shown in the group velocity curve in Fig. 2. Again, the direct horizontally polarized pure transverse wave (T_p) is less observable than its once-reflected counterpart (T_pT_p) due to the same reason. The cylindrical Rayleigh wave (R) and its dispersive behavior are also clearly observable, and a head wave (H) is observed. Similarly, the time arrival of every observed wave is in agreement with that calculated by the corresponding ray trajectory (Fig. 4) and group wave velocity (Fig. 2). The once reflected longitudinal wave (LL) is observable, but the marked direct longitudinal wave (L) is hardly discernible. This can be explained by the different directivities of the two regimes for the longitudinal wave generation.[8]

The experimental and calculated displacements are further compared at the epicenter ($z=0$) and non-epicenter ($z=1.6$ mm) positions of the laser point detection, respectively. As shown in Figs. 7(a) and 7(b), the experimental and theoretical waveforms are in agreement. The time, shape, and relative amplitude of most marked wave arrivals are almost identical, in spite of the poor signal-to-noise ratio for this regime. Under both cases, the LL, T_pT_p, H, and R waves are clearly observable. Moreover, the direct transverse waves T_p

and T_q almost disappear, because the directivity of the generated transverse wave also contributes less for this regime.[8] For a non-epicenter observation, these two waves likely appear as the directivity shows nonzero amplitude.

Specifically, the wave resulting from the proximity of the cusp D is also clearly discernible in theory and experiment for both positions of the epicenter and the non-epicenter with the observation angle of $\alpha=15°$ in Fig. 2. As shown in Fig. 6, its amplitude increases as the observation angle α increases from 0° to 15°; the diffraction effect reaches its maximum near cusp edge. This is also true for the ablation generation in Figs. 3(a) and 3(b), even though the overlap with the L wave makes it difficult to observe. The D wave is totally overlapped by the L wave for the epicenter observation in Fig. 5(a). As shown in Figs. 6(a) and 6(b), the amplitude evolution of the D wave is similar to that for the ablation regime shown in Figs. 3(a) and 3(b). The D wave and the cuspidal shape of the T_q and T_qT_q wave arrivals for a thermoelastic generation were not observed for an isotropic cylinder.[19] Due to the presence of the D wave, the L wave predicted by the directivity of the thermoelastic generation at the non-epicenter direction is hardly discernible.

VI. CONCLUSION

A theoretical solution is presented to predict the acoustic field generated by a laser point pulse in either the ablation or the thermoelastic regime at any point of a homogeneous and transversely isotropic cylinder. Experimental and theoretical radial displacements under either regime are obtained and compared for a composite cylinder. Good agreement is observed in the time, shape, and relative amplitude (i) of the cylindrical Rayleigh waves with different roundtrips, and (ii) of the various longitudinal and transverse bulk waves propagating through the cylinder or reflected at the free circular surface. The focusing effects that anisotropy gives rise to are observed under either regime. These results pave the way to the nondestructive control of cylindrical parts made of composite material. They will also be helpful to identify useful waves when dealing with inverse problems for the nondestructive evaluation of cylindrical parts. The inverse problem of measuring without contact the five independent stiffness coefficients of fiber reinforced composite cylinders is now in progress.

ACKNOWLEDGMENTS

This work was done at Laboratoire de Mécanique Physique, Université Bordeaux 1. Y.P. was supported by CNRS K.C. Wong fellowships and by the National Natural Science Foundation of China under Grant No. 10234020.

[1] I. Mirsky, "Wave propagation in transversely isotropic circular cylinders: Theory and numerical results," J. Acoust. Soc. Am. **37**, 1016–1026 (1965).
[2] R. G. Payton, *Elastic Wave Propagation in Transversely Isotropic Media* (Nijhoff, The Hague, The Netherlands, 1983).
[3] M. J. Berliner and R. Solecki, "Wave propagation in fluid-loaded, transversely isotropic cylinders: Analytical formulation and numerical results," J. Acoust. Soc. Am. **99**, 1841–1853 (1996).
[4] C. P. Lusher and W. N. Hardy, "Axisymmetric free vibrations of a transversely isotropic finite cylindrical rod," J. Appl. Mech. **55**, 855–862 (1988).
[5] J. Zemanek, "An experimental and theoretical investigation of elastic wave propagation in a cylinder," J. Acoust. Soc. Am. **51**, 265–283 (1972).
[6] F. Honarvar and A. N. Sinclair, "Acoustic wave scattering from transversely isotropic cylinders," J. Acoust. Soc. Am. **100**, 57–63 (1996).
[7] F. Honarvar and A. N. Sinclair, "Nondestructive evaluation of cylindrical components by resonance acoustic spectroscopy," Ultrasonics **36**, 845–854 (1998).
[8] C. B. Scruby and L. E. Drain, *Laser Ultrasonics: Techniques and Applications* (Adam Hilger, New York, 1990).
[9] A. Viktorov, *Rayleigh and Lamb Waves* (Plenum Press, New York, 1967).
[10] D. Royer, E. Dieulesaint, X. Jia, and Y. Shui, "Optical generation and detection of surface acoustic waves on a sphere," Appl. Phys. Lett. **52**, 706–708 (1988).
[11] X. Wu, M. Qian, and J. H. Cantrell, "Dispersive properties of cylindrical Rayleigh waves," Appl. Phys. Lett. **83**, 4053–4055 (2003).
[12] W. Hu and M. Qian, "Propagating properties of cylindrical Rayleigh waves generated by a pulsed laser line source," Chin. Phys. Lett. **21**, 1294–1297 (2004).
[13] R. Burridge, "Lamb's problem for an anisotropic half-space," Q. J. Mech. Appl. Math. **24**, 81–98 (1971).
[14] C.-Y. Wang and J. D. Achenbach, "Lamb's problem for solids of general anisotropy," Wave Motion **24**, 227–242 (1996).
[15] A. G. Every, K. Y. Kim, and A. A. Maznev, "The elastodynamic response of a semi-infinitive anisotropic solid to sudden surface loading," J. Acoust. Soc. Am. **102**, 1346–1355 (1997).
[16] C. Bescond and M. Deschamps, "Dynamic surface response of a semi-infinite anisotropic elastic medium to an impulsive force," J. Acoust. Soc. Am. **103**, 114–124 (1998).
[17] H. J. Maris, "Effect of finite phonon wavelength on phonon focusing," Phys. Rev. B **28**, 7033–7037 (1983).
[18] Y. Pan, C. Rossignol, and B. Audoin, "Acoustic waves generated by a laser line pulse in a transversely isotropic cylinder," Appl. Phys. Lett. **82**, 4379–4381 (2003).
[19] Y. Pan, C. Rossignol, and B. Audoin, "Acoustic waves generated by a laser point source in an isotropic cylinder," J. Acoust. Soc. Am. **116**, 814–820 (2004).
[20] A. Rahman and F. Ahmad, "Representation of the displacement in terms of scalar functions for use in transversely isotropic materials," J. Acoust. Soc. Am. **104**, 3675–3676 (1998).
[21] D. A. Hutchins, *Physical Acoustics* (Academic, New York, 1988), Vol. **18**, pp. 21–123.
[22] L. R. F. Rose, "Point-source representation for laser-generated ultrasound," J. Acoust. Soc. Am. **75**, 723–732 (1984).
[23] Y. H. Berthelot and I. J. Busch-Vishniac, "Thermoacoustic radiation of sound by a moving laser source," J. Acoust. Soc. Am. **81**, 317–327 (1987).
[24] H. Uberall, *Physical Acoustics* (Academic, New York, 1973), Vol. **10**, pp. 1–60.
[25] F. Reverdy and B. Audoin, "Elastic constants determination of anisotropic materials from phase velocities of acoustic waves generated and detected by lasers," J. Acoust. Soc. Am. **109**, 1965–1972 (2001).
[26] M. Deschamps and O. Poncelet, "Inhomogeneous plane wave and the most energetic complex ray," Ultrasonics **40**, 293–296 (2002).

Pressure-sensitive paint as a distributed optical microphone array[a)]

James W. Gregory[b)] and John P. Sullivan
School of Aeronautics and Astronautics, Purdue University, West Lafayette, Indiana 47907

Sameh S. Wanis and Narayanan M. Komerath
School of Aerospace Engineering, Georgia Institute of Technology, Atlanta, Georgia 30332

(Received 1 June 2005; revised 27 October 2005; accepted 31 October 2005)

Pressure-sensitive paint is presented and evaluated in this article as a quantitative technique for measurement of acoustic pressure fluctuations. This work is the culmination of advances in paint technology which enable unsteady measurements of fluctuations over 10 kHz at pressure levels as low as 125 dB. Pressure-sensitive paint may be thought of as a nano-scale array of optical microphones with a spatial resolution limited primarily by the resolution of the imaging device. Thus, pressure-sensitive paint is a powerful tool for making high-amplitude sound pressure measurements. In this work, the paint was used to record ensemble-averaged, time-resolved, quantitative measurements of two-dimensional mode shapes in an acoustic resonance cavity. A wall-mounted speaker generated nonlinear, standing acoustic waves in a rigid enclosure measuring 216 mm wide, 169 mm high, and 102 mm deep. The paint recorded the acoustic surface pressures of the (1,1,0) mode shape at ~1.3 kHz and a sound pressure level of 145.4 dB. Results from the paint are compared with data from a Kulite pressure transducer, and with linear acoustic theory. The paint may be used as a diagnostic technique for ultrasonic tests where high spatial resolution is essential, or in nonlinear acoustic applications such as shock tubes. [DOI: 10.1121/1.2140935]

PACS number(s): 43.38.Zp, 43.25.Zx, 43.25.Gf, 43.20.Ks [AJZ] Pages: 251–261

I. INTRODUCTION

Optical microphones are transducers that modulate light in response to acoustic signals. Most prior instances of optical microphone designs involve the use of some mechanical membrane to modulate the light. Bilaniuk[1] has classified optical microphone transduction techniques into three categories—intensity modulating,[2,3] polarization modulating,[4] and phase modulating.[1] Often these optical microphones are interrogated through fiber optics. The primary advantage of this type of setup is that electrical connections are not required, allowing optical microphones to be used in harsh experimental environments. There are some drawbacks to this type of microphone, however. The typical sensitivity of these optical transducers is not as good as traditional microphones. Furthermore, the fiber-optic interrogation bundle must be positioned close to the sensing membrane element, and these devices are limited to point measurements.

Pressure-sensitive paint (PSP) is detailed in this article as an alternative form of optical microphone. The paint is similar to optical microphones in that it modulates light intensity in response to an acoustic signal. It is fundamentally different, however, in that the paint does not have any mechanical membranes or moving parts. Instead, pressure-sensitive paint modulates the light intensity through a repeatable chemical interaction of the sensing layer with atmospheric oxygen. A photodetector such as a CCD camera or photomultiplier tube (PMT) is employed for interrogation of the paint. Since the paint is composed of nano-scale chemical sensors, the microphone spatial density is quite high. Thus, pressure-sensitive paint serves as a nano-distributed optical microphone array with a spatial resolution limited only by the pixel resolution of the photodetector. The high spatial resolution and fast response allows the paint to be used for high-frequency applications where the characteristic wavelengths are small.

McGraw *et al.*[5] recently demonstrated pressure-sensitive paint as a form of optical microphone. They calibrated the paint for intensity and frequency response, and measured acoustic pressure fluctuations in a standing-wave tube. McGraw's paint formulation involved a chemical sensor of platinum tetra(pentafluorophenyl)porphine (PtTFPP) mixed with a polymer and applied to thin-layer chromatography plate. With this formulation they resolved pressure fluctuations as low as 6 Pa in a frequency range of 150–1300 Hz. Their measurements, however, were limited to the end plate of a one-dimensional standing wave tube where light intensity was integrated over a large area. By integrating light over a large area they were able to improve the signal-to-noise ratio of their measurements, but sacrificed the ability to make two-dimensional measurements. One of the characteristic advantages of pressure-sensitive paint is the ability to make two-dimensional measurements with high spatial resolution. Sakaue has also demonstrated acoustic measurements with pressure-sensitive paint.[6] He developed a paint formu-

[a)]A small portion of this work was presented in "Fluidic Oscillator as a Dynamic Calibration Tool," at the 22nd AIAA Aerodynamic Measurement Technology & Ground Testing Conference, St. Louis, MO, June 2002.

[b)]Electronic mail: jim.gregory@alumni.purdue.edu

lation incorporating PtTFPP deposited on an anodized aluminum surface. Sakaue's measurements were also in a one-dimensional standing wave tube, although the PSP was positioned along the length of the tube. His data were recorded at very acoustic high pressures, on the order of 172 dB.

When used as a distributed optical microphone array, pressure-sensitive paint can provide quantitative mode-shape visualization data. Previous methods for determining acoustic mode shapes have been either qualitative or quantitative methods. Galaitsis developed a qualitative visualization method based on the refraction of light through water.[7] His experiments involved a rectangular cavity partially filled with water. The standing waves inside the cavity deformed the water such that a time-averaged image of the mode shape could be recorded by the varying refraction of light passing through the water. Chinnery *et al.* have recently employed schlieren imaging techniques for the visualization of mode shapes in cylindrical cavities at ultrasonic frequencies.[8]

Quantitative methods for determining mode shapes have required microphone measurements. Either a large array of microphones is required, or more commonly, a small array that can be traversed throughout the region of interest. Smith suggested the use of microphone measurements at multiple locations within an enclosure.[9] He computed the transfer function between signals from multiple microphones at different locations in order to determine the mode shape. Nieter and Singh developed a concept whereby the transfer function between a driving speaker and multiple microphone measurements was used to calculate the mode shape.[10] Their experiments used a traversing microphone within a cylindrical resonance cavity, with the results showing good agreement with linear acoustic theory. In subsequent work, Kung and Singh determined mode shapes in three-dimensional cavities through microphone measurements on the cavity boundary.[11] Knittel and Oswald,[12] as well as Whear and Morrey,[13] developed a technique using an array of two or three microphones to calculate a time-resolved spatial derivative of pressure. They coupled this information with accelerometer data for the loudspeaker cone to determine the mode shapes using structural modal analysis software.

In the current work a rigid, rectangular cavity excited by a single-frequency sound source was chosen as a benchmark application for evaluating the capabilities of PSP for acoustics measurements. The advantage of the rectangular enclosure is that the pressure field is well-known from linear acoustic theory.[14] Furthermore, high-amplitude pressure waves may be generated through resonant amplification, enabling the use of a relatively low-power compression driver to generate measurable pressures. The cavity used in this work was originally developed and used for acoustic shaping experiments in microgravity, where acoustic radiation forces were used to collect particles into desired surfaces.[15] Theoretical[16] and numerical[17] solutions are available for high-amplitude, nonlinear wall pressures in resonant enclosures, but an experimental technique specific to this cavity is needed. Thus, pressure-sensitive paint was used to verify the surface pressure distribution in a rigid enclosure.

II. PAINT DEVELOPMENT

A. Characteristics of pressure-sensitive paint

Pressure-sensitive paint is an oxygen-sensitive optical measurement technique, traditionally developed for aerodynamics applications.[18,19] The oxygen-sensing molecule, known as the luminophore, interacts with oxygen atoms in the test gas in a reversible process that alters the luminescent intensity of the paint. According to Henry's law, the oxygen concentration within the paint layer is proportional to the local partial pressure of oxygen, which is proportional to absolute pressure of air. Thus, the oxygen sensor forms the basis for a pressure-sensitive paint.

In a typical pressure-sensitive paint test, the luminophore molecules are excited to a heightened energy state by illuminating the paint with light of a specific wavelength. This light is best tuned to the absorption spectrum of the paint, and is typically in the ultraviolet to blue range of the spectrum. Before excitation, electrons of the luminophore molecule are in the ground state. When the paint is illuminated, photons are absorbed by the luminophore molecules and the luminophore electrons are elevated to a heightened vibrational state. These electrons in the higher state can release their energy through several mechanisms which return the energy of the molecule back to its ground state. For pressure-sensitive paint applications, the relevant and dominant energy transfer mechanisms are oxygen quenching, phosphorescence, and radiationless decay. For quasisteady quenching, these mechanisms are denoted by the rate constants k_Q, k_P, and k_{NR}, respectively. Oxygen quenching occurs when oxygen molecules in the test gas collide with the activated luminophore molecules. An energy transfer occurs from the luminophore to the oxygen, as the oxygen is easily elevated to a heightened energy state. The oxygen molecules subsequently release this energy through long-wavelength infrared radiation or vibrational relaxation. Phosphorescence of the luminophore (also referred to as luminescence) is the radiative release of energy at a longer wavelength than the excitation light. Nonradiative transfer of energy involves an intersystem transfer from the triplet state to the singlet state, and subsequent vibrational relaxation. Thus, the primary physical mechanisms of energy transfer of interest in pressure-sensitive paint applications are phosphorescence and oxygen quenching. Oxygen quenching is related to the local acoustic pressure, while phosphorescence is measured by photodetectors.

The rate of phosphorescent emission of a pressure-sensitive paint (I) may be expressed as a first-order differential equation,[18]

$$\tau \frac{dI}{dt} + I = \tau k_P \Phi_T a(t), \tag{1}$$

where Φ_T is the triplet quantum yield (the fraction of absorbed photons that produces luminophore molecules in the triplet excited state), and $a(t)$ is the photon absorption rate. The development of Eq. (1) assumes that the lifetime of the luminescent decay is much faster than the characteristic time scale of the pressure fluctuations, which is valid for the sub-

ject acoustics application. The luminescent lifetime τ is given by

$$\tau = \frac{1}{k_{\mathrm{NR}} + k_P + k_Q}, \tag{2}$$

and the quenching constant is related to the local oxygen concentration $[O_2]$ by

$$k_Q = \kappa_Q [O_2], \tag{3}$$

where κ_Q is the quenching rate constant. Thus, the quasi-steady form of Eq. (1) is given by

$$I = \tau k_P \Phi_T a = \frac{k_P \Phi_T a}{k_{\mathrm{NR}} + k_P + \kappa_Q [O_2]}. \tag{4}$$

An intensity ratio may be obtained when Eq. (4) is expressed as a ratio between the test condition and vacuum conditions (the complete absence of oxygen):

$$\frac{I_0}{I} = \frac{k_{\mathrm{NR}} + k_P + \kappa_Q [O_2]}{k_{\mathrm{NR}} + k_P} = 1 + K_{\mathrm{SV}} [O_2]. \tag{5}$$

Here the subscript 0 indicates vacuum conditions, and K_{SV} is the Stern-Volmer constant.[20] Equation (5) expresses the essence of the pressure-sensitive paint technique: measured light intensity from the paint is inversely proportional to the oxygen concentration.

In practical applications it is often infeasible to use vacuum as a reference condition (I_0). Thus, an arbitrary reference condition (I_{ref}) is often used by taking the ratio of Eq. (5) at the test condition and a practical reference point such as atmospheric conditions. This yields the Stern-Volmer relation,

$$\frac{I_{\mathrm{ref}}}{I} = A + B \frac{P}{P_{\mathrm{ref}}}, \tag{6}$$

which is common in aerodynamic applications of pressure-sensitive paint. Here the oxygen concentration $[O_2]$ has been replaced by pressure P since local oxygen concentration varies with air pressure. A and B are the Stern-Volmer calibration coefficients, which are typically sensitive to temperature.

B. Morphology

Conventional pressure-sensitive paint formulations are composed of oxygen-sensitive luminophore molecules embedded in a polymer matrix. The polymer serves as a mechanical binder to hold the luminophore to the model of interest. The properties of most polymers inhibit the diffusion of oxygen within the binder and delay quenching of the luminophore. Sakaue *et al.* have shown that the response time of conventional paint formulations can be as long as a few seconds.[21] These slow response characteristics preclude the use of traditional paint formulations for acoustic measurements. Therefore, a new morphology has been developed to enable rapid response times.

The time response of paint formulations may be modeled by one-dimensional diffusion of a gas through the polymer binder. The relevant parameters controlling the response time τ_{resp} are given by[22,23]

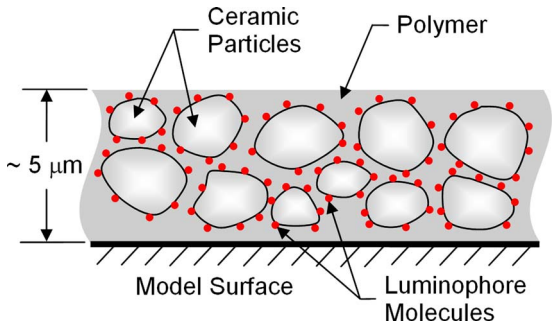

FIG. 1. Morphology of the polymer/ceramic pressure-sensitive paint formulation.

$$\tau_{\mathrm{resp}} \propto \frac{h^2}{D}, \tag{7}$$

where h is the paint thickness and D is the gas diffusion constant for the binder. According to Eq. (7), the time response of pressure-sensitive paints may be improved by reducing the paint thickness or by increasing the diffusivity of the binder matrix. As the paint thickness is decreased, the amount of light emitted by the paint also decreases with a concomitant decrease in signal-to-noise ratio. Also, the gas diffusion constant of many polymers is so low that even very thin paint films will still exhibit unacceptably slow response times. Thus, a decrease in paint thickness is not an ideal solution for optimizing the paint response. A better solution is to significantly increase the gas diffusion constant of the matrix binder. This concept has led to a new class of pressure-sensitive paints based on *porous* binders.

Porous pressure-sensitive paints are based upon a matrix structure that is porous and relatively open to the test gas. The open structure allows for oxygen molecules to freely move in and out of the binder by gas diffusion processes. This is accomplished by drastically increasing the surface area of the binder, which enlarges the air-binder interface. This surface area enhancement modifies the diffusion coefficient shown in Eq. (7), creating an effective diffusion coefficient (D_{eff}) that is related to the fractal dimension of the porous structure.[24] Thus, the response time decreases as the value of the effective diffusion coefficient increases.

Three types of porous binders have recently been developed for aerodynamic testing: thin-layer chromatography plate,[25] anodized aluminum,[22,26,27] and polymer/ceramic.[28,29] Thin-layer chromatography plate is commonly used in chemistry laboratories and is composed of a thin layer ($\sim$250 μm) of silica gel. The disadvantages of the thin-layer chromatography plate are that it is fragile and limited to simple shapes. Anodized aluminum is created through an electrochemical process by etching small pores ($\sim$10-nm diameter) on an aluminum surface. The luminophore is deposited directly on the porous surface by chemical and physical adsorption. Anodized aluminum provides the fastest paint response times, but is limited by the choice of material and cannot be sprayed onto a model. Polymer/ceramic PSP is a hybrid that uses a small amount of polymer with a large amount of ceramic particles, as shown in Fig. 1. The resulting aggregate is a highly porous surface that allows for rapid

diffusion of the test gas. The primary advantage of polymer/ceramic paint is that it may be sprayed on a model, and offers reasonable response times.

Polymer/ceramic was selected for the current investigation because of its robust mechanical properties. The particular formulation created for acoustic testing is a water-based paint that was sprayed on one wall of the cavity. A slurry mixture was prepared by mixing 1.8 g of 0.4 μm rutile titanium dioxide (DuPont R-900) for every gram of distilled water. In order to separate any TiO_2 agglomerates, 12 mg of dispersant (Rohm & Haas D-3021) was added for every gram of water. The resulting slurry mixture was ball-milled for 1 h to mechanically break up TiO_2 agglomerates. The polymer (Rohm & Haas B-1035) was then stirred into the slurry mixture at a 3.5% weight ratio. The resulting polymer/ceramic formulation was then sprayed directly onto the test article. The chemical sensor, known as the luminophore, is the active ingredient of the paint formulation that is sensitive to local oxygen concentration. The luminophore selected for these tests was Tris(Bathophenanthroline) Ruthenium Dichloride (GFS Chemicals, CAS # 36309-88-3). This luminescent molecule was chosen because of its characteristically fast lifetime—approximately 5 μs at atmospheric conditions.[30] The luminophore was dissolved in methanol, sprayed over the binder, and allowed to leach into the polymer/ceramic structure.

C. Dynamic response characteristics

The polymer/ceramic paint morphology has been tailored to optimize the frequency response characteristics of the paint. Before being applied to acoustic testing, however, the response characteristics must be evaluated in some manner. The fluid-dynamic flow field of a fluidic oscillator was used to demonstrate the fast response characteristics of these paints. A fluidic oscillator produces an oscillating jet when supplied with pressurized air, where the oscillation frequency varies with the supply pressure.[31] The wave form of the oscillating jet approximates a square wave. As such, the flow field is rich in high-frequency content, and is ideal for calibrating the frequency response of the paint sensor. The pressure field of the impinging fluidic jet is a hydrodynamic pressure fluctuation ($P/P_{\text{atm}} \cong 1.6$), rather than an acoustic pressure fluctuation. The pressure levels induced by the fluidic jet are much greater than typical sound pressures. There is no expected difference in the frequency response characteristics of the paint due to the excitation mechanism (i.e., hydrodynamic versus acoustic) because the quenching mechanism remains the same. Gregory and Sullivan[23] have shown that large-amplitude pressure fluctuations near the frequency response limit of the paint may induce a nonlinear response. Low-level pressure fluctuations such as acoustic pressures typically are not affected by the nonlinear response characteristics. Thus, it is presumed that the response for acoustic pressures will be at least as fast as the hydrodynamic response.

In the dynamic calibration experiments, the paint was excited with a 404-nm diode laser and the intensity response was recorded with a PMT. The paint response was compared with measurements from a collocated Kulite pressure transducer. Power spectra of the two signals are shown in Fig. 2. The 5.3-kHz fundamental frequency from the fluidic oscillator is clearly shown as the dominant peak in both the Kulite and pressure-sensitive paint power spectra. Higher-order harmonics are visible up through the fourth harmonic for the Kulite and the third harmonic for the PSP. Spurious harmonics at 2.7 and 8.0 kHz are also present in the Kulite data, but not in the pressure-sensitive paint data. This is an artifact of the large scale of the Kulite (~2.5 mm) relative to the hydrodynamic jet diameter (~1.5 mm), while the diameter of the laser spot for PSP is much smaller (~0.5 mm). Thus, the absence of these spurious harmonics in the paint signal's power spectrum is not due to a deficiency in the paint response. The peak magnitudes in the paint spectrum correlate well to the Kulite peak magnitudes, with the largest difference occurring at 10.5 kHz where the paint signal is only 2 dB down from the Kulite response. The signal-to-noise ratio of the instrumentation employed in these experiments was low, rendering the higher-frequency content of the flow field undetectable. The noise floor at −15 dB was higher than any frequency component above 20 kHz. Thus, the paint's frequency response is flat to at least 15 kHz, and beyond this point the data are inconclusive because of the high noise level in the paint measurements. These response characteristics are sufficient for the current study, where the frequency of interest is on the order of 1.3 kHz.

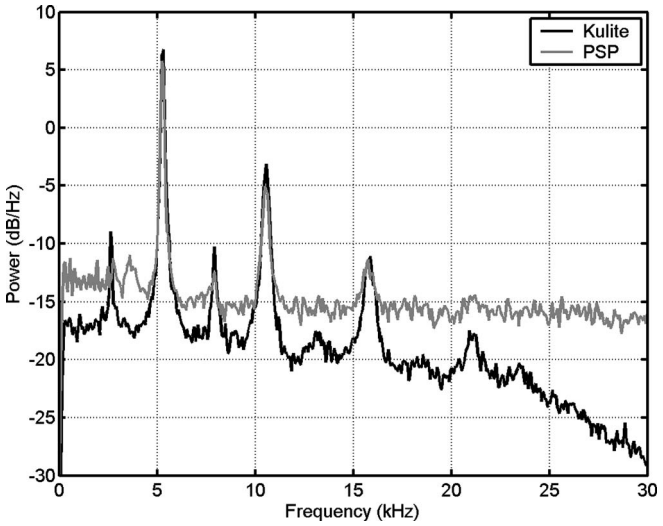

FIG. 2. Dynamic calibration of polymer/ceramic pressure-sensitive paint with a fluidic oscillator.

D. Sensitivity

The luminophore molecules employed in porous paint formulations exhibit a nonlinear intensity response when subjected to a wide range of pressures, as shown in Fig. 3. The sensitivity is relatively high at very low ambient pressures, but the response is less sensitive near atmospheric conditions. When the paint is subjected to small pressure changes at atmospheric conditions, however, the response may be considered linear and Eq. (6) serves as a good description of the intensity response. The linear calibration co-

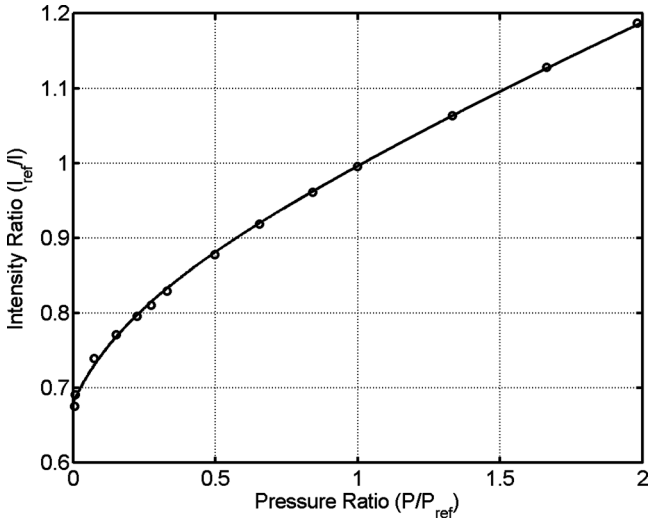

FIG. 3. Typical calibration of polymer/ceramic pressure-sensitive paint over a range from vacuum to two atmospheres. Although the response is nonlinear over this broad range, it may be approximated by a linear fit over the small acoustic pressures about ambient conditions.

efficients at atmospheric conditions for the polymer/ceramic paint are $A=0.791$ and $B=0.209$. The slope of the calibration curve (B) is somewhat lower than the $B=0.66$ sensitivity of the paint developed by McGraw *et al.*[5] Note that this diminished sensitivity is a consequence of the porous structure of the paint formulation that enables fast response times, making the luminophore molecules nearly quenched at atmospheric conditions. Despite having a lower sensitivity, the frequency response of the polymer/ceramic paint formulation ($\geqslant$15 kHz) is significantly greater than the response of McGraw's formulation (3.55 kHz).

The sensitivity of the paint formulation establishes a limit on the minimum detectable pressure change that can be resolved by the system. This minimum level also depends on the quality of the photodetector and digitizing equipment used for the measurements. Pressure-sensitive paint measurements are inherently absolute, rather than ac-coupled. The chemistry and optics of the system are unable to separate the pressure fluctuations from the mean pressure. Thus, there is no way to offset the signals to remove the paint response to the mean pressure before the signals are recorded. For example, a strong acoustic signal with a pressure amplitude of 283 Pa (140 dB sound pressure level) and a mean atmospheric pressure of 101.3 kPa produces a maximum pressure ratio of ±0.28%. The intensity response of the polymer/ceramic paint to this pressure fluctuation is ±0.058%. If a 14-bit photodetection system is used to record this signal, the maximum bit change that will be recorded is ±10 counts (out of a possible 16 384!).

Such a small change in measured signal is easily masked by the noise in the measurement system. Thus, the signal-to-noise ratio of the photodetector, along with the sensitivity of the paint, are the limiting factors that establish the minimum detectable level (Liu *et al.*).[32] In the photon shot noise limited case, the signal-to-noise ratio is related to the photoelectron capacity by[32]

$$\mathrm{SNR} = \sqrt{\frac{V}{G\hbar\nu B_d}} = \sqrt{n_{\mathrm{pe}}}, \tag{8}$$

where V is the photodetector output, G is the system gain, $\hbar$ is Planck's constant, ν is the frequency, B_d is the electrical bandwidth of the detection electronics, and n_{pe} is the total number of photoelectrons collected over the integration time. An expression for the minimum detectable level is then given by[32]

$$\frac{(\Delta P)_{\min}}{P} = \frac{1}{\sqrt{(n_{\mathrm{pe\ ref}})_{\max}}}\left[1 + \frac{A}{B}\frac{P_{\mathrm{ref}}}{P}\right] \times \left[1 + A + B\frac{P}{P_{\mathrm{ref}}}\right]^{1/2}, \tag{9}$$

where A and B are the linear calibration coefficients, P is approximately equal to P_{ref} for acoustics measurements, and $(n_{\mathrm{pe\ ref}})_{\max}$ is the full-well electron capacity of the CCD sensor. The 14-bit CCD sensor used in the current work has a full-well capacity of 255 000 electrons. When used with the polymer/ceramic paint formulation, this measurement system has a minimum detectable level of ±1.34% (±1.36 kPa at atmospheric conditions). Thus, the minimum resolvable pressure change is dependent upon the full-well capacity of the photodetector. This minimum level may be improved by averaging multiple images, because photon shot noise is a random noise source. If N images are averaged, then the minimum detectable level is reduced by a factor of $N^{1/2}$. Yet another method for improving the minimum level is averaging pixels in a region, known as binning. This has the disadvantage of reduced

TABLE I. Theoretical minimum-detectable-level of pressure-sensitive paint, with 100 images averaged.

	Scroggin's polymer/ceramic formulation[a] ($\geqslant$15 kHz response)		McGraw's paint formulation[b] (3.55 kHz response)	
Photodetector full-well electron capacity	Minimum pressure amplitude (Pa)	Minimum SPL (dB, ref 20 μPa)	Minimum pressure amplitude (Pa)	Minimum SPL (dB, ref 20 μPa)
32 000	383.3	142.6	121.4	132.6
150 000	177.0	135.9	56.0	125.9
255 000	135.8	133.6	43.0	123.6
500 000	97.0	130.7	30.7	120.7

[a]References 28 and 29.
[b]Reference 5.

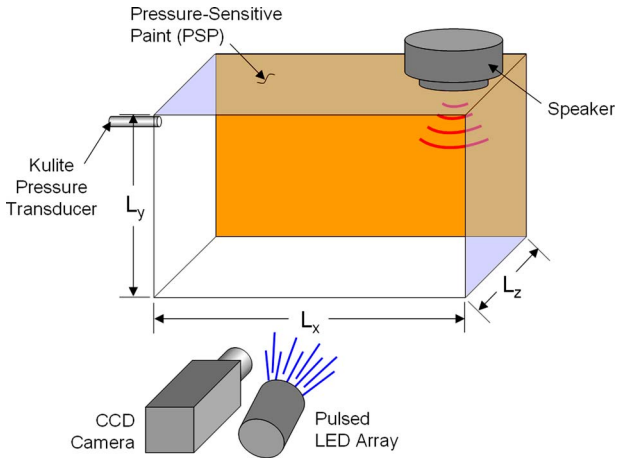

FIG. 4. Experimental setup of the cavity with pressure-sensitive paint.

spatial resolution, however. A summary of these effects is presented in Table I, with a comparison of Scroggin's polymer/ceramic paint formulation[28,29] with McGraw's paint formulation[5] when 100 images are averaged. The sensitivity of McGraw's paint is about three times that of the polymer/ceramic paint, yielding a 10-dB improvement in minimum detectable level, but at the expense of frequency response. Also evident in Table I is how the quality of the photodetector, expressed as full-well electron capacity, improves the minimum detectable level. The lower full-well electron capacities correspond to earlier camera designs,[33] while the higher values correspond to higher performance devices.

The main challenge in using pressure-sensitive paint for acoustic measurements is thus to resolve small intensity changes. Conversely, one advantage is that the paints do not have a rated maximum pressure that can be resolved. Microphones and piezoresistive pressure transducers have an upper pressure limit based on the mechanical properties of the diaphragm. The burst pressure can limit the usefulness of these conventional transducers for some nonlinear measurements, but pressure-sensitive paint is not limited in this regard.

III. EXPERIMENTAL SETUP

The experimental setup for the cavity pressure measurements is shown in Fig. 4. The cavity is made of 12.7-mm-thick acrylic, with overall dimensions of 216 mm length (L_x), 169 mm height (L_y), and 102 mm depth (L_z). The sound source used to drive the oscillations was a 100 -W compression driver typically used on emergency vehicles (Southern Vehicle Products, D-60). The driver was mounted in the upper right-hand corner of the cavity ($x/L_x \approx 0.9$, $y/L_y = 1$, $z/L_z \approx 0.5$), flush with the inner cavity wall and facing downwards. The corner is the most efficient location for exciting a rectangular cavity because it is always a pressure anti-node for any mode. A Kulite pressure transducer (XCQ-062-15D) was mounted in the forward upper-left corner, as shown in Fig. 4. The transducer signal was high-pass filtered at 500 Hz and low-pass filtered at 50 kHz. The Kulite measured the pressure fluctuations at the antinode, and provided a reference signal for phase-locking the pressure-sensitive paint data to the resonant oscillations.

The cavity was mounted with the x dimension horizontal and the y dimension vertical, with the speaker on the upper surface as shown in Fig. 4. The back surface of the cavity was a removable lid painted with polymer/ceramic PSP and bathophen ruthenium luminophore. Pressure-sensitive paint measurements were made with a Photometrics 14-bit CCD camera and an ISSI LM2 pulsed LED array ($\lambda \approx 470$ nm) for illumination. A 590-nm long-pass colored-glass filter was mounted on the camera to separate the excitation light from the paint luminescence. A camera shutter speed of 185 ms was selected in order to acquire sufficient luminescence from the paint. Since the acoustic pressure field is unsteady, phase-locking techniques were required to record time-resolved pressure-sensitive paint data. The pulsing of the LED array was synchronized with the pressure fluctuations measured by the Kulite pressure transducer through the gating function on a triggered oscilloscope. A variable delay was added to the oscilloscope's TTL pulse with a Berkeley Nucleonics BNC-555 pulse/delay generator. Phase-locked time histories were recorded by varying the delay throughout the oscillation cycle. Thus, this system makes phase-averaged measurements of the unsteady pressure field. The excitation pulse width was typically 1.0% of the oscillation period, and each delay step was 8.3% of the period. Thus, there were 12 time steps evenly spaced throughout the complete oscillation cycle.

IV. DATA REDUCTION

Data reduction techniques were developed in order to successfully resolve acoustic-level pressures. The fidelity of pressure-sensitive paint measurements is primarily limited by shot noise in the CCD camera. Furthermore, the temperature sensitivity of PSP is a source of significant bias errors in most paint measurements. These two factors combined account for most of the errors in paint measurements.[32] Another potential source of error in pressure-sensitive paint measurements is any misalignment of the test object between the reference and test condition images. Particularly when low-level pressures are being measured, image misalignment errors can be substantial. These sources of error were reduced through use of the data acquisition and reduction techniques discussed as follows.

A. Shot noise

Random errors in the paint's intensity signal are primarily attributable to shot noise in the CCD sensor. Shot noise is related to the electrical noise generated when the sensor converts the photons to an electrical signal, and in the digitization of that signal. Since shot noise is a random error, it may be reduced through averaging.[34] The error decreases with the square root of the number of samples acquired. Image averaging is a straightforward technique for reducing shot noise, but offers diminishing returns as the number of samples increases. In the current tests, 100 images were averaged to compile a single speaker-on image for each phase delay and test condition. The reference image was also an

average of 100 images. Thus, the random shot noise for both the speaker-on and reference images was reduced by an order of magnitude by averaging. This in turn improves the minimum detectable level by 20 dB.

B. Temperature effects

In aerodynamic testing in wind tunnels, temperature variations can be a significant source of error for pressure-sensitive paint measurements. If there is an unknown temperature change between the reference and test condition images, the temperature effect will produce a bias of unknown magnitude in the pressure data. Researchers have compensated for the temperature effect by using a temperature-sensitive paint to correct the luminescent data.[35] An alternative technique is to use a bi-luminophore paint, which allows acquisition of the pressure and temperature data simultaneously without having to repaint the model.[36,37]

The maximum temperature fluctuation induced by sound pressure fluctuation is given by[14]

$$T' = T_0 \frac{\gamma - 1}{\gamma} \frac{P'}{P_0}. \tag{10}$$

Thus, for a ±500-Pa pressure fluctuation at atmospheric pressure (101.3 kPa) and temperature (298 K), the maximum temperature fluctuation will be ±0.42 K. The temperature sensitivity of polymer/ceramic pressure-sensitive paint is given as 1.24% change in intensity per degree Kelvin.[38] Despite these factors, temperature-induced errors are negligible in the current set of experiments. The painted acrylic surface has a fairly large heat capacity, making the temperature oscillations in the paint layer several orders of magnitude less than the maximum fluctuation in the test gas. McGraw *et al.*[5] made a similar argument for their paint tests, and showed experimentally that temperature gradients induced by high-amplitude acoustic fields could be safely neglected. Furthermore, Sakaue[6] showed a temperature gradient of less than 0.01 K across the entire painted surface of the cavity, even when driving at high sound pressure levels (172 dB). This represents an error in sound pressure of about 7 Pa. Thus, temperature gradients and fluctuations are considered negligible, and explicit temperature-correction schemes are unnecessary for the subject work.

C. Image misalignment

Any slight displacement of the cavity between the speaker-on and reference images can cause substantial errors, particularly if there are significant spatial inhomogenaities in the paint layer. Image registration techniques are one attempt at mitigating this issue.[39] A more effective and straightforward correction, however, is to limit or eliminate the model motion. In these tests, the cavity was securely fixed to the table with rubber mounts and clamps. The rubber provided a certain amount of damping and traction to prevent motion of the box induced by speaker vibrations. Furthermore, it was important to minimize the vibrations in the lab. Data quality was significantly enhanced when images were acquired in a quiet, vibration-free environment.

D. Data reduction procedure

A total of 200 images were acquired for each phase-locked position within the oscillation cycle. The images were acquired in 20 sets of 10 images, each set consisting of 5 speaker-on and 5 speaker-off conditions. Each image was normalized by the average intensity value of the painted surface. The 100 speaker-on images were averaged together, as were the 100 speaker-off images. An intensity ratio was calculated by dividing the speaker-off averaged image by the speaker-on averaged image. This scheme was repeated for all 12 phase delays to compile a time history throughout the oscillation cycle. The intensity images were then converted to pressure through an *in situ* calibration from the Kulite pressure transducer. The pressure data were then spatially filtered with a two-dimensional low-pass spatial filter with a frequency cutoff of 3 wavelengths per dimension. This filter is useful in this application because sinusoidal fluctuations are anticipated in the resonance cavity, and any higher spatial frequencies will be due only to nonlinear effects and should not exceed the third harmonic. After spatial filtering, a temporal low-pass filter was applied to the pressure time-history at each pixel location. The filter was a third-order Chebyshev-II filter with the stop-band 20-dB down and a cutoff frequency of 5 kHz.

V. RESULTS

The (1,1,0) mode within the cavity was excited by a corner-mounted loudspeaker and the paint response was recorded. The pressure-sensitive paint results are then compared with linear acoustic theory as well as measured data from a conventional piezoresistive pressure transducer.

A. Linear modal theory

Despite the fact that the acoustic pressures in the cavity are so high that nonlinear effects are anticipated, linear modal theory provides a good first approximation of the sound field. Pierce has derived modal theory for a rigid-walled enclosure, based on a solution of the Helmholtz equation.[14] The resulting expression is the following spatiotemporal response for the sound pressure:

$$p(x,y,z,t) = \cos\left(\frac{n_x \pi x}{L_x}\right)\cos\left(\frac{n_y \pi y}{L_y}\right)\cos\left(\frac{n_z \pi z}{L_z}\right)e^{-i\omega(n)t}. \tag{11}$$

Here n_x, n_y, and n_z are the mode numbers; L_x, L_y, and L_z are the cavity dimensions; and the resonance frequency for a particular mode is given by

$$\omega(n) = c\pi\sqrt{\left(\frac{n_x}{L_x}\right)^2 + \left(\frac{n_y}{L_y}\right)^2 + \left(\frac{n_z}{L_z}\right)^2}, \tag{12}$$

where c is the speed of sound. The dimensions of the subject cavity were L_x=0.216 m, L_y=0.169 m, and L_z=0.102 m and the experiments were performed at room temperature (24.1 °C). With these parameters, Eq. (12) indicates that the resonant frequency should be 1298 Hz for the (1,1,0) mode. Equation (11) yields the pressure distribution inside the cavity volume. The calculated surface-pressure field

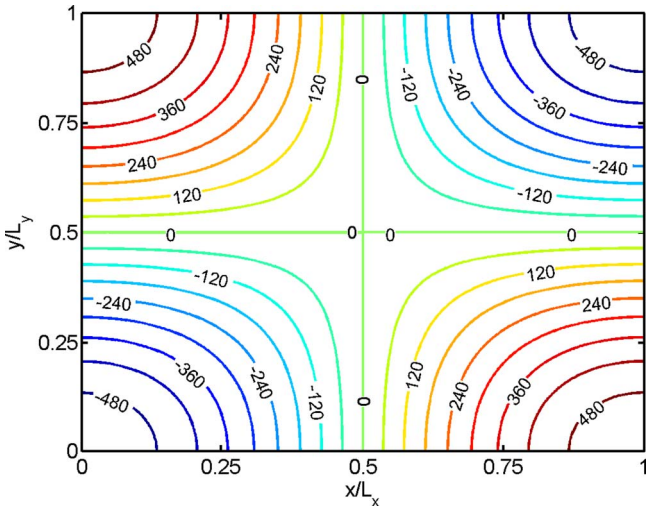

FIG. 5. Analytical solution for the (1,1,0) mode shape in a rectangular cavity. ω=1298 Hz, L_x=0.216 m, L_y=0.169 m, and L_z=0.102 m. Pressure (Pa) is scaled to match the magnitude of experimental results.

on the cavity wall is shown in Fig. 5, with the amplitude scaled to match the experimental data. The nodal lines in the pressure field are along the central axes of the x and y coordinates (x is horizontal and y is vertical in the figure).

B. Pressure-sensitive paint results

The frequency of the driving signal was adjusted such that a maximum pressure amplitude was obtained near the resonant frequency for the (1,1,0) mode. The tuned driving frequency was 1286 Hz, which is within 1% of the predicted resonance frequency. Figure 6 shows pressure-sensitive paint data for the (1,1,0) mode shape at an SPL of 145.4 dB. This pressure map represents one phase-averaged point within the oscillation period, at the condition when the anti-node pressure is nearly maximum. The pressure distribution compares favorably with the general distribution from linear theory shown in Fig. 5. There are some minor differences between the paint data and the theoretical solution: the nodal lines are slightly curved, and the pressure in the center of the reso-

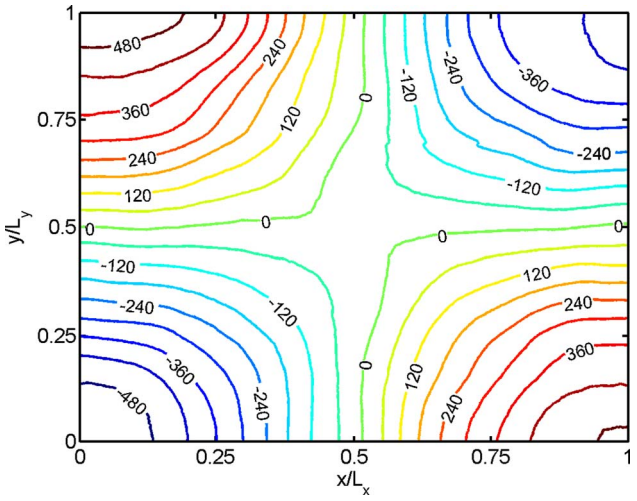

FIG. 6. Pressure-sensitive paint data for the (1,1,0) mode shape at 145.4 dB and ω=1286 Hz. Pressure is expressed in Pascals.

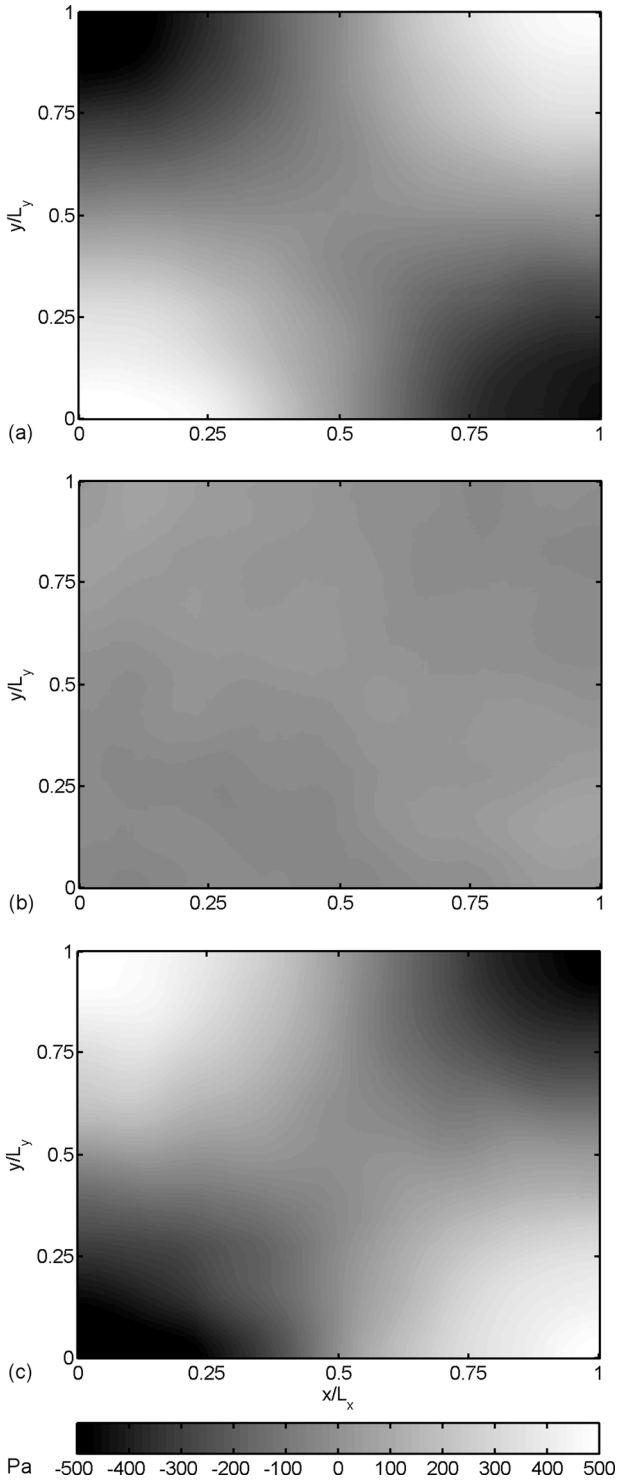

FIG. 7. Pressure-sensitive paint data for the (1,1,0) mode shape at 145.4 dB and ω=1286 Hz. Three phase-averaged time steps are represented: (a) 0°, (b) 90°, and (c) 180°.

nance cavity is slightly lower than ambient pressure. Furthermore, the maximum amplitudes in the left corners are slightly greater than the pressure amplitudes in the right corners. These differences may be attributed to nonlinear effects at the high sound pressure levels of these tests (145.4 dB).

Figure 7 shows the spatial pressure distribution at three time steps, separated by 90° phase within the oscillation cycle. Figures 7(a) and 7(c) show the antinode pressures at

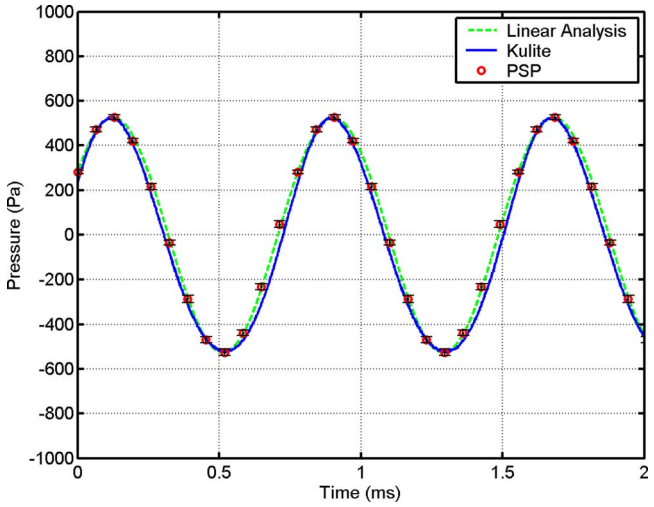

FIG. 8. Pressure time-history comparison between pressure-sensitive paint, Kulite pressure transducer measurements, and linear theory. PSP data were taken from one corner of the resonance cavity, and the Kulite transducer was also corner-mounted. Error bars on the PSP data indicate an average uncertainty of ±12.5 Pa.

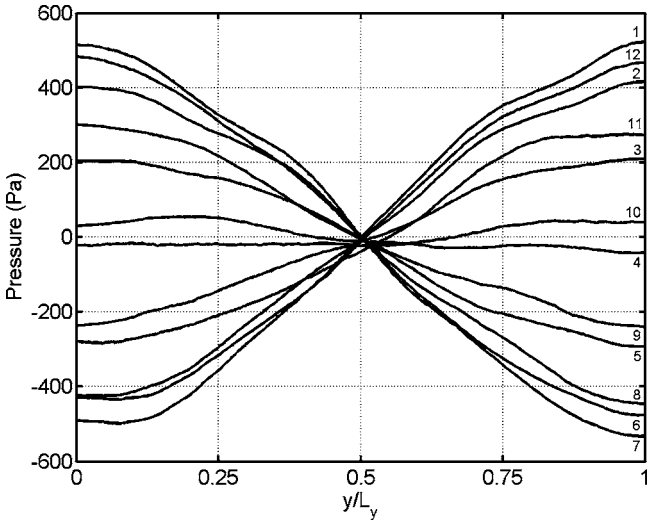

FIG. 10. Vertical cross section of the pressure-sensitive paint data at $x/L_x=0$. The curves represent twelve time steps equally spaced throughout the period, and are sequentially numbered. The node is clearly visible at $y/L_y=0.5$ and exhibits very little motion.

their maxima and minima. Figure 7(b), however, shows a nearly uniform pressure across the cavity, as expected. The uniform pressure distribution at this time step confirms the isothermal assumption.

One sample time-history from the paint data at a single point is shown in Fig. 8. The signal from the Kulite pressure transducer is compared with the analytical solution and the pressure-sensitive paint data points. The paint data results from averaging the signal in a 10-pixel square window in the bottom, left corner of the cavity ($x/L_x \approx 0, y/L_y \approx 0$). The error bars on the PSP data are estimated from the standard deviation of the 100-sample average, yielding a mean uncertainty of ±12.5 Pa. The pressure time-history within the cavity is slightly nonlinear, as evidenced by the slight differences between the Kulite transducer measurement and the linear theory. These slight nonlinearities are to be expected at the moderately high pressure levels at which the cavity was driven. Data shown in Fig. 9 provide an indication of how well the pressure-sensitive paint resolves the nonlinearities present in the acoustic field. The solid curve represents the

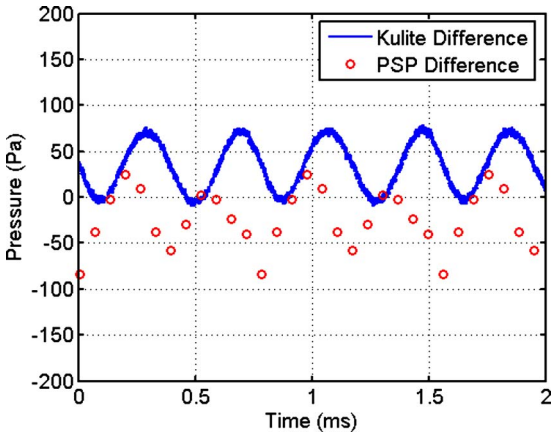

FIG. 9. Difference between Kulite transducer data and linear theory, compared with PSP difference from linear theory.

difference between the Kulite transducer data and the linear theory, indicating the level of nonlinearity. The data points are the difference between the PSP data and the linear theory. The paint data have a bias error between 50 and 100 Pa, when compared to the Kulite data. This bias error may be due to uncertainty in the magnitude and time scale of the *in situ* calibration process, and ultimately is about one order of magnitude larger than the 115.8 Pa minimum detectable level predicted by Eq. (9).

A cross section of the paint data along the left vertical edge ($x/L_x=0$) of the cavity is shown in Fig. 10. Each curve represents a separate time step, spaced equally throughout the period of 777 μs. The node is clearly visible at the midpoint of the wall ($y/L_y=0.5$), where the pressure fluctuations are nearly zero. There is some distortion visible in the spatial wave form, but the data largely resemble the linear numerical results of Vanhille and Campos-Pozuelo.[17] A pressure plot of the phase-averaged rms pressure fluctuations is shown in Fig. 11. This plot also indicates the node locations across the end wall of the resonance cavity, taking into account the entire cycle of the pressure fluctuation. This plot is a concise representation of the large volume of data generated by the pressure-sensitive paint measurements.

C. Discussion

The level of the pressure amplitudes measured in these experiments is on the order of 500 Pa. It is estimated that this pressure-sensitive paint system and data reduction methodology are capable of reliably resolving pressure amplitudes as low as 50 Pa (125 dB). Since a 10-pixel square region was averaged from the 100-image average at each data point, the theoretical SNR was improved by a factor of 100. Thus, the minimum detectable level for this test was 115.8 dB, which is 9 dB lower than the experimentally estimated minimum of 125 dB.

A unique characteristic of porous paint formulations can be employed to improve the pressure sensitivity. Figure 3

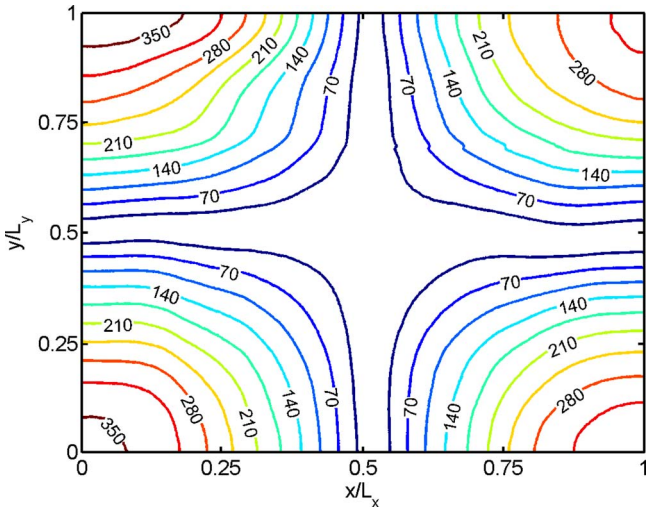

FIG. 11. rms pressure data (Pa) as measured by pressure-sensitive paint for the (1,1,0) mode shape.

shows that the slope of the calibration curve near vacuum conditions is approximately 3.7 times higher than the slope at atmospheric conditions. If the mean pressure can be reduced, then the higher sensitivity of the paint formulation at these pressures can be advantageously exploited. A second alternative is to alter the test gas within the resonance cavity. If an inert gas such as nitrogen or argon at atmospheric pressure is injected with trace amounts of oxygen, then the resulting gas mixture approximates air at low mean pressures as sensed by the paint.

One significant advantage of the current test is that the pressure field is repeatable, which allows for phase-averaging techniques to be employed. If a transient pressure field must be measured, then other techniques and instrumentation can be utilized. A high-speed CCD camera may be used, although the lower signal-to-noise ratio of these cameras will establish a higher minimum-detectable-level. Alternatively, a point measurement could be acquired with a laser-scanning system for illumination and a photomultiplier tube for detection. This type of system offers much higher light intensity, which improves the signal-to-noise ratio for real-time measurements.

A hallmark of the polymer/ceramic paint utilized in these tests is that it is a very bright paint formulation. The titanium dioxide particles present in the paint not only enhance the response time, but also serve as reflective particles that make the paint much brighter than most other formulations. This allows for a very short shutter exposure time (185 ms), which decreases thermal noise in the image. The total amount of light integrated by the camera was 185 ms: 100 images were acquired at 185-ms each, but the excitation light was pulsed such that the paint was illuminated for 1% of the exposure time. This contrasts with the 4-s of light required for Brown's tests of a NACA 0012 airfoil in a low-speed wind tunnel.[34] He found that rms error was adequately reduced by averaging 8 wind-on images, with a 500 ms exposure for each image. The total pressure gradient over the airfoil surface was about 4 kPa. The significant limiting error source in his tests was a temperature change as the wind tunnel cooled down after the run. In the current acoustic PSP tests, which are not hindered by temperature problems, the resolved pressure gradient is on the order of 1 kPa and the total integrated light is 185 ms.

VI. CONCLUSIONS

Pressure-sensitive paint was used to measure sound pressure fluctuations at a frequency of about 1.3 kHz. The (1,1,0) mode shape within a rigid, rectangular cavity was effectively resolved with the PSP system. This work overcomes two significant challenges that have limited pressure-sensitive paint measurements of acoustic pressures in the past. First, the excellent frequency response characteristics ($\geqslant$15 kHz) of the porous paint formulations have allowed time-resolved measurements of the unsteady fluctuations. The second challenge addressed was the sensitivity limitation of pressure-sensitive paints. Data acquisition and reduction techniques were developed to extend the resolvable pressure limitation of most paints. Pressure amplitudes on the order of 500 Pa (145 dB) were measured, and it is estimated that this system is capable of measuring pressure amplitudes as low as 50 Pa (125 dB). Furthermore, the paint system has no theoretical limit on the maximum pressure levels that can be measured, making the system ideal for nonlinear acoustics measurements. The paint measurements in the current tests compared exceptionally well with both linear modal theory and experimental measurements with a Kulite pressure transducer. These tests demonstrate the utility of pressure-sensitive paint for making acoustics measurements. The pressure-sensitive paint data provide a complete time-history of the pressure at over 137 000 pixel locations across the 365-cm^2 area of the cavity. As such, the paint system is a distributed array of nano-scale optical microphones. The pressure-sensitive paint system described in this work may be applied to tests where high spatial resolution is required, such as nonlinear acoustics, ultrasonic measurements, and acoustics in MEMS devices.

ACKNOWLEDGMENTS

Funding for this work was provided by the NASA Graduate Student Researchers Program through NASA Glenn Research Center and NASA Langley Research Center. The Boeing Company has loaned the CCD camera that was used in these tests. The authors also wish to thank Luc Mongeau for his comments and suggestions. Funding for this work was provided by the NASA Graduate student Researchers Program Center. The Boeing Company has loaned the CCD camera that was used in these tests. The authors would like to thank Tim Bencic of the Optical Instrumentation Technology Branch at NASA Glenn, who provided lab space for the dynamic calibration experiments, as well as discussions that were the progenitor for this work. The authors also wish to thank Luc Mongeau for his comments and suggestions.

[1]N. Bilaniuk, "Optical microphone transduction techniques," Appl. Acoust. **50**, 35–63 (1997).
[2]D. Garthe, "Fiber- and integrated-optical microphones based on intensity modulation by beam deflection at a moving membrane," Sens. Actuators,

A **A37–A38**, 484–488 (1993).
[3]A. Hu and F. W. Cuomo, "Theoretical and experimental study of a fiber optic microphone," J. Acoust. Soc. Am. **91**, 3049–3056 (1992).
[4]E. L. Vinogradova, O. A. Kapustina, V. N. Reshetov, V. D. Svet, and G. N. Yakovenko, "Characteristics of an optical microphone using a nematic liquid crystal," Sov. Phys. Acoust. **31**, 10–12 (1985).
[5]C. M. McGraw, H. Shroff, G. Khalil, and J. B. Callis, "The phosphorescence microphone: A device for testing oxygen sensors and films," Rev. Sci. Instrum. **74**, 5260–5266 (2003).
[6]H. Sakaue, "Anodized aluminum pressure sensitive paint for unsteady aerodynamic applications," Ph.D. dissertation, School of Aeronautics and Astronautics, Purdue University, West Lafayette, IN 2003.
[7]A. G. Galaitsis, "Visualization of the time-average pressure distribution in a rectangular resonant cavity," J. Acoust. Soc. Am. **52**, 1569–1571 (1972).
[8]P. A. Chinnery, V. F. Humphrey, and C. Beckett, "The schlieren image of two-dimensional ultrasonic fields and cavity resonances," J. Acoust. Soc. Am. **101**, 250–256 (1997).
[9]D. L. Smith, "Experimental techniques for acoustic modal analysis of cavities," Internoise 129–132 (1976).
[10]J. J. Nieter and R. Singh, "Acoustic modal analysis experiment," J. Acoust. Soc. Am. **72**, 319–326 (1982).
[11]C.-H. Kung and R. Singh, "Experimental modal analysis technique for three-dimensional acoustic cavities," J. Acoust. Soc. Am. **77**, 731–738 (1985).
[12]J. D. Knittel and L. J. Oswald, "An experimental technique for acoustic modal analysis in three-dimensional cavities," SAE paper 870974, Society of Automotive Engineers, 1987, pp. 205–217.
[13]F. R. Whear and D. Morrey, "A technique for experimental acoustic modal analysis," J. Mech. Eng. Sci. **210**, 143–151 (1996).
[14]A. D. Pierce, *Acoustics—An Introduction to Its Physical Principles and Applications* (Acoustical Society of America, Woodbury, NY, 1989).
[15]S. Wanis, A. Sercovich, and N. M. Komerath, "Acoustic shaping in microgravity: Higher order surface shapes," AIAA 99-0954, 37th Aerospace Sciences Meeting and Exhibit, American Institute of Aeronautics and Astronautics, Reno, NV, 1999.
[16]A. B. Coppens and J. V. Sanders, "Finite-amplitude standing waves within real cavities," J. Acoust. Soc. Am. **58**, 1133–1140 (1975).
[17]C. Vanhille and C. Campos-Pozuelo, "Numerical simulation of two-dimensional nonlinear standing acoustic waves," J. Acoust. Soc. Am. **116**, 194–200 (2004).
[18]J. H. Bell, E. T. Schairer, L. A. Hand, and R. D. Mehta, "Surface pressure measurements using luminescent coatings," Annu. Rev. Fluid Mech. **33**, 155–206 (2001).
[19]T. Liu and J. P. Sullivan, *Pressure and Temperature Sensitive Paints* (Springer, New York, 2004).
[20]O. Stern and M. Volmer, "Uber die Abklingungszeit der Fluoreszenz," Phys. Z. **20**, 183–188 (1919).
[21]H. Sakaue, J. W. Gregory, J. P. Sullivan, and S. Raghu, "Porous pressure-sensitive paint for characterizing unsteady flowfields," AIAA J. **40**, 1094–1098 (2002).
[22]H. Sakaue and J. P. Sullivan, "Time response of anodized aluminum pressure-sensitive paint," AIAA J. **39**, 1944–1949 (2001).
[23]J. W. Gregory and J. P. Sullivan, "The effect of quenching kinetics on the unsteady response of pressure-sensitive paint," AIAA J. (to be published).
[24]T. Liu, N. Teduka, M. Kameda, and K. Asai, "Diffusion timescale of porous pressure-sensitive paint," AIAA J. **39**, 2400–2402 (2001).
[25]A. E. Baron, J. D. S. Danielson, M. Gouterman, J. R. Wan, J. B. Callis, and B. McLachlan, "Submillisecond response times of oxygen-quenched luminescent coatings," Rev. Sci. Instrum. **64**, 3394–3402 (1993).
[26]K. Asai, Y. Iijima, H. Kanda, and T. Kunimasu, "Novel pressure-sensitive coating based on anodic porous alumina," 30th Fluid Dynamics Conference, Okayama, Japan 1998 (in Japanese).
[27]N. Teduka, M. Kameda, Y. Amao, and K. Asai, "Experimental investigation on the time response of pressure-sensitive paint," Proceedings of the 31st JSASS Annual Meeting, 2000, pp. 218–221 (in Japanese).
[28]A. M. Scroggin, E. B. Slamovich, J. W. Crafton, N. Lachendro, and J. P. Sullivan, "Porous polymer/ceramic composites for luminescence-based temperature and pressure measurement," Mater. Res. Soc. Symp. Proc. **560**, 347–352 (1999).
[29]A. M. Scroggin, "Processing and optimization of doped polymer/ceramic composite films for luminescence-based pressure and temperature measurement in aerodynamic applications," M.S. thesis, School of Materials Engineering, Purdue University, West Lafayette, IN, 1999.
[30]T. Liu, B. T. Campbell, S. P. Burns, and J. P. Sullivan, "Temperature- and pressure-sensitive luminescent paints in aerodynamics," Appl. Mech. Rev. **50**, 227–246 (1997).
[31]J. W. Gregory, H. Sakaue, and J. P. Sullivan, "Fluidic oscillator as a dynamic calibration tool," AIAA 2002-2701, 22nd Aerodynamic Measurement Technology and Ground Testing Conference, American Institute of Aeronautics and Astronautics, St. Louis, MO, 2002.
[32]T. Liu, M. Guille, and J. Sullivan, "Accuracy of pressure-sensitive paint," AIAA J. **39**, 103–112 (2001).
[33]R. D. LaBelle and S. D. Garvey, "Introduction to high performance CCD Cameras," 16th International Congress on Instrumentation in Aerospace Simulation Facilities (ICIASF'95 Record), 1995, pp. 30.1–30.5.
[34]O. C. Brown, "Low-speed pressure measurements using a luminescent coating system," Ph.D. dissertation, Department of Aeronautics and Astronautics, Stanford University, Stanford, CA 2000.
[35]M. A. Woodmansee and J. C. Dutton, "Treating temperature-sensitivity effects of pressure-sensitive paint measurements," Exp. Fluids **24**, 163–174 (1998).
[36]C. Klein, R. H. Engler, S. D. Fonov, and O. Trinks, "Pressure sensitive paint measurements on a wing model in a low-speed wind tunnel," ICIASF'99: 18th International Conference on Instrumentation in Aerospace Simulation Facilities, 14–17 June 1999, *ICIASF Record, International Congress on Instrumentation in Aerospace Simulation Facilities* (IEEE, Piscataway, NJ, 1999), p. 22-1.
[37]C. S. Subramanian, T. R. Amer, D. M. Oglesby, and J. Burkett, "New self-referencing pressure-sensitive-paint measurement," AIAA J. **40**, 582–584 (2002).
[38]J. W. Gregory, "Unsteady pressure measurements in a turbocharger compressor using porous pressure-sensitive paint," M.S. thesis, School of Aeronautics and Astronautics, Purdue University, West Lafayette, IN, 2002.
[39]J. H. Bell and B. G. Mclachlan, "Image registration for pressure-sensitive paint applications," Exp. Fluids **22**, 78–86 (1996).

Decentralized harmonic active vibration control of a flexible plate using piezoelectric actuator-sensor pairs

Matthieu Baudry, Philippe Micheau, and Alain Berry[a)]
G.A.U.S, Mechanical Engineering Department, Université de Sherbrooke, Sherbrooke, Québec J1K 2R1, Canada

(Received 11 February 2005; revised 20 August 2005; accepted 24 October 2005)

We have investigated decentralized active control of periodic panel vibration using multiple pairs combining PZT actuators and PVDF sensors distributed on the panel. By contrast with centralized MIMO controllers used to actively control the vibrations or the sound radiation of extended structures, decentralized control using independent local control loops only requires identification of the diagonal terms in the plant matrix. However, it is difficult to *a priori* predict the global stability of such decentralized control. In this study, the general situation of noncollocated actuator-sensor pairs was considered. Frequency domain gradient and Newton-Raphson adaptation of decentralized control were analyzed, both in terms of performance and stability conditions. The stability conditions are especially derived in terms of the adaptation coefficient and a control effort weighting coefficient. Simulations and experimental results are presented in the case of a simply supported panel with four PZT-PVDF pairs distributed on it. Decentralized vibration control is shown to be highly dependent on the frequency, but can be as effective as a fully centralized control even when the plant matrix is not diagonal-dominant or is not strictly positive real (not dissipative). © *2006 Acoustical Society of America.* [DOI: 10.1121/1.2139624]

PACS number(s): 43.40.-r, 43.40.Vn, 43.40.Dx [JGM] Pages: 262–277

I. INTRODUCTION

Active control is an efficient tool for attenuating low frequency vibrations in structures whose vibration response or sound radiation needs to be globally reduced. This technique has been applied to control lumped and distributed parameter structures.[1] Usually, the vibration response is sensed at a number of locations on the structure and modified by a number of local actuators using a *centralized* controller. The sensors and the actuators must be located in order to have sufficient authority to sense and control structural vibrations. In simple situations, such as the active damping of a limited number of weakly damped structural modes, this approach is very effective. However, its application to more complicated situations involving forced response of a large number of structural modes is more challenging: in such a case, a centralized control strategy involves modeling a large number of secondary transfer functions, requires cumbersome wiring, and is prone to instability due to plant uncertainty or individual actuator or sensor failure.

The problem under study in this article is the active control of bending vibrations of a panel and the control strategy investigated is the use of independent control loops between an individual PVDF sensor and an individual PZT actuator instead of a centralized controller.[2] Piezoelectric materials are good candidates for decentralized active vibration control because under the pure bending assumption they can form collocated, dual actuator-sensor pairs.[3,4] Decentralized control approaches were also recently applied to the active control of free-field sound radiation using loudspeaker-microphone pairs.[5,6] The main advantage of such a decentralized control strategy is its reduced complexity, reduced processing requirement, ease of implementation, and robustness to individual control unit failure. However, performance and stability of decentralized control are difficult to predict *a priori*.

Decentralized control strategies in the context of active vibration or vibroacoustic control has recently been studied by Elliott and colleagues.[7,3,8–10] Under the assumption of collocated and dual actuator-sensor pairs, decentralized control has the very attractive property that each local feedback loop (with the other feedback loops being active) is stable regardless of the local feedback gains applied,[3] leading to a globally stable and robust implementation. When applied to globally reducing the vibration response of panels, or sound transmission through panels, decentralized control leads to control performance very similar to a fully centralized control structure.[8,11,9,10] However, piezoelectric strain actuators (PZT) and strain sensors (PVDF) cannot, strictly speaking, be collocated and dual because of coupling through extensional excitation.[12] Hence, the main objective of this article is to analyze performance and stability of decentralized vibration control using the general situation of noncollocated actuator-sensor PZT-PVDF pairs.

The specific situation investigated here is the active control of a reverberant system (a weakly damped bending plate) under a periodic excitation. For such disturbance, the feedback controller and the x-LMS MIMO feedforward controller can both be seen as an equivalent resonant controller.[13] The similarity between feedback and feedforward comes from the fact that the equivalent compensator has one undamped mode at the disturbance frequency to provide the high loop gain necessary for the rejection of the disturbance frequency. Hence, without loss of generality, the control

[a)]Electronic mail: alain.berry@usherbrooke.ca

 0001-4966/2006/119(1)/262/16/$22.50

problem can be addressed with an harmonic controller which adjusts complex gains (amplitude and the phase of the sinusoidal control inputs with respect to the amplitude and phase of the sensor signals). The feedback law can be tuned with two parameters: the adaptation coefficient which specifies the convergence rate, and the control effort weighting which limits the amplitude of the control input. Decentralized control is the special case where the gain matrix is diagonal, in contrast with a fully centralized control where the gain matrix is fully populated.

The problem of decentralized controller is to ensure the stability of the whole system.[14] Decentralized control was studied in the context of large structures, and it was established that a solution to the decentralized problem exists if and only if a solution exists to the centralized problem.[15] For x-lms feedforward, the Gershgorin theorem is useful to derive a *sufficient* condition of stabilization:[7] the diagonal dominance of the matrix gain. The same condition can be derived from the small gain theorem for feedback controllers. However, this diagonal dominance condition proves to be too conservative to be applied in practice. More adequate necessary and sufficient stability conditions were derived in the active free-field sound control problem.[5] The objective of this article is to extend this previous analysis by providing a set of simple analytical tools to *a priori* predict closed loop stability of active vibration control using piezoelectric actuators and sensors.

Section II introduces the problem, and Sec. III details the plant modeling. The controller synthesis in terms of minimization of a quadratic criterion is presented in Sec. IV, together with the conditions of stability related to the requirement of a positive definite plant matrix at the disturbance frequency. Section V presents the implementation of the harmonic controller using a complex envelope controller.[16] Finally, experimental results presented in Sec. VI illustrate the effectiveness of the proposed analytical tools.

II. THE PROBLEM

The physical system under study is a flexible panel under forced harmonic oscillation, whose vibration response or sound radiation needs to be globally reduced. To this end, the vibration response is sensed at a number of locations on the structure, and modified by a number of local actuators on it (Fig. 1). The control strategy investigated here is the use of N independent control loops Γ_i between an individual sensor and an individual actuator instead of an $N\times N$ centralized controller. The controller is implemented in the frequency domain. A general block-diagram form of the controller is shown in Fig. 2 (ω_0 is the angular frequency of the disturbance, $\mathbf{d}$ is the disturbance vector measured by the N sensors, $\mathbf{y}$ is the error signal at the sensors, $\mathbf{u}$ is the control inputs at the N actuators, and $\mathbf{H}$ is the $N\times N$ transfer function matrix between actuators and sensors). In order to reject the frequency ω_0, the controller $\mathbf{\Gamma}$ restricts to a matrix of complex gains at ω_0. In the general case of a central controller, the control matrix has off-diagonal components Γ_{ij}. In the case of decentralized control, the control matrix is diagonal, $\mathbf{\Gamma}=\mathrm{diag}(\Gamma_{ii})$. In the following, the controller $\mathbf{\Gamma}$ is iteratively

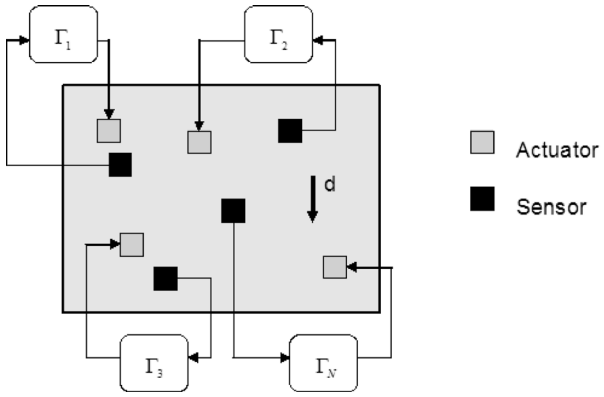

FIG. 1. Physical configuration under study: A flexible panel controlled by N independent loops.

adapted in order to minimize a given error criterion. Since it is assumed that the disturbance has a fixed frequency and that the error is slowly varying in time (slow convergence), the time variations of the error phasor are slow, and it is therefore possible to implement the controller adaptation at a much slower rate than the disturbance frequency. The demodulation and modulation blocks shown in Fig. 2 are used to, respectively, extract the phasor of the error $\mathbf{y}$, and synthesize the oscillatory control input $\mathbf{u}$ at the disturbance frequency. The demodulation and modulation blocks are described in more detail in Sec. V.

III. PLANT MODELING

We consider a rectangular, simply supported panel equipped with N surface-mounted, identical actuator-sensor pairs. Each pair consists of a rectangular piezoceramic (PZT) actuator and a rectangular polyvinylidene fluoride (PVDF) sensor, which are not necessarily collocated on the panel. In the following analysis, pure bending response is assumed, therefore, the effect of extensional deformation of the panel on the actuator-sensor transfer functions is not considered. Applying an oscillatory voltage (of angular frequency ω_0) on an individual PZT actuator generates forced bending vibrations of the panel which are sensed by all PVDF films. The transfer function between actuator j and sensor i is defined by

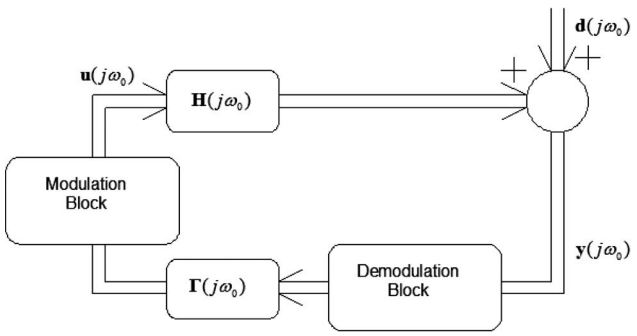

FIG. 2. Block diagram of the frequency domain controller.

$$H_{ij}(\omega_0) = \frac{V_i^{(s)}(\omega_0)}{V_j^{(a)}(\omega_0)}, \tag{1}$$

where $V_i^{(s)}$ is the output voltage of the PVDF sensor and $V_j^{(a)}$ is the input voltage of the PZT actuator. The transverse displacement of the panel $w(x,y,\omega_0)$ is decomposed over its eigenfunctions Φ_{mn},

$$w(x,y,\omega_0) = \sum_{m=1}^{\infty}\sum_{n=1}^{\infty} W_{mn}(\omega_0)\phi_{mn}(x,y), \tag{2a}$$

$$\phi_{mn}(x,y) = \sin(\gamma_m x)\sin(\gamma_n y), \tag{2b}$$

$$\omega_{mn} = \sqrt{\frac{\tilde{E}_p h^3}{12\mu(1-\nu_p^2)}}(\gamma_m^2+\gamma_n^2), \tag{2c}$$

$$\gamma_m = \frac{m\pi}{L_x}, \quad \gamma_n = \frac{n\pi}{L_y}, \tag{2d}$$

where ω_{mn} is the natural angular frequency of bending mode (m,n). Equation (2) assumes a homogeneous, isotropic panel. Also, $\tilde{E}_p = E_p(1+\eta)$ (E_p is the complex Young's modulus of the panel, η is the structural loss factor), μ, ν_p, L_x, L_y are the mass per unit area, Poisson's ratio, and dimensions of the panel, respectively. The complex modal amplitudes W_{mn} under the action of an individual actuator j are given by[1,17]

$$W_{mn}(\omega_0) = -\frac{\gamma_m^2+\gamma_n^2}{\gamma_m\gamma_n}\frac{d_{31}}{4M_p}\frac{C_0 V_j^{(a)}(\omega_0)}{4M_p t_a(\omega_{mn}^2-\omega_0^2)} \times [\cos(\gamma_m x_{1j}^{(a)}) - \cos(\gamma_m x_{2j}^{(a)})][\cos(\gamma_n y_{1j}^{(a)}) - \cos(\gamma_n y_{2j}^{(a)})], \tag{3}$$

where $M_p = L_x L_y \mu$ is the mass of the panel, d_{31} is the strain coefficient of the piezoceramic (it is assumed that the actuator provides equal free strains in the x and y directions, that is $d_{31}=d_{32}$), t_a is its thickness, $x_{1j}^{(a)}$, $x_{2j}^{(a)}$, $y_{1j}^{(a)}$, $y_{2j}^{(a)}$ are the positions of the limits of the piezoceramic on the panel, and C_0 is a coefficient related to the bending moment applied by the PZT actuator, $C_0 = E_p K^f h^2/6$ where[1,17]

$$K^f = \frac{3Kr(r+2)}{4+8Kr+12Kr^2+2Kr^3+4K^2r^4} \tag{4}$$

and $r=2t_a/h$, $K=[E_a(1-\nu_p)]/[E_p(1-\nu_a)]$ where E_a and ν_a are the Young's modulus and Poisson's ratio of the piezoelectric actuator, respectively. It should be noted that Eqs. (3) and (4) are based on several assumptions related to the piezoelectric actuation of the panel: (i) the applied moment distribution is constant over the area covered by the PZT actuator (in reality, the moment vanishes at the edges of the actuator, modifying stress distribution in the panel within about four actuator thicknesses from the boundary.[17,18] This edge effect may also slightly affect the strain measured by a PVDF sensor located in the immediate vicinity of the PZT actuator). (ii) The preceding formulation assumes a PZT actuator on one side of the panel only; the asymmetric actuation of the panel generates not only bending but also extensional response of the panel (the extensional component is not taken into account in the following analysis, especially in terms of the PVDF sensor response). (iii) Finally, the PZT actuator is assumed to be perfectly bonded to the panel and the bonding layer is assumed to have a negligible thickness.

The closed circuit charge equation of an extended piezoelectric PVDF sensor i bonded to the flexible panel is

$$q(\omega_0) = -\int_{x_{1i}^{(s)}}^{x_{2i}^{(s)}}\int_{y_{1i}^{(s)}}^{y_{2i}^{(s)}} e_{3l}\epsilon_l^{(s)} dxdy, \tag{5}$$

where $x_{1i}^{(s)}$, $x_{2i}^{(s)}$, $y_{1i}^{(s)}$, $y_{2i}^{(s)}$ are the positions of the limits of the piezoelectric sensor on the panel, e_{3l} are the piezoelectric coefficients, and $\epsilon_l^{(s)}$ are the strain components in the sensor. If pure bending strain is assumed in the panel (that is, the extensional strain response of the panel is neglected), Eq. (5) takes the form [19]

$$q(\omega_0) = \frac{h+t_s}{2}\int_{x_{1i}^{(s)}}^{x_{2i}^{(s)}}\int_{y_{1i}^{(s)}}^{y_{2i}^{(s)}}\left(e_{31}\frac{\partial^2 w(x,y,\omega_0)}{\partial x^2} + e_{32}\frac{\partial^2 w(x,y,\omega_0)}{\partial y^2} + 2e_{36}\frac{\partial^2 w(x,y,\omega_0)}{\partial x\partial y}\right)dxdy, \tag{6}$$

where t_s is the thickness of the PVDF film. Assuming a zero skew angle ($e_{36}=0$) and identical sensitivity in the x and y directions ($e_{31}=e_{32}$), and using Eqs. (2) and (3), Eq. (6) becomes

$$q(\omega_0) = -e_{31}\frac{h+t_s}{2}\sum_{m,n} W_{mn}\frac{\gamma_m^2+\gamma_n^2}{\gamma_m\gamma_n}[\cos(\gamma_m x_{1i}^{(s)}) - \cos(\gamma_m x_{2i}^{(s)})][\cos(\gamma_n y_{1i}^{(s)}) - \cos(\gamma_n y_{2i}^{(s)})]. \tag{7}$$

Finally, the voltage output of the PVDF sensor measured through a high impedance circuit is given by

$$V_i^{(s)}(\omega_0) = -\frac{q(\omega_0)}{C_s}, \tag{8}$$

where $C_s = \xi_s(S/t_s)$ is the sensor capacitance and ξ_s, S are its dielectric permittivity and area, respectively. Finally, combining Eqs. (3), (7), and (8), the PZT-PVDF transfer function H_{ij} of Eq. (1) can be calculated. The application of decentralized vibration control using PZT-PVDF pairs empirically depends on the relative magnitude of off-diagonal coefficients H_{ij} $(i \neq j)$ and diagonal coefficients H_{ii} of the matrix **H**. In Sec. VI, both diagonal and off-diagonal coefficients of **H** are examined and compared to measured values.

Note that in the case of an isolated, *collocated* PZT-PVDF pair [that is $(x_{1j}^{(a)}, x_{2j}^{(a)}, y_{1j}^{(a)}, y_{2j}^{(a)}) = (x_{1i}^{(s)}, x_{2i}^{(s)}, y_{1i}^{(s)}, y_{2i}^{(s)})$], and under the preceding assumption of pure bending, it can be easily shown that the product of the actuator input voltage $V_j^{(a)}$ and the sensor output voltage rate $\dot{V}_i^{(s)}$ is proportional to the power supplied to the panel: such a collocated PZT-PVDF pair is therefore *dual*. In such a case a simple proportional feedback loop between each collocated pair would provide an unconditionally stable feedback control.[3] However, the coupling of both the PZT and PVDF with extensional deformation of the panel makes the analysis more complicated. When considering extensional deformation, it turns out that a collocated PZT-PVDF pair is no longer dual in the general case. In any case, the following analysis involves noncollocated actuator-sensor pairs, therefore the du-

ality of actuators and sensors is not *a priori* required.

IV. CONTROLLER SYNTHESIS

A. Control objective

When the system is in steady state (all transients have vanished) the error vector $\mathbf{y}=[y_1 y_2 \ldots y_N]^T$ measured by the N PVDF sensors is given by

$$\mathbf{y} = \mathbf{d} + \mathbf{H}\mathbf{u}, \tag{9}$$

where $\mathbf{u}=[u_1 u_2 \ldots u_N]^T$ is the complex control input vector at the N PZT actuators and $\mathbf{d}=[d_1 d_2 \ldots d_N]^T$ is the disturbance at the N PVDF sensors. The problem is to adjust the complex inputs to the N PZT actuators to minimize the measured signal from each of the N PVDF sensors. The trivial solution of this problem, $\mathbf{u}_{\text{opt}}^{p}=-\mathbf{H}^{-1}\mathbf{d}$, cannot be implemented in practice because of uncertainty on the matrix $\mathbf{H}$, the disturbance $\mathbf{d}$, and measurement noise. The usual approach is to rather derive an optimal command $\mathbf{u}_{\text{opt}}$ with respect to an error criterion, $J(\mathbf{u},\mathbf{y})$, in order to apply iterative methods of minimization. A quadratic criterion can be defined as the sum of power outputs plus the power of the control weighted effort:

$$J(\mathbf{u}) = \mathbf{y}^H\mathbf{y} + \mathbf{u}^H\mathbf{R}\mathbf{u}, \tag{10}$$

where the superscript ^{H} denotes the Hermitian transpose and $\mathbf{R}$ is a positive definite matrix. The introduction of the weighting control matrix, $\mathbf{R}$, in the criterion leads to a trade off of the optimal command between the active attenuation and the "magnitude" of the control input. Two types of weighting matrices $\mathbf{R}$ will be considered in this article: The first type penalizes the power of the control inputs, $\mathbf{R}=\beta\mathbf{I}$, while the second type penalizes the power of the control signals that are measured by the error sensors: $\mathbf{R}=\beta\mathbf{H}^H\mathbf{H}$ ($\beta>0$).

For the quadratic criterion (10) and the linear system (9), the gradient vector is $\nabla_{\mathbf{u}}J=2\mathbf{H}^H\mathbf{y}+2\mathbf{R}\mathbf{u}$ and the Hessian matrix is $[\Delta_{\mathbf{u}}J]=2\mathbf{H}^H\mathbf{H}+2\mathbf{R}$. The optimal command $\mathbf{u}_{\text{opt}}$ is defined as the command that minimizes J. The minimum of J is obtained when $\nabla_{\mathbf{u}}J(\mathbf{u}_{\text{opt}})=0$ and $[\Delta_{\mathbf{u}}J]>0$. It can be easily established that

$$\mathbf{u}_{\text{opt}} = -(\mathbf{H}^H\mathbf{H}+\mathbf{R})^{-1}\mathbf{H}^H\mathbf{d}, \tag{11}$$

$$J_{\min} = \mathbf{d}^H[\mathbf{I}-\mathbf{H}(\mathbf{H}^H\mathbf{H}+\mathbf{R})^{-1}\mathbf{H}^H]\mathbf{d}. \tag{12}$$

If the weighting matrix is in the form $\mathbf{R}=\beta\mathbf{H}^H\mathbf{H}$, Eq. (12) takes the form $J_{\min}=[\beta/(1+\beta)]\mathbf{d}^H\mathbf{d}$. Hence, the attenuation level at the error sensors provided by the active control is

$$\text{Att}_{dB} = 10\log_{10}\left(\frac{\beta}{1+\beta}\right). \tag{13}$$

Equation (13) clearly reveals the effect of the weighting β on the attenuation performance: A large weighting coefficient β has the effect of decreasing the optimal attenuation Att_{dB} while decreasing the control effort $\mathbf{u}_{\text{opt}}$. Hence, the weighting coefficient should be chosen small ($\beta\ll 1$) in order to obtain a significant active attenuation. The limiting case of $\beta=1$ leads to an attenuation of 3 dB of the criterion. In addition, the following sections will demonstrate that the introduction of a small control effort weighting in the criterion can have a stabilizing effect on decentralized vibration control.

B. Design of the controller

One of the most useful iterative methods of minimization is the steepest-descent (or gradient) algorithm. It is used to iteratively adjust the command $\mathbf{u}$ in the opposite direction of the gradient of the criterion in order to reach a minimum: $\mathbf{u}(k+1)=\mathbf{u}(k)-\mu_g\nabla_{\mathbf{u}}J$ where μ_g is the adaptation coefficient of the algorithm. For the criterion defined by Eq. (10), the gradient algorithm takes the form

$$\mathbf{u}(k+1) = \mathbf{u}(k) - 2\mu_g(\mathbf{H}^H\mathbf{y}(k) + \mathbf{R}\mathbf{u}(k)). \tag{14}$$

The main problem of the steepest-descent algorithm is that the adaptation rate directly depends on the local gradient: when the gradient is small, the adaptation becomes very slow. A faster convergence to the optimal command can be obtained with the Newton algorithm by multiplying the gradient by the inverse of the Hessian matrix: $\mathbf{u}(k+1)=\mathbf{u}(k)-\mu_N[\Delta_{\mathbf{u}}J]^{-1}\nabla_{\mathbf{u}}J$ where μ_N is the adaptation coefficient of the Newton algorithm. For the criterion defined by Eq. (10), the Newton algorithm takes the form

$$\mathbf{u}(k+1) = \mathbf{u}(k) - \mu_N(\mathbf{H}^H\mathbf{H}+\mathbf{R})^{-1}(\mathbf{H}^H\mathbf{y}(k) + \mathbf{R}\mathbf{u}(k)). \tag{15}$$

Both the gradient (14) and Newton algorithms (15) are therefore special forms of the generic update equation

$$\mathbf{u}(k+1) = (\mathbf{I}-\mu\mathbf{W})\mathbf{u}(k) - \mu\mathbf{C}\mathbf{y}(k), \tag{16}$$

where $\mu=2\mu_g$, $\mathbf{C}=\mathbf{H}^H$ and $\mathbf{W}=2\mathbf{R}$ for the gradient algorithm; $\mu=\mu_N$, $\mathbf{C}=(\mathbf{H}^H\mathbf{H}+\mathbf{R})^{-1}\mathbf{H}^H$, $\mathbf{W}=(\mathbf{H}^H\mathbf{H}+\mathbf{R})^{-1}\mathbf{R}$ for the Newton algorithm. Therefore, it is appropriate to define distinct weighting matrices $\mathbf{R}$ for the gradient and Newton algorithms: $\mathbf{R}=\beta\mathbf{I}$ with β a real positive number for the gradient algorithm, and $\mathbf{R}=[\beta/(1-\beta)]\mathbf{H}^H\mathbf{H}$ for the Newton algorithm. In such a way, the matrix $\mathbf{W}$ in Eq. (16) is the same diagonal matrix for both the gradient and the Newton algorithms: $\mathbf{W}=\beta\mathbf{I}$. However, the penalization is in terms of the control inputs for the gradient algorithm, while it is in terms of the control signals that are measured by the error sensors for the Newton algorithm. Moreover, for the Newton algorithm, the matrix $\mathbf{C}$ is simplified to $\mathbf{C}=\mathbf{H}^{-1}$. In the following, centralized and decentralized versions of the update equation (16) are analyzed.

C. Proposed controllers

A perfect measurement of the plant matrix $\mathbf{H}$ is necessary to rigorously implement the iterative algorithms (16), however only an estimation $\hat{\mathbf{H}}$ of $\mathbf{H}$ is available in practice. When the matrix $\mathbf{C}$ is built from the complete estimate of the plant matrix $\hat{\mathbf{H}}$ (both diagonal and off-diagonal coefficients), then Eq. (16) provides the update of a centralized controller. In what follows, it is assumed that for centralized control, both the diagonal and off-diagonal coefficients of $\mathbf{H}$ are perfectly estimated, therefore $\hat{\mathbf{H}}=\mathbf{H}$ for centralized control.

The case of a decentralized controller corresponds to N independent update equations that take into account only the diagonal coefficients of the plant matrix. This is formally equivalent to a biased estimation of the complete matrix $\mathbf{H}$, $\hat{\mathbf{H}}=\mathrm{diag}(H_{ii})$ for all $i=1,\ldots,N$; in other words, the off-diagonal coefficients are forced to 0 and the diagonal coefficients are assumed to be perfectly estimated. Therefore, decentralized control derived from the gradient algorithm corresponds to $\mathbf{C}=\mathrm{diag}(H_{ii}^{*})$, where H_{ii}^{*} denotes the complex conjugate of H_{ii}. On the other hand, decentralized control derived from the Newton algorithm corresponds to $\mathbf{C}=\mathrm{diag}(1/H_{ii})$. Note that decentralized control derived from the Newton algorithm does not need the inversion of the complete plant matrix, but only the inverse of its diagonal elements.

In summary, Eq. (16) is the general update equation that applies to the four cases investigated in this article: the control matrix is $\mathbf{C}=\hat{\mathbf{H}}^{H}$ for the gradient algorithm, $\mathbf{C}=\hat{\mathbf{H}}^{-1}$ for the Newton algorithm, $\hat{\mathbf{H}}=\mathbf{H}$ for centralized control, and $\hat{\mathbf{H}}=\mathrm{diag}(H_{ii})$ for decentralized control. For the four cases, the weighting matrix is $\mathbf{W}=\beta\mathbf{I}$.

The main limitation of decentralized control is that both the Hessian and the gradient of the criterion are approximated from only the diagonal elements of the plant matrix. Hence, the estimated gradient computes a biased direction for searching the optimal command. In the worst case, the controller may search the minimum of the criterion in its opposite direction and never reach it: the system is unstable. The following sections address the conditions of stability of the controlled system.

D. Conditions of stability

It is possible to establish the condition of asymptotic stability of the closed loop system described by Eqs. (16) and (9). If we consider that the closed loop system is stable, then the command $\mathbf{u}(k)$ converges to $\mathbf{u}_{\infty}=-(\mathbf{CH}+\mathbf{W})^{-1}\mathbf{Cd}$ [obtained by imposing $\mathbf{u}(k+1)=\mathbf{u}(k)$ in Eq. (16)]. It is then possible to re-express Eqs. (16) and (9) as an autonomous linear discrete-time system:

$$\mathbf{x}(k+1)=\mathbf{A}\mathbf{x}(k), \tag{17}$$

where $\mathbf{x}(k)=\mathbf{u}(k)-\mathbf{u}_{\infty}$ [or $\mathbf{x}(k)=\mathbf{y}(k)-\mathbf{y}_{\infty}$] and $\mathbf{A}=\mathbf{I}-\mu(\mathbf{CH}+\mathbf{W})$. Such a discrete-time dynamic system is called stable when $\mathbf{x}(k)$ tends exponentially to zero when $k\to\infty$ for any initial condition such that $\mathbf{x}(0)\neq\mathbf{0}$. The *necessary and sufficient condition* of stability of the closed loop system is that the matrix $\mathbf{A}$ is *Schur* stable: all its eigenvalues lie within the interior of the unit circle in the complex plane: $|\lambda_i(\mathbf{A})|<1$ for all i.

In the special case of $\mathbf{A}=\mathbf{I}-\mu\mathbf{B}$ with $\mathbf{B}=\mathbf{CH}+\mathbf{W}$ and $\mu>0$, the condition of Schur stability becomes $|1-\mu\lambda_i(\mathbf{B})|<1$ for all $i=1,\ldots,N$. Hence, the Schur stability condition leads to the necessary and sufficient condition of stability

$$\mu<\frac{2\Re(\lambda_i(\mathbf{B}))}{|\lambda_i(\mathbf{B})|^2},\quad \forall\, i=1,\ldots,N, \tag{18}$$

where $\Re(\lambda_i)$ designates the real part of the complex eigenvalue λ_i. An important interpretation of the above-noted condition is that it introduces an upper bound for the adaptation coefficient in the iterative algorithm,

$$\mu_{\max}=\frac{2\Re(\lambda_i(\mathbf{B}))}{|\lambda_i(\mathbf{B})|^2}.$$

The main implication of Eq. (18) is that the real part of all eigenvalues of $\mathbf{B}$ must necessarily be positive, $\Re(\lambda_i)>0$ for all i. In the following, and in the context of this article, the term "μ-stabilization" refers to the *necessary* condition of stability: if $\Re(\lambda_i(\mathbf{B}))>0$ for all i then it is possible to obtain stable control with an appropriate tuning of the adaptation coefficient μ. When all eigenvalues of $\mathbf{B}$ are located in the open right complex half plane, the matrix theory literature often refers to the concept of *positive stability*. In control theory literature, the matrix $-\mathbf{B}$ is said to be *Hurwitz stable*: the associated autonomous continuous time system $\dot{\mathbf{x}}(t)=-\mathbf{B}\mathbf{x}(t)$ is stable.

An alternative and simpler method of analyzing the "μ-stabilization" of the closed loop system is derived from the following theorem (Ref. 20, p. 88). *If* $\mathbf{B}\in C^{N\times N}$ *with* $n_0(\mathbf{B})=0$ *and if the Hermitian nonsingular matrix* $\mathbf{P}\in C^{N\times N}$ *satisfies the condition* $\mathbf{PB}+\mathbf{B}^{H}\mathbf{P}=-\mathbf{Q}$ *with* $\mathbf{Q}\geqslant 0$ *then* $\mathrm{In}\,\mathbf{B}=\mathrm{In}\,\mathbf{P}$. The inertia of a matrix $\mathbf{B}$, denoted $\mathrm{In}\,\mathbf{B}$ is defined by the triple $[n_{+}(\mathbf{B}),n_0(\mathbf{B}),n_{-}(\mathbf{B})]$ where $n_{+}(\mathbf{B})$ is the number of eigenvalues of $\mathbf{B}$ in the open right complex half-plane, $n_0(\mathbf{B})$ is the number of purely imaginary eigenvalues of $\mathbf{B}$, $n_{-}(\mathbf{B})$ is the number of eigenvalues of $\mathbf{B}$ in the open left complex half-plane. According to the theorem, choosing $\mathbf{P}=\mathbf{I}$ and assuming that $\mathbf{B}^{H}+\mathbf{B}$ is positive definite, then $\mathrm{In}\,\mathbf{B}=(N,0,0)$ [meaning that $\Re(\lambda_i(\mathbf{B}))>0$]. Consequently, if $\mathbf{B}$ is a "strictly positive-real" (SPR) matrix (that is, $\mathbf{B}^{H}+\mathbf{B}$ is positive definite) it is possible to find a μ which achieves stable control of the overall closed-loop system. Moreover, when $\mathbf{B}$ is a SPR matrix, this implies that $V(\mathbf{x})=\mathbf{x}^{H}\mathbf{x}$ is a quadratic Liapunov function for the system $\dot{\mathbf{x}}(t)=-\mathbf{B}\mathbf{x}(t)$. Therefore $dV/dt\leqslant 0$, the matrix $-\mathbf{B}$ is said to be *Hurwitz diagonally stable* (this is also referred to as Volterra stability, Voltera-Liapunov stability or VL-stability, or dissipativity).[20] Hence, the necessary condition of $\mathbf{B}$ SPR means that in the limiting case of $\mu\to 0$, $-\mathbf{B}$ must be Hurwitz diagonally stable. The diagonal stability is a stronger requirement than just stability; in our case diagonal stability means that the sum of power outputs measured by the PVDF sensors monotonously decreases with time when μ is very small.

From a purely mathematical point of view, the concept of strictly positive-real matrix $\mathbf{B}$ has the advantage of simplifying the stability analysis and of providing some physical insight. For example, we consider the case of centralized control, a perfectly estimated plant matrix and no effort weighting ($\mathbf{R}=\mathbf{0}$). In the case of the centralized Newton algorithm, $\mathbf{C}=\mathbf{H}^{-1}$, then $\mathbf{CH}=\mathbf{I}$ is SPR (its eigenvalues are 1). In the case of the centralized gradient algorithm, $\mathbf{C}=\mathbf{H}^{H}$, then $\mathbf{CH}=\mathbf{H}^{H}\mathbf{H}$ is a SPR matrix (because $\mathbf{H}^{H}\mathbf{H}$ is a Hermitian positive definite matrix). Consequently, centralized control with perfect system estimation will always be stable.

The case of decentralized control is more interesting. The consideration of only the diagonal coefficients of the plant matrix $\mathbf{H}$ is formally equivalent to a biased estimation of the complete matrix $\mathbf{H}$. In the case of imperfect plant

estimation, the eigenvalues of $\mathbf{CH}$ are not necessarily real and positive, therefore the condition $\Re(\lambda_i(\mathbf{B}))>0$ suggests that control effort weighting $\mathbf{W}$ may be necessary to stabilize the control. The following sections investigate the effect of effort weighting on the stability of decentralized control.

E. Decentralized control without effort weighting, $\mathbf{W}=\mathbf{0}$

When $\mathbf{W}=\mathbf{0}$, the disturbance rejection is theoretically perfect but "μ-stabilization" of the closed loop system is possible if and only if $\Re(\lambda_i(\mathbf{CH}))>0$, this condition is verified if $\mathbf{CH}$ is a strictly positive-real (SPR) matrix. In order to illustrate the role of the decentralized compensator $\mathbf{C}$, two cases are considered in this section for the plant matrix: $\mathbf{H}$ is a SPR matrix and $\mathbf{H}$ is not SPR.

(1) When $\mathbf{H}$ is a SPR matrix, the "μ-stabilization" in decentralized or centralized *is guaranteed*. Disturbance rejection is possible without any estimation of the plant matrix $\mathbf{H}$: with $\mathbf{C}=\mathbf{I}$, the matrix $\mathbf{CH}=\mathbf{H}$ is SPR, therefore a sufficiently small adaptation coefficient μ will necessarily ensure closed loop stability. A SPR plant matrix $\mathbf{H}$ for all frequencies physically corresponds to a *dissipative* plant.[21] The SPR condition is obtained in a linear undamped flexible structure with dual-collocated actuator-sensor pairs (passive operator), without poles on the imaginary axis (strictly stable linear system) and without null eigenvalues (dissipativity condition).[22] In other words, the dual collocation of actuators and sensors and the intrinsic damping in the plant imply the SPR condition at any frequency. In contrast, the configuration of distributed and noncollocated actuator-sensor pairs results in a non-PR plant matrix $\mathbf{H}$ (and consequently to a non-SPR $\mathbf{H}$), leading to more difficult control situations.

(2) When $\mathbf{H}$ is not SPR, the role of the diagonal compensator matrix $\mathbf{C}$ can be to ensure a SPR matrix $\mathbf{CH}$. A necessary (but not sufficient) condition for $\mathbf{CH}$ to be SPR is that the real part of diagonal elements of $\mathbf{CH}$ are strictly positive: $\Re(C_iH_{ii})>0$. With the assumption of perfect estimation of the diagonal coefficients of the plant matrix, $\hat{H}_{ii}=H_{ii}$, this necessary condition is always verified in decentralized control because $C_iH_{ii}=|h_{ii}|^2$ for the gradient algorithm and $C_iH_{ii}=1$ for the Newton algorithm. However, in the case of a biased estimation of the diagonal coefficients of the plant matrix, this condition may be not verified. For example, if we consider the Newton algorithm with a phase-shift error ϕ of the diagonal coefficient, $H_{ii}=\hat{H}_{ii}\exp^{j\phi}$, then the diagonal coefficients of $\mathbf{CH}$ have a real part $\Re(H_{ii}/\hat{H}_{ii})=\cos(\phi)$ which is negative when the phase error is such that $\pi/2>\phi>3\pi/2(\mathrm{mod}\ 2\pi)$: therefore, an individual control unit can be unstable (with the other units being inactive). In this case, since the corresponding diagonal coefficient C_iH_{ii} is not strictly positive, the whole system is not SPR (it may still be stable, though).

To summarize, the main role of the diagonal compensator $\mathbf{C}$ in decentralized control is to compensate the phase of the diagonal coefficients of the plant matrix $\mathbf{H}$ in order to ensure a SPR matrix $\mathrm{diag}(C_iH_{ii})$. Along these lines, we can conclude that any compensator of the form $\mathbf{C}=\mathbf{K}\hat{\mathbf{H}}^H$ with $\hat{\mathbf{H}}=\mathrm{diag}(H_{ii})$, and $\mathbf{K}$ a diagonal positive matrix is a candidate for decentralized control. For example, $K_{ii}=1$ corresponds to the gradient algorithm and $K_{ii}=1/|H_{ii}|^2$ corresponds to the Newton algorithm.

F. Decentralized control with effort weighting, $\mathbf{W}\neq\mathbf{0}$

In situations where it exists at least one negative eigenvalue $\Re(\lambda_i(\mathbf{CH}))<0$, then, according to Eq. (18), the weighting matrix $\mathbf{W}=\beta\mathbf{I}$ must be included in the criterion to ensure a stable closed loop. The weighting coefficient β that ensures theoretical μ-stabilization of the convergence process should satisfy

$$\beta>-\Re(\lambda_i(\mathbf{CH}))\quad\forall\, i. \tag{19}$$

Therefore, the minimum value of β is $\beta=\max(-\Re(\lambda_i(\mathbf{CH})))$. The main drawback of weighting the control effort is to decrease the active attenuation. For example, Eq. (13) shows that $\beta=1$ leads to a 3 dB attenuation of the criterion after control. In practical situations, values of β should be kept much lower than unity in order to maintain satisfactory control performance.

G. Positive definite and diagonal dominance

In case of a perfect estimation of the diagonal coefficients of the plant matrix, the Gershgorin theorem can be applied to derive a *sufficient* condition of μ-stabilization. The Gershgorin theorem states that "the eigenvalues of a complex matrix $\mathbf{B}$ are within disks in the complex plane whose centers are the diagonal coefficients B_{ii} of $\mathbf{B}$ and whose radii are the sums of the modulus of off-diagonal coefficients B_{ij} with $i\neq j$." When B_{ii} is a real positive number and $\Sigma_{j=1,j\neq i}^{m}|B_{ij}|<B_{ii}$, then all these disks lie within the right-hand side of the complex plane, therefore all eigenvalues of $\mathbf{B}$ have a positive real part: $\Re(\lambda_i(\mathbf{B}))>0$; therefore, the system is μ-stabilizable. A matrix such that $\Sigma_{j=1,j\neq i}^{m}|B_{ij}|<B_{ii}$ for all i is called diagonal dominant. Consequently, a sufficient condition of μ-stabilization is that the matrix $\mathbf{B}=\mathbf{CH}+\mathbf{W}$ is diagonal dominant and $\mathrm{diag}(B_{ii})>0$.

It can be easily established that the condition $\mathbf{CH}$ diagonal dominant is equivalent to the condition $\mathbf{H}$ diagonal dominant for the gradient and Newton algorithms, $|H_{ii}|>\Sigma_{j=1,j\neq i}^{m}|H_{ij}|$ for all i. Therefore, if $\mathbf{H}$ is diagonal dominant then $\mathbf{CH}$ is SPR and the decentralized control is μ-stabilizable without control effort weighting. The condition that $\mathbf{H}$ is diagonal dominant is easy to test in practice. However this condition is fairly restrictive because the phase of transfer functions between actuators and sensors is not considered. For example, in the case where the number of actuator-sensor pairs $N\rightarrow\infty$, the diagonal dominant condition will be never satisfied even if the matrix $\mathbf{CH}$ is SPR or the system is *dissipative*. The plant $\mathbf{H}$ does not necessarily need to be diagonal dominant in order to make decentralized control effective.

To summarize, the various conditions of μ-stabilization [to obtain $\mathbf{A}=\mathbf{I}-\mu(\mathbf{CH}+\mathbf{W})$ Schur stable by tuning μ] are

TABLE I. The various conditions of stability of the closed loop system.

Ref.	Condition	Type	Interpretation
C0	$\lvert\lambda_i(\mathbf{I}-\mu(\mathbf{CH}+\beta\mathbf{I})\rvert<1$	Necessary and sufficient	The system is unstable if $\mu>\mu_{\max}$
C1	$\Re(\lambda_i(\mathbf{CH}+\beta\mathbf{I}))>0$	Necessary for C0	The system is stable if $\mu\to 0$
C2	$\Re(\lambda_i(\mathbf{CH}))>0$	Sufficient for C1	Effort weighting β not necessary
C3	$\mathbf{CH}+\beta\mathbf{I}$ SPR	Sufficient for C1	Diagonal stability when $\mu\to 0$
C4	$\mathbf{CH}$ SPR	Sufficient for C2	Diagonal stability and β not necessary
C5	C_iH_{ii} SPR	Necessary for C4	Each individual unit is stable
C6	$\mathbf{H}$ SPR	Sufficient for C4	The system is dissipative
C7	$\mathbf{H}$ dd	Sufficient for C4	Low interaction between units

presented in Table I as a function of the plant matrix $\mathbf{H}$, the control matrix $\mathbf{C}$, the effort weighting coefficient β, and the adaptation coefficient μ.

V. CONTROL IMPLEMENTATION

A. Implemented harmonic controller

In the preceding sections, the inherent delay of the control system in processing the error signal $\mathbf{y}$ and generating the next control input $\mathbf{u}$ has not been taken into account. In practice, the implementation of a frequency-domain control used demodulation and modulation blocks that extract the phasor of the error $\mathbf{y}$ and generate the oscillatory control input, respectively (Fig. 2). This section presents the practical signal processing to implement the decentralized harmonic controllers.

In order to extract the phasor Y_i from the real oscillatory signal $y_i(t)$ provided by sensor i, a complex demodulation is applied. The method involves translating the signal y_i in the frequency domain, from the harmonic frequency ω_0, to 0 (rad/s), by multiplication with the complex sine wave of frequency ω_0. A low-pass filter, f, is applied to this complex signal in order to extract the phasor of interest:

$$Y_i(t)=f(t)\otimes(y_i(t)\exp(-j\omega_0 t)), \tag{20}$$

where $\otimes$ denotes the convolution operator. The cut-off frequency of the low-pass filter is set equal to $\omega_c \ll \omega_0$ and its static gain is set to 1, $\lvert f(0)\rvert=1$. Because of the low-pass filtering, the complex signal $Y_i(t)$, called the complex envelope, is localized in the low frequency domain. Hence, according to the Shannon criterion, $Y_i(t)$ can be sampled without aliasing at a rate $\omega_e<2\omega_0$. The discrete downsampled output of the complex envelope is $Y_i[k]=Y_i(kT_e)$ with $T_e=2\pi/\omega_e$ the sampling period and k the discrete time.

In order to generate each command signal $u_i(t)$ from each phasor U_i (Fig. 2), a complex modulation is used. First, the causal low-pass filtering f is applied to generate $U_i(t)$ from the downsampled dicrete-time signal $U_i[k]$. Then, the signal is translated in the frequency domain from 0 (rad/s) to the harmonic frequency, ω_0, and the real part is extracted to generate the command signal:

$$u_i(t)=2\Re(U_i(t)\exp(j\omega_{0t})). \tag{21}$$

In order to provide insight into the controller implementation, its equivalent form is developed. In the continuous time domain, Eq. (16) can be written by considering the finite difference approximation with $T_e\to 0$ and $\mu\to 0$:

$$\frac{\mathbf{U}(k+1)-\mathbf{U}(k)}{T_e}\approx\frac{d\mathbf{U}(t)}{dt}=-a\mathbf{U}(k)-b\mathbf{CY}(k), \tag{22}$$

where $b=\mu/T_e$ and $a=b\beta$. The Laplace Transform of Eq. (22) gives the equivalent compensator in terms of the complex envelopes $\mathbf{U}$ and $\mathbf{Y}$:

$$\mathbf{U}(s)=-\frac{b}{s+a}\mathbf{CY}(s). \tag{23}$$

By introducing Laplace transforms of Eqs. (20) and (21) in Eq. (23), the equivalent decentralized compensator is obtained in terms of the real oscillatory signals u_i and y_i:

$$\frac{u_i(s)}{y_i(s)}=-\frac{bN(s)}{(s+a)^2+\omega_0^2} \tag{24}$$

with $N(s)=Cf^2(s-j\omega_0)(s+a+j\omega_0)+C^*f^2(s+j\omega_0)(s+a-j\omega_0)$.

The numerator $N(s)$ includes bandpass filtering f, centered at ω_0; the denominator includes two weakly damped poles close to the harmonic frequency ω_0: $s_0=-a+j\omega_0$ and $s_0^*=-a-j\omega_0$. The feedback loop gain at the disturbance frequency, ω_0, is approximately bC_{ii}/a. It is tuned with the μ parameter: with $\mu=0$ there is no feedback loop ($b=0$) and no control. The maximal adaptation coefficient, $\mu_{\max}$ defined by Eq. (18), is equivalent to the critical feedback gain: the stability is marginal for this value. When $\beta=0$, Eq. (24) is the expression of a resonant controller because the added pole is undamped: the compensator is characterized by an infinite gain at ω_0. According to the Wohan's Principle,[23] this allows perfect rejection of the harmonic disturbance because the compensator includes a model of the harmonic generator: it is able to generate a sinusoidal wave form at the disturbance frequency even when the error is null. When it exists at least one negative eigenvalue $\Re(\lambda_i(\mathbf{CH}))<0$, the compensator poles should be damped for the purpose of adding stability robustness: the increase of β in Eq. (24) moves the compensator poles from the imaginary axis to the left side of the complex plane. According to Siever,[13] the equivalent controller is independent of the methodology chosen (analog, adaptive, classical, modern method); for example, a MIMO adaptive feedforward algorithm (usually called x-lms) will also present complex poles centered at the disturbance frequency.[5]

TABLE II. Panel data.

Parameter	Value
Thickness	$h=3.18\times10^{-3}$ m
Length	$L_x=48\times10^{-2}$ m
Width	$L_y=42\times10^{-2}$ m
Young's modulus	$E_p=68.5\times10^{9}$ Pa
Poisson's coefficient	$\nu_p=0.33$
Density	$\rho=2700$ kg m^{-3}
Loss factor	$\eta=5.0\times10^{-3}$

TABLE III. BM-500 PZT actuator and PVDF sensor data.

Parameter	PZT actuator	PVDF sensor
Thickness	$t_a=1.02\times10^{-3}$ m	$t_s=28\times10^{-6}$ m
Length	$L_x^{(a)}=2.54\times10^{-2}$ m	$L_x^{(s)}=1\times10^{-2}$ m
Width	$L_y^{(a)}=2.54\times10^{-2}$ m	$L_y^{(s)}=1.5\times10^{-2}$ m
Young's modulus	$E_a=61.1\times10^{9}$ Pa	
Poisson's coefficient	$\nu_a=0.29$	
Piezoelectric coefficient	$d_{31}=-1.9\times10^{-10}$ C/N	
Piezoelectric coefficient		$e_{31}=46\times10^{-3}$ C m^{-2}
Capacitance		$C_s=5\times10^{-10}$ F

B. Stability analysis of the implemented controller

When the controller slowly adapts the control inputs ($\mu\to0$) in comparison to the dynamics of the low-pass filters, the influence of modulation and demodulation blocks is negligible and closed loop stability can be analyzed using Eq. (9). However, in the general case, the low-pass filtering operations induce transients in the modulation and demodulation processes and they must be taken into account by modifying Eq. (9) as follows:

$$\mathbf{y}(k)=\mathbf{d}+\mathbf{H}\phi(q^{-1})\mathbf{u}(k), \tag{25}$$

where $\phi(q^{-1})=\phi_0+\phi_1q^{-1}+\cdots+\phi_dq^{-d}$ is the impulse response of the filters and q^{-1} is the delay operator. The impulse response coefficients are computed from the downsampled discrete-time impulse response of the two lowpass filters in series: $\phi_n=(f\star f)(nT_e)$ for $n=0,1,2,\cdots,d$. In other words, the impulse response of the combined modulation and demodulation blocks are represented by a finite impulse response (FIR) filter with $d+1$ coefficients. This FIR filter has an unitary static gain, $\phi(1)=\phi_0+\phi_1+\cdots+\phi_d=1$, because $|f(\omega)|\approx1$ for $\omega\approx0$. Consequently, the steady state version of Eq. (25) is Eq. (9). In other words, Eq. (25) describes the transients due to the signal processing operations (modulation and demodulation), but not the transients due to the physical system.

Similar to Eq. (17), Eq. (25) can be re-expressed as a discrete time autonomous system of state variable $\mathbf{x}(k)$:

$$\mathbf{x}(k+1)=(1-\mu\beta)\mathbf{x}(k)-\mu\mathbf{CH}\phi(q^{-1})\mathbf{x}(k), \tag{26}$$

where $\mathbf{x}(k)=\mathbf{u}(k)-\mathbf{u}_\infty$. By introducing the expression of $\phi(q^{-1})$, Eq. (26) takes the form of a difference equation

$$\mathbf{x}(k+1)=[(1-\mu\beta)\mathbf{I}-\mu\phi_0\mathbf{CH}]\mathbf{x}(k)-\mu\sum_{i=1}^{d}\phi_i\mathbf{CH}\mathbf{x}(k-i). \tag{27}$$

The condition for which $\mathbf{x}$ converges to $\mathbf{x}_\infty$ is more difficult to establish in the case of Eq. (27) than in the case of Eq. (17). It is necessary to re-express Eq. (27) in an augmented state space form

$$\mathbf{z}(k+1)=\mathbf{A}_d\mathbf{z}(k), \tag{28}$$

where $\mathbf{z}(k)=[\mathbf{x}(k)\mathbf{x}(k-1)\ldots\mathbf{x}(k-d)]^t$ is the new state vector, and the evolution matrix is

$$\mathbf{A}_d=\begin{bmatrix}(\mathbf{I}-\mu\mathbf{W})-\mu\mathbf{F}_0 & -\mu\mathbf{F}_1 & \cdots & -\mu\mathbf{F}_{d-1} & -\mu\mathbf{F}_d\\ \mathbf{I} & \mathbf{O} & \cdots & \mathbf{O} & \mathbf{O}\\ \vdots & \ddots & \ddots & \vdots & \vdots\\ \mathbf{O} & \mathbf{O} & \cdots & \mathbf{I} & \mathbf{O}\end{bmatrix}$$

with $\mathbf{F}_i=\phi_i\mathbf{CH}$.

The necessary and sufficient condition of stability is that the matrix $\mathbf{A}_d$ is Schur stable: all its eigenvalues are inside the unit circle in the complex plane.

When the weighting coefficient β is fixed, the stability condition consists of finding the maximum adaptation coefficient $\mu_{\max}$ such that $\forall\mu<\mu_{\max}:\sup|\lambda_i(\mathbf{A}_d(\mu))|<1$ and $|\lambda_i(\mathbf{A}_d(\mu_{\max}))|=1$. Considering the complexity of the matrix $\mathbf{A}_d$, this search was done numerically.

VI. SIMULATION AND EXPERIMENTAL RESULTS

A. Comparison of plant model with measured data

The prediction of $\mathbf{H}$, presented in Sec. III was first compared to experimental data in the case of a simply supported 48 cm$\times$42 cm aluminum panel instrumented with 4 BM-500 2.54 cm$\times$2.54 cm, 1-mm-thick PZT actuators and 41.5 cm$\times$1 cm, 28-μm-thick PVDF sensors. Tables II and III list the panel, actuator, and sensor data. Table IV shows the calculated and measured natural frequencies of the panel in the [0–800 Hz] range. The positions of actuator and sensor pairs on the panel (subsequently referred to as positions

TABLE IV. Natural frequencies of the panel.

m	1	2	1	2	3	1	3	2	4	3	4	1
n	1	1	2	2	1	3	2	3	1	3	2	4
f_{mn}, calculated (Hz)	77	177	208	308	344	425	474	525	577	692	708	730
f_{mn}, measured (Hz)	80	176	206	292	337	425	455	517	571	676	705	719

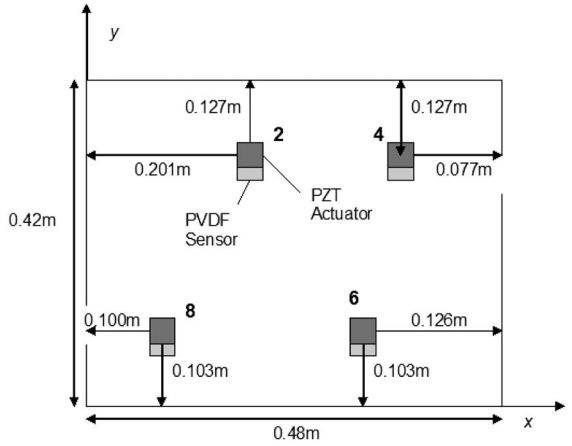

FIG. 3. Positions of the 4 PZT-PVDF pairs on the panel.

2, 4, 6, and 8) are shown in Fig. 3. The actuator positions were selected randomly in order to excite as many panel modes as possible in the [0–800 Hz] frequency range. Note however that in this configuration, PZT 2 and 4 do not effectively excite the panel modes $n=3$, and PZT 6 and 8 are not effective for panel modes $n=4$. A PVDF sensor was bonded close to each PZT to form a pair (their separation was of the order of 1 mm). The PZT-PVDF transfer functions were measured using a (0–800 Hz) white noise input signal sequentially driving the PZT actuators; the charge response of the PVDF sensors was amplified and converted to a voltage output through high input impedance filters. The following transfer functions do not include the input gain of the high voltage PZT amplifier and the output gain of the PVDF filters. On the other hand, a structural loss factor of the panel of 5×10^{-3} was considered in the simulations; this value was adjusted to fit the measured response on resonance of selected panel modes.

Figure 4 shows examples of measured and predicted transfer functions H_{28}, H_{48}, H_{66}, H_{88}. The agreement is generally good for the off-diagonal terms H_{28}, H_{48} (with the prediction slightly overestimating the measured values), but much less satisfactory for the diagonal terms H_{66}, H_{88}. In this case the prediction largely underestimates the magnitude of the transfer function off-resonance. This leads to a measured **H** which is more diagonally dominant than the calculated **H**, and therefore an *a priori* more viable implementation of decentralized control. Possible explanations for the underestimation of direct transfer by the theory are bending near-field

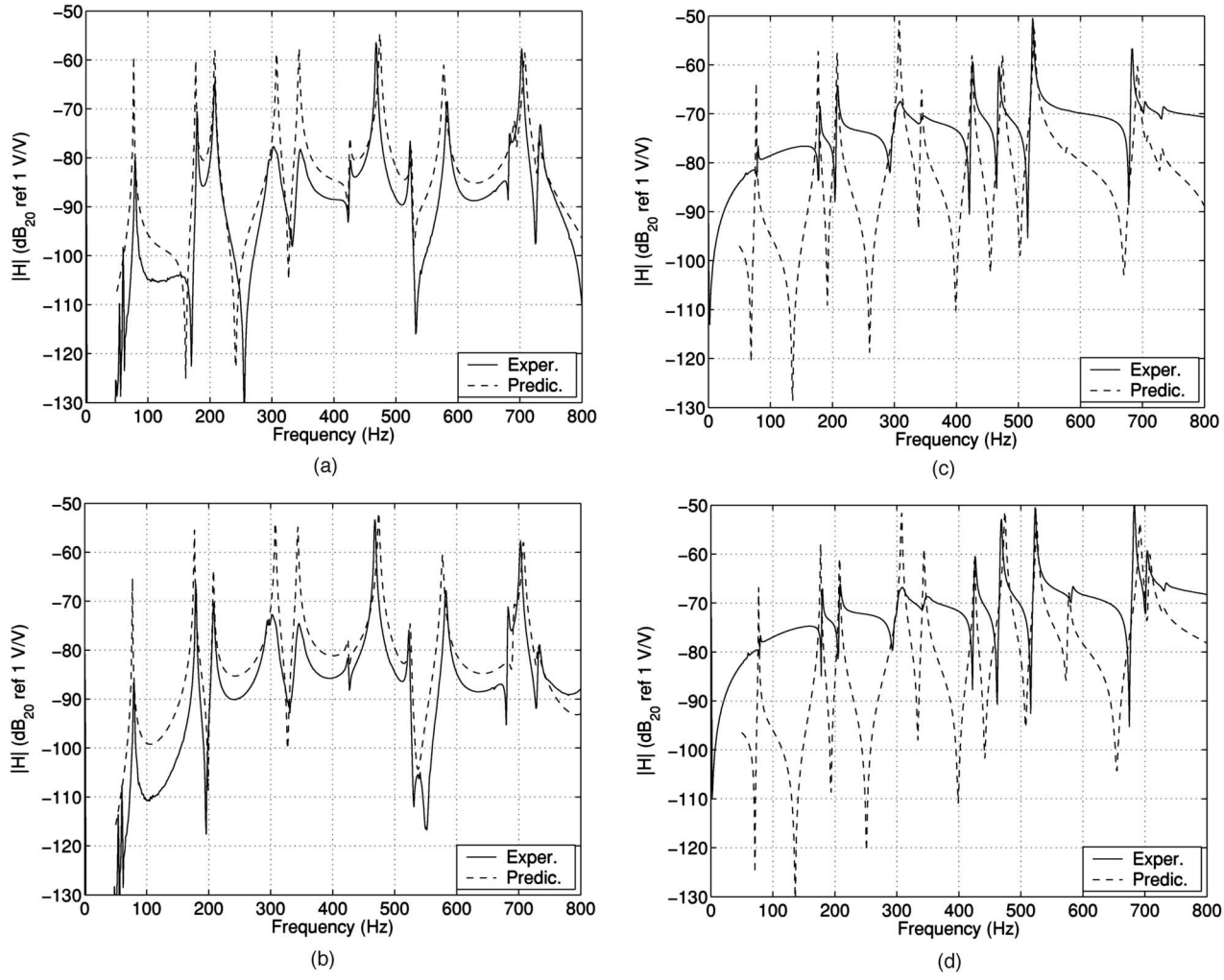

FIG. 4. Magnitude of transfer function matrix coefficients between PZT actuators and PVDF sensors. Off-diagonal coefficients (a) H_{28}, (b) H_{48}; Diagonal coefficients (c) H_{66}, (d) H_{88}. Solid line: experimental. Dashed line: predicted.

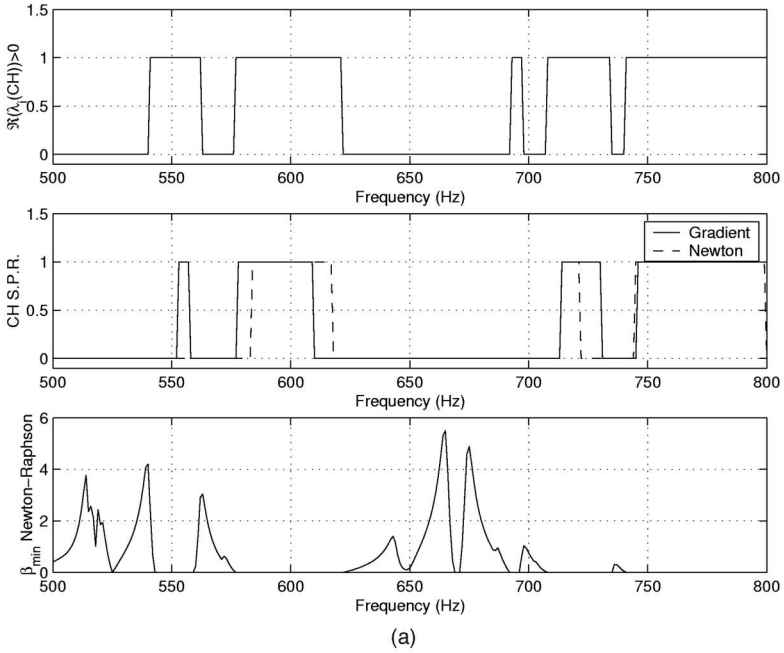

FIG. 5. Stability indicators of decentralized control derived from (a) theoretical and (b) measured plant matrix **H**: condition of **H** diagonal dominant, condition of **CH** SPR, minimum control effort weighting β.

effects of the PZT actuators and the effect of extensional excitation of the panel by the PZT actuators, which were not accounted for in the model.

B. Predicted stability indicators for decentralized control

For the physical configuration with four control units shown in Fig. 3, the various stability conditions listed in Table I were tested for decentralized control. The stability conditions are derived from the *theoretical* plant matrix or the *measured* plant matrix **H**. In this case, the plant matrix was measured by driving the PZT actuators with a pure sine in the frequency range from 500 to 800 Hz, with a 10 Hz step. The amplitude of the actuator signal was automatically adjusted in order to obtain the largest possible output signal from the PVDF sensors without saturation. Figure 5 presents predicted stability of decentralized control derived from either the theoretical or measured plant matrix **H** in the frequency range 500–800 Hz. The presented stability indicators are the diagonal dominant property of **H**, the condition of $\Re(\lambda_i(\mathbf{CH}))>0$, the condition **CH** strictly positive real (SPR), and the minimum control effort weighting β according to Eq. (19).

In the case of stability derived from the theoretical plant matrix, the sufficient condition of **H** being diagonal dominant is never verified in the frequency range investigated: the interaction between PZT-PVDF pairs is large at all frequencies. In the case of stability derived from the measured plant matrix, the diagonal dominant condition is verified in some frequency intervals. This is consistent with the observations

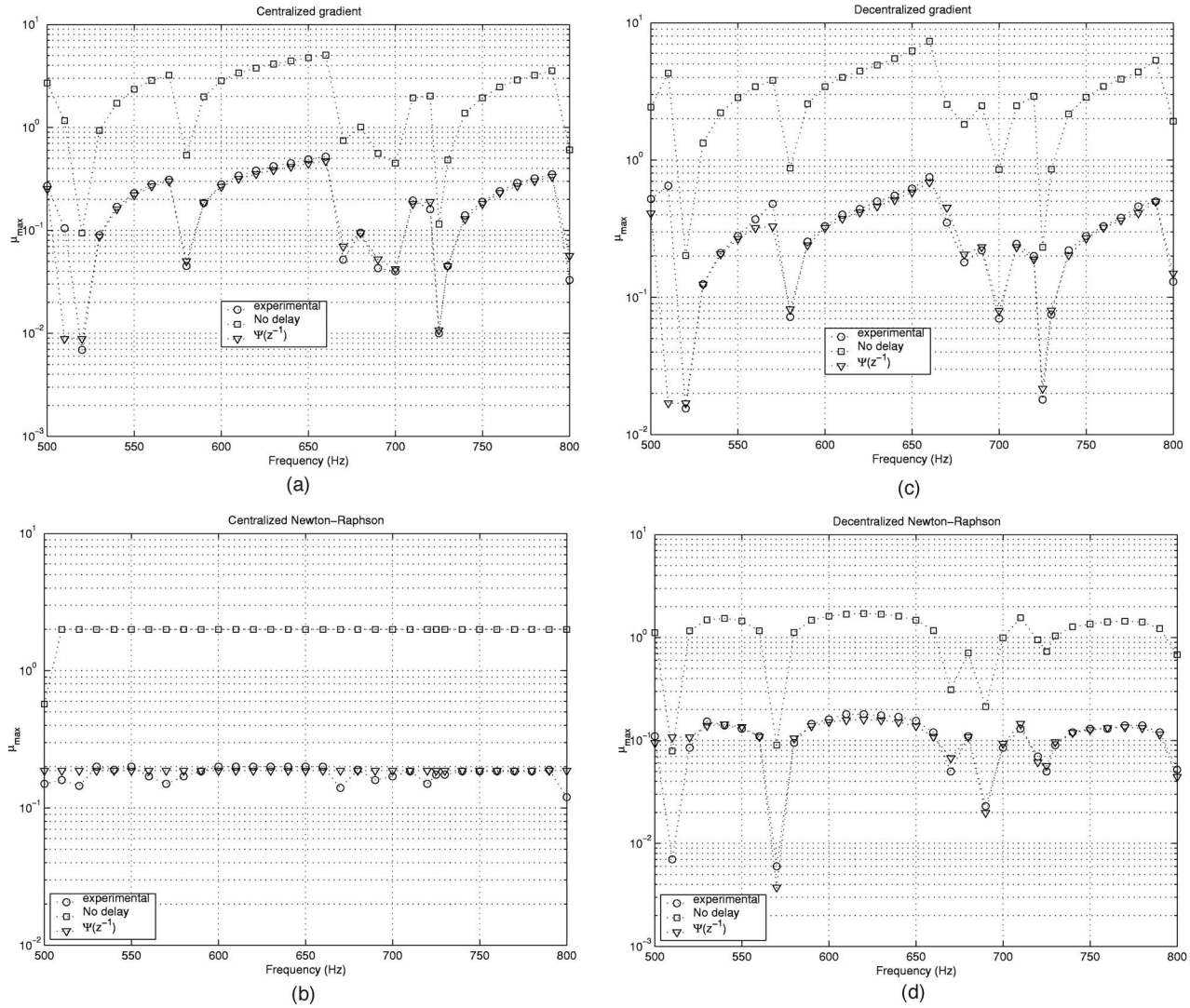

FIG. 6. Maximum value of the adaptation coefficient $\mu_{\max}$ for centralized or decentralized gradient and Newton-Raphson adaptation in the case of 4 PZT-PVDF pairs on the panel. (a) Centralized gradient; (b) centralized Newton-Raphson; (c) decentralized gradient; (d) decentralized Newton-Raphson.

derived from the plant matrix components H_{ij} in Fig. 4. The measured plant matrix tends to be not diagonal dominant close to resonances of panel modes.

The condition that the matrix **CH** is SPR guarantees that μ-stabilization of the closed loop system is possible without requiring control effort weighting (β=0). This condition is presented in Fig. 5 for decentralized Newton, for which $\mathbf{C}=\mathrm{diag}(1/H_{ii})$. In the case of stability derived from the theoretical plant matrix and for the Newton algorithm, the **CH** matrix is SPR only in some frequency intervals included in those of the condition $\Re(\lambda_i(\mathbf{CH}))>0$; accordingly, the minimum value of β is predicted to be larger than 0 only when $\Re(\lambda_i(\mathbf{CH}))<0$. Note that for the gradient algorithm, the condition $\Re(\lambda_i(\mathbf{CH}))>0$ is verified at all frequencies, therefore the minimal value of β is predicted to be null (not shown in the figure). Stability derived from the measured **H** is less stringent: for decentralized Newton, **CH** always verifies $\Re(\lambda_i(\mathbf{CH}))>0$ except at 500 Hz and in the frequency range 670–690 Hz. At these frequencies, control effort weighting is necessary in order to stabilize the closed-loop system, $\beta_{\min}>0$ for both the gradient and Newton algorithms. Note that at frequencies for which $\beta_{\min}>0$, **H** is not diagonal dominant, but the inverse is not true: for example, at 800 Hz, the experimental and theoretical matrices **H** are not diagonal dominant but the associated **CH** matrix is SPR for the gradient algorithm, and both gradient and Newton algorithms are μ-stable because $\Re(\lambda_i(\mathbf{CH}))>0$. The hierarchy between the conditions is verified: the diagonal dominance of **H** or the SPR of **CH** are sufficient, but not necessary conditions of closed-loop stability.

Note also that the minimum value of the effort weighting coefficient β required to stabilize the Newton algorithm is large, and usually larger than for the gradient algorithm (a value of β=1 reduces the attenuation at the error sensors to 3 dB). Hence, the control performance obtained with the weighted Newton is expected to be smaller than the performance of the weighted gradient.

C. Predicted and measured stability limits

The decentralized and centralized controllers were implemented in a rapid prototyping dSPace system. The

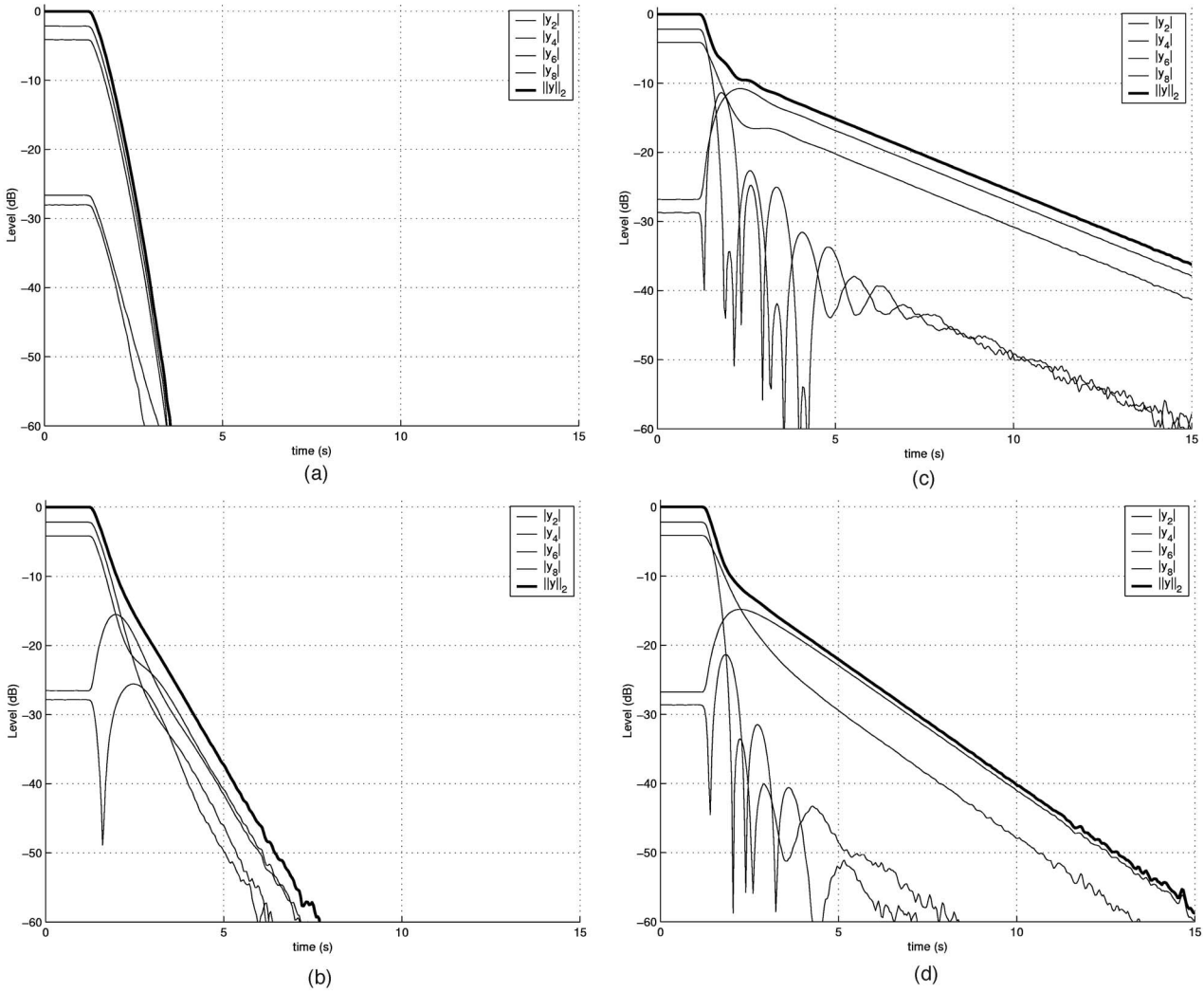

FIG. 7. Experimental results at 550 Hz for the case of **H** SPR and diagonal dominant. No control effort weighting ($\beta=0$). The levels are normalized by $\|\mathbf{y}(0)\|_2$. (a) Centralized Newton-Raphson ($\mu=0.08$); (b) decentralized Newton-Raphson ($\mu=0.05$); (c) centralized gradient ($\mu=0.15$); (d) decentralized gradient ($\mu=0.15$).

sampling frequency was set to 5 kHz. For the analysis and synthesis of the complex envelopes, the low-pass FIR filters were implemented with 4 Butterworth second-order filters in order to ensure an attenuation of 40 dB outside ±7.5 Hz. Consequently, the complex envelopes were under sampled at 25 Hz without aliasing. The identification of the plant matrix was performed for each frequency with an harmonic input of the PZT actuators (with the disturbance off) and under steady-state response of the system. The identified plant matrix was used to perform the active centralized/decentralized control of the plate. Steady-state harmonic response of the system can be assumed for the control due to the slow dynamics of the FIR filters (and the slow dynamics of the controller-low value of μ) against the dynamics of a low damped mode in the considered narrow frequency band.[24] This point is experimentally verified with the results presented in Fig. 6 where the dynamics of the filters limit the maximum value of the adaptation coefficient.

Figure 6 shows the predicted and measured stability limits of the centralized and decentralized controllers in the case of the 4 PZT-PVDF control pairs shown in Fig. 3, in the frequency range [500–800 Hz]. Note that the predicted stability limit was obtained from the *measured* plant matrix **H**. The maximum adaptation coefficient, $\mu_{\max}$, observed experimentally for the various controllers is also reported. Two cases of low-pass filter dynamic response were examined in the prediction: (i) a unitary frequency response, $\phi_0=1$ and $\phi_i=0$ for $i>0$ [in this case, no filter delay is assumed, and the stability limit was obtained from Eq. (18)]; (ii) the measured impulse response of the low-pass filters $\phi(q^{-1})$ [in this case, the stability limit was derived from the eigenvalues of the matrix $\mathbf{A}_d$ in Eq. (28)].

In the case of the *centralized* gradient and Newton algorithms, the **CH** matrix is always SPR, therefore the control effort weighting was set to zero: $\beta=0$. The maximum adaptation coefficient $\mu_{\max}$ turns to be frequency-independent for the centralized Newton, its predicted value being 2 in the case of a zero loop delay and close to 0.02 in the case of the loop delay induced by the low-pass filters. The negative impact of the time-delay, or filtering, is clearly apparent in this

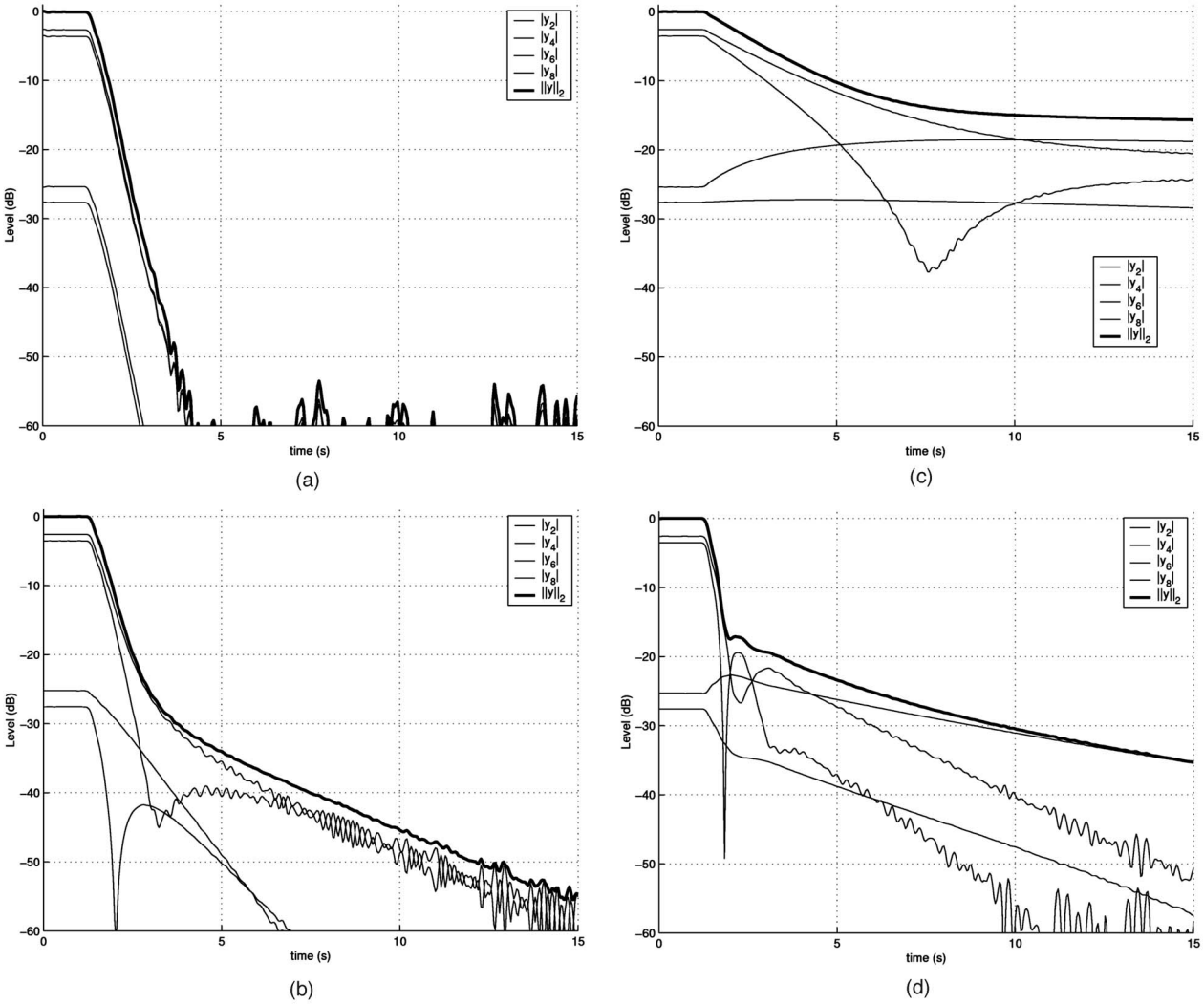

FIG. 8. Experimental results at 520 Hz for the case of **H** not SPR and not diagonal dominant, but **CH** SPR. No control effort weighting ($\beta=0$). The levels are normalized by $\|\mathbf{y}(0)\|_2$. (a) Centralized Newton ($\mu=0.05$); (b) decentralized Newton-Raphson ($\mu=0.03$); (c) centralized gradient ($\mu=0.001$); (d) decentralized gradient ($\mu=0.01$).

computation. The value of $\mu_{\max}=2$ in the case of a zero loop delay is consistent with convergence analysis derived from Eq. (16). As expected, when loop delay is increased, the critical feedback gain is reduced. The experimental values of $\mu_{\max}$ are close to the values predicted when the measured impulse response of low-pass filters is included in the loop. It is clear that $\mu_{\max}$ is largely overestimated if no loop delay is included. In the case of centralized gradient, the values of $\mu_{\max}$ are frequency-dependent: when $\mathbf{C}=\mathbf{H}^H$, Eq. (18) becomes $\mu_{\max}<2/\sigma^2_{\max}$, where $\sigma^2_{\max}$ is the largest eigenvalue of $\mathbf{H}^H\mathbf{H}$. Therefore, at resonance of panel modes, the system presents a high gain and the adaptation coefficient must be reduced. The time-delay induced by low-pass filters still decreases the critical value of μ. The agreement between experimental and predicted values of $\mu_{\max}$ when the measured impulse response of low-pass filters is included in the loop is again very good.

In the case of *decentralized* control, the matrix **CH** is not SPR for all frequencies in the [500–800 Hz] range, therefore a strictly positive control effort weighting coefficient β has to be introduced at certain frequencies. The same value of β was used in the experiments and the prediction [1.5 times the minimum value computed with Eq. (18)]. It appears that in this case $\mu_{\max}$ is frequency-dependent for both the gradient and Newton algorithms.

The following sections detail the control results obtained at frequencies where: (i) **H** is diagonal dominant, (ii) $\Re(\lambda_i(\mathbf{CH}))>0$, the closed loop is μ-stable without effort weighting; (iii) $\Re(\lambda_i(\mathbf{CH}))<0$, control effort weighting is necessary. In all cases, the primary disturbance is a transverse point force provided by an electrodynamic shaker at location $x=35$ cm, $y=17$ cm in the coordinate system of Fig. 3.

D. Experimental results for a case H diagonal dominant

At the disturbance frequency of 550 Hz, the measured plant matrix **H** is diagonal dominant (see Fig. 5), and SPR. The diagonal dominant condition of **H** is a sufficient condition to guarantee that the matrix **CH** is positive definite, and that the system is μ-stable without control effort weighting,

$\beta=0$. Consequently, the eigenvalues associated to the decentralized gradient algorithm, $\lambda_i(\mathrm{diag}(\mathbf{H})^H\mathbf{H})=\{0.70, 0.41, 0.27, 0.10\}$, are close to the eigenvalues of the centralized gradient $\lambda_i(\mathbf{H}^H\mathbf{H})=\{0.85, 0.41, 0.29, 0.06\}$. Similarly, the eigenvalues associated to the decentralized Newton algorithm, $\Re(\lambda_i(\mathbf{CH}))=\{1.36, 1.26, 0.78, 0.59\}$, are close to the eigenvalues of the centralized Newton (equal to unity).

Figure 7 shows the measured convergence of the error measured by each of the PVDF sensors, for centralized Newton, decentralized Newton and decentralized gradient. In this case, $\beta=0$ since the closed-loop system is μ-stable without control effort weighting. For equal adaptation coefficients, the decentralized Newton algorithm converges at a rate similar to the centralized Newton, because the associated eigenvalues are similar. Moreover, the convergence rate is similar for of all PVDF sensors in the case of the centralized and decentralized Newton. For the decentralized gradient, the convergence rate varies from one PVDF sensor to another: the largest eigenvalue of **CH** is associated in this case with the fastest convergence mode and the smallest eigenvalue of **CH** corresponds to the slowest convergence mode. The ratio of the largest to the smallest eigenvalue defines the condition number of **CH**, and is representative of the convergence rate of the algorithm. It was experimentally verified that in this case, decentralized Newton converges faster $[\mathrm{cond}(\mathbf{CH})=2.43]$ than decentralized gradient $[\mathrm{cond}(\mathbf{CH})=7.23]$ for equal adaptation coefficients μ.

E. Experimental results for a case CH is SPR

At the frequency of 520 Hz, the disturbance is close to the natural frequency of the (2,3) plate mode. The plant matrix **H** measured at this frequency is not diagonal dominant: the interaction between control units is significant. The transverse velocity field of the panel due to the primary point force driving the panel at 520 Hz is presented on the right-hand side of Fig. 9. It appears that at this frequency, PZT actuator 2 is close to a vibration node and leads to a low response of PVDF sensor 2($|H_{22}|=0.36$), but PZT actuator 8, close to an antinode, leads to a high response of PVDF sensor 2: $|H_{82}|=0.63$. Consequently, the diagonal dominant condition cannot be respected. Moreover, the plant matrix is not SPR, $\lambda_i(\mathbf{H}^H+\mathbf{H})=\{5.41, 0.97, 0.51, -0.67\}$, the system is not dissipative: it is necessary to introduce the diagonal compensator matrix **C**. Consequently, it is not possible to conclude on the closed-loop stability without investigation of the positiveness of **CH**. The matrices **CH** associated with the decentralized gradient and newton algorithms are both SPR; consequently, the stability can be diagonal for $\mu\to 0$: the decentralized algorithms are predicted μ-stable.

Figure 8 shows the measured convergence of the error measured by each of the PVDF sensors, for centralized Newton, decentralized Newton, and decentralized gradient. β is set to 0 since the closed-loop system is μ-stable without control effort weighting. The centralized gradient algorithm converges less rapidly than the decentralized gradient because the condition number of $\mathbf{H}^H\mathbf{H}$ is large in comparison to the condition number of $\mathrm{diag}(\mathbf{H})^H\mathbf{H}$. In other words, the panel resonance leads to an ill-conditioned matrix, which implies that the centralized gradient $[\mathrm{cond}(\mathbf{CH})=97]$ is slower than the decentralized gradient $[\mathrm{cond}(\mathbf{CH})=45]$. On the other hand, the Newton algorithm is seen to have the largest convergence rates, $\mathrm{cond}(\mathbf{CH})=6$ for the decentralized algorithm and $\mathrm{cond}(\mathbf{CH})=1$ for the centralized algorithm.

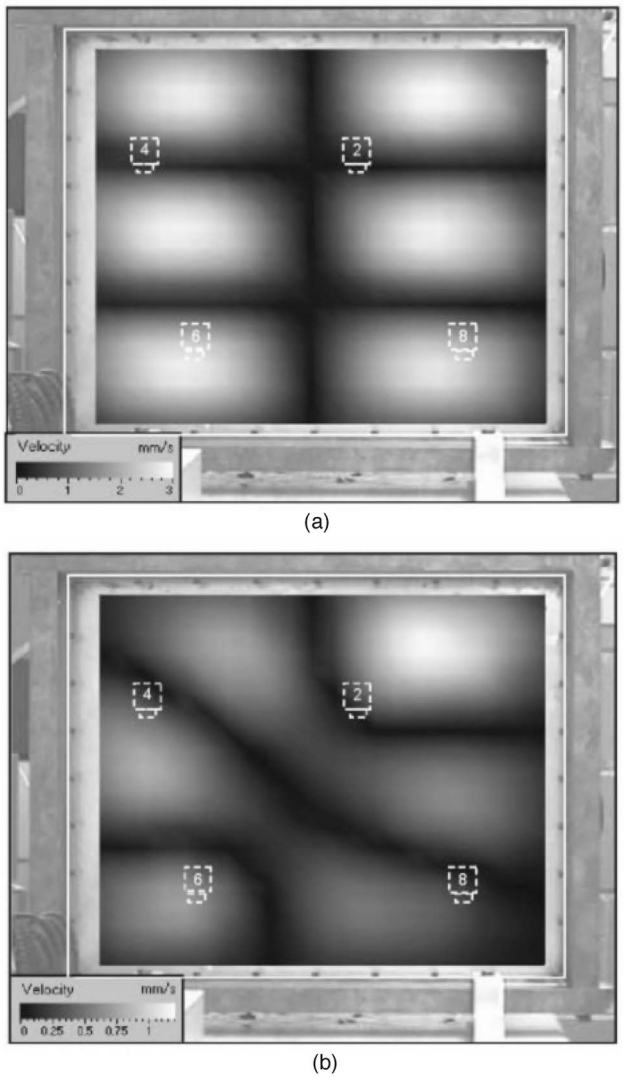

FIG. 9. Transverse velocity field of the panel measured by Doppler laser vibrometry at 520 Hz. (a) Control off; (b) decentralized gradient control on. Note that the amplitude scale is increased by a factor about 3.

Figure 9 shows the transverse vibration field of the panel at 520 Hz with the control off and after convergence of the decentralized gradient algorithm. A significant decrease of the panel response is observed not only at the sensor locations, but also over the whole panel area.

F. Experimental results for a case with effort weighting β

At the frequency of 680 Hz, the measured plant matrix **H** is not diagonal dominant (for example, $|H_{11}|=0.26$ but $|H_{14}|=0.59$)), **H** is not SPR, and the matrices **CH** corresponding to decentralized gradient and decentralized Newton are not SPR: there exist eigenvalues such that $\Re(\lambda_i(\mathbf{CH}))=-0.05$ for the gradient algorithm, and $\Re(\lambda_i(\mathbf{CH}))=-0.5$ for the Newton algorithm. In order to guarantee that the matrix

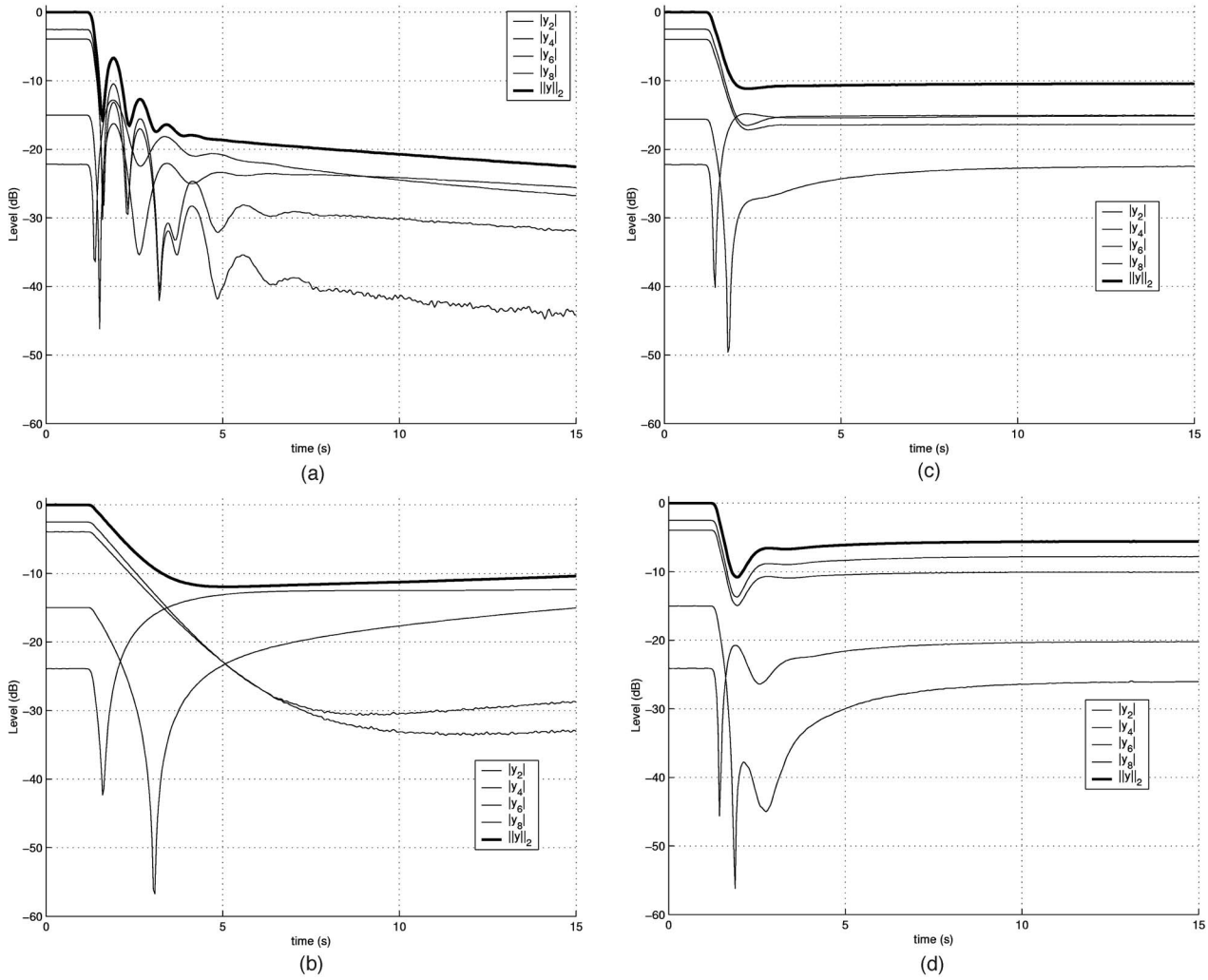

FIG. 10. Experimental results at 680 Hz for the case of **CH** not SPR and not diagonal dominant. The levels are normalized by $\|\mathbf{y}(0)\|_2$. (a) Centralized gradient (μ=0.05, β=0.0); (b) decentralized gradient (μ=0.02, β=0.0); (c) decentralized gradient (μ=0.05, β=0.3); (d) decentralized Newton (μ=0.04, β=1.0).

$\mathbf{B}=\mathbf{CH}+\beta\mathbf{I}$ is SPR, a control effort weighting coefficient must be introduced: a value of β=0.3 was chosen for the gradient algorithm and β=0.7 for the Newton algorithm. Figure 10 shows the measured convergence of the error measured by each of the PVDF sensors, for various control algorithms. Decentralized gradient is seen to diverge when β =0 and when a relatively small value μ=0.02 of the adaptation coefficient is chosen. On the other hand, applying an effort weighting β=0.3 has the effect of stabilizing the decentralized gradient when μ=0.05. This is done however at the detriment of a smaller attenuation of the error signals (of the order of 10 dB). On the other hand, the performance of decentralized Newton is marginal in this case, because of the relatively large effort weighting applied.

VII. CONCLUSIONS

We have analyzed the performance and stability of decentralized active control of panel vibration using multiple pairs combining PZT actuators and PVDF sensors distributed (and not necessarily collocated) on the panel. The stabilization condition of the closed loop by adjusting the convergence coefficient was especially investigated through an adjustable control effort term in the quadratic cost function. Various necessary or sufficient conditions derived from the plant matrix have been obtained to analyze the stability of decentralized gradient and decentralized Newton-Raphson algorithms; these conditions were summarized in Table I from the most restrictive to the less restrictive condition. Figure 11 illustrates the hierarchy between the three cases investigated in the experiments: at 550 Hz the plant matrix is diagonal dominant, hence the stability is ensured by the low interaction between units; at 520 Hz the plant matrix is not SPR, hence the stability is ensured by the diagonal compensator; at 680 Hz the stability requires a control effort weighting term, consequently perfect rejection cannot be reached.

While the diagonal dominance of the plant matrix **H** provides a sufficient condition for closed loop μ-stability, it is not a necessary condition. Therefore, decentralized vibration control is achievable even in the presence of strong interaction between control units. Also, the collocation of dual actuator-sensor pairs has the very attractive property to theoretically provide a SPR plant matrix **H**, but this is also a sufficient condition of μ-stability. Finally, the necessary con-

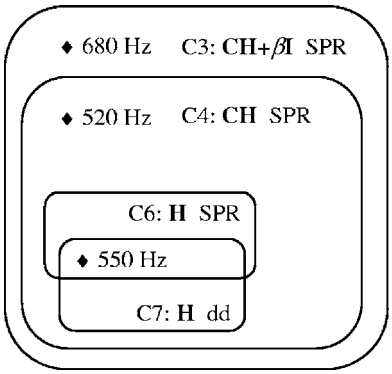

FIG. 11. The hierarchy of stability conditions shows that at 550 Hz the system is diagonal dominant and SPR (in C6 and C7). At 520 Hz **H** is not SPR and not dd but **CH** is SPR (in C4 but not in C6 nor C7). At 680 Hz only C3 is satisfied, control effort weighting is necessary to stabilize the closed loop.

dition of μ-stability (the real part of the eigenvalues of **CH** being positive) can be interpreted as a tolerance on the collocation of dual actuator-sensor pairs.

[1]C. R. Fuller, S. J. Elliot, and P. A. Nelson, *Active Control of Vibration* (Academic, London, 1996).
[2]B. Petitjean and I. Legrain, "Feedback controllers for active vibration suppression," J. Struct. Control. **3**, 111–127 (1996).
[3]S. J. Elliott, "Distributed control of sound and vibration," in Proceedings of ACTIVE04, Williamsburg, VA, 2004.
[4]J. Q. Sun, "Some observations on physical duality and collocation of structural control sensors and actuators," J. Sound Vib. **194**, 765–770 (1996).
[5]E. Leboucher, P. Micheau, A. Berry, and A. L'Espérance, "A stability analysis of a decentralized adaptive feedback active control system of sinusoidal sound in free space," J. Acoust. Soc. Am. **111**, 189–199 (2002).
[6]C. Bordier, "Controle actif de sources inaccessibles," Ph.D. thesis, Université Aix-Marseille, 2003.
[7]S. J. Elliott and C. Boucher, "Interaction between multiple feedforward active control systems," IEEE Trans. Speech Audio Process. **2**, 521–530 (1994).
[8]P. Gardonio, E. Bianchi, and S. J. Elliott, "Smart panel with multiple decentralised units for the control of sound transmission," Proceedings of Active, 2002.
[9]O. N. Engels, W. P. Baumann, and S. J. Elliott, "Centralised and decentralised feedback control of kinetic energy," in Proceedings of ACTIVE04, Williamsburg, VA, 2004.
[10]O. N. Baumann, W. P. Engels, and S. J. Elliott, "A comparison of centralised and decentralised control for the reduction of kinetic energy and radiated sound power," in Proceedings of ACTIVE04, Williamsburg, VA, 2004.
[11]P. Gardonio, E. Bianchi, and S. J. Elliott, "Smart panel with multiple decentralised units for the control of sound transmission. I. Theoretical predictions. II. Design of the decentralised control units. III. Control system implementation," J. Sound Vib. **274**, 163–232 (1996).
[12]S. J. Elliott, P. Gardonio, T. C. Sors, and M. J. Brennan, "Active viboacoustic control with multiple local feedback loops," J. Acoust. Soc. Am. **111**, 908–915 (2002).
[13]L. A. Sievers and A. H. Flotow, "Comparison and extensions of control methods for narrow-band disturbance rejection," IEEE Trans. Signal Process. **40**, 2377–2391 (1992).
[14]M. Morari and E. Zafiriou, *Robust Process Control* (Prentice Hall, Englewood Cliffs, NJ, 1989).
[15]G. West-Vukovich and E. J. Davison, "The decentralized control of large flexible space structures," IEEE Trans. Autom. Control **29**, 866–879 (1984).
[16]P. Micheau and P. Coirault, "Adaptive controller using filter banks to reject multi-sinusoidal disturbance," Automatica **36**, 1659–1664 (2000).
[17]E. K. Dimitriadis, C. R. Fuller, and C. A. Rogers, "Piezoelectric actuators for distributed vibration excitation of thin plates," J. Vibr. Acoust. **113**, 100–107 (1991).
[18]J. H. Kim, S. B. Choi, C. C. Cheong, S. S. Han, and J. K. Lee, "h_{inf} control of structure-borne noise of a plate featuring piezoceramic actuators," ASME Smart Material Structures **8**, 1–12 (1999).
[19]C. K. Lee and F. C. Moon, "Modal sensors/actuators," J. Appl. Mech. **57**, 434–441 (1990).
[20]E. Kaszkurewicz and A. Bhaya, *Matrix Diagonal Stability in Systems and Computation* (Birkhauser, Boston, 1999).
[21]J.-J. Slotine and W. Li, *Applied Nonlinear Control* (Prentice Hall, Englewood Cliffs, NJ, 1991).
[22]K. B. Scribner, L. A. Sievers, and A. H. Flotow, "Active narrow-band vibration isolation of machinery noise from resonant substructures," J. Acoust. Soc. Am. **167**, 17–24 (1993).
[23]B. A. Francis and W. Wonham, "The internal model principle of control theory," Automatica **12**, 457–465 (1976).
[24]P. Micheau and S. Renault, "Active control of the complex envelope associated with a low damped mode," Mech. Syst. Signal Process. **20**(3), 646–661 (2006).

Effects of porous covering on sound attenuation by periodic arrays of cylinders

Olga Umnova[a)]
Acoustics, Audio and Video Group, School of Computing, Science and Engineering, The University of Salford, Salford, Lancs. M5 4WT, United Kingdom

Keith Attenborough
Department of Engineering, University of Hull, Hull HU6 7RX, United Kingdom

Chris M. Linton
Department of Mathematical Sciences, Loughborough University, Leics. LE11 3TU, United Kingdom

(Received 10 May 2005; revised 31 August 2005; accepted 12 October 2005)

The acoustic transmission loss of a finite periodic array of long rigid cylinders, without and with porous absorbent covering, is studied both theoretically and in the laboratory. A multiple scattering model is extended to allow for the covering and its acoustical properties are described by a single parameter semi-empirical model. Data from laboratory measurements and numerical results are found to be in reasonable agreement. These data and predictions show that porous covering reduces the variation of transmission loss with frequency due to the stop/pass band structure observed with an array of rigid cylinders with similar overall radius and improves the overall attenuation in the higher frequency range. The predicted sensitivities to covering thickness and effective flow resistivity are explored. It is predicted that a random covered array also gives better attenuation than a random array of rigid cylinders with the same overall radius and volume fraction. © *2006 Acoustical Society of America.* [DOI: 10.1121/1.2133715]

PACS number(s): 43.50.Gf, 43.20.Fn [DKW] Pages: 278–284

I. INTRODUCTION

Interest in applications of periodic arrays of cylinders for noise control has increased since publication of the measured transmission spectra of a minimalistic sculpture.[1] When the density of scattering elements is large enough, the structure does not support sound propagation through it at the frequencies of the stop bands that appear in its transmission spectrum. Measurements on periodic arrays of cylinders[2] have shown the potential of using these kinds of structures for noise control. One possible advantage in using such periodic arrays instead of conventional noise barriers is that the structures are relatively transparent. Another possibility is that they could be formed from trees, since trees can be arranged in periodic arrays. Hence useful noise control could be achieved by natural means.[3]

A 7.2-m-long, 1.1-m-wide periodic (triangular) array of hollow cylindrical PVC rods with diameter 16 cm and with an array filling fraction, i.e., the volume fraction of cylinders in the array, of 47%, has been shown[2] to give a maximum attenuation close to 25 dB at some frequencies in the range between 800 Hz and 4 kHz. However the transmission loss spectrum was found to have a peaky character and there were frequencies at which measured attenuation minima were less than 7 dB. For noise control applications, the problem arises of how to reduce the frequency dependence of the attenuation without reducing the overall value. It has been suggested[2] that the effect of covering the elements by the sound absorptive materials should be investigated. This study is the main subject of the present paper.

Previous publications devoted to the study of the properties of sonic crystals refer to two theoretical approaches for predicting the transmission and reflection properties of the periodic arrays: the infinite array "sonic crystal" approach, which involves the computation of the dispersion bands using a plane-wave expansion method,[4,5] and the multiple scattering approach.[6,7] The second approach is more useful for practical applications as it allows computations for finite arrays and direct comparisons with data.

Section II presents a review of the model used to describe multiple scattering by regular arrays and the modifications necessary to allow for porous coverings on the array elements. In Sec. III, laboratory measurements on arrays of rigid and covered cylinders are described. Data for the insertion loss at different frequencies are compared with model predictions for the arrays of rigid and covered cylinders. Section IV presents conclusions and suggestions for further research.

II. THE MODEL

In this paper we follow a previously published multiple scattering approach.[8] However, we assume that a line source is located at the origin of the coordinate system instead of a source of plane wave excitation. Suppose that there are N cylinders of radius a_j^{out}. We will introduce $N+1$ polar coordinate systems in the (x,y) plane normal to the cylinder axes: (r,θ) centered at the origin and (r_j,θ_j), $j=1,\ldots,N$, centered

a)Electronic mail: o.umnova@salford.ac.uk

 0001-4966/2006/119(1)/278/7/$22.50

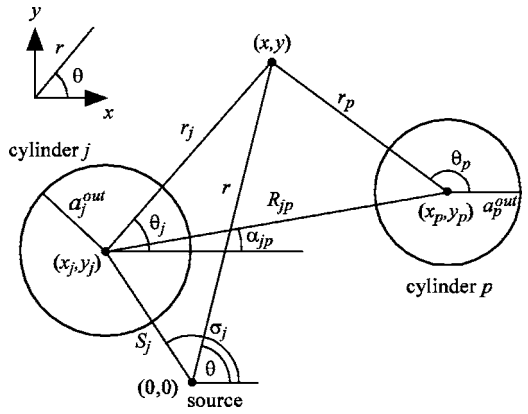

FIG. 1. Plan view of two cylinders and corresponding Cartesian and polar coordinates.

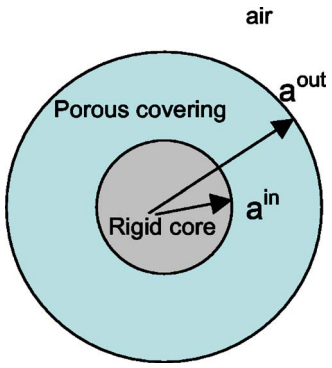

FIG. 2. (Color online) Cross section of the cylinder covered with porous material.

at (x_j, y_j), the center of the jth cylinder (Fig. 1). The center-to-center spacing between the jth and pth cylinders is denoted by R_{jp} and the distance of the center of the jth cylinder from the origin is denoted by S_j.

Exterior to the cylinders the pressure field is ϕ, where

$$\nabla^2\phi + k_0^2\phi = 0,$$

and $k_0 = \omega/c_0$ is the wave number in air.

Each cylinder scatters the waves which are incident upon it. To take account of all such scattering we express the total field as the sum of the incident wave represented by a Hankel function, $\phi_i = H_0^{(1)}(k_0 r)$, and a general outgoing wave emanating from each cylinder. Thus the total field exterior to the cylinders can be written

$$\phi = H_0(k_0 r) + \sum_{j=1}^{N}\sum_{n=-\infty}^{+\infty} A_n^j Z_n^j H_n^{(1)}(k_0 r_j) e^{in\theta_j}, \tag{1}$$

for some set of unknown coefficients A_n^j.

The factors Z_n^j are introduced for later convenience and determined by the boundary conditions on the cylinder surface.

If the cylinders are rigid

$$Z_n^j = \frac{J_n'(k_0 a_j^{\text{out}})}{H_n^{(1)\prime}(k_0 a_j^{\text{out}})}. \tag{2}$$

Using Graf's addition theorem[9] (for Bessel functions we can show that, as long as $r_p < R_{jp}$ for all $j \neq p$ and $r_p < S_p$, we can write):

$$\begin{aligned}\phi(r_p,\theta_p) = &\sum_{m=-\infty}^{\infty} J_m(k_0 r_p) H_m^{(1)}(k_0 S_p) e^{im\theta_p} e^{-im(\pi+\sigma_p)} \\ &+ \sum_{n=-\infty}^{\infty} A_n^p Z_n^p H_n^{(1)}(k_0 r_p) e^{in\theta_p} + \sum_{\substack{j=1\\ \neq p}}^{N}\sum_{n=-\infty}^{\infty} A_n^j Z_n^j \\ &\times \sum_{m=-\infty}^{\infty} J_m(k_0 r_p) H_{n-m}^{(1)}(k_0 R_{jp}) e^{im\theta_p} e^{i(n-m)\alpha_{jp}}.\end{aligned}$$

The geometrical restriction implies that this expression is only valid if the point (r_p, θ_p) is closer to the center of cylinder p than to the centers of any of the other cylinders or the source.

This is certainly true on the surface of cylinder p and so the above equation can be used to apply the boundary conditions on each cylinder.

The cross section of the single element of the array with porous covering is shown in Fig. 2. The field in the region $a_p^{\text{in}} < r_p < a_p^{\text{out}}$ can be represented by

$$\phi_{\text{in}}(r_p,\theta_p) = \sum_{n=-\infty}^{\infty} A_n^p (X_n^p H_n^{(1)}(k(\omega) r_p) + Y_n^p J_n(k(\omega) r_p)),$$

where $k(\omega)$ is the complex wave number in the porous material and factors X_n^p and Y_n^p are introduced for later convenience.

We apply boundary conditions of continuity of pressure and particle velocity on the outer surface of the cylinder p:

$$\begin{aligned}&\phi|_{r_p=a_p^{\text{out}}} = \phi_{\text{in}}|_{r_p=a_p^{\text{out}}}, \\ &\frac{1}{\rho_0}\left.\frac{\partial\phi}{\partial r_p}\right|_{r_p=a_p^{\text{out}}} = \frac{\Omega}{\rho(\omega)}\left.\frac{\partial\phi_{\text{in}}}{\partial r_p}\right|_{r_p=a_p^{\text{out}}},\end{aligned} \tag{3}$$

where $\rho(\omega)$ is complex density of porous material and Ω is its porosity.

At the interface between porous covering and the rigid core of the cylinder the condition of zero velocity is applied:

$$\left.\frac{\partial\phi_{\text{in}}}{\partial r_p}\right|_{r_p=a_p^{\text{in}}} = 0.$$

This boundary condition leads to a relationship between coefficients X_n^p and Y_n^p:

$$Y_n^p = -X_n^p \frac{H_n^{(1)\prime}(k(\omega) a_p^{\text{in}})}{J_n'(k(\omega) a_p^{\text{in}})}.$$

Application of boundary conditions for pressure and velocity on the outer surface of cylinder p allows elimination of coefficients X_n^p and after using the orthogonality of the functions $e^{im\theta_p}$, $m = 0, \pm 1, \pm 2, \ldots$, these boundary conditions lead to an infinite system of equations for coefficients A_m^p:

$$A_m^p + \sum_{\substack{j=1 \\ \neq p}}^{N} \sum_{n=-\infty}^{\infty} A_n^j Z_n^j e^{i(n-m)\alpha_{jp}} H_{n-m}^{(1)}(k_0 R_{jp})$$

$$= -H_m^{(1)}(k_0 S_p) e^{-im(\pi+\sigma_p)}, \quad (4)$$

$$p = 1, \ldots, N, \quad m = 0, \pm 1, \pm 2, \ldots .$$

which can be solved by truncation. These equations differ from those for rigid cylinders only by the factors Z_n^j which are now given by

$$Z_n^j = \frac{J_n(k_0 a_j^{\text{out}}) - Z(\omega) J_n'(k_0 a_j^{\text{out}}) F_n(k_0 a_j^{\text{out}}, k(\omega) a_j^{\text{in}})}{H_n^{(1)}(k_0 a_j^{\text{out}}) - Z(\omega) H_n^{(1)\prime}(k_0 a_j^{\text{out}}) F_n(k_0 a_j^{\text{out}}, k(\omega) a_j^{(\text{in})})}, \quad (5)$$

where

$$F_n(x,y) = \frac{J_n(x) H_n^{(1)\prime}(y) - H_n^{(1)}(x) J_n'(y)}{J_n'(x) H_n^{(1)\prime}(y) - H_n^{(1)\prime}(x) J_n'(y)}$$

and $Z(\omega) = \rho(\omega) k_0 / \Omega k(\omega) \rho_0$ is the normalized characteristic impedance of porous material.

In principle, the model could be used for arrays of cylinders with different outer radii and different thickness of porous covering. However, since the measurements reported later have used arrays of identical cylinders, the simplified version of the model has been used for computations.

Equation (5) is expressed in terms of characteristic impedance $Z(\omega)$ and propagation constant $k(\omega)$, so, effectively, these quantities replace the porosity and the complex density function introduced by the boundary conditions (3). Although various models are available to provide $k(\omega)$ and $Z(\omega)$ as a function of frequency, since a fibrous woollen felt has been used in the measurements, the single parameter empirical Delany and Bazley model,[10] derived from data for fibrous materials, has been found suitable. According to this model,

$$Z(\omega) = 1 + 0.00571 \left(\frac{\rho_0 \omega}{2\pi\sigma} \right)^{-0.754} + i 0.087 \left(\frac{\rho_0 \omega}{2\pi\sigma} \right)^{-0.732},$$

$$k(\omega) = \frac{\omega}{c_0} \left(1 + 0.0928 \left(\frac{\rho_0 \omega}{2\pi\sigma} \right)^{-0.7} + i 0.189 \left(\frac{\rho_0 \omega}{2\pi\sigma} \right)^{-0.597} \right), \quad (6)$$

where σ represents the flow resistivity of the material.

The numerical procedure for finding the total field at a certain point requires solving the system of equations (4) by truncation and finding the pressure by summation using expression (1). For rigid cylinders, factors Z_n^j are determined from Eq. (2). If the cylinders are covered by porous material, the factors Z_n^j are determined from Eqs. (5) and (6).

III. MEASUREMENTS AND COMPARISONS OF NUMERICAL RESULTS WITH DATA

Measurements have been carried out in a semi-anechoic chamber and far from any reflecting surfaces.

A free field $\frac{1}{4}$ in. B&K microphone was positioned centrally behind the array and orientated at right angles to the source and receiver path (grazing incidence) to avoid directivity effects at high frequencies (Fig. 3). The distance between the array and the microphone was varied between 3 and 11.5 cm.

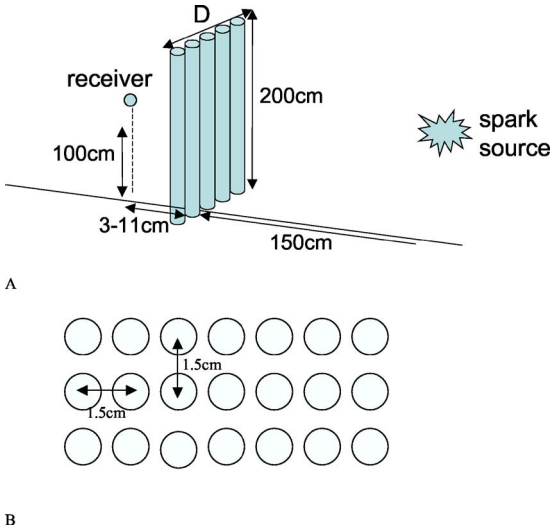

FIG. 3. (Color online) Measurement arrangement (a) and array geometry (b).

Sparks associated with air breakdown between high voltage electrodes have been used to provide acoustic pulses. The spark source was positioned 1.5 m away from the scattering array and 1 m above the ground. The acoustic pulses had a duration of about 60 μs and a central frequency of approximately 15 kHz [Figs. 4(a) and 4(b)]. Most of the acoustic energy of the pulse was contained between 1 and 50 kHz. Outside this range the signal/noise ratio was too low for reliable results. Consequently the transmission loss measurements were limited to the range between 1 and 50 kHz. Pressure measurements were made in the free field and then

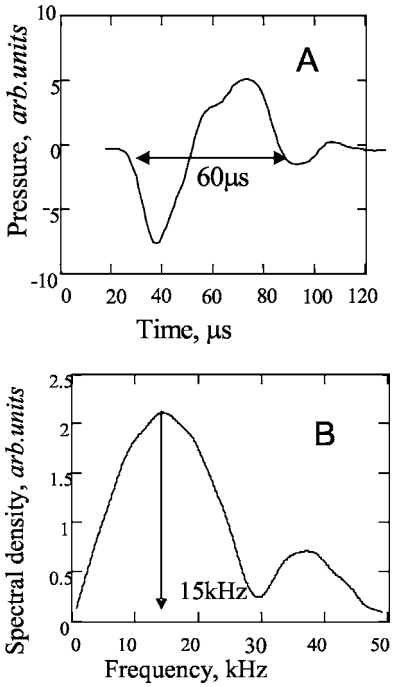

FIG. 4. Wave form (a) and spectrum (b) of the pulse generated by the spark source, distance from the source 150 cm.

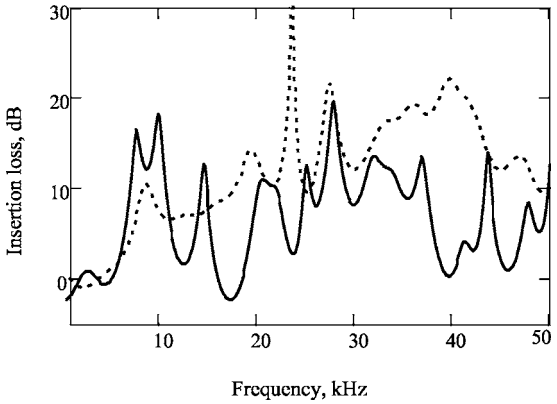

FIG. 5. Effect of the porous covering on the attenuation spectrum at 3 cm from the regular array. The solid line represents data for rigid cylinders; the broken lines represents data for rigid cylinders covered with felt.

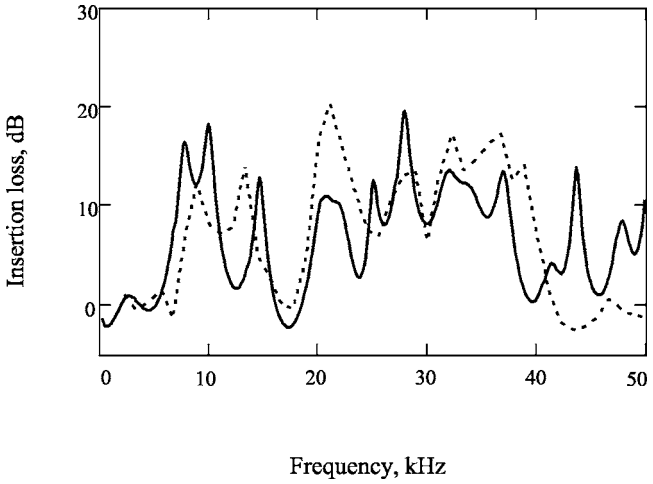

FIG. 6. Measurements (solid line) and model predictions for the insertion loss of the array of rigid cylinders for a receiver 3 cm from the array.

in the presence of the array. The spectral content of the signals was determined by Fourier transform. The insertion loss due to the array has been obtained from the ratio of the spectral density of the transmitted field in the presence of the array and that measured in the free field. The free field pressure data at various distances from the source are consistent with spherically spreading waves. However, since the model [Eqs. (1)–(5)] is valid only for two-dimensional geometry, the cylinders were sufficiently long (2 m) that the receiver/array distance (maximum 11.5 cm) was always much shorter than the cylinder length. The rigid cylinders were aluminum rods with a diameter of $\frac{3}{8}$ in. (0.953 cm) mounted between two rectangular supporting plates. Each absorbing cylinder had a $\frac{1}{4}$ in. (0.635 cm) diameter aluminum rod as a core and this was covered by a layer of woollen felt. The thickness of the felt was close to 0.175 cm so that the diameter of the covered cylinders (0.98 cm) was close to that of the rigid cylinders used for the data comparison.

The cylinders were arranged in a square lattice, i.e., they were placed in identical rows so that the inter-row distance was equal to the intercylinder distance within a row. This distance was chosen to be 1.5 cm. The filling fraction of the rigid cylinder array was approximately 32% whereas the filling fraction of the corresponding square array of covered cylinders was 33%. Since the filling fractions of both arrays were more or less the same, any measured differences in their acoustical performance could be attributed exclusively to the presence of covering. The filling fraction of the rigid cylinder array was high enough for a stop/pass band structure to be noticeable in the attenuation spectrum. The arrays consisted of three rows with seven cylinders in each row. This was the minimum number of rows needed for the stop/ pass bands to be observed when using rigid cylinders.

Figure 5 compares the measured insertion losses of the arrays of rigid and covered rods at 3 cm from the array. The presence of covering is seen to destroy the pass/stop band structure and to make the attenuation more uniform in frequency. In addition the sound absorbing nature of the porous covering provides stronger attenuation for most of the frequencies except in the first stop band. Between 10 and 50 kHz the minimum attenuation for the array of covered rods is 6.6 dB (at 10 864 Hz) and the mean value for the attenuation is 13.9 dB. In the same frequency range the minimum attenuation of the array of rigid cylinders is −2.2 dB (at 17 212 Hz) and the mean attenuation is 6.9 dB.

Figure 6 compares data and predictions for the array of rigid cylinders. The agreement is generally good taking into account the idealization of the geometry and the source used in the model. To make similar comparisons for the array of covered cylinders the acoustical characteristics of the porous covering material are required. Since the material was not convenient for impedance tube measurements, surface impedance values have been deduced from measurements of the complex excess attenuation, i.e., the ratio between the pressures measured by the receiver arranged above the felt layer and in the free field.[11] The complex excess attenuation (EA) is related to the spherical wave reflection coefficient Q by

$$\mathrm{EA} = 1 + Q\frac{R_1}{R_2}e^{ik_0(R_2-R_1)},$$

where R_1 and R_2 are the direct path length from the source to receiver and the path length through the specular reflection point. The relationship between the spherical wave reflection coefficient Q and the surface impedance Z of the porous layer is obtained from

$$Q = R(1 - F(w)) + F(w),$$

$$R = \frac{1 - Z_s\cos(\Theta)}{1 + Z_s\cos(\Theta)},$$

$$F(w) = 1 + i\sqrt{\pi}we^{-w^2}\,\mathrm{erfc}(-iw),$$

$$w = \sqrt{\frac{ik_0R_2}{2}}\frac{1 + Z_s\cos(\Theta)}{Z_s},$$

where Θ is angle of incidence for the ground reflected beam.

Hence the surface impedance Z_s can be deduced from the excess attenuation data using a numerical method to search for complex roots.

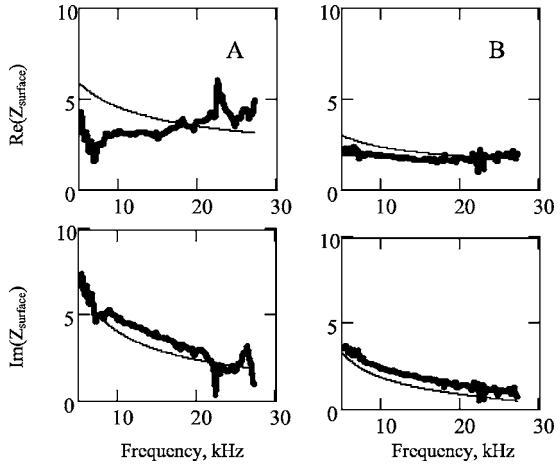

FIG. 7. Surface impedance of single (a) and double (b) layer of felt. Points—data, lines—predictions, using Delany and Bazley model for characteristic impedance and propagation constant with $\sigma = 2.3 \times 10^4$ Pa s/m^2.

The surface impedance Z_s of the hard-backed porous layer of thickness d is related to the propagation constant $k(\omega)$ and the characteristic impedance of the material $Z(\omega)$:

$$Z_s = \frac{Z(\omega)}{\cos(\Theta_T)} \coth(-ik(\omega)d\cos(\Theta_T)),$$
$$\Theta_T = \sin^{-1}\left(\sin(\Theta)\frac{k_0}{k(\omega)}\right), \tag{7}$$

where Θ_T is the refraction angle.

Using Eqs. (6) and (7) and a least-squares method, the value of the flow resistivity parameter σ in the Delany and Bazley model has been adjusted to fit the surface impedance data for both single ($d = 0.175$ cm) and double ($2d = 0.35$ cm) layers of felt. Figure 7 shows the surface impedance data and the best-fit predictions. It appears that the Delany and Bazley model (6) with $\sigma = 23$ kPa s m^{-2} provides a good approximation to the characteristic impedance and the propagation constant in the frequency range of interest. The poorer agreement of the model predictions with data for single layer felt is probably due to experimental error (since the single layer has a higher impedance, the same % error in measurements will produce larger absolute discrepancies between data and predictions). Notice however that even in this case $\sigma = 23$ kPa s m^{-2} still gives the best fit. The results presented here are limited by the extent to which the Delany and Bazley model is applicable. For example, other work[12] has shown that this model overestimates the attenuation constant within a rigid-porous material for a given flow resistivity. Moreover, since the felt used for the covering does not correspond to the type of fibrous material (i.e., glass fiber) for which the Delany and Bazley model was intended, the best fit flow resistivity represents an *effective* value. Nevertheless, in the absence of other required material parameters for the felt, for the purposes of demonstrating and predicting the effects of porous covering, the Delany and Bazley model is considered adequate.

Comparisons between predictions and data for the insertion loss of the array of covered cylinders are shown in Fig. 8 for the microphone was positioned either 3 cm from the array or 11.5 cm from the array. This change in distance from the array does not appear to affect the attenuation significantly. The mean attenuation between 10 and 50 kHz is 14.0 dB with the receiver 11.5 cm from the array. This is very close to that (13.9 dB) observed with the receiver 3 cm from the array. The sensitivity of the results to the thickness of the porous covering has been studied numerically by performing computations for various covering thickness while keeping the outer radius of the cylinder constant, thus keeping the filling fraction of the array constant. According to the predictions in Fig. 9, increase in the covering thickness does

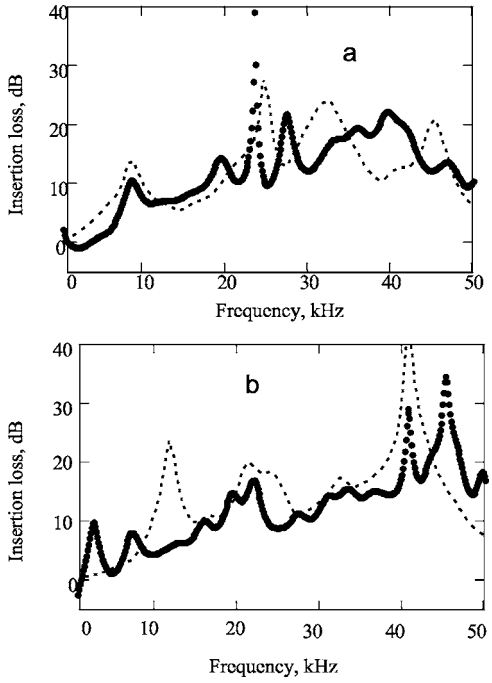

FIG. 8. Data (points) and predictions (broken lines) for the attenuation spectrum due to an array of covered rods (0.175 cm covering thickness) (a) at a receiver 3 cm from the array, (b) at a receiver 11.5 cm from the array.

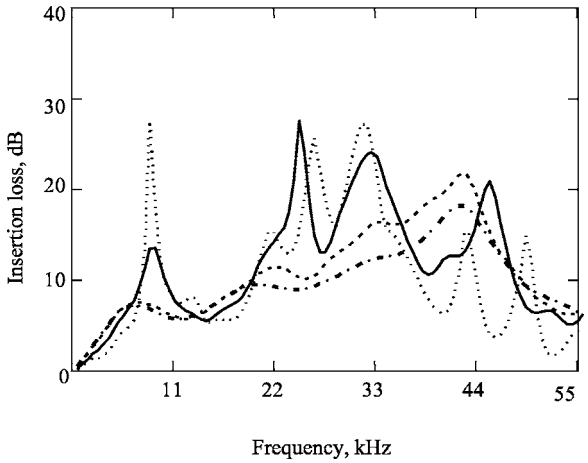

FIG. 9. Predicted insertion losses at 3 cm from regular arrays with 33% filling fraction and different felt covering thickness. The dotted line represents predictions with 0.088 cm covering thickness; the solid line represents predictions with 0.175 cm covering thickness; the broken line represents predictions with 0.35 cm covering thickness; the dashed dotted line represents predictions with 0.438 cm covering thickness.

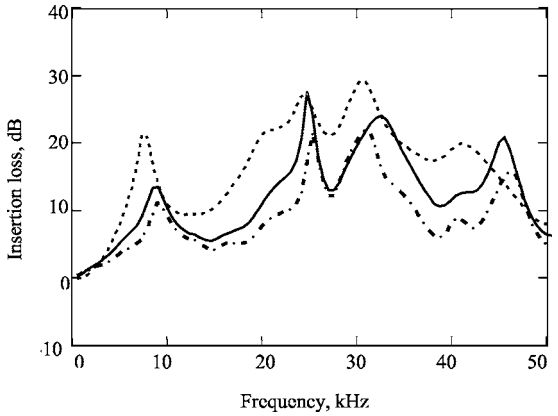

FIG. 10. Predicted insertion losses at 3 cm from regular arrays of cylinders covered by different flow resistivity materials. All dimensions are as in Fig. 6. The solid line—$\sigma=23\,000$ Pa s/m^2 (felt), dashed dotted line—$\sigma=11\,500$ Pa s/m^2, dashed line—$\sigma=69\,000$ Pa s/m^2.

not necessarily mean improved attenuation. A covering thickness increased to 5/2 of its original value (0.438 cm), corresponding to nearly all of the cylinders consisting of porous material, does not show the best performance in any frequency range. This suggests that there is an optimum thickness for a given flow resistivity.

Figure 10 shows predictions for $\sigma=11.5$, 23 and 69 kPa s m^{-2}. The largest mean attenuation corresponds to the highest flow resistivity value. On the other hand, when the flow resistivity and hence the surface impedance of the covering are sufficiently high the results should be comparable with those for acoustically hard cylinders. Indeed, for the given array, it has been found that the hard cylinders prediction is recovered when $\sigma=10^4$ kPa s m^{-2}.

It should be noted that Delany and Bazley model predictions for higher effective flow resistivity values may not be valid in the frequency range of interest here. Indeed the Delany and Bazley model is only applicable when $10^{-2}<\rho_0\omega/2\pi\sigma<1$. This means that, strictly speaking, increasing the effective flow resistivity value would move the range of the model applicability into the higher frequency range. Thus for $\sigma=10^4$ kPa s m^{-2} the model can only be applied for frequencies higher than 100 kHz which is well outside the measured range. Consequently a more sophisticated model for the acoustical properties of the porous covering would be needed to find the optimum flow resistivity value.

To predict the effect of randomizing the array, each cylinder center has been moved at random from its location in regular array (x_j,y_j).[13] Hence the coordinates of each cylinder in the perturbed array are

$$x_j' = x_j + \tau\gamma_j(l-a^{\text{out}})\cos(2\pi\gamma_j),$$

$$y_j' = y_j + \tau\gamma_j(l-a^{\text{out}})\sin(2\pi\gamma_j),$$

where γ_j are random numbers from the interval $[0,1]$ and parameter τ determines the proportion of the maximum permissible displacement $(l-a^{\text{out}})$ of the cylinders, here l is the half distance between the cylinder centers in the lattice. In the computations it was assumed that $\tau=0.9$ so that the imposed order of disorder was relatively high. Since different results are obtained for each "random" array, computations of the transmitted field have been carried out for 20 arrays and the results have been averaged. Figure 11 compares the attenuation of regular arrays with those with randomized positions of cylinders. For both arrays of rigid cylinders and cylinders covered with felt the effects of the randomness are noticeable for frequencies higher than the first attenuation band as observed elsewhere.[13] The imposed random perturbations in the positions of cylinders tend to make the stop/pass band structure less pronounced but do not destroy it completely as happens when the cylinders are distributed completely randomly within the area occupied by the array.[7] A randomized array of cylinders covered by single layer of felt is still predicted to provide better attenuation than a similarly random array of hard cylinders. The difference in averaged attenuation is approximately 4.7 dB.

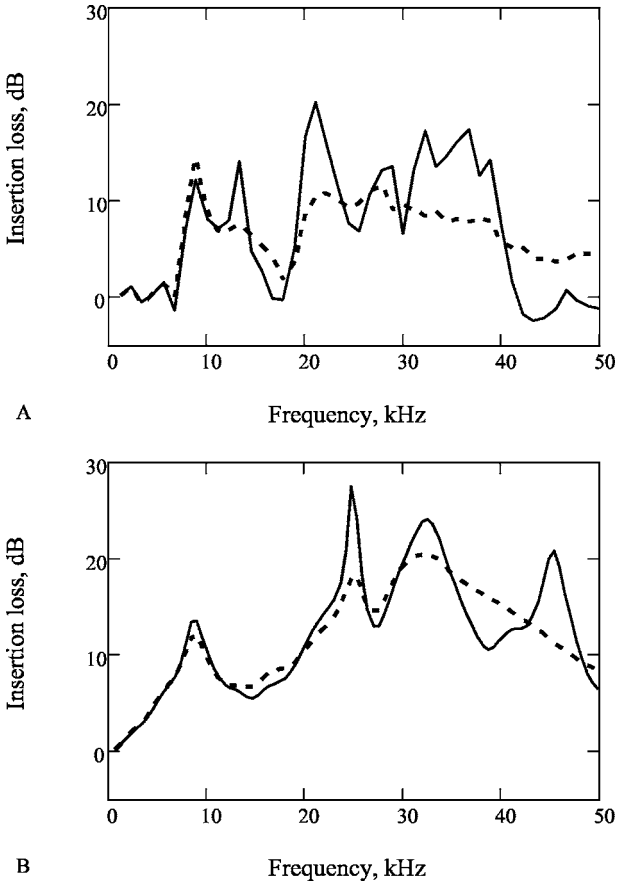

FIG. 11. Predicted effects of randomized positioning of the cylinders within an array on the insertion loss at 3 cm from the array. Array dimensions are as for Fig. 6. (a) Array of rigid cylinders, (b) array of cylinders covered with felt. Solid lines—regular array, dashed lines—randomized array.

IV. CONCLUSIONS

Laboratory measurements and numerical simulations of the transmission loss of regular cylinder arrays, using a multiple scattering model modified to allow for the porous covering, have shown that covering the cylinders with a porous material makes the array insertion loss more uniform in frequency. Moreover, arrays with covered elements provide higher averaged attenuation than similar arrays of rigid cylinders. Numerical simulations have shown that the insertion

loss depends strongly on the covering thickness and that a thicker porous covering does not necessarily mean better attenuation. On the other hand, increasing the flow resistivity of the covering material by a factor of 3 is predicted to improve the array performance. These results suggest that it might be possible to optimize the array attenuation through choice of covering material and its thickness. It might be worthwhile to explore the use of multiple layers for impedance matching in the porous covering also.

In the laboratory measurements considerable attenuation has been achieved in the frequency range between 10 and 50 kHz by the array with a filling fraction of 33%. To achieve a similar attenuation in noise control applications that would involve a lower frequency range, the geometry of the cylinder arrays would have to be scaled accordingly. If it is supposed that lowering the frequencies by a certain factor will mean that the distances should be increased by the same factor, to offer a useful attenuation in the frequency range between 300 Hz and 1.5 kHz the distance between cylinders and rows should be approximately 45 cm and the cylinders diameter would have to be approximately 30 cm. In an artificial array intended for outdoor use the choice of porous material would be limited by the ability to withstand weathering and fibrous materials may not be suitable. Consequently simulations and measurements using more robust materials such as porous concrete are needed. The potential for use of periodic arrays of trees has been demonstrated already[3] but there may be possibilities for exploiting species with high porosity and/or roughness of bark. Finally, the performance of arrays in which trees are surrounded by foliage might be simulated through a covered cylinder model of the kind presented here.

ACKNOWLEDGMENTS

We are grateful to Dr. Q. Qin, University of Hull, for the complex excess attenuation measurements and deduction of the felt impedance. The work was supported by EPSRC Grant No. GR/S35592 while O.U. was at the University of Hull.

[1] R. Martinez-Sala, J. Sancho, J. V. Sanchez, V. Gomez, J. Llinares, and F. Meseguer, "Sound attenuation by sculpture," Nature (London) **378**, 241 (1995).

[2] J. V. Sanchez-Perez, C. Rubio, R. Martinez-Sala, R. Sanchez-Grandia, and V. Gomez, "Acoustic barriers based on periodic arrays of scatterers," Appl. Phys. Lett. **81**, 5240–5242 (2002).

[3] R. Martinez-Sala, C. Rubio, L. M. Garcia-Raffi, J. V. Sanchez-Perez, E. A. Sanchez-Perez, and J. Llinares, "Control of noise by trees arranged like sonic crystals," J. Sound Vib. (to be published).

[4] J. V. Sanchez-Perez, D. Caballero, R. Martinez-Sala, C. Rubio, J. Sanchez-Dehesa, F. Meseguer, J. Llinarez, and F. Galvez, "Sound attenuation by a two-dimensional array of rigid cylinders," Phys. Rev. Lett. **80**, 5325–5328 (1998).

[5] D. Caballero, J. Sanchez-Dehesa, C. Rubio, R. Martinez-Sala, J. V. Sanchez-Perez, F. Messeguer, and J. Llinares, "Large two-dimensional sonic band gaps," Phys. Rev. E **60**, R6316–R6319 (1999).

[6] Y.-Y. Chen and Z. Ye, "Theoretical analysis of acoustic stop bands in two-dimensional periodic scattering arrays," Phys. Rev. E **64**, 036616 (2001).

[7] Y.-Y. Chen and Z. Ye, "Acoustic attenuation by two-dimensional arrays of rigid cylinders," Phys. Rev. Lett. **87**, 184301 (2001).

[8] C. M. Linton and D. V. Evans, "The interaction of waves with arrays of vertical cylinders," J. Fluid Mech. **215**, 549–569 (1990).

[9] I. S. Gradshteyn and I. M. Ryzhik, *Tables of Integrals, Series and Products* (Academic, New York, 1965), p. 979, Eq. WA394(6).

[10] M. E. Delany and E. N. Bazley, "Acoustic properties of fibrous absorbent materials," Appl. Acoust. **3**, 105–116 (1970).

[11] P. Boulanger, K. Attenborough, and Q. Qin, "Effective impedance of surfaces with porous roughness: Models and data," J. Acoust. Soc. Am. **117**, 11146–11156 (2005).

[12] J-F Allard, *Sound Propagation in Porous Media* (Elsevier Applied Science, New York, 1993).

[13] G. Duclos and A. H. Clement, "Wave propagation through arrays of unevenly spaced vertical piles," Ocean Eng. **31**, 1655–1668 (2004).

Wave reflection and transmission reduction using a piezoelectric semipassive nonlinear technique

D. Guyomar, A. Faiz, L. Petit, and C. Richard
Institut National des Sciences Appliquées de Lyon, Laboratoire de Génie Electrique et Ferroélectricité, Villeurbanne 69621, France

(Received 7 February 2005; revised 1 August 2005; accepted 2 November 2005)

This study addresses the problem of noise reduction using piezoelements. The nonlinear technique, synchronized switch damping (SSD), is implemented. The device is a pulse-tube termination equipped with piezoelements, which allows performant damping of the vibration resulting from an incident acoustic wave. Due to this damping, both reflected and transmitted wave are reduced. In the semipassive damping approach proposed in this paper, energy degradation is strongly enhanced when the piezoelements are continuously switched from open to short circuit synchronously to the strain. This technique has been developed following two strategies. The first is SSD on a short circuit in which the piezoelement is always in open circuit, except for a very brief period at each strain extremum where it is short-circuited. The second approach is SSD on an inductor. The process is very similar, except that instead of forcing the voltage to zero, the voltage is exactly reversed using a controlled oscillating discharge of the piezoelement capacitor on an inductor during switch drive. Due to this switching mechanism, a phase shift appears between the strain and the resulting voltage, thus creating energy dissipation. Following SSD on an piezoelement, attenuations of 15 dB in reflection and 7 dB in transmission were obtained. © *2006 Acoustical Society of America.* [DOI: 10.1121/1.2141361]

PACS number(s): 43.50.Ki, 43.55.Wk, 43.55.Rg, 43.38.Fx [KAC] Pages: 285–298

I. INTRODUCTION

Wave control and the development of anechoic systems in air are of major interest for improving acoustic comfort. Currently, passive control techniques (Gibson, 1987), which consist of using absorbing materials such as insulating wool, glass, or rubber, are effective at high frequency, but the principal limitation of this approach is the mass and volume, particularly in the low-frequency range. Moreover, the variations of loss angle with temperature or frequency due to viscoelastic behavior of the considered materials are also an important drawback.

Active control techniques have been used for several years and applied in noise control (Ho, 2000). The most common practice is the use of antinoise, which utilizes interference of sound waves. This method has been successfully applied to reduce the noise level experienced by passengers in the compartment of a motorcar (Peiffer, 2005). Its main drawback is the complexity of the global system and global power requirements. To bypass these problems, some approaches have proposed a combination of the active and passive noise reduction techniques (Lee, 2002), but these are only valid for the transmitted pressure and require an increase in panel mass.

As excitation noise on one side causes the structure to vibrate, the vibration becomes a secondary source of noise on the other. Many studies reported the suppression of noise transmission by proper control of transmitting structure vibration damping (Ho, 2000; Hong, 2001). For plate or beam structures, many techniques have been tested to dampen vibrations using piezoelectric elements. The piezoelectric elements, attached to the vibrating structure, are stressed and generate electric energy due to the piezoelectric effect. Degradation or transfer of this energy results in control and reduction of the vibration.

Passive techniques are the most commonly applied vibration control strategies due to ease of integration, and their simplicity and compactness. The piezoelectric elements are connected to specific electrical impedances, used as dissipating shunts. The most efficient method is the tuned shunt, where an L-R-C circuit is formed by adding an inductor and resistor in series with the inherent capacitance of the piezoelectric elements. Addition of this network results in a damped electromechanical resonance. Optimal damping is obtained by tuning the electric resonance to the frequency of the unwanted structural mode (Hagood, 1991). This method gives good results but has several disadvantages. First, it is a monomodal technique and multimodal damping needs the use of complex shunt circuits (Wu, 1998). For low-frequency modes, the optimal value of the inductor is generally very large and reaches tens or hundreds of henry. Another drawback of the tuned passive method is its sensitivity to environmental factors, such as temperature, which cause drifts in the resonance frequencies. The resonant circuit can be detuned, reducing the damping performance.

To address the drawbacks, several semipassive or active–passive techniques have been proposed. Their common goal is to maintain the compactness of the passive technique combined with a stand-alone character. Two approaches are particularly interesting.

(a) Continuous dissipative techniques

As in the purely passive case, part of the mechanical energy is continuously dissipated in a shunt circuit.

However, in this case, active control action leads to multimodal and/or broadband damping. In the solid-state tunable piezoelectric absorber, developed by Davis and Lesieutre (1998, 2000), a passive capacitive shunt circuit is used to electrically adjust the piezoelectric element's effective stiffness and then to tune the device's resonance frequency. In the approach proposed by Morgan and Wang (2002), an adaptive tuning inductor, a negative resistance, and a coupling enhancement setup are combined in a system with multimodal damping ability. Other complex shunt circuits have been used for multimodal damping strategies (Browning and Wynn, 1993; Wu, 1998).

(b) Semipassive switching shunt techniques

Different switching techniques have been investigated over the last 5 years, known as semipassive in the sense that there is no introduction of an active driving element. Only a small amount of energy is necessary to supply the electronic control necessary to monitor the vibration and drive one or many switches. The first technique of this type was proposed by Clark (2000). This method is based on switching the active piezoelement from an open circuit to a short circuit state at specific times synchronously with the structure's vibration. These methods are referred to as state switching, for adjusting the stiffness of the piezoelectric structure, or pulse switching, depending on the control strategy. The term "state switching" was introduced by Larson (1998), who used this technique to increase the frequency band of an acoustic transducer. This approach consists of changing the transducer stiffness through piezoelectric shunting at times of minimum strain. Following the Clark (2000) approach, whose switching sequence is different, the piezoelement is short-circuited at each peak of the strain and held in short circuit until the mechanical energy in the piezoelement vanishes. This switching action has the effect of removing the electrical potential energy converted from the mechanical strain through the piezoelectric effect, thus removing part of the mechanical energy from the particular structural mode.

Another performant damping technique known as synchronized switch damping (SSD) was developed at the same time (Richard, 1999, 2000). In this technique, as in the previous method, semipassive nonlinear voltage processing is used to extract mechanical energy using piezoelectric coupling. In the synchronized switch damping on a short-circuit (SSDS) strategy (Richard, 1999), the piezoelement is always in open circuit, except for a very brief period at each strain extremum, where it is short-circuited. The extracted energy in this case is exactly four times the energy extracted following Clark's strategy. This results from the fact that the piezoelement voltage magnitude is exactly twice the unprocessed voltage for the same vibration amplitude. The damping effect can be assimilated to electrically induced dry friction, performing quite well in the low-frequency regime. In the synchronized switch damping on an inductor (SSDI) strategy (Richard, 2000), processing is nearly the same, except that instead of forcing the voltage to zero at each strain extremum, the voltage is exactly inversed using a controlled oscillating discharge of the piezoelement capacitor on an inductor during the switch drive. The consequence is a charge accumulation on the piezoelement capacitance leading to a greater magnification, as well as a time shift, of the voltage. Consequently, the resulting nonlinear voltage is exactly in phase with the velocity, thus optimizing the piezoelectric energy extraction capability. These techniques have been numerically compared for a monomodal excitation, and SSDI was demonstrated to be nearly optimal (Niederberger, 2004). Finally, it should be mentioned that Corr and Clark (2003) adapted the SSDI approach (also called pulse switching) to the case of a multimodal vibration using a numerical processing to accurately define the switch instants depending on the targeted modes.

Previous work by Larson *et al.* (1998) on the state-switching concept has been successfully adapted to vibration damping in a rather different way—proposed as the state-switching absorber (SSA) by Cunefare *et al.* (2000). This device is a simple spring mass-damper attached to the structure by a piezoelectric spring and capable of altering its stiffness state nearly instantaneously by modifying the electrical boundary conditions with a control switch. This device is attached to the structure in areas of maximum displacement and the switching strategy is defined to maximize the energy extracted from the structure that will be degraded by the SSA damper. For this purpose, when the force exerted by the active spring on the base is opposite to the base motion, it is set to a stiffer value to optimize the force and, therefore, the energy transferred from the structure to the SSA. Inversely, the spring is set to a smaller stiffness when the force helps the base motion to release less energy to the structure. According to Larson *et al.* (1998) and Cunefare (2002), the great advantage of the SSA technique is that switching occurs only when there is no potential energy in the spring, which corresponds to zero strain. Unlike SSD, this last condition allows the avoidance of any mechanical transient of the voltage or stress step due to the rapid potential energy change in the device. This technique has been applied to various cases and was shown to be an interesting multimodal approach if associated with a proper damper location (Holdhusen, 2004).

The purpose of this paper is to describe a new application merging the nonlinear SSD damping technique and acoustic control. The proposed approach is oriented toward the development of anechoic coatings for underwater application or acoustic control of rooms using thin lightweight panels. The basic idea is similar to applications using active skins made of piezoelectric composite with 1–3 (Bao *et al.*, 1990) or 0–3 connectivity (Lafleur, 1991), and implementing active as well as passive shunt techniques (Zhang, 2001) to control reflection and transmission losses. The principal objective consists of limiting either the backscattered or transmitted energy by proper damping of the structure excited by incoming acoustic pressure energy.

The application described in this paper consists of a pulse-tube termination equipped with a piezoelectric transducer excited with incoming pressure. The piezoelectric ele-

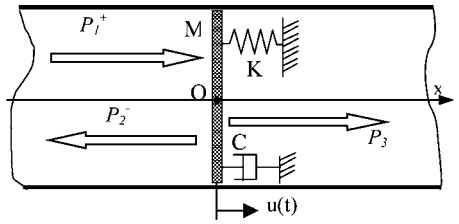

FIG. 1. Spring-mass model of a membrane-acting wall. The spring K represents the piezoelectric element acting as the suspension. C stands for the various mechanical losses. P_1, P_2, and P_3 are the incident, reflected, and transmitted pressure waves, respectively.

ment is associated with a switching circuit implementing SSD (or pulse switching) to control vibration damping of the wall. This results in attenuation of both the reflected and transmitted pressure waves. The switching control device is synchronized with the voltage itself, does not use any sensor, and is simple enough to be installed close to the transducer. Moreover, the required power is very low, which would allow the system to be self-powered, using part of the incoming energy. The performance of the system depends on the amount of mechanical energy stored temporarily in the termination and that could be transformed. The system mainly performs well around the mechanical resonance of the termination when large displacements occur, which can be greatly reduced by the proposed nonlinear damping system. In the technique proposed here, the main advantage is simplicity of design, its low profile, and light weight, with good performance and adaptability.

In this paper, a model of the proposed acoustic termination is first proposed. Then, the nonlinear SSD processing used is comprehensively described and theoretical analytical solutions of the termination motion and reflected and transmitted pressure given. Simulation of both reflection and transmission damping performances are also proposed. The experimental setup is finally described and the experimental performance is analyzed and discussed.

II. ANECHOIC TERMINATION SYSTEM

The considered anechoic termination is schematically represented in Fig. 1. It consists of a rigid membrane with an inertia mass M, subject to an incidental pressure P_1.

This membrane is attached to spring K working as a piezoelectric suspension, and damper C representing the global mechanical losses. The reflected wave is P_2 and transmitted wave is P_3. Here, $u(t)$ represents the one-dimensional displacement of the membrane.

P_1, P_2, P_3, and $u(t)$ are oriented along the same O_x axis, corresponding to the propagation direction.

This membrane is a rigid separation wall (or tube termination wall) separating the incident and transmitted semi-infinite media. P_1 and P_3 are traveling waves propagating is the positive O_x direction, while P_2 is a traveling wave propagating in the negative O_x direction.

A. Acoustic coupling aspect

If $u_i(x,t)$ is the particle velocity associated with the traveling pressure waves $P_i(x,t)$ and Z the acoustic impedance of the propagation medium, then

$$\begin{cases} P_1 = Z \,.\, u_1(t,x) \\ P_2 = -Z \,.\, u_2(t,x) \\ P_3 = Z \,.\, u_3(t,x). \end{cases} \tag{1}$$

The flow equilibrium on each side of the membrane at $x=0$ leads to

$$\begin{cases} u_1(0,t) + u_2(0,t) = \dfrac{\partial u}{\partial t} \\ u_3(0,t) = \dfrac{\partial u}{\partial t}, \end{cases} \tag{2}$$

where u is the membrane axial displacement.

B. Mechanical aspect

Membrane M is supposed to be bound to the base by a piezoelectric insert. At low frequency, or for wavelengths much larger than the size of the structure, the differential equation that governs the motion $u(t)$ of the membrane mass is

$$Mu = -F_P + A(P_1 + P_2 - P_3) - Cu, \tag{3}$$

where F_P is the piezoelement suspension reaction force and A the membrane area.

For simplification, the piezoelectric element on which the membrane is attached is a disk with a cross-sectional area and thickness represented by Υ and L, respectively.

According to the piezoelectric state equations restrained to the motion in direction 3 (axis of the disk), the mechanical stress T_3 and electric displacement D_3 can be written as

$$\begin{cases} T_3 = c_{33}^E S_3 - e_{33} E_3 \\ D_3 = e_{33} S_3 + \varepsilon_{33}^S E_3, \end{cases} \tag{4}$$

where S_3 and E_3 are the mechanical strain and electric field along direction 3, respectively, c_{33}^E is stiffness of the short-circuited equivalent piezoelectric element, c_{33}^D is stiffness of the open-circuited equivalent piezoelectric element. ε_{33}^s is clamped permittivity of the piezoelectric element, and e_{33} is piezoelectric coefficient of the piezoelectric element.

For frequencies lower than piezoelectric disk resonances, Eq. (4) can be expressed as a function of global variables, taking account of the piezoelectric element geometry

$$F_P = \Upsilon T_3 = \Upsilon c_{33}^E S_3 - \Upsilon e_{33} E = \frac{\Upsilon c_{33}^E}{L} u - \frac{\Upsilon e_{33}}{L} V, \tag{5}$$

$$Q_p = \Upsilon D_3 = \Upsilon e_{33} S_3 + \Upsilon \varepsilon_{33}^S E = \frac{\Upsilon e_{33}}{L} u + \frac{\Upsilon \varepsilon_{33}^S}{L} V, \tag{6}$$

where F_P and Q_P are, respectively, the global mechanical force and electric charge related to membrane displacement u and piezoelectric voltage V.

K^E and K^D are the elastic stiffness in the short and open circuit, respectively, C_0 is the piezoelectric element blocked capacitance and α is the global electromechanical voltage coefficient of the structure, with

$$K^E = \frac{\Upsilon c_{33}^E}{L}; \quad C_0 = \frac{\Upsilon \varepsilon_{33}^s}{L}; \quad \alpha = \frac{\Upsilon e_{33}}{L}; \quad K^D = \frac{\Upsilon c_{33}^D}{L}. \quad (7)$$

These equations can be written as

$$\begin{cases} F_P = K^E u - \alpha V \\ Q_P = \alpha u + C_0 V. \end{cases} \quad (8)$$

Therefore, the equilibrium of the membrane can be summarized as

$$Mu + Cu + K^E u = \alpha V + A(P_1 + P_2 - P_3), \quad (9)$$

which can be rewritten as

$$u + \frac{C}{M}u + \frac{K^E}{M}u = \frac{\alpha}{M}V + \frac{A}{M}P_T \quad (10)$$

or

$$u + 2\xi\omega_0 u + \omega_0^2 u = \frac{\alpha}{M}V + \frac{A}{M}P_T, \quad (11)$$

with $P_T = P_1 + P_2 - P_3$, $\xi = C/2M\omega_0$, and $\omega_0^2 = K^E/M$, where ω_0 is the short-circuited angular resonance frequency of the vibrating membrane, P_T is the global differential pressure, and ξ is the suspension mechanical damping.

As previously stated, in the development proposed here the piezoelectric element is dissociated from the membrane and is given a disk shape to establish simple electromechanical equations of the transducer.

This analysis is valid for any piezoelectric element geometry or assembly with, of course, a proper calculation of the α, K^E, and M constants. This electromechanical model can be extended to the case of the piezoelectric buzzer, which will be used in the experimental implementation of this electro-active membrane. In this case, various constants can be predicted with comprehensive modeling (such as field emission microscopy, FEM), or identified.

C. SSD technology (SSDS and SSDI)

The principle of the proposed method consists of briefly switching the piezoelements on a specific shunt circuit, which can either be a short circuit (SSDS) or an inductor (SSDI), to modify the piezoelement voltage. The switch trigger is synchronized with each extremum of the displacement and the switch is closed (see Sec. II C 2) for a period of time much smaller than the vibration period (see Fig. 2), typically 20–30 times shorter than the main vibration period. Without any switching, the piezoelectric voltage is simply proportional to the displacement. When the switching process is on, the piezoelement voltage is distorted, magnified, and time shifted.

1. SSDS switching current

At each extremum of the piezoelement displacement, the blocked capacitance C_0 is charged with a voltage V_0. The corresponding global electric charge is Q_0. For SSDS, at time t_0 where the switch is closed, this charge flows through the switch following a time constant dependent on the switch impedance. This transient discharge current is very brief and its integral is equal to the total initial charge Q_0. For an initial simplified analysis, this transient current will be considered as a Dirac pulse function centered at time t_0 with a weigh equal to Q_0; thus,

$$I_{\mathrm{SSDS}}(t) = C_0 V_0 \delta(t - t_0). \quad (12)$$

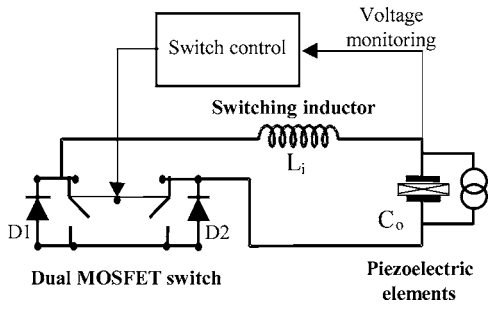

FIG. 2. Electronic circuit used for the SSDI damping technique. The inductor can be replaced by a simple short-circuit or resistor for SSDS operation.

2. SSDI switching current

In the SSDI case, the charged piezoelement is initially connected to an inverting inductor L_i. In this case, an oscillating discharge of the charged capacitance C_0 takes place through the inductor L_i. The pulsation ω_L of this pseudo-oscillation can be approximated by

$$\omega_L = \frac{1}{\sqrt{L_i C_0}}. \quad (13)$$

Since the oscillating network is not perfect (impedance of the transistor, losses of the inductor), the voltage oscillation can be approximated by

$$V(t) = V_0 e^{(-\omega_L/2Q_L)(t-t_0)} \cos(\omega_i(t - t_0)). \quad (14)$$

In this last equation, the inversion quality factor Q_L is related to the parasitic resistance R_L by

$$Q_L = \frac{L_i \omega_i}{R_L}. \quad (15)$$

In the proposed process, the oscillation is stopped by opening the switch after half a period T_L when the current is null and the voltage reaches the first inverted extremum voltage V_0', which is defined as

$$V_0' = -V_0 e^{(-\omega_L T_L/4Q_L)} = -V_0 e^{(-\pi/2Q_L)} = -aV_0, \quad (16)$$

where $a = e^{(-\pi/2Q_L)}$ is the inversion coefficient, related to the logarithmic decrement D by

$$D = \frac{\omega_L}{2Q_L} T_L = \frac{\pi}{Q_L} = -2 \ln a. \quad (17)$$

During this oscillation semiperiod, the total charge flowing through the switch, which is also the switching current integral, is Q_{SSDI}, defined as

$$Q_{SSDI} = (1+a)C_0V_0. \tag{18}$$

For an initial simplified analysis, as in the previous case, the transient current will be considered as a Dirac pulse function centered at time t_0 with a weigh equal to $(1+a)C_0V_0$; thus,

$$I_{SSDI}(t) = (1+a)C_0V_0\delta(t-t_0). \tag{19}$$

Note that in each case, right after the SSDS or SSDI transient state, the circuit is released open and the piezoelement capacitance continues to be charged by piezoelectric effect without change in the polarity since the piezoelement and the structure are in motion, and this motion, after reaching a maximum, sets out again in the opposite direction.

Finally, note that SSDS can be considered as a degraded SSDI process for which the inversion coefficient is null.

D. Nonlinear semipassive voltage and control function

In accordance with the above-mentioned equations, the electric charge Q appearing on the electrodes of the piezoelectric element is

$$Q(t) = C_0V(t) + \alpha u(t); \tag{20}$$

while it is held open-circuited,

$$I(t) = \frac{dQ(t)}{dt} = 0. \tag{21}$$

Therefore,

$$\frac{\partial V}{\partial t} = -\frac{\alpha}{C_0}\frac{\partial u}{\partial t}, \text{ and then}$$

$$\int_{-aV_{i-1}}^{V_i} \partial V = -\frac{\alpha}{C_0}\int_{u_{i-1}}^{u_i} \partial u = -\gamma\int_{u_{i-1}}^{u_i} \partial u, \tag{22}$$

where V_i and u_i stands for the voltage and displacement at time t_i just before switching, respectively, as illustrated in Fig. 3.

The voltage V_i is related to the displacement u_i, and to the previous voltage and displacement V_{i-1} and u_{i-1} by

$$V_i = -\frac{\alpha}{C_0}(u_i - u_{i-1}) - aV_{i-1}. \tag{23}$$

When the circuit is closed, as previously stated, a transient current I_i is established whose integral corresponds to the charge Q_i held by the piezoelement at time t_i,

$$I_i(t) = Q_i(1+a)\delta(t-t_i). \tag{24}$$

The total current $I(t)$ is the sum of the various I_i values, such as

$$I(t) = \sum_i I_i(t) = \sum_i Q_i(1+a)\delta(t-t_i), \tag{25}$$

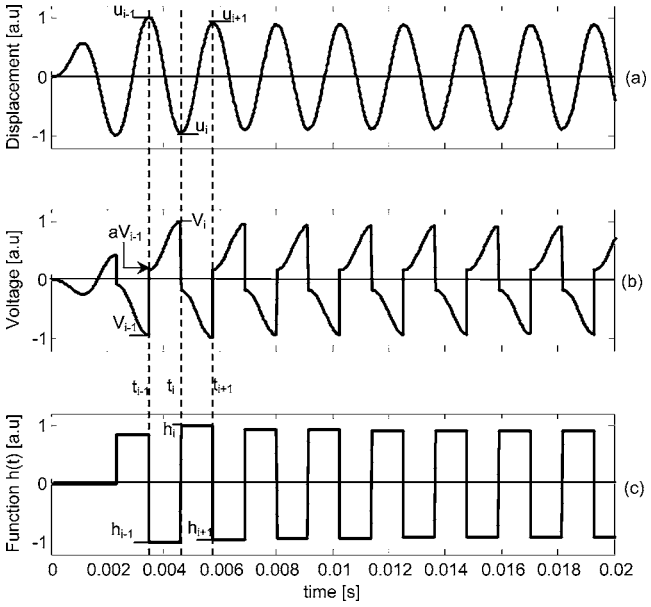

FIG. 3. Illustration of the membrane displacement (a), piezoelectric element voltage (b), and SSD nonlinear control function $h(t)$ (c). Switching on the first extremum has been omitted for readability.

$$I(t) = \sum_i C_0V_i(1+a)\delta(t-t_i). \tag{26}$$

Therefore, the total current is

$$I(t) = -\frac{\partial Q}{\partial t} = -C_0\frac{\partial V}{\partial t} - \alpha\frac{\partial u}{\partial t} = \sum_i C_0V_i(1+a)\delta(t-t_i). \tag{27}$$

Therefore,

$$\frac{\partial V}{\partial t} = -\frac{\alpha}{C_0}\frac{\partial u}{\partial t} - \sum_i V_i(1+a)\delta(t-t_i), \tag{28}$$

and then

$$V(t) = -\frac{\alpha}{C_0}u(t) - \sum_i V_i(1+a)H(t-t_i), \tag{29}$$

where $H(t)$ is the Heaviside step function.

Voltage and control function can be defined as follows:

(i) At $t=0$ $\quad u=0$ and $V=0$.

(ii) At $t=t_1$ $\quad V_1 = -\frac{\alpha}{C_0}u_1$ according to Eq. (23). (30)

(iii) At $t=t_2$ $\quad V_2 = -\frac{\alpha}{C_0}(u_2-u_1) - aV_1$

$$= -\frac{\alpha}{C_0}(u_2-u_1) + a\frac{\alpha}{C_0}u_1, \tag{31}$$

$$V_2 = -\frac{\alpha}{C_0}u_2 + \frac{\alpha}{C_0}(1+a)u_1. \tag{32}$$

(iv) At $t=t_3$ $V_3=-\frac{\alpha}{C_0}(u_3-u_2)-aV_2$

$$=-a(1+a)\frac{\alpha}{C_0}u_1+(1+a)\frac{\alpha}{C_0}u_2-\frac{\alpha}{C_0}u_3. \tag{33}$$

(v) At $t=t_4$ $V_4=-\frac{\alpha}{C_0}(u_4-u_3)-aV_3$

$$=a^2(1+a)\frac{\alpha}{C_0}u_1-a(1+a)\frac{\alpha}{C_0}u_2+(1+a)\frac{\alpha}{C_0}u_3-\frac{\alpha}{C_0}u_4, \tag{34}$$

and more generally

(vi) At $t=t_i$ $V_i=-\frac{\alpha}{C_0}u_i+\frac{\alpha}{C_0}\sum_{k=1}^{i-1}(1+a)(-a)^{i-k-1}u_k.$ (35)

Thus Eq. (29) becomes

$$V(t)=-\frac{\alpha}{C_0}u(t)-\sum_i\left[-\frac{\alpha}{C_0}u_i+\frac{\alpha}{C_0}\sum_{k=1}^{i-1}(1+a)\times(-a)^{i-k-1}u_k\right](1+a)H(t-t_i), \tag{36}$$

which can be rewritten as

$$V(t)=-\frac{\alpha}{C_0}[u(t)+h(t)], \tag{37}$$

with

$$h(t)=\sum_i\left[-u_i+\sum_{k=1}^{i-1}(1+a)(-a)^{i-k-1}u_k\right](1+a)H(t-t_i)=-\sum_i(u_i+h_i)(1+a)H(t-t_i)=\sum_i(h_{i+1}-h_i)H(t-t_i) \tag{38}$$

and

$$h_i=\sum_{k=1}^{i-1}-(1+a)(-a)^{i-k-1}u_k. \tag{39}$$

Here, $h(t)$ can be seen as a self-generated nonlinear control function resulting from the switch sequence. It is illustrated in Fig. 3 for a simple transient case.

The total piezoelectric element voltage is the sum of two functions, $u(t)$ and $h(t)$. In the case of the steady-state regime, $h(t)$ is a square signal whose amplitude will be derived in the next section.

Finally, considering Eqs. (1), (2), and (37), the motion equation (10) can be written as follows:

$$u+\left(\frac{C}{M}+\frac{2AZ}{M}\right)u+\left(\frac{K^E}{M}+\frac{\alpha^2}{MC_0}\right)u=-\frac{\alpha^2}{MC_0}h(t)+\frac{2A}{M}P_1|_{x=0}, \tag{40}$$

or more generally:

$$u+2\zeta\omega_1u+\omega_1^2u=-(\omega_1^2-\omega_0^2)h(t)+\frac{2A}{M}P_1|_{x=0}, \tag{41}$$

with

$$\alpha^2/MC_0=(\omega_1^2-\omega_0^2). \tag{42}$$

As previously stated, ω_0 is the eigenfrequency with short-circuit conditions (resonance), and ω_1 is the eigenfrequency for open-cicuit (antiresonance conditions). Note that these frequencies are related to the electromechanical coupling coefficient k by $\omega_0^2=(1-k^2)\omega_1^2$.

ζ is the open-circuit damping coefficient deduced from the time decay of the excited transducer. The terms $[(C/M)+(2AZ/M)]$ are representative of mechanical losses of the electroacoustic transducer plus damping due to both the reflected and transmitted acoustic power.

The differential equation (41) presents a known elementary solution, which is

$$u(t)=\left[-(\omega_1^2-\omega_0^2)h(t)+\frac{2A}{M}P_1\right]\times S(t), \tag{43}$$

with

$$S(t)=\frac{e^{-\zeta\omega_1 t}}{\omega_1\sqrt{1-\zeta^2}}\sin(\omega_1\sqrt{1-\zeta^2}t)H(t), \tag{44}$$

$$u(t)=-(\omega_1^2-\omega_0^2)h(t)\times S(t)+\frac{2A}{M}p_1\times S(t). \tag{45}$$

Therefore,

$$u(t)=-(\omega_1^2-\omega_0^2)\int_0^t h(\tau)S(t-\tau)d\tau+\frac{2A}{M}\int_0^t P_1(\tau)S(t-\tau)d\tau=u_{\mathrm{SSD}}(t)+u_{\mathrm{SC}}(t), \tag{46}$$

where u_{SC} is the response of the piezoelectric transducer termination in open circuit to the incoming pressure wave. Following Eq. (46), the displacement without control u_{SC} is easy to obtain for a given incident pressure P_1 and known impulsional response of the membrane. Here, u_{SSD} can be calculated from the $h(t)$ function, defined by Eq. (38), and the same impulsional response. The integration of Eq. (45) is performed numerically by computing $h(t)$ for each time step, and defining the various switching times t_i by implementing extremum detection on $u(t)$. We can consider u_{SSD} as the response of the open-circuited piezoelectric transducer to the $h(t)$ control voltage function self-generated by the SSD switching process. The reflected and transmitted pressure P_2 and P_3 are derived a second time from the expression of $p_1(t)$ and the solution $u(t)$ from Eqs. (1) and (2).

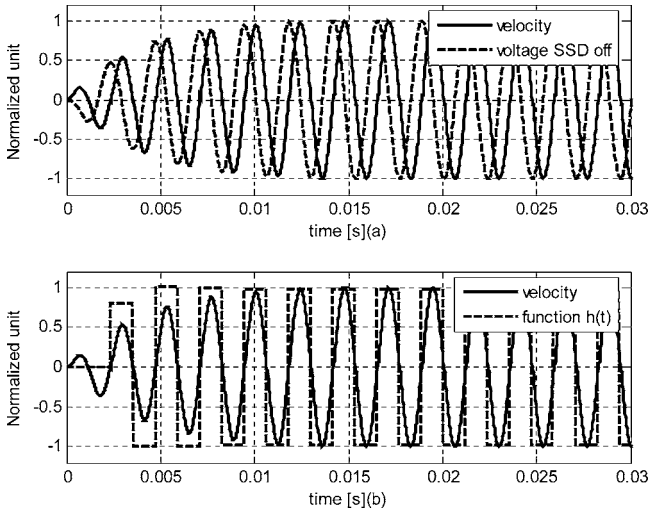

FIG. 4. (a) The open-circuit voltage and the velocity. (b) The resulting $h(t)$ function appears to be exactly in phase with the velocity.

III. ENERGETIC ANALYSIS

To establish the energy balance, the dynamic equilibrium equation (40) is multiplied by the velocity and mass, and integrated over the time variable, leading to

$$\int_0^t Muu\,dt + \int_0^t (C + 2AZ)u^2 dt + \int_0^t K^E uu\,dt = -\frac{\alpha^2}{C_0}\int_0^t (u+h)u\,dt + \int_0^t 2AP_1 u\,dt. \quad (47)$$

In the case of a sinusoidal excitation with a period T, this can be written over a period as

$$\underbrace{\left[\frac{1}{2}Mu^2\right]_0^T + \left[\frac{1}{2}K^E u^2\right]_0^T}_{E_m} + \int_0^T Cu^2 dt + \int_0^T 2AZu^2 dt + \frac{\alpha^2}{C_0}\int_0^T hu\,dt + \frac{\alpha^2}{C_0}\int_0^T uu\,dt = \int_0^T 2AP_1 u\,dt. \quad (48)$$

The first two terms correspond to the kinetic and elastic energies, which are reactive energies. The third term is a dissipative term corresponding to viscous losses. The fourth term corresponds to the energy extracted by the piezoelectric element. As illustrated in Fig. 4(a), representing the open-circuit voltage and the speed nearly in quadrature, this extracted energy term is null in the open circuit. When the switching process is used, according to Eq. (37) the voltage is a function of the displacement and of the self-generated control function $h(t)$. In this case and considering Eqs. (1) and (2), Eq. (48) becomes

$$\underbrace{\left[\frac{1}{2}Mu^2\right]_0^T + \left[\frac{1}{2}K^E u^2\right]_0^T}_{E_m} + \int_0^T Cu^2 dt + \frac{\alpha^2}{C_0}\int_0^T hu\,dt + \frac{\alpha^2}{C_0}\int_0^T uu\,dt + \int_0^T AP_3 u\,dt + \int_0^T AP_2 u_2\,dt = \int_0^T AP_1 u_1\,dt. \quad (49)$$

The fourth and fifth terms result from the SSD nonlinear process. As mentioned previously, $h(t)$ is nearly a square function equal to h_i sign(u) (between two consecutive switching times t_i and t_{i+1}). This is illustrated in Fig. 4(b). If, for orthogonality reasons, the fifth term is null, the fourth term is obviously dissipative and can be assimilated to a quasi-dry-friction dissipation term. The sixth and seventh terms correspond, respectively, to transmitted and reflected acoustic energies. Finally, the right-hand term corresponds to the energy injected by the impinging acoustic wave. Taking apart the mechanical reactive energy term, it remains

$$E_V + E_S + E_{ac} = \underbrace{\int_0^T Cu^2 dt}_{\text{Viscous friction damping}} + \underbrace{\frac{\alpha^2}{C_0}\int_0^T hu\,dt}_{\text{dry friction damping by SSD}} + \underbrace{\int_0^T P_2 u_2\,dt + \int_0^T P_3 u\,dt}_{\text{Acoustic energy}} = \int_0^T AP_1 u_1\,dt = E_d. \quad (50)$$

The term E_V corresponds to viscous damping (mechanical losses), while E_{ac} corresponds to the acoustic energy and E_S corresponds to the nonlinear control. This energy, withdrawn from the mechanical system, is directly dissipated during the short-circuit (SSDS) or in the switching and inverting device (SSDI).

A. Calculation of the related switching energy in the permanent regime

Assuming a monochromatic displacement $u(t) = U_M \sin(\omega t)$ in the permanent regime, the viscous damping energy E_V can be derived as

$$E_V = \int_0^T Cu^2 dt = \pi C\omega U_M^2 = 2\pi\xi\frac{K^E}{1-k^2}\frac{\omega}{\omega_1}U_M^2 = 2\pi\xi K^D\frac{\omega}{\omega_1}U_M^2. \quad (51)$$

The term of the switching-related energy is null if the voltage $V(t)$ and displacement $u(t)$ are in phase. It is obviously optimized both with the phase shift and with the voltage amplitude.

According to Eq. (37), the voltage is decomposed between two components: $h(t)$, which is in phase with the velocity and the displacement.

The energy E_S, dissipated during a one-period vibration by the SSD process, becomes

$$E_S = \frac{\alpha^2}{C_0}\int_0^T h(t)u(t)dt + \frac{\alpha^2}{C_0}\int_0^T u(t)u(t)dt = \frac{\alpha^2}{C_0}\int_0^T h(t)u(t)dt. \quad (52)$$

Since the second term clearly vanishes for orthogonality reasons, for the SSDI case at two consecutive extrema of the

TABLE I. Nonlinear control function amplitude and extracted energy E_S.

Control type	a	h_m	E_S
SSDS	0	U_M	$4K^E k^2 U_M^2$
SSDI	<1	$U_M \frac{(1+a)}{(1-a)}$	$4K^E k^2 U_M^2 \frac{(1+a)}{(1-a)}$

displacement in the permanent regime, we have

$$\begin{cases} h_i = -h_{i-1} \\ u_i = -u_{i-1}. \end{cases} \tag{53}$$

Using the h_i definition, Eq. (39) becomes

$$\begin{cases} h_i = -(1+a)\sum_{k=1}^{i-1} (-a)^{i-1-k} u_k \\ h_{i-1} = -(1+a)\sum_{k=1}^{i-2} (-a)^{i-2-k} u_k. \end{cases} \tag{54}$$

Therefore, considering Eqs. (53) and (54) simultaneously leads to

$$h_i = \frac{1+a}{1-a} u_i, \tag{55}$$

and $h(t)$ is therefore a square function with amplitude,

$$h(t) h_m = \frac{1+a}{1-a} u_m. \tag{56}$$

It is important to note that this square control function amplitude increases with the inversion performance and is ideally very large if a approaches 1.

The voltage amplitude is

$$V_m = -\frac{\alpha}{C_0}\left(u_m + \frac{1+a}{1-a} u_m\right). \tag{57}$$

The dissipated energy can be written, after calculation, by

$$E_S = 4K^E k^2 U_M^2 \frac{(1+a)}{(1-a)}. \tag{58}$$

Finally, it is remarkable that this energy can be very high and the damping very strong if the quality factor Q_L is high, which means a value of the inversion coefficient a close to 1. The coupling factor k of the considered vibration mode is also of great importance, since k^2 quantities the part of mechanical energy effectively converted into electrical energy.

These results for the permanent regime are summarized in Table I.

Figures 5(a) and 5(b) are, respectively, illustrations of the relevant waveforms for the SSDS and SSDI cases in the permanent regime. Figure 5(c) illustrates the decomposition of the voltage as the sum of the two functions $u(t)$ and $h(t)$.

B. Energy diagram (u, V)

The force exerted by the piezoelectric element on the membrane and related to the voltage (piezoelectric effect) is

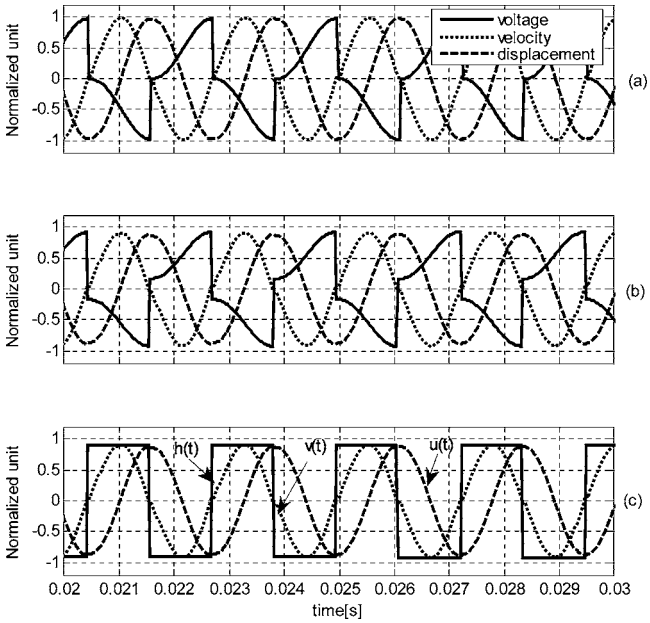

FIG. 5. Illustrations of the piezoelectric element voltage functions in the permanent regime for SSDS (a) and SSDI (b), and of the decomposition of the voltage function $V(t)$ as the sum of the two functions $h(t)$ and $u(t)$ (c).

$$F = -\alpha V(t) = \frac{\alpha}{C_0}[u(t) + h(t)]. \tag{59}$$

The mechanical work resulting from this force is

$$dw = F\, du = -\alpha V\, du. \tag{60}$$

The energy extracted by the piezoelectric element due to the voltage $V(t)$ appearing on the piezoelectric element is

$$w = \int -\alpha V\, du. \tag{61}$$

This energy is proportional to the surface circumscribed in the cycles representing the state of the system in the plane $[u(t), V(t)]$.

Figure 6 illustrates these energy cycles also representing

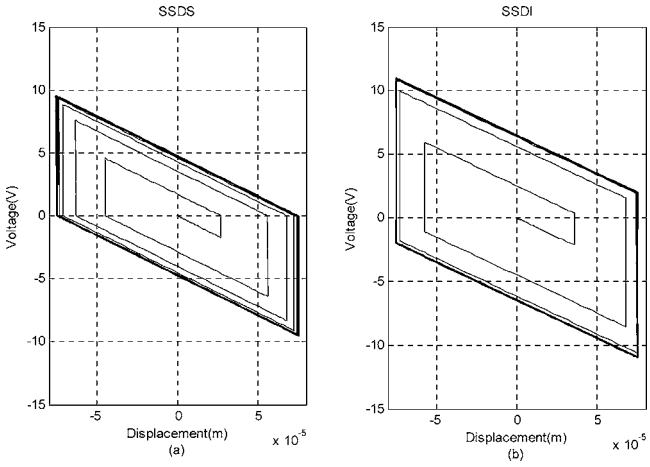

FIG. 6. Diagram illustrating the variation in piezoelectric element voltage versus piezoelectric element displacement for an incoming two-period pressure tone burst. The area circumscribed by the plot cycle is proportional to the energy extracted by the nonlinear switching process for SSDS (a) and SSDI (b) control for each period.

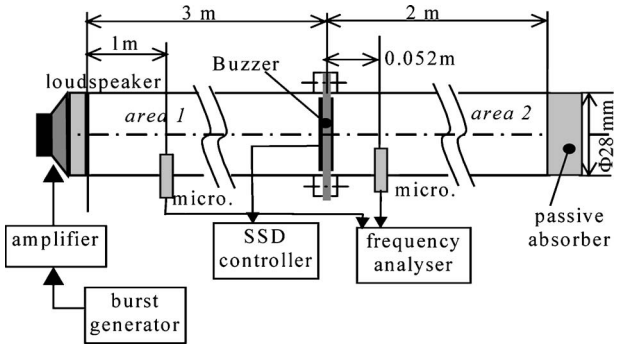

FIG. 7. Experimental setup: a brass pulse tube with a separator wall consisting of a piezoelectric buzzer driven by the SSD control board.

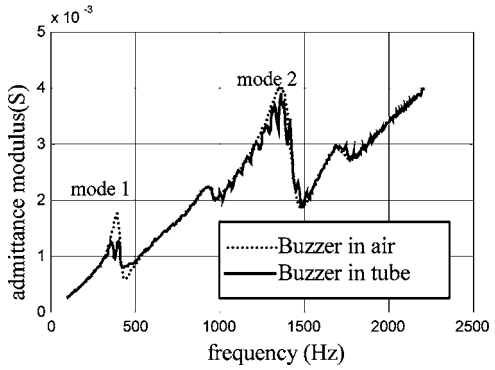

FIG. 8. Plot of admittance (modulus) versus the frequency for the buzzer used as the anechoic separation. The plot is limited to the low-frequency band and shows the two lower resonance modes.

the extracted and dissipated energies for SSDS [Fig. 6(a)] and SSDI [Fig. 6(b)]. Each loop represents one period. The vertical segments correspond to the commutation times at each piezoelectric strain or membrane displacement extrema. It is remarkable that the area of the SSDI cycle is larger than that of SSDS for a given vibration amplitude thanks to the inversion process. This illustrates that the SSDI control is more performing than the SSDS type. In this case represented here the SSDI to SSDS cycle area ratio is approximately 1.5. According to the extracted energy definitions given in Table I, this ratio should be equal to 1.5 for an inversion coefficient $a=0.2$ corresponding to the experimental case. This means that the SSDI energy extraction performance is 50% better than SSDS.

IV. EXPERIMENTAL SETUP

The experimental setup shown in Fig. 7 consists of a 28-mm-diameter tube, 5 m in length and split into two sections by a separation wall. The tube is equipped with a loudspeaker (VISATON FRWS 5) at one extremity. A passive rock-foam absorber is placed at the other extremity to cancel any reflection and simulate an infinite rear medium. Two microphones (AV-JEFE TCM110, 5 mm in diameter with a 5.6-mV/Pa sensitivity) are used to monitor the traveling pressure waves: the first is installed 1 m from the loudspeaker and the second is installed 52 mm behind the separation wall. The latter is simply a piezoelectric buzzer (a 50-mm-diameter MURATA "buzzer" Ceramitone VSB50EW-0301B). The buzzer terminals are connected to the SSD controller, made from an extremum detection stage driving two MOSFET transistor switches (Richard, 1999). The specific buzzer exhibits a first bending mode short-circuit resonance at 399 Hz. As the wavelength is close to 1 m for this frequency range, only a two-period tone burst will be considered to allow the correct separation of the various echoes.

The buzzer admittance spectrum is given in Fig. 8. It shows two resonant modes in the specific frequency band ($f_0=399$ and $f_0'=1400$ Hz). An additional resonant mode (900 Hz) is visible due to the clamping system that secures the buzzer to the separation wall.

V. SIMULATIONS

Numerical software has been developed following the model presented in the previous section. For a given impinging wave $P_1(t)$, the differential equation (41) is solved with a numerical approach by computing the integrals of Eq. (46). Once the displacement $u(t)$ solution is obtained, both the reflected and transmitted pressures are computed. To ensure the proper significance of the model, several parameters of the system have to be identified first.

A. Parameter identification

The various parameters of Eq. (40) are identified from the following transducer characterization procedure. The resonance and antiresonance frequencies and blocked capacitance C_0 are obtained from impedance mesurements. The resonance and antiresonance frequencies for each mode correspond, respectively, to the maximum of the real part of the admittance and impedance spectrum plot. The blocked capacitance of the buzzer C_0 is obtained from the equivalent circuit parameter identification, based on the admittance spectrum around the buzzer's first resonance. Parameter γ is the coefficient of proportionality between the voltage applied to the transducer and the displacement of the buzzer, measured directly with a laser Doppler vibrometer. This measurement is performed in a harmonic regime distant from the transducer resonance frequency and in the center of the buzzer membrane. However, the buzzer membrane displacement is not uniform because it is deformed in flexure mode and its deformed shape is approximately a section of a sphere. Therefore the displacement, necessary for the calculation of the γ coefficient, is corrected to ensure proper acoustic flow in agreement with the assumption of the model. As the axial displacement is very small compared to the membrane radius, the corrected displacement can be considered half the measured value. Parameter C is obtained from the open-circuit damping coefficient, deduced from the time decay of the excited buzzer *in vacuo*. The damping coefficient ζ is deduced from this measurement and from acoustic impedance of air.

Finally, the equivalent mass M, the global stiffness K^E, and electromechanical coefficient α are obtained, using the following relations:

TABLE II. Numerical data characterizing the experimental setup.

Parameter	Data
f_0	399 Hz
f_1	426 Hz
γ	5.5×10^4 V/m
C_o	360 nF
K^E	7783.2 N/m
M	1.2 mg
C	0.0609

$$\begin{cases} K^E = \dfrac{\alpha^2}{C_0}\dfrac{f_0^2}{f_1^2 - f_0^2} \\ \alpha = \gamma C_0 \\ M = \dfrac{K^E}{4\pi^2 f_0^2}. \end{cases} \tag{62}$$

Various numerical data, representative of the experimental setup and used in the proposed calculations, are assembled in Table II.

B. Simulation results

In the following simulations, Figs. 9 and 10 show the theoretical reflected and transmitted pressure signals, respectively, for an incident 426-Hz perfect two-period tone burst in the transient regime.

Three cases are considered for the reflected pressure (Fig. 9). The first case corresponds to the open-circuited buzzer, then the buzzer voltage is driven using the SSDS and the SSDI approaches. In this last case, the inversion coefficient a is approximately equal to 0.2. This value is rather small due to the poor quality of the inversion inductance used in the experiments. The pressure amplitude is normalized to the incoming pressure P_1. The propagating time delay in the tube is not taken into account, and both transmitted and reflected pulses start at $t=0$.

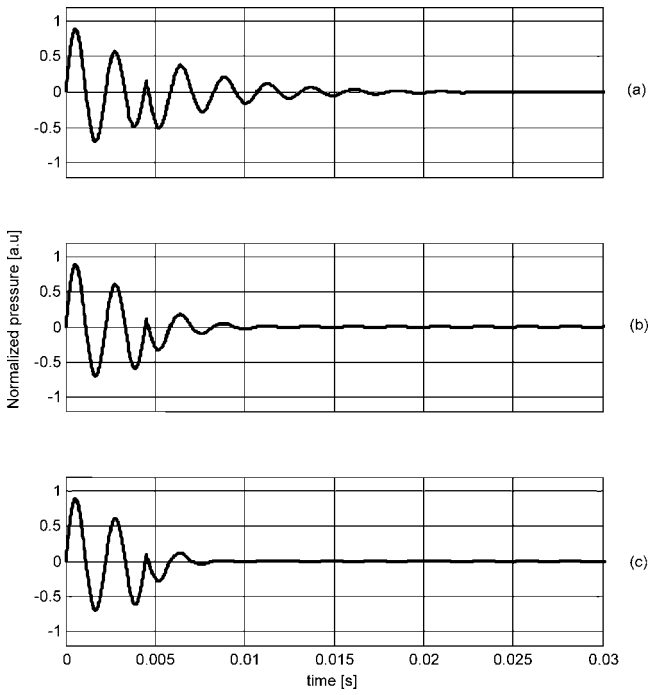

FIG. 9. Numerical simulations of the reflection damping performance. The reflected pressure P_2 with the noncontrolled buzzer (a) is compared with pressure P_2 with the buzzer controlled by the SSDS (b) and SSDI (c) processes (amplitudes are normalized to the amplitude of the echo on a stiff aluminum reflector).

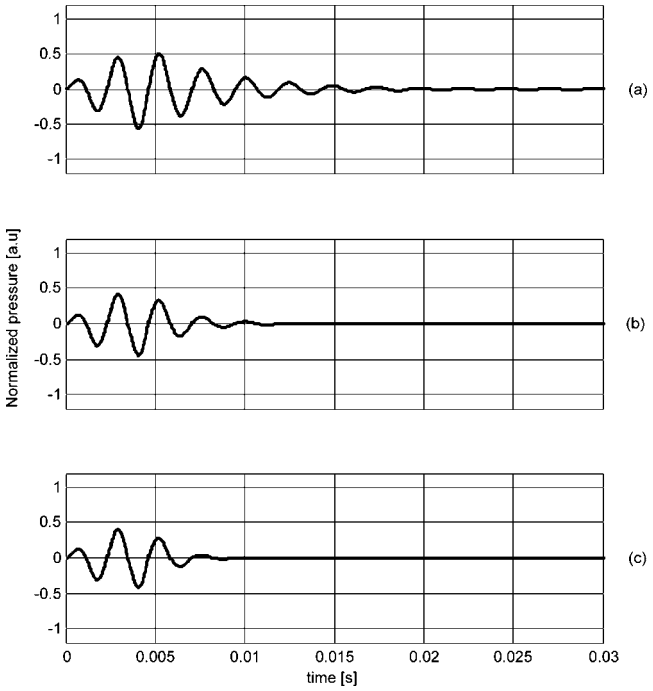

FIG. 10. Numerical simulations of the pressure transmitted through the buzzer. The incoming pressure wave amplitude is equal to unity. The noncontrolled buzzer response (a) is compared to the SSDS (b) and SSDI (c) cases (amplitudes are normalized to the incident wave amplitude).

In the reflection case, it is clear that part of the incoming wave energy is converted into vibration energy in the buzzer. This energy is dissipated either by viscous losses or by both reflection and transmission during the panel ringing. In the SSD controlled case, this ringing is strongly reduced, thus limiting the reflected energy. This is clearer in the transmission case, where the transmitted pulse amplitude is even more reduced. Clearly, the SSDI approach appears to be slightly more performing than the SSDS in both cases.

C. Energy balance simulation

The principle of absorbing termination is illustrated in Figs. 11 and 12, showing the energy flows and balance by integration of Eq. (50) in the transient regime. According to previous simulations, the incoming pressure wave is still a two-period tone burst centered at the transducer antiresonance frequency. When the SSD damping is not active (Fig. 11), the switching energy E_S is equal to zero; thus, the impinging energy E_d is only dissipated through viscous losses E_v, and the acoustic energy E_{ac} is retrieved as reflected and transmitted energy. In the SSDI case (Fig. 12), the voltage $V(t)$ develops and the self-control function $h(t)$ is established acting as a mechanical dry friction damping force. This results in greater energy extracted E_S from the vibrating buzzer and therefore in lower reflected and transmitted energies E_{ac}. This efficient energy extraction mechanism can be seen by a

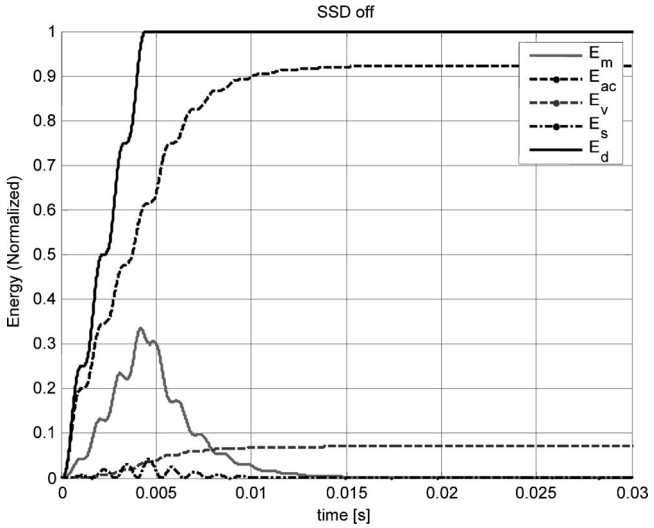

FIG. 11. Numerical simulations of energy balance in the case of Fig. 9 and Fig. 10 without nonlinear control. E_d is the incoming energy; E_m is the mechanical energy stored in the termination. Switch extracted energy E_S is compared to mechanical losses E_v and to reflected and transmitted acoustic energy E_{ac}.

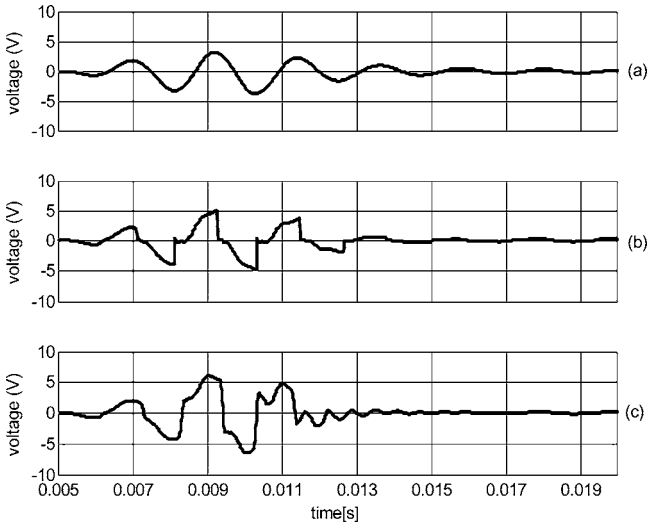

FIG. 13. Experimental piezoelectric element voltage waveforms for a two-period acoustic pressure incident tone burst in the transient regime. Comparison of the noncontrolled buzzer voltage (a) with the SSDS (b) and SSDI (c) cases.

smaller peak in the mechanical energy (kinetic+elastic) stored in the transducer, as well as a shorter transient regime. The reflected and transmitted energies are both lower in amplitude, as well as quicker to reach the final value. In this controlled case, the transmitted and reflected energy is nearly twice smaller than in the uncontrolled case.

VI. EXPERIMENTAL INVESTIGATIONS

Figure 13 illustrates the various voltage waveforms obtained across the piezoelectric element in a transient regime for an incident two-period tone burst. Figure 13(a) illustrates the uncontrolled open-circuit case, while Figs. 13(b) and 13(c) illustrate the SSDS and the SSDI cases, respectively.

In the SSDS case, according to the principle described in Sec. II C, the piezoelectric element capacitance is briefly discharged at each voltage extremum, then released open. The switching device does not operate for the low-amplitude ringing, since the voltage is lower than the detection circuit threshold. However, total free ringing appears to be attenuated while the first period voltage amplitude is magnified and time shifted. This is even clearer for the SSDI case. There, the voltage is inversed (a=0.2) for each voltage maximum above the threshold. The first voltage period amplitudes are nearly twice the uncontrolled amplitude and nearly in quadrature, and no low-frequency ringing is apparent. Higher frequency ripples (third harmonics) are apparent, however, a consequence of the sharp edges due to the voltage inversion process.

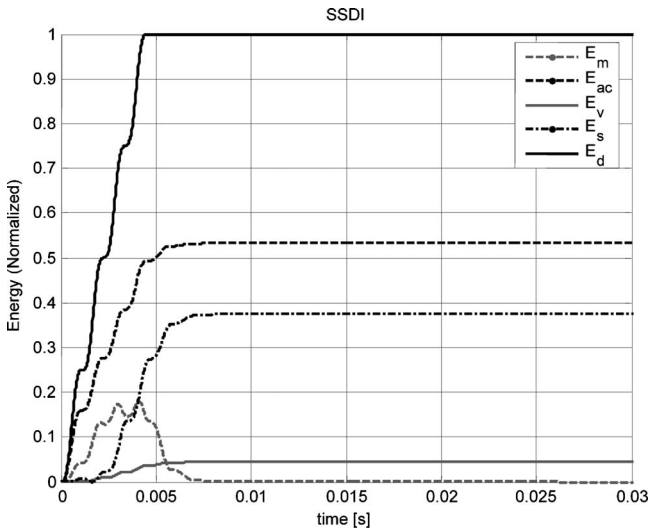

FIG. 12. Numerical simulations of energy balance in the case of Fig. 9 and Fig. 10 with nonlinear control (SSDI) emphasizing lower acoustic energy for larger extracted energy.

A. SSD damping performance in reflection

Figure 14 shows the experimental reflected pressure signal in the transient regime in three cases: first, a stiff massive aluminum reflector (SR) is used for quasiperfect reflection and as a reference. Then, the reflector is replaced by the open-circuited buzzer (SSD off) and, finally, the buzzer voltage is driven following the SSDI approach. The use of a buzzer instead of a stiff plate reduces the echo amplitude significantly, while combined use of SSDI limits the reflected echo duration of the controlled buzzer. The SSDS case is not represented because it is very close to the uncontrolled case.

The results plotted in Fig. 14. are normalized to the maximum amplitude of the echo on the stiff aluminum reflector. Moreover, the impinging sound wave is not a perfect tone burst, as in the theoretical case represented in Fig. 9. The response of the loudspeaker and the dispersive character of the tube leads to the more modulated wave, represented in Fig. 14. For this reason, the proposed comparison will be more qualitative. However, uncontrolled and controlled echoes on the buzzer termination can be compared more quantitatively.

In both cases (reflected and transmitted pressure), part of the provided energy is directly reflected and another part is

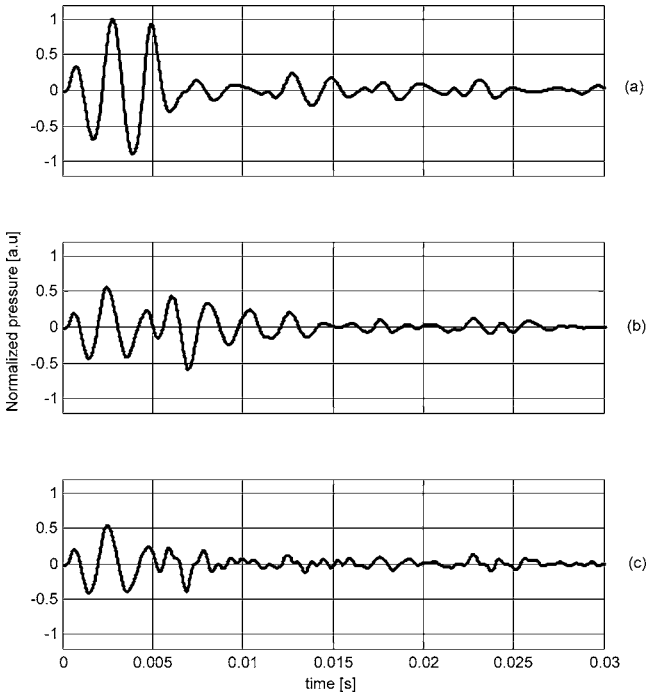

FIG. 14. Experimental reflected pressure plots in the transient state. The microphone voltage waveform is plotted in the case of: (a) a stiff aluminum reflector (SR); (b) the uncontrolled buzzer (SSD off); and (c) the buzzer associated with SSDI control (SSDI).

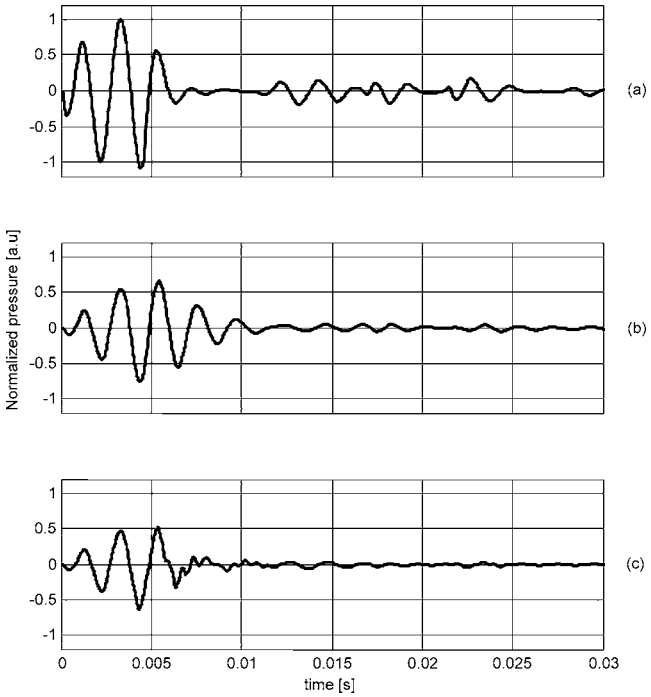

FIG. 16. Experimental transmitted pressure in the transient state. The transmitted pressure is plotted without the termination (a), with the uncontrolled buzzer termination (b), and with the buzzer controlled by SSDI (c). (Acoustic pressures are normalized to the incident acoustic pressure amplitude.)

transmitted to the buzzer, resulting in oscillations. If no damping is induced, the buzzer will restore the energy of the vibration as ringing. In the case of the SSD control, this energy is extracted and subsequent buzzer vibrations are damped, resulting in lower ringing and much lower reflected pressure power. This point is illustrated in Fig. 15, which represents the power spectral densities of the signals represented in Fig. 14. For the buzzer controlled by the SSDI approach, the reflected maximum power density is one-third of the noncontrolled case (SSD off). Due to the nonlinear switching process used in the SSDI technique, odd harmonics appear in the piezoelement voltage. This phenomenon can be harmful if the frequency of one of these harmonics is coincident with a resonant mode of the transducer. This point is illustrated in Fig. 15 with clear emerging peaks at frequencies close to 1400 Hz. The amplitude of the odd harmonics of the piezoelectric element voltage spectrum directly depends on the voltage inversion edge slope, which is related to the inversion angular frequency ω_L, defined by Eq. (13). Hence, a large inversion inductance value leads to a "smoothed" edge and limits the risk of energy rejection.

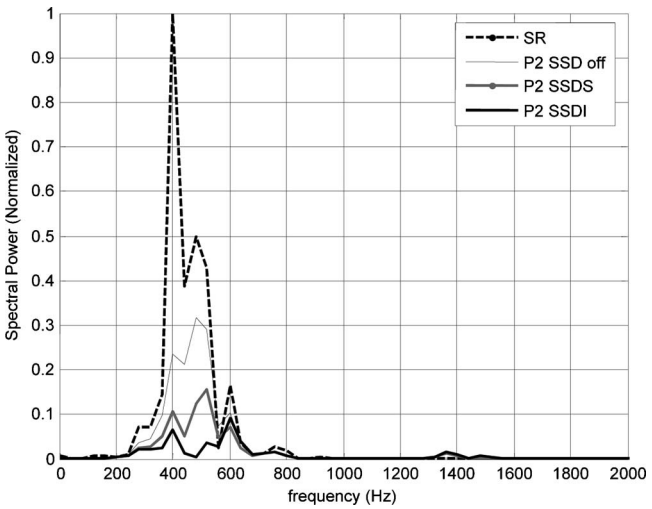

FIG. 15. Normalized spectral power density of the reflected pressure represented in Fig. 14. The inversion inductance is 160 mH, allowing low inversion frequency and leading to smooth edge and low high-frequency rejection.

This approach shows that, compared to a perfect reflector, a 15-dB echo reflection is obtained at the buzzer antiresonance frequency when SSDI is active. A 10-dB echo reflection attenuation is obtained for this same frequency compared to the uncontrolled buzzer.

B. SSD damping performance in transmission

Figure 16 shows the experimental transmitted pressure in the transient regime. The agreement with the theoretical predictions is rather good. A large decrease in transmitted pressure is observed when the SSDI approach is operational. The main difference is due to the fact that the experimental incident tone burst is more smoothed by the propagation in the tube than considered theoretically in Fig. 10. Another difference is that the reflection at the end of the tube is also apparent in Fig. 16(a). The pulse transmitted through the uncontrolled buzzer termination [Fig. 16(b)] is also in good agreement with the predictions. It presents both a reduced direct transmission amplitude and a longer ringing as the buzzer vibrates. This ringing is emphasized by the fact that the impinging wave is tuned to the buzzer resonance. Direct transmission and ringing are both reduced when the buzzer

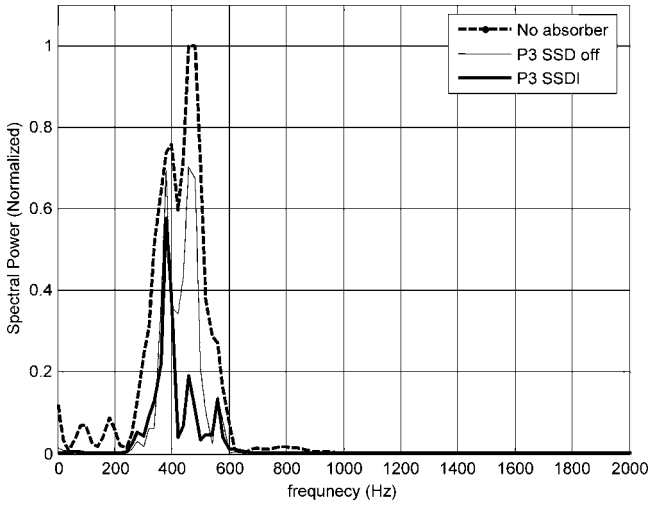

FIG. 17. Normalized spectral power density of the transmitted pressure represented in Fig. 16. without termination, with the uncontrolled and then the controlled buzzer termination.

voltage is controlled following the SSDI approach in Fig. 16(c). Both the direct transmission and the subsequent ringing are strongly attenuated. Figure 17 shows the corresponding power spectral densities. For the controlled buzzer, the maximum transmitted power density is one-fifth of the case without the isolation termination at the buzzer antiresonance frequency. This corresponds to a 7-dB attenuation of the transmitted acoustic power.

C. Quantitative comparison and discussion

Both from the experimental and theoretical data, the total rms value of the various pressure signals is evaluated on the whole pulse. Table III summarizes these amplitudes for the reflected and transmitted acoustic pressures. The amplitudes are normalized to the incoming pressure pulse, considered as unity. The incoming pressure pulse is a two-period tone burst at the buzzer termination antiresonance frequency. The SSDS case was not evaluated experimentally under these conditions.

An overall good agreement can be observed between the theoretical and experimental results. Using a controlled buzzer termination allows the attenuation of both the reflected and transmitted waves. The uncontrolled buzzer reflects 60% of the incoming energy and transmits 30%. The same buzzer with the SSDI control reflects only 35% and transmits 17% of the incoming energy. The experimental results appear to be a little better, the difference is mainly due to a smoother experimental pulse and therefore with an incident energy more centered on the buzzer resonance frequency. In the experimental case, 20% of the incident energy is reflected while 10% is transmitted, corresponding, respectively, to a 7- and 10-dB global attenuation. The buzzer termination can be considered as a thin and lightweight energy absorption cell when it is excited at its resonance frequency. For the transmission case, the thin buzzer is a rather good reflector except at its resonance frequency, where its own resonant motion radiates most of the vibrational energy. Adding SSDI vibration damping allows a strong reduction in the resonance and, therefore, the transmitted energy, even at the buzzer resonance frequency.

TABLE III. rms total amplitude of the various pressure pulses represented in Figs. 9, 10, 14, and 16. The incoming pressure amplitude is taken as unity.

		Theoretical	Experimental
Reflection	Perfect reflector	1	1
	SSD off	0.78	0.68
	SSDS	0.73	···
	SSDI	0.59	0.44
Transmission	No absorber	1	1
	SSD off	0.54	0.47
	SSDS	0.44	···
	SSDI	0.42	0.31

VII. CONCLUSION

SSD nonlinear piezoelectric-enhanced control was shown to be a high-performance method for addressing the problem of acoustic control. Both reflected and transmitted waves were shown to be attenuated for a thin wall consisting of a piezoelectric buzzer. The proposed control technique is simple, lightweight, and compact. It does not require any operative power, as opposed to the classical active systems. Only a small amount of energy is required to drive an integrated switch. Moreover, the device can be self-powered, using the energy of the vibration to start and pursue the damping operation. No sensor is required since the piezoelectric element is used both as a sensor and as an actuator through monitoring and control of the piezoelectric voltage.

In the proposed technique, incident acoustic energy is converted into vibrational energy in the separation wall. The proposed effective vibration damping solution allows extraction of this energy before acoustic transmission.

The main drawback of the technique is a performance strongly affected by the frequency band of the wall "transducer" and the possibility of energy feedback at higher modes. The latter point can be efficiently addressed with a proper choice of inductor invertion, including active inductance. The first point has to be addressed by a sound design of the piezoelectric actuator, including piezoelectric patch placement, piezoelectric material performances, etc.

Current work focuses on the extension of this technique to the development of active skin panels, including anechoic damping on a given frequency band. Association of various skin panels on a large surface is an ongoing objective for architectural acoustic control. One of the main interests of the proposed technique is its great potential for excellent performance at low frequency with a very low profile, thin and light panel device. Another objective is the control of large panels using various piezoelectric patches focusing on differents modes. A final important point concerns the extension of the proposed switching technique to multimodal and complex voltage signals.

Bao, X. Q., Varadan, V. K., and Howarth, T. R. (**1990**). "Design model of a bilaminar piezoceramic composite actuator for an active acoustic attenuation control system," J. Acoust. Soc. Am. **87**, pp. 1350–1352.
Browning, D. R., and Wynn, W. D. (**1993**). "Multiple-mode piezoelectric

passive damping experiments for an elastic plate," Proceedings 11th Int. Modal Analysis Conf. (Kissimmee, FL), pp. 1520–1526.
Clark, W. W. (**2000**). "Vibration control with state-switching piezoelectric materials," J. Intell. Mater. Syst. Struct. **11**, 263–271.
Clark, W. W., and Corr, L. R. (**2003**). "A novel semi-active multi-modal vibration control law for a piezoceramic actuator," Trans. ASME, J. Vib. Acoust. **125**, 214–222.
Cunefare, K. A. (**2002**). "State-switched absorber for vibration control of point-excited beams," J. Intell. Mater. Syst. Struct. **13**, 97–105.
Cunefare, K. A., De Rosa, S., Sadegh, N., and Larson, G. (**2000**). "State-switched absorber for semiactive structural control," J. Intell. Mater. Syst. Struct. **11**, 300–310.
Davis, C. L., and Lesieutre, G. A. (**1998**). "An actively-tuned solid state piezoelectric vibration absorber," Proceedings of the SPIE-The International Society for Optical Engineering, **3327**, 169–182.
Davis, C. L., and Lesieutre, G. A. (**2000**). "An actively-tuned solid state vibration absorber using capacitive shunting of piezoelectric stiffness," J. Sound Vib. **232**, 601–617.
Gibson, W. C., and Johnson, C. D. (**1987**). "Optimisation methods for design of viscoelastic damping treatments," Proceedings of the ASME Conference on Vibration and Noise **5**, 279–286.
Hagood, W. N., and Flotow, A. V. (**1991**). "Damping of structural vibrations with piezoelectric material and passive electric networks," J. Sound Vib. **146**, 234–268.
Ho, S. (**2000**). "Active control of plate-through noise transmission," Dynamics and Design Conference 2000, JSME, CD-ROM proceedings, Paper No. 746.
Holdhusen, M., and Cunefare, K. A. (**2004**). "Optimization of a state-switched absorber applied to a continuous vibrating system," Proceedings, SPIE Smart Structures and Materials Conf.: Passive Damping and Isolation, **5386**, 319–328.
Hong, J. (**2001**). "Active control of radiated sound from a vibrating plate," Proceedings of DETC, ASME, Vib-21481.
Lafleur, L. D., Shields, F. D., and Hendrix, J. E. (**1991**). "Acoustically active surfaces using piezorubber," J. Acoust. Soc. Am. **90**, 1230–1237.
Larson, G. D., Rogers, P. H., and Munk, W. (**1998**). "State switched transducers: A new approach to high-power low frequency, underwater projectors," J. Acoust. Soc. Am. **103**(3), 1428–1441.
Lee, J. K., Kim, J., and Rhee, Ch. J. (**2002**). "Noise reduction of passive and active hybrid panels," Smart Mater. Struct. **11**, 940–946.
Morgan, R. A., and Wang, K. W. (**2002**). "Active-passive piezoelectric absorbers for systems under multiple non-stationary harmonic excitations," J. Sound Vib. **255**(4), 685–700.
Niederberger, D., Morari, M., and Pietrzko, S. (**2004**). "A new control approach for switching shunt damping," Proceedings, SPIE Smart Structures and Materials Conf.: Passive Damping and Isolation **5386**, 426–437.
Peiffer, A., Storm, S., Roder, A., Maier, R., and Frank, P. (**2005**). "Active vibration control for high speed train bogies," Smart Mater. Struct. **14**, 1–18.
Richard, C., Guyomar, D., Audigier, D., and Ching, G. (**1999**). "Semi-passive damping using continuous switching of a piezoelectric device," Proceedings of the SPIE Smart Struct. and Mat Conf., Passive Damping and Isolation, San Diego, **3672**, 104–111.
Richard, C., Guyomar, D., Audigier, D., and Bassaler, H. (**2000**). "Enhanced semi passive damping using continuous switching of a piezoelectric device on an inductor," Proceedings, SPIE Smart Structures and Materials Conf.: Passive Damping and Isolation **3989**, 288–299.
Wu, S. (**1998**). "Method for multiple shunt damping of structural vibration using a single PZT transducer," Proceedings, SPIE Smart Structures and Materials Conf.: Passive Damping and Isolation, San Diego **3327**, 159–168.
Zhang, J. M., Chang, W., Varadan, V. K., and Varadan, V. K. (**2001**). "Passive underwater acoustic damping using shunted piezoelectric coating," Smart Mater. Struct. **10**, 414–420.

Subjective assessment of listening environments in university classrooms: Perceptions of students

Susan M. Kennedy and Murray Hodgson
School of Occupational and Environmental Hygiene, University of British Columbia, 3rd Floor, 2206 East Mall, Vancouver, B.C. V6T 1Z3, Canada

Lisa Dillon Edgett and Noelle Lamb
School of Audiology and Speech Sciences, University of British Columbia, 5804 Fairview Avenue, Vancouver, B.C. V6T 1Z3, Canada

Rod Rempel
School of Occupational and Environmental Hygiene, University of British Columbia, 3rd Floor, 2206 East Mall, Vancouver, B.C. V6T 1Z3, Canada

(Received 7 July 2005; revised 24 October 2005; accepted 25 October 2005)

A questionnaire is developed to evaluate perception of the listening environment by university students. The objectives were to develop a questionnaire-based measurement tool, derive a measure of perceived classroom-listening quality, use the questionnaire to investigate factors that enhance, impair, or do not affect perceived listening quality, and consider the implications for classroom design. The questionnaire was administered to over 5700 students in 30 classrooms at one university. Physical and acoustical measurements were also performed in each classroom. The questionnaire included items that recorded aspects of student perception, as well as individual, course-, and instructor-specific factors. Responses to 19 perception items generated a perception of listening ease (PLE) score for each student and a classroom-average score. Decreased PLE was associated with women, English-second-language students, those with hearing impairment, students not interested in the course material, and those who found the material difficult. Increased PLE was associated with higher speech transmission index, acceptable lighting, temperature and seating, better instructor voice, increased visual-aid use, and easier course material. Results indicate that PLE is a useful measure of student perception of the classroom-listening environment, and that optimal classroom acoustical design must take into consideration "in-use" conditions, as well as classroom physical characteristics.
[DOI: 10.1121/1.2139629]

PACS number(s): 43.55.Hy [NX] Pages: 299–309

I. INTRODUCTION

In university classrooms, learning occurs primarily through verbal communication. The physical characteristics of the acoustical environment are key factors in the success of this communication, although other factors, such as the characteristics of the speaker and the listener, and the learning circumstances, also play a role.

Considerable research has demonstrated that successful verbal communication is related to the relative levels of the received speech signal and background noise, and the classroom reverberation.[1] These depend, in part, on the geometry and acoustical characteristics of the classroom surfaces, furnishings, and occupants. One composite measure of the physical characteristics of a room, calculated from the speech-signal level, background-noise level, and reverberation time, is the speech transmission index (STI).[2]

The relationship between these physical parameters and communication success has been studied using various tests of "speech intelligibility" (SI). SI tests are typically performed under controlled conditions, by evaluating the percentage of specific speech material—often single words—correctly understood by a panel of listeners, with or without competing noise.[1,3–5]

Comparisons between SI and STI in the same classroom have indicated good correlation between these composite measures.[2,6,7] However, in these studies considerable effort was directed at minimizing experimental variation due to nonacoustical and typically variable factors such as language, motivation, lighting, etc. However, even in a controlled setting, Cox *et al.*[8] found significant differences in SI in the same room when comparing six different "normal" talkers. Further, of four simulated environments (a quiet living room, a classroom, and social events in two settings) studied by Cox *et al.*, SI was most reduced for all talkers and all speech features in the classroom environment.

Therefore, although STI and SI values provide useful data on the potential influence of objective physical characteristics on classroom communication, the extent to which either approach accurately reflects the total listening experience of students and instructors in a classroom during typical classroom use is not known. Qualitative descriptors (poor, excellent, etc.) of conditions for verbal communication are sometimes associated with various ranges of measured quantities,[2] but they are derived from controlled studies using simple speech material, and their significance to actual classrooms during use is not known.

A possible reason for this gap in the literature is the lack of standardized measurement tools for evaluating the uncontrolled communication experience (including the speaker, room, and listener) during typical classroom use. Questionnaires have been developed to determine the adverse effect of external noise on students and teachers.[4,9] However, until recently, there were few studies that evaluated how classroom users perceive the overall success of the acoustical conditions in the classroom environment, and these generally considered primary- and or secondary-school settings. In order to fill the gap, we developed a questionnaire to measure university-student perception of classroom-listening environments. Details of the questionnaire development, and preliminary results, have been presented (see Ref. 10)—the present journal article describes the work more fully and extends it by using multivariable regression modeling to examine relationships between overall perceptions of classroom-listening quality and both objective and subjective factors that may influence perception.

More recently, several groups of investigators have reported results from studies in which questionnaires were used to assess classroom environments. Wilson *et al.*[11] used a questionnaire to determine the reactions of primary-school teachers to their listening environments and to the addition of ceiling absorption, as well as factors that might affect the reactions. Astolfi *et al.*[12] used teacher and student questionnaires to investigate environmental comfort, including acoustical quality (noise-source intensity and annoyance, consequences of the acoustical environment, teacher voice problems, and student perception of teacher voice clarity and speech comprehension) in secondary-school classrooms. Dockrell and Shield[13] performed a large-scale questionnaire survey of teacher and children perceptions of awareness and annoyance of noise environments in primary schools. Meis *et al.*[14] used a questionnaire to study perception of the quality of the acoustical environments in university classrooms. Respondents rated a number of environmental attributes on scales bounded by opposite-extreme descriptors. Results were correlated with the results of reverberation-time measurements. Hagen *et al.*[15] used a similar questionnaire to measure the reactions of primary-school children to their classroom acoustical environments before and after "improvement" by the addition of sound absorption and/or a sound-field-amplification system.

In the present work, we developed and applied a questionnaire aimed at generating a global measure of the subjective perception of the listening environment by students in university classrooms and at capturing relevant personal and environmental characteristics that may modify this perception. Our specific research objectives were to investigate demographic, instructional, and environmental factors (including physical-acoustical characteristics of the classroom) that enhance, impair, or do not affect perceived classroom-listening quality, and to consider the implications of the work for classroom design.

Here we report results from administering the questionnaire to over 5700 university students from a stratified random sample of university classrooms in which comprehensive measures of the physical-acoustical environments were also made.

II. METHODS

A. Questionnaire development

The questionnaire was developed using standard methods,[16] including a comprehensive literature review, structured interviews with context experts and classroom users, item development, several stages of pilot testing with structured feedback to evaluate construct validity, and reproducibility testing. The final questionnaire contains 73 items, in three parts. Part 1 contains 23 items on student perception of the classroom-listening environment (subsequently used to construct a summary score of "perceived listening ease"); part 2 contains items about potential modifying characteristics of the classroom, the instructor, the course, and where the student typically sat in the room; and part 3 asks demographic information about the respondent. In parts 1 and 2, most items used a five-point response scale bounded at both ends by the words "almost always" and "rarely." One item used a visual analogue scale (i.e., a straight line bounded by descriptive words, on which the subject is asked to place a mark). The complete questionnaire is available from the authors; part 1 is included in the Appendix.

B. Questionnaire administration

A stratified random sample of 30 classrooms was drawn from a list of all classrooms on the University of British Columbia (UBC) campus in which five or more classes were scheduled (with 10 each from classrooms with fewer than 30 seats, between 30 and 80 seats, and between 81 and 300 seats). One of the two UBC classrooms with more than 300 seats was also chosen at random; it replaced one randomly chosen 81–300 seat classroom. For each classroom that was chosen, each instructor scheduled to teach classes in that classroom during one term was contacted for consent to participate in the study. Consent was obtained from all but ten instructors. The final number of participating classes was 107, in 30 classrooms.

Questionnaire administration took place over a two-month period in the Autumn term. Questionnaires were filled out during the first ten minutes of class time and were collected immediately by the researcher. It was not possible to keep a systematic record of refusals; however, the difference between the number of questionnaires distributed and the number returned was less than 5%.

C. Physical measurements, empirical prediction, and STI calculation

Acoustical measurements were made in the classrooms for the purpose of obtaining the values of physical quantities that characterize their acoustical environments physically. It was considered that values relevant to the "in-use" conditions—that is, the occupied classroom—were of most relevance, and had to be obtained. However, since acoustical measurements are difficult in occupied classrooms, class-

rooms were measured in the unoccupied condition; values of relevant quantities were corrected to the occupied condition by theoretical considerations. Following is a brief description of the measurements performed and the subsequent calculations—full details are found elsewhere.[17–19]

In each classroom, two to nine receiver locations (depending on the size of the room) distributed throughout the student seating area were considered. Measurements were made of 1-kHz octave-band early-decay times using a speech source located at the typical teaching position; for each class, these were then corrected to the occupied condition based on the known number of students in the class. Total A-weighted speech levels associated with a typical male or female instructor (corresponding to the gender of the instructor for each class) were determined using empirical formulas developed in previous work,[19] and these too were corrected to the occupied condition. Total A-weighted occupied-classroom ventilation-system and student-activity noise levels were predicted by previously developed empirical formulas.[19] Total A-weighted background-noise levels were calculated by energetic summation. The resulting 1-kHz early-decay times and A-weighted signal-to-noise level differences were used to calculate values of speech transmission index for each receiver position in the occupied classroom, using a simplified version of the procedure developed by Steeneken and Houtgast.[2] In eight classes, student and instructor questionnaire responses confirmed that a speech-reinforcement system had been used most of the time. In an attempt to account for this in the STI calculations, signal-to-noise level differences were forced to a value of 20 dB on the assumption that the speech-reinforcement system amplified the instructor's speech enough to render the effect of the background noise negligible. Weighted class-average STI values were calculated for each class in each room, using weights based on the proportion of students in each class typically sitting at each of the various receiver positions.

D. Data analysis

A total of 5738 questionnaires were returned. Data analyses used SAS-PC statistical-analysis software (SAS Institute, Cary, NC). Questionnaires missing key demographic variables, more than 50% of the listening-environment response variables, or missing either one of the two composite classroom rating variables were excluded ($n=245$), leaving 5493 analyzable questionnaires. Of these, the proportion with missing values for individual items ranged from less than 0.1 to 1.4%, with no apparent clustering; therefore, missing values were substituted by the mean value for the item from all other questionnaires. One five-item section about classroom activities hampered by a poor listening environment had a large number of "non–applicable" responses; therefore, responses to these items were collapsed into one variable (the number of yes responses divided by the number of applicable responses) and then standardized to a five-point scale. A "perceived listening ease" (PLE) score was calculated as the sum of responses to each of 19 items in Part 1, after each item was standardized to a five-point scale (or rescaled in the case of item 4a) from 0 to 4, in which 4 represents a "better" environment. The final sum was then standardized to a 100-point scale. Prior to settling on a simple additive score for PLE, we tested several different approaches to combining responses to the questions in Part 1, using a randomly selected sample of 500 questionnaires. These included using several different approaches to weighting correlated answers—simply using the answer to question 4a alone or combining 4a and 4b, and using factor analysis instead of an additive (or weighted average) summary score. In brief, we found that weighted average scores gave results similar to those found using a simple additive approach, that using only question 4 responses was not as informative (i.e., less variability was explained by predictive models) as using a score that incorporated all responses in Part 1, and that results from factor analysis were much more difficult to interpret than results using a summary score and they did not appear to provide additional insights into factors associated with subjective perception of the listening environment.

To evaluate factors that may influence PLE, univariable and multivariable linear-regression analyses were carried out with the PLE score as the dependent variable, and classroom-environment variables, course and instructor variables, and personal factors as potential explanatory variables. Environmental variables included the class-average physical measurements (STI, early-decay time, signal-to-noise ratio, and measures of classroom size), seating capacity, the reported level of background noise present due to classroom equipment (e.g., projector, lab equipment), reported suitability of the seating, classroom air, temperature, and lighting, and the ratio of classroom floor area to the number of students (as a measure of crowding). Course and instructor variables included speed, loudness, articulation and accent of the instructor's voice, the normal position of the instructor in the classroom, whether or not a microphone was used, the instructors use of visual aids, the type of material being taught (math and science, language, other), whether the course was an elective or required, whether the course was undergraduate or graduate level, and student report of frequency of attendance, ease of the course material, interest in the material, and whether or not the student typically did required reading prior to class. Personal factors included age, gender, age at which English was first learned, reported hearing impairment, reported uncorrected vision impairment, and the frequency of ear infections and episodes of flu or allergy affecting the ears since the beginning of the course.

Multivariable models were built using a "best subsets" procedure for groups of variables evaluated in the following order: classroom environmental factors, instructor factors, course factors, and personal factors. Model "goodness of fit" was evaluated based on *adjusted* R^2 values and the principle of parsimony (i.e., choosing a simpler model where the change in adjusted R^2 was small). Explanatory factors were only considered for inclusion in the multivariable models if they were associated with PLE in univariate analysis with $p<0.20$. To control for multicollinearity for highly correlated predictor variables (e.g., STI and many of the reported classroom characteristics), the choice of which to include was based on a combination of strength of association in univariable models and on existing theory. Regression diag-

TABLE I. Relevant physical characteristics of 30 UBC classrooms studied.

Quantity	Unit	Mean (standard deviation)	Range
Seating capacity		107 (111)	19–498
Volume	m^3	570 (837)	106–4036
Source/receiver distance	m	6.4 (4.2)	1.0–19.7
Unoccupied 1-kHz early-decay time	s	1.13 (0.41)	0.54–1.83
Number of students		54 (59)	3–279
Occupied 1-kHz early-decay time	s	0.70 (0.24)	0.34–1.31
Occupied A-weighted signal-to-noise ratio	dB	9.0 (5.1)	−0.5 to 20.0
Occupied STI[a] (unweighted)		0.56 (0.06)	0.34–0.71

[a]Speech transmission index, STI (occupied), averaged over $n=9$ receiver positions in each room, adjusted for the total number of students in the class, the gender of the instructor, and microphone use where applicable (but not weighed for the number of students typically sitting in each receiver position)—see Sec. II for details.

nostics (examination of influence and residual plots) were carried out on the final models.

III. RESULTS

A. Characteristics of participants

The participants ranged from first-year to post-graduate students, with a mean age of 21.5 years, and with approximately equal numbers of men and women ($n=2538:2955$, M:F). Typical of our region, one-third of the students reported that English was not their first language, and almost 6% had only learned English after age 16. About 4% of students reported being aware of having a hearing impairment; 1% reported that this was of moderate or greater severity. Almost all students (98%) reported that they attended class most of the time, but 20% found the course material uninteresting, and 24% found the material difficult.

B. Characteristics of the classrooms

The classrooms studied varied from small lecture rooms with volumes around 100 m^3 and as few as 20 seats, to large auditoria with volumes over 3000 m^3 and over 500 seats. The volume-to-surface-area ratios varied from 0.7 to 2.4 m, and classroom shapes varied considerably. Classroom average STI values (weighted for typical student positions in the rooms) ranged from 0.49 to 0.72 with a mean of 0.62 (SD: 0.7). Details are presented in Table I.

C. Subjective perception of the listening environment

Table II presents the responses of the students to the individual questions used to generate the PLE score. "Students talking" was the factor most commonly reported as interfering with listening, followed by intermittent noises in the building, but outside the classroom. In contrast, constant noises within or outside the building, and noise due to the heating and ventilating system, or to projectors or lab equipment, were less likely to be reported as interfering with the listening environment. The most commonly reported adverse consequence of a poor listening environment was the failure to hear questions asked by other students in the class. Individual PLE scores ranged from 1.0 to 94.7 with a mean of 64.2; class-average PLE scores were less variable than the individual scores, ranging from 42.5 to 89.0.

D. Potential modifying factors

Table III records the responses to questions about general characteristics of the classrooms and the instructors that may have influenced the student perception. Almost 33% of respondents rated the level of background noise associated with students as high or very high, whereas only 5% reported high background noise due to teaching or lab equipment. Over 25% of respondents rated temperature, seating, and "classroom air, in general" as unacceptable. The voice of the instructor was rated as fast or very fast by 28% of students, but only 8% reported that they found the instructor's accent or articulation difficult to understand. Visual aids were commonly used and instructors tended to move around, rather than lecture from one fixed position.

E. Perceived listening ease scores

Tables IV and V show class-average and individual PLE scores stratified by selected classroom, class, and personal factors expected *a priori* to influence PLE. PLE score was higher in smaller and less crowded classrooms and in classrooms with measured STI values greater than 0.55. On average, lower PLE scores were reported by women, students whose mother tongue was not English, those with moderate to severe hearing impairment, students not interested in the course material, and those who found the course material difficult.

Table VI shows results from multivariable analyses in which all possible factors that might influence PLE were considered together. The table shows actual and standardized coefficients. The actual coefficients reflect the predicted change in PLE associated with a one unit change in the factor; standardized coefficients reflect the predicted change in PLE for each factor after standardizing for differences in the variance of the factors. Factors associated with a significant reduction in PLE included microphone use in the classroom, math or science course material, and moderate to severe hearing impairment. Increased PLE was associated with

TABLE II. Perception of listening ease (PLE)[a] questionnaire items.

% reporting interference with listening "much of the time or always"	
How often…interferes with ability to hear	%
Students talking in the classroom	26.0
Students moving about in the classroom	19.1
Noise from projectors or lab equipment	4.0
Noise from heating/ventilating systems	10.0
Noises outside the classroom, in the building	
Constant	10.4
Intermittent	22.6
Noises outside the building	
Constant	9.4
Intermittent	17.7
How often experience…as a result of poor listening environment	
Miss points made in class due to noise	13.4
Concentration broken	25.1
Fail to hear questions from other students	55.0
Ask instructor to repeat points	10.8
Increased fatigue	23.5
Leave class feeling frustrated	12.2
Increased effort to hear	23.8
Ask questions for clarification (not understanding)	13.2
% reporting this activity adversely affected (yes/no)	
Activity affected by the listening environment? (yes/no)	%
Lectures ($n=5337$)	46.0
In class essays, exams, tests ($n=4319$)	43.6
Question periods ($n=3886$)	58.0
Class discussions ($n=3009$)	51.5
Guest speakers ($n=2865$)	44.5
Overall rating of this classroom:	mean (sd)
compared to other university classrooms (scale: 0 to 4)	2.4 (0.9)
compared to an ideal listening environment (scale: 0 to 100)	60.5 (22.9)
PLE score, individual	64.2 (15.6)
PLE score, class average ($n=107$)	66.4 (8.9)

[a]PLE is calculated as the sum of responses to each of 19 items (each standardized to scale from 0 to 4, where 4 indicates a better listening environment), then standardized to a 100-point scale.

higher STI values, acceptability of the classroom lighting, temperature, seating, better articulation, easier to understand accent, louder voice from the instructor, increased use of visual aids, and course material that was reported to be easier to understand. Models that considered the individual components of STI (early-decay time and signal-to-noise ratio) instead of STI indicated that both components were significantly associated with PLE, but the model with STI alone was superior to the model with its components (i.e., explained a greater proportion of the overall variance in PLE). Factors tested in the models but *not* associated with PLE in multivarable models included student age, home department and year of study, whether or not the course was required or elective, reported attendance record, whether the student reported doing assigned readings or not, the student's level of interest in the course material, reported visual impairment, reported frequency of ear infections, flu, or allergy, reported mild hearing impairment, loudness of the instructor's voice, and how often the instructor moved around the room or spoke directly facing the class.

IV. DISCUSSION

In summary, a questionnaire to investigate the subjective perception of students to listening environments in university classrooms was developed and applied to a large, heterogeneous population of students. A global measure of perceived listening quality was constructed and factors associated with this subjective perception were evaluated.

Our study population was as heterogeneous as is possible on a single university campus with a large proportion of non-English native speakers and a broad mix of subject matters and levels of interest represented by the courses. The proportion of students reporting a hearing impairment was similar to that expected in a general population of this age range.[20] Therefore, the results from this large study are likely to be well generalized to any similarly aged population of classroom users.

The physical characteristics of the classrooms studied here are similar to those reported at other universities and elsewhere. Other studies have dealt with pre-university classrooms and students with either normal or impaired hearing.[21]

TABLE III. Responses to questionnaire items on factors that may modify student perception of the listening environment.

Questionnaire item	%
Level of background noise (% rating this factor as high or very high)[a]	
from students	32.8
from teaching or lab equipment	4.5
from ventilation, heating, lighting, etc.	12.4
Other environmental factors (% rating this factor as unacceptable)	
lighting	10.7
temperature	26.1
seating	24.6
classroom air	27.8
Voice of instructor	
speed (% fast or very fast)	28.5
loudness (% soft or very soft)	18.7
accent (% difficult/very difficult to understand)	8.1
articulation (% difficult/very difficult to understand)	8.1
Instructor's activities	
speaks toward listeners (% rarely)	3.2
moves about the room while speaking (% rarely)	39.5
uses visual aids (% rarely)	12.7
uses a microphone (% rarely)	72.1

[a]In this part of the questionnaire, respondents were asked to report the *level* of background noise without reference to whether or not they felt it interfered with their ability to hear in this classroom.

TABLE IV. PLE scores—according to class and classroom characteristics.

	Class-average PLE score[a]
	mean (sd)
Classroom size	
<30 seats (n=31 classes/9 rooms)	72.7 (7.1)
30–80 seats (n=33 classes/10 rooms)	67.1 (5.6)
>80 seats (n=43 classes/11 rooms)	64.8 (5.0)
p-value[b]	<0.0001
Room area/number of students	
>3 m^2/student (n=53 classes)	69.8 (6.5)
<3 m^2/ student (n=54 classes)	65.7 (6.2)
p-value	0.001
Course type	
languages (n=16 classes)	69.9 (6.8)
humanities/social sciences (n=47 classes)	68.4 (6.1)
math/physical or biological sciences (n=44 classes)	66.3 (7.0)
p-value	0.1
Microphone used[c]	
No (n=94 classes)	68.6 (6.4)
Yes (n=13 classes)	61.7 (5.6)
p-value	0.0004
STI (occupied)[d]	
>0.60 (n=25 classes)	70.1 (7.4)
0.55–0.60 (n=51 classes)	68.6 (6.3)
<0.55 (n=31 classes)	64.5 (5.4)
p-value	0.003

[a]average of the *classroom*-average PLE values (n=107).
[b]p-value from analysis of variance comparing values across the groups identified.
[c]Microphone used sometimes, often, or always.
[d]STI (occupied), averaged over n=9 receiver positions in each room, adjusted for the total number of students in the class, the gender of the instructor, and microphone use where applicable (but not weighed for the number of students typically sitting in each receiver position); see Sec. II for details.

TABLE V. PLE scores—according to personal characteristics of respondents.

	Individual PLE score
	mean (sd)
Age	
35 or younger (n=5386)	64.2 (15.6)
>age35 (107)	67.8 (17.2)
p-value[a]	0.02
Gender	
Men (n=2538)	64.8 (15.5)
Women (n=2955)	63.8 (15.6)
p-value	0.01
English language fluency	
English mother tongue (n=3673)	65.7 (15.3)
Learned English age 15 or earlier (n=1461)	61.2 (15.3)
Learned English after age 15 (n=292)	61.6 (17.3)
p-value	<0.0001
Hearing impairment (reported)	
None (n=5203)	64.3 (15.5)
Mild (n=135)[b]	66.4 (15.7)
Moderate, severe, or profound (n=70)	57.7 (21.2)
p-value	0.0006
Interest in course material	
Interested or very interested (n=2831)	65.8 (15.7)
Neutral or not interested (n=2662)	62.5 (15.3)
p-value	<0.0001
Difficulty of course material	
Does not find course material difficult (n=4151)	65.1 (15.4)
Finds material difficult or very difficult (n=1291)	61.7 (16.0)
p-value	<0.0001
Chooses seat in class in order to hear better	
Rarely (n=1786)	72.3 (13.2)
sometimes (n=1817)	62.1 (14.4)
always or almost always (n=1886)	58.6 (15.6)
p-value	<0.0001

[a]p-value from analysis of variance comparing values across the groups identified.
[b]p=0.30 comparing mild hearing impairment to no reported hearing impairment (Scheffé post-hoc test for multiple comparisons).

Results of speech-intelligibility tests ranging from 32% to 93% have been reported;[1,3–5] many classrooms had insufficient signal-to-noise ratios and excessive reverberation. Pekkarinen and Viljanen[22] measured STI values from 0.44 to 0.81 in unoccupied classrooms and from 0.60 to 0.81 in occupied classrooms. Again, classrooms often had excessive noise levels and reverberation.

The objective of the questionnaire-development phase of this study was to create a valid instrument suitable for scoring classroom-user perception of the listening environment during typical classroom use, and for recording environmental and personal factors that may modify this perception. Given the absence of an existing objective gold standard for measuring perception of the listening environment by users, the validity of the questionnaire and of the PLE score can only be assessed indirectly.[23]

In this study, PLE was associated with factors expected to be linked to subjective perception of the quality of the listening environment, including personal factors such as moderate to severe hearing impairment and mother tongue, environmental factors such as room size, crowding, and physical acoustical characteristics (measured by STI), and numerous characteristics of the speaker's voice and the material being delivered. The small but significant gender difference in PLE (with men reporting slightly higher scores) is unexplained by these data, although it should be noted that the size of the difference between women and men was small (1.8 points) compared to other factors. For comparison, since the environmental factors were measured on a scale from 0 to 4, the average difference in PLE between a student rating projector noise as very high compared to very low was about 18 points (i.e., four times the coefficient in the model).

PLE was also associated with student perception of the quality of room lighting, temperature, and seating, factors that are not expected to influence the room acoustics. This suggests that respondents were not completely able to separate their perceptions of overall environmental quality of the classrooms from the "acoustical" quality; however, these more general environmental factors could also contribute to the "listening environment" through indirect pathways (e.g., contributing to increased noise generated by student movement).

Individual components of our results are similar to those found in other studies in which questionnaires have been

TABLE VI. Factors associated with PLE–multivariable models.[a]

Dependent variable:	Individual PLE coefficient (se)	standardized coefficient[b]	p
Intercept	10.3 (2.0)	0	<0.0001
Personal characteristics			
gender (1=female,2=male)	1.8 (0.36)	0.058	<0.0001
English mother tongue (0=no,1=yes)	3.3 (0.38)	0.098	<0.0001
moderate to severe hearing impairment (0=no,1=yes)	−3.8 (1.6)	−0.027	0.02
Room characteristics			
crowding: room area/number of students (range: 1.1–11.9 m^2/student)	1.2 (0.14)	0.106	<0.0001
STI,[c] occupied, weighted (range: 0.34–0.71)	17.9 (2.9)	0.073	<0.0001
reported background noise from projectors, other equipment (0 to 4, 4=least noisy)	4.6 (0.21)	0.259	<0.0001
room lighting acceptability (0 to 4, 4=best)	1.7 (0.19)	0.113	<0.0001
room temperature acceptability (0 to 4, 4=best)	1.2 (0.15)	0.095	<0.0001
room seating acceptability (0 to 4, 4=best)	1.3 (0.16)	0.103	<0.0001
Course material/instructor characteristics			
instructor's articulation (0 to 4, 4=easiest to understand)	1.6 (0.26)	0.102	<0.0001
instructor's accent (0 to 4, 4=easiest to understand)	0.76 (0.25)	0.050	0.003
loudness of instructor's voice (0 to 4, 4=loudest)	0.92 (0.21)	0.052	<0.0001
visual aid use (0 to 4, 4=most frequent)	0.43 (0.15)	0.033	0.005
course material ease (0 to 4, 4=easiest to understand)	0.87 (0.20)	0.055	<0.0001
course type: math or physical/biological sciences (0=no,1=yes)	−1.7 (0.42)	−0.053	<0.0001
microphone used (0=no,1=sometimes or more often)	−4.1 (0.42)	−0.123	<0.0001
Model R-squared	***0.30***		

[a]Coefficients (standard errors) and p values for the hypothesis that the coefficient=0, from multiple linear-regression models—see Sec. II for details.
[b]Standardized coefficient is computed by dividing the regular regression coefficient by the ratio of PLE standard deviation to the factor standard deviation.
[c]STI (occupied), calculated for n=2 to 11 receiver positions in each of 107 classes, weighted according to the number of students reporting typically sitting at each receiver position.

used. Hétu *et al.*[4] found that a high proportion of school teachers find noise to be detrimental to their work. Wilson *et al.*[11] found that while noise outside the classroom was the biggest source of annoyance, in-class student noise was significant. One-third of teachers reported voice strain and the need to raise their voices when teaching. Adding sound absorption to the ceiling improved the perceived classroom quality. Astolfi *et al.*[12] found students in the classroom, and external transportation, to be the biggest sources of noise. The main consequences were reduced teacher-voice perception and reduced concentration. However, the annoyance associated with noise sources was low, apparently because teachers compensated for noise by raising their voices. Thus, many teachers reported hoarse voices and the need to raise their voices while teaching. Dockrell and Shield[13] found that children's ability to hear in class was mainly affected by noise outside the classrooms, and when working in groups. Transportation noise was the most often heard source. Meis *et al.*[14] found that classrooms with the highest reverberation times at low frequencies were judged to be more "reverberant" and "unpleasant." Those with the highest reverberation times at mid-frequencies were rated more "pleasant," "distinct," and "transparent." Hagen *et al.*[15] found that either ceiling absorption, a sound-field amplification system, or both, improved perceived classroom quality.

A strength of our study is that the questionnaire was designed so that the items used to calculate the global PLE score are separate from the items that record potential modifying factors (i.e., the instructor characteristics, the respondent demographics, and the academic level and preparation of the respondent). Therefore, although the questionnaire was designed for university students, it should be possible to modify parts 2 and 3 of the questionnaire to allow it to be applied to other adult populations. Part 1 of the questionnaire (which generates the PLE score) could be used for other adult populations; however, it would be necessary for a modified questionnaire to be subjected to additional verification for face and content validity and reproducibility if it were to be used for a younger age group.

Although previous work at our university[24] found STI values in occupied UBC classrooms ranging from 0.35 to 0.86, the rooms studied here had somewhat less variability in STI values (ranging from 0.34 to 0.71). Based on previously published equations linking STI and SI, this would correspond to predicted SI levels (for controlled situations) of 84–97%.[17] However, the results of multivariable modeling for PLE from this study indicate that, although there was a statistically significant association between PLE and STI in these rooms, if all other factors in the model are held constant (e.g., at their midpoints), predicted PLE varies only from 49.6 to 56.2 when comparing a classroom with STI of 0.34 to one with STI of 0.71. This suggests that, in actual classroom situations, many factors in addition to the physical acoustical characteristics of the classroom play an important

role in the user's subjective perception of the quality of the listening environment. For example, predicted PLE from this study would be 31.0 for the challenging environment scenario of a student in a crowded math classroom, who learned English as a second language and who reports difficulty with the course material, who has difficulty understanding the accent and articulation of the instructor, and who rates the classroom lighting, seating, and temperature as poor (for a female student without hearing impairment, holding STI constant at 0.52, and other factors at their midpoint). In contrast, predicted PLE would be 78.6 for the scenario of an English-mother-tongue student in an uncrowded social-science classroom, who reports no difficulty with the course material, no difficulty understanding the instructor's voice, and who rates the classroom lighting, seating, and temperature as excellent (holding STI and other factors constant as above). Since STI quantifies classroom quality with respect to verbal communication, the small variation of PLE with STI could also indicate that verbal communication quality is only a minor component of overall classroom listening quality.

Our results have implications for classroom design. Although it may seem reasonable to design a classroom to optimize verbal communication from a single lecturing position at the front of the class to a group of listeners, our results suggest that this notion of a typical classroom does not capture important components of the listening environment. Fewer than 15% of respondents in this study reported frequent difficulties associated with failure of communication from the instructor to the student—i.e., missing points, asking for points to be repeated, asking questions for clarification due to failure to hear, etc. In contrast, the items identified as most influential with respect to a poor listening environment were those associated with other people—i.e., noise due to students talking and moving about. Noises outside the classroom were also important, especially when they were intermittent. For example, one could anticipate interference from noise due to other students in the hallway, when a classroom door is left open. The most commonly reported activities that were adversely influenced by a poor listening environment were question and discussion periods and over 50% of students reported frequent difficulties with failure to hear questions from other students. Therefore, optimal classroom acoustical design needs to take into consideration the "in-use" (occupied) conditions, as well as the physical and acoustical characteristics of the unoccupied classroom.

According to the results of this study, classroom listening quality can be improved by increasing classroom STI. As discussed in more detail elsewhere,[17,25] this involves controlling external and internal noise, promoting adequate speech levels, and optimizing reverberation. The design optimization of classroom reverberation should take into account typical classroom occupancies and the absorption contributed by the occupants.[26] Classrooms should be designed for effective communication between students, and from students to the instructor, as well as from the instructor to the students. Classrooms should have flexible and accessible seating, and not be overcrowded. They should be designed to avoid the need for a speech-reinforcement system to amplify voices; research has shown that this is possible in any classroom, unless instructors have quiet voices.[17] Voice training for instructors may be an effective option to increase speech levels and ensure clear articulation. Finally, the quality of a classroom's lighting, seating, and air should be sufficiently high.

V. CONCLUSION

In this study, we have developed a questionnaire-based score (PLE) to measure subjective perception, by users, of the listening environment in a classroom, and we evaluated physical, personal, and other factors that may modify how respondents score a classroom. The study population was heterogeneous, suggesting good external generalizability within the age range of this study. PLE was associated with both objective and subjective factors, with variable environmental factors at least as important as fixed physical measures or personal factors in predicting PLE. Finally, the questionnaire results indicate that communication between students in the classroom is as important to the students as communication from the instructor in determining subjective perception of listening ease.

These results point to the conclusion that acoustical design criteria need to take into account the "in-use" (occupied) characteristics of classrooms, in addition to physical characteristics of the unoccupied classrooms. The PLE score may be useful to other researchers in the field of classroom acoustics, as an adjunct to speech-intelligibility tests, and to measured or predicted physical parameters, in these complex environments.

ACKNOWLEDGMENTS

The authors thank the instructors of each of the courses, who willingly gave up class time to allow students to participate in this study, and the content experts who assisted in the initial stages of questionnaire development.

APPENDIX: PERCEPTION OF LISTENING EASE QUESTIONNAIRE

Part 1: The listening environment in this classroom

These questions ask about your experience with the listening environment in *this classroom*. When answering, please think about this course in this classroom, since the term began in September. Please circle the most appropriate number response for each question. **If no response seems exactly correct, please indicate the one that seems closest**.

1. There are many possible sources of noise that may affect the listening environment in a classroom. Please indicate **how often each of the following *interferes with your ability to hear***, in this classroom, for this course:

	ALMOST ALWAYS				RARELY
Students talking within the classroom:	1	2	3	4	5
Students moving or shuffling in the classroom:	1	2	3	4	5

Noise from classroom equipment (projectors, lab equipment):	1	2	3	4	5
Ventilation/air conditioning/ heating or lighting equipment:	1	2	3	4	5
Noises (from people or equipment) outside the classroom, but inside the building:					
- Noises that are present most of the time:	1	2	3	4	5
- Noises occurring only once in a while:	1	2	3	4	5
Noises (from people or equipment) outside the building:					
- Noises that are present most of the time:	1	2	3	4	5
- Noises occurring only once in a while:	1	2	3	4	5

2. Here is a list of consequences that some students have told us they have experienced as a result of a poor listening environment in a classroom. These may or may not apply to you. Please indicate how often the items listed below relate to *your listening experience in this classroom*, for this course:

	ALMOST ALWAYS				RARELY
I find I miss major points made in class due to noise:	1	2	3	4	5
I find my concentration broken:	1	2	3	4	5
I *fail to hear* questions asked by other students:	1	2	3	4	5
I find I have to ask for repetition of points made by the instructor:	1	2	3	4	5
I experience increased fatigue:	1	2	3	4	5
I leave class feeling frustrated:	1	2	3	4	5
I have to increase my effort during class:	1	2	3	4	5
I ask questions for clarification rather than for understanding:	1	2	3	4	5

3. Certain course activities may be affected by the listening environment more than others.

Please tell us whether or not your ability to *generally perform well* during each of the following activities is affected by the listening environment in this classroom.

	NO, my ability to *generally perform well* during this activity ***IS NOT*** affected by the listening environment in this classroom.	YES, my ability to *generally perform well* during this activity ***IS*** affected by the listening environment in this classroom.	Not applicable. This activity does not occur in this classroom or this course.
Lectures:	---	---	---
In-class essays, exams, tests:	---	---	---
Question periods:	---	---	---
Guest speakers:	---	---	---
Class discussions:	---	---	---

4. Please provide an **overall rating** for the listening environment of this classroom:

a) with respect to the **IDEAL** listening environment:

(Place a mark on the following line to show your rating)

WORST POSSIBLE LISTENING ENVIRONMENT	BEST POSSIBLE LISTENING ENVIRONMENT
|----------	----------|

b) with respect to **OTHER CLASSROOMS** in a university setting:

(Circle the appropriate number)

WORST 15%				BEST 15%
1	2	3	4	5

Part 2 asks about the room, and about the course material and its presentation. THIS IS NOT A COURSE OR INSTRUCTOR EVALUATION. We simply need to know about presentation style in order to interpret your answers about the listening environment.

Part 3 asks some general questions about you, so that we can interpret the results appropriately.

A complete copy of the questionnaire, including parts 2 and 3, can be obtained from the authors.

[1]A. K. Nabelek and I. V. Nabelek, "Classroom acoustics and speech perception," in *Handbook of Clinical Audiology*, edited by J. Katz (Williams and Wilkins, Baltimore, MD, 1974), pp. 624–637.

[2]H. J. M. Steeneken and T. Houtgast, "A physical method for measuring speech-transmission quality," J. Acoust. Soc. Am. **67**, 318–326 (1980).

[3]M. Ross, "Classroom acoustics and speech intelligibility," in *Handbook of Clinical Audiology*, edited by J. Katz (Williams and Wilkins, Baltimore, MD, 1974), pp. 756–771.

[4]R. Hétu, C. Truchon-Gagnon, and S. Bilodeau, "Problems of noise in school settings: A review of literature and the results of an exploratory study," J. Speech Lang. Path. Audiol. **14**, 31–39 (1990).

[5]C. C. Crandall and J. J. Smaldino, "An update of classroom acoustics for children with hearing impairment," Volta Review **96**, 291–306 (1994).

[6]J. S. Bradley, "Speech intelligibility studies in classrooms," J. Acoust. Soc. Am. **80**, 846–854 (1986).

[7]T. Houtgast and H. J. M. Steeneken, "The modulation transfer function in acoustics as a predictor of speech," Acustica **28**, 66–73 (1973).

[8]R. M. Cox, G. C. Alexander, and C. Gilmore, "Intelligibility of average talkers in typical listening environments," J. Acoust. Soc. Am. **81**, 1598–1606 (1987).

[9]P. Blake and S. Busby, "Noise levels in New Zealand classrooms: Their impact on hearing and teaching." N. Z. Med. J. **107**, 357–358 (1994).

[10]M. R. Hodgson and S. M. Kennedy, "Factors related to perceived acoustical quality in university classrooms," J. Acoust. Soc. Am. **101**, (5, Pt. 2), 3051 (1997).

[11]J. Wilson, M. Valentine, K. Halstead, K. McGunnigle, G. Dodd, A. Hellier, J. Wood, and R. Simpson, *Classroom Acoustics—A New Zealand Perspective* (The Oticon Foundation in New Zealand, 2002).

[12]A. Astolfi, V. Corrado, M. Filippi, and S. Viazzo, "Classroom acoustic assessment: Analysis of subjective analysis and measured indices," *Proc. Euronoise 2003*, Paper 392 (2003).

[13]J. E. Dockrell and B. Shield, "Children's perceptions of their acoustic environment at school and at home," J. Acoust. Soc. Am. **115**, 2964–2973 (2004).

[14]M. Meis, C. Nocke, S. Hoffman, and B. Becker, "Subjective evaluation of speech and noise in learning environments in the realm of classroom acoustics: Results from laboratory and field experiments," J. Acoust. Soc. Am. **117**,(4, Part 2), 2437 (2005).

[15]M. Hagen, J. Kahlert, C. Hemmer-Schanze, L. Huber, and M. Meis, "Developing an acoustic school design: Steps to improve hearing and listening at schools," J. Building Acoustics **11**, 293–307 (2004).

[16]M. Sudman and A. Bradbum, *Asking Questions: A Practical Guide to Questionnaire Design* (Jossey-Bass, San Francisco, 1982).

[17]M. R. Hodgson, "Rating, ranking and understanding acoustical quality in

university classrooms," J. Acoust. Soc. Am. **112**, 568–575 (2002).
[18]M. R. Hodgson, "Empirical prediction of speech levels and reverberation in classrooms," J. Build. Acoust. **8**, 1–14 (2001).
[19]M. R. Hodgson, R. Rempel, and S. Kennedy, "Measurement and prediction of typical speech and background noise levels in university classrooms during lectures," J. Acoust. Soc. Am. **105**, 226–233 (1999).
[20]Health and Welfare Canada, *The Health of Canadians: Report of the Canadian Health Survey* (Health and Welfare Canada, Ottawa, 1981).
[21]M. Picard and J. S. Bradley, "Revisiting speech interference in classrooms," Audiology **40**, 221–224 (2001).
[22]E. Pekkarinen and V. Viljanen, "Acoustic conditions for speech communication in classrooms," Scand. Audiol. **20**, 263 (1991).
[23]L. Del Greco, W. Walop, and R. H. McCarthy, "Questionnaire development: 2. Validity and reliability," Can. Med. Assoc. J. **136**, 699–700 (1987).
[24]M. R. Hodgson, "Experimental investigation of the acoustical characteristics of university classrooms," J. Acoust. Soc. Am. **106**, 1810–1819 (1999).
[25]M. R. Hodgson and J. S. Bradley, "Sound in rooms," in *Noise and Vibration Control Engineering*, 2nd ed., edited by I. Ver (John Wiley & Sons, 2005), Chap. 7.
[26]M. R. Hodgson and E.-M. Nosal, "Effect of noise and occupancy on optimum reverberation times for speech intelligibility in classrooms," J. Acoust. Soc. Am. **111**, 931–939 (2002).

Ternary and quadriphase sequence diffusers

Trevor J. Cox[a] and James A. S. Angus[b]
Acoustics Research Centre, University of Salford, Salford M5 4WT, United Kingdom

Peter D'Antonio[c]
RPG Diffusor System Inc., 651-c Commerce Drive, Upper Marlboro, Maryland 20774

(Received 16 June 2005; revised 25 October 2005; accepted 26 October 2005)

A room acoustic diffuser breaks up reflected wavefronts, and this can be achieved by presenting a spatially varying surface impedance. In hybrid surfaces, varying impedance is achieved by patches of absorption and reflection, giving reflection coefficients nominally of 0 and 1. These surfaces are hybrids, absorbing some of the incident sound while diffusing any reflected energy. A problem with planar hybrid surfaces is that specular energy is only removed by absorption. By exploiting interference, by reflecting waves out-of-phase with the specular energy, it is possible to diminish the specular energy further. This can be achieved by using a diffuser based on a ternary sequence that nominally has reflection coefficients of 0, −1, and +1. Ternary sequences are therefore a way of forming hybrid absorber-diffusers that achieve better scattering performance without additional absorption. This paper discusses methods for making ternary sequence diffusers, including giving sequence generation methods. It presents prediction results based on Fourier and boundary element method models to examine the performance. While ternary diffusers have better performance than unipolar binary diffusers at most frequencies, there are frequencies at which the performances are the same. This can be overcome by forming diffusers from four-level, quadriphase sequences.
 [DOI: 10.1121/1.2139632]

PACS number(s): 43.55.−n, 43.20.El [NX] Pages: 310–319

I. INTRODUCTION

Diffusers can be used to improve the acoustics of enclosed spaces to make music more beautiful and speech more intelligible.[1] Early research in diffusers began by considering nonabsorbing surfaces, such as Schroeder diffusers.[2] Recent developments have concerned the development of "diffsorbers" of hybrid absorber-diffusers; these are surfaces where partial absorption is inherent in the design, and any reflected sound is dispersed. In hybrid surfaces, wavefront dispersal is achieved via a spatial distribution of impedances, which is achieved by patches of absorbing and reflecting material. These surfaces are hybrids somewhere between pure absorbers and nonabsorbing diffusers, usually providing sound diffusion at high frequencies, and crossing over to absorption below some cutoff frequency.

The use of absorptive patches to generate dispersion is not particularly new. In studio spaces, people have been arranging absorption in patches rather than solid blocks for many years. In recent times, however, a new breed of surface has been produced, where the absorbent patches are much smaller, and the arrangement of these patches is determined by a pseudorandom sequence to maximize the dispersion generated. For instance, the binary amplitude diffsorber (BAD) panel[3–5] is a flat hybrid surface with the location of the absorbent patches determined by a maximum length sequence (MLS). Figure 1 shows a typical construction for a device designed to scatter in a single plane.

A problem with planar hybrid absorber-diffusers is that energy can only be removed from the specular reflection by absorption. While there is diffraction caused by the impedance discontinuities between the hard and soft patches, this is not a dominant mechanism except at low frequencies. At high frequencies, when the patch becomes smaller than half the wavelength, the specular reflection is only attenuated by about 6 dB for a surface with 50% absorptive area. To improve performance, it is necessary to exploit interference and reflect waves out-of-phase with the specular energy. This can be achieved by using a diffuser based on a ternary sequence.

In the next section, a brief outline of a simple theory for sound scattering is given; this is needed to understand the diffuser design. Section III then outlines the principles behind the construction of a ternary sequence diffuser. Section IV then details various construction methods that can be used to make the diffusers and also includes some results for the scattering performance based on a simple prediction model. Repeating diffuser units concentrates energy in diffraction lobes, which can degrade scattering performance, consequently Sec. V examines how repetition can be avoided in ternary diffusers using modulation techniques. Up to this point, rather narrow and short sequences have been used to outline the general principles. In Sec. VI, longer sequences that are more useful for application are considered and more accurate prediction models are used. For many frequencies, ternary sequence diffusers have improved performance over diffusers based on unipolar binary sequences. However, at even multiples of the design frequency, the performances of the two diffuser types are the same. Consequently, Sec. VII examines how this is solved using quadriphase (four-level) sequences. Up until this point, the paper will only have dealt

[a]Electronic mail: t.j.cox@salford.ac.uk
[b]Electronic mail: j.a.s.angus@salford.ac.uk
[c]Electronic mail: pdantonio@rpginc.com

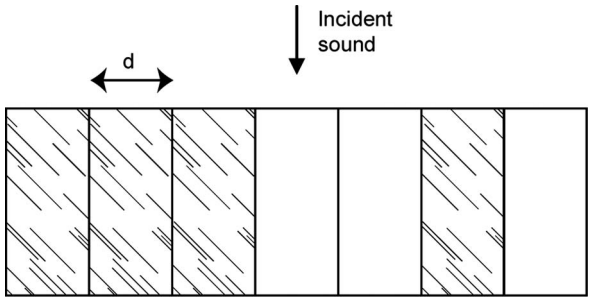

FIG. 1. A binary amplitude diffuser where the white patches are made of hard material and are reflecting, and the shaded patches are made of absorbent material and so are absorbing. Based on an $N=7$ MLS {1 1 1 0 0 1 0}.

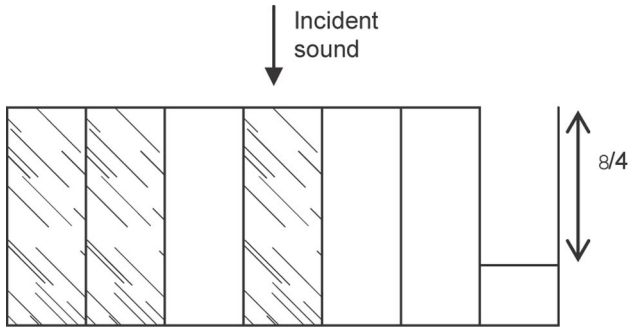

FIG. 2. A ternary diffuser based on the sequence {1 1 0 1 0 0 −1}. The last well is a quarter of a wavelength deep at the design frequency to provide a reflection coefficient of −1.

with diffusers that scatter in a single plane, and so in Sec. VIII appropriate methods for constructing ternary sequence diffusers that scatter hemispherically are given.

II. THEORY

Consider a flat diffuser surface with a distribution of reflection coefficients R_n. The diffuser is illuminated with a plane wave normal to the surface. When the observer is in the far field, this results in a far-field pressure, $p(\theta)$ of

$$p(\theta) = \sum_{n=0}^{N-1} R_n e^{-jn\Omega}, \tag{1}$$

where $\Omega = kd\sin(\theta)$, d is the spacing of the patches (see Fig. 1), k is the wave number, and θ is the angle of reflection with respect to the normal to the surface of the diffuser. This equation is a discrete Fourier transform, which means that the far-field polar pattern is related to the reflection coefficients by a Fourier transform relationship. What is needed is to find structures with reflection coefficients that have uniform magnitude Fourier transforms, such as Schroeder diffusers.[2] The Wiener-Khinchin theorem states that the squared Fourier transform magnitude of a sequence is equal to the Fourier transform of its autocovariance (or autocorrelation function). Thus a sequence of reflection coefficients whose autocovariance is a Kronecker delta function will form a good diffuser, because the autospectrum will be uniform.

III. A SIMPLE TERNARY DIFFUSER

Figure 1 shows a typical hybrid absorber-diffuser. The hard and soft patches produce reflection coefficients that are nominally either 1 (hard) or 0 (absorbing). By changing the relative proportion of hard and soft patches on the surface, it is possible to control the absorption coefficient. By changing the ordering of the patches, it is possible to control how the reflected sound is distributed. If a periodic arrangement of patches is used, then the autocovariance will contain a series of peaks, and so the autospectrum will be uneven. From Eq. (1), this means that at each frequency the reflected sound will be concentrated in particular directions due to spatial aliasing; these are grating lobes. If a good pseudorandom sequence is used to choose the patch order, one with a delta-function like autocovariance—say a Barker sequence[6]—then the scattering will be more even.

However, whatever the arrangement of the patches, at high frequency, the best that can be achieved is an attenuation of 7 dB of the specular reflection lobe, because 3/7 of the surface forms a flat plane surface that reflects mostly unaltered by the presence of the absorbing material. For the specular reflection direction, $\theta=0$, the scattered pressure is simply a sum of the reflection coefficients R_n. So unless some of these coefficients are negative, the suppression of the specular lobe is limited. Figure 1 is an example of a "unipolar" binary diffuser because the sequence of reflection coefficients is only in one direction with respect to zero; i.e., it is composed of 0's and 1's. (Schroeder's original maximum length sequence diffuser[2] was bipolar, because the binary sequence was composed of −1's and +1's).

Ternary diffusers offer a chance to introduce some negative reflection coefficients. An example of a ternary diffuser is shown in Fig. 2. The final well has a depth of a quarter of a wavelength at the design frequency, f_0, and so at odd multiples of this frequency the well has a reflection coefficient, $R=-1$. Therefore, the surface reflection coefficient distribution is a sequence of −1's, 0's, and +1's. The well produces waves out-of-phase with the sections of the diffuser producing the specular energy (the patches with $R=+1$), thus enabling better reduction of the specular energy. In this case, the suppression of the specular lobe will be up to $\approx 20\log_{10}(7/2) \approx 11$ dB.

IV. SEQUENCES

To compare the performance of unipolar binary and ternary sequences, it is necessary to construct some diffusers, and for this sequences with the best patch order are needed. For diffusers with a small number of patches, it is possible to find the sequences with the best autocovariance by an exhaustive search of all possible combinations using a computer. The computer judges the quality of each sequence's autocovariance using a merit factor.[6] For the unipolar case, there can be no cancellation within the autocovariance calculation because $R=0$ or 1; in this case, the merit factor used for optical sequences is appropriate; this is the maximum value of the out-of-phase autocovariance function. For the ternary sequence, there can be cancellation when calculating the out-of-phase autocovariance values, and so the merit factor is the total out-of-phase energy.

There are many combinations of patches that are not useful because they would form diffusers that are too absorbing or too reflecting, and so these sequences are excluded from the search. (It is assumed that the $R=-1$ wells are nonabsorbing, however, as shall be seen later, they can generate absorption by putting significant energy into the reactive field in conjunction with the $R=1$ patches.) In the results presented below, there were four reflecting and three absorbing elements. The sequences shown in Figs. 1 and 2 are the result of this search; however, there are many more length 7 sequences of equally good merit.

With a larger number of patches, it is not possible to construct the ternary diffuser by searching all combinations. Consequently, methods from number theory must be drawn upon. However, many of the ternary sequences that have been generated for other applications are inappropriate because they do not have the right balance of −1, 0, and +1 elements. Many sequences have very few zero elements in them and consequently the diffusers made from these sequences would not be very absorbing. This arises because most applications of number theory try to maximize the efficiency of the sequence—efficiency in this context meaning the power carried by a signal based on the sequence. In the case of hybrid diffusers, more zero terms are required in a sequence; fortunately, there is a method that can achieve this.

A. Correlation identity derived ternary sequences

Correlation identity derived ternary sequences[7] have a nominal absorption coefficient of ≈ 0.5 provided that the design parameters are chosen correctly. They are formed from two MLSs of length $N=2^m-1$, with the constraint that the order of the sequences $m \neq 0 \bmod 4$.

First it is necessary to find a pair of MLSs with suitable cross-covariance properties. The process is to form an MLS, and then sample this sequence at a different rate to form a complementary sequence. For example, if the sample rate Δn is 2, then every second value from the original signal is taken. The sample rate is chosen using either $\Delta n=2^k+1$ or $\Delta n=2^{2k}-2^k-1$. A parameter e is defined as $e=\gcd(m,k)$ where gcd( ) is the greatest common divisor. This must be chosen so that m/e is odd as this gives the correct distribution of cross-covariance values.

Under these conditions, the two MLSs have a cross-covariance $S_{ab}(\tau)$, which has three values,

$$S_{ab}(\tau)=\begin{cases} -1+2^{(m+e)/2} & \text{occurs} \quad 2^{m-e-1}+2^{(m-e-2)/2} \quad \text{times} \\ -1 & \text{occurs} \quad 2^m-2^{(m-e)}-1 \quad \text{times} \\ -1-2^{(m+e)/2} & \text{occurs} \quad 2^{m-e-1}-2^{(m-e-2)/2} \quad \text{times}. \end{cases} \tag{2}$$

The total number of 1's and −1's in the sequence will be given by $\approx N(1-2^{-e})$. This is therefore the amount of reflecting surface on the diffuser, and so at high frequency, when the wavelength $\lambda < d$, it would be anticipated that the absorption coefficient of the diffuser, α, would be $\approx 1-2^{-e}$. If the aim is to achieve a diffuser with $\alpha \approx 0.5$, this means choosing $e=1$, which means the order of the MLS, m, must be odd.

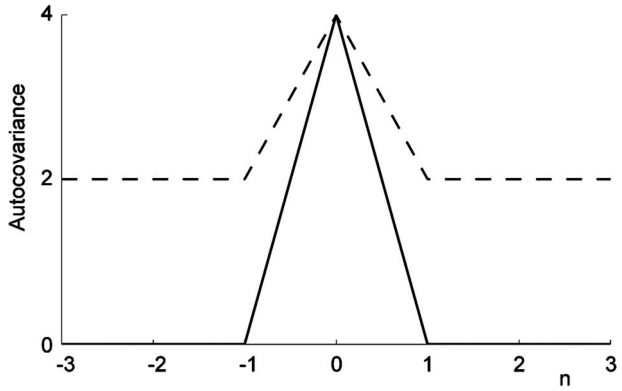

FIG. 3. Autocovariance for two sequences:– – –, unipolar binary and —, ternary.

Consider an example of $N=31=2^5-1$. e is required to be a divisor of m so that m/e is odd and this can be achieved with $k=1$ as this makes $e=\gcd(k,m)=1$. A possible sample rate is $\Delta n=3$.

The first part of the first MLS used was {1 0 0 0 0 1 0 0 1 0 1 1 0 0 1 1 1 1 1 ⋯}. Taking every third value then gives the second MLS: {1 0 0 0 0 1 1 0 0 1 0 0 1 1 1 1 1 0 1 ⋯}. This then gives a cross-covariance where $S_{ab}=7$, −1, or −9 (7 occurs 10 times, −1 occurs 15 times, and −9 occurs 6 times).

The ternary sequence c_n is formed from this cross-covariance, a rather surprising and remarkable construction method—the sequence is $2^{-(m+e)/2}(S_{ab}(\tau)+1)$. This sequence has an ideal autocovariance with a peak value of 2^{m-e} and out-of-phase values that are zero. Applying this to the above pair of MLSs yields the ternary sequence {0 0 1 1 −1 1 −1 0 0 0 1 1 0 1 −1 −1 0 1 0 ⋯}.

The autocovariance indicates the advantages that might be expected from ternary sequence diffusers in comparison to unipolar binary sequence diffusers. The autocovariance functions for the ternary and unipolar binary sequences are shown in Fig. 3. The binary sequence has constant out-of-phase values, but they are not zero. This leads to diffusers with a significant specular component in their polar pattern. Perfection can be achieved using a ternary sequence as the out-of-phase values are all zero.

In terms of scattering, the ternary sequence has the better reflection coefficient autospectrum because it is constant; this is shown in Fig. 4. It would be anticipated that the scattering from the ternary sequence would be more even with reflection angle if one repeat of the device was tested. For a periodic structure, that is, one in which many repeats of the diffuser are placed side by side but not an infinite number, this will result in all the grating lobes having the same energy for the ternary sequence. For the binary sequence, on the other hand, the specular lobe will have a higher level when compared to the other lobes.[1] (Note: The autospectra for MLS usually seen in the literature have a reduced $N_f=0$ value, however this is for bipolar sequences.)

Figure 5 shows the scattering from the ternary and unipolar binary diffusers alongside the scattering from a plane surface. A simple Fourier prediction model is used.[1] $d=10$ cm. Figure 5(a) is at the design frequency. As expected,

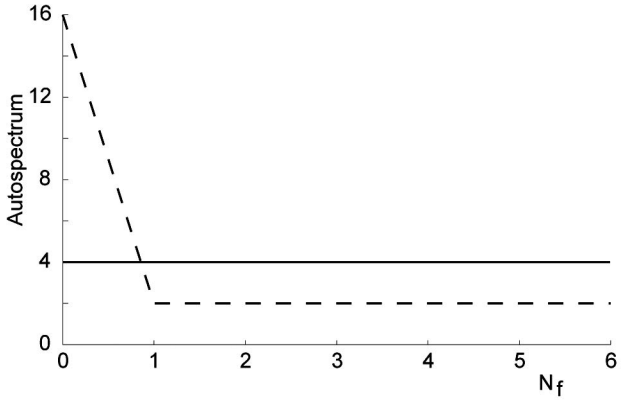

FIG. 4. Autospectrum for two sequences:– – –, unipolar binary and —, ternary.

the ternary diffuser has three lobes all of the same energy, whereas the specular lobe is not so well suppressed for the unipolar binary diffuser. Figure 5(b) shows the case one octave higher. At this frequency, the last well in the ternary sequence no longer has a reflection coefficient of −1. Now the well is half a wavelength deep, and the reflection coefficient is +1. In fact, the sequence of reflection coefficients is now the same as for the unipolar binary sequence, and hence the two diffusers have the same polar responses. Hence, the ternary diffuser provides better scattering than the unipolar binary diffuser at odd multiples of the design frequency and the same scattering at even multiples of the design frequency. This trend continues at higher frequencies as illustrated by the plot of diffusion coefficient versus frequency in Fig. 6.

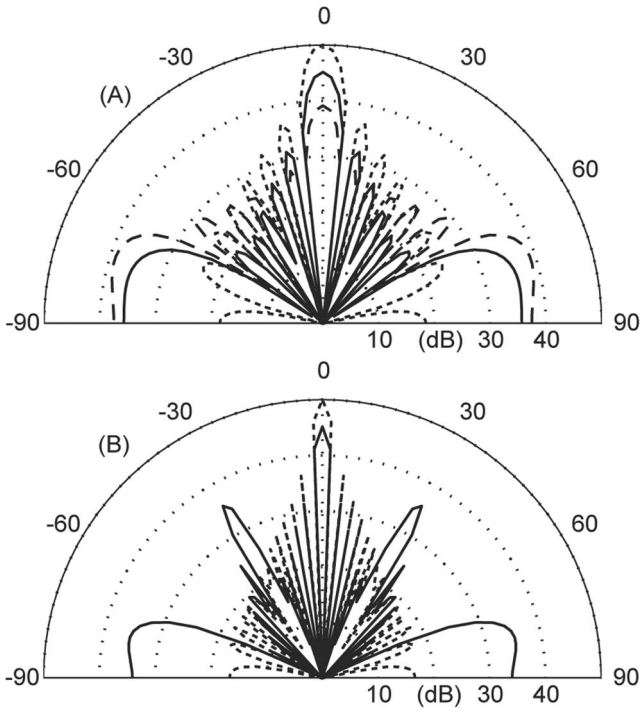

FIG. 5. The predicted scattered polar response from three surfaces: —, unipolar binary diffuser; – – –, ternary diffuser; and ……, plane surface. (a) At the design frequency and (b) twice the design frequency. In (b), the two diffuser responses are identical and overlay each other.

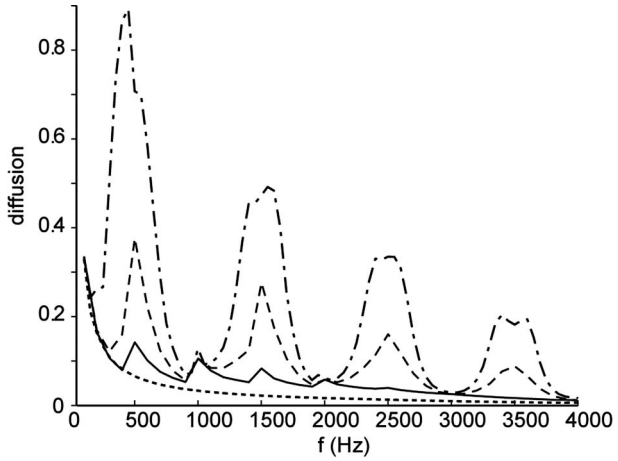

FIG. 6. Predicted diffusion coefficient as a function of frequency for four surfaces: —, periodic unipolar binary diffuser; – – –, periodic ternary diffuser; –·–·, modulated ternary diffuser; and ……, plane surface.

The diffusion coefficient is evaluated using AES-4id-2001,[8] and a higher value indicates better dispersion.

So far the performance has only been discussed at harmonics of the design frequency. Between these frequencies, the phase of the reflection coefficient offered by the well of fixed depth is neither 180° nor 0°. The waves reflected from this well will be partly out-of-phase with the waves from the parts of the diffuser with $R=+1$. Consequently, the performance is improved over the unipolar binary diffuser for these in-between frequencies, a finding confirmed by Fig. 6.

V. MODULATION AND PERIODICITY

The overall performance could be improved at many frequencies by removing the repetition of the diffusers as this would remove the defined grating lobes. This could be achieved either by using much longer sequences or by modulating two sequences.[9,10] Using one long sequence is normally avoided because of manufacturing cost, and so the use of modulation is considered here.

For Schroeder diffusers, one method is to modulate a diffuser with its inverse.[1] Two sequences are chosen that produce the same magnitude of scattering, but with opposite phase. So if the first ternary sequence is {1 1 0 1 0 0 −1}, then the complementary sequence used in modulation is the inverse of this {−1 −1 0 −1 0 0 1}. Given these two base diffusers, a pseudorandom sequence is used to determine the order these diffusers are used; this reduces repetition.

Figure 7 shows the scattering at the design frequency for a periodic and modulated arrangement of the ternary sequences illustrating the removal of the three lobes via modulation. Figure 6 shows the diffusion coefficient versus frequency. This shows that great improvement can be achieved but only over certain bandwidths. At even multiples of the design frequency, the two base shape reflection coefficients are identical, and so at these frequencies the structure is periodic and grating lobes reduce performance. Consequently, while inverting a sequence is good for modulating Schroeder diffusers, they are not optimal here.

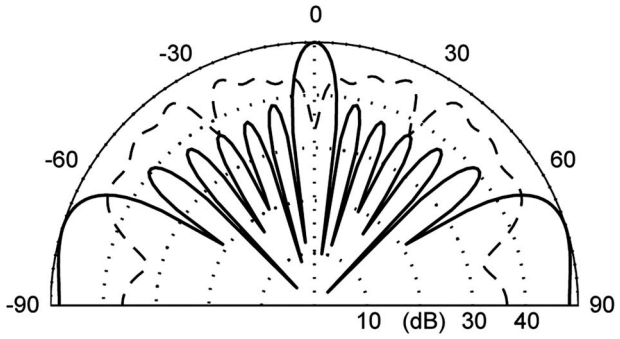

FIG. 7. The predicted scattered polar response from two ternary diffuser arrangements at their design frequency: —, periodic and – – –, modulated.

Single base shape asymmetric modulation[11] is where a single sequence is used, but the order of the sequence is reversed between different diffusers. For example, if the first ternary sequence is {1 1 0 1 0 0 −1}, then the second sequence used is {−1 0 0 1 0 1 1}. An added advantage of this method is that only one base shape needs to be made. At even multiples of the design frequency, the reflection coefficients all revert to 0 and 1, but the structure will not be completely periodic. However, it is found that periodicity is only partly removed, and that the grating lobes are still present because the two sets of reflection coefficient are very similar. Consequently, when choosing a sequence for asymmetrical modulation, it is necessary to find ones that are as asymmetric as possible at even multiples of the design frequency.

VI. BOUNDARY ELEMENT MODELING

Having established the general principles, more exacting predictions will be presented using boundary element methods (BEMs). BEMs have been shown to give accurate results for hybrid surfaces before when compared with measurements[12] and also to give accurate results for Schroeder diffusers.[13] Consequently, it would be anticipated that the BEM will be accurate for ternary diffusers. The model used here is a 2D BEM based on the standard Helmholtz-Kirchhoff integral equation. The open well in the ternary diffuser is modeled assuming plane-wave propagation in the well, and using an element at the well entrance with the appropriate surface impedance. Previous experience[13] indicates this is a reasonable model, but becomes less accurate for oblique incidence and reflection. For the absorptive patches, the impedance was modeled using an empirical formulation[14] for mineral wool with a flow resistivity of 50000 N m^{-4} and a porosity of 0.98. The scattering was predicted in the far field at discrete frequencies. The results were converted into 1/3 octave bands by integrating the scattered energy from nine discrete frequencies within each 1/3 octave band using Simpson's rule. The source was normal to the surface.

Two diffusers were used. The first was an $N=31$ unipolar binary diffuser based on a MLS. A little over ten periods of the device were used, the patch width was 2 cm, and the total width was 6.3 m. The second diffuser was an $N=31$ ternary diffuser, with the same overall dimensions and patch size. The wells were set to be 8.5 cm deep and so the design frequency was 1 kHz.

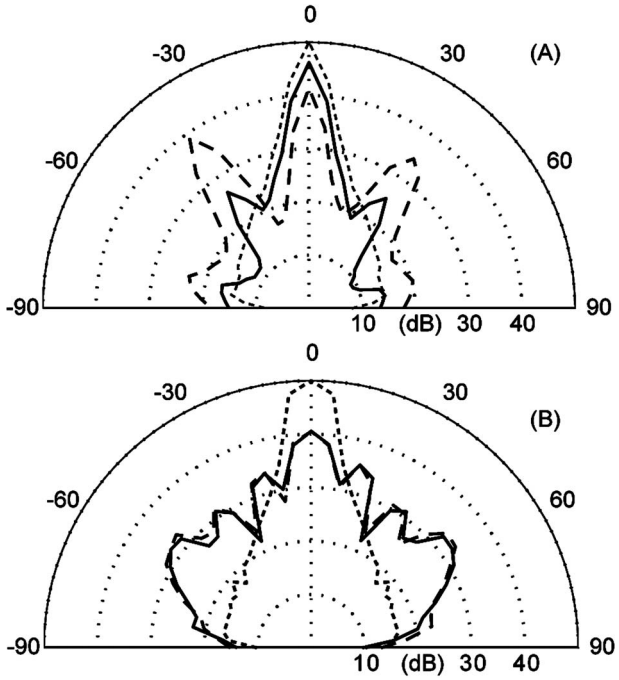

FIG. 8. Scattering from three diffusers predicted using a BEM model. —, binary diffuser; – – –, ternary diffuser; and ……, plane surface, for the 1/3 octave whose center frequency is (a) the design frequency and (b) twice the design frequency.

A. Results

Figure 8(a) shows the scattering for the 1/3 octave band centered on the design frequency, Fig. 8(b) shows the scattering at an octave higher. The results confirm the simple analysis provided earlier. At even multiples of the design frequency, the scattering from the unipolar binary and ternary diffusers is similar. At odd multiples of the design frequency, the ternary diffuser offers more even scattering and a reduced specular lobe. It is also found that at frequencies that are not multiples of the design frequency, the ternary diffuser is better than the unipolar binary diffuser.

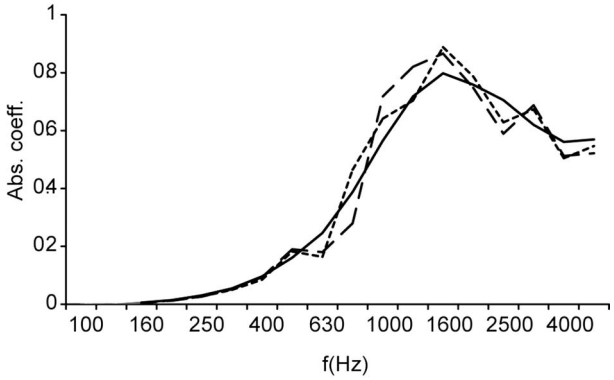

FIG. 9. Predicted absorption coefficient for three surfaces: —, binary diffuser; – – –, ternary diffuser; and ……, quadriphase diffuser estimating using a BEM model.

Using the BEM results, it is possible to estimate the normal incidence absorption coefficients. The results in Fig. 9 are typical for hybrid absorber-diffusers. The low-frequency response is dominated by the onset of the absorption provided by the mineral wool. At high frequency the absorption coefficient is determined by the open area and is about 0.5. As the system is essentially a perforated resonant absorber, there is a peak of absorption at midfrequency. The absorption coefficient response is less smooth for the ternary diffuser. It is assumed that this is due to reflections from wells providing out-of-phase reflections when compared to other parts of the diffuser, and therefore the waves can combine to put energy into the reactive field. Overall, however, the absorption is similar for all diffuser types.

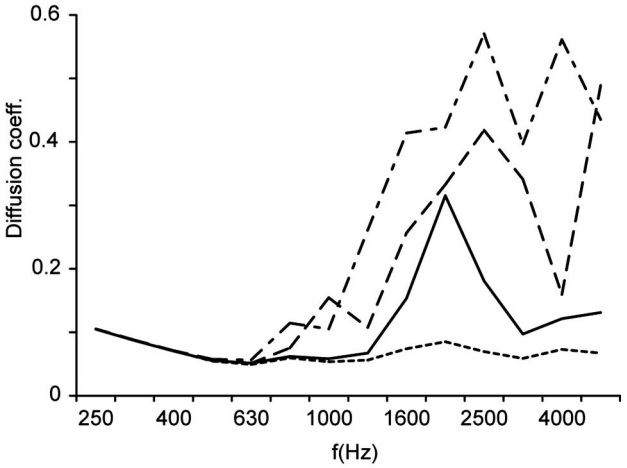

FIG. 10. Predicted diffusion coefficient for three diffusers and a plane surface: —, binary diffuser; – – –, ternary diffuser; –·–·, quadriphase diffuser; and ……, plane surface.

VII. QUADFFUSERS

A. Design

It is impossible to greatly improve the performance of the ternary diffusers at even multiples of the design frequency when the diffuser only has reflection coefficients of 0 and 1. To overcome this, more well depths need to be used. For only a few absorbent wells and many different depth wells, it would be possible to use index sequences.[15] However, this would complicate the construction of the surface, and the absorption coefficient would be relatively small. Another solution would be to use active elements. It has been shown[16] that with active impedance technologies it is possible to create $R=-1$ across a 3–4 octave bandwidth. However, this can only be achieved at low- to midfrequencies due to limitations of the active technologies, and, furthermore, active diffusers are very expensive. Another solution would be to bend and shape the diffuser so the front face was no longer flat, and therefore use corrugation to break up the specular reflection; this works well for binary amplitude diffusers.[17]

Another simple approach is to use one more well depth. Consequently, diffusers with four different reflection coefficients will be considered. At the design frequency, these coefficients should be $R=-1$, 0, +1, and ξ. It is assumed that the last coefficient, ξ, is generated by a rigid walled well of a certain depth, and consequently $|\xi|=1$, and the well purely causes a change in the phase of the reflection. In choosing an appropriate value for ξ, it is necessary to consider not just the design frequency f_0, but also the effects at multiples of the design frequency, because the idea behind introducing this additional wave depth is to improve performance at even multiples of the design frequency. For instance, if $\angle\xi=\pi/2$ at f_0, then at $2f_0$, the reflection coefficient would be -1. However, at $4f_0$, the reflection coefficient would be +1 and so a poor performance at this frequency would be expected. Using a depth related by relatively prime fractions, e.g., 1/2, 1/3, 1/5, 1/7, etc. to the $\lambda/4$ well depth, or maybe prime rationals, e.g., 1/2, 3/5, 7/11, etc., ensures that there are no frequencies in the audible frequency range for which all the nonabsorbing parts of the diffuser reflect in phase. Consequently, at the design frequency the $R=-1$ wells are set to a depth of $\lambda/4$, and the $R=\xi$ wells are set to $\lambda/6$. This puts the frequency at which these two well types radiate in phase at $24f_0$.

Choosing an appropriate number sequence for this design is no longer simple. While there are quadriphase sequences in number theory, these do not normally have zero terms in them. For a 31-element diffuser, there are too many combinations to exhaustively search all combinations. Consequently, the approach used is to adapt the current ternary sequence. It is assumed that the same open area is required, and consequently the zeros in the sequence will be maintained in their current locations. Then all that remains is to determine which -1's and 1's in the sequence need to be changed to $\lambda/6$ wells. In the original ternary sequence, there are 16 -1's and 1's, and consequently it is possible to search all possible combinations to find the best arrangement. The search is for the best average merit factor for the first five harmonics of the design frequency, as these are in the frequency range (1–5 kHz) of interest here.

B. Results

Figure 10 shows the diffusion coefficient versus frequency response predicted using the BEM. The use of multiple well depths in the quadriphase diffuser produces better scattering than the other diffusers except at 1 kHz, where the ternary diffuser performs better. However, this diffusion response needs to be reviewed alongside the absorption coefficients shown in Fig. 9. Only above $\approx$2 kHz is the diffusion performance of these devices important, because in the frequency range 1–2 kHz the devices are essentially just absorbers, and below 1 kHz the surface has a decreasing effect on the sound wave because of insufficient absorption. At frequencies, such as 4 kHz, where the unipolar and ternary diffusers produce identical scattering, the quadriphase diffuser is performing better. The scattering at 4 kHz is shown in Fig. 11; the design is working as expected. The absorption coefficient (Fig. 9) is similar to that for ternary diffusers.

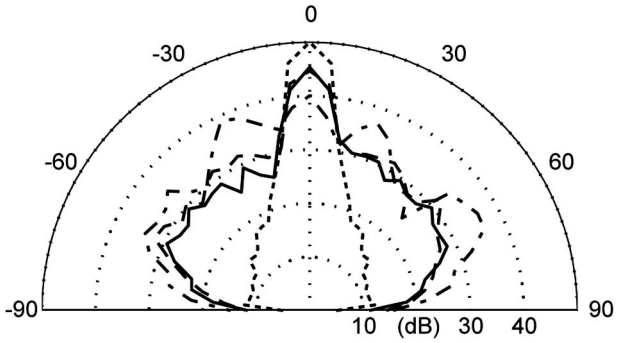

FIG. 11. Predicted scattering for three diffusers and a plane surface at four times the design frequency: —, unipolar binary diffuser; – – – , ternary diffuser; –·–·–, quadriphase diffuser; and ……, plane surface.

VIII. HIGHER DIMENSION ARRAYS

So far this paper has been concerned with diffusers that scatter in one plane. However, there are many applications where diffusers with hemispherical reflection patterns are required. To form hemispherical diffusers, two-dimensional ternary sequences (in number theory these would be called sequence arrays) are needed. There are a variety of methods for making multidimensional binary[18] and ternary arrays.[19]

Consider constructing a ternary diffuser of dimensions (in terms of number of patches) of $N \times M$. There should be $\approx NM/2$ zeros in the sequence for a nominal 50% absorption. Whether a sequence can be constructed depends on the values of N and M. There are three standard construction methods: folding, modulation (Kronecker product in number theory), and periodic multiplication. Even so, there will be many array sizes that cannot be made with ideal two-dimensional autocovariance properties.

A. Folding

Schroeder[20] showed that a folding technique called the Chinese Remainder Theorem could be applied to phase grating diffusers based on polyphase sequences. D'Antonio[4] used the same technique for a binary hybrid diffuser. References 1 and 5 give comprehensive descriptions of the process. The folding process wraps a 1D sequence into a 2D array while preserving the autocovariance properties. This can also be applied to ternary sequences. To use this method, N and M must be co-prime. The requirement for 50% absorptive patches means a correlation identity derived ternary sequence must be used with length $NM=2^m-1$, with m being odd.

The folding technique can be viewed as an indexing process. The 1D sequence, a_k, will be indexed using $k=1,2,3,4,\ldots,NM$. The elements of the 2D array, $b_{p,q}$, are given by $b_{p,q}=a_k$ with $p=k \bmod N$ and $q=k \bmod M$, where (p,q) are the coordinates of the elements in the folded array.

Consider a real ternary sequence with $N=9$ and $M=7$: $a_k=\{0,0,0,0,1,0,0,0,0,0,1,0,-1,0,0,0,0,0,-1,0,0,0,0,1,0,0,0,0,0,0,0,0,1,0,0,0,0,0,0,0,1,0,0,0,0,0,0,0,1,1,1,0,1,-1,0,0,1,0,-1,0,0,0,0,0,1,-1,0,0,-1,0,0,-1,0,0\}$.

The folded 2D array is then

$$\begin{Bmatrix} 0 & 0 & 0 & 1 & -1 & 0 & 0 \\ 0 & 0 & 0 & 1 & -1 & 0 & 0 \\ 0 & 0 & 0 & 0 & 0 & 0 & 0 \\ 0 & 1 & 0 & 0 & 0 & -1 & 0 \\ 1 & 0 & -1 & 0 & 0 & 0 & 0 \\ 0 & 0 & 1 & 0 & 1 & 1 & 1 \\ 1 & 0 & -1 & 0 & 0 & 0 & 0 \\ 0 & 1 & 0 & 0 & 0 & -1 & 0 \\ 0 & 0 & 0 & 0 & 0 & 0 & 0 \end{Bmatrix}.$$

The autocovariance of this array is ideal; it is a Kronecker delta-function.

The number of sequences that can be constructed using this method with 50% absorbent patches is rather limited (only 7×73, 23×89, $7\times31\times151$, 217×151, 31×1057, or 7×4681 for $NM\leqslant2^{16}$), and consequently other construction methods are needed. However, the folding process will be useful again later because it will allow the resizing of other arrays.

B. Modulation

Modulation was a process that was used to allowed diffusers to be arranged in a nonperiodic fashion by modulating one or more base shapes with a binary sequence. Another way of viewing the outcome of this process is that it forms a single longer length sequence. A very similar process can be used to form arrays using ternary and binary sequences and arrays.

1. Ternary and binary modulation

By modulating a ternary sequence with a perfect aperiodic binary array, a ternary array with ideal autocovariance properties can be obtained. (Note, it is important to modulate the array by the sequence and not vice versa.) Consider a length 7 correlation identity derived ternary sequence $a=\{1,1,0,1,0,0,-1\}$. This is used to modulate the perfect aperiodic binary array, $b:b=\left\{\begin{smallmatrix}-1 & -1\\ -1 & 1\end{smallmatrix}\right\}$ to form a 2×14 length array, c, given by

$$c = \begin{Bmatrix} -1 & -1 & -1 & -1 & 0 & 0 & -1 & -1 & 0 & 0 & 0 & 0 & 1 & 1 \\ -1 & 1 & -1 & 1 & 0 & 0 & -1 & 1 & 0 & 0 & 0 & 0 & 1 & -1 \end{Bmatrix}.$$

This array has ideal periodic autocovariance properties. As the binary array has no zeros, the modulated array has the same proportion of absorbent patches as the original ternary sequence, 40% in this case. For long sequences, the proportion tends toward 50%.

An issue that is not often discussed in the number theory literature is the imbalance between the distribution of −1 and 1's in a sequence. This is important to the diffusers because the proportion of −1 and 1's changes the amount of attenuation of the specular reflection. In this case, the modulation has produced an array with a more even balance of −1 and 1's than the original ternary sequence, and consequently it would be expected to perform better at attenuating the specular reflection.

There is only one known perfect aperiodic binary sequence, the one shown above. Consequently, 2×14, 2×62, 2×254, 14×146, 46×178, and 2×16382 are the array sizes that can be constructed by this method with $\approx50\%$ efficiency for $NM\leqslant2^{16}$; again the allowable array sizes are rather few. Furthermore, as the resulting array sizes have N and M, which are not co-prime, it is not possible to refold these arrays to get other sizes.

2. Ternary and ternary modulation

The efficiency (proportion of zeros) of the derived array by modulation is a product of the efficiency of the original array and sequence. Consequently, it is possible to modulate a ternary array by a ternary sequence, provided the product of their efficiencies is about 50%. Two aperiodic perfect ternary arrays with 67% zeros are

$$d_1=\begin{Bmatrix}1&0&1\\1&0&-1\end{Bmatrix},\quad d_2=\begin{Bmatrix}1&1\\0&0\\1&-1\end{Bmatrix}. \tag{3}$$

Consequently, if either of these is combined with a perfect periodic ternary sequence with 75% zeros, the overall design goal of an array with 50% zeros is achieved.

In this case, the correlation identity derived ternary sequences are not useful because they have too low an efficiency. On the other hand, some Ipatov ternary sequences and those based on the Singer difference sets are appropriate.[21,22] If the efficiency goal is set to be between 45% and 55%, then there are four Ipatov ternary sequences that can be used of length 13, 121, 31, and 781. While these achieve an efficiency of about 50%, respectively, there is an imbalance between the number of +1 and −1 in the sequence, leading to somewhat less than optimal specular reflection absorption, so these are not considered further.

By combining two binary sequences based on Singer difference sets, it is possible to form a ternary sequence with the desired efficiency and a better balance of −1's and 1's. Difference sets are used to form sequences with the best possible autocovariance. The Singer difference set is a particular class of difference sets, and has the following parameters:

$$(N,k,\gamma)=\left(\frac{q^{2r+1}-1}{q-1},\frac{q^{2r}-1}{q-1},\frac{q^{2r-1}-1}{q-1}\right), \tag{4}$$

where N is the length of the sequence, k the number of 1's in the two binary sequences formed, and γ the maximum out-of-phase autocovariance of the two binary sequences. q and r are constants and are specified below. The efficiency of the ternary sequence formed by combining the binary sequences is approximately given by $(q-1)/q$. Since the requirement is to find a sequence with 75% efficiency, $q=4$ is used. This meets a necessary requirement that $q=2^s$, where s is an integer.

The possible sequences are $N=21,341,5461,\ldots$, which are the cases for $r=1$, 2, and 3. Consider the case of $N=21$, for example. The two Singer difference sets for this case are $D1=\{3,6,7,12,14\}$ and $D2=\{7,9,14,15,18\}$, where the numbers in the brackets indicate the locations of the 1's in the sequence. The unipolar binary sequence for $D1$ is $a=\{0,0,1,0,0,1,1,0,0,0,0,1,0,1,0,0,0,0,0,0,0\}$ and for $D2$ is $b=\{0,0,0,0,0,0,1,0,1,0,0,0,0,1,1,0,0,1,0,0,0\}$.

To form the ternary sequence, the cross-correlation between these two sequences is found: $s_{ab}=\{2,0,0,1,0,2,1,1,0,2,2,0,1,2,1,2,0,2,2,2,2\}$. The final sequence, c, is then given by

$$c=q^{1-r}\left(s_{ab}-\frac{q^{2r-1}-1}{q-1}\right), \tag{5}$$

which in this case yields $c=\{1,-1,-1,0,-1,1,0,0,-1,1,1,-1,0,1,0,1,-1,1,1,1,1\}$. This sequence has ideal autocovariance properties.

Having obtained the necessary ternary sequence, it is now possible to form the array. The sequence c is modulated with the first perfect aperiodic ternary array d_1 shown in Eq. (3) to form an array that has size 63×2 and has ideal autocovariance properties with a maximum value of 64. Hence, the absorption coefficient at high frequency in this case is nominally 0.51. The array has 28 values at −1 and 36 values at +1, and so there is good attenuation of the specular reflection at odd multiples of the design frequency.

Array sizes that are square will be more useful, because if the 63×2 diffuser is used periodically, the small repeat distance in one direction will reduce performance. By applying the Chinese Remainder Theorem in reverse, it is possible to unfold this array into a 126×1 sequence, and then refold it into two other array sizes 18×7 and 14×9, which are squarer.

3. Periodic multiplication

The final design process is to use periodic multiplication. Two arrays can be multiplied together to form a larger array. Consider array 1 to be $b_{p,q}$ of size $N_b\times M_b$, which has an efficiency of E_b, and array 2 to be $c_{p,q}$ of size $N_c\times M_c$, which has an efficiency of E_c. Then the new array is a product of the periodically arranged arrays, $b_{p,q}\cdot c_{p,q}$ of size $N_bN_c\times M_bM_c$, and the efficiency will be E_bE_c. A necessary condition is that N_b and N_c are co-prime, and so are M_b and M_c, otherwise the repeat distance for the final arrays will be the least common multiples of N_b and N_c in one direction and M_b and M_c in the other.

For example, the ternary sequence derived previously from Singer difference sets, c, can be folded into an array that is 7×3,

$$\begin{matrix}\{1,&0,&1\\0,&1,&0\\-1,&1,&-1\\-1,&1,&-1\\1,&0,&1\\-1,&1,&-1\\1,&0,&1\},\end{matrix}$$

which has an efficiency of 76%. This can then be multiplied by the ternary array d_2, which has an efficiency of 67% to form a 21×6 array with ideal autocovariance properties and an efficiency of 51%. There is a slight imbalance between

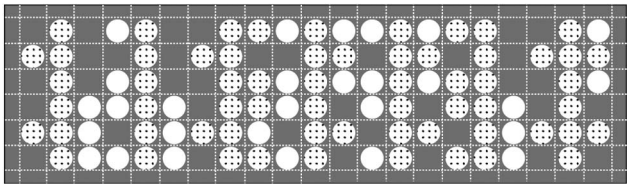

FIG. 12. A visualization of a 21×6 ternary array mask. The white holes open up to nonabsorbing wells ($R=-1$), the shaded holes open up to mineral wool ($R=0$), and the rest of the mask is reflecting ($R=1$).

the number of −1 and 1's with 28 and 36, respectively, of each. Figure 12 shows a visualization of a mask for this sequence.

This multiplication process can involve a binary array multiplied by a ternary array, or two ternary arrays multiplied together. Except for the perfect 2×2 binary array, perfect binary arrays will have an imbalance between the number of +1 and −1 terms, which could lead to an imbalance in the final array design and insufficient attenuation of the specular reflection lobe. In general, perfect binary arrays of size $N\times M$ have NM mod $4=0$ and $NM=(2k)^2$, where k is an integer, and they have an imbalance of $\sqrt{NM}$.

C. Array discussions

Once the array is formed, any periodic section can be chosen and many other manipulations can be done and still preserve the good autocovariance. Procedures that can be done on their own or in combination include the following.

(i) Using a cyclic shift to move the pattern around. $c_{p,q}=b_{p+u,q+v}$, where u and v are integers and the indexes $p+u$ an $q+v$ are taken modulo N and M, respectively.

(ii) Mirror image the array $c_{p,q}=b_{\pm p,\pm q}$.

(iii) Invert the sequence $c_{p,q}=-b_{p,q}$.

(iv) Rotation by 90° $c_{p,q}=b_{q,p}$.

(v) Under sample the array, $c_{p,q}=b_{up,vq}$, provided both u,N and v,M are co-prime.

These will not change the acoustic performance, but may change the visual aesthetic. It can also help to make the array more asymmetric, which can be useful in modulation.

The main problem in forming these arrays is that there is only a limited set of arrays, which provide ideal autocovariance properties, the required efficiency to give the desired absorption coefficient, and a reasonable balance between the number of −1's and 1's in the sequence leading to good suppression of the specular lobe. In work on binary sequences,[23] it has been shown that relaxing the requirement for ideal autocovariance enables more different length sequences to be formed. This should also be possible for the ternary sequence case. For example, where there are a large number of elements in a sequence, it may be possible to truncate the sequence, losing one or two elements, and still gain good (but not ideal) autocovariance properties. This type of truncation might then give the right sequence length for folding into an array with the desired size.

IX. CONCLUSIONS

The performance of a new sort of room acoustic diffuser that is based on ternary sequences has been discussed. The rationale and performance of these have been analyzed using simple prediction models and concepts, as well as more accurate boundary element models. By adding wells to hybrid diffuser surfaces, thus forming ternary diffusers, a useful improvement in performance is achieved for a modest depth penalty. While this produces an improved performance for odd multiples of the design frequency, at even multiples the performance of the ternary structures is the same as for the hybrid diffuser surfaces made from unipolar binary sequences. Using two different well depths reduces this problem and allows more broadband improvements in scattering. A method for obtaining the design sequence for these four-level (quadriphase) diffusers is discussed. Design methods for transforming the sequences into arrays and thus producing hemispherical diffusers have been outlined. While there are a number of methods available for construction, the number of different arrays available with ideal autocovariance properties is rather small. Future work will undertake measurements to confirm the performance of the surfaces, and examining methods of construction so the surfaces can be easily and cheaply made.

[1]T. J. Cox and P. D'Antonio, *Acoustic Absorbers and Diffusers: Theory, Design and Application* (Spon Press, 2004).

[2]M. R. Schroeder, "Diffuse sound reflection by maximum-length sequences," J. Acoust. Soc. Am. **57**, 149–150 (1975).

[3]J. A. S. Angus, "Sound diffusers using reactive absorption grating," Proceedings of the 98th Convention of the Audio Engineering Society, paper no. 3953 (1995).

[4]P. D'Antonio, "Planar binary amplitude diffusor," U.S. Pat. No. 5,817,992 (1998).

[5]J. A. S. Angus and P. D'Antonio, "Two dimensional binary amplitude diffusers," Proceedings of the Audio Engineering Society, paper no. 5061 (D-5) (1999).

[6]P. Fan and M. Darnell, *Sequence Design for Communication Applications* (John Wiley and Sons, Inc., 1996).

[7]P. Fan and M. Darnell, *Sequence Design for Communication Applications* (John Wiley and Sons, Inc., 1996), pp. 180–183.

[8]AES-4id-2001, "AES Information document for room acoustics and sound reinforcement systems—Characterisation and measurement of surface scattering uniformity," J. Audio Eng. Soc. **49**, 149–165 (2001).

[9]J. A. S. Angus, "Using grating modulation to achieve wideband large area diffusers," Appl. Acoust. **60**, 143–165 (2000).

[10]J. A. S. Angus and C. I. McManmon, "Orthogonal sequence modulated phase reflection gratings for wide-band diffusion," J. Audio Eng. Soc. **46**, 1109–1118 (1998).

[11]P. D'Antonio and T. J. Cox, "Aperiodic tiling of diffusers using a single asymmetric base shape," Proceedings of the 18th ICA, paper Mo2.B2.3 (2004).

[12]L. Xiao, T. J. Cox, and M. R. Avis, "Active diffusers: Some prototypes and 2D measurements," J. Sound Vib. **285**, 321–339 (2005).

[13]T. J. Cox and Y. W. Lam, "Prediction and evaluation of the scattering from quadratic residue diffusers," J. Acoust. Soc. Am. **95**, 297–305 (1994).

[14]M. E. Delaney and E. N. Bazley, "Acoustical properties of fibrous absorbent materials," Appl. Acoust. **3**, 105–116 (1970).

[15]M. R. Schroeder, "Phase gratings with suppressed specular reflections," Acustica **81**, 364–369 (1995).

[16]L. Xiao, T. J. Cox, and M. R. Avis, "Maximum length sequence and Bessel diffusers using active technologies," J. Sound Vib. **289**, 807–829 (2006).

[17]T. J. Cox and P. D'Antonio, "Optimized planar and curved diffsorbors," Proceedings of the 107th Convention of the Audio Engineering Society, paper no. 5062, New York (1999).

[18]T. J. Cox and P. D'Antonio, "Optimized planar and curved diffsorbors," Proceedings of the 107th Convention of the Audio Engineering Society, paper no. 5062, New York (1999), pp. 297–310.

[19]M. F. M. Antweiler, L. Bomer, and H. D. Luke, "Perfect ternary arrays," IEEE Trans. Inf. Theory **36**, 696–705 (1990).

[20]M. R. Schroeder, *Number theory in science and communication: With*

applications in cryptography, physics, digital information, computing, and self-similarity (Springer, 1997).
[21]M. R. Schroeder, *Number theory in science and communication: With applications in cryptography, physics, digital information, computing, and self-similarity* (Springer, 1997), pp. 178–183.
[22]V. P. Ipatov, "Ternary sequences with ideal autocorrelation properties," Radio Eng. Electron. Phys. **24**, 75–79 (1979).
[23]H. D. Luke, H. D. Schotten, and H. Hadinejad-Mahram, "Binary and quadriphase sequences with optimal autocorrelation properties: A survey," IEEE Trans. Inf. Theory **49**, 3271–3282 (2003).

Calibration of the pressure sensitivity of microphones by a free-field method at frequencies up to 80 kHz

Allan J. Zuckerwar[a] and G. C. Herring[b]
NASA Langley Research Center, Hampton, Virginia 23681

Brian R. Elbing
University of Michigan, Ann Arbor, Michigan 48109

(Received 14 April 2005; revised 2 November 2005; accepted 3 November 2005)

A free-field (FF) substitution method for calibrating the pressure sensitivity of microphones at frequencies up to 80 kHz is demonstrated with both grazing and normal-incidence geometries. The substitution-based method, as opposed to a simultaneous method, avoids problems associated with the nonuniformity of the sound field and, as applied here, uses a $\frac{1}{4}$-in. air-condenser pressure microphone as a known reference. Best results were obtained with a centrifugal fan, which is used as a random, broadband sound source. A broadband source minimizes reflection-related interferences that can plague FF measurements. Calibrations were performed on $\frac{1}{4}$-in. FF air-condenser, electret, and microelectromechanical systems (MEMS) microphones in an anechoic chamber. The uncertainty of this FF method is estimated by comparing the pressure sensitivity of an air-condenser FF microphone, as derived from the FF measurement, with that of an electrostatic actuator calibration. The root-mean-square difference is found to be ±0.3 dB over the range 1–80 kHz, and the combined standard uncertainty of the FF method, including other significant contributions, is ±0.41 dB. [DOI: 10.1121/1.2141360]

PACS number(s): 43.58.Vb, 43.38.Kb [NHF] Pages: 320–329

I. INTRODUCTION

Society has an interest[1,2] in noise reduction for those airports that are in or near metropolitan areas. The frequency range 1–5 kHz is of key importance when considering the reduction of the public annoyance due to commercial air traffic. Furthermore, a significant fraction of noise-reduction research is done by means of wind tunnel testing, rather than more expensive field testing. The acoustic wavelength will scale as a function of r, a characteristic scale length, and the dependence on r can vary considerably, depending on specific conditions. Confident interpretation of wind-tunnel data is possible only if the dependence on r is known and accounted for in the transformation between full-scale flight conditions and scaled-down facility conditions. For the particular example of linear scaling[3] (invariant Strouhal number) and a 1/20-scale model, the 1–5 kHz region is transformed to the 20–100 kHz region. Thus the acoustic frequency range 20–100 kHz becomes important for noise reduction work carried out with small-scale models in wind tunnels. Microphones used in these studies must be calibrated at these ultrasonic frequencies before they can be used to measure unknown sound sources. Historically, an electrostatic actuator (EA) has been used to calibrate air-condenser microphones at these high frequencies.

If imaging of unknown acoustic sources is also of interest, then the microphone cost becomes an issue. A typical acoustic array may use 100 or more microphones at a substantial cost per microphone channel. To address the cost issue, low-cost Panasonic WM-60A electret microphones have recently been considered[4] for acoustic arrays. The pressure sensitivity is appropriate for this type of application. However, these electret microphones are not adaptable to the EA. In addition, other technologies such as microelectromechanical systems (MEMS) microphones, which would allow higher packing densities in microphone arrays, are also not adaptable to the EA. Thus the need arises for high-frequency calibration techniques for microphone types that are not compatible with the venerable EA. In this paper, a substitution-based, free-field (FF) calibration method is demonstrated to derive the pressure sensitivity of the amplitude response of various microphones out to frequencies of 80 kHz. A standard air-condenser pressure microphone is used as the known reference. Two sound sources, a centrifugal fan and a tweeter driven by either frequency sweeps or random noise, were used. FF calibration design issues, procedures, results, and uncertainties for several of the above-mentioned microphones are discussed.

II. MICROPHONE CALIBRATION METHODS

Over the years, several methods have been developed for microphone calibration. A summary of the more common methods is presented in Table I. The pressure sensitivity of a microphone is the voltage per unit sound pressure that the microphone will produce when a completely uniform pressure is incident on the microphone diaphragm. This is the appropriate sensitivity, for example, when the microphone is installed in a small cavity (compared to the acoustical wavelength) or is flush-mounted in a large baffle. In contrast, the

[a]Present address: Analytical Services and Materials, Inc., Hampton, Virginia 23666.
[b]Electronic mail: g.c.herring@larc.nasa.gov

TABLE I. Common methods of microphone calibration.

Method	Sensitivity type	Frequencies	Limitations
Coupler	Pressure	Low-frequency	Cavity modes
Reciprocity[a]			
Substitution			
Simultaneous			
Pistonphone	Pressure	Low-frequency	Limited No. of frequencies, SPLs
Electrostatic actuator	Pressure	Wideband	Accessible, conductive diaphragm
Free-field	Free-field	Wideband	Diffraction/reflections
Reciprocity			High-frequency reciprocal transducer
Substitution			Source stability
Simultaneous			Uniformity of pressure field

[a]Primary calibration method.

FF sensitivity of a microphone is the voltage per unit sound pressure produced when a traveling wave incident on the diaphragm is isolated from boundaries. This FF sensitivity is different from the pressure sensitivity because of diffraction of the incident wave, which leads to a spatially varying resultant sound field over the face of the diaphragm. If the microphone is mounted in free space with minimal mounting hardware, it exhibits its diffraction-related FF sensitivity. The difference between a microphone's FF and pressure responses is shown in Fig. 1. Thus measurements in the FF require a frequency-dependent correction C to yield the pressure response.

Table I also lists the limitations of each method. Coupler-based methods are confined to relatively low frequencies because of the increasing spectral density of cavity modes with increasing frequency.[5] In the example shown in Fig. 2, calibration of a microphone would become problematic at frequencies approaching 30 kHz or higher. A pistonphone provides a constant and known volume velocity to a microphone inserted in a coupler at a variety of fixed frequencies over the audio range, but again is limited to low frequencies. For higher frequencies, the EA has long been

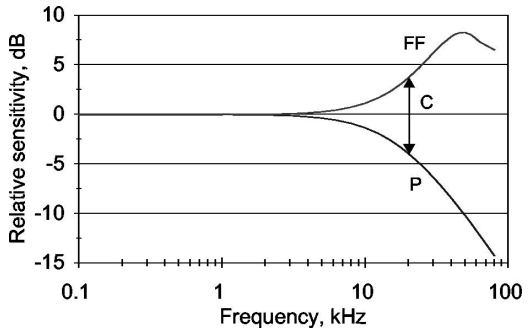

FIG. 1. Typical pressure sensitivity (P) and free-field sensitivity (FF) of an air-condenser microphone. The correction C is the frequency-dependent difference between the two sensitivities. It depends on the microphone diameter and is shown here for a $\frac{1}{2}$ in. microphone at normal incidence.

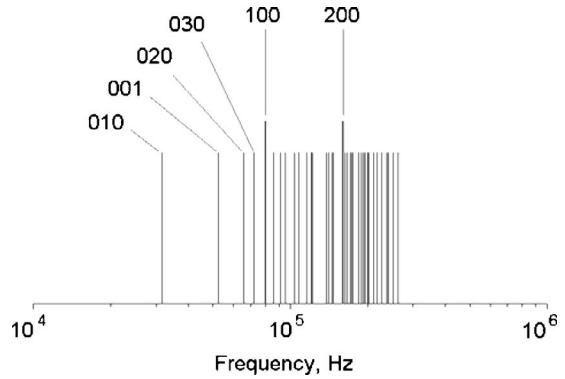

FIG. 2. Mode locations of a cylindrical cavity having a diameter of 6.35 mm × height of 2.14 mm. The modal designations (ijk) refer to the axial, radial, and azimuthal modes, respectively.

used to calibrate air-condenser microphones up to frequencies exceeding 100 kHz, but requires an accessible, conductive diaphragm. Many newer microphone types fail to meet this requirement and thus are not compatible with the EA. This is the appropriate situation for the FF technique to be considered for high-frequency calibration. Specific precautions to minimize or eliminate the diffraction problem are discussed in more detail in a later section of this article.

Both the coupler and FF methods can both be executed using reciprocity, simultaneous, or substitution procedures, each encumbered with its own particular difficulty. The reciprocity method requires a reciprocal transducer that operates efficiently as both a transmitter and a receiver at high frequencies, especially in the FF. The simultaneous method, whereby both the known reference and unknown test microphones are tested at the same time, requires the sound field to be spatially uniform at all frequencies. The substitution method, whereby the two microphones are tested sequentially in the same location to avoid the spatial nonuniformity problem, requires a temporally stable sound source since the two measurements are no longer made simultaneously. Since this was deemed the least problematic requirement to fulfill, substitution was chosen as the preferred high-frequency calibration method in this study.

Time selective techniques have been demonstrated to remove the reflections from the time response and thus eliminate the attendant contribution to the measurement uncertainty.[6,7] These, however, have not been applied to calibration of the microphone pressure sensitivity nor to measurements above 30 kHz.

III. CALIBRATION STANDARDS AND KEY SPECIFICATIONS

Upon close inspection of existing standards[8,9] for microphone calibration, it is apparent that all are written with low-frequency calibrations or FF sensitivity in mind. Thus there is no published national or international standard for microphone pressure-sensitivity calibration in the ~20–100 kHz frequency range other than the EA.[10] In this section, several parameters that will affect the quality of a high-frequency, FF microphone calibration are discussed.

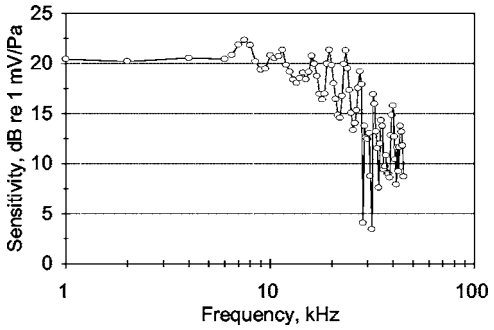

FIG. 3. Free-field measurement of the pressure sensitivity of an electret condenser microphone using a tweeter excited at discrete frequencies. Open circle: datum point at a discrete frequency.

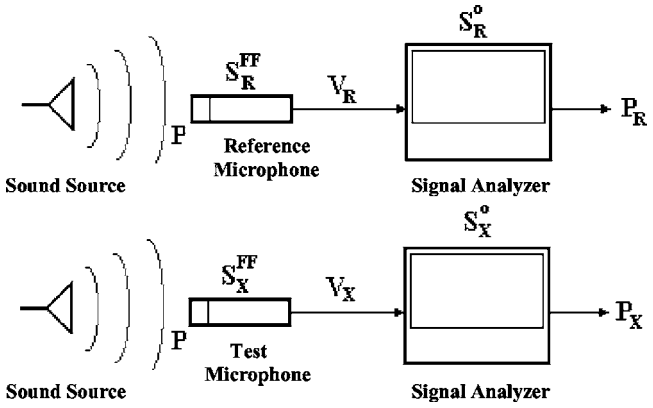

FIG. 4. Principle of the free-field substitution method.

One important problem that arises in a typical FF calibration is a frequency-dependent systematic error that generates an oscillatory pattern on the microphone response spectrum. An example of this oscillatory systematic error is shown in Fig. 3 for a FF calibration of a Panasonic WM60A electret microphone. A distinct modulation of the sensitivity is seen at frequencies of 10 kHz and higher. In this study, five possible different frequency-dependent causes were considered as origins for this sensitivity variation: (1) interference from room resonances; (2) reflections from nearby mounting structure and subsequent interference between the incident and reflected acoustic waves; (3) modal breakup[11] in the diaphragm of the sound source; (4) difference in diffraction[12] between the unknown test and the known reference microphones; (5) differences in the acoustic center location[13] and acoustic impedance between the unknown test and the known reference microphones. It was determined in this study that item (2), reflections and subsequent interference, was the primary reason for the occurrence of the oscillatory systematic errors that can occur.

Five different countermeasures can be used to help minimize or eliminate the systematic error due to these interference effects: (1) to perform the calibrations in a suitable anechoic chamber and cover the mounting structure with an absorbing foam to minimize reflections; (2) to keep all mounting hardware far away from, or behind, the test microphone to minimize significant reflections; (3) to choose the source-microphone separation distance L such that $d^2/(\lambda L) \gg 1$, where d=source size and λ=acoustic wavelength, to ensure placement of the test microphone beyond the Fresnel region of the source; (4) to use a broadband source that exhibits minimal phase coherence at all frequencies of interest, in order to suppress the build-up of standing waves, and to minimize interference between any reflected and incident waves near the microphone diaphragm; (5) if a phase-coherent tonal source must be used to achieve a large enough signal-to-noise ratio (SNR), then to use a grazing-angle, rather than a normal-angle, incidence to minimize interference effects in the vicinity of the microphone diaphragm. Thus key specifications for any FF calibration procedure should include the geometry (i.e., normal or grazing incidence), the bandwidth characteristics of the source, SNR, and the source-microphone separation distance. Because the microphone response to grazing incidence more closely matches the pressure response, the correction from FF to pressure sensitivity is accordingly smaller than the correction for normal incidence.

IV. PRINCIPLE OF THE FF SUBSTITUTION METHOD

Figure 4 illustrates the principle of the substitution method. The calibrations are performed in an anechoic chamber with a sound source, the test and reference microphones, and a signal analyzer. The reference and test microphones are tested sequentially. The symbols in the figure are defined as follows:

P = the acoustic pressure in the undisturbed sound field;
S_R^{FF}, S_X^{FF} = the FF sensitivity of the reference and test microphones, in mV/Pa;
V_R, V_X = the output voltage of the reference and test microphones;
S_R^o, S_X^o = the sensitivity of the reference and test microphones at a reference frequency, as determined for example by a pistonphone at 250 Hz;
P_R, P_X = the pressure reading for the reference and test microphones as displayed by the analyzer.

Then it follows:

$$P_R = \frac{V_R}{S_R^o} = \frac{S_R^{FF} P}{S_R^o} = \frac{C S_R^P P}{S_R^o}, \tag{1}$$

$$P_X = \frac{V_X}{S_X^o} = \frac{S_X^{FF} P}{S_X^o} = \frac{C S_X^P P}{S_X^o}, \tag{2}$$

where C is the correction factor for converting from FF to pressure sensitivity. Upon taking ratios, and expressing the result in dB, one finds the pressure sensitivity M_X^P of the test microphone (the M's are the microphone sensitivities in dB re 1 mV/Pa),

$$M_X^P = L_X - L_R + M_R^P + M_X^o - M_R^o, \tag{3}$$

where

L_R, L_X = the measured FF pressure levels P_R, P_X, in dB re 20 μPa;

M_R^P = the known pressure sensitivity of the reference microphone, as determined by the electrostatic actuator.

The validity of Eq. (3) rests upon two assumptions: first, that the sound pressure is the same at the reference and test microphone diaphragms. This implies that the microphone-diaphragm distance and diaphragm height is matched for the two microphone measurements as closely as possible; that the source and microphone are fixed firmly to the chamber floor or to a common base plate (to make their separation immune to displacement by foot traffic); and finally that the source remain sufficiently stable between the two measurements so as not to cause significant measurement error. It is imperative that the measurements on the reference and test microphones take place with minimum delay after the exchange of microphones.

The second assumption is that the correction factor C for diffraction be the same for both microphones. Since diffraction is primarily a geometric effect, this implies that both microphones must present the same surface geometry to the sound field. If the test and reference microphones are of dissimilar geometries, then one or both of the microphone mounts must be modified (e.g., encased in an adapter) to match each other in size and shape. Further, it is important that the size of the microphone holder and stand be minimized as much as practical.

An advantage of the substitution method is that the frequency calibration does not depend upon the frequency spectrum of the source, for frequency-dependent variations in amplitude are expected to cancel. However, if the source spectrum has structure, as may be expected of a pistonlike source (e.g., loudspeaker), then the error related to source stability is most sensitive in the regions where structure is most prominent. A disadvantage of the substitution method is that the sound source and detector must be very stable and repeatable over the time period between testing of the test and reference microphones.

V. EXPERIMENTAL SETUP

In the experimental setup for the FF calibration method, indicated schematically in Fig. 4, two sound sources were used for testing: a centrifugal fan (Campanella Associates RSS-10U) and a tweeter (Motorola KSN1078). A signal analyzer (B&K 2035), remotely located in a control room, was used to record the data. This performs a fast Fourier transform on the signal, which allows for the data to be recorded in the frequency domain on a 3.5 in. floppy disk for subsequent processing on a spreadsheet. All calibrations were performed in a $2.1 \times 2.5 \times 3.7$-m anechoic chamber, having a cutoff frequency of 210 Hz and an A-weighted ambient noise level of 15 dB.

A. Sound sources

The centrifugal fan is a wideband noise source that produces approximately random noise. A wideband source minimizes the chance of interference between the incident wave and unwanted reflected waves, and allows for data to be collected simultaneously over the entire frequency range.

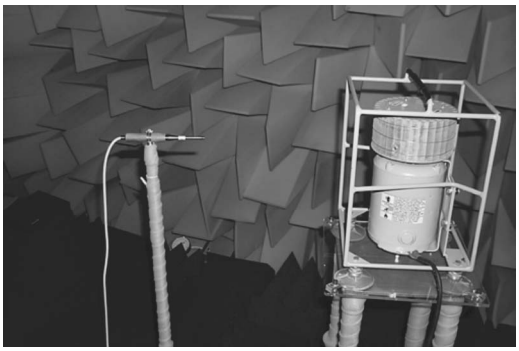

FIG. 5. Calibration setup using the centrifugal fan (right) and microphone (left) in an anechoic chamber. The centrifugal fan platform and microphone stand are attached rigidly to a base-plate (not shown) on the floor.

The disadvantage of this sound source is that the SNR is small compared to a typical tonal source. This ratio can be increased by moving the microphone closer to the centrifugal fan. The manufacturer's specifications state that a microphone should not be used within 0.5 m of the fan to prevent systematic errors due to windage from the fan. Calibrations were typically much better when moved inside of the half-meter separation because the SNR was larger. Figure 5 shows a typical experimental setup for an air condenser microphone. Figure 6(a) shows the emission spectrum of the centrifugal fan, which reveals no structure except for a small region near 10 kHz. A "1-over-R" test was performed to verify that the centrifugal fan behaves as a point source. Figure 6(b) shows the results of the "1-over-R" test. The results show that the centrifugal fan still acts as a point

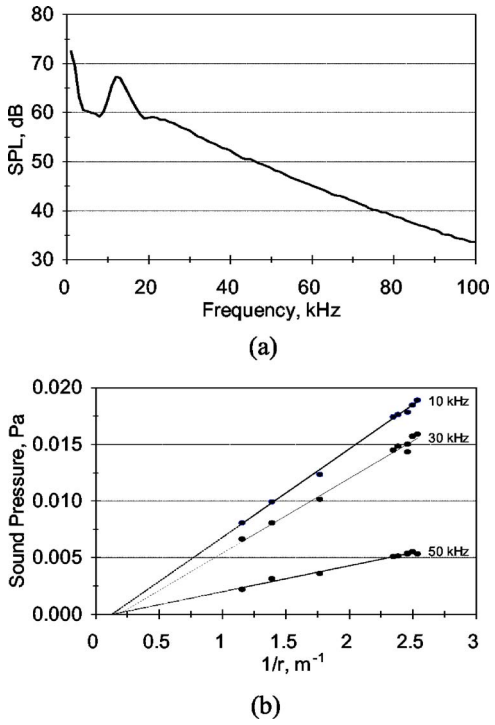

FIG. 6. Properties of the centrifugal fan (Campanella Associates Reference Sound Source RSS-101U): (a) acoustical emission spectrum calibrated by the manufacturer with a Larson-Davis type 2520 microphone at a distance of 0.5 m; (b) sound pressure versus reciprocal distance from the fan at frequencies of 10, 30, and 50 kHz. Circles: in-house measurement. Lines: best fit.

source with a separation of 0.4 m, which is less than the separations used for all calibrations presented here.

The response of the tweeter was inconsistent below 1 kHz, but had exceptional performance above 1 kHz until the output rolled off at about 60 kHz; it could still be used at 80 kHz. Two types of electrical input were used to excite the tweeter: swept tones and random noise. With tones, testing could be done with either a frequency-sweep function or temporally-fixed tones. Sweeping of the tones is superior because the time interval required to complete the calibration is significantly reduced when compared with using fixed tones. The reduced time is an advantage because heating of the voice coil affects the input impedance (and hence the acoustic output) of the tweeter. The only advantage to using fixed tones is that it allows the maximum SNR, which, for example, is important for the calibrating low-sensitivity piezoresistive microphones. The disadvantage of using fixed tones is that the chance of generating interference effects on the response profile, as in Fig. 3, is increased.

The random-noise input signal has the advantage of being able to complete the calibration faster than sweeping tones, but the accuracy of the calibration is reduced due to the lower SNR of the acoustic input.

B. Microphones and their mounting

An air-condenser $\frac{1}{4}$-in. pressure microphone (B&K type 4136), with the protective grid removed, was used as the reference microphone for every calibration. The dual-channel microphone power supply (B&K type 2807) was turned on at least 24 h prior to a calibration. The second channel was used for the calibration of other air-condenser microphones.

For the nonair condenser microphones (MEMS & electrets) an alternative setup was used. These microphones were powered from a dc power supply (Agilent E3630A), located in the anechoic chamber. The output signal from the microphone was then fed into a single channel instrumentation amplifier (Pacific Instruments SA1A), having a very low output impedance, and from there to the signal analyzer.

The setup for the tweeter was the same for both the white noise and tone signals, with the exception of the input-signal generator. The white-noise signal generator was a multifunction synthesizer (Agilent 8904A) and the tonal signal generator was a function generator (HP 3314A). The driver-signal was amplified with a wideband power amplifier (B&K 2713).

Mounting of the microphone is a critical step in the FF calibration method. One of the primary assumptions is that both the reference and test microphones encounter the same pressure field. Two factors dictate the validity of this assumption: temporal stability of the sound source and repeatable positioning of the microphone. The positioning of the microphones entails both the orientation to the sound source and the geometry of the microphone.

The orientation of the microphone to the sound source has to be carefully implemented because variations in position between tests can have significant effects on the results. To improve the ability for the microphones to be accurately positioned, both the sound source and the microphone stand were fixed to a baseboard. This kept the setup rigidly fixed in place throughout testing. Even with the sound source stand and the microphone stand fixed in place, careful measurements still had to be made when mounting the microphones. The height from the ground to the microphone, distance from the microphone diaphragm to the source and to the mounting post, were all adjustable. The height from the ground to the microphone diaphragm center was fixed at 1.25 m, which also corresponds to the center of the sound source. The distances between the microphone diaphragm and source and between the microphone diaphragm and the mounting post are summarized in Table II. With the distances listed in Table II, typical sound SPLs (128 Hz band) generated at the microphone diaphragm were the following: centrifugal fan, 55–60 dB at 10 kHz and 33–38 dB at 80 kHz; tweeter, 75–80 dB at 10 kHz and 60–68 dB at 80 kHz, sweep being slightly higher than white noise excitation.

TABLE II. Typical distances (meters): diaphragm-source and diaphragm-mounting post.

	Normal incidence		Grazing incidence	
Source	Diaphragm-source	Diaphragm-mounting post	Diaphragm-source	Diaphragm-mounting post
Centrifugal fan	0.406[a]	0.102[b]	0.508	Not applicable
Tweeter	0.406	0.089[b]	0.495	Not applicable

[a]Measured to center of fan.
[b]For the SiSonic microphone SP0101Z the diaphragm-mounting post distance was 0.051 m.

The other aspect of proper microphone mounting is the geometry of the microphone mount. Since the pressure sensitivity was determined here by FF measurements, the geometry associated with the test and reference microphones had to be nearly identical. Through experience it was determined that there are two key considerations when considering the geometry of the microphone mount. First is the shape and size of the microphone diaphragm surface. Testing was done with both $\frac{1}{4}$-in. microphones as well as with varied diaphragm arrangements. These variations included a recessed diaphragm (electret) and a rectangular shaped surface with the diaphragm mounted in the middle (MEMS). The variations produced good results when careful consideration was given to replication of the shape and size. The second key consideration for the microphone mount is the presence of reflecting surfaces near the microphone diaphragm. In practice any solid surface, like the microphone stand, should be placed at least 10 diaphragm diameters behind the microphone.[15]

C. Procedure

A requirement for the FF method described here is that a reference microphone be selected that can be calibrated using the EA method. Reliance of the FF method upon the EA is acceptable since the purpose of the FF method is to calibrate "special microphones" that cannot be mated to the EA. This requires that the reference microphone has a flat, conducting

diaphragm. Once the reference microphone has been properly calibrated with the EA, the FF calibration can be performed on the test microphone.

Before the FF calibration, both the reference and test microphones were calibrated with a fixed pistonphone (B&K type 4228) at 250 Hz. The test microphone was flush mounted in a holder, designed to retain the correct coupler volume of the pistonphone. These pistonphone measurements were taken immediately prior to the FF calibration. Measurements of the chamber environment were also recorded. The main environmental parameters are temperature, atmospheric pressure, and relative humidity. These data are used to make small corrections to the calibration and in the uncertainty analysis.

The method for the start up of the sound source varies based on the source. If the centrifugal fan was used, then the fan was left on for approximately 5 min to allow the source to reach an equilibrium state. The tweeter was used shortly after being turned on. It is important to note that the tweeter should be employed in a regular routine. Since the output can vary over time as a result of an increase in temperature of the tweeter, the accuracy of the calibration will depend on the time duration from start to finish. Thus if the time delay between starting the tweeter and data acquisition is repeatable and if there is adequate time for the tweeter to cool down in between runs, the calibration will be more accurate.

Four data runs are required for a calibration of the test microphone. The first two runs are performed with the test microphone, first with the sound source on and second with the sound source turned off. The latter two runs are performed similarly for the reference microphone. Then the acoustic pressure P_R for the reference microphone in Eq. (1) is corrected to

$$P_R = \sqrt{P_R^2(\text{meas}) - P_R^2(\text{bg})},$$

where meas and bg refer to the runs with and without the source turned on. The acoustic pressure P_X for the test microphone in Eq. (2) is corrected similarly. In this work, the background subtraction was always carried out, even if the signal was more than 20 dB above the background.

After the FF data had been collected for all four test runs a second pistonphone reading was taken for each microphone. The first pistonphone reading and this later reading were used for an average sensitivity at a fixed frequency of 250 Hz. Thus the absolute sensitivity over the entire spectrum is fixed to the pistonphone reading. In addition to the pistonphone measurements, the environmental conditions (temperature, pressure, relative humidity) were also repeated.

An independent calibration is desirable for additional confidence and validation of the FF method. The calibrator used here, B&K type 4226 Multifunction Acoustic Calibrator (MAC), operates over the range of 31.5 Hz to 16 kHz at octave intervals (except for an intermediate frequency at 12.5 kHz). The FF method did produce some calibrations that were stable down to 1 kHz (i.e., agree with the MAC), but the 1 kHz endpoint could not be consistently obtained with the FF method.

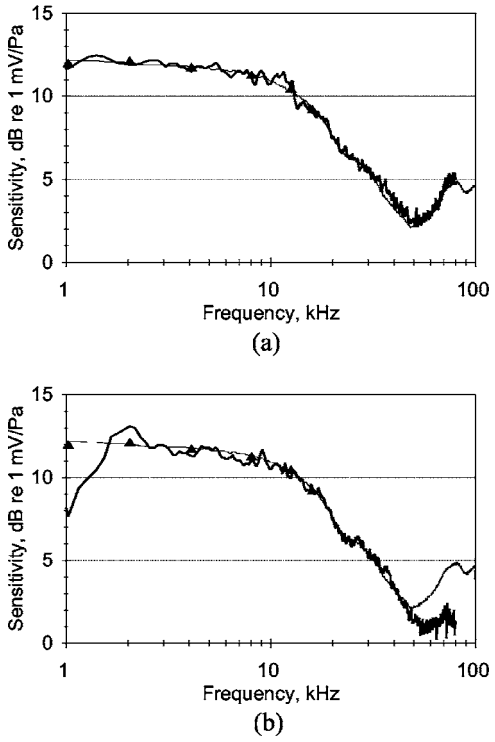

FIG. 7. Pressure sensitivity of a B&K type 4939 $\frac{1}{4}$-in. free-field microphone as calibrated by the free-field method (heavy line), EA (light line), and Multifunction Acoustic Calibrator (B&K type 4226, triangles). Source: centrifugal fan. Incidence: (a) normal, (b) grazing.

VI. RESULTS

This section is organized into two parts: (A) proof of the FF calibration concept, whereby the FF calibration method is tested on a microphone for which the electrostatic actuator (EA) calibration is known; and (B) FF calibrations on microphones having geometries unsuited to an EA calibration. The signal analyzer was operated in the "Autospectrum" mode over the frequency range 0–102.4 kHz with a frequency resolution of 128 Hz. Typical test conditions were 20.5 °C, 101 900 Pa, and 54% for the temperature, pressure, and relative humidity. Despite small variations in these parameters, the difference in air absorption at 80 kHz between the reference and test microphone measurements never exceeded 0.088 dB over the source-microphone path.[9]

A. Proof of the free-field calibration concept

To prove the concept, a series of calibrations was performed on a test microphone for which the wideband pressure sensitivity by the EA method is known, namely a $\frac{1}{4}$-in. FF air-condenser microphone (B&K type 4939). The first test was performed with the centrifugal fan at normal incidence, in accord with the specification of prior standards.[8–10] The result is shown in Fig. 7(a). Agreement between the FF and EA spectra is excellent, the difference not exceeding ±0.5 dB. The difference is greatest in the vicinity of 10 kHz, where the emission spectrum reveals structure [Fig. 6(a)]. The FF spectrum follows the inflection point at about 20 kHz, the sensitivity minimum at 50 kHz, and in this case appears to remain well-behaved at frequencies down to 1 kHz. The discrete calibration points (triangles) obtained

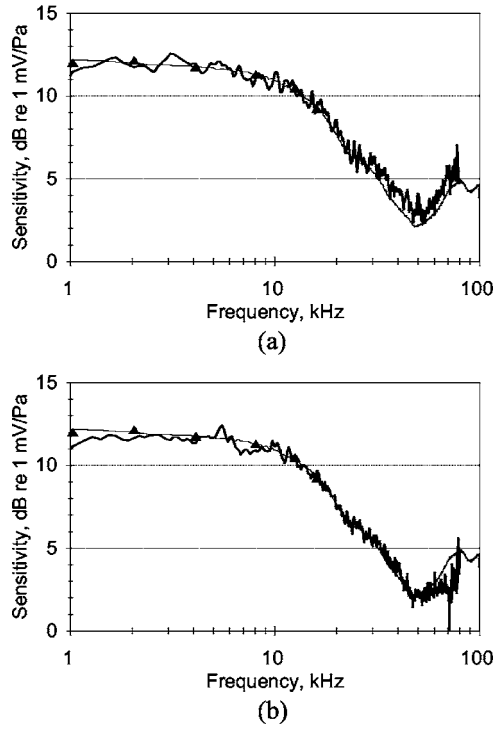

FIG. 8. Pressure sensitivity of a B&K type 4939 $\frac{1}{4}$-in. free-field microphone as calibrated by the free-field method (heavy line), EA (light line), and Multifunction Acoustic Calibrator (B&K type 4226, triangles). Source: tweeter excited by white noise. Incidence: (a) normal, (b) grazing.

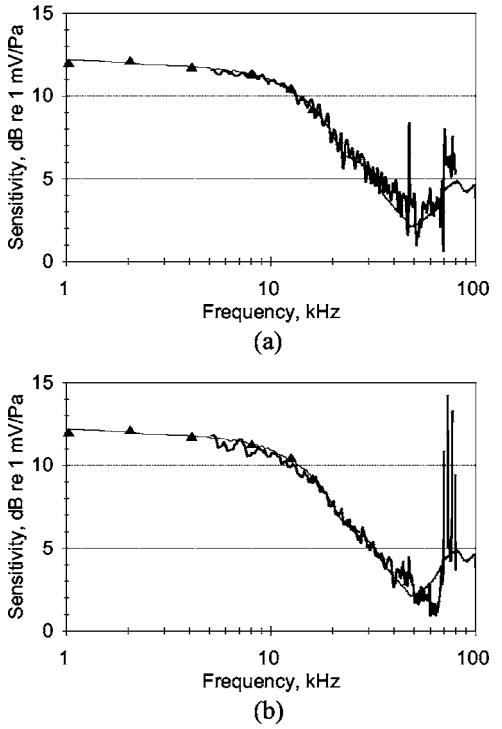

FIG. 9. Pressure sensitivity of a B&K type 4939 $\frac{1}{4}$-in. free-field microphone as calibrated by the free-field method (heavy line), EA (light line), and Multifunction Acoustic Calibrator (B&K type 4226, triangles). Source: tweeter excited by linear frequency sweep (5–102.4 kHz over a sweep time of 120 s). Incidence: (a) normal, (b) grazing.

with the MAC also reveals excellent consistency with the other two calibration methods. Figure 7(b) shows the results for grazing incidence. Here agreement between the FF and EA spectra lies within ±0.5 dB only within the interval 3–50 kHz.

For some test microphones it is desirable to increase the SPL to ensure adequate SNR. Here the use of a tweeter will prove useful. However, there will be some sacrifice in accuracy because the tweeter response shows structure across the frequency spectrum. In Fig. 8 the tweeter is excited by white noise. The FF pressure sensitivity of the microphone at (a) normal and (b) grazing incidence shows agreement with the EA to ±1 dB, except in a small region near 80 kHz. A small oscillatory pattern is evident, especially in the normal response.

Alternatively, one can drive the tweeter with a frequency sweep, which improves the SPL especially at the higher frequencies. In Figs. 9(a) and 9(b) the sweep frequency ranges from 5 to 102.4 kHz linearly over a sweep time of 120 s. The responses are similar to those obtained from white noise. They may be somewhat better in the low-kHz range, but show spikes at the upper end of the spectrum. Otherwise, agreement with the EA appears to lie also within ±1 dB.

B. Free-field calibrations on microphones unsuited to an EA calibration

A calibration was performed on an electret condenser microphone, Panasonic WM-60A. The cartridge is 6 mm in diameter and contains a small hole (~2 mm) for acoustic access to a recessed diaphragm. A felt pad covering the hole was removed prior to calibration. The unavailability of access to the diaphragm precluded the possibility of an EA calibration. The cartridge was installed in a tube of dimensions 6.35 mm o.d. × 50.8 mm length, which contained a circuit board to accommodate the needed circuit components. The supply voltage was 5.00 V in series with an 8.2 kΩ resistor on the circuit board. The assembled microphone was fitted into a microphone holder, which was tapered on the microphone end to resemble a conventional $\frac{1}{4}$-in. condenser microphone adapter, as shown in Fig. 10(a).

The results of the calibrations using the centrifugal fan, tweeter excited by white noise, and tweeter excited by a frequency sweep, are shown in Figs. 11(a)–11(c), respectively. The heavy and light lines represent normal and grazing incidence in each figure. Results for grazing are for the most part slightly lower than for normal. Figure 11(a) shows the adverse effect of low SNR for grazing incidence as early as 40 kHz, where nevertheless the sensitivity lies well beyond the −3 dB point. Grazing shows slightly better agreement with the MAC the whole way down to 1 kHz. Figures 11(b) and 11(c) reveal good agreement between normal and grazing, as well as with the MAC, at frequencies down to about 3 kHz. The normal incidence, however, shows an unexplained spike in the response slightly below 50 kHz. Except for the spike, the calibrations from 3 kHz to the frequency where the sensitivity drops 20 dB agrees with each other to within ±1 dB.

A second microphone is a microelectromechanical system (MEMS) capacitive microphone, SiSonic SP0101Z, manufactured by Knowles Acoustics. The rectangular cartridge has dimensions of 6.50 × 6.25 × 2.37 mm. A small

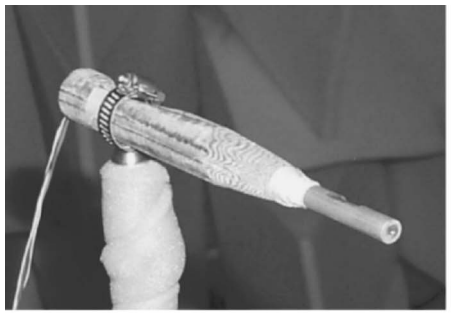

(a)

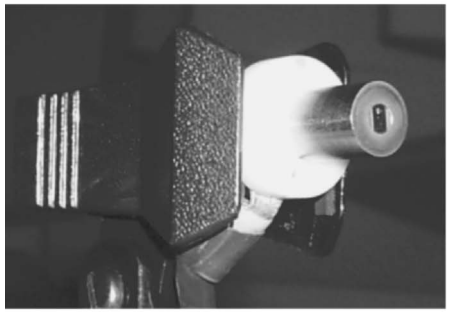

(b)

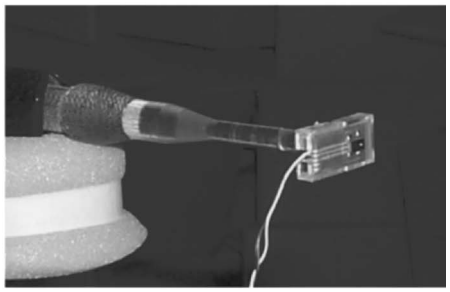

(c)

FIG. 10. Mounting arrangement of test microphones unsuited to an electrostatic actuator calibration: (a) Electret condenser microphone (Panasonic WM-60A), (b) MEMS microphone (SiSonic SP0101Z) in adapter, (c) MEMS microphone (SiSonic Ultrasonic Prototype) on a circuit board/adapter.

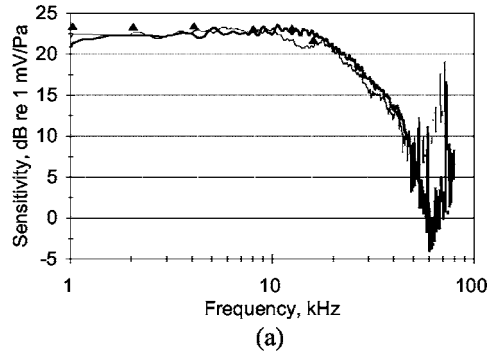

(a)

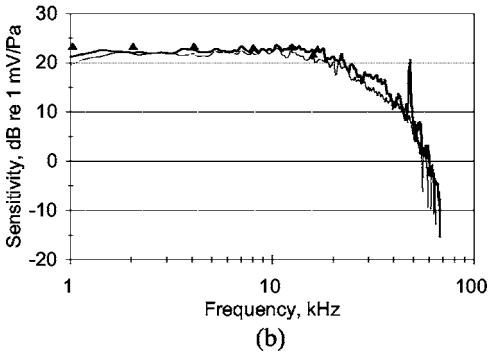

(b)

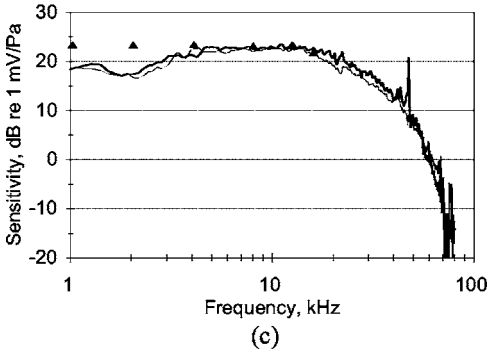

(c)

FIG. 11. Pressure sensitivity of electret condenser microphone (Panasonic WM-60A). Sound sources: (a) centrifugal fan, (b) tweeter excited by white noise, (c) tweeter excited by swept tones. Triangles: multifunction acoustic calibrator data (B&K type 4226). Light line: grazing incidence. Heavy line: normal incidence.

hole on one face renders acoustic access to the recessed diaphragm, an arrangement unsuited to an EA calibration, while the opposite face contains four solder pads for electrical contacts. A cylindrical adapter, 12.7 mm (1/2 in.) in diameter, was fabricated with a rectangular recess to seat the cartridge flush with the surface, and provided with spring-loaded contacts to make electrical contacts through an access hole in the adapter [see Fig. 10(b)]. Finally a sleeve pressing against the corners of the cartridge provided enough tension to hold the cartridge in place. The adapter was designed to permit calibration with the MAC; but an unfavorable length-to-diameter ratio did not appear to have an adverse influence on the FF calibration, at least by the centrifugal fan. A matching cylindrical adapter was made for the $\frac{1}{4}$-in. reference microphone.

The results are shown for the centrifugal fan and tweeter in Figs. 12(a) and 12(b). The centrifugal fan yields excellent agreement among normal incidence, grazing incidence, and the MAC, all within ±1 dB of each other. The calibration reveals diaphragm resonances near 15 and 35 kHz. The tweeter calibrations meet the ±1 dB uncertainty specification only from 3 kHz to just over the first peak at about 18 kHz. Significant differences occur in the region between the peaks from 18 to 35 kHz. Below 3 kHz the white noise calibration (dotted line) veers far astray. The unfavorable length-to-diameter ratio of the adapter may be the culprit.

The final microphone unsuited to an EA calibration is another MEMS microphone, "SiSonic Ultrasonic Prototype," having the same size but a greater bandwidth than the above. The microphone, as delivered, was mounted on a small rectangular circuit board, 24.2 mm L. × 11.7 mm W. Since the microphone could not be detached from the circuit board, the latter was inserted into a rectangular fixture at the end of a support rod, which provided adequate separation from the microphone stand. This arrangement is shown in Fig. 10(c). The fixture, 26.8 mm L. × 14.2 mm W., served as an acoustic baffle. The reference microphone was flush-mounted in a similar baffle of the same dimensions. The geometry is unsuited to a MAC calibration. Because the baffle precluded a

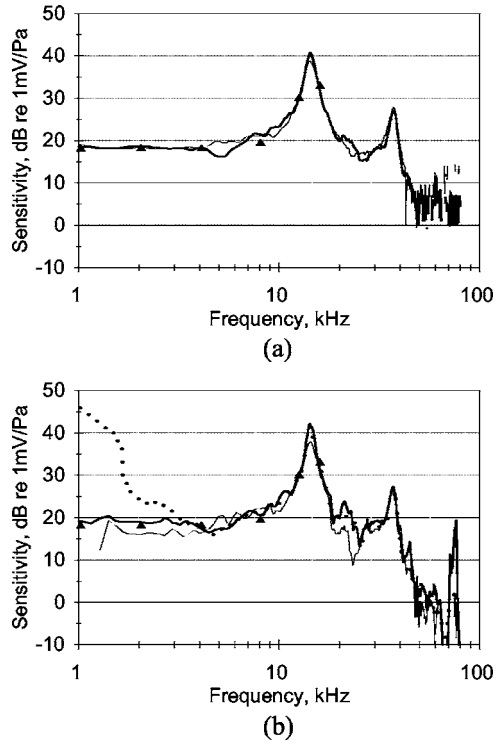

FIG. 12. Pressure sensitivity of MEMS microphone (SiSonic SP0101Z). Sound sources: (a) centrifugal fan, (b) tweeter excited by swept tones (solid lines) and white noise (dotted line, normal incidence). Triangles: Multifunction Acoustic Calibrator data (B&K type 4226). Light line: grazing incidence. Heavy line: normal incidence.

conventional pistonphone calibration as well, the sensitivity of the test microphone at a reference frequency was obtained by matching FF sound pressures between the test and reference microphones at 2 kHz. The result is $M_X^0 = 4.2$ mV/Pa.

The best results of the FF calibration were obtained using the centrifugal fan and tweeter excited by white noise, as shown in Fig. 13. The fundamental diaphragm resonance is seen to be shifted to about 30 kHz. Agreement between the two sound sources is within ±1 dB from 2 to 50 kHz.

VII. ESTIMATE OF THE CALIBRATION UNCERTAINTY

For normal incidence and the FF microphone of Sec. VI A and Fig. 7, the rms differences between the EA and the FF methods are $\pm 0.3, \pm 0.8$, and ± 1.0 dB over the 1–80 kHz range for the fan, white-noise, and tweeter sweep methods. Contributions to the combined uncertainty of the FF method are summarized in Table III. These values might realistically be considered reasonable estimates for the uncertainty of a test microphone that is nearly geometrically identical to the reference microphone. One might cautiously expect that the nongeometrically-identical microphones of Sec. VI B may have slightly larger uncertainties due to additional reflection-related problems.

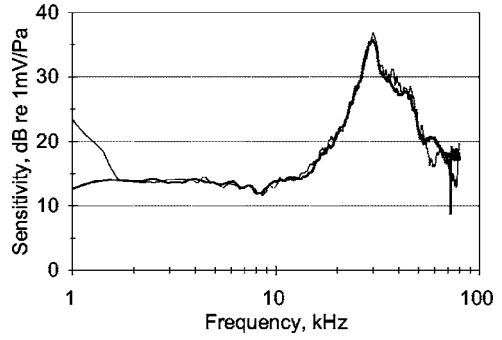

FIG. 13. Pressure sensitivity of MEMS microphone (SiSonic Ultrasonic Prototype). Sound sources: centrifugal fan at normal incidence (heavy line), tweeter excited by white noise at normal incidence (light line).

TABLE III. Contributions to the measurement uncertainty.

	Uncertainty contribution	Standard uncertainty dB
I	Electrostatic actuator	
	Cross talk	0.15
	Radiation loading	0.07
	Pistonphone	0.20
	Microphone-source separation	0.017
	Microphone orientation	0.10
	Air attenuation	0.088
II	Pressure measurement	
	Centrifugal fan	0.30
	Tweeter, white noise	0.80
	Tweeter, frequency sweep	1.00
III	Combined standard uncertainty	
	Centrifugal fan	0.41
	Tweeter, white noise	0.85
	Tweeter, frequency sweep	1.04

In Table III, group I contributions are independent of the acoustic source. The dominant contributions to the EA calibration are "cross-talk" and loading of the microphone diaphragm by the radiation impedance. The relative uncertainty of cross-talk,[14] from one frequency to the next, was determined through a measurement of the EA response with and without the polarization voltage over the frequency range 1–80 kHz. The uncertainty due to radiation loading[10] is based on theoretical estimates of the ratio of radiation impedance to diaphragm stiffness reactance. It is noted that this ratio falls off dramatically with decreasing diaphragm diameter, because the equivalent volume (varying inversely with diaphragm stiffness) reveals a disproportionate decrease (factor 40 from $\frac{1}{2}$ in. to $\frac{1}{4}$ in.). The microphone-source separation uncertainty is 0.001 m out of a separation of 0.5 m. The uncertainty due to orientation of the microphones is based on the effect of an angular deviation of 2° upon the FF correction factor at 50 kHz (worst case). The uncertainty due to air attenuation, based on ambient changes between reference and test microphone measurements, is evaluated at 80 kHz (worst case) according to Annex B of Ref. 15.

Group II contributions depend upon the sound source. For each source the rms deviation of the FF from the EA sensitivity of the proof-of-concept condenser microphone (Sec. VI A) was computed over the measured frequency range. This procedure accounts for imperfect cancellation of effects due to diffraction and acoustic pressure mismatch at the microphones.

The entries under group III are the combined standard uncertainties for each source, based on summation in quadrature according to the specification of Ref. 16.

VIII. SUMMARY

The free-field substitution method has proved effective for calibrating microphone pressure sensitivity at frequencies out to at least 80 kHz and is applicable to microphones unsuited to an EA calibration. Best results were obtained with a centrifugal fan at normal incidence. For a microphone with a relatively low SNR, however, a tweeter excited either by white noise or a frequency sweep will provide a higher SPL but the overall accuracy will be reduced.

The selection of specific instruments for testing does not imply endorsement by the National Aeronautics and Space Administration.

ACKNOWLEDGMENTS

We are pleased to thank W.R. Noack and R.M. Faison, Wyle Laboratories, for performing the electrostatic actuator calibrations, and S.M. Bartram and W.M. Humphreys, NASA Langley Research Center, for fabricating equipment used in the anechoic chamber and for helpful comments on the manuscript.

[1]S. Fidell, R. Horonjeff, J. Mills, E. Baldwin, S. Teffeteller, and K. Pearsons, "Aircraft noise annoyance at three joint air carrier and general aviation airports," J. Acoust. Soc. Am. **77**, 1054–1068 (1985).

[2]G. M. Lilley, "The prediction of airframe noise and comparison to experiment," J. Sound Vib. **239**, 849–859 (2001).

[3]D. G. Crighton, "Airframe noise," in *Aeroacoustics of Flight Vehicles: Theory and Practice*, edited by H. H. Hubbard, NASA Reference Publication 1258, Vol. **I**, (August 1991), p. 394.

[4]W. M. Humphreys, Jr., C. H. Gerhold, A. J. Zuckerwar, G. C. Herring, and S. M. Bartram, "Performance analysis of a cost-effective electret condenser microphone directional array," paper AIAA 2003–3195, 9th AIAA/CEAS Aeroacoustics Conference, Hilton Head, SC, 12–14 May 2003.

[5]U. S. Shirahtti and M. J. Crocker, "Standing Waves," in *Encyclopedia of Acoustics*, edited by M. Crocker (Wily, New York, 1997), Vol. **I**, Chap. 7, pp. 81–89.

[6]S. B. Figueroa, K. Rasmussen, and F. Jacobsen, "Time-selective technique for free-field reciprocity calibration of condenser microphones," J. Acoust. Soc. Am. **114**, 1467–1476 (2003).

[7]O.-H. Bjor, "Measurement of microphone freefield response," Noise Control Eng. J. **52**, 72–77 (2004).

[8]ANSI S1.15-2005/Part 2, "Measurement Microphones—Part 2: Primary method for Pressure Calibration of Laboratory Standard Microphones by the Reciprocity Technique," Standards Secretariat, Acoustical Society of America, Melville, NY (2005).

[9]CEI/IEC 61094-5: 2001, "Measurement microphones—Part 5: Methods for pressure calibration of working standard microphones," International Electrotechnical Commission, Geneva (2001).

[10]CEI/IEC 61094-6: 2004, "Measurement microphone—part 3: Electrostatic actuators for determination of frequency response," International Electrotechnical Commission, Geneva (2004).

[11]B. M. Starobin, "Loudspeaker design," in *Encyclopedia of Acoustics*, edited by M. Crocker (Wily, New York, 1997), Vol. **IV**, Chap. 160, pp. 1903–1924.

[12]F. Wiener, "The diffraction of sound by rigid disks and rigid square plates," J. Acoust. Soc. Am. **21**, 334–347 (1949).

[13]F. Jacobsen, S. B. Figueroa, and K. Rasmussen, "A note on the concept of acoustic center," J. Acoust. Soc. Am. **115**, 1468–1473 (2004).

[14]E. Fredericksen, "Electrostatic Actuator," in *AIP Handbook of Condenser Microphones*, edited by G. S. K. Wong and T. F. W. Embleton (AIP Press, New York, 1995), Chap. 15.

[15]CEI/IEC 61094-3: 2001, "Measurement microphones—Part 3 Primary method for free-field calibration of laboratory standard microphones by the reciprocity technique," International Electrotechnical Commission, Geneva (2001).

[16]ISO, *Guide to the Expression of Uncertainty in Measurement*, International Organization for Standardization, Geneva, Switzerland (1993). See also Ref. 9, Annex D.

A specialized fast cross-correlation for acoustical measurements using coded sequences[a)]

John N. Daigle
Department of Electrical Engineering, Anderson Hall, University of Mississippi, University, Mississippi 38677

Ning Xiang[b)]
School of Architecture, Rensselaer Polytechnic Institute, Troy, New York 12180

(Received 18 July 2005; revised 22 October 2005; accepted 2 November 2005)

In acoustics applications, binary maximal-length sequences and related sequences are increasingly used for acoustics system identification tasks. A number of coded sequences, such as binary maximal-length related sequences and ternary sequences possess two-valued or pulselike autocorrelation functions. It is this correlation property that is exploited in most of acoustical applications. However, the length of some of these sequences is not directly suitable for FFT-based cross-correlation algorithms. This paper explores using standard FFTs to calculate the cross-correlation between two periodic finite-length sequences of equal length, where the lengths of the sequences are not a power of 2. We apply our specialized correlation algorithm to analyze data collected in a room-acoustic environment to simultaneously obtain impulse responses between multiple sources and multiple receivers. © *2006 Acoustical Society of America.* [DOI: 10.1121/1.2141236]

PACS number(s): 43.60.Dh, 43.60.Ek, 43.58.Gn, 43.55.Mc [EJS] Pages: 330–335

I. INTRODUCTION

Maximal-length sequences and related coded signals have been increasingly used in acoustical applications.[1–7] Recent works[6,7] have reported on the application of binary maximal-length sequences (MLS) and MLS-related sequences in acoustical measurements such as using simultaneous sound sources. The simultaneous measurement technique can meet some critical requirements encountered in outdoor sound propagation research to investigate sound propagation near the ground surface in outdoor environment.[8,9] This paper shows how periodic cross-correlations, in general, and channel impulse responses of acoustical systems, in particular, may be obtained via judicious application of conventional FFT techniques even in the case where the length of coded sequences to be evaluated is not suitable for conventional FFT algorithms.[10] The practical significance of this algorithm for acousticians is to increase efficiency of the correlation measurement technique, particularly for those applications where a large number of simultaneous sound or vibration sources and receivers are needed.

Many types of coded sequences are suitable for use as excitation signals for this purpose; examples include MLS (binary and higher prime), and Legendre sequences.[1,11] Each of these possesses a two-valued periodic autocorrelation function (PACF). In addition, MLS-related sequences, such as reciprocal MLS pairs,[6] Gold, and Kasami sequences[7,12] have a similar correlation property; their PACFs contain a single peak at zero-lag and low-valued side lobes relative to the peak, and the periodic cross-correlation functions (PCCF) with other sequences can arrive at low values of the same amplitude as those in the side lobes of the PACF. It is this correlation property that is exploited in determining channel impulse responses and in many other applications, such as simultaneous multiple acoustic source measurements for room-acoustic investigations,[6] and acoustic tomography.[7,8] Performing the cross-correlation via discrete Fourier transforms is computationally inefficient [order of L^2, denoted in this paper as $O(L^2)$], but the length (L) of some of these sequences is not directly suitable for FFT-based cross-correlation algorithms [$O(L \log_2 L)$]. The length of the binary periodic MLS is $L=2^N-1$, only one point less than the suitable length for FFT. Applying binary MLS in underwater experiments, Birdsall and Mertzger[3] have explored the efficacy of zero-padding one point to obtain a suitable length for FFTs. They explore the effect of locating this additional point at all possible points within the sequence, but, in the end, the approach yields unacceptable errors with a spectral compensation.

There exists a fast algorithm, called the *fast MLS transform* (FMT), dedicated to binary MLS.[6,13] The acoustical measurement techniques using MLS based on this fast algorithm has been frequently reported in major acoustical journals.[2,6,14–16] The efficiency of the FMT is based on the fact that binary MLS matrix is permutationally similar to the Hadamard matrix[17,18] in such a way that a fast Hadamard transform can be adopted for a high efficiency of cross-correlation calculation. This paper refers to this algorithm as the *Hadamard transform-based fast MLS-transform* (HT-FMT). The HT-FMT on acoustics responses to the MLS excitation directly results in impulse responses of the acoustical

[a)]Aspects of this work have been presented at the 18th ICA, Kyoto, Japan.
[b)]Author to whom correspondence should be addressed. Electronic mail: xiangn@rpi.edu; Tel: (518)-276-6464; Fax: (518)-276-3034.

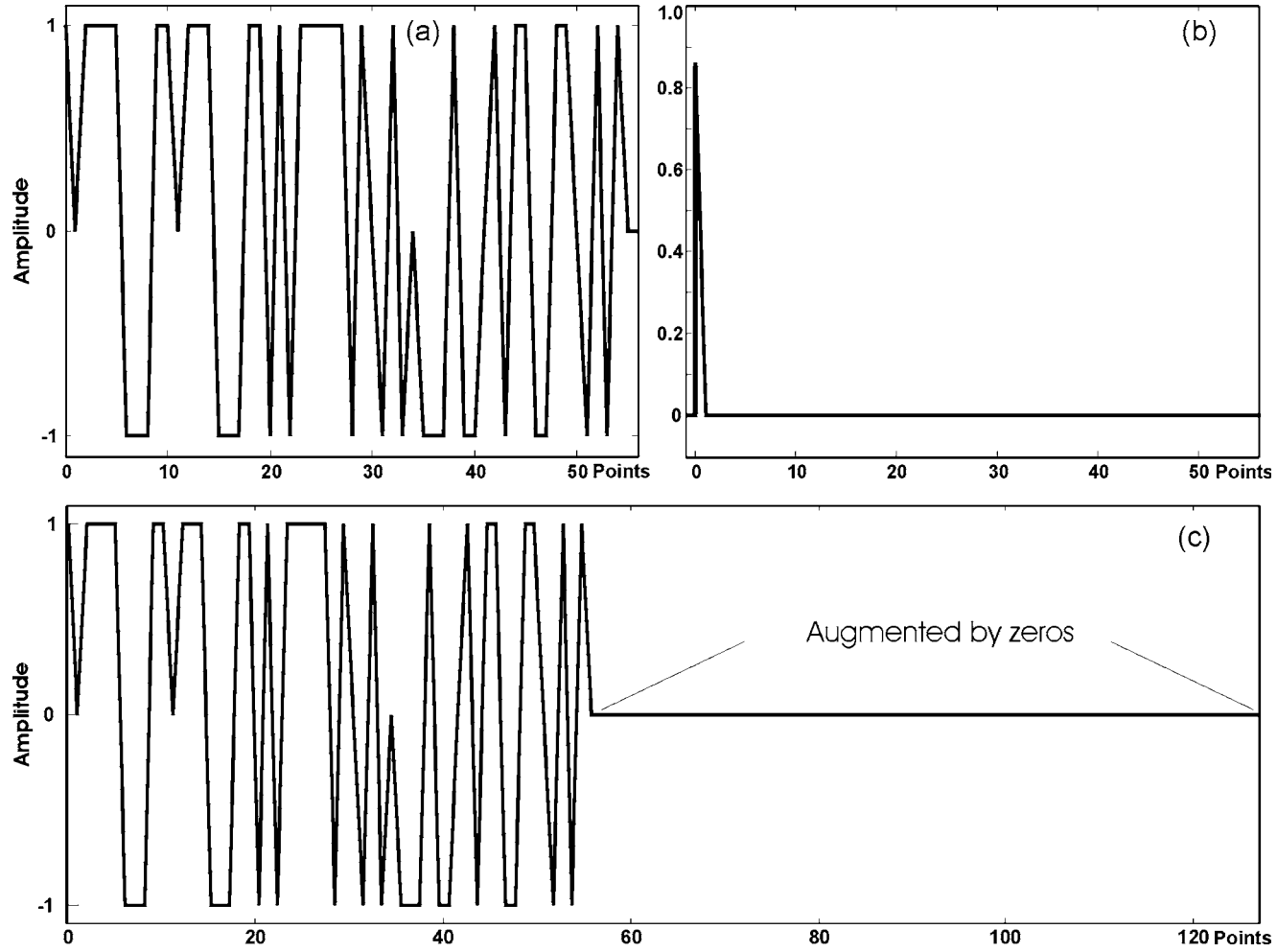

FIG. 1. (a) Ternary sequence of length 57. (b) Its autocorrelation function is two-valued (0.86, 0.0). (c) Augmented sequence of length 128 by zeros.

systems in the time domain. However, the HT-FMT can be applied only to binary M-sequences. Standard FFTs have not yet been successfully applied to cross-correlation of other sequences possessing the desired correlation property. While there exists techniques for efficiently computing FFTs of sequences of arbitrary length, such as Bluestein's algorithm (BFFT),[19] we explore the use of standard FFTs in calculating the periodic cross-correlation between two periodic sequences of equal finite length, where the lengths of the sequences are not equal to a positive power of 2. In our approach we do not actually compute the FFTs of the original sequences, and, as we shall see, this yields a more efficient computational algorithm.

In the next section, we discuss the general problem of computing PCCFs and explain our approach to computing PCCFs of arbitrary-length (finite) sequences using FFTs. We then present a number of examples that illustrate the application of our approach. Finally, we draw some conclusions.

II. COMPUTATION OF CROSS CORRELATION FUNCTIONS

Let $\mathcal{I}$ denote the set of integers and consider two sequences, $x[\cdot]=\{x[i], i\in\mathcal{I}\}$ and $y[\cdot]=\{y[i], i\in\mathcal{I}\}$ such that $x[i]=y[i]=0$ for $i\ni\{0,1,\ldots,L-1\}$ and $x[i]$ and $y[i]$ have arbitrary values for $i\in\{0,1,\ldots,L-1\}$. Define the sequences $x_I[\cdot]$ and $y_I[\cdot]$, $I\geqslant L$ to be the sequences $x[\cdot]$ and $y[\cdot]$ repeated at intervals of length I. If $I>L$, then we refer to the sequences $x_I[\cdot]$ and $y_I[\cdot]$ as *augmented* sequences of $x_L[\cdot]$ and $y_L[\cdot]$, respectively. As an example, Fig. 1(a) illustrates a ternary sequence, say $t_L[\cdot]$ with $L=57$, and its augmented sequence $t_I[\cdot]$ with $I=128$ as shown in Fig. 1(c). In particular, define

$$x_L(i)=\sum_{j=-\infty}^{\infty} x[i-jL] \quad \text{and} \quad y_L(i)=\sum_{j=-\infty}^{\infty} y[i-jL]. \tag{1}$$

We wish to determine the periodic cross-correlation between $x_L[\cdot]$ and $y_L[\cdot]$, where L cannot be represented as a positive power of 2. In order to do this, we make use of the augmented sequences.

It is well-known[20] that the periodic cross-correlation

$$R_{x_I,y_I}[\cdot]=\mathcal{D}^{-1}(X_L[\cdot]Y_L^*[\cdot]), \tag{2}$$

where $\mathcal{D}$ denotes the discrete Fourier transform (DFT) operator and $X_L[\cdot]=\mathcal{D}(x_L[\cdot])$ and $Y_L^*[\cdot]=\mathcal{D}^*(y_L[\cdot])$. Y^* stands for complex conjugate of Y. Similarly, if $I=2^N$ for some positive integer N, then

$$R_{x_I,y_I}[\cdot] = \mathcal{F}^{-1}(X_I[\cdot]Y_I^*[\cdot]), \tag{3}$$

where $\mathcal{F}$ denotes the fast Fourier transform (FFT) operator, $\mathcal{F}^{-1}$ the inverse FFT (IFFT), and $X_I[\cdot]=\mathcal{F}(x_I[\cdot])$ and $Y_I^*[\cdot]=\mathcal{F}^*(y_I[\cdot])$. The FFT is significantly more efficient computationally than the DFT $\{O[L\log_2(L)]$ versus $O(L^2)\}$. But if L does not have the form 2^N for some positive integer N, then the standard FFT cannot be used directly. We demonstrate below a technique for using the standard FFT as a primary computational tool for arbitrary values of L.

Let $R_{x,y}(k)$ denote the cross-correlation between $x[i]$ and $y[i]$ at offset k; that is,

$$R_{x,y}[k] = \sum_{i=-\infty}^{\infty} x[i]y[i+k] = \sum_{i=\max\{0,-k\}}^{\min\{L-1,L-1-k\}} x[i]y[i+k], \tag{4}$$

where (4) follows from the fact that $x[i]$ and $y[i]$ are zero for $i \ni \{0,1,\ldots,L-1\}$. Now, if $k<0$, then $\max\{0,-k\}=-k$ and $\min\{L-1,L-1-k\}=L-1$. Similarly, if $k\geqslant 0$, then $\max\{0,-k\}=0$ and $\min\{L-1,L-1-k\}=L-1-k$, thus

$$R_{x,y}[k] = \begin{cases} \sum_{i=-k}^{L-1} x[i]y[i+k] & \text{for } k<0, \\ \sum_{i=0}^{L-1-k} x[i]y[i+k] & \text{for } k\geqslant 0. \end{cases} \tag{5}$$

Thus, we readily see that $R_{x,y}[k]=0$ for $k \ni \{0,\pm 1,\ldots,\pm(L-1)\}$.

Now, define $R_{x,y_I}[k]$ to be the cross-correlation between $x[i]$ and $y_I[i]$ at offset k, it follows from (4) that

$$R_{x,y_I}[k] = \sum_{j=-\infty}^{\infty} R_{x,y}[k-jI]. \tag{6}$$

Similarly, since the cross-correlation of two sequences, $a[\cdot]$ and $b[\cdot]$, each having period I is defined as

$$R_{a,b}[k] = \lim_{\ell\to\infty} \frac{1}{2\ell I} \sum_{i=-\ell I}^{\ell I-1} a[i]b[i+k], \tag{7}$$

we find that

$$R_{x_I,y_I}[k] = \sum_{j=-\infty}^{\infty} R_{x,y}[k-jI]. \tag{8}$$

Now, let us determine the value of $R_{x_I,y_I}[k]$ over the period $k\in\{0,1,\ldots,I-1\}$ in terms of $R_{x,y}[k]$. Since $R_{x,y}[k]=0$ for $k \ni \{0,\pm 1,\ldots,\pm(L-1)\}$ and $I\geqslant L$, it follows that with $j<0$, $R_{x,y}[k-jL]=0$ for $k\geqslant 0$. Similarly, with $j>1$, $R_{x,y}[k-jL]=0$ for $k<I$. Therefore, we find that for $0\leqslant k\leqslant I-1$,

$$R_{x_I,y_I}[k] = R_{x,y}[k] + R_{x,y}[k-I]. \tag{9}$$

In particular, if $I\geqslant 2L$, then (9) can be written as follows:

$$R_{x_I,y_I}[k] = \begin{cases} R_{x,y}[k], & 0\leqslant k\leqslant L-1, \\ 0, & L\leqslant k\leqslant I-L, \\ R_{x,y}[k-I], & I-L<k\leqslant I-1. \end{cases} \tag{10}$$

Equation (10) can be rewritten as

$$R_{x,y}[k] = \begin{cases} R_{x_I,y_I}[I+k], & -(L-1)\leqslant k\leqslant -1, \\ R_{x_I,y_I}[k], & 0\leqslant k\leqslant L-1, \\ 0 & \text{else}. \end{cases} \tag{11}$$

The point of (10) and (11) is that if I is chosen to be at least $2L$, then $R_{x_L,y_L}[\cdot]$ can be obtained from $R_{x_I,y_I}[\cdot]$. Thus, if we choose $I=2^N$, where N is the minimum value yielding $I\geqslant 2L$, then $R_{x_I,y_I}[\cdot]$ can be computed from (3). Next, $R_{x,y}[\cdot]$ can be computed using (11), and finally, $R_{x_L,y_L}[\cdot]$ can be computed from (10) by using L in place of I.

As an example, we take a ternary sequence $\{t\}=\{1\ 0\ 1\ 1\ 1\ 1\ -1\ -1\ -1\ 1\ 1\ 0\ 1\ 1\ 1\ -1\ -1\ -1\ 1\ 1\ -1\ 1\ -1\ 1\ 1\ 1\ 1\ 1\ -1\ 1\ 0\ -1\ 1\ -1\ 0\ -1\ -1\ -1\ 1\ 1\ -1\ 0\ 1\ -1\ 1\ 1\ -1\ -1\ 1\ 1\ 0\ -1\ 1\ -1\ 1\ 0\ 0\}$ (Ref. 21) of length $L=57$ as shown in Fig. 1(a) to demonstrate the described method in calculating its periodic autocorrelation function. The sequence $\{t\}$ contains 8 zeros in its period, so the zero-lag autocorrelation value amounts to $(57-8)/57=0.86$. Its periodic autocorrelation function is a two-valued function of $\{0.86,0.0\}$ as shown in Fig. 1(b). After augmenting the original sequence to $\{t_{128}\}$ with $t_i=0$ for $i \ni \{0,56\}$ as shown in Fig. 1(c) we can find from (3),

$$R_{t_{128},t_{128}}[\cdot] = \mathcal{F}^{-1}(T_{128}[\cdot]T_{128}^*[\cdot]), \tag{12}$$

as shown in Fig. 2(a). Figure 2(a) clearly demonstrates that a cross-correlation between sequences of unsuitable length using a direct FFT-method in (3) and (12) will not provide correct results no matter how many zeros are padded to the sequences in order to get a suitable length for FFT operations. For this reason, we find from (11),

$$R_{t,t}[k] = \begin{cases} R_{t_{128},t_{128}}[128+k], & -56\leqslant k\leqslant -1, \\ R_{t_{128},t_{128}}[k], & 0\leqslant k\leqslant 56, \\ 0 & \text{else}. \end{cases} \tag{13}$$

Finally, we find from (11), for $0\leqslant k\leqslant 56$

$$R_{t,t}[k] = R_{t_{128},t_{128}}[k] + R_{t_{128},t_{128}}[k+128-57]. \tag{14}$$

The two terms on the right-hand side of (14) are shown in Fig. 2(b), the addition of which results in exactly the correct PACF as shown in Fig. 1(b).

The described algorithm can be summarized in the following three major steps:

(1) Augment the MLS-related sequences and other sequences $m[\cdot]$ of length L (not suitable for FFT) to $\hat{m}[\cdot]$ and the response $y[\cdot]$ to $\hat{y}[\cdot]$ by zeros, respectively to form a suitable length $I=2^N$ for FFT operations, I is the first power of 2 that exceeds $2L$.

(2) Cross-correlate the two augmented sequences of length I using the *FFT*,

$$\hat{h}[\cdot] = \mathcal{F}^{-1}\{\mathcal{F}(\hat{m}[\cdot])\mathcal{F}^*(\hat{y}[\cdot])\}. \tag{15}$$

(3) Add the first L and the last L points in $\hat{h}[\cdot]$ to form the resulting $h[\cdot]$ of L points,

$$h_k = \hat{h}_k + \hat{h}_{k+I-L}, \quad 0\leqslant k<L. \tag{16}$$

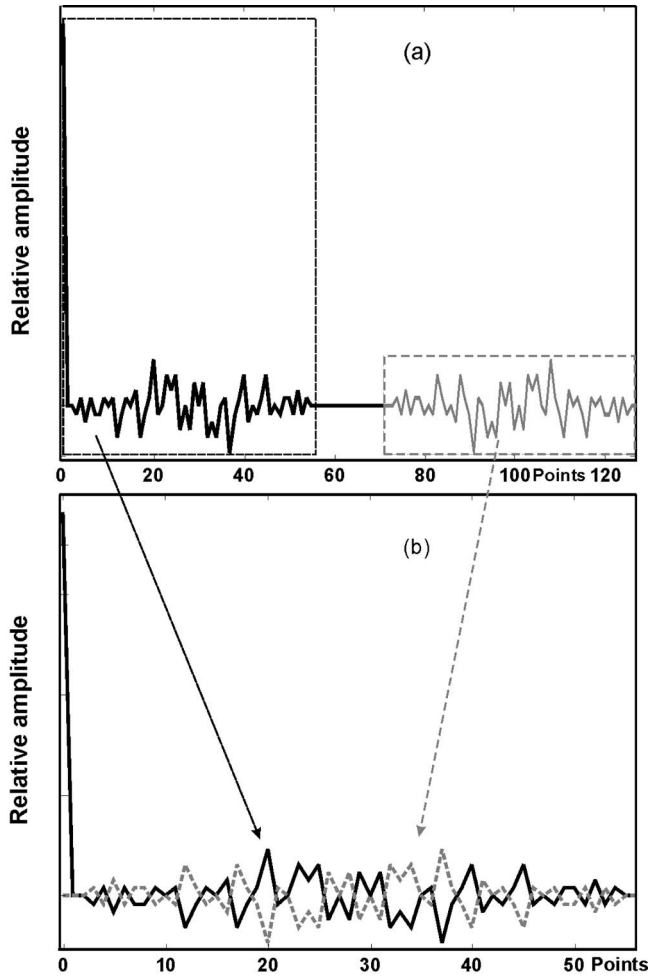

FIG. 2. Combining process illustrated using ternary sequence of length 57. (a) (Auto) correlation function evaluated using the augmented sequence to 128 points. (b) Combination (addition) of the first 57 and the last 57 points according to (14) results in the correct auto-correlation function of length 57 as shown in Fig. 1(b).

Using this method the FMT can be performed economically with a computational load of $O[I\log_2(I)]$. The FFT-based FMT algorithm is computationally more expensive than the HT-based FMT since the fast Hadamard transform consists solely of $O[L\log_2(L)]$ addition operations. However, the additional computation load will be less and less noticeable with the modern, fast developing computer technology. More importantly, it is of practical significance when other digital sequences have to be applied in acoustical experiments as the next section elaborates.

We emphasize here that our contribution is an algorithm to find the cross-correlation of two sequences of arbitrary length, not to find the FFTs of the original sequences. That is, our procedures do not yield FFTs of the original sequences, and consequently, we do not add anything whatever to the literature on computation of FFTs of sequences of arbitrary length. By contrast, the BFFT algorithm[19] is specifically designed to compute the FFT of a sequence of arbitrary length. But, the BFFT algorithm requires three applications of the standard FFT algorithm to a sequence of the same length as our extended sequence in addition to miscellaneous convolutions to produce the coefficients. Thus, while the BFFT algorithm is efficient for finding the FFTs of sequences such as our original sequences, its application to our particular case would result in a computational penalty of a factor of at least 3.

We note in passing that, depending on the value of L, it may be more efficient to compute the FFT of the original sequences by developing a specialized FFT routine. In particular, suppose that $N=r_1,r_2,\ldots,r_p$ where $\{r_1,r_2,\ldots,r_p\}$ is the set of prime factors of N. Then, it is possible to develop a specialized FFT routine that requires $N\Sigma_{i=1}^{p}r_i$ operations,[22,23] as opposed to N^2 for the DFT. For example, if $N=57$, then $N=3\times19$. Hence, the specialized FFT for a 57 point sequence requires $57(19+3)=1254$ operations, while using a DFT requires $57^2=3249$ and our technique based on standard FFTs requires $128\times14=1792$ operations. Similarly, if $N=255=3\times5\times17$, then a specialized FFT routine would require $255\times(3+5+17)=6275$ operations while our technique based on standard FFTs requires $512\times18=9216$ operations. On the other hand, if $N=127$, then N is prime and a 127 point DFT routine requires $127^2=16129$ operations while our technique based on standard FFTs requires $256\times16=4096$ operations. Although there exist a dedicated fast Fourier transform for prime lengths,[24] which is suitable for binary Legendre sequences,[11] but only a few MLS-related sequences have a prime length, such as $2^{17}-1$, a so-called Mersenne number. Therefore, the prime-length FFT has limited applications. Thus, the value of developing a specialized FFT routine depends on the length of the sequence.

III. EXPERIMENTAL EXAMPLES

This section presents an experimental example to illustrate the application of the above-described algorithm in acoustical measurements. Unlike the application in spread spectrum technology where some desired code is used to modulate a digital data sequence before modulating a carrier, the coded signals here in acoustical applications are directly used to drive acoustic sources at a rate that is sufficiently high to cover the frequency range of interest according to the sampling theorem. In order to measure room impulse responses from two separate sound sources simultaneously in the Russell Sage Hall at Rensselaer Polytechnic Institute, Troy, New York, a pair of Kasami sequences of degree 20 were used to drive the sound sources simultaneously at a sampling frequency of 50 kHz. Two microphones were used to receive the steady-state room acoustic responses to the excitations. Figure 3 shows the first 1.2 s of the four room impulse responses of the channels between the two sound sources and the two microphones. Note that a preferred pair of MLSs or MLSs drawn from the maximum connect set[7] might also be applied to this case, but with increasing number of simultaneous sources, these MLSs cannot meet the need, while enough number of Kasami or Gold sequences can be easily constructed to cope with the required number of sources.[7] In addition, Kasami or Gold sequences are combined sequences, to which the HT-FMT can no longer be applied.

When calculating the cross-correlation between the acoustic (microphone) steady-state response to the Kasami-

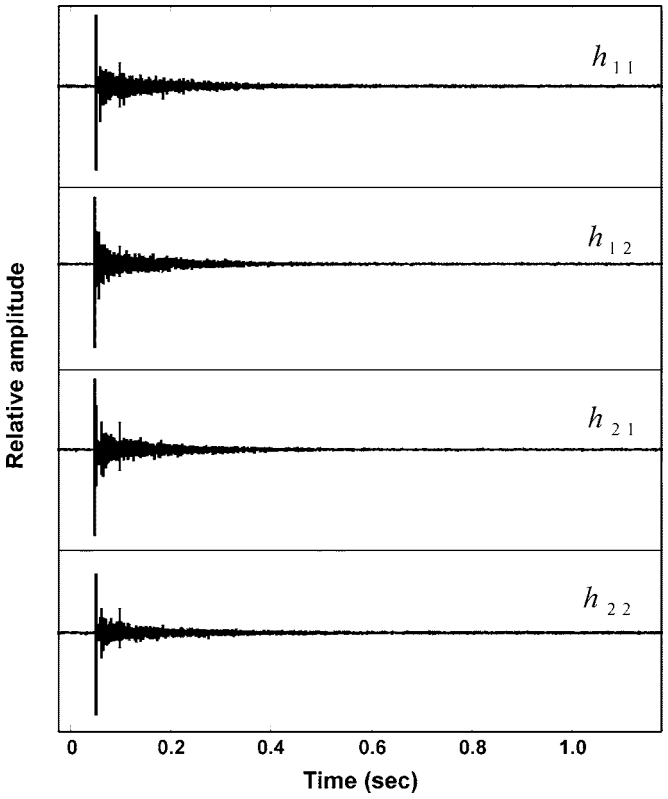

FIG. 3. Room impulse responses measured using the specialized FFT techniques in the Russell Sage Hall, RPI. Two separate sound sources are excited simultaneously by two Kasami sequences of degree 20. Two microphones measure the room acoustic responses to the Kasami sequence excitations. The specialized FFT-based cross-correlation algorithm results in four room impulse responses.

sequence and the original Kasami-sequence, the described algorithm is applied resulting in a desired room impulse response. This example exactly demonstrates the application of our algorithm to a case where the Hadamard-transform-based fast M-sequence transform cannot be applied and where use of the DFT is computationally grossly inefficient. It is easy to verify that the impulse response are identical to those obtained by direct cross-correlation.

IV. SUMMARY AND CONCLUSIONS

We have shown how periodic cross-correlations, in general, and channel impulse responses of acoustical systems, in particular, may be obtained via specialized application of conventional FFT techniques even in the case where the length of sequences to be evaluated are not of length p^N, where p is a prime. Conventional FFTs cannot directly process periodic cross-correlations of coded signals, such as ternary sequences, binary or higher prime maximum-length sequences, Gold, and Kasami sequences, which are increasingly used in acoustic system identification tasks. We have argued that our techniques can provide substantial computational improvements over direct DFT techniques in a practical situation, specifically when it is desirable or even mandatory simultaneously to obtain impulse responses between multiple sound/vibration sources and one or several receivers.

The application of Kasami sequences or Gold sequences[7] is of particular interest when a large number of sound sources need to be driven simultaneously so that the measurement can be accomplished in the same time interval as those using a single source channel. As stated previously, Kasami and Gold sequences are combinations between binary maximal-length sequences and their derived sequences.[7] The combination can easily provide a large number of sequences of the same length with desired correlation properties as suitable for simultaneous source excitations.

The ability to efficiently analyze room impulse responses using Kasami sequences is especially important in cases where it is desired to measure simultaneously the impulse responses at a point from a number of different sources. In that case, one can easily construct enough distinct Kasami sequences to meet the need,[7] but neither the Hadamard-transform-based fast M-sequence transform nor the conventional FFT algorithm applied directly to the sequences can accomplish the processing. The specialized correlation algorithm described in this paper is simple to use. It involves only zero-padding of the original sequences, performing two conventional FFTs and one conventional IFFT, and simple addition to obtain the final result. This algorithm is also applicable to binary MLSs, so the fast MLS-transform can also be performed based on the specialized FFT-based correlation algorithm, then termed FFT-based FMT. The computation load of each single impulse response is, however, $3O(I \log_2 I)$. One can always carry out one FFT of the augmented excitation sequence once and store the results in memory before a large number of measurements using the same excitation sequence need to be performed so that the computation load is reduced to $2O(I \log_2 I)$.

ACKNOWLEDGMENTS

The authors thank Professors Dr. Hans D. Lüke and Dr. Mendel Kleiner for their valuable advice and inspiration. The authors would like to thank the associate editor and the reviewers for their insightful and constructive comments.

[1]M. R. Schroeder, "Integrated-impulse method measuring sound decay without using impulses," J. Acoust. Soc. Am. **66**, 497–500 (1979).
[2]J. Borish and J. B. Angell, "An efficient algorithm measuring the impulse response using pseudorandom noise," J. Audio Eng. Soc. **31**, 478–488 (1983).
[3]T. G. Birdsall and K. Metzger Jr., "Factor inverse matched filtering," J. Acoust. Soc. Am. **79**, 91–99 (1986).
[4]H. DeFerrari and H. Hien, "M-sequences and bi-static active sonar," J. Acoust. Soc. Am. **116**, 2647[A] (2004).
[5]W. Munk, P. Worchester, and C. Wunsch, *Ocean Acoustic Tomography* (Cambridge University Press, Cambridge, 1995).
[6]N. Xiang and M. R. Schroeder, "Reciprocal maximum-length sequence pairs for acoustic dual source measurements," J. Acoust. Soc. Am. **113**, 2754–2761 (2003).
[7]N. Xiang, J. N. Daigle, and M. Kleiner, "Simultaneous acoustic channel measurement via maximal-length-related sequences," J. Acoust. Soc. Am. **117**, 1889–1894 (2005).
[8]D. K. Wilson, A. Ziemann, V. E. Ostashev, and A. G. Voronovich, "An Overview of Acoustic Travel-Time Tomography in the Atmosphere and its Potential Applications," Acta. Acust. Acust. **87**, 721–730 (2001).
[9]A. Ziemann, K. Arnold, and A. Raabe, "Acoustic Tomography as a Method to Identify Small-Scale Land Surface Characteristics," Acta. Acust. Acust. **87**, 731–737 (2001).
[10]J. Cooley and J. Tukey, "An algorithm for the machine calculation of complex Fourier series," Math. Comput. **19**, 297–301 (1965).

[11]M. R. Schroeder, *Number Theory in Science and Communication*, 2nd enl. ed. (Springer-Verlag, Berlin, 1991).
[12]D. V. Sarwate and M. B. Pursley, "Cross-correlation Properties of Pseudorandom and Related Sequences," Proc. IEEE **68**, 593–619 (1980).
[13]N. Xiang, "Using M-sequences for determining the impulse responses of LTI-systems," Signal Process. **28**, 139–152 (1992).
[14]W. T. Chu, "Impulse-response and reverberation-decay measurements made by using a periodic pseudorandom sequence," Appl. Acoust. **29**, 193–205 (1990).
[15]R. Burkard, Y. Shi, and K. E. Hecox, "A comparison of maximum length and Legendre sequences for the derivation of brain-stem auditory-evoked responses at rapid rates of stimulation," J. Acoust. Soc. Am. **87**, 1656–1664 (1990).
[16]M. Garai, "Measurement of the sound-absorption coefficient *in-situ*: The reflection method using periodic pseudo-random sequences of maximum length," Appl. Acoust. **39**, 119–139 (1993).
[17]M. Cohn and A. Lempel, "On fast M-sequences transforms," IEEE Trans. Inf. Theory **IT.23**, 135–137 (1977).
[18]A. Lempel, "Hadamard and M-sequence transforms are permutationally similar," Appl. Opt. **18**, 4064–4065 (1979).
[19]L. I. Bluestein, "A linear filtering approach to the computation of the discrete Fourier transform," (1968), reprinted in "Papers on Digital Signal Processing," edited by A. V. Oppenheim (MIT Press, Cambridge, MA, 1969), pp. 171–172.
[20]A. V. Oppenheim, R. W. Schafer, and J. R. Buck, *Discrete-Time Signal Processing*, 2nd ed. (Prentice-Hall, Englewood Cliffs, 1999).
[21]H. D. Lüke, *Korrelationssignale* English translation "Correlation Signals" (Springer-Verlag, Berlin, 1992).
[22]G. Dahlquist and Å. Björck, *Numerical Methods* (Prentice-Hall, Englewood Cliffs, 1974), translated by N. Anderson.
[23]G. D. Bergland, "The fast Fourier transform recursive equations for arbitrary length records," Math. Comput. **21**, 236–238 (1967).
[24]C. M. Rader, "Discrete Fourier transform when the number of data samples is prime," Proc. IEEE **56**, 1107–1108 (1968).

The array invariant

Sunwoong Lee[a] and Nicholas C. Makris[b]
Massachusetts Institute of Technology, Department of Mechanical Engineering, Cambridge, Massachusetts 02139

(Received 16 February 2005; revised 14 August 2005; accepted 17 October 2005)

A method is derived for instantaneous source-range estimation in a horizontally stratified ocean waveguide from passive beam-time intensity data obtained after conventional plane-wave beamforming of acoustic array measurements. The method has advantages over existing source localization methods, such as matched field processing or the waveguide invariant. First, no knowledge of the environment is required except that the received field should not be dominated by purely waterborne propagation. Second, range can be estimated in real time with little computational effort beyond plane-wave beamforming. Third, array gain is fully exploited. The method is applied to data from the Main Acoustic Clutter Experiment of 2003 for source ranges between 1 to 8 km, where it is shown that simple, accurate, and computationally efficient source range estimates can be made. © *2006 Acoustical Society of America.* [DOI: 10.1121/1.2139074]

PACS number(s): 43.60.Fg, 43.60.Jn, 43.30.Bp [WLS] Pages: 336–351

I. INTRODUCTION

It has long been known that multi-modal dispersion in a shallow water waveguide degrades the performance of bearing estimates by conventional plane-wave beamforming. This is due to the advent of spurious effects unique to the waveguide environment, such as multiple peaks and beam spreading in the beamformer output.[1–3] Attempts, on the other hand, have been made to localize sources submerged in ocean waveguides by exploiting multi-modal interference using methods such as matched field processing (MFP).[4–6] Apart from being computationally expensive, MFP techniques require accurate knowledge of the wave propagation environment. They are susceptible to large systematic errors from mismatch when adequate environmental information is not available.[7,8]

The range of a source in a horizontally stratified ocean waveguide can sometimes also be estimated by the much simpler waveguide invariant method,[9–11] which employs only incoherent processing of acoustic intensity data as a function of range and bandwidth. The waveguide invariant method, however, requires knowledge of certain "invariant" parameters, which unfortunately often vary significantly with ocean sound speed structure. It also requires a sufficiently large number of waveguide modes to significantly contribute to the measured field because these cause the interference structure necessary to produce a unique solution. Sufficiently dense sampling of the intensity data in source-receiver range is also necessary to provide an unambiguous solution. When the application involves single-sensor measurements, joint ambiguity in source-receiver range and velocity is an inherent limitation of the waveguide invariant method. This ambiguity can disappear when spatial sensor arrays of sufficient horizontal aperture are used. None of the usual benefits of increased signal-to-noise ratio at the array output appear, however, because only incoherent processing of the spatial samples can be performed.

Here we show that instantaneous source range estimation is possible in a horizontally stratified ocean waveguide by a computationally inexpensive method that has significant advantages over the waveguide invariant because it requires neither *a priori* knowledge of environmental parameters nor multiple modes in the received field, and fully exploits the coherent gain possible with receivers of finite spatial aperture.[12] Since the new approach takes advantage of invariant properties of passive beam-time intensity data obtained after conventional plane-wave beamforming of underwater acoustic array measurements, we call it the *array invariant* method. We show that maximum beam-time intensity migrates along an angle that is invariant to environmental parameters but follows a known and unique dependence on source-receiver range. Horizontal source localization is also achieved when the receiving array has sufficient horizontal aperture to resolve source bearing. The formulation introduced here is specifically for broadband transient source signatures. A more general but involved formulation that can treat continuous broadband noise signatures is possible.[13]

The array invariant method is derived in Sec. II. Illustrative examples are presented in Sec. III. In Sec. IV, source localization by the array invariant method is experimentally demonstrated using data from the Main Acoustic Clutter 2003 Experiment (MAE). Comparisons between the array invariant method and other acoustic techniques for source range estimation in the ocean, such as the waveguide invariant method and MFP, are presented in Sec. V.

II. DERIVATION OF THE ARRAY INVARIANT

Analytic expressions are derived for the migration of peak intensity through a beam-time intensity image generated from acoustic array measurements made in an ideal waveguide. It is then shown that the expressions are approxi-

[a]Electronic address: sunwoong@mit.edu
[b]Electronic address: makris@mit.edu

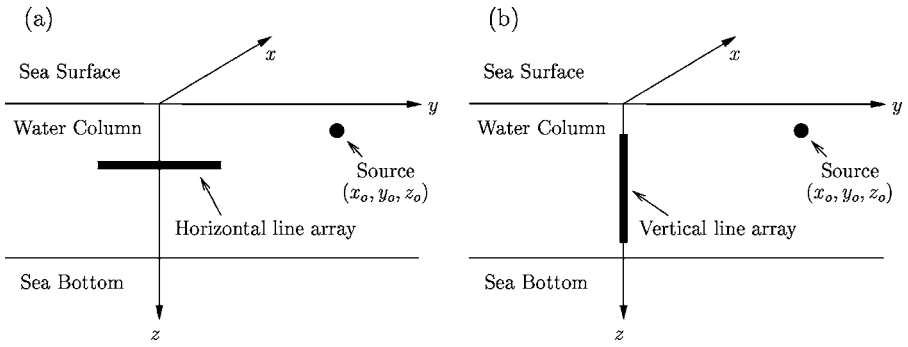

FIG. 1. The geometry of the coordinate system for a horizontal line array (a), or a vertical line array (b). The horizontal line array is aligned parallel to the y-axis. The vertical line array is located along the z-axis. A source is located at (x_o, y_o, z_o).

mately valid for typical horizontally stratified ocean waveguides, where they can be used for instantaneous source localization.

A. Beam-time migration for horizontal arrays in stratified waveguides

The measurement and coordinate geometry of Fig. 1(a) shows a horizontal line array parallel to the y axis, with array center at $(0,0,z)$, and source at (x_o, y_o, z_o). We define $\mathbf{r} = x\hat{i}_x + y\hat{i}_y$, and $r = |\mathbf{r}|$, where $\hat{i}_x$ and $\hat{i}_y$ are unit vectors in the x and y directions, respectively. The wavenumber vector $\mathbf{k}$ is decomposed into $k_x = -k \sin\phi \cos\theta$, $k_y = -k \sin\phi \sin\theta$, and $k_z = -k \cos\phi$, where $k = |\mathbf{k}|$, and elevation angle ϕ and bearing θ are shown in Fig. 2.

The pressure P at frequency f due to a source at $(\mathbf{r_o}, z_o)$ can be expressed using normal mode theory as

$$P(\mathbf{r},z,f) = 4\pi Q(f) \frac{i}{\sqrt{8\pi\rho(z_o)}} e^{-i\pi/4} \times \sum_n u_n(z_o) u_n(z) \frac{e^{ik_{rn}|\mathbf{r}-\mathbf{r_o}|}}{\sqrt{k_{rn}|\mathbf{r}-\mathbf{r_o}|}}, \quad (1)$$

where $Q(f)$ is the source spectrum, ρ is the density, k_{rn} is the horizontal wavenumber of the nth mode, and u_n is the mode shape of the nth mode which satisfies $\int_0^\infty u_m(z) u_n^*(z)/\rho(z) dz = \delta_{mn}$. Using the far-field approximation $|\mathbf{r}-\mathbf{r_o}| \simeq r_o - y \sin\theta_o$, where θ_o is source bearing, the beamformed pressure P_B can be expressed as a function of array scan angle θ,

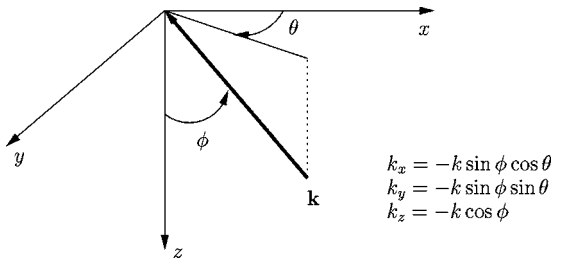

FIG. 2. Definition of the elevation angle ϕ and the bearing θ of plane waves. The angles are defined in the "coming from" direction.

$$P_B(s,f) = \int_{-\infty}^{\infty} T(v) P(v,z,f) e^{i2\pi v \sin\theta} dv = 4\pi Q(f) \frac{i}{\sqrt{8\pi\rho(z_o)}} e^{-i\pi/4} \times \sum_n u_n(z_o) u_n(z) \frac{e^{ik_{rn}r_o}}{\sqrt{k_{rn}r_o}} B(s-s_n), \quad (2)$$

where $s = \sin\theta$, $v = ky/2\pi$, $s_n = \sin\phi_n \sin\theta_o$, and $\sin\phi_n = k_{rn}/k$. For evanescent modes, $\phi_n = \pi/2 - i\phi_n'$ where $\phi_n' = \ln[k_{rn}/k + \{(k_{rn}/k)^2 - 1\}^{(1/2)}]$. The beam pattern $B(s)$ is the spatial Fourier transform of the array taper function $T(v)$.[14] This far-field formulation is valid when the source-receiver range exceeds the square of the aperture divided by the wavelength.

The time-domain expression for the beamformed pressure $P_B(s,t)$ is obtained by taking the inverse Fourier transform of Eq. (2),

$$P_B(s,t) = 2\,\mathrm{Re}\left\{ \int_0^\infty P_B(s,f) e^{-i2\pi ft} df \right\} = 2\,\mathrm{Re}\{P_{B+}(s,t)\}, \quad (3)$$

where $\mathrm{Re}\{\cdot\}$ represents the real part. The complex beamformed pressure $P_{B+}(s,t)$ can then be approximated using the method of stationary phase[3,15–17] when $k_{rn}r_o \gg 1$, as given in Eq. (A6) in Appendix A. The stationary phase approximation for Eq. (3) simplifies to Eq. (A8) if the relative phase shifts between the different frequency components of the source spectrum are negligible, which occurs when $Q(f) = |Q(f)|$, such as in an impulsive or Gaussian signal. This is the simplifying approximation that limits the present formulation to the domain of transient signals, which is clearest for introducing the concepts. A more general formulation for continuous broadband noise is possible,[13] as noted in Sec. I. The complex beamformed pressure in Eq. (3) can then be approximated as

$$P_{B+}(s,t) \simeq \frac{4\pi i}{\sqrt{8\pi\rho(z_o)}} e^{-i\pi/4} \times \sum_n |Q(\tilde{f})| \tilde{u}_n(z_o) \tilde{u}_n(z) \frac{\tilde{B}(s-\tilde{s}_n)}{\sqrt{\tilde{k}_{rn}r_o}} F_n(\tilde{f}), \quad (4)$$

where $\tilde{f}$ is the frequency component within the source band that satisfies

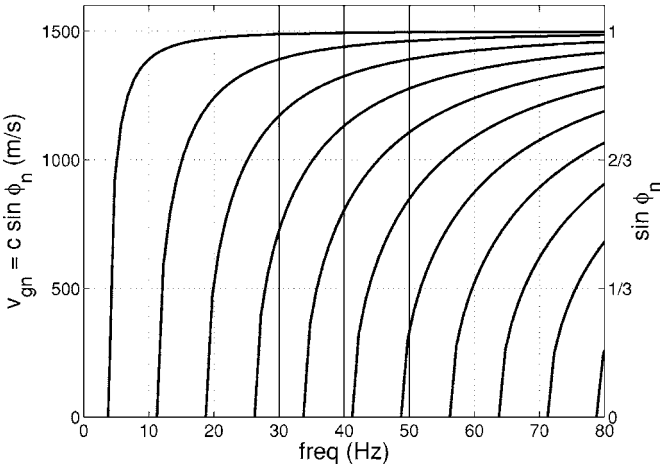

FIG. 3. Group velocity v_{gn} and modal elevation angle sin ϕ_n as a function of frequency in an ideal waveguide. The water depth and the sound speed are 100 m and 1500 m/s, respectively, and the boundaries are assumed to be pressure release. The vertical lines at 30, 40, and 50 Hz will be referred to in Fig. 5.

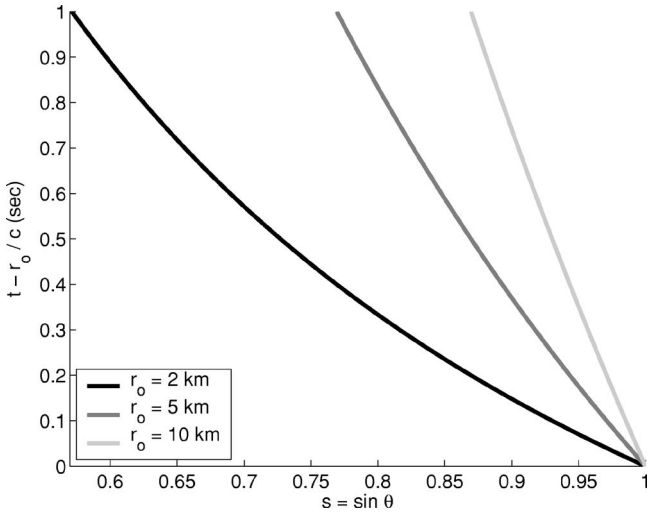

FIG. 4. The beam-time migration lines $\tilde{s}_n(t)$ as a function of reduced travel time $t-r_o/c$ and array scan angle θ for various source ranges over the full 0 to 80-Hz frequency band shown in Fig. 3. The sound speed c is 1500 m/s and source bearing θ_o is $\pi/2$. It can be seen that all the $\tilde{s}_n(t)$ merge to a single beamformer migration line $\tilde{s}(t)$.

$$t = \frac{r_o}{v_{gn}(\tilde{f})}, \tag{5}$$

v_{gn} is the group velocity of the nth mode, and $\tilde{u}_n, \tilde{k}_{rn}, \tilde{B}, \tilde{s}_n, \tilde{v}_{gn}, \tilde{\phi}_n$ are the corresponding values of $u_n, k_{rn}, B, s_n, v_{gn}, \phi_n$ at $f=\tilde{f}$. The function $F_n(\tilde{f})$ in Eq. (4) is given in Eq. (A9) of Appendix A. The bearing of peak beamformed pressure for the nth mode at time t is specified by

$$\tilde{s}_n(t) = \sin \tilde{\phi}_n(t) \sin \theta_o, \tag{6}$$

which is the zero of the argument of the beam pattern $\tilde{B}(s-\tilde{s}_n)$ in Eq. (4). Equations (5) and (6) enable the temporal migration of the maximum beamformer output angle to be determined in any horizontally stratified ocean waveguide. These equations are significant because they lead directly to source localization in an ocean waveguide by the new array invariant method.

B. Array invariant for horizontal arrays in ideal waveguides

Here we show that the bearing of peak beamformed pressure $\tilde{s}_n(t)$, given in Eq. (6) for any given mode at any time, is an observable from which source range can be estimated. This is done by first noting that group velocity and modal elevation angle are related by

$$[v_{gn}]^{-1} = \frac{1}{2\pi}\frac{d}{df}\sqrt{k^2 - k_{zn}^2} = \frac{1}{2\pi}\frac{dk}{df}\frac{k}{k_{rn}} = [c \sin \phi_n]^{-1} \tag{7}$$

for an ideal isovelocity waveguide with pressure-release or rigid boundaries since the vertical wavenumber of the nth mode k_{zn} is not a function of f. This is illustrated in Fig. 3. Then Eqs. (5) and (7) can be used to express Eq. (6) as

$$\tilde{s}_n(t) \equiv \tilde{s}(t) = \frac{r_o}{ct} \sin \theta_o, \tag{8}$$

which shows that the $\tilde{s}_n(t)$ merge to a single beamformer migration line $\tilde{s}(t)$ for all mode numbers if the source bandwidth is sufficiently large. For fixed source bearing, the beamformer migration line changes only as a function of source range as can be seen in Eq. (8) and as illustrated in Fig. 4.

If the bandwidth of the source signal is not sufficiently large, $\tilde{s}_n(t)$ may appear as discrete line segments along the trajectory described by the right-hand side of Eq. (8). This is due to the discrete nature of the waveguide modes. An example is shown in Fig. 5(a) for a source signal in the 30 to 40-Hz band. For a given frequency band, the length of an $\tilde{s}_n(t)$ segment is greater for higher-order modes. This is because they exhibit more dispersion than lower-order modes, as can be deduced from Fig. 3 by noting that the change in group velocity across the band increases with mode number.

For a given mode and $\tilde{s}_n(t)$ segment, the $\tilde{s}_n(t)$ will migrate to a different part of the $\tilde{s}(t)$ curve when the frequency band of the source signal changes. This is because both the group velocity and elevation angle of the given mode change as a function of frequency. This is illustrated in Fig. 5(b), where the source frequency is now in the 40 to 50-Hz band. Comparison of Figs. 5(a) and 5(b) shows that the $\tilde{s}_n(t)$ for a given mode migrates to an earlier segment with greater scan angle because both group velocity v_{gn} and elevation angle ϕ_n for that mode have increased with the positive shift in the bandwidth. This migration is constrained to occur within the $\tilde{s}(t)$ curve given by Eq. (8), which completely determines the peak beam-time migration in an ideal waveguide. If the source signal occupies the entire 30 to 50-Hz band, the $\tilde{s}_n(t)$ for individual modes overlap to form the continuous $\tilde{s}(t)$, as shown in Fig. 5(c).

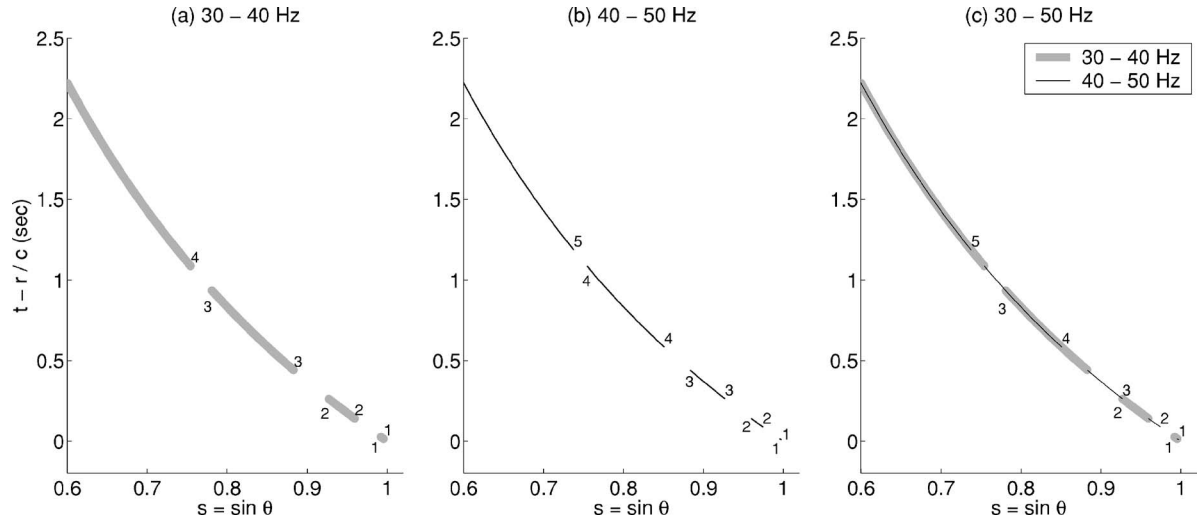

FIG. 5. (a) The beam-time migration lines $\tilde{s}_n(t)$ for modes in the 30 to 40-Hz band shown in Fig. 3 as a function of reduced travel time $t-r_o/c$ and array scan angle θ for a source at $r_o=5$ km and $\theta_o=\pi/2$. The beam-time migration lines $\tilde{s}_n(t)$ appear as discrete line segments. The beginning and end of each $\tilde{s}_n(t)$ segment is marked by mode number n. (b) The same as (a), but for modes in the 40 to 50-Hz band. As group velocity and elevation angle of a given mode changes, $\tilde{s}_n(t)$ for that mode migrates to a different location in the beam-time plot. This migration is constrained to occur within the $\tilde{s}(t)$ curve given by Eq. (8). (c) The same as (a), but for modes in the 30 to 50-Hz band. As the frequency band of the source increases, $\tilde{s}_n(t)$ for the individual modes overlap to form the continuous $\tilde{s}(t)$.

We define an array invariant χ_h for a horizontal linear receiver array as

$$\chi_h \equiv \frac{d\tilde{s}^{-1}(t)}{dt} = \frac{c}{r_o \sin\theta_o}. \tag{9}$$

For fixed source bearing, Eq. (9) is independent of source frequency band, mode number, source depth, receiver depth, and waveguide depth. Also, Eq. (9) is valid for both pressure release and rigid boundary ideal waveguides.

Source range can now be estimated using

$$\hat{r}_o = \frac{c}{\hat{\chi}_h \sin\hat{\theta}_o}, \tag{10}$$

based on direct measurements of the array invariant $\hat{\chi}_h$ and source bearing $\hat{\theta}_o$ obtained from beam-time intensity data. Since Eq. (10) is a unique one-to-one mapping of $\hat{r}_o$ from $\hat{\chi}_h$ for fixed $\hat{\theta}_o$, range inversion using the array invariant does not suffer from ambiguity, as is common in MFP.

The array invariant method differs significantly from the waveguide invariant method in that the array invariant does not rely on modal interference. Application of the waveguide invariant is not possible, for example, if there is only one mode propagating in a waveguide. The array invariant, however, is still applicable if the solitary mode causes sufficient dispersion in the source band, as can be seen in Eq. (8) and Fig. 4. In most practical applications, the combined dispersion of multiple modes is needed for robust source localization as will be shown in Sec. III.

C. Array invariant for horizontal arrays in stratified waveguides

For general horizontally stratified waveguides, the relationship between group velocity and horizontal wavenumber is

$$[v_{gn}]^{-1} = \frac{1}{2\pi}\frac{d}{df}\sqrt{k^2(z)-k_{zn}^2(z)},$$

which leads to the relation

$$v_{gn} = \frac{c(z)\sin\phi_n(z)}{1+\dfrac{c(z)}{2\pi}\cos\phi_n(z)\dfrac{dk_{zn}(z)}{df}} \tag{11}$$

between group velocity and modal elevation angle. By substituting Eq. (11) into Eq. (6), the peak beam-time migration line $\tilde{s}_n(t)$ for a given mode can be written explicitly as

$$\begin{aligned}\tilde{s}_n(z,t) &= \sin\tilde{\phi}_n(z,t)\sin\theta_o \\ &= \frac{r_o}{c(z)t}\sin\theta_o\left\{1+\frac{c(z)}{2\pi}\cos\tilde{\phi}_n(z)\left[\frac{dk_{zn}(z)}{df}\right]_{f=\tilde{f}}\right\}.\end{aligned} \tag{12}$$

The second term in the bracket in Eq. (12) is the correction term for the beamformer migration when there is variation in sound speed structure versus depth. This correction term for the nth mode is negligible when

$$\left|\frac{1}{2\pi}\left[\frac{dk_{zn}(z)}{df}\right]_{f=\tilde{f}}\right| \ll |c(z)\cos\tilde{\phi}_n(z)|^{-1}, \tag{13}$$

as can be seen in Eq. (12). It will be shown in Sec. III that most of the modes propagating in shallow-water waveguides satisfy Eq. (13), since change of the vertical wavenumber

versus frequency is typically negligible for frequencies not near modal cut-off. We refer to modes that do not satisfy Eq. (13) as waterborne modes. This terminology for waterborne modes is similar to that used by Ref. 18. While Eq. (13) is not satisfied near modal cut-off frequencies, modal contributions near cut-off are negligible since the corresponding modal amplitudes decay rapidly as r_o increases.[19]

Equation (12) is then independent of mode number, and can be approximated as

$$\tilde{s}(z,t) \simeq \frac{r_o}{c(z)t} \sin\theta_o, \tag{14}$$

where the departure from Eq. (8) is that sound speed at the receiver depends on receiver depth.

An array invariant for a general horizontally stratified waveguide is then defined as

$$\chi_h \equiv \frac{d\tilde{s}^{-1}(z,t)}{dt} \simeq \frac{c(z)}{r_o \sin\theta_o}, \tag{15}$$

where source range can again be estimated from Eq. (10) but with $c(z)$ substituted for c. The sound speed dependence of Eq. (15) is not an impediment since the sound speed at receiver depth can be readily measured by expendable bathythermographs (XBT). If such measurements are not available, $c(z)=1490$ m/s can be used for range estimation, which leads to only 3% error for the typical range of sound speeds, roughly 1440 to 1540 m/s, encountered in continental shelf waveguides.[20]

An array invariant can also be defined in another way. In practical shallow-water waveguides, the maximum extent of the exact beam-time migration line $\tilde{s}_n(z,t)$ along the beam-time migration line for non-waterborne modes $\tilde{s}(z,t)$ is limited by the time of the latest modal arrival, which is bounded by the minimum group velocity at the Airy phase. This maximum extent is typically sufficiently small that $d\tilde{s}(z,t)/dt$ can be expanded around $t=r_o/c(z)$, and only the zeroth-order term

$$\chi_l \equiv \frac{d\tilde{s}(z,t)}{dt} \simeq -\frac{c(z)}{r_o} \sin\theta_o \tag{16}$$

need be retained. Equation (16) defines an array invariant χ_l that is more convenient for practical use, and is a good approximation unless the seafloor is impenetrable. It will be used for source range estimation in Secs. III and IV.

D. Array invariant for vertical arrays in stratified waveguides

The array invariant method can also be used to instantaneously estimate source range from vertical line array measurements. The sound speed across the aperture of the array is taken to be approximately constant. The geometry is shown in Fig. 1(b). The beamformed pressure of the vertical array as a function of array scan angle ϕ is

$$P_{B,v}(s_v,f) = 4\pi Q(f) \frac{i}{\sqrt{8\pi}\rho(z_o)} e^{-i\pi/4} \sum_n u_n(z_o) \frac{e^{ik_{rn}r_o}}{\sqrt{k_{rn}r_o}} \times [N_n^+ B(s_v - s_{v,n}) + N_n^- B(s_v + s_{v,n})], \tag{17}$$

where $s_v=\cos\phi$, $s_{v,n}=\cos\phi_n$. Here, N_n^+ and N_n^- are the plane-wave amplitudes of the nth mode that satisfy $u_n(z) = N_n^+ e^{ik_{zn}z} + N_n^- e^{-ik_{zn}z}$ at the receiver depths z spanned by the array. For evanescent modes, $s_{v,n}$ does not lie in real space since $\cos\phi_n = i\sinh\phi_n'$. The time-domain complex beamformed pressure is approximated as

$$\tilde{P}_{B,v+}(s_v,t) \simeq \frac{4\pi i}{\sqrt{8\pi}\rho(z_o)} e^{-i\pi/4} \sum_n |Q(\tilde{f})| \tilde{u}_n(z_o) \frac{e^{i\tilde{k}_{rn}r_o}}{\sqrt{\tilde{k}_{rn}r_o}} \times [\tilde{N}_n^+ \tilde{B}(s_v - \tilde{s}_{v,n}) + \tilde{N}_n^- \tilde{B}(s_v + \tilde{s}_{v,n})] F_n(\tilde{f})$$

by the stationary phase method, where $\tilde{N}_n^+, \tilde{N}_n^-, \tilde{s}_{v,n}$ are the corresponding values of $N_n^+, N_n^-, s_{v,n}$ at the frequencies $\tilde{f}$ that satisfy Eq. (5).

For an ideal waveguide, group velocity and elevation angle are related by $v_{gn}=c\sqrt{1-\cos^2\phi_n}$, which can be obtained from Eq. (7). The beam-time migration line for a vertical array in an ideal waveguide then obeys

$$\pm\tilde{s}_{v,n}(t) \equiv \pm\tilde{s}_v(t) = \pm\sqrt{1-\left(\frac{r_o}{ct}\right)^2}, \tag{18}$$

and the migration lines $\tilde{s}_{v,n}(t)$ for all the modes merge to a single line $\tilde{s}_v(t)$. The signs specify whether the migration is vertically up or down. This is due to the symmetry of up and down-going plane-wave components of the modes when the sound speed across the array aperture is constant.

An array invariant χ_v for vertical arrays can be defined as

$$\chi_v \equiv \frac{d}{dt}[1-\tilde{s}_v^2(t)]^{-1/2} = \frac{c}{r_o}, \tag{19}$$

using Eq. (18). Source range can then be estimated as $\hat{r}_o = c/\hat{\chi}_v$, after measuring $\hat{\chi}_v$ from the migration of $\tilde{s}_v(t)$ in the given beam-time intensity data set. Linearization of $d\tilde{s}_v(t)/dt$ using a Taylor series expansion is not appropriate for vertical arrays since the zeroth-order term of $d\tilde{s}_v(t)/dt$ at $t=r_o/c$ is not finite.

The array invariant approach for vertical arrays can be applied in a general horizontally stratified waveguide when the sound speed $c(z)$ is constant across the aperture of the array. Using Eq. (11) and relation (13), the beam-time migration line in this scenario is

$$\pm\tilde{s}_{v,n}(z,t) \equiv \pm\tilde{s}_v(z,t) \simeq \pm\sqrt{1-\left(\frac{r_o}{c(z)t}\right)^2}, \tag{20}$$

from which the array invariant becomes

$$\chi_v \equiv \frac{d}{dt}[1-\tilde{s}_v^2(z,t)]^{-1/2} \simeq \frac{c(z)}{r_o}, \tag{21}$$

so that source range can be estimated as $\hat{r}_o = c(z)/\hat{\chi}_v$.

Equations (20) and (21) are also good approximations if the sound speed is not constant along the array aperture in

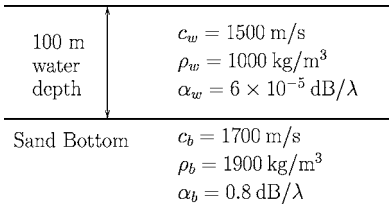

FIG. 6. The Pekeris waveguide with sand bottom, where c_w, ρ_w, and α_w are the sound speed, density, and attenuation of the water column, and c_b, ρ_b, and α_b are those of the sea-bottom.

general horizontally stratified waveguides so long as the variation of $k_{zn}(z)$ along the aperture of an array satisfies

$$|k_{zn}(z)(z-z_c) - k_{zn}(z_c)(z-z_c)| < \frac{\pi}{4}, \tag{22}$$

where z_c is the center depth of an array. The worst case would then occur at either end of the array for waves propagating parallel to the z-axis. Equation (22), with the approximation $1/c(z) = 1/(c(z_c)+\Delta c(z)) \simeq c^{-1}(z_c)(1-\Delta c(z)/c(z_c))$ where $\Delta c(z)$ is the sound speed difference at z_c and depths z spanned by the array, leads to a more practical condition

$$|\Delta c(z)| < \frac{c(z_c)}{2L/(\lambda(z_c)/2)} \tag{23}$$

for the sound speed variation along the array aperture for source range estimation using Eq. (21), where $\lambda(z_c) = k(z_c)/2\pi$ and L is the array aperture. For a typical vertical array aperture of $L = 64\lambda(z_c)/2$ and $c(z_c) = 1490$ m/s, Eq. (23) requires that the relatively benign condition $|\Delta c(z)| < 11$ m/s must be satisfied for Eqs. (20) and (21) to be good approximations.

III. ILLUSTRATIVE EXAMPLES BY SIMULATION

A. Horizontal array

Instantaneous source range estimation by the array invariant method is illustrated by a number of examples involving typical continental shelf environments and array configurations. The first example employs a horizontal receiving array in a Pekeris waveguide. The environmental parameters are shown in Fig. 6. The detection geometry is defined by $z = 30$ m, $z_o = 50$ m, $r_o = 5$ km, and $\theta_o = 60°$. The source signal is impulsive in the time-domain and bandlimited to 390 to 440 Hz by a Tukey filter.[21] The source level is 219 dB *re* 1 μPa at 1 m. The array aperture L is 94.5 m, and is tapered by a Hann window. The source, receiver, and geoacoustic parameters of the seabed are chosen for consistency with the field experiment described in Sec. IV.

The acoustic field from the impulsive source is measured as a time-series on each hydrophone sensor of the horizontal array. The hydrophone time-series data are converted to beam-time data by standard time-domain beamforming. Only the beam-time sound pressure level $L_{\text{bt}}(s,t) = 20\log|P_B(s,t)/1\ \mu\text{Pa}|$, which forms a two-dimensional image as shown in Fig. 7(a), is necessary for range estimation by the array invariant method.

The source range estimate

$$\hat{r}_o = -\frac{c(z)}{\hat{\chi}_l}\sin\hat{\theta}_o \tag{24}$$

is then a function of the estimates $\hat{\theta}_o$ and $\hat{\chi}_l$ based on the $L_{\text{bt}}(s,t)$ data. As noted in Sec. II C, the assumption $c(z) = 1490$ m/s is employed if no local sound speed measurements are available.

The source bearing estimate $\hat{\theta}_o$ is taken as the scan angle that corresponds to the global maximum of the beam-time sound pressure level data $L_{\text{bt}}(s,t)$. This is typically a good approximation in any continental shelf environment because (1) the global maximum is dominated by contributions from the earliest arrivals corresponding to the lowest-order modes, which typically suffer the least attenuation and dispersion, and (2) these modes typically satisfy $\sin\phi_n \simeq 1$ so that the global maximum occurs at $\sin\phi_n \sin\theta_o \simeq \sin\theta_o$, as can be seen from Eq. (6). The location of the global maximum is found by an automated exhaustive search through the $L_{\text{bt}}(s,t)$ data, leading to the estimate $\hat{\theta}_o = 59.8°$, which is consistent with the value obtained by inspection of Fig. 7(a), and is within a fraction of a degree of the true bearing.

The array invariant χ_l is estimated from the data by first finding

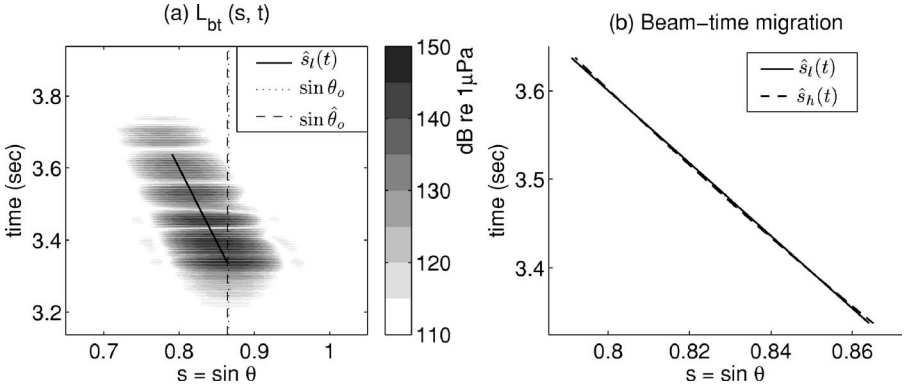

FIG. 7. (a) Beam-time image $L_{\text{bt}}(s,t)$ with true source range $r_o = 5$ km and bearing $\theta_o = 60°$ in the Pekeris sand waveguide. The dotted and dashed vertical lines are at $\sin\theta_o$ and $\sin\theta_o$, respectively, where $\hat{\theta}_o$ is the scan angle of the array corresponding to the global maximum of the $L_{\text{bt}}(s,t)$ data. The black solid line is the linear least squares fit $\hat{s}_l(t)$ of peak intensity angle versus time using Eq. (26). (b) The black solid line is the same $\hat{s}_l(t)$ as shown in (a), and the black dashed line is the linear least squares fit $\hat{s}_h(t)$ using Eq. (28). The two least squares fits are nearly identical to each other.

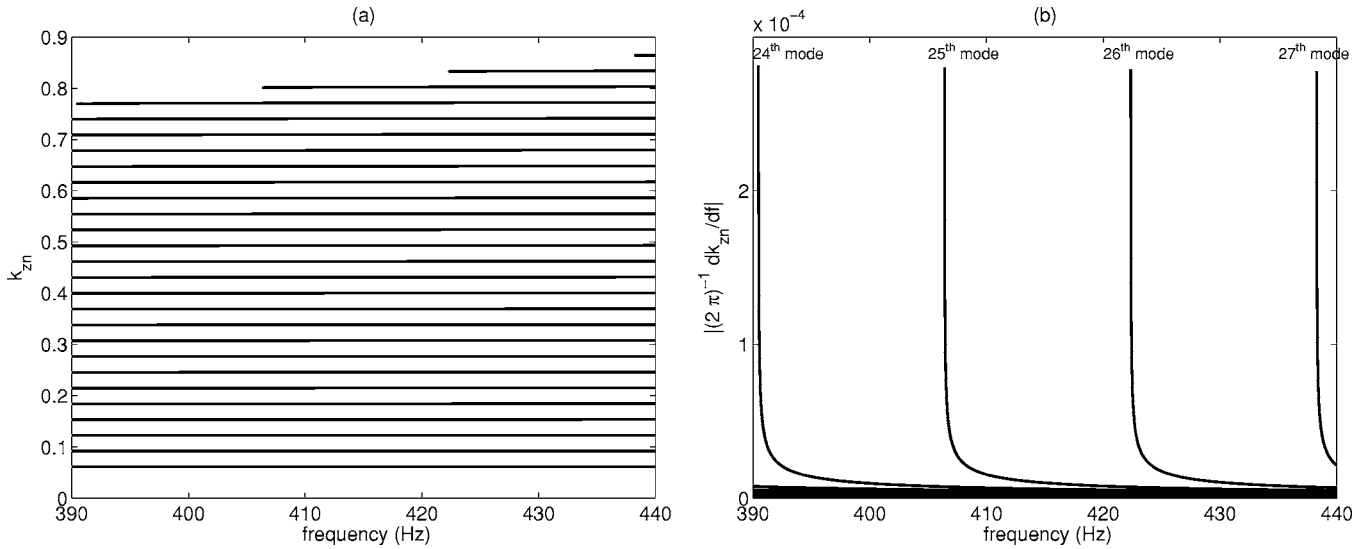

FIG. 8. (a) Vertical wavenumber k_{zn} versus frequency for modes in the Pekeris sand waveguide of Fig. 6. Each horizontal line corresponds to a specific mode. Higher-order modes have higher wavenumbers. (b) Frequency derivatives of k_{zn}. This figure shows that k_{zn} is effectively a constant function of frequency so that relation (13) is satisfied for the Pekeris waveguide except near mode cut-off.

$$s_{\max}(t) = \arg\max_{s} L_{\mathrm{bt}}(s,t)$$

by an automated peak detection algorithm. A least squares estimate of $\hat{\chi}_l$ is then found under the linear approximation

$$\hat{s}_l(t) = \hat{\chi}_l t + d_l \tag{25}$$

from Eq. (16), where d_l is a constant intercept. By this approach, the array invariant estimate $\hat{\chi}_l$ would explicitly be the first element of the vector

$$[\hat{\chi}_l \quad d_l]^T = (\mathbf{T}^T\mathbf{T})^{-1}\mathbf{T}^T\mathbf{S_1}, \tag{26}$$

where $\mathbf{S_1}=[s_{\max}(t_1), s_{\max}(t_2), \cdots, s_{\max}(t_N)]^T$, $\mathbf{T}=[(t_1, t_2, \cdots, t_N)^T\mathbf{1}^T]$, $t_j=t_1+(j-1)\Delta t_s$, Δt_s is the sample spacing in time, and $\mathbf{1}$ is an $1\times N$ matrix given by $\mathbf{1}=[1, 1, \cdots, 1]$. Other methods of estimation could be used such as the maximum likelihood or the Radon transform method. If the received field undergoes circular complex Gaussian fluctuations due to transmission through a random waveguide, or due to a random source, the least squares estimate of the log transformed beam-time intensity data is approximately the maximum likelihood estimator.[22,23]

The linear least squares fit $\hat{s}_l(t)$ of Eq. (25) is overlain on the $L_{\mathrm{bt}}(s,t)$ data in Fig. 7(a). The slope of the fitted line is the array invariant estimate, $\hat{\chi}_l=-0.244$. The corresponding source range estimate is then $\hat{r}_o \simeq 5.3$ km, from Eq. (24), which is within 6% of the true range $r_o=5$ km.

A slightly more accurate source range estimate can be obtained from

$$\hat{r}_o = \frac{c(z)}{\hat{\chi}_h \sin\hat{\theta}_o}, \tag{27}$$

where a least squares estimate of $\hat{\chi}_h$ is found under the approximation $\hat{s}_h^{-1}(t)=\hat{\chi}_h t+d_h$ from Eq. (15), with

$$[\hat{\chi}_h \quad d_h]^T = (\mathbf{T}^T\mathbf{T})^{-1}\mathbf{T}^T\mathbf{S_h}, \tag{28}$$

$\mathbf{S_h}=[s_{\max}^{-1}(t_1), s_{\max}^{-1}(t_2), \cdots, s_{\max}^{-1}(t_N)]^T$, and d_h as a constant intercept. The resulting least squares fit is shown in Fig. 7(b), where $\hat{\chi}_h=0.355$. The estimate of source range is then $\hat{r}_o \simeq 4.9$ km, from Eq. (27), which is within 2% of the true range.

In these examples, we do not use knowledge of the environment to estimate source range. This is necessary to show that the array invariant method can be used for range estimation simply by use of Eqs. (24), (27), and incoherent beam-time data $L_{\mathrm{bt}}(s,t)$.

The array invariant method works because relation (13) is satisfied in the given Pekeris waveguide environment as can be seen in Fig. 8, where the vertical wavenumber of the 27 propagating modes and their frequency derivatives are plotted. The vertical wavenumbers are nearly constant except near modal cutoff frequencies. Relation (13) is then satisfied for all modes except near cutoff, as can be seen in Fig. 8(b). The components near cutoff, however, do not contribute to the acoustic pressure as noted in Sec. II C, and can be neglected.

The array invariant method also works because the exact beam-time migration line $\tilde{s}_n(z,t)$ is well approximated by the least squares fits. The exact beam-time migration line $\tilde{s}_n(z,t)$, calculated using Eq. (12), is shown in Fig. 9(a) as a black line. The temporal extent of $\tilde{s}_n(z,t)$ is limited by the time of the latest modal arrival in the source band, as discussed in Sec. II C. The detailed shape of $\tilde{s}_n(z,t)$ is plotted in Fig. 9(b), which shows that $\tilde{s}_n(z,t)$ can be well approximated by the least squares fits given in Eqs. (26) and (28).

B. Vertical array

Here we show that source range can be instantaneously estimated using the array invariant for vertical arrays with a

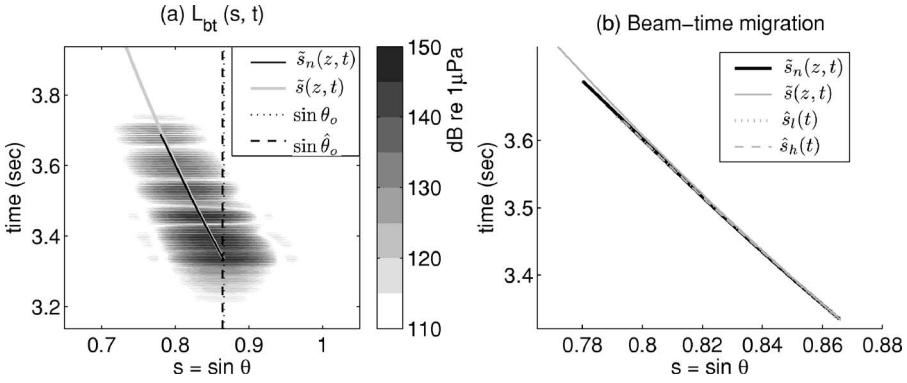

FIG. 9. (a) Beam-time image $L_{\mathrm{bt}}(s,t)$ identical to that in Fig. 7. The black solid line is the exact beam-time migration line $\tilde{s}_n(z,t)$ given in Eq. (12), for modes up to $n=23$. The last four modes with mode cut-off in the 390 to 440-Hz band, as shown in Fig. 8, are neglected. The gray solid line is the beam-time migration line for non-waterborne modes $\tilde{s}(z,t)$ from Eq. (14). (b) The black and gray solid lines are the detailed shapes of the same $\tilde{s}_n(z,t)$ and $\tilde{s}(z,t)$ shown in (a). The two least squares fits $\hat{s}_l(t)$ and $\hat{s}_h(t)$ in Fig. 7, overlain as gray dashed and dotted lines, show good agreement with the exact beam-time migration line $\tilde{s}_n(z,t)$.

Pekeris waveguide example. The environmental parameters are shown in Fig. 6. The detection geometry is defined by $z_c=50$ m, $z_o=50$ m, and $r_o=5$ km. The source signal is impulsive in the time domain and bandlimited in 390 to 440 Hz by a Tukey filter. The source level is 219 dB *re* 1 μPa at 1 m. The array aperture L is 94.5 m, and is tapered by a Hann window.

The acoustic field from the impulsive source is measured as a time-series on each element of the vertical array. The time-series data are converted to beam-time data by standard time-domain beamforming. The beam-time sound pressure level $L_{\mathrm{bt}}(s_v,t)=20\log|P_B(s_v,t)/1\ \mu\mathrm{Pa}|$ is shown in Fig. 10(a). The $L_{\mathrm{bt}}(s_v,t)$ data are symmetric with respect to array broadside, where $s_v=0$, since each mode is composed of an up and a down-going plane wave component with equal amplitude in the water column. Only $L_{\mathrm{bt}}(s_v>0,t)$ is shown in Fig. 10(a). Resolution of lower-order modes is significantly better for the vertical array than the horizontal array since equivalent plane waves are incident near broadside in the former.[24]

Source range can be estimated from

$$\hat{r}_o=\frac{c(z)}{\hat{\chi}_v}, \tag{29}$$

where a least squares estimate of $\hat{\chi}_v$ is found with the approximation $[1-\hat{s}_v^2(t)]^{-1/2}=\hat{\chi}_v t+d_v$ from Eq. (21), by

$$[\hat{\chi}_v \quad d_v]^T=(\mathbf{T}^T\mathbf{T})^{-1}\mathbf{T}^T\mathbf{S}_\mathbf{v}, \tag{30}$$

where $\mathbf{S}_\mathbf{v}=[(1-s_{\max}^2(t_1))^{-1/2},(1-s_{\max}^2(t_2))^{-1/2},\cdots,(1-s_{\max}^2(t_N))^{-1/2}]^T$, and d_v is a constant intercept. Since the beam-time intensity is symmetric with respect to the $s_v=0$ axis, $s_{\max}(t)$ can be found either from

$$s_{\max}(t)=\arg\max_{s_v>0} L_{\mathrm{bt}}(s_v,t),$$

or from

$$s_{\max}(t)=\arg\max_{s_v<0} L_{\mathrm{bt}}(s_v,t).$$

The resulting least squares fit is overlain in Fig. 10(a) as a black line, where $\hat{\chi}_v=0.312$. The corresponding source

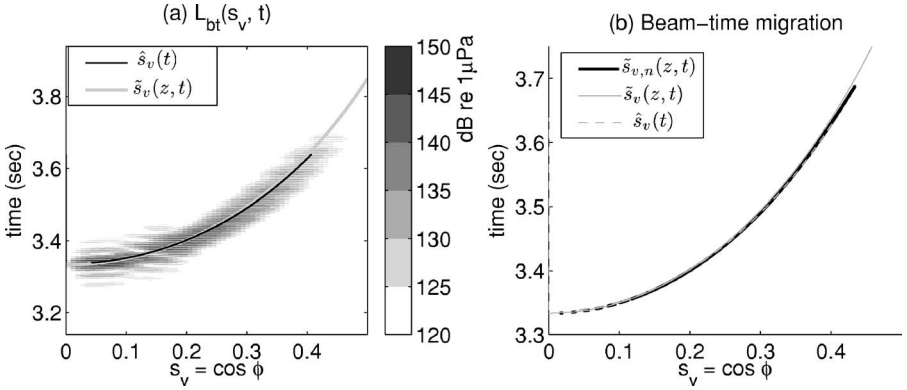

FIG. 10. (a) Beam-time image $L_{\mathrm{bt}}(s_v,t)$ for $r_o=5$ km in the Pekeris sand waveguide. The black solid line is the linear least squares fit $\hat{s}_v(t)$ of peak intensity versus time calculated using Eq. (30). The gray solid line is the beam-time migration line for non-waterborne modes, $\tilde{s}_v(z,t)$, in Eq. (18). (b) The black solid line is the exact beam-time migration line $\tilde{s}_{v,n}(z,t)$. The gray solid and dashed lines are $\tilde{s}_v(z,t)$ and $\hat{s}_v(t)$ in (a), respectively. It can be seen that the exact beam-time migration line $\tilde{s}_{v,n}(z,t)$ can be well approximated by the least squares fit $\hat{s}_v(t)$.

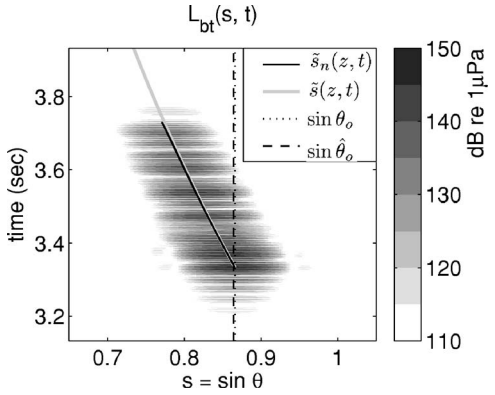

FIG. 11. The same as Fig. 9(a), but for the 150-m deep Pekeris sand waveguide. The exact beam-time migration line $\tilde{s}_n(z,t)$ is plotted for the first 36 modes of the 41 propagating modes. It can be seen by comparison of Fig. 9(a) and Fig. 11 that the exact beam-time migration line $\tilde{s}_n(z,t)$ in a Pekeris waveguide is invariant over the waveguide depth.

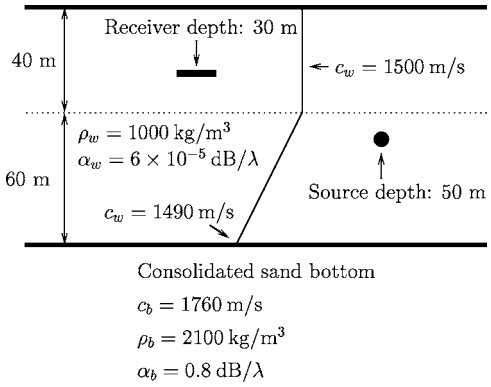

FIG. 12. Horizontally stratified waveguide with linear sound speed gradient. The sound speed is constant up to 40-m depth, and linearly decreases to 1490 m/s at 100-m depth. The density and attenuation of the water column are the same as those in Fig. 6, but the geoacoustic parameters of the sea-bottom are assumed to be different.

range estimate is then $\hat{r}_o \simeq 4.8$ km, from Eq. (29), which is within 4% of the true range $r_o = 5$ km.

C. Environmental invariance

Here we illustrate the environmental invariance of the range estimation equations (24) and (27) with some examples. We first note that the array invariants χ_l and χ_h are effectively identical for the 100-m deep Pekeris waveguide of Fig. 9, and for the 150-m deep Pekeris waveguide of Fig. 11. This is because the migration of $\tilde{s}_n(z,t)$ in response to the given change in waveguide depth occurs only within $\tilde{s}(z,t)$, as discussed in Sec. II. From this example, it can also be deduced that the same invariance holds over frequency. This is because the dispersion relation in a Pekeris waveguide with water depth H effectively depends only on the nondimensional parameter Hf/c_w for fixed ρ_b/ρ_w and c_b/c_w, as shown in Fig. 4–10 of Ref. 15.

The next example illustrates that array invariants are insensitive to the detailed sound speed profile of the water column and the geoacoustic parameters of the sea-bottom. Figure 12 shows an ocean waveguide with a sound speed gradient in the water column. The sound speed changes linearly from 1500 m/s at $z=40$ m to 1490 m/s at $z=100$ m. The sea-bottom is assumed to be a consolidated sand bottom with geoacoustic parameters given in Fig. 12. The true source range and bearing with respect to the receiver array are identical to those in Sec. III A.

The vast majority of modes satisfy relation (13), and the exact beam-time migration line $\tilde{s}_n(z,t)$ effectively span the entire $\tilde{s}(z,t)$ line shown in Fig. 13. Only the negligible portion of the line $\tilde{s}_n(z,t)$ at its temporal inception arises from waterborne modes that violate relation (13), as can be seen from Figs. 14 and 15. Source range can then be estimated following the same procedure in Sec. III A, by estimating $\hat{\chi}_l$ or $\hat{\chi}_h$ and using Eqs. (26) or (28).

IV. EXPERIMENTAL DEMONSTRATION OF THE ARRAY INVARIANT

We demonstrate the performance of the array invariant method at range estimation with field data acquired during the MAE of 2003 conducted in the New Jersey Strataform area. Water depth typically varied from 70 to 80 m, and source range from 1 to 8 km for the data considered.

A. Source, receiver geometry, and environmental parameters

The MAE was conducted in the New Jersey Strataform area to identify the causes of acoustic clutter in continental shelf environments.[25,26] Broadband source signals were

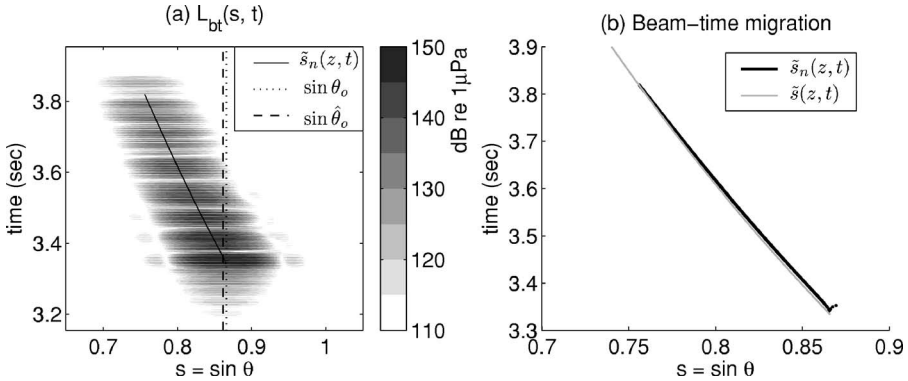

FIG. 13. Beam-time image $L_{bt}(s,t)$ for $r_o=5$ km and $\theta_o=60°$ in the environment shown in Fig. 12. The exact beam-time migration line $\tilde{s}_n(z,t)$ is plotted for the first 27 modes of the 31 propagating modes. The exact beam-time migration line $\tilde{s}_n(z,t)$ is nearly identical to that of the Pekeris waveguide shown in Fig. 9, and it effectively spans the entire $\tilde{s}(z,t)$ line.

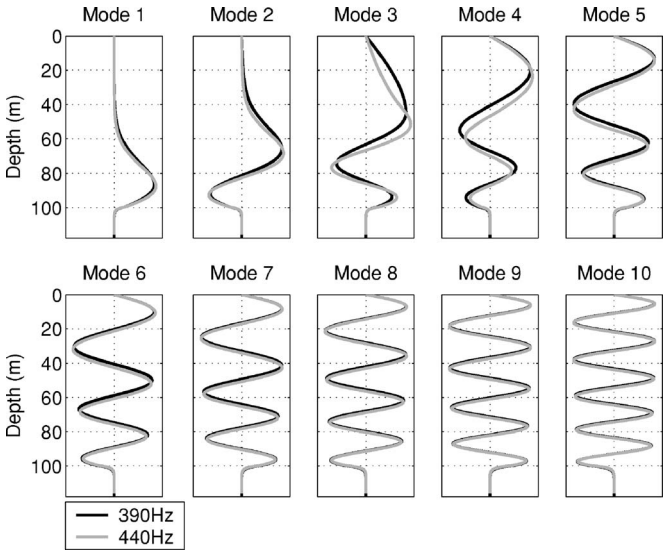

FIG. 14. Mode shape of the first ten modes at 390 and 440 Hz, for the environment shown in Fig. 12. Only the first three modes are waterborne since they are trapped in the refract-bottom-reflect sound speed channel between $z=40$ m and 100 m shown in Fig. 12.

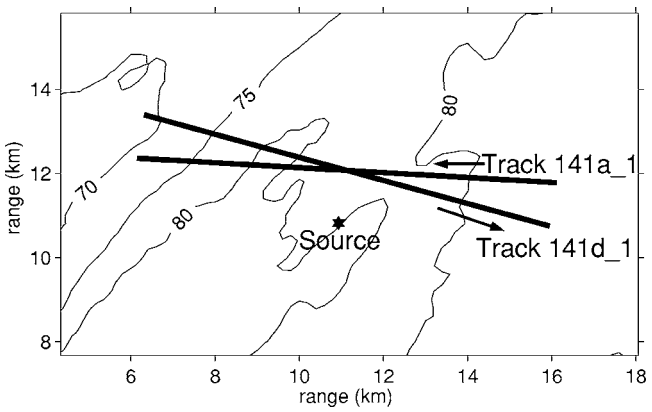

FIG. 16. The source position and the two receiver ship tracks on May 7, 2003. The source to receiver distance varied from 1 km to 6 km. The depth contour of the sea-bottom in meters is also shown in the figure. The arrows show the heading of the receiver ship along the tracks. The origin of the coordinates in Figs. 16 and 17 is at 38.955°N and 73.154°W.

transmitted from R/V Endeavor. A horizontal linear receiver array was towed along linear tracks by R/V Oceanus. The positions of the source and the tracks used in the present analysis are shown in Figs. 16 and 17. The positions of both research vessels were accurately measured by Global Positioning System (GPS).

Bathymetry is also plotted in Figs. 16 and 17. The seafloor has an extremely benign slope, typically less than 1°, as can be seen in Fig. 4 of Ref. 26. The seabed is mostly composed of sand with geoacoustic parameters given in Fig. 6.[25,26] Two or three XBTs were deployed per track from R/V Oceanus. The sound speed profiles measured by the XBTs are shown in Fig. 18.

The receiver was a horizontal line array with aperture $L=94.5$ m for the frequency band of the present analysis. Receiver array depth typically varied from 35 to 45 m for the tracks considered here. The source was a seven-element vertical line array with a 10-m aperture with center depth at 38.1 m. As will be shown later in this section, this vertical source array significantly suppressed the amplitudes of the higher-order modes by generating a narrow vertical beam of sound with roughly 6° 3-dB beamwidth. The source transmitted 1-second duration linear frequency modulated signals in the 390 to 440-Hz band every 50 seconds, roughly 100 transmissions per track.[25] The signal measured by the receiving array was tapered by a Hann window, beamformed, and then matched filtered with a replica signal. As shown in Appendix A, the array invariant derived for impulsive sources can also be applied to non-impulsive sources if the received field is phase conjugated by matched filtering. As noted in

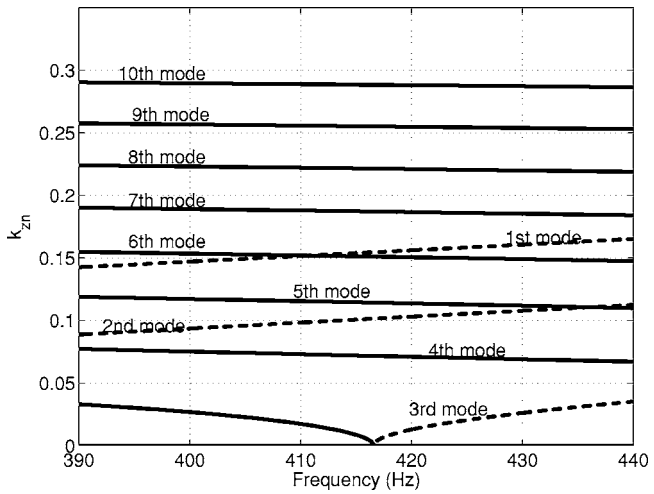

FIG. 15. Vertical wavenumber k_{zn} of the first ten modes in the environment shown in Im. 12. The solid lines represent Re$\{k_{zn}\}$, and the dashed lines represent Im$\{k_{zn}\}$. Only the first three modes are waterborne, and exhibit rapid change of k_{zn} versus frequency.

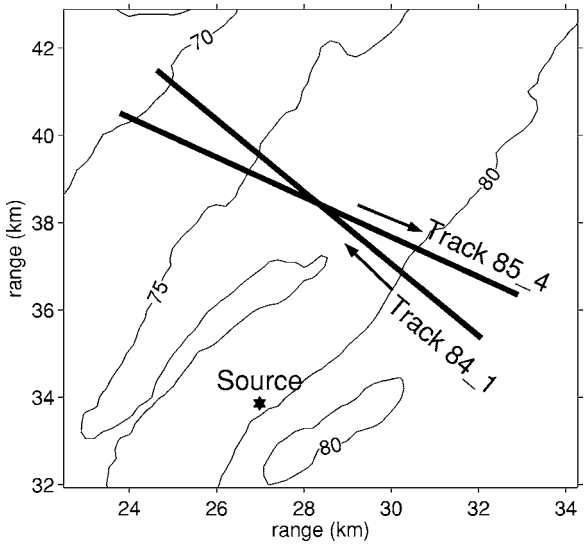

FIG. 17. The source position and the two receiver ship tracks on May 1, 2003. The source to receiver distance varied from 4 km to 8 km.

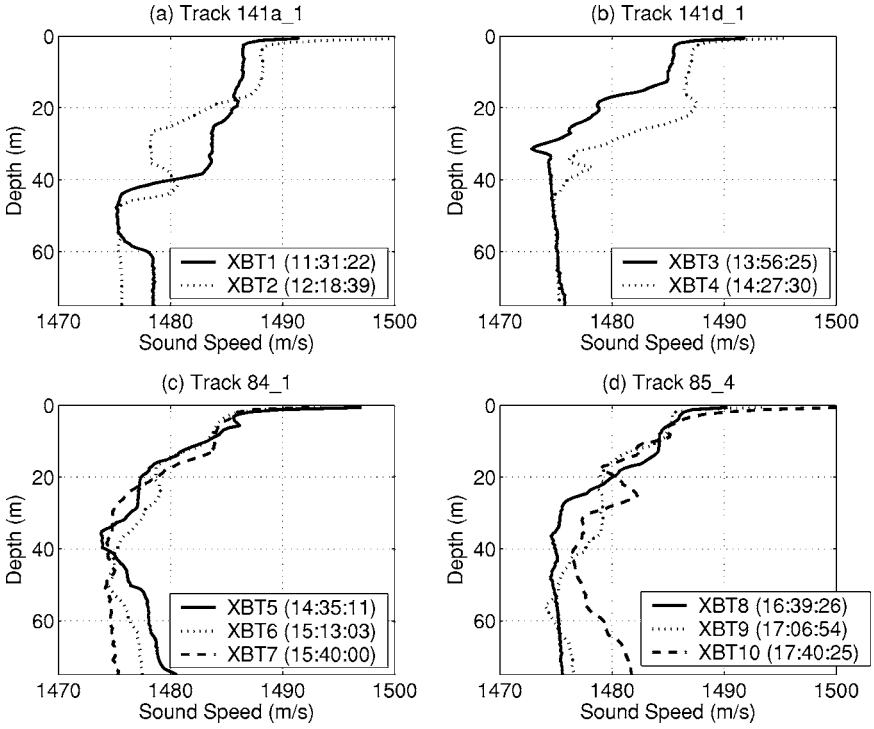

FIG. 18. Sound speed profiles measured by XBT's during the MAE 2003. Two XBTs were deployed for tracks 141a_1 and 141d_1 [(a) and (b)], and three XBTs were deployed for tracks 84_1 and 85_4 [(c) and (d)]. The Greenwich Mean Time of the deployment are shown in the parentheses.

Sec. I, a more general formulation that can treat arbitrary broadband signals that are not necessarily impulsive is possible.[13]

B. Instantaneous range estimation by the array invariant method

We show that source range can be instantaneously and accurately estimated using the array invariant method from field data. The measured beam-time sound pressure level data $L_{\mathrm{bt}}(s,t)$, obtained after time-domain beamforming and matched filtering of the acoustic field received on the horizontal array for a source transmission from Track 141d_1, is imaged in Fig. 19(a). The range and bearing of the source with respect to receiver coordinates are r_o=3.6 km and θ_o =−65° by GPS measurement. The linear least squares fit of the beam-time migration line $\hat{s}_l(t)$, calculated using Eq. (26), is overlain on Fig. 19(a). The slope of the fitted line is the array invariant estimate, $\hat{\chi}_l$=0.339. The source range r_o is then estimated as $\hat{r}_o=-c(z)\sin\hat{\theta}_o/\hat{\chi}_l\simeq 4.1$ km from Eq. (24). This is within 14% of the true range, which is sufficient for many practical applications.

A corresponding simulation is shown in Fig. 19(b). The simulated $\tilde{s}_n(z,t)$, overlain in Fig. 19(b), shows good agreement with the least squares fit of the beam-time migration line $\hat{s}_l(t)$ in Fig. 19(a). Figure 20 shows that vertical wavenumber is effectively a constant function of frequency so that relation (13) is satisfied for the MAE waveguide, which implies that the array invariant method should work well as shown in the example in Fig. 19.

We show that source range can be consistently and robustly estimated using the array invariant method with experimental field data. Source range was estimated 241 times for ranges between 1 and 8 km over a 6-hour period using MAE data. High correlation was found between source range

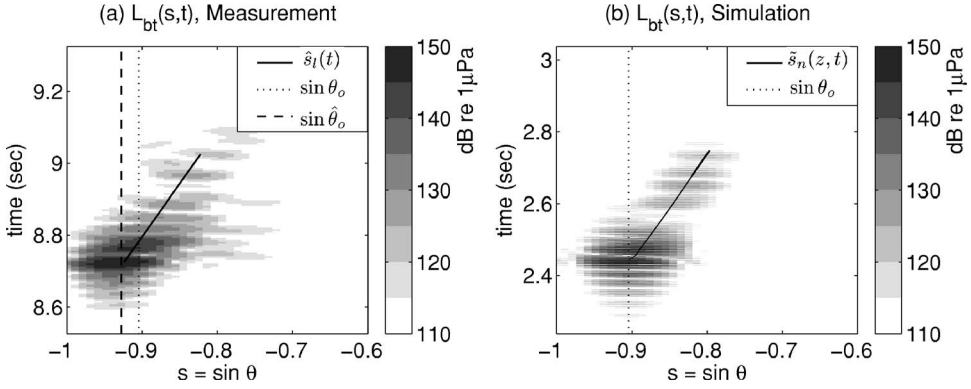

FIG. 19. (a) The beam-time sound pressure level image $L_{\mathrm{bt}}(s,t)$ measured during the MAE 2003. The dotted vertical line is at $\sin\theta_o$, and the dashed vertical line is at $\sin\hat{\theta}_o$, where θ_o=−65° and $\hat{\theta}_o$=−68°. The slanted line is the linear least squares fit of peak beam-time migration. The receiver depth is 39.7 m. (b) Simulation of the measurement shown in (a) using the sound speed profile in Fig. 18(b) XBT3. The positions of $\sin\theta_o$ and $\sin\hat{\theta}_o$ are nearly identical. The slant line is $\tilde{s}_n(z,t)$ up to the 20th mode.

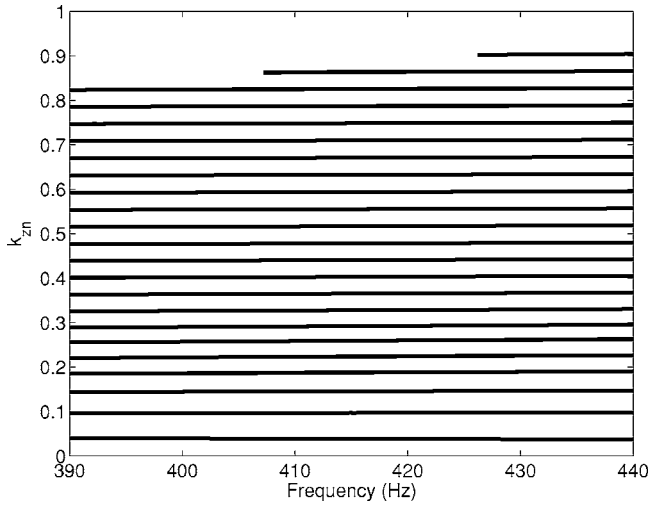

FIG. 20. Vertical wavenumbers k_{zn} at $z=39.7$ m calculated using the sound speed profile in Fig. 18(b) XBT3. This figure shows that relation (13) is satisfied for the MAE waveguide so that the array invariant method should be applicable. This is because the vertical wavenumber is effectively a constant function of frequency.

estimates using the array invariant method and ranges measured by GPS. The range estimates $\hat{r}_o$ using the array invariant method are shown in Fig. 21 along with the GPS measured ranges r_o for tracks 141a_1, 141d_1, 84_1, and 85_4. Only ping transmissions that have $20° < |\hat{\theta}_o| < 75°$ were used in range estimation since the array invariant for a horizontal array is insensitive to r_o at broadside incidence, and since the endfire resolution of a horizontal linear array is significantly worse than the near-broadside resolution.

Figure 22 shows range estimates $\hat{r}_o$ versus GPS measured ranges r_o for all four tracks. The solid line in Fig. 22 is the linear regression of $\hat{r}_o$ with respect to r_o. The regression coefficient and the correlation coefficient of 0.946 and 0.835, respectively, are high and indicate that the data have significantly supported the array invariant range estimation model.

The root mean square (rms) error of all range estimates determined by the array invariant method is 25% of the source range. The accuracy of this particular experimental configuration shows that the array invariant is of extreme practical value.

Even greater accuracy can be achieved for similar measurement scenarios if the source is omnidirectional. The vertical linear source array used in this experiment significantly degraded performance by suppressing higher-order modes, especially at long ranges. This is not typical of mobile sources that are detected and tracked in operational systems. Comparison of simulations in Fig. 9 and Fig. 19(b) shows that the amplitudes of the higher-order modes are significantly reduced by the beampattern of the source. This is especially noticeable since $r_o=5$ km in Fig. 9, whereas $r_o=3.6$ km in Fig. 19(b). This also appears in the experimental measurement in Fig. 19(a) where peak amplitude decays rapidly with increasing arrival time.

The length of the receiver array used in the MAE was roughly $64\lambda/2$, one-half the length of many standard arrays. Using a more typical $128\lambda/2$ aperture array would increase the range resolution by a factor of 2, since the range resolution of the array invariant method is roughly proportional to receiving array beamwidth.

Uncertainties in array position, tilt, and shape can also introduce range estimation error. Our numerical simulations show that a 1° tilt in both the horizontal and vertical, which was typical in the MAE,[25,26] can cause roughly a 10% error in the current source range estimates.

V. COMPARISON OF THE ARRAY INVARIANT METHOD TO OTHER RANGE ESTIMATION TECHNIQUES

It has been suggested that the interference pattern of incoherent acoustic intensity measured as a function of range and frequency can be used for source localization in shallow-water waveguides by the waveguide invariant method, provided that the values of the invariant parameters are known accurately.[9,10] The waveguide invariant parameter β_{mn} between two propagating modes m and n is defined as

$$\beta_{mn} = -\frac{v_{pm}^{-1} - v_{pn}^{-1}}{v_{gm}^{-1} - v_{gn}^{-1}}. \tag{31}$$

For an ideal waveguide with perfectly reflecting boundaries or for a waveguide with an n^2-linear sound speed profile, the waveguide invariant parameters are approximately equal to 1 and -3, respectively. Equation (31) shows that the waveguide invariant requires multiple modes in its fundamental definition, whereas the array invariant does not require multiple modes as discussed in Sec. II B.

Range estimation using the waveguide invariant can lead to large errors if the distribution of β_{mn} is not known *a priori* since uncertainty in r_o is proportional to uncertainly in β_{mn}. Incoherent intensity interference patterns measured during the MAE and corresponding waveguide invariant parameters are provided in Figs. 23 and 24, respectively, where it can be seen that β_{mn} can vary from 1 by more than a factor of 2. This variation of β_{mn} will lead to more than a factor of 2 error in range estimates if $\beta_{mn}=1$ is assumed without *a priori* knowledge of the waveguide invariant parameters. The waveguide invariant parameters also can suffer from large temporal and spatial variation. This is demonstrated in Fig. 24, where roughly a factor of 2 change in β_{mn} is shown to have occurred in less than 2 hours.

Range estimation using MFP techniques also requires accurate knowledge of the environmental parameters. For example, Fig. 9 in Ref. 7 shows that a very common uncertainty of only ±6 m/s sound speed mismatch in the water column results in intolerable MFP ambiguity in a 100-m deep shallow-water waveguide with a source at 5-km range.

The array invariant, waveguide invariant, and MFP techniques for passive source range estimation all fit into a similar category. This is because they all work even when the source is in the far-field of the receiver since they all rely on

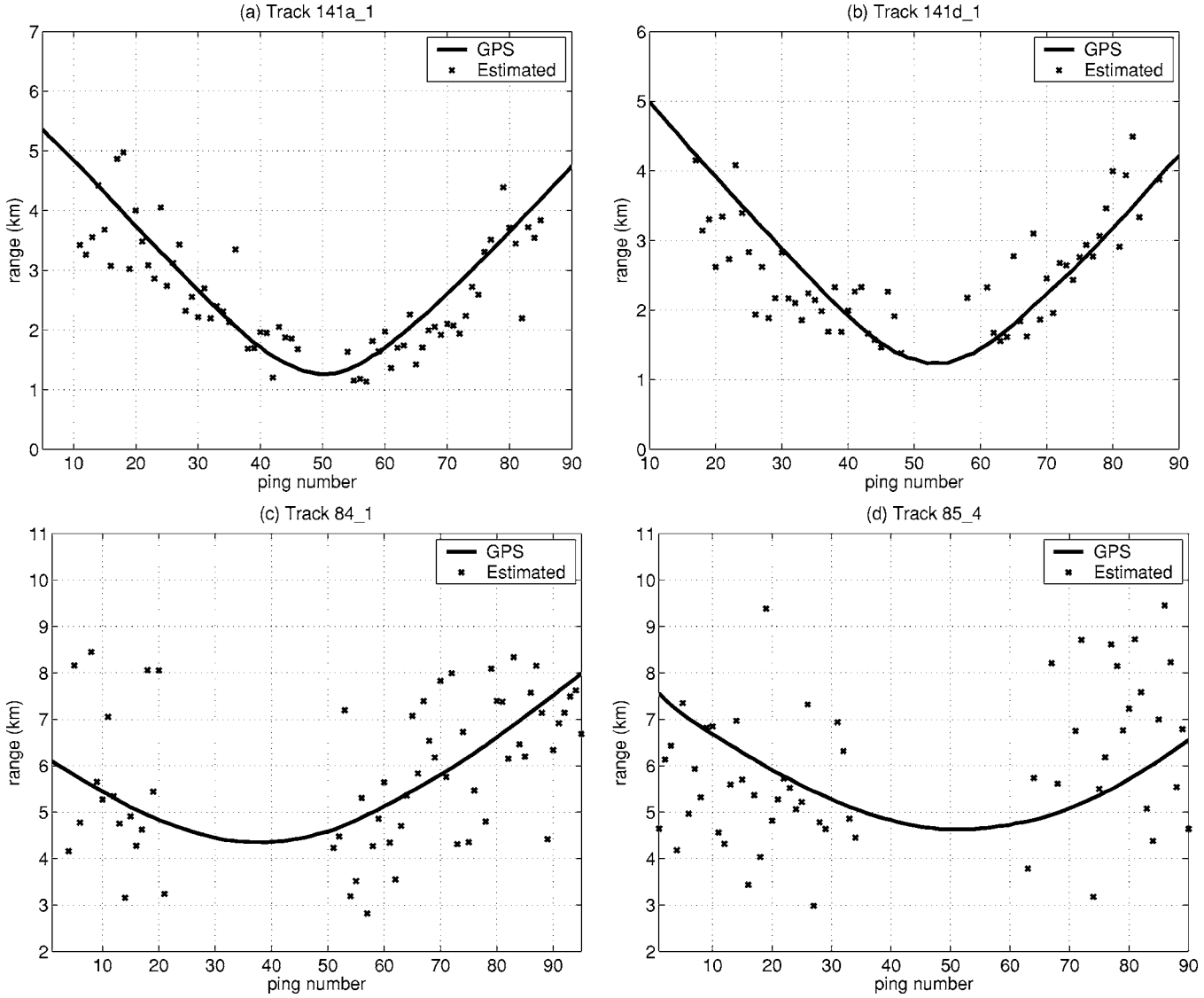

FIG. 21. Experimental range estimates using the array invariant method. The solid lines show r_o measured by GPS. The cross marks show $\hat{r}_o$ estimated by the array invariant method. (a) Track 141a_1: 66 range estimates are shown, and 3 noise-corrupted data are ignored. The rms error e_{rms} is 0.6 km. (b) Track 141d_1:58 range estimates are shown, and 4 noise-corrupted data is ignored. The rms error e_{rms} is 0.6 km. (c) Track 84_1: 61 range estimates are shown, and 8 noise-corrupted data are ignored. The rms error e_{rms} is 1.4 km. (d) Track 85_4: 56 range estimates are shown, and 6 noise-corrupted data are ignored. The rms error e_{rms} is 1.7 km.

the waveguide effects such as modal dispersion or interference. While near-field techniques for source localization, such as focusing or triangulation, may have better range resolution than any of these far-field waveguide techniques, they require an extended aperture or combination of widely separated apertures, which limits their practicality.

VI. CONCLUSION

The array invariant method has been introduced for instantaneous source range estimation in an ocean waveguide. The method exploits the dispersive behavior of guided wave propagation. It has been shown that the array invariant method does not require *a priori* knowledge of the environmental parameters, nor does it require extensive computations. The ability to make simple and accurate range estimates by the array invariant method has been demonstrated with data from the MAE of 2003.

APPENDIX A: STATIONARY PHASE APPROXIMATION APPLIED TO BEAMFORMING IN A WAVEGUIDE

The method of stationary phase has long been used in guided wave propagation problems to obtain the time-domain response at a receiver,[15,16] and to obtain the time-domain solution of the scattered field[3,17] by a broadband source. The stationary phase approximation used here is explicitly given in Appendix A 1, and applied to beamforming in a waveguide in Appendix A 2.

1. General stationary phase approximation

Let

$$I(x) = \int_a^b g(f) e^{ix\psi(f)} df, \tag{A1}$$

and let $\psi(f)$ satisfy $\psi^{(\nu)}(\tilde{f}) \neq 0$ and $\psi^{(1)}(\tilde{f}) = \psi^{(2)}(\tilde{f}) = \cdots = \psi^{(\nu-1)}(\tilde{f}) = 0$ at $f = \tilde{f}$, where $\psi^{(\nu)}(f)$ is the νth derivative of

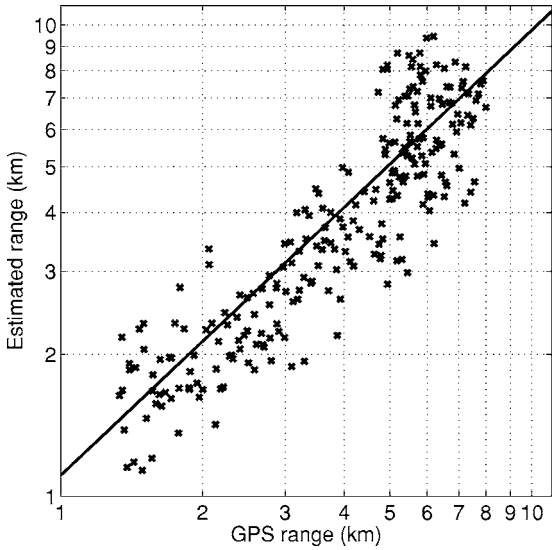

FIG. 22. Experimental range estimates using the array invariant method. The range estimates $\hat{r}_o$ versus GPS measured ranges r_o for tracks 141a_1, 141d_1, 84_1, and 85_4 plotted in logarithmic scale. The solid line is the linear regression $\hat{r}_o = a + br_o$, where the regression coefficient $b = 0.946$ and the intercept $a = 161$ m. The correlation coefficient is 0.835.

$\psi(f)$ with respect to f for positive integer ν. Then $\psi(f)$ can be expanded into the Taylor series as

$$\psi(f) \simeq \psi(\tilde{f}) + \frac{\psi^{(\nu)}(\tilde{f})}{\nu!}(f-\tilde{f})^{\nu}$$

near $f=\tilde{f}$, and Eq. (A1) can be approximated as

$$I(x) \simeq \begin{cases} 2g(\tilde{f})e^{ix\psi(\tilde{f})+\mathrm{sgn}(\psi^{(\nu)}(\tilde{f}))i\pi/2\nu}\left[\dfrac{\nu!}{x|\psi^{(\nu)}(\tilde{f})|}\right]^{1/\nu}\dfrac{\Gamma(1/\nu)}{\nu} & \text{if } \nu \text{ is even,} \\ 2g(\tilde{f})e^{ix\psi(\tilde{f})}\left[\dfrac{\nu!}{x|\psi^{(\nu)}(\tilde{f})|}\right]^{1/\nu}\dfrac{\Gamma(1/\nu)}{\nu}\cos\left(\dfrac{\pi}{2\nu}\right) & \text{if } \nu \text{ is odd,} \end{cases} \tag{A2}$$

for $x \gg 1$.[27] Solutions for the special cases of $\nu=2$ and $\nu=3$ can be found in Ref. 16. The error term introduced by the approximation in Eq. (A2) vanishes at a rate of $1/x$ and therefore is negligible for sufficiently large x.[27]

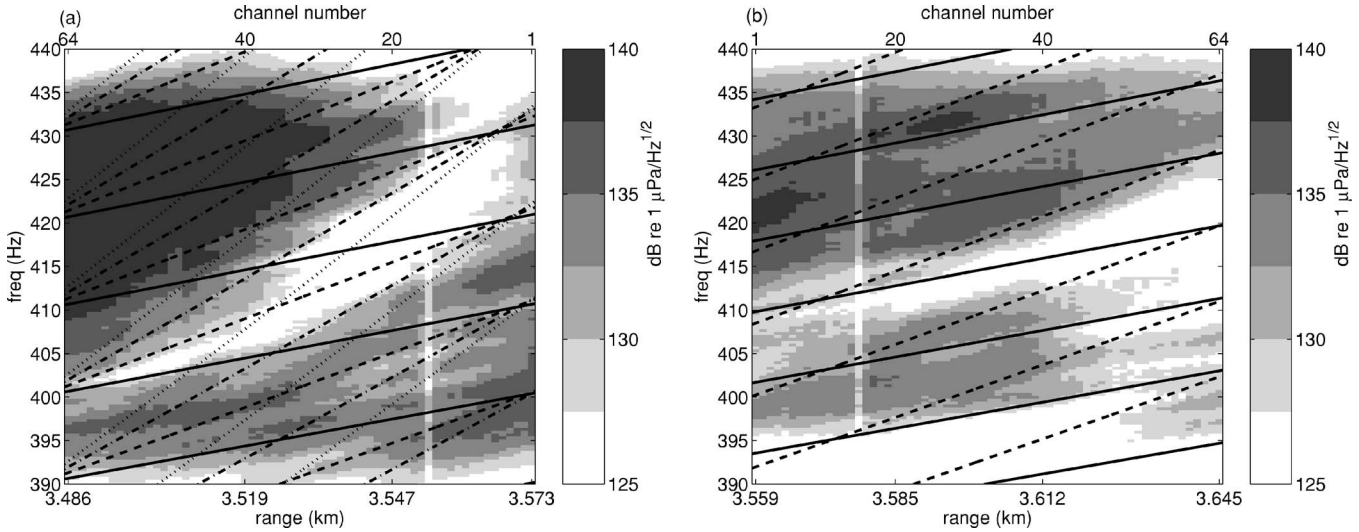

FIG. 23. Incoherent acoustic intensity measured over the array aperture during the MAE 2003. (a) is one of the measurements from Track 141a_1, and (b) is the incoherent intensity of the same data shown in Fig. 19 from Track 141d_1. The receiver array has 64 channels, the number of which are shown on top of the figures. The range from each channel to the source is shown at the bottom of the figures. The black lines are the interference patterns for $\beta_{mn}=1$ (—) $\beta_{mn}=2$ (---), $\beta_{mn}=3$ (-·--), and $\beta_{mn}=4$ (···), respectively, calculated using Eq. (31). Variation of β_{mn} from 1 by more than a factor of 2 can be observed.

2. Application of the stationary phase approximation for array beamforming

The complex beamformed pressure $P_{B+}(s,t)$ of Eq. (3) can be rewritten as

$$P_{B+}(s,t) = \frac{4\pi i}{\sqrt{8\pi\rho(z_o)}} e^{-i\pi/4} \sum_n \int_0^\infty |Q(f)| u_n(z_o) u_n(z) \times \frac{B(s-s_n)}{\sqrt{k_{rn} r_o}} e^{i r_o \psi_n(f)} df, \tag{A3}$$

where

$$\psi_n(f) = k_{rn} - \frac{2\pi f t - \angle Q(f)}{r_o}, \tag{A4}$$

and $|Q(f)|$ and $\angle Q(f)$ are the magnitude and phase of $Q(f)$. Then $\psi_n'(f)$ is zero at the frequency f that satisfies

$$t = \frac{r_o}{v_{gn}(\tilde{f})} + \frac{1}{2\pi} \frac{d}{df} \angle Q(f) \Big|_{f=\tilde{f}}, \tag{A5}$$

where $\tilde{f}$ is the dominant frequency component that arrives at the receiver array at time t. The first term in the right-hand side of Eq. (A5) is the travel time of the nth mode at $f=\tilde{f}$. The second term is the relative phase shift of the source spectrum, or the relative source time delay of the frequency component $\tilde{f}$. The stationary phase approximation of Eq. (A3) is then

$$P_{B+}(s,t) \simeq \frac{4\pi i}{\sqrt{8\pi\rho(z_o)}} e^{-i\pi/4} \sum_n |Q(\tilde{f})| \tilde{u}_n(z_o) \tilde{u}_n(z) \times \frac{\tilde{B}(s-\tilde{s}_n)}{\sqrt{\tilde{k}_{rn} r_o}} F_n(\tilde{f}), \tag{A6}$$

where

$$F_n(\tilde{f}) = \begin{cases} e^{i[\tilde{k}_{rn} r_o - \{2\pi\tilde{f}t - \angle Q(\tilde{f})\}/r_o + \mathrm{sgn}(\psi_n''(\tilde{f}))\pi/4]} \left[\dfrac{2\pi}{r_o \psi_n''(\tilde{f})} \right]^{1/2} & \text{if } \psi_n''(\tilde{f}) \neq 0, \\ e^{i[\tilde{k}_{rn} r_o - \{2\pi\tilde{f}t - \angle Q(\tilde{f})\}/r_o]} \left[\dfrac{6}{r_o |\psi_n'''(\tilde{f})|} \right]^{1/3} \dfrac{\Gamma(1/3)}{3} & \text{if } \psi_n''(\tilde{f}) = 0. \end{cases} \tag{A7}$$

The phase term of the source spectrum in Eq. (A3) can be eliminated when the time duration of the source is much smaller than the time spread of the source due to waveguide dispersion so that the relative phase difference is negligible. Equation (A3) then simplifies to

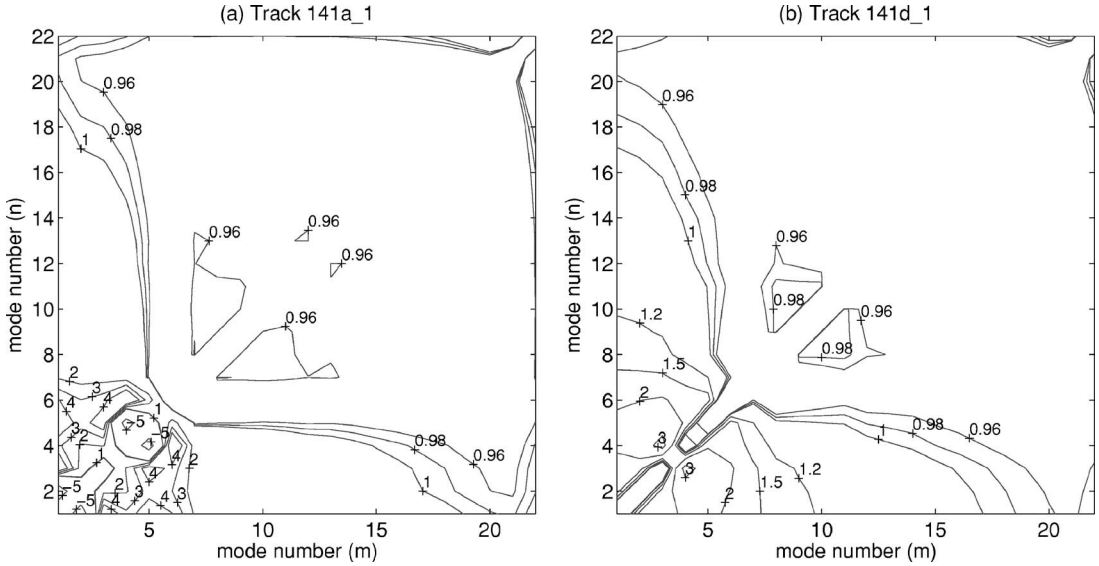

FIG. 24. (a) Track 141a_1: The waveguide invariant parameters β_{mn} calculated using the sound speed profile in Fig. 18(a) XBT2 at $f=415$ Hz. (b) Track 141d_1: The waveguide invariant parameters β_{mn} calculated using the sound speed profile in Fig. 18(b) XBT3 at $f=415$ Hz. It can be seen that roughly a factor of 2 change in β_{mn} has occurred in less than 2 hours.

$$P_{B+}(s,t) \simeq \frac{4\pi i}{\sqrt{8\pi\rho(z_o)}} e^{-i\pi/4} \sum_n |Q(\tilde{f})| \tilde{u}_n(z_o)\tilde{u}_n(z) \times \frac{\tilde{B}(s-\tilde{s}_n)}{\sqrt{\tilde{k}_{rn} r_o}} F_n(\tilde{f}) \tag{A8}$$

for $Q(f)=|Q(f)|$, where

$$F_n(\tilde{f}) = \begin{cases} e^{i(\tilde{k}_{rn} r_0 - 2\pi\tilde{f}t) - i\,\mathrm{sgn}(\tilde{v}'_{gn})\pi/4} \sqrt{\dfrac{(\tilde{v}_{gn})^2}{r_o|\tilde{v}'_{gn}|}} & \text{if } \tilde{v}'_{gn} \neq 0, \\ e^{i(\tilde{k}_{rn} r_0 - 2\pi\tilde{f}t)} \left[\dfrac{3(\tilde{v}_{gn})^2}{\pi r_o[\tilde{v}''_{gn}]} \right]^{1/3} \dfrac{\Gamma(1/3)}{3} & \text{if } \tilde{v}'_{gn} = 0. \end{cases} \tag{A9}$$

Similar results can be obtained if the received field is matched filtered with the transmitted signal. The matched filter output P_M of the beamformed field P_B is

$$P_M(s,t) = 2\,\mathrm{Re}\left\{ K \int_0^\infty P_B(s,f) Q^*(f) e^{-i2\pi ft} df \right\} = 2\,\mathrm{Re}\{P_{M+}(s,t)\}, \tag{A10}$$

where $K=[\int_{-\infty}^{\infty}|Q(f)|^2 df]^{-1/2}$. Again using the method of stationary phase,

$$P_{M+}(s,t) \simeq \frac{4\pi K i}{\sqrt{8\pi\rho(z_o)}} e^{-i\pi/4} \sum_n |Q(\tilde{f})|^2 \times \tilde{u}_n(z_o)\tilde{u}_n(z) \frac{\tilde{B}(s-\tilde{s}_n)}{\sqrt{\tilde{k}_{rn} r_o}} F_n(\tilde{f}), \tag{A11}$$

where $\tilde{f}$ satisfies Eq. (5). The function $F_n(\tilde{f})$ in Eq. (A11) is identical to that for impulsive sources given in Eq. (A9).

[1] C. S. Clay, "Array steering in a layered waveguide," J. Acoust. Soc. Am. **33**(7), 865–870 (1961).
[2] Y. Y. Wang, C. S. Clay, and E. C. Shang, "Bearing determination in a waveguide," J. Acoust. Soc. Am. **82**(1), 233–237 (1987).
[3] N. C. Makris and P. Ratilal, "A unified model for reverberation and submerged object scattering in a stratified ocean waveguide," J. Acoust. Soc. Am. **109**(3), 909–941 (2001).
[4] H. P. Bucker, "Use of calculated sound field and matched field detection to locate sound sources in shallow water," J. Acoust. Soc. Am. **59**, 368–373 (1976).
[5] A. B. Baggeroer, W. A. Kuperman, and H. Schmidt, "Matched field processing: Source localization in correlated noise as an optimum parameter estimation problem," J. Acoust. Soc. Am. **83**(2), 571–587 (1988).
[6] H. Schmidt, A. B. Baggeroer, W. A. Kuperman, and E. K. Sheer, "Environmentally tolerant beamforming for high-resolution matched field processing: Deterministic mismatch," J. Acoust. Soc. Am. **88**(4), 1851–1862 (1990).
[7] C. Feuillade, D. R. DelBalzo, and M. M. Rowe, "Environmental mismatch in shallow-water matched-field processing: Geoacoustic parameter variability," J. Acoust. Soc. Am. **85**(6), 2354–2364 (1989).
[8] G. B. Smith, H. A. Chandler, and C. Feuillade, "Performance stability of high-resolution matched-field processors to sound-speed mismatch in a shallow-water environment," J. Acoust. Soc. Am. **93**(5), 2617–2626 (1993).
[9] S. D. Chuprov, "Interference structure of a sound field in a layered ocean," in *Acoustics of the Ocean: Current Status (in Russian)*, edited by L. M. Brekhovskikh and I. B. Andreevoi (Nauka, Moscow, 1982), pp. 71–91.
[10] L. M. Brekhovskikh and Y. Lysanov, *Fundamentals of Ocean Acoustics*, 3rd ed. (Springer, New York, 2003).
[11] G. L. D'Spain and W. A. Kuperman, "Application of waveguide invariants to analysis of spectrograms from shallow water environments that vary in range and azimuth," J. Acoust. Soc. Am. **106**(5), 2454–2468 (1999).
[12] S. Lee and N. C. Makris, "A new invariant method for instantaneous source range estimation in an ocean waveguide from passive beam-time intensity data," J. Acoust. Soc. Am. **116**(4), 2646 (2004).
[13] S. Lee and N. C. Makris, "Range estimation of broadband noise sources in an ocean waveguide using the array invariant," J. Acoust. Soc. Am. **117**(4), 2577 (2005).
[14] L. E. Kinsler, A. R. Frey, A. B. Coppens, and J. V. Sanders, *Fundamentals of Acoustics*, 4th ed. (Wiley, New York, 2000).
[15] W. M. Ewing, W. S. Jardetzky, and F. Press, *Elastic Waves in Layered Media* (McGraw-Hill, New York, 1957).
[16] J. Miklowitz, *The Theory of Elastic Waves and Waveguides* (North–Holland, Amsterdam, 1978).
[17] P. Ratilal, "Remote sensing of submerged objects and geomorphology in continental shelf waters with acoustic waveguide scattering," Ph.D. thesis, Massachusetts Institute of Technology, Cambridge, MA, 2002.
[18] T. C. Yang, "Beam intensity striations and applications," J. Acoust. Soc. Am. **113**(3), 1342–1352 (2003).
[19] C. T. Tindle, "Virtual modes and mode amplitudes near cutoff," J. Acoust. Soc. Am. **66**(6), 1423–1428 (1979).
[20] R. J. Urick, *Principles of Underwater Sound*, 3rd ed. (McGraw–Hill, New York, 1983).
[21] F. J. Harris, "On the use of windows for harmonic analysis with the discrete Fourier transform," Proc. IEEE **66**(1), 51–83 (1978).
[22] N. C. Makris, "A foundation for logarithmic measures of fluctuating intensity in pattern recognition," Opt. Lett. **20**(19), 2012–2014 (1995).
[23] N. C. Makris, "The effect of saturated transmission scintillation on ocean acoustic intensity measurements," J. Acoust. Soc. Am. **100**(2), 769–783 (1996).
[24] M. Zanolin, I. Ingram, A. Thode, and N. C. Makris, "Asymptotic accuracy of geoacoustic inversions," J. Acoust. Soc. Am. **116**(4), 2031–2042 (2004).
[25] N. C. Makris, "Main acoustic clutter experiment cruise report," Technical Report, Office of Naval Research (2003).
[26] P. Ratilal, Y.-S. Lai, D. T. Symonds, L. A. Ruhlmann, J. A. Goff, C. W. Holland, J. R. Preston, E. K. Scheer, M. T. Garr, and N. C. Makris, "Long-range acoustic imaging of the continental shelf environment: The Acoustic Clutter Reconnaisance Experiment 2001," J. Acoust. Soc. Am. **117**(4), 1977–1998 (2005).
[27] C. M. Bender and S. A. Orszag, *Advanced Mathematical Methods for Scientists and Engineers* (McGraw–Hill, New York, 1978).

A miniaturized adaptive microphone array under directional constraint utilizing aggregated microphones

Mitsuharu Matsumoto[a] and Shuji Hashimoto[b]
Department of Applied Physics, Waseda University, 55N-4F-10A, 3-4-1 Okubo, Shinjiku-ku, Tokyo 169-8555 Japan

(Received 2 May 2005; revised 21 October 2005; accepted 2 November 2005)

This paper introduces a miniaturized microphone array using the Directionally Constrained Minimization of Power (DCMP) method, which utilizes the transfer functions of microphones located at the same place, namely aggregated microphones. The phased microphone array realizes a noise reduction and direction of arrival (DOA) estimation system according to differences in the arrival time, phase shift, and/or the level of the sound wave for each microphone. Hence it is difficult to miniaturize the microphone array. The objective of our research is to miniaturize the system size using aggregated microphones. In this paper, we first show that the phased microphone array system and the proposed aggregated microphone system can be described within the same framework. We then apply a microphone array under directional constraint to the aggregated microphones and compare the proposed method with the microphone array. We show the directional pattern of the aggregated microphones. We also show the experimental results regarding DOA estimation. © *2006 Acoustical Society of America.* [DOI: 10.1121/1.2141232]

PACS number(s): 43.60.Fg, 43.60.Mn, 43.60.−c [EJS] Pages: 352–359

I. INTRODUCTION

Microphone array has a long history and has been studied for a long time.[1–5] The applications of microphone array include sound focusing, noise reduction, and direction of arrival (DOA), etc. It can be applied to hearing aids,[6] robot audition,[7–9] speech enhancement,[10] and so on. The delay-and-sum array[11] and the adaptive microphone array[12–14] are well known as conventional sound focusing or noise reduction techniques with a microphone array. High-resolution algorithms, including the minimum variance method,[15] the minimum norm method,[16] and the multiple signal classification (MUSIC) method,[17] etc. are well known as conventional DOA techniques.

All the algorithms of microphone array, namely phased microphone arrays in this paper, basically utilize the differences in the arrival time, phase shift, and/or the level of the sound wave among the microphones. Hence, the size of phased microphone arrays depends on the wavelength of the target sound. It is difficult to miniaturize the phased microphone arrays. The objective of our research is to make a miniaturized sound focusing and localization system.

In our previous study, the authors proposed another type of microphone array not utilizing the difference in the position of the microphones, but utilizing the differences in the transfer function of the microphones,[18,19] namely *aggregated microphones*. In this method, all the microphones are located at the same position, and directional microphones are arranged to differentiate the microphone transfer function. Hence it is easy to miniaturize the system. This feature is useful when applied to small robots, conference systems, and so on.

The proposed aggregated microphone method and phased microphone array can be described within the same framework. Hence, various techniques in phased microphone array are applicable to the aggregated microphones. The authors have already reported the multiple signal classification utilizing aggregated microphones.[20] In this paper, we apply the Directionally Constrained Minimization of Power (DCMP) algorithm to the aggregated microphones in order to verify the applicability of the aggregated microphones. The DCMP algorithm of Takao *et al.*[13,14] can be used to suppress the side-lobe echoes while maintaining the desired signal. The same principle is also used in Capon's minimum variance method.[15] Hence, the DCMP algorithm can be applied not only to noise reduction but also to DOA estimation. This idea is further utilized in a variety of Generalized Sidelobe Canceling (GSC) algorithms by Griffiths and Jim,[21]

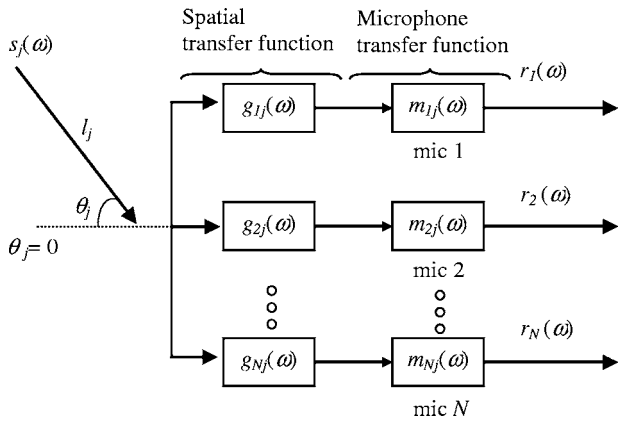

FIG. 1. Problem formulation.

[a]Phone: +81-3-5286-3233; FAX: +81-3-3202-7523; electronic mail: matsu@shalab.phys.waseda.ac.jp
[b]Phone: +81-3-5286-3233; FAX: +81-3-3202-7523; electronic mail: shuji@waseda.jp

which assures the response in the desired direction by controlling the weight of output that does not contain the desired signal.

In the next section, we formulate the problem of the N microphone system and explain the difference between phased microphone arrays and aggregated microphones. In Sec. III, we show a model that includes noise and reflected sounds, and the algorithm of the DCMP used by aggregated microphones. In Sec. IV, we show the directional pattern of the aggregated microphones to investigate their performance. We also show the experimental results of DOA estimation.

II. PROBLEM FORMULATION

A. Problem formulation

Figure 1 depicts a sound system with N microphones including the transfer functions of the ith microphone besides the spatial transfer functions from the sound source to the ith microphone ($i=0,1,\ldots,N$).

In the following discussions, we consider a two-dimensional plane where the coordinate is represented as (x,y) by an orthogonal coordinate system and the direction θ and distance l are measured from the origin as

$$\theta = \tan^{-1}\left(\frac{y}{x}\right), \tag{1}$$

$$l = \sqrt{x^2 + y^2}. \tag{2}$$

To clarify the difference between the phased microphone array and the proposed aggregated microphones, we suppose a sound but no reflected sounds in this section. A sound $s_j(\omega)$ is generated by the sound source at position $\boldsymbol{C}_j=(X_j,Y_j)$, where

$$X_j = l_j \cos\theta_j, \tag{3}$$

$$Y_j = l_j \sin\theta_j, \tag{4}$$

ω represents the angular frequency and j is the suffix to be consistent with Sec. III.

In Fig. 1, $g_{ij}(\omega)$, $i=1,2,\ldots,N$, represents the spatial transfer function from a sound source for direction θ_j and the distance l_j to the ith microphone at position $\boldsymbol{c}_i=(x_i,y_i)$ where ω and N represent the angular frequency and the number of microphones, respectively.

$m_{ij}(\omega)$ represents the transfer function of the ith microphone at angular frequency ω and the direction θ_j. According to the model in Fig. 1, the measured signal at the ith microphone $r_i(\omega)$ can be expressed as follows:

$$r_i(\omega) = m_{ij}(\omega) g_{ij}(\omega) s_j(\omega) (i = 1,2,\ldots,N). \tag{5}$$

B. Outline of phased microphone arrays and aggregated microphones

We first describe the characteristics of phased microphone arrays and aggregated microphones. Figure 2 depicts a phased microphone array system and the proposed aggregated microphone system.

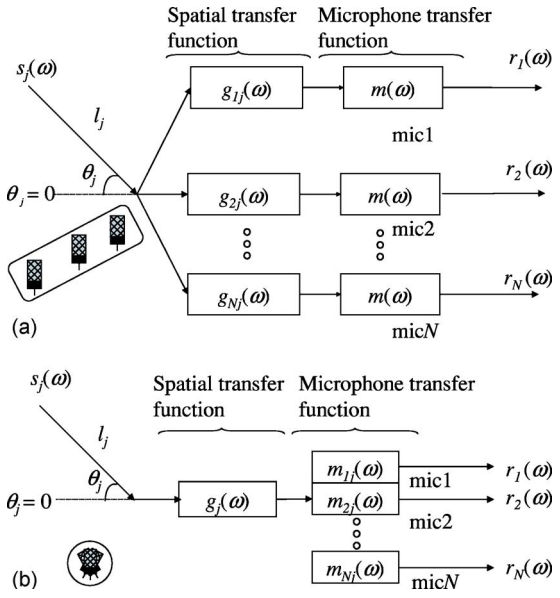

FIG. 2. Phased microphone array system and aggregated microphone system. (a) Phased microphone arrays; (b) Aggregated microphones.

In phased microphone arrays, omnidirectional microphones are usually assumed to make constant the transfer function of the microphone $m_{ij}(\omega)$. In phased microphone arrays, the microphones are arranged at different positions in order to differentiate the spatial transfer functions $g_{ij}(\omega)$ for all the microphones.

On the other hand, in the aggregated microphone system, we use directional microphones so that we can obtain the different transfer functions of the microphones. If all the microphones are located at almost the same position, the spatial transfer function $g_{ij}(\omega)$ can be regarded as constant. Therefore, noise reduction and/or DOA estimation are achieved by utilizing the different transfer functions of the microphones $m_{ij}(\omega)$ without considering the spatial transfer functions.

C. Mathematical restrictions of phased microphone arrays

A general model of the phased microphone arrays with N microphones is placed on an x-y plane as shown in Fig. 3. $\boldsymbol{O}$ represents the origin. Generally, the following conditions are assumed in the phased microphone array system.

Condition 1: (Position differences) All the microphones are located at different positions,

$$\forall i,j\ c_i \neq c_j\ (i,j = 1,2,\ldots,N, i \neq j). \tag{6}$$

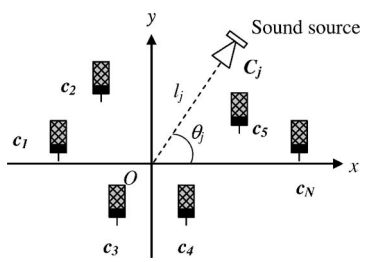

FIG. 3. General model of phased microphone array with N microphones.

Condition 2: (Omnidirectional microphones) The directivity of the microphones is identical for all the angles,

$$\forall i \ \forall\ \theta m_{ij}(\omega) = m(\omega)\text{:Identical for } \theta_j (i = 1,2, \ldots ,N). \tag{7}$$

Under these conditions, we can rewrite the problem formulation in Eq. (5) as follows: If the sound is expressed by a complex sinusoidal wave with the angular frequency ω, $g_{ij}(\omega)$ can be expressed as

$$g_{ij}(\omega) = \exp(-j\omega\tau_{ij}) g_j(\omega), \tag{8}$$

where τ_{ij} is the time delay of the ith microphone for the origin regarding the jth sound. $g_j(\omega)$ represents the spatial transfer function from a sound source $\boldsymbol{C}_j$ to the origin $\boldsymbol{O}$. The received sound of the ith microphone $r_i(\omega)$ can then be expressed as

$$r_i(\omega) = \exp(-j\omega\tau_{ij}) m_{ij}(\omega) g_j(\omega) s_j(\omega). \tag{9}$$

According to Eq. (7), $r_i(\omega)$, can be expressed as

$$r_i(\omega) = \exp(-j\omega\tau_{ij}) m(\omega) g_j(\omega) s_j(\omega). \tag{10}$$

In phased microphone arrays, the influence of the transfer function of microphones is usually disregarded. Because of this simplification, $m(\omega)$ is usually assumed to be 1. Hence, the received signal of the ith microphones in the phased array $r_i(\omega)$ can be expressed as follows:

$$r_i(\omega) = \exp(-j\omega\tau_{ij}) s'_j(\omega), \tag{11}$$

where

$$s'_j(\omega) = g_j(\omega) s_j(\omega) \tag{12}$$

represents the sound at the origin $\boldsymbol{O}$.

The vector of the received sound $\boldsymbol{r}(\omega)$ can be expressed as follows:

$$\begin{aligned} \boldsymbol{r}(\omega) &= [r_1(\omega), r_2(\omega), \ldots , r_N(\omega)]^T \\ &= [\exp(-j\omega\tau_{1j}) s'_j(\omega), \exp(-j\omega\tau_{2j}) s'_j(\omega), \\ &\quad \ldots \exp(-j\omega\tau_{Nj}) s'_j(\omega)] \\ &= \boldsymbol{d}_j(\omega) s'_j(\omega), \end{aligned} \tag{13}$$

where

$$\boldsymbol{d}_j(\omega) = [\exp(-j\omega\tau_{1j}), \exp(-j\omega\tau_{2j}), \ldots , \exp(-j\omega\tau_{Nj})]^{\mathrm{T}} \tag{14}$$

and $[\ ]^{\mathrm{T}}$ represents the transpose.

It should be noted that $\exp(-j\omega\tau_{ij})$ is independent of the spatial transfer function $g_j(\omega)$ and the sound source $s_j(\omega)$. It depends on the relation between the position of the sound source and the position of the ith microphone. $g_j(\omega)$ and $s_j(\omega)$ are common to all the microphones. The characteristics of $\exp(-j\omega\tau_{ij})$ can be controlled by changing the position of the ith microphone. The phased microphone array can realize the noise reduction and the DOA estimation by utilizing the relation between the position of the sound source and the position of each microphone.

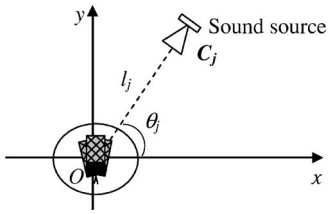

FIG. 4. General model of the aggregated microphones.

D. Mathematical restrictions of aggregated microphones

In our method, N small microphones are located at the origin $\boldsymbol{O}$.

The microphones utilized in the aggregated microphones array are different kinds of small directional microphones. The same kind of directional microphones can also be utilized if the prepared microphones are located in different rotated directions as shown in Fig. 4. The size of the prepared microphone system is significantly small in comparison with the wavelength of the sound because N microphones are located at the same position. $r_i(\omega)$ can then be expressed as

$$r_i(\omega) = m_{ij}(\omega) g_j(\omega) s_j(\omega) = m_{ij}(\omega) s'_j(\omega). \tag{15}$$

The vector of the received sound $\boldsymbol{r}(\omega)$ can be expressed as follows:

$$\begin{aligned} \boldsymbol{r}(\omega) &= [m_{1j}(\omega) s'_j(\omega), m_{2j}(\omega) s'_j(\omega), \ldots , m_{Nj}(\omega) s'_j(\omega)]^T \\ &= \boldsymbol{m}_j(\omega) s'_j(\omega), \end{aligned} \tag{16}$$

where

$$\boldsymbol{m}_j(\omega) = [m_{1j}(\omega), m_{2j}(\omega), \ldots , m_{Nj}(\omega)]^T. \tag{17}$$

It should be noted that directional microphones are utilized for the aggregated microphones. If we use directional microphones, we can realize a sound system similar to the phased microphone array.

Comparing Eqs. (11) and (15), $\exp(-j\omega\tau_{ij})$ in Eq. (11) can be considered as a substitution for $m_{ij}(\omega)$ in Eq. (15), thus the proposed method can be used in the same theoretical framework as the phased microphone array system. We can assume that the difference in the spatial transfer function to each microphone is minimal as the microphones are aggregated. It is necessary for this method to satisfy the following conditions:

Condition 1: (Observability) For every direction, the transfer functions of the microphones are nonzero,

$$\forall\, \theta\ m_{ij}(\omega) \neq 0 \quad (i = 1,2, \ldots ,N). \tag{18}$$

Condition 2: (Independence of direction) For each direction, the ratios of the transfer functions of the microphones are different.

$$\forall\, \theta_i,\ \forall\ \theta_j\ (\theta_i \neq \theta_j) \boldsymbol{m}_i(\omega) \neq \alpha \boldsymbol{m}_j(\omega). \tag{19}$$

According to conditions (18) and (19), it is necessary to differentiate the transfer functions of microphones $m_{ij}(\omega)$ for all the microphones. The conditions can be satisfied easily, as $m_{ij}(\omega)$ is not a real number but a complex number.

III. MICROPHONE ARRAY UNDER DIRECTIONAL CONSTRAINT

A. Phased microphone array

In this section, we consider a situation with two or more sounds. We suppose L signals $s'_j(\omega)$ from the angle $\theta_j (j=1,2,\ldots,L)$ and the distance l_j from the origin. $s'_j(\omega)$ includes J desired signals and K undesired signals $(J+K=L)$, including reflected sounds. We suppose $K<N$. We first consider the constraint for the direction θ_j.

The received signal of the phased microphone arrays $r_i(\omega)$ can be represented as follows:

$$r_i(\omega)=\sum_{j=1}^{L}\exp(-j\omega\tau_{ij})s'_j(\omega)+n_i(\omega), \tag{20}$$

where $n_i(\omega)$ represents the noise signal regarding the ith microphone.

Consider that $y(\omega)$ represents the following linear combination of received sounds. $y(\omega)$ can be represented as follows:

$$\begin{aligned} y(\omega)&=\sum_{i=1}^{N}w_i^*r_i(\omega)=\sum_{i=1}^{N}w_i^*\sum_{j=1}^{L}\exp(-j\omega\tau_{ij})s'_j(\omega)\\ &\quad+\sum_{i=1}^{N}w_i^*n_i(\omega)=\sum_{j=1}^{L}\boldsymbol{d}_j^T\mathbf{w}^*s'_j(\omega)+\boldsymbol{w}^H\boldsymbol{n}(\omega), \end{aligned}\tag{21}$$

where

$$\boldsymbol{w}=[w_1,w_2,\ldots,w_N]^T, \tag{22}$$

$$\boldsymbol{n}(\omega)=[n_1(\omega),n_2(\omega),\ldots,n_N(\omega)]^T \tag{23}$$

stand for the weight vector and the noise vector, respectively. w_i and $[\ ]^*$ represent the ith weight and the complex conjugate, respectively. $[\ ]^H$ represents the conjugate transpose. To obtain the sound from (θ_j,l_j) at the origin, $y(\omega)$ is constrained as follows:

$$y(\omega)=s'_j(\omega). \tag{24}$$

According to formulations (21) and (24), the constraint of $y(\omega)$ can be expressed as follows:

$$\boldsymbol{d}_j^T\boldsymbol{w}^*=1 \quad (j=1,2,\ldots,J). \tag{25}$$

Hence, the constraint can be expressed as

$$\boldsymbol{D}^T\boldsymbol{w}^*=\boldsymbol{H}, \tag{26}$$

where

$$\boldsymbol{D}=[\boldsymbol{d}_1,\boldsymbol{d}_2,\ldots,\boldsymbol{d}_J], \tag{27}$$

$$\boldsymbol{H}=[1,1,\ldots,1]^T. \tag{28}$$

$\boldsymbol{H}$ is the N-dimensional constant vector.

The basic idea of DCMP is minimizing the output power under the constraints (26)–(28).

The average output power $P(\omega)$ of $y(\omega)$ is then given by

$$P(\omega)=E[|y(\omega)|^2]=\tfrac{1}{2}\boldsymbol{w}^H\boldsymbol{R}\boldsymbol{w}, \tag{29}$$

where

$$\boldsymbol{R}=E[\boldsymbol{r}^H(\omega)\boldsymbol{r}(\omega)]. \tag{30}$$

$E[x]$ represents the expectation of x. Hence, the constraint regarding DCMP can be expressed as

$$\min P(\omega) \tag{31}$$

$$\text{subject to } \boldsymbol{D}^T\boldsymbol{w}^*=\boldsymbol{H}. \tag{32}$$

We can obtain the optimum weight $\boldsymbol{w}_{\text{opt}}$ by the Lagrange multiplier method as follows:

$$\boldsymbol{w}_{\text{opt}}=\boldsymbol{R}^{-1}\boldsymbol{D}(\boldsymbol{D}^H\boldsymbol{R}\boldsymbol{D})^{-1}\boldsymbol{H}^*. \tag{33}$$

The output power $P(\omega)$ of $y(\omega)$ can be expressed as follows:

$$P(\omega)=\tfrac{1}{2}\boldsymbol{w}_{\text{opt}}^H\boldsymbol{R}\boldsymbol{w}_{\text{opt}}=\tfrac{1}{2}\boldsymbol{H}^T(\boldsymbol{D}^H\boldsymbol{R}^{-1}\boldsymbol{D})^{-1}\boldsymbol{H}^*. \tag{34}$$

In the phased microphone arrays, the microphones are arranged at different positions in order to differentiate the spatial transfer functions $g_{ij}(\omega)$ for all the microphones.

B. Aggregated microphones

In the same situation as the sounds supposed in the previous section, the received signal of the aggregated microphones $r_i(\omega)$ can be represented as follows:

$$r_i(\omega)=\sum_{j=1}^{L}m_{ij}(\omega)s'_j(\omega)+n_i(\omega). \tag{35}$$

In the formulation with the aggregated microphones, the DCMP algorithm can be described by replacing the time-delay $\exp(-j\omega\tau_{ij})$ with the microphone transfer function $m_{ij}(\omega)$.

We consider that $y(\omega)$ represents the following linear combination of the received sounds $r(\omega)$:

$$\begin{aligned} y(\omega)&=\sum_{i=1}^{N}w_i^*r_i(\omega)\\ &=\sum_{i=1}^{N}w_i^*\sum_{j=1}^{L}m_{ij}(\omega)s'_j(\omega)+\sum_{i=1}^{N}w_i^*n_i(\omega)\\ &=\sum_{j=1}^{L}\boldsymbol{m}_j^T\boldsymbol{w}^*s'_j(\omega)+\boldsymbol{w}^H\boldsymbol{n}(\omega). \end{aligned}\tag{36}$$

In the same way as for the phased microphone array, the constraint regarding the aggregated microphones utilizing the DCMP method can be expressed as follows:

$$\min P(\omega) \text{ subject to } \boldsymbol{M}^T\boldsymbol{w}^*=1, \tag{37}$$

where

$$\boldsymbol{M}=[\boldsymbol{m}_1,\boldsymbol{m}_2,\ldots,\boldsymbol{m}_K]. \tag{38}$$

We can obtain the optimum weight by having it agree with the phased microphone arrays utilizing the DCMP method. We can obtain the optimum weight $\boldsymbol{w}_{\text{opt}}$ as

$$\boldsymbol{w}_{\text{opt}}=\boldsymbol{R}^{-1}\boldsymbol{M}(\boldsymbol{M}^H\boldsymbol{R}\boldsymbol{M})^{-1}\boldsymbol{H}^*. \tag{39}$$

It should be noted that $-(\boldsymbol{M}^H\boldsymbol{R}^{-1}\boldsymbol{M})^{-1}$ also exists, because $\boldsymbol{R}$ is the positive definite matrix and $\boldsymbol{m}_j$ $(j=0,1,\ldots,J)$ is lin-

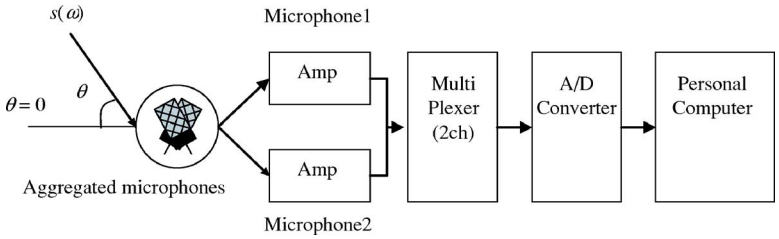

FIG. 5. Experimental environment and block diagram of the aggregated microphones system.

early independent [refer to condition (19)]. The output power $P(\omega)$ of $y(\omega)$ can be expressed as follows:

$$P(\omega) = \tfrac{1}{2}\boldsymbol{w}_{\mathrm{opt}}^{H}\boldsymbol{R}\boldsymbol{w}_{\mathrm{opt}} = \tfrac{1}{2}\boldsymbol{H}^{T}(\boldsymbol{M}^{H}\boldsymbol{R}^{-1}\boldsymbol{M})^{-1}\boldsymbol{H}^{*}. \tag{40}$$

In our method, it is necessary to differentiate the transfer functions of microphones $m_{ij}(\omega)$ for all the microphones so that $\boldsymbol{m}_j$ $(j=1,2,\ldots,J)$ is mutually independent. As is well known, this method can be utilized as the DOA estimation system.

To estimate the DOA, we first calculate the optimum weight for all the angles in advance. When an unknown sound was generated from an unknown angle, we calculate the power $P(\omega,\theta)$ as follows:

$$P(\omega,\theta) = \tfrac{1}{2}(\boldsymbol{m}^{H}(\omega,\theta)\boldsymbol{R}^{-1}\boldsymbol{m}(\omega,\theta)), \tag{41}$$

where $\boldsymbol{m}(\omega,\theta)$ represents the transfer function of the microphone for the angle θ. θ is the objective angle when we find θ so that $P(\omega,\theta)$ has the maximum value.

IV. EXPERIMENT

A. Experimental conditions

Figure 5 depicts the block diagram of the experimental aggregated microphones system. We use two directional capacitor microphones (RP-VC200, Panasonic). Each microphone is connected to a computer through an amplifier (AT-MA2, Audio-technica) and A/D converter (DAQCard-AI-16E-4, National Instruments). All the amplifier gains are unified into +20 dB. The process is performed for sounds sampled with a sample frequency of 22050 Hz and 16 bit resolution. The window size of the FFT is 1024/22050 ms.

$r_1(\omega)$ and $r_2(\omega)$ are acquired for the angle θ in the range of 0°–350° at 10° intervals. The transfer functions of the microphone are measured in advance as the calibration of the aggregated microphones. We obtained the transfer function of the microphone utilizing sound generated at $l=1$ m. The transfer functions of the microphones measured in this way include not only the transfer functions of the microphones but also the spatial transfer function from the sound to the origin. Hence, we investigate the influence of the path change in the following section about DOA estimation.

B. The directional pattern of the aggregated microphones

In this section, we investigate the directional pattern of the aggregated microphones to show that a null-point is made for the angle of the undesired sound by the microphone array utilizing aggregated microphones, just as for the microphone array utilizing the phased array. We obtain the optimum weight $\boldsymbol{w}_{\mathrm{opt}}$ as follows.

We suppose the desired signal $s_1'(\omega)$ from the angle $\theta_1(J=1)$, the undesired signal $s_2'(\omega)$ from the angle $\theta_2(K=1)$ and the noise signal $n(\omega)$. In this situation, the constraint can be expressed as follows:

$$\min P(w)$$

$$\text{subject to } \boldsymbol{m}_1^{T}\boldsymbol{w}_{\mathrm{opt}}^{*} = 1. \tag{42}$$

The optimum weight $\boldsymbol{w}_{\mathrm{opt}}$ can be expressed as follows:

$$\boldsymbol{w}_{\mathrm{opt}} = \gamma\boldsymbol{R}^{-1}\boldsymbol{M}. \tag{43}$$

The received signal $r(\omega)$ can be expressed as

$$r(\omega) = \begin{bmatrix} m_{11}(\omega) \\ m_{21}(\omega) \end{bmatrix} s_1'(\omega) + \begin{bmatrix} m_{12}(\omega) \\ m_{22}(\omega) \end{bmatrix} s_2'(\omega) + \begin{bmatrix} n_1(\omega) \\ n_2(\omega) \end{bmatrix}. \tag{44}$$

The correlation matrix $\boldsymbol{R}(\omega)$ can be expressed as follows:

$$\begin{aligned} \boldsymbol{R} &= E[\boldsymbol{r}(\omega)\boldsymbol{r}^{H}(\omega)] \\ &= P_1\begin{bmatrix} m_{11}(\omega)m_{11}^{*}(\omega) & m_{11}(\omega)m_{21}^{*}(\omega) \\ m_{11}^{*}(\omega)m_{21}(\omega) & m_{21}(\omega)m_{21}^{*}(\omega) \end{bmatrix} \\ &\quad + P_2\begin{bmatrix} m_{12}(\omega,\theta_2)m_{12}^{*}(\omega) & m_{12}(\omega)m_{22}^{*}(\omega) \\ m_{12}^{*}(\omega,\theta_2)m_{22}(\omega) & m_{22}(\omega)m_{22}^{*}(\omega) \end{bmatrix} \\ &\quad + P_n\begin{bmatrix} 1 & 0 \\ 0 & 1 \end{bmatrix}, \end{aligned} \tag{45}$$

where P_1, P_2, and P_n, respectively, represent the power of the desired signal, the undesired signal, and the noise signal as follows:

$$P_1 = E[|s_1'(\omega)|^2], \tag{46}$$

$$P_2 = E[|s_2'(\omega)|^2], \tag{47}$$

$$P_n = E[|n(\omega)|^2], \tag{48}$$

$$n(\omega) = n_1(\omega) = n_2(\omega). \tag{49}$$

Figure 6 depicts the directional patterns of two microphones with frequencies of 500 Hz, 1000 Hz, 2000 Hz, and 4000 Hz. In the experiment, two microphones are set with the directivities shown in Fig. 6. We measured the transfer function of two microphones in the silent room in advance.

To obtain the optimum weight, P_1, P_2, and P_n are modified as follows:

$$P_1 = 1, \tag{50}$$

$$P_2 = 1, \tag{51}$$

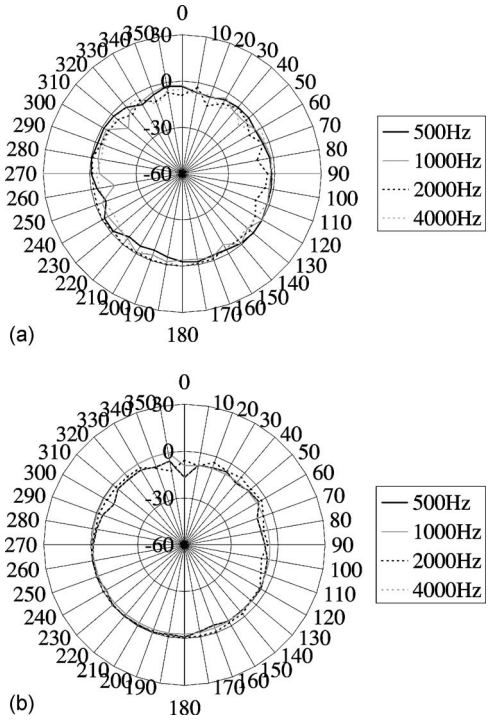

FIG. 6. The directional pattern of two microphones. (a) The directional pattern of microphone 1; (b) The directional pattern of microphone 2.

$$P_n = 0.01. \tag{52}$$

Figure 7 depicts the directional pattern of aggregated microphones with frequencies of 500 Hz, 1000 Hz, 2000 Hz, and 4000 Hz. We calculate the correlation matrix utilizing recorded sounds to measure the directional pattern.

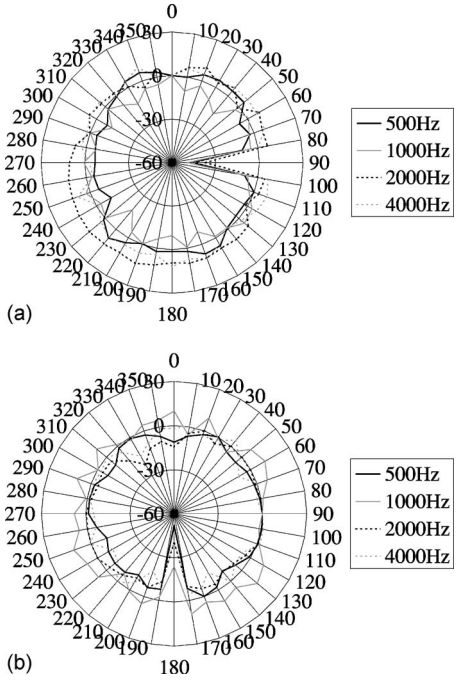

FIG. 7. Directional pattern of the proposed method with aggregated microphones. (a) The desired angle $\theta_1=0°$, undesired angle $\theta_2=90°$; (b) The desired angle $\theta_1=90°$, undesired angle $\theta_2=180°$.

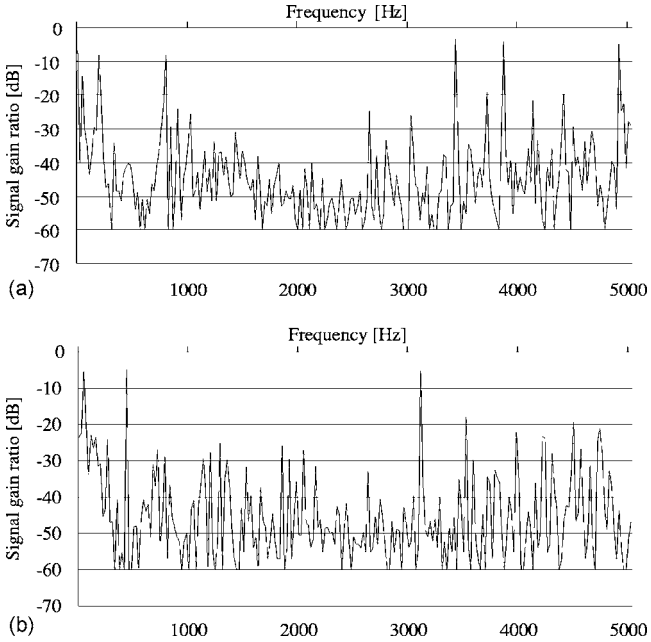

FIG. 8. Signal to noise ratio from 0 Hz to 5000 Hz. (a) The directional angle $\theta_1=0°$, undesired angle $\theta_2=90°$. (b) The directional angle $\theta_1=90°$, undesired angle $\theta_2=180°$.

The system's response to noise is low in the direction of the undesired signal and high in the direction of the desired signal.

To investigate the frequency response to the undesired and desired signals of a microphone array utilizing aggregated microphones, we show the ratio to the desired angle and the undesired angle in Fig. 8. Figure 8 depicts the signal gain ratio to the desired angle and the undesired angle from 0 Hz to 5000 Hz.

In Figs. 7(a) and 8(a), the desired signal direction is set as 0°. The undesired signal direction is set as 90°. In Figs. 7(b) and 8(b), the desired signal direction is set as 90°. The undesired signal direction is set as 180°.

A null-point can be seen at the undesired angle as shown in Fig. 7. The response to the undesired signal is lower than the response to the desired signal by more than 30 dB at almost all the frequencies as shown in Fig. 8. These results indicate that we can realize a miniaturized microphone array similar to phased microphone array that utilize the DCMP method.

C. Direction of arrival estimation

The results of the DOA estimation are shown in this section. In this experiment, the following sound is used as the sound source:

(1) Continuous sinusoidal waves with frequencies of 500 Hz, 1000 Hz, 2000 Hz, and 4000 Hz;
(2) Band-limited white noise up to 10000 Hz.

The sound was generated from 180°. We conducted the following three experiments for DOA estimation:

Experiment 1: An experiment in the silent room (l = 1 m).

In this experiment, the DOA was estimated when sound was generated at $l=1$ m in the silent room. The length, width, and height of the room were 6.77 m, 6.25 m, and 2.84 m, respectively. The reverberation time was 72 ms. This experiment was conducted to evaluate the basic performance of aggregated microphones.

Experiment 2: An experiment in an ordinary room ($l=1$ m).

In this experiment, the DOA was estimated when sound was generated at $l=1$ m in an ordinary room. The length, width and height of the room were 4.27 m, 3.45 m, and 2.40 m, respectively. The reverberation time was 212 ms. This experiment was conducted to evaluate the influence of reflected sounds.

Experiment 3: An experiment in the silent room ($l=0.5$ m).

In this experiment, the DOA was also estimated in the silent room. However the sound was generated at $l=0.5$ m. If the positions of the microphones are changed, the influence of the reflected sounds or the path of the sound is also changed. This experiment was to investigate the influence of the path change between the sound source and the microphone. Figures 9 and 10 depict the results of these experiments. Figure 9 depicts the output of $P(\omega,\theta)/\max[P(\omega,\theta)]$ for the continuous sinusoidal waves of 500 Hz, 1000 Hz, 2000 Hz, and 4000 Hz. Figures 9(a)–9(c) represent the results of Experiments 1, 2, and 3, respectively. We can see a peak at 180° in all the figures, while in Experiment 3 in particular, the sharpness of the peak is relatively less than in the results of the other two experiments. Figure 10 depicts the number of peaks in the frequency domain with regard to angle θ. We can see a peak at 180°, while some peaking is seen at other angles.

The influence of the reflected sounds and the path change is considerable and needs to be improved. However, it is considered that Figs. 9 and 10 indicate the possibility of minimizing the size of microphone array.

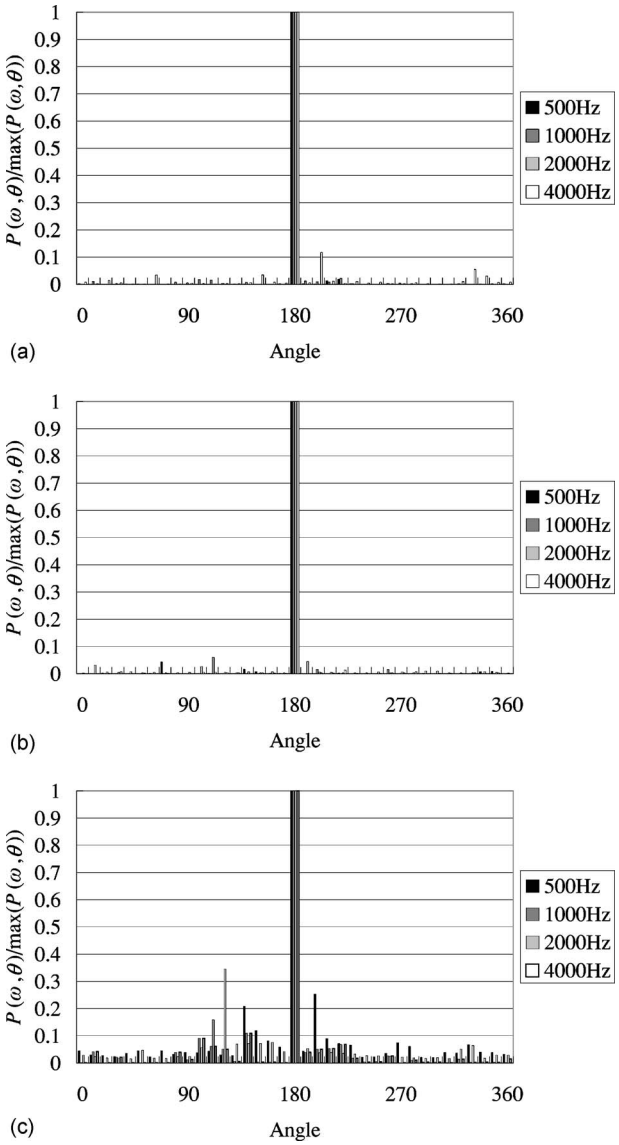

FIG. 9. The output of $P(\omega,\theta)/\max(P(\omega,\theta))$ related to the ideal sinusoidal wave with 500 Hz, 1000 Hz, 2000 Hz, and 4000 Hz from 180°. (a) The experiment in the silent room ($l=1$ m); (b) The experiment in the ordinary room ($l=1$ m); (c) The experiment in the silent room ($l=0.5$ m).

V. CONCLUSION

We proposed a miniaturized microphone array under the Directionally Constrained Minimum Power (DCMP) algorithm that utilizes the transfer functions of microphones located in the same place, namely, aggregated microphones. It was demonstrated that a microphone array and the proposed system can be described within a similar framework. We showed the directional pattern of adaptive array under the DCMP algorithm for aggregated microphones. The same null-point was seen for the undesired signal as when using the phased microphone array. We also showed the experimental results of DOA estimation by aggregated microphones to verify the performance of the proposed method and the influence of the reflected sounds and the path change. These experimental results show that the aggregated microphones utilizing the DCMP method have a performance similar to the phased array utilizing the DCMP method, while minimizing the system size. However, it was observed that reflected sound and the path change affect the precision of utilizing the aggregated microphones utilizing the DCMP method.

In this method, we also have to obtain the transfer functions of the microphones in advance. This is one of the points in this method that needs improvement. Future tasks include the simplification of this process. We also need to estimate changes in the performance of the aggregated microphones in response to changes in the directional pattern of the prepared directional microphones. This is also considered to be a subject for future work.

ACKNOWLEDGMENTS

This work was supported in part by the "The innovative research on symbiosis technologies for humans and robots in an elderly-dominated society," the 21st Century Center of Excellence (COE) Program, the Japan Society for the Pro-

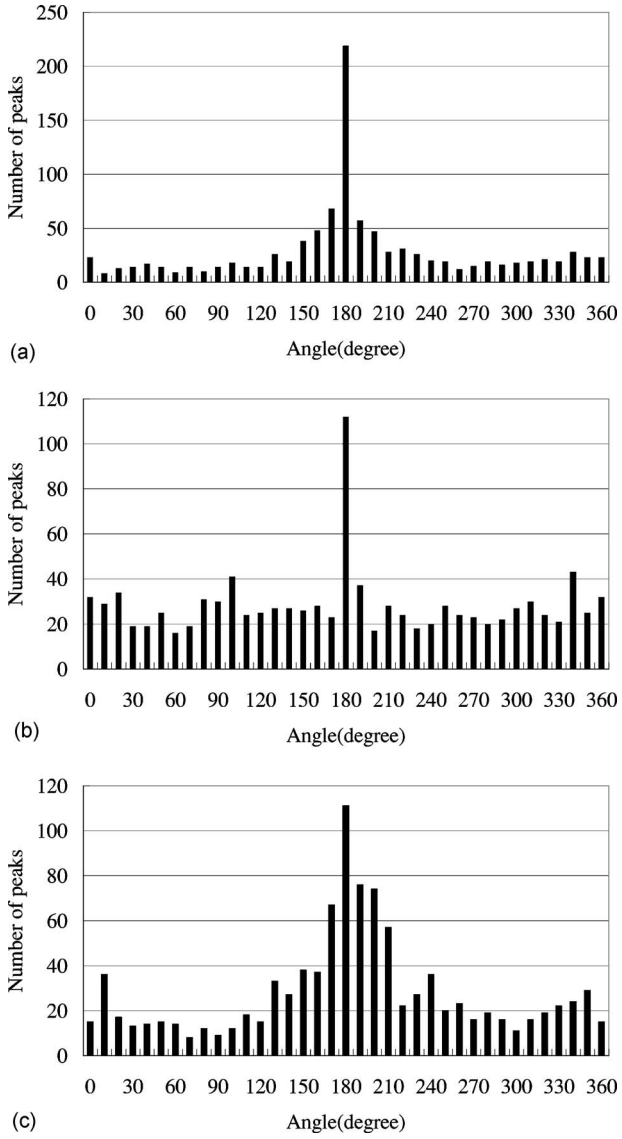

FIG. 10. The peak histogram with regard to various frequencies when white noise was generated from 180°. (a) The experiment in the silent room (l =1 m); (b) The experiment in the ordinary room (l=1 m); (c) The experiment in the silent room (l=0.5 m).

motion of Science. This work was also supported in part by the "Establishment of Consolidated Research Institutes for Advanced Science and Medical Care," the Encouraging Development of Strategic Research Centers Program, the Special Coordination Funds for Promoting Science and Technology, and the Ministry of Education, Culture, Sports, Science and Technology, Japan.

[1]K. Sasaki and K. Hirata, "3D-localization of a stationary random acoustic source in near-field by using 3 point-detectors," Trans of the Society of Instrument and Control Engineers **34**(10), 1329–1337 (1998).
[2]Y. Yamasaki and T. Itow, "Measurement of spatial information in sound fields by the closely located four point microphone method," J. Acoust. Soc. Jpn. **10-2**, 101–110 (1990).
[3]J. Huang, N. Ohnish, and N. Sugie, "Spatial localization of sound sources: azimuth and elevation estimation," in *Proceedings of the IEEE Instrumentation and Measurement Technology Conference*, 1998, pp. 330–333.
[4]H. F. Silverman, in "An algorithm for determining talker location using a linear microphone array and optical hyperbolic fit," *Proceedings of the Speech and Natural Language Workshop*, 1990, pp. 151–156.
[5]S. Azuma, S. Uchikoshi, and K. Kido, "Studies on the spatial distribution of sensitivity in arc-arrayed microphone system," J. Acoust. Soc. Jpn. **40-10**, 677–683 (1985).
[6]A. Wang, K. Yao, R. E. Hudson, D. Korompis, and F. Lorenzelli, "Microphone Array for Hearing Aid and Speech Enhancement Applications," *International Conference on Application-Specific Systems, Architectures, and Processors (ASAP '96)*, 1996, pp. 231–239.
[7]T. Nishiura, M. Nakamura, A. Lee, H. Saruwatari, and K. Shikano, "Talker Tracking Display on Autonomous Mobile Robot with a Moving Microphone Array," in *Proceedings of the 8th International Conference on Auditory Display (ICAD2002)*, 2002, pp. 244–247.
[8]J.-M. Valin, J. Rouat, and F. Michaud, "Enhanced robot audition based on microphone array source separation with post-filter," in *Proceedings of the IEEE/RSJ International Conference on Robots and Intelligent Systems*, 2004.
[9]J.-M. Valin, F. Michaud, B. Hadjou, and J. Rouat, "Localization of simultaneous moving sound sources for mobile robot using a frequency-domain steered beamformer approach," *IEEE International Conference on Robotics and Automation*, 2004.
[10]H. Luts, J. Maj, W. Soede, and J. Wouters, "Better speech perception in noise with an assistive multi-microphone array for hearing aids," Ear Hear. **25**, 411–420 (2004).
[11]K. Kiyohara, Y. Kaneda, S. Takahashi, H. Nomura, and J. Kojima, "A microphone array system for speech recognition," in *Proceedings of the IEEE International Conference on Acoustics, Speech, and Signal Processing ICASSP'97*, 1997, pp. 215–218.
[12]Y. Kaneda and J. Ohga, "Adaptive microphone-array system for noise reduction," IEEE Trans. Acoust., Speech, Signal Process. **ASSP-34**(6), 1391–1400 (1986).
[13]K. Takao, M. Fujita, and T. Nishi, "An adaptive antenna array under directional constraint," IEEE Trans. Antennas Propag. **24**, 662–669 (1976).
[14]K. Takao and N. Kikuma, "Tamed adaptive antenna array," IEEE Trans. Antennas Propag. **34**, 388–394 (1986).
[15]J. Capon, "High resolution frequency-wavenumber spectrum analysis," Proc. IEEE **57**, 2408–2418 (1969).
[16]S. S. Reddi, "Multiple source location: A digital approach," IEEE Trans. Aerosp. Electron. Syst. **AES-15**, 95–105 (1979).
[17]R. O. Schmidt, "Multiple emitter location and signal parameter estimation," IEEE Trans. Antennas Propag. **AP-34**, 276–280 (1986).
[18]M. Matsumoto and S. Hashimoto, "Aggregated Microphones Method for Sound Localization," Technical Report of Mathematical Modeling and Problem Solving, **48**, 3–6 (2004).
[19]M. Matsumoto and S. Hashimoto, "Aggregated Microphones Method for Sound Focusing and Localization," *Technical Report of IEICE*, pp. 7–12, 2004.
[20]M. Matsumoto and S. Hashimoto, "Multiple signal classification by aggregated microphones," IEICE Trans. Fundamentals **E88-A**(7), (2005).
[21]L. J. Griffiths and C. W. Jim, "An alternative approach to linearly constrained adaptive beam-forming," IEEE Trans. Antennas Propag. **30**, 27–34 (1982).

Algorithms for computing the time-corrected instantaneous frequency (reassigned) spectrogram, with applications

Sean A. Fulop[a)]
Department of Linguistics, California State University, Fresno, California 93740-8001

Kelly Fitz
School of Electrical Engineering and Computer Science, Washington State University, Pullman, Washington 99164-2752

(Received 9 June 2005; revised 7 October 2005; accepted 11 October 2005)

A modification of the spectrogram (log magnitude of the short-time Fourier transform) to more accurately show the instantaneous frequencies of signal components was first proposed in 1976 [Kodera *et al.*, Phys. Earth Planet. Inter. **12**, 142–150 (1976)], and has been considered or reinvented a few times since but never widely adopted. This paper presents a unified theoretical picture of this time-frequency analysis method, the *time-corrected instantaneous frequency spectrogram*, together with detailed implementable algorithms comparing three published techniques for its computation. The new representation is evaluated against the conventional spectrogram for its superior ability to track signal components. The lack of a uniform framework for either mathematics or implementation details which has characterized the disparate literature on the schemes has been remedied here. Fruitful application of the method is shown in the realms of speech phonation analysis, whale song pitch tracking, and additive sound modeling. © *2006 Acoustical Society of America.* [DOI: 10.1121/1.2133000]

PACS number(s): 43.60.Hj [EJS] Pages: 360–371

I. INTRODUCTION

The purpose of this paper is the detailed description and unification of a number of time-frequency analysis methods gracing the literature over the past 30 years. Though given different names at different times, it will be shown that these methods arrive at the same end, viz. a representation of the time-varying instantaneous frequencies of the separable amplitude and/or frequency modulated (AM/FM) line components comprising a signal. This representation will herein be called by the descriptive name of time-corrected instantaneous frequency (TCIF) spectrogram.

Section II presents an historical overview of the literature on spectrograms, the short-time Fourier transform, and the subsequent development of the ideas which underlie the time-corrected instantaneous frequency spectrogram. Section III describes three methods for computing this representation that have been published,[1–3] unifying their theoretical underpinnings and providing detailed step-by-step algorithms which cannot be found in the original more theory-oriented papers. The performance of the TCIF spectrogram in relation to conventional spectrograms will be illustrated using a speech signal. Section IV then presents a number of applications of the TCIF spectrogram to signal analysis and modeling. The close examination of phonation in speech, pitch tracking of whale songs, and sound modeling for the purpose of flexible and efficient resynthesis are the three application areas illustrated and discussed.

The chief contributions of this paper are the provision of step-by-step algorithms for and unification of disparate methods for computing the time-corrected instantaneous frequency spectrogram that have been published in the past, the provision of a uniform theoretical perspective on the TCIF spectrogram with concern for its proper physical interpretation, and the illustration of the great superiority of the technique over traditional time-frequency distributions for certain selected applications. Past publications on this subject have not been sufficiently accessible to many applied acoustics researchers. At least one of the methods treated has recently had program code published,[4] but here the method is reduced to its essential steps without relying on particular programming schemes. It is thus hoped that the algorithms presented here, together with their illustrations, will provide the material necessary to foster widespread adoption of this promising and underused technology.

II. BRIEF HISTORY OF THE TCIF SPECTROGRAM

The history of the TCIF spectrogram naturally begins with and is to some degree intertwined with the development of the spectrogram itself. While the spectrogram is now typically described as a logarithmic plot (in dB) of the squared magnitude of the short-time Fourier transform, in truth the spectrogram itself predated the first recognition of this transform by more than 20 years. It is now part of acoustical lore that the first "Sound Spectrograph" device was developed at Bell Labs shortly before World War II, was closely held following the outbreak of war, and was finally described in the open literature following the war's end.[5] At that point the short-time spectra it produced were understood from the empirical perspective of analog filters, and the description of its output was not put into strict mathematical terms.

[a)]Electronic mail: sfulop@csufresno.edu

The first mathematical approach to the kind of "time-frequency representation" that would eventually subsume the spectrogram was put forth by Gabor,[6] in apparent ignorance of the existence of the spectrograph device (in fairness, Gabor mentioned it in a footnote added following the acceptance of his paper). Gabor's work developed what was in essence an approximation to a digital (discrete in time and frequency) version of a spectrogram with Gaussian windows, a so-called expansion of a signal in Gaussian elementary signals on a time-frequency grid. Gabor did not characterize this representation as a short-time power spectrum; that equivalence would be shown much later.

At this point, two parallel literature streams developed, neither citing the other for some time. In an effort to analyze the spectrogram, the short-time power spectrum was given its first rigorous mathematical treatment by Fano,[7] but this was limited to a particular (and at the time impractical) form of the window. The first short-time power spectrum allowing for an arbitrary continuous window function was derived by Schroeder and Atal;[8] while this took the form of the squared magnitude of an analog short-time Fourier transform, the fact that it involved a generalized kind of Fourier transform pair remained unstated.

After some time, other researchers took up where Gabor had left things. Lerner[9] generalized Gabor's approximate digital signal expansion to allow arbitrary elementary signals. Helstrom[10] completed a derivation of an exact continuous expression for the expansion of a signal in Gaussian elementary signals, corresponding to Gabor's "digital" representation. This treatment was generalized to arbitrary elementary signals (which now can be seen as equivalent to spectrogram window functions) by Montgomery and Reed,[11] who went on in their paper to prove that this really was a new class of two-dimensional transforms standing in an invertible transform-pair relation to the signal, thus marking the first derivation of what we now call the short-time Fourier transform.

The theory behind the time-corrected instantaneous frequency spectrogram begins with a paper by Rihaczek,[12] who summarized some of the previous papers and quickly dismissed the now-ubiquitous short-time Fourier transform as a minor curiosity because it fails to capture the time-frequency energy distribution which he, like Gabor 22 years earlier, was seeking to represent. Achieving this goal involved deriving the *complex energy density* of the signal as a function of time and frequency, and then integrating over it within a time-frequency "cell" to yield the energy distribution within the cell. Rihaczek went on to show that, in accordance with the principle of stationary phase, the significant contributions to the integral come from the points where the phase is stationary. For the time integration, this condition yields the instantaneous frequency,[13] assuming just one AM/FM signal component is significant within the cell. For the frequency integration, the stationary phase condition yields the group delay, pinpointing the primary "event time" of the time-frequency area covered by the cell.

These facts form the foundation of the time-corrected instantaneous frequency spectrogram, and also justify this name for it. To see how to use them, however, one must note that the digital form of the short-time Fourier transform of a signal provides, in effect, a filtered analytic signal at each frequency bin, thereby decomposing the original signal into a number of component signals (one for each frequency bin) whose instantaneous frequency can then be computed using Rihaczek's equations. More exposition of this can be found in Nelson,[2] who used the term *channelized instantaneous frequency* to refer to the vector of simultaneous instantaneous frequencies computed over a single frame of the digital short-time Fourier transform.

It is first assumed that a signal can be written as the sum of general AM/FM components:

$$f(t) = \sum_n A_n(t) e^{i(\Omega_n(t)+\phi_n)}. \tag{1}$$

The channelized instantaneous frequency of a signal as a continuous function of time and frequency is defined as

$$\mathrm{CIF}(\omega, T) = \frac{\partial}{\partial T} \arg(\mathrm{STFT}_h(\omega, T)), \tag{2}$$

where STFT_h is the continuous short-time Fourier transform using window function h.

An analogous relation holds for the quantized time axis of the digital short-time Fourier transform; one can treat each time index (i.e., frequency vector) as a frequency "signal" whose group delay can be computed using Rihaczek's equations, thus yielding a new vector of corrected event times for each cell. Again following Nelson,[2] the *local group delay* of a signal as a continuous function of time and frequency is given by

$$\mathrm{LGD}(\omega, T) = -\frac{\partial}{\partial \omega} \arg(\mathrm{STFT}_h(\omega, T)). \tag{3}$$

These facts were first recognized by Kodera *et al.*,[1] who suggested reassigning the time-frequency points of a digital spectrogram matrix (i.e., the squared magnitude of the digital short-time Fourier transform) to new time-frequency locations matching the instantaneous frequency and group delay of the signal component resolved at each time-frequency cell in the matrix. The magnitude to be plotted at the new location would be the same as the original spectrogram magnitude at the corresponding cell. So, Rihaczek's theory would be put into practice under the name "modified moving window method," but the work failed to attract the attention of the community.

One problem involves devising a method to compute the phase derivatives in the digital domain, which might first be attempted with a naïve implementation by finite difference approximation. This is, it seems, the actual technique employed by Kodera *et al.*[1,14] An algorithm for implementing this is provided in the following, and its performance on a test signal is exemplified as a benchmark. Stemming from concerns over the accuracy of the finite difference estimates (concerns which may be unfounded, as will be observed in the sequel), at least two other methods[2,3] for computing the partial phase derivatives have been devised over the years. These two methods are also provided with step-by-step algorithms here, and their performance relative to the naïve

benchmark is anecdotally and mathematically evaluated. A third independent method was also published,[15] but this seems to be a partial foreshadowing of the method of Auger and Flandrin,[3] and so will not be separately treated here. A host of more distantly related work on increasing precision in time-frequency analysis has also been published over the years[16] but also will not be considered because the contributions do not directly modify the spectrogram as closely as our main subject, the TCIF spectrogram.

In the past decade or so, a small but growing number of applied researchers have adopted one or another of these techniques. The technique of Nelson,[2] for instance, was employed by Fulop *et al.*[17] to show the fine time-frequency structure of click sounds in a Bantu language. The technique of Auger and Flandrin,[3] meanwhile further expounded,[4] has been employed in papers by Plante *et al.*[18,19] to perform speech spectrography, Hainsworth *et al.*[20] for the analysis of musical sounds for the purpose of automatic classification, Niethammer *et al.*[21] for the imaging of Lamb waves, and Fitz and Haken[22] to perform additive sound modeling. In addition, two independent recent papers[23,24] describe equivalent theories of spectrographic reassignment using instantaneous frequency only (no time correction is performed), and each appears to be a reinvention that does not rely on any of the prior literature just reviewed.

None of the applied papers just mentioned describe in any detail how their particular version of the time-corrected instantaneous frequency spectrogram is actually computed, and some of the papers proffer inaccuracies about just how the new spectrogram should be interpreted. This situation has put unwanted obstacles in the way of widespread adoption of the technology, and some colleagues have privately expressed outright disapproval of it stemming from unease or misunderstanding about what it is. It is apparent that the time is nigh for a more thoroughgoing comparative account of the various ways in which this new spectrographic tool can be computed, as well as a discussion of its proper physical interpretation, so that future researchers can make clearly informed choices about what precisely to do.

III. THREE METHODS FOR COMPUTING THE TIME-CORRECTED INSTANTANEOUS FREQUENCY SPECTROGRAM

One of the most important application areas of this technology is the imaging and measurement of speech sound. It has been found to be particularly useful for analyzing the fine scale time-frequency features of individual pulsations of the vocal cords during phonation, so one example of this kind of short signal will be adopted as a test signal for the demonstration of the algorithms.

The source-filter theory of speech production models phonation as a deterministic process, the excitation of a linear filter by a pulse train. The filter resonances of the mouth "ring" after excitation by each pulse, yielding the formants of a speech sound. One can observe these formants as they are excited by the individual glottal pulsations in Fig. 1, which pictures a portion of a vowel [e] produced with *creaky* phonation having extremely low airflow and fundamental frequency to enhance the accuracy of the source-filter model.

Figure 2 shows a conventional spectrogram of the test signal, which is one vocal cord pulsation excised from the previous signal. This and all subsequent examinations of this signal are computed using 7.8 ms windows and 78 μs frame advance. While it is possible to observe the numerous formant frequencies as they resonate, the conventional spectrogram shows an extreme amount of time-frequency "smearing" owing to the short window length employed and high magnification. A major goal of the time-corrected instantaneous frequency spectrogram is to move away from the pure time-frequency domain which attempts to show an energy distribution, and instead work to track the instantaneous frequency of each significant AM/FM line component constituting the signal frames.

A. Methods computing the finite difference approximation

1. Spectrogram reassignment

Both the original proposal of Kodera *et al.*[1] and the later independent developments by Nelson[2] compute the channelized instantaneous frequency and local group delay using their definitions in Eqs. (2) and (3) by means of finite difference approximations. The only real disparity between the two approaches is in the details of how to compute this finite difference, so they can be described with a single algorithmic out-line. It can be presumed that Kodera *et al.*[1] computed the finite differences of the short-time Fourier transform phases literally, e.g.,

$$\mathrm{CIF}(\omega,T) = \frac{\partial}{\partial T}\arg(\mathrm{STFT}_h(\omega,T)) \approx \frac{1}{\epsilon}\left[\phi\left(T+\frac{\epsilon}{2},\omega\right)-\phi\left(T-\frac{\epsilon}{2},\omega\right)\right]. \quad (4)$$

With the CIF and LGD matrices in hand, the frequency and time locations of each point in the digital short-time Fourier transform of the signal are reassigned to new locations according to

$$(\omega,T)\mapsto[\mathrm{CIF}(\omega,T),T+\mathrm{LGD}(\omega,T)]. \quad (5)$$

This form of the reassignment is obtained when the short-time Fourier transform of the signal $f(T)$ is defined following Nelson[2] as

$$\mathrm{STFT}_h(\omega,T)=\int_{-\infty}^{\infty} f(t+T)h(-t)e^{-i\omega t}dt. \quad (6)$$

This form of the transform is equivalent modulo a phase factor $e^{i\omega t}$ to the more standard form in which the window is time-translated with the signal held to a fixed time. This important difference between the two forms of the short-time Fourier transform propagates into the local group delay in the expressions and algorithms presented here, so that the value computed from the phase derivative of the above-defined short-time Fourier transform provides a *correction* to the signal time for the reassignment rather than a new time value that supersedes the signal time.

A later approach to reassigning the power spectrum and spectrogram using the same general ideas was developed by

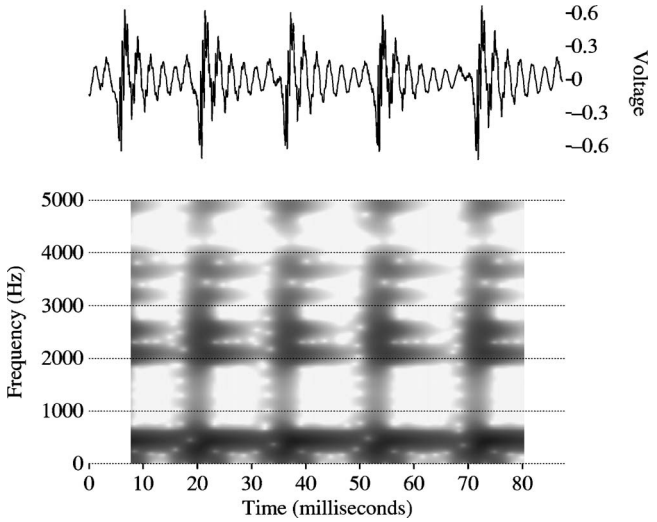

FIG. 1. Vocal cord pulsations during a *creaky voiced* production of the vowel [e], "day," wave form and conventional spectrogram shown.

Nelson.[25,26,2] Nelson's stated goal was the estimation of the desired partial derivatives without finite differencing, since it was assumed that phase unwrapping was important in extracting acceptable performance from that method, and phase unwrapping can present well-understood difficulties in certain circumstances.

The primary insight of Nelson was that each of the two partial derivatives of the short-time Fourier transform phase can be estimated by means of point-by-point multiplication of two related transform surfaces. Nelson[2] states that the self-cross-spectral surface C defined in Eq. (7) encodes the channelized instantaneous frequency in its complex argument, and that analogously the surface L defined in Eq. (8) encodes the local group delay in its complex argument,

$$C(\omega,T,\epsilon)=\mathrm{STFT}\left(\omega,T+\frac{\epsilon}{2}\right)\mathrm{STFT}^{*}\left(\omega,T-\frac{\epsilon}{2}\right), \tag{7}$$

$$L(\omega,t,\epsilon)=\mathrm{STFT}\left(\omega+\frac{\epsilon}{2},T\right)\mathrm{STFT}^{*}\left(\omega-\frac{\epsilon}{2},T\right). \tag{8}$$

Let us demonstrate that the argument of C does indeed provide the same approximation to the STFT phase derivative as the finite difference, since no derivation can be found in the literature:

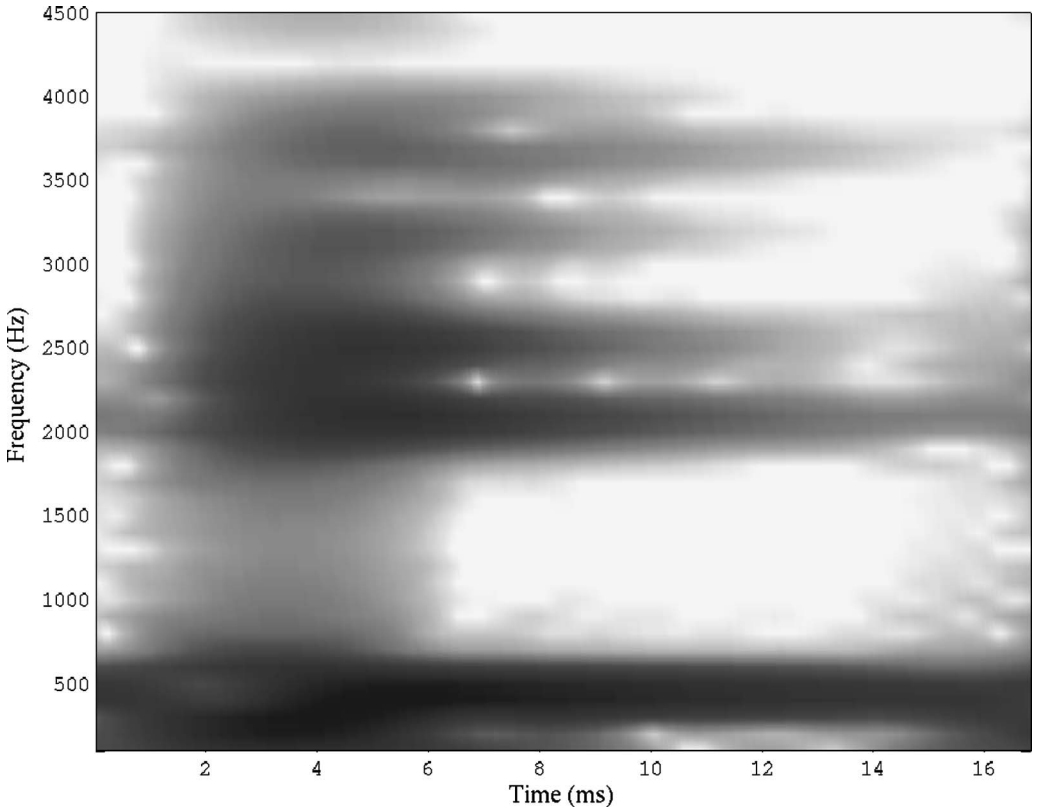

FIG. 2. Conventional spectrogram of a single vocal cord pulsation from the vowel [e]. Computed using 7.8 ms windows and 78 μs frame advance.

$$\frac{1}{\epsilon}\arg[C(\omega,T,\epsilon)] = \frac{1}{\epsilon}\arg\left(\mathrm{STFT}\left(\omega,T+\frac{\epsilon}{2}\right)\mathrm{STFT}^{*}\left(\omega,T-\frac{\epsilon}{2}\right)\right) \tag{9}$$

$$= \frac{1}{\epsilon}\arg\left(M\left(\omega,T+\frac{\epsilon}{2}\right)e^{j\phi(\omega,T+\epsilon/2)}M\left(\omega,T-\frac{\epsilon}{2}\right)e^{-j\phi(\omega,T-\epsilon/2)}\right) \tag{10}$$

where $M(\cdot)$ is the magnitude of the short-time Fourier transform and $\phi(\cdot)$ is its phase,

$$= \frac{1}{\epsilon}\arg\left(M\left(\omega,T+\frac{\epsilon}{2}\right)M\left(\omega,T-\frac{\epsilon}{2}\right)e^{j[\phi(\omega,T+\epsilon/2)-\phi(\omega,T-\epsilon/2)]}\right), \tag{11}$$

and because M is always real,

$$= \frac{1}{\epsilon}\left[\phi\left(\omega,T+\frac{\epsilon}{2}\right)-\phi\left(\omega,T-\frac{\epsilon}{2}\right)\right]. \tag{12}$$

An analogous derivation holds for the other surface L. Given this, it is possible to write the following estimates:

$$\mathrm{CIF}(\omega,T) \approx \frac{1}{\epsilon}\arg[C(\omega,T,\epsilon)], \tag{13}$$

$$\mathrm{LGD}(\omega,T) \approx \frac{-1}{\epsilon}\arg[L(\omega,T,\epsilon)]. \tag{14}$$

It is important to note that in a digital implementation of Nelson's procedure the resulting CIF and LGD values are approximations to the same degree of precision as with the original method of Kodera *et al.*,[1] but this procedure automatically takes care of phase unwrapping. It might also be noted that while the reassigned locations of STFT magnitudes computed here do diminish unwanted time-frequency smearing and focus tightly on individual components, two components cannot be separated if they are closer than the classical uncertainty limit that is determined by the length of the analysis window, as was first elucidated by Gabor.[6]

2. Algorithm using the finite difference approximations

The input to the procedure is a signal; its output is a time-corrected instantaneous frequency spectrogram, presented as a three-dimensional (3D) scatterplot showing time on the x axis, channelized instantaneous frequency on the y axis, and short-time Fourier transform log magnitude on the z axis. The plotted points can have their z-axis values linked to a colormap, and then when the 3D plot is viewed directly down the z axis the image will look similar to a conventional spectrogram.

(1) First, one builds two matrices `S` and `Sdel` of windowed signal frames of length `win_size` (user-supplied to the procedure) time samples, with `Sdel` having frames that are delayed by one sample with respect to `S`. For the present purposes a standard Hanning window function will suffice, but other windows may be more appropriate for other applications. The windowed signal frames overlap by the same user-input number of points in each of the matrices.

(2) One next computes three short-time Fourier transform matrices; each column is `fftn`-length Fourier transform of a signal frame computed with a fast Fourier transform function called `fft`. The length value `fftn` is supplied by the user. The difference between `fftn` and `win_size` is zero-padded up to `fftn` for the computation.

`STFTdel=fft(Sdel)`

`STFT=fft(S)`

`STFTfreqdel` is just `STFT` rotated by one frequency bin—this can be accomplished by shifting the rows in `STFT` up by one step and moving the former last row to the new first row.

(3) Here are the computational steps at which the original proposal and Nelson's method differ.

(a) In the original method, compute the channelized instantaneous frequency matrix by a direct finite difference approximation. It is possible to define the phase angle in relation to the usual principal argument (required to be a value between $-\pi$ and π here) so that phase unwrapping is a by-product (taking the principle angle mod 2π should do the trick, so long as the mod function output is defined to take the sign of its second argument),

$$\mathrm{CIF} = \frac{-\mathtt{Fs}}{2\pi} \times \mathrm{mod}((\arg(\mathtt{STFTdel}) - \arg(\mathtt{STFT})), 2\pi), \tag{15}$$

where `Fs` is the sampling rate (in Hz) of the signal. This yields a matrix of `CIF` rows, one for each frequency bin (discrete channel) in the STFT matrices.

(b) Alternatively, compute Nelson's cross-spectral matrix:

`C=STFT`$\times$`STFTdel`*,

where the notation X^{*} for complex X indicates the complex conjugate (pointwise if X is a matrix of complex numbers). The notation $A \times B$ for matrices A, B denotes a point-by-point product, not a matrix multiplication.

`C` is a matrix of complex numbers; each row's phase angles equal the channelized instantaneous frequencies in the channel indexed by that row. Then compute the channelized instantaneous frequency:

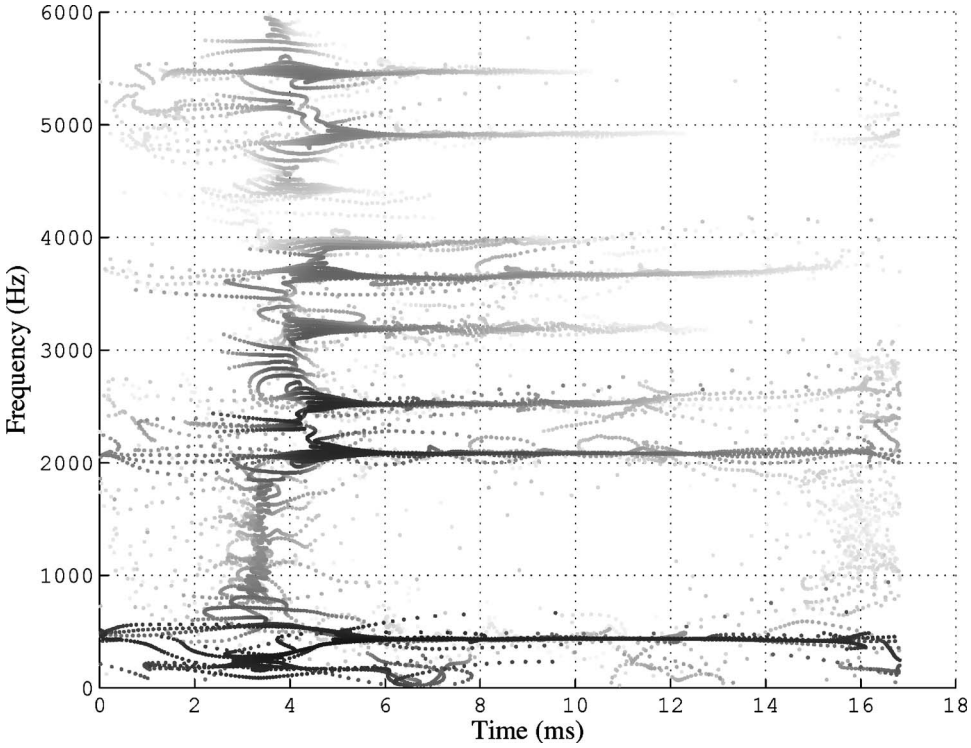

FIG. 3. Time-corrected instantaneous frequency spectrogram computed with finite difference approximations.

$$\mathrm{CIF} = \frac{\mathtt{Fs}}{2\pi} \times \arg(\mathtt{C}), \tag{16}$$

where Fs is the sampling rate (in Hz) of the signal.

(4) Compute the local group delay matrix by finite difference approximation, analogously.

(a) For the original method:

$$\mathrm{LGD} = \frac{\mathtt{fftn}}{2\pi\mathtt{Fs}} \times (\mathrm{mod}(\arg(\mathtt{STFTfreqdel}) - \arg(\mathtt{STFT})), 2\pi). \tag{17}$$

This yields a matrix of LGD columns, one for each time step in the STFT matrices.

(b) Alternatively, compute Nelson's cross-spectral matrix:

L=STFT×STFTfreqdel*

L is also a matrix of complex numbers; each column's phase angles equal the local group delay values over all the frequencies at the time index of the column. Now compute the local group delay:

$$\mathrm{LGD} = \frac{-\mathtt{fftn}}{2\pi\mathtt{Fs}} \times \arg(\mathtt{L}). \tag{18}$$

For subsequent plotting, each STFT matrix value is positioned on the *x* axis at its corrected time by adding to its signal time the corresponding (i.e., coindexed) value in the LGD matrix, plus an additional time offset equal to win_size/2Fs. The offset is required because this LGD computation corrects the time relative to the leading edge of the analysis window, but it is conventional to reference the signal time to the center of the window. Each STFT matrix value is positioned on the *y* axis at its instantaneous frequency value found at the coindexed element in the CIF matrix.

3. Performance on a test signal

It is apparent from Fig. 3 that, in comparison to the above-shown conventional spectrogram, the instantaneous frequencies of the line components (vowel formants, in this instance) are successfully highlighted, and the time correction by the local group delay is significant and shows the event time of the glottal impulse to a much higher degree of precision. It is important to emphasize that while this technique has been said to "increase the readability of the spectrogram,"[3] since it no longer plots a conventional time-frequency representation it also eliminates some spectrographic information such as the spread of energy around the components (bandwidth). (This "bandwidth" information in a spectrogram is as much or more a result of the window function as it is of the actual energy distribution in the signal, but it could of course be kept and used somehow in a modified TCIF spectrogram if so desired.) What is now plotted is the instantaneous frequency of the (assumed) single dominant line component in the vicinity of each frequency bin in the original short-time Fourier transform, the occurrence time of which is also corrected by the group delay. When there is more than one significant line component within one frequency bin, these cannot be resolved, and a weighted average of these will be plotted. When there is not significant energy within a particular time-frequency cell in the short-time Fourier transform matrix, a point with a meaningless location will be plotted somewhere, but it is not so easy to remove these troublesome points by clipping because the "significance" of a point is relative to the amplitudes of nearby components. A more sophisticated technique for re-

moving points that do not represent actual components has been suggested,[2,27] but cannot be considered in this paper.

The TCIF spectrogram for the above-mentioned signal computed using the Nelson method is by all measures indistinguishable from that shown in Fig. 3, so it would be redundant to print it. After considerable testing, we conclude that the two methods of approximating the phase derivatives are equally successful in practice. In addition, their computational complexity is similar, in that they each require the computation of two short-time Fourier transforms from the signal.

The time-corrected instantaneous frequency spectrogram can reasonably be viewed as an excellent solution to the problem of tracking the instantaneous frequencies of the components in a multicomponent signal.[24] In many common applications of spectrography (e.g., imaging and measuring the formants of speech sounds, as well as tracking the harmonics of periodic sounds), the solution to this problem is actually more relevant than what a conventional time-frequency distribution shows. In particular it should be emphasized that, while the frequencies that can be measured in a conventional spectrogram are constrained to the quantized frequency bin center values, the channelized instantaneous frequency of the dominant component near a bin is not quantized, and can be arbitrarily accurate under ideal separability of the components, even at fast chirp rates.

B. The method of Auger and Flandrin

1. Theory of the method

The method of Kodera *et al.* was further developed by Auger and Flandrin,[3] but the digital implementation details were somewhat difficult to tease out from their theory-focused paper. Digital implementations (MATLAB programs) which included the ability to create time-corrected instantaneous frequency spectrograms were ultimately released to the public domain by these authors on the Internet and have since been published,[4] though these have not been consulted or used here.

At the root of this technique there lies a rigorously derived pair of analytical expressions for the desired partial phase derivatives which invoke two new transforms using modifications of the window function $h(t)$, viz. a derivative window $dh(t)/dt$ and a time-product window $t \cdot h(t)$. Referring to the present choice of definition of the short-time Fourier transform in Eq. (6), the Auger-Flandrin equations must be written as follows; note the importance of using two different time variables T and t:

$$\mathrm{CIF}(\omega,T) = \Im\left\{ \frac{\mathrm{STFT}_{dh/dt}(\omega,T) \times \mathrm{STFT}_h^*(\omega,T)}{|\mathrm{STFT}_h(\omega,T)|^2} \right\} + \omega, \tag{19}$$

$$\mathrm{LGD}(\omega,T) = \Re\left\{ \frac{\mathrm{STFT}_{t\cdot h}(\omega,T) \times \mathrm{STFT}_h^*(\omega,T)}{|\mathrm{STFT}_h(\omega,T)|^2} \right\}. \tag{20}$$

These expressions can be sampled in a discrete implementation, to yield values of the derivatives at the STFT matrix points. Thus the resulting CIF and LGD computations are not estimates in the sense provided by the other two methods. It is easy to show empirically, however, that there is virtually no apparent difference between the results of this method and those of the finite difference methods.

2. Algorithm computing the Auger-Flandrin reassigned spectrogram

(1) A time ramp and frequency ramp are constructed for the modified window functions, and these depend in detail on whether there is an odd or even number of data points in each frame. Accordingly, the following algorithm should be used to obtain the ramps and the special windows:

1: if mod(`win_size`, 2) then
2: Mw=(`win_size`−1)/2
3: `framp`=[(0:Mw),(−Mw:−1)] (using MATLAB colon notation for a sequence of numbers stepping by one over the specified range)
4: `tramp`=(−Mw:Mw)
5: else
6: Mw=`win_size`/2
7: `framp`=[(0.5:Mw−0.5),(−Mw+0.5:−0.5)]
8: `tramp`=(−Mw+0.5:Mw−0.5)
9: end if
10: `Wt`=`tramp`×`window`
11: `Wdt`=−imag(`ifft`(`framp`×`fft`(`window`))); (`ifft` is the inverse transform function to `fft`)

(2) One next builds three matrices of windowed signal frames of length `win_size` time samples. The matrix `S` has its frames windowed by the nominal function `window`. The matrix `S_time` has its frames windowed by `Wt`, while the matrix `S_deriv` has its frames windowed by `Wdt`. The windowed signal frames overlap by a user-supplied number of points.

(3) One next computes three corresponding short-time Fourier transform matrices in the above-described customary manner:

```
STFT=fft(S)
STFT_time=fft(S_time)
STFT_deriv=fft(S_deriv)
```

(4)

$$\mathrm{CIF} = -\,\mathtt{Fs} \times \frac{\Im(\mathtt{STFT\_deriv} \times \mathtt{STFT}^*)}{|\mathtt{STFT}|^2} + \mathtt{fbin} \tag{21}$$

where `Fs` is the sampling rate (in Hz) of the signal and `fbin` is a column vector of frequency bin values resulting from the Fourier transform, to be added pointwise. Once again the notation $A \times B$ for matrices A, B denotes a point-by-point product.

(5)

$$\mathrm{LGD} = \frac{\Re(\mathtt{STFT\_time} \times \mathtt{STFT}^*)}{\mathtt{Fs} \times |\mathtt{STFT}|^2} \tag{22}$$

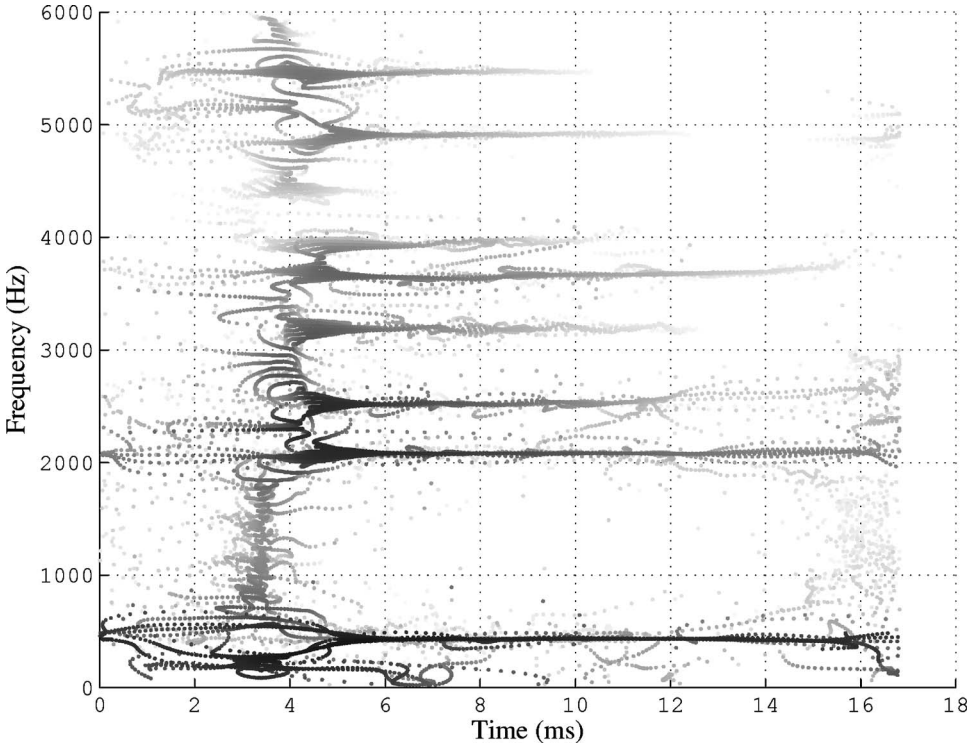

FIG. 4. Time-corrected instantaneous frequency spectrogram computed with the Auger-Flandrin equations.

3. Performance on the test signal

It is sufficient to note for our purposes that any differences that can be detected in any way between Figs. 3 and 4 are very minute and affect chiefly points that show computational artifacts rather than true signal components. No signal has yet been found to betray significant sizable differences between the Auger-Flandrin method and either of the finite-difference methods. Considering the computational load, the last and most exact method requires one more short-time Fourier transform matrix than the other methods. Theoretically the Auger-Flandrin technique is more exact, yet the advantage is in no way apparent for this or any other test signal that we have tried.

IV. APPLICATIONS

A. Examining phonation

As mentioned earlier, the phonation process involves the repetitive acoustic excitation of the vocal tract air chambers by pulsation of the vocal cords, which in an idealized model provide spectrally tilted impulses. As the test signal shows, the time-corrected instantaneous frequency spectrogram provides an impressive picture of the formant frequencies and their amplitudes following excitation by a single such impulse. The test signal was produced using creaky phonation, which has a very low airflow and is quite pulsatile, to render the process as purely acoustic as possible.

Under more natural phonatory conditions, the process is significantly aeroacoustic, meaning that the higher airflow cannot be neglected and has clearly observable effects on the excitation of resonances. The manifold effects can easily be observed by comparing Fig. 5 with any of the preceding, even though the vowel in the former was still pronounced with an artificial degree of vocal cord stiffness.

To exaggerate the aerodynamic aspect of glottal excitation, one can pronounce a vowel with an obviously breathy voice, in which the vocal cords never completely close during the glottal cycles and an audible flow of turbulent air is permitted to pass through at all times. It has long been known in practical acoustic phonetics that breathy voiced sounds yield formants whose frequencies are more difficult to measure. From Fig. 6 one can see why—the acoustic output of the process no longer conforms to a simple source-filter model, and has apparently been modified by other forces. This is expected from basic considerations of aeroacoustics when excitation by sources within the flow (turbulence) competes in importance with the more ideal excitation by vocal cord pulsation.

B. Tracking the pitch of whale songs

One of the main pieces of information about whale songs and calls that interests bioacousticians is of course, the melody, or pitch track, of the songs. Whale songs, however, have infamous features that spoil conventional pitch tracking methods, including intervals of disrupted periodicity and occasional chirps with considerably fast frequency modulation. Figure 7 shows a long frame (40 ms) time-corrected instantaneous frequency spectrogram of a portion of a Humpback whale song (thanks to Gary Bold of the University of Auckland for sharing this Humpback recording with us). The hydrophone signal is quite noisy, but the fundamental and second harmonic of the periodic portions of the song are easy to see and measure in this representation. The initial chirp is too fast for conventional pitch tracking algorithms to follow, but in the figure it is shown as a line component with no difficulty.

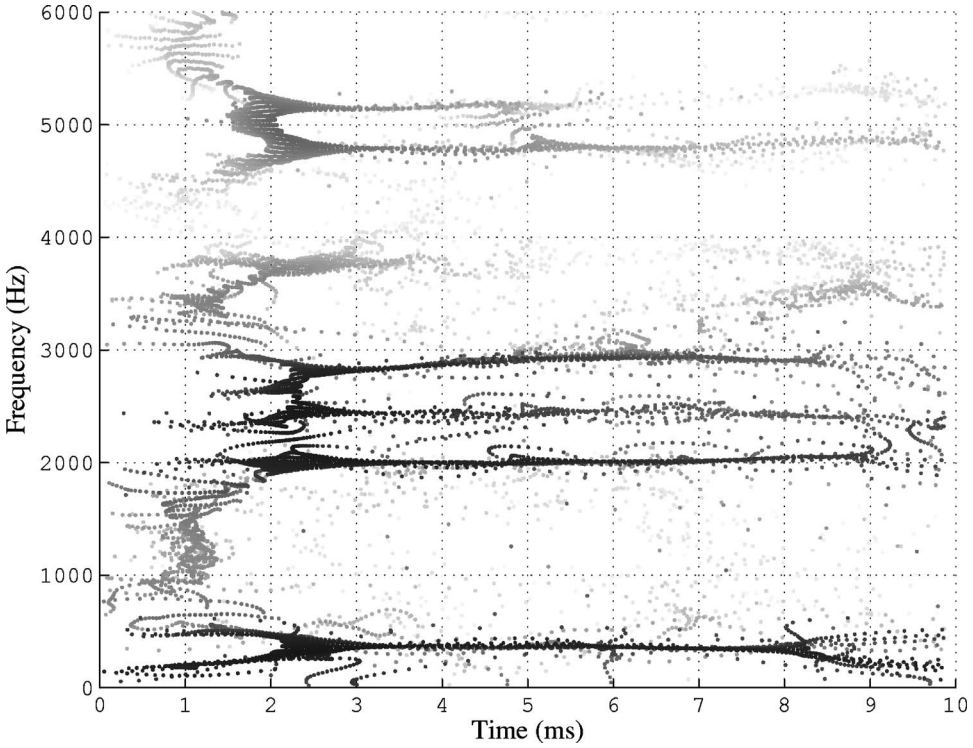

FIG. 5. Time-corrected instantaneous frequency spectrogram of one glottal pulsation from the vowel [e] pronounced with stiff modal phonation. Computed using the Nelson method with 5.9 ms windows and 78 μs frame advance.

C. Sound modeling and resynthesis

Sound modeling goes beyond analysis or transformation of the sample data to construct something not present in the original wave form. In sound modeling, one attempts to extract a complete set of features to compose a sufficient description of all perceptually relevant characteristics of a sound. One further strives to give structure to those features such that the combined features and structure (the model) form a sufficient description of a family of perceptually similar or related sounds.

The models are intended to be sufficient in detail and fidelity to construct a perceptual equivalent of the original sound based solely on the model. Furthermore, deformations of the model should be sufficient to construct sounds differing from the original only in predictable ways. Examples of such deformations are pitch shifting and time dilation.

Traditional additive sound models represent sounds as a collection of amplitude- and frequency-modulated sinusoids. These models have the very desirable property of easy and intuitive manipulability. Their parameters are easy to under-

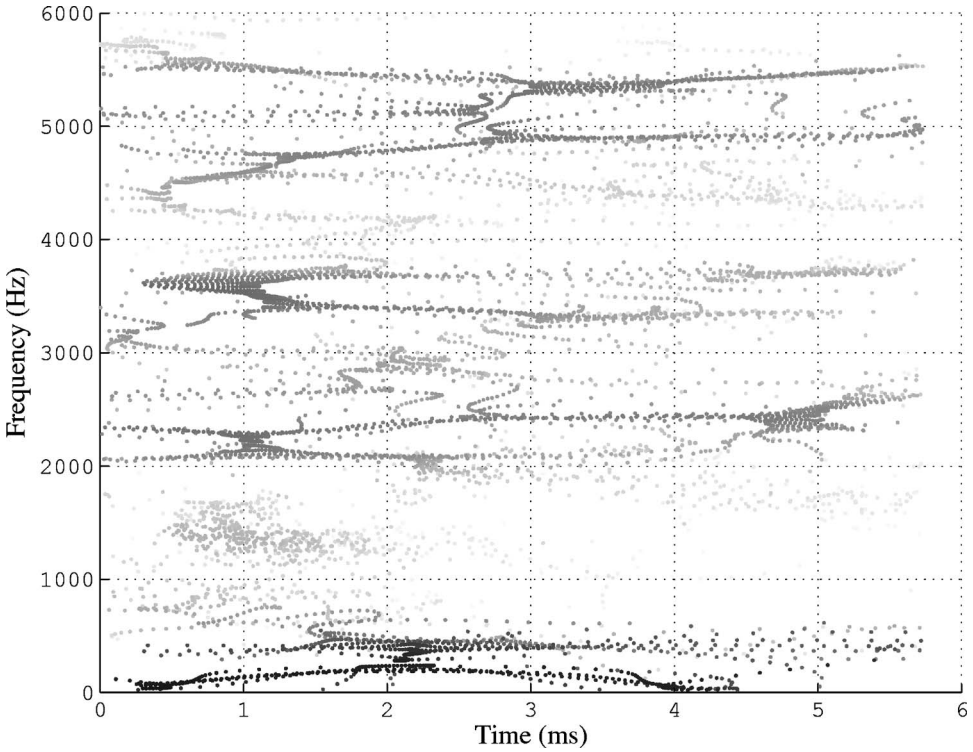

FIG. 6. Time-corrected instantaneous frequency spectrogram of one glottal pulsation from the vowel [e] pronounced with breathy phonation. Computed using the Nelson method with 5.9 ms windows and 78 μs frame advance.

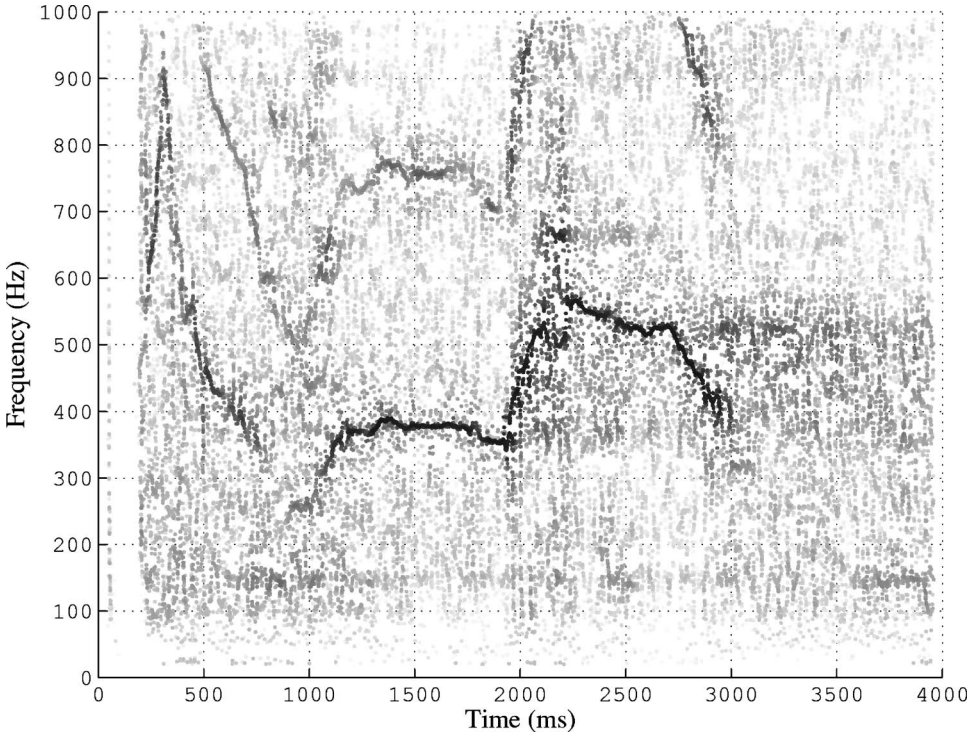

FIG. 7. Time-corrected instantaneous frequency spectrogram of a song segment produced by a Humpback whale. Computed using the Nelson method with 40 ms windows and 4.5 ms frame advance.

stand and deformations of the model data yield predictable results. Unfortunately, for many kinds of sounds, it is extremely difficult, using conventional techniques, to obtain a robust sinusoidal model that preserves all relevant characteristics of the original sound without introducing artifacts.

The *reassigned bandwidth-enhanced additive* sound model[22] is a high-fidelity representation that allows manipulation and transformation of a great variety of sounds, including noisy and nonharmonic sounds. This sound model combines sinusoidal and noise energy in a homogeneous representation, obtained by means of the time-corrected instantaneous frequency spectrogram. The amplitude and frequency envelopes of the line components are obtained by following ridges on a TCIF spectrogram. This model yields greater precision in time and frequency than is possible using conventional additive techniques, and preserves the temporal envelope of transient signals, even in modified reconstruction.

Figure 8 shows the conventional spectrogram of an acoustic bass tone. The long analysis window is needed to resolve the harmonic components in the decay of the bass tone, which are spaced at approximately 73.4 Hz. This

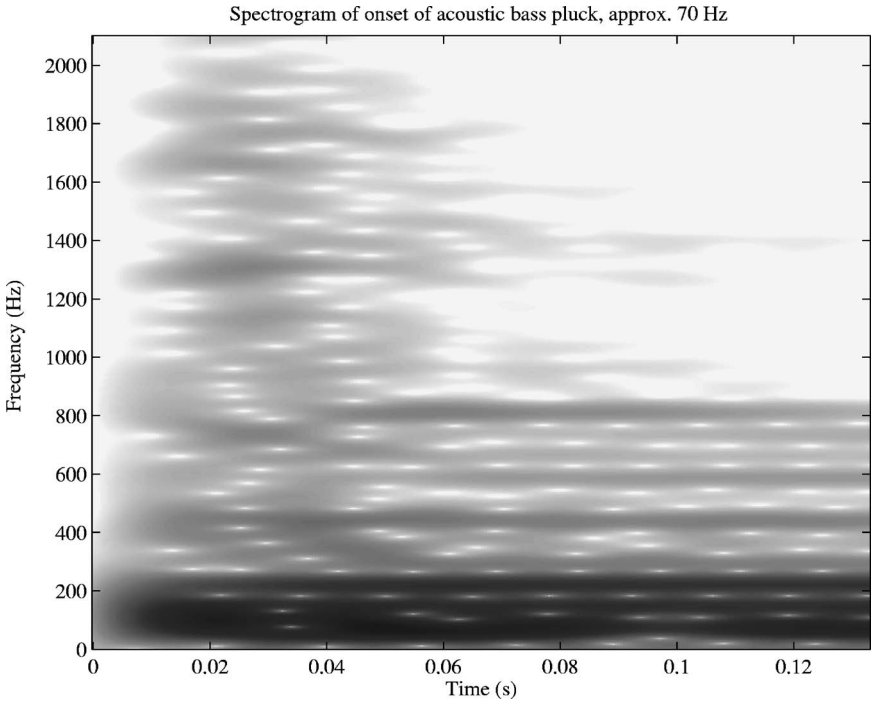

FIG. 8. Conventional spectrogram of acoustic bass pluck, computed using a Kaiser window of 1901 samples at 44.1 kHz with a shaping parameter to achieve 66 dB of sidelobe rejection.

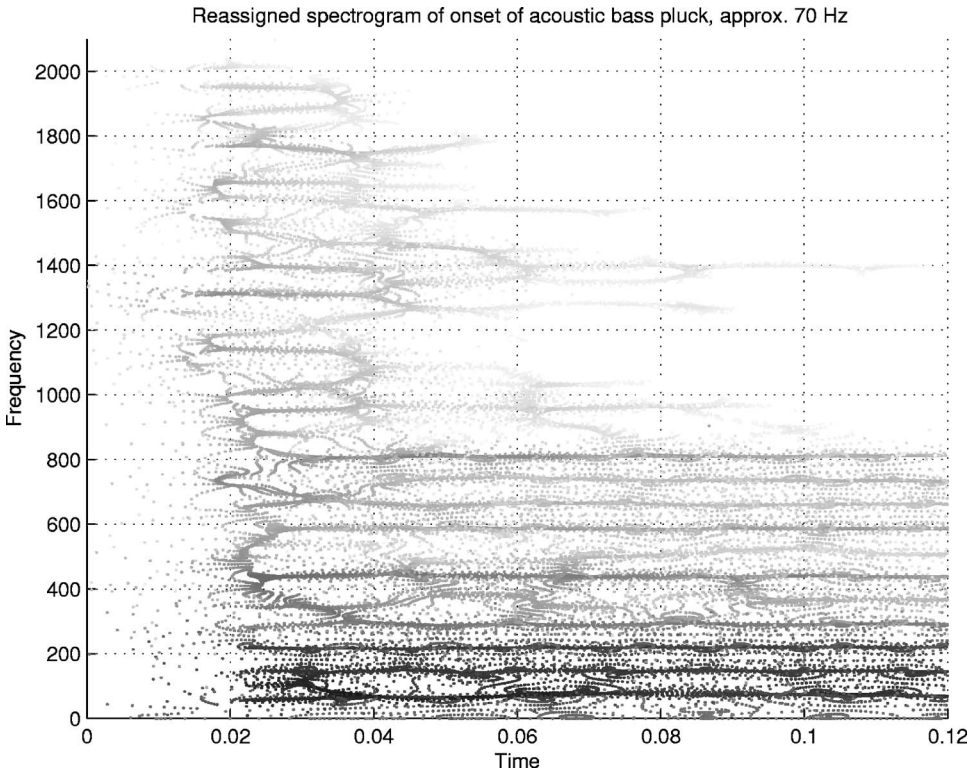

FIG. 9. TCIF spectrogram of acoustic bass pluck, computed with the same window parameters as Fig. 8.

acoustic bass sound is difficult to model because it requires very high temporal resolution to represent the abrupt attack without smearing. In fact, in order to capture the transient behavior of the attack, a window much shorter than a single period of the wave form (approximately 13.6 ms) is needed, on the order of 3 ms. Any window that achieves the desired temporal resolution in a conventional approach will fail to resolve the harmonic components.

Figure 9 shows a TCIF spectrogram for the same bass tone as above. From this reassigned spectral data, a robust model of the bass tone that captures both the harmonic components in the decay and the transient behavior of the abrupt attack can be constructed. Again it is prudent to emphasize that this single attack transient has been located in time to a high level of precision; this is not to suggest that two closely spaced transients could be resolved if they both fell within a single analysis frame.

V. CONCLUSION

The time-corrected instantaneous frequency spectrogram has gone by many names, and has so far remained little-known and underappreciated in the signal processing and acoustic literature. This is suspected to be due to the widely scattered research papers often containing perfunctory explanations of the proper interpretation of this signal representation, and subsequent natural confusion in the community about its precise nature and relationship to well-understood time-frequency representations. In short, the TCIF spectrogram is not an ordinary time-frequency representation at all, in that it is not a two-dimensional invertible transform, or even a two-dimensional function, and it does not endeavor to show the overall distribution of signal energy in the time-frequency plane. Rather, it is a different way of examining the time-frequency makeup of a signal by showing only the instantaneous frequencies of its AM/FM line components as revealed by a particular choice of analysis frame length. For many applications such as those exemplified here, focusing solely on the line components is oftentimes more valuable than the time-frequency energy distribution.

ACKNOWLEDGMENTS

This work was supported in part by a Research Incentive Grant from the University of Chicago Department of Computer Science while S. A. F. was a Visiting Assistant Professor with the Departments of Linguistics and Computer Science. The authors are grateful to Mike O'Donnell for introducing them to each other.

[1]K. Kodera, C. de Villedary, and R. Gendrin, "A new method for the numerical analysis of non-stationary signals," Phys. Earth Planet. Inter. **12**, 142–150 (1976).
[2]D. J. Nelson, "Cross-spectral methods for processing speech," J. Acoust. Soc. Am. **110**, 2575–2592 (2001).
[3]F. Auger and P. Flandrin, "Improving the readability of time-frequency and time-scale representations by the reassignment method," IEEE Trans. Signal Process. **43**, 1068–1089 (1995).
[4]P. Flandrin, F. Auger, and E. Chassande-Mottin, "Time-frequency reassignment: From principles to algorithms," in *Applications in Time-Frequency Signal Processing*, edited by A. Papandreou-Suppappola (CRC Press, Boca Raton, FL, 2003), pp. 179–203.
[5]R. K. Potter, "Visible patterns of sound," Science **102**, 463–470 (1945).
[6]D. Gabor, "Theory of communication," J. Inst. Electr. Eng., Part 3 **93**, 429–457 (1946).
[7]R. M. Fano, "Short-time autocorrelation functions and power spectra," J. Acoust. Soc. Am. **22**, 546–550 (1950).
[8]M. R. Schroeder and B. S. Atal, "Generalized short-time power spectra and autocorrelation functions," J. Acoust. Soc. Am. **34**, 1679–1683 (1962).
[9]R. M. Lerner, "Representation of signals," in *Lectures on Communication System Theory*, edited by E. J. Baghdady (McGraw-Hill, New York, 1961), pp. 203–242.

[10]C. W. Helstrom, "An expansion of a signal in Gaussian elementary signals," IEEE Trans. Inf. Theory **IT-12**, 81–82 (1966).
[11]L. K. Montgomery and I. S. Reed, "A generalization of the Gabor-Helstrom transform," IEEE Trans. Inf. Theory **IT-13**, 344–345 (1967).
[12]A. W. Rihaczek, "Signal energy distribution in time and frequency," IEEE Trans. Inf. Theory **IT-14**, 369–374 (1968).
[13]J. R. Carson, "Notes on the theory of modulation," Proc. IRE **10**, 57–64 (1922).
[14]K. Kodera, R. Gendrin, and C. de Villedary, "Analysis of time-varying signals with small *BT* values," IEEE Trans. Acoust., Speech, Signal Process. **ASSP-26**, 64–76 (1978).
[15]D. H. Friedman, "Instantaneous-frequency distribution vs. time: An interpretation of the phase structure of speech," in Proceedings of the IEEE-ICASSP, 1985, pp. 1121–1124.
[16]R. G. Stockwell, L. Mansinha, and R. P. Lowe, "Localization of the complex spectrum: The *S* transform," IEEE Trans. Signal Process. **44**, 998–1001 (1996).
[17]S. A. Fulop, P. Ladefoged, F. Liu, and R. Vossen, "Yeyi clicks: Acoustic description and analysis," Phonetica **60**, 231–260 (2003).
[18]F. Plante, G. Meyer, and W. A. Ainsworth, "Speech signal analysis with reallocated spectrogram," in Proceedings of the IEEE Symposium on Time-Frequency and Time-Scale Analysis, 1994, pp. 640–643.
[19]F. Plante, G. Meyer, and W. A. Ainsworth, "Improvement of speech spectrogram accuracy by the method of reassignment," IEEE Trans. Speech Audio Process. **6**, 282–287 (1998).
[20]S. W. Hainsworth, M. D. Macleod, and P. J. Wolfe, "Analysis of reassigned spectrograms for musical transcription," in IEEE Workshop on Applications of Signal Processing to Audio and Acoustics, 2001.
[21]M. Niethammer, L. J. Jacobs, J. Qu, and J. Jarzynski, "Time-frequency representation of Lamb waves using the reassigned spectrogram," J. Acoust. Soc. Am. **107**, L19–L24 (2000).
[22]K. Fitz and L. Haken, "On the use of time-frequency reassignment in additive sound modeling," J. Audio Eng. Soc. **50**, 879–893 (2002).
[23]T. Nakatani and T. Irino, "Robust and accurate fundamental frequency estimation based on dominant harmonic components," J. Acoust. Soc. Am. **116**, 3690–3700 (2004).
[24]T. J. Gardner and M. O. Magnasco, "Instantaneous frequency decomposition: An application to spectrally sparse sounds with fast frequency modulations," J. Acoust. Soc. Am. **117**, 2896–2903 (2005).
[25]D. J. Nelson, "Special purpose correlation functions for improved signal detection and parameter estimation," in Proceedings of the IEEE Conference on Acoustics, Speech and Signal Processing, 1993, pp. 73–76.
[26]D. J. Nelson and W. Wysocki, "Cross-spectral methods with an application to speech processing," in *SPIE Conference on Advanced Signal Processing Algorithms, Architectures, and Implementations IX* [Proc. SPIE **3807**, 552–563].
[27]D. J. Nelson, "Instantaneous higher order phase derivatives," Digit. Signal Process. **12**, 416–428 (2002).

Transducer sensitivity compensation using diagonal preconditioning for time reversal and Tikhonov inverse filtering in acoustic systems

Pierre M. Dumuid, Ben S. Cazzolato, and Anthony C. Zander
ANVC Group, School of Mechanical Engineering, The University of Adelaide, South Australia 5005

(Received 30 March 2005; revised 12 October 2005; accepted 13 October 2005)

Filters are commonly used in sound reproduction and communication systems as a means of compensating for the response of the electro-acoustic plant. Two commonly used filter designs in the field of acoustics are the time reversal filter and the Tikhonov inverse filter. In this paper the influence of transducer sensitivities on the performance of these filters is examined. It is shown that the sensitivity of the transducers can negatively affect the performance of the resulting filter. To compensate for the decrease in performance, diagonal preconditioning can be implemented in the system. It is shown that by using diagonal matrices, which minimize the condition number of the system, the loss in performance arising from unbalanced sensitivities is minimized. This paper proposes an algorithm to find such a set of diagonal matrices and results are presented showing the improvements in performance arising from the modified filter design. © *2006 Acoustical Society of America.* [DOI: 10.1121/1.2139069]

PACS number(s): 43.60.Pt, 43.60.−c, 43.38.Md [TDM] Pages: 372–381

I. INTRODUCTION

The control of transmissions through electro-acoustic systems has been an active topic of research for many years. Transmission through a system generally involves the design of a filter that manipulates input signals, such that when the output signals from the filter are transmitted through the physical system, the input signals are reproduced at the receiver. The design of such a filtering system depends on the type of physical system. The types of physical systems examined in this paper are multi-channel linear time-invariant (LTI) systems. Various designs of such filters exist for multi-channel LTI systems. Of particular interest in this work is that of designing a filter from measured impulse response functions (IRFs) of the system.[1–5] Two such filter designs are time reversal filters and Tikhonov inverse filters. When designing such filters, it is important to understand the influences various components of the system have on the resulting filter. A typical system contains a set of sensitivities for the transmitting and receiving elements. In this paper, it is shown that the choice of transducer sensitivity has a considerable influence on the resulting filters. This paper examines this influence for both time reversal and Tikhonov inverse filter designs. An algorithm is then given that generates more appropriate transducer sensitivities, and results are presented showing the improvement to the system performance.

II. BACKGROUND THEORY

The design of the multi-channel filter discussed in this paper is based on the system presented in Fig. 1. This figure shows input signals, $\mathbf{u}(z)$, transformed by the filter, $\mathbf{A}(z)$, to produce a set of signals, $\mathbf{d}(z)$, that are desired to be replicated by the signals, $\mathbf{w}(z)$, being the output of the electro-acoustic system denoted by $\mathbf{C}(z)$. In order to achieve this, a filter $\mathbf{H}(z)$ is designed based on $\mathbf{C}(z)$ and $\mathbf{A}(z)$. In general, the transfer matrix $\mathbf{A}(z)$ is a delay [i.e., $\mathbf{A}(z)=z^{-m}\mathbf{I}$]. This problem can be expressed as

$$\mathbf{w}(z) = \mathbf{C}(z)\mathbf{v}(z) \tag{1}$$

with the objective that

$$\mathbf{w}(z) = \mathbf{A}(z)\mathbf{u}(z). \tag{2}$$

In order to achieve this objective, a filter $\mathbf{H}(z)$ is designed that relates $\mathbf{w}(z)$ to $\mathbf{u}(z)$ according to

$$\mathbf{w}(z) = \mathbf{C}(z)\mathbf{H}(z)\mathbf{u}(z). \tag{3}$$

A solution to achieving this objective proposed by Kirkeby *et al.*[6,7] solved the problem by minimizing the cost function

$$J(z) = \mathbf{e}^{\mathrm{T}}(z^{-1})\mathbf{e}(z) + k\mathbf{v}^{\mathrm{T}}(z^{-1})\mathbf{v}(z). \tag{4}$$

The filter that minimizes this function is given by [Ref. 6, Eq. (8)]

$$\mathbf{H}(z) = (\mathbf{C}^{\mathrm{T}}(z^{-1})\mathbf{C}(z) + k\mathbf{I})^{-1}\mathbf{C}^{\mathrm{T}}(z^{-1})\mathbf{A}(z), \tag{5}$$

where k is a weighting term used to limit the energy of the transducer signal $\mathbf{v}(z)$. The solution given in Eq. (5) requires the calculation of the matrix,

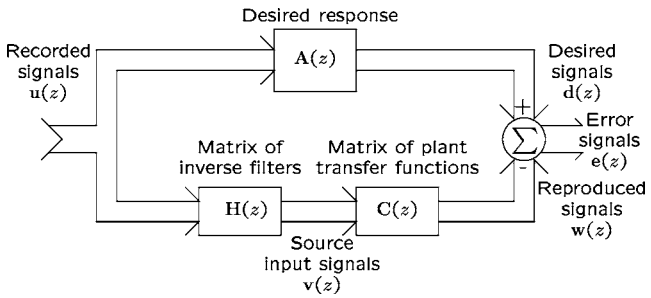

FIG. 1. Generic inverse filter system schematic (Ref. 6, Fig. 1).

$$(\mathbf{C}^{\mathrm{T}}(z^{-1})\mathbf{C}(z)+k\mathbf{I})^{-1}\mathbf{C}^{\mathrm{T}}(z^{-1}). \tag{6}$$

This matrix was observed by Elliot *et al.*[8] to be the Tikhonov inverse of the matrix $\mathbf{C}(z)$, and will hereafter be called the Tikhonov inverse filter (TIF). An extensive discussion of the Tikhonov inverse of a matrix can be found in Ref. 9. This paper will be devoted to the filter designed when $\mathbf{A}(z)=\mathbf{I}$.

Kirkeby *et al.*[6] showed that an increase in k results in an increase in the decay rate of the poles in the filter. By setting k appropriately, the length of the filters (the time at which the impulse response of the system has decayed to below the noise floor), could be reduced to fit within a finite number of points, N_{FFT}. The calculation of the filter was then possible in the frequency domain using the fast Fourier transform (FFT) without the problem of wraparound occurring when performing the inverse FFT. Calculation of the filter by this technique proved to be considerably faster than equivalent calculations performed using time domain techniques. The calculations performed in the frequency domain are given by

$$\mathbf{H}_k(\omega_i)=(\mathbf{C}^{\mathrm{H}}(\omega_i)\mathbf{C}(\omega_i)+k\mathbf{I})^{-1}\mathbf{C}^{\mathrm{H}}(\omega_i), \tag{7}$$

where $\mathbf{C}(\omega_i)$, $i\in[1,N_{\mathrm{FFT}}]$ and $\mathbf{H}_k(\omega_i)$, $i\in[1,N_{\mathrm{FFT}}]$ are the frequency domain representation of the system and Tikhonov inverse filter, respectively.

When implementing a filter design, the entire electro-acoustic system often includes sensitivities for the transmitting and receiving elements. By denoting the transmitter and receiver sensitivities as α_i, $i\in[1,N]$ and β_j, $j\in[1,M]$, respectively, the transfer matrix of the system with the sensitivities included can be expressed as

$$\begin{aligned}\mathbf{C}_{\mathrm{g}}(\omega)&=\begin{bmatrix}\beta_1 & 0 & \cdots & 0\\ 0 & \beta_2 & & \vdots\\ \vdots & & \ddots & 0\\ 0 & \cdots & 0 & \beta_{\mathrm{M}}\end{bmatrix}\\ &\quad\times\mathbf{C}(\omega)\begin{bmatrix}\alpha_1 & 0 & \cdots & 0\\ 0 & \alpha_2 & & \vdots\\ \vdots & & \ddots & 0\\ 0 & \cdots & 0 & \alpha_{\mathrm{N}}\end{bmatrix}\\ &=\boldsymbol{\beta}\mathbf{C}(\omega)\boldsymbol{\alpha}.\end{aligned} \tag{8}$$

A question raised by this form is: What influence do the sensitivities have on the resulting filters? This paper aims to address this question whereby it will be shown that the selection of $\boldsymbol{\alpha}$ and $\boldsymbol{\beta}$ to achieve the smallest condition number for $\mathbf{C}_{\mathrm{g}}(\omega)$ also decreases the high regularization that results from a poor choice of sensitivities.

In single-channel systems, the coherence between the input and the output of the system is maximized by setting the sensitivity of the transmitters to the maximum possible to reduce the noise from the electro-acoustic portion of the system, typically the largest source of noise in an acoustic system. With a multi-channel time reversal or Tikhonov inverse filter design, the level of the input signals to the electro-acoustic system is actually determined by the filter design that is developed considering both the channel and the sensitivities. If the sensitivities for each channel are set to their maximum based purely on maximizing the coherence between the input and output of the electro-acoustic system, this does not directly correspond to maximizing the coherence between the input and output of the entire system incorporating the inverse filter, the sensitivities, and the electro-acoustic system. The algorithm presented in this paper will produce the optimal set of sensitivities that provide the most balanced coherence for all channels.

III. INFLUENCE OF DIAGONAL PRECONDITIONING ON THE PERFORMANCE OF THE TIKHONOV REGULARIZED INVERSE FILTER

A. An "equally responsive system"

The influence of diagonal preconditioning on the Tikhonov inverse filter for the conditions $k=0$, and k tending toward infinity, shall be examined. The examination shall be performed for a system $\mathbf{C}(\omega)$ that is "equally responsive." A system shall be defined to be "equally responsive" when a signal transmitted from each input results in a similar level of excitation at the receivers.

When $k=0$ (i.e., no regularization) the filter created using Eq. (5) is found to be

$$\begin{aligned}\mathbf{H}(\omega)&=(\boldsymbol{\alpha}\mathbf{C}^{\mathrm{H}}(\omega)\boldsymbol{\beta}\boldsymbol{\beta}\mathbf{C}(\omega)\boldsymbol{\alpha})^{-1}\boldsymbol{\alpha}\mathbf{C}^{\mathrm{H}}(\omega)\boldsymbol{\beta}\\ &=\boldsymbol{\alpha}^{-1}(\mathbf{C}^{\mathrm{H}}(\omega)\boldsymbol{\beta}^2\mathbf{C}(\omega))^{-1}\mathbf{C}^{\mathrm{H}}(\omega)\boldsymbol{\beta}.\end{aligned} \tag{9}$$

If $\boldsymbol{\beta}=\mathbf{I}$ (i.e., equal receiver sensitivities), then Eq. (9) shows that the signal amplitude for transmitter i will be scaled by $1/\alpha_i$. The filter will thus create a set of signals that generates a higher signal level for the weaker transmitter. It then follows that the dynamic range will be fully used only for the output channel with the smallest sensitivity (assuming all the transducers have the same input dynamic range). When the matrix $\mathbf{C}$ is square, Eq. (9) can be reduced to

$$\mathbf{H}=\boldsymbol{\alpha}^{-1}(\mathbf{C}^{\mathrm{H}}(\omega)\mathbf{C}(\omega))^{-1}\mathbf{C}^{\mathrm{H}}(\omega)\boldsymbol{\beta}^{-1}, \tag{10}$$

showing that a similar attenuation is applied to the input signal according to the choice of receiver sensitivities, $\boldsymbol{\beta}$.

When regularization is included, it can be noted from Eq. (7) that as k is increased, $(\mathbf{C}_{\mathrm{g}}^{\mathrm{H}}\mathbf{C}_{\mathrm{g}}+k\mathbf{I})^{-1}$ tends toward $(1/k)\mathbf{I}$ and, as a result, the resulting filter approaches

$$\mathbf{H}(\omega)=\frac{1}{k}\mathbf{C}_{\mathrm{g}}^{\mathrm{H}}(\omega) \tag{11}$$

$$=\frac{1}{k}\boldsymbol{\alpha}\mathbf{C}^{\mathrm{H}}(\omega)\boldsymbol{\beta}, \tag{12}$$

which can be observed to be a scaled version of the frequency domain representation of the multi-channel time reversal filter.[10–12] This filter design results in the signal to transducer i being scaled by α_i, and the signal transmitted to receiver j being scaled by β_j. It then follows that the dynamic range will only be fully used for the output channel with the largest sensitivity.

It has been shown that at the two extremities of $k=0$ and $k\to\infty$ [denoted hereafter as inverse filtering (IF) and time reversal filtering (TRF)], the full dynamic range of the transducer will only be effectively used if the transducer sensitivi-

ties are equal for an "equally responsive system." It can then be noted that if the system is not equally responsive (i.e., positioning a microphone close to a pressure node), it would be desirable to find an alternative set of sensitivities that would transform the total system into an equally responsive system.

B. Influence of diagonal preconditioning on the total system

With reference to Fig. 1, the total system transfer function, being the combination of the filter and the system, is given by

$$\mathbf{T}(\omega) = \mathbf{C}(\omega)\mathbf{H}(\omega). \tag{13}$$

The influence that the transducer sensitivities have on the total system for IF and TRF can be observed by inserting Eqs. (9) and (12) into Eq. (13). The system transfer functions for IF and TRF are given by

$$\mathbf{T}_{\mathrm{IF}} = \boldsymbol{\beta}\mathbf{C}\boldsymbol{\alpha}\mathbf{H}_{\mathrm{IF}} = \boldsymbol{\beta}\mathbf{C}\boldsymbol{\alpha}((\boldsymbol{\alpha}\mathbf{C}^{\mathrm{H}}\boldsymbol{\beta}\boldsymbol{\beta}\mathbf{C}\boldsymbol{\alpha})^{-1}\boldsymbol{\alpha}\mathbf{C}^{\mathrm{H}}\boldsymbol{\beta}) = \mathbf{I} \tag{14}$$

and

$$\mathbf{T}_{\mathrm{TRF}} = \boldsymbol{\beta}\mathbf{C}\boldsymbol{\alpha}\mathbf{H}_{\mathrm{TR}} = \boldsymbol{\beta}\mathbf{C}\boldsymbol{\alpha}(\boldsymbol{\alpha}\mathbf{C}^{\mathrm{H}}\boldsymbol{\beta}) = \boldsymbol{\beta}\left(\sum_{i=1}^{\mathrm{N}} \alpha_i^2 \begin{bmatrix} c_{1i} \\ c_{2i} \\ \vdots \end{bmatrix} \begin{bmatrix} c_{1i}^* & c_{2i}^* & \cdots \end{bmatrix}\right)\boldsymbol{\beta}, \tag{15}$$

respectively, and the matrix

$$\begin{bmatrix} c_{1i} \\ c_{2i} \\ \vdots \end{bmatrix} \begin{bmatrix} c_{1i}^* & c_{2i}^* & \cdots \end{bmatrix} \tag{16}$$

is the transfer matrix due to the ith transmitter. It is thus observed that the variation of the transducer sensitivities have no influence on the total response for an IF but considerable influence on the TRF.

Considering that $\mathbf{C}^{\mathrm{H}}\mathbf{C}$ is diagonally dominant,[13] Eq. (15) shows that the transducer sensitivities $\boldsymbol{\beta}$ result in the signal at the jth receiver being scaled by β_j^2, and the sensitivities $\boldsymbol{\alpha}$ result in the scaling of the ith transfer matrix by α_i^2. Since the Tikhonov inverse filter has a nonzero regularization parameter, it is considered reasonable to assume that the transmission channels would also be unequally scaled.

C. Examination of the transfer matrix according to the singular values

In this section, the influence of the transducer sensitivities on the TIF will be examined according to the singular values decomposition (SVD) of the system matrix, given by

$$\mathbf{C}(\omega) = \mathbf{U}(\omega)\boldsymbol{\Sigma}(\omega)\mathbf{V}^{\mathrm{H}}(\omega) = \sum_{i=1}^{N} \sigma_i \mathbf{u}_i(\omega)\mathbf{v}_i^{\mathrm{H}}(\omega), \tag{17}$$

where $\mathbf{U}(\omega)$ and $\mathbf{V}(\omega)$ are unitary matrices, $\boldsymbol{\Sigma}(\omega)$ is a diagonal matrix of singular values, σ_i, $i \in [1, N]$, and $\mathbf{u}_i(\omega)$ and $\mathbf{v}_i(\omega)$ are the corresponding basis vectors within the unitary matrices. The inverse filter with no regularization can then be expressed as

$$\mathbf{H}_{\mathrm{IF}}(\omega) = \mathbf{V}(\omega)\boldsymbol{\Sigma}^{-1}(\omega)\mathbf{U}^{\mathrm{H}}(\omega) = \sum_{i=1}^{N} \frac{\mathbf{v}_i(\omega)\mathbf{u}_i^{\mathrm{H}}(\omega)}{\sigma_i} \tag{18}$$

and the addition of the regularization results in the filter

$$\mathbf{H}_{\mathrm{TIF}}(\omega) = \mathbf{V}(\omega)\boldsymbol{\Sigma}_{\mathrm{TIF}}(\omega)\mathbf{U}^{\mathrm{H}}(\omega) = \sum_{i=1}^{N} \left(\frac{\sigma_i^2}{\sigma_i^2 + k}\right)\frac{\mathbf{v}_i(\omega)\mathbf{u}_i^{\mathrm{H}}(\omega)}{\sigma_i}, \tag{19}$$

where the subscript TIF denotes Tikhonov inverse filter. In subsequent equations the frequency dependence (ω) is implied, but not shown. In Eq. (19) it can be seen that the magnitude of k compared to σ_i^2 [the singular values of $\mathbf{C}(\omega)\mathbf{C}^{\mathrm{H}}(\omega)$] determines the effectiveness of the "basis vector coupling" between $\mathbf{u}_i$ and $\mathbf{v}_i$.[14] Basis vector coupling is physically described as follows: $\mathbf{u}_i$ is considered similar to a mode shape that, when excited, results in an excitation of the receivers with a phase and amplitude, $\mathbf{v}_i$, scaled according to the coupling factor of σ_i.

When the sensitivities are included, the filter becomes

$$\mathbf{C}_{\mathrm{g}} = \boldsymbol{\beta}\mathbf{U}\boldsymbol{\Sigma}\mathbf{V}^{\mathrm{H}}\boldsymbol{\alpha} \tag{20}$$

$$= \mathbf{U}_{\mathrm{g}}\boldsymbol{\Sigma}_{\mathrm{g}}\mathbf{V}_{\mathrm{g}}^{\mathrm{H}}, \tag{21}$$

where $\mathbf{U}_{\mathrm{g}}$, $\mathbf{V}_{\mathrm{g}}$, and $\boldsymbol{\Sigma}_{\mathrm{g}}$ are the unitary and singular matrices of the new system. The basis vector coupling matrices, $\mathbf{u}_i\sigma_i\mathbf{v}_i^{\mathrm{H}}$, have been converted to $\boldsymbol{\beta}\mathbf{u}_i\sigma_i\mathbf{v}_i^{\mathrm{H}}\boldsymbol{\alpha}$. Since the set of vectors, $\boldsymbol{\beta}\mathbf{u}_i$, $i \in [1, \mathrm{M}]$ and $\boldsymbol{\alpha}\mathbf{v}_i$, $i \in [1, \mathrm{N}]$ (being the transformation of the original basis vectors); cannot be simply scaled to form another orthonormal set, it can be concluded that there is no trivial solution to relate the singular values of $\mathbf{C}$ to that of $\mathbf{C}_{\mathrm{g}}$.

In this work, the goal is to determine a new set of sensitivities that reduce the regularization that results from a poor choice of sensitivities. Given a fixed regularization parameter, k, Eq. (19) shows that to reduce the effect of the regularization on the singular values, sensitivities should be chosen that result in the largest singular values possible. This strategy by itself is unrealistic since the problem is unconstrained since $\boldsymbol{\alpha}$ and $\boldsymbol{\beta}$ can be chosen to scale the singular values by any desired amount, x, by using a set of scaling matrices,

$$\boldsymbol{\alpha} = x\mathbf{I}, \quad \boldsymbol{\beta} = \mathbf{I}. \tag{22}$$

It can further be shown using Eq. (19) that the change in regularization that results from the equal scaling of the sensitivities by x can equivalently be achieved by selecting a different regularization parameter, $k' = x^2k$. Thus, the objective of adjusting the sensitivities should not be to scale the singular values, but to minimize the condition number, being the ratio of the largest singular value to the smallest singular value.

D. Diagonal preconditioning

In Secs. III B and III C, two optimization techniques have been proposed, the former to achieve an equally respon-

sive system and the latter to reduce the condition number of the matrix. In the former technique, the transducer sensitivities are chosen such that every input signal to the system excites the outputs of the system with the same magnitude. This can be expressed as

$$|\boldsymbol{\beta}\mathbf{C}\boldsymbol{\alpha}\mathbf{e}_1|_2 = |\boldsymbol{\beta}\mathbf{C}\boldsymbol{\alpha}\mathbf{e}_2|_2 = \cdots = |\boldsymbol{\beta}\mathbf{C}\boldsymbol{\alpha}\mathbf{e}_N|_2, \tag{23}$$

where $|\cdot|_2$ is the norm-2 (or Euclidean length) of a vector, and the vectors $\mathbf{e}_1, \ldots, \mathbf{e}_N$ are the standard basis vectors for $\mathbb{R}_N$. This condition can be achieved by setting

$$\beta_i = 1, \qquad \alpha_j^2 = \frac{1}{\sum_{j=1}^{M} |c_{ij}|^2}. \tag{24}$$

By using this scaling, the resulting filters will equalize the signals transmitted, but not the signals received. In order to achieve equal signal levels at the receivers, a further condition can be imposed: for a simultaneous unit input on all the channels, the energy at each output is to be equal. To achieve this, a set of diagonal matrices, $\boldsymbol{\alpha}$ and $\boldsymbol{\beta}$, are chosen such that

$$r_1^2 = r_2^2 = \cdots = r_M^2, \tag{25}$$

where

$$\begin{bmatrix} r_1 \\ r_2 \\ \vdots \\ r_M \end{bmatrix} = \boldsymbol{\beta}\mathbf{C}\boldsymbol{\alpha} \begin{bmatrix} 1 \\ 1 \\ \vdots \\ 1 \end{bmatrix}. \tag{26}$$

A solution that achieves this is

$$\alpha_j = 1, \qquad \beta_i^2 = \frac{1}{\sum_{i=1}^{N} |c_{ij}|^2}. \tag{27}$$

When the conditions in Eqs. (24) and (27) are met, the system responds equally, and thus Tikhonov inverse filtering can be found to effectively use the full dynamic range of all the transducers within the system.

In Sec. III C it was shown that a suitable choice of diagonal matrices was the set that minimized the condition numbers of the system. Van der Sluis[15] discussed that minimization of the condition number could not be expected to be easily achieved, however it was shown in Ref. 15, Theorem 3.5, that the condition number of the matrix $\boldsymbol{\alpha}\mathbf{C}$ was upper bounded to be a factor of $\sqrt{m}$ from the minimum when all the rows have equal two-norms, and the condition number of $\mathbf{C}\boldsymbol{\beta}$ was upper bounded to be a factor of $\sqrt{n}$ from the minimum when all the columns have equal two-norms for an $m \times n$ matrix. From Eqs. (24) and (27), the diagonal matrices that best use the dynamic range of the transducers also results in a matrix of equal two-norm of both the row and columns. Thus the design techniques presented in Secs. III B and III C have the same solution, being that of diagonal matrices that result in $\mathbf{C}_g$ having rows and columns of equal two-norm.

Finding a set of diagonal matrices that achieve equal two-norms of both the columns and rows simultaneously is a nontrivial problem. In order to approximate such a condition, Ruiz[16] showed that an algorithm involving the iterative application of Eqs. (24) and (27) converges to a set of diagonal matrices that results in equal two-norms of both row and columns of the combined matrices. A variation of the algorithm by Ruiz[16] is proposed and used hereafter to calculate an optimal set of diagonal matrices:

Algorithm 1:

$$\hat{\mathbf{C}}^{(0)} = \mathbf{C}, \quad \boldsymbol{\beta}^{(0)} = \mathbf{I}, \quad \boldsymbol{\alpha}^{(0)} = \mathbf{I}$$

for $k = 0, 1, 2, \ldots$, until convergence do

$$\mathbf{D}_R = \mathrm{diag}\left(\sqrt{|\mathbf{r}_i^{(k)}|_2}\right)_{i=1,\ldots,m},$$

$$\mathbf{D}_C = \mathrm{diag}\left(\sqrt{|\mathbf{c}_j^{(k)}|_2}\right)_{j=1,\ldots,n},$$

$$\hat{\mathbf{C}}^{(k+1)} = \mathbf{D}_R^{-1}\hat{\mathbf{C}}^{(k)}\mathbf{D}_C^{-1},$$

$$\boldsymbol{\beta}^{(k+1)} = \boldsymbol{\beta}^{(k)}\mathbf{D}_R^{-1}, \quad \text{and} \quad \boldsymbol{\alpha}^{(k+1)} = \boldsymbol{\alpha}^{(k)}\mathbf{D}_C^{-1},$$

where $\mathbf{r}_i^{(k)}$ and $\mathbf{c}_j^{(k)}$ are the ith row and jth column of the matrix $\hat{\mathbf{C}}^{(k)}$, respectively. For the experimental results given in Sec. IV, it was found that adequate convergence of the algorithm was reached after 20 iterations.

E. Preconditioning within the controller

So far the implementation of sensitivity compensation has only been discussed with respect to scaling within the analog domain. In this section the concept of scaling the signal within the digital domain will be presented. To develop a filter for use in the digital domain, it is observed that the filter, $\mathbf{H}_g$, is designed such that

$$[\boldsymbol{\beta}\mathbf{C}\boldsymbol{\alpha}]\mathbf{H}_g \simeq \mathbf{I}, \tag{28}$$

where the square brackets have been included to define the analog domain. It then follows that

$$\boldsymbol{\beta}^{-1}\boldsymbol{\beta}\mathbf{C}\boldsymbol{\alpha}\mathbf{H}_g \simeq \boldsymbol{\beta}^{-1}, \qquad [\mathbf{C}]\boldsymbol{\alpha}\mathbf{H}_g\boldsymbol{\beta} \simeq \mathbf{I}. \tag{29}$$

Thus an inverse filter for use in the digital domain is given by

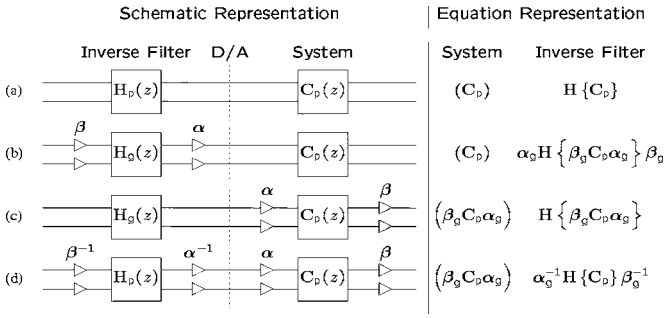

FIG. 2. Diagonal preconditioning systems: (a) no diagonal preconditioning, (b) digital preconditioning, (c) analog preconditioning, and (d) scaled version of the Tikhonov inverse filter.

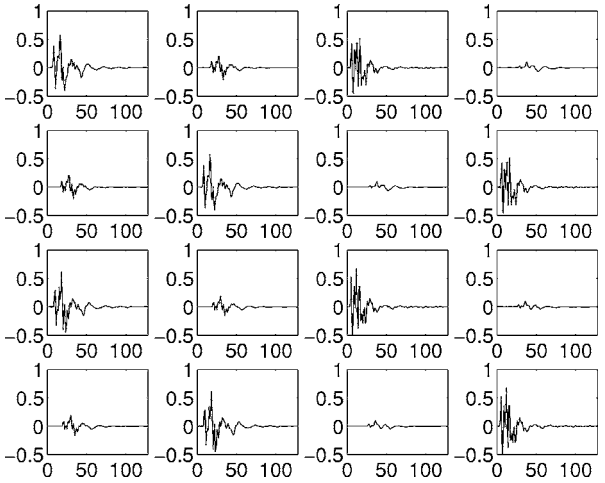

FIG. 3. The impulse responses $c_{rs}(n)$ of the system (replica of Ref. 7, Fig. 3) showing the response amplitudes versus sample, n. In this figure, the subfigure at row i, column j corresponds to the IRF of the channel between transmitter j and receiver i.

$$\mathbf{H}_{\text{digital}} = \boldsymbol{\alpha}\mathbf{H}_{\text{g}}\boldsymbol{\beta} = \boldsymbol{\alpha}((\boldsymbol{\beta}\mathbf{C}\boldsymbol{\alpha})^{\text{H}}(\boldsymbol{\beta}\mathbf{C}\boldsymbol{\alpha}) + k\mathbf{I})^{-1}(\boldsymbol{\beta}\mathbf{C}\boldsymbol{\alpha})^{\text{H}}\boldsymbol{\beta}$$
$$= (\mathbf{C}^{\text{H}}\boldsymbol{\beta}^2\mathbf{C} + k\boldsymbol{\alpha}^{-2})^{-1}\mathbf{C}^{\text{H}}\boldsymbol{\beta}^2. \quad (30)$$

The digital and analog implementations are shown in Figs. 2(b) and 2(c). When applying diagonal preconditioning in the analog domain, $\boldsymbol{\alpha}$ and $\boldsymbol{\beta}$ are chosen to transform the system $\mathbf{C}_{\text{g}}(z)$ into an equally responsive system such that the signals at the input and output of the system have relatively equal amplitudes. However, if the scaling is performed within the digital domain, the amplitude of the signals at the D/A and A/D converters are

$$\mathbf{s}_{\text{D/A}}(z) = \boldsymbol{\alpha}\mathbf{v}(z) \quad (31)$$

and

$$\mathbf{s}_{\text{A/D}}(z) = \boldsymbol{\beta}^{-1}\mathbf{w}(z), \quad (32)$$

respectively, showing that the filter does not make effective use of the D/A and A/D converters. Thus the only benefit to using diagonal preconditioning in the digital domain is to reduce the unequal regularization on the singular values that results from a poor choice of sensitivities.

IV. AN EXAMPLE ANALYSIS

In this section, a simulation will be used to demonstrate the concept of diagonal preconditioning. The simulation used is a replica of that performed by Kirkeby *et al.*[7] in which a filtering system is designed that utilizes four speakers to generate a set of desired signals at four points surrounding a dummy head. For a detailed overview of the physical configuration, see Ref. 7. The simulation utilizes transfer functions created by Gardner and Martin[17] which are freely available for download from the MIT Media Laboratory website (World Wide Web Address: http://sound.media.mit.edu/KEMAR.html). The impulse responses that describe the system are shown in Fig. 3. It should be observed that due to symmetry in the experiment, the impulse response matrix can be written in the form

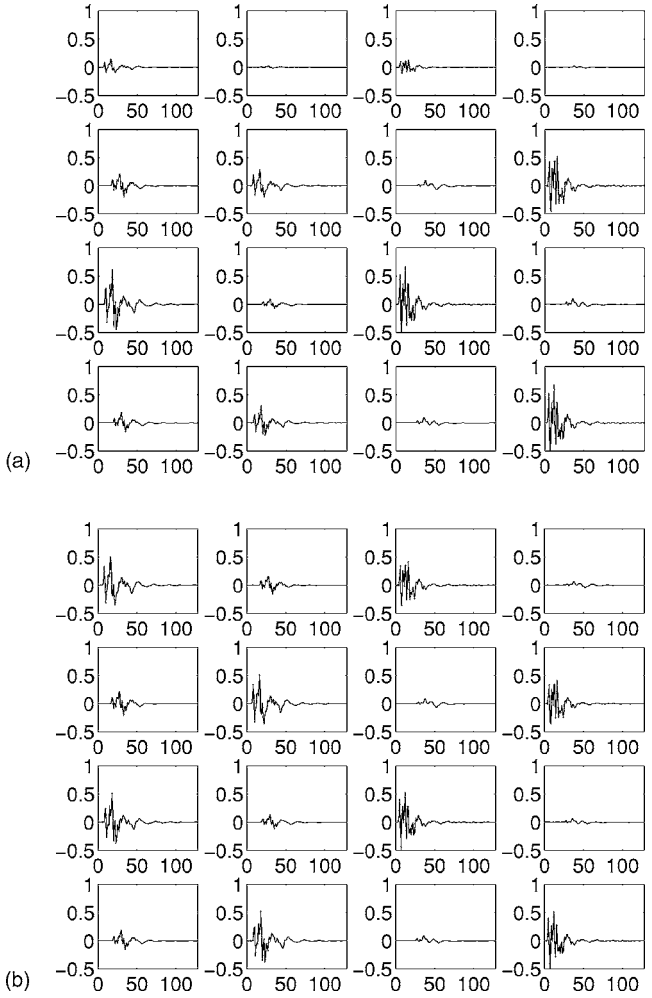

FIG. 4. The impulse responses $c(n)$. In these figures, the subplot at row i, column j corresponds to the IRF of the channel between transmitter j and receiver i. (a) Poorly scaled system, $\mathbf{C}_{\text{p}}$. (b) Poorly scaled system after application of gain compensation, $\boldsymbol{\beta}_{\text{g}}\mathbf{C}_{\text{p}}\boldsymbol{\alpha}$.

$$\mathbf{C}(z) = \begin{bmatrix} c_1(n) & c_2(n) & c_3(n) & c_4(n) \\ c_2(n) & c_1(n) & c_4(n) & c_3(n) \\ c_5(n) & c_6(n) & c_7(n) & c_8(n) \\ c_6(n) & c_5(n) & c_8(n) & c_7(n) \end{bmatrix}. \quad (33)$$

It can be observed from Fig. 3 that the energies of $c_1(n)$, $c_3(n)$, $c_5(n)$, and $c_7(n)$ are relatively equal, and similarly the energies of $c_2(n)$, $c_4(n)$, $c_6(n)$, and $c_8(n)$ are relatively equal. From this it can be concluded that the norm-2 of the rows

TABLE I. Energy within the rows and columns of the transfer matrices.

System	Rows	Columns
Poor scaled system ($\mathbf{C}_{\text{p}}$)	$[0.70 \quad 0.44 \quad 0.77 \quad 1.00]^{\text{T}}$	$[0.24 \quad 0.81 \quad 1.00 \quad 0.86]$
Compensated ($\boldsymbol{\beta}_{\text{g}}\mathbf{C}_{\text{p}}\boldsymbol{\alpha}_{\text{g}}$)	$[1.00 \quad 0.98 \quad 1.00 \quad 0.98]^{\text{T}}$	$[0.98 \quad 1.00 \quad 0.98 \quad 1.00]$

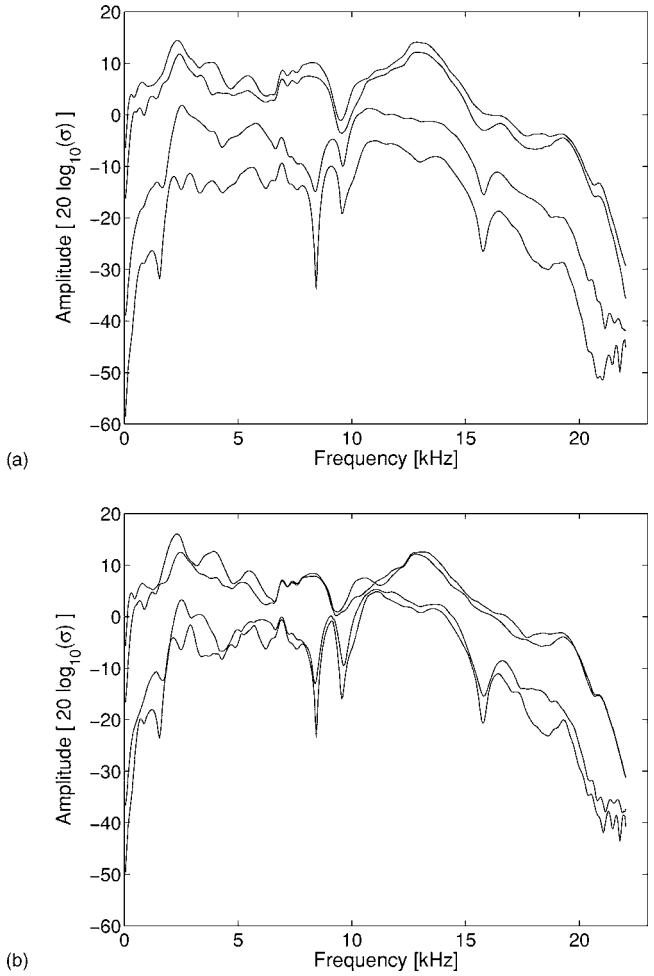

FIG. 5. The singular values of $\mathbf{C}(\omega)$. (a) Poorly scaled system, $\mathbf{C}_\mathrm{p}$. (b) Poorly scaled system after application of gain compensation, $\boldsymbol{\beta}_\mathrm{g}\mathbf{C}_\mathrm{p}\boldsymbol{\alpha}$.

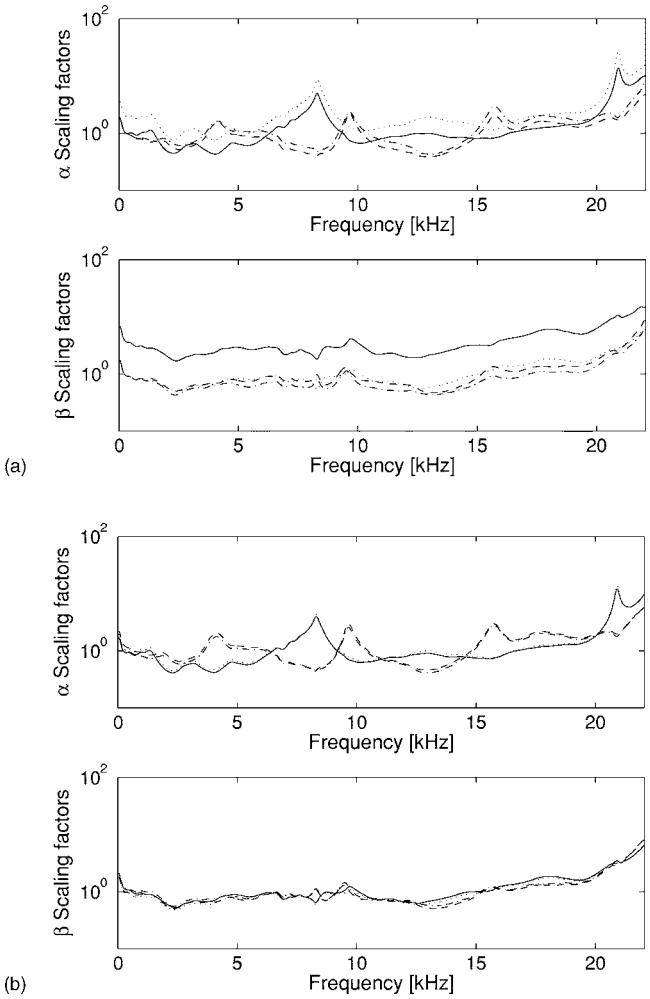

FIG. 6. Optimal values of $\boldsymbol{\alpha}$ and $\boldsymbol{\beta}$ with respect to frequency, calculated using the preconditioning algorithm; ———x_1, $\cdots x_2$, -·-·-x_3, - - -x_4, where $x=\boldsymbol{\alpha}$ and $\boldsymbol{\beta}$, respectively. (a) Poorly scaled system, $\mathbf{C}_\mathrm{p}$. (b) Poorly scaled system after application of gain compensation, $\boldsymbol{\beta}_\mathrm{g}\mathbf{C}_\mathrm{p}\boldsymbol{\alpha}$.

and columns of this matrix are likely to be fairly similar, and thus the system is equally responsive. To examine the influence of diagonal preconditioning, a set of gains will be used to cause the system to be poorly scaled, and then, to demonstrate the proposed technique, a set of gains will be calculated using Algorithm 1 to compensate for the poor scaling.

The set of gains arbitrarily chosen to create a system with a poor choice of sensitivities is given by

$$\boldsymbol{\alpha}_\mathrm{p}=\begin{bmatrix}1.00 & 0 & 0 & 0\\ 0 & 0.50 & 0 & 0\\ 0 & 0 & 1.00 & 0\\ 0 & 0 & 0 & 1.00\end{bmatrix},$$
$$\boldsymbol{\beta}_\mathrm{p}=\begin{bmatrix}0.25 & 0 & 0 & 0\\ 0 & 1.00 & 0 & 0\\ 0 & 0 & 1.00 & 0\\ 0 & 0 & 0 & 1.00\end{bmatrix}, \tag{34}$$

with the resulting IRFs shown in Fig. 4(a). This system will be denoted as $\mathbf{C}_\mathrm{p}$, where the subscript p denotes *poorly scaled*. The scaling introduced physically corresponds to transmitter 2 having half the sensitivity of the other transmitters and receiver 1 having a sensitivity a quarter that of the other elements. A set of compensating gains was then calculated by applying Algorithm 1 to the system energy matrix,

$$\mathbf{E}=\begin{bmatrix}\sqrt{\sum_n c_{11}^2(n)} & \sqrt{\sum_n c_{12}^2(n)} & \sqrt{\sum_n c_{13}^2(n)} & \sqrt{\sum_n c_{14}^2(n)}\\ \sqrt{\sum_n c_{21}^2(n)} & \sqrt{\sum_n c_{22}^2(n)} & \sqrt{\sum_n c_{23}^2(n)} & \sqrt{\sum_n c_{24}^2(n)}\\ \sqrt{\sum_n c_{31}^2(n)} & \sqrt{\sum_n c_{32}^2(n)} & \sqrt{\sum_n c_{33}^2(n)} & \sqrt{\sum_n c_{34}^2(n)}\\ \sqrt{\sum_n c_{41}^2(n)} & \sqrt{\sum_n c_{42}^2(n)} & \sqrt{\sum_n c_{43}^2(n)} & \sqrt{\sum_n c_{44}^2(n)}\end{bmatrix}. \tag{35}$$

The resulting compensation gains are

$$\boldsymbol{\alpha}_\mathrm{g}=\begin{bmatrix}1.06 & 0 & 0 & 0\\ 0 & 1.85 & 0 & 0\\ 0 & 0 & 0.99 & 0\\ 0 & 0 & 0 & 0.83\end{bmatrix},$$
$$\boldsymbol{\beta}_\mathrm{g}=\begin{bmatrix}3.30 & 0 & 0 & 0\\ 0 & 0.96 & 0 & 0\\ 0 & 0 & 0.79 & 0\\ 0 & 0 & 0 & 0.93\end{bmatrix}. \tag{36}$$

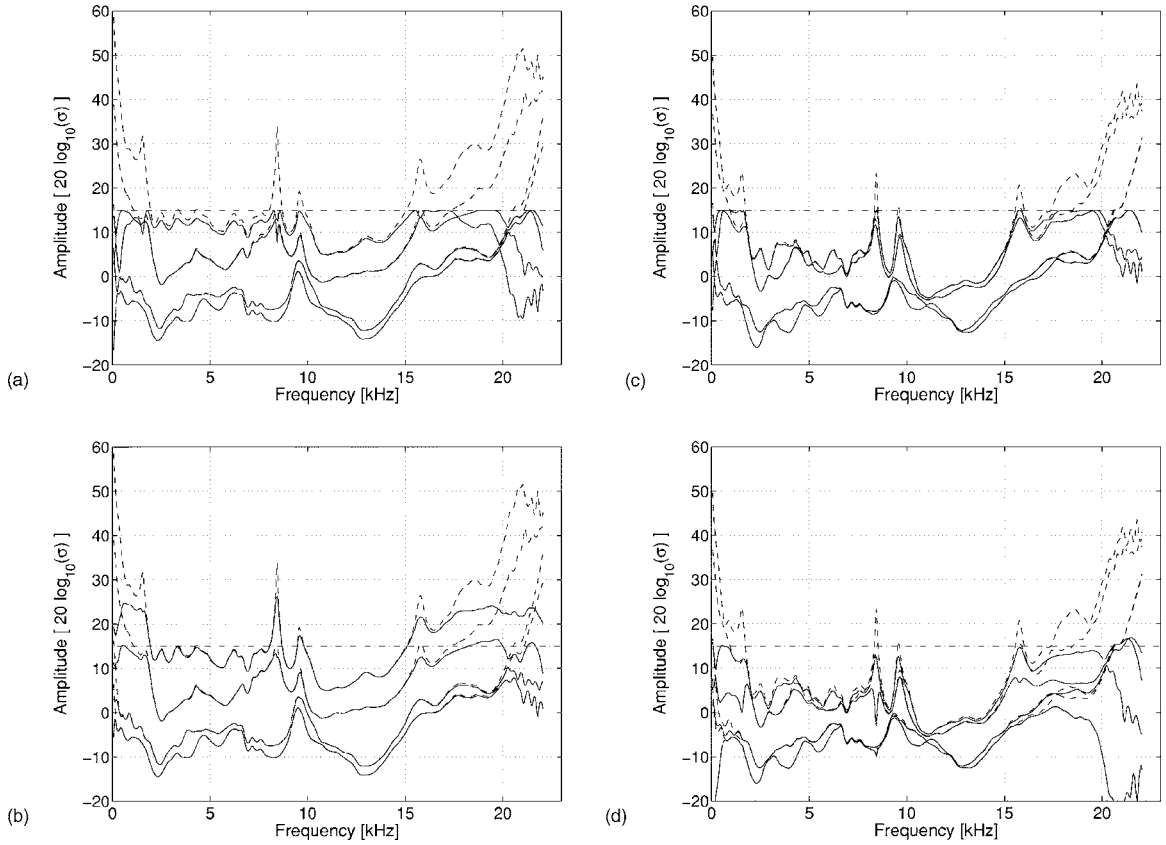

FIG. 7. The singular values of the $\mathbf{H}_{\mathrm{TIF}}(\omega_n)$ for $k=0.008$, ———with regularization; - - - without regularization, -·-·- singular value limit, $1/2\sqrt{k}$. (a) No preconditioning, $\mathbb{H}\{\mathbf{C}_\mathrm{p}\}$. (b) Digital preconditioning, $\boldsymbol{\alpha}_\mathrm{g}^{-1}\mathbb{H}\{\boldsymbol{\beta}_\mathrm{g}\mathbf{C}_\mathrm{p}\boldsymbol{\alpha}_\mathrm{g}\}\boldsymbol{\beta}_\mathrm{g}^{-1}$. (c) Analog preconditioning, $\mathbb{H}\{\boldsymbol{\beta}_\mathrm{g}\mathbf{C}_\mathrm{p}\boldsymbol{\alpha}_\mathrm{g}\}$. (d) No preconditioning, scaled $\boldsymbol{\alpha}_\mathrm{g}^{-1}\mathbb{H}\{\mathbf{C}_\mathrm{p}\}\boldsymbol{\beta}_\mathrm{g}^{-1}$.

Figure 4(b) shows the IRFs of the system after sensitivity compensation has been applied (i.e., the application of $\boldsymbol{\alpha}_\mathrm{p}\boldsymbol{\alpha}_\mathrm{g}$ and $\boldsymbol{\beta}_\mathrm{p}\boldsymbol{\beta}_\mathrm{g}$ to the initial system.) Table I shows the energy within the rows and columns of both systems, normalized such that the largest energy level is unity. As the energy within each row and each column for the sensitivity-compensated system are of similar magnitude (in contrast to that of the poorly scaled system), the algorithm is thus observed to work as desired.

The singular values of the two systems as a function of frequency are shown in Fig. 5. It can be observed in this figure that when the system is poorly scaled, the spread of the singular values is much larger than that obtained when compensation gains are used.

Figure 6 shows the sensitivities, $\boldsymbol{\alpha}$ and $\boldsymbol{\beta}$, that would result in the optimal scaling for each particular frequency. It can be observed that with gain compensation, the spread of these curves is reduced. If the system is to be used for band-limited operation, then in practice a choice of sensitivities would be found by averaging the $\boldsymbol{\alpha}$ and $\boldsymbol{\beta}$ over the desired bandwidth of operation.

In Sec. III E it was shown that diagonal preconditioning could be performed in either the digital or analog domain. To understand the results obtained using diagonal preconditioning, various forms of diagonal preconditioning shall be examined, and these are illustrated in Fig. 2. In order to compare the performance of the filter with and without diagonal preconditioning, the system that the filters are compensating for should be identical. Figure 2 shows that when diagonal preconditioning is implemented in the digital domain [Fig. 2(b)], the system being compensated is the same as that for the implementation without preconditioning [Fig. 2(a)]. However, when diagonal preconditioning is implemented in the analog domain [Fig. 2(c)], the system being compensated is different. In order to have a benchmark against which the performance of the analog implementation can be compared, a new filter has been introduced, being the Tikhonov inverse filter formed from the system with no preconditioning scaled for a system with poor sensitivities using the same method and assumptions used to obtain Eq. (30). This filter is shown in Fig. 2(d).

The singular value curves of the filters presented in Fig. 2 are shown in Fig. 7. These curves represent the "basis vector coupling" discussed in Sec. III C. Figures 7(a) and 7(b) show the singular values of the filters that are designed to compensate for the coupling in Fig. 5(a), while Fig. 7(c) and 7(d) show the singular values of the filters designed to compensate for the coupling represented in Fig. 5(b).

Figures 7(a) and 7(c) show that the filters do not have any singular values that exceed 15 dB. This limit can be explained with reference to Eqs. (18) and (19) where regularization changes the singular value from $1/\sigma_i$ to $\sigma_i^2/(\sigma_i^2+k)\sigma_i$. A plot of these functions is given in Fig. 8 for $k=0.008$. In this figure, the regularization is observed to limit the singular value to 15 dB. In the Appendix it is shown that

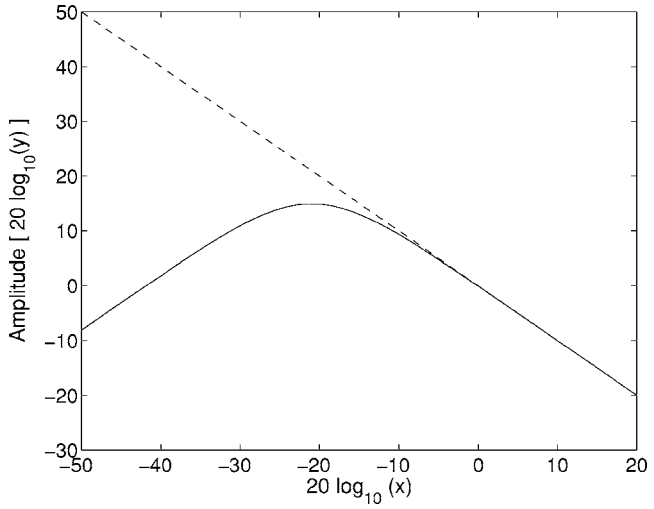

FIG. 8. Influence of regularization of singular values; - - - $y=1/x$, ——— $y=x^2/(x^2+0.008)x$.

for a regularization parameter of k, the maximum singular value possible is $1/2\sqrt{k}$, obtained when $\sigma_i=\sqrt{k}$. When σ_i is greater than $\sqrt{k}$, the singular values of the filter can be observed to mirror about $1/2\sqrt{k}$ as in Fig. 8. This limit is shown in Fig. 7 and is labeled the singular value limit. Comparing Figs. 7(a) and 7(b), it is observed that the singular values are no longer limited at 15 dB, but rather a regularization is evident that takes into account the poor choice of sensitivities in the system.

Figures 7(b) and 7(d) show the singular value curves of the filter designed for a system with appropriately chosen sensitivities for the transducers. Comparing these two filters, it can be observed that the filter designed using poor sensitivities [Fig. 7(d)] has been regularized considerably compared to the filter designed for a correctly scaled system [Fig. 7(b)]. This regularization is visible on the lowest curve above 15 kHz, where such heavy regularization is unwarranted.

Figure 9 shows the resulting IRFs of the filter when the filters are normalized such that the largest peak is ±1. By implementing diagonal preconditioning in the analog domain [Fig. 9(c)], the amplitude of the IRFs are fairly similar, resulting in better use of the dynamic range of the transducers, whereas when diagonal preconditioning is implemented in the digital domain, the magnitude of the IRFs suffer as they are required to compensate for the poor sensitivities given by Eq. (34). Figure 9(d) shows the system response obtained when the filter is designed using poor sensitivities and scaled to be implemented for a system with a better choice of sensitivities. The filter is observed to make poor use of the channels compared to the filter [Fig. 9(c)] designed with correct

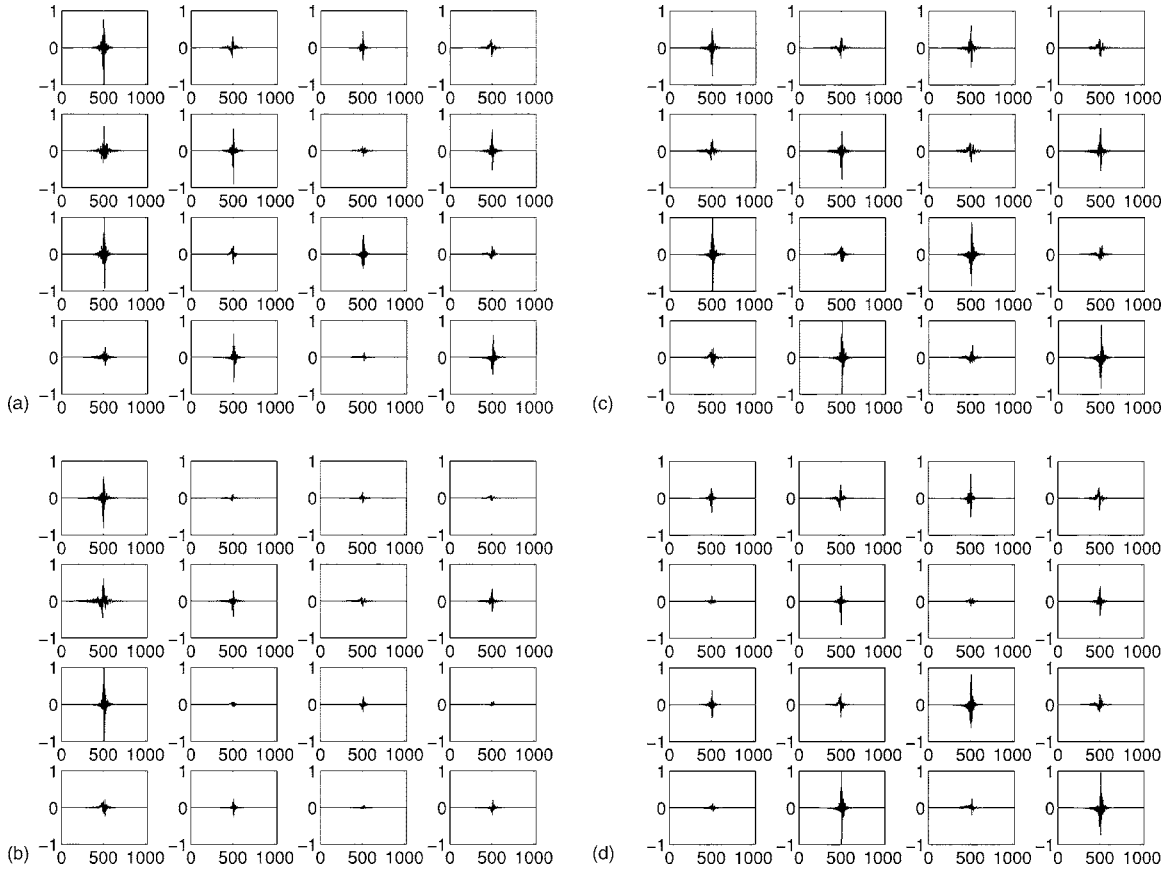

FIG. 9. The impulse responses of the filters for $k=0.008$. The unit on the x axis is samples. In these figures, the subplot at row i, column j corresponds to the IRF of the filter between virtual source j and transmitter i. These impulse responses have been normalized such that the largest peak value of each filter is ±1. (a) No preconditioning, $\mathbb{H}\{\mathbf{C}_p\}$. (b) Digital preconditioning, $\boldsymbol{\alpha}_g^{-1}\mathbb{H}\{\boldsymbol{\beta}_g\mathbf{C}_p\boldsymbol{\alpha}_g\}\boldsymbol{\beta}_g^{-1}$. (c) Analog preconditioning, $\mathbb{H}\{\boldsymbol{\beta}_g\mathbf{C}_p\boldsymbol{\alpha}_g\}$. (d) No preconditioning, scaled $\boldsymbol{\alpha}_g^{-1}\mathbb{H}\{\mathbf{C}_p\}\boldsymbol{\beta}_g^{-1}$.

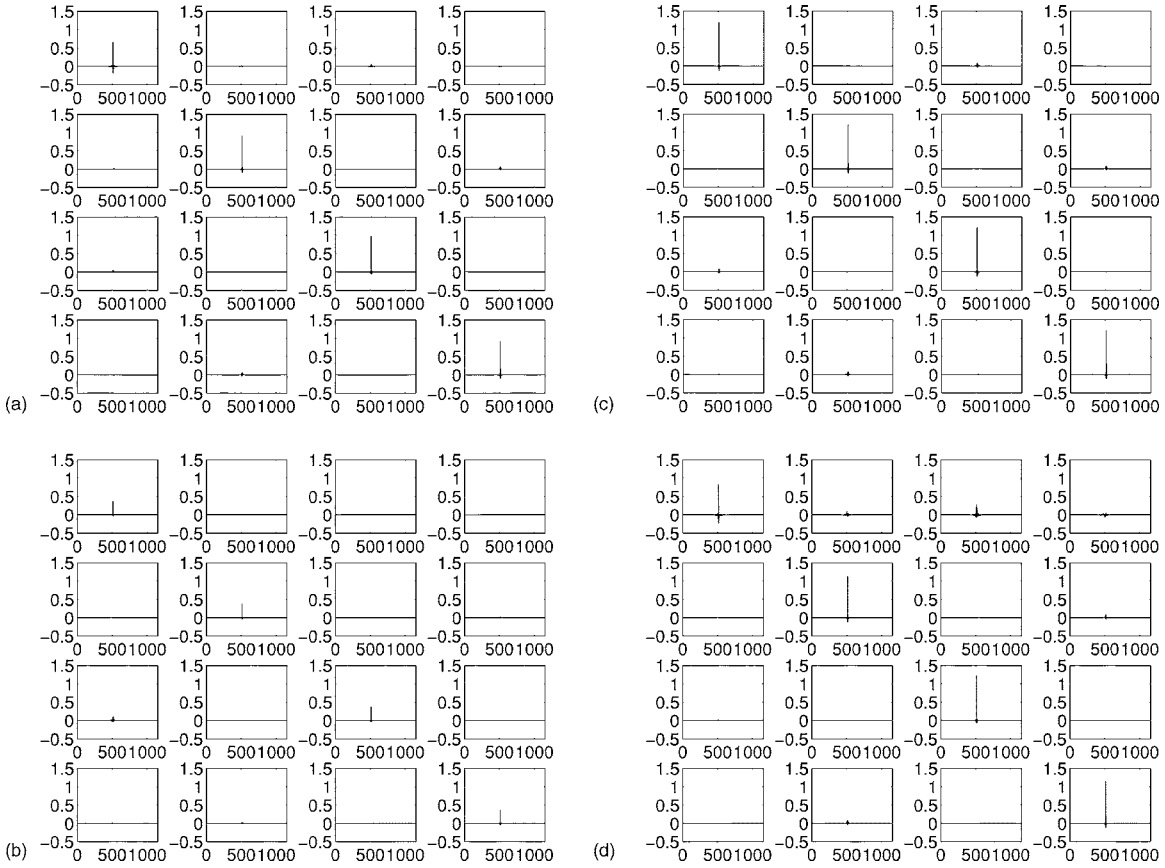

FIG. 10. The impulse responses of the complete system for $k=0.008$. The unit on the x axis is samples. In this figure, the subplot at row i, column j corresponds to the IRF of the entire system between virtual source j and receiver i. (a) No preconditioning, $\mathbb{H}\{\mathbf{C}_p\}$. (b) Digital preconditioning, $\boldsymbol{\alpha}_g^{-1}\mathbb{H}\{\boldsymbol{\beta}_g\mathbf{C}_p\boldsymbol{\alpha}_g\}\boldsymbol{\beta}_g^{-1}$. (c) Analog preconditioning, $\mathbb{H}\{\boldsymbol{\beta}_g\mathbf{C}_p\boldsymbol{\alpha}_g\}$. (d) No preconditioning, scaled $\boldsymbol{\alpha}_g^{-1}\mathbb{H}\{\mathbf{C}_p\}\boldsymbol{\beta}_g^{-1}$.

sensitivities. Applying scaling to compensate for transducer sensitivities is thus not as effective as setting the transducer sensitivities to the optimal values.

Figure 10 shows the IRFs of the entire system from the desired signal, $\mathbf{u}(z)$, to the received signal, $\mathbf{w}(z)$, using the filters shown in Fig. 9. In Fig. 10(a) it is observed that because of the effort required to transmit to receiver 1 the regularization has reduced the quality of the response and also the level of the signal received. When the sensitivities obtained using Algorithm 1 are used [Figs. 10(b) and 10(c)], it is observed that the magnitude of the pulse and the quality are much more similar over all the channels. The implementation of diagonal preconditioning in the digital domain [Fig. 10(b)] is shown to have a better response across all receivers at the cost of reducing the signal level. Figure 10(d) shows the system response obtained when the filter is designed using poor sensitivities and scaled to be implemented for a system with a better choice of sensitivities. It can be observed that the performance of this filter is much worse than that given in Fig. 10(c), being the filter designed for the properly scaled system.

Figure 11 shows the frequency response functions (FRFs) of the entire system from the desired signal to be received, $\mathbf{u}(z)$, to the actual signal received, $\mathbf{w}(z)$, using the filters shown in Figs. 9(a) and 9(c). The system response of Figs. 9(b) and 9(d) have not been included, as they have very similar spectra to the filters shown in Figs. 9(c) and 9(a), respectively. Comparing Figs. 11(a) and 11(b), the frequency response at the first receiver is noticeably improved with little change observed in the cross-talk cancellation, observable in the off-diagonal FRFs.

V. CONCLUSION

In this paper it has been demonstrated that the choice of sensitivities used within the amplifying stages of an acoustic system can have a significant influence on the performance of a filter designed using the Tikhonov inverse filtering method. An algorithm has been presented that generates a set of gains that can compensate for poorly selected receiver and transmitter sensitivities. It has been shown that improvements in performance can be obtained by using the compensated sensitivities.

ACKNOWLEDGEMENT

Thanks are given to Professor Phillip Nelson who provided an insightful conversation in regards to the Tikhonov inverse filtering.

APPENDIX: MAXIMUM SINGULAR VALUE OF A TIKHONOV INVERSE FILTER

In Sec. III C it was shown that the addition of Tikhonov regularization changes the singular values of the filter from

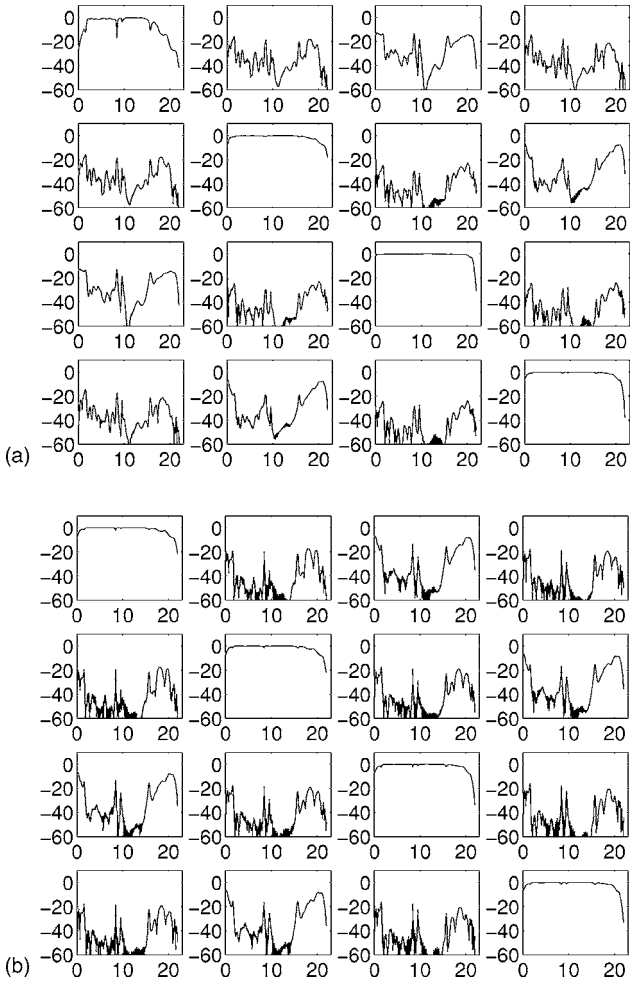

FIG. 11. The frequency responses of the complete system for $k=0.008$. The unit on the abscissa is kHz, and the unit on the ordinate is dB. In these figures, the subplot at row i, column j corresponds to the FRF of the entire system between virtual source j and transmitter i.

$$\sigma_{\mathrm{IF}} = \frac{1}{\sigma_i} \tag{A1}$$

to

$$\sigma_{\mathrm{TIF}} = \frac{\sigma_i^2}{(\sigma_i^2 + k)\sigma_i}. \tag{A2}$$

Figure 8 shows a plot of these two functions when $k=0.008$. In this figure, the singular values are observed to be limited to 15 dB. The maximum singular value for any k can be found by determining σ_{TIF} when $(\partial/\partial\sigma_i)\sigma_{\mathrm{TIF}}=0$, where

$$\frac{\partial}{\partial\sigma_i}\sigma_{\mathrm{TIF}} = \frac{1}{(\sigma_i^2 + k)} - \frac{2\sigma_i^2}{(\sigma_i^2 + k)^2} = \frac{(\sigma_i^2 + k) - 2\sigma_i^2}{(\sigma_i^2 + k)^2} \tag{A3}$$

Setting $(\partial/\partial\sigma_i)\sigma_{\mathrm{TIF}}=0$,

$$\begin{aligned} &(\sigma_i^2 + k) - 2\sigma_i^2 = 0, \\ &\sigma_i = \sqrt{k}. \end{aligned} \tag{A4}$$

Inserting σ_i into Eq. (A2), we obtain

$$\sigma_{\mathrm{TIF}} = \frac{1}{2\sqrt{k}}. \tag{A5}$$

[1] Y. Kim and P. A. Nelson, "Spatial resolution limits for the reconstruction of acoustic source strength by inverse methods," J. Sound Vib. **265**, 583–608 (2003).

[2] J. Mourjopoulos, "On the variation and invertibility of room impulse response functions," J. Sound Vib. **102**, 217–228 (1985).

[3] S. Neely and J. Allen, "Invertibility of a room impulse response," J. Acoust. Soc. Am. **66**, 165–169 (1979).

[4] P. A. Nelson, F. Orduña Bustamante, and H. Hamada, "Inverse filter design and equalization zones in multichannel sound reproduction," IEEE Trans. Speech Audio Process. **3**, 185–192 (1995).

[5] P. Roux and M. Fink, "Time reversal in a waveguide: Study of the temporal and spatial focusing," J. Acoust. Soc. Am. **107**, 2418–2429 (2000).

[6] I. Kirkeby, P. Nelson, H. Hamada, and F. Orduña Bustamante, "Fast deconvolution of multi-channel systems using regularisation," Technical Report 255, Institute of Sound and Vibration Research, Southhampton S017 1BJ, England (1996).

[7] O. Kirkeby, P. Nelson, H. Hamada, and F. Orduña Bustamante, "Fast deconvolution of multichannel systems using regularization," IEEE Trans. Speech Audio Process. **6**, 189–195 (1998).

[8] S. J. Elliot, C. C. Boucher, and P. A. Nelson, "The behaviour of a multiple channel active control system," IEEE Trans. Signal Process. **40**, 1042–1052 (1992).

[9] P. C. Hansen, *Rank-Deficient and Discrete Ill-Posed Problems: Numerical Aspects of Linear Inversion, SIAM Monographs on Mathematical Modeling and Computation* (Society for Industrial and Applied Mathematics, Philadelphia, PA, 1998).

[10] D. Jackson and D. Dowling, "Phase conjugation in underwater acoustics," J. Acoust. Soc. Am. **89**, 171–181 (1991).

[11] W. A. Kuperman, W. S. Hodgkiss, H. C. Song, T. Akal, C. Ferla, and D. R. Jackson, "Phase conjugation in the ocean: Experimental demonstration of an acoustic time-reversal mirror," J. Acoust. Soc. Am. **103**, 25–40 (1998).

[12] C. Prada, S. Manneville, D. Spoliansky, and M. Fink, "Decomposition of the time reversal operator: Detection and selective focusing on two scatterers," J. Acoust. Soc. Am. **99**, 2067–2076 (1996).

[13] M. Tanter, J.-L. Thomas, and M. Fink, "Time reversal and the inverse filter," J. Acoust. Soc. Am. **108**, 223–234 (2000).

[14] M. Tanter, J.-F. Aubry, J. Gerber, J.-L. Thomas, and M. Fink, "Optimal focusing by spatio-temporal inverse filter. I. Basic principles," J. Acoust. Soc. Am. **110**, 37–47 (2001).

[15] A. Van der Sluis, "Condition numbers and equilibration of matrices," Numer. Math. **14**, 14–23 (1969).

[16] D. Ruiz, "A scaling algorithm to equilibrate both rows and columns norms in matrices," Technical Report RAL-TR-2001-034, Rutherford Appleton Laboratory (2001).

[17] B. Gardner and K. Martin, "HRTF measurements of a KEMAR dummy-head microphone," Technical Report 280, MIT Media Lab Perceptual Computing, MIT Media Lab, E15-401D, Cambridge, MA 02139 (1994).

Scan-based near-field acoustical holography and partial field decomposition in the presence of noise and source level variation

Moohyung Lee[a] and J. Stuart Bolton[b]
Ray W. Herrick Laboratories, School of Mechanical Engineering, Purdue University, 140 S. Intramural Drive, West Lafayette, Indiana 47907-2031

(Received 29 October 2004; revised 2 August 2005; accepted 8 September 2005)

Practical holography measurements of composite sources are usually performed using a multireference cross-spectral approach, and the measured sound field must be decomposed into spatially coherent partial fields before holographic projection. The formulations by which the latter approach have been implemented have not taken explicit account of the effect of additive noise on the reference signals and so have strictly been limited to the case in which noise superimposed on the reference signals is negligible. Further, when the sound field is measured by scanning a subarray over a number of patches in sequence, the decomposed partial fields can suffer from corruption in the form of a spatially distributed error resulting from source level variation from scan-to-scan. In the present work, the effects of both noise included in the reference signals, and source level variation during a scan-based measurement, on partial field decomposition are described, and an integrated procedure for simultaneously suppressing the two effects is provided. Also, the relative performance of two partial field decomposition formulations is compared, and a strategy for obtaining the best results is described. The proposed procedure has been verified by using numerical simulations and has been applied to holographic measurements of a subsonic jet. [DOI: 10.1121/1.2133717]

PACS number(s): 43.60.Sx, 43.50.Yw, 43.60.Cg [EGW] Pages: 382–393

I. INTRODUCTION

Since near-field acoustical holography (NAH) was introduced in 1980,[1] it has been developed into a useful tool for noise source characterization. That usefulness comes from the fact that the sound field in a three-dimensional space can be reconstructed from data measured on a relatively small, two-dimensional surface. Since the holographic projection of the sound field throughout a homogeneous medium is performed by using the Helmholtz equation, it is required that the sound field on the hologram surface be fully coherent. One way to satisfy the latter requirement is by measuring the sound field at all points on the hologram surface simultaneously, i.e., the coherent sound field is obtained by evaluating the temporal Fourier transforms of single and, in principle, infinite time histories captured simultaneously by an array of field microphones. This method, referred to as a "snapshot" measurement, is especially useful when time-varying, nonstationary signals (e.g., impulsive signals) are to be measured since the time-dependent nature of the reconstructed field can be animated.[2,3] However, a very large number of microphones must be available to perform a "snapshot" measurement, which often makes such a measurement impractical.

Alternatively, a "scan-based" procedure can be used to visualize statistically stationary noise sources. This method reduces the number of microphones required to perform a complete measurement by making it possible to scan a microphone array over a number of patches in sequence (while simultaneously making measurements at an array of fixed reference microphones), thus capturing the sound field over the entire hologram surface in a number of steps. Recently, a new procedure for obtaining the coherent field on the hologram surface when using a scan-based measurement was suggested.[4] In that method, the acoustic transfer matrix (assumed to be time invariant) between a fixed array of reference microphones and the field microphones is obtained in a scanning measurement, and the coherent field is then obtained by using the measured reference signals in conjunction with the acoustic transfer matrix.

When a sound field comprising a superposition of fields radiated by incoherent or partially coherent subsources is measured by using a cross-spectral approach based on the use of references, the total measured field must be decomposed into a set of coherent partial fields that are mutually incoherent, each of which can then be projected onto a surface of interest as desired. The resulting projected fields can be added together on a quadratic basis to construct the total sound field. In the latter method, it is required that the number of references should be, in principle, at least equal to the number of incoherent sources. The signals measured by the references (which are assumed to be linearly related to the source signals) are used as the basis for decomposition since the source signals themselves cannot be measured directly in most practical cases. A multireference, cross-spectral procedure of this kind was first described by Hald.[5] In his implementation, referred to as spatial transformation of sound fields (STSF), the composite sound field is decomposed into a set of mutually incoherent partial fields with the help of singular value decomposition (i.e., the virtual coherence method). The partial coherence method based on Cholesky

[a]Electronic mail: leemoohy@ecn.purdue.edu
[b]Electronic mail: bolton@purdue.edu

decomposition has also been used in this role.[6,7] Since the two methods differ in the way that the sound field is decomposed, the resulting partial fields are different, but the total sound fields that result are the same in either case under ideal circumstances. If individual subsources are well-separated spatially, the partial coherence method can provide physically meaningful partial fields when reference microphones are placed close to each of the subsources. However, *a priori* knowledge of the source nature (i.e., source location, directivity, and so on) is necessary in that case, and the reference signals must be properly reordered before the decomposition is performed. For these reasons, the use of the partial coherence method has been limited. Postprocessing procedures have recently been suggested to address the latter problem.[8,9] Those methods allow "virtual references" to be positioned arbitrarily close to significant sources after a measurement has been performed with a sufficient, but nonoptimally placed, set of references.

When a scan-based measurement is performed, the measured sound field is likely to be corrupted by a spatially distributed error due to the scan-to-scan source level variation that is characteristic of realistic sources. Kwon *et al.* discussed this effect and proposed a partial field decomposition formulation, based on the use of the acoustic transfer matrix, that compensates for source level variation.[10]

When partial field decomposition is to be performed, the reference cross-spectral matrix must not be contaminated by significant levels of noise; otherwise, the levels of the partial fields calculated by using either of the formulations described by Hald[5] and by Kwon *et al.*[10] will be underestimated, thus causing the resulting total sound field to be itself underestimated. Also, the implementation of the generalized inverse involved in the Hald and Kwon *et al.* formulations was not discussed in the specific case when the reference cross-spectral matrix is fully ranked and its singular values gradually decrease to small values owing to the effects of additive noise on the reference signals.

In Sec. II of this article, the effects of measurement noise and source level variation on partial field decomposition will be discussed first, and a regularization procedure for implementing the generalized inverse involved in the previously proposed formulation for correcting for source level variation is presented in order to accommodate noise-contaminated estimates of the reference cross-spectral matrix. It will be shown that spurious effects in partial field decomposition related both to source level variation and measurement noise can be suppressed by the combined use of the latter formulation with a measurement scheme that involves a relatively large number of reference microphones. In Sec. III, numerical simulation results performed by using a three-monopole model will be presented to demonstrate the validity of the proposed procedure. In Sec. IV, the application of the procedure to NAH measurements of the sound field radiated by a subsonic jet will be described. Finally, a summary and conclusions are presented in the final two sections.

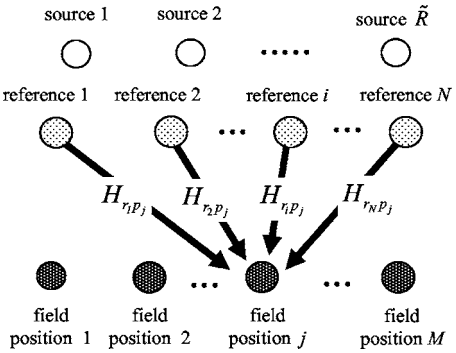

FIG. 1. Relation between the source, the reference, and the field microphone signals in a multireference measurement.

II. THEORY

A. Approach to multireference NAH

In this subsection, the basis of multireference NAH will be reviewed briefly. To begin, when a sound field description is based on the use of multiple references, the sound field on the hologram surface can be expressed as a linear combination of reference signals multiplied by appropriate transfer functions (the $H_{r_ip_j}$ in Fig. 1),[7] i.e., in matrix form, the field is expressed as

$$\mathbf{p} = \mathbf{H}_{rp}^{\mathrm{T}}\mathbf{r}, \tag{1}$$

where $\mathbf{H}_{rp}$ is the acoustic transfer matrix that relates the reference signals and the measured field microphone signals on the hologram surface, $\mathbf{r}=[r_1,\ldots,r_N]^{\mathrm{T}}$ and $\mathbf{p}=[p_1,\ldots,p_M]^{\mathrm{T}}$ are the Fourier transforms of the time histories measured by the references and by the field microphones on the hologram surface, respectively, N is the number of references, M is the total number of measurement points on the hologram surface, and the superscript T denotes the transpose operator. When statistically random sources are considered, Eq. (1) can be expressed more naturally in terms of cross-spectral matrices,[11] i.e.,

$$\mathbf{C}_{pp} = \mathbf{C}_{rp}^{\mathrm{H}}\mathbf{C}_{rr}^{-1}\mathbf{C}_{rp} = \mathbf{H}_{rp}^{\mathrm{H}}\mathbf{C}_{rr}\mathbf{H}_{rp}, \tag{2}$$

where

$$\mathbf{H}_{rp} = \mathbf{C}_{rr}^{-1}\mathbf{C}_{rp}, \tag{3}$$

and where the superscript H denotes the Hermitian operator, the inverse represents the generalized inverse to accommodate rank-deficient matrices, and $\mathbf{C}_{rr}$, $\mathbf{C}_{rp}$, and $\mathbf{C}_{pp}$ are cross-spectral matrices defined as

$$\mathbf{C}_{rr} = \mathrm{E}[\mathbf{r}^{*}\mathbf{r}^{\mathrm{T}}], \tag{4}$$

$$\mathbf{C}_{rp} = \mathrm{E}[\mathbf{r}^{*}\mathbf{p}^{\mathrm{T}}], \tag{5}$$

$$\mathbf{C}_{pp} = \mathrm{E}[\mathbf{p}^{*}\mathbf{p}^{\mathrm{T}}]. \tag{6}$$

In the latter equations, the superscript * denotes the complex conjugate and $\mathrm{E}[\cdot]$ represents the expectation operator. Note that a harmonic time dependence, $e^{-i\omega t}$, is assumed when $\mathbf{r}$ and $\mathbf{p}$ are evaluated by using the temporal Fourier transform.

In order to project the total sound field onto a surface of interest, the composite sound field must be decomposed into a set of coherent partial fields that are mutually incoherent. When using a virtual coherence method, the decomposition is performed with the help of singular value decomposition (SVD), i.e.,

$$\mathbf{C}_{rr} = \mathbf{U}\boldsymbol{\Sigma}\mathbf{V}^{\mathrm{H}} = \mathbf{U}\boldsymbol{\Sigma}\mathbf{U}^{\mathrm{H}}, \tag{7}$$

where $\boldsymbol{\Sigma}$ is a diagonal matrix composed of the singular values, λ_i, $\mathbf{U}$ and $\mathbf{V}$ are unitary matrices that comprise the left and right singular vectors, respectively, and $\mathbf{U}$ and $\mathbf{V}$ are here identical since $\mathbf{C}_{rr}$ is a positive semi-definite Hermitian matrix. The singular values of the reference cross-spectral matrix represent the autospectral amplitudes of virtual references, i.e., rearrangement of Eq. (7) yields

$$\boldsymbol{\Sigma} = \mathbf{U}^{\mathrm{H}}\mathbf{C}_{rr}\mathbf{U} = \mathrm{E}[\mathbf{v}^{*}\mathbf{v}^{\mathrm{T}}] = \mathbf{C}_{vv}, \tag{8}$$

where $\mathbf{v}$ is the virtual reference vector and $\mathbf{C}_{vv}$ is the virtual reference cross-spectral matrix. The decomposed partial fields (subject to the condition that $\mathbf{C}_{pp}=\hat{\mathbf{P}}^{*}\hat{\mathbf{P}}^{\mathrm{T}}$) are then expressed as

$$\hat{\mathbf{P}} = \mathbf{C}_{rp}^{\mathrm{T}}\mathbf{U}^{*}\boldsymbol{\Sigma}^{-1/2} = \mathbf{C}_{vp}^{\mathrm{T}}\boldsymbol{\Sigma}^{-1/2} \tag{9}$$

$$= \mathbf{H}_{rp}^{\mathrm{T}}\mathbf{U}^{*}\boldsymbol{\Sigma}^{1/2} = \mathbf{H}_{vp}^{\mathrm{T}}\boldsymbol{\Sigma}^{1/2}, \tag{10}$$

where the ith column vector of $\hat{\mathbf{P}}$ represents the ith partial field, and $\mathbf{C}_{vp}$ and $\mathbf{H}_{vp}$ represent, respectively, the cross-spectral matrix and the acoustic transfer matrix between the virtual references and the measured field microphone signals on the hologram surface.

B. Approach to scan-based NAH

The cross-spectral approach described above is usually implemented by using a scan-based measurement since the number of microphones required for a complete measurement can be reduced. In the latter approach, as many reference cross-spectral matrices are obtained during the course of the measurement as there are scans performed. To help minimize statistical error, it is desirable to average the reference cross-spectral matrix over all the scans. Thus, Eqs. (9) and (10) should be expressed as

$$\hat{\mathbf{P}} = \mathbf{C}_{rp(\mathrm{scan})}^{\mathrm{T}}\mathbf{U}_{(\mathrm{avg})}^{*}\boldsymbol{\Sigma}_{(\mathrm{avg})}^{-1/2} \tag{11}$$

$$= \mathbf{H}_{rp(\mathrm{scan})}^{\mathrm{T}}\mathbf{U}_{(\mathrm{avg})}^{*}\boldsymbol{\Sigma}_{(\mathrm{avg})}^{1/2}, \tag{12}$$

where the subscripts (scan) and (avg) denote the properties obtained from cross-spectral matrices estimated during each scan and averaged over all the scans, respectively.[10] However, when the sound field on the hologram surface is obtained by using scan-based measurements, the reference cross-spectral matrices may vary from scan-to-scan owing both to source level variation and measurement noise. In particular, the partial fields calculated by using Eq. (11) may be corrupted by a spatially distributed error when the source level varies. In contrast, the acoustic transfer matrix, $\mathbf{H}_{rp}$, calculated during each scan [i.e., by using Eq. (3)] is essentially independent of source level since it represents amplitude and phase information *relative* to the sources.[10] When the acoustic transfer matrix is assumed to be independent of source level and when measurement noise is entirely negligible, the effect of source level variation can, in principle, be suppressed by using Eq. (12).

C. Properties in the presence of noise

Data obtained directly from real measurements are inevitably contaminated by various kinds of noise (e.g., background noise, instrument noise, statistical error,[11] sensor positioning error,[12,13] and so on), however small. Thus, the measured spectra are here defined to be the sum of noise-free spectra and the noise-related spectra, i.e.,

$$\mathbf{C}_{rr} = \tilde{\mathbf{C}}_{rr} + \mathbf{C}_{rr}^{\delta}, \tag{13}$$

$$\mathbf{C}_{rp} = \tilde{\mathbf{C}}_{rp} + \mathbf{C}_{rp}^{\delta}, \tag{14}$$

where $\mathbf{C}_{rr}^{\delta}$ and $\mathbf{C}_{rp}^{\delta}$ denote additive noise matrices and terms marked with a $\sim$ represent noise-free properties. If it is assumed that all noise components included in the signals are perfectly uncorrelated with each other and with the signals from the actual sources, and that an infinite amount of averaging is performed, the noise-related cross-spectral terms vanish except for the diagonal terms of $\mathbf{C}_{rr}^{\delta}$ (i.e., the autospectra of the noise components). In practice, however, not all of the above conditions are met and so $\mathbf{C}_{rr}^{\delta}$ is not a diagonal matrix: it may therefore be written as

$$\mathbf{C}_{rr}^{\delta} = \begin{bmatrix} \mu_1^2 & \Delta_{12} & \cdots & \Delta_{1N} \\ \Delta_{12}^{*} & \mu_2^2 & \cdots & \Delta_{2N} \\ \vdots & \vdots & \ddots & \vdots \\ \Delta_{1N}^{*} & \Delta_{2N}^{*} & \cdots & \mu_N^2 \end{bmatrix}. \tag{15}$$

In this case, the results of the SVD are

$$\boldsymbol{\Sigma} = \tilde{\boldsymbol{\Sigma}} + \boldsymbol{\Sigma}^{\delta} = \begin{bmatrix} \boldsymbol{\Sigma}_s & \mathbf{0} \\ \mathbf{0} & \boldsymbol{\Sigma}_n \end{bmatrix} \tag{16}$$

and

$$\mathbf{U} = \tilde{\mathbf{U}} + \mathbf{U}^{\delta} = [\mathbf{U}_s\ \mathbf{U}_n]. \tag{17}$$

In Eqs. (16) and (17), $\boldsymbol{\Sigma}^{\delta}$ and $\mathbf{U}^{\delta}$ represent error terms introduced by measurement noise, and $\mathbf{U}^{\delta}$, in particular, is nonzero either when the levels of the reference noise autospectra are different (i.e., μ_i^2 is not constant) or when nonzero off-diagonal terms appear in $\mathbf{C}_{rr}^{\delta}$ (i.e., the Δ_{ij}'s). The matrices $\boldsymbol{\Sigma}_s$ and $\boldsymbol{\Sigma}_n$ are R-by-R and $(N$-$R)$-by-$(N$-$R)$ diagonal matrices, respectively, where R is the number of singular values required to describe the total sound field, and $\mathbf{U}_s$ and $\mathbf{U}_n$ are matrices whose columns are the singular vectors corresponding to $\boldsymbol{\Sigma}_s$ and $\boldsymbol{\Sigma}_n$, respectively. Note that, when the reference signals are contaminated by noise, none of the singular values will be zero, thus causing the reference cross-spectral matrix to be fully ranked (but still weakly ill-conditioned), and the value of R is likely to be larger than the actual number of subsources (i.e., $\tilde{R}$ in Fig. 1).

In a scan-based measurement in the presence of noise and source level variation, the reference cross-spectral matrix singular values and vectors calculated during individual scans differ, i.e., when $i \neq j$,

$$\mathbf{\Sigma}_{(\mathrm{scan})_i} \approx \mathbf{\Sigma}_{(\mathrm{scan})_j}, \tag{18}$$

$$\mathbf{U}^{\mathrm{H}}_{s(\mathrm{scan})_i}\mathbf{U}_{s(\mathrm{scan})_j} \approx \mathbf{I}, \tag{19}$$

$$\mathbf{U}^{\mathrm{H}}_{n(\mathrm{scan})_i}\mathbf{U}_{s(\mathrm{scan})_j} \approx \mathbf{0}. \tag{20}$$

The latter three relations would all be equalities in the absence of both noise and source level variation. Note that the product $\mathbf{U}^{\mathrm{H}}_{n(\mathrm{scan})_i}\mathbf{U}_{n(\mathrm{scan})_j}$ yields an arbitrary matrix whose value lies between $\mathbf{0}$ and $\mathbf{I}$ depending on the degree to which the reference signals measured during successive scans are contaminated by measurement noise. Another useful relation is

$$\mathbf{C}^{\mathrm{H}}_{rp(\mathrm{scan})}\mathbf{U}_{n(\mathrm{scan})} \approx \mathbf{0}. \tag{21}$$

The Hermitian product of the matrices $\mathbf{C}_{rp(\mathrm{scan})}$ and $\mathbf{U}_{n(\mathrm{scan})}$, which belong to the source subspace and the noise subspace, respectively, would be zero in the absence of noise, but in practice the cancellation is not perfect owing to the existence of finite levels of measurement noise.

D. Effect of measurement noise and source level variation on partial field decomposition

In this subsection, the effects of measurement noise and source level variation on partial field decomposition are described in detail. In the presence of measurement noise as considered here, the generalized inverse (e.g., the Moore-Penrose inverse) yields the ordinary inverse since the reference cross-spectral matrix is not singular.

The partial fields calculated by using Eq. (11) can be expressed in expanded form by using Eqs. (16) and (17) as

$$\begin{aligned}\hat{\mathbf{P}} &= \mathbf{C}^{\mathrm{T}}_{rp(\mathrm{scan})}\mathbf{U}^{*}_{(\mathrm{avg})}\mathbf{\Sigma}^{-1/2}_{(\mathrm{avg})} \\ &= \mathbf{C}^{\mathrm{T}}_{rp(\mathrm{scan})}[\mathbf{U}^{*}_{s(\mathrm{avg})}\mathbf{U}^{*}_{n(\mathrm{avg})}]\begin{bmatrix}\mathbf{\Sigma}^{-1/2}_{s(\mathrm{avg})} & \mathbf{0} \\ \mathbf{0} & \mathbf{\Sigma}^{-1/2}_{n(\mathrm{avg})}\end{bmatrix} \\ &= \Big[\underbrace{\mathbf{C}^{\mathrm{T}}_{rp(\mathrm{scan})}\mathbf{U}^{*}_{s(\mathrm{avg})}\mathbf{\Sigma}^{-1/2}_{s(\mathrm{avg})}}_{\text{the first } R \text{ partial fields}}\ \underbrace{\mathbf{C}^{\mathrm{T}}_{rp(\mathrm{scan})}\mathbf{U}^{*}_{n(\mathrm{avg})}\mathbf{\Sigma}^{-1/2}_{n(\mathrm{avg})}}_{\text{the last } (N-R) \text{ partial fields}}\Big].\end{aligned} \tag{22}$$

Since the first R partial fields represent the main components of the total sound field, only those partial fields are of interest. It can be seen that those partial fields are associated with the terms that are principally related to the source signals. However, the effect of measurement noise is still included in those terms, and, in particular, when the autospectral noise terms are significant, the levels of the calculated partial fields are smaller than those in a noise-free case since the singular values are overestimated (i.e., $\lambda_i > \tilde{\lambda}_i$). The noise term included in $\mathbf{C}_{rp(\mathrm{scan})}$ can be expected to be small when a sufficient amount of averaging is performed, but the source level variation still has an impact on $\mathbf{C}_{rp(\mathrm{scan})}$.

The partial fields calculated by using Eq. (12) can be expressed in explicit form as

$$\begin{aligned}\hat{\mathbf{P}} &= [\mathbf{C}^{-1}_{rr(\mathrm{scan})}\mathbf{C}_{rp(\mathrm{scan})}]^{\mathrm{T}}\mathbf{U}^{*}_{(\mathrm{avg})}\mathbf{\Sigma}^{1/2}_{(\mathrm{avg})} = [\mathbf{U}_{(\mathrm{scan})}\mathbf{\Sigma}^{-1}_{(\mathrm{scan})}\mathbf{U}^{\mathrm{H}}_{(\mathrm{scan})}\mathbf{C}_{rp(\mathrm{scan})}]^{\mathrm{T}}\mathbf{U}^{*}_{(\mathrm{avg})}\mathbf{\Sigma}^{1/2}_{(\mathrm{avg})} \\ &= \Big[\underbrace{\mathbf{C}^{\mathrm{T}}_{rp(\mathrm{scan})}\mathbf{U}^{*}_{s(\mathrm{scan})}\mathbf{\Sigma}^{-1}_{s(\mathrm{scan})}\mathbf{U}^{\mathrm{T}}_{s(\mathrm{scan})}\mathbf{U}^{*}_{s(\mathrm{avg})}\mathbf{\Sigma}^{1/2}_{s(\mathrm{avg})} + \mathbf{C}^{\mathrm{T}}_{rp(\mathrm{scan})}\mathbf{U}^{*}_{n(\mathrm{scan})}\mathbf{\Sigma}^{-1}_{n(\mathrm{scan})}\mathbf{U}^{\mathrm{T}}_{n(\mathrm{scan})}\mathbf{U}^{*}_{s(\mathrm{avg})}\mathbf{\Sigma}^{1/2}_{s(\mathrm{avg})}}_{\text{the first } R \text{ partial fields}} \\ &\quad \underbrace{\mathbf{C}^{\mathrm{T}}_{rp(\mathrm{scan})}\mathbf{U}^{*}_{s(\mathrm{scan})}\mathbf{\Sigma}^{-1}_{s(\mathrm{scan})}\mathbf{U}^{\mathrm{T}}_{s(\mathrm{scan})}\mathbf{U}^{*}_{n(\mathrm{avg})}\mathbf{\Sigma}^{1/2}_{n(\mathrm{avg})} + \mathbf{C}^{\mathrm{T}}_{rp(\mathrm{scan})}\mathbf{U}^{*}_{n(\mathrm{scan})}\mathbf{\Sigma}^{-1}_{n(\mathrm{scan})}\mathbf{U}^{\mathrm{T}}_{n(\mathrm{scan})}\mathbf{U}^{*}_{n(\mathrm{avg})}\mathbf{\Sigma}^{1/2}_{n(\mathrm{avg})}}_{\text{the last } (N-R) \text{ partial fields}}\Big].\end{aligned} \tag{23}$$

In Eq. (23), the multiplications by $\mathbf{\Sigma}^{-1}_{(\mathrm{scan})}$ and $\mathbf{\Sigma}^{1/2}_{(\mathrm{avg})}$ implement the correction for source level variation. However, in addition to the noise effect embedded in the source-related terms as in the case of Eq. (11), the first R partial fields are corrupted by the second term that features the noise-related singular values (i.e., $\mathbf{\Sigma}_{n(\mathrm{scan})}$). In that term, the two quantities, $\mathbf{C}^{\mathrm{T}}_{rp(\mathrm{scan})}\mathbf{U}^{*}_{n(\mathrm{scan})}$ and $\mathbf{U}^{\mathrm{T}}_{n(\mathrm{scan})}\mathbf{U}^{*}_{s(\mathrm{avg})}$ are themselves not likely to be significant, but their multiplication by $\mathbf{\Sigma}^{-1}_{n(\mathrm{scan})}$ causes the second term to be amplified to a significant level. Therefore, in summary, the use of Eq. (12) allows the effect of source level variation to be corrected, but the latter formulation is more sensitive to noise effects than is Eq. (11).

E. Regularization procedure for implementing the generalized inverse in the presence of noise

In the presence of measurement noise, the generalized inverse is not well defined since the singular values tend to decrease gradually to small but nonzero values. In this subsection, a regularization procedure for treating the small, noise-related singular values and its practical implementation in the two partial field decomposition formulations discussed above are described.

First, in the case of Eq. (11), the first R partial fields are not corrupted by the noise-related singular values as shown in Eq. (22), thus eliminating the need to incorporate a regularization procedure. That is, the inverse in the latter formu-

lation can be implemented by using the ordinary inverse, and the first R partial fields that result can be used to construct the total sound field.

In contrast, when implementing Eq. (12), a regularization procedure is necessary in practice. In principle, regularization needs to be applied only when the latter formulation is implemented in conjunction with a scan-based measurement. Either in a noise-free case or when all the matrices are obtained at one time, the second term in the first R partial fields vanishes automatically since $\mathbf{U}_{n(\mathrm{scan})}$ and $\mathbf{U}_{s(\mathrm{avg})}$ are orthogonal, thus yielding $\mathbf{U}^{\mathrm{T}}_{n(\mathrm{scan})}\mathbf{U}^{*}_{s(\mathrm{avg})}=\mathbf{0}$ in that case; however, even in that case, the floating point error that depends on machine precision may still be problematical. The corruption of the partial fields caused by the noise-related singular values can be addressed simply by setting $\mathbf{\Sigma}^{-1}_{n(\mathrm{scan})}=\mathbf{0}$, and Eq. (23) then becomes

$$\hat{\mathbf{P}}=\Big[\underbrace{\mathbf{C}^{\mathrm{T}}_{rp(\mathrm{scan})}\mathbf{U}^{*}_{s(\mathrm{scan})}\mathbf{\Sigma}^{-1}_{s(\mathrm{scan})}\mathbf{U}^{\mathrm{T}}_{s(\mathrm{scan})}\mathbf{U}^{*}_{s(\mathrm{avg})}\mathbf{\Sigma}^{1/2}_{s(\mathrm{avg})}}_{\text{the first } R \text{ partial fields}}\quad\underbrace{\mathbf{C}^{\mathrm{T}}_{rp(\mathrm{scan})}\mathbf{U}^{*}_{s(\mathrm{scan})}\mathbf{\Sigma}^{-1}_{s(\mathrm{scan})}\mathbf{U}^{\mathrm{T}}_{s(\mathrm{scan})}\mathbf{U}^{*}_{n(\mathrm{avg})}\mathbf{\Sigma}^{1/2}_{n(\mathrm{avg})}}_{\text{the last } (N-R) \text{ partial fields}}\Big]. \tag{24}$$

The procedure described above corresponds to evaluating the regularized inverse of an ill-posed matrix by truncated singular value decomposition (TSVD).[14] Thus Eq. (12) can be written in a more general form as

$$\begin{aligned}\hat{\mathbf{P}}&=[\mathbf{C}^{+}_{rr(\mathrm{scan})}\mathbf{C}_{rp(\mathrm{scan})}]^{\mathrm{T}}\mathbf{U}^{*}_{(\mathrm{avg})}\mathbf{\Sigma}^{1/2}_{(\mathrm{avg})}\\&=[\mathbf{U}_{(\mathrm{scan})}\mathbf{\Sigma}^{+}_{(\mathrm{scan})}\mathbf{U}^{\mathrm{H}}_{(\mathrm{scan})}\mathbf{C}_{rp(\mathrm{scan})}]^{\mathrm{T}}\mathbf{U}^{*}_{(\mathrm{avg})}\mathbf{\Sigma}^{1/2}_{(\mathrm{avg})},\end{aligned} \tag{25}$$

where $\mathbf{\Sigma}^{+}$ is the regularized inverse of $\mathbf{\Sigma}$ defined as

$$\mathbf{\Sigma}^{+}=\begin{bmatrix}\mathbf{\Sigma}_s & \mathbf{0}\\ \mathbf{0} & \mathbf{\Sigma}_n\end{bmatrix}^{+}\equiv\begin{bmatrix}\mathbf{\Sigma}^{-1}_{s} & \mathbf{0}\\ \mathbf{0} & \mathbf{0}\end{bmatrix}. \tag{26}$$

For the sake of computational efficiency, Eq. (25) can be expressed in a reduced form since only the first R partial fields are of interest, i.e.,

$$\hat{\mathbf{P}}_{(1:R)}=[\mathbf{U}_{s(\mathrm{scan})}\mathbf{\Sigma}^{-1}_{s(\mathrm{scan})}\mathbf{U}^{\mathrm{H}}_{s(\mathrm{scan})}\mathbf{C}_{rp(\mathrm{scan})}]^{\mathrm{T}}\mathbf{U}^{*}_{s(\mathrm{avg})}\mathbf{\Sigma}^{1/2}_{s(\mathrm{avg})}. \tag{27}$$

It has been shown here that the corruption of the partial fields caused by the noise-related singular values can be avoided by incorporating a proper regularization of the reference cross-spectral matrix, if necessary, but the resulting partial fields are still in error due to the error embedded in the source-related terms. In the following subsection, it will be shown that the latter effect can be suppressed by increasing the number of references used in the measurements.

F. Effect of the number of references

When a cross-spectral approach is implemented for a composite source, the number of references should be at least equal to the number of incoherent sources contributing to the total sound field. In the ideal case (i.e., in the absence of measurement noise and if the references are positioned so that all sources are sensed), the number of incoherent physical sources is equal to the rank of the reference cross-spectral matrix. However, in practice, the number of incoherent sources that is determined by inspection of the magnitudes of the singular values is usually larger than the actual number of sources since additional artificial sources are introduced by the presence of noise in the measured reference cross-spectral matrix.[15] In the usual implementation of NAH, the number of references required is determined simply by counting the number of singular values greater than the background noise level.[16] In that case, it must also be ensured that each source signal is sensed by at least one reference to ensure that the number of references required for an accurate measurement is determined appropriately. That is, the position as well as the number of references is an important factor when the component subsources are localized and directional.[17] In practice, it is desirable to use a larger number of references than the actual number of subsources both to ensure a higher likelihood of sensing all the source signals and to allow the effects of measurement noise to be reduced, as will be described next.

The singular values of the measured cross-spectral matrix (i.e., the λ_i's) are perturbed by noise, and the effect of the noise can be significant in the special case when the noise autospectra measured by the references are large (e.g., when the reference microphones are exposed to flow). The latter effect of noise can be suppressed, however, by increasing the number of references.[18] Since the sum of the singular values is equal to the sum of the diagonal terms of the reference cross-spectral matrix, an increase in the number of references causes the levels of singular values related to the source signals to become larger while the levels of the singular values related to the noise components remain nearly the same, thus resulting in a clearer separation of the source- and noise-related singular values. In addition, noise included in the singular vectors can be suppressed when a large number of references are used. Thus, perhaps paradoxically, as the number of references is increased, the number of partial fields (or virtual references) required to accurately describe the total sound field approaches the actual number of subsources from above.

G. Selection of a cutoff singular value

In this subsection, a procedure for determining the number of singular values to be retained is described. When a matrix is fully ranked due to the effects of measurement

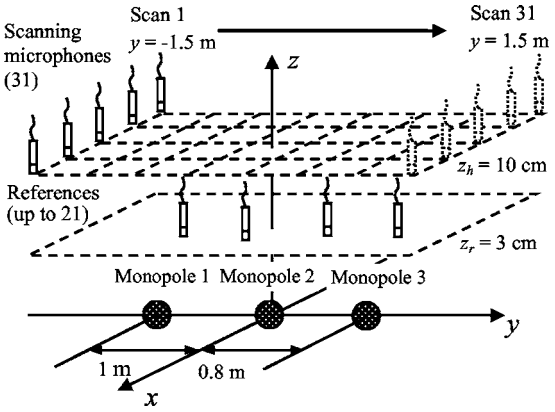

FIG. 2. Geometry of numerical simulation model.

noise, the number of significant singular values can be chosen by finding a numerical (or pseudo-) rank that is determined by counting the number of singular values greater than a threshold. When noise effects are not significant, setting a threshold is relatively easy since noise-related singular values are usually well separated from source-related singular values. However, when gradually decreasing singular values are observed, as in the examples considered here, a methodology for determining the optimal number of singular values to be retained needs to be established. In this work, the latter was achieved by finding the number of partial fields required to construct the total sound field: the virtual coherence function can be used to guide the latter task.[6] The virtual coherence function is defined as

$$\gamma^2_{j:i} = \frac{|C_{v_i p_j(\text{scan})}|^2}{C_{v_i v_i(\text{scan})} C_{p_j p_j(\text{scan})}}, \tag{28}$$

where $C_{v_i p_j}$ represents the (i,j)th element of $\mathbf{C}_{vp}$. The subscripts i and j denote the ith partial field and the jth measurement point, respectively. Since the virtual coherence function represents the contribution of each partial field (associated with each virtual reference) to the total sound field, the number of significant partial fields can be determined by finding the value of R that causes the sum of the virtual coherence functions to approach unity over the entire hologram surface, i.e.,

$$\sum_{i=1}^{R} \gamma^2_{j:i} \approx 1 \quad \text{for all } j = 1,2,\ldots,M. \tag{29}$$

When the latter is true, the singular values smaller than the Rth can be discarded when Eq. (25) is implemented. This procedure allows the choice of the optimal cutoff singular value that minimizes the noise included in the decomposed partial fields.

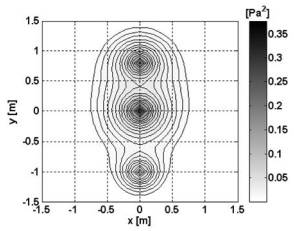

FIG. 3. Spatial distribution of the autospectrum of the total sound field created by three monopoles in the noise-free case.

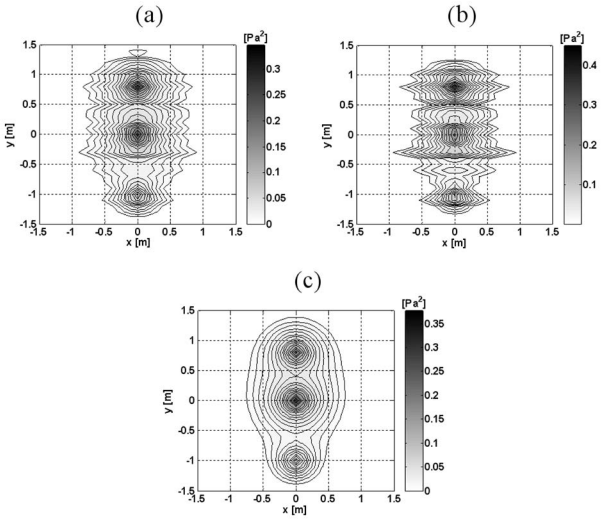

FIG. 4. Spatial distribution of the autospectrum of the total sound field in the case when the effect of source level variation is considered (6 references were used): (a) measured, (b) calculated by using Eq. (11), and (c) calculated by using Eq. (25).

Note finally that the number of partial fields that make a significant contribution to the total sound field is not, in general, equal to the number of references required to perform an accurate measurement in the presence of measurement noise. Also, when both reference and field microphone signals contain measurement noise, the use of the virtual coherence function might be limited; while the effects of noise included in the reference signals are suppressed as the number of references increases, the sum of the virtual coherence functions converges to a level (smaller than unity) that is dependent on the levels of noise sensed by the field microphones: that level, rather than unity, can be used as a benchmark against which to judge the required number of references, so long as all the sources are sensed by the references.

III. NUMERICAL SIMULATION

Numerical simulations were performed to illustrate the effects of noise and source level variation on partial field decomposition. Three mutually uncorrelated monopoles lo-

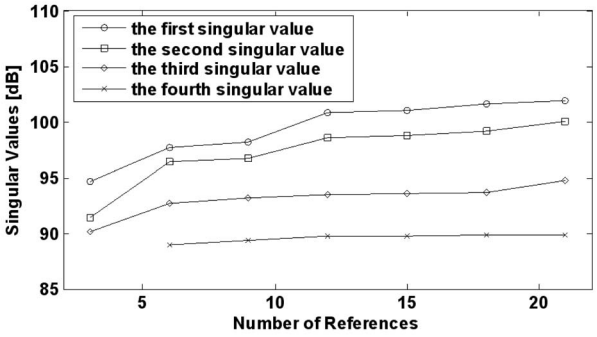

FIG. 5. The singular values of the noise-contaminated reference cross-spectral matrix with respect to the number of references in the case when the effect of autospectral noise is considered.

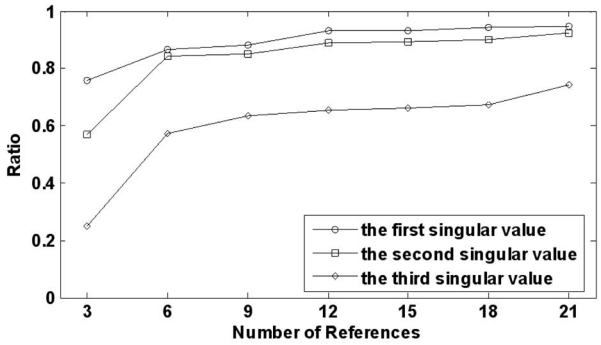

FIG. 6. The ratio of the singular values calculated from the noise-free reference cross-spectral matrix to those calculated from the noise-contaminated reference cross-spectral matrix ($\tilde{\lambda}_i/\lambda_i$), with respect to the number of references in the case when the effect of autospectral noise is considered.

cated on the source plane (i.e., $z=0$ cm) were used to create a sound field at a frequency of 1 kHz (see Fig. 2). Reference microphones were positioned arbitrarily on a plane 3 cm in the z direction from and parallel with the source plane, the sound field on the planar hologram surface (i.e., $z=10$ cm) was sampled at 31-by-31 measurement points in 31 steps (i.e., the field was sampled by using a line array that was scanned in the y direction), and the spatial sampling interval was 10 cm in both the x and y directions. In Fig. 3, the total sound field created by the three monopoles on the hologram plane is shown. Three different simulations were performed to illustrate the effects of source level variation and additive noise. Note that noise was added only to the reference signals since it is the reference cross-spectral matrix that plays a crucial role in partial field decomposition. In all cases, the total sound fields obtained by summing quadratically the resulting, meaningful partial fields are compared since they also reflect the effects of noise and source level variation included in the partial fields.

A. Source level variation from scan-to-scan

In the first case, the effect of source level variation from scan to scan was considered. The latter effect has already been discussed in Ref. 10, but, in this subsection, a more detailed discussion that quantifies the degree to which the latter effect corrupts the partial field decomposition results is presented. The simulation was performed by using 6 references in a noise-free condition. To simulate the effect of source level variation, the levels of the three monopoles at

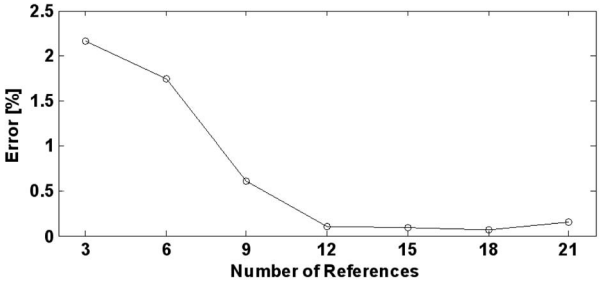

FIG. 7. Error in the singular vectors [Eq. (30)] of the reference cross-spectral matrix with respect to the number of references in the case when the effect of autospectral noise is considered.

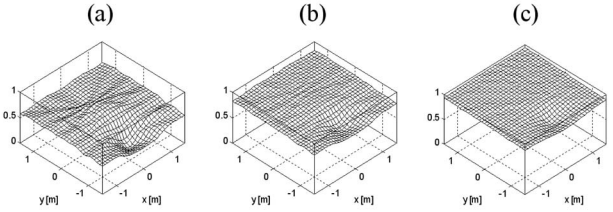

FIG. 8. The sum of the virtual coherence functions of the first 3 partial fields in the case when the effect of autospectral noise is considered: (a) when 3 references were used, (b) when 6 references were used, and (c) when 21 references were used.

each scan were varied by a factor c_g, and it was assumed that their levels varied at the same rate. The value of c_g at each scan was chosen arbitrarily within the range 0.7 to 1.4 (i.e., ±1.5 dB, approximately) under the constraint that its value averaged over all the scans was unity so that the averaged cross-spectral matrix corresponded statistically to that which would be obtained when the sources were perfectly stationary. In this case, the singular vectors remain the same over all the scans, and the singular values other than those associated with the sources are zero.

In Fig. 4, the "measured" sound field and the total sound fields obtained by using Eqs. (11) and (25) are presented. When Eq. (11) was used, it was observed that the effect of source level variation was not corrected: in fact, it was amplified [compare Figs. 4(a) and 4(b)]. The latter can be explained by examining the dimension of the sound field calculated by using Eq. (11). The dimension of the autospectrum of the measured sound field is $c_g[\mathrm{Pa}^2_{(\mathrm{avg})}]$, which is mathematically incorrect. In comparison, when Eq. (11) is used, the dimension is $[\mathrm{Pa}^4_{(\mathrm{scan})}/\mathrm{Pa}^2_{(\mathrm{avg})}]=c_g^2[\mathrm{Pa}^2_{(\mathrm{avg})}]$. Thus, when using Eq. (11), the effect of source level variation is increased by a factor of c_g compared with the measured sound field. In contrast, when Eq. (25) is used, the dimension is $[\mathrm{Pa}^2_{(\mathrm{avg})}]$. As expected then, it was observed that the effect of source level variation was corrected when Eq. (25) was used [compare Figs. 3 and 4(c)].

B. Measurement noise in the reference cross-spectral matrix

1. Autospectral noise component

In the second case, noise autospectra [i.e., the μ_i^2's in Eq. (15)] with levels ranging between 87 and 89.8 dB (the signal-to-noise ratios of the 21 reference signals ranged from

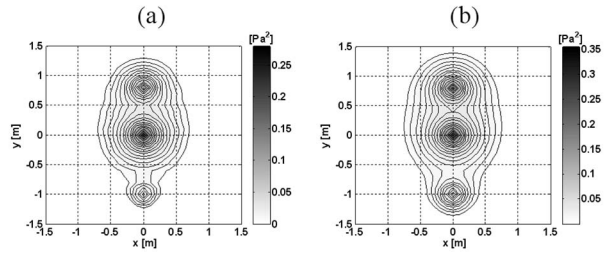

FIG. 9. Spatial distribution of the autospectrum of the total sound field calculated by using Eq. (25) in the case when the effect of autospectral noise is considered: (a) when 3 references were used and (b) when 21 references were used.

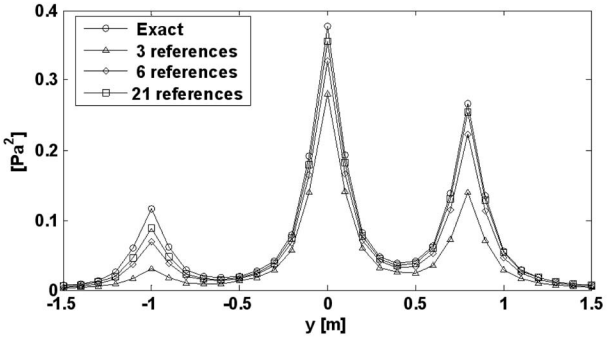

FIG. 10. Comparison of the total mean square pressure calculated by using Eq. (25) when various numbers of references were used as a function of y at $x=0$ m in the case when the effect of autospectral noise is considered.

−10.2 to 9.2 dB) were added to the diagonal terms of the noise-free reference cross-spectral matrix. In this case, the singular vectors were affected by the latter noise since noise autospectra having different levels were added, and the singular values calculated from the noise-contaminated cross-spectral matrix are larger than those calculated from the noise-free cross-spectral matrix (i.e., $\lambda_i > \tilde{\lambda}_i$).

In Figs. 5 and 6, it is shown that the effect of the latter noise on the singular values can be reduced by increasing the number of references. In Fig. 5, the singular values of the reference cross-spectral matrix constructed by using various numbers of references are compared. It can be seen that the distinction between the singular values associated with the source signals (i.e., the first 3 singular values) and the singular values associated with noise was clearer when a larger number of references were used. In Fig. 6, the ratio of the singular values calculated from the noise-free reference cross-spectral matrix to those calculated from the noise-contaminated reference cross-spectral matrix (i.e., $\tilde{\lambda}_i/\lambda_i$) with respect to the number of references is shown. It was observed that the ratios of the first 3 singular values approached unity as the number of references increased and that the rate of convergence of the third singular value (i.e., when the signal-to-noise ratio was low) to unity was slow. Thus it can be concluded that a larger number of references are required as the amount of noise increases.

The noise effect included in the singular vectors can also be suppressed by increasing the number of references, thus causing the singular vectors obtained from the noise-contaminated reference cross-spectral matrix to approach the

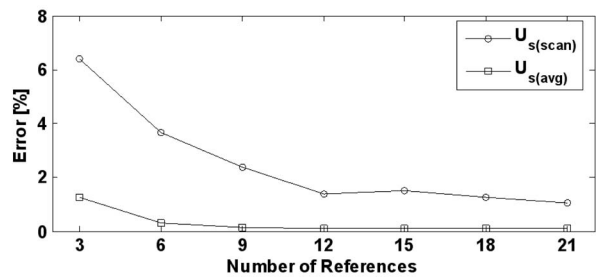

FIG. 11. Error in the singular vectors (Eq. (30)) of the reference cross-spectral matrix with respect to the number of references in the case when the effect of cross-spectral noise is considered.

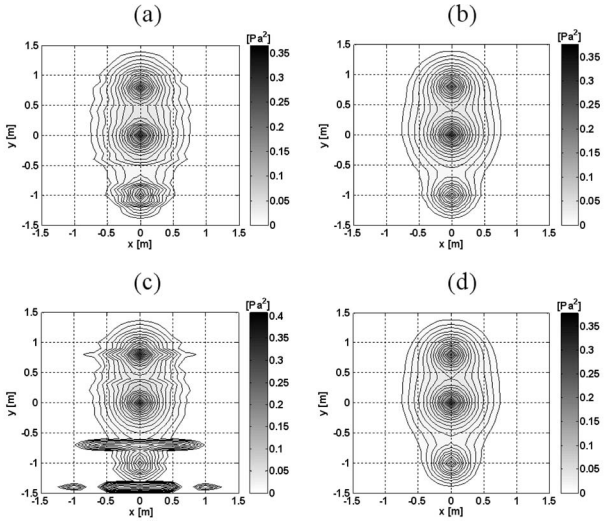

FIG. 12. Spatial distribution of the autospectrum of the total sound field in the case when the effect of cross-spectral noise is considered: (a) calculated by using Eq. (25) (6 references were used), (b) calculated by using Eq. (25) (21 references were used), (c) calculated by using Eq. (12) (21 references were used), and (d) calculated by using Eq. (11) (3 references were used).

singular vectors obtained in the noise-free case The latter effect is illustrated in Fig. 7, where the error is defined as

$$\text{Error}\ (\%) = \frac{\|\mathbf{U}_s^{\mathrm{H}}\tilde{\mathbf{U}}_s\|_{F(i\neq j)}}{\|\mathbf{U}_s^{\mathrm{H}}\tilde{\mathbf{U}}_s\|_{F(i=j)}} \times 100. \tag{30}$$

In Eq. (30), $\|\cdot\|_{F(i\neq j)}$ and $\|\cdot\|_{F(i=j)}$ denote Frobenius norms[19] that are evaluated by using only off-diagonal and diagonal terms, respectively. Since $\tilde{\mathbf{U}}_s$ is a unitary matrix (i.e., $\tilde{\mathbf{U}}_s^{\mathrm{H}}\tilde{\mathbf{U}}_s = \mathbf{I}$), the error would be zero in the noise-free case and should increase as the effect of noise becomes larger. Note that this error does not always decrease monotonically: i.e., when the signal-to-noise ratios of the additional reference signals are poor, their addition may actually cause the error to increase; but, in general, the noise effect included in the singular vectors decreases as the number of references increases as can be seen in Fig. 7.

In Fig. 8, the sums of the virtual coherence functions calculated by using three different numbers of references are compared. When 3 references were used, the sum of the virtual coherence functions was poor, i.e., less than unity [see Fig. 8(a)], but a significant improvement was observed when 21 references were used [see Fig. 8(c)]. This result confirms that the effect of noise autospectra can be reduced by using a relatively large number of references.

In Fig. 9, the total sound fields calculated by using Eq. (25) when 3 and 21 references were used are shown, and, in Fig. 10, the total sound fields obtained when various numbers of references were used are compared as a function of y at $x=0$. In both figures, it can be seen that the results approached those in the noise-free case as the number of references increased.

Finally, although not presented here, the result obtained using Eq. (11) was almost the same in this case since the level of the sources remained the same over all the scans.

TABLE I. Comparison of the characteristics of the two partial field decomposition formulations.

	Cross-spectral method $\hat{\mathbf{P}}=\mathbf{C}^{\mathrm{T}}_{rp(\mathrm{scan})}\mathbf{U}^{*}_{(\mathrm{avg})}\boldsymbol{\Sigma}^{-1/2}_{(\mathrm{avg})}$ [Eq. (11)]	Acoustic transfer matrix-based method $\hat{\mathbf{P}}=[\mathbf{C}^{+}_{rr(\mathrm{scan})}\ \mathbf{C}_{rp(\mathrm{scan})}]^{\mathrm{T}}\mathbf{U}^{*}_{(\mathrm{avg})}\boldsymbol{\Sigma}^{1/2}_{(\mathrm{avg})}$ [Eq. (25)]
Autospectral noise	Large number of references required during a measurement	
Source level variation	Not corrected	Corrected
Cross-spectral noise	Less sensitive, so a relatively small number of references can be used	More sensitive, so either the use of a relatively large number of references or a relatively large amount of averaging is needed
Regularization	Not necessary	Necessary

2. Cross-spectral noise component

In the third case, noise was added to the off-diagonal terms of the reference cross-spectral matrix [i.e., the Δ_{ij}'s in Eq. (15)]. The amount of noise added was 4.6% of the root mean square of the off-diagonal terms in the noise-free reference cross-spectral matrix. In this case, the singular values from the fourth to the smallest (that would be zero in the noise-free case) were not zero, i.e., energy from the true sources "leaked" into noise-related artificial sources (the latter also happened in the second case but cannot be observed clearly due to the larger influence of the noise autospectra). The contribution of the artificial sources to the total sound field may or may not be significant depending on the amount of noise. If their levels are comparable to those of the actual sources, they should be included to account for all the energy radiating from the sources. In this simulation, however, the overall contribution of the artificial sources was not significant, so only the first 3 singular values were included when Eq. (25) was implemented.

In Fig. 11, errors defined by Eq. (30) are shown with respect to the number of references and are compared in two cases: first, the error between the noise-free singular vectors and those obtained from the reference cross-spectral matrix constructed during the 16th scan (i.e., $\mathbf{U}_{s(\mathrm{scan})_{16}}$) was calculated, and, second, the error between the noise-free singular vectors and those obtained from the averaged reference cross-spectral matrix (i.e., $\mathbf{U}_{s(\mathrm{avg})}$) was calculated. It can be seen that the errors decreased as the number of references increased and that the error calculated when the averaged reference cross-spectral matrix was used was smaller than when the reference cross-spectral matrix constructed at a single scan was used.

In Fig. 12, the total sound fields calculated in the various cases are shown. Figures 12(a) and 12(b) compare the total sound fields calculated by using Eq. (25) when 6 and 21 references were used. Both results showed good overall agreement with the exact result, but it can be observed that the effect of noise included in the singular vectors was reduced when a larger number of references were used. In Fig. 12(c), the total sound field obtained by using Eq. (12) is shown. Note that Eq. (12), when referred to in this and following sections, represents the acoustic transfer matrix-based formulation without a regularization procedure as distinct from Eq. (25). The latter result confirmed that it is necessary to apply a regularization procedure when partial field decomposition is performed based on the use of the acoustic transfer matrix. In Fig. 12(d), the result obtained by using Eq. (11) when 3 references were used is shown. The result was better than that in Fig. 12(a) even though a smaller number of references were used. The latter result can be explained by the fact that Eq. (11) only makes use of the singular vectors of the averaged reference cross-spectral matrix, which was found to include a smaller cross-spectral noise effect (see Fig. 11). Thus, it might be said that it is more efficient to use Eq. (11) than Eq. (25) to suppress the effect of cross-spectral noise components when the sources remain "perfectly" stationary during each scan.

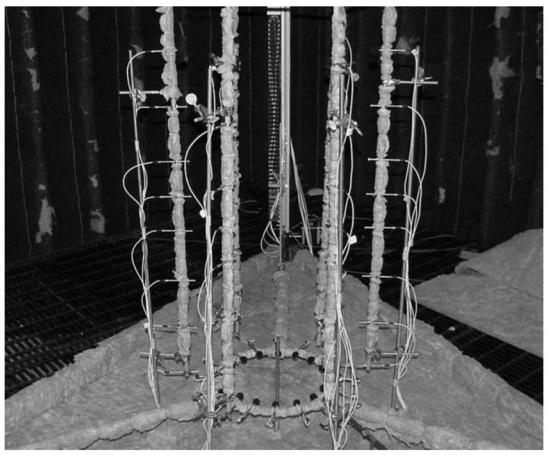

FIG. 13. Experimental setup for jet noise measurement.

IV. EXPERIMENTAL RESULTS

The procedure presented in the present work was applied to NAH measurements of a subsonic jet. The consider-

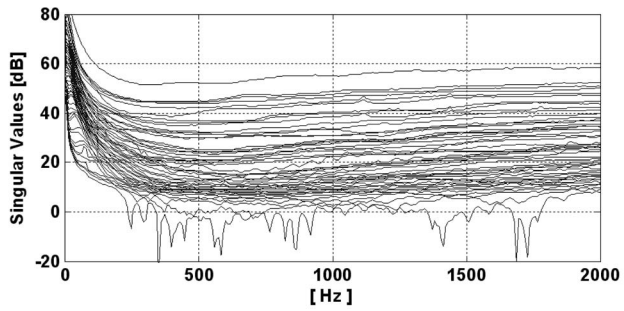

FIG. 14. The singular values of the reference cross-spectral matrix averaged over all the scans with respect to frequency when 48 references were used (experiment).

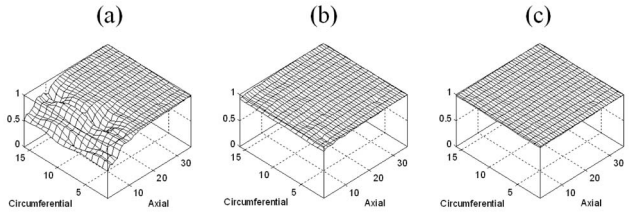

FIG. 15. The sum of the virtual coherence functions at 1 kHz when 48 references were used (experiment): (a) when the first 5 partial fields were used, (b) when the first 11 partial fields were used, and (c) when the first 20 partial fields were used.

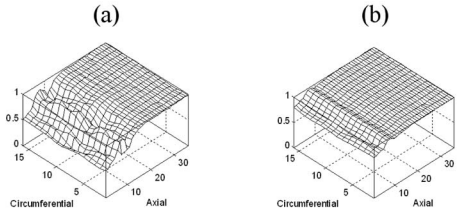

FIG. 17. The sum of the virtual coherence functions at 1 kHz when 18 references were used (experiment): (a) when the first 5 partial fields were used and (b) when the 18 partial fields were used.

ation of that type of source is particularly appropriate in the present context since jet noise sources comprise a relatively large number of subsources that are localized, directional, and random in nature. Also, the measured reference signals are likely to be corrupted by the effects of entrained flow exterior to the main jet plume.

In the measurement, an 0.8-cm-diameter burner nozzle with a sharp exit was used to generate a subsonic free jet flow. Six fixed, linear arrays, each holding 8 reference microphones (Larson Davis TMS426B01), were positioned around the jet plume, and 16 field microphones (Larson Davis TMS426B01) were traversed axially in 3-cm increments to sample a 30-cm-diameter cylindrical hologram surface in 36 steps (see Fig. 13). The measurement bandwidth was 8192 Hz with a frequency resolution of 8 Hz and the spectra were estimated by using 400 averages with 50% overlap. Results are presented for the first and the second partial fields at 1 kHz.

In Figs. 14 and 15, the singular values of the reference cross-spectral matrix averaged over all scans and the sum of the virtual coherence functions are shown. The first 11 partial fields were found to be the main contributors to the sound field [see Fig. 15(b)], and, based on the observation that the sum of the virtual coherence functions calculated by using 20 partial fields reached essentially unity at all points, singular values smaller than the 20th singular value were discarded when implementing Eq. (25).

The effects of reference array configuration are illustrated by a comparison with results obtained when 18 references were used (three references were chosen from each linear array). When 18 references were used, the separation between the source- and noise-related singular values was reduced (compare Figs. 14 and 16), and the sum of the virtual coherence functions calculated by using the complete set of 18 partial fields was smaller than that calculated by using the first 11 partial fields generated when using 48 references [compare Figs. 15(b) and 17(b)] even though the number of references in the former case was still larger than the number of significant partial fields. These comparisons demonstrate the benefit of using a number of references that is substantially larger than the actual number of significant partial fields.

In Fig. 18, the scan-to-scan source level variation is illustrated: the vertical axis represents the sum of the reference autospectra at each scan. The latter levels would be equal to a constant if the source were perfectly stationary. In Figs. 19(a) and 19(b), the first 2 partial fields calculated by using Eqs. (11) and (25) are compared. It can be seen that the partial fields calculated by using Eq. (11) included a spatial error whose shape corresponded to the source level variation while the use of Eq. (25) suppressed the latter effect.

A comparison of the results shown in Figs. 20(a), 20(c), 21(a), and 21(c) illustrates the combined effects of the regularization of the reference cross-spectral matrix and correction for source level variation. Those results confirm that partial field decomposition based on the acoustic transfer matrix can be significantly corrupted in the absence of a proper regularization procedure. In Figs. 20(b), 20(d), 21(b), and 21(d), the partial fields after wave number filtering are compared to demonstrate the importance of regularization as proposed here. In this study, modified Tikhonov regularization was used in conjunction with the Mozorov discrepancy principle.[20] Since regularization implemented as wave number filtering in a holographic projection procedure is a low-pass filtering process, it can remove only high wave number noise components, not spurious low wave number noise components, particularly those in the radiation region. The latter effect can be observed by comparing the wave number

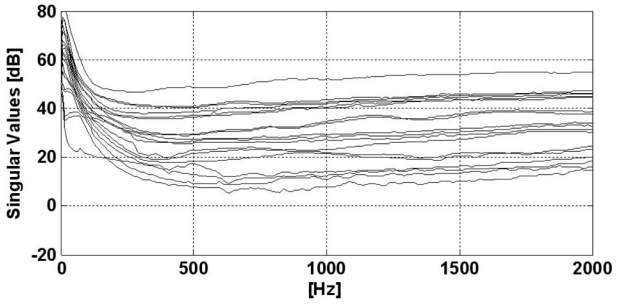

FIG. 16. The singular values of the reference cross-spectral matrix averaged over all the scans with respect to frequency when 18 references were used (experiment).

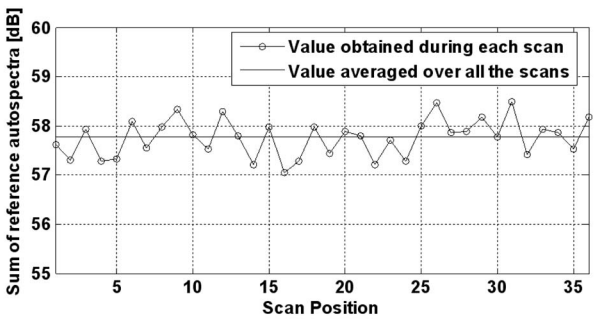

FIG. 18. Scan-to-scan source level variation at 1 kHz (experiment).

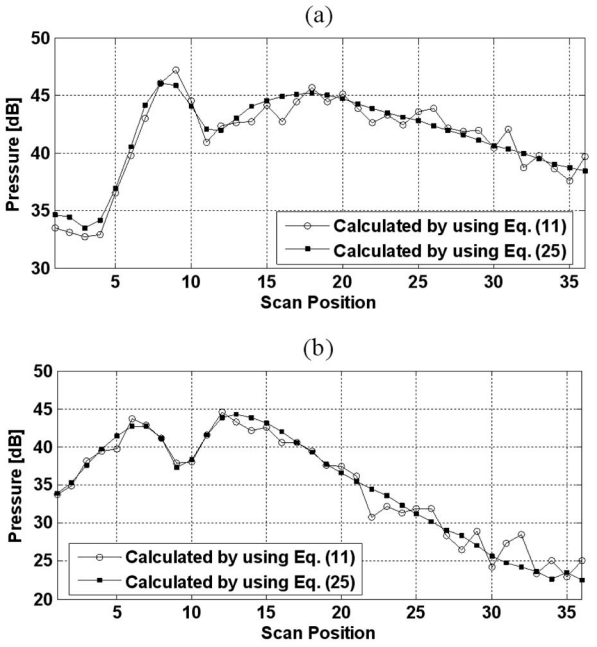

FIG. 19. Comparison of the partial fields calculated by using Eqs. (11) and (25) at 1 kHz (experiment): (a) the first partial field and (b) the second partial field. Results are shown at one angular section and the horizontal axis corresponds to the axial direction.

spectra presented in Figs. 22 and 23. From the results presented here, it can be concluded that regularization with an optimally chosen cutoff singular value is necessary to avoid corruption of the partial fields resulting from the combined effects of the use of Eq. (12) and measurement noise.

V. SUMMARY

In this section, a summary is provided along with a comparison between the cross-spectral method [i.e., Eq. (11)] and the acoustic transfer matrix-based method [i.e., Eq. (25)] for

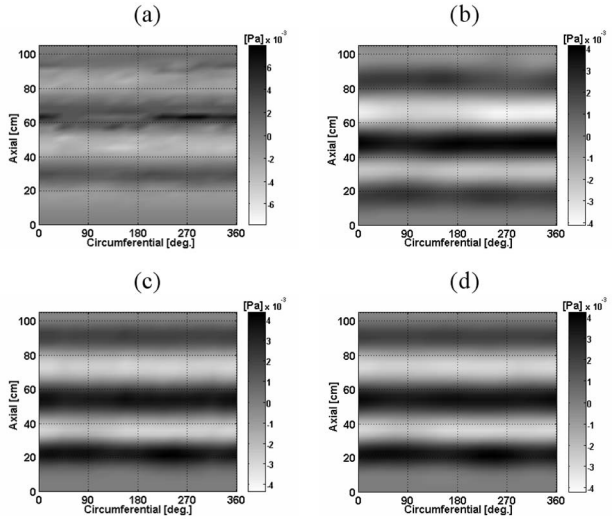

FIG. 20. The spatial distribution of the real part of the first partial field at 1 kHz (experiment): (a) calculated by using Eq. (12) without wave number filtering, (b) calculated by using Eq. (12) with wave number filtering, (c) calculated by using Eq. (25) without wave number filtering, and (d) calculated by using Eq. (25) with wave number filtering.

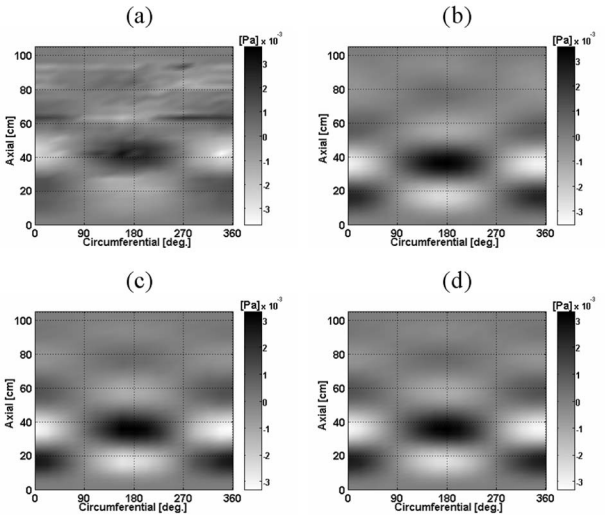

FIG. 21. The spatial distribution of the real part of the second partial field at 1 kHz (experiment): (a) calculated by using Eq. (12) without wave number filtering, (b) calculated by using Eq. (12) with wave number filtering, (c) calculated by using Eq. (25) without wave number filtering, and (d) calculated by using Eq. (25) with wave number filtering.

partial field decomposition in order to help establish the best strategy for various situations. In Table I, the characteristics of those two partial field decomposition formulations are compared. The autospectral noise components measured by the reference microphones affect mainly the levels of the calculated partial fields. When the latter noise levels are significant, thus making the singular values biased, both formulations require the use of a large number of references during a measurement to avoid underestimation of the partial field results. Since Eq. (11) does not correct for the effect of source level variation, the use of Eq. (25) should generally be preferred. In the case of perfectly stationary sources, however, Eq. (11) has advantages over Eq. (25): first, Eq. (11) is less sensitive to cross-spectral noise components than Eq.

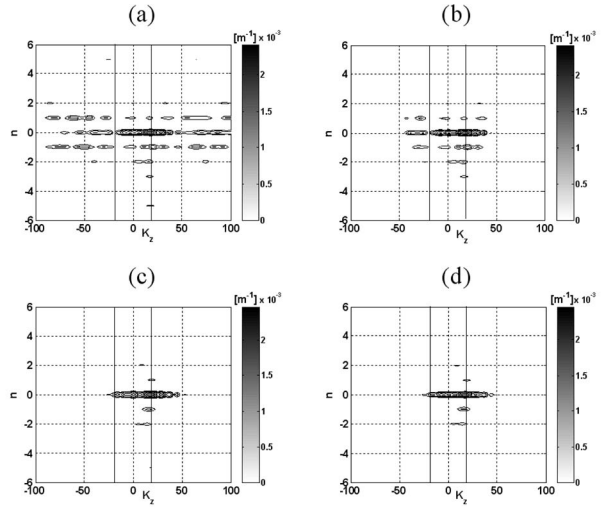

FIG. 22. The wave number spectrum of the first partial field at 1 kHz (experiment): (a) calculated by using Eq. (12) without wave number filtering, (b) calculated by using Eq. (12) with wave number filtering, (c) calculated by using Eq. (25) without wave number filtering, and (d) calculated by using Eq. (25) with wave number filtering. The vertical lines represent the extent of the radiation region at 1 kHz.

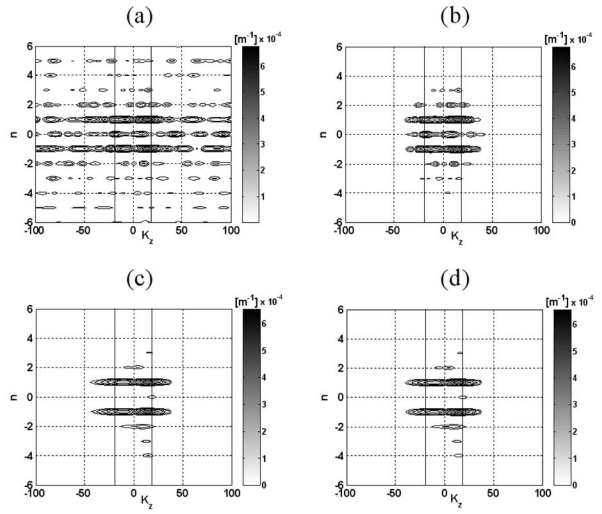

FIG. 23. The wave number spectra of the second partial field at 1 kHz (experiment): (a) calculated by using Eq. (12) without wave number filtering, (b) calculated by using Eq. (12) with wave number filtering, (c) calculated by using Eq. (25) without wave number filtering, and (d) calculated by using Eq. (25) with wave number filtering. The vertical lines represent the extent of the radiation region at 1 kHz.

(25) since Eq. (11) involves only the averaged reference cross-spectral matrix. Therefore, Eq. (11) can suppress the latter noise more effectively, thus allowing the use of a smaller number of references during a measurement than when Eq. (25) is used. Second, its implementation is simple since a regularization procedure is not required.

In summary, the use of a larger number of references than the expected or previously identified number of independent subsources is always recommended, and the choice between the two formulations considered here should be made based on the significance of the effects of measurement noise and source level variation.

VI. CONCLUSIONS

In this study, the effects of noise in the reference signals and source level variation on partial field decomposition in the context of scan-based, near-field acoustical holography were discussed. First, it was shown that both autospectral and cross-spectral noise can be suppressed by increasing the number of references used during measurements since the use of a larger number of references results in a clearer separation between the source- and noise-related signals. Second, it was shown that the previously proposed partial field decomposition formulation, based on the use of the acoustic transfer matrix, for correcting for source level variation is sensitive to the effects of measurement noise, thus requiring a proper regularization procedure to be incorporated. In this work, truncated singular value decomposition was used to perform the regularization, and the optimal cutoff singular value was determined with the help of the virtual coherence function. Without the latter procedure, the effect of slight variations of the singular vectors of the reference cross-spectral matrix obtained during each scan can be amplified to a significantly large level by the effect of the ill-conditioned reference cross-spectral matrix. In particular, spurious low wave number components may appear in the radiation region which cannot be removed by conventional regularization procedures. Both the numerical simulations and the experimental results were presented to demonstrate that the combined use of a relatively large number of references during a measurement and the acoustic transfer matrix-based partial field decomposition formulation with a regularization procedure can successfully suppress the effects of both noise in the reference signals and source level variation. Finally, the relative performance of the two approaches to partial field decomposition was summarized.

[1]E. G. Williams, J. D. Maynard, and E. J. Skudrzyk, "Sound source reconstructions using a microphone array," J. Acoust. Soc. Am. **68**, 340–344 (1980).
[2]J. Hald, "Non-stationary STSF," B&K technical review No. 1 (2000).
[3]J. Hald, "Time domain acoustical holography and its applications," Sound Vib. **35**, 16–25 (2001).
[4]H.-S. Kwon, Y.-J. Kim, J. S. Bolton, J.-G. Suh, and S.-J. Suh, "Generalized scan-based nearfield acoustical holography and its application," *Proceedings of INTER-NOISE 2003*, paper no. 1111 (2003).
[5]J. Hald, "STSF—A unique technique for scan-based near-field acoustic holography without restrictions on coherence," B&K technical review No. 1 (1989).
[6]D. L. Hallman and J. S. Bolton, "A comparison of multi-reference nearfield acoustical holography procedures," *Proceedings of NOISE-CON 94*, pp. 929–934(1994).
[7]H.-S. Kwon and J. S. Bolton, "Partial field decomposition in near-field acoustical holography by the use of singular value decomposition and partial coherence procedures," *Proceedings of NOISE-CON 98*, pp. 649–654 (1998).
[8]K.-U. Nam and Y.-H. Kim, "A partial field decomposition algorithm and its examples for near-field acoustic holography," J. Acoust. Soc. Am. **116**, 172–185 (2004).
[9]Y.-J. Kim, J. S. Bolton, and H.-S. Kwon, "Partial sound field decomposition in multireference near-field acoustical holography by using optimally located virtual references," J. Acoust. Soc. Am. **115**, 1641–1652 (2004).
[10]H.-S. Kwon, Y.-J. Kim, and J. S. Bolton, "Compensation for source nonstationarity in multireference, scan-based near-field acoustical holography," J. Acoust. Soc. Am. **113**, 360–368 (2003).
[11]J. S. Bendat and A. G. Piersol, *Random Data: Analysis and Measurement Procedures*, 3rd ed. (Wiley, New York, 2000).
[12]G. P. Carroll, "The effect of sensor placement errors on cylindrical near-field acoustic holography," J. Acoust. Soc. Am. **105**, 2269–2276 (1999).
[13]K.-U. Nam and Y.-H. Kim, "Errors due to sensor and position mismatch in planar acoustic holography," J. Acoust. Soc. Am. **106**, 1655–1665 (1999).
[14]P. C. Hansen, *Rank-Deficient and Discrete Ill-Posed Problems* (SIAM, Philadelphia, PA, 1998).
[15]M. S. Kompella, P. Davies, R. J. Bernhard, and D. A. Ufford, "A technique to determine the number of incoherent sources contributing to the response of a system," Mech. Syst. Signal Process. **8**, 363–380 (1994).
[16]S. H. Yoon and P. A. Nelson, "A method for the efficient construction of acoustic pressure cross-spectral matrices," J. Sound Vib. **233**, 897–920 (2000).
[17]M. Lee, J. S. Bolton, and L. Mongeau, "Holographic visualization of a subsonic jet," *Proceedings of INTER-NOISE 2004*, paper no. 459 (2004).
[18]K.-U. Nam and Y.-H. Kim, "Low coherence acoustic holography," *Proceedings of INTER-NOISE 2003*, paper no. 229 (2003).
[19]G. H. Golub and C. F. V. Loan, *Matrix Computations*, 3rd ed. (Johns Hopkins U.P., Baltimore, MD, 1996).
[20]E. G. Williams, "Regularization methods for near-field acoustical holography," J. Acoust. Soc. Am. **110**, 1976–1988 (2001).

A hydromechanical biomimetic cochlea: Experiments and models

Fangyi Chen[a)]
Department of Electrical and Computer Engineering, Hearing Research Center, Boston University, Boston, Massachusetts 02215

Howard I. Cohen
Department of Physiology and Biophysics, Boston University, School of Medicine, Boston, Massachusetts 02118

Thomas G. Bifano
Department of Manufacturing Engineering, Boston University, Boston, Massachusetts 02215

Jason Castle, Jeffrey Fortin, and Christopher Kapusta
General Electric Global Research Center, Niskayuna, New York 12309

David C. Mountain and Aleks Zosuls
Department of Biomedical Engineering, Hearing Research Center, Boston University, Boston, Massachusetts 02215

Allyn E. Hubbard[b)]
Department of Electrical and Computer Engineering, Department of Biomedical Engineering, Hearing Research Center, Boston University, Boston, Massachusetts 02215

(Received 11 May 2005; revised 1 November 2005; accepted 3 November 2005)

The construction, measurement, and modeling of an artificial cochlea (ACochlea) are presented in this paper. An artificial basilar membrane (ABM) was made by depositing discrete Cu beams on a piezomembrane substrate. Rather than two fluid channels, as in the mammalian cochlea, a single fluid channel was implemented on one side of the ABM, facilitating the use of a laser to detect the ABM vibration on the other side. Measurements were performed on both the ABM and the ACochlea. The measurement results on the ABM show that the longitudinal coupling on the ABM is very strong. Reduced longitudinal coupling was achieved by cutting the membrane between adjacent beams using a laser. The measured results from the ACochlea with a laser-cut ABM demonstrate cochlear-like features, including traveling waves, sharp high-frequency rolloffs, and place-specific frequency selectivity. Companion computational models of the mechanical devices were formulated and implemented using a circuit simulator. Experimental data were compared with simulation results. The simulation results from the computational models of the ABM and the ACochlea are similar to their experimental counterparts. © *2006 Acoustical Society of America.* [DOI: 10.1121/1.2141296]

PACS number(s): 43.64.Bt, 43.64.Kc, 43.60.Qv [BLM] Pages: 394–405

I. INTRODUCTION

The cochlea, which is highly frequency selective, handles acoustic phenomena hydromechanically, resulting in an audible frequency range of typically 20 Hz to 20 kHz for humans. Although the biological cochlea is an active mechanism, in which amplification takes place (Dallos, 1996), the passive (aged or slightly damaged) cochlea is still a valuable hearing asset. A passive artificial hydromechanical implementation of a cochlea, therefore, should be able to mimic at least some useful aspects of cochlear signal processing functionality. Modern micromachining technology offers the technology with which to build such a device. In this paper, we describe the construction and characterization of a hydromechanical artificial cochlea (ACochlea). Our goal in this paper is twofold. One is to demonstrate cochlea-like features in the experimental results taken from a prototype device. The other is to use mathematical models[1] to understand the behavior of the prototype and investigate ways to improve its performance.

To mimic salient cochlear signal processing features, electronic chips have been built using both analog (for a review see Yang, 2004) and digital circuits (for a review see Leong *et al.*, 2003). Most of the analog implementations are improved versions of the electronic cochlea originally proposed by Lyon and Mead (1988). In these implementations, a cascade of second-order filters was built using subthreshold

[a)]Current address: Oregon Hearing Research Center, Oregon Health & Science University, Portland, Oregon 97239-3098. Electronic mail: chenfa@ohsu.edu
[b)]Author to whom correspondence should be addressed: Allyn E. Hubbard, Boston University, Department of Electrical and Computer Engineering, 8 Saint Mary's Street, Boston, Massachusetts 02215. Electronic mail: aeh@bu.edua

MOSFET technology. This implementation, however, suffers stability and accuracy problems from transistor mismatching and temperature sensitivity.

The digital implementations to approximate the cochlear frequency response are built as digital filters, either coded into a field programmable gate array (FPGA), designed into an application-specific integrated circuit (ASIC), or programmed on a digital signal processing (DSP) chip. The digital implementation typically requires more transistors than a comparable analog implementation, so the number of output channels from a single digital chip is likely to be more limited. Another problem is that, while a larger number of output channels can be achieved with increasingly potent chips, or by using multiple chips, the power consumption can become unattractively high.

A mechanical implementation of an artificial cochlea should be able to mimic cochlear signal processing functionality in a more natural way. The desired behavior should be the result of material properties and construction geometry, not circuit behavior. In theory, the mechanical signal processor does not require external power other than the acoustic power from the impinging sound, although electrical power will be needed for instrumentation and post-processing.

The history of building a mechanical structure for simulating cochlear behavior can be divided into two periods. During the first period, mechanical cochleae were built to study and help understand cochlear behavior. Because of the difficulties building and driving such a small device, these early mechanical cochleae were typically one or two orders of magnitude larger than a human cochlea. A *scaling* technique was adopted in those designs, wherein all the dimensions of the human cochlea were multiplied by a scale factor. However, the material properties of these artificial cochleae were usually not scaled properly due to the lack of materials with the required properties. Some of the important works of this period are as follows. von Bekesy (1960) built a mechanical cochlea to study the traveling wave. Tonndorf (1959) adopted a similar structure to study beats in the cochlea. Chadwick and Adler (1975) constructed a mechanical cochlear model to examine their theory of the cochlea. Much later, Lechner (1993) implemented an ACochlea with a Polyvinylidene Fluoride (PVF_2 or PVDF) bending transducer, which is mounted on beams on the artificial basilar membrane (ABM) to obtain an electrical output from the vibrational activity. Lechner also added actuators to a beam to simulate the active response in the cochlea. About the same time, Zhou *et al.* (1993), proposed the first life-sized physical mechanical cochlea. In this device, an isotropic polymer membrane was put on a steel template to build the ABM. Two plastic chambers were constructed to mimic the cochlear scalae.

The second period begins in the mid-1990s. With improved micromachining technology, efforts to build practical devices to mimic the cochlear function were carried out and reported. Haronian and Macdonald (1996) proposed a microelectromechanically based frequency signature sensor (MEM-FSS). An array of beams of gradually varying lengths was etched on a silicon substrate. However, no fluid coupling exists in this structure. Thus, the structure can only mimic the basilar membrane (BM), since the fluid coupling is a key element for the cochlea mechanical signal processing. Although they did model the squeezed air between beams as a coupling spring and dashpot, they treated this coupling as a local factor to influence the adjacent beam resonating quality, but not a longitudinal energy coupling mechanism. Tanaka *et al.* (1998) described a fish-boned structure, where different lengths of silicon beams lie on a core backbone of the same material. This core backbone was used to transfer vibrations along the device, simulating the fluid channel's function. The input to the device is at the end of the core backbone, which is too stiff to match it properly to the acoustic input signal. Lim *et al.* (2000) published their work on a mechanical cochlea made by laying an isotropic film over a slotted silicon wafer and surrounding it with fluid channels. They demonstrated the traveling-wave feature by showing the phase plot at two locations along their ACochlea. The magnitude response shown is rather irregular and does not show the expected high-frequency roll off. The author offered the isotropy of the ABM as the major reason for this problem. Hemmert *et al.* (2003) proposed a fluid-filled MEMS-based mechanical cochlea. In this model, the BM is built using an epoxy-based photoresist, which possesses stiffness close to the biological material. The authors used the impulse response at two very closely spaced locations to demonstrate the existence of a traveling wave.

Recently, Wittbrodt *et al.* (2004) proposed a new design continuing Lim's effort (Lim *et al.*, 2000). Aluminum fibers were deposited on a soft membrane to produce the anisotropic ABM. In 2002, White and Grosh (2002) reported their microelectromechanical-system (MEMS) cochlea, which used a single fluid channel and a BM made of silicon beams. Silicon-nitride beams were used in a newer version of this work to reduce the residue tension on the beams (White and Grosh, 2005). Both the silicon and silicon-nitride beams are much stiffer than their biological counterpart. White and Grosh (2005) presented the measurement results from their ACochlea. The phase response from measurements on this device demonstrated the traveling wave delay. However, the magnitude response shows very shallow high-frequency rolloff with ripples. The authors cited the difficulty in achieving strong enough anisotropy on the ABM as a reason for the shallow high-frequency rolloff. To obtain an electrical output from the beam vibration, White and Grosh (2002) used piezoresistive material and later (White and Grosh, 2005) used a capacitive sensing technique.

The above review demonstrates some of the challenges in building an ACochlea. The first challenge is the fabrication. Here the key is to build an anisotropic BM with stiffness similar to the biological material. The second challenge is to properly drive the small device and demonstrate the cochlea-like features in the experimental results. Those features include a slow traveling wave, sharp rolloff at the high-frequency end of the beam vibration spectrum, and the gradually decreasing cutoff frequency of the beam vibration spectrum along the length of the ACochlea.

The passive hydromechanical cochlea is typically simplified to be an elongated box with two fluid channels and a membrane partition between them (Peterson and Bogert,

1950; Zwislocki, 1950). The membrane partition is sometimes simply called the "basilar membrane". It is the BM, in fact, whose stiffness is critical to cochlear frequency sensitivity (von Bekesy, 1960). Zwislocki (1950) proposed a transmission-line-based model for his simplified cochlear mechanical structure. His theory explained the presence of a traveling wave as well as the tonotopicity of the cochlea. These two important features of cochlear behavior were originally measured by von Bekesy (1960). Zwislocki (1950) noted that the stiffness gradient on the BM, and the presence of the fluid channel, are keys to the hydromechanical signal processing in the cochlea. The interaction of the fluid mass and the BM stiffness results in the passive cochlear response, which present a series of low-pass filters with gradually varying cutoff frequencies.

Two devices are described in this paper: One is an ABM and the other is an ACochlea built around the ABM. The ABM is the most important functional part of the ACochlea, since it provides tonotopicity, i.e., positional frequency selectivity. We also provide computational models of the devices. Results from those devices are presented to characterize their performance and to help us to understand their behavior. The measured results on our ACochlea demonstrate some cochlea-like features, such as the slow traveling wave, tonotopicity, and the sharp high frequency roll-off. The model results mimic the performance of the devices.

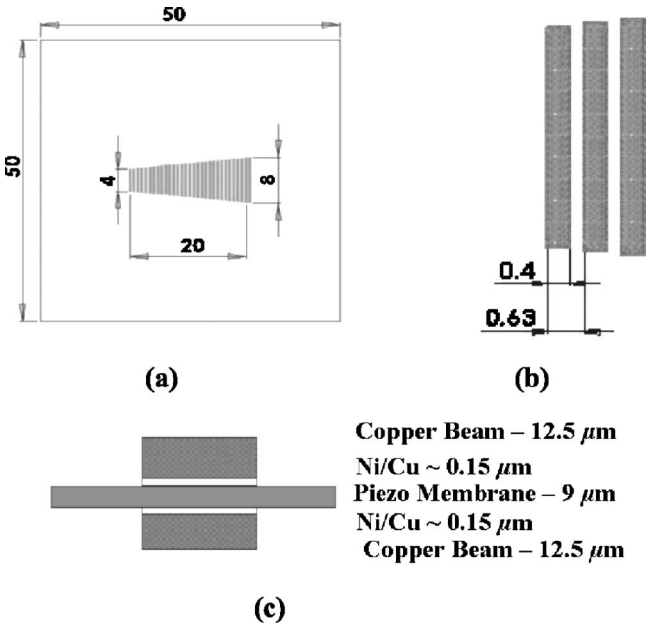

FIG. 1. The membrane structure of a 32-beam ABM, not to scale. The dimensions in this figure are in mm unless specified otherwise. (a) The layout schematic. This panel shows how the beams are arrayed on the membrane substrate. (b) Zoom-in view of the beam structure. (c) A schematic of the cross-sectional view of a beam section.

II. METHODS

A. Device design and fabrication

We constructed our ACochlea with our ABM and a fluid channel. The constituents of the ABM include a membrane substrate with beams and the frame supporting it. On the membrane substrate, a Cu beam array with gradually increasing length is designed to produce the stiffness gradient, which is a key component for the cochlear mechanical signal processing. The beam array has a trapezoidal profile. Frames support the membrane. The frames have a slotted window of the same shape as the profile of the Cu beam array. When the membrane is sandwiched by the frame, the edge of the slotted window clamps the beams and forms an open channel on each side of the membrane. This open channel is covered by a Plexiglas structure to form the ACochlear fluid channel. Two windows on this Plexiglas structure provide accessibility to the fluid channel, one for providing mechanical input and the other for fluid filling.

1. ABM materials and structure

The fabrication and assembling of the ABM took place in General Electric's Global Research Center (GE-GRC) facility in Niskayuna, NY. The membrane substrate is made of piezofilm procured from Measurement Specialties, Inc. of Hampton, VA. The piezo film at the beam serves as a mechanical transducer. The current design uses a 9 μm thick PVDF film premetalized with ~1500 angstroms Ni/Cu on both sides.

During the fabrication, a 100 mm diameter sheet of the piezofilm was first attached to a hoop around the outside, using a laminating process. This process induces a slight pretension in the film, which achieves a smooth surface so that standard photolithography can be used to form the beam array and the circuitry to connect the piezosensors. The smooth surface is also needed in assembling the ABM.

AZ1512, a positive photoresist, is then spun onto both sides of the stretched film. Next, vias are drilled through the stretched frame using the ESI laser system. These vias will be used later for precision alignment pins and alignment locations for the circuitry. Using a laser exposure system, the outline of the circuitry is patterned into the resist on both sides of the frame. AZ351, an aqueous developer (Clariant Corporation, Somerville, NJ) is used to develop the resist and to expose the metal circuitry for electroplating. The developing time is about 3–5 min. If interconnections between both sides of the film are necessary, the ESI laser system can be used to drill through the material to form fused vias.

Since the metallization of the PVDF film is very thin, the circuitry is electroplated with Cu to about 12.5 μm thick. This gives the device rigidity for probing and the correct beam modulus. Following plate-up, the resist is stripped from both sides and then redeposited for the next patterning step. After developing, the device is wet etched in a 30% nitric acid bath to remove the Ni/Cu metallization. Etching takes about 1 min, depending on the concentration of the solution. This in turn exposes the PVDF film and defines the circuitry. Once etching is complete the remaining resist can be stripped to expose the completed circuit.

Figure 1(a) is a schematic view of the membrane substrate, showing a beam array in the middle. The circuitry to connect beams is not shown here for simplicity. The beam length increases progressively from 4 mm at one end to 8 mm at the other end. This length gradient produces the stiffness gradient. There are 32 beams on this sample. Figure

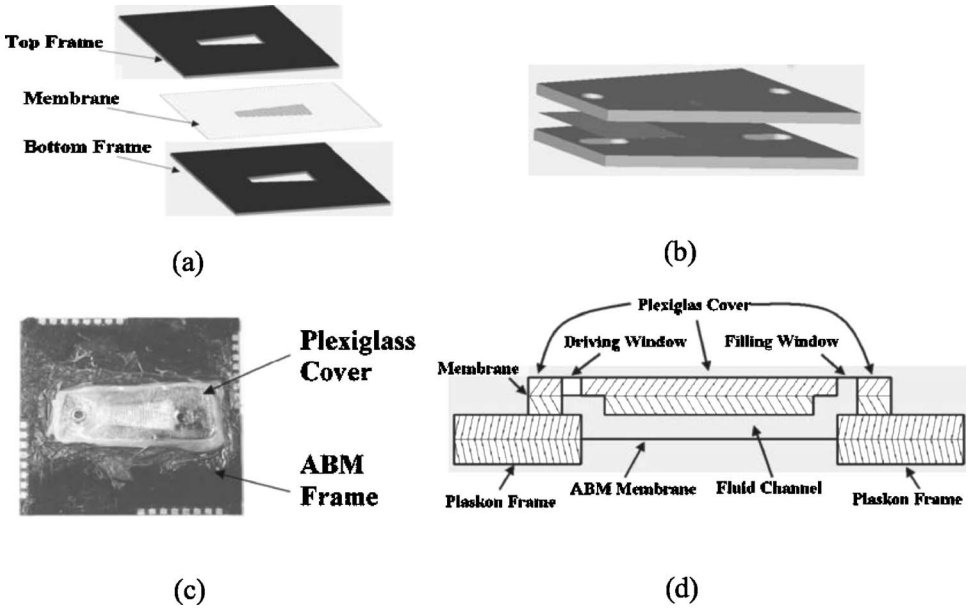

FIG. 2. The constituents of the ACochlea. (a) The ABM. The membrane substrate of the ABM is sandwiched by two Plaskon (a plastic material) frames. Each frame has a trapezoidal slot of the same size as the profile of the beam array. (b) The Plexiglas cover. The cover encloses the trapezoidal slot on the frame of the ABM, forming the ACochlear fluid channel. (c) Photo of the assembled ACochlea. The ACochlea is made by gluing the Plexiglas cover onto the frame of the ABM. The four-row connectors at the edge of the frame are to obtain electrical output from the piezoelectric beams. (d) Schematic of a cross-section view of the ACochlea. This panel demonstrates the relationship between the Plexiglas cover, the ABM, and how the canals on the bottom piece of the cover connect the windows to the ACochlear fluid channel.

1(b) shows a zoom-in view of the beams. On the sample under discussion, the beams are equally spaced along the ABM, each being 400 μm wide. They are spaced 630 μm center to center, resulting in a gap of 230 μm between the edges of adjacent beams. Figure 1(c) shows a schematic cross-sectional view of a beam section, noting the thickness dimensions of the layers. This figure shows that the two Cu layers, each of 12.5 μm thickness, are coated on both sides of the piezomembrane.

The Young's modulus of the Cu is about 30–50 times greater than that of the piezomembrane (110 GPa vs. 2–4 GPa). Hence this structure is expected to produce strong anisotropy. However, a later study showed that the pretension on the membrane during the fabrication greatly reduces the anisotropy. Therefore, a laser system (model #5200 from ESI in Portland, OR) was used to provide controlled, sharp, precision cutting or slitting of the film. The spot size of this triple YAG laser is about 18 μm. The laser slices through the membrane, resulting in a cut of about 100 μm width in the membrane between beams.

The frame of the ABM is made of plaskon (Amco Plastic Materials, Inc. in Farmingdale, NY), a thermo set epoxy widely used in the electronics industry as an encapsulant. It was chosen because of its ease of fabrication. The plaskon is molded into a large substrate, 6 in. by 6 in., and approximately 1 mm thick. The thickness will dictate the depth of the ACochlear fluid channel, as we will discuss in Sec. II A 2. If a different substrate thickness is needed, the plaskon can be lapped thinner or molded to the desired thickness. Post-molding, the plaskon is cleaned with an acetone wipe followed by a propanol wipe. This allows better adhesion to the adhesive layer. The adhesive layer is a 3M™ high-temperature acrylic film, similar to a double-sided tape. The adhesive is applied to the appropriate sides of the plaskon and trimmed with a razor blade. The adhesion process is used to sandwich the membrane substrate in the assembly of the ABM.

2. Assembly of the ABM

Figure 2(a) shows how two identical Plaskon frames are used to support the membrane substrate. The frames were cut by the laser into the same shape as the membrane substrate. A trapezoidal window, which is of the same size as the profile of the Cu beam array on the membrane substrate, was opened on the frames.

A laminating process is used to create this sandwich. The plaskon pieces are attached to the prestretched membrane by removing the release sheet from the 3M™ adhesive and adhering the plaskon part to the PVDF film. Precise alignment with pins permits the two long edges of the trapezoidal windows to firmly clamp the far tip edges of the Cu beams. In this way, the frames support the membrane substrate, while the window exposes the beam array. Because of the frame thickness, typically 1 mm on both sides of the beam array, we create the fluid channel by covering one open channel using the Plexiglas cover and filling it with water. The fluid channel is 4 and 8 mm wide at the small and large end, 20 mm long, and 1 mm high. The fluid channel provides longitudinal energy coupling.

3. Assembly of the Plexiglas cover

Figure 2(b) illustrates the assembly of the Plexiglas cover and how it forms a closed fluid channel. This cover is about 35 mm long, 10 mm and 15 mm wide at the small and large ends, respectively. Windows are opened on each end. A 2 mm window accommodates the piezostack driver to stimulate the ACochlea. The channel is filled through the other window and sealed with Vaseline.

On the bottom of the Plexiglas piece [Fig. 2(b)], two channels, each of about 3 mm long and 2 mm wide, are opened to provide a connection between the windows and the ACochlear fluid channel. Between the top and bottom pieces, a soft membrane is placed underneath the driving window. This membrane is sandwiched by the top and bottom Plexiglas pieces by applying Krazy Glue®. The mem-

brane window separates the ACochlear fluid channel from the air and provides an interface for the piezodriver.

4. Constituents of the ACochlea and the method to fill the fluid channel

Figure 2(c) shows the assembled ACochlea. The Plexiglas cover is adhered to the Plaskon surface over the ABM using a commercially available, quick setting, epoxy adhesive (Plastic Welder™ from Devcon). Figure 2(d) shows a schematic of the cross-section view along the longitudinal axis. This view shows that the driving and filling window are connected to the ACochlear fluid channel through the two canals on the bottom piece of the Plexiglas cover. To fill the fluid channel, the whole ACochlea, as shown in Fig. 2(c), is placed in a vessel and submerged in water and degassed using a vacuum.

5. Efficacy of the design of our ACochlea

Our device is designed to mimic the passive cochlear mechanical signal processing features of the cochlea, not its size, shape, or material properties. Only the top open channel of the ABM is covered. The bottom of the ABM is exposed to the air, so that our laser instrument could monitor the beam's vibrational activity. When a double channel implementation was used, where both channels were covered by a Plexiglas piece, the plastic cover, and the fluid absorbed, deflected and scattered the laser light, both during incidence and reflection, degrading the signal-to-noise ratio of the measurement. Theoretical analyses (Patuzzi, 1996) and the modeling study by an author (Chen, 2005) show that the single channel cochlea offers behavior very similar to its double channel counterpart.

B. Experimental measurements

We measure both the ACochlea and ABM responses by recording the vibration of the beams along the ABM. However, because of the different structure of the ACochlea and ABM, very different driving methods were adopted. Figure 3 shows a block diagram of the experimental setup for testing the acoustic properties of the ABM.

1. Schematic of the test system and the procedures for ABM measurements

In the setup shown in Fig. 3, a pulse signal is generated from an HP8114A Pulse Generator to drive the speaker with a 6 V, 32 μs, 10 per second signal. The interval of almost 100 ms allows sufficient time for the acoustic signal to die out. The speaker generates a peak sound pressure of about 1.0 Pa peak amplitude having approximately a 30 kHz bandwidth. A Brüel and Kjaer Condenser Microphone Type 4138 placed 2–3 mm from the beams measures the sound pressure near the beams. Simultaneously, the beam vibration is observed and measured by a Laser Doppler Vibrometer (LDV) system from Polytec PI, Auburn, MA. The laser head of the LDV system is 750 mm from the ABM, on the other side from the microphone. Both the amplified microphone signal and LDV output signal are sampled by a Tektronix digital oscilloscope model TDS420A.

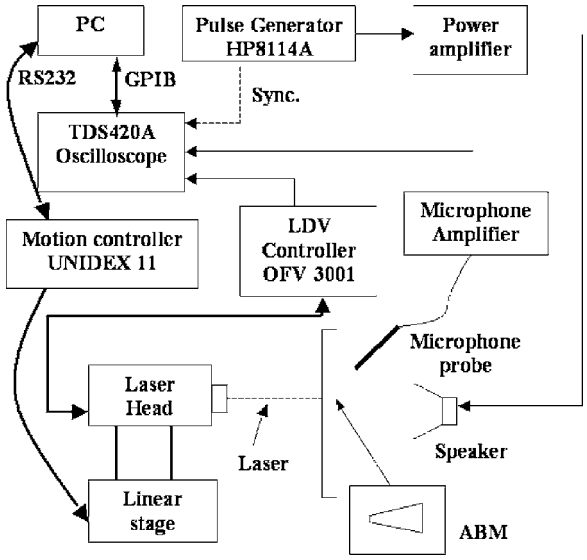

FIG. 3. Experimental setup for the ABM measurement. The pulse generator HP8114A generates a stimulus to drive the speaker through a power amplifier. The resulting sound pressure, which is measured by a B & K 1/8th in. microphone, makes the beams on the ABM vibrate. This vibration is detected by the laser from the laser head OFV303. The detected vibration signal is then decoded in the LDV controller OFV3001. The decoded vibration signal and the sound pressure signal were sampled by a digital oscilloscope TDS420A. A PC reads data from the oscilloscope through a General Purpose Interface Bus (GPIB). To measure the vibration at different locations along the ABM, the laser head is placed on a motorized linear stage ATS302. The linear stage is controlled by a remote controller Unidex 11, which has a keyboard to manually manipulate the motion of the stage. The controller also has an RS-232 interface with the PC, which allows for the automatic control.

The samplings are triggered by a synchronizing signal from the pulse generator. The measurement is averaged over approximately 100 repetitions. Using the GPIB protocol a PC reads the sampled data from the TDS420A. A Fast Fourier Transform (FFT) is used to calculate the sound pressure spectrum and the beam velocity spectrum from the time domain data. The beam sensitivity spectrum is calculated by dividing the beam velocity spectrum by the sound pressure spectrum. The impulse response of the beam sensitivity is calculated by doing an inverse FFT (IFFT) on the resulting sensitivity spectrum. The laser head of the LDV system is placed on a linear translation stage, an ATS302, manufactured by Aerotech Inc. of Pittsburg, PA. It is controlled by another Aerotech product, a motion controller, the Unidex 11. Computer interfacing is done through an RS-232 connection. Through the controller, the stage and the laser can be moved laterally with an accuracy of 2 μm over in a range of 50 mm.

2. Single beam measurement

Modal frequencies of the beam vibration were examined to investigate if the tension force on the beam is significant. Haronian (Haronian and MacDonald, 1996) and White (White and Grosh, 2002) also explored tensioning on the beams of their ABMs, by checking the relationship between modal frequencies. The measurement procedure is the same

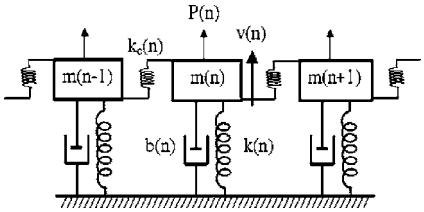

FIG. 4. The mechanical model of the ABM. In this model, each beam is modeled as a mechanical resonator with a mass component, $m(n)$, a damper, $b(n)$, and a spring, $k(n)$. The spring, $k_c(n)$, connecting two beam resonators, represents the coupling between beams through the membrane substrate.

as that used for the ABM measurement, except that the ABM is mounted so that the beam is in the horizontal direction and the laser scans along the length of the beam.

3. ACochlea measurement

The basic experimental setup shown in Fig. 3 is also used to measure the ACochlear response, but using a piezostack driver. The driver head, a cylindrical steel post of 10 mm length and 2 mm in diameter, was glued on top of the stack driver. The piezostack was then glued on an aluminum post, which was mounted on an XYZ micromanipulator to move the driver head into the driving window. The piezostack driver's vibration was measured before it was advanced into the driving window. The load of the ACochlea should not influence the vibration of the driver, because the acoustic impedance of the driver is at least 100 times larger than that of the ACochlea, as calculated using our mathematical models. Their outputs track the ACochlear and piezodriver response well.

We also tested an ACochlea built using an ABM where the piezofilm between beams was sliced completely through, to reduce longitudinal coupling. The cuts allow slow water leakage from the ACochlear fluid channel. Measurements typically had to be done within 30-45 min, before significant leakage would occur.

C. Simulation methods

1. Mechanical model of the ABM

Here the ABM model is introduced using its mechanical schematic. Each metal beam is represented by a damped mass-spring oscillator. Contrary to the classical cochlear model (von Bekesy, 1960), where the coupling between the BM sections is ignored, most models of artificial cochlea include longitudinal coupling. Lim (Lim *et al.*, 2000) indicated that the longitudinal coupling can influence the slope of the high-frequency rolloff of the artificial cochlea responses. White and Grosh (White and Grosh, 2005) also use the longitudinal stiffness to account for the shallow rolloff in their measurements. Here a spring is used to represent the coupling action of the membrane between the beams. Figure 4 shows the mechanical schematic of three adjacent beams.

2. Circuit model of the ACochlea

Figure 5 shows a circuit model of the ACochlea, which is a two-dimensional version of a traditional transmission-line structure (Peterson and Bogert, 1950; Zwislocki, 1950);

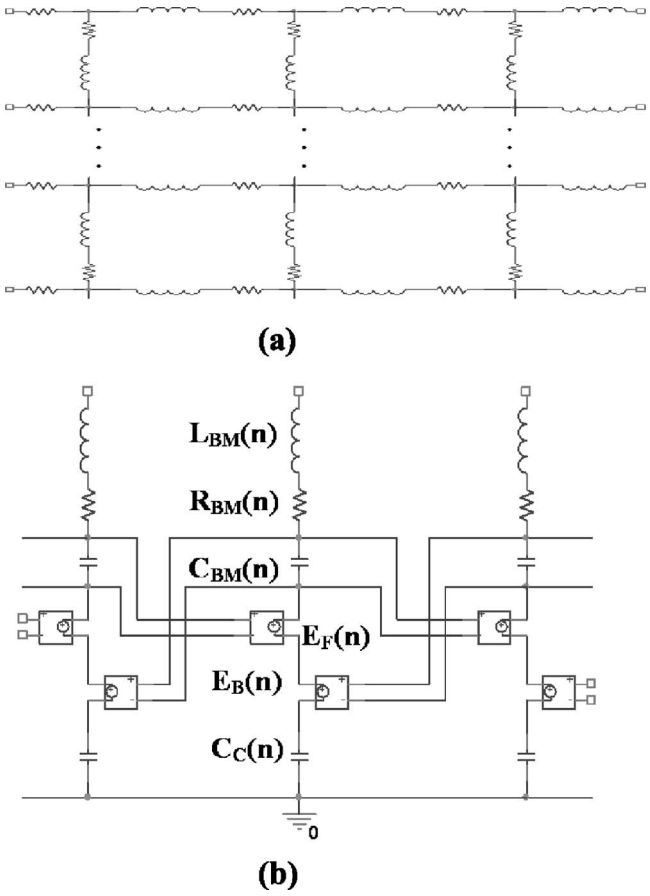

FIG. 5. The circuit schematic for three adjacent beam sections of the ACochlear model. (a) The fluid channel model. The inductors and resistors here represent the fluid inertia and viscosity, respectively. (b) The ABM model. This is the circuit (acoustic units) implementation of the mechanical model shown in Fig. 4. The dashpot damper $b(n)$, spring $k(n)$, and mass $m(n)$ are replaced by resistance $R_{\mathrm{BM}}(n)$, capacitance $C_{\mathrm{BM}}(n)$, and inductance $L_{\mathrm{BM}}(n)$, respectively. The values of the circuit components for a beam section are determined by the beam geometry and its material characteristics. The effect of the interstage spring $k_c(n)$ between beams is represented by two voltage controlled voltage sources (VCVSs), $E_F(n)$ and $E_B(n)$, and the capacitor $C_C(n)$. This seemingly complex circuit is necessary to match the force equation of the mechanical coupling. The value of the coupling components is determined by the geometry of the membrane and the pretension on the membrane. The floating nodes at the bottom of the fluid model are connected to those on the top of the ABM model, forming the ACochlear model.

(see Hubbard and Mountain, 1996) for a review. Figure 5(a) shows the fluid channel, modeled as a two-dimensional matrix of inductors and resistors, representing the inertia and the viscosity of the fluid, respectively. Figure 5(b) shows a circuit model for the ABM, which represents the mechanical model shown in Fig. 4, now based on the electroacoustic analogy. Each beam is modeled as a series of circuit components, and is called a beam section. A middle section receives input both from the one before it and the one after it, affecting the longitudinal coupling. The fluid channel model is constructed with an equal number of sections and connected one-to-one with the ABM model, forming the ACochlea model. Table I lists the corresponding components in the acoustical model and the circuit model, as well as their dimensional units.

The stiffness of the beam section is due to the bending and the pretension on the beam, and labeled T_y to distinguish

TABLE I. Corresponding components in the acoustical model and the circuit model, as well as their dimensional units. Note that the components in the mechanical model are in acoustic units. k_C is the coupling spring that represents the longitudinal coupling, which is represented in the circuit model by two VCVSs and a coupling capacitor. Although the unit of the VCVS is Pa, the gain of VCVSs is dimensionless.

Acoustic	Circuit	Unit
P: pressure	v: voltage	Pa
V: volume velocity	i: current	M^3/s
m: mass	L_{BM}: inductor	kg/m^4
k: spring	$1/C_{BM}$: capacitor	$kg/(m^4\ s^2)$
b: damper	R_{BM}: resistor	$kg/(m^4\ s)$
k_C: coupling spring	E_B: VCVS	Pa
	E_F: VCVS	Pa
	$1/C_C$: capacitor	$kg/(m^4\ s^2)$

it from the longitudinal tension (T_x) on the membrane. The stiffness due to bending is calculated by assuming a clamped–clamped boundary condition on the sandwich structure shown in Fig. 1(c). The stiffness due to the pretension T_y is calculated from a string equation. The value of T_y is estimated in the single beam measurement by observing how the modal frequencies of a beam section deviate from those of an ideal clamped–clamped beam.

In each beam section, the value of the capacitor $C(n)$, which is a volume compliance, is calculated using the square of the beam surface area divided by the total stiffness. The value of inductor $L(n)$ is calculated from the beam acoustic mass, which is the mass of the beam scaled by the square of the beam surface area. The value of the damper, $R(n)$, is calculated from $L(n)$ and $C(n)$ by assigning a quality factor, Q.

The membrane between beams is modeled as a string with tension, represented by the coupling spring $Kc(n)$. By assigning a pretension T_x, the coupling spring value is calculated by knowing the length and the cross-section area of the membrane. Three coupling components $E_F(n)$, $E_B(n)$, and $C_C(n)$ are used to represent the coupling spring in order to satisfy the mechanical equations. The values of Q and T_x are estimated in the ABM study by matching the measured results with modeling results of a proper Q and T_x. [See Chen (2005) for details.]

III. EXPERIMENTAL RESULTS

A. The ABM

1. Results from an ABM with membrane coupling between beams

We measured beam vibration at the middle of each beam on a 64-beam ABM. Figures 6(a) and 6(c) show the spectra of the ABM response. Figure 6(a) shows the spectrum of Beam #32 and Fig. 6(c) shows a gray-scale map of the spectra of all the beams, from Beam #1 at the small, narrower end to Beam #64 at the large, wider end. Figure 6(a) is a cross-section view of Fig. 6(c) at Beam #32. Although Fig. 6(a) exhibits a seemingly irregular spectrum, by looking at the gray-scale map in Fig. 6(c), one can see that there is a pattern in how the spectrum of each beam relates to the others.

Figures 6(b) and 6(d) show the impulse response of the ABM. Figure 6(b) is the impulse response of Beam #32. The figure shows two distinct times when the beam oscillation is strong. The first oscillation lasts from 0.0 to 0.5 ms; the second one starts aggressively at about 1.3 ms and gradually decays in amplitude. A third region of oscillation appears at around 2.8–3.3 ms.

Figure 6(d) shows two distinct triangular-shaped regions, as annotated by the dashed lines. The first is shaped like a right triangle and is positioned at the leftmost side of the 3-D map; the second one is in the middle of the map and has an isosceles triangular shape, although its right-hand edge is not very clear. Figure 6(b) is a cross-sectional line graph through Fig. 6(d) at Beam #32.

2. Results from an ABM with cuts in the membrane between beams

To confirm that the longitudinal coupling on the membrane between beams results in the high-frequency ripples in the ABM spectra, the membrane between beams on a 32-beam ABM was cut using the laser. Figure 7(a) shows the spectrum of Beam #16 and Fig. 7(b) shows a gray-scale spectrum map of all 32 beams. In Fig. 7(a), a clear resonance peak occurs at about 2.8 kHz. The second peak that is the third mode of beam vibration occurs at about 10 kHz. The second mode is not observed because we measured in the middle of the beam, where the second mode has a node; and because the beam is driven by a uniformly distributed pressure (Chen, 2005). This symmetric force tends to suppress the even modes. This is shown in Fig. 8 and discussed later.

B. Single beam

Figure 8(a) shows the vibration spectra of a beam from the 32-beam ABM, with cuts through the membrane, measured at the quarter-length point along the beam. This point is chosen to best observe the second mode. Figure 8(b) shows the 3-D spectral map of the all beam's vibration characteristics.

C. ACochlea

The measured results on an ACochlea, made using an ABM with cuts between beams, are presented in Fig. 9. Figure 9(a) shows the time domain displacement response of Beams #6, 16, and 26. Figures 9(b) and 9(c) show, respectively, the magnitude and phase of the ratio of the beam displacement spectrum to the driver displacement spectrum. (The driver displacement spectrum of the piezostack driver was measured before it was advanced into the driving window).

D. The piezomembrane output

The piezomembrane voltage output from a beam on an ACochlea was measured using the impulse stimulation. We recorded both the displacement of the membrane and the piezoelectrical output of the beam. Figures 10(a) and 10(b) show the time domain response of the displacement and the electrical output from a beam. The electrical output of the

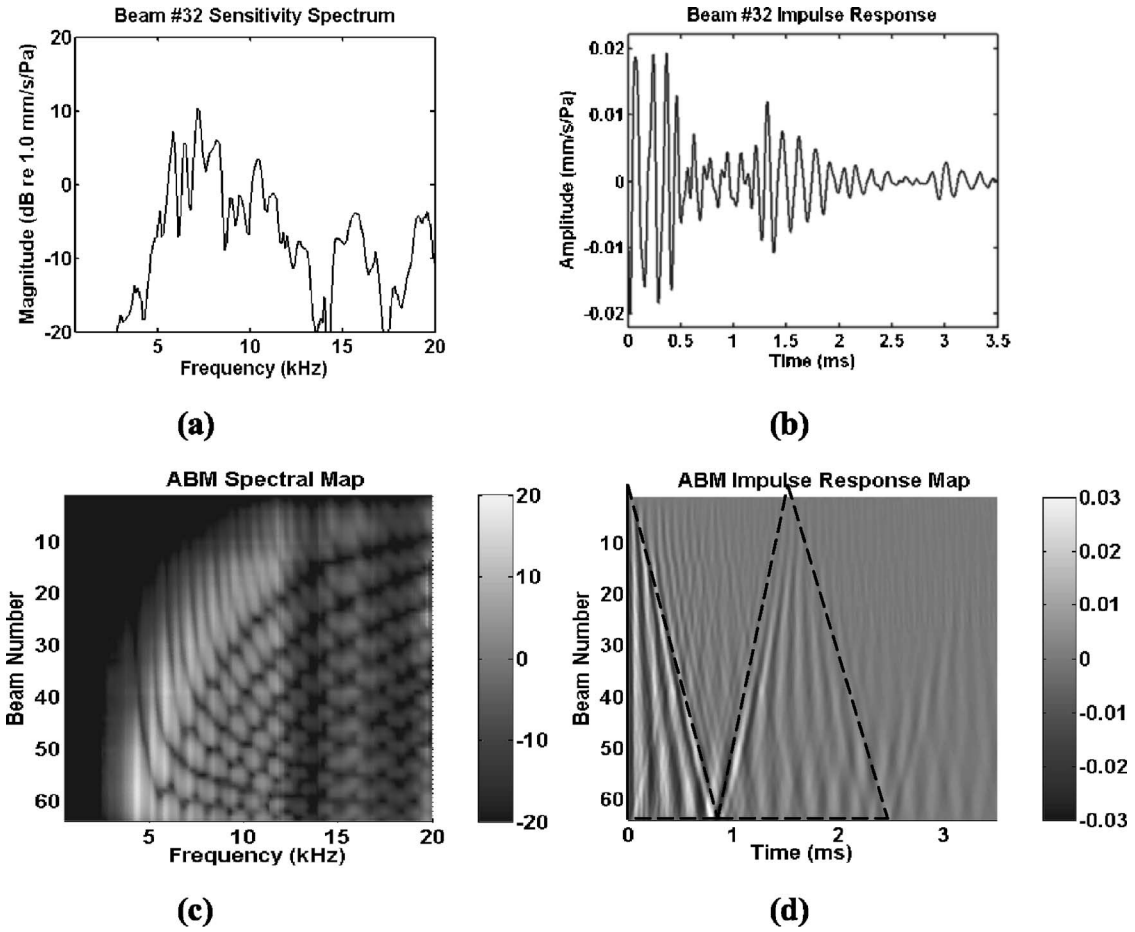

FIG. 6. The velocity sensitivity spectra and the impulse response of a single beam (#32) as well as that of all 64 beams. (a) Magnitude response of the velocity sensitivity spectrum of Beam #32. This spectrum was calculated by scaling the Beam #32 velocity spectrum by the sound pressure spectrum, which was previously smoothed using a median filter to avoid introducing noise. In the test, time domain responses of the sound pressure and the beam response were recorded and their spectra were calculated by taking the FFT of the time domain response. (b) Impulse response of Beam #32. This impulse response is calculated by doing an inverse FFT of the complex spectrum, whose magnitude is shown in (a). (c) A 3-D map of the sensitivity spectrum of all 64 beams. The *X* axis is the frequency and the *Y* axis is the beam number. The magnitude of the velocity of a specific beam at a specific frequency is represented by the gray scale at the corresponding position in the map. Light is highest, dark is lowest. In the *Y* axis, Beam #1 is at the small end of the ABM and Beam #64 is at the large end. (d) A 3-D map of the impulse response of the 64 beams. The *X* axis here is the time. NOTE: In (a) and (c), to get better resolution, dB is used as the unit, where 0 dB is equivalent to 1.0 mm/s/Pa.

piezomembrane shows a response that is similar to the displacement signal. A spike in the electrical output at about 1 ms is due to electrical coupling directly from the driver signal to the piezo-output to the measurement amplifier. This spike signal was manually removed before calculating the electrical output spectrum. Figure 10(c) shows the sensitivity spectrum of the piezo-output. The sensitivity is about 30 mV/μm at 2 kHz, where the beam vibration is at its maximum.

IV. COMPARISIONS OF MODELING AND EXPERIMENTAL RESULTS

A. ABM

The ABM model [Fig. 5(b)] was used to simulate the ABM response. An ac analysis was used to generate the spectral map of the beam responses. An ac voltage source was applied to each beam section, simulating a unit pressure applied to the ABM. The current on each beam section, which represents the volume velocity of the beam, was scaled by the area of the beam to obtain the linear velocity. In Figs. 11(a) and 11(b), the beam response from the simulation, Fig. 11(b), is compared with the calculated beam frequency response from the measured data, Fig. 11(a). Both figures exhibit a wide arching bright band from about 3 to 12 kHz, which is called the major band and represents the beam resonance. Orderly patterned, high-frequency ripples at frequencies above the major band are due to the longitudinal coupling through the membrane between beams.

In the model, the longitudinal tension T_x on the ABM membrane substrate determines the degree of the longitudinal coupling. The modeling study shows that a high T_x on the ABM results in the high-frequency ripples in the frequency map. A smaller T_x will enhance the magnitude of resonant peaks in the major band, with reduction of the response to the right of the major band. Given a relatively limited range of geometries, fluids, and material properties, for which the model is valid, T_x is a critical parameter.

B. ACochlea

Using the ACochlear model shown in Fig. 5, an analysis was performed to calculate the ACochlear model frequency

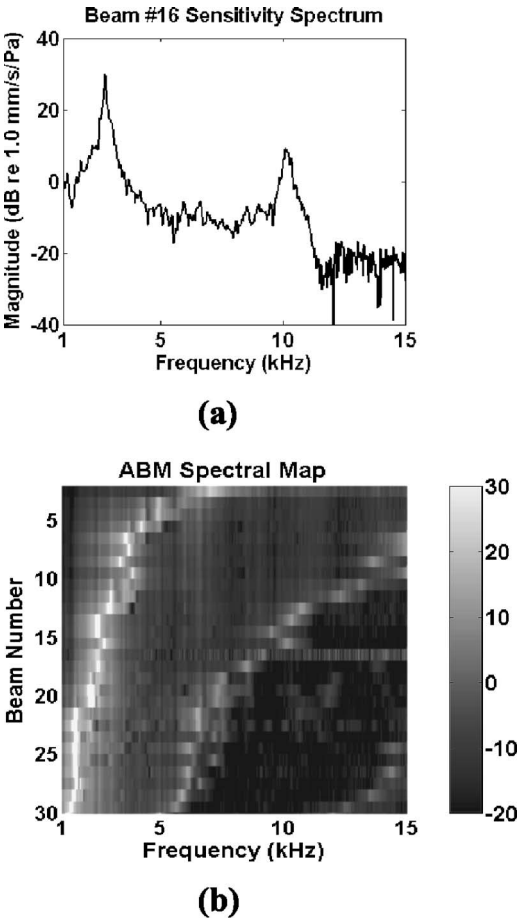

FIG. 7. Measured results on the beams of a 32-beam ABM with cuts through the membrane between beams. (a) The velocity sensitivity spectrum of Beam #16. (b) A three-dimensional map of the beam sensitivity spectrum. The peaks at about 2.8 and 10 kHz in Fig. 7 (a) are the first and third mode of the beam vibration, respectively. Correspondingly, there are two bright bands in the gray-scale map in Fig. 7 (b). A dB scale is used here, and 0 dB corresponds to 1 mm/s/Pa.

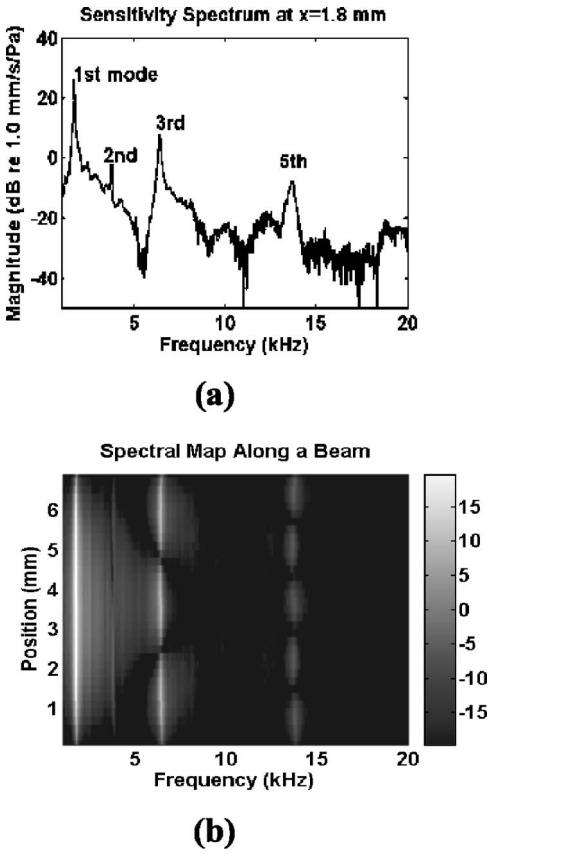

FIG. 8. The velocity sensitivity spectrum of a beam on the 32-beam ABM with cuts through the membrane. (a) Velocity sensitivity spectrum at a location 1.8 mm from the end of the beam. This is about one-quarter the length of the beam. (b) A 3-D spectral map. The *Y* axis marks the positions along the lengthwise direction of the beam. Corresponding to the peaks shown in (a), this map demonstrates the first mode with a long light line at 1.73 kHz, the third mode with three light spots at 6.38 kHz, and the fifth mode with five light spots at 13.7 kHz. The second mode—at 3.79 kHz—can be discerned if one looks for two light, vertical lines at that frequency. The fourth mode is not discernible from Fig. 10(b).

responses to compare with their experimental counterparts. The ratio of the linear velocity of the beam vibration to the piezodriver velocity was calculated to establish the beam transfer response. Figure 12 shows the spectral plots of four equally spaced beams, comparing the measured and modeling results. Figure 12(a) compares the magnitude responses of the four beams; Fig. 12(b) compares their phase responses.

V. DISCUSSION

A. ABM

The results presented in Sec. II A demonstrate the effect of coupling on the membrane substrate of the ABM. First, the spring coupling via the membrane between beams supports a wave propagating along the ABM. In Fig. 6(d), the left edge of the second triangular region changes from 0.9 ms at Beam #64 to about 1.8 ms at Beam #1. This indicates a wave traveling from the large end to the small end, because the wave is a result of the spring coupling due to the membrane substrate rather than due to a mass coupling. Second, the spring coupling also contributes to the rippling appearance of the beam vibration spectra, as shown in Fig. 6(c). The modeling results shown in Fig. 11(b) demonstrate that a larger coupling will produce larger ripples in the spectra. The measurement results in Fig. 7 also support this conclusion by showing that removing the coupling can eliminate the rippling.

In Fig. 7(b), the gray-scale spectral map demonstrates the frequency selectivity of the ABM. The resonant frequency of the beams does not change smoothly with beam number. This is most likely due to a nonmonotonic tension along the beams. As discussed in the single-beam measurement, the tension in the lengthwise direction of the beam contributes to the beam stiffness. The fabrication process, such as Cu deposition and prestretching the membrane during the assembling of ABM, could introduce nonmonotonic tension on beams. The laser cutting may also result in a nonmonotonic change in the pretension on the beam. This change of the pretension will result in a nonmonotonic change in the beam stiffness, and thus affect the expected, monotonic change in resonant frequency of the beam.

B. Single beam

In Sec. II B, we demonstrated the existence of vibrational modes of a single beam. The relationship of the modal

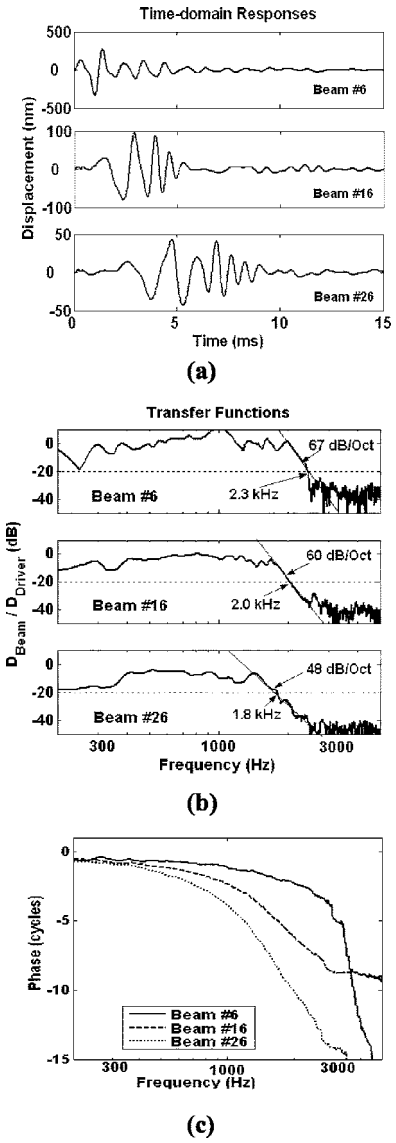

FIG. 9. Displacement measured on beams along the ACochlea made up using the ABM with cuts in the membrane between beams. (a) Time domain response. (b) Transfer function: Magnitude of the ratio of the beam displacement spectrum and the driver displacement spectrum. This high impedance of the driver results in negligible changes on its response after loading with the ACochlea. The frequency where the value of the magnitude response is about −20 dB is defined as the cutoff frequency of that beam. Those frequencies are 2.3, 2.0, and 1.8 kHz for Beams #6, #16, and #26. In the figure, we also marked the slope of the high-frequency rolloff of the response. The response of Beam #16 has a slope of 60 dB/octave. (c) The phase response of the ratio. Phase plots from Beam #6, Beam #16, and Beam #26 show a steady increasing delay until the signal is lost in noise.

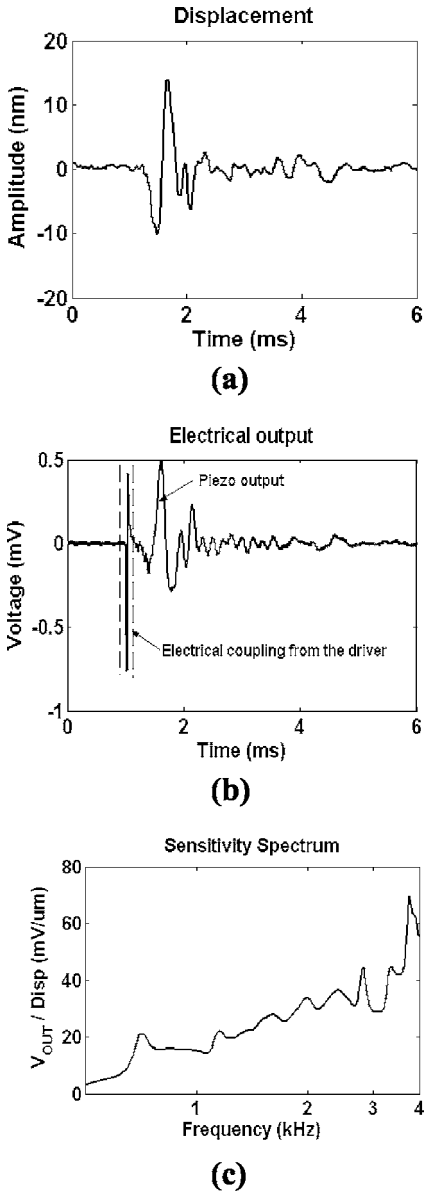

FIG. 10. The impulse response of a beam on an ACochlea. (a) Displacement output. (b) Electrical output. (c) Spectrum of the piezoresponse. This was calculated by scaling the piezoelectric output spectrum by the beam displacement spectrum.

frequencies can be used to ascertain the behavior of the beam (von Bekesy, 1960). Haronian (Haronian and MacDonald, 1996) indicated that the beam in their MEM-FSS behaves like a string instead of an expected clamped–clamped beam. Here we compare the modal frequencies from experimental results with those estimated from the theory for both a string and a pure clamped–clamped beam. For easy comparison, we normalize the higher frequencies using the first mode frequency. From Fig. 8, we note the frequencies of the first, second, third, and fifth modes to be 1.73, 3.79, 6.38, and 13.7 kHz. The normalized frequencies are 1.0, 2.69, 3.69, and 7.92. For a string, the higher mode frequencies are integer multiples of the first mode, so the corresponding normalized frequencies are 1.0, 2.0, 3.0, and 5.0. For a pure clamped–clamped beam, they are 1.0, 2.75, 5.40, and 13.3. Figure 13 plots the normalized frequencies in these three cases. Thus, the beam behavior is somewhere between a string and a clamped–clamped beam. This behavior of the beam is primarily due to the pretension on the beam, T_y.

It is well known that the stiffness of a pure clamped–clamped beam is inversely proportional to the cube of its length. However, the stiffness of a string is inversely proportional only to its length. For the ABM with the same width gradient, a string-like beam array will result in a much smaller stiffness gradient than a pure beam array. The string-like feature of the beam reduces the ABM stiffness gradient, which reduces the frequency range of the ACochlea made using this ABM.

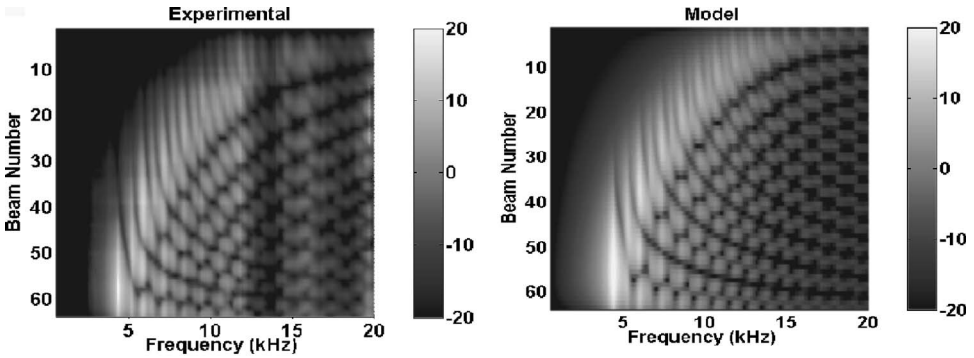

FIG. 11. A comparison of the velocity sensitivity (unit: dB *re* 1.0 mm/s/Pa) spectra of the 64-beam ABM between the measured and modeled results. (a) Spectral map of the measured result. (b) Spectral map from the modeling result. The spectra were calculated using the ABM circuit model, as shown in Figure 5(b). In the simulation, model parameters were adjusted away from their theoretical values to produce the best match to the experimental results.

C. ACochlea

The experimental results from our ACochlea, as shown in Fig. 9, demonstrate clear traveling wave features. The time domain responses in Fig. 9(a) show the steadily increasing delay from Beam #6 to #26. The delay is also demonstrated in Fig. 9(c) by the increasing phase lag from Beam #6 to #26. The time domain response in Fig. 9(a) demonstrates the widening of the period of the oscillation. Correspondingly, the magnitude response in Fig. 9(b) shows a progressively decreasing cutoff frequency, viz. from about 2.3 kHz at Beam #6, to about 2.0 kHz at Beam #16, and to about 1.8 kHz at Beam #26. This steady decrease of the roll-off frequency as a function of distance along its length demonstrates the tonotopic feature of the ACochlea.

In Fig. 9(b), the magnitude responses show high-frequency rolloffs of 67, 60, and 48 dB/octave for Beams #6, 16, and 26, respectively. The spectra also show a shallow slope in the low-frequency range. These features, a shallow slope in the low-frequency range and much steeper slope at the high-frequency end, are also features of cochlear responses.

Figure 9(b) shows a small cutoff frequency range from Beam #6 to Beam #26. Two reasons mainly account for this narrow frequency range. The first reason is the small stiffness gradient on the ABM. In our ABM, the large end is only twice as wide as the small end, compared, for example, to about six times in the human BM (Wever, 1938). This small width gradient, as well as the lack of a thickness gradient in our ABM, results in a much smaller stiffness gradient than that in the human cochlea. Additionally, the presence of the pretension on the beam, T_y, which results in a string-like behavior on beams, also results in the reduction of the stiffness gradient along the ABM, as discussed in Sec. IV B. The second reason is the coupling due to the residue from the membrane cutting. We have observed residue that bridges the cuts between beams (Chen, 2005). Simulations on the ACochlear model show that 1% of the original longitudinal tension on the membrane significantly reduces the frequency range of the ABM.

Figure 12 shows a good match between the measured and modeling results. Also, they both show ripples in the low-frequency range, which are due to reflections at the end of both the ACochlea and its model. Our ACochlear model is a vetted representation of our Acochlea.

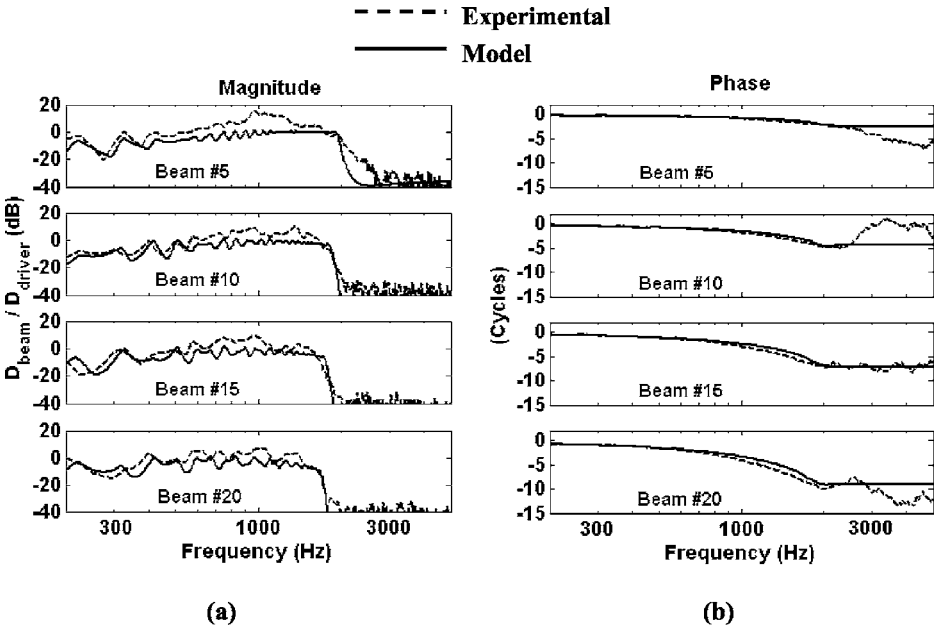

FIG. 12. A comparison of the transfer functions of the ACochlear model with the measured transfer functions from the ACochlea. The solid lines represent the modeling results and the dashed lines represent the measured results. (a) Transfer function: Magnitude in dB of the displacement ratio of the beam vibration to the driver displacement. (b) Phase response of the ratio. The phase plots of Beams #10, #15, and #20 show irregularity at frequencies above 2 kHz. This is due to the unwrapping process of the phase response. In that frequency range, the responses are near the noise level, as shown in the magnitude plots.

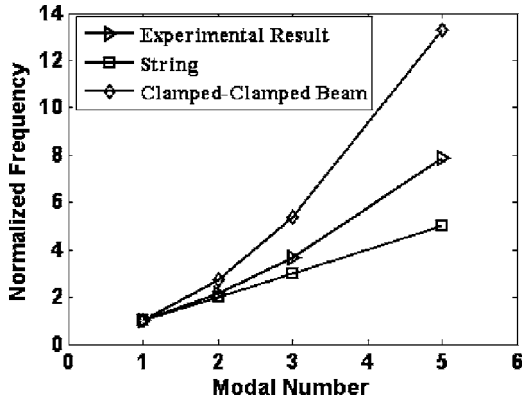

FIG. 13. A comparison of the normalized frequencies from measurements of a beam on an ABM with cuts in the membrane between beams, and those from the theoretical calculations of both a string and a pure clamped–clamped beam. Only first, second, third, and fifth modes are compared because the fourth mode is not discernible in the experimental results. The normalized frequencies from the measurements lie between two theoretical cases, which indicate that the beam vibrates neither like a string nor a pure clamped–clamped beam.

D. Piezomembrane

As shown in Fig. 10, the sensitivity of the piezofilm is about 30 mV/μm, which is not very high. This is largely because when the beam vibrates, the membrane is compressed/extended at the edge but is extended/compressed in the middle of the beam. Charges generated by these contradictory deformations partly cancel each other, reducing the piezosensitivity. A possible solution would be to attach the piezomembrane only at the edge of the beam. Lechner (Lechner, 1993) employed this design in his piezosensor.

VI. CONCLUSIONS

We have presented the construction, measurements, and the modeling of an artificial cochlea. The measurement results from this ACochlea demonstrate some cochlea-like features. The modeling results for both the ABM and the ACochlea show patterns similar to their experimental counterparts. Thus, we believe that we know how to evaluate the incorporation of various materials, rather than build a new ACochlea for every material proposed.

Future work is needed to make the ACochlea useful as a practical acoustic sensor. A large width gradient of the ABM will help increase its stiffness gradient and thus the frequency range of the ACochlea, which is likely a critical performance criterion. The tension on the membrane substrate both affects longitudinal coupling and reduces the ABM stiffness gradient. Both factors will deteriorate the frequency selectivity of our ACochlea. Materials and fabrication processes are needed to produce a membrane substrate with minimum tension. Additionally an artificial middle ear is needed to convert acoustic signals into a vibrating driver, eliminating the need for the piezostack driver, while properly matching the low impedance acoustic interface to the high impedance fluid interface of the ACochlea. A cover on the lower side of the Acochlea, creating a closed, water tight, underside channel using a cover would have virtually no effect on performance.

ACKNOWLEDGMENTS

The authors would like to thank two anonymous reviewers for their relevant comments. This work was supported by DARPA Contract No. N0001400C0314 and NIH Grant No. R01 DC00029.

[1]Note that in this paper, we limit the usage of the word "model" only to refer to the computational model. Any mechanical cochlear model will be identified as a mechanical cochlea, or an artificial cochlea, or simply ACochlea.

Chadwick, R. S., and Adler, D. (**1975**). "Experimental observations of a mechanical cochlear model," J. Acoust. Soc. Am. **58**, 706–710.

Chen, F. (2005). "A hydro-mechanical biomimetic cochlea: experiments and models" Ph.D dissertation, Boston University.

Dallos, P. (**1996**). "Overview: cochlear neurobiology," in *The Cochlea*, edited by P. Dallos, A. N. Popper, and R. R. Fay (Springer-Verlag, New York), Vol. 8, pp. 1-5.

Haronian, D., and MacDonald, N. C. (**1996**). "A micromechanics-based frequency-signature sensor," Sens. Actuators, A **53**, 288–298.

Hemmert, W., Durig, U., Despont, M., Drechsler, U., Genolet, G., Vettiger, P., and Freeman, D. M. (**2003**). "A life-sized, hydrodynamical, micromechanical inner ear," in *Biophysics of the Cochlea: From Molecules to Models*, edited by A. W. Gummer (World Scientific, Singapore), pp. 409–416.

Hubbard, A. E., and Mountain, D. C. (**1996**). "Analysis and synthesis of cochlear mechanical function using models," in *Auditory Computation*, edited by H. L. Hawkins, T. A. McMullen, A. N. Popper, and R. R. Fay (Springer-Verlag, New York), Vol. 6, pp. 62–120.

Lechner, T. P. (**1993**). "A hydromechanical model of the cochlea with nonlinear feedback using PVF2 bending transducer," Hear. Res. **66**, 202–212.

Leong, M. P., Jin, C. T., and Leong, P. H. (2003). "*An FPGA-based electronic cochlea*," EURASIP Journal on Applied Signal Processing **7**, 629–638.

Lim, K. M., Fitzgerald, A. M., Steele, C. R., and Puria, S. (**2000**). "Building a physical cochlear model on a silicon chip," in *Recent Developments in Auditory Mechanics*, edited by H. Wada, T. Takasaka, K. Ikeda, K. Ohyama, and T. Koike (World Scientific, Singapore), pp. 223–229.

Lyon, R. F., and Mead, C. (**1988**). "An analog electronic cochlea," IEEE Trans. Acoust., Speech, Signal Process. **ASSP–36**, 1119–1134.

Patuzzi, R. (**1996**). "Cochlear micromechanics and macromechanics," in *The Cochlea*, edited by P. Dallos, A. N. Popper, and R. R. Fay (Springer-verlag, New York), Vol. **8**, pp. 186–257.

Peterson, L. C., and Bogert, B. P. (**1950**). "A dynamic theory of the cochlea," J. Acoust. Soc. Am. **22**, 369–381.

Tanaka, K., Abe, M., and Ando, S. (1998). "*A novel mechanical cochlea fishbone with dual sensor/actuator characteristics*," IEEE/ASME Trans. Mechatron. **3**, 98–105.

Tonndorf, J. (**1959**). "Beats in cochlear models," J. Acoust. Soc. Am. **31**, 608–619.

von Bekesy, G. (**1960**). *Experiments in Hearing* (McGraw-Hill, New York).

Wever, E. G. (**1938**). "The width of the basilar membrane in man," Ann. Otol. Rhinol. Laryngol. **47**, 37–47.

White, R. D., and Grosh, K. (**2002**). "Design and characterization of a MEMS piezoresistive cochlear-like acoustic sensor," *IMECE'02, 2002 ASME International Mechanical Engineering Congress and Exposition*, New Orleans, LA.

White, R. D., and Grosh, K. (**2005**). "Microengineered hydromechanical cochlear model," Proc. Natl. Acad. Sci. U.S.A. **102**, 1296–1301.

Wittbrodt, M. J., Steele, C. R., and Puria, S. (**2004**). "Fluid–structure interaction in a physical model of the human cochlea," *148th Meeting of the Acoustical Society of America*, San Diego, CA.

Yang, Z. (2004). "Low-frequency analog integrated circuit design using current-mode techniques," Ph.D dissertation, Boston University.

Zhou, G., Bintz, L., Anderson, D. Z., and Bright, K. E. (**1993**). "A life-sized physical model of the human cochlea with optical holographic readout," J. Acoust. Soc. Am. **93**, 1516–1523.

Zwislocki, J. (**1950**). "Theory of the acoustical action of the cochlea," J. Acoust. Soc. Am. **22**, 778–784.

Auditory-nerve first-spike latency and auditory absolute threshold: A computer model

Ray Meddis[a)]
Centre for the Neural Basis of Hearing at Essex, Department of Psychology, University of Essex, Colchester, CO4 3SQ, United Kingdom

(Received 30 June 2005; revised 25 October 2005; accepted 25 October 2005)

A computer model of the auditory periphery was used to address the question of what constitutes the physiological substrate of absolute auditory threshold. The model was first evaluated to show that it is consistent with experimental findings that auditory-nerve fiber spikes can be predicted to occur when the running integral of stimulus pressure reaches some critical value [P. Heil and H. Neubauer, J. Neurosci. **15**, 7404–7415 (2001)]. It was then modified to examine two ways in which the accumulation and clearance of receptor presynaptic calcium might explain this effect. Both methods gave results that matched the animal data. It was also shown how the rate of clearance of presynaptic calcium could be used to explain the origin of differences between low and high spontaneous-rate fiber types. When spiking activity is aggregated across a number of similar high spontaneous-rate fibers and used as the input to a model of a cochlear nucleus coincidence neuron, its response can be used to judge whether or not a stimulus is present. A simulated psychophysical experiment then demonstrated that this simple decision procedure can reproduce measurements of absolute auditory threshold for tones in quiet where the threshold is a joint function of both time and level. [DOI: 10.1121/1.2139628]

PACS number(s): 43.64.Bt, 43.64.Ld, 43.66.Ba, 43.66.Cb [BLM] Pages: 406–417

I. INTRODUCTION

The physiological basis of auditory absolute threshold is not known. Psychophysical thresholds are lower for longer stimuli and must therefore involve some kind of integration across time (see Eddins and Green, 1995 for a review). The physiological nature and anatomical location of this integrator is also unknown, and this is a major problem for computer models of the auditory system that seek to explain psychophysical phenomena in terms of a physiological substrate.

A number of studies in mammals (Clock *et al.*, 1998; Gersuni, 1965; Viemeister *et al.*, 1992) have used 2 interval, 2 alternative forced-choice (2I2AFC) paradigms to estimate absolute threshold on the basis of auditory-nerve (AN) fiber spike counts. These estimates show a similar trading relationship between stimulus level and duration to that found in behavioral measurements. Clock *et al.* (1993) used a similar paradigm but based threshold estimates on the spike counts of primary-like and chopper neurons in the ventral cochlear nucleus (CN) and showed a decline in threshold between stimulus durations of 8 and 128 ms. These animal studies show that the AN and CN responses are consistent with the phenomenon of temporal integration at absolute threshold. However, they do not identify the nature or location of the integrator. These experiments also carry the implication (but do not prove) that the temporal integration takes the form of spike counting at some anatomical location more central than the AN or CN.

However, Heil and Neubauer (2001) have presented evidence of a long-duration (>100 ms) example of temporal integration occurring at a very early stage in the auditory processing sequence, probably as early as the inner hair cell (IHC). Using single-fiber AN recordings, they showed that the latency to the first spike following stimulus onset is a function of both the amplitude and onset duration of the stimulus. For example, if two pure-tone stimuli have equal amplitudes but onset ramps of different duration, the stimulus with the shallower ramp will produce a later first spike. Heil and Neubauer showed that the best predictor of first-spike latency was the running integral of the stimulus pressure envelope. The first spike occurred when this integral reached a critical value, T_c (see Fig. 1). This critical value was consistent over time within a single fiber but varied meaningfully between fibers; for example, it was higher for low spontaneous rate (LSR) than for high spontaneous rate (HSR) fibers.

Heil and Neubauer (2003) went on to argue that the time constants of integration revealed by their observations were similar to those observed in the measurement of auditory thresholds. They make the radical argument that the temporal integrator is located *before* the AN. The computer modeling study below aims to demonstrate in physiological terms how temporal integration at this early stage could give rise to the time/duration trade-off observed in behavioral studies of absolute threshold.

Heil and Neubauer reasoned that the integrator must involve the accumulation of presynaptic calcium in the IHC. During acoustic stimulation, the receptor potential rises and calcium flows proportionately into the IHC in its presynaptic regions. It is this calcium that promotes the release of transmitter substance that initiates a postsynaptic action potential in the auditory-nerve fiber. This process constitutes a "leaky integrator" because the calcium is cleared from the presyn-

a)Electronic mail: rmeddis@essex.ac.uk

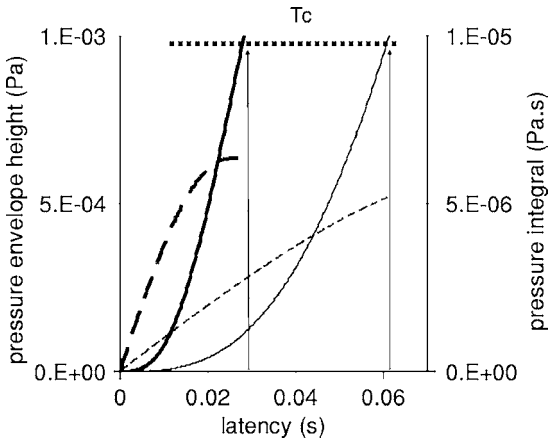

FIG. 1. General scheme of pressure integration paradigm. Dashed lines show two stimulus ramps (pressure: left ordinate). Continuous lines show the integral of stimulus pressure (pressure × time: right ordinate) for the two ramps. Predicted latency is the time, L, at which the integral of the pressure exceeds a critical threshold value, T_c.

aptic region almost (but not quite) as quickly as it arrives. They reasoned that the difference between LSR fibers and HSR fibers might be related to the rate at which the calcium builds up. In HSR fibers, it builds up quickly and this results in an early first spike. In LSR fibers the buildup of calcium is slower and the first spike is delayed.

It will be reported that this process was studied using an existing computer model of the auditory periphery (Sumner *et al.*, 2002, 2003a, 2003b, Holmes *et al.*, 2004, Meddis and O'Mard, 2005). The published model already incorporates a process where HSR fiber types were distinguished from LSR fiber types in terms of the rate of influx of calcium into the IHC. However, Heil and Neubauer also argue that it is not clear whether this faster accumulation of calcium in HSR fibers is the result of a higher rate of calcium influx into HSR synaptic regions or a slower rate of clearance. Both possibilities will be evaluated below and shown to be equally applicable. In the first "calcium influx" case, the published model was used. In the second "calcium clearance" case, the original model was used but different parameters were used to simulate the difference between fiber types.

It was then necessary to establish a direct connection between these processes and behavioral threshold. At first sight, this is straightforward. Near threshold, the first-spike latency will determine whether or not the stimulus provokes a detection decision. If the duration of the stimulus is shorter than the expected first-spike latency, then no spike will occur and the stimulus will be undetected. If, however, the same stimulus is presented at a greater intensity, the first spike will occur at an earlier time which is more likely to be before the end of the stimulus. In the absence of spontaneous activity, the detection of the stimulus could depend on a single spike occurring in a single fiber. Unfortunately, the fibers with the lowest thresholds are also the fibers with the highest rate of spontaneous activity (e.g., Liberman and Kiang, 1978; Winter *et al.*, 1990). This creates the problem of how the auditory system distinguishes between spontaneous spikes and stimulus-driven spikes.

In this computer modeling study, it is proposed that the problem can be solved by combining spikes across a group of similar AN fibers. In the proposed model, a number of model HSR AN fibers supply input to a model CN neuron that is configured as a "coincidence detector," one that responds only when a number of input spikes occur almost simultaneously. In quiet, the HSR fibers spike at random with respect to one another and do not trigger a response in the CN unit. When the AN fiber activity is driven by an acoustic stimulus, the spike activity is correlated. In particular, the first spikes will occur at similar times because similar fibers have similar expected first-spike latencies. As a consequence, spontaneous spikes will not cause a response in the CN unit, but stimulus-driven spikes will do so and the stimulus will be detected. It will be shown that this model displays the expected trade-off between stimulus level and duration when tested in a psychophysical 2I2AFC paradigm.

Only one other relevant modeling study has been published (Krishna, 2002). He used a more schematic computer model successfully to simulate first-spike latency data. His model was successful because it includes an explicit "integration module" with a critical threshold function. Although the model is physiologically inspired, this integration module was not associated with any specific physiological function except that the author explicitly *ruled out* the possibility that it could be calcium dynamics. This rejection was based on the grounds that the time constants of calcium dynamics were too short. The following study will show that this widely held objection is not well founded. Indeed, the rapid dynamics of presynaptic calcium are ideally suited to the long time scales of the first-spike latency effect.

II. COMPUTER MODEL

The input to the computer model of the auditory periphery is an arbitrary acoustic stimulus. Its output is a stream of spiking events in one or more parallel AN fibers all innervating the same location on the cochlear partition. The complete peripheral model consists of a cascade of six stages estimating: (1) stapes velocity; (2) BM velocity; (3) IHC receptor potential; (4) IHC presynaptic calcium currents; (5) transmitter release events at the IHC-AN synapse; and (6) AN spiking response including refractory effects. The output of the peripheral model is used as input to a second model of a single cochlear nucleus chopper neuron. Throughout this study all AN fibers have a best frequency of 4 kHz and all stimuli are 4-kHz tones. The basilar-membrane response in this implementation of the model is linear up to 40 dB SPL. As a consequence, BM nonlinearity does not feature in the evaluation of absolute threshold where most stimuli are presented well below this level.

A complete description of the model equations and parameters is given in the Appendix. Except where specified, all equations and parameters are exactly as specified in the most recent previously published evaluations of the component modules. The model was implemented using routines from a library of C-code modules in the Development System for Auditory Modeling (DSAM) which is published by

the University of Essex, UK. The full model of the auditory periphery was implemented as a program sequence using the AUDITORY MODELLING SYSTEM (AMS) application.[1] The MATLAB programming language was used to create the sequence of stimuli, to initiate a model run, and to collect, analyze, and display the results. The model was evaluated at a sampling rate of 100 kHz.

A. Presynaptic calcium

Two models of calcium dynamics are evaluated below. The first model (calcium influx) identifies the difference between AN fiber types in terms of different rates of influx of calcium into the cell and assumes, for example, that LSR fibers have the lowest rate of calcium influx for a given receptor potential. The second model (calcium clearance) assumes a fixed rate of influx for all fiber types, but defines the differences between fibers in terms of the rate at which calcium is cleared from the presynaptic site. LSR fibers, for example, have the fastest rate of clearance of presynaptic calcium.

1. Calcium influx model

Calcium concentration, $[Ca^{2+}](t)$, is modeled as a first-order low-pass filtered function of the trans-membrane calcium current, $I_{Ca}(t)$

$$\frac{d[Ca^{2+}](t)}{dt} = I_{Ca}(t) - [Ca^{2+}](t)/\tau_{Ca}, \tag{1}$$

where τ_{Ca} is the time constant of calcium clearance and

$$I_{Ca}(t) = G_{Ca}^{max} m_{I_{Ca}}^3(t)(V(t) - E_{Ca}), \tag{2}$$

where $V(t)$ is the receptor potential, E_{Ca} is the reversal potential for calcium, and G_{Ca}^{max} is the maximum calcium conductance in the vicinity of the synapse, $m_{I_{Ca}}(t)$ is the fraction of calcium channels that are open and is a function of the receptor potential (see the Appendix for the determination of $m_{I_{Ca}}$). The probability that an available transmitter vesicle will be released into the synaptic cleft is proportional to the cube of the $[Ca^{2+}]$ concentration

$$k(t) = \max(([Ca^{2+}]^3(t) - [Ca^{2+}]_{thr}^3)z, 0), \tag{3}$$

where z is a scalar and $[Ca^{2+}]_{thr}^3$ is a threshold parameter. Both G_{Ca}^{max} and $[Ca^{2+}]_{thr}^3$ are changed when modeling the difference between LSR and HSR fibers. This model is unchanged from its previously published form.

2. Calcium clearance hypothesis

Evaluation 2 investigates Heil and Neubauer's proposal that differences between AN fibers might alternatively be explained in terms of differences in the rate of calcium clearance. To evaluate this proposal the same model was used except that the time constant of calcium clearance, τ_{Ca}, was changed when modeling the difference between fibers, while G_{Ca}^{max} was held constant and $[Ca^{2+}]_{thr}^3$ was set to zero. This allows us to simplify Eq. (3) so that the relationship between calcium levels and transmitter release is more transparent.

$$k(t) = z\,Ca^3(t). \tag{4}$$

In this version, only τ_{Ca} ic changed when modeling the difference between LSR and HSR fiber types.

III. EVALUATION 1: CALCIUM INFLUX MODEL

Heil and Neubauer (2001, 2003) measured the "latency to first spike" of single AN fibers in cat in response to pure tones. Both the level of the tones and the steepness of the onset ramp were varied. The following demonstration replicates their experimental procedure in detail using the computer model of the guinea pig periphery. Model parameters were unchanged from Sumner *et al.*, 2002, 2003a and 2003b, but incorporated small changes described in Meddis and O'Mard (2005). All parameters are given in the Appendix and the rate/level functions for this model are shown in Fig. 3(A) (below).

Pure-tone stimuli at BF (4 kHz) of 200-ms duration were shaped with cosine-squared rise and fall functions with seven different rise times equally spaced on a log scale between 1.7 and 170 ms. They were presented at levels that varied between 0 and 90 dB SPL in 10-dB steps. Each stimulus was presented 20 times and the mean latency to first spike was measured for each presentation. Latencies were measured between the beginning of the stimulus onset ramp and the first spike that occurred after that time. If no spike occurred before the end of any stimulus on any of the 20 trials, the mean latency for that combination of level and ramp duration was treated as indeterminate. Each trial began with a 50-ms period of silence which was used to assess the spontaneous firing rate. Figure 2 (top row) shows model first-spike latencies measured as a function of both level and ramp duration.

Heil and Neubauer showed that the mean latencies (L) for the animal data could be predicted, L_{pred}, by the sum of two quantities, L_{min} and L_c, where L_{min} is a minimum latency common to all measurements for that fiber and L_c is the delay before the integral of the pressure envelope reaches a critical threshold value T_c (measured in Pa s). These two free parameters, L_{min} and T_c, were estimated by finding the least-squares best fit between the logarithms of the predicted and actual latencies (see Heil and Neubauer, 2001, for a full account of the relevant procedures and justification). Measured latencies were used in the calculations only if these were shorter than half the average interval between spikes during spontaneous activity. Figure 2 (bottom row) plots the actual latencies of the present model against the latencies predicted by Heil and Neubauer's formula as a function of tone level and ramp duration.

HSR, MSR, and LSR model fibers all show the expected effect and the plots are virtually identical with those given by Heil and Neubauer [2001, Figs. 2(B), 5(A)–(D), 6(A) and (C)]. The small deviations from the predicted line (diagonal) for short and long predicted latencies are also a characteristic of the animal data [Heil and Neubauer, 2001, Figs. 6(A) and (C)] and are not a shortcoming of the model. These deviations reflect the fact that the calcium integration system is "leaky" and, as a consequence, is not a perfect integrator of stimulus pressure. Heil and Neubauer [2001, Fig. 8(D)] ob-

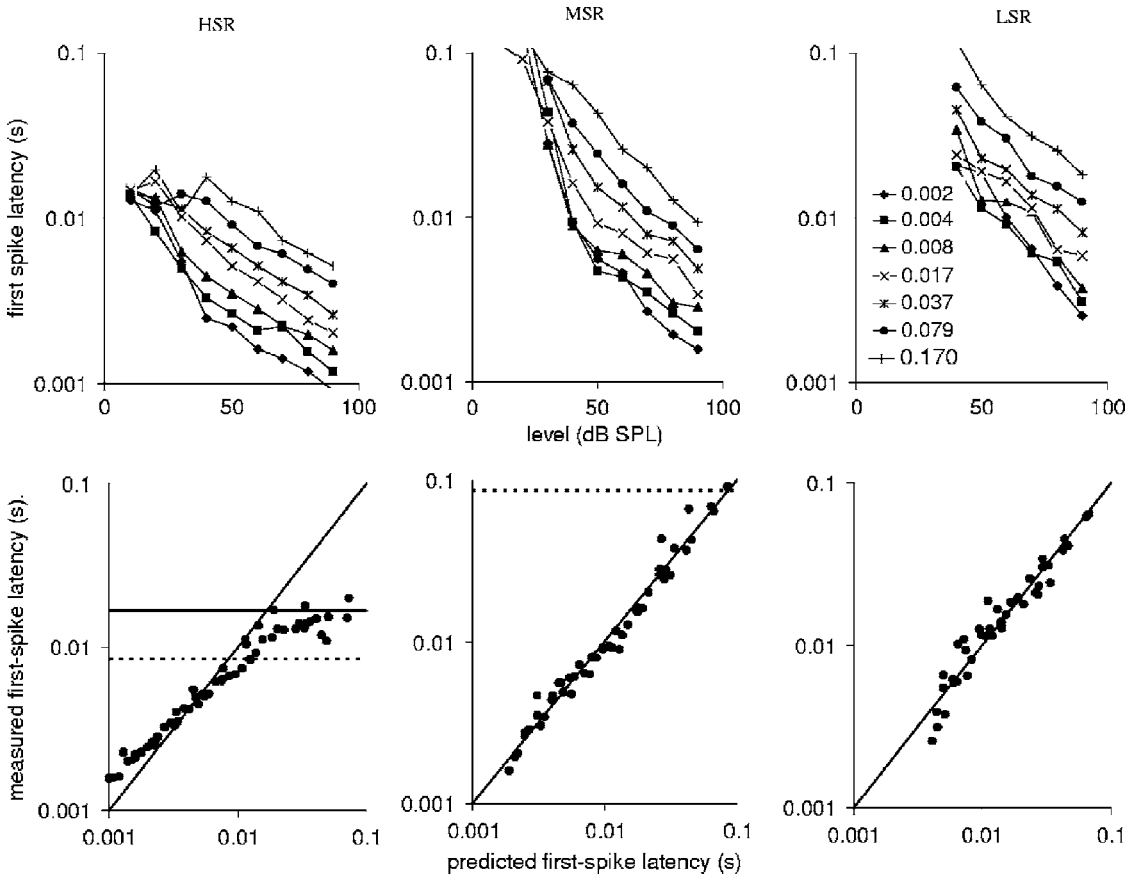

FIG. 2. Model AN first-spike latencies using the calcium influx model for HSR, MSR, and LSR fiber types. Top row: first-spike latencies as a function of tone level (x axis) and onset ramp duration (see the legend). Bottom row: first-spike latencies as a function of predicted latencies using the prediction function $L_{\text{pred}}=L_{\text{min}}+L_c$ (see the text). The horizontal continuous line represents the expected latency during spontaneous activity (1/spontaneous rate). Horizontal dotted lines indicate the cutoff criterion for omitting data from the best-fit analysis for the prediction function. The best-fit values for L_{min} are 1, 2, and 3 ms for HSR, MSR, and LSR fibers, respectively. The corresponding values for T_c are 5.3E-6, 1.7E-5, and 1E-4 Pa s.

tained critical threshold integrals (T_c) in the region 1E −7 to 1E−4 Pa s. The values shown in Fig. 2 are comfortably within that region. They also found that T_c was greater for LSR than HSR fibers. This was also true of the model data.

IV. EVALUATION 2: CALCIUM CLEARANCE MODEL

Heil and Neubauer speculated that the rate of clearance of calcium from the presynaptic region might also be a critical parameter determining first-spike latency, and that the variation in spontaneous rate across nerve fibers might be explained in terms of differences in the rate of calcium clearance. In the calcium influx model, the calcium clearance time constant (τ_{Ca}) is fixed while the rate of calcium influx per unit of time varies across fiber types. To test the new hypothesis (that influx is fixed while τ_{Ca} varies across fiber types), the model was run again varying τ_{Ca} while holding other parameters constant.

Figure 3 shows the rate-level function for both the original calcium influx model and the calcium clearance version of the model. The results show that both models give a useful account of the differences between fiber types similar to

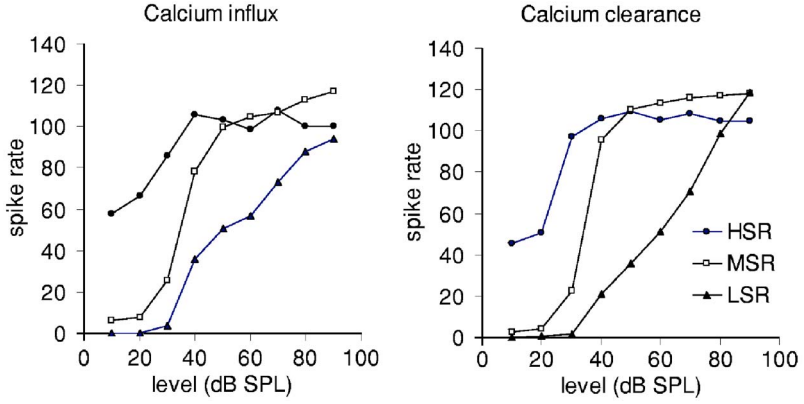

FIG. 3. Rate-level functions for the original and modified calcium influx models. Rate is based on all spikes during presentation of a 200-ms pure tone presented at CF (4 kHz). Tones had a 17-ms cosine-squared onset ramp. In the calcium clearance model, τ_{Ca} values were 0.35, 0.15, and 0.075 ms for HSR, MSR, and LSR fibers, respectively.

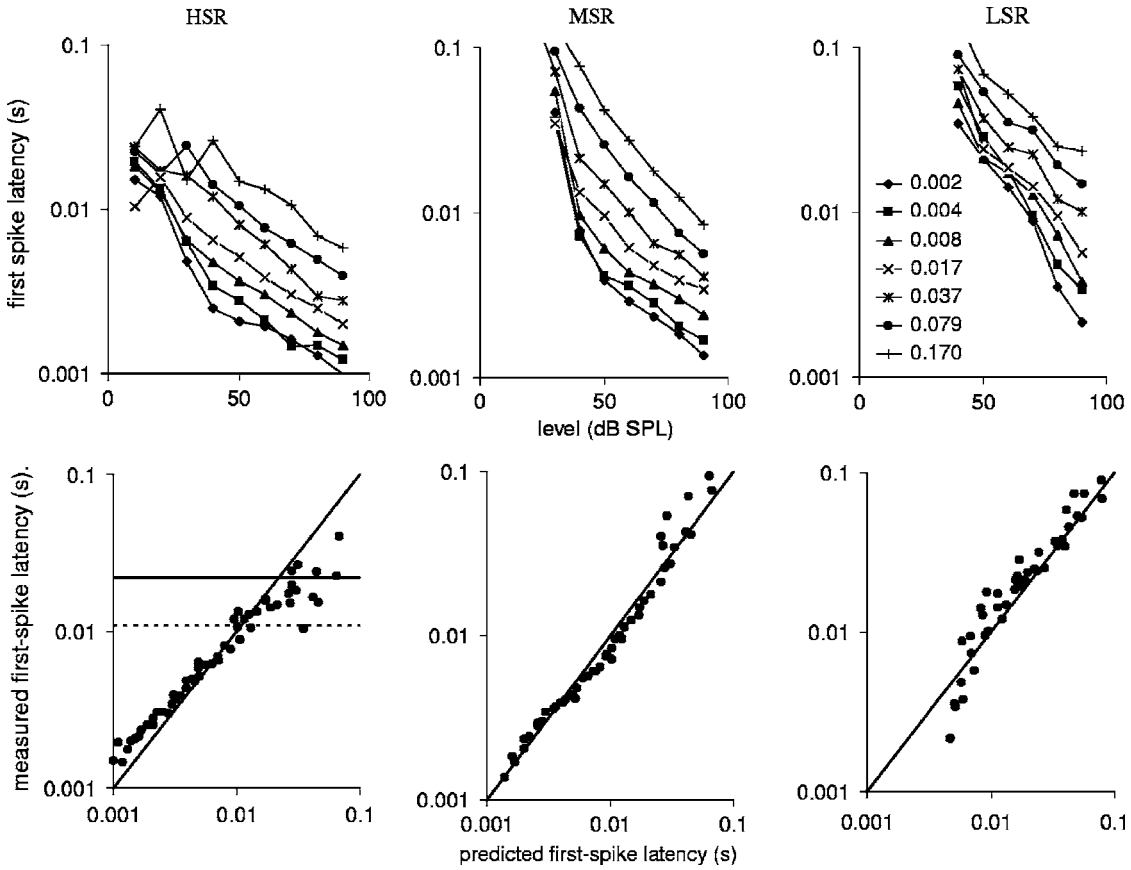

FIG. 4. Model first-spike latency using the calcium clearance model for HSR, MSR, and LSR fiber types. (See Fig. 2 for explanation). The best-fit values for $L_{\min}$ are 1, 1, and 6 ms for HSR, MSR, and LSR fibers, respectively. The corresponding values for T_c are 5.3*E*-6, 1.7*E*-5, and 1*E*-4 Pa s.

those observed in laboratory studies. HSR fibers have higher spontaneous rates, a lower rate threshold, and a lower saturation threshold than LSR fibers. The differences in the shape of the rate-level functions are similar to the differences observed between LSR and HSR fibers in mammalian physiological studies (Liberman and Kiang, 1978; Winter *et al.*, 1990).

First-spike latency data for the same three fiber types are shown in Fig. 4. They show the same pattern as the data in Fig. 2. Once again, the critical pressure integral required to fit the response of the modified model lies within the range observed by Heil and Neubauer and the critical pressure integral, T_C, increases across the HSR-LSR spectrum. In conclusion, both the calcium-influx model and clearance models are able to simulate both the first-spike latency effect and the differences between fiber types. They are, therefore, both candidate explanations in terms of presynaptic calcium dynamics.

The central difference between the two models is, of course, an empirical issue. The question as to whether the low spontaneous firing rate of LSR fibers is caused by different rates of clearance or different rates of calcium influx is more properly decided by further laboratory observation. In evaluations 3 and 4 below, both models were tested and gave approximately the same results. The illustrations below use only the calcium-clearance model for the only reason that it is slightly simpler. By dispensing with the calcium threshold parameter, $[Ca^{2+}]^3_{thr}$, it requires only one parameter to distinguish HSR and LSR fibers while the calcium influx version uses two [see Sumner *et al.* (2002, Fig. 5)].

For both models, it should also be noted that the critical threshold integral, T_c, as estimated from the first-spike latencies, is *not* a parameter of the model but an emergent property. When the presynaptic calcium level rises, the probability of release of a transmitter vesicle rises as a function of the third power of the calcium level. As a consequence, the probability of a release event increases very rapidly. However, there is no "trigger" calcium threshold, *per se*, in the model, only the *appearance* of one.

V. EVALUATION 3: COINCIDENCE DETECTION

The first-spike latency data provide evidence that temporal integration of a kind is taking place at an early stage in the auditory system. The integration takes place over relatively long time periods (more than 100 ms). This suggests that the first-spike latency might be related to the temporal integration observed in psychophysical studies. One possibility is that the nervous system fails to detect low-intensity, short sounds because the time taken to accumulate enough presynaptic calcium to initiate a spike is greater than the duration of the signal. If the signal is too weak or too short, no spike is initiated before the end of the signal and no detection occurs.

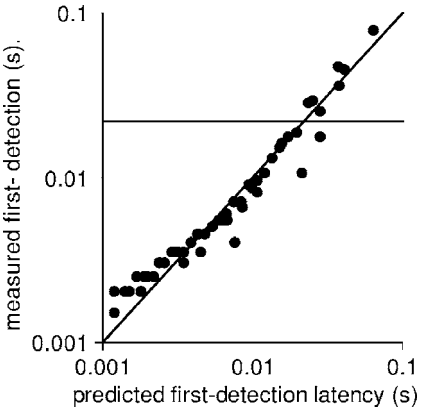

FIG. 5. First-spike latency of a model *CN coincidence neuron* plotted against predicted first-spike latency. The neuron receives input from 20 model HSR fibers. The horizontal continuous line is the "expected latency" (1/spontaneous rate) of the AN fibers used as input.

The next stage of the model addresses the problem of how to distinguish spontaneous AN spikes from spikes that are stimulus driven using the principle outlined in the Introduction. The model is extended so that 20 HSR AN model fibers are used as input into a coincidence-detector neuron. This consists of two stages; a low-pass filter to simulate dendritic smoothing followed by a simple computer model of the neuron soma (MacGregor, 1987) described in the Appendix and elsewhere (Hewitt and Meddis, 1993; Wiegrebe and Meddis, 2004). This unit has a spontaneous rate of 1.5 spikes/s. When acoustically stimulated, it responds with a sustained chopper firing pattern. The dendritic filter has a low-pass cutoff of 200 Hz which equates to a time constant of approximately 0.7 ms. As a result, the CN unit responds only when the input fibers generate spikes very close together in time. This is roughly equivalent to a previous implementation of the same principle (Meddis and O'Mard, 2005) where the inputs were simply aggregated into 0.5-ms bins and a minimum count criterion applied.

In this evaluation, the protocol of stimulus presentation is exactly the same as that used in evaluations 1 and 2 except that latency is based on the first spike produced by the CN neuron. The results are shown in Fig. 5 where the diagonal line shows the predicted latency estimated using the same procedure used earlier with AN fibers. The coincidence latencies are a good fit to the prediction, and the correspondence between predicted and actual latencies shows a greatly extended temporal range. For HSR AN fibers the relationship between first-spike latency and pressure integral is valid only up to approximately 10 ms (see Fig. 4). This is because the spontaneous activity of the fiber introduces an upper limit to the length of intervals occurring between successive spikes. When the coincidence criterion is used, this limitation is removed because the coincidence neuron does not respond to spontaneous AN spikes. The figure shows that the relationship remains valid up to at least 100 ms.

VI. EVALUATION 4: CN AND PSYCHOPHYSICAL THRESHOLDS

The results obtained in evaluation 3 suggest that the coincidence detection model might be capable of temporal integration over the longer time scales that characterize *psychophysical* paradigms. A low-intensity stimulus will produce a coincidence event with a long latency. If that stimulus is short, the coincidence event will not occur before its termination. As a result, the length of the signal will be critical in determining whether it is detected at all. To evaluate this possibility, the absolute threshold of the model was measured as a function of stimulus duration. The procedure was based as closely as possible on a 2I2AFC psychophysical experiment described by Florentine *et al.* (1988).

In the same evaluation, the model response is compared to the results of a corresponding animal study (Clock *et al.*, 1993) where CN unit responses were recorded in a 2I2AFC paradigm. They also drew attention to a statistical complication associated with the method of counting CN unit spikes. They began by assuming that the decision was made by an "ideal observer" with complete knowledge of the time of the onset and offset of the stimulus so that probe-spike counts were restricted to the time that the probe was on ("probe-count" measure). However, it cannot always be assumed that the decision process always knows exactly when a stimulus will occur or how long it will last. For example, in the experiment with human listeners, the stimuli (irrespective of their length) were presented during a 550-ms inspection window, and listeners would need to base their decision on spike activity throughout the whole period ("window-count" measure). The statistical nature of the decision is, in principle, different for the two measures. Clock *et al.* studied both approaches and both will be considered below.

Absolute thresholds were measured using a 2I2AFC paradigm following as closely as possible the protocol of Florentine *et al.* (1988). On each trial, two independent 550 -ms observation intervals were used; one silent interval and one containing a probe tone presented central to the observation window. The model's task was to use the output of the coincidence detection neuron to choose which interval contained the stimulus. Threshold measurements were made using a two-down, one-up adaptive procedure which converges on the signal level yielding 70.7%-correct responses (Levitt, 1971). The probe level started at 50 dB SPL and was reduced by steps of 5 dB until the first reversal, after which the step size was reduced to 2 dB. A run was terminated after five reversals and thresholds were calculated using the average level of the last two reversals. Stimuli were pure tones presented at CF (4 kHz) with rise times of 1 ms. Separate threshold estimates were made for signal durations of 2, 4, 8, 16, 32, 64, 128, 256, and 512 ms.

For each of the two observation intervals, the model made an independent decision as to whether a stimulus was or was not present. A "yes" decision was made if the neuron generated *at least one spike* during the counting period. Separate decisions were made for the stimulus and control condition. If only one interval generated a yes response, that interval was chosen. If the same decision was made for both intervals, either yes for both or "no" for both, the model chose one of the two alternatives at random. In the example below, the spontaneous rate of the CN neuron was very low (<2 spikes/s). Near threshold, the spike count was typically zero or 1. A special provision was made for occasions arising

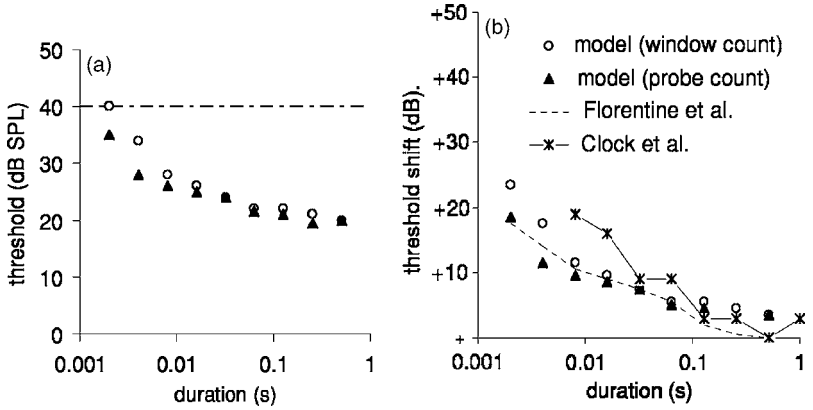

FIG. 6. (a) Absolute threshold of a model cochlear nucleus coincidence neuron as a function of signal duration. Thresholds are based on total spike counts in the 500-ms observation window (open circles) or exclusively when the probe was playing (filled triangles). Each threshold is the mean of 20 trials. Stimuli are CF (4-kHz) tones. The horizontal dotted line indicates the level at which basilar-membrane compression begins in the basilar-membrane stage of the model. (b) Threshold shift representation of the same data. Also shown are human data (Florentine *et al.*, 1988; dashed line) and animal CN unit thresholds (Clock *et al.*, 1993; asterisks). The human data are adjusted to give 0-dB shift at the longest duration. The model data are shifted so that the middle durations approximately match the human data. This emphasizes the slope differences at the longest and shortest durations.

at the beginning of the trial when the stimulus was well above threshold and the spike count for the stimulus-present condition was very large with respect to the stimulus-absent condition. In the event of a yes/yes outcome when the discrepancy in the counts was very large, the decision was given in favor of the window yielding the larger count in order to move the stimulus level more quickly towards the threshold region. Once in the threshold region, this principle was no longer needed.

The model was exactly the same as that described in evaluation 3. Figure 6(a) shows absolute threshold as a function of signal duration based on both methods of calculating spike counts (see above). Threshold decreases monotonically between 2 and 512 ms. All but one of the thresholds are below the compression threshold for the basilar-membrane simulation (horizontal dotted line). Nonlinearity of response was, therefore, unlikely to contribute to the determination of the threshold. The probe-count and window-count datasets are similar except at very short durations when the precise knowledge of the time and duration of the stimulus produces a small but consistent reduction of threshold.

Figure 6(b) compares the same data with the psychophysical thresholds of Florentine *et al.* (1988, Fig. 1; mean of five listeners) and the physiological measurements of Clock *et al.* (1993) based on single unit measurements in the CN. The model data have been adjusted slightly so that they are close to the human data in the mid-duration range. The model data fit the human data reasonably well up to 64 ms. Both the model and the human data have roughly level functions at very long durations. However, the leveling begins earlier for the model data. It is difficult to know how significant these differences are. The reduction in threshold between 100 and 500 ms is very small for the psychophysical data nine other studies reviewed by Florentine *et al.* (1988) are inconsistent in this region.

Clock *et al.* speculated that the spike counts based on the probe period alone might be subject to a statistical artifact because the observation window was changing in size across different signal conditions. They measured the mean (M) and standard deviation (SD) statistics of spike counts and found that the ratio SD/M decreased with duration up to 128 ms and then leveled out at long durations. This means that an "ideal observer" who takes advantage of knowledge of the time of occurrence of the probe should show an improved ability to distinguish between signal and noise up to 128 ms. This is consistent with the model response where the probe count showed lower thresholds for the shortest stimuli. The best fit to human data at short durations is obtained using the probe-count method and is, therefore, consistent with the idea that the human observer is taking advantage of knowledge of the expected time and duration of delivery of the probe during the observation window.

VII. DISCUSSION

Evaluation 1 showed that a previously published model of IHC synapse function could simulate the basic first-spike latency findings of Heil and Neubauer (2001). The model first-spike latency could be predicted on the basis of the integral of the stimulus pressure envelope between the onset of the tone stimulus and the time of the first spike. The pressure integral (T_c) at which the first spike typically occurred was lower for HSR than LSR fibers. This is also in agreement with the animal data. The model latencies can be attributed to the accumulation of presynaptic calcium during tone presentation. The effect was shown to operate at least up to tone durations of 200 ms.

Evaluation 2 modified the model so that fiber type was controlled using the rate of clearance of calcium from the presynaptic region. This model generated realistic rate-level functions for the different fiber types and was also able to simulate the first-spike latency data. In terms of performance, there was little to distinguish the two models. However, the modified model gave a simpler account of the IHC calcium dynamics and dispensed with the use of a specific threshold parameter. As a consequence, it is easier to see that the threshold differences between the fiber types are emergent properties rather than fixed properties of the model. In gen-

eral terms, the modeling work supports the conjecture of Heil and Neubauer that first-spike latency is determined by the accumulation of presynaptic calcium, but it does not help decide whether these differences are caused by different rates of calcium influx or clearance. It does show, however, that both possibilities are worthy of further investigation.

Evaluation 3 linked first-spike latency with absolute perceptual threshold by extending the model to include a CN coincidence neuron whose input was 20 HSR fibers. The neuron was tuned to be all but unresponsive to uncorrelated spontaneous activity but responsive to correlated stimulus-driven activity. CN latencies also showed a strong relationship to integrated pressure. However, this relationship remained valid over longer stimulus durations in the CN model than with the AN HSR fiber model. A relationship to integrated pressure was visible up to 100 ms in this test.

Evaluation 4 explored a possible link between AN first-spike latency and absolute perceptual threshold by simulating a psychophysical experiment (Florentine *et al.*, 1988) but substituting the model CN unit for the human listener. The model data were similar in number of respects to the human data. While the meaning of the correspondence can easily be overstated, it is clear that a coincidence detecting neuron receiving input from similar HSR fibers could show temporal integration up to 500 ms. The slope of the threshold-duration function is, however, less steep than the psychophysical data after 64 ms. The modeling result is similar to the measurements of Clock *et al.* (1993) in the CN.

This evaluation also addresses the more general issue of detecting isolated stimuli where the system has little prior knowledge of the stimulus timing. In a probe-count (ideal observer) condition, it was assumed that the system knew exactly when the stimulus will occur and how long it would be. In contrast, a window-count method assumed only that a stimulus of unknown duration would occur within a period of time that might be considerably longer than the stimulus. The probe-count approach produced lower thresholds for shorter stimuli than the window-count method but both showed a similar trading relationship between duration and level.

Until recently, it has been a common view that temporal integration must take place relatively late in the auditory processing sequence because the long duration of the integration period contrasts with the short time constants typically found in peripheral physiological processes. However, this is based on a misunderstanding; "leaky integrator" systems with short time constants are capable of integrating over long time periods if the input rate is rising and the time constant of clearance is fast.

A possible counterexample to the hypothesis modeled here is the finding of Gerken (1979) that the behavioral threshold in cat for brief electrical pulses delivered to electrodes in the CN of a cat decreased by 7.6 dB per tenfold (1.5 dB per octave) increase in the number of pulses. If this involves the same mechanism as psychophysical auditory temporal integration, then it would firmly locate the integration mechanism *after* the IHC/AN synapse, and the relationship between first-spike latency and integrated pressure could be seen as irrelevant. Unfortunately, the pulse data are open to a range of interpretations. One is that each threshold level pulse (taken as a separate entity) is associated with a small probability of eliciting a detection. As the number of pulses is increased, the probability that *at least one* pulse will be detected will increase proportionately. Accordingly, any interpretation of these data in terms of temporal integration should be treated with caution.

In this study, a sustained chopper unit was used as the decision neuron in the cochlear nucleus. Clock's results show that both primary-like and chopper units show the time-duration trade-off, and either could have been chosen for this project. The chopper unit also had the convenience of a low spontaneous rate (1.5 sp/s), which made it easier to illustrate the application of the coincidence principle. Nothing in this study rules out other possibilities.

Of course, the presence of any spontaneous activity in the decision unit will render the detection process less reliable. In principle, at least, additional decision reliability can be achieved by repeating the coincidence-detection process at a higher level, such as the inferior colliculus, so that the higher unit is insensitive to spontaneous activity in the CN. This may be part of the explanation as to why both the animal CN data and the model CN data did not show the expected decline in threshold beyond stimulus durations of 64 ms. The small amount of spontaneous activity would be expected to produce some random spike events during these longer stimuli and to raise thresholds proportionately.

However, the primary purpose of this study is not to identify the specific circuits involved but to show that the psychophysical data on thresholds for tones in silence are consistent with the idea that some temporal integration takes place in the IHC rather than later in the processing chain. In this respect, the current modeling exercise using only one CN neuron is primarily a practical demonstration that the temporal integration underlying thresholds in quiet might be taking place as early as the IHC. Neuronal processes subsequent to the AN are used in the model but theirs is a *decision function*. In the model at least, the temporal integration is complete before the AN.

The term "temporal integration" is used in psychophysics with reference to a wide range of suprathreshold phenomena (such as gap detection, loudness, and sensitivity to amplitude modulation) and also to the numerous theories that have been proposed to explain them (Eddins and Green, 1995). This model study concerns itself exclusively with the detection of pure tones in silence, and it is not suggested here that the calcium dynamics of the IHC can be used to explain the full range of phenomena in this class.

Empirical methods will eventually decide the question of what mechanisms underpin first-spike latency and psychophysical temporal integration at absolute threshold. However, the question of how we link the physiological substrate to absolute auditory threshold is a conceptual matter and well suited to exploration by modeling methods. The conventional view that equates the rate threshold of single AN fibers with behavioral threshold is clearly inadequate because threshold also depends on stimulus duration. The problem of stimulus detection near absolute threshold is further complicated by the presence of spontaneous activity in the nerve fiber. The

model evaluated here presents one solution to this problem by suggesting that the relevant units in the cochlear nucleus respond only when multiple AN fibers fire in synchrony. In this respect, it is convenient for the model that the temporal integration component has already taken place in the IHC/AN synapse. As a consequence, the level at which sound induces a response in at least one CN unit is a function of both time and level.

ACKNOWLEDGMENTS

This manuscript and the modeling has benefited substantially from the challenging and insightful comments of Brian Moore, Peter Heil, and Heinrich Neubauer on a much earlier version of this manuscript. Chris Sumner and Enrique Lopez-Poveda also contributed useful comments on a later manuscript. Lowel O'Mard contributed valuable computational support throughout.

APPENDIX: COMPUTATIONAL DETAILS

1. Middle-ear filtering

A cascade of two linear bandpass Butterworth filters was used to model the response of the guinea pig middle ear. The first filter is second order with an upper cutoff of 25 kHz and a lower cutoff of 4 kHz. The second filter is third order with upper- and lower-cutoffs of 30 and 0.7 kHz. Both have unit gain in the passband. The filter output is transformed into stapes velocity by applying a scalar of $1.4E{-}4$ m s^{-1} Pa^{-1}.

2. Mechanical filtering: DRNL filter

The filtering of the BM is modeled with a "dual-resonance-nonlinear" (DRNL) filter architecture that has been described and evaluated more fully elsewhere (Meddis *et al.*, 2001; Lopez-Poveda and Meddis, 2001; Sumner *et al.*, 2003b). The input is stapes velocity, $x(t)$. The DRNL filter consists of two parallel pathways, one linear and the other nonlinear, whose outputs are summed to produce an output, $v(t)$ representing the velocity of the cochlear partition in m s^{-1}.

The *nonlinear* pathway consists of the following cascaded sequence: (1) three identical first-order gammatone filters; (2) a compression function; (3) three more identical gammatone filters, and (4) four first-order Butterworth low-pass filters. The compression in the nonlinear pathway is described by

$$v_t = \mathrm{SIGN}(x_t) \times \mathrm{MIN}(a|x_t|, b|x_t|^{\upsilon}), \tag{A1}$$

where a and b are parameters specific to a particular BM location (see Table I). The compression exponent, υ, was 0.1. The *linear* pathway consists of the following cascaded sequence: (1) a gain function; (2) a cascade of three identical gammatone filters; (3) a cascade of four Butterworth low-pass filters. For both pathways the cutoff frequency of the low-pass filters was set to the CF of the corresponding gammatone filters.

TABLE I. Coefficients for computing parameters of the guinea pig DRNL filters as a function of CF_{nl}. Source: Sumner *et al.* (2003b).

$\log(\text{parameter}) = p_0 + m\log(CF_{nl})$	p_0	M
Bandwidth of nonlinear path, BW_{nl} (Hz).	0.8	0.58
Compression parameter, a	1.87	0.45
Compression parameter, b	−5.65	0.875
Center frequency of linear path, CF_{lin} (Hz).	0.339	0.895
Bandwidth of linear path, BW_{lin} (Hz).	1.3	0.53
Linear path gain, G_{lin}.	5.68	−0.97

The CF of the nonlinear path gammatone filters (CF_{nl}) is set to the desired CF of the filter as a whole. The other parameters of the system are set relative to CF_{nl} using the formula

$$\log(\text{parameter}) = p_0 + m\log(CF_{nl}). \tag{A2}$$

Table I shows the parameters p_0 and m used to compute the parameters a, b, the bandwidths of the component gammatone filters in linear (BW_{lin}) and nonlinear (BW_{nl}) pathways, the gain of the linear filter (G_{lin}), and the center frequency of the linear filter (CF_{lin}).

3. IHC receptor potential

The displacement of the IHC cilia, $u(t)$, as a function of BM velocity, $v(t)$, is given by

$$\tau_c \frac{du(t)}{dt} + u(t) = \tau_c C_{\mathrm{cilia}} v(t), \tag{A3}$$

where C_{cilia} is a gain factor and τ_c is a time constant. The cilia displacement determines the apical conductance $G(u)$. The total apical conductance is given by

$$G(u) = G_{\mathrm{cilia}}^{\max}\left[1 + \exp\left(-\frac{u(t)-u_0}{s_0}\right) \times \left[1 + \exp\left(-\frac{u(t)-u_1}{s_1}\right)\right]\right]^{-1} + G_a, \tag{A4}$$

where $G_{\mathrm{cilia}}^{\max}$ is the transduction conductance with all channels open, and G_a is the passive conductance in the apical membrane. s_0, u_0, s_1, and u_1 are constants determining the exact shape of the nonlinearity. G_a is computed as

$$Ga = G0 - G_{\mathrm{cilia}}^{\max}\left[1 + \exp\left(\frac{u_0}{s_0}\right)\left[1 + \exp\left(\frac{u_1}{s_1}\right)\right]\right]^{-1}, \tag{A5}$$

where $G0$ is the resting conductance. See Table II.

The membrane potential of the cell body is modeled with a passive electrical circuit analog

$$C_m \frac{dV(t)}{dt} + G(u)(V(t) - E_t) + G_k(V(t) - E_k') = 0, \tag{A6}$$

where $V(t)$ is the intracellular IHC potential; C_m is the cell capacitance; G_k is the voltage-invariant basolateral membrane conductance; E_t is the endocochlear potential; and $E_k' = E_k + E_t R_p/(R_t + R_p)$ is the reversal potential of the basal current E_k corrected for the resistance (R_t, R_p) of the supporting cells.

TABLE II. IHC receptor potential. Source: Sumner *et al.* (2002, Table I). Note that *s*1 was previously given incorrectly as $5E-7$.

Et, endocochlear potential (V)	$100E-3$
Ek, potassium reversal potential (V)	$-70.45E-3$
*G*0, resting conductance (S)	$1.974E-9$
Gk, potassium conductance (S)	$18E-9$
$Rp/(Rt+Rp)$, correction factor (Ω)	$40E-3$
$G_{\text{cilia}}^{\max}$, max. mechanical conductance (S)	$8E-9$
s_0, displacement sensitivity (m^{-1})	$85E-9$
u_0, displacement offset (m)	$7E-9$
s_1, displacement sensitivity (m^{-1})	$5E-9$
u_1, displacement offset (m)	$7E-9$
C_m, total capacitance (F)	$6E-12$
τ_c cilia/BM time constant (s)	$2.13E-3$
C_{cilia}, cilia/BM coupling gain (dB)	16

4. Calcium controlled transmitter release function

Depolarization of the IHC membrane leads to an increase in the calcium current, I_{Ca},

$$I_{\text{Ca}}(t) = G_{\text{Ca}}^{\max} m_{I_{\text{Ca}}}^3(t)(V(t) - E_{\text{Ca}}), \tag{A7}$$

where E_{Ca} is the reversal potential for calcium and $G_{\text{Ca}}^{\max}$ is the calcium conductance in the vicinity of the synapse, with all the channels open. $m_{I_{\text{Ca}}}(t)$ is the fraction of calcium channels that are open. Its steady state value, $m_{I_{\text{Ca}},\infty}$, is modeled by a Boltzmann function

$$m_{I_{\text{Ca}},\infty} = [1 + \beta_{\text{Ca}}^{-1} \exp(-\gamma_{\text{Ca}} V(t))]^{-1}, \tag{A8}$$

where β_{Ca} and γ_{Ca} are constants chosen to reflect published observations of calcium currents (see Table III), and $m_{I_{\text{Ca}}}(t)$ is a low-pass filtered function of $m_{I_{\text{Ca}},\infty}$

$$\tau_m \frac{dm_{I_{\text{Ca}}}(t)}{dt} + m_{I_{\text{Ca}}}(t) = m_{I_{\text{Ca}},\infty}, \tag{A9}$$

where τ_m is a calcium current time constant.

TABLE III. Parameters for control of presynaptic calcium levels. Source: Sumner *et al.* (2002, Table II).

		Calcium influx.	Calcium clearance
E_{Ca}, reversal potential (V)		0.066	0.066
β_{Ca}		400	400
γ_{Ca}		130	130
τ_m, calcium current time constant (s)		$1E-4$	$1E-4$
τ_{Ca}, calcium clearance time constant (s)			
	HSR	$1E-4$	$3.5E-4$
	MSR	$1E-4$	$1.5E-4$
	LSR	$1E-4$	$0.75E-4$
z, converts from $[Ca^{2+}]^3$ to probability		$2E33$	$2E42$
$G_{\text{Ca}}^{\max}$, maximum Ca^{2+} conductance			
	HSR	$7.2E-9$	$8E-9$
	MSR	$2E-9$	$8E-9$
	LSR	$1.6E-9$	$8E-9$
$[Ca^{2+}]_{\text{thr}}$, threshold			
	HSR	0	Not used
	MSR	$3.3E-14$	
	LSR	$1.4E-11$	

TABLE IV. IHC transmitter release parameters. Source: Meddis and O'Mard (2005).

y, replenishment rate (s^{-1})	3
l, loss rate (s^{-1})	2580
x, reprocessing rate (s^{-1})	30
r, recovery rate (s^{-1})	6580
M, maximum free transmitter quanta	10

Presynaptic calcium concentration $[Ca^{2+}](t)$ is modeled as a first-order low-pass filtered function of calcium current, $I_{\text{Ca}}(t)$. This has been changed slightly from the previous published formula to match units. This requires a change to $G_{\max}$ scalar but is otherwise equivalent.

$$\frac{d[Ca^{2+}](t)}{dt} = I_{\text{Ca}}(t) - [Ca^{2+}](t)/\tau_{[\text{Ca}]}, \tag{A10}$$

where τ_{Ca} is a time constant. The probability of the release of transmitter is proportional to the cube of $[Ca^{2+}]$ concentration

Original published model (calcium influx model):

$$k(t) = \max(([Ca^{2+}]^3(t) - [Ca^{2+}]_{\text{thr}}^3)z, 0), \tag{A11}$$

where $[Ca^{2+}]_{\text{thr}}$ is a threshold constant, z is a scalar for converting calcium levels into release rate.

In the calcium clearance model, the calcium threshold has been removed, leaving the the more transparent expression

$$k(t) = z\{[Ca^{2+}]^3(t)\}. \tag{A12}$$

See Table IV.

5. Quantal and probabilistic model of synaptic adaptation

More detailed accounts of transmitter release in a probabilistic form can be found in Hewitt and Meddis (1991) and Sumner (2002, 2003a, and 2003b). A description of the quantal version is found in Sumner (2002).

Individual vesicles of neurotransmitter (probably glutamate) are released from an *immediate presynaptic* store containing $q(t)$ transmitter vesicles into the synaptic cleft, $c(t)$, at a rate, $k(t)$, that is dependent on calcium concentration, $[Ca^{2+}](t)$. In the cleft, the transmitter disperses and some is lost from the system at a rate *l*. The remaining transmitter in the cleft is taken back into the cell into a reprocessing store containing $w(t)$ vesicles at a rate *r*. Here, it is repackaged into vesicles that are returned to the immediate store at a rate *x*. Additionally, $q(t)$ is continuously replenished with new transmitter vesicles at a rate $y[M-q(t)]$, where *M* represents the maximum number of transmitter quanta that can be held in the immediate store.

Neurotransmitter in the immediate store is quantal, and enters and leaves the immediate store stochastically. The stochastic transport of neurotransmitter is described by the function $N(n,\rho)$, in which each of *n* quanta has an equal probability of release, $\rho \cdot dt$, in a single simulation epoch. In the cleft and reprocessing stores, transmitter is a continuous quantity. This means, for instance, that the contents of the

TABLE V. MacGregor point neuron parameters Source: modified from Wiegrebe and Meddis (2004) to use international units.

Dendritic low-pass cutoff (Hz)	100
τ_m, membrane time constant (s)	$5E-4$
τ_{Gk}, potassium recovery time constant (s)	$4E-4$
b, increment in G_k (Siemens/s)	8000
$Th0$, resting threshold (V)	$16E-3$
E_k potassium reversal potential (V)	−10
R, membrane resistance (ohms)	$60E6$

reprocessing store must contain at least enough transmitter to make one vesicle before a quantum can rejoin the immediate store. The output from the synapse into the cleft is a stream of discrete events indicating vesicle releases, $N[q(t),k(t)]$.

The flow of transmitter between stores is simulated by the following equations:

$$\frac{dq(t)}{dt} = N(w(t),x) + N([M - q(t)],y) - N(q(t),k(t)), \tag{A13}$$

$$\frac{dc(t)}{dt} = N(q(t),k(t)) - lc(t) - rc(t), \tag{A14}$$

$$\frac{dw(t)}{dt} = rc(t) - N(w(t),x). \tag{A15}$$

Initial values for the variable quantities are found as follows (Meddis *et al.*, 1990):

$$c_0 = k_0 ym/[y(l+r) + k_0 l], \tag{A16}$$

$$q_0 = c_0(l+r)/k_0, \tag{A17}$$

$$w_0 = c_0 r/x. \tag{A18}$$

6. Auditory nerve response

An absolute refractory period lasting 0.75 ms was applied. Thereafter, a release event was converted into a spike on a probabilistic basis as a function of time since the last spike

$$P_{\text{conversion}} = 1 - \exp(t/0.0006). \tag{A19}$$

Each spike is counted and added to a peristimulus time histogram (PSTH) with a 0.0005-s bin width. When multiple fibers are used, all spikes are aggregated in the same PSTH. This then serves as the input to the next stage.

7. Sustained chopper model

The CN unit model is based on MacGregor's (1987) point neuron model. It consists of two stages: (1) input at the dendrites and (2) spike generation at the soma. The dendritic input stage applies a first-order low-pass filter to the AN PSTH to produce a representation of input current, $I(t)$, to the soma assuming a current input of 300 nA per spike when there are 20 fibers. If more fibers are used this value must be adjusted *pro rata*. See Table V.

The trans-membrane potential at the soma, E, is represented as a deviation from resting potential, E_r, and tracked using the equation

$$dE(t)/dt = -E(t)/\tau_m + I(t)\cdot R + Gk(t)\cdot[Ek - E(t)], \tag{A20}$$

where τ_m is the membrane time constant, R is the cell membrane resistance, E_k is the potassium reversal potential (relative to E_r), and $Gk(t)$ is the cell potassium conductance

$$dGk(t)/dt = -Gk(t)/\tau Gk + (b\cdot s), \tag{A21}$$

where τ_{Gk} is the potassium time constant, b is the increase in G_k following an action potential indicated when $s=1$. An action potential is initiated when the membrane potential exceeds a threshold $E(t) > Th0$. This threshold was fixed throughout. The original MacGregor neuron provides for the possibility that the $Th0$ can vary over time. This has been omitted here by setting his parameter c to 0.

[1]DSAM: Development software for Auditory Modeling, a library of compiled C-code routines for auditory modeling. AMS: auditory modeling system, an application for creating running and displaying complex auditory models using DSAM routines. This software is available from the authors. (http://www.essex.ac.uk/psychology/hearinglab/)

Clock, A. E., Salvi, R. J., Saunders, S. S., and Powers, N. L. (**1993**). "Neural correlates of temporal integration in the cochlear nucleus of the chinchilla," Hear. Res. **71**, 37–50.

Clock, A. E., Salvi, R. J., Wang, J., and Powers, N. L. (**1998**). "Threshold-duration functions of chinchilla auditory nerve fibers," Hear. Res. **119**, 135–141.

Eddins, D. A., and Green, D. M. (**1995**). "Temporal integration and temporal resolution," in *Hearing*, edited by B. C. J. Moore (Academic, San Diego), pp. 207–242.

Florentine, M., Fastl, H., and Buus, S. (**1988**). "Temporal integration in normal hearing, cochlear impairment, and impairment simulated by masking," J. Acoust. Soc. Am. **84**, 195–203.

Gerken, G. M. (**1979**). "Temporal summation of pulsate brain stimulation in normal and deafened cats," J. Acoust. Soc. Am. **66**, 728–734.

Gersuni, G. V. (**1965**). "Organization of afferent flow and the process of external signal discrimination," Neuropsychologia **3**, 95–109.

Heil, P., and Neubauer, H. (**2001**). "Temporal integration of sound pressure determines thresholds of auditory nerve fibers," J. Neurosci. **15**, 7404–7415.

Heil, P., and Neubauer, H. (**2003**). "A unifying basis of auditory thresholds based on temporal summation," Proc. Natl. Acad. Sci. U.S.A. **100**, 6151–6156.

Hewitt, M. J., and Meddis, R. (**1991**). "An evaluation of eight computer models of mammalian inner hair-cell function," J. Acoust. Soc. Am. **90**, 904–917.

Hewitt, M. J., and Meddis, R. (**1993**). "Regularity of cochlear nucleus stellate cells: A computational modeling study," J. Acoust. Soc. Am. **93**, 3390–3399.

Hewitt, M. J., and Meddis, R. (**1994**). "A Computer model of amplitude-modulation sensitivity of single units in the inferior colliculus," J. Acoust. Soc. Am. **95**, 2145–2159.

Holmes, S., Sumner, C., O'Mard, L. P., and Meddis, R. (**2004**). "The temporal representation of speech in a nonlinear model of the guinea pig cochlea," J. Acoust. Soc. Am. **116**, 3534–3545.

Krishna, B. S. (**2002**). "A unified mechanism for spontaneous-rate and first-spike timing in the auditory nerve," J. Comput. Neurosci. **13**, 71–91.

Levitt, H. (**1971**). "Transformed up and down methods in psychology," J. Acoust. Soc. Am. **49**, 467–477.

Liberman, M. C., and Kiang, N. Y. S. (**1978**). "Acoustic trauma in cats. Cochlear pathology and auditory-nerve activity," Acta Otolaryngol. Suppl. **358**, 1–63.

Lopez-Poveda, E. A., and Meddis, R. (**2001**). "A human nonlinear cochlear filterbank," J. Acoust. Soc. Am. **110**, 3107–3118.

MacGregor, R. J. (**1987**). *Neural and Brain Modeling* (Academic, San Diego).
Meddis, R., and O'Mard, L. P. (**2005**). "A computer model of the auditory nerve response to forward masking stimuli," J. Acoust. Soc. Am. **117**, 3787–3798.
Meddis, R., Hewitt, M. J., and Shackleton, T. (**1990**). "Implementation details of a computational model of the inner hair-cell/auditory-nerve synapse," J. Acoust. Soc. Am. **87**, 1813–1818.
Meddis, R., O'Mard, L. P., and Lopez-Poveda, E. A. (**2001**). "A computational algorithm for computing nonlinear auditory frequency selectivity," J. Acoust. Soc. Am. **109**, 2852–2861.
Sumner, C. J., Lopez-Poveda, E. A., O'Mard, L. P., and Meddis, R. (**2003a**). "Adaptation in a revised inner-hair cell model," J. Acoust. Soc. Am. **113**, 893–901.
Sumner, C. J., O'Mard, L. P., Lopez-Poveda, E. A., and Meddis, R. (**2003b**). "A nonlinear filter-bank model of the guinea-pig cochlea," J. Acoust. Soc. Am. **113**, 3264–3274.
Sumner, C. J., O'Mard, L. P., Lopez-Poveda, E. A., and Meddis, R. (**2002**). "A revised model of the inner-hair cell and auditory nerve complex," J. Acoust. Soc. Am. **111**, 2178–2189.
Viemeister, N. F., Shivapuja, G., and Recio, A. (**1992**). "Physiological correlates of temporal integration," in *Auditory Physiology and Perception*, edited by Y. Cazals, K. Horner, and L. Demany (Pergamon, Oxford), pp. 323–329.
Wiegrebe, L., and Meddis, R. (**2004**). "The representation of periodic sounds in simulated sustained chopper units of the ventral cochlear nucleus," J. Acoust. Soc. Am. **115**, 1207–1218.
Winter, I. M., Robertson, D., and Yates, G. K. (**1990**). "Diversity of characteristic frequency rate-intensity functions in guinea pig auditory nerve fibers," Hear. Res. **45**, 191–202.

Influence of primary-level and primary-frequency ratios on human distortion product otoacoustic emissions[a)]

Tiffany A. Johnson,[b)] Stephen T. Neely, Cassie A. Garner, and Michael P. Gorga
Boys Town National Research Hospital, Omaha, Nebraska 68131

(Received 3 May 2005; revised 11 October 2005; accepted 12 October 2005)

The combined influence of primary-level differences (L_1-L_2) and primary-frequency ratio (f_2/f_1) on distortion product otoacoustic emission (DPOAE) level was investigated in 20 normal-hearing subjects. DPOAEs were recorded with continuously varying stimulus levels [Neely *et al.* J. Acoust. Soc. Am. **117**, 1248–1259 (2005)] for the following stimulus conditions: f_2=1, 2, 4, and 8 kHz and f_2/f_1=1.05 to 1.4; various L_1-L_2, including one individually optimized to produce the largest DPOAE. For broadly spaced primary frequencies at low L_2 levels, the largest DPOAEs were recorded when L_1 was much higher than L_2, with L_1 remaining relatively constant as L_2 increased. As f_2/f_1 decreased, the largest DPOAEs were observed when L_1 was closer to L_2 and increased as L_2 increased. Optimal values for L_1-L_2 and f_2/f_1 were derived from these data. In general, average DPOAE levels for the new L_1-L_2 and f_2/f_1 were equivalent to or larger than those observed for other stimulus combinations, including the L_1-L_2 described by Kummer *et al.* [J. Acoust. Soc. Am. **103**, 3431–3444 (1998)] and those defined by Neely *et al.* in which L_1-L_2 was evaluated, but f_2/f_1 was fixed at 1.2. © *2006 Acoustical Society of America.* [DOI: 10.1121/1.2133714]

PACS number(s): 43.64.Jb, 43.64.Yp [BLM] Pages: 418–428

I. INTRODUCTION

Distortion product otoacoustic emissions (DPOAEs) have been used to assess normal and impaired cochlear function in humans (e.g., Stover *et al.*, 1996; Janssen *et al.*, 1998; Kummer *et al.*, 1998; Abdala 2000, 2003; Dorn *et al.*, 2001; Gorga *et al.*, 1993, 2002, 2003; Abdala and Fitzgerald, 2003; Neely *et al.*, 2003) and are commonly used as a clinical tool for the objective prediction of auditory status (e.g., Gorga *et al.*, 1997; Norton *et al.*, 2000). The level of the DPOAE recorded in the ear canal depends on the frequency and level characteristics of the stimuli used to elicit the DPOAE. The choice of stimulus parameters, therefore, may influence the success with which DPOAEs can be used to assess cochlear function and predict auditory status. It may be more important to focus on maximizing DPOAE level rather than other DPOAE measures such as signal-to-noise ratio (SNR) on the assumption that DPOAE level is correlated with cochlear function. Additionally, while DPOAE phase may be important for basic research applications (e.g., Shera and Guinan, 1999), current clinical applications of DPOAE measures depend on DPOAE level (or SNR), but largely ignore phase measurements.

A number of previous investigations have examined the influence of stimulus parameters on the DPOAE (e.g., Harris *et al.*, 1989; Brown and Gaskill, 1990; Gaskill and Brown, 1990; Hauser and Probst, 1991; Whitehead *et al.*, 1995a, c), resulting in recommendations for stimulus conditions likely to yield robust emissions in human ears. A constant level relation of L_1-L_2=10 or 15 dB has been used in some cases (Gorga *et al.*, 1993, 1997), although recent work reported by Kummer *et al.* (1998) suggests that setting $L_1=0.4L_2+39$ results in the largest DPOAE level at each L_2, independent of frequency (Kummer *et al.*, 2000). A primary-frequency ratio of 1.22 has been recommended as optimal (Harris *et al.*, 1989; Gaskill and Brown, 1990; Brown *et al.*, 1994), although variability in the frequency ratio producing the largest DPOAE across stimulus frequency has been reported (Harris *et al.*, 1989).

The majority of previous parametric investigations of the DPOAE stimulus space, especially those involving humans, have focused on a restricted region of the level and/or frequency space. Although Mills (2002) described a comprehensive investigation of the four-dimensional stimulus space in gerbils, similar investigations have not been completed in humans. This is due, in part, to the time involved in recording DPOAEs in response to a large number of stimulus combinations.

Neely *et al.* (2005) described a novel method of recording DPOAE responses using continuously varying stimulus levels, which was validated by comparing results with it to more traditional measurements in which L_1 and L_2 were set to discrete values. Using this new method, Neely *et al.* were able to more fully explore the two-dimensional L_1, L_2 space in a group of normal-hearing subjects and were able to determine an individually optimized primary-level difference (L_1-L_2). Larger DPOAE levels were recorded when the individually optimized L_1-L_2 was used, as compared to DPOAE levels obtained with the relation recommended by Kummer *et al.* (1998). Furthermore, in contrast to the findings reported by Kummer *et al.* (2000), where the optimal L_1-L_2 was found to be independent of f_2, Neely *et al.* found a systematic effect of f_2 on the optimal L_1-L_2. Specifically, the optimal L_1-L_2 for low-level stimuli increased with f_2. When

[a)]Portions of this work were presented at the 28th Midwinter Meeting of the Association for Research in Otolaryngology, New Orleans, LA, February 2005.

[b)]Electronic mail: johnsonta@boystown.org

f_2=8 kHz, the optimal L_1-L_2 resulted in DPOAE levels that were approximately 10 dB higher than those observed with the approach to setting stimulus level recommended by Kummer *et al.* (1998). These differences decreased as f_2 decreased and, on average, were only 2 dB when f_2=1 kHz.

Although the reason for the discrepancy between the Neely *et al.* (2005) results and the results reported by Kummer *et al.* (1998, 2000) is not clear (it may be due, in part, to differences in recording paradigms), a question arising from the Neely *et al.* data is whether the variation in optimal L_1-L_2 with f_2 can be attributed to differences in cochlear frequency selectivity along the length of the basilar membrane. Direct observation of basilar-membrane motion in lower animals suggests that the spatial distribution of excitation patterns is more localized at the base of the cochlea than at the apex (e.g., Robles and Ruggero, 2001). The observation in Neely *et al.* (2005) that the L_1-L_2 for maximum DPOAE level is larger for f_2=8 kHz than for f_2=1 kHz is consistent with the idea that excitation patterns for the eliciting stimuli (i.e., the two primaries) are more spatially separated when f_2=8 kHz than when f_2=1 kHz, requiring an increase in the level of f_1 in order to generate "optimized" overlap at the f_2 place.

The purpose of the present study was to provide a more complete investigation of the stimulus parametric space in humans and to further investigate the trends observed by Neely *et al.* (2005). We hypothesized that differences in frequency resolution as a function of f_2 might underlie the effect of f_2 on the primary-level difference producing the largest DPOAE. Stated another way, more sharply defined representation of high-frequency primaries at the cochlear base might result in less effective overlap between f_2 and f_1, requiring an increase in L_1 relative to L_2 in order to maximize the interaction between primaries and the generation of distortion. In contrast, broader cochlear representation for lower frequencies might result in greater overlap (for the same f_2/f_1); under these conditions, maximum distortion might be produced when there was less difference between L_1 and L_2, compared to high-frequency conditions. Furthermore, we predicted that, for any stimulus frequency, a broader cochlear representation would occur as level increased; thus, we hypothesized that an interaction might occur among f_2/f_1, L_1-L_2, and L_2. A related goal was to determine the stimulus parameters producing the largest DPOAE levels in a group of normal-hearing subjects, with the expectation that those conditions might have use in the clinical application of DPOAEs.

II. METHODS

A. Subjects

Twenty normal-hearing subjects participated in this project. Normal hearing was defined as thresholds $\leqslant$10 dB HL (ANSI, 1996) for the octave frequencies from 0.25 through 8 kHz. Normal 226-Hz tympanograms were required just prior to each session in which DPOAE data were collected.

B. Procedures

All DPOAE data were collected using custom-designed software (SYSRES, Neely and Stevenson, 2002) that controlled a 24-bit soundcard (CardDeluxe, Digital Audio Labs) housed in a PC. An ER-10C probe-microphone system was used to present stimuli and record DPOAE responses. Stimuli were calibrated *in situ* in sound pressure level at the plane of the probe. While concerns exist for pressure calibrations in the ear canal (Siegel, 1994; Siegel and Hirohata, 1994; Neely and Gorga, 1998), those same concerns apply for other approaches to selecting stimulus conditions for DPOAE measurements. *In situ* pressure calibration represents one of the sources of variability in our DPOAE measurements. The variability associated with *in situ* pressure calibration is acknowledged and accepted as inherent in current standard calibration methods. This variability is addressed in our study by including subjects (N=20) with a range of different ear canal dimensions.

DPOAEs were recorded in response to pairs of primary tones (f_1,f_2) whose levels (L_1,L_2) varied continuously. The frequency of f_2 varied in octave steps from 1 to 8 kHz. Responses for a total of eight primary-frequency ratios (f_2/f_1), ranging from 1.05 to 1.40 in steps of 0.05, were recorded for each subject. The continuous-level method has been described previously (Neely *et al.*, 2005). Briefly, the levels of f_1 and f_2 are continuously amplitude modulated in dB. The DPOAE level is extracted using a frequency-domain, heterodyne technique (Kim *et al.*, 2001). As in our previous work with the continuous-level method (e.g., Neely *et al.*, 2005), DPOAE responses were recorded using two different stimulus paths, a Lissajous path and a linear path, each of which is described below.

In the Lissajous-path condition, the levels of the primary stimuli were continuously amplitude modulated over a 33-s time course, which was repeated. L_2 ranged from 17 to 69 dB SPL and L_1 ranged from 43 to 76 dB SPL. In each half of the 66-s stimulus buffer, 23 cycles of L_1 modulation and 17 cycles of L_2 modulation were presented. Stimulus and DPOAE levels were determined by summing the two halves of the buffer. Noise levels (at the $2f_1$-f_2 frequency) were determined by subtracting the halves. These stimulus conditions allowed us to rapidly record DPOAE responses for stimulus conditions representing a broad L_1, L_2 space. The rapid collection of data for the Lissajous-path stimulus results in a smoothing of the DPOAE response levels. As a consequence, the DPOAE levels obtained with this stimulus can be compared in relative terms across L_1, L_2 combinations; however, as will be seen below, DPOAE levels obtained with this stimulus cannot be compared to those obtained with more traditional stimulus and recording parameters. The reader is referred to Neely *et al.* (2005) for more information regarding the Lissajous-path stimuli.

The responses to the Lissajous-path stimuli were used to determine the optimal, linear L_1, L_2 relationship for each subject and each f_2/f_1 combination (as described below). The DPOAE levels recorded for the Lissajous-path stimuli also were used to compare the responses obtained for a variety of linear L_1, L_2 paths, including the frequency-

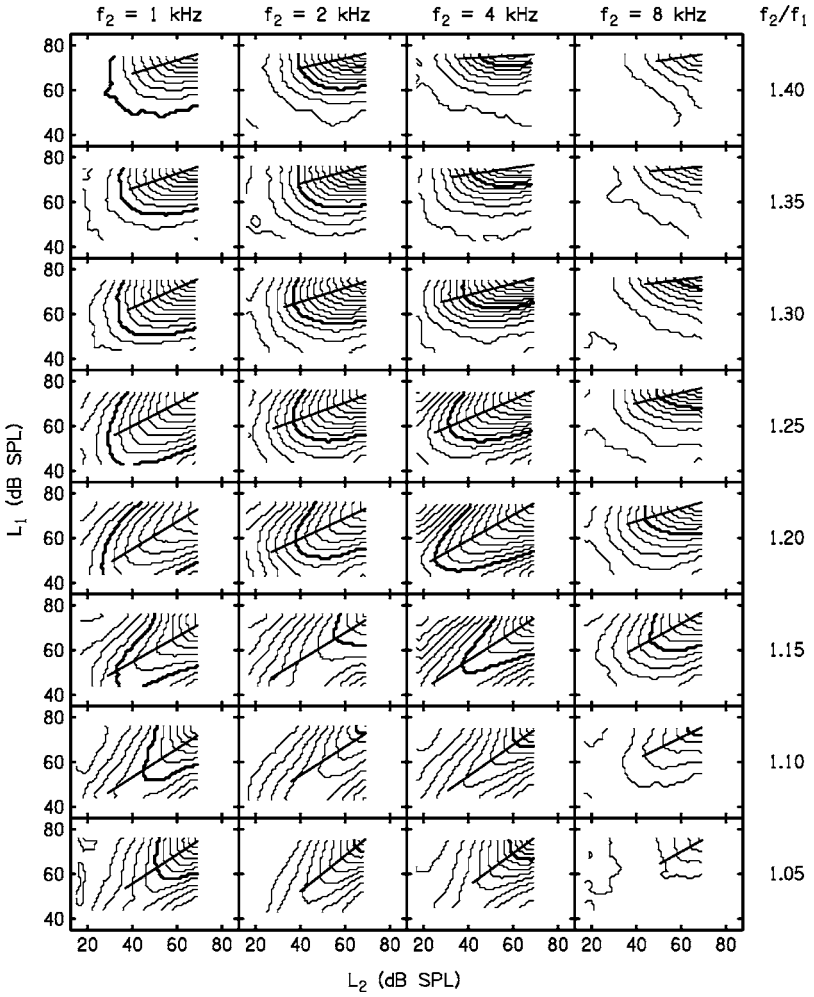

FIG. 1. Contour plots representing DPOAE level in L_1, L_2 stimulus space. Each column represents data for a different f_2 and each row represents a different f_2/f_1, as indicated on the figure. The contours are spaced in 2-dB increments of DPOAE level. As a reference, the contour corresponding to −6 dB SPL is indicated with a thicker line. The maximum DPOAE level in panels without a reference (f_2=8 kHz, f_2/f_1=1.40, 1.35, 1.05) is −8 dB SPL. The slanting, straight lines in each panel describe the L_1, L_2 relationship producing the largest DPOAE level at each L_2. Our approach for fitting this line is described in the text.

independent relation recommended by Kummer *et al.* (1998) and the frequency-dependent paths described in Neely *et al.* (2005).

Each individual's optimal path was determined from the response to Lissajous-path stimuli by identifying the L_1 producing the largest DPOAE for each L_2. A linear function was fit to the subset of these L_1, L_2 values producing responses with a signal-to-noise ratio (SNR) $\geqslant$12 dB. Pilot data suggested that a 12-dB SNR represented a reasonable compromise between the need to fit a function over a range of L_2 levels and the desire to minimize the influence of noise on the line fits. The resulting equation describes the optimal, linear path through L_1, L_2 space. This procedure was repeated for each f_2 and f_2/f_1 combination, resulting in a total of 32 optimal linear paths for each subject ($4f_2 \times 8f_2/f_1$).

For each subject, DPOAE I/O functions were recorded along these 32 optimal linear L_1, L_2 paths. The optimal linear-path I/O functions were recorded using continuously varying stimulus levels, in a manner similar to that used to record responses to the Lissajous-path stimuli. However, these I/O functions were obtained with more slowly varying stimulus levels such that only one cycle of L_1 and L_2 modulation was presented in each half of the 66-s stimulus buffer. As for the Lissajous-path stimuli, the stimulus and DPOAE levels were obtained by summing the two halves of the buffer and the noise was obtained from the difference. L_2 varied continuously from −20 to 80 dB SPL and L_1 varied according to each individual's optimal linear path. For certain conditions (typically the smallest and largest frequency ratios) in several subjects, we were unable to determine an optimal L_1, L_2 relationship because the DPOAE levels were too small to fit a valid linear function to the Lissajous-path responses (i.e., points with $\geqslant$12-dB SNR extended over less than a 10-dB L_2 range). For these conditions in these subjects, the optimal linear L_1, L_2 path condition was not tested.

All data were collected in a sound-treated room. During data collection, subjects relaxed or slept in a reclining chair. They were asked to remain quiet throughout the test session and breaks were provided as needed. These data were typically collected in three test sessions, with each session lasting 2 h.

III. RESULTS

A. Responses to Lissajous-path stimuli

DPOAE levels in L_1, L_2 stimulus space for each f_2 and f_2/f_1 are shown as contour plots in Fig. 1. These data represent the DPOAE levels obtained for the Lissajous-path stimuli averaged across all 20 subjects. Each column represents data for a different f_2, from f_2=1 kHz (left column) to f_2=8 kHz (right column). Each row represents data for a different f_2/f_1, with f_2/f_1=1.40 in the top row, decreasing to

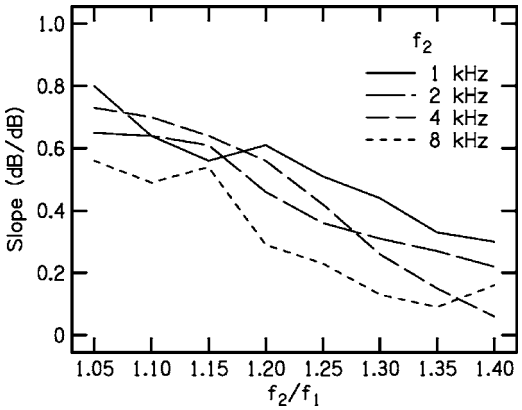

FIG. 2. The slope of the average, optimal path as a function of f_2/f_1. The parameter is f_2.

$f_2/f_1=1.05$ in the bottom row. The contours are spaced in 2-dB increments of DPOAE level, with the maximum DPOAE level represented by the contours in the upper right portion of each panel. As a reference, the contours corresponding to a DPOAE level of −6 dB SPL (a level that exists in all but three panels) are indicated with a thicker line than the other contours. There is no reference line for the conditions where $f_2=8$ kHz and $f_2/f_1=1.40$, 1.35, or 1.05. Here, the maximum DPOAE level was −8 dB SPL. Also shown as solid sloping lines in each panel are the average optimal linear L_1, L_2 stimulus paths obtained by averaging the coefficients for each subject's optimal path for each f_2 and f_2/f_1 combination. The length of the average optimal-path line in each panel indicates the L_2 range over which the SNR was $\geqslant$12 dB, the minimum SNR requirement for points included in our optimal-line fit. For certain conditions, typically the largest and smallest frequency ratios, the average optimal-path line includes data from less than 20 subjects because not every subject produced DPOAEs with SNRs exceeding 12 dB.

In general, the slope of the optimal path becomes steeper as the primaries are more closely spaced at each f_2. When the primaries are broadly spaced ($f_2/f_1=1.35$ or 1.40), the largest DPOAE levels were obtained when L_1 was much bigger than L_2 at low levels of L_2 and increased slowly as L_2 increased. For more closely spaced primaries, the largest DPOAE levels were obtained when L_1 was more similar in level to L_2 and increased more rapidly with L_2.

The slope of the optimal path and its relation to f_2/f_1 and f_2 is summarized in Fig. 2. Here, the slope of the average optimal path is plotted as a function of f_2/f_1 with f_2 as the parameter. As shown in Fig. 1, the slope of the average optimal path decreases as f_2/f_1 increases at each f_2. This change in slope is consistent with expected changes in relative response growth at the f_2 place as the spacing between the two primaries increases. Additionally, for frequency ratios greater than 1.15, the slope of the optimal path tends to decrease as f_2 increases from 1 to 8 kHz, suggesting that, for a given frequency ratio, the overlap between the primaries at the f_2 place decreases as f_2 increases.

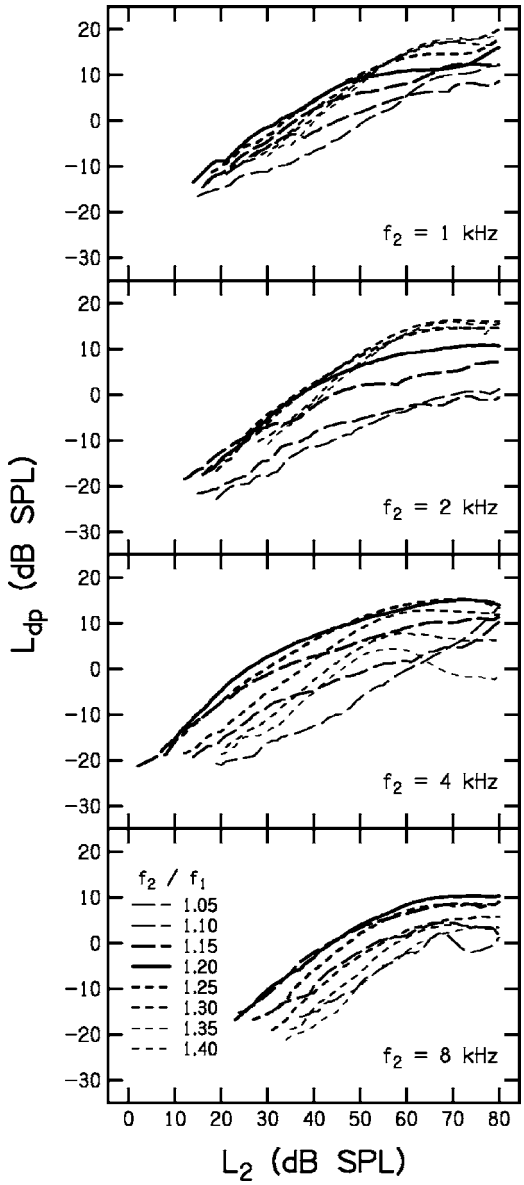

FIG. 3. DPOAE level (L_{dp}) is plotted as a function of L_2 with primary-frequency ratio as a parameter. Each panel represents a different f_2, as indicated. The solid line in each panel represents DPOAE level for $f_2/f_1=1.20$. Shorter dashes correspond to $f_2/f_1>1.20$ and longer dashes correspond to $f_2/f_1<1.20$. The line thickness represents the distance the frequency ratio is from 1.20, with $f_2/f_1=1.05$ and 1.40 indicated by the thinnest dashed lines.

B. Responses to linear-path stimuli

DPOAE I/O functions, averaged across subjects, are shown in Fig. 3. Each panel represents data for a different f_2 with f_2/f_1 as the parameter. These data were obtained with L_1 set according to each subject's optimal path for each f_2/f_1 at each f_2. Data were included in Fig. 3 only for those conditions on the averaged I/O function where the SNR was $\geqslant$6 dB. This SNR criterion was invoked in this and subsequent figures (Figs. 4–6), in order to plot only those points that were reliably measured with minimal influence from noise. The solid, thick line represents the I/O function for $f_2/f_1=1.20$. The longer dashed lines are for $f_2/f_1<1.20$ and the shorter dashes are for $f_2/f_1>1.20$. The thickness of the dashed lines indicates the distance the frequency ratio is

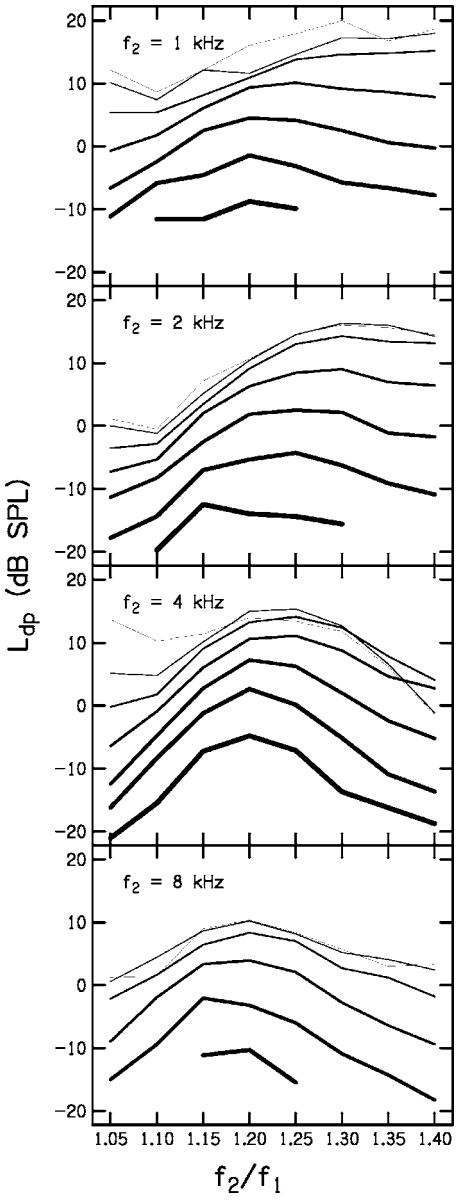

FIG. 4. Mean DPOAE level (L_{dp}) as a function of frequency ratio. Each panel represents data for a different f_2. Here, the parameter is L_2, with decreasing line thickness indicating increasing L_2 in 10-dB increments of L_2. When f_2=8 kHz, data for L_2=30 to 80 dB SPL are plotted; for all other f_2 frequencies data are plotted for L_2 ranging from 20 to 80 dB SPL.

from 1.20, with the dashed lines becoming progressively thinner as f_2/f_1 approaches either 1.05 or 1.40. The thinnest lines are for frequency ratios of 1.05 and 1.40. For f_2=4 and 8 kHz, the maximum DPOAE level for essentially all L_2 was achieved when f_2/f_1=1.20. Both increases and decreases in f_2/f_1 resulted in reductions in DPOAE level relative to the levels observed when f_2/f_1=1.20. However, for f_2=1 and 2 kHz, there was an interaction between optimal f_2/f_1 and L_2. For $L_2<40$ dB SPL, maximum DPOAE level occurred when f_2/f_1=1.20; for $L_2>40$ dB SPL, frequency ratios greater than 1.20 resulted in an increase in DPOAE level, achieving a maximum increase of approximately 5 dB.

An alternative view of the effect of frequency ratio as stimulus level is varied is shown in Fig. 4. Here, the DPOAE I/O functions shown in Fig. 3 are replotted as DPOAE level

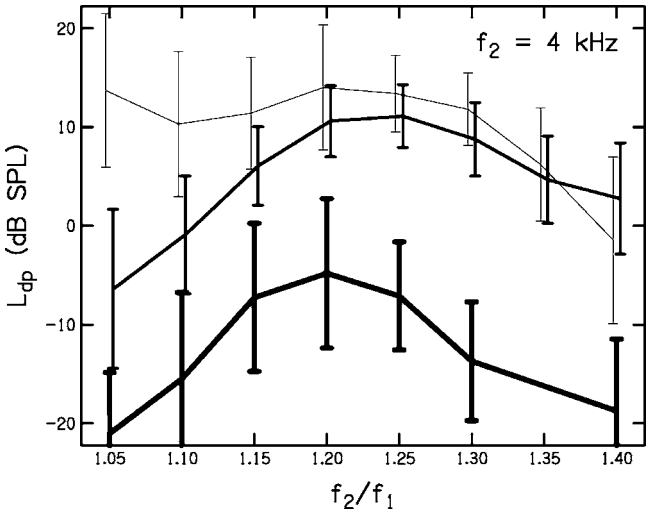

FIG. 5. Mean DPOAE level (L_{dp}) as a function of frequency ratio when f_2=4 kHz and L_2=20, 50, and 80 dB SPL (indicated with decreasing line thickness). Errors bars represent ±1 standard deviation.

versus f_2/f_1 functions with L_2 as the parameter. Plots like these have sometimes been referred to as DPOAE frequency or filter functions (e.g., Stover *et al.*, 1999). Each panel represents data for a different f_2, with line thickness decreasing as L_2 increases. As in Fig. 3, only points where the SNR was 6 dB or greater are plotted. The lines are shown for 10-dB increments of L_2. For f_2=1, 2, and 4 kHz, L_2 ranges from 20 to 80 dB SPL. L_2 ranges from 30 to 80 dB SPL for f_2

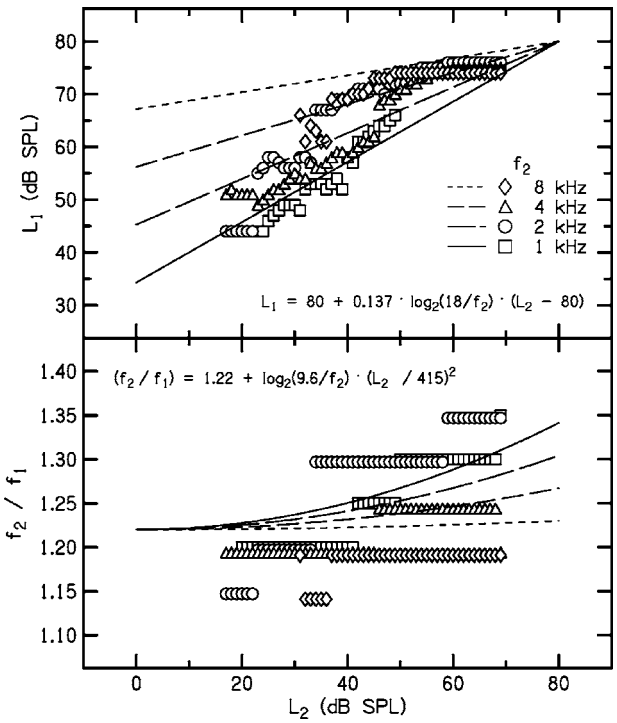

FIG. 6. Our approach to specifying optimal stimulus parameters. The upper panel plots L_1 as a function of L_2 while the lower panel plots f_2/f_1 as a function of L_2. The parameter is f_2, as indicated within the upper panel. The symbols shown in each panel correspond to the L_1 (upper panel) or f_2/f_1 (lower panel) producing the largest DPOAE at each L_2. The lines in each panel represent the best fit to the stimulus conditions producing the maximum DPOAE according to the approach described in the text. The equations describing these lines are shown as an inset in each panel.

=8 kHz, a consequence of the reduced range over which reliable measurements were possible at this f_2. For f_2 =8 kHz, f_2/f_1=1.20 resulted in the maximum DPOAE levels for all L_2's except 40 dB SPL. For all other f_2 frequencies, the f_2/f_1 producing the largest DPOAE increased with L_2. These data suggest that it is possible to obtain larger DPOAE levels if f_2/f_1 is varied with L_2, in addition to varying L_1 (e.g., Kummer *et al.*, 1998; Neely *et al.*, 2005), although the size of the effect is small, compared to the influence of L_1 variation.

Data describing the intersubject variability in DPOAE level are plotted in Fig. 5. Here, a portion of the data shown in Fig. 4 (f_2=4 kHz, L_2=20, 50, and 80 dB SPL) have been replotted with the addition of error bars representing ±1 standard deviation. In general, the variability across subjects is less for the high-level stimuli (L_2=50 and 80 dB SPL) and for frequency ratios between 1.15 and 1.30. Standard deviations for other stimulus conditions (i.e., the complete set of f_2 and L_2 shown in Fig. 4) are similar to those shown in Fig. 5, suggesting similar intersubject variability across stimulus condition.

C. Optimal stimulus parameters

Figure 6 summarizes our approach for specifying stimulus conditions that (on average) elicit larger DPOAE levels than those obtained when only L_1-L_2 is varied. The upper panel plots L_1 as a function of L_2, while the lower panel plots f_2/f_1 as a function of L_2. The parameter in each panel is f_2, shown with different symbols as indicated in the upper panel. Data points are plotted at values that represent the maximum responses to the Lissajous-path stimuli shown in Fig. 1. As in previous figures, data are included only if the SNR ⩾6 dB. The values of L_1 and f_2/f_1 at which each symbol in Fig. 6 is plotted can be viewed as the stimulus conditions resulting in the maximum average DPOAE level for each L_2 and f_2. However, using the stimulus conditions described by the individual data points limits the degree to which these data can be used to generalize to stimulus conditions for f_2 frequencies other than those tested in this study. Therefore, equations describing the relations among stimulus parameters were developed.

In specifying the form of these equations, emphasis was placed on developing as simple a model as possible that also provided a reasonable fit to the data. Changes in f_2/f_1 with L_2 and f_2 were motivated by data shown in Fig. 4, where larger frequency ratios produced bigger DPOAE levels as either f_2 decreased or L_2 increased. An additional constraint on the model was that the relationship between L_1 and L_2 be described by a straight line in the same manner as previous descriptions of the relationship between L_1 and L_2 (e.g., Kummer *et al.*, 1998, 2000; Neely *et al.*, 2005). For a particular f_2 and L_2 combination, L_1 is set according to

$$L_1 = 80 + a \log_2(b/f_2) \cdot (L_2 - 80).$$

Likewise, f_2/f_1 is set according to

$$f_2/f_1 = c + \log_2(d/f_2) \cdot (L_2/e)^2.$$

The equation parameters were determined first by constraining L_1=80 dB SPL when L_2=80 dB SPL. The five additional parameters (a–e) were determined by minimizing the sum of the squared deviations between the DPOAE levels obtained with freely varying stimulus parameters (which we refer to as L_{dmax}) and the DPOAE levels obtained for stimulus parameters specified by the equations shown in each panel (which we refer to as L_{dpar}). The final parameter values are shown in the equations plotted on Fig. 6. These parameters represent the values resulting in the smallest squared deviation between L_{dmax} and L_{dpar}. Functions derived from these equations are shown as solid (1 kHz) and dashed (2, 4, and 8 kHz) lines in the figure, the shorter the dash, the higher the f_2.

In Fig. 6, the fit between the solid/dashed lines and the individual data points suggests that the stimulus parameters recommended by these two equations deviate from the stimulus parameters associated with L_{dmax} and that perhaps these equations do not provide a good representation of the stimulus conditions producing the largest DPOAEs. However, the method by which we determined the equation parameters placed an emphasis on equating DPOAE levels for L_{dmax} and L_{dpar} rather than fitting the freely varying stimulus parameters. The extent to which L_{dmax} and L_{dpar} differ is shown in Fig. 7, which, in the final analysis, probably represents a better test of the appropriateness of using these equations to select stimulus conditions that optimize response level.

DPOAE I/O functions for L_{dmax} and L_{dpar} are plotted in Fig. 7, along with I/O functions using the L_1, L_2 relations described by Kummer *et al.* (1998) and Neely *et al.* (2005). For these latter two functions, the frequency ratio is fixed at 1.20, which is the frequency ratio used in the two previous studies. The horizontal lines between −10 and −20 dB SPL represent the noise level. Again, only points with SNR ⩾6 dB are shown. Data obtained with the Kummer *et al.* stimulus conditions are shown as solid lines. The corresponding response levels for the Neely *et al.* stimulus conditions are shown as the longest dashed lines. The DPOAE levels for the L_{dmax} condition are represented by the shortest dash and the DPOAE levels for the L_{dpar} condition are shown as dashed lines intermediate in length to those used for L_{dmax} and those used to depict the DPOAE levels for the Neely *et al.* stimulus conditions. For all conditions, the DPOAE and noise levels were taken from the response to the Lissajous-path stimuli. Recall that because these data were collected rapidly with associated smoothing of the response, the DPOAE levels are not directly comparable to levels obtained with more traditional stimulus and response conditions. Therefore, the I/O functions shown in Fig. 7 should be evaluated in relative terms and not in relation to those shown in Fig. 3 or elsewhere in the DPOAE literature.

If we use the Kummer *et al.* levels as the reference point (measured under conditions in which both f_2/f_1 and L_1-L_2 were independent of f_2), the other I/O functions describe the extent to which it is possible to increase the DPOAE level by adjusting only the L_1-L_2 (Neely *et al.*) or by varying both

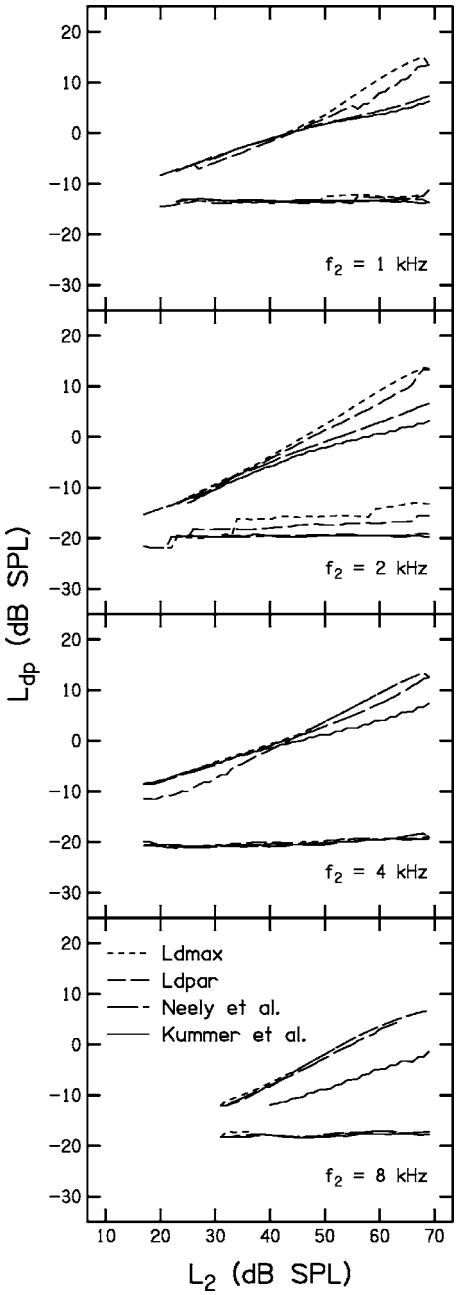

FIG. 7. DPOAE level (L_{dp}) as a function of L_2. Each panel represents a different f_2. The parameter is the stimulus condition used to record the DPOAE, as indicated in the legend. The nearly horizontal lines near the bottom of each panel represent the corresponding noise levels.

L_1-L_2 and f_2/f_1 (L_{dmax}, L_{dpar}) as a function of f_2. In general, the DPOAE levels for the Kummer *et al.* condition are equivalent to or less than those recorded for any of the other three conditions. For f_2=8 kHz, Neely *et al.*, L_{dpar}, and L_{dmax} all produce equivalent DPOAE levels, which might be expected given the similarity in stimulus conditions for Neely *et al.*, L_{dpar}, and L_{dmax}. This observation also provides further validation of the results observed in Neely *et al.* (2005) regarding the optimal relationship between L_1 and L_2 when f_2=8 kHz. As f_2 decreases from 4 to 1 kHz, L_{dpar} and L_{dmax} produce increasingly larger DPOAE levels relative to Neely *et al.* While the stimulus conditions for L_{dmax} (as expected) always produce responses that are equal to or greater than those produced by the stimulus conditions for L_{dpar}, the differences seldom exceed a few dB. When f_2=4 kHz and L_2 $<$40 dB HL, DPOAE levels associated with L_{dpar} are less than those associated with the other three sets of stimulus conditions, suggesting that L_{dpar} may not be a good choice for specifying stimulus conditions for this f_2 and L_2. This observation also suggests that it might be possible to improve our approach to specifying stimulus parameters for L_{dpar}. However, even with the L_{dpar} stimulus conditions at f_2=4 kHz, DPOAEs were recorded with a positive SNR for L_2=17 dB SPL. Furthermore, for all other combinations of f_2 and L_2, the response levels for L_{dpar} exceeded the levels achieved with the approach recommended by Kummer *et al.* (1998), were equal to or greater than the levels achieved by Neely *et al.* (2005), and were only slightly less than the maximum levels achieved by freely varying stimulus conditions (L_{dmax}). We, therefore, view the stimulus conditions associated with L_{dpar} as representing an acceptable compromise between achieving the maximum possible DPOAE levels (L_{dmax}) and specifying a simple stimulus model that can be generalized to other f_2 frequencies.

When f_2=2 kHz, the noise levels associated with L_{dmax} and L_{dpar} increase as stimulus levels increase, which can be attributed to changes in DPOAE frequency with changes in f_2/f_1. As f_2/f_1 increases, the frequency at which the DPOAE is measured decreases. When f_2=1 and 2 kHz, frequency ratios exceeding 1.25 are recommended for the highest stimulus levels. For these conditions, the DPOAE was recorded at lower frequencies (because $2f_1$-f_2 decreases as f_2/f_1 increases). Noise levels increase as $2f_1$-f_2 decreases (Gorga *et al.*, 1993), which occurs when either f_2 decreases or f_2/f_1 increases. At 2 kHz, the shift in the DPOAE frequency appears to be associated with larger increases in noise level than for other f_2 frequencies.

Data in support of this interpretation are shown in Fig. 8, where the noise level averaged across the entire DPOAE I/O function is plotted as a function of frequency ratio. Each panel represents data for a different f_2 with the noise levels for each primary-level path as the parameter. The triangles represent the noise levels when the Kummer *et al.* (1998) primary-level relation is used at each frequency ratio (recall that this level ratio is the same for all f_2 frequencies). The circles represent the corresponding noise levels when the Neely *et al.* (2005) primary-level relations are used; in this case, a different primary-level relation is specified at each f_2, but the same level relation is used for each frequency ratio within an f_2. Finally, the squares represent the case when the average optimal paths are used to specify the L_1, L_2 relationship. These paths correspond to the average optimal paths plotted on the contour plots in Fig. 1; in this case, a different primary-level relation is used at each f_2 and f_2/f_1.

As expected, there is a tendency for overall noise levels to increase as f_2 decreases (going from bottom to top in Fig. 8). Within each panel, the primary determining factor for noise level is the frequency ratio; within a given frequency ratio, there is no difference in noise level across the three primary-level paths. For f_2=1 and 2 kHz, the noise level increases as frequency ratio increases. When f_2=4 kHz, the noise level remains relatively constant across frequency ra-

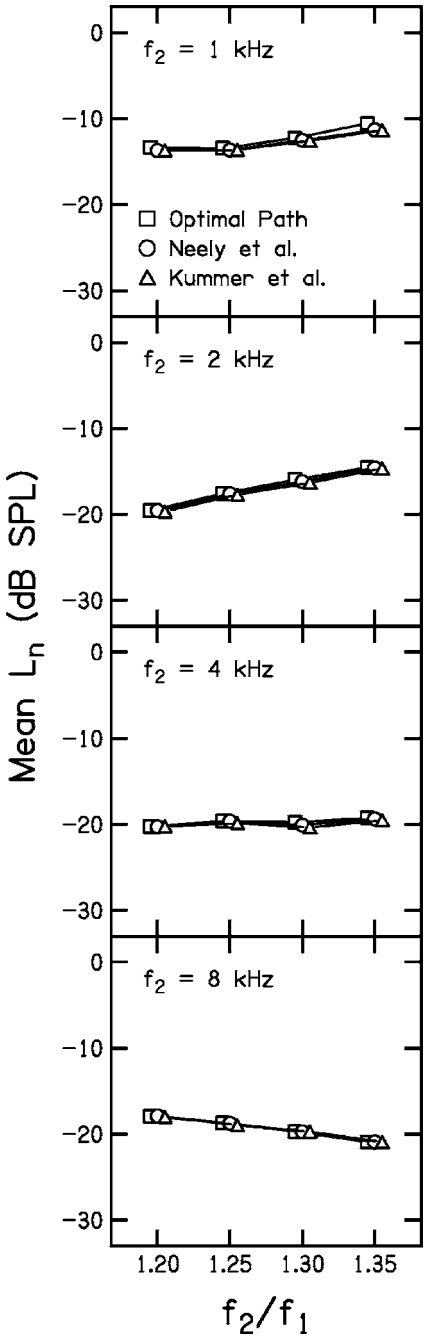

FIG. 8. DPOAE noise levels (L_n) as a function of frequency ratio with each panel corresponding to a different f_2. Each symbol corresponds to a different L_1,L_2 path as indicated in the legend.

tio. For f_2=8 kHz, the noise level decreases by 2–3 dB between f_2/f_1=1.20 and f_2/f_1=1.35. The decrease in noise level with increases in f_2/f_1 for f_2=8 kHz was unexpected given previous observations (e.g., Gorga *et al.*, 1993), and the mechanism responsible for this change at 8 kHz is unclear. For f_2=2 kHz, the increase is approximately 5 dB, which is a larger effect than was observed for the other frequencies.

IV. DISCUSSION

The results described above summarize a broad exploration of the DPOAE parametric space in humans. These results suggest that it is possible to record larger DPOAE levels in normal-hearing human ears if the L_1, L_2 and f_2/f_1 relations are allowed to vary with both L_2 and f_2. Extensive parametric investigations for individual subjects are impractical due to the significant time involved in collecting these data. However, we have described an approach to specifying optimal stimulus conditions that are expected, on average, to result in larger DPOAE levels in normal-hearing human subjects.

A. Frequency dependence of average, optimal L_1, L_2 difference

The data displayed in Figs. 1 and 2 demonstrate systematic variations in the average optimal L_1, L_2 stimulus path as both f_2 and f_2/f_1 are varied. Two trends are apparent in these data. First, across f_2, the slope of the optimal path decreases with increasing frequency ratio (which corresponds to broader frequency spacing of the primaries). Second, within a given frequency ratio, there is a trend for the optimal-path slope to increase with decreasing f_2. These results suggest that if we increase the separation of the two primaries in the cochlea either by presenting high-frequency stimuli, for which we presume there is sharper frequency resolution, or by increasing the frequency ratio, an increase in L_1 is necessary to produce "optimal" overlap of the primaries at the f_2 place. The shallower optimal-path slope and higher intercept represent this compensation. The higher intercept is a result of the increase in L_1 for low-level stimuli, which is necessary because of the increased separation in the cochlear representation of the primaries for large frequency ratios or high f_2 frequencies. The shallow slope reflects a subsequent slow change in L_1 as L_2 increases.

The shallower optimal-path slope for broadly spaced primaries is also consistent with expected changes in growth of response to f_1 at the f_2 place. In the generation of DPOAEs, the primary nonlinear interaction is believed to occur near the f_2 place (e.g., Brown and Kemp, 1984; Harris *et al.*, 1992). Response growth for the f_2 primary is, therefore, expected to be nonlinear. As the frequency ratio is increased, a larger L_1 would be needed for low levels of L_2 and response growth for the f_1 primary at the f_2 place would be expected to become increasingly more linear. This linearizing of the f_1 response at the f_2 place results in relatively little change in L_1 for relatively large changes in L_2. Stated another way, as frequency ratio increases, the response to the f_1 primary grows increasingly more rapidly than the response to the f_2 primary at the f_2 place. This results in the need for a smaller increase in f_1 relative to f_2 for the same relative representation at the f_2 place. This interpretation is consistent with arguments made in the psychoacoustics literature to explain differences in growth of masking for on- versus off-frequency maskers (e.g., Stelmachowicz *et al.*, 1987; Oxenham and Plack, 1997) and in the DPOAE suppression literature to explain differences in growth of suppression for on-versus-off-frequency suppressors (e.g., Gorga *et al.*, 2002).

Changes in the optimal-path slope across f_2 also are consistent with expected variations in frequency resolution and cochlear nonlinearity as a function of frequency. Direct observation of basilar-membrane motion in lower animals sug-

gests broader tuning at the cochlear apex as compared to its base (e.g., Cooper and Rhode, 1997; reviewed in Robles and Ruggero, 2001). While the extent to which cochlear nonlinearity differs between the base and the apex remains controversial [contrast, for example, the behavioral data of Oxenham and Plack (2000) with behavioral data of Plack and Drga (2003)], more recent evidence points to similar cochlear nonlinearity at both the base and apex (e.g., Nelson and Schroder, 2004; Oxenham and Dau, 2004). Additionally, data from the chinchilla suggest nonlinear responses at the apex, but also suggest that they are more distributed and less sharply tuned than those observed at the base (Cooper and Rhode, 1997). In the present data, the lowest f_2 frequency for which measurements were made was 1 kHz, so these data do not represent responses from extreme apical regions of the cochlea. However, the observation of consistently steeper optimal L_1, L_2 relationships for $f_2=1$ kHz as compared to $f_2=8$ kHz suggest more similar growth of response for the f_1 primary at the f_2 place when $f_2=1$ kHz than when $f_2=8$ kHz. This would be expected if there were more broadly tuned responses with more distributed nonlinearity in the apical regions of the cochlea.

B. Interactions between primary-level ratios and primary-frequency ratios

As discussed above, one hypothesis at the outset of this investigation was that differences in frequency resolution along the length of the cochlea might underlie the frequency dependence of the optimal L_1-L_2 observed in Neely *et al.* (2005). If this hypothesis was true, the optimal L_1-L_2 for each f_2 might be more similar if the frequency ratio was adjusted to maintain more consistent overlap at the f_2 place. The present results suggest that our hypothesis was too simplistic. If it were possible to compensate for differences in frequency resolution between the base and apex by varying either the primary-frequency or primary-level ratio, the optimal-path I/O functions in Fig. 3 would be superimposed. The horizontal and vertical offsets to these I/O functions suggest that it is not entirely possible to compensate for differences in basilar-membrane frequency selectivity by either decreasing f_2/f_1 or increasing L_1.

We had anticipated that frequency ratios <1.20 would be optimal for the higher frequency stimuli, particularly $f_2=8$ kHz. However, frequency ratios less than 1.20 were rarely associated with maximum DPOAE level (see Figs. 3 and 4). Additionally, for frequency ratios <1.20 there was a decrease in DPOAE level for all f_2 frequencies except 1 kHz (see Fig. 4). This decrease in level for $f_2/f_1<1.20$ occurs despite optimizing the L_1-L_2 to produce the maximum DPOAE level. One possible mechanism for this observation is that the primaries may be suppressing each other and possibly the DPOAE component for frequency ratios less than 1.20, thus counterbalancing the increase in DPOAE level associated with more "optimal" overlap of the cochlear representation of the primaries. This explanation has been proposed in the modeling work of Kanis and de Boer (1997) and Lukashkin and Russell (2001). Experimental observations in support of this view also have been reported by Cooper and Rhode (1997), based on direct observations of basilar-membrane motion under conditions of single- and two-tone stimulation.

The observation of a less steep decline in DPOAE level for $f_2/f_1<1.20$ when $f_2=1$ kHz (see Fig. 4) also may be consistent with the two-tone suppression interpretation. Cooper and Rhode (1997) observed an essentially flat frequency-ratio function for $f_2/f_1<1.40$ in mechanical responses in the apical region of chinchilla cochlea. This observation was in contrast to the more sharply tuned frequency-ratio function in the basal region of guinea pig cochlea. They attributed this difference in frequency-ratio tuning between the base and apex to the observation in their own work (Cooper and Rhode, 1996) and the work of Delgutte (1990), that two-tone suppression is stronger in the base than in the apex. The flatter frequency-ratio function when $f_2=1$ kHz as compared to higher f_2 frequencies in the present data suggest less suppression among the primaries and the DPOAE component when $f_2=1$ kHz.

C. Optimal stimulus parameters

The stimulus conditions associated with the maximum DPOAE levels (see Fig. 6), as well as our model for describing them, are consistent with hypothesized interactions among f_2/f_1, L_1-L_2, and L_2. As described above, frequency resolution is sharper for high frequencies than for low frequencies. However, for a given frequency, a broader cochlear representation is expected as level is increased. Therefore, larger frequency ratios were required for maximum DPOAE levels as either f_2 decreased or L_2 increased. Although the largest DPOAE levels were obtained using freely varying stimulus combinations (L_{dmax}), the time required to determine the stimulus conditions resulting in L_{dmax} for individual subjects may argue against its use. The DPOAE levels obtained from stimulus conditions described by the equations shown in Fig. 6 were less than L_{dmax} for some conditions, but were greater than those obtained by allowing only L_1-L_2 to vary (e.g., Kummer *et al.*, 1998; Neely *et al.*, 2005). These equations may have an added benefit in that they could be used to specify stimulus conditions for f_2 frequencies other than the ones used in this study.

The manner in which stimulus level is calibrated is expected to have an influence on the optimal stimulus parameters for recording DPOAEs. It has been shown that differences in sound pressure level exist at the tympanic membrane (TM) when stimuli are calibrated at the plane of the probe as compared to the plane of the TM, or when using an isovoltage strategy (e.g., Siegel, 1994; Siegel and Hirohata, 1994; Whitehead *et al.*, 1995b). These differences are most pronounced for frequencies exceeding 2–3 kHz and are variable across individuals. They are a consequence of the presence of standing waves in the ear canal, which vary with probe-insertion depth and ear-canal geometry for an individual ear. There is no simple method for accounting for these calibration errors, although Neely and Gorga (1998) suggest calibrating in acoustic intensity rather than acoustic pressure as a way to avoid standing-wave influences on stimulus level. Unfortunately, acoustic intensity calibrations

have not been widely utilized. While the optimal stimulus parameters described here may not generalize to alternate calibrations strategies, they are expected to result, on average, in the largest DPOAE levels in subjects with normal hearing for applications where stimulus levels are calibrated at the plane of the measurement probe. Furthermore, it may be of value to note the calibration was the same, regardless of which stimulus paradigm (Kummer *et al.*, 1998; Neely *et al.*, 2005; the present approach) was used to set stimulus conditions.

Investigations of the complete DPOAE parametric space are rarely attempted in humans because of the time involved in recording DPOAE responses for the large number of stimulus conditions that are necessary to explore the stimulus space. Mills (2002) described results from a comprehensive investigation of the DPOAE parametric space in the Mongolian gerbil. Similarly comprehensive investigations in humans are impractical. Parametric investigations in humans typically focus on a restricted region of the primary level or frequency space (e.g., Harris *et al.*, 1989; Gaskill and Brown, 1990; Kummer *et al.*, 1998; Neely *et al.*, 2005). The equations shown in Fig. 6, however, may obviate the need for comprehensive evaluations of stimulus conditions in individual subjects. Although the fits of these equations to the data shown in Fig. 6 may not appear compelling, the more important observation is how close the DPOAE levels were for the L_{dmax} and L_{dpar} stimulus conditions. Thus, the stimulus conditions defined by L_{dpar} may be a good compromise in that they do not require a complete exploration of the primary-level and primary-frequency-ratio space with every subject and they can be used with f_2 frequencies other than the ones used in the present study.

ACKNOWLEDGMENTS

This work was supported by the NIH NIDCD R01-DC02251, T32-DC00013, and P30-DC04662. Manuscript preparation was also supported by NIH NIDCD F32 DC007536. The authors would like to thank Darcia Dierking for her assistance with data collection and Hongyang Tan for her assistance with the analyses of these data.

Abdala, C. (**2000**). "Distortion product otoacoustic emission ($2f_1$-f_2) amplitude growth in human adults and neonates," J. Acoust. Soc. Am. **107**, 446–456.

Abdala, C. (**2003**). "A longitudinal study of distortion product otoacoustic emission ipsilateral suppression and input/output characteristics in human neonates," J. Acoust. Soc. Am. **114**, 3239–3250.

Abdala, C., and Fitzgerald, T. S. (**2003**). "Ipsilateral distortion product otoacoustic emission ($2f_1$-f_2) suppression in children with sensorineural hearing loss," J. Acoust. Soc. Am. **114**, 919–931.

ANSI (**1996**). ANSI 3.6-1996, "Specifications for audiometers" (American National Standards Institute, New York).

Brown, A. M., and Gaskill, S. A. (**1990**). "Measurement of acoustic distortion reveals underlying similarities between human and rodent mechanical responses," J. Acoust. Soc. Am. **88**, 840–849.

Brown, A. M., and Kemp, D. T. (**1984**). "Suppressibility of the $2f_1$-f_2 stimulated acoustic emissions in gerbil and man," Hear. Res. **13**, 29–37.

Brown, A. M., Sheppard, S. L., and Russell, P. T. (**1994**). "Acoustic distortion products (ADP) from the ears of term infants and young adults using low stimulus levels," Br. J. Audiol. **28**, 273–280.

Cooper, N. P., and Rhode, W. S. (**1996**). "Two-tone suppression in apical cochlear mechanics," Aud. Neurosci. **3**, 123–134.

Cooper, N. P., and Rhode, W. S. (**1997**). "Mechanical responses to two-tone distortion products in the apical and basal turns of the mammalian cochlea," J. Neurophysiol. **78**, 261–270.

Delgutte, B. (**1990**). "Two-tone rate suppression in auditory-nerve fibers: Dependence on suppressor frequency and level," Hear. Res. **49**, 225–246.

Dorn, P. A., Konrad-Martin, D., Neely, S. T., Keefe, D. H., Cyr, E., and Gorga, M. P. (**2001**). "Distortion product otoacoustic emission input/output functions in normal-hearing and hearing-impaired human ears," J. Acoust. Soc. Am. **110**, 3119–3131.

Gaskill, S. A., and Brown, A. M. (**1990**). "The behavior of the acoustic distortion product, $2f_1$-f_2, from the human ear and its relation to auditory sensitivity," J. Acoust. Soc. Am. **88**, 821–839.

Gorga, M. P., Neely, S. T., Dorn, P. A., and Konrad-Martin, D. (**2002**). "The use of distortion product otoacoustic emission suppression as an estimate of response growth," J. Acoust. Soc. Am. **111**, 271–284.

Gorga, M. P., Neely, S. T., Dierking, D. M., Dorn, P. A., Hoover, B. M., and Fitzpatrick, D. F. (**2003**). "Distortion product otoacoustic emission suppression tuning curves in normal-hearing and hearing-impaired human ears," J. Acoust. Soc. Am. **114**, 263–278.

Gorga, M. P., Neely, S. T., Ohlrich, B., Hoover, B., Redner, J., and Peters, J. (**1997**). "From laboratory to clinic: A large scale study of distortion product otoacoustic emissions in ears with normal hearing and ears with hearing loss," Ear Hear. **18**, 440–455.

Gorga, M. P., Neely, S. T., Bergman, B., Beauchaine, K. L., Kaminski, J. R., Peters, J., and Jesteadt, W. (**1993**). "Otoacoustic emissions from normal-hearing and hearing-impaired subjects: Distortion product responses," J. Acoust. Soc. Am. **93**, 2050–2060.

Harris, F. P., Probst, R., and Xu, L. (**1992**). "Suppression of the $2f_1$-f_2 otoacoustic emission in humans," Hear. Res. **64**, 133–141.

Harris, F. P., Lonsbury-Martin, B. L., Stagner, B. B., Coats, A. C., and Martin, G. K. (**1989**). "Acoustic distortion products in humans: Systematic changes in amplitude as a function of f_2/f_1 ratio," J. Acoust. Soc. Am. **85**, 220–229.

Hauser, R., and Probst, R. (**1991**). "The influence of systematic primary-tone level variation L_2-L_1 on the acoustic distortion product emission $2f_1$-f_2 in normal human ears," J. Acoust. Soc. Am. **89**, 280–286.

Janssen, T., Kummer, P., and Arnold, W. (**1998**). "Growth behavior of the $2f_1$-f_2 distortion product otoacoustic emission in tinnitus," J. Acoust. Soc. Am. **103**, 3418–3430.

Kanis, L. J., and de Boer, E. (**1997**). "Frequency dependence of acoustic distortion products in a locally active model of the cochlea," J. Acoust. Soc. Am. **101**, 1527–1531.

Kim, D. O., Dorn, P. A., Neely, S. T., and Gorga, M. P. (**2001**). "Adaptation of distortion product otoacoustic emission in humans," J. Assoc. Res. Otolaryngol. **2**, 31–40.

Kummer, P., Janssen, T., and Arnold, W. (**1998**). "The level and growth behavior of the $2f_1$-f_2 distortion product otoacoustic emission and its relationship to auditory sensitivity in normal hearing and cochlear hearing loss," J. Acoust. Soc. Am. **103**, 3431–3444.

Kummer, P., Janssen, T., Hulin, P., and Arnold, W. (**2000**). "Optimal L_1-L_2 primary tone level separation remains independent of test frequency in humans," Hear. Res. **146**, 47–56.

Lukashkin, A. N., and Russell, I. J. (**2001**). "Origin of the bell-like dependence of the DPOAE amplitude on primary frequency ratio," J. Acoust. Soc. Am. **110**, 3097–3106.

Mills, D. M. (**2002**). "Interpretation of standard distortion product otoacoustic emission measurements in light of the complete parametric response," J. Acoust. Soc. Am. **112**, 1545–1560.

Neely, S. T., and Gorga, M. P. (**1998**). "Comparison between intensity and pressure as measures of sound level in the ear canal," J. Acoust. Soc. Am. **104**, 2925–2934.

Neely, S. T., and Stevenson, R. (**2002**). "SYSRES," Tech. Memo. 19, Boys Town National Research Hospital, Omaha, NE.

Neely, S. T., Gorga, M. P., and Dorn, P. A. (**2003**). "Cochlear compression estimates from measurements of distortion-product otoacoustic emissions," J. Acoust. Soc. Am. **114**, 1499–1507.

Neely, S. T., Johnson, T. A., and Gorga, M. P. (**2005**). "Distortion-product otoacoustic emission measured with continuously varying stimulus level," J. Acoust. Soc. Am. **117**, 1248–1259.

Nelson, D. A., and Schroder, A. C. (**2004**). "Peripheral compression as a function of stimulus level and frequency region in normal-hearing listeners," J. Acoust. Soc. Am. **115**, 2221–2233.

Norton, S. J., Gorga, M. P., Widen, J. E., Folsom, R. C., Sininger, Y., Cone-Wesson, B., Vohr, B. R., Mascher, K., and Fletcher, K. (**2000**). "Identification of neonatal hearing impairment: Evaluation of transient

evoked otoacoustic emission, distortion product otoacoustic emission, and auditory brain stem response test performance," Ear Hear. **21**, 508–528.
Oxenham, A. J., and Dau, T. (**2004**). "Masker phase effects in normal-hearing and hearing-impaired listeners: Evidence for peripheral compression at low signal frequencies," J. Acoust. Soc. Am. **116**, 2248–2257.
Oxenham, A. J., and Plack, C. J. (**1997**). "A behavioral measure of basilar-membrane nonlinearity in listeners with normal and impaired hearing," J. Acoust. Soc. Am. **101**, 3666–3675.
Oxenham, A. J., and Plack, C. J. (**2000**). "Effects of masker frequency and duration in forward masking: Further evidence for the influence of peripheral nonlinearity," Hear. Res. **150**, 258–266.
Plack, C. J., and Drga, V. (**2003**). "Psychophysical evidence for auditory compression at low characteristic frequencies," J. Acoust. Soc. Am. **113**, 1574–1586.
Robles, L., and Ruggero, M. A. (**2001**). "Mechanics of the mammalian cochlea," Physiol. Rev. **81**, 1305–1352.
Shera, C. A., and Guinan, J. J., Jr. (**1999**). "Evoked otoacoustic emissions arise by two fundamentally different mechanisms: a taxonomy for mammalian OAEs," J. Acoust. Soc. Am. **105**, 782–798.
Siegel, J. H. (**1994**). "Ear-canal standing waves and high-frequency sound calibration using otoacoustic emission probes," J. Acoust. Soc. Am. **95**, 2589–2597.
Siegel, J. H., and Hirohata, E. T. (**1994**). "Sound calibration and distortion product otoacoustic emissions at high frequencies," Hear. Res. **80**, 146–152.
Stelmachowicz, P. G., Lewis, D. E., Larson, L. L., and Jesteadt, W. (**1987**). "Growth of masking as a measure of response growth in hearing-impaired listeners," J. Acoust. Soc. Am. **81**, 1881–1887.
Stover, L., Gorga, M. P., Neely, S. T., and Montoya, D. (**1996**). "Toward optimizing the clinical utility of distortion product otoacoustic emission measurements," J. Acoust. Soc. Am. **100**, 956–967.
Stover, L. J., Neely, S. T., and Gorga, M. P. (**1999**). "Cochlear generation of intermodulation distortion revealed by DPOAE frequency functions in normal and impaired ears," J. Acoust. Soc. Am. **106**, 2669–2678.
Whitehead, M. L., McCoy, M. J., Lonsbury-Martin, B. L., and Martin, G. K. (**1995a**). "Dependence of distortion-product otoacoustic emissions on primary levels in normal and impaired ears. I. Effects of decreasing L_2 below L_1," J. Acoust. Soc. Am. **97**, 2346–2358.
Whitehead, M. L., Stagner, B. B., Lonsbury-Martin, B. L., and Martin, G. K. (**1995b**). "Effects of ear-canal standing waves on measurements of distortion-product otoacoustic emissions," J. Acoust. Soc. Am. **98**, 3200–3214.
Whitehead, M. L., Stagner, B. B., McCoy, M. J., Lonsbury-Martin, B. L., and Martin, G. K. (**1995c**). "Dependence of distortion-product otoacoustic emissions on primary levels in normal and impaired ears. II. Asymmetry in L_1,L_2 space," J. Acoust. Soc. Am. **97**, 2359–2377.

Signal-to-noise ratio and frequency analysis of continuous loop averaging deconvolution (CLAD) of overlapping evoked potentials

Özcan Özdamar
Department of Biomedical Engineering, College of Engineering, University of Miami, Coral Gables, Florida 33124 and Department of Otolaryngology, Pediatrics and Neuroscience, Miller School of Medicine, University of Miami, Miami, Florida 33101

Jorge Bohórquez
Department of Biomedical Engineering, College of Engineering, University of Miami, Coral Gables, Florida 33124

(Received 3 June 2005; revised 6 October 2005; accepted 12 October 2005)

In this study, a frequency domain formulation of continuous loop averaging deconvolution (CLAD) of overlapping evoked potentials is developed and applied for the extraction of transient responses from recordings obtained at high stimulation rates. This formulation allows for a faster execution of CLAD by using fast Fourier transform algorithms. The frequency characteristics of the deconvolution filter depends exclusively on the stimulus sequence and determines whether the noncoherent noise is amplified or attenuated in different frequencies. A formula for calculating the signal-to-noise ratio (SNR) achieved by the deconvolution process is developed. The newly developed theory and the methodology is applied to the extraction of the auditory brainstem and middle latency responses using various sequences. The effects of the sequence used and the number of sweeps averaged in ongoing acquisition on SNR are examined by using single sweep recordings. The results verify the deconvolution theory and the methodology and show its limitations. Depending on the frequency characteristics of the sequence, the deconvolution process can amplify or attenuate the EEG noise. Proper selection of the stimulus sequence can increase the SNR enhancement obtained with conventional averaging. © *2006 Acoustical Society of America.* [DOI: 10.1121/1.2133682]

PACS number(s): 43.64.−q, 43.64.Ri [BLM] Pages: 429–438

I. INTRODUCTION

Auditory evoked responses (AERs) are almost exclusively acquired using conventional averaging to increase the signal-to-noise ratio (SNR) of the acquired brain waves. In general, transient evoked responses require the infrequent presentation of the stimulus so the waves generated by it disappear before the next stimulus is presented. Steady-state responses, on the other hand, require the presence of frequent stimuli such that the frequency component of the response stays constant in the frequency domain. When the stimuli are presented before the effects of the previous response disappear, overlapping of the response components occurs. This wrapping problem is a frequent occurrence whenever adaptation or stimulus rate studies are conducted or when the stimulus rate is increased to achieve rapid acquisition of the AERs. Overlapping of the different response components creates complex and often unidentifiable waveforms that hinder the scientific and clinical applicability of evoked responses.

A solution to the overlap problem was first offered by Eysholdt and Schreiner (1982) who used the unique autocorrelation property of maximum length sequences (MLSs) to deconvolve overlapping auditory brainstem responses (ABRs) obtained at high rates. The method was later adopted by several auditory researchers who expanded the application and applied it to other classes of AERs and otoacoustic emissions (OAEs) (Burkard *et al.*, 1990; Lasky *et al.*, 1992; Picton *et al.*, 1992; Thornton, 1993a; Bell *et al.*, 2001).

The MLS method, however, has a few limitations and works only when stimuli are presented with a preset MLS sequence. Since only a handful of such sequences are available in MLS or similar sequences (e.g., Legendre), only a few different mean rates could be achieved for a given minimum pulse interval (MPI). The sequence length and MPI can be varied by zero padding and/or changing the sampling frequency to achieve mean rates as high as 1000 Hz (Burkard *et al.*, 1996a, b). The MPI at such high rate is 0.5 ms, which runs the risk of temporal overlap of acoustic click waveforms. The interstimulus interval (ISI) patterns of the MLS sequences are fixed and cannot be changed. They contain a wide but uneven distribution of ISIs which may generate a different result than a regularly spaced conventional stimulus sequence due to adaptation (Burkard *et al.*, 1996a, b).

To provide a more general solution to the overlap problem, we recently developed a new method called continuous loop averaging deconvolution (CLAD) which can utilize a very wide set of sequences (Özdamar *et al.*, 2003a, b; Delgado and Özdamar, 2004). CLAD uses a time-domain approach to develop a set of simultaneous equations for a given sequence. These equations are solved by matrix algebra and a solution generally exists as long as the resulting matrix of coefficients is invertable (i.e., not singular). In this approach,

sequences are randomly chosen and the resulting simultaneous equations are solved using matrix algebra. Not all solvable sequences, however, yield workable results since some sequences cause the generation of high levels of low-frequency (sloping) or high-frequency (ripples) noise by enhancing the EEG noise already present in the recording.

In this study we develop a generalized theory to explain the origin of such undesirable noise and a fast computational method to deconvolve the overlapping responses in the frequency domain. Thus, a trial and error approach to sequence generation is replaced with a noise-analysis-based approach. A similar frequency domain solution has been very recently proposed for quasi-steady-state sequences with similar results (Jewett *et al.*, 2004). In this study we further develop a generalized method to calculate the signal-to-noise ratio (SNR) for any sequence and analyze the noise attenuation and amplification characteristics of averaged deconvolution processes. The developed method and the results give insight for the proper design of sequences for the application of fast stimulus rates in basic research and clinical diagnosis.

II. THEORY AND COMPUTATION

Let $\{t_n\}$ be an N sequence of stimulus time positions in an acquisition buffer of length T and N be the number of stimuli presented within the acquisition buffer. Time positions are defined as $0 \leqslant t_n \leqslant T-1$, $n=1,\ldots,N$. Let $v(t), t=0,\ldots,T-1$ be the measured evoked response to all N stimuli. Let $a(t), t=0,\ldots,T-1$ be a transient evoked response of time length T. Let us assume that T is large enough that $a(t)=0$ for $t>T$ and $a(t)$ represents the elementary response to a single stimulus in infinite time.

A. Circular convolution formulation

Assuming that there is no adaptation in responses and each stimulus evokes the same response, the total measured response, $v(t)$, is the periodic superposition of all the N elementary responses, $a(t)$:

$$v(t) = \sum_{n=1}^{N} a(t - t_n). \tag{1}$$

This equation assumes that the signal $a(t)$ wraps around in a circular fashion with period T (Delgado and Özdamar, 2004), so the term $(t-t_n)$ should be interpreted as $[(t-t_n)$ modulus $T]$.

Equation (1) can be expressed in the familiar form of a standard convolution equation:

$$v(t) = a(t) * s(t), \tag{2}$$

where $s(t)$ is the stimulus sequence function. Convolution of the elementary responses with the stimulus sequence expressed above can be expressed in a matrix form as

$$\vec{v}(t) = [M] \times \vec{a}(t), \tag{3}$$

where matrix M represents the stimulus sequence $s(t)$ diagonally shifted in consecutive rows for performing convolution. Equation (3) can be solved by inverting the matrix M (Delgado and Özdamar, 2004) to obtain the unwrapped signal as shown below:

$$\vec{a}(t) = [M]^{-1}\vec{v}(t). \tag{4}$$

Each column of the inverted matrix corresponds to the impulse deconvolution function and $a(t)$ can be easily obtained by performing the matrix multiplication operation shown in Eq. (4).

B. Deconvolution in the frequency domain

If we compute the Fourier transform (FT) to the both sides of (2), we obtain

$$V(f) = A(f)S(f). \tag{5}$$

The signal $a(t)$ can be then computed using (5):

$$a(t) = \mathrm{FT}^{-1}\left(\frac{V(f)}{S(f)}\right) \quad if\ [S(f) \neq 0]\ \forall f. \tag{6}$$

The above deconvolution is possible only if the frequency domain transfer function does not have any zero values. Time domain convolution and the frequency domain deconvolution processes are shown below in Fig. 1.

C. Response acquisition to a stimulus sequence

In Fig. 2 evoked response acquisition for a stimulus sequence is outlined. The top left section (A) shows a typical arrangement of the electrode positions for a right ear monaural stimulus presentation. The resulting recording is the summation of the spontaneous EEG which is primarily responsible for the noise and the convolved evoked response in response to the stimulus sequence shown on the top right section (B). Since the EEG noise is much greater than the overlapped evoked response, several sweeps (K sweeps in this case) are averaged to decrease the effects of noise as shown in the bottom of the figure. Thus, a convolved evoked response linearly added to an averaging attenuated noise is recorded.

D. Computational methods and limitations

The deconvolved evoked response $a(t)$ can be computed by first converting both the measured response $v(t)$ and the stimulus sequence $s(t)$ to the frequency domain and then using Eq. (6) as displayed in Fig. 3. The denominator of Eq. (6) determines if a solution is possible and shows the characteristics of the response. If the $S(f)$ is zero, no solution is possible. This corresponds to isochronic sequences in which no solution exists [in the time domain, matrix M is singular and cannot be inverted (Delgado and Özdamar, 2004)]. The inverse of the denominator $[1/S(f)]$ is named the deconvolution filter $[H(f)]$ and is analyzed individually to examine the noise characteristics of the deconvolution process. The time domain version of this function is the deconvolution impulse response and corresponds to a column or row of the deconvolution matrix in the CLAD formulation.

Overlap (convolution) of evoked responses occurs in the brain due to the simultaneous activation of multiple generators. EEG noise is added to this process during acquisition.

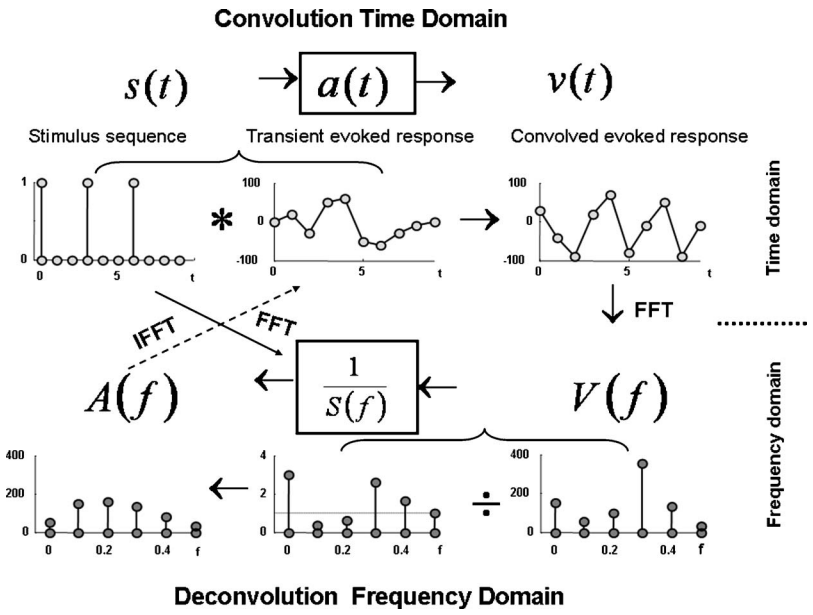

FIG. 1. Convolution (overlapping) of the elementary responses to a stimulus sequence in the time domain produces a convolved response (top) and the deconvolution of the convolved response into the elementary response in the frequency domain (bottom). A ten-point elementary response $a(t)=\{0,20,-30,50,60,-50,-60,-30,-10,0\}$ and three stimuli sequence $s(t)=\{1\ 0\ 0\ 1\ 0\ 01\ 0\ 0\ 0\}$ are shown as an example taken from Delgado and Özdamar (2004). The deconvolution process expressed in the frequency domain is used to recover the original unwrapped time domain signal $a(t)$.

During the numerical deconvolution process both the signal and the noise are affected by the deconvolution filter. Since the effects of the convolution and the deconvolution processes annihilate each other, the deconvolution process leaves the elementary signal untouched while the noise is affected by both the characteristics of the deconvolution filter and the averaging process. Thus, noise attenuation (or amplification) of the deconvolution averaging process depends solely on the stimulus sequence frequency characteristics and the number of sweeps averaged.

E. SNR computation

Signal-to-noise ratio (SNR) in a process is generally defined as the ratio of the signal power (signal variance),σ_s^2, to the noise power, σ_n^2. $\mathrm{SNR}_{\mathrm{amp}}$ can also be defined in the amplitude sense by taking the ratio of the square root of signal and noise power expressed as below [Eq. (10)] where c_g is the gain factor due to any noise reduction process (amplification or attenuation):

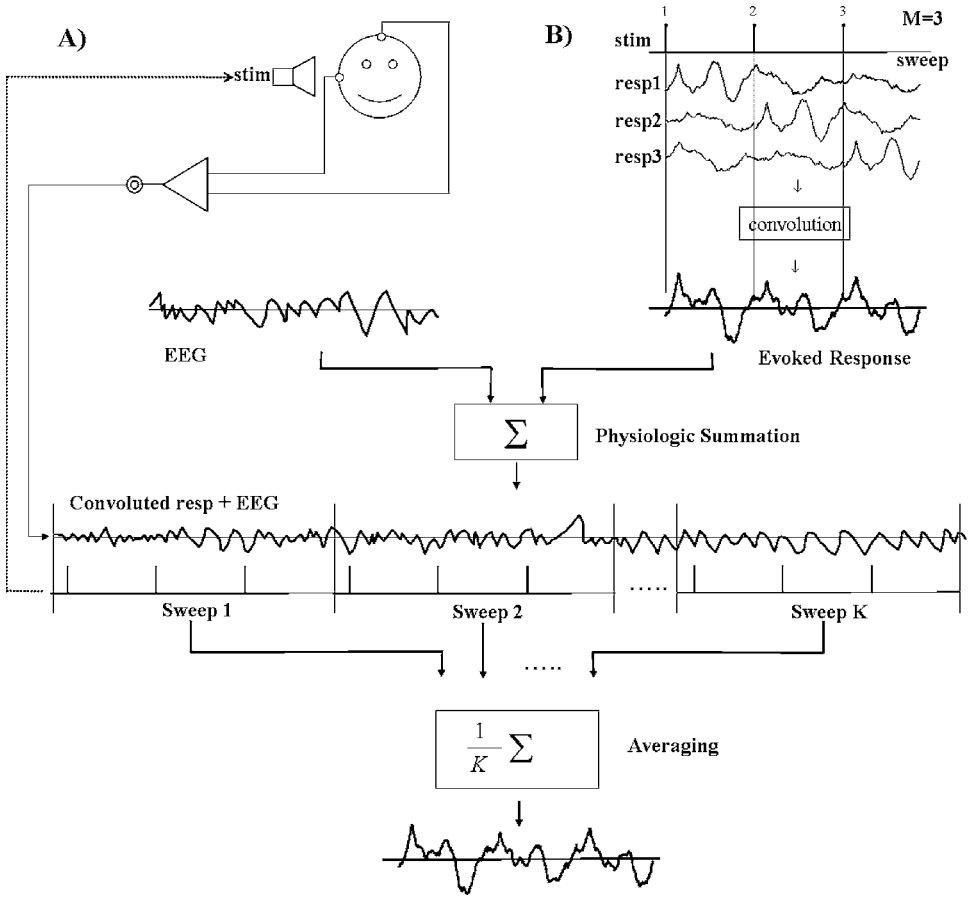

FIG. 2. Overlapping (convolution) of the evoked responses with high rate stimulation (top right) with the superposition of EEG (top left) during averaging operation (bottom). The averaged response shown on the bottom contains a convolved averaged response with residual noise attenuated with conventional averaging.

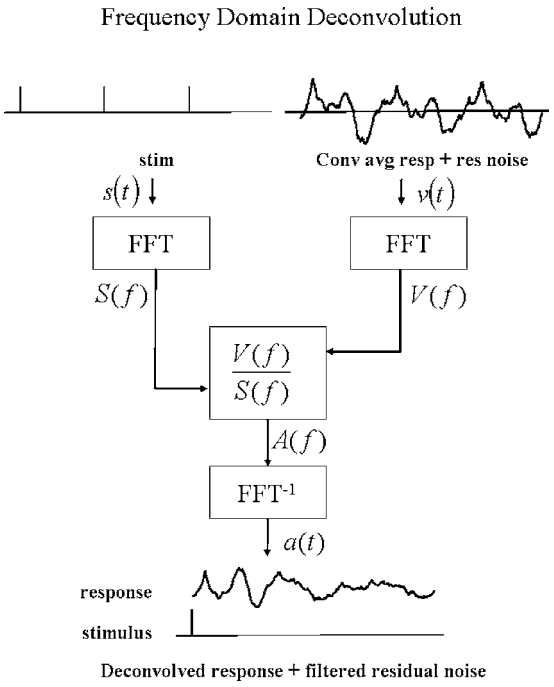

FIG. 3. Block diagram of the deconvolution process in the frequency domain. The convolved response obtained from a subject with the three stimuli sequence shown in Fig. 2 is deconvolved to compute the unwrapped evoked response shown in the bottom.

$$\mathrm{SNR}_{\mathrm{amp}} = \frac{\sigma_s}{c_g \sigma_n}. \tag{7}$$

In conventional averaging, noise is attenuated in proportion to the number of sweeps averaged as stated below (Özdamar and Delgado, 1996),

$$c_g = c_{\mathrm{avg}} = \frac{1}{\sqrt{K}}, \tag{8}$$

where K is the number of sweeps averaged.

When the deconvolution process is implemented, a deconvolution gain factor, c_{dec}, needs to be incorporated into the formula as stated in Eq. (9) below:

$$c_g = c_{\mathrm{dec}} c_{\mathrm{avg}} = c_{\mathrm{dec}} \frac{1}{\sqrt{K}}. \tag{9}$$

Noise attenuation due to deconvolution using the MLS procedure has been a controversial issue. While some researchers have doubted any noise attenuation advantage, others offered noise reduction estimations (Marsh, 1992; Thornton, 1993b; Bell *et al.*, 2001, 2002). In this study we will develop a general method to calculate the noise attenuation factor due to the filtering of the deconvolution process for any stimulus sequence. In an accompanying paper (Bohórquez and Özdamar, 2006), a general formula for noise attenuation will be derived for any MLS deconvolution using the method developed here.

Deconvolution transfer function $H(f)$ can be expressed as the inverse of the stimulus transfer function, $S(f)$ as shown below [Eq. (10)]:

$$H(f) = 1/S(f). \tag{10}$$

The deconvolution gain factor c_{dec} is essentially a summation of all the gain factors for each frequency band other than the dc component ($i=0$). Using Parseval's theorem and assuming that $N(f)$ is constant for all frequencies, the noise gain factor due to deconvolution can be expressed as below:

$$c_{\mathrm{dec}} = \sqrt{\frac{1}{F}\sum_{i=1}^{F} H(f)H^*(f)} = \sqrt{\frac{1}{F}\sum_{i=1}^{F} \frac{1}{S(f)S^*(f)}}, \tag{11}$$

where F is the Nyquist frequency.

In this study, the magnitude of the deconvolution filter which shows the noise gain factor for each frequency band is plotted as a function of frequency. When the noise gain factor is bigger than one, noise is amplified which is not desirable. When it is less than one, noise is attenuated and SNR is increased. In Fig. 1 the deconvolution frequency response $|H(f)|$ shows the amplified frequencies ($f=0.1$ and 0.2) and the attenuated frequencies ($f=0.3$ and 0.4). The gain at the Nyquist frequency ($f=0.5$) is equal to one which keeps the noise at the same level. For this filter the deconvolution gain factor is computed to be 1.48 which indicates an overall amplification of noise if present.

The overall SNR formula for the deconvolution averaging is given as follows:

$$\mathrm{SNR}_{\mathrm{tot}} = \frac{1}{\sqrt{K}} \frac{\sigma_s}{c_{\mathrm{dec}} \sigma_n}. \tag{12}$$

III. EXPERIMENTAL METHODS

A. Response acquisition

In this study two types of human recordings were obtained to verify the validity of the equations developed in the previous section. The purpose of the first study was to demonstrate the effects of the filtering characteristics of the sequences on the deconvolved response. This was achieved by generating stimulus sequences with similar rate and length characteristics but different filter functions. For the second study, the goal was to demonstrate the characteristics of the noise as a function of the sweeps averaged. This required the recording of the data in single sweep mode and performing averaging off-line. For comparisons with the theoretical results, rms values were computed for estimating noise and signal amplitudes. In both studies, recording parameters were chosen such that both auditory brainstem responses (ABRs) and middle latency responses (MLRs) were recorded simultaneously using monaural stimulation. Five young normal-hearing adult subjects with no history of neurological problems participated in two studies. In both studies stimuli were delivered monaurally to the subject's ear at 92 dB SPL using ER-3A insert phones (EtymoticResearch, Elk Grove Village, IL). Acoustic calibration was done in a 2-cc acoustic coupler using a precision sound level meter (Quest Model 1800) to measure peak dB SPL levels. Scalp AER recordings were obtained with differential amplifiers (noninverting: forehead; inverting: ipsilateral mastoid; common: contralateral mastoid) and stored digitally for later processing and analysis.

The first part of the study was conducted using the Smart-EP averaging system (Intelligent Hearing Systems,

TABLE I. Stimulus time occurrences and their properties of the ten sequences used in the first study. Buffer size is 1024 points which corresponds to 204.8 ms sweep time.

Sequence no.	Sequence	No. of stimuli	Average Rate (/s)	Interpulse interval (ms)			
				min	max	mean	st. d.
1	1, 137, 273, 409, 545, 681, 817	7	34.18	27.20	41.60	29.26	5.44
2	1, 129, 257, 385, 513, 641, 769, 957	8	39.06	13.60	37.60	25.60	6.41
3	1, 129, 257, 385, 513, 641, 769, 901	8	39.06	24.80	26.40	25.60	0.43
4	1, 129, 257, 385, 513, 641, 769, 993	8	39.06	6.40	44.80	25.60	10.26
5	1, 129, 261, 393, 525, 657, 789, 921	8	39.06	20.80	26.40	25.60	1.96
6	1, 149, 281, 393, 501, 661, 785, 921	8	39.06	20.80	32.00	25.60	3.97
7	1, 61, 245, 317, 469, 517, 565, 785	8	39.06	9.60	48.00	25.60	11.09
8	1, 129, 257, 385, 513, 641, 769	7	34.18	25.60	51.20	29.26	9.68
9	1, 229, 257, 377, 413, 521, 633, 877	8	39.06	5.60	48.80	25.60	15.68
10	1, 25, 217, 297, 385, 661, 885	7	34.18	4.80	55.20	29.26	17.84

Miami FL) using routine procedures (gain: 100 000; electrodes: filters: 10–1500 Hz, 6 dB/oct). For this study, ten different sequences with identical lengths (1024) and similar rates (34 and 39/s) were designed. A rate around 40 Hz was chosen so large ABRs and MLRs can be elicited at a fairly high rate known to generate large steady-state responses. The exact time occurrences of these sequences, their average rates, and their interstimulus interval properties are listed in Table I.

The acquisition program was modified to allow acquiring and averaging of responses without any loss of data using the special stimulus buffer. Data was acquired with 200 μs sampling time (5-kHz sampling frequency) into a 1024-point acquisition buffer (T) and averaged in real time. The duration of the acquisition buffer and the deconvolved response were 204.8 ms. A total of 1024 sweeps were averaged for each recording. Two averages were obtained for each sequence. No single sweep responses were saved for this study.

The second part of the study was conducted using the NeuroScan System (Compumedics, El Paso, TX) using the sequence {1 43 71 87 151 185 221} with length $L=256$. Fifteen zeros were padded to each data point to increase the length of the sweep to $L=4096$. Sampling frequency of system was set to 20 kHz, creating a 204.8-ms sweep time. This acoustic stimulation resulted in a 37.4/s average rate. For this study stimuli were 1000-kHz tone pips (1-ms rise and fall times, 5-ms duration) generated according to the above sequence.

Acoustic stimulation for the second study was achieved by using a laptop computer which generated the sounds delivered to the subject's ear. The trigger points were recorded in one of the channels of the NeuroScan machine. NeuroScan allowed continuous recording of EEG responses to individual sweeps. Recordings were done with 100 000/ amplification at 1–1000 Hz(12 dB/oct); sampling frequency was at 20 kHz and 1500 sweeps were recorded. Sweep-by-sweep averaging and deconvolution were done offline.

B. SNR computation in ongoing deconvolution averaging

In clinical applications, it is desirable to observe the ongoing evoked response averaging to monitor the effects of noise and the patient's EEG state. This can be done by displaying signal and noise sweep-by-sweep and plotting the resultant SNR as a function of sweeps averaged (Özdamar and Delgado, 1996). For deconvolution averaging this can be done by displaying Eq. (12) as a function of K, the number of sweeps averaged. For each sweep averaged, signal and cumulative noise magnitude should be estimated. Cumulative noise estimate magnitude can be estimated as follows [Eq. (13)] by finding the standard deviation of the whole recorded EEG signal $v(t)$ since evoked response is only a small fraction of this response:

$$\sigma_n(K) \cong \sqrt{\frac{(\sigma_{v1}^2 + \sigma_{v2}^2 + \cdots + \sigma_{vK}^2)}{K}} = \sqrt{\frac{\sum_{k=1}^{K} \sigma_{vk}^2}{K}}. \tag{13}$$

The variance of $v(t)$ for the kth sweep is computed as follows:

$$\sigma_{vk}^2 = \frac{\sum_{t=1}^{T} v_k^2(t)}{T}. \tag{14}$$

The signal estimate is computed as the deconvolved averaged signal from Eq. (6) as follows:

$$\sigma_s(K) \cong \sqrt{\frac{\sum_{t=1}^{T} a_K^2(t)}{T}}, \tag{15}$$

where $a_K(t)$ is the deconvolved signal at the end of the Kth sweep.

IV. RESULTS

A. Effects of stimulus sequence filter characteristics on AER recordings

For the first study ten stimulus sequences with similar rates and length characteristics were designed. The deconvolution filter characteristics of the stimulus sequences used in this study are listed in Table II in the order of decreasing c_{dec} values. Three seven-stimulus sequences (#1, 8, and 10) had the same average rate of 34.18/s. The first sequence (#1), however, had a high noise amplifying gain with a low noise attenuating gain (9.18 vs. 0.66) in contrast to other sequences

TABLE II. Characteristics of the ten sequences used in the first study.

Sequence No.	Noise amplifying gain (Bad SNR)	Noise attenuating gain (Good SNR)	Bandwidth ratio (attenvation/amplitude)	Noise gain factor c_{dec}
1	9.18	0.66	1.20	6.21
2	9.44	0.59	2.48	5.08
3	6.26	0.63	1.81	3.18
4	2.77	0.58	2.37	1.59
5	2.54	0.59	2.16	1.51
6	3.72	0.48	6.77	1.41
7	2.80	0.50	6.77	1.11
8	⋯	0.94	Infinite	0.94
9	2.47	0.50	8.18	0.94
10	1.86	0.47	4.32	0.91

(#8 and 10) which has none or 1.86 noise amplifying gain with high noise attenuating gains of 0.94 and 0.47, respectively. The total noise attenuating factors for these three filters were 6.21, 0.94, and 0.91, respectively. The other seven eight-stimulus sequences (#2, 3, 4, 5, 6, 7, and 9) were chosen to reflect various noise characteristics and have an average rate of 39.06/s. Their total noise gain factors ranged from a high of 5.08 to a low of 0.94.

The time occurrences and the ISI histograms of the sequences are shown on the left two columns of Fig. 4. The deconvolution filter characteristics of these sequences are shown in the third column. Figures show the transfer function of the deconvolution filter having high resonances when the sequence tends to be isochronic. As a consequence this results in noise amplification at specific frequency bands. Conversely, when the stimulation sequence has more jitter, the deconvolution filter tends to be flatter in the frequency domain.

The fourth column of Fig. 4 displays the deconvolved responses obtained from one subject. As observed, the first three rows represents high noise gain sequences ($c_{dec} > 3.0$) and ABR-MLR components cannot be recognized in the deconvolved responses. The type of noise contaminating the response can be predicted from the deconvolution filter characteristics displayed in the third column. The frequency of the oscillatory noise observed in the first two responses (1 and 2) corresponds to the frequencies of the peaks observed in the deconvolution filter. The third response shows the effects of high noise in the low frequencies as reflected by the low-frequency sloping line. The seventh response show the insidious noise gain at 40 Hz which increases the amplitude of the P_a response artificially which may be mistaken as a real physiological response.

Generally the deconvolution filter displays high resonances at certain frequencies when the sequence tends to be isochronous. As a consequence, this results in noise amplification at those specific frequency bands. Conversely, when the stimulation sequence has more jitter, the deconvolution filter tends to be flatter in the frequency domain. This is not always the case, however, as shown in the eighth response (missing click) where no noise amplification is observed.

B. Signal and noise characteristics as a function of sweeps averaged

The time characteristic of the sequence used for the second study is plotted in Fig. 5(A). This sequence presented at 20 kHz produced a 37.4/s average rate and a 204.8-ms sweep time. A sample EEG to this sequence is shown in Fig. 5(B). The deconvolved response to this sweep is given in Fig. 5(C). As easily observed, trace 5(C) (deconvolved response) has a reduced amplitude compared to trace 5(B) (convolved response). The averaged convolved and deconvolved responses to 1435 sweeps are shown in Figs. 5(D) and 5(E), respectively. Again reduction of noise in the averaged deconvolved response is easily observable.

The frequency response of the stimulus sequence shown in Fig. 6 (top) is plotted for frequencies up to 300 Hz. The deconvolution gain factor c_{dec} of this sequence is 0.5186 and it has very few noise amplification bands as seen in the figure. Average rms amplitudes of the convolved and deconvolved recorded EEG responses as a function of frequency are plotted in Fig. 6 (middle). As expected most of the EEG energy is below 50 Hz. The bottom portion of Fig. 6 shows the experimentally obtained magnitude ratios of the convolved responses to deconvolved responses for each frequency band. The similarity of theoretical and experimental frequency function is striking, confirming the validity of the deconvolution theory.

V. DISCUSSION

In this study a frequency domain analysis of the generalized theory of the deconvolution of overlapping evoked potentials is presented. The present study extends the matrix-based operations of the time-domain based CLAD (Delgado and Özdamar, 2004) procedure into the frequency domain and characterizes the operations as transfer functions. The deconvolution or cross-correlation procedures have been described in the literature primarily as pertaining to special sequences such as MLS (Chan *et al.*, 1992; Van Veen and Lasky, 1994). Only recently these procedures have been extended to arbitrary sequences (Delgado and Özdamar, 2004; Jewett *et al.*, 2004) without a general explanation of the SNR characteristics of such procedures. The generalized theory and mathematical formulation developed in this study lead naturally to the SNR analysis of the deconvolution procedure for any given stimulus sequence. The deconvolution gain factor, c_{dec} given in Eq. (11), gives an overall description of the gain (attenuation or amplification) that can be achieved by a given stimulus sequence. The overall SNR of the CLAD deconvolution procedure is given by Eq. (12), which combines the number of sweeps averaged conventionally as well as the deconvolution gain factor achieved by the stimulus-sequence-dependent procedure and the signal and noise variances.

As clearly explained in this study, the deconvolution process is very strongly dependent on the frequency characteristics of the stimulus sequence and the EEG signals recorded. The particular gain value of the stimulus sequence at a given frequency determines whether the incoming EEG noise is amplified ($c_{dec} > 1$) or attenuated ($c_{dec} < 1$) as illus-

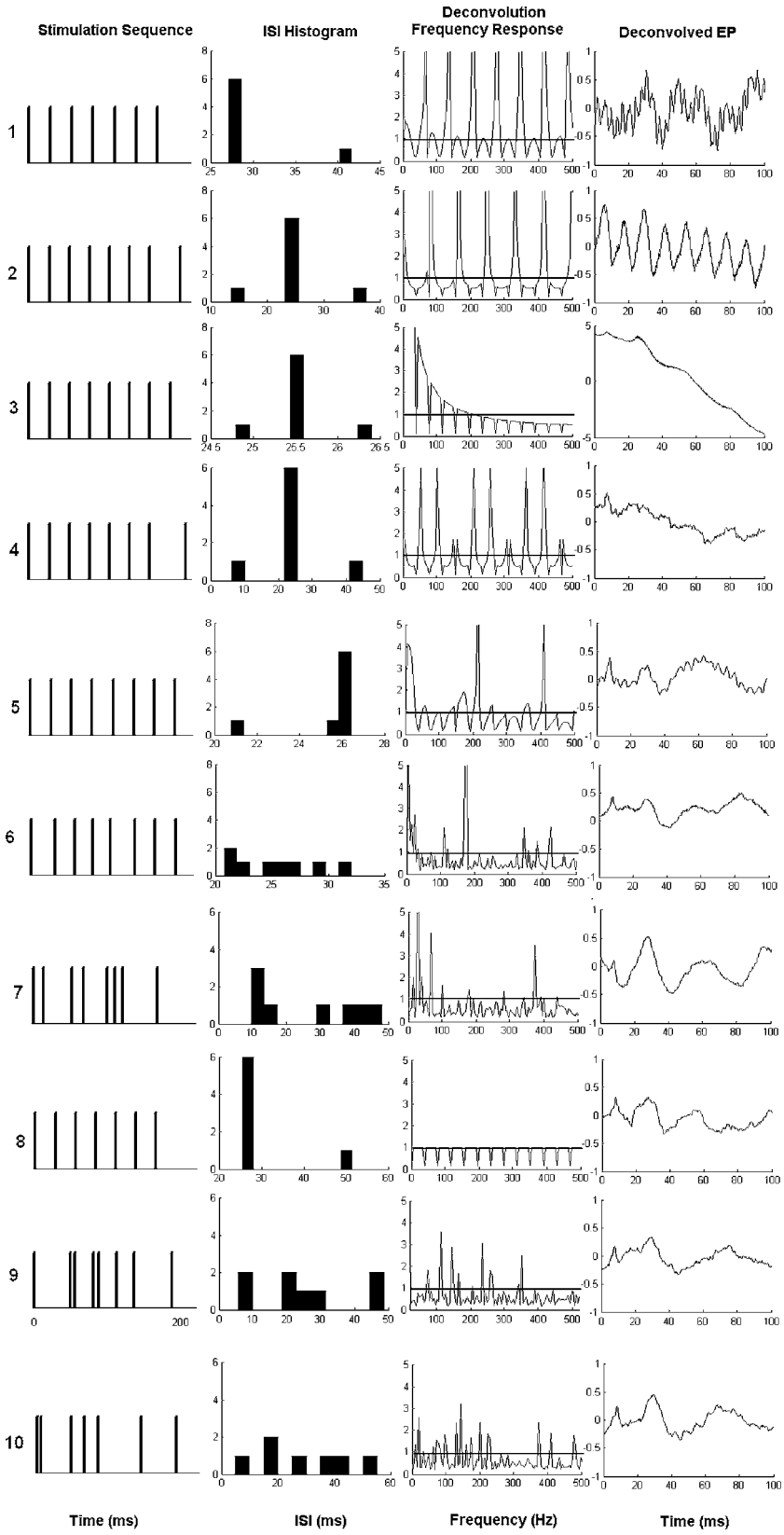

FIG. 4. Examples of different stimulus sequences (first column), their interstimulus interval histograms (second column), frequency responses of the sequences (third column), and the deconvolved responses obtained from a subject (fourth column). Noise gain factor of the deconvolution process is displayed in the third column. The horizontal line at 1.0 gain separates the noise amplification region (top) from the noise attenuation region (bottom). Time domain, frequency domain, and the SNR characteristics of each sequence are listed in Tables I and II.

trated in Fig. 4. Consequently a low overall c_{dec} value is not a guarantee for satisfactory noise attenuation if a large amplification value exists at a frequency where there is a dominant EEG presence. Sequences with deconvolution gain factors less than one at all frequencies naturally occur for all pseudorandom sequences such as the MLS and guarantee the attenuation of the EEG noise. The treatment of the noise characteristics of such sequences and the formulation of SNR will be developed in our accompanying article (Bohórquez and Özdamar, 2006).

The time-domain deconvolution method developed in our previous study (Delgado and Özdamar, 2004) and ex-

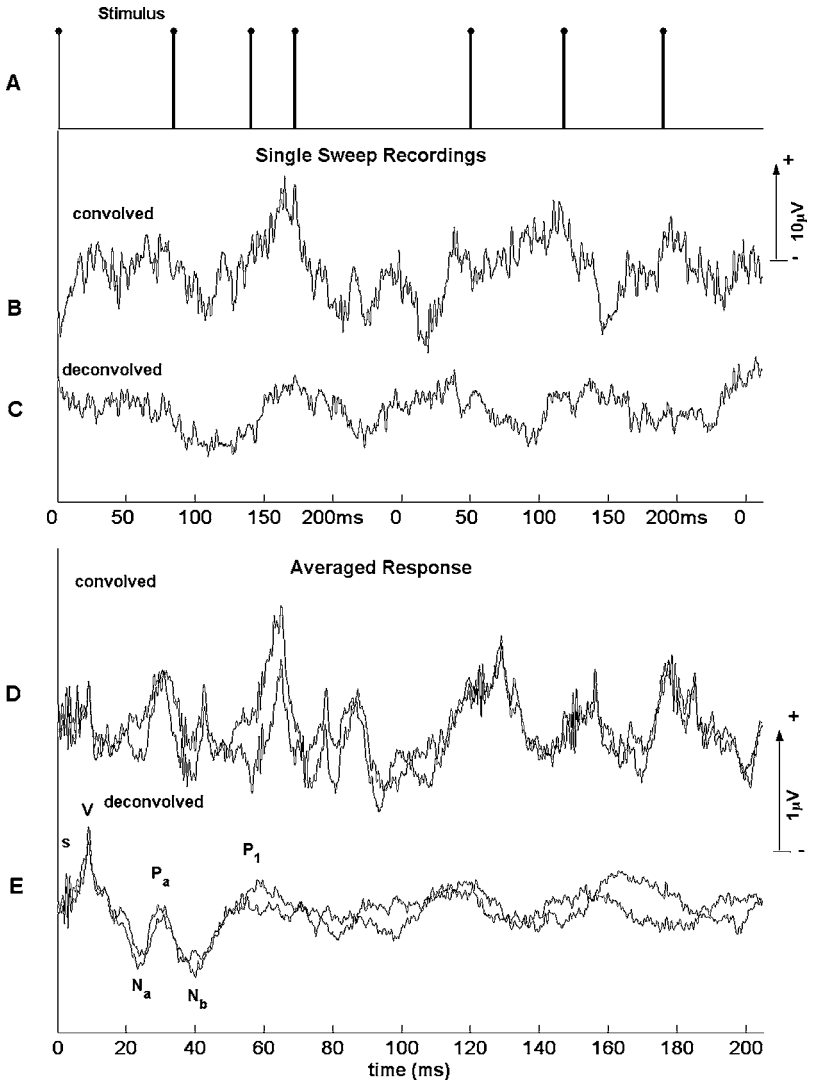

FIG. 5. Single sweeps and averaged recordings and their deconvolutions of a 37.4/s mean rate sequence. Time display of the sequence (A); a sample single sweep recording (B) and its deconvolution (C); averaged single sweep recording (D) and its deconvolution (E). The sequence (L=4096, N=7) duration is 204.8 ms and 1435 sweeps are averaged. Noise level in responses is reduced for this sequence after deconvolution as observed in both deconvolved single sweep (C) and averaged (E) recordings. Major peaks of the ABR (V) and MLR (N_a, P_a, N_b, and P_1) are labeled. S is the stimulus artifact and can be observed in the averaged original (convolved) and deconvolved recordings.

tended to the frequency domain in this study is a powerful strategy to separate overlapping evoked potentials acquired at high speeds. This method enables us to record EPs potentially at all rates possibly limited only by the absolute refractory period of the action potentials and the length of the stimulus. The use of high stimulus rates in ABRs, as a "stress test" for the auditory system, has long been recognized as a potential facilitator in the diagnosis of many diseases and disorders involving the auditory pathways (e.g., Hecox *et al.*, 1981). Overlapping of ABRs at stimulation rates greater than 100 Hz has limited the potential utility of this stress test and deconvolution techniques with arbitrary sequences (Delgado and Özdamar, 2004; Jewett *et al.*, 2004) and MLS have been used to overcome this barrier (e.g., Jiang *et al.*, 2003; Lasky *et al.*, 1992; Lina-Granade *et al.*, 1994; Leung *et al.*, 1998). The MLS method, however, offers a limited solution to this problem due to the availability of few specific stimulus sequences. Due to the high jitter of these sequences, the adaptation effects vary a lot, thus possibly smearing the obtained responses (Picton *et al.*, 1992). Also the maximum average rate cannot be attained easily due to this high jitter range without reducing MPI to intervals where acoustic overlapping might be a problem. With a minimum of 1 ms MPI, the maximum attainable mean rate for a MLS sequence is 500 Hz. Using properly designed CLAD sequences this upper limit can be extended towards 1000 Hz (Özdamar *et al.*, 2003a).

The overlapping problem gains even more importance when later occurring AERs, such as MLRs, late latency responses (LLRs), or event-related potentials (ERPs), are considered. The overlap of waveforms is easily observed in recording MLRs at rates above 10 to 15 Hz and is recognized as the primary (if not exclusive) generator of the 40-Hz auditory steady-state responses (ASSRs) (e.g., Galambos *et al.*, 1981). Our recent CLAD studies show that the P_a component of the MLR persists even at stimulation rates as high as 500 Hz (Özdamar *et al.*, 2003b; Delgado and Özdamar, 2004). However, whether high-rate MLRs could be useful in diagnosis, as high-rate ABRs, remains to be seen.

The deconvolution technique using the MLS has been frequently proposed to shorten the acquisition time in recording EPs. This proposition, however, has been controversial due to the lack of firm theoretical formulation and the somewhat ubiquitous nature of the experimental results (Burkard *et al.*, 1990; Marsh, 1992; Thornton and Slaven, 1993; Van Veen and Lasky, 1994; Bell *et al.*, 2001). The adaptation of the AEP components at high rates causes latency shifts and amplitude reductions. Thus, any gain obtained by the use of

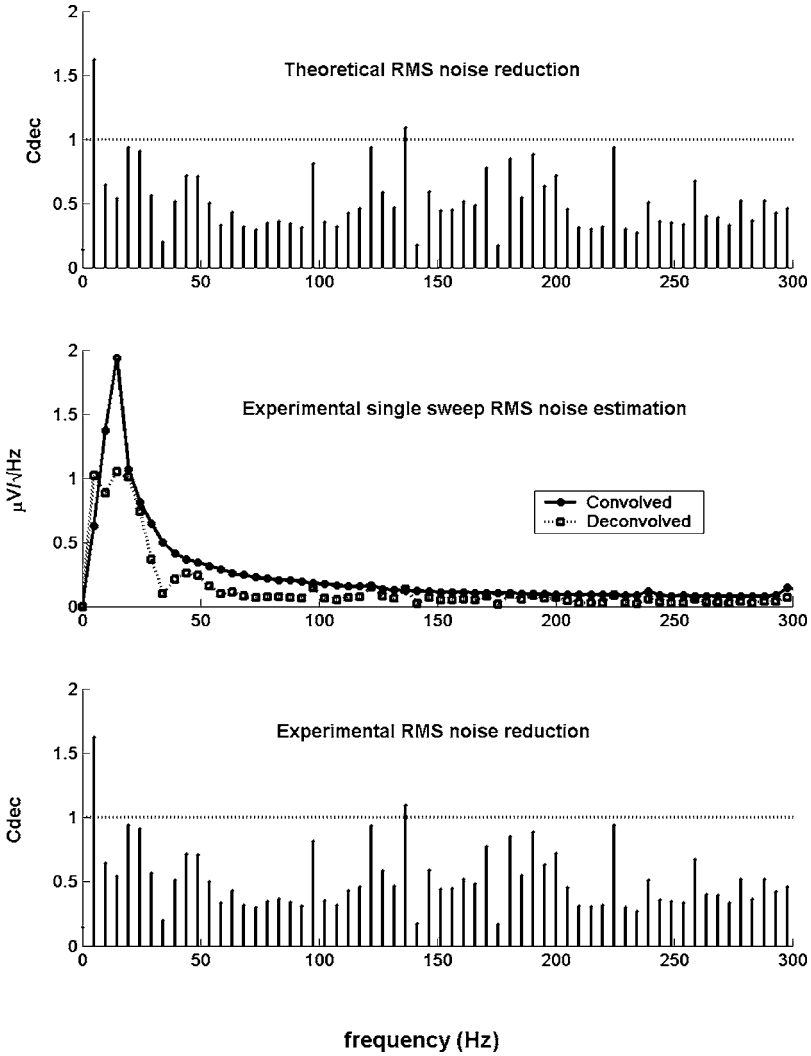

FIG. 6. Computed sequence transfer function (top), averaged rms value per frequency bin of the averaged convolved (circles) and deconvolved recording shown in the previous figure (middle), and the ratio of the convolved to deconvolved amplitudes per frequency bin (bottom). Only the low-frequency portion (<300 Hz) where most of the energy occurs is displayed for clarity.

deconvolution averaging can be lost by the adaptation process. Given the inherent variability of the evoked response recordings, experimental approaches to the resolution of this proposal cannot be expected to give clear proof of such shortening of acquisition time. This study clearly shows that such shortening is possible if proper sequences are chosen and the amplitude reduction does not generate a counter effect. The recent study of Bell and colleagues (2001) indicates this might be possible in MLS recording of MLRs. This issue now can be resolved by careful studies of the adaptation characteristics of P_a and P_b (or P_1) components of the MLRs at high stimulus rates.

Until the development of the revolutionary MLS method, the evoked potential researchers tried to resolve the overlap problem by avoiding it. The simplest method is to use high ISIs, so no overlap is generated. For auditory EPs, however, this approach is only possible if the ISI is kept longer than 1 s. For ABR and MLR, such slow rates are not practical for any application. One quick solution is to increase the high-pass (HP) cutoff points of the filter settings to eliminate the low-frequency LLRs. This bandwidth limiting approach generates some distortion of the waveforms but has been effectively used for ABR or MLR recordings. For MLRs, 10-Hz high-pass cutoff eliminates most of the LLRs and makes recordings at rates up to 10–15 Hz possible. Above such rates, the P_a component starts overlapping with P_1 and itself and the ABR waves generating steady-state responses. For ABR, 100 Hz is typically used as the high-pass cutoff value even though it eliminates the low-frequency component (slow ABR) of the ABR. Under such conditions, rates up to 100 Hz are possible. Higher rates which could be of diagnostic value could not be recorded without significant overlap.

The overlap problems in LLR and ERP can be particularly serious since individual components can last up to 1 s or more and responses are greatly influenced and distorted by the preceding stimuli. The overlapping of late latency-evoked potentials has long been known to result from the mathematical convolution process with no general solution at constant stimulation rates. When a behavioral response is elicited in response to stimuli, cognitive and/or motor responses are also generated which cause more overlap of responses. Early on, Hansen (1983) recognized the problem and developed a frequency domain matrix-based method to separate the stimulus locked and response locked waveforms. This method uses alignment of the stimulus locked and response locked averages to separate the individual responses based on their occurrence distributions. This method, however, is very specific to separation of stimulus and response locked waveforms and cannot be used if each

waveform has overlapping responses due to different generators. Since response is only loosely related to stimulus, periodicity of the buffer is not maintained which is required for solution in the frequency domain.

Recording of the P_3 component of the ERP can be especially problematic due to its long latency and high amplitude. To alleviate the overlap problem in ERPs, Woldorff (1993) developed a series of algorithms [collectively termed the adjacent response (Adjar) technique] to estimate and remove the residual distortion. This solution, however, is iterative and approximate and cannot be easily used in all applications (Talsma and Woldoff, 2005). Deconvolution methods for ERP described above have stayed as isolated studies with little application because of their lack of generality. Further development of the theory of deconvolution of overlapping responses generated by multiple stimulus sequences is needed for such cognitive applications.

The theory and the method of deconvolution developed in this study ignore the individual adaptation effect on each stimulus in the sequence. The procedure finds the averaged response of the differently adapted individual responses. This adaptation effect can be minimized by decreasing the amount of jitter in the sequences. Further development of the multiple sequence deconvolution theory suggested above might bring a solution to the individual adaptation problem as well.

Bell, S. L., Allen, R., and Lutman, M. E. (**2001**). "The feasibility of maximum length sequences to reduce acquisition time of the middle latency response," J. Acoust. Soc. Am. **109**, 1073–1081.

Bell, S. L., Allen, R., and Lutman, M. E. (**2002**). "Optimizing the acquisition time of the middle latency response using maximum length sequences and chirps," J. Acoust. Soc. Am. **112**, 2065–2073.

Bohórquez, J., and Özdamar, Ö. (2006). "Signal-to-noise-ratio analysis of Maximum Length Sequence (MLS) deconvolution of overlapping evoked responses," to be submitted.

Burkard, R., McGee, J., and Walsh, E. J. (**1996a**). "Effects of stimulus rate on the feline brain-stem auditory evoked response during development I. Peak latencies," J. Acoust. Soc. Am. **100**, 978–990.

Burkard, R., McGee, J., and Walsh, E. J. (**1996b**). "Effects of stimulus rate on the feline brain-stem auditory evoked response during development. I. Peak amplitudes," J. Acoust. Soc. Am. **100**, 991–1002.

Burkard, R., Shi, Y., and Hecox, K. E. (**1990**). "A comparison of maximum length sequences and Legendre sequences for the derivation of brainstem auditory evoked responses at rapid rates of stimulation," J. Acoust. Soc. Am. **87**, 1656–1664.

Chan, F. H. Y., Lam, F. K., Poon, P. W. F., and Du, M. H. (**1992**). "Measurement of human BAERs by the maximum length sequence technique," Med. Biol. Eng. Comput. **30**, 32–40.

Delgado, R. E., and Özdamar, Ö. (**2004**). "Deconvolution of evoked responses obtained at high stimulus rates," J. Acoust. Soc. Am. **115**, 1242–1251.

Eysholdt, U., and Schreiner, C. (**1982**). "Maximum Length Sequences—a fast method for measuring brainstem evoked responses," Audiology **21**, 242–250.

Galambos, R., Makeig, S., and Talmachoff, P. J. (**1981**). "A 40 Hz auditory potential recorded from the human scalp," Nicolet Potentials **1**, 8–12.

Hansen, J. C. (**1983**). "Separation of overlapping waveforms having known temporal distributions," J. Neurosci. Methods **9**, 127–139.

Hecox, K., Cone, B., and Blaw, M. (**1981**). "Brainstem auditory evoked response in the diagnosis of pediatric neurologic diseases," Neurology **31**, 832–840.

Jewett, D. L., Caplovitz, G., Baird, B., Trumpis, M., Olson, M. P., and Larson-Prior, L. J. (**2004**). "The use of QSD (q-sequence deconvolution) to recover superposed, transient evoked-responses," Clin. Neurophysiol. **115**, 2754–2775.

Jiang, Z. D., Brossi, D. M., Wang, J., Xu, X, Chen, G. Q., Shao, X. M., and Wilkonson, A. R. (**2003**). "Time course of brainstem pathophysiology during first month in term infants after perinal asphyxia, revealed by MLS BAER latencies and intervals," Pediatr. Res. **54**, 680–687.

Lasky, R. E., Perlman, J., and Hecox, K. E. (**1992**). "Maximum Length Sequence Auditory Evoked Brainstem Responses in Human Newborns and Adults," J. Am. Acad. Audiol **3**, 383–389.

Leung, S.-M., Slaven, A., Thornton, R. D., and Brickley, G. J. (**1998**). "The use of high stimulus rate auditory brainstem responses in estimation of hearing threshold," Hear. Res. **123**, 201–205.

Lina-Granade, G., Collet, L., and Morgon, A. (**1994**). "Auditory-evoked brainstem responses elicited by maximum-length sequences in normal and sensorineural ears," Audiology **33**, 218–236.

Marsh, R. (**1992**). "Signal to Noise Constraints on Maximum Length Sequence Auditory Brain Stem Responses," Ear Hear. **13**, 396–400.

Özdamar, Ö, and Delgado, R. E. (**1996**). "Measurement of signal and noise characteristics in ongoing auditory brainstem response averaging," Ann. Biomed. Eng. **24**, 702–715.

Özdamar, Ö., Delgado, R. E., Thombre, K. V., Yavuz, E., and Anderson, M. (**2003a**). "Acquisition of ABRs at very high stimulation rate using CLAD (Continuous Loop Algorithm Deconvolution)," ARO Abstr. **40**, 44.

Özdamar, Ö., Delgado, R. E., Yavuz, E., Thombre, K. V., and Acikgoz, N. (**2003b**). "Deconvolution of auditory evoked potentials obtained at high stimulus rates," Proc. 1st Int. IEEE EMBS Conf. Neural Engineering, Capri, Italy, pp. 285–288.

Picton, T. W., Champagne, S. C., and Kellet, A. J. C. (**1992**). "Human auditory evoked potentials using maximum length sequences," Electroencephalogr. Clin. Neurophysiol. **84**, 90–100.

Talsma, D., and Woldorff, M. G. (**2005**). "Methods for estimating and removal of artifacts and overlap in ERP waveforms," in *Event-Related Potentials: A Methods Handbook*, edited by T. H. Handy (MIT, Cambridge, MA), pp. 115–148.

Thornton, A. R. D. (**1993a**). "High rate otoacoustic emissions," J. Acoust. Soc. Am. **94**, 132–136.

Thornton, A. R. D. (**1993b**). "Click evoked otoacoustic emissions: new techniques and applications," Br. J. Audiol. **27**, 109–115.

Thornton, A. R. D., and Slaven, A. (**1993**). "Auditory brainstem responses recorded at fast stimulation rates using maximum length sentences," Br. J. Audiol. **27**, 205–210.

Van Veen, B. D., and Lasky, R. E. (**1994**). "A framework for assessing the relative efficiency of stimulus sequences in evoked response measurements," J. Acoust. Soc. Am. **96**, 2235–2243.

Woldorff, M. G. (**1993**). "Distortion of ERP averages due to overlap from temporally adjacent ERPs: Analysis and correction," Psychophysiology **30**, 98–119.

Audition in sciaenid fishes with different swim bladder-inner ear configurations

John U. Ramcharitar,[a] Dennis M. Higgs,[b] and Arthur N. Popper
Department of Biology & Neuroscience and Cognitive Science Program, University of Maryland, College Park, Maryland 20742

(Received 7 April 2005; revised 23 September 2005; accepted 13 October 2005)

We investigated how morphological differences in the auditory periphery of teleost fishes may relate to hearing capabilities. Two species of western Atlantic sciaenids were examined: weakfish (*Cynoscion regalis*, Block and Schneider) and spot (*Leiostomus xanthurus*, Lacepede). These species differ in the anatomical relationship between the swim bladder and the inner ear. In weakfish, the swim bladder has a pair of anterior horns that terminate close to the ear, while there are no extensions of the swim bladder in spot. Thus, the swim bladder in spot terminates at a greater distance from the ear when compared to weakfish. With the use of the auditory brainstem response technique, *Cynoscion regalis* were found to detect frequencies up to 2000 Hz, while *Leiostomus xanthurus* detected up to 700 Hz. There were, however, no significant interspecific differences in auditory sensitivity for stimuli between 200 and 700 Hz. These data support the hypothesis that the swim bladder can potentially expand the frequency range of detection. © *2006 Acoustical Society of America.* [DOI: 10.1121/1.2139068]

PACS number(s): 43.64.−q, 43.64.Ri, 43.64.Ha, 43.66.Cb [WWA] Pages: 439–443

I. INTRODUCTION

Fish hearing may involve two paths of sound stimulation in the ear (Fay and Popper, 1974). All fish are able to use a "direct" stimulation pathway where the displacement component of sound waves causes relative motion between the otoliths and sensory epithelia of the inner ear. Such direct detection primarily works at frequencies below 500–600 Hz (Dijkgraaf, 1960; Popper and Fay, 1999). Many species (often referred to as "hearing specialists") have also evolved the ability to use an "indirect" detection pathway for hearing by reradiating the pressure component of sound waves to stimulate the inner ear (Dijkgraaf, 1960; van Bergeijk, 1967; Fay and Popper, 1974; Kalmijn, 1988; Rogers and Cox, 1988), thereby extending the detectable auditory bandwidth to several thousand Hertz (e.g., von Frisch, 1938; McCartney and Stubbs, 1971; Fay and Popper, 1974; Hawkins and Myrberg, 1983; Mann *et al.*, 1997). It has been postulated that this pressure detection occurs via swim bladders and other gas bubbles which are located close to the ear or which are brought into proximity to the ear by specialized extensions (e.g., Dijkgraaf, 1960; Fay and Popper, 1974; Denton and Blaxter, 1976; Coombs and Popper, 1979; Crawford, 1993; Yan *et al.*, 2000).

The sciaenids are a very large group of commercially important marine fishes that have a diversity of swim bladder configurations. Among western Atlantic sciaenids, there are three general types of swim bladder-ear relationships. In species such as weakfish (*Cynoscion regalis*), spotted seatrout (*Cynoscion nebulosus*), and silver perch (*Bairdiella chrysoura*), the swim bladder has anterior horns that terminate close to the ear (Chao, 1978; Ramcharitar *et al.*, 2004). In other species such as the spot (*Leiostomus xanthurus*) and black drum (*Pogonias chromis*), the swim bladders are further from the ear, and they lack anterior horns or diverticulae (Chao, 1978; Davorec, 1983; Ramcharitar and Popper, 2004). Species such as Atlantic croaker (*Micropogonias undulatus*) represent an intermediate group in which the swim bladder possesses anteriorly directed diverticulae that approach but do not touch the ear (Chao, 1978; Ramcharitar and Popper, 2004). This interspecific diversity in swim bladder-inner ear relationship makes sciaenids good models for investigating structure-function relations in the teleost auditory system.

Ramcharitar *et al.* (2001) demonstrated that a correlation exists between swim bladder-ear configuration and two aspects of inner ear morphology in several sciaenid species. It was found that *M. undulatus* and *C. nebulosus* have significant rostral expansion of their saccular sensory epithelia, as well as more stereocilia per sensory hair cell ciliary bundle on these epithelia, than do *L. xanthurus* and kingfish (*Menticirrhus americanus*). These interspecific variations in inner ear ultrastructure correlated with swim bladder-ear relationships among the four species, as the swim bladder of both *M. undulatus* and *C. nebulosus* have anterior extensions that approach the ear, while those of *L. xanthurus* and *M. americanus* do not terminate near the ear.

In addition, recent studies have shown correlations between structure and function in the auditory systems of several sciaenid species (Ramcharitar *et al.*, 2004; Ramcharitar and Popper, 2004). *Bairdiella chrysoura*, a sciaenid species with a close association between the swim bladder and inner ear and with several specializations of the otolithic end organs, responds to sounds up to 4 kHz (Ramcharitar *et al.*,

[a]Current address: Department of Anatomy and Cell Biology, The George Washington University, 2300 Eye St., Washington, DC 20037. Electronic mail: anajxr@gwumc.edu
[b]Current address: Department of Biology, University of Windsor, Windsor, CA N9B 3P4.

2004). Also, hearing sensitivity of *B. chrysoura* is comparable to that of the goldfish, a well-known "hearing specialist" (Ramcharitar *et al.*, 2004). It also has been demonstrated that sciaenid species with different swim bladder-inner ear arrangements also show differences in frequency selectivity (Ramcharitar and Popper, 2004).

The vast majority of studies on the potential contribution of the swim bladder to audition have used species at the extremes of the spectrum of auditory capability (e.g., Fay and Popper, 1974; Denton and Blaxter, 1976; Crawford, 1993; Yan *et al.*, 2000). Sciaenid fishes exhibit a continuum in the degree of separation between the swim bladder and the otic capsule, and, therefore, comparative work on these species may add critically to our understanding of form and function in the teleost inner ear. In this study, the auditory brainstem responses of *C. regalis* and *L. xanthurus* were investigated, and these data together with those of other sciaenids support a role for the swim bladder in frequency range of detection.

II. MATERIALS AND METHODS

All animals were obtained from the Rutger's Marine Field Station, Tuckerton, NJ or from the Delaware Bay (courtesy of the Public Service Enterprise Group). Ten individuals per species were used in this study. *C. regalis* were 7.2–12.0 cm total length, while *L. xanthurus* were 7.2–12.5 cm total length. Methods used have been described in detail in previous studies (Ramcharitar *et al.*, 2004; Ramcharitar and Popper, 2004) and were approved by the University of Maryland Institutional Animal Care and Use Committee.

A. Gross dissections

After anesthesia and fixation, ventral dissections were performed to quantify swim bladder proximity to the ear. The swim bladder-ear distance was measured as the minimum distance between the rostral extent of the swim bladder and the caudal edge of the otic capsule. In the case of weakfish, this distance was measured from the rostral tips of the swim bladder horns. On average, five individuals per species (of comparable size) were used for these measurements.

The position of the brainstem was also determined using gross dissections. Dorsal dissections were performed to expose the brain and rostral region of the spinal cord. Once the brainstem was mapped, landmarks on the external surface of the fishes were then identified to make electrode placement consistent between physiology experiments.

B. Auditory brainstem response

Fish were suspended in a plastic bucket (19 L, depth =45 cm) filled with water above (about 35 cm) an underwater speaker (UW-30, Underwater Sound Inc., Oklahoma City, OK, USA). A recording electrode was placed subdermally on the dorsal surface of the fish just over the brainstem, and a reference electrode was positioned approximately 1 cm rostral to this recording electrode. Additionally, there was a ground electrode near the body of the fish. Electrodes were stainless steel (Rochester Electro-Medical Inc., Tampa, FL, USA) and insulated with fingernail polish.

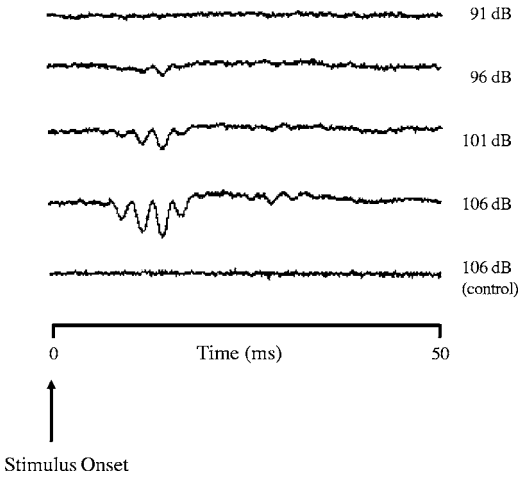

FIG. 1. Examples of ABR traces from *Leiostomus xanthurus* at a test frequency of 300 Hz. Stimulus intensity levels are stated in dB (*re*: 1 μPa) to the right of each trace. The auditory threshold is defined as the minimum sound intensity level at which an ABR is evoked. In this example, the auditory threshold is judged to be 96 dB (*re*: 1 μPa), the first trace showing a response. The ABR emerges as a series of downward negative peaks within the first 20 ms of stimulus onset (which is at 0 ms). The bottom trace is from a dead fish at a test frequency of 300 Hz at 106 dB (*re*: 1 μPa).

Sounds were played and responses were collected using a Tucker-Davis Technologies Inc. (TDT; Gainesville, FL) physiological apparatus using SigGen and BioSig software (TDT). Acoustic stimuli were generated by a computer with TDT software and then delivered to the UW-30 underwater speaker via a power amplifier. Tone burst stimuli were used at 100-Hz intervals from 200–1500 Hz. Tones were 10 ms in duration with a 2-ms rise and fall time. Sound intensity levels at each frequency were increased in 5 dB steps from 60 to 125 dB *re*: 1 μPa until a typical ABR waveform was observed (series of negative peaks within the first 20 ms of stimulus onset, see Fig. 1). The sound intensity levels used were checked and calibrated (calibration sensitivity of −195 dB *re*: 1 V/μPa; ±3 dB, 0.02–10 kHz, omnidirectional; model 902; Interocean Systems, Inc., San Diego, CA, USA). The lower and upper limits of the sound delivery system were determined to be 60 and 125 dB (*re*: 1 μPa), respectively. Signal waveform across the frequency and sound intensity range used were also analyzed periodically to ensure that distortion did not occur. For each test condition, 400 responses of alternating phase were averaged.

C. Controls

Occasionally our system was checked using goldfish, a species for which there are established behavioral audiograms (reviewed in Fay, 1988; Higgs, 2002). In each test case, the expected frequency range of detection was achieved for this teleost. On several occasions, experiments were performed using euthanized fish and also with no fish in the setup in order to establish that the identified ABR responses

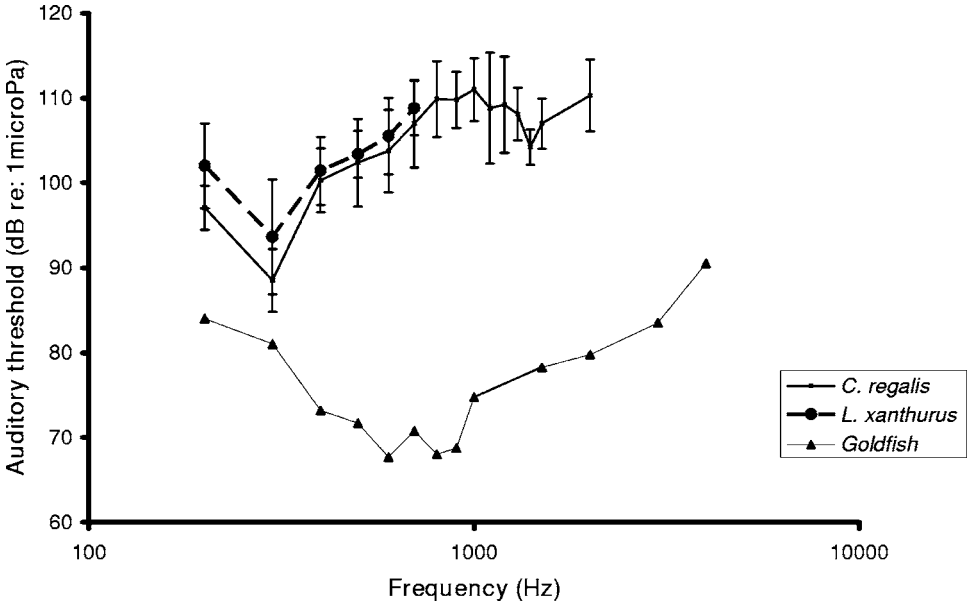

FIG. 2. Audiograms of *Leiostomus xanthurus* and *Cynoscion regalis*. Auditory thresholds are expressed as "mean±standard deviation." The frequency axis is in log scale. Weakfish detected tones up to 2 kHz while spot were sensitive to signals up to 700 Hz. The audiogram of goldfish is included for comparison and calibration (Higgs, 2002). For all three species, the same apparatus, stimuli, and auditory threshold criteria were used.

were not artifacts. These tests confirmed that our data were reliable. Responses were never obtained from dead fish (Fig. 1) or when fish were not in the apparatus.

D. Statistical analysis

All statistical analyses were done as analyses of variance (ANOVA) with the Tukey *posthoc* test as follow-up when significant differences were found (Zar, 1984). For all tests, $\alpha=0.05$ was used as the significance level.

III. RESULTS

A. Swim bladder-inner ear relationships

In *C. regalis*, the minimum distance between the rostral extent of the swim bladder and the otic capsule was 0.22 ± 0.05 mm cm^{-1}, while in *L. xanthurus*, the distance was 0.74 ± 0.06 mm cm^{-1} (distance normalized and expressed per centimeter of fish). Thus the distance was significantly less in *C. regalis* than in *L. xanthurus* ($p<0.05$).

B. Auditory brainstem responses

The auditory brainstem response trace characteristics were similar in *L. xanthurus* and *C. regalis*. Responses emerged as a series of negative peaks within the first 20 ms of stimulus onset (Fig. 1). There were interspecific differences in the auditory bandwidth of *L. xanthurus* and *C. regalis* (Fig. 2). Relative to *L. xanthurus*, *C. regalis* had a broader frequency range of detection. In our experimental setup, *L. xanthurus* detected tones up to 700 Hz, while *C. regalis* detected tones up to 2 kHz. In the frequency range 200–700 Hz, there were no statistical differences in auditory thresholds between the two species investigated (Fig. 2, $p>0.05$).

C. Mass of saccular otoliths

There were statistically significant differences in saccular otolith mass between *C. regalis* and *L. xanthurus*. The otoliths of *C. regalis*, expressed per centimeter of fish to account for differences in fish size, were larger (4.87 ± 0.51 mg cm^{-1} fish) than those of *L. xanthurus* (1.69 ± 0.14 mg cm^{-1} fish).

IV. DISCUSSION

In this study, we found that frequency range of detection correlated with swim bladder proximity to the inner ear. *C. regalis*, a species in which the swim bladder terminates near the ear, has a bandwidth almost three times wider than *L. xanthurus*, a species in which the swim bladder is distant from the ear. Compared to goldfish, however, a well-studied hearing specialist, the auditory thresholds of *C. regalis* were relatively high (Fig. 2). In earlier studies, it has been suggested that the swim bladder enhances sensitivity as well as bandwidth of hearing (von Frisch, 1938; Poggendorf, 1952; Fay and Popper, 1974, 1975). However, results from these sciaenids suggest that the major role of the swim bladder in these species is to only increase sensitivity at higher frequencies (e.g., above 700 Hz) and that this, in effect, increases the bandwidth of frequencies over which *C. regalis* can detect sound. Thus, our data, in part, support the hypothesis that the swim bladder may enhance audition when in close proximity to the ear (van Bergeijk, 1967; Kalmijn, 1988; Rogers and Cox, 1988) but suggest that this enhancement may not be over the whole range of hearing of the species.

Sciaenids can be divided into three nontaxonomic "groups" based on swim bladder-ear associations (close, intermediate, and distant), and these correlate with observed differences in frequency range of detection. The data presented for *C. regalis* and *L. xanthurus*, when pooled with those for *B. chyrsoura* (Ramcharitar *et al.*, 2004), *M. undulatus*, and *P. chromis* (Ramcharitar and Popper, 2004), support an association between swim bladder-ear distance and frequency range of detection (Fig. 3). Interestingly, of these five species, *B. chyrsoura* demonstrates auditory thresholds similar to those of the goldfish (Ramcharitar *et al.*, 2004), and it also has the closest swim bladder-ear association. Therefore, sciaenids are good models for investigating

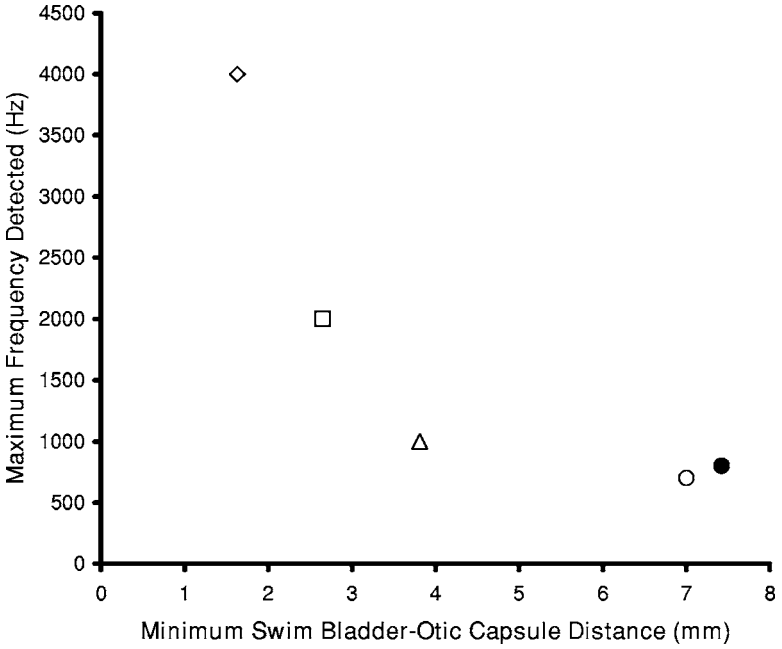

FIG. 3. Relationship between swim bladder-otic capsule distance and maximum frequency detected in sciaenid fishes. These averaged data points include (◦) *Leiostomus xanthurus* and (□) *Cynoscion regalis* (current study), (◇) *Bairdiella chrysoura* (Ramcharitar *et al.*, 2004), and (△) *Micropogonias undulatus* and (•) *Pogonias chromis* (Ramcharitar and Popper, 2004). In general, detection bandwidth improves with proximity of the swim bladder to the inner ear. For all species, the same apparatus, stimuli, and auditory threshold criteria were used.

structure-function relationships in the auditory systems of teleost fish.

Like the sciaenids (although with substantially less interspecific variability), the Atlantic squirrelfish (holocentrids) show three general categories of swim bladder-ear configurations (Nelson, 1955; Popper, 1977). Species in the subfamily Myripristinae have a direct connection between the ear and the anterolateral projections of the swim bladder, while those in the subfamily Holocentrinae can be divided into two groups, one with intermediate swim bladder-ear distances (genus *Holocentrus*) and one in which the swim bladder is relatively distant from the ear (genera *Adioryx* and *Flammeo*). Hearing differences among these categories of squirrelfish may be related to differences in the peripheral auditory system (Tavolga and Wodinsky, 1963; Coombs and Popper, 1979, 1981). Coombs and Popper (1979) demonstrated that *Adioryx* (no swim bladder-ear connections) has higher auditory thresholds and a more restricted range of frequency detection compared to *Myripristis* (direct swim bladder-ear connections), and when compared to data for *Holocentrus* (Tavolga and Wodinsky, 1963), a species with an intermediate swim bladder-ear relationship, it was found that the latter species had hearing abilities that were intermediate, as was predicted.

Interestingly, the auditory thresholds of weakfish and spot were not significantly different for the test frequency range of 200–700 Hz. If the swim bladder in weakfish were in fact stimulating the ear, it would have been expected that this species would show better sensitivity than spot across their common detection range, i.e., 200–700 Hz. Numerous studies on "hearing specialists," including otophysan species [in these, the anterior part of the swim bladder is mechanically coupled to the inner ear by an intervening chain of ossicles, the Weberian ossicles (Weber, 1820)], indicate a reduction in hearing sensitivity when the Weberian ossicles, swim bladder, or otic gas bladder are ablated (e.g., von Frisch, 1938; Poggendorf, 1952; Fay and Popper, 1974, 1975; Fletcher and Crawford, 2001). However, as first observed by Poggendorf (1952), no change in frequency detection range results from such ablation procedures. There is, however, evidence that development of the swim bladder-ear connection coincides with enhanced auditory bandwidth but no change in sensitivity in zebrafish (*Danio rerio*; Higgs *et al.*, 2003), supporting the enhanced frequency detection seen in the current study. Additionally, in one study (Ladich and Wysoki, 2003), a small reduction in frequency range of detection has been reported for goldfish when its Weberian apparatus is ablated. It is possible that auditory sensitivity is enhanced only when the swim bladder is physically coupled to the inner ear.

The differences observed in frequency detection range between *C. regalis* and *L. xanthurus* may be due in part to morphological differences in inner ear ultrastructure. In particular, a correlation between bundle morphology (height and stereocilia density) and frequency detection has been established for several vertebrate taxa (e.g., Köppl *et al.*, 1998; Gleich and Manley, 2000), although not yet for fish. Studies of inner ear ultrastructure of sciaenid species with different swim bladder-inner ear configurations have shown that species in which this relationship was close also tend to have more stereocilia per bundle on their saccular sensory epithelia (Ramcharitar *et al.*, 2001). As such, the otolithic organs may be frequency tuned. Given the interspecific distinctions in the shapes of the saccular epithelia and their associated ciliary bundle morphology which correlate with swim bladder-inner ear proximity, it is reasonable to propose that these differences may account for (at least in part) the variations observed in frequency range of detection. Further studies on the ultrastructure of the saccular epithelium of the weakfish may shed light on this.

The differences in saccular otolith morphology between *C. regalis* and *L. xanthurus* do not appear to impart differential sensitivity to the species. It has been proposed that larger otoliths are likely to confer greater sensitivity to low fre-

quencies (Lychakov and Rebane, 2000), but no significant differences in sensitivity were observed for the frequency range 200–700 Hz. While it is still possible that otolith size may account for sensitivity differences at even lower frequencies (i.e., <200 Hz), and especially in terms of direct detection of particle motion (largely untested), it is also possible that interspecific differences in saccular otolith size may be responsible, in part, for differences observed here in auditory bandwidth by imparting more displacement when coupled with the pressure transduction provided by the swim bladder. This is supported by recent data from the sleeper goby (Lu and Xu, 2002) which reveal that bilateral removal of the saccular otoliths significantly reduces hearing sensitivity. This hypothesis and the general function of the otolith *vis a vis* size and shape need exploration.

In conclusion, the data presented for *C. regalis* and *L. xanthurus* support the hypothesis that teleost fish with swim bladders that lie in close proximity to the inner ear tend to detect sounds at higher frequencies than species lacking such proximity. This correlation between form and function in the teleost auditory system is exemplified by data for several sciaenid species including spot, weakfish, silver perch, Atlantic croaker, and black drum (Fig. 3). While further investigations are needed, we hypothesize that the general relationship in Fig. 3 will hold for other groups of fishes as well, thus demonstrating the functional role of peripheral specializations. This model may also be useful in determining auditory bandwidth in species that are not amenable to physiological testing, such as endangered or even extinct species.

Chao, L. N. (**1978**). "A basis for classifying western Atlantic sciaenidae," NOAA Tech. Rep. Cir. 415.

Coombs, S., and Popper, A. N. (**1979**). "Hearing differences among Hawaiian squirrelfish related to differences in the peripheral auditory system," J. Comp. Physiol., A **132**, 203–207.

Coombs, S., and Popper, A. N. (**1981**). "Comparative frequency selectivity in fishes: simultaneously and forward-masked psychophysical tuning curves," J. Acoust. Soc. Am. **71**, 133–141.

Crawford, J. D. (**1993**). "Central auditory neurophysiology of sound producing mormyrid fish: the mesencephalon of *Pollimyrus isidori*," J. Comp. Physiol., A **172**, 1–14.

Davorec, J. E. (**1983**). "Sciaenid fishes of western peninsula Florida," Florida Department of Natural Resources MRL, St. Petersburg, FL.

Denton, E. J., and Blaxter, J. H. S. (**1976**). "The mechanical relationship between the clupeid swim bladder, inner ear and lateral line," J. Mar. Biol. Assoc. U.K. **56**, 787–807.

Dijkgraaf, S. (**1960**). "Hearing in bony fishes," Proc. R. Soc. London, Ser. B **152**, 51–54.

Fay, R. R. (**1988**). *Hearing in Vertebrates: A Psychophysics Databook* (Hill-Fay, Winnetka, IL).

Fay, R. R., and Popper, A. N. (**1974**). "Acoustic stimulation of the ear of the goldfish," J. Exp. Biol. **61**, 243–260.

Fay, R. R., and Popper, A. N. (**1975**). "Modes of stimulation of the teleost ear," J. Exp. Biol. **62**, 379–387.

Fletcher, L. B., and Crawford, J. D. (**2001**). "Acoustic detection by sound producing fishes (*Mormyridae*): the roll of gas-filled tympanic bladders," J. Exp. Biol. **204**, 175–183.

Gleich, O., and Manley, G. A. (**2000**). "Hearing organs of birds and crocodilian," in *Comparative earing: Birds and Reptiles*, edited by R. J. Dooling, R. R. Fay, and A. N. Popper (Springer-Verlag, New York), pp. 70–138.

Hawkins, A. D., and Myrberg, A. A. (**1983**). "Hearing and sound communication underwater," in *Bioacoustics – A Comparative Approach*, edited byB. Lewis (Academic, London), pp. 347–405.

Higgs, D. M. (**2002**). "Development of the fish auditory system: How do changes in auditory structure affect function?" Bioacoustics **12**, 180–182.

Higgs, D. M., Rollo, A. K., Souza, M. J., and Popper, A. N. (**2003**). "Development of form and function in peripheral auditory structures of the zebrafish (*Danio rerio*)," J. Acoust. Soc. Am. **113**, 1145–1154.

Kalmijn, A. J. (**1988**). "Hydrodynamic and acoustic field detection," in *Sensory Biology of Aquatic Animals*, edited by A. Atema, R. R. Fay, A. N. Popper, and W. N. Tavolga (Springer-Verlag, New York), pp. 131–149.

Köppl, C., Gleich, O., Schwabedissen, G., Siegl, E., and Manley, G. A. (**1998**). "Fine structure of the basillar papilla of the emu: implications for the evolution of avian hair cell types," Hear. Res. **355**, 99–112.

Ladich, F., and Wysoki, L. E. (**2003**). "How does tripus extirpation affect auditory sensitivity in goldfish?." Hear. Res. **182**, 119–129.

Lu, Z., and Xu, Z. (**2002**). "Effects of removal of saccular otoliths on hearing sensitivity in the sleeper goby (*Dormitator latifrons*)," J. Comp. Physiol., A **188**, 595–602.

Lychakov, D. V., and Rebane, Y. T. (**2000**). "Otolith regularities," Hear. Res. **143**, 83–102.

Mann, D. M., Lu, Z., and Popper, A. N. (**1997**). "A clupeid fish can detect ultrasound," Nature (London) **389**, 341.

McCartney, B. S., and Stubbs, A. R. (**1971**). "Measurements of the acoustic target strengths of fish in dorsal aspect including swim bladder resonance," J. Sound Vib. **15**, 397–420.

Nelson, E. M. (**1955**). "The morphology of the swim bladder and auditory bulla in the Holocentridae," Zoologica (N.Y.) **37**, 121–130.

Poggendorf, D. (**1952**). "Die absolute Hörschwelle des Zwergwelses (*Amiurus nebulosus*) und Beiträge Zur Physik des Weberschen Apparates der Ostariophysan." Z vergl. Physiol. **34**, 222–257.

Popper, A. N. (**1977**). "A scanning electron microscopic study of the sacculus and lagena in the ears of fifteen species of teleost fishes," J. Morphol. **153**, 397–418.

Popper, A. N., and Fay, R. R. (**1999**). "The auditory periphery in fishes," in *Comparative Hearing: Fish and Amphibians*, edited by R. R. Fay and A. N. Popper (Springer-Verlag, New York), pp. 43–100.

Ramcharitar, J., and Popper, A. N. (**2004**). "Masked auditory thresholds in sciaenid fishes: a comparative study," J. Acoust. Soc. Am. **116**, 1687–1691.

Ramcharitar, J., Higgs, D. M., and Popper, A. N. (**2001**). "Sciaenid inner ears: a study in diversity," Brain Behav. Evol. **58**, 152–162.

Ramcharitar, J. U., Deng, X., Ketten, D., and Popper, A. N. (**2004**). "Form and function in the unique inner ear of a teleost: the silver perch (*Bairdiella chrysoura*)," J. Comp. Neurol. **475**, 531–539.

Rogers, P. H., and Cox, M. (**1988**). "Underwater sound as a biological stimulus," in *Sensory Biology of Aquatic Animals*, edited by A. Atema, R. R. Fay, A. N. Popper, and W. N. Tavolga (Springer-Verlag, New York), pp. 131–149.

Tavolga, W. N., and Wodinsky, J. (**1963**). "Auditory capacities in fishes. Pure tone thresholds in nine species of marine teleosts," Bull. Am. Mus. Nat. Hist. **126**, 177–240.

van Bergeijk, W. A. (**1967**). "The evolution of vertebrate hearing," Contrib Sens Physiol. **2**, 1–49.

von Frisch, K. (**1938**). "The sense of hearing in fish," Nature (London) (London) **141**, 8–11.

Weber, E. H. (**1820**). "De aure et auditu hominis et animalium, Pars I," De Aure Animalium Aquatilium. Leipzig.

Yan, H. Y., Fine, M. L., Horn, N. S., and Coton, W. E. (**2000**). "Variability in the role of the gasbladder in fish audition," J. Comp. Physiol., A **186**, 435–445.

Zar, J. H. (**1984**). *Biostatistical analysis*, 2nd ed. (Prentice-Hall, Englewood Cliffs, NJ).

Level dependence of auditory filters in nonsimultaneous masking as a function of frequency

Andrew J. Oxenham[a] and Andrea M. Simonson
Research Laboratory of Electronics, Massachusetts Institute of Technology, Cambridge, Massachusetts 02139

(Received 1 March 2005; revised 2 November 2005; accepted 4 November 2005)

Auditory filter bandwidths were measured using nonsimultaneous masking, as a function of signal level between 10 and 35 dB SL for signal frequencies of 1, 2, 4, and 6 kHz. The brief sinusoidal signal was presented in a temporal gap within a spectrally notched noise. Two groups of normal-hearing subjects were tested, one using a fixed masker level and adaptively varying signal level, the other using a fixed signal level and adaptively varying masker level. In both cases, auditory filters were derived by assuming a constant filter shape for a given signal level. The filter parameters derived from the two paradigms were not significantly different. At 1 kHz, the equivalent rectangular bandwidth (ERB) decreased as the signal level increased from 10 to 20 dB SL, after which it remained roughly constant. In contrast, at 6 kHz, the ERB increased consistently with signal levels from 10 to 35 dB SL. The results at 2 and 4 kHz were intermediate, showing no consistent change in ERB with signal level. Overall, the results suggest changes in the level dependence of the auditory filters at frequencies above 1 kHz that are not currently incorporated in models of human auditory filter tuning.
 [DOI: 10.1121/1.2141359]

PACS number(s): 43.66.Ba, 43.66.Dc [AK] Pages: 444–453

I. INTRODUCTION

Frequency selectivity, or the ability to distinguish simultaneous sounds of different frequencies, is a fundamental property of the auditory system. From the earliest days of psychoacoustic research, it has generally been assumed that frequency selectivity measured behaviorally reflects the tuning properties of the cochlea. This assumption is supported by various lines of indirect evidence, such as marked changes in frequency selectivity in the presence of hearing losses diagnosed to be of cochlear origin (e.g., Moore and Glasberg, 1986), many qualitative similarities between human behavioral frequency selectivity and physiological studies of auditory-nerve tuning in other mammals (e.g., Moore, 1978), and animal studies showing similar estimates of filter bandwidth using behavioral and neural measures (e.g., Evans, 2001).

Recently, Shera *et al.* (2002) provided more direct evidence of a correspondence between cochlear tuning and behavioral frequency selectivity in humans. They used a measure based on stimulus-frequency otoacoustic emissions (SFOAEs) to predict cochlear tuning, and measured psychophysical frequency selectivity using a forward masker and a low-level probe. They found a good correspondence between the SFOAE predictions and the psychophysical measures. Although this general finding was in line with earlier studies in animals (Evans, 2001), two aspects of the data were surprising. First, both measures suggested that cochlear tuning in humans was considerably sharper than that found in two mammals (cat and guinea pig) that are often used in auditory experiments. Second, the estimated tuning was sharper and had a different dependence on characteristic frequency (CF) than many earlier psychophysical estimates of tuning: instead of the relative bandwidth staying roughly constant above 1 kHz (e.g., Glasberg and Moore, 1990), tuning was found to sharpen considerably, such that the 8-kHz filter had a Q_{ERB} (CF divided by the equivalent rectangular bandwidth or ERB) nearly twice that of the 1-kHz filter. This sharpening of tuning with increasing CF is also observed in the auditory-nerve tuning curves of other mammals. Shera *et al.* (2002) ascribed the differences between their results and those of previous psychophysical studies to their use of nonsimultaneous masking, which reduced possible suppression effects (Delgutte, 1990a,b), and—perhaps more importantly—to their use of a low-level (10 dB SL) probe tone (see Oxenham and Shera, 2003).

The use of a low-level probe tone provided estimates of tuning that were readily comparable to a large body of neural tuning curve data in animals, and they resulted in the conclusion that human cochlear tuning may be sharper than that of other mammals, such as cat and guinea pig. However, the use of a low-level probe tone does not provide a full description of frequency selectivity because of the inherent nonlinearities present in the cochlea, including increases in filter bandwidth with level that are often observed in physiological studies of tuning (Ruggero *et al.*, 1997). Increases in bandwidth with increasing level have been observed in many psychophysical studies of frequency selectivity using simultaneous masking (e.g., Weber, 1977; Rosen and Stock, 1992; Rosen *et al.*, 1998; Hicks and Bacon, 1999; Glasberg and Moore, 2000). In one of the more recent studies, Glasberg and Moore (2000) found that the dependence of the auditory filters on level was similar at all frequencies above about 1 kHz. However, as they used simultaneous masking, it is

[a]Electronic mail: oxenham@mit.edu

not clear to what extent their results are due to the effects of suppression, rather than to changes in the underlying cochlear tuning, such as would be measured by neural tuning curves (Delgutte, 1990a; Moore and Vickers, 1997; Oxenham and Plack, 1998).

Fewer studies have examined changes in frequency selectivity with level using nonsimultaneous masking, where suppression is not thought to play a role. Studies that did use nonsimultaneous masking have employed either psychophysical tuning curves (Moore *et al.*, 1984; Nelson and Freyman, 1984; Nelson *et al.*, 1990; Nelson, 1991) or the notched-noise technique (Glasberg and Moore, 1982). The studies using psychophysical tuning curves have concluded that the masker level at the tip of the tuning curve (i.e., when the masker and signal frequencies are very similar) determines the bandwidth and shape of the filter, and that other variables, such as the gap between the masker and signal, and the signal level, have no effect once the effects of masker level have been accounted for (e.g., Nelson and Freyman, 1984). Furthermore, these studies indicate that the filter shape remains roughly constant for masker levels (at the tip of the tuning curve) up to about 60 dB SPL (Nelson *et al.*, 1990), above which it broadens. Consistent with this, Glasberg and Moore (1982), using a notched-noise masker, found that over the three fixed masker levels (30, 40, and 50 dB SPL spectrum level) and three fixed signal levels (roughly 10, 15, and 20 dB SL), there was no change in filter bandwidth with level. Interestingly, all the studies mentioned used a signal frequency of 1 kHz. To our knowledge, there are no published studies that have used the notched-noise technique to investigate frequency selectivity in nonsimultaneous masking as a function of level for frequencies other than 1 kHz.

The lack of data on the level dependence of frequency selectivity as a function of signal frequency in nonsimultaneous masking is an important omission, particularly given the large changes in tuning with frequency that can occur at low levels (Shera *et al.*, 2002; Oxenham and Shera, 2003). Information on how human cochlear filter shapes change as a function of frequency and level will be crucial in developing and refining computational models of the human auditory periphery. Interestingly, there is also a dearth of systematic data from physiological studies on this topic. Basilar-membrane tuning data are limited mainly to the basal turn of the cochlea, and thus to relatively high CFs (e.g., Ruggero *et al.*, 1997). Although some data from lower CFs in the apical turn exist (Cooper and Rhode, 1995; Rhode and Cooper, 1996), it is not yet clear to what extent the cochlea was damaged in those preparations. There are limited data on the effect of level on neural tuning curves as a function of CF. One problem is that most auditory-nerve fibers have relatively small dynamic ranges, making a study of level effects difficult, because of saturation effects. One study to show some sample neural tuning curves at CFs of around 200, 500, 1500, and 5000 Hz with different rate criteria found little systematic effect of level on bandwidth over the range of criteria tested (Liberman and Mulroy, 1982). Another approach, which is less susceptible to saturation effects, is to use the reverse-correlation (revcor) technique to derive the tuning characteristics of individual neurons (Moller, 1977; Harrison and Evans, 1982; Carney and Yin, 1988). However, this technique is limited to relatively low CFs, at which phase locking to the stimulus fine structure is still strong. Thus, basilar-membrane data are generally limited to high CFs, whereas auditory-nerve data are often limited to low CFs, making it difficult to provide a general survey of level effects in tuning across a wide range of CFs.

Here, we investigate the dependence of auditory filter bandwidths on level at signal frequencies ranging from 1 to 6 kHz using nonsimultaneous masking. We used the notched-noise technique, which has been shown to provide estimates that are in good agreement with estimates of human cochlear tuning using otoacoustic emissions (Shera *et al.*, 2002). Measuring filter shapes at a fixed signal level is closer to the technique used in derived neural and basilar-membrane tuning curves, and has also been shown to provide more consistent estimates of tuning as a function of level than estimates based on a fixed masker spectrum level (e.g., Rosen *et al.*, 1998). However, even if the derived filters are based on a fixed signal level, the data can be collected either with a fixed signal or fixed masker level (Rosen *et al.*, 1998). Both paradigms have some advantages. Collecting data using a fixed signal level and an adaptively varying masker level provides a direct estimate of filter tuning that requires no further transformations, whereas collecting data using a fixed masker level and adaptively varying signal level may require a transformation of the data before tuning estimates for a filter at a given level can be made. In a study of auditory filter shapes in forward masking at 1 kHz, Glasberg and Moore (1982) tested both methods for about a 10-dB range of signal levels and found no significant difference between the two methods. On the other hand, it is possible that for higher signal levels and wide notch widths, a fixed signal level paradigm might lead to somewhat uncomfortable masker levels, which in turn might bias listeners toward responding wrongly, because they realize (consciously or unconsciously) that wrong answers lead to lower and perhaps less objectionable levels. This could be the case, even though listeners are made aware during the process of informed consent that the level cannot exceed safe limits, and that if anything makes them feel uncomfortable they should inform the experimenter immediately.

In this study, we estimated filter shapes using both methods. In the first study, a fixed masker level paradigm was used over a wide range of masker notch widths and masker levels using signal frequencies of 1 and 6 kHz. In the second study, a fixed signal level paradigm was used to test a more limited range of notch widths at more signal frequencies (1, 2, 4, and 6 kHz). The studies were undertaken at different times and with different subjects. In agreement with the data of Glasberg and Moore (1982) no significant differences in estimated filter bandwidths emerged at the two frequencies for which both methods were used (1 and 6 kHz). Overall, we were able to estimate auditory filter bandwidths in nonsimultaneous masking at signal frequencies of 1, 2, 4, and 6 kHz for signal levels ranging from 10 to 35 dB SL. Both experiments were consistent in showing a markedly different dependence of filter tuning on level at the different signal

frequencies, in contrast to expectations based on the results from simultaneous-masking studies in the same frequency range (Glasberg and Moore, 2000).

II. EXPERIMENT

A. Stimuli

The signal was a tone burst of 20-ms total duration, gated on and off with 10-ms raised-cosine ramps (no steady state). The signal was immediately preceded and followed by noise maskers with total durations of 200 ms, each gated with 5-ms raised-cosine ramps. The beginning and end of the signal temporally abutted the offset and onset of the forward and backward masker, respectively. In this way, the paradigm was similar to simultaneous masking with a brief probe, with the difference that the masker was interrupted for the duration of the signal. Each masker consisted of two bands of Gaussian noise centered below and above the signal frequency (f_s), each with a bandwidth of $0.25f_s$. Each noise burst was generated independently in the spectral domain and was bandlimited by setting all spectral components outside the desired passband to zero. In this way, the slope of the filtering was limited only by the spectral spread caused by the 5-ms onset and offset ramps of the masker. The spectral notch width was defined as the deviation (Δf) of the closer edge of each noise from the signal frequency, divided by the signal frequency, i.e., $\Delta f/f_s$. The exact signal and masker levels, as well as the notch widths used, depended on whether the masker or signal level was adaptively varied. These differences are described in the following two subsections.

All stimuli were generated digitally at a sampling rate of 32 kHz and were played out via a LynxStudio LynxOne soundcard at 24-bit resolution. The maskers and signal were passed through different programmable attenuators (TDT PA4) before being mixed (TDT SM3) and passed through a headphone buffer (TDT HB6). The stimuli were presented monaurally in a double-walled sound-attenuating booth via Etymotic Research ER2 insert earphones, which are designed to provide a flat frequency response at the eardrum up to about 14 kHz.

1. Fixed masker level

In each run, the masker spectrum level and notch width were fixed, and the signal level was adaptively varied to track threshold. The signal frequency was either 1 or 6 kHz. There were seven conditions in which the notch was placed symmetrically about the signal frequency; values of $\Delta f/f_s$ were 0 (no spectral notch), 0.05, 0.1, 0.15, 0.2, 0.3, and 0.4. Four asymmetric conditions were also tested, where the upper and lower normalized deviations were 0.1 and 0.3, or 0.2 and 0.4, and vice versa. This provided a total of 11 different notch widths. Masker levels were chosen at each notch width in order to cover as wide a range of signal levels as possible, between 10 and 40 dB SL for each subject individually. This enabled us to reconstruct filter functions for any given signal level between about 10 and 40 dB SL, as described in the Sec. II D. In general, at least four masker spectrum levels were tested for each notch width, usually in steps of 10 dB, with levels ranging from −10 to 50 dB SPL spectrum level. This corresponded to maximum overall masker levels of about 77 and 85 dB SPL at 1 and 6 kHz, respectively.

2. Fixed signal level

In each run, the signal level was fixed at 10, 15, 20, 25, or 30 dB above absolute threshold, as measured individually for each subject, and the masker spectrum level was varied adaptively. Pilot runs showed that notched noises with normalized deviations greater than 0.2 often resulted in the signal being detectable even at the highest allowable masker levels. Because of this, only symmetrically placed notches were tested with normalized deviations of 0, 0.05, 0.1, 0.15, and 0.2. This allowed us to estimate the bandwidth of the filter tip, but limited our ability to derive the entire shape of the filter. However, because of the reduced number of notch widths, we were able to test more signal frequencies. Frequencies tested were 1, 2, 4, and 6 kHz. The maximum allowable masker level in any run was 60 dB SPL spectrum level, corresponding to a maximum overall level ranging from 87 dB SPL at 1 kHz to 95 dB SPL at 6 kHz.

B. Procedure

All thresholds were measured using a three-interval, three-alternative forced-choice method with a two-down, one-up (fixed masker level) or two-up, one-down (fixed signal level) adaptive procedure that tracks the 70.7%-correct point on the psychometric function (Levitt, 1971). Intervals were marked on a virtual response box on a flat-panel monitor located in the booth. Responses were made via the computer keyboard or mouse, and feedback was provided after each trial. The initial step size was 8 dB, which was reduced to 4 dB after the first two reversals in the direction of the tracking procedure. The final step size of 2 dB was reached after a further four reversals, and threshold was defined as the mean signal level at the remaining six reversals. Runs in which the standard deviation across the last six reversals exceeded 4 dB were discarded and were repeated at a later time. Each reported threshold represents the mean of at least two valid runs. If the standard error of the mean was 2 dB or more, up to four additional runs were included, until the standard error was less than 2 dB. For values based on six runs, an outlier was excluded if threshold was more than 4 standard deviations from the mean of the other five runs. This procedure eliminated less than 1% of all runs.

Initially, thresholds in quiet were measured for the 20-ms signal at 1, 2, 4, and 6 kHz. Following this, thresholds in the presence of the notched noise were measured. The conditions were presented using a randomized block design, with all conditions being run once before any were repeated. Thresholds for all masker levels (or signal levels in the fixed signal level paradigm) of a given notch width were run together in random order, and all notch widths for a given signal frequency were measured before proceeding to the next signal frequency. The presentation orders of levels, signal frequencies, and notch widths were randomized independently for each subject and each repetition.

TABLE I. Absolute thresholds in dB SPL for the 20-ms signals used in the experiments. Subjects 1–4 were tested only at 1 and 6 kHz.

		Signal frequency (kHz)			
Subject	Ear tested	1	2	4	6
S1	R	27	⋯	⋯	26
S2	R	22	⋯	⋯	23
S3	R	24	⋯	⋯	21
S4	R	22	⋯	⋯	25
S5	R	21	25	20	22
S6	L	28	26	24	28
S7	R	22	22	14	17
S8	L	24	27	29	20
S9	R	22	22	19	23

C. Subjects

Four normal-hearing listeners (two males, two females), aged between 19 and 24 years, served as subjects in the fixed masker level experiment, and five normal-hearing subjects (two males, three females, including author AS), aged between 20 and 39 participated in the fixed signal level experiment. They all had audiometric thresholds of 15 dB HL or less at frequencies of 250, 500, 1000, 2000, 4000, 6000, and 8000 Hz. They received at least 2 h of training before the data were collected. The total number of 2-h sessions ranged from 8 to 12. Initially, five subjects were used in both paradigms, but one subject who participated in the fixed masker level experiment, despite having a normal audiometric threshold at 6 kHz (measured using long-duration tones with TDH39 headphones), had an absolute threshold for the 20-ms signal at 6 kHz that was 10 dB or more higher than that of the other subjects. Because of this, his data were not analyzed further. The absolute thresholds of the nine remaining subjects for the 20-ms signals are shown in Table I.

D. Results

1. Fixed masker level

The mean data using the fixed masker levels are shown in Fig. 1, with results using a 1- and 6-kHz signal shown in the left and right panels, respectively. Signal level at threshold is plotted as a function of masker spectrum level, with notch width as a parameter. For clarity, only six of the 11 notch widths are shown, as described in the legend. Only points that include data from all four subjects are included in the figure. As expected, signal thresholds increase with masker level and with decreasing masker notch width. Some differences between 1 and 6 kHz are apparent in these raw data. At 1 kHz, once the signal level exceeds about 30 dB SPL, the masking curves are roughly parallel to one another, with the possible exception of the two asymmetric conditions, which diverge somewhat, indicating slightly greater filter asymmetry at higher levels. At 6 kHz, differences in the slopes of the different curves are more marked, suggesting greater changes in tuning as a function of level. The pattern of data from individual subjects was very similar to the average data shown in Fig. 1.

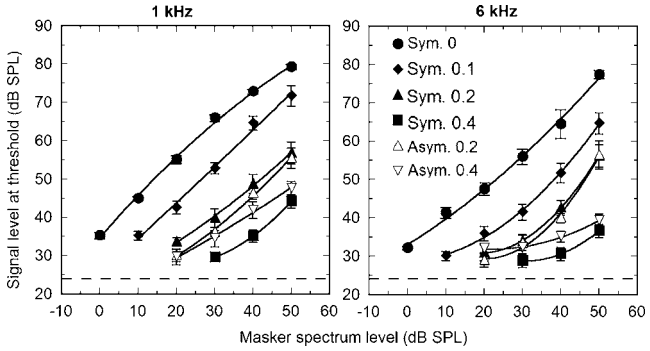

FIG. 1. Mean signal thresholds of four subjects as a function of masker spectrum level, from the fixed masker level experiment. The left and right panels show data from a signal frequency of 1 and 6 kHz, respectively. The different symbols represent data from different masker spectral notch widths. Filled symbols represent symmetric notches and open symbols represent asymmetric notches. Up-pointing arrows represent conditions where the center of the masker's spectral notch was higher than the signal frequency; down-pointing arrows represent conditions where the center of the spectral notch was lower than the signal frequency. Data points falling within 5 dB of absolute threshold have been omitted. The numbers in the legend denote the normalized frequency deviation between the lower edge of the spectral notch and the signal. Error bars denote ±1 standard error between subjects. The curves show second-order polynomial fits to the data. The dashed horizontal lines represent the mean absolute threshold (23.8 dB SPL at both frequencies).

As an initial step in deriving the underlying auditory filter shapes, iso-signal-level curves were calculated from both the individual data and the data pooled across individuals. This was achieved by fitting a second-order polynomial to each of the notch-width data sets, relating signal level at threshold to masker spectrum level. Conditions that resulted in signal thresholds within 5 dB of absolute threshold were excluded from the analysis to reduce the effects of approaching absolute threshold on the masking function. For each subject and signal level, the polynomials were solved to find the masker levels at each notch width corresponding to a given signal level from 10 to 40 dB above the absolute threshold (dB SL) of each subject in 5-dB steps.[1] The procedure can be visualized by imagining a horizontal line on the graph in Fig. 1, and picking all the x values (masker levels) at which the horizontal line intersects with the different masking functions. Finally, all the masker levels corresponding to a given signal level were collected across notch widths to provide a curve that plots masker spectrum level as a function of notch width. These transformations were performed on individual data sets and on the data pooled across all four subjects. In the pooled case, the polynomials were fitted to the individual mean data points, rather than to the raw data from each repetition, so that the data from all subjects would carry equal weight in the fitting procedure. The dB SL values were based on the absolute threshold values averaged across the four subjects. The threshold values derived from the polynomial fits to the pooled data are plotted in Fig. 2 for signal levels of 10, 20, and 30 dB SL. The left panels show data at 1 kHz, and the right panels show data at 6 kHz. These transformed data were then used to derive auditory filter shapes. Note that only relatively narrow notch widths (normalized deviations of 0.2 or less) include masker levels below the maximum measured spectrum level of

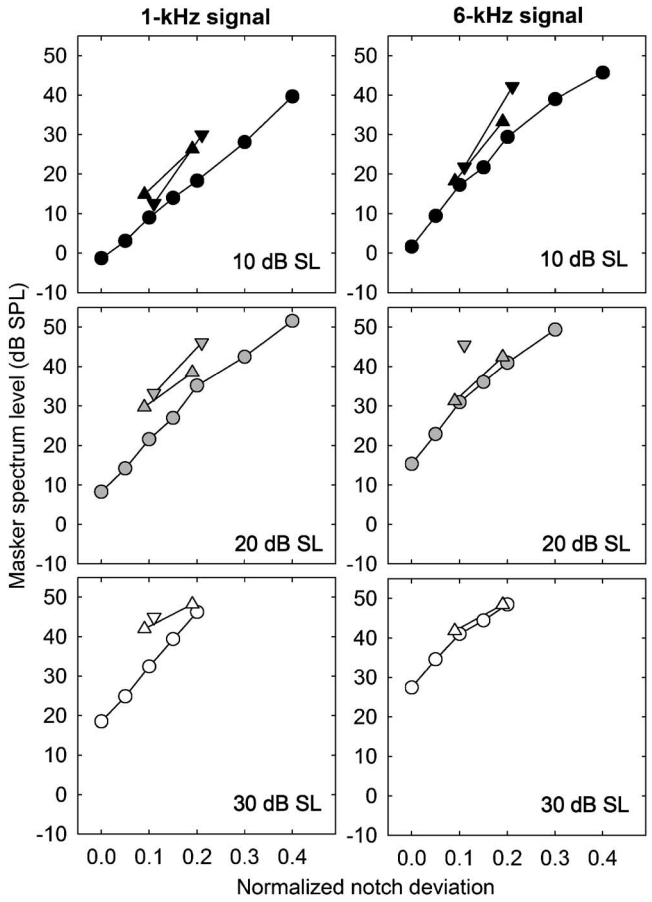

FIG. 2. Transformed data from the fixed masker level experiment, pooled across subjects, showing masker spectrum level at threshold as a function of masker notch width. The abscissa shows the frequency difference between the signal and the nearest spectral edge of the notched noise, divided by the signal frequency. Left and right panels show data from 1 and 6 kHz, respectively. The three rows show results from three different signal levels, as shown in the panels. Data from symmetric spectral notches are shown as circles. Data from the asymmetric notches are shown as triangles: upward-pointing triangles denote points where the spectral edge of the lower-frequency noise band was closer to signal frequency, and downward-pointing triangles denote conditions where the spectral edge of the higher-frequency noise band was closer to the signal frequency.

50 dB SPL for signal levels of 20 dB SL or more. Thus, in examining the effects of level on auditory filter bandwidth, we are limited to relatively narrow notch widths.

2. Fixed signal level

The results from the fixed signal level paradigm needed no transformation before being used to derive auditory filter shapes at each signal level. The mean data are plotted in Fig. 3, with the results from each signal frequency in a separate panel. For clarity, only the results using signal levels of 10, 20, and 30 dB SL are shown. As expected, the masker level required to mask the signal increases with increasing masker notch width and with increasing signal level. At the higher signal frequencies of 4 and 6 kHz there is a trend for the function relating masker level to masker notch width to be shallower at higher than at lower signal levels, with the three curves at each frequency converging somewhat at the wider notch widths. In contrast, the functions at 1 kHz appear, if anything, to diverge somewhat with increasing notch width. These effects are quantified in the following sections by deriving auditory filters from the data.

III. DERIVING AUDITORY FILTERS

A. Model implementation and fitting procedures

Before being processed by simulated auditory filters, the stimuli were passed through a middle-ear function described by Moore *et al.* (1997). As the insert earphones used in this study (Etymotic Research ER2) are designed to produce a flat transfer function at the eardrum for frequencies up to about 14 kHz, no outer-ear transfer function was incorporated into the simulations. The filter shapes were derived using the basic rounded exponential (roex) shape (Patterson and Nimmo-Smith, 1980), with methods similar to those described in many previous studies (e.g., Glasberg and Moore, 1990; 2000). Both the roex(p) (Patterson *et al.*, 1982) and a variant of the roex(p,w,t) (Glasberg *et al.*, 1984; Rosen *et*

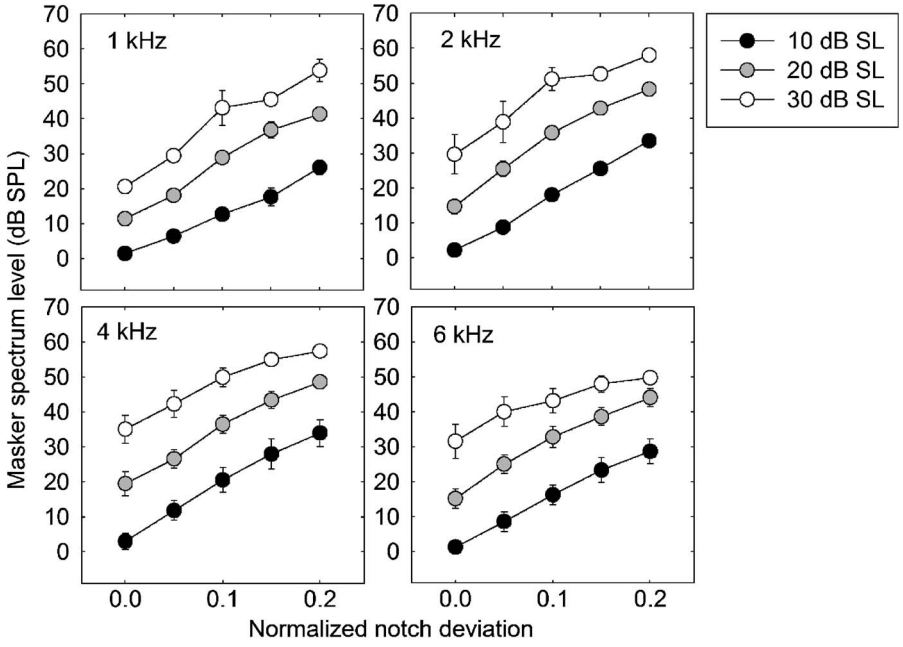

FIG. 3. Mean thresholds of five subjects from the fixed signal level experiment. The different panels show the results using different signal frequencies. Black, gray, and white symbols represent signal levels of 10, 20, and 30 dB SL, respectively. Error bars represent ±1 standard error of the mean.

al., 1998; Glasberg and Moore, 2000; Oxenham and Shera, 2003) were tested. The equation for each side of the roex(p) filter is

$$W(g) = (1 + pg)\exp(-pg), \quad (1)$$

where W is the filter weighting function, g is the normalized deviation from the center frequency ($|\Delta f|/f_c$), and p is the parameter determining the slope of the filter. The value for p can either be the same on both sides of the filter to produce a symmetric filter, or can be allowed to differ on either side of the filter (p_u for the upper side and p_l for the lower side). We used the symmetric roex(p) in cases with limited numbers of notch widths (normalized deviations of 0.2 or less), where the tails of the filter and the filter asymmetry were poorly (or not at all) defined. In cases with a wider range of symmetric and asymmetric notch-width data, we continued to use the roex(p) function to describe the upper side of the filter, but used the roex(p,w,t) filter to describe the lower side

$$W(g) = (1 - w)(1 + p_l g)\exp(-p_l g) + w(1 + p_l g/t)\exp(-p_l g/t). \quad (2)$$

In line with Oxenham and Shera (2003), we refer to this hybrid as the roex(p,w,t,p) model. The difference between Eqs. (1) and (2) [and the difference between the upper and lower sides of the roex(p,w,t,p) filter] is that Eq. (2) has two slopes instead of one. This can be important in describing accurately how thresholds change at wider notch widths, but it comes at the expense of an additional two parameters. The parameter t determines the factor by which the second (tail) slope is shallower than the first (tip) slope; the parameter w determines the relative weights of the first and second slopes, or the point on the filter function at which the second slope begins to dominate. The roex(p,w,t,p) filter has been used in a number of recent studies and is favored because it more closely resembles the shape of auditory neural tuning curves (Rosen *et al.*, 1998; Glasberg and Moore, 2000; Oxenham and Shera, 2003). Also, Rosen *et al.* (1998) found that this shape was the most efficient in terms of giving a low rms error, while maintaining a small number of free parameters.

The data from all notch widths at a single signal level were used to derive a filter shape. A multidimensional nonlinear minimization routine [Nelder-Mead, as implemented in MATLAB (Mathworks, Natick, MA)] was used to find the best-fitting parameters of the filters in the least-squares sense. It was assumed that the signal was detected using the output of the filter with the best signal-to-noise ratio (SNR). In most situations this was also the filter centered at the signal frequency. However, in some cases the filter that had the best SNR was centered somewhat away from the signal frequency, although its CF was always within 10% of the signal frequency. The "efficiency" of the detector, K, is the threshold SNR at the output of the detection filter averaged across all conditions at a given signal level. The minimization routine was driven by the sum of squared deviations of the actual thresholds from the predicted thresholds, based on a constant K value, which was set so that the mean of all the predicted thresholds was equal to the mean of the obtained thresholds. To guard against the minimization routine finding local spurious minima, we often reran the fits using different starting parameter values. This was done for all the fits to the pooled data.

By fitting the data from each signal level with a separate filter function, we assume that the filter shapes at each signal level are independent of each other, and that the signal-to-noise ratio at threshold (K) can vary as a function of signal level. In contrast, Rosen and colleagues (Rosen and Baker, 1994; Rosen *et al.*, 1998) have argued that it is preferable to fit all the data across all signal levels within a single model that allows the filter parameters to vary systematically with level according to a polynomial equation. They found that allowing K to vary with signal level did not improve the model predictions, and were thus able to treat it as a constant across all signal levels. Their approach has the advantage that it reduces the number of free parameters, thereby increasing the stability of the fits. The assumption of a constant K across all signal levels is also well justified for the simultaneous-masking paradigm used by Rosen and colleagues. However, it is not possible to assume a constant K with nonsimultaneous masking, unless some further modeling is introduced to take account of the nonlinear growth of forward and backward masking (e.g., Jesteadt *et al.*, 1982; Oxenham and Moore, 1995; Plack and Oxenham, 1998). Also, because forward masking can involve rather abrupt transitions in masking growth as a function of level (e.g., Plack and Oxenham, 1998), it was decided to allow the filter parameters to vary independently at different signal levels.

B. Auditory filter shapes at low signal levels

Our fixed masker level data for the lowest two signal levels (10 and 15 dB SL) were the only data sets that incorporated the full complement of notch widths, extending out to normalized deviations of 0.4. This allowed us to fit the roex(p,w,t,p) to the data, and to compare the resulting filter bandwidths to those in an earlier study, using just forward masking with a fixed signal level (Oxenham and Shera, 2003). The parameters and ERBs for the filters derived from the pooled data are shown in Table II, along with the mean ERBs taken from fitting filter shapes to the individual data.

The ERB values for a signal level of 10 dB SL are generally larger (implying poorer tuning) than the mean ERBs of Oxenham and Shera (2003), which were 98 and 360 Hz at 1 and 6 kHz, respectively. However, a statistical comparison of the present ERBs and those of Oxenham and Shera (2003) revealed that these differences were not significant (two-tailed t-tests; $p > 0.05$ at both frequencies). When equating the masker levels for the on-frequency masking condition (no notch) (Nelson *et al.*, 1990)—Oxenham and Shera's (2003) data are more comparable to our data with a signal level of 15 rather than 10 dB SL. The filter parameters with a 15-dB SL signal are shown in the second row of Table II. The ERBs tend to be somewhat smaller (narrower) and the standard deviation across listeners is somewhat lower. For the 15-dB SL condition, the ERB at 1 kHz was similar to

TABLE II. Parameters for the filters fitted to the data from the fixed masker level experiment, pooled across subjects. The parameters are from Eqs. (1) and (2) to describe the upper and lower slopes of the filter, respectively. The error term (rms) is an indication of the goodness of fit. The right-most two columns show the mean and standard deviation of the ERBs derived from filter fits to the individual data.

		Pooled filter parameters								
Frequency	level (dB SL)	p_l	p_u	t	$10\log(w)$	$10\log(K)$	ERB (Hz)	rms (dB)	Mean of individual filters ERB (Hz)	s.d.
1 kHz	10	40.2	29.7	2.01	−13.7	14.4	**119**	1.6	**121**	24.0
	15	40.1	42.1	2.30	−18.1	15.2	**98**	1.6	**102**	20.3
6 kHz	10	44.0	43.4	2.80	−25.6	4.54	**550**	1.5	**531**	155
	15	41.4	63.0	3.94	−30.73	2.47	**481**	0.7	**478**	85.4

that found by Oxenham and Shera (2003), while the ERB at 6 kHz was somewhat broader. Again using two-tailed *t*-tests, differences between the two studies in ERB estimates failed to reach statistical significance at the 0.05 level. The 10- and 15-dB SL signal conditions in the fixed-masker-level paradigm were the only ones to be analyzed with a roex(p,w,t,p) model, as these were the two signal levels where almost all the masker levels fell below 50 dB SPL spectrum level.[2]

C. Auditory filter bandwidths as a function of level

For signal levels above 15 dB SL in the fixed masker level conditions, and for all signal levels in the fixed signal level condition, only notches with spectral gaps between the masker edge and the signal of $0.2f_s$ or less were used to derive auditory filters. Because of the reduced number of notch widths (5), and the lack of asymmetric notches, the simple symmetric roex(p) model, with one parameter to describe the filter shape, was used to fit the data [i.e., Eq. (1) for both sides of the filter]. While this method does not provide for very detailed filter shapes, it provides a more robust fit and avoids the danger of "overfitting" the data with too many free parameters.

Each individual data set from the fixed masker level and fixed signal level paradigms was fitted using roex(p) filters, as described above. The resulting ERBs are shown in Fig. 4. Dotted lines show individual fits from the fixed signal level paradigm and dashed lines show individual fits from the fixed masker level paradigm. The heavy solid lines represent the mean ERBs, averaged across listeners (and groups at 1 and 6 kHz) for the level range over which data were collected in both groups (10 to 30 dB SL).

When considering only notch widths of 0.2 or less, the ERB values are somewhat higher than when all notch widths are considered. For instance, the pooled ERB for the 1-kHz, 15-dB SL signal in the fixed masker level paradigm was 96 Hz with all points included using the roex(p,w,t,p) filter, whereas the ERB from the same data using only notch widths of 0.2 or less was 113 Hz using the roex(p) filter. This is primarily a consequence of the simpler filter model, in which one filter slope must account for the whole filter, commonly leading to an underestimate of the slope near the tip and an overestimate near the tail. Thus, the values shown in Fig. 4 should not be taken as accurate estimates of absolute cochlear tuning. Similarly, it is not appropriate to compare absolute ERB values from this analysis with those from previous studies. Nevertheless, the simple model provides a quantitative way of estimating *changes* in filter bandwidth over a wider range of levels than is possible with the more complex model.

1. Comparing fixed masker level and fixed signal level paradigms

The common conditions (1 and 6 kHz) allowed us to test for any significant differences between the two groups and methods (fixed masker level vs fixed signal level). No difference was expected, given that Glasberg and Moore (1982) had found none when comparing ERBs derived from notched-noise forward masking for signal levels between 8 and about 23 dB SL. However, according to our initial hypothesis, a difference might emerge at high masker levels, where subjects might start responding incorrectly to lower the level of the masker in the fixed signal level conditions. A repeated-measures analysis of variance (ANOVA) was carried out on the normalized ERB values (ERB divided by the signal frequency) with signal level (10 through 30 dB SL)

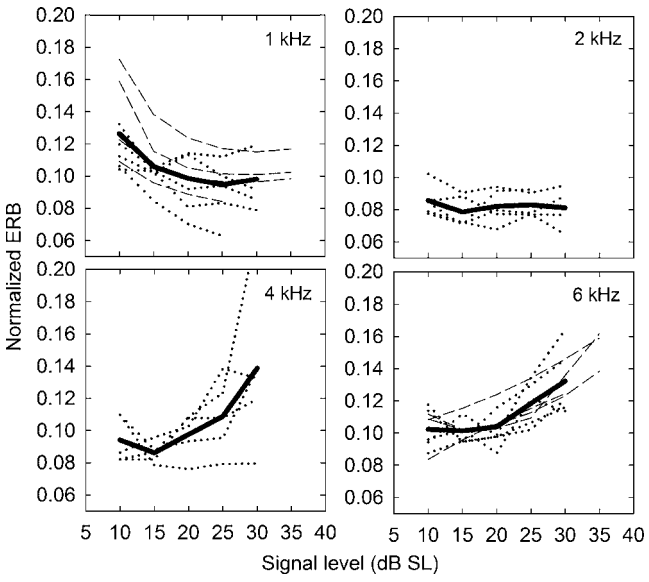

FIG. 4. Equivalent rectangular bandwidths (ERBs), derived by fitting the roex(p) filter model to symmetric notch widths between 0 and 0.2 to signal levels between 10 and 35 dB SL. Dashed lines represent individual fits using a fixed masker level paradigm; dotted lines represent individual fits using a fixed signal level paradigm. The heavy solid lines represent the mean ERB values, averaged across both sets of subjects where applicable.

and frequency (1 or 6 kHz) as within-subject factors and masking paradigm as a between-subjects factor. Masker paradigm did not have a significant main effect, nor were the interactions between paradigm and frequency or signal level significant ($p > 0.2$ in all cases). Thus, consistent with Glasberg and Moore (1982), the ERBs derived from fixing the signal level or fixing the masker level in the experimental paradigm were the same, so long as the data were analyzed in terms of signal level.

2. Effects of signal frequency on ERB level dependence

Despite some intersubject variability, some general trends are apparent in the data shown in Fig. 4. For both experimental paradigms at 1 kHz, there is an apparent *decrease* in ERB, particularly as the signal level is increased from 10 to 15 dB SL, and continuing slightly up to 25 dB SL. This trend was confirmed by subjecting the data using the 1-kHz signal between 10 and 30 dB SL to a one-way repeated-measures ANOVA with signal level as the within-subjects factor and group as the between-subjects factor. The effect of level was highly significant overall [$F(3.5, 24.6) = 13.4$, $p < 0.001$],[3] and there were both significant linear and quadratic trends, reflecting the general decrease in ERBs with increasing level. This finding was unexpected, given that Glasberg and Moore (1982) had found no significant effect of level on ERBs at 1 kHz in forward masking. However, the trend we observed seemed robust and was apparent in both experimental paradigms. The effect can also be observed in the raw and transformed data of the fixed signal level and fixed masker level paradigms, respectively. In Fig. 2, considering only notch widths up to 0.2, it can be seen that the slope of the function for the 1-kHz signal (left panel) is shallower for the 10-dB SL signal level than for the 20- or 30-dB SL signal levels. Similarly, in Fig. 3, the slopes for the 1-kHz signal (upper-left panel) seem shallower at 10 dB SL than at the higher two levels. We currently have no good explanation for this effect.

At 2 kHz, ERBs remained roughly constant over the level range tested. This was confirmed by a repeated-measures ANOVA, showing no significant effect of level on the ERB [$F(4, 16) = 0.77$, $p > 0.5$]. At 4 kHz, the data were rather variable, with one subject showing no change in ERB as function of level and another showing a very dramatic increase in ERB. Overall, the effect of level on the ERB at 4 kHz failed to reach significance [$F(2.0, 8.2) = 3.1$, $p = 0.1$]. In contrast, at 6 kHz, all nine subjects showed a consistent increase in ERB with increasing level, and the effect of level was significant for the pooled data [$F(2.7, 19.2) = 12.9$, $p < 0.001$], as were linear and quadratic trends ($p < 0.01$). Overall, the mean ERB increased by more than 30% between 10 and 30 dB SL and increased further for the three subjects for whom an ERB could be estimated at a signal level of 35 dB SL.

The results suggest that the dependence of ERB on level varies as a function of signal frequency between 1 and 6 kHz, with the broadening of the ERB as a function of level becoming increasingly pronounced with increasing signal frequency.

3. Changes in filter shape as a function of level

One important question is how the shape (and not just the ERB) of the filter changes with level. In the simple roex(p) model, increases in bandwidth are associated with decreases in the slopes of the filter. Another way a filter's ERB can increase is for the tuning of the filter tip to remain constant, while its gain decreases relative to the gain of the filter tail (e.g., Rosen *et al.*, 1998; Glasberg and Moore, 2000; Gorga *et al.*, 2003), which can be implemented in the roex(p, w, t) model by an increase in value of the weighting parameter, w. Our data with only 5 data points per signal level above 15 dB SL are generally too limited to permit a serious evaluation of a model with three free filter parameters. However, we carried out an analysis involving two free filter parameters using the roex(p, r) model, the equation for which is

$$W(g) = (1 - r)(1 + pg)\exp(-pg) + r, \tag{3}$$

where r represents a limit to the filter's dynamic range. This allowed us to determine whether the changes in ERB found with the roex(p) model could be attributed more to the tip or tail of the filter. This analysis was carried out at the 1- and 6-kHz signal frequencies, which were the frequencies that were tested for both groups of subjects, and which showed significant effects of level on the ERB. At the 1-kHz signal frequency, using the roex(p, r) filter shape, the effect of level on p values was found to be significant [$F(2.0, 16.4) = 3.87$, $p = 0.041$], but there was no significant effect of level on the r values [$F(2.4, 19.2) = 0.015$, $p > 0.5$]. In contrast, at the 6-kHz signal frequency, there was no significant effect of level on the p values [$F(3.7, 29.7) = 0.48$, $p > 0.5$], but a significant effect on the r values [$F(1.7, 13.8) = 6.86$, $p = 0.01$]. This suggests that at 6 kHz the increase in ERB found in the original analysis may be ascribed to the decrease in filter tip gain, relative to the tail, as proposed in other psychophysical studies using simultaneous masking (Glasberg and Moore, 2000) and physiological studies using otoacoustic emissions (Gorga *et al.*, 2003).

IV. DISCUSSION

Earlier studies using simultaneous masking have also found changes in level dependence as a function of frequency (e.g., Moore and Glasberg, 1987; Hicks and Bacon, 1999; Glasberg and Moore, 2000). In one of the more recent such studies, Glasberg and Moore (2000) concluded that level dependence (or, in their model, maximum filter gain) increased up to about 1 kHz and remained constant thereafter. On the other hand, an analysis by Baker *et al.* (1998) suggested that level dependence continued to increase with signal frequency up to 6 kHz. Both these studies used simultaneous masking. The pattern of our results is more in line with those found in Baker *et al.*'s study (1998). However, both earlier studies showed increasing ERB with increasing level at all signal frequencies tested. Here, a marked and significant increase (at least for signal levels up to 35 dB SL) was only observed at the highest signal frequency of 6 kHz. A possible reason for this apparent discrepancy is that the

results were based on simultaneous masking, while ours were based on nonsimultaneous masking. However, a more detailed study is required to confirm this conjecture. In any case, to the extent that nonsimultaneous masking better reflects cochlear tuning, as measured physiologically, it seems that pronounced differences occur between 1 and 6 kHz, which are not captured by current phenomenological models of human auditory filtering (e.g., Glasberg and Moore, 2000; Meddis *et al.*, 2001). One study measured psychophysical tuning curves as a function of level at both 1 and 3 kHz (Green *et al.*, 1981). They found level independence over a 20-dB range of signal levels at both frequencies. However, some aspects of their experiment, such as the abrupt gating of their 10-ms signal (with no onset or offset ramps), the limited number of conditions tested at 3 kHz, and their use of a tonal masker, which can produce so-called "confusion" effects in some cases (e.g., Neff, 1986), make their results somewhat difficult to interpret.

An earlier study, which examined human cochlear tuning only at very low levels, found that filter tuning sharpened considerably as the signal frequency was increased from 1 to 8 kHz (Shera *et al.*, 2002; see also Oxenham and Shera, 2003). Our data suggest that the improvement in tuning with increasing frequency may be a purely low-level phenomenon, and even that the reverse may be true at higher levels. For instance, in the earlier data, the normalized ERB decreased by a factor of about 1.6 as the signal frequency increased from 1 to 6 kHz. Although somewhat variable, our data at 10 dB SL go in the same direction with a decrease in normalized ERB by a factor of about 1.4 for both the full (Table I) and limited (Fig. 4) sets of notch widths. In contrast, at 30 dB SL the present data show that the normalized ERB *increases* by a factor of about 1.3 between signal frequencies of 1 and 6 kHz, and by about 1.5 at 35 dB SL for those subjects for whom data could be collected that level. These data thus confirm the conjecture of Shera *et al.* (2002) and Oxenham and Shera (2003), that their revised estimates of human cochlear tuning are only valid at very low stimulus levels.

What accounts for these changes in filter properties at different signal frequencies? One possibility is that the properties of the "cochlear amplifier," and its role in determining tuning, vary as a function of place along the cochlear partition. It has long been thought that cochlear gain and nonlinearity decrease in the apex of the cochlea, corresponding to low CFs. More recent psychophysical studies suggest that cochlear compression remains relatively constant across a wide range of CFs, at least in humans (Lopez-Poveda *et al.*, 2003; Plack and Drga, 2003; Plack and O'Hanlon, 2003; Oxenham and Dau, 2004). However, all these studies agree that cochlear compression is less frequency specific at low CFs. This suggests that while the cochlear amplifier may provide substantial *gain* at low CFs, it may not play such an important role in determining *tuning* at low CFs. The conjecture that different mechanisms determine tuning at low and high CFs is consistent with the observation that the shapes of neural tuning curves differ between low and high CFs. In particular, high-CF tuning curves exhibit clearly defined "tip" and "tail" portions, which have been hypothesized to derive from (at least) two separate modes of IHC excitation (e.g., Mountain and Cody, 1999; Lin and Guinan, 2000), whereas low-CF (including 1000 Hz) tuning curves show a more uniform shape, with no clearly discernible tail portion (e.g., Liberman, 1978). Other evidence for differences between apical and basal cochlear mechanics can be found in data from auditory-nerve-fiber group delays (Pfeiffer and Molnar, 1970) and from otoacoustic emissions (Shera and Guinan, 2003). Finally, it should *not* be concluded that there is no increase in filter bandwidth with level at frequencies of 1 and 2 kHz. Studies using psychophysical tuning curves have been able to measure tuning at levels higher than we attained in the present study, and have found increases in filter bandwidth once the masker level exceeds about 60 dB SPL (Nelson and Freyman, 1984; Nelson *et al.*, 1990; Nelson, 1991). To our knowledge, no similar studies have been done at higher signal frequencies.

In summary, our nonsimultaneous-masking data reveal a striking difference between the level dependence of the ERB as the signal frequency increases from 1 to 6 kHz: filter bandwidths decreased somewhat with increasing level at 1 kHz, remained constant at 2 kHz, showed a tendency to increase at 4 kHz, and increased consistently at 6 kHz. A similar level dependence has not been reported in earlier studies using simultaneous masking, where changes in tuning with level appear not to vary as much with frequency for signal frequencies of 1 kHz and above (Glasberg and Moore, 2000). The difference between our and previous results may be due to our use of nonsimultaneous masking, which may better reflect cochlear tuning as measured physiologically (e.g., Shera *et al.*, 2002).

ACKNOWLEDGMENTS

This work was supported by the National Institutes of Health (R01 DC 03909). We thank Christophe Micheyl, Xuedong Zhang, and Chris Shera for helpful comments on previous versions of this manuscript and Bertrand Delgutte for useful discussions. Brian Moore, Richard Baker, an anonymous reviewer, and the associate editor, Armin Kohlrausch, also provided many helpful comments during the review process.

[1]In a few cases (5 out of 88), second-order polynomial functions did not produce a real solution to individual data at either the highest or lowest signal level, because the function reached a maximum (or minimum) before crossing the relevant signal level. In these cases, a linear function was fitted, and the solution from the linear function was used to replace the complex values. This procedure was not required when using the pooled data.

[2]A few exceptions occurred at 6 kHz, where at 15 dB SL the masker level predicted by the polynomial function was higher than the highest masker level used in the experiment (50 dB SPL spectrum level, or 85 dB SPL overall level). In cases where the extrapolation was 3 dB or less (two data points each in S1 and S3), the extrapolated points were included; in the single case where the extrapolation exceeded 3 dB, the point (0.4 notch width for S2), the data point was not included in the filter fitting procedure. No such extrapolations were necessary when the polynomial functions were fitted to the pooled data.

[3]The F values and degrees of freedom reported in this paper incorporate the Huynh–Feldt correction for sphericity where applicable.

Baker, R. J., Rosen, S., and Darling, A. M. (**1998**). "An efficient characterisation of human auditory filtering across level and frequency that is also physiologically reasonable," in *Psychophysical and Physiological Advances in Hearing*, edited by A. R. Palmer, A. Rees, A. Q. Summerfield, and R. Meddis (Whurr, London), pp. 81–87.

Carney, L. H., and Yin, T. C. (**1988**). "Temporal coding of resonances by low-frequency auditory nerve fibers: Single-fiber responses and a population model," J. Neurophysiol. **60**, 1653–1677.

Cooper, N. P., and Rhode, W. S. (**1995**). "Nonlinear mechanics at the apex of the guinea-pig cochlea," Hear. Res. **82**, 225–243.

Delgutte, B. (**1990a**). "Physiological mechanisms of psychophysical masking: Observations from auditory-nerve fibers," J. Acoust. Soc. Am. **87**, 791–809.

Delgutte, B. (**1990b**). "Two-tone suppression in auditory-nerve fibers: Dependence on suppressor frequency and level," Hear. Res. **49**, 225–246.

Evans, E. F. (**2001**). "Latest comparisons between physiological and behavioural frequency selectivity," in *Physiological and Psychophysical Bases of Auditory Function*, edited by J. Breebaart, A. J. M. Houtsma, A. Kohlrausch, V. F. Prijs, and R. Schoonhoven (Shaker, Maastricht), pp. 382–387.

Glasberg, B. R., and Moore, B. C. J. (**1982**). "Auditory filter shapes in forward masking as a function of level," J. Acoust. Soc. Am. **71**, 946–949.

Glasberg, B. R., and Moore, B. C. J. (**1990**). "Derivation of auditory filter shapes from notched-noise data," Hear. Res. **47**, 103–138.

Glasberg, B. R., and Moore, B. C. J. (**2000**). "Frequency selectivity as a function of level and frequency measured with uniformly exciting notched noise," J. Acoust. Soc. Am. **108**, 2318–2328.

Glasberg, B. R., Moore, B. C. J., Patterson, R. D., and Nimmo-Smith, I. (**1984**). "Dynamic range and asymmetry of the auditory filter," J. Acoust. Soc. Am. **76**, 419–427.

Gorga, M. P., Neely, S. T., Dierking, D. M., Dorn, P. A., Hoover, B. M., and Fitzpatrick, D. F. (**2003**). "Distortion product otoacoustic emission suppression tuning curves in normal-hearing and hearing-impaired human ears," J. Acoust. Soc. Am. **114**, 263–278.

Green, D. M., Shelton, B. R., Picardi, M. C., and Hafter, E. R. (**1981**). "Psychophysical tuning curves independent of signal level," J. Acoust. Soc. Am. **69**, 1758–1762.

Harrison, R. V., and Evans, E. F. (**1982**). "Reverse correlation study of cochlear filtering in normal and pathological guinea pig ears," Hear. Res. **6**, 303–314.

Hicks, M. L., and Bacon, S. P. (**1999**). "Psychophysical measures of auditory nonlinearities as a function of frequency in individuals with normal hearing," J. Acoust. Soc. Am. **105**, 326–338.

Jesteadt, W., Bacon, S. P., and Lehman, J. R. (**1982**). "Forward masking as a function of frequency, masker level, and signal delay," J. Acoust. Soc. Am. **71**, 950–962.

Levitt, H. (**1971**). "Transformed up–down methods in psychoacoustics," J. Acoust. Soc. Am. **49**, 467–477.

Liberman, M. C. (**1978**). "Auditory-nerve response from cats raised in a low-noise chamber," J. Acoust. Soc. Am. **63**, 442–455.

Liberman, M. C., and Mulroy, M. J. (**1982**). "Acute and chronic effects of acoustic trauma: Cochlear pathology and auditory nerve pathology," in *New Perspectives on Noise-induced Hearing Loss*, edited by R. P. Hamernik, D. Henderson, and R. Salvi (Raven, New York), pp. 105–135.

Lin, T., and Guinan, J. J., Jr. (**2000**). "Auditory-nerve-fiber responses to high-level clicks: Interference patterns indicate that excitation is due to the combination of multiple drives," J. Acoust. Soc. Am. **107**, 2615–2630.

Lopez-Poveda, E. A., Plack, C. J., and Meddis, R. (**2003**). "Cochlear nonlinearity between 500 and 8000 Hz in listeners with normal hearing," J. Acoust. Soc. Am. **113**, 951–960.

Meddis, R., O'Mard, L. P., and Lopez-Poveda, E. A. (**2001**). "A computational algorithm for computing nonlinear auditory frequency selectivity," J. Acoust. Soc. Am. **109**, 2852–2861.

Moller, A. R. (**1977**). "Frequency selectivity of single auditory-nerve fibers in response to broadband noise stimuli," J. Acoust. Soc. Am. **62**, 135–142.

Moore, B. C. J. (**1978**). "Psychophysical tuning curves measured in simultaneous and forward masking," J. Acoust. Soc. Am. **63**, 524–532.

Moore, B. C. J., and Glasberg, B. R. (**1986**). "Comparisons of frequency selectivity in simultaneous and forward masking for subjects with unilateral cochlear impairments," J. Acoust. Soc. Am. **80**, 93–107.

Moore, B. C. J., and Glasberg, B. R. (**1987**). "Formulae describing frequency selectivity as a function of frequency and level and their use in calculating excitation patterns," Hear. Res. **28**, 209–225.

Moore, B. C. J., and Vickers, D. A. (**1997**). "The role of spread of excitation and suppression in simultaneous masking," J. Acoust. Soc. Am. **102**, 2284–2290.

Moore, B. C. J., Glasberg, B. R., and Baer, T. (**1997**). "A model for the prediction of thresholds, loudness, and partial loudness," J. Audio Eng. Soc. **45**, 224–240.

Moore, B. C. J., Glasberg, B. R., and Roberts, B. (**1984**). "Refining the measurement of psychophysical tuning curves," J. Acoust. Soc. Am. **76**, 1057–1066.

Mountain, D. C., and Cody, A. R. (**1999**). "Multiple modes of inner hair cell stimulation," Hear. Res. **132**, 1–14.

Neff, D. L. (**1986**). "Confusion effects with sinusoidal and narrowband-noise forward maskers," J. Acoust. Soc. Am. **79**, 1519–1529.

Nelson, D. A. (**1991**). "High-level psychophysical tuning curves: Forward masking in normal-hearing and hearing-impaired listeners," J. Speech Hear. Res. **34**, 1233–1249.

Nelson, D. A., and Freyman, R. L. (**1984**). "Broadened forward-masked tuning curves from intense masking tones: Delay-time and probe level manipulations," J. Acoust. Soc. Am. **75**, 1570–1577.

Nelson, D. A., Chargo, S. J., Kopun, J. G., and Freyman, R. L. (**1990**). "Effects of stimulus level on forward-masked psychophysical tuning curves in quiet and in noise," J. Acoust. Soc. Am. **88**, 2143–2151.

Oxenham, A. J., and Dau, T. (**2004**). "Masker phase effects in normal-hearing and hearing-impaired listeners: Evidence for peripheral compression at low signal frequencies," J. Acoust. Soc. Am. **116**, 2248–2257.

Oxenham, A. J., and Moore, B. C. J. (**1995**). "Additivity of masking in normally hearing and hearing-impaired subjects," J. Acoust. Soc. Am. **98**, 1921–1934.

Oxenham, A. J., and Plack, C. J. (**1998**). "Suppression and the upward spread of masking," J. Acoust. Soc. Am. **104**, 3500–3510.

Oxenham, A. J., and Shera, C. A. (**2003**). "Estimates of human cochlear tuning at low levels using forward and simultaneous masking," J. Assoc. Res. Otolaryngol. **4**, 541–554.

Patterson, R. D., and Nimmo-Smith, I. (**1980**). "Off-frequency listening and auditory filter asymmetry," J. Acoust. Soc. Am. **67**, 229–245.

Patterson, R. D., Nimmo-Smith, I., Weber, D. L., and Milroy, R. (**1982**). "The deterioration of hearing with age: Frequency selectivity, the critical ratio, the audiogram, and speech threshold," J. Acoust. Soc. Am. **72**, 1788–1803.

Pfeiffer, R. R., and Molnar, C. E. (**1970**). "Cochlear nerve fiber discharge patterns: Relationship to the cochlear microphonic," Science **167**, 1614–1616.

Plack, C. J., and Drga, V. (**2003**). "Psychophysical evidence for auditory compression at low characteristic frequencies," J. Acoust. Soc. Am. **113**, 1574–1586.

Plack, C. J., and O'Hanlon, C. G. (**2003**). "Forward masking additivity and auditory compression at low and high frequencies," J. Assoc. Res. Otolaryngol. **4**, 405–415.

Plack, C. J., and Oxenham, A. J. (**1998**). "Basilar-membrane nonlinearity and the growth of forward masking," J. Acoust. Soc. Am. **103**, 1598–1608.

Rhode, W. S., and Cooper, N. P. (**1996**). "Nonlinear mechanics in the apical turn of the chinchilla cochlea *in vivo*," Aud. Neurosci. **3**, 101–121.

Rosen, S., and Baker, R. J. (**1994**). "Characterising auditory filter nonlinearity," Hear. Res. **73**, 231–243.

Rosen, S., and Stock, D. (**1992**). "Auditory filter bandwidths as a function of level at low frequencies (125 Hz–1 kHz)," J. Acoust. Soc. Am. **92**, 773–781.

Rosen, S., Baker, R. J., and Darling, A. (**1998**). "Auditory filter nonlinearity at 2 kHz in normal hearing listeners," J. Acoust. Soc. Am. **103**, 2539–2550.

Ruggero, M. A., Rich, N. C., Recio, A., Narayan, S. S., and Robles, L. (**1997**). "Basilar-membrane responses to tones at the base of the chinchilla cochlea," J. Acoust. Soc. Am. **101**, 2151–2163.

Shera, C. A., and Guinan, J. J. (**2003**). "Stimulus-frequency-emission group delay: A test of coherent reflection filtering and a window on cochlear tuning," J. Acoust. Soc. Am. **113**, 2762–2772.

Shera, C. A., Guinan, J. J., and Oxenham, A. J. (**2002**). "Revised estimates of human cochlear tuning from otoacoustic and behavioral measurements," Proc. Natl. Acad. Sci. U.S.A. **99**, 3318–3323.

Weber, D. L. (**1977**). "Growth of masking and the auditory filter," J. Acoust. Soc. Am. **62**, 424–429.

Auditory filter nonlinearity across frequency using simultaneous notched-noise masking

Richard J. Baker[a)]
Human Communication and Deafness Division, School of Psychological Science, Humanities Devas Street, University of Manchester, Oxford Road, Manchester M13 9PL, United Kingdom

Stuart Rosen
Department of Phonetics and Linguistics, University College London, 4 Stephenson Way, London NW1 2HE, United Kingdom

(Received 15 July 2003; revised 11 August 2005; accepted 27 October 2005)

Psychoacoustic masking experiments have been widely used to investigate cochlear function in human listeners. Here we use simultaneous notched-noise masking experiments in normal hearing listeners to characterize the changes in auditory filter shape with stimulus level over the frequency range 0.25–6 kHz. At each frequency a range of fixed signal levels (30–70 dB SPL) and fixed masker levels (20–50 dB SPL spectrum level) are used in order to obtain accurate descriptions of the filter shapes in individual listeners. The notched-noise data for individual listeners are fitted with two filter shape models: a rounded exponential (roex) shape in which the filter skirt changes as a linear function of probe-tone level and the other, in which the gain of the tip filter relative to the filter tail changes as a function of signal level [Glasberg and Moore, J. Acoust. Soc. Am. **108**, 2318–2328 (2000)]. The parameters for these fitted models are then described with a simple set of equations that quantify the changes in auditory filter shape across level and frequency. Both these models fitted the data equally well and both demonstrated increasing tip-tail gain as frequency increased. © *2006 Acoustical Society of America.* [DOI: 10.1121/1.2139100]

PACS number(s): 43.66.Ba, 43.66.Dc, 43.64.Bt [GDK] Pages: 454–462

I. INTRODUCTION

The fundamental properties of the cochlea as a frequency analyzer have been widely studied both from physiological and psychoacoustical points of view. It is now generally accepted that the filtering properties of the cochlea are nonlinear in that the "auditory filters" broaden with increasing stimulus level.

In physiological terms, measurement of basilar membrane (BM) motion has clearly demonstrated compressive nonlinear behavior that is manifest as sharply tuned excitation at low levels with broader tuning at high levels (or in the "damaged" cochlea) associated with a basalward spread of excitation along the BM (Rhode, 1971; Ruggero and Rich, 1991; Ruggero *et al.*, 1997; Russell and Nilsen, 1997). It is thought that normally functioning outer hair cells (OHCs) in the cochlea provide saturating electromechanical amplification of the traveling wave (e.g., Davis, 1983; Ruggero, 1991; Dallos, 1992; Russell and Nilsen, 1997) and that damage to the OHCs reduces or abolishes this nonlinear enhancement of tuning (e.g., Ruggero and Rich, 1991; Murugasu and Russell, 1995; Ruggero *et al.*, 1996). For a sinusoidal signal this nonlinear enhancement of tuning is restricted to a relatively narrow region of the BM specific to the stimulus frequency (Russell and Nilsen, 1997). If measurements are made more basally to the characteristic place for that signal the response appears to grow in a more linear manner. Similarly, for BM measurements at a single place, the response for a tone well below the characteristic frequency (CF) for that place is linear (e.g., Ruggero *et al.*, 1997). However, such measurements have mainly involved the basal regions of the cochlear, and there is evidence that for apical regions the BM compression is not restricted to the CF region in the same way (Rhode and Cooper, 1996).

The broadening of auditory filters with increasing stimulus level has also been widely documented in psychoacoustic studies of masking (e.g., Weber, 1977; Pick, 1980; Lutfi and Patterson, 1984; Glasberg and Moore, 1990; Rosen and Stock, 1992; Rosen and Baker, 1994; Moore and Glasberg, 1987; Baker *et al.*, 1998; Rosen *et al.*, 1998; Hicks and Bacon, 1999; Glasberg and Moore, 2000). Many of these studies have used the notched-noise masking technique (Patterson, 1976) to estimate the effective "filter shape" and to quantify how the filters broaden as a function of stimulus level. Studies by Moore and colleagues have attempted to describe the change in auditory filter bandwidth across frequency and across level with the aim of deriving realistic "excitation patterns" (Moore and Glasberg, 1983, 1987; Glasberg and Moore, 1990). More recently Rosen and colleagues have developed a procedure for fitting a filter shape model to notched-noise data such that the shape can be an explicit polynomial function of either the signal level or the masker level (Rosen and Baker, 1994; Rosen *et al.*, 1998). Using this "POLYFIT" procedure Rosen and colleagues have argued that the aspect of the signal that determines the shape of the filter is more closely related to the signal level rather than the masker spectrum level. Glasberg and Moore (2000) took a similar approach but explicitly fitted a model which

a)Electronic mail: richard.baker@manchester.ac.uk

had "tip" and "tail" filters where the gain of the tip relative to the tail was described by a function that could be linear at low and high levels and nonlinear in between (see also Glasberg *et al.*, 1999). Glasberg and Moore (2000) supported the findings of Rosen and colleagues that a signal-level-dependent model fitted the data better than a model in which the parameters depended on the masker level. Interestingly, for the data sets analyzed by Glasberg and Moore (2000), using a more "realistic" function to describe the tip-tail gain produced relatively small changes in the goodness-of-fit compared to the linear function used by Rosen and colleagues (apart from at 250 Hz where the linear function was worse). While these studies all concentrated on describing the filter shape, Irino and Patterson (1997) derived the "gammachirp" as a level dependent time-domain description of human auditory filtering and showed that it could also be used to describe notched-noise masking data using only four free parameters in the fitted model. These studies that have tried to characterize level dependent changes in filter shape across frequency show that the level dependency is somewhat less at lower frequencies. This has been attributed to a decrease in BM nonlinearity at the lower frequencies. Such a suggestion has also been put forward to explain the decrease in "cochlear compression" estimated from growth of masking (GoM) experiments (Stelmachowicz *et al.*, 1987; Oxenham and Plack, 1997; Plack and Oxenham, 1998; Bacon *et al.*, 1999; Plack and Oxenham, 2000). However, as Plack and Oxenham (2000) point out, such a procedure is dependent on the "*differential* compression between the signal and the masker" and that any compression of the masker in addition to that of the signal will cause an underestimation of the degree of cochlear compression. Given the results of Rhode and Cooper (1996), which suggest that the nonlinearity is more spread out in the apical region of the cochlear, it is to be expected that such measures of relative compression between the effectiveness of on- and off-frequency will underestimate compression at the lower frequencies.

More recently, studies based on forward masking, and in particular using temporal masking curves (Nelson *et al.*, 2001) have suggested that the degree of compression derived from such masking experiments is independent of frequency, with compression at 250 Hz being similar to that at higher frequencies (Lopez-Poveda *et al.*, 2003; Plack and Drga, 2003; Nelson and Schroder, 2004).

The aim of the present study is to use a comprehensive set of simultaneous masked notched-noise thresholds to characterize the nature of auditory filtering in individual listeners and to use these data to derive relatively simple quantitative descriptions of auditory filtering across level and frequency. While a subset of the notched-noise data used here was presented by Baker *et al.* (1998) and also analyzed by Glasberg and Moore (2000) these two studies only used data averaged across two listeners. Here we employ data from a larger group of listeners and concentrate on the analysis of individual listeners' filter shapes with the aim of generalizing across frequency. We also consider the effect of the middle ear transfer function on the derived filter shapes. Finally, these notched-noise data sets are fitted using the *signal-level-dependent* (SLD) model of Glasberg and Moore (2000) and these are compared with the filter shapes obtained using the POLYFIT procedure of Rosen and colleagues.

While this study utilizes simultaneous masking, it is important to acknowledge that such a technique will underestimate both the frequency selectivity and any derived measure of cochlear compression compared to BM measurements (and forward masking experiments). Such differences are attributable to the effect of suppression, in addition to masking, when the masker and stimulus are presented simultaneously (e.g., Delgutte, 1990; Moore and Vickers, 1997; Moore *et al.* 1999).

II. METHODS

A. Listeners

A total of 10 normally hearing listeners (thresholds $<$20 dB HL 0.25–8 kHz) were used for the study (4 male, 6 female). These listeners were aged between 20 and 37 years old. Two of the listeners completed the full set of measurements at each of the seven frequencies. A further two listeners completed two of the frequencies each and the remaining six listeners completed measurements at just one frequency.

B. Masked threshold estimation

Masked thresholds were determined for sinusoidal probe tones at each of a range of seven frequencies in the presence of notched-noise maskers with variable notch widths. The probe tone frequencies used were: 0.25, 0.5, 1, 2, 3, 4, and 6 kHz. Four listeners took part at each of the frequencies apart from 3 and 6 kHz where only two listeners took part (these two also completed measurements at each of the other frequencies). The notches were placed both symmetrically and asymmetrically about the relevant probe frequency and either the probe level or the noise level could be varied to determine the thresholds. A two-interval, two-alternative forced-choice paradigm with feedback together with a three-down, one-up tracking procedure was used to estimate the 79% point on the psychometric function. Listeners responded on a button box, with illuminated buttons indicating presentation intervals and providing feedback. From a starting level at which the probe was clearly audible, the varying sound, either probe or masker, was initially changed in 5 dB steps, with step size decreasing by 1 dB after each turnaround. Once the step size reached 2 dB, it remained constant for a further eight turnarounds, the mean of which was taken as the threshold. For each particular combination of notch width and fixed probe or fixed masker level, two thresholds per listener were typically obtained. Threshold measurements where the standard deviation of the last eight turnarounds exceeded 3 dB were rejected and the measurement repeated. Also, where two measurements of the same condition in the same listener differed by more than 3 dB, a further measurement was taken and the average of all measurements used.

C. Stimulus configuration

The outside edges of the masker noise were fixed at $f_0 \pm (0.8 \times f_0)$. For example, the outside edges of the noise

were placed at 0.4 and 3.6 kHz when a 2 kHz probe tone was being used. A maximum of 16 different notch conditions were used (6 symmetric and 10 asymmetric). The frequencies of the edges of the notch are specified in normalized frequency units relative to the probe frequency (f_0) as given by $(|f-f_0|)/f_0$. In the symmetric conditions, both notch edges were placed at normalized values of 0.0, 0.1, 0.2, 0.3, 0.4, and 0.5. In the asymmetric condition one of the notch edges was set at a normalized value of 0.0, 0.1, 0.2, 0.3, and 0.4, while the other was set to 0.2 normalized units further away (0.2, 0.3, 0.4, 0.5, and 0.6).

When the masker level was fixed, masker spectrum levels (N_0) ranging from 20 to 50 dB SPL in 10 dB steps were used (for 2 kHz probe N_0 spectrum levels of 60 dB SPL were also used for three of the four subjects). When the probe level was fixed, probe levels (P_s) ranging from 30 to 70 dB SPL, again in 10 dB steps, were used. Blocks of 16 threshold measurements were used where all 16 notch widths were measured for one frequency and signal or masker level, with a maximum of 9 different level conditions used at each frequency. The order of presentation within blocks was randomized, and one block took approximately 40–60 min to complete. The order of conditions was also randomized. At each of the seven probe frequencies there were a total of 144 level/notch possible combinations (with each threshold measured at least twice). There were a total of 24 listener/frequency combinations giving approximately 7000 masked threshold measurements in total ($144\times24\times2$).

D. Stimulus generation

All the stimuli were computer generated at a sampling frequency of 40 kHz. The time wave form of the probe was calculated independently of the masker and consisted of a steady state portion of 360 ms plus 20 ms raised-cosine onsets and offsets. The probe was temporally centered within the masker which consisted of a 460 ms steady-state portion with 20 ms raised-cosine-squared[1] onset and offsets. To generate the masker, the desired frequency spectrum was defined by setting all the spectral components (spaced at intervals of 1.22 Hz) within the appropriate frequency limits to have equal amplitudes while those outside were set to zero. Nonzero components had their phases randomized uniformly in the range of $0-2\pi$ rad. An inverse FFT was then applied to generate the time wave form. At the start of each threshold determination, a 3.2768 s buffer of noise was generated for use during that test. On each trial, a 500 ms portion of the buffer was chosen randomly for each of the two masker intervals within each trial.

The probe and masker were played out through separate channels of a stereo 16 bit D-A converter and attenuated independently under computer control before being electrically mixed (PA4 and SM3 from Tucker-Davis Technologies). The signal was then sent via a balanced line to a final amplifier in a sound-treated room where it was presented monaurally to the right ear via Etymotic ER2 insert earphones. Calibrations were carried out using a B&K 4157 ear simulator [conforming to IEC 711 and ANSI S3.25/1979 (ASA 39/179)] with a B & K DB 2012 ear canal extension.

E. Analyses

1. Level dependent filter shapes

At each frequency a variety of models were fitted to each listener's data individually, using the POLYFIT procedure. All of the models were variants of the asymmetric roex(p,w,t) model. For a more detailed discussion of the fitting procedure the reader is referred to Rosen *et al.* (1998). In this paper we will concentrate on a simple model that characterizes the dominant aspects of auditory filter nonlinearity and yet allows simple parametrization of the filter shapes across frequency. In this relatively simple model, the upper half of the filter was described with a roex(p) shape where the "p_u" parameter is independent of signal level. The lower half of the filter shape is described by a complete roex(p_l,w_l,t_l) shape in which the "w" parameter is allowed to vary with signal level—a linear function of probe-tone level. Such a simplified model was chosen as it described the major changes in filter shape with level, allows simple interpretation of parameter behavior across frequency, and is akin to the SLD(*wlin*) model of Glasberg and Moore (2000). In fitting the filter shapes to the data it is also necessary to estimate k, a level independent parameter representing the signal-to-noise ratio necessary for detection at the output of the filter. Finally, we also used the ability of POLYFIT to estimate an absolute threshold (A) that is never allowed to vary with level. Thus, in total, there are 7 free parameters in the model fitted to data at a single frequency: p_l, p_u, t_l, k, A, and the two parameters w_{l1} and w_{l2} which describe the straight line relationship between w_l and probe-tone level. In using this procedure to fit the filter shapes the gain at the center frequency is assumed to be zero and the attenuation at other frequencies is expressed relative to this. The solid lines in Fig. 1 show examples of predicted thresholds using this roex model.

2. Corrections for middle ear transfer functions

In order to consider the properties of the cochlear filtering processes on their own it is necessary to separate these processes from the frequency dependent effects of the outer and middle ear. This can be achieved by applying a weighting function to the representation of the masker spectrum in the fitting procedure. For example, in the present study a flat spectrum noise was delivered to the tympanic membrane. However, the middle ear transfer function will reduce the amplitude of this signal entering the cochlea for frequencies below about 400 Hz and above about 4 kHz. By applying an appropriate weighting to the representation of the noise in the fitting process, the fitting procedure can take into account the fact that outside these frequency ranges less masker energy will be entering the cochlea. This was carried out as part of the filter fitting procedure in a manner similar to that described by Glasberg and Moore (1990) using the middle ear transfer function measured in human cadavers as described by Puria *et al.* (1997). This function is approximated by Puria *et al.* (1997) as a bandpass filter with slopes of −8 dB/octave above 4 kHz and 4 dB/octave below 400 Hz, although here we use a smoothed version of their actual transfer function rather than these approximations. No cor-

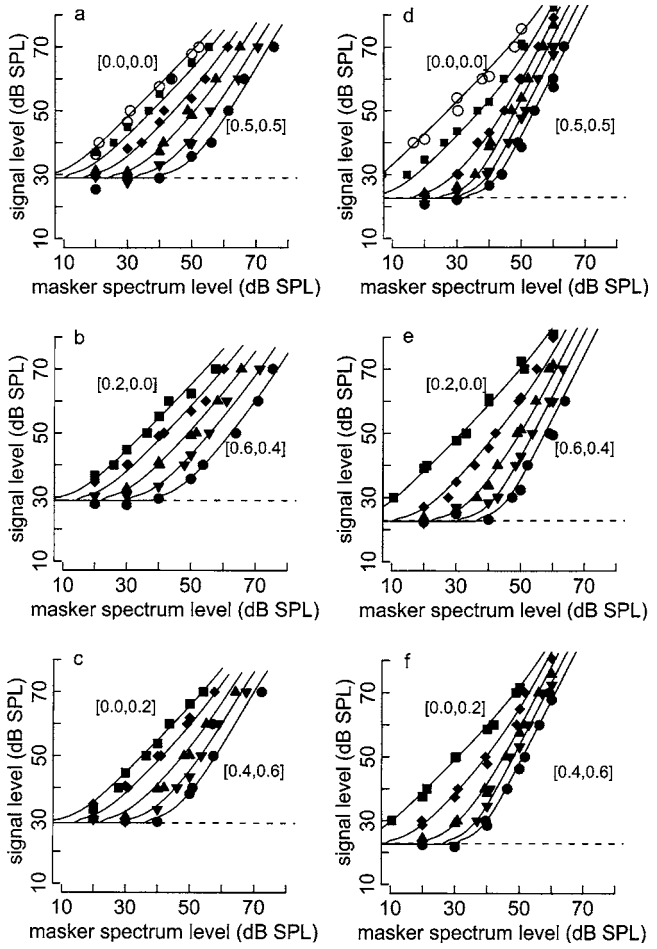

FIG. 1. Examples of growth of masking functions from listener AD. (a)–(c) Functions for 250 Hz signal. (d)–(f) Functions for the 2000 Hz signal. (a), (d) GoM functions for symmetric notches. (b), (e) GoM functions for notches with the lower edge furthest from the signal and plots. (c), (f) GoM functions for notches with the upper edge furthest from the signal. The two extreme notch conditions are indicated on each plot. The solid lines show the predicted thresholds from the filter shapes fitted to the data using the POLYFIT procedure. The horizontal dashed line represents the absolute threshold of the listener estimated using this procedure. For each frequency the GoM functions are separated into three separate plots for clarity. However, the predicted values shown in each of the three plots are based on the same POLYFIT model fitted to all 16 notch conditions together.

rections for the headphone or the ear canal transfer functions were used as the ER2 insert earphones give a flat frequency response at the eardrum.

3. SLD fits

In addition to using the POLYFIT procedure to fit filter shapes to the individual listeners' data—the SLD (signal-level-dependent) procedure described by Glasberg and Moore (2000) was also used to fit the data both with and without the middle ear weighting function. The model used in this procedure is based on the roex(p,w,t) filter model except that the gain of the tip filter relative to the tail filter is allowed to vary in a way similar to that of the basilar membrane input-output function. One gain parameter ($G_{\max}$) describes the maximum gain at low signal level. The other model parameters are invariant with level.

III. RESULTS

A. Growth of masking functions

Example plots of growth of masking (GoM) functions can be seen in Fig. 1 from listener AD at tone frequencies of 0.25 and 2 kHz. In Fig. 1 the probe tone level at threshold is plotted against masker spectrum level for the different notch conditions and for both fixed tone and fixed masker conditions. The solid lines represent the fits to the data estimated using the POLYFIT procedure and the dashed horizontal lines represent the absolute threshold estimated from the data using the same procedure.

These GoM functions clearly demonstrate the changing shape of the auditory filters as the signal level increases—the GoM functions tend to converge indicating a broadening of the filters. For a linear filter the GoM functions would be parallel (above absolute threshold). Notice from the examples shown in Fig. 1 that for the 2 kHz wide-notch conditions the GoM functions are approximately parallel, whereas the GoM functions for the narrower notches show more curvature. One possible interpretation of this is that the nonlinearity at this frequency is limited to passband of the filter and that the filter skirts are more linear. For the 250 Hz conditions shown in Fig. 1, there appears to be less of a distinction in the degree of convergence of the GoM functions which may suggest that the nonlinearity is more distributed across the whole of the filter bandwidth.

B. Fitted filter shapes

At each frequency the POLYFIT procedure was used to fit filter shapes to each listener's data sets individually both with and without the middle ear weighting function as described above. The mean rms error in the fit was 1.594 dB (s.d.=0.292) for the unweighted fits and 1.607 dB (s.d. =0.303) for the weighted fits. Regression analysis was used to describe how the fitted parameters varied across frequency. Those parameters derived using the middle-ear weighting in the fitting are plotted as a function of frequency in Fig. 2.

For each of these the regressions, a linear dependency on logarithmic frequency is required ($p<0.01$) except when the middle ear weighting is applied in which case parameter p_u is independent of frequency [see Fig. 2(a)] and parameter t_l requires a quadratic term to describe its relationship with frequency [$p<0.001$, Fig. 2(d)]. The regression equations that describe how the parameters vary across frequency for both the weighted and unweighted fits are given in the upper half of Table I.

The w_{l2} parameter indicates the rate at which w_l changes with level (i.e., the rate of change of the tip-tail ratio with increasing signal level). The value of w_{l2} generally increases with frequency. The mean value is 0.517 (s.d.=0.06) at 0.25 kHz and 0.616 (s.d=0.01) at 6 kHz. If this value of w_{l2} is presumed to represent a change in the tip-tail ratio with signal level then they correspond to relative compression ratios between the filter tip and skirt of 2.1:1 and 2.6:1 respectively.

Figure 3 shows the filter shapes derived from the "unweighted" equations given in Table I for signal levels of 30,

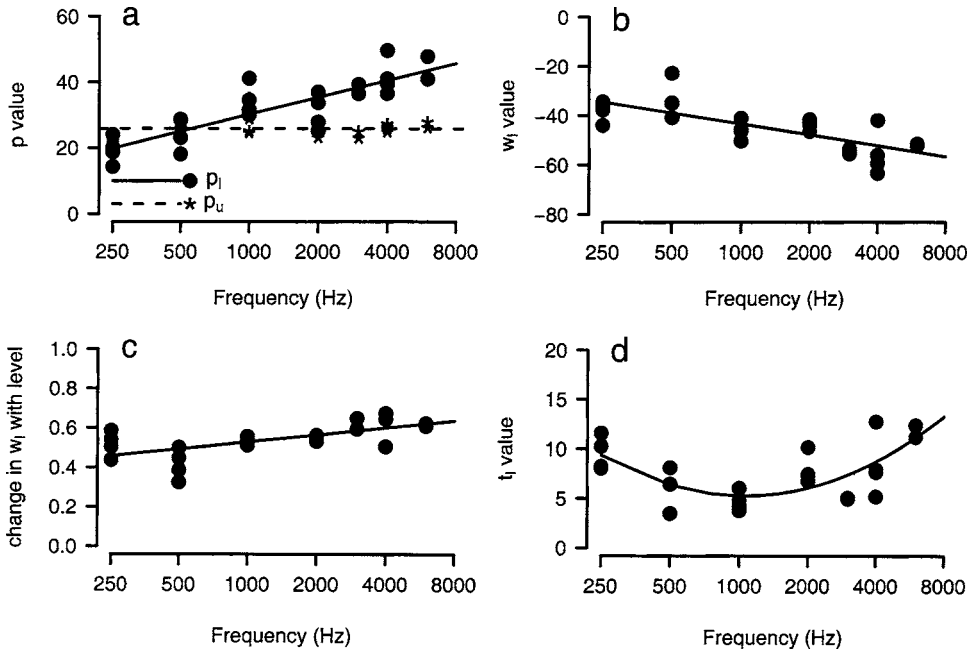

FIG. 2. Variation of the fitted parameters across frequency (middle ear weighting function applied during fitting). Parameters p_l and p_u are shown in (a), w_{l1} in (b), w_{l2} in (c), and t_l in (d). Note that w_{l2} gives the rate of change in the w_l parameter with level. The w_{l1} and w_{l2} parameters are combined to describe w_l as a function of signal level: $w_l = w_{l1} + w_{l2} \times$ (signal level). Note, p_u is invariant with frequency while t_l shows a quadratic dependency on frequency. The equations for the fitted regression lines are given in Table I.

50, and 70 dB SPL (dashed lines), along with those derived from the filter shapes fitted with the middle ear weighting (solid lines). Figure 3(a) shows the filters as described by the roex equations (i.e., normalized to 0 dB at the center frequency). Figure 3(b) follows Rosen *et al.* (1998) and shows the filters normalized to 0 dB at 0.4× center frequency (cf). Such figures allow visualization of the decrease in gain at cf as signal level increases. However, as discussed earlier, the assumption of linearity well below cf is probably not entirely valid at the lower frequencies.

From Fig. 3 it is obvious that the main effect of applying the middle ear transfer function is one of making the low-frequency side of the filters shallower except at the highest frequencies. A similar effect has previously been shown by Glasberg and Moore (1990) where corrections for the middle ear transfer function were based on minimum audible field measurements and on the 100 phon equal loudness contour.

C. Equivalent rectangular bandwidths (ERBs)

From the above-described fitted filter shapes the equivalent rectangular bandwidth was calculated for each individual listener/frequency condition for signal levels of 30, 50, and 70 dB SPL. These calculations were carried out for both the unweighted and weighted filter shapes. The mean and standard deviations of these ERBs are given in Table II.

From Table II we can see that, in addition to the increase in ERB with frequency, the ERB changed little between 30

TABLE I. Equations describing the fitted model parameters as a function of log frequency. The upper panel shows the equations describing the POLYFIT parameters, while the lower panel shows the equations describing the parameters obtained using the SLD procedure of Glasberg and Moore (2000). The second column gives the regression equations for the filter parameters obtained without compensation for the middle ear transfer function. The right-hand column gives the equations obtained when compensation for the middle ear transfer function was used in the fitting procedure. For each of the equations shown the p value associated with the regression was less than 0.05. The bottom rows of the POLYFIT table show how the w_{l1} and w_{l2} parameters, which are used to describe w_l as a function of signal level, vary across frequency. For the POLYFIT model the w_{l1} and w_{l2} parameters are combined to describe w_l as a function of signal level: $w_l = w_{l1} + w_{l2} \times$ (signal level).

Parameter	No middle ear correction	Middle ear correction
	POLYFIT	
p_l	$p_l = [13.57 \times \log_{10}(f)] - 9.31$	$p_l = [17.23 \times \log_{10}(f)] - 21.50$
p_u	$p_u = [6.02 \times \log_{10}(f)] + 7.22$	$p_u = 25.85$
t_l	$t_l = [-3.43 \times \log_{10}(f)] + 20.10$	$t_l = [10.4 \times \log_{10}(f)^2] - [62.7 \times \log_{10}(f)] + 100.1$
w_{l1}	$w_{l1} = [-15.75 \times \log_{10}(f)] + 5.96$	$w_{l1} = [-14.73 \times \log_{10}(f)] + 0.83$
w_{l2}	$w_{l2} = [0.14 \times \log_{10}(f)] + 0.095$	$w_{l2} = [0.119 \times \log_{10}(f)] + 0.17$
	SLD	
p_l	$p_l = 13.24 \times \log_{10}(f) - 8.576$	$p_l = [16.73 \times \log_{10}(f)] - 20.04$
p_u	$p_u = [4.34 \times \log_{10}(f)] + 11.57$	$p_u = 24.98$
t_l	$t_l = 10.03$	$t_l = [5.53 \times \log_{10}(f)^2] - [30.8 \times \log_{10}(f)] + 29.2$
$G_{\max}$	$G_{\max} = [10.01 \times \log_{10}(f)] + 15.50$	$G_{\max} = [12.87 \times \log_{10}(f)] + 5.20$

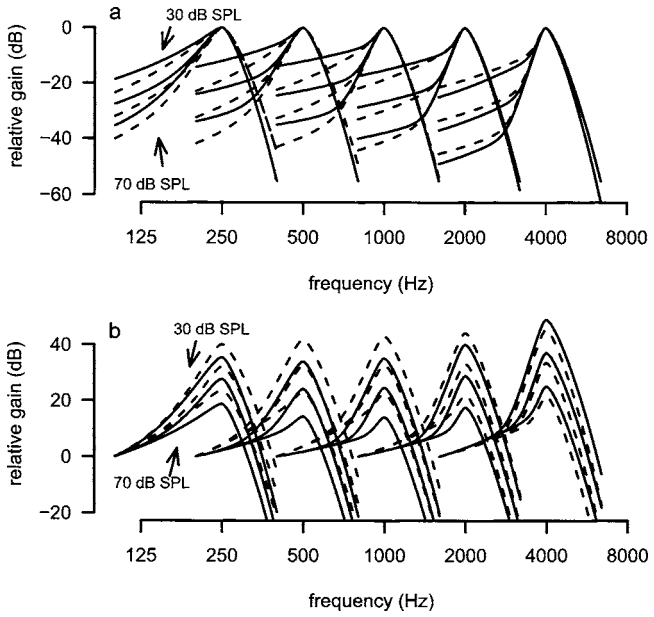

FIG. 3. Filter shapes derived from the set of POLYFIT equations given in Table I. The solid lines show the filter shapes obtained with the middle ear weighting taken into account in the fitting procedure. The dashed lines represent the filter shapes obtained without applying the middle ear weighting function. At each frequency the parameter values are calculated using these equations and the filter shapes plotted for probe-tone levels of 30, 50, and 70 dB SPL. The upper plot shows the filter shapes normalized to have 0 dB gain at the center frequency. The lower plot shows the same filter shapes normalized to give 0 dB gain at 0.4 × center frequency. Filter shapes at 3 and 6 kHz are omitted for clarity.

and 50 dB SPL signal levels but increased more markedly between 50 and 70 dB SPL. This constant filter bandwidth at lower levels is likely to be due to the fact that the ERB calculation is dominated by energy in the passband of the filter while the dominant changes in the above-described filter shapes are in the filter skirts. It is only at the higher signal levels that the skirt is high enough relative to the filter tip for it to have an influence on the ERB calculation (Baker and Rosen, 2002). Notice also, from Table II that the application of the middle ear weighting function has relatively little effect on the ERB apart from at low frequencies and high signal levels. This should be expected from Fig. 3 where it can be seen that the middle-ear weighting raises the low-frequency skirt of the filter at these low frequencies and that the tip-tail distinction is much less pronounced.

D. SLD fits

The SLD procedure described by Glasberg and Moore (2000) was also used to fit the listeners' individual data sets and the fitted parameters were described as a function of frequency. The fitted p_l and p_u parameters showed similar variations with frequency to those obtained with the POLYFIT procedure. The lower half of Table I shows the regression equations that describe how the fitted parameters vary across frequency. Again, applying the middle ear weighting caused the t_l parameter to take on a quadratic form. Note that the "w" parameters given by the POLYFIT procedure are now replaced by a single fitted parameter—$G_{\max}$, which defines the form of the tip to tail gain function. The upper plot of Fig. 4 shows the variation in $G_{\max}$ with frequency. The mean values of $G_{\max}$ generally increase with frequency from 37 dB (s.d. =3.5) at 0.25 kHz to 49 dB (s.d.=1.8) at 6 kHz.

Using the equations from the lower part of Table I for the middle-ear-weighted fits, filter shapes were derived using the procedure described by Glasberg and Moore (2000). This procedure is not the same as used earlier to generate Fig. 3. For each filter shape in Fig. 3 the shape of the filter is defined by the level of the signal at the filter's CF. Glasberg and

TABLE II. Equivalent rectangular bandwidths expressed in hertz, with standard deviations in brackets. The ERBs were calculated from the filter shapes for each individual listener at the three signal levels shown and the mean and standard deviation calculated across the listeners at each frequency. The ERBs are shown both with and without the use of middle ear weighting in the filter fitting procedure. The second from bottom row shows the ERB values from Glasberg and Moore (1990) and the bottom row shows the ERB values calculated from the SLD fits to the data in the current study using the level-independent p parameters to calculate the ERB.

		Frequency (kHz)						
	Signal level	0.25	0.5	1.0	2.0	3.0	4.0	6.0
No middle ear weighting	30 dB SPL	49.2 (5.9)	79.5 (6.9)	128.7 (17.9)	277.5 (38.9)	402.6 (19.5)	492.6 (38.2)	678.2 (50.9)
	50 dB SPL	50.6 (5.4)	83.1 (7.4)	133.7 (18.9)	287.3 (41.3)	408.0 (18.9)	497.0 (41.0)	686.3 (49.6)
	70 dB SPL	60.8 (4.0)	108.9 (24.8)	185.9 (38.6)	403.2 (71.0)	502.3 (10.8)	563.7 (66.7)	810.3 (25.2)
With middle ear weighting	30 dB SPL	50.7 (6.8)	81.6 (9.0)	131.4 (18.1)	282.6 (43.87)	409.2 (23.0)	502.0 (36.2)	716.0 (49.2)
	50 dB SPL	52.2 (6.3)	89.3 (11.2)	135.7 (19.1)	291.2 (43.4)	413.4 (22.4)	505.4 (38.6)	721.5 (48.3)
	70 dB SPL	68.2 (5.7)	141.2 (45.8)	182.7 (41.7)	400.3 (87.5)	488.8 (0.03)	555.8 (60.9)	815.5 (27.3)
	Glasberg and Moore (1990)	51.7	78.7	132.6	240.6	348.5	456.5	672.3
	SLD model	49.1 (6.9)	79.5 (8.5)	139.0 (17.1)	287.5 (40.3)	437.9 (31.1)	528.2 (26.3)	716.2 (50.3)

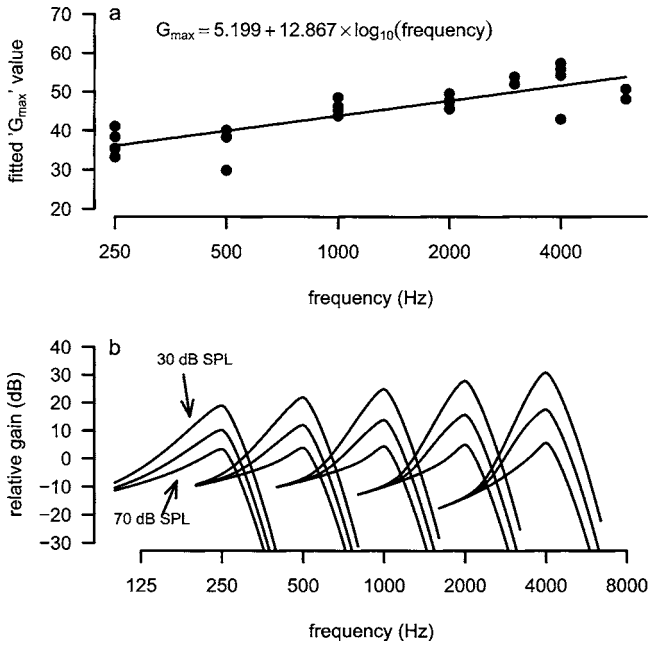

FIG. 4. The upper plot shows the variation of the fitted "G_{max}" parameters following the fitting procedure of Glasberg and Moore (2000) using the middle ear weighting function described in the text. The lower plot shows the derived filter shapes for the weighted fits following the procedure of Glasberg and Moore (2000). Filter shapes are plotted for probe-tone levels of 30, 50, and 70 dB SPL. Filter shapes at 3 and 6 kHz are omitted for clarity.

Moore (and Fig. 4 of the present study) use an iterative procedure in which the shape of the filter depends on the filter's own output. Thus for a filter centered on 1 kHz and a signal of 0.5 kHz, the filter will attenuate the signal, this will lead to a decrease in the filter output and thus an increase in the gain of the tip portion of the filter. This difference can most easily be seen if the 4 kHz filter in Fig. 3(b) is compared with that of Fig. 4(b). In Fig. 3(b) there is a pronounced transition region between the tip and tail. In Fig. 4(b) this is not as evident, as this is the region where level dependent gain effectively broadens the filter. In terms of how well the two models fit the data, the average rms errors for the POLYFIT and the SLD middle-ear-weighted fits are 1.61 dB (s.d. =0.30) and 1.68 dB (s.d.=0.30), respectively. Thus there is very little to choose from in terms of the difference in goodness of fit of the two models to the data.

E. Filter shapes and the extent of nonlinearity at low frequencies

For high signal frequencies the filter shapes from the POLYFIT procedure show a clear "linear" low frequency tail region. For example, in the 4 kHz filter shown in Fig. 3(b), the nonlinear passband of the "tip-filter" does not spread down to the low frequencies. This also seems to be reflected in the GoM functions as discussed earlier (e.g., 2 kHz plots in Fig. 1). For the 250 Hz filter shape however, the nonlinear passband appears to spread right down to the tail of the filter suggesting that the response may still be nonlinear at 0.4 $\times$CF. This can be more clearly seen from the SLD fits shown in the lower plot of Fig. 4, where the gain curves of the 250 Hz filters fail to converge at 0.4$\times$CF.

In addition, the model filter shape used in the POLYFIT procedure in this study is restricted to a roex(p,w,t) on the low frequency side in which only the w parameter is allowed to vary with level. Such restriction of the filter shape, while allowing a straightforward description of the parameters across frequency, may not be ideal for all signal frequencies. If these constraints are relaxed and each of the parameters p_l, w_l, and t_l are allowed to be linear functions of probe-tone level (p_u remains independent of level) then the relative compression estimated at 250 Hz changes from a mean of 0.625 (s.d.=0.095) to 0.461 (s.d.=0.150). If this is repeated for each signal frequency the change in compression across frequency is no longer significant. However, when such a model is fitted to the data of individual subjects not all the parameters are constrained in the fitting process for every subject which thus makes interpolation of the parameters across frequency difficult.

IV. DISCUSSION

This study attempts to characterize how the signal-level-dependent auditory filter shapes measured with notched-noise masking change across frequency. When the filter shapes are fitted to individual subjects' masked thresholds the general patterns of fitted parameters are similar across the subjects. This has allowed the fitted parameters to be described as functions of signal frequency.

The filter shapes themselves follow the same pattern as those described by Rosen *et al.* (1998) at 2 kHz, although in the present study the complexity of the fitted filter shapes is limited to the lower w parameter being allowed to vary with level. By removing the effect of middle ear filtering in the fitting procedure a similar pattern was also observed to that shown by Glasberg and Moore (1990) using a weighting function derived from minimum audible field measurements. The main effect of applying this middle ear weighting function is one of raising the low-frequency skirts for the low-frequency filters (see Fig. 3). This is as expected, since compensating for the transfer function effectively "removes" some of the low-frequency masker in the fitting procedure and thus a raised filter skirt is then required to account for the masked thresholds. In terms of the actual filter shapes, correcting for the middle ear transfer function means that the tip-to-tail gain increases more dramatically with increasing frequency [see Fig. 3(b)] as a result of this change in filter asymmetry.

Quantifying the frequency selectivity of the ear with a single parameter has traditionally been done using the ERB. While it has been known for some time that the ERB increases with frequency (e.g., Glasberg and Moore, 1990), the ERB, as a descriptor of frequency selectivity, is somewhat limited in that it is dominated by the tip of the filter shape and thus does not correlate well with changes in the filter tails. This can be clearly seen in Table II, where the ERB for three different signal levels (at the seven frequencies) is given. It is only at the higher signal levels, when the low frequency skirt of the filter approaches the tip, that the ERB changes with increasing signal level. The ERB values for the

lower level signals are similar to those of Glasberg and Moore (1990). In addition, ERB values calculated from SLD fits to the data are also similar to those derived from the POLYFIT procedure at these low stimulus levels. The main discrepancy arises at higher levels where calculating the ERB using just the p values ($\mathrm{ERB}=[2/p_l+2/p_u]/f$—Patterson and Nimmo-Smith, 1980; Glasberg and Moore, 2000) fails to take into account the effect of the raised filter skirt. The ERBs derived using the POLYFIT models take into account the effect of the filter skirt (i.e., changes in w_l and t_l). While the ERB values derived for low stimulus levels are commensurate with other simultaneous masking studies, these values are considerably larger that those obtained in nonsimultaneous masking where the influence of suppression is thought to be less. For example, Shera *et al.* (2002) have compared forward-masked psychoacoustic measures of cochlear tuning with measurements derived from stimulus frequency otoacoustic emission measurements and noted bandwidths approximately half those measured in simultaneous masking experiments.

Fitting the SLD model of Glasberg and Moore (2000) to the notched-noise data generally revealed similar patterns to the POLYFIT model. The passband characteristics of these two fitted models were very similar, as were the errors in the goodness of fit. It can be argued that the SLD model is "better" for two reasons—first, it involves one fewer fitted parameters and, second, the function that describes the tip-tail gain is somewhat more realistic than the linear function describing the w parameter in the POLYFIT model. The shape of the SLD gain function ensures that the tip-tail gain can never become negative as could be the case when w is a linear function of stimulus level (although in practice the POLYFIT procedure prevents this from happening). However, over the range of signal levels used in this study (fixed tone levels of 30–70 dB SPL), the gain function for the SLD model is approximately a straight line, decreasing with increasing level. The fact that both these functions can be described by straight lines for the range of levels over which the data constrain the fitted models explains why the two models fit the data equally well. What this does imply, however, is that for this range of stimulus levels there is no indication that the filtering, as measured in this study, is becoming linear either at low or at high signal levels.

While there is a clear level dependence of the filter shapes at all of the frequencies used in this study, there is some evidence that, for these simultaneous masking paradigms at least, the degree of nonlinearity increases with increasing frequency. (e.g., differences in the rate of change of w_l with level, or changes in $G_{\max}$). Such behavior is at odds with the findings of recent studies that have utilized forward masking paradigms and demonstrated that the underlying compression ratios appear to be independent of frequency (e.g., Lopez-Poveda *et al.*, 2003; Plack and Drga, 2003; Nelson and Schroder, 2004). However, at least some of this discrepancy may be accounted for by the varying extent of the nonlinear region at each cf as suggested by Plack and Oxenham (2000). At the higher filter frequencies the nonlinear passband of the filter is relatively narrow and thus in the wider notch-noise conditions the masker will fall into the linear tail regions of the filter. For the lower frequency filters there is no clear distinction between the tip and tail of the filter—the filters appear to still show some degree of nonlinearity even at $0.4\times$cf. This would mean that, even for the widest notch widths used in this study, the masker would still be undergoing some degree of compression and thus any estimate of relative compression between the tip and tail at these lower frequencies would underestimate the degree of underlying cochlear compression.

ACKNOWLEDGMENTS

This work was supported, in part, by the Wellcome Trust (Grant No. 046823/Z/96). We thank Brian Glasberg and Brian Moore for supplying us with their modified versions of the POLYFIT software that allowed the SLD model to be fitted to the data and Gerald Kidd, Chris Plack, and Brian Glasberg for their invaluable reviewers comments.

[1]A 20 ms raised-cosine ramp was accidentally applied twice to the masker in the computer program. This is approximately equivalent to a single application of a 15 ms raised-cosine ramp.

Bacon, S. P., Boden, L. N., Lee, J., and Repovsch, J. L. (**1999**). "Growth of simultaneous masking for fm<fs: effects of overall frequency and level," J. Acoust. Soc. Am. **106**, 341–350.

Baker, R. J., and Rosen, S. (**2002**). "Auditory filter nonlinearity in mild/moderate hearing impairment," J. Acoust. Soc. Am. **111**, 1330–1339.

Baker, R. J., Rosen, S., and Darling, A. (**1998**). "An efficient characterisation of human auditory filtering across level and frequency that is also physiologically reasonable," in *Psychophysical and Physiological Advances in Hearing*, edited by A. R. Palmer, A. Rees, A. Q. Summerfield, and R. Meddis (Whurr, London), pp. 81–87.

Dallos, P. (**1992**). "The active cochlea," J. Neurosci. **12**, 4575–4585.

Davis, H. (**1983**). "An active process in cochlear mechanics," Hear. Res. **9**, 79–90.

Delgutte, B. (**1990**). "Physiological mechanisms of psychophysical masking: Observations from auditory-nerve fibers," J. Acoust. Soc. Am. **87**, 791–809.

Glasberg, B. R., and Moore, B. C. J. (**1990**). "Derivation of auditory filter shapes from notched-noise data," Hear. Res. **47**, 103–138.

Glasberg, B. R., and Moore, B. C. J. (**2000**). "Frequency selectivity as a function of level and frequency measured with uniformly exciting notched noise," J. Acoust. Soc. Am. **108**, 2318–2328.

Glasberg, B. R., Moore, B. C. J., and Stone, M. A. (**1999**). "Modelling changes in frequency selectivity with level," in *Psychophysics, Physiology and Models of Hearing*, edited by T. Dau, V. Hohmann, and B. Kollmeier (World Scientific, Singapore)

Hicks, M. L., and Bacon, S. P. (**1999**). "Psychophysical measures of auditory nonlinearities as a function of frequency in individuals with normal hearing," J. Acoust. Soc. Am. **105**, 326–338.

Irino, T., and Patterson, R. (**1997**). "A time-domain, level-dependent auditory filter: The gammachirp," J. Acoust. Soc. Am. **101**, 412–419.

Lopez-Poveda, E. A., Plack, C. J., and Meddis, R. (**2003**). "Cochlear nonlinearity between 500 and 8000 Hz in listeners with normal hearing," J. Acoust. Soc. Am. **113**, 951–960.

Lutfi, R. A., and Patterson, R. D. (**1984**). "On the growth of masking asymmetry with stimulus intensity," J. Acoust. Soc. Am. **76**, 739–745.

Moore, B. C. J., and Glasberg, B. R. (**1983**). "Suggested formulae for calculating auditory-filter bandwidths and excitation patterns," J. Acoust. Soc. Am. **74**, 750–753.

Moore, B. C. J., and Glasberg, B. R. (**1987**). "Formulae describing frequency selectivity as a function of frequency and level, and their use in calculating excitation patterns," Hear. Res. **28**, 209–225.

Moore, B. C. J., and Vickers, D. A. (**1997**). "The role of spread of excitation and suppression in simultaneous masking," J. Acoust. Soc. Am. **102**, 2284–2290.

Moore, B. C. J., Vickers, D. A., Plack, C. J., and Oxenham, A. J. (**1999**). "Inter-relationship between different psychoacoustic measures assumed to

be related to the cochlear active mechanism," J. Acoust. Soc. Am. **106**, 2761–2778.
Murugasu, E., and Russell, I. J. (**1995**). "Salicylate ototoxicity: The effects on basilar membrane displacement, cochlear microphonics, and neural rsponses in the basal turn of the guinea pig cochlea," Aud. Neurosci. **1**, 139–150.
Nelson, D. A., and Schroder, A. C. (**2004**). "Peripheral compression as a function of stimulus level and frequency region in normal-hearing listeners," J. Acoust. Soc. Am. **115**, 2221–2233.
Nelson, D. A., Schroder, A. C., and Wojtczak, M. (**2001**). "A new procedure for measuring peripheral compression in normal-hearing and hearing impaired listeners," J. Acoust. Soc. Am. **110**, 2045–2064.
Oxenham, A. J., and Plack, C. J. (**1997**). "A behavioural measure of basilar membrane nonlinearity in listeners with normal and impaired hearing," J. Acoust. Soc. Am. **101**, 3666–3675.
Patterson, R., and Nimmo-Smith, I. (**1980**). "Off-frequency listening and auditory filter asymmetry," J. Acoust. Soc. Am. **67**, 229–245.
Patterson, R. D. (**1976**). "Auditory filter shapes derived with noise stimuli," J. Acoust. Soc. Am. **59**, 640–654.
Pick, G. F. (**1980**). "Level dependence of psychophysical frequency resolution and auditory filter shape," J. Acoust. Soc. Am. **68**, 1085–1095.
Plack, C. J., and Drga, V. (**2003**). "Psychophysical evidence for auditory compression at low characteristic frequencies," J. Acoust. Soc. Am. **113**, 1574–1586.
Plack, C. J., and Oxenham, A. J. (**1998**). "Basilar-menbrane nonlinearity and growth of forward masking," J. Acoust. Soc. Am. **103**, 1598–1608.
Plack, C. J., and Oxenham, A. J. (**2000**). "Basilar-membrane nonlinearity estimated by pulsation threshold," J. Acoust. Soc. Am. **107**, 501–507.
Puria, S., Peake, W. T., and Rosowski, J. J. (**1997**). "Sound-pressure measurements in the cochlea vestibule of human-cadaver ears," J. Acoust. Soc. Am. **101**, 2754–2770.
Rhode, W. S. (**1971**). "Observations of the vibration of the basilar membrane in squirrell monkeys using the Mossbauer technique," J. Acoust. Soc. Am. **49**, 1218–1231.
Rhode, W. S., and Cooper, N. P. (**1996**). "Nonlinear mechanics in the apical turn of the chinchilla cochlea in vivo," Aud. Neurosci. **3**, 101–121
Rosen, S., and Baker, R. J. (**1994**). "Characterising auditory filter nonlinearity," Hear. Res. **73**, 231–243.
Rosen, S., Baker, R. J., and Darling, A. (**1998**). "Auditory filter nonlinearity at 2 kHz in normal hearing listeners," J. Acoust. Soc. Am. **103**, 2539–2550.
Rosen, S., and Stock, D. (**1992**). "Auditory filter bandwidth as a function of level at low-frequencies (125 Hz–1 kHz)," J. Acoust. Soc. Am. **92**, 773–781.
Ruggero, M. A. (**1991**). "Physiology and coding of sound in the auditory nerve," in *The Mammalian Auditory Pathway: Neurophysiology*, edited by A. N. Popper and R. R. Fay (Springer, New York).
Ruggero, M. A., and Rich, N. C. (**1991**). "Furosemide alters organ of Corti mechanics: Evidence for feedback of outer hair cells upon the basilar membrane," J. Neurosci. **11**, 1057–1067.
Ruggero, M. A., Rich, N. C., Recio, A., Narayan, S. S., and Robles, L. (**1997**). "Basilar-membrane responses to tones at the base of the chinchilla cochlea," J. Acoust. Soc. Am. **101**, 2151–2163.
Ruggero, M. A., Rich, N. C., Robles, L., and Recio, A. (**1996**). "The effects of acoustic trauma, other injury and death on basilar-membrane responses to sound," in *Scientific Basis of Noise-Induced Hearing Loss*, edited by A. Axelsson, H. Borchgrevink, R. P. Hamernik, P. A. Hellstrom, D. Henderson, and R. Salvi (Thieme Medical, New York), pp. 23–35.
Russell, I. J., and Nilsen, K. E. (**1997**). "The location of the cochlea amplifier: spatial representation of a single tone on the guinea pig basilar membrane," Proc. Natl. Acad. Sci. U.S.A. **94**, 2660–2664.
Shera, C. A., Guinan, J. J., and Oxenham, A. J. (**2002**). "Revised estimates of human cochlear tuning from otoacoustic and behavioural measurements," Proc. Natl. Acad. Sci. U.S.A. **99**, 3318–3323.
Stelmachowicz, P. G., Lewis, D. E., Larson, L. L., and Jesteadt, W. (**1987**). "Growth of masking as a measure of response growth in hearing-impaired listeners," J. Acoust. Soc. Am. **81**, 1881–1887.
Weber, D. L. (**1977**). "Growth of masking and the auditory filter," J. Acoust. Soc. Am. **62**, 424–429.

Sound source localization in real sound fields based on empirical statistics of interaural parameters[a)]

Johannes Nix[b)] and Volker Hohmann
Medizinische Physik, Carl von Ossietzky Universität Oldenburg, D-26111 Oldenburg, Germany

(Received 12 July 2004; revised 20 October 2005; accepted 24 October 2005)

The role of temporal fluctuations and systematic variations of interaural parameters in localization of sound sources in spatially distributed, nonstationary noise conditions was investigated. For this, Bayesian estimation was applied to interaural parameters calculated with physiologically plausible time and frequency resolution. Probability density functions (PDFs) of the interaural level differences (ILDs) and phase differences (IPDs) were estimated by measuring histograms for a directional sound source perturbed by several types of interfering noise at signal-to-noise ratios (SNRs) between −5 and +30 dB. A moment analysis of the PDFs reveals that the expected values shift and the standard deviations increase considerably with decreasing SNR, and that the PDFs have non-Gaussian shape at medium SNRs. A d' analysis of the PDFs indicates that elevation discrimination is possible even at low SNRs in the median plane by integrating information across frequency. Absolute sound localization was simulated by a Bayesian maximum *a posteriori* (MAP) procedure. The simulation is based on frequency integration of broadly tuned "detectors." Confusion patterns of real and estimated sound source directions are similar to those of human listeners. The results indicate that robust processing strategies are needed to exploit interaural parameters successfully in noise conditions due to their strong temporal fluctuations. [DOI: 10.1121/1.2139619]

PACS number(s): 43.66.Ba, 43.66.Pn, 43.66.Qp, 43.72.Dv [AK] Pages: 463–479

I. INTRODUCTION

The filtering of acoustical signals by the human body, head, and pinna is characterized by the head-related transfer functions (HRTFs) and depends on both direction and distance of the sound source (Blauert, 1983; Shaw, 1997). A set of HRTFs for the left and right ears characterizes the physical differences between signals recorded at the ear canal entrances. These differences are generally quantified by the frequency-dependent interaural parameters, i.e., the interaural level differences (ILDs) and the interaural time differences (ITDs). Interaural parameters measured from different directions exhibit a rich variety of possible features for sound localization (Wightman and Kistler, 1989b) and have therefore been considered in many physiological and psychoacoustical models of binaural processing. Jeffress (1948) proposed a "place theory" of sound localization based on the ITDs, which suggests a physiological mechanism for coincidence detection. Influenced by Jeffress's hypothesis, ITDs have been used in many psychoacoustic experiments and models of binaural detection to characterize interaural timing (Breebaart *et al.*, 1999; Colburn, 1996; Durlach and Colburn, 1978). Responses of neurons to ITDs were also considered in physiological studies of binaural processing (Brugge, 1992; Caird and Klinke, 1987; Joris and Yin, 1996; Clarey *et al.*, 1992; Kuwada and Yin, 1987). Alternatively, interaural phase differences (IPDs), which are the frequency-domain representation of ITDs, have been used to quantify interaural timing cues (Kuwada and Yin, 1983; Malone *et al.*, 2002; Spitzer and Semple, 1991). IPDs were used as well in recent quantitative physiological models (Borisyuk *et al.*, 2002). Whether IPD or ITD representations of interaural timing cues are more physiologically relevant for auditory processing in mammals is still an open question (McAlpine and Grothe, 2003). Regarding the processing of ILDs, there is a wide consensus that a combination of excitatory ipsilateral and inhibitory contralateral interactions takes place (Colburn, 1996). Interaural timing information and ILDs are then combined for sound localization (Brugge, 1992). In the barn owl (tyto alba) it has been shown that a topotopic map of auditory space exists, which performs such a combination (Knudsen, 1982).

Interaural parameters have also been used as basic parameters for sound source localization algorithms (Neti *et al.*, 1992; Albani *et al.*, 1996; Datum *et al.*, 1996; Duda, 1997; Janko *et al.*, 1997; Chung *et al.*, 2000; Liu *et al.*, 2000), "cocktail-party" processors (Bodden, 1993), and binaural directional filtering algorithms (Kollmeier *et al.*, 1993; Kollmeier and Koch, 1994; Wittkop *et al.*, 1997). The aim of such algorithms is to estimate the directions of the sound sources on a short-term basis and use this information for speech enhancement techniques like Wiener filtering (Bodden, 1996). A short-term analysis of interaural parameters is commonly used in these approaches. It is also assumed that the auditory system initially evaluates interaural parameters on a short-term basis for exploiting binaural information.

[a)]Part of this research was presented at the 137th meeting of the Acoustical Society of America [V. Hohmann and J. Nix, "Application of localization models to noise suppression in hearing aids," J. Acoust. Soc. Am.**105**, 1151 (1999)].

[b)]Electronic mail: johannes.nix@uni-oldenburg.de

For localization of signals in noise or of nonstationary signals, the information available for sound localization differs from the information in the HRTFs. In contrast to the stationary and anechoic conditions in which HRTFs are measured, the interaural parameters derived from subsequent windows in a short-term analysis fluctuate due to the statistics of the signal and due to the influence of noise, if present. As a consequence, the information about source location in the short-term values of the interaural parameters is likely to be degraded as compared to the information content of the set of HRTFs itself. These fluctuations have a close relationship with the properties of the HRTFs, e.g., spectral notches of the HRTFs for certain directions can lead to stronger fluctuations at these frequencies. Therefore, fluctuations can be used to retrieve additional information on the sound source direction.

Probability density functions of interaural parameters have been evaluated in several studies on binaural detection (Domnitz and Colburn, 1976; Henning, 1973; Zurek, 1991). However, these experiments do not allow us to draw conclusions about localization performance in noisy environments. Although fluctuations of interaural parameters have been explicitly considered in models of sound localization (Duda, 1997; Wittkop *et al.*, 1997), empirical data on the amount of fluctuations are still missing. The aim of the present study is to characterize fluctuations of interaural parameters in realistic listening conditions and to study their possible implications for sound localization.

The approach chosen here is to simulate the possible effective signal processing involved in binaural sound localization and to use *a priori* knowledge about statistical properties of the interaural parameters to estimate the sound source directions. This *a priori* knowledge is gathered empirically by observation of histograms of a large amount of short-term interaural parameter values. Consequences of the observed statistics for modeling sound source localization are discussed using the framework of detection theory and Bayesian analysis. It was not in the focus of these analyses to construct a detailed model of human sound localization, but to gain knowledge about the relevant properties of real-world signals.

II. METHODS

A. Assumptions

Several general assumptions are made in this study: First, only binaural cues derived from the amplitude ratio and the phase difference of the left and right signals are used for simulating sound source localization.

Second, the sound to be localized is assumed to be speech coming from a constant direction without reverberation. The noise is assumed to be a noise field as found in real environments without preferred directions and to be incoherent between different frequencies. The long-term signal-to-noise ratio is known, however the shape of the short-term magnitude spectra of the participating sound sources is not known.

The global structure of the processing is in line with current auditory peripheral modeling approaches: First, a short-term frequency analysis with resolution similar to the auditory critical bandwidth is performed. Interaural parameters are then calculated for the set of frequency bands as a function of time. Second, binaural information is integrated across the different frequency bands. In contrast to most models mentioned in the Introduction, this integration is defined as a combination of probabilities. Because time domain and frequency domain representation of a signal are equivalent in terms of information content, the IPDs as frequency-domain representation of the interaural timing carry approximately the same information as the narrow-band ITDs. To represent interaural timing, the IPDs are used here in addition to the ILDs. Finally, a temporal integration with a longer time constant is performed. The time constants of the model are a 16-ms window for the analysis of interaural parameters, followed by a moving average with 8-ms time constant, and, subsequent to the computation of probabilities, a 100-ms window for the integration of statistical information, similar to the time constants found by Wagner (1991). The long-term integration consists of a simple moving average; statistical estimation procedures of a much higher complexity are possible and may be required to explain localization of several concurrent sound objects. However, they are disregarded here because this study focuses on localization of a single directional source.

Using short-term analysis of nonstationary signals to evaluate interaural parameters has important consequences on the amount of temporal fluctuations, especially if framing prior to ITD detection is assumed. As an example, Fig. 1 shows schematically the time course of the level at the left

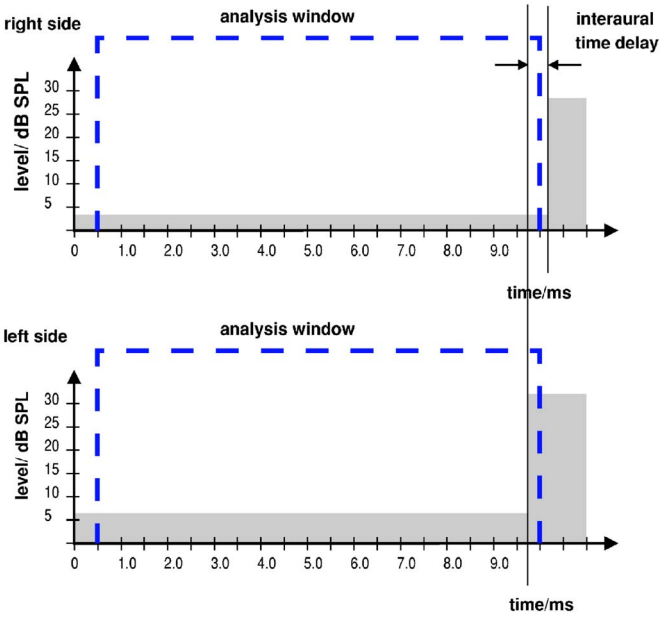

FIG. 1. (Color online) The diagram shows the effect of fluctuations of a single signal with a fixed interaural time delay on the observed ILDs for the framework of a short-term analysis of both ear signals. As long as the signal is constant, an ILD of about 3 dB is observed. In the example, a sudden increase in level occurs close to the end of the analysis window. This increase is caught in the temporal window of the ipsilateral side, but not the one of the contralateral side. Because the ILD and IPD values are weighted according to their amplitude, the higher ILD near the end of the analysis window gains a high weight. A temporal fluctuation of the observed short-term ILDs is the result.

and right ear canal entrance. The source is assumed to be on the left side. Therefore, we usually expect the level at the left side to be higher than the level at the right side, resulting in a stationary level difference of about 3 dB for our example. Now consider what happens if the signal has a sudden increase in level of about 25 dB near the end of the analysis window. At the left side, part of the additional energy enters the short-term analysis window, but not at the right side. Because the increase by 25 dB means a more than tenfold increase in the amplitude, the observed intensity-weighted level difference is much larger than one would expect because of the sound source direction. The same is valid for level-weighted estimates of interaural timing parameters, when analyzed by a windowed short-term analysis.

B. Computation of interaural parameters in the frequency domain

In this work, the interaural parameters are represented in the frequency domain by the interaural transfer function (ITF) (Duda, 1997). It is defined by the HRTFs, $H_r(\alpha,\phi,f)$ and $H_l(\alpha,\phi,f)$, which are functions of azimuth α, elevation ϕ, and frequency f; r and l denote left and right side. As the elevation of a sound source, we define the angle to the horizontal plane; as the azimuth, we define the angle between the projection of the source onto the horizontal plane, and the median plane. The ITF is defined as the quotient of the left and right HRTFs, assuming both have nonzero gains:

$$I(\alpha,\phi,f)=\frac{H_r(\alpha,\phi,f)}{H_l(\alpha,\phi,f)}. \tag{1}$$

Interaural timing can be characterized by the phase of the ITF,

$$\arg I(\alpha,\phi,f), \tag{2}$$

by the *interaural phase delay* t_p,

$$t_p(\alpha,\phi,f)=-\frac{\arg I(\alpha,\phi,f)}{2\pi f}, \tag{3}$$

and by *the interaural group delay*, t_g,

$$t_g(\alpha,\phi,f)=-\frac{1}{2\pi}\frac{d\arg I(\alpha,\phi,f)}{df}. \tag{4}$$

If one nonstationary sound source with spectrum $S(f,t)$ is present, t denoting the time variable, the spectra of the signals which arrive, filtered by the HRTFs, at the left and right ear canals are approximately

$$F_r(\alpha,\phi,f,t)\approx S(f,t)H_r(\alpha,\phi,f), \tag{5}$$

$$F_l(\alpha,\phi,f,t)\approx S(f,t)H_l(\alpha,\phi,f). \tag{6}$$

We do not write this as an identity because of the possible windowing effects for nonstationary sources discussed above.

If we assume $F_l(\alpha,\phi,f,t)$ and $F_r(\alpha,\phi,f,t)$ to be nonzero, the time-dependent quotient transfer function $\hat{I}(\alpha,\phi,f)$ can be computed based on the binaural signals as an approximation to the ITF:

$$\hat{I}(\alpha,\phi,f,t)=\frac{F_r(\alpha,\phi,f,t)}{F_l(\alpha,\phi,f,t)}. \tag{7}$$

Here, the ILD Δ_L and the IPD Δ_θ are defined as amplitude and phase of $\hat{I}(\alpha,\phi,f)$.

Because, with X^* being the complex conjugate of X,

$$\hat{I}(\alpha,\phi,f,t)=\frac{F_r(\alpha,\phi,f,t)F_l(\alpha,\phi,f,t)^*}{|F_l(\alpha,\phi,f,t)|^2}, \tag{8}$$

the IPDs can be computed from the interaural cross-power spectrum without unwrapping. $F_r(\alpha,\phi,f,t)/F_l(\alpha,\phi,f,t)$ is, according to the cross-correlation theorem (a generalized form of the Wiener-Khintchine theorem), identical to the Fourier transform of the short-term interaural cross-correlation function.

C. Description of interaural parameters as random variables

It is assumed that short-term interaural parameters form a stochastic process. It is described by the vector random variable of interaural parameters $\vec{\boldsymbol{\Delta}}$ whose instances $\vec{\Delta}$ consist of the set of ILD and IPD variables in all frequency bands at a certain point of time. Writing $\Delta_{L,b}$ for the ILD of band b, and $\Delta_{\theta,b}$ the IPD of band b, $\vec{\Delta}$ is defined as

$$\vec{\Delta}=(\Delta_{L,1},\Delta_{L,2},\ldots,\Delta_{L,B},\Delta_{\theta,1},\Delta_{\theta,2},\ldots,\Delta_{\theta,B}). \tag{9}$$

Assuming that B frequency bands are analyzed, $\vec{\Delta}$ is $2B$-dimensional. In the following, we disregard the temporal characteristics of $\vec{\boldsymbol{\Delta}}$, e.g., temporal correlations, and focus on the probability density function (PDF) of $\vec{\boldsymbol{\Delta}}$. The PDF of the random variable $\vec{\boldsymbol{\Delta}}$ is determined by the properties of the sound field at both ears. In principle, this PDF could be calculated analytically, requiring knowledge about the anechoic HRTFs, the power spectral density statistics of the sources, room acoustics, and the distribution of incidence directions of the noise sources. In practice, however, an analytical derivation is not feasible because the required statistics are not available.

In this study, the PDF is therefore estimated empirically by measuring the time series of short-term interaural parameters calculated from actual binaural recordings of directional sound sources. The normalized histogram of the series is then regarded as being an estimate of the PDF of the underlying random process. We denote the PDF of $\vec{\boldsymbol{\Delta}}$ given the direction λ as $p(\vec{\Delta}|\lambda)$, where λ is one of N_λ possible discrete directions. As $p(\vec{\Delta}|\lambda)$ is a $2B$-dimensional PDF, and histograms with N_K categories require about $(N_K)^{2B}$ observations, its empirical estimation is not feasible for $B=43$, because the number of observations required would be too high. Therefore, only the histograms of the components of $\vec{\Delta}$ are observed, and it is assumed that the components of $\vec{\boldsymbol{\Delta}}$ can be treated as statistically independent. In this case, the joint PDF is calculated by multiplication of the component PDFs

$$p(\vec{\Delta}|\lambda) = \prod_{b=1}^{2B} p_b(\Delta_b|\lambda), \tag{10}$$

where the component or marginal PDFs $p_b(\Delta_b|\lambda)$ are estimated by the histograms of the respective variables Δ_b.

In addition to approximating the PDF of $\vec{\mathbf{\Delta}}$ by the product of its marginals, stationarity, and ergodicity of the random process are assumed. Because the statistics of spectral power densities of speech cannot be assumed to be Gaussian, and interaural parameters are the result of a nonlinear operation on the spectral power densities, it can not be assumed, in general, that the resulting PDF has a Gaussian shape.

D. Data acquisition

1. Signals

The signals used in this study are an additive superposition of one directional sound source recorded in an anechoic room (the target signal) and spatially distributed noises recorded in real listening environments.

All signals were recorded binaurally in one individual male subject using hearing aid microphones mounted in in-the-ear (ITE) hearing aids (Siemens Cosmea M). The devices were fitted to the subject's ear canals with ear molds, allowing for a reproducible positioning of the microphones. They were positioned at the ear canal entrance, ensuring that most of the binaural information would be recorded; however, the effect of the concha may have been underestimated due to the size of the devices. The usable frequency range of the hearing aid microphone was between 100 Hz and about 8 kHz.

A nonstationary speech signal was generated as the target signal. Continuous speech from four different talkers was recorded at a sampling frequency of 25 kHz through a single microphone and added together to yield a speech signal with almost no pauses but still significant amplitude modulations. It included one female and three male talkers. One male read a German text and the other talkers read English texts. From this recording a segment of 20-s duration was selected as a target in which all talkers were present.

In the next step, directional information was generated by taking binaural recordings of the target signal in an anechoic room. The position of the source was set by means of a free-field apparatus (Otten, 2001). The apparatus consists of two loudspeakers attached to a movable arc of 3.6-m diameter, which can be positioned with stepping motors at all azimuths and at all elevations between −30° and 85°. Positions of the loudspeakers and generation of signals were controlled by a personal computer. The subject sat in the center of the arc on a stool and was instructed to move his head and arms as little as possible. The head was supported by a headrest. The error of direction is estimated to be about 3° in the azimuth and elevation, mostly the result of head movements and to a lesser extent due to position uncertainty. Recordings of the target signal on digital audio tape (DAT) were taken at 430 positions, ranging in azimuths from 0° to 355° in 5° steps at elevations of −15°, 0°, 15°, and 30°. For azimuths in the range of −15° to 15° and 165° to 195°, additional elevations of −10°, −5°, 5°, 10°, and 20° were measured. Three breaks were scheduled during the session in order to change the tapes and to permit the subject to take a rest and move around. All elevations for each azimuth were recorded without a break.

TABLE I. List of the 27 signal conditions chosen for the analysis of interaural parameters. Each condition includes a superposition of a directional target signal from 430 directions and a spatially distributed noise at a specific signal-to-noise ratio. The target signal in silence was included as well.

Target signal	Noise	SNR/dB
speech	silence	⋯
	station concourse	15, 5
	cafeteria	30, 20, 15, 10, 12, 5, 3, 2, 1, 0, −1, −2, −5
	metal workshop 1	15, 5
	metal workshop 2	15
	car interior noise	15, 5
	outdoor market	15, 5
	traffic noise 1	15, 5
	traffic noise 2	15, 5

In addition to the recordings of the target signal, spatially distributed noise signals were recorded in eight different real environments. By using the same subject, the same microphones, and the same recording equipment, it was assured that the anechoic HRTFs and the transfer functions of the equipment were equal in all recordings. The selected noise environments were a densely populated university cafeteria, an outdoor market, inside a moving car, a city street with traffic noise (two different recordings), a train station concourse, and a metal workshop with various machinery operating, such as a milling cutter, grinding wheel, and lathe (two different recordings). The goal was to record situations in which many nonstationary noise sources were impinging on the listener from different directions at the same time and in which no source was dominant for more than about 1 s. The level of the noise was not measured during the recording session but was ensured to be well above the noise floor associated with the recording equipment so that the interaural parameters were determined by the environmental noise rather than the recording noise. Segments of 25-s duration which met these criteria were selected as spatially distributed noise samples.

The DAT recordings of the target and all noise signals were sampled at 25 kHz with 16-bit resolution and stored on a computer. For further processing and analysis of the interaural parameters, 27 different target-noise conditions were selected. Each condition consists of a set of 430 signals covering the different directions of incidence. They were generated by digitally adding a target and a noise signal at various signal-to-noise ratios (SNRs, defined explicitly in the next paragraph) in the range between +30 and −5 dB as well as in silence. The conditions are listed in Table I. Especially for the condition of a speech target mixed with cafeteria noise, a broad range of SNRs were selected to ensure good coverage of this important communication situation.

The SNR was defined as the difference in decibels of the level associated with the target and noise signals. The levels

were calculated from the digitized recordings by averaging the overall rms (root mean square) levels across both ears on a linear scale and transforming this average to decibels. For a specified SNR, the recorded signals were scaled appropriately for each direction, target, and noise type and then added. Using this definition, the SNR was controlled at ear level and did not vary with direction. As the SNR is expected to influence the distribution of interaural parameters, this definition seems more appropriate than defining the SNR at the source level which would have introduced SNR variations with direction due to the influence of the HRTFs. This issue will be discussed later on in this paper.

2. Calculation of interaural parameters and their distributions

Interaural parameters, i.e., ILDs and IPDs, were calculated using a windowed short-term fast Fourier transform (FFT) analysis (Allen and Rabiner, 1977; Allen, 1977) with a subsequent averaging across broader frequency bands.

Time segments with a length of 400 samples were taken from the left and right signals with an overlap of 200 samples. This corresponds to a total window duration of 16 ms and a window time shift of 8 ms, resulting in a frame rate of 125 Hz. The segments were multiplied by a Hann window, padded with zeros for a total length of 512 samples and transformed with a fast Fourier transform (FFT). The short-term FFT spectra of left and right channels are denoted as $F_l(f,k)$ and $F_r(f,k)$, respectively. The indices f and k denote the frequency and time index of the spectrogram, respectively. The FFT bins were grouped to 43 adjacent frequency channels so that, according to the transformation from frequency to the equivalent rectangular bandwidth (ERB) of auditory filters given by Moore (1989), a bandwidth of at least 0.57 ERB was reached. These frequency bands covered the range of center frequencies from 73 Hz to 7.5 kHz, i.e., 3.3 to 32.6 ERB. Because at low frequencies the frequency resolution of the FFT, 48.8 Hz, does not allow for a channel bandwidth of 0.57 ERB, the low-frequency channels have bandwidths of up to 1.37 ERB; the first band which includes more than one FFT bin has a center frequency of 634 Hz, and the average bandwidth is 0.76 ERB.[1]

Let $f_u(b)$ and $f_h(b)$ denote the lowest and highest FFT frequency index belonging to a frequency channel b, respectively. Frequency averaging was then performed by adding up the squared magnitude spectrum and the complex-valued cross spectrum of left and right FFT results across the FFT bins belonging to each channel:

$$F_{rr}(b,k) = \sum_{f=f_u(b)}^{f_h(b)} |F_r(f,k)|^2, \tag{11}$$

$$F_{ll}(b,k) = \sum_{f=f_u(b)}^{f_h(b)} |F_l(f,k)|^2, \tag{12}$$

$$F_{rl}(b,k) = \sum_{f=f_u(b)}^{f_h(b)} F_r(f,k)F_l(f,k)^*. \tag{13}$$

These parameters were filtered by a recursive first-order low-pass filter with the filter coefficient $\gamma = e^{-\Delta T/\tau_a}$, corresponding to a time constant of $\tau_a = 8$ ms, the frame shift being $\Delta T = 8$ ms:

$$\overline{F_{rr}(b,k)} = (1-\gamma)F_{rr}(b,k) + \gamma\overline{F_{rr}(b,k-1)}, \tag{14}$$

$$\overline{F_{ll}(b,k)} = (1-\gamma)F_{ll}(b,k) + \gamma\overline{F_{ll}(b,k-1)}, \tag{15}$$

$$\overline{F_{rl}(b,k)} = (1-\gamma)F_{rl}(b,k) + \gamma\overline{F_{rl}(b,k-1)}. \tag{16}$$

The binaural parameters, i.e., the ILD Δ_L and IPD Δ_θ, were then calculated as follows:

$$\Delta_L(b,k) = 10 \log \left| \frac{\overline{F_{rr}(b,k)}}{\overline{F_{ll}(b,k)}} \right|, \tag{17}$$

$$\Delta_\theta(b,k) = \arg \overline{F_{rl}(b,k)}. \tag{18}$$

It should be noted that Eq. (13) describes an intensity-weighted average of the phase difference across the FFT bins belonging to one channel. The cyclical nature of the IPDs is accounted for by taking the complex-valued average.

The time series of the binaural parameters from each signal were sorted into histograms employing 50 nonzero bins in an adjusted range from up to a −50 to 50 dB level difference and up to a $-\pi$ to $+\pi$ phase difference, respectively. No special effort was made to detect outliers, except speech pauses that were discarded using a threshold criterion.

In each of the 27 different target-noise conditions described earlier, histograms of the ILD and IPD variables in each of the 43 frequency channels for each of the 430 directions were calculated, resulting in a total of 36 980 histograms per condition. The histograms were normalized so that they could be used as an estimate of the marginals of the PDF of the underlying process.

The processing described above was implemented on a VME-Bus-based digital signal processor (DSP) system, made up of five DSPs (Texas Instruments TMS320C40) that were attached to a SUN SPARC host system. The signals were read from hard disk and copied in blocks to the memory of the DSP system. The DSPs carried out the calculations and the results (i.e., the histograms of interaural parameters) were transferred back to the host system and stored on hard disk. The system allows for taking input signals from either hard disk or A/D converters, ensuring real-time processing and calculation of binaural parameters and its distributions. A detailed description of the system can be found in Wittkop *et al.* (1997).

E. d' analysis of differences in interaural parameters

We assume that a classification system discriminates between two directions with a Bayesian criterion on the basis of the observed values of short-term interaural parameters. No further information loss is assumed. In this case and with the further approximation of a Gaussian PDF, the detectability d' of differences in interaural parameters for two different

directions can be calculated as the difference in mean values of the respective distributions divided by the geometric mean of their standard deviation. This measure was calculated from the first moments of the empirical univariate distributions of either ILDs or IPDs, neglecting the deviation from a Gaussian shape.

F. Moment analysis

The marginal PDF estimates were further analyzed by means of descriptive statistics, (i.e., calculation of higher-order moments of the distributions). Following Tukey's rule (Sachs, 1992) for the estimation of the nth moment, at least 5^n samples of a random variable should be taken. Here, at least 1875 samples were evaluated (15-s duration at 125-Hz sampling frequency), so that the first four moments can be estimated according to Tukey's rule. Linear moments, namely expected value, standard deviation, skew, and kurtosis (sometimes also called kurtosis excess), were used for the linear ILD variable. For the distributions of the IPD variable, trigonometric moments as defined by Fisher (1993, p. 41) were used to calculate the mean phase angle, vector strength, circular standard deviation, circular skew, and circular kurtosis (see the Appendix for definitions). By using the trigonometric moments, no unwrapping of the IPDs is required.

G. Bayesian analysis for sound localization

From an information theoretic point of view, the extraction of directional information from the noisy short-term interaural parameters can be described as a Bayesian maximum *a posteriori* (MAP) estimate, which derives the most probable direction based on *a priori* knowledge of the PDF of the parameters for all directions. From Bayes's formula, the conditional probability for each direction λ out of N_λ possible directions is calculated given the parameter vector $\vec{\Delta}$ [cf. Eq. (9)] as

$$P(\lambda|\vec{\Delta}) = \frac{P(\vec{\Delta}|\lambda)P(\lambda)}{\sum_{\lambda=1}^{N_\lambda}[P(\vec{\Delta}|\lambda)P(\lambda)]}, \tag{19}$$

where $P(\vec{\Delta}|\lambda)$ is the conditional probability[2] of $\vec{\Delta}$ given the direction λ and $P(\lambda)$ is the *a priori* probability for the occurrence of the direction λ. From Eq. (10) and under the assumption that all directions λ are equally probable, this formula yields

$$P(\lambda|\vec{\Delta}) = \frac{\prod_{b=1}^{2B} P_b(\Delta_b|\lambda)}{\sum_{\lambda=1}^{N_\lambda}\prod_{b=1}^{2B} P_b(\Delta_b|\lambda)}. \tag{20}$$

The right-hand side arguments are all known, as the $P_b(\Delta_b|\lambda)$ are estimated from the empirical analysis for all b and λ. The marginal distributions $P_b(\Delta_b|\lambda)$ form the *a priori* knowledge used to calculate the probability of all directions. The direction chosen as the most probable, given an observation of the parameter vector $\vec{\Delta}$ and assuming that one source is present in the given noise field, is then

$$\hat{\lambda} = \underset{\lambda\in[1,\ldots,N_\lambda]}{\arg\max}\ P(\lambda|\vec{\Delta}). \tag{21}$$

Using Eqs. (20) and (21), the *a posteriori* probability of all directions can be calculated and the most probable direction can be selected from one observation of parameter $\vec{\Delta}$ and the known distributions of its components for the different directions. A new set of probabilities can be calculated from every time frame so that an ongoing estimate of the most probable direction results.

The statistical localization model described above has been applied to several types of signals and spatially distributed noises. Results for a 25-s segment of speech from a single talker (different from the four-talker target signal) in cafeteria noise at 5 dB SNR are reported below. The distributions of the four-talker target and the cafeteria noise sample at 5 dB SNR were used as reference distributions[3] in Eq. (20).

The *a posteriori* probabilities were calculated for the total signal length, yielding 3200 samples of the probabilities for each of the 430 probed directions. The *a posteriori* probabilities were smoothed by a first-order, low-pass filter with 100-ms time constant, and the most probable direction was determined from the smoothed probabilities. The estimates for the most probable direction are plotted into a normalized histogram, which describes the probability that a specific direction is detected as the most probable direction, given the real direction. This plot can be described as a "decision histogram," displaying deviations and confusions in the estimates in one view.

III. RESULTS

A. Distributions of interaural parameters

In this section, the empirical results on the statistics of short-term interaural parameters are described. Specifically, the dependence of the distributions on frequency, SNR, direction, and noise type is analyzed. Due to the large amount of data, the parameter space covered in this analysis had to be restricted. The signal conditions pertaining to speech in silence and speech in cafeteria noise at a moderate-to-low SNR of 5 dB were used as primary examples for one lateral direction and one direction near the median plane (0° elevation). Results for low frequencies are reported for the IPD variable (340 and 540 Hz), and results for medium and high frequencies are reported for the ILD variable (830 Hz and 2.88 kHz).

1. Dependence on frequency

Figure 2 shows percentiles of the distribution of the ILD variable as a function of frequency for the different conditions pertaining to speech in silence (upper panel), speech in cafeteria noise at 5 dB SNR (middle panel), and car interior noise at 5 dB SNR (lower panel).

In each condition, the 5, 10, 25, 50, 75, 90, and 95 percentiles of the distributions are plotted for −15° azimuth (lines) and +85° azimuth (symbols) and 0° elevation. The widths of the distributions can be assessed, e.g., by considering the vertical difference between the 95 percentile line and the 5 percentile line. For the case of silence, the widths of the distributions reveal that the parameter fluctuation is considerable, even though no additional noise is present,

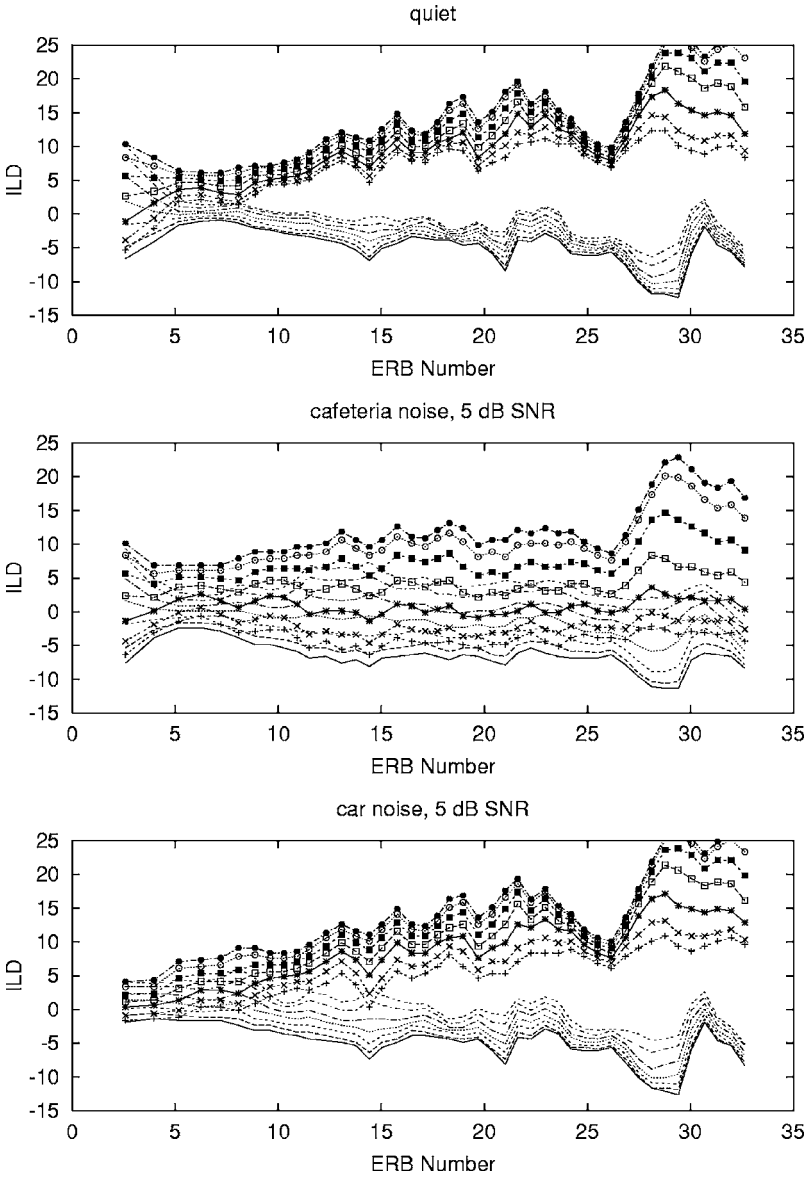

FIG. 2. Distribution percentiles for the interaural level difference (ILD) as a function of frequency for three different conditions: speech target in silence (upper panel), in cafeteria noise (5 dB SNR, mid panel), and in car interior noise (5 dB SNR, lower panel). Each panel shows 5, 10, 25, 50, 75, 90, and 95 percentiles for −15° azimuth (symbols) and +85° azimuth (lines) and 0° elevation. Percentiles are calculated by integration from the negative towards positive parameter values.

which is due to the statistics of the signal in short time frames. The width depends on both the frequency and the direction of the target. It is especially high in the lowest two frequency bands (50 and 100 Hz) because the band level of the speech is close to the recording noise level in these bands. The distributions are narrow as compared to the mean difference between these directions, except for the low frequencies of up to 8 ERB (310 Hz). In the noise conditions, however, the distributions are significantly broadened so that they overlap for the different directions. The broadening extends across the whole frequency range in the cafeteria-noise condition because the long-term frequency spectra of target and noise are nearly the same and the frequency-specific SNR is almost constant. In the car interior noise, the broadening is restricted to the lower frequency region, because the noise has a $1/f$ type of spectrum with primarily low-frequency content. The SNR of the remaining frequencies is higher than for the cafeteria noise at the same overall SNR.

2. Dependence on signal-to-noise ratio (SNR)

In order to clarify the influence of noise on the distributions of interaural parameters, their dependence on SNR was studied. Figures 3 and 4 show the distributions of the ILDs and IPDs, respectively, for the speech target in cafeteria noise. Distributions are plotted for two directions (15° and 60° azimuth 0° elevation) and two frequencies (IPDs: 340 and 540 Hz; ILDs: 830 Hz and 2.88 kHz). For the ILDs, each of the four plots shows distributions for the SNR values of −5, −2, −1, 0, 1, 2, 3, 5, 10, 15, 20, and 30 dB, and in silence. The curves are separated for clarity by relative shifting in y direction by 0.025 (ILDs), the uppermost curve in each plot showing the distributions in silence.

In silence, the ILD distributions (Fig. 3) are relatively narrow and show little overlap between directions at both frequencies (upper versus lower panels, respectively). The ILD increases significantly with frequency for both directions (left versus right panels, respectively). It is therefore a distinctive parameter for the direction. However, the distributions "decay" with decreasing SNR due to the influence of the noise. Specifically, the variance increases and the mean value is shifted towards zero. The distributions are skewed at medium SNRs. These effects are due to the nonlinear superposition of the PDFs of the target, which has a nonzero mean

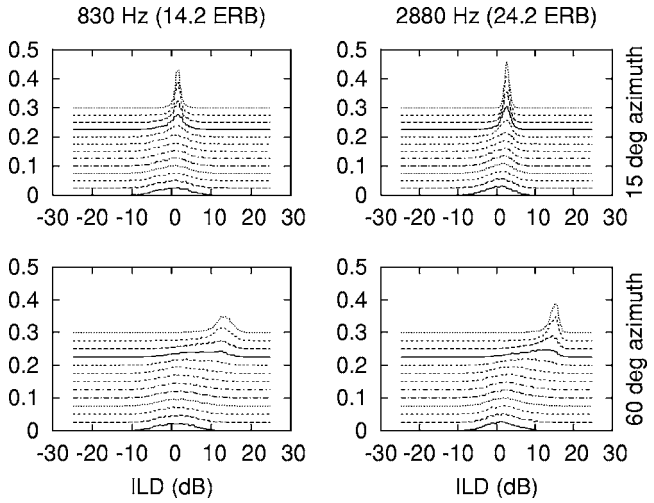

FIG. 3. Histograms of ILD values, i.e., number of observations of a specific ILD normalized to the total count, for the speech target in cafeteria noise. The left panels are for a frequency of 830 Hz and the right panels are for 2.88 kHz. The upper panels are for 15° azimuth and the lower panels are for 60° azimuth (0° elevation, respectively). Each panel shows the distributions for the SNR values of −5, −2, −1, 0, 1, 2, 3, 5, 10, 15, 20, and 30 dB and in silence. The curves are shifted in this order successively by 0.025 in the y direction for clarity.

and a low variance due to its directionality, and of the noise, which has a zero mean and higher variance because of its diffusiveness. Both the increased variance and the systematic shift of the mean value towards zero lead to a reduction of the variation of the distributions with direction and frequency. The systematic shift is especially large for the lateral direction of 60° azimuth (lower panels). In this case, the observed level difference at low SNRs approaches the difference between the noise level at the contralateral ear and the source level at the ipsilateral ear rather than the large level difference expected from the anechoic HRTFs.

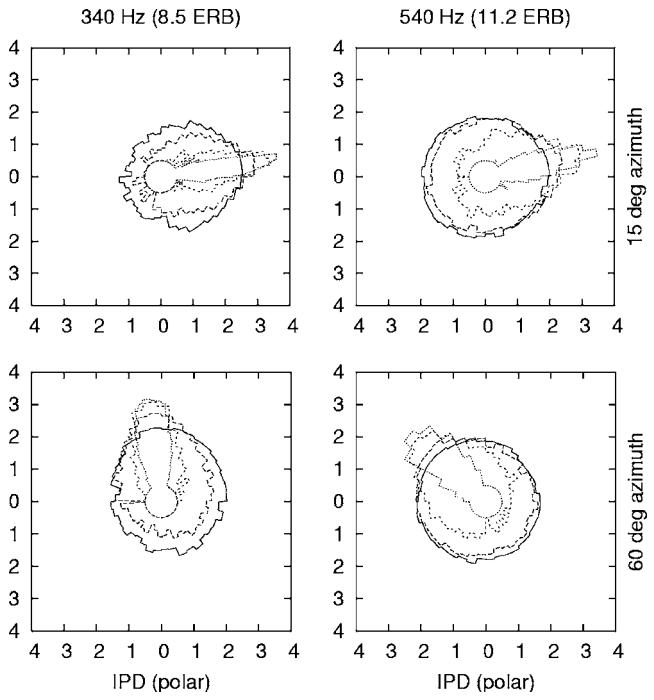

FIG. 4. Polar plots showing histograms of the interaural phase difference (IPD). The frequency subbands are 340 Hz (left panels) and 540 Hz (right panels), the azimuths 15° (upper panels) and 60° (lower panels); the elevation was 0°. The angle parameter of the plot shows the angle of the IPD, in counter-clockwise orientation, and the angle 0° corresponds to the half-axis with $y=0$, $x>0$. The radius parameter of the curve, r, shows the relative frequency of occurrence h of this IPD value. To make the differences visible, the frequencies of occurrence are logarithmically transformed according to $r=4.5+\log_{10} h$. The maximum radii of each curve are ordered as the SNR values at which the histograms were measured. The SNRs are, in the order from the largest maximum to the smallest, silence, 20, 5, and −5 dB.

Figure 4 shows the corresponding histograms of the IPD variable; because the variable is cyclical, the histogram is plotted in a polar diagram. The angular parameter of the plot shows the IPD, in counter-clockwise orientation, and the IPD 0° corresponds to the half-axis with $y=0$, $x>0$. The radius of the curve, r, shows the relative frequency of occurrence h of this IPD value. To make the differences visible, the frequencies of occurrence are logarithmically transformed according to $r=4.5+\log_{10} h$. The curves are directly superposed without offset. The maximum radii of each curve are ordered as the SNR values in which the histograms were measured. The figure shows that for the IPD variable the PDFs "decay" as well, converging to a uniform circular distribution with decreasing SNR. The variation of the mean value with decreasing SNR is much smaller than for the ILD variable.

The higher-order moments of the ILD distributions at 830 Hz and 2.88 kHz and 60° azimuth (lower left and right panel in Fig. 3) are listed in Table II. Both frequencies behave similarly. The mean values and standard deviations show the broadening and shifting described above. Due to the nonlinear superposition of the PDFs of target and noise, the standard deviations show a nonmonotonic behavior. They increase and then decrease slightly with decreasing SNRs. Skew and kurtosis are significantly different from 0 at high SNRs and converge towards zero with decreasing SNRs. Again, nonmonotonic behavior is observed with decreasing SNRs.

The corresponding higher-order moments of the IPD distributions for the frequencies 340 and 540 Hz are shown in Table III. The mean values depend less on the SNR, whereas the standard deviations show a monotonic increase with decreasing SNRs at both frequencies. Nonzero skew and kurtosis values are observed especially at the lower frequency. For a Gaussian PDF, both parameters would be zero because a nonzero skew indicates an asymmetrical distribution and a positive kurtosis indicates a distribution with a sharper maximum and wider shoulders than the normal distribution. Here, the skew varies between 0.3 and 2.0, and the kurtosis has values up to 30.9, which is a very large difference in shape from Gaussian PDFs.

The analysis of higher-order moments shows that non-Gaussian PDFs have to be assumed in general for the distributions of the interaural parameters. Whether the small deviations from Gaussian shape at low SNRs are still relevant for the retrieval of binaural information remains to be further analyzed.

3. Dependence on direction

The HRTF-derived interaural parameters of stationary, undisturbed signals show a clear dependence on direction,

TABLE II. Moments derived from the distributions of the ILD variable at 830 Hz (left columns) and 2.88 kHz (right columns) at various SNR. The target-noise condition was speech at 60° azimuth and 0° elevation in cafeteria noise. Moments are $\bar{x}$ expected value, σ standard deviation, s skew, and K kurtosis.

		f=830 Hz				f=2880 Hz			
Noise type	SNR (dB)	$\bar{x}$(dB)	σ(dB)	$s(1)$	$K(1)$	$\bar{x}$(dB)	σ(dB)	$s(1)$	$K(1)$
cafeteria	silence	12.83	2.52	−0.92	1.78	14.63	1.68	−2.03	8.04
cafeteria	30	11.68	3.59	−1.26	2.35	14.09	2.15	−1.63	4.09
cafeteria	20	8.82	5.05	−0.70	0.12	11.78	3.81	−1.08	1.20
cafeteria	15	6.82	5.46	−0.31	−0.48	9.64	4.56	−0.58	−0.31
cafeteria	12	5.61	5.53	−0.12	−0.54	8.08	4.84	−0.33	−0.53
cafeteria	10	4.83	5.51	−0.02	−0.52	7.02	4.93	−0.17	−0.55
cafeteria	5	3.13	5.21	0.10	−0.21	4.49	4.83	0.13	−0.27
cafeteria	3	2.59	5.03	0.11	−0.21	3.63	4.66	0.21	−0.11
cafeteria	2	2.32	4.94	0.10	−0.17	3.22	4.55	0.24	−0.01
cafeteria	1	2.08	4.86	0.08	−0.15	2.82	4.50	0.17	0.24
cafeteria	0	1.87	4.77	0.08	−0.13	2.52	4.36	0.25	0.09
cafeteria	−1	1.67	4.69	0.05	−0.13	2.21	4.27	0.23	0.12
cafeteria	−2	1.49	4.61	0.04	−0.12	1.93	4.17	0.21	0.11
cafeteria	−5	1.04	4.42	−0.01	−0.11	1.24	3.93	0.11	0.05

and extensive sets of data exist on this in the literature (e.g., Wightman and Kistler, 1989a). Therefore, the direction dependence of the expected values of the short-term interaural parameters, which are associated with the HRTF-derived parameters, is not shown here. Instead, higher-order moments of the distributions are considered.

Data not shown here reveal that the ILD standard deviations depend strongly on the azimuth (for 15 dB SNR, they vary from about 2 to 5 dB at azimuth angles from 15° to 90°) and only moderately on the elevation (about 1 dB variation from −20° to 45° elevation at 15 dB SNR). Standard deviations are high for lateral directions, where the ILDs themselves are large. For the IPD variable, however, the vector strength is high for the lateral directions (i.e., for this frequency, the short-term phase vectors are more congruent in time than for the more central directions). For an SNR of 5 dB, the variation in the vector strength is from about 0.18 to 0.52 for a variation in azimuth from 15° to 90° and for a variation in elevation from −20° to 45°. It is clear from this analysis of the second moments that the fluctuation of the short-term interaural parameters depends strongly on the direction at a fixed SNR. IPDs and ILDs behave differently in this aspect.

4. Dependence on noise condition

The moments of the distribution of the ILD variable at 830 Hz and 2.88 kHz and of the IPD distributions at 340 and 540 Hz for various target-noise conditions are listed in Table IV. The target was always speech at 60° azimuth and 0° elevation and the SNR was 15 dB. The moments for the speech target in silence are included as a reference.

The data for the ILD show that the parameter values lie in a narrow range as compared to the deviation from the

TABLE III. Same as Table II, but for the IPD variable at 340 and 540 Hz. The moments are ϕ expected value of phase angle, σ_z standard deviation, s_z skew, and K_z kurtosis (see the Appendix for definitions).

	f=340 Hz				f=540 Hz			
SNR (dB)	ϕ(rad)	σ_z(rad)	$s_z(1)$	$K_z(1)$	ϕ(rad)	σ_z(rad)	$s_z(1)$	$K_z(1)$
silence	1.69	0.12	0.43	4.77	2.40	0.17	0.74	21.11
30	1.69	0.14	0.29	10.56	2.42	0.32	−0.05	23.74
20	1.67	0.26	2.00	30.92	2.46	0.60	−0.39	6.69
15	1.65	0.38	1.59	17.84	2.51	0.82	−0.23	2.99
12	1.63	0.48	1.24	11.79	2.55	0.96	−0.18	1.77
10	1.62	0.55	1.06	8.57	2.58	1.05	−0.16	1.27
5	1.54	0.77	0.62	3.64	2.71	1.28	−0.13	0.53
3	1.50	0.86	0.45	2.46	2.77	1.37	−0.10	0.35
2	1.47	0.91	0.44	1.99	2.79	1.41	−0.10	0.29
1	1.43	0.96	0.39	1.61	2.82	1.45	−0.09	0.23
0	1.39	1.02	0.36	1.27	2.85	1.48	−0.09	0.20
−1	1.35	1.07	0.32	1.02	2.88	1.51	−0.07	0.17
−2	1.29	1.13	0.30	0.80	2.92	1.54	−0.06	0.14
−5	1.08	1.28	0.24	0.36	3.03	1.61	−0.03	0.09

TABLE IV. Distribution moments of the ILD variable at 830 Hz (left table entry) and 2.88 kHz (right table entry) and for the IPD variable at 340 and 540 Hz for various target-noise conditions. The target was always speech at 60° azimuth and 0° elevation and the SNR was 15 dB. The "speech in silence" condition is listed as a reference. The noise condition "inside car" is listed separately, the data for all other noise conditions listed in Table I were averaged and the mean and standard deviation are given.

		f=830 Hz				f=2880 Hz			
Noise type ILD	SNR (dB)	$\bar{x}$(dB)	σ(dB)	$s(1)$	$K(1)$	$\bar{x}$(dB)	σ(dB)	$s(1)$	$K(1)$
—	silence	12.83	2.52	−0.92	1.78	14.63	1.68	−2.03	8.04
mean	15	6.64	5.55	−0.37	−0.34	9.56	4.47	−0.65	0.24
(std)	15	(2.07)	(0.73)	(0.20)	(0.21)	(0.84)	(0.50)	(0.15)	(0.48)
inside car	15	12.43	2.95	−0.84	2.67	14.58	1.83	−1.03	14.03
		f=340 Hz				f=540 Hz			
IPD	(dB)	$\bar{x}_z$(rad)	σ_z(rad)	$s_z(1)$	$K_z(1)$	$\bar{x}_z$(rad)	σ_z(rad)	$s_z(1)$	$K_z(1)$
—	silence	1.69	0.12	0.43	4.77	2.40	0.17	0.74	21.11
mean	15	1.67	0.29	1.18	20.91	2.45	0.59	−0.15	8.10
(std)		(0.02)	(0.08)	(0.81)	(5.38)	(0.07)	(0.15)	(0.88)	(4.57)
inside car	15	1.68	0.18	2.10	25.14	2.41	0.21	0.92	25.47

values in the silent condition. This shows that the influence of the noise type on the distributions is small relative to the influence of the SNR (cf. Table II). The only significant deviation is observed for the car interior noise, where the parameters resemble those of the silent condition. The mean value for the IPD variable is similar in all noise conditions and deviates little from the silent condition. For the standard deviation, an increase is observed, which is larger at the higher frequency. The skew and kurtosis, however, vary across noise conditions more than for the ILDs. Nevertheless, similar noise types have a similar impact on these parameters.

It can be concluded from the analysis of the moments of the distributions that different types of spatially distributed noise have a similar influence on the distribution of short-term interaural parameters. The SNR is therefore the most relevant parameter for the quantification of the noise's impact on mean and variance. However, the higher-order moments (i.e., skew and kurtosis) vary with the noise condition, especially for the IPD variable.

B. Simulation results

A probabilistic approach of directional information extraction from short-term interaural parameters is studied in this section. Both discrimination of directions and absolute localization are considered.

1. d' analysis of differences in interaural parameters

Figure 5 shows single-band d' derived from two different target directions as a function of SNR and in silence for the speech in cafeteria noise condition. Data are plotted for the ILD variable at 830 Hz (+) and 2.88 kHz (□) and for the IPD variable at 340 Hz (×) and 540 Hz (∗).

In the upper panel of Fig. 5, the two target directions are 0° and 5° azimuth in the horizontal plane. In silence, d' is greater than 1 in all cases except for the ILD variable at 830 Hz. However, d' decreases significantly with decreasing SNRs and reaches a value of about 0.2 on average at an SNR of 5 dB. Assuming that the observations in different frequency bands are statistically independent, and that the ILDs vary systematically with small azimuth changes, the d' increases with a factor of the square root of the number of observations. The number of observations required to detect a difference in direction (i.e., $d'=1$) is about 25 in this case.

In the lower panel of Fig. 5, the differences in interaural parameters arise from a shift in elevation from 0° to 15° in the median plane. The d' is lower than in the case of azimuth

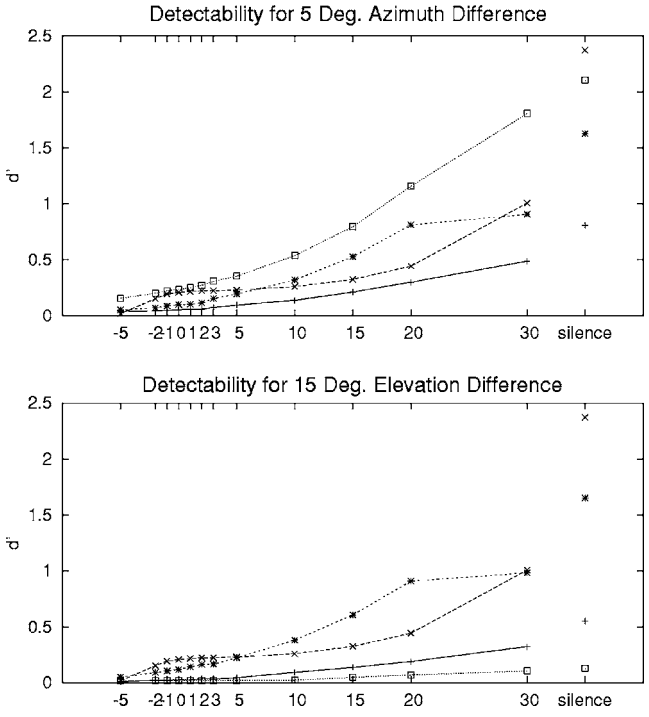

FIG. 5. d' of differences in interaural parameters derived from two different target directions as a function of SNR. In the upper panel, the two target directions were at 0° and 5° azimuth in the horizontal plane. In the lower panel, the differences in interaural parameters arise from a shift in elevation from 0° to 15° in the median plane. The target-noise condition was speech in cafeteria noise. Each plot shows data for the ILD variable at 830 Hz (+) and 2.88 kHz (□), and for the IPD variable at 340 (×) and 540 Hz (∗).

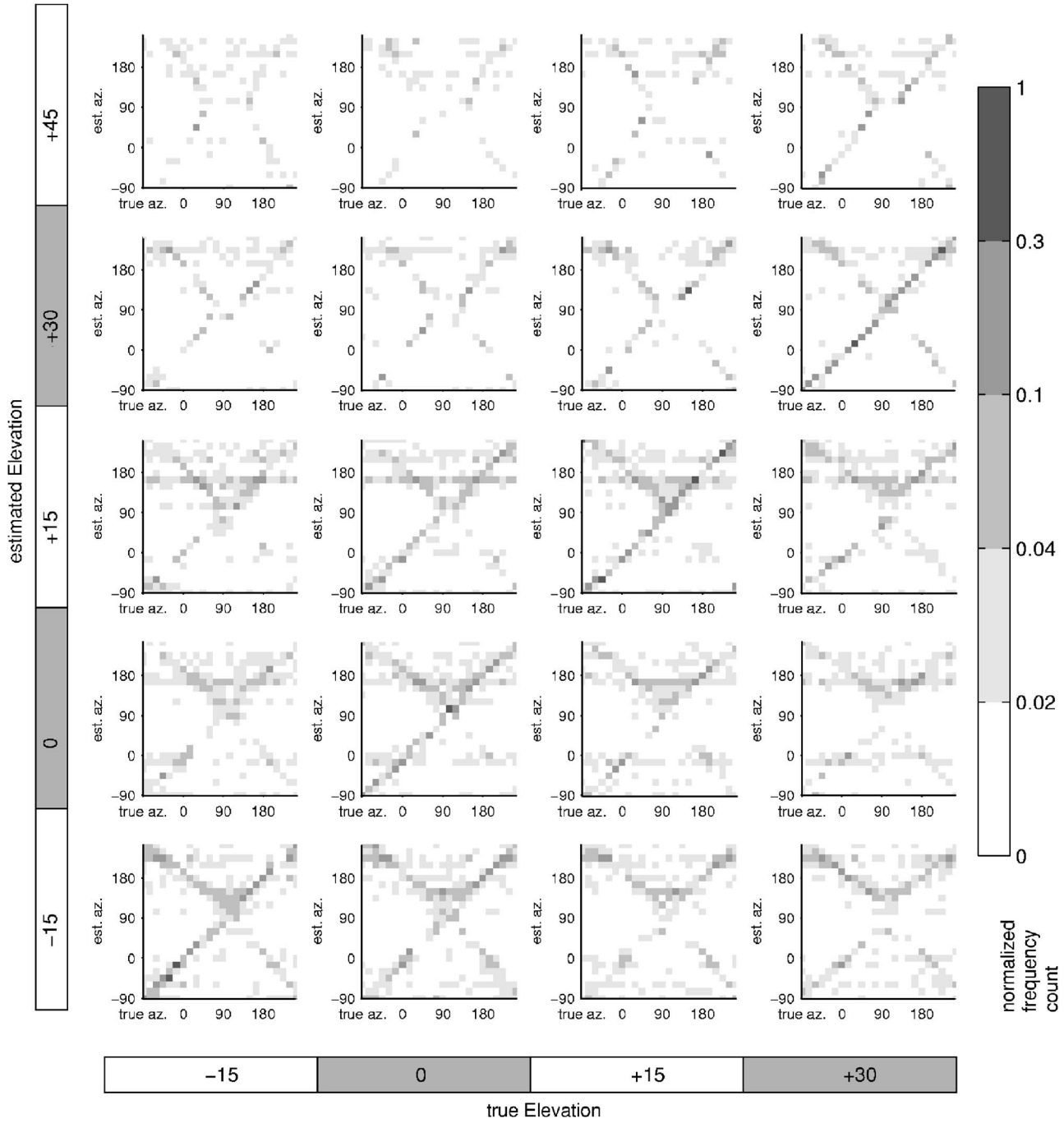

FIG. 6. Decision histogram for the target-noise condition "speech in cafeteria noise" at 5 dB SNR. The *y* axis represents the detected direction and the *x* axis the real direction of the target. Plotted is the normalized frequency count of localization decisions as an estimate of the probability that a specific direction is detected as the most probable direction, given the real direction. Each box in the plot gives real and estimated azimuth for a given combination of real and estimated elevation. If all decisions are correct, a diagonal intersecting the lower left plot's origin should result.

variation. At 5 dB SNR, d' is on average 0.1. In this case, about 100 independent observations, combined across time, frequency, or both, are needed to reach a d' of 1.

2. Simulation of absolute sound localization

Figure 6 gives the decision histogram in columns for each direction as a gray-scale-coded frequency count. The condition is speech in cafeteria noise at 5 dB SNR. Each small rectangle in the plot represents a real and estimated azimuth for a given combination of real and estimated elevation. Real azimuths are varied along the *x* axis of the subplots, estimated azimuths along the *y* axis of the subplot. Each real elevation is represented in a column of subplots and each estimated elevation in a row of subplots. If all decisions are correct, a black diagonal intersecting the plot's origin should result. Decisions plotted on parallel lines intersecting the *y* axis at different elevation boxes signify elevation confusions, whereas perpendicular diagonal lines indicate front-back confusions. Most pixels away from the diagonal are white, indicating that less than 2% of the direction estimates were given for this real/estimated direction combination. If for a fixed "true" direction estimates would

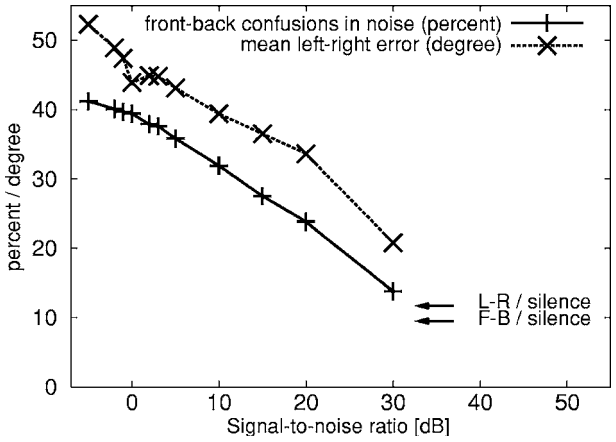

FIG. 7. Percentage of front-back confusions (+) and rms error of the angle to the median plane (×) of the Bayes localization simulation as function of SNR. The target-noise condition is speech in cafeteria noise. Data were averaged for all target directions. An estimate was considered a front-back confusion if the total angle of error was decreased by at least 15° when mirroring the azimuth coordinate at the frontal plane.

be evenly distributed across all possible directions, a white column across all subplots would result. The top row of the subplots is mostly white because the elevation value of 45° did not occur in the test data.

The percentage of front-back confusions, averaged across all target directions, was calculated from the decision histogram for the target-noise condition "speech in cafeteria noise" as a function of the SNR. A directional estimate was defined as a front-back confusion if the total angle of error was decreased by at least 15° when mirroring the azimuth coordinate at the frontal plane. Additionally, the direction estimates and the true directions were transformed to the angle to the median plane, also known as the "left-right" coordinate (Wightman and Kistler, 1989b), and the rms value of the error across all tested directions was evaluated. Figure 7 shows the percentage of confusions (+) and the rms error of the angle to the median plane (×). The percentage of confusions increases from 9.5% in silent conditions to 41.2% at the lowest SNR of −5 dB, while the rms value of the left-right coordinate has a value of 11.7% in silent conditions, which rises to 52.3% at −5 dB SNR.

For a real-world application of the Bayes localization algorithm, its robustness against changes in the noise environment is crucial. The dependence of the distributions of interaural parameters on the SNR was found to be especially high so that the localization accuracy might be lowered, if the reference distributions used in Eq. (20) did not match the test stimuli in SNR. The localization accuracy for the target-noise condition "speech in cafeteria noise" has therefore been evaluated for different SNRs with *a priori* information measured at the same SNR ("matched" condition) and at different SNRs ("unmatched" condition). Data are shown in Table V.

The rows show the percentage of front-back confusions for the different test SNRs. The columns give the SNR of the reference distributions that were used as *a priori* knowledge. The conditions with optimal information form the diagonal of the matrix (same data as in Fig. 7). For a test SNR of 10 dB (fifth row), the percentage is lowest for the optimal condition, i.e., a reference SNR of 10 dB. However, the percentage is only slightly higher for an unmatched reference SNR. With a fixed reference SNR of 15 dB (fourth column), the dependence on the test SNR is similar to the dependence with matched references (entries on the diagonal). Usually, very small differences among data in the same row are observed. However, if the reference condition which was measured in silence is tested at medium SNRs, the percentage of confusions increases from 9.5% to 34.2% (first row).

IV. DISCUSSION

A. Consequences of parameter distributions for sound localization

The analysis described in the last section reveals significant variations of short-term interaural parameters in silent environments and especially in noise conditions, justifying their statistical description as random variables. The empirical approach of estimating probability distributions from observations of ILD and IPD time series from actual binaural recordings seems to be sufficient for the characterization of random variables, because it reveals the most relevant dependencies of their PDFs on the sound field properties.

The description of short-term interaural parameters as random variables has several consequences for the extraction

TABLE V. Percentage of front-back confusions for the Bayes localization algorithm for the target-noise condition "speech in cafeteria noise." Rows show the data for the different tested SNR. The columns give the SNR of the reference distributions that were used as *a priori* knowledge. The conditions with optimal information form the diagonal of the matrix.

	Silence	30	20	15	10	5	3	2	0	−2	−5
Silence	9.5			34.2							
30		13.8		11.4							
20			23.8	22.3							
15				27.5							
10	34.2	33.2	33.6	32.9	31.9	32.0	32.4	31.8	35.7	34.7	35.0
5				37.1		35.8					
3				37.9			37.6				
2				39.0				37.9			
0				39.6					39.4		
−2				40.1						40.1	
−5				41.4							41.2

of directional information from short-term interaural parameters. First, the parameters fluctuate because of the nonstationarity of the signals and their nonlinear combination. Therefore, information retrieval at low SNRs can only be performed in a statistical sense and requires a certain number of observations of short-term interaural parameter values. Second, directional information can be retrieved with *a priori* knowledge of the statistics of the interaural parameters. Restriction of the *a priori* knowledge to the interaural parameters derived from anechoic HRTFs can lead to much larger errors, as Table V shows. Third, the detectability of systematic variations of interaural parameters with direction might be reduced due to their fluctuations. The amount of fluctuations is mainly a function of SNR and source direction and in the examined cases does not depend much on the noise type so that a general quantification of this effect as a function of SNR seems appropriate. Fourth, the systematic variation of the ILDs with direction itself is reduced due to the shift in mean values, i.e., the bias. Due to the SNR-dependent bias, it can be assumed that the large and significant ILD values observed in anechoic HRTFs from lateral directions cannot be fully exploited for localization or discrimination of directional sources in noise without taking into account the SNR. Finally, the direction dependence of higher-order moments possibly has to be taken into account. It could in principle be exploited for direction estimation, if an analysis of higher-order statistics is included.

B. Detectability of differences in interaural parameters

The d' analysis shows that at moderate-to-low SNRs of about 15 dB or below, the physical difference in interaural parameters induced by significant variations of direction, according to our assumptions, is not detectable on the basis of the observation of either one of the variables alone. However, discrimination is possible by integration of the information across frequency, time, or both. The coarse estimate given above shows that the number of observations necessary for the detection of 5° azimuth or 15° elevation difference is in the range of the number of frequency bands in a critical band analysis of interaural parameters. In order to reach the same number of observations by temporal integration, time windows of about 400 to 800 ms would be needed, which are much larger than psychoacoustically derived time constants of localization in humans (Stern and Bachorski, 1983). Some authors discussed that interaural cues caused by asymmetries between the pinnae may be sufficient also for sound source localization along the "cones of confusion" and the median plane (Searle *et al.*, 1975). However, as these asymmetries provide only small cues, it still has to be understood in which situations they are relevant.

If such an integration mechanism is used by the human hearing system, it can be assumed that the physically defined d' is perceptually relevant, because at moderate-to-low SNRs, the standard deviation of the IPDs at low frequencies and of the ILDs at medium-to-high frequencies is larger than the human just-noticeable differences (jnd's) in ILDs and IPDs in the respective frequency regions (cf. Ito *et al.*, 1982; Stern *et al.*, 1983). It can thus be assumed that the external noise is the limiting factor in this range of SNRs rather than internal noise associated with neural processing.

The notion that frequency integration is needed to ensure detectability, although physically founded here, coincides with the physiological studies by Brainard *et al.* (1992) in barn owls that demonstrated binaural information processing in multiple frequency bands and subsequent frequency integration. Directional ambiguities have been shown to be resolved by this integration. The assumption of frequency integration is supported by psychophysical findings showing that the localization accuracy increases with increasing bandwidth of the stimulus (e.g., Butler, 1986).

C. Simulation of absolute localization

Figure 6 shows that the confusion pattern is qualitatively similar to the patterns of human performance found, e.g., by Good and Gilkey (1996). Confusions occur mainly as elevation errors or front-back confusions. Hardly any confusions occur that could not be explained by this typical pattern. At lower SNRs, localization of lateral directions becomes more blurred, which is not shown here.

Good and Gilkey obtained human data for a single noise masker in the front and a click train from different directions. The SNR was defined relative to the detection threshold of the target for the condition where the target was in the front, other directions were tested with the same free field sound level. That means that the SNR at the ear canal entrance varied for different directions of the sound source. Due to the different target-noise condition and the different definition of the SNR, the results are not directly comparable. The diffuse cafeteria condition with a single talker target is probably more difficult to localize at the same SNR than the single-noise source condition using a click train as a target employed for the psychophysical experiments. Also, the psychoacoustic experiment was performed at a constant free-field SNR for each trial block. Because human pinnae enhance the high-frequency part of the spectrum of sounds from frontal directions (Shaw, 1997), there is a systematic direction dependence of the SNR at the ear canal entrance, so that detectability may have been used by the subjects as a cue to estimate the sound source azimuth. A more thorough comparison of the confusion patterns of the algorithm and in humans using the same stimulus configuration is therefore indicated. However, it can be concluded from the data illustrated here that the localization accuracy of the model is qualitatively similar to the one in humans. The relatively good estimation of elevations and front-back directions in the median plane with binaural input only can be explained by the fact that the algorithm is able to exploit asymmetries of the pinnae by the across-frequency integration of probabilities.

Table V suggests that the performance of the algorithm depends mainly on the SNR of the test condition and only slightly on the reference SNR. This finding shows that the Bayes localization model is robust against changes of the SNR of the reference condition. Its performance decreases only slightly if the *a priori* knowledge does not match the actual target-noise condition to be analyzed. The results

show that the distribution of interaural parameters as measured here could be one possible robust source of *a priori* information.

There are several reasons why human subjects probably are able to use binaural information in a more efficient way. First, the proposed MAP estimator disregards possible correlations between frequency channels, because in Eq. (10) the multidimensional PDF is approximated as a product of its marginals. Jenison (2000) has shown that a maximum-likelihood estimator with knowledge of the response covariance structure is able to perform better on a correlated population response than an estimator assuming independence. This might be relevant here, because the auditory system effectively possesses not only 43 frequency channels, but many thousands of nerve fibers with overlapping receptive fields. Second, the measured distributions include small variations of the interaural parameters due to head movements during the recording. These measurement errors decrease the localization performance at high SNRs. Third, humans use frequencies of at least up to 10 kHz for sound localization, and the high-frequency ILDs are probably particularly important, while the frequencies used here do not exceed 8 kHz. Fourth, the simulation does not include the interaural group delay, corresponding to time differences of the envelopes, which can be computed, e.g., according to Eq. (4). So far, the role of high-frequency ITDs has not been clarified completely (Macpherson and Middlebrooks, 2002); for high frequencies, envelope delays are probably more important. Therefore, it is possible that including some representation of interaural envelope delays improves localization performance. Fifth, humans can use monaural cues for sound localization in some circumstances. This can especially improve discrimination of directions on the median plane. Because monaural cues are not evaluated in the simulation, the distinction of front-back directions and elevations along the "cone of confusion" is probably worse than the performance of humans at the same SNR. Sixth, the used resolution of the histograms of IPDs is in part of the cases coarser than psychoacoustically observed jnd's; this should only affect localization at high SNRs. On the other hand, there is one aspect which may improve the performance of the algorithm as compared to human subjects, i.e., that humans cannot extract the fine structure of waveforms beyond 2 kHz. However, at higher frequencies, the IPDs are not only strongly disturbed by noise, but also become highly ambiguous. Taking all preceding aspects into account, humans probably can use the binaural information in a more efficient way, especially for directions close to the median plane, and for higher frequencies. A preprocessing model which better matches human binaural processing including interaural envelope delays, and excluding IPDs for channels at 1.5 kHz and higher, can possibly explain most of the localization ability of humans by binaural parameters alone.

It should be noted that the Bayesian approach is equivalent to the one of Duda (1997) if one assumes that the distributions are Gaussian with constant variance. In this case, the MAP procedure reduces to a least-squares fit, which would not need the *a priori* knowledge of all distributions. In contrast, Eq. (20) allows a more general approach which is able to take noise explicitly into account.

D. Frequency integration of probabilities

Most models of lateralization or localization combine short-term correlation values over frequency by a summation or multiplication (e.g., Stern *et al.*, 1988; Shackleton *et al.*, 1992; Stern and Trahiotis, 1997; Braasch and Hartung, 2002; Braasch, 2002b, a). Neurophysiological findings support that, for some species, after the detection of interaural parameters, a frequency integration is performed. This has been shown by Brainard *et al.* (1992) in the barn owl. Interaural cue detection followed by frequency integration has been used also successfully by frequency-domain models and technically motivated algorithms of sound localization (Duda, 1997; Wittkop *et al.*, 1997; Nakashima *et al.*, 2003). In contrast to the models cited above, the quantities which are integrated across frequency in the model presented here are *probabilities*, which takes, according to the assumptions stated, the available information into account in an optimum way.

E. Statistical representation of interaural timing

Because interaural parameters are considered in the frequency domain in narrow frequency bands, the interaural phase differences (IPDs) are used to describe timing differences. IPDs have several advantages over ITDs: For signals filtered by narrow-band auditory filters, the interaural cross-correlation function (ICCF) becomes nearly periodic. In the case that the signal is nonstationary or contains additional noise, the maximum of the ICCF, which is used frequently to estimate the ITD, is not well defined (Lyon, 1983; Stern *et al.*, 1988; Schauer *et al.*, 2000). This ambiguity of the maximum of the ICCF is directly related to the ambiguity of the phase in the frequency domain. This can be explained by the fact that, according to Eq. (8), both representations are linked by the combination of the generalized Wiener-Khintchine theorem (cross-correlation theorem) and the Wiener-Lee relation, and therefore have equal information content. Consequently, the probability density function (PDF) of ITD estimates based on the ICCF would have several maxima. While it is possible to describe such multimodal PDFs by histograms, there is no well-established approach to characterize it by a few parameters.

Contrarily, the statistics of the IPDs can be described neatly by statistics of cyclical data as defined by Fisher (1993); the expected value and variance can be calculated robustly, and empirically observed PDFs can be approximated well by the von Mises distribution. The phase difference is represented in the complex plane. Therefore, the error-prone operation of unwrapping the phase of noisy signals (Tribolet, 1977) is not necessary. This advantage of the IPDs has shown to become especially important in noise, as demonstrated by technical algorithms for robust sound localization (Liu *et al.*, 2000; Nakashima *et al.*, 2003).

F. Possible physiological representations of interaural timing

The processing structure sketched here aims to be a possible description of important features of the binaural auditory system. Clearly, the actual signal processing in binaural processing of interaural timing is still being discussed and may vary between different species. However, the explicit consideration of external noise, as proposed here, might be relevant for modeling physiological data.

Harper and McAlpine (2004), e.g., showed that when assuming a population code for distributions of IPDs for humans, as measured in indoor and outdoor sound fields, there are consequences for optimum distributions of best IPDs of auditory nerve fibers. Fitzpatrick *et al.* (1997) propose a population code based on the observation that localization of sounds is much more accurate than the spatial sensitivity of single neurons. Population codes have been proposed also, e.g., by Hancock and Delgutte (2004). The statistical data as well as the Bayesian approach described here could help to develop such models further, and eventually to decide which model matches neural data best.

The approach described here is solely based on the physical properties of the interaural parameters and subsequent Bayesian estimation. However, there is an interesting similarity with physiological models and data. When taking the logarithm of Eq. (20), the log probability $\log P(\lambda|\vec{\Delta})$ can be interpreted as an activity that is a sum of the activities (log probabilities) derived from the frequency bands. Frequency-specific activities are generated by the log distributions $\log P_b(\Delta_b|\lambda)$ from the observed parameter Δ_b. In terms of neural processing, the log distributions can be interpreted as optimum tuning curves of neurons sensitive to single-channel ILDs and IPDs. These narrow-band tuning curves are rather broad due to the external noise. The tuning curve sharpens by summation across frequency, which is equivalent to multiplication of probabilities, and a precise and robust localization is possible, although the basic tuning curves are unspecific. Measuring the "response" for ITD of narrow-band stimuli would yield periodic tuning curves. Also, with progressive frequency integration, ITD tuning curves would become less periodic and their shape should become more similar to a wideband cross-correlation function, the bandwidth corresponding to the bandwidth of the receptive fields. Therefore, the width and shape of the tuning curves could be interpreted as useful to increase the robustness in noise. The observed deviations of the parameter distributions from Gaussian shapes suggest that properties of physiologically observed tuning curves for interaural parameters, such as asymmetry (skewedness), might be an adaptation to increase the robustness with real-world stimuli.

The interpretation of the log distributions as activation tuning curves and well-defined *a priori* information can be regarded as a major advantage of the Bayesian localization model compared to other approaches that use neural nets in combination with common training rules (e.g., Neti *et al.*, 1992; Datum *et al.*, 1996; Janko *et al.*, 1997; Chung *et al.*, 2000). In neural nets, the training procedure is less well defined and sources of information used by the net are less clear than those in the approach described here.

G. Comparison to other approaches for sound localization

The general approach employed here is not restricted to the specific ILD and IPD analysis carried out here, but is also applicable to more specific computational models of human binaural signal processing. Small nonlinearities in the extraction of binaural information by the models is acceptable for this type of analysis, as it has been shown here that the physically defined parameters are nonlinear functions of the sound field as well. Additional nonlinearities induced by the models (e.g., level dependencies) could add some additional uncertainty, which is processed by the fuzzy information processing strategy proposed here in the same way as the nonlinearity in the physical parameters.

V. CONCLUSIONS

In noise conditions, the observed random variation of short-term, narrow-band interaural parameters (ILDs and IPDs) with time is large compared to the systematic variation induced by a change of direction of the sound source of several degrees in azimuth. Additionally, noise fields cause a systematic shift of the average values of these parameters. Because of the stochastic temporal variability, integration of information across frequency, or time, or both, is necessary to estimate directions from interaural parameters in such conditions.

A way to achieve this integration is the combination of statistical information across frequency. A Bayesian approach was used for this, which takes the estimated probability density functions (PDFs) of ILDs and IPDs from a reference noise condition as *a priori* information. These *a priori* PDFs were measured and evaluated for a large number of conditions. The shapes of the observed distributions depend mainly on the SNR, azimuth, and elevation. The noise environment has a smaller influence on the shape of the distributions. This influence is most notable at medium SNRs. Using the Bayesian approach, the azimuth and elevation can be estimated robustly. The elevation can be estimated even in the median plane at SNRs as low as 5 dB. The localization performance depends mainly on the SNR in the test condition.

The high level of external noise in combination with the hypothesis of integrating probabilities in the neural system could explain why tuning curves of neurons sensitive to interaural timing found in physiological measurements are broad, unspecific, and often asymmetric, while the behavioral localization performance is robust and accurate. External noise with realistic statistical properties should be explicitly considered in physiological measurements and models of binaural processing.

ACKNOWLEDGMENTS

We are grateful to Birger Kollmeier for his substantial support and contribution to this work. We thank the members of the Oldenburg Medical Physics Group, especially Thomas Wittkop, Stephan Albani, and Jörn Otten, for providing tech-

nical support and for important discussions. Ronny Meyer prepared additional material which helped to discuss the results. Also, we are grateful to the staff of the Hearing Research Center at the Department of Biomedical Engineering, Boston University, for fruitful and motivating discussions during a visit from the second author. Thanks to Armin Kohlrausch, Fred Wightman, two anonymous reviewers, Steve Greenberg, Hermann Wagner, and Jesko Verhey for helpful suggestions and comments on earlier versions of this manuscript. This work was supported by DFG (European Graduate School Psychoacoustics), BMBF (Center of Excellence on Hearing Technology, 01 EZ 02 12), and DFG (SFB TR 31).

APPENDIX: MOMENT COEFFICIENTS AND PARAMETERS OF DISTRIBUTIONS OF CYCLIC RANDOM VARIABLES

The first moment μ_1 of the PDF $f(\theta)$ of a circular variable θ is

$$\mu_1 = \int_{-\pi}^{\pi} e^{i\theta} f(\theta) d\theta \tag{A1}$$

$$= \varrho e^{i\phi}. \tag{A2}$$

The argument ϕ of μ_1 denotes the *mean phase angle* and the absolute value ϱ denotes the *vector strength* or *resultant length*. The *circular standard deviation* σ_z is defined as

$$\sigma_z = \sqrt{-2 \log \varrho} \tag{A3}$$

(Fisher, 1993). The *circular variance* ν is defined as $\nu = 1 - \varrho$.

The vector strength can assume values between 0 and 1. If ϱ equals 1, the distribution has the shape of a delta function and all phase values are coincident. By way of contrast, $\varrho = 0$ could mean that the random variable is uniformly distributed at all phase values, or that the distribution has two peaks at an angular difference of π, for example.

Analogous to the central moments for the linear case, trigonometric central moments μ_p of order p can be defined as

$$\mu_p = \int_{-\pi}^{\pi} e^{ip(\theta-\phi)} f(\theta) d\theta. \tag{A4}$$

The imaginary part of the second central trigonometric moment $\mathcal{T}[\mu_2]$ can be used to calculate the *circular skew*

$$s_z = \frac{\mathcal{T}[\mu_2]}{\nu^{3/2}}, \tag{A5}$$

and the real part $\mathcal{R}[\mu_2]$ defines the *circular kurtosis*:

$$K_z = \frac{\mathcal{R}[\mu_2] - \varrho^4}{\nu^2}. \tag{A6}$$

Using these quantities it is possible to describe distributions of circular variables by a few descriptive parameters as in the linear case.

[1]Taking into account the effect of the 400-point Hann window, an effective average bandwidth of 0.96 ERB results.

[2]Probabilities $P(\Delta)$ are given in capital letters here and can be calculated by multiplying the probability density $p(\Delta)$ with the parameter interval $\delta\Delta$. This factor is omitted here, because it is constant and does not change the results.

[3]Specifically, the reference distributions were clustered using the hierarchical Ward technique (Ward, 1963; Kopp, 1978) so that for each of the 36 980 histograms (43 frequencies, 430 directions, and 2 parameters), 1 out of 550 samples of the marginal distributions was used. For simplicity, the influence of this data reduction technique on the localization accuracy is not discussed here. However, its application shows that a noticeable reduction of the *a priori* information is possible.

Albani, S., Peissig, J., and Kollmeier, B. (**1996**). "Model of binaural localization resolving multiple sources and spatial ambiguities," in *Psychoacoustics, Speech and Hearing Aids*, edited by B. Kollmeier (World Scientific Publishing, Singapore), pp. 227–232.

Allen, J. B. (**1977**). "Short term spectral analysis, synthesis and modification by discrete Fourier transform," IEEE Trans. Acoust., Speech, Signal Process. **ASSP-25**(3), 235–238.

Allen, J. B., and Rabiner, L. R. (**1977**). "A unified approach to short-time Fourier analysis and synthesis," in *Proceedings of the IEEE*, Vol. **65** (IEEE, New York).

Blauert, J. (**1983**). *Spatial Hearing—The Psychophysics of Human Sound Localization* (MIT, Cambridge, MA).

Bodden, M. (**1993**). "Modeling human sound source localization and the cocktail-party-effect," Acta Acust. (Beijing) **1**(1), 43–55.

Bodden, M. (**1996**). "Auditory demonstrations of a cocktail-party-processor," Acta Acust. (Beijing) **82**(2), 356–357.

Borisyuk, A., Semple, M. N., and Rinzel, J. (**2002**). "Adaptation and inhibition underlie responses to time-varying interaural phase cues in a model of inferior colliculus neurons," J. Neurophysiol. **88**(4), 2134–2146.

Braasch, J. (**2002a**). "Auditory Localization and Detection in Multiple-Sound Source Scenarios," Ph.D. thesis, Ruhr-Universität Bochum, Düsseldorf, VDI-Verlag. Fortschritts-Berichte VDI Reihe 10 Nr. 707.

Braasch, J. (**2002b**). "Localization in presence of a distracter and reverberation in the frontal horizontal plane. II. Model algorithms," Acta. Acust. Acust. **88**, 956–969.

Braasch, J., and Hartung, K. (**2002**). "Localization in presence of a distracter and reverberation in the frontal horizontal plane. I. Psychoacoustical data," Acta. Acust. Acust. **88**, 942–955.

Brainard, M. S., Knudsen, E. I., and Esterly, S. D. (**1992**). "Neural derivation of sound source location: Resolution of spatial ambiguities on binaural cues," J. Acoust. Soc. Am. **91**, 1015–1027.

Breebaart, J., van de Par, S., and Kohlrausch, A. (**1999**). "The contribution of static and dynamically varying ITDs and IIDs to binaural detection," J. Acoust. Soc. Am. **106**, 979–992.

Brugge, J. F. (**1992**). "An overview of central auditory processing," in *The Mammalian Auditory Pathway: Neurophysiology*, edited by A. N. Popper and R. R. Fay, Vol. **2** of *Springer Handbook on Auditory Research* (Springer Verlag, New York), Chap. 1, pp. 1–33.

Butler, R. A. (**1986**). "The bandwidth effect on monaural and binaural localization," Hear. Res. **21**(1), 67–73.

Caird, D., and Klinke, R. (**1987**). "Processing of interaural time and intensity differences in the cat inferior colliculus," Exp. Brain Res. **68**(2), 379–392.

Chung, W., Carlile, S., and Leong, P. (**2000**). "A performance adequate computational model for auditory localization," J. Acoust. Soc. Am. **107**, 432–445.

Clarey, J. C., Barone, P., and Imig, T. J. (**1992**). "Physiology of thalamus and cortex," in *The Mammalian Auditory Pathway: Neurophysiology*, edited by A. N. Popper and R. R. Fay, Vol. **2** of *Springer Handbook on Auditory Research* (Springer Verlag, New York), Chap. 5, pp. 232–334.

Colburn, H. S. (**1996**). "Computational models of binaural processing," in *Auditory Computation*, edited by H. L. Hawkins, T. A. McMullen, A. N. Popper, and R. R. Fay, Vol. **6** of *Springer Handbook of Auditory Research* (Springer, New York), Chap. 8, pp. 332–400.

Datum, M. S., Palmieri, F., and Moiseff, A. (**1996**). "An artificial neural-network for sound localization using binaural cues," J. Acoust. Soc. Am. **100**, 372–383.

Domnitz, R. H., and Colburn, H. S. (**1976**). "Analysis of binaural detection models for dependence on interaural target parameters," J. Acoust. Soc. Am. **59**, 598–601.

Duda, R. O. (**1997**). "Elevation dependence of the interaural transfer function," in *Binaural and Spatial Hearing in Real and Virtual Environments*, edited by R. H. Gilkey and T. R. Anderson (Erlbaum, Mahwah, NJ), Chap. 3, pp. 49–75.

Durlach, N. I., and Colburn, H. S. (**1978**). "Binaural phenomena," in *Handbook of Perception—Hearing*, edited by E. C. Carterette and M. P. Friedman (Academic, New York), Vol. **4**, Chap. 10, pp. 365–466.

Fisher, N. I. (**1993**). *Statistical Analysis of Circular Data* (Cambridge U.P., Cambridge).

Fitzpatrick, D., Batra, R., and Stanford, T. (**1997**). "A neural population code for sound localization," Nature (London) **388**, 871–874.

Good, M. D., and Gilkey, R. H. (**1996**). "Sound localization in noise: The effect of signal-to-noise ratio," J. Acoust. Soc. Am. **99**, 1108–1117.

Hancock, K. E., and Delgutte, B. (**2004**). "A physiologically based model of interaural time difference discrimination," J. Neurosci. **24**(32), 7110–7117.

Harper, N. S., and McAlpine, D. (**2004**). "Optimal neural population coding of an auditory spatial cue," Nature (London) **430**, 682–686.

Henning, G. B. (**1973**). "Effect of interaural phase on frequency and amplitude discrimination," J. Acoust. Soc. Am. **54**, 1160–1178.

Ito, Y., Colburn, H. S., and Thompson, C. L. (**1982**). "Masked discrimination of interaural time delays with narrow-band signal," J. Acoust. Soc. Am. **72**, 1821–1826.

Janko, J. A., Anderson, T. R., and Gilkey, R. H. (**1997**). "Using neural networks to evaluate the viability of monaural and interaural cues for sound localization," in *Binaural and Spatial Hearing in Real and Virtual Environments*, edited by R. H. Gilkey and T. R. Anderson (Erlbaum, Mahwah, NJ), Chap. 26, pp. 557–570.

Jeffress, L. A. (**1948**). "A place theory of sound localization," J. Comp. Physiol. Psychol. **41**, 35–39.

Jenison, R. L. (**2000**). "Correlated cortical populations can enhance sound localization performance," J. Acoust. Soc. Am. **107**, 414–421.

Joris, P. X., and Yin, T. C. T. (**1996**). "Envelope coding in the lateral superior olive. I. Sensitivity to interaural time difference," J. Neurophysiol. **73**(3), 1043–1062.

Knudsen, E. I. (**1982**). "Auditory and visual maps of space in the optic tectum of the owl," J. Neurosci. **2**, 1177–1194.

Kollmeier, B., and Koch, R. (**1994**). "Speech enhancement based on physiological and psychoacoustical models of modulation perception and binaural interaction," J. Acoust. Soc. Am. **95**, 1593–1602.

Kollmeier, B., Peissig, J., and Hohmann, V. (**1993**). "Real-time multi-band dynamic compression and noise reduction for binaural hearing aids," J. Rehabil. Res. Dev. **30**(1), 82–94.

Kopp, B. (**1978**). "Hierarchical classification III: Average-linkage, median, centroid, WARD, flexible strategy," Biom. J. **20**(7/8), 703–711.

Kuwada, S., and Yin, T. C. T. (**1983**). "Binaural interaction in low-frequency neurons in inferior colliculus of the cat. I. Effects of long interaural delays, intensity, and repetition rate on interaural delay function," J. Neurophysiol. **50**(4), 981–999.

Kuwada, S., and Yin, T. C. T. (**1987**). "Physiological studies of directional hearing," in *Directional Hearing*, edited by W. A. Yost and G. Gourevitch (Springer, New York), Chap. 6, pp. 146–176.

Liu, C., Wheeler, B. C., O'Brien, Jr., W. D., and Bilger, R. C. (**2000**). "Localization of multiple sound sources with two microphones," J. Acoust. Soc. Am. **108**, 1888–1905.

Lyon, R. F. (**1983**). "A computational model of binaural localization and separation," in *Proceedings of the International Conference on Acoustics, Speech and Signal Processing ICASSP'83*, Vol. **3** (IEEE, New York).

Macpherson, E. A., and Middlebrooks, J. C. (**2002**). "Listener weighting of cues for lateral angle: The duplex theory of sound localization revisited," J. Acoust. Soc. Am. **111**, 2219–2236.

Malone, B. J., Scott, B. H., and Semple, M. N. (**2002**). "Context-dependent adaptive coding of interaural phase disparity in the auditory cortex of awake macaques," J. Neurosci. **22**(11), 4625–4638.

McAlpine, D., and Grothe, B. (**2003**). "Sound localization and delay lines—do mammals fit the model?" Trends Neurosci. **26**(7), 347–350.

Moore, B. C. J. (**1989**). *An Introduction to the Psychology of Hearing*, 3rd ed. (Academic, New York), Vol. **1**, Chap. 3, pp. 100–101.

Nakashima, H., Chisaki, Y., Usagawa, T., and Ebata, M. (**2003**). "Frequency domain binaural model based on interaural phase and level differences," Acoust. Sci. & Tech. **24**(4), 172–178.

Neti, C., Young, E. D., and Schneider, M. H. (**1992**). "Neural network models of sound localization based on directional filtering by the pinna," J. Acoust. Soc. Am. **92**, 3140–3156.

Otten, J. (2001). "Factors influencing acoustical localization," Ph.D. thesis, Universität Oldenburg, Oldenburg, Germany.

Sachs, L. (**1992**). *Angewandte Statistik (Applied Statistics)*, 7 ed. (Springer, Berlin).

Schauer, C., Zahn, T., Paschke, P., and Gross, H. M. (**2000**). "Binaural sound localization in an artificial neural network," in *Proc. International Conference on Acoustics, Speech and Signal Processing (ICASSP) 2000*, Vol. **2** (IEEE, New York).

Searle, C. L., Braida, L. D., Cuddy, D. R., and Davis, M. F. (**1975**). "Binaural pinna disparity: Another localization cue," J. Acoust. Soc. Am. **57**, 448–455.

Shackleton, T., Meddis, R., and Hewitt, M. J. (**1992**). "Across frequency integration in a model of lateralization," J. Acoust. Soc. Am. **91**, 2276–2279.

Shaw, E. A. (**1997**). "Acoustical features of the human external ear," in *Binaural and Spatial Hearing in Real and Virtual Environments*, edited by R. H. Gilkey and T. R. Anderson (Erlbaum, Mahwah, NJ), Chap. 2, pp. 25–47.

Spitzer, M. W., and Semple, M. N. (**1991**). "Interaural phase coding in auditory midbrain: Influence of dynamic stimulus features," Science **254**(5032), 721–724.

Stern, R. M., and Bachorski, R. J. (**1983**). "Dynamic cues in binaural perception," in *Hearing—Physiological Bases and Psychophysics*, edited by R. Klinke and R. Hartmann (Springer, Heidelberg), pp. 209–215.

Stern, R. M., and Trahiotis, C. (**1997**). "Models of binaural perception," in *Binaural and Spatial Hearing in Real and Virtual Environments*, edited by R. H. Gilkey and T. R. Anderson (Erlbaum, Mahwah, NJ), Chap. 24, pp. 499–531.

Stern, R. M., Zeiberg, A. S., and Trahiotis, C. (**1988**). "Lateralization of complex binaural stimuli: A weighted-image model," J. Acoust. Soc. Am. **84**, 156–165.

Stern, Jr., R. M., Slocum, J. E., and Phillips, M. S. (**1983**). "Interaural time and amplitude discrimination in noise," J. Acoust. Soc. Am. **73**, 1714–1722.

Tribolet, J. M. (**1977**). "A new phase unwrapping algorithm," IEEE Trans. Acoust., Speech, Signal Process. **ASSP-25**(2), 170–177.

Wagner, H. (**1991**). "A temporal window for lateralization of interaural time difference by barn owls," J. Comp. Physiol., A **169**, 281–289.

Ward, Jr., J. H. (**1963**). "Hierarchical grouping to optimize an objectice function," J. Am. Stat. Assoc. **58**(301), 236–244.

Wightman, F. L., and Kistler, D. J. (**1989a**). "Headphone simulation of free-field listening. I: Stimulus synthesis," J. Acoust. Soc. Am. **85**, 858–867.

Wightman, F. L., and Kistler, D. J. (**1989b**). "Headphone simulation of free-field listening. II: Psychophysical validation," J. Acoust. Soc. Am. **85**, 868–878.

Wittkop, T., Albani, S., Hohmann, V., Peissig, J., Woods, W. S., and Kollmeier, B. (**1997**). "Speech processing for hearing aids: Noise reduction motivated by models of binaural interaction," Acust. Acta Acust. 83(4), 684–699.

Zurek, P. M. (**1991**). "Probability distributions of interaural phase and level differences in binaural detection stimuli," J. Acoust. Soc. Am. **90**, 1927–1932.

Frequency discrimination of complex tones; assessing the role of component resolvability and temporal fine structure[a)]

Brian C. J. Moore,[b)] Brian R. Glasberg, and Helen J. Flanagan
Department of Experimental Psychology, University of Cambridge, Downing Street, Cambridge CB2 3EB, England

Joe Adams
Faculty of Music, University of Cambridge, West Road, Cambridge CB3 9DP, England

(Received 25 May 2005; revised 11 October 2005; accepted 14 October 2005)

Thresholds for discriminating the fundamental frequency (F0) of a complex tone, F0DLs, are small when low harmonics are present, but increase when the number of the lowest harmonic, *N*, is above eight. To assess whether the relatively small F0DLs for *N* in the range 8–10 are based on (partly) resolved harmonics or on temporal fine structure information, F0DLs were measured as a function of *N* for tones with three successive harmonics which were added either in cosine or alternating phase. The center frequency was 2000 Hz, and *N* was varied by changing the mean F0. A background noise was used to mask combination tones. The value of F0 was roved across trials to force subjects to make within-trial comparisons. *N* was roved by ±1 for every stimulus, to prevent subjects from using excitation pattern cues. F0DLs were not influenced by component phase for *N*=6 or 7, but were smaller for cosine than for alternating phase once *N* exceeded 7, suggesting that temporal fine structure plays a role in this range. When the center frequency was increased to 5000 Hz, performance was much worse for low *N*, suggesting that phase locking is important for obtaining low F0DLs with resolved harmonics. © *2006 Acoustical Society of America.* [DOI: 10.1121/1.2139070]

PACS number(s): 43.66.Hg, 43.66.Nm, 43.66.Fe [JHG] Pages: 480–490

I. INTRODUCTION

The pitch of a periodic complex tone usually corresponds to its fundamental frequency (F0), even when the fundamental component is not present (Schouten, 1940), which has been called the phenomenon of the "missing fundamental." The pitch evoked by a group of harmonics is called residue pitch, virtual pitch, or low pitch. A low pitch can be heard even when the fundamental component is masked by low-frequency noise (Licklider, 1956), which proves that the pitch is not produced by a distortion component at F0.

Several classes of model have been proposed to explain the perception of the low pitch of complex tones. In one class, the pattern-recognition models (de Boer, 1956; Thurlow, 1963; Goldstein, 1973; Terhardt, 1974), it is assumed that two stages are involved. The first stage is a frequency analysis to determine the frequencies (or "pitches" in Terhardt's terminology) of some of the individual sinusoidal components of the complex tone. This might depend on both place and temporal analysis (Srulovicz and Goldstein, 1983; Shamma, 1985; Shamma and Klein, 2000). The second stage is a pattern recognizer which determines the pitch of the complex tone from the frequencies of the resolved components. For this class of model, it should only be possible for the auditory system to derive a low pitch when there is at least one resolvable harmonic.

An alternative class of model is based on temporal analysis of the waveforms evoked on the basilar membrane (Schouten, 1940; de Boer, 1956). The lower harmonics in a complex tone are partially resolved by the basilar membrane, each leading to a peak in response at the appropriate place. The waveform evoked on the basilar membrane by a resolved low harmonic reflects the periodicity of that harmonic, and the pattern of phase locking evoked at the place of maximal response to the harmonic is similar to what would be evoked by a sine wave with the same frequency as the harmonic. However, higher harmonics interfere on the basilar membrane. The temporal pattern of the waveform evoked by high harmonics reflects the F0 of periodic sounds. Temporal theories assume that pitch is derived from the temporal pattern of neural spikes arising from one or more points on the basilar membrane where harmonics are interfering. According to these theories, interference of harmonics on the basilar membrane is required for a low pitch to be heard.

Research has shown that a low pitch can be perceived both when only low resolved harmonics are present and when only high unresolved harmonics are present (Ritsma, 1962; 1963; Moore and Rosen, 1979; Moore and Glasberg, 1988; Houtsma and Smurzynski, 1990; Shackleton and Carlyon, 1994; Kaernbach and Bering, 2001). This has led to models in which information from both low and high harmonics is used to determine low pitch (Moore, 1982; van Noorden, 1982; Meddis and Hewitt, 1991; Meddis and O'Mard, 1997).

[a)]Part of this work was presented at the 28th Midwinter meeting of the Association for Research in Otolaryngology

[b)]Electronic mail: bcjm@cam.ac.uk

 0001-4966/2006/119(1)/480/11/$22.50

Accepting that a (weak) low pitch can be derived from the temporal waveform evoked on the basilar membrane by a group of high unresolved harmonics, the question arises as to whether the pitch is determined by the envelope or by the temporal fine structure. This has been assessed using amplitude-modulated (AM) tones. Consider an AM tone with carrier frequency fc and modulation frequency fm. The spectrum of this sound contains components with frequencies $fc-fm$, fc, and $fc+fm$. Consider a case where, initially, fc is an integer multiple of fm, for example $fc=2000$ Hz and $fm=200$ Hz. In this case the sound has a low pitch corresponding to 200 Hz. If now fc is shifted upwards (say to 2030 Hz) keeping fm fixed, the envelope repetition rate remains the same (200 Hz), but a slight upward shift in pitch is heard (de Boer, 1956; Schouten *et al.*, 1962; Patterson, 1973; Moore and Moore, 2003). This has been explained in terms of the temporal fine structure of the waveform (either of the stimulus itself, or the waveform evoked on the basilar membrane). The time interval between peaks in the temporal fine structure close to adjacent envelope maxima is slightly reduced by the upward shift in fc, and the shifted pitch corresponds to this time interval.

Moore and Moore (2003) modified the stimuli used to assess the role of temporal fine structure so as to eliminate possible cues related to shifts in the excitation pattern with shifts in fc. They used complex tones with more than three components and passed the tones through a fixed bandpass filter. They assessed the effect on pitch of shifting all components upwards in frequency by a fixed amount, keeping the spacing between components (and therefore the envelope repetition rate) the same. They showed that when the nominal harmonic number of the lowest component in the complex tone, N, was relatively high (N above about 14), there was no shift in pitch, whereas when N was 9, significant pitch shifts occurred. Moore and Moore argued that, when a complex tone contains only very high harmonics, the pitch is determined from the envelope periodicity rather than from the temporal fine structure. The pitch shift found when N was 9 could be explained either in terms of a sensitivity to the temporal fine structure or in terms of a pattern-matching process to (partially) resolved harmonics.

Hall *et al.* (2003) also studied the relative importance of envelope and temporal fine structure cues. They compared modulation-rate discrimination thresholds for amplitude-modulated (AM) and quasi-frequency-modulated (QFM) tones. Thresholds were similar for AM and QFM tones whose carrier fell in a low spectral region, but as the spectral region of the carrier frequency increased, performance worsened more rapidly for QFM than for AM tones. Hall *et al.* argued that when components occupy relatively low spectral regions, phase locking both to the fine structure and to the envelope can be used as a cue. However, as the spectral region occupied by the components increases, phase locking to the fine structure becomes less robust, whereas phase locking to the envelope remains as a potentially strong cue. In the study of Hall *et al.* the modulation rate was fixed at 100 or 200 Hz and performance was measured for several carrier frequencies over the range 1500 to 6000 Hz. Hence, in their study it was not possible to separate the effects of carrier frequency *per se* from the effects of harmonic number (determined by the ratio of carrier to modulation frequency).

The ability to detect changes in F0 for a harmonic complex tone is usually good when the tone contains low resolved harmonics and poor when the tone contains only high unresolved harmonics (Hoekstra and Ritsma, 1977; Moore and Glasberg, 1988; Houtsma and Smurzynski, 1990; Shackleton and Carlyon, 1994; Kaernbach and Bering, 2001; Bernstein and Oxenham, 2003, 2005). It is usually assumed that performance is good for tones containing low harmonics because these harmonics are resolved in the peripheral auditory system, although Bernstein and Oxenham (2003) presented evidence suggesting that resolvability *per se* is not the critical factor. Performance may be poor for very high harmonics because only information about the temporal envelope of the stimulus is available, temporal fine structure information being lost, the evidence for which was described earlier (Moore and Moore, 2003).

If complex tones are filtered or synthesized so as to contain only a few harmonics, F0 discrimination is usually good when N is below 8. However, as N is increased above 8, performance starts to worsen, until it reaches a plateau of relatively poor performance when N is 12–13 (Hoekstra and Ritsma, 1977; Bernstein and Oxenham, 2003). The question addressed in this paper is: what mechanisms underlie the F0 discrimination of complex tones when N is in the range 8–11, where performance is still relatively good? The good performance in this range might occur because the harmonics are still partially resolved. Data on the audibility of individual partials in steady complex tones (Plomp, 1964; Plomp and Mimpen, 1968; Moore and Ohgushi, 1993) suggest that the lowest five harmonics can be "heard out" with high accuracy, but accuracy decreases for harmonics above the fifth, and harmonics above the eighth cannot be heard out at all. However, in studies in which the "target" harmonic was pulsed on and off, it has been reported that harmonics up to about the 11th could be heard out (Gibson, 1970; Bernstein and Oxenham, 2003). If this estimate is correct, then the good F0 discrimination for tones with lowest harmonics in the range 8–11 might depend on (partially) resolved harmonics. Also, the pitch-shift effect found for stimuli with components in this range (Schouten *et al.*, 1962; Moore and Moore, 2003) could be explained in terms of the best-fitting fundamental frequency obtained via a pattern-recognition process (Goldstein, 1973). An alternative possibility is that, in this range, listeners can extract information from the temporal fine structure of the sound and not just the envelope. Use of temporal fine structure information could lead to greater precision in the estimation of F0 than use of envelope information.

In the present experiment, we assessed the two possibilities discussed above by comparing F0 discrimination for complex tones with components added in two different phase relationships. One, cosine phase, was chosen to give waveforms on the basilar membrane with a high peak factor (ratio of peak to root-mean-square value), which should lead to optimal use of temporal fine structure information, since there are only a few high-amplitude peaks in the fine structure in each stimulus period. This is illustrated in the upper

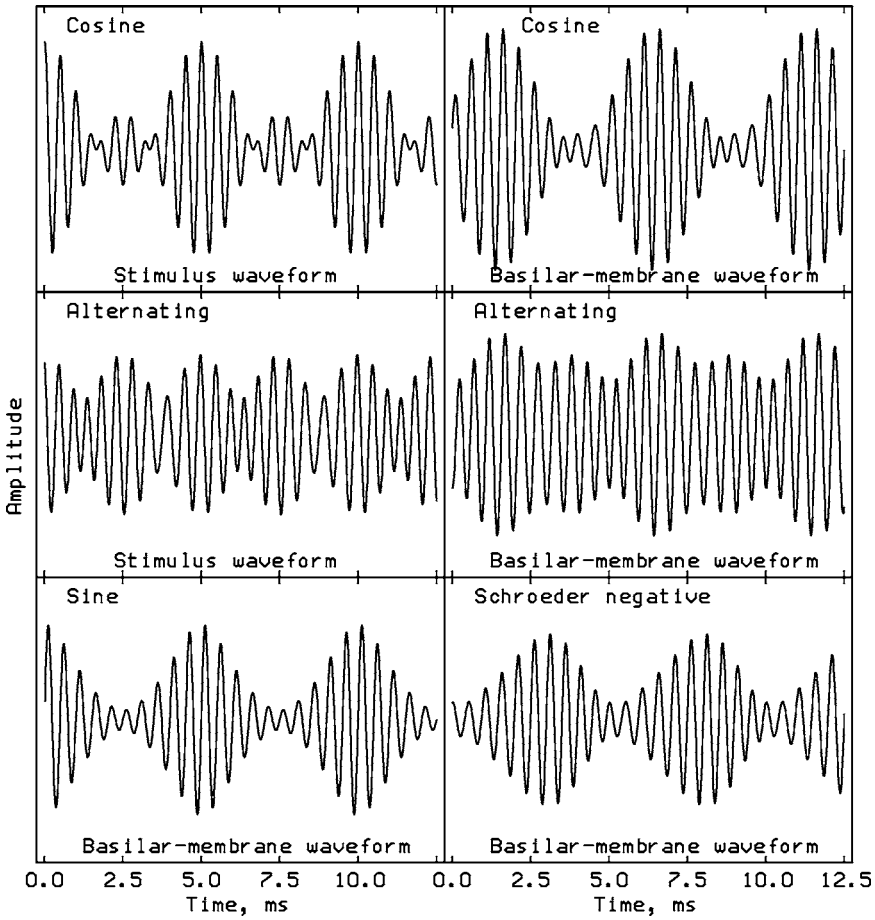

FIG. 1. The top and middle rows illustrate the effect of component phase on the waveforms of three-component complex tones. The top-left trace shows the waveform of a cosine-phase stimulus (the 9th, 10th, and 11th harmonics of a 200-Hz F0) and the top-right trace shows a simulation of the waveform evoked by that stimulus on the basilar membrane at the place tuned to 2000 Hz, calculated as described by Alcántara *et al.* (2003). The middle two traces show corresponding waveforms for an alternating-phase stimulus. The lower two traces simulate basilar-membrane waveforms evoked by 11-component stimuli similar to those used by Houtsma and Smurzynski (1990). The tones contained harmonics 9–19 of a 200-Hz F0. For the bottom-left trace, the components were added in sine phase. For the bottom-right trace, the components were added in Schroeder-negative phase.

traces of Fig. 1; the left trace shows the waveform of one of the stimuli (the 9th, 10th, and 11th harmonics of a 200-Hz F0) and the right trace shows a simulation of the waveform evoked by that stimulus on the basilar membrane, calculated as described by Alcántara *et al.* (2003) and assuming that the curvature of the phase response of the auditory filter centered at 2000 Hz is 2.5×10^{-5} rad/Hz^2 (Lentz and Leek, 2001; Oxenham and Dau, 2001). The other, alternating phase, was chosen to give waveforms with lower peak factors, with many fine structure peaks of similar magnitude, which should lead to poorer use of temporal fine structure information. This is illustrated in the middle traces of Fig. 1 (the lower traces are explained later). Note that the envelope of the alternating-phase stimulus has two peaks per period. For alternating-phase stimuli with many high harmonics, this can lead to a near-octave shift in pitch relative to a stimulus with sine-phase or cosine-phase components (Patterson, 1987; Shackleton and Carlyon, 1994). However, for our three-component stimuli, while the simulated basilar-membrane waveform still has two envelope peaks per period, one of these envelope peaks is markedly bigger than the other. Informal listening by the experimenters and some of the musically trained subjects indicated that, for a given F0, the pitch of our alternating-phase stimuli was the same as that of the cosine-phase stimuli (although the pitch of the former was often less clear).

It is generally assumed that the relative phase of the components in a complex tone does not affect pitch perception when the components are resolved, but can affect pitch perception when they are not resolved (Moore, 1977; Carlyon and Shackleton, 1994; Shackleton and Carlyon, 1994; Houtsma and Smurzynski, 1990; Bernstein and Oxenham, 2005). Hence, we expected to find no effect of component phase when the complex tones contained only low harmonics, but poorer F0 discrimination for alternating than for cosine phase when the tones contained only very high harmonics (say above the 14th). The question of interest was: would there be a phase effect when the lowest harmonic was in the range 8–11? If so, this would imply that the harmonics were unresolved, and this, combined with the pitch-shift effect described earlier, would provide evidence for a role of temporal fine structure derived from unresolved harmonics. If there was not a phase effect, this would support the idea that the good F0 discrimination for harmonics in that range is linked to partial resolution of the harmonics.

In experiment 1, all complex tones had frequency components centered at 2000 Hz, a frequency for which temporal fine structure is represented in the auditory nerve of the chinchilla (Javel, 1980) and the cat (Cariani and Delgutte, 1996a, b) and probably in humans (Moore, 1973). We chose this center frequency as pilot experiments had shown that many subjects did not clearly perceive a low pitch when the center frequency was lower (e.g., 1000 Hz) and the harmonic numbers were relatively high, whereas all subjects reported hearing a low pitch when the center frequency was 2000 Hz and the components were added in cosine phase. In experiment 2, the complex tones were centered at 5000 Hz, a frequency for which phase locking is very weak, and temporal fine struc-

ture information would probably be unusable. The comparison of results for the two frequencies was intended to give some insight into the relative effectiveness of temporal fine structure and temporal envelope information.

There are two previous experiments that have some resemblance to the ones reported here. Houtsma and Smurzynski (1990) measured F0DLs as a function of N for complex tones with 11 harmonics, which were added either in sine phase or Schroeder negative phase (Schroeder, 1970). F0DLs were smaller for the sine-phase than for the Schroeder-negative-phase stimuli for $N=13$ and higher (although the statistical significance of the phase effect was not assessed), but there was no phase effect for $N=7$ or 10. Values of N between 10 and 13 were not used. There are four ways in which the experiments of Houtsma and Smurzynski differ from our experiments. First, their F0 was always close to 200 Hz, so the spectral region occupied by the harmonics varied with N. This means that it is impossible to separate the effect of spectral region from the effect of harmonic number. In contrast, we used stimuli centered on two fixed spectral regions, one where phase locking is available and one where it is not. Second, their use of complex tones with many harmonics makes it difficult to determine which harmonics were most important in determining the F0DLs. We used stimuli with only three harmonics. Third, the use of Schroeder negative phase may not have been optimal for minimizing the use of temporal information; Houtsma and Smurzynski pointed out that the two phases used by them "were merely chosen as two rather convenient phase configurations for which some elementary masking data exist and on the basis of which one might expect different pitch behavior." This is illustrated by the two lower traces in Fig. 1. These show simulations of basilar membrane responses at a place tuned to 2000 Hz, calculated in the way described earlier, for stimuli similar to those used by Houtsma and Smurzynski. In both cases, the complex tones contained harmonics 9 to 19 of a 200-Hz F0. For the left trace, the components were added in sine phase, while for the right trace they were added in Schroeder-negative phase. Both waveforms have a single distinct envelope maximum per period, and the peak factors of the waveforms are similar for the two cases, being 2.37 for the sine-phase complex and 2.16 for the sine-phase complex. In contrast, the phases of the stimuli used by us were specifically chosen, based on simulations of the waveforms on the basilar membrane (Alcántara *et al.*, 2003), so as to give waveforms with high peak factors (cosine phase) and low peak factors (alternating phase) on the basilar membrane. Finally, we used values of N spaced in steps of 1 instead of the steps of 3 used by Houtsma and Smurzynski.

The other experiment that is comparable to ours was published recently by Bernstein and Oxenham (2005). They compared F0 discrimination for multiple-component complex tones filtered into two frequency regions, a "low" region, for which phase-locking information was thought to be available, and a "high" region, for which phase-locking information was thought to be "greatly reduced." Components in the complex tones were added in either sine phase or random phase. For $N>15$, F0DLs were larger for random-phase than for sine-phase stimuli. For $N\approx 10$, there was a small phase effect for stimuli in the high spectral region but no phase effect for stimuli in the low spectral region. No values of N between 10 and 15 were tested. Generally, the patterns of performance were similar for the two frequency regions, which led Bernstein and Oxenham to conclude "This implies that phase locking to the stimulus fine structure did not play a significant role overall in F0 discrimination for the stimuli used in this experiment." However, they did note that the stimuli used in the "high" spectral region had audible components extending down to 3.28 kHz "where phase-locking to the stimulus fine structure might still have been available." The results reported here show clear differences between the results for center frequencies of 2000 and 5000 Hz, consistent with a strong role of temporal fine structure information for the lower center frequency. Our experiments also differ from that of Bernstein and Oxenham in our use of closely spaced values of N, and of stimuli with only three harmonics; this allowed us to determine more precisely which harmonics were required to observe an effect of phase on F0DLs.

II. EXPERIMENT 1: CENTER FREQUENCY 2000 HZ

A. Method

Thresholds for the discrimination of F0 (F0DLs) were measured using a two-interval two-alternative forced-choice procedure. Subjects had to indicate, by pressing one of two buttons, which of the two intervals contained the stimulus with higher F0, and feedback was provided after each trial by lights on the response box. For a given center F0, $F0_c$, and a given difference, $\Delta F0$, one stimulus in a trial had an F0 of $F0_c+0.5\Delta F0$ and the other had an F0 of $F0_c-0.5\Delta F0$. A three-down, one-up geometric tracking procedure was used to estimate the 79% correct point on the psychometric function (Levitt, 1971). Twelve turnpoints were obtained. A run started with a relatively large value of $\Delta F0$, typically 20% of $F0_c$. In most cases, this was sufficiently large to ensure that the difference was easily discriminable. The value of $\Delta F0$ was increased or decreased by a factor of 1.414 until four turnpoints had occurred. Then, the factor was reduced to 1.189 and eight further turnpoints were obtained. The geometric mean of the frequency differences at the last eight turnpoints was taken as the estimate of threshold for that run. At least three estimates were obtained for each combination of stimulus condition and F0. In cases where the variability of the three estimates was high, up to five additional runs were obtained, and the final threshold was taken as the geometric mean of all estimates.

B. Stimuli

Each complex tone contained three successive equal-amplitude harmonics, each with a level of 60.2 dB SPL (overall level of 65 dB SPL). The nominal frequency of the center component was 2000 Hz. The nominal number, N, of the lowest harmonic ranged from 6 to 15. N was varied by changing the mean $F0_c$. To force subjects to make within-trial comparisons, rather than making comparisons with a long-term memory for F0, the value of $F0_c$ was roved by

±10% across trials. To reduce the ability of subjects to perform the task by comparing the pitches of individual resolved harmonics (for example the lowest harmonic or highest harmonic), or from using excitation pattern cues for unresolved harmonics (Moore and Moore, 2003), the value of N was roved by ±1 independently for each of the two intervals within each forced-choice trial (Houtsma and Smurzynski, 1990). For example, for a value of N of 8, the harmonic numbers in each interval were selected randomly from 7, 8, 9 or 8, 9, 10 or 9, 10, 11, independently of which interval had the higher F0.

The components in the complex tones were added with two different starting phases. In one condition, cosine phase, all components started at a positive peak in the waveform. In the other condition, alternating phase, the phase of the middle component was shifted by 90°. Each tone had rise/fall times of 20 ms and a steady-state duration of 480 ms. The silent interval between the two tones within a trial was 500 ms.

To prevent discrimination of F0 based on combination tones, a continuous background noise was presented during each run. The noise was "threshold equalizing noise" (Moore *et al.*, 2000) designed to give equal masked thresholds at all frequencies over the range 50 to 2800 Hz; the upper cutoff frequency was 3000 Hz. The noise was synthesized by adding sinusoidal components spaced at 0.1-Hz intervals with appropriate amplitudes and random phases. The resulting 10-s noise segment was seamlessly recycled to give continuous noise and recorded onto CDR. During the experiment the noise was replayed from the CDR. The noise spectrum level (*re* 20 μPa) was 6 dB at 2000 Hz, corresponding to a level per ERB_N of 30 dB SPL, where ERB_N stands for the average value of the equivalent rectangular bandwidth of the auditory filter for young normal-hearing listeners at moderate sound levels (Glasberg and Moore, 1990).

The complex tones were generated digitally on-line using a Tucker-Davis Technologies (TDT) system II. The tones were played through a 16-bit digital-to-analog converter (TDT, DD1) at a 50-kHz sampling rate, low-pass filtered at 8 kHz (Kemo VBF8/04), attenuated (TDT, PA4), mixed with the noise (TDT, SM3), and presented via a headphone buffer (TDT, HB6), a manual attenuator (Hatfield 2125), and one earpiece of a Sennheiser HD580 headset.

C. Subjects and training

Five normal hearing subjects were tested (three males and two females), four of whom had some musical training. Their ages ranged from 20 to 35 years. All subjects had absolute thresholds better than 20 dB HL over the range of audiometric frequencies from 250 to 8000 Hz. All subjects except author HF were paid for their services. Pilot experiments showed that subjects initially found the randomization of harmonic number to be very distracting, and they often performed poorly even when N was 6 or 7, because they based their judgments on the shift in frequency of the lowest harmonic rather than the shift in F0. To overcome this problem, subjects were initially trained using complex tones with seven harmonics (each with a level of 60.2 dB SPL), initially without and then with randomization of ±1 for the number of the lowest harmonic. For tones with more harmonics, the change in F0 was more salient, and the randomization of harmonic number was less distracting. Once subjects achieved stable performance for the complex tones with seven harmonics, even when N was randomized, the number of harmonics was reduced to three. Subjects were given at least 3 h of training using complex tones with three harmonics (i.e., the stimuli to be used in the main experiment) before data were accepted.

D. Results and discussion

Figure 2 shows the results for each subject and the geometric mean across subjects (bottom-right panel). Results for the cosine-phase stimuli are shown by open circles and results for the alternating-phase stimuli are shown by filled circles. The pattern of results for the cosine-phase stimuli is similar to that found by Hoekstra and Ritsma (1977) for discrimination of the rate of click trains passed through a $\frac{1}{3}$-oct filter centered at 2000 Hz. F0DLs are small for the lowest harmonic numbers ($N=6$ or 7) and increase progressively as N is increased to about 12. The F0DLs then flatten off. There is no clear effect of component phase for $N=6$ or 7. However, alternating phase led to higher F0DLs than cosine phase for harmonic numbers of 8 and above.

A within-subjects analysis of variance (ANOVA) was conducted on the logarithms of the F0DLs (as the standard deviation of the F0DLs was roughly proportional to the mean value of the F0DLs) with factors lowest harmonic number ($N=6$ to 15) and phase (cosine or alternating). Both main effects were significant: for harmonic number, $F(9,36)=24.59$, $p<0.001$; for phase, $F(1,4)=93.09$, $p<0.001$. The interaction of harmonic number and phase was also significant: $F(9,36)=2.64$, $p<0.02$. *Posthoc* tests of the effect of phase, using the least-significant-differences (LSD) test, showed no significant effect for $N=6$ or 7. The effect of phase was significant at $p<0.02$ for $N=10$ to 15 and significant at $p<0.001$ for $N=8$ and 9.

Bernstein and Oxenham (2003) also assessed the effect of component phase on F0 discrimination as a function of the number of the lowest harmonic in complex tones. In contrast to us, they did not find a significant effect of phase or a significant interaction of phase with harmonic number. This may be due to several differences between the experiments: (1) They compared sine phase and random phase rather than the cosine and alternating phase used by us. (2) They used complex tones with 12 components, which would have evoked activity over a range of places along the basilar membrane, with different waveforms at different places. (3) They tested different subjects for the sine-phase and random-phase conditions.

Our results are broadly consistent with those of Houtsma and Smurzynski (1990), although they found no phase effect (sine phase versus Schroeder negative phase) when N was 10 and a clear phase effect when N was 13 (no intermediate values were assessed). The lack of a phase effect for $N=10$ (while we found a clear effect) may have occurred because the waveform evoked on the basilar membrane by the com-

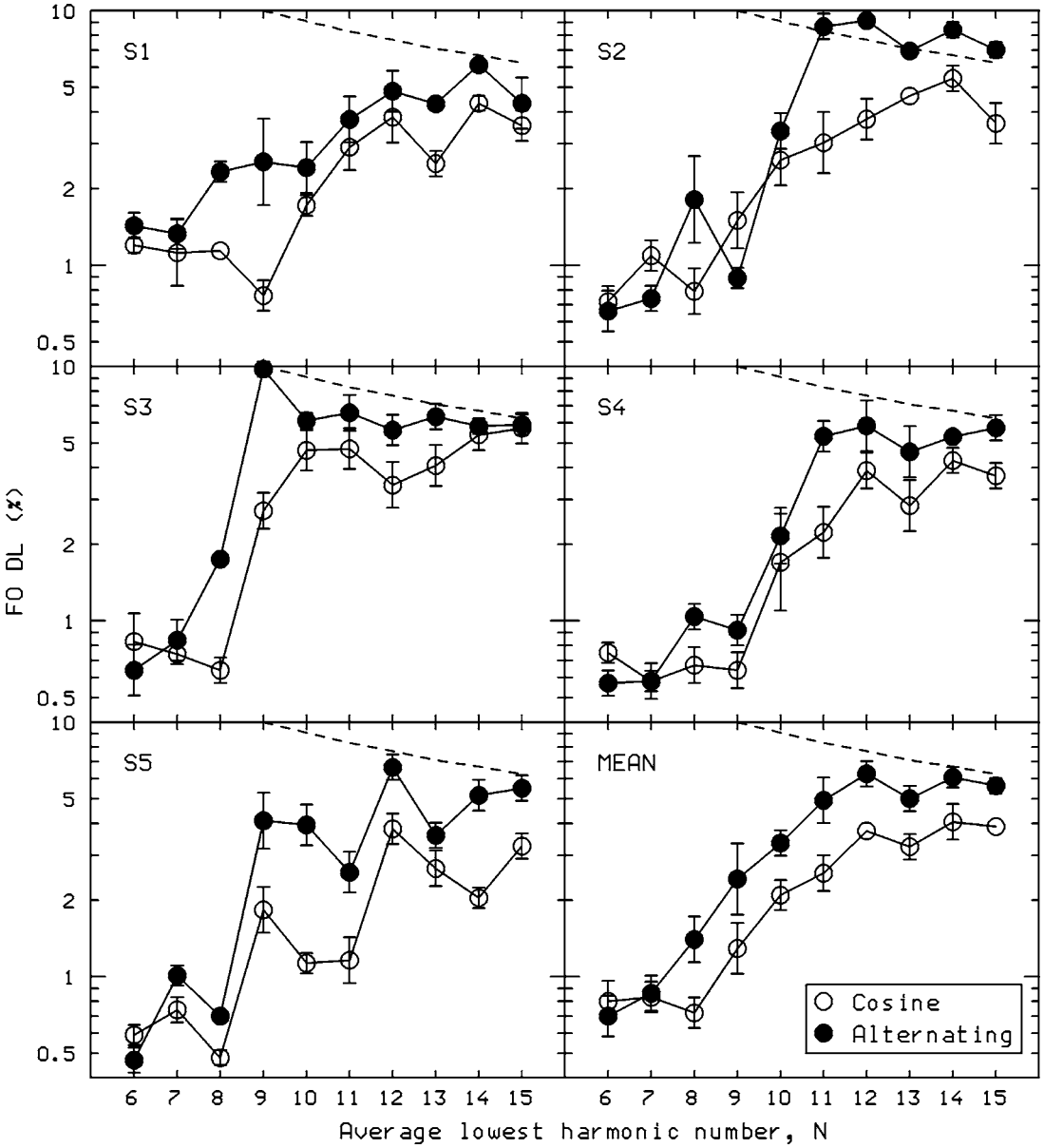

FIG. 2. Individual and mean (bottom-right) results for experiment 1 (harmonics centered at 2000 Hz). F0DLs, expressed as a percentage of $F0_c$, are plotted on a logarithmic scale as a function of the average number, N, of the lowest harmonic. Open and filled circles show results for components added in cosine phase and alternating phase, respectively. Error bars in the results for individual subjects show ± one standard error (SE) of the mean across repeated runs. Error bars in the mean results show ± one standard error (SE) of the mean across subjects. The dashed lines show the smallest F0DLs that could be achieved if performance were based on discrimination of the frequency of the lowest harmonic in the complex tones.

plex tone with components added in Schroeder negative phase probably still had distinct envelope peaks and dips, allowing effective use of temporal information (see the bottom-right trace in Fig. 1).

Our results are also broadly consistent with those of Bernstein and Oxenham (2005) for the "low" spectral region; they measured F0DLs for complex tones with many components added either in sine phase or random phase. However, they found a significant effect of phase only for $N>10$, whereas we found a significant effect for $N=8$ to 10. Again, the lack of a phase effect in their data for $N=10$ may have occurred because random phase was not optimal for minimizing the use of temporal information; with random phase and many harmonics there is a reasonable probability of a waveform with a high peak factor at some point along the basilar membrane.

For our data, the absence of a phase effect for low harmonic numbers ($N=6$ or 7) is as expected and is consistent with the assumption that harmonics up to about the fifth to eighth are resolved in the auditory system. However, F0DLs were smaller for cosine than for alternating phase once the number of the lowest harmonic was 8 or more, which suggests that the components were not resolved when N was 8 or more. The relatively small F0DLs for $N=8-11$, combined with the phase effect, and combined with earlier data showing a "pitch shift" effect for harmonic numbers in this range (Moore and Moore, 2003), lead to the interpretation that temporal fine structure plays a role in F0 discrimination for $N=8-11$.

One concern with these results is whether the subjects based their judgments on spectral differences between stimuli, rather than on the differences in F0. The randomiza-

tion of N by ±1 was intended to reduce the usefulness of spectral cues. However, when ΔF0 was large, spectral cues might still have been used. Consider the F0DLs that would be expected if subjects performed the task by comparing the frequency of the lowest harmonic in the tones across the two intervals in a forced-choice trial. As a limiting case, assume that this comparison could be made perfectly. Since harmonic $N+1$ was centered at 2000 Hz, the mean frequency separation between adjacent harmonics, $F0_c$, was equal to $2000/(N+1)$. For $\Delta F0 < F0_c$, a strategy of comparing the frequency of the lowest harmonic in the two tones within a trial would lead to only 6/9 (66.7%) correct,[1] which is well below the "target" of 79.4% correct tracked by the psychophysical procedure. However, for $\Delta F0 = F0_c$, the strategy would lead to 7/9 (77.8%) correct, and if ΔF0 were a little greater than $F0_c$, the strategy would lead to 8/9 (88.9%) correct, which is greater than the "target" of 79.4% correct. The dashed lines in Fig. 2 are defined by $\Delta F0 = F0_c$. If subjects based their decisions on the frequency of the lowest harmonic, and were perfectly able to discriminate the frequency of that harmonic, the measured F0DLs should lie slightly above the dashed line. Imperfect discrimination of the frequency of the lowest harmonic would lead to F0DLs further above the line.

For the cosine-phase stimuli, the F0DLs fall below the dashed line for all values of N for all subjects, indicating that subjects did not base their decisions on the frequency of the lowest harmonic. For the alternating-phase stimuli, the F0DLs fall well below the dashed line for low values of N, but for higher values of N the F0DLs approach and in one case (S2) lie above the dashed line. For alternating-phase stimuli with high N, subjects may have partly based decisions on the frequency of the lowest harmonic, possibly because the low pitch was very weak.

III. EXPERIMENT 2: CENTER FREQUENCY 5000 HZ

A. Rationale

The F0DLs measured in experiment 1 were smaller for cosine than for alternating phase even when N was high (14 or 15) and temporal fine structure information was probably not used (Hall *et al.*, 2003; Moore and Moore, 2003). Presumably, the phase effect for these high harmonics reflects the influence of phase on the envelopes of the waveforms on the basilar membrane. We have argued that the phase effect for N in the range 8–11 probably reflects the use of temporal fine structure cues. This argument is based on two facts: (1) performance was relatively good for $N=8-11$ and (2) pitch shift effects occur for harmonics in this range (Schouten *et al.*, 1962; Moore and Moore, 2003). However, it is difficult to be sure that temporal fine structure was involved. As a further way of assessing the role of temporal fine structure, as opposed to envelope cues, experiment 1 was repeated, but with the nominal center frequency shifted to 5000 Hz. At this frequency, phase locking is very weak (Palmer and Russell, 1986) and temporal fine structure information would probably be unusable.

B. Procedure, stimuli, and subjects

The procedure and stimuli were the same as for experiment 1, except that the nominal center frequency was 5000 Hz. The background threshold-equalizing noise used to mask combination tones had an upper cutoff frequency of 8000 Hz.

Five new subjects (four males and one female) were recruited for this experiment, all of whom were music students. Their ages ranged from 20 to 23 years. All subjects had absolute thresholds better than 20 dB over the range of audiometric frequencies from 250 to 8000 Hz. All subjects except author JA were paid for their services. Training was conducted in a similar way to that described for experiment 1.

C. Results and discussion

Figure 3 shows the results for each subject and the geometric mean across subjects (bottom-right panel). Results for the cosine-phase stimuli are shown by open circles and results for the alternating-phase stimuli are shown by filled circles. Note that the range of values on the ordinate is different for Figs. 2 and 3, reflecting the generally higher F0DLs when the center frequency was 5000 Hz. However, to facilitate comparison, the ratio of maximum to minimum values on the ordinate is the same for Figs. 2 and 3. The results of experiment 2 are somewhat more erratic than for experiment 1, although the mean results are fairly orderly. The pattern of results is very different from that found in experiment 1. It is also very different from that found by Bernstein and Oxenham (2005) for the "high" spectral region, probably because the high region in their experiment included the frequency range down to 3280 Hz, a frequency at which phase locking still occurs. For our data, F0DLs tended to decrease with increasing harmonic number, rather than to increase over the range $N=8-12$. The phase effect was smaller and less consistent than for experiment 1 and than found by Bernstein and Oxenham (2005) for the "high" spectral region. In the mean data for experiment 2 there is no phase effect for $N=6$ or 7, and a small but reasonably consistent phase effect for $N=9$ and above.

A within-subjects ANOVA was conducted on the logarithms of the F0DLs with factors lowest harmonic number ($N=6$ to 15) and phase (cosine or alternating). Both main effects were significant: for harmonic number, $F(9,36)=6.66$, $p<0.001$; for phase, $F(1,4)=29.82$, $p<0.01$. The interaction of harmonic number and phase was not significant: $F(9,36)=1.11$, $p>0.05$. *Posthoc* tests of the effect of phase, using the least-significant-differences (LSD), showed no significant effect for $N=6$, 7, 8, 12, 13, or 14. The effect of phase was significant at $p<0.05$ for $N=9$, 10, 11, and 15.

The dashed lines in Fig. 3 show the limit of performance that would be expected if subjects based decisions on the frequency of the lowest harmonic. For the cosine-phase stimuli, the F0DLs mostly fall below the dashed lines, indicating that performance was not based entirely on the frequency of the lowest harmonic; presumably information derived from the temporal envelope was used. However, for the alternating-phase stimuli and for $N>9$, the F0DLs often fell

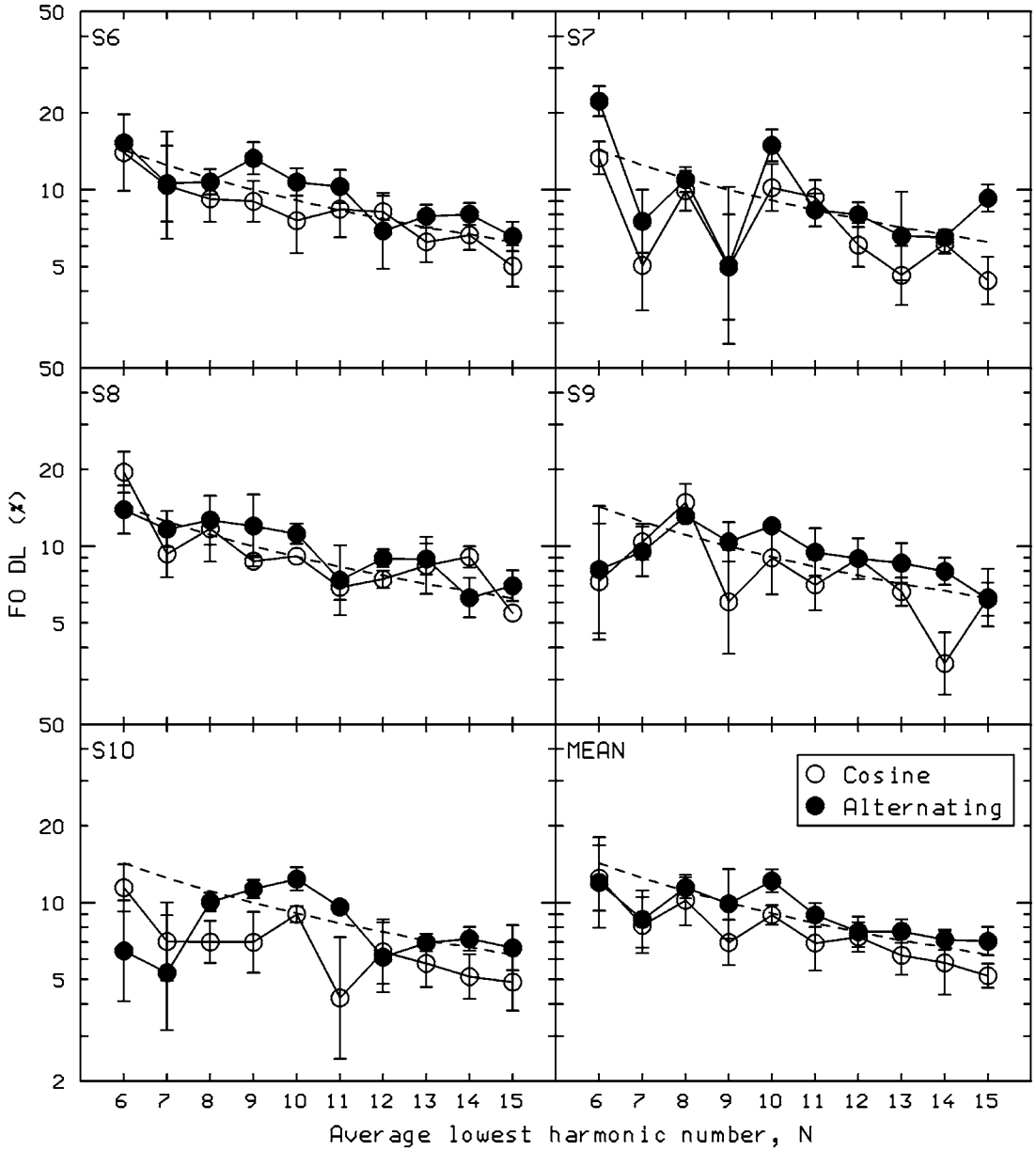

FIG. 3. As Fig. 2, but showing the results for experiment 2 (harmonics centered at 5000 Hz).

close to or a little above the dashed line, indicating that performance may have been based partly or exclusively on the frequency of the lowest harmonic. Possibly, the phase effect for high N would have been larger if this spectral cue had not been available.

The absence of a phase effect for $N=6$ or 7 suggests that the components in the complex tones were resolved for these values of N. Despite this, F0 discrimination was very poor, F0DLs being around 10%. This indicates that the presence of resolved harmonics is not sufficient to give good F0 discrimination. Rather, it appears that temporal information (phase locking) is required. This is consistent with previous work suggesting that the coding of the frequencies of individual components within complex tones (with harmonics below 5000 Hz) depends at least partly on temporal information (Moore *et al.*, 1984; Hartmann and Doty, 1996; de Cheveigné, 1999).

For $N=9$ or 10, there was a clear phase effect in experiment 2, but performance was much poorer than for experiment 1. This is consistent with our argument that the relatively good performance found in experiment 1 for intermediate harmonic numbers reflects the use of temporal fine structure information. When such information is not available (experiment 2), performance is much poorer. In experiment 2, the decrease in F0DLs with increasing N over the range 8–15 may reflect three effects. First, it may reflect the use of spectral cues, especially for the alternating-phase stimuli, as described above. Second, when spectral cues were not used, it may be connected with the salience of the distracting spectral changes produced by the randomization of N. As the mean value of N increased, the change in frequency of the lowest component produced by randomizing N by ±1 became smaller (for example a change by +1 for $N=8$ corresponds to a change in frequency of 555.6 Hz, whereas a change by +1 for $N=15$ corresponds to a change in frequency of 312.5 Hz). Hence, the distracting effect

would have decreased with increasing N. The third effect is connected with the influence of auditory filtering. For the higher values of N, all harmonics would be well within the passband of the auditory filter centered on the harmonics, and so the waveform at the output of the filter (equivalent to a specific place on the basilar membrane) would be minimally affected by the amplitude and phase response of the filter. For the lower values of N, the outer harmonics would lie closer to the edge of the passband of the filter, and the nonlinear phase response of the filter (Lentz and Leek, 2001; Oxenham and Dau, 2001) might lead to a reduction of the peak factor of the waveform at the output of the filter, at least for the cosine-phase stimuli. The reduced peak factor would impair the ability to extract the periodicity of the temporal envelope.

When the frequencies of the harmonics of a complex tone fall within the range where phase-locking information is available (as in experiment 1), F0DLs may be relatively small when low harmonics are present because the temporal information is relatively independent in different frequency channels. Each component produces maximum excitation at a different place on the basilar membrane, and the temporal information derived from each place is different from that at the other places. This helps to resolve ambiguities in the temporal information and leads to a clear estimate of F0 (Moore, 2003). In contrast, when only a few intermediate or high harmonics are present, the information carried in the interspike intervals is ambiguous. The waveform on the basilar membrane is not greatly different from the stimulus waveform, and there are several peaks in the temporal fine structure close to each envelope peak. Each of the peaks in the temporal fine structure has the potential to evoke nerve spikes. For such a stimulus, many different interspike intervals are present, only one of which corresponds to F0 (Javel, 1980; Cariani and Delgutte, 1996a, b). This leads to an ambiguous and unclear pitch. The ambiguity can be decreased by increasing the number of harmonics, which leads to distinctly different waveforms at different points along the basilar membrane and results in a clearer pitch (Houtsma and Smurzynski, 1990; Kaernbach and Bering, 2001).

The finding of a phase effect for $N=8$ and above when the center frequency was 2000 Hz appears to be inconsistent with the conclusion of Gibson (1970) and Bernstein and Oxenham (2003) that harmonics up to about the 10th or 11th are resolved for complex tones with F0=100 or 200 Hz, when those tones contain equal-amplitude successive harmonics. However, it is possible that harmonics with numbers in the range 8–11 are partially resolved, but still interact sufficiently to convey information about F0 in the temporal fine structure of the waveform on the basilar membrane. Thus, our finding of an effect of phase on F0 discrimination for $N=8-12$ does not necessarily rule out the possibility that harmonics in that range are resolved to a small extent. However, it is worth noting that, for the center frequency of 2000 Hz, the effects of phase on the F0DLs were at least as large for $N=8$ and 9 as for higher values of N. This suggests that the components were already interacting strongly for $N=8$ and 9. It is worth considering, therefore, whether the task used by Bernstein and Oxenham (2003) provides a good measure of harmonic resolvability.

Bernstein and Oxenham used a task similar to that of Moore and Ohgushi (1993) in which subjects heard a pure tone followed by a complex tone and were asked to indicate whether the pure tone was higher or lower in frequency than a comparison tone contained within the complex. However, unlike the task used Moore and Ohgushi, Bernstein and Oxenham pulsed the comparison tone on and off, while the other components in the complex tone were presented as a single longer burst. The pulsing of the comparison tone was intended to promote the segregation of the comparison tone from the other components in the complex. However, it may have had other effects, for example producing a release from adaptation to the comparison tone [Viemeister and Bacon (1982); note, however, that Bernstein and Oxenham argued that release from adaptation should not affect peripheral resolvability]. In any case, pulsing a component within a complex tone on and off will produce a change in the basilar-membrane waveform at the place tuned to the pulsed harmonic, and this may lead to the percept of a change in that frequency region. This may have been sufficient to allow subjects to perform the task of Bernstein and Oxenham even when the pulsed harmonic was not actually resolved.

We have argued that, for N in the range 8–11, subjects are able to use information related to the temporal fine structure of the stimuli, whereas for very high N (14 or 15) only envelope information or spectral cues are available. A possible explanation for the loss of temporal fine structure information with increasing N is related to the precision with which interspike intervals in a given neuron can be measured by the auditory system. It seems reasonable to assume that this precision follows Weber's law, i.e., a given interspike interval, t, can be measured with a standard deviation, $\sigma(t)$, which is proportional to t. Consider the temporal pattern of neural spikes evoked by a complex tone with F0=200 Hz and with three harmonics centered at 2000 Hz. There will be many interspike intervals close to 5 ms (the true period), and there will be other intervals corresponding to 5 ± 0.5 ms, e.g., 4, 4.5, 5.5, and 6 ms (Javel, 1980; Cariani and Delgutte, 1996a, b). Provided that $\sigma(t)$ is less than about $0.05t$, it will be possible for the auditory system to extract the interval, t, corresponding to 5 ms. Assume now that the F0 is decreased to 125 Hz, keeping the center frequency the same. Now the true period is 8 ms, and there will be competing intervals such as 7, 7.5, 8.5, and 9 ms. If $\sigma(t)$ is only a little less than $0.05t$, the standard deviation $\sigma(t)$ associated with the estimation of the interval of 8 ms will exceed 0.25 ms. In this case, the auditory system will no longer reliably be able to distinguish the interval of 8 ms from the nearby intervals of 7.5 and 8.5 ms; temporal fine structure information will be lost and only envelope information will remain.

IV. CONCLUSIONS

(1) For complex tones whose lowest harmonic number, N, was 6 or 7, F0DLs were independent of component phase, consistent with the idea that the harmonics for

such tones are resolved in the auditory system. F0DLs for such tones were small (around 0.8%) when the harmonics were centered at 2000 Hz (experiment 1) but were relatively large (around 10%) when the harmonics were centered at 5000 Hz. This suggests that the presence of resolved harmonics is not sufficient to give good F0 discrimination. Rather, temporal information (phase locking) is required.

(2) For complex tones whose lowest harmonic number, N, was in the range 8–11, F0DLs were smaller when the components were added in cosine phase than when they were added in alternating phase. This is consistent with the idea that the harmonics were not resolved and that F0DLs depended on temporal information. When the harmonics were centered at 2000 Hz, F0DLs increased as N was increased from 8 to 12. This is consistent with a progressive loss of temporal fine structure information over this range. When the harmonics were centered at 5000 Hz, F0DLs decreased slightly as N was increased from 8 to 12. This is consistent with the absence of temporal fine structure information at this center frequency, forcing subjects to rely solely on envelope cues or spectral cues.

ACKNOWLEDGMENTS

This work was supported by the Medical Research Council (UK) and by the Grindley Fund. We thank Bob Carlyon and Hedwig Gockel for helpful discussions and Tom Baer, Hedwig Gockel, John Grose, Christian Kaernbach, and an anonymous reviewer for helpful comments on an earlier version of this paper.

[1]This footnote derives the proportion correct that would be achieved for different values of ΔF0, assuming that judgments were based on the change in frequency of the lowest harmonic, and that discrimination of the frequency of that harmonic was perfect. In any given trial, there were three possible values of N for each stimulus (randomly drawn from $N_{\text{nom}}-1$, N_{nom}, and $N_{\text{nom}}+1$, where N_{nom} is the nominal value of N), and nine possible combinations of N for the two stimuli in a trial. For three of those combinations, N was the same for the two stimuli in a trial, so subjects would score perfectly. For another three combinations, the frequency shift produced by the change in N would be in the same direction as the frequency shift produced by the change in F0, so subjects would again score perfectly. We consider next the outcomes for the remaining three combinations, for three ranges of ΔF0.

(1) $\Delta F0 < F0_c$: subjects would be consistently wrong. Hence, the overall proportion correct is $(3+3)/9=6/9$.

(2) $\Delta F0 = F0_c$: for two of the combinations, the frequency shift produced by the change in N would exactly cancel the frequency shift produced by the change in F0, and subjects would guess and score 50% correct on average. For the final combination (corresponding to a difference in N of 2 across stimuli), subjects would be consistently wrong. Hence, the overall proportion correct is $(3+3+(0.5\times2))/9=7/9$.

(3) $\Delta F0 > F0_c$ but $< 2F0_c$: for two of the combinations, the frequency shift produced by the change in N would be smaller than the frequency shift produced by the change in F0, and subjects would score perfectly. For the final combination (corresponding to a difference in N of 2 across stimuli), subjects would be consistently wrong. Hence, the overall proportion correct is $(3+3+2)/9=8/9$.

Alcántara, J. I., Moore, B. C. J., Glasberg, B. R., Wilkinson, A. J. K., and Jorasz, U. (**2003**). "Phase effects in masking: Within-versus across-channel processes," J. Acoust. Soc. Am. **114**, 2158–2166.

Bernstein, J. G., and Oxenham, A. J. (**2003**). "Pitch discrimination of diotic and dichotic tone complexes: harmonic resolvability or harmonic number?" J. Acoust. Soc. Am. **113**, 3323–3334.

Bernstein, J. G., and Oxenham, A. J. (**2005**). "An autocorrelation model with place dependence to account for the effect of harmonic number on fundamental frequency discrimination," J. Acoust. Soc. Am. **117**, 3816–3831.

Cariani, P. A., and Delgutte, B. (**1996a**). "Neural correlates of the pitch of complex tones. I. Pitch and pitch salience," J. Neurophysiol. **76**, 1698–1716.

Cariani, P. A., and Delgutte, B. (**1996b**). "Neural correlates of the pitch of complex tones. II. Pitch shift, pitch ambiguity, phase invariance, pitch circularity, rate pitch and the dominance region for pitch," J. Neurophysiol. **76**, 1717–1734.

Carlyon, R. P., and Shackleton, T. M. (**1994**). "Comparing the fundamental frequencies of resolved and unresolved harmonics: Evidence for two pitch mechanisms?," J. Acoust. Soc. Am. **95**, 3541–3554.

de Boer, E. (1956). "On the "residue" in hearing," Ph.D. thesis, University of Amsterdam.

de Cheveigné, A. (**1999**). "Pitch shifts of mistuned partials: A time-domain model," J. Acoust. Soc. Am. **106**, 887–897.

Gibson, L. (1970). "The ear as an analyzer of musical tones," 80th Meeting of the Acoustical Society of America p. 63.

Glasberg, B. R., and Moore, B. C. J. (**1990**). "Derivation of auditory filter shapes from notched-noise data," Hear. Res. **47**, 103–138.

Goldstein, J. L. (**1973**). "An optimum processor theory for the central formation of the pitch of complex tones," J. Acoust. Soc. Am. **54**, 1496–1516.

Hall, J. W., Buss, E., and Grose, J. H. (**2003**). "Modulation rate discrimination for unresolved components: temporal cues related to fine structure and envelope," J. Acoust. Soc. Am. **113**, 986–993.

Hartmann, W. M., and Doty, S. L. (**1996**). "On the pitches of the components of a complex tone," J. Acoust. Soc. Am. **99**, 567–578.

Hoekstra, A., and Ritsma, R. J. (**1977**). "Perceptive hearing loss and frequency selectivity," in *Psychophysics and Physiology of Hearing*, edited by E. F. Evans and J. P. Wilson (Academic, London).

Houtsma, A. J. M., and Smurzynski, J. (**1990**). "Pitch identification and discrimination for complex tones with many harmonics," J. Acoust. Soc. Am. **87**, 304–310.

Javel, E. (**1980**). "Coding of AM tones in the chinchilla auditory nerve: Implications for the pitch of complex tones," J. Acoust. Soc. Am. **68**, 133–146.

Kaernbach, C., and Bering, C. (**2001**). "Exploring the temporal mechanism involved in the pitch of unresolved harmonics," J. Acoust. Soc. Am. **110**, 1039–1048.

Lentz, J. J., and Leek, M. R. (**2001**). "Psychophysical estimates of cochlear phase response: masking by harmonic complexes," J. Assoc. Res. Otolaryngol. **2**, 408–422.

Levitt, H. (**1971**). "Transformed up-down methods in psychoacoustics," J. Acoust. Soc. Am. **49**, 467–477.

Licklider, J. C. R. (**1956**). "Auditory frequency analysis," in *Information Theory*, edited by C. Cherry (Academic, New York).

Meddis, R., and Hewitt, M. (**1991**). "Virtual pitch and phase sensitivity of a computer model of the auditory periphery. I. Pitch identification," J. Acoust. Soc. Am. **89**, 2866–2882.

Meddis, R., and O'Mard, L. (**1997**). "A unitary model of pitch perception," J. Acoust. Soc. Am. **102**, 1811–1820.

Moore, B. C. J. (**1973**). "Frequency difference limens for short-duration tones," J. Acoust. Soc. Am. **54**, 610–619.

Moore, B. C. J. (**1977**). "Effects of relative phase of the components on the pitch of three-component complex tones," in *Psychophysics and Physiology of Hearing*, edited by E. F. Evans and J. P. Wilson (Academic, London).

Moore, B. C. J. (**1982**). *An Introduction to the Psychology of Hearing*, *2nd Ed.* (Academic, London).

Moore, B. C. J. (**2003**). *An Introduction to the Psychology of Hearing*, *5th Ed.* (Academic, San Diego).

Moore, B. C. J., and Glasberg, B. R. (**1988**). "Effects of the relative phase of the components on the pitch discrimination of complex tones by subjects with unilateral and bilateral cochlear impairments," in *Basic Issues in Hearing*, edited by H. Duifhuis, H. Wit, and J. Horst (Academic, London).

Moore, B. C. J., and Ohgushi, K. (**1993**). "Audibility of partials in inharmonic complex tones," J. Acoust. Soc. Am. **93**, 452–461.

Moore, B. C. J., and Rosen, S. M. (**1979**). "Tune recognition with reduced

pitch and interval information," Q. J. Exp. Psychol. **31**, 229–240.
Moore, B. C. J., Glasberg, B. R., and Shailer, M. J. (**1984**). "Frequency and intensity difference limens for harmonics within complex tones," J. Acoust. Soc. Am. **75**, 550–561.
Moore, B. C. J., Huss, M., Vickers, D. A., Glasberg, B. R., and Alcántara, J. I. (**2000**). "A test for the diagnosis of dead regions in the cochlea," Br. J. Audiol. **34**, 205–224.
Moore, G. A., and Moore, B. C. J. (**2003**). "Perception of the low pitch of frequency-shifted complexes," J. Acoust. Soc. Am. **113**, 977–985.
Oxenham, A. J., and Dau, T. (**2001**). "Towards a measure of auditory-filter phase response," J. Acoust. Soc. Am. **110**, 3169–3178.
Palmer, A. R., and Russell, I. J. (**1986**). "Phase-locking in the cochlear nerve of the guinea-pig and its relation to the receptor potential of inner hair-cells," Hear. Res. **24**, 1–15.
Patterson, R. D. (**1973**). "The effects of relative phase and the number of components on residue pitch," J. Acoust. Soc. Am. **53**, 1565–1572.
Patterson, R. D. (**1987**). "A pulse ribbon model of monaural phase perception," J. Acoust. Soc. Am. **82**, 1560–1586.
Plomp, R. (**1964**). "The ear as a frequency analyzer," J. Acoust. Soc. Am. **36**, 1628–1636.
Plomp, R., and Mimpen, A. M. (**1968**). "The ear as a frequency analyzer II," J. Acoust. Soc. Am. **43**, 764–767.
Ritsma, R. J. (**1962**). "Existence region of the tonal residue. I.," J. Acoust. Soc. Am. **34**, 1224–1229.
Ritsma, R. J. (**1963**). "Existence region of the tonal residue. II.," J. Acoust. Soc. Am. **35**, 1241–1245.
Schouten, J. F. (**1940**). "The residue and the mechanism of hearing," Proc. K. Ned. Akad. Wet. **43**, 991–999.
Schouten, J. F., Ritsma, R. J., and Cardozo, B. L. (**1962**). "Pitch of the residue," J. Acoust. Soc. Am. **34**, 1418–1424.
Schroeder, M. R. (**1970**). "Synthesis of low peak-factor signals and binary sequences with low autocorrelation," IEEE Trans. Inf. Theory **IT-16**, 85–89.
Shackleton, T. M., and Carlyon, R. P. (**1994**). "The role of resolved and unresolved harmonics in pitch perception and frequency modulation discrimination," J. Acoust. Soc. Am. **95**, 3529–3540.
Shamma, S., and Klein, D. (**2000**). "The case of the missing pitch templates: how harmonic templates emerge in the early auditory system," J. Acoust. Soc. Am. **107**, 2631–2644.
Shamma, S. A. (**1985**). "Speech processing in the auditory system II: Lateral inhibition and the central processing of speech evoked activity in the auditory nerve," J. Acoust. Soc. Am. **78**, 1622–1632.
Srulovicz, P., and Goldstein, J. L. (**1983**). "A central spectrum model: a synthesis of auditory-nerve timing and place cues in monaural communication of frequency spectrum," J. Acoust. Soc. Am. **73**, 1266–1276.
Terhardt, E. (**1974**). "Pitch, consonance, and harmony," J. Acoust. Soc. Am. **55**, 1061–1069.
Thurlow, W. R. (**1963**). "Perception of low auditory pitch: a multicue mediation theory," Psychol. Rev. **70**, 461–470.
van Noorden, L. P. A. S. (**1982**). "Two-channel pitch perception," in *Music, Mind and Brain*, edited by M. Clynes (Plenum, New York).
Viemeister, N. F., and Bacon, S. P. (**1982**). "Forward masking by enhanced components in harmonic complexes," J. Acoust. Soc. Am. **71**, 1502–1507.

Factors affecting the use of noise-band vocoders as acoustic models for pitch perception in cochlear implants

Johan Laneau[a)]
Laboratory for Experimental ORL, K.U.Leuven, Kapucijnenvoer 33, B 3000 Leuven, Belgium

Marc Moonen
ESAT-SCD, K.U.Leuven, Kasteelpark Arenberg 10, B 3001 Leuven, Belgium

Jan Wouters
Laboratory for Experimental ORL, K.U.Leuven, Kapucijnenvoer 33, B 3000 Leuven, Belgium

(Received 30 June 2004; revised 10 October 2005; accepted 11 October 2005)

Although in a number of experiments noise-band vocoders have been shown to provide acoustic models for speech perception in cochlear implants (CI), the present study assesses in four experiments whether and under what limitations noise-band vocoders can be used as an acoustic model for pitch perception in CI. The first two experiments examine the effect of spectral smearing on simulated electrode discrimination and fundamental frequency (F0) discrimination. The third experiment assesses the effect of spectral mismatch in an F0-discrimination task with two different vocoders. The fourth experiment investigates the effect of amplitude compression on modulation rate discrimination. For each experiment, the results obtained from normal-hearing subjects presented with vocoded stimuli are compared to results obtained directly from CI recipients. The results show that place pitch sensitivity drops with increased spectral smearing and that place pitch cues for multi-channel stimuli can adequately be mimicked when the discriminability of adjacent channels is adjusted by varying the spectral slopes to match that of CI subjects. The results also indicate that temporal pitch sensitivity is limited for noise-band carriers with low center frequencies and that the absence of a compression function in the vocoder might alter the saliency of the temporal pitch cues. [DOI: 10.1121/1.2133391]

PACS number(s): 43.66.Hg, 43.66.Ts, 43.66.Fe [RAL] Pages: 491–506

I. INTRODUCTION

Previous studies have shown that noise-band vocoders can be used as an acoustic model for speech perception in cochlear implants (Blamey *et al.*, 1984b; Dorman and Loizou, 1997, 1998; Friesen *et al.*, 2001; Nelson *et al.*, 2003). These studies have indicated that at least good qualitative agreement exists between the model results and the results obtained from cochlear implant (CI) subjects as long as the number of channels is below eight. More recently, several studies have used noise-band vocoders to study pitch perception in CI (Green *et al.*, 2002) or pitch-related tasks (Fu *et al.*, 1998; Faulkner *et al.*, 2000; Xu *et al.*, 2002; Kong *et al.*, 2004). However, it is generally unknown whether noise-band vocoders provide a valid acoustic model to study pitch perception in CI. It has been shown that speech perception relies on different mechanisms than pitch perception (Smith *et al.*, 2002). Smith *et al.* showed that while speech perception is mostly based upon envelope information in broad frequency bands, pitch perception is based upon the fine structure within every frequency band. The principal goal of the present study was to assess the validity of noise-band vocoders as acoustic models for pitch perception in CI subjects. Valid models are defined here as models for which the average pitch discrimination performance does not differ significantly from the average performance obtained from CI subjects on any of a number of different tasks. In order to find such a model, pitch discrimination results from post-lingual CI subjects are compared to results from normal-hearing (NH) subjects listening to noise-band vocoder processed signals for different parameters of the noise-band vocoder.

There are several benefits of using acoustic models in parallel to performing experiments directly with cochlear implant recipients. First, the results obtained from cochlear implant patients are generally more prone to inter- and intra-subject variability (Friesen *et al.*, 2001). Possible reasons for this higher variability might be the different etiologies of the patients, differences in duration of auditory deprivation leading to various amounts of degeneration of the auditory functions, and the high variability in peripheral processes, such as neural excitation profiles, between subjects and even within subjects. A second benefit of using acoustic models is the fact that in acoustic models most of the parameters can be changed independently, whereas in cochlear implant patients some these factors are fixed, such as width of excitation pattern or implant insertion depth. Third, comparing the results of NH subjects using acoustic models, on the one hand, and cochlear implant patients, on the other hand, reveals some details of the basic functioning of the auditory system. Basic mechanisms of the auditory system can be more solidly founded when the results in electrical and acoustical hearing reveal the same trends (Carlyon *et al.*, 2002). Fourth, com-

[a)]Electronic mail: johan.laneau@philips.com

paring results obtained through acoustic models and results obtained directly from CI recipients also allows indicating the cause of limitations in CI recipients' performance. Finally, there is a practical benefit to acoustic models because the pool of NH subjects is vastly more extended than the pool of CI subjects, and research interfaces to stimulate acoustically are more easily available than research interfaces to stimulate implants directly.

Previously several acoustic models have been developed and used to study pitch perception in cochlear implants through NH subjects. First, noise-band vocoders are most often used (Fu *et al.*, 1998; Faulkner *et al.*, 2000; Green *et al.*, 2002; Xu *et al.*, 2002; Kong *et al.*, 2004) because temporal and place pitch cues appear to be accurately modeled. Modulation of noise carriers elicits weak purely temporal pitch percepts that correspond to the modulation frequency (Burns and Viemeister, 1976). Moreover, the difference limens in rate discrimination for CI resemble the modulation rate discrimination of noise carriers as a function of frequency (Shannon, 1983a; Blamey *et al.*, 1984a). Furthermore, the place pitch cues can be modeled by changing the center frequency of the noise band because the pitch of a steady-state noise band corresponds approximately to its center frequency (Stover and Feth, 1983; Dai *et al.*, 1996; Zwicker and Fastl, 1999).

Whereas noise-band vocoder signals sound very stochastic, CI subjects never define the perceived sound as noisy but rather qualify the perceived sound of single channels as beeps. To accommodate for this fact a second acoustic model was developed that uses pure tones as carriers for the different channels in the resynthesis of the vocoder (Dorman *et al.*, 1997). More recently, such a vocoder was used to study the pitch perception through discrimination of lexical tones for two different sound processing schemes (Lan *et al.*, 2004). The sinusoidal vocoder might be less accurate in modeling pitch perception in CI because adjacent channels are extremely well discriminable in the model while in general CI subjects can have problems discriminating adjacent channels (Nelson *et al.*, 1995). Furthermore, amplitude modulation of a pure-tone carrier generates sidebands which can be detected when the sidebands are spaced wide enough to be resolved by the peripheral filters of the normal ear (Kohlrausch *et al.*, 2000), while this is impossible in CI subjects.

A third acoustic model was proposed to study the purely temporal pitch percepts and uses harmonic complexes that are band-pass filtered in relatively high-frequency regions so that all harmonics are unresolved (McKay and Carlyon, 1999; Carlyon *et al.*, 2002; van Wieringen *et al.*, 2003; Deeks and Carlyon, 2004). Using this scheme place and temporal pitch cues can be adjusted independently by varying the center frequency of the band-pass filter and the fundamental frequency of the harmonic complex, respectively. However, the model is restricted to lower pulse rates because for higher pulse rates the harmonics become resolved.

The present study examines the factors that affect the use of a noise-band vocoder as an acoustic model of pitch perception in CI. Four experiments are described. The first two experiments examine the effect of spectral smearing on pitch perception of noise-band vocoded signals in NH subjects. These experiments focus on spectral or mimicked place pitch cues. The amount of spectral smearing is changed by varying the spectral slope of the noise bands in the vocoder. The first experiment (experiment 1) assesses center frequency discrimination for noise bands, simulating electrode discrimination. The second experiment (experiment 2) measures fundamental frequency (F0) discrimination. In the third experiment (experiment 3) F0-discrimination results for postlingually deafened CI subjects from Laneau *et al.* (2004) are compared to F0-discrimination results for NH subjects for two different vocoders to assess the effect of spectral mismatch. Both temporal and place pitch cues are evaluated in this experiment. In the last experiment (experiment 4) the effect of the absence of amplitude compression in the vocoder is assessed on modulation rate discrimination, focusing on temporal pitch discrimination.

II. EXPERIMENT 1: THE EFFECT OF SPECTRAL SMEARING ON SIMULATED ELECTRODE DISCRIMINATION

A. Subjects

Five NH subjects (S1–S5) aged between 24 and 39 participated in this and all further experiments of the presented study. All subjects were members of the departmental staff and one subject was the first author of this paper. All subjects had experience in psychophysical studies with similar stimuli.

The results of the NH subjects will be compared to the results of four adult postlingually deafened CI subjects that performed equivalent tasks. The results of the CI subjects have been reported in Laneau and Wouters (2004). All CI subjects were implanted with the Nucleus CI24 implant and were relatively good performers. Some of the subjects' relevant details can be found in Table I. Although some subjects had relatively short implant experience, their pitch discrimination performance was expected to asymptote because they already participated in previous psychophysical studies assessing pitch perception including training sessions.

B. Presentation

In this and all further experiments of the present study, the acoustical stimuli were routed via a desktop PC and a 24-bit PCI sound card (Lynx ONE, Lynx Studio Technology) to a mixer-amplifier (Eurorack MX1604A) and played to the right earpiece of a TDH39 headphone. The APEX program controlled stimulus playback and response collection (Geurts and Wouters, 2000). The attenuated intensity of the stimuli was adjusted to be at a comfortable level, which in most cases was approximately 70 dB SPL. The subjects were seated in a double-walled soundproof booth.

C. Methods

Simulated place pitch discrimination was measured using the acoustical analogy of electrode discrimination based on a noise-band vocoder: center frequency discrimination for

TABLE I. Relevant information about each of the CI subjects who participated in the experiments.

Subject	Duration of profound deafness (years)	Etiology	Speech processor	Clinical speech processing strategy	Age (years)	Implant experience (year;month)
CI1	11	Hereditary	ESPrit	Speak	19	1;11
CI2	3	Unknown	ESPrit	Speak	21	3;2
CI3	30	Progressive	SPrint	ACE	54	0;8
CI4	32	Progressive	ESPrit 3G	ACE	49	0;6

noise bands. The center frequency discrimination was assessed as a function of the slope of the noise bands and at two different reference center frequencies.

Stimuli consisted of white noise filtered with a custom designed filter. This filter (CISIM filter) is loosely based upon the physiology of electrical stimulation through a cochlear implant. The center frequency of the filter is set to the frequency corresponding to the cochlear location of a simulated electrode. The shape of the frequency response of the filter is designed to mimic the exponential decay of current density along the basilar membrane (Black and Clark, 1980). The magnitude of the desired frequency response of the CISIM filter was thus set to decay exponentially with increasing distance between the characteristic point corresponding to the frequency and the position of the stimulating electrode. The space constant of the exponential decay (λ) and the position of the simulated electrode ($x_{\text{electrode}}$) are two free parameters. Consequently the desired frequency response of the CISIM filter is given by

$$F_{\text{CISIM}}(x(f)) = \exp\left(\frac{-|x_{\text{electrode}} - x(f)|}{\lambda}\right). \quad (1)$$

The conversion of distance along the cochlea to frequency $x(f)$ was done using Greenwood's formula (1990). The desired frequency response was calculated for 400 frequencies spaced equidistantly from 1 to 34 mm, assuming a 35-mm cochlea. The obtained desired frequency response was approximated using a 150-tap linear phase FIR filter using the FIR2 command in Matlab.

Center frequency discrimination was measured at two reference center frequencies 565 and 2643 Hz (corresponding to cochlear locations of 10.75 and 20.5 mm; cochlear length is expressed from apex to base and assuming a 35-mm cochlea), and for ten different space constants: $\lambda = 0.5$, 0.67, 1, 1.33, 2, 2.5, 3.33, 5, 10, and 20 mm. Stimuli were 500 ms long including 10-ms linear on- and off-ramps and were sampled at 20 kHz.

Discrimination was measured using a two-interval two-alternative forced choice (2I-2AFC) constant stimuli paradigm. The subjects were presented with a reference and a comparison stimulus in random order, and they were asked to indicate the highest in pitch. The center frequency of the reference stimulus corresponded to one of the two reference center frequencies tested. The center frequency of the comparison stimulus was higher than that of the reference stimulus, corresponding to a shift towards the base of the cochlea. For space constants (λ) of 2 mm up to 20 mm three comparison stimuli were used with cochlear locations (corresponding to their center frequencies) shifted 0.75, 1.5, or 2.25 mm towards the base from the cochlear location of the reference stimulus. This corresponds to shifts of one, two, or three electrodes in the Nucleus CI24 device. For space constants (λ) of 0.5 up to 1.33 mm, five comparison stimuli were used and the shifts were 0.1875, 0.375, 0.5625, 0.75, or 1.5 mm towards the base. This corresponds to shifts of $\frac{1}{4}$, $\frac{1}{2}$, $\frac{3}{4}$, 1, or 2 electrodes in the Nucleus CI24 device. Note that a shift of 0.75 mm corresponds to a relative change of center frequency of approximately 12% and that the relative center frequency is roughly proportional to the shift. The intensity of the stimuli was randomly attenuated over a 20-dB range to minimize loudness cues. No feedback was presented to the subjects.

The trials were presented in blocks. Each block contained trials for a given space constant and for both reference center frequencies. Every trial was repeated ten times per block, and this led to 60 or 100 trials per block for space constants greater or smaller than 2 mm, respectively. Every block was presented twice to the subjects; hence every subject was presented 20 blocks.

Just noticeable differences (jnd's) of simulated electrode position were estimated for each combination of reference center frequency and space constant. Using a nonlinear least squares fitting routine, a normal cumulative distribution function was fitted to the average proportion of trials where the comparison stimulus was indicated as higher than the reference stimulus as a function of distance between cochlear locations of comparison and reference stimulus. The jnd was set to the distance that resulted in a proportion of 75% correct according to the fitted curve. If the listener could not perform the task, the discrimination threshold was arbitrarily set to 75 mm for the statistical analysis. This procedure is identical to that used in Laneau and Wouters (2004).

D. Results and discussion

Figure 1 shows the average jnd's (expressed in mm) of the subjects as a function of the space constant for both reference center frequencies. The logarithms of the jnd's were used for averaging and to obtain a normal distribution for the statistical analysis.

A repeated measures analysis of variance (ANOVA) was performed on the logarithms of the estimated jnd data with

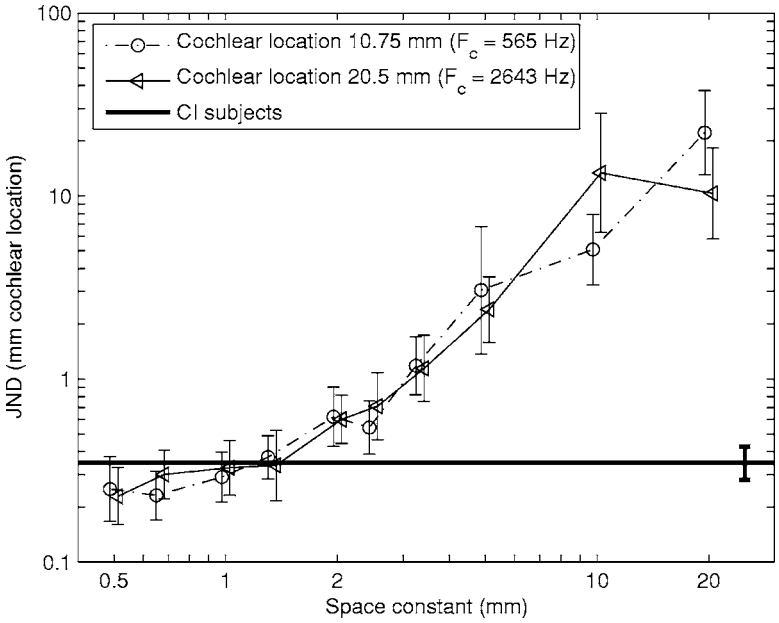

FIG. 1. Results for simulated electrode discrimination using the CISIM filter. Electrode discrimination was simulated by discrimination of center frequency of noise bands. Just noticeable differences were estimated as a function of the spectral overlap between the noise bands and expressed as distance shift in cochlear position. As the space constant decreases, the noise bands become narrower with less overlap, and the discrimination improves. The error bars indicate ±1 standard error of the mean of the intersubject variability. There was no significant difference between the two simulated insertion depths. The average result of electrode discrimination of four Nucleus CI24 subjects as measured in a separate study (Laneau and Wouters, 2004) is added with the horizontal solid line. The standard error of the mean for the CI subjects is approximately 0.07 electrodes.

the reference center frequency and the space constant as factors. There was a significant effect of space constant ($p = 0.002$). No other effects were significant.

The variation of jnd as a function of space constant is qualitatively equivalent to the resonance frequency discrimination of filtered noise (Gagne and Zurek, 1988). Gagne and Zurek found that when the Q factor of the noise-shaping filter was decreased, the center frequency discrimination was impaired. Similarly in the present experiment, increasing the space constant resulted in an increase of place pitch jnd's. Gagne and Zurek also found that the difference limen expressed relative to the center frequency is roughly constant when the Q factor or spectral slope was held constant. This is also found in the present study in that there is no difference between the results obtained at both reference center frequencies and noting that a shift in cochlear position corresponds to a constant relative frequency difference.

The jnd's measured by Gagne and Zurek are, however, significantly smaller than the jnd's obtained in the present study, especially for large space constants. (In comparing the jnd's, the d' values derived from the jnd's of both studies were assumed to vary linearly with distance along the basilar membrane.) For the larger space constants it is, however, hard to compare the two filter shapes, since for low values of Q the resonance filters of Gagne and Zurek become low-pass filters with a steeper slope compared to the slopes of the filters of the present study. Part of the lower sensitivity in the present study is also most probably due to the relatively large range of intensity roving in the present study while Gagne and Zurek did not rove the intensity of their stimuli. Also differences between subjects of the two studies might have contributed to the lower sensitivity reported in the present study. In the present study a large variability in subjects' performance is observed (see Fig. 1 and below) which is mainly caused by the performance of two NH subjects performing relatively poorly on pitch discrimination (see experiment 4).

Using the present custom-made CISIM filter there was no difference in place pitch sensitivity across reference center frequency or equivalent simulated electrode position. Similarly, in cochlear implants place pitch sensitivity is not significantly different at different electrode locations (Nelson *et al.*, 1995).

The place pitch discrimination of the CI subjects was measured in Laneau and Wouters (2004). In this study, electrode discrimination was measured for single- and multichannel stimuli. The experimental procedure was very similar to the procedure used for the present simulated electrode discrimination experiment. In the cochlear implant experiment it was, however, impossible to change the space constant (λ) of the decay of the excitation pattern. The average jnd for electrode discrimination of the four CI subjects is added as a solid horizontal line to Fig. 1 for comparison. The average performance of the NH subjects matches the average CI performance for a space constant of approximately 1 mm. Note that the filter designed based on a space constant of 1 mm has relatively steep slopes of approximately 40 dB/oct.

III. EXPERIMENT 2: THE EFFECT OF SPECTRAL SMEARING ON F0 DISCRIMINATION

In experiment 2, F0 discrimination of stylized synthetic vowels was measured in NH subjects for different amounts of spectral smearing in the noise-band vocoder. The vocoder processing was designed such that only spectral pitch (or mimicked place pitch) cues were useful for the subject. The subjects and equipment for stimulus presentation were the same as in experiment 1.

A. Methods

1. Stimuli

The stimuli consisted of stylized vowels processed with a noise-band vocoder. The unprocessed stylized vowels were a subset of the original stimuli used in the comparison study (Laneau *et al.*, 2004). Stylized vowels were generated by

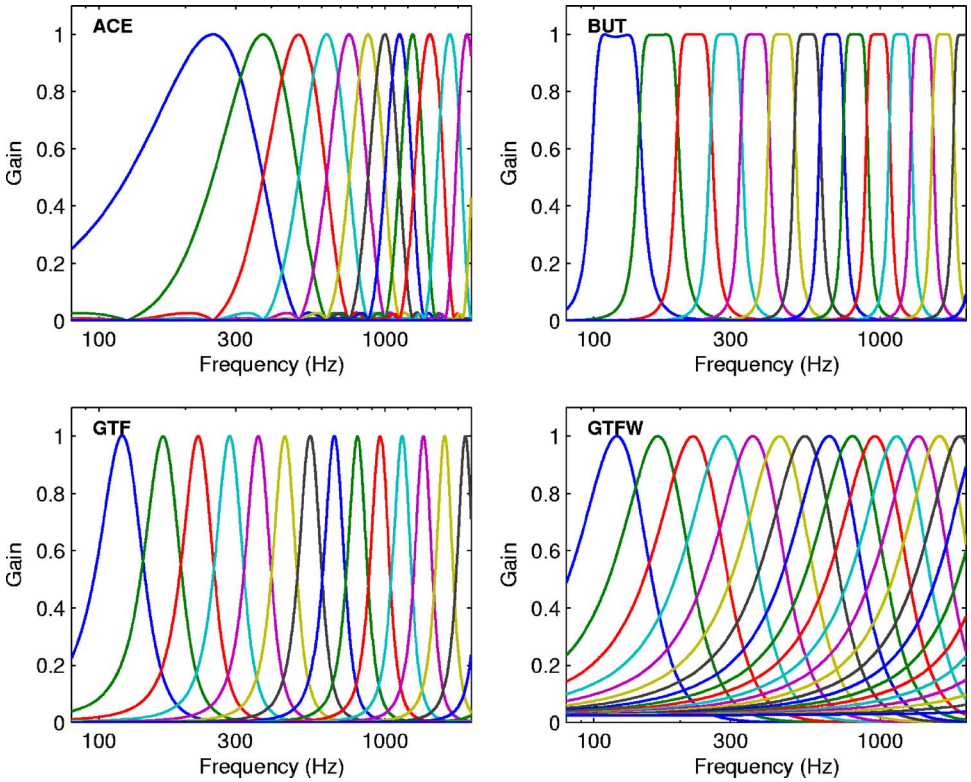

FIG. 2. (Color online) Details of the frequency response of the four analysis filter banks used in the present study.

passing a pulse train through a low-pass filter and a single resonator. The low-pass filter was a second-order IIR filter with a cutoff of 50 Hz and the output of the low-pass filter resembled the glottal volume velocity. The resonator was a second-order IIR resonating filter that created a formant in the spectrum. The details of both filters can be found in Laneau *et al.* (2004). The formant frequency was set at 300, 350, 400, 450, or 500 Hz while the bandwidth of the resonator was fixed at 100 Hz.

These single formant stimuli (SFS) were created with fundamental frequencies 133, 140, 150, 165, 180, 210, 250, 325, and 450 Hz. The sampling frequency was 16 kHz. All stimuli were 500 ms long and had equal rms power.

2. Processing—analysis

The analysis part of the vocoder is identical to the analysis stage of the processing in the study of Laneau *et al.* (2004) with the Gammatone filter bank. The Gammatone filterbank (GTF) has 22 bands and its frequency response is shown in Fig. 2. The GTF filter bank is based upon a model for the filtering of the normal ear (Patterson *et al.*, 1995). The GTF filter bank consists of 22 fourth order IIR gammatone band-pass filters with center frequencies spaced to simulate auditory filters distributed equidistantly along the length of the basilar membrane. The bandwidth of the filters was set to the ERB_N of the respective auditory filter (Glasberg and Moore, 1990).

In order to obtain a condition mainly focusing on spectral pitch (simulating place pitch), the envelopes of the filter outputs were low-pass filtered at 10 Hz so that all fluctuations causing temporal pitch cues were removed. More details of the implementation of the GTF filter bank and the envelope extraction are given in Laneau *et al.* (2004).

Finally, maxima selection was performed in two steps. First, the obtained envelopes were resampled from the audio sampling rate to 900 Hz (the stimulation rate per channel in the CI). Then, for each time slot (sampled at 900 Hz) only the 8 most intense channels of the 22 channels were retained, while the other channels were set to zero. In contrast to CI processing, no compression of the envelopes was included in the noise-band vocoder schemes.

3. Processing—resynthesis

In the resynthesis stage, the output of the analysis stage is upsampled to 30 kHz and then modulated with noise bands. These noise bands are generated by filtering white Gaussian noise through a bank of 22 CISIM filters, to simulate an electrode array consisting of 22 electrodes spaced 0.75 mm apart, as the Cochlear Nucleus CI24(M) electrode array. The space constant λ of the 22 CISIM filters was set to 2, 1.33, 1, 0.8, 0.67, 0.5, 0.33, or 0.25 mm, in order to assess the effect of changing the slope of the resynthesis filters (space constants or equivalently changing the channel discrimination) on place pitch cues for F0 discrimination. The center frequency of the lowest channel was set at 1148 Hz, corresponding to the cochlear location of a simulated electrode array inserted relatively shallow to 20 mm from the round window. This was done to minimize the negative effect of the peripheral auditory filters on temporal pitch sensitivity (Hanna 1992). Consequently, the center frequencies of the 22 noise-band carriers in the CISIM vocoder ranged from 1148 Hz up to 11 410 Hz, and the center frequencies of adjacent carriers were separated by approximately 12%.

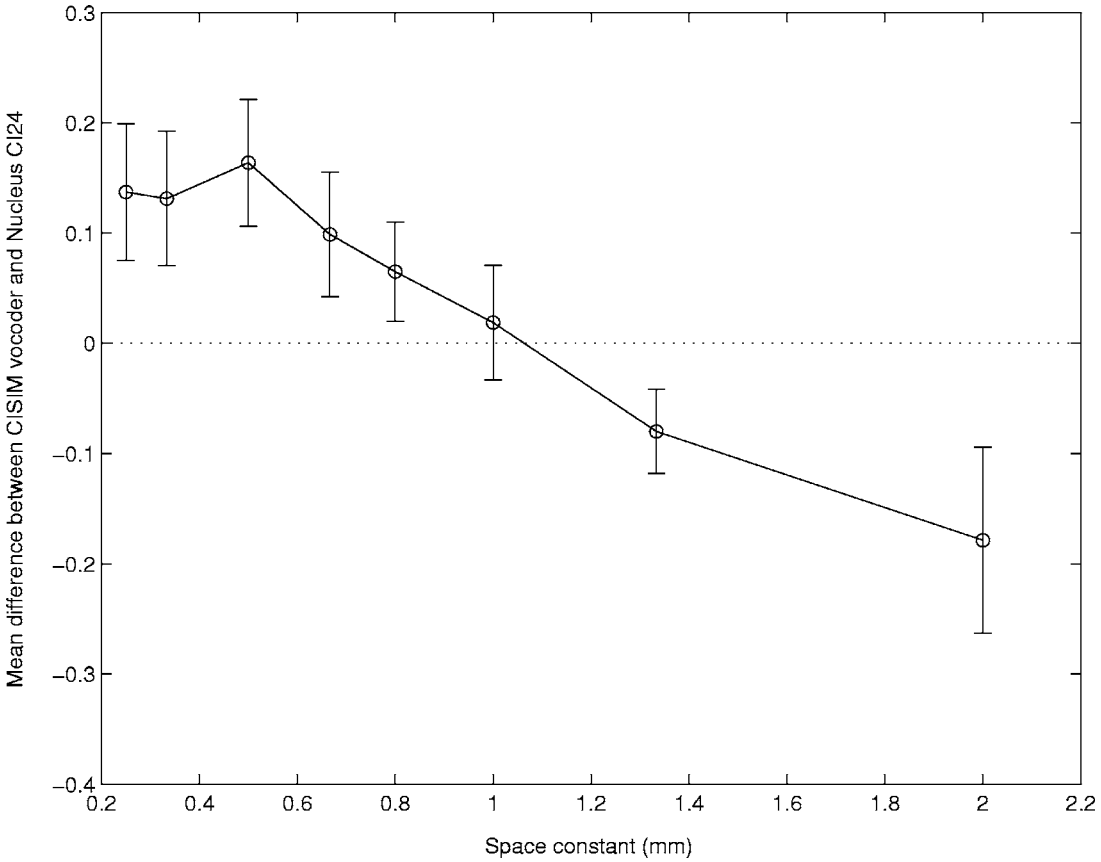

FIG. 3. The mean difference between the average psychometric curve of the CI subjects and the average psychometric curve of the NH subjects with the CISIM vocoder as a function of the space constant of the CISIM filters. Positive values indicate that the psychometric curves for the NH subjects were on average higher than for the CI subjects and consequently had better F0 discrimination and vice versa. All stimuli were processed with the GTF filter bank and with the envelopes low-pass filtered at 10 Hz. The best correspondence between the vocoder and CI results is a space constant of 1 mm. The error bars indicate ±1 standard error of the mean of the five NH subjects.

4. Procedure

F0 discrimination was measured in a 2I-2AFC procedure using the method of constant stimuli. The subjects were presented with two stimuli separated by a 500-ms silent gap and were asked to indicate which of the two intervals contained the stimulus with higher pitch, while ignoring the loudness cues. No feedback was presented to enforce subjects to use their intuitive sense of pitch and to prevent the subjects from using other cues than pitch. Both stimuli in a trial had the same formant frequency but one stimulus' F0 frequency was set at the reference frequency (133 Hz) and the F0 of the other stimulus was set at a higher frequency.

The trials were presented in blocks in random order, where each block contained only stimuli processed with the same space constant (or amount of spectral smearing). Each block contained trials with every comparison frequency for all five formant frequencies, and within each block each trial was repeated twice. Different formant frequencies were included per block in order to prevent the subject from identifying and learning the reference stimulus based upon other cues. To minimize loudness cues, the intensity of the stimuli was randomly attenuated over a 20-dB range.

B. Results and discussion

The psychometric curves were averaged across the 5 NH subjects and the difference was calculated between the average psychometric curve of the NH subjects and the average psychometric curve obtained for CI subjects in the same condition (Laneau *et al.*, 2004). For each space constant, the mean difference is calculated and this mean error is shown in Fig. 3 as a function of space constant. Positive values indicate that the F0 discrimination was better for the NH subjects using the CISIM vocoder than for the CI subjects. Negative values indicate that the CI subjects were able to discriminate better F0 differences than the NH subjects using solely place pitch cues.

NH listeners were better able to make use of place pitch cues using the vocoder with small space constants, or easily discriminable adjacent channels, than the CI subjects. However, by increasing the channel overlap the effect of the place pitch cues decreased and ultimately became less salient in the vocoder than in the CI subjects. The closest correspondence between the results using the CISIM vocoder and the CI results is obtained for a space constant of 1 mm. This is the value for the space constant that was also found to optimally mimic electrode discrimination (see experiment 1).

IV. EXPERIMENT 3: THE EFFECT OF SPECTRAL MISMATCH ON F0 DSICRIMINATION

A. Methods

In order to asses the effect of spectral mismatch on F0 discrimination of noise-band vocoded signals, F0 discrimina-

tion of stylized synthetic vowels was measured in NH subjects for two different noise-band vocoders: the standard vocoder and the CISIM vocoder. The subjects and equipment for stimulus presentation were the same as in experiment 1. The results obtained with each vocoder are compared to the results for CI subjects from the comparison study (Laneau *et al.*, 2004). The stimuli are the same as in experiment 2.

1. Processing—analysis

The analysis part of the vocoder is identical for both noise-band vocoders tested in the present experiment and is identical to the analysis stage of the processing in the comparison study (Laneau *et al.*, 2004). Four different filter banks were used to process the stimuli in the analysis stage: ACE, GTF, BUT, and GTFW. The filter banks differ in spectral resolution for the low frequencies and in the shape of the individual filters. All filter banks have 22 bands and their frequency response is shown in Fig. 2. One filter bank (ACE) is identical to the filter bank currently implemented in the commercial speech processor of Nucleus devices (Cochlear Ltd., 2002). It consists of a 128-point fast Fourier transform (FFT) with a Hamming window. The center frequencies of the resulting frequency bins are spaced by 125 Hz, and their bandwidth is approximately 250 Hz. The 64 frequency bins are summed together to form 22 channels with an approximately logarithmic frequency resolution. The three other filter banks resemble more closely the frequency analysis of the normal human ear and have more resolution in the low frequencies compared to the ACE filter bank. The GTF filter bank is described in experiment 2. The BUT and GTFW are derived from this filter bank by changing the filters' shape and bandwidth, respectively. The GTF, BUT, and GTFW filter banks all consist of 22 fourth-order IIR band-pass filters with center frequencies spaced approximately equidistantly along the length of the basilar membrane. The filters of the GTFW filter bank were fourth-order gammatone filters, while Butterworth filters were used for the BUT filter bank. The bandwidth of the GTFW filter bank was set to half the filter's center frequency. For the BUT filter bank the bandwidth was set to have crossover frequencies at 3 dB down from the pass band.

In order to separate the effects of temporal and place pitch cues, the envelopes of the filter outputs were obtained under two different conditions. In one condition, including both temporal and place pitch cues, the envelope contained modulations up to 200 Hz. In the other condition, including place pitch cues but without temporal pitch cues, the envelope was low-pass filtered at 10 Hz so that all fluctuations causing temporal pitch cues were removed. More details of the implementation of the four filter banks and the envelope extraction are given in Laneau *et al.* (2004). Further processing in the analysis stage is the same as in experiment 2.

2. Processing—resynthesis

The specification of the noise bands, serving as carriers in the resynthesis stage of the noise-band vocoders, differs between the two vocoders: standard vocoder and CISIM vocoder.

a. Standard vocoder. In the standard vocoder the output of the analysis stage is up-sampled to 16 kHz using sample-and-hold resampling and then modulated with noise bands. These noise bands are generated by filtering white Gaussian noise through fourth-order Butterworth band-pass filters. The cutoff frequencies of the resynthesis filters are set equal to the crossover frequencies of the filters of the analysis filter bank. Consequently, the resynthesis filters differ depending on the filter bank used in the analysis.

For the BUT and ACE filter bank the crossover frequencies of the analysis filter bank were determined analytically. For the GTF filter bank the cutoff frequencies of the resynthesis filter bank were set to 23 frequencies spaced evenly along the basilar membrane between 100 and 8000 Hz, where the conversion between place along the basilar membrane and frequency was calculated using Greenwood's formula (Greenwood, 1990). The standard vocoder is not used with the GTFW filter bank.

b. CI-simulation vocoder (CISIM). The main difference of the CISIM vocoder with the standard vocoder was the frequency response of the resynthesis filters. The CISIM vocoder used 22 CISIM filters, as described in experiment 2. The space constant of the 22 CISIM filters was set to 1 mm, because for this value the performance of the simulated place pitch discrimination in NH subjects was closest to the performance of the CI subjects (see experiments 1 and 2).

In contrast to the standard vocoder, the resynthesis filters were now kept fixed independent of the analysis filter bank. This resembles more closely CI operation because when the sound processing scheme is altered, the channels perceived by the subject do not immediately change accordingly because the electrodes remain at the same location and the current spread does not alter. It is noted, however, that after some time CI subjects do tend to adapt to new schemes (Fu *et al.*, 2002). Such adaptation is not active in Laneau *et al.* (2004), which reports on an acute experiment.

3. Procedure

The test procedure was identical to the procedure of experiment 2. The trials were presented in blocks. The conditions resulting from the combinations of type of envelope extraction (with or without temporal pitch cues) and filter bank (ACE, GTF, BUT, or GTFW) were presented into separate blocks. The block contents, number of trial repetitions, and the loudness roving were as in experiment 2.

For the standard vocoder the F0 of the comparison stimuli only ranged up to 250 Hz and the GTFW filter bank was not included, while for the CISIM vocoder the fundamental frequency of the comparison stimuli ranged up to 450 Hz, as in the comparison study (Laneau *et al.*, 2004). In summary, 12 blocks of 60 trials containing stimuli processed with the standard vocoder and 16 blocks of 80 trials containing stimuli processed with the CISIM vocoder were presented to every subject.

4. Data analysis

A measure of the effect of temporal and place pitch cues was derived from the proportions of correctly ranked trials. Because no significant effect of the formant frequencies was found (Laneau *et al.*, 2004), the proportions were averaged over the different formant frequencies. The resulting average

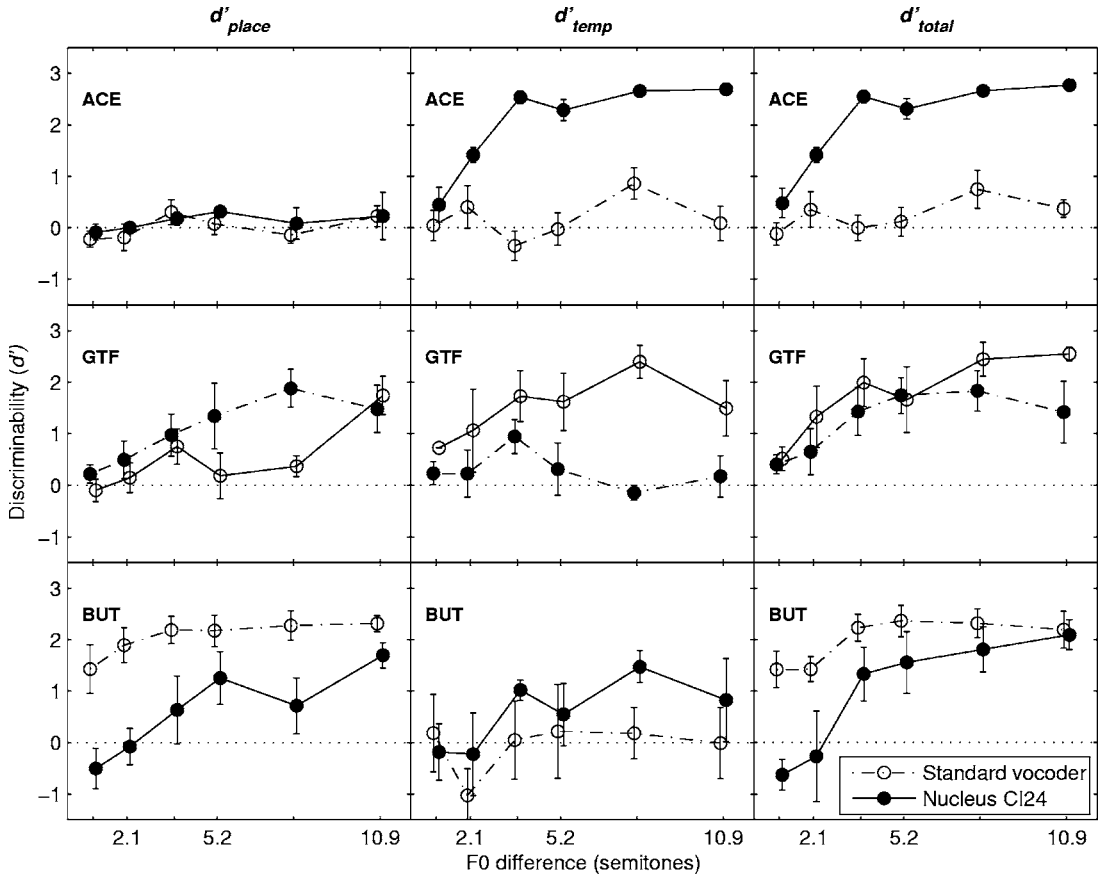

FIG. 4. The average effect of the place pitch cues, the temporal pitch cues, and the combined temporal and place pitch cues for F0 discrimination present in the stimuli processed with the standard vocoder for the ACE, GTF, and BUT filter banks. The results are averaged over the five NH subjects. The average result for four CI subjects from Laneau *et al.* (2004) is included for comparison. The error bars indicate ±1 standard error of the mean of the intersubject variability.

proportions were transformed into d' values, taking into account an adjustment for perfect performance. For perfect performance (for all proportions equal to one), half a trial error was introduced as suggested by MacMillan and Creelman (1991).

The d'_{place} values were estimated from the condition where the temporal fluctuations in the envelopes above 10 Hz were filtered out and represent an estimate of the effect of place pitch cues. The d'_{total} values were estimated from the condition where temporal fluctuations in the envelopes were present up to 200 Hz and represent an estimate of the combined effect of temporal and place pitch cues. The effect of the pure temporal pitch cues (d'_{temp}) was calculated by taking the difference between the effect of the combined pitch cues and the effect of the place pitch cues using the following formula:

$$d'_{\text{temp}} = \text{sign}(X)^* \sqrt{|X|} \quad \text{with} \quad X = \text{sign}(d'_{\text{total}})(d'_{\text{total}})^2 - \text{sign}(d'_{\text{place}})(d'_{\text{place}})^2.$$

In this formula, temporal and place pitch cues are assumed independent and negative d' values are possible (Laneau, 2005).

In order to compare the results obtained with the vocoder and the results obtained for CI subjects, the d' values for place pitch cues, temporal pitch cues, and combined temporal and place pitch cues were calculated for the results of the NH subjects using the vocoders and for the results of four CI subjects (Laneau *et al.*, 2004). For both vocoders, a repeated measures ANOVA was performed on the d' values with two within-subject factors (analysis filter bank and F0-difference) and one intersubject factor (separating NH subjects from CI subjects). This analysis was performed for d'_{place}, d'_{temp}, and d'_{total} separately.

B. Results

1. Standard vocoder

Figure 4 displays the effects of place pitch cues, temporal pitch cues, and combined pitch cues in the left, middle, and right columns, respectively, obtained with the standard vocoder. Each row of panels shows results of stimuli processed with a different analysis filter bank. The average results for four CI subjects (Laneau *et al.*, 2004) are included in the figures for comparison.

(i) The repeated measures ANOVA performed on the d'_{place} values (shown in the left column of Fig. 4) comparing the vocoder results with the CI results indicate that there was a significant difference between the results obtained with the vocoder and the results obtained with the CI subjects ($p=0.048$). Moreover, this difference depended significantly on the analysis filter bank ($p=0.042$). The place pitch cues had a signifi-

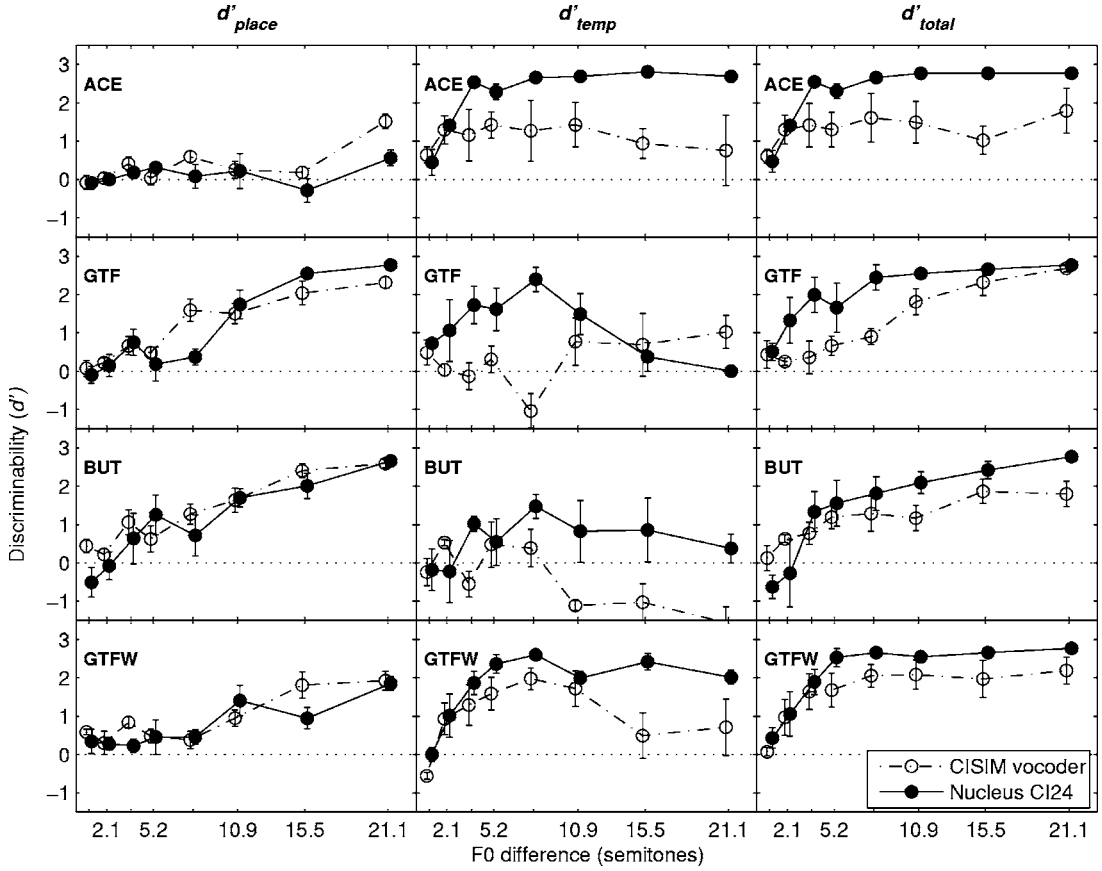

FIG. 5. The average effect of the place pitch cues, the temporal pitch cues, and the combined temporal and place pitch cues for F0 discrimination present in the stimuli processed with the CISIM vocoder for different filter banks and as a function of relative F0 difference. The results are averaged over the five NH subjects. The error bars indicate ±1 standard error of the mean of the intersubject variability. The average result for four CI subjects from Laneau *et al.* (2004) is included for comparison.

cantly larger effect in the NH subjects than in the CI subjects. The largest difference between the standard vocoder results and CI results occurred for the BUT filter bank, where the standard vocoder allowed the subjects to discriminate frequency differences smaller than a semitone (approximately 5%) solely based upon place pitch cues. For the ACE filter bank the place pitch cues did not allow F0 discrimination with either the standard vocoder or with the CI.

(ii) The analysis of the d'_{temp} values (shown in the middle column of Fig. 4) indicated that the temporal pitch cues had significantly different effects for the NH subjects with the standard vocoder than for the CI subjects ($p=0.002$). The perceived pitch effect of adding temporal modulations in the envelope up to 200 Hz was smaller for the NH subjects with the standard vocoder than for the CI subjects.

(iii) The combined effects of both temporal and place pitch cues (d'_{total} shown in the right column of Fig. 4) were also compared between the standard vocoder and the CI. Although there is no significant difference for F0 discrimination with combined place and temporal pitch cues between the CI subjects and NH subjects with the standard vocoder over all the filter banks ($p=0.295$), there is a significant difference depending on the processing filter bank used ($p=0.001$). For example, the ACE filter bank led to the best performance in the CI subjects but to the worst performance in the NH subjects using the standard vocoder. Similarly, while the BUT filter bank led to the best performance in NH subjects, it had the worst performance of all filter banks in the CI subjects.

2. CISIM vocoder

Figure 5 shows the effect the place pitch cues (d'_{place}), the effect of the temporal pitch cues (d'_{temp}), and the effect of the combined place and temporal pitch cues (d'_{total}) averaged over the five NH subjects for the CISIM vocoder, in the right, middle and left columns, respectively. Each row of panels shows the results for a different analysis filter bank. The average results for four CI subjects (Laneau *et al.*, 2004) are included in each figure for comparison.

(i) The statistical analysis of the perceptual effect of the place pitch cues (d'_{place}), showed no significant difference between the CISIM vocoder and the CI results ($p=0.412$). There were significant effects of the filter bank ($p=0.002$), the relative F0 difference ($p<0.001$), and a significant interaction effect between the filter bank and the relative F0 difference ($p=0.023$).

(ii) The analysis of the amount of effect of temporal pitch cues (d'_{temp}) showed that both the filter bank and the relative F0 difference had a significant effect on performance ($p=0.002$, and $p=0.032$, respectively). There was a significant difference between the results obtained with the CISIM vocoder and with the CI subjects ($p=0.028$). However the procedure for obtaining these results (with the CISIM vocoder or with CI subjects) did not interact significantly with either F0 difference or analysis filter bank.

(iii) The analysis of the effects of the combined place and temporal pitch cues (d'_{total}) showed only a significant effect of the relative F0 difference ($p<0.001$). There was no significant overall difference between the CISIM data and the results obtained from the CI subjects ($p=0.140$).

The CISIM vocoder performed well in modeling the effect of the place pitch cues present in the CI results. There is no significant difference between the results obtained from NH subjects with the CISIM vocoder and from CI subjects for the condition where only place pitch cues were present. Moreover, the comparison in performance over the four different analysis filter banks leads to similar results when using the CISIM vocoder results or the CI results: The effect of the place pitch cues was largest for the BUT and GTF filter banks, while for the ACE filter bank there was almost no effect of place pitch cues.

However, the effects of the temporal pitch cues were smaller with the CISIM vocoder than those present in the CI results. For both the ACE and GTFW filter bank F0-discrimination performance improved by adding temporal modulations in the envelopes up to 200 Hz. Temporal pitch cues thus had an effect for these filter banks, although the effect is smaller than the effect found in the CI subjects. It should also be noted that the intersubject variability is greater for the CISIM vocoder than for the CI results. For the GTF and BUT filter bank no clear benefit in F0 discrimination is obtained by providing temporal modulations in the envelopes up to 200 Hz for the CISIM vocoder. Even more, for the BUT filter bank for large F0 differences the F0-discrimination performance dropped after adding the temporal fluctuations.

In summary, the CISIM vocoder and the CI provide the approximately equivalent place pitch cues for F0 discrimination, but the CISIM vocoder provides less effective temporal pitch cues than the CI. Consequently, the CISIM vocoder provides less effective pitch cues in total (combined place and temporal pitch cues) for F0 discrimination than the CI, although not significantly.

C. Discussion

In most noise-band vocoders used for CI research white noise is modulated before the resynthesis filters are applied (e.g., Shannon *et al.*, 1995). In the present study the modulation of the noise is performed after the filtering for two reasons. First, the band-pass filtering may reduce the depth of the modulation of the envelope for higher modulation frequencies. And, second, the different group delays of the resynthesis filters alter the phase relations between the modulations on the different channels.

Neither the standard nor the CISIM vocoder was completely suitable as acoustic models for CI. For the standard vocoder neither the effects of the place pitch cues nor the effects of the temporal pitch were correctly modeled. For the CISIM vocoder the effect of the temporal pitch cues was somewhat underestimated, but the effects of the place pitch cues were accurately modeled for all analysis filter banks. In the next sections we discuss the possible factors affecting the results for place pitch cues and temporal pitch cues for both vocoders.

1. Place pitch cues

With the standard vocoder the NH subjects obtained better F0 discrimination than the CI subjects when the discrimination was solely based on place pitch cues. This higher pitch sensitivity using the standard vocoder was most likely caused by the relatively high-frequency resolution of the vocoder processed signals and the fact that there is no spectral mismatch in the standard vocoder. The resynthesis filters of the standard vocoder were relatively steep and did not overlap. Consequently, the spectrum of the signals was relatively little smeared by the standard vocoder. In contrast, excitation patterns of adjacent channels in CI probably had shallow slopes and overlapped greatly because of the current spread along the cochlea (Shannon, 1983b). Such overlap would smear the resulting excitation pattern and consequently weakened the place pitch differences between the compared signals.

The high performance of the NH subjects with the BUT filter bank using purely place pitch cues was likely due to the fact that for the BUT filter bank the analysis and resynthesis filters were identical. In this way the spectrum was least distorted for the BUT filter bank and the spectrum was minimally warped along the cochlea. Presenting the correct frequency to the correct place of stimulation is crucial for NH subjects to obtain good frequency discrimination (Oxenham *et al.*, 2004).

For the CISIM vocoder the slopes of the resynthesis filters were set to obtain equal channel discrimination using the CISIM vocoder as found in CI subjects (see experiment 1 and 2). With this adjusted channel discrimination, the results of the NH subjects with the CISIM vocoder successfully model the results of CI subjects in an F0-discrimination task based solely on place pitch cues independent of the analysis filter bank used.

2. Temporal pitch cues

Although amplitude-modulated noise is known to elicit pitch percepts (Burns and Viemeister, 1976) and the sensitivity to temporal pitch in CI is similar to the sensitivity of rate discrimination of amplitude-modulated noise (Blamey *et al.*, 1984a), the effect of the temporal pitch cues was smaller for the NH subjects using the vocoders than for CI subjects. This limited temporal pitch sensitivity using the vocoder was most probably caused by a combination of factors. The most

important factors are the absence of envelope compression/expansion in the vocoder, the poor pitch sensitivity of some of the NH subjects in the present study, the ringing of the peripheral auditory filters of the normal ear, and the possible interference between the channel envelope and the noisy envelope inherent in the narrow noise band.

The first factor that most probably contributed to the limited effect of the temporal pitch cues using the noise-band vocoders is the absence of any compression/expansion of the envelopes in the vocoders. In the CI system the envelopes are compressed to accommodate for the reduced dynamic range and the steep loudness growth of CI subjects. However, even with compression, the resulting modulation depth in the neural excitation pattern may be larger for CI subjects compared to the modulation depth in the excitation pattern of NH subjects listening to the vocoders. This is because excitation is an expansive function of the input for electrical stimulation, while it is a compressive function for acoustic stimulation (Zeng and Shannon, 1994). Consequently, the relative reduced modulation depth may have impaired the effectiveness of the temporal pitch cues for the NH subjects because lower modulation depths lead to poorer modulation rate discrimination (Patterson *et al.*, 1978; Grant *et al.*, 1998). This hypothesis is tested and confirmed in experiment 4.

In experiment 4 it is shown that NH listeners with a vocoder require more modulation depth to achieve the same performance of modulation rate discrimination compared to CI subjects (see Fig. 7). This difference in perception has different effects for the four analysis filter banks. For the ACE and GTFW filter banks the modulation depth present in the stimuli ranged from 59% up to 65% for the ACE filter bank and from 35% up to 60% for the GTFW filter bank. The modulation depth was calculated using the "in-phase" method from Laneau *et al.* (2004). For these analysis filter banks the modulation depth was sufficient to elicit temporal pitch cues in the three NH subjects (S2, S4, and S5) and in all four CI subjects. For the GTF and BUT filter banks the modulation depth of the reference stimuli ranged from approximately 10% to 33%, and from 11% to 36%, respectively. This modulation depth was insufficient to generate discriminable temporal pitch percepts in any of the NH subjects while in contrast it was sufficient for at least some stimuli for the three better CI subjects. Although the modulations for the GTF and BUT filter bank were undiscriminable in rate for the NH subjects, they were still detectable. The required modulation depth for modulation detection at 133 is in the order of 10% for NH subjects (Bacon and Viemeister, 1985). The presence of these fluctuations may have elicited a roughness sensation (Zwicker and Fastl, 1999) that may have interfered with the place pitch cues and resulted in negative temporal pitch cues for the BUT filter bank and for some subjects with the GTF filter bank (see the middle column of Fig. 5).

This difference for rate discrimination as a function of modulation depth between the vocoder and the CI subjects may be overcome by the insertion of an additional compression/expansion stage into the vocoder. An expansion stage would increase the modulation depth and thus provide more effective temporal pitch cues. This suggested compression/expansion stage is not equivalent to the compression stage found in CI systems. The suggested compression/expansion stage is intended to overcome any residual differences in loudness growth (or more specifically perceptual modulation depth) between the CI with compression and the vocoder.

The second factor contributing to the difference in effectiveness of the temporal pitch cues between NH listeners and CI subjects is the relatively poor performance in pitch related tasks of two of the NH subjects. In experiment 4, two NH listeners, S1 and S3, were unable to perform the pitch discrimination task while this task is within the limits of normal performance for most NH subjects (Patterson *et al.*, 1978; Grant *et al.*, 1998). Futhermore, these same subjects also performed below average performance on another modulation rate discrimination task reported in Laneau (2005). There is no clear reason why these two subjects performed so poorly at modulation rate discrimination tasks.

A third reason why the effect of temporal pitch cues was lower in the NH subjects using the vocoder compared to the effect in CI is the peripheral filtering of the normal ear. Hanna (1992) showed that at low center frequencies the smaller bandwidth of the peripheral filters limits the effect of the temporal pitch cues. This effect is largest for the standard vocoder because for the standard vocoder the spectral region of the output signal is matched to the spectral region of the input signal and the original stimuli in the present study only contained energy in the lower frequencies because of the relatively low formant frequencies and the maxima selection in the processing. Consequently, the output signals of the standard vocoder in the present study only contained lower frequencies where the limiting effect of the peripheral filters exists. The F0-related modulations in the envelope of the different channels of the standard vocoder can be obscured by the modulations already present on the basilar membrane. Due to the limited bandwidth of the basilar membrane at lower frequencies the effective modulation depth of the F0-related modulations can be reduced.

This effect is absent for the CISIM vocoder because the center frequencies of the resynthesis filters are shifted up in frequency with respect to the center frequencies of the analysis filters. The stimuli processed with the CISIM vocoder contained energy at higher frequencies where the effect of the temporal pitch cues is not limited by the peripheral filters of the normal ear. There was a significant increase in the effect of temporal pitch cues between the standard and the CISIM vocoder ($p=0.031$) for the filter bank with sufficient modulation depth (ACE) and for the three better performing NH subjects.

Summarizing the three previous factors, a noise band vocoder can be used as an acoustic model for temporal pitch research in cochlear implants for NH subjects with relatively good pitch sensitivity, for stimuli with enough modulation depth, and for a vocoder with noise bands at higher frequencies (i.e., the CISIM vocoder). This is shown in Fig. 6 where the average effect of the temporal pitch cues (d'_{temp}) for subjects S2, S4, and S5 are depicted for the ACE and GTFW filter banks obtained with the CISIM vocoder. There exists

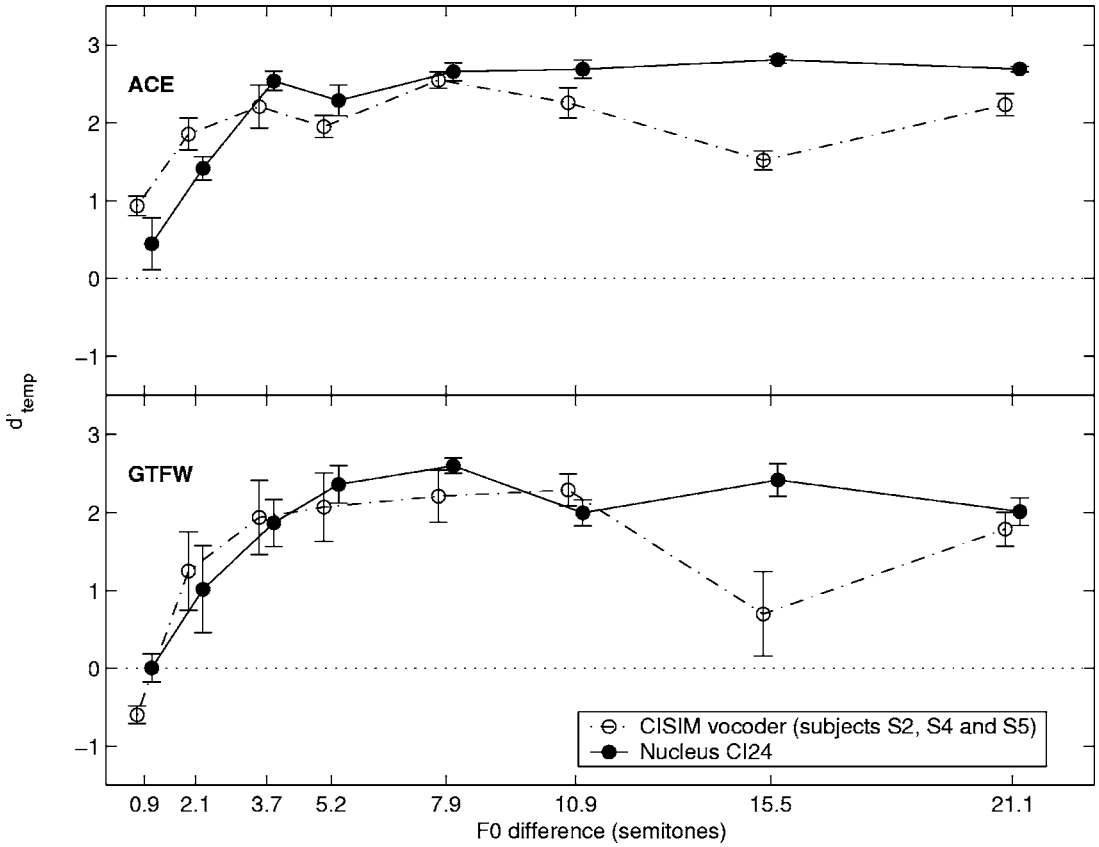

FIG. 6. The amount of effect of the temporal pitch cues for F0 discrimination for stimuli processed with the CISIM vocoder for filter banks ACE and GTFW and as a function of relative F0 difference. The results are averaged over NH subjects S2, S4, and S5 who have relatively good temporal pitch sensitivity. The results for four CI subjects from Laneau *et al.* (2004) are included for comparison. For this reduced set of conditions and for these subjects, the CISIM vocoder succeeds in modeling the CI data. The error bars indicate ±1 standard error of the mean of the intersubject variability.

relatively good correspondence between the results obtained with the CISIM vocoder for these subjects and for the results obtained with the four CI subjects from Laneau *et al.* (2004) added to the figure for comparison.

Finally, a fourth factor may have contributed to the poor effectiveness of the temporal pitch cues for the NH listeners using the vocoder compared to the CI subjects. The noise-band carriers of the vocoder have inherent random envelope fluctuations, creating an "external" variability. These random modulations may interfere with the envelope modulations in the analysis-channel envelopes related to the F0 and eliciting the temporal pitch cues (Formby and Muir, 1988; Hanna, 1992). Therefore, a deterministic carrier with limited envelope modulations in the temporal pitch frequency range might be more suitable as a carrier for a vocoder intended as an acoustic model for pitch sensation in CI (Carlyon *et al.*, 2002; van Wieringen *et al.*, 2003; Deeks and Carlyon, 2004).

V. EXPERIMENT 4: MODULATION RATE DISCRIMINATION

A. Methods

To assess the effect of the absence of a compression/expansion stage in the vocoder on temporal pitch cues, the minimal modulation depth required to discriminate a 20% change in modulation frequency (approximately 3.2 semitones) was measured in the same five NH subjects using the CISIM vocoder and in the four CI subjects of Laneau *et al.* (2004). For the CI subjects, the stimuli consisted of amplitude-modulated pulse trains presented interleaved on the three most apical channels with 900 pulses per second per channel. A dc-shifted sinusoid was compressed using the standard compression function to accommodate for loudness growth in Nucleus CI24 subjects (Laneau *et al.*, 2004) and used to modulate the amplitude of the pulses of the three channels. The modulation was in phase across the three channels and the modulation depth was varied adaptively. The subjects were presented two signals in random order on each trial: one was modulated at 133 Hz and the other at approximately 160 Hz. Subjects were asked to indicate the higher in pitch. After two consecutive correct answers the modulation depth was decreased by 1 dB and after each incorrect answer the modulation depth was increased again by 1 dB, leading to an asymptotic average of 71% correct responses (Levitt, 1971). The procedure was continued until eight reversals were obtained and the mean of the last four reversals was taken as the result for that particular run. The three best runs out of five runs were retained for each subject. Intensity was roved identically as in Laneau *et al.* (2004) by randomly varying the electrical output gain from 85% up to 110% of the dynamic range, to minimize loudness cues.

For the NH subjects, stimuli consisted of the sum of three modulated noise bands filtered with CISIM filters with

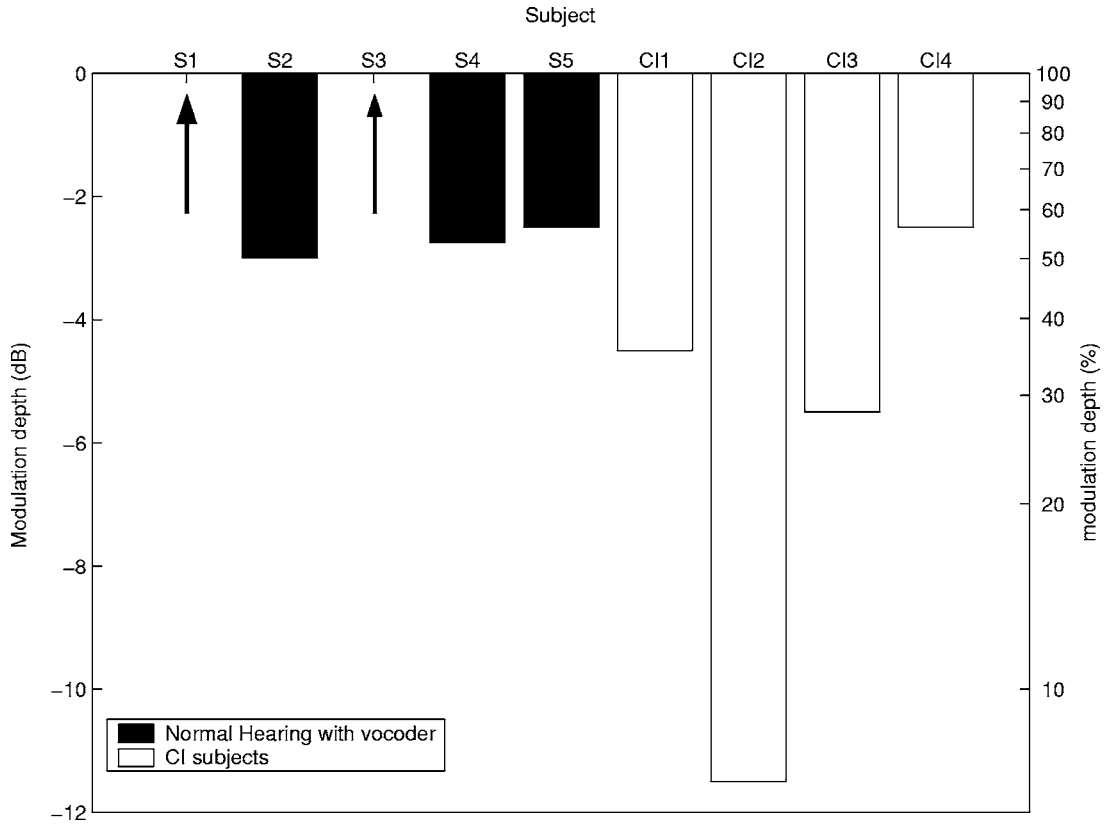

FIG. 7. Minimal required modulation depth to discriminate a 20% modulation rate difference on three simultaneously stimulated channels. The filled bars show the results of the NH subjects (S1–S5) where the modulation depth was measured using modulated noise bands (CISIM filters with space constant 1 mm). The open bars show the results of the CI subjects (CI1–CI4) where pulse trains were modulated. The arrows for subjects S1 and S3 indicate that they were unable to correctly rank the 20% modulation rate difference above chance level even for 100% modulation depth. The results show that the required modulation depth for rate discrimination is generally lower for the CI subjects compared to the NH subjects.

space constant of 1 mm and center frequencies of 1148, 1291, and 1451 Hz, corresponding to the cochlear locations of the three most apical electrodes of the simulated electrode array of the CISIM vocoder (15, 15.75, and 16.5 mm, respectively). The modulation was sinusoidal and in-phase over the three channels. The procedure was identical to the procedure for the CI subjects. Intensity was roved over a 20-dB range. No compression or expansion of the envelope was included for the acoustical stimuli.

B. Results and discussion

Figure 7 shows the results for both the NH subjects and the CI subjects. Two of the NH subjects (S1 and S3) were unable to discriminate the rate difference even at 100% modulation depth. CI subjects CI1, CI2, and CI3 require the smallest modulation depth to discriminate the 20% modulation rate difference. CI subject CI4 is comparable in performance to the better NH subjects. In general, CI subjects thus require less modulation depth compared to NH subjects with the CISIM vocoder to discriminate the 20% difference in modulation rate.

VI. GENERAL DISCUSSION

Our results indicate that the relative contributions of spatial and temporal pitch cues for F0 discrimination can be altered by varying the width of the single-channel excitation patterns. Narrower excitation patterns with steeper slopes elicit highly salient place pitch cues and with very narrow excitation patterns these place pitch cues may become more salient than the temporal pitch cues.

In currently used CI systems F0 discrimination is mediated by temporal pitch cues more than by place pitch cues (Geurts and Wouters, 2001; Green *et al.*, 2002; Laneau *et al.*, 2004). However, the present results suggest that narrower excitation patterns may provide more salient place pitch cues. Narrower excitation patterns were reported using bipolar or tripolar stimulation compared to the monopolar mode used in most current CI systems (Hartmann and Kral, 2004). Ultimately, these narrow excitation patterns may elicit place pitch cues which are more salient than the temporal pitch cues. This might enhance F0 discrimination in CI subjects whereas the limit for the temporal pitch cues appears to be reached (Green *et al.*, 2004).

In most studies using vocoders to investigate the effects of processing for pitch perception (or pitch-related tasks) in CI subjects the carriers of the vocoders are spectrally matched, as in the standard vocoder in the present study, i.e., the analysis filters and the resynthesis filters are identical for noise-band vocoders (Fu *et al.*, 1998; Faulkner *et al.*, 2000; Green *et al.*, 2002; Xu *et al.*, 2002; Green *et al.*, 2004; Qin and Oxenham, 2005; Kong *et al.*, 2004; Fu *et al.*, 2004) or pulse-train vocoders (Deeks and Carlyon, 2004), or the frequency of the sinusoidal carrier is set at the center frequency

of the analysis filters for sinusoidal vocoders (Lan *et al.*, 2004; Fu *et al.*, 2004). First, our results indicate that the place (or spectral) pitch cues with the spectrally matched vocoders are more salient than those found in the CI subjects, especially for the case where analysis and resynthesis filters were completely identical as in the BUT condition for the standard vocoder. This suggests that the spectral pitch cues found in the mentioned vocoder studies may have been stronger than what may be obtained in CI subjects, especially when many channels are used in the vocoder. Second, our results also indicate that the temporal pitch cues obtained with the standard vocoder are less salient than the cues CI subjects can use because of the peripheral filtering in the normal ear. This suggests that with the spectrally matched vocoders of most other studies the obtained temporal pitch cues may be smaller than what may be found in CI subjects because the channels with center frequencies below 1 kHz are less effective in providing salient temporal pitch cues. Taken together the last two findings, it is possible that the spectral pitch cues were relatively more important than the temporal pitch cues with the vocoders than what may be obtained with CI subjects, especially as the number of channels would be high and the spectral resolution would be good. For sinusoidal vocoders the relative contribution of the spectral pitch cues may be even more exaggerated as the excitation profile of sinusoids is very narrow and this leads to very discriminable spectral pitch cues.

Pitch or F0 discrimination solely based upon place pitch cues was strongly affected in the present study by spectral smearing (see Fig. 3). This is in contrast with the smaller effect of spectral smearing on speech perception. Spectral smearing only affects speech understanding when the slopes of the noise-band carriers of the vocoder are more shallow than 18 dB/oct (Shannon *et al.*, 1998). This observation is consistent with the higher spectral resolution needed for melody recognition than for speech understanding (Smith *et al.*, 2002).

There exists, however, a difference between the amount of spectral smearing necessary to replicate CI subjects' speech perception performance and the amount of spectral smearing necessary to replicate CI subjects' pitch discrimination performance. The mean speech-in-noise recognition thresholds of implant users are close to those of NH subjects listening to four-channel spectrally smeared (with 6 dB/oct resynthesis filters) noise-band vocoded speech (Fu and Nogaki, 2005). In the present study the place pitch performance was matched for a 22-channel noise-band vocoder with slopes of 40 dB/oct (the CISIM vocoder). The cause of this difference in smearing necessary for matching CI performance is unknown, but two factors may be important. First, in the CISIM vocoder the spectrum is spectrally shifted and compressed along the cochlear axis. This probably affected performance because for a vocoder with a matched spectrum and shallower slopes (the standard vocoder in this study) the performance of place pitch discrimination was better even though the slopes of the carriers were shallower (24 dB/oct). This is similar to the reduced speech understanding for spectrally shifted and compressed speech (Fu and Shannon, 1999; Baskent and Shannon, 2003). In the studies assessing the effect of spectral smearing on speech perception the spectrum was not warped along the cochlear axis. Second, channel interactions in CI subjects may be greater during speech than during the stationary signals used in the present study because dynamic stimuli may cause stronger channel interactions (Chatterjee, 2003).

Only postlingually deafened CI subjects participated in the pitch discrimination experiments that were used to verify the acoustic model. However, both place pitch and temporal pitch mechanisms can be impaired in prelingually deafened subjects that were implanted at a relatively late age (approximately after 12 years of age) (Busby *et al.*, 1993; Busby and Clark, 2000a, b). In those subjects often no pitch ordering across the electrode array is observed (Busby and Clark, 2000b). Therefore, the acoustic model presented in this study is not likely to be generalized to this particular group of CI subjects. For prelingually deafened CI subjects that were implanted early in life, normal pitch perception can be observed (Busby and Clark, 2000a, b). In contrast to the previous group of subjects, these subjects experience auditory sensations in the "critical period" of their brain development and this allows for at least partial maturation of their auditory system (Hartmann and Kral, 2004). It may thus be possible to extend the present acoustic model to also include early-implanted prelingually deafened CI subjects, although this remains to be verified in future experiments. The model thus appears applicable for postlingually deafened CI subjects and early-implanted prelingually deafened subjects. These two groups constitute the major portion of all CI subjects.

The application of the presented acoustic model (the CISIM vocoder) to CI subjects in general may be complicated by the fact that the CI subjects participating in this study were all relatively good performers with very good electrode discrimination compared to other postlingually deafened CI subjects (Nelson *et al.*, 1995). Second, as already mentioned, the performance on the pitch discrimination task of some of the NH subjects in this study was poorer than that of other NH subjects on similar tasks reported in other studies. Because of these two factors the pitch discrimination obtained with the acoustic model may be somewhat too optimistic to replicate CI performance in general. Especially the length constant λ could be considered somewhat longer, or equivalently more spectral smearing, in more general applications of the model or a compressive function, might be used to limit the effectiveness of temporal pitch cues.

VII. CONCLUSIONS

Although noise-band vocoders have been proven to provide a successful acoustic model to study speech perception in cochlear implants, it may not be straightforward to extend the model for pitch perception research in CI. The results of the present study indicated that both temporal and place pitch sensitivity can be affected by parameters of the noise-band vocoder.

1. The degree of spectral overlap between adjacent resynthesis filters of the vocoder is inversely proportional to the place pitch sensitivity subjects obtain with the vocoder.

2. The discrimination of noise bands based on place pitch cues and as a function of simulated mm shifts is independent of center frequency for noise bands filtered with the CISIM filter.
3. If the discrimination of adjacent channels with the vocoder, or equivalently single-channel place pitch sensitivity, is adjusted (by varying the spectral overlap of the channels) to match the electrode discrimination performance in CI subjects, then the place pitch sensitivity with the vocoder matches the place pitch sensitivity of CI subjects also for complex multi-channel stimuli.
4. Temporal pitch sensitivity is limited for lower frequency channels of the vocoder. For noise bands having lower center frequencies the peripheral auditory filters limit the modulation depth and consequently the temporal pitch sensitivity. A noise band vocoder where the resynthesis filters all have high center frequencies (e.g., mimicking a shallow insertion depth) may overcome this effect of the peripheral auditory filters.
5. There is large variation in subjects' performance on pitch discrimination tasks, even for NH subjects.
6. A compression/expansion stage in the vocoder has to be adjusted to the effect of the compression in the CI system. The resulting modulation depths in the neural excitation pattern with electrical stimulation and with acoustical stimulation may differ if the CI compression is insufficient or too high. An extra compression or expansion function in the vocoder may compensate for these differences.

Taking these factors into account, a noise-band vocoder may be used as an acoustic model for pitch perception research in CI. Nevertheless, one has to take great care with the interpretation of the results because noise bands differ fundamentally from the deterministic pulse trains used in cochlear implants. Even for the CISIM vocoder, which was specifically designed to mimic pitch discrimination performance of CI subjects, the obtained results differed from the CI results for at least some conditions or subjects. This outcome limits the noise-band vocoder as a general model for electric hearing with a CI.

ACKNOWLEDGMENTS

We thank the subjects for their enthusiastic cooperation. We also thank Fred Wightman and Bob Shannon for valuable comments on earlier versions of this manuscript. This study was partly supported by the Flemish Institute for the Promotion of Scientific-Technological Research in Industry (Project No. IWT 020540), by the Fund for Scientific Research—Flanders/Belgium (Project No. G.0233.01), and by Cochlear Ltd.

Bacon, S. P., and Viemeister, N. F. (**1985**). "Temporal-modulation transfer-functions in normal-hearing and hearing-impaired listeners," Audiology **24**, 117–134.

Baskent, D., and Shannon, R. V. (**2003**). "Speech recognition under conditions of frequency-place compression and expansion," J. Acoust. Soc. Am. **113**, 2064–2076.

Black, R. C., and Clark, G. M. (**1980**). "Differential electrical excitation of the auditory nerve," J. Acoust. Soc. Am. **67**, 868–874.

Blamey, P. J., Dowell, R. C., Tong, Y. C., and Clark, G. M. (**1984a**). "An acoustic model of a multiple-channel cochlear implant," J. Acoust. Soc. Am. **76**, 97–103.

Blamey, P. J., Dowell, R. C., Tong, Y. C., Brown, A. M., Luscombe, S. M., and Clark, G. M. (**1984b**). "Speech processing studies using an acoustic model of a multiple-channel cochlear implant," J. Acoust. Soc. Am. **76**, 104–110.

Burns, E. M., and Viemeister, N. F. (**1976**). "Non-spectral pitch," J. Acoust. Soc. Am. **60**, 863–869.

Busby, P. A., and Clark, G. M. (**2000a**). "Electrode discrimination by early-deafened subjects using the cochlear limited multiple-electrode cochlear implant," Ear Hear. **21**, 291–304.

Busby, P. A., and Clark, G. M. (**2000b**). "Pitch estimation by early-deafened subjects using a multiple-electrode cochlear implant," J. Acoust. Soc. Am. **107**, 547–558.

Busby, P. A., Tong, Y. C., and Clark, G. M. (**1993**). "Electrode position, repetition rate, and speech perception by early- and late-deafened cochlear implant patients," J. Acoust. Soc. Am. **93**, 1058–1067.

Carlyon, R. P., van Wieringen, A., Long, C. J., Deeks, J. M., and Wouters, J. (**2002**). "Temporal pitch mechanisms in acoustic and electric hearing," J. Acoust. Soc. Am. **112**, 621–633.

Chatterjee, M. (**2003**). "Modulation masking in cochlear implant listeners: envelope versus tonotopic components," J. Acoust. Soc. Am. **113**, 2042–2053.

Cochlear Ltd (**2002**). "Nucleus implant communicator (NIC) system overview," N95291 Iss.1, Cochlear Ltd.

Dai, H. P., Nguyen, Q., Kidd, G., Feth, L. L., and Green, D. M. (**1996**). "Phase independence of pitch produced by narrow-band sounds," J. Acoust. Soc. Am. **100**, 2349–2351.

Deeks, J. M., and Carlyon, R. P. (**2004**). "Simulations of cochlear implant hearing using filtered harmonic complexes: implications for concurrent sound segregation," J. Acoust. Soc. Am. **115**, 1736–1746.

Dorman, M. F., and Loizou, P. C. (**1997**). "Speech intelligibility as a function of the number of channels of stimulation for normal-hearing listeners and patients with cochlear implants," Am. J. Otol. **18**, S113-S114.

Dorman, M. F., and Loizou, P. C. (**1998**). "The identification of consonants and vowels by cochlear implant patients using a 6-channel continuous interleaved sampling processor and by normal-hearing subjects using simulations of processors with two to nine channels," Ear Hear. **19**, 162–166.

Dorman, M. F., Loizou, P. C., and Rainey, D. (**1997**). "Speech intelligibility as a function of the number of channels of stimulation for signal processors using sine-wave and noise-band outputs," J. Acoust. Soc. Am. **102**, 2403–2411.

Faulkner, A., Rosen, S., and Smith, C. (**2000**). "Effects of the salience of pitch and periodicity information on the intelligibility of four-channel vocoded speech: Implications for cochlear implants," J. Acoust. Soc. Am. **108**, 1877–1887.

Formby, C., and Muir, K. (**1988**). "Modulation and gap detection for broadband and filtered noise signals," J. Acoust. Soc. Am. **84**, 545–550.

Friesen, L. M., Shannon, R. V., Baskent, D., and Wang, X. (**2001**). "Speech recognition in noise as a function of the number of spectral channels: Comparison of acoustic hearing and cochlear implants," J. Acoust. Soc. Am. **110**, 1150–1163.

Fu, Q. J., and Nogaki, G. (**2005**). "Noise susceptibility of cochlear implant users: the role of spectral resolution and smearing," J. Assoc. Res. Otolaryngol. **6**(1), 19–27.

Fu, Q. J., and Shannon, R. V. (**1999**). "Recognition of spectrally degraded and frequency-shifted vowels in acoustic and electric hearing," J. Acoust. Soc. Am. **105**, 1889–1900.

Fu, Q. J., Chinchilla, S., and Galvin, J. J. (**2004**). "The role of spectral and temporal cues in voice gender discrimination by normal-hearing listeners and cochlear implant users," J. Assoc. Res. Otolaryngol. **5**, 253–260.

Fu, Q. J., Shannon, R. V., and Galvin, J. J., III (**2002**). "Perceptual learning following changes in the frequency-to-electrode assignment with the Nucleus-22 cochlear implant," J. Acoust. Soc. Am. **112**, 1664–1674.

Fu, Q. J., Zeng, F. G., Shannon, R. V., and Soli, S. D. (**1998**). "Importance of tonal envelope cues in Chinese speech recognition," J. Acoust. Soc. Am. **104**, 505–510.

Gagne, J. P., and Zurek, P. M. (**1988**). "Resonance-frequency discrimination," J. Acoust. Soc. Am. **83**, 2293–2299.

Geurts, L., and Wouters, J. (**2000**). "A concept for a research tool for experiments with cochlear implant users," J. Acoust. Soc. Am. **108**, 2949–2956.

Geurts, L., and Wouters, J. (**2001**). "Coding of the fundamental frequency in continuous interleaved sampling processors for cochlear implants," J. Acoust. Soc. Am. **109**, 713–726.
Glasberg, B. R., and Moore, B. C. (**1990**). "Derivation of auditory filter shapes from notched-noise data," Hear. Res. **47**, 103–138.
Grant, K. W., Summers, V., and Leek, M. R. (**1998**). "Modulation rate detection and discrimination by normal hearing and hearing-impaired listeners," J. Acoust. Soc. Am. **104**, 1051–1060.
Green, T., Faulkner, A., and Rosen, S. (**2002**). "Spectral and temporal cues to pitch in noise-excited vocoder simulations of continuous-interleaved-sampling cochlear implants," J. Acoust. Soc. Am. **112**, 2155–2164.
Green, T., Faulkner, A., and Rosen, S. (**2004**). "Enhancing temporal cues to voice pitch in continuous interleaved sampling cochlear implants," J. Acoust. Soc. Am. **116**, 2289–2297.
Greenwood, D. D. (**1990**). "A cochlear frequency-position function for several species—29 years later," J. Acoust. Soc. Am. **87**, 2592–2605.
Hanna, T. E. (**1992**). "Discrimination and identification of modulation rate using a noise carrier," J. Acoust. Soc. Am. **91**, 2122–2128.
Hartmann, R., and Kral, A. (**2004**), *Cochlear Implants: Auditory Prostheses and Electric Hearing*, edited by F. G. Zeng, A. N. Popper, and R. R. Fay (Springer-Verlag, New York, 2004), Chap. 6, pp. 213–285.
Kohlrausch, A., Fassel, R., and Dau, T. (**2000**). "The influence of carrier level and frequency on modulation and beat-detection thresholds for sinusoidal carriers," J. Acoust. Soc. Am. **108**, 723–734.
Kong, Y. Y., Cruz, R., Jones, J. A., and Zeng, F. G. (**2004**). "Music perception with temporal cues in acoustic and electric hearing," Ear Hear. **25**, 173–185.
Lan, N., Nie, K. B., Gao, S. K., and Zeng, F. G. (**2004**). "A novel speech-processing strategy incorporating tonal information for cochlear implants," IEEE Trans. Biomed. Eng. **51**, 752–760.
Laneau, J. (**2005**). "When the deaf listen to music—pitch perception with cochlear implants," Ph.D. dissertation, Katholieke Universiteit Leuven, Belgium (http://hdl.handle.net/1979/57).
Laneau, J., and Wouters, J. (**2004**). "Multi-channel place pitch sensitivity in cochlear implant recipients," J. Assoc. Res. Otolaryngol. **5**, 285–294.
Laneau, J., Moonen, M., and Wouters, J. (**2004**). "Relative contributions of temporal and place pitch cues to fundamental frequency discrimination in cochlear implantees," J. Acoust. Soc. Am. **116**, 3606–3619.
Levitt, H. (**1971**). "Transformed up-down methods in psychoacoustics," J. Acoust. Soc. Am. **49**, 467–477.
Macmillan, N. A., and Creelman, C. D. (**1991**). *Detection Theory: A User's Guide* (Cambridge U. P., Cambridge).
McKay, C. M., and Carlyon, R. P. (**1999**). "Dual temporal pitch percepts from acoustic and electric amplitude-modulated pulse trains," J. Acoust. Soc. Am. **105**, 347–357.
Nelson, P. B., Jin, S. H., Carney, A. E., and Nelson, D. A. (**2003**). "Understanding speech in modulated interference: Cochlear implant users and normal-hearing listeners," J. Acoust. Soc. Am. **113**, 961–968.
Nelson, D. A., Van Tasell, D. J., Schroder, A. C., Soli, S., and Levine, S. (**1995**). "Electrode ranking of 'place pitch' and speech recognition in electrical hearing," J. Acoust. Soc. Am. **98**, 1987–1999.
Oxenham, A. J., Bernstein, J. G. W., and Penagos, H. (**2004**). "Correct tonotopic representation is necessary for complex pitch perception," Proc. Natl. Acad. Sci. U.S.A. **101**, 1421–1425.
Patterson, R. D., Allerhand, M. H., and Giguere, C. (**1995**). "Time-domain modeling of peripheral auditory processing: a modular architecture and a software platform," J. Acoust. Soc. Am. **98**, 1890–1894.
Patterson, R. D., Johnson-Davies, D., and Milroy, R. (**1978**). "Amplitude-modulated noise—detection of modulation versus detection of modulation rate," J. Acoust. Soc. Am. **63**, 1904–1911.
Qin, M. K., and Oxenham, A. J. (**2005**). "Effects of envelope-vocoder processing on F0 discrimination and concurrent-vowel identification," Ear Hear. **26**(5), 451–460.
Shannon, R. V. (**1983a**). "Multichannel electrical stimulation of the auditory nerve in man. I. Basic psychophysics," Hear. Res. **11**, 157–189.
Shannon, R. V. (**1983b**). "Multichannel electrical-stimulation of the auditory-nerve in man. 2. Channel interaction," Hear. Res. **12**, 1–16.
Shannon, R. V., Zeng, F. G., and Wygonski, J. (**1998**). "Speech recognition with altered spectral distribution of envelope cues," J. Acoust. Soc. Am. **104**, 2467–2476.
Shannon, R. V., Zeng, F. G., Kamath, V., Wygonski, J., and Ekelid, M. (**1995**). "Speech recognition with primarily temporal cues," Science **270**, 303–304.
Smith, Z. M., Delgutte, B., and Oxenham, A. J. (**2002**). "Chimaeric sounds reveal dichotomies in auditory perception," Nature (London) **416**, 87–90.
Stover, L. J., and Feth, L. L. (**1983**). "Pitch of narrow-band signals," J. Acoust. Soc. Am. **73**, 1701–1707.
van Wieringen, A., Carlyon, R. P., Long, C. J., and Wouters, J. (**2003**). "Pitch of amplitude-modulated irregular-rate stimuli in acoustic and electric hearing," J. Acoust. Soc. Am. **114**, 1516–1528.
Xu, L., Tsai, Y. J., and Pfingst, B. E. (**2002**). "Features of stimulation affecting tonal-speech perception: Implications for cochlear prostheses," J. Acoust. Soc. Am. **112**, 247–258.
Zeng, F. G., and Shannon, R. V. (**1994**). "Loudness-coding mechanisms inferred from electric-stimulation of the human auditory-system," Science **264**, 564–566.
Zwicker, E., and Fastl, H. (**1999**). *Psychoacoustics: Facts and Models, 2* (Information Sciences, Springer-Verlag, Berlin).

Perception of amplitude modulation by hearing-impaired listeners: The audibility of component modulation and detection of phase change in three-component modulators

Aleksander Sek[a)]
Institute of Acoustics, Adam Mickiewicz University, 85 Umultowska, 61-614 Poznan, Poland

Brian C. J. Moore[b)]
Department of Experimental Psychology, University of Cambridge, Downing Street, Cambridge CB2 3EB, England

(Received 4 August 2005; revised 24 October 2005; accepted 25 October 2005)

Two experiments were conducted to assess whether hearing-impaired listeners have a reduced ability to process suprathreshold complex patterns of modulation applied to a 4-kHz sinusoidal carrier. Experiment 1 examined the ability to "hear out" the modulation frequency of the central component of a three-component modulator, using the method described by Sek and Moore [J. Acoust. Soc. Am. **113**, 2801–2811 (2003)]. Scores were around 70–80% correct when the components in the three-component modulator were widely spaced and when the frequencies of the target and comparison different sufficiently, but decreased when the components in the modulator were closely spaced. Experiment 2 examined the ability to hear a change in the relative phase of the components in a three-component modulator with harmonically spaced components. The frequency of the central component, f_c, was either 50 or 100 Hz. Scores were about 70% correct when the component spacing was $\leqslant 0.5 f_c$, but decreased markedly for greater spacings. Performance was only slightly impaired by randomizing the overall modulation depth from one stimulus to the next. For both experiments, performance was only slightly worse than for normally hearing listeners, indicating that cochlear hearing loss does not markedly affect the ability to process suprathreshold complex patterns of modulation. © *2006 Acoustical Society of America.*
[DOI: 10.1121/1.2139631]

PACS number(s): 43.66.Mk, 43.66.Nm, 43.66.Sr [AJO] Pages: 507–514

I. INTRODUCTION

The perception of amplitude modulation (AM) plays an important role in many aspects of auditory perception, including speech perception (Plomp, 1983; Shannon *et al.* 1995) and the ability to analyze mixtures of sounds arising from different sources (Darwin and Carlyon, 1995). Hearing-impaired people often have difficulty in understanding speech in the presence of background sounds (Plomp, 1978, 1994; Moore, 1998) and it is possible that part of this difficulty stems from abnormalities in the processing of amplitude modulation. This possibility is assessed in the present experiments.

Previous studies of AM perception by hearing-impaired people have mostly focused on the detection of AM (Formby, 1982; Bacon and Gleitman, 1992; Moore *et al.*, 1992; Moore and Glasberg, 2001) or the discrimination of AM rate (Formby, 1986; Grant, 1998). Overall, the results from these studies suggest that performance is not usually adversely affected by cochlear hearing loss, except when a portion of the carrier is inaudible. Here, we focus on the perception of complex patterns of modulation applied to a single carrier for modulation depths well above threshold. We start with a review of previous related studies.

Moore *et al.* (1996) tested listeners with unilateral hearing loss. They were presented with an amplitude-modulated sinusoid to one ear, and were asked to adjust the AM depth of a sinusoid presented alternately to the other ear, so as to match the perceived modulation depth. The results indicated that the perceived amount of modulation in the impaired ear was "magnified" compared to that in the normal ear, and it was argued that this was a manifestation of loudness recruitment (Steinberg and Gardner, 1937), probably resulting from the loss of fast-acting compression on the basilar membrane (Rhode and Robles, 1974, Moore and Glasberg, 1997, 2004).

Tandetnik *et al.* (2001) measured second-order modulation detection thresholds in normally hearing and hearing-impaired listeners. Second-order modulation is modulation applied to the modulation depth of an AM signal, i.e., modulation of the modulator. The second-order modulation thresholds were measured as a function of the frequency of the modulation applied to the modulation depth (referred to as f'_m), using values of f'_m from 1 to 11 Hz, and a fixed first-order modulation frequency of 16 Hz. The audio-frequency carrier was broadband white noise. The thresholds for the hearing-impaired listeners were within the normal range for $f'_m = 3, 5$, and 11 Hz, and were higher (poorer) than normal for $f'_m = 1$ and 7 Hz. These results suggest that cochlear hearing loss may have some deleterious effect on the ability to

a)Electronic mail: oleksek@amu.edu.pl
b)Author to whom correspondence should be addressed. Electronic mail: bcjm@cam.ac.uk

process complex temporal envelopes, but the effect is not large. In a later study using a 2-kHz sinusoidal carrier, detection thresholds for second-order AM were found to be essentially the same for normally hearing and hearing-impaired listeners (Füllgrabe *et al.*, 2003).

Turner *et al.* (1995) used "noise-vocoder" processing to compare the ability of hearing-impaired and normally hearing listeners to identify speech on the basis of temporal envelope cues in a few spectral regions. They found that performance did not differ significantly for the two groups. However, recent unpublished data obtained in our laboratory indicate that hearing-impaired listeners often perform more poorly than normally hearing listeners when trying to understand "noise-vocoded" speech when background sounds are present.

Although most of the studies described above suggest that the ability of hearing-impaired listeners to process amplitude modulation is nearly normal, there is at least one study suggesting that this may not be the case. Lorenzi *et al.* (1997) measured the ability to detect 100-Hz sinusoidal AM applied to a white noise carrier, as a function of the frequency of a masking sinusoidal AM applied to the same noise carrier. For listeners with normal hearing, the modulation masking patterns had a broad bandpass characteristic with a peak at 100 Hz. One listener with a moderate hearing loss also showed a broadly tuned pattern with a peak at 100 Hz. However, the two other listeners with moderate or mild-to-severe hearing loss showed broader patterns with more of a lowpass characteristic. These results suggest that frequency selectivity in the modulation domain can be reduced in listeners with sensorineural hearing loss.

In the present experiments, we examine the ability of hearing-impaired listeners to process complex patterns of suprathreshold modulation imposed on a single sinusoidal carrier, i.e., we examine within-channel modulation processing. The two tasks used (Sek and Moore, 2003) were originally designed to test the concept that the envelopes of the outputs of the auditory filters are fed to a second array of overlapping bandpass filters tuned to different envelope modulation rates. This set of filters is usually called a "modulation filter bank" (MFB) (Dau *et al.*, 1997a, 1997b). The main purpose of the present experiments was not to test the concept of the MFB, but rather to use the two tasks as measures of the ability of hearing-impaired listeners to process complex suprathreshold patterns of AM imposed on a single sinusoidal carrier. This allowed us to examine modulation processing while avoiding possible confounding effects of reduced frequency selectivity in hearing-impaired listeners. It also allowed us to avoid confounding effects of variations in audibility with frequency, which can occur when a broadband carrier is used.

II. EXPERIMENT 1: "HEARING OUT" COMPONENT MODULATION

In our first experiment, we assessed the extent to which hearing-impaired listeners can "hear out" the component modulations in a complex modulator, in the same way that spectral components in a complex sound can be heard out in the audio-frequency domain (Plomp, 1964; Plomp and Mimpen, 1968; Soderquist, 1970; Moore and Ohgushi, 1993). Performance was measured as a function of the frequency separation of the modulator components. The method was identical to that used by Sek and Moore (2003) with normally hearing listeners, so it is described only briefly here.

TABLE I. For each hearing-impaired listener, the table shows hearing loss at 4 kHz, test level, gender/age, and likely etiology of the hearing loss.

Listener	HL at 4 kHz (dB)	Test level (dB SPL)	Gender/Age (years)	Etiology
S1	60	85	M/62	Noise exposure
S2	40	83	M/55	Infection
S3	50	88	F/68	Antibiotics
S4	50	85	M/47	Head injury
S5	65	90	M/53	Antibiotics
S6	65	80	F/69	Unknown
S7	80	96	F/73	Presbycusis (?)
S8	75	93	M/71	Noise exposure

A. Listeners and test levels

Eight hearing-impaired listeners were tested. All were paid for their services. The air-bone gap in the audiogram was always $\leqslant$10 dB, indicating that the hearing losses were sensorineural, presumably cochlear, in origin. Only one ear was tested for each listener. This was the ear that had a hearing loss closest to 50 dB at the test frequency of 4 kHz. The hearing loss at 4 kHz ranged from 40 to 80 dB. The level of the 4-kHz sinusoidal carrier was chosen to give a comfortable loudness for each listener. Initially, the carrier was presented with a level of 80–85 dB SPL for listeners with hearing loss at 4 kHz up to 65 dB, and 85–90 dB SPL for listeners with hearing loss at 4 kHz greater than 65 dB. Listeners were asked to indicate whether the carrier was at a comfortable level. If the carrier was judged too soft, the level was increased, while if it was judged too loud, the level was decreased.

Generally, the required adjustments were small (±2 to 4 dB). Table I shows, for each listener, the hearing loss at 4 kHz, the test level, the gender and age, and the probable etiology of the hearing loss.

Listeners were trained both on the task for this experiment and the task for experiment 2 (described later), on alternate days. Training lasted 4–6 days with about 2.5 h of training per day. Following training, performance appeared to be stable for all listeners.

B. Method and stimuli

To maximize the likelihood that listeners could perform the task, we used a modulator containing only three components, with relatively wide frequency spacings between the components. We assessed whether listeners could hear out the central component of this complex modulator. The carrier was a 4-kHz sinusoid. To avoid any influence of resolvable spectral sidebands (Sek and Moore, 1994; Kohlrausch *et al.*, 2000; Moore and Glasberg, 2001), the highest modulation frequency used was 190 Hz, which is less than one-half of the "normal" bandwidth of the auditory filter, ERB_N, at

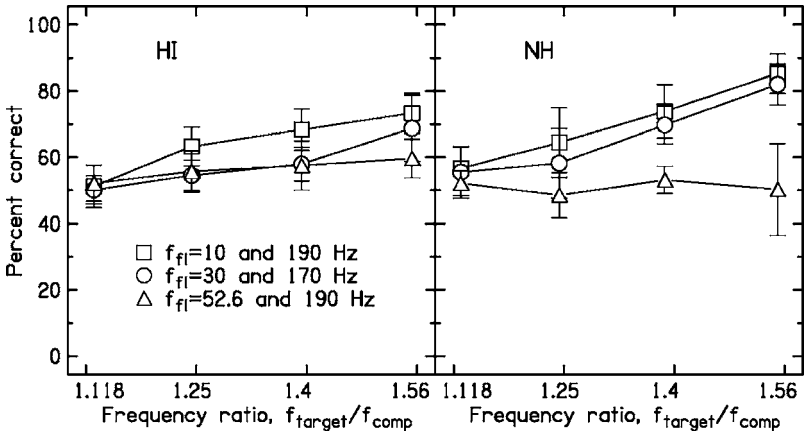

FIG. 1. The left panel shows mean results of experiment 1 for the hearing-impaired listeners tested here. The right panel shows mean results for the same conditions for the normally hearing listeners tested by Sek and Moore (2003). The percent correct identification of the target is plotted as a function of the ratio of f_{target} and f_{comp}, using as numerator whichever of the two was the larger. Each symbol denotes one pair of frequencies for the flanking modulator components, as indicated by the key. Error bars indicate ±1 standard deviation (SD) across listeners.

4 kHz (Glasberg and Moore, 1990). Since hearing-impaired listeners usually have auditory-filter bandwidths that are larger than normal (Pick *et al.*, 1977; Glasberg and Moore, 1986), it was very unlikely that the listeners would be able to "hear out" any spectral sidebands (Moore and Glasberg, 2001).

The task was designed so that listeners could not perform it by judging the mean rate of the complex modulator. On each trial, three modulated stimuli were presented. The modulator of the first stimulus contained three components. Within a run, the frequencies of the outer two components (called "flanking" components) were fixed and the frequency of the central ("target") component, f_{target}, was drawn randomly from one of five possible values: 80, 89.4, 100, 111.8, and 125 Hz. The modulators of the second and third stimuli contained just a single component. In one of these, selected at random, the modulation frequency was equal to that of the target. In the other, the ("comparison") modulation frequency, f_{comp}, was randomly selected from one of the four other possible values of the target. Listeners were required to indicate whether the second or third stimulus contained a modulation component that was present in the first stimulus. Feedback was provided by lights on the response box indicating the correct interval. Listeners were seated in a double-walled sound-attenuating chamber.

The results were analyzed in terms of the ratio between f_{target} and f_{comp}, taking as the numerator whichever of these two was the larger. The smallest ratio was equal to 1.118. This was chosen as it is somewhat larger than the threshold for detection of a change in modulation frequency of a sinusoidal carrier (Lee, 1994; Lemanska *et al.*, 2002; Füllgrabe and Lorenzi, 2003). A run started with five trials using the easiest condition, with the largest ratio of f_{target} and f_{comp}. Scores for these initial five trials were discarded. Then each possible value of f_{target} was paired with each possible value of f_{comp} two times, giving a total of 40 scored trials per run. Data presented are the result of at least 17 runs per listener (more usually, 20–23 runs).

Stimuli were generated using a Tucker-Davis Technologies (TDT) array processor (TDT-AP2) in a host PC, and a 16-bit digital-to-analog converter (TDT-DD1) operating at a 50-kHz sampling rate. The stimuli were attenuated (TDT-PA4) and sent through an output amplifier (TDT-HB6) to a Sennheiser HD580 earphone. Each modulator component had a modulation index of 0.33. This was chosen so as to avoid overmodulation of the three-component modulator, while ensuring that the modulation was clearly audible. The starting phase of each modulator component was chosen randomly for each and every stimulus.

On each trial, the carrier was presented in three bursts separated by silent intervals of 400 ms. Each burst had a 20-ms raised-cosine rise and fall, and an overall duration (including rise/fall times) of 1000 ms. The modulation was applied during the whole of the carrier. The flanking component modulation frequencies were 10 and 190 Hz, 30 and 170 Hz, and 52.6 and 190 Hz. These values were also used by Sek and Moore (2003). The first pair of flanking frequencies was chosen to be widely spaced, so that it would be possible to hear out the middle component even if selectivity in the modulation domain was very poor. The components were equally spaced from the central target component (100 Hz) on a linear frequency scale. The second pair was chosen to be closer in modulation frequency to the target component, while keeping the components symmetrically placed (on a linear frequency scale) around the frequency of the central target component. This was done to assess the ability to hear out the central modulation component under more difficult conditions. For the third pair, the components were equally spaced from the central target component on a logarithmic scale.

C. Results and discussion

The pattern of the results was similar across the eight listeners, and mean results across listeners are shown in the left panel of Fig. 1; the right panel shows the mean results for normally hearing listeners obtained by Sek and Moore (2003) for the same stimuli, but using a carrier level of 70 dB SPL. Percent-correct scores are plotted as a function of the ratio f_{target}/f_{comp}, with the frequencies of the flanking components as parameter. For the smallest ratio f_{target}/f_{comp}, scores for the hearing-impaired listeners are close to the chance level of 50%. However, scores increase as the ratio increases, and for a ratio of 1.56 the mean scores are all above 50%. Performance was better for the widest spacing of the flanking modulator components (10 and 190 Hz) than for the two smaller spacings.

A within-subjects analysis of variance (ANOVA) was

conducted on the percent correct scores for the hearing-impaired listeners, with factors ratio f_{target}/f_{comp} and frequencies of the flanking components. There was a significant main effect of the ratio f_{target}/f_{comp}; $F(3,21)=28.55$, $p<0.001$. This suggests an ability to hear out the target modulation in the complex modulator when f_{target} and f_{comp} differ sufficiently. There was also a significant main effect of the frequencies of the flanking components; $F(2,14)=18.74$, $p<0.001$. Post hoc tests, based on the least-significant differences test, showed that performance was significantly better ($p<0.01$) for the 10- and 190-Hz flanking components than for either of the other two combinations of flanking components. There was no significant difference in scores between the 30- and 170-Hz combination and the 52- and 190-Hz combination. There was a significant interaction between the two main factors; $F(6,42)=2.42$, $p=0.042$. This reflects the fact that the improvement in performance with increasing value of the ratio f_{target}/f_{comp} was greater for the 10- and 190-Hz combination of flanking components than for either of the other two combinations. However, post hoc tests showed that the improvement in performance with increasing value of the ratio f_{target}/f_{comp} was significant ($p<0.01$) for all three pairs of flanking components.

The pattern of results was very similar for the hearing-impaired listeners tested here and the normally hearing listeners tested by Sek and Moore (2003). For the largest ratio f_{target}/f_{comp}, the normally hearing listeners performed slightly better than the hearing-impaired listeners when the flanking component frequencies were 10 and 190 Hz, and 30 and 170 Hz, but the reverse was true when the flanking component frequencies were 52.6 and 190 Hz. To assess whether the difference between the two groups was significant, an ANOVA was conducted on the mean percent correct scores for each group, with the following factors: ratio f_{target}/f_{comp}, frequencies of the flanking components, and group membership. The error variance was estimated from the three-way interaction term. The main effect of group membership was significant; $F(1,6)=6.39$, $p=0.045$. There was also a significant interaction between group membership and the frequencies of the flanking components; $F(2,6)=11.77$, $p=0.008$. This reflects the finding that performance was affected more by the frequencies of the flanking components for the normal than for the impaired listeners.

In summary, the results indicate that the hearing-impaired listeners had some ability to hear out the target modulation in the complex modulator when the flanking components were widely spaced in frequency from the target, and when f_{target} and f_{comp} differed sufficiently. The ability is comparable to, but slightly worse than, that found for normally hearing listeners. Performance for both groups was never perfect even for the widest spacing of the modulator components, which is consistent with the relatively broad tuning of the modulation filters inferred from experiments on modulation masking (Dau *et al.*, 1997a, 1997b; Ewert and Dau, 2000) and on forward masking of AM (Wojtczak and Viemeister, 2005).

III. EXPERIMENT 2: THE DETECTION OF CHANGES IN MODULATOR COMPONENT PHASE

A. Background

In the audio-frequency domain, listeners are more sensitive to within-channel phase changes than to across-channel phase changes (Zwicker, 1952; Patterson, 1987; Uppenkamp *et al.*, 2001; Moore, 2003). Hence, changes in phase sensitivity with changes in the frequency spacing of the components probably reflect the influence of the frequency selectivity of the auditory system. Applying this rationale to the modulation domain, one would expect high sensitivity to component phase for closely spaced modulator components, and poorer sensitivity for widely spaced components. Such a pattern of results was observed by Sek and Moore (2003) for normally hearing listeners in a task requiring detection of a change in relative modulator phase of a three-component modulator.

One complicating factor when interpreting phase effects in the modulation domain is that the internal representation of the envelopes of sounds may be distorted by the presence of nonlinearities in the auditory system, such as basilar-membrane compression (Rhode and Robles, 1974) and neural saturation and adaptation effects (Shofner *et al.*, 1996). These nonlinearities can result in the introduction of components in the effective modulation spectrum that were not present in the stimulus itself (Moore *et al.*, 1999; Verhey *et al.*, 2003; Sek and Moore, 2004; Füllgrabe *et al.*, 2005), and they can also result in differences in effective "internal" root-mean-square (RMS) value of the modulator when the relative phases of modulator components are changed. Like Sek and Moore (2003), we included a condition in which the modulation depth of all components was fixed, and a condition in which the effective modulation depth was made unreliable as a cue by randomizing the overall modulation depth from one stimulus to the next. Comparison of the results for the two conditions provides an indication of the extent to which effective modulation depth was used as a cue when there was no randomization of modulation depth.

B. Listeners

Eight hearing-impaired listeners were tested; they were the same as for experiment 1. All listeners were paid for their services.

C. Stimuli

The equipment and earphone were the same as for experiment 1. The carrier was again a 4-kHz sinusoid, and its level for each listener was the same as for experiment 1. Listeners were required to discriminate two three-component complex modulators differing only in the relative phases of their components. Each modulator component was of equal amplitude. The center component of the modulator had a frequency, f_c, of 50 or 100 Hz. The spacing of the components was 5, 15, 25, 35, or 45 Hz for the 50-Hz f_c, and 10, 30, 50, 70, or 90 Hz for the 100-Hz f_c. For one modulator, the starting phase was 0° (sine phase) for all components. We refer to this as 0-phase. The waveforms for the 0-phase

modulator had relatively high peak factors; see Sek and Moore (2003) for details. For the other modulator, the lowest component was phase-shifted by 180° or π radians (the other two components starting at 0°). We refer to this as π-phase. The waveforms for this modulator had lower peak factors than for the 0-phase modulator.

On each trial, three stimuli were presented. Durations and levels were the same as for experiment 1. In one set of conditions, the modulation index m of each component was fixed at 0.2. In another set of conditions, each modulator component had the same value of m, but the value of m was randomly varied from one stimulus to the next, over a range of ±3 dB in terms of 20 log m (on a uniform scale in terms of log m); the value of m varied between 0.1416 and 0.2825.

D. Procedure

A three-interval three-alternative forced-choice task was used. Two intervals contained the 0-phase stimulus. The other interval, selected at random from the three intervals, contained the π-phase stimulus. The task of the listener was to select the interval that was different from the other two. Feedback was given via lights on the response box. A run started with five trials using the smallest frequency spacing of the modulator components; pilot trials indicated that performance was relatively good for this spacing. Then, in successive trials, stimuli with each frequency spacing were presented once, in ascending order. This sequence was repeated ten times to give a total of 55 trials per run. Results from the first five trials of each run were discarded. For each listener, each modulator center frequency, and each modulation-depth condition (fixed or randomized), 20 runs were obtained.

E. Results

The pattern of results was reasonably similar across listeners, and mean results across listeners are shown in the top two panels of Fig. 2. Performance worsened with increasing frequency separation of the modulator components, for all listeners. However, even for the largest frequency separation, scores for all listeners remained above the score that would be achieved by guessing (33.3%). For f_c=100 Hz, performance for listeners 1 and 2 was somewhat poorer when the modulation depth was randomized (squares) than when it was fixed, suggesting that, when the modulation depth was fixed, these listeners may have made some use of a cue related to the change in "internal" modulation depth. For the other listeners, and for all listeners when f_c=50 Hz, there was no consistent effect of randomizing the modulation depth.

The data for the hearing-impaired listeners were subjected to a within-subjects ANOVA with factors modulator center frequency (50 or 100 Hz), spacing of the components relative to the center frequency (five values), and randomization of modulation depth (absent or present). The main effect of center frequency was significant; $F(1,7)=10.49$, $p=0.014$. Overall performance was a little better for $f_c=100$ Hz (64%) than for f_c=50 Hz (59%). The main effect of frequency spacing of the components was significant; $F(4,28)=85.88$, $p<0.001$. The main effect of randomization

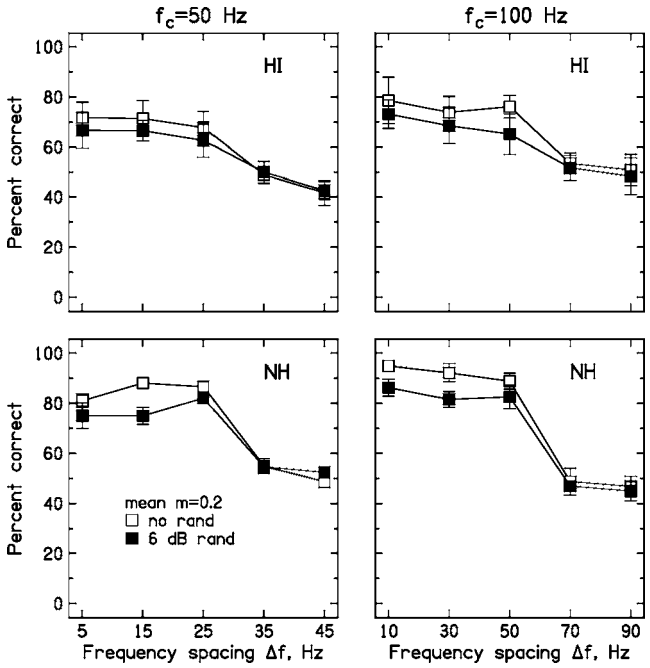

FIG. 2. The top two panels show the mean results for the hearing-impaired listeners tested here, for modulator center frequencies of 50 Hz (left) and 100 Hz (right). The lower two panels show corresponding mean results for the same conditions for the normally hearing listeners tested by Sek and Moore (2003). Error bars indicate ±1 SD across listeners.

was also significant; $F(1,7)=13.21$, $p=0.008$. The mean score was 63.5% with no randomization and 59.5% with randomization. Finally, the interaction of randomization and frequency spacing of the components was significant, reflecting the fact that randomization of the modulation depth had a larger effect for small spacings than for large spacings; $F(4,28)=4.47$, $p=0.006$. No other interactions were significant.

The lower two panels of Fig. 2 show the mean results for the normally hearing listeners tested by Sek and Moore (2003) using a carrier level of 70 dB SPL. The results are similar for the two groups, except that the hearing-impaired listeners performed slightly more poorly overall than the normally hearing listeners. To assess whether the difference between the two groups was significant, an ANOVA was conducted on the mean percent correct scores for each group, with such factors as modulator center frequency (50 or 100 Hz), spacing of the components relative to the center frequency (five values), randomization of modulation depth (absent or present), and group membership. The error variance was estimated from the three-way and four-way interaction terms. The main effect of group membership was significant; $F(1,17)=85.81$, $p<0.001$. There was also a significant interaction between group membership and spacing of the components; $F(4,17)=11.47$, $p<0.001$. This reflects the finding that performance changed more with spacing of the components for the normal than for the impaired listeners.

F. Discussion

Sek and Moore (2003) considered various possible cues that might be used in the phase-discrimination task. Given

the small size of the effect of randomization of modulation depth, they argued that listeners did not perform the task using a cue based on the effective internal depth of the modulation. Another possible cue introduced by nonlinearities in the auditory system is a distortion component at the envelope or "beat" rate of the modulation, which is determined by the spacing between modulator components (Sek and Moore, 2004; Füllgrabe *et al.*, 2005). The strength of this component might vary with the phase of the modulator components, and this could be used as a cue to discriminate the phase changes (possibly mediated via analysis with an MFB). However, in several of the conditions of our experiment, the distortion component would have coincided in frequency with a component that was already present. Given that the distortion component appears to be weak in amplitude relative to the primaries, it is unlikely that the change in effective modulation depth of the distortion component would provide a useful cue in the phase discrimination task, especially in the condition where the modulation depth was randomized.

Sek and Moore (2003) also considered and rejected as possible cues the ratio of the maximum value to the minimum value of the modulator (max-min) (Forrest and Green, 1987; Strickland and Viemeister, 1996) and the crest factor or the skewness of the modulator (Lorenzi *et al.*, 1999).

It seems likely, as argued by Sek and Moore (2003) and Ewert *et al.* (2002), that listeners are sensitive to changes in the shape of the modulator waveform at the output of the modulation filter centered on (or close to) the central component of the modulator. This shape would be influenced by the relative phase of the components. When the modulator components are widely spaced (spacing greater than $0.5f_c$), they interact less at the output of the modulation filter, so the sensitivity to modulator phase is reduced. However, because of the broad tuning of the modulation filters, some interaction occurs even for wide spacings. This can explain why performance remained above chance for the largest spacing used. It was not possible to use much larger spacings, since if the spacing exceeds f_c, one of the modulator components has a negative frequency.

IV. GENERAL DISCUSSION

In both experiments, the pattern of results obtained for the hearing-impaired listeners was similar to that obtained previously for normally hearing listeners. This suggests that the processing of suprathreshold complex patterns of modulation is not greatly affected by cochlear hearing loss. However, for both experiments, the hearing-impaired listeners tested here did perform slightly and significantly more poorly overall than the normally hearing listeners tested by Sek and Moore (2003). Also, for both experiments, performance of the hearing-impaired listeners was affected less by the frequencies of the flanking components than performance of the normally hearing listeners. This is consistent with the idea that the hearing-impaired listeners had slightly reduced frequency selectivity in the modulation domain, consistent with the modulation-masking results of Lorenzi *et al.* (1997). It is not obvious why this should be the case, since the MFB is usually assumed to occur relatively centrally in the auditory system (Rees and Møller, 1983; Liegeois-Chauvel *et al.*, 2004), and there is no obvious reason why the operation of central mechanisms should be affected by cochlear hearing loss (Füllgrabe *et al.*, 2003). While poorer selectivity in the modulation domain for hearing-impaired listeners might explain the reduced effect of the spacing of the flanking components in experiment 2, it does not account for the poorer overall performance; reduced selectivity would lead to more interaction of components, which would be expected to lead to better discrimination of the relative phase of the components.

It is of interest to consider other factors that might have affected the performance of the impaired listeners tested here. As described in the Introduction, cochlear hearing loss usually leads to a loss of fast-acting compression on the basilar membrane (Ruggero *et al.*, 1997). For suprathreshold modulation depths, this can lead to a perceived amount of modulation that is greater than normal (Moore *et al.*, 1996). One might argue that in a person with cochlear hearing loss, the effective modulation depth at the input to central mechanisms is greater than normal. This might lead to an advantage in some modulation-processing tasks, and may account for why detection of AM is sometimes better than normal when the comparison is made at equal (low) SLs (Bacon and Gleitman, 1992; Moore *et al.*, 1992). On the other hand, for normally hearing listeners, the high-frequency side of the excitation pattern is processed almost linearly, at least for high characteristic frequencies (Robles and Ruggero, 2001). If a large effective modulation depth is beneficial in a specific task, a normally hearing listener can obtain that benefit by using information from the high-frequency side of the excitation pattern (Zwicker, 1956), at least when the carrier is at a relatively high level. The normally hearing listeners of Sek and Moore (2003) were tested using a carrier level of 70 dB SPL, which would have been sufficient to allow them to use information from the high-frequency side of the excitation pattern. One might therefore argue that differences in basilar-membrane compression between normal and hearing-impaired listeners should have little effect on performance.

Another factor that may have affected the relative performance of the normally hearing listeners tested by Sek and Moore (2003) and the hearing-impaired listeners tested here is the relatively low SL of the stimuli for the latter, which ranged from 15 to 43 dB SL (mean=27 dB SL). Performance on many tasks, including the detection of AM, worsens at very low SLs (Kohlrausch *et al.*, 2000). However, there is little information on the influence of SL on the processing of suprathreshold amounts of AM. The relatively low SL of the stimuli in our experiments might have led to slightly poorer-than-normal performance simply because relatively few neurons are excited at low SLs, so the neural code is relatively sparse. Put another way, neural "noise" may have a greater influence at low SLs than at high SLs.

A final possible reason for the slightly poorer-than-normal performance of the hearing-impaired listeners is connected with the fact that they were older than the normally hearing listeners tested by Sek and Moore (2003). It has been

suggested that age can have adverse effects on temporal processing (Wingfield *et al.*, 1985). However, Takahashi and Bacon (1992) found that there were no significant effects of age on performance in a variety of modulation processing tasks once the effect of hearing loss was taken into account (except for a very modest correlation between age and modulation detection sensitivity at low modulation frequencies). Furthermore, in our data there was no clear trend for the older listeners (S7 and S8, aged 73 and 71, respectively) to perform more poorly than the younger listeners (S4 and S5, aged 47 and 53, respectively). Thus it seems unlikely that age had a major influence on the results.

Overall, the results of the present experiments indicate that hearing impairment has relatively little effect on the ability to process complex suprathreshold patterns of modulation, although the impaired listeners may have slightly reduced frequency selectivity in the modulation domain.

V. CONCLUSIONS

We have described two experiments assessing the ability of listeners with cochlear hearing loss to process suprathreshold amounts of AM applied to a 4-kHz sinusoidal carrier presented at a comfortable listening level. Experiment 1 examined the ability to "hear out" the modulation frequency of the central component of a three-component modulator. All listeners showed some ability to perform the task when the components in the modulator were widely spaced and when the frequencies of the target and comparison differed sufficiently. Scores were poorer when the two flanking components were closer to the central target component frequency of 100 Hz. This is consistent with the relatively broad tuning of the modulation filters inferred from experiments on modulation masking. The pattern of the results was very similar to that found earlier for normally hearing listeners, although performance overall was slightly poorer than for normally hearing listeners (Sek and Moore, 2003).

Experiment 2 examined the ability to hear a change in the relative phase of the components in a three-component modulator with harmonically spaced components. The frequency of the central component, f_c, was either 50 or 100 Hz. Performance was good (70–80% correct) when the component spacing was $\leqslant 0.5 f_c$, but worsened markedly for frequency spacings greater than that. This is broadly the pattern of results predicted from the concept of the MFB. Performance was only slightly impaired by randomizing the overall modulation depth from one stimulus to the next. This suggests that listeners did not use the overall effective internal depth of the modulation as a cue. Again, the pattern of the results was very similar to that found earlier for normally hearing listeners, although performance overall was slightly poorer than for normally hearing listeners (Sek and Moore, 2003).

It may be concluded that the ability to process complex suprathreshold patterns of AM is affected only slightly by cochlear hearing loss.

ACKNOWLEDGMENTS

This work was supported by the Wellcome Trust and by the MRC. We thank Christian Füllgrabe for helpful discussions and Brian Glasberg for help with statistical analyses. We also thank Associate Editor Andrew Oxenham, Christian Lorenzi, and an anonymous reviewer for helpful comments on an earlier version of this paper.

Bacon, S. P., and Gleitman, R. M. (**1992**). "Modulation detection in subjects with relatively flat hearing losses," J. Speech Hear. Res. **35**, 642–653.

Darwin, C. J., and Carlyon, R. P. (**1995**). "Auditory grouping," In *Hearing*, edited by B. C. J. Moore (Academic Press, San Diego).

Dau, T., Kollmeier, B., and Kohlrausch, A. (**1997a**). "Modeling auditory processing of amplitude modulation. I. Detection and masking with narrowband carriers," J. Acoust. Soc. Am. **102**, 2892–2905.

Dau, T., Kollmeier, B., and Kohlrausch, A. (**1997b**). "Modeling auditory processing of amplitude modulation. II. Spectral and temporal integration," J. Acoust. Soc. Am. **102**, 2906–2919.

Ewert, S. D., and Dau, T. (**2000**). "Characterizing frequency selectivity for envelope fluctuations," J. Acoust. Soc. Am. **108**, 1181–1196.

Ewert, S. D., Verhey, J. L., and Dau, T. (**2002**). "Spectro-temporal processing in the envelope-frequency domain," J. Acoust. Soc. Am. **112**, 2921–2931.

Formby, C. (1982). "Differential sensitivity to tonal frequency and to the rate of amplitude modulation of broad-band noise by hearing-impaired listeners," Ph.D. thesis, Washington University, St. Louis.

Formby, C. (**1986**). "Frequency and rate discrimination by Meniere patients," Audiology **25**, 10–18.

Forrest, T. G., and Green, D. M. (**1987**). "Detection of partially filled gaps in noise and the temporal modulation transfer function," J. Acoust. Soc. Am. **82**, 1933–1943.

Füllgrabe, C., and Lorenzi, C. (**2003**). "The role of envelope beat cues in the detection and discrimination of second-order amplitude modulation," J. Acoust. Soc. Am. **113**, 49–52.

Füllgrabe, C., Meyer, B., and Lorenzi, C. (**2003**). "Effect of cochlear damage on the detection of complex temporal envelopes," Hear. Res. **178**, 35–43.

Füllgrabe, C., Moore, B. C. J., Demany, L., Ewert, S. D., Sheft, S., and Lorenzi, C. (**2005**). "Modulation masking produced by second-order modulators," J. Acoust. Soc. Am. **117**, 2158–2168.

Glasberg, B. R., and Moore, B. C. J. (**1986**). "Auditory filter shapes in subjects with unilateral and bilateral cochlear impairments," J. Acoust. Soc. Am. **79**, 1020–1033.

Glasberg, B. R., and Moore, B. C. J. (**1990**). "Derivation of auditory filter shapes from notched-noise data," Hear. Res. **47**, 103–138.

Grant, K. W. (**1998**). "Modulation rate detection and discrimination by normal-hearing and hearing-impaired listeners," J. Acoust. Soc. Am. **104**, 1051–1060.

Kohlrausch, A., Fassel, R., and Dau, T. (**2000**). "The influence of carrier level and frequency on modulation and beat-detection thresholds for sinusoidal carriers," J. Acoust. Soc. Am. **108**, 723–734.

Lee, J. (**1994**). "Amplitude modulation rate discrimination with sinusoidal carriers," J. Acoust. Soc. Am. **96**, 2140–2147.

Lemanska, J., Skrodzka, E., and Sek, A. (**2002**). "Discrimination of the amplitude modulation rate," Arch. Acoust. **27**, 3–22.

Liegeois-Chauvel, C., Lorenzi, C., Trebuchon, A., Regis, J., and Chauvel, P. (**2004**). "Temporal envelope processing in the human left and right auditory cortices," Cereb. Cortex **14**, 731–740.

Lorenzi, C., Berthommier, F., and Demany, L. (**1999**). "Discrimination of amplitude-modulation phase spectrum," J. Acoust. Soc. Am. **105**, 2987–2990.

Lorenzi, C., Micheyl, C., Berthommier, F., and Portalier, S. (**1997**). "Modulation masking in listeners with sensorineural hearing loss," J. Speech Lang. Hear. Res. **40**, 200–207.

Moore, B. C. J. (**1998**). *Cochlear Hearing Loss* (Whurr, London).

Moore, B. C. J. (**2003**). *An Introduction to the Psychology of Hearing*, 5th ed. (Academic Press, San Diego).

Moore, B. C. J., and Glasberg, B. R. (**1997**). "A model of loudness perception applied to cochlear hearing loss," Aud. Neurosci. **3**, 289–311.

Moore, B. C. J., and Glasberg, B. R. (**2001**). "Temporal modulation transfer functions obtained using sinusoidal carriers with normally hearing and hearing-impaired listeners," J. Acoust. Soc. Am. **110**, 1067–1073.

Moore, B. C. J., and Glasberg, B. R. (**2004**). "A revised model of loudness perception applied to cochlear hearing loss," Hear. Res. **188**, 70–88.
Moore, B. C. J., and Ohgushi, K. (**1993**). "Audibility of partials in inharmonic complex tones," J. Acoust. Soc. Am. **93**, 452–461.
Moore, B. C. J., Sek, A., and Glasberg, B. R. (**1999**). "Modulation masking produced by beating modulators," J. Acoust. Soc. Am. **106**, 908–918.
Moore, B. C. J., Shailer, M. J., and Schooneveldt, G. P. (**1992**). "Temporal modulation transfer functions for band-limited noise in subjects with cochlear hearing loss," Br. J. Audiol. **26**, 229–237.
Moore, B. C. J., Wojtczak, M., and Vickers, D. A. (**1996**). "Effect of loudness recruitment on the perception of amplitude modulation," J. Acoust. Soc. Am. **100**, 481–489.
Patterson, R. D. (**1987**). "A pulse ribbon model of monaural phase perception," J. Acoust. Soc. Am. **82**, 1560–1586.
Pick, G., Evans, E. F., and Wilson, J. P. (**1977**). "Frequency resolution in patients with hearing loss of cochlear origin," in *Psychophysics and Physiology of Hearing*, edited by E. F. Evans and J. P. Wilson (Academic Press, London).
Plomp, R. (**1964**). "The ear as a frequency analyzer," J. Acoust. Soc. Am. **36**, 1628–1636.
Plomp, R. (**1978**). "Auditory handicap of hearing impairment and the limited benefit of hearing aids," J. Acoust. Soc. Am. **63**, 533–549.
Plomp, R. (**1983**). "The role of modulation in hearing," in *Hearing—Physiological Bases and Psychophysics*, edited by R. Klinke and R. Hartmann (Springer, Berlin).
Plomp, R. (**1994**). "Noise, amplification, and compression: Considerations of three main issues in hearing aid design," Ear Hear. **15**, 2–12.
Plomp, R., and Mimpen, A. M. (**1968**). "The ear as a frequency analyzer II," J. Acoust. Soc. Am. **43**, 764–767.
Rees, A., and Møller, A. R. (**1983**). "Responses of neurons in the inferior colliculus of the rat to AM and FM tones," Hear. Res. **10**, 301–310.
Rhode, W. S., and Robles, L. (**1974**). "Evidence from Mössbauer experiments for non-linear vibration in the cochlea," J. Acoust. Soc. Am. **55**, 588–596.
Robles, L., and Ruggero, M. A. (**2001**). "Mechanics of the mammalian cochlea," Physiol. Rev. **81**, 1305–1352.
Ruggero, M. A., Rich, N. C., Recio, A., Narayan, S. S., and Robles, L. (**1997**). "Basilar-membrane responses to tones at the base of the chinchilla cochlea," J. Acoust. Soc. Am. **101**, 2151–2163.
Sek, A., and Moore, B. C. J. (**1994**). "The critical modulation frequency and its relationship to auditory filtering at low frequencies," J. Acoust. Soc. Am. **95**, 2606–2615.
Sek, A., and Moore, B. C. J. (**2003**). "Testing the concept of a modulation filter bank: The audibility of component modulation and detection of phase change in three-component modulators," J. Acoust. Soc. Am. **113**, 2801–2811.
Sek, A., and Moore, B. C. J. (**2004**). "Estimation of the level and phase of the simple distortion tone in the modulation domain," J. Acoust. Soc. Am. **116**, 3031–3037.
Shannon, R. V., Zeng, F.-G., Kamath, V., Wygonski, J., and Ekelid, M. (**1995**). "Speech recognition with primarily temporal cues," Science **270**, 303–304.
Shofner, W. D., Sheft, S., and Guzman, S. J. (**1996**). "Responses of ventral cochlear nucleus units in the chinchilla to amplitude modulation by low-frequency, two-tone complexes," J. Acoust. Soc. Am. **99**, 3592–3605.
Soderquist, D. R. (**1970**). "Frequency analysis and the critical band," Psychonomic Sci. **21**, 117–119.
Steinberg, J. C., and Gardner, M. B. (**1937**). "The dependency of hearing impairment on sound intensity," J. Acoust. Soc. Am. **9**, 11–23.
Strickland, E. A., and Viemeister, N. F. (**1996**). "Cues for discrimination of envelopes," J. Acoust. Soc. Am. **99**, 3638–3646.
Takahashi, G. A., and Bacon, S. P. (**1992**). "Modulation detection, modulation masking, and speech understanding in noise in the elderly," J. Speech Hear. Res. **35**, 1410–1421.
Tandetnik, S., Garnier, S., and Lorenzi, C. (**2001**). "Measurement of first- and second-order modulation detection thresholds in listeners with cochlear hearing loss," Br. J. Audiol. **35**, 355–364.
Turner, C. W., Souza, P. E., and Forget, L. N. (**1995**). "Use of temporal envelope cues in speech recognition by normal and hearing-impaired listeners," J. Acoust. Soc. Am. **97**, 2568–2576.
Uppenkamp, S., Fobel, S., and Patterson, R. D. (**2001**). "The effects of temporal asymmetry on the detection and perception of short chirps," Hear. Res. **158**, 71–83.
Verhey, J. L., Ewert, S. D., and Dau, T. (**2003**). "Modulation masking produced by complex tone modulators," J. Acoust. Soc. Am. **114**, 2135–2146.
Wingfield, A., Poon, L. W., Lombardi, L., and Lowe, D. (**1985**). "Speed of processing in normal aging: Effects of speech rate, linguistic structure and processing time," J. Gerontol. **40**, 579–585.
Wojtczak, M., and Viemeister, N. F. (**2005**). "Forward masking of amplitude modulation: Basic characteristics," J. Acoust. Soc. Am. **118**, 3198–3210.
Zwicker, E. (**1952**). "Die Grenzen der Hörbarkeit der Amplitudenmodulation und der Frequenzmodulation eines Tones (The limits of audibility of amplitude modulation and frequency modulation of a pure tone)," Acustica **2**, 125–133.
Zwicker, E. (**1956**). "Die elementaren Grundlagen zur Bestimmung der Informationskapazität des Gehörs (The foundations for determining the information capacity of the auditory system)," Acustica **6**, 356–381.

Horizontal localization with bilateral hearing aids: Without is better than with

Tim Van den Bogaert[a)]
Lab exp. ORL, K. U. Leuven, Kapucijnenvoer 33, B-3000 Leuven, Belgium

Thomas J. Klasen
ESAT-SCD, K. U. Leuven, Kasteelpark Arenberg 10, B-3001 Leuven, Belgium

Marc Moonen
ESAT-SCD, K. U. Leuven, Kasteelpark Arenberg 10, B-3001 Leuven, Belgium

Lieselot Van Deun
Lab exp. ORL, K. U. Leuven, Kapucijnenvoer 33, B-3000 Leuven, Belgium

Jan Wouters
Lab exp. ORL, K. U. Leuven, Kapucijnenvoer 33, B-3000 Leuven, Belgium

(Received 23 November 2004; revised 12 September 2005; accepted 27 October 2005)

This paper studies the effect of bilateral hearing aids on directional hearing in the frontal horizontal plane. Localization tests evaluated bilateral hearing aid users using different stimuli and different noise scenarios. Normal hearing subjects were used as a reference. The main research questions raised in this paper are: (i) How do bilateral hearing aid users perform on a localization task, relative to normal hearing subjects? (ii) Do bilateral hearing aids preserve localization cues, and (iii) Is there an influence of state of the art noise reduction algorithms, more in particular an adaptive directional microphone configuration, on localization performance? The hearing aid users were tested without and with their hearing aids, using both a standard omnidirectional microphone configuration and an adaptive directional microphone configuration. The following main conclusions are drawn. (i) Bilateral hearing aid users perform worse than normal hearing subjects in a localization task, although more than one-half of the subjects reach normal hearing performance when tested unaided. For both groups, localization performance drops significantly when acoustical scenarios become more complex. (ii) Bilateral, i.e., independently operating hearing aids do not preserve localization cues. (iii) Overall, adaptive directional noise reduction can have an additional and significant negative impact on localization performance. [DOI: 10.1121/1.2139653]

PACS number(s): 43.66.Qp, 43.66.Pn, 43.66.Ts [RAL] Pages: 515–526

I. INTRODUCTION

Selective hearing is a useful mechanism for extracting desired signals in complex acoustic environments, such as a cocktail party. The ability to understand speech in these complex scenarios has been largely attributed to the binaural processing strategy used in the auditory system (Bronkhorst and Plomp, 1988, 1989). Information from both ears interacts at various subcortical structures thereby providing the listener with the information needed to reconstruct the auditory scene. This helps the listener to stay focussed on one sound source and to cancel out unwanted sound sources. This paper studies one of the binaural processes, namely sound localization. The main mechanisms used for sound localization are fairly well known. Localization involves binaural processing of very small differences in time (10–700 μs), intensity (0–20 dB), and spectrum between the two ears (Stevens and Newman, 1936; Blauert, 1997; Gilkey and Anderson, 1997; Hartmann, 1999; Langendijk and Bronkhorst, 2002). Extensive psychoacoustical research has been done on localization: Experiments to measure localization performance of normal hearing (Makous and Middlebrooks, 1990; Hofman and Van Opstal, 1998; Lorenzi *et al.*, 1999b) and hearing impaired subjects (Hausler *et al.*, 1983; Noble *et al.*, 1994; Lorenzi *et al.*, 1999a) with different stimuli and in different test conditions, experiments under headphones with isolated or conflicting cues (Wightman and Kistler, 1992; Lorenzi *et al.*, 1999b), comparing performance of a monaural hearing aid or cochlear implant configuration with a bilateral hearing aid or cochlear implant configuration (Dillon, 2001; Van Hoesel and Tyler, 2003), and many others. Although a lot of work has been done on localization with normal hearing and hearing impaired subjects, little work has questioned the effect of a bilateral hearing aid system on the binaural potential of the hearing aid user. In the human auditory system, the acoustical input signals of both ears are linked to the binaural centers where the binaural cues are interpreted and processed. Adding independently working hearing aids, each using its own compression scheme, introducing its own time delay (in the order of 5 to 10 ms) (Dillon *et al.*, 2003) and

[a)]Electronic mail: tim.vandenbogaert@uz.kuleuven.ac.be

having independent noise reduction schemes, could have a destructive effect on the binaural cues. Correspondingly, the hearing aid user's localization performance and speech perception in a complex environment could also be degraded.

In the work of Hausler *et al.* (1983), the question was raised as to whether hearing aids could have an impact on sound localization performance. Noble and Byrne (1990) tested localization performance in the frontal horizontal and vertical planes with bilateral behind the ear (BTE), in the ear (ITE), and in the canal (ITC) hearing aids with omnidirectional microphone configurations. A normal hearing group was used as a reference. Intrasubject analysis did not show significant differences between unaided and aided performance for all three groups. These analyses were done on an error measure in which both vertical and horizontal errors were included. No statistical analysis on only horizontal or on only vertical localization errors was presented in the study. However, Noble and Byrne stated that for the control group, i.e. a group of six normal hearing subjects, horizontal localization performance dropped from nearly 100% correct unaided to 73% correct wearing BTE hearing aids. In the same study, it is mentioned that the hearing aid users tended to show poorer aided than unaided localization performance in the frontal horizontal plane, except for the ITE hearing aid users, when wearing their own hearing aids. The difference in horizontal localization performance was not quantified in the study.

Later, Noble *et al.* (1998) and Byrne *et al.* (1998) showed that better performance could be obtained by using open earmolds instead of closed earmolds for subjects with a moderate high-frequency (and a severe low-frequency loss) or a moderate low-frequency (and a severe high-frequency) hearing loss. By using open earmolds, the subject can use the direct soundfield in the region of the moderate hearing loss for localization. For subjects with a moderate high-frequency loss, improvement in the vertical plane was found. For subjects with a moderate low to midfrequency hearing loss, improvement in the horizontal plane was found and performance was restored to unaided performance. These studies suggest that bilateral BTE hearing aids do not preserve localization cues. In all three studies, a broadband pink noise target stimulus was used and no jammer sources were present.

The available processing power in hearing aids increases as technology evolves. One of the main benefits is that more complex noise reduction algorithms can be implemented, improving speech understanding performance in acoustically challenging scenarios. In recent years, good results have been obtained using adaptive filtering techniques. These techniques adapt according to changes in noise scenario or acoustic condition, but are typically designed and evaluated monaurally. An important question is whether using these techniques bilaterally can have an impact on a binaural process, in particular on localization.

This paper studies localization performance of bilateral BTE hearing aid users in the frontal horizontal plane. The main cues for sound localization in these tests are interaural time differences (ITD) and interaural level differences (ILD). This study questions and quantifies the effect of current signal processing techniques on localization performance. By using low-and high-frequency stimuli, it tries to determine which cues are being affected by the different signal processing strategies. The following research questions are addressed in this paper: (i) How well do bilateral hearing aid subjects, relative to normal hearing persons, perform on a localization task using low-frequency, high-frequency and broadband signals and what is the influence of jammer sources on localization performance? (ii) Do modern digital hearing aids preserve localization cues and hence can hearing aid users use the full potential of their binaural processing capabilities? (iii) Do noise reduction systems have an influence on localization performance? The noise reduction technique tested was an adaptive directional microphone configuration, which is implemented in today's state of the art hearing aids. Data were gathered from hearing impaired subjects with and without hearing aids to test the impact of their hearing aids. A group of normal hearing subjects was used as a reference. The hearing aids were fitted with a nonadaptive omnidirectional microphone configuration and an adaptive directional microphone configuration. Low-frequency, high-frequency, and broadband signals were used to separate the effects on ITD and ILD processing. Jammer sources were added to the condition with the broadband signal to evaluate the impact of the noise reduction system.

II. METHODS

A. Subjects

Prior to the study with the hearing impaired subjects, a similar study was performed with ten normal hearing subjects between 20 and 25 years old (average age: 22 years old). Mean audiometric data of the normal hearing subjects are given in Table I. These subjects have a maximum hearing threshold of 20 dB hearing level (HL) on all octave frequencies starting from 125 Hz up to 8000 Hz. The relevant data of the normal hearing group will be described and used as a reference for the hearing impaired group.

Ten hearing impaired subjects, ranging from 44 to 79 years old, participated in this study. All of them are experienced bilateral hearing aid users. Six of them use Phonak, Switzerland, Perseo hearing aids, three use GNResound, Denmark, Canta7 hearing aids, and one of the test persons uses Widex, Denmark, Diva hearing aids. The settings of their everyday hearing aids were copied into another pair of hearing aids of the identical brand and type, and monaural spectral enhancement techniques were switched off in the Canta7 and Perseo devices. Audiometric data of the hearing impaired subjects are given in Table I. The mean absolute difference between left and right hearing loss is less than 10 dB for all subjects, except for subject ML who has a larger asymmetrical hearing loss. The subjects used their own earmolds with a venting between 1 and 3 mm, except for subject ML who used an open venting on her best ear for otological reasons. The amplification levels of all subjects did not show big asymmetrical settings (<7 dB difference between the mean left and right amplification levels at an input level of 50 dB sound pressure level (SPL) (G50) and <7 dB difference for the mean left and right amplification

TABLE I. The audiometric data (in dB HL) of the 10 hearing impaired (HI) subjects and the mean audiometric data of the 10 normal hearing (NH) subjects.

		Right ear (Hz)							Left ear (Hz)						
Subject	Hearing aid type	250	500	1 k	2 k	4 k	6 k	8 k	250	500	1 k	2 k	4 k	6 k	8 k
AP	Perseo 211	55	50	45	40	55	60		35	35	45	55	60	60	
BG	Canta 7	35	35	40	40	45	30		40	35	35	35	35	25	
BJ	Perseo 211	25	35	40	40	45	55		35	40	45	45	60	60	
CH	Perseo 111	45	35	35	50	80	100		40	30	35	70	80	105	
DH	Perseo 211	30	30	40	40	40	45		35	30	45	50	45	50	
MA	Canta 7	15	10	30	55	60	45		25	25	30	55	55	45	
ML	Diva	35	55	65	60	70	80		15	25	35	40	55	75	
SM	Canta 7	45	40	35	45	55	60		50	50	40	60	55	60	
VP	Perseo 111	25	30	35	35	50	60		20	20	30	35	45	55	
VM	Perseo 211	50	50	45	50	50	45		50	55	50	50	50	50	
Mean HI		36	37	41	46	55	58		35	35	39	50	54	59	
StDev HI		13	13	10	8	12	20		12	11	7	11	12	21	
Mean NH		−3	1	4	3	3		14	4	5	8	5	10		11
StDev NH		9	6	7	7	5		6	6	4	3	5	7		6

levels at an input level of 80 dB SPL (G80) at all frequencies), except for subject ML who had asymmetrical amplification levels to compensate for the asymmetrical hearing loss. However, this subject did not show a bias with (on average 5°) or without hearing aids (on average 2°), and showed results similar to all other subjects.

B. Setup

Tests were carried out in a reverberant room with dimensions 6 m × 3 m × 3.5 m (length × width × height) and a reverberation time, *T*60, of 0.54 s as determined for a speech weighted noise spectrum. Test persons were placed inside an array of 13 single-cone speakers with a cone diameter of 10 cm. The speakers were located in the frontal horizontal plane at angles ranging from −90° to +90° relative to the subject, a spacing of 15° was used. The speakers were placed at a distance of 1 m of the subject and were labeled 1 to 13. The target signal was played through one of the 13 speakers using a LYNXONE soundcard and a programmable electronic switch box. This switch box, together with the whole test procedure, is controlled by our test software, referred to as "advanced localization procedure" (ALP). The test operator loads the test into the program and enters the responses of the subject by clicking the appropriate buttons. The full test procedure is stored by the program, together with the calculated performance measures. Two other, YAMAHA CBX-S3 powered speakers were present in the test room to create the noise scenario to evaluate localization performance with the noise reduction system. They were placed at a distance of 1 m from the subject at an angle of −90° to +90° relative to the subject. An illustration of the test setup is given in Fig. 1.

C. Stimuli

Earlier studies show that localization of high and low frequencies rely on different binaural processing strategies. Low frequencies ($f < 1000$ Hz) do not generate a large ILD, because the head shadow effect is small for such wavelengths. When localizing low-frequency sounds, ITD information is primarily used. When the wavelength of a sinusoid is smaller than the diameter of the head, timing information becomes ambiguous. For high frequencies ($f > 1500$ Hz), the localization system is based on ILD information and ITD information of the low-frequency envelope of the signal (Moore, 1997a; Hartmann, 1999). To obtain information about both binaural processing paths, a 200 ms 1/3 octave low-frequency noise band ($fc = 500$ Hz) and a 200-ms 1/3 octave high-frequency noise band were chosen as target stimuli. In the first study with normal hearing subjects, a 200 ms 1/3 octave high-frequency noise band centered at 5000 Hz ($fc = 5000$ Hz) was used. When testing hearing impaired persons, this stimulus proved to be useless due to the inaudibility of the stimulus to some test persons. Therefore, a

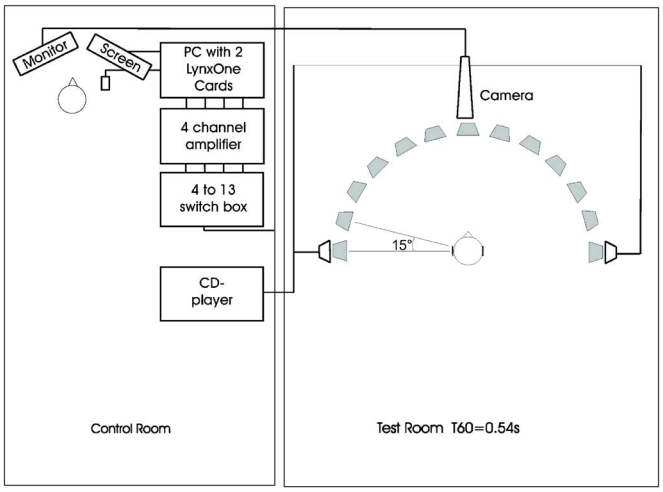

FIG. 1. An overview of the used test setup. The "4 to 13 switch box" is connected to the array of 13 (gray colored) loudspeakers and enables the test program to play target sounds from a personal computer on the speakers (connections are not drawn for reasons of clarity). The compact disk players are connected to the 2 YAMAHA (noncolored) speakers located at ±90° and −90° of the subject. These are used to create the noise scenario. A camera is used to monitor the subject.

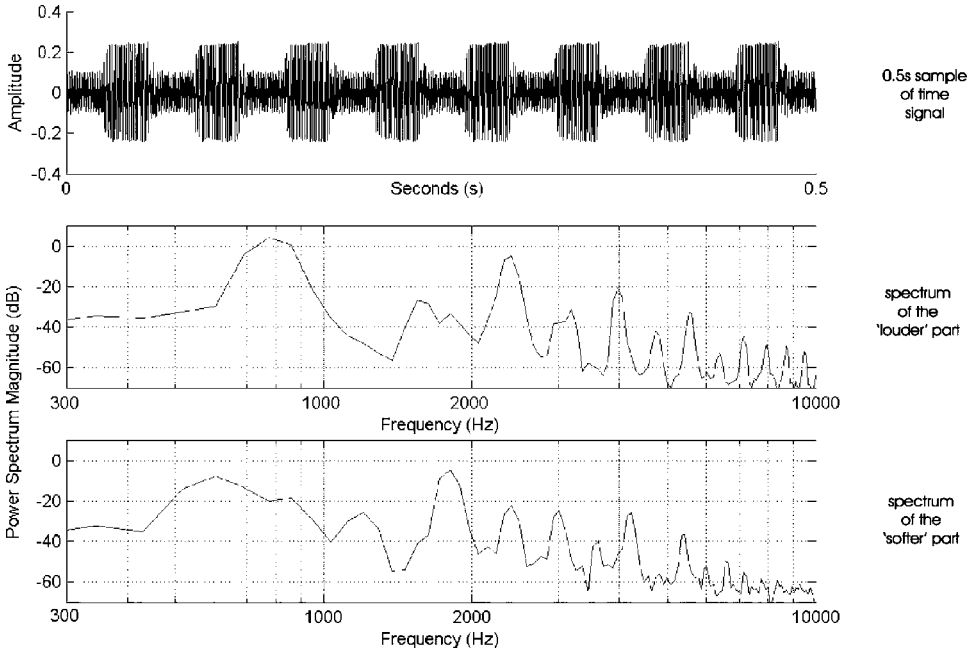

FIG. 2. Up: The time structure of a 0.5 s sample of the used telephone ringing signal which alternates between a "softer" and a "louder" fragment. Middle: The power spectral density of the louder part of the telephone ringing signal. Down: The power spectral density of the softer part of the telephone ringing signal.

200 ms 1/3 octave high-frequency noise band centered at 3150 Hz was used for the hearing impaired subjects. Still, the data of the 5000 Hz test with the normal hearing subjects are given and compared with the 3150 Hz test with the hearing impaired subjects. We believe that this remains a fair comparison for three reasons. First, frequencies are well above 1500 Hz, meaning that the same localization mechanisms are being used. Second, the center frequencies—3150 Hz and 5000 Hz—are separated by less than an octave. Third, the minimum audible angle for frequencies in both stimuli are similar, with the 5000 Hz noise band having a slightly smaller minimal audible angle at the left and right most sides of the head (starting from 60°) (Moore, 1997b) which would give the normal hearing group a slight disadvantage. The third stimulus was a 1 s broadband telephone ringing signal. This is the alerting signal of a telephone, it contains both low and high frequencies and includes a lot of transients which should make localization easier. The time structure and the spectrum of this signal is shown in Fig. 2. An interesting fact is that human subjects are very familiar with and highly trained on localizing a telephone signal in their daily lives.

All target signals are cosine windowed with a rise and fall time of 50 ms. The telephone stimulus was tested in silence, as well as with a multitalker babble source located at the left and the right side of the subject. When tests were carried out with hearing aids or with normal hearing subjects, stimuli were presented at 65 dB SPL. For the noise scenario, the two noise sources were set at 62 dB SPL giving a signal-to-noise ratio (SNR) of 0 dB in the center of the speaker array. Sound level calibrations were done in absence of the subject. To estimate the impact of signal processing in bilateral hearing aids, tests with and without hearing aids are compared. To rule out the effect of audibility, tests were carried out at equal sensation levels with and without hearing aids. The amplification level of the stimuli was corrected until the subject confirmed that an equal sensation level was obtained with and without hearing. Afterwards, the noise level was corrected to keep the SNR of 0 dB. Because of the extra amplification in the unaided condition, the results do not reflect a "daily life" comparison between the aided and unaided condition. However, they should reflect the auditory ability of the subject to use binaural cues.

D. Test protocol

Subjects sat inside the array of 13 speakers and the chair was elevated until the ears reached the level of the 13 speakers. For the first tests with normal hearing (the test with the low- and high-frequency noise band), four repetitions were used per speaker resulting in 52 presented trials per test. Due to lack of time, all the other tests (all tests with the hearing impaired and both tests with the telephone signal for the normal hearing) have three repetitions on each speaker resulting in 39 presented trials per test. The stimuli were presented randomly and were roved with a roving level of 4 dB (between −4 dB and 0 dB). All subjects were instructed to keep their head fixed and pointed to 0° during stimulus playback. They were watched on a monitor. The task was to identify the speaker where the target sound was heard. Hearing aid users were tested without their hearing aids, with their hearing aids using an omnidirectional microphone configuration and with their hearing aids using an adaptive directional microphone configuration. Three different stimuli were used. Two different acoustical scenarios were tested with the broadband stimulus (in silence and with multitalker babble sources). All four test scenarios were performed twice for each test subject. Two sessions were held on different dates for test-retest purposes, and all tests were completed during each session. One subject had one shorter visit in which not all scenarios were tested, combined with a longer session in which some tests were repeated twice. The tests that had to be done twice were performed in the beginning and at the end of the second session. No influence was seen

on the test results. One test took about 5 min, and one session including all scenarios took less than 1.5 h. Subjects had a break after every six tests and could take a break whenever they felt tired. In total, 320 individual test runs were completed ($4 \times 4 \times 10 \times 2$).

E. Performance measures

Different error measures have been used in previous localization studies (Noble and Byrne, 1990; Lorenzi *et al.*, 1999b; Van Hoesel *et al.*, 2002). We will focus on two commonly used error measures:

(1) Root-mean-square (rms) error

$$\text{rms}(^\circ) = \sqrt{\frac{\sum_{i=1}^{n} (\text{stimulus} - \text{response})^2}{n}}, \quad (1)$$

(2) Mean Absolute Error (MAE)

$$\text{MAE}(^\circ) = \frac{\sum_{i=1}^{n} |\text{stimulus} - \text{response}|}{n}, \quad (2)$$

where n is the number of presented stimuli. When using MAE, all errors are weighted equally, while in the rms error large errors have a bigger impact than small errors. The smallest nonzero error a subject can make during one test run equals 2.40° rms and 0.38° MAE (with $n=39$ trials per test run). Statistical analysis has been performed on both error measures, showing similar results. Throughout this manuscript, the data will be reported in detail only using the rms error measure. The mean and standard deviation of the MAE values will be given for the different subject categories for all tested conditions. This gives the reader the opportunity to compare with other work where MAE error measures have been used. Throughout this paper, statistical analysis will be shown only for rms values.

III. RESULTS AND ANALYSIS

First, the data and statistical analysis of the normal hearing persons are presented, followed by the data and analysis of the hearing impaired subjects. The data shown for each subject are the average over test and retest conditions. This is done because no statistical difference is found between test and retest conditions for both the normal hearing and the hearing impaired subjects. All statistical analyses are performed using SPSS 10.0 with test and retest separated in a repeated-measures ANOVA. A standard significance level of 0.05 is used throughout the manuscript. The different test conditions are identified as follows: For the hearing-impaired group, the three hearing aid conditions are: No—without hearing aids; o—with hearing aids with an omnidirectional configuration; and a—with hearing aids with an adaptive directional configuration. The normal hearing group is identified as nh. The stimulus conditions are identified as follows: 500 Hz—1/3 octave low-frequency band; 3150 Hz or 5000 Hz—1/3 octave high-frequency band; ts—wideband telephone signal in silent condition; and tblr—telephone signal with babble jammer on the left and right. The data and statistical analysis will motivate the discussion in Sec. IV.

TABLE II. The individual rms data with the mean MAE and rms data of the normal hearing subjects for the four different test conditions. All data are in units of degrees (°)

rms error (°)	ts	tblr	500 Hz	5000 Hz
TVS	10.5	12.5	14.3	22.9
SB	6.1	12.1	14.4	22.8
SVD	10.4	11.6	15.3	23.1
LD	5.3	13.6	15.8	21.5
LVDP	5.3	9.9	10.5	14.0
KH	3.3	11.6	11.0	16.4
HD	9.9	13.0	14.0	25.4
EBI	4.5	12.0	12.3	21.9
EBO	10.0	11.1	16.4	24.2
DVS	2.4	10.3	11.2	21.0
Mean rms	6.8	11.8	13.5	21.3
stdev	3.1	1.1	2.1	3.5
Mean MAE	3.5	7.3	8.7	14.3
stdev	2.6	0.9	1.9	2.9

Note: stdev=Standard deviation.

A. Normal hearing subjects

The data of the normal hearing subjects are given in Table II and represented in Figs. 3–5. Table II shows the individual rms results and the mean rms and MAE results of the normal hearing subjects. It shows that all normal hearing subjects perform better with the low-frequency narrow-band signal (average rms error: 13.5°) than with the high-frequency narrow-band signal (average rms error: 21.3°).

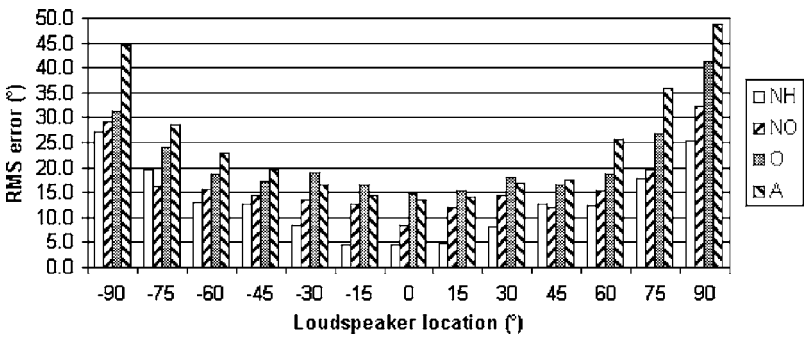

FIG. 3. The error bars show the rms error per speaker when accumulating all responses of the different test conditions per stimulus location. This was done for the group of normal hearing subjects (NH), the group of hearing impaired subjects without hearing aids (NO), with hearing aids using an omnidirectional configuration (O), and an adaptive directional configuration (A).

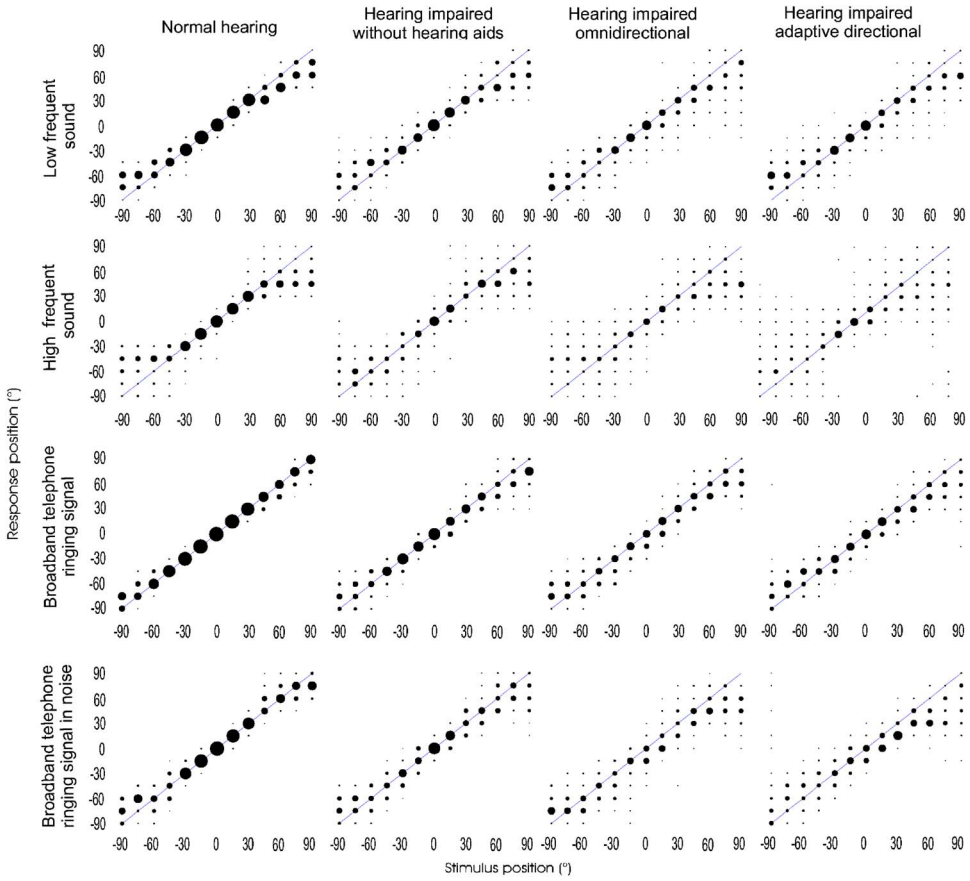

FIG. 4. All responses given by the normal hearing subjects and the hearing impaired subjects with and without hearing aids for the different stimuli and acoustical conditions. The surface of the circles is proportional to the amount of responses given by the subjects.

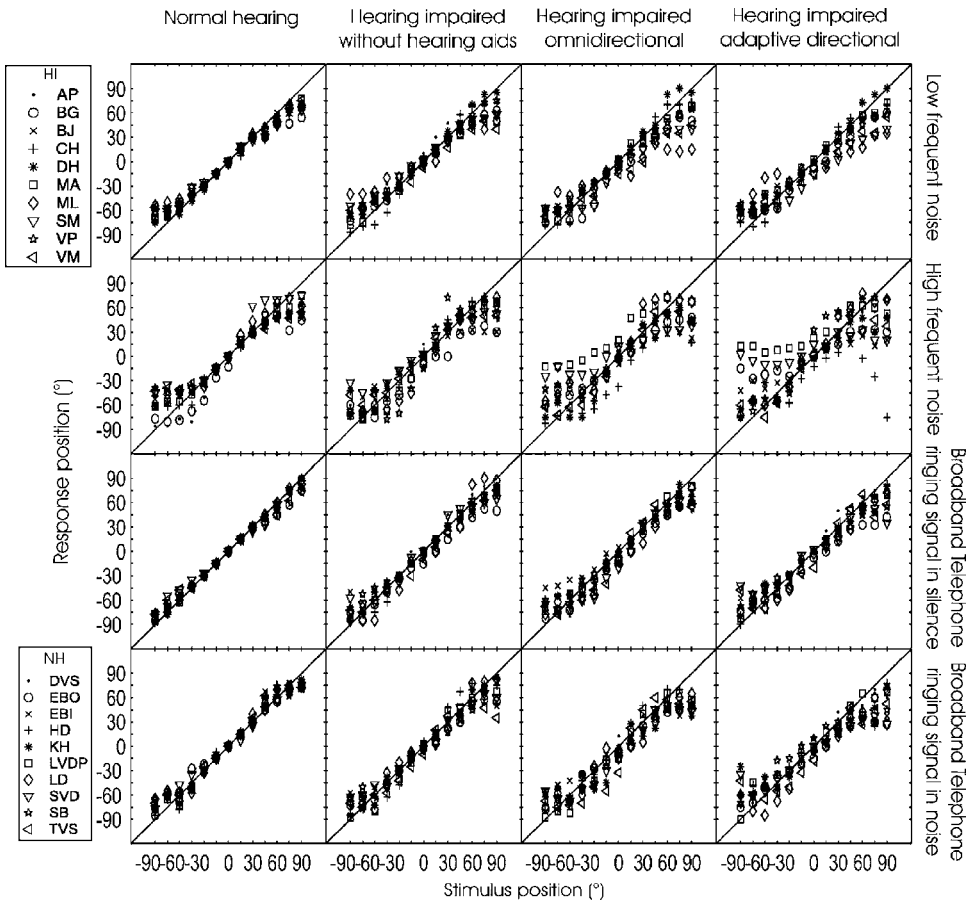

FIG. 5. The mean responses given by the different normal hearing subjects and the different hearing impaired subjects with and without hearing aids for the different stimuli and acoustical conditions.

TABLE III. The individual rms data with the mean rms and MAE data of the hearing impaired subjects for the four different test signals and three different hearing aid settings.

	ts			tblr			500 Hz			3150 Hz		
rms (°)	No HA	Omni	Adapt	No HA	Omni	Adapt	No HA	Omni	Adapt	No HA	Omni	Adapt
AP	12.6	16.5	19.6	14.3	18.3	17.1	16.5	17.3	18.6	21.7	21.3	21.3
BG	18.2	15.6	24.4	15.7	18.4	26.8	14.8	20.2	16.4	28.3	23.4	37.4
BJ	15.3	19.4	16.3	18.0	24.6	26.4	16.8	14.4	16.4	29.3	30.9	35.7
CH	12.1	12.9	8.3	16.6	18.0	28.2	12.4	12.8	14.1	18.2	33.7	61.5
DH	8.1	15.0	10.6	9.7	28.9	31.1	11.6	13.8	13.1	18.2	23.4	22.8
MA	8.5	10.2	12.4	12.1	15.8	14.2	15.8	15.0	15.5	14.3	39.0	49.6
ML	14.6	14.8	15.0	15.4	16.9	19.8	27.1	38.4	35.0	16.9	22.6	18.3
SM	16.2	19.4	25.9	16.3	24.7	31.1	18.7	25.0	27.1	25.0	36.9	47.5
VP	13.3	17.5	17.5	14.4	21.1	25.4	14.5	15.6	18.8	31.9	26.8	29.2
VM	11.0	20.1	24.9	20.8	26.3	29.3	21.3	27.8	26.3	20.3	21.4	26.6
Mean rms	13.0	16.1	17.5	15.3	21.3	25.0	17.0	20.0	20.1	22.4	27.9	35.0
stdev	3.3	3.1	6.2	3.0	4.5	5.9	4.5	8.1	7.1	5.9	6.7	14.1
Mean MAE	8.8	11.7	12.4	10.6	15.9	17.8	12.1	15.1	15.4	16.0	21.4	25.7
stdev	2.9	3.0	5.2	2.5	3.8	4.1	4.2	7.2	7.1	5.2	6.5	10.3

Note: stdev=Standard deviation.

Also, all subjects perform better with the transient broadband signal (average rms error: 6.8°) than with both narrow-band signals. Performance drops for all tested subjects when noise is added to the scenario with the broadband telephone ringing signal (average rms error: 11.8°). These statements are confirmed by a two-way repeated-measures ANOVA (with Bonferroni adjustment for multiple comparisons).

The ANOVA is carried out on the normal hearing data with the factors "test signal" (500 Hz noise band, 5000 Hz noise band, and telephone in silence and telephone with babble from left and right) and "test-retest." A main effect for the factor test signal is observed (lower bound, $p < 0.001$). No main effect was seen for the factor test-retest for the standard 0.05 level (lower bound, $p=0.330$) and no significant interaction between the two factors was found (lower bound, $p=0.225$). For the standard 0.05 level, all four different test signals are significantly different from each other (all $p \leqslant 0.003$), except for the 500 Hz and the "telephone with babble" condition ($p=0.066$).

The data can also be interpreted per angle of incidence. The white error bar in Fig. 3 shows the rms error per speaker when accumulating all responses of the normal hearing subjects over the different test conditions. This illustrates that normal hearing subjects have a very good performance in the most frontal area of the horizontal plane (rms error $<10°$ and $>80\%$ correct answers for every angle in the area between $-30°$ and $+30°$). At the sides, sensitivity drops and localization starts to detoriate. The same tendency can be seen in the left column of Fig. 4, which shows all responses given by the normal hearing subjects under the different test conditions. However, these figures should be interpreted with caution because they represent an accumulation of the responses of the different test subjects on a localization task, which is a subject dependent process. The left column of Fig. 5 illustrates the distribution of the mean response given by each subject for each speaker location and for each test condition. This figure shows that the similarity between the mean responses given by the different normal hearing subjects was relatively high for most test conditions. Only the high-frequency stimulus showed larger dissimilarities, especially at the sides of the head.

B. Hearing impaired subjects

Hearing impaired subjects were tested in the same conditions as the normal hearing except for the fact that the 5000 Hz stimulus was replaced by a 3150 Hz stimulus. All tests were performed with six stimuli in total per condition (three each for test and retest). Figures 3–5 illustrate the data obtained from the hearing impaired subjects. The individual results of the hearing impaired subjects are given in Table III.

A two-way repeated-measures ANOVA (with Bonferroni adjustment for multiple comparisons) was carried out on the hearing impaired data on the factors test signal (500 Hz noise band, 3150 Hz noise band, and telephone in silence and telephone with babble from left and right), "hearing aid" setting (omnidirectional, adaptive directional, and no-hearing aid), and test-retest. A main effect for the factor test signal (lower bound, $p=0.011$) and the factor hearing aid setting (lower bound, $p=0.001$) is observed. No main effect is observed for the factor test-retest (lower bound, $p=0.095$). No significant interactions are found at the standard 0.05 significance level (test signal*hearing aid setting, lower bound, $p=0.185$; test signal*retest, lower bound, $p=0.487$; hearing aid setting*retest, lower bound, $p=0.209$, and hearing aid setting*test signal*retest, lower bound, $p=0.414$). Pairwise comparisons for the factor hearing aid setting show a significantly better performance without hearing aids (no) compared to both conditions with hearing aids. No significant difference at the standard 0.05 level was found between the omnidirectional (o) and adaptive directional condition (a) although the p value is very close to the 0.05 bound (p

TABLE IV. p values (with Bonferroni adjustment) of the pairwise comparison for hearing impaired subjects. Conditions without hearing aids (no), with hearing aids with an omnidirectional microphone (o), and with hearing aids with an adaptive directional microphone (a) are compared with each other (*=significant for a significance level of 0.05).

	45°/−45°	±60°/±90°	Full
General (Four conditions)			
no vs o	0.038*	0.002*	0.002*
no vs a	0.014*	0.001*	0.001*
o vs a	0.998	0.046*	0.053
500 Hz			
no vs o	0.092	0.371	0.133
no vs a	0.320	0.040*	0.032*
o vs a	0.625	1.000	1.000
3150 Hz			
no vs o	1.000	0.105	0.284
no vs a	0.441	0.071	0.098
o vs a	1.000	0.333	0.120
ts			
no vs o	0.014*	0.227	0.046*
no vs a	0.060	0.095	0.059
o vs a	1.000	0.637	1.000
tblr			
no vs o	0.038*	0.004*	0.016*
no vs a	0.012*	0.084	0.002*
o vs a	0.458	0.009*	0.044*

=0.053). The p values of all pairwise comparisons are summarized in the column "Full" of Table IV. Because the assumption was made that the two main horizontal localization mechanisms (ITD and ILD) have a different contribution to the localization performance with the different stimuli, a separate analysis on each signal is done for the hearing impaired group. This could give better insight into the distortion of cues by hearing aids. For each signal, a repeated-measures ANOVA is performed with the factors hearing aid setting (no-hearing aid, omnidirectional, and adaptive directional) and test-retest. Each time a Bonferroni adjustment was used for multiple comparisons. The p values of the pairwise comparisons discussed below are summarized in the column labeled Full of Table IV.

The low-frequency noise band. There is a main effect for the factor hearing aid setting (lower bound, $p=0.037$). No interaction with the factor 'test-retest' is observed ($p=0.310$). The setup without hearing aids outperformed the setup with the adaptive directional microphone significantly (on average by 3.1°). Although the mean difference between the omnidirectional configuration and the no-hearing-aid condition is 3.0°, no significant difference for the standard 0.05 level is found between these conditions. The mean performance of the omnidirectional and adaptive directional configuration was very similar for this test signal. No significant difference between these conditions is observed.

High-frequency noise band. There is a main effect for the factor hearing aid setting (lower bound, $p=0.042$). No interaction is observed (lower bound, $p=0.202$). Large differences in the mean results between the different conditions are observed; however, no significant differences are found in the pairwise comparisons.

Broadband telephone ringing signal in silence. There is a main effect for the factor hearing aid setting (lower bound, $p=0.043$). No interaction is observed (lower bound, $p=0.289$). The no-hearing-aid condition is significantly better than the omnidirectional condition (on average 3.1°). No significant difference is found between the no-hearing-aid and adaptive directional condition for the standard 0.05 level, although the p value lies close to the level of significance ($p=0.059$). No difference is found between the omnidirectional and adaptive directional condition ($p=1$).

Broadband telephone ringing signal with babble from left and right. A main effect is found for the factor hearing aid setting (lower bound, $p=0.002$). No interaction is observed (lower bound, $p=0.509$). Statistical significant differences are found in all pairwise comparisons, with the no-hearing-aid condition performing better than both hearing aid conditions (on average 6.0° and 9.7°), and the omnidirectional configuration performing better than the adaptive directional configuration (on average 3.7°).

Another aspect that seems to make a distinction between the data obtained with the adaptive directional microphone configuration and the other configurations is the presence of left-right confusions for the extreme left and right angles (Fig. 4). Several subjects experienced this problem for stimuli presented at ±90° when they were tested with the adaptive directional microphone. This was found for the high-frequency noise band (subjects SM, MA, VM, and CH) and for the telephone signal in noise (subjects DH, VM, CH, and BG).

An evaluation per angle of incidence is shown in Fig. 3. This shows the rms error per speaker location when accumulating the responses of the hearing impaired subjects on the different stimulus conditions, and was done for the three different hearing aid conditions (omnidirectional, adaptive directional, and without hearing aids). Figures 3 and 4 illustrate that hearing impaired subjects have a better localization performance in the frontal region compared to the region at the sides of the head, which is in agreement with the data of the normal hearing subjects. However, it is important to note that when using hearing aids, a decrease in performance is observed not only at the sides of the head, but also in front of the listener. These figures should be interpreted with caution. They represent an accumulation of the responses given by the different hearing impaired subjects on a localization task, which is a subject dependent process. A large intersubject variance is present in the hearing impaired data, especially with hearing aids. This is illustrated in Fig. 5, which gives the mean response of each subject on each stimulus location for each test condition.

C. Hearing impaired without hearing aids versus normal hearing

When evaluating the normal hearing and the hearing impaired subjects, one can clearly see differences in performance (Table II versus Table III, Fig. 3–5. In this section, the

data of the normal hearing group are compared with the best condition of the hearing impaired group, being the condition without hearing aids. The data of all four test signals (low-frequency, high-frequency, telephone ringing signal, and telephone ringing signal in noise) are included in a repeated-measures ANOVA. A between-subjects factor—subjects—is introduced which separates the group of normal hearing and hearing impaired persons. There is a main effect present for the factor test signal (lower bound $p<0.001$) and no effect is found for the factor test-retest. No interactions are found (signal*subjects, lower bound $p=0.129$, signal*retest, lower bound $p=0.214$, and signal*retest*subjects, lower bound $p=0.182$). The group of normal hearing subjects perform better than the hearing impaired group without hearing aids ($p=0.005$). This can also be seen when comparing the data of the normal hearing and the hearing impaired in Figs. 3 and 4. The pairwise comparisons of the factor test signal show the same results as described in the normal hearing section. There is a better performance when using the broadband stimulus compared to both narrow-band stimuli ($p<0.001$ for both the low- and high-frequency stimulus) and compared to the broadband stimulus in noise ($p=0.001$). There is also a better performance when using the low-frequency stimulus compared to the high-frequency stimulus ($p<0.001$). Another difference between the normal hearing and the hearing impaired subjects is the larger consistency between the different subjects in the normal hearing group compared to the hearing impaired group (Fig. 5).

IV. DISCUSSION

Three research questions were raised in the introduction of this manuscript. The results and analyses from the previous section will be used to answer these questions.

A. Normal hearing and hearing impaired performance

Section III describes and quantifies the localization performance of normal hearing and hearing impaired subjects in the frontal horizontal plane. Hearing impaired subjects were tested in three different conditions: Without their hearing aids (no), with hearing aids with an omnidirectional microphone configuration (o), and with hearing aids with an adaptive directional microphone configuration (a). Overall, the average performance with the low-frequency stimulus (mainly ITD) was better than performance with the high-frequency (mainly ILD) stimulus (Secs. III A and III C). Test results improved when using the broadband stimulus compared to high- or low-frequency stimuli. This can be explained by the possibility to use both ILD and ITD cues and by the time structure of the broadband signal. The length of the stimulus could also have affected localization performance. When using a 1 s signal, slight head movements can occur during stimulus playback which would give the subject an extra advantage. When adding jammer sources with a SNR of 0 dB, performance drops significantly for both the hearing impaired subjects and the normal hearing subjects. This confirms the results of the study of Lorenzi *et al.* (1999b).

Statistical analysis (Sec. III C) showed a better performance of the normal hearing subjects compared to the hearing impaired subjects (Sec. III C Figs. 3 and 4). Although the two subject groups were not age matched, 64% of the individual scores of the hearing impaired subjects without hearing aids are within two standard deviations, and 39% are within one standard deviation of the results of the normal hearing group (when comparing the data of the same test conditions). In the study of Lorenzi *et al.* (1999a), it was also mentioned that a considerable percentage of the hearing impaired subjects (between two and three subjects out of four) can reach normal hearing performance on a binaural task. This leads us to conclude that some hearing impaired subjects are able to use binaural cues which is important to motivate further research on binaural signal processing for hearing aids.

It was also shown that for both the normal hearing as the hearing impaired subjects, localization is more accurate in front of the listener than at the left and right side of the listener (Figs. 3 and 4) which agrees with the data of Makous and Middlebrooks (1990) and Carlile *et al.* (1997). However, in these studies, the decrease in accuracy at the sides of the head was less pronounced which might be explained by the difference in the experimental setup. The hearing impaired subjects, who were using their own hearing aids, and are therefore highly trained on localizing sound sources with these devices in their daily lives, were not able to localize half of the targets correctly in the most frontal region (from $-45°$ to $+45°$), whereas normal hearing subjects have a near 100% score in this region (Secs. III B and III A).

B. Do bilateral hearing aids preserve localization cues?

To answer this question, tests were performed with hearing impaired subjects with and without hearing aids. By using equal sensation levels (for restoring audibility), a comparison can be made between performance when all binaural information is present and performance with hearing aids. Throughout the different tests, four out of eight comparisons between unaided and aided conditions showed significant better performance unaided than aided for a significance level of $p=0.05$ (and six out of eight for a significance level of $p=0.1$) (see Table IV). A general analysis confirmed that performance without hearing aids is significantly better than with hearing aids (Sec. III B). This can be related to the data of Noble *et al.* (1998) and Byrne *et al.* (1998) obtained with open earmolds, allowing the subjects to use binaural cues of the direct sound instead of the output of the hearing aid. Moreover, when comparing with normal hearing performance, only 36% of the individual test results with hearing aids fall within 2 standard deviations of the results of the normal hearing subjects, and only 20% of the individual test results fall within 1 standard deviation of the results of the normal hearing subjects. These percentages are considerably smaller than the numbers shown in the previous section for the hearing impaired subjects without hearing aids. This confirms that hearing aid users localize better without their hearing aids than with their hearing aids.

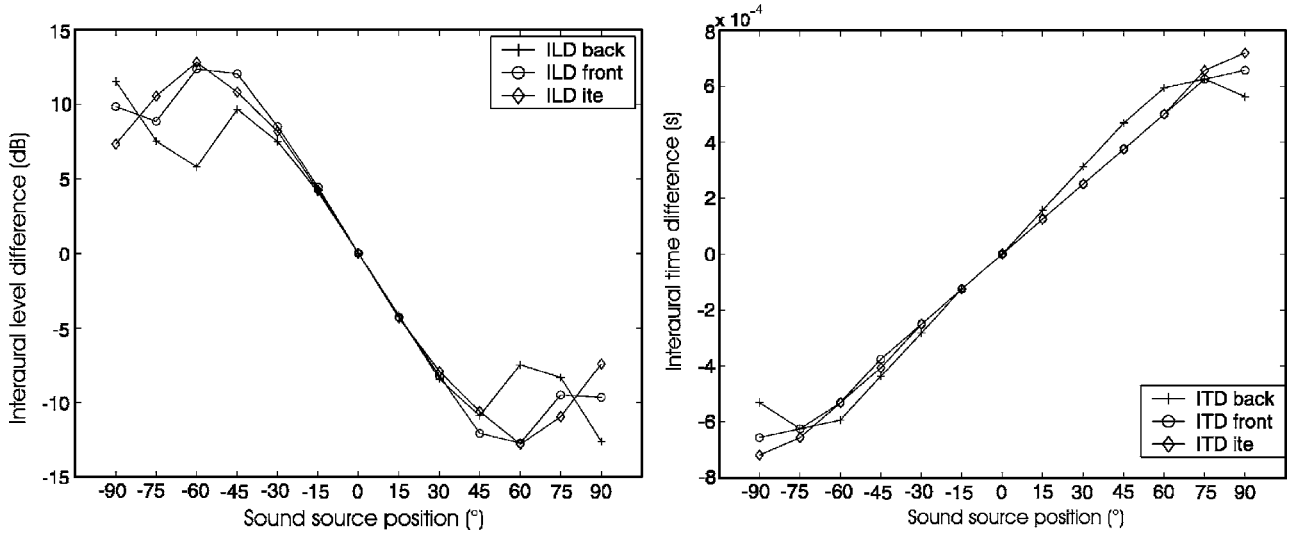

FIG. 6. ITD and ILD measurements with two Canta7 BTE hearing aids prototypes on a CORTEX manikin in anechoic conditions. Interaural time and level differences were measured between the ITE microphones of a CORTEX manikin (ITD ite, ILD ite), between the front omnidirectional microphones of the BTE devices (ITD front and ILD front), and between the back omnidirectional microphones of the BTE devices (ITD back and ILD back). Measurements were made using a broadband white-noise stimulus.

Extra measurements were made to quantify the influence of microphone position on interaural cues. On a BTE hearing aid, the microphones are positioned relatively far from the eardrum, which may influence the interaural cues given to the listener. One could assume that this is the reason for the degradation in horizontal localization performance. To quantify this influence, physical measurements are made using the microphones of BTE hearing aid devices and in the ear microphones (ITE) of a manikin under anechoic conditions. A 01 dB CORTEX MK2 manikin, a dummy head with torso built according to the IEC 959 standard, is used with two G.R.A.S. IEC 711 ear simulators. A G.R.A.S. 40AG pressure microphone is located in each ear simulator. The BTE devices are two Canta7 dual microphone shells with direct microphone outputs. All recordings are made using an eight-channel G.R.A.S. 12AG preamplifier and two synchronized LYNXONE soundcards with a sampling rate of 48 kHz. A broadband white-noise signal is recorded simultaneously with all six microphones (two CORTEX MK2 in the ear and four BTE microphones). ITDs and ILDs are calculated between the two ITE microphones of the manikin the two omnidirectional microphones located at the front of the BTE devices and between the two omnidirectional microphones located at the back of the BTE devices.

The measured ITDs are calculated using a cross correlation function and are given in the left part of Fig. 6. This illustrates that the ITDs between the BTE microphone pairs do not fully agree with the data of the ITE microphone pair, which represents the ITD information at the eardrums of a human listener. Moreover, the distortion is dependent on the microphone placement on the BTE. The front microphone pair shows a distortion of ITD information only around −90° and +90°. The back microphone pair shows larger distortions and generates almost similar ITDs for the area from −60° to −90° and from 60° to 90° which could have an effect on localization performance. These measurements were done using a broadband white-noise. Interaural cues are, however, to some extent frequency dependent (Blauert, 1997 and Kuhn, 1977). A frequency specific analysis was done to get a clear comparison between the interaural measurements and the localization measurements described earlier. These analyses made clear that most of the ITD distortion shown in Fig. 6 (at angles beyond ±60°) is generated by relatively high frequencies ($f > 1$ kHZ). Lower frequencies showed smaller differences between the ITE and BTE measurements, but showed the same tendency as the broadband measures shown in Fig. 6 with the front microphone pair having a smaller influence on the ITD information (<40 μs ITD distortion over all angles) compared to the back microphone pair and with the back microphones producing almost similar ITDs for the angles at the most left and right side of the head.

The right part of Fig. 6 shows the ILD cues generated by a broadband white-noise stimulus. The distortion generated by the back microphone pair is again more pronounced than the distortion by the front microphone pair, and is mainly located at the most left and right angles. The measured ILDs for low frequencies are much smaller (less than 7 dB for frequencies below 1000 Hz). For these frequencies, the measured maximum distortion relative to the ITE condition was <1.5 dB for the front microphone pair and <3 dB for the back microphone pair over all angles. For higher frequencies (>1 kHz and <5 kHz), the measured ILDs were much larger (maximum: 17 dB). Only at the sides of the head (starting from ±60°) were the high-frequency ILDs measured at the front BTE microphones very different than the ILDs generated by the ITE microphones (maximum measured difference around 7 dB at an angle of 75°). The back microphones showed larger deviations than the front microphones, especially at the sides of the head (>5 dB difference at the sides of the head starting from ±45° with a maximum difference of 8 dB at 75°).

In general, both ITD and ILD distortions are relatively small, especially if one would assume that the hearing aid manufacturer uses the front microphone as the reference mi-

crophone. To rule out the effect of microphone placement, the data were split into two parts: The data of the area where the impact of the microphone position is almost negligible (from −45° to 45°) and the remaining data for which the distortion could be (although unlikely) generated by the microphone position. The statistical analysis of Sec. III was repeated for these two subareas, the p values of the pairwise comparisons are summarized in Table IV. This table shows that—for the telephone ringing signal in silence and for the telephone signal in noise—performance of the subjects with hearing aids is already significantly lower than without hearing aids for a standard 0.05 significance level. A general analysis of the four test conditions confirms that performance in the area between −45° and 45° is already worse with than without hearing aids. This suggests that the drop in localization performance cannot be explained only by microphone positioning. Moreover, it can be linked to the work of Noble and Byrne (1990) (see Sec. I) where no significant differences in localization performance were found when comparing BTE, ITE, and ITC hearing aids. Because microphone positioning seems insufficient to explain the difference in localization performance, the data strongly suggest that the signal processing of hearing aids introduces interaural cue distortion when used in a bilateral hearing aid configuration. Further, more fundamental research is needed on the separate signal processing blocks of an hearing aid to pinpoint the exact blocks that cause the interaural distortion which could lead to a better design of hearing aids for bilateral hearing impaired subjects.

C. Can noise reduction systems have an influence on localization performance?

Although most test scenarios in this study do not show a significant difference between the adaptive directional microphone configuration and the omnidirectional microphone configuration (Table IV), a trend of the omnidirectional microphone configuration performing better than the adaptive directional microphone configuration can be observed in most test conditions (Table III and Fig. 4). Analysis showed that the overall effect was not significant (but close to significance) for a significance level of $p=0.05$ ($p=0.053$). However, the adaptive directional microphone is significantly different from the omnidirectional microphone configuration when directional noise is added at ±90° ($p=0.044$) (Table IV). The adaptive directionality has a negative impact only in this test condition, probably because the noise sources were playing continuously throughout this test. Therefore, the noise reduction system had plenty of time to adapt to a steady filtering operation. In the other tests, very short sounds were used which could have given the noise reduction system not enough time to adapt to a steady filtering operation. Two reasons might explain the negative affect of the adaptive directional microphone. First, an adaptive directional microphone creates a directional pattern depending on the noise scenario. It searches for the most dominant noise source (normally the search area is restricted to the rear horizontal plane) and puts a null in this direction. When testing with babble jammer sources at the left and right side of the subject, the adaptive directional microphone will try to cancel out these directions. It can be assumed that the ILD perception of the stimulus, around ±90°, could be degraded by this filtering operation. This would explain why the difference between the omnidirectional and the adaptive directional microphone configuration is only significant in the area from 60° to 90° and not in the area from −45° to 45° (Table IV, general analysis, and tblr analysis). Second, the directional filter introduces a phase relationship between the input and output of the hearing aid. ITDs would be distorted if left and right hearing aids have a different phase relationship. These are two suggestions and further research is needed to clarify why an adaptive directional microphone affects localization performance. However, the results of the tests indicate that a noise reduction system can have an influence on binaural cues. Therefore, when designing noise reduction systems for hearing aids, more attention should be given to bilateral usage, in general, and more specifically to the preservation of interaural cues.

To get a better insight on the type of interaural distortion experienced by hearing aid users (ITD or ILD), low- and high-frequency stimuli were used. When comparing the omnidirectional condition with the condition without hearing aids in Table III, it shows that four out of ten subjects have a large decrease in performance for the 500 Hz stimulus when using hearing aids (subjects BG, ML, SM, and VM) which could indicate distortion of time cues by the hearing aids. On the other hand, five subjects out of ten show a large decrease in performance for the 3150 Hz stimulus (subjects CH, DH, MA, ML, and SM) which could indicate distortion of level cues. So, some subjects seem to experience problems with level cues, some with time cues, and some do not experience problems at all when localizing a high- and low-frequency stimulus with an omnidirectional configuration (e.g., subject AP). Strangely enough, subject AP, who had no decrease in performance with both low- and high-frequency stimuli did show a decrease in performance with the transient broadband signal and the broadband signal with jammer sounds. When comparing the omnidirectional with the adaptive directional microphone configuration in Table III, it shows that only small differences are present for the 500 Hz stimulus, but that large differences are present for the 3150 Hz stimulus for five out of ten subjects (subjects BG, BJ, CH, MA, and SM). This could indicate that, for these subjects, the extra distortion given by an adaptive directional microphone is mainly ILD distortion. However, these analyses should be interpreted with the necessary caution. The reader should pay attention to the fact that these systems are multiband processing devices. Different subbands can be processed inside the hearing aid in a different way. This would not only lead to the possibility of interaural cue distortion, but also to the possibility of generating interfering interaural cues over the different frequency channels. How the auditory system of the different subjects would react to these interfering cues is an unknown factor when interpreting the data. Therefore, caution is advised when extrapolating data of narrow-band signals to broadband signals. Also, no attention has been given to spectral cues. It is known that high frequency spectral cues improve localization performance and are especially useful

for vertical localization and for resolving front-back confusions. The influence of spectral cues was not studied but can be assumed to be limited because of the nature of the task (no front-back ambiguities or vertical localization), the high-frequency loss of the subjects, and the limited frequency bandwidth at the output of BTE hearing aids. Monaural spectral enhancement techniques were switched off in this study which might influence (enhance or degrade) localization performance in real-life situations.

V. CONCLUSIONS

Three research questions are addressed in this paper. First, the localization performance of normal hearing and hearing impaired subjects in the frontal horizontal plane is quantified. The group of hearing impaired subjects localized sounds less accurately than the normal hearing subjects. However, it is shown that the hearing impaired subjects can still use binaural cues which motivates further research on binaural hearing aid systems. Second, current state of the art bilateral hearing aids have a negative impact on binaural cues, thereby degrading localization performance. The decrease in localization performance with hearing aids could not be fully explained by microphone placement which indicates that the different signal processing blocks inside a hearing aid distort interaural cues. More fundamental research should be done on these separate building blocks. Third, noise reduction techniques, such as an adaptive directional microphone, can have an additional significant negative impact on localization performance. Whether a significant drop in localization performance occurred with the noise reduction technique depended on the stimulus and noise scenario used in the localization test. The fact that hearing aid users receive distorted binaural cues could lead to degraded speech perception in noisy listening situations, in which binaural cues are important. The main conclusion seems to be that using two monaural hearing aids is a suboptimal solution for a bilateral hearing aid user. More research should be done on preserving binaural acoustical cues in noise reduction algorithms and hearing aids, in general.

ACKNOWLEDGMENTS

This research was funded by a Ph.D grant of the Institute for the Promotion of Innovation through Science and Technology in Flanders (IWT-Vlaanderen). The authors would like to thank Lies Royackers for helping out with the tests. Thanks are also extended to Mark Laureyns and Kristin De Klerck of Dialogue Leuven, Roel Vangelder of Lapperre hearing systems Leuven, and Katleen Devoecht of UZ Leuven for contacting the test subjects. Many thanks to all the hearing aid users and normal hearing subjects who participated in this study.

Blauert, J. (**1997**). *Spatial hearing, the psychophysics of human sound localization*. The MIT Press, Cambridge, MA.

Bronkhorst, A. W., and Plomp, R. (**1998**). "The effect of head-induced interaural time and level differences on speech intelligibility in noise," J. Acoust. Soc. Am. **83**(4), 1508–1516.

Bronkhorst, A. W., and Plomp, R. (**1989**). "Binaural speech intelligibility in noise for hearing impaired listeners," J. Acoust. Soc. Am. **86**(4), 1374–1383.

Byrne, D., Sinclair, S., and Noble, W. (**1998**). "Open earmold fittings for improving aided auditory localization for sensorineural hearing losses with good high-frequency hearing," Ear Hear. **19**(1), 62–71.

Carlile, S., Leong, P., and Hyams, S. (**1997**). "The nature and distribution of errors in sound localization by human listeners," Hear. Res. **114**, 179–196.

Dillon, H. (**2001**). *Hearing aids*, Boomerang Press, Sydney.

Dillon, H., Keidser, G., and Silberstein, H. (**2003**). "Sound quality comparisons of advanced hearing aids," Hear. J. **56**(4), 1–6.

Kuhn, G. F. (**2003**). "Model of the interaural time differences in the azimuthal plane," J. Acoust. Soc. Am. **62**(1), 157–167.

Gilkey, R. H. and Anderson, T. R. (**1997**). *Binaural and spatial hearing in real and virtual environments*. Lawrence Erlbaum associates, Mahwah, NJ.

Hartmann, W. M. (**1999**). "How we localize sound," Phys. Today **11**, 24–29.

Hausler, R., Colburn, S., and Marr, E. (**1983**). "Sound localization in subjects with impaired hearing," Acta Oto-Laryngol. **400**, 1–62.

Hofman, P. M., and Van Opstal, J. (**1998**). "Spectro-temporal factors in two-dimensional human sound localization," J. Acoust. Soc. Am. **103**(5), 2634–2648.

Langendijk, E. H. A., and Bronkhorst, A. W. (**2002**). "Contribution of spectral cues to human sound localization," J. Acoust. Soc. Am. **112**(4), 1583–1596.

Lorenzi, C. S., Gatehouse, S., and Lever, C. (**1999a**). "Sound localization in noise in hearing impaired listeners," J. Acoust. Soc. Am. **105**(6), 3454–3463.

Lorenzi, C. S., Gatehouse, S., and Lever, C. (**1999b**). "Sound localization in noise in normal hearing listeners," J. Acoust. Soc. Am. **105**(3), 1810–1820.

Makous, J. C., and Middlebrooks, J. C. (**1990**). "Two-dimensional sound localization by human listeners," J. Acoust. Soc. Am. **87**(5), 2188–2200.

Moore, B. C. J. (**1997a**). *An introduction to the psychology of hearing*, Chap. 8: Spatial hearing and related phenomena, Academic, New York, 297–345.

Moore, B. C. J. (**1997b**). *An introduction to the psychology of hearing*, Chap. 7: Space perception, Academic, New York, 223–267.

Noble, W., Sinclair, S., and Byrne, D. (**1998**). "Improvements in aided sound localization with open earmolds: Observations in people with high-frequency hearing loss," J. Am. Acad. Audiol **9**(1), 25–34.

Noble, W., Byrne, D., and Lepage, B. (**1994**). "Effects on sound localization of configuration and type of hearing impairment," J. Acoust. Soc. Am. **95**(2), 992–1005.

Noble, W., and Byrne, D. (**1990**). "A comparison of different binaural hearing aid systems for sound localization in the horizontal and vertical planes," Br. J. Audiol. **24**, 335–346.

Stevens, S. S., and Newman, E. B. (**1936**). "The localization of actual sources of sound," Am. J. Psychol. **48**, 297–306.

Van Hoesel, R. J. M., and Tyler, R. S. (**2003**). "Speech perception, localization, and lateralization with bilateral cochlear implants," J. Acoust. Soc. Am. **113**(3), 1617–1630.

Van Hoesel, R., Ramsden, R., and O'Driscoll, M. (**2002**). "Sound direction identification, interaural time delay discrimination, and speech intelligibility advantages in noise for a bilateral cochlear implant user," Ear Hear. **23**(2), 137–149.

Wightman, F. L., and Kistler, D. J. (**1992**). "The dominant role of low-frequency interaural time differences in sound localization," J. Acoust. Soc. Am. **91**(3), 1648–1661.

Distortion product otoacoustic emission (DPOAE) in tinnitus patients

E. Ozimek[a] and A. Wicher
Institute of Acoustics, A. Mickiewicz University, Poznań, Poland

W. Szyfter and E. Szymiec
ENT Department, Karol Marcinkowski University of Medical Sciences, Poznań, Poland

(Received 7 April 2005; revised 6 October 2005; accepted 3 November 2005)

The aim of this study was to determine the effect of tinnitus (experiment I) and the combined effect of tinnitus and sensorineural hearing loss (experiment II) on the distortion product otoacoustic emission (DPOAE) for two age groups of tinnitus patients. Tinnitus patients with normal earing, along with normal-hearing control subjects, participated in experiment I. They were divided into two age groups, below 50 and above 50 years. Experiment I showed that the DPOAE levels in the tinnitus patients were lower than those in the normal-hearing (nontinnitus) subjects. The differences depended on the frequency and the age of the patients, suggesting the confounding influence of presbyacusis. The second group of tinnitus patients with increasing and notch-like hearing loss participated in experiment II. They were also divided into two age groups, below 50 and above 50 years. The data from experiment II showed that DPOAE activity well reflects the increasing and notch-like hearing loss functions up to about 40 dB HL. The effect of age on the DPOAE level was clearly noted only for the tinnitus patients with clinically normal-hearing thresholds and was ambiguous for the tinnitus patients with hearing loss. © *2006 Acoustical Society of America.* [DOI: 10.1121/1.2141297]

PACS number(s): 43.66.−x, 43.64.Jb [BLM] Pages: 527–538

I. INTRODUCTION

Otoacoustic emissions (OAEs) are sound signals produced by the cochlea which can be measured in the outer ear canal (Kemp, 1978, 1982, 1986; Probst *et al.*, 1991; Robinette and Glattke, 2002). They reflect some activity of the outer hair cells (OHCs) and are closely related to the signal-transduction function of the cochlea (Probst *et al.*, 1991; Robinette and Glattke, 2002). The question arises: what is the relation of OAEs to tinnitus manifested as sound sensation without external stimulation? Tinnitus is often defined as phantom auditory perception (Jastreboff, 1990; Jastreboff and Hazell, 1993). This effect is usually associated with hearing losses induced by noise exposure or with aging processes. Different hypotheses have been proposed for the tinnitus mechanism, however, none has yet been proved (Tonndorf, 1987; Eggermont, 1990; Jastreboff, 1990; Eggermont and Roberts, 2004). It is usually assumed that tinnitus results from abnormal neural activity of the auditory pathway perceived as a real sound and the majority of tinnitus cases are associated with cochlear dysfunction. There are also some suggestions based on magnetoencephalography studies in tinnitus subjects that their auditory cortex exhibits abnormal representation of the frequency region related to the tinnitus pitch (Mühlnickel *et al.*, 1998). These data point to some relationship between tinnitus and abnormal neural activity in the cortical tonopic map.

The transiently evoked otoacoustic emissions (TEOAEs) were found to be less suppressible in tinnitus patients compared to subjects with similar hearing impairments, but showing no tinnitus (Attias *et al.*, 1996). One explanation of this observation may be a hyperactivity of the outer hair cells (OHCs) resulting from pathological cochlear activity. OHC impairments affecting the impedance change of the cochlear system are assumed to be responsible for generation of inner-ear standing waves, which may affect both spontaneous OAEs and tinnitus (Zweig and Shera, 1995). The swelling of OHCs related to an increase in magnitude and gain of their electromotility is supposed to also be important in hearing disorders associated with tinnitus (Sziklai and Dallos, 1997).

Distortion product OAEs (DPOAEs) are assumed to be caused by the compressive nonlinearity of cochlear micromechanics based on the specific activity of OHCs. They originate in a relatively limited area of the cochlea, since primary tones (f_1,f_2) are usually close together. The cubic distortion tone (CDT), i.e., $2f_1$-f_2, is associated with the two traveling waves related to f_1 and f_2. Thus, by changing the stimulus frequencies, it is possible to test different parts of the cochlea. Since DPOAEs come from different regions of the cochlea, they can interact with each other, depending on their relative magnitudes and phases, resulting in some effects often difficult for interpretation (Whitehead *et al.*, 1992a, b; Mills *et al.*, 1993; Lonsbury-Martin *et al.*, 2002).

Hitherto there have been only a few, not always consistent, reports on tinnitus and DPOAEs. DPOAE levels in tinnitus patients showing normal hearing have been reported to be lower or higher than those in normal-hearing individuals without tinnitus (Norton *et al.*, 1990; Mitchell *et al.*, 1993; Shiomi *et al.*, 1997; Gouveris, 2005). Some authors suggest that, in tinnitus patients with sensorineural hearing loss, ei-

[a]Electronic mail: ozimaku@main.amu.edu.pl

ther a decrease or an increase in DPOAEs can be obtained (Janssen and Arnold, 1995; Janssen *et al.*, 1998). Such an equivocal statement on the relation between hearing loss and DPOAE level in tinnitus patients is difficult to explain.

It is known that increasing hearing loss in nontinnitus patients is usually associated with a decreasing magnitude of DPOAEs, which tend to disappear for large losses (Martin *et al.*, 1990; Gorga *et al.*, 1993, 1997; Kimberley *et al.*, 1994). However, the relation between tinnitus and DPOAEs and the effect of the shape of the hearing loss function on DPOAEs have not been fully established, to date. Thus, the basic aim of the present study was to estimate the effect of tinnitus alone (experiment I) and the combined effects of tinnitus and sensorineural hearing loss on the DPOAE level (experiment II). This experiment was performed for tinnitus patients with normal-hearing threshold and with two different configurations of hearing loss. The DPOAE responses obtained for the tinnitus patients were compared to those of a control group of normal-hearing subjects. Results of the study are expected to be relevant to the application of DPOAE measures for the clinical evaluation of hearing status in aging tinnitus patients.

II. APPARATUS AND MEASUREMENT PROCEDURE

A. Apparatus and method

The DPOAE measurements for tinnitus ears were made with a Bio-Logic Scout Sport System (v. 3.02), model 3.33.00, (Bio-Logic Systems Corp., Mundelein, Illinois). The stimuli were delivered to the ear canal via an ear probe with insert transducers and the ear canal sound pressure was measured using a miniature microphone. Fast Fourier transform software separated the ear canal sound into its discrete frequency components so that DPOAEs at the $2f_1$-f_2 frequency could be extracted.

The DPOAE frequency functions (DPgrams) were collected in response to pairs of primary tones (f_1 and f_2; $f_2/f_1=1.22$), at $\frac{1}{8}$ octave steps, in the f_2 frequency range from 1.22 to about 10 kHz. The f_1 frequency was related to the audiometric frequency f_a except for 250, 500, and 1000 Hz, since DPOAE measurements were not possible at these lower frequencies due to relatively high noise floor, while f_2 could be expressed by f_a according to the formula $f_2=1.22f_1=1.22f_a$ (the f_2 frequency is presented on the abscissa of the DPgrams).

DPOAE level was determined as the level of the $2f_1$-f_2 component. Primary tones were presented at the sound pressure levels of $L_1=65$ dB SPL and $L_2=55$ dB SPL. Such levels of the primaries were selected since they permit the most accurate classifications of the cochlear status (Whitehead *et al.*, 1995a,b; Stover *et al.*, 1996). Earlier studies used either equilevel primary tones (Nelson and Kimberly, 1992) or a special stimulus level algorithm $L_1=0.4L_2+39$ dB (Kummer *et al.*, 1998). The DPgrams were accepted as valid when the signal-to-noise ratios exceeded 3 dB. DPOAEs were measured starting form 1.5 kHz since patient noise limited measurement of low-frequency DPOAE components.

To check the measurement system for the presence of distortion, a check for artifacts was made using hyperdermic syringe set at 2.3 cc. It was found that at the sound pressure levels of primary tones equal to 70 dB SPL, the level of nonlinear components produced by the measurement system was below −25 dB SPL. Thus, the main contribution to the noise floor level came from the patient's (biological) noise. DPOAE measurements were performed in a double-walled sound-proof room. The patients were asked to remain quiet during the measurements.

Next, the tinnitus pitch and tinnitus loudness were measured. Different methods to evaluate tinnitus pitch and loudness have been proposed in literature (Mitchel *et al.*, 1993; Henry and Meikle, 2000; Tyler, 2000; Andersson, 2003). In our experiment the tinnitus matching stimuli were presented to the ipsilateral ear using the same audiometer as in the hearing threshold measurements, with the subject positioned in a sound-proof booth. Depending on the sensation of the tinnitus pitch, pure tones or narrow band-pass noises were used as matching stimuli. They were presented at a level corresponding to the tinnitus loudness. The subject in the matching procedure was asked to concentrate on the predominant pitch of tinnitus. The tinnitus pitch was assessed using $\frac{1}{3}$-oct steps. Each patient made ten tinnitus pitch matches to the frequency of an external stimuli (to pure tone or band-pass noise). The stimuli were selected to match as closely as possible the perceived tinnitus pitch in each individual case. The pitch matching experiment was limited to 8 kHz since the tinnitus subjects provided variable frequency matches above this frequency, which were not reliable.

Thereafter, minimal masking level of tinnitus (MML) with white noise was performed. It allowed a determination of how loud a masking sound needs to be to mask the tinnitus. The level of the masking stimuli was presented ipsilaterally, first at a low value and then its level was increased in 2-dB steps until the tinnitus sensation was not audible. Such a masking run was terminated by a button push from the patient. Each patient completed ten MML tests.

B. Patients

Tinnitus patients (in total 87 persons) were selected from those treated at the Center of Laryngological Rehabilitation Medical University in Poznan.

To estimate the effect of tinnitus on the DPOAE level (experiment I), considerable effort was made to select such patients who suffered from tinnitus, but exhibited normal hearing according to ANSI (1996) standards. Normal hearing was defined as audiometric thresholds of 20 dB HL or better for half-octave frequencies from 250 to 8000 Hz. Keeping in mind the effect of age on DPOAEs (Lonsbury Martin *et al.*, 1991; Strouse *et al.*, 1996; Ozimek *et al.*, 2004), which is complex and can result from a dysfunction of OHCs, cochlear degeneration, etc., the tinnitus patients selected for experiment I ($N=33$) were divided into two age groups: tinnitus normal hearing—age $\leqslant 50$ years ($TNH_{\leqslant 50}$) ($N=18$, age range =17–47 years, median =27 years, quartiles =23 and 38 years) and tinnitus normal hearing—age >50 years ($TNH_{>50}$) ($N=15$, age range =51–57 years, median =54 years, quartiles =51 and 56 years). The age of the

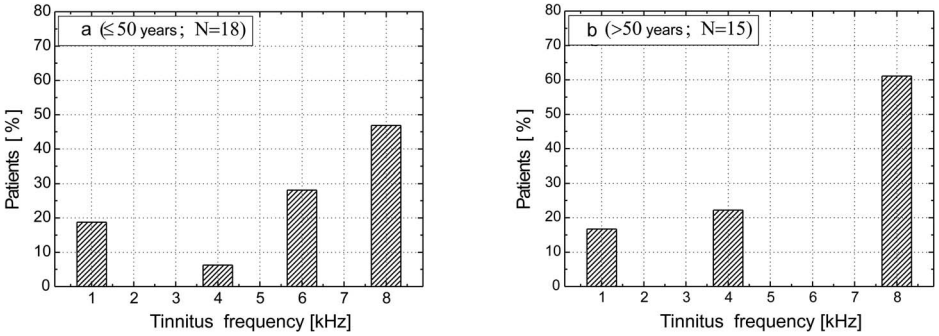

FIG. 1. Distributions of the tinnitus pitch for two age groups (a to 50 years, b above 50 years) with clinically normal-hearing thresholds. *N*=number of patients.

normal-hearing subjects ($N=14$) determined as a normal-hearing group (NH) ranged from 23–36 years, median =29 years, quartiles =26 and 31 years.

The remaining number of the tinnitus patients ($N=54$), who exhibited sensorineural hearing losses, participated in experiment II. They were also divided into two age groups. The first one (up to 50 years) was named $THL_{\leqslant 50}$ and the second one (above 50 years) as $THL_{>50}$. In each of these groups two classes of sensorineural hearing losses were distinguished: (1) increasing hearing loss characterized by a sloping audiogram for higher frequencies and (2) notch-like hearing loss for which a significant minimum on the audiogram is observed. In the $THL_{\leqslant 50}$ group, 12 patients (age range =40–50 years, median =46 years, quartiles =43 and 49 years) revealed the increasing hearing losses and 10 patients (age range =31–50 years, median =44 years, quartiles =40 and 46 years) presented notch-like hearing losses. Similarly, in the $THL_{>50}$ group, 21 patients (age range =51–75 years, median =61 years, quartiles =55 and 66 years) exhibited increasing hearing losses and 11 patients (age range =55–58 years, median =60 years, quartiles =56 and 66 years) exhibited notch-like hearing losses. All hearing losses were cochlear in origin and stable. Overall, 35 patients were female and 52 male; 60 patients reported binaural location of tinnitus, whereas in 27 it was monaural; 54 patients exhibited a tonal and 33 a band-noise-like tinnitus.

Before DPOAE data were collected, clinical pure-tone basic audiometric and middle-ear testing had been performed. The audiometric testing (AC 40, Interacoustics) comprised measurements of hearing thresholds and bone conduction thresholds at half-octave frequencies from 250 to 8000 Hz, with a minimum step size of 5 dB. To increase reliability of the threshold data, three threshold measurements were made for each tinnitus patient and all estimates were averaged. The middle-ear testing consisted of immittance measurements. Immittance parameters comprising peak middle-ear pressure, compliance, and base volume (ear-canal volume) were measured by means of a tympanometer (SD-30, Siemens). Such testing was important since middle ear pressure changes are likely to influence the mechanical properties of the ossicular chain and the tympanic membrane, which can affect signal transmission of DPOAEs through the middle ear. An increase in ear pressure is usually associated with greater attenuation of the middle ear system. Negative pressure usually affects transmission of both low and high frequencies and the effect of this pressure is generally greater than that of an equivalent positive pressure (Robinson and Haughton, 1991; Naeve *et al.*, 1992; Zhang and Abbas, 1997).

III. RESULTS

There were no significant differences in the values for compliance, middle ear pressure, or the volume of the outer-ear canal between any of the subject groups. Thus, the middle ear transmission systems of the tinnitus patients, regardless of age and hearing status, and the control subjects were normal according to routine clinical measures.

A. Experiment I. Tinnitus and DPOAE

Experiment I was aimed at determining the effect of tinnitus on DPOAE levels.

1. Tinnitus pitch and masking level

Distributions of the measured tinnitus pitch and tinnitus masking level in two age groups (a$\leqslant$50 years, b$>$50 years) with clinically normal-hearing thresholds are shown in Figs. 1 and 2, respectively.

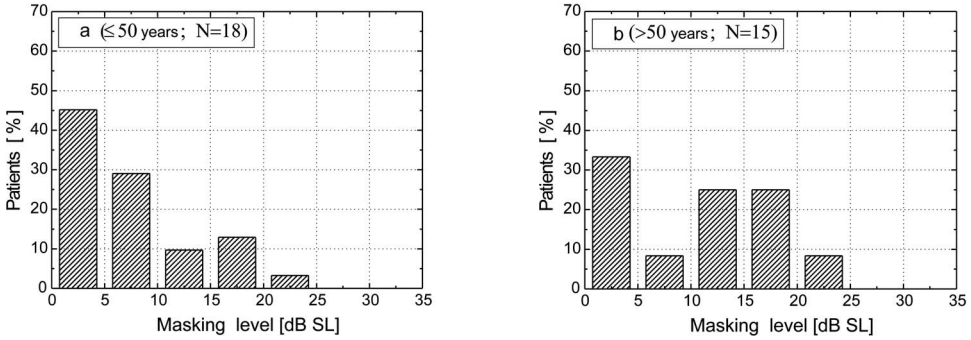

FIG. 2. Distributions of the tinnitus masking levels for two age groups (a to 50 years, b above 50 years) with clinically normal-hearing thresholds. *N*=number of patients.

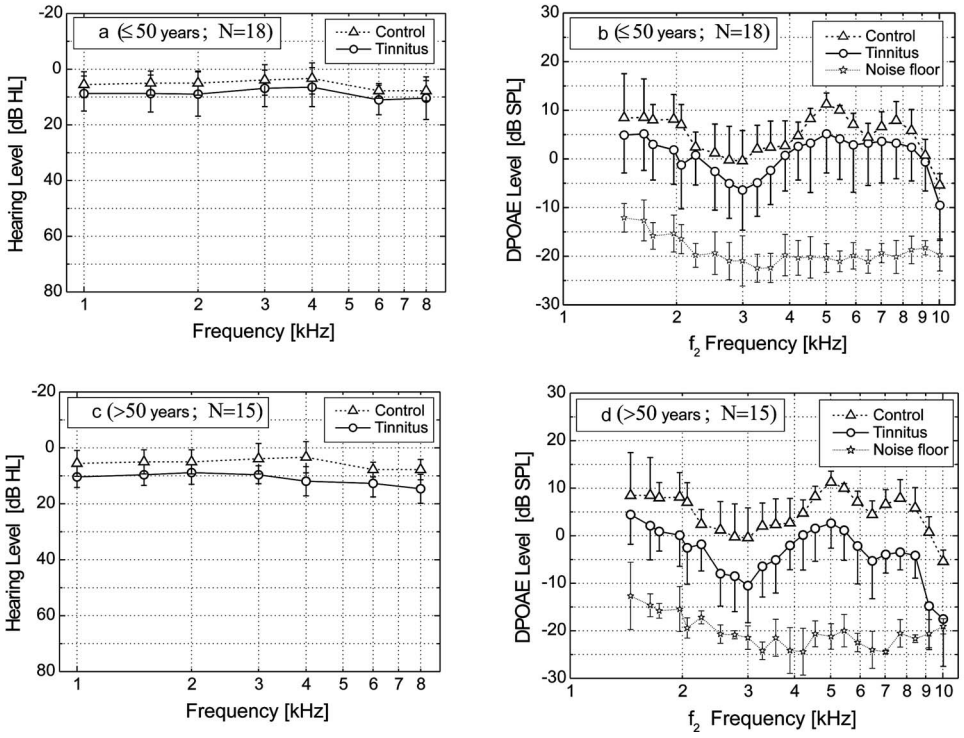

FIG. 3. Hearing loss functions (audiograms) averaged across patients for two tinnitus age groups (a to 50 years and c above 50 years) and the corresponding DPgrams (b to 50 years and d above 50 years). Solid lines show the audiograms and DPgrams for the tinnitus patients and broken lines show the audiograms and DPgrams for the normal-hearing subjects (control group). Corresponding noise floors are depicted below with thin dotted lines. Vertical bars specify the ±1 standard deviations. For clarity, only half length of the vertical bars are presented in panels (b) and (d). *N*=number of patients.

According to Fig. 1, the tinnitus appeared in almost 50% of cases at the highest frequency around 8 kHz and in the remaining cases at 1, 4, and 6 kHz. In this experiment, as noted above, almost 36% of tinnitus patients perceived tinnitus as a tonelike sensation and in 64% patients as a noiselike sensation.

As Fig. 2 shows, the distributions of the tinnitus masking levels for the patients aged up to 50 and above 50 had sloping forms that did not exceed 25 dB SL. Similarly, tinnitus sensation levels obtained by Anderson (2003) were not higher than 16 dB SL and the tinnitus loudness obtained by Gouveris *et al.* (2005) was within the range of 10–26 dB HL.

2. Hearing threshold and DPOAE response

Figure 3 (left column) presents averaged audiometric thresholds (audiograms) for the two age-distinct tinnitus groups with normal hearing ($a \leqslant 50$ years, $c > 50$ years). The corresponding averaged DPOAE responses are presented in the right column ($b \leqslant 50$ years, $d > 50$ years). The solid lines correspond to audiograms and DPgrams for tinnitus patients, the broken lines to normal-hearing no-tinnitus subjects (non-tinnitus group) and the thin dotted lines (the lowest in the right panels) represent the levels of the noise floor.

As follows from Fig. 3, the audiometric threshold for normal-hearing control subjects did not exceed 10 dB HL. The corresponding thresholds for the tinnitus patients aged below 50 was 2–3 dB higher than that of the normal-hearing subjects, and for the tinnitus patients above 50 it was on average 5–10 dB higher. Some elevation of the threshold was seen for the older tinnitus group for the highest frequency region. However, the hearing thresholds were still below 20 dB HL, implying normal [according to ANSI (1996) standards] hearing sensitivity for the older tinnitus group. Our extensive audiometric and middle-ear testing comprising the basic otology examination and the immittance measurements performed excluded individuals with symptoms of subclinical hearing pathology in this group of patients, which would affect their hearing sensitivity.

Figure 3(a) shows that the conventional audiometric thresholds are quite similar for the normal-hearing (NH) and the tinnitus group aged below to 50 ($TNH_{\leqslant 50}$). This fact is supported by the ANOVA analysis (see Table I) which revealed no statistically significant differences between the audiograms of the NH and $TNH_{\leqslant 50}$ groups ($[F(1,217) = 3.16;\ p \leqslant 0.0768]$).

Despite the similarity in the audiograms, differences in

TABLE I. ANOVA analysis results related to the audiograms and DPgrams for the tinnitus subject groups ⩽50 and >50 years old with normal-hearing thresholds (TNH). (Bold fonts present statistically significant data.)

Factors	Audiograms	DPgrams
$TNH_{\leqslant 50}$ referred to NH	$F(1,217)=3.16;\ p \leqslant 0.0768$	$\boldsymbol{F}(1,575)=26.80;\ \boldsymbol{p} \leqslant 0.0000$
$TNH_{>50}$ referred to NH	$F(1,140)=0.58;\ p \leqslant 0.4467$	$\boldsymbol{F}(1,414)=210.28;\ \boldsymbol{p} \leqslant 0.0000$
Age: $TNH_{\leqslant 50}$ and $TNH_{>50}$	$F(1,245)=1.88;\ p \leqslant 0.1722$	$\boldsymbol{F}(1,805)=157.94;\ \boldsymbol{p} \leqslant 0.0000$
$TNH_{\leqslant 50} * TNH_{>50}$	$F(6,245)=1.05;\ p \leqslant 0.3914$	$\boldsymbol{F}(22,805)=1.67;\ \boldsymbol{p} \leqslant 0.0273$

the DPOAE levels between these groups, associated with a larger variability in the emission level, were observed in the tinnitus ears over the entire frequency range. These differences are statistically significant [$F(1,575)=26.80$; $p \leqslant 0.000\,00$]. The maximum level difference in DPOAEs of the order of 6 dB SPL appeared at 3 and 5 kHz. Taking into regard that the groups NH and $TNH_{\leqslant 50}$ had a similar age median (for NH the median was 29 years, while for $TNH_{\leqslant 50}$ it was 27 years) one can possibly state that for the $TNH_{\leqslant 50}$ group, the tinnitus alone was responsible for decreased DPOAE levels.

Larger differences between the DPOAE levels were found when comparing the mean DPOAE responses for the NH and $TNH_{>50}$ groups [Fig. 3(d)], despite the fact that the audiograms for these groups were within normal limits, and there were no statistical differences between them. For higher frequencies above 5 kHz, the difference between the DPOAE levels amounted to about 10 dB. As follows from the ANOVA analysis, the difference in the DPOAE averages between the groups $TNH_{>50}$ and NH was statistically significant [$F(1,414)=210.28$; $p \leqslant 0.0000$]. This implies that the difference was mainly due to the tinnitus and not the difference in the hearing thresholds. The age difference between the two groups may have some effect estimated on the basis of a comparison of the DPOAE levels for the $TNH_{<50}$ and $TNH_{>50}$ groups, in which median ages were almost twice as different (for $TNH_{\leqslant 50}$ the median was 27 years, while for $TNH_{>50}$ it was 54 years). Comparing the DPgrams corresponding to these groups, it can be seen that the older group DPOAE levels were lower than those of the younger group by about a few decibels up to 5 kHz and increased above 5 kHz. According to the statistical analysis for the $TNH_{<50}$ and $TNH_{>50}$ groups there was no difference between the audiograms, but there was a statistically significant difference in the DPOAE levels [$F(1,805)=157.94$; $p \leqslant 0.0000$]. This result infers that the age difference between the groups $TNH_{<50}$ and $TNH_{>50}$ affected the DPOAE magnitudes. The question arises if the different number of subjects in the groups tested might affect the result of the ANOVA test. According to Rankin (1974), the errors in estimation of the probabilities related to the variance analysis are insignificant as long as the ratio between the size of the largest and the smallest groups is below 3:1. In our experiments, the ratios of subjects in the largest and the smallest groups were less than 2:1. This supports the possibility that the differences in the numbers of subjects in the groups tested had no significant effect on the ANOVA results.

To characterize the DPOAE decrease, the slope $s = [\text{DPOAE level}]/[\Delta f]$ was calculated for the frequency range (Δf). Between 1.5 and 3 kHz, the DPOAE level for $TNH_{\leqslant 50}$ exhibited a continuous decrease from 5 to −6 dB, that is by 11 dB, which corresponds to a slope of about 0.007 dB/Hz. Appropriate data for $TNH_{>50}$ were DPOAE level decreased from 4 to −10 dB, that is by 14 dB, which corresponds to a slope of about 0.009 dB/Hz. For the normal-hearing subjects the slope of the DPOAE response within the same frequency region amounted to about 0.0046 dB/Hz.

Our data did not indicate any particular effect of the tinnitus frequency on the magnitude of the DPgram. As Fig. 1 shows, the tinnitus appeared mainly at a frequency of about 4, 6, and 8 kHz (tinnitus around 1 kHz can be neglected since it is out of the measuring range of the DPOAE). None of the specific changes in DPOAE levels were found at those frequencies.

B. Experiment II. Tinnitus combined with hearing loss and the DPOAE response

Experiment II was undertaken to assess the effect of hearing loss on the DPOAE response in the tinnitus ears. At the beginning of the experiment the tinnitus pitch and tinnitus intensity level in the patients participating in the experiment were evaluated.

1. Tinnitus pitch and masking level data

Distributions of the tinnitus pitch in the two distinctly aged tinnitus groups (a, c to 50 years ($THL_{\leqslant 50}$), b, d above 50 years ($THL_{>50}$) with two different hearing loss functions (increasing and notch-like) are shown in Fig. 4. The distributions of the tinnitus masking level corresponding to these data are shown in Fig. 5.

As can be seen from Fig. 4, the tinnitus pitch for the ears with increasing hearing loss appeared mainly at 6 and 8 kHz (a, b) and for the ears with the notch-like hearing loss at the frequencies 4, 6 and 8 kHz (c, d). The tinnitus was mostly associated with frequency regions in which the losses reached their maxima: 60 dB HL (increasing hearing loss) and 40 dB HL (notch-like hearing loss). In this experiment about 78% of patients perceived tinnitus as a tone-like sensation and in 22% patients received it as a noise-like sensation.

The distributions of the tinnitus masking levels displayed rather irregular shapes with unique maximal values. For the tinnitus group aged below 50, these values did not exceed 20 dB SL for the increasing hearing loss [Fig. 5(a)] and 30 dB SL for the notch-like hearing loss [Fig. 5(c)]. The consecutive maximum value for the older tinnitus group (above 50 years) was equal 20 dB SL for both the increasing [Fig. 5(b)] and notch-like hearing loss [Fig. 5(d)].

2. Hearing loss function and DPOAE response

In order to compare the effect of the form of hearing loss function on the DPOAE response, two groups of tinnitus patients were chosen representing two types of hearing loss function: increasing [Figs. 6(a) and 7(a)] and notch-like [Fig. 6(c) and 7(c)]. To check the possible effect of age on the DPOAE, each group of patients with hearing loss was divided into two age categories: to 50 years ($THL_{\leqslant 50}$) and above 50 years ($THL_{>50}$). The measured DPgrams (averaged across patients in each group) corresponding to these hearing loss functions are presented in Figs. 6(b) and 6(d) (for $THL_{\leqslant 50}$) and in Figs. 7(b) and 7(d) (for $THL_{>50}$), respectively. The solid lines correspond to audiograms and DPgrams for tinnitus patients, and the broken lines represent the normal hearing subjects, with the thin dotted lines (in the right column) indicating the level of the related noise floors.

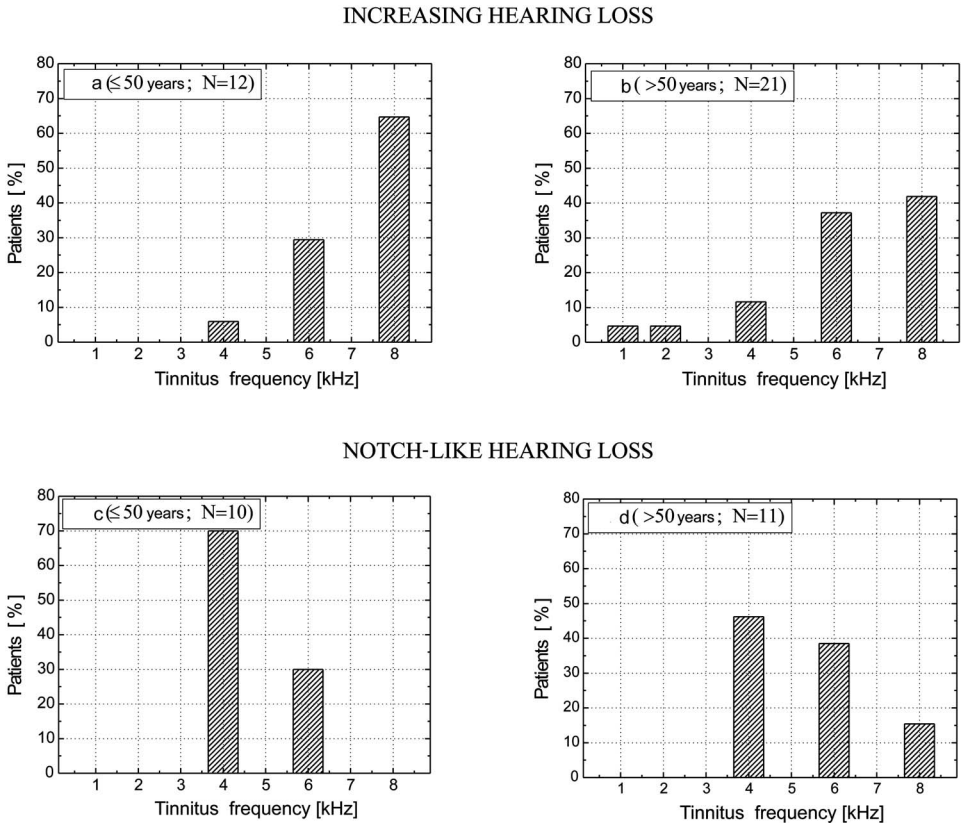

FIG. 4. Distributions of the tinnitus pitch for two age groups (a and c to 50 years, b and d above 50 years) and for two types of the hearing loss function: increasing (a, b) and notch-like (c, d). *N*=number of patients.

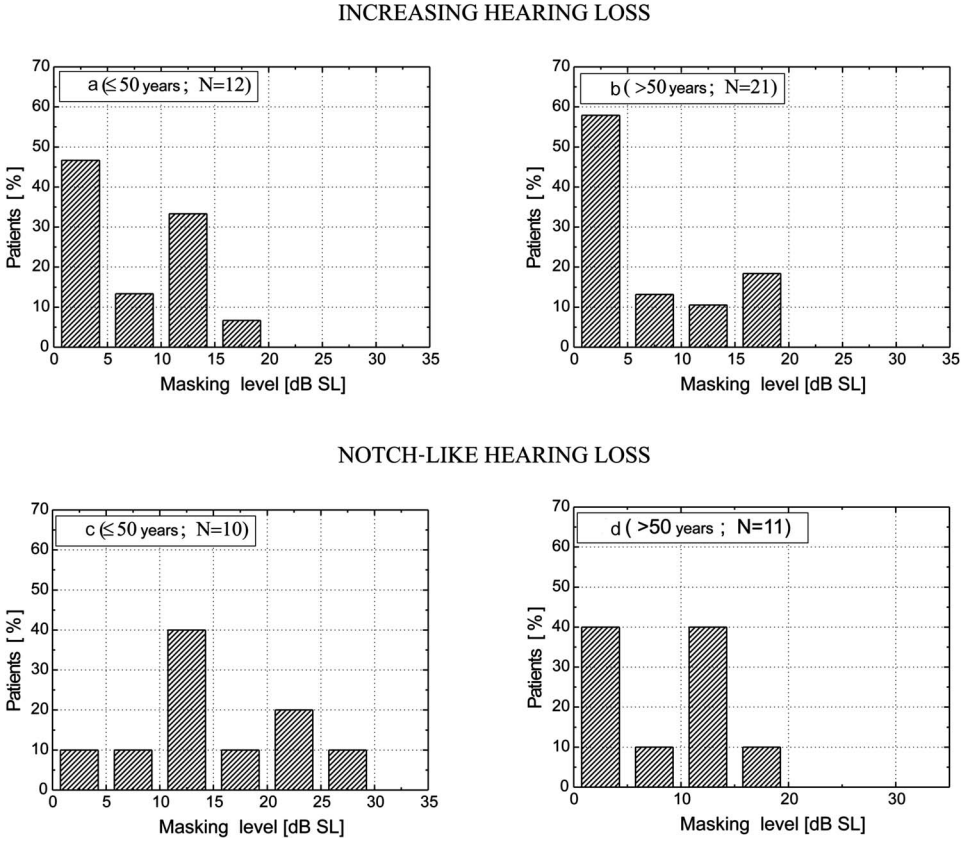

FIG. 5. Distributions of the tinnitus masking levels for two age groups (a and c to 50 years, b and d above 50 years) and for two types of the hearing loss function: increasing (a, b) and notch-like (c, d). N=number of patients

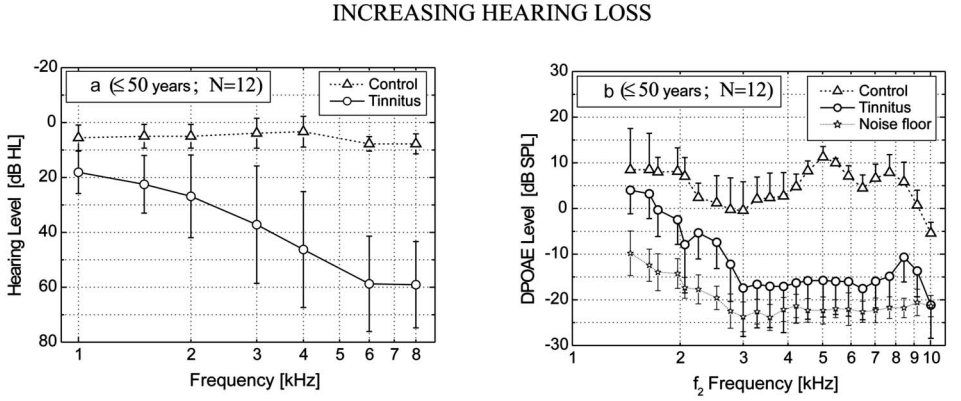

FIG. 6. Two types of the hearing loss functions (audiograms): increasing and notch-like (left column, a, c), and the corresponding DPgrams (right column, b, d) averaged across the tinnitus patients aged up to 50 years. Solid lines show the audiograms and DPgrams for the tinnitus patients and broken lines show the audiograms and DPgrams for the normal-hearing subjects (control group). Corresponding noise floors are depicted with thin dotted lines. Vertical bars specify the ±1 standard deviations. For clarity, only half length of the vertical bars are presented in panels (b) and (d). *N*=number of patients.

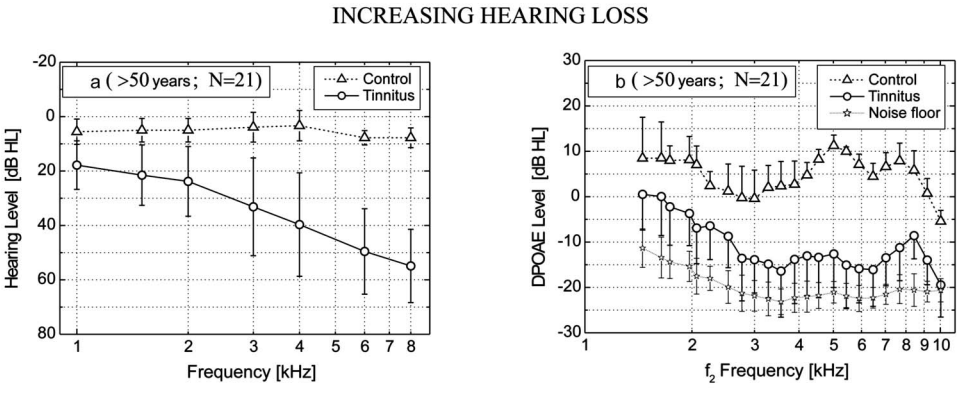

FIG. 7. As in Fig. 6, but for the tinnitus patients aged above 50.

The effect of increasing hearing loss on the DPgram revealed that the DPOAE levels decreased from about 4 to −16 dB [Fig. 6(b)] within the range to 3 kHz, while the hearing loss versus frequency function systematically increased up to about 38 dB HL [Fig. 6(a)]. Further increases in hearing loss above 38 dB HL (up to 60 dB HL) did not cause a decrease in the DPOAE level, however, the DPOAE could still be recorded around −16 dB SPL. Similar relations are observed in the older tinnitus group with increasing hearing loss [Figs. 7(a) and 7(b)]. To quantify the DPOAE decrease, the slope $s=[\text{DPOAE level}]/[\Delta f]$ was calculated for a chosen frequency range (Δf), over which DPOAE response and hearing sensitivity showed a similar decreasing tendency. According to Figs. 6(a) and 6(b), the hearing sensitivity and DPOAE level decreased within the frequency range $\Delta f=1.5$–3 kHz about 17 and 20 dB, respectively. This corresponds to the slope s being equal to 0.0113 and 0.0133 dB/Hz, respectively. The DPOAE slope was about 12% greater than the slope of the hearing loss function. For the older tinnitus group [Figs. 7(a) and 7(b)] similar calculations yielded the following results: an 11–and 15–dB decrease corresponding to 0.0073– and 0.010–dB/Hz slopes, respectively. In this case, the DPOAE slope was about 14% greater than the slope of the related hearing loss function. These data show that for the increasing hearing loss, if the slope of the hearing loss function diminishes in the frequency range of interest, the slope of the DPOAE response also decreases and is slightly steeper.

With respect to the effect of the tinnitus pitch on the DPOAE level, the group of patients with increasing hearing loss (sloping audiogram) classified their tinnitus as being high pitched with a frequency around 6 and 8 kHz. No effect of the tinnitus pitch on the DPOAE response was observed about 6 kHz. However, some DPOAE maxima were observed at 8 kHz corresponding to the tinnitus pitch, in the group aged to 50 years and above 50 years [see Figs. 6(b) and 7(b)] despite almost 60 dB HL hearing loss.

The DPOAE responses for two different tinnitus age groups showing the notch-like hearing loss are generally similar and reproduce quite well the hearing loss functions in the notch frequency region. The hearing sensitivity, starting from 1.5 kHz, systematically decreased versus increasing frequency reaching at 4 kHz its minimum of 40 dB HL [for the tinnitus group to 50 years, Fig. 6(c)] and 60 dB HL [for the tinnitus group above 50 years, Fig. 7(c)]. Above 4 kHz and up to 8 kHz, the hearing sensitivity increased by about 15 and 22 dB, respectively for these groups. Similar courses are shown by the DPOAE responses. The DPOAE levels from 2 kHz systematically decreased reaching their minima about −17 dB [Fig. 6(d)] and −22 dB [Fig. 7(d)] in the range of 3–4 kHz. Next the DPOAE level increased by about 13 dB with frequency increasing to 8 kHz (for the tinnitus group to 50 years) and 15 dB (for the tinnitus group above 50 years).

The slope calculation, similarly as for the patients exhibiting the increasing hearing loss, was made for the left and right parts of the notch type of hearing loss and the related DPOAE response. According to Fig. 6(c), the decrease in the left part of the notch (between 2 and 4 kHz) and the increase in the right part of the notch (between 4 and 7 kHz) of the hearing loss function amounted to 23 and 15 dB HL. They correspond to the slope s of 0.0115 and 0.005 dB/Hz, respectively. Clearly, the slope of the notch on the low-frequency side was about two times greater than the one on the high-frequency side. The calculations performed for the DPOAE notch [Fig. 6(d)] showed that for the left part of the notch, a level decrease, within the range of 1.5–3 kHz, was 18 dB, and, for the right part, a level increase, within the range of 4–7 kHz, was 14 dB SPL. The slopes s of the DPOAE notch branches corresponded to 0.012 and 0.005 dB/Hz, thus showing almost the same values as for the hearing loss function. This indicates that the notch shape of the DPOAE reflects quite well the hearing loss notch.

The calculations made for the tinnitus group above 50 [Figs. 7(c) and 7(d)] indicated a decrease in the left part of the notch (between 2 and 4 kHz) and an increase in the right part of the notch (between 4 and 7 kHz) of the hearing loss function [Fig. 7(c)] of 38 and 20 dB HL, respectively. These data correspond to the slopes s of the left and right parts of the notch of 0.019 and 0.0067 dB/Hz. The slopes of the left and right segments of the notch of the hearing loss function were larger for the older tinnitus group than for the younger one. This difference can be accounted for by the deeper hearing loss notch (of about 20 dB) in the older tinnitus group. The same calculation made for the DPOAE notch [Fig. 7(d)] gave, for the left part of the DPOAE notch, the level decrease (within the range of 2–4 kHz) of 22 dB and, for the right part, the level increase (within the range of 5–8 kHz) of 12 dB SPL. The slopes s of the DPOAE notch branches corresponded to 0.011 and 0.004 dB/Hz, respectively, which was a little lower than for the younger tinnitus group. As one can appreciate, a steeper slope of the hearing loss notch segments occurring in the tinnitus group above 50 years did not changed the steepness of the related DPOAE notch. This implies that the hearing loss shaped as a notch affects the DPOAE response only when the loss is limited to about 40 dB HL (observed for the tinnitus group below 50 years).

The tinnitus pitch data for patients showing the notch-like hearing loss were concentrated at about 4 and 6 kHz. The tinnitus masking levels did not exceed 30 dB SL. The correlation coefficient estimated a possible relationship between the depth in the DPOAE for the notch-like hearing loss and the maximum of the tinnitus pitch. It can be seen that for the $\text{TNH}_{<50}$ group the deepest part of the notch was localized in the range 3–4 kHz that corresponded to the maximum of the tinnitus pitch. It was found that for this group of patients the correlation coefficient was −0.79, suggesting some relationship between the notch-depth frequency and the tinnitus pitch. A weaker correlation was found for the older tinnitus group ($\text{TNH}_{>50}$) which exhibited a wider trough over the range of 4–6 kHz. In this case, the correlation coefficient was −0.43.

The obtained DPgrams were subjected to the two-way ANOVA, shown in Table II with hearing loss and age as factors.

As shown in Table II, there were significant effects of the shape of the hearing loss function on the DPOAE response: $[F(1,460)=541.64;\ p\leqslant 0.0000]$ for the $\text{THL}_{\leqslant 50}$ pa-

TABLE II. ANOVA analysis results related to the audiograms and DPgrams for the tinnitus groups with specific hearing loss (THL). (Bold fonts present statistically significant data.)

Factors	Audiograms	DPgrams
Increasing: $THL_{\leqslant 50}$ referred to NH	$\boldsymbol{F}(1,161)=225.94;\ \boldsymbol{p}\leqslant 0.0000$	$\boldsymbol{F}(1,460)=541.64;\ \boldsymbol{p}\leqslant 0.000$
Increasing: $THL_{>50}$ referred to NH	$\boldsymbol{F}(1,364)=222.00;\ \boldsymbol{p}\leqslant 0.0000$	$\boldsymbol{F}(1,598)=456.53;\ \boldsymbol{p}\leqslant 0.000$
Age: Increasing $THL_{\leqslant 50}$ and $THL_{>50}$	$\boldsymbol{F}(1,413)=5.22;\ \boldsymbol{p}\leqslant 0.0022$	$\boldsymbol{F}(1,874)=12.14;\ \boldsymbol{p}\leqslant 0.0005$
Notch: $THL_{\leqslant 50}$ referred to NH	$\boldsymbol{F}(1,140)=195.30;\ \boldsymbol{p}\leqslant 0.0000$	$\boldsymbol{F}(1,391)=423.13;\ \boldsymbol{p}\leqslant 0.000$
Notch: $THL_{>50}$ referred to NH	$\boldsymbol{F}(1,105)=431.45;\ \boldsymbol{p}\leqslant 0.000$	$\boldsymbol{F}(1,253)=515.44;\ \boldsymbol{p}\leqslant 0.000$
Age: Notch $THL_{\leqslant 50}$ and $THL_{>50}$	$\boldsymbol{F}(1,133)=58.52;\ \boldsymbol{p}\leqslant 0.0001$	$\boldsymbol{F}(1,460)=22.86;\ \boldsymbol{p}\leqslant 0.0000$

tients and $[F(1,598)=456.53;\ p\leqslant 0.0000]$ for those of the $THL_{>50}$ group for the increasing hearing loss condition. For the notch-like hearing loss, these values were $[F(1,391)=423.13;\ p\leqslant 0.000]$ for the $THL_{\leqslant 50}$ group and $[F(1,253)=515.44;\ p\leqslant 0.000]$ for the $THL_{>50}$ group. The effect of age difference between $THL_{\leqslant 50}$ and $THL_{>50}$ for increasing hearing loss was statistically significant both for the audiograms $[F(1,413)=5.22;\ p\leqslant 0.0022]$ and DPgrams $[F(1,874)=12.14;\ p\leqslant 0.0005]$. Similar relations were also observed for the notch-like hearing loss ($[F(1,133)=58.52;\ p\leqslant 0.0001]$ and $[F(1,460)=22.86;\ p\leqslant 0.0000]$, respectively).

IV. DISCUSSION

The data from experiment I showed that DPOAE levels decrease in tinnitus ears with clinically normal hearing when compared to DPOAE levels in normal hearing (nontinnitus) ears. The mean DPgram for tinnitus ears revealed a clear reduction in the emission over a limited frequency range localized mainly around 3 and 5 kHz for $TNH_{\leqslant 50}$, and around 3 and above 5 kHz for $TNH_{>50}$. Shiomi *et al.* (1997), studying tinnitus ears with normal hearing, also reported a reduction in the DPOAE level over a limited frequency range of 4–7 kHz. These findings suggest different cochlear signal processing in ears with and without tinnitus. To account for reduced DPOAEs in tinnitus ears one can assume that these ears had a number of malfunctioning OHCs that could be identified easier by the sensitive DPOAE measure than by routine audiometric testing. This supposition is supported by the data obtained in animal models of noise-induced hearing loss, which indicate that a behavioral threshold shift was evident only when about 50% of OHCs were missing (Bohne and Clark, 1982).

The above-mentioned reduction in the DPOAE levels in the tinnitus ears with clinically normal hearing is not consistent with the findings of other studies (Norton *et al.*, 1990; Mitchell *et al.*, 1995), which suggest that the DPOAE levels in tinnitus ears might be lower or higher, depending on the frequency range, than the DPOAE levels in normal ears (without tinnitus). Gouveris *et al.* (2005) recently showed that tinnitus ears with normal hearing exhibit decreased DPOAE levels over the middle frequency range and increased levels at high frequencies compared to DPOAEs in ears without tinnitus.

For the tinnitus patients with clinically normal hearing, DPOAE levels depended on the age of patients as follows from a comparison of Figs. 3(b) and 3(d). As seen from these plots, the mean DPOAE level was lower for the older tinnitus group ($TNH_{>}50$) than for the younger one ($TNH_{\leqslant 50}$), despite the fact that for these two groups, the audiograms were clinically normal and there was no significant statistical difference between these data sets. One can assume that the age-related decrease in DPOAE generation observed in the older tinnitus patients resulted either from reduced OHC activity or from OHC losses. This decrease is in agreement with the findings of a number of investigators (Lonsbury-Martin *et al.*, 1991; Ozimek *et al.*, 2004) who also reported an age effect on the DPOAE response mainly for the higher frequencies. The reduction of DPOAE level as a result of aging is also consistent with the histopathological observations reported for some animal models, for which aging effects on cochlear structures resulted in progressive OHC losses (Hawkins *et al.*, 1985; Bohne *et al.*, 1990).

As mentioned above, despite the fact that the hearing thresholds of the two tinnitus groups tested were assumed to be clinically normal according to ANSI (1996) standards, their general auditory system activity (particularly that of the older tinnitus patients) was deteriorated from the DPOAE point of view relative to that of the "normal" hearing system. Thus, the classical definition of clinically "normal" hearing does not comprise the subtle changes in the cochlea micromechanism associated with the tinnitus. The decrement observed in the high-frequency DPOAEs due to aging might be considered to be a more sensitive indicator of cochlear state, suggesting an onset of the presbyacusis process in tinnitus patients.

The decrease in DPOAEs with increasing age observed for the tinnitus patients is also in agreement with the effect of aging on the spontaneous otoacoustic emissions (SOAEs) and transiently evoked otoacoustic emissions (TOAEs) (Bonfils, 1989). Bonfils (1989) found that the prevalence of SOAEs decreased with age in a group of older patients exhibiting close to normal hearing thresholds. A similar age-related decrease was found in TEOAE levels (Bonfils *et al.*, 1988). The TEOAEs varied systematically as a function of age, which is related to the decrease in hearing sensitivity caused by presbyacusis. Other reports, however, have failed to support the DPOAE-age-related dependence. For ex-

ample, Stover and Norton (1993) found that DPOAEs were related to hearing sensitivity and frequency, but not to age. Similarly, Strouse *et al.* (1996) found no consistent age effects on DPOAEs.

It is difficult to explain the above conflicting data concerning the effect of age on the DPOAEs. However, it is worth noting that the age-related decrease in the DPOAE level reported here was clearly seen for the tinnitus patients with normal-hearing thresholds. This effect, however, was not so obvious for the tinnitus patients with hearing loss tested in experiment II, regardless of the shape of the hearing loss function. Comparing the DPOAE responses presented in Figs. 6(b) and 6(d) (age group below 50 years) with those in Figs. 7(b) and 7(d) (age group above 50 years), it is not possible to conclude definitely a decrease in the DPOAE levels in the older tinnitus group. Aging is usually related to hearing loss (presbycusis), which is a complex issue since it may result from degeneration of the cochlea, external effects such as noises or ototoxic drugs, intrinsic diseases, or all these elements taken together. The presence of a hearing loss confounds to some extent the age effect on the DPOAEs since both factors (age and hearing loss) have a similar origin resulting from dysfunction of OHCs activity and/or their loss (sensory presbyacusis). The age-related cochlea may also be affected by a strial atrophy, which is a substantive factor in metabolic presbycusis resulting from a pathophysiological mechanism (Schuknecht *et al.*, 1974; Gratton *et al.*, 1996; Mills, 2001). A more in-depth study of strial presbycusis, as an important factor in cochlear aging, might add new insights into age-related hearing loss linked to DPOAE changes.

One can also suppose that the cochlear and possible cortical processing of auditory information differ in some aspects between patients of different ages being either affected or not affected by hearing loss, which would result in conflicting data on the effects of age on DPOAEs. Perhaps a more thorough look into cochlear and cortical processing of auditory information could be obtained by simultaneous measurements of the DPOAE and auditory brainstem responses (ABRs) (Durrant and Collet, 2002) for patients representing different age groups and different types of hearing loss.

The results of experiment II indicate a correspondence between the configuration of the increasing and the notch-like hearing loss functions and the DPOAE responses in the tinnitus ears. For the increasing hearing loss, the hearing level increases, within the range 1.5–3 kHz, by about 16 dB HL for the tinnitus group below 50 and by about 12 dB HL for the older group. A related reduction in the DPOAE level assigned to those groups of patients was also observed. Within the frequency range to 3 kHz, the DPOAE responses showed a systematic level decrease from 4 to −16 dB SPL in the tinnitus patients below 50 and from 1 to −14 dB SPL in the older tinnitus group. For higher frequencies (above 3 kHz), despite a further increase in the hearing loss up to almost 60 dB HL, the DPOAE level remained the same of about −15 dB SPL. Thus, for a decreasing hearing sensitivity, a good correspondence between the hearing loss and DPOAE functions exists only when the hearing loss did not exceed a value of about 40 dB HL.

A good correspondence was also found between the notch-like hearing loss and the DPOAE function. At 4 kHz, where the hearing losses for both tinnitus groups reached their minimum (40 dB HL for the group below 50, and 60 dB HL for the older tinnitus group) the DP levels were really low, reaching −16 and −21 dB SPL for the two groups, respectively. Below and above this frequency region, where hearing sensitivity continuously increased, the DP level also rose by more than 15 dB. For the tinnitus group below 50, the steepness of the left branches of the notch of the hearing loss and DPOAE functions was about 0.012 dB/Hz and for the right ones it was 0.004 dB/Hz. For the older tinnitus group, a steeper slope of the hearing loss notch (due to the larger loss by about 60 dB HL) was observed, however, it did not influence the steepness of the DPOAE notch. This finding supports the statement on the limited (to about 40 dB HL) correspondence between the hearing loss and the DPOAE functions.

The results of experiment II clearly showed a decrease in the DPOAEs in the tinnitus ears exhibiting hearing losses. It is consistent with the general finding presented in other papers reporting that the DPOAE level is reduced in the ears with hearing loss (Martin *et al.*, 1990; Stover *et al.*, 1996; Gorga *et al.*, 1993, 1997, 2002). However, it is not in agreement with the findings of Janssen and Arnold (1995) and Janssen *et al.* (1998) who showed that in tinnitus patients with sensorineural hearing loss, DPOAE responses were nonuniform. In some tinnitus ears they tested, the DPOAE level decreased with increasing hearing loss. Other ears, however, exhibited a poor or even inverse relationship between the DPOAE level and the hearing loss, i.e., displayed a surprising increase in the DPOAE level with increasing hearing loss. They assumed that in those ears a reinforced mechanical distortion was generated by a hypothetical cochlear hyperactivity that was a source of the DPOAE and the tinnitus.

The relationship between DPOAEs and hearing level was also discussed in papers related to hearing losses due to noise exposure (Martin *et al.*, 1990) and some unspecified factors (Kimberley and Nelson, 1989). Other authors (Lonsbury-Martin and Martin, 1990; Martin *et al.*, 1990; Nelson and Kimberly, 1992; Gorga *et al.*, 1993; Lonsbury-Martin *et al.*, 1993) found a rather weak relationship between hearing sensitivity and DPOAE responses. We suppose that some role in these ambiguities in DPOAE activity versus hearing loss might be assigned to different cochlear impairments in the tinnitus ears tested.

A characteristic feature of the DPOAE response was a specific dip (minimum) at about 3–4 kHz. A similar dip was found by others (Lonsbury-Martin *et al.*, 1991; Gorga *et al.*, 1993; Strouse *et al.*, 1996). An attempt was made to interpret the appearance of such a dip to cancellation effects associated with the generation of the otoacoustic emissions (Whitehead *et al.*, 1992a; Mills *et al.*, 1993; Mills, 1997).

Another problem with DPOAEs is a large number of different parameters that may affect the DPOAE response.

For example a change in the frequency ratio of primaries causes complex changes in the level and phase of the cubic distortion products (Whitehead *et al.*, 1992a). The reasons for these changes are not well established. The DPOAE response also depends on the magnitude ratio of the f_1 and f_2 primaries and the criteria of choosing the best ratio still remain unclear (Mills *et al.*, 1993; Mills and Rubel, 1994; Whitehead *et al.*, 1995a, b; Kummer *et al.*, 1998).

In conclusion, our data indicate that the DPOAE level in the tinnitus patients with clinically normal-hearing thresholds are lower than that in the normal-hearing subjects (without tinnitus). The level difference changes with frequency and depends on the age of the patients, suggesting that the DPOAE response may be helpful in determination of the onset of presbyacusis in tinnitus patients. The presence of tinnitus combined with sensorineural hearing loss reduces DPOAEs. The data also imply that age affects DPOAEs, but that this effect is rather independent of hearing loss. One has to remember that the tinnitus, whose etiology has not been well established yet, and the hearing loss are only two aspects of cochlear dysfunction. Given the complexity of the cochlea, one can expect that cochlear dysfunction is generally a multidimensional problem, which often makes it difficult to interpret DPOAE data. Further study of the association of tinnitus and DPOAEs may reveal more information about the cochlear and neural functions of the hearing system.

ACKNOWLEDGMENTS

This work was supported by a grant from the State Committee for Scientific Research (KBN) No. 2 P05D 122 26 and a grant from the A. Mickiewicz University. We thank two anonymous reviewers for useful comments and remarks on the earlier version of this manuscript.

Andersson, G. (**2003**). "Tinnitus loudness matching in relation to annoyance and grading of severity," Auris Nasus Larynx **30** (2), 129–133.

ANSI (**1996**). ANSI S3.6-1996 "*Specifications for Audiometers*" (American National Standards Institute, New York).

Attias, J., Bresloff, L., and Furman, V. (**1996**). "The influence of the efferent auditory system on otoacoustic emission in noise induced tinnitus: Clinical relevance," Acta Oto-Laryngol. **116**, 534–539.

Bohne, B. A., and Clark, W. W. (**1982**). "Growth of hearing loss and cochlear lesion with increasing duration of noise exposure," in *New Perspectives of Noise-Induced Hearing Loss*, edited by R. P. Hammernick, D. Hendrson, and R. Salvi (Raven, New York), pp. 283–301.

Bohne, B. A., Gruner, M. M., and Harding, G. W. (**1990**). "Morphological correlates of aging in the chinchilla cochlea," Hear. Res. **48**, 79–91.

Bonfils, P. (**1989**). "Spontaneous otoacoustic emissions: Clinical interest," Laryngoscope **99**, 752–756.

Bonfils, P., Bertrand, Y., and Uziel, A. (**1988**). "Evoked otoacoustic emissions: Normative data and presbycusis," Audiology **27**, 27–35.

Durrant, J. D., and Collet, A. L. (**2002**). "Integrating otoacoustic emission and electrophysiological measures," in *Otoacoustic Emissions—Clinical Application*, edited M. S. Robinette and T. J. Glattke (Stuttgart, New York).

Eggermont, J. J. (**1990**). "On the pathophysiology of tinnitus; a review and a peripheral model," Hear. Res. **48**, 111–124.

Eggermont, J. J., and Roberts, L. E. (**2004**). "The neuroscience of tinnitus," Trends Neurosci. **27**, 676–682.

Gorga, M. P., Neely, S. T., and Dorn, P. A. (**2002**). "Distortion product otoacoustic emission in relation to hearing loss," in *Otoacoustic Emissions Clinical Applications*, edited by M. S. Robinette and T. J. Glattke (Thieme, New York), pp. 243–272.

Gorga, M. P., Neely S. T., Ohlrich B., Hoover B., Redner J., and Peters J. (**1997**). "From laboratory to clinic: a large scale study of distortion product otoacoustic emissions in ears with normal hearing and ears with hearing loss," Ear Hear. **18**, 440–455.

Gorga, M. P., Neely, S. T., Bergman, B., Beauchaine, K. L., Kaminski, J. R., Peters, J., and Jesteadt, W. (**1993**). "Otoacoustic emissions from normal-hearing and hearing-impaired subjects: distortion product responses," J. Acoust. Soc. Am. **93**, 2050–2060.

Gouveris, H., Maurer, J., and Mann, W. (**2005**). "DPOAE-grams in patients with acute tonal tinnitus," Otolaryngol.-Head Neck Surg. **132** (4), 550–553.

Gratton M. A., Schmiedt R. A., and Schulte B. A. (**1996**). "Age-related decreases in endocochlear potential are associated with vascular binormalities in the stria vascularis," Hear. Res. **102**, 181–190.

Hawkins, J. E., Miller, J. M., Rouse, R. C., Davis, J. A., and Rarey, K. (**1985**). "Inner ear histopathology in aging rhesus monkeys (*Macaco mulatto*)," in *Behavior and Pathology of Aging in Rhesus Monkeys*, edited by R. T. Davis and C. W. Leathers (Liss, New York), pp. 137–154.

Henry, J. A., and Meikle, M. B. (**2000**). "Psychoacoustic measures of tinnitus," J. Am. Acad. Audiol **11**, 138–155.

Janssen, T., and Arnold, W. (**1995**). "Growth functions of distortion product otoacoustic emissions in cochlear tinnitus," Oto-Rhino-Laryngol. Nova **5**, 127–144.

Janssen, T., Kummer, P., and Arnold, W. (**1998**). "Growth behavior of the 2*f*1-*f*2 distortion product otoacoustic emission in tinnitus," J. Acoust. Soc. Am. **103**, 3418–3430.

Jastreboff, P. J. (**1990**). "Phantom auditory perception (tinnitus); mechanism of generation and perception," Neurosci. Res. (NY) **8**, 221–254.

Jastreboff, P. J., and Hazell, J. W. P. (**1993**). "A neurophysiological approach to tinnitus: clinical implication," Br. J. Audiol. **27**, 7–17.

Kemp, D. T. (**1978**). "Stimulated acoustic emissions from within the human auditory system," J. Acoust. Soc. Am. **64**, 1386–1391.

Kemp, D. T. (**1982**). "Cochlear echoes: Implications for noise-Induced hearing loss," in *New Perspectives on Noise Induced Hearing Loss*, edited by R. P. Hamernick, D. Henderson, and R. Salvi (Raven, New York), pp. 189–207.

Kemp D. T. (**1986**). "Otoacoustic emissions, traveling waves, and cochlear mechanisms," Hear. Res. **21**, 95–104.

Kimberley, B. P., and Nelson, D. A. (**1989**). "Distortion product emissions and sensorineural hearing loss," J. Otorhinolaryngol. **18**, 365–369.

Kimberley, B. P., Hernadi, I., Lee, A. M., and Brown, D. K. (**1994**). "Predicting pure tone thresholds in normal and hearing-impaired ears with distortion product otoacoustic emissions and age," Ear Hear. **15**, 199–209.

Kummer, P., Janssen, T., and Arnold, W. (**1998**). "The level and growth behavior of the $2f_1$-$2f_2$ distortion product otoacoustic emission and its relationship to auditory sensitivity in normal hearing and cochlear hearing loss," J. Acoust. Soc. Am. **103**, 3431–3444.

Lonsbury-Martin, B. L., and Martin, G. K. (**1990**). "The clinical utility of distortion-product otoacoustic emissions," Ear Hear. **11**, 144–154.

Lonsbury-Martin, B. L., and Martin, G. K. (**2002**). "Distortion Product Otoacoustic Emissions," in *Otoacoustic Emissions Clinical Application*, edited by M. S. Robinette and T. J. Glattke (Thieme, New York), pp. 116–142.

Lonsbury-Martin, B. L., Cutler, W. M., and Martin, G. K. (**1991**). "Evidence for the influence of aging on distortion-product otoacoustic emissions in humans," J. Acoust. Soc. Am. **89**, 1749–1759.

Lonsbury-Martin, B. L., McCoy, M. J., Whitehead, M. L., and Martin, G. K. (**1993**). "Clinical testing of distortion-product otoacoustic emissions," Ear Hear. **1**, 11–22.

Martin, G. K., Ohlms, L. A., Franklin, D. J., Harris, F. P., and Lonsbury-Martin, B. L. (**1990**). "Distortion product otoacoustic emissions: III. Influence of sensorineural hearing loss," Ann. Otol. Rhinol. Laryngol. **99**, 30–42.

Mills, D. M. (**1997**). "Interpretation of distortion product otoacoustic emission measurements. I. Two stimulus tones," J. Acoust. Soc. Am. **102**, 413–429.

Mills, D. M. (**2001**). "Distortion product otoacoustic emissions and neural responses measure different things: Using the difference for differential diagnosis of cochlear dysfunction," Abstract, *XVIIth Biennial Symposium of the International Evoked Response Audiometry Study Group*.

Mills, D. M., and Rubel, E. D. (**1994**). "Variation of distortion product otoacoustic emissions with furosemide injection," Hear. Res. **77**, 183–199.

Mills, D. M., Norton, S. J., and Rubel, E. D. (**1993**). "Vulnerability and adaption of distortion product otoacoustic emissions to endocochlear po-

tential variation," J. Acoust. Soc. Am. **94**, 2108–2122.
Mitchell, C. R., Lilly, D. J., and Henry, J. (**1995**). "Otoacoustic emissions in subjects with tinnitus and normal hearing," in *Proceedings of the 5th International Tinnitus Seminar*, edited by G. Reich and J. Vernon (Am. Tinnitus Association, Portland), pp. 180–185.
Mitchell, C. R., Vernon, J. A., and Creedon, T. A. (**1993**). "Measuring tinnitus parameters: Loudness, pitch, and maskability," J. Am. Acad. Audiol **4**, 139–151.
Mühlnickel, W., Elbert, T., Taub, E., and Flor, H. (**1998**). "Reorganization of auditory cortex in tinnitus," Proc. Natl. Acad. Sci. U.S.A. **95**, 10340–10343.
Naeve, S. L., Margolis, R. H., Levine, S. C., and Fournier, E. M. (**1992**). "Effect of ear-canal air pressure on evoked otoacoustic emissions," J. Acoust. Soc. Am. **91**, 2091–2095.
Nelson, D. A., and Kimberley, B. P. (**1992**). "Distortion-product emissions and auditory sensitivity in human ears with normal hearing and cochlear hearing loss," J. Speech Hear. Res. **35**, 1142–1159.
Norton, S. J., Schmidt, A. R., and Stover L. J. (**1990**). "Tinnitus and otoacoustic emissions: Is there a link?" Ear Hear. **11**, 159–166.
Ozimek, E., Wicher, A., Szyfter, W., and Szymiec, E. (**2004**). "The age-related changes in DPOAEs in tinnitus patients," in *Structures–Waves—Human Health*, edited by R. Panuszka (Polish Acoustical Society, Krakow), Vol. XIII, No. 2, pp. 120–124.
Probst, R., Lonsbury-Martin, B. L., and Martin, G. K. (**1991**). "A review of otoacoustic emissions," J. Acoust. Soc. Am. **89**, 2027–2067.
Rankin, N. O. (**1974**). "The harmonic mean method for one-way and two-way analyses of variance," Biometrika **61**, 117–129.
Robinette, M. S., and Glattke, T. J. (**2002**). *Otoacoustic Emissions—Clinical Applications*. Thieme, New York, Stuttgart.
Robinson, P. M., and Haughton, P. M. (**1991**). "Modification of evoked otoacoustic emissions by changes in pressure in the external ear," Br. J. Audiol. **25**, 131–133.
Schuknecht, H. F., Watanuki, K., Takahashi, T., Belal, A. A., Kimura, Jr., R. S., Jones, D. D., and Ota, C. Y. (**1974**). "Atrophy of the stria vascularis, a common cause for hearing loss," Laryngoscope **84**, 1777–1821.
Shiomi, Y., Tsuji, J., Naito, Y., Fujiki, N., and Yamamoto, N. (**1997**). "Characteristic of DPOAE audiogram in tinnitus patients," Hear. Res. **108**, 83–88.
Stover, L., and Norton, S. J. (**1993**). "The effects of aging on otoacoustic emissions," J. Acoust. Soc. Am. **94**, 2670–2681.
Stover, L., Gorga, M. P., Neely, S. T., and Montoya, D. (**1996**). "Towards optimizing the clinical utility of distortion product otoacoustic emission measurements," J. Acoust. Soc. Am. **100**, 956–967.
Strouse, A. L., Ochs, M. T., and Hall, J. W. (**1996**). "Evidence against the influence of aging on distortion-product otoacoustic emissions," J. Am. Acad. Audiol **7**, 339–345.
Sziklai, L., and Dallos, P. (**1997**). "Hyposmotic induces magnitude and gain change in the electromotile performance of isolated outer hair cells," Acta Oto-Laryngol. **117**, 222–225.
Tonndorf, J. (**1987**). "The analogy between tinnitus and pain: a suggestion for a physiological basis of chronic tinnitus," Hear. Res. **28**, 271–275.
Tyler, R. S. (**2000**). "The psychoacoustical measurement of tinnitus," in *Tinnitus handbook*, edited by R. S. Tyler (Singular, Thomson Learning, San Diego), pp. 149–179.
Whitehead, M. L., Lonsbury-Martin, B. L., and Martin, G. K. (**1992a**). "Evidence for two discrete sources of $2f_1$-f_2 distortion-product otoacoustic emissions in rabbit. I: Differential dependence on stimulus parameters," J. Acoust. Soc. Am. **91**, 1587–1607.
Whitehead, M. L., Lonsbury-Martin, B. L., and Martin, G. K. (**1992b**). "Evidence for two discrete sources of $2f_1$-f_2 distortion-product otoacoustic emissions in rabbit. II: Differential physiological vulnerability," J. Acoust. Soc. Am. **92**, 2662–2682.
Whitehead, M. L., McCoy, M. J., Lonsbury-Martin, B. L., and Martin, G. K. (**1995a**). "Dependence of distortion-product otoacoustic emissions on primary levels in normal and unpaired ears. I. Effects of decreasing L_2 below L_1," J. Acoust. Soc. Am. **97**, 2346–2358.
Whitehead, M. L., Stagner, B. B., McCoy, M. J., Lonsbury-Martin, B. L., and Martin, G. K. (**1995b**). "Dependence of distortion-product otoacoustic emissions on primary levels in normal and unpaired ears. II. Asymmetry in L_1, L_2 space," J. Acoust. Soc. Am. **97**, 2359–2377.
Zhang, M., and Abbas, P. J. (**1997**). "Effects of middle ear pressure on otoacoustic emission measures," J. Acoust. Soc. Am. **102**, 1032–1038.
Zweig, G., and Shera, C. A. (**1995**). "The origin of periodicity in the spectrum of evoked otoacoustic emissions," J. Acoust. Soc. Am. **98**, 2018–2047.

The effect of glottal angle on intraglottal pressure

Sheng Li
The Key Laboratory of Biomedical Information Engineering of Ministry of Education, and Department of Biomedical Engineering, School of Life Science and Technology, Xi'an Jiaotong University, Xi'an 710049, People's Republic of China

Ronald C. Scherer
Department of Otolaryngology—Head and Neck Surgery, University of Cincinnati Medical Center, P.O. Box 670528, Cincinnati, Ohio 45267-0528

MingXi Wan,[a] SuPin Wang, and HuiHui Wu
The Key Laboratory of Biomedical Information Engineering of Ministry of Education, and Department of Biomedical Engineering, School of Life Science and Technology, Xi'an Jiaotong University, Xi'an 710049, People's Republic of China

(Received 22 May 2004; revised 7 October 2005; accepted 11 October 2005)

Intraglottal pressure distributions depend upon glottal shape, size, and diameter. This study reports the effects of varying glottal angle on intraglottal and transglottal pressures using a three-dimensional Plexiglas™ model with a glottis having nine symmetric glottal angles and a constant minimal glottal diameter of 0.06 cm. The empirical data were supported by computational results using FLUENT. The results suggested that (1) the greater the convergent glottal angle, the greater outward driving forces (higher intraglottal pressures) on the vocal folds; (2) flow resistance was greatest for the uniform glottis, and least for the 10° divergent glottis; (3) the greatest negative pressure in the glottis and therefore the greatest pressure recovery for diverging glottal shapes occurred for an angle of 10°; (4) the smaller the convergent angle, the greater the flow resistance; (5) FLUENT was highly accurate in predicting the empirical pressures of this model; (6) flow separation locations (given by FLUENT) for the divergent glottis moved upstream for larger flows and larger glottal angles. The results suggest that phonatory efficiency related to aerodynamics may be enhanced with vocal fold oscillations that include large convergent angles during glottal opening and small (5°–10°) divergent angles during glottal closing. © *2006 Acoustical Society of America.* [DOI: 10.1121/1.2133491]

PACS number(s): 43.70.Aj, 43.70.Bk [AL] Pages: 539–548

I. INTRODUCTION

The oscillation of the vocal folds during phonation depends on their tissue characteristics, their initial positions, and the intraglottal air pressure distributions throughout the cycle (Titze, 1994). The dynamic air pressures on the surface of the vocal folds act as external driving forces during phonation, and have significant influence on the motion of the vocal folds (Ishizaka and Flanagan, 1972; Ishizaka and Matsudaira, 1972; Titze, 1986). Another driving force is the shear force resulting from air viscosity near the tissue surface, which is determined by the velocity distribution within the glottis (Alipour *et al.*, 1996; Deverge *et al.*, 2003). Pressure and velocity information in laryngeal models help to improve our understanding of phonation and test the calculations of aerodynamic forces within computer simulations of speech.

Recordings of human phonation suggest that adequate modeling of phonation requires specification of a wide range of glottal configurations in phonation (Titze, 1974; Gauffin *et al.*, 1983; Guo and Scherer, 1993), which includes the inferior-superior and anterior-posterior lengths of the glottal duct, the minimal glottal diameter, glottal symmetry, glottal linearity, the curvature of the vocal folds at the glottal entrance and exit locations, and the glottal angle [Gauffin *et al.*, 1983; Scherer *et al.*, 2001a, 2001b, 2002; Li *et al.* (unpublished a, b).

Physical models of laryngeal function can be made with precise geometry of the vocal folds and the glottis, and can be used to control the transglottal pressures and the motion of the vocal folds. They therefore have been used to study flow resistance, intraglottal pressure distributions, velocity distributions, and acoustic generation (Alipour *et al.*, 1996; Alipour and Scherer, 2000; Mongeau *et al.*, 1997; Kucinschi, 2004). Studies with static geometries and constant volume flows depend upon the validity of the quasisteady approximation when the results are to be applied to dynamic models. Numerous studies, both theoretical and empirical, support the quasisteady assumption for phonation (Flanagan, 1972; Binh and Gauffin, 1983; Mongeau *et al.*, 1997; Zhang *et al.*, 2002) except possibly near glottal opening and closing (Pelorson *et al.*, 1994; Pelorson, 2001; Kucinschi, 2004), whereas others caution that the quasisteady assumption may not be valid (McGowan, 1993; Pedley, 1983) or at least for the jet flow structure rather than for volume flow (Kucinschi,

[a]Electronic mail: mxwan@mail.xjtu.edu.cn

2004). The work presented here assumes that there remains useful validity to static laryngeal modeling with constant volume flows.

During any given phonation cycle, the glottis takes on a variety of shapes. The primary general shapes appear to be the rectangular, convergent, and divergent. The *rectangular* shape corresponds to the medial surface of the vocal folds being parallel to each other, also called a uniform glottal duct, or a glottis with an angle of 0°. When the glottis is *convergent*, as it is during glottal opening during the phonatory cycle, the glottal diameter is larger inferiorly and smaller superiorly. A *divergent* glottal shape occurs typically during glottal closing and has a narrower portion inferiorly and a wider portion superiorly. Each of the primary glottal shapes may yield unique pressure-flow characteristics.

Several previous studies have motivated the use of the chosen glottal angles in this study. Guo and Scherer (1993) adopted the penalty finite element method to simulate steady airflows through a model of the larynx. The transglottal pressures and flows for nine glottal angles [40°, 20°, 10°, and 5° (divergent), 0° (uniform), −5°, −10°, −20°, and −40° (convergent)] were explored for a minimal glottal diameter of 0.04 cm. The results suggested that the computational method should be sufficient to study glottal aerodynamics.

Unsteady flow through *in vitro* models of the glottis was studied in some detail based on a quasisteady boundary-layer model by Hofmans *et al.* (2003). A 20°-diverging model and 10°-diverging model were explored by means of a combined experimental, numerical, and theoretical study, the results indicating that the vocal fold model with a diffuser angle of 20° exhibited highly unsteady flow behavior, and the vocal fold model with a diffuser angle of 10° acted as a well-designed diffuser.

Scherer and Shinwari (2000) reported an unpublished study on pressure distributions for nine glottal angles (the same angles as used by Guo and Scherer, 1993) for transglottal pressures of 3, 5, 10, and 15 cm H_2O using a Plexiglas™ model (M5) which had 14 pressure taps on the vocal folds. The results gave rather complete pressure distributions, and suggested that the most efficient glottal diffuser angle was between 5° and 10° divergent. An oblique glottal angle was studied by Scherer *et al.* (2001a) and replicated nearly exactly by Shinwari *et al.* (2003). The study reported intraglottal pressure distributions for model M5 with a glottis having a 10° divergence angle and either a symmetric orientation or an oblique angle of 15°. The study showed that the right and left glottal wall pressures differed for both the symmetric and the oblique glottis, suggesting that there are asymmetric wall pressures in asymmetric glottal ducts.

The purpose of this study was to obtain pressure distributions in a physical glottal model when the glottis takes on different convergent, uniform, and divergent shapes, to better understand the aerodynamics of phonation. Earlier published studies have not examined in detail the pressure distributions for a wide range of glottal angles in a three-dimensional model. This study does so. In addition, this study uses a commercial computational code, FLUENT (Fluent, Inc., Lebanon, NH), to test its ability to match the empirical data, which it does well, as will be shown. The results provide information relevant to vocal fold driving pressures, as well as data for validation of other computational models of phonation.

II. METHODS

A. Plexiglas™ model

The model used in this research was a nonvibrating laryngeal airway model made from Plexiglas™. Relative to a similitude analysis (Streeter and Wylie, 1975) and for the convenience of fabrication of the model and recording experimental data, the model had linear dimensions 1.732 times that of a normal male larynx (hereafter, only the human size dimensions will be stated, except where indicated otherwise). Figures 1(a) and 1(b) show the planform or coronal (a) and side elevation or lateral (b) views of the model, respectively. The sub-, supra-, and glottal portions were formed by using four parts: the top, bottom, and left and right sections. The model was symmetric about two axes. A three-dimensional airway rendering of a side elevation view for a 40° divergent glottal angle is shown in Fig. 1(c). A synthetic resin fixed the four parts. Two vocal fold pieces were embedded into the airway duct. Since a synthetic resin hermetically sealed the model, and the side faces of the vocal folds touched the corresponding faces of the other two sides, this embedded construction prevented air leakage between the glottis and the inlet and outlet tunnel.

Typically in static physical models of the larynx the superior vocal fold surface angle is set with an angle of 0°, although there have been exceptions [for example, Gauffin *et al.* (1983) used a positive slope, but did not study this feature parametrically]. A recent study based on laminagraphic tracings (Agarwal *et al.*, 2003) indicates that the superior vocal fold surface angle during phonation ranges from about −10° to 25° for nonsinger subjects, where a positive angle means that the lateral portion of the surface is lower, more inferior, than the medial portion. A related study [Li *et al.* (unpublished a)] suggests that, for constant entrance and exit glottal radii, the intraglottal pressures are unchanged for superior vocal fold surface angles up to approximately −70°. In the study reported here, a negative angle of −45° was used (see Fig. 1), which allowed easier construction. Thus, the intraglottal pressures reported here should be approximately equal to those found in a model with a 0° superior vocal fold surface angle, given that the entrance and exit radii were the same for the two models.

The glottis itself is the slit between the two vocal folds. The minimal glottal diameter was adjustable by a movable handle outside the glottal duct (Fig. 1). The indentations of the larynx at the anterior and posterior ends partially mimic the presence of the arytenoid cartilages posteriorly and the anterior commissure anteriorly (Hirano *et al.*, 1988).

There were nine pairs of vocal fold pieces. Figure 2 indicates the general design of the vocal folds. The shape and size of the vocal folds were well defined. The anterior-posterior glottal length was held constant at 1.210 cm. The eighteen vocal folds (nine pairs) were fabricated out of Plexiglas™ using precision machinery to provide nine symmetric

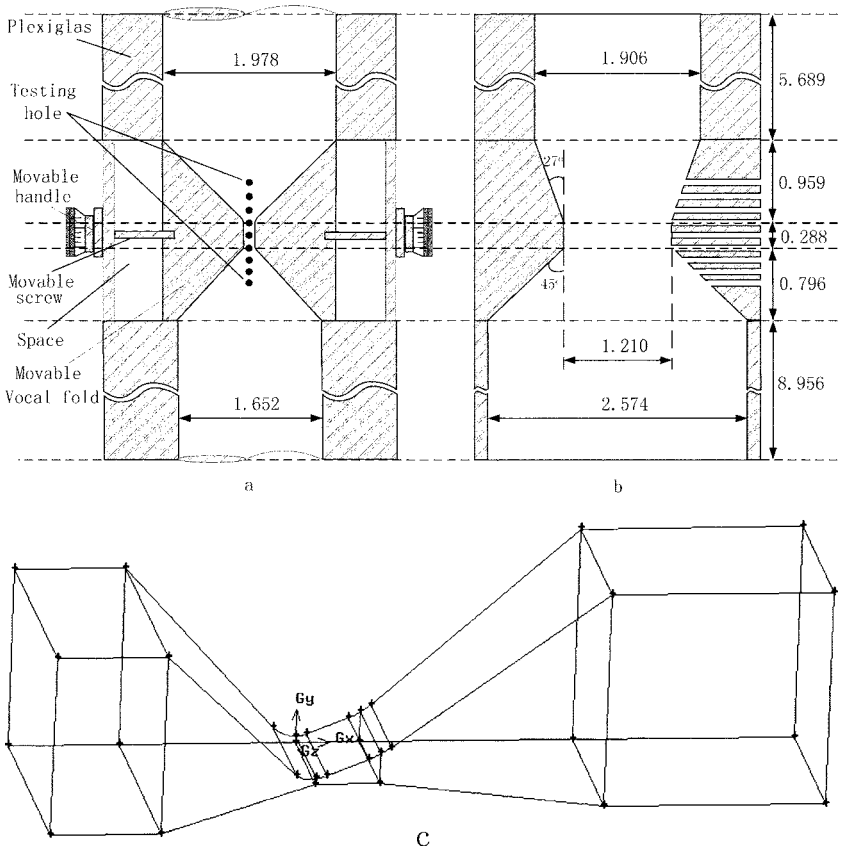

FIG. 1. The planform (a) and side elevation (b) of the Plexiglas™ model, and a three-dimensional perspective of the computational airway (in GAMBIT) (c). Note that (c) represents a quarter of the model. All measures are in human values in centimeters or degrees. The dimensions of the model were 1.732 times greater than human size values.

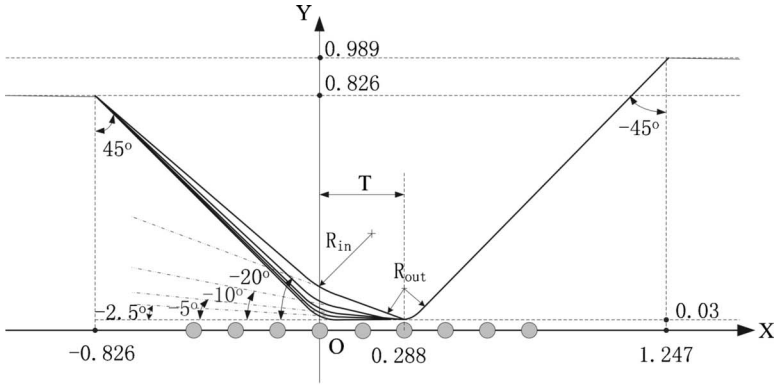

General vocal fold surface design equations:

(a) $R_{in} = R_0 \tan((135^\circ + (\varphi/2))/2) / \cos(\varphi/2)$, $R_{out} = 0.144$, $R_0 = 0.07$, $T = 0.288$
Where φ is the convergent glottal angle, T is glottal thickness.

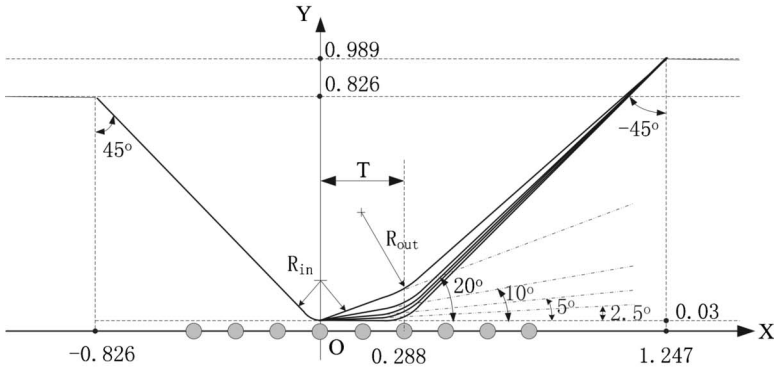

General vocal fold surface design equations:

(b) $R_{in} = 0.144$, $R_{out} = R_0 \tan((135^\circ + (\varphi/2))/2) / \cos(\varphi/2)$, $R_0 = 0.07$, $T = 0.288$
Where φ is the divergent glottal angle, T is glottal thickness.

FIG. 2. (a) Schematic of the design of the convergent vocal fold pieces. The shapes of the vocal folds shown are for uniform and the four convergent glottal angles of −5°, −10°, −20°, and −40° (corresponding to −2.5°, −5°, −10°, and −20° half-angles as shown). R_{in} is 0.1690, 0.1802, 0.1931, 0.2254, and 0.3360 cm for the 0°, 5°, 10°, 20°, and 40° convergent glottal angles, respectively. The 45° inferior vocal fold surface angle is only for the uniform glottal angle. (b) Schematic of the design of the divergent vocal fold pieces. The shapes of the vocal folds shown are for uniform and the four divergent glottal angles of 40°, 20°, 10°, and 5° (corresponding to 20°, 10°, 5°, and 2.5° half-angles shown). R_{out} is 0.1690, 0.1802, 0.1931, 0.2254, and 0.3360 cm for the 0°, 5°, 10°, 20°, and 40° divergent glottal angles, respectively. The −45° superior vocal fold surface angle is only for the uniform glottal angle. All distance measures are human sizes in centimeters.

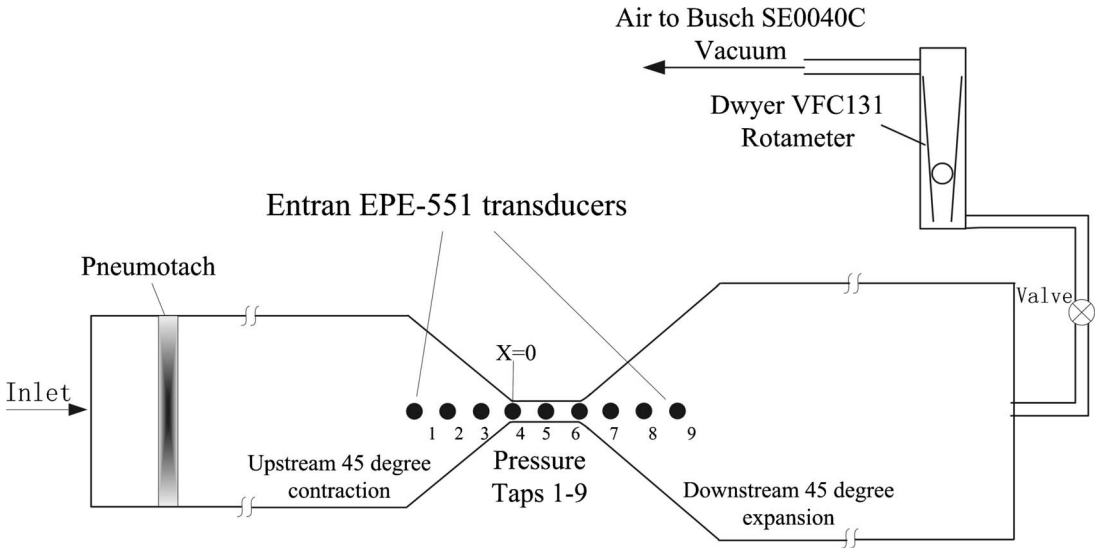

FIG. 3. Schematic of the mechanical larynx model and experimental setup.

glottal angles, namely, 40°, 20°, 10°, and 5° divergent, 0° (uniform), and −5°, −10°, −20°, and −40° convergent.

The sole minimal glottal diameter was set at 0.06 cm by adjusting the movable handle outside the glottal duct and measuring the glottal diameter with feeler gauges.

In order to measure pressures inside the Plexiglas™ model, nine cylindrical ducts were made on the midline plane of the top wall of the model (Figs. 1 and 3; this location was along the "posterior" wall in the vicinity of the vocal folds, not along the vocal fold medial surface as is typically done in such experiments). The diameter of each duct was 0.0704 cm human size (0.1220 cm in the model) so that the cylindrical extension of a calibrated Entran EPE-551 pressure transducer (0.1040 cm outside diameter and 6 cm long) could fit snugly into the ducts. The distance between the centers of each hole was 0.1440 cm human size.

In this study pressure distributions along the medial vocal fold surfaces will be reported. These pressures will be given by FLUENT, a computational fluid dynamics program. The empirical pressures along the top wall of the model will be compared to the pressures indicated by FLUENT at those locations, and will be shown to be nearly identical, thus giving justification for using FLUENT to obtain the intraglottal pressure estimations. Advantages of this approach include (1) the lack of the need to drill numerous pressure taps into the rather small model used (and the associated difficulties in drawing pressure lines from the model), and (2) the essentially continuous pressure distributions that are thereby obtained.

B. Experimental arrangement

Figure 3 is a schematic of the experimental arrangement used for the model. Straws were placed at the entrance of the inlet section to smooth and laminarize the flow. The outlet section was connected to a flowmeter (Dwyer Model VFC131) by means of 50 cm of flexible tubing with a 2.5 cm inside diameter. A vacuum source (Busch Model SE0040C) with variable speed drew the air through the model.

When the pressure reading was to be taken at a pressure tap location, the external screw that closes that tap was taken out, and the cylindrical pressure transducer extension was placed down the channel, such that the end of the extension was located about 2–3 mm away from the inner surface of the top side of the model. For the pressure measurement at the next pressure tap, the cylindrical extension was withdrawn, the external screw replaced, and the procedure repeated for the new pressure tap. The pressure data were recorded on a computer using a 12-bit A-823PGL Microdigit A/D device recording at 10 000 samples/s.

The pressure distributions were obtained by time averaging the pressure at each tap location for 20-s intervals (100 000 samples), while the minimal glottal diameter was set at 0.06 cm and the transglottal pressure held constant at 5 cm H_2O, a pressure value expected in human soft phonation. For each of the pressure measures, the operator waited approximately 3 min before recording the value, so that random disturbances were avoided.

Some pressure taps were not perpendicular to the surface (Fig. 1), which may have introduced a small measurement error, but no more than approximately 1% of the kinetic pressure (Rayle, 1958).

Because the Plexiglas™ model was larger than human size by a factor of 1.732, the corresponding pressures in the model were less than human size by a factor of $(1.732)^{-2}$, the corresponding velocities in the model were less than human size by a factor of 1.732, and the volume flows in the model were 1.732 times larger than human size values, as determined by similitude analysis (Streeter and Wylie, 1975).

C. Computational method

To obtain a detailed description of the flow and pressure fields, steady flow through the model was obtained numerically. A commercially available computational fluid dynamics code called FLUENT, based on the control-volume technique, was used to numerically solve the Navier-Stokes equations for laminar, incompressible airflow physics occur-

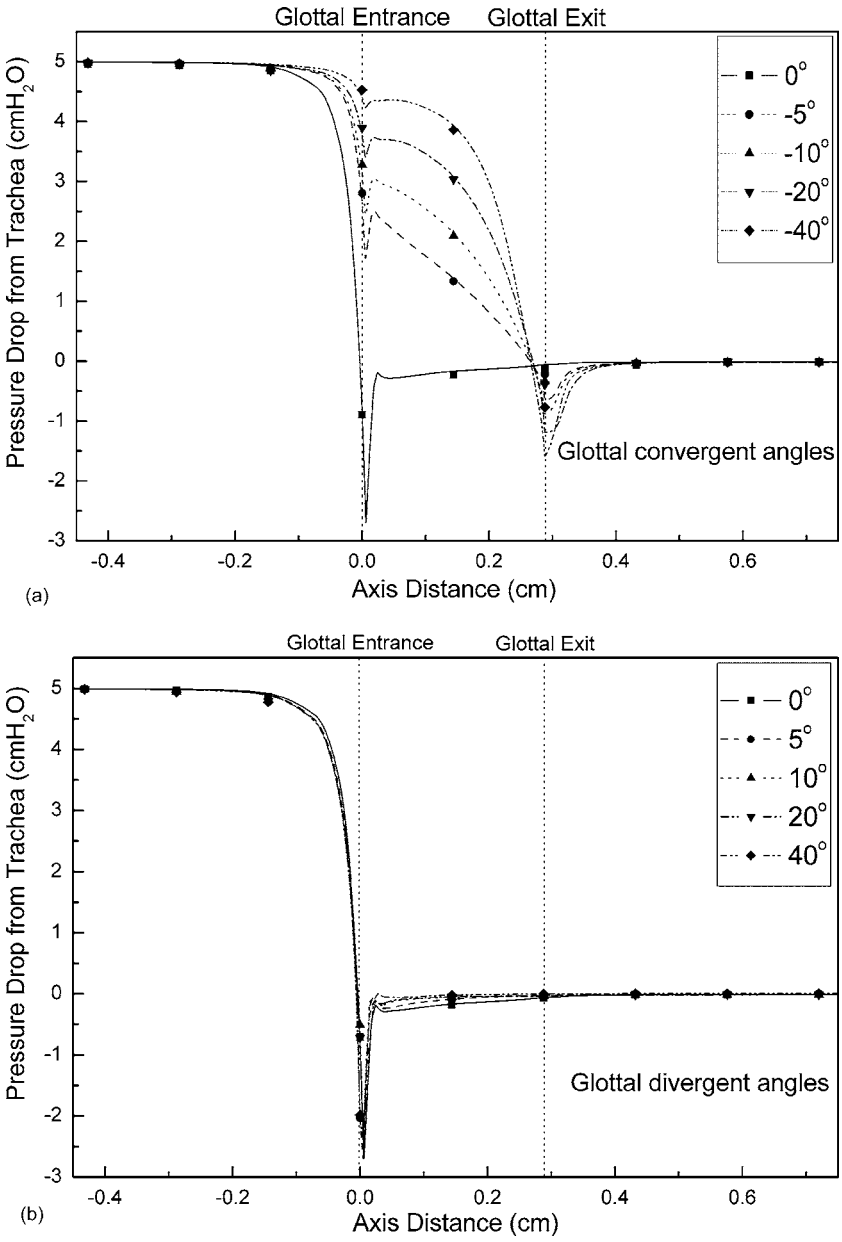

FIG. 4. Empirical one-dimensional pressure distributions on the midline surface of the top side of the model for nine representative glottal angles for a 0.06 cm minimal glottal diameter and 5 cm H_2O transglottal pressure. The estimated pressure distributions using FLUENT for each glottal angle condition are also shown as the lines. Pressures and distances are in human values rather than in model values. Zero on the horizontal axis refers to the axial location of the glottal entrance. (a) For four convergent glottal angles of −5°, −10°, −20°, and −40° and uniform; (b) for four divergent glottal angles of 5°, 10°, 20°, and 40° and uniform.

ring inside the three-dimensional symmetric geometries. This use of FLUENT, then, is for constant shapes, not for vibrating vocal folds. Furthermore, the code as used does not produce turbulence. The input data for FLUENT included grid point coordinates, element topology, and boundary conditions. The grids used in the simulations contained both structured and unstructured meshes. In these simulations, grids containing between 820 000 and 830 000 nodes were used. Since the glottal section in the model was most important for this study, the interval size of the mesh element was selected to be 0.015 cm for the glottal section, whereas it was 0.03 cm for the inlet and outlet tunnel. The fluid material was defined as air (density of 1.225 kg/m^3 and viscosity of 1.7894×10^{-5} kg/m s). The boundary conditions of the model included an inlet pressure of 5 cm H_2O and outlet pressure of 0 cm H_2O. All computational runs were performed unsteady with a time step of 10^{-5} s to obtain second-order solutions for momentum and pressure, with residuals of less than 10^{-4} and solutions that were grid-independent. The flow field was assumed to be symmetric across the midline of the glottis in this study, and therefore only the quarter flow field was modeled.

III. RESULTS

A. Pressure distributions

The goal of this project was to obtain the pressures along the vocal fold surfaces in the upstream-downstream direction (i.e., the intraglottal wall pressures) in order to make statements concerning patterns of driving forces on the vocal folds. However, pressure taps were not made in the vocal folds themselves, but along the wall (top side) of the model "posterior" to the glottis. The estimates of the intraglottal wall pressures therefore relied on the accuracy of FLUENT. This accuracy was tested by comparing FLUENT predictions with the pressures on the top side of the model. Figure 4 shows the empirical one-dimensional pressure distributions along the midline surface of the top side of the model [the

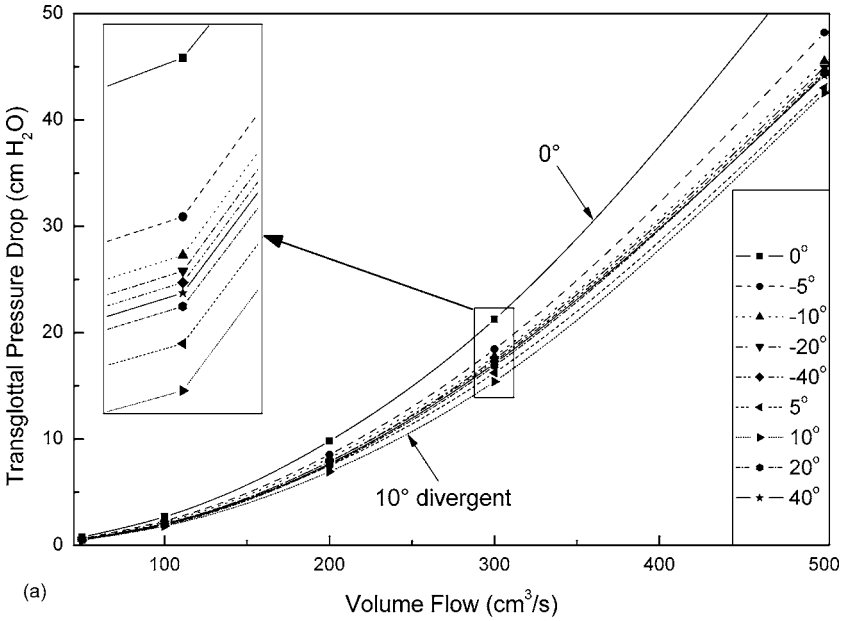

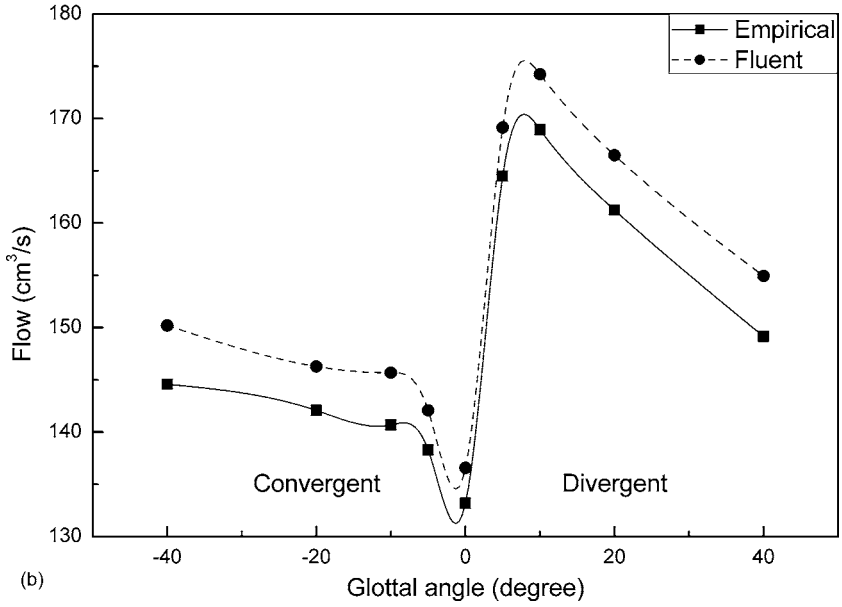

FIG. 5. (a) The empirical translaryngeal pressure-flow data for different volume flow rates and glottal angles for 0.06 cm minimal glottal diameter. Positive angles are divergent, negative angles are convergent. (b) The comparison between the empirical flows and FLUENT flows for a transglottal pressure of 5 cm H_2O. The empirical pressure distributions were obtained by time averaging the pressure for 20-s intervals (100 000 samples). Pressures and volume flow rates are in human values rather than in model values. The lines connecting the data are spline fits.

side with the pressure taps seen on the right side of Fig. 1(b)] for the nine glottal angles and a transglottal pressure of 5 cm H_2O. The corresponding predicted pressure distributions using FLUENT are also shown in Fig. 4 as the lines, which match the data points closely. The average difference between the FLUENT and empirical pressure values was 0.0261 cm H_2O (SD=0.0334 cm H_2O), and the greatest difference was 0.1179 cm H_2O. This closeness of FLUENT predictions with the empirical pressures suggests that the pressures along the vocal folds in the axial direction predicted by FLUENT should also be valid for this model (as they were for the data in a more restricted model given by Scherer *et al.*, 2001a).

Before showing the pressure distributions, the overall transglottal pressure-flow relations will be discussed. The empirical transglottal pressure-flow data for the nine glottal angles are plotted in Fig. 5. The transglottal pressure was obtained by taking the difference in pressures between tap 1 and tap 9. The uniform glottis created the largest pressure drop for any specific flow due to the relatively high viscous loss in the glottis. The least pressure drop (and least flow resistance) corresponded to the 10° divergent glottal angle for any given flow (consistent with Hofmans *et al.*, 2003, and Fulcher *et al.*, in press). For a given flow value, all divergent angles gave lower transglottal pressures than for all convergent angles. Figure 5(b) gives the empirical and FLUENT flow values for each glottal angle for the 5 cm H_2O condition. This figure is consistent with Fig. 5(a) in that all divergent angles had greater flows than all convergent angles. Also, the figure indicates that FLUENT predicted flows to be about 2%–4% higher than the empirical flows.

The FLUENT-predicted pressure distributions on the centerline and along the mid-portion of the glottal walls of the model are shown in Fig. 6. In general, the pressures on the medial vocal folds increased as the convergent angle increased. For example, an increase from −5° convergent to −40° convergent raised the intraglottal pressures midway along the glottis from approximately 1.6 cm H_2O to 4.3 cm

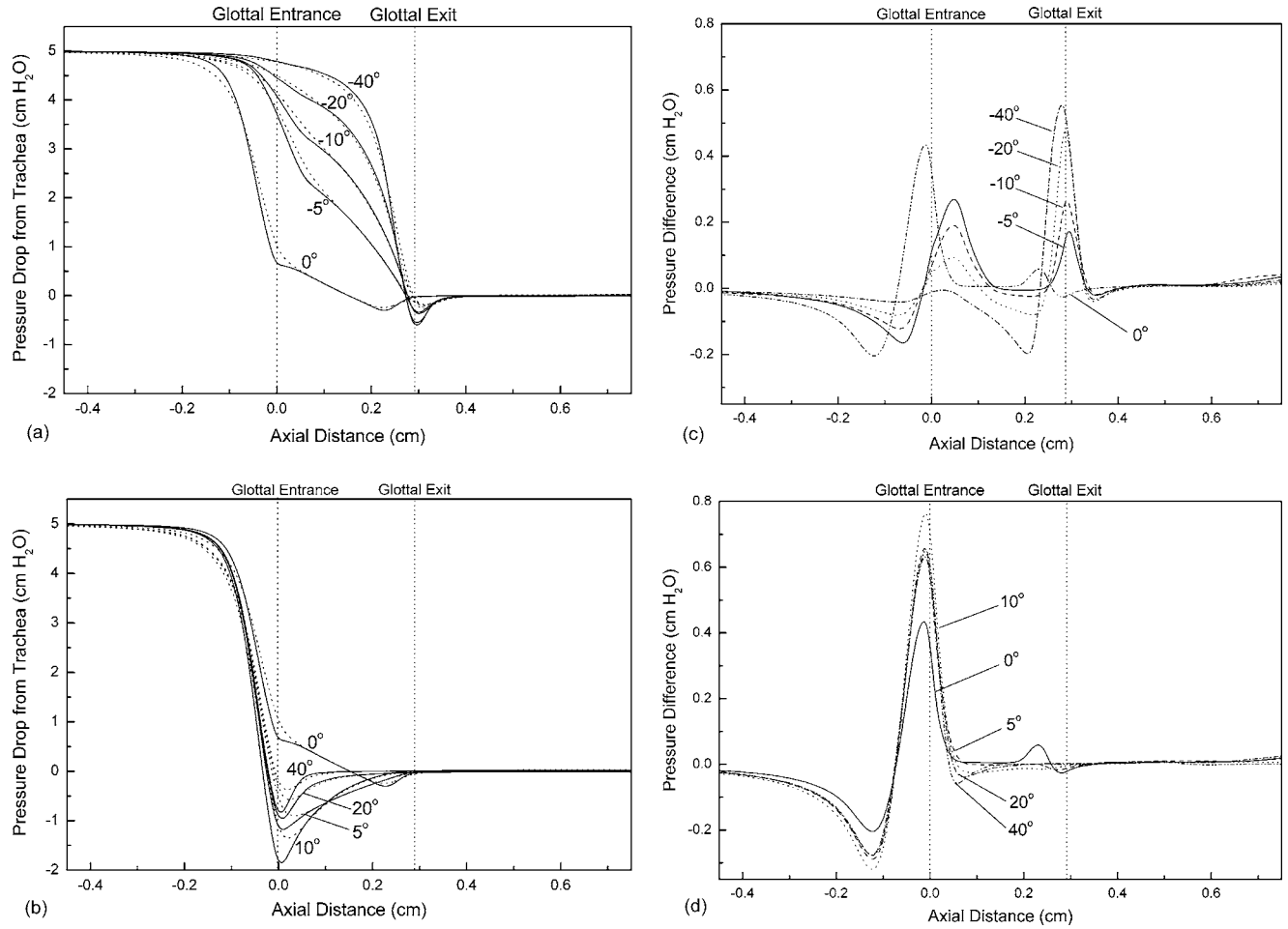

FIG. 6. The predicted one-dimensional wall pressure distributions (using FLUENT) on the surface of the vocal folds (shown by solid lines) and the predicted pressures on the centerlines of the model (shown by dashed lines) for 0.06 cm minimal glottal diameter for 5 cm H_2O transglottal pressure drops. Pressures and distances are in human values rather than in model values. The zero of the horizontal axis refers to the glottal entrance location. Positive valued angles are for the divergent glottis, negative for convergent; (a) for four convergent glottal angles of −5°, −10°, −20°, −40° and uniform; (b) for four divergent glottal angles of 5°, 10°, 20°, 40° and uniform; (c) the difference between the centerline pressures and the wall pressures in the glottis for the four convergent glottal angles and uniform; (d) the difference between the centerline pressures and the wall pressures in the glottis for the four divergent glottal angles uniform.

H_2O, nearly a tripling of the outward driving pressure. The pressures for the divergent glottal angles varied depending on the size of the angle. The 10° divergent angle gave the lowest dip in pressures, followed by the 5° divergence, then the 20° divergence, and finally the 40° divergence. The results for the divergence angles were consistent with diffuser flow (Kline, 1959). The wall pressure distributions therefore would create different positive or negative resultant pressure forces to push the vocal folds away from each other during glottal opening and to pull the vocal folds toward each other during glottal closing, depending upon the angle created at any moment (the pressure would also depend, of course, on the transglottal pressure and glottal diameter prevailing at the time). These pressures are the external driving forces of great importance in vocal fold oscillation (Ishizaka and Flanagan, 1972).

Figure 6 shows that the centerline pressure distributions were approximately equal to the wall pressure distributions within the glottis except near the glottal entrance and glottal exit. At glottal entrance and exit, there was radial curvature that would create curved streamlines with a pressure gradient providing lower pressures toward the wall (Massey, 1979). As indicated in Figs. 6(c) and 6(d), these pressure differences were greatest for the largest angle, −40°, for the convergent cases at glottal exit (0.55 cm H_2O), and for the most efficient diffuser, 10°, for the divergent cases (0.78 cm H_2O) at glottal entrance.

B. Separation points

For the divergent glottal angles, separation of the flow within the glottis was expected. However, as the angle changed for the constant 5 cm H_2O, the separation point location changed. The separation points using the FLUENT data were obtained, and for the 5°, 10°, 20°, and 40° divergent cases, the distance from glottal entry (zero in Fig. 6) and the separation locations were 0.27, 0.175, 0.06, and 0.04 cm, respectively, as shown by arrows in Fig. 7. Thus, the separation point moved more upstream as the angle increased. The separation point was near the glottal exit (at 0.288 cm, Fig.

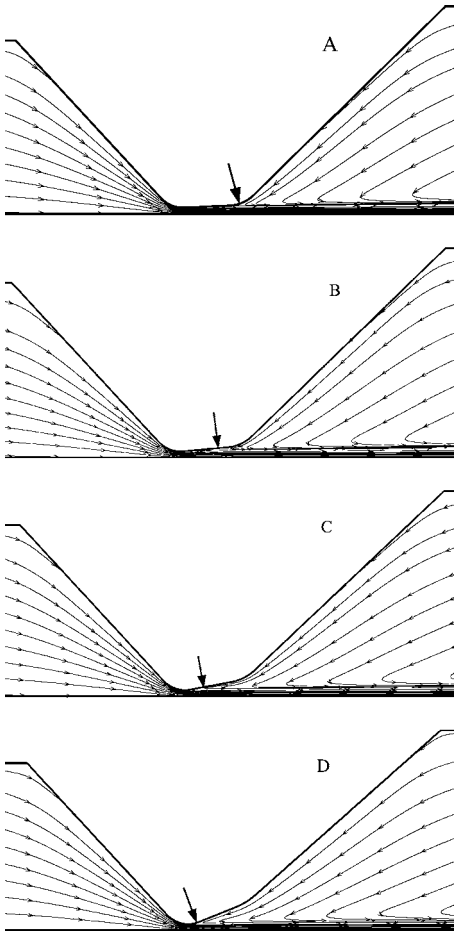

FIG. 7. Separation point locations for the four divergent angles, 5 cm H_2O, and 0.06 cm minimal glottal diameter, as predicted by FLUENT. A: 5°; B: 10°; C: 20°; D: 40° included glottal angle.

2) for the smallest divergent angle of 5°, and was close to the entrance (at 14% of the axial glottal length) for the largest angle (40°). There was reverse flow (air moving upstream) just past the separation points.

IV. DISCUSSION

In general, as convergent glottal angles increased, flow resistance decreased and intraglottal pressures increased. For divergent glottal angles, flow resistance was least and intraglottal pressure recovery the greatest for 10°, suggesting that it was the most "efficient" divergence angle. Increasing flow resistance and decreasing intraglottal pressure recovery then followed for 5°, 20°, and 40° divergence. The flow resistance results are consistent with Fulcher *et al.* (in press), and the intraglottal pressure distributions are consistent with Guo and Scherer (1993) who used a different glottal diameter (0.04 cm). The phonatory implication for these results would be that greater outward glottal opening forces are obtained for larger convergent angles, and greater negative closing forces are obtained for divergent angles in the 5°–10° range. The 5°–10° angles may be viewed as favorable angles relative to phonation if they occur during glottal closing when the flow needs to be relatively high with rightward skewing while providing a relatively high pull in the glottis to close the glottis *aerodynamically*. A theory of efficient phonation from an aerodynamic point of view would therefore include the concept of relatively large convergent angles and relatively small to mid range (5°–10°) divergent angles at critical points of the phonatory cycle. It is noted that this suggestion is offered with only limited data relative to glottal diameter (here only one diameter, 0.06 cm). It is also noted that the uniform glottal angle gave the greatest flow resistance, and from a phonatory point of view would be an efficient angle to have near glottal closure in order to reduce the flow even more (aerodynamically).

For the diameter used in this study, 0.06 cm, FLUENT appears to have been a valid computational method to obtain pressures. The results in the more limited study by Guo and Scherer (1993) were similar using a different computational scheme (penalty finite element method, chosen at the time for its alleged pressure accuracies), thus suggesting that both of these methods may be viable for other glottal aerodynamic studies. Also, the results here, wherein empirical data and computational prediction match well, constitute results for testing other computational schemes, at least when the flow in the glottis is considered nonturbulent.

Flow separation points in the divergent glottis can be estimated with the use of FLUENT. The basic reason to determine the location of the separation point is to estimate the location in the glottis where pressures have risen to the prevailing pressure *downstream* of the glottis (Pelorson *et al.*, 1994; Lucero, 1999). That is, it has been assumed that if one can determine the separation point in a divergent glottis for the prevailing angle, minimal diameter, and transglottal pressure, one can assume that the pressures needed are those from glottal entry to the separation point, because it is safe to assume that at the separation point the pressure equals that above the glottis. This assumption, however, does not appear to be correct, as pointed out by Hofmans (1998) and Shinwari *et al.* (2003). The separation point occurs on the rising side of the pressure (recovery) in the glottis, as close observation of the results here indicate. Combining the information in Figs. 6 and 7 indicates that the separation point for 5°, 10°, 20°, and 40° divergence occurred not at zero pressure (the prevailing downstream pressure), but at pressures of −0.075, −0.238, −0.388, and −0.275 cm H_2O, or at 6.5%, 13.0%, 41.9%, and 34.4% of the pressure dip at glottal entry, respectively, for this 5 cm H_2O transglottal pressure.

Extending the results using FLUENT beyond the empirical 5 cm H_2O case presented here resulted in Table I, wherein the separation points are given for the 0.06 cm minimal diameter, but for increasing flow rates, corresponding to pressures below and above 5 cm H_2O. It can be seen that the separation point location monotonically moved upstream (toward the glottal entrance) when either angle or flow increased, consistent with Alipour and Scherer (2004). For the 5° case, the separation point remained near the glottal exit as flow increased. The 10° divergence case consistently corresponded to the lowest transglottal pressure at each flow rate. Thus, the 5° and 10° cases both appear to correspond to "efficient" diffusers, the 5° case relative to delayed flow

TABLE I. FLUENT predicted flow separation points on the glottal walls and the corresponding transglottal pressures for four divergent glottal angles and five flow values for a minimal diameter of 0.06 cm, measured from the glottal entrance (length of the glottal duct was 0.288 cm).

Flow (cm^3/s)	Separation points (cm) for four divergent glottal angles (°)				Transglottal pressures (cm H_2O) for four divergent glottal angles (°)			
	5	10	20	40	5	10	20	40
50	0.279	0.262	0.105	0.052	0.542	0.536	0.548	0.554
100	0.273	0.240	0.075	0.045	1.918	1.863	1.971	2.067
200	0.266	0.160	0.056	0.039	7.663	7.084	7.728	7.784
300	0.261	0.122	0.052	0.035	16.495	15.636	17.213	17.389
500	0.258	0.095	0.050	0.033	43.464	42.925	43.813	44.632

separation and second to the 10° in least flow resistance, and the 10° case relative to the least flow resistance (typically the most efficient diffusers have angles in the 7°–12° range, Kline, 1959).

V. CONCLUSIONS

A Plexiglas™ model of the larynx was used to study laryngeal pressures for various glottal angles. The experimental data were well supported by the computational fluid dynamics code FLUENT for laminar flow, and FLUENT was then used to predict glottal pressures for convergent, uniform, and divergent glottal shapes, and flow separation locations for the divergent angles.

The results suggest that, for the same transglottal pressure of 5 cm H_2O and a minimal glottal diameter of 0.06 cm, larger convergent glottal angles corresponded to increased pressure force on the medial surface of the vocal folds and decreased flow resistance, whereas divergent glottal angles created the greatest negative intraglottal pressure and least flow resistance for the 10° divergent angle, followed by the 5°, 20°, and 40° angles. Flow resistance was greater for all convergent angles compared to all divergent angles for the 5 cm H_2O transglottal pressure case. These results suggest that, for aerodynamically efficient phonation, it may be important to have large convergent angles during glottal opening, and relatively small divergent glottal angles during glottal closing.

Separation points given by FLUENT for divergent glottal angles moved toward the glottal entrance as the angle increased or the flow increased, consistent with steady flow results in diffusers. The location of the separation point occurred on the increasing pressure recovery curve, ranging from 6.5% to 41.9% of the pressure recovery dip, suggesting that pressure recovery miscalculations may well occur if the separation point location were set to be equal to the prevailing downstream (supraglottal) pressure.

The glottal dimensions used in this study were limited to one minimal glottal diameter (0.06 cm) and symmetric glottal configurations. A more complete set of glottal geometries and transglottal pressures are necessary to establish intraglottal pressure, velocity, and volume flow effects in dynamic models of phonation, especially models that predict effects for pathological conditions.

ACKNOWLEDGMENTS

This work was supported in part by the National Natural Science Foundation of China (Grant Nos. 30070212 and 69925101) and the National Institutes of Health (Grant No. R01 DC03577). We also want to thank the participants from the E.N.T. Department, the Second Hospital, Xi'an Jiaotong University, for helping with data acquisition and analysis.

Agarwal, M., Scherer, R. C., and Hollien, H. (**2003**). "The false vocal folds: Shape and size in frontal view during phonation based on laminagraphic tracings," J. Voice **17**, 97–113.

Alipour, F., and Scherer, R. C. (**2004**). "Flow separation in a computational oscillating vocal fold model," J. Acoust. Soc. Am. **116**, 1710–1719.

Alipour, F., and Scherer, R. C. (**2000**). "Pressure-flow relationship in a Hemilarynx mechanical model," in *Proceedings of the Fifth Seminar on Speech Production: Models and Data & CREST Workshop on Models of Speech Production: Motor Planning and Articulatory Modelling* (Kloster Seeon, Bavaria, Germany), pp. 189–192.

Alipour, F., Scherer, R. C., and Knowles, J. (**1996**). "Velocity distributions in glottal models," J. Voice **10**, 50–58.

Binh, N., and Gauffin, J. (**1983**). "Aerodynamic measurements in an enlarged static laryngeal model," STL-QPSR **2–3**, Dept. of Speech Communications and Music Acoustics, R. Inst. Tech. Stockholm, 36–60.

Deverge, M., Pelorson, X., Vilain, C., Lagree, P.-Y., Chentouf, F., Willems, J., and Hirschberg, A. (**2003**). "Influence of collision on the flow through in-vitro rigid models of the vocal folds," J. Acoust. Soc. Am. **114**, 3354–3362.

Flanagan, J. L. (**1972**). *Speech Analysis, System, and Perception*, 2nd ed. (Springer, New York).

Fulcher, L. P., Scherer, R. C., Zhai, G., and Zhu, Z. (**in press**). "Analytic representation of volume flow as a function of geometry and pressure in a static physical model of the glottis," J. Voice.

Gauffin, J., Binh, N., Ananthapadmanabha, T. V., and Fant, G. (**1983**). "Glottal geometry and volume velocity waveform," in *Vocal Fold Physiology: Contemporary Research and Clinical Issues*, edited by D. M. Bless and J. H. Abbs (College Hill, San Diego), pp. 194–201.

Guo, C. G., and Scherer, R. C. (**1993**). "Finite element simulation of glottal flow and pressure," J. Acoust. Soc. Am. **94**, 688–700.

Hirano, M., Kiyokawa, K., and Kuria, S. (**1988**). "Laryngeal muscles and glottis shaping," in *Vocal Physiology: Voice Production, Mechanisms and Functions*, edited by O. Fujimura (Raven, New York), pp. 49–65.

Hofmans, G. C. J. (**1998**). *Vortex Sound in Confined Flows* (Technische Universiteit Eindhoven, Eindhoven).

Hofmans, G. C. J., Groot, G., Ranucci, M., Graziani, G., and Hirschberg, A. (**2003**). "Unsteady flow through in-vitro models of the glottis," J. Acoust. Soc. Am. **113**, 1658–1675.

Ishizaka, K., and Flanagan, J. L. (**1972**). "Synthesis of voiced sounds from a two-mass model of the vocal cords," Bell Syst. Tech. J. **51**, 1233–1268.

Ishizaka, K., and Matsudaira, M. (1972). "Fluid mechanical considerations of vocal cord vibration," SCRL Monograph No. 8, Speech Communications Research Laboratory, Inc., Santa Barbara.

Kline, S. J. (**1959**). "On the nature of stall," J. Basic Eng. **81**, 302–322.

Kucinschi, B. R. (2004). "An analysis of the flow through a driven mechanical model of the vocal folds," dissertation, University of Toledo.

Li, S., Scherer, R. C., Minxi, W., Wang, S., and Wu, H., "The effects of inferior and superior vocal fold surface angles on vocal fold pressure distributions," J. Acoust. Soc. Am. (in press).
Li, S., Scherer, R. C., Wan, M., Wang, S., and Wu, H., "The effects of entrance radii on intraglottal pressure distributions in the divergent glottis," J. Acoust. Soc. Am. (in press).
Lucero, J. C. (**1999**). "A theoretical study of the hysteresis phenomenon at vocal fold oscillation onset-offset," J. Acoust. Soc. Am. **105**, 423–431.
Massey, B. S. (**1979**). *Mechanics of Fluids*, 4th ed. (Van Nostrand Reinhold, New York).
McGowan, R. S. (**1993**). "The quasisteady approximation in speech production," J. Acoust. Soc. Am. **94**, 3011–3013.
Mongeau, L., Franchek, C., Coker, R., and Kubli, R. A. (**1997**). "Characteristics of a pulsating jet through a small modulated oriface, with applications to voice production," J. Acoust. Soc. Am. **102**, 1121–1134.
Pedley, T. J. (**1983**). "Wave phenomena in physiological flows," Appl. Math. (Germany) **32**, 267–287.
Pelorson, X. (**2001**). "On the meaning and accuracy of the pressure-flow technique to determine constrictions within the vocal tract," Speech Commun. **35**, 179–190.
Pelorson, X., Hirschberg, A., Wijnands, A. P. J., and Auregan, Y. (**1994**). "Theoretical and experimental study of quasisteady-flow separation within the glottis during phonation. Application to a modified two-mass model," J. Acoust. Soc. Am. **96**, 3416–3431.
Rayle, R. E. (1958). "Influence of orifice geometry on static pressure measurements," Am. Soc. Mech. Eng., paper 59-A-234.
Scherer, R. C., and Shinwari, D. (**2000**). "Glottal pressure profiles for a diameter of 0.04 cm," J. Acoust. Soc. Am. **107**, 2905.
Scherer, R. C., Shinwari, D., Witt, K. J. D., Zhang, C., Kucinschi, B. R., and Afjeh, A. A. (**2001a**). "Intraglottal pressure profiles for a symmetric and oblique glottis with a divergence angle of 10 degrees," J. Acoust. Soc. Am. **109**, 1616–1630.
Scherer, R. C., Shinwari, D., Witt, K. J. D., Zhang, C., Kucinschi, B., and Afjeh, A. A. (**2002**). "Intraglottal pressure profiles for a symmetric and oblique glottis with a uniform duct," J. Acoust. Soc. Am. **112**, 1253–1256.
Scherer, R. C., Witt, K. J. D., and Kucinschi, B. R. (**2001b**). "The effect of exit radii on intraglottal pressure distributions in the convergent glottis," J. Acoust. Soc. Am. **110**, 2267–2269.
Shinwari, D., Scherer, R. C., J.DeWitt, K., and Afjeh, A. A. (**2003**). "Flow visualization and pressure distributions in a model of the glottis with a symmetric and oblique divergent angle of 10 degrees," J. Acoust. Soc. Am. **113**, 487–497.
Streeter, V. L., and Wylie, E. B. (**1975**). *Fluid Mechanics* (McGraw-Hill, New York).
Titze, I. R. (**1986**). "Mean intraglottal pressure in vocal fold oscillation," J. Phonetics **14**, 359–364.
Titze, I. R. (**1994**). *Principles of Voice Production* (Prentice-Hall, Englewood Cliffs, NJ).
Titze, I. R. (**1974**). "The human vocal cords: A mathematical model Part II," Phonetica **29**, 1–21.
Zhang, Z., Mongeau, L., and Frankel, S. H. (**2002**). "Experimental verification of the quasisteady approximation for aerodynamic sound generation by pulsating jets in tubes," J. Acoust. Soc. Am. **112**, 1652–1663.

Testing the assumptions of linear prediction analysis in normal vowels

M. A. Little[a)]
Applied Dynamical Systems Research Group, Oxford Centre for Industrial and Applied Mathematics, and Pattern Analysis Research Group, Engineering Science, Oxford University, United Kingdom

P. E. McSharry
Oxford Centre for Industrial and Applied Mathematics and Engineering Science, Oxford University, United Kingdom

I. M. Moroz
Applied Dynamical Systems Research Group, Oxford Centre for Industrial and Applied Mathematics, Oxford University, United Kingdom

S. J. Roberts
Pattern Analysis Research Group, Engineering Science, Oxford University, United Kingdom

(Received 11 March 2005; revised 26 July 2005; accepted 2 November 2005)

In this paper we develop an improved surrogate data test to show experimental evidence, for all the simple vowels of U.S. English, for both male and female speakers, that Gaussian linear prediction analysis, a ubiquitous technique in current speech technologies, cannot be used to extract all the dynamical structure of real speech time series. The test provides robust evidence undermining the validity of these linear techniques, supporting the assumptions of either dynamical nonlinearity and/or non-Gaussianity common to more recent, complex, efforts at dynamical modeling speech time series. However, an additional finding is that the classical assumptions cannot be ruled out entirely, and plausible evidence is given to explain the success of the linear Gaussian theory as a weak approximation to the true, nonlinear/non-Gaussian dynamics. This supports the use of appropriate hybrid linear/nonlinear/non-Gaussian modeling. With a calibrated calculation of statistic and particular choice of experimental protocol, some of the known systematic problems of the method of surrogate data testing are circumvented to obtain results to support the conclusions to a high level of significance. [DOI: 10.1121/1.2141266]

PACS number(s): 43.70.Gr, 43.25.Ts, 43.60.Wy [DOS] Pages: 549–558

I. INTRODUCTION

In this paper we develop an improved method of surrogate data testing (a formal hypothesis test), and thereby demonstrate more reliable experimental evidence that the assumptions of Gaussian linear prediction of speech time series cannot explain all the dynamics of real, normal vowel speech time series. By making a calibrated calculation of the simple non-Gaussian measure of *time-delayed mutual information* (a generalization of the concept of autocorrelation), while ensuring that the *surrogates* contain no detectable non-Gaussianity, Fig. 1 demonstrates that, for a simple, stationary, normal vowel time series of a certain length, the null hypothesis of a Gaussian stochastic process is false to a high level of significance.

The core of most modern, established speech technology is the classical linear theory of speech production (Fant, 1960), bringing together the well-developed subjects of linear digital signal processing and linear acoustics to process and analyze speech time series. The biophysical, acoustic assumption that the vocal tract can be modeled as a linear resonator leads naturally to the use of digital filtering and linear prediction analysis (Markel and Gray, 1976), techniques that are based upon classical statistical signal processing, in turn, relying upon a cluster of mathematical results from linear systems theory and Gaussian, ergodic random processes. With these methods, it is possible to separate the vocal tract resonances from the driving force of the vocal folds during voiced sounds such as vowels [this technique is demonstrated in, for example, Wong *et al.* (1979)].

However, the biomechanics of speech cannot be entirely linear (Kubin, 1995). There are several potential sources of nonlinearity in speech. A list of these should include turbulent gas dynamics (Teager and Teager, 1989), but also nonlinear vocal fold dynamics due to the interaction between nonlinear aerodynamics and the vocal folds (Story, 2002), feedback between vocal tract resonances and the vocal folds (Quatieri, 2002), and nonlinear vocal fold tissue properties (Chan, 2003). This list is certainly not exhaustive. Simplified vocal fold models also show hysteresis (Lucero, 1999), and in pathological cases, evidence for nonlinear bifurcations have been observed in experiments on excised larynxes, and nonlinear models have replicated these observations (Herzel *et al.*, 1995).

[a)]Electronic mail: littlem@maths.ox.ac.uk. Group website http://www.maths.ox.ac.uk/ads

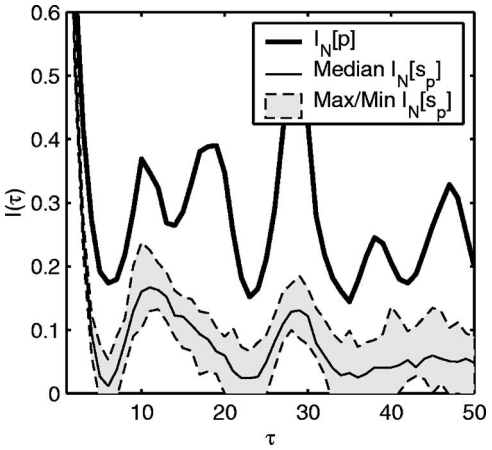

FIG. 1. A plot of the nonlinear statistic applied to a particular, simple vowel showing a significant discrepancy between the metric applied to linear surrogates (a thin black line shows the median value, and the shaded area is bounded by the minimum/maximum values) and the original speech signal (thick black line). The discrepancy demonstrates that to a significance level of 95%, there exists shared dynamical information between samples at most time delays τ that cannot be accounted for by a purely Gaussian, linear model. (Vowel code name mbjk0_si2128_ao; see the text).

More recently, there has been growing interest in applying tools from nonlinear and non-Gaussian time series analysis to speech time series attempting to characterize and exploit these nonlinear/non-Gaussian phenomena (Kubin, 1995). Algorithms for finding fractal dimensions (Maragos and Potamianos, 1999) and Lyapunov exponents (Banbrook *et al.*, 1999) have both been applied, giving evidence to support the existence of nonlinearities and possibly chaos in speech. Tools that attempt to capture other nonlinear effects have been developed and applied [Maragos *et al.*, 2002]. Speech time series have been analyzed using higher-order statistics such as the bicoherence and bispectrum (Fackrell, 1996), providing evidence against the existence quadratic nonlinearities detectable with third-order statistical moments, although higher-order moments were not investigated. Further, Bayesian Markov chain Monte Carlo methods (Godsill, 1996) have also been used. There have been several attempts to capture nonlinear dynamical structure in speech. Thus, local linear (Mann, 1999), global polynomial (Kubin, 1995), regularized radial basis function (Rank, 2003), and neural network (Wu *et al.*, 1994) methods have all been used to try to build compact models that can regenerate speech time series, with varying degrees of success.

There are, however, formidable numerical, theoretical, and algorithmic problems associated with the calculation of nonlinear dynamical quantities such as Lyapunov exponents or attractor dimensions for real speech time series, casting doubt over whether a nonlinear description can be justified by the data (McSharry, 2005). Circumventing some of these difficulties, the method of surrogate data testing is a formal hypothesis test allowing an estimate of the likelihood that the null hypothesis of Gaussianity and/or linearity is true.

By this method, Tokuda *et al.* (2001) detected deterministic nonlinear structure in the intercycle dynamics of several Japanese vowels using a specific phase-space nonlinear statistic and spike-and-wave surrogates. Work reported by Miyano *et al.* (2000) used the surrogate data test applied to a Japanese vowel from one male and one female speaker using Fourier surrogates and the same phase-space statistic. In related work on animal vocalizations, surrogate analysis tests have been carried out using a globally nonlinear versus linear prediction statistic and Fourier surrogates (Tokuda *et al.*, 2002). These studies report significant evidence of deterministic nonlinear structure. Improving the reliability of these results for speech time series is our main aim in the present study, since one of the problems with the surrogate data test is that it is easy to spuriously discount the null hypothesis, as discussed in general by Kugiumtzsis (2001) and McSharry *et al.* (2003). This is because any systematic errors inadvertently introduced while carrying out the test cause a *bias toward rejection* of the null hypothesis.

The organization of this paper is as follows. In Sec. II we motivate the construction of a surrogate data test method with improved reliability, and in Sec. III we explain the statistic used. In Sec. IV we detail the method used to construct the surrogates, and in Sec. V we apply the method to an example of a known, nonlinear dynamical system. In Sec. VI we then apply the method to normal vowels. Finally, in Sec. VII we interpret the results obtained, and Sec. VIII contains a summary and suggestions for future work.

II. PROBLEMS WITH SURROGATE DATA TESTS AGAINST GAUSSIAN LINEARITY IN SPEECH

In the classical linear modeling of speech, as common to most current speech technology (Kleijn and Paliwal, 1995), given an acoustic speech pressure time series, it is typically formally assumed that, over a short interval in time,[1] the vocal fold behavior can be represented as a (short-time) stationary, ergodic, zero-mean, Gaussian random process (Proakis and Manolakis, 1996) that acts as a driving input to a linear digital filter, forcing the filter into resonance. Assuming Gaussianity makes it possible to use the efficient *Yule–Walker* equations to find the linear prediction coefficients (Proakis and Manolakis, 1996). In wider circles this amounts to the use of what is known as a linear AR, or autoregressive process.

It is, however, an open question as to whether real speech time series actually do support these assumptions, leading to the need for a test of the following null hypothesis: that the data has been generated by a (short-time) stationary, ergodic, zero-mean, Gaussian random process driving a linear resonator. The desire is to obtain sufficient significance that the null hypothesis can be rejected, achieved by generating an appropriate number of surrogates using the Fourier transform method (Schreiber and Schmitz, 2000). Using this method, the surrogates have the same power spectrum [and thus autocorrelation, by the Wiener-Khintchine theorem (Proakis and Manolakis, 1996)], as the original speech time series, yet have only linear, Gaussian statistical dependencies at different time lags (the specifics of the particular surrogate data analysis technique used are discussed further in the next section).

There follows a discussion of a number of systematic errors that arise with the use of these techniques that motivate the development of a more reliable approach.

First, there are problems with the use of Fourier surrogates due to periodicity artifacts, as used by Miyano *et al.* (2000), introduced because only the finite, *cyclic* autocorrelation is preserved, not the autocorrelation of a theoretically infinite duration (Schreiber and Schmitz, 2000). Similarly, for spike-and-wave surrogates, as used by Tokuda *et al.* (2001), the cyclic autocorrelation can differ systematically from the original. Discontinuities can also be introduced if the ends and gradients of each cycle are not matched, so that the high-frequency energy characteristics of the surrogates are different from the original (Small *et al.*, 2001). Therefore, this could lead to false rejection of the null hypothesis because the nonlinear statistic might be sensitive to differences in the cyclic autocorrelation (and hence frequency characteristics), between the original and the surrogates (Kugiumtzsis, 2001). It is at least necessary to discount this possibility.

Second, each additional free parameter in the algorithm used to calculate the nonlinear statistic increases the likelihood that the results of the test will depend upon the choice of these free parameters (Kugiumtzsis, 2001). Since the statistic used to obtain the results in both the cited studies of Miyano *et al.* (2000) and Tokuda *et al.* (2001) requires the choice of several free parameters, varying these may produce a different result, leading again to the spurious rejection of the null hypothesis. Discounting this is also necessary, but for the cited statistic the systematic investigation of such a large parameter space poses formidable challenges.

Third, in the cited studies, the algorithm used to compute the nonlinear statistic is not shown to be insensitive to other, simpler aspects of the time series such as the overall amplitude or mean value (McSharry *et al.*, 2003). Then, for example, if the surrogates all have a different amplitude than the original time series, the nonlinear statistic might reflect this feature as well rather than just the existence of structure consistent or inconsistent with the null hypothesis. This will nearly always lead to the spurious rejection of the null hypothesis, guarding against this possibility is one aim of the present study.

Finally, with the cited studies, analytic values of the statistic are not available for some relevant processes, and so cross-checks of the numerical results with known cases cannot be carried out (for example, to ensure that the surrogates really do conform to the null hypothesis).

Circumventing these pitfalls, in this study we introduce an improved surrogate test, carrying out several precautions in the preparation of the original time series and choice of surrogate generation method, and in the choice, and algorithm, for a calculation of the statistic.

III. CHOICE OF STATISTIC

From information theory, a particular metric, the two-dimensional time-delayed mutual information (Fraser and Swinney, 1986) allows the detection of correlations between different time-lagged samples of the time series that cannot be detected by linear statistics based upon second-order moments. Thus, rejection of the null hypothesis is confirmation that the time series is generated by a Markov process with non-Gaussian transition probabilities. Note that a specific example of such a process is a purely deterministic nonlinear dynamical system (but a rejection of the null hypothesis does not discriminate a deterministic from a stochastic process).

An additional merit to this statistic is the known analytic expression of this value for various linear, Gaussian processes, used to cross-check numerical calculations (Palus, 1995).

For a function, or time series, $u(t)$, the time-delayed mutual information is

$$I[u](\tau) = \int_{-\infty}^{\infty}\int_{-\infty}^{\infty} p_{0,\tau}(u,v)\ln p_{0,\tau}(u,v)\mathrm{d}u\,\mathrm{d}v - 2\int_{-\infty}^{\infty} p_0(u)\ln p_0(u)\mathrm{d}u, \tag{1}$$

and by defining the time delay operator,

$$D^{\tau}u(t) = u(t+\tau), \tag{2}$$

then $p_0(u)$ is the probability density of the undelayed time series $D^0u(t)$, and $p_{0,\tau}(u,v)$ is the joint probability density of $D^0u(t)$ with a time-delayed copy $D^{\tau}u(t)$. Equation (1) is a metric of statistical dependence and so is zero only when the samples at time lag zero and τ are statistically independent, and positive otherwise.

For the null hypothesis of a linear, ergodic, zero-mean Gaussian process, with knowledge of the covariance matrix:

$$\mathbf{C} = \begin{bmatrix} \sigma_{0,0} & \sigma_{\tau,0} \\ \sigma_{0,\tau} & \sigma_{\tau,\tau} \end{bmatrix}, \tag{3}$$

where $\sigma_{i,j}$ is the covariance between $D^iu(t)$ and $D^ju(t)$, and the analytic value of the mutual information is given by

$$I_L[u](\tau) = \frac{1}{2}\ln\sigma_{0,0} + \frac{1}{2}\ln\sigma_{\tau,\tau} - \frac{1}{2}\ln\lambda_1 - \frac{1}{2}\ln\lambda_2, \tag{4}$$

where λ_1 and λ_2 are the eigenvalues of $\mathbf{C}$.

For an independent, identically distributed, zero-mean Gaussian process $e(t)$ of variance σ^2, the mutual information is

$$I[e](\tau) = \begin{cases} \frac{1}{2}[\ln(2\pi\sigma^2)+1], & \text{if } \tau = 0; \\ 0, & \text{otherwise.} \end{cases} \tag{5}$$

Note that $I_L[u]=I[e]$ if there are no linear autocorrelations in a time series of variance σ^2. Typically, the integral expression for $I[u]$ is approximated using summations over discrete probabilities of partitions of u (Kantz and Schreiber, 1997), precluding the direct comparison between the value of this expression with the analytical expression $I_L[u]$ (Paluš, 1995). However, calculating the integral numerically gives one way that a direct comparison may be achieved, using (first-order Euler) discrete numerical integration:

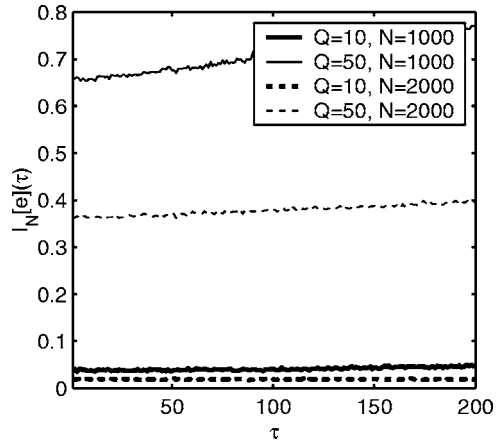

FIG. 2. Calibrating the nonlinear mutual information metric on an independent, identically distributed, Gaussian process of the same number of samples N and number of partitions Q of a particular time series. The metric varies systematically with these two parameters, and hence is adjusted to cancel out this parametric dependency.

$$I_N[u](\tau) \approx \sum_{i=1}^{Q}\sum_{j=1}^{Q} p_{0,\tau}(u_i,u_j)\ln p_{0,\tau}(u_i,u_j)\Delta u^2 - 2\sum_{i=1}^{Q} p_0(u_i)\ln p_0(u_i)\Delta u, \quad (6)$$

with $u_i = i\,\Delta u + u_{\min}$ and Q the number of uniform discretisation intervals Δu that subdivide the full range of the time series.[2]

Numerical estimation of the densities $p_0(u_i)$ and $p_{0,\tau}(u_i,u_j)$ can then be carried out by using a quantization, or box operator:

$$\delta_{\Delta u}(u,w) = \begin{cases} 1, & \text{if } w - \Delta u/2 \leqslant u < w + \Delta u/2 \\ 0, & \text{otherwise,} \end{cases} \quad (7)$$

where w is the quantization center, and Δu is the quantization interval. Then the estimated densities are

$$p_0(u_i) = \frac{1}{N\Delta u}\sum_{n=1}^{N} \delta_{\Delta u}[D^0 u(n), u_i] \quad (8)$$

and

$$p_{0,\tau}(u_i,u_j) = \frac{1}{(N-\tau)\Delta u^2}\sum_{n=1}^{N-\tau} \delta_{\Delta u}[D^0 u(n), u_i] \times \delta_{\Delta u}[D^\tau u(n), u_j]. \quad (9)$$

Here, N is the length of the time series. In the limit of small Δu, $I_N[u]$ converges to $I[u]$.

The estimation of the densities $p_0(u)$ and $p_{0,\tau}(u,v)$ from the data is biased due to the finite time series length N and the finite partitions Q. Thus $I_N[u]$ systematically overestimates $I[u]$, this overestimate varies with the parameters N and Q, as suggested by Paluš (1995). Such variation can be analytically approximated as a series expansion; see, for example, Herzel and Grosse (1997) and Schürmann (2004). The typical variation of $I_N[u]$ upon N and Q is demonstrated in Fig. 2.

One approach to cancel out the effect of such variation is to use the truncated analytic, series expansions and thus correct for the deviations. However, for large ranges of values of N and Q, the truncation leads to further systematic error, therefore the approach taken in this study is to cancel out the variation upon N and Q by calibration with the known analytic case $I[e]$. For any pair of parameters $\{N,Q\}$, the calculation of $I_N[e]$ over a large number of realizations of $e(t)$ allows the comparison of this with the analytic expression $I[e]$. Finding a best-fit straight line through the mean numerical value $I_N[e]$ for $0 < \tau < \tau_{\max}$ (with $\tau_{\max}$ being the largest lag of interest, typically 200), and subsequently subtracting this line from the values $I_N[u]$ achieves this calibration. Note that this best-fit straight line is usually not horizontal, there is a small, upward slope.

The calibrated calculation of $I_N[u]$ now allows application of this and the metric $I_L[u]$ to a time series. If the time series has linear, Gaussian correlations then $I_N[u] \approx I_L[u]$ for all values of N and Q, to within the magnitude of the errors introduced by box quantization, finite duration sample correlation matrix estimates $\mathbf{C}$ and discretization error due to finite summation approximation of the continuous integrals in $I[u]$. The most important application of this calibrated calculation of $I_N[u]$ is to test that the surrogates, are, to within these expected errors, consistent with the null hypothesis. For surrogate time series $s_u(t)$ of $u(t)$, if $I_N[s_u]$ and $I_L[s_u]$ stay within the expected tolerance given the above errors, this instills confidence that the surrogates actually allow a test against a linear Gaussian process.

IV. CHOICE OF SURROGATE CONSTRUCTION METHOD

In addition to the particular statistic used, the results of a surrogate data test can depend upon the time series data chosen, the methods used to construct the surrogates, and the interactions between them [Kugiumtzsis (2001)]. Surrogate construction requires consideration of all these factors. In this particular application, and with the chosen statistic, periodicity artifacts must be avoided by ensuring that the end points and gradients of each time series match as closely as possible Schreiber and Schmitz (2000). Otherwise, $I_L[u]$ and $I_L[s_u]$ do not coincide, as their covariance matrices differ systematically.

The Fourier transform method (Schreiber and Schmitz, 2000) is used, starting with an initial, randomized shuffle of the time series. Shuffling destroys as much of the original dynamical structure in the time series as possible. Imposition of the desired spectral amplitudes from the original time series forces the same cyclic autocorrelation as the original signal, followed by amplitude adjustment to that of a Gaussian process of zero mean and unit variance.

Note that this is slightly different to the typical practice of constraining the probability density using amplitude adjustment to be the same as that of the original time series. Amplitude adjustment was designed as a palliative measure to circumvent the problem that certain statistics can vary systematically with the overall amplitude, as discussed earlier. In the present study, the nonlinear mutual information

calculation is insensitive to the overall amplitude, since the numerical probability densities are estimated over the full scale of the time series.

However, for the present application and choice of statistic, surrogates are required with amplitude distributions constrained to be the same as a Gaussian process, rather than to be the same as the original time series. This is because the test is against the null hypothesis of a linear, Gaussian-driven process, using the nonlinear mutual information metric, and for any Gaussian-driven linear process, the amplitude distribution is also Gaussian (this is a consequence of the fact that any linear combination of Gaussian processes is also Gaussian). The nonlinear mutual information is of course sensitive to the entropy of the distribution of the time series, and the original speech time series have a non-Gaussian distribution [this has been demonstrated empirically using various tests, for example, by the use of higher-order statistical moments (Kubin, 1995)]. Therefore, surrogates generated by constraining the amplitude distribution to be the same as the original, non-Gaussian speech time series will be inconsistent with the required null hypothesis of this study, and this inconsistency is then detected by the nonlinear mutual information metric.[3]

For this reason, in practice, constraining the amplitude distribution to be the same as the original, non-Gaussian speech time series gives, as predicted by theory, a slight, overall increase to the nonlinear mutual information calculation on the surrogates. Although this is small enough that it does not affect the final results, ensuring that theory and practice are in accord by using amplitude distributions constrained to be Gaussian is of more importance here.

Finally, a finding of this study is no difference to the results with the use of the IAAFT (Iterative Amplitude Adjusted Fourier Transform) method (Schreiber and Schmitz, 2000), and so for the sake of computational simplicity this technique is not used.

V. APPLICATION TO A TOY EXAMPLE

Having described the method, in this section we demonstrate ruling out the null hypothesis of a linear, stochastic, Gaussian process on a toy, deterministic nonlinear example.

Figure 3(a) shows, plotted against the discrete time index $n=1, 2 \ldots$, the time series $y(n)$ of an order two, autoregressive process [called an AR(2) process], and Fig. 3(b) the x-coordinate time series $x(n)$ of the Lorenz system, a simple, third-order nonlinear differential system, for a set of parameters in the chaotic regime. For these two systems, Fig. 4(a) plots both I_L and I_N for the AR(2) process, demonstrating that the two metrics do indeed agree, showing no significant nonlinearity/non-Gaussianity in this time series. Figure 4(b) plots the same for the Lorenz time series, showing that, after a certain time lag τ, the linear and nonlinear metrics begin to diverge significantly and very quickly. This instills confidence that I_L and I_N behave as expected. Figure 4(a) shows that the accumulated sources of error in the calibrated calculation of I_N amount to a small discrepancy in the value over

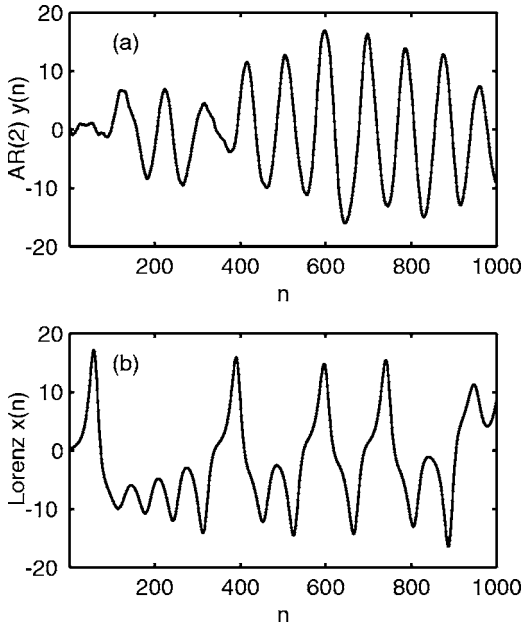

FIG. 3. Time series of nonlinear versus linear processes: (a) an order two, Gaussian AR process; (b) the Lorenz system.

all time lags, but that, unlike Fig. 4(b), the two values always track each other to within a certain small amount, as noted by Palus (1995).[4]

In all real-world time series some kind of observation noise must be expected. In order to simulate this, Fig. 5(a) shows the Lorenz time series corrupted by zero mean Gaussian noise of around 30% of the maximum amplitude.

Quantification of the significance of the test is best measured using rank-order statistics, because the form of the distribution of the statistic I_N is unknown, Schreiber and Schmitz (2000). Requiring a probability of false rejection of the null hypothesis of $P\%$, generating $M=(0.01P)^{-1}-1$ sur-

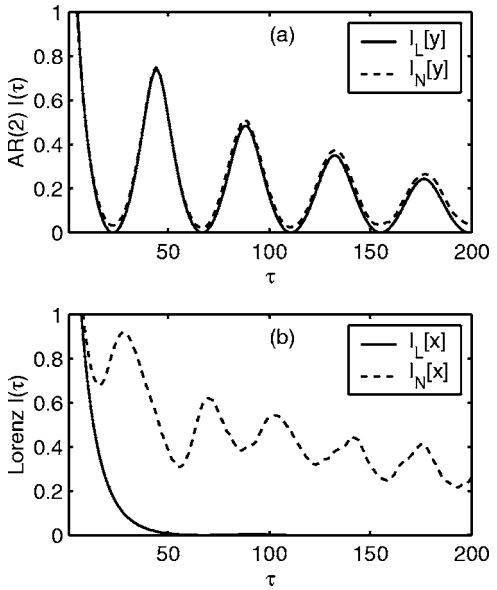

FIG. 4. (a) Linear and nonlinear mutual information metrics coincide for a purely linear, Gaussian stochastic process; (b) linear and nonlinear mutual information metrics diverge for a nonlinear, deterministic process. Here $Q=20$ and $N=6538$.

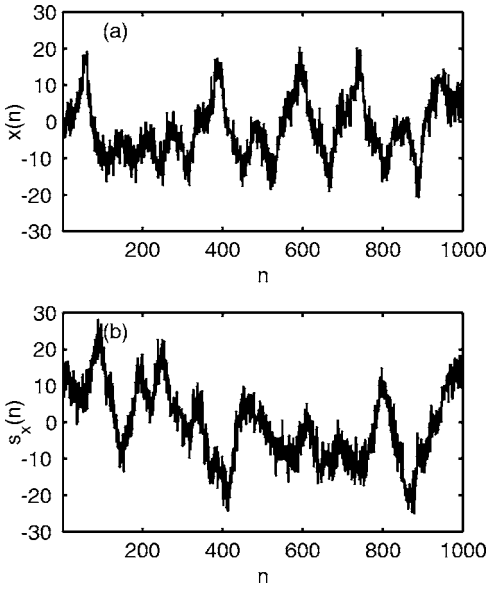

FIG. 5. (a) Nonlinear Lorenz time series corrupted by Gaussian observation noise; (b) a suitable, linear stochastic surrogate for the above.

rogates allows the (one-sided) test of the null hypothesis to a significance level of $S=100\%-P\%$. The probability that I_N is largest on the original time series is $P\%$, as intended. This study sets a significance level of $S=95\%$, so that $P=5\%$ and hence $M=19$ surrogates are generated, one of which is shown in Fig. 5(b).

Although familiarity with the Lorenz system might allow the detection of the difference by eye, $x(n)$ and $s_x(n)$ are very similar, and as shown in Fig. 6(a) the linear statistics $I_L[x]$ and $I_L[s_x]$ are practically indistinguishable, and the full extent of variation of $I_L[s_x]$ is very small. Furthermore, Fig. 6(b) shows that the nonlinear metric on the surrogates $I_N[s_x]$ tracks the linear metric on the surrogates to within numerical error. Therefore, the surrogates cannot be separated from the original by the linear metric, and the nonlinear metric on the surrogates agrees with the linear metric on the surrogates. Hence, confidence is obtained that only linear statistical dependencies are present in the surrogates. Yet, Fig. 6(c) shows that the nonlinear metric on the original $I_N[x]$ is larger than the value of this statistic on the surrogates, for most time lags $\tau>10$.

This demonstrates that the test is indeed capable of ruling out the null hypothesis for the chaotic system. There are interesting complications in the details though. For a certain range of low lags (say, $\tau\leqslant 10$), the results do not warrant confidence in rejecting the null hypothesis, because I_L and I_N on the surrogates differ systematically, noted in Kugiumtzsis (2001).

VI. APPLICATION TO NORMAL VOWELS

Having demonstrated that by being selective and avoiding known systematic errors in the use of surrogate data methods, ruling out the null hypothesis where it is indeed known to be false is possible, taking into account the conditions under which the test can be said to be valid. The next step is the application of this method to 20 normal, nonpathological vowel time series from the TIMIT database

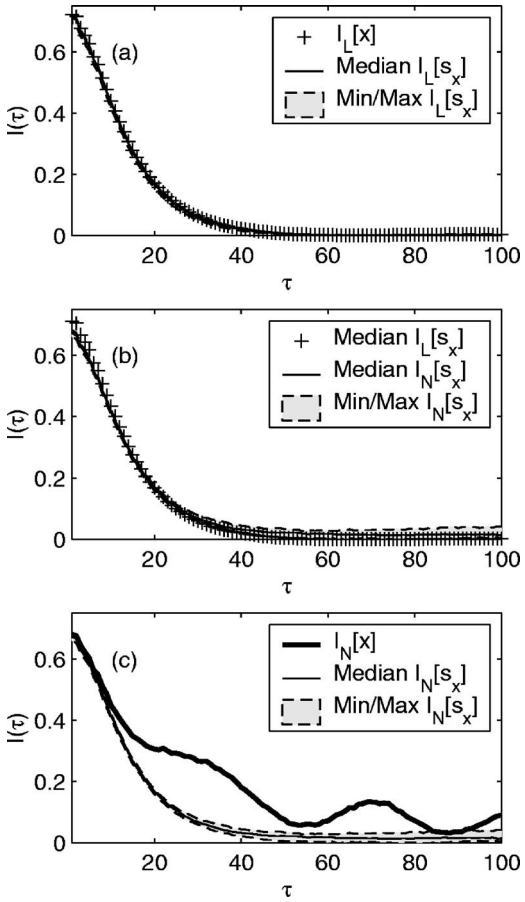

FIG. 6. Establishing the difference between the Lorenz system and linear, Gaussian surrogates using the cross-application of both linear and nonlinear metrics. (a) Check that surrogates conform to the null hypothesis. Linear mutual information metric on the surrogates has a negligible spread of values, and the median linear metric over all the surrogates coincides with that of the original time series. (b) Check that the nonlinear metric gives the same values as the linear metric for the surrogates that have only linear, Gaussian statistical dependencies. The median of the linear metric on the surrogates tracks the nonlinear metric on the surrogates to within numerical error. (c) Detecting the difference between the deterministic Lorenz time series and the Gaussian linear surrogates. The nonlinear metric on the original time series is the largest value of the nonlinear metric. Combined with the cross-checks in (a) and (b), and given 19 surrogates, the null hypothesis for the Lorenz time series can be ruled out, with a significance level of 95%. Here $Q=20$ and $N=6358$.

(Fisher *et al.*, 1986) which have been carefully selected to be as short and stationary as possible. These represent ten different U.S. English sounds from randomly selected male and female speakers, covering all the principal, simple vowels. Diphthongs are avoided since they are considered to be nonstationary in the sense that the vocal tract resonances are changing with time. All the time series are recorded under quiet acoustic conditions with minimal background noise, with 16 bits and sample rate 16 kHz. The time series have been normalized to an amplitude range of ±1. Table I lists the vowels and their code names, and Table II lists the TIMIT source audio file names and lengths in samples of each time series.[5] The time series are therefore all approximately 63 ms long. Finally, Figs. 7 and 8 shows plots of all the time series $p(t)$.

Figure 9 picks out one of the time series for closer inspection of the associated surrogates. By eye it is fairly easy

TABLE I. Vowels and code names used in this study.

Example	Code name
f**a**rther	/aa/
b**i**rd	/er/
b**ea**t	/iy/
b**i**t	/ih/
b**a**t	/ae/
b**e**t	/eh/
b**oo**t	/uw/
p**u**t	/uh/
p**o**t	/ao/
b**u**t	/ah/

to separate the surrogates from the original. However, for this same vowel, Fig. 10 shows that the linear metric is identical on both the original time series and the surrogates, and the surrogates are consistent with the null hypothesis as measured by the nonlinear metric. Therefore the surrogates are consistent with the null hypothesis. Figure 1 shows, again for this same sample vowel, the nonlinear statistic applied to the surrogates and the original speech time series.

Figures 11 and 12 show plots comparing the nonlinear metric (calculated with $Q=20$) applied to a selection of the original speech time series ($I_N[p]$, thick black line), with the median of the nonlinear metric applied to all corresponding surrogates ($I_N[s_p]$, thin, solid black line). The minimum and maximum values of the nonlinear metric for the surrogates are shown (filled gray area with dotted outlines). Over all the time series and at all time lags $1 \leqslant \tau \leqslant 50$, there are only two instances out of $50 \times 20 = 1000$ time lags where the nonlinear metric on the original time series is not the largest value.

VII. DISCUSSION

Figures 11 and 12 show specific examples of the result that there are an insignificant number of cases where the nonlinear metric on the original is not the maximum value. Simultaneous cross-checks show that the surrogates are indistinguishable using second-order statistics, from the original, and, to within the numerical error associated with the

TABLE II. Sound file sources and sample lengths of time series.

Time series code name	TIMIT file name	Length in samples
faks0_sx223_aa	TEST/DR1/FAKS0/SX223.WAV	1187
msjs1_sx369_aa	TEST/DR1/MSJS1/SX369.WAV	914
fcft0_sa1_er	TEST/DR4/FCFT0/SA1.WAV	1106
mrws0_si1732_er	TRAIN/DR1/MRWS0/SI1732.WAV	948
fdac1_si844_iy	TEST/DR1/FDAC1/SI844.WAV	1143
mreb0_si2005_iy	TEST/DR1/MREB0/SI2005.WAV	1148
fmaf0_si2089_ih	TEST/DR4/FMAF0/SI2089.WAV	1023
mbwm0_sa1_ih	TEST/DR3/MBWM0/SA1.WAV	1151
fjwb1_sa2_ae	TRAIN/DR4/FJWB1/SA2.WAV	1280
mstf0_sa1_ae	TRAIN/DR4/MSTF0/SA1.WAV	1053
fdkn0_sx271_eh	TRAIN/DR4/FDKN0/SX271.WAV	1261
mbml0_si1799_eh	TRAIN/DR7/MBML0/SI1799.WAV	1213
mdbp0_sx186_uw	TRAIN/DR2/MDBP0/SX186.WAV	951
fmjb0_si547_uw	TRAIN/DR2/FMJB0/SI547.WAV	1036
futb0_si1330_uh	TEST/DR5/FUTB0/SI1330.WAV	1043
mcsh0_sx199_uh	TEST/DR3/MCSH0/SX199.WAV	1051
fcal1_si773_ao	TEST/DR5/FCAL1/SI773.WAV	983
mbjk0_si2128_ao	TEST/DR2/MBJK0/SI2128.WAV	930
fmgd0_sx214_ah	TEST/DR6/FMGD0/SX214.WAV	971
mdld0_si913_ah	TEST/DR2/MDLD0/SI913.WAV	997

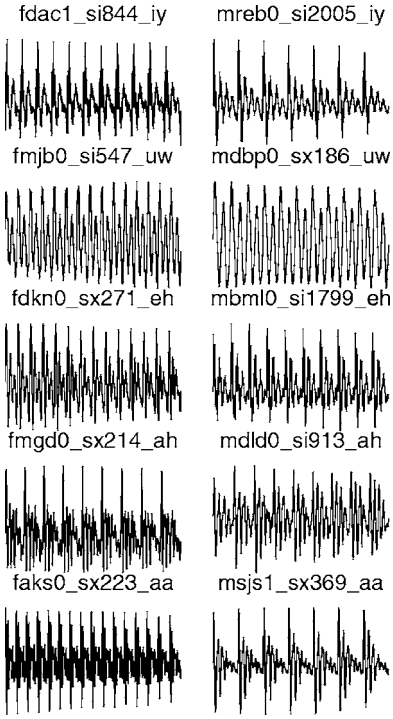

FIG. 7. Time series of the first set of vowels used in this study. The code names are described in Table II. For clarity, the axes labels have been removed, the horizontal axis is time index n, the vertical axis is speech pressure $p(n)$.

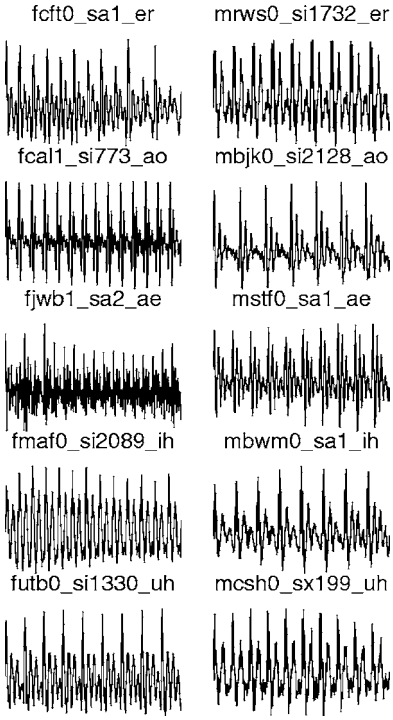

FIG. 8. Time series of the second set of vowels used in this study. The code names are described in Table II. For clarity, the axes labels have been removed, the horizontal axis is time index n, the vertical axis is speech pressure $p(n)$.

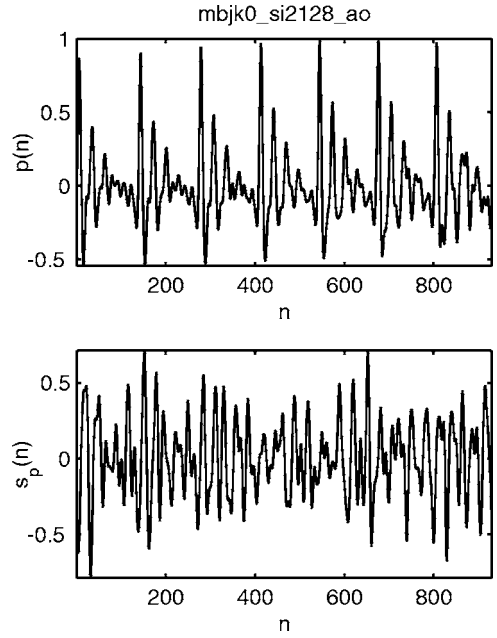

FIG. 9. (Top) Time series of a sample vowel from the set, (bottom) one corresponding surrogate.

computation of the linear and nonlinear metrics, contain no detectable non-Gaussianity. The broad conclusion is that the linear Gaussian null hypothesis can be rejected for most lags for all the vowels tested.

There are, however, interesting details that are worth pointing out. It appears that in most cases the nonlinear metric applied to the speech time series follows the broad peaks and troughs of the mutual information in the surrogates, with

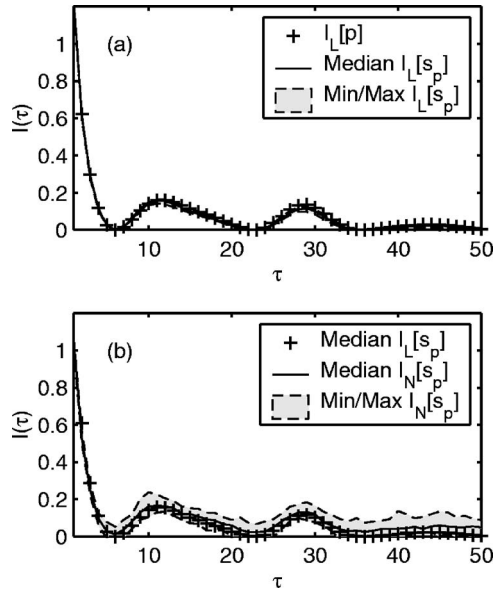

FIG. 10. Surrogate cross-checks for the same sample vowel as selected for Fig. 9. (a) Check that surrogates conform to the null hypothesis. Linear mutual information metric on the surrogates has a negligible spread of values, and the median linear metric over all the surrogates coincides with that of the original time series. (b) Check that the nonlinear metric gives the same values as the linear metric for the surrogates that have only linear, Gaussian statistical dependencies. The median of the linear metric on the surrogates tracks the nonlinear metric on the surrogates to within numerical error.

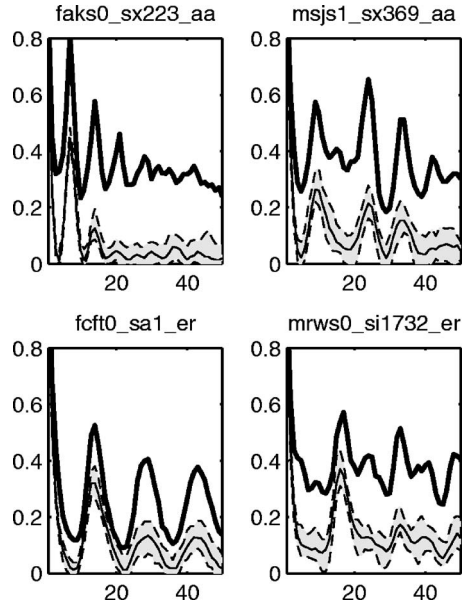

FIG. 11. Diverging nonlinear mutual information metrics for simple vowels /aa/ and /er/ and their surrogates. For clarity, the axes labels have been removed, the horizontal axis is time lag τ, the vertical axis is mutual information $I(\tau)$.

some obvious exceptions. It is the opinion of the authors that this is an indication that the autocorrelation is, to some extent, broadly indicative of the general statistical dependence between samples at specific time lags. This is perhaps one of the reasons why Gaussian linear prediction is a useful technique—since it can capture a broad picture of the dynamical structure of the vowel sounds. However, clearly linear prediction cannot represent all the structure.

A further observation is that this kind of tracking is apparently absent from the comparison between linear and nonlinear metrics applied to the chaotic Lorenz time series, seen

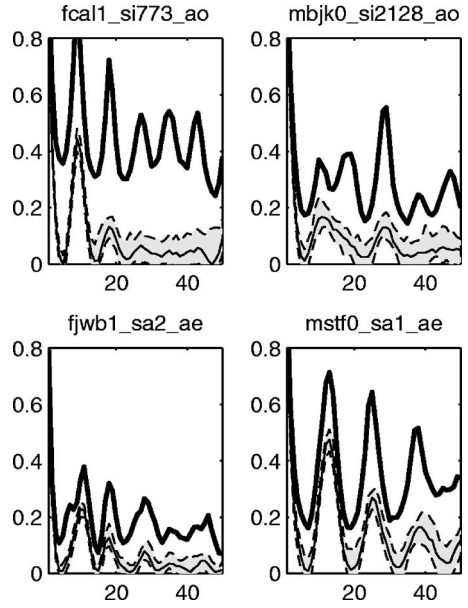

FIG. 12. Diverging nonlinear mutual information metrics for simple vowels /ao/ and /ae/ and their surrogates. For clarity, the axes labels have been removed, the horizontal axis is time lag τ, the vertical axis is mutual information $I(\tau)$.

in Fig. 4. Also, as seen in most of the curves in Figs. 11 and 12, for very small lags ($\tau < 4$) the nonlinear and linear metrics mostly coincide and the null hypothesis cannot be comfortably rejected.

One alternative interpretation is that the detected non-Gaussianity is actually spectral nonstationarity in the time series. A deliberate precaution of this study is being careful to select short segments of speech that appear to be as regular as possible. However, an additional check carried out, that of calculating the power spectral densities at the beginning, middle, and end of the time series, shows that the spectral differences are very slight. Even so, some of the vowels are more irregular than others. Comparing, for example, faks0_sx223_aa against fjwb1_sa2_ae in Figs. 7 and 8, the former might be considered more stationary than the latter. However, Fig. 11 shows that, even for the apparently stationary vowel faks0_sx223_aa, the level of non-Gaussianity is significant (and, in fact, even more so than the case for vowel fjwbl_sa2_ae; see Fig. 12). In conclusion, therefore, any slight spectral nonstationarity in the vowel time series that could not be eradicated is not a significant factor in the detection of non-Gaussianity.

VIII. CONCLUDING REMARKS

In this paper we provide evidence, using an improved surrogate data test method, that the linear Gaussian theory of speech production cannot be the whole explanation for the dynamical structure of simple vowels. It reaches this conclusion by first identifying (Sec. II) and circumventing (Secs. III and IV) certain systematic problems with the use of the surrogate data analysis test method that affect other studies. It demonstrates the effectiveness of the method on a known nonlinear time series (Sec. V). The application to real speech time series demonstrates that the null hypothesis of Gaussian-driven linearity is false, to a high level of significance (Sec. VI).

Although the calibrated calculation of I_N leads to agreement with I_L to within a small discrepancy, more satisfactory would be to avoid the calibration altogether. To this end, a complete theoretical explanation of the systematic divergence of this algorithm from the analytic values would be of value, and perhaps also a more sophisticated calculation of $I_N[u]$ involving adaptive partitioning and the use of higher-order numerical integration.

Careful selection of time series where the linear correlations are stationary over the duration is important, but the duration of approximately 60 ms is twice as long as the normal frame size used in speech coders. To provide more incentive for the use of sophisticated nonlinear/non-Gaussian methods in practical speech coding, it might be preferable to test the assumptions over shorter time scales. This study finds that applying the test over such short time scales is problematic for the calculation of I_N since it starts to vary substantially from I_L, and confidence is weakened that the surrogates are consistent with the null hypothesis. Improvements suggested in the previous paragraph might enable this test to be carried out.

Although this paper avoids spectral nonstationarity, nonstationarity may be measured by many other quantities, such as running mean, variance, and higher-order moments, which could be used as additional checks to assess nonstationarity of non-Gaussian correlations in the speech data (Fackrell, 1996). This would probably require, however, longer time series, making it harder to find natural speech data for which nonstationarity can be avoided.

It would also be interesting to apply the same technique to other speech time series, for example, consonants that are supposed to be turbulent yet still amenable to linear prediction analysis (Kubin, 1995). Diphthongs are supposed to be generated by nonstationary linear dynamics, but perhaps a nonlinear predictor may model these dynamics more naturally. The application of this test to these vowel sounds might be possible. Pathological speech time series are believed to exhibit signs of chaos, and this method might be adapted to the detection of such complex dynamics. For whispering and shouting, the dynamics might diverge from linearity further.

Finally, these results could have implications in LPAS speech coding standards that rely upon Gaussian code books (Kroon and Kleijn, 1995). Although use of linear prediction analysis increases the Gaussianity of the residual with respect to the original speech signal (Kubin, 1995), this paper suggests that the residual will never be exactly Gaussian. Improvements to the quality of speech coders may be obtained by appropriate, non-Gaussian code books.

ACKNOWLEDGMENTS

Max Little would like to thank Professor Stephen McLaughlin for helpful discussions about nonlinear speech processing, and Reason Machete for interesting insights. He acknowledges the EPSRC, UK for financial support.

[1]For commercial speech coding standards, typically 20–30 ms, which amounts to a maximum of around 480 samples at a sample rate of 16 kHz (Kroon and Kleijn, 1995).

[2]Subsequent reference to I_N as the "nonlinear metric," even though it more accurately describes non-Gaussianity, provides an expressive shorthand.

[3]This is mostly because the entropy features significantly in the calculation of the nonlinear mutual information at all time lags, even if the statistical dependencies at other time lags could be jointly Gaussian and therefore completely characterized by the autocorrelation.

[4]There is also a small variation in the linear metric since it depends upon the *sample* covariance matrix estimate from the time series.

[5]Microsoft WAV files of these time series and software to carry out the calibrated surrogate data test are available from the URL http://www.maths.ox.ac.uk/~littlem/surrogates/.

Banbrook, M., McLaughlin, S., and Mann, I. (**1999**). "Speech characterization and synthesis by nonlinear methods," IEEE Trans. Speech Audio Process. **7**, 1–17.

Chan, R. (**2003**). "Constitutive characterization of vocal fold viscoelasticity based on a modified Arruda–Boyce eight-chain model," J. Acoust. Soc. Am. **114**, 2458–2458.

Fackrell, J. (1996). "Bispectral analysis of speech signals," Ph.D. thesis, Edinburgh University, UK.

Fant, G. (**1960**). *Acoustic Theory of Speech Production* (Mouton, s'Gravenhage).

Fisher, W., Doddington, G., and Goudie-Marshall, K. (**1986**). "The DARPA speech recognition research database: Specifications and status," in *Proceedings of the DARPA Workshop on Speech Recognition*, pp. 93–99.

Fraser, A. and Swinney, H. (**1986**). "Independent coordinates for strange attractors from mutual information," Phys. Rev. A **33**, 1134–1140.

Godsill, S. (**1996**). "Bayesian enhancement of speech and audio signals which can be modeled as ARMA processes," Int. Statist. Rev. **65**(1), 1–21.
Herzel, H. and Grosse, I. (**1997**). "Correlations in DNA sequences: The role of protein coding segments," Phys. Rev. E **55**, 800–810.
Herzel, H., Berry, D., Titze, I., and Steinecke, I. (**1995**). "Nonlinear dynamics of the voice: Signal analysis and biomechanical modeling," Chaos **5**, 30–35.
Kantz, H. and Schreiber, T. (**1997**). *Nonlinear Time Series Analysis* (Cambridge University Press, Cambridge).
Kleijn, W. and Paliwal, K. (**1995**). "An introduction to speech coding," in *Speech Coding and Synthesis*, edited by W. B. Kleijin and K. K. Paliwal (Elsevier Science, Amsterdam), Chap. 1, pp. 1–47.
Kroon, P., and Kleijn, W. (**1995**). "Linear-prediction based analysis-by-synthesis coding," in *Speech Coding and Synthesis*, edited by W. B. Kleijin and K. K. Paliwal (Elsevier Science, Amsterdam), Chap. 3, pp. 79–119.
Kubin, G. (**1995**). "Nonlinear processing of speech" in *Speech Coding and Synthesis*, edited by W. B. Kleijin and K. K. Paliwal (Elsevier Science, Amsterdam), Chap. 16, pp. 557–610.
Kugiumtzsis, D. (**2001**). "On the reliability of the surrogate data test for nonlinearity in the analysis of noisy time series," Int. J. Bifurcation Chaos Appl. Sci. Eng. **11**, 1881–1896.
Lucero, J. (**1999**). "A theoretical study of the hysteresis phenomenon at vocal fold oscillation onset–offset," J. Acoust. Soc. Am. **105**, 423–431.
Mann, I. (1999). "An investigation of nonlinear speech synthesis and pitch modification techniques," Ph.D. thesis, Edinburgh University, UK.
Maragos, P., and Potamianos, A. (**1999**). "Fractal dimensions of speech sounds: Computation and application to automatic speech recognition," J. Acoust. Soc. Am. **105**, 1925–1932.
Maragos, P., Dimakis, A., and Kokkinos, I. (**2002**). "Some advances in nonlinear speech modeling using modulations, fractals, and chaos," in *Proceedings of the 14th International Conference on Digital Signal Processing*, DSP **2002**, Vol. **1**, pp. 325–332.
Markel, J. and Gray, A. (**1976**). *Linear Prediction of Speech* (Springer-Verlag New York).
McSharry, P. (**2005**). "The danger of wishing for chaos," Nonlin. Dyn., Psych., and Life Sci. **9**(4), 375.
McSharry, P., Smith, L., and Tarassenko, L. (**2003**). "Prediction of epileptic seizures: Are nonlinear methods relevant?," Nat. Med. **9**, 241–242.
Miyano, T., Nagami, A., Tokuda, I., and Aihara, K. (**2000**). "Detecting nonlinear determinism in voiced sounds of Japanese vowel /a/," Int. J. Bifurcation Chaos Appl. Sci. Eng. **10**, 1973–1979.
Paluš, M. (**1995**). "Testing for nonlinearity using redundancies: Quantitative and qualitative aspects," Physica D **80**, 186–205.
Proakis, J., and Manolakis, D. (**1996**). *Digital Signal Processing: Principles, Algorithms, and Applications* (Prentice-Hall, Englewood Cliffs, NJ).
Quatieri, T. (**2002**). *Discrete-Time Speech Signal Processing*, Prentice-Hall Signal Processing Series.
Rank, E. (**2003**). "Application of Bayesian trained RBF networks to nonlinear time-series modeling," Signal Process. **83**, 1393–1410.
Schreiber, T. and Schmitz, A. (**2000**). "Surrogate time series," Physica D **142**, 346–382.
Schürmann, T. (**2004**). "Bias analysis in entropy estimation," J. Phys. A **37**, 295301.
Small, M., Yu, D., and Harrison, R. (**2001**). "Surrogate test for pseudoperiodic time series data," Phys. Rev. Lett. **87**, 188101.
Story, B. H. (**2002**). "An overview of the physiology, physics and modeling of the sound source for vowels," Acoust. Sci. & Tech. **23**(4), 195–206.
Teager, H. M., and Teager, S. M. (1989). "Evidence for nonlinear sound production mechanisms in the vocal tract," *Speech Production and Speech Modelling*, NATO Advanced Study Institute Series D Vol. **55**, pp. 241–261.
Tokuda, I., Miyano, T., and Aihara, K. (**2001**). "Surrogate analysis for detecting nonlinear dynamics in normal vowels," J. Acoust. Soc. Am. **110**(6), pp. 3207–3217.
Tokuda, I., Riede, T., Neubauer, J., Owren, M., and Herzel, H. (**2002**). "Nonlinear analysis of irregular animal vocalizations," J. Acoust. Soc. Am. **111**, 2908–2919.
Wong, D., Markel, J., and Gray, A. (**1979**). "Least squares glottal inverse filtering from the acoustic speech waveform," IEEE Trans. Acoust., Speech, Signal Process. **27**, pp. 350–355.
Wu, L., Niranjan, M., and Fallside, F. (**1994**). "Fully vector quantized neural network-based code-excited nonlinear predictive speech coding," IEEE Trans. Speech Audio Process. **2**, 482–489.

Speech perception from monaural and binaural information

John F. Culling, Barrie A. Edmonds, and Kathryn I. Hodder
School of Psychology, Cardiff University, Tower Building, Park Place, Cardiff, CF10 3AT United Kingdom

(Received 13 September 2005; revised 7 October 2005; accepted 2 November 2005)

Two experiments explored the concept of the binaural spectrogram [Culling and Colburn, J. Acoust. Soc. Am. **107**, 517–527 (2000)] and its relationship to monaurally derived information. In each experiment, speech was added to noise at an adverse signal-to-noise ratio in the NoSπ binaural configuration. The resulting monaural and binaural cues were analyzed within an array of spectro-temporal bins and then these cues were resynthesized by modulating the intensity and/or interaural correlation of freshly generated noise. Experiment 1 measured the intelligibility of the resynthesized stimuli and compared them with the original NoSo and NoSπ stimuli at a fixed signal-to-noise ratio. While NoSπ stimuli were $\approx$50% intelligible, each cue in isolation produced similar (very low) intelligibility to the NoSo condition. The resynthesized combination produced $\approx$25% intelligibility. Modulation of interaural correlation below 1.2 kHz and of amplitude above 1.2 kHz was not as effective as their combination across all frequencies. Experiment 2 measured three-point psychometric functions in which the signal-to-noise ratio of the original NoSπ stimulus was increased in 3-dB steps from the level used in experiment 1. Modulation of interaural correlation alone proved to have a flat psychometric function. The functions for NoSπ and for combined monaural and binaural cues appeared similar in slope, but shifted horizontally. The results indicate that for sentence materials, neither fluctuations in interaural correlation nor in monaural intensity are sufficient to support speech recognition at signal-to-noise ratios where 50% intelligibility is achieved in the NoSπ configuration; listeners appear to synergistically combine monaural and binaural information in this task, to some extent within the same frequency region. [DOI: 10.1121/1.2140806]

PACS number(s): 43.71.An, 43.66.Pn, 43.66.Dc [PFA] Pages: 559–565

I. INTRODUCTION

When speech and interfering noise have different interaural time delays or phases, the speech is easier to understand than when they are presented with identical interaural parameters (Licklider, 1948; Schubert, 1956). The improvement in intelligibility is known as binaural advantage. It mirrors improvements in detection thresholds for tonal signals in similar binaural configurations known as the binaural masking level difference (BMLD). It would appear that the binaural system provides some additional information about the speech signal beyond that available by listening with one ear. However, while the BMLD has been intensively investigated, very little research has been directed to identifying the nature of binaurally derived speech information and the way in which it is combined with information derived monaurally.

Levitt and Rabiner (1967b) developed a technique for predicting the magnitude of the binaural advantage for speech. This technique assumed that the binaural system reduced the effective level of the masking noise in each frequency band in accordance with the BMLD of a pure tone at the same frequency and in the same binaural configuration; if the BMLD was 5 dB, then the effective masker level was reduced by 5 dB. For a given binaural configuration, the model used measurements of the pure-tone BMLD at each frequency and the articulation index (Kryter, 1962) to predict the SRT that would result from using that binaural configuration with speech signals. This model produced accurate predictions of their speech intelligibility measurements (Levitt and Rabiner, 1967a). However, the model is rather agnostic about the level of processing at which listeners combine monaural and binaural information; it simply assumes an effective equivalence between binaural unmasking and reduced monaural masking, which is, as they noted, "reasonable…at an empirical level." It would be interesting to determine whether monaural and binaural information is combined before or after word recognition.

Akeroyd and Summerfield (2000) addressed the combination of monaural and binaural cues in the specific context of vowel identification from formant information. In their experiments, formants were represented either by prominent frequency bands in the amplitude spectrum of a broadband noise or by interaurally decorrelated subbands of that noise. Akeroyd and Summerfield demonstrated that two formants encoded in these different forms could be combined to produce accurate identification of the vowel they represent, where information from either cue alone would leave the vowel ambiguous. Akeroyd and Summerfield's demonstration begins to explore the nature of the cues provided by each system and proves that information derived independently from each cue can be integrated. Although the stimuli employed were somewhat schematic, they reflect a situation that probably arises frequently in everyday listening, where binaural information is recovered effectively at low frequencies, but not at high frequencies. Vowel identification may therefore often rely upon a first formant frequency derived from binaural cues and a second formant frequency that is better represented by monaural cues. The present investiga-

tion looks at the same cues as Akeroyd and Summerfield, but using more naturalistic stimuli, derived from sentences embedded in noise, and also tests, to some degree, the integration of these cues within the same frequency region, as well as across frequency. The cues involved are temporal modulations within individual frequency channels in the amplitude and in the interaural coherence of the stimulus.

One consequence of adding a signal to a more-intense noise with a different interaural time delay is that the interaural coherence of the stimulus (the maximum interaural correlation[1] as a function of delay) is reduced at the frequency of the signal. As the intensity of the signal is increased the interaural coherence of the stimulus is reduced. In the widely used NoSπ binaural configuration, where the noise has zero interaural delay, the interaural coherence and the interaural correlation will be identical for negative signal-to-noise ratios. Consequently, it is often sufficient to consider only the interaural correlation (without applying any delays). Supporting the notion that interaural coherence/correlation is the cue used by the binaural system to produce binaural advantage, Culling *et al.* (2001) showed that direct manipulation of the interaural correlation of one subband of an otherwise diotic broadband noise generates the illusion of an embedded sound at the frequency of this subband. Further, they found that the lower the interaural correlation, the louder is the illusory sound. This experiment shows that the auditory system interprets reduced correlation as evidence of an additional sound. The perceived loudness increases as correlation is reduced, which is consistent with the expected effect of an increase in the level of that sound on the correlation.

In order to explain binaural advantage for complex, time-varying signals, such as speech, Culling and Colburn (2000) proposed a conception of binaural processing, in which spectro-temporal variations in signal intensity are recovered from the combined speech and noise by analyzing the interaural coherence of the stimulus within a sliding temporal window for each frequency channel. Based on measurements of binaural frequency selectivity (Kohlrausch, 1988) and temporal acuity (Culling and Summerfield, 1998), the frequency channels were modeled by a gammatone filterbank (Patterson *et al.*, 1987, 1988) followed by a sliding analysis window of asymmetric, Gaussian shape, and 110 -ms duration. In Culling and Colburn (2000), this analysis was followed by an interaural coherence measurement, giving a physical measure of cue strength. However, a further refinement to the model is to perceptually scale the interaural coherence values according to the sensitivity of the binaural system. Such a scaling provides the basis on which the brain encodes the intensity of the stimuli it detects using the binaural system. Culling *et al.* (2001) measured listeners' sensitivity function using cumulative d' to the interaural correlation of one subband in an otherwise diotic noise. Culling (2000) employed this sensitivity function to predict the salience of the Fourcin pitch as a function of the size of interaural delays and the number of noises used to generate the pitch. Thus, the output of the model is a salience measure that can be used to address suprathreshold as well as threshold data.

In the present investigation, the purpose was not to model human binaural processing, but to isolate the cues to which this model is sensitive and investigate listeners' ability to use such cues for speech recognition. In this way, we seek to underpin the claim that the model provides a plausible account of human proficiency at understanding speech in noise in the NoSπ configuration. In particular, the model assumes that the only information needed from the binaural system is the coherence, and not, for instance, the location of the speech or of the noise. If the spectro-temporal pattern of coherence is simulated and listeners can exploit the simulated binaural cues successfully, the contention that coherence is the only important cue receives some support. For this purpose, a method was developed for the analysis and resynthesis of monaural and binaural cues.

II. EXPERIMENT 1

Experiment 1 measured the intelligibility of speech in six different conditions. Two of these were real speech-and-noise mixtures in the NoSo and NoSπ binaural configurations. Three more were based upon the NoSπ stimuli and generated by analyzing and resynthesizing specific cues using the method outlined below. These conditions were (1) "binaural" using stimuli with resynthesized binaural cues, (2) "monaural" using stimuli with resynthesized monaural cues, and (3) "combined" using stimuli with both resynthesized binaural and monaural cues. Since effective binaural processing of speech in noise is known to be largely limited to low frequencies (Levitt and Rabiner, 1967a, b), a sixth "split" condition explored the possibility that binaural cues operate mainly below 1.2 kHz, while monaural cues operate mainly above 1.2 kHz. This condition was identical to the binaural stimuli below this frequency and identical to the monaural stimuli above it.

A. Analysis and resynthesis method

The general analysis and resynthesis method began with an input speech waveform (16-bit quantization; 20-kHz sampling rate) and a specified signal-to-noise ratio (SNR). Brown noise (i.e., with a −6-dB/oct roll-off) was generated and added to the speech in the NoSo and NoSπ binaural configurations at the desired SNR. The resulting stereo waveforms were both stored and the NoSπ waveform was analyzed as follows.

The left- and right-ear channels were each filtered in the frequency domain into 30 spectrally contiguous, logarithmically spaced frequency bands between 0.1 and 10 kHz. To filter out each band, the complete waveform was transformed into the frequency domain and all frequency bins outside the passband were set to zero amplitude before inverse Fourier transformation. The frequency resolution of this analysis was roughly equivalent to human frequency selectivity (Moore and Glasberg, 1983), but using rectangular passbands. The time waveform from each resulting frequency band was recovered by inverse Fourier transform and then windowed using a series of 50% overlapping Hanning windows of 100-ms equivalent-rectangular duration (200 ms in total duration). Two statistics were measured from the resulting

spectro-temporal bins: (1) the rms power of each bin for the left channel and (2) the correlation coefficient (Pearson's r) for corresponding bins from the left- and right-hand channels.

The stimuli of the monaural, binaural, and combined conditions contained only noise. These noises were manipulated in order to introduce the speech cues that had been determined using the analysis above. The cues were introduced as follows. Two freshly generated, independent Brown noises of equal duration to the original speech waveform were filtered and windowed in a similar fashion to the speech-noise mixture in order to produce two spectro-temporal arrays of noise bins. The measured interaural correlations and rms powers of the corresponding bins in the speech-noise mixture were imposed on the noise bins. Corresponding bins from the two noises were orthogonalized using the Gram-Schmidt method (Culling *et al.*, 2001, Appendix I), so that they had an interaural correlation of zero and equal rms power. To recreate the original pattern of interaural correlation changes (binaural condition), each pair of noise bins was then mixed[2] so that their interaural correlation exactly matched that of the corresponding pair of spectro-temporal bins from the speech-noise mixture. To recreate the original power spectrogram (monaural condition), the rms power of each noise bin was measured and then the sample values were scaled so as to match the power of the corresponding spectro-temporal bin from the speech-noise mixture. Both of these operations were independent, so each speech-noise mixture stimulus was resynthesized from noise alone with monaural cues, binaural cues, or both.

The binaural cues alone result in the perception of muffled speech embedded in the background noise. When the content of the sentence is known, the content of the sentence can also be "followed," but, as the experiments below demonstrate, without prior knowledge, it is very difficult to understand a novel speech sample from binaural cues alone.

B. Stimuli

The stimuli were based on 60 sentences from the Harvard sentence list (M.I.T. recordings of voice DA), which are equalized in overall level. Each sentence was processed into the six different forms described above using an original SNR of −20 dB. A further ten sentences were prepared for use as practice stimuli in the NoSo and NoSπ binaural configurations. The SNRs for these practice stimuli ranged from −12 to −20 dB in 2-dB steps. The presentation level was approximately 57 dB (A).

C. Procedure

Twelve listeners with no reported hearing defects and all native speakers of English each attended a single hour-long session, during which they listened to 70 sentences. The first ten sentences were a practice, which was identical for each listener. The ten practice sentences alternated between the NoSo and NoSπ binaural configurations and decreased in SNR by 2 dB on every other trial, such that the SNR matched that of the test stimuli by the end of the practice. In the subsequent 60 trials listeners received ten sentences in each of the six conditions in randomized sequence. The stimulus materials were rotated through these conditions from one listener to the next, so that each sentence was represented equally in each of the conditions.

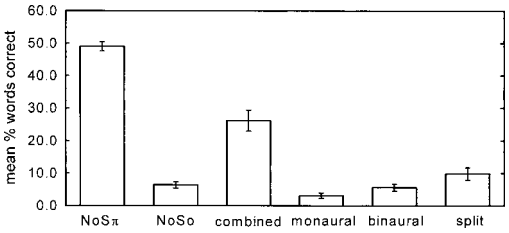

FIG. 1. Results from experiment 1. Percentage of words correctly recognized in six conditions: NoSπ, NoSo, "combined," (resynthesized combination of the monaural and binaural cues of amplitude and correlation modulation), "monaural" (resynthesized monaural cues only), "binaural" (resynthesized binaural cues only), and "split" (resynthesized binaural cues below 1.2 kHz and monaural cues above 1.2 kHz). Error bars are one standard error of the mean.

Listeners were seated in a single-walled IAC booth within a sound-treated room and made responses on a computer terminal, whose keyboard was within the booth. The screen could be seen through the booth's window. Listeners were invited to replay each stimulus (by pressing the "?" key) up to ten times before attempting a transcription. However, they were advised that no further benefit should be expected after listening three or four times to each stimulus. Once they had listened enough, they typed in their transcription and pressed the return key. The correct transcript then appeared on the screen, beneath their own, and they counted the number of words correctly transcribed and indicated the total with a single keypress, 0–9. Five of the sentences contained ten words, but it was very rare for all ten to be correctly transcribed. In this situation, listeners were instructed to press "9."

D. Results

The mean percentage of words correctly recognized in each condition is shown in Fig. 1. These are averages across listeners and represent the total number of words recognized from the ten sentences presented in a given condition. Since the sentences were not all of equal length, some variance arises from differences in the maximum possible score for a given listener in a given condition, but this effect is counterbalanced across conditions by the rotation of materials, as are any variations in the intrinsic intelligibility of different sentence lists. An analysis of variance showed that the six conditions differed significantly $[F(5,55)=119,\ p<0.001]$. However, Tukey HSD pairwise comparisons indicated that the NoSo, monaural, binaural, and split conditions did not differ significantly, while the NoSπ and combined conditions differed from these and from each other ($q>10$, $p<0.01$, in each case). The NoSπ condition is therefore significantly better than any other. The combined condition displayed a marked superiority over the monaural and binaural conditions, but was still worse than the NoSπ condition, from whose stimuli it was derived.

E. Discussion

The low recognition rate in the binaural condition of experiment 1 indicates that binaural cues alone are insufficient to facilitate substantial intelligibility. Indeed many of the correctly recognized words probably occurred by chance; the words "a" and "the" accounts for about 50% of correct words in the more difficult conditions. Nonetheless, some transcripts show unambiguous evidence of intelligibility, supporting the principle that the binaural spectrogram can support a low, but measurable, level of speech communication. Of 120 attempted transcripts from the 12 subjects, the most accurate was "we all have a new day's decision" for "we now have a new base for shipping." Aside from the four correct words, there is a matching prosodic structure, the correct number of syllables, and many phonemes within incorrect words either match or have the correct manner of articulation.

Although both monaural and binaural cues alone gave poor intelligibility, it is striking that their combination resulted in a large increase in scores. For instance, in the combined condition, "raise the sail and steer the ship northward" was transcribed quite accurately by one listener as "raise the sail, steer the ship upward." The proposed direction of movement suggests that this listener was not, while making these transcriptions, making very great use of semantic constraints. The success of the combined condition suggests two possibilities. One is that there is some form of perceptual interaction between the two types of cue, whereby one cue corroborates or reinforces the other. The other is that there is simply a highly nonlinear relationship between the information gained about the stimulus and the chance of correctly identifying a whole word. Experiment 2 was designed to address this question.

Although speech recognition was markedly improved by the combination of monaural and binaural cues in the combined condition it still did not match that of a real mixture of speech and noise in the NoSπ condition. When frequency bands above and below 1.2 kHz were encoded with different perceptual cues (split condition), performance was not significantly better than when the individual cues were provided at all frequencies (monaural and binaural conditions). This outcome suggests that monaural and binaural cues are exploited to some extent from the same frequency regions. Since it is known from the work of Levitt and Rabiner (1967a, b) that the contribution of the binaural system at high frequencies is very limited, one must conclude that substantial monaural information is normally extracted from the band below 1.2 kHz, and that this information remains useful to speech intelligibility when corresponding binaural information is also available.

III. EXPERIMENT 2

In experiment 1, listeners showed markedly higher identification rates when provided with both monaural and binaural cues, compared to either cue in isolation. If information from monaural and binaural cues is independent and is combined at the lexical level, then the size of this improvement should conform to an equation offered by Boothroyd and Nittrouer (1988), which sums log error rates:

$$\log(1-p_c)=\log(1-p_m)+\log(1-p_b). \quad (1)$$

The equation is adapted so that, p_m, p_b, and p_c are the proportions of words correct in the monaural, binaural, and combined conditions, respectively. One implication of this equation is that when two independent sources of information are combined, the resulting psychometric function is predicted to be steeper than that produced when either cue is available individually. If this equation is applied to the results of experiment 1, the predicted score for the combined condition is only 9%, compared to the observed 27%. However, the method of scoring based on all the words is probably not best adapted to this form of analysis, since there are substantial opportunities to get common words such as "the" right by chance. Therefore, experiment 2 employed a scoring method that used a fixed number of content words. In addition, the signal-to-noise ratio of the original NoSπ stimulus was varied, so that a three-point psychometric could be measured for each condition.

A. Stimuli

The stimuli were generated in a similar manner to those of experiment 1, but in order to accommodate testing at three SNRs, the number of conditions was reduced to four, NoSπ, monaural cues only, binaural cues only, and combined monaural and binaural cues. In addition, the quantity of starting speech material had to be increased to 120 sentences for experimental materials and another 20 for practice. The three SNRs for the original speech-noise mixture were −20, −17, and −14 dB. SNR thus increased in 3-dB steps from that used for experiment 1. With four binaural conditions and three SNRs, there were 12 conditions in all. The presentation level was approximately 57 dB (A).

B. Procedure

Sixteen listeners each attended one 75-min session. During a session, they listened to 20 practice stimuli including five examples from all four conditions at declining SNR as in experiment 1. They then listened to 120 experimental stimuli (10 examples $\times$ 4 conditions $\times$ 3 SNRs). The 120 stimuli were divided into three blocks. Each successive block used stimuli based on a lower SNR. As in experiment 1, each listener heard ten sentences in each condition, and the sentences were rotated around the conditions from one listener to the next. Unlike experiment 1, listeners heard each sentence three times and scoring was based upon five keywords, indicated to the listeners with the use of capital letters in the transcript.

C. Results

The results are plotted as psychometric functions in Fig. 2. The abscissa represents the SNR of the NoSπ stimuli and the SNR of the NoSπ stimuli on which the other three conditions were based. The four stimulus types differed significantly $[F(3,45)=340,\ p<0.0001]$. The NoSπ condition showed significantly higher intelligibility than all other con-

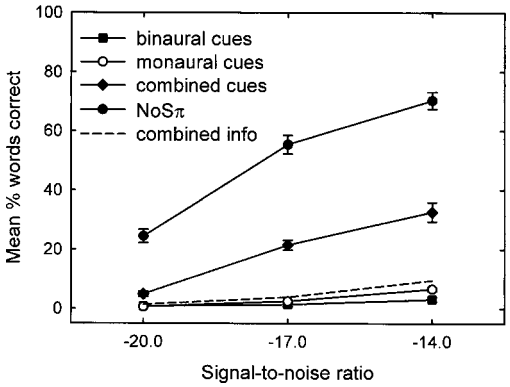

FIG. 2. Results from experiment 2. Percentage of words correctly recognized as a function of signal-to-noise ratio in four conditions: NoSπ (filled circles), resynthesized binaural cues only (filled squares), resynthesized monaural cues (open circles), resynthesized combination of monaural and binaural cues (filled diamonds), and expected scores from combined monaural and binaural cues (dashed line). Error bars are one standard error of the mean.

ditions ($q>24$, $p<0.001$, in each case). The combined cues also gave significantly higher intelligibility than either monaural or binaural cues ($q>13$, $p<0.001$, in each case).

Two of the four conditions showed a substantial improvement in intelligibility with increasing SNR, but the monaural-cue and binaural-cue conditions showed little or no improvement. This is reflected in a significant main effect of SNR [$F(2,30)=188$, $p<0.0001$], but an interaction between SNR and condition [$F(6,90)=55.0$, $p<0.0001$]. Simple main effects showed significant improvement with SNR for the NoSπ condition [$F(2,30)>240$, $p<0.0001$], combined-cue condition [$F(2,30)>86$, $p<0.0001$], and a small but significant improvement in the monaural-cue condition [$F(2,30)>4.2$, $p<0.05$], but not for the binaural-cue condition.

Predictions of performance in the combined condition based on that from the monaural and binaural conditions using Eq. (1) are shown by a dashed line in Fig. 2. These predictions are substantially lower than the observed level of performance in the combined condition.

D. Discussion

The results of experiment 2 indicate not only that isolated binaural cues cannot support full speech intelligibility, but that there is no sign of any improvement with increasing SNR. Even the monaural-cue condition shows only the slightest of improvements across this range of SNRs. The substantial superiority of the combined cue condition over both the binaural-cue and monaural-cue conditions suggests that the information furnished by these two cues is in some way complementary. The fact that the predictions based on Eq. (1) fall well below the observations in the combined condition indicates that information from the two types of cue is not combined at the lexical level and probably occurs at a lower level of processing. The exact nature of that complementarity remains elusive.

Because the individual-cue psychometric functions are so flat, it is not possible to make a comparison of slopes. However, the results clarify and amplify those of experiment 1. The combined cues produced growing intelligibility with SNR, while the corresponding individual cues supported only the slightest improvement. A remarkable feature of the data from experiment 2 is that the intelligibility furnished by the binaural system did not seem to grow at all with increasing SNR, so it may be the case while that the binaural system provides some information that contributes to intelligibility, it rarely provides sufficient information to support the accurate identification of words. It is tempting to speculate that this information is fairly constant in usefulness over a wide range of SNRs and the shape of the psychometric function for combined cues is therefore determined only by the increasing value of monaural cues.

Finally, it is noteworthy that at the most adverse SNR used in experiment 2, listeners did not recognize as many words as in experiment 1, which used the equivalent SNR. This difference may have arisen from three sources. First, in experiment 2 these stimuli were presented within the context of an experiment that included much more favourable SNRs and this may have reduced the level of effort that the listeners were prepared to devote to the more difficult stimuli. Second, experiment 2 used a different scoring system based on keywords correct, rather than all correct words. This may have reduced scores on some of the more difficult conditions, for which articles accounted for many of the correct words (in the monaural and binaural conditions, correct words were 51% articles, 15% verbs, 5% personal pronouns, 10% adjectives, 9% prepositions, and 10% nouns). Third, listeners only had three opportunities to repeat the stimulus in experiment 2 compared to up to ten in experiment 1.

IV. GENERAL DISCUSSION

The experiments in this study have explored the plausibility of a theory of binaural unmasking for speech put forward by Culling and Colburn (2000). This theory suggested that listeners detect spectro-temporal variations in interaural coherence and treat these as a perceptual surrogate for the spectro-temporal variations in the energy of the speech signal. The results offer support for the theory in that (1) stimuli designed to provide listeners with this cue in isolation facilitated measurable, if very low, intelligibility, and (2) when these cues were combined with monaural cues, a substantial increase in intelligibility was observed, mirroring the effect of binaural advantage. This said, it is disappointing that the isolated binaural cues did not facilitate greater speech recognition, and that the resynthesis of combined monaural and binaural cues did not fully emulate the intelligibility of speech in noise in the NoSπ configuration. It is not clear whether these failings arise from a limitation of the theory or of the signal processing.

It is possible that there was some lack of fidelity in reproducing the pattern of amplitude and interaural correlation changes from the original stimulus and that this introduced informational noise to the cues the listeners were using. An obvious possibility here is that analysis windows of 100 ms, while being appropriate for the binaural cues, are very long compared to the 10-ms temporal resolution of the monaural system (Plack and Moore, 1990). Another is that

the Fourier-based method of filtering produced excessive ringing. Alternatively there may be some additional cue, perhaps provided by the fine temporal structure of the stimulus that listeners lacked when they were not listening to a real speech-noise mixture. Some attempts were made to address these possibilities, but no clear leading candidate emerged. First, analysis within shorter windows did not yield an audible improvement (not formally tested). Second, visual inspection of spectrograms of the frequency bands produced by rectangular-passband, frequency-domain filtering did not reveal ringing that seemed likely to be significant at the 100-ms time scale on which the processing was based. Third, a simple test of the integrity of the stimuli was to subtract one channel from the other. For NoSπ stimuli, this will recover the original speech waveform, but for the binaural cues and combined cues conditions, it results in a spectro-temporally modulated noise similar to those generated by Shannon *et al.* (1995), but with a modulation spectrum that is low-pass filtered at just 10 Hz. These stimuli sounded like an individual with some serious glottal pathology, but were nonetheless highly intelligible. It is possible that fine temporal structure makes a difference. An obvious possibility is that the presence of the target talker's fundamental frequency allows the auditory system to select the harmonics of that fundamental frequency. Although a persuasive idea, it runs against current theories of fundamental frequency processing that suggest a process of harmonic cancellation, rather than selection (de Cheveigné, 1997).

The reliance of Culling and Colburn's theory on measurement of interaural coherence implicitly limits its scope to speech recognition in unmodulated noise. This is because the direct relationship between interaural coherence and signal intensity is disturbed if the masker is modulated. For present purposes, it is convenient to remain within this constraint, because it facilitates the form of resynthesis used here. However, a better theory would more successfully predict performance with modulated maskers, such as competing speech. van de Par *et al.* (2001) argued that subtractive mechanisms such as Durlach's (1963) E-C model are more robust in modulated maskers. An improved form, therefore, of Culling and Colburn's model might employ a mechanism similar to Culling and Summerfield's (1995) mE-C model within each spectro-temporal bin. Such a model would equalize the level and interaural delay independently within each spectro-temporal bin and return the residue from cancellation as a measure of the signal intensity.

ACKNOWLEDGMENTS

The authors would like the Hanse Wissenschaftskolleg, which supported Culling with a fellowship during the course of this study, the editor, Peter Assmann, and the two reviewers, Chris Darwin and Wes Grantham, for their valuable comments on the manuscript.

[1]Throughout the present article "interaural correlation" may be taken to mean the Pearson's product-moment correlation, r (also known as the normalized covariance), of the waveforms at the two ears. At high frequencies and particularly for narrow stimulus bandwidths, the adopted definition of correlation can make a material difference to predictive models and the normalized interaural correlation has been found to facilitate better fitting models of interaural discrimination data than the normalized covariance (Bernstein, and Trahiotis, 1992, 1996a, b; Bernstein *et al.* 1999). However, for the broadband, mainly low-frequency stimuli used here, it makes little difference, so Pearson's r is employed here, as it is the more familiar.

[2]Mixing was performed using the "two-noise" method, in which one channel contains noise N_1 and the other mixture of the two noises, N_1 and N_2, in the following proportions: $\rho N_1 + \sqrt{1-\rho^2} N_2$.

Akeroyd, M. A. and Summerfield, A. Q. (**2000**). "Integration of monaural and binaural evidence of vowel formants," J. Acoust. Soc. Am. **107**, 3394–3406.

Bernstein, L. R., and Trahiotis, C. (**1992**). "Measurements of interaural envelope correlation and its relation to binaural unmasking at high frequencies," J. Acoust. Soc. Am. **91**, 306–316.

Bernstein, L. R., and Trahiotis, C. (**1996a**). "On the use of the normalized correlation as an index of interaural envelope correlation," J. Acoust. Soc. Am. **100**, 1754–1763.

Bernstein, L. R., and Trahoitis, C. (**1996b**). "The normalized correlation: Accounting for binaural detection across center frequency," J. Acoust. Soc. Am. **100**, 3774–3784.

Bernstein, L. R., van de Par, S., and Trahiotis, C. (**1999**). "The normalized correlation: Accounting for NoS thresholds obtained with Gaussian and 'low-noise' masking noise," J. Acoust. Soc. Am. **106**, 870–876.

Boothroyd, A., and Nittrouer, S. (**1988**). "Mathematical treatment of context effects in phoneme and word recognition," J. Acoust. Soc. Am. **84**, 101–114.

Culling, J. F. (**2000**). "Dichotic pitches as illusions of binaural unmasking. III. The existence region of the Fourcin pitch," J. Acoust. Soc. Am. **107**, 2201–2208.

Culling, J. F., and Colburn, H. S. (**2000**). "Binaural sluggishness in the perception of tone sequences and speech in noise," J. Acoust. Soc. Am. **107**, 517–527.

Culling, J. F., and Summerfield, Q. (**1995**). "Perceptual separation of concurrent speech sounds: Absence of across-frequency grouping by common interaural delay," J. Acoust. Soc. Am. **98**, 785–797.

Culling, J. F., and Summerfield, Q. (**1998**). "Measurements of the binaural temporal window using a detection task," J. Acoust. Soc. Am. **103**, 3540–3553.

Culling, J. F., Colburn, H. S., and Spurchise, M. (**2001**). "Interaural correlation sensitivity," J. Acoust. Soc. Am. **110**, 1020–1029.

de Cheveigné, A. (**1997**). "Concurrent vowel identification III: A neural model of harmonics interference cancellation," J. Acoust. Soc. Am. **101**, 2857–2865.

Durlach, N. I. (**1963**). "Equalization and cancellation theory of binaural masking level differences," J. Acoust. Soc. Am. **35**, 1206–1218.

Kohlrausch, A. (**1988**). "Auditory filter shape derived from binaural unmasking experiments," J. Acoust. Soc. Am. **84**, 573–583.

Kryter, K. (**1962**). "Methods for the calculation and use of the articulation index," J. Acoust. Soc. Am. **34**, 1684–1697.

Levitt, H., and Rabiner, L. R. (**1967a**). "Binaural release of masking for speech and gain in intelligibility," J. Acoust. Soc. Am. **42**, 601–608.

Levitt, H., and Rabiner, L. R. (**1967b**). "Predicting binaural gain in intelligibility and release from masking for speech," J. Acoust. Soc. Am. **42**, 820–828.

Licklider, J. C. R. (**1948**). "The influence of interaural phase relations on the masking of speech by white noise," J. Acoust. Soc. Am. **20**, 150–159.

Moore, B. C. J., and Glasberg, B. R. (**1983**). "Suggested formulae for calculating auditory-filter bandwidths and excitation patterns," J. Acoust. Soc. Am. **74**, 750–753.

Patterson, R. D., Nimmo-Smith, I., Holdsworth, J., and Rice, P. (1987). "An efficient auditory filterbank based on the gammatone function," paper presented to the IOC speech group on auditory modeling at RSRE, 14–15 December.

Patterson, R. D., Nimmo-Smith, I., Holdsworth, J., and Rice, P. (1988). "Spiral VOS final report, Part A: The auditory filter bank," Cambridge Electronic Design, Contract Report (APU 2341).

Plack, C. J. and Moore, B. C. J. (**1990**). "Temporal window shape as a function of frequency and level," J. Acoust. Soc. Am. **87**, 2178–2187.

Schubert, E. D. (**1956**). "Some preliminary experiments on binaural time delay and speech intelligibility," J. Acoust. Soc. Am. **28**, 895–901.
Shannon, R. V., Zeng, F.-G., Kamath, V., Wygonski, J., and Ekied, M. (**1995**). "Speech recognition with primarily temporal cues," Science **270**, 303–304.
van de Par, S., Trahiotis, C., and Bernstein, L. R. (**2001**). "A consideration of the normalization that is typically included in correlation-based models of binaural detection," J. Acoust. Soc. Am. **109**, 830–833.

Perceptual similarity of regional dialects of American English

Cynthia G. Clopper,[a] Susannah V. Levi, and David B. Pisoni
Department of Psychological and Brain Sciences, Indiana University, Bloomington, Indiana 47405

(Received 24 May 2005; revised 31 October 2005; accepted 2 November 2005)

Previous research on the perception of dialect variation has measured the perceptual similarity of talkers based on regional dialect using only indirect methods. In the present study, a paired comparison similarity ratings task was used to obtain direct measures of perceptual similarity. Naive listeners were asked to make explicit judgments about the similarity of a set of talkers based on regional dialect. The talkers represented four regional varieties of American English and both genders. Results revealed an additive effect of gender and dialect on mean similarity ratings and two primary dimensions of perceptual dialect similarity: geography (northern versus southern varieties) and dialect markedness (many versus few characteristic properties). The present findings are consistent with earlier research on the perception of dialect variation, as well as recent speech perception studies which demonstrate the integral role of talker gender in speech perception. [DOI: 10.1121/1.2141171]

PACS number(s): 43.71.Bp [ARB] Pages: 566–574

I. INTRODUCTION

A growing body of research has shown the importance of indexical properties in spoken language processing. Abercrombie (1967) described indexical properties of speech as those aspects of the signal which provide an index about the talker as an individual and as a member of social groups based on gender, ethnicity, and regional background. Research on the perception of the indexical properties of speech has typically involved one of two approaches. The first approach is to explore the interaction between indexical and linguistic properties in speech processing tasks, such as word recognition (Goldinger, 1996; Nygaard *et al.*, 1994) or sentence intelligibility (Nygaard and Pisoni, 1998). The second is to ask naive listeners to make explicit judgments about talkers' identity and social group membership, including judgments of talker similarity based on voice quality, gender, and regional dialect. The current study employed the latter method to directly assess naive listeners' perception of indexical properties of speech.

In one early study of the perception of talker similarity, Walden *et al.* (1978) asked naive listeners to rate the similarity of pairs of male talkers based on single word utterances using a seven-point similarity scale. A multidimensional scaling analysis of the results revealed two primary dimensions of within-gender talker similarity, word duration and F0. More recently, Kreiman and her colleagues (Kreiman *et al.*, 1994) asked trained linguists and speech-language pathologists to listen to pairs of male talkers with voice disorders and rate the relative breathiness and roughness of each pair using seven-point dissimilarity scales. Using multidimensional scaling techniques, they found that breathiness and roughness were the two primary dimensions of similarity for both the breathiness and the roughness ratings, suggesting that these two factors are integral components of judgments of disordered voices. More recently, Remez and his colleagues (Remez *et al.*, 2004) examined the role of dialect mismatch on the perceptual similarity of a set of female talkers. Listeners in Brooklyn, NY, and Bloomington, IN, were asked to rate the similarity of two sets of female talkers. One group of talkers was native to Brooklyn and the other group was native to Bloomington. The authors found that the listeners' region of origin had an effect on the perception of talker similarity. However, they did not observe any strong acoustic correlates of perceptual talker similarity for the two listener groups.

All three of these studies exploring talker similarity used within-gender comparisons. However, gender appears to be a very salient indexical property for naive listeners. Lass *et al.* (1976) reported that gender identification performance based on sustained isolated vowels was very good in normal, whispered, and filtered conditions. Therefore, the limited design of the previous studies may have been warranted to avoid interactions between gender and voice quality in assigning similarity ratings.

Perceptual ratings directly related to gender similarity have also been obtained in several recent studies which explored the acoustic correlates of "masculine-sounding" speech. In one of these studies, Gaudio (1994) asked naive listeners to rate gay and straight male talkers on a seven-point gay-straight scale using a single-interval task. He found that participants were highly accurate in their judgments across several different reading styles. Using a two-interval task, Avery and Liss (1996) asked naive listeners to make relative masculinity judgments with a single talker as the reference throughout the experiment. The authors found that the relative masculinity judgments were correlated with several acoustic properties of the speech samples, including F0. Taken together, these studies suggest that F0 may also play a role in explicit judgments of gender similarity across a set of speakers with a range of gender prototypicality [see also Strand (1999)].

[a]Present address: Department of Linguistics, Northwestern University, Evanston, IL 60208.

Unlike voice quality and gender, however, the perception of dialect similarity has not received much attention in speech perception research. Clopper (2004) indirectly examined dialect similarity using an auditory free classification task. Naive listeners were asked to group unfamiliar talkers by dialect similarity using sentence-length speech samples. The listeners were permitted to make as many groups as they wanted with as many talkers in each group as they wanted. Multidimensional scaling analyses revealed three primary dimensions of similarity that were consistent across two sets of stimulus materials: geography (northern versus southern), markedness (varieties with many distinguishing features versus varieties with few characteristic properties), and gender.

Sociolinguists and dialectologists have also studied dialect similarity, using computational and survey methods. For example, Nerbonne and his colleagues (Nerbonne and Heeringa, 2001; Nerbonne *et al.*, 1996) used string comparison metrics, such as Levenshtein distances, to compute dialect similarity scores for more than 100 Dutch dialects. In Japan, Mase (1999) used a map task to obtain judgments of dialect similarity from naive participants. He showed his participants a map of Japan and asked them to indicate where people spoke the same as them, where they spoke a little differently, where they spoke quite differently, and where they spoke an unintelligibly different variety. In general, his results were comparable to the more traditional dialect boundaries drawn by Japanese dialectologists.

The purpose of the current set of experiments was to explicitly examine perceptual dialect similarity using a two-interval similarity ratings task with a set of talkers from several different regional varieties of American English. Previous research on the perception of dialect variation by Clopper and her colleagues (Clopper, 2004; Clopper *et al.*, 2005a) has shown that naive listeners are able to accurately classify unfamiliar talkers with above chance performance in six-alternative forced-choice categorization tasks.

Experiment 1 was a replication of these earlier studies using a smaller set of talkers with fewer response alternatives. The reduction in response alternatives was motivated by results of our earlier perception research and by production work in sociolinguistics (e.g., Labov, 1998). A clustering analysis of Clopper's (2004) free classification data suggested that naive listeners have four primary perceptual categories for regional varieties of American English: Northeast, North, South, and Midland/West. The Northeast dialect included Mid-Atlantic talkers and r-less New England talkers. New England talkers who were not r-less were perceptually similar to Midland and Western talkers. In our previous work (Clopper, 2004; Clopper *et al.*, 2005a), we interpreted these perceptual similarity findings in terms of the markedness of the different varieties. As noted above, markedness refers to the extent to which a given dialect has unique characteristics that differentiate it from the other dialects of American English. In this sense, Northern, Southern, Mid-Atlantic, and r-less New England varieties are "marked" because they have many features that distinguish them from other dialects. However, Midland, Western, and r-ful New England varieties are considered less marked because they have fewer characteristic properties.

These perceptual results are also consistent with Labov's (1998) division of American English into three broad dialect categories (North, South, and the "Third Dialect"), based on the vowel systems of the different varieties. The "Third Dialect" includes New England, the Midland, and the West; Mid-Atlantic is treated as an exception. Each of the other primary dialects is also composed of subdialects, such as the Inland North in the Northern dialect or the Coastal Southeast in the Southern dialect. In addition, intradialect variation exists between talkers in all regions, such that some talkers are more likely to produce the characteristic properties of their dialect than others. However, the regions defined by Labov (1998) provide a picture of regional variation of the United States painted with a broad stroke that is supported by the perception of dialect variation by naive listeners.

Based on the earlier perception and production research, we selected talkers from the following four broad regional varieties of American English for the current study: Mid-Atlantic, North, South, and "General American."[1] We predicted that naive listeners would perform somewhat better on the four-alternative categorization task than the previous six-alternative tasks because some of the more confusable dialects were eliminated as response alternatives and because chance performance was higher in the new task with fewer alternatives.

Experiment 2 used a direct two-interval dialect similarity ratings task with the same set of talkers as in experiment 1. We expected that naive listeners would assign overall higher similarity ratings to pairs of talkers from the same dialect region than to pairs of talkers from different dialect regions and that the patterns of perceptual similarity would reflect the primary dimensions of dialect similarity reported in the earlier free classification experiment by Clopper (2004), including geography, markedness, and gender.

II. EXPERIMENT 1

A. Methods

1. Listeners

Thirty-seven Indiana University undergraduates participated as listeners in experiment 1. Prior to data analysis, data from nine participants were excluded: two were bilingual, two had one or more parents whose first language was not English, two had a history of a hearing or speech disorder, one did not complete the entire experiment, one was significantly older than the other participants, and one performed statistically at chance across both blocks and all four groups of talkers. The remaining 28 listeners were all 18–25-year-old monolingual native speakers of American English with native English-speaking parents and no history of speech or hearing disorders reported at the time of testing. The residential history of the listeners varied, but the majority ($N=16$) had lived in the Midwest (Midland or North dialect region) for their entire lives. The remainder were either lifetime residents of another region ($N=2$) or had lived in multiple different dialect regions before attending Indiana University in Bloomington ($N=10$). The listeners received partial credit in a psychology course for participating.

2. Talkers

The talkers in experiment 1 were a subset of the talkers included in the Nationwide Speech Project (NSP) corpus (Clopper and Pisoni, unpublished). The NSP corpus includes recordings of five male and five female lifetime residents of six dialect regions in the United States: New England, Mid-Atlantic, North, Midland, South, and West. Thirty-two talkers were selected for the current study. In particular, four males and four females were randomly selected from each of the Mid-Atlantic, Northern, and Southern regions. The remaining four male and four female talkers comprised the set of "General American" talkers and were randomly drawn from the New England, Midland, and Western regions. Thus, the 32 talkers in experiment 1 represented both genders and four dialects of American English: Mid-Atlantic, North, South, and General American.

The Northern dialect is characterized by the Northern Cities Chain Shift (NCCS), which involves the clockwise rotation of the low and low-mid vowels, beginning with the fronting and raising of /æ/. Other aspects of the NCCS include backing of /ɛ/ and /ʌ/, fronting and lowering of /ɔ/, and fronting of /ɑ/ (Clopper *et al.*, 2005b; Labov, 1998). The Southern dialect is characterized by the fronting of the high back vowels /u/, /ʊ/, and /ow/, /ɑy/ and /oy/ monophthongization, and the Southern Vowel Shift (SVS), which includes the peripheralization of the front lax vowels /ɪ/ and /ɛ/, and the centralization of the front tense vowels /i/ and /ey/ (Clopper *et al.*, 2005b; Labov, 1998; Thomas, 2001). The Mid-Atlantic dialect is traditionally characterized by the raising of /ɔ/ (Labov, 1972), but the Mid-Atlantic talkers included in the NSP corpus did not exhibit this particular vowel shift. Instead, they showed evidence of backing /ʌ/ and /ɑ/ and fronting /ɔ/ (Clopper *et al.*, 2005). General American, or "the Third Dialect," is characterized by the merger of the low back vowels /ɑ/ and /ɔ/ (Labov, 1998). Several recent acoustic analyses also suggest that /u/ fronting is spreading to regions beyond the South, including the West and Midland regions (Clopper *et al.*, 2005b; Thomas, 2001). Finally, r-lessness is a prominent property of both New England and coastal Southern dialects, but none of the New England or Southern talkers in the NSP corpus exhibited r-lessness in their speech.

3. Stimulus materials

Two different sentences from each talker were selected for the stimulus materials in experiment 1, for a total of 64 different stimulus items. The sentences were short, meaningful English sentences taken from the Speech Perception in Noise test (Kalikow *et al.*, 1977). All of the sentences were "high probability" sentences, which means that the final word was semantically predictable from the preceding context. The sentences for each talker were selected to include dialect-specific vowel shifts, so that regional variation was present in the stimulus materials. For example, sentences for the Northern talkers frequently contained fronted /æ/ or raised /ɑ/ and sentences for the Southern talkers often contained monophthongal /ɑy/ or fronted /u/. A complete list of the test sentences is included in the Appendix. No sentence was repeated during the course of the experiment.

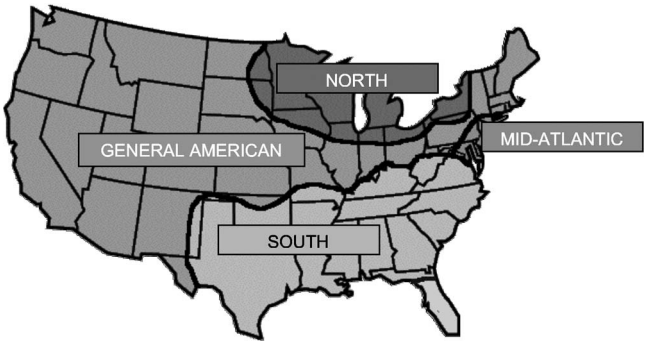

FIG. 1. Response alternatives in the four-alternative forced-choice categorization task. In the colored map that the participants saw, Mid-Atlantic was magenta, North was red, South was orange, and General American was green.

4. Procedure

The listeners were seated in a quiet testing room at personal computers equipped with headphones (Beyerdynamic DT100) and a mouse. On each trial, the listeners heard a single sentence produced by one of the talkers and were asked to identify which region of the United States the talker was from. The regions were presented on a color-coded labeled map of the United States, as shown in Fig. 1. The listeners were permitted to hear each sentence as many times as they wanted before making their response, but they did not receive any feedback about the accuracy of their responses.

The experiment was divided into two blocks. Each block contained one sentence produced by each talker, for a total of 32 trials per block. The sentences were randomly assigned to the first or second block for each listener and the trials were presented in random order within each block. The stimuli were presented over headphones at a comfortable listening level (approximately 70 dB SPL). The listeners made their responses by clicking on the labeled button for the region that they thought each talker was from. The experiment took approximately 15 min to complete.

B. Results

A summary of the listeners' categorization performance in experiment 1 is shown in Fig. 2. In a four-alternative task, chance performance is 25% and a binomial test confirmed that overall performance was statistically above chance ($p < 0.05$). The listeners' performance was above chance for all four talker groups.

A repeated measures ANOVA with talker dialect (Mid-Atlantic, North, South, or General American) and experimental block (first or second) as within-subject factors revealed a significant main effect of talker dialect [$F(3,81) = 11.3$, $p < 0.001$]. *Post hoc* paired comparison t tests revealed that performance on the General American talkers was significantly better than performance on the Mid-

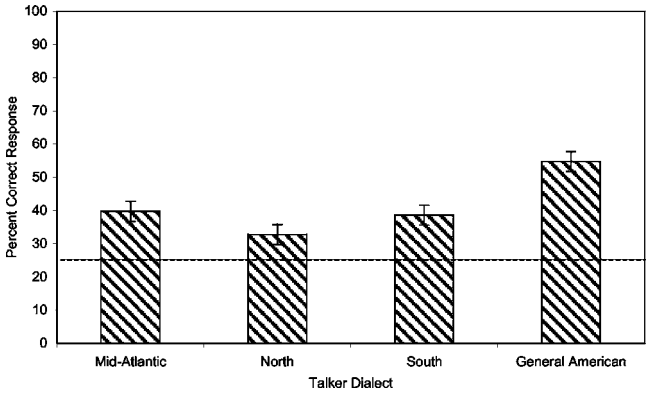

FIG. 2. Percent correct responses in the four-alternative forced-choice categorization task for each of the four talker dialect groups, collapsed across experimental block. Error bars indicate standard error. Chance performance (25%) is indicated by the dashed line.

Atlantic, Northern, and Southern talkers (all $p<0.001$). Performance on the Mid-Atlantic talkers was significantly better than performance on the Northern talkers ($p=0.03$). Performance on the Southern talkers did not differ significantly from performance on either the Mid-Atlantic or the Northern talkers. The main effect of experimental block and the dialect $\times$ block interaction were not significant.

To assess the effects of talker gender on performance, a paired sample t test was conducted on the mean accuracy scores for male and female talkers, collapsed across talker dialect and experimental block. The male and female talkers were categorized with 40% and 43% accuracy, respectively. This difference was not significant [$t(27)=1.08$, n.s.]. Thus, talker gender did not affect dialect categorization performance.

As expected, overall raw percent correct scores were higher on this task than on the earlier six-alternative forced-choice task using stimulus materials from the same speech corpus (Clopper, 2004). Performance cannot be compared directly using percent correct scores, however, because the different number of response alternatives in the two tasks altered the level of chance performance (17% in the six-alternative task versus 25% in the four-alternative task). In order to compare the previous results to those obtained in the current experiment, the data from each listener were converted into a relative information transmitted score (Miller, 1953; Miller and Nicely, 1955), using the equation in (1), where p_i is the probability of stimulus category i, p_j is the probability of response alternative j, and p_{ij} is the probability of response j given stimulus i. These information transmitted scores provide another index of performance accuracy, beyond raw percent correct, which normalizes the data for the number of response alternatives and the participants' response biases:

$$T(\mathrm{x},\mathrm{y}) = \frac{-\sum p_{ij} \log_2 (p_i p_j / p_{ij})}{-\sum p_i \log_2 (p_i)}. \quad (1)$$

Information transmitted scores were also calculated from the earlier six-alternative data. The mean information transmitted scores were 14% (SD=7%) and 15% (SD=6%) in the current four-alternative categorization experiment and the earlier six-alternative task, respectively. An independent samples t test revealed no significant difference across the two tasks in terms of relative information transmitted [$t(125)=-0.77$, n.s.].

C. Discussion

Overall performance in the four-alternative forced-choice dialect categorization task was approximately 42% correct, which is significantly above chance performance (25%). While this overall level of accuracy is higher than that reported in the previous studies of dialect categorization using six alternatives (e.g., Clopper, 2004; Clopper *et al.*, 2005a), the information transmitted analysis revealed that performance across the two tasks was comparable when the different levels of chance performance were accounted for. Thus, explicit dialect categorization is a difficult task for naive listeners, regardless of whether they are presented with four or six response alternatives.

The finding that naive listeners were able to perform above chance on these tasks, however, suggests that they were able to reliably classify talkers from different regions of the United States. We would therefore also expect them to be able to make consistent similarity judgments between pairs of talkers in a paired comparison similarity ratings task. Experiment 2 was designed to obtain explicit direct judgments of regional dialect similarity for all possible pairwise comparisons of the set of 32 talkers used in experiment 1.

III. EXPERIMENT 2

A. Methods

1. Listeners

One hundred and seven Indiana University undergraduates participated as listeners in experiment 2. Prior to data analysis, data from 14 listeners were removed. Seven participants knew one or more of the talkers by name, two did not finish the experiment, two did not meet our residential history requirements, one reported a history of a hearing or speech disorder, one had one or more parents whose first language was not English, and one had previously participated in a related experiment during the same semester. The remaining 93 listeners were all 18–25-year-old monolingual native speakers of American English with no history of hearing or speech disorders reported at the time of testing. In addition, both parents of each listener were also native speakers of English. The listeners each received $15 for participating.

The listeners were assigned to four different groups, based on their residential history. Twenty-four of the listeners, who had lived only in the Midland dialect region, were assigned to the Non-Mobile Midland group. Similarly, 24 listeners who had lived only in the Northern dialect region prior to attending school in Bloomington, IN, were assigned to the Non-Mobile North group. The remaining 45 listeners had lived in more than one dialect region prior to attending Indiana University. Of these 45 Mobile listeners, the 21 whose parents lived in the Northern dialect region at the time

of testing were assigned to the Mobile North group and the 24 whose parents lived in the Midland dialect region at the time of testing were assigned to the Mobile Midland group.

2. Talkers

The same 32 talkers were used in experiment 2 as in experiment 1.

3. Stimulus materials

The same 64 stimulus items were used in experiment 2 as in experiment 1.

4. Procedure

The listeners were seated in a quiet testing room in front of personal computers equipped with headphones (Beyerdynamic DT100) and a mouse. On each trial, the listeners heard two sentences produced by two different talkers separated by 500 ms of silence. They were then asked to indicate how likely it was that the two talkers came from the same part of the United States using a scale from 1 ("Not at all likely") to 7 ("Very likely"). The listeners were asked to make a direct and explicit dialect similarity judgment, with higher numbers reflecting greater dialect similarity than lower numbers. The listeners did not receive any feedback about their responses.

One sentence from each talker was randomly selected and assigned to List A. The remaining sentence from each talker was assigned to List B (see the Appendix). Each listener heard the stimulus items from either List A or List B, so that there was a perfect one-to-one relationship between sentence content and talker throughout the experiment for each listener. Half of the listeners in each listener group heard the List A sentences and half of the listeners in each listener group heard the List B sentences.

Each listener heard all 32 talkers paired with each of the other talkers one time, for a total of 496 trials. Of the 496 trials, 112 included two talkers from the same dialect region ("same-dialect" trials) and the remaining 384 trials included two talkers from different dialect regions ("different-dialect" trials). In addition, 240 trials included two talkers with the same gender ("same-gender" trials) and the remaining 256 trials included one male and one female talker ("different-gender" trials). The order of presentation of the talkers within each pair was determined randomly, as was the order of presentation of the trials. The experiment was divided into eight blocks, with a short break provided after every 62 trials. Experiment 2 took approximately 75 min to complete.

B. Results

Figure 3 shows the mean similarity ratings for same-dialect and different-dialect pairs for each of the four listener groups. Performance across the four listener groups was highly consistent and all four groups showed overall higher similarity ratings for same-dialect pairs than different-dialect pairs. An initial inspection of the data revealed that all but three (3%) of the listeners used the entire seven-point scale in making their judgments and that the responses were approximately normally distributed between 1 and 7. Therefore, no normalization was necessary and the analyses were conducted on the raw perceptual ratings scores.

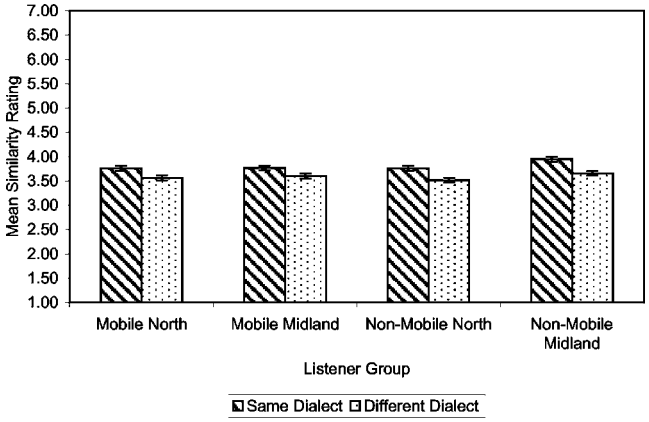

FIG. 3. Mean similarity ratings for same-dialect and different-dialect trials for each of the four listener groups, collapsed across experimental block and stimulus list. Error bars indicate standard error.

A repeated measures ANOVA with dialect (same-dialect versus different-dialect) and block (first through eighth) as within-subject factors and stimulus list (List A versus List B) and listener group (Mobile North, Mobile Midland, Non-Mobile North, or Non-Mobile Midland) as between-subject factors revealed a significant main effect of dialect $[F(1,595)=41.6,\ p<0.001]$. The same-dialect pairs were rated higher than the different-dialect pairs. *Post hoc* paired comparison *t* tests revealed that this effect was highly significant for all four listener groups (all $p<0.001$). The main effect of block was also significant $[F(7,595)=2.7,\ p=0.009]$, but *post hoc* Tukey tests did not reveal any significant pairwise comparisons. The main effects of stimulus list and listener group were not significant.

Two of the interactions were also significant. First, the dialect × stimulus list interaction was significant $[F(1,595)=17.4,\ p<0.001]$. While the overall ratings did not differ between List A and List B, *post hoc t* tests revealed that different-dialect pairs were rated more similar for List A than List B stimuli (List A $M=3.75$, SD=0.50; List B $M=3.42$, SD=0.59; $p<0.001$). Ratings for same-dialect pairs for List A and List B were not significantly different (List A $M=3.83$, SD=0.59; List B $M=3.79$, SD=0.73; n.s.). The second significant interaction was the block × stimulus list interaction $[F(7,595)=3.7,\ p=0.001]$. Once again, while the overall ratings did not differ across the two stimulus lists, *post hoc t* tests revealed that overall ratings were higher for List A than List B in blocks 3–7 (all $p<0.02$). Ratings did not differ across the two lists for blocks 1, 2, and 8. Taken together these two interactions suggest that the sentences included in List A may have been more difficult to discriminate based on dialect, although the primary findings are robust across both stimulus sets. None of the other two- or three-way interactions were significant.

A repeated measures ANOVA with gender (same-gender versus different-gender) and dialect (same-dialect versus different-dialect) as within-subject factors was conducted to

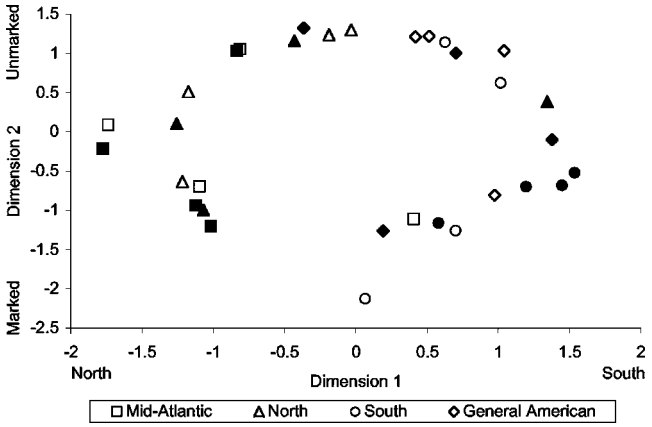

FIG. 4. Multidimensional scaling solution. Filled symbols represent male talkers and open symbols represent female talkers.

assess the effects of talker gender in the similarity ratings task. The repeated measures ANOVA revealed significant main effects of gender [$F(1,92)=39.7$, $p<0.001$] and dialect [$F(1,92)=23.0$, $p<0.001$]. As in the previous analysis, same-dialect pairs were rated significantly higher than different-dialect pairs. In addition, same-gender pairs were rated significantly higher than different-gender pairs. The gender $\times$ dialect interaction was not significant.

To examine the similarity ratings in more detail and obtain measures of the underlying similarity space, a multidimensional scaling analysis was conducted. For each listener, a 32×32 talker similarity matrix was constructed by assigning the similarity rating assigned to each talker pair to one cell of the matrix. The 93 talker similarity matrices were then submitted to an INDSCAL analysis to explore the role of individual listener differences in the perceptual similarity of the talkers. Two-, three-, and four-dimensional solutions were obtained using INDSCAL with mean stress values of 0.37, 0.28, and 0.23, respectively. While these results suggest an "elbow" at the three-dimensional solution, the two-dimensional solution was selected for interpretation and discussion for two reasons. First, the two-dimensional solution was highly interpretable and the addition of the third dimension did not contribute meaningfully to the analysis. Second, the two-dimensional model required fewer free parameters and was therefore preferable as a more parsimonious analysis, despite its lower overall level of fit to the data.

The two dimensions of the multidimensional scaling solution are plotted in Fig. 4. Each symbol represents a different talker. The shapes represent the four different dialect groups (squares for Mid-Atlantic, triangles for North, circles for South, and diamonds for General American). Male talkers are indicated by the filled symbols and female talkers are represented by the open symbols. Dimension 1 separates the Northern and Mid-Atlantic talkers on the left and the Southern and General American talkers on the right. The first dimension can therefore be interpreted as distinguishing the North from the South (or non-North). The second dimension separates the Mid-Atlantic and Southern talkers at the bottom from the Northern and General American talkers on the top, which can be interpreted in terms of dialect markedness.[2] Marked dialects contain many characteristic properties that distinguish them from other dialects, whereas unmarked dialects contain fewer characteristic features. In Fig. 4, the perceptually marked dialects are at the bottom (Mid-Atlantic and Southern) and the perceptually less-marked dialects are at the top (Northern and General American). Thus, the two underlying dimensions extracted from the INDSCAL analysis can be described in terms of geography (north versus south) and markedness (marked versus unmarked).

TABLE I. Mean normalized subject weights from the INDSCAL analysis for each of the four listener groups and each of the two stimulus lists for each of the two dimensions.

	Dimension 1 geography	Dimension 2 markedness
Mobile North	0.50	0.50
Mobile Midland	0.49	0.51
Non-Mobile North	0.51	0.49
Non-Mobile Midland	0.51	0.49
List A	0.48	0.52
List B	0.53	0.47

The INDSCAL analysis also returned dimension weights for each of the 93 listeners. The mean normalized weights for each listener group and each stimulus list are shown in Table I. Two-way ANOVAs on the normalized subject weights for each dimension with listener group (Mobile North, Mobile Midland, Non-Mobile North, or Non-Mobile Midland) and stimulus list (List A versus List B) as the factors revealed a significant main effect of stimulus list for both dimensions [$F(1,92)=14.9$, $p<0.001$ for dimension 1 and $F(1,92)=14.9$, $p<0.001$ for dimension 2]. The listeners who heard stimulus materials from List B attended more to the first dimension than the listeners who heard stimulus materials from List A. The participants who heard List A, however, attended more to the second dimension than the participants who heard List B. Thus, the stimulus list interactions reported above may reflect different strategies employed by the listeners in the two groups. Linguistic markedness was more salient for the listeners who were responding to List A stimulus materials, whereas geography was more salient for the listeners who were responding to List B stimulus materials.

The main effect of listener group was not significant. However, an inspection of the mean normalized subject weights suggests that the Mobile listeners tended to weight both dimensions equally, whereas the Non-Mobile listeners attended more to the geographic dimension (dimension 1) than the markedness dimension (dimension 2). The Non-Mobile listeners attended to the geographic dimension more than the Mobile listeners and to the markedness dimension less than the Mobile listeners, although neither of these differences were significant by independent sample t tests. In general, the dimension weights were highly consistent across the listener groups, with more attention paid to geography than markedness.

C. Discussion

The results of the paired comparison similarity ratings task demonstrate that naive listeners' direct judgments about the perceptual similarity of the dialect of two talkers reflect the regional background of the talkers. The initial analysis of the mean ratings revealed that the listeners consistently rated pairs of talkers from the same dialect region as more similar than pairs of talkers from different regions. This finding was consistent across all four listener groups, all eight blocks of trials, and both sets of stimulus materials. It is important to emphasize here that the paired comparison task was designed such that all of the similarity judgments were made across two different sentences, which means that the listeners were required to judge dialect similarity in the absence of identical linguistic content.

Talker gender was also found to be an important component in the similarity judgments, however. In particular, same-gender pairs were consistently rated as more similar than different-gender pairs, regardless of whether they were same-dialect or different-dialect pairs. This result is a classic "additive" effect, which suggests that gender and dialect are independent factors that contribute to the judgment of dialect similarity (Sternberg, 1998). Unlike the earlier free classification study (Clopper, 2004), in which gender emerged as one of the primary dimensions of perceptual similarity in the multidimensional scaling analysis, gender was not an important dimension in the INDSCAL analysis of the similarity ratings data. Given that the listeners were not given any specific instructions regarding the role of gender in determining dialect similarity, however, the gender effect on the overall mean similarity ratings suggests that naive listeners are unable to selectively ignore talker gender when making judgments about regional dialect (see also Mullennix and Pisoni, 1990).

The multidimensional scaling analysis uncovered two dimensions of perceptual dialect similarity: geography (north versus south) and markedness. These perceptual dimensions create a space in which the Southern talkers are located in the Marked Southern quadrant (bottom right in Fig. 4), the General American talkers are located in the Unmarked Southern/Non-Northern quadrant (top right in Fig. 4), the Northern talkers are located in the Unmarked Northern quadrant (top left in Fig. 4), and the Mid-Atlantic talkers are located in the Marked Northern quadrant (bottom left in Fig. 4). Although descriptively the Northern dialect is linguistically marked due to the Northern Cities Chain Shift, the perception of the NCCS by Midwestern listeners is more variable. Some listeners, particularly in the Northern dialect region, do not appear to perceive the shifted Northern vowels as distinct from the unmarked vowels produced by Midland talkers (Clopper, 2004; Niedzielski, 1999). The result of this variation in perception is that the Northern talkers appear primarily in the Unmarked Northern quadrant of the space. The two dimensions revealed by the multidimensional scaling analysis are also consistent with the recent findings obtained using a free classification task (Clopper, 2004). These studies provide converging evidence for two primary dimensions of perceptual dialect similarity: geography and markedness.

IV. GENERAL DISCUSSION

The results of experiments 1 and 2 confirm that naive listeners can make explicit judgments about both the identity and the similarity of regional varieties of American English. Overall performance in the four-alternative forced-choice categorization experiment was approximately 42%, which is statistically above chance. In the paired comparison similarity ratings task, the listeners assigned higher similarity ratings to pairs of talkers from the same dialect region than to pairs from different dialect regions. The results of the multidimensional scaling analysis on the similarity ratings were interpretable in terms of the observed linguistic attributes of the four dialects. The two dimensions served to divide the similarity space into four quadrants that approximately corresponded to the four dialects.

An examination of the response biases in the four-alternative forced-choice task in experiment 1 revealed a positive bias for General American responses, but no strong negative biases for the remaining three response alternatives. In our earlier study (Clopper, 2004), we found a positive response bias for the Midland, but negative response biases for New England and West. We argued that the listeners' lack of personal experience with New England and Western talkers led to these negative response biases, whereas familiarity with Midland speech and the location of the listeners in the Midland dialect region at the time of the experiment contributed to a positive response bias (Clopper, 2004). The positive response bias for General American in the current experiment can be attributed to similar factors. In addition, the listeners may have chosen this category more often simply because it covered a larger geographic area than the other categories. Regardless of the factors involved, however, while Midland in the six-alternative task and General American in the four-alternative task were treated as defaults and thus were selected as a response more often than the other response alternatives, negative response biases for less familiar dialects such as New England and West were eliminated in the four-alternative task. Further research is needed with listeners from other geographic areas to determine how the listener's region of origin affects the perception of subvarieties of General American English.

The emergence of gender as a statistically significant factor in the overall perceptual ratings merits discussion. Listeners were not given any explicit instructions about the role that talker gender should play in their similarity judgments. However, gender was found to interact with dialect in an additive manner, so that ratings on same-gender pairs were consistently higher overall than ratings on different-gender pairs, regardless of the dialects of the two talkers. The finding that gender interacts with dialect perception is not too surprising, however. First, gender and dialect are known to interact in speech production. For example, women tend to be more advanced in adopting vowel shifts such as the Northern Cities Chain Shift (e.g., Eckert, 1989). We there-

fore might expect listeners to be aware of those within-dialect gender differences and that their responses might reflect that awareness. Second, gender has repeatedly been shown to interact with the perception of the linguistic properties of speech. For example, Strand (1999) found that both talker gender and gender prototypicality affected the perception of /s/ and /ʃ/. And, Mullennix and Pisoni (1990) found indirect evidence of the effects of talker gender on speech perception in a Garner speeded classification task. They reported that variation in talker gender interfered with listeners' performance in a phoneme classification task and led to slower response times than when talker gender was held constant across trials. Taken together, these studies all suggest that talker gender is very difficult to selectively ignore when listeners are asked to make explicit judgments about other aspects of the speech signal.

V. CONCLUSIONS

The results of the current study demonstrate that naive listeners can make explicit judgments about the similarity of pairs of talkers based on regional dialect. These findings are consistent with previous research on the perception of indexical properties of speech which has consistently found that both experienced and naive listeners can make explicit judgments about properties of unfamiliar talker's voices, including voice quality (Kreiman *et al.*, 1994; Remez *et al.*, 2004; Walden *et al.*, 1978), gender (Lass *et al.*, 1976), and sexual orientation (Avery and Liss, 1996; Gaudio, 1994), and suggest that social group properties such as regional, ethnic, and social dialect are also integral components of speech perception and spoken language processing. Dialect variation is a significant source of variability in speech and naive listeners can make explicit judgments about this source of variation in the speech of unfamiliar talkers.

ACKNOWLEDGMENTS

This work was supported by NIH NIDCD T32 Training Grant No. DC00012 and NIH NIDCD R01 Research Grant No. DC00111 to Indiana University.

APPENDIX: STIMULUS MATERIALS

Key: Mid-Atlantic (AT), North (NO), South (SO), Midland (MI), New England (NE), West (WE), General American (GA).

Talker	List A	List B
AT1	He rode off in a cloud of dust.	Ruth poured herself a cup of tea.
AT2	The car drove off the steep cliff.	Ruth had a necklace of glass beads.
AT3	Paul hit the water with a splash.	My son has a dog for a pet.
AT5	The cow gave birth to a calf.	Banks keep their money in a vault.
AT6	The glass had a chip on the rim.	I ate a piece of chocolate fudge.
AT7	The heavy rains caused a flood.	Cut the meat into small chunks.
AT9	Throw out all this useless junk.	Watermelons have lots of seeds.
A18	Kill the bugs with this spray.	Please wipe your feet on the mat.
NO0	Tighten the belt by a notch.	That job was an easy task.
NO2	The cabin was made of logs.	They tracked the lion to his den.
NO3	Peter dropped in for a brief chat.	Wash the floor with a mop.
NO4	The cut on his knee formed a scab.	Raise the flag up the pole.
NO5	The shepherd watched his flock of sheep.	The story had a clever plot.
NO6	The swimmer's leg got a bad cramp.	Paul took a bath in the tub.
NO8	The flashlight casts a bright beam.	The mouse was caught in the trap.
NO9	Bob was cut by the jackknife's blade.	Paul was arrested by the cops.
SO1	A bicycle has two wheels.	The landlord raised the rent.
S10	We swam at the beach at high tide.	The guests were welcomed by the host.
SO2	My jaw aches when I chew gum.	The sick child swallowed the pill.
S22	Spread some butter on your bread.	Playing checkers can be fun.
SO5	Get the bread and cut me a slice.	The scarf was made of shiny silk.
SO6	The judge is sitting on the bench.	We camped out in our tent.
SO7	Greet the heroes with loud cheers.	The bride wore a white gown.
SO8	For dessert he had apple pie.	She cooked him a hearty meal.
M12 (GA)	The lion gave an angry roar.	The chicken pecked corn with its beak.
MI3 (GA)	He was scared out of his wits.	The detectives searched for a clue.
MI8 (GA)	He's employed by a large firm.	The bloodhound followed the trail.
NE1 (GA)	The shepherds guarded their flock.	A spoiled child is a brat.
NE7 (GA)	The doctor prescribed the drug.	To open the jar, twist the lid.
NE8 (GA)	Unlock the door and turn the knob.	Keep your broken arm in a sling.
WE2 (GA)	She shortened the hem of her skirt.	Our seats were in the second row.
WE8 (GA)	The witness took a solemn oath.	The super highway has six lanes.

[1]We have chosen to refer to this fourth dialect as "General American" for several reasons. First, in experiment 1, we needed to provide a label to our listeners for this region and "General American" was both nontechnical and intuitive for our listeners. Second, while we recognize that this term can imply a national norm or standard, we have not encountered an alternative that avoids this problem while maintaining descriptive adequacy. Thus, in this paper, "General American" is defined as the combination of r-less New England, Midland, and Western varieties and is comparable to Labov's (1998) "Third Dialect." It is not intended to carry any prestige, standard, or normative value.

[2]This dimension could also be interpreted as an East versus West dimension with the Southern and Mid-Atlantic dialects in the East and the Northern and General American dialects in the West. However, this interpretation seems to suggest that the Southern dialect is limited to the eastern United States when, in fact, it extends all the way across the southern part of the country into Texas. In addition, our interpretation of this dimension in terms of markedness is more consistent with our previous research on the perceptual similarity of dialect variation (e.g., Clopper, 2004).

Abercrombie, D. (**1967**). *Elements of General Phonetics* (Aldine, Chicago).

Avery, J. D., and Liss, J. M. (**1996**). "Acoustic characteristics of less-masculine-sounding speech," J. Acoust. Soc. Am. **99**, 3738–3748.

Clopper, C. G. (2004). "Linguistic experience and the perceptual classification of dialect variation," Indiana University Ph.D. dissertation.

Clopper, C. G., and Pisoni, D. B., "The Nationwide Speech Project: A new corpus of American English dialects," Speech Commun. (unpublished).

Clopper, C. G., Conrey, B. L., and Pisoni, D. B. (**2005a**). "Effects of talker gender on dialect categorization," J. Lang. Soc. Psychol. **24**, 182–206.

Clopper, C. G., Pisoni, D. B., and de Jong, K. (**2005b**). "Acoustic characteristics of the vowel systems of six regional varieties of American English," J. Acoust. Soc. Am. **118**, 1661–1676.

Eckert, P. (**1989**). "The whole woman: Sex and gender differences in variation," Lang. Var. Change **1**, 245–267.

Gaudio, R. P. (**1994**). "Sounding gay: Pitch properties in the speech of gay and straight men," Am. Speech **69**, 30–57.

Goldinger, S. D. (**1996**). "Words and voices: Episodic traces in spoken word identification and recognition memory," J. Exp. Psychol. Learn. Mem. Cogn. **22**, 1166–1183.

Kalikow, D. N., Stevens, K. N., and Elliott, L. L. (**1977**). "Development of a test of speech intelligibility in noise using sentence materials with controlled word predictability," J. Acoust. Soc. Am. **61**, 1337–1351.

Kreiman, J., Gerratt, B. R., and Berke, G. S. (**1994**). "The multidimensional nature of pathologic vocal quality," J. Acoust. Soc. Am. **96**, 1291–1302.

Labov, W. (**1972**). *Sociolinguistic Patterns* (Univ. of Pennsylvania, Philadelphia).

Labov, W. (**1998**). "The three dialects of English," in *Handbook of Dialects and Language Variation*, edited by M. D Linn (Academic, San Diego), pp. 39–81.

Lass, N. J., Hughes, K. R., Bowyer, M. D., Waters, L. T., and Bourne, V. T. (**1976**). "Speaker sex identification from voiced, whispered, and filtered isolated vowels," J. Acoust. Soc. Am. **59**, 675–678.

Mase, Y. (**1999**). "Dialect consciousness and dialect divisions: Examples in the Nagano-Gifu boundary region," in *Handbook of Perceptual Dialectology*, edited by D. R. Preston (John Benjamins, Amsterdam), pp. 71–99.

Miller, G. A. (**1953**). "What is information measurement?" Am. Psychol. **8**, 3–11.

Miller, G. A., and Nicely, P. E. (**1955**). "An analysis of perceptual confusions among some English consonants," J. Acoust. Soc. Am. **27**, 338–352.

Mullennix, J. W., and Pisoni, D. B. (**1990**). "Stimulus variability and processing dependencies in speech perception," Percept. Psychophys. **47**, 379–390.

Nerbonne, J., and Heeringa, W. (**2001**). "Computational comparison and classification of dialects," Dialectol. Geolinguist. **9**, 69–83.

Nerbonne, J., Heeringa, W., van den Hout, E., van der Kooi, P., Otten, S., and van de Vis, W. (**1996**). "Phonetic distance between Dutch dialects," in *Papers from the 6th CLIN Meeting*, edited by G. Durieuz, W. Daelemans, and S. Gillis (Univ. of Antwerp, Center for Dutch Language and Speech, Antwerp), pp. 185–202.

Niedzielski, N. (**1999**). "The effect of social information on the perception of sociolinguistic variables," J. Lang. Soc. Psychol. **18**, 62–85.

Nygaard, L. C., and Pisoni, D. B. (**1998**). "Talker-specific learning in speech perception," Percept. Psychophys. **60**, 355–376.

Nygaard, L. C., Sommers, M. S., and Pisoni, D. B. (**1994**). "Speech perception as a talker-contingent process," Psychol. Sci. **5**, 42–46.

Remez, R. E., Wissig, S. C., Ferro, D. F., Liberman, K., and Landau, C. (**2004**). "A search for listener differences in the perception of talker identity," J. Acoust. Soc. Am. **116**, 2544.

Sternberg, S. (**1998**). "Discovering mental processing stages: The method of additive factors," in *An Invitation to Cognitive Science: Methods, Models, and Conceptual Issues*, edited by D. Scarborough and S. Sternberg (MIT, Cambridge, MA), pp. 703–864.

Strand, E. A. (**1999**). "Uncovering the role of gender stereotypes in speech perception," J. Lang. Soc. Psychol. **18**, 86–100.

Thomas, E. R. (**2001**). *An Acoustic Analysis of Vowel Variation in New World English* (Duke U. P., Durham, NC).

Walden, B. E., Montgomery, A. A., Gibeily, G. J., Prosek, R. A., and Schwartz, D. M. (**1978**). "Correlates of psychological dimensions in talker similarity," J. Speech Hear. Res. **21**, 265–275.

Differentiation of speech and nonspeech processing within primary auditory cortex[a)]

D. H. Whalen[b)]
Haskins Laboratories, 300 George Street, New Haven, Connecticut 06511

Randall R. Benson
Department of Neurology-UHC 8D, Wayne State University, 4201 St. Antoine, Detroit, Michigan 48201

Matthew Richardson
Haskins Laboratories, 300 George Street, New Haven, Connecticut 06511

Brook Swainson
Haskins Laboratories, 300 George Street, New Haven, Connecticut 06511, and Department of Psychology, University of Connecticut, Storrs, Connecticut 06269

Vincent P. Clark
Department of Psychology, Logan Hall, 1 University of New Mexico, MSC03 2220, Albuquerque, New Mexico 87131-1161

Song Lai
Department of Radiology, Thomas Jefferson University, COB Room 140R, 909 Walnut Street, Philadelphia, Pennsylvania 19107

W. Einar Mencl
Haskins Laboratories, 300 George Street, New Haven, Connecticut 06511

Robert K. Fulbright and R. Todd Constable
Department of Diagnostic Radiology, Yale University School of Medicine, 333 Cedar Street, Fitkin-B, New Haven, Connecticut 06510

Alvin M. Liberman[c)]
Haskins Laboratories, 300 George Street, New Haven, Connecticut 06511

(Received 19 November 2004; revised 23 October 2005; accepted 25 October 2005)

Primary auditory cortex (PAC), located in Heschl's gyrus (HG), is the earliest cortical level at which sounds are processed. Standard theories of speech perception assume that signal components are given a representation in PAC which are then matched to speech templates in auditory association cortex. An alternative holds that speech activates a specialized system in cortex that does not use the primitives of PAC. Functional magnetic resonance imaging revealed different brain activation patterns in listening to speech and nonspeech sounds across different levels of complexity. Sensitivity to speech was observed in association cortex, as expected. Further, activation in HG increased with increasing levels of complexity with added fundamentals for both nonspeech and speech stimuli, but only for nonspeech when separate sources (release bursts/fricative noises or their nonspeech analogs) were added. These results are consistent with the existence of a specialized speech system which bypasses more typical processes at the earliest cortical level. © *2006 Acoustical Society of America.* [DOI: 10.1121/1.2139627]

PACS number(s): 43.71.An, 43.71.Es [ALF] Pages: 575–581

I. INTRODUCTION

Is there a specialization for phonetic perception, separate from ordinary audition? Although it is clear that all acoustic signals are processed by the ear and brainstem nuclei, the neural processing occurring at higher levels of the brain has been the subject of theoretical debate. Most researchers assume an "acoustic theory" in which there is an acoustic analysis of the speech signal which is not differentiated for speech until the auditory signal is matched to speech templates in auditory association cortex (Darwin, 1984; Diehl and Kluender, 1989; Bregman, 1990; Stevens, 1998). An alternative "speech specific" theory holds that the speech signal is processed as speech from the earliest stage in cortical processing, with the acoustic signal being interpreted in relation to its possible origin as gestures of the vocal tract

[a)]Portions of this work were presented at the annual meeting of the Linguistic Society of America, January, 2000, Chicago, Illinois, and January 2003, Atlanta, Georgia and the Cognitive Neuroscience Society meeting, March, 2003, New York City.

[b)]Author to whom correspondence should be addressed. Electronic mail: whalen@haskins.yale.edu

[c)]Deceased.

rather than as acoustic signals *per se* (Liberman and Mattingly, 1985; 1989; Browman and Goldstein, 1992; Fowler, 1994). The present experiments looked for neurological evidence to distinguish the two positions.

Neurological evidence may distinguish the two theories because auditory theories state explicitly that the acoustic signal receives a complete auditory description before being considered for interpretation as speech. The sounds of speech are not immediately separated from those of other sounds (Darwin and Culling, 1990), and thus auditory theories hold that sounds are separated first into various acoustic categories and assigned to sources (Bregman, 1990). According to Patterson *et al.*, "Sounds in the natural world fall broadly into three categories: **transients, tones and noises**.… the auditory system constructs internal ***auditory images*** of sounds, and the images of transients, tones and noises exhibit large, characteristic differences. Humans produce all three categories of sounds when they speak…" (Patterson *et al.*, 2000, p. 155). Similarly, Diehl and Kluender conclude that "listeners perceive speech *sounds* (i.e., acoustic/auditory events) rather than articulatory events as such" (Diehl and Kluender, 1989, p. 140). The primitives of speech are typically assumed to be those properties that are represented in the mammalian auditory system (Kuhl and Miller, 1978; Kluender and Lotto, 1994).

Behavioral evidence indicates that speech perception is not dependent on auditory primitives of this sort, however. One of the earliest observations was that the transitions for [d] in [di] versus [du] in a synthetic rendition go in opposite directions but are heard as the same sound (Liberman *et al.*, 1967). Nonspeech equivalents of those transitions are heard as distinct rising or falling patterns. In addition, the rate at which the phonemes of speech occur is far higher than that at which acoustic events can be segregated and sequenced (Liberman and Mattingly, 1985). And, the various acoustically defined segments of speech violate most of the "laws" of perceptual grouping and yet are grouped nonetheless (Remez *et al.*, 1994). A theoretical explanation is that speech constitutes a perceptual module whose output is quite distinct from its input, much as sound localization transforms time and intensity differences into locations on the azimuth (Liberman and Whalen, 2000). The present experiments adds direct imaging of the speech perception process to the behavioral evidence.

Inputs from subcortical auditory structures synapse largely in transverse temporal gyrus (TTG), also known as Heschl's gyrus (HG), about two-thirds of which constitutes the primary auditory cortex (PAC) (Shepherd, 1994; Rademacher *et al.*, 2001). There is disagreement about the anatomic extent of PAC, but its location within TTG is well established. PAC is weakly tonotopic (Wessinger *et al.*, 1997; Talavage *et al.*, 2004) but is, in acoustic theories, the site of preliminary acoustic analysis. Speech-specific theories assume that this stage is unnecessary—indeed, actively counterproductive—for speech and so would be superseded. It has recently become possible to look for patterns of activation in normal, functioning brains with positron emission tomography (PET) or functional magnetic resonance imaging (fMRI), and various studies have discovered areas that are primarily sensitive to speech (Demonet *et al.*, 1992; Zatorre *et al.*, 1992; Fiez *et al.*, 1995; Binder *et al.*, 1996; 1997; Belin *et al.*, 2000). However, such findings do not distinguish the two theories, since the associative area would presumably be active in the matching of acoustics to stored representations of speech categories in either theory. Differences in acoustic complexity in the present stimuli, if they turn out to correlate with increases in activation, could allow us to dissociate the two theories: More complex acoustic signals should, on acoustic theories, require more activation of PAC than simple signals, regardless of their status as speech. Speech-specific theories predict that only nonspeech will elicit such a correlation.

Such a result was found in our earlier work (Benson *et al.*, 2001). There, we contrasted two complexity dimensions, one for speech and one for nonspeech. The stimuli were nonsense syllables [isolated vowels (V), consonant-vowel syllables (CVs) or CVCs] for the speech, and piano notes, chords, and chord progressions for the nonspeech (see Fig. 1). In a passive listening task, activation was found to increase along with complexity in a variety of brain regions. Most important for the current discussion are those correlations in HG (and likely PAC) and posterior STG. Activation for each voxel for each listener was correlated with the complexity dimension. Thus, the degree of correlation was independent of the overall level of activation, allowing us to see correlations in different regions even if the region might have been below the cutoff level of the more global analysis.

We found that activation for nonspeech correlated positively with complexity across HG and thus most or all of PAC, but there was virtually no correlation in HG for the speech complexity dimension. Speech complexity correlated strongly with activation in posterior STG, while nonspeech complexity correlated in anterior STG. The magnitude of acoustic complexity differences manifested in the speech and nonspeech dimensions is unlikely to be exactly the same (if indeed there is a scale on which the difference can even be captured). However, the simplest stimuli were similar (largely steady-state, harmonically structured patterns for both vowels and notes), while the high end was, if anything, more different for speech, given the noises and bursts in the CVs and CVCs. Thus, the number of acoustically different components was higher for the speech, and yet the nonspeech stimuli were the ones that increasingly engaged PAC.

The complexity dimensions in our previous study were matched fairly well spectrally but contained one major difference: The nonspeech dimension added more fundamental frequencies (*F*0s) while the speech continuum added other sources (bursts and fricative noises). The present study presented listeners with two new continua along with the original ones. In this way, the differences that might have occurred only due to the presence of one type of sound or the other will occur with both speech and nonspeech. A similar analysis of brain activation was carried out.

II. EXPERIMENT

Although the stimuli of Benson *et al.* (2001) varied complexity within speech and nonspeech dimensions, the

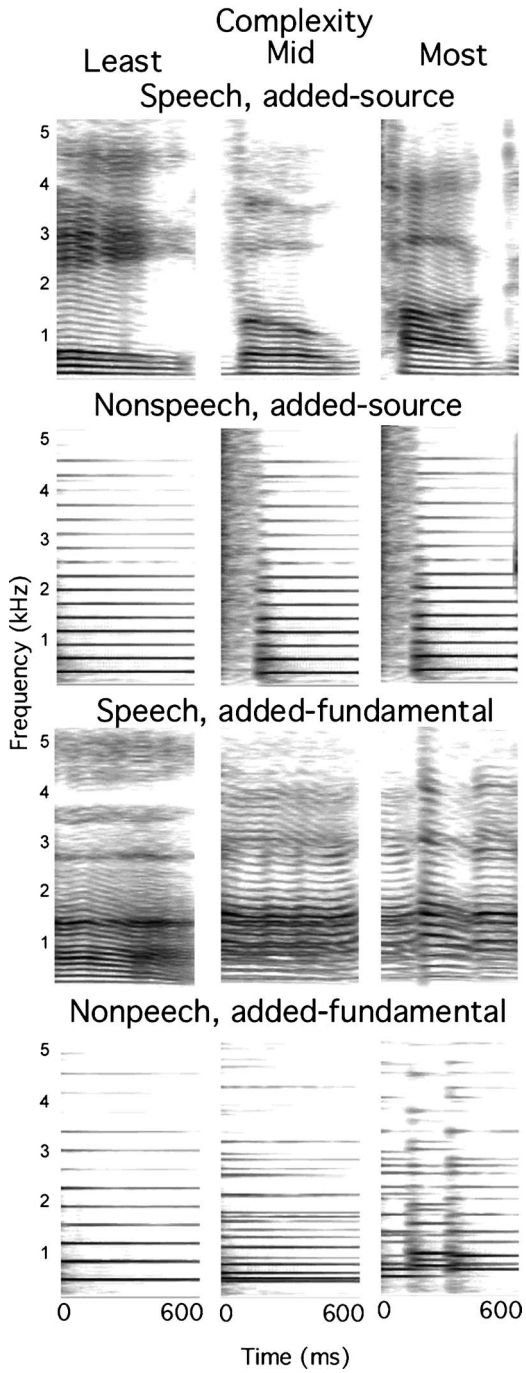

FIG. 1. Examples of stimuli. Each panel is a spectrogram representing time (in ms) on the *x* axis and frequency (in kHz) on the *y* axis, with intensity displayed as darkness of the image. The first row is the vowel syllable /e^{j}/ (as in "say"), CV syllable /vo^{w}/ ("voh"), and CVC syllable /tɑg/ ("tog"). The next row shows a note (F_4) by itself, then with swishsnare sound, then with a swishsnare at the beginning and a clave at the end. The next row shows a vowel syllable /ɑ/ (as in "ma"), then the vowel /ɑ/ said by three talkers simultaneously on different fundamentals, and finally the vowel /ɑ/ said by three talkers simultaneously, but at three different fundamentals within the syllable. The bottom row shows a note (F_4), a chord ($E_4G_4B_4$), and a chord progression ($G_4C_5Eflat_4, D_5F_5Aflat_5, C_5Eflat_5G_5$).

two dimensions were not completely equivalent. An extension was therefore run with two additional dimensions, one each for speech and nonspeech. These dimensions equated acoustic features more closely than previously.

A. Method

1. Stimuli

Our stimuli contrasted speech and nonspeech across two kinds of complexity (Fig. 1). The basic speech sounds were syllables (V, CV, and CVC); the basic nonspeech sounds were piano notes, piano chords, and combinations of notes and percussion sounds. The first complexity dimension was created by adding new sources of sound (and spectral movement within the base sound). For speech, the stimuli of Benson *et al.* (2001) were used. There were five instances at each level of complexity: V's—/ɑ, e^{j}, i^{j}, o^{w}, u^{w}/; CV's—/tɑ, ze^{j}, gi^{j}, vo^{w}, du^{w}/; and CVC's—/tɑg, ze^{j}k, gi^{j}p, vo^{w}s, du^{w}t/. These had naturally occurring added sources (fricative noises and stop bursts) for the CV and CVC syllables. Further, the formant transitions added another kind of spectral complexity. For the nonspeech, the added sources were percussion sounds. The simplest level (corresponding to the V syllables) was that of the notes; the midlevel of complexity added a percussion sound to the onset of the note (similar to the CV syllables), while the most complex had a percussion sound at both the onset and offset of the note. The five notes of our previous study were used (C4, D4, E4, F4, and G4). The onset percussion sound was a swishsnare, a slapsnare, a triangle, a slapsnare, and a block for those five notes, respectively. The offset percussion sounds (which always cooccurred with the onset percussion sounds, analogous to the CVC syllables) were a clave, a triangle, a block, a swishsnare, and a timbale, respectively. There was no further acoustic complexity, in that the nonspeech stimuli had no analogs of the formant transitions in the speech. Thus, if anything, there was somewhat less acoustic complexity in the nonspeech continuum than in the speech continuum. All stimuli were 600 ms in duration. The duration of the note was reduced by an amount equivalent to the duration of the percussion sound(s). The spectral content of the percussion sounds was similar to that of the release bursts and fricative noises of the speech.

The second complexity dimension increased complexity by adding fundamental frequencies and fundamental frequency changes. The nonspeech version was the original nonspeech dimension from Benson *et al.* (2001). The least complex stimulus was a note, the midlevel was a chord, and the most complex was a chord progression (three chords in succession) (Fig. 1). The piano chords were as follows: the major triad (0–4–7) C4E4G4, the minor triad (0–3–7) D4F4A4, the diminished triad (0–3–6) E4G4B$^{\flat}$4, the major triad 2nd inversion (0–5–9) F4B$^{\flat}$4D5, the minor triad 2nd inversion (0–5–8) G4C5E5. The chord progressions contained three chords, the first of which was one of the five chords just described. The next chord had a higher first note, and the third chord had a first note intermediate in pitch between that of the first and second chords. (Full specification can be found in Benson *et al.*, 2001.) The added-fundamental speech dimension consisted of the five vowels used before with added fundamentals achieved by combining multiple voices together. The least complex level consisted of the five vowels spoken by a single voice; the midlevel was composed of a combination of three voices with different

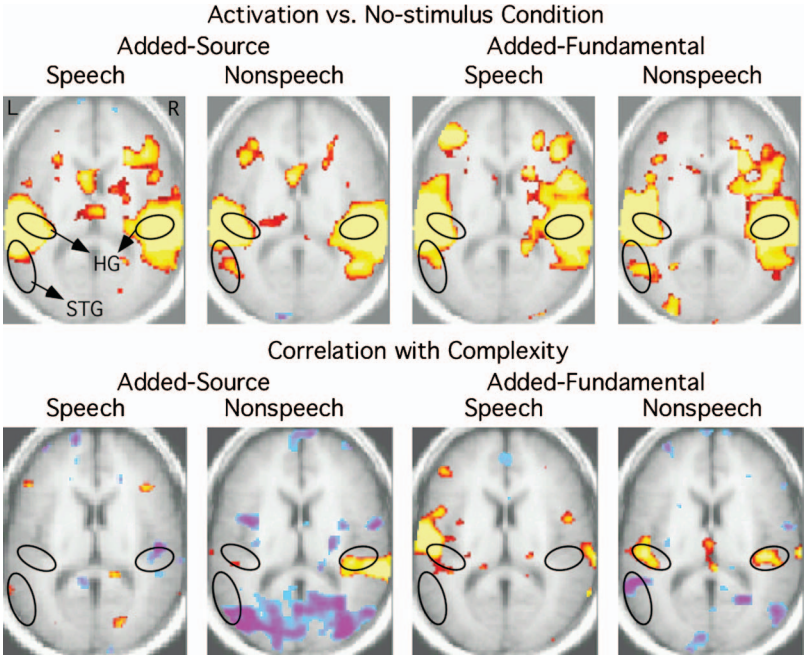

FIG. 2. Top row: Activation versus the no-stimulus condition for added-source speech, added-source nonspeech, added-fundamental speech, and added-fundamental nonspeech, respectively. Bottom row: Correlation of each complexity dimension with activation; panels are ordered as in top row. Approximate location of Heschl's gyrus (including PAC) is outlined in the pair of black ovals labeled "HG" in the first panel. Major area of correlation with speech complexity in Benson *et al.* (2001) is outlined in the oval labeled "STG" in the first panel. Significance threshold is 0.05. Each image is in neurologic convention, so that the left hemisphere is on the left.

*F*0's saying the vowel (equivalent to the chords); or the most complex was composed of those three voices saying the vowel, but changing *F*0 twice during the course of the syllable, once up, once down (equivalent to the chord progression) (Fig. 1).

All speech stimuli were recorded from native speakers of English. Piano notes and chords were recorded from a Yamaha Clavinova Digital Piano CLP-611 ("Piano 1" sound) Roland RD-250s. The percussion sounds were derived from the same sampling synthesizer. Because the number of dimension was twice that of our original study, the natural/synthetic dimension of Benson *et al.* (2001) was omitted from the current set so that the experiment could be run in a single session; this dimension had provided little interpretable data in any event.

All stimuli were 600 ms in duration. The nonspeech stimuli were specified to be that duration. The speech stimuli were all close to that duration initially and were digitally edited to be 600 ms.

2. Participants

Sixteen right-handed native speakers of English participated in the study, eight male and eight female. None had any reported speech, hearing, or language problems, and all gave informed consent. None were trained musicians or pianists. They were paid for their participation.

3. Procedure

The equipment was a GE Signa 1.5 T scanner (General Electric Corp., Waukesha, WI) equipped for echoplanar (EPI) imaging. Twenty contiguous, interleaved oblique-axial 7-mm slices were collected using a single-shot gradient-echo echoplanar sequence (flip angle=90°, echo time=40 ms, repetition time=3 s, field of view=20 cm, 64×64 matrix). An electrical pulse (TTL) at the start of the scan triggered the stimulus sequence from Psyscope (on a Macintosh computer). To shorten the runs, stimuli were not interleaved as before; our own experience and the results of the study indicate that the stimuli were still audible. After discarding the first 12 s (four images) to allow magnetization stabilization, the functional images were corrected for motion using SPM96, then spatially smoothed in-plane using a Gaussian kernel of FWHM=3.125 mm using the Yale University MRI Software Package (Skudlarski *et al.*, 1998). Regression analysis extracted effects of interest—correlations to levels of complexity—from the individual participants, with run offsets and drift accounted for. The analysis across participants tested the difference of these extracted parameters from zero, implementing mixed model analysis of variance.

A block of stimuli consisted of 15 items, three repetitions of each of the five types of a single category randomized. Stimuli were presented one every 2 s (thus with 1400 ms of silence between stimuli), occurring randomly with respect to the bursts of scanner noise (due to timing drift across the session). After the 15 items of one block were completed, items for the next block continued without pause. Because the simplest levels of each added-source and added-fundamental series were the same (e.g., the "V" stimuli were the simplest for both speech series), there were only 10 blocks rather than the expected 12. Four repetitions of a baseline block in which no auditory stimuli were presented was also included, during which only scanner noise was audible. Nine runs of each of the 14 blocks, which were pseudorandomized between runs, were obtained in one session.

B. Results

Figure 2 shows activations above the no-stimulus condition and the correlations with the complexity dimension. Two regions (one bilateral) are indicated, HG, defined anatomically, and the portion of pSTG that correlated with speech complexity in Benson *et al.* (2001) (see the ovals in each panel in Fig. 2). Most of HG, presumably including most of

PAC, was activated above the no-stimulus condition for all four complexity dimensions (Fig. 2). This supports the interpretation of Benson *et al.* (2001) that the lack of activation vs. the no-stimulus condition reported there was due to a lack of power in the no-stimulus condition, not a lack of use of HG for all the stimuli. Direct comparison of speech and nonspeech in these areas shows a significant difference in the areas examined in Benson *et al.* (2001).

Figure 2 shows the correlation of activation for each voxel with increases in the added-source speech stimuli (equivalent to the original speech dimension). There is no correlation with complexity in the left HG, and a negative correlation in the right. There is a region of correlation within the relevant part of pSTG. The added-fundamental speech condition shows a sizable portion of HG that correlates on the left, but the speech area does not show a correlation. The added-fundamental nonspeech dimension (equivalent to the original Benson *et al.* (2001) nonspeech dimension) correlates in HG bilaterally; there is a negative correlation in the speech area of STG. The added-source nonspeech dimension correlates with activation in HG bilaterally.

To confirm the correlations in HG, we performed a region of interest (ROI) analysis on just this region, defined anatomically as HG for each participant as in Dhankhar *et al.*, (1997): one or two short gyri of the superior surface of the STG that originate from the circular sulcus in the posterior insular area and that follow an obliquely anterior course to the lateral aspect of the STG. Included in the ROI for HG, forming its posterior margin, was the transverse temporal sulcus (TTS), immediately posterior to and parallel with HG. The average correlation with complexity was significant in the left HG for added-fundamental speech [$t(15)=4.82$, $p<0.001$], and both nonspeech dimensions [$t(15)=3.68$ and 2.99, both $p<0.01$], but not for the added-source speech [$t(15)=0.31$, not significant]. In the right, added-fundamental speech was significant [$t(15)=2.45$, $p<0.05$], as were both nonspeech dimensions [$t(15)=4.84$ and 4.20, both $p<0.001$], but the added-source speech had a negative correlation [$t(15)=-2.57$, $p<0.05$]. The conglomerate effect of small correlations resulted in a significant effect in the *a priori* ROI in one case (added-fundamental speech, right) where there was no apparent correlation in the average map.

III. DISCUSSION AND CONCLUSION

Our results confirm that certain areas of association cortex are selectively active for speech relative to nonspeech, but they also reveal differentiation within HG. Furthermore, no part of HG shows increased activity with increasing complexity of the added-source speech—as posterior temporal cortex does—but does increase with increasing nonspeech (and added-fundamental) complexity. This differentiation within HG and likely PAC is compatible with a distinction between the acoustic and speech-specific theories of speech perception. At the earliest cortical level of processing of acoustic stimuli, speech sounds are treated differently from nonspeech sounds. That is, they may not engage PAC in the same way that acoustically similar nonspeech sources do, and so speech may not receive a full auditory representation in PAC. The representation that PAC would give is often at odds with the information that is relevant to the speech percept (Remez *et al.*, 1994). Increases in processing in PAC were found for the added-source nonspeech, indicating that the present methodology can reflect this kind of activation when it is present.

If preliminary acoustical analysis occurs in PAC, as is suggested by animal and recent human data, then speech sounds do not receive a full auditory description. Indeed, the animal literature would lead us to expect that just the types of acoustic elements in the speech stimuli should have resulted in PAC activation (Schreiner *et al.*, 2000). Rapid transitions such as those that signal the presence of consonants in speech activate analogs of human PAC in cats (Heil *et al.*, 1992), rats (Ricketts *et al.*, 1998), ferrets (Nelken and Versnel, 2000), and monkeys (Bieser, 1998). Here, rapid frequency modulations in speech elicited increases in activation only in association cortex. While a lack of homology between human and primate PAC is possible, such an outcome is difficult to incorporate in a theory that claims that all sounds receive a full acoustic analysis before being processed as speech. Rather, the results are consistent with a theory in which speech processes are specialized and immediately linguistic.

Our passive listening task allowed us to avoid the disparities between overt decisions based for speech versus nonspeech, which will always differ in difficulty. Although passive tasks do not always generate the same level of activation as active tasks, the results are comparable when activation is present (e.g., Specht *et al.*, 2003). In the present case, ensuring that the task demands of each type of stimulus were the same was of utmost importance; the patterns of activation indicate that the passive listening was still showing the areas involved in processing the signals.

A similar case of superseding primary processing has recently been reported in primary visual cortex (or V1) (Murray *et al.*, 2002). When visual elements were presented at random, V1 was less active when those elements formed a figure than when they did not. This was true both for static lines and for visual gating stimuli in which the number of line segments was identical in both random and figural cases. Murray *et al.* conclude that the higher-level organization is actively subtracted from the representation in V1. They do not discuss whether the patterns are necessarily formed from the elements extracted in the primary regions or whether (as we argue for speech) the elements may be of a different sort altogether. The results nonetheless support a mechanism by which higher level perception can affect processing at a lower level.

The difference in area covered by the correlation with speech complexity across the two studies is likely due to experimental changes. The synthetic condition of Benson *et al.* (2001) was omitted from the current experiment to make the session tractable. Synthetic speech may require more resources to process than natural speech: which would increase the overall activation. The number of blocks was also re-

duced, which is likely to restrict the area as well (Huettel and McCarthy, 2001), although the power was increased in each block in the ratio of stimuli to TR.

Some of the nonsense items used may have activated nearby lexical items ("dog" for "tog," e.g.) or may have been misperceived as the item itself. Such activation is likely to affect only the association areas which are not the primary focus of this study. If a highly interactive approach to speech perception is assumed, then it might be that the earliest cortical levels would also be influenced by such lexical involvement. However, it would seem that such involvement would only increase activation, not reduce it. Given that our results show no correlation with complexity for HG in the relevant series (the added-source speech), the possible ancillary activation of lexical representations seems not to have affected our results.

The new speech dimension (added-fundamental) elicited activation patterns that were more similar to nonspeech than to speech, but this is not unexpected for syllables containing only vowels. Such syllables are less categorical (Fry *et al.*, 1962; Pisoni, 1975) and less strongly lateralized (Shankweiler and Studdert-Kennedy, 1967) than those with consonants. Further, the added fundamentals may have increased the perception of a nonspeech event, even though the source was a vocal tract. This dual nature of vowels is probably important to vocal music, where the nonlinguistic aspects of *F*0 can be most easily manipulated. Thus, the ROI analysis showed a positive correlation with added-fundamental speech in HG, even though the added-source speech dimension was nonsignificant in the left (and significantly negative in the right). The acoustically equivalent added-source nonspeech dimension was positively correlated in both the left and right HG, indicating that the area (including PAC) does intrinsically expend more resources with such signals.

Although these results are consistent with other studies of speech areas (e.g., Belin *et al.*, 2000; Vouloumanos *et al.*, 2001), two studies have found activation within speech areas for stimuli with rapidly moving transitions (Scott *et al.*, 2000; Thivard *et al.*, 2000). However, both contain substantial speech information in their nonspeech stimuli. Thivard *et al.* (2000) used analogs of speech formant transitions, ones that cover the frequency regions appropriate to *F*2 and *F*3 of speech. These were claimed to be "similar to vocal sounds in structure but with no phonemic value" (p. 2969). But, in fact, after a small bit of familiarity, it is quite easy to identify phonemic content in their transition stimuli. The voice quality is strange, because there is no equivalent of *F*1, resulting in a quality similar to that of sine-wave speech (Remez *et al.*, 1981; 1994). Participants in their experiment heard the stimuli at least four times and were likely hearing them as speech during the experiment if not at the very beginning. Thus, this study only shows that these unusual speech stimuli are processed in the speech areas. With Scott *et al.* (2000), the "rotated speech" stimuli were also claimed not to have intelligible phonemic content, but for at least some of their stimuli, this was not the case (selected stimuli can be heard at http://www.phon.ucl.ac.uk/home/brain/). Even if the phonemic content is debatable, the stimuli were claimed to "preserve intonation" (p. 2401). If so, those aspects of the stimuli should be processed in a speech area, thus making these results also consistent with the account given here: At the earliest cortical level (HG), speech information is immediately passed on to a specialized system that is not dependent on the auditory analysis provided by PAC.

Earlier behavioral studies showed precedence of speech processes over nonspeech processes (Whalen and Liberman, 1987; Xu *et al.*, 1997), but the structure of the auditory pathway seemed to argue against such a model. Results for another specialized system, sound localization, also indicate the existence of dedicated neural regions (Tian *et al.*, 2001). The present results and those in the visual domain (Murray *et al.*, 2002) indicate that earlier pathways can be influenced by later ones, leading to what could be termed "postemption," since priority is taken by the specialized process but at a later time. Results with elaborated nonspeech percepts competing with speech percepts indicate that only temporal priority (of 50 ms, in this case) allows the nonspeech system to compete successfully with the speech system, indicating that there is a time limit on the precedence of the speech system (Whalen and Liberman, 1996). The current neuroimaging evidence is consistent with an account in which this precedence includes a suppression of the earlier cortical treatment of speech in PAC in favor of a specialized representation centered in STG.

ACKNOWLEDGMENTS

This research is dedicated to the memory of Alvin M. Liberman. Helpful comments were provided by Ken Pugh, Carol A. Fowler, Michael Studdert-Kennedy, Annette Jenner, Bruno Galantucci, and three anonymous reviewers. This work was supported by NIH grants HD-01994 and DC-00403 to Haskins Laboratories.

Belin, P., Zatorre, R. J., Lafaille, P., Ahad, P., and Pike, B. (**2000**). "Voice-selective areas in human auditory cortex," Nature (London) **403**, 309–312.

Benson, R. R., Whalen, D. H., Richardson, M. Swainson, B. Clark, V., Liberman, A. M. (**2001**). "Parametrically dissociating speech and nonspeech perception in the brain using fMRI," Brain Lang **78**, 364–396

Bieser, A. (**1998**). "Processing of twitter-call fundamental frequencies in insula and auditory cortex of squirrel monkeys," Exp. Brain Res. **122**, 139–148.

Binder, J. R., Frost, J. A., Hammeke, T. A., Rao, S. M., and Cox, R. W. (**1996**). "Function of the left planum temporale in auditory and linguistic processing," Brain **119**, 1239–1247.

Binder, J. R., Frost, J. A., Hammeke, T. A., Cox, R. W., Rao, S. M., and Prieto, T. E. (**1997**). "Human brain language areas identified by functional magnetic resonance imaging," J. Neurosci. **17**, 353–362.

Bregman, A. S. (**1990**). *Auditory Scene Analysis* (MIT Press, Cambridge, MA).

Browman, C. P., and Goldstein, L. M. (**1992**). "Articulatory phonology: An overview," Phonetica **49**(3–4), 155–180.

Darwin, C. J. (**1984**). "Auditory processing and speech perception," in *Attention and Performance X: Control of Language Processes*, edited by H. Bouma and D. G. Bouwhuis, pp. 197–209.

Darwin, C. J., and Culling, J. F. (**1990**). "Speech perception seen through the ear," Speech Commun. **9**, 469–475.

Demonet, J.-F., Chollet, F., Ramsay, S., Cardebat, D., Nespoulous, J.-L., Wise, R. J. S., Rascol, A., and Frackowiak, R. (**1992**). "The anatomy of phonological and semantic processing in normal subjects," Brain **115**, 1753–1768.

Dhankhar, A., Wexler, B. E., Fulbright, R. K., Halwes, T., Blamire, A. M., and Shulman, R. G. (**1997**). "Functional magnetic resonance imaging assessment of the human brain auditory cortex response to increasing word

presentation rates," J. Neurophysiol. **77**, 476–483.
Diehl, R. L., and Kluender, K. R. (**1989**). "On the objects of speech perception," Ecological Psychol. 1, 121–144.
Fiez, J. A., Raichle, M. E., Miezin, F. M., Petersen, S. E., Tallal, P., and Katz, W. F. (**1995**). "PET studies of auditory and phonological processing: Effects of stimulus characteristics and task demands," J. Cogn Neurosci. **7**, 357–375.
Fowler, C. A. (**1994**). "Invariants, specifiers, cues: An investigation of locus equations as information for place of articulation," Percept. Psychophys. **55**, 597–610.
Fry, D. B., Abramson, A. S., Eimas, P. D., and Liberman, A. M. (**1962**). "The identification and discrimination of synthetic vowels," Lang Speech **5**, 171–189.
Heil, P., Rajan, R., and Irvine, D. R. F. (**1992**). "Sensitivity of neurons in cat primary auditory-cortex to tones and frequency-modulated stimuli II. Organization of response properties along the isofrequency dimension," Hear. Res. **63**, 135–156.
Huettel, S. A., and McCarthy, G. (**2001**). "The effects of single-trial averaging upon the spatial extent of fMRI activation," NeuroReport **12**, 2411–2416.
Kluender, K. R., and Lotto, A. J. (**1994**). "Effects of first formant onset frequency on [-voice] judgments result from auditory processes not specific to humans," J. Acoust. Soc. Am. **95**, 1044–1052.
Kuhl, P. K., and Miller, J. D. (**1978**). "Speech perception by the chinchilla: Identification functions for synthetic VOT stimuli," J. Acoust. Soc. Am. **63**, 905–917.
Liberman, A. M., and Mattingly, I. G. (**1985**). "The motor theory of speech perception revised," Cognition **21**, 1–36.
Liberman, A. M., and Mattingly, I. G. (**1989**). "A specialization for speech perception," Science **243**, 489–494.
Liberman, A. M., and Whalen, D. H. (**2000**). "On the relation of speech to language," Trends in Cognitive Sciences **4**, 187–196.
Liberman, A. M., Cooper, F. S., Shankweiler, D. P., and Studdert-Kennedy, M. (**1967**). "Perception of the speech code," Psychol. Rev. **74**, 431–461.
Murray, S. O., Kersten, D., Olshausen, B. A., Schrate, P., and Woods, D. L. (**2002**). "Shape perception reduces activity in human primary visual cortex," Proceedings of the National Academy of Sciences of the United States of America 99, 15164–15169.
Nelken, I., and Versnel, H. (**2000**). "Responses to linear and logarithmic frequency-modulated sweeps in ferret primary auditory cortex," Eur. J. Neurosci. **12**, 549–562.
Patterson, R. D., Uppenkamp, S., Norris, D., Marslen-Wilson, W., Johnsrude, I., and Williams, E. (**2000**). "Phonological processing in the auditory system: A new class of stimuli and advances in fMRI techniques," in Proceedings of the 6th International Conference of Spoken Language Processing (ICSLP), edited by Chinese Academy of Science, Beijing, pp. 1–4.
Pisoni, D. B. (**1975**). "Auditory short-term memory and vowel perception," Mem. Cognit. **3**, 7–18.
Rademacher, J., Morosan, P., Schormann, T., Schleicher, A., Werner, C., Freund, H.-J., and Zilles, K. (**2001**). "Probabilistic mapping and volume measurement of human primary auditory cortex," Neuroimage **13**, 669–683.
Remez, R. E., Rubin, P. E., Pisoni, D. B., and Carrell, T. D. (**1981**). "Speech perception without traditional speech cues," Science **212**, 947–950.
Remez, R. E., Rubin, P. E., Berns, S. M., Pardo, J. S., and Lang, J. M. (**1994**). "On the perceptual organization of speech," Psychol. Rev. **101**, 129–156.
Ricketts, C., Mendelson, J. R., Anand, B., and English, R. (**1998**). "Responses to time-varying stimuli in rate auditory cortex," Hear. Res. **123**, 27–30.
Schreiner, C. E., Read, H. L., and Sutter, M. L. (**2000**). "Modular organization of frequency integration in primary auditory cortex," Annu. Rev. Neurosci. **23**, 501–529.
Scott, S. K., Blank, C. C., Rosen, S., and Wise, R. J. S. (**2000**). "Identification of a pathway for intelligible speech in the left temporal lobe," Brain **123**, 2400–2406.
Shankweiler, D. P., and Studdert-Kennedy, M. (**1967**). "Identification of consonants and vowels presented to left and right ears," Q. J. Exp. Psychol. **19**, 59–63.
Shepherd, G. (**1994**). *Neurobiology*, 3rd ed. (Oxford University Press, New York).
Skudlarski, P., Constable, R. T., and Gore, J. C. (**1998**). "ROC analysis of statistical methods used in functional MRI: Individual subjects," Neuroimage **9**, 311–329.
Specht, K., Willmes, K., Shah, N. J., and Jancke, L. (**2003**). "Assessment of reliability in functional imaging studies," J. Magn. Reson Imaging **17**, 463–471.
Stevens, K. N. (**1998**). *Acoustic phonetics* (MIT Press, Cambridge, MA).
Talavage, T. M., Sereno, M. I., Melcher, J. R., Ledden, P. J., Rosen, B. R., and Dale, A. M. (**2004**). "Tonotopic organization in human auditory cortex revealed by progressions of frequency sensitivity," J. Neurophysiol. **91**, 1282–1296.
Thivard, L., Belin, P., Zilbovicius, M., Poline, J.-B., and Samson, Y. (**2000**). "A cortical region sensitive to auditory spectral motion," NeuroReport **11**, 2979–2972.
Tian, B., Reser, D., Durham, A., Kustov, A., and Rauschecker, J. P. (**2001**). "Functional specialization in Rhesus monkey auditory cortex," Science **292**, 290–293.
Vouloumanos, A., Kiehl, K. A., Werker, J. F., and Liddle, P. F. (**2001**). "Detection of sounds in the auditory stream: Event-related fMRI evidence for differential activation to speech and nonspeech," J. Cogn Neurosci. **13**, 1–12.
Wessinger, C. M., Buonocore, M. H., Kussmaul, C. L., and Mangun, G. R. (**1997**). "Tonotopy in human auditory cortex examined with functional magnetic resonance imaging," Hum. Brain Mapp **5**, 18–25.
Whalen, D. H., and Liberman, A. M. (**1987**). "Speech perception takes precedence over nonspeech perception," Science **237**, 169–171.
Whalen, D. H., and Liberman, A. M. (**1996**). "Limits on phonetic integration in duplex perception," Percept. Psychophys. **58**, 857–870.
Xu, Y., Liberman, A. M., and Whalen, D. H. (**1997**). "On the immediacy of phonetic perception," Psychol. Sci. **8**, 358–362.
Zatorre, R. J., Evans, A. C., Meyer, E., and Gjedde, A. (**1992**). "Lateralization of phonetic and pitch discrimination in speech processing," Science **256**, 846–849.

Perceived speech rate: The effects of articulation rate and speaking style in spontaneous speech

Jacques Koreman
Institute of Phonetics, Saarland University, P.O. Box 151150, D-66041 Saarbrücken, Germany

(Received 14 June 2004; revised 11 October 2005; accepted 11 October 2005)

In this study, the effect of articulation rate and speaking style on the perceived speech rate is investigated. The articulation rate is measured both in terms of the *intended* phones, i.e., phones present in the assumed canonical form, and as the number of actual, *realized* phones per second. The combination of these measures reflects the deletion of phones, which is related to speaking style. The effect of the two rate measures on the perceived speech rate is compared in two listening experiments on the basis of a set of intonation phrases with carefully balanced intended and realized phone rates, selected from a German database of spontaneous speech. Because the balance between input-oriented (effort) and output-oriented (communicative) constraints may be different at fast versus slow speech rates, the effect of articulation rate is compared both for fast and for slow phrases from the database. The effect of the listeners' own speaking habits is also investigated to evaluate if listeners' perception is based on a projection of their own behavior as a speaker. It is shown that listener judgments reflect both the intended and realized phone rates, and that their judgments are independent of the constraint balance and their own speaking habits. © *2006 Acoustical Society of America.* [DOI: 10.1121/1.2133436]

PACS number(s): 43.71.Es, 43.71.Gv, 43.71.Bp, 43.72.Kb [DOS] Pages: 582–596

I. INTRODUCTION

The segmental and prosodic characteristics of speech rate have been investigated quite extensively. The prosodic characteristics mainly concern pausing behavior and phonetic and phonological intonational properties. Fast speech characteristically has fewer and shorter pauses (Goldman-Eisler, 1968; see Butcher, 1981, and Lass, 1970, for the effect of pauses on the perceived speech rate) and fewer F0 resets (Trouvain and Grice, 1999). These observations support the idea that speech is divided into fewer prosodic units at fast rates than at normal or slow rates. Further, the complexity of pitch accents varies between speech rates, with fewer bitonal pitch accents and more monotonal ones in fast than in slow speech (cf. Rietveld and Gussenhoven, 1987, for its effect on the perceived speech rate). Also, the F0 range is generally reduced in fast speech, although there is substantial variation across speakers (Fougeron and Jun, 1998; Kohler, 1986).

Segmental effects of speech rate are reflected in the articulation rate, which by definition excludes pauses (Crystal and House, 1990) and is defined as the number of production units (often phones or phonemes, but also syllables, morae, or words) per unit time. In the present article, the relationship between the perceived speech rate and two different measures of segmental articulation rate—"intended" and "realized"—is under investigation. Due to the importance of the definition of these terms for the interpretation of the results, the two measures need to be considered in some detail prior to the presentation of our experiments. This discussion cannot offer an ultimate solution to all terminological issues, but it aims to identify the underlying theoretical problems and to clarify the operationalization of the two rate measures used here. These are derived from the hypothesized "canonical" and the actual, realized forms of the words in an utterance. The resulting calculable speech rate measures will be termed *intended* and *realized* rate, respectively (cf. "linguistic" and "phonetic" segments in Den Os, 1985).

The experimental issue under consideration is whether the perceived speech rate is determined by the number of actually realized speech sounds per unit time or whether it is dependent on the number of potentially realizable units according to some underlying, ideal(ized) form of the words, presumably defined in the speaker-listener's mental lexicon. For the latter concept the terms "canonical" and "intended" are used. There can be objections to the word "canonical" to refer to a more abstract representation. *Canonical* itself means "regular," "accepted or approved" (Funk and Wagnalls, 1973). In the present context the term could be interpreted as the accepted norm for the realization of a word in its everyday use, but this is not necessarily an indication of its hypothesized, underlying structure. The canonical form is often also referred to as the lexicon form, but it is not clear whether it can also be assumed to be the segmental representation in the speaker-listeners' *mental* lexicon, nor whether this representation is identical for each individual speaker (cf. Bromberger and Halle, 2000). To elicit a word in its canonical form, speakers may be requested to produce the word in citation form, i.e., the segment sequence which is produced when the word is articulated clearly and in isolation. But at the same time it is not certain that the citation form is really a good indicator of the canonical form: it may be overarticulated in the sense of a "spelling pronunciation." For German, the language in which the experiments presented here were carried out, the status of schwa is particularly interesting in this respect and has been discussed extensively by Kohler and his colleagues (Wesener, 1999; Kohler, 2001; Kohler and Rodgers, 2001). The present-day realiza-

tion of schwa, for instance, which is historically present in the *-en* suffix of many verbal and adjectival forms, depends on the dialect region of the speaker. In most dialect regions it is realized as a syllabic nasal (this is the norm in Standard German—cf. Duden, 2000, p. 38 ff.), but in some dialects it is realized as schwa, in others still as schwa plus nasal. To decide whether schwa is part of the (non speaker-specific) canonical form, Kohler and Rodgers (2001) statistically analyze the (Northern) German Kiel Corpus (IPDS, 1994; IPDS, 1995-1997), setting a threshold on the relative frequency of its realization in different contexts. In contexts in which schwa only occurs rarely in the actual, realized form, as in poststress "plosive+schwa+apical nasal" syllables, Kohler concludes that "schwa-less and at the same time place-assimilated forms have become the canonical entries for the speaker group as a whole" (Kohler, 2001, p. 10; see also Wesener, 1999, p. 332). Kohler and his co-workers clearly commit themselves, therefore, to a definition of the canonical form in terms of its observable everyday, concrete use. Of course, a statistical measure such as used by Kohler is a useful descriptive tool, but evidence for the psychological status of schwa needs to be derived (if this is possible at all) from psycholinguistic experiments. This problem can be generalized to the status of other phones as part of the canonical form. The reliance on a statistical measure based on the direct phonetic context further ignores the role of other factors like the situational and dialog context on the realization of utterances, which would probably lead to different canonical forms for many words. In the present paper, the *intended* form is defined as the abstract, "full" canonical form that may be hypothesized to be stored in language users' mental lexicon, including schwa and other rarely realized segments. Since these segmentally more elaborate forms do occur in our data, their realizations represent *de facto* the more careful end of the articulatory continuum from "clear" to "sloppy."[1] Whether they belong to others' idea of "canonical," "underlying," or "intended" forms is not critical for the present study.

The realized form can differ substantially from the underlying form. This is demonstrated by the possible realizations of the phrase "I do not know"—from very clear realizations of the intended form to more sloppy realizations typical of a conversational speaking style, including "dunno" or even more strongly reduced, mainly vocalic, realizations (Hawkins, 2003). As Hawkins convincingly demonstrates, the realization depends on the contextual setting in which a conversation takes place. In his H&H ("hyper"- and "hypo"-articulation) theory, Lindblom (1990) describes the interaction between articulation rate and reduction as the result of system- and output-oriented constraints on speech production. The speaker is presented as striving for minimal effort leading to sloppy or hypospeech (cf. Lindblom, 1963; Gay, 1981), but also willing to resort to clear or hyperspeech if it is required by the situation to get his message across. The example from Hawkins shows that the underlying, canonical form cannot be taken to be "intended" in a literal sense, i.e., it is not claimed here that it is always the speaker's intention to realize this form. In fact, system-oriented control as discussed in H&H theory implies that the speaker does *not* always intend to invest all the effort necessary to produce an unreduced form of the word.

Looking at the example from a speech perception standpoint, Hawkins claims that "speech perception does not demand early reference to abstract, linguistic units" (p. 373). This, too, calls the status of the so-called "intended form" into question and takes exemplars as the basis for speech perception. Although the terminology in the main part of this article is taken from the abstract-form view ("intended," "canonical"), it should be stressed that the experimental results are compatible with both views. The controversy between the abstract-form versus exemplar-based models is, however, relevant to the interpretation of the results and will therefore be taken up again in Sec. V.

Clearly, articulation rate cannot be dealt with without also considering speaking style (which will be used here in the restricted sense of articulatory precision or clarity). It should be pointed out that in our operationalization of the realized rate only the number of actual, realized segments per second is counted. Incomplete reductions, i.e., quantitative (e.g., vowel shortening) and qualitative (e.g., the substitution of long, tense by short, lax vowels) reductions which do not entail the deletion of a complete phone segment, do not affect the realized phone rate and are therefore not taken into consideration here. It is expected that realizations with more numerous deletions also show a greater number of incomplete reductions, since these can be considered as a less extreme but otherwise similar effect of a sloppy articulation—but their effect on the perceived speech rate is not investigated here.

Although it is clear that articulation rate and speaking style are related phenomena, their joint effects on the perceived speech rate have, to our knowledge, not been investigated in controlled experiments using unmodified, natural speech. In this paper, the following hypotheses are tested:

First, because segmental reduction is often related to a higher speech rate, it is hypothesized that utterances with many deletions (as the most extreme form of reduction) are interpreted by listeners as spoken at a higher speech rate than utterances of an equivalent realized articulation rate with no or very few deletions.

Second, the balance of input- and output-oriented constraints is different for fast and slow speech. In contrast to clear speech at lower intended articulation rates, the lack of reductions at fast intended articulation rates may be interpreted as hyperspeech and the greater perceived articulatory effort may be interpreted as an indication of faster speech. Conversely, the presence of reductions at lower intended articulation rates, where input-oriented constraints are weak, may be interpreted as hypospeech or even "slurred" articulation, and may therefore be perceived as slower. Exploring this extension of H&H theory, the perceived speech rates of two sets of carefully selected stimuli with high and low intended articulation rates are compared.

A third hypothesis tested here is that the perceived speech rate depends on the listeners' own speaking habits. Speech which is judged as fast by slow speakers may be

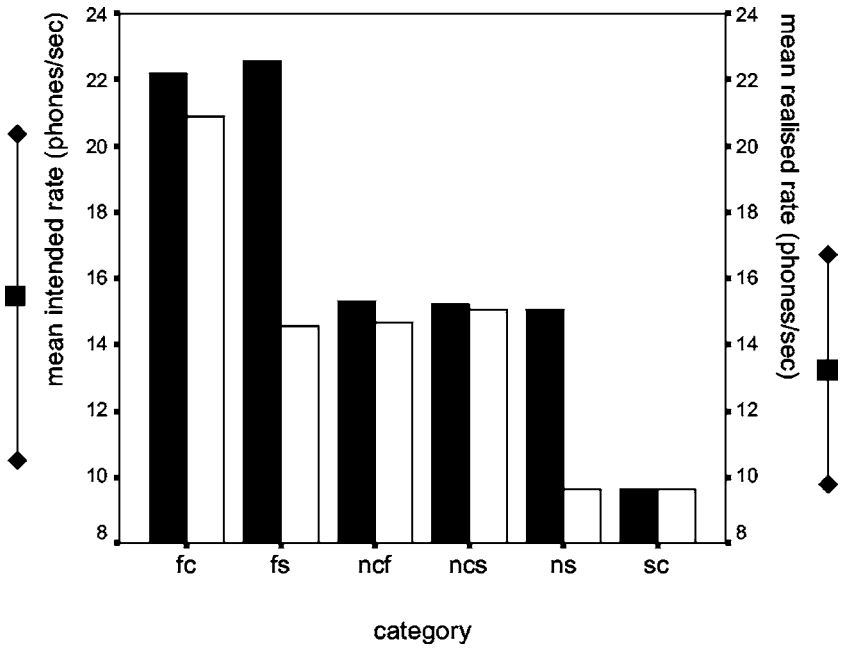

FIG. 1. Average intended (filled bars) and realized phone rates (white bars) in phones/s of stimuli from six rate categories (with means and standard deviations for intended and realized rates in the prosodically labeled part of the Kiel Corpus of Spontaneous Speech indicated on the vertical axes).

judged differently by fast speakers and vice versa. Also, clear and sloppy speakers may differ in their evaluation of phone deletions in speech utterances.

The above hypotheses are investigated in two listening experiments using intonation phrases from the German Kiel Corpus of Spontaneous Speech (IPDS, 1995-1997). The first experiment (*comparison* experiment) evaluates the effect of measured articulation rate and speaking style (clear versus sloppy) on the perceived speech rate in direct comparisons between the two intonation phrases in each stimulus pair. Listeners' ability to judge the speech rate of the individual phrases is investigated in a second experiment (*scaling* experiment). Further, the evaluation of speech rate in this experiment is related to the listeners' own speaking habits. Because it can be hypothesized that other factors such as hesitations, the relative number of function versus content words in an utterance, and the intonation patterns affect the perceived speech rate of the specific stimuli used in the experiments, the generalizability of the results from our controlled experiments is examined. This is done by comparison with the perceived speech rates labeled in the entire database from which the stimuli are selected.

II. METHOD

In two experiments, the influence of the intended and realized articulation rates on the perceived speech rate is investigated. In the first experiment, listeners compare which of two stimuli is faster (or whether they are equally fast). In a scaling experiment carried out immediately after the first experiment, each of the stimuli is then judged separately on a continuous scale for perceived speech rate. Before presenting the two experiments, the stimuli are described in some detail. The participants in both tasks were selected on the basis of their own speech rate as subjectively perceived by the experimenters. Speakers who were judged as either particularly fast or as particularly slow were invited to participate in the listening experiments.

A. Stimuli

The stimuli consist of intonation phrases (without pauses) selected from the German Kiel Corpus of Spontaneous Speech (IPDS, 1995–1997). The corpus contains high-quality recordings of conversations in which two speakers schedule one or more appointments. Despite the recording setup, in which the speakers have to press a button to obtain the floor, the speaking style is very natural. The reason for choosing intonation phrases is that the articulation rate within an intonation phrase can be assumed to have a relatively stable pattern (Dankovičová, 1999).

The intonation phrases and the segments they contain are manually labeled for a large part of the Kiel Corpus (see Sec. IV below). The segmental labels of the intonation phrases take the canonical form as a point of departure and indicate the changes to the canonical form which lead to the observed, realized form (see the Appendix). The intended and realized articulation rates can therefore be derived from the transcriptions by counting the number of intended and realized phones in an intonation phrase, respectively, and dividing them by its duration. In order to control for the effect of phrase duration (cf. Pfitzinger, 1999), only phrases with a duration between 1 and 1.5 s were selected. They were carefully matched within each set of phrases for which pairwise comparisons were made.

The selected phrases vary systematically in their intended and realized articulation rates, which allows us to separately evaluate the effect of articulation rate (fast versus slow) and speaking style (clear versus sloppy) on the perceived speech rate. Two sets of stimuli were selected (with five phrases for each of the six stimulus categories described below), one set from the fast and the other from the slow half of the Kiel Corpus (cf. Fig. 1).

Set 1: Comparison of fast with normal speech

FC: *Fast, clear* phrases have both high intended and high

realized phone rates. Intended phone rates are between 1 and 2 standard deviations above the sample mean computed across the prosodically labeled part of the database from which our stimuli were selected. The realized phone rates are close to the intended phone rates, with few phone deletions (maximally 8%). The realized phone rates of these phrases are about 2–3 standard deviations above the sample mean. This category is considered as typical hyperspeech, because the phrases are spoken fast both from the point of view of their intended rate as well as the actual articulator speed, as reflected in the realized phone rate.

FS: The intended phone rates for the *fast but sloppy* phrases are similar to those of the clear phrases, but 35%–40% of the intended phones are not realized. The realized phone rate is therefore much lower than in the fast, clear category, namely within 1 standard deviation from the sample mean.

NCf: A third category of *normal, clear phrases for comparison with fast intended phrases* was selected from the database, for which both the intended and the realized phone rates are similar to the realized phone rates of fast, sloppy speech. The phrases are spoken clearly, with a low percentage of phone deletions, comparable to those in the FC category. Their intended phone rates are within about 0.5 standard deviations of the sample mean. As is the case for the other categories, each of the phrases in the NCf category was carefully matched, also in terms of its duration, with the comparison phrases from the other two categories.

The stimuli in the FS category were selected on the basis of the numerous deletions, as in the phrase "Nee, da habe ich schon einen anderen Termin," which is realized as [ne:, da: a:b ɪ ʃõ: n a̰nɐn tɛɐmi:n] (with only 20 out of 32 intended phones being realized). In many of the FS stimuli, schwa deletion (plus assimilation) occurs: "eig*e*ntlich," "würd*e* es," "Ihn*e*n," "pass*e*n," "ein*e*n," "mach*e*n," "vorschlag*e*n," and "hab*e* ich" (the stimuli are listed in the Appendix, together with the transcriptions of the intended and realized phones). As expected, many of the schwas in the stimuli which were selected for the FC category on the basis of their low deletion rate are actually realized (high articulatory precision), even in clear reduction contexts like in "Revisionstreff*e*n," "mach*e*n" (cf. Kohler and Rodgers, 2001). But, in general, far fewer intuitive deletion contexts are found in the FC stimuli. One could hypothesize that if there is no opportunity for deletion, this should not affect the perceived speech rate, i.e., given the identical intended rates for the FC and FS categories, they should be judged equal. On the other hand, following Kohler's argument, it could also be argued that the lack of deletions, particularly in some of the contexts mentioned above, can be considered as hyperarticulation at a fast speech rate. Like the fast, clear stimuli (FC), the normal, clear (NCf) stimuli contain only few deletion contexts, and there are also a few contexts like "gan*z sch*lecht" and "d*e*n" where no deletion occurs, although the context seems appropriate for it. If the listeners derive their speech rate judgments solely from the actual speech rate without taking the canonical form into consideration, then the stimuli in the NCf category should be judged as equally fast as those in the FS category, which have the same realized phone rate.

Set 2: Comparison of slow with normal speech

To mirror the intonation phrases selected from the faster half of the database, another set of stimuli were selected from the slower half of the database. Comparison of the results for the two stimulus sets allows us to test the hypothesis that the different balance between input- and output-oriented constraints at fast versus slow rates affects the perceived speech rate. The clearly spoken phrases at slower rates are not necessarily considered as hyperspeech and may therefore have a different effect on the perceived speech rate compared to fast, clear utterances. Conversely, the pressure from the point of view of ease of articulation to reduce or delete segments is less at slower articulation rates, because there is more time to realize the segments at normal and slow than at high articulation rates. The set of stimuli from the slower half of the intended articulation rate range (normal to slow) offers an opportunity to examine whether the same regularities in speech rate judgments are found at faster and slower measured rates. The following stimulus categories were selected:

NCs: *Normal, clearly* spoken phrases were selected for comparison with other phrases with intended rates in the *slow half* of the articulation rate range. The intended and realized phone rates are similar to those of the NCf category, but the phrases are different ones. This is done in order to provide an optimal match with the phrases in the two following categories (also in terms of their durations).

NS: *Normal but sloppy* intonation phrases have intended phone rates close to the sample mean and 35%–40% of the intended phones are not realized (as in the FS category). This results in fairly slow realized phone rates between −0.5 and −1.5 standard deviations from the sample mean. Of all the categories in the experiment, this is the clearest instantiation of hypospeech, because at a normal intended articulation rate the pressure to reduce or delete segments is less than in the FS category.

SC: Finally, a category of *slow*, *clear* phrases is defined. The phrases are matched to the NS phrases in their realized phone rate. The intended phone rates are similar to the realized phone rates and lie between −1 and −2 standard deviations from the sample mean.

As in the NCf category, the stimuli in the NCs category hardly show any deletions. All schwas are realized, even in deletion contexts like in "wär*e*," "ließ*e* sich," or "mach*e*n," except for a single schwa deletion in the final syllable of "dreizehnt*e*n" (cf. Kohler and Rodgers, 2001). Even the prevocalic glottal stops in "und" and "ich" are fully realized, with additional laryngealization of the vowel (Kohler, 1994; Wesener, 1999). As in the fast half of the database, the sloppy stimuli in the slower half (NS) contain many deletion contexts, like "hab*e*n," "klein*e*n," "Aug*e*nblick," "morg*e*n,"

"ein*e*m," "hätt*e*n," and "erst*e*n," all of which are realized without a schwa, and with assimilation where applicable. The stimuli in the SC category, which are very slow, contain few deletion contexts, and when they do the deletable segments are phonetically realized, like the schwa in "nehm*e*n" or the prevocalic glottal stops in "am," "und," and "auf." The presence of a clear glottal stop is quite usual for any of the normal and slow clear categories, whereas they are not realized (or, rarely, as creak in the following segment) in fast clear or in sloppy speech. Figure 1 displays the intended and realized speech rates of the six stimulus categories.

B. Listeners and their speaking habits

Since it was hypothesized that listeners' own speaking habits may affect their perception of speech rate, the 12 subjects for our listening experiments (five male and seven female in the age range 20–80, with an average age of 33) were selected on the basis of the subjective impression of their speech rate (subjective speech rate: fast or slow) in a consensus judgment by six advanced students in the Institute of Phonetics. There were thus two subjectively allocated listener groups: eight fast speakers and four slow speakers.

In order to also obtain a more objective estimate of the listeners' speech behavior, and particularly in order to see whether the subjective judgments (which may also be based on speech properties such as pausing and intonation) are related to the intended and realized *articulation* rates, each subject first read aloud a German text ("Die Buttergeschichte") and then retold the story in his/her own words. Both versions of the text (read and retold) were recorded onto audio tape and then digitized at a sampling frequency of 10 kHz and with a 16-bit amplitude resolution. The recordings were subsequently divided into interpause stretches (ips). These were used instead of intonation phrases (used as stimuli in the listening experiments) because they are easier to determine. In the main, they correspond to intonation phrases. The differentiation of the speakers in terms of their speaking habits in a spontaneous speech task was based on the retold stories.

The intended and realized phone rates were computed for each ips and an *articulatory precision index* (api) was computed by dividing the realized phone rate by the intended phone rate (low api values indicate more deletions). The duration of each ips was also measured. Subsequently, the data were analyzed to see whether the subjective speech rate (as perceived by the judges) is reflected in the subjects' measured speech behavior. Finally, the subjects were also divided into objective articulation rate/speaking style categories on the basis of the measures taken from their speech.

1. Objective basis of subjective speech rate groups

As was pointed out in the Introduction, many factors beside articulation rate are likely to affect the perception of speech rate, so it is necessary to verify whether the division into fast and slow speakers on the basis of the judges' subjective impression of speech rate is (also) reflected in the measures used in this study. Because some of the ips contain disfluencies which would affect the articulation rate measures, these are analyzed first, before continuing to evaluate the intended and realized phone rates as well as the articulatory precision index for the fluently spoken ips.

TABLE I. Disfluencies in ips of speakers subjectively perceived as fast and slow for read and retold stories

	Read		Retold	
Disfluency	Fast	Slow	Fast	Slow
Stutter	0	0	0	2
Slip of the tongue	3	2	8	0
Interruption	4	0	1	0
Hesitation	1	1	5	4
Lengthening	2	0	23	4
Filled pause	1	0	6	4
Laughter	1	0	4	0
Total	12	3	47	14

A total of 76 disfluencies were observed in the 683 ips. They are divided into seven categories: stutters, slips of the tongue, interruptions, hesitations, lengthenings, filled pauses, and laughters. As expected, fewer disfluencies occur for read than for retold stories. Given the low number of disfluencies, chi square tests are not appropriate, but the pattern shown for the retold stories in Table I suggests that subjectively slow speech is characterized by relatively (i.e., after division by the total number of disfluencies for each column) more stutters and hesitations or filled pauses, while subjectively fast speech contains more slips of the tongue, lengthenings, and laughters.

To prevent these disfluencies from biasing our measures, only fluent ips are used for further analysis. Short ips with a duration of less than half a second are also excluded (2.2% of the read and 9.6% of the retold ips), because the small number of phones in these ips can lead to unreliable estimates, particularly because final lengthening will have a strong effect on the average number of phones per second.

For the read and retold stories, the duration of each ips is measured. Further, their intended and realized phone rates and the articulatory precision index are computed. t tests for the fluent ips with a duration of at least half a second show that fast and slow speakers have ips of approximately the same duration when reading aloud, but when they retell the story the durations of the ips for fast speakers (1.7 s on average) are significantly shorter ($t=2.4$, $df=217$, $p<0.05$) than for slow speakers (average: 2.1 s). In both the reading and retelling tasks, the intended (reading: $t=10.3$, $df=356$, $p<0.001$; retelling: $t=4.0$, $df=217$, $p<0.001$) and realized phone rates (reading: $t=8.3$, $df=230.6$, $p<0.001$; retelling: $t=5.9$, $df=217$, $p<0.001$) differ significantly for fast and slow speakers. As expected, the fast speakers have higher phone rates than slower ones. The articulatory precision index, which is highly significant in the reading task ($t=4.3$, $df=356$, $p<0.001$; with lower articulatory precision, i.e., more deletions, for fast than for slow speakers), is not significant in the retelling task. These results in general confirm that articulation rate properties, both intended and realized, go hand in hand with the subjectively perceived speech rate.

TABLE II. Three groupings of the speakers into four categories on the basis of the measured intended and realized rate and the articulatory precision in a retold text (dashes indicate combinations which do not occur).

Grouping		Category 1	2	3	4
1	intended rate	fast	fast	slow	slow
	realized rate	fast	slow	fast	slow
2	intended rate	–	fast	slow	–
	articulatory precision		sloppy	clear	
3	realized rate	fast	fast	slow	slow
	articulatory precision	clear	sloppy	clear	sloppy

The subjective speech rate will be used later to analyze the results from the listening experiments for the effect of speaking habits on the perceived speech rate.

2. Objective rate and style

Because the subjective impression of speech rate (viz. as either slow or fast) is in all likelihood not just based on articulation rate, but is probably also influenced by pausing behavior and other prosodic characteristics of the speakers as well as by disfluencies, an objective grouping of the subjects is obtained on the basis of cluster center analyses performed on measures reflecting the subjects' articulation behavior. Two groups (fast, slow) are created on the basis of the median values of the measured intended phone rates in the retold story; the same is done for the realized phone rates (fast, slow) as well as for the articulatory precision index values (clear, sloppy). Each two out of the three variables are combined to derive subject categories which reflect different articulation rates and speaking styles in a manner which is similar to the way the stimuli selected from the Kiel Corpus were categorized. These speaker groupings, which are summarized in Table II, are used in some of the later analyses. The clustering confirms that factors other than the intended and realized rates also influence the subjectively perceived speech rate, because one of the speakers with a slow subjectively perceived speech rate belongs to category 1 of grouping 1 (category 2 of groupings 2 and 3), while one of the speakers with a fast subjectively perceived speech rate belongs to category 4 of grouping 1 (category 3 of groupings 2 and 3).

C. Comparison experiment

Two experiments were carried out. The goal of the first, comparison experiment is to see how the different articulation rates and speaking styles in stimulus pairs affect the listeners' judgments of speech rate. The Experimenter software (Altman, 1992) was used to carry out the comparison experiment. In order to obtain a judgment of perceived speech rate which is not affected by the intelligibility of the stimuli, the two intonation phrases were first orthographically displayed on a computer screen for 3.5 s, followed by a beep and a silent pause of 0.5 s. Then the stimulus pair was played, separated by a silence interval of 0.5 s. The stimuli, which were set to equal loudness levels and adjusted for each listener to a comfortable volume, were played to the listeners over loudspeakers in a sound-treated room. After presentation of a stimulus pair the subject had 5 s to respond by pressing one of three keys on the keyboard for "first stimulus faster" (key: ←), "second stimulus faster" (key: →) or "both stimuli equally fast" (key: ↓). Both the response and the response time were registered.

All possible combinations of the six categories shown in Fig. 1 were compared, giving 15 comparisons. Five sets of six phrases were selected from the database. The total number of stimulus pairs was therefore 5 (sets) $\times$ 15 (comparisons) = 75 per listener. The word content of the phrases was always different and with a few exceptions the phrases were all produced by different speakers. The stimulus pairs were offered in pseudo-randomized order. The listeners were divided into two equal groups, which heard the stimuli within each pair in opposite orders. The stimuli were preceded and followed by, as well as interspersed with, filler items. Because the responses of the comparison experiment constitute nominal data which is mainly suitable for qualitative analysis, metrical data were collected in a scaling experiment, which is described in the following section.

D. Scaling experiment

The scaling experiment serves a double aim. First, it tests whether listeners are able to make consistent judgments of speech rate when they are required to judge each stimulus phrase by itself. Second, the speech rate judgments of the individual intonation phrases can be related to the listeners' own speech behavior. The same 30 intonation phrases as in the comparison experiment (5 sets $\times$ 6 categories) were used for the scaling experiment. The stimuli were offered in two blocks, each containing all the stimuli, but in a different randomized order. The blocks were preceded by five and followed by four filler items. Each phrase was shown on the computer screen for 1.75 s before it was played to the listener. As in the comparison experiment, the stimuli were played over loudspeakers in a sound-treated room. After hearing the phrase, the listener scored the perceived speech rate on a continuous scale from −3 ("too slow") to 3 ("too fast") by marking the position on the scale with a vertical line. The intermediate full values were labeled with "very slow" (−2), "quite slow" (−1), "normal" (0), "quite fast" (1), and "very fast" (2). The positions of the vertical lines were later measured with a precision of one decimal—thus metrical data are obtained, which are more suited to quantitative analysis than the data obtained from the comparison experiment. The extremes of the scale, which contain a subjective judgment, were not used by any of the listeners. After scoring a stimulus, the listener hit return to continue with the next stimulus.

III. RESULTS

A. Comparison experiment

For ease of interpretation, the results from the multiple comparisons between all stimulus categories are condensed into four types of stimulus pairs. In set A, both the intended

TABLE III. Comparison of intended (ipr) and realized phone rates (rpr) within the stimulus pairs for four conditions (see text), with the number of listener judgments and the compared rate conditions in their intrinsic order (cf. Fig. 1).

Condition	ipr	rpr	No. of judgments	Rate categories compared
A	different	different	480	FC-NCf, FC-NCs, FC-NS, FC-SC, FS-NS, FS-SC, NCf-SC, NCs-SC
B	same	different	180	FC-FS, NCf-NS, NCs-NS
C	different	same	180	FS-NCf, FS-NCs, NS-SC
D	same	same	60	NCf-NCs

and the realized articulation rates of the two intonation phrases in a stimulus pair are different. In set B, only the realized articulation rate is different, while in set C there is only a difference in intended rate. In set D, finally, both the intended and realized articulation rates of the two intonation phrases are the same. Table III lists the sets to which each of the comparisons between the categories in Fig. 1 belongs. Irrespective of actual order of presentation, results are given as percentage "stimulus faster" with respect to the *intrinsic order* of categories given in the column "rate categories compared" in Table III.

The perceived speech rate differences for each of the four sets are shown in Fig. 2. As expected, when both the intended and realized articulation rates of the two phrases are different, a large number of "first stimulus faster" responses is found [Fig. 2(A)], with relatively few "equal" responses. Figures 2(B) and 2(C) show that the effect of the intended and the realized rate is virtually the same: Relatively more "equal" responses are given when only one of the two measured rates differs for the two phrases, but the first stimulus of a pair is considered faster three to four times as often as the second. This is not the case when both the intended and

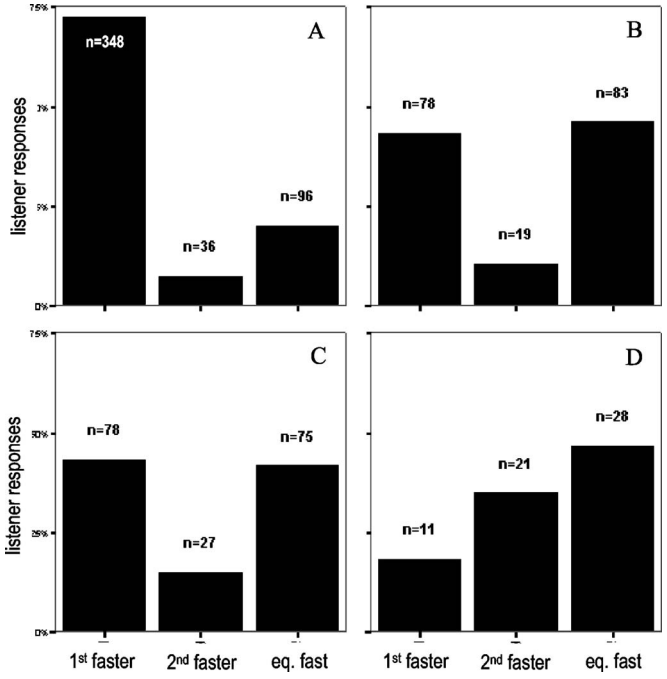

FIG. 2. Listener responses (percentages) to stimuli with different intended and realized rates (A), only different realized rates (B) or intended rates (C), or with both equal (D).

the realized rates of the two phrases in the stimulus pair are the same [Fig. 2(D)]: Although the percentage of "equal" responses is similar to that in Figs. 2(B) and 2(C), there are fewer "first stimulus faster" than "second stimulus faster" responses (intrinsic order). The results confirm those reported in Koreman (2003), where a different set of 20 listeners carried out the same experiment.

Of course, the effect for the stimuli in set A, shown in Fig. 2, is not only large because both the intended and realized rates of the stimuli in each pair differ, but also because this stimulus set contains comparisons between phrases with extreme articulation rate differences (e.g., FC-SC), while this is not true for the other stimulus sets. But the clear perceptual effect of differences in intended and realized rates is consistently reproduced when each two stimulus categories are compared separately (Fig. 3). If there is a difference in either the intended or the realized rate between the two stimuli in a pair, this difference is used by the listeners to determine which stimulus is faster (cf. Table III). The greater the distance from the top-left to bottom-right diagonal (the greater the differences in intended and/or realized articulation rates), the clearer the difference between the stimuli is perceived. This is true for the difference between the "first stimulus faster" and "second stimulus faster" responses, where an increasing preference towards "first stimulus faster" responses can be observed (black bars), as well as for the reduction in "equal" responses (dark gray bars). In one condition, namely NCf-NCs, phone rates are compared for stimuli which are similar in their intended as well as in their realized rates. As expected, the listeners are not able to decide which of the two stimuli was spoken faster, resulting in a large number of "equal" responses and even a reversal of "first stimulus faster" and "second stimulus faster" responses. Possible reasons why there are many "first stimulus faster" and "second stimulus faster" responses instead of only "equal" responses are that the listeners are encouraged by the task to judge one of the two stimuli as faster, but also that in the absence of segmental cues the listeners rely on stimulus properties which were not controlled in the present experiment, such as local speech rate, disfluencies, and intonational characteristics. There is no qualitative difference between stimulus comparisons from the fast half (dashed graphs) and the slow half of the database (dotted graphs).

For a more quantitative evaluation of how sure the listeners are that their response is correct, a certainty measure is derived for each listener across the five comparisons between each two categories. The measure is a Bayesian estimate of

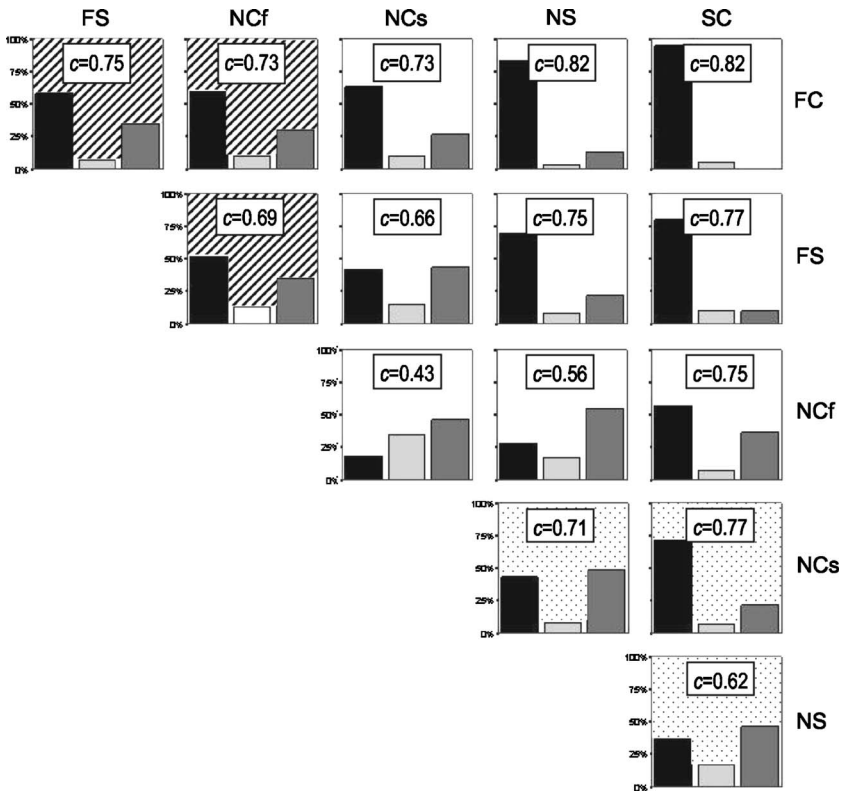

FIG. 3. Number of "first stimulus faster" (black bars), "second stimulus faster" (light gray bar), and "both stimuli equal" (dark gray bars) averaged for each stimulus pair. Rows indicate the category of the first stimulus in a pair, while columns show the category of the second stimulus (intrinsic order). The graphs with the dashed backgrounds represent comparisons between stimuli from the fast half of the database, while the ones with a dotted background are for stimulus comparisons for the slow half of the database. Certainty values c in each graph are derived from the size of the bars and indicate how certain the listeners are that their response is correct (see text).

the Bernoulli probability (Collings, 1997, p. 26), assuming a prior probability of 0.5; "equal" responses are considered as failed trials (but do affect the certainty measure), so that the certainty of giving the correct response can be computed as $c=(1+s1)/(2+s1+s2)$, where s1 is the number of "first stimulus faster" and s2 the number of "second stimulus faster" responses.[2] The lowest certainty value ($c=0.44$) is obtained for the comparison between NCf and NCs categories, where no difference ($c=0.50$) is expected. An analysis of variance ($F(14,165)=7.3$, $p<0.001$) with Tukey-HSD *posthoc* tests shows that this value is significantly lower ($p<0.05$) than that for all categories which differ in *either* intended or realized rate (or both)—except for the comparison of the NCf and NS categories, from which it does not differ significantly. The certainty values are indicated in Fig. 3. As can be seen from the figure, the certainty values increase as the distance between two compared categories (as recognizable from Fig. 1) increases. The same analysis for the four conditions in Fig. 2 showed a significant main effect ($F(3,176)=25.8$, $p<0.001$), with a significantly decreasing certainty value (Tukey-HSD *posthoc* tests at $p<0.05$) from condition A-D, except for the comparison between conditions B (only realized rates of the two stimuli different) and C (only the intended rates different). The results from the scaling experiment will show further differences between the perceived rates for the stimulus categories.

B. Scaling experiment

1. Comparison with the results of the first experiment

The stimuli were judged by the listeners in two blocks in the scaling experiments. The identified rates for repetitions of identical stimuli showed a high and significant correlation ($r=0.88$, $n=360$, $p<0.001$). An analysis of variance of the *average* rate scores across the two stimulus repetitions, with the five stimuli in each stimulus category as repeated measures, shows that the stimulus category affects the identified rate ($F(20,264)=11.1$, $p<0.001$). Each of the stimulus categories is significantly different from each other category, as shown by *posthoc* Tukey-HSD tests (all $p<0.001$), with two exceptions: (1) the two categories NCf and NCs are not significantly different, as expected, and (2) the average identified rates for stimuli from category FS are not significantly different from those for NCs stimuli, but this is mainly caused by one stimulus (they do differ significantly from the NCf stimuli). The results are in perfect agreement with those from the comparison experiment. The farther apart two categories are in their intrinsic order (as shown in Fig. 1), the greater the difference in average perceived speech rate (see Table IV). The slightly (but not significantly) higher average identified rate for the NCs stimuli than for the NCf stimuli supports the results from the comparison experiment, where comparison between the two categories led to more "second stimulus faster" (NCs faster than NCf) responses.

For the three response categories, significant differences are found both in the identified rates ($F(2,879)=109.5$, $p<0.001$) and in the reaction times for the responses ($F(2,879)=15.0$, $p<0.001$). In most stimulus comparisons, the choice for "first stimulus faster" is clear and the differ-

TABLE IV. Means and standard deviations of the identified rate for each stimulus category in a scaling experiment

	FC	FS	NCf	NCs	NS	SC
mean	1.12	0.40	−0.08	0.03	−0.58	−1.14
sd	0.58	0.65	0.74	0.78	0.75	0.66

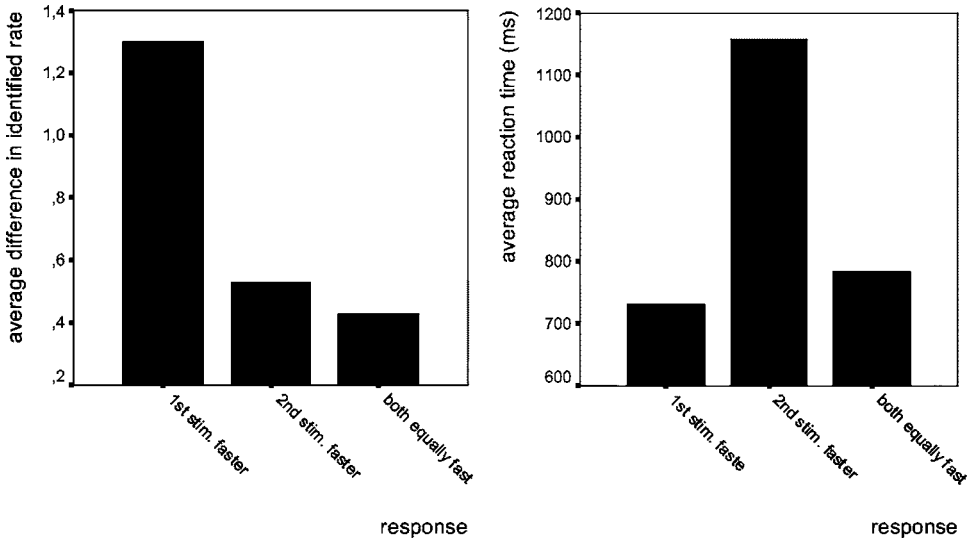

FIG. 4. Average differences in identified rate (left) and average response times (right) for each judgment.

ence in perceived speech rate of the stimuli is large, as shown by the first column in Fig. 4 (left). The differences in identified rate are small when listeners perceive the second stimulus as faster than or equally fast as the first one (second and third columns). The average differences in identified rate are significantly smaller for these two response categories than for the "first stimulus faster" category (Tukey-HSD *post hoc* test, $p<0.001$). There are also obvious differences in response time to the stimulus pairs in the comparison experiment (Fig. 4, right). If the listeners base their judgments on the measured rates only, the second stimulus should never be judged as faster (because the results are always presented for the intrinsic order of the stimulus categories). When listeners nevertheless judge the second stimulus as faster than the first one, they take a long time for their response (second column). This is a clear indication of the uncertainty about their judgment. The difference with the other two categories is significant at $p<0.001$ in a Tukey-HSD *posthoc* test.

2. Comparison with the listeners' speaking habits

An analysis of variance of the average identified rate of the stimuli with the stimulus categories (with NCf and NCs merged into a single category NC) and the subjective speech rate of the subjects (fast or slow, as judged by the experimenters) as independent variables confirms the influence of stimulus category on the identified rate ($F(16,248)=6.3$, $p<0.001$). The subjective speech rate, however, does not affect the perceived rate of the stimuli, nor is there an interaction between subjective speech rate and stimulus category. Also after standardizing the identified rate values for each speaker (by computing their z-score values) in order to compensate for a different use of the perception scale among individual listeners, there is no interaction between subjective speech rate and stimulus category.

The subjective speech rate of the subjects, which was used above, is partly based on other cues beside articulation rate (although this, too, was shown to differ). In order to use a more objective grouping of the subjects according to their speaking habits, the groupings shown in Table II (which are based on the speakers' *measured* articulation rates) were used to replace the subjective speech rate in the previous analysis of variance (but note that with only 12 subjects in total the tests are not very powerful). Several of the suggested groupings lead to significant differences for these "objective rate" clusters, but in all *posthoc* analyses fast, clear speakers group with slow, sloppy speakers. As with the subjective speech rate, there are no significant interactions between stimulus category and objective rate, either for the raw identified rate values or for their standardized (z-score) values.

IV. COMPARISON WITH DATABASE ANALYSIS

Using spontaneous speech stimuli in perception experiments has the advantage that the results are representative of conversational speech. But it also has the disadvantage that other variables cannot always be completely controlled. It was assumed that for the selection of our stimuli they constitute random variables in our experimental design. Careful inspection of the stimuli in terms of the hesitations, intonational properties (number and type of accents as well as the contours which connect them; boundary tones), and the relative number of function and content words did not show any *systematic* differences between the stimulus categories which could constitute an alternative explanation for our results.

The rationale for the analysis of the database from which the stimuli were selected in terms of the intended and realized rates of all the intonation phrases is that a confirmation of the differences found in the perception experiments gives further support for their perceptual relevance. At the time of analysis a total of 1329 files from the Kiel Corpus of Spontaneous Speech had been prosodically labeled. The files were divided up into intonation phrases on the basis of the prosodic labels (only one phrasing level was used), resulting in 5779 intonation phrases after exclusion of intonation phrases with only nonspeech material or hesitations. For intonation phrases with extreme perceived speech rates, the perceived rate was indicated by the labelers. The labels RM for rate minus and RP for rate plus were used when (part of) an intonation phrase was considered to be spoken particularly slowly or fast, respectively. The rest of the intonation phrases

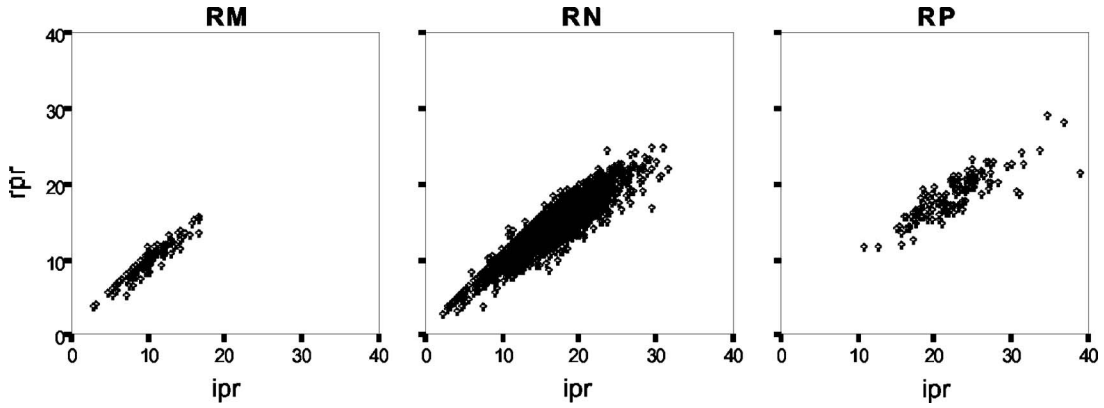

FIG. 5. Scatterplot of intended (ipr) versus realized rate (rpr) in phones per second for all intonation phrases with a minimum duration of 0.5 s perceived as slow (RM), normal (RN), and fast (RP).

were labeled by us as rate normal (RN)—though this does not preclude variation in rate, since it was from these phrases that all the stimuli in the two listening experiments were taken. As in the analysis of the subjects' speaking habits, only intonation phrases with a duration of at least half a second are analyzed ($n=4736$). This reduces the data by 18%, but only 8 out of 137 fast and 2 out of 116 slow intonation phrases are less than half a second long. The fact that the labelers only rarely use the labels RM and RP for short intonation phrases supports Pfitzinger's observation that "using speech signal segments of less than 500 ms hindered the assessment of speech rate" (Pfitzinger, 1999, p. 893).

For each intonation phrase, the number of intended and realized phones per second was determined.[3] There is a strong and highly significant correlation between the two rates (overall correlation: $r=0.93$, $n=4736$, $p<0.001$). Figure 5 shows scatterplots of the data for slow (RM: $r=0.95$, $n=114$, $p<0.001$), normal (RN: $r=0.92$, $n=4493$, $p<0.001$), and fast (RP: $r=0.85$, $n=129$, $p<0.001$) perceived speech rates.

The considerable overlap in the measured phone rates of the different perceived rate categories indicates that factors other than articulation rate also determine the perceived speech rate. Nevertheless, an analysis of variance with subsequent Tukey-HSD *posthoc* tests shows that both the intended ($F(2,4733)=298.0$, $p<0.001$) and realized phone rates ($F(2,4733)=253.8$, $p<0.001$) as well as the articulatory precision index values ($F(2,4733)=45.1$, $p<0.001$) differ significantly for the three perceived rates. Figure 6 shows that, as expected, both the intended and the realized speech rate increase with perceived speech rate, while the articulatory precision index decreases.

V. DISCUSSION

As the results from the comparison experiment have shown, differences between the stimuli in intended and realized phone rates are clearly perceived [Fig. 2(A)]. Even if only the intended, canonical rate of two phrases differs (with identical realized rates), listeners perceive a difference in speech rate. In this case, the phrase with the faster intended rate is perceived as faster [Fig. 2(C)]. The experiment shows therefore that the perceived speech rate is not solely determined by actual articulatory events, but also by the listener's knowledge of what articulations are implied by a particular utterance.

On the other hand, knowledge of the implied articulations is not used to normalize differences in the realized ar-

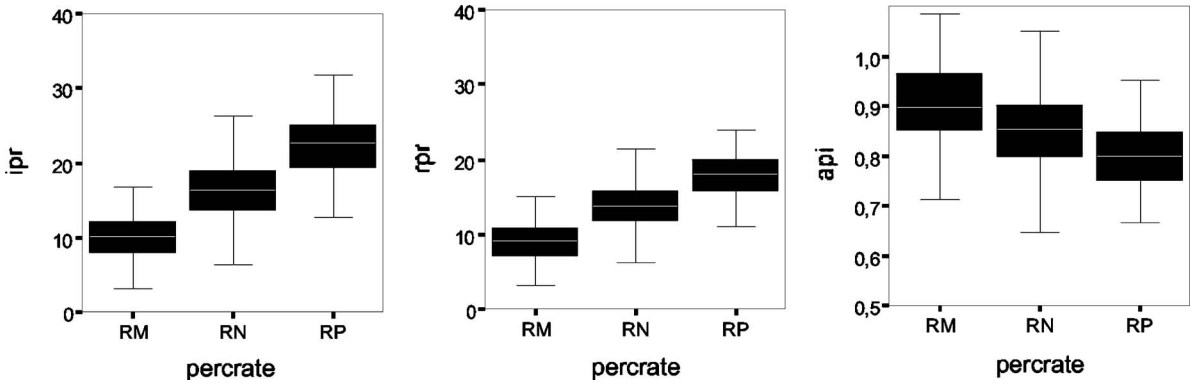

FIG. 6. Boxplots of intended (ipr) and realized phone rates (rpr) in phones per second as well as articulatory precision index (api) values for intonation phrases perceived as slow (RM), normal (RN), and fast (RP).

ticulation rates away. If this were the case, the perceived speech rate would have been entirely determined by the intended rate. As was noted in the description of the stimuli, the difference in realized rate between the FC and FS categories, and also between the NCs and NS categories (also NCf-NS), is at least in part caused by the lack of reduction contexts in the clear phrases. If listeners were to compensate for this when they judge speech rate, the stimuli should be considered equally fast. In reality, the higher realized articulation rates in clearly spoken phrases is taken at face value and interpreted as an indication of faster speech [Fig. 2(B)].

These results, and corroborating evidence from the scaling experiment showing differences between all stimulus categories except NCf-NCs (but also FS-NCs), clearly support hypothesis 1 that both the intended and the realized rate affect the perceived speech rate (see the Introduction). The significant differences in intended and realized rates between fast (RP), normal (RN), and slow (RM) speech in the extended database analysis seem to support the role of both rates for the perception of speech rate.

There are two possible interpretations of the joint contribution of intended and realized rates to the perceived rate. In the first interpretation it is assumed that the intended form has a real, psychological status. Listeners combine the actual, realized phone rate with their knowledge of the intended, canonical form to determine the perceived speech rate. But instead of claiming direct reference to listeners' knowledge of the intended form, there is a second possible explanation of our results within exemplar-based approaches to speech perception. If we do not want to assume reference to abstract units in speech perception before or simultaneously with the construction of meaning (Hawkins, 2003)—and this certainly does not seem necessary for the task—one must assume that the perceived speech rate is determined after the meaning of an utterance has been established (on the basis of the realized speech signal and the situational context in which it is produced), possibly by referring to functional groupings for the context. These functional groupings must then be indexed with information about the speech rate directly, or with information from which speech rate judgments can be derived, e.g., information about the time pressure under which conversations take place in which the observed realized forms have been used before, or information about the level of formality. The results from the listening experiments presented in this study are fully compatible with both theories.

The differences in perceived rate between categories from the faster half of the database (FC-FS-NCf) are the same as those in comparisons for the slower half (NCs-NS-SC). In general, there is no evidence that a difference in the balance between input- and output-oriented constraints at faster versus slower articulation rates in any way affects listeners' perception of speech rate (cf. hypothesis 2 in the Introduction). Although it was hypothesized that hyperspeech may be a typical fast speech phenomenon, clear speech in the slower half of the database has the same effect of making the utterance sound faster than an utterance with the same intended, but a lower realized rate (cf. the dashed with the dotted graphs in Fig. 3). The same is true for hypospeech: although it was suggested this may be more typical for slow speech, sloppiness has the same perceptual effect at high intended rates, making the utterance sound slower (cf. Fig. 3). There is no evidence from the perception experiments, therefore, to support the second hypothesis.

The results from the scaling experiment show that listeners do not only distinguish between articulation rates when two stimuli are presented for comparison (first experiment), but they can also judge them in isolation (second experiment). There is, however, no evidence that the perception of speech rate depends on the speaker-listener's own speaking habits. Subjectively fast speakers do not judge stimuli any differently from subjectively slow speakers. And although the effect of the objective groupings for the listeners' speech behavior on the identified rate of the stimuli was significant, these groupings are not consistent with the hypothesized effects of articulation rate and articulatory precision on the perceived rate of the stimuli. In particular, slow speakers were expected to evaluate the stimuli as faster on average than fast speakers, and sloppy speakers were expected to consider clear stimuli as faster (more hyperarticulated) than clear speakers, particularly in the case of fast, clear speech. But, in fact, fast, clear speakers group with slow, sloppy speakers in all statistical tests. This clearly contradicts our hypothesis. Thus, perceived speech rate does not seem to be a projection of the listener's own speech behavior.

The results presented in this paper described the effects of articulation rate and speaking style on the perceived speech rate. Of course, the perceived speech rate is also affected by other factors which still need to be investigated. For instance, *local* variation within an intonation phrase was not taken into consideration, although this may influence the perceived speech rate. Also, quantitative and qualitative phone reductions which do not affect the number of phones (e.g., vowel shortening or reductions from long, tense to short, lax vowels) and are therefore not reflected in our measures are likely to influence the perceived speech rate. Many of the deletions and reductions can be described using a small set of well-known phonological rules, such as schwa deletion, (nasal) assimilation and lenition of pre-vocalic glottal stops into laryngealized vowel onsets, or complete deletion of glottal stops (cf. Zellner, 1998; Kohler, 2001; Brinckmann and Trouvain, 2002). Further phonetic analysis of the database for the type of deletions and reductions at the different rates and subsequent evaluation of their perceptual effects are needed. The fact that other signal properties besides the articulation rate measures investigated here do affect the perceived speech rate is reflected in the discrepancy between the subjective and objective speaker groupings (cf. section on objective rate and style) as well as in the considerable overlap (shown in the section on database analysis) between normal and slow measured rates (RN and RM) and also between normal and fast measured rates (RN and RP) in the database. This stresses the importance of a phonetic analysis of the effect of nonsegmental properties such as disfluencies, the relative number of function versus content words in an utterance, and the intonation patterns at different perceived rates in the whole database to arrive at a more complete

understanding of the speech characteristics which affect the perceived speech rate.

ACKNOWLEDGMENTS

The author should like to thank Dominik Bauer, Fabian Brackhane, Tamara Hausmann, Anja Moos, Olga Trifsik, and Steven Webber for their perseverance in running the experiments. Further thanks are due to Bistra Andreeva, Bill Barry, Andrew Morris, and Markus Pospeschill for discussion, as well as to the anonymous reviewers for their helpful comments on an earlier version of this paper.

APPENDIX: STIMULI AND THEIR TRANSCRIPTIONS

Intonation phrases for each of the stimulus categories used in this study, selected from the files of Kiel Corpus of Spontaneous Speech, together with their orthographic, intended, and realized phone transcriptions as well as their duration (dur), intended (ipr), and realized phone rates (rpr) and their articulatory precision index values (api). Phone counts are based on the conventions used in the Kiel Corpus transcriptions.

FC (fast clear)

File:	g114a009.s1h	api=1.00
Orthographic:	"…Revisionstreffen zu machen?"	dur=1.00 s
Intended:	/ʁɛvɪzjo:nstʁɛfən tsu: maχən/	ipr=22.98 phones/s
Realized:	[ʁɛvɪzjo:nstʁɛfən tsu: maχən]	rpr=22.98 phones/s
File:	g312a012.s1h	api=0.92
Orthographic:	"Und wann sind Sie dann wieder zurück?"	dur=1.19 s
Intended:	/ʔʊnt van zɪnt zi: dan vi:dɐ tsʊʁʏk/	ipr=21.85 phones/s
Realized:	[ʊnd van zɪnt zi: dan vi:ɐ tsʊʁʏk]	rpr=20.17 phones/s
File:	g077a003.s1h	api=0.94
Orthographic:	"Ich weiß ja nicht direkt, wie lange das dauert…"	dur=1.49 s
Intended:	/ʔɪç vaɪs ja: nɪçt dɪʁɛkt, vi: laŋə das daʊɐt/	ipr=20.78 phones/s
Realized:	[i̯ç vaɪs ja: niç dɪʁɛkt, vi: laŋə das daʊɐd]	rpr=19.44 phones/s
File:	g113a011.s1h	api=0.93
Orthographic:	"…nämlich von Montag, dem neunzehnten…"	dur=1.33 s
Intended:	/nɛ:mlɪç fɔn mo:nta:k, de:m nɔɪntse:ntən/	ipr=21.06 phones/s
Realized:	[nɪmɪç fɔn mo:nta:χ, de:m nɔɪntse:ntn]	rpr=19.55 phones/s
File:	g197a009.s1h	api=0.92
Orthographic:	"…würde mir ganz gut in den Kram…"	dur=1.12 s
Intended:	/vʏɐdə mi:ɐ gants gu:t ʔɪn de:n kʁa:m/	ipr=23.07 phones/s
Realized:	[vʏɐdə mi:ɐ gants gu:t i̯n ne:ŋ kʁa:m]	rpr=21.29 phones/s

FS (fast sloppy)

File:	g077a005.s1h	api=0.65
Orthographic:	"und da habe ich wieder eigentlich…"	dur=1.09 s
Intended:	/ʔʊnt da: ha:bə ʔɪç vi:dɐ ʔaɪgəntlɪç/	ipr=23.78 phones/s
Realized:	[ʊn da: ha:b i̯ç vi:ɐ a̯ɪŋl̩ɪç]	rpr=15.55 phones/s
File:	g147a005.s1h	api=0.64
Orthographic:	"Würde es Ihnen da es gut passen?"	dur=1.10 s
Intended:	/vʏɐdə ʔɛs ʔi:nən da: ʔɛs gu:t pasən/	ipr=22.78 phones/s
Realized:	[vʏɐ əs i̯:n da: s gu:t pasn]	rpr=14.58 phones/s
File:	g211a012.s1h	api=0.63
Orthographic:	"Ich hätte hier einen Vorschlag zu machen…"	dir=1.49 s
Intended:	/ʔɪç hɛtə hi:ɐ ʔaɪnən fo:ɐʃla:k tsu: maχən/	ipr=20.19 phones/s
Realized:	[ç hɛtə hi:ɐ n fo:ɐʃla:χ ts maχŋ]	rpr=12.79 phones/s
File:	g086a018.s1h	api=0.65
Orthographic:	"Ich würde Ihnen daher vorschlagen…"	dur=1.24 s
Intended:	/ʔɪç vʏɐdə ʔi:nən da:he:ɐ fo:ɐʃla:gən/	ipr=20.19 phones/s
Realized:	[ɪç vʏɐdə i:n dahe:ɐ fɔɐʃla:ŋ]	rpr=13.66 phones/s
File:	g193a009.s1h	api=0.62
Orthographic:	"Nee, da habe ich schon einen anderen Termin."	dur=1.25 s
Intended:	/ne:, da: ha:bə ʔɪç ʃo:n ʔaɪnən ʔandɐʁən tɛɐmi:n/	ipr=25.69 phones/s
Realized:	[ne:, da: a:b ɪ ʃõ: n a̯nɐn tɛɐmi:n]	rpr=16.06 phones/s

NCf (normal clear, for comparison with fast stimuli)

File:	g115a011.s1h	api=1.00
Orthographic:	"Das wird ja ganz schlecht."	dur=1.15 s
Intended	/das vɪɐt ja: gants ʃlɛçt/	ipr=15.63 phones/s
Realized:	[das vɪɐt ja: gants ʃlɛçt]	rpr=15.63 phones/s

NCf (normal clear, for comparison with fast stimuli)

File:	g121a003.s1h	api=1.00
Orthographic:	"Samstag bis Montag."	dur=1.09 s
Intended:	/zamsta:k bɪs mo:nta:k/	ipr=14.64 phones/s
Realized:	[zamssa:χ bɪs mo:nta:k]	rpr=14.64 phones/s
File:	g212a007.s1h	api=0.94
Orthographic:	"Bis Mittwoch, den achten?"	dur=1.33 s
Intended:	/bɪs mɪtvɔχ, de:n ʔaχtən/	ipr=13.52 phones/s
Realized:	[bɪs mɪtvɔχ, de:n ʔa̰χtn]	rpr=12.77 phones/s
File:	g195a001.s1h	api=0.94
Orthographic:	"Nee, Samstag bin ich schon…"	dur=1.22 s
Intended:	/ne:, zamsta:k bɪn ʔɪç ʃo:n/	ipr=14.71 phones/s
Realized:	[ne:, zamssa:χ bɪn ɪç ʃo:n]	rpr=13.89 phones/s
File:	g091a024.s1h	api=0.92
Orthographic:	"Wie wäre es mit Ende November?"	dur=1.34 s
Intended:	/vi: vɛ:ʁə ʔɛs mɪt ʔɛndə no:vɛmbɐ/	ipr=17.89 phones/s
Realized:	[vi: ve:ʁ əs mɪt ʔɛ̰ndə no:vɛmbɐ]	rpr=16.40 phones/s

NCs (normal clear, for comparison with slow stimuli)

File:	g312a019.s1h	api=1.00
Orthographic:	"…gleich drei Termine fertig."	dur=1.14 s
Intended:	/glaɪç dʁaɪ tɛɐmi:nə fɛɐtɪç/	ipr=15.83 phones/s
Realized:	[glaɪç dʁaɪ tɛɐmi:nə fɛɐtɪç]	rpr=15.83 phones/s
File:	g105a010.s1h	api=1.00
Orthographic:	"Ja, das wäre günstig…"	dur=1.13 s
Intended:	/ja: das vɛ:ʁə gʏnstɪç/	ipr=14.17 phones/s
Realized:	[ja: das vɛ:ʁə gʏnstɪç]	rpr=14.17 phones/s
File:	g117a005.s1h	api=1.00
Orthographic:	"Und ich denke mal…"	dur=1.08 s
Intended:	/ʔʊnt ʔɪç dɛŋkə ma:l/	ipr=13.84 phones/s
Realized:	[ʔʊ̰nt ʔɪ̰ç dɛŋkə ma:l]	rpr=13.84 phones/s
File:	g254a007.s1h	api=0.95
Orthographic:	"Bis zum dreizehnten Juli?"	dur=1.46 s
Intended:	/bɪs tsʊm dʁaɪtse:ntən ju:li:/	ipr=14.40 phones/s
Realized:	[bɪs tsʊm dʁaɪtse:ntn ju:li:]	rpr=13.71 phones/s
File:	g075a002.s1h	api=1.00
Orthographic:	"…ließe sich dann schnell machen…"	dur=1.07 s
Intended:	/li:sə zɪç dan ʃnɛl maχən/	ipr=17.69 phones/s
Realized:	[li:sə zɪç dan ʃnɛl maχən]	rpr=17.69 phones/s

NS (normal sloppy)

File:	g215a001.s1h	api=0.67
Orthographic:	"Dann haben wir half nur…"	dur=1.17 s
Intended:	/dan ha:bən vi:ɐ halt nu:ɐ/	ipr=15.43 phones/s
Realized:	[dan ha:m vi:ɐ halt nu:ɐ]	rpr=10.29 phones/s
File:	g072a008.s1	api=0.67
Orthographic:	"Kleinen Augenblick…"	dur=1.06
Intended:	/klaɪnən ʔaʊgənblɪk/	ipr=14.10 phones/s
Realized:	[klaɪn a̰ʊŋblɪk]	rpr=9.40 phones/s
File:	g317a006.s1h	api=0.62
Orthographic:	"…den wir morgen haben…"	dur=1.16 s
Intended:	/de:n vi:ɐ mɔʁgən ha:bən/	ipr=13.82 phones/s
Realized:	[de:n vi:ɐ mɔʁŋ ha:m]	rpr=8.64 phones/s
File:	g105a005.s1h	api=0.59
Orthographic:	"…um neun Uhr in einem Hotel…"	dur=1.48 s
Intended:	/ʔʊm nɔɪn ʔu:ɐ ʔɪn ʔaɪnəm ho:tɛl/	ipr=14.86 phones/s
Realized:	[ʊ̰m nɔɪn ṵ:ɐ ɪ̰n m ho:tɛl]	rpr=8.78 phones/s
File:	g142a008.s1h	api=0.65
Orthographic:	"Hätten Sie in der ersten…?"	dur=1.18 s
Intended:	/hɛtən zi: ʔɪn de:ɐ ʔɛ:ʁstən/	ipr=17.03 phones/s
Realized:	[hɛtn zi: ɪn de:ɐ ɛ̰:ʁstn]	rpr=11.07 phones/s

SC (slow clear)

File:	g251a024.s1h	api=1.00
Orthographic:	"…zum Beispiel am…"	dur=1.28 s
Intended:	/tsʊm baɪʃpi:l ʔam/	ipr=10.15 phones/s
Realized:	[tsʊm baɪʃpi:l ʔa̯m]	rpr=10.15 phones/s
File:	g253a004.s1h	api=1.00
Orthographic:	"Und freitags?"	dur=1.17 s
Intended:	/ʔʊnt fʁaɪta:ks/	ipr=9.38 phones/s
Realized:	[ʔʊnt fʁaɪta:ks]	rpr=9.38 phones/s
File:	g217a006.s1h	api=1.00
Orthographic:	"…beschäftigt…"	dur=1.08 s
Intended:	/bəʃɛftɪçt/	ipr=8.38 phones/s
Realized:	[bəʃɛftɪçt]	rpr=8.38 phones/s
File:	g311a007.s1h	api=1.00
Orthographic:	"…den vielleicht auf…"	dur=1.34 s
Intended:	/de:n fɪlaɪçt ʔaʊf/	ipr=8.94 phones/s
Realized:	[de:n fɪlaɪçt ʔa̯ʊf]	rpr=8.94 phones/s
File:	g085a004.s1h	api=1.00
Orthographic:	"…Dienstag nehmen?"	dur=1.07 s
Intended:	/di:nsta:k ne:mən/	ipr=11.22 phones/s
Realized:	[di:nsta:k ne:mən]	rpr=11.22 phones/s

[1]As others, we shall use the terms "clear" and "sloppy" as an opposition to describe the speaker's care of articulation, although the first term refers to perception—its articulatory counterpart could be "precise" or even "overprecise" if the possibility of spelling pronunciations is included. No negative connotations are intended with the word "sloppy," even if in everyday use it may imply that the speaker is *too* careless of his/her articulation.

[2]For the five comparisons between the categories FC and FS, for instance, listener HR responded twice with "first stimulus faster," once with "second stimulus faster," and twice with "equal" (response code 2-1-2), so that $c=(1+2)/(2+2+1)=0.6$. The same number of "first stimulus faster" responses, but with more "equal" responses, as in response code 2-0-3, would result in $c=0.75$, i.e., a higher certainty, because there are no "second stimulus faster" responses which go against expectation. If the subject always (five times for each comparison between two stimulus categories) responds with "first stimulus faster" (response code 5-0-0), this results in $c=0.86$; if (s)he consistently chooses "second stimulus faster (response code 0-5-0), $c=0.14$. Both response codes 0-0-5 and 2-2-1 result in $c=0.5$ (uncertainty).

[3]The number of intended and realized syllables per second as well as the number of orthographic words per second were also derived. The correlation between syllable and phone rates varied between $r=0.79$ and $r=0.88$ ($p<0.001$). The correlation between the orthographic word rate and the other four measures was between $r=0.49$ and $r=0.62$ ($p<0.001$).

Altman, G. (**1992**). *Experimenter. A Toolkit for Multi-Modal Psycholinguistic Experimentation on the Apple Macintosh* (Laboratory of Experimental Psychology, University of Sussex).

Brinckmann, C., and Trouvain, J. (**2002**). "The role of duration models and symbolic representation for timing in speech synthesis," Int. J. Speech Technolo. **6**, 21–31.

Bromberger, S., and Halle, M. (**2000**). "The ontology of phonology (revised)," in *Phonological Knowledge: Conceptual and Empirical Issues*, edited by N. Burton-Roberts, P. Carr, and G. Docherty (Oxford U. P., Oxford).

Butcher, A. (**1981**). "Phonetic correlates of perceived tempo in reading and spontaneous speech," *Work in Progress*, University of Reading, Vol. 3, pp. 105–117.

Collings, S. N. (**1997**). *Fundamentals of Statistical Inference, Unit 9. Decision Theory and Bayesian Inference*, course M341, pp. 7–45 (Open U. P., Walton Hall, Milton Keynes).

Crystal, T. H., and House, A. S. (**1990**). "Articulation rate and the duration of syllables and stress groups in connected speech," J. Acoust. Soc. Am. **88**, 101–112.

Dankovičová, J. (**1999**). "Articulation rate variation within the intonation phrase in Czech and English," *Proc. 14th Int. Congress of Phonetic Sciences (ICPhS)*, San Francisco, Vol. 1, pp. 269–272.

Den Os, E. (**1985**). "Perception of speech rate, a scaling experiment," Prog. Rep. Inst. Phonetics Utrecht (PRIPU) **10**, 35–43.

Duden (**2000**). *Duden: Aussprachewörterbuch* (Mannheim, Dudenverlag).

Fougeron, C., and Jun, S.-A. (**1998**). "Rate effect on French intonation: Prosodic organization and phonetic realization," J. Phonetics **26**, 45–69.

Funk and Wagnalls (**1973**). *Standard Dictionary of the English Language, International Edition* (Funk & Wagnalls, New York).

Gay, T. (**1981**). "Mechanisms in the control of speech rate," Phonetica **38**, 148–158.

Goldman-Eisler, F. (**1968**). *Psycholinguistics* (Academic Press, London).

Hawkins, S. (**2003**). "Roles and representations of systematic fine phonetic detail in speech understanding," J. Phonetics **31**, 373–405.

IPDS (**1994**). *The Kiel Corpus of Read Speech, CD-ROM #1* (Institut für Phonetik und digitale Sprachverarbeitung, Kiel), www.ipds.uni-kiel.de/forschung/kielcorpus.en.html, last viewed: 10.06.2004.

IPDS (**1995–1997**). *The Kiel Corpus of Spontaneous Speech, CD-ROM #2–4* (Institut für Phonetik und digitale Sprachverarbeitung, Kiel), www.ipds.uni-kiel.de/forschung/kielcorpus.en.html, last viewed: 10.06.2004.

Kohler, K. J. (**1986**). "Parameters of speech rate perception in German words and sentences: Duration, F0 movement and F0 level," Lang Speech **29**, 115–139.

Kohler, K. J. (**1994**). "Glottal stops and glottalization in German," Phonetica **51**, 38–51.

Kohler, K. J. (**2001**). "Articulatory dynamics of vowels and consonants in speech communication," J. Int. Phonetic Assoc. **31**(1), 1–16.

Kohler, K. J., and Rodgers, J. (**2001**). "Schwa deletion in German read and spontaneous speech," Arb. Inst. Phonetik Dig. Signalverarbeitung Universität Kiel (AIPUK) **35**, 97–123.

Koreman, J. (**2003**). "The perception of articulation rate," *Proc. 15th Int. Congress of Phonetic Sciences (ICPhS)*, Barcelona.

Lass, N. J. (**1970**). "The significance of intra- and intersentence pause times in perceptual judgments of oral reading rate," J. Speech Hear. Res. **13**, 777–784.

Lindblom, B. (**1963**). "Spectrographic study of vowel reduction," J. Acoust. Soc. Am. **35**, 1773–1781.

Lindblom, B. (**1990**). "Explaining phonetic variation: A sketch of the H&H theory," in *Speech Production and Speech Modelling*, edited by W. J. Hardcastle and A. Marchal (Kluwer Academic Publishers, Dordrecht).

Pfitzinger, H. R. (**1999**). "Local speech rate perception in German speech," *Proc. 14th Int. Congress of Phonetic Sciences (ICPhS)*, San Francisco, Vol. 2, pp. 893–896.

Rietveld, T., and Gussenhoven, C. (**1987**). "Perceived speech rate and intonation," J. Phonetics **15**, 273–285.

Trouvain, J., and Grice, M. (**1999**). "The effect of tempo on prosodic struc-

ture," *Proc. 14th Int. Congress of Phonetic Sciences (ICPhS)*, San Francisco, Vol. 2, pp. 1067–1070.
Wesener, T. (**1999**). "The phonetics of function words in German spontaneous speech," Arb. Inst. Phonetik Dig. Signalverarbeitung Universität Kiel (AIPUK) **34**, 327–377.
Zellner, B. (**1998**). "Temporal structures for fast and slow speech rate," *Proc. 3rd ESCA/COCOSDA Workshop on Speech Synthesis*, Jenolan Caves, pp. 143–146.

First-language phonotactics in second-language listening

Andrea Weber[a)]
Saarland University, Saarbrücken, Germany

Anne Cutler
Max Planck Institute for Psycholinguistics, Nijmegen, The Netherlands

(Received 25 July 2005; revised 27 October 2005; accepted 31 October 2005)

Highly proficient German users of English as a second language, and native speakers of American English, listened to nonsense sequences and responded whenever they detected an embedded English word. The responses of both groups were equivalently facilitated by preceding context that both by English and by German phonotactic constraints forced a boundary at word onset (e.g., *lecture* was easier to detect in *moinlecture* than in *gorklecture*, and *wish* in *yarlwish* than in *plookwish*). The American L1 speakers' responses were strongly facilitated, and the German listeners' responses almost as strongly facilitated, by contexts that forced a boundary in English but not in German (*thrarshlecture, glarshwish*). The German listeners' responses were significantly facilitated also by contexts that forced a boundary in German but not in English (*moycelecture, loitwish*), while L1 listeners were sensitive to acoustic boundary cues in these materials but not to the phonotactic sequences. The pattern of results suggests that proficient L2 listeners can acquire the phonotactic probabilities of an L2 and use them to good effect in segmenting continuous speech, but at the same time they may not be able to prevent interference from L1 constraints in their L2 listening. © *2006 Acoustical Society of America.* [DOI: 10.1121/1.2141003]

PACS number(s): 43.71.Hw, 43.71.Es [ARB] Pages: 597–607

I. INTRODUCTION

A speaker of English who does not know the word *lope* is nonetheless likely to parse the sequence *lope for* correctly, because any other boundary assignment would give rise to an un-English syllable: *lowpf or* would yield a postvocalic /pf/ cluster, and *low pfor* would yield a prevocalic /pf/ cluster. English speakers know from experience that the cluster /pf/ does not occur in either position in their language. Phonotactic constraints on the possible structures that syllables may assume constitute part of the implicit knowledge that listeners have amassed about the phonology of their language. Such knowledge can be usefully exploited when new words are encountered.

In fact, phonotactic knowledge is useful in all listening situations, even if no unfamiliar words are presented. The rules and probabilities applying to the sequencing of phonemes provide a rich source of information for listeners. They can tell listeners where the speech signal definitely contains word or syllable boundaries, as in the above-noted example; but they can also tell where such boundaries are more versus less likely to occur. This potential source of information in the recognition of continuous speech (by human listeners or by machines) was pointed out many years ago (e.g., Church, 1987; Lamel and Zue, 1984; Harrington, Watson, and Cooper, 1989). Its use by human listeners has been amply attested in perceptual experiments. Several such experiments have used the wordspotting task, which is particularly suited for examining detection of word boundaries. In a wordspotting experiment, listeners attempt to find real words embedded in nonsense input. For instance, in the string *obzel crivthish dullfim* they should detect the word *dull*. The relative difficulty of detection associated with a particular boundary can affect the speed with which listeners correctly detect the embedded word, and indeed the likelihood of the word being detected at all.

Sequencing constraints are easy to manipulate in a wordspotting experiment. If *dull* were to be presented in *dullfbim* instead of *dullfim*, for instance, we would expect detection to be harder, since the sequence /fb/ should contain a word boundary (as in: *we found the gulf bigger than expected*) and thus there would be no natural boundary aligned with the edge of the word *dull*. In consequence, we would expect listeners to take longer finding *dull*, or perhaps not to find it at all. The study that first clearly showed this effect was carried out in Dutch. McQueen (1998) showed that listeners detected *vel* "rim" faster and more accurately in *velbroel* versus *velmroel*, and *rok* "skirt" likewise faster and more accurately in *fimrok* versus *fidrok*. The sequence /mr/ in each of these pairs must contain a boundary in Dutch, just as in English; this information helps listeners find *rok* in *fimrok*, but hinders them with *vel* in *velmroel*.

Dumay, Frauenfelder, and Content (2002) established that constraints of the same type affect wordspotting in French; thus *lac* "lake" is easier to spot in *zunlac*, in which its edge is aligned with a phonotactically obligatory syllable boundary, than in *zuglac*, in which this is not the case.

Probabilistic information can be used in the same way: van der Lugt (2001), in an analogous experiment in Dutch, showed that words with common onsets are easier to spot than words with rare onsets—e.g., it is easier to find *galg* "gallows" in *piengalg* than *geur* "aroma" in *piengeur*. In

[a)]Electronic mail: aweber@coli.uni.sb.de

Dutch, many words begin *ga-* but very few begin *geu-*; van der Lugt argued that listeners translate their experience of this pattern in the vocabulary into probabilistic heuristics for finding word boundaries in speech.

Both kinds of information are also used by Korean listeners; word boundaries are prohibited in Korean in the sequence [dʒi], legal but not highly likely in the sequence [di], and highly likely in the sequence [nni]; correspondingly, Korean listeners detect words like *imin* "migration" more easily in [pjodimin] than in [pjodʒimin] and easiest of all in [pjonnimin] (Warner *et al.*, 2005).

Sensitivity to legality or probability of phoneme sequences also appears in phoneme detection in many languages (e.g., Gow, 2001, for English; Hallé *et al.* 1998, for French; Otake *et al.* 1996, for Japanese; Weber, 2001, for German; Yip, 2000, for Cantonese), as well as in artificial language learning (Saffran, Newport, and Aslin, 1996), goodness ratings of nonsense words (Vitevitch *et al.* 1997), lexical decision and word repetition (Vitevitch and Luce, 1999). Note that the nature of transitional probability effects depends upon the task that listeners have to carry out—thus although van der Lugt (2001) found that many words beginning in the same way makes spotting such words easier, lexical decision and repetition responses are slower for words with many onset competitors (Vitevitch, 2002).

The ability to exploit such rules and probabilities comes, of course, from linguistic experience. What is relevant is experience with a particular language, because phonotactic syllable boundary constraints and probabilities are specific to particular vocabularies. Thus English may proscribe both pre- and postvocalic /pf/ clusters, but other languages happily allow them in both positions. German is one such language—*Kopf* "head" and *Pferd* "horse" are both German words. Similarly, for McQueen's (1998) Dutch listeners, *vel* was particularly easy to find in *velbroel* and *rok* particularly hard in *fidrok* because /b/ and /d/ (and all voiced obstruents) do not occur in syllable-final position in Dutch. Therefore a syllable boundary had to precede these sounds. This obviously is not true of English, in which voiced obstruents may occur syllable-finally, so that words like *bulb* and *feed* are perfectly legal.

The language-specificity of phonotactic sequencing constraints has two consequences for the relevance of such information in second-language listening. First, native (L1) listeners' greater experience with the language should better enable them to make use of this kind of information than second-language (L2) listeners, who will have enjoyed much less relevant experience. Experiments with listening to totally unfamiliar languages have shown that phoneme sequence effects shown by L1 listeners do not appear with naive listeners (Otake *et al.*, 1996; Weber, 2001). Thus it is not the case that these effects are primarily signal-driven; they are experience-driven, and L2 listeners will have had less of the relevant experience than L1 listeners.

A second, and potentially more dangerous, consequence of the language-specificity of phonotactics is the potential transfer of the L1 phonotactic knowledge to L2 listening. Just as L2 listeners show effects of the L1 phonemic inventory in L2 phonetic processing (see Strange, 1995, for reviews), so might L1 phonotactics interfere and in consequence hinder L2 listening, when L2 listeners hear sequences that are prohibited syllable-internally in the L1 but not in the L2, or are allowed syllable-internally in the L1 but prohibited in the L2. Since the smallest viable word in any language is a syllable, segmentation of continuous speech into its component words necessarily makes reference to syllable boundaries (Norris *et al.*, 1997). Thus a German speaker of English might not readily perceive that *lope for* has to contain a syllable boundary between /p/ and /f/, because the /pf/ sequence can occur syllable-internally in German. An English speaker of German, in contrast, might falsely posit a boundary between /p/ and /f/ in *die Pferde* or *Kopf auf*, on the grounds that a boundary must occur in a /pf/ sequence in English.

The present study tests whether L1 phonotactic effects in L2 listening do indeed occur. We confronted L2 listeners—Germans listening to English—with phonotactic sequences that in their L1, German, would signal a boundary (but that should not be informative in the L2, English). The listeners were highly proficient in English, though their accumulated experience with the language would not match that of an L1 speaker of the same age. We asked—using the task that McQueen (1998), van der Lugt (2001), Dumay *et al.* (2002), and Warner *et al.* (2005) had shown to be sensitive to lexical segmentation via phonotactic information—whether the listeners would be influenced by the German constraints when listening to English. We compared their responses in this condition with conditions involving sequences that would indeed signal a boundary in English, and sequences that would signal a boundary in both languages or in neither language, and we also compared their responses with those of American English L1 listeners. We also ascertained what acoustic information the materials contained that might potentially signal the presence of a word or syllable boundary, and we determined whether the presence of this information was correlated with the pattern of each listener group's responses.

II. MATERIALS CONSTRUCTION

With the wordspotting paradigm it is possible to compare detection of the same word in different contexts. This is a particularly valuable feature of this paradigm in the present case, because with L2 listening it is hard to control the properties of words that experimenters usually attempt to keep constant in lexical processing experiments. Word frequency counts, for example, may not reflect the experience of L1 and L2 listeners in the same way. Such controls are unnecessary, however, if the manipulations of interest can be accomplished within items.

To make this possible, we required English words that could be placed in four different preceding contexts: one in which the preceding phoneme provided a phonotactically clear boundary in both English and German, one in which the preceding phoneme provided a clear boundary in English but not in German, one in which the preceding phoneme provided a clear boundary in German but not in English, and one in which the preceding phoneme provided a clear bound-

ary in neither language. For the latter two cases it was thus necessary to select words beginning with phonemes that could be the second element in more than one kind of English cluster. This severely constrains the range of available words. It rules out exploiting the pf- case, for example, because /f/ hardly occurs as second element in a cluster in English words (*sphere, sphinx*). We chose to use words beginning with /l/ and /w/. These phonemes make it possible to construct all four types of context.

In both English and German, words can begin with the singleton consonant /l/, and its pronunciation in syllable onset position is analogous in the two languages. Such close parallels cannot be achieved with /w/, since this labiovelar approximant does not occur in German; instead, German has the voiced fricative /v/, e.g., in cognate words (E: *winter, wool, warm*; G: *Winter, Wolle, warm*). Substitution of /v/ for /w/ is perhaps the most noticeable marker of a German accent in English (*ve have vays…*), suggesting that the English sound is assimilated to the German category. These two onset phonemes thus provide a further interesting contrast regarding the application of phonotactic constraints, since one can be directly mapped to L1 constraints, while the other can only be mapped via prior assimilation of the L2 sound to a L1 category.

English and German phonotactic constraints differ (Giegerich, 1992; Wiese, 1996). In English, words may begin with /s/, and there are many /s/-initial clusters (*sleep, swim, sport, stand, script*, etc.). Thus a word preceded by a context ending with /s/ is not aligned with a phonotactically clear boundary. The situation is quite different in German. Words in standard German may not begin with /s/. Thus a word beginning with a consonant is aligned with a clear boundary if the preceding context ends with /s/. In contrast, German words may begin with /ʃ/, and there are many /ʃ/-initial clusters (*Schlaf, schwimmen, Sport, stehen, Schrift*, etc.). A word preceded by a context ending with /ʃ/ is thus not aligned with a clear boundary. Again, there is a contrast with English, that has no native words beginning with /ʃ/-initial clusters (only a couple of Yiddish loanwords in American English, such as *schlep*). Thus a word beginning with a consonant has a very strong probability of being aligned with a clear boundary if the preceding context ends with /ʃ/.

The phonemes /s/ and /ʃ/, plus /t/ for some w-words, thus provided our cross-linguistically mismatching boundaries: /sl/, /sw/, and /tw/ are possible onset clusters in English but not in German, /ʃl/ and /ʃw/ are impossible onsets in native English words but are possible in analogous German words. The two other boundary conditions were: phonotactically clear in both languages (/nl, ml, nw, mw, lw/ are impossible onsets in English, and impossible either directly or in analogue in German), and phonotactically clear in neither language (/pl, kl, fl, kw/ are all possible onsets in English and, directly or analogously, in German). Again, cognates abound: E: *plan, clear, flame, quality*; G: *Plan, klar, Flamme, Qualität*). All our selected words were thus preceded by four contexts, supporting No boundary, an English boundary, a German boundary, and a Common boundary, respectively. For *lecture*, this produced *gorklecture* (No), *thrarshlecture* (E), *moycelecture* (G), *moinlecture* (C); for *wish, plookwish* (No), *glarshwish* (E), *loitwish* (G), *yarlwish* (C).

From the CELEX lexical database (Baayen, Piepenbrock, and van Rijn, 1993) we selected 68 words, 36 l-initial and 32 w-initial, mono- or bisyllabic (e.g., *lunch, lecture, wish, weapon*); all words and their contexts are listed in the Appendix. As far as possible, these words contained no other embedded English or German words, though it was not possible to avoid some embeddings leaving a single-consonant residue, such as *lea* in *league*; such embeddings are usually overlooked in wordspotting: Norris *et al.*, 1997). Each word was provided with four monosyllabic preceding contexts as described earlier; some contexts were used for several words. Contexts could contain /l/ and /w/. All context monosyllables contained long vowels, diphthongs or vowels plus /r/, so that they would be phonotactically legal syllables without their coda; thus the internal structure of the context syllable did not itself force a particular segmentation (e.g., *moyce lecture* and *moy slecture* are both permissible segmentations in English).

A further 55 nonsense sequences were constructed that began with context syllables similar to those in the experimental items, and contained, embedded in final position, an English word beginning with a consonant other than /l/ or /w/ (e.g., *hooshdonkey*). A further 251 bi- or trisyllabic nonsense sequences without embedded word were also constructed (e.g., *crivthish*); these sequences could contain /l/ or /w/, and the first syllable could end with any of the sounds in the boundary sequences in the experimental items. These were filler materials for the wordspotting study.

All 272 (68×4) experimental items and 306 fillers were recorded via a Sennheiser ME64 microphone onto Digital Audio Tape in a sound-attenuated booth by a phonetically trained female native speaker of American English (born in the Midwest, who had lived as a child and teenager in four different states). The speaker was instructed to avoid any clear syllable boundaries in her productions. Subsequently, the speaker also recorded the 136 (68×2) experimental sequences potentially ambiguous in English twice each, without pause but with different intended syllable boundaries (e.g., *gor clecture, gork lecture, moy slecture, moyce lecture, ploo kwish, plook wish, loy twish, loit wish*). These additional productions were for acoustic analysis to establish the dimensions of variation that might potentially cue boundaries in the experimental materials.

The recordings, initially sampled at 44.1 kHz, were downsampled to 16 kHz and stored on disk. Using XWAVES software, measurements were made of segmental durations in each target word and its context, as well as in the additional clear-boundary productions of the 136 potentially ambiguous sequences. Also using XWAVES software, the initial syllable was removed from each of the 272 experimental sequences and 306 fillers. This manipulation produced the stimuli for a control experiment using the lexical decision task.

III. ACOUSTIC ANALYSES

Existing literature on acoustic cues to juncture motivated five measurements in the clear-boundary productions of the

potentially ambiguous (No boundary, German boundary) sequences. The aim of these measurements was to identify features of our speaker's production that might vary across items in the experimental materials, and thereby affect the ease of detection of the embedded words. Not all measurements applied to all stimuli.

(a) *Glottalization*. Spectrograms of the boundary sequences /kl, pl, tw, kw/ (63 pairs) [1] were examined for signs of glottalization of the stop consonant, a potential marker of syllable-finality (e.g., *loit wish*; Pierrehumbert, 1994).
(b) *Stop VOT*. For the same sequences, we measured the duration from stop burst onset to onset of voicing; this was expected to be longer in sequences with no boundary, i.e., with a string-initial stop (*loy twish*; Keating, Wright, and Zhang, 1999).
(c) *Fricative duration*. For the sequences /fl, sl, sw/ (58 pairs) we measured fricative duration from the offset of voicing of the preceding vowel to the offset of high-frequency fricative noise. Conflicting predictions were motivated for this measure; it might be longer when the sequence contained no boundary so that the fricative was string-initial (e.g., *moy slecture*; Klatt, 1974), or shorter in the same sequences containing a boundary due to shortening of phonemes within a cluster (Haggard, 1973).
(d) *Duration of /l/*. For the sequences /fl, sl, pl, kl/ (68 pairs) we measured duration of the voiced portion of /l/, from the onset of voicing to a rise in the second formant and an increase in amplitude of the third formant. This measure was expected to be longer when the sequence contained a boundary so that the /l/ was in a singleton onset rather than a cluster (*moyce lecture*; Haggard, 1973).
(e) *Vowel duration*. For all items (120 pairs), we measured duration of the vowel in the first syllable. Vowels were defined as beginning at the onset of voicing after voiceless obstruents. and as beginning at the onset of the second and third formant after voiced segments. When the vowel in the context syllable was followed by /r/, /r/ was included in the vowel duration measurement. Vowels were expected to be longer when the two-consonant boundary sequence did not contain a boundary, i.e., when the measured vowel was syllable-final (e.g., *moy slecture*; Lehiste, 1960).

Results and discussion.

(a) *Glottalization* is apparently not a feature of our speaker's productions; it was observed on only two productions (both /tw/ sequences containing a boundary).

The mean durations for measures (b) to (e) are given in Table I. Two-factor analyses of variance (ANOVA) were conducted on each value set, with consonant sequence as between-items factor and boundary placement as within-items factor.

(b) *Stop VOT* showed no boundary placement effect ($F[1,60]=2.86$, $p>0.09$).
(c) *Fricative duration* showed an interaction between boundary placement and consonant sequence (the only interaction of these factors); boundary placement was therefore analyzed in each consonant sequence separately. Fricatives were significantly longer before a boundary in the case of /fl/ ($F[1,10]=24.89$, $p<0.001$) and /sl/ ($F[1,33]=47.77$, $p<0.001$), but not in the case of /sw/ ($F[1,12]=1.13$).
(d) *Duration of /l/* was increased by a boundary in the consonant sequence ($F[1,64]=126.92$, $p<0.001$).
(e) *Vowel duration* was increased when there was no boundary in the consonant sequence ($F[1,115]=117.03$, $p<0.001$).

TABLE I. Mean durations in milliseconds for the two intended syllabifications.

Measure	Boundary in consonant sequence (*moyce lecture*)	No boundary in consonant sequence (*moy slecture*)
VOT (stops; e.g., [t] in *loitwish*)	85	79
fricative duration (e.g., [s] in *moyslecture*)	153	136
voiced duration of /l/ (e.g., [l] in *moyslecture*)	44	24
First syllable vowel duration (all items; e.g., [ɔɪ] in *moyce, loit*)	150	177

Duration of the vowel in the context syllable, and, for /l/-initial targets, duration of /l/ and duration of a preceding fricative, are therefore factors that, if they vary in our speaker's productions of the wordspotting materials, might produce effects on listeners' responses. Recall that the speaker, a trained phonetician, had tried in producing those materials to avoid durational differences between the conditions. Inspection of the acoustic measures of the experimental materials (performed for the English, German, and No boundary conditions only) showed that to a considerable degree she was successful in this. The measured duration of the context vowel, which in the clear-boundary productions was shorter when the word was aligned with a boundary (*moyce lecture*) than when it was not (*moy slecture*), was not shorter in the English or German boundary constraint conditions than in the No boundary condition, for either word type; it was slightly longer. Thus if listeners attended to this information, it could counteract the effects of the phonotactic boundary constraints.

For /l/-initial targets, the duration of the voiced portion of /l/ (in the clear-boundary productions, longer when the word was aligned with a boundary) also patterned in the wrong direction for the English boundary condition (at 22.6 ms it was 10% shorter than the 26.8 ms of the No boundary productions of the same items). However /l/ was on average 32% longer (35.5 ms) in the German boundary condition than in the No boundary condition. The duration of a preceding fricative in the boundary constraint conditions could not be compared with the No boundary condition, which had no fricative, but the average duration differed by

TABLE II. Control lexical decision experiment with American English participants: (a) mean RTs in milliseconds, measured from item offset, and (b) mean percentage of missed responses, with standard errors of each mean, as a function of word-initial phoneme and boundary context in the wordspotting materials from which the items were excised.

Measure	Initial sound	Common boundary	English boundary	German boundary	No boundary
(a) RT	l-words	401 (18.4)	382 (18.5)	372 (18.3)	361 (17.2)
	w-words	354 (22.4)	394 (21.4)	399 (22.2)	348 (15.9)
(b) Miss	l-words	14.7 (1.9)	16.5 (2.1)	11.6 (2.1)	12.5 (1.8)
	w-words	11.2 (2.2)	14.6 (2.5)	16.4 (3.3)	11.0 (2.0)

only 4% in the German (137.2 ms) versus the English boundary condition (142.3 ms). These analyses suggest that for some words in some conditions, acoustic variation in the wordspotting materials may provide listeners with useful information.

IV. CONTROL DATA FROM LEXICAL DECISION

The wordspotting task resembles lexical decision (in which listeners decide whether a spoken form is a real word), but the focus is on the effects of the adjacent context rather than on properties of the word itself. Although in a typical wordspotting experiment the same word is presented in different contexts, natural productions of the items can lead to differences in the acoustic form of the word across contexts. A standard way of controlling for such effects is to excise the words from their contexts and present them for lexical decision. The task is the same—respond whenever a real word is heard—but the context is removed while the acoustic form of the word remains. If the different contexts had different effects on the acoustic goodness of the word itself, in a way that would affect ease of recognition and so confound the wordspotting data, this should be apparent in lexical decision responses to the words alone.

Participants. Forty native speakers of American English, students at the University of South Florida, took part in the experiment in return for course credit or a small monetary compensation.

Materials and Procedure. The excised real words (*lecture, wish, donkey*, etc.) and nonwords (*thish*, etc.) formed four lists, each list containing one truncated version of each of the 68 experimental words and all 306 truncated filler items. The first 14 items in each list formed a practice set. No version of an experimental word occurred in more than one list; the four types of context were counterbalanced across lists. Ten listeners heard each list over headphones. They were asked to press a response button whenever they spotted a real English word, and to repeat aloud each word that they had found. This form of the lexical decision task mimicked the word-spotting task as closely as possible. Stimulus presentation and response collection was controlled by a portable computer running NESU experimental control software. Both response times (RT; measured from item onset) and accuracy were recorded.

Results and discussion. In any lexical decision task responses cannot be made until word offset (*donkey* could always turn out to be *donkeef*). Hence the measured whole-word duration was subtracted from the recorded RTs to give RTs from that point.[2] Table II shows the mean RT from word offset for detections which were accompanied by a correct oral response, and the mean miss rate (no response, response without correct oral report), as a function of the original context from which the word had been excised. ANOVAs were conducted across participants and across items to test for effect of original context on these responses. Across items, all main effects and interactions were insignificant in RTs and miss rates; across participants, the only significant effect was Condition ($F[3,108]=3.26$, $p<0.03$ for RTs, $F[3,108]=3.22$, $p<0.03$ for miss rates). Subsequent t-tests showed that the words excised from the No boundary condition (predicted to be hardest in wordspotting) produced faster RTs than words in the other three conditions, and fewer misses than words in the English boundary condition. The acoustic form of the words thus did not differ across contexts in any way likely to produce the pattern of results we predict in wordspotting; on the contrary, acoustic effects, if operative, would tend to work against our predictions.

V. WORDSPOTTING EXPERIMENTS

Participants. Ninety-six participants were tested. Forty-eight were L1 listeners, native speakers of American English, mostly students at the University of South Florida; they took part in the experiment in return for course credit or a small monetary compensation. These participants had no knowledge of German. The other forty-eight were native speakers of German, students of English translation and interpretation at the University of Heidelberg, Germany; they received a small monetary compensation for taking part. These participants had received an average of 15 years of training in English as a foreign language, beginning at a mean age of 11. Their knowledge of English was in consequence excellent.

Materials and Procedure. The wordspotting materials, comprising four versions of each of the 68 experimental words with appended context, and 306 filler items, were arranged in four lists, each list containing one version of each of the 68 experimental words and all 306 filler items. The first 14 items in each list formed a practice set. No version of an experimental word occurred in more than one list; the four types of context were counterbalanced across lists. The order of the lists was the same as in the lexical decision experiment; the order was pseudo-random, with each experimental item occurring after at least one filler item containing no real word.

TABLE III. Wordspotting experiments: (a) mean RTs in milliseconds, measured from item offset, and (b) mean percentage of missed responses, with standard errors of each mean, for American English L1 listeners vs German listeners as a function of word-initial phoneme and boundary constraint exercised by the context.

		Boundary constraint			
		Common boundary (*moinlecture*)	English boundary (*thrarshlecture*)	German boundary (*moycelecture*)	No boundary (*gorklecture*)
(a) RT					
English	l-words	482 (22.5)	543 (24.3)	516 (23.6)	596 (26.1)
L1 listeners	w-words	466 (25.9)	468 (21.2)	593 (31.8)	528 (30.9)
German	l-words	608 (33.6)	662 (33.5)	651 (31.9)	676 (34.1)
listeners	w-words	542 (27.5)	589 (29.2)	570 (26.7)	678 (36.8)
(b) Miss					
English	l-words	11.9 (1.6)	17.2 (2.2)	18.3 (1.9)	26.0 (2.8)
L1 listeners	w-words	16.9 (2.8)	17.3 (2.4)	24.3 (2.6)	24.6 (3.0)
German	l-words	18.6 (2.1)	24.2 (2.6)	24.5 (2.5)	33.1 (3.0)
listeners	w-words	19.9 (2.5)	20.4 (2.6)	22.2 (2.5)	32.1 (3.0)

In each participant group, 12 listeners heard each list over headphones. They were asked to press a response button whenever they spotted a real English word at the end of one of the nonsense sequences, and to repeat aloud each word that they had found. Their response times and accuracy were recorded. Except for the brand of portable computer used, all aspects of the testing setup were the same in each location. Stimulus presentation and timing were as for the lexical decision experiment.

The crucial predictions for the wordspotting results concern the relative effect of the different boundary constraints across the listener groups. First, we predict that both listener groups should show significant effects of common boundary constraints. We test this by comparing RT and accuracy in the Common boundary condition (*lecture* in *moinlecture*) with the No boundary condition (*lecture* in *gorklecture*); responses in the Common condition should be faster and more accurate. Second, English-speaking L1 listeners should show an effect of English constraints, and our highly proficient L2 listeners may do so. We test this by comparing RT and accuracy in the English boundary condition (*lecture* in *thrarshlecture*) with the No boundary condition; responses in the English condition should be faster and more accurate. Third, German boundary constraints may affect German listeners (but should not affect L1 listeners). We test this by comparing RT and accuracy in the German boundary condition (*lecture* in *moycelecture*) with the No boundary condition; any effect should show up as faster and more accurate responses in the German condition.

Results and discussion. Table III shows the mean RTs (again adjusted to measure from word offset) for detections accompanied by a correct oral response, and mean miss rates (no response, response before word offset, or response without correct oral response), for each listener group in the four conditions. Seven words have been removed from these results (six missed by 50% or more of the German listeners, and one, *leisure*, with multiple pronunciations—rhyming with *measure* or *seizure*—known to our listener group), leaving 61 experimental words. It can be seen that, unsurprisingly, the L1 participants produced overall faster RTs and lower miss rates than the L2 participants. It is noteworthy, though, that both the RT and miss rate distributions for the two listener groups overlap; that is, these German listeners had, with the exception of the seven excluded words, little trouble performing the wordspotting task in their L2.

ANOVAs were conducted across participants (F1) and across items (F2) to examine the effects of participant language, context and word-initial phoneme. The first two comparisons were within-item and the last two within-participant. There was a main effect of language (L1 listeners were faster and more accurate: F1 $[1,88]=9.8$, $p<0.005$, F2 $[1,59]=82.1$, $p<0.001$ for RTs, F1 $[1,88]=5.94$, $p<0.02$, F2 $[1,59]=9.65$, $p<0.005$ for miss rates) and of context (F1 $[3,264]=19.33$, $p<0.005$, F2 $[3,177]=82.1$, $p<0.001$ for RTs, F1 $[3,264]=27.12$, $p<0.001$, F2 $[3,177]=8.02$, $p<0.001$ for miss rates), but not of word-initial phoneme. Initial phoneme also did not interact with either of the other main effects, but language and context did interact (F1 $[3,264]=2.63$, $p=0.05$, F2 $[3,177]=2.63$, $p=0.05$, RTs only).

The crucial predictions, as described earlier, concern the relative effects of context in each listener group, i.e., the components of the language by context interaction, and we test the predictions for each context type in turn via separate t-tests, across the mean RTs and miss rates for participants (tl) and items (t2), for each listener group. Because the ANOVA also revealed a three-way interaction between the effects (F1 $[3,264]=6.47$, $p<0.001$, F2 $[3,177]=8.05$, $p<0.001$, RTs only), separate ANOVAs were additionally conducted for each listener group. The main effect of context remained significant and the main effect of initial phoneme remained insignificant in each of these analyses, but the interaction between context and initial phoneme differed: it was insignificant for the German listeners but significant for the L1 listeners (F1 $[3,132]=8.43$, $p<0.001$, F2 $[3,177]$

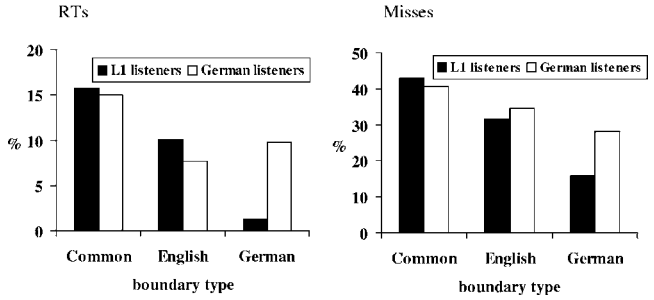

FIG. 1. Wordspotting results: effect of boundary type, expressed as mean percentage reduction in RT and miss rate, for each listener group in each boundary constraint condition (Common, English, German) compared with the No boundary condition.

$=7.42$, $p<0.001$). To understand this interaction we carried out separate t-tests examining the context effects separately for each word type for this listener group.

The effects for each listener group of each constraint type (Common, English, German) are displayed in Fig. 1 as the percentage reduction in RT and miss rate compared with the No boundary condition. Because the average RT and average miss rate of the two listener groups were significantly different, as can only be expected in a comparison of L1 vs L2, displaying the reduction as a percentage better allows comparison of the effect size across the two groups. The higher the bar in Fig. 1, the larger the effect size; it can be seen that a common boundary has a large effect for both groups (i.e., responses are significantly faster and more accurate when there is a common boundary than when there is no boundary), an English boundary also has an effect for both groups, but a German boundary has more effect for German listeners.

Common constraints. The first set of t-tests compared responses in the Common boundary condition and the No boundary condition; as predicted, for both listener groups, responses in the Common condition were faster and more accurate (for L1 listeners, $t1[47]=5.25$, $p<0.001$, $t2[60]=5.06$, $p<0.001$ for RTs and $t1[47]=4.32$, $p<0.001$, $t2[60]=3.51$, $p<0.001$ for miss rates; for German listeners, $t[47]=4.53$, $p<0.001$, $t2[60]=3.77$, $p<0.001$ for RTs and $t[47]=5.73$, $p<0.001$, $t2[60]=3.98$, $p<0.001$ for miss rates). The difference between these two conditions was also highly significant for both the l-words and the w-words in the separate t-tests on the L1 listeners' RTs.

English constraints. The second set of t-tests compared responses in the English boundary condition versus the No boundary condition; as predicted, L1 listeners' responses were faster and more accurate in the English boundary condition ($t1[47]=2.81$, $p<0.01$, $t2[60]=3.01$, $p<0.005$ for RTs and $t1[47]=3.58$, $p<0.001$, $t2[60]=2.36$, $p<0.025$ for miss rates). This effect also held for RTs to l-words, and for w-words was significant across items ($p<0.05$) although not ($p=0.067$) across participants. The German listeners' responses also were faster and more accurate in the English boundary condition, though the RT effect across items narrowly missed significance ($t1[47]=2.08$, $p<0.05$, $t2[60]=1.81$, $p=0.075$ for RTs and $t1[47]=4.19$, $p<0.001$, $t2[60]=3.08$, $p<0.003$ for miss rates). Thus these highly proficient L2 listeners were able to make use of boundary constraints in their L2.

German constraints. The third set of t-tests compared the German boundary condition to the No boundary condition. The German listeners responded faster and more accurately in the German boundary condition ($t1[47]=2.83$, $p<0.01$, $t2[60]=2.25$, $p=0.03$ for RTs and $t1[47]=4.13$, $p<0.001$, $t2[60]=3.1$, $p<0.003$ for miss rates). For L1 listeners, this overall comparison was insignificant across both items and participants for RTs, and insignificant across items though significant across participants for miss rates ($t1[47]=2.07$, $p<0.05$). Separate t-tests across word type revealed the L1 listeners' RTs to l-words to be faster in the German boundary condition than in the No boundary condition (t1 $p<0.005$, t2 $p<0.005$), but their RTs to w-words to be slower in the German boundary condition than in the No boundary condition (t1 $p=0.068$, t2 $p<0.04$).[3] This latter difference between l-words and w-words is presumably the source of the significant interaction of context and initial phoneme for these listeners' RTs, noted above.

The wordspotting results thus showed that common boundary constraints affected both listener groups' responses equivalently, English constraints affected L1 listeners' responses strongly and German listeners' responses almost as strongly, while German constraints affected only the German listeners' responses.

The fact that the L1 listeners' response pattern in the latter comparison was exactly opposite for l-words versus w-words suggests that these differences may not reflect the phonotactic information but some other factor. In search of such a factor, we conducted correlations of the acoustic measures with listeners' RTs. The only significant correlations were with /l/ duration: the longer the /l/, the faster l-words were spotted, both by L1 listeners ($r[101]=-0.24$, $p<0.015$) and German listeners ($r[101]=-0.33$, $p<0.001$). Since segmental lengthening is known to be a cue to word boundaries in running speech (Shatzman and McQueen, in press), we would predict that this correlation in the results of wordspotting (which measures segmentation) would have no counterpart in the results of the control lexical decision experiment (which measures recognition of the same tokens without segmentation being needed). Indeed, the lexical decision RTs showed no significant correlation with /l/ duration ($r[101]=-0.08$, $p>0.4$).

It appears that both listener groups could take advantage of subtle acoustic cues to boundaries where these were available. As described earlier, however, the only comparison in which the /l/-duration cue was usefully available was the comparison between the German boundary context and the No boundary context, with the cue here clearly favoring the words in the German boundary context. The result was that L1 listeners and L2 listeners alike detected the words more rapidly in this context. No acoustic cues favored detection of w-words in the German boundary context over the No boundary context, however. In the absence of acoustic cues, the phonotactic cues had a clear facilitatory effect for the German listeners, but not for the L1 listeners.

VI. GENERAL DISCUSSION

Figure 1 says it all: The advantage of a common phonotactic boundary constraint in a spoken sequence is robust and almost identical for both our listener groups, the advantage of an English-only boundary constraint is again robust and not significantly different for the L1 versus the L2 listener groups, but the advantage of a German-only boundary constraint is robust only for the German-native L2 listeners. Thus first-language phonotactic constraints can influence second-language listening. German listeners to English found it easier to spot English words embedded in a nonsense context like *moycelecture*, where the word-initial phoneme could not be combined with the preceding phoneme to form a syllable-initial cluster in German, than when the preceding phoneme plus word-initial phoneme could be a syllable-initial cluster in either English or German (e.g., *gorklecture*). This facilitatory effect appeared for words beginning both with /l/ and with /w/. This pattern did not appear in the responses of American English listeners to the same materials.

Words aligned with a boundary signaled by a constraint common to both English and German (e.g., *moinlecture*) were easiest to detect, for both L1 and German listeners. Words aligned with a highly likely boundary in English only (e.g., *thrarshlecture*) were likewise easy for both L1 and German listeners to detect. These results replicate for American English the effects of phonotactic constraints on word segmentation already demonstrated with the same listening task in Dutch (McQueen, 1998), French (Dumay *et al.*, 2002) and Korean (Warner *et al.*, 2005). More significantly, the latter result shows that experienced L2 listeners can exploit constraints specific to their L2.

The finding that the common boundary constraints affected both listener groups' responses equivalently is open to alternative interpretations. It could mean that each listener group was making use of English boundary constraints or, in principle, it could mean that each listener group was making use of the boundary constraints appropriate for their L1. However, the finding that English boundary constraints affected German listeners' responses almost as strongly as they affected the responses of L1 listeners is unambiguous evidence that with those items the German listeners were able to exploit their knowledge of the probabilities relevant to the L2.

This is good news for L2 listeners: in this respect it is possible for L2 listening to approach the level of L1 listening. These listeners, it is true, were very proficient indeed in their L2; we cannot say on the basis of the present results exactly how much L2 experience is necessary for the efficient exploitation of L2 boundary constraints which do not apply in the L1. But note that the constraints in the English-boundary condition not only did not apply in German, they were equivalent to the No boundary condition if interpreted in terms of German phonotactics; in *thrarshlecture, lecture* is preceded by /ʃ/, and /ʃl/ is just as good a possible onset in German as /pl/ or /kl/ -*Schlaf, Plan, klar*. In this case the German listeners were thus able to suppress or ignore the probabilities of their L1 while listening to their L2. Moreover, they applied this English-only constraint not only to the set of w-words such as *weapon* and *wish*, that putatively show less phonetic resemblance to their L1, but also to the l-words such as *lunch* and *lecture*, even though the /ʃl/ boundary sequence was in this case phonetically very close indeed to potential L1 sequences.

Much less good news for L2 listeners emerges from the results from the German-only boundary condition. Even though these listeners are highly proficient in the L2, and even though they are clearly sensitive to the L2 probabilities, nevertheless they also show sensitivity to a boundary cue from their L1 which is absolutely not informative in the L2 they are listening to. Again, they applied this boundary constraint in the detection of both l-words—where it was putatively the case that the constraint could be translated directly from the L1—and w-words, where, as we argued earlier, application of the constraint can only proceed via a prior assimilation of the L2 category /w/ to the L1 category /v/. Evidence from German pronunciation of English suggests that such assimilation does occur; our results suggest that it does not inhibit further application to the L2 category of rules pertaining to the L1 category.

Acoustic correlates of the realization of word-initial /l/ were exploited by listeners of both groups in finding the words. The fact that both groups made similar use of these cues is again good news for L2 listening, though probably to be expected given that domain-initial strengthening effects appear consistently across languages (Keating *et al.*, 2003). As it happened, these acoustic cues provided useful evidence in the German-only boundary condition to a greater extent than in other conditions. The result of this was that the American English L1 listeners' detection of the l-words was facilitated in this condition. The fact that their responses to w-words were not facilitated in this condition—if anything, they showed the reverse pattern, although for w-words the difference did not reach our criterion of significance—strongly suggests that the German phonotactic constraints were having no facilitatory effect at all for this listener group. The facilitation in the l-words arose from the acoustic cues alone. Note that Kirk (2000), in a wordspotting study with American English, found that allophonic cues on the initial phoneme of an word affected how rapidly the word could be detected; *rock* in *voodrock*, for instance, was spotted more rapidly if the /dr/ sequence was pronounced without retroflexion than if it was pronounced with the retroflex articulation characteristic of an onset cluster. Our results with l-words provide further evidence that listeners are able to make good use of such cues in segmentation. We could find no such cues in the realization of the w-words. The German listeners' responses, significantly affected even for the w-words by the presence of the German-only boundary constraint, emphasize the relevance of this constraint in their L2 listening.

It is well known that L2 listening is influenced by expectations from the L1. Thus a mismatch between L1 and L2 phoneme repertoires can lead to L2 categories being interpreted in terms of distinctions used in the L1 (see Strange, 1995, for an overview). These phoneme confusions can cause pseudo-homophony, as when no difference can be per-

ceived between, for instance, *write* and *light* (Cutler and Otake, 2004; Pallier, Colomé, and Sebastián-Gallés, 2001). They further cause an increase in word activation (Broersma, 2002; Sebastián-Gallés, Echeverría, and Bosch, 2005), which can multiply several times the amount of lexical competition involved in a given word recognition situation (Cutler, 2005). To add to the L2 listener's word recognition problems, the native vocabulary may even be activated during listening to the L1 (Spivey and Marian, 1999; Weber and Cutler, 2004).

The segmentation of continuous speech in a second language is similarly subject to inappropriate influence from the L1. Thus English listeners do not segment their native language syllable by syllable or mora by mora, but French listeners to English apply syllabic segmentation, just as they do in listening to their L1 (Cutler *et al.*, 1986), and Japanese listeners to English apply moraic segmentation, just as for their L1 (Cutler and Otake, 1994). Inappropriate application of L1 phonotactic constraints in L2 listening thus joins the range of interference effects that L2 listeners must attempt to overcome in segmenting spoken language.

It should perhaps not be surprising that phonotactic constraints are well-anchored in listening, given that language acquisition studies have demonstrated that these constraints belong to the earliest information acquired about the mother tongue. Late in the first year of life, before they begin to talk, babies show evidence of a preference for speech that meets the sequencing constraints of their language over speech that does not (Jusczyk *et al.*, 1993; Jusczyk, Luce, and Charles-Luce, 1994). They also prefer legal over illegal word boundary clusters within their own language (Friederici and Wessels, 1993). Adult listeners, as we saw, are sensitive not simply to gross differences between legal and illegal patterns (Gow, 2001; Halle *et al.*, 1998; Otake *et al.*, 1996; Weber, 2001), but also to finer-grained differences in probabilities of acceptable sequences (Saffran *et al.*, 1996; van der Lugt, 2001; Vitevitch *et al.*, 1997; Yip, 2000).

However, our results indicate that listeners' knowledge of phonotactic probabilities is not always translated into the ability to exploit the information to maximum effect in on-line listening. The German listeners' responses in the English boundary condition showed that they had good mastery of the English probabilities and also of the difference between the probabilities of English and German (since they did not treat the sequences in this condition in the way appropriate for German). Nevertheless they were apparently unable to suppress the German boundary constraint probabilities in sequences such as *moycelecture* or *loitwish*. One possible interpretation of this asymmetry is that there is a difference between the effect of a positive boundary constraint (/sl/ in the L1 must always contain a boundary, /ʃl/ in the L2 should always contain a boundary) versus the effect of probabilities indicating that a boundary is unnecessary (/ʃl/ in the L1 and /sl/ in the L2 may be word-initial). In the spoken-word recognition model Shortlist (Norris *et al.*, 1997), which explicitly incorporates a role for phonotactic segmentation information, such a stronger effect of positive boundary information would indeed be predicted: Only clear boundary cues play a role in the model, so that strings with ambiguous boundaries (e.g., *moycelecture*) must be resolved via competition between alternative word candidates. A recent study by Altenberg (2005) indeed shows that in parsing potentially ambiguous sequences Spanish listeners to English exploit positive boundary cues (e.g., a glottal stop before the initial vowel in *grave at*) far better than negative cues (e.g., the absence of a glottal stop before the medial vowel in *grey vat*).

Further, there is converging evidence that L2 listeners do not always capitalize maximally upon their phonological knowledge of the L2 in on-line recognition of spoken language. Broersma (2005) found that Dutch listeners to English performed within the L1 range on forced-choice categorization of syllable-final voiced versus voiceless obstruents (/s,z/, /p,b/, etc.). Despite this evidence that Dutch listeners can indeed distinguish voicing contrasts in syllable-final position, Cutler *et al.* (2004) found that listeners from the same population produced many syllable-final voicing errors in an open phonemic identification task, and Broersma (2002) observed many false-alarm positive responses due to voicing misperception in the same listener group's lexical decision performance (such that, for instance, *cheece* or *glope* was accepted as a word of English). Thus proficiency in distinguishing L2 contrasts in a forced-choice task may not be applied in other listening situations.

We note that visual word recognition also can be affected by such asymmetric application of the same type of phonotactic knowledge. Altenberg and Cairns (1983) asked English monolinguals and English-German bilinguals to rate nonwords such as *smatt* (legal in English but illegal in German) as potential English words. The ratings of both the bilinguals and the monolinguals were only influenced by phonotactic legality in English, suggesting that their knowledge of phonotactic constraints was equivalent. But when asked to decide whether a visually presented item was an English word or not (lexical decision), the bilinguals did not show the same pattern of response times as the monolinguals did. Bilinguals' decisions were affected by the phonotactic legality of the stimuli in both German and English, while monolinguals' decisions were only affected by phonotactic legality in English.

Mastery of a second language, in short, requires not only knowledge of the sequencing probabilities of the L2, but also the ability to translate this knowledge into on-line segmentation and recognition decisions. Our results suggest that the knowledge can be adequately mastered by L2 users—at least, by proficient L2 users such as those in our German listener group. However, translation of the knowledge into useful application is not necessarily achieved even by listeners with high proficiency. Especially positive cues to the presence of an L1 boundary can still provide unwanted interference in L2 listening.

ACKNOWLEDGMENTS

This research was supported by a doctoral fellowship from the Max Planck Society to A.W., with additional support from the NWO-SPINOZA project "Native and Non-native Listening" to A.C. We thank Winifred Strange and

Elaine Griffiths for making it possible to test the Florida and Heidelberg participants, respectively. We further thank Dianne Bradley, Taehong Cho, James Jenkins, James McQueen, Holger Mitterer, Kanae Nishi, and Natasha Warner for assistance and helpful commentary. Parts of the research were presented to the workshop "Spoken Word Access Processes" in Nijmegen, May 2000, and to the Sixth International Conference on Spoken Language Processing, Beijing, October 2000.

APPENDIX

Target-bearing materials used in the wordspotting study. The seven words excluded from the analysis are marked with two asterisks.

Embedded words with initial /l/

Common boundary	English boundary	German boundary	No boundary	Embedded word
/dʒimlæns/	/ðiʃlæns/	/blɔɪslæns/	/θiplæns/	lance
/fumlɔft/	/prarʃlɔft/	/forslɔft/	/zarplɔft/	loft
/dʒanlɪrɪk/	/diʃlɪrɪk/	/nɔslɪrɪk/	/narplɪrɪk/	lyric
/rinled/	/rarʃled/	/birsled/	/bɔkled/	lead**
/dɔɪnlɔs/	/nuʃlɔs/	/tirslɔs/	/mɔklɔs/	loss
/jɔɪnlardʒ/	/giʃlardʒ	/ðaʊslardʒ/	fuklardʒ/	large
/garnlɛʒər/	/frarʃlɛʒər/	/fərslɛʒər/	/garflɛʒər/	leisure**
/paʊnlɛtər/	/ruʃlɛtər/	/puslɛtər/	/jiflɛtər/	letter
/marnlup/	/griʃlup/	/hoʊslup/	/narflup/	loop
/pumlɪft/	/narʃlɪft/	/rirslɪft/	/nuplɪft/	lift
/fumlord/	/kriʃlord/	/mɔɪslord/	/jarplord/	lord
/pərnlɔndri/	/parʃlɔndri/	/borslɔndri/	/farplɔndri/	laundry
/gɔɪnlaf/	/priʃlaf/	/krirslaf/	/ʃorklaf/	laugh
/funlɛŋθ/	/zarʃlɛŋθ/	/joʊslɛŋθ/	/gukleŋθ/	length
/harnlʊntʃ/	/riʃlʊntʃ/	/faʊslʊntʃ/	/jorklʊntʃ/	lunch
/waʊnlɪst/	/farʃlɪst/	/gɔɪslɪst/	/buflɪst/	list
/hɔɪnlɛvəl/	/dʒiʃlɛvəl/	/buslɛvəl/	/parflɛvəl/	level
/parnlʌst/	/grarʃlʌst/	/pɔɪslʌst/	/darflʌst/	lust
/dʒimlɔ/	/θiʃlɔ/	/grirslɔ/	/marplɔ/	law
/fumlɑdʒɪk/	/jiʃlɑdʒɪk/	/hɔɪslɑdʒɪk/	/darplɑdʒɪk/	logic
/wɔɪnlɔn/	/tarʃlɔn/	/θirslɔn/	/jiplɔn/	lawn
/punlidʒən/	/darʃlidʒən/	/buslidʒən/	/ruklidʒən/	legion
/zarnlʌv/	/briʃlʌv/	/paʊslʌv/	/fuklʌv/	love
/ðaʊnlɪnən/	/dʒiʃlɪnən/	/kɔɪslɪnən/	/dɪklɪnən/	linen
/rarnlɛft/	/trarʃlɛft/	/jorslɛft/	/rarflɛft/	left
/ʃaʊnlɛðɛr/	/buʃlɛðər/	/hirslɛðər/	/marflɛðər/	leather
/marnlaʊndʒ/	/krarʃlaʊndʒ/	/nɔɪslaʊndʒ/	/trarflaʊndʒ/	lounge
/pumlɑk/	/garʃlɑk/	/mərslɑk/	/fuplɑk/	lock
/dʒimlɛnz/	/frarʃlɛnz/	/torslɛnz/	/rarplɛnz/	lens
/zɔɪnlæg/	/drarʃlæg/	/rərslæg/	/garplæg/	lag
/farnlʌk/	/briʃlʌk/	/dorslʌk/	/wuklʌk/	luck
/jaʊnlig/	/karʃlig/	/jɔɪslig/	/nɔklig/	league
/mɔɪnlɛkʃər/	/θrarʃlɛkʃər/	/mɔɪslɛkʃər/	/gorklɛkʃər/	lecture
/rərnlɑdʒ/	/fuʃlɑdʒ/	/dɔɪslɑdʒ/	/krarflɑdʒ/	lodge
/parnlaʊs/	/driʃlaʊs/	/foʊslaʊs/	/tarflaʊs/	louse
/faʊnlɛpərd/	/dʒarʃlɛpərd/	/gaʊslɛpərd/	/giflɛpərd/	leopard

Embedded words with initial /w/

/pirlworm/	/flarʃworm/	/gɔɪtworm/	/zorkworm/	warm
/ʃirlwɛl/	/narʃwɛl/	/mɔɪtwɛl/	/mɔkwɛl/	well
/narlwor/	/farʃwor/	/mirtwor/	/plukwor/	war
/jarlwɔsp/	/gruʃwɔsp/	/nutwɔsp/	/ðikwɔsp/	wasp

Embedded words with initial /w/

/tarlwʊmən/	/fuʃwʊmən/	/θaʊswʊmən/	/horkwʊmən/	woman
/pɔɪnwɛðər/	/darʃwɛðər/	/dɔswɛðər/	/jikwɛðər/	weather
/zaʊnwərm/	/griʃwərm/	/grərswərm/	/rukwərm/	worm
/pumwaɪf/	/riʃwaɪf/	/blirswaɪf/	/nɔkwaɪf/	wife
/girlwund/	/larʃwund/	/gaʊtwund/	/θikwund/	wound
/narlword/	/tarʃword/	/tʃutword/	/fukword/	ward
/darlwɔk/	/fruʃwɔk/	/nirtwɔk/	/borkwɔk/	walk
/jarlwɪʃ/	/glarʃwɪʃ/	/lɔitwɪʃ/	/plukwɪʃ/	wish
/mirlwul/	/ðiʃwul/	/gorswul/	/bukwul/	wool**
/hərnworp/	/ruʃworp/	/drirsworp/	/pukworp/	warp
/fɔɪnwərd/	/guʃwərd/	/glɔɪswərd/	/gukwərd/	word
/fumwɪn/	/nuʃwɪn/	/fərswɪn/	/θɔkwɪn/	win
/rarlworf/	/priʃworf/	/hɔɪtworf/	/dukworf/	wharf**
/parlweɪ/	/guʃweɪ/	/putweɪ/	/nukweɪ/	way
/kirlwæg/	/giʃwæg/	/lirtwæg/	/ðikwæg/	wag**
/rarlwɪŋ/	/klarʃwɪŋ/	/fɔitwɪŋ/	/jɔkwɪŋ/	wing
/birlwərs/	/muʃwərs/	/glirswərs/	/gorkwərs/	worse**
/ʃɔɪnwɛpən/	/rarʃwɛpən/	/fɔswɛpən/	/horkwɛpən/	weapon
/funwʊd/	/plarʃwʊd/	/mirswʊd/	/frukwʊd/	wood
/dʒimwum/	/puʃwum/	/plurswum/	/ʃorkwum/	womb**
/nirlwɛt/	/kluʃwɛt/	/mɔɪtwɛt/	/bukwɛt/	wet
/hirlwɑtʃ/	/jiʃwɑtʃ/	/ʒɔɪtwɑtʃ/	/lukwɑtʃ/	watch
/dirlwɛdiŋ/	/parʃwɛdɪŋ/	/hirtwɛdiŋ/	/jɔkwɛdiŋ/	wedding
/marlwəri/	/buʃwəri/	/pirtwəri/	/dɔkwəri/	worry
/girlwik/	/luʃwik/	/krərswik/	/prukwik/	week
/dərnwɪntər/	/prarʃwɪntər/	/nərswɪntər/	/mukwɪntər/	winter
/θaʊnwɪnd/	/parʃwɪnd/	/θrirswɪnd/	/zorkwɪnd/	wind
/pumwɪdθ/	/pruʃwɪdθ/	/pərswɪdθ/	/jikwɪdθ/	width

[1]Seven items excluded from the wordspotting results have also been excluded from these acoustic analyses. One further item, *wing*, was omitted by mistake from the recording session. The acoustic analyses are thus based on 60 items.

[2]The seven items excluded from the wordspotting results have also been excluded from the lexical decision analyses.

[3]A reviewer of this paper suggested that /t/-final contexts of w-words might have been fricated, rendering these items particularly difficult for English L1 listeners but possibly particularly easy for German listeners who might have been unfamiliar with this allophonic variation, so that they would hear it as an affricate rather than a stop, and thus be more likely to postulate a boundary. Inspection of the mean responses for the 14 w-words that had /t/-final contexts in the German boundary condition revealed that, contrary to this prediction, they were not relatively more difficult in this condition than in other conditions for English L1 listeners, and they were not relatively easier in this condition than in other conditions for German listeners (in fact they were harder). However, there was indeed some frication in these items; measured duration and amplitude of the fricated portion did not correlate with English L1 listeners' responses, but German listeners responded more rapidly the longer the fricated portion ($t[13]=0.54$, $p<0.05$). An analysis of the German listeners' results in the German boundary condition for items with /s/-final contexts only (i.e., omitting the 14 items with /t/-final contexts) showed responses to be still significantly faster ($t2[46]=2.14$, $p<0.04$) and more accurate ($t2[46]=3.12$, $p<0.003$) in this condition than in the No boundary condition.

Altenberg, E. P. (**2005**). "The perception of word boundaries in a second language," Second Lang. Res. **21**, 325–358

Altenberg, E. P., and Cairns, H. S. (**1983**). "The effects of phonotactic constraints on lexical processing in bilingual and monolingual subjects," J. Verbal Learn. Verbal Behav. **22**, 174–188.

Baayen, H., Piepenbrock, R., and van Rijn, H. (1993). "The CELEX Lexical database," Philadelphia: Linguistic Data Consortium, University of Pennsylvania (CD-ROM).

Broersma, M. (**2002**). "Comprehension of non-native speech: Inaccurate phoneme processing and activation of lexical competitors," in Proceedings of the Seventh International Conference on Spoken Language Processing,

Denver, CO, pp. 261–264.
Broersma, M. (**2005**). "Perception of familiar contrasts in unfamiliar positions," J. Acoust. Soc. Am. **117**, 3890–3901.
Church, K. W. (**1987**). "Phonological parsing and lexical retrieval," Cognition **25**, 53–69.
Cutler, A. (**2005**). "The lexical statistics of word recognition problems caused by L2 phonetic confusion," in Proceedings of INTERSPEECH 2005, Lisbon, pp. 413–416.
Cutler, A., Mehler, J., Norris, D. G., and Seguí, J. (**1986**). "The syllable's differing role in the segmentation of French and English," J. Mem. Lang. **25**, 385–400.
Cutler, A., and Otake, T. (**1994**). "Mora or phoneme? Further evidence for language-specific listening," J. Mem. Lang. **33**, 824–844.
Cutler, A., and Otake, T. (**2004**). "Pseudo-homophony in non-native listening," 147th Meeting of the Acoustical Society of America (ASA), New York.
Cutler, A., Weber, A., Smits, R., and Cooper, N. (**2004**). "Patterns of English phoneme confusions by native and non-native listeners," J. Acoust. Soc. Am. **116**, 3668–3678.
Dumay, N., Frauenfelder, U. H., and Content, A. (**2002**). "The role of the syllable in lexical segmentation in French: Wordspotting data," Brain Lang **81**, 144–161.
Friederici, A. D., and Wessels, J. M. I. (**1993**). "Phonotactic knowledge and its use in infant speech perception," Percept. Psychophys. **54**, 287–295.
Giegerich, H. J. (**1992**). *English Phonology: An introduction* (Cambridge University Press, Cambridge).
Gow, D. (**2001**). "Assimilation and anticipation in continuous spoken word recognition," J. Mem. Lang. **45**, 133–159.
Haggard, M. (**1973**). "Abbreviation of consonants in English pre- and post-vocalic clusters," J. Phonetics **1**, 9–24.
Hallé, P., Seguí, J., Frauenfelder, U., and Meunier, C. (**1998**). "Processing of illegal consonant clusters: A case of perceptual assimilation?," J. Exp. Psychol. Hum. Percept. Perform. **24**, 592–608.
Harrington, J., Watson, G., and Cooper, M. (**1989**). "Word boundary detection in broad class and phoneme strings," Comput. Speech Lang. **3**, 367–382.
Jusczyk, P. W., Friederici, A. D., Wessels, J. M., Svenkerud, V. Y., and Jusczyk, A. M. (**1993**). "Infants' sensitivity to the sound patterns of native language words," J. Mem. Lang. **32**, 402–420.
Jusczyk, P. W., Luce, P. A., and Charles-Luce, J. (**1994**). "Infants' sensitivity to phonotactic patterns in the native language," J. Mem. Lang. **33**, 630–645.
Keating, P., Cho, T., Fougeron, C., and Hsu, C. (**2003**). "Domain-initial strengthening in four languages," in *Laboratory Phonology VI*, edited by J. Local, R. Odgen, and R. Temple (Cambridge University Press, Cambridge), pp. 145–163.
Keating, P., Wright, R., and Zhang, J. (**1999**). "Word-level asymmetries in consonant articulation," UCLA Working Papers in Phonetics **97**, 157–173.
Kirk, C. (**2000**). "Syllabic cues to word segmentation," in Proceedings of the Workshop on Spoken Word Access Processes (SWAP), edited by A. Cutler, J. M. McQueen, and R. Zondervan (Nijmegen, The Netherlands), pp. 131–134.
Klatt, D. H. (**1974**). "The duration of [s] in English words," J. Speech Hear. Res. **17**, 51–63.
Lamel, L., and Zue, V. W. (**1984**). "Properties of consonant sequences within words and across word boundaries," Proceeding IEEE Int. Conf. Acoust, Sp., Sig. Processing (ICASSP), pp. 42.3.1–42.3.4.
Lehiste, I. (**1960**). "An acoustic-phonetic study of internal open juncture," Phonetica **5**, 1–54.
McQueen, J. M. (**1998**). "Segmentation of continuous speech using phonotactics," J. Mem. Lang. **39**, 21–46.
Norris, D., McQueen, J. M., Cutler, A., and Butterfield, S. (**1997**). "The possible-word constraint in the segmentation of continuous speech," Cogn. Psychol. **34**, 191–243.
Otake, T., Yoneyama, K., Cutler, A., and van der Lugt, A. H. (**1996**). "The representation of Japanese moraic nasals," J. Acoust. Soc. Am. **100**, 3831–3842.
Pallier, C., Colomé, A., and Sebastián-Gallés, N. (**2001**). "The influence of native-language phonology on lexical access: Exemplar-based versus abstract lexical entries," Psychol. Sci. **12**, 445–449.
Pierrehumbert, J. (**1994**). "Knowledge of variation," in Papers of the 30th Regional Meeting of the Chicago Linguistic Society, Chicago, University of Chicago, pp. 232–256.
Saffran, J. R., Newport, E. L., and Aslin, R. N. (**1996**). "Word segmentation: The role of distributional cues," J. Mem. Lang. **35**, 606–621.
Sebastián-Gallés, N., Echeverría, S., and Bosch, L. (**2005**). "The influence of initial exposure on lexical representation: Comparing early and simultaneous bilinguals," J. Mem. Lang. **52**, 240–255.
Shatzman, K. B., and McQueen, J. M. (in press). "Segment duration as a cue to word boundaries in spoken-word recognition," Percept. Psychophys..
Spivey, M., and Marian, V. (**1999**). "Cross talk between native and second languages: Partial activation of an irrelevant lexicon," Psychol. Sci. **10**, 281–284.
Strange, W. (**1995**). *Speech Perception and Linguistic Experience: Issues in Cross-Language Research* (York, Timonium, MD).
van der Lugt, A. H. (**2001**). "The use of sequential probabilities in the segmentation of speech," Percept. Psychophys. **63**, 811–823.
Vitevitch, M. S. (**2002**). "Influence of onset density on spoken-word recognition," J. Exp. Psychol. Hum. Percept. Perform. **28**, 270–278.
Vitevitch, M. S., and Luce, P. A. (**1999**). "Probabilistic phonotactics and neighborhood activation in spoken word recognition," J. Mem. Lang. **40**, 374–408.
Vitevitch, M. S., Luce, P. A., Charles-Luce, J., and Kemmerer, D. (**1997**). "Phonotactics and syllable stress: Implications for the processing of spoken nonsense words," Lang Speech **40**, 47–62.
Warner, N., Kim, J., Davis, C., and Cutler, A. (**2005**). "Use of complex phonological patterns in processing: Evidence from Korean," J. Linguistics **41**, 353–387.
Weber, A. (**2001**). "Help or hindrance: How violation of different assimilation rules affects spoken-language processing," Lang Speech **44**, 95–118.
Weber, A., and Cutler, A. (**2004**). "Lexical competition in non-native spoken-word recognition," J. Mem. Lang. **50**, 1–25.
Wiese, R. (**1996**). *The Phonology of German* (Clarendon, Oxford).
Yip, M. C. W. (**2000**). "Recognition of spoken words in continuous speech: Effects of transitional probability," in Proceedings of the Sixth International Conference on Spoken Language Processing, Beijing, China pp. 758–761.

Beamformer performance with acoustic vector sensors in air

Michael E. Lockwood[a] and Douglas L. Jones
Beckman Institute for Advanced Science and Technology, University of Illinois at Urbana—Champaign, 405 North Mathews Avenue, Urbana, Illinois 61801

(Received 12 April 2005; revised 25 July 2005; accepted 14 October 2005)

For some time, compact acoustic vector sensors (AVSs) capable of sensing particle velocity in three orthogonal directions have been used in underwater acoustic sensing applications. Potential advantages of using AVSs in air include substantial noise reduction with a very small aperture and few channels. For this study, a four-microphone array approximating a small (1 cm^3) AVS in air was constructed using three gradient microphones and one omnidirectional microphone. This study evaluates the signal extraction performance of one nonadaptive and four adaptive beamforming algorithms. Test signals, consisting of two to five speech sources, were processed with each algorithm, and the signal extraction performance was quantified by calculating the signal-to-noise ratio (SNR) of the output. For a three-microphone array, robust and nonrobust versions of a frequency-domain minimum-variance (FMV) distortionless-response beamformer produced SNR improvements of 11 to 14 dB, and a generalized sidelobe canceller (GSC) produced improvements of 5.5 to 8.5 dB. In comparison, a two-microphone omnidirectional array with a spacing of 15 cm yielded slightly lower SNR improvements for similar multi-interferer speech signals. © *2006 Acoustical Society of America.* [DOI: 10.1121/1.2139073]

PACS number(s): 43.72.Dv, 43.66.Pn, 43.66.Ts [DOS] Pages: 608–619

I. INTRODUCTION

To reduce interference from undesirable acoustic sources in air, beamforming algorithms most commonly utilize signals from two or more spatially separated acoustic microphones. These sensors are usually omnidirectional; their sensitivity to sound does not vary with the direction of the source. Fixed-weight beamforming techniques, i.e., those techniques that apply the same filter coefficients to the signal over time, typically rely upon a specific, predetermined spacing of array sensors to provide good interference rejection. This spacing is a significant fraction of the lowest wavelength at which the array is intended to operate, necessitating the use of large arrays to process low-frequency sounds. Pressure sensors are most common for sensing acoustic sources in air, while particle-velocity sensors, such as hot-wire anemometers, are less common, less sensitive, and more difficult to implement.

For underwater acoustic sources, the wavelengths are longer than for the same source in air due to higher underwater propagation speeds, and sensor arrays must be of larger physical aperture. However, the increased density of water over that of air allows velocity sensors to be more easily implemented. At low frequencies, a neutrally buoyant mass suspended in water is moved directly by the particle velocity of the water (Leslie *et al.*, 1956), and this motion may be measured in three dimensions by one sensor, in one location. Such a device, referred to as an acoustic vector sensor (AVS), is capable of measuring three orthogonal directional components of an acoustic signal simultaneously in the same location. A smaller implementation for sensing particle velocity on one axis is described by Josserand and Maerfeld (1985). A similar three-axis sensor is described by White (1961) and utilizes three velocity sensors, oriented orthogonally, and one pressure sensor. This system appears to have been intended for use in seismic exploration. An overview of more recent techniques and work in the field of multicomponent seismic recording is given by Stewart *et al.* (2002).

A large body of literature details the development of underwater acoustic vector sensors and associated signal-processing algorithms. These techniques are closely related to those used to process electromagnetic signals received by arrays of directional antennas. An advantage of vector sensors is that a single sensor, sensing acoustic pressure and the three components of particle velocity at a single location, can be used to determine the direction of arrival (DOA) of a sound source in three dimensions without ambiguity, while four spatially separated pressure sensors are required for the same task. Cox and Zeskind (1992) described bearing estimation and adaptive null steering using an underwater array of two orthogonal dipole sensors and one omnidirectional sensor. D'Spain *et al.* (1992) implemented minimum-variance direction finding and beamforming using a 16-element array of underwater vector and pressure sensors.

After the usefulness of vector sensors had been shown, their theoretical capabilities were bounded and performance comparisons with conventional arrays were made. Nehorai and Paldi (1994) presented methods for localizing sources using acoustic vector sensors, evaluated their performance, and derived expressions for the Cramer-Rao bound of the estimation errors. Hochwald and Nehorai (1996) determined the maximum number of sources that can be identified using an array of vector sensors. Hawkes and Nehorai (1998) detailed the advantages of beamforming with vector-sensor arrays and implemented optimal beamforming methods (1998),

[a]Electronic mail: melockwo@uiuc.edu

examined the effects of placement on vector-sensor performance (1999), investigated vector-sensor performance near a reflecting boundary (2000), and evaluated correlations between sensors in different types of noise fields (2001). Wong and Zoltowski described source localization algorithms for underwater sensors with unknown locations (1997a), for underwater sensors that are uniformly but sparsely spaced (1997b), and for underwater sensors with uniform spacing and arbitrary orientation (1999c). They also described an extension of the MUSIC algorithm to underwater acoustic vector sensors. Extensions of the ESPRIT algorithm to antenna and underwater arrays are detailed in Wong and Zoltowski (1999); Wong and Zoltowski (2000); and Tichavsky *et al.* (2001). Wong and Chi (2002) examined the beam patterns of underwater acoustic vector sensors for a single source distant from reflecting boundaries. Chen and Zhao examined direction of arrival (DOA) estimation using MVDR beamforming with vector sensors (2004).

While the literature for underwater acoustic vector sensors is clearly well developed, there is a general absence of published work concerning the performance of acoustic vector sensors in air. The potential advantages of using such a sensor in air include the ability to determine the direction of arrival of sound sources (Mohan *et al.*, 2003b) or to perform beamforming based on signals from a single vector sensor, rather than a much larger array of spatially separated sensors. The combination of a vector sensor and a frequency-domain beamformer (Lockwood *et al.*, 2003), working to suppress interfering sound sources, also appears worthy of study, because these beamformers have been shown to substantially reduce nonstationary interference while utilizing as few as two spatially separated sensors (Lockwood *et al.*, 2004).

Sensors suitable for use in the construction of a small vector-sensor array exist and are commercially produced. Therefore, the goals of this study are (1) to demonstrate, for the first time, the advantageous use of beamforming algorithms with an acoustic vector sensor in air and (2) to evaluate the performance of time- and frequency-domain beamformers used to process real recorded signals from the array.

Using commercially available gradient and omnidirectional microphones, a small array of four microphones was constructed to approximate an acoustic vector sensor in air. This array contained three orthogonally oriented gradient microphones and one omnidirectional microphone mounted in close proximity to each other, or collocated. Recorded calibration signals were used to create artificial acoustic scenes with multiple speech sources.

Robust and nonrobust adaptive implementations of a frequency-domain minimum-variance beamforming algorithm (Lockwood *et al.*, 2004) and the widely used generalized sidelobe canceling algorithm (Griffiths and Jim, 1981) were used to suppress a varying number of interfering speech sources and to improve the signal-to-noise ratio (SNR) of a target signal originating from a known direction. One fixed beamformer was also implemented.

The effectiveness of the noise suppression was quantified using three SNR metrics: a traditional SNR calculation, a second metric that penalized for distortion of the target signal, and a third that weighted frequency bands according to their contributions to speech intelligibility. Results show that both the adaptive time- and frequency-domain algorithms can produce significant improvements in the SNR of the signals. However, the frequency-domain algorithms produce more SNR improvement, especially for test signals with multiple interfering sound sources. In other experiments not reported here, this array was successfully used to extract acoustic signals and localize their sources, in the frequency range between 300 Hz and 11 kHz, that were produced by and recorded in the field from military vehicles.

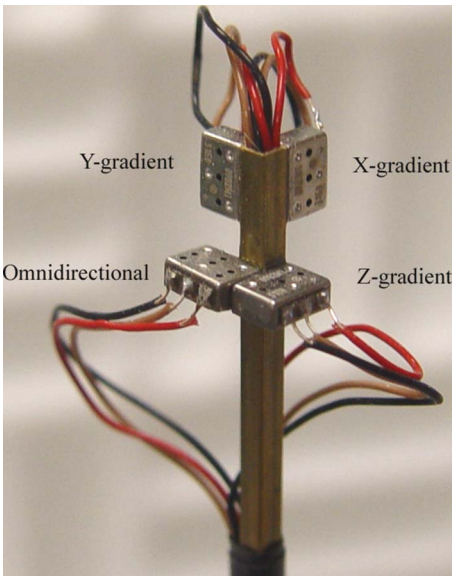

FIG. 1. (Color online) Collocated four-microphone array approximating an acoustic vector sensor in air. The top two and bottom right microphones have gradient responses; the microphone at bottom left has an omnidirectional response. Each sensor is $5.6 \times 4 \times 2.3$ mm.

II. EXPERIMENTAL METHODS

A. Calibration and data collection

The four-sensor AVS array is pictured in Fig. 1. The three gradient sensors (Knowles NR-3158) were positioned such that their directions of maximum response were oriented in the *X*, *Y*, and *Z* directions. The sensors have useful directivity between 300 Hz and 11 kHz, sufficient for work involving speech signals. The omnidirectional microphone was a Knowles EK-3132. The four microphones are glued to a thin, square, metal tube, such that the complete four-sensor assembly occupies a volume of less than 1 cm^3 (not including batteries to provide bias voltage). With gradients arranged in three orthogonal directions, this array is capable of discriminating between sound sources in both elevation and azimuth.

Calibration signals were recorded in a grass-covered outdoor field with no large reflecting objects nearby. All test signals were played from a self-powered loudspeaker (Mackie HR624). For sources at 0° elevation, the loudspeaker tweeter was located approximately 18 in. above the ground. For sources with nonzero elevation, the speaker was elevated up to 6 ft on a stand. For both zero and nonzero elevations, the microphone array was placed such that the sensors were approximately 18 in. above the ground on a

rotating platform, approximately 3 m from the loudspeaker. The sensor assembly was rotated in 15° intervals in azimuth, and recordings were made after each rotation such that 24 recordings were made covering all 360°.

Calibration signals were recorded at 44.1 kHz and consisted of 0.5 s of white noise followed by 0.5 s of silence, followed by 44 periods of a length-4095 maximal-length sequence (MLS). The white-noise signal allowed easy verification of time alignment across all recorded channels (via simple correlation). The MLS sequence was then used to calculate a length-4095 impulse response for each microphone for each direction of arrival.

B. Steering vectors and matching filters

For the frequency-domain algorithms to function properly, the amplitude and phase relationships between the recorded channels must be known for the direction of arrival of the target signal. These relationships are referred to as the "steering vector." For each frequency band k, the "steering vector" for the frequency-domain minimum-variance beamforming algorithm (FMV) and robust FMV algorithms is a $C \times 1$ vector of the frequency-domain representation of the impulse responses for each of the C channels. Steering vectors were calculated for each of 1024 frequency bands.

The time-domain algorithms were implemented assuming identical sensors. Therefore, matching filters were applied to compensate each channel to the response of the omnidirectional sensor. These filters were calculated by dividing the frequency-domain representation of the impulse response of the omnidirectional microphone by that of the other sensor (one of the gradient microphones). The resulting frequency-domain filter was then converted to the time domain, truncated to 1001 points (which experimentally gave the best results), and applied to the appropriate channel. A delay filter was applied to the omnidirectional channel to maintain time alignment.

C. Test materials

A series of high-context sentences from the revised R-SPIN test (Bilger *et al.*, 1984) were originally recorded on digital audio tape (DAT) at a sampling rate of 48 kHz, quantized to 16 bits. These sentences and the impulse responses measured during calibration were downsampled to 22.05 kHz. For each sensor, the sentences were convolved with the corresponding impulse response from that sensor for the desired simulated azimuth of the signal. The impulse responses were truncated to 1001 samples before convolution was performed. (The signals were downsampled to 22.05 kHz because the frequencies of interest for the sensors were between 300 Hz and 11 kHz and because it reduced the length of the test signal, thereby reducing the processing time.) The test signals were the digital superposition of one target speech source and one or more interfering speech sources.

To evaluate the performance of the beamforming algorithms, four groups of test signals were synthesized with sources placed at various azimuths and the same elevation (0°). The first group consisted of 24 tests, in which the target signal and one interfering signal were located within 15° of each other in azimuth. The sources are moved around the array in azimuth in 15° increments (maintaining the 15° spacing between sources), resulting in the 24 tests. The varying location of the target signal shows the effect on the beamforming algorithms of the microphones' varying responses for different azimuths. The second through fourth groups of signals consisted of the target signal and two (tests 25–30), three (tests 31–36), or four (tests 37–42) interfering speech signals, respectively. The source locations are listed in Table I. The SNR for all test signals before processing varied from approximately −10 to 0.5 dB, allowing algorithm performance to be evaluated over a range of SNR.

TABLE I. Source locations for two-dimensional tests.

Test no.	Target Azimuth	Interferer 1 azimuth	Interferer 2 azimuth	Interferer 3 azimuth	Interferer 4 azimuth
1	0°	345°			
2–24	15° to 345°, 15° increments	Target Az.−15°			
25	0°	60°	300°		
26	285°	315°	45°		
27	330°	270°	15°		
28	30°	0°	75°		
29	60°	330°	30°		
30	0°	345°	15°		
31	0°	60°	300°	270°	
32	285°	315°	45°	0°	
33	330°	270°	15°	75°	
34	30°	0°	75°	345°	
35	60°	330°	30°	300°	
36	0°	345°	15°	330°	
37	0°	60°	300°	270°	75°
38	285°	315°	45°	0°	15°
39	330°	270°	15°	75°	300°
40	30°	0°	75°	345°	315°
41	60°	330°	30°	300°	15°
42	0°	345°	15°	330°	30°

For the multi-interferer tests, all sources are located in the front half-plane. This constraint, together with placing all sources at an elevation of 0°, prevents spatial ambiguities from affecting the two- or three-channel processing. Ambiguities arise when the relationships of the amplitudes of the signals received by the microphones are not unique for a particular direction or directions. Additionally, the constraints on the source locations allow easier comparisons to be made between the results of this study and the results of previous studies that use some of the same algorithms.

Due to the placement of the sources along the azimuthal plane, the Z gradient, with its maxima oriented in the vertical directions, receives a relatively low-amplitude signal that does not vary appreciably in amplitude with azimuth. Therefore, for the tests described above, the chosen two-microphone array included the X- and Y- gradient microphones (XY), and the chosen three-microphone array included the omnidirectional microphone and the X- and Y-gradient microphones (XYO). This combination has an ambiguity, but only when sources are located off the azimuthal plane.

TABLE II. Source locations for three-dimensional tests.

Test no.	Target elevation, azimuth	Interferer 1 elevation, azimuth	Interferer 2 elevation, azimuth	Interferer 3 elevation, azimuth
1	0°, 0°	39°, 0°	0°, 315°	0°, 75°
2	39°, 0°	0°, 0°	0°, 315°	0°, 75°

For completeness, two additional test signals were created with source locations varying in azimuth and elevation (Table II). The signals were processed with a subset of the algorithms using signals from both three and four microphones to demonstrate that sources could be extracted in both azimuth and elevation. For these tests, the three-microphone arrays included both the *XYO* configuration described above and a configuration with the *X*, *Y*, and *Z* gradients (*XYZ*).

D. Performance metrics

The performance metrics adopted for this study are similar to those used by Lockwood *et al.* (2004). Results are presented in terms of three SNR-based metrics after processing. The value of the metric before and after processing is presented so that the improvement in the metric may be observed.

A standard definition of the SNR is to compute the ratio of signal and noise energy. The input SNR, or SNR before processing, is calculated in the following manner:

$$\mathrm{SNR}_{IN} = 10 \log_{10} \left(\frac{\sum_{c=1}^{C} [\sum_{v=1}^{V} t_{u,c}(v)^2]}{\sum_{c=1}^{C} [\sum_{v=1}^{V} i_{u,c}(v)^2]} \right), \tag{1}$$

where V is the number of time samples, C is the number of microphone channels, and $t_{u,c}(v)$ and $i_{u,c}(v)$ are the target and interference signals before processing. The sum of squares (energy) is computed separately for each channel, and then the energies are summed for the SNR calculation. (Summing across channels before squaring amounts to a form of conventional beamforming, possibly canceling some interference.)

Because all signals were recorded individually, the target and interference signals received by each microphone before and after processing are known. The SNR_{IN} calculation yields the SNR after microphone reception, including the directional effects of the microphones. The conventional output SNR (SNR_{OUT}) is easily calculated in the same manner using the monaural output signal from each beamformer decomposed into target and interference portions.

The second metric is the frequency-weighted SNR gain (FWSNR). A frequency-domain weighting is applied to the input and output signals; this weighting increases emphasis on the low frequencies so that each of 20 frequency bands contributes equally to intelligibility (French and Steinberg, 1947). The frequency weighting is described by Link and Buckley (1993) as

$$W_{\mathrm{AI}}(f) = \frac{1}{1 + (f/1925)^2}, \tag{2}$$

where the function is weighted such that the area under the curve is unity. The FWSNR gain is then calculated by computing the SNR gain for the frequency-weighted signals.

The third metric, the SNR including distortion penalty (SNRD), is the ratio of the target output power to output interference plus target distortion power:

$$\mathrm{SNRD}_{OUT} = 10 \log_{10} \left(\frac{\sum_{i=1}^{V} t_p(v)^2}{\sum_{i=1}^{V} [y_p(v) - \sum_{c=1}^{C} g_c t_{u,c}(v)]^2} \right), \tag{3}$$

where $t_p(v)$ represents the processed target signal, $y_p(v)$ represents the monaural output signal from the beamformer, and g_c represents the gains applied by the algorithm (effectively the steering vector) to the unprocessed target signal in each channel. The SNRD takes into account the quality of the target signal after it has been processed by treating distortion as noise, and thus is reduced if the target signal is distorted. Therefore, this metric will indicate poorer algorithm performance if portions of the target signal are distorted (usually attenuated) due to correlated source reflections or look-direction errors.

III. ALGORITHMS

Four adaptive beamforming algorithms and one fixed beamforming algorithm were evaluated. The adaptive algorithms consisted of two frequency-domain beamformers and two time-domain beamformers. Three of the adaptive algorithms (GSC, RGSC, FMV) are minimum-variance distortionless-response (MVDR) beamformers with markedly different implementations. A fourth is a robust minimum-variance beamformer modified to allow a small amount of target distortion. For signals composed of statistically stationary, uncorrelated sources and with no microphone mismatch, the three MVDR beamformers all, in theory, converge to identical solutions given sufficient time. However, for the speech signals used in this study, their performance is markedly different due to the nonstationary nature of speech and mismatch between sensors. All signal processing and algorithm implementation was done using Matlab (The Mathworks, Inc., Natick, MA). Floating-point calculations were performed with 64-bit precision.

The adaptive algorithms were allowed to continuously adapt for the entire duration of the test signal due to the nonstationary nature of the speech signals used for testing. We believe that this more closely approximates the use of the beamformer in an acoustic environment where sources change position unpredictably and often quickly. This is in contrast to other evaluation techniques that involve preadaptation of the beamformer before the onset of the stimulus signal, followed by fixing the weights and processing the stimulus with no further adaptation.

The adaptive algorithm parameters (Table III) were adjusted for best performance in terms of the SNR metric [Sec. II D, Eq. (1)]. The test signals were processed with many

TABLE III. Algorithm parameters for best performance. For the FMV and RFMV algorithms, N is the FFT length, F is correlation length in FFTs, M is the regularization value, and the vector $\boldsymbol{\beta}$ controls robustness. For the GSC and RGSC algorithms, K_{GSC} is the length of the adaptive filter, α_{sum} is the adaptive step-size parameter, and β is the tap-weight leakage parameter.

	Processing Algorithm			
Microphones	FMV	RFMV	GSC	RGSC
(2), *X*-, *Y*-gradients	$N=1024$ $F=100$ $M=1.03$	$N=1024$ $F=50$ $M=1.005$ $\boldsymbol{\beta}=[50\ 50\ 25\ 25]$	$K_{GSC}=101$ $\alpha_{sum}=0.02$	$K_{GSC}=101$ $\alpha_{sum}=0.05$ $\beta=0.999$
(3), *X*-, *Y*-gradients, omni.	$N=1024$ $F=100$ $M=1.03$	$N=1024$ $F=60$ $M=1.005$ $\boldsymbol{\beta}=[100\ 100\ 100\ 100\ 100\ 100]$	$K_{GSC}=101$ $\alpha_{sum}=0.01$	$K_{GSC}=101$ $\alpha_{sum}=0.005$ $\beta=0.9999$
(4), *X*-, *Y*-, *Z*-gradients, omni.	$N=1024$ $F=100$ $M=1.03$	$N=1024$ $F=60$ $M=1.01$ $\boldsymbol{\beta}=[50\ 50\ 50\ 50\ 50\ 50\ 50\ 50]$	$K_{GSC}=101$ $\alpha_{sum}=0.01$	$K_{GSC}=101$ $\alpha_{sum}=0.01$ $\beta=0.9999$

different sets of parameters for each combination of algorithm and number of microphones used. The results were first averaged for each number of interferers (two, three, or four). These three numbers were then averaged to produce an overall performance figure. The parameter set that produced the best overall SNR was chosen as optimal; SNR, SNRD, and FWSNR are all reported for that parameter set.

A. FMV algorithm

The first algorithm was the frequency-domain minimum-variance distortionless-response (FMV) algorithm, as implemented by Lockwood *et al.* (2004). It was selected because it provided much better performance when processing nonstationary speech-on-speech signals from small arrays (two elements). In this earlier study, the FMV algorithm was used to process signals from two microphones separated by ~15 cm. For such an array, the *time delay* between sensors (in each frequency band) is the primary cue utilized by the algorithm. However, the FMV algorithm can utilize arbitrary steering vectors that include amplitude differences, and thus it is especially well suited to processing signals from collocated microphone arrays, such as acoustic vector sensors (AVSs). For these arrays, the primary cue utilized by the algorithm is the *amplitude difference* between sensors.

The FMV algorithm is constrained to pass signals that exhibit the relationships represented in the steering vectors with unity gain (thus the term distortionless response). This is referred to as a "hard" constraint, and any error in the steering vectors results in attenuation of the target signal. This attenuation is greatly reduced and the beamforming performance improved by the use of multiplicative regularization applied to the diagonal terms of the correlation matrix for each frequency band (Lockwood *et al.*, 2004).

B. Robust FMV algorithm

The second algorithm is the robust FMV algorithm (RFMV). This is a modification of the FMV algorithm such that it is more robust to errors in the calculated steering vectors compared to the actual microphone response. This algorithm effectively implements a "soft" constraint by reformulating the variance minimization problem into a nonlinear convex quadratic programming problem, as proposed by Wu and Zhang (1999), that can be solved with appropriate techniques. (In this case a quadratic solver was used in Matlab.)

The constraint allows the effective gain to be 1.00 or slightly larger for signals that exhibit relationships between microphones that are very close to those represented in the steering vectors. Therefore some target distortion is introduced in the form of amplification (rather than attenuation of the target signal). The hope is that allowing a small amount of distortion will permit greater freedom to choose (calculate) filter coefficients, and these coefficients will reduce the interfering signals to a greater extent than if they had been calculated using a hard constraint (as with the FMV, GSC, and RGSC). Thus, signal distortion is traded for improvements in the SNR gain.

C. GSC algorithm

The third algorithm is the generalized sidelobe canceller (GSC), as implemented by Greenberg (1998). It was selected because it has been used frequently in other studies of interference suppression relating to hearing aids (Greenberg and Zurek, 1992; Welker *et al.*, 1997; Greenberg *et al.*, 2003), making it a standard to which others have been compared. Greenberg modified the original GSC of Griffiths and Jim (1981) to limit target distortion when the target source was strong. The update equation for this time-domain algorithm is

$$\mathbf{W}_{\text{new}} = \mathbf{W}_{\text{old}} + \frac{\alpha_{\text{sum}}}{K_{\text{GSC}}[\sigma_e^2(n) + \sigma_x^2(n)]} e(n)\mathbf{x}_G(n), \quad (4)$$

where α_{sum} is a step size parameter, n is an index of the current sample, $\mathbf{W}_{\text{old}}$ is the previous set of time-domain filter coefficients, e is the processed output, $\mathbf{x}_G$ is a vector of samples of the signal passed by the blocking matrix (mostly interference), K_{GSC} is the filter length, and σ_e^2 and σ_x^2 represent the average powers (updated every sample) of e and $\mathbf{x}_G$, respectively.

For certain test signals the target source originates from a direction such that it is received weakly by one of the directional microphones. In the case of two-channel processing, one channel then contains the target and interference signals and the other mainly interference. This results in poor conditioning of the blocking matrix in the GSC algorithm, which can magnify microphone mismatch and result in poor performance and high target distortion. Therefore the algorithm was modified slightly for these situations to function as an adaptive noise canceller. For the noise canceller the target was never present in one channel, so the matrix becomes either [0 1] or [1 0], depending on which sensor is receiving very little of the target signal. This occurs for tests 5, 10, and 21, for which the target and interference signals are at azimuths of 60° and 45°, 130° and 125°, and 300° and 285°, respectively. This is a practical (though *ad hoc*) processing strategy because in reality the array can be calibrated for all directions, and the best processing strategy chosen for certain ranges of azimuths. A similar strategy is used for the three-channel processing (utilizing the x- and y-gradient microphones and the omnidirectional microphone). The four-channel processing always uses the conventional GSC algorithm.

D. Robust GSC algorithm

The fourth algorithm is a robust variation of the generalized sidelobe canceller (GSC), as implemented by Greenberg (1998). For our applications, this technique reduces to a very simple implementation. A multiplicative factor, β, of less than unity is applied to the filter weights at each iteration. This is referred to as tap-weight leakage and has been shown to increase robustness in the presence of microphone mismatch (Jablon, 1986). The update equation is

$$\mathbf{W}_{\text{new}} = \beta\mathbf{W}_{\text{old}} + \frac{\alpha_{\text{sum}}}{K_{\text{GSC}}[\sigma_e^2(n) + \sigma_x^2(n)]} e(n)\mathbf{x}_G(n). \quad (5)$$

As with the GSC above, the robust GSC is implemented as a noise canceller for some test signals for the two- and three-channel implementation.

E. Fixed (conventional) beamformer

The final algorithm is a fixed beamformer, referred to as a conventional beamformer (CBF), implemented in the frequency domain. This filter applies the (normalized) impulse response for each sensor for the target direction to the test signal, effectively implementing a maximum ratio combiner. This beamformer was implemented in the frequency domain via 1024-point FFTs (fast Fourier transforms) and inverse FFTs, but alternatively it could have been implemented as a time-domain filter. To be useful, the adaptive algorithms should outperform the CBF, or at worst they should provide comparable performance.

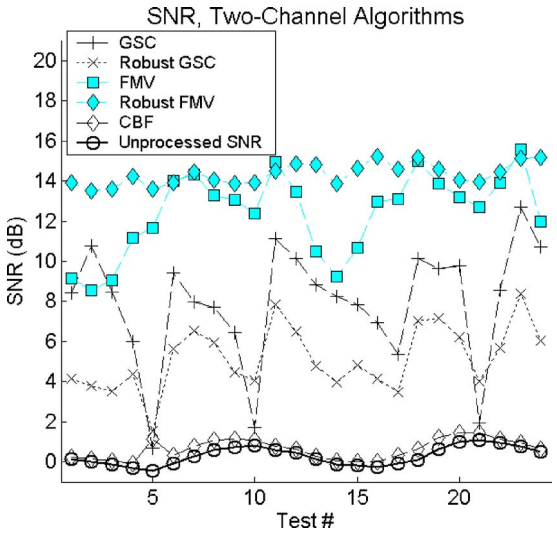

FIG. 2. (Color online) Individual test results for all 24 one-interferer tests. Both sources are speech, and the interferer is only 15° from the target for these tests.

IV. RESULTS AND DISCUSSION

A. Two-microphone signal results

Figure 2 shows the results, in terms of SNR, for processing the first set of 24 tests, each containing one interfering source. For conciseness, all other results are averaged for each number of interferers, but the individual results are shown here to illustrate the variability of the processing results with the azimuth angle of the sources. Results are in terms of SNR; the SNR gain is the difference between the unprocessed and processed SNRs. Note the dips in GSC and robust GSC performance for tests 5, 10, and 21, for which the noise canceller strategy was employed; without it, much smaller increases and even decreases were observed for these test signals. Also notable in this figure is the consistency in performance of the RFMV algorithm, while the FMV algorithm performance falls for some tests. The CBF provides little gain for the one-interferer signals, but actually outperforms the GSC for test 5.

The results for the two-channel algorithms, averaged for each number of interferers, are shown in Figs. 3(a) and 3(b) for the SNR and SNRD metrics, respectively. All four algorithms produce substantial improvements in the SNR and SNRD of the test signals, with the exception of the one-interferer tests for the CBF. This first result is important, because it shows that these beamforming algorithms, using signals from two commercially available gradient sensors that are separated by less than a centimeter, can improve the SNR of the test signals consisting of multiple speech sources by up to 14 dB. Improvements of up to 10 dB are observed for test signals that consisted of five speech sources. This is

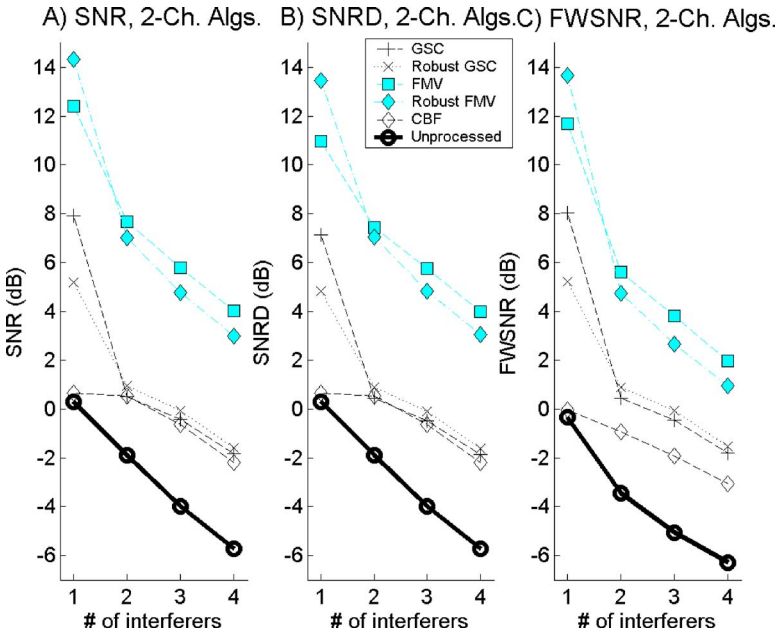

FIG. 3. (Color online) (a) SNR after processing with the two-channel algorithms. (b) SNRD after processing with the two-channel algorithms. (c) FWSNR after processing with the two-channel algorithms.

significant, given the difficulty that has traditionally been encountered in processing such statistically nonstationary signals.

The FMV and RFMV (frequency-domain) algorithms produce substantially more improvement in the SNR than the GSC and RGSC time-domain algorithms for all numbers of interferers. The RFMV has an advantage over the FMV for the one-interferer tests, while the FMV performs slightly better for tests with two or more interferers. By allowing the algorithm to depart slightly from the imposed constraint (passing the target signal with unity gain), the robust FMV produces higher SNR gains, albeit with more target distortion.

Overall, the FMV and RFMV outperform the GSC and RGSC by 4–9 dB for the one-interferer tests and by 5–7 dB for two or more interferers. The time-domain GSC and RGSC algorithms perform comparably to the CBF for tests with two or more interferers, indicating that the two adaptive algorithms are behaving much as fixed beamformers and are unable to function effectively in the presence of the multiple interfering speech sources.

For the SNRD metric, the results are quite similar to those of the SNR, but with a decrease in performance of 1 to 1.5 dB for the FMV, RFMV, and GSC algorithms for the one-interferer tests. This indicates that the algorithms are slightly distorting the target signal while providing large gains in the SNR. For these tests, the metric is especially sensitive to target distortion because most of the interferer energy is successfully removed from the output signal.

Distortion in the case of the GSC algorithm is mainly due to errors present in the matching filters that are applied to the microphone signals prior to processing. These errors effectively cause slight differences in the target signal across channels, and this is measured as distortion. For the FMV and RFMV algorithms, the distortion arises mainly due to the effects of circular convolution. Examination of the calculated frequency-domain weights reveals that the effective time-domain filter is not zero at the end of the filter, and a small amount of energy is being "wrapped" around to the other end of the filter. Applying these weights causes distortion of the target signal, particularly for tests in which the target signal is nearly absent in one channel due to it being located near a directional response minimum of a sensor. These problems can be avoided at the expense of additional computation (Joho and Moschytz, 2000).

The results for the FWSNR metric are similar to the SNR metric, but the improvement in FWSNR for the FMV and RFMV algorithms is 1–2 dB less than with the SNR metric for tests with two or more interferers. (The unprocessed FWSNR is reduced for these tests as well.) The improvement for the GSC and RGSC algorithms is approximately 1 dB more than with the SNR metric for tests with two or more interferers. This suggests either that the FMV and RFMV perform slightly better at high frequencies or the GSC and RGSC perform slightly better at low frequencies. However, the frequency-domain algorithms maintain a significant performance advantage over the time-domain algorithms. It is also noted that the optimization of the algorithm parameters was performed for the SNR metric, not the FWSNR metric, so a different choice of algorithm parameters may change these results.

B. Three-sensor results

Compared to the two-channel SNR results, the three-channel frequency-domain algorithms, utilizing the X- and Y-gradient microphones and the omnidirectional microphone (XYO), generally offer improved performance for signals with multiple interfering sources and comparable performance with one interferer [Fig. 4(a)]. The time-domain algorithms' performances generally improve by 1–2.5 dB for all numbers of interferers. A 2.5-dB improvement is noted for the RGSC algorithm for the one-interferer tests. The FMV and RFMV performance rises by about 1.5–3 dB for tests with two or more interferers. The performance advantage of the FMV and RFMV over the GSC and RGSC algorithms

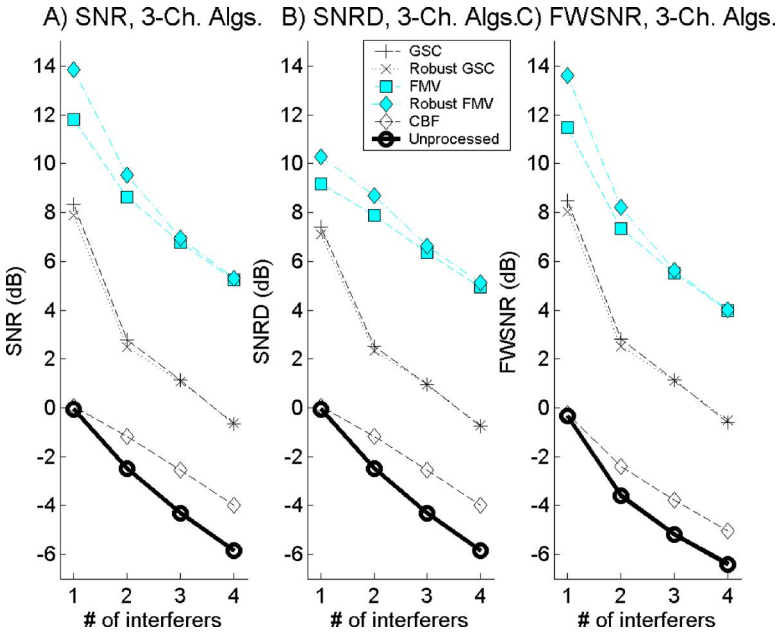

FIG. 4. (Color online) (a) SNR after processing with the three-channel algorithms. (b) SNRD after processing with the three-channel algorithms. (c) FWSNR after processing with the three-channel algorithms.

remains approximately 5–7 dB for the tests with multiple interfering sources and drops slightly to 3.5–6 dB for the single-interferer tests. Performance of the CBF drops 1.5–2 dB for multiple interferer tests.

For the one-interferer tests, the RFMV algorithm has approximately a 2-dB advantage over the FMV, because it allows some target distortion. This decreases to 1 dB for the two-interferer tests. For tests with two or more interferers, the performance of the RFMV is comparable with that of the FMV, in terms of SNR.

The results show that the algorithms utilize the extra information provided by the omnidirectional microphone. A two-microphone system has sufficient degrees of freedom for perfect source cancellation when there are two sources; three microphones may result in more adaptation noise when there are only two sources, reducing performance. Additionally, the matrix inverse used by the FMV and RFMV is less stable in the event the matrix is reduced rank, which could lead to other problems. However, the results indicate that the extra information provided by the addition of the omnidirectional sensor results in a performance advantage (in terms of SNR) for signals with three or more sources.

Compared to the SNRD results for the two-channel algorithms, the SNRD results [Fig. 4(b)] for the time-domain algorithms rise by 1–2 dB for the multiple-interferer tests. For the one-interferer tests, the RGSC performance improves by about 2 dB. The performances of the RFMV and FMV algorithms decline by 3.5 and 2 dB, respectively, for one-interferer tests, due to increased target distortion.

Comparing the SNRD results to the SNR results [Figs. 4(a) and 4(b)], the most notable change is that for the FMV and RFMV for the one-interferer tests, the SNRD is 3–4 dB lower than the SNR. This indicates good suppression of interference but with some distortion of the target signal. Results for the FWSNR are similar to those for the two-channel algorithms; compared to the SNR results, the gain of the frequency-domain algorithms is decreased by approximately 1 dB for the multi-interferer tests, while the gain for the time-domain algorithms is increased by approximately 1 dB.

C. Four-sensor results

The SNR for the GSC and RGSC algorithms after processing the four-channel signals [Fig. 5(a)] decreases by approximately 1 dB for tests with one interferer, compared to the three-channel SNR results [Fig. 4(a)]. The performance of the RGSC algorithm declines slightly for multiple-interferer tests. Otherwise, performances are quite similar. This indicates that the extra channel of information is not useful for these tests and algorithms. This is not surprising, as these tests have sources that lie in the direction of a spatial null of the added microphone (Z-gradient), because the elevation of all the sources is 0°.

Compared to the three-sensor SNRD results, the SNRD metric declines by 1.5–2 dB for the FMV algorithm, remains nearly constant for the RFMV algorithm, and declines by about 1–1.5 dB for the GSC and RGSC algorithms. Thus, the extra signal (from the Z-gradient) used in processing may result in higher distortion of the target signal than the three-channel signal. This indicates that little, if any, new information is provided by this channel in the test signals considered here, in which all sources are in the azimuthal plane.

Compared to the SNR results for the four-channel algorithm, the SNRD results decline for the RFMV algorithm for the one-, two-, and three-interferer tests. FMV performance declines for all tests, most notably for the one-interferer tests, for which performance declines to that of the time-domain algorithms. In terms of FWSNR, the results for the frequency-domain algorithms decline slightly compared to SNR. Gains for the time-domain algorithms improve by 1–2 dB for multi-interferer signals.

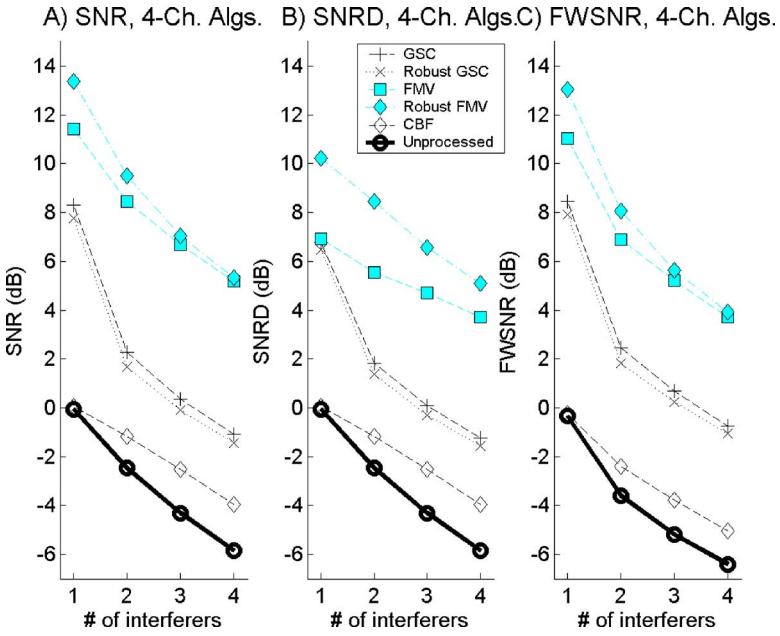

FIG. 5. (Color online) (a) SNR after processing with the four-channel algorithms. (b) SNRD after processing with the four-channel algorithms. (c) FWSNR after processing with the four-channel algorithms.

D. Three-dimensional test results

Two tests with four interferers were created; the positions of the sources are summarized in Table II. These tests had either a target or interfering source at 39° elevation, 0° azimuth. The signals from the three gradient microphones (*XYZ*), from the *X*- and *Y*-gradients and the omni (*XYO*), and from all four microphones (*XYZO*) were processed with the FMV algorithm to verify the effectiveness of the processing for signals with sources located in three dimensions. Results, in terms of all three performance metrics, are summarized in Table IV. The algorithms produce between 10.2 and 15.46 dB of improvement in the SNR of the signal (averaged over the two tests). This indicates that the FMV algorithm can effectively extract speech signals in three dimensions amidst multiple interfering speech sources.

In terms of all three metrics, the *XYZO* array configuration produces the best performance, followed closely by the *XYZ* configuration. This indicates that using all sensors may be important when sources are located off the azimuthal plane. This is not surprising, because using all four sensors eliminates all spatial ambiguities. Performance for the *XYO* configuration is markedly reduced, indicating that the *Z*–gradient is important in processing signals with sources in three dimensions.

TABLE IV. Performance for three-dimensional tests processed with the FMV algorithm. Each value is the average of the results from two test signals.

Array configuration	Average SNR gain (dB)	Average SNRD gain (dB)	Average FWSNR gain (dB)
XYZ	14.75	13.72	15.03
XYO	10.20	9.75	10.23
XYZO	15.46	14.37	15.63

E. Discussion

Collectively, the test results reveal that the FMV, RFMV, GSC, and RGSC algorithms can produce significant improvements in the signal-to-noise ratio of the test signals generated from the recordings made with the vector acoustic sensor in air. While other techniques utilize the time delay between sensors as the primary processing cue (and therefore require apertures of significant size), excellent results can be obtained with the much smaller vector sensor by utilizing gain differences between differently oriented directional sensors as the primary processing cue.

Additionally, these substantial gains in SNR are obtained for signals that contain multiple interfering speech sources that are by nature nonstationary. Thus, the processing algorithms can adapt with sufficient speed to maintain good performance in the presence of rapidly changing interference signals while utilizing mainly amplitude cues. It is in this area that the frequency-domain algorithms gain their advantage over their time-domain counterparts. The frequency-domain algorithms adapt independently in each frequency band, resulting in faster overall adaptation and improved performance (Lockwood *et al.*, 2004), even without time-delay information.

In general, for test signals with sources in the azimuthal plane, performance for the algorithms improves when the number of channels increases from two to three when the number of sources is greater than two, and decreases slightly when it changes from three to four (for the SNR metric). In general, beamformer performance is expected to increase when channels with useful information are added, as in the case of the omnidirectional microphone for the three-channel signals, and decrease otherwise due to increased adaptation error. The channel added for the four-channel signals is the *Z*-gradient channel, for which the microphone has response maxima in the ±*Z* directions. The sources in this study generally lie in the *X*-*Y* plane (elevation angle of 0°) and therefore are received with minimum amplitude by this sensor.

Therefore, little useful information is added, as this channel is quite similar to the omnidirectional channel for the test signals used in this study, but with significantly more inherent system noise.

When the sources are not located on the *X*-*Y* plane (the elevation angle is not 0°), results show that adding the *Z*-gradient provides significant improvements in performance. An important benefit may be gained by adding the omnidirectional sensor as well; it can be shown that by utilizing signals from all four sensors during processing, all spatial ambiguities can be eliminated because the amplitude relationships of the sensors are unique for any direction. Therefore, this small sensor array, combined with a multichannel frequency-domain beamformer, appears to be an effective system for performing signal extraction and noise suppression in a crowded environment with sources varying in position in both azimuth and elevation.

The robust GSC algorithm offered little advantage over the conventional GSC algorithm. It was hoped that robustness to microphone mismatch would improve the performance of the algorithm, but this was not observed experimentally. Both algorithms worked best with a relatively short filter length (see Table III) of length 101, when compared to the optimal FFT length of 1024 for the FMV and RFMV algorithms. The most likely cause of this is that the longer filter lengths were less able to adapt to the rapid changes in the sources, while the shorter filters could adapt more quickly. In general, the GSC adapts more slowly than the FMV when processing speech signals (Lockwood *et al.*, 2004).

The robust FMV algorithm does offer improved performance over the FMV, especially as the number of microphones increases and for single-interferer tests. This indicates that the robust algorithm is better able to cope with the increasing number of channels and overdetermined situations. As the number of channels increases, the matrix inversion required for this algorithm becomes more sensitive to channel mismatch, and the robust algorithm is likely better able to cope with this mismatch. In terms of algorithm parameters, the RFMV operates best both with a shorter correlation length (F) and a smaller regularization value (M) than the FMV algorithm. This seems logical, as the regularization term introduces error in the correlation matrix that acts to make the FMV algorithm more robust in the case of microphone mismatch. The RFMV has built-in robustness and requires little error to be introduced. A small amount does appear to provide a benefit in terms of SNR performance, though, and likely helps avoid instability in the matrix inversion.

In Lockwood *et al.* (2004), signals with two to four interfering sources, recorded with a two-element, omnidirectional 15-cm array in the least-reverberant room were processed with the FMV algorithm, yielding an average gain in SNR of 7–8 dB. In this study, the improvements in SNR for the frequency-domain algorithms are approximately 9–10 dB for two-channel signals, and nearly 12 dB for three-channel signals. This indicates that the performance attainable with the small acoustic vector sensor array and speech sources is at least comparable to that obtained with an array of two spatially separated sensors for environments with minimal reverberation.

Other experiments have shown the capability of the FMV algorithm to extract the signal of a military vehicle in the presence of other acoustic sources, and the capability of a localization algorithm (Mohan *et al.*, 2003a) to accurately localize both vehicles and gunfire with high accuracy. This suggests that this type of array, constructed with suitable sensors with useful directionality in a frequency range below that of the commercial gradients used in this study, could be useful in applications requiring the localization and extraction of vehicle sounds, particularly at lower frequencies where the most energy is radiated by the engine exhaust.

V. CONCLUSION

An approximation of an acoustic vector sensor in air has been constructed using commercially available gradient microphones and has been used to record test signals consisting of multiple speech sources. Robust and nonrobust versions of the frequency-domain minimum-variance distortionless-response beamformer (FMV) provide improvements in the signal-to-noise ratio of 11–14 dB for a three-microphone array. Robust and nonrobust versions of the generalized sidelobe canceller (GSC) provide improvements of approximately 5.5–8.5 dB. A fixed conventional beamformer (CBF) provides improvements of 1.5–2 dB.

The improvements in SNR for all the adaptive algorithms are positive and substantial, indicating that adaptive beamforming can successfully be accomplished with an array of essentially collocated, directional microphones. To our knowledge, such a result has not been shown for such a compact microphone array. Additionally, this result was obtained through processing test signals containing multiple, statistically nonstationary (speech) sources. The beamformers were allowed to adapt throughout the processing (rather than being preadapted at the beginning of a test signal), which we believe to be the most common and realistic use case in practical applications. Results from Lockwood *et al.* (2004) are most readily comparable to those presented here; that study reported improvements of 7–8 dB for similar two-channel speech test signals processed with the FMV algorithm and ~4 dB for time-domain algorithms. However, the array had a spacing of 15 cm, compared to a much smaller size of 1 cm^3 for the collocated array. The collocated array appears to offer similar or slightly better performance while utilizing a much smaller array.

As discussed by Lockwood *et al.* (2004), other studies (Hoffman *et al.*, 1994; Kates and Weiss, 1996; Greenberg *et al.*, 2003) allowed the algorithms under test to converge for 1–2 s before processing was started. The study by Greenberg *et al.* allows the algorithms to converge in the noise-only condition, with the target signal absent. It is unclear what the effects of moving sources, or, equivalently, a quick turn of the array wearer's head, would have on the processing algorithms, but performance would surely be degraded. (Greenberg *et al.* did include a "roving" noise condition,

where interferers changed location, but the adaptive algorithms were not evaluated for SRT gain for those signals.)

The only study in which the algorithm was not allowed to preadapt was by Berghe and Wouters (1998), which evaluated an adaptive processing strategy used with a two-microphone endfire directional microphone array with 3-cm spacing, implemented on a BTE hearing aid. Results were provided only for the case of a single interfering noise source, for which an improvement in SRT of 5–6 dB was obtained.

Perhaps a more important observation is that all the studies mentioned above, with the exception of Lockwood *et al.* (2004), test algorithms under conditions in which there are always at least as many sensors as sources. This represents a condition where fully converged adaptive algorithms should be able to cancel stationary interfering sources almost completely. In effect, these are ideal conditions for the operation of adaptive algorithms, and we believe this represents an unrealistic test of the algorithms/array systems. Our evaluation of our smaller array included numerous tests with more sources than sensors, and no preadaptation of the algorithms was allowed. We believe this is more representative of real conditions under which such an array system might operate.

Signals from a spatially compact array such as the one used for this study may have interesting properties in reverberant environments. Reflected sound arriving at spatially separated sensors generally results in the decorrelation of the signals. However, the decorrelation effect observed with a collocated array may be different than with a spatially separated array. Future work in reverberant environments is required to answer this question. Additionally, the capabilities of the algorithms and array should be evaluated with a more extensive battery of test signals containing sources that do not lie exclusively on the *X*-*Y* plane. In theory, this can be accomplished with two different combinations of three microphones, the *X*-, *Y*-, and *Z*-gradient microphones, or alternatively the *X*- and *Y*-gradient and the omnidirectional microphone.

ACKNOWLEDGMENTS

This research was supported by a grant from the Defense Advanced Research Projects Agency (ARO Contract No. DAAD17-00-0149, administered by the Army Research Office) and a grant from the National Institutes of Health (NIDCD Contract No. R01 DC005762-02).

Berghe, J. V., and Wouters, J. (**1998**). "An adaptive noise canceller for hearing aids using two nearby microphones," J. Acoust. Soc. Am. **103**, 3621–3626.

Bilger, R. C., Nuetzel, J. M., Rabinowitz, W. M., and Rzeckzowski, C. (**1984**). "Standardization of a test of speech perception in noise," J. Speech Hear. Res. **27**, 32–48.

Chen, H. W., and Zhao, J. W. (**2004**). "Wideband MVDR beamforming for acoustic vector sensor linear array," IEE Proc., Radar Sonar Navig. **151**(3), 158–162.

Cox, H., and Zeskind, R. M. (**1992**). "Adaptive cardioid processing," Proceedings of the 26th Asilomar Conference on Signals, Systems and Computers, Vol. **2**, pp. 1058–1061.

D'Spain, G. L., Hodgkiss, W. S., Edmonds, G. L., Nickles, J. C., Fisher, F. H., and Harriss, R. A. (**1992**). "Initial analysis of the data from the vertical DIFAR array," OCEANS '92 Proceedings, Vol. **1**, pp. 346–351.

French, N. R., and Steinberg, J. C. (**1947**). "Factors governing the intelligibility of speech sounds," J. Acoust. Soc. Am. **19**, 90–119.

Greenberg, J. E. (**1998**). "Modified LMS algorithms for speech processing with an adaptive noise canceller," IEEE Trans. Speech Audio Process. **6**, 338–351.

Greenberg, J. E., and Zurek, P. M. (**1992**). "Evaluation of an adaptive beamforming method for hearing aids," J. Acoust. Soc. Am. **91**, 1662–1676.

Greenberg, J. E., Desloge, J. G., and Zurek, P. M. (**2003**). "Evaluation of array-processing algorithms for a headband hearing aid," J. Acoust. Soc. Am. **113**, 1646–1657.

Griffiths, L. J., and Jim, C. W. (**1981**). "An alternative to linearly constrained adaptive beamforming," IEEE Trans. Antennas Propag. **AP-30**, 27–34.

Hawkes, M., and Nehorai, A. (**1998**). "Acoustic vector-sensor beamforming and Capon direction estimation," IEEE Trans. Signal Process. **46**, 2291–2304.

Hawkes, M., and Nehorai, A. (**1999**). "Effects of sensor placement on acoustic vector-sensor array performance," IEEE J. Ocean. Eng. **24**, 33–40.

Hawkes, M., and Nehorai, A. (**2000**). "Acoustic vector-sensor processing in the presence of a reflecting boundary," IEEE Trans. Signal Process. **48**, 2981–2993.

Hawkes, M., and Nehorai, A. (**2001**). "Acoustic vector-sensor correlations in ambient noise," IEEE J. Ocean. Eng. **26**, 337–347.

Hochwald, B., and Nehorai, A. (**1996**). "Identifiability in array processing models with vector-sensor applications," IEEE Trans. Signal Process. **44**, 83–95.

Hoffman, M. W., Trine, T. D., Buckley, K. M., and Van Tasell, D. J. (**1994**). "Robust adaptive microphone array processing for hearing aids: Realistic speech enhancement," J. Acoust. Soc. Am. **96**, 759–770.

Jablon, N. K. (**1986**). "Adaptive beamforming with the generalized sidelobe canceller in the presence of array imperfections," IEEE Trans. Antennas Propag. **AP-34**, 996–1012.

Joho, M., and Moschytz, G. S. (**2000**). "Connecting partitioned frequency-domain filters in parallel or in cascade," IEEE Trans. Circuits Syst., II: Analog Digital Signal Process. **47**, 685–698.

Josserand, M. A., and Maerfeld, C. (**1985**). "PVF2 velocity hydrophones," J. Acoust. Soc. Am. **78**, 861–867.

Kates, J. M., and Weiss, M. R. (**1996**). "A comparison of hearing-aid array-processing techniques," J. Acoust. Soc. Am. **99**, 3138–3148.

Leslie, C. B., Kendall, J. M., and Jones, J. L. (**1956**). "Hydrophone for measuring particle velocity," J. Acoust. Soc. Am. **28**, 711–715.

Link, M. J., and Buckley, K. M. (**1993**). "Prewhitening for intelligibility gain in hearing aid arrays," J. Acoust. Soc. Am. **93**, 2139–2145.

Lockwood, M. E., Jones, D. L., Su, Q., and Miles, R. N. (**2003**). "Beamforming with collocated microphone arrays," J. Acoust. Soc. Am. **114**, 2451.

Lockwood, M. E., Jones, D. L., Bilger, R. C., Lansing, C. R., O'Brien, W. D. Jr., Wheeler, B. C., and Feng, A. S. (**2004**). "Performance of time- and frequency-domain binaural beamformers based on recorded signals from real rooms," J. Acoust. Soc. Am. **115**, 379–391.

Mohan, S., Lockwood, M. E., Jones, D. L., Su, Q., and Miles, R. N. (**2003a**). "Sound source localization with a gradient array using a coherence test," J. Acoust. Soc. Am. **114**, 2451.

Mohan, S., Kramer, M. L., Wheeler, B. C., and Jones, D. L. (2003b). "Localization of nonstationary sources using a coherence test," 2003 IEEE Workshop on Statistical Signal Processing, pp. 470–473.

Nehorai, A., and Paldi, E. (**1994**). "Acoustic vector-sensor array processing," IEEE Trans. Signal Process. **42**, 2481–2491.

Stewart, R. R., Gaiser, J. E., Brown, R. J., and Lawton, D. C. (**2002**). "Converted-wave seismic exploration: Methods," Geophysics **67**, 1348–1363.

Tichavský, P., Wong, K. T., and Zoltowski, M. D. (**2001**). "Near-field/far-field azimuth and elevation angle estimation using a single vector hydrophone," IEEE Trans. Signal Process. **49**, 2498–2510.

Welker, D. P., Greenberg, J. E., Desloge, J. G., and Zurek, P. M. (**1997**). "Microphone-array hearing aids with binaural output-part II: a two-microphone adaptive system," IEEE Trans. Speech Audio Process. **5**, 543–551.

White, J. E. (1961). "Directional sound detection," U. S. Patent #2,982,942.

Wong, K. T., and Chi, H. (**2002**). "Beam-patterns of an underwater acoustic vector hydrophone," IEEE J. Ocean. Eng. **27**(3), 628–637.

Wong, K. T., and Zoltowski, M. D. (**1997a**). "Closed-form underwater acoustic direction-finding with arbitrarily spaced vector hydrophones at

unknown locations," IEEE J. Ocean. Eng. **22**, 566–575.
Wong, K. T., and Zoltowski, M. D. (**1997b**). "Extended-aperture underwater acoustic multisource azimuth/elevation direction-finding using uniformly but sparsely spaced vector hydrophones," IEEE J. Ocean. Eng. **22**, 659–672.
Wong, K. T., and Zoltowski, M. D. (**1997c**). "Uni-vector-sensor ESPRIT for multisource azimuth elevation and polarization estimation," IEEE Trans. Antennas Propag. **45**, 1467–1474.
Wong, K. T., and Zoltowski, M. D. (**1999**). "Root-MUSIC-based azimuth-elevation angle-of-arrival estimation with uniformly spaced but artibrarily oriented velocity hydrophones," IEEE Trans. Signal Process. **47**, 3250–3260.
Wong, K. T., and Zoltowski, M. D. (**2000**). "Self-initiating MUSIC-based direction finding in underwater acoustic particle velocity-field beamspace," IEEE J. Ocean. Eng. **25**, 262–273.
Wu, S. Q., and Zhang, J. Y. (1999). "A new robust beamforming method with antennae calibration errors," IEEE Wireless Communications and Networking Conference, Vol. **2**, pp. 869–872.

Rainforests as concert halls for birds: Are reverberations improving sound transmission of long song elements?

Erwin Nemeth[a)]
Konrad Lorenz Institute for Comparative Ethology, Austrian Academy of Sciences, Savoyenstrasse 1a, A–1160 Wien, Austria

Torben Dabelsteen
Department of Animal Behaviour, Zoological Institute, University of Copenhagen, Tangensvej 16, DK-2200 Copenhagen, Denmark

Simon Boel Pedersen
Department of Animal Behaviour, Zoological Institute, University of Copenhagen, Tangensvej 16, DK-2200 Copenhagen, Denmark

Hans Winkler
Konrad Lorenz Institute for Comparative Ethology, Austrian Academy of Sciences, Savoyenstrasse 1a, A–1160 Wien, Austria

(Received 14 April 2005; revised 9 September 2005; accepted 14 October 2005)

In forests reverberations have probably detrimental and beneficial effects on avian communication. They constrain signal discrimination by masking fast repetitive sounds and they improve signal detection by elongating sounds. This ambivalence of reflections for animal signals in forests is similar to the influence of reverberations on speech or music in indoor sound transmission. Since comparisons of sound fields of forests and concert halls have demonstrated that reflections can contribute in both environments a considerable part to the energy of a received sound, it is here assumed that reverberations enforce also birdsong in forests. Song elements have to be long enough to be superimposed by reflections and therefore longer signals should be louder than shorter ones. An analysis of the influence of signal length on pure tones and on song elements of two sympatric rainforest thrush species demonstrates that longer sounds are less attenuated. The results indicate that higher sound pressure level is caused by superimposing reflections. It is suggested that this beneficial effect of reverberations explains interspecific birdsong differences in element length. Transmission paths with stronger reverberations in relation to direct sound should favor the use of longer signals for better propagation. © *2006 Acoustical Society of America.* [DOI: 10.1121/1.2139072]

PACS number(s): 43.80.Ev, 43.80.Lb [JAS] Pages: 620–626

I. INTRODUCTION

Acoustic signals are always altered by the environment. Frequencies can be absorbed and temporal characteristics can be heavily distorted. Variation in acoustic conditions have led to contrasting predictions of vocal signal structures in different environments.[1–6] The low-pitched, whistlelike songs of rainforest birds are an example of adaptation of signal structure to habitat.[1,3] Low frequencies transmit farther and slow amplitude or frequency modulations are less affected by reverberations.[7] Contrary to this detrimental effect of reverberations, possible positive effects of reverberations on avian communication in forests have rarely been suggested.[3,7] One experimental exception, which deserves more attention, is an investigation of the song of the green hylia (*Hylia prasina*) in an African tropical forest.[8] This species sings almost pure notes, and it was shown that test sounds with narrow bandwidth are more elongated by echoes than sounds with broader spectral distribution. Since males of this species reacted stronger to longer notes, it was concluded that the elongation of signals with narrow bandwidth is a beneficial consequence of reverberations on birdsong transmission.

Reverberations have always played a crucial part in architectural acoustics[9] and research results in this scientific field might have inspired some bioacoustic studies. In two recent studies Sakai and his co-workers compared the acoustic qualities of sound fields in forests and concert halls.[10,11] Though they were interested in the sound fields related to human hearing preferences, their results could be important to explain the adaptive design of long-range acoustic signals in animals. According to Sakai *et al.*[11] both in concert halls and in forests the energy of reflected waves in relation to the energy of direct waves increases with distance. In a concert hall the energy of the reflected sound equals the energy of the direct sound after a few meters. In a deciduous forest reflected sound energy comes up to the energy of direct sound after 40 m;[10] in a bamboo forest it reaches the same value already after 10 m.[11] The estimated values are dependent on the location of the loudspeaker and microphone, the mea-

[a)]Electronic mail: e.nemeth@klivv.oeaw.ac.at

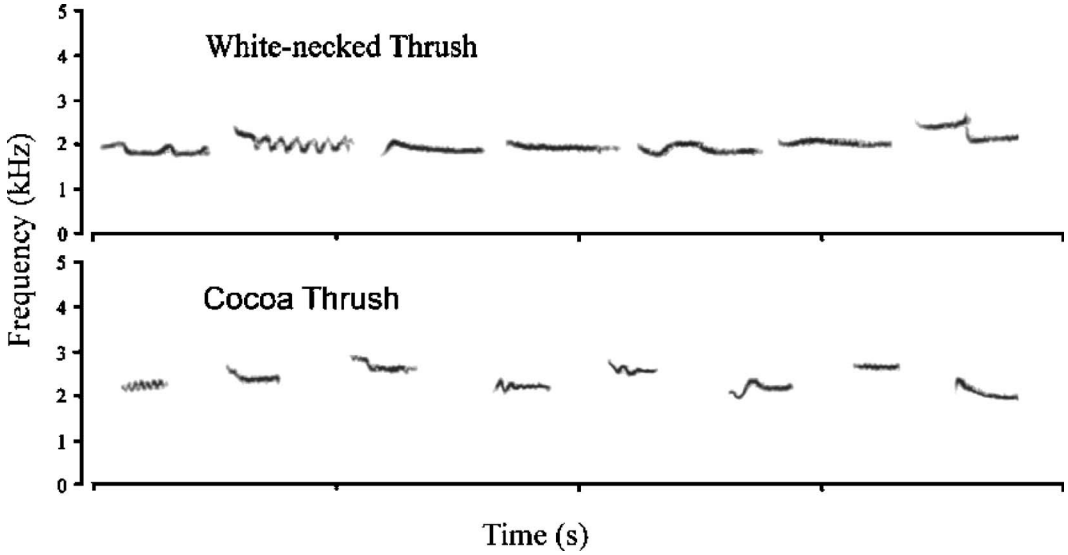

FIG. 1. Spectrograms of song elements used for transmission experiments. Time resolution is 43.1 ms, frequency resolution is 23.2 Hz. The hatch marks on the *x* axis represent 1 s. Note that the lower frequency of the white-necked thrush songs is not related to larger body weight, like described for other species;[20,35] the cocoa thrush (71.4 g) is about 40% heavier than the white-necked thrush (51.1 g).[36]

surement methods, and the frequencies measured. Nevertheless, they imply that reflected sound in forests can contribute a considerable part of the energy to the amplitude of sound signals. If signals are long enough to be superimposed by reflections, they should therefore have a higher sound pressure level (SPL) than shorter sounds.

Within the framework of a study of songs of rainforest birds we found a possible example for this kind of signal enforcement. We noticed that song elements of the white-necked thrush (*Turdus albicollis*) have nearly double the length of song elements of the sympatric cocoa thrush [*Turdus fumigatus orinocensis*; element length, mean±s.e. (ms): white-necked, 444±16, $n=16$; cocoa, 223±10.2, $n=32$]. Transmission experiments showed that the longer song elements of the white-necked thrush were less attenuated (see Sec. III and Fig. 2).

To test the effect of reverberations on signal length we examined SPL in shortened song elements and artificial tones. However, even if we show that longer signals are less attenuated, this could be caused by other reasons and it is not yet a conclusive evidence for an effect of reflected sound. Therefore, it would be preferable to assess reverberations themselves. Though it was not possible to measure reverberations that superimposed signals, we measured at least a tail-to-signal ratio (TSR)[12] in the transmitted birdsong elements. The TSR describes how much energy the echoic tail contains in comparison with the preceding signal. On transmissions paths where the TSR ratio is higher we also expect a stronger influence of reverberations on the signal. Finally, our results are discussed in relation to an optimal signal design in birdsong.

II. METHODS

A. Study site and birds

The study was conducted in 1996 and 1997 in a primary rainforest (3°10′27″ N, 65°40′19″ W, 105 m a.s.l.) in southern Venezuela. Song post heights were estimated from spontaneously singing birds in the immediate neighborhood of the test site [song post heights; mean±s.e. (m): white-necked, 2.8±1.97, $n=18$; cocoa, 11.6±2.70, $n=22$]. These observations confirmed descriptions in the literature, which describe *T. fumigatus* as a species of the midstorey, while *T. albicollis* is known to live closer to the ground.[13] The specific status of the cocoa thrush is uncertain. Observed and captured birds were identified as the subspecies *Turdus fumigatus orinocensis*,[13] but the songs appeared more similar to recordings of Hauxwell's thrush (*Turdus hauxwelli*).[14] The species has not been recorded from this area and until further investigation we assume that the species is a subspecies of *T. fumigatus*.

B. Transmission experiments and analysis

The transmission of thrush song elements was part of more extensive transmission experiments and details about the experimental setup, recording equipment, and weather conditions that have already been described.[15] We selected seven and eight song elements for the two thrush species from high quality recordings made at close distances (<10 m). The song elements for transmission experiments were collected from only two individuals. We therefore have to note that we consider here mainly the effect of element length and we are not able to present an extensive comparison of song features in these two species. However, the interspecific difference in element length is also found in other recordings.[14,16] (See Fig. 1).

All songs were digitized (sample frequency 44 100 Hz). Frequency and time characteristics were measured with AVISOFT SONOGRAPH PRO. All of the selected elements have a rather narrow bandwidth [threshold criterion: −25 dB from the peak of the amplitude spectrum; bandwidth (Hz), mean±s.e.: white-necked 393±67; cocoa thrush: 375±38].

Test sounds were transmitted over three distances (17.5, 37, and 54.5 m) at two heights (2 and 12 m). The micro-

phone and loudspeaker were always at the same height. The order of transmission paths was randomly chosen. In each trial, the sequence of test sounds was randomized and repeated eight times. We refer to the experimental recordings as the *observation sounds*. For each test sound and each transmission path we selected the first four repetitions that were not superimposed by other sounds; when not possible, only two or three replicates were selected (altogether 368 observations). Filtered[17] observation sounds were compared with non-degraded *models*, which were recorded in an anechoic room. We measured signal-to-noise ratio (SNR), excess attenuation (EA), and blur ratio.[17] The lowest SNR value was 15.9 dB. Detailed results for SNR and blur ratio are not reported here. EA is the level of attenuation in excess of that predicted by spherical spreading. The tail-to-signal ratio (TSR),[12] which expresses the amount of elongation with trailing echoes, was calculated from the energy of the observation sound (Ey) and the energy of the echoic tail (Et). The energy of the signal was measured by a forward integration over the squared signal (energy accumulated over time); the energy of echoes was measured by backward integration over the tail from the end, where the sound disappears in background noise. In both integrations background noise was subtracted and the result was expressed as tail-to-signal ratio, $\mathrm{TSR}=10\log(\mathrm{Et}/\mathrm{Ey})$.[12] Filtering of signals and acoustical analysis of song elements were performed by the customized program SIGPRO 1.4.

To test the influence of signal length on attenuation we examined the transmission properties of the first part of song elements cut to the shortest element in both species (190 ms). Since the difference in attenuation of elements could be due to a different song structure at the beginning of the elements, we investigated also transmitted sinus tones with a length of 500 ms and a constant amplitude within the frequency range of both species (1.5, 2, 2.5, 3, and 3.5 kHz). The artificial sounds provided a better quantification of a possible dependence of attenuation on signal length and signal frequency. The SPL of the sinus tones was measured as root mean square (rms) levels in dB of each model sound and each observation sound on each transmission path for four replicates (when possible, minimum was two replicates). For each sound we measured the SPL of the first 50, 100, 150, 200, 250, 300, 350, 400, 450, and 500 ms. SPL was corrected for the frequency-dependent output level of the loudspeaker, which was measured in an anechoic chamber. SNR was always more than 20 dB. Both observation and model sounds were filtered with FFT filters (Hamming-Filter, sampling rate 44 100 Hz, FFT size=8192, bandwidth=200 Hz). SPLs of model sounds in relation to observation sounds were used to calculate EA values. The rms values were measured with COOL EDIT PRO.

The estimation of EA of sinus tones differs from the method used for song elements. Song element measurements are based on the cross correlation of the amplitude functions transmitted with un-degraded sound to account for changes in frequency and amplitude patterns of transmitted signals.[17] In the sinus tones there are no frequency changes and we measured all energy of the respective frequency within the duration of the signal. Therefore, we avoided a quantitative comparison of attenuation values between these two groups of test sounds.

C. Statistical analysis

Seven sounds of the white-necked thrush and eight sounds of the cocoa thrush with up to four replicates produced 368 measurements. For species comparison we analyzed in a three-factor ANOVA [species(2) × height(2) × distance(3)] the average attenuation values of test sounds sorted on species. The EA values of sinus tones were subjected to a four-factor ANOVA [height(2) × distance(3) × signal length(10) × frequency(5)]. Here four replications per transmission and path resulted in 1180 measurements.

III. RESULTS

The song of the white-necked thrush was on average 1.9 dB less attenuated at all distances and heights (Fig. 2, ANOVA, species, $F_{1,9}=40.4$, $p<0.001$). This difference in excess attenuation (EA) between species increased with distance reaching 3.5 dB at 54.5 m (ANOVA, distance × species, $F_{2,90}=7.8$, $p<0.05$).

Shortened song elements were significantly more attenuated than complete ones and the species difference was decreased (Fig. 2). In the white-necked thrush shortened song elements were on average 0.7 dB more attenuated at all distances and heights (paired t test, $t=-8.69$, $d.f.=156$, $p<0.001$). When we interpret the species difference in attenuation we should also consider frequency differences between species. The test sounds of the white-necked thrush had lower frequencies than those of the cocoa thrush [mean ± standard error (Hz): white-necked, 1921 ± 189; cocoa, 2283 ± 178; Mann-Whitney U test, $n_1=7$, $n_2=8$, $p<0.01$]. EA values increased with the frequency of the peak spectral amplitude of each test sound both in complete (Spearman rank correlation, $r=0.74$, $n=15$, $p<0.01$) and shortened elements (Spearman rank correlation, $r=0.64$, $n=15$, $p<0.01$). Therefore, both frequency and duration of the song may be responsible for the species difference in EA.

TSR was higher in the song elements of the cocoa thrush [ANOVA, species, $F_{2,89}=79.8$, $p<0.001$, height, $F_{2,89}=115.9$, $p<0.001$; Figs. 3(c)]. TSR was significantly higher at greater distances and at lower heights [ANOVA, distance, $F_{2,89}=79.8$, $p<0.001$, height, $F_{2,89}=43.4$, $p<0.001$; Figs. 3(a) and 3(b)]. TSR was higher when there were higher levels of excess attenuation (Pearson correlation, $r_{TSR,EA}=0.74$, $n=365$, $p<0.001$).

As the song elements the transmitted sinus tones were more attenuated with increasing distance and decreasing height (ANOVA, distance, $F_{2,1180}=429.4$, $p<0.001$, height, $F_{2,1180}=4798.3$, $p<0.001$). Attenuation varied significantly with signal length (ANOVA, signal length, $F_{9,1180}=43.9$, $p<0.001$). EA decreased with duration at all heights and distances [Figs. 4(a) and 4(b)]; the difference between 50 and 500 ms was on average 2.6 dB (ANOVA, *posthoc* Scheffé test, $p<0.001$]; between 50 and 250 ms it was 2.2 dB (ANOVA, *posthoc* Scheffé test, $p<0.01$). EA decreased at all frequencies with signal length and varied with frequency

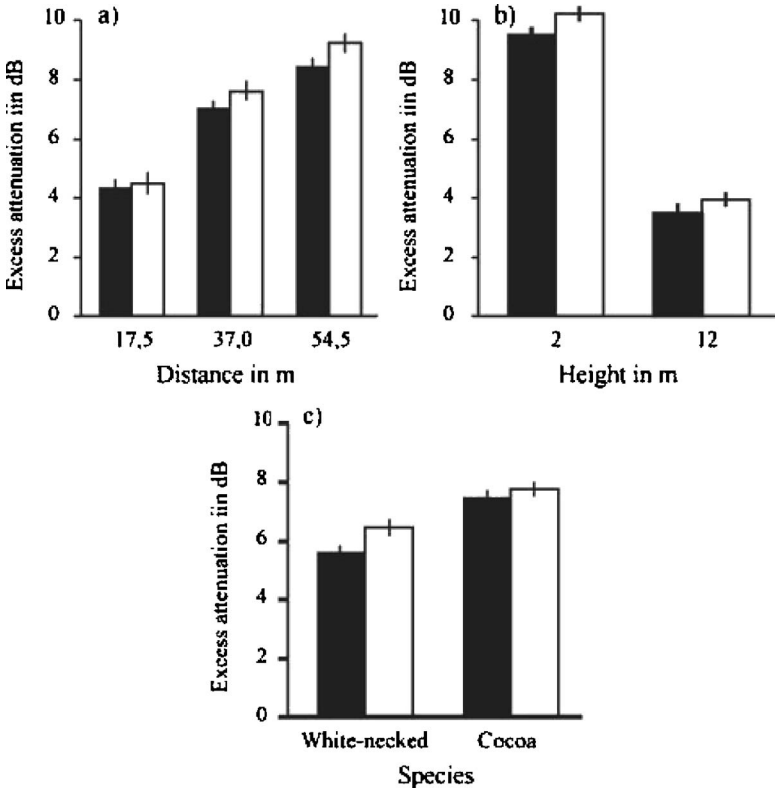

FIG. 2. Excess attenuation values (means±s.e.) of song elements. Main effect factors: (a) distance, (b) height, and (c) species. Black columns=complete song elements, white columns=shortened song elements derived by analyzing only the first 190 ms of the sounds.

[ANOVA, frequency, $F_{4,1180}=426.6$, $p<0.001$; Fig. 4(c)]. The decrease of EA in sinus tones with signal length was steeper, and differences between shorter and longer elements were greater at lower height and greater distance [Figs. 4(a) and 4(b)]. For example, at a distance of 54.5 m and a height of 2-m height the SPLs of a 500-ms-long signal were on average 4 dB higher than those of a 50-ms-long signal (*post-thoc* Scheffé test, $p<0.001$).

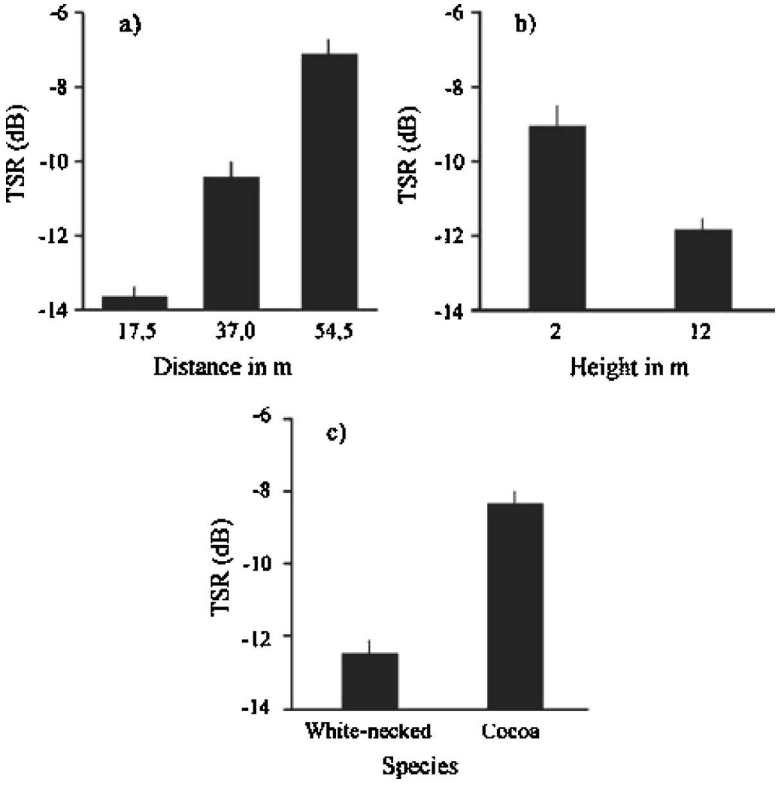

FIG. 3. Tail-to-signal ratio (TSR) in dB (means±s.e.) of song elements. Main effect factors: (a) distance, (b) height, and (c) species.

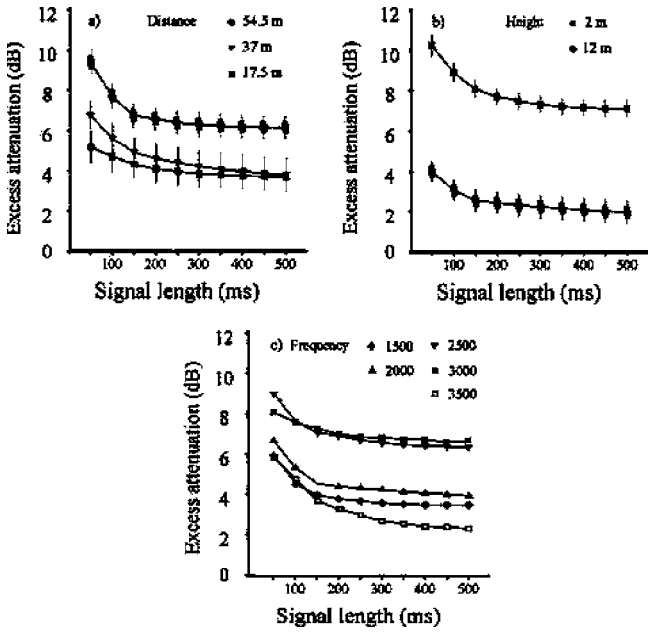

FIG. 4. Excess attenuation values for sinus tones (means±s.e.). Two–way interactions (a) signal length × distance, (b) signal length × height, and (c) signal length × frequency. In (c) data points are horizontally shifted to allow a better inspection of the standard errors.

IV. DISCUSSION AND CONCLUSIONS

A. Are reverberations the cause of less attenuation?

Longer sounds were significantly less attenuated. The attenuation of the sinus tones is fast decreasing in the first 150 ms and then approaches slowly at a minimum 500 ms. The reduced attenuation of longer signals in a forest seems thus similar to the reinforcement of signal amplitude in rooms, where the SPL of continuous sound is increased by superimposing reflections to a steady-state value.[18] Consequently, it is highly probable that reflections cause the increase of SPL with element length.

Another argument for the influence of reverberations are the TSRs of the song elements. We found higher TSRs closer to the ground and at larger distances. At these transmission paths overall EA of signals was higher (Fig. 2), and thus direct sound was more attenuated compared to reflected sound. On the same transmission paths attenuation of sinus tones decreased stronger with signal length (Fig. 3). The varying slopes of attenuation can thus be explained by a differential influence of reflected sound. TSRs were higher in song elements of the cocoa thrush. This species has shorter song elements and consequently more of the reflected energy was located in the echoic tail. The results of our tail measurements confirm those found in transmission experiments with song elements of the wren *Troglodytes troglodytes*[12] or the blackcap *Sylvia atricapilla*.[19] There, in temperate forests, signal length, distance, and height influenced the TSRs in a similar way. The higher TSRs at larger distances correspond also to the findings of Sakai *et al.*, where energy of reflected sound in relation to the energy of direct sound increased with distance.[10,11]

The positive effect of reflected sound on SPL of longer sounds differs from the benefits of reverberations described by Slabbekoorn and his co-workers.[8] They investigated the effect of reverberation on the length and amplitude of the echoic tail in 100- to 300-ms-long signals with different frequency slopes varying from 30 000 to 150 Hz/s. Their results show that tails were longer and louder in signals with shallower slope. They conclude that signals with narrow bandwidths are better for sound transmission because they are benefiting from reverberations. We agree with their conclusion that longer tails are probably beneficial for sound transmission. But their result that the tail is louder in narrow-bandwidth sounds seems to be influenced by their measurement method. In all experimental sounds tail length and amplitude were measured at the same frequency (3800 Hz) within a bandwidth of a few Hz. Since signals with shallower slope had more energy within this small measurement bandwidth, they produced more reflections and longer tails within this frequency range.

In our measurements we estimated SPLs within the total frequency range of the respective sounds (song elements or sinus tones) and we show that SPLs are increasing with signal length. Our results do not allow us to infer an influence of signal bandwidth on sound intensity. However, narrow-bandwidth signals and their reflections can have advantages in acoustic communication. Since long elements with constant frequency confine energy to a narrow bandwidth, they enhance the signal-to-noise ratio in the receiver.[20]

B. Predictions for adaptive birdsong design

When we try to predict an optimal signal structure for long-range acoustic communication we have to consider that adaptation to the environment does not mean necessarily a design for maximum transmission. Degradation and attenuation of signals are not always a disadvantage, since birds act in a communication network[21] and they have to mitigate a trade-off between intended receivers and nonintended eavesdroppers.[22] Degraded signals can carry information about location ("ranging"), which might or might not be intended to be transmitted.[21,23] It has been shown that birds can encode different information into particular acoustic parameters that differ in their transmission distances.[23] For example, in the song of the white–browed warbler (*Basileuterus leucoblepharus*) species identity is encoded in sound structures that resist sound attenuation and degradation, while individuality, identity, ranging, and perhaps motivation are found in acoustic parameters that are more easily modified by propagation.[24] However, even if there are many functions of birdsong that require different transmission pathways, we still can assume that at least some parts of birdsong are designed to be easily detected at a long range.

If song length is an adaptive feature in birdsong, then forest birds should use signals long enough to be enforced by reflected sound. The optimal duration of song elements will depend on the temporal characteristics of reverberations on the specific transmission path. In our experiments on all transmission heights the increase of sound level with signal length was especially steep until 150 ms. Therefore the song elements of both thrush species seem to exploit most of the reverberant energy, though variation at different transmission

heights is still large enough to produce a species difference in attenuation (Fig. 2). The measured values are valid only for the analyzed transmission paths at our study site and we expect other values for other distances or in forests with different acoustics. Moreover, we found a height-dependent variation in our results with a stronger influence of reflected sound at lower height. We can thus assume that birds that sing closer to the ground should utter longer song elements. Shorter song element length in higher perching species, as in our two thrush species, was described in five sympatric antbird species[15] and found in a comparison of birdsongs in suboscine rainforest birds.[26] The acoustic differences within different layers of a forest from the ground to the canopy are probably similar to a gradient from closed to more open habitats, where longer elements are found more often in forests.[27] Reverberations are almost lacking in open habitats[3,4,6] and therefore there should be no beneficial effect of longer elements. However, we did not broadcast our sounds in a nonforested habitat and further experiments would be necessary to analyze the effects of signal length on attenuation in the vocalizations of grassland species.

Element length could also be determined by beak morphology that constrains temporal song structure in sound production.[28,29] Since faster song pace in suboscine canopy birds is indeed positively correlated with body mass and beak size,[26] shorter song elements may be caused by morphological constraints. An alternative explanation for shorter song elements, however, could be that smaller birds have smaller territories and communicate over shorter transmission paths, where signals are less affected by reflected sound.

Another reason for long song elements could be located in the receiver. Longer durations of signals improve signal detections by temporal summation. This process describes the summation or integration of sound over time. It is a widespread phenomenon in birds,[30,31] and could be a reasonable explanation for the adaptive value of long song elements in long-range communication.[32]

In conclusion, our experiments have demonstrated a beneficial effect of reflected sound on birdsong transmission in forests and we give an additional argument for the adaptation of acoustic signals to habitat acoustics.[1–6,33] Though birdsong structures have certainly evolved under a multitude of selective conditions, our results support other recent studies that stress environmental factors in the evolution of vocal signal structures.[25,26,34]

ACKNOWLEDGMENTS

N. Goeth assisted in the field experiments. H. Weix and O. Larsen commented on the planning of the experiments. D. Hohenwarter and A. Niemczanowskie from the Institute of Technology in Vienna helped with the calibration of the equipment. D. Deutsch and A. Noll from the Acoustic Research Institute of the Austrian Academy of Sciences enabled the digital transfer of data to the computer. G. Tebb, R. Wagner, and R. Pappenheim made useful comments on the manuscript. We are very grateful to all of them. The work was supported by the Austrian Science Foundation Project No. P11563-Bio.

[1]C. Chappius, "Un example de l'influence du millieu sur les emissions vocals des oiseaux: L'evolution des chants en fôret equatorial," Terre Vie **2**, 183–202 (1971).
[2]A. Jilka and B. Leisler, "Die Einpassung dreier Rohrsänger (Acrocephalus schoenobaenus, A. scirpaceus, A. arundinaceus) in ihre Lebensräume in Bezug auf das Frequenzspektrum ihrere Reviergesänge," J. Orn. **115**, 192–212 (1974).
[3]E. S. Morton, "Ecological sources of selection in avian sounds," Am. Nat. **109**, 17–43 (1975).
[4]K. Marten and P. Marler, "Sound transmission and its significance for animal vocalizations. 1. Temperate Habitats," Behav. Ecol. Sociobiol. **2**, 271–290 (1977).
[5]P. M. Waser and M. S. Waser, "Experimental studies of primate vocalizations: Specializations for long-distance propagation," Z. Tierpsychol **43**, 239–263 (1977).
[6]R. H. Wiley and D. G. Richards, "Physical constraints on the evolution on acoustic communication in the atmosphere: Implications for the evolution of animal vocalizations," Behav. Ecol. Sociobiol. **3**, 69–94 (1978).
[7]D. G. Richards and R. H. Wiley, "Reverberations and amplitude fluctuations in the propagation of sound in a forest: Implications for animal communication," Am. Nat. **126**, 87–100 (1980).
[8]H. Slabbekoorn, J. Ellers, and T. B. Smith, "Birdsong and sound transmission: The benefits of reverberations," Condor **104**, 564–573 (2002).
[9]L. Beranek, *Concert Halls and Opera Houses, How They Sound* (Acoustical Society of America, New York, 1996).
[10]H. Sakai, S. Sato, and Y. Ando, "Orthogonal acoustical factors of sound fields in a forest compared with those in a concert hall," J. Acoust. Soc. Am. **104**, 1491–1497 (1998).
[11]H. Sakai, S. Shibato, and Y. Ando, "Orthogonal acoustical factors of a sound field in a bamboo forest," J. Acoust. Soc. Am. **109**, 2827–2830 (2001).
[12]J. Holland, T. Dabelsteen, J. S. B. Pedersen, and A. L. Paris, "Potential ranging cues contained within the energetic pauses of transmitted wren song," Bioacoustics 12, 2–20 (2002).
[13]R. S. Ridgely and G. Tudor, *The Birds of South America. Volume I. The Oscines Passerines* (Oxford U. P., Oxford, 1989).
[14]J. W. Hardy and T. A. Parker III, *Voices of the New World Thrushes* (ARA Records, Gainesville, 1992).
[15]E. Nemeth, H. Winkler, and T. Dabelsteen, "Differential degradation of antbird songs in a neotropical rainforest: Adaptation to perch height?" J. Acoust. Soc. Am. **110**, 3263–3274 (2001).
[16]P. Boesman, *Birds of Venezuela* (Bird Songs International, Enschede, 1999).
[17]T. Dabelsteen, O. N. Larsen, and S. B. Pedersen, "Habitat-induced degradation of sound signals: Quantifying the effects of communication sounds and bird location on blur ratio excess attenuation and signal-to noise ratio in blackbird song," J. Acoust. Soc. Am. **93**, 2206–2230 (1993).
[18]K. H. Kutruff, "Sound in enclosures," in *Handbook of Acoustics*, edited by M. J. Crocker (Wiley, New York, 1998), pp. 925–938.
[19]N. Mathevon, T. Dabelsteen, and S. H. Blumenrath, "Are high perches in the blackcap *Sylvia* atricapilla song or listening posts? A sound transmission study," J. Acoust. Soc. Am. **117**, 442–449 (2005).
[20]M. J. Ryan and E. A. Brenowitz, "The role of phylogeny, and ambient noise in the evolution of bird song," Am. Nat. **126**, 87–100 (1985).
[21]P. K. McGregor and T. Dabelsteen, "Communication Networks," in *Ecology and Evolution of Acoustic Communication in Birds*, edited by D. E. Kroodsma and E. H. Miller (Cornell U. P., Ithaca, NY, 1996), pp. 409–426.
[22]J. E. Endler, "Evolutionary implications of the interaction between animal signals and their environment," in *Animal Signals*, edited by Y. Espmark, T. Amundsen, and G. Rosenqvist (Tapir Academic, Trondheim, 2000), pp. 11–46.
[23]E. S. Morton, "Predictions from the ranging hypothesis for the evolution of long distance signals in birds," Behaviour **99**, 65–86 (1986).
[24]N. Mathevon, T. Aubin, T. Dabelsteen, and J. M. E. Vielliard, "Are communication activities shaped by environmental constraints in reverberating and absorbing forest habitat?" An. Acad. Bras. Ciênc. **76**, 259–263 (2004).
[25]T. Aubin, N. Mathevon, M. L. Silvia, J. M. E. Vielliard, and F. Sebe, "How a simple and stereotyped signal transmits individual information: The song of the white-browed warbler Basileuterus leucoblepharus," An. Acad. Bras. Ciênc. **76**, 335–344 (2004).
[26]N. Seddon, "Ecological adaptation and species recognition drives vocal evolution in Neotropical Suboscine birds," Evolution (Lawrence, Kans.)

59, 200–215 (2005).
[27]A. V. Badyaev and E. S. Leaf, "Habitat associations and song characteristics in Phylloscopus and Hippolais Warblers," Auk **114**, 40–46 (1997).
[28]M. G. Palacios and P. L. Tubaro, "Does beak size influence acoustic frequencies in woodcreepers?" Condor **102**, 553–560 (2000).
[29]J. Podos, "Correlated evolution of morphology and vocal signal structure in Darwin's finches," Nature (London) (London) **409**, 185–188 (2001).
[30]R. J. Dooling, "Temporal summation of pure tones in birds," J. Acoust. Soc. Am. **65**, 1058–1060 (1979).
[31]R. J. Dooling and M. H. Searcy, "Temporal integration of acoustic signals by the Budgerigar (*Melopsittacus undulatus*)," J. Acoust. Soc. Am. **77**, 1917–1920 (1985).
[32]G. M. Klump, "Bird communication in a noisy world," in *Ecology and Evolution of Acoustic Communication in Birds* (Cornell U. P., Ithaca, NY, 1996), pp. 321–338.
[33]R. H. Wiley, "Associations of song properties with habitats for territorial oscine birds of eastern North America," Am. Nat. **138**, 973–993 (1991).
[34]H. Slabbekoorn and T. B. Smith, "Habitat-dependent song divergence in the little greenbul: An analysis of environmental selection pressures on acoustic signals," Evolution (Lawrence, Kans.) **56**, 1849–1858 (2002).
[35]D. Wallschläger, "Correlation of song frequency and body weight in passerine birds," Experientia **36**, 412 (1990).
[36]J. B. Dunning, "Body masses of birds of the world," in *CRC Handbook on Body Masses*, edited by J. B. Dunning (CRC, Boca Raton, FL, 1993), pp. 3–312.

Vocal behavior of resident killer whale matrilines with newborn calves: The role of family signatures

Brigitte M. Weiß[a] and Friedrich Ladich
Department of Neurobiology and Behavior, University of Vienna, Althanstrasse 14, 1090 Vienna, Austria

Paul Spong and Helena Symonds
OrcaLab, Hanson Island, BC, Canada

(Received 22 April 2005; revised 29 July 2005; accepted 5 October 2005)

Studies of the vocal behavior of resident killer whales or orcas, *Orcinus orca*, in British Columbia have shown that matrilines have unique call repertoires consisting of up to 17 different call types. These call types cannot be attributed exclusively to specific behaviors, and their function in social contexts is poorly understood. This study investigated the change in call patterns of three resident matrilines in a changed social environment, before and up to one year after the birth of a calf. Acoustic data were collected with a network of hydrophones and were supplemented by visual observations. Call use changed distinctly after the birth of a calf in all three observed matrilines. All call types that were recorded in control situations were also recorded in postbirth situations; however, aberrant versions of discrete calls and excitement calls made up a higher proportion of calls after birth. Most conspicuously, family-specific call types occurred significantly more frequently in the days following a birth in two of the three matrilines and gradually returned to prebirth values within 2 weeks. Their increased use after a calf's birth may facilitate the learning process of this "acoustic family badge" and thereby help to recognize and maintain cohesion with family members. © *2006 Acoustical Society of America.* [DOI: 10.1121/1.2130934]

PACS number(s): 43.80.Ka [WWA] Pages: 627–635

I. INTRODUCTION

All mobile species, in which associating with particular conspecifics is advantageous, must develop strategies to maintain group cohesion. This is particularly important if mothers and their dependent offspring frequently separate, e.g., during foraging trips (Janik and Slater, 1998). The fish-eating killer whales or orcas, *Orcinus orca*, in the coastal waters of the northeastern Pacific Ocean, termed *residents*, live in the most stable groups documented among mammals. Offspring of both sexes travel with their mothers throughout their lives, and dispersal from a family (hereafter termed "matriline") has not been documented in over 25 years of intensive observations (Bigg *et al.*, 1990; Ford *et al.*, 2000).

Resident orcas emit a variety of vocalizations, including echolocation clicks, tonal whistles, and pulsed calls. The most common vocalizations are "discrete calls," which are highly stereotyped pulsed calls that can be divided into distinct call types (Ford, 1989). Studies of the vocal behavior of residents showed that "pods," social units comprised of one or more closely related matrilines, have unique vocal repertoires of 7 to 17 discrete call types (Ford, 1991; Strager, 1995). Moreover, acoustic similarities within groups apparently reflect common ancestry (Barrett-Lennard, 2000; Yurk *et al.*, 2002). Closely related matrilines share most or all of their call repertoire, but may differ in relative production rate and certain structural variables of shared calls (Miller and Bain, 2000). Ford (1991) found that these dialects remain stable at the level of the vocal repertoire, since he detected no differences in the call types used by selected groups over a 30-year period. None of the discrete call types showed a significant linear change in their relative production rate over a 16-year period (Presi, 2002). On a structural level, Deecke *et al.* (2000) detected significant changes in one of two studied call types over a 12–13-year period. Their study also showed that the call was modified in a similar fashion in the two studied matrilines, thereby retaining the dialect differences between the groups.

Ford (1989) examined the role of discrete calls in the communication system of pods and found that no call type was exclusively associated with particular behavioral categories. He suggested that discrete calls function as signals to maintain pod cohesion and that the use of pod-specific signals enhances the efficiency of intrapod communication. Using the group's calls might provide an individual with an acoustic "badge" of pod affiliation, which could be important for its acceptance by the group and continued access to the benefits of group living. Also, individual- or group-specific signals may be used to discriminate between relatives and nonrelatives and might thus function as a mechanism for avoiding inbreeding (Sayigh *et al.*, 1990; Ford, 1991; Barrett-Lennard, 2000).

Vocal signals function in maintaining group cohesion in a variety of species (birds: Hausberger, 1997; primates: Elowson and Snowdon, 1994; cetaceans: Sayigh *et al.*, 1990; Weilgart and Whitehead, 1993; Janik and Slater, 1998), and a consensus is emerging that avian and mammalian species living in complex social environments have at least some vocalizations, generally used in affiliative contexts, that are responsive to changes in social environment. For instance,

[a]Electronic mail: a9400355@unet.univie.ac.at

convergence of calls among birds within a flock has been reported for a number of species (Mundinger, 1970; Mammen and Nowicki, 1981; Nowicki, 1989). Pygmy marmosets (*Cebuella pygmaea*) of all age groups changed the structure of their trill calls when housed together with a novel group (Elowson and Snowdon, 1994), and Smolker *et al.* (1993) reported vocal convergence among a coalition of three male bottlenose dolphins. Captive bottlenose dolphins, that were voluntarily separated from their group, primarily produced individually distinct signature whistles. The remaining group also used primarily their signature whistles if one animal was in a separate pool, while the group used almost only nonsignature whistles when together (Janik and Slater, 1998). Similarly, bottlenose dolphin mothers and calves produced their signature whistles at high rates when forcibly separated in the wild (Sayigh *et al.*, 1990), and during voluntary separations calves often whistled as if to signal their intention to reunite with the mother (Smolker *et al.*, 1993). Social factors not only influenced use of signature whistles in juvenile and adult bottlenose, it also affected signature whistle development in bottlenose dolphin calves (see Tyack and Sayigh, 1997).

A study on the vocal development of a captive orca calf showed that the calf selectively learned some of its mother's calls, but none of the other unrelated pool mates' calls in the first year after birth (Bowles *et al.*, 1988). However, social influences on the use of discrete calls are poorly understood, since captive studies often cannot provide a naturalistic social background (see Caldwell *et al.*, 1990; Hausberger, 1997), and field studies of orcas face severe methodological limitations. Methods that allow assigning calls to known individuals are relatively new and difficult to apply (Miller and Tyack, 1998), and data collection in the wild depends on chance occasions, when situations are clearly definable and comparable.

The aim of the present study was to investigate the influence of the birth of a calf on the vocal repertoire of the three matrilines (A12, A30, and A36) comprising A1 pod of the Northern resident community. Birthdates of several calves in all three matrilines are known unusually precisely, and they also possess identified and easily distinguishable family-specific call types, which makes them ideal subjects for this study. In order to analyze these rare social events, acoustic data were collected with a network of permanent remote, radio-transmitting hydrophones and supplemented by visual observations.

II. MATERIAL AND METHODS

A. Study animals

The Northern Resident Community consists of more than 200 individually known orcas in three acoustic clans. It is regularly found in the study area of Johnstone Strait and adjacent waters off Vancouver Island, British Columbia, from July to October and occasionally through the rest of the year (Bigg *et al.*, 1990). New calves are observed every year but knowledge of precise birthdates is rare as most calves are born outside of the study area. A1 pod is the most commonly observed pod and consists of three matrilines, named A12, A30, and A36 (Ford *et al.*, 2000). Between 1989 and 2001 these were observed with a total of six newborn calves, whose birthdates were known with a maximum error of six days (Table I). In all cases, we assumed an age of one day for the day a calf was first sighted. The calf born to A36 in 1993 did not live long enough to have an ID number assigned.

TABLE I. Life history parameters of the individuals belonging to A1 pod in the studied timeframe (1989–2002). ID numbers according to Ford *et al.* (2000). Max.age=maximum age of the calf (in days) when first seen. m =male, f=female, ?=unknown.

Matriline	ID	Sex	Born–Died	Mother	First seen	max.age
A12	A12	f	1941	?		
	A31	m	1958–1997	A12		
	A33	m	1971	A12		
	A34	f	1975	A12		
	A55	m	1989	A34	18 October 1989	0
	A62	f	1993	A34	01 November 1993	4
	A67	?	1996	A34	10 November 1996	6
	A74	?	2000	A34	09 October 2000	0
A30	A30	f	1947	A2		
	A6	m	1964–1999	A30		
	A38	m	1970	A30		
	A39	m	1975	A30		
	A50	f	1984	A30		
	A54	f	1989	A30		
	A72	?	1999	A50		
	A75	?	2001	A54	06 September 2001	1
A36	A36	f	1947–1997	A1		
	A32	m	1964	A36		
	A37	m	1977	A36		
	A46	m	1982	A36		
	no ID	?	1993–1993	A36	20 November 1993	4

B. Field observations and recordings

Visual and acoustic data were obtained at the research station OrcaLab on Hanson Island, which is located centrally in the study area. Additional visual data were obtained through a network of observers: Orcalab volunteers stationed at field stations, other independent researchers, and whale watch operators. All data were reconciled daily. The waterways were routinely surveyed with spotting scopes; visual observations were done on an opportunistic basis, whenever whales were seen or heard within the vicinity of a station. Upon sighting, the number and identity of individuals (Ford *et al.*, 2000), group composition, group cohesion, direction of movement, and behavioral state (travel, motionless, forage, or socialize) were recorded. As long as whales were within visual range, changes in any of the above parameters, as well as times when the whales passed key landmarks, were noted.

Acoustic data were collected with a network of up to six radio-transmitting, various custom-made hydrophone stations (overall system frequency response 10 Hz to 15 kHz) monitoring the underwater acoustic environment of the area continuously, 24 hours a day and year-round (Fig. 1). At OrcaLab, the mixed output of radio receivers tuned to the specific frequencies of the remote transmitters was recorded on

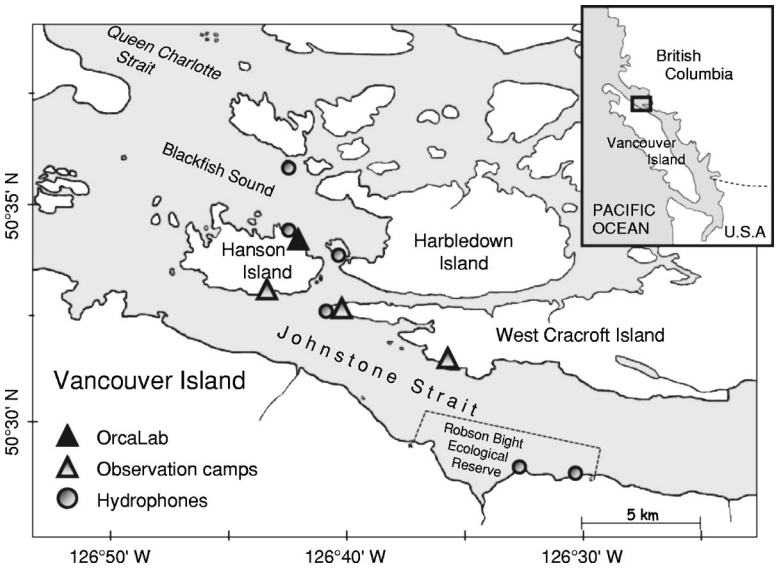

FIG. 1. Summer core area of the Northern Resident community with land-based observation sites and the OrcaLab hydrophone network.

a two-channel audio cassette recorder (Sony Professional Walkman WM-D6C or Sony TCD-D3), whenever whales were vocal. Use of mixer controls allowed distinction of hydrophone stations and thus basic tracking of group movements. Mixer settings were recorded in logbooks together with acoustic and visual information.

C. Acoustic analyses

We analyzed all available recordings of focal matrilines traveling with a young calf of known age, as well as recordings of the A30 matriline when they returned into the study area in the summer after A75's birth. We only used recordings for further analysis that allowed definite attribution of calls to the respective matriline. This excluded night-time recordings as well as those where one or more additional matrilines were seen and/or heard within range of the same hydrophone as the focal matriline. As controls we chose recordings of the same matrilines with no calves younger than 1 year present. These were chosen from several different days, where no other than the focal matriline was present in the core recording area. The predominant behaviors in the selected recordings were foraging or traveling.

Calls were classified by simultaneous acoustic and visual inspection of sonagrams, generated with Cool Edit 2000 (Syntrillium Software Corporation) or Raven 1.2 (Cornell Lab of Ornithology). Call classification followed that of Ford (1987, 1989, 1991), with the addition of two call subtypes: a rendition of call N5 (Ford, 1987), hereafter termed N5iii, and a subtype of the N9 call, hereafter termed N9iv, that was not previously described by Ford (see Sec. III and Figs. 5 and 6).

D. Statistical analyses

Recordings with more than 5% of calls not both visually and acoustically recognizable because of poor signal-to-noise ratio were excluded from statistical analysis to avoid a bias towards call types of higher amplitude (see Miller and Tyack, 1998). The remaining data were split into samples of 100 continuous calls. To increase the data set, we also included recordings in which less than 100, but a minimum of 75, calls remained after final selection. We determined percentages of call use per call type and sample. Data were analyzed using the SPSS® statistical program (Pfeifer, 1991). Data were $\log(x+1)$ transformed and tested separately for each matriline with multivariate ANOVAs comparing call rates across ages. For the A12 matriline, we used the identity of the calf as a covariate. Where necessary, we used Bonferroni *posthoc* corrections. For *posthoc* tests, A30 data for days 4+5, 15+20, 73+74, as well as 332–365 were pooled because of insufficient sample size. Duration and frequency of N9 subtypes were not normally distributed (Shapiro-Wilk, all parameters $p<0.05$) and were compared with Mann-Whitney U test. All statistical tests were two tailed.

III. RESULTS

A. Basic call patterns

Call patterns in the absence of young calves did not differ markedly from those described by Miller and Bain (2000). The most frequent call types in all three matrilines were types N4 and N9. Call types N11, N12, N13, and N27 were included in the category "other" [Figs. 2(a), 3(a), and 4(a)] because of their low rate of occurrence (usually less than 0.5%) in any context. Call type N47 is specific to the A1 pod (Ford, 1989) and therein almost exclusively produced by the A30 matriline. All three matrilines, but in particular the A12 matriline, produced a rendition of call type N5, first described by Ford (1987). This N5iii, also known as "A12special" among local researchers, is a relatively long call ($\bar{X}\pm SD=1.18\pm0.13$ s, $n=23$) with a sharp initial rise of the fundamental of the repetition rate to 1118 ± 63 Hz and a gradual rise to 1709 ± 185 Hz (Fig. 5). The call repertoire of the A36 matriline was characterized by a high proportion of N5 calls and the exclusive use of subtype N9iv. Compared to the A1-typical N9 (see Ford, 1989), N9iv is significantly shorter (N9iv: $\bar{X}\pm SD=0.69\pm0.06$ s, $n=15$; N9i: $\bar{X}\pm SD=0.91\pm0.05$ s, $n=8$; MWU: $Z=-3.81$, $n=23$, $p<0.001$) and, after the initial buzz, shows a steeper rise towards the

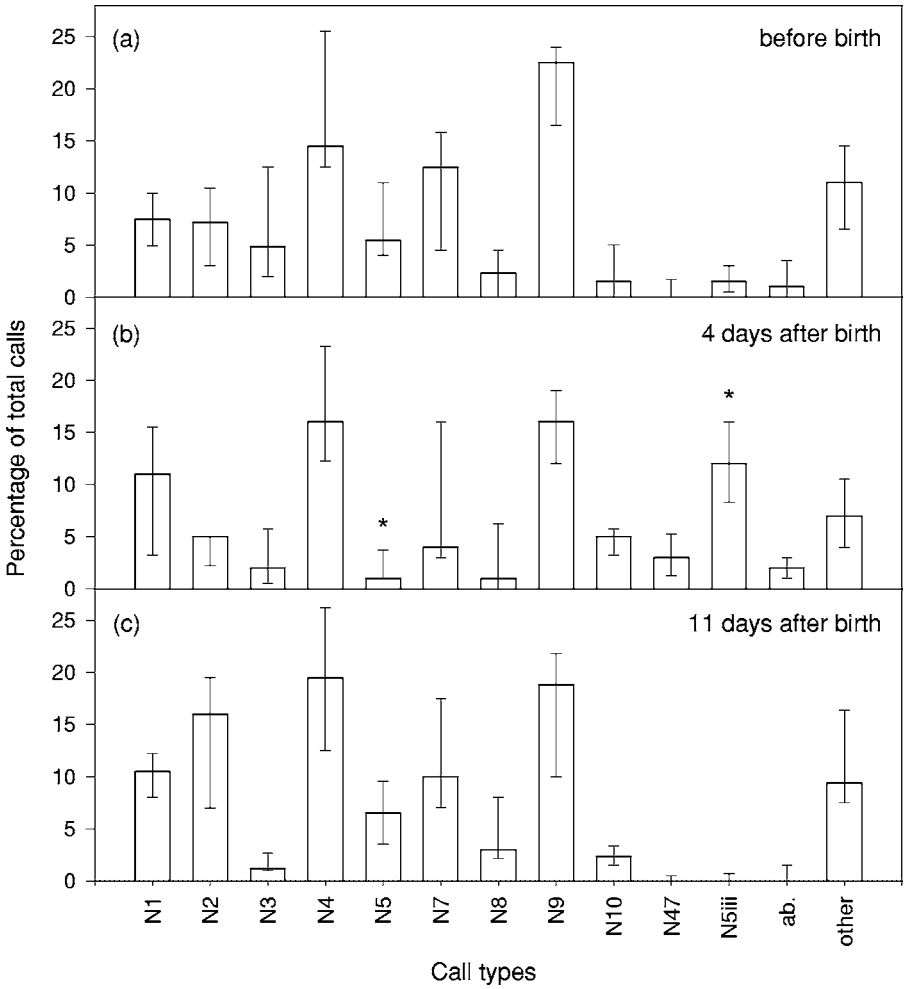

FIG. 2. Call use of the A12 matriline (a) before the birth of a calf, (b) four days after the birth of the calf A74, and (c) 11 days after birth of the calf A67. N(1–47)=call types after Ford (1989). ab.=aberrant. Bars show median percentage of total calls and first and third quartiles. Asterisks mark significant differences to prebirth values: $^{*}=p<0.05$. N (calls)=(a) 782, (b) 814, and (c) 374.

end (N9iv: from 1419±76 Hz to 2118±45 Hz, $\bar{X}\pm$SD; N9i: from 1165±44 Hz to 1385±47 Hz, $\bar{X}\pm$SD; MWU: $Z=-3.88$, $n=23$, $p<0.001$), which gives it a "squeaky" quality (Fig. 6).

B. Call patterns after the birth of a calf

1. A12 matriline

Eight control samples from six different days and 15 samples for four different calves, spanning from an age of 3 to 11 days, were of sufficient quality to be further analyzed. Age of the calves significantly influenced the occurrence of call types N5 (ANOVA: $F_{5,22}=3.469$, $p=0.024$) and N5iii (ANOVA: $F_{5,22}=6.284$, $p=0.002$). The identity of the calf had no significant effect (ANOVA: $F_{14,3}=2.059$, $p=0.302$). Sample numbers only allowed *posthoc* comparisons between recordings before birth [Fig. 2(a)] and recordings at ages of 4 days [calves A62+A74, Fig. 2(b)] and 11 days [calf A67, Fig. 2(c)]. N5 calls made up a significantly smaller proportion of calls 4 days, but not 11 days after birth as compared to prebirth recordings ($F_{2,19}=5.469$, after Bonferroni correction: control vs. 4 days: $p=0.016$, control vs. 11 days $p=1.0$). On the contrary, N5iii calls were used significantly more frequently when 4-day-old calves were present than before or 11 days after birth. Values did not differ significantly before and 11 days after birth ($F_{2,19}=8.201$, after Bonferroni correction: control vs. 4 days: $p=0.03$, 4 days vs. 11 days: $p=0.005$, control vs. 11 days: $p=0.548$). Also, there was a tendency for aberrant calls to occur more often 4 days after birth ($F_{2,19}=3.495$, control vs. 4 days: $p=0.082$).

2. A30 matriline

The most extensive data set was available for the calf A75, with 19 samples from 10 different control days and 47 samples for ages of 1 to 365 days. The matriline showed significant variation in the use of call types N2, N7, N10, and N47, aberrant calls as well as excitement calls at different ages of the calf; because of the large number of aberrant N47 calls, we analyzed them separately from other aberrant calls (N2: $F_{11,65}=3.037$, $p=0.003$, N7: $F_{11,65}=2.046$, $p=0.041$; N10: $F_{11,65}=5.500$, $p<0.001$; N47: $F_{11,65}=6.584$, $p<0.001$; N47 aberrant: $F_{11,65}=5.321$, $p<0.001$; other aberrant calls: $F_{11,65}=2.319$, $p=0.020$; excitement calls: $F_{11,65}=3.381$, $p=0.001$). Most strikingly, the use of N47 calls increased dramatically on the first day after birth and gradually returned to prebirth values within 2 weeks (Fig. 3, Table II). Also, excitement calls were almost absent from all recordings except for day 1 after birth. The use of N10 calls did not differ from controls in the first 2 days following the birth but increased significantly thereafter and remained elevated even 1 year later (Fig. 3). N2 calls occurred significantly less often 1 day and 1 year after birth, but not in between. *Posthoc* analyses

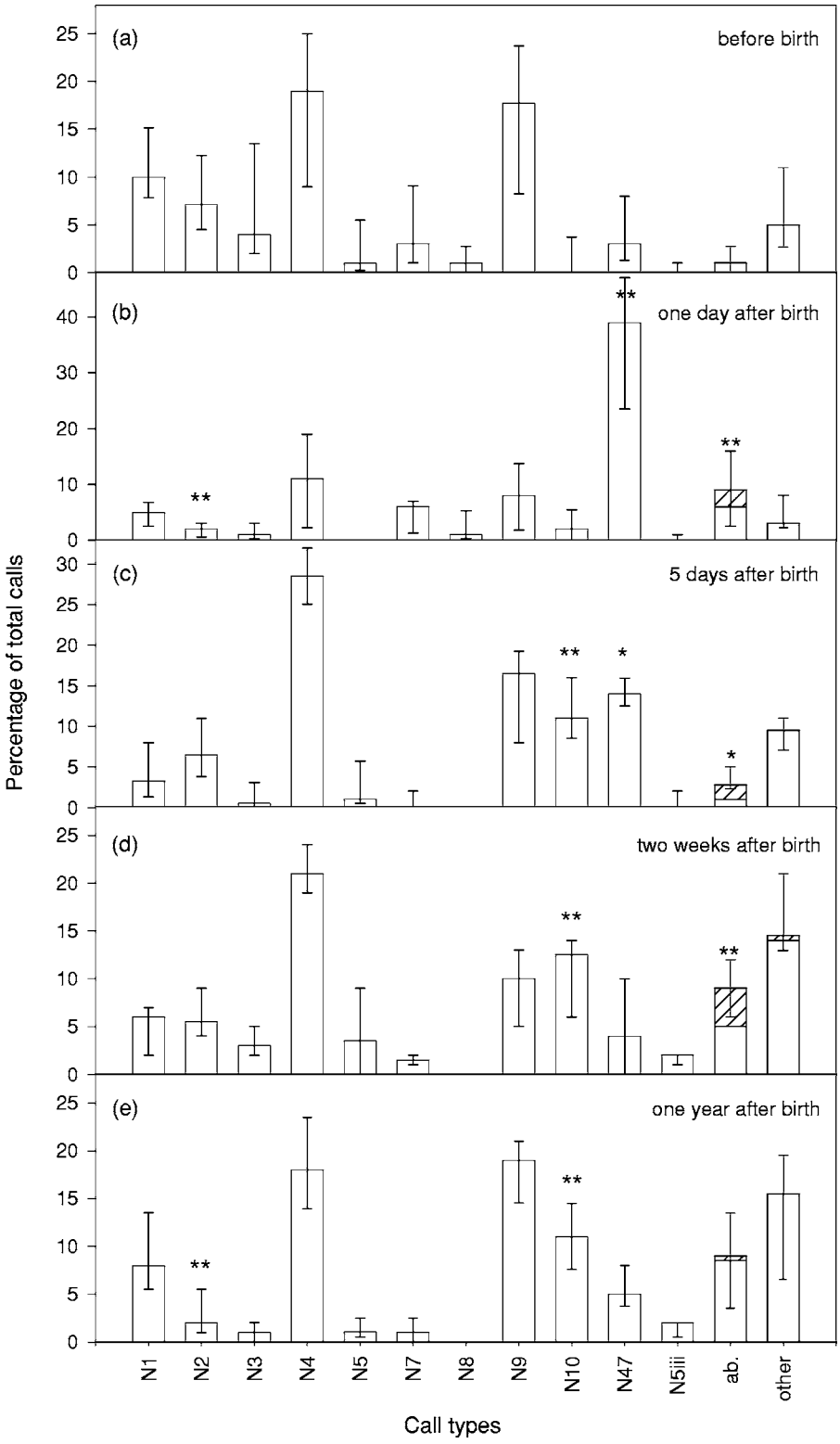

FIG. 3. Call use of the A30 matriline (a) before the birth of a calf, (b) 1 day, (c) 5 days, (d) 2 weeks, and (e) 1 year after the birth of the calf A75. N(1–47)=call types after Ford (1989). ab.=aberrant. Hatched portions of aberrant calls indicate the proportion of aberrant N47s, hatched portions of other calls indicate the proportion of excitement calls. Bars show median percentage of total calls and first and third quartiles. Note the different scalings on the *y* axis. Asterisks mark significant differences to pre-birth values: $^{*}=p<0.05$, $^{**}=p<0.01$. N (calls) =(a) 1859, (b) 1181 (c) 377, (d) 600, and (e) 1186.

revealed no further statistical differences between ages for call type N7 and for aberrant calls, except for aberrant N47s, which occurred significantly more often in the first 2 weeks after birth (Fig. 3 and see Table II).

3. A36 matriline

Data selection yielded 12 prebirth samples from 11 different days and 5 samples from 20 November 1993, when the A36 matriline was observed traveling through Blackney Pass with a newborn calf. In the presence of the calf, excitement calls (Ford, 1991) made up the highest proportion of produced calls with almost 20% (Fig. 4), while they usually were emitted at less than 0.5% ($F_{1,16}=80.220$, $p<0.001$). Also, the use of aberrant calls increased significantly when the calf was present ($F_{1,16}=9.475$, $p=0.008$). Rates of N3 calls and N8 calls were found to be significantly lower when the matriline was traveling with the calf than in control situa-

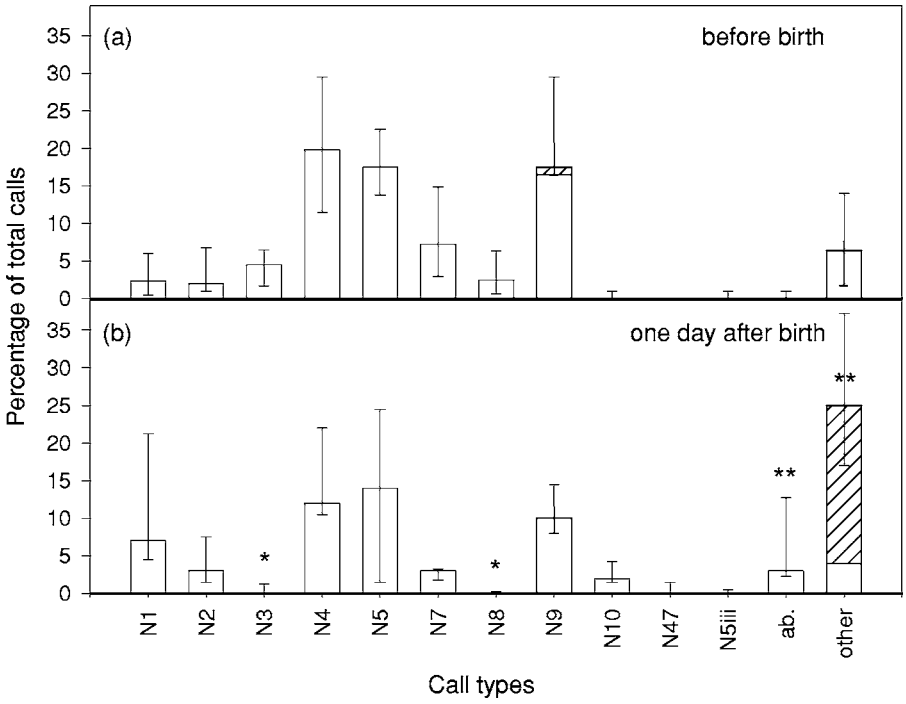

FIG. 4. Call use of the A36 matriline (a) before the birth of a calf and (b) 1 day after the birth of a calf. N(1–47)=call types after Ford (1989). ab.=aberrant. Hatched portions of N9 calls indicate the proportion of A36-specific subtypes; hatched portions of other calls indicate the proportion of excitement calls. Bars show median percentage of total calls and first and third quartiles. Asterisks mark significant differences to prebirth values: $^{*}=p<0.05$, $^{**}=p<0.01$. N(calls)=(a) 1128 and (b) 500.

tions (N3: $F_{1,16}=7.805$, $p=0.014$; N8: $F_{1,16}=6.941$, $p=0.019$).

IV. DISCUSSION

A. Comparison between matrilines

In all three studied matrilines we observed distinct changes in call use in the days after the birth of a calf. The most striking difference was the dramatic increase of the family-typical call N47 in the A30 matriline 1 day after the calf A75 was born. N47s were the most frequently used calls when the calf was 1 day old, with N47—call rates dropping gradually in the following days. They were still significantly higher than before birth on day 4–5, but were back to normal after 2 weeks. This fits well with the pattern found in the A12 matriline. Again, the use of the family-specific call, N5iii, was affected by the birth of calves. When the family was recorded 4 days after the birth of A74, they emitted their family-typical call at similar rates as the A30s did when A75 was 4–5 days old. Another calf born into the A12 matriline, A67, was 11–16 days old when the family was recorded on its own and, as in the A30s, the family-specific call type was no longer used at higher rates than before birth. Among the 88 calls analyzed when A55 of the A12 matriline was 3 days old, there was not a single A12special. It is possible that the N5iii call subtype only became noticable as the family grew in number with successive calves and became more independent of the other A1 matrilines, but this idea remains yet to be tested. In a recording of the A12s with A62 at an age of 8–11 days, the A12special was still the second most frequently used call type. However, for the latter two calves, sample sizes were too small to be taken into account on their own.

In contrast to the A12s and A30s, the A36 matriline did not increase the use of their "family badge," N9iv, but instead showed a very high rate of excitement calls. An in-

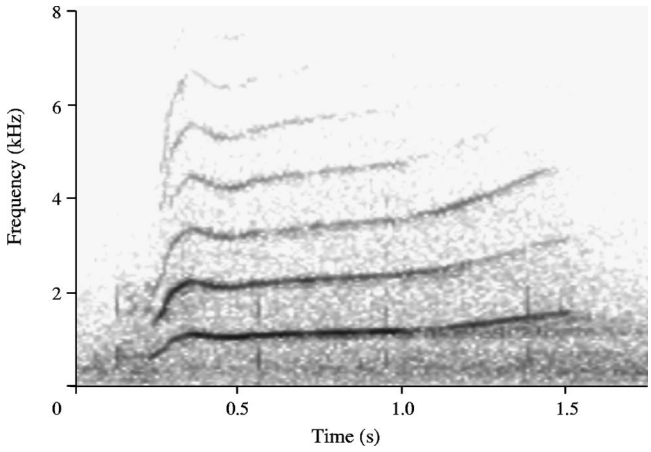

FIG. 5. Sonagram of call subtype N5iii, produced by the A12 matriline, with a filter bandwith of 64.5 Hz.

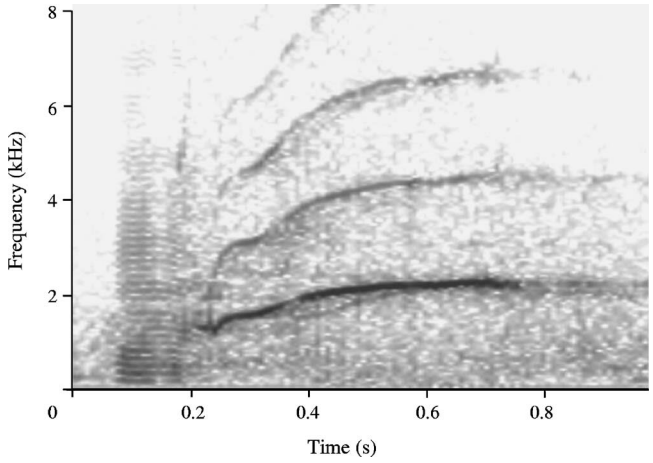

FIG. 6. Sonagram of call subtype N9iv, produced by the A36 matriline, with a filter bandwith of 82.4 Hz.

TABLE II. Significant differences in A30 call use before and several days after birth (day 1–365). >: call rates higher than on, <: call rates lower than on, p values are Bonferroni corrected. N47 ab.=N47 aberrant, exc. =excitement calls.

Call type	day		day	p
N2	prebirth	>	1	0.001
	prebirth	>	365	0.005
N10	prebirth	<	5	0.001
	prebirth	<	15	<0.001
	prebirth	<	73	0.002
	prebirth	<	365	<0.001
	1	>	5	0.019
	1	>	15	0.004
	1	>	73	0.04
	1	>	365	0.001
N47	prebirth	<	1	<0.001
	prebirth	<	2	0.004
	prebirth	<	5	0.032
	1	>	15	<0.001
	1	>	73	0.005
	1	>	365	<0.001
	2	>	15	0.004
	2	>	365	*0.061*
	5	>	15	0.026
N47 ab.	prebirth	<	1	<0.001
	prebirth	<	2	0.002
	prebirth	<	5	0.028
	prebirth	<	15	0.001
	1	>	73	0.045
exc.	prebirth	<	1	<0.001
	1	>	2	0.023
	1	>	5	0.003
	1	>	15	0.007
	1	>	73	0.003
	1	>	365	<0.001

crease in excitement calls was also observed in the A30s 1 day after the birth of A75, but the change was not nearly as strong as in the A36s. A general state of excitement after a birth likely is one reason why we observed elevated rates of aberrant calls in all three matrilines. Bowles *et al.* (1988) observed a variety of vocalizations not yet resembling discrete call structure in a captive orca calf at an age of 12–15 days. While not able to produce "proper" call types yet, the calves in this study may already have produced aberrant versions of discrete calls.

Other changes affected call types N2, N3, and N8, which all decreased in use in the days following birth, but otherwise showed no obvious pattern between matrilines. Likely one explanation is the significant increase of usually only infrequently used call types, which necessarily caused other call types to make up smaller proportions of overall calls than in the usual call repertoires. Only in the A30 matriline we observed an increase of call type N10 by day 5 and in any recordings thereafter. Rates of N10s were still higher than before birth at the end of the study, one year after the birth of A75. While all the short-time changes were very likely caused directly by the birth of a calf, it is difficult to say whether this long-time change was, too, or whether it was an independent shift in the A30s call pattern (Presi, 2002) that just coincided with the birth of A75.

B. Signature signals and family badges

Group- or individual-specific vocal signals are effective means of maintaining contact with group members (f.i. bats: Boughman and Wilkinson, 1998), especially in the aquatic environment, where visual signals can only serve in short distance communication. Orcas, as well as other cetacean species, however, often separate over distances of several hundred meters or more during foraging (Ford *et al.*, 2000) and need reliable means for maintaining or reestablishing spatial proximity. Bottlenose dolphins, for instance, rely on signature whistles with individually distinct frequency contours (see Tyack, 1997), while sperm whales use group-specific rhythmic click patterns called codas (Weilgart and Whitehead, 1997). Ford (1989) suggested that also the family-specific vocal dialects of the studied population of resident orcas serve that function. Resident orcas frequently come together in large aggregations where several matrilines are present at one time and engage in a high degree of social activity and movement. Group- or individual-specific vocal signals might therefore help ensure that individual members can locate and coordinate with other family members. Social communication and coordination with members of other groups would likewise be ensured and further enhanced. The family-typical call types or subtypes seem to be particularly well suited for this task.

Maintaining contact with its mother is of critical importance for a young calf. Orca calves can swim well at birth and may become separated by tens of meters from their mothers, on whom they are completely dependent. For instance, bottlenose dolphin mothers and calves both whistle at high rates when temporarily separated (Sayigh *et al.*, 1990). It is thus not surprising that the most obvious change we observed in the vocal patterns of the studied matrilines was generally a dramatic increase in the use of their most distinct calls. Both in the A12 and in the A30 matriline this effect ceased after approximately 2 weeks. It is very unlikely that the calves were able to produce these calls at that point in time: A captive orca calf was first found to produce discrete call types at an age of 1 year (Bowles *et al.*, 1988). Neonate sperm whales produce clicks that are very different from adult clicks (Madsen *et al.*, 2004), whereas older animals use patterned click sequences that more closely resemble adult codas (see Weilgart and Whitehead, 1997), and even bottlenose dolphin calves only develop distinct signature whistles at an age of 1.5–2.5 months of age (Caldwell and Caldwell, 1979). However, a high exposure to the family-specific call type in the first days after birth may enhance its recognition and thereby facilitate keeping up or reestablishing spatial proximity between calves and their mothers or other immediate family members. This may become increasingly important when infants begin to separate further away from their mothers (Smolker *et al.*, 1993; Baird, 2000). It remains crucial even later in life, as resident orca offspring bond with their mother for life and dispersal from the natal group has

not been documented in over 30 years of research (Barrett-Lennard, 2000, Ford *et al.*, 2000, OrcaLab, unpublished data).

The importance of acoustic and other social factors in vocal acquisition has been documented in a variety of species (e.g., birds: Baptista and Gaunt, 1997; cotton-top tamarins *Saguinus oedipus*: Snowdon *et al.*, 1997), including cetaceans (see Tyack and Sayigh, 1997). For instance, those wild bottlenose dolphin calves that showed higher levels of synchronized surfacing with their mothers during the period of whistle development developed their signature whistles more rapidly than others. Bottlenose dolphin calves whose acoustic environment consisted mainly of their mothers' signature whistle had a more rapid whistle development than calves being less exposed to the mother's signature (Tyack and Sayigh, 1997). Also, the captive orca calf studied by Bowles *et al.* (1988) learned its mother's most frequently used call types faster than other call types. Studying the vocal behavior of matrilines and newborns might lead to more in-depth investigations of what happens to vocal behavior when an individual is separated from its group temporarily. On one occasion, the adult male A6 from the A30 matriline was observed trailing his family who had travelled about 2 km ahead and, upon following, the separated male emitted the family-specific N47 call continuously (Spong *et al.*, 1993). Detailed analyses of such rare events promise further important insights into the role of family dialects for maintaining and reestablishing family bonds.

In conclusion, births of calves into resident orca matrilines were followed by a general state of excitement as well as a dramatic increase in family-specific call rates. This supports the idea that discrete calls in orcas indeed function as family badges and suggests that the family may actively enhance vocal learning of a signal that is crucial for recognizing and maintaining contact with the family.

ACKNOWLEDGMENTS

We wish to thank Anna Spong and OrcaLab assistants for continuous recording and observation efforts. Also, we are grateful for the contributions of observers, researchers, and whale-watchers in the Johnstone Strait area, especially the late Dr. Michael Bigg, Graeme Ellis, and John Ford. The manuscript benefitted from comments of two referees. The study was supported by a doctoral scholarship of the Austrian Academy of Sciences to B.M.W.

Baird, R. W. (**2000**). "The killer whale: Foraging specialization and group hunting," in *Cetacean Societies: Field Studies of Dolphins and Whales*, edited by J. Mann, R. C. Connor, P. L. Tyack, and H. Whitehead (Univ. of Chicago, Chicago), pp. 127–153.

Baptista, L. F., and Gaunt, S. L. L. (**1997**). "Social interaction and vocal development in birds," in *Social Influences on Vocal Development*, edited by C. T. Snowdon and M. Hausberger (Cambridge U. P., Cambridge), pp. 23–40.

Barrett-Lennard, L. G. (**2000**). "Population structure and mating patterns of killer whales, *Orcinus orca*, as revealed by DNA analysis," Ph.D. thesis, University of British Columbia, Vancouver.

Bigg, M. A., Olesiuk, P. F., and Ellis, G. M. (**1990**). "Social organization and genealogy of resident killer whales (*Orcinus orca*) in the coastal waters of British Columbia and Washington State," Rep. Int. Whal. Comm. **12**, pp. 383–405.

Boughman, J. W., and Wilkinson, G. S. (**1998**). "Greater spear-nosed bats discriminate group mates by vocalizations," Anim. Behav. **55**, 1717–1732.

Bowles, A. E., Young, W. G., and Asper, E. D. (**1988**). "Ontogeny of stereotyped calling of a killer whale calf, *Orcinus orca*, during her first year," Rit Fiskideildar **11**, 251–275.

Caldwell, M. C., and Caldwell, D. K. (**1979**). "The whistle of the Atlantic bottlenosed dolphin (*Tursiops truncatus*)-ontogeny," in *Behavior of Marine Animals, 3, Cetaceans*, edited by H. E. Winn and B. L. Olla (Plenum, New York), pp. 369–401.

Caldwell, M. C., Caldwell, D. K., and Tyack, P. L. (**1990**). "A review of the signature whistle hypothesis for the Atlantic bottlenose dolphin, *Tursiops truncatus*," in *The Bottlenose Dolphin: Recent Progress in Research*, edited by S. Leatherwood and R. Reeves (Academic, San Diego), pp. 199–234.

Deecke, V. B., Ford, J. K. B., and Spong, P. (**2000**). "Dialect change in resident killer whales (*Orcinus orca*): Implications for vocal learning and cultural transmission," Anim. Behav. **60**, 629–638.

Elowson, A. M., and Snowdon, C. T. (**1994**). "Pygmy marmosets, *Cebuella pygmaea*, modify vocal structure in response to changed social environment," Anim. Behav. **47**, 1267–1277.

Ford, J. K. B. (**1987**). A catalogue of underwater calls produced by killer whales (*Orcinus orca*) in British Columbia. Canadian Data Report of Fisheries and Aquatic Science, Vol. **633**.

Ford, J. K. B. (**1989**). "Acoustic behavior of resident killer whales (*Orcinus orca*) off Vancouver Island, British Columbia," Can. J. Zool. **67**, 727–745.

Ford, J. K. B. (**1991**). "Vocal traditions among resident killer whales (*Orcinus orca*) in coastal waters of British Columbia," Can. J. Zool. **69**, 1454–1483.

Ford, J. K. B., Ellis, G. M., and Balcomb, K. C. (**2000**). *Killer Whales: The natural history and genealogy of Orcinus orca in British Columbia and Washington*, 2nd ed. (UBC, Vancouver).

Hausberger, M. (**1997**). "Social influences on song acquisition and sharing in the European starling (*Sturnus vulgaris*)," in *Social Influences on Vocal Development*, edited by C. T. Snowdon and M. Hausberger (Cambridge U. P., Cambridge), pp. 128–156.

Janik, V. M., and Slater, P. J. B. (**1998**). "Context-specific use suggests that bottlenose dolphin signature whistles are cohesion calls," Anim. Behav. **56**, 829–838.

Madsen, P. T., Carder, D. A., Au, W. W. L., Nachtigall, P. E., Møhl, B., and Ridgway, S. H. (**2004**). "Sound production in neonate sperm whales (L)," J. Acoust. Soc. Am. **113**, 2988–2991.

Mammen, D. L., and Nowicki, S. (**1981**). "Individual differences and within-flock convergence of chickadee calls," Behav. Ecol. Sociobiol. **9**, 179–186.

Miller, P. J. O., and Bain, D. E. (**2000**). "Within-pod variation in the sound production of a pod of killer whales, *Orcinus orca*," Anim. Behav. **60**, 617–628.

Miller, P. J. O., and Tyack, P. L. (**1998**). "A small towed beamforming array to identify vocalizing resident killer whales (*Orcinus orca*) concurrent with focal behavioral observations," Deep-Sea Res., Part II **45**, 1389–1405.

Mundinger, P. C. (**1970**). "Vocal imitation and individual recognition of finch calls," Science **168**, 480–482.

Nowicki, S. (**1989**). "Vocal plasticity in captive black-capped chickadees: The acoustic basis and rate of call convergence," Anim. Behav. **37**, 64–73.

Pfeifer, A. (**1991**). *Datenanalyse mit SPSS/PC+4.0. (Data analysis with SPSS/PC 4.0)* (Oldenburg Verlag GmbH, Munich).

Presi, P. (**2002**). "Changes in the vocal repertoire of resident killer whales," M.Sc. thesis, University of Zurich.

Sayigh, L. S., Tyack, P. L., Wells, R. S., and Scott, M. D. (**1990**). "Signature whistles of free-ranging bottlenose dolphins *Tursiops truncatus*: Stability and mother—offspring comparison," Behav. Ecol. Sociobiol. **26**, 247–260.

Smolker, R. A., Mann, J., and Smuts, B. B. (**1993**). "Use of signature whistles during separations and reunions by wild bottlenose dolphin mothers and infants," Behav. Ecol. Sociobiol. **33**, 393–402.

Snowdon, C. T., Elowson, A. M., and Roush, R. S. (**1997**). "Social influences on vocal development in New World primates," in *Social Influences on Vocal Development*, edited by C. T. Snowdon and M. Hausberger (Cambridge U. P., Cambridge), pp. 234–248.

Spong, P., Symonds, H., Gaetz, W. C., Jantzen, K., and Weinberg, H. (**1993**). "A neural network method for recognition of individual *Orcinus orca*

based on their acoustic behavior: Phase 1," Oceans 1993, Conference of the IEEE, Victoria, BC.
Strager, H. (**1995**). "Pod-specific call repertoires and compound calls of killer whales, *Orcinus orca* Linnaeus, 1758, in the waters of northern Norway," Can. J. Zool. **73**, 1037–1047.
Tyack, P. L. (**1997**). "Development and social functions of signature whistles in bottlenose dolphins *Tursiops truncatus*," Bioacoustics 8, 21–46.
Tyack, P. L., and Sayigh, L. S. (**1997**). "Vocal learning in cetaceans," in *Social Influences on Vocal Development*, edited by C. T. Snowdon and M. Hausberger (Cambridge U. P., Cambridge), pp. 208–233.
Weilgart, L., and Whitehead, H. (**1993**). "Coda vocalizations in sperm whales (*Physeter macrocephalus*) off the Galapagos Islands," Can. J. Zool. **71**, 744–752.
Weilgart, L., and Whitehead, H. (**1997**). "Group-specific dialects and geographical variation in coda repertoire in South Pacific sperm whales," Behav. Ecol. Sociobiol. **40**, 277–285.
Yurk, H., Barrett-Lennard, L., Ford, J. K. B., and Matkin, C. O. (**2002**). "Cultural transmission within maternal lineages: Vocal clans in resident killer whales in southern Alaska," Anim. Behav. **63**, 1103–1119.

Monaural and binaural hearing directivity in the bottlenose dolphin: Evoked-potential study

Vladimir V. Popov,[a] Alexander Ya. Supin,[b] Vladimir O. Klishin, and Tatyana N. Bulgakova
Institute of Ecology and Evolution of the Russian Academy of Sciences, 33 Leninsky Prospect, 119071 Moscow, Russia

(Received 27 June 2005; revised 14 October 2005; accepted 1 November 2005)

Hearing thresholds as a function of sound-source azimuth were measured in bottlenose dolphins using an auditory evoked potential (AEP) technique. AEP recording from a region next to the ear allowed recording monaural responses. Thus, a monaural directivity diagram (a threshold-vs-azimuth function) was obtained. For comparison, binaural AEP components were recorded from the vertex to get standard binaural directivity diagrams. Both monaural and binaural diagrams were obtained at frequencies ranging from 8 to 128 kHz in quarter-octave steps. At all frequencies, the monaural diagram demonstrated asymmetry manifesting itself as: (1) lower thresholds at the ipsilateral azimuth as compared to the symmetrical contralateral azimuth and (2) ipsilateral shift of the lowest-threshold point. The directivity index increased with frequency: at the ipsilateral side it rose from 4.7 to 17.8 dB from 11.2 to 128 kHz, and from 10.5 to 15.6 dB at the contralateral side. The lowest-threshold azimuth shifted from 0° at 90–128 kHz to 22.5° at 8–11.2 kHz. The frequency-dependent variation of the lowest-threshold azimuth indicates the presence of two sound-receiving apertures at each head side: a high-frequency aperture with the axis directed frontally, and a low-frequency aperture with the axis directed laterally. [DOI: 10.1121/1.2141093]

PACS number(s): 43.80.Lb [WWA] Pages: 636–644

I. INTRODUCTION

Dolphins and whales have unique hearing abilities (rev. Au, 1993; Au *et al.*, 2000; Supin *et al.*, 2001). Among these abilities, high sensitivity and a wide frequency range are mostly known. Apart from that, acute frequency tuning and high temporal resolution are also characteristic of the dolphin's hearing. One more important feature of hearing is its spatial selectivity, which is the ability to detect and discriminate spatial positions of sound sources. To a large extent, the spatial selectivity is based on directional sensitivity of hearing, which is the dependence of hearing sensitivity on the direction to the sound source. An acute receiving beam, being directed to a certain sound source, allows minimizing the perception of other interfering sounds.

Directional sensitivity in dolphins was measured in a number of psychophysical studies (Zaitseva *et al.*, 1975; Au and Moore, 1984). However, in those studies masked thresholds were measured as a function of angular distance between the probe and masker sound sources, instead of direct measurements of thresholds as a function of the sound source position. The directivity indices of the receiving beam calculated from those results at frequencies of 30, 60, and 120 kHz were 10.4, 15.3, and 20.6 dB, respectively (Au and Moore, 1984). It should be noted, however, that results obtained in that sort of experimental paradigm depend both on the sound source position relative to the head axis (which gives the true receiving beam pattern) and on the mutual position of the probe and masker sources. The discrimination of the mutual position of two sound sources may involve some mechanisms apart from the receiving beam width. Indeed, experiments with the use of a minimum audible angle (MAA) paradigm (Renaud and Popper, 1975) and another similar paradigm (Dubrovskiy, 1990) demonstrated the ability to discriminate sound sources separated by a few angular degrees, which is much less than the receiving beam width.

Direct measurements of the receiving beam pattern (i.e., thresholds as a function of the azimuth sound source position) were performed by the evoked-potential method in a few dolphin species (Popov and Supin, 1988, 1990; Popov *et al.*, 1992). The −3-dB beam width varied from ±6° to ±12°.

In the studies mentioned above, contributions of the right and left ears to both the behavioral and evoked-potential responses were not separated, so, neglecting a possible small difference between the two ears, the threshold-vs-azimuth function was adopted to be symmetrical by definition. The actual (monaural) threshold-vs-azimuth function of each ear may be asymmetric, and the pattern of the monaural receiving beam may be important for the real directional selectivity and binaural interactions.

The evoked potential technique allows separate recording of responses from the right and left dolphin ears. This kind of recording has made it possible to measure monaural directional sensitivity (Popov and Supin, 1992). The monaural receiving beam has been shown to be substantially asymmetric, with the peak of sensitivity shifted ipsilaterally and with lower thresholds at all ipsilateral azimuths as compared to the symmetrical contralateral azimuths. That investigation was performed with the use of wide-band clicks, so no data could be obtained concerning the monaural receiving beam dependence on frequency. Later on an attempt was made

[a]Electronic mail: popov_vl@sevin.ru
[b]Electronic mail: alex_supin@sevin.ru

(Supin and Popov, 1993) to investigate the monaural receiving beam with the use of tonal stimuli of different frequencies but only three frequency values (30, 60, and 100 kHz) were tested in that study, which was insufficient for a detailed investigation of monaural spatial directivity as a function of frequency.

In the present study we performed a more detailed investigation of how monaural hearing sensitivity of a dolphin depends on two variables, the sound frequency and sound-source azimuth. For comparison, standard binaural hearing sensitivity dependence on these two variables was investigated as well. For this purpose, the evoked-potential technique was used.

II. METHODS

A. Subjects

The experimental animals were two adult bottlenose dolphins *Tursiops truncatus*, males, kept in the Utrish Marine Station of the Russian Academy of Sciences on the Black Sea. The animals were housed in an on-land seawater pool $9 \times 4 \times 1.2$ m. The use and care of the animals adhered to the guidelines of "Ethical Principles of the Acoustical Society of America for Research Involving Human and Non-Human Animals in Research and Publishing and Presentations."

B. Experimental conditions

During the experiments, each animal was placed into a circular experimental tank filled with seawater, 6 m in diameter, 0.45 m deep (Fig. 1). The animal (1) on a stretcher (2) was positioned in such a way that the main part of its body was in water but the blowhole and a part of its back were above water. The stretcher was made of 30-mm cell fish net thus being entirely sound-transparent. The animal's head was near the center of the tank. A sound-emitting transducer (3) was mounted on a bar (4), which laid on a support (5) and could be rotated around a center above the animal's melon tip. The transducer was located at a distance of 1.2 m from the rotation center. At the mid-distance (0.6 m) between the rotation center and transducer there were baffles (6) extending 15 cm upward of the bottom and 15 cm downward from the water surface; thus, the 15-cm slit in between the baffles was open for direct sound to spread from the transducer to the head whereas the paths for sound reflected from the bottom and surface were blocked by baffles. Rotation of the bar allowed the placement of the transducer at varying azimuth angles relative to the longitudinal head axis. Since the rotation center coincided with the tank center, the distance from transducer to the tank walls was 1.8 m. Therefore, the path for sounds reflected from the walls to the animal's head was at least 3.6 m longer (the delay at least 2.4 ms longer) than the direct way from the transducer. The position of the animal's head was monitored by a video camera (7).

C. Acoustic stimulation

The acoustic stimuli were short sound pips [Fig. 2(a)], which were designed by modulation of a carrier frequency by one cycle of a cosine envelope. Carrier frequencies varied

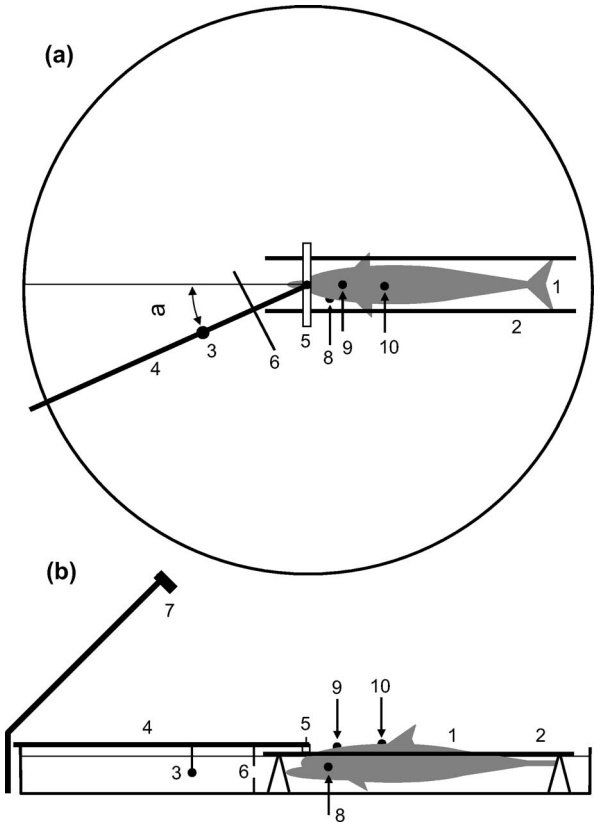

FIG. 1. Experimental design. (a) Top view. (b) Side view. Explanations in the text.

from 8 to 128 kHz by $\frac{1}{4}$-octave steps, i.e., 8, 9.5, 11.2, 13.5, 16, 19, 22.5, 27, 32, 38, 45, 54, 64, 76, 90, 108, and 128 kHz. The frequency of the cosine envelope was always 8 times as low as the carrier cycle, that is, from 1 kHz at the

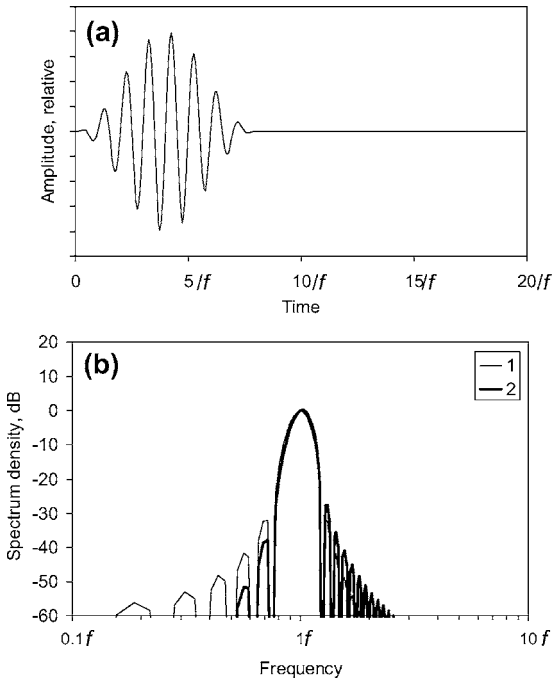

FIG. 2. Stimulus waveform (a) and spectrum (b). 1, spectrum of electric signal; 2, spectrum of acoustic signal when transformed through the transducer frequency response with a slope of 12 dB/oct.

8-kHz carrier to 16 kHz at the 128-kHz carrier. Thus, at all carrier frequencies, the pip contained a constant number (eight) of carrier cycles, and the pip spectrum was constant as expressed on a relative frequency scale [Fig. 2(b)(1)]. The main loop width of the spectrum was ±0.25 of the carrier frequency, and outside this loop the spectrum level did not exceed −30 dB. The deformation of the spectrum by the transducer frequency response was considered as insignificant because, even at the steepest part of the response (12 dB/oct), the spectrum level outside the main loop was not higher than −28 dB [Fig. 2(b)(2)].

The signals were digitally synthesized at an update rate of 500 kHz and stored in computer memory. For presentation, they were played at a rate of 16 per second, amplified, attenuated and transmitted through a B&K-8104 transducer. The transducer was placed at a distance of 1.2 m from the melon tip of the animal, at a depth of 22 cm (the middepth between the tank bottom and water surface). The azimuth position of the transducer varied within a range of ±90° from the longitudinal head axis, by steps of 7.5° within a range of ±30° and by steps of 15° within a range of 30°–90°.

The sound-play channel was calibrated both before and(or) after the experiments by positioning a calibrated receiving B&K 8103 hydrophone at the same location as the animal's head.

D. Evoked-potential recording

Evoked potentials were recorded noninvasively using 1-cm stainless-steel disk electrodes secured at the body surface by rubber suction cups. For monaural response recording, the active electrode was placed on the lateral part of the head, near the auditory meatus (although closed, the meatus is visible at the head surface as a small spot and therefore easily identified), underwater [Fig. 1(8)]. This electrode position is the best to record the monaural component of the auditory brainstem response. For binaural response recording, the active electrode was placed at the vertex midline, 6–7 cm behind the blowhole [Fig. 1(9)]. The reference electrode was placed near the dorsal fin, above the water surface [Fig. 1(10)]. The recorded potentials were amplified, bandpass filtered between 200 and 5000 Hz (6 dB/oct slopes beyond cut-off points), digitized using a 12-bit A/D converter, and averaged using a standard personal computer. Each evoked response was collected by averaging 1000 poststimulus sweeps.

III. RESULTS

A. Monaural evoked-potential waveform and threshold determination

Typical evoked-potential (EP) waveforms obtained at the lateral position of the recording electrode are presented in Fig. 3. Similar to EP waveforms described in dolphins earlier (Supin *et al.*, 2001), these EPs were composed of a sequence of rapid potential waves lasting 0.5–1 ms each. A distinctive feature of the EPs at the lateral electrode position was the presence of a short-latency component, which is marked by arrows in Fig. 3. Its onset latency was as short as 2.0–2.1 ms and the peak latency was around 2.5 ms. Taking into consideration the acoustic delay of the stimulus (0.8 ms at the distance of 1.2 m), the physiological onset latency of this component was 1.2–1.3 ms.

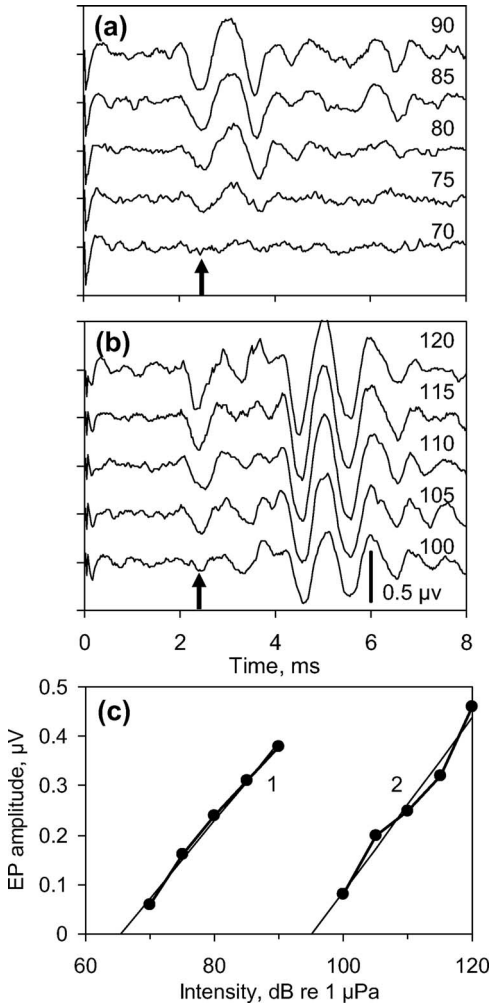

FIG. 3. Examples of monaural evoked responses and threshold determination. (a) Sound source position 15° ipsilateral to the recording side. (b) Sound source position 15° contralateral to the recording side. Stimulus intensities (dB re 1 μPa) are indicated near the records. The upward headed arrow points the monaural response component. (c) Amplitude-vs-intensity functions of the monaural component; 1, ipsilateral; 2, contralateral sound-source position; straight lines, regression line approximating the function within a 20-dB intensity range.

This early component demonstrated true monaural properties, that is, its amplitude and sensitivity was quite different at ipsi- and contralateral positions of the sound source relative to the side of recording. Figure 3 presents EP recorded at sound-source positions of 15° ipsilateral (a) and 15° contralateral (b) relative to the recording side. Both sets of evoked potential records demonstrate that with the stimulus intensity decrease, the amplitude of the early EP component decreased until the response disappeared in noise. However, to evoke a response of certain particular amplitude, the ipsilateral sound-source position required intensities about 30 dB lower than those at the contralateral position. Thus, even if assume some contribution of the contralateral ear to the response, its sensitivity and threshold were determined by the ipsilateral ear.

Note, that at the contralateral sound-source position,

high-amplitude ABR components of longer latency (the main positive peak latency at 4.5–4.6 ms) appeared. These later waves might represent either a response of ipsilateral auditory structures to sound reflected from the tank walls, or a binaural response, or both. Because of the delay, these late waves could be easily separated from the early monaural component.

To estimate monaural thresholds, only the early monaural component was used. Its zero-to-peak amplitude was plotted as a function of sound pressure [Fig. 3(c)]. The oblique part of the plot was approximated by a straight regression line, and this line was extrapolated to the zero-amplitude value. The sound pressure corresponding to the zero response amplitude was adopted as an arbitrary threshold measure. The thresholds obtained this way were much lower at ipsilateral sound-source positions than at the symmetric contralateral positions. Figure 3(c) shows that thresholds obtained differed by 29.6 dB at symmetric ipsi- and contralateral sound-source positions (65.5 and 95.1 dB SPL, respectively).

Using this threshold determination procedure, thresholds were measured as a function of azimuth at different pip carrier frequencies. At each combination of azimuth (by steps of 7.5 to 15°, as described above) and frequency (by quarter-octave steps) measurements were repeated three times, and the results were averaged.

B. Monaural threshold-vs-azimuth functions

Figure 4 presents measured thresholds as a function of sound-source azimuth, keeping pip carrier frequency as a parameter. Although the tested frequencies were varied by quarter-octave steps, only half-octave separated curves are shown in Fig. 4 to avoid overloading the figure; intermediate frequency values gave intermediate function forms.

The main features demonstrated by the threshold-vs-azimuth functions were as follows:

(1) All the functions featured a certain preferred azimuth of the lowest threshold (the best sensitivity); with deviation from this preferred azimuth, thresholds increased.
(2) The acuteness of directional sensitivity depended on frequency: it was the lowest at the lowest tested frequency (8 kHz) and the highest at the highest frequency (128 kHz).
(3) All the functions were asymmetric relative to the midline. A manifestation of the asymmetry was higher thresholds at all contralateral sound-source positions than at the symmetric ipsilateral positions; this difference increased from lower to higher frequencies.
(4) Another manifestation of the asymmetry was that the lowest-threshold point was not located at the midline but was shifted to the ipsilateral direction; this shift diminished from lower to higher frequencies.

To quantitatively characterize the asymmetry of the threshold-vs-azimuth curves, two of their parameters were plotted as functions of stimulus frequency: the threshold variation span as a difference between the lowest and the highest thresholds (separately for the ipsi- and contralateral branches) [Fig. 5(a)] and the position of the lowest-threshold point [Fig. 5(b)]. Note that though Fig. 4 exemplified only frequencies with half-octave steps, Fig. 5(a) presents results of measurements in more detail with $\frac{1}{4}$-oct steps.

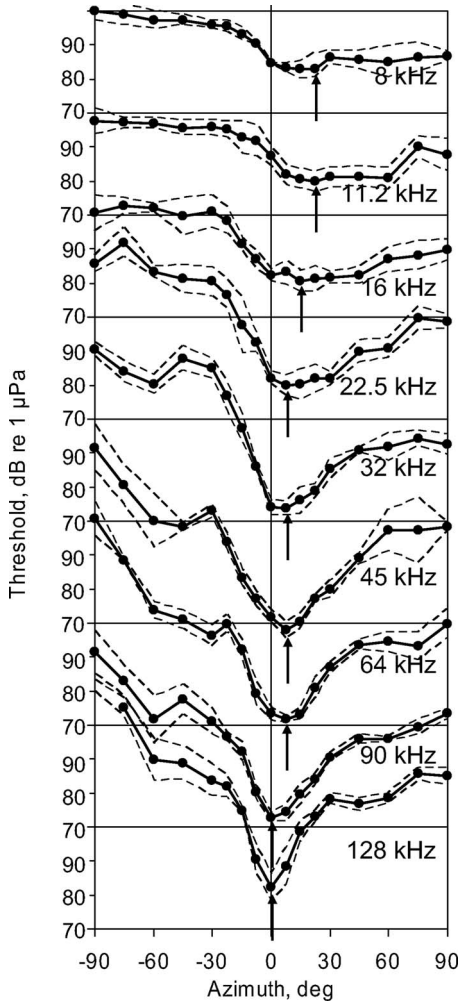

FIG. 4. Monaural directivity diagrams (threshold-vs-azimuth functions) at stimulus frequencies from 8 to 128 kHz, as indicated. Solid lines with dot symbols, means of three measurement runs; thin dashed lines, standard errors. Negative azimuth, contralateral; positive, ipsilateral to the recording side. Upward-headed arrows mark the lowest-threshold points.

The threshold variation span monotonously increased with frequency, from 17.2 dB at 8 kHz to 59.4 dB at 128 kHz at the contralateral side and from 10.5 dB at 8 kHz to 33.3 dB at 128 kHz at the ipsilateral side. Both these functions could be satisfactorily approximated by straight regression lines on the log frequency scale with slopes of 11.1 (r^2=0.81) and 5.8 (r^2=0.84) dB/oct, respectively.

As to the position of the lowest-threshold point, it could be determined with accuracy no better than the step of azimuth variation, which was 7.5°. The deviation of this position from the midline decreased with frequency from 22.5° at frequencies of 8–11.2 kHz to 0° at frequencies of 90–128 kHz [Fig. 5(b)]. This function could be approximated by a straight regression line (r^2=0.88) with a slope of 5.75 deg/oct.

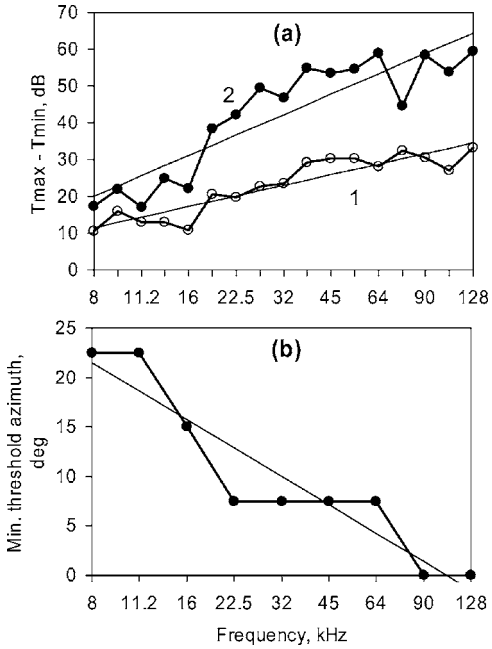

FIG. 5. (a) Dependence of threshold span (the difference between the lowest and the highest threshold) on stimulus frequency. 1, ipsilateral branch of the diagram; 2, contralateral branch; straight lines, approximating regression lines. (b) Dependence of the lowest-threshold azimuth on stimulus frequency; straight line, approximating regression line.

C. Interaural threshold difference

Subtraction of the left from right branches of plots presented in Fig. 4 resulted in functions that show ipsi- to contralateral sensitivity difference as a function of azimuth. Assuming as a first approximation that two ears are of equal sensitivity at symmetrical azimuths, this function may be adopted as interaural threshold difference (IThD) dependence on azimuth. The functions are presented in Fig. 6 at a few stimulus frequencies with half-octave steps.

The functions were nonmonotonous. Within a frequency range from low (8 kHz) to middle (32 kHz) frequencies, IThD increased. At a frequency of 32 kHz IThD reached a maximum (27–29 dB) at azimuth of 22.5°–30° and 90°, however at intermediate azimuth of 60°–75° it was lower (18–19 dB). With further frequency increase up to 128 kHz, IThD at large azimuths (75°–90°) remained almost constant, but at smaller azimuths (7.5°–45°) IThD fell by several times. Thus, the steepest IThD-vs-azimuth gradient was observed at intermediate frequencies and at small azimuths. Within an azimuth range of ±7.5°, IThD gradient exceeded 1 dB/deg at frequencies from 22.5 to 64 kHz, and reached 1.6–1.7 dB/deg at frequencies of 22.5–32 kHz.

D. Binaural threshold-vs-azimuth functions

For comparison, threshold-vs-azimuth functions were measured also in standard conditions, when contributions of the right and left ears to the measured responses were not separated. For that, thresholds were evaluated for AEPs recorded from the vertex, at the head midline, where potentials generated by the right and left halves of the brain are equally recorded. Threshold evaluation was done in the same manner as described above, except measuring the peak-to-peak amplitude of the largest positive-negative AEP wave instead of the earliest component (Fig. 7). Duration of this wave was also short enough (about 1 ms) to avoid contamination by similar responses evoked by reflected sounds.

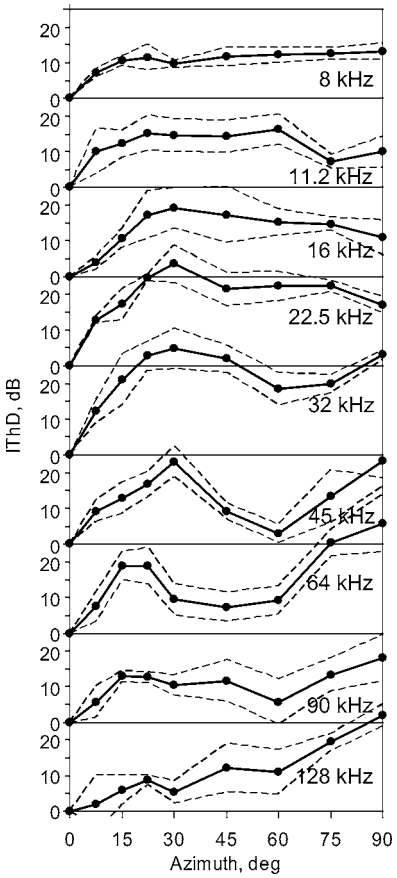

FIG. 6. Interaural threshold difference (IThD) dependence on azimuth at frequencies from 8 to 128 kHz, as indicated. Solid lines with dot symbols, means of three measurement runs; thin dashed lines, standard errors.

The functions obtained in such a way for frequencies from 8 to 128 kHz, with half-octave steps, are presented in Fig. 8. All the functions were almost symmetrical, which is an indication of insignificant sensitivity difference between the right and left ears.

Similar to the monaural functions, acuteness of the binaural functions was dependent on frequency: it was the lowest at the lowest tested frequency (8 kHz) and the highest at the highest frequency (128 kHz).

A remarkable feature of the obtained binaural threshold-vs-azimuth functions was the presence of two peaks (threshold minima) in some of them. The functions were obviously one-peaked at high frequencies (90–128 kHz), but with lowering the frequency, the peak became flattened (64 kHz) and then dissociated into two peaks (45 kHz and lower). The most obvious dissociation was observed at intermediate frequencies (22.5–32 kHz). In these functions, the lowest-threshold points were separated as far as ±22.5°. At frequencies of 16 kHz and lower, the flattened function form made it difficult to evaluate the exact peak positions. Nevertheless a little better sensitivity at the azimuths of ±15 to 30° rather than at the zero (midline) azimuth could be noticed.

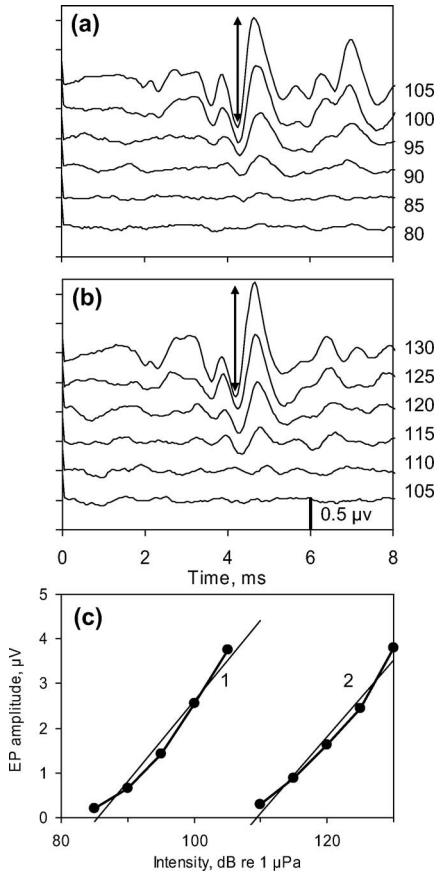

FIG. 7. Examples of binaural evoked responses and threshold determination. (a) Sound source position at the. (b) Sound source position at 30° azimuth. Stimulus intensities (dB re 1 μPa) are indicated near the records. The double-headed arrows show the peak-to-peak measured wave. (c) Amplitude-vs-intensity functions of the monaural component; 1, midline; 2, 30° azimuth; straight lines, regression line approximating the function within a 20-dB intensity range.

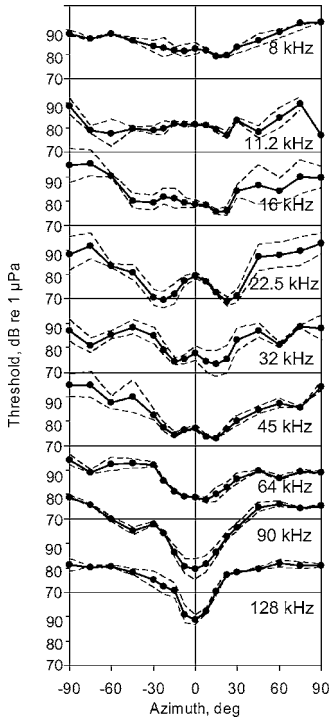

FIG. 8. Binaural directivity diagrams (threshold-vs-azimuth functions) obtained with the vertex recording at stimulus frequencies from 8 to 128 kHz, as indicated. Solid lines with dot symbols, means of three measurement runs; thin dashed lines, standard errors. Negative azimuth, left; positive, right.

IV. DISCUSSION

A. Acuteness of monaural directivity diagram

A commonly adopted measure of the acuteness of the receiving beam is the directivity index. It is the ratio of the power P_0 received by an omnidirectional receiver to the power P_d received by a directional receiver in an isotropic sound field,

$$DI = 10 \log(P_0/P_d) = 10 \log \frac{4\pi}{\int_0^{2\pi} \int_{-\pi/2}^{\pi/2} (P(\theta,\varphi)/P_0) \sin\theta d\theta d\varphi} \quad (1)$$

where $P(\theta,\phi)/P_0$ is the beam pattern of the directional receiver in the power domain, θ and ϕ are elevation and azimuth. Since we measured thresholds as a function of azimuth only, our data do not allow computing the directivity index according to Eq. (1) but they allow computing the partial directivity index in the azimuth plane. For that, Eq. (1) may be reduced to

$$DI = 10 \log \frac{2\pi}{\int_0^{2\pi} (P(\phi)/P_0) d\phi}. \quad (2)$$

For computing the directivity index from discrete threshold data, Eq. (2) was substituted with

$$DI = 10 \log \frac{2\pi}{\sum_{-\pi}^{\pi} 10^{(T_\phi - T_0)/10} \delta\phi} \quad (3)$$

for the complete azimuth plane or

$$DI = 10 \log \frac{\pi}{\sum_{0}^{\pi} 10^{(T_\phi - T_0)/10} \delta\phi} \quad (4)$$

for an ipsi- or contralateral half-plane, where T_0 is the lowest threshold of the directivity diagram (dB-measure) and T_ϕ is the threshold at an azimuth ϕ.

Figure 9 presents directivity index as a function of frequency computed as described above for frequencies from 11.2 to 128 kHz. The lower frequency limit of 11.2 kHz was adopted since the sound power received from the caudal semicircle was not really measured in our experiments but at this and higher frequencies it could be neglected because even at ±90° the thresholds were at least 10 dB higher (i.e., the received power was an order of magnitude less) than at the optimal azimuth. Indices were computed for the overall azimuth circle (1) and separately for the ipsilateral (2) and contralateral (3) semicircles. The plots demonstrate an increase of the directivity index with frequency; within a range from 11.2 to 128 kHz, the directivity index rose from

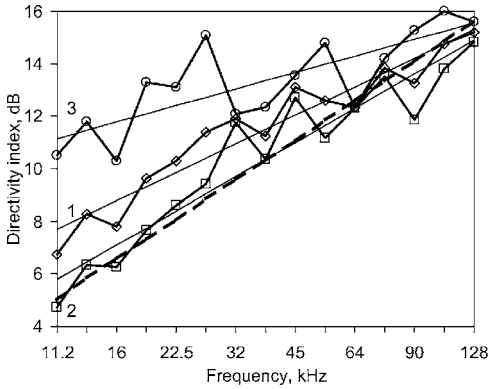

FIG. 9. Directivity indices of monaural diagrams. 1, of the complete diagram; 2, of the ipsilateral branch; 3, of the contralateral branch. Straight lines, approximating regression lines.

6.7 to 15.2 dB for the overall circle, from 4.7 to 14.8 dB within the ipsilateral semicircle and from 10.5 to 15.6 within the contralateral semicircle. Being approximated by straight regression lines, these functions had slopes of 2.01, 2.42, and 1.17 dB/oct, respectively.

It was of interest to compare the directivity indices with those of an equivalent receiving aperture. Computation of the directivity index of an aperture is considered in detail by Au (1993). In the azimuth plane, the receiving beam of an aperture (in the sound-pressure domain) is

$$\frac{p(\phi)}{p_0} = \frac{\sin \Psi}{\Psi}, \tag{5}$$

where $\psi = (kw \sin \phi)/2$, $k = 2\pi/\lambda = 2\pi f/c$ (the wave number), λ is the wavelength, f is the frequency, and c is the velocity. The directivity index of the aperture is

$$DI = 10 \log \frac{2\pi}{\int_{-\pi}^{\pi} \left(\frac{p(\phi)}{p_0} \right)^2 d\phi}. \tag{6}$$

If $p(\varphi)$ falls to a negligible value within an azimuth range where $\sin \varphi \approx \varphi$, Eq. (6) may be reduced to a simple expression

$$DI \approx 10 \log \frac{2\pi}{\frac{c^2}{\pi^2 f^2 w^2} \int_{-\infty}^{\infty} \frac{\sin^2(\pi w f \phi / c)}{\phi^2} d\phi} = \frac{2\pi w f}{c}, \tag{7}$$

where w is the aperture width, f is the sound frequency, and c is the sound velocity. That is, directivity index depends on frequency with a rate of 3 dB/oct. This prediction is rather close to the found slope of *DI*-vs-frequency dependence at the ipsilateral side (2.42 dB/oct) but markedly differs from that at the contralateral side (1.17 dB/oct). Thus, for the ipsilateral side, the found directivity index dependence on frequency may be satisfactory approximated by a receiving aperture of a certain width. The best correlation with the experimental data according to the least-mean-square criterion was found at $w = 6.8$ cm. However, for the contralateral side the interpretation of data in terms of a receiving aperture is not appropriate. Probably, perception of sounds from the contralateral side is determined to a large extent by shadowing which is not proportional to the sound frequency.

B. Best-sensitivity azimuth dependence on frequency

An intriguing feature of the obtained monaural directivity diagrams was the lowest-threshold azimuth dependence on frequency: from around 22.5° at low frequencies to around 0° at high frequencies. We determined the best-sensitivity azimuth with a step of 7.5°, so only four values of the best-sensitivity azimuth were detected (0°, 7.5°, 15°, and 22.5°, see Fig. 5), but it is reasonable to suppose that actually this value depends gradually on frequency within a certain azimuth range. This feature hardly can be explained by a model based on a single receiving aperture since an aperture is always the most sensitive at its axis.

A possible way to explain these data is to adopt the presence of two (or more) sound-conducting pathways with different frequency responses: a high-frequency receiver with the axis close to the midline and a low-frequency receiver with an axis deviated from the midline. With two such receiving pathways, their relative weights may change depending on frequency, thus resulting in variation of the lowest-threshold azimuth.

Some indications of multiple sound-conducting pathways in dolphins have been previously noted. The most popular hypothesis implies that sounds reach the dolphin's ear through an acoustic window and then through a fatty channel in the lower jaw (Norris, 1968; Bullock *et al.*, 1968; McCormick *et al.*, 1970, 1980; rev. Au, 1993). On the other hand, measurements of acoustic delays of auditory evoked potentials indicated an acoustic window next to the bulla (Popov and Supin, 1992). But these two hypotheses may be complementary rather than contradictory. Detailed measurements of acoustic delays of auditory evoked potentials at different azimuths and sound frequencies may be interpreted as an indication of more than one sound-conduction pathway to the dolphin's ear (Popov *et al.*, 1992). More than one sound-conduction pathway may be provided by a few lobes of fatty tissues connecting to the bulla (Ketten, 2000). The data presented herein may serve as a further (though still not ultimate) argument in favor of multiple sound-conducting pathways.

C. Interaural threshold difference (IThD) dependence on frequency

Contrary to the directivity index which increased monotonously with sound frequency, the IThD dependence on frequency was not monotonous: within a frontal sector of around ±30°, IThD was maximal at intermediate frequencies (around 32 kHz) and diminished at both lower and higher frequencies. Correspondingly, IThD gradient (dB/deg) was the highest within the same frequency range (22.5–64 kHz). This is a consequence of the fact that IThD depended on both acuteness and asymmetry of the directivity function. In turn, the acuteness and asymmetry depended on frequency in opposite manners: the acuteness increased whereas asymmetry decreased with frequency. As a result, the best combination

of the acuteness and asymmetry resulting in the maximal IThD was achieved at intermediate frequencies.

IThD gradient (dB/deg) may be very important for binaural location of the sound-source position. The higher the IThD gradient, the better angular resolution may be provided by comparison of sound levels perceived by the right and left ear (interaural intensity difference, IID). With this respect, it is noteworthy that the highest IThD gradient within the frontal sector was observed not at the highest but at intermediate frequencies, that is at frequencies of high sensitivity. If the gradient is g (dB/deg) and IThD-detection threshold is d (dB), then the expectable angular threshold $\alpha = d/g$ (deg). According to data obtained with the use of local sound stimulation (Moore *et al.*, 1995), minimal detectable IID in the bottlenose dolphin is around 1 dB. With this threshold, and with IThD gradient of 1.7 dB/deg, the dolphin is expected to detect the sound-source position relative to the head axis with accuracy better than 1°.

D. Binaural directivity diagrams

A remarkable feature of the binaural directivity diagrams described herein is their two-peak form at middle frequencies, that is, lower thresholds at nonzero right and left azimuth and a little higher threshold at the zero azimuth (midline). It corresponds well to the form of monaural diagrams. Indeed, at any sound-source position, the binaural threshold is expected to be equal to the lower of the two monaural thresholds, either the left or right. Therefore, if monaural diagrams feature the lowest threshold at an azimuth deviated from the midline, the binaural diagram must demonstrate the same. Indeed, combination of monaural directivity diagrams (see Fig. 4) with their mirror images results in the lowest threshold functions with two minima at frequencies of 64 kHz and lower (Fig. 10). Although the resulting minimum-threshold curves do not coincide exactly with the binaural directivity diagrams (see Fig. 8) which may be a result of inevitable data scatter, they demonstrate qualitatively the principle of forming the two-peak binaural directivity diagrams.

It is somewhat surprising that this feature of binaural directivity diagrams was never described before, although a few studies described binaural directivity diagrams in dolphins. In all the preceding studies (see the Introduction), the directivity diagram was described as featuring one best-sensitivity peak at the zero azimuth (midline). We do not have sufficient data for a definite explanation of this contradiction. However, it should be noted that the two-peak form of a binaural directivity diagram, if it exists, might be easily missed because of a combination of a few unfavorable circumstances. (i) The dip in between the two diagram peaks is rather small. (ii) A two-peak diagram may be observed only within a limited range of middle frequencies since at high frequencies it really does not exist (monaural diagrams feature the maximum sensitivity near midline) and at low frequencies the exact peak positions are difficult to detect because of flattening the diagrams. (iii) A small inconsistency of the head position relative to the sound source during measurements may smooth down the peak-and-dip pattern. (iv) If the threshold criterion is too conservative, i.e., actually the diagram is based on suprathreshold responses, responses from the right and left ears may summate at the midline sound-source position, thus mimicking a threshold decrease. Retrospectively, it is hardly possible to find out which of these circumstances did, and which did not, take place in the earlier studies. So, only future detailed studies can show whether the described two-peak waveform of binaural directivity diagrams is a common feature of the dolphin's hearing or an exception that appeared in the present study for some particular reason.

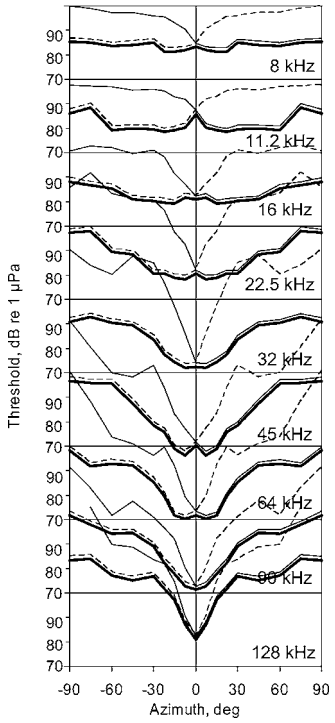

FIG. 10. Model of the origin of a two-peak binaural directivity diagram. Thin lines reproduce monaural directivity diagrams (see Fig. 4); thin dashed lines, their mirror images assumed as diagrams of the contralateral ear; solid line, a binaural diagram as determined by the least thresholds of the two monaural diagrams.

ACKNOWLEDGMENTS

The study was supported by the Russian Foundation for Basic Research Grant No. 03-04-48117 and the Russian President Grant No. NSh-2152.2003.4. Assistance of the Utrish Marine Station staff is greatly appreciated. Valuable comments of Paul Nachtigall are greatly appreciated.

Au, W. W. L. (**1993**). *The Sonar of Dolphins* (Springer-Verlag, New York).

Au, W. W. L. and Moore, P. W. B. (**1984**). "Receiving beam patterns and directivity indices of the Atlantic bottlenose dolphin *Tursiops truncatus*," J. Acoust. Soc. Am. **75**, 255.

Au, W. W. L., Popper, A. N., and Fay, R. (**2000**). *Hearing by Whales and Dolphins* (Springer-Verlag, New York).

Bullock, T. H., Grinnell, A. D., Ikezono, F., Kameda, K., Katsuki, Y., Nomoto, M., Sato, O., Suga, N., and Yanagisava, K. (**1968**). "Electrophysiological studies of the central auditory mechanisms in cetaceans," Z. Vergl. Physiol. **59**, 117.

Dubrovskiy, N. A. (**1990**). "On the two auditory systems in dolphins," in *Sensory Abilities of Cetaceans. Laboratory and Field Evidence*, edited by J. A. Thomas and R. A. Kastelein (Plenum, New York), pp. 233–254.

Ketten, D. R. (**2000**). "Cetacean ears," in *Hearing by Whales and Dolphins*,

edited by W. W. L. Au, A. N. Popper, and R. R. Fay (Springer, New York), pp. 43–108.
McCormick, J. G., Wever, E. G., Palin, G., and Ridgway, S. H. (**1970**). "Sound conduction in the dolphin ear," J. Acoust. Soc. Am. **48**, 1418.
McCormick, J. G., Wever, E. G., Ridgway, S. H., and Palin, G. (**1980**). "Sound reception in the porpoise as it relates to echolocation," in *Animal Sonar Systems*, edited by R. G. Busnel and J. F. Fish (Plenum, New York), pp. 449–467.
Moore, P. W. B., Pawlosky, D. A., and Dankiewicz, L. (**1995**). "Interaural time and intensity difference thresholds in the bottlenose dolphin (*Tursiops truncates*)," in *Sensory Systems of Aquatic Mammals*, edited by R. A. Kastelein, J. A. Thomas, and P. E. Nachtigall (De Spil Publishers, Woerden, The Netherlands), pp. 11–23.
Norris, K. S. (**1968**). "The evolution of acoustic mechanisms in odontocete cetaceans," in *Evolution and Environment*, edited by E. T. Drake (Yale University, New Haven), pp. 297–324.
Popov, V. V. and Supin, A. Ya. (**1988**). "Diagram of auditory directionality in the dolphin *Tursiops truncatus* L," Dokl. Biol. Sci. **300**, 323.
Popov, V. V., and Supin, A. Ya. (**1990**). "Electrophysiological studies of hearing in some cetaceans and manatee," in *Sensory Abilities of Cetaceans: Laboratory and Field Evidence*, edited by J. A. Thomas and R. A. Kastelein (Plenum, New York), pp. 405–415.
Popov, V. V. and Supin, A. Ya. (**1992**). "Electrophysiological study of the interaural intensity difference and interaural time-delay in dolphins," in *Marine Mammal Sensory Systems*, edited by J. A. Thomas, R. A. Kastelein, and A. Ya. Supin (Plenum, New York, London), pp. 257–267.
Popov, V. V., Supin, A. Ya., and Klishin, V. O. (**1992**). "Electrophysiological study of sound conduction in dolphins," in *Marine Mammal Sensory Systems*, edited by J. A. Thomas, R. A. Kastelein, and A. Ya. Supin (Plenum, New York, London), pp. 269–276.
Renaud, D. L. and Popper, A. N. (**1975**). "Sound localization by the bottlenose porpoise *Tursiops truncatus*," J. Exp. Biol. **63**, 569.
Supin, A. Ya. and Popov, V. V. (**1993**). "Direction-dependent spectral sensitivity and interaural spectral difference in a dolphin: Evoked potential study," J. Acoust. Soc. Am. **96**, 3490.
Supin, A. Ya., Popov, V. V., and Mass, A. M. (**2001**). *The Sensory Physiology of Aquatic Mammals* (Kluwer, Boston).
Zaytseva, K. A., Akopian, A. I., and Morozov, V. P. (**1975**). "Noise resistance of the dolphin auditory analyzer as a function of noise detection," Biofizika **20**, 519.

Automated categorization of bioacoustic signals: Avoiding perceptual pitfalls

Volker B. Deecke
Marine Mammal Research Unit, University of British Columbia, 2202 Main Mall, Vancouver, BC V6T 1Z4 Canada and Cetacean Research Lab, Vancouver Aquarium Marine Science Centre, P.O. Box 3232, Vancouver, BC V6B 3X8, Canada

Vincent M. Janik
Sea Mammal Research Unit, Gatty Marine Laboratory, University of St. Andrews, Fife KY16 8LB, United Kingdom and Centre for Social Learning and Cognitive Evolution, School of Biology, University of St. Andrews, Fife KY16 9TS, United Kingdom

(Received 6 June 2005; revised 21 September 2005; accepted 13 October 2005)

Dividing the acoustic repertoires of animals into biologically relevant categories presents a widespread problem in the study of animal sound communication, essential to any comparison of repertoires between contexts, individuals, populations, or species. Automated procedures allow rapid, repeatable, and objective categorization, but often perform poorly at detecting biologically meaningful sound classes. Arguably this is because many automated methods fail to address the nonlinearities of animal sound perception. We present a new method of categorization that incorporates dynamic time-warping and an adaptive resonance theory (ART) neural network. This method was tested on 104 randomly chosen whistle contours from four captive bottlenose dolphins (*Tursiops truncatus*), as well as 50 frequency contours extracted from calls of transient killer whales (*Orcinus orca*). The dolphin data included known biologically meaningful categories in the form of 42 stereotyped whistles produced when each individual was isolated from its group. The automated procedure correctly grouped all but two stereotyped whistles into separate categories, thus performing as well as human observers. The categorization of killer whale calls largely corresponded to visual and aural categorizations by other researchers. These results suggest that this methodology provides a repeatable and objective means of dividing bioacoustic signals into biologically meaningful categories. [DOI: 10.1121/1.2139067]

PACS number(s): 43.80.−n, 43.60.Np, 43.80.Lb, 43.80.Ka [WWA] Pages: 645–653

I. INTRODUCTION

A. Categorization of sound patterns by humans and computers

A widespread problem in the study of animal sound communication lies in dividing the patterns that make up the acoustic repertoire of an individual or group into biologically relevant categories. We refer to this process as categorization to distinguish it from classification, the process of assigning sound patterns to predefined categories. Biologically meaningful categorization is fundamental to any study attempting to compare repertoires between contexts, individuals, populations, or species. Historically, such categorization was usually carried out by human observers who sorted the sound patterns into categories according to their perceived similarity. Categorization by human observers requires the subjects to decide which features are important in defining categories and how these features should be weighted. Humans use their natural pattern recognition skills to solve such tasks. However, the judgments and decisions made on weighting different features in a pattern can differ between individuals (Jones *et al.*, 2001) and can be difficult to quantify since humans are not usually aware of the threshold values they use (e.g., Rendell and Whitehead, 2003). This makes it difficult to compare acoustic repertoires between studies conducted by different people. One way of solving this problem is to use several observers. One can then use categories that observers agreed on and measure threshold values that distinguish these categories. However, this is a time-consuming process that limits the amount of data included in any comparison. Thus, an automated method that categorizes sound patterns in a biologically meaningful way would be an extremely valuable analytical tool.

Categorization of animal sounds has usually been based on the patterns of frequency modulation over time. Approaches to achieve automated classification have included clustering schemes based on various measures of similarity (e.g., Symmes *et al.*, 1979; Chabot, 1988), principal components analyses (e.g., Clark, 1982; Cerchio and Dahlheim, 2001), or combinations of these procedures (e.g., Nowicki and Nelson, 1990; Elowson and Hailman, 1991). However, such standard methods often fall far short of observer ratings in accuracy and frequently fail to detect biologically meaningful categories (see Janik, 1999). We argue here that this poor performance of current methods is largely due to failure to consider two fundamentals of acoustic perception when measuring the similarity of sound patterns: flexibility in the time domain and the exponential perception of sound frequency.

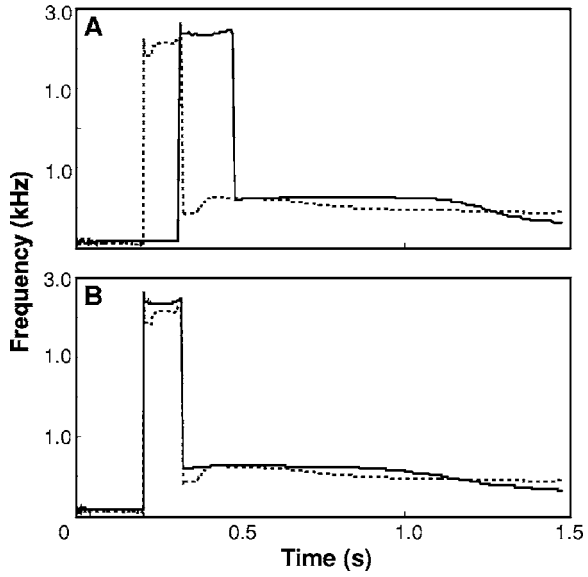

FIG. 1. Matching a frequency contour (pulse-repetition rate as a function of time) of a pulsed call of transient killer whales (solid line) to a reference contour (dotted line) using standardization of call length [panel (a)] and dynamic time warping [local extension and compression of the time axis of the frequency contour to maximize frequency overlap—panel (b)]. The match (given as the average similarity in frequency in percent for all points of the two contours) is 69.9% using standardization, but 86.9% using dynamic time warping.

B. Time and frequency resolution in the auditory perception of birds and mammals

Any categorization scheme of sound patterns requires a measure of the similarity of sounds. Traditional similarity measures have included spectrogram cross correlation (e.g., Clark *et al.*, 1987), hidden Markov models (e.g., Clemins *et al.*, 2005), or measures of the distance between frequency contours (e.g., Buck and Tyack, 1993). The first shortcoming of any study using spectrograms or frequency contours (plots of the fundamental frequency of a vocalization over time) is that, in order to compare two entire sound patterns using most traditional distance measures, they need to be standardized for time. This can have the effect of rating two sound patterns as very similar even though their lengths might differ by an order of magnitude. In addition, for signals with strong frequency modulation, temporal standardization can have the effect of generating artificially low similarity values for signals that are in fact very similar in shape, but instead differ only slightly in the length of different components so that equivalent sections of the signals do not overlap (see Fig. 1). Animals are relatively insensitive to such slight differences in the duration of sound patterns. Dooling (1982) suggests that birds are ten times more sensitive to changes in the frequency of sounds than they are to changes in their duration. Small differences in the duration of certain acoustic features are therefore often insignificant to the animal and any analysis of sound patterns must allow for this.

The other main feature of vertebrate auditory perception that needs to be considered when developing automated methods of acoustic categorization is that tonal frequency is not perceived on a linear but on an logarithmic scale. Humans perceive the difference between two tones with frequencies that differ by a factor of 2 (an octave) as being the same regardless of whether the two tones have frequencies of 110 and 220 Hz or 880 and 1760 Hz. This logarithmic perception of frequency is reflected by the distribution of hair cells sensitive to different frequencies in the inner ear and appears to be common to all terrestrial vertebrates (e.g., Müller, 1991; Smolders *et al.*, 1995; Vater and Siefer, 1995; Manley *et al.*, 1999). This means that acoustic features with higher fundamental frequencies can exhibit greater absolute frequency variation before they are perceived as different compared to features with low fundamental frequencies. Frequency measurements should therefore be log-transformed before comparison, or differences in frequencies should be expressed as relative rather than absolute values. Any scheme that fails to account for the logarithmic perception of frequency runs the risk of biasing categorization towards an inflated number of categories of high-frequency sound patterns.

C. Unsupervised learning in artificial neural networks

In this paper we introduce and test a novel method of call categorization that allows for flexibility in the time domain and accounts for the logarithmic perception of sound frequency. It uses an adaptive resonance theory (ART) neural network that is unsupervised in its learning phase. Supervised and unsupervised learning describe two different applications of self-organizing artificial neural networks. Supervised learning is a method of automated classification, where an artificial neural network learns to classify unknown patterns using information extracted from a training set of identified patterns. For example, artificial neural networks can be trained in this way to distinguish between the vocal patterns of different identified individuals (e.g., Reby *et al.*, 1997; Campbell *et al.*, 2002; Terry and McGregor, 2002), social groups (e.g., Deecke *et al.*, 1999), or species (e.g., Phelps and Ryan, 1998; Parsons and Jones, 2000), or between vocal patterns given in response to clearly identifiable stimuli [e.g., predator-specific calls (Placer and Slobodchikoff, 2000)]. In contrast, unsupervised learning describes a series of artificial neural network algorithms that can be used to categorize patterns without prior training—they are the self-organizing analogs of traditional clustering schemes. The main advantage of unsupervised learning is that, for a new pattern to be assigned to a category, it must only be compared to a small subset of reference patterns (or neighboring patterns in the case of self-organizing maps) rather than all other patterns in the data set. Unsupervised learning algorithms therefore lend themselves to the analysis of large data sets where computing time is limiting, or to situations where categorization must happen in real time.

The most common algorithms for unsupervised learning are self-organizing maps [SOM, e.g., Kohonen (1988)], competitive learning (e.g., Grossberg, 1987), and adaptive resonance theory (ART) neural networks (e.g., Carpenter and Grossberg, 1987). The categorization algorithm used in this study is based on an ART2 neural network (Carpenter and Grossberg, 1987). ART2 is an unsupervised learning algorithm in which a given pattern is compared to a set of refer-

ence patterns. If the input pattern resembles one of the reference patterns with a certain degree of similarity (called the vigilance), the input is assigned to the category represented by this reference pattern and the reference pattern itself is updated and made even more similar to the current input pattern. If the input pattern does not resemble any reference pattern sufficiently, it becomes the reference pattern for a new category. ART2 neural networks have the advantage that they do not require assumptions about the frequencies of patterns in different categories. In contrast, competitive learning algorithms and self-organizing maps assume that input patterns are evenly distributed between categories and therefore tend to split frequent input patterns into finer categories. For this reason, ART neural networks lend themselves to the categorization of behavior patterns where equal distribution can rarely be assumed.

D. Objectives

Our objective for this study is to develop and test an automated method for categorizing stereotyped vocal patterns of animals using test data sets of vocalizations of bottlenose dolphins and killer whales. Both of these species produce a variety of structurally distinct stereotyped sound patterns and dividing these into meaningful sound categories is an important first step before vocal repertoires, or the structure of given sound types, can be compared between individuals and populations, behavior contexts, or over time. While the methodology is developed using data sets from two species of toothed whales, our hope is that it can be applied to the vocalizations of a wide variety of species.

In order to allow for variation in the lengths of different components of the sounds, similarities between input and reference patterns were calculated using dynamic time-warping (e.g., Sakoe and Chiba, 1978; Buck and Tyack, 1993). Dynamic time-warping is an algorithm developed for the automated recognition of human speech that allows limited compression and expansion of the time axis of a signal to maximize frequency overlap with a reference signal (see Fig. 1 for an illustration of dynamic time-warping). To account for exponential perception of frequency in this analysis, we expressed similarity of contours as their relative similarity in frequency.

We test the performance of this method on two categorization problems. The first is a set of frequency contours of bottlenose dolphin whistles described in detail by Janik (1999). Bottlenose dolphins produce a variety of whistles, including stereotyped signature whistles which are individually distinctive. Since signature whistles represent biologically defined categories and their structure has been shown to convey important information (i.e., identity of the caller) to the animals (Janik and Slater, 1998; Sayigh *et al.*, 1999), we aim to use this data set to test whether the categories determined by our analysis are congruent with categories known to be perceived as meaningful by bottlenose dolphins.

The second data set consists of frequency contours of killer whale calls. The pulsed calls of killer whales are highly stereotyped and can be divided easily and consistently into categories by human observers (e.g., Ford, 1989, 1991). We present the categorization performance and investigate the vigilance parameter that controls the fineness of categorization and therefore the number of categories established. We also show how optimality of categorization can be achieved without prior knowledge of the underlying categories by selecting a vigilance parameter for the neural network that minimizes variation within categories while maximizing differences between categories.

II. METHODS

A. Data sets, acoustic analysis, and contour extraction

Both the dolphin whistle and killer whale call data sets consist of frequency contours extracted from spectrograms of calls or whistles. Dolphin whistles are tonal signals and frequency contours therefore give the fundamental frequency of a whistle as a function of time. The recordings for our study were collected in 1996 from a social group consisting of two female and two male bottlenose dolphins held at Zoo Duisburg in Germany. We recorded whistles with two Dowty SSQ 904 hydrophones connected to a Marantz CP430 tape recorder (system frequency response: 1–20 kHz±3 dB). Time resolution of the extracted frequency contours was 10 ms. For details on the recording and selection of bottlenose dolphin whistles and on the extraction of frequency contours see Janik *et al.* (1994); Janik and Slater (1998), and Janik (1999).

The frequency contours of killer whale calls were generated from a sample of calls digitized from field recordings of transient killer whales. Recordings were made with a variety of hydrophones on Type II audio cassette tapes, digital audio tape, or reel-to-reel tape. Frequency responses of the recording systems were 1–16 kHz±3 dB or better. We rated the quality of each call from the spectrogram on a scale from one to five, taking into account signal-to-noise ratio, echoes, and reverberation, as well as background noise. In order to avoid categorization due to noise artifacts (e.g., faint call elements that were missed), calls of the three lowest quality categories were excluded from this analysis. Since killer whale calls are pulsed signals (Schevill and Watkins, 1966), frequency contours give the pulse-repetition rate rather than fundamental frequency. We used the sidewinder algorithm (Deecke *et al.*, 1999) to extract frequency contours from spectrograms of killer whale calls, with the difference that for the current analysis the contours were not standardized for time. Time resolution for these frequency contours was also 10 ms.

B. ARTwarp—Combining dynamic time-warping and adaptive resonance theory

The neural network used in this analysis was an ART2 neural network for the categorization of analog input patterns. The computer script was a simulation of the ART2 algorithm of Carpenter and Grossberg (1987). However, this algorithm was modified in two ways. First, the similarity between frequency contours and the set of reference contours was calculated using dynamic time-warping to ensure maximum overlap in the frequency domain. Second, if a fre-

quency contour matched a reference contour better than the critical similarity (vigilance), this reference contour was then modified in three ways to be more similar to the input pattern. (1) The frequency content of the reference contour was made more similar to the time-warped frequency contour by adding a proportion (10%) of the difference between reference contour and time-warped input contour. (2) The relative lengths of different components of the reference contour were modified to be more similar to the current frequency contour by applying a warping function that stretched or compressed the time axis by a proportion (10%) of the inverse of the original warping function generated when input and reference contour were compared. (3) The length of the reference contour was made more similar to the current input contour. The extent of the change in length (number of points) was given by the learning rate (10% of the difference in our case). To increase or decrease the number of frequency points, the frequency measurements in the contour were interpolated at a number of equally spaced points corresponding to the new length of the contour. If the current input pattern did not match any of the reference patterns better than the critical similarity, it became the reference contour for a new category. All frequency contours were repeatedly presented to the neural network until they consistently matched the same reference contour (i.e., no reclassifications occurred between iterations).

The dynamic time-warping algorithm used in this study was that applied by Sakoe and Chiba (1978) and Buck and Tyack (1993) with the difference that the algorithm allowed horizontal and vertical jumps of three frequency points in the contour [rather than two points as in Sakoe and Chiba (1978) and Buck and Tyack (1993)]. A frequency contour can therefore be "sped up" or "slowed down" in parts by a factor of 3 to fit the reference contour. In addition, the algorithm calculated the relative frequency similarity (S) in percent between both frequency contours rather than the total square difference of Sakoe and Chiba (1978) or the average square difference of Buck and Tyack (1993). This was done by dividing the smaller frequency value by the larger value at each point and multiplying by 100:

$$S(i) = \frac{\min[M(i),N(i)]}{\max[M(i),N(i)]} \times 100,$$

where M is the reference pattern and N the input pattern. Like Buck and Tyack (1993), we also divided the total difference by the length of the reference contour. The measure of similarity therefore gives the average relative similarity in frequency for the reference and input contour after time warping.

C. Experiment I: Categorization of bottlenose dolphin whistles

The level of critical similarity (vigilance) for the analysis of dolphin whistles was obtained by categorizing only the signature whistles of one individual [individual A of Janik (1999)] and increasing the vigilance in steps of 1% until the analysis split these signature whistles into two categories. The critical vigilance (96%) is the highest value that still recognizes the whistles as a single category. The entire data set was then categorized using this vigilance parameter and the resulting categories were analyzed to test whether the signature whistle categories were recognized.

D. Experiment II: The appropriate fineness of categorization

In this experiment, we categorized a sample of 50 frequency contours randomly chosen from all calls with the two highest quality scores in the transient killer whale data set. These calls came from 25 recordings of different groups. Unlike the bottlenose dolphin whistles, this data set does not contain any sound categories known *a priori* to be biologically meaningful. Therefore the method to determine the appropriate fineness of categorization used for the dolphin whistles could not be applied. In the absence of identifiable categories, we wanted to find the categorization that would explain a maximum of the variation in call structure with a minimum number of call categories. To do this, we initially set the vigilance to zero. At this level, call categories are assigned only by call length [since any two contours whose length differs by more than a factor of 3 are automatically assigned a similarity of zero; see Buck and Tyack (1993)]. The vigilance was then increased to 100% in 50 logarithmic steps and the sample of contours was categorized. At a vigilance of 100%, each frequency contour is assigned to its own category. For each categorization, we determined the number of categories generated. In order to investigate patterns of within-category and between-category variation, we calculated the similarity matrix for all frequency contours in the data. This matrix contained similarity values of all possible pairwise comparisons of contours using dynamic time-warping. Using this matrix, we could determine the average similarity of contours in the same category (within-category variation), as well as the average similarity of contours in different categories (between-category variation) for each categorization. The categorization where a minimum number of distinct categories explain a maximum amount of difference in the frequency contours can then be identified by plotting the ratio of within-category and between-category variation and determining the number of categories where this ratio levels off (i.e., adding additional categories does little to explain additional variation). This is analogous to the variance ratio criterion (e.g., Calinski and Harabasz, 1974; Everitt *et al.*, 2001; Schreer *et al.*, 1998; Rendell and Whitehead, 2003) to determine the optimal number of groups in cluster analysis.

E. Visualization of neural network performance

In order to illustrate how the ARTwarp algorithm categorizes the discrete calls of killer whales from frequency contours, we used the neural network to categorize a sample of 20 frequency contours, small enough so that it could be graphed on a single page. These were randomly chosen from the two highest quality categories in the data set of transient killer whale calls. The vigilance parameter used in this analysis was the optimum value determined in experiment II.

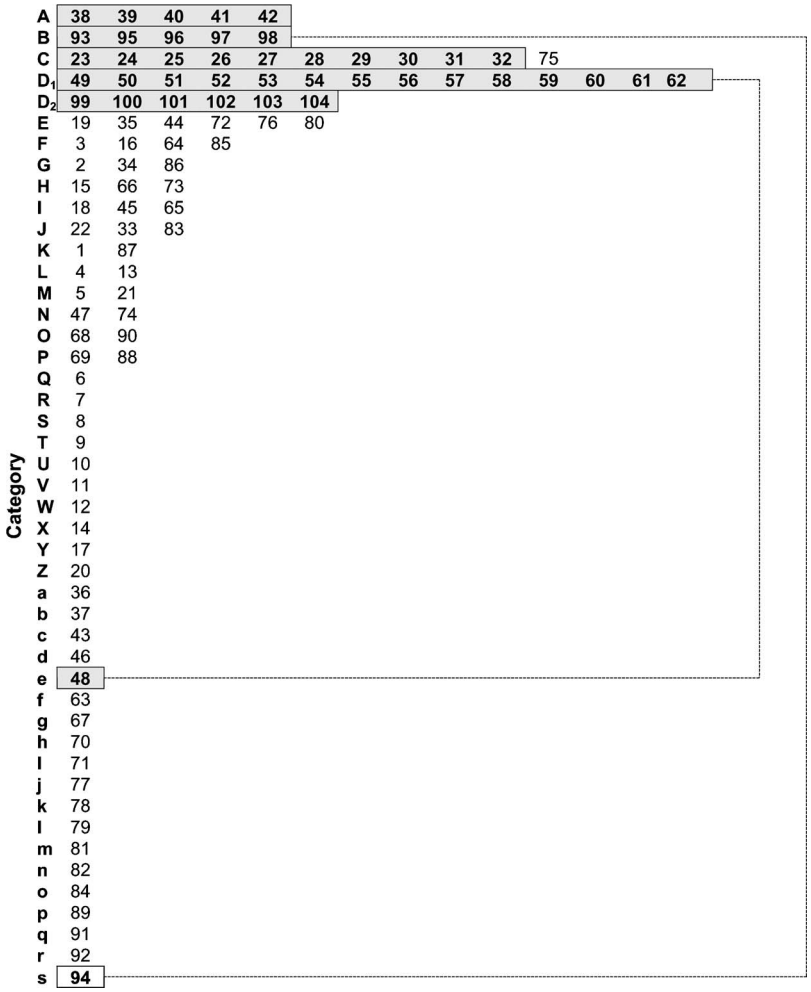

FIG. 2. Categorization of frequency contours of bottlenose dolphin whistles using an ART2 neural network and dynamic time warping to calculate similarity. Numbers represent individual whistle contours. Signature whistles are shown in bold and boxes identify signature whistles from the same individual. Signature whistle categories that were split by the analysis are linked with dotted lines. See Janik (1999) for visual representations of the whistle contours.

III. RESULTS

A. Experiment I: Categorization of bottlenose dolphin whistles

The categorization of the data set of bottlenose dolphin whistles is shown in Fig. 2. Using a vigilance of 96%, the analysis divided the 104 whistle contours into 46 categories each containing between 1 and 14 contours (mean: 2.26, standard deviation: 2.62 contours). With regard to the behaviorally defined categories of signature whistles recorded from each of the five dolphins in isolation, the analysis correctly clustered two whistle types (A and D2) into individual categories but made three errors while categorizing the other three whistle types: It added an additional whistle (no. 75) to the category containing the contours of whistle type C. In the case of whistle types B and D_1, a single contour was not assigned to the category containing the whistle types, but was put in a category of its own.

B. Experiment II: The appropriate fineness of categorization

The effects of increasing the vigilance parameter on the categorization of transient killer whale calls are illustrated in Fig. 3. With higher vigilance the analysis generated an increasing number of categories. Both the average similarity of frequency contours within a category and the average similarity of contours in different categories increased as more and more categories were added. However, they did so at different rates. Initially the rate of increase in the between-category similarity was relatively low and the rate of increase in the within category variation was high. At a critical point, however, the rate of increase in the within-category similarity slowed (since new categories explain little additional variation) and the rate of increase in the between-category similarity increased (since more and more natural clusters in the data set were divided between categories). Adding further categories after this critical point does little to improve the categorization. The plot of the ratio of within and between-category variation [Fig. 3(b)] therefore leveled off abruptly at a vigilance of 81.24%. At this point the analysis generated ten categories.

C. Visualization of neural network performance

The frequency contours used in this experiment, as well as the resulting call categories, are shown in Fig. 4. The analysis divided the 20 contours into six categories each containing between two and seven calls. The categories were largely consistent with the call types established by Ford (1984) and Ford and Morton (1991): Category 1 contained calls classified as T08i, category 2 represents the T04 call type of Ford (1984) and the T03ii call type of Ford and Morton (1991), category 3 is equivalent to the T01 call type,

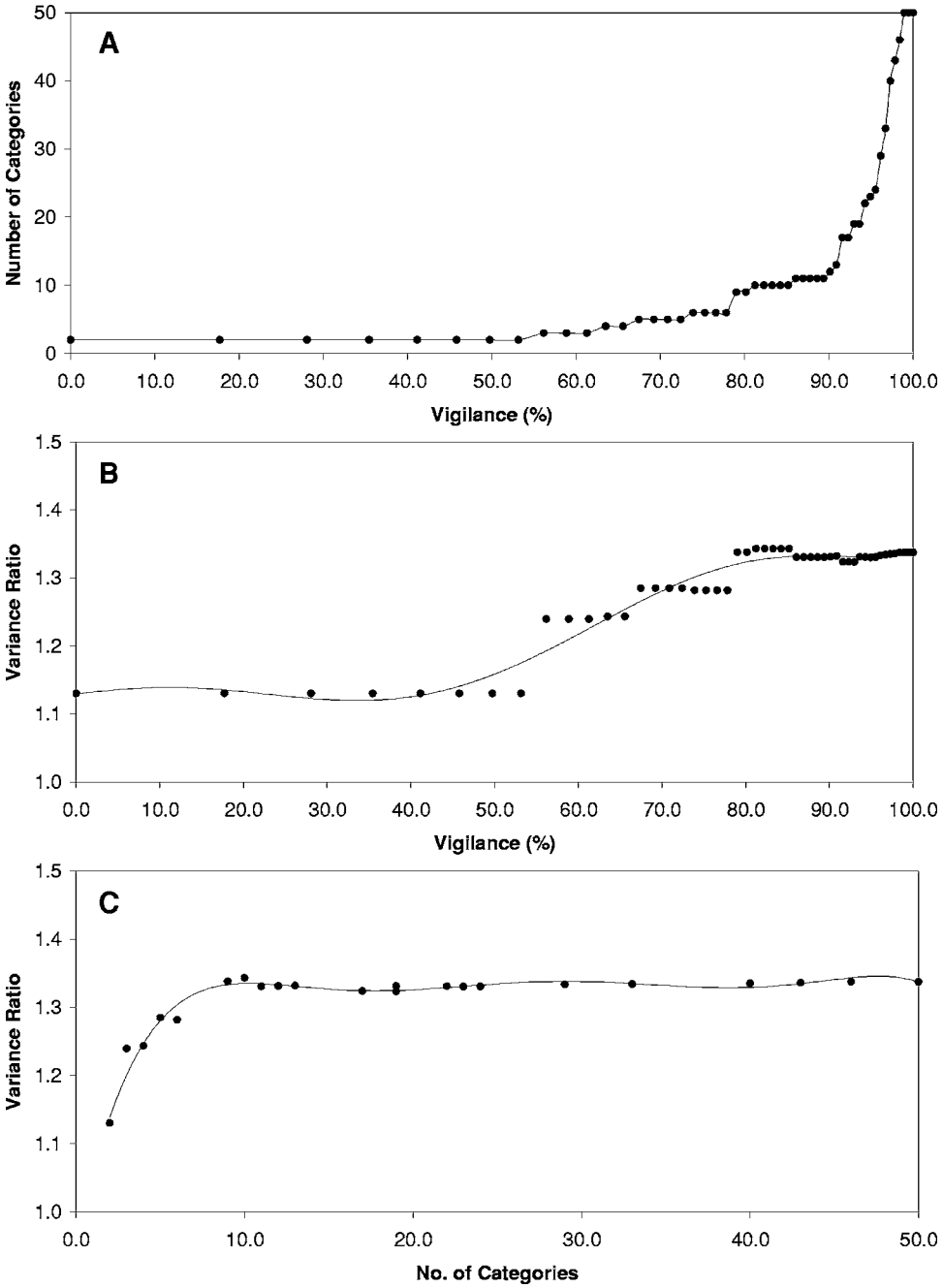

FIG. 3. Effect of the vigilance on the categorization of 50 frequency contours from calls of transient killer whales. Panel (a) shows the increase in the number of categories generated with increasing vigilance. Panel (b) shows the change in the variance ratio (ratio of within- to between-category variance) with increasing vigilance and panel (c) shows the change in the variance ratio with increasing numbers of categories. This ratio reached a maximum at a vigilance of 81.24% (10 categories). Trend lines in panels (b) and (c) are sixth-order polynomials.

and category 4 represents the T07 call type of Ford and Morton (1991). Category 5 contained calls classified as subtype T07ii by Ford and Morton (1991) and category 6 is equivalent to their T02 call type.

IV. DISCUSSION

A. Categorization of bottlenose dolphin whistles

The automated categorization combining dynamic time-warping with an ART2 neural network was able to recognize biologically meaningful categories in our data set of bottlenose dolphin whistles. While the analysis was not designed to detect individual signature whistles and identify them as such (a problem of *classification*, not categorization) it did recognize the stereotyped signature whistles as uniform signal categories to a high degree. By doing so, our method performed much better than any of the statistical procedures tested by Janik (1999), none of which proved satisfactory at detecting these biologically significant signal categories. Our automated categorization even performed marginally better at detecting the signature whistle categories in the data set of bottlenose dolphin whistles than did the human observers of Janik (1999) who made on average 3.4 mistakes. Interestingly, the neural network did not agree with the human observers in the categorization of nonsignature whistles. In general, the automated analysis created finer categories containing fewer contours for this subset. Janik (1999) identified four combinations of nonsignature whistles common to the categorization of all five observers and none of these combinations occur in the neural network categorization. Since we have no external validation for appropriate classification of nonsignature whistles, it is impossible to say which catego-

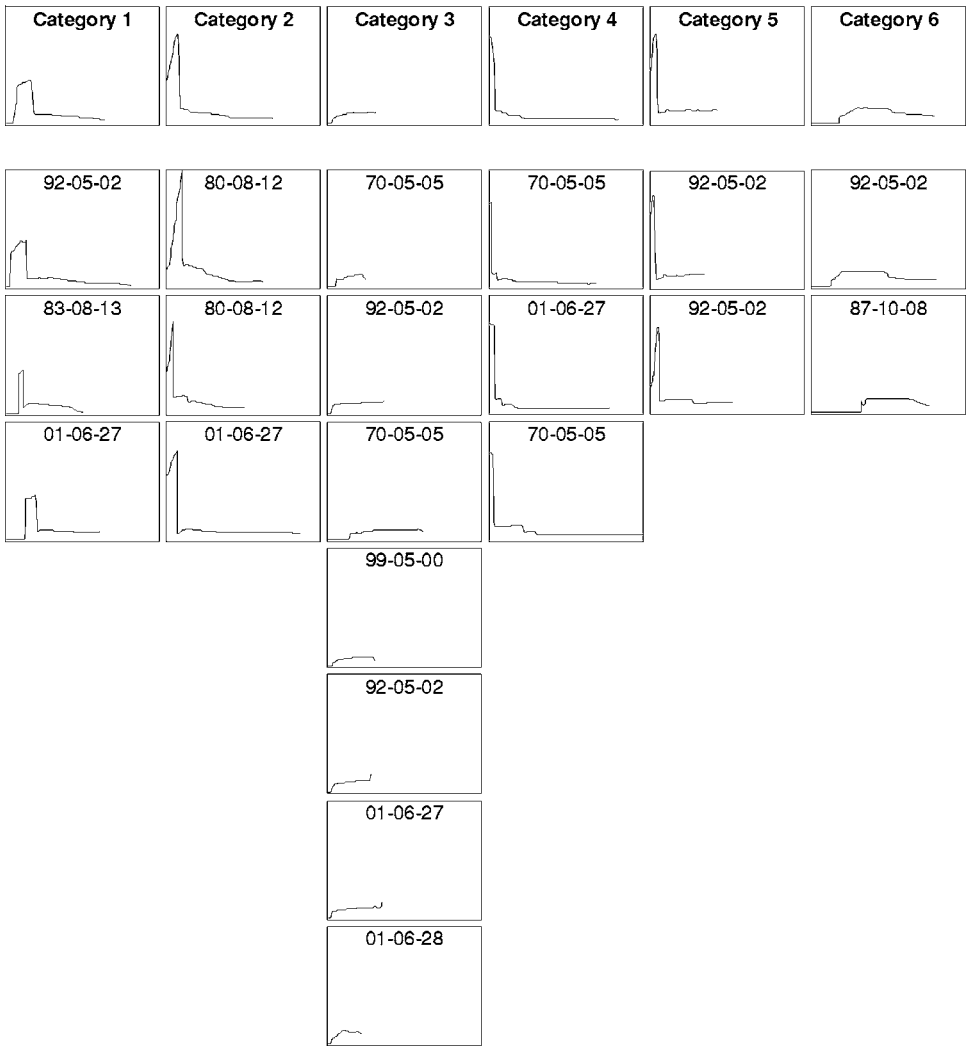

FIG. 4. Results of the categorization of frequency contours from 20 randomly chosen calls of transient killer whales. All frequency contours in the same column were assigned to the same call type by the analysis. The reference contours representing each category are shown in the first row. Labels give the recording session (in the format yy-mm-dd) for each frequency contour.

rization scheme is of greater biological relevance here.

The two signature whistles that were assigned to separate categories from the rest of their whistle types are both shorter than the other whistles of the same type and may represent truncated versions of the individuals' signature whistles. If this is the case, relaxing the endpoint constraint during dynamic time-warping [i.e., permitting the time-warped contour to be shorter in duration than the reference contour and calculating frequency similarity only for the section of overlap with the reference contour; see Parsons (1987)] would improve classification for these contours.

B. Choosing the vigilance parameter

Most automated analytic procedures require the investigator to choose some parameters that control their performance. In the automated categorization described here, the performance depends to a large degree on the vigilance of the neural network. This parameter controls the fineness of categorization, that is, the size and number of categories that are generated. It has no influence on which patterns are rated as similar in the analysis. Note that the problem of deciding on the appropriate fineness of categorization is shared by categorization of behavior using human observers: we refer to observers as "joiners" or "splitters" depending on how fine their behavior categories tend to be. As an example, Saulitis (1993) divides the surface behavior of killer whales into 14 categories, whereas Ford (1989) distinguishes between only five behavior categories. We have no information on the extent to which this difference is due to differences in the behavior of killer whale populations studied by the two researchers, or differences in the fineness of categorization considered appropriate to describe the observed behavioral variation by the authors. The advantage of the automated procedure is obviously that the fineness of categorization can be quantified for each analysis.

The categorization of bottlenose dolphin whistles demonstrates that where biologically relevant sound categories can be identified *a priori*, these can be used to determine the vigilance parameter appropriate for categorization. Such biologically defined categories may be sound patterns specific to certain individuals or populations or to clearly defined contexts, such as isolation from group members (Symmes *et al.*, 1979; Janik, 1999) or the presence of a food source (Judd and Sherman, 1996; Roush and Snowdon, 2000) or a predator (e.g., Placer and Slobodchikoff, 2000). Human observers frequently use such information from predefined categories to determine the appropriate resolution for behavioral categorization.

In many categorization problems, it is desirable to ex-

plain a maximum amount of the observed acoustic variation using a minimum number of sound categories. In situations where acoustic variation is difficult to quantify, this can be hard to achieve. However, wherever measures of acoustic similarity are readily available, simple algorithms can help to determine the appropriate number of categories for analysis. In situations where no external validation of categories is available, calculating the ratio of variation within to variation between categories for a large number of vigilance values provides a useful approach to determining the appropriate fineness of categorization. This is time consuming for large samples of sound patterns but, as demonstrated in experiment II, categorization of a randomly selected subset will generally allow identification of the appropriate vigilance parameter. Applying alternative goodness of fit measures, such as the Bayesian information criterion or Aikake's information criterion (e.g., Kuha, 2004), to categorizations with increasing vigilance setting may similarly help to identify the appropriate fineness of categorization in future studies.

C. Applicability to other categorization problems in the study of behavior

While this method has so far only been tested on the vocalizations of toothed whales, these results should also encourage its application to analyses of vocal behavior in other species. Unsupervised learning algorithms have been applied successfully to the categorization and classification of a variety of bioacoustic signals (e.g. Leinonen *et al.*, 1993; Terry and McGregor, 2002) and allowing for differences in the length of acoustic signals and their components by incorporating dynamic time-warping may prove useful in these and other situations as well. As described here, our analysis is currently limited to vocalizations that can be described adequately by frequency contours. This includes the sound signals of many species of amphibians, birds, and mammals. However, in species with vocalizations that are broadband (e.g., Campbell *et al.*, 2002), or where relevant information is encoded in the harmonic content (e.g., Weiss and Hauser, 2002), frequency contours alone are inadequate to describe vocal patterns. Fortunately, dynamic time-warping can also be used to compare spectrograms [it was in fact first developed to classify human speech patterns from spectrograms (see Sakoe and Chiba, 1978)] and the neural network component of the analysis could easily be adapted to deal with the two-dimensional format of spectrograms rather than one-dimensional frequency contours, making the analysis applicable to the categorization of vocal behavior in a wide variety of species.

Since it was developed to address peculiarities of acoustic perception, the methodology as described in this study is probably of limited value to categorize behaviors other than those that are acoustic. Nonetheless, elements applied in the current analysis may prove useful elsewhere: the ART2 neural network can be used with similarity measures other than dynamic time-warping in a wide variety of categorization problems. Conversely, dynamic time-warping and its extension of hidden Markov models will be useful in any situation where the trajectory of change in a behavioral parameter is more important than the precise timing of the change. The categorization of dive profiles from aquatic birds and mammals (e.g., Schreer *et al.*, 1998; Lesage *et al.*, 1999; Malcolm and Duffus, 2000) may prove to be a valuable example. In addition, much if not most of sensory perception is nonlinear in scale (usually exponential or logarithmic), and this is important to bear in mind when quantifying the strength and quality of behavioral stimuli for categorization. This study therefore serves to illustrate the importance of obtaining and applying relevant information about the sensory perception of study animals when designing categorization schemes for the study of their behavior.

V. CONCLUSIONS

Our results suggest that automated categorization of bioacoustic signals can present a powerful alternative to categorization by human observers, as long as the importance of the time domain and the frequency domain in the auditory perception of the study species is understood and any peculiarities in the way time and frequency parameters are perceived are considered. Automated methods such as the one used in our study are particularly useful in situations were large data sets need to be analyzed and where the size of acoustic repertoires must be compared between individuals, social groups or species, or over time.

ACKNOWLEDGMENTS

We thank the staff of Zoo Duisburg for the opportunity to work with their animals and for their support during the recording of dolphin whistles, especially Roland Edler, Reinhard Frese, Manuel García Hartmann, Friedrich Ostenrath, and Ulf Schönfeld. Recordings for the analysis of killer whale vocalizations were generously supplied by Nancy A. Black, John K. B. Ford, P. Dawn Goley, Dan McSweeney, Paul Spong, and Richard L. Ternullo. The ART2 neural network algorithm was adapted from a program originally written by Aaron Garrett, and Mary Royerr helped with statistical aspects of this paper. Earlier drafts of this manuscript benefited from comments by Karen E. McComb, John K. B. Ford, Michael J. Ritchie, and Peter J. B. Slater. V.M.J was funded by a Royal Society University Research Fellowship, and V.B.D received financial support from a DAAD Doktorandenstipendium aus Mitteln des 3. Hochschulsonderprogramms during part of this study.

Buck, J. R., and Tyack, P. L. (**1993**). "A quantitative measure of similarity for *Tursiops truncatus* signature whistles," J. Acoust. Soc. Am. **94**, 2497–2506.

Calinski, T., and Harabasz, J. (**1974**). "A dendrite method for cluster analysis." Commun. Stat: Theory Meth. **3**, 1–27.

Campbell, G. S., Gisiner, R. C., Helweg, D. A., and Milette, L. L. (**2002**). "Acoustic identification of female Steller sea lions (*Eumetopias jubatus*)," J. Acoust. Soc. Am. **111**, 2920–2928.

Carpenter, G. A., and Grossberg, S. (**1987**). "ART 2: Self-organization of stable category recognition codes for analog input patterns," Appl. Opt. **26**, 4919–4930.

Cerchio, S., and Dahlheim, M. E. (**2001**). "Variation in feeding vocalizations of humpback whales (*Megaptera novaeangliae*) from Southeast Alaska," Bioacoustics 11, 277–295.

Chabot, D. (**1988**). "A quantitative technique to compare and classify humpback whale (*Megaptera novaeangliae*) sounds," Ethology **77**, 89–102.

Clark, C. W. (**1982**). "The acoustic repertoire of the southern right whale, a quantitative analysis," Anim. Behav. **30**, 1060–1071.

Clark, C. W., Marler, P., and Beeman, B. (**1987**). "Qualitative analysis of animal vocal phonology and application to swamp sparrow song," Ethology **76**, 101–115.
Clemins, P. J., Johnson, M. T., Leong, K. M., and Savage, A. (**2005**). "Automatic classification and speaker identification of African elephant (*Loxodonta africana*) vocalizations," J. Acoust. Soc. Am. **117**, 956–963.
Deecke, V. B., Ford, J. K. B., and Spong, P. (**1999**). "Quantifying complex patterns of bioacoustic variation: Use of a neural network to compare killer whale (*Orcinus orca*) dialects," J. Acoust. Soc. Am. **105**, 2499–2507.
Dooling, R. J. (**1982**). "Auditory perception in birds," in *Acoustic Communication in Birds*, edited by E. D. Kroodsma, E. H. Miller, and H. Ouellet (Academic, London), pp. 95–131.
Elowson, A. M., and Hailman, J. P. (**1991**). "Analysis of complex variation: Dichotomous sorting of predator-elicited calls of the Florida scrub jay," Bioacoustics 3, 295–320.
Everitt, B. S., Landau, S., and Leese, M. (**2001**). *Cluster Analysis*, 4th ed. (Arnold, London), pp. 102–105.
Ford, J. K. B. (**1984**). "Call Traditions and Vocal Dialects of Killer Whales (*Orcinus orca*) in British Columbia," (Ph.D. dissertation, University of British Columbia, Vancouver, BC).
Ford, J. K. B. (**1989**). "Acoustic behaviour of resident killer whales (*Orcinus orca*) off Vancouver Island, British Columbia," Can. J. Zool. **67**, 727–745.
Ford, J. K. B. (**1991**). "Vocal traditions among resident killer whales (*Orcinus orca*) in coastal waters of British Columbia, Canada," Can. J. Zool. **69**, 1454–1483.
Ford, J. K. B., and Morton, A. B. (**1991**). "Vocal behaviour and dialects of transient killer whales in coastal waters of British Columbia, California and southeast Alaska," in *Abstracts of the Ninth Biennial Conference on the Biology of Marine Mammals* (Society for Marine Mammalogy, Chicago, IL).
Grossberg, S. (**1987**). "Competitive learning: From interactive activation to adaptive resonance," Cogn. Sci. **11**, 23–63.
Janik, V. M. (**1999**). "Pitfalls in the categorization of behaviour: A comparison of dolphin whistle classification methods," Anim. Behav. **57**, 133–143.
Janik, V. M., and Slater, P. J. B. (**1998**). "Context-specific use suggests that bottlenose dolphin signature whistles are cohesion calls," Anim. Behav. **56**, 829–838; Printer's Erratum: Anim. Behav.57, 1173.
Janik, V. M., Dehnhardt, G., and Todt, D. (**1994**). "Signature whistle variations in a bottlenosed dolphin, *Tursiops truncatus*," Behav. Ecol. Sociobiol. **35**, 243–248.
Jones, A. E., Ten Cate, C., and Bijleveld, C. J. H. (**2001**). "The interobserver reliability of scoring sonagrams by eye: A study on methods, illustrated on zebra finch songs," Anim. Behav. **62**, 791–801.
Judd, T. M., and Sherman, P. W. (**1996**). "Naked mole-rats recruit colony mates to food sources," Anim. Behav. **52**, 957–969.
Kohonen, T. (**1988**). "The self-organizing map," Proc. IEEE **78**, 1464–1480.
Kuha, J. (**2004**). "AIC and BIC: Comparisons of assumptions and performance," Sociolog. Methods Res. **33**, 188–229.
Leinonen, L., Hiltunen, T., Torkkola, K., and Kangas, J. (**1993**). "Self-organized acoustic feature map in detection of fricative-vowel coarticulation," J. Acoust. Soc. Am. **93**, 3468–3472.
Lesage, V., Hammill, M. O., and Kovacs, K. M. (**1999**). "Functional classification of harbor seal (*Phoca vitulina*) dives using depth profiles, swimming velocity, and an index of foraging success," Can. J. Zool. **77**, 74–87.
Malcolm, C. D., and Duffus, D. A. (**2000**). "Comparison of subjective and statistical methods of dive classification using data from a time-depth recorder attached to a gray whale (*Eschrichtius robustus*)," J. Cetacean Res. Manage. **2**, 177–182.
Manley, G. A., Koppl, C., and Sneary, M. (**1999**). "Reversed tonotopic map of the basilar papilla in *Gekko gecko*," Hear. Res. **131**, 107–116.
Müller, M. (**1991**). "Frequency representation in the rat cochlea," Hear. Res. **51**, 247–254.
Nowicki, S., and Nelson, D. A. (**1990**). "Defining natural categories in acoustic signals: comparison of three methods applied to 'chick-a-dee' call notes," Ethology **86**, 89–101.
Parsons, S., and Jones, G. (**2000**). "Acoustic identification of twelve species of echolocating bat by discriminant function analysis and artificial neural networks," J. Exp. Biol. **203**, 2641–2656.
Parsons, T. W. (**1987**). *Voice and Speech Processing* (McGraw-Hill, New York).
Phelps, S. M., and Ryan, M. J. (**1998**). "Neural networks predict response biases of female túngara frogs," Proc. R. Soc. London, Ser. B **265**, 279–285.
Placer, J., and Slobodchikoff, C. N. (**2000**). "A fuzzy-neural system for identification of species-specific alarm calls of Gunnison's prairie dogs," Behav. Processes **52**, 1–9.
Reby, D., Lek, S., Dimopoulos, I., Joachim, J., Lauga, J., and Aulagnier, S. (**1997**). "Artificial neural networks as a classification method in the behavioural sciences," Behav. Processes **40**, 35–43.
Rendell, L. E., and Whitehead, H. (**2003**). "Comparing repertoires of sperm whale codas: A multiple methods approach," Bioacoustics 14, 61–81.
Roush, R. S., and Snowdon, C. T. (**2000**). "Quality, quantity, distribution and audience effects on food calling in cotton-top tamarins," Ethology **106**, 673–690.
Sakoe, H., and Chiba, S. (**1978**). "Dynamic programming algorithm optimization for spoken word recognition," IEEE Trans. Acoust., Speech, Signal Process. **ASSP-26**, 43–49.
Saulitis, E. L. (**1993**). "The Behavior and Vocalizations of the 'AT' Group of Killer Whales (*Orcinus orca*) in Prince William Sound, Alaska," (M.Sc. thesis, University of Alaska, Fairbanks, AK).
Sayigh, L. S., Tyack, P. L., Wells, R. S., Solow, A. R., Scott, M. D., and Irvine, A. B. (**1999**). "Individual recognition in wild bottlenose dolphins: A field test using playback experiments," Anim. Behav. **57**, 41–50.
Schevill, W. E., and Watkins, W. A. (**1966**). "Sound structure and directionality in *Orcinus* (killer whale)," Zoologica (N.Y.) (N.Y.) **51**, 70–76.
Schreer, J. F., Hines, R. J. O., and Kovacs, K. M. (**1998**). "Classification of dive profiles: A comparison of statistical clustering techniques and unsupervised artificial neural networks," J. Agric. Biol. Environ. Stat. **3**, 383–404.
Smolders, J. W. T., Ding-Pfennigdorff, D., and Klinke, R. (**1995**). "A functional map of the pigeon basilar papilla: Correlation of the properties of single auditory nerve fibres and their peripheral origin," Hear. Res. **92**, 151–169.
Symmes, D., Newman, J. D., Talmage-Riggs, G., and Katz Lieblich, A. (**1979**). "Individuality and stability of isolation peeps in squirrel monkeys," Anim. Behav. **27**, 1142–1152.
Terry, A. M. R., and McGregor, P. K. (**2002**). "Census and monitoring based on individually identifiable vocalizations: The role of neural networks," Animal Conservation **5**, 103–111.
Vater, M., and Siefer, W. (**1995**). "The cochlea of *Tadarida brasiliensis*: Specialized functional organization in a generalized bat," Hear. Res. **91**, 178–195.
Weiss, D. J., and Hauser, M. D. (**2002**). "Perception of harmonics in the combination long call of cottontop tamarins, *Sanguinus oedipus*," Anim. Behav. **64**, 415–426.

In vitro ultrasonic characterization of human cancellous femoral bone using transmission and backscatter measurements: Relationships to bone mineral density

F. Jenson and F. Padilla[a)]
Laboratoire d'Imagerie Paramétrique, Université Paris VI, UMR CNRS 7623, 15 rue de l'Ecole de Medecine, 75006 Paris, France

V. Bousson, C. Bergot, and J -D. Laredo
Laboratoire de Radiologie Expérimentale, UMR CNRS 7052, Faculté de Médecine Lariboisière-Saint Louis, 10 avenue de Verdun, 75010 Paris, France

P. Laugier
Laboratoire d'Imagerie Paramétrique, Université Paris VI, UMR CNRS 7623, 15 rue de l'Ecole de Medecine, 75006 Paris, France

(Received 9 February 2005; revised 27 September 2005; accepted 29 September 2005)

Thirty-eight slices of pure trabecular bone 1-cm thickness were extracted from human proximal femurs. A pair of 1-MHz central frequency transducers was used to measure quantitative ultrasound (QUS) parameters in transmission [normalized broadband ultrasound attenuation (nBUA), speed of sound (SOS)] and in backscatter [broadband ultrasound backscatter (BUB)]. Bone mineral density (BMD) was measured using clinical x-ray quantitative computed tomography. Site-matched identical region of interest (ROIs) of 7×7 mm^2 were positioned on QUS and QCT images. This procedure resulted in 605 ROIs for all the specimens data pooled together. The short-term precision of the technique expressed in terms of CV was found to be 2.3% for nBUA, 0.3% for SOS and 4.5% for BUB. Significant linear correlation between QUS and BMD were found for all the 605 ROIs pooled, with r^2 values of 0.73, 0.77, and 0.58 for nBUA, SOS, and BUB, respectively (all $p < 0.05$). For the BUB, the best regression was obtained with a polynomial fit of second order ($r^2 = 0.63$). An analysis of measurements errors was developed. It showed that the residual variability of SOS is almost completely predicted by measurements errors, which is not the case for BUA and BUB, suggesting a role for micro-architecture in the determination of BUA and BUB.
 [DOI: 10.1121/1.2126936]

PACS number(s): 43.80.−n, 43.80.Ev, 43.80.Jz, 43.80.Qf [FD] Pages: 654–663

I. INTRODUCTION

X-ray-based measurement of bone mineral density (BMD) represents the gold standard for osteoporosis diagnosis and *in vivo* assessment of fracture risk. Other noninvasive modalities have been developed such as high resolution magnetic resonance imaging (MRI) (Link and Bauer, 2002; Majumdar, 2002), peripheral quantitative computed tomography (pQCT) (Laib *et al.*, 1998; Pistoia *et al.*, 2001), and quantitative ultrasound (QUS) of peripheral skeletal sites (Langton *et al.*, 1984; Laugier *et al.*, 1994; Barkmann *et al.*, 2000a,b; Bossy *et al.*, 2003). Absence of ionizing radiation, low cost, and portability are actual advantages of the ultrasound technology over x-ray or MR-based technologies. In addition, because QUS parameters such as speed of sound, attenuation, or backscatter coefficients are closely related to bone materials and structural properties (Ashman and Rho, 1988; Bouxsein and Radloff, 1997; Njeh *et al.*, 1997), they may provide useful information for the characterization of bone and prediction of bone strength in addition to BMD (Hodgskinson *et al.*, 1997).

Several ultrasonic devices are currently available for the measurement of the slope of frequency-dependent attenuation (so-called broadband ultrasound attenuation or BUA) and speed of sound (SOS) at peripheral skeletal sites including the heel, finger phalanges, and distal radius (Njeh *et al.*, 1999). The most widely documented technique is transverse transmission at the heel. Numerous retrospective or prospective studies indicate that QUS at the heel predicts fracture outcomes as well as x-ray densitometry measurements (Gluer *et al.*, 1996; Hans *et al.*, 1996; Bauer *et al.*, 1997; Huang *et al.*, 1998; Thompson *et al.*, 1998).

One of the most important limitations of QUS methods clinically available today is their limited range of measured skeletal sites: only peripheral sites can be measured and central skeletal sites such as the femur or the spine, the most important fracture sites, cannot be assessed. However, the risk of fracture is best predicted by analyzing the site where the fracture occurs. For example, BMD of the proximal femur has the best ability to predict hip fractures (Marshall *et al.*, 1996). Peripheral QUS measurements are therefore not optimal for predicting fracture risk at clinical relevant sites such as the femoral neck. We hypothesize that performing

a)Author to whom correspondence should be addressed. Electronic mail: padilla@lip.bhdc.jussieu.fr

measurements directly at the hip is required to reach optimal sensitivity of QUS measurements to hip fracture risk prediction.

The ultrasonic properties of human proximal femur and their relationships to material and structural bone properties are not well known. A few studies reported the ability of QUS *in vitro* to predict mechanical properties of cancellous bone specimens from bovine (Turner and Eich, 1991; Njeh *et al.*, 1996, 1997) femoral heads. The data indicate that SOS correlates well to bone density and mechanical properties. Njeh *et al.* (1997) showed that BMD and SOS were independent significant predictors of both stiffness and strength and that BMD, if used in conjunction with ultrasound velocity, could be able to improve osteoporosis risk assessment. Two other studies document the relationship between proximal femur BUA and proximal femur BMD in bovine (Duquette *et al.*, 1997) and human samples (Padilla *et al.*, 2004). BUA at the proximal femur has been found to correlate with site-matched BMD values (Padilla *et al.*, 2004).

In the present paper, we extend the systematic investigation of ultrasonic properties of human trabecular bone performed at the calcaneus to the femur which is a potential target for future *in vivo* fracture risk assessment with QUS technologies (Roberjot *et al.*, 1996; Laugier *et al.*, 1997; Droin *et al.*, 1998; Chaffaï *et al.*, 2000a,c). The aims of this study are to determine ultrasonic properties of human proximal femur, to assess the spatial heterogeneity of ultrasonic properties at this skeletal site, and to determine whether QUS measured in transmission and in backscatter correlate with bone mineral density (BMD) measured using quantitative computed tomography (QCT).

In Sec. II of this paper we describe bone specimens, the methods to measure QUS parameters and BMD, as well as characteristics of the data acquisition and data analysis. The experimental results are presented in Sec. III. In Sec. IV, the results are discussed and compared to the state of knowledge of ultrasonic properties of human trabecular bone of the calcaneus.

II. MATERIAL AND METHODS

A. Bone specimens

Measurements were performed on 38 human femurs removed from fresh cadavers with age ranging from 45 to 95 years (mean=74±11 years, 25 males and 13 females). Each femur was excised and the soft tissues removed manually. Then the specimens were immediately stored at −20 °C. The bone specimens were prepared in several steps. The femoral head and the diaphysis were first removed leaving the proximal part of the femur (neck and trochanter). Slices of trabecular bone with parallel faces and thickness ranging from 0.85 to 1.35 cm were cut from the proximal femur, in the plane defined by the cephalo-caudal and medio-lateral directions (Fig. 1) using a circular saw under continuous irrigation, leading to an orientation of the trabeculae mainly in planes parallel to the faces. Each sample's thickness was measured using an electronic caliper. The specimens were defatted using a dichloromethane ($C_2H_2Cl_2$) solution (immersion for two or three days) and water jet. To remove any air bubbles trapped in the defatted samples, they were vacuum-degassed under water in a desiccator before ultrasonic measurements.

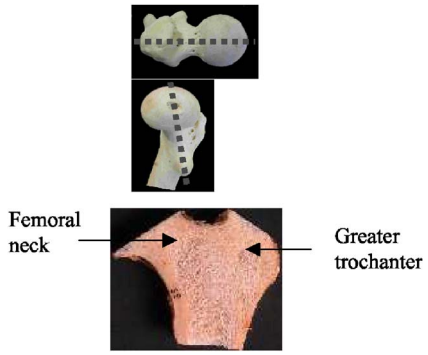

FIG. 1. (Color online) Position of the slice on the complete specimen.

B. Ultrasonic measurements

Ultrasonic measurements were performed in immersion using a pair of focused broadband transducers (1-MHz center frequency, 29 mm in diameter, focal length of 35 mm, V391, Panametrics Inc, Waltham, MA). The beam width at half maximum was approximately 3 mm. The −20-dB frequency bandwidth was 0.4–1.2 MHz. Emission and reception of the signals were performed using a plug-in ultrasonic pulser-receiver, amplifier, and digitizer (SFT 4001H PCI, Sofratest, Ecquevilly, France). Both transducers were mounted coaxially, separated by twice the focal length, in a through-transmission normal incidence configuration (direction of the ultrasound beam perpendicular to the faces of the specimens). The measured specimen was placed in the focal zone. Two stepping motors mounted on a crossed slide assembly (Motion Controller, MM4006, Newport, Irvine, CA) moved the specimen transversally in the ultrasonic beam. Transmitted and backscattered radio-frequency (rf) signals were recorded along 2-D scans in steps of 1 mm (Motion Controller, MM4006, Newport, Irvine, CA). The size of the scans were chosen to fit the sample size. Radiofrequency signals were amplified, time averaged, and digitized at 60 MHz.

The transmitted signals were computed to obtain the SOS (m/s) and the slope of the frequency-dependent attenuation, called the normalized BUA (nBUA, dB/MHz.cm). Both parameters were obtained using a through-transmission method that has been widely described elsewhere (Laugier *et al.*, 1997; Chaffaï *et al.*, 2000a; Wear, 2000). Briefly, the ratio of the Fourier transform of the signal transmitted through the sample to that of a reference signal transmitted through water was computed. The log-magnitude of the ratio gave the frequency-dependent attenuation coefficient while the phase of the ratio yielded the phase velocity. The slope of a linear regression fit of the attenuation coefficient between 0.4 and 0.8 MHz gave the BUA value. This frequency bandwidth fits the usual frequency bandwidth of commercial devices. Normalizing by the sample thickness resulted in the nBUA. The phase velocity was obtained following the method proposed by Sachse and Pao (1978) and extensively described by Droin *et al.* (1998) in the case of bone. This method was preferred to a time domain derivation in order to

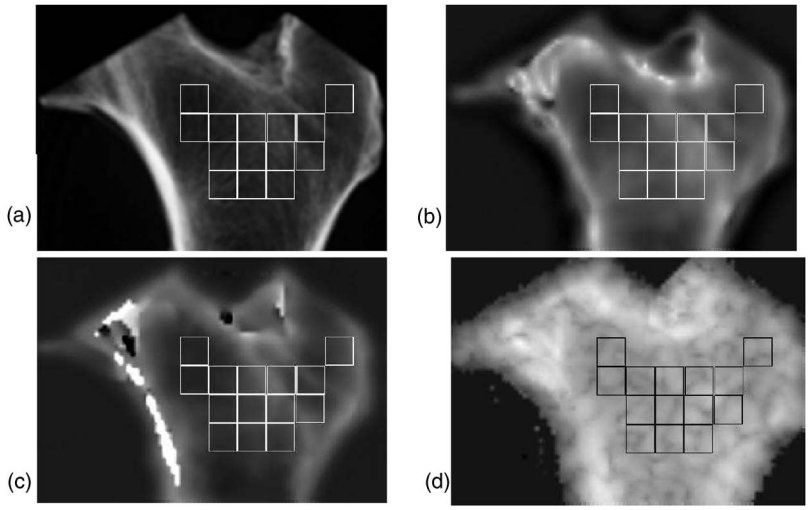

FIG. 2. QCT and QUS images in one representative specimen and positioning of the square ROIs. (a) BMD, (b) nBUA, (c) SOS, and (d) BUB. The gray scales are 77–173 $g.cm^{-3}$, 10.2–33.2 dB/cm.MHz, 1495–1554 m/s, and −19.2–−8.3 dB from black to white for BMD, nBUA, SOS, and BUB, respectively.

avoid frequency dispersion related errors (Droin *et al.*, 1998). Due to strong frequency dependence of the velocity in cancellous bone (Strelitzki *et al.*, 1996; Droin *et al.*, 1998; Wear *et al.*, 2000a), SOS was defined as the phase velocity taken at the center frequency of the initial pulse (i.e., 0.9 MHz). Use was made of individual thickness of the specimen to calculate phase velocity. Ultrasound measurements were made at room temperature which was measured to be 19.5±1 °C (i.e., the speed of sound in pure water was estimated to 1480 m/s).

The backscattered signals were computed to obtain the integrated backscatter coefficient, the so-called broadband ultrasound backscatter (BUB in dB). Measurements were performed using a substitution method (Chaffaï *et al.*, 2000c). First, a reference echo was acquired on a plane reflector (steel plate) placed at a distance equal to the position of the scattering volume of the specimen under study. Then, an echo signal was acquired from the scattering of the incident pulse onto a bone specimen. This signal was time weighted using a Hamming function in order to keep only the part of the signal backscattered from a volume approximately 8 mm in length placed in the center of the specimen. Then the backscatter coefficient $\sigma(f)$ was calculated by computing the ratio of the frequency power spectrum of the time-gated echo signal to the power spectrum of the reference signal. Corrections were made to compensate for attenuation, Hamming gate function, and frequency-dependent scattering volume (diffraction). The detailed calculation may be found in a previous paper (Chaffaï *et al.*, 2000c). With this method, the intrinsic backscatter coefficient of the scattering volume is obtained, and it is independent of the characteristics of the measuring device and of experimental conditions. Finally, the BUB was obtained by computing the average of $\sigma(f)$ over the frequency bandwidth.

C. QCT bone density measurements

Quantitative computed tomography of the specimens was performed using a four-row CT scanner (SOMATOM Volume Zoom 4, Siemens, Germany). The defatted specimens were scanned in air, at 80 kV and 120 mAs. They were fixed vertically in order to perform the acquisition of a centered 8-mm-thick slice in the coronal plane of each femur. The reconstruction field was 110 mm^2 (matrix 512×512, pixel size 215 μm^2), the kernel B40. To convert Hounsfield units (HU) into bone mineral density, a solid calibration phantom was placed below the specimens and scanned simultaneously with them. With this procedure, approximately the same volume of trabecular bone was investigated with ultrasound and x rays.

D. Image analysis

Images analysis was made using Image J vl.29[1] (free software). This software was used to select site-matched identical ROIs (regions of interest) on QUS and QCT images. Several manual steps were necessary in order to first match QCT and QUS images: (a) extraction of a subimage from the QCT image that could fit the QUS image at best, (b) correction for both translational and rotation differences between QCT and QUS images using a bilinear interpolation for the rotational correction, and (c) resampling QUS images to upgrade QUS images spatial sampling to that of QCT images using cubic spleen interpolation. Identical site-matched ROIs were then selected from QCT and QUS images (Fig. 2). This was made possible using the absolute coordinates on the images. The average value of each parameter (nBUA, SOS, BUB, BMD) was then calculated for each selected ROI. To avoid any acoustic diffraction edge artifact, a distance of 5 mm was left between bone edges and ROI edges (Laugier *et al.*, 1997). For a similar reason, Ward's triangle (a triangular area within the femoral neck in which the trabeculae are normally thin and loosely arranged) was excluded when containing a void after visual inspection of the samples. Several nonoverlapping adjacent square ROIs, 7 mm in lateral dimension, were selected. A variable number of ROIs could be analyzed for each specimen according to its size. This procedure resulted in 605 ROIs for all the specimens' data pooled together.

E. Short-term precision

The short-term precision of QUS parameters was assessed by measuring a representative group of four specimens five times each with intermediate repositioning. The

mean QUS parameter values were calculated within identical ROIs on the five images of each specimen. For each ROI, the precision for specimen i was expressed using the coefficient of variation (CV_i), defined as the standard deviation (SD_i) divided by the mean value $\bar{x}_i$ of the five readings (Glüer *et al.*, 1995). The technique's precision error was given by the root-mean square average of the individual precision errors expressed on a percentage basis:

$$CV = \frac{\sqrt{\sum_{i=1}^{n} SD_i^2/n}}{\sum_{i=1}^{n} \bar{x}_i/n} \times 100,$$

where $n=4$ is the number of specimens.

Coefficient of variation is a classical definition of relative precision. However, it does not take into account the impact of the value to which it is normalized and, thus, it does not allow the comparison between different modalities. In order to be able to compare the precision of different variables, the standardized *CV* (*sCV*) was computed following the definition given by Miller *et al.* (1993) as the ratio of absolute precision (root mean square of the standard deviation) over the range (5 to 95 percentiles) of the measured parameter. The range was derived from the data obtained for the entire sample size (605 ROIs in our case).

F. Statistical data analysis

The relationship between QUS and BMD was first assessed for each of the 38 specimens individually, and then for the 605 ROIs from all specimens pooled together. These relationships were investigated using linear least-square regression analysis, except for the relationships between BUB and BMD over the 605 ROIs where the best correlation was obtained using a nonlinear regression as explained in the next section. All statistical computations were processed with Matlab (Mathworks, Natick, MA).

The intraspecimen regional variations of QUS parameters and BMD was assessed by a coefficient of variation (CV_i^r) for specimen number i, defined as the standard deviation (SD_i^r) divided by the mean value $\bar{x}_i^r$ of the N_i readings for that specimen (N_i is the number of ROIs for specimen number i). A mean coefficient of variation (CV_r) was derived from the ratio of the root-mean-square average standard deviation of the values obtained for all the ROIs within a given specimen to the mean value for all specimens.

III. RESULTS

A. Short-term precision

The short-term precision of the technique expressed in terms of CV was found to be 2.3% for nBUA, 0.3% for SOS, and 4.5% for BUB. For comparison, the CV obtained for the BUA on the intact femur specimens ranged from 1.6% to 2.5% depending on the location of the ROI (Padilla *et al.*, 2004). The standardized CV for nBUA, SOS, and BUB were found to be 0.9%, 3.4%, and 6%, respectively.

TABLE I. Descriptive statistics for BMD.

Specimens	No. of ROIs	BMD (mg/cm^3)		
		Mean	Standard deviation	Min - Max
1	14	120	27	77 - 173
2	14	206	94	45 - 320
3	10	70	29	31 - 134
4	17	44	11	28 - 62
5	14	123	22	98 - 166
6	14	112	38	48 - 165
7	14	78	22	39 - 108
8	16	119	30	67 - 169
9	18	90	23	55 - 146
10	16	66	18	43 - 100
11	11	73	39	26 - 136
12	9	101	34	41 - 162
13	24	82	31	38 - 143
14	18	58	32	32 - 175
15	16	87	24	44 - 152
16	12	126	38	70 - 172
17	19	95	37	45 - 177
18	13	127	15	99 - 154
19	15	181	67	80 - 269
20	23	79	23	45 - 143
21	24	74	27	30 - 138
22	16	100	15	78 - 127
23	16	113	29	74 - 158
24	15	173	67	61 - 274
25	25	122	38	55 - 188
26	19	81	50	35 - 258
27	19	125	59	64 - 292
28	13	70	21	44 - 118
29	12	94	31	65 - 162
30	11	120	32	87 - 207
31	12	44	24	22 - 106
32	9	104	22	77 - 134
33	17	148	50	84 - 227
34	18	89	20	58 - 128
35	24	69	29	31 - 139
36	18	128	47	56 - 221
37	15	52	13	33 - 82
38	15	107	38	42 - 171
605 ROIs pooled	605	100	50	22 - 320
Between specimen		101	36	44 - 206

B. Descriptive statistics

Tables I–IV list the descriptive statistics for BMD, BUA, SOS, and BUB respectively. Mean values, standard deviation, and minimum and maximum values are given for each of the 38 specimens individually. The results for the 605 ROIs pooled are given in the next to last line. Finally, the results after averaging over each of the specimens are given in the last line.

Figure 2 shows QUS and QCT images in one representative specimen. The images clearly illustrate the main structures of the trabecular network in the proximal femur and show similar patterns despite the lower spatial resolution of QUS images (~3 mm) compared to QCT (~215 μm). In particular, there can be seen a region of lower BMD and QUS parameters localized in the neck. In some extreme

TABLE II. Descriptive statistics for nBUA.

Specimens	nBUA (dB/cm*MHz)		
	Mean	Standard deviation	Min - Max
1	21.0	7.0	10.2 - 33.2
2	23.4	12.6	2.6 - 42
3	7.4	3.8	1.7 - 15
4	4.4	3.4	0.4 - 12.6
5	12.2	4.2	3.8 - 17.9
6	17.2	10.8	3 - 42
7	9.2	4.4	1.2 - 14.7
8	17.4	7.1	5.7 - 28.2
9	10.6	3.8	4.7 - 15.8
10	6.7	3.6	2.2 - 16
11	16.1	11.9	1.6 - 34.8
12	13.9	6.8	2.8 - 24.7
13	8.9	4.6	1.9 - 17
14	6.9	8.0	0.9 - 36.9
15	10.9	4.4	2.7 - 19.7
16	17.1	8.9	5.9 - 31.4
17	12.5	5.9	2.4 - 26.8
18	25.6	5.2	16.1 - 34.2
19	29.9	12.1	5.8 - 48.4
20	8.5	4.4	2.6 - 21
21	10.1	8.0	0.4 - 29.1
22	13.2	5.1	4.8 - 22.6
23	16.9	8.6	5.2 - 33.7
24	19.2	14.3	3.1 - 50
25	14.5	7.2	4 - 33
26	10.7	9.5	1.8 - 45.8
27	16.9	10.8	5.2 - 42.2
28	7.7	3.4	2.4 - 13.5
29	8.4	3.4	3.9 - 14.3
30	20.1	7.7	9.1 - 35.7
31	4.6	4.8	1.7 - 18.9
32	9.0	5.2	1.9 - 16.6
33	10.9	8.9	1.1 - 26.5
34	10.9	4.7	4.8 - 20.6
35	9.5	6.7	0.9 - 21.8
36	22.7	12.5	1.4 - 42.5
37	4.8	3.1	0.1 - 9.7
38	16.2	12.3	0.8 - 42.8
605 ROIs pooled	13.1	9.5	0.1 - 50
Between specimens	13.3	6.1	4.4 - 29.9

TABLE III. Descriptive statistics for SOS.

Specimens	SOS (m/s)		
	Mean	Standard deviation	Min - Max
1	1523	20	1495 - 1554
2	1530	32	1490 - 1593
3	1500	7	1494 - 1518
4	1484	4	1479 - 1492
5	1506	8	1499 - 1527
6	1505	30	1474 - 1570
7	1501	16	1480 - 1528
8	1501	16	1481 - 1528
9	1491	7	1481 - 1507
10	1486	6	1478 - 1501
11	1508	25	1483 - 1556
12	1502	18	1483 - 1542
13	1493	8	1484 - 1513
14	1478	23	1461 - 1563
15	1491	8	1479 - 1508
16	1512	25	1480 - 1554
17	1501	17	1481 - 1544
18	1531	17	1500 - 1558
19	1595	74	1496 - 1739
20	1490	7	1481 - 1509
21	1491	15	1475 - 1532
22	1494	10	1482 - 1518
23	1509	21	1479 - 1544
24	1516	45	1480 - 1663
25	1512	20	1488 - 1559
26	1495	26	1479 - 1594
27	1538	83	1483 - 1788
28	1494	6	1484 - 1502
29	1487	5	1481 - 1497
30	1524	27	1479 - 1561
31	1490	11	1481 - 1519
32	1487	10	1473 - 1499
33	1497	18	1483 - 1535
34	1489	7	1479 - 1504
35	1489	11	1478 - 1524
36	1528	39	1485 - 1615
37	1488	7	1478 - 1507
38	1505	26	1479 - 1549
605 ROIs pooled	1510	31	1451 - 1772
Between specimens	1504	21	1478 - 1595

cases, this region (the Ward's triangle) contained almost no trabecular material and was excluded from the analysis. The central part of the specimen and the great trochanter region have higher values of BMD and QUS parameters. The localization of these regions is quite difficult on the BUB images due to the speckle noise.

The heterogeneity of BMD and QUS values is confirmed by the analysis of the intraspecimen regional variability. The CV_r was found to be 32% for BMD, 57% for nBUA, 1.3% for SOS, and 18% for BUB. Over the 605 ROIs, the values of QUS parameters range from 0.1 to 50 dB/MHz.cm for BUA, from 1451 to 1772 for SOS, and from −38 to −1 dB for BUB. These results match those found at the calcaneum (Laugier *et al.*, 1997). At first glance, the intraspecimen regional variability of SOS (1.3%) seems to be much lower than the variability of the other parameters. From this value, it may be concluded erroneously that SOS is less sensitive to changes in trabecular structure and material properties than BMD or nBUA. However, the CV_r value is strongly determined by the mean value it is normalized to and, thus, it does not allow a direct comparison between different variables that exhibit a different range of variation. The value of SOS in cancellous bone is close to the value of SOS in water (approximately 1480 m/s) which acts like a threshold. In order to compensate for the influence of SOS in water, this threshold value has to be subtracted from SOS values given in Table III. After that correction, the SOS specimen regional variability (CV_r) increases to 48%, comparable to the value found for BUA or BMD.

C. Correlation between QUS and BMD

Table V lists the results of the correlation (r^2 and RMSE) between QUS parameters and BMD when the analy-

TABLE IV. Descriptive statistics for BUB.

Specimens	BUB (dB)		
	Mean	Standard deviation	Min - Max
1	−14.6	3.5	−19.2 - −8.3
2	−11.3	4.8	−20.8 - −3.4
3	−23.9	2.5	−27.8 - −20.3
4	−25	4.9	−34.6 - −16.7
5	−19.1	2.1	−23.4 - −16.5
6	−15.1	4.2	−23.9 - −7.7
7	−22.1	3.4	−27.8 - −15.5
8	−14.7	2.8	−20.5 - −11.4
9	−17.2	2.2	−21.8 - −13.4
10	−24.6	2	−26.4 - −19.9
11	−18.8	6.7	−28.6 - −11.2
12	−18.7	3.1	−24.2 - −14.6
13	−22.1	3.5	−27.7 - −16.5
14	−20.7	6	−27.5 - −5.9
15	−18.1	2.6	−23.5 - −14.7
16	−16.7	3.6	−24.5 - −12.3
17	−19.2	2.8	−29 - −16
18	−10.9	2.5	−14.5 - −6.5
19	−5.2	7	−16.7 - 6.8
20	−18.3	3.6	−24.6 - −6.9
21	−19.9	4.4	−27.4 - −9.6
22	−15.3	2.1	−18 - −11.8
23	−16.6	3.1	−21.4 - −10.8
24	−15.6	7.2	−24.7 - −1.4
25	−16.1	3.2	−23 - −8.7
26	−22.3	4.9	−27.3 - −5.1
27	−14.8	4.6	−21.9 - −4.3
28	−22.1	3.1	−29.3 - −17.4
29	−20.4	2.5	−24.9 - −14.8
30	−12.8	3.7	−18.5 - −7.6
31	−24	3.1	−27.4 - −16.2
32	−19	3.6	−24.6 - −12.5
33	−21	6.1	−30.7 - −11.7
34	−19	4	−23.5 - −7.4
35	−21.9	4	−28.5 - −15
36	−14.1	5.6	−24.2 - −2.9
37	−25.9	4.1	−37.8 - −20
38	−15.6	4.2	−23.5 - −7.9
605 ROIs pooled	−18.3	5.8	−38 - 7
Between specimens	−18.2	4.4	−24.2 - −9.6

TABLE V. Pearson correlation coefficients between QUS parameters and BMD. (a) nBUA vs. BMD, (b) SOS vs. BMD, and (c) BUB vs. BMD. All $p < 5.10^{-2}$ except (n.s.) not significant.

Specimens	nBUA/BMD		BUB/BMD		SOS/BMD	
	r^2	RMSE (dB/MHz*cm)	r^2	RMSE (dB)	r^2	RMSE (m/s)
1	0.82	3.1	0.61	2.3	0.81	8.9
2	0.68	7.5	0.44	3.7	0.68	18.7
3	0.69	2.3	0.61	1.6	0.57	4.8
4	0.63	2.2	0.63	3.1	0.50	2.9
5	0.54	3.0	$0.10^{n.s.}$	2.1	$0.23^{n.s.}$	7.3
6	0.75	5.6	0.63	2.7	0.76	15.4
7	0.89	1.5	0.78	1.6	0.74	8.5
8	0.96	1.4	0.72	1.5	0.76	8.1
9	0.62	2.4	$0.11^{n.s.}$	2.1	0.82	3.3
10	0.78	1.8	$0.14^{n.s.}$	1.9	0.81	2.9
11	0.92	3.5	0.78	3.3	0.91	7.8
12	0.74	3.7	$0.30^{n.s.}$	2.8	0.80	8.7
13	0.70	2.5	0.45	2.7	0.36	6.4
14	0.83	3.4	0.48	4.4	0.73	12.5
15	0.67	2.6	0.41	2.0	0.27	7.0
16	0.82	3.9	0.58	2.4	0.73	13.9
17	0.69	3.4	0.24	2.5	0.81	7.8
18	0.71	2.9	$0.15^{n.s.}$	2.4	0.94	4.4
19	0.84	5.0	0.84	2.8	0.76	37.4
20	0.66	2.6	0.41	2.8	0.33	5.8
21	0.87	3.0	0.83	1.9	0.65	9.0
22	0.73	2.7	0.27	1.9	0.63	6.1
23	0.82	3.8	0.54	2.2	0.92	5.9
24	0.74	7.6	0.76	3.7	0.49	33.2
25	0.73	3.8	$0.12^{n.s.}$	3.0	0.34	16.3
26	0.93	2.6	0.82	2.2	0.92	7.4
27	0.85	4.2	0.61	3.0	0.93	22.8
28	0.58	2.3	$0.21^{n.s.}$	2.9	0.48	4.5
29	0.74	1.8	$0.14^{n.s.}$	2.5	0.46	3.9
30	0.77	3.9	0.51	2.7	$0.3^{n.s.}$	24.2
31	0.77	2.4	0.42	2.5	0.61	7.2
32	0.69	3.1	0.67	2.2	0.59	6.5
33	0.83	3.7	0.66	3.7	0.72	9.6
34	0.85	1.9	0.72	2.2	0.81	3.2
35	0.82	2.9	0.79	1.9	0.77	5.1
36	0.77	6.2	0.74	2.9	0.88	13.9
37	0.83	1.3	0.53	2.9	0.50	5.0
38	0.66	7.50	0.56	2.89	0.75	13.51
Mean	0.76	3.40	0.60	2.57	0.68	10.25
Standard deviation	0.10	1.62	0.16	0.65	0.19	7.96
605 ROIs pooled	0.73	5	0.58	3.7	0.77	16.7

sis was conducted separately for each of the 38 specimens and for pooled data. Highly statistically significant relationships were noted between the three QUS parameters and BMD for most of the specimens. The slope of the frequency-dependent attenuation is significantly correlated to BMD: the values of r^2 for the relationship between nBUA and BMD were found between 0.54 and 0.96 (all $p < 0.05$). Similarly, the speed of sound significantly correlated with BMD with r^2 values between 0.27 and 0.94 (all $p < 0.05$), except for two specimens (number 5 and 30) for which no significant correlation was found. For these two particular specimens, measurement errors occurred during the ultrasound scan for the measurement of SOS, and the two specimens were excluded from the analysis. Finally, BUB is less correlated to BMD than transmission QUS parameters but still significantly: r^2 values were found between 0.24 and 0.84 (all $p < 0.05$), except for eight specimens (numbers 5, 9, 10, 12, 18, 25, 28, and 29) for which no significant correlation was found. For these specimens, the lack of correlation may be explained by the weak intraspecimen variability of BUB (the standard deviation for these eight specimens range from 2 to 3.2 dB, while the standard deviation over the 38 specimens is 4.4 dB). When pooling the values of BUB for these eight specimens, the range of values of BUB is increased and the correlation between BUB and BMD becomes significant.

The scatter plots showing relationships between acoustic parameters and bone mineral density are presented in Fig. 3

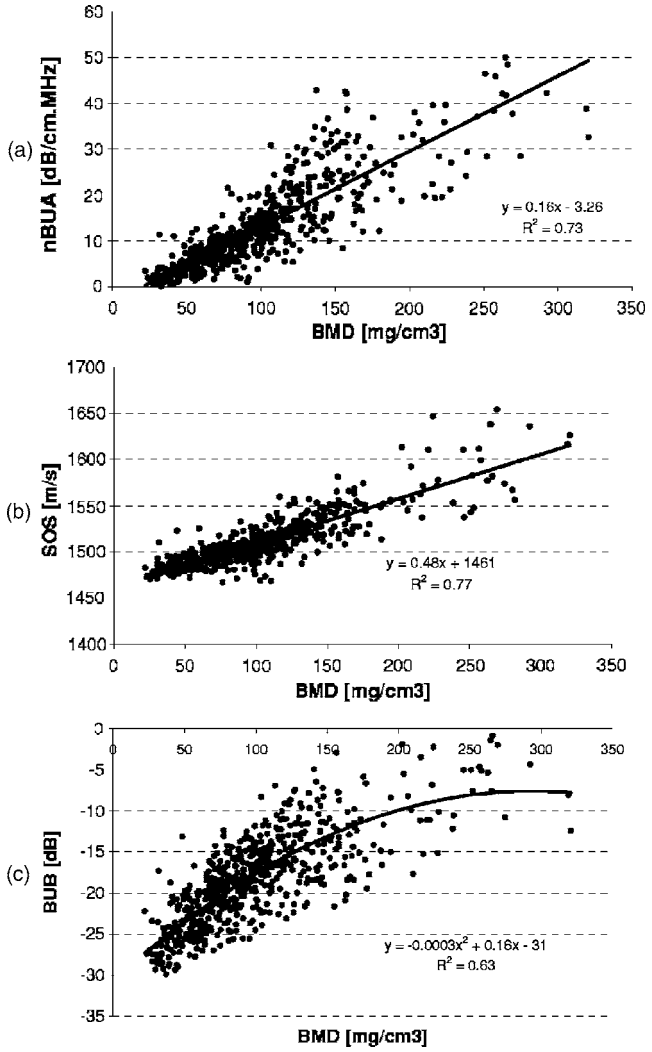

FIG. 3. Scatter plots showing relationships between acoustic parameters and bone mineral density (for the 605 ROIs). (a) nBUA vs. BMD, (b) SOS vs. BMD, and (c) BUB vs. BMD.

(all data pooled). Significant linear correlations were found for the three QUS parameters, with r^2 values of 0.73, 0.77, and 0.58 for nBUA, SOS, and BUB, respectively (all $p < 0.05$). For the BUB, the best regression was obtained with a polynomial fit of second order, leading to an r^2 value of 0.63. This polynomial fit is plotted in Fig. 3.

IV. DISCUSSION

The present study protocol is similar to that used in a previous study by our group on the ultrasonic properties of human calcaneus bone specimens. However, a few differences between both studies have to be highlighted. The study on femur specimens was performed on a larger sample size ($N=38$ for the femur versus $N=15$ for the calcaneus). Second, the femur bone specimens have been selected to cover a wider range of porosity values (96%–67% for the femur and 97%–85% for the calcaneus, see below).

A. Short-term precision

The short-term precision of the technique was found to be comparable to the *in vitro* reproducibility at the calcaneus for the transmission measurements [2% for BUA, 0.1% for SOS (Laugier *et al.*, 1997; Padilla *et al.*, 2004)] as well as for the backscatter measurements [2.8% for BUB (Chaffaï *et al.*, 2002)]. Moreover, Padilla *et al.* (2004) have found comparable *in vitro* short-term precision for BUA on intact femur specimens. For all measured parameters, the precision remained much smaller than the regional variations. This suggests that the observed variations are actual and not caused by errors.

B. Descriptive statistics

The measured values of nBUA and SOS were found to be slightly higher than typical values measured on trabecular bone at the calcaneus [6–20 dB/MHz.cm and 1485–1550 m/s for BUA and SOS, respectively (Laugier *et al.*, 1997; Chaffaï *et al.*, 2000c)].

C. Relationships between QUS and BMD

Strong correlations were found in our study between transmission QUS parameters and BMD. This result is similar to previous studies comparing QUS to BMD at site-matched ROIs at the calcaneus (Graffmans *et al.*, 1996; Chappard *et al.*, 1997; Laugier *et al.*, 1997; Cheng *et al.*, 1999; Langton and Langton, 2000; Louis *et al.*, 2000) or femur (Padilla, 2004). Although QUS does not measure BMD directly (like, for example, DXA does), such high correlations of coefficients between nBUA, SOS, and BMD are consistent with *in vivo* findings (Cheng, 1999) and reinforce the idea that QUS in transmission mainly primarily reflects BMD (Laugier *et al.*, 1997; Nicholson *et al.*, 1998). On the other side, BUB is less correlated to BMD. This result may be explained partly by the inherent statistical properties of signals backscattered by random media such as cancellous bone. The statistical variations in the backscatter signal is due to random phase of the elementary waves scattered by each single trabeculae. A significant amount of the unexplained variance of BUB may be accounted for by the statistical variance of random interference noise (Wear, 2001). On the other hand, the study of backscatter is important, because it can provide information regarding bone micro-structure (Jenson *et al.*, 2003; Wear and Laib, 2003). In addition, skeletal sites which are difficult to reach by transmission, such as the greater trochanter, for example, could be evaluated by such reflection techniques. Further studies should focus on the practical implementation of *in vivo* backscatter QUS measurement in order to enhance signal-to-speckle-noise ratio.

Note that, similarly to what has been reported previously for the calcaneus (Laugier *et al.*, 1997), when the nBUA values are plotted against corresponding BMD values [Fig. 3(a)], an increasing dispersion of the values around the regression line is found at higher nBUA and BMD values. To explain this effect, the slopes of the regression between nBUA and BMD were computed individually for each specimen (data not shown). It was observed that the interspecimen variability of this slope was higher for high than for low values of nBUA and BMD. Therefore, when the data for all

the specimens are pooled together, the dispersion around the regression line is higher for high than for low values of nBUA and BMD.

The increase of the dispersion of nBUA values around the regression line has an impact on the estimation of BUB. The frequency-dependent attenuation curves are used to compensate for attenuation when estimating the backscatter coefficient. Consequently, the same dispersion effect is observed for BUB: there is an increased dispersion as a function of BMD on the scatterplot for BUB when the 605 ROIs are pooled together [Fig. 3(c)].

The best model for BUB was obtained using a polynomial fit of second order. This is in agreement with scattering models developed for soft tissues which indicate a nonlinear dependence of BUB with the amount of scatterers (Yagi and Nakayama, 1980). This result opens very interesting prospects for future models of scattering by trabecular bone.

A better prediction was reached for transmission QUS parameters (nBUA and SOS) compared to backscatter. While the regression models could explain 73% and 77% of the variance of nBUA and SOS, respectively, only 63% of the variance of BUB was accounted for. Because BUB is a variable affected by substantial speckle noise, a lower prediction was expected compared to transmission variables. Still, a significant part of the variance of QUS variables (27% for BUA, 23% SOS, and some of the 37% left for BUB) is unexplained. Part of this unexplained variability is certainly due to errors in experimental procedures (QUS and BMD measurements, image processing). In order to sort out all these contributions, we propose to describe and quantify each of these error sources:

(1) The measurement precision includes errors in the measurement of both BMD and QUS parameters. Typical precision for BMD measurement of approximately 1% was obtained on a femur phantom (Tothill *et al.*, 1995). The short-term precision in QUS measurement was estimated by computing the coefficient of variation (CV) as described in Sec. II. An averaged CV of 2.3%, 0.3%, and 4.5% was found for the nBUA, SOS, and BUB respectively. Temperature could fluctuate of ±1 °C. These temperature fluctuations have moderate effects on the measure of nBUA and BUB, but have to be taken into account in the measurement of speed of sound (Wear *et al.*, 2000a; Nicholson and Bouxsein, 2002). The speed of sound in water was taken at 1480 m/s corresponding to a temperature of 19.5 °C. Yet, fluctuations of ±1 °C in room temperature result in an error of ±3.5 m/s in the estimate of the speed of sound in water according to the expression given by Kaye and Laby (1973) for the speed of sound in distilled water. This imprecision was added to our model.

(2) Other types of errors include several factors responsible for discrepancies between size and location of bone volumes that contribute to the estimate of QUS and BMD for a given ROI. The BMD measurements provide images with high spatial resolution (215 μm) while the spatial resolution is approximately 3 mm for QUS measurements (due to the size of the focal spot of the ultrasonic beam). In addition, BMD measurements were made on 8-mm-thick slices while the total thickness (from 0.85 to 1.35 cm) of the sample was investigated with QUS in transmission. Thus, for a given size of ROI, bone volume contributing to QUS measurements will be systematically larger than bone volume contributing to BMD measurements. This error, systematic for QUS measurements, is difficult to quantify but should remain low if spatial homogeneity of bone at the scale of ROI size is assumed. The positioning of the ROIs is thought to have a more significant contribution due to several manual steps in the image analysis process (described in Sec. II) and to the limited resolution of QUS images. In order to quantify these contributions, we have proceeded to simulations in a way that will be described now. A set of ROIs was chosen within a specimen. Next, the QUS image was translated and rotated in steps of 1 mm and 1°, respectively. After each move, the variation of the QUS parameter averaged on each ROI was computed. We found that the error on the QUS parameter (averaged over the ROIs) increased approximately linearly for moves and rotations up to 3 mm and 3° with a slope, depending on the sample, of approximately 10% by mm and 3% by degree for nBUA. The final step was to estimate the accuracy of the positioning algorithm. The precision is essentially limited by the transducers resolution, i.e., the size of the focal spot. We estimated our precision to 1 mm in both translational directions and1° in rotation. Finally, this corresponds to a precision of $\sigma_{\text{Positioning}}=14\%$ on the averaged nBUA (the values for SOS and BUB are given in Table VI).

A model to study the influence of the different errors on the coefficient of determination r^2 between QUS and BMD is now proposed. First, a set of nBUA values that are perfectly determined by values of BMD was chosen. A linear regression was then computed after adding a noise on each type of data (nBUA and BMD). In the case of a nonexistent noise, the coefficient of determination resulting from the linear regression would be necessarily equal to one. The noise was generated using a Gaussian distribution with standard deviation linked to both measurement and positioning errors ($\sigma^2 = \sigma^2_{\text{measurement}} + \sigma^2_{\text{positioning}}$). The contributions of each error source to the coefficient of determination are given in Table VI. These results show that an important amount of variability of QUS not predicted by BMD could be explained by error sources. This is especially true for SOS, where almost all of the residual variability is explained by measurement errors. On the contrary, measurement errors explain at best a quarter of the residual variability of nBUA and BUB. As mentioned earlier, interference noise is a potential contributor to the unexplained variance of BUB. From a physical point of view, it should not be surprising that parameters other than BMD have an influence on BUA and BUB like, for example, the micro-architecture of bone.

TABLE VI. Estimated determination coefficients using a model of random noise on QUS and BMD parameters. The QUS and BMD are initially perfectly correlated. A random noise ($\sigma^2=\sigma^2_{\text{measurement}}+\sigma^2_{\text{positioning}}$) is then added and the determination coefficients are estimated from the new scatter plot. (a) nBUA vs. BMD, (b) SOS vs. BMD, and (c) BUB vs. BMD.

(a)

$\sigma_{\text{positioning}}$	$\sigma_{\text{measurement,nBUA}}$	$\sigma_{\text{measurement,BMD}}$	R^2	RMSE (dB/cm.MHz)
2 dB/cm*MHz	0	0	0.94	1.95
0	0.3 dB/cm*MHz	0	1	0.32
0	0	1 mg/cm^3	1	0.15
2 dB/cm*MHz	0.3 dB/cm*MHz	1 mg/cm^3	0.94	2
	Experimental model		0.73	5

(b)

$\sigma_{\text{positioning}}$	$\sigma_{\text{measurement,SOS}}$	$\sigma_{\text{measurement,BMD}}$	$\sigma_{\text{temperature}}$	R^2	RMSE (m/s)
10.5 m/s	0	0	0	0.86	10.4
0	4.5 m/s	0	0	0.97	4.5
0	0	1 mg/cm^3	0	1	0.5
0	0	0	7 m/s	0.94	6.8
10.5 m/s	4.5 m/s	1 mg/cm^3	7 m/s	0.8	13.7
	Experimental model			0.77	16.7

(c)

$\sigma_{\text{positioning}}$	$\sigma_{\text{measurement,BUB}}$	$\sigma_{\text{measurement,BMD}}$	R^2	RMSE (dB)
0.92 dB	0	0	0.96	0.95
0	0.82 dB	0	0.96	0.85
0	0	1 mg/cm^3	1	0.08
0.92 dB	0.82 dB	1 mg/cm^3	0.92	1.24
	Experimental model (linear correlation)		0.58	3.7

V. CONCLUSION

This study is a part of the systematic investigation of ultrasonic properties of the human femoral bone. Slices of pure trabecular bone extracted from human femurs were investigated. A strong correlation between quantitative ultrasound parameters measured in transmission (slope of the frequency-dependent attenuation and speed of sound) and bone mineral density was demonstrated. This result is in agreement with previous papers dealing with the calcaneus or intact femur specimens.

The correlation between bone mineral density and quantitative integrated backscatter coefficient has been found to be significant but lower than with transmitted QUS. This point is in agreement with scattering models that predict that the backscatter coefficient is directly related to the microarchitecture of the medium and sensitive to others parameters than BMD.

The study of the relationships between QUS, BMD, and micro-architecture parameters will be the object of a forthcoming paper.

ACKNOWLEDGMENTS

This work was supported by the European Commission (Contract No. QLK6-CT-2002-02710). The authors are grateful to Dr. Robin Cleveland for valuable discussions and for correction of the manuscript.

[1]http://rsb.info.nih.gov/ij/

Ashman, R. B., and Rho, J. Y. (**1988**). "Elastic modulus of trabecular bone material," J. Biomech. **21**(3), 177–181.

Barkmann, R., Lusse, S., Stampa, B., Sakata, S., Heller, M., and Gluer, C. C. (**2000a**). "Assessment of the geometry of human finger phalanges using quantitative ultrasound in vivo," Osteoporosis Int. **11**(9), 745–755.

Barkmann, R., Kantorovich, E., Singal, C., Hans, D., Genant, H., Heller, M., and Glüer, C. (**2000b**). "A new method for quantitative ultrasound measurements at multiple skeletal sites," J. Clin. Densitom. **3**, 1–7.

Bauer, D. C., Glüer, C. C., Cauley, J. A., Vogt, T. M., Ensrud, K. E., Genant, H. K., and Black, D. M. (**1997**). "Broadband ultrasound attenuation predicts fractures strongly and independently of densitometry in older women," Arch. Intern Med. **157**, 629–634.

Bossy, E., Talmant, M., and Laugier, P. (**2004**). "Bi-directional axial transmission can improve accuracy and precision of ultrasonic velocity measurement in cortical bone: a validation on test materials," IEEE Trans. Ultrason. Ferroelectr. Freq. Control **51**(1), 71–9;.

Bouxsein, M. L., and Radloff, S. E. (**1997**). "Quantitative ultrasound of the calcaneus reflects the mechanical properties of calcaneal trabecular bone," J. Bone Miner. Res. **12**(5), 839–846.

Chaffaï, S., Padilla, F., Berger, B., and Laugier, P. (**2000a**). "*In vitro* measurement of the frequency dependent attenuation in cancellous bone between 0.2 - 2 MHz," J. Acoust. Soc. Am. **108**, 1281–1289.

Chaffaï, S., Peyrin, F., Berger, G., and Laugier, P. (2000b). "Numerical Investigation of the frequency dependence of ultrasonic backscatter in trabecular bone," 2000 IEEE Ultrasonics Symposium.

Chaffaï, S., Roberjot, V., Peyrin, F., Berger, G., and Laugier, P. (**2000c**). "Frequency dependence of ultrasonic backscattering in cancellous bone: autocorrelation model and experimental results," J. Acoust. Soc. Am. **108**(5), 2403–2411.

Chaffaï, S., Peyrin, F., Nuzzo, S., Porcher, R., Berger, G., and Laugier, P. (**2002**). "Ultrasonic characterization of human cancellous bone using transmission and backscatter measurements: relationships to density and microstructure," Bone (N.Y.) (N.Y.) **30**(1), 229–237.

Chappard, C., Laugier, P., Fournier, B., Roux, C., and Berger, G. (**1997**). "Assessment of the relationship between broadband ultrasound attenuation and bone mineral density at the calcaneus using BUA imaging and DXA," Osteoporosis Int. **7**(4), 316–322.

Cheng, S., Suominen, H., Ollikainen, S., Goll, J., Sipila, S., Taaffe, D., Fuerst, T., Njeh, C. F., and Genant, H. K. (**1999**). "Comparison of ultrasound and bone mineral density assessment of the calcaneus with different regions of interest in healthy early menopausal women," J. Clin. Densitom. **2**(2), 117–126.

Droin, P., Berger, G., and Laugier, P. (**1998**). "Velocity dispersion of acoustic waves in cancellous bone," IEEE Trans. Ultrason. Ferroelectr. Freq. Control **45**, 581–592.

Duquette, J., Lin, J., Hoffman, A., Houde, J., Ahmadi, S., and Baran, D. (**1997**). "Correlations among bone mineral density, broadband ultrasound attenuation, mechanical indentation testing, and bone orientation in bovine femoral neck samples," Calcif. Tissue Int. **60**(2), 181–186.

Glüer, C. C., Blake, G., Lu, Y., Blunt, B. A., Jergas, M., and Genant, H. K. (**1995**). "Accurate Assessment of Precision Errors: How to Measure the Reproducibility of Bone Densitometry Techniques," Osteoporosis Int. **5**, 262–270.

Gluer, C. C., Cummings, S. R., Bauer, D. C., Stone, K., Pressman, A., Mathur, A., and Genant, H. K. (**1996**). "Osteoporosis: association of recent fractures with quantitative US findings," Radiology **199**(3), 725–732.

Graafmans, W. C., Van Lingen, A., Ooms, M. E., Bezemer, P. D., and Lips, P. (**1996**). "Ultrasound measurements in the calcaneus: precision and its relation with bone mineral density of the heel, hip, and lumbar spine," Bone (N.Y.) **19**(2), 97–100.

Hans, D., Dargent-Moline, P., Schott, A. M., Sebert, J. L., Cormier, C., Kotski, P. O., Delmas, P. D., Pouilles, J. M., Breart, G., and Meunier, P. J. (**1996**). "Ultrasonographic heel measurements to predict hip fracture in elderly women: the Epidos prospective study," Lancet **348**(9026), 511–514.

Hodgskinson, R., Njeh, C. F., Currey, J. D., and Langton, C. M. (**1997**). "The ability of ultrasound velocity to predict the stiffness of cancellous bone in vitro," Bone (N.Y.) **21**(2), 183–190.

Huang, C., Ross, P. D., Yates, A. J., Walker, R. E., Imose, K., Emi, K., and Wasnich, R. D. (**1998**). "Prediction of fracture risk by radiographic absorptiometry and quantitative ultrasound: a prospective study," Calcif. Tissue Int. **63**(5), 380–384.

Jenson, F., Padilla, F., and Laugier, P. (**2003**). "Prediction of frequency-dependent ultrasonic backscatter in cancellous bone using statistical weak scattering model," Ultrasound Med. Biol. **29**(3), 455–464.

Kaye, G. W. C., and Laby, T. H. (**1973**). *Table of Physical and Chemical Constants* (Longman, London).

Laib, A., Hauselmann, H. J., and Ruegsegger, P. (**1998**). "In vivo high resolution 3D-QCT of the human forearm," Technol. Health Care **6**(5–6), 329–337.

Langton, C. M., and Langton, D. K. (**2000**). "Comparison of bone mineral density and quantitative ultrasound of the calcaneus: site-matched correlation and discrimination of axial BMD status," Br. J. Radiol. **73**(865), 31–35.

Langton, C. M., Palmer, S. B., and Porter, S. W. (**1984**). "The measurement of broadband ultrasonic attenuation in cancellous bone," Eng. Med. **13**(2), 89–91.

Laugier, P., Giat, P., and Berger, G. (**1994**). "Broadband ultrasonic attenuation Imaging: A new imaging technique of the os calcis," Calcif. Tissue Int. **54**, 83–86.

Laugier, P., Droin, P., Laval-Jeantet, A. M., and Berger, G. (**1997**). "In vitro assessment of the relationship between acoustic properties and bone mass density of the calcaneus by comparison of ultrasound parametric imaging and QCT," Bone (N.Y.) **20**, 157–165.

Link, T. M., and Bauer, J. S. (**2002**). "Imaging of trabecular bone structure," Semin. Musculoskelet. Radiol. **6**(3), 253–261.

Louis, O., Kaufman, L., and Osteaux, M. (**2000**). "Quantitative ultrasound of the calcaneus with parametric imaging: correlation with bone mineral density at different sites and with anthropometric data in menopausal women," Eur. J. Radiol. **35**(1), 65–69.

Majumdar, S. (**2002**). "Magnetic resonance imaging of trabecular bone structure," Top. Magn. Reson. Imaging 13(5), 323–334.

Marshall, D., Johnell, O., and Wedel, H. (**1996**). "Meta-analysis of how well measures of bone mineral density predict occurrence of osteoporotic fractures," BMJ 312(7041), 1254–1259.

Miller, C. G., Herd, R. J., Ramalingam, T., Fogelman, I., and Blake, G. M. (**1993**). "Ultrasonic velocity measurements through the calcaneus: which velocity should be measured?" Osteoporosis Int. **3**(1), 31–35.

Nicholson, P. H., and Bouxsein, M. L. (**2002**). "Effect of temperature on ultrasonic properties of the calcaneus in situ," Osteoporosis Int. **13**(11), 888–892.

Nicholson, P. H., Muller, R., Lowet, G., Cheng, X. G., Hildebrand, T., Ruegsegger, P., van der Perre, G., Dequeker, J., and Boonen, S. (**1998**). "Do quantitative ultrasound measurements reflect structure independently of density in human vertebral cancellous bone?" Bone (N.Y.) **23**(5), 425–431.

Njeh, C. F., Hodgskinson, R., Currey, J. D., and Langton, C. M. (**1996**). "Orthogonal relationships between ultrasonic velocity and material properties of bovine cancellous bone," Med. Eng. Phys. **18**(5), 373–381.

Njeh, C. F., Hans, D., Fuerst, T., Glüer, C. C., and Genant, H. K. (**1999**). "*Quantitative Ultrasound: Assessment of Osteoporosis and Bone Status*. (Martin Dunitz, London).

Njeh, C. F., Kuo, C. W., Langton, C. M., Atrah, H. I., and Boivin, C. M. (**1997**). "Prediction of human femoral bone strength using ultrasound velocity and BMD: an in vitro study," Osteoporosis Int. **7**(5), 471–474.

Padilla, F., Akrout, L., Kolta, S., Latremouille, C., Roux, C., and Laugier, P. (**2004**). "In vitro ultrasound measurement at the human femur," Calcif. Tissue Int. **75**(5), 421–30.

Pistoia, W., van Rietbergen, B., Laib, A., and Ruegsegger, P. (**2001**). "High-resolution three-dimensional-pQCT images can be an adequate basis for in-vivo microFE analysis of bone," J. Biomech. Eng. **123**(2), 176–183.

Roberjot, V., Laugier, P., Droin, P., Giat, P., and Berger, G. (**1996**). "Measurement of integrated backscatter coefficient of trabecular bone," IEEE Ultrasonics Symposium.

Sachse, W., and Pao, Y. H. (**1978**). "On the determination of phase and group velocities of dispersive waves in solids," J. Appl. Phys. **49**, 4320–4327.

Strelitzki, R., Clarke, A. J., and Evans, J. A. (**1996**). "The measurement of the velocity of ultrasound in fixed trabecular bone using broadband pulses and single-frequency tone bursts," Phys. Med. Biol. **41**(4), 743–753.

Thompson, P. W., Taylor, J., Oliver, R., and Fisher, A. (**1998**). "Quantitative ultrasound (QUS) of the heel predicts wrist and osteoporosis-related fractures in women age 45-75 years," J. Clin. Densitometry **1**(3), 219–225.

Tothill, P., Fenner, J. A., and Reid, D. M. (**1995**). "Comparisons between three dual-energy X-ray absorptiometers used for measuring spine and femur," Br. J. Radiol. **68**(810), 621–629.

Turner, C. H., and Eich, M. (**1991**). "Ultrasonic velocity as a predictor of strength in bovine cancellous bone," Calcif. Tissue Int. **49**(2), 116–119.

Wear, K. (**2000a**). "Temperature dependence of ultrasonic attenuation in human calcaneus," Ultrasound Med. Biol. **26**(3), 469–472.

Wear, K. A. (**2000b**). "The effects of frequency-dependent attenuation and dispersion on sound speed measurements: applications in human trabecular bone," IEEE Trans. Ultrason. Ferroelectr. Freq. Control **47**(1), 265–273.

Wear, K. A. (**2001**). "Fundamental precision limitations for measurements of frequency dependence of backscatter: applications in tissue-mimicking phantoms and trabecular bone," J. Acoust. Soc. Am. **110**(6), 3275–3282.

Wear, K. A., and Laib, A. (**2003**). "The dependence of ultrasonic backscatter on trabecular thickness in human calcaneus: theoretical and experimental results," IEEE Trans. Ultrason. Ferroelectr. Freq. Control **50**(8), 979–986.

Wear, K. A., Stuber, A. P., and Reynolds, J. C. (**2000**). "Relationships of ultrasonic backscatter with ultrasonic attenuation, sound speed and bone mineral density in human calcaneus," Ultrasound Med. Biol. **26**(8), 1311–1316.

Yagi, S. I., and Nakayama, K. (**1980**). "Acoustical scattering in weakly inhomogeneous dispers media: theoretical analysis," J. Acoust. Soc. Jpn. **36**, 496.